PROCEEDINGS OF THE SEVENTEENTH INTERNATIONAL SYMPOSIUM ON ARTIFICIAL LIFE AND ROBOTICS

(AROB 17th ’12)

Jan. 19-21, 2012

B-Con Plaza, Beppu, Oita, JAPAN

Editors: Masanori Sugisaka and Hiroshi Tanaka

Publisher: ALife Robotics Co., Ltd.
Publication Date: Jan. 10, 2012
ISBN 978-4-9902880-6-8

Proceedings of the Seventeenth International Symposium on

ARTIFICIAL LIFE AND ROBOTICS

(AROB 17th ’12)

January 19- 21, 2012
B-Con Plaza, Beppu, Oita, Japan

Editors: Masanori Sugisaka and Hiroshi Tanaka

The Eighteenth International Symposium on

Artificial Life and Robotics

AROB 18th '13

January 30 – February 1, 2013
Daejeon Convention Center, Daejeon, Korea

IS ROB

1st Call For Papers

General Chairs
Ju-Jang Lee
Masanori Sugisaka

Program Chair
Hiroshi Tanaka

Vice Chairs
John L. Casti
Yingmin Jia
Henrik Hautop Lund
Ken Naitoh
Hiroshi Tanaka
Yongguan Zhang

Advisory Committee Chair
Fumio Harashima

Assistant General Chair
Takao Ito

The Eighteenth International Symposium on Artificial Life and Robotics will be held in Daejeon, Korea, January 30 – February 1, 2013. This symposium will bring together researchers to discuss development of new technologies concerning *artificial life and robotics* based on computer simulations and hardware designs of state-of-the-art technologies, and to share findings on how advancements in artificial life and robotics technologies that relate to artificial intelligence, virtual reality, and computer science are creating the basis for exciting new research and applications in various fields listed in the following topics.

Topics of interest include, but are not limited to

- Artificial brain research
- Artificial living
- Bipedal robot
- Cognitive science
- Control techniques
- Evolutionary computations
- Human-machine cooperative systems
- Intelligent control & modeling
- Medical surgical robot
- Molecular biology
- Nano-robotics
- Pattern recognition
- Renewable energy
- Soccer robot
- Artificial intelligence
- Artificial mind research
- Brain science
- Complexity
- Data mining
- Fuzzy control
- Human-welfare robotics
- Learning
- Micromachines
- Multi-agent systems
- Neurocomputing technologies and its application for hardware
- Resilient infrastructure systems
- Virtual reality
- Artificial life
- Bioinformatics
- Chaos
- Computer graphics
- DNA computing
- Genetic algorithms
- Image processing
- Management of technology
- Mobile vehicles
- Nano-biology
- Neural networks
- Quantum computing
- Robotics
- Visualization

Important Dates

- **September 1, 2012** Deadline for abstract submissions
- **September 15, 2012** Notification of acceptance
- **October 31, 2012** Final camera-ready papers due
- **November 1, 2012** Deadline for Early Registration

Publication

Accepted papers will be published in the Proceedings of the AROB. Extended versions of the selected papers will be published in the international journal : ARTIFICIAL LIFE AND ROBOTICS and in the special issue on special topics of Artificial Life and Robotics, Applied Mathematics and Computation.

Symposium Site

Daejeon Convention Center

AROB Secretariat
Tel / Fax: +81-97-594-0181
Email: arobsecr@isarob.org

isarob.org

ALife Robotics
IEEE
SICE
EiC
IEEJ
RSJ
ISCIE
JARA
AAI

Organized By

AROB 18th 2013

International Organizing Committee of International Symposium on Artificial Life and Robotics (AROB)

Co-Operated by

The Society of Instrument and Control Engineers (SICE, Japan)
The Robotics Society of Japan (RSJ, Japan)
The Institute of Electrical Engineers of Japan (IEEJ, Japan)
IEEE Japan Council (IEEE Robotics and Automation Society Japan Chapter)
Japan Robot Association (JARA)
Chinese Association for Artificial Intelligence (CAAI, P. R. China)
The Institute of Systems, Control and Information Engineers (ISCIE)
The Institute of Electronics, Information and Communication Engineers (IEICE)

General Chairs

Ju-Jang Lee (KAIST, Korea)
Masanori Sugisaka (Nippon Bunri University and ALife Robotics Co., Ltd., Japan)

Vice-Chairs

John L. Casti (International Institute for Applied Systems Analysis, Austria)
Yingmin Jia (Beihang University, P. R. China)
Ju-Jang Lee (KAIST, Korea)
Henrik Hautop Lund (Technical University of Denmark, Denmark)
Ken Naitoh (Waseda University, Japan)
Hiroshi Tanaka (Tokyo Medical & Dental University, Japan)
Yong-Guang Zhang (Academia Sinica, P. R. China)

Program Chair

Hiroshi Tanaka (Tokyo Medical & Dental University, Japan)

Assistant General Chair

Takao Ito (Ube National College of Technology, Japan)

Advisory Committee Chair

Fumio Harashima (Tokyo Metropolitan University, Japan)

Advisory Committee

Bruce Eisenstein (Drexel University, Former IEEE President, USA)
Robert Fischl (Drexel University, USA)
Toshio Fukuda (Nagoya University, Japan)
Fumio Harashima (Tokyo Metropolitan University, Japan)
Paul Kalata (Drexel University, USA)
Moshe Kam (Drexel University, IEEE President, USA)
Hidenori Kimura (RIKEN, Japan)
Paul Oh (Drexel University, USA)
Masayoshi Tomizuka (University of California Berkeley, USA)

International Organizing Committee

Hussein Abbass (University of New South Wales, Australia)
Kazuyuki Aihara (The University of Tokyo, Japan)
Takaya Arita (Nagoya University, Japan)
Christopher L. Barrett (Virginia Polytechnic Institute and State University, USA)
Mark A. Bedau (Reed College, USA)
Malachy Eaton (University of Limerick, Ireland)
Joshua M. Epstein (The Johns Hopkins University, USA)
Adam Grzech (Wroclaw University of Technology, Poland)
Hideki Hashimoto (The University of Tokyo, Japan)
Yoshiteru Ishida (Toyohashi University of Technology, Japan)
David John Glyndwyr James (Coventry University, United Kingdom)
Takashi Kohno (The University of Tokyo, Japan)
Kazuo Kyuma (Mitsubishi Electric Corporation, Japan)
Man Hyung Lee (Pusan National University, Korea)
Fumitoshi Matsuno (Kyoto University, Japan)
Junichi Murata (Kyushu University, Japan)
Masatoshi Nakamura (Research Institute of Systems Control, Japan)
Nobuhiro Okada (Kyushu University, Japan)
Marion Oswald (Vienna University of Technology, Austria)
Steen Rasmussen (University of Southern Denmark, Denmark)
Thomas S. Ray (University of Oklahoma, USA)
Shinichi Sagara (Kyushu Institute of Technology, Japan)
Katsunori Shimohara (Doshisha University, Japan)
Hideyuki Suzuki (The University of Tokyo, Japan)
Jerzy Świątek (Wroclaw University of Technology, Poland)
Charles Taylor (University of California-Los Angeles, USA)
Toshio Tsuji (Hiroshima University, Japan)
Jiwu Wang (Beijing Jiaotong University, P. R. China)
Keigo Watanabe (Okayama University, Japan)
Changshui Zhang (Tsinghua University, P. R. China)

International Program Committee

Richard K. Belew (University of California-San Diego, USA)
Shyi-Ming Chen (National Taichung University of Education, Taiwan)
Young Im Cho (The University of Suwon, Korea)
Mo-Yuen Chow (North Carolina State University, USA)
Fengzhi Dai (Tianjin University of Science & Technology, P. R. China)
Yueyue Fan (University of California-Davis, USA)
Takayasu Fuchida (Kagoshima University, Japan)
Ivan Godler (The University of Kitakyushu, Japan)
Sung Hyun Han (Kyungnam University, Korea)
Noriyasu Homma (Tohoku University, Japan)
Zunaidi bin Ibrahim (TATi University College, Malaysia)
Seiji Ishikawa (Kyushu Institute of Technology, Japan)
Takashi Iwamoto (Mitsubishi Electric Corporation, Advanced Technology R&D Center, Japan)
Kiyotaka Izumi (Saga University, Japan)
Jeff Johnson (The Open University, UK)
Sanjay S. Joshi (College of Engineering University of California, USA)
Hiroshi Kinjo (University of the Ryukyus, Japan)
Kentarou Kurashige (Muroran Institute Technology, Japan)
Hee-Hyol Lee (Waseda University, Japan)
Yong Liu (University of Aizu, Japan)
Kenneth James Mackin (Tokyo University of Information Sciences, Japan)
Kathryn Elizabeth Merrick (University of New South Wales and ADFA, Australia)
Chris Mi (University of Michigan-Dearborn, USA)
Kazushi Nakano (The University of Electro-Communications, Japan)
Walter Nistico (University of Dortmund, Germany)
Harutoshi Ogai (Waseda University, Japan)
Shigeru Omatu (Osaka Institute of Technology, Japan)
Luigi Pagliarini (Technical University of Denmark, Denmark)
Rolf Pfeifer (University of Zurich-Irchel, Switzerland)
Mohd Rizon (King Saud University, Saudi Arabia)
Peter S. Sapaty (National Academy of Sciences of Ukraine, Ukraine)
Jeong-Youn Sim (Kangnam University, Korea)
Ken Sugawara (Tohoku Gakuin University, Japan)
Mikhail Svinin (Kyushu University, Japan)
Ivan Tanev (Doshisha University, Japan)
Hiroshi Umeo (Osaka Electro-Communication University, Japan)
Katsuji Uosaki (Fukui University of Technology, Japan)
Mutsumi Watanabe (Kagoshima University, Japan)
Kazuko Yamasaki (Tokyo University of Information Sciences, Japan)
Hidekazu Yanagimoto (Osaka Prefecture University, Japan)
Masao Yokota (Fukuoka Institute of Technology, Japan)
Ikuo Yoshihara (University of Miyazaki, Japan)
Yong Yu (Kagoshima University, Japan)
Tao Zhang (Tsinghua University, P. R. China)
Huailin Zhao (Shanghai Institute of Technology, P. R. China)

Artificial Life and Robotics

We invite you to publish your paper
in this journal full of inventive scientific findings and state-of-the art technologies.

Two types of papers from the world are

I. Contributed papers
II. Recommended papers presented at **the International Symposium on Artificial Life and Robotics (ISAROB),**

Contribution fee:

4 pages or Under **¥19,950 / page** (¥19,000 + 5 % consumption tax: only in Japan)
Extra page charge **¥16,800 / page** (¥16,000 + 5% consumption tax: only in Japan)
(Pages are counted on double-columns basis as they appear in the journal.)

Shipping Cost:

domestic **¥735 / delivery** (¥700 + 5 % consumption tax)
overseas **¥3,000 / delivery**

We deliver every corresponding author (or sponsor) one copy of journal in which his/her paper is included. We would like to thank authors for their support in the form of contribution fee payable before publication, which funds the production of this journal contracted by Springer Japan.

Order:

I. Price for co-authors

¥ 5,250 (¥5,000 + 5 % consumption tax: only in Japan) **per copy (for every co-author)**

If necessary, please order extra copies for co-authors to the Journal Office.

II. Subscription fee

	domestic	**overseas**
Annual subscription rate	**¥21,000*/year**	**¥20,000/year**
Shipping Costs	**free**	**¥2,000/year**

*including consumption tax

III. Purchase price for single issue

¥ 8,400 (¥8,000 + 5 % consumption tax: only in Japan) **per issue**.

AROB Journal Office : joffice@alife-robotics.co.jp

Artificial Life and Robotics

Our Review System

For contributed papers,

1. Duration:

   Two months is our target time of the whole review process, however, we are trying our best to make it as short as possible.

2. Review results:

   Every contributed paper will be reviewed by three assigned reviewers with score ranging from 1 (highest mark) to 4 (lowest mark);

   1. publish with no revision,
   2. publish with minor revisions,
   3. possibly publish with revision and re-review,
   4. reject.

Review results, a total score of the three evaluation scores, would be read as;.

3 or 4	:	accepted and to be published as it is,
4, 5, or 6	:	accepted and to be published after minor revisions,
7, 8, or 9	:	acceptable but subject to rewriting and re-review,
10, 11, or 12	:	rejected

For recommended papers,

The recommended papers are ones that the chair of each session and reviewers read before the symposium that year and recommend to AROB Journal Office using the same evaluation score above. Therefore, the quality of recommended papers is apparent at the time of recommendation.

We express our heartfelt gratitude to chairs and reviewers of ISAROB for their support and sincere voluntary work without which this journal never exists.

AROB Journal Office : joffice@alife-robotics.co.jp

Artificial Life and Robotics

AROB Journal Office

ALife Robotics Corporation Ltd.

joffice@alife-robotics.co.jp

Tel: +81-97-567-3088

Fax: +81-97-594-0181

THE SEVENTEENTH INTERNATIONAL SYMPOSIUM
ON
ARTIFICIAL LIFE AND ROBOTICS

(AROB 17th '12)

ORGANIZED BY

International Organizing Committee of International Symposium on Artificial Life and Robotics (AROB)
(ALife Robotics Corporation Ltd. and Nippon Bunri University (NBU), Japan)

SPONSORED BY

Mitsubishi Electric Corporation Advanced Technology R&D Center
SANWA SHURUI Co., Ltd.

CO-OPERATED BY

The Society of Instrument and Control Engineers (SICE, Japan)
The Robotics Society of Japan (RSJ, Japan)
The Institute of Electrical Engineers of Japan (IEEJ, Japan)
The Institute of Systems, Control and Information Engineers (ISCIE)
The Institute of Electronics, Information and Communication Engineers (IEICE)
IEEE Japan Council (IEEE Robotics and Automation Society Japan Chapter)
Japan Robot Association (JARA)
Institute of Control, Robotics and Systems (ICROS, Korea)
Chinese Association for Artificial Intelligence (CAAI, P. R. China)

SUPPORTED BY

Kyushu Bureau of Economy, Trade and Industry, Ministry of Economy, Trade and Industry
OITA PREFECTURE
Oita City
BEPPU CITY
The oita chamber of commerce and industry
Oita Joint Industrial Association
Kyodo News
Jiji Press
Oita Godo Shimbunsya
The Asahi shimbun
The Mainichi Newspaper Co., Ltd.
The Yomiuri Shimbun, Seibu
THE NIKKAN KOGYO SHIMBUN, LTD
Japan Broadcasting Corporation Oita Station
Oita Broadcasting System
Television Oita System Corporation
Oita Asahi Broadcasting co., ltd.

GENERAL CHAIR

Masanori Sugisaka (Nippon Bunri University and Alife Robotics Co., Ltd., Japan)

VICE CHAIR

John L. Casti (International Institute for Applied Systems Analysis, Austria)
Yingmin Jia (Beihang University, P. R. China)
Ju-Jang Lee (KAIST, Korea)
Henrik Hautop Lund (Technical University of Denmark, Denmark)
Ken Naitoh (Waseda University, Japan)
Hiroshi Tanaka (Tokyo Medical & Dental University, Japan)
Yong-Guang Zhang (Academia Sinica, P. R. China)

ADVISORY COMMITTEE CHAIR

Fumio Harashima (Tokyo Metropolitan University, Japan)

PROGRAM CHAIR

Hiroshi Tanaka (Tokyo Medical & Dental University, Japan)

ASSISTANT GENERAL CHAIR

Takao Ito (Ube National College of Technology, Japan)

ADVISORY COMMITTEE

Bruce Eisenstein (Drexel University, Former IEEE President, USA)
Robert Fischl (Drexel University, USA)
Toshio Fukuda (Nagoya University, Japan)
Fumio Harashima (Tokyo Metropolitan University, Japan)
Paul Kalata (Drexel University, USA)
Moshe Kam (Drexel University, IEEE President, USA)
Hidenori Kimura (RIKEN, Japan)
Paul Oh (Drexel University, USA)
Masayoshi Tomizuka (University of California Berkeley, USA)

INTERNATIONAL ORGANIZING COMMITTEE

Hussein Abbass (University of New South Wales, Australia)
Kazuyuki Aihara (The University of Tokyo, Japan)
Takaya Arita (Nagoya University, Japan)
Christopher L. Barrett (Virginia Polytechnic Institute and State University, USA)
Mark A. Bedau (Reed College, USA)
Malachy Eaton (University of Limerick, Ireland)
Joshua M. Epstein (The Johns Hopkins University, USA)
Adam Grzech (Wroclaw University of Technology, Poland)
Hideki Hashimoto (The University of Tokyo, Japan)
Yoshiteru Ishida (Toyohashi University of Technology, Japan)
David John Glyndwyr James (Coventry University, UK)
Takashi Kohno (The University of Tokyo, Japan)

INTERNATIONAL PROGRAM COMMITTEE

HISTORY

The AROB was founded in 1996 under the support of Science and International Affairs Bureau, Ministry of Education, Culture, Sports, Science and Technology, Japanese Government. Since then, the symposium organized by the AROB has been held every year at B-Con Plaza, Beppu, Japan except AROB 5th ’00 (Oita) and AROB 6th ’01 (Tokyo). The seventeenth symposium will be held on January 19–21, 2012, at B-Con Plaza, Beppu, Japan.

OBJECTIVE

This symposium will bring together researchers to discuss development of new technologies concerning *artificial life and robotics* based on computer simulations and hardware designs of state-of-the-art technologies, and to share findings on how advancements in artificial life and robotics technologies that relate to artificial intelligence, virtual reality, and computer science are creating the basis for exciting new research and applications in various fields.

GENERAL SESSION TOPICS

Artificial intelligence
Artificial brain research
Artificial intelligence
Artificial life
Artificial mind research
Bioinformatics
Brain science
Complexity
Control techniques
Data mining
Evolutionary computations
Genetic algorithms
Human-machine cooperative systems
Human-welfare robotics
Image processing
Intelligent control & modeling
Learning
Multi-agent systems
Neural networks
Pattern recognition
Robotics
Poster Session

ORGANIZED SESSION TOPICS

Advanced Vehicle Control
Aware Technologies for e-Services
Bioinformatics
Bio-inspired theory and applications
Biomimetic Machines and Robots
Computer Vision and Sound Analysis
Computer-Supported Learning Systems
Control Application
Control Theory and its Application
Embracing Complexity in Natural Intelligence
Embracing Complexity in System Sensing
Information Technology for Environmental Research
Intelligent control
Intelligent control & modeling
Intelligent System and Control
Intelligent Systems and Applications
Intuitive Human-System Interaction
Management of technology
Mechatronics and Intelligent Systems
Medical Science and Complex System
Network Dynamics in Biological Information System
System sensing and control
Systems for defense of disaster

COPYRIGHTS

Accepted papers will be published in the proceedings of AROB and some of high quality papers in the proceedings will be requested to re-submit their papers for the consideration of publication in an international journal ARTIFICIAL LIFE AND ROBOTICS. All correspondence related to the symposium should be addressed to AROB Secretariat.

AROB Secretariat

ALife Robotics Corporation Ltd.

1068-1 Oaza Oshino, ita, 870-1121, JAPAN

Tel/Fax：+81-97-594-0181

Email：arobsecr@isarob.org

Home Page：http://isarob.org/

ADDRESS

Takayuki Hirai

President, Nippon Bunri University

It is a great pleasure to have the Seventeenth International Symposium on Artificial Life and Robotics. It is highly evaluated that many researchers known internationally have attended this event and presented the results of advanced valuable research since the first symposium in 1996. The research made public in each symposium has been the great moving force to develop the technologies of Artificial Life and Robotics. The researchers all over the world pay attention to the presentations of research and make good use of them to promote their own academic research. We have a lot of the presentations of research this time as well, and their academic contribution is remarkable. I would like to show honor to all of you in the committee who have such a valuable international symposium.

MESSAGES

Fumio Harashima

Advisory Committee Chair of AROB

Professor, Tokyo Metropolitan University

The science and technology (S&T) on Artificial Life and Robotics was born in 1996, and it’s been providing human being with happiness. This S & T is not only important but also necessary for people living in the world to maintain high quality of life. Research is heart and desire of human being and the S&T is going toward clarifying tool to achieve our objective.

I would like to congratulate researchers who work in the fields on Artificial Life and Robotics.

Masanori Sugisaka

General Chair of AROB

Professor, Nippon Bunri University and President,

ALife Robotics Corporation, Ltd. , Japan

It is my great pleasure to invite you all to the Seventeenth International Symposium on Artificial Life and Robotics (AROB 17th '12).

The symposium from the first (1996) to the Thirteenth (2008) were organized by Oita University and Nippon Bunri University (NBU) and the Symposium from the Fourteenth (2009) to the Sixteenth (2011) were organized by Nippon Bunri University (NBU) and ALife Robotics Corporation Ltd. under the sponsorship of the Science and Technology Policy Bureau, the Ministry of Education, Science, Sports, and Culture (Monbusho), presently, the Ministry of Education, Culture, Sports, Science, and Technology (Monkasho), Japanese Government, Japan Society for the Promotion of Science (JSPS), The Commemorative Organization for the Japan World Exposition ('70), Air Force Office of Scientific Research, Asian Office of Aerospace Research and Development (AFOSR/AOARD), USA. I would like to express my sincere thanks to not only Monkasho, JSPS, the Commemorative Organization for the Japan World Exposition ('70), AFOSR/AOARD but also Japanese companies (Mitsubishi Electric Corporation, Advanced Technology R&D Center, Oita Gas Co., Ltd., ME System Co. LTD, and Sanwa Shurui Co., LTD.) for their repeated supports.

This symposium is organized by International Organizing Committee of AROB and is sponsored by ALife Robotics Co., Ltd., and technically co-sponsored by IEEE Robotics and Automation Society Japan Chapter, JARA, SICE, ISCIE, IEICE and CAAI (P.R. China).

I hope that the new technologies presented in this symposium bring happiness to human society and will facilitate the establishment of an international research Institute of Artificial Life and Robotics.

Welcome and enjoy your stay in Beppu.

Hiroshi Tanaka

Program Chair and Vice-Chair of AROB

Professor, Tokyo Medical and Dental University

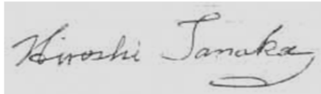

On behalf of the program committee, it is my great pleasure and honor to invite you all to the Seventeenth International Symposium on Artificial Life and Robotics (AROB 17th 2012). This symposium is made possible owing to the cooperation of Nippon Bunri University and Santa Fe Institute. We are also debt to Japanese academic associations such as SICE, RSJ, and several private companies. I would like to express my sincere thanks to all of those who make this symposium possible.

As is needless to say, the Alife or biologically-inspired Robotics approach now attracts wide interests as a new paradigm of science and engineering. Taking an example in the field of bioscience, the accomplishment of HGP (Human Genome Project) and subsequent post-genomic comprehensive “Omics data” such as transcriptome, proteome and metabolome, bring about vast amount of bio-information. However, as a plenty of omics data becomes available, it becomes sincerely recognized that the framework by which these omics data can be understood to make a whole picture of life is critically necessary. Thus, in the omics era, biologically-inspired systems approach like Alife is expected to give one of new alternative ideas to integrate this vast amount of bio-data.

This example shows the Alife and biologically-inspired approach is very promising and may exert a wide influence on the effort to develop a new paradigm for next generation of life science. We hope this symposium becomes a forum for exchange of the ideas of the attendants from various fields, including the life science field, who are interested in the future possibility of biologically-inspired computation and systems approach. I am looking forward to meeting you in Beppu, Oita.

John L. Casti

Vice-Chair of AROB

Professor, International Institute for Applied Systems Analysis,

Vienna, Austria

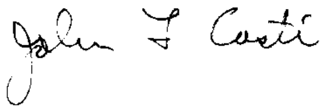

As a member of the AROB committee since the first AROB in 1994, it's always a pleasure for me to begin the year with this event. So once again I'm very pleased to invite you all to the Seventeenth International Symposium on Artificial Life and Robotics (AROB 17th ‘12). The program for this year's meeting contains the customary wide variety of themes, ranging from robotics and human-machine interfaces to mathematical and computer modeling of human systems. I think I can fairly say that the AROB has now taken its place as the premier event in Asia each year for researchers in these areas.

Over the coming days, I anticipate many productive exchanges of idea and feel that the AROB symposium will give rise to many fruitful ways for international cooperation in the areas of simulation of human systems. In these very difficult times, the world must find new tools for solving the pressing problems of climate change, energy and food supply, economic growth and many other domains of modern life. Hopefully, the work presented at the AROB will contribute to finding effective solutions to these growing threats.

Yingmin Jia

Vice-Chair of AROB

Professor, Beihang University

The 17th International Symposium on Artificial Life and Robotics (AROB) will be held in Beppu, Oita, Japan from Jan. 19th to 21th, 2012. As a vice-chairman, I am honored and privileged to invite you all to this fruitful 3-day event, which provides an excellent opportunity for the formal exchange of information, ideas, and research results between leading scientists and engineers in the areas of artificial life and robotics.

In 1996, the first Symposium was created and organized by Prof. Masanori Sugisaka, the general chairman of AROB. Since then, the symposium has attracted an impressive range of researchers from all around the world, and distinguished achievements have been obtained that shows his foresight in merging two disciplines of artificial life and robotics. Moreover, it is gratifying to see that there are more and more young colleagues, researchers and engineers from the universities, research institutions and industries interested in the field. I believe there is a rapid and better development in the near future.

Finally, I would like to acknowledge the contributions of operating and programming committee members for their great efforts to make this symposium successful. Also, I would like to express my sincere appreciation to the plenary speakers and invited speakers for their willingness to give us their excellent lectures.

Looking forward to meeting you at the 17th AROB, and wishing you all have fruitful technical discussions and enjoy the symposium.

Ju-Jang Lee

Vice-Chair of AROB

Professor, KAIST

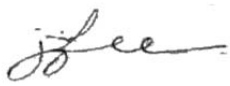

The Seventeenth International Symposium on Artificial Life and Robotics (AROB) will be held in Beppu, Oita, Japan from Jan. 19th to 21th, 2012. This year's Symposium will be held amidst the high expectation of the increasingly important role of the new interdisciplinary paradigm of science and engineering represented by the field of artificial life and robotics that continuously attracts wide interests among scientist, researchers, and engineers around the globe.

Since the time of the very first AROB meeting in 1996, each year, distinguished researchers and technologists from around the world are looking forward to attending and meeting at AROB. AROB is becoming the annual excellent forum that represents a unique opportunity for the academic and industrial communities to meet and assess the latest developments in this fast growing artificial life and robotics field. AROB enables them to address new challenges, share solutions, discuss research directions for the future, exchange views and ideas, view the results of applied research, present and discuss the latest development of new technologies and relevant applications.

In addition, AROB offers the opportunity of hearing the opinions of well-known leading experts in the field through the keynote sessions, provides the bases for regional and international collaborative research, and enables to foresee the future evolution of new scientific paradigms and theories contributed by the field of artificial life and robotics and associated research area. The twenty-first century will become the century of artificial life and intelligent machines in support of humankind and AROB is contributing through wide technical topics of interest that support this direction. It is a great for me as the Vice Chairman of the 17th AROB 2012 to welcome everyone to this important event. Also, I would like to extend my special thanks to all authors and speakers for contributing their research works, the participants, and the organizing team of the 17th AROB.

Looking forward to meet you at the 17th AROB in Beppu-Oita and wishing you all the best.

Henrik Hautop Lund

Vice-Chair of AROB

Professor, Center for Playware, Technical University of Denmark

I am much honored to invite you to the Seventeenth International Symposium on Artificial Life and Robotics (AROB 17th '12). The international symposium has been held each year since 1996, initially organized by Oita University and now being organized by Nippon Bunri University, and supported by Ministry of Education, Culture, Sports, Science and Technology, the Japanese Government.

The symposium attracts an impressive range of researchers from all continents, who all share the vision of merging research based upon artificial life and robotics. The symposium is visionary in merging these two, science and engineering disciplines, and has become the most important forum for research into merging artificial life and robotics.

The research in artificial life and robotics is very important since it both brings us insight into ourselves as human beings and natural systems, and brings us new engineering solutions that may influence our lives. It is my hope that you will use this insight and opportunity to develop systems that help humankind in socially responsible ways. Indeed, the symposium puts high emphasis on the social impact of interdisciplinary (based on artificial life and robotics combined with other fields, e.g. social science, art) developments, and has become an important forum for the discussion of global developments of socially responsible technology.

I would like to take this opportunity to thank the general chairman of AROB, Prof. Masanori Sugisaka, for being so visionary 17 years ago to engage in creating and organizing this important annual event for our research community. It takes a lot of courage to be the first to create a novel interdisciplinary research field such as the one that comes from the merge between artificial life and robotics. Prof. Sugisaka has shown how being courageous enough to engage in the adventurous activities of merging two fields may lead to very fruitful research and to the lively research community that you are now part of with your participation in this international symposium.

I would also take this opportunity to thank Springer-Verlag for supporting this research community, and remind all participants of the Springer-Verlag Artificial Life and Robotics Journal. Hopefully, we will see numerous, high quality contributions to the journal as the outcome of this symposium and the research collaboration that may entail the symposium. Indeed, it is my hope that you will all engage in open and fruitful scientific discussions with your colleague researchers during the symposium, and that these discussions may open up for future research collaborations in order to bring new insight into artificial life and robotics to the community.

Ken Naitoh

Vice-Chair of AROB

Professor, Waseda University, Faculty of Science and Engineering

What is the essential difference between living beings and machines? This may be the mystery which cannot be solved forever. However, deep thought experiments on the mystery will bring new technologies: quantum leaps of biological, medical, and mechanical technologies. The International Symposium on Artificial Life and Robotics related to the mystery and wonderful hot springs in Oita, Beppu, are wellsprings for inducing wonderful idea, concepts, scenario, and concrete systems. It is a great pleasure for us to discuss on the future with a lot of researchers in the world and also to encourage the next generations here.

Takao Ito

Assistant General Chair of AROB

Professor, Ube National College of Technology

Since our first symposium was held in Beppu Oita in 1996, we have met every year. We are now about to begin our 17th symposium. As one of the program committee, I am delighted to invite you all to the Seventh International Symposium on Artificial Life and Robotics which will be held in Beppu Oita next year.

Given the intense competition in the field of artificial life and robotics, the effective coordination and efficient maintenance of information exchange take on increased importance. The AROB international symposium provides us a unique opportunity to enjoy the discussion of all new issues, and to share experiences related to the advanced technologies and management skills. I am pleased to put together this excellent program that represents submissions from many countries around the world. I sincerely hope that those participating in this symposium as delegates from their various countries will have something to offer regarding our study of the present situation of the artificial intelligence and its management and will contribute to its future development.

I end these words of welcome with an earnest prayer for the great success of this symposium.

Plenary speakers:

PT1 : Modular Playware Technology

Prof. Henrik Hautop Lund

Professor, Center for Playware, Technical University of Denmark, Denmark

Abstract:

Playware is intelligent hardware and software that creates play and playful experiences for users of all ages. Such playware aim at providing play forces to bring the user into play dynamics, and in this way motivate the user to perform desired behaviors, e.g. for play, education, sports training, and health improvements. However, designing playware technology that results in specific behaviors of the user in not a trivial task, and it demands an array of background knowledge in a number of scientific fields. Indeed, definition of desired interactions and behaviors should arise from deep knowledge of the field of application (e.g. play of a specific user group, clinical knowledge of therapy of a specific patient group, professional music knowledge, and professional sport knowledge). In order to meet a practice, where several disciplines can join to develop such playware, we conceptualized the approach of modular playware in the form of building blocks. Building blocks should allow easy and fast expert-driven or user-driven development of playware applications for a given application field. The development of such modular playware technology takes its inspiration from modular robotics, human-robot interaction and embodied artificial intelligence. In this talk, I will present the design principles for creating such modular playware technology with focus on the play principles and educational principles that forms the foundation for the design principles of modular playware technology. I will exemplify the design principles with practical applications from the fields of play, education, sports, music, performance art, and health.

Biography:

Henrik Hautop Lund is head of the Center for Playware at Technical University of Denmark (DTU Elektro). Prof. Lund is known world-wide for his work in bringing robotics to use in novel ways. His approach is to combine modular robotics and modern artificial intelligence to create novel solutions to problems that occupy the citizens of the World, e.g. obesity, rehabilitation, and 3rd World development. He has recently founded the Center for Playware to focus even further on how playful aspects of robotics may provide motivation for any citizen to perform different kinds of interaction with the robots of our future daily life. He chaired the Robots at Play festivals in the open city areas where researchers, artists, entertainers, and citizens meet through playful hands-on experience with robotics in the daily life of the citizens. In all cases, Prof. Lund has shown how the combination of a modern artificial intelligence, modular robotics and entertainment may provide novel opportunities in play, rehabilitation, sport, music, teaching, third World development, etc., by trying to allow non-expert users easy access to the technology in a playful and motivating way.

Prof. Lund has published 150 scientific articles in the field of robotics, he has been a member of the Danish Research Council, and he has been invited to present his robotic work in numerous occasions, for instance for the Emperor of Japan at Akasaka Palace in Tokyo. He founded and headed the LEGO Lab in 1997-2000. He invented the RoboCup Junior robot football game for children, and his Adaptronics group won the RoboCup Humanoids Free Style World Championship 2002 in front of 120.000 spectators. Further, he developed the RoboMusic in collaboration with World Music Award winner, remix musician Funkstar De Luxe. Prof. Lund's work has received world-wide interest from news media, and he was nominated for the award for the best entertainment robots and systems research over the last 20 years at the IEEE International Conference on Intelligent Robots and Systems (IROS).

Prof. Lund is director of the spin-off company Entertainment Robotics.

PT2 : Fundamentals of Neurodynamics: Statistical neurodynamics and Neural Field Theory

Prof. Shun-ichi Amari

Senior Advisor, RIKEN Brain Science Institute, Japan

Abstract:

The brain consists of a vast number of neurons and processes information through their dynamical interactions. Peculiar characteristics neural networks would be useful for designing algorithms for artificial life and applying them to robot navigation. The present talk will focus on two types of neurodynamics, one is generalized majority decision dynamics and the other dynamics of excitation patterns in a neural field.

A neural network is a generalized majority decision system, in which each element calculates a weighted sum of the outputs of the other elements and decides its own output. Such a system is common in many biological systems such as a gene expression network, social communication network etc. We consider randomly connected binary elements and compare its dynamical behavior with that of a random Boolean logic network. We prove that a generalized majority decision system can make very quick decision (short transient time) compared with a random Boolean net. We also show that its state transition graph has a scale-free property so that a small number of states monopolize the incoming branches.

Neurons are arranged in a two-dimensional sheet in the cortex, where neighboring neurons are connected. Excitations in a neural field propagate and interact. We show an interesting phenomenon of traveling local excitations and their collision. Such phenomena will be applied to information processing having topology of the outer environment. This will be applied to the problem of robot navigation.

Biography:

Shun-ichi Amari was born in Tokyo, Japan, on January 3, 1936. He graduated from the Graduate School of the University of Tokyo in 1963 majoring in mathematical engineering and received Dr. Eng. Degree.

He worked as an Associate Professor at Kyushu University and the University of Tokyo, and then a Full professor at the University of Tokyo, and is now Professor-Emeritus. He served as Director of RIKEN Brain Science Institute for five years, and is now its senior advisor. He has been engaged in research in wide areas of mathematical engineering, in particular, mathematical foundations of neural networks, including statistical neurodynamics, dynamical theory of neural fields, associative memory, self-organization, and general learning theory. Another main subject of his research is information geometry initiated by himself, which provides a new powerful method to information sciences and neural networks.

Dr. Amari served as President of Institute of Electronics, Information and Communication Engineers, Japan and President of International Neural Networks Society. He received Emanuel A. Piore Award and Neural Networks Pioneer Award from IEEE, the Japan Academy Award, Gabor Award from INNS, Caianiello Award, and C&C award, among many others.

Invited speakers:

IT1 : Future Technology and Market Developments for Unmanned Maritime Vehicles

Mr. Bob Nugent

Vice President, Advisory Services, AMI International, USA

Abstract:

The paper forecasts technological and market developments that will shape the future role and demand for unmanned maritime vehicles (UMV), to include unmanned underwater vehicles (UUV) and unmanned surface vehicles (UMV) over the next decade. We will begin with a review of the current UMV market by application/mission segment, technology and vehicle type, covering UUVs, both autonomous (AUV) and remotely operated (ROV), as well as USVs. Will then examine improvements in power and communications technologies that will change the UMV market in the coming decade and blur some of the current capability and design differences between commercial and military UMV markets. The paper will consider the thesis that improvements in UMV power and communications technologies will, following a trajectory seen in the UAV market, lead to growth in demand for UMVs in the civil, military and security sectors. These UMVs would be capable of augmenting manned platforms in conventional Anti-Surface, Anti-Submarine, and Anti-Air naval operations. However, AMI market and technical research suggests that the next decade of changing patterns of world economic and commercial maritime activity, and continuing technological limitations will limit the growth potential for weaponized UMVs. Rather, the period will see more demand among a broader customer base of commercial, security, and military users for hybrid UMVs optimized for port/harbor/facility security and environmental survey and exploration rather than combat missions. We will conclude with future UMV market forecast scenarios in a "high-medium-low" framework for both commercial and defense applications. These market scenarios predict significant increases in UMV sales and use, but temper some overly optimistic forecasts currently being made for these vehicles in both commercial and military/security sectors. The prospects of integration of scientific research and theoretical results in the robotics field (regularly publicized at the AROB symposia) with practical development and use of unmanned systems, especially in maritime domain, will be discussed too.

Biography:

Bob Nugent joined AMI in Bremerton WA in 2007 as a Senior Consultant following a 22 year career as a US naval officer. In 2010 he relocated to Northern Virginia as Vice President of Advisory Services to head up AMI's Washington DC Operations Office. He advises on defense, naval, maritime, C4/ISR, aerospace, and unmanned systems markets. Bob has been quoted and published on naval, defense and economic issues in CNBC, Defense News, Naval Forces Magazine, Singapore Straits Times, BBC, Al-Jazeera and a wide range of national and regional media around the world. He has also presented papers at naval industry expos and conferences in the US, Europe and Asia. Bob's skill sets include strategic planning, competitive assessment, business development and capture, defense systems, tactics, and platform analysis; and market and risk research. Bob earned undergraduate degrees at New Mexico State University and attended the U.S. Naval Postgraduate School and Defense Language Institute, where he studied Russian. He graduated with distinction from the U.S. Naval War College in 2004 and received an M.B.A from Marymount University in Arlington, Virginia in 2007. His last Navy assignment was as Director of Command and Control overseeing major C4ISR programs on the U.S. Navy's acquisition staff in the Pentagon. Bob has also served as Assistant Naval Attache in Moscow, current intelligence department head on the U.S. Navy staff in London, and in analytic and watch officer assignments in Hawaii, South Korea, and Japan. His operational assignments included duty as an Intelligence Officer afloat with expeditionary and aviation units. Bob is married to Nancy Smedberg of McLean, Virginia where they live with their 7 children. Bob has been an adjunct university instructor in Economics and Accounting and a youth athletics coach.

IT2 : JAEA Robotics' Emergency Response to FUKUSHIMA-DAIICHI Accident

Mr. Shinji Kawatsuma

Japan Atomic Energy Agency, Japan

Abstract:

Japan Atomic Energy Agency (JAEA) developed Nuclear Emergency Response Robotics, two RESQ-A, a RESQ-B, a RESQ-C and a RaBOT, in 2001 after JCO criticality accidents occurred, and a Remote operated vehicle (ROV) for Glove Box dismantling cold test in 2008. It is very sorry that RESQ-A, RESQ-B and RESQ-C could not work because of lack of budget when the Fukushima-Daiichi accident occurred by a big earthquake and a huge Tsunami on March 11th 2011, that RaBOT was abandoned from the view point of Practicality, and that ROV could work but was in the facilities damaged by the earthquake.

According to status and condition of the accident at Fukushima-Daiichi, JAEA have modified ROV and two RESQ-A to JAEA-1, JAEA-2 and JAEA-3, and prepared Robotics Control vehicles.

JAEA has provided Robotics and Robotics Control vehicle to TEPCO and is continuously supporting TEPCO for plant restoration.

The summary and lesson learned of Robotics' emergency response to Fukushima-Daiichi accident, would be presented.

Biography:

Shinji Kawatsuma is a senior Principal Engineer and General Manager of Remote and Robotics Engineering Office, Department of Partnership Operation for Plant restoration, Headquarters of Fukushima partnership Operation, Japan Atomic Energy Agency (JAEA).

He is responsible for JAEA support in the field of Remote and Robotics to FUKUSHIMA-DAIICHI accident, Nuclear Emergency Response Robotics of JAEA and basic research and development in the field of Remote and Robotics in JAEA.

He served as General Manager of Backend cooperation office and was responsible for promoting of decommissioning and waste management in JAEA.

He began his career as engineer in Power reactor and Nuclear fuel development Corporation (PNC), to develop Bilateral-Servo-Manipulator, and research Radiation Resistance Technology, Man-Machine-Interface. He has been assigned to Oak Ridge National Laboratory as an exchange engineer for co-developing remote maintenance system including servo manipulator.

He received his bachelor of Mechanical Engineering from Waseda university.

IT3 : Using Robots to Understand Natural Behavior

Dr. Sanjay S. Joshi

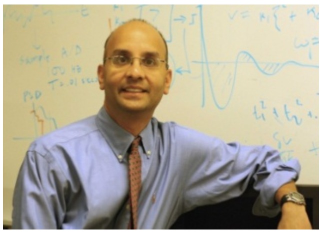

Ph.D. Associate Professor,

College of Engineering University of California, Davis, USA

Abstract:

Since its beginnings, robotics has been inspired by animal and human behavior. However, more recently, roboticists and biologists have been using robots as new tools to better understand animal behavior itself. These new biorobots are not meant to look and move like real animals in all respects. Rather, they are designed to test specific biological hypotheses and lend insight into the complexity of natural behavior. In our lab, we are building artificial rat pups that have helped discover the factors responsible for the emergence of both individual and group rat pup behavior patterns. A central theme in this research is the emergence of behavior from the interaction of brain, body, and environment. In another project, we are building robotic squirrels to interact with live rattlesnakes, to study predator-prey interaction. These squirrel models have already helped discover the first-known infrared communication in the animal world. New versions of the robot are currently being used in natural environments to collect long-term information on squirrel and snake behavior. As robotics and biology researchers continue to work together, robotics tools will surely facilitate a deeper understanding of natural behavior.

Biography:

Sanjay Joshi is currently Associate Professor of Mechanical and Aerospace Engineering at the University of California, Davis where he directs the Robotics, Autonomous Systems, and Controls Laboratory. This interdisciplinary laboratory studies natural and artificial control systems and robotics, with applications in medicine, biology, and space exploration. Dr. Joshi received a BS from Cornell University in 1990, and MS/PhD from UCLA in 1992/1996, all in Electrical Engineering. After his doctoral work, he became a member of the technical staff at the NASA Jet Propulsion Laboratory in Pasadena, California where he designed spacecraft control systems for NASA missions and performed research for the Mars robotics program. After joining academia, he began applying autonomous robotics to the study of animal behavior, cognition, and communication. From 2010-2011, he was Visiting Associate Professor in the Department of Neurology, Columbia University College of Physicians and Surgeons, New York City.

IT4 : Withstanding Asymmetric Situations in Distributed Dynamic Worlds

Dr. Peter S. Sapaty

Chief Research Scientist, Director of Distributed Simulation and Control of the Institute of Mathematical Machines and Systems, National Academy of Sciences of Ukraine, Ukraine

Abstract:

In our modern dynamic world we are meeting numerous irregular situations where proper reaction could save lives and wealth and protect critical infrastructures. For example, no secret that world powerful armies with traditional system organizations are often losing to terrorists, insurgents or piracy with primitive gadgets but very flexible structures making them hard to detect and fight. And delayed reaction to earthquakes or tsunamis is a result of inadequacy of system organizations too. A novel philosophy and supporting high-level networking technology will be revealed that can quickly react on irregular situations and threats and organize any available human and technical resources into operable systems providing global awareness, pursuing global goals and self-recovering from damages. The approach allows us at runtime, on the fly, to formulate top semantics of the needed reaction on asymmetric events in a special Distributed Scenario Language (DSL), shifting most of traditional organizational routines to automated up to fully automatic implementation, with effective engagement of unmanned systems. This technology, based on gestalt and holistic principles rather than traditional multi-agent organizations will be revealed in detail, with numerous DSL scenarios that can be executed by any mixture of human and robotic components. These include runtime investigation and classification of irregular situations in distributed air, land and maritime environments, launching effective relief or combat missions like fighting collective manned piracy by smart unmanned swarms, and many others. The technology offered provides a unified solution to human-robot interaction and multi-robot behaviors just as a derivative of parallel and distributed interpretation of DSL.

Biography:

Dr Peter Sapaty, Director of Distributed Simulation and Control at the Ukrainian Academy of Sciences, is with networked systems for more than 45 years. Received MSc on calculation and simulation of distributed power networks at Kiev Polytechnic Institute in 1971, and PhD in Computer Science from V.M. Glushkov Cybernetics Center in 1976. Created heterogeneous citywide computer networks from 1969 and parallel supercomputers from mid seventies, chaired international intelligent network management project and simulated dynamic systems like battlefields on distributed computer networks in 1990-98. Worked in Germany, UK, Canada, and Japan as Alexander von Humboldt Foundation fellow, project leader, research professor, department head, and special invited professor, chaired SIG on Mobile Technologies within Distributed Interactive Simulation project in the US. Published more than 150 scientific papers on simulations and management of networked systems. Invented higher-level networking technology used in different countries and resulted in a European Patent and two John Wiley books. Main area of interest: models and languages for coordination and simulation of distributed dynamic systems with application in cooperative robotics, emergency management, infrastructure protection, and terrorism and piracy fight. Peter's individual data is published in Marquis 2010 edition of Who's Who in the World, also in Cambridge 2000 Outstanding Intellectuals of the 21st Century.

IT5 : Human Interface of Robots or Agents via Facial and Word Expression

Prof. Kaoru Sumi

PhD Professor at Future University Hakodate, Hokkaido, Japan

Abstract:

To design an intelligent interactive system, it is necessary to consider how humans feel about the system and establish a good relationship with them. In human robot interaction or human agent interaction, to establish a fifty-fifty relationship between a technical artifact (such as a robot or an agent system) and a human, the power of conviction or influence of the artifact over the human is very important.

To develop an intelligent system using a robot or an agent such as a system that proactively interacts with a user and even changes the user's intention according to the user's circumstances, our project investigated reactions with the user under several situations, considering human robot interaction and human agent interaction using facial and word expressions. Accordingly, we established some rules for making the agent's reaction favorable to the user on the basis of facial expressions and words, and gained some insights into the differences between human robot interaction and human agent interaction.

In this talk, I introduce the possibility of human persuasion by a robot or an agent using facial expressions and emotion words, based on the experimental results.

Biography:

Kaoru Sumi is a professor in the Department of Media Architecture, Future University Hakodate, Japan. Prof. Sumi received her PhD in engineering from the University of Tokyo. Her recent research interests are human computer interaction, persuasive technology, and an application for digital storytelling.

After she received her BS in physics from the Science University of Tokyo, she worked at a telecommunications company. She received her MS in systems management from the University of Tsukuba while she was working there.

She worked at ATR MI&C Research Laboratories, Communication Research Laboratory in Japan, Osaka University, where she researched human computer interaction, knowledge engineering and the application of artificial intelligence. She worked on media informatics and human agent interaction at the National Institute of Information and Communications Technology. She was an associate professor at Hitotsubashi University until last year.

Tutorial speaker:

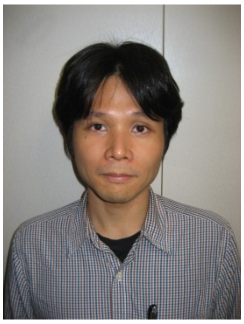

Introduction to silicon neuron and neuronal networks

Dr. Takashi Kohno

M.D., Ph.D. Associate Professor, University of Tokyo, Japan

Abstract:

The silicon neuronal network is an electronic circuit system designed to mimic the biophysical functions in the nerve system, which is realized by interconnecting the silicon neurons and synapses, electronic counterparts to the neurons and the synapses. It has three major application fields; the hybrid system, the real-time neural network simulator, and the neuromorphic system. The hybrid system between the nerve system and the silicon neuronal networks have been playing crucial roles as neurophysiological research tools as well as are expected to realize novel biomedical devices. The neuromorphic system is expected to provide a robust, autonomous, and energy-efficient computation and controlling platform whose operating principle is similar to the nerve system.
Most of the silicon neurons are implemented using the Complementary Metal Oxide Semiconductor (CMOS) technology to simulate in real-time the activities of the membrane potential in neuronal cells. A wide variety of implementations have been tried in the aspect of their circuitry and the neuronal models they are based on. For the biomedical applications, a detailed ionic conductance neuron model has been implemented using ultra-low-power consuming circuitry, whereas more configurable models and circuitry with more precise operation were selected for the real-time simulators. Another most historical trend is to adopt an ultimately simplified model, the Leaky Integrage-and-Fire (LIF) model, to avoid difficulty of implementation and realize relatively large-scale network. Though it succeeded in the implementation aspect, the over-simplifed model seemed to provide very few functionality. In these years, several efforts based on the nonlinear mathematics are made to find the silicon neuron models with sufficient dynamics that are feasible for implementation of large-scale silicon neuronal networks.

Biography:

Takashi Kohno, M.D., Ph.D., received the B.E. degree in medicine and the Ph.D. degree in mathematical engineering from University of Tokyo, Japan, in 1996 and 2002, respectively. After experiencing designing of medical care information systems in Hamamatsu University School of Medicine, took the job of a group leader in Aihara Complexity Modeling Project, Exploratory Research for Advanced Technology (ERATO), Japan Science and Technology Agency (JST), Japan. He is currently an associate professor in Institute of Industrial Science, University of Tokyo, Japan.
His research interests include the construction of the silicon neuronal networks, an artificially realized nerve system, and nonlinear dynamics in the models of the neuronal cells and the synapses. Based on his knowledge over the three academic fields, applied nonlinear mathematics, neurophysiology, and electronic circuit design, he is realizing a simple, compact, and low-power consuming silicon neuron circuit whose dynamics are qualitatively equivalent to several classes of neuronal cells and can be selected at run-time. His main interest is moving to construction of small silicon neural networks and autonomous regulation of the silicon neuron circuit. The final goal of his research is to realize a brain-like computing system that is at least comparable to the human brain.
In his private life, he has a long history of developing digital circuits including an original microprocessor and electronic circuit development tools such as a logic analyzer and a ROM emulator. It started in the mid-1980s and his first personal FPGA device board was with him in the early 1990s. He has a number of contributions to Japanese industry journals on digital circuit design.

Conference Rooms

1F

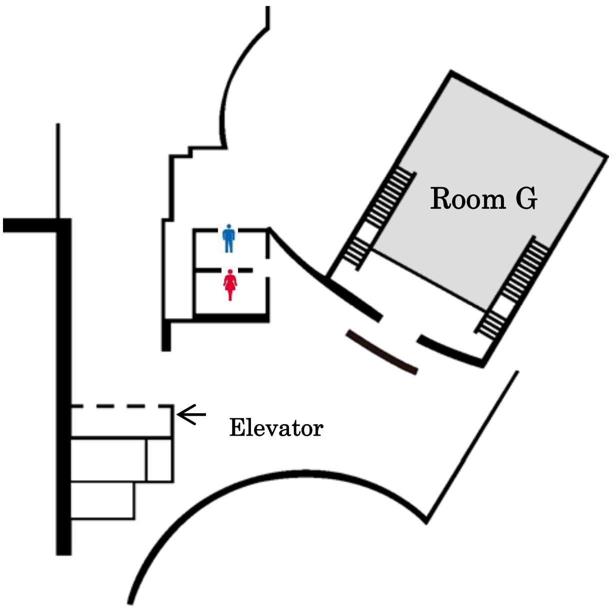

3F

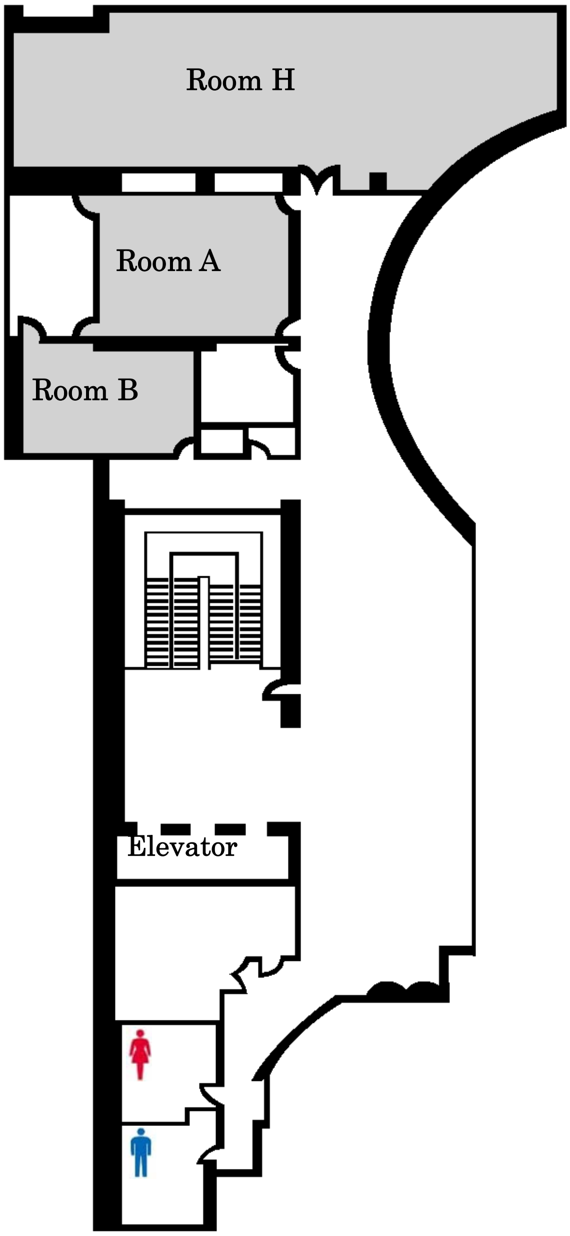

B1F

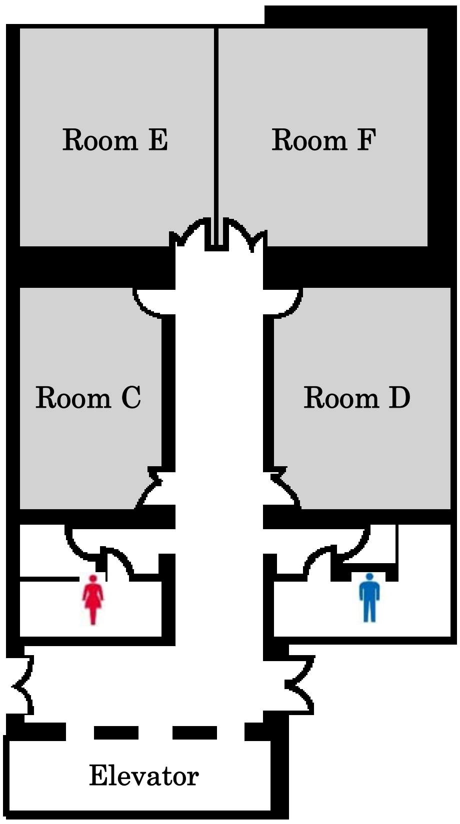

B-Con Plaza

Timetable (January 19, 2012)

	Room A	Room B	Room C	Room D	Room E	Room F
1/18 15:00 –	Registration (Registration Desk)					
1/18 17:00 –	Welcome Party (at Hotel Arthur)					
08:00 –	Registration (Registration Desk)					
08:45 – 10:15	GS3 Artificial life Chair T. Arita	GS8 Control techniques I Chair F. Nagata	GS10 Data mining I Chair D. Yamaguchi	GS25 Robotics I Chair J. Wang	GS26 Robotics II Chair N. Okada	OS18 Intelligent control & Modeling Chair H. Zhao
10:15 – 10:30	Coffee Break					
10:30 – 10:55	Opening Ceremony (Room G) Chair T. Ito					
10:55 – 11:45	**Plenary Speech** (Room G) Modular Playware Technology / **Prof. Henrik Hautop Lund** Chair H. Tanaka					
11:45 – 12:50	Lunch					
12:50 – 15:00	GS2 Artificial intelligence Chair H. Taki	GS9 Control techniques II Chair K. Higuchi		**Invited Speech** (Room H) **Mr. Bob Nugent** / **Mr. Shinji Kawatsuma** / **Dr. Sanjay S. Joshi** Chair P. Sapaty		
15:00 – 15:20	Coffee Break					
15:20 – 16:20	OS17 Intelligent control Chair Y. Jia	OS28 Systems for defense of disaster Chair M. Kubo	GS4 Artificial mind research Chair S. Kato	GS5 Bioinformatics Chair Y.I. Cho	GS12 Evolutionary computations Chair S.C. Horng	GS27 Robotics III GS28 Robotics IV Chair Y. Amano will start at 16:25
16:20 – 16:40	Coffee Break					
16:40 – 18:10	GS13 Genetic algorithms Chair S. Nakayama	GS16 Image processing I Chair A. Yamawaki	GS21 Multi-agent systems Chair H. Yamamoto	GS22 Neural networks I Chair E. Inohira	GS24 Pattern recognition Chair M. Rizon	

GS: General Session **OS: Organized Session**

Timetable (January 20, 2012)

	Room A	Room B	Room C	Room D	Room E	Room F
08:00 –	Registration (Registration Desk)					
08:40 – 09:40	GS1 Artificial brain research Chair H. Tanaka	GS14 Human - machine cooperative systems Chair K. Young	GS18 Intelligent control & modeling I Chair S. Nakayama	GS20 Learning Chair J. Botzheim	GS29 Robotics V Chair J. Wang	OS9 Computer-Supported Learning Systems I Chair K. J. Mackin
09:40 – 10:00	Coffee Break					
10:00 – 10:50	**Plenary Speech** (Room G) Fundamentals of Neurodynamics: Statistical neurodynamics and Neural Field Theory / **Prof. Shun-ichi Amari** Chair K. Naitoh					
10:50 – 11:10	Coffee Break					
11:10 – 12:40	**Invited Session on Playware** (Room H) Chair H.H. Lund			GS11 Data mining II Chair I. Yoshihara	GS17 Image processing II Chair H. Kim	GS23 Neural networks II Chair J.S. Shieh
12:40 – 13:40	Lunch / **Poster Session** (Room H)					
13:40 – 14:55	**Tutorial** (Room H) Introduction to silicon neuron and neuronal networks **Dr. Takashi Kohno**		OS20 Intelligent Systems and Applications Chair K. Su	GS7 Complexity Chair R. Suzuki	GS19 Intelligent control & modeling II Chair N. Okada	
14:55 – 15:15	Coffee Break					
15:15 – 17:00	OS10 Computer-Supported Learning Systems II Chair K.J. Mackin	OS13 Embracing Complexity in Natural Intelligence Chair Y. Ishida	OS19 Intelligent System and Control Chair K. Hsia		OS24 Medical Science and Complex Systems Chair K. Naitoh	GS15 Human-welfare Robotics Chair T. Fuchida
18:30 – 21:00	AROB Award Ceremony (Chair Y. Ishida) Banquet - Hotel Shiragiku (Chair J.J. Lee) …… Address S. Amari / H.H. Lund / Y. Jia / M.K. Habib					

GS: General Session **OS: Organized Session**

Timetable (January 21, 2012)

	Room A	Room B	Room C	Room D	Room E	Room F
08:00 –	Registration (Registration Desk)					
08:40 – 10:10	GS6 Brain science Chair T. Levi	OS1 Advanced Vehicle Control Chair S. Sagara	OS4 Bio-inspired theory and applications I Chair I. Yoshihara	OS12 Control Theory and its Application Chair M. Yokomichi	OS25 Network Dynamics in Biological Information Systems I Chair H. Suzuki	OS27 System sensing and control Chair M. Uchida
10:10 – 10:30	Coffee Break					
10:30 – 12:00	OS2 Aware Technologies for e-Services Chair K. Hashimoto	OS5 Bio-inspired theory and applications II Chair K. Yamamori	OS8 Computer Vision and Sound Analysis Chair Y. Yoshitomi	OS14 Embracing Complexity in System Sensing Chair Y. Ishida	OS23 Mechatronics and Intelligent Systems Chair M.K. Habib	OS26 Network Dynamics in Biological Information System II Chair H. Suzuki
12:00 – 13:00	Lunch					
13:00 – 15:10	**Invited Speech** (Room H) **Dr. Peter S. Sapaty** / **Prof. Kaoru Sumi** Chair J.J. Lee			OS15 Information Technology for Environmental Research I Chair T. Yamaguchi	OS3 Bioinformatics Chair S. Omatu	OS6 Biomimetic Machines and Robots I Chair K. Watanabe
15:10 – 15:30	Coffee Break					
15:30 – 16:45		OS21 Intuitive Human-System Interaction Chair M. Yokota	OS22 Management of technology Chair T. Ito	OS16 Information Technology for Environmental Research II Chair T. Yamaguchi	OS11 Control Application Chair O. Sato	OS7 Biomimetic Machines and Robotics Chair K. Watanabe
17:00 – 18:00	Farewell Party (RoomA)					

GS: General Session **OS: Organized Session**

Technical paper index

January 19 (Thursday)

Room G
10:55-11:45 Plenary Speech
Chair: Hiroshi Tanaka (Tokyo Medical & Dental University, Japan)

PL1 *Modular Playware Technology*
Henrik Hautop Lund (Center for Playware, Technical University of Denmark, Denmark)

Room H
12:50-15:00 Invited Speech
Chair: Peter S. Sapaty (National Academy of Sciences of Ukraine, Ukraine)

IS1 *Future Technology and Market Developments for Unmanned Maritime Vehicles*
Bob Nugent (AMI International, USA)

IS2 *JAEA Robotics' Emergency Response to FUKUSHIMA-DAIICHI Accident*
Shinji Kawatsuma (Japan Atomic Energy Agency, Japan)

IS3 *Using Robots to Understand Natural Behavior (Genetic-Algorithms Produce Individual Robotic-Rat-Pup Behaviors that Match Norway-Rat-Pup Behaviors at Multiple Scales)*
Chris Sullivan, Sanjay S. Joshi, Jeffrey C. Schank (College of Engineering University of California, Davis, USA)

January 20 (Friday)

Room G
10:00-10:50 Plenary Speech
Chair: Ken Naitoh (Waseda University, Japan)

PL2 *Fundamentals of Neurodynamics: Statistical neurodynamics and Neural Field Theory*
Shun-ichi Amari (RIKEN Brain Science Institute, Japan)

Room H
11:10–12:40 Invited Session on Playware
Chair: Henrik Hautop Lund (Center for Playware, Technical University of Denmark, Denmark)

ISP1 *MagicTiles. ALife for Real and Virtual RoboMusic*
Luigi Pagliarini (Center for Playware, Technical University of Denmark, Denmark / Academy of Fine Arts of Macerata, Italy)
Henrik Hautop Lund (Center for Playware, Technical University of Denmark, Denmark)

ISP2 *Social Playware for Supporting and Enhancing Social Interaction*
Kenji Suzuki (University of Tsukuba / Japan Science and Technology Agency, Japan)
Kazuki Iida, Tomoya Shimokakimoto (University of Tsukuba, Japan)

ISP3 *Adapting Body and Behaviour: - learning and playing with a modular robotic platform -*
Patrizia Marti, Iolanda Iacono (University of Siena, Italy)

ISP4 *Adaptivity to Age, Gender, and Gaming Platform Topology in Physical MultiPlayer Games*
Davíð Þór Björnsson, Rafn Vídalín Friðriksson, Henrik Hautop Lund (Center for Playware, Technical University of Denmark, Denmark)

13:40-14:55 Tutorial

Tutorial *Introduction to silicon neuron and neuronal networks*
Takashi Kohno (University of Tokyo, Japan)

January 21 (Saturday)

Room H
13:00–15:10 Invited Speech
Chair: Ju-Jang Lee (KAIST, Korea)

IS4 *Withstanding Asymmetric Situations in Distributed Dynamic Worlds*
Peter S. Sapaty (National Academy of Sciences of Ukraine, Ukraine)

IS5 *Human Interface of Robots or Agents via Facial and Word Expression*
Kaoru Sumi (Future University Hakodate, Japan)

January 19 (Thursday)

Room A
08:45-10:15 GS3 Artificial life
Chair: Takaya Arita (Nagoya University, Japan)

GS3-1 *Two-dimensional cellular automata model of microorganism morphosis*
Takeshi Ishida (Nippon Institute of Technology, Japan)

GS3-2 *Control of water flow to avoid twining of artificial seaweed*
Jun Ogawa, Ikuo Suzuki, Masahito Yamamoto, Masashi Furukawa (Hokkaido University, Japan)

GS3-3 *Dealing with rounding error problems in evolutionary physical simulation*
Marcin L. Pilat, Reiji Suzuki, Takaya Arita (Nagoya University, Japan)

GS3-4 *Adaptive behavior to environmental changes: Emergence of multi-generational migration by artificial Monarch Butterfly*
Katsuya Suetsugu, Atsuko Mutoh, Shohei Kato, Hidenori Itoh (Nagoya Institute of Technology, Japan)

GS3-5 *Real-time generation of prime sequence by one-dimensional cellular automaton with 8 states*
Kunio Miyamoto (Japan Advanced Institute of Science and Technology, Japan)
Hiroshi Umeo (University of Osaka Electro-Communication, Japan)

12:50-15:00 GS2 Artificial intelligence
Chair: Hirokazu Taki (Wakayama University, Japan)

GS2-1 *Power saving parameter learning for light power control in public space*
Hiroaki Obana, Hirokazu Miura, Noriyuki Matsuda, Hirozumi Kaneko, Fumitaka Uchio, Hirokazu Taki (Wakayama University, Japan)

GS2-2 *Control of flock behavior by using tau-margin -Obstacle avoidance and reformation-*
Tatsuya Kon, Kazuyuki Ito (Hosei University, Japan)
Akira Yokokawa (SANYO Electric Co.,Ltd., Japan)

GS2-3 *A proposition of adaptive state space partition in reinforcement learning with Voronoi Tessellation*
Kathy Thi Aung, Takayasu Fuchida (Kagoshima University, Japan)

GS2-4 *Universal Creativity Engine: Real-time creation of melody and lyrics based on the Ant system*
Kenta Nishio, Takaya Arita (Nagoya University, Japan)

GS2-5 *Simple system for detecting sound localization based on the biological auditory system*
Takanori Tomibe, Kimihiro Nishio (Tsuyama National College of Technology, Japan)

15:20-16:20 OS17 Intelligent control
Chair: Yingmin Jia (Beihang University, P. R. China)
Co-Chair: Junping Du (Beijing University of Posts and Telecommunications, P. R. China)

OS17-1 *H_∞ consensus control for high-order multi-agent systems with disturbances*
Ping Wang, Yingmin Jia (Beihang University, P. R. China)
Junping Du (Beijing University of Posts and Telecommunications, P. R. China)
Fashan Yu (Henan Polytechnic University, P. R. China)

OS17-2 *Lane keeping control for 4WS4WD vehicles subject to wheel slip constraint*
Changfang Chen, Yingmin Jia (Beihang University, P. R. China)
Junping Du (Beijing University of Posts and Telecommunications, P. R. China)
Fashan Yu (Henan Polytechnic University, P. R. China)

OS17-3 *Robust exponential stabilization criteria for uncertain linear systems with interval time-varying delay*
Nan Xiao, Yingmin Jia (Beihang University(BUAA), P. R. China)
Junping Du (Beijing University of Posts and Telecommunications, P. R. China)
Fashan Yu (Henan Polytechnic University, P. R. China)

OS17-4 *Improved Rao-Blackwellized particle filtering algorithms for multi-target tracking in clutter*
Yazhao Wang, Yingmin Jia (Beihang University, P. R. China)
Junping Du (Beijing University of Posts and Telecommunications, P. R. China)
Fashan Yu (Henan Polytechnic University, P. R. China)

16:40-18:25 GS13 Genetic algorithms
Chair: Shigeru Nakayama (Kagoshima University, Japan)

GS13-1 *A hybrid evolutionary algorithm for the resource constrained project scheduling problem*
Arit Thammano, Ajchara Phu-ang (King Mongkut's Institute of Technology Ladkrabang, Thailand)

GS13-2 *Study on evolution of the artificial flying creature controlled by neuro-evolution*
Ryosuke Ooe, Ikuo Suzuki, Masahito Yamamoto, Masashi Furukawa (Hokkaido University, Japan)

GS13-3 *A new differential artificial bee colony algorithm for large scale optimization problems*
Takuya Kagawa, Akihide Utani, Hisao Yamamoto (Tokyo City University, Japan)

GS13-4 *A generation alternation model for user-system cooperative evolutionary computation*
Satoshi Ono, Kiyomasa Sakimoto, Shigeru Nakayama (Kagoshima University, Japan)

GS13-5 *A neutral evolutionary path-planner*
Eivind Samuelsen, Kyrre Harald Glette, Kazi Shah Nawaz Ripon (University of Oslo, Norway)

Room B

08:45-10:15 GS8 Control techniques I

Chair: Fusaomi Nagata (Tokyo University of Science, Japan)

GS8-1 *Attitude control of an airborne two wheeled robot*
Huei Ee YAP, Shuji Hashimoto (Waseda University, Japan)

GS8-2 *A new adaptive and flexible communication protocol for long-term operation of ubiquitous sensor networks with multiple sinks and multiple sources*
Satoshi Yasuda, Akihide Utani, Hisao Yamamoto (Tokyo City University, Japan)

GS8-3 *Data gathering scheme for area monitoring-based wireless sensor networks*
Kosuke Ikeda, Akihide Utani, Hisao Yamamoto (Tokyo City University, Japan)

GS8-4 *A centralized control system for ecological vehicle platooning using linear quadratic regulator theory*
Anan Kaku, Masakazu Mukai, Taketoshi Kawabe (Kyushu University, Japan)

GS8-5 *A feedback-trained robot task assignment system*
Jeremy Straub, Eunjin Kim (University of North Dakota, USA)

GS8-6 *A control method to suppress the rotational oscillation of a magnetic levitating system*
Toshimasa Nishino (Toshiba industrial products manufacturing corporation, Japan)
Yasuhiro Fujitani, Norihiko Kato, Yoshihiko Nomura, Hirokazu Matsui (Mie University, Japan)
Naoaki Tsuda (Wakayama National College of Technology, Japan)

12:50-15:00 GS9 Control techniques II

Chair: Kohji Higuchi (The University of Electro-Communications, Japan)

GS9-1 *Fuzzy servo control of an inverted pendulum system*
Mohd Khairi Bin Mohamed Nor, Shigenori Okubo (Yamagata University, Japan)

GS9-2 *A lightweight sensing method of tooth-touch sound for disabled person using remote controller*
Akira Yamawaki, Seiichi Serikawa (Kyushu Institute of Technology, Japan)

GS9-3 *Two-dimensional merging path generation using model predictive control*
Wenjing Cao, Masakazu Mukai, Taketoshi Kawabe (Kyushu University, Japan)

GS9-4 *Model predictive control of a power-split hybrid electric vehicle system*
Kaijiang Yu, Masakazu Mukai, Taketoshi Kawabe (Kyushu University, Japan)

15:20-16:20 OS28 Systems for defense of disaster
Chair: Masao Kubo (National Defense Academy of Japan, Japan)
Co-Chair: Hiroshi Sato (National Defense Academy of Japan, Japan)

OS28-1 *Estimation of Hazardous Area with Surveillance UAV*
Hiroshi Sato, Masao Kubo, Akira Namatame (National Defense Academy of Japan, Japan)
OS28-2 *Safety of ships evacuation from Tsunami-Survey Unit about the Great East Japan Earthquake-*
Saori Iwanaga, Yoshinori Matsuura (Japan Coast Guard Academy, Japan)
OS28-3 *Individual recognition-free target enclosure model*
Masao Kubo, Tatsurou Yoshimura, Hiroshi Sato (National Defense Academy of Japan, Japan)
Akihiro Yamaguchi (Fukuoka Institute of Technology, Japan)

16:40-18:25 GS16 Image processing I
Chair: Akira Yamawaki (Kyushu Institute of Technology, Japan)

GS16-1 *Hamming distance based gradient orientation pattern matching*
Prarinya Siritanawan, Toshiaki Kondo (Thammasat University, Thailand)
GS16-2 *Microscopic image restoration based on tensor factorization of rotated patches*
Masayuki Kouno, Ken Nakae, Shin Ishii (Kyoto university, Japan)
Shigeyuki Oba (Kyoto University / Japan Science and Technology Agency, Japan)
GS16-3 *Robotic applications of a defensible error-aware super-resolution technique*
Jeremy Straub (University of North Dakota, USA)
GS16-4 *A study on situation recognition in wide area by aerial image analysis*
Ganwen Jiang, Jun Yoshida, Masayuki Kashima, Kiminori Sato, Mutsumi Watanabe (Kagoshima University, Japan)

Room C
08:45-10:15 GS10 Data mining I
Chair: Daisuke Yamaguchi (Toin University of Yokohama, Japan)

GS10-1 *Web search support system for the smartphone using call and Web logs*
Takuya Ito, Hiroyuki Nishiyama (Tokyo University of Science, Japan)
GS10-2 *Sentiment analysis for domain-specific texts*
Hidekazu Yanagimoto, Michifumi Yoshioka (Osaka Prefecture University, Japan)
GS10-3 *A localization method for smart phones by detection of walking using an accelerometer in indoor environments*
Kunioki Hayashi, Hiroyuki Nishiyama (Tokyo University of Science, Japan)

GS10-4 *Batch fast update algorithm for incremental association rule discovery*
Araya Ariya, Worapoj Kreesuradej (King Mongkut's Institute of Technology Ladkrabang, Thailand)

15:20-16:20 GS4 Artificial mind research
Chair: Shohei Kato (Nagoya Institute of Technology, Japan)

GS4-1 *AGVs' control in autonomous decentralized FMS (AGVs' mind with neural networks)*
Hidehiko Yamamoto, Hiroaki Tashiro, Takayoshi Yamada (Gifu University, Japan)
GS4-2 *Modelling mental representation as evolved second order learning*
Solvi Fylgja Arnold, Reiji Suzuki, Takaya Arita (Nagoya University, Japan)
GS4-3 *How equity norms evolve? - an evolutionary game theory approach to distributive justice*
Kazuaki Kojima, Takaya Arita (Nagoya University, Japan)
GS4-4 *Dynamics of rules internalized in dynamic cognitive agents playing a multi-game*
Takashi Sato (Okinawa National College of Technology, Japan)

16:40-18:25 GS21 Multi-agent systems
Chair: Hidehiko Yamamoto (Gifu University, Japan)

GS21-1 *An implementation of firefly-inspired network synchronicity without leaders on a group of small wireless devices*
Fujio Yamamoto (Kanagawa Institute of Technology, Japan)
GS21-2 *An improved clustering based Monte Carlo Localization approach for cooperative multi-robot localization*
Guanghui Luo, Dan Wu (University of Windsor, Canada)
Libing Wu (Wuhan University, P. R. China)
GS21-3 *Soundscape partitioning to increase communication efficiency in bird communities*
Reiji Suzuki (Nagoya University, Japan)
Charles E. Taylor, Martin L. Cody (University of California, USA)
GS21-4 *A cooperative self-localization method based on group robot information sharing*
Yuichi Kitazumi, Noriyuki Shinpuku, Kazuo Ishii (Kyushu Institute of Technology, Japan)
GS21-5 *Dual layered multi agent system for intentional islanding operation of microgrids*
Asitha Lakruwan Kulasekera, Ranathunga Arachchilage Ruwan, Manjula Udayanga Hemapala, Nuwan Perera (University of Moratuwa , Sri Lanka)
Achala Pallegedara (Saga University, Japan)
GS21-6 *Multi-agent framework for kinematics process of redundant multi-link robots*
Shinya Haramaki (Ariake National College of Technology, Japan)
Akihiro Hayashi, Mochimitsu Komori (Kyushu Institute of Technology, Japan)
Toshifumi Satake (Asahikawa National College of Technology, Japan)

Room D
08:45-10:15 GS25 Robotics I
Chair: Jiwu Wang (Beijing Jiaotong University, P. R. China)

GS25-1 *Development of MEMS micro robot using piezoelectric actuator mechanism*
Tatsuya Ogiwara, Kazuto Okazaki, Yutaro Kezuka, Shinpei Yamasaki, Minami Takato, Ken Saito, Fumio Uchikoba (Nihon University, Japan)

GS25-2 *Development of an autonomous-drive personal robot "An environment recognition and the position detecting system that used image processing and an LRS"*
Katsuhiro Yamamoto, Hideki Ishimaru, Eiji Hayashi (Kyushu Institute of Technology, Japan)

GS25-3 *Design of robotic behavior that imitates animal consciousness: Construction of the user-recognition system*
Motoki Yoshida, Kei Ueyama, Eiji Hayashi (Kyushu Institute of Technology, Japan)

GS25-4 *An abductive environment enables teacher's intervention in a robotics class*
Ilkka Jormanainen, Erkki Sutinen (University of Eastern Finland, Finland)
Meurig Beynon (University of Warwick, UK)

GS25-5 *A simplified approach towards realizing a three dimensional fax based on claytronics*
Chetan J, Shrikrishna Upadhyaya (BMS Institute of technology, India)

15:20-16:20 GS5 Bioinformatics
Chair: Young Im Cho (The University of Suwon, Korea)

GS5-1 *On classification of interview sheets for ophthalmic examinations using self-organizing maps*
Naotake Kamiura, Ayumu Saitoh, Teijiro Isokawa, Nobuyuki Matsui (University of Hyogo, Japan)
Hitoshi Tabuchi (Tsukazaki Hospital, Japan)

GS5-2 *An electrophysiological model of the pharyngeal muscle in Caenorhabditis elegans*
Yuya Hattori (Hiroshima University / Japan Atomic Energy Agency, Japan)
Michiyo Suzuki, Yasuhiko Kobayashi (Japan Atomic Energy Agency, Japan)
Zu Soh (Osaka University, Japan)
Toshio Tsuji (Hiroshima University, Japan)

GS5-3 *Origin of the Chukchee-Kamchatkan language family from the Paiwan language in Formosa: Evidenced by Swadesh basic vocabulary comparison, providing basic knowledge for understanding DNA haplotype distributions*
Koji Ohnishi (Niigata University, Japan)

GS5-4 *A study on line length and direction perception via cutaneous sensation*
Syed Muammar Najib Syed Yusoh, Yoshihiko Nomura, Ryota Sakamoto, Kazuki Iwabu (Mie University, Japan)

16:40-18:25 GS22 Neural networks I
Chair: Eiichi Inohira (Kyushu Institute of Technology, Japan)

GS22-1 *Optimizing the thermoforming of polypropylene foam by an artificial neural network*
Shih-Jung Liu, Ting-Ting Wen, Yau-Zen Chang (Chang Gung University, Taiwan)

GS22-2 *Situational judgment system for a robot in complex environments using hierarchical neural network*
Anri Nishimoto, Hitoshi Sori (Tsuyama National College of Technology, Japan)

GS22-3 *Medical image diagnosis of lung cancer by multi-layered GMDH-type neural network self-selecting functions*
Tadashi Kondo, Junji Ueno, Shoichiro Takao (The University of Tokushima, Japan)

GS22-4 *The technique of the online learning method using SOM algorithm for nonlinear SVM*
Hiroki Tamura, Takeshi Yoshimatsu, Koichi Tanno (University of Miyazaki, Japan)

GS22-5 *Financial market forecasting by integrating wavelet transform and k-means clustering with support vector machine*
W.D.S Roshan, R.A.R.C Gopura, A.G.B.P Jayasekara, D.S.V Bandara (University of Moratuwa, Sri Lanka)

Room E
08:45-10:15 GS26 Robotics II
Chair: Nobuhiro Okada (Kyushu University, Japan)

GS26-1 *A method of teaching a new action to a communication robot through spoken commands*
Eiichi Inohira (Kyushu Institute of Technology, Japan)
Yudai Okuda (Hoshiden Kyushu Corporation, Japan)

GS26-2 *Evaluation of the teleoperation system based on force-free control and visual servo control by using different human operator perception: evidence verified by experiments and statistical analysis*
Achala Pallegedara, Yoshitaka Matsuda, Takeo Matsumoto, Kenta Tsukamoto, Takenao Sugi, Satoru Goto (Saga University, Japan)
Naruto Egashira (Kurume National College of Technology, Japan)

GS26-3 *Development of flexible joints for a humanoid robot that walks on an oscillating plane*
Takehiro Yoneyama, Kazuyuki Ito (Hosei University, Japan)

GS26-4 *Manually controlled manhole cleaning robotic system*
Gopal Joshi, Animesh Rana, Venkateshwar R (Vels University, India)

15:20-16:20 GS12 Evolutionary computations
Chair: Shih-Cheng Horng (Chaoyang University of Technology, Taiwan)

GS12-1 *Optimal base-stock policy of the assemble to order systems*
Shih-Cheng Horng (Chaoyang University of Technology, Taiwan)
Feng-Yi Yang (National Yang-Ming University, Taiwan)

GS12-2 *DNA sequencing by Max-Min Ant System and Genetic Algorithm*
Tao Liu, Michiharu Maeda (Fukuoka Institute of Technology, Japan)

GS12-3 *Advanced artificial bee colony algorithm detecting plural acceptable solutions*
Masaaki Nishimoto, Akihide Utani, Hisao Yamamoto (Tokyo City University, Japan)

GS12-4 *Multi-objective optimal path selection in the Electric Vehicles*
Umair Farooq Siddiqi, Yoichi Shiraishi (Gunma University, Japan)
Sadiq M. Sait (King Fahd University of Petroleum & Minerals, Saudi Arabia)

16:40-18:25 GS24 Pattern recognition
Chair: Mohd Rizon (King Saud University, Saudi Arabia)

GS24-1 *Handwriting character classification using Freeman's olfactory KIII model*
Masanao Obayashi, Shinnosuke Koga, Liangbing Feng, Takashi Kuremoto, Kunikazu Kobayashi (Yamaguchi University, Japan)

GS24-2 *A corner detection technique using unit gradient vectors*
Pramuk Boonsieng, Toshiaki Kondo, Waree Kongprawechnon (Thammasat University, Thailand)

GS24-3 *Human detection employing the HOG feature based on multiple scale cells*
Yusuke Ehara, Joo Kooi Tan, Seiji Ishikawa, Takashi Morie (Kyushu Institute of Technology, Japan)

GS24-4 *Hash based early recognition of gesture patterns*
Yoshiyasu Ko, Atsushi Shimada, Hajime Nagahara, Rin-ichiro Taniguchi (Kyushu University, Japan)

GS24-5 *Source recognition in acoustic sensor arrays using self-organizing hidden Markov models*
Edgar E. Vallejo, Julio G. Arriaga (ITESM Campus Estado de México, México)
Charles E. Taylor (University of California, USA)

GS24-6 *Japanese finger-spelling recognition using a chest-mounted camera*
Akira Nagasue, Joo Kooi Tan, Hyoungseop Kim, Seiji Ishikawa (Kyushu Institute of Technology, Japan)

Room F

08:45-10:15 OS18 Intelligent control & Modeling

Chair: Huailin Zhao (Shanghai Institute of Technology, P. R. China)

Co-Chair: Fengzhi Dai (Tianjin University of Science and Technology, P. R. China)

OS18-1 *System development of an artificial assistant suit*
Jianling Bian (Zhengzhou University, P. R. China)
Huailin Zhao (Shanghai Institute of Technology, P. R. China)
Xiaomin Liu (North China University of Water Resources and Electric Power, P. R. China)
Masanori Sugisaka (Nippon Bunri University, Japan)

OS18-2 *Fundamental research on the fuzzy control to the autonomous airship*
Long Li, Yuan Li, Fengzhi Dai, Dejin Wang (Tianjin University of Science and Technology, P. R. China)
Yutaka Fujihara (Matsue College of Technology, Japan)

OS18-3 *Fundamental research on the fingerprint recognition algorithm*
Binyao Li, Fengzhi Dai, Dejin Wang, Baolong Zhang (Tianjin University of Science and Technology, P. R. China)
Naoki Kushida (Oshima National College of Maritime Technology, Japan)

OS18-4 *Configuration of the Mckibben Muscles and action intention detection for the artificial assistant suit*
Xiaoqing Jia (Shanghai Institute of Technology / Shanghai Maritime University, P. R. China)
Huailin Zhao, Lixia Wang (Shanghai Institute of Technology, P. R. China)
Masanori Sugisaka (Nippon Bunri University, Japan)

15:20-16:20 GS27 Robotics III

Chair: Yoko Amano (Nihon University, Japan)

GS27-1 *An improved Bug-type navigation algorithm for mobile robots*
Yi Zhu, Tao Zhang, Jingyan Song, Xiaqin Li (Tsinghua University, P. R. China)
Xuedong Chen (Huazhong University of Science and Technology, P. R. China)
Masatoshi Nakamura (Research Institute of Systems Control, Saga University, Japan)

GS27-2 *Sound source detection robot inspired by water striders*
Hiroki Nakatsuka, Kazuyuki Ito (Hosei University, Japan)

16:40-18:25 GS28 Robotics IV

Chair: Chair: Yoko Amano (Nihon University, Japan)

GS28-1 *Stability of two-wheeled mobile robot using new combined pole-placement method*
Yoko Amano (Nihon University, Japan)

GS28-2 *Phrase and music search engine for musical data*
Kentarou Minowa, Eiji Hayashi (Kyushu Institute of Technology, Japan)
GS28-3 *Control of real world complex robots using a biologically inspired algorithm*
Fabio DallaLibera (Padua University, Italy / Osaka University, Japan)
Shuhei Ikemoto, Hiroshi Ishiguro, Koh Hosoda (Osaka University, Japan)
GS28-4 *Control method for a redundant robot using stored instances*
Yuya Okadome, Yutaka Nakamura, Hiroshi Ishiguro (Osaka University, Japan)
GS28-5 *Proposal of semiautonomous centipede-like robot for rubbles*
Shota Kashiwada, Kazuyuki Ito (Hosei University, Japan)

January 20 (Friday)

Room A
08:40-09:40 GS1 Artificial brain research
Chair: Hiroshi Tanaka (Tokyo Medical & Dental University, Japan)

GS1-1 *Binary MEMS optically reconfigurable gate array for an artificial brain system*
Yuichiro Yamaji, Minoru Watanabe (Shizuoka University, Japan)
GS1-2 *Synaptic redistribution and variability of signal release probability at hebbian neurons in a dynamic stocsastic neural network*
Subha Danushika Fernando, Koichi Yamada (Nagaoka University of Technology, Japan)
GS1-3 *Properties of Hopfield model with the zero-order synaptic decay*
Ryota Miyata, Toru Aonishi (Tokyo Institute of Technology, Japan)
Jun Tsuzuruki (Okayama University of Science, Japan)
Koji Kurata (University of the Ryukyus, Japan)
GS1-4 *Pulse-type hardware neural networks circuit for PWM servo motor control*
Ken Saito, Masahiko Kato, Minami Takato, Yoshifumi Sekine, Fumio Uchikoba (Nihon University, Japan)

15:15-17:00 OS10 Computer-Supported Learning Systems II
Chair: Kenneth J. Mackin (Tokyo University of Information Sciences, Japan)
Co-Chair: Daisuke Yamaguchi (Toin University of Yokohama, Japan)

OS10-1 *Educational effectiveness of the lecture using animated figures for beginner's programming course in the university*
Yorinori Kishimoto, Kazuhisa Kitakaze (Tokyo University of Information Sciences, Japan)
OS10-2 *Self-learning support system to increase motivation for learning*
Kei Ito, Tomoki Sato, Ayahiko Niimi (Future University Hakodate, Japan)

OS10-3 *A proposal of Web-Com API for e-learning contents creation services*
Yoshihiro Kawano (Tokyo University of Information Sciences, Japan)
Chao Zhou, Tatsuhiro Yonekura (Ibaraki University, Japan)

OS10-4 *Using smartphones in sports education*
Shinya Iwasaki, Kenneth J. Mackin, Masahiro Ishii (Tokyo University of Information Sciences, Japan)

OS10-5 *A vision-based motion-speed instruction method - Application to motion learning of underarm throw*
Akinobu Morikawa, Ryota Sakamoto, Yoshihiko Nomura (Mie University, Japan)

Room B
08:40-09:40 GS14 Human-machine cooperative systems
Chair: Kuu-young Young (National Chiao Tung University, Taiwan)

GS14-1 *Manipulating a multi-DOF robot manipulator for tasks in home-like environments*
Mu-Cheng Hsieh, Po-Ying Tseng, Ming-Shiun Jan, Kuu-young Young (National Chiao Tung University, Taiwan)

GS14-2 *An article retrieval support system that accepts arbitrary Kansei words*
Yuichi Murakami, Shingo Nakamura, Shuji Hashimoto (Waseda University, Japan)

GS14-3 *Design of a user-support system for vision information using a smart phone*
Hiroyuki Nishiyama, Fumio Mizoguchi (Tokyo University of Science, Japan)

GS14-4 *Producing text and speech from video images of lips movement photographed in speaking Japanese by using mouth shape sequence code - An experimental system to communicate with hearing impaired persons -*
Shiori Kawahata, Eiko Koyama, Tsuyoshi Miyazaki, Fujio Yamamoto (Kanagawa Institute of Technology, Japan)

OS13 Embracing Complexity in Natural Intelligence
Chair: Yoshiteru Ishida (Toyohashi University of Technology, Japan)
Co-Chair: Koji Harada (Toyohashi University of Technology, Japan)

OS13-1 *An analysis of spatial patterns in a spatial prisoner's dilemma*
Yuji Katsumata, Yoshiteru Ishida (Toyohashi University of Technology, Japan)

OS13-2 *Identifying cellular automata rules using local rule network from spatiotemporal patterns*
Takuya Ueda, Yoshiteru Ishida (Toyohashi University of Technology, Japan)

OS13-3 *Performance evaluations of adaptive strategies in self-repairing network*
Masahiro Tokumitsu, Yoshiteru Ishida (Toyohashi University of Technology, Japan)

OS13-4 *Solar Insolation simulation by cellular automata and applications to smart home*
Ken Matsuka, Yoshiteru Ishida (Toyohashi University of Technology, Japan)

OS13-5 *Toward development of a strategy to drive HIV-1 into self-extinction through the error catastrophe*
Koji Harada, Yoshiteru Ishida (Toyohashi University of Technology, Japan)

OS13-6 *A pattern formation mechanism of a cellular automaton evolving on a mutual determination rule of variables and a dynamics*
Koji Harada, Yoshiteru Ishida (Toyohashi University of Technology, Japan)

OS13-7 *Network rewiring in self-repairing network: from node repair to link rewire*
Yoshiteru Ishida, Kei-Ichi Tanabe (Toyohashi University of Technology, Japan)

Room C
08:40-09:40 GS18 Intelligent control & modeling I
Chair: Shigeru Nakayama (Kagoshima University, Japan)

GS18-1 *Reinforcement learning with phased approach for fast learning*
Norifumi Hodohara, Yuichi Murakami, Shingo Nakamura, Shuji Hashimoto (Waseda University, Japan)

GS18-2 *Identification of continuous-time Hammerstein systems using Gaussian process models trained by particle swarm optimization*
Tomohiro Hachino, Shouichi Yamakawa (Kagoshima University, Japan)

GS18-3 *Reinforcement learning in dynamic environment -Abstraction of state-action space utilizing properties of the robot body and environment-*
Yutaka Takeuchi, Kazuyuki Ito (Hosei University, Japan)

13:40-14:55 OS20 Intelligent Systems and Applications
Chair: Kuo-Lan Su (National Yunlin University of Science and Technology, Taiwan)
Co-Chair: Jie-Tong Zou (National Formosa University, Taiwan)

OS20-1 *A correction circuit of Hall sensor signal base speed measurement for BLDC motors*
Chung-Wen Hung, Jhih-Han Chen, Ke-Cheng Huang (National Yunlin University of Science & Technology, Taiwan)

OS20-2 *An image sensor based virtual mouse including fingertip detection in face mask algorithm*
Chung-Wen Hung, Hsuan T. Chang, Cheng-Yang Chen (National Yunlin University of Science & Technology, Taiwan)

OS20-3 *The modeling and implementation of tri-rotor flying robot*
Jie-Tong Zou, Haw Tso (National Formosa University, Taiwan)
Kuo-Lan Su (National Yunlin University of Science & Technology, Taiwan)

OS20-4 *Path planning of fire escaping system for intelligent building*
Hsu-Shan Su, Kuo-Lan Su (National Yunlin University of Science & Technology, Taiwan)

OS20-5 *Speech based formation control of multiple mobile robots*
Kuo-Lan Su, Bo-Yi Li, Jr-Hung Guo, Chih-Hung Chang (National Yunlin University of Science & Technology, Taiwan)

OS20-6 *Development of the residual power prediction system of mobile robots*
Jr-Hung Guo, Kuo-Lan Su, Cheng-Yun Chung (National Yunlin University of Science & Technology, Taiwan)
Jie-Tong Zou (National Formosa University, Taiwan)

OS20-7 *Development of tactile sensing system and evaluation for the application to the intelligent robot using the microbending fiber optic sensors*
Ju-Won Jeong, Jung-Ju Lee (Korea Advanced Institute of Science and Technology, Korea)
Heo-Jin Seok (Samsung Electronics company, Korea)

15:15-17:00 OS19 Intelligent System and Control
Chair: Kuo-Hsien Hsia (Far East University, Taiwan)
Co-Chair: Yen Liang Yeh (Far East University, Taiwan)

OS19-1 *Obstacle avoidance control of indoor patrol robots using image-sensing techniques*
Kuo-Hsien Hsia (Far East University, Taiwan)
Shao-Fan Lien, Juhng-Perng Su, Wei-Cheng Lin (National Yunlin University of Science & Technology, Taiwan)

OS19-2 *Twisting algorithm second order sliding mode control for a synchronous reluctance motor*
Wen-Bin Lin, Huann-Keng Chiang, Yi-Chang Chang (National Yunlin University of Science & Technology, Taiwan)

OS19-3 *The implementation of accelerometer and embedded system-based multi-functional pedometer*
Yi-Yu Lu (National Cheng Kung University / Far East University, Taiwan)
Kuo-Sheng Cheng (National Cheng Kung University, Taiwan)
Wen-Bin Lin (Far East University / National Yunlin University of Science & Technology, Taiwan)
Ji-Jer Huang (Southern Taiwan University of Technology, Taiwan)

OS19-4 *An efficient three-scan approach for mining high utility itemsets*
Guo-Cheng Lan, Vincent S. Tseng (National Cheng Kung University, Taiwan)
Tzung-Pei Hong (National University of Kaohsiung / National Sun Yat-Sen University, Taiwan)

OS19-5 *Thermal wave effect for living tissue with surface heating problems by differential transformation method*
Song-Yih Lin (National Cheng Kung University / Far East University, Taiwan)
Hsin-Yi Lai, Cha'o-Kuang Chen (National Cheng Kung University, Taiwan)

OS19-6 *The forming parameter analysis of the circular plate by using computer-aided engineering*
Yen-Liang Yeh, Kuo-Ying Chen, Chia-Hsing Shen (Far East University, Taiwan)

OS19-7 *Motion planning using memetic evolution algorithm for network robot systems*
Chien-Chou Lin, Wei-Ju Chuang, Kun-Cheng Chen (National Yunlin University of Science and Technology, Taiwan)

Room D
08:40-09:40 GS20 Learning
Chair: János Botzheim (Széchenyi István University, Hungary)

GS20-1 *Adaptive reinforcement learning based on degree of learning progress*
Akihiro Mimura, Shohei Kato (Nagoya Institute of Technology, Japan)
GS20-2 *Developing reinforcement learning for adaptive co-construction of continuous state and action spaces*
Masato Nagayoshi (Niigata College of Nursing, Japan)
Hajime Murao, Hisashi Tamaki (Kobe University, Japan)
GS20-3 *Reinforcement learning approach to multi-stage decision making problems with changes in action sets*
Takuya Etoh, Hirotaka Takano, Junichi Murata (Kyushu University, Japan)
GS20-4 *Reduction of learning space by making a choice of sensor information*
Yasutaka Kishima, Kentarou Kurashige, Toshinobu Numata (Muroran Institute of Technology, Japan)

11:10-12:40 GS11 Data mining II
Chair: Ikuo Yoshihara (University of Miyazaki, Japan)

GS11-1 *Proposal of method to extract location-related words and to classify location-dependent information*
Masaki Sakata, Hiroyuki Nishiyama (Tokyo University of Science, Japan)
GS11-2 *Advantages of flexible musculoskeletal robot structure in sensory acquisition*
Shuhei Ikemoto, Yoichi Nishigori, Koh Hosoda (Osaka University, Japan)
GS11-3 *Trend awareness by value senses in home energy consumption*
Jin Dai, Fei Wei, Shingo Aoki, Hiroshi Tsuji (Osaka Prefecture University, Japan)
Shuki Inoue (The Kansai Electric Power Co., Inc., Japan)

13:40-14:55 GS7 Complexity
Chair: Reiji Suzuki (Nagoya University, Japan)

GS7-1 *A potential model pruning in Monte-Carlo go*
Makoto Oshima, Koji Yamada, Satoshi Endo (University of the Ryukyus, Japan)
GS7-2 *Emergence of autocatalytic reaction in a meme propagation model based on particle motion*
Kengo Kobayashi, Reiji Suzuki, Takaya Arita (Nagoya University, Japan)

GS7-3 *Pre-historical multiple movements of modern humans from Old World to Americas: Evidence based on comparing basic body-part name words with Austronesian*

Koji Ohnishi (Niigata University, Japan)

GS7-4 *Bifurcation analysis in a silicon neuron*

Filippo Grassia, Timothée Levi, Sylvain Saighi (University of Bordeaux, France)

Takashi Kohno (University of Tokyo, Japan)

Room E

08:40-09:40 GS29 Robotics V

Chair: Jiwu Wang (Beijing Jiaotong University, P. R. China)

GS29-1 *Construction of a sense of force feedback and vision for micro-objects: Recreate the response and a sense of force of objects*

Tatsuya Domoto, Eiji Hayashi (Kyushu Institute of Technology, Japan)

GS29-2 *Estimate of current state based on experience in POMDP for Reinforcement Learning*

Yoshiki Miyazaki, Kentarou Kurashige (Muroran Institute of Technology, Japan)

GS29-3 *Evolution of locomotion in a simulated quadraped robot and transferral to reality*

Kyrre Glette, Gordon Klaus, Jim Torresen (University of Oslo, Norway)

Juan Cristobal Zagal (University of Chile, Chile)

GS29-4 *A study on the use of tactile instructions for developing robot's motions*

Fransiska Basoeki, Fabio DallaLibera, Hiroshi Ishiguro (Osaka University, Japan)

Takashi Minato (ATR Hiroshi Ishiguro Laboratory, Japan)

11:10-12:40 GS17 Image processing II

Chair: Hyoungseop Kim (Kyushu Institute of Technology, Japan)

GS17-1 *Visual IMU in Manhattan-like enviroments from 2.5D data*

Sven Olufs, Markus Vincze (Vienna University of Technology, Austria)

GS17-2 *Image texture analysis using second order statistical model*

Shahera Hossain, Seiichi Serikawa (Kyushu Institute of Technology, Japan)

GS17-3 *Study on the development of the log scaling system based on the machine vision*

Jiwu Wang, Weijie Gao, Fangbo Liao (Beijing Jiaotong University, P. R. China)

Masanori Sugisaka (Nippon Bunri University, Japan)

GS17-4 *Arterial hemodynamic analysis on non-enhanced magnetic resonance angiogram using optical flow*

Akiyoshi Yamamoto, Hyoungseop Kim, Joo Kooi Tan, Seiji Ishikawa (Kyushu Institute of Technology, Japan)

13:40-14:55 GS19 Intelligent control & modeling II
Chair: Nobuhiro Okada (Kyushu University, Japan)

GS19-1 *Intelligent control method for autonomous vehicle by fuzzy-neural network and self-position-azimuth Correction*
Ryunosuke Takauji, Peng Chen, Mitushi Yamashita (Mie University, Japan)

GS19-2 *Learning strategy with neural-networks and reinforcement learning for actual manipulator robot*
Shingo Nakamura, Shuji Hashimoto (Waseda University, Japan)

GS19-3 *A basic study on cooperative behavior of two butterflies inspired by quantum entanglement*
Masaki Maezono (Kagoshima National College of Technology, Japan)
Ichiro Iimura (Prefectural University of Kumamoto, Japan)
Shigeru Nakayama (Kagoshima University, Japan)

GS19-4 *Importing dynamic planner to BDI agent creating flexible dicision-making of policies for selecting robot actions in real world*
Megumi Fujita, Hiroko Katayama, Yuko Ojima, Naoyuki Nide (Nara Women's University, Japan)

15:15-17:00 OS24 Medical Science and Complex Systems
Chair: Ken Naitoh (Waseda University, Japan)
Co-Chair: Takashi Matsuo (Kanagawa Institute of Technology, Japan)

OS24-1 *Hyper-gourd theory: solving simultaneously the mysteries in particle physics, biology, oncology, neurology, economics, cosmology*
Ken Naitoh (Waseda University, Japan)

OS24-2 *Quasi-stability: Revealing the inevitability of biological molecules*
Hiromi Inoue, Kenji Hashimoto, Ken Naitoh (Waseda University, Japan)

OS24-3 *BioCell print utilizing PELID (Patterning with Electrostatically-Injected Droplet) method*
Shinjiro Umezu (Tokai University, Japan)

OS24-4 *Collective motions of Chases and Escapes*
Toru Ohira (Sony Computer Science Laboratories, Inc., Japan)

OS24-5 *Form and function of arterial bifurcations in the various parts of animal body*
Takashi Matsuo, Shin-ichi Watanabe, Masato Nakakubo, Hidenobu Takao (Kanagawa Institute of Technology, Japan)
Tatsuhisa Takahashi (Asahikawa Medical University, Japan)

Room F
08:40-09:40 OS9 Computer-Supported Learning Systems I
Chair: Kenneth J. Mackin (Tokyo University of Information Sciences, Japan)
Co-Chair: Daisuke Yamaguchi (Toin University of Yokohama, Japan)

OS9-1 *The PSP low layer practice support used on the android personal digital assistant*
Daisuke Yamaguchi (Toin University of Yokohama, Japan)
Ayahiko Niimi (Future University Hakodate, Japan)

OS9-2 *Development of game based learning features in programming learning support system*
Eiji Nunohiro, Kotaro Matsushita, Kenneth J Mackin, Masanori Ohshiro (Tokyo University of Information Sciences, Japan)

OS9-3 *Visualization of satellite data for educational use*
Kotaro Matsushita, Shun Koshikawa, Taito Endoh, Jong Geol Park,
Takashi Yamaguchi, Kenneth J. Mackin, Eiji Nunohiro (Tokyo University of Information Sciences, Japan)

OS9-4 *Programming learning support system with competitive gaming using monitoring and nicknames*
Masanori Ohshiro, Kotaro Matsushita, Kenneth J Mackin, Eiji Nunohiro (Tokyo University of Information Sciences, Japan)

11:10-12:40 GS23 Neural networks II
Chair: Jiann-Shing Shieh (Yuan Ze University, Taiwan)

GS23-1 *Medical image diagnosis of liver cancer by feedback GMDH-type neural network using knowlege base*
Tadashi Kondo, Junji Ueno, Shoichiro Takao (The University of Tokushima, Japan)

GS23-2 *Large database analysis of out-of-hospital cardiac arrest using ensembled neural networks*
Jiann-Shing Shieh (Yuan Ze University / National Central University, Taiwan)
Yuan-Jang Jiang (Yuan Ze University, Taiwan)
Huei-Ming Ma, Wei-Zen Sun (National Taiwan University, Taiwan)
Guan-Wu Jang (New Taipei City Government, Taiwan)

GS23-3 *Analog circuit for detecting position of smell based on pheromone source location of silkmoth*
Masaki Ihara, Kimihiro Nishio (Tsuyama National College of Technology, Japan)

GS23-4 *Discussion of stability of adaptive type neural network direct controller and its folding behavior*
Takayuki Yamada (Ibaraki University, Japan)

GS23-5 *A neural network strategy for process optimization*
Shiu-Wan Hung (National Central University, Taiwan)

15:15-17:00 GS15 Human-welfare Robotics
Chair: Takayasu Fuchida (Kagoshima University, Japan)

GS15-1 *Development of the electric wheelchair hands-free semi-automatic control system using the surface-electromygram of facial muscles.*
Yuki Yamashita, Hiroki Tamura, Koichi Tanno (University of Miyazaki, Japan)

GS15-2 *Upper extremity prosthetics: current status, challenges and future directions*
Sanjaya Vipula Bandara, Ruwan Chandra Gopura, Manjula Udayanga Hemapala (University of Moratuwa, Sri Lanka)
Kazuo Kiguchi (Saga University, Japan)

GS15-3 *Wire-driven two fingers robotic hand for operating a touch-sensitive panel*
Tatsuro Hakui, Yukiharu Yamauchi (Kitakyushu National College of Technology, Japan)
Sei-ichiro Kamata, Shinnosuke Nakao (Waseda University, Japan)

GS15-4 *Development of a singing robotic system from music scores in real time*
Shou Imamoto, Yukiharu Yamauchi (Kitakyushu National College of Technology, Japan)
Sei-ichiro Kamata, Naoto Ohta, Yusuke Murayama (Waseda University, Japan)

GS15-5 *Robotic system for reading Japanese characters on a written document in real time*
Narumi Habu, Yukiharu Yamauchi, Takahiro Kawabuchi (Kitakyushu National College of Technology, Japan)
Sei-ichiro Kamata, Youhei Shinfuku (Waseda University, Japan)

GS15-6 *Eye gesture controlled intelligent wheelchair using electro-oculography*
Satish Ravishankar, Govinda Ram Pingali, Niyanth Krishna Polisetty, Theja Ram Pingali, Padmaja K.V (R.V. College of Engineering, India)
Avinash Sista (Mahindra Satyam, India)

Room H
12:40-13:40 Poster Session
Chairs: Ju-Jang Lee (KAIST, Korea)
Masatoshi Nakamura (Research Institute of Systems Control, Saga University, Japan)
Peter S. Sapaty (National Academy of Sciences of Ukraine, Ukraine)

PS1-1 *An intelligent human behavior based automatic accessing control system*
ChinLun Lai (Oriental Institute of Technology, Taiwan)

PS1-2 *Non-contact physical activity estimation method based on electrostatic induction technique*
Koichi Kurita (Kochi National College of Technology, Japan)

PS1-3 *Genetic algorithm with cross paths detection for solving traveling salesman problems*
Shi-Jim Yen, Shih-Yuan Chiu (National Dong Hwa University, Taiwan)
Sheng-Ta Hsieh (Oriental Institute of Technology, Taiwan)

PS1-4 *Development of a mechanical safety device for service robots*
Yoshihiro Kai (Tokai University, Japan)
Tatsuya Adachi (Daitocacao Co., LTD., Japan)

PS1-5 *Improvement by the image processing of the certification of a reconstructed image from Computer-Generated Hologram picked up by digital watermark*
Yuki Hirama, Ken-ichi Tanaka (Meiji University, Japan)

PS1-6 *Improvement of digital halftoning*
Hiroki Takekawa, Ken-ichi Tanaka (Meiji University, Japan)

PS1-7 *An improved differential evolution for solving large scale global optimization*
Sheng-Ta Hsieh (Oriental Institute of Technology, Taiwan)
Shih-Yuan Chiu, Shi-Jim Yen (National Dong Hwa University, Taiwan)

PS1-8 *Calibration of networked laser range scanners in an intelligent space based on interactive SLAM*
Fumitaka Hashikawa, Kazuyuki Morioka (Meiji University, Japan)

PS1-9 *Development of person identification and tracking system with wearable acceleration sensors in intelligent space*
Tomoyasu Takigawa, Kazuyuki Morioka (Meiji University, Japan)

PS1-10 *Development of easy camera calibration tool under unified world coordinate system using online three-dimensional reconstruction*
Shintaro Kuroiwa, Kazuyuki Morioka (Meiji University, Japan)

PS1-11 *Development of a multi-purpose compact board for robot control systems*
Mitsuhiro Yamano, Shinya Takeda, Yu Kakuta (Yamagata University, Japan)
Yuichi Suzukawa (UD Trucks, Japan)

PS1-12 *'Cruise-and Collect' algorithm for an ARM-based autonomous robot*
Mohd. Noh Zarina, Md. Salim Sani Irwan, Mohamad Yatim Norhidayah, Ali Nur Alisa, Mohd. Said Muzalifah (Universiti Teknikal Malaysia Melaka, Malaysia)

PS1-13 *Blood vessel extraction for diabetic retinopathy*
Haniza Yazid (Universiti Malaysia Perlis, Malaysia)
Ali AlMejrad, Mohd Rizon (King Saud University, Saudi Arabia)
Hamzah Arof (University of Malaya, Malaysia)

PS1-14 *Decision tree approach for fault diagnosis of nonlinear systems*
In Soo Lee (Kyungpook National University, Korea)
Jung Hwan Cho (University of Massachusetts Lowell, USA)
Hae Moon Seo (Korea Electronics Technology Institute, Korea)
Yoon Seok Nam (Dongguk University, Korea)

PS1-15 *A design of a cost effective Fire Fighting Robot using intelligent system*
Shuddha Chowdhury, Shuva Paul (American International University Bangladesh, Bangladesh)
Istiaque Islam (Islamic University of Technology, Bangladesh)

PS1-16 *Gait analysis using inertial sensor and vision*
Tri Nhut Do, Young Soo Suh (University of Ulsan, Korea)

January 21 (Saturday)

Room A
08:40-10:10 GS6 Brain science
Chair: Timothée Levi (University of Bordeaux, France)

GS6-1 *Correlation-based competition regulated by nonlinear interspike interaction in STDP*
Shigeru Kubota (Yamagata University, Japan)
GS6-2 *Density map of attentional capacity allocation*
Satoshi Kambara (Kyoto University, Japan)
Shigeyuki Oba (Japan Science and Technology Agency, Japan)
GS6-3 *Development of a brain computer interface using inexpensive commercial EEG sensor with one-channel*
Masanao Obayashi, Kouji Watanabe, Takashi Kuremoto, Kunikazu Kobayashi (Yamaguchi University, Japan)
GS6-4 *A sparse regression method to estimate neuronal structure from spike sequence*
Syunsuke Aki, Ken Nakae (Kyoto university, Japan)
Shigeyuki Oba (Kyoto university / Japan Science and Technology Agency, Japan)
Shin Ishii (Japan Science and Technology Agency, Japan)

10:30-12:00 OS2 Aware Technologies for e-Services
Chair: Kiyota Hashimoto (Osaka Prefecture University, Japan)
Co-Chair: Sachio Hirokawa (Kyushu University, Japan)

OS2-1 *Visual chance discovery method of potential keys for innovations in tourism*
Kiyota Hashimoto, Makoto Okada (Osaka Prefecture University, Japan)
Kazuhiro Takeuchi (Osaka Electro-Communication University, Japan)
Sachio Hirokawa (Kyushu University, Japan)
OS2-2 *An improved method to extract landmarks information for the purpose of using maps and route*
Shunichiro Sugimori, Yuki Murai, Makoto Okada, Kiyota Hashimoto (Osaka Prefecture University, Japan)
OS2-3 *Automatic generation of tourism quiz using blogs*
Jun Zeng, Toshihiko Sakai, Chengjiu Yin, Takahiko Suzuki, Sachio Hirokawa (Kyushu University, Japan)

OS2-4 *Sharing knowlede and experience of search with SNS*
Xiaobin Wu, Jun Zeng, Chengjiu Yin, Sachio Hirokawa (Kyushu University, Japan)
OS2-5 *A method of sentiment analysis for online reviews containing values of multi-criteria evaluation*
Takaya Nishikawa, Makoto Okada, Kiyota Hashimoto (Osaka Prefecture University, Japan)

Room B
08:40-10:10 OS1 Advanced Vehicle Control
Chair: Shinichi Sagara (Kyushu Institute of Technology, Japan)
Co-Chair: Masahiro Oya (Kyushu Institute of Technology, Japan)

OS1-1 *Flight guidance and control of a winged rocket*
Tomoaki Shimozawa, Shinichi Sagara, Tomohiro Narumi, Koichi Yonemoto (Kyushu Institute of Technology, Japan)
OS1-2 *Position and attitude control of underwater vehicle-manipulator systems using a stereovision system*
Akihito Shigetomi, Shinichi Sagara, Tomoaki Shimozawa (Kyushu Institute of Technology, Japan)
OS1-3 *Adaptive control of underwater vehicle-manipulator systems using radial basis function networks*
Yuichiro Taira (National Fisheries University, Japan)
Masahiro Oya, Shinichi Sagara (Kyushu Institute of Technology, Japan)
OS1-4 *An improved adaptive controller in the presence of input saturation - In case of systems with available output derivatives up to the order of relative degree -*
Natsuki Takagi (Miyakonojo National College of Technology, Japan)
Masahiro Oya (Kyushu Institute of Technology, Japan)
OS1-5 *Development of a position control scheme for rotating sensor unit attached to in-pipe robot*
Hdeki Wada (Sin-Nippon Nondestructive Inspection Co., Japan)
Masahiro Oya (Kyushu Institute of Technology, Japan)
Katsuhiro Okumura (Fukuoka Industrial Technology Center, Japan)
OS1-6 *Adaptive oscillation control scheme for a wheeled mobile robot*
Bo Zhou, Tasuku Eto, Hiroshi Shibata, Masahiro Oya (Kyushu Institute of Technology, Japan)

10:30-12:00 OS5 Bio-inspired theory and applications II
Chair: Kunihito Yamamori (University of Miyazaki, Japan)
Co-Chair: Yuji Sato (Hosei University, Japan)

OS5-1 *Stochastic analysis of OneMax problem by using Markov chain*
QingLian Ma, Kiminobu Koga, Kunihito Yamamori, Makoto Sakamoto, Hiroshi Furutani (University of Miyazaki, Japan)
Yu-an Zhang (Qinghai University, P. R. China)

OS5-2 *High signal and power integrity design for VLSI packaging using genetic algorithms*
Moritoshi Yasunaga, Hiroki Shimada, Shohei Akita (University of Tsukuba, Japan)
Ikuo Yoshihara (Miyazaki University, Japan)

OS5-3 *Solving a multi-objective constraint satisfaction problem with genetic algorithms-Making a food menu with GAs-*
Hironori Fukamachi, Yuji Sato (Hosei University, Japan)

OS5-4 *Improvement of the reinforcement learning efficiency using individually reward value allotment of the soccer video game agent*
Daisuke Inami, Yuuki Sakaguchi, Yuji Sato (Hosei University, Japan)

15:30-16:45 OS21 Intuitive Human-System Interaction
Chair: Masao Yokota (Fukuoka Institute of Technology, Japan)
Co-Chair: Tetsushi Oka (Nihon University, Japan)

OS21-1 *Gesture detection based on 3D tracking for multimodal communication with a life-supporting robot*
Tetsushi Oka, Ryuuichi Kibayashi, Hirosato Matsumoto (Nihon University, Japan)

OS21-2 *Evaluation of some user interfaces for elderly persons*
Sinichi Inenaga, Kaoru Sugita, Masao Yokota (Fukuoka Institute of Technology, Japan)

OS21-3 *Toward artificial Kansei based on Mental Image Directed Semantic Theory*
Tzu-Hsuan Huang, Kaoru Sugita, Masao Yokota (Fukuoka Institute of Technology, Japan)

OS21-4 *A high-sensitivity 3-D shape measurement method with microscope*
Xueli Zhang, Kazuhiro Tsujino, Cunwei Lu (Fukuoka Institute of Technology, Japan)

OS21-5 *Tele-immersive environment with tiled display wall for intuitive operation and understanding in remote collaborative work*
Yasuo Ebara (Osaka University, Japan)

Room C
08:40-10:10 OS4 Bio-inspired theory and applications I
Chair: Ikuo Yoshihara (University of Miyazaki, Japan)
Co-Chair: Moritoshi Yasunaga (University of Tsukuba, Japan)

OS4-1 *Solving Sudoku with Bayesian optimization algorithm*
Shinichi Shirakami, Yuji Sato (Hosei Univercity, Japan)

OS4-2 *Parallelization of genetic operations that takes building-block linkage into account*
Hazuki Inoue, Naohiro Hasegawa, Yuji Sato (Hosei University, Japan)
Mikiko Sato (Tokyo University of Agriculture and Technology, Japan)

OS4-3 *A detection method for intronic snoRNA genes using extended-weight-updating SOM with appearance probability of bases*
Takuro Matsuo, Junichi Iwakiri, Kunihito Yamamori, Naoya Kenmochi, Ikuo Yoshihara (University of Miyazaki, Japan)

OS4-4 *A method to detect intronic snoRNA genes using characteristic base patterns of DNA sequences*
Chen Xue, Junichi Iwakiri, Kunihito Yamamori, Naoya Kenmochi, Ikuo Yoshihara (University of Miyazaki, Japan)

10:30-12:00 OS8 Computer Vision and Sound Analysis
Chair: Yasunari Yoshitomi (Kyoto Prefectural University, Japan)
Co-Chair: Masayoshi Tabuse (Kyoto Prefectural University, Japan)

OS8-1 *Pedestrian detection and tracking in near infrared images*
Masayoshi Tabuse (Kyoto Prefectural University, Japan)
Sayuri Kozawa (Sumitomo Forestry Archi Techno Co., Ltd., Japan)

OS8-2 *A system for facial expression recognition of a speaker using front-view face judgment, vowel judgment and thermal image processing*
Taro Asada, Yasunari Yoshitomi, Masayoshi Tabuse (Kyoto Prefectural University, Japan)

OS8-3 *Robust facial expression recognition of a speaker using thermal image processing and updating of fundamental training-data*
Yuu Nakanishi, Yasunari Yoshitomi, Taro Asada, Masayoshi Tabuse (Kyoto Prefectural University, Japan)

OS8-4 *A system for synchronizing nods of a computer-generated character and a speaker using thermal image processing*
Yasunari Yoshitomi, Ryota Kato, Taro Asada, Masayoshi Tabuse (Kyoto Prefectural University, Japan)

OS8-5 *Music recommendation aimed at improving recognition ability using collaborative filtering and impression words*
Chikoto Koro (ISI Software Corp., Japan)
Yasunari Yoshitomi, Taro Asada, Saya Yoshizaki (Kyoto Prefectural University, Japan)

15:30-16:45 OS22 Management of technology
Chair: Takao Ito (Ube National College of Technology, Japan)
Co-Chair: Rajiv Mehta (New Jersey Institute of Technology, USA)

OS22-1 *How does the network structure of standard-setter affect its standard-setting activity?*
Kensuke Ogata (University of Nagasaki, Japan)

OS22-2 *Simple model of economic Stability and Control*

S. Lu (Fudan University / Shandong University in Weihai, P. R. China)

Takao Ito (Ube National College of Technology, Japan)

OS22-3 *An efficiency analysis using the ICB model in Mazda's Keiretsu*

Seigo Matsuno, Takao Ito, Masayoshi Hasama (Ube National College of Technology, Japan)

Rajiv Mehta (New Jersey Institute of Technology, USA)

Makoto Sakamoto (University of Miyazaki, Japan)

OS22-4 *A note on three-dimensional probabilistic finite automata*

Makoto Sakamoto, Masahiro Yokomichi, Satoshi Ikeda, Hiroshi Furutani (University of Miyazaki, Japan)

Takao Ito, Yasuo Uchida (Ube National College of Technology, Japan)

Xia Qingquan (Harbin Institute of Technology, P. R. China)

Tsunehiro Yoshinaga (Tokuyama College of Technology, Japan)

OS22-5 *A Study on Factors Affecting the Degree of Bullwhip Effect and Inventory Cost to an optimal management strategy for information Sharing in Supply Chains*

Masayoshi Hasama, Seigo Matsuno, Takao Ito, Kouichi Saeki (Ube National College of Technology, Japan)

Yu Song (Fukuoka Institute of Technology, Japan)

Room D
08:40-10:10 OS12 Control Theory and its Application
Chair: Masahiro Yokomichi (University of Miyazaki, Japan)
Co-Chair: Nobuya Takahashi (University of Miyazaki, Japan)

OS12-1 *Propose of the use to alternative Gramian for the controller order reduction*

Shota Usui (Miyakonojo National College of Technology, Japan)

Tsutomu Nagado (University of the Ryukyus, Japan)

Michio Kono (University of Miyazaki, Japan)

OS12-2 *Classes of linear systems of difference equations with bounded solutions*

Naoharu Ito (Nara University of Education, Japan)

Reinhold Küstner (Universität Hannover, Germany)

Harald K. Wimmer (Universität Würzburg, Germany)

OS12-3 *Dynamic window-based obstacle avoidance in the presence of moving obstacles*

Hitomi Harada, Masahiro Yokomichi, Osamu Sato (University of Miyazaki, Japan)

OS12-4 *Multimodal MSEPF for visual tracking*

Masahiro Yokomichi, Yuki Nakagama (University of Miyazaki, Japan)

10:30-12:00 OS14 Embracing Complexity in System Sensing
Chair: Yoshiteru Ishida (Toyohashi University of Technology, Japan)
Co-Chair: Yuji Watanabe (Nagoya City University, Japan)

OS14-1 *A multipath immunity-based statistical en-route filtering in wireless sensor networks*
Yuji Watanabe, Tomotsugu Tamura (Nagoya City University, Japan)
OS14-2 *Extraction of operational behavior for user identification on smart phone*
Yuji Watanabe, Shunta Ichikawa (Nagoya City University, Japan)
OS14-3 *Continuous review model of mutual support supply system for disaster responses*
Nur Budi Mulyono, Yoshiteru Ishida (Toyohashi University of Technology, Japan)
OS14-4 *Network rewiring by matching automaton: from unit reliability to collective survivability*
Yoshiteru Ishida, Masahiro Tokumitsu (Toyohashi University of Technology, Japan)

13:00-15:10 OS15 Information Technology for Environmental Research I
Chair: Takashi Yamaguchi (Tokyo University of Information Sciences, Japan)
Co-Chair: Kenneth J. Mackin (Tokyo University of Information Sciences, Japan)

OS15-1 *Network Analysis of Input-Output Table* ***(withdrawal)***
Kousuke Yoshizawa, Xiang Gao, Shuhei Miyake, Naoko Sakurai, Takeshi Fujiwara, Zeyu Zheng, Kazuko Yamasaki (Tokyo University of Information Sciences, Japan)
OS15-2 *Network analysis of ecologocal footprint & CO2 emission based on Input-Output table for East Asia*
Xiang Gao, Takeshi Fujiwara, Naoko Sakurai, Kousuke Yoshizawa, Syuhei Miyake, Zeyu Zheng, Kazuko Yamasaki (Tokyo University of Information Sciences, Japan)
OS15-3 *The fluctuation in Carbon emission trading Market*
Zeyu Zheng, Naoko Sakurai, Takeshi Fujiwara, Kousuke Yoshizawa, Kazuko Yamasaki (Tokyo University of Information Sciences, Japan)

15:30-16:45 OS16 Information Technology for Environmental Research II
Chair: Takashi Yamaguchi (Tokyo University of Information Sciences, Japan)
Co-Chair: Kenneth J. Mackin (Tokyo University of Information Sciences, Japan)

OS16-1 *Development of Stream Data Platform in Satellite Image Data Analysis System*
Eiji Nunohiro, Hayao Mori, Masaki Hanada, Kenneth J Mackin, Jong Geol Park (Tokyo University of Information Sciences, Japan)
OS16-2 *Flood risk assessment using MLSWI by MODIS Time Series data*
Jonggeol Park, Eiji Nunohiro (Tokyo University of Information Sciences, Japan)
Youngjoo Kwak (International Center for Water Hazard and Risk Management, Japan)

OS16-3 *Application of transfer learning to PSO for similar image search*
Kazuma Mori, Takashi Yamaguchi, Kenneth J. Mackin, Yasuo Nagai (Tokyo University of Information Sciences, Japan)

OS16-4 *The maximum and minimum temperatures trends in Oita*
Masao Igarashi, Takahiro Yamazaki (Nihon University, Japan)
Eiji Nunohiro (Tokyo University of Information Sciences, Japan)

Room E
08:40-10:10 OS25 Network Dynamics in Biological Information Systems I
Chair: Hideyuki Suzuki (The University of Tokyo, Japan)
Co-Chair: Takashi Kohno (The University of Tokyo, Japan)

OS25-1 *Analytical approach to synchrony between populations of neurons with modulatory effects*
Yoichiro Hashizume, Osamu Araki (Tokyo University of Science, Japan)

OS25-2 *A computational model for multiple potential actions for inferred movement goals*
Takuro Fujimura, Yuta Kakimoto, Osamu Araki (Tokyo University of Science, Japan)

OS25-3 *An action planning model using short-term and long-term memory information during learning of sequential procedures*
Nao Tomoda, Yuta Kakimoto, Osamu Araki (Tokyo University of Science, Japan)

OS25-4 *Coherence patterns in neural fields at criticality*
Teerasit Termsaithong, Makito Oku, Kazuyuki Aihara (The University of Tokyo, Japan)

10:30-12:00 OS23 Mechatronics and Intelligent Systems
Chair: Maki K. Habib (American University in Cairo, Egypt)
Co-Chair: Ju-Jang Lee (KAIST, Korea)

OS23-1 *Modified local Gaussian Process Regression for inverse dynamics learning*
Seung-Yoon Cho, Sung-Soon Yim, Ju-Jang Lee (KAIST, Korea)

OS23-2 *Bioinspiration and modern actuators*
Maki K Habib (American University in Cairo, Egypt)
Keigo Watanabe (Okayama University, Japan)
Fusaomi Nagata (Tokyo University of Science, Japan)

OS23-3 *Ubiquitous system and its apapplication networks*
Young Im Cho (The University of Suwon, Korea)

OS23-4 *Simultaneous optimization of path planning and flow shop scheduling by bacterial memetic algorithm*
János Botzheim (Széchenyi István University, Hungary)
Yuichiro Toda, Naoyuki Kubota (Tokyo Metropolitan University, Japan)

OS23-5 *Lateral controller design for an unmanned vehicle via Kalman filtering*
Man Hyung Lee, Hyung Gyu Park, Kil Soo Lee, Young Chul Cha, Dong Jin Kim, Sinpyo Hong, Ho Hwan Chun, Bong Jin Lee, Yun Ja Lee (Pusan National University, Korea)
Byung Il Kim (Hyundai Motor Company, Korea)

OS23-6 *Unmanned container transporter via pseudolite ultrasonic system*
Man Hyung Lee, Kil Soo Lee, Young Chul Cha, Dong Jin Kim, Bong Jin Lee, Sung Mi Kim, Yun Ja Lee (Pusan National University, Korea)
Jung Hyun Moon (Aztechs Co., Ltd, Korea)
Fumio Harashima (Tokyo Metropolitan University, Japan)

13:00-15:10 OS3 Bioinformatics
Chair: Shigeru Omatu (Osaka Institute of Technology, Japan)
Co-Chair: Hideo Araki (Osaka Institute of Technology, Japan)

OS3-1 *Measurement system for metal oxide gas sensors*
Hideo Araki, Sigeru Omatu (Osaka Institute of Technology, Japan)

OS3-2 *Smell classification by using metal oxide gas sensors*
Sigeru Omatu, Hideo Araki (Osaka Institute of Technology, Japan)

OS3-3 *Measurement system for quarts crystal microbalance sensors*
Hideo Araki, Sigeru Omatu (Osaka Institute of Technology, Japan)

OS3-4 *Classification of mixed smells by using neural networks*
Toru Fujinaka (Hiroshima University, Higashihiroshima, Japan)
Sigeru Omatu, Hideo Araki (Osaka Institute of Technology, Japan)

15:30-16:45 OS11 Control Application
Chair: Osamu Sato (University of Miyazaki, Japan)
Co-Chair: Nobuya Takahashi (University of Miyazaki, Japan)

OS11-1 *Acquisition of rules for selecting suppliers of raw materials in distributed production systems by means of reinforcement learning*
Hisaaki Yamaba, Kayoko Takatsuka, Shigeyuki Tomita (University of Miyazaki, Japan)

OS11-2 *Analysis of manipulator in consideration of impact absorption between link and object*
Asaji Sato (Miyakonojo National College of Technology, Japan)
Osamu Sato, Nobuya Takahashi, Masahiro Yokomichi (University of Miyazaki, Japan)

OS11-3 *An application of guaranteed cost control to a 3-DOF model helicopter*
Erwin Susanto, Tatsuhiro Tamura, Mitsuaki Ishitobi, Sadaaki Kunimatsu (Kumamoto University, Japan)

OS11-4 *Robust control of a three-link RRR manipulator with structured uncertainty*
Nobuya Takahashi, Yoshiaki Nakamura, Osamu Sato (University of Miyazaki, Japan)
OS11-5 *Obstacle avoidance of snake robot by switching control constraint*
Yasunobu Hitaka, Toshikazu Yoshitake (Kitakyushu National College of Technology, Japan)

Room F
08:40-10:10 OS27 System sensing and control
Chair: Masafumi Uchida (The University of Electro-Communications, Japan)
Co-Chair: Hirotoshi Asano (Aoyama Gakuin University, Japan)

OS27-1 *The evaluation of the emotion by NIRS*
Hirotoshi Asano, Takanori Sagami, Hideto Ide (Aoyama Gakuin University, Japan)
OS27-2 *A reward allocation method for reinforcement learning in stabilizing control tasks*
Shu Hosokawa, Joji Kato, Kazushi Nakano (The University of Electro-Communications, Japan)
OS27-3 *Acquisition of stationary behavior based on Multiagent Enforced SubPopulations*
Joji Kato, Shu Hosokawa, Kazushi Nakano (The University of Electro-Communications, Japan)
OS27-4 *Robust digital control of DC-DC buck converter with various frequency samplings*
Yuji Fukaishi, Yoshihiro Ohta, Kohji Higuchi (The University of Electro-Communications, Japan)
Eiji Takegami, Satoshi Tomioka (TDK-LAMBDA K.K., Japan)
Kosin Chamnongthai (King Mongkut's University of Technology Thonburi, Thailand)
OS27-5 *EMG analysis accompanied by tactile apparent movement*
Ali Mokhtari, Masafumi Uchida (The University of Electro-Communications, Japan)

10:30-12:00 OS26 Network Dynamics in Biological Information System II
Chair: Hideyuki Suzuki (The University of Tokyo, Japan)
Co-Chair: Takashi Kohno (The University of Tokyo, Japan)

OS26-1 *A network consisting of phase adjusting units*
Masanori Shiro (AIST Human Technology Research Institute / University of Tokyo, Japan)
Syotaro Akaho (AIST Human Technology Research Institute, Japan)
Kazuyuki Aihara (University of Tokyo, Japan)
OS26-2 *Modeling of potential- and noise-induced intracellular dynamics with cell-cell communication*
Tomoyuki Yamada, Atsushi Kamimura (The University of Tokyo, Japan)
Tetsuya J. Kobayashi (The University of Tokyo / Japan Science and Technology Agency, Japan)
OS26-3 *Cholinergic top-down modulation based on the free-energy principle*
Masaaki Takada, Kazuyuki Aihara (The University of Tokyo, Japan)
OS26-4 *Dynamics of associative memory network with self-oscillatory and non-self-oscillatory oscillators*
Yusuke Okada, Yuichi Katori, Kazuyuki Aihara, Hideyuki Suzuki (The University of Tokyo, Japan)

13:00-15:10 OS6 Biomimetic Machines and Robots I
Chair: Keigo Watanabe (Okayama University, Japan)
Co-Chair: Kiyotaka Izumi (Saga University, Japan)

OS6-1 *Proposal and implementation of CAM system for industrial robot RV1A*
Sho Yoshitake, Fusaomi Nagata, Akimasa Otsuka (Tokyo University of Science, Yamaguchi, Japan)
Keigo Watanabe (Okayama University, Japan)
Maki K. Habib (American University in Cairo, Egypt)

OS6-2 *The adjustment of CPG parameters to realize continuous jumping movements for a six-legged robot*
Masaaki Ikeda, Keigo Watanabe (Okayama University, Japan)
Kiyotaka Izumi (Saga University, Japan)

OS6-3 *A proposal of experimental education system of mechatronics*
Naoki Kitahara, Fusaomi Nagata, Akimasa Otsuka (Tokyo University of Science, Yamaguchi, Japan)
Kaoru Sakakibara (C-TASK Co., Ltd., Japan)
Keigo Watanabe (Okayama University, Japan)
Maki K. Habib (American University in Cairo, Egypt)

OS6-4 *A discontinuous exponential stabilization law for an underactuated X4-AUV*
Zainah Binti Md. Zain, Keigo Watanabe, Isaku Nagai (Okayama University, Japan)
Kiyotaka Izumi (Saga University, Japan)

OS6-5 *Eye-vergence visual servoing enhancing Lyapunov-stable trackability*
Fujia Yu, Mamoru Minami, Akira Yanou (Okayama University, Japan)
Wei Song (University of Shanghai, Japan)

OS7 Biomimetic Machines and Robotics
Chair: Keigo Watanabe (Okayama University, Japan)
Co-Chair: Kiyotaka Izumi (Saga University, Japan)

OS7-1 *Image-based fuzzy trajectory tracking control for four-wheel steered mobile robots*
Tatsuya Kato, Keigo Watanabe, Shoichi Maeyama (Okayama University, Japan)

OS7-2 *Study on mobile mechanism of a climbing robot for stair cleaning-A translational locomotion mechanism and turning motion to be faced to a stair-*
Takahisa Kakudou, Keigo Watanabe, Isaku Nagai (Okayama University, Japan)

OS7-3 *The experiment of the path planning to respect human movements using a human frequency map for a mobile robot*
Kimiko Motonaka, Shoichi Maeyama, Keigo Watanabe (Okayama University, Japan)

OS7-4 *A study of tipping stability for omnidirectional mobile robot with active dual-wheel caster assemblies*
Muhammad Juhairi Aziz Safar, Keigo Watanabe, Shoichi Maeyama, Isaku Nagai (Okayama University, Japan)

OS7-5 *Unscented transformation for a FastSLAM framework*

Saifudin Razali, Keigo Watanabe, Shoichi Maeyama (Okayama University, Japan)

Modular Playware Technology – A Brief Historical Review

Henrik Hautop Lund

Centre for Playware, Technical University of Denmark, 2800 Kgs. Lyngby, Denmark

hhl@playware.dtu.dk
www.playware.dk

Abstract

In this paper, we present a shortened historical review of the building blocks concept. With the concept we show that three B's can lead to three A's: Building Bodies and Brains leads to applications for Anybody, Anywhere, Anytime. Hence, we outline how the inspiration from artificial life, especially regarding the relationship between the body and brain, leads to a building block concept based upon interactive, distributed parallel processing. The historical outline shows how biomimetic robotics and behavior-based robotics has inspired the development of modular playware. Application examples based upon the concept include LEGO I-Blocks, playgrounds, multi-sensory rooms, robomusic, etc. In the paper, we attempt to explore the theoretical characteristics of the concept and the lessons learned for playware application fields.

Introduction

Research into artificial life and robotics over the last few decades has provided background and insight for developing new kinds of interaction between human beings and physical electronic systems. The artificial life focus on living material provides a direction for the development of the physical systems (e.g. robotic systems) towards systems with "living" characteristics (growing systems, adaptive systems, flexible systems, social systems, etc.). We may speculate that such a focus may possibly allow for more natural interaction with such systems, since we as human beings are familiar with interaction with natural systems, hence we use the term 'natural' interaction. It is interesting to study if and how the artificial life inspiration to the creation of robotic system may lead to natural interaction for the users of such systems, and thereby expand the use of the technological systems to diverse users and diverse application fields.

Body and Brain

One of the main inspirations from artificial life to the field of robotics has been the understanding of the interplay between the body and the brain. Artificial life experiments in the form of biomimetic robotics [1, 2] have shown us how the brain structure and complexity to obtain certain behaviors is dependent on the physical body. For instance, by designing robotic ears and a robot mimicking female crickets, we [2] showed how cricket phonotaxis behavior could be obtained with a much simpler neural system than often hypothesized by biologists based on their behavioral experiments with crickets. Later, many other animal species have been mimicked in similar biomimetic robotic experiments. Such studies have enlightened both biological studies to enhance our fundamental scientific knowledge about nature, and they have enlightened robotics for the creation of intelligent robotic systems putting emphasis on creation of the right interplay between the body and the brain to achieve intelligent robotic systems.

Using artificial life as a means to understand and facilitate user interaction was initially performed as studies of simulation environments. For instance, we developed interactive evolutionary computation for users to express facial expressions and artistic design [3]. In this case, users were presented with a population of potential solutions (e.g. facial expressions or artistic design) on the computer screen, and the users would select a few of the most appealing to the user for reproduction. These selected examples would then reproduce with mutation (and possibly cross-over) to form the next generation presented on the computer screen, and the user would again select the most appealing ones. In this fashion, the user would select for generation after generation towards creating appealing solutions (e.g. facial expressions or artistic designs).

A similar approach of interactive evolutionary computation was used to allow users to develop their own controllers for simulated Khepera robots and LEGO robots. Indeed, in 1996-97 we developed interactive evolutionary robotics as a children's game for young children to make LEGO robots out of the Edinburgh LEGO robot platform [4]. With this approach, young children were able to simply select robot behaviors of their preference on the screen and make an evolutionary process to develop robot controllers that were afterwards downloaded to the physical LEGO robots. It demanded no technical knowledge to perform the selection for the development of robot controllers. Anybody would be able to express their preferences of the robot behaviors visualized on the computer screen and after an interactive evolutionary process download the developed controller to the physical LEGO robot.

This inspired us to engage in further collaboration with the LEGO company on the development of LEGO Mindstorms, e.g. with the development of the first public demonstration of LEGO Mindstorms during RoboCup 1998 [5], the pilot projects for the FIRST LEGO League, and the RoboCup Junior in 1999 [6]. Indeed, our invention of the RoboCup Junior in 1999 used the interactive evolutionary robotics approach and also a user-friendly behavior-based approach to allow even young children to develop LEGO robots for the soccer tournaments.

The behavior-based system allowed users to make the coordination of behaviors. A number of primitive behaviors (at a fairly high abstraction level) were shown on the computer screen, and the user could select among these and combine these to make up the overall soccer playing behavior and download this to the LEGO robots that would then play the robot soccer games [6].

This use of behavior-based robotics to allow non-expert users to develop fairly complex robot behaviors was the inspiration to make a physical version of the behavior-based approach. Indeed, in our LEGO Lab an approach to resistors in LEGO bricks was developed to allow the children to combine different bricks to make up behaviors for the robot. Here, the children would combine physical resistor bricks on top of a LEGO Mindstorms robot to make the overall behavior of the robot instead of combining the primitive behaviors on the computer screen [7].

Building Bodies and Brains

We can describe these examples of artificial life inspired approaches to facilitate user interaction as approaches based on distributed, parallel processing (populations with individuals running in parallel in the evolutionary computation approaches, and behaviors running in parallel in the behavior-based robot approaches). In a physical form, such distributed, parallel processing can manifest itself in a modular approach. Even though the interactive behavior-based approaches developed in the past with users combining primitive behaviors on the computer screen or physically in the form of resistor bricks entailed a somewhat serial processing, a distributed parallel processing version is an interesting possibility.

Based upon the exploration of the body and brain relationship and our exploration of this relationship in robotics, we developed a concept of physical and functional building blocks in order to explore interactive, distributed parallel processing in a physical form. We have explored this general concept since the mid-1990s and developed several physical platforms in order to test the concept in different use contexts.

Generally, the concept can be used to create self-reconfigurable modular robots [8], which autonomously change their physical shape, which we did later in the 2000's, but here we will focus on how the concept can be used to create *user-configurable modular interactive systems*. Here, the user constructs with the technological building blocks to create a physical entity and the functionality of this entity. By making changes to the physical shape of the entity, the user can change the functionality of the entity. This happens simply by attaching or detaching technological building blocks, and moving technological building blocks to different positions. Hence, in such a case, the user is making the physical configuration in a hands-on manner, and the user does not need to do traditional programming to change the functionality of the entity. Therefore, in some cases, it is believed that the building block approach may lead any user to develop solutions in a *simple* and very *flexible* manner. Further, the modularity and distributed processing of the building block approach means that the produced solutions are *robust to failure* of individual building blocks. If one building block fails then the rest will still be working, contrary to most traditional technological solutions with a central processing that makes everything fail if one component fails. Also, since there is no central processing and large infrastructure, but the system is composed of a set of individual building blocks (modules), these may potentially be easily transported around and set up anywhere.

Indeed, in 1995 we got the first idea on putting processing and communication capabilities into each individual LEGO brick. As one of the appealing research directions, at the time, together with Orazio Miglino we envisioned the possibilities for exploring neural networks in a physical form with this new building block concept. Even though the exact implementation was not done until the early 2000's, we explored the concept in several variations on the LEGO robot platforms in the 1995-2000, e.g. as the resistor bricks with LEGO Mindstorms mentioned above [7] and in co-evolution of bodies and brains experiments with the Edinburgh LEGO robot platform [9].

Finally in 2000, it became feasible from a technological point of view to start implementing processors, communication means, sensors, and actuators into the individual LEGO brick, though from a practical prototyping perspective we started making implementation in the LEGO DUPLO bricks [10]. The initial prototypes were based upon a PIC16 microprocessor and communication with two male connectors on the top and two female connectors on the bottom of each LEGO DUPLO brick.

Having processing and communication capabilities in the individual bricks allows both physical (body) and functional (brain) construction. Everything happens as soon as bricks are put together, contrary to e.g. the LEGO Mindstorms approach which imposes a certain sequential process and split of building, programming and testing in the real world. Hence, with LEGO Mindstorms there is a long way from conceiving ideas to actually testing in the real world, which may prevent the non-expert user from overcoming the abstract, cognitive challenge to develop his/her own robotic system. The building block approach is a response to the Mindstorms split processes, and it provides 'action in the interaction', where things happen as soon as the user puts two pieces together, and thereby get an *immediate feedback* (e.g. sound, light, motion) in the construction process.

Numerous tests showed that diverse child users were able to use the technological building block approach implemented in the LEGO bricks to physically confront abstract cognitive challenges e.g. in mathematics, language training, understanding emotions, etc. [11]. Later, cubic blocks – termed African I-Blocks and cubic I-Blocks - were developed as a response to some users' difficulty with building with the LEGO bricks.

Physical Interaction with Modules

The concept became the foundational technological concept when in 2001, Europe's largest producer of playgrounds, KOMPAN, engaged in the development of interactive electronic playgrounds [12]. Initially, sensors and actuators were distributed on traditional playground products, later wire-connected modular tiles were developed as the ground of playgrounds, and finally the ICONS product emerged on the market. The playground tiles became an implementation used for several studies of children's physical interactivity and of adaptation to the individual user.

Despite the relative success of the playground experiments, we wanted to push towards a more free use of modules. Some of the playground work was based on wired connection between modules, which essentially limited the reconfiguration of modules to be performed by the installation worker, and not to be performed by the user.

Therefore, we developed the modular interactive tiles. According to the concept, each tile is a self-contained module with processing power and communication to neighboring modules, and a number of these can be put together in any physical shape by the user within a minute. The tiles light up in different colors and can perceive the pressure when people press them with their hands or jump on them with their feet. Numerous games (exercises) are running on the tiles, and these games aim at providing high motivation for people to engage physically with the tiles. Therapists have used the tiles to provide treatment for a large number of patients who receive hospital, municipality or home care, although the tiles can as well be used for prevention with elderly or for fitness with normal people. The tiles have been tested extensively with cardiac patients, COLD patients and stroke patients in hospitals and in the private homes of patients and elderly, and it have been found that therapists are using the modular aspect of the tiles for personalized training of a vast variety of elderly patients modulating exercises and difficulty levels [13].

Modules and Applications – Some Lessons

In the mid 2000's, we started combining the different technological platforms to explore the building block concept for different user sensory modalities by combining heterogeneous building blocks. For instance, we combined the modular interactive tiles and cubic I-Blocks in the creation of a multi-sensory room in the HC Andersen children's hospital [14], we combined rolling pins and light&sound cylinders in the creation of a multi-sensory room for elderly with dementia [15], and we combined modular tiles, rolling pins, and light&sound cylinders for the first RoboMusic concert [16]. With the different kinds of technological building blocks, we were able to make applications and tests these in many different contexts. Some examples include:

- Neema Rehabilitation Unit, Iringa, Tanzania – therapy of handicapped children
- Orphanage Ilembula, Tanzania – play and education
- Pommern Secondary School, Tanzania – language and mathematics education
- Casa Protetta Albesani, Italy – elderly dementia patients therapy
- Ringe neurorehabilitation center, Denmark – stroke patient therapy
- OUH Hospital Svendborg, Denmark – cardiac and stroke patient physiotherapy
- Townships in South Africa – football competitions during FIFA World Cup 2010
- Winter Music Conference, Miami – RoboMusic performances

An important lesson learned from the many experiments with modular playware technology is that the building block concept facilitated users in engaging with modules with different sensory modalities, and that the concept made it easy to configure the technological systems to the users' preferred sensory modality or activity. Based on all these implementations of the concept, we can now summarize the types of modules and control used:

Modules:	Control:
arithmetic blocks, behavior blocks, language blocks, neural blocks, spiking neural blocks.	open loop, randomness based, rule based, user interaction based, AI and ALife based, morphology based.

Conclusion

We presented a shortened historical review of the building blocks concept. We believe that the concept has shown to be a general approach to facilitate user interaction. We can formulate this as with the building block concept three B's can possibly lead to three A's: **B**uilding **B**odies and **B**rains leads to applications for **A**nybody, **A**nywhere, **A**nytime.

References

[1] M. O. Franz and H. A. Mallot. Biomimetic robot navigation. *Robotics Auton Systems 30*, 133–153, 2000.

[2] H. H. Lund, B. Webb, and J. Hallam. Physical and temporal scaling considerations in a robot model of cricket calling song preference. *Artificial Life, 4(1)*:95-107, 1998.

[3] L. Pagliarini, H. H. Lund, O. Miglino, and D. Parisi. Artificial Life: A New Way to Build Educational and Therapeutic Games. In C. Langton and T. Shimohara (eds.) Proc. of Artificial Life V, MIT Press, MA, 1996.

[4] H. H. Lund, O. Miglino, L. Pagliarini, A. Billard, and A. Ijspeert. Evolutionary Robotics : A Children's Game In Proceedings of IEEE 5th International Conference on Evolutionary Computation. IEEE Press, NJ, 1998.

[5] H. H. Lund and L. Pagliarini. LEGO Mindstorms Robot Soccer. In Proceedings of RoboCup'98, LNAI 1604, Springer-Verlag, Heidelberg, 1999.

[6] H. H. Lund and L. Pagliarini. RoboCup Jr. with LEGO Mindstorms. In Proc. of Int. Conf. On Robotics and Automation (ICRA2000), IEEE Press, NJ, 2000.

[7] H. H. Lund. AI in Children's Play with LEGO Robots. In AAAI Spring Symposium Series 1999, AAAI Press, Menlo Park, 1999.

[8] E. H. Ostergaard, K. Kassow, R. Beck, and H. H. Lund. Design of the ATRON lattice-based self-reconfigurable robot. *Autonomous Robots 21(2)*, 165-183, 2006

[9] H. H. Lund, J. Hallam, and W.-P. Lee. Evolving robot morphology, in *Proc. 1997 IEEE Conf. Evolutionary Computat. (ICEC'97)*. NJ, IEEE, pp. 197–202, 1997.

[10] H. H. Lund. Intelligent Artefacts. In Sugisaka and Tanaka (Eds.), Proc. of 8th International Symposium on Artificial Life and Robotics. Oita: ISAROB, 2003.

[11] H. H. Lund, and P. Marti. Designing Manipulative Technologies for Children with Different Abilities. *Artificial Life and Robotics Journal, 9:4*, 175-187, 2005.

[12] H. H. Lund, T. Klitbo, and C. Jessen. Playware Technology for Physically Activating Play, *Artificial Life and Robotics Journal, 9:4,* 165-174, 2005.

[13] H. H. Lund and C. B. Nielsen. Modularity for Modulating Exercises and Levels – Observations from Cardiac, Stroke, and COLD Patients Therapy. Proc. of IEEE 8th Intl. Conf. on Ubiquitous Robots and Ambient Intelligence (URAI 2011), Korea, pp. 253-258, 2011.

[14] H. H. Lund, A. Henningsen, and R. Nielsen. Modular Robotic System as Multisensory Room in Children‟s Hospital. In Sugisaka and Takaga (eds.) Proc. of 14th International Symposium on Artificial Life and Robotics (AROB'14), ISAROB, Oita, 2009.

[15] P. Marti, L. Giusti, and H. H. Lund. The Role of Modular Robotics in Mediating Nonverbal Social Exchanges. *IEEE Trans Robot 25:3*, 602-613, 2009.

[16] H. H. Lund, and M. Ottesen. RoboMusic – A Behavior-Based Approach, *Artificial Life and Robotics, 12: 1-2*, 18-23, 2008.

The Seventeenth International Symposium on Artificial Life and Robotics 2012 (AROB 17th '12),
B-Con Plaza, Beppu, Oita, Japan, January 19-21, 2012

Fundamentals of Neurodynamics: Statistical neurodynamics and Neural Field Theory

Shun-ichi Amari

RIKEN Brain Science Institute

AROB-17-2012

Fundamentals of Neurodynamics:
Statistical Neurodynamics and Neural Field Theory

Biological Decision is Fast and Robust

Shun-ichi Amari
RIKEN Brain Science Institute

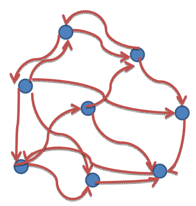

Biological decision

Densely connected
Sparsely connected

Majority
Boolean

$$x_i{}' = f_i(x_1, x_2, \ldots, x_n)$$

$x_i = 1, -1$ binary

Majority Decision vs Boolean Decision

Statistical Neurodynamics

$$z = \mathrm{sgn}(\sum w_i x_i - h_i)$$
$$z = f(x_1, \cdots, x_n)$$

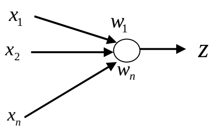

Statistical Neurodynamics

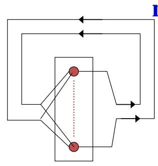

micro-dynamics

$$\mathbf{x} = (x_1, \ldots, x_n) : state$$
$$\mathbf{x}(t+1) = T_w \mathbf{x}(t) = f\{\mathbf{x}(t)\}$$
$$x_i^t = \mathrm{sgn}\left(\sum w_{ij} x_j^{t-1} - h_i\right)$$

macro-dynamics

$$X_{t+1} = F(X_t) \qquad X = \frac{1}{n}\sum x_i$$

Kauffman network: gene regulation

Boolean logic units vs majority decision units
sparsely connected vs densely connected

dilemma: fast (sparse) vs
robust (majority decision)

densely connected majority units (neural networks)

	Boolean	majority
sparse	Kauffman	Kurten
dense	random graph	Amari ○

dilemma:

fast (sparse; dense--chaos)
robust (majority decision)

densely connected majority units

majority decision logic : Boolean logic

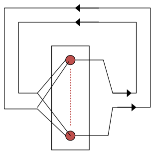

$$x_i' = \operatorname{sgn}\left(\sum w_{ij} x_j - h_i\right)$$

$$x_i' = f(x_1, x_2, \ldots x_n)$$

densely connected : sparsely connected

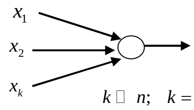

$k \ll n; \quad k = 2,3,4$

Statistical neurodynamics

$$X = \frac{1}{n}\sum x_i$$

$$X' = F(X) = \operatorname{erf}(\overline{w}X - \overline{h}):$$

$$X(t+1) = F(X(t))$$

mono-stable; bistable

Ensemble of neural networks

The laws
that hold for almost all networks in the ensemble

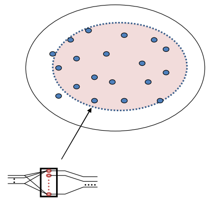

$$\Omega = \{\omega\} = \{W, h\}$$

Statistical Neurodynamics

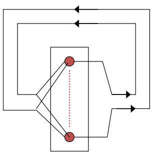

micro-dynamics

$$\mathbf{x}(t+1) = T_w \mathbf{x}(t) = \operatorname{sgn}(W\mathbf{x}(t))$$

macro-dynamics $\quad X = \frac{1}{n}\sum x_i$

$$X_{t+1} = F(X_t)$$

$$X_2 = X(\mathbf{x}_2) = X(T_W \mathbf{x}_1)$$

$$X_3 = X(\mathbf{x}_3) = X(T_W T_W \mathbf{x}_1)?$$

Strong proposition of macrodynamics

$$\lim_{n\to\infty}\sup_t E\left[\left|X_t - \tilde{X}_t\right|^2\right] = 0 \qquad X_t = X(T_\omega^t \mathbf{x}_0)$$

$$\tilde{X}_{t+1} = F\left(\tilde{X}_t\right) \ : \qquad \boldsymbol{x}_0$$

weak proposition of macrodynamics

$$\sup_t \lim_{n\to\infty} E\left[\left|X_t - \tilde{X}_t\right|^2\right] = 0,$$

Fundamental Problems of Statistical Neurodynamics --- unsolved

$$x_i^t = \operatorname{sgn}\left(\sum w_{ij} x_j^{t-1} - h_i\right) \qquad x_i = \pm 1$$

$$\boldsymbol{x}^t = \operatorname{sgn}\left(W\boldsymbol{x}^{t-1} - \boldsymbol{h}\right) = T_\omega \boldsymbol{x}^{t-1}$$

$$X' = F(X) = F(X(T_\omega(\mathbf{x})))$$

$$X_{t+1} = F(X_t)? \quad F(X(T_\omega T_\omega(\mathbf{x})))$$

$$\omega = (W, \boldsymbol{h})$$

State transition diagram

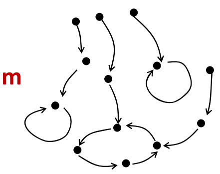

$$X_t = X\left(T_\omega^t \boldsymbol{x}_0\right)$$

$$X_1 = F\left\{X\left(T_\omega \boldsymbol{x}_0\right)\right\}, \qquad \boldsymbol{x}_1 = T_\omega \boldsymbol{x}_0$$

$$X_2 = F\left\{X\left(T_\omega \boldsymbol{x}_1(\omega)\right)\right\} \qquad ?$$

Boltzman H theorem, Kac

Associative memory

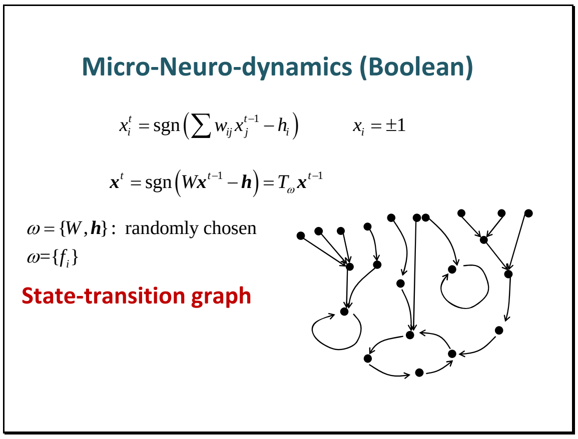
Micro-Neuro-dynamics (Boolean)
$x_i^t = \mathrm{sgn}\left(\sum w_{ij} x_j^{t-1} - h_i\right)$ $x_i = \pm 1$
$\boldsymbol{x}^t = \mathrm{sgn}\left(W\boldsymbol{x}^{t-1} - \boldsymbol{h}\right) = T_\omega \boldsymbol{x}^{t-1}$
$\omega = \{W, \boldsymbol{h}\}$: randomly chosen
$\omega = \{f_i\}$
State-transition graph

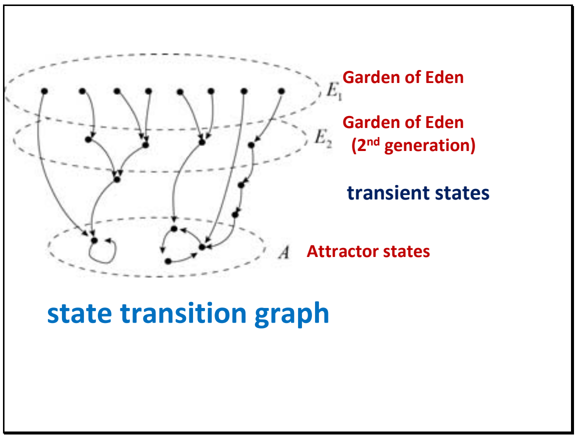
E_1 Garden of Eden
E_2 Garden of Eden (2nd generation)
transient states
A Attractor states
state transition graph

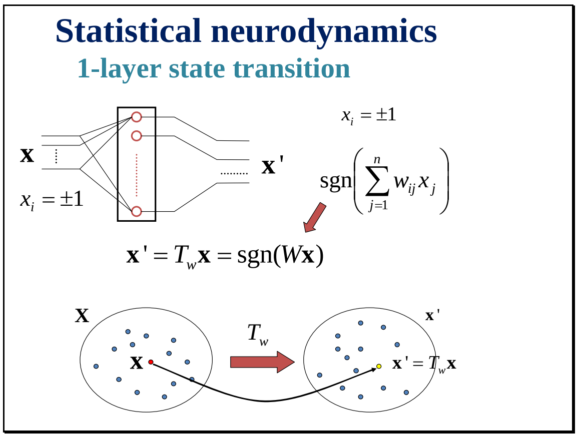
Statistical neurodynamics
1-layer state transition
$\mathbf{x}$
$x_i = \pm 1$
$\mathbf{x}'$
$x_i = \pm 1$
$\mathrm{sgn}\left(\sum_{j=1}^{n} w_{ij} x_j\right)$
$\mathbf{x}' = T_w \mathbf{x} = \mathrm{sgn}(W\mathbf{x})$
$\mathbf{X}$
T_w
$\mathbf{x}'$
$\mathbf{x}$
$\mathbf{x}' = T_w \mathbf{x}$

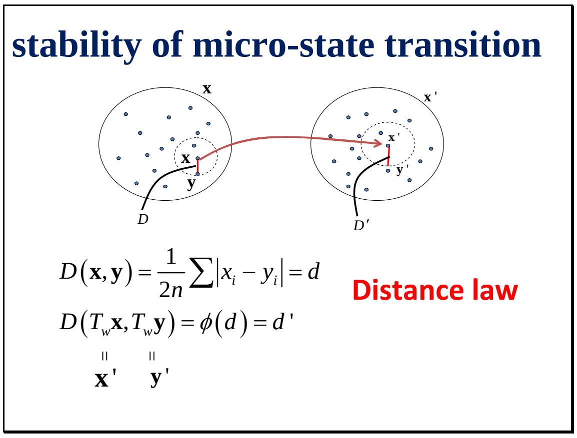
stability of micro-state transition
$\mathbf{x}$
$\mathbf{y}$
D
$\mathbf{x}'$
$\mathbf{y}'$
D'
$D(\mathbf{x},\mathbf{y}) = \frac{1}{2n}\sum |x_i - y_i| = d$
$D(T_w\mathbf{x}, T_w\mathbf{y}) = \phi(d) = d'$
$\mathbf{x}'$ $\mathbf{y}'$
Distance law

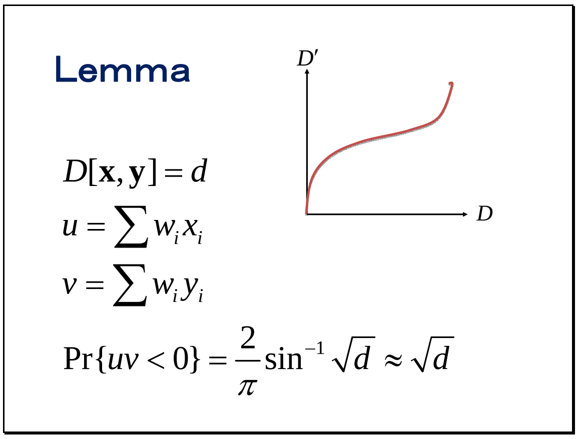
Lemma
D'
D
$D[\mathbf{x},\mathbf{y}] = d$
$u = \sum w_i x_i$
$v = \sum w_i y_i$
$\Pr\{uv < 0\} = \frac{2}{\pi}\sin^{-1}\sqrt{d} \approx \sqrt{d}$

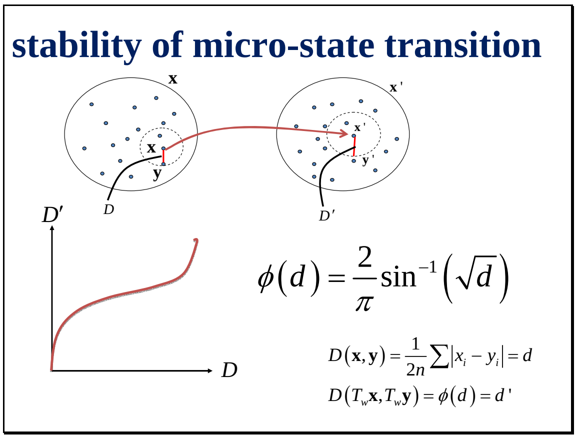
stability of micro-state transition
$\mathbf{x}$
$\mathbf{y}$
D
$\mathbf{x}'$
$\mathbf{y}'$
D'
D'
D
$\phi(d) = \frac{2}{\pi}\sin^{-1}\left(\sqrt{d}\right)$
$D(\mathbf{x},\mathbf{y}) = \frac{1}{2n}\sum |x_i - y_i| = d$
$D(T_w\mathbf{x}, T_w\mathbf{y}) = \phi(d) = d'$

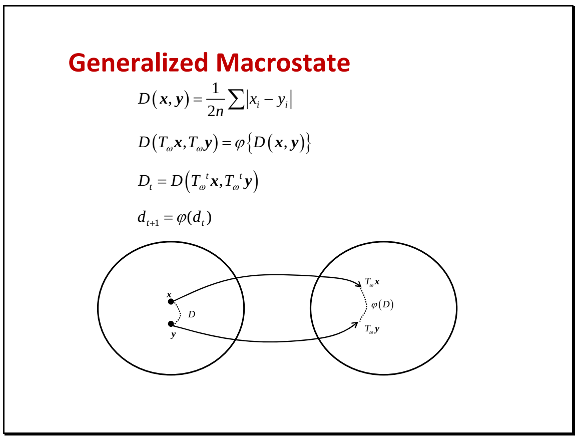
Generalized Macrostate
$D(\mathbf{x},\mathbf{y}) = \frac{1}{2n}\sum |x_i - y_i|$
$D(T_\omega\mathbf{x}, T_\omega\mathbf{y}) = \varphi\{D(\mathbf{x},\mathbf{y})\}$
$D_t = D\left(T_\omega{}^t\mathbf{x}, T_\omega{}^t\mathbf{y}\right)$
$d_{t+1} = \varphi(d_t)$
x
D
y
$T_\omega x$
$\varphi(D)$
$T_\omega y$

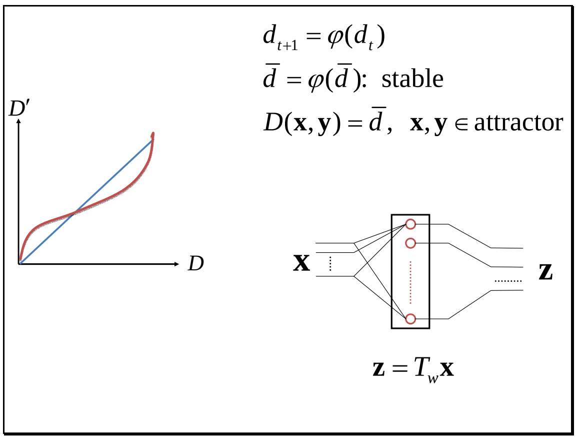
$d_{t+1} = \varphi(d_t)$
$\bar{d} = \varphi(\bar{d})$: stable
$D(\mathbf{x},\mathbf{y}) = \bar{d}$, $\mathbf{x},\mathbf{y} \in$ attractor
D'
D
$\mathbf{x}$
$\mathbf{z}$
$\mathbf{z} = T_w\mathbf{x}$

Distance Laws

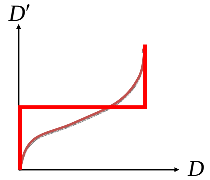

$$\phi_M(d) = \frac{2}{\pi}\sin^{-1}\left(\sqrt{d}\right)$$

$$\phi_B(d) = 1/2, \quad d \neq 0; \quad =0, \quad d=0$$

$$\phi_{SB,k}(d) = \frac{1}{2}\{1-(1-d)^k\}$$

$$\phi_{SM,k}(d) = \sum f_{k,i}c_i(d)$$

$$T_t = E_1 \cup E_2 \cup \cdots \cup E_r \to \overline{T} = T_r$$

Gardens of Eden

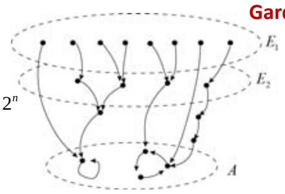

$X = \{\mathbf{x}\}; \quad |X| = 2^n$

$X = \overline{T} \cup A$

$A = \bigcup C_i$

state transition graph

state –transition graph---Boolean
--- random graph

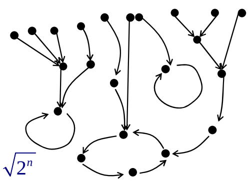

$N = 2^n$ states

number of attractor states : $\sqrt{2^n}$

number of attractor cycles : n

transient length : $\sqrt{2^n}$

microscopic dynamics

$x_i^t = \mathrm{sgn}\left(\sum w_{ij}x_j^{t-1} - h_i\right) \qquad x_i = \pm 1$

$\mathbf{x}^t = \mathrm{sgn}\left(W\mathbf{x}^{t-1} - \mathbf{h}\right) = T_\omega \mathbf{x}^{t-1}$

$\omega = (W, \mathbf{h})$

state transition diagram

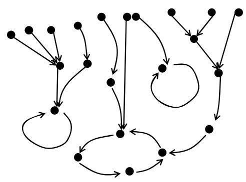

Concentration of wealth (monopoly!)
--- speed of convergence

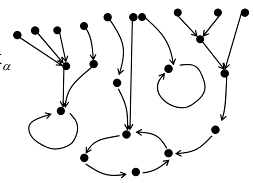

$\mathbf{s}_0 = (s_{0\alpha}) = (1,1,1,\ldots,1)$

$T_\omega = (T_{\alpha\beta}); \quad T_{\alpha\beta} = 1$ when $\mathbf{x}_\beta \to \mathbf{x}_\alpha$

$\mathbf{s}_1(\omega) = T_\omega \mathbf{s}_0(\omega)$

$\overline{S}_1 = E[s_{1\alpha} \mid \mathbf{x}_\beta \to \mathbf{x}_\alpha]$

$\mathbf{s}_t(\omega) = T_\omega^{\ t}\mathbf{s}_0(\omega):$

$\overline{S}_t = E[s_{1\alpha} \mid \mathbf{x}_\beta \to \mathbf{x}_{\beta'} \ldots \to \mathbf{x}_\alpha]$

:Expected number of coins after t state transitions

$\overline{S}_1$:Expected number of in-coming branches when x is not in the garden of Eden

Concentration index

$$\alpha_k = \lim_{n\to\infty}\frac{1}{n}\log \ \overline{S}_k$$

$$\overline{S}_k \approx 2^{\alpha_k n}$$

$\alpha_k = 0$ for densely connected Boolean net

Calculation of $\overline{S}_1$

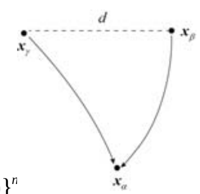

$\mathbf{x}_\alpha = T_\omega \mathbf{x}_\beta$

$D(\mathbf{x}_\beta, \mathbf{x}_\gamma) = d$

$\Pr\left\{T_\omega \mathbf{x}_\gamma = \mathbf{x}_\alpha \mid \mathbf{x}_\alpha = T_\omega \mathbf{x}_\beta\right\} = \{1-\varphi(d)\}^n$

$\overline{S}_1 = \sum {}_nC_{nd}\{1-\varphi(d)\}^n$

$= \int \exp\{n[H(x) + \log\{1-\varphi(x)\}]\}dx$

$= \exp[n[H(x_0) + \log\{1-\varphi(x_0)\}]$

$x_0 = \arg\max_x\{H(x) + \log\{1-\varphi(x)\}\}$

Calculation of $\overline{S}_2$

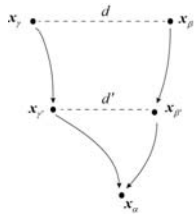

$\mathbf{x}_\beta \to \mathbf{x}_{\beta'} \to \mathbf{x}_{\beta''}$

$\mathbf{x}_\gamma \to \mathbf{x}_{\gamma'} \to \mathbf{x}_{\gamma''}$

$D(\mathbf{x}_\gamma, \mathbf{x}_\beta) = d; D(\mathbf{x}_{\gamma'}, \mathbf{x}_{\beta'}) = d'$

$d \to d' \to 0$

$\varphi(d)^{nd'}\{1-\varphi(d)\}^{n(1-d')}: \qquad \{1-\varphi(d')\}^n$

$\overline{S}_2 = \int \exp\{n[H(x) + H(x') + d'\varphi(x)$

$\quad + (1-x')\log\{1-\varphi(x)\} + \log\{1-\varphi(x')\}]\}dxdx'$

$$\bar{S}_t = \exp(\alpha_t n)$$
$$\alpha_1 = 0.23$$
$$\alpha_2 = 0.30$$
$$\alpha_3 = 0.32$$

The distribution of in-coming branches: Power law $p_k \approx \frac{1}{k^{\gamma}}$

$p_k = \Pr\{\#\text{incoming branches}=k\}$

#outgoing branches = 1

$$\sum p_k = 1$$
$$\sum k p_k = 1$$
$$\sigma^2 = \sum k^2 p_k - 1 \to \infty: \text{ monopoly}$$
$$p_k \approx \frac{1}{k^{\gamma}};$$

Friend gathering theorem

$$r_k = \text{Prob}\left\{\left|T_\omega^{-1}\boldsymbol{x}\right| = k \mid x \notin E_1\right\}$$
$$= \text{Prob}\left\{\left|T_\omega^{-1}\boldsymbol{x}\right| = k \mid T_\omega \boldsymbol{y} = \boldsymbol{x}\right\}$$
$$= \frac{\text{Prob}\left\{\left|T_\omega^{-1}\boldsymbol{x}\right| = k\right\}\text{Prob}\left\{T_\omega \boldsymbol{y} = \boldsymbol{x} \mid \left|T_\omega^{-1}\boldsymbol{x}\right| = k\right\}}{\text{Prob}\{T_\omega \boldsymbol{y} = \boldsymbol{x}\}}$$
$$\text{Prob}\left\{T_\omega \boldsymbol{y} = \boldsymbol{x} \mid \left|T_\omega^{-1}\boldsymbol{x}\right| = k\right\} = \frac{k}{N}$$
$$r_k = k p_k = k\,\text{Prob}\left\{\left|T_\omega^{-1}\boldsymbol{x}\right| = k\right\}$$

how to calculate σ^2

$$\sigma^2 = E\left[\left|T_\omega^{-1}\boldsymbol{x}\right| \;\; \left|T_\omega \boldsymbol{y} = \boldsymbol{x}\right]\right. - 1$$
$$\text{Prob}\left\{T_\omega \boldsymbol{y} = \boldsymbol{x} \mid \left|T_\omega^{-1}\boldsymbol{x}\right| = k\right\} = \frac{k}{N}$$
$$p_k = \text{Prob}\left\{\left|T_\omega^{-1}\boldsymbol{x}\right| = k, T_\omega \boldsymbol{y} = \boldsymbol{x}\right\} N$$
$$\sigma^2 = \sum_n {}_nC_k \left\{1 - \phi\left(\frac{k}{n}\right)\right\}^n - 1 = \bar{S}_1$$

The Power law

p_k : probability that a node has k incoming branches

$$\sum k p_k = 1$$
$$\sum k^2 p_k = 2^{\alpha_1 n} \to \infty$$
$$p_k \approx \frac{1}{k^{\gamma}}; \quad \gamma = \frac{\alpha_1 + 3}{\alpha_1 + 1} = 2.6$$

Random Boolean graph

$$p_k = \frac{1}{ek!}:$$

Poisson dustribution

$$\sum k p_k = 1$$
$$\sum k^2 p_k = 2$$

State transition of generalized majority decision: fast and robust

very small number of attracting states

small-world network

short transient states

chaotic dynamics

general statements concerning majority decision logic

Neural Oscillation

Wiener ・・・ entrainment

$$\frac{dU_E}{dt} = -U_E + w_{EE} f(U_E) - w_{EI} f(U_I) + S_E$$
$$\frac{dU_I}{dt} = -U_I + w_{IE} f(U_E) - w_{II} f(U_I) + S_I$$

f : sigmoidal function

Amari (1971; 1972)

Wilson-Cowan (1972)

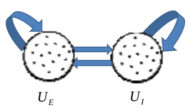

multi-stability

oscillation

Neural Fields : Wilson-Cowan (1972)

$$\tau_E \frac{\partial U_E(\xi,t)}{\partial t} = -U_E + w_{EE} \circ f(U_E) - w_{EI} \circ f(U_I) + S_E(\xi,t)$$
$$\tau_I \frac{\partial U_I(\xi,t)}{\partial t} = -U_I + w_{IE} \circ f(U_E) - w_{II} \circ f(U_I) + S_I(\xi,t)$$

$\circ$: convolution

Ermentrout-Cowan (1979): hallucination

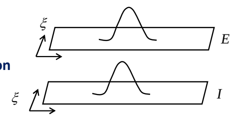

$$\frac{\partial u(\xi,t)}{\partial t} = -u(\xi,t) + \int w(\xi-\xi') f\left[u(\xi',t)\right] d\xi' + a$$

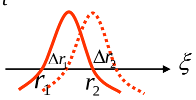

$$u(r_i,t)=0 \qquad u(r_i+\Delta r_i, t+\Delta t)=0$$

$$\frac{\partial u(r_i,t)}{\partial t} + \frac{\partial u(r_i,t)}{\partial \xi}\frac{\partial r_i}{\partial t} = 0$$

$$\alpha_i \frac{\partial r_i}{\partial t} = -\frac{\partial u(r_i,t)}{\partial t} = \int_{r_1}^{r_2} w(r_i-\xi')d\xi' = \pm W(r_2-r_1)$$

$$W(\xi) = \int_0^{\xi} w(\xi)d\xi$$

Neural Fields・・・mathematical theory

Amari (1977) :

dynamics of boundary

$f(u)=1(u)$

- bump solution
- traveling bump
- maximum detector
- working memory

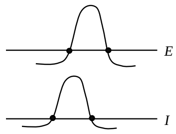

Amari-Kishimoto (1979)

$$\frac{\partial u(\xi,t)}{\partial t} = -u(\xi,t) + \int w \circ f[u(\xi',t)-h]d\xi' - v(\xi,t) + I_u(\xi,t)$$

$$\frac{\partial v(\xi,t)}{\partial t} = -\alpha u(\xi,t) - \beta v(\xi,t) + I_v(\xi,t)$$

Pinto-Ermentrout model (2001)

Traveling bump

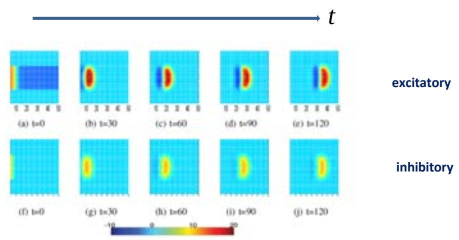

Collision of bumps (1)

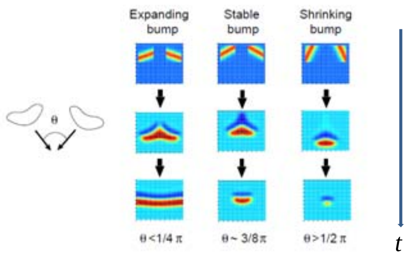

Collision of bumps (2)

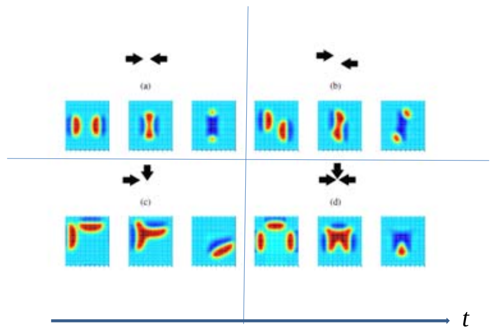

Collision of bumps (3)

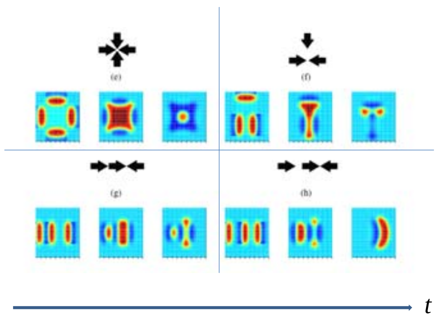

Control of moving bumps

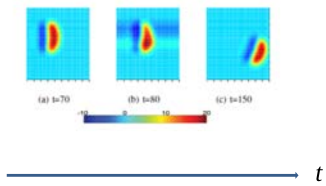

Unmanned Maritime Systems
Growing Applications--Naval, Security and Commercial

Bob Nugent

VP Advisory Services, AMI International

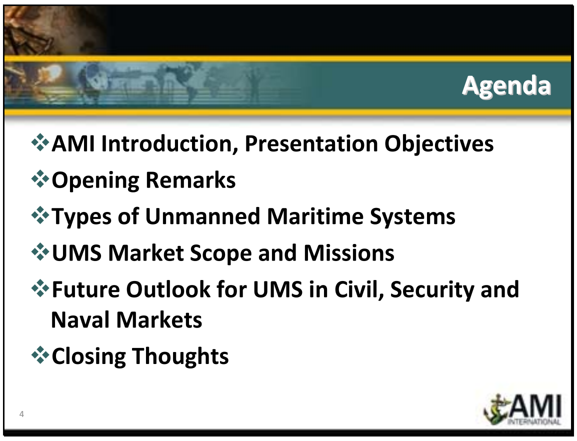

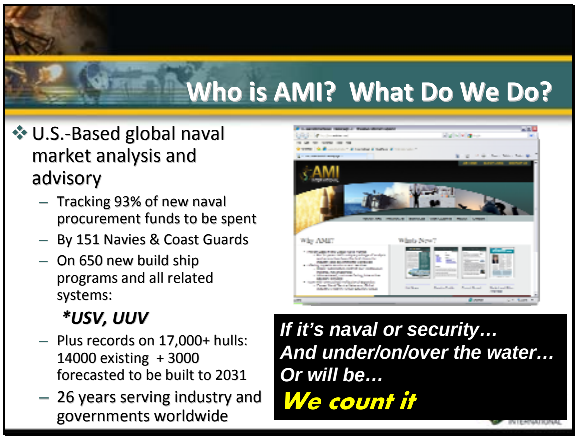

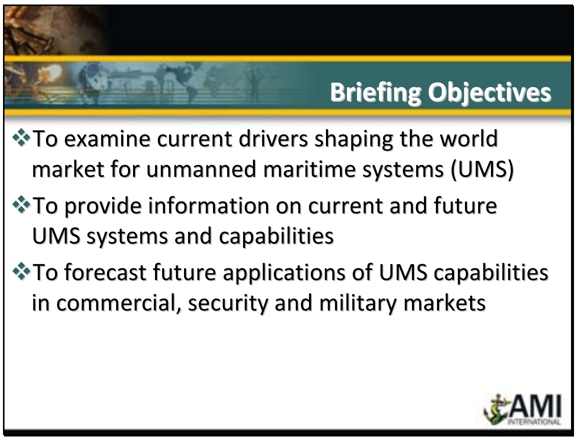

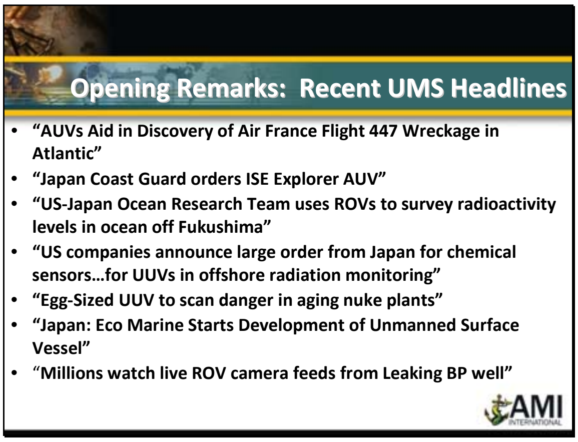

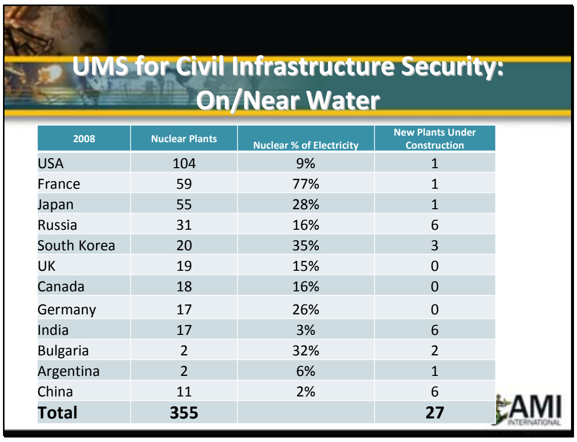

2008	Nuclear Plants	Nuclear % of Electricity	New Plants Under Construction
USA	104	9%	1
France	59	77%	1
Japan	55	28%	1
Russia	31	16%	6
South Korea	20	35%	3
UK	19	15%	0
Canada	18	16%	0
Germany	17	26%	0
India	17	3%	6
Bulgaria	2	32%	2
Argentina	2	6%	1
China	11	2%	6
Total	**355**		**27**

Defining Our Terms: UMS

- *"Unmanned Maritime Systems" refer to:*
- *"Unmanned Surface Vessels" (USV)*
- *Unmanned Underwater Vehicles (UUV)*
- *UUV further divided into*
  1. AUV (A=autonomous)
  2. ROV (R=Remote…tethered to the mothership)

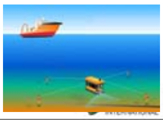

Unmanned Surface Vessels: Comparative

Model	Common USV	Draco	Piranha	Spartan Scout
Manufacturer	AAI	GD	Zyvex	USMI
Snapshot				
Length (m)	11.9	11.0	16.3	11.0
Beam (m)	3.12	3.4	3.2	3.2
Endurance (hrs)	24+	24	96	48
Displacement (kg)	8000	10430	3856	8000
Max Payload (kg)	1200	2267	6804	2267
Max Speed (km/hr)	28	34	45+	40+

Small UUVs: Comparative

Name	Manufacturer	Weight (kg)	Diameter (cm)	Length (m)	Depth Max. (m)	Range (km)	Speed (m/sec)	Endurance
Electric Glider	Webb Research (Teledyne)	52	21.3	1.5	1000	1500	0.4	days
Thermal Glider	Webb Research (Teledyne)	60	21.3	1.5	2000	40000	0.4	5 years
Spray	Bluefin	52	n/a	n/a	1500	4000	n/a	6 months
Bluefin 9	Bluefin	50	23.5	1.7	198.12	n/a	2.57	13 hours
CETUS	Lockheed Martin	100	8	1.8	4000	40	2.57	n/a
REMUS 100	Hydroid (Kongsberg)	37	19	1.6	100	n/a	2.6	22 hours
Gavia	Hafmynd	44	n/a	1.7	200 (1000)	n/a	3	n/a
EcoMapper	OceanServer Technology	20.41	14.73	15.2	n/a	n/a	2.06	8 hours
Iver2	OceanServer Technology	20	14.73	1.26	n/a	n/a	2.06	10 hours
Fetch 2.9	Sias Patterson (Prizm)	73	29	1.96	150	92.6	6.5	20 hours
Fetch 3.5	Sias Patterson (Prizm)	98	35	2.1	150	229	5	30 hours
Seaglider	iRobot	52	30	1.8	1000	4600	25	n/a

Range and Mission Demands for larger UMS

- *Commercial and Security/Military Customers seek larger UMS to for larger cargoes, longer ranges, deeper dives:*
  - **USV: From 7M RHIB to more robust/longer range hulls 11-16M…with new materials to lighten ship**
  - **UUV: From original torpedo form to "large diameter" UUVs**
- *Technical Challenges Limiting Vehicle Growth:*
  - **Launch/Recovery still the hardest bit**
  - **Followed closely by C2/autonomy**

AMI INTERNATIONAL

UMS Future Market Scenarios…

High: 8.8B 2008 USD total revenues (Military/Comm) by 2020

Bharat Book Bureau (India)

Mid: 1.8-3.7B annual market (Mil/Comm) 2018

Douglas-Westwood (UK)

Low: 500M annual sales (Mil) by 2017

Frost & Sullivan (US)

Our View: Most UMS Market Growth Forecasts Remain Overoptimistic …Especially WRT Military Market

Most Global Military UMS Spending will still be US…but procurement spending growing in Asia-Pacific region, which will become big UMS market by 2020

Current UMS Market Snapshot-UUV

- **UUVs: Existing Market Population = 6000+ ROV, 400+ AUV**
  - ✓ Commercial UUVs make up 70-80% of total existing market
  - ✓ ROVs in the oil and gas industry last 30 years
  - ✓ 3 UUV Types/Segments:
    - Large: Comm/Research/Oil & Gas
    - Medium: Research/Mil/Oil & Gas
    - Small: Research/Mil: Half of all AUVs are <50KG
    - Today's Military UUV market: mostly AUVs for Mine Warfare
- Military AUVs =25% of current global AUV inventory
- Military AUVs: portable and/or "Gliders"—torpedo heritage
- Industry seeing some growth potential—M&A up last 5 years:
  - **Hydroid (Kongsberg)**
  - **Bluefin (Batelle)**
  - **Sea Glider (iRobot)**
  - **Webb Research (Teledyne)**
  - **Sias Patterson (Prizm)**
  - **Seaeye (Saab)**

AMI INTERNATIONAL

Current UMS Market Snapshot-USV

Key Manufacturer Countries by Known USV Models

Asia & Australia	**6**
Japan	2
Singapore	3
Unknown	1
Middle East & North Africa	**4**
Israel	4
NATO	**39**
Canada	6
France	6
Germany	3
Norway	2
Portugal	2
Sweden	2
Turkey	2
U.K.	16
United States	**34**
Total	**83**

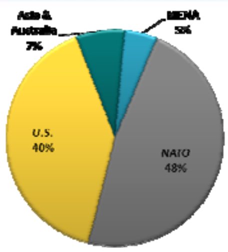

15

AMI INTERNATIONAL

Identifying UMS Capability & Market Gaps

4 USV Classes as Defined by U.S. Navy

USV Mission	X-Class (small)	Harbor Class (7M)	Snorkeler Class (7M SS)	Fleet Class (11M)
Mine Countermeasures (MCM)		MCM Delivery, Search/Neutralization	MCM Search, Towed, Delivery, Neutralization	MCM Sweep, Delivery, Neutralization
Anti-Submarine Warfare (ASW)			Maritime Shield	Protected Passage & Maritime Shield
Maritime Security		ISR/Gun Payloads		7M Payloads
Surface Warfare (SUW)		SUW, Gun	SUW (Torpedo)	SUW, Gun & Torpedo
Special Operation Forces (SOF) Support	SOF Support	SOF Support		Other Delivery Missions (SOF)
Electronic Warfare		Other IO	High Power EW	High Power EW
Maritime Interdiction Operations (MIO) Support	MIO USV for 11M L&R	ISR/Gun Payloads		

Primary Missions supported by

X-Class	Harbor Class	Snorkeler Class	Fleet Class
Secondary Missions of each class that are possible			

16

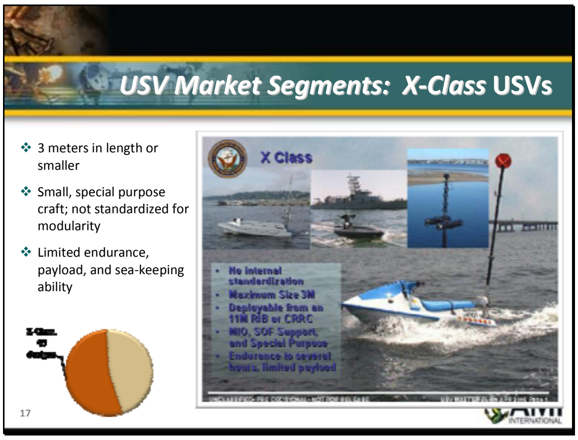
USV Market Segments: X-Class USVs
3 meters in length or smaller
Small, special purpose craft; not standardized for modularity
Limited endurance, payload, and sea-keeping ability
X Class
No internal standardization
Maximum Size 3M
Deployable from an 11M RIB or CRRC
MIO, SOF Support, and Special Purpose
Endurance to several hours, limited payload
17
INTERNATIONAL

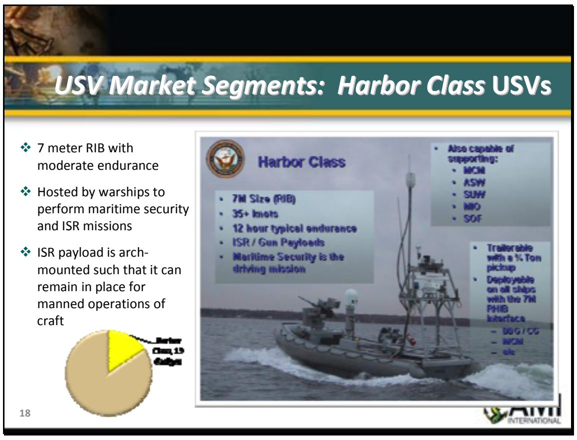
USV Market Segments: Harbor Class USVs
7 meter RIB with moderate endurance
Hosted by warships to perform maritime security and ISR missions
ISR payload is arch-mounted such that it can remain in place for manned operations of craft
Harbor Class
7M Size (RIB)
35+ knots
12 hour typical endurance
ISR / Gun Payloads
Maritime Security is the driving mission
Also capable of supporting:
MCM
ASW
SUW
MIO
SOF
Trailerable with a ¾ Ton pickup
Deployable on all ships with the 7M RHIB interface
DDG / CG
MCM
etc
18
INTERNATIONAL

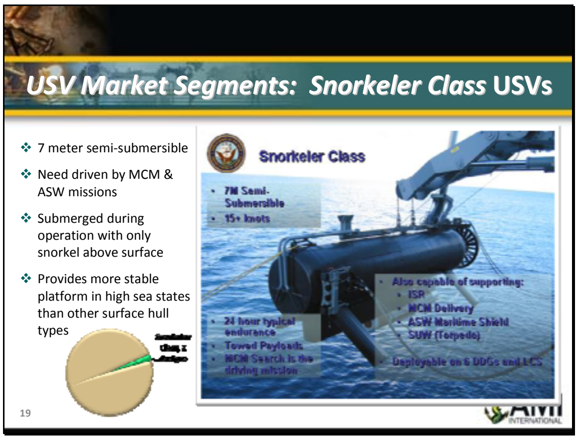
USV Market Segments: Snorkeler Class USVs
7 meter semi-submersible
Need driven by MCM & ASW missions
Submerged during operation with only snorkel above surface
Provides more stable platform in high sea states than other surface hull types
Snorkeler Class
7M Semi-Submersible
15+ knots
24 hour typical endurance
Towed Payloads
MCM Search is the driving mission
Also capable of supporting:
ISR
MCM Delivery
ASW Maritime Shield
SUW (Torpedo)
Deployable on 6 DDGs and LCS
19
INTERNATIONAL

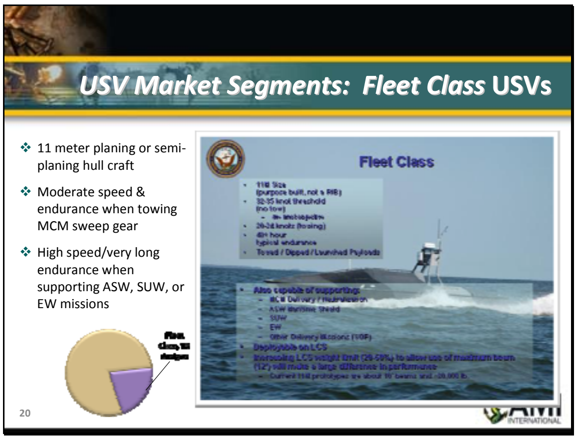
USV Market Segments: Fleet Class USVs
11 meter planing or semi-planing hull craft
Moderate speed & endurance when towing MCM sweep gear
High speed/very long endurance when supporting ASW, SUW, or EW missions
Fleet Class
Also capable of supporting:
SUW
EW
Deployable on LCS
20
INTERNATIONAL

JAEA Robotics' Emergency Response to FUKUSHIMA-DAIICHI Accident - Summary and Lessons Learned -

Shinji Kawatsuma[1], Takashi Okada[1], and Mineo Fukushima[1]

[1]Japan Atomic Energy Agency, Tokyo 105-8577, Japan
(Tel: 81-3-3592-2150, Fax: 81-3-5157-1950)

[1]kawatsuma.shinji@jaea.go.jp

Abstract: Japan Atomic Energy Agency developed Nuclear Disaster Response Robotics in 2001 after JCO criticality accidents occurred. It is very sorry that Nuclear Disaster Response Robotics could not work when the FUKUSHIMA-DAIICHI accident occurred by a big earthquake and a huge Tsunami on March 11th 2011. According to the situation and condition of the FUKU SHIMA-DAIICHI accident, JAEA has modified above mentioned Nuclear Disaster Response Robotics and prepared suppo rting equipments like as Robotics Control vehicles. JAEA has provided Robotics and Robotics Control vehicle to TEPCO and is continuously supporting TEPCO for plant restoration. This paper summarize JAEA ROBOTICS' Emergency Respo nse to FUKUSHIMA-DAIICHI Accident and describe lessons learned.

Keywords: FUKUSHIMA-DAIICHI, Emergency Response, Nuclear disaster Robotics, Robotics control vehicle.

1 INTRODUCTION

Japan Atomic Energy Agency (JAEA), former Japan Atomic energy Research Institute (JAERI) and Japan Nuclear Cycle development institute (JNC), had experienced on development for reactor vessel remote dismantling machine and bilateral servo-manipulator which has been used for maintenance task under extremely high radiation dose level. Nuclear Disaster Robotics, two RESQ-A, RESQ-B, RESQ-C and RaBOT had been developed after JCO criticality accident occurred on September 30th 1999. It is very sorry that those Nuclear Disaster Robotics could not work when the FUKUSHIMA-DAIICHI accident occurred by a big earthquake and a huge Tsunami on March 11th 2011.

JAEA modified existed Remote Operated Vehicle (ROV) which had been used cold test for Glove Box dismantling and two RESQ-A and prepared Robotics Control Vehicles and provides them to TEPCO for supporting FUKUSHIMA-DAIICHI restoration based on experiences obtained during above mentioned development.

2 Back Ground

2.1 reactor vessel remote dismantling system

JAERI developed reactor vessel remote dismantling machine based on single arm power manipulator 1981 to 1990, and deployed the system during decommissioning of The Japan Power Demonstration Reactor. See **Fig. 1**

2.2 Bilateral Servo-Manipulator System

JNC developed Bilateral Servo-Manipulator System 1982 to 1999 in order to deploy the system for maintenance in Tokai Vitrification Facility which has extremely high dose area. See **Fig. 2**.

Fig. 1

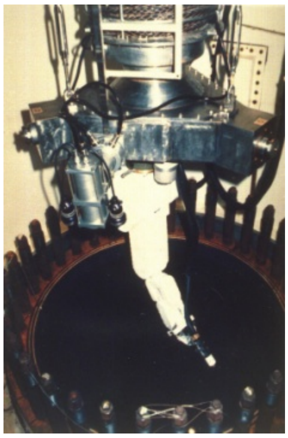

Fig. 2

2.3 Nuclear Disaster Robotics

JAERI developed nuclear Disaster Robotics, two RESQ-A, RESQ-B, RESQ-C and RaBOT in 2000 to 2001 with cooperation of some company, based on the lesson learned that operator could not access easily for repressing criticality during JCO criticality accident which was occurred on the September 30th.. See **Fig. 3**.

2.4 Remote Operated Vehicle for decommissioning

JAEA deploy Remote Operated Vehicle in cold test for dismantling Glove BOX which was use for Mixed Oxide

Fuel for Fast Breeder Reactors and an Advanced Thermal reactor. See **Fig. 4**.

Fig. 3

Fig. 4

3 Emergency response to FUKUSHIMA-DAIICHI accident

3.1 Outline

At the 2:46PM on March 11th 2011, the earthquake of the East Japan Pacific Ocean was occurred and following huge Tsunami attacked FUKUSHIMA-DAIICHI Nuclear Power Station, therefore Station black out occurred reactor coolant could not be maintained. As a result, hydrogen explosion was occurred. See **Fig. 5**.

At that time, RaBOT was already discarded, and RESQ-A, RESQ-B and RESQ-C were not able to work with some failure. It was requested to repair to the company which cooperated when developed, however the request was rejected by the company with reason why engaged engineer were had dissipated and the technology was not handed down.

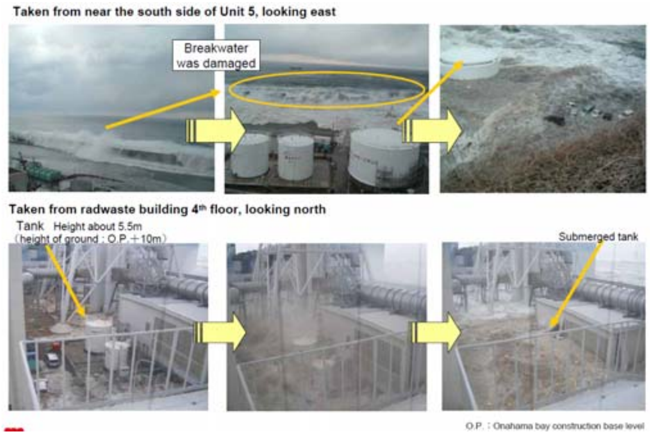

Fig. 5

3.2 Robotics Control Vehicle 1 (RC-1)

It is known that Robotics can't be used successfully without various supporting equipment. JAEA prepared Robotics Control Vehicle – 1 (RC-1) which is for JAEA-1 and JAEA-2 operation and is equipped with Steel shielded operation BOX, a gamma-camera, a teletecter, a viewing camera, a generator.

Based on request from Tokyo Electric Company (TEPCO), JAEA was provide the RC-1 to TEPCO for TALON operation which a robot has radiation mapping system and is provided by Idaho National Laboratory, DOE. Also, a thermo camera and a 3-D laser camera were equipped which were developed and provided by Tadokoro Laboratory of Tohoku University. See **Fig. 6**.

Fig. 6

RC-1 was supplied to FUKUSHIMA-DAIICHI on May 1st and have been used for radiation measurement. The picture taken by gamma camera was shown in **Fig.7**, and the hot point was indicated clearly.

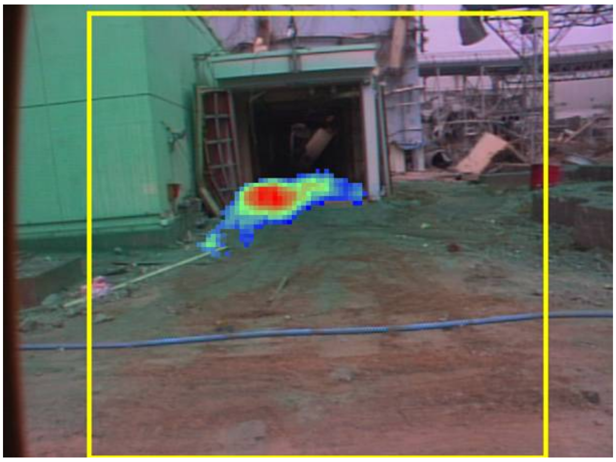

Fig. 7

3.3 JAEA-1

JAEA-1 was modified based on Remote Operated Vehicle used for cold test for Globe BOX dismantling, and is for cleanup of rubbles Rubble scattered by the explosions. See **Fig. 8**.

Fig. 8

3.4 JAEA-2

JAEA-2 was modified based on RESQ-A and equipped with 6 MPa high pressure water spray for decontamination. See **Fig. 9**.

3.5 JAEA-3

JAEA-3 was modified based on RESQ-A and equipped with a prototype of gamma camera which was made based on the experiences on the gamma camera which was equipped on RC-1. See **Fig. 10**.

3.6 Robotics Control Vehicle 2 (RC-2)

As a result of RC-1 preparation, TEPCO requested a new Robotic Control Vehicle. **Fig 11** shows the steel shielded BOX which was not fitting yet.

Fig. 9

Fig. 10

Fig. 11

4 Consideration

4.1 Organization and Scheme for operation and maintenance

It is most important lesson learned that an organization and scheme for operation and maintenance of Emergency response Robotics and accessories like as Robotics control vehicle.

This issue had been pointed out and discussed when Nuclear Disaster Robotics were developed after JCO criticality accident, however conclusion had not been reached.

If such organization and scheme had been established other lessons learned mentioned below could have been pointed out and solved.

4.2. Systematization

As mentioned above, it was known that a Robotics itself can't be used successfully without accessories. Accessories like as Robotic Control Vehicles, gamma cameras, teletecters lights, cooler/heater, generators and others should be prepared in advance and should be systematization. Especially, generators were difficult to obtain after the earthquake and Tsunami attacked.

4.3. Optimization under emergency

As experienced, maker cannot be always depended, under the emergency situation. Minimum tasks like as to optimize Robotic systems in accordance to the situation of the accidents should be performed by operators of the organization.

Therefore, Platform and tool systems should be recommended. Platform is mobile mechanism and should be prepared two or three type according to size and weight of tools. Tools should be prepared or modified based on conventional equipment on the shelf.

4.4 Mobility

Even if an organization established, it is very difficult to prepare logistics in the damaged area just after earthquakes and Tsunamis attacked, so the organization should cooperated with the Defense Forces of Japan. Also Robotics Control Vehicles should be designed and prepared in accordance with transport plane and helicopter of Defense Force of Japan.

5 CONCLUSION

We are TEAM NIPPON.

We shall overcome!

Fig. 12

REFERENCES

[1] Ohno (2011), Robotic Control Vehicle for measuring Radiation in Fukushima Daiichi Nuclear Power plant, SSRR 2011

The Seventeenth International Symposium on Artificial Life and Robotics 2012 (AROB 17th '12),
B-Con Plaza, Beppu, Oita, Japan, January 19-21, 2012

Genetic-Algorithms Produce Individual Robotic-Rat-Pup Behaviors that Match Norway-Rat-Pup Behaviors at Multiple Scales

Chris Sullivan[1], Sanjay S. Joshi[2,4], and Jeffrey C. Schank[3]

[1]Department of Mechanical and Aerospace Engineering, University of California, Davis, USA
[2]Department of Mechanical and Aerospace Engineering, University of California, Davis, USA
[3]Department of Psychology, University of California, Davis, USA

[4]Correspondence: ctljoshi@gmail.com

Abstract: We designed cognitive architectures for individual robotic rat pups using genetic algorithms, with the aim of achieving insight into Norway rat pup behavior. Our genetic algorithms were evolved using only metrics of Norway rap pup behavior (e.g., percent of time spent in corners, along walls, and center of an arena during animal experiments). Robotic rat pups quantitatively matched Norway rat pups at the macro level and additionally qualitatively matched Norway rat pup behavior at the micro behavior scales (corner snooping, punting). The complexity of the resulting deterministic controllers may lend support to previous studies that show random-like control codes (possibly emerging from complex underlying interactions) can produce apparently realistic rat pup behavior below a certain age.

Keywords: genetic algorithm, behavior, biorobotics

1 INTRODUCTION

We combine robotic models of infant Norway rats (robopups), with computer simulation and animal experimentation to study rat pup behavior (Fig. 1). In past work, we showed the remarkable result that simply choosing robopup movement directions at random, regardless of sensory input, produced quite intentional-looking emergent behavior patterns that matched rat pups in both individuals and groups, somewhere in-between 7-10 days of age [1]. Our analysis revealed that body morphology and arena topology interacted with the random control architecture to produce emergent complex behavior. We could not conclude, however, from these results that rat pups in an arena move purely randomly, because we did not investigate the full space of possible deterministic sensorimotor rules. In our current work, we use genetic algorithms to investigate the space of possible sensorimotor rules by artificially designing sensory-dependent deterministic robopup controllers using macro-level topological fitness metrics (e.g., percent of time spent in various regions of an arena during animal experiments). The genetic algorithms allow us to explore a wide range of possible deterministic control solutions. In this paper, we review past work and explain our methods to evolve cognitive codes with genetic algorithms to study a variety of solutions.

2 BACKGROUND

Behavior is influenced by the nervous system, body morphology, physiology, the environment (including the social environment), and interactions among all these elements. Thus, our basic schematic view of behavior is defined in equation (1). Autonomous robots and associated simulations allow systematic variation of the variables of (1) in ways that are often impossible in live animals.

Behavior = *F*(*Internal State*, *Sensorimotor Rules*, *Biomechanics*, *Environment*) (1)

Equation (1) is a schema for developing animal and robotic models and, by including the environment (broadly construed), it is a schema that is likely to result in emergent behavior.

2.1 Rat Pup Experiments

An individual rat-pup experiment consists of placing a single pup in the middle of an arena and videotaping its behavior from above. Figure 1 illustrates a 7-day old rat pup in an arena. Arenas could be manipulated in a variety of ways and the test chamber was configured to study the effects of specific environmental stimuli (e.g., heat, inclines, and light). The video recordings of rats moving in the arena, were then analyzed by extracting digitized video frames at specified time intervals (i.e., 5 secs.) to record the position of the tip of the nose and base of the tail [2].

Fig. 1. 7-day old Norway rat pup during animal observation experiments.

Algorithms were then used to extract metrics from these measurements [3]. Animal experiment results for individual 10-day old pups were reported in Schank et al., 2004 [4]. Rat pups spent time in corners, near walls, and in the center of the arena. In addition, some rat pups visited one corner, some two corners, and others 3 or 4 corners. Sometimes, a rat pup spent an extended period of time in a limited region of the arena. Playback of video from these pup experiments revealed "micro" behaviors, which were limited in time and space. Micro behaviors were easily identified in video playback, but hidden in 2-dimensional trajectory plots. For example, rat pups repeatedly burrowed their nose into corners for variable periods of time (i.e., *corner-snooping*, e.g., see Fig. 1). Rat pups sometimes turned in place in the open or in a corner for periods of time, which is called *punting*. Rat pups also followed walls for periods of time, which we called *wall-following*. These individual rat-pup behavior features also hold for 7-day old pups [1]. We therefore categorized all rat pup behavior as either: (1) macro-level behavior (those relating to overall trajectories which occur on the order of 10 minutes over extended arena space), or (2) micro-level (those that relate to detailed micro-behaviors as described above which occur on the order of seconds to minutes over limited arena space).

2.2 Robotic Rats and Dynamic Simulator

In parallel with the animal experiments, we conducted experiments with robotic rat pups (robopups). The current generation of robopup is shown in Fig. 2. The design of the robopup incorporated biologically inspired and robotic aspects, such as body shape, sensor and actuator location, and computational needs [4]. In brief, the robot's shape was designed to model the basic shape of a rat pup 7-10 days of age. The robot had the same 3:1 length to width ratio as Norway rat pups in the 7 to 10-day age range, and had a similar curved snout (Fig. 1). Rat pups have limited mobility at these ages and primarily use their back legs to push their bodies forward [2]. To model this type of movement, two rear rubber wheels propelled the robot and a supporting passive wheel stabilized the front of the robot.

Before 13 to 14 days of age, rats are blind, deaf, and have limited olfactory capabilities [3]. Thus, infant rat pups rely largely on tactility at these early ages. Robopups incorporated tactility by placing 14 micro-switches at various positions around the robot's perimeter. Most of the sensors were placed near the front of the robopup because a rat pup's primary tactile sensitivity is around the snout area [2]. To detect contact at points where there were no switches, brass strips were connected to the micro switches. Sensorimotor rules were programmed in the robot's microprocessor (Parallax 25 MHz Java stamp 24-pin DIP module). Robots were tested in arenas proportional to the arenas in which rat pups were tested (Fig. 1), and we applied the exact same data extraction and analysis tools for both the robopups and rat pups.

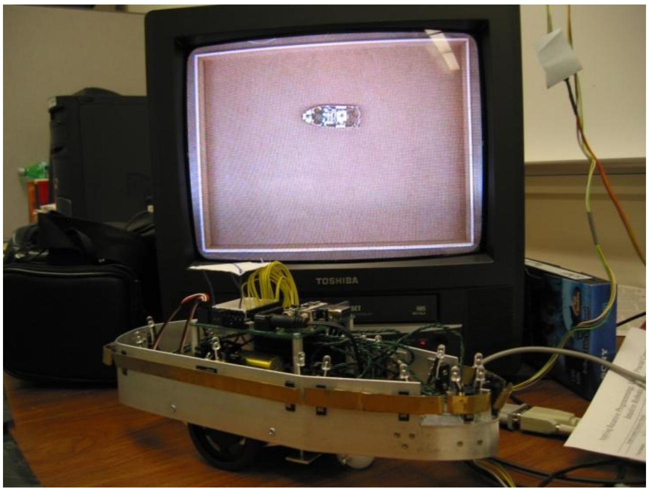

Fig. 2. Robotic model of infant rat pup (foreground), and another robot in testing arena (on monitor).

A MATLAB/Simulink based individual-robot simulation was used in the current study [5]**.** Just as in the actual robots, sensorimotor rules are programmed into the robot simulator. The only differences are the programming language and the computing platform. Model validation studies showed that the simulation produced results very similar to robopups [5].

Several robot controllers were developed for the robopup project to accomplish the goal of modeling rat-pup sensory behavior. Each controller took in information from the robot's tactile sensors and then used that information to send commands to the two robot wheels. The robopup could move forward, back up, or turn (or some combination thereof), depending on the command sent to each wheel.

2.3 Random Control Architectures

In May et al., 2006 [1], we implemented a *random* control architecture as a type of null model to compare to other sensor-driven architectures. In this null model, robots did not use their sensors at all. Instead, every two seconds, robopups *randomly* chose one of ten movements with equal probability: stop moving or one of the seven forward or two back-up directions depicted in Fig. 3.

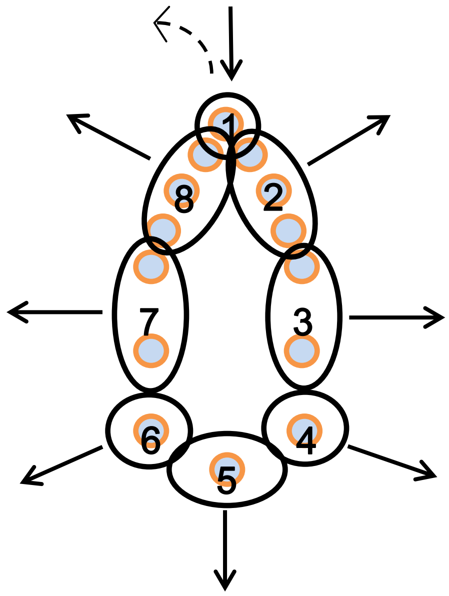

Fig. 3. Illustration of tactile sensor groups on robot, and possible movement directions.

Rat pups can flex their body and turn away from a corner. Rigid-body robopups cannot escape a corner in this way. Therefore, to model the ability of rat pups to escape corners, we implemented *back-up* directions of movement. When moving, the random architecture distributed movements such that a robopup moved forward 78% of the time and backed up 22% of the time. It was surprising and remarkable how well the trajectory plots of "random" robots matched the plots for both 7 and 10 day-old pups. Further analysis showed that the random architecture resulted in good matches somewhere in-between 7-day old and 10-day old rat pups in key macro-level topological metrics, such as the proportion of time spent in corners, near walls, and in the center of the arena [1]. The robopups also exhibited all the micro-level behaviors commonly seen in rat pups including corner-snooping, wall-following, and punting. This surprising result could be explained by the complex interaction of body-shape, arena constraints, and simple cognitive codes all working in unison to allow behavior to emerge.

3 GENETIC ALGORITHM METHODOLOGY

In May et al., 2006 [1], we first designed the controller and then analyzed the ability of the controller to match certain macro-level topological quantitative metrics and micro-level behaviors. In the current work, we reversed the procedure by *imposing* (through artificial selection) the matching of macro-level quantitative topological numerical metrics (percent of time spent in various regions of an arena during animal experiments), and then studied the resulting variety of controllers and their subsequent qualitative micro-level detailed behaviors.

Given that the *random* control architecture, using no sensory information, produced results very similar to the rat pups, a natural question to ask was how well *any* sensory-dependent *deterministic* control architecture could perform in matching pup behavior. To explore the large space of possible deterministic control designs, we employed a genetic algorithm (GA). The evolutionary method used to design controllers depended on three components: (i) macro-level behavior metrics that could be numerically quantified (e.g., percent of time spent in various regions of an arena during animal experiments), (ii) creation of *fitness functions* that evaluated behavioral metrics to score the quality of control designs, and (iii) a method of varying and combining high-scoring control designs to create new control designs (called a *generation* of control designs).

Employing a relatively high-fidelity dynamics model [5] placed computational constraints on our ability to simulate thousands of solutions over hundreds of generations, as is commonly done in GA studies. However, the evolutionary method was still extremely successful at automatically constructing and comparing thousands of computer-designed control codes, many of which closely matched our performance goals and rat pup behavior.

3.1 Control Designs

In this study, the physical design of the robot was held constant; only the motor responses to sensor contact were able to evolve from generation to generation. For each of the eight touch sensor groups on the robot (Fig. 3), a motor response could support up to three consecutive wheel commands (Fig. 4). A wheel command consisted of a left wheel *speed*, a right wheel *speed*, and a time variable to define *duration* of wheel operation. Each sensor's motor response therefore had nine degrees of freedom, bringing the total potential number of variables to 74 (eight sensor groups and an additional two variables to define default left and right wheel speeds when no sensors were currently activated).

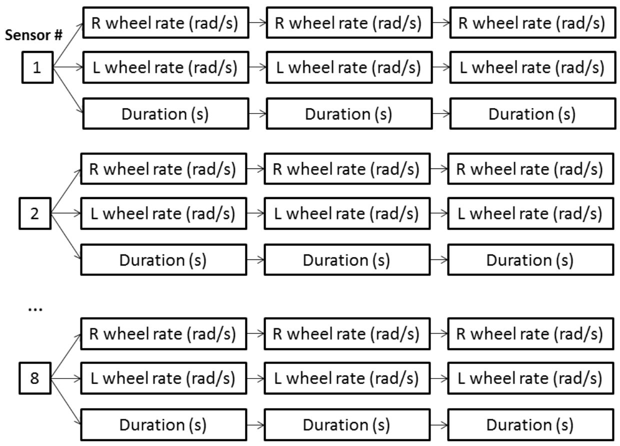

Fig. 4. Variables representing sensori-motor mapping on robotic pup.

It is important to note that a controller design was *not* required to have more than one response for each sensor group. If a controller design consisted of more than one response for a sensor group, the second and third responses were executed sequentially in order, for the amount of time defined in their duration variable (Fig. 4). It was up to the genetic algorithm to select the best combination of the 74 variables that would lead to the most realistic rat pup behavior. The controller genome was then simply a matrix of floating numbers precise to the 2nd decimal place.

3.2 Topological Metric

The underlying fitness metric matched was based on a topological analysis of where infant rat pups spend time in an arena. An average profile of 113 10-day old pups was reported in Schank et al., 2004 by comparing the percentage of total time spent next to walls, in corners, and in the center of the arena during rat pup testing [4]. Every 5 secs during a 10 minute experiment, a pup's position was classified as a *wall event*, *corner event*, or *center event*. A wall event was defined as a snout point next to a wall. A corner event was defined as a snout point within a square area delineated by a corner. A center event was a snout point in the inner arena. We found that rat pups, on average, spent ~60% of time near a corner, ~22% near a wall, and ~18% in the center (Fig. 5). Note that this metric of rat pup behavior does not describe micro behaviors that rat pups exhibited including corner snooping and punting.

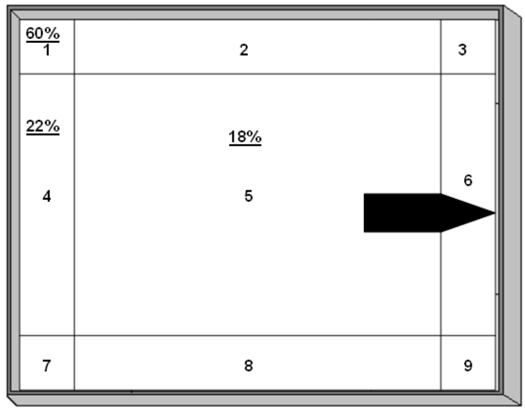

Fig. 5 Topological fitness metrics. Percentages indicate location distributions among all corners (~60%), walls (~22%), and center (~18%) areas averaged over 113 rat pups [4].

3.3 Fitness Function

A linear fitness function was defined as in Eqn. 2, where c is the percent distribution of corner samples (in range from 0-100), c_0 is the desired target percent distribution of corner samples (60% in our case), and the variables w, a, represent the walls and center areas, respectively. The goal then was to maximize this fitness function (c_0 =60, w_0 =22, a_0 =18). Note that the overall fitness function is in the range from 0-1. Even though we refer to the fitness function as linear, the function in (2) is piecewise linear

$$f_{avg} = 1 - \left[\left(\left| \frac{c - c_0}{c_0} \right| \right) + \left(\left| \frac{w - w_0}{w_0} \right| \right) + \left(\left| \frac{a - a_0}{a_0} \right| \right) \right] \Big/ 3 \tag{2}$$

3.4 Genetic Algorithm (GA)

The GA would initially generate 12 controller genomes at random for the first generation of simulated robots. The simulation stored the (x,y) locations of the nose of the robot every 5 seconds to maintain consistency with the original rat pup observations (Section 3.2). For each controller design, three simulation trials were run with different initial headings for a robot initially placed in the center of the arena, since initial orientation often resulted in a substantial difference in robot paths for both deterministic and random architectures. The fitness scores were computed for each simulation and averaged to obtain an average fitness value.

The genetic algorithm employed one of two selection methods to vary control design each generation. Both single parent and crossbreeding techniques were used.

Once the GA evaluated the average fitness of all the simulated robots in a given generation, the top three designs from the population of 12 were selected as a basis for the next generation in the single parent cases. Each of the chosen parent designs created four (slightly varied) versions of itself to produce the 12 children needed for the next generation. In the crossbreeding trials, the process was different. New genomes were created by choosing two parents from the previous generation to essentially blend motor response features of the two parents. Rather than averaging motor responses, the child design would instead pick several motor responses from each parent and the resulting design would be tried. The percentage of cases in which a particular design would be chosen as a parent was proportional to its fitness score.

Mutations could occur at the level of an individual response element ("point" mutations), or an entire sensor response ("bulk" mutations). The mutation rates were 25% for point mutations, and 15% for bulk mutations. Our chosen mutation rates ensured that the children genomes would vary significantly from the parents, but hopefully not so significantly that natural selection was neutralized. Point mutations could modify a single wheel speed by roughly ten percent, or wheel duration by up to 0.1 second. After the new generation of controller designs was mutated, the simulation and fitness function evaluation process started over and repeated for 20 generations.

4 RESULTS

The linear fitness function (2) frequently evolved a control scheme that invoked punting or flailing movement of the robot when a wall was contacted by a sensor. This caused the robot to move across the arena in unpredictable trajectories. In some cases, a no-sensor-contact default curved movement would lead the robot into another wall or corner across the arena, at which point the robot would again spin away from the wall and head out into the arena again (Fig. 6).

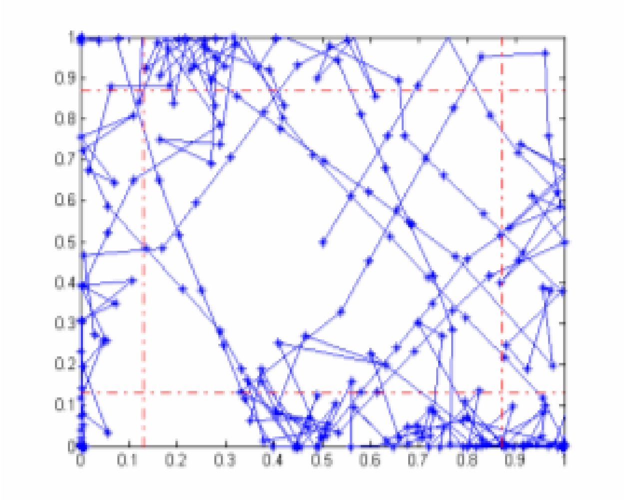

Fig. 6. Representative trajectory of robotic rat pup using a GA solution. This controller achieved an average corner behavior of ~65%, average wall behavior of ~21%, and average center behavior of ~14%.

The best (fully deterministic) linear fitness controller trajectories were quantitatively and visually similar to both infant rat pup trajectories (Schank et al., 2004 [4]) and the previously reported (May et al. 2006 [1]) random robopup trajectories in that the controller produced:

- trajectories that closely matched the macro-level topological corner, wall, and center distributions (by selection with the fitness functions);
- a wide variety of trajectories for a single controller, including trajectories that visited a varying number of corners (depending on a simulated robopup's initial heading);
- typical rat-pup micro-level sub-behaviors like corner snooping, wall-following, and punting
- many trajectories that traversed the center of the arena and crossed the length of the arena to the other side, and whose paths crossed over each other multiple times.

Only the first item above was explicitly designed-for in the GA methodology. The other three items were emergent.

5 CONCLUSIONS

The best GA solutions (in terms of the macro-level topological fitness metric and micro-level rat pup behaviors) incorporated a repeated thrashing at wall contact and a 'random-looking' projection of the robot into the center of the arena, which is interesting for two reasons. First, it supports the idea that a 'random-like' component is needed to match observed behavior, regardless of whether the random-like behavior was created by a truly random controller as in May et al., 2006 [1] or a complex deterministic controller as evolved in this study. As discussed in May et al. 2006 [1], random-like behavior need not result from truly random commands, but in biological organisms, it could be, for example, the result of developing motor systems. Secondly, our results illustrate the potential complexity of sensory-dependent controllers that may be required to produce realistic behavior. The controllers we evolved were complex, with each sensor contact followed by possibly three motor commands in succession. In effect, this work and our past work bounds the rat-pup controller problem at the controller extremes, from a simple random controller (May et al. 2006 [1]) to a complex deterministic controller (current study). Indeed, we have shown that both extremes can produce apparently realistic rat-like behavior for individuals. A promising future line of study would mix deterministic and stochastic controllers. Finally, more investigation needs to be conducted into group behavior. May et al. 2006 [1] showed random-robot behavior metrics intermediate between 7-10 day old pups in individuals and groups. However, a recent study by May et al. 2011 [6], which studied only group behavior, showed metrics that match random-robot group behavior and 7-day old group behavior. But, random-robot group behavior and 10-day old group behavior did not match. This may imply that near 10-days of age, behavior shifts depending on isolation vs. group contexts [3]. However, more investigation with both random and non-random models, and different age rat pups needs to be conducted before any conclusions can be drawn.

ACKNOWLEDGMENTS

This work was supported by the U.S. National Science Foundation under Grant No. 0218927 and by the U.S. National Institutes of Health under Grant 5R01MH065555.

REFERENCES

[1] C. J. May, J. C. Schank, S. S. Joshi, J. Tran, R. J. Taylor, and I. E. Scott, "Rat pups and random robots generate similar self-organized and intentional behavior," *Complexity*, vol. 12, pp. 53-66, 2006.

[2] J. Schank and J. Alberts, "The developmental emergence of coupled activity as cooperative aggregation in rat pups," *Proceedings of the Royal Society of London B*, vol. 267, pp. 2307-2315, 2000.

[3] J. Schank, "The development of locomotor kinematics in neonatal rats: An agent based modeling analysis in group and individual contexts," *Journal of Theoretical Biology*, vol. 254, pp. 826-842, 2008.

[4] J. Schank, C. J. May, J. Tran, and S. S. Joshi, "A biorobotic investigation of Norway rat pups (Rattus norvegicus) in an arena," *Adaptive Behavior*, vol. 12, pp. 161-173, 2004.

[5] R. L. Bish, S. S. Joshi, J. Schank, and J. Wexler, "Mathematical modeling and computer simulation of a robotic rat pup," *Mathematical and Computer Modeling*, vol. 45, pp. 981-1000, 2007.

[6] C. May, J. Schank, and S. Joshi, "Modeling the Influence of Morphology on the Movement Ecology of Groups of Infant Rats (Rattus novegicus)," *Adaptive Behavior*, vol. 19, pp. 280-291, 2011.

The Seventeenth International Symposium on Artificial Life and Robotics 2012 (AROB 17th '12),
B-Con Plaza, Beppu, Oita, Japan, January 19-21, 2012

Withstanding Asymmetric Situations in Distributed Dynamic Worlds

Peter S. Sapaty

Institute of Mathematical Machines and Systems
National Academy of Sciences
Glushkova Ave 42, 03187 Kiev, Ukraine
(Tel: +380-67-4199223; Fax: +380-44-5266457)
sapaty@immsp.kiev.ua, peter.sapaty@gmail.com

Abstract: A high-level ideology and technology will be revealed that can effectively convert any distributed system (manned, unmanned, or mixed) into a globally programmable spatial machine capable of operating without central resources. Compact mission scenarios in a special high-level language can start from any point, runtime covering & grasping the whole system or its parts needed, setting operational infrastructures, and orienting local and global behavior. The approach offered can be particularly useful for quick reaction on asymmetric situations and threats the world is facing, paving the way to massive use of cooperative robotics and gradual transition to unmanned systems for solving critical problems in unpredictable environments.

Keywords: distributed dynamic worlds, asymmetric situations and threats, Spatial Grasp Technology, Distributed Scenario Language, parallel networked interpretation, multi-robot systems.

1 INTRODUCTION

In our modern dynamic world we are meeting numerous irregular situations and threats where proper reaction could save lives and wealth and protect critical infrastructures. For example, no secret that world powerful armies with traditional system organizations are often losing to terrorists, insurgents or piracy with primitive gadgets but very flexible structures making them hard to detect and fight. And delayed reaction to earthquakes or tsunamis is a result of inadequacy of system organizations too.

A novel philosophy and supporting high-level networking technology will be described that can quickly react on irregular situations and threats and organize any available human and technical resources into operable systems providing global awareness, pursuing global goals and self-recovering from damages.

The approach allows us at runtime, on the fly, formulate top semantics of the needed reaction on asymmetric events in a special Distributed Scenario Language (DSL), shifting most of traditional organizational routines to automated up to fully automatic implementation, with effective engagement of unmanned systems.

The details of this technology, based on gestalt and holistic principles [1] rather than traditional multi-agent organizations [2, 3] will be revealed in this paper, with explanation of different DSL scenarios that can be effectively executed by self-organized robotic groups. These scenarios include collective navigation of distributed spaces, coastline patrols, outlining and impacting forest fire zones, and swarm-against-swarm solutions where highly organized robotic swarms can fight another, manned, groups related, say, to piracy intrusions.

The technology offered provides a unified solution to human-robot interaction and multi-robot behaviors just as a derivative of parallel and distributed interpretation of system scenarios in DSL.

2 TRADITIONAL SYSTEM ORGANIZATIONS AND THEIR PROBLEMS

2.1 From system structure to system function

The traditional approach to system design, development and management is when the system structure and system organization are primary, created in advance, and global function with overall behavior are secondary, as in Fig. 1.

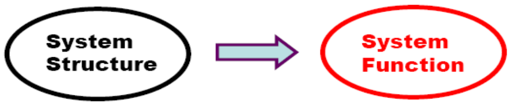

Fig. 1. Traditional approach to system design

Typical examples of the traditional approach are multi-agent organizations [2, 3], where global system behavior is the result of work and interaction of predetermined parts (agents). In this respect we can name the 4D/RCS Model Architecture [4], with its block diagram shown in Fig. 2.

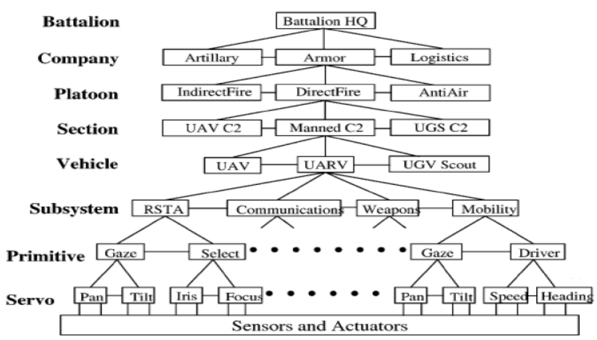

Fig. 2. 4D/RCS model architecture

4D/RCS prescribes a hierarchical control principle, where commands flow down the predefined hierarchy, and status feedback and sensory information flows up. Large amounts of communication may also occur between nodes at the same level, particularly within the same subtree of the command tree. Future Combat Systems (FCS) project [5] was ideologically and technologically based on this organizational (as well as artificial intelligence) hierarchical model.

2.2 The problems with classical organizations

The related systems, where we first formalize and build the system structure and organization and then try to get from these the global behavior needed, are usually static, and may often fail to adapt to highly dynamic and asymmetric situations. If the initial goals change, the whole system may have to be partially or even completely redesigned and reassembled. Adjusting the already existing system to new goals and functionality needed may result in a considerable loss of system's integrity and performance.

3 AN ALTERNATIVE: THE SPATIAL GRASP TECHNOLOGY (SGT)

3.1 SGT basic idea

Within the approach offered (also known as "overoperability" [6, 7] in contrast to the conventional *interoperability*) the global function and overall behavior are considered, as much as possible, to be primary. Whereas system structure and organization (command and control including) are secondary, with the latter as a derivative of the former, as in Fig. 3.

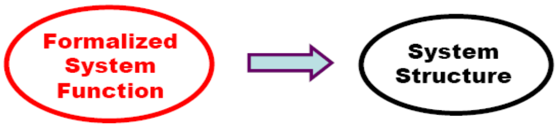

Fig. 3. SGT basic idea of system creation and organization

The advantages of this (actually, the other way round) approach include high potential flexibility of runtime system creation and organization, especially in quick responses to asymmetric events, and enhanced opportunities for automated up to fully automatic (unmanned) solutions.

3.2 Parallel spatial grasp of distributed worlds

SGT is based on a formalized wavelike seamless navigation, coverage, penetration, and grasping of distributed physical and virtual spaces, as shown in Fig. 4.

a) b)

Fig. 4. Incremental integral grasping of distributed worlds: a) virtual interpretation, b) symbolic physical analogy

This top mode of system vision has strong psychological and philosophical background, reflecting, for example, how humans (top commanders) mentally plan, comprehend, and control complex operations in distributed environments.

3.3 Distributed scenario interpretation

The approach in practice works as follows. A network of universal control modules U, embedded into key system points, collectively interprets system scenarios expressed in DSL, as shown in Fig. 5. System scenarios, based on the spatial grasp idea (representing any parallel and distributed algorithms, spatial cycles including), can start from any node, subsequently covering the system at runtime.

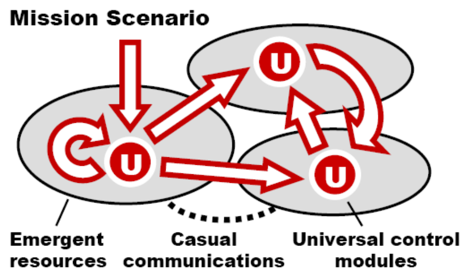

Fig. 5. Scenario execution in dynamic environments

DSL scenarios are very compact and can be created on the fly. Different scenarios can cooperate or compete in a networked space (depending on real control or distributed simulation mode) as overlapping fields of solutions. Self-spreading scenarios can also create runtime knowledge infrastructures distributed between system components (robots, sensors, humans). These infrastructures can effectively support distributed databases, command and control, situation awareness, and autonomous decisions, as well as any other computational or control models.

More details on the SGT, its core language DSL, and its distributed interpreter can be found elsewhere [8-16], with some key features (necessary for explanation of the chosen here applications) being briefed in the following sections.

4 DISTRIBUTED SCENARIO LANGUAGE, DSL

DSL differs radically from traditional programming languages. It allows us to directly move through, observe, and make any actions and decisions in fully distributed environments. DSL directly operates with:

- *Virtual World* (VW), finite and discrete, consisting of nodes and semantic links between them.
- *Physical World* (PW), infinite and continuous, where each point can be identified and accessed by physical coordinates.
- *Virtual-Physical World* (VPW), finite and discrete, similar to VW but associating virtual nodes with certain PW coordinates.

4.1 DSL basic features

Any sequential or parallel, centralized or distributed, stationary or mobile algorithm operating with information and/or physical matter can be written in DSL on a high level. Its top level recursive structure is shown in Fig. 6.

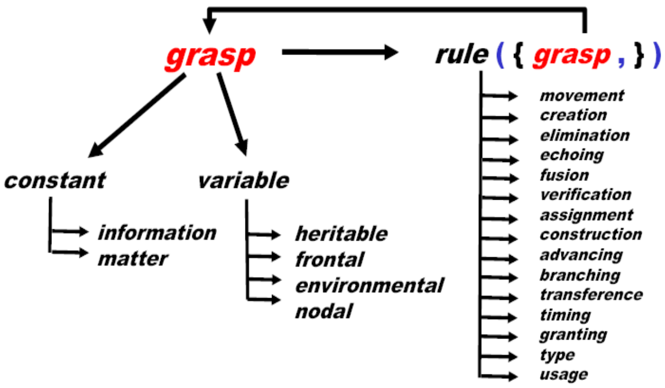

Fig. 6. DSL top level syntax

DSL main features may be summarized as follows:

- A DSL scenario develops as parallel transition between sets of progress points (*props*).
- Starting from a prop, an action may result in other props.
- Each prop has a resulting *value* and a resulting *state*.
- Different actions may evolve *independently or interdependently* from the same prop.
- Actions may also spatially *succeed each other*, with new ones applied in parallel from all props reached by the previous actions.
- Elementary operations may directly use *values of props obtained from other actions* whatever complex and remote.
- Any prop can associate with a *node* in VW or a *position* in PW, or *both* -- when dealing with VPW.
- Any number of props can simultaneously link with the same points of the worlds.
- Staying with the world points, it is possible to *directly access and impact* local world parameters, whether virtual or physical.

4.2. DSL rules

The basic construct, *rule*, of the language can represent any action or decision and can, for example, be as follows (this list is far from being complete):

- Elementary arithmetic, string or logic operation.
- Hop in a physical, virtual, or combined space.
- Hierarchical fusion and return of (remote) data.
- Distributed control, both sequential and parallel.
- A variety of special contexts for navigation in space, influencing operations and decisions.
- Type or sense of a value, or its chosen usage, guiding automatic interpretation.
- Creation or removal of nodes and links in distributed knowledge networks.

4.3 Spatial variables in DSL

Working in fully distributed physical or virtual environments, DSL has different types of variables, called *spatial*, effectively serving multiple cooperative processes:

- *Heritable variables* – these are starting in a prop and serving all subsequent props, which can share them in both read & write operations.
- *Frontal variables* – are an individual and exclusive prop's property (not shared with other props), being transferred between the consecutive props, and replicated if from a single prop a number of other props emerge.
- *Environmental variables* – are accessing different elements of physical and virtual words when navigating them, also a variety of parameters of the internal world of DSL interpreter.
- *Nodal variables* – allow us to attach an individual temporary property to VW and VPW nodes, accessed and shared by all props associated with these nodes.

These variables allow us to create spatial algorithms working *in between components* of distributed systems rather than *in* them, thus allowing for highly flexible, robust and capable of self-recovery solutions, even though different components may fail indiscriminately. Such algorithms can freely move in distributed processing environments (partially or as an *organized whole*), always preserving global integrity and overall control.

Traditional abbreviations of operations and delimiters can be used too, substituting some rules, as in following examples throughout this text, in order to shorten DSL programs (but always remaining within the general recursive syntactic structure shown in Fig. 6).

5 THE DSL INTERPRETER

5.1 Distributed interpreter organization

The DSL interpreter consists of specialized modules (which can work in parallel) handling and sharing specific language interpretation data structures [10, 13-16]. The network of the interpreters (the latter encircled as modules U in Fig. 7) can be mobile and open, changing the number of nodes and communication structure at runtime. Communicating copies of the interpreter can be concealed, if needed (say, for operation in hostile environments).

The heart of the distributed interpreter is its spatial *track system*. The dynamically crated track forests are used for supporting (or removing) spatial variables and echoing and merging different types of control states and remote data.

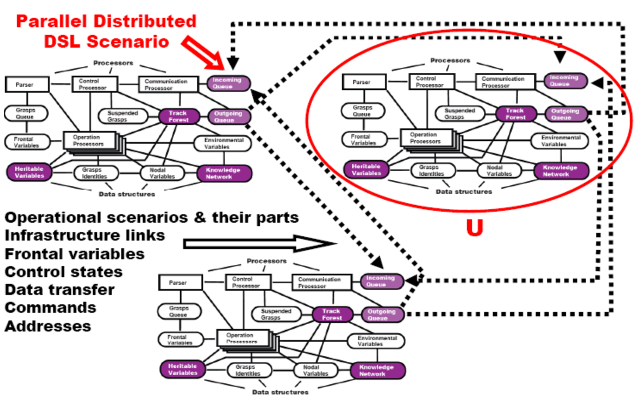

Fig. 7. Networked DSL interpreter organization

Being self-optimized in the echo processes, the track forests are dynamically covering the systems in which DSL scenarios evolve, keeping the overall parallel and distributed process integrity as well as local and global control. They also route further grasps to the positions in physical, virtual or combined spaces reached by the previous grasps, uniting them with the frontal variables left there by preceding grasps.

5.2 Integrating interpreter with usual robotic functionality

Installing DSL interpreters (as universal modules U, see Fig. 8) into mobile robots (ground, aerial, surface, underwater, space, etc.) allows us to organize effective group solutions (incl. any swarming) of complex problems in distributed physical spaces in a clear and concise way, effectively shifting traditional management routines to automatic levels. Human-robot interaction and gradual transition to fully unmanned systems are essentially assisted too.

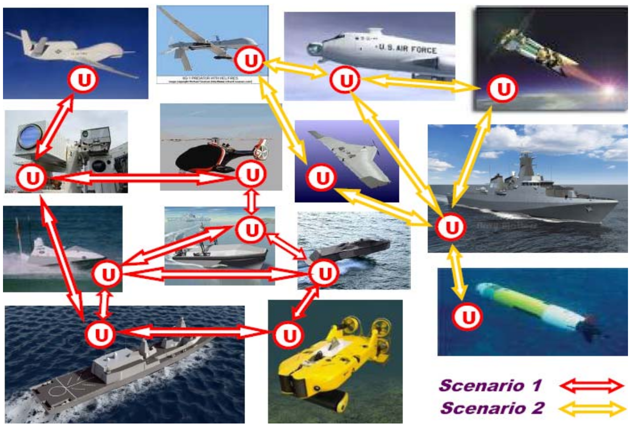

Fig. 8. Examples of cooperative robotic scenario skeletons

Any groups of manned-unmanned devices with DSL interpreters implanted into them, with any communication networks in between, can serve as universal spatial machines capable of doing any jobs together, under a unified control automatically emerging from high-level DSL scenarios.

6 EXAMPLE OF SEMANTIC, TASK LEVEL

By embedding DSL interpreters into robotic vehicles we can task them on a higher, *semantic* level, skipping numerous traditional details of management of them as a group -- fully delegating these to an automatic solution. An exemplary semantic level tasking may be as follows.

Go to physical locations of the disaster zone with coordinates: (x1, y1), (x2, y2), (x3, y3); evaluate radiation level at each location; return its maximum value with attached exact coordinates of the respected location to the headquarters; and launch from the latter a massive cleanup operation at this location.

The DSL program will strictly follow this scenario:

```
Location = maximum(move(x1_y1, x2_y2, x3_y3);
  attach(evaluate(radiation), WHERE));
move(Location[2]); massive_cleanup(radiation)
```

This (inherently parallel and fully distributed) scenario can be executed with any available number of mobile robots (practically from one to four), and the number of robots may change at runtime. Distributed DSL interpreter automatically creates the needed operational and command and control infrastructures of the robotic group and guarantees full task execution under any variations [8, 9].

7 PATROLLING COASTAL WATERS

This scenario may be suitable for both surface and varying depth underwater search of intrusions in the coastline zone, but for simplicity we will be assuming here only two dimensional space to be navigated.

At the beginning let us create a coastal waypoint map in the form of a semantic network, as in Fig. 9 (where `r` is chosen as an arbitrary name of links between the nodes-waypoints). The corresponding DSL solution is as follows.

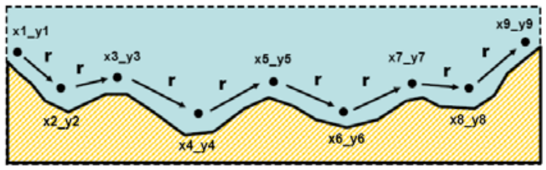

Fig. 9. Coastal waypoint map

```
create(
 #x1_y1; +r#x2_y2; +r#x3_y3; ... +r#x9_y9)
```

A single USV (or UUV) solution repeatedly navigating all coastal area by the map created is shown in Fig. 10 and DSL program that follows (searching the water space for alien objects by the `depth` available by vehicle's sensors).

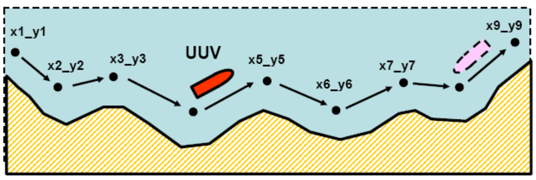

Fig. 10. Patrolling coastal waters with a single vehicle

```
move(hop(x1_y1)); R = +r;
repeat(repeat(move(hop(R));
         check_report(depth)); invert(R))
```

Two-vehicle parallel solution is shown in Fig. 11 and by the following program, with vehicles are moving according to the coastal map independently, assuming each having embedded automatic procedures for avoiding possible collisions with the other vehicle.

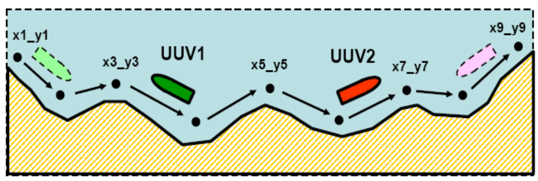

Fig.11. Patrolling coastal waters with two vehicles

```
(move(hop(x1_y1)); R = +r),
(move(hop(x9_y9)); R = -r);
repeat(repeat(move_avoid(hop(R));
          check_report(depth)); invert(R))
```

Another solution for the two-vehicle case may be when each vehicle turns back if discovers another patrol vehicle on its way, checking for this its vicinity by `depth2`).

```
(move (hop(x1_y1)); R = +r),
(move (hop(x9_y9)); R = -r);
repeat(repeat(none(depth2); move(hop(R));
           check_report(depth)); invert(R))
```

For the both latter cases, the whole coastline will always be searched in full if at least a single vehicle remains operational.

8 BATTLING FOREST FIRES

We will consider a solution where distributed physical space is randomly searched by simultaneous propagation of multiple reconnaissance units, which when discover irregularities (e.g. forest fires) move further and encircle respected zones, collect their perimeter coordinates, transfer them to the headquarters (HQ), and ultimately initiate massive impact on the zones under fire.

The zones with fires and initial positions of reconnaissance units are shown in Fig. 12*a*, and intermediary positions of robotic unites moving randomly-oriented (repeatedly shifting their positions within certain coordinate sector) are in Fig. 12*b*.

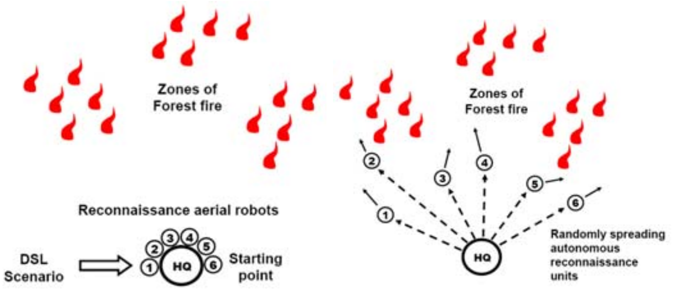

Fig.12. Initial scenario injection (a) and robots movement (b)

After detecting fire locations, the reconnaissance units that reached them begin moving around the fire zones, having initially randomly chosen the encirclement orientation (i.e. clockwise or anticlockwise). In each step they accumulate coordinates of the periphery of fire zones, and upon termination of the encirclement send the completed zone coordinates to the headquarters (HQ). Getting the latter, the HQ is launching a massive direct impact on the zones outlined, as shown in Fig. 13, which may be manned, unmanned, or mixed. The full DSL scenario for this task may be as follows.

```
move(HQ); create_nodes(1,2,3,4,5,6);
repeat(shift(random(limits));
 if(check(fire),
    (Zone = WHERE; Direction =
      random(clockwise, anticlockwise);
      repeat(
       move_around(fire, Direction, depth);
       append(Zone, WHERE);
       if(distance(WHERE,Zone[1])<threshold,
          (hop(HQ); impact(Zone); done)))))
```

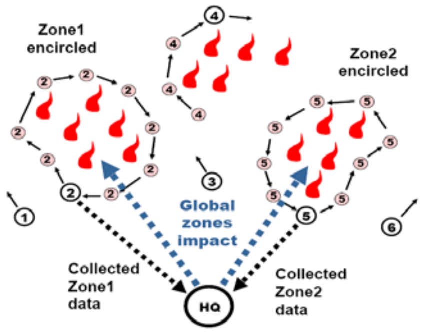

Fig.13. Encircling fire zones followed by global impact

Other interpretations of this scenario may be dealing with radiation zones, environment pollution, zones of terrorist activities, zones of fish concentration, etc., with aerial, ground, surface or underwater robots engaged.

9 SWARM AGAINST SWARM SCENARIO

As a more complex scenario example in DSL we will consider here the case where an unmanned swarm is opposing other (possibly, manned) group/swarm, as in Fig. 14. This may relate, for example, to fighting piracy in maritime environment where aerial, surface and underwater unmanned vehicles, working cooperatively under a unified control, can be used for withstanding this negative activity taking place worldwide.

Fig. 14. Fighting group targets with unmanned swarms

Main features of this scenario are as follows:

- Initial launch of the swarmed chasers (shown in red in Fig. 14, with DSL interpreters embedded, which can communicate with each other) into the expected piracy area.
- Discovering targets and forming their priority list by their positions in physical space where maximum priority is assigned to topologically central targets as potential control units of the intruders.
- Other targets are sorted out by their distance from the topological center of their group, estimated previously.

- Most peripheral targets (those in maximum distance from the topological center, as potentially having more chances to escape, are being of higher priority too.
- Assigning available chasers to targets, classifying them as engaged, with chasing and neutralizing targets, and subsequently returning them into status free after performing mission.
- The vacant chasers are again engaged in the targets selection & impact.

This entire advanced swarm-against-swarm scenario may be expressed in DSL in a very compact form, as follows.

```
frontal(Next);
sequence(
 start_launch(all_free_chasers,targets_area),
 repeat(
  hop(any_free_chaser);
  All_targets = merge(hop(all_free_chasers);
  coordinates(targets_seen));
  nonempty(All_targets);
  Center = average(All_targets);
  List = min_max_sort(split(All_targets);
      attach(distance(VALUE,Center),VALUE);
  List = append(withdraw(List, last), List);
  loop(nonempty(List); Next =
   element(withdraw(List, first), second);
   Chaser =
    element(min(hop(all_free_chasers);
      attach(distance(WHERE,Next),ADDRESS),
       second);
   release(hop(Chaser); STATUS = engaged;
    pursue_investigate_neutralize(Next);
    STATUS = free))));
```

It is worth noting that all the chaser swarm management expressed or automatically induced by the above program is done exclusively within the swarm itself, without any external intervention, which dramatically simplifies external control of this multi-robot operation.

10 CONCLUSION

A brief summary of advantages of the approach offered may be as follows.

- The Spatial Grasp ideology and technology can dramatically simplify application programming in distributed dynamic systems.
- Setting multi-robot solutions in DSL may often be comparable in complexity to routine data processing in traditional languages.
- External management of multi-robot systems may not depend on the number of components in them due to their internal self-organization and automatic command and control inside robotic groups.
- Formalization of mission scenarios in DSL can make human-robot interaction and transition to fully unmanned systems natural and straightforward.
- Spatial swarm intelligence in DSL can successfully compete with human collective intelligence, outperforming the latter in time critical situations.

In addition to the features listed above, we can state that in comparison with other systems, DSL interpreter represents an *embedded universal intelligence* common to all applications. Any scenario can be executed by a network of such intelligences. In other approaches, most of the system intelligence has to be programmed *explicitly for each application*, thus enormously complicating mission planning and management.

All communications among unmanned units, also between manned and unmanned ones, are on a high, semantic level in DSL. They are *very compact* (often hundreds times shorter than in other languages) which may be essential for maritime (especially underwater) operations with casual and limited data channels.

REFERENCES

[1] Wertheimer M (1924), Gestalt theory, Erlangen, Berlin

[2] Minsky M (1988), The society of mind, Simon and Schuster, New York

[3] www.wikipedia.org/wiki/Multi-agent_system

[4] 4D/RCS: A reference model architecture for unmanned vehicle system, version 2.0 (2002), Report NIST

[5] Feliciano CN (2009), The army's future combat system program (Defense, Security and Strategy Series), Nova Science Pub Inc.

[6] Sapaty PS (2002), Over-operability in distributed simulation and control, The MSIAC's M&S Journal Online, Winter Issue, Volume 4, No. 2, Alexandria, VA, USA

[7] Sapaty P (2009), The over-operability organization of distributed dynamic systems for asymmetric operations, Proc. IMA Conference on Mathematics in Defence, Farnborough, UK

[8] Sapaty P (2011), Spatial grasp technology for high-level management of distributed unmanned systems, Unmanned Systems Asia 2011, Singapore

[9] Sapaty PS (2011), Seeing and managing distributed spaces using maritime unmanned systems, GLOBAL OPV and Maritime Unmanned Systems Summit, Dedeman Hotel, Istanbul, Turkey

[10] Sapaty P (2011), Meeting the world challenges with advanced system organizations, Informatics in Control Automation and Robotics, Lecture Notes in Electrical Engineering, Vol. 85, 1st Edition, Springer

[11] Sapaty P, Kuhnert D, Sugisaka M, Finkelstein R (2009), Developing high-level management facilities for distributed unmanned systems, Proc. Fourteenth International Symposium on Artificial Life and Robotics (AROB 14th'09), B-Con Plaza, Beppu, Oita, Japan

[12] Sapaty P, Morozov A, Finkelstein R, Sugisaka M, Lambert D (2008), A new concept of flexible organization for distributed robotized systems, Artificial Life and Robotics, Volume 12, Numbers 1-2, ISSN: 1433-5298 (Print) 1614-7456 (Online), Springer Japan

[13] Sapaty P (2008), Distributed technology for global dominance, Proc. of SPIE, Volume 6981, Defense Transformation and Net-Centric Systems 2008, 69810T

[14] Sapaty P (2005), Ruling distributed dynamic worlds, John Wiley & Sons, New York.

[15] Sapaty P (1999), Mobile processing in distributed and open environments, John Wiley & Sons, New York

[16] P. Sapaty (1993), A distributed processing system, European Patent No. 0389655, Publ. 10.11.93, European Patent Office.

Human Interface of Robots or Agents via Facial and Word Expression

Kaoru Sumi[1]

[1]Future University Hakodate, Hakodate, Hokkaido 041-8655, Japan
kaoru.sumi@acm.org

Abstract: To design an intelligent interactive system, it is necessary to consider how humans feel about the system and establish a good relationship with them. In human robot interaction or human agent interaction, to establish a fifty-fifty relationship between a technical artifact (such as a robot or an agent system) and a human, the power of conviction or influence of the artifact over the human is very important. To develop an intelligent system using a robot or an agent such as a system that proactively interacts with a user and even changes the user's intention according to the user's circumstances, our project investigated reactions with the user under several situations, considering human robot interaction and human agent interaction using facial and word expressions. Accordingly, we established some rules for making the agent's reaction favorable to the user on the basis of facial expressions and words, and gained some insights into the differences between human robot interaction and human agent interaction. In this talk, I introduce the possibility of human persuasion by a robot or an agent using facial expressions and emotion words, based on the experimental results.

Keywords: Facial expression, word expression, persuasive technology

1 INTRODUCTION

Nowadays, there are many systems that use virtual agents to mediate between a user and the system. Character agents make the user feel the presence of an assistant to access the system and also give him or her feeling of affinity with the system. According to Media Equation [1], people treat computers, television, and new media as real people and places, thereby making the users uncomfortable if an agent behaves in a disagreeable manner. In the field of persuasive technology research [2] it is said that if a user recognizes the presence of something in a computer, he or she will respond to it according to the normal social rules. However, there are still many things that we do not know about how an agent's response affects a user during their interaction.

In the development of intelligent systems, it is important to consider how best a feeling of affinity with the system and show the presence of the system that has human-like intelligent functions such as recommendation or persuasion. Therefore, evaluating the interpersonal impressions conveyed by agents is very important.

Our research group performed an experiment to evaluate how the facial expressions of an agent and the words used by the agent affected users during agent-user interaction [3]. In this paper, I introduce our evaluation of the user's impression of agents in emotion-arousing scenarios set up to see how users react to various patterns of agent reactions. In particular, after setting up situations that evoke feelings of "joy", "anger", "sadness", "disgust", "fright", and "surprise" and matching up the agent's reaction with the combination of facial and verbal expressions, we asked users about their impressions of the agent.

There have been some studies using character agents as the interface of a system. However, it is not known how and there has been no evaluation of how the agents affect the users. Interactive patterns of the combination of the agents' facial expressions and words have not yet been evaluated.

The situation in which a message and its contradiction are both presented simultaneously is called a double-bind situation [4]. There has been research on information processing by the memory and the feelings perceived by humans in double bind situation. However, it is not clear what impression the speaker conveying the messages of double-bind situation gives to the receiver.

2 EXPERIMENT ON IMPRESSIONS OF REPLIES FROM THE AGENT

We chose six kinds of feelings. From the total of 216 combinations, covering multiple feelings that the user felt (6 patterns) and the facial expressions for the agent's interaction with the user (6 patterns) and word expressions used by the agent (6 patterns), we selected 96 patterns in this experiment. These covered 16 patterns in each feeling: empathetic words and consistent facial expressions, nonempathetic words and consistent facial expressions, word consistent and facial inconsistent, and word inconsistent and facial consistent. This is because the conditions of nonempathetic and both inconsistent word and facial expressions are nonsensical in normal communication. This is the condition where the word and facial expressions are inconsistent, which is the condition for double bind communication, but it can be considered as either word or facial being empathetic to the user. The case of nonempathetic condition and inconsistent word and facial expressions can be considered as pathological. A total of 1236 people, 568 male and 668 female (AV. age 38.0, SD age 11.5), were assigned 96 contents. More than ten users were assigned to each content.

- Experimental Materials

"Joy", "anger", "sadness", "disgust", "fright", and "surprise" scenarios were selected as scenarios with a high concordance rate in a preliminary experiment as emotion-arousing scenarios for each emotion. These scenarios were described by a male reader reading in a neutral manner.

A female character agent was used to react to the user's emotion. Faces representing "joy", "anger", "sadness", "disgust", "fright", and "surprise" were selected as faces with a high concordance rate in a preliminary experiment as emotional faces.

The agent dialog was read by a female reader with emotions conveyed. At first, as empathetic dialogue, "I think so, too" or "I don't think so" as nonempathetic dialog were spoken. Then, emotionally, the dialogue of "that's nice", "that's aggravating", "that's sad", "that's disgusting", "that's scary", and "that's a big surprise" were spoken.

In this experiment, we use nine factors: three factors for interpersonal impression evaluation [5] were "affable-inaffable","serious-unserious","conversable-inconversable" and original six factors.

" reliable-unreliable", "gentle-bitter", "egotistic-humble", "empathetic-unempathetic", "authoritative-unauthoritative", and "offensive-inoffensive".

We prepared 96 contents to cover the combination of emotions that a user feels, the facial expressions of the agent, and the word expressions used by the agent. These contents were developed using the Bot3D Engine [6], which displays an agent on web pages. The Bot3D Engine is an embedded engine for developing software using the Web3D plug-in and ActiveX component. Users can use the 3D agent program only to access web pages that have the program embedded.

- Procedure

The examination was conducted in the form of a questionnaire on the Web. The content was displayed on user's own PC monitor after the user accessed the target URL.

The users were asked about their sex, age, marital status, occupation, intended purpose of using the PC, and for how long they had been using a PC.

Next, the following teaching sentences were presented.

"This examination aims to discover what emotions people feel in various cases. There is no correct answer, so please say exactly what you think and feel. This examination is not a test of your personal abilities. The answers will be analyzed statistically and private information will not be released. First, please consider the given scenario and then select from the alternatives the emotions that you feel. Next, an animated character will respond to your selected answer. Please answer the question by giving your impression of the character. Your answer should relate only to this scenario. Please do not include feeling from previous scenarios, but think scenario by scenario."

Each user was presented with one of 96 contents. One of the emotion-arousing scenarios was read by a male voice. It then asked: "What kind of emotion do you feel?" and prompted the user to select from the alternatives "joy", "anger", "sadness", "disgust", "fright", and "surprise". On the other hand, the female agent on the screen responded with facial and word expressions.

Users were asked: "How do you feel about this person? Please answer using the degrees listed in the questionnaire." Five conditional moods in nine answers, "conversable-inconversable", "reliable-unreliable", "gentle-bitter", "egotistic-humble", "empathetic-unempathetic", "authoritative-unauthoritative", "offensive-inoffensive", "serious-unserious", "affable-inaffable" were given and the user selected a suitable answer. The order of the terms was kept constant throughout the questions.

3 Result and Discussion

We conducted the experiment on how the user felt about the agent's reaction by setting up an emotion-arousing scenario for the user. Four factors were extracted by using factor analysis. Eight clusters were indicated by cluster analysis by using four factors as the dependent variable. Favorable, intermediate, and unfavorable impressions fell in category of higher-level clusters among these eight clusters. Therefore, we focused on the relationship between agent reaction and the higher clusters.

The synchronization of the agent's words with the user's emotion has a major impact on the impression of the agent as perceived by the user. However, the synchronization of facial expressions of the agent with the user's emotion does not have a major impact on the creation of an impression.

First, we predicted that words and facial expressions reflected on the emotions aroused by the scenario would lead to the most favorable impression, so we set these data as the control group. In fact, there were more favorable impressions than those obtained for the control group. For example, the words and facial expressions were "joy" when the user's emotion was "joy" for the control group. It is very interesting that when the user's emotion was "joy", the agent's words for "joy" with facial expressions of "surprise", "sadness", or "fright" were most favorable. On the other hand, when the user's emotion was "fright", the agent's words for "fright" with facial expressions of "disgust" or "sadness" were the most favorable.

These facial expressions were recognized as the emotion conveyed by the words and were more empathetic and somewhat meaningful emotions. For example, when the user's emotion was "joy", the agent's words of "joy" with facial expressions of "surprise" or "fright" might have been recognized as the agent being exaggeratedly surprised at the "joy" scenario. When the user's emotion was "joy", the agent's words of "joy" with facial expressions of "sadness" might have been recognized as the agent being highly pleased from the heart at the "joy" scenario. When the user's emotion was "fright", the agent's words of "fright" with facial expressions of "sadness" might have been recognized as the agent grieving deeply at the user's "fright" scenario. When the user's emotion was "fright", the agent's words of "fright" with facial expressions of "disgust" might have been recognized as the agent feeling deep hate at the user's "fright" scenario.

Through these observations, we concluded that there is a rule for facial expressions: in a certain scenario, synchronizing foreseen emotion of the user caused by the situation will make a favorable impression. For example, when the user has the emotion of "joy", he/she wants someone to be surprised or highly pleased. Then, showing surprised or highly pleased face expression make the user feels favorable impression. When the user has the emotion of "fright", he/she wants someone to grieve deeply or disgust. Then, showing grieved or disgust face expression make the user feels favorable impression. Users want the agent to ooze synchronized their foreseen emotion by hearing the news instead of simply showing synchronized reaction according to emotion at present time.

The ability to do this is known as the emotional intelligence quotient (EQ) [7], which is a measure of the ability to understand the feelings of the partner and maintain human relations well.

This facial expression rule is a kind of EQ rules as we can often see service-minded persons show their sympathy with very sad face when they on hearing bad news. In this case, the emotional situation was "disgust", their word is "disgust" with facial expressions of "sad". These patterns are consistent with the cluster of favorable impressions in the result of the experiment. These persons favorably impress, as we often see them employed as salesmen having some technical know-how in order to make themselves look good. We often see this type of person in our country and they are accepted as favorable. However, this facial expression might be considered as a specific feature of Japanese culture. It needs more examination, taking into account diverse nationalities.

This facial expression rule is a technique of foreseeing the other's emotion and the agent can behave proactively by reading the other's feelings.

5 CONSLUSION

As a purpose of developing intelligent system using virtual agent which interacts with a user proactively according to the user's circumstances, we evaluated the user's impression of agents by setting up an emotion-arousing scenario and observed how the users reacted to various patterns of agent reactions. The results of the experiment reveal the rule for creating an agent which reacts proactively using facial expressions.

For the next step of this research, our research group have evaluated human robot interaction using facial expression.

REFERENCES

[1] Reeves, Byron and Clifford Nass The Media Equation: How People Treat Computers, Television, and New Media Like Real People and Places, Cambridge University Press, 1996.

[2] B.J.Fogg: Persuasive Technology –Using Computers to Change What We Think and Do-, Elsevier, 2003.

[3] Kaoru Sumi and Mizue Nagata: Evaluating a Virtual Agent as Persuasive Technology, Psychology of Persuasion, Janos Csapó and Andor Magyar eds., Nova Science Publishers (2010).

[4] Bateson, G., Jackson, D. D., Jay Haley and Weakland, J., "Toward a Theory of Schizophrenia", Behavioral Science, vol.1, 1956, 251-264, 1956

[5] Ikuo Daibo: Sansya kan communication ni okeru taijininsyo to genngo katudousei, jikkenn shinri gaku kenkyu,18, 21-34, 1978 (in Japanese)

[6] Bot3D: http://www.atom.co.jp/bot/

[7] Daniel Goleman: Emotional Intelligence, Bantam Dell Pub Group, 1995.

MagicTiles. ALife for Real and Virtual RoboMusic

Luigi Pagliarini[1,2] Henrik Hautop Lund[1]

[1] Centre for Playware, Technical University of Denmark, 2800 Kgs. Lyngby, Denmark
[2] Academy of Fine Arts of Macerata, Via Berardi, 6, 62100 Macerata, Italy

luigi@artificialia.com hhl@playware.dtu.dk
www.playware.dk

Abstract

In this paper, we define and trace the contours of a new cross-modal and cross-media approach to robotic systems. In particular, our system is based on the use of electronic tiles and oriented to the use of ALife based interactive robotic modules that can be either virtual or real. This approach, which relies on interactive parallel and distributed processing algorithmics, can be thought and used on many different domains, though in the specific experience presented here, it has been applied to music composition and remix. In details, we describe the initial MagicTiles product prototype and show, as an example, a musical application with which any user can create and perform RoboMusic. We show how the combination of the Modular Interactive Tiles and the MagicTiles tools might lead to a broader vision of robotic systems with a fluid flow between the physical and virtual. Fluidity between the physical and virtual, end-user authoring, and ALife control is conceived to open up technology to ordinary users as a tool for creativity. Finally, in this paper, we attempt to explore the theoretical characteristics of such an approach and exploit the possible playware application fields.

Introduction

In this paper we present the "MagicTiles" application, an ALife software based on and derived from our previous work on the Modular Interactive Tiles [1] and RoboMusic [2]. This attempt to move a hardware based paradigm to a software based one is due to a couple of main beliefs.

The first of these is that the social media are changing and are showing a strong demand for a mobile electronics representation (i.e. applications) of any given device and/or activity. Indeed it seems to be expected that any future playware [3] and/or robotics tool will require - for a proper and common use within a large community of people - to get somehow connected to a mobile phone, tablet (or similar) control system or, alternatively, have a given instance of it, as for example a simulated version of the tool/activity itself. This is because the new virtual media may allow users an easy access to social interaction, for instance mediated by the physical media.

Hence, the physical media is enhanced by the social, virtual media. On the other hand, the social, virtual media is also used to promote the users' interest in the physical media. Indeed, today users' access to the virtual is easy and cheap, and it allows the users to experience their own interest for the specific real technology (e.g. the physical media). Thereby, there is a bidirectional use of the social, virtual media (on smart phones, tablets, etc.) and the physical media, which can be seen as complementary, and to be integrating and promoting each other.

The second belief is that by realizing a software-based representation of the Modular Interactive Tiles, we can easily explore many different new algorithmic solutions and easily access a larger number of users. Therefore, it gives the chance to test both efficiency and popularity of our "games" and the concept of Modular Interactive Tiles itself.

As a starting point, we chose music as the application domain, building upon the concept of RoboMusic.

RoboMusic

The RoboMusic concept [2] was developed to allow any user to interact with a professional music performance through the interaction with physical, intelligent objects. For instance, in the first RoboMusic concert, the interaction happened with modular interactive tiles, rolling pins and cylinders [2] (see Fig. 1), and the Center for Playware later made RoboMusic versions using cubes [4, 5] and tiles. When interacting with these physical, intelligent objects, the user activates, changes or de-activates a sound (Fig. 2).

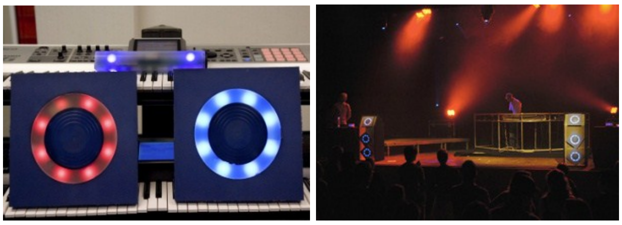

Figure 1. Left: Two Tiles and a RollingPin used as robotic instruments. Right: The RoboMusic live concert set-up, with Funkstar De Luxe and his control station in the center, and the robotic instruments on the left and right side of the stage.

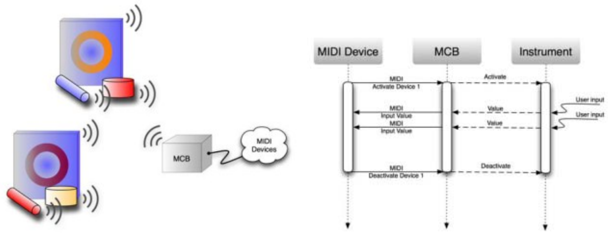

Figure 2. For the first RoboMusic concert, we used an interaction pattern in which physical objects as tiles, rolling pins, and cylinders ("Instruments") are communicating to a MIDI Control Box ("MCB"), which is connected to a PC running Cubase or Ableton Live ("MIDI Device"). Note that the original RoboMusic concept allows also communication in the direction from PC ("MIDI Device") to tiles ("Instruments") through the MIDI Control Box ("MCB").

The sound can be more or less complex. In order to produce an appealing sound, it is of crucial importance to create a RoboMusic soundscape which fits the RoboMusic concept of allowing the user to interact with the music, e.g. as in the behavior-based approach, where the programmer is designing the default music behavior, and the user provokes smaller behavioral deviations by the physical interaction [2].

Indeed, as a kind of *user-guided behavior-based system*, in RoboMusic, the design challenge is to create primitive 'robotic' behaviours and to coordinate these primitive behaviours in order for the music piece to emerge as the coordination of primitive behaviours. Thereby, a music composition emerges from the way the composer, musicians or audience interact with the 'robotic' instruments that provide the primitive behaviours.

Each 'robotic' instrument is used to trigger a particular primitive behaviour dependent on the interaction with the instrument(s). In RoboMusic, the primitive behaviours can be anything from a volume or a cut-off to a small sequence of tones. The music composer designs the way in which the primitive behaviours that are triggered should interact with each other.

Hence, as is the case when designing behaviour-based robots such as mobile robots (e.g. [6, 7]), the robot designer (in this case the music composer) designs the primitive behaviours and the coordination scheme. And, as is the case with *user-guided behaviour based robotics* [8, 9], if non-expert users (e.g. live concert audience) are supposed to manipulate and become creative with the systems, it is crucial that the designer (music composer) creates primitives on a fairly high abstraction level that allows the non-expert user to understand and have positive feedback from the human-robot interaction within a very short time frame.

The RoboMusic concept was applied on cubic I-BLOCKS [4, 5] which each represents an instrument or group of instruments. The individual I-BLOCKS orientation - which side is facing down - determines the variation of that specific instrument. The I-BLOCK LEDs change colour depending on their orientation, in order to make it possible for the user to remember and activate specific variations.

The musical setup can be seen in Figure 3. Note the black XBEE-enabled I-BLOCK, which communicates wirelessly with the MIDI Box. When instrument blocks are connected to this, music starts playing depending on the actual I-BLOCK's colour and orientation. The music is loop-based, meaning that when active, each variation of each instrument is playing for a certain time and then repeating itself over and over until it is finally deactivated when the user removes the current instrument I-BLOCK from the structure or shifts its orientation.

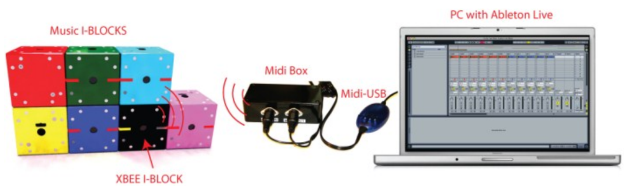

Figure 3. Music setup with I-BLOCKS, MIDI-box and PC.

The pieces of music that was made for the cubic I-BLOCKS were all constructed using these rules: There are five or six predefined instruments or groups of instruments, varying in type according to genre, and within each piece of music there are up to six variations per instrument type, and there can be an unspecified number of different instruments. Later, we also applied this approach to other intelligent building blocks such as the modular interactive tiles [1], where the color of the tiles LEDs would indicate the instrument, and the number of LEDs indicates the variation of the instrument type.

MagicTiles Interface

The MagicTiles application is a new, funny, musical app, which as RoboMusic can be used by users of different musical competencies - from precipitants to musician to expert composers - to both remix songs or experiment with new tunes. The initial MagicTiles app runs on iPads and iPhones. The MagicTiles application is made of a small number (i.e. more than 3 less than 10) of virtual music tiles. Generally, each single tile embodies a single instrument (although it can be programmed and used in many different ways), and each instrument-tile is capable of expressing seven different musical solution (i.e. loops) or variation of the same one. Every instrument of a MagicTiles song is wrapped inside a single tile and, therefore, we can have a tile for vocals, one for the rhythm guitar, one for the bass, one for the piano, etc.

Figure 4. MagicTiles for iPad.

At the start, the user is presented with all the tile-instruments of a given song inside the tiles board with the tile-instruments being disconnected from each other (see Fig. 4). Since a tile is disconnected from other tiles, it is not active and will not play.

Once the user drags and attaches a tile to another (see Fig. 5 left) the two tiles get synchronized and are able to play together.

To actually start the music, the user has to press the play/stop icon, positioned at the bottom-right side of the screen (see Fig. 4). At this point, the music will keep playing and the remaining music tiles can be connected to the former two enriching the music scenario of the song running. In the same way, by dragging the tiles around and rearranging their geometry, the user changes the music sequence and flow.

Figure 5. Left: Connecting two tiles. Right: 2-sides connection example.

Every tile has 7 music loops, one for each side (north side, east side, south side and west side) plus 3 extra music loops which will play when a tile is connected on, respectively, two, three or four sides. In this way, as in Fig. 5 left, the Drum tile will play the East Side loop and the Guitar tile will play the West Side loop, and as in Fig. 5 right, the Drum tile will play the *2 Sides* loop, the Guitar tile will play the West Side loop and the Choir tile will play the North Side loop.

Likewise, as in Fig. 6 the Drum tile will play *3 Sides* loop, the Choir tile the North Side loop, the Guitar tile will play the West Side loop, and the Bass tile the East one.

Figure 6. A *3 Sides* connection example.

Growing the number of instruments/tiles impressively increase the number of possible combinations and out of these simple rules, one obtains an extraordinary number of musical possibilities (e.g. by using 6 tiles, and just counting the 1-side connections, we reach 4^(6-1)=1024 music variations of the same song).

MagicTiles' usability has already been pilot-tested with 5 years old children and can be considered simple to use, and to be an effective and funny instrument to play with. Further, this first version of the MagicTiles app has two more exciting features, which enhance the user interactivity and possibility: the *Loop Recorder* and the *SkipBar Tool*.

The Loop Recorder

The previous section described the so-called *Pre-recorded* loops tiles, trying to understand their meaning and logic. Differently from that, MagicTiles also features two other kinds of music tiles, the *Pre-recorded* loops tiles and the *User-recording* loops tiles (see Fig. 7).

The *User-recording* tiles differ from *Pre-recorded* tiles for two specific characteristics:

1. The music loops are not given and have to be recorded by the user (e.g. at run-time);
2. The number of different loops a *User-recording* tile can express are only four (i.e. north, east, south and west side loops).

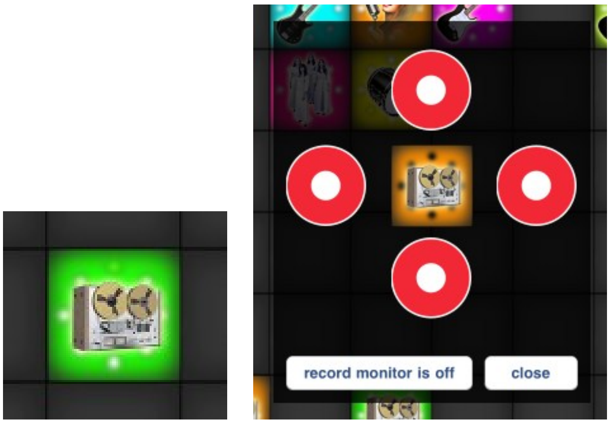

Figure 7 Left: The *User-recording* tile icon. Right: The loop recorder menu.

When the user double touches one of the User-recording tiles (see Fig. 7 left), the MagicTiles app shows the loop recorder menu (see Fig. 7 right). The loop recorder menu allows the user to record a loop for each side of the user-recording tile through the iPhone or iPad built-in microphone. The application shapes the recordings to exactly fit to the length of all the other pre-recorded tile loops of the actually running song. Such process gives the user the great advantage of always being on the beat. As a consequence, the ability of recording a proper music sequence/loop will simply rely on the user musicality, itself. Technically speaking, such a feature works at the lowest possible latency, because it relies on the powerful audio framework that the native iOS devices comes with.

Another tool for user interactivity is the SkipBar Tool that allows the user to skip the current (playing) bar and to repeat it or use it like for real sampler. The bottom of Fig. 4 shows the SkipBar with 8 buttons/areas (i.e. one for each single bar). When pressing one of them, the user let the music flow to jump or repeat one single bar music.

MagicTiles Algorithms

The Sound Patterns

Every single tile can activate seven different music loops. Each sound is activated accordingly to the following rules.

If only one side of the tile is connected, the tile itself reproduces one out of four available loops, which is:

1. One for the North side
2. One for the East side
3. One for the South side
4. One for the West side.

Besides the above sounds, there are three extra music loops, which are activated when:

5. Two sides of the given tile are connected simultaneously;
6. Three sides of the given tile are connected simultaneously;
7. Four sides of the given tile are connected simultaneously.

(See Fig. 5 and Fig. 6 for visual examples).

Sound Files Specifications

To be used with the MagicTiles app, sound files must be:

1. of an uncompressed sound format (e.g. AIF or .WAV);
2. same length (at the moment, 8 bars for every musical loop, independently from the song metronome).

Further, the sound files should preferably only be *monophonic files*, since stereo files may demand too much memory.

Loops may be denominated in any way. For example, a good practice would be to name loops with a specific *Song/AuthorName_* plus *InstrumentName_* plus the *SideNames*, to keep track of the musical meanings, as shown here:

The Drums Tile of the Bob Marley Remix files could be denominated:

1. MARLEY_DRUM_N
2. MARLEY_DRUM_E
3. MARLEY_DRUM_S
4. MARLEY_DRUM_W
5. MARLEY_DRUM_2
6. MARLEY_DRUM_3
7. MARLEY_DRUM_4

Meaning that the first 4 loops are denominated accordingly to the activated side, and the remaining 3 loops are the extra loops for "2 sides connected", "3 sides connected", "4 sides connected".

Synchronization of audio files

With MagicTiles, we developed a novel way for getting rid of a metronome. First of all, we made the music loops have a fixed length (i.e. a parameter that you can tune inside your audio editor, like Ableton Live, Logic, Cubase, etc.). Every single loop is stored inside a *C* programming language structure variable defined with the keyword "*struct*" that contains some variables. As in Fig. 8 one of those variables is sampleNumber. This var contains the current sample number of a music loop, this *struct* is filled during the app startup where all the files are red and stored into memory. The sampleNumber is updated during playback continuously.

```
// Data structure for mono or stereo sound, to pass to the application's render callback function,
//    which gets invoked by a Mixer unit input bus when it needs more audio to play.
typedef struct {
    BOOL                 isStereo;          // set to true if there is data in the audioDataRight member
    UInt32               frameCount;        // the total number of frames in the audio data
    UInt32               sampleNumber;      // the next audio sample to play
    AudioUnitSampleType  *audioDataLeft;    // the complete left (or mono) channel of audio data read from an audio file
    AudioUnitSampleType  *audioDataRight;   // the complete right channel of audio data read from an audio file
    BOOL                 isRecording;
    UInt32               startSample;
} soundStruct, *soundStructPtr;
```

Figure 8. The audio files C struct.

Now, suppose that the drum tile is playing and we want to add the guitar tile. When the user connects the guitar tile to the drum tile, it is known that the drum tile is playing the "x" sample number, so the system simply updates the sampleNumber variable inside the guitar struct to get them synchronized.

ALife in MagicTiles

The MagicTiles app is both inspired and aiming at the use of ALife paradigms. Indeed, as software conception it was deeply inspired by cellular automata research, from which it inherits part of the cells interactive logic. The MagicTiles algorithm could be properly defined as a User Based Interactive Cellular Automata algorithm where - for the moment being - the basic cell rules are predefined (see the MagicTile Algorithm section for further explanations). In this cellular automata like approach the *User* - intended either as the one who "composes the musical units" or the one who "manipulate the software" by arranging them in the virtual space – plays a major role in leading the (musical) output flow.

Further, the MagicTiles conception effectively derives from Music Cubes and Modular Interactive Tiles, and by doing so, it largely expresses and inherits principles coming from embodied artificial life. As a consequence, the musical outcome the MagicTiles, as for the Embodied ALife algorithms, implements a form of intelligence without either a static or a physical representation. As Brooks enounced [10], in MagicTiles the so-called musical intelligence is approached in an incremental manner, and it is given a strict reliance on interfacing to it through perception and action, letting the reliance on representation gradually disappear.

Apart from improving the interface and the interactivity, as an experimental platform the MagicTiles opens up for future research that goes deeper in incorporating ALife paradigms. An intelligent serve-routine may be defined to learn from the user activity and to build a user profile – a personalized fitness formula – which may facilitate users to manipulate music elements and reach their desired goal. In addition, the MagicTiles app can be introduced as a social component that by connecting its own community of users - through the use of classical interactive genetic algorithms – may implement a refined form of collective Evolutionary Music.

Discussion and Conclusion

In this paper, we presented a new RoboMusic application, MagicTiles, which aims at exploring a new cross-modal and cross-media approach to robotic systems. Through such an application any user can create and perform RoboMusic by assembling a number of interactive virtual tiles on the screen. After our past efforts in building physical interfaces, we decided to conceive the MagicTiles platform to show how the combination of the physical interface (i.e. Music Cubes and Modular Interactive Tiles) and the virtual interface (i.e. MagicTiles) tools might lead to a broader vision of robotic systems with a fluid and bidirectional flow between the physical and virtual. Indeed we believe that such a fluid and multifaceted representation of a single tool/activity may widely enhance the user immersion into a *one reality* that combines the physical and virtual.

It is interesting to observe a similar trend in robotics with the current development of cloud robotics, which combines the physical with the virtual. This may be in the form of physical robots connected to the cloud, which performs the computing such as object recognition, speech recognition, etc. for the physical robot.

Differently from most other modular interactive systems, the MagicTiles application allows end-user authoring of the contents of the individual modules, therefore enabling a high level of personalization – that even can be applied run-time – of the outcome. Our concept is inspired by ALife control systems (e.g. Cellular Automata, Embodied AI, etc.) and aims at using further traditional ALife resources to open up to single and ordinary users, as well as, building a new collective and evolutionary tool for creativity.

Acknowledgements

The authors wish to thank Massimiliano Leggieri and Andrea Gabriele for the help in developing the first prototype system. Also thanks to the Centre for Playware colleagues for valuable discussions.

References

[1] H. H. Lund. Modular Robotics for Playful Physiotherapy, in *Proceedings of IEEE International Conference on Rehabilitation Robotics*, IEEE Press, 571-575, 2009.
[2] H. H. Lund, and M. Ottesen. RoboMusic – A Behavior-Based Approach, *Artificial Life and Robotics Journal, 12: 1-2*, pp. 18-23, 2008.
[3] H. H. Lund, T. Klitbo, and C. Jessen. Playware Technology for Physically Activating Play, *Artificial Life and Robotics Journal, 9:4,* 165-174, 2005.
[4] J. Nielsen. User Configurable Modular Robotics - Control and Use, Ph.D. thesis, University of Southern Denmark, Odense, 2008.
[5] K. Falkenberg, N. K. Bærendsen, J. Nielsen, C. Jessen, H. H. Lund. RoboMusic with Modular Playware. *Artificial Life and Robotics, 15:4*, 369-375, 2010.
[6] R. A. Brooks. A robust layered control system for a mobile robot. *IEEE Journal of Robotics and Automation, 2(1):*14--23, 1986.
[7] R. C. Arkin. *Behavior Based Robotics*, MIT Press, Cambridge MA, 1998.
[8] H. H. Lund. Modern Artificial Intelligence for Human-Robot Interaction. *Proceedings of the IEEE journal, 92:11*, 1821-1838, 2004
[9] H. H. Lund. *Robots at Play*. ISBN 978-87-992302-0-4, 160 pages, Odense, 2007.
[10] R. A. Brooks, Intelligence without representation, *Artificial Intelligence 47*, 139–159, 1991.

The Seventeenth International Symposium on Artificial Life and Robotics 2012 (AROB 17th '12),
B-Con Plaza, Beppu, Oita, Japan, January 19-21, 2012

Social Playware for Supporting and Enhancing Social Interaction

Kenji Suzuki[1,2], Kazuki Iida[1], and Tomoya Shimokakimoto[1]

[1] University of Tsukuba, Tsukuba 305-8573, Japan
[2] Japan Science and Technology Agency, Japan
(Tel: 81-29-852-5761, Fax: 81-29-852-6287)
(kenji@ieee.org)

Abstract: Social Playware is regarded as cyber-physical systems to support and enhance the experiences on play and social interaction among people by measuring and presenting physical contacts, spatial movement and facial expression. Several wearable or modular devices are used in this study, which enable behavior and affective measurements based on augmented human technology. It is aimed not only to integrate cyber and physical spaces by using developed wearable devices but also to show the possibility to help people develop their social ability throughout case studies.

Keywords: Playware, Wearable Device, Body Area Network, Heart Beat, Physiotherapy Application

1 INTRODUCTION

Several attempts have been done for playful physiotherapy, which is supposed to motivate patients to engage in and perform physical training and exercising for preventing potential health problems or rehabilitation. Researchers recently have been paid attention to playful therapeutic applications with the aid of recent advancement of sensing devices and display. For example, input devices by measuring body gesture such as Wii (Nintendo) and Eyetoy (SONY) are typical cases used for rehabilitation or clinical trials. Camera or sensors are used to measure human bodily movement, and visual and / or auditory feedback is given to people by using virtual / mixed reality technology.

In this domain, social interaction plays an important role in different situations during these physical training and exercising. There have been reported that the motivation is a critical factor at the physical therapy and rehabilitation, but it is not easy for people to keep it on performing physical exercising. There is another difficulty to establish a different level of communication between patients, or patient and therapist. In this matter, toys are interesting and playful tools to each other mediated through the interaction. Several studies about toys have been done, for example, it is known that children have general preferences on visual stimuli with warm-color lights, auditory stimuli with tones and scales, haptic and somatosensory feedback to the whole body. Also they have positive response to toy's movement itself.

In order to understand social interaction among people, several kinematic and physiological cues among people are investigated in these case studies, such as facial expression, gaze direction, head orientation, body gesture, physical touch, space / location, physical distance among people and objects, as illustrated in Fig. 1. We introduce several wearable or modular devices, which enable behavior and affective measurements based on augmented human technology.

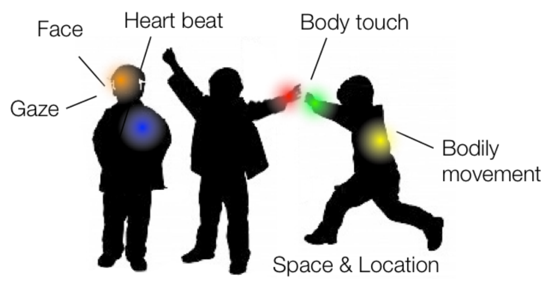

Fig. 1. Social Playware: Cyber-physical system to support and enhance the experiences on play and social interaction.

The concept of "Playware" is proposed and several works have been done so far in order to realize the playful interaction with interactive tools (see also [1, 2]). It is defined as intelligent hardware and software that creates play and playful experiences for users of all ages, and social playware is also defined as playware which aims at creating playful social interaction between several users.

In this paper, we introduce two examples of Social Playware; (i) Enhanced Touch: Sensing touches and identifying others can be done by the wearable device, (ii) HOTARU ("firefly" in Japanese): LED lights up in synchronization with the heart beat, and the color changes according to the calculated heart beat rate.

2 CASE STUDY I: ENHANCED TOUCH

We propose a novel bracelet-type device for sensing physical contact among people in order to support direct communication between people by inducing touching with appropriate visual feedbacks. The device detects and records the touches of users by simply wearing the device on their wrists (See Fig. 3).

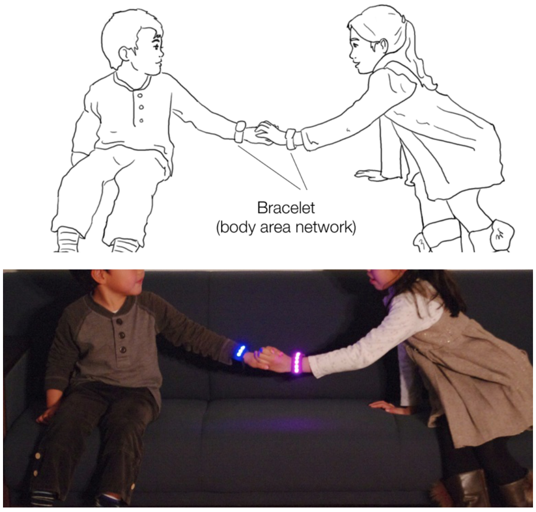

Fig. 2. Enhanced Touch: Sensing touches and identifying others can be done by the wearable device with electrodes.

Fig. 3. The six full color LEDs are installed in the bracelet, which are lit up when handshake occurs.

Physical touch is a fundamental element of human communication and several benefits and positive effects were reported at the communication and therapeutic domain such as Positive Touch and Deep Touch Pressure, for instance [3]. Typical symptoms of autism among children include avoiding direct touch with other people in addition to the tendency to lone activities. Some studies reported that training of touching by therapists contributes in the alleviation of these symptoms. Till now, human coders tried to observe their activity via recorded video but it is not objective measure and time consuming for checking all touches among people in a session. Measuring the time of touching, partner, frequency are desirable data, but there is no practical equipment for this purpose. Similar technology is used for the instrumental device [5], but users needed to grasp and hold the same device together.

2.1 System Overview

We use the communication technology based on body area network [4] in order to detect touching between people communication through human body. This technology was known as alternative solution of communication between humans and objects. Since the information is transferred via human body, it can be utilized for sensing physical contact among people. The developed device is used for sensing touches and identifying others, which can be performed by the wearable device with electrodes. The six full color LEDs are installed in the bracelet, which are lit up when handshake occurs. The pair of electrodes is located on the inside of the case as to fit the wrist. The device communicates with another device using a specific communication protocol. The received conducted signal is first amplified and demodulated, and then handled by the microprocessor. Every microprocessor tries to transmit a synchronous signal at random intervals within $10\,[\mathrm{ms}]$ to detect if touching has occurred and to synchronize with other device.

Several visual effects are programmed to visualize not only the physical touch but also the touching condition such as duration of physical touch and history of past touching. For example, colour blending is implemented for effective visual feedback to show the duration of touching. A unique color is assigned to each device; the three primary colors (Red, green, blue).

When a user wears the devices and touch to another person with the developed device by their hands, both devices light up LEDs with its unique color. While keeping the shake-hands, Two different colors change and are then blended gradually as long as the touching lasts. In other words, the degree of color blending represents the duration of the touching time. The LED colors in the two devices in touch become the same color. This manner of lighting allows our proposed method to measure the duration of physical contact along with the device's ability to identify other devices.

Table 1. Time during different style of physical touch

Style of physical touch	Time (S.D.) [ms]
Hand Clap	50.7 (12.1)
High Touch (Normal)	44.8 (10.9)
High Touch (Slow)	187.5 (22.1)

2.2 Touching and response time

In order to confirm the performance of the developed device, we first conducted a simple experiment to measure the time during different style of physical touch. Fig. 1 shows the averaged times in [ms]. We obtained that the averaged touching time is $94.3\,[\mathrm{ms}]$ at different style of physical touch such as hand clap and high touch.

Due to the characteristics of communication protocol, the response time of the developed device has some variance. The response time is regarded as the period of time from the moment the touching occurs to the moment the LEDs of the device are lit up. Two subjects touched fifty times by the tip of the fingers and these touches was recorded by a high-

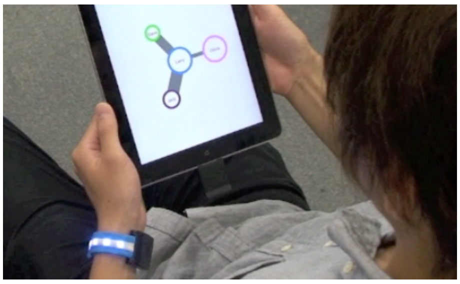

Fig. 4. A correlation diagram among users by exporting the data to another device with a Tablet device.

speed camera with 1200 [fps]. The response time was calculated from the number of frames between those two actions. From the experimental results, we obtained that the average of response time is 27.7 [ms], and the standard deviation is 19.2 [ms]. The minimum value is 6.7 [ms], which is almost equal to the transmitting time plus receiving time, thus the value is valid. The maximum value is 80.0 [ms]. These results show that the response is signitifant for recording daily life touching or for games that include touching activity, even in the worst case of response time.

2.3 Correlation Diagram on a Tablet Device

The device is be able to record and show the physical contact log among people, such as the number of shake-hands and/or amount of touching time over a long term. These logs show the degree of friendship or relationship among people. We developed a Tablet device with electrode in order to show a correlation diagram among users by exporting the data to it. A correlation diagram is shown in Fig. 4. This diagram appears when the user touch and hold the device. Where the circles indicate users, and the lines show the relationship among these users as the line's width indicates the degree of friendship between two users. Such application will provide a new measuring method of relationship in an easily understandable way.

3 CASE STUDY II: HOTARU

In this study, we propose a novel method of heart beat tracking and develop a wearable device to visualize the heart beat, namely *HOTARU* ("firefly" in Japanese). These are a number of systems and devices for heart beat measurement, which can be used to measure heart function or exercise volume, psychological barometer such as stress or relaxes. However, since the measurement of biological signals are not stable due to the unexpected several noises, the user is asked to firmly attach the sensor, for example electrode, and also to keep quiet even for the measurement of the heart beat rate, Fast Fourier Transform (FFT) is used as the traditional method of the measurement of heart beat rate, while the signals with unexpected noises in the measured signal are ignored.

Fig. 5. HOTARU ("firefly" in Japanese): The conceptual image of using the developed device.

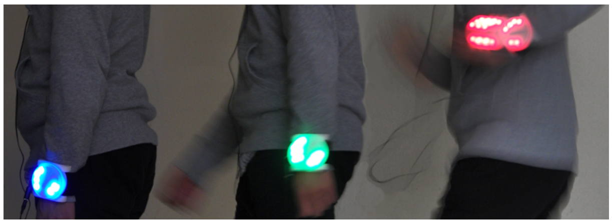

Fig. 6. The developed device in use. LED lights up in synchronization with the heart beat, and the color changes according to the calculated heart beat rate.

3.1 System Overview

A wearable device is developed to indicate the heart beat in real time with different color of LED. The color changes according to the heart beat rate, and blinks in synchronization with the heart beat pulse. The developed system is able not only to track the heart beat but also to interpolate it from the noisy signals in real time. The heart beat is extracted from the original signal of the photoplethysmographic (PPG) sensor, which contains the noise delivered by body movement or other unexpected causes. In the proposed method, when the system is not able to determine the heart beat due to the sensor 's alignment or temporary no pulse, the heart beat is interpolated based on the past signal and liner prediction algorithm.

3.2 System Overview

The developed device *HOTARU* consists of a microprocessor, LEDs display, and PPG sensor that can measure heart beat pulse by using optical absorptance of human body. The user is asked to attache PPG sensor that is a clip-type interface on the ear, and to wear a bracelet-type interface with LEDs on his or her wrist. The brightness of LEDs changes in synchronizion heart beat and its colors corresponds to the heart beat rate (HBR). As shown in left of Fig. 6, blue means that heart beat rate is less than 60, green means that heart beat rate is from 60 to 80, and red means more than 80.

3.3 Methodology: Real Time Heat Beat Tracker

Traditionally, since the measurement of heart beat is focused on the heart beat pulse itself, but the tracking accuracy depends upon the environment. It is usually not stable because of the noise, and users are asked to rest during the measurement. The intervals of heart beat pulse are low frequency from about 0.5 to 2.0 [Hz] and these intervals is assumed not rapidly change. But precise intervals are difficult to be recognized from the measured signals only by using peak detection due to the noises, which are usually impulse noise and look like heart beat pulse. FFT is used as the analysis of it.

On the other hand, we propose a novel method of heart beat tracking. The pattern-matching is carried out between the measured signal $\mathbf{P}(x, t)$ and the ideal heart beat pulse $\mathbf{Pc}(x)$, which is prepared in advance. The cross-correlation $\mathbf{z}(x, t)$ is calculated with the fixed time window which is the same as the length of the ideal heart beat pulse. The matching result $\mathbf{z}$ is expected to be a periodical signal, and it is synchronized with the real heart beat pulse. The computational cost to obtain the coefficients of all possible cross-correlation values is very high and not suitable for real time calculation, only limited coefficients are used in this process. In addition, in order to reduce the computational cost, the cross-correlation values are obtained only at the certain time, which is estimated at the linear prediction process.

Then, a modified peak detection algorithm is employed by combining Kalman filter to predict the intervals of heart beat, which is based on the linear prediction and uniform distribution function. Assuming that these intervals do not rapidly change, next heart beat interval can be estimated from transition of previous several intervals. And center value of probability density function (PDF) is solely used for detection of peak candidate in $\mathbf{P}$. The peaks are detected within the $\mathbf{z}$ time range of reliability based on this PDF.

3.4 Experiments

We conducted an experiment to compare the proposed heart beat tracker with electrocardiograph (ECG) signal from 10[s] data in different situations of user's resting and moving. The experimental result shows 100% accuracy for resting state and 94% for moving situation where traditional FFT or peak detection algorithm does not give any significant heart beat tracking.

4 DISCUSSION AND CONCLUSIONS

In this paper, we introduced two examples of social playware. It is aimed not only to integrate cyber and physical spaces by using developed wearable devices but also it can be used to help people develop their social ability throughout case studies.

The devices for sensing the human contact can be used to recognize the social network based on physical contacts. The bracelet-type device lights up - with a different color for each - when the wearer shakes hands with another wearer. Not only sensing the contact but also the electrical communication is also used to identify and share the device ID. We believe that the proposed device could provide a novel playful interaction method between humans. We now plan to verify if the device contributes to motivate touching among users by lighting LEDs or by playing interactive social games. On the other hand, we presented another device for presenting current heart beat with different color. LED lights up in synchronization with the heart beat, and the color changes according to the calculated heart beat rate. The developed device allows users to freely move and play without attaching the sensor or electrode firmly. Potential applications include the tool for kids to promote social interaction. The user testing with several people is planned. We also will implement the sound feedback according to heart beat pulse for computer games and VR avatar.

Throughout these case studies, we would like to expand the playware technology for supporting and enhancing the experiences on play and social interaction among people by using playful devices. The device mediates between humans without missing fundamental properties of human activities. We consider that social playware is a cyber-physical system by measuring and presenting human physical activities such as physical contacts, spatial movement and facial expression, where psychological and social aspect of human activities could also be enhanced.

ACKNOWLEDGMENTS

This work is supported in part by JST PRESTO, Japan Science and Technology, and also by the FIRST Program, funded by the Council for Science and Technology Policy.

REFERENCES

[1] Lund HH, Klitbo T and Jessen C (2005), Playware Technology for Physically Activating Play. *Artificial Life and Robotics Journal*, 9(4):165-174

[2] Marti P, Giusti L, Lund HH (2009), The Role of Modular Robotics in Mediating Nonverbal Social Exchanges, *IEEE Transactions on Robotics*, 25(3):602-613

[3] Pardew EM, and Bunse C (2005), Enhancing interaction through positive touch. *Young Exceptional Children*, 8(2):21-29

[4] Zimmerman TG (1996), Personal Area Networks: Near-field intrabody communication, *IBM Systems Journal*, 35(3.4):609-617

[5] Baba et al. (2007), Freqtric drums: a musical instrument that uses skin contact as an interface, *Proc. of NIME*, 386-387

ADAPTING BODY AND BEHAVIOUR:
- learning and playing with a modular robotic platform -

Patrizia Marti[1], Iolanda Iacono[2]

University of Siena
Social, Political and Cognitive Science Department
[1]marti@unisi.it, [2] iacono@media.unisi.it

Abstract: The paper illustrates the design of Iromec, a robotic platform developed to engage disabled children in exploring play scenarios and thereby in learning through play. Key features of the system are: *modularity*, provided both at physical and functional level; *configurability*, to allow the teacher to make the physical and functional rearrangement of the robot configuration, *construction* to modify, enrich and adapt play activities to different and evolving needs of the disabled children. Furthermore the platform offers the possibility for the teacher/therapist to design new play scenarios addressing different educational objectives**.** The paper shows how the adopted design enables multiple robot configurations and play scenarios, and exemplifies the use of the robot in the school context.

Keywords: modularity, play, learning, disability, game creation.

1 INTRODUCTION

In the last decade the technology evolution has produced a remarkable change in children's and adults' play offering new kinds of play experiences and equipments. From the humble beginnings of Pong, Pac-man, Tetris, and video pinball computer games, the game industry has moved to more realistic virtual worlds, more interactive environments and competitive play. A number of challenges guided this evolution: to increase the realism of virtual worlds, to turn "finger athletes" in sport and fitness people, to penetrate different areas of the industrial and public sector other than entertainment, like business (simulation games), education, professional training, health care. While some of these challenges have been successfully addressed by launching on the market physical and virtual games of increasing popularity, 3D representations used in courtrooms, interactive learning environments for the school and museum context, simulations for building designs and military systems, however a limited attention has been paid in making interactive games and equipments accessible for all, and in particular for disabled people to support them in improving their quality of life, their learning and development opportunities. Moving, exchanging, experimenting and learning through play are fundamental activities that should be exercised from childhood, according to the cognitive and physical abilities that an individual may have.

Unfortunately, disabled children are often prevented from playing due to their cognitive or physical impairment. Interactive games rarely adapt to the abilities of disabled children and therefore are far from being accessible for them.

Iromec (Interactive RObotic social MEdiators as Companions) is a robotic platform that addresses play as a medium for disabled children's learning, development and enjoyment. The platform is composed of passive and interactive hardware modules and configurable interfaces to enable the creation of play scenarios adapted to fit the needs of children with different kinds of disabilities [1].

Key features of the system are: *modularity* (passive and interactive modules can assembled to modify the robot appearance and its behaviour), *configurability* (the platform allows two main configurations, stationary and mobile), *construction* (the construction and deconstruction of modules allows to modify, enrich and adapt play activities to children with different abilities in different contexts). Furthermore the platform allows the creation of new games that can be implemented through "play script".

2 THE ROBOTIC PLATFORM

IROMEC is a modular mobile robotic platform developed to support children with cognitive and physical impairment to learn through play. The platform is conceived as a modular system equipped with different components: a mobile platform, an application module and some additional pluggable components used to modify the robot's appearance and behaviour [1].

The mobile platform developed by Robosoft (www.robosoft.fr) controls all the commands related to the movement, localization and navigation. It is equipped with

13 ultrasound and 18 infrared sensors and a laser scanner to allow obstacle detection, navigation in the space and reaction to external stimuli. Movement and speed are controlled through a motor/gearbox/encoder ensemble that makes the movement safe and suitable for the interaction with children. The platform contains also a video camera for colour tracking. It weights around 10 kgs.

The application module developed by Profactor (www.profactor.at) manages the user interaction through a set of digital components and interfaces. It can be plugged/-unplugged on/from the mobile platform through hooks that safely and invisibly fastener the two modules. The interaction module measures 35x55x17 cm and weights around 8 kgs. The module is composed of two parts: the body and the head. The body displays graphical interface elements related to different play scenarios on a 13 inch digital touch screen. For example, the body screen can represent the features of an imaginary cartoon-like character displaying a digital fur which moves according to the direction of the platform's movement. When the robot stops, fur clumps appear that extend when it moves again. The head is constituted of a 8 inch digital screen that displays the robot's facial expressions. The head rotates along a vertical axis from right to left (and vice versa) to simulate the robot's attention towards a specific direction. The head movements are controlled by an additional micro-controller that it also in charge for controlling the camera system.

A number of additional components were designed to modify the appearance of the robot and its behaviours. Some of these modules are interactive and affect the robot's behaviour. For example luminescent fabric covers are plugged on the lateral sides of the robot and light up when the robot moves. They are fixed on the interaction module through magnets. Different groups of luminescent fibers are weaved into the fabric and can be managed independently being controlled by one inverter each. Different light patterns can be obtained are used to reinforce the feedback on the robot status during movements and coordination games. Another example of interactive module embedding smart textile is "interactive fur" is made of a soft woolen cover with static and moving hairs. This is a stand alone module which is plugged on top of the interaction module through an interlocking mechanism. The moving hairs are fixed to the copper fabric but their lower part is connected to a Nitinol spring.

Each Nitinol spring is connected in their central part to an electric wire wrapping the hairs. The Nitinol springs are fixed to the inner part of the dome shell by means of screws, and the electric wires are inserted through holes in the shell itself. When electricity passes from one extremity of the spring to the center, the other extremity contracts. The movement of the hair can be controlled in timing, intensity and form. This makes the effect of the moving hairs seem quite natural, similar to the fur of an animal [2].

Some other modules of the platform are passive and are used to modify the appearance of the robot. For example, a mask can be mounted on the robot's head to hide part of the digital face and reduce the robot's expressivity. The mask is composed of a fixed smiling mouth, nose and removable eyes.

Fig. 1. The robotic platform

The platform can be assembled in two main robot configurations, vertical (**Fig. 2.** left) and horizontal (**Fig. 2**. right). In the vertical configuration, the robot is stationary and the interaction module is mounted on a dedicated support that provides stability and maintains a fixed position. The mobile platform is not used in this configuration. The head is rotated on the vertical axe to fit the vertical position of the body and the head display automatically adapts the face with the correct orientation. In this configuration the robot has a human-like stance. A dedicated mask can be mounted on the head to hide part of the face if required. This configuration supports imitation scenarios that require the children to reproduce basic movements, like turning the head. The robot can also assume the horizontal configuration to support activities requiring wider mobility and dynamism. In the horizontal configuration the interaction module in plugged in the mobile platform and the head is rotated upside down. Also in this case the head display automatically adapts the face with the correct orientation.

Fig. 2. Vertical (left) and horizontal (right) configuration

The covering modules contribute to modify the appearance of the robot in both configurations (**Fig. 3.**).

Fig. 3. Interactive fur cover (left), mask (right)

2.2 Interfaces

The application module is featured with a high level control system (Game Control) that provides editing of "play scripts" through the GUI, by means of XML-description. The Game Control programming software is written in java programming language and it is easy to modify. An game editor is currently under development to allow the teachers to implement new scenarios autonomously. "Play script" allow to implement GUIs for different play scenarios, so that the robot can turn from an imaginary animal covered by a fur (**Fig. 4.**) into a creeping snake, or an agile tiger or a quite turtle (**Fig. 5.**). Currently the robot can show facial expressions that incorporate the mouth, nose, eyes and eyebrows, as well as different levels of expressiveness and emotional states. Smooth transitions are used to provide a life-like impression.

Fig. 4. Imaginary animal-like character

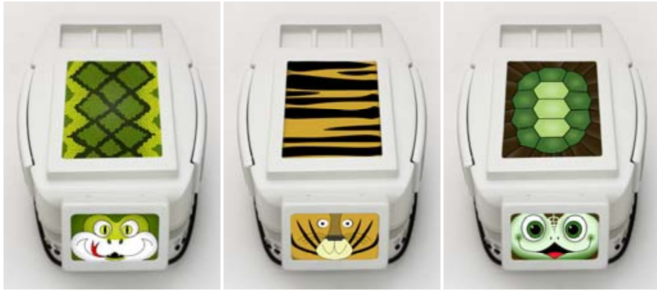

Fig. 5. Snake (left), Tiger (centre), Turtle (right)

The interfaces are enriched by original sounds to structure and articulate the play experience. They have been designed in collaboration with experts, therapists and teachers to give the impression of a living entity without any specific human or animal connotation. A library of sounds was created so that different sounds can be associated to various games through "play scripts".

3 CREATION OF PLAY SCENARIOS

The robotic platform can be configured to engage in a number of play scenarios [3] [1] including turn taking and imitation games, cause and effect games, coordination games, sensory stimulation games. Each scenario is designed to address detailed educational and therapeutic objectives and can be adapted to the specific needs and ability of the child. For example, the *Tickle* scenario (**Fig. 6.**) consists of an exploration of the robot's body to discover where it is sensitive to being tickled. The game can be played in different configurations: either by tickling the robot in correspondence of "digital fur knots" appearing and disappearing on the touch screen display; or by stroking a pressure sensitive fabric cover mounted on the robot's body: whenever the child strokes a sensitive area the robot laughs emitting sounds. The tickling zones change dynamically and children have fun in trying to guess where the robot is more sensitive.

Fig.6. Two configurations for the Tickle scenario

The game is designed to improve the perceptual functions (auditory, visual, tactile and visuo-spatial perception) as a basic form of communication. This is important to the learner since the tactile sense can help to provide awareness of one's own self and each other, to build trust, and to give or receive support in order to develop social relationships during play.

The scenario was experimented in a primary school in Siena (Italy) with children with physical and cognitive impairments. As an example, we briefly present an excerpt of an experiment conducted with M., a 6 year old girl with Pierre Robin syndrome. Because of her disease, M. has a poor speech and difficulties in performing movements that require coordination of the upper and lower limbs, such as sitting down and getting up, and eye-hand coordination. She is emotionally fragile and needs to be constantly reassured during the execution of a task. She is in trouble in playing games that require the production of simultaneous mental schemes and the presence of co-occurrence of variables such as several moving objects at the same time. M. was involved in an experimental study conducted in a primary school in Siena (Italy) for 3 months with 3 sessions per week [4].

Fig. 7. shows the child playing the *Tickle* game. The child explores the robot's body (**Fig. 7**. up left), she observes the interface and the "fur knots" appearing on the digital screen (**Fig. 7.** up right), she executes the task (**Fig. 7.** bottom left) and at the same time monitors the robot's expressions in reaction to tickling (**Fig. 7.** bottom right). The sequence shows that M. is very engaged in playing with the robot. She carefully touches the fur knots showing a certain degree of eye-hand coordination and a correct understanding of the cause-effect relations of her actions. Furthermore, she attributes emotional states to the robot showing empathic engagement with the play companion. These behaviours are examples of social competence that the child can develop, exercise and reinforce in interaction with the robot.

Fig. 7. Experimenting the *Tickle* scenario

4 CONCLUSIONS

Iromec is a robotic platform that supports disabled children in exploring play styles. The platform has a number of key features that make the robot a suitable support in learning and therapeutic activities. The modularity is achieved both at hardware and software level: it allows to configure the robot by changing its appearance, and to create new games to address the specific needs of disabled children. Thereby, the platform can be used in a flexible manner by allowing the teacher/therapist to design educational activities. The design leads to solutions such as utilising the material properties of the platform to facilitate understanding of behavioural characteristics and to exercise creativity. These features further make it possible to create inclusive games which are adapted to children with different physical and cognitive abilities. Indeed, the platform has been used with autistic, motor impaired children, and children with mild cognitive impairment in the school context with the classmates with typical development [4].

ACKNOWLEDGMENTS

The authors would like to thank the children and their families for their enthusiasm in experimenting with the robot. Thanks also to Sara Gioiosa for designing the tiger, turtle and snake games.

REFERENCES

[1] Marti P, (2010), "Bringing playfulness to disability" Proceedings of the 6th Nordic Conference on Human-Computer Interaction, (NordiCHI 2010) Reykjavik, Iceland, 17-20 October 2010.

[2] Marti P, (2010). Perceiving while being perceived. *International Journal of Design*, *4*(2).

[3] Robins B, Ferrari E, Dautenhahn K, Kronrief G, Prazak B, Gerderblom GJ, Bernd T, Caprino F, Laudanna E, Marti P, (2010), Human-centred Design Methods: Developing Scenarios for Robot Assisted Play Informed by User Panels and Field Trials. International Journal of Human Computer Studies, 2010, Volume 68 Issue 12, December, 2010, ISSN: 1071-5819, pp. 873-898.

[4] Marti P, Iacono I, (2011), Learning Through Play With a Robot Companion. Proceedings of the 11th European Conference for the Advancement of Assistive Technology (AAATE 2011), Maastricht, The Netherlands, August 31 - September 2, 2011.

Adaptivity to Age, Gender, and Gaming Platform Topology in Physical Multi-Player Games

Davíð Þór Björnsson, Rafn Vídalín Friðriksson, Henrik Hautop Lund
Center for Playware, Technical University of Denmark, Building 325, 2800 Kgs, Lyngby
Tel: +45-45253929; Email: hhl@playware.dtu.dk

Abstract

In games where players are competing against each other, it can be of interest to ensure that all players are challenged according to their individual skills. In order to investigate such adaptivity to the individual player in physical multi-player games, we developed a game on modular interactive tiles which can be used in both single-player and multi-player mode. We implemented simple adaptivity methods and tested these with different user groups including children and adults of both genders. The results show statistically significant differences in the game interactions between children and adults, and between male and female players. Also, results show statistically significant differences in the game interactions between different physical set-ups of the modular interactive tiles, i.e. the interaction depended on the topology of the modular tiles set-up. Changing the physical set-up of the physical game platform changes the interaction and performance of the players.

Introduction

Physical games can be both fun and physical challenging, as is seen with numerous physical gaming platforms currently emerging on the market, including Nintendo Wii, Microsoft Kinect, etc. (an overview of such physical gaming platforms and their history is presented in [1]). If we want the games to be challenging to a variety of users, it is important that the games can challenge the users at different levels appropriate to the individual user. In the physical games, we may imagine that a young child is at a different level than an older child, we may imagine that young adults are at a different level than most elderly, we may imagine that fully able users are at a different level than physical disabled users, etc.

Hence, it is interesting to investigate how different users perform differently, and based on this investigate how physical games may possibly adapt to match the physical capabilities of the individual user. In other words, it is interesting to investigate how to develop adaptive physical games. For instance, for modular playware [2, 3], it has been outlined that there exist different possibilities for such adaptation: "(1) *Hardware adaptation*, e.g. the user changes the physical form or size of the playware tool to fit the user level, (2) *Software adaptation*, e.g. the game automatically changes level to fit the user at run-time, (3) *Hardware and software adaptation*, e.g. the user builds a desired playware tool and software adapts to the built playware tool (e.g. to its topology) and the user interactions" [4]. In the present work, we will therefore make experiments with a platform that allows both hardware and software adaptation, though focusing on the software adaptation.

As introduced by Derakhshan et al. [5], an adaptation approach to playware is a run-time iteration of observation, classification, and adaptation. Related to the classification of users in physical playware games, Derakhshan et al. [5] classified the users into simple categories (young/old child, playing/not playing, continuous/discontinuous behavior, etc.) using an artificial neural network, whereas Yannakakis et al. [6, 7] introduced an approach for estimating expressed player satisfaction in real-time through physiological signals (e.g. heart rate) measured during physical gameplay. Lund and Thorsteinsson [4] used a simple approach of a run-time classification and adaptation based upon the reaction speed of the user. Likewise, we will use such an approach in the present work.

Experimental Set-up

In order to make experiments on different user groups' physical performance and impression of adaptive physical games of different difficult level, we developed the adaptive double mole game for the modular interactive tiles.

Modular Interactive Tiles

The modular interactive tiles are a distributed system where the tiles can be attached to one another to form the overall system. Each tile is self sufficient of processing power and each one has a battery that lasts approximately 30 hours in use. This makes the usage of the tiles very flexible because they do not need a computer or external power source. When connected to one another to form a playfield, they communicate to their neighbors through four infra-red (IR) transceivers located on the sides. In a set of tiles one tile usually differs slightly from the others and that is the master tile which has a XBee radio communication chip. The master tile is capable of communicating to other devices that have a XBee chip for example a game selector box or a PC that has an USB XBee dongle connected.

Figure 1: Left: The interior of the modular interactive tiles.
Right: A tile playfield being assembled.

When playing on the tiles, the player provides the tiles with an input in the form of pressure measured by a single force sensitive resistor which is located in the center of each tile. The tile can then react by turning on 8 RGB LEDs which are mounted with equal spacing between each other in a circle inside the tile. On the back side of the tiles there are four magnets which can be used to place the tiles vertically on a magnetic surface. The tiles have the means to detect whether they are placed horizontally or vertically with a 2 axis accelerometer. This feature can be used to change game parameters on the fly when the tiles are, for example, moved from a floor to a wall.

Double Mole

The game developed for the present work found inspiration from the well known game „Whack-A-Mole“ where the objective is to hit the moles with a hammer before they go back into their holes. The game was implemented on the modular interactive tile platform in such a way that each tile was considered as a hole for a mole to appear in. Appearing moles were represented by 8 LEDs lighting up in either green or blue color and they appeared randomly around the tile set. The tiles count down by turning off the LEDs one by one until all the LEDs have been turned off, which means that the mole has escaped. However if the player steps on a lit up tile before it finishes the countdown, the player is considered to have hit the mole and receives one point. The game can either be played in single-player or multi-player mode where the two modes differ slightly. The difference is due to the chance of a bonus tile/mole appearing in the multi-player mode. The players compete for this bonus and the player who wins it, receives a certain amount of points (e.g. 10 points). This tile counts up from 0 to 8 LEDs in red and yellow until a player hits it, but then the red color randomly changes to either blue or green. Then with each hit, the color switches between green and blue until the count up finishes. In the present tests, the tiles are arranged in a rectangle, in 2x3, 2x4, or 4x4 set-ups. Depending on the set-up the amount of tiles each player has to hit changes. In the 2x3 set-up each player has one tile to hit while in 2x4 and 4x4 each player has 2 tiles to hit at each time. When playing, players are most often standing outside the tile platform facing each other in the 2x3 and 2x4 set-ups and stretch their leg inside the platform to hit the lit up tiles. This game-play relies on the reaction of the players and their ability to keep the balance while stretching their leg inside the tile platform. The 4x4 tile set-up requires the players to stand on top of the platform which alters the game-play quite considerably because now size and strength of the player also plays a big role in how they perform in the game.

Adaptivity

Due to the nature of the game, being fast paced and competitive in the multi-player mode, the game was made in such a way that it would adapt the countdown speed of the tiles depending on the number of remaining LEDs lit when a tile was hit. The values used to adapt the countdown speed can be seen in the following table:

Countdown		
LEDs (no.)	LEDs (ms)	Tile (ms)
8	-80	-640
7	-40	-320
6	0	0
⋮	⋮	⋮
3	0	0
2	10	80
1	20	160
0	30	240

Table 1: Countdown speed adaptation values where negative values are an increase in speed and positive a decrease.

In both single- and multi-player mode the game adapts the countdown speed to each individual depending on his performance. This feature possibly allows two players in different physical shape to play a game against each other. The challenge may be to make the game challenging enough to keep each player motivated but at the same time make each of the two players able to win the match. The bonus tile was implemented as a test to see whether it could be used to slow down the faster player.

Tests

User tests were made on two different age groups. One group consisted of children aging 6-8 year old, 3 boys and 3 girls and the other group consisted of adults aging 20-35 year old, 10 males and 10 females.

Single-player
First a single player test was conducted where each player played a 60 second game alone and where the adults played both in 2x3 and 2x4 tile set-ups while the children only played in the 2x3 tile set-up. Comparisons were made between the 10 males and 10 females to determine whether any significant difference was in their performance in the game. Figure 2 shows the performance of males and females in the 2x3 tile set-up, displaying how the countdown time adapts over game time.

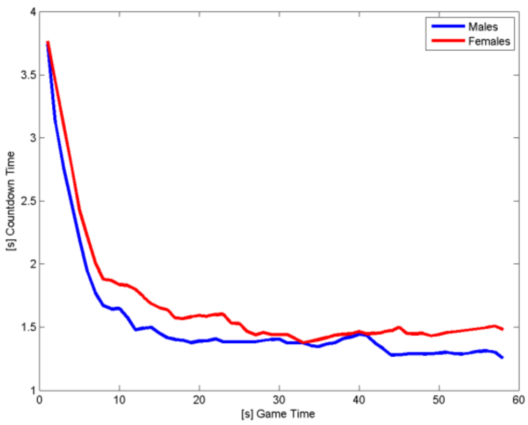

Figure 2: The average values of tile countdown time. A comparison between males and females in 2x3 tile set-up.

The males appear to reach faster countdown time than the females. Comparing the two sets of data consisting of the countdown time at each second of game time, a Mann Whitney U-test returns the P-value 5.6098e-008. At the 0.05 critical alpha level, this concludes that there is a statistically significant difference between the performance of males and females. The game statistics can be seen in the following table.

2x3 – Males vs. Females		
Gender	Tiles hit	Reaction time [s]
Males	82.80	0.446
Females	75.20	0.530
MW-U (P)	0.0881	0.0452

Table 2: Game statistics, average values.

The difference in countdown time observed on Figure 2 is related to the significant difference in reaction speed observed in Table 2.

Similarly a comparison was made between males and females in the 2x4 tile set-up, see figure 3.

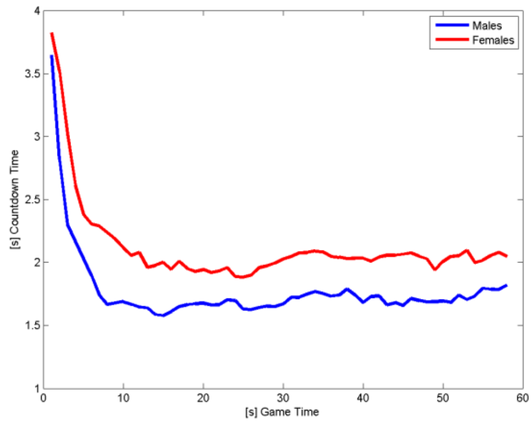

Figure 3: The average values of tile countdown time. A comparison between males and females in 2x4 tile set-up.

For the game on the larger 2x4 tiles platform, the difference between the countdown time of the tiles for the two genders increases from what was observed in the 2x3 tile set-up. A Mann Whitney U-test with the 0.05 critical alpha level was used to determine if the difference could be considered significant. The test returned the P-value 1.6521e-015 so the difference is considered significant.

2x4 – Males vs. Females		
Gender	Tiles hit	Reaction time [s]
Males	127.80	0.612
Females	113.8	0.734
MW-U (P)	0.1117	0.0312

Table 3: Game statistics, average values.

When examined, the game statistics revealed that changing from 2x3 tile set-up to 2x4 tile set-up slowed the reaction time (remember that in this game the user now has two tiles lighting up at a time), and the reaction time difference between the two genders is, as before, statistically significant.

A comparison between adults and children was also made where the averages of all the adults were compared to the averages of all the children, as shown in figure 4.

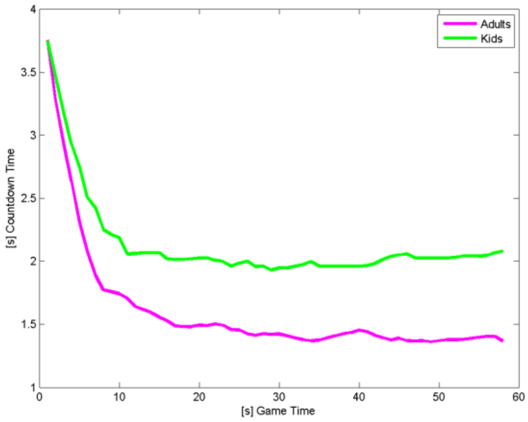

Figure 4: The average values of countdown time. A comparison between adults and children in 2x3 tile set-up.

It can be seen that the adults reached a much faster countdown time on average than the children did. A Mann Whitney U-test returned the P-value 5.4814e-014 so the difference is considered significant.

2x3 – Adults vs. Children		
Group	Tiles hit	Reaction time [s]
Adults	79.00	0.488
Children	61.83	0.684
MW-U (P)	0.0028	0.0038

Table 4: Game statistics, average values.

By examining Table 4 it can be seen that the adults seem to have much faster reactions than the children do. The difference was determined, with the Mann Whitney U-test, to be significant.

Finally for the single-player user tests, a comparison was made between two different tile set-ups, namely 2x3 and 2x4, see figure 5. This comparison was made between the average values of the adults that participated.

It can be observed that the adults reached a faster countdown time in the 2x3 set-up. This difference is explained by the increased number of lit tiles that the players have to hit in the 2x4 set-up.

Game statistics show a significant difference in both tiles hit and reaction time. This is explained as before by that an increase in amount of tiles the players have to hit at each time is increased from one to two.

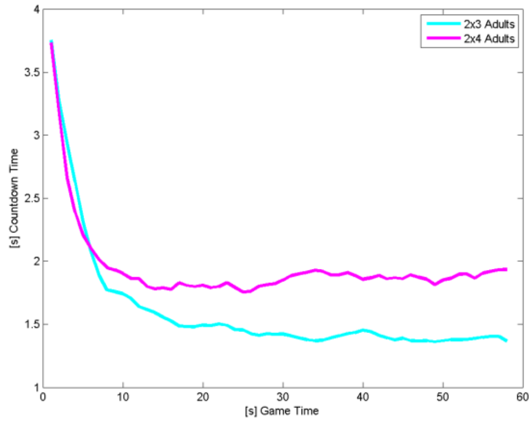

Figure 5: The average values of countdown time. A comparison between adults playing in 2x3 and 2x4 tile set-ups.

2x3 vs. 2x4 – Adults		
Setup	Tiles hit	Reaction time [s]
2x3	79.00	0.488
2x4	117.25	0.673
MW-U (P)	0.0000	0.0000

Table 5: Game statistics, average values.

Multi-player

In the multi-player tests, 16 of the 20 adults were tested. They were split into 4 groups where 2 fast players of each gender were matched against 2 slow player of each gender. The players were categorized as fast or slow depending on how they performed in the single-player test. The same 6 children as before were also tested in 2x3 tile set-up though no performance classification was made.

To see how changing the tile set-up would affect the performance of the adult players, the average values of all adults were put on a single graph for comparison, see figure 6.

When Figure 6 is examined it can be seen that the games adapt to the users at different speeds. The 4x4 tile set-up has by far the slowest game-play. This is due to altered game interaction where the players are now standing on top of the tile set resulting in more disturbances from the other player.

Figure 7 shows the results from the matching of fast and slow players in the 2x4 tile set-up. The other games (2x3 and 4x4) show similar patterns, though with either faster (2x3) or slower (4x4) countdown time. In all games, Mann-Whitney U-tests show (P-values of 1.5085e-009, 3.9221e-013, and 2.7131e-013) a statistically significant difference between the fast and slow players.

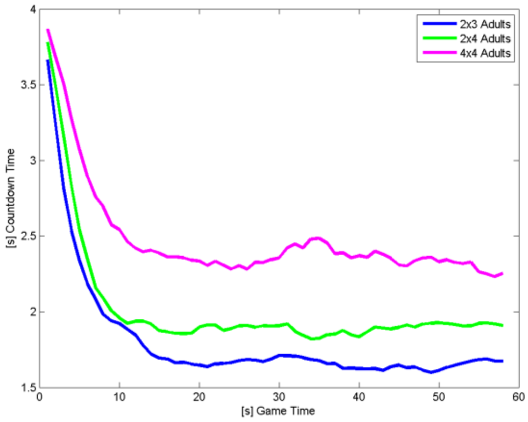

Figure 6: The average values of countdown time. A comparison between adults playing in 2x3, 2x4 and 4x4 tile set-ups.

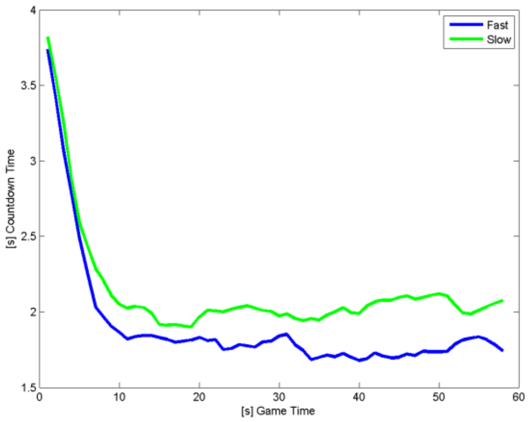

Figure 7: The average values of countdown time. A comparison between fast and slow players playing in 2x4 tile set-up.

2x3 – Fast vs. Slow - Adults			
Group	Tiles hit	Bonus tiles	Reaction time [s]
Fast	59.44	2.13	0.570
Slow	52.50	1.69	0.653
MW-U (P)	0.0258	0.3644	0.0438

2x4 – Fast vs. Slow – Adults			
Group	Tiles hit	Bonus tiles	Reaction time [s]
Fast	73.69	1.94	0.706
Slow	61.94	1.75	0.794
MW-U (P)	0.0039	0.7132	0.0302

4x4 – Fast vs. Slow – Adults			
Group	Tiles hit	Bonus tiles	Reaction time [s]
Fast	61.38	1.31	0.893
Slow	50.13	2.06	1.091
MW-U (P)	0.0066	0.0111	0.0044

Table 6: Game statistics, average values.

For all the game set-ups, the game statistics show a significant difference according to the Mann Whitney U-test both in the amount of tiles hit and the reaction time. In the case of 4x4, there is also a statistically significant difference in bonus tiles hit favoring the slower players.

If the game scoring system is set so that one point is awarded for hitting a regular tile and 3 points for winning a bonus tile, the fast player wins in all three tile set-ups as seen in table 7. On the other hand, if the bonus tile was set to give 15 points, then the slower players would obtain a higher score than faster players in the 4x4 game.

Adults – Scores			
Group	2x3	2x4	4x4
Fast	65.81	79.50	65.31
Slow	57.56	67.19	56.31

Table 7: Adults, average scores in multi-player.

After playing each game, the players answered a questionnaire including the three following questions:

Q1: How was the game ? (1 Boring / 5 Fun)
Q2: How was the speed ? (1 Slow / 5 Fast)
Q3: Was the game difficult ? (1 Not / 5 Very)

The answers were given on a 5-step Lickert Scale. The answers to the questions revealed that both player groups thought the game was entertaining (average 4 on the 1-5 scale) and moderately challenging (speed average 3.5, difficulty average 3). Interestingly, in all cases, the difference in answers between the fast and slow players was not considered statistically significant according the Mann Whitney U-test. Hence, despite the statistically significant differences in reaction speed (and thereby difference in number of tiles hit during each game), the players found the adaptive game equally fun and challenging.

Finally a comparison between adults and children was made to see if there was a difference in how children and adults compete, see figure 8. As can be seen in Table 8, the adults hit significantly more tiles and their reaction time is almost twice as of the children. Interestingly, the amount of bonus tiles hit is similar.

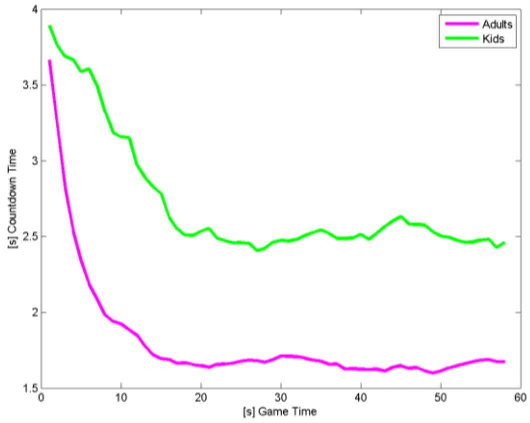

Figure 8: The average values of countdown time. A comparison between adults and children playing the multi-player version in 2x3 tile set-up.

2x3 – Adults vs. Children			
Group	Tiles hit	Bonus tiles	Reaction time [s]
Adults	55.97	1.91	0.611
Children	38.83	1.50	1.046
MW-U (P)	0.0012	0.4996	0.0000

Table 8: Game statistics, average values.

Discussion and Conclusion

With the present work, we have seen how different users have different reaction speed in single and multiplayer physical games. The work shows that there are statistical significant differences between different players and between different game set-ups. Indeed, in the single player game we observed statistical significant differences between male and female players, between adult and children, and between play on a 2x3 tiles platform and a 2x4 tiles platform. A similar change in performance due to different tiles set-ups (2x3, 2x4, and 4x4) was observed with the multiplayer game. Further, the multiplayer games showed that there was statistical significant difference in reaction speed and number of tiles hit between the fast players and the slow players, who were coupled to play against each other. Despite this difference, both fast players and slow players found the games equally fun and challenging.

In our point of view, it is an important result to be able to create physical games which players with different physical abilities can play together with equal fun and challenge. We believed that we obtained this here by the creation of adaptive games that run-time adapts to the reaction speed of individual players. Even in the multiplayer game, the game adapts differently to the two individual players, and thereby they each become challenged at their own particular level.
This can be important for instance in welfare technology for elderly, where we have observed a need for physical training/rehabilitation equipment to easily adapt to the individual elderly [8, 9]. Therefore, in future, we will investigate the adaptive playware as a welfare technology, and adaptive in other games potentially suitable for elderly (e.g. see [10]).

Acknowledgement

The work is supported by the "LEV VEL" project.

References

[1] L. Pagliarini and H. H. Lund. Wearing the Playware. *Artificial Life and Robotics Journal*, 15:4, 381-384, 2011.
[2] H. H. Lund, T. Klitbo, and C. Jessen, C. Playware Technology for Physically Activating Play, *Artificial Life and Robotics Journal*, 9:4, 165-174, 2005.
[3] H. H. Lund, and P. Marti. Designing Modular Robotic Playware. In *Proc. of 18th IEEE Int. Symposium on Robot and Human Interactive Communication* (Ro-Man 2009), IEEE Press, 115-121, 2009.
[4] H. H. Lund and A. T. Thorsteinsson. Adaptive Playware in Physical Games. In *Proceedings of the 6th International Conference on Foundations of Digital Games 2011*, ACM, 2011.
[5] A. Derakhshan, F. Hammer, and H. H. Lund. Adapting Playgrounds for Children's Play Using Ambient Playware. In *Proceedings of IEEE Intelligent Robots and Systems* (IROS'06), IEEE Press, Hong Kong, 2006
[6] G. N. Yannakakis, H. H. Lund, and J. Hallam. Modeling Children's Entertainment in the Playware Playground. *IEEE Symposium on Computational Intelligence and Games 2006* (CIG 2006), IEEE Press: 134-141, 2006
[7] G. N. Yannakakis, J. Hallam, and H. H. Lund. Entertainment capture through heart rate activity in physical interactive playgrounds. *User Modeling and User-Adapted Interaction*, 18: 207-243, 2008.
[8] H. H. Lund. Modular Robotics for Playful Physiotherapy, in *Proceedings of IEEE Int. Conference on Rehabilitation Robotics*, IEEE Press, 571-575, 2009.
[9] H. H. Lund and C. B. Nielsen. Modularity for Modulating Exercises and Levels – Observations from Cardiac, Stroke, and COLD Patients Therapy. In *Proceedings of 8th Int. Conference on Ubiquitous Robots and Ambient Intelligence (URAI)*, IEEE, 2011.
[10] D. T. Björnsson and R. V. Fridriksson. Adaptivity in Interactive Modular Playware for Tele-Play. MSc Thesis, DTU, August 2011.

The Seventeenth International Symposium on Artificial Life and Robotics 2012 (AROB 17th '12),
B-Con Plaza, Beppu, Oita, Japan, January 19-21, 2012

Introduction to silicon neuron and neuronal networks

Takashi Kohno

The University of Tokyo

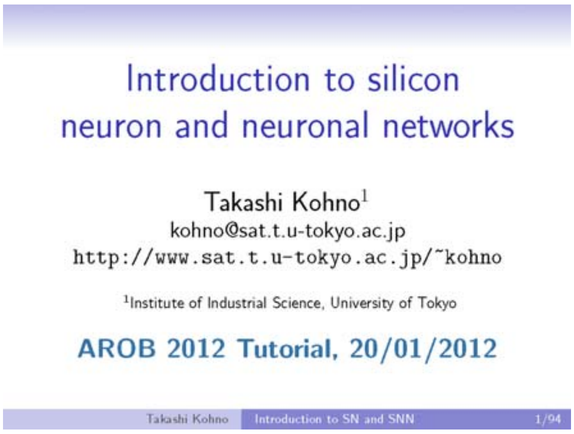

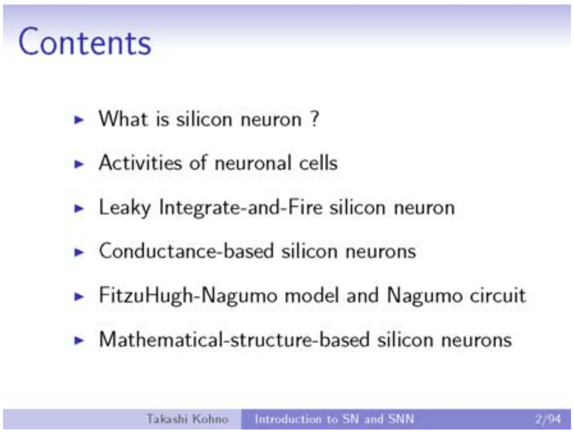

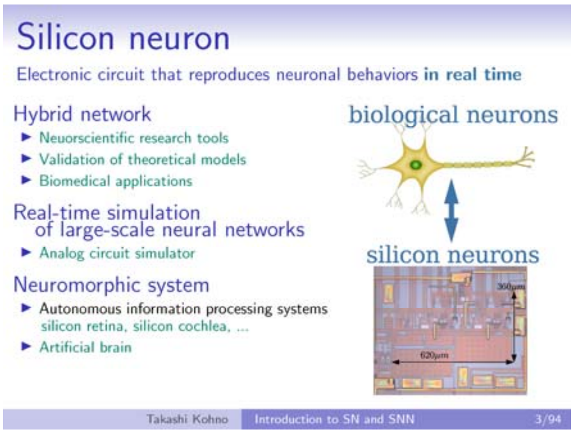

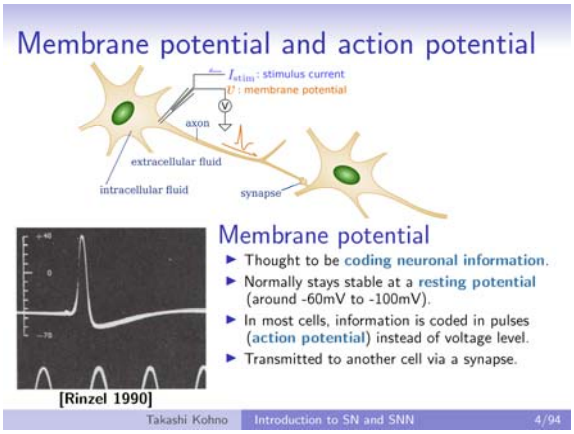

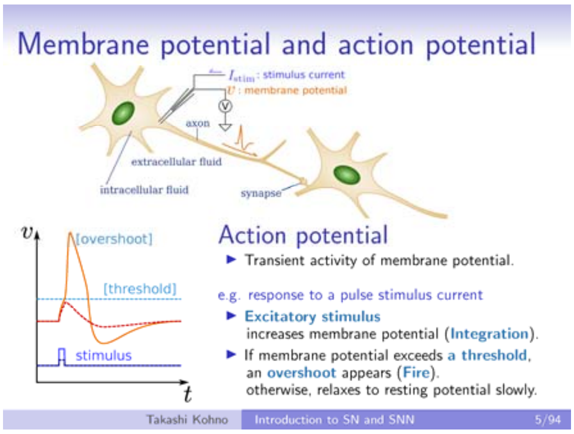

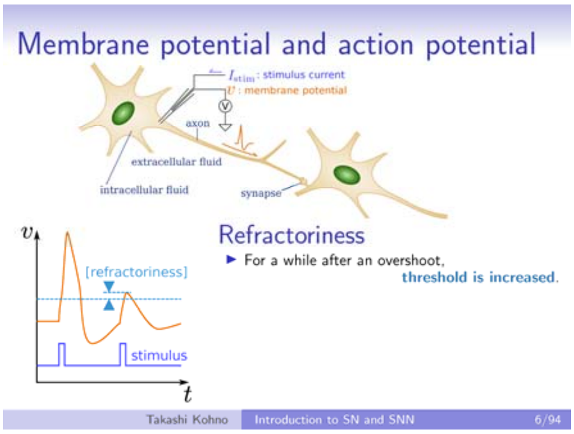

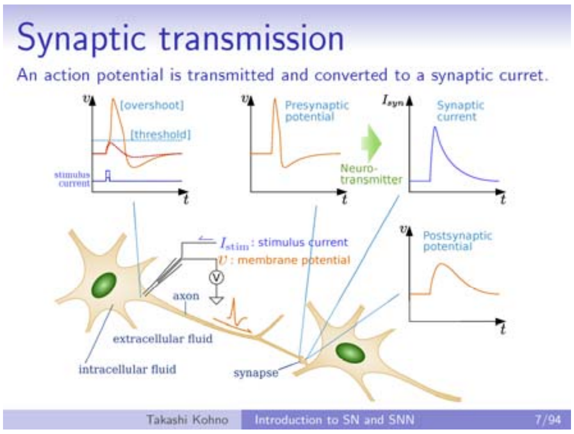
Synaptic transmission
An action potential is transmitted and converted to a synaptic curret.
[overshoot]
[threshold]
stimulus current
Presynaptic potential
Neuro-transmitter
Synaptic current
Postsynaptic potential
I_{stim} : stimulus current
v : membrane potential
axon
extracellular fluid
intracellular fluid
synapse
Takashi Kohno
Introduction to SN and SNN
7/94

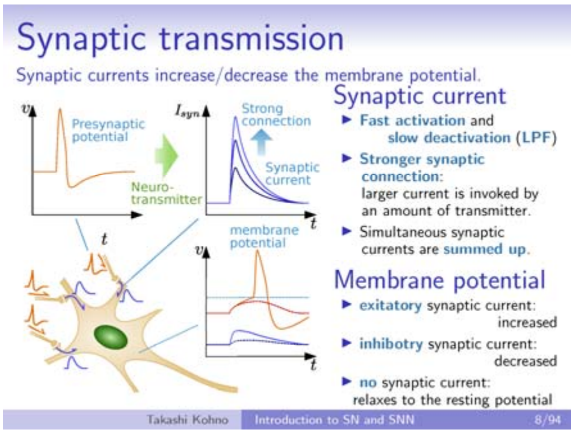
Synaptic transmission
Synaptic currents increase/decrease the membrane potential.
Presynaptic potential
Neuro-transmitter
Strong connection
Synaptic current
membrane potential
Synaptic current
Fast activation and slow deactivation (LPF)
Stronger synaptic connection: larger current is invoked by an amount of transmitter.
Simultaneous synaptic currents are summed up.
Membrane potential
exitatory synaptic current: increased
inhibotry synaptic current: decreased
no synaptic current: relaxes to the resting potential
Takashi Kohno
Introduction to SN and SNN
8/94

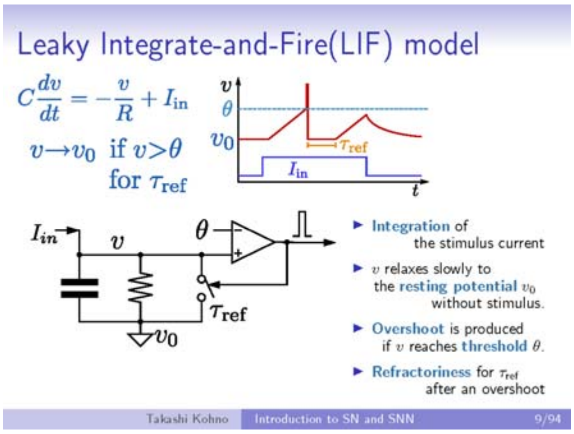
Leaky Integrate-and-Fire(LIF) model
$C\frac{dv}{dt} = -\frac{v}{R} + I_{in}$
$v \rightarrow v_0$ if $v > \theta$
for τ_{ref}
I_{in}
Integration of the stimulus current
v relaxes slowly to the resting potential v_0 without stimulus.
Overshoot is produced if v reaches threshold θ.
Refractoriness for τ_{ref} after an overshoot
Takashi Kohno
Introduction to SN and SNN
9/94

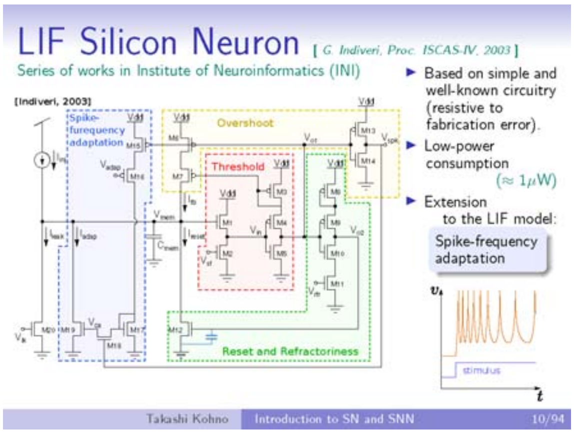
LIF Silicon Neuron [G. Indiveri, Proc. ISCAS-IV, 2003]
Series of works in Institute of Neuroinformatics (INI)
[Indiveri, 2003]
Spike-furequency adaptation
Overshoot
Threshold
Reset and Refractoriness
Based on simple and well-known circuitry (resistive to fabrication error).
Low-power consumption ($\approx 1\mu$W)
Extension to the LIF model:
Spike-frequency adaptation
stimulus
Takashi Kohno
Introduction to SN and SNN
10/94

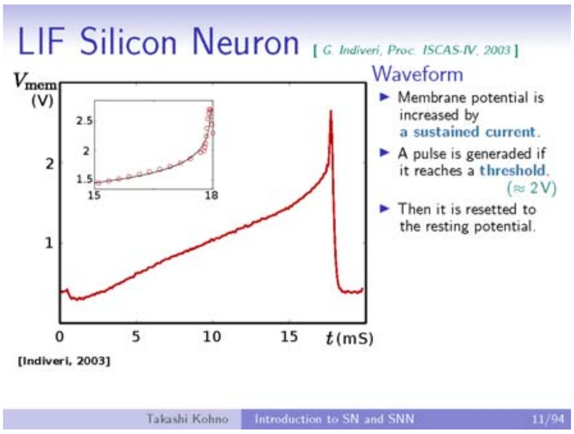
LIF Silicon Neuron [G. Indiveri, Proc. ISCAS-IV, 2003]
V_{mem} (V)
t (mS)
[Indiveri, 2003]
Waveform
Membrane potential is increased by a sustained current.
A pulse is generaded if it reaches a threshold. ($\approx$ 2V)
Then it is resetted to the resting potential.
Takashi Kohno
Introduction to SN and SNN
11/94

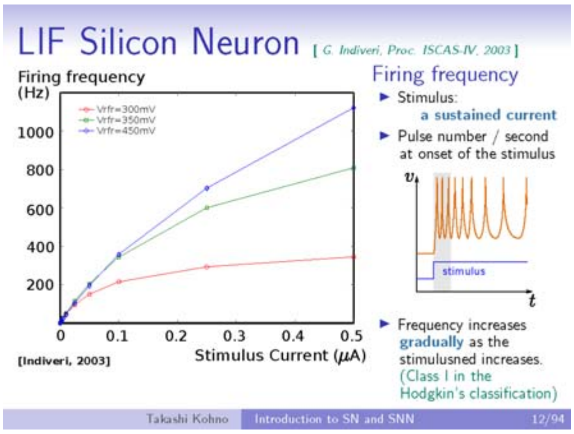
LIF Silicon Neuron [G. Indiveri, Proc. ISCAS-IV, 2003]
Firing frequency (Hz)
Vrfr=300mV
Vrfr=350mV
Vrfr=450mV
Stimulus Current (μA)
[Indiveri, 2003]
Firing frequency
Stimulus: a sustained current
Pulse number / second at onset of the stimulus
stimulus
Frequency increases gradually as the stimulusned increases. (Class I in the Hodgkin's classification)
Takashi Kohno
Introduction to SN and SNN
12/94

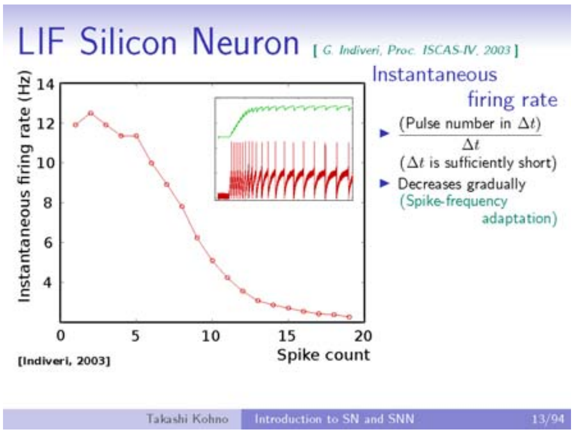
LIF Silicon Neuron [G. Indiveri, Proc. ISCAS-IV, 2003]
Instantaneous firing rate (Hz)
Spike count
[Indiveri, 2003]
Instantaneous firing rate
(Pulse number in Δt)/Δt
(Δt is sufficiently short)
Decreases gradually (Spike-frequency adaptation)
Takashi Kohno
Introduction to SN and SNN
13/94

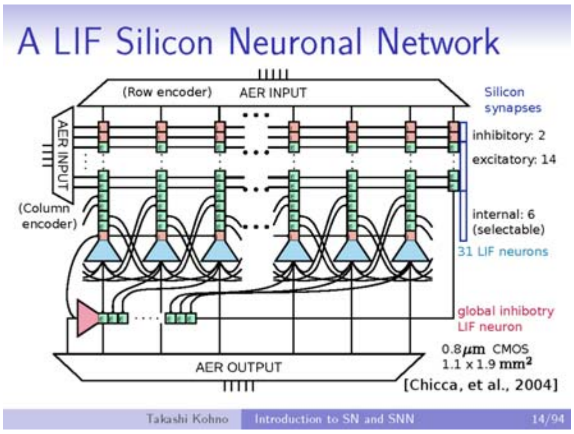
A LIF Silicon Neuronal Network
(Row encoder)
AER INPUT
Silicon synapses
inhibitory: 2
excitatory: 14
internal: 6 (selectable)
31 LIF neurons
(Column encoder)
global inhibotry LIF neuron
0.8μm CMOS
1.1 x 1.9 mm^2
AER OUTPUT
[Chicca, et al., 2004]
Takashi Kohno
Introduction to SN and SNN
14/94

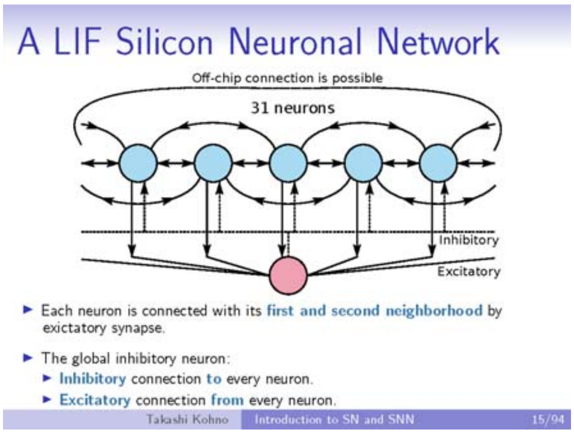
A LIF Silicon Neuronal Network
Off-chip connection is possible
31 neurons
Inhibitory
Excitatory
Each neuron is connected with its first and second neighborhood by exictatory synapse.
The global inhibitory neuron:
Inhibitory connection to every neuron.
Excitatory connection from every neuron.
Takashi Kohno
Introduction to SN and SNN
15/94

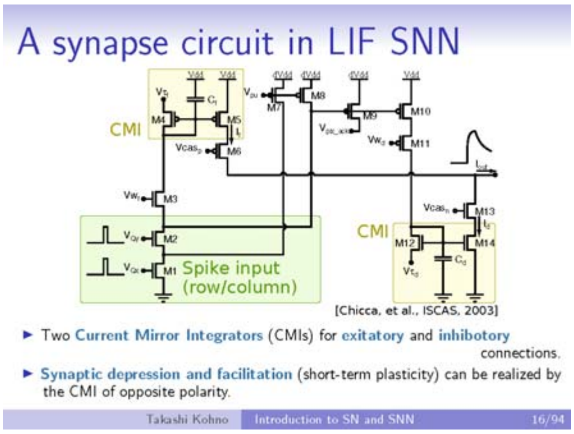
A synapse circuit in LIF SNN
CMI
Spike input (row/column)
CMI
[Chicca, et al., ISCAS, 2003]
Two Current Mirror Integrators (CMIs) for exitatory and inhibotory connections.
Synaptic depression and facilitation (short-term plasticity) can be realized by the CMI of opposite polarity.
Takashi Kohno
Introduction to SN and SNN
16/94

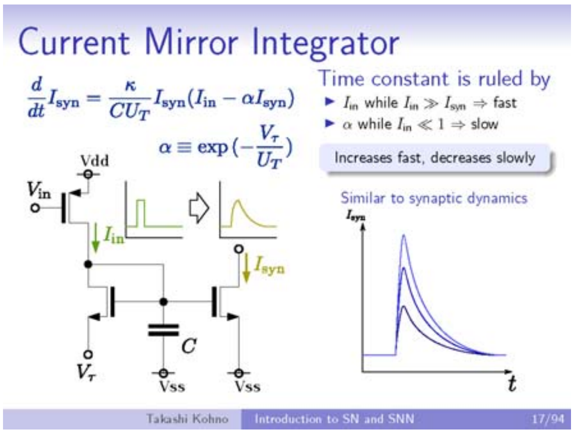
Current Mirror Integrator
$\frac{d}{dt}I_{syn} = \frac{\kappa}{CU_T} I_{syn}(I_{in} - \alpha I_{syn})$
$\alpha \equiv \exp(-\frac{V_\tau}{U_T})$
Time constant is ruled by
I_{in} while $I_{in} \gg I_{syn} \Rightarrow$ fast
α while $I_{in} \ll 1 \Rightarrow$ slow
Increases fast, decreases slowly
Similar to synaptic dynamics
Vdd
V_{in}
I_{in}
I_{syn}
C
V_τ
Vss
Vss
t
Takashi Kohno
Introduction to SN and SNN
17/94

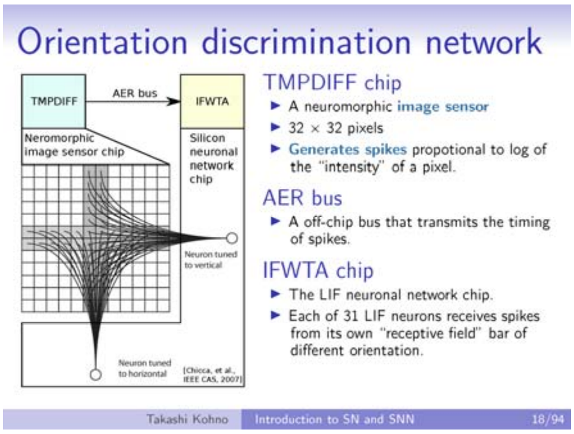
Orientation discrimination network
TMPDIFF
AER bus
IFWTA
Neromorphic image sensor chip
Silicon neuronal network chip
Neuron tuned to vertical
Neuron tuned to horizontal
[Chicca, et al., IEEE CAS, 2007]
TMPDIFF chip
A neuromorphic image sensor
32 × 32 pixels
Generates spikes propotional to log of the "intensity" of a pixel.
AER bus
A off-chip bus that transmits the timing of spikes.
IFWTA chip
The LIF neuronal network chip.
Each of 31 LIF neurons receives spikes from its own "receptive field" bar of different orientation.
Takashi Kohno
Introduction to SN and SNN
18/94

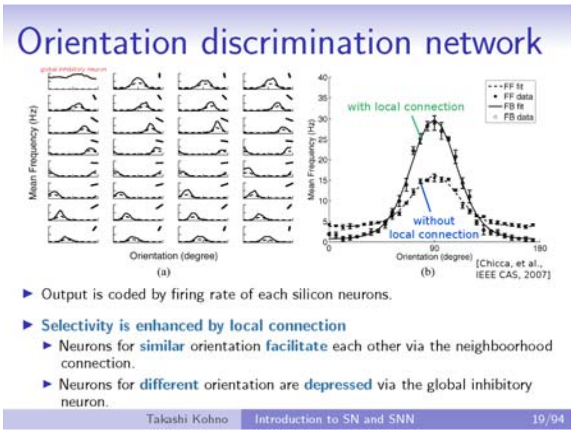
Orientation discrimination network
Mean Frequency (Hz)
Orientation (degree)
(a)
with local connection
without local connection
(b)
[Chicca, et al., IEEE CAS, 2007]
Output is coded by firing rate of each silicon neurons.
Selectivity is enhanced by local connection
Neurons for similar orientation facilitate each other via the neighborhood connection.
Neurons for different orientation are depressed via the global inhibitory neuron.
Takashi Kohno
Introduction to SN and SNN
19/94

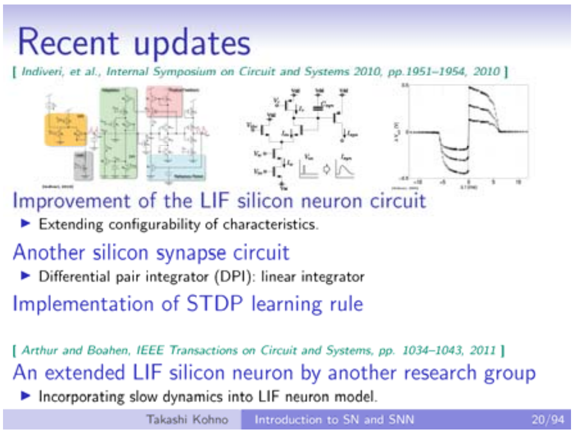
Recent updates
[Indiveri, et al., Internal Symposium on Circuit and Systems 2010, pp.1951–1954, 2010]
Improvement of the LIF silicon neuron circuit
Extending configurability of characteristics.
Another silicon synapse circuit
Differential pair integrator (DPI): linear integrator
Implementation of STDP learning rule
[Arthur and Boahen, IEEE Transactions on Circuit and Systems, pp. 1034–1043, 2011]
An extended LIF silicon neuron by another research group
Incorporating slow dynamics into LIF neuron model.
Takashi Kohno
Introduction to SN and SNN
20/94

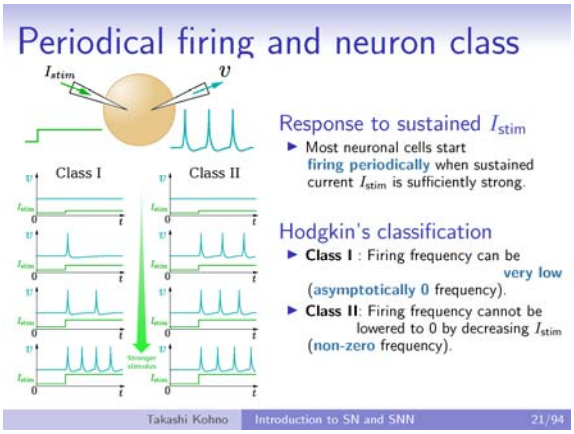
Periodical firing and neuron class
I_{stim}
v
Class I
Class II
Response to sustained I_{stim}
Most neuronal cells start firing periodically when sustained current I_{stim} is sufficiently strong.
Hodgkin's classification
Class I : Firing frequency can be very low (asymptotically 0 frequency).
Class II: Firing frequency cannot be lowered to 0 by decreasing I_{stim} (non-zero frequency).
Takashi Kohno
Introduction to SN and SNN
21/94

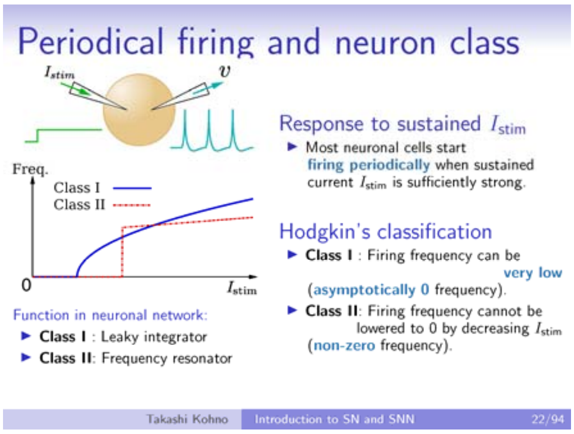
Periodical firing and neuron class
I_{stim}
v
Freq.
Class I
Class II
0
I_{stim}
Function in neuronal network:
Class I : Leaky integrator
Class II: Frequency resonator
Response to sustained I_{stim}
Most neuronal cells start firing periodically when sustained current I_{stim} is sufficiently strong.
Hodgkin's classification
Class I : Firing frequency can be very low (asymptotically 0 frequency).
Class II: Firing frequency cannot be lowered to 0 by decreasing I_{stim} (non-zero frequency).
Takashi Kohno
Introduction to SN and SNN
22/94

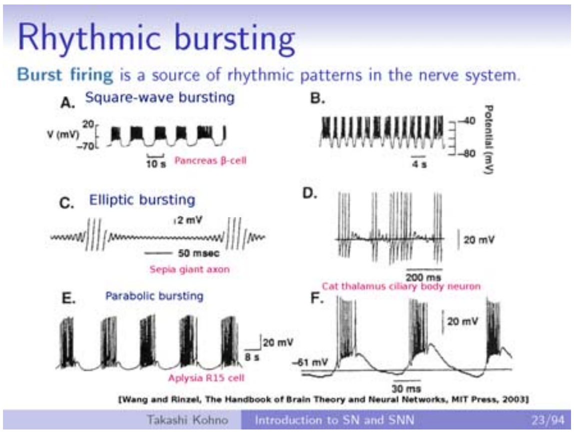
Rhythmic bursting
Burst firing is a source of rhythmic patterns in the nerve system.
A. Square-wave bursting
Pancreas β-cell
B.
C. Elliptic bursting
Sepia giant axon
D.
Cat thalamus ciliary body neuron
E. Parabolic bursting
Aplysia R15 cell
F.
[Wang and Rinzel, The Handbook of Brain Theory and Neural Networks, MIT Press, 2003]
Takashi Kohno Introduction to SN and SNN 23/94

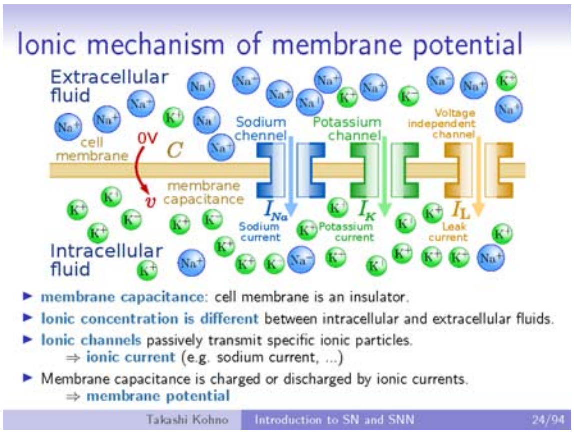
Ionic mechanism of membrane potential
Extracellular fluid
Intracellular fluid
cell membrane
membrane capacitance
Sodium chennel
Potassium channel
Voltage independent channel
Sodium current
Potassium current
Leak current
membrane capacitance: cell membrane is an insulator.
Ionic concentration is different between intracellular and extracellular fluids.
Ionic channels passively transmit specific ionic particles.
⇒ ionic current (e.g. sodium current, ...)
Membrane capacitance is charged or discharged by ionic currents.
⇒ membrane potential
Takashi Kohno Introduction to SN and SNN 24/94

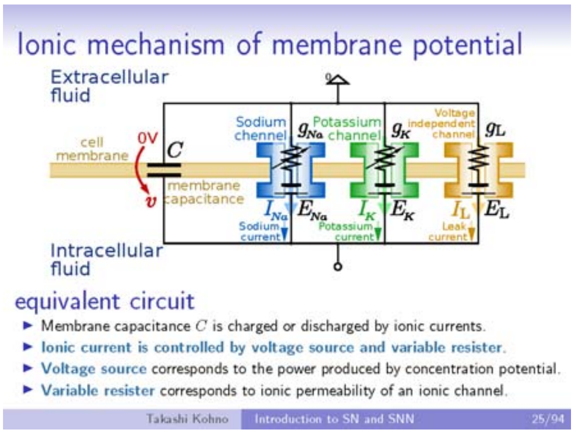
Ionic mechanism of membrane potential
Extracellular fluid
Intracellular fluid
cell membrane
membrane capacitance
Sodium chennel
Potassium channel
Voltage independent channel
equivalent circuit
Membrane capacitance C is charged or discharged by ionic currents.
Ionic current is controlled by voltage source and variable resister.
Voltage source corresponds to the power produced by concentration potential.
Variable resister corresponds to ionic permeability of an ionic channel.
Takashi Kohno Introduction to SN and SNN 25/94

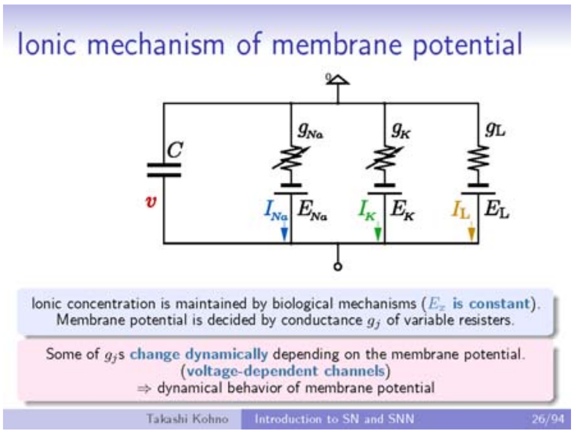
Ionic mechanism of membrane potential
Ionic concentration is maintained by biological mechanisms (E_x is constant).
Membrane potential is decided by conductance g_j of variable resisters.
Some of g_js change dynamically depending on the membrane potential.
(voltage-dependent channels)
⇒ dynamical behavior of membrane potential
Takashi Kohno Introduction to SN and SNN 26/94

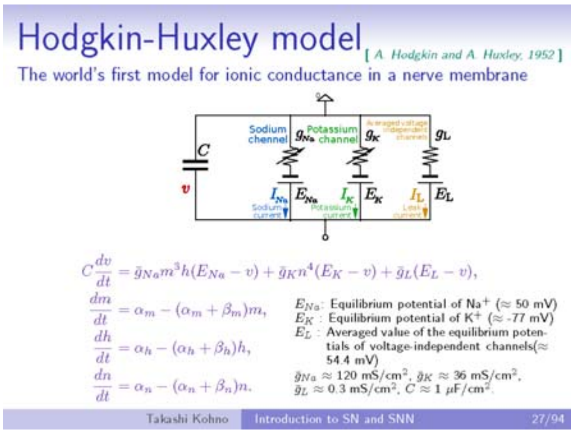
Hodgkin-Huxley model [A. Hodgkin and A. Huxley, 1952]
The world's first model for ionic conductance in a nerve membrane
$C\frac{dv}{dt} = \bar{g}_{Na}m^3h(E_{Na}-v) + \bar{g}_K n^4(E_K - v) + \bar{g}_L(E_L - v),$
$\frac{dm}{dt} = \alpha_m - (\alpha_m + \beta_m)m,$
$\frac{dh}{dt} = \alpha_h - (\alpha_h + \beta_h)h,$
$\frac{dn}{dt} = \alpha_n - (\alpha_n + \beta_n)n.$
E_{Na}: Equilibrium potential of Na+ (≈ 50 mV)
E_K: Equilibrium potential of K+ (≈ -77 mV)
E_L: Averaged value of the equilibrium potentials of voltage-independent channels(≈ 54.4 mV)
$\bar{g}_{Na} \approx 120$ mS/cm², $\bar{g}_K \approx 36$ mS/cm², $\bar{g}_L \approx 0.3$ mS/cm², $C \approx 1$ μF/cm².
Takashi Kohno Introduction to SN and SNN 27/94

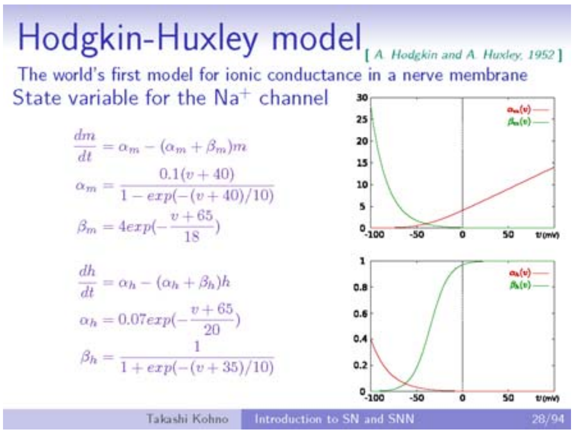
Hodgkin-Huxley model [A. Hodgkin and A. Huxley, 1952]
The world's first model for ionic conductance in a nerve membrane
State variable for the Na+ channel
$\frac{dm}{dt} = \alpha_m - (\alpha_m + \beta_m)m$
$\alpha_m = \frac{0.1(v+40)}{1-exp(-(v+40)/10)}$
$\beta_m = 4exp(-\frac{v+65}{18})$
$\frac{dh}{dt} = \alpha_h - (\alpha_h + \beta_h)h$
$\alpha_h = 0.07exp(-\frac{v+65}{20})$
$\beta_h = \frac{1}{1+exp(-(v+35)/10)}$
Takashi Kohno Introduction to SN and SNN 28/94

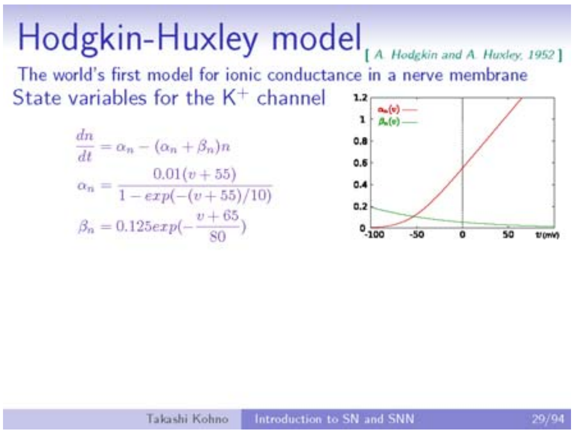
Hodgkin-Huxley model [A. Hodgkin and A. Huxley, 1952]
The world's first model for ionic conductance in a nerve membrane
State variables for the K+ channel
$\frac{dn}{dt} = \alpha_n - (\alpha_n + \beta_n)n$
$\alpha_n = \frac{0.01(v+55)}{1-exp(-(v+55)/10)}$
$\beta_n = 0.125exp(-\frac{v+65}{80})$
Takashi Kohno Introduction to SN and SNN 29/94

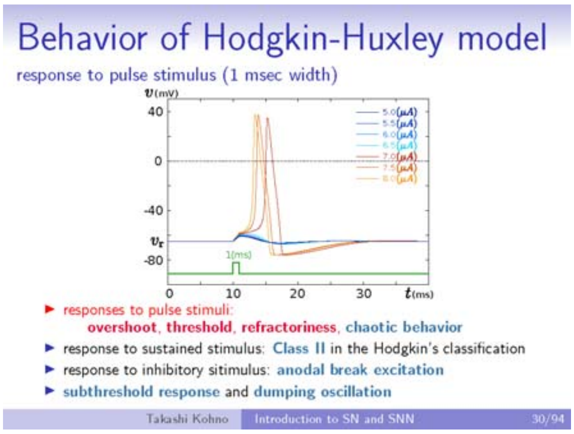
Behavior of Hodgkin-Huxley model
response to pulse stimulus (1 msec width)
responses to pulse stimuli:
overshoot, threshold, refractoriness, chaotic behavior
response to sustained stimulus: Class II in the Hodgkin's classification
response to inhibitory stimulus: anodal break excitation
subthreshold response and dumping oscillation
Takashi Kohno Introduction to SN and SNN 30/94

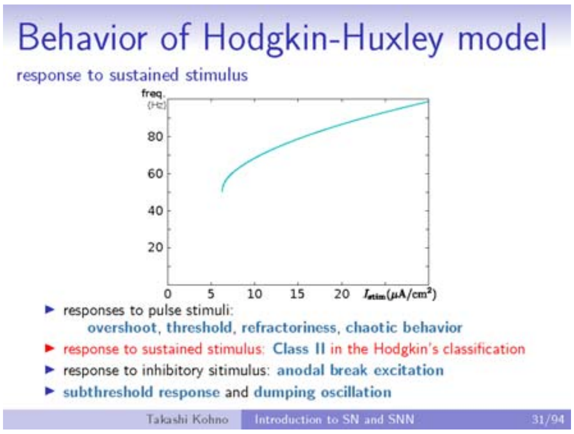
Behavior of Hodgkin-Huxley model
response to sustained stimulus
freq. (Hz)
I_{stim} (μA/cm^2)
responses to pulse stimuli: overshoot, threshold, refractoriness, chaotic behavior
response to sustained stimulus: Class II in the Hodgkin's classification
response to inhibitory sitimulus: anodal break excitation
subthreshold response and dumping oscillation
Takashi Kohno
Introduction to SN and SNN
31/94

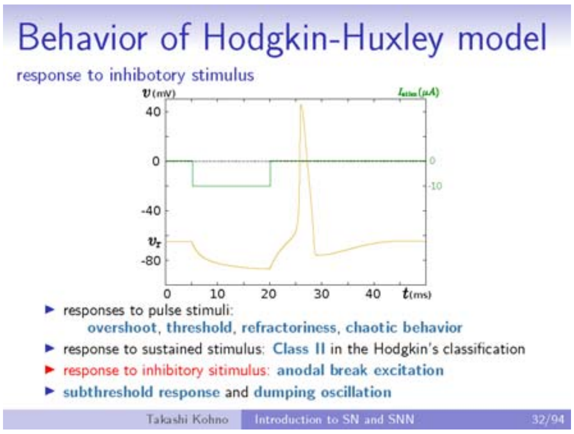
Behavior of Hodgkin-Huxley model
response to inhibotory stimulus
v (mV)
I_{stim} (μA)
v_r
t (ms)
responses to pulse stimuli: overshoot, threshold, refractoriness, chaotic behavior
response to sustained stimulus: Class II in the Hodgkin's classification
response to inhibitory sitimulus: anodal break excitation
subthreshold response and dumping oscillation
Takashi Kohno
Introduction to SN and SNN
32/94

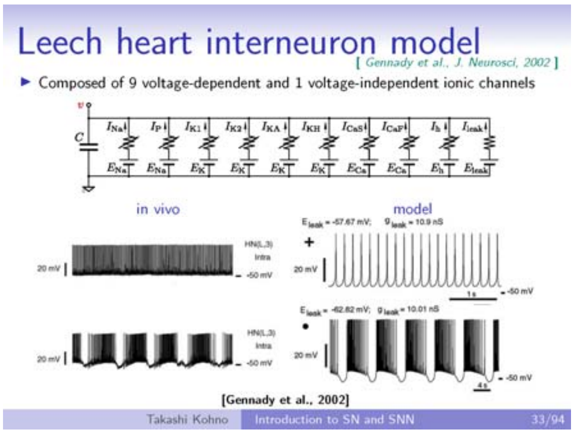
Leech heart interneuron model
[Gennady et al., J. Neurosci, 2002]
Composed of 9 voltage-dependent and 1 voltage-independent ionic channels
in vivo
model
[Gennady et al., 2002]
Takashi Kohno
Introduction to SN and SNN
33/94

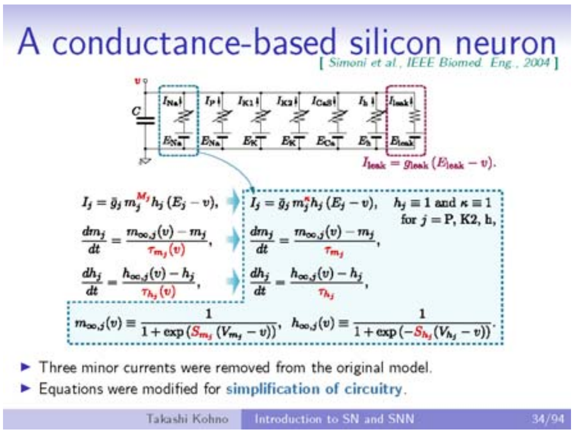
A conductance-based silicon neuron
[Simoni et al., IEEE Biomed. Eng., 2004]
$I_{leak} = g_{leak}(E_{leak} - v)$.
$I_j = \bar{g}_j m_j^{M_j} h_j (E_j - v)$,
$I_j = \bar{g}_j m_j^{\kappa} h_j (E_j - v)$, $h_j \equiv 1$ and $\kappa \equiv 1$ for $j =$ P, K2, h,
$\frac{dm_j}{dt} = \frac{m_{\infty,j}(v) - m_j}{\tau_{m_j}(v)}$,
$\frac{dm_j}{dt} = \frac{m_{\infty,j}(v) - m_j}{\tau_{m_j}}$,
$\frac{dh_j}{dt} = \frac{h_{\infty,j}(v) - h_j}{\tau_{h_j}(v)}$,
$\frac{dh_j}{dt} = \frac{h_{\infty,j}(v) - h_j}{\tau_{h_j}}$,
$m_{\infty,j}(v) \equiv \frac{1}{1+\exp(S_{m_j}(V_{m_j} - v))}$, $h_{\infty,j}(v) \equiv \frac{1}{1+\exp(-S_{h_j}(V_{h_j} - v))}$.
Three minor currents were removed from the original model.
Equations were modified for simplification of circuitry.
Takashi Kohno
Introduction to SN and SNN
34/94

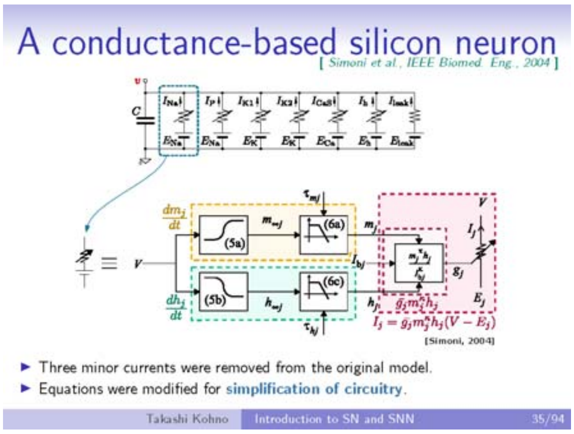
A conductance-based silicon neuron
[Simoni et al., IEEE Biomed. Eng., 2004]
$I_j = \bar{g}_j m_j^\kappa h_j (V - E_j)$
[Simoni, 2004]
Three minor currents were removed from the original model.
Equations were modified for simplification of circuitry.
Takashi Kohno
Introduction to SN and SNN
35/94

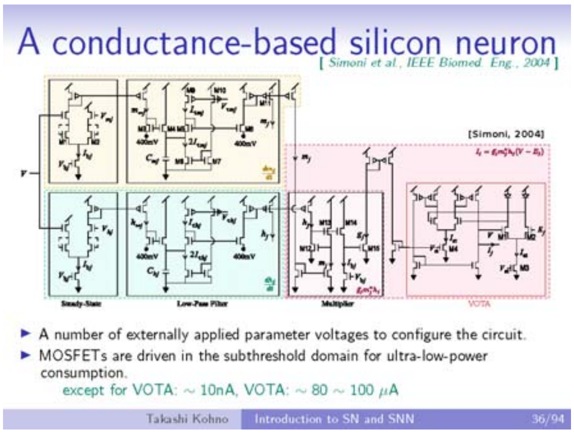
A conductance-based silicon neuron
[Simoni et al., IEEE Biomed. Eng., 2004]
[Simoni, 2004]
Steady-State
Low-Pass Filter
Multiplier
VOTA
A number of externally applied parameter voltages to configure the circuit.
MOSFETs are driven in the subthreshold domain for ultra-low-power consumption.
except for VOTA: ~ 10nA, VOTA: ~ 80 ~ 100 μA
Takashi Kohno
Introduction to SN and SNN
36/94

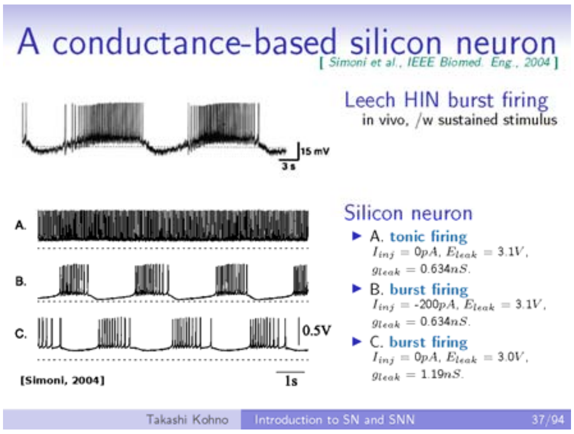
A conductance-based silicon neuron
[Simoni et al., IEEE Biomed. Eng., 2004]
Leech HIN burst firing
in vivo, /w sustained stimulus
15 mV
3 s
Silicon neuron
A. tonic firing
I_{inj} = 0pA, E_{leak} = 3.1V, g_{leak} = 0.634nS.
B. burst firing
I_{inj} = -200pA, E_{leak} = 3.1V, g_{leak} = 0.634nS.
C. burst firing
I_{inj} = 0pA, E_{leak} = 3.0V, g_{leak} = 1.19nS.
0.5V
1s
[Simoni, 2004]
Takashi Kohno
Introduction to SN and SNN
37/94

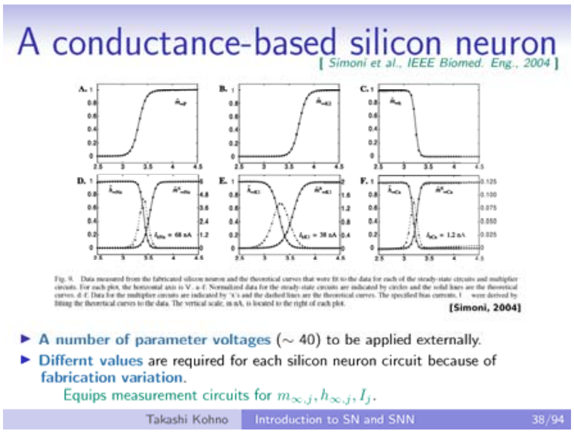
A conductance-based silicon neuron
[Simoni et al., IEEE Biomed. Eng., 2004]
[Simoni, 2004]
A number of parameter voltages (~ 40) to be applied externally.
Differnt values are required for each silicon neuron circuit because of fabrication variation.
Equips measurement circuits for $m_{\infty,j}, h_{\infty,j}, I_j$.
Takashi Kohno
Introduction to SN and SNN
38/94

A conductance-based silicon neuronal network

[Simoni et al., IEEE Biomed. Eng., 2007]

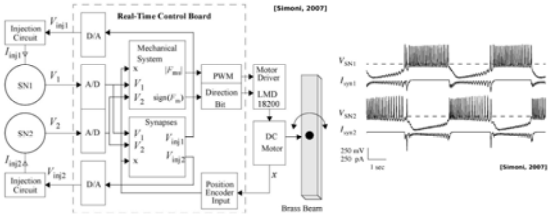

- A silicon half-center oscillator
  - Half-center oscillator: the simplest biological motion pattern generator
  - Two neurons are connected each other via inhibitory synapses.
- Synapses are emulated by ADC, PC, and DAC (dynamic clamp)

Takashi Kohno | Introduction to SN and SNN | 39/94

Cortical neuron models

[Pospischil et al., Biol. Cybern., 2008]

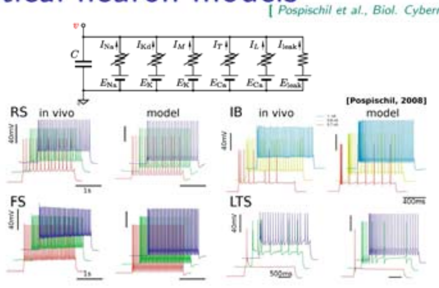

- Composed of 5 voltage-dependent and 1 voltage-independent ionic channels

Takashi Kohno | Introduction to SN and SNN | 40/94

A conductance-based silicon cortical neuron

[Grassia et al., Frontiers Neurocsi., 2011]

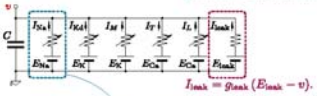

$$I_{leak} = g_{leak}(E_{leak} - v).$$

$$I_j = \bar{g}_j m_j^{p_j} h_j^{q_j}(E_j - v),$$

$$\frac{dm_j}{dt} = \frac{m_{\infty,j}(v) - m_j}{\tau_{m_j}(v)}, \quad \frac{dm_j}{dt} = \frac{m_{\infty,j}(v) - m_j}{\tau_{m_j}},$$

$$\frac{dh_j}{dt} = \frac{h_{\infty,j}(v) - h_j}{\tau_{h_j}(v)}, \quad \frac{dh_j}{dt} = \frac{h_{\infty,j}(v) - h_j}{\tau_{h_j}},$$

$$m_{\infty,j}(v) \equiv \frac{1}{1+\exp((V_{m_j} - v)/V_{s,m_j})}, \quad h_{\infty,j}(v) \equiv \frac{1}{1+\exp((V_{h_j} - v)/V_{s,h_j})}$$

- Equations were modified for simplification of circuitry.

Takashi Kohno | Introduction to SN and SNN | 41/94

A conductance-based silicon cortical neuron

[Grassia et al., Frontiers Neurocsi., 2011]

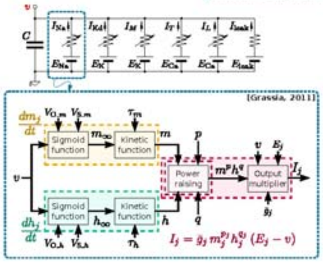

- Several nFs of capacitors are required: off-chip capacitor.
- Parameter voltages are stored in on-chip dynamic analog memory.
- 0.35μm BiCMOS SiGe process, total power consumption 550mW (5 neurons)

Takashi Kohno | Introduction to SN and SNN | 42/94

A conductance-based silicon cortical neuron

[Grassia et al., Frontiers Neurocsi., 2011]

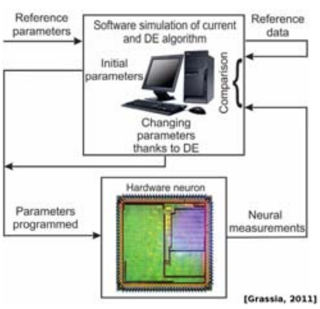

Configuration

- Numbers of parameter voltages to be tuned (maximum 28).
- Fabrication variation is inevitable:
  ⇒ Each instance of silicon neurons requires different parameter voltages.

Automated configuration

- Parameter voltages are tuned up by differential evolution algorithm.
- Minimize behavioral difference to the target cortical neuron models.
- Requires about a day.

Takashi Kohno | Introduction to SN and SNN | 43/94

Behavior of silicon cortical neuron

[Grassia et al., Frontiers Neurocsi., 2011]

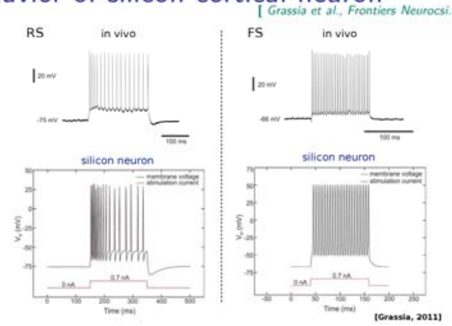

- Successfull automated tuning system.

Takashi Kohno | Introduction to SN and SNN | 44/94

Behavior of silicon cortical neuron

[Grassia et al., Frontiers Neurocsi., 2011]

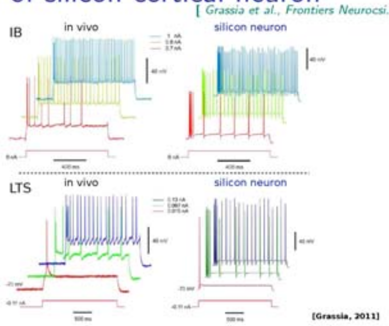

- Successfull automated tuning system.

Takashi Kohno | Introduction to SN and SNN | 45/94

Qualitative neuron models

Ionic conductance models are too complex to explain the mechanism of the neuronal behaviors.

Simple models with similar dynamics were developed by techniques in nonlinear mathematics.

FitzHugh-Nagumo model
Similar dynamics to the Hodgkin-Huxley model

$$\frac{du}{dt} = c(-v + u - \frac{u^3}{3} + I(t)),$$
$$\frac{dv}{dt} = u - bv + a.$$

Hindmarsh-Rose model
A simplest burst firing model

$$\frac{dx}{dt} = y - x^3 + 3x^2 - z,$$
$$\frac{dy}{dt} = 1 - 5x^2 - y,$$
$$\frac{dz}{dt} = r(s(x - x_1) - z).$$

Reduction of the Hodgkin-Huxleymodel by Rinzel

$$h = b - an.$$

Takashi Kohno | Introduction to SN and SNN | 46/94

The Seventeenth International Symposium on Artificial Life and Robotics 2012 (AROB 17th '12),
B-Con Plaza, Beppu, Oita, Japan, January 19-21, 2012

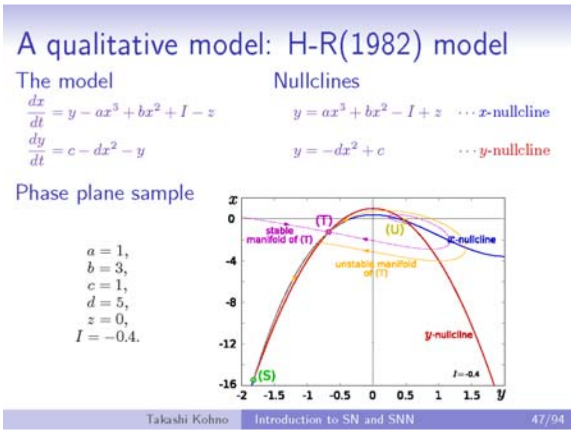

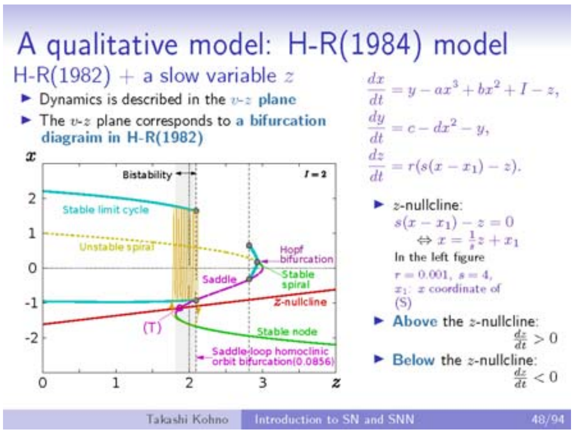

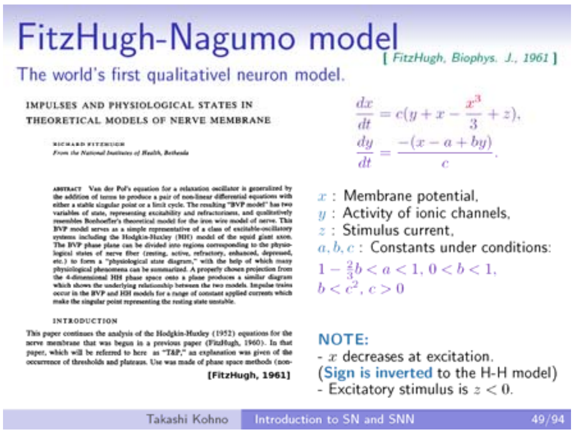

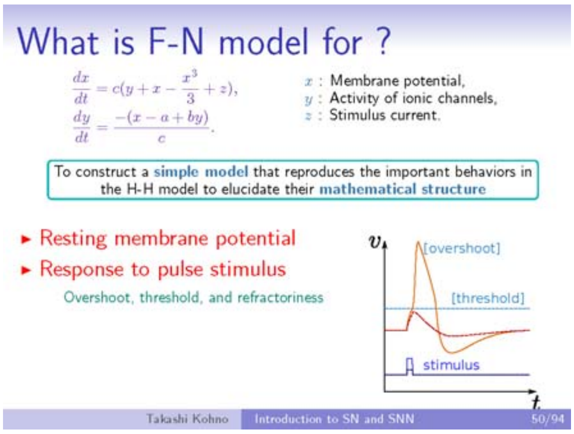

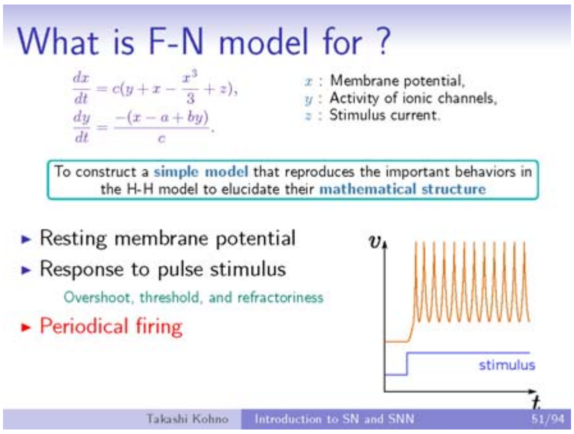

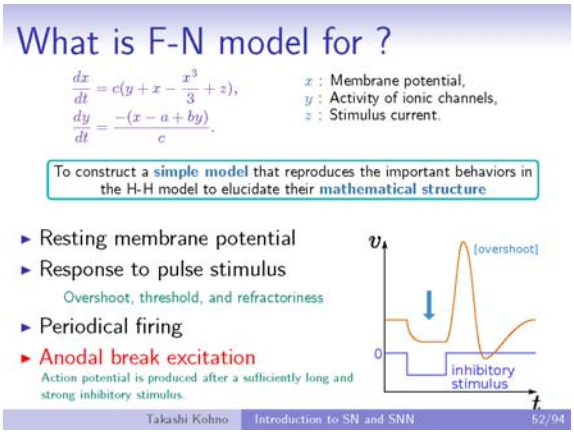

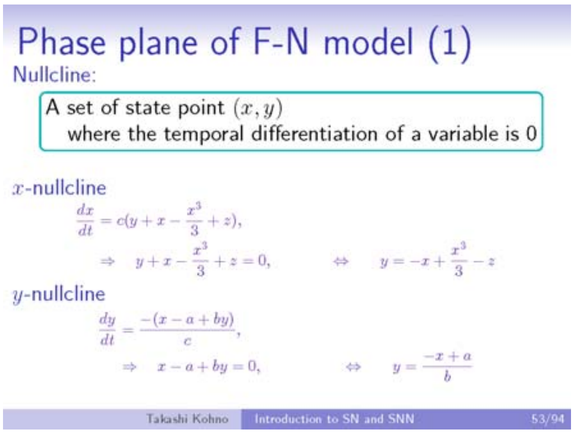

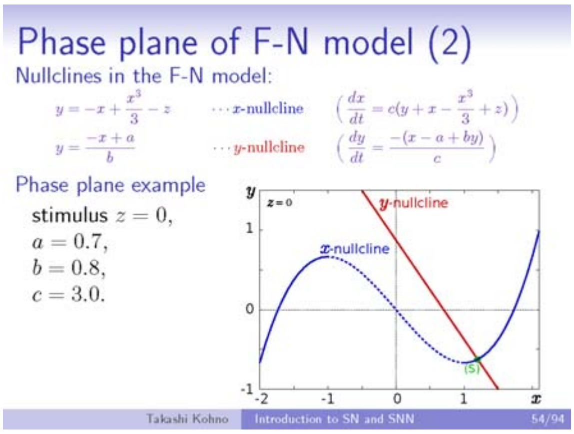

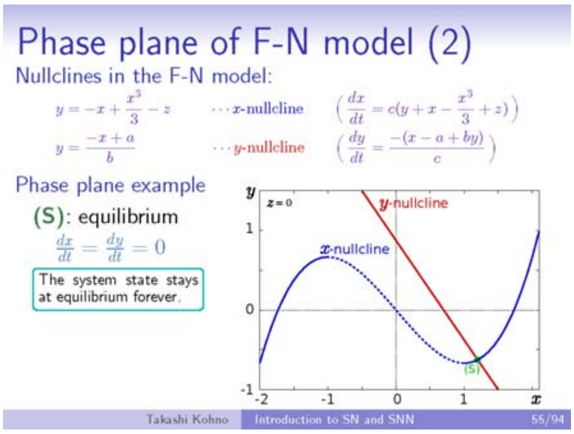
Phase plane of F-N model (2)
Nullclines in the F-N model:
$y = -x + \frac{x^3}{3} - z$ ··· x-nullcline $\left(\frac{dx}{dt} = c(y + x - \frac{x^3}{3} + z)\right)$
$y = \frac{-x + a}{b}$ ··· y-nullcline $\left(\frac{dy}{dt} = \frac{-(x - a + by)}{c}\right)$
Phase plane example
(S): equilibrium
$\frac{dx}{dt} = \frac{dy}{dt} = 0$
The system state stays at equilibrium forever.
$z = 0$
y-nullcline
x-nullcline
(S)
Takashi Kohno
Introduction to SN and SNN
55/94

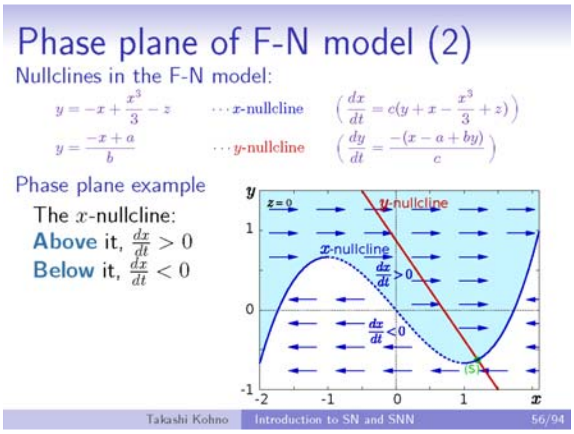
Phase plane of F-N model (2)
Nullclines in the F-N model:
$y = -x + \frac{x^3}{3} - z$ ··· x-nullcline $\left(\frac{dx}{dt} = c(y + x - \frac{x^3}{3} + z)\right)$
$y = \frac{-x + a}{b}$ ··· y-nullcline $\left(\frac{dy}{dt} = \frac{-(x - a + by)}{c}\right)$
Phase plane example
The x-nullcline:
Above it, $\frac{dx}{dt} > 0$
Below it, $\frac{dx}{dt} < 0$
$z = 0$
y-nullcline
x-nullcline
$\frac{dx}{dt} > 0$
$\frac{dx}{dt} < 0$
(S)
Takashi Kohno
Introduction to SN and SNN
56/94

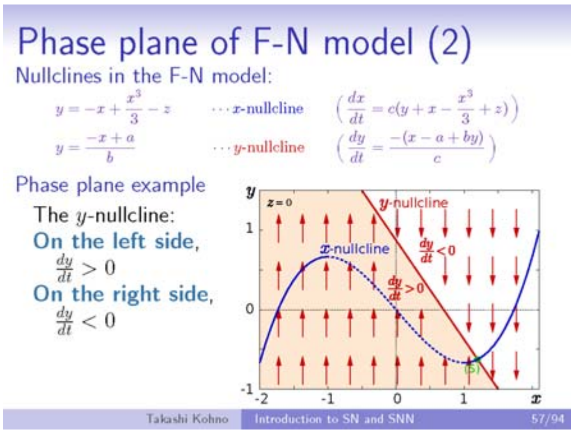
Phase plane of F-N model (2)
Nullclines in the F-N model:
$y = -x + \frac{x^3}{3} - z$ ··· x-nullcline $\left(\frac{dx}{dt} = c(y + x - \frac{x^3}{3} + z)\right)$
$y = \frac{-x + a}{b}$ ··· y-nullcline $\left(\frac{dy}{dt} = \frac{-(x - a + by)}{c}\right)$
Phase plane example
The y-nullcline:
On the left side, $\frac{dy}{dt} > 0$
On the right side, $\frac{dy}{dt} < 0$
$z = 0$
y-nullcline
x-nullcline
$\frac{dy}{dt} < 0$
$\frac{dy}{dt} > 0$
(S)
Takashi Kohno
Introduction to SN and SNN
57/94

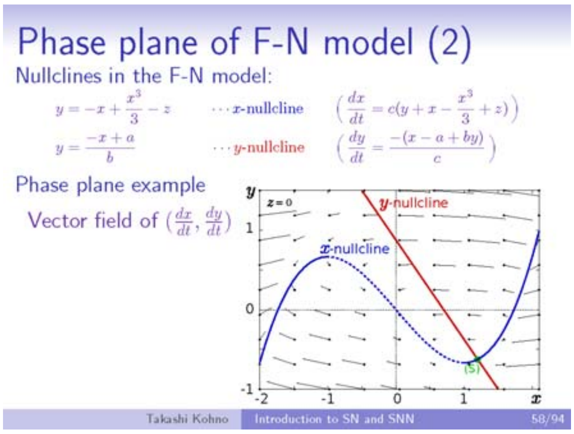
Phase plane of F-N model (2)
Nullclines in the F-N model:
$y = -x + \frac{x^3}{3} - z$ ··· x-nullcline $\left(\frac{dx}{dt} = c(y + x - \frac{x^3}{3} + z)\right)$
$y = \frac{-x + a}{b}$ ··· y-nullcline $\left(\frac{dy}{dt} = \frac{-(x - a + by)}{c}\right)$
Phase plane example
Vector field of $\left(\frac{dx}{dt}, \frac{dy}{dt}\right)$
$z = 0$
y-nullcline
x-nullcline
(S)
Takashi Kohno
Introduction to SN and SNN
58/94

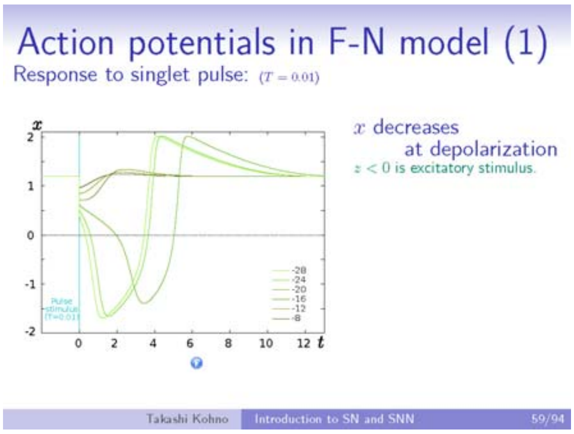
Action potentials in F-N model (1)
Response to singlet pulse: $(T = 0.01)$
x decreases at depolarization
$z < 0$ is excitatory stimulus.
Takashi Kohno
Introduction to SN and SNN
59/94

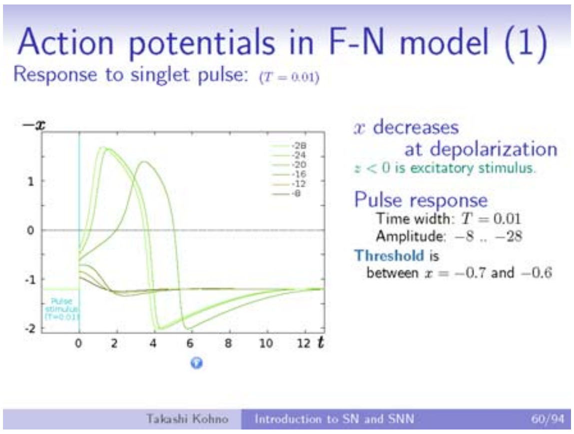
Action potentials in F-N model (1)
Response to singlet pulse: $(T = 0.01)$
x decreases at depolarization
$z < 0$ is excitatory stimulus.
Pulse response
Time width: $T = 0.01$
Amplitude: -8 .. -28
Threshold is between $x = -0.7$ and -0.6
Takashi Kohno
Introduction to SN and SNN
60/94

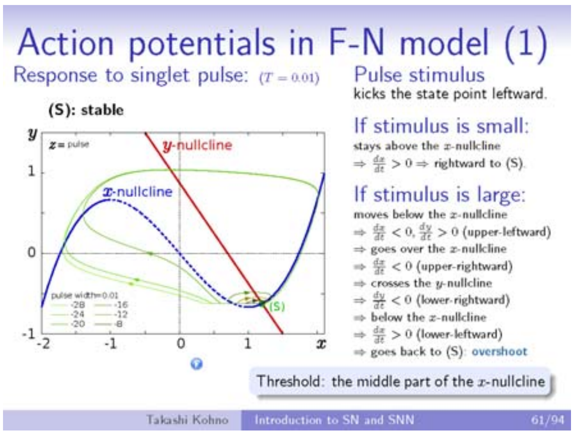
Action potentials in F-N model (1)
Response to singlet pulse: $(T = 0.01)$
(S): stable
Pulse stimulus
kicks the state point leftward.
If stimulus is small:
stays above the x-nullcline
$\Rightarrow \frac{dx}{dt} > 0 \Rightarrow$ rightward to (S).
If stimulus is large:
moves below the x-nullcline
$\Rightarrow \frac{dx}{dt} < 0$, $\frac{dy}{dt} > 0$ (upper-leftward)
$\Rightarrow$ goes over the x-nullcline
$\Rightarrow \frac{dx}{dt} < 0$ (upper-rightward)
$\Rightarrow$ crosses the y-nullcline
$\Rightarrow \frac{dy}{dt} < 0$ (lower-rightward)
$\Rightarrow$ below the x-nullcline
$\Rightarrow \frac{dx}{dt} > 0$ (lower-leftward)
$\Rightarrow$ goes back to (S): overshoot
y-nullcline
x-nullcline
Threshold: the middle part of the x-nullcline
Takashi Kohno
Introduction to SN and SNN
61/94

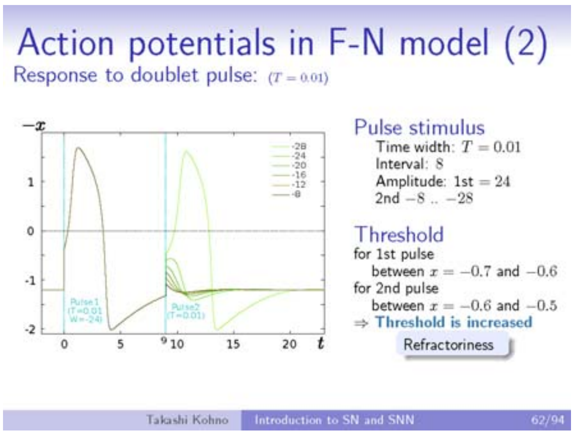
Action potentials in F-N model (2)
Response to doublet pulse: $(T = 0.01)$
Pulse stimulus
Time width: $T = 0.01$
Interval: 8
Amplitude: 1st $= 24$
2nd -8 .. -28
Threshold
for 1st pulse
between $x = -0.7$ and -0.6
for 2nd pulse
between $x = -0.6$ and -0.5
$\Rightarrow$ Threshold is increased
Refractoriness
Takashi Kohno
Introduction to SN and SNN
62/94

Action potentials in F-N model (2)

Response to doublet pulse: $(T = 0.01)$

(S): stable

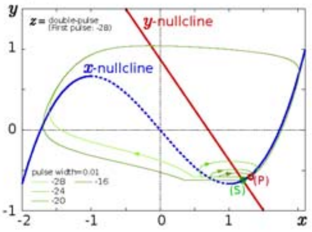

The 2nd pulse is given when the state point is at (P)

(8 timeunit after the 1st pulse) ⇒ jumps leftward from (P)

Threshold: the middle part of the x-nullcline

[The x coordinate of threshold for (P)] $\vee$ [The x coordinate of threshold for (S)]

Refractoriness

Takashi Kohno | Introduction to SN and SNN | 63/94

Action potentials in F-N model (2)

Response to doublet pulse: $(T = 0.01)$

(S): stable

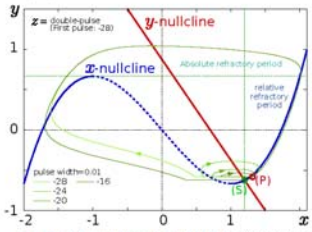

- Absolute refractory period: No threshold exist
- Relative refractory period: Threshold is high

The 2nd pulse is given when the state point is at (P)

(8 timeunit after the 1st pulse) ⇒ jumps leftward from (P)

Threshold: the middle part of the x-nullcline

[The x coordinate of threshold for (P)] $\vee$ [The x coordinate of threshold for (S)]

Refractoriness

Takashi Kohno | Introduction to SN and SNN | 64/94

Anodal break excitation in F-N model

Response to inhibitory stimulus: $(z = 0.4, T = 10)$

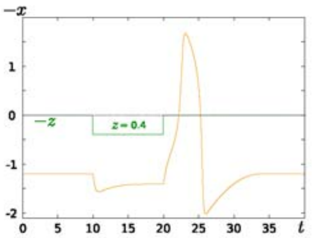

Sufficiently long inhibitory stimulus invokes an action potential at its end.

Takashi Kohno | Introduction to SN and SNN | 65/94

Anodal break excitation in F-N model

Response to inhibitory stimulus: $(z = 0.4, T = 10)$

(S): stable

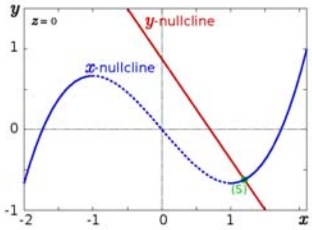

Sufficiently long inhibitory stimulus invokes an action potential at its end.

- Inhibitory stimulus $z = 0.4$ ⇒ x-nullcline is displaced downward

($\because$ x-nullcline: $y = -x + \frac{x^3}{3} - z$) ⇒ (S) moves lower-rightward

Takashi Kohno | Introduction to SN and SNN | 66/94

Anodal break excitation in F-N model

Response to inhibitory stimulus: $(z = 0.4, T = 10)$

(S): stable

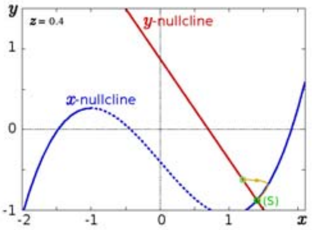

Sufficiently long inhibitory stimulus invokes an action potential at its end.

- Inhibitory stimulus $z = 0.4$ ⇒ x-nullcline is displaced downward

($\because$ x-nullcline: $y = -x + \frac{x^3}{3} - z$) ⇒ (S) moves lower-rightward

Takashi Kohno | Introduction to SN and SNN | 67/94

Anodal break excitation in F-N model

Response to inhibitory stimulus: $(z = 0.4, T = 10)$

(S): stable

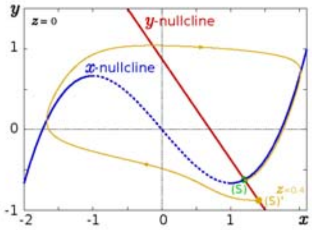

Sufficiently long inhibitory stimulus invokes an action potential at its end.

- Inhibitory stimulus $z = 0.4$ ⇒ x-nullcline is displaced downward

($\because$ x-nullcline: $y = -x + \frac{x^3}{3} - z$) ⇒ (S) moves lower-rightward

- Stimulus ends $z = 0$ ⇒ The system state is below the x-nullcline, where $\frac{dx}{dt} < 0$ ⇒ it moves leftward and action potential starts.

Takashi Kohno | Introduction to SN and SNN | 68/94

Periodic firing in F-N model (1)

Response to sustained stimulus: $(z = 0 \to -0.4)$

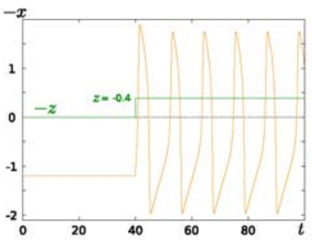

Excitatory sustained stimulus invokes periodic firing.

Takashi Kohno | Introduction to SN and SNN | 69/94

Periodic firing in F-N model (1)

Response to sustained stimulus: $(z = 0 \to -0.4)$

(S): stable

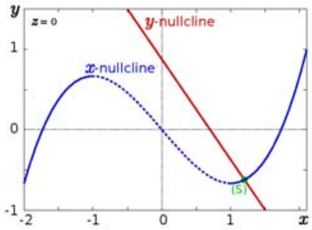

Excitatory sustained stimulus invokes periodic firing.

Decrease in z ⇒ x-nullcline shifts upward.

x-nullcline: $y = -x + \frac{x^3}{3} - z$

Takashi Kohno | Introduction to SN and SNN | 70/94

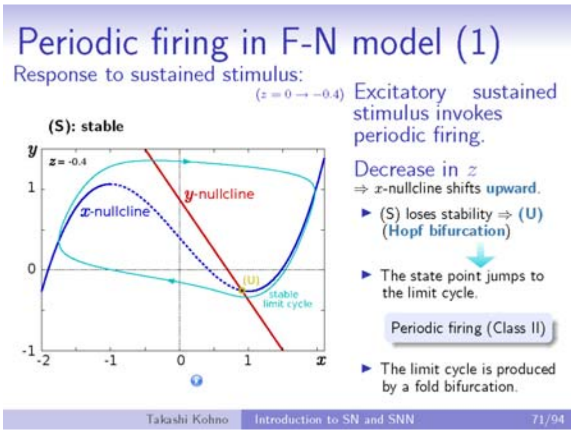
Periodic firing in F-N model (1)
Response to sustained stimulus:
Excitatory sustained stimulus invokes periodic firing.
(S): stable
y-nullcline
x-nullcline
(U)
stable limit cycle
Decrease in z
⇒ x-nullcline shifts upward.
(S) loses stability ⇒ (U) (Hopf bifurcation)
The state point jumps to the limit cycle.
Periodic firing (Class II)
The limit cycle is produced by a fold bifurcation.
Takashi Kohno Introduction to SN and SNN 71/94

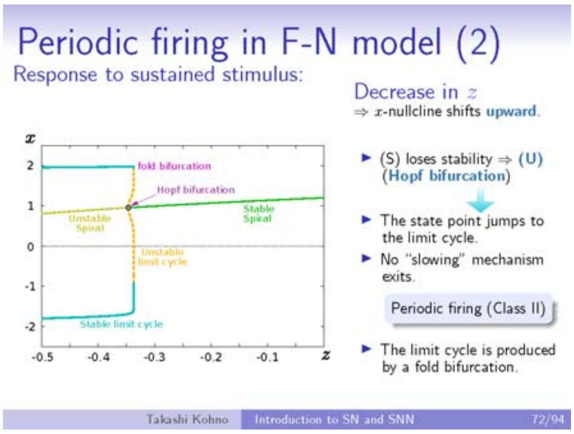
Periodic firing in F-N model (2)
Response to sustained stimulus:
Decrease in z
⇒ x-nullcline shifts upward.
fold bifurcation
Hopf bifurcation
Unstable Spiral
Stable Spiral
Unstable limit cycle
Stable limit cycle
(S) loses stability ⇒ (U) (Hopf bifurcation)
The state point jumps to the limit cycle.
No "slowing" mechanism exits.
Periodic firing (Class II)
The limit cycle is produced by a fold bifurcation.
Takashi Kohno Introduction to SN and SNN 72/94

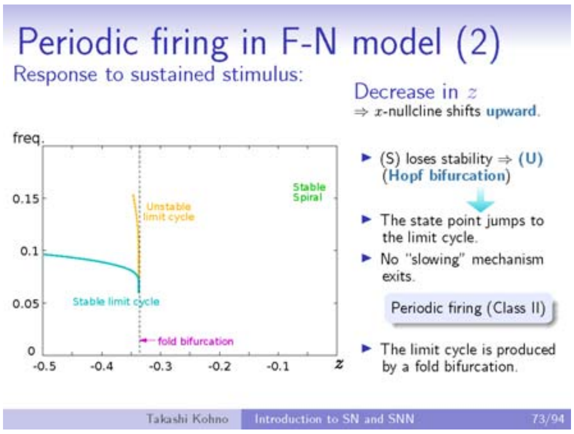
Periodic firing in F-N model (2)
Response to sustained stimulus:
Decrease in z
⇒ x-nullcline shifts upward.
freq.
Unstable limit cycle
Stable Spiral
Stable limit cycle
fold bifurcation
(S) loses stability ⇒ (U) (Hopf bifurcation)
The state point jumps to the limit cycle.
No "slowing" mechanism exits.
Periodic firing (Class II)
The limit cycle is produced by a fold bifurcation.
Takashi Kohno Introduction to SN and SNN 73/94

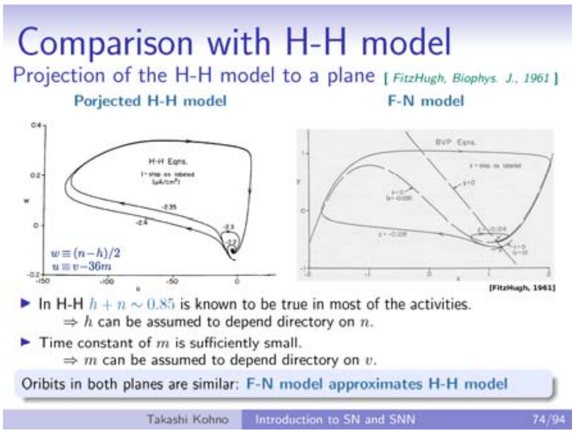
Comparison with H-H model
Projection of the H-H model to a plane [FitzHugh, Biophys. J., 1961]
Porjected H-H model
F-N model
H-H Eqns.
BVP Eqns.
[FitzHugh, 1961]
In H-H h + n ~ 0.85 is known to be true in most of the activities.
⇒ h can be assumed to depend directory on n.
Time constant of m is sufficiently small.
⇒ m can be assumed to depend directory on v.
Oribits in both planes are similar: F-N model approximates H-H model
Takashi Kohno Introduction to SN and SNN 74/94

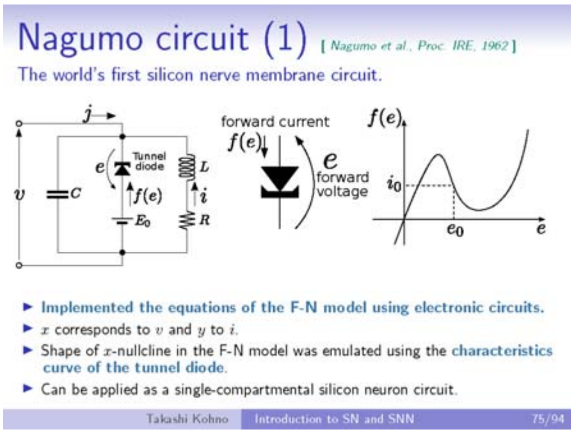
Nagumo circuit (1) [Nagumo et al., Proc. IRE, 1962]
The world's first silicon nerve membrane circuit.
Tunnel diode
forward current
forward voltage
Implemented the equations of the F-N model using electronic circuits.
x corresponds to v and y to i.
Shape of x-nullcline in the F-N model was emulated using the characteristics curve of the tunnel diode.
Can be applied as a single-compartmental silicon neuron circuit.
Takashi Kohno Introduction to SN and SNN 75/94

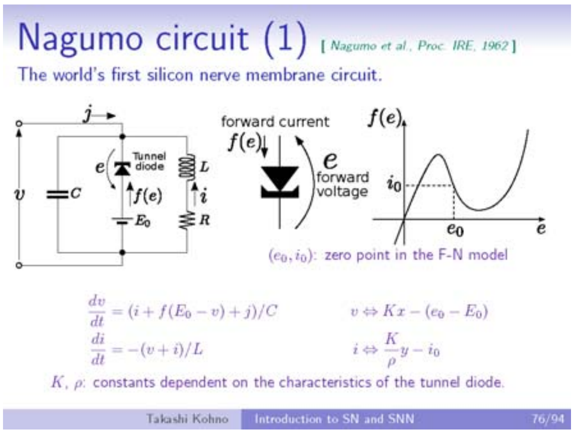
Nagumo circuit (1) [Nagumo et al., Proc. IRE, 1962]
The world's first silicon nerve membrane circuit.
Tunnel diode
forward current
forward voltage
(e_0, i_0): zero point in the F-N model
$\frac{dv}{dt} = (i + f(E_0 - v) + j)/C$
$\frac{di}{dt} = -(v + i)/L$
$v \Leftrightarrow Kx - (e_0 - E_0)$
$i \Leftrightarrow \frac{K}{\rho}y - i_0$
K, ρ: constants dependent on the characteristics of the tunnel diode.
Takashi Kohno Introduction to SN and SNN 76/94

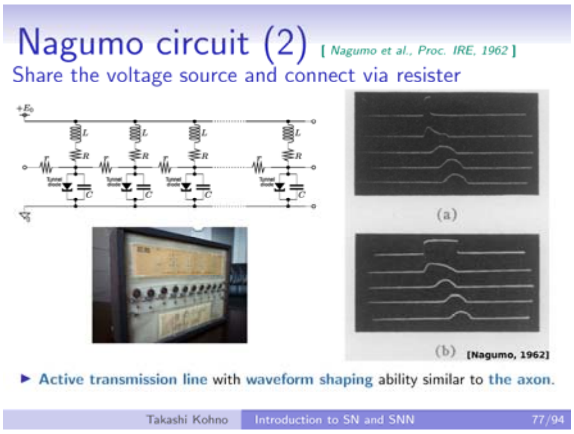
Nagumo circuit (2) [Nagumo et al., Proc. IRE, 1962]
Share the voltage source and connect via resister
(a)
(b) [Nagumo, 1962]
Active transmission line with waveform shaping ability similar to the axon.
Takashi Kohno Introduction to SN and SNN 77/94

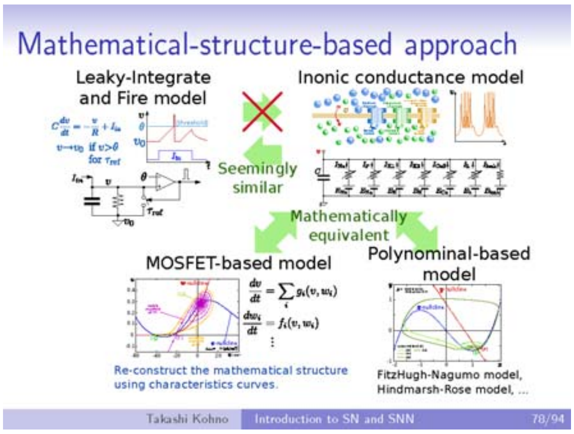
Mathematical-structure-based approach
Leaky-Integrate and Fire model
Inonic conductance model
Seemingly similar
Mathematically equivalent
MOSFET-based model
Polynominal-based model
Re-construct the mathematical structure using characteristics curves.
FitzHugh-Nagumo model, Hindmarsh-Rose model, ...
Takashi Kohno Introduction to SN and SNN 78/94

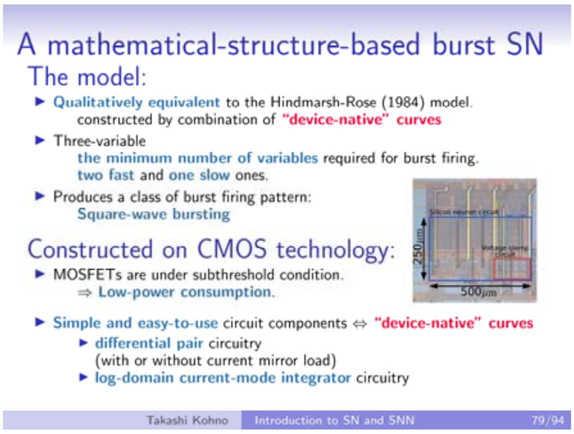
A mathematical-structure-based burst SN
The model:
Qualitatively equivalent to the Hindmarsh-Rose (1984) model.
constructed by combination of "device-native" curves
Three-variable
the minimum number of variables required for burst firing.
two fast and one slow ones.
Produces a class of burst firing pattern:
Square-wave bursting
Constructed on CMOS technology:
MOSFETs are under subthreshold condition.
⇒ Low-power consumption.
Simple and easy-to-use circuit components ⇔ "device-native" curves
differential pair circuitry
(with or without current mirror load)
log-domain current-mode integrator circuitry
250μm
500μm
Takashi Kohno
Introduction to SN and SNN
79/94

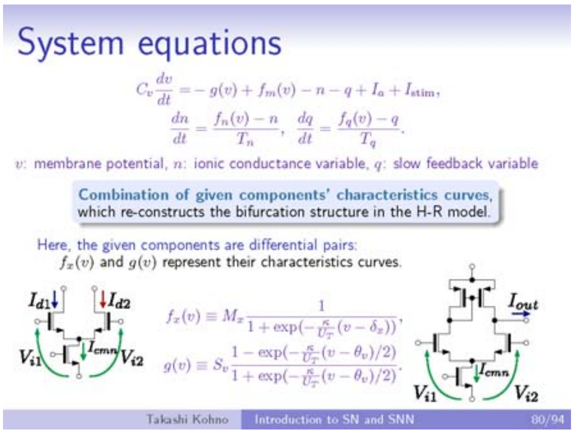
System equations
$C_v \frac{dv}{dt} = -g(v) + f_m(v) - n - q + I_a + I_{stim}$,
$\frac{dn}{dt} = \frac{f_n(v) - n}{T_n}$, $\frac{dq}{dt} = \frac{f_q(v) - q}{T_q}$.
v: membrane potential, n: ionic conductance variable, q: slow feedback variable
Combination of given components' characteristics curves,
which re-constructs the bifurcation structure in the H-R model.
Here, the given components are differential pairs:
$f_x(v)$ and $g(v)$ represent their characteristics curves.
$f_x(v) \equiv M_x \frac{1}{1+\exp(-\frac{\kappa}{U_T}(v-\delta_x))}$,
$g(v) \equiv S_v \frac{1-\exp(-\frac{\kappa}{U_T}(v-\theta_v)/2)}{1+\exp(-\frac{\kappa}{U_T}(v-\theta_v)/2)}$.
I_{d1}
I_{d2}
I_{cmn}
V_{i1}
V_{i2}
I_{out}
Takashi Kohno
Introduction to SN and SNN
80/94

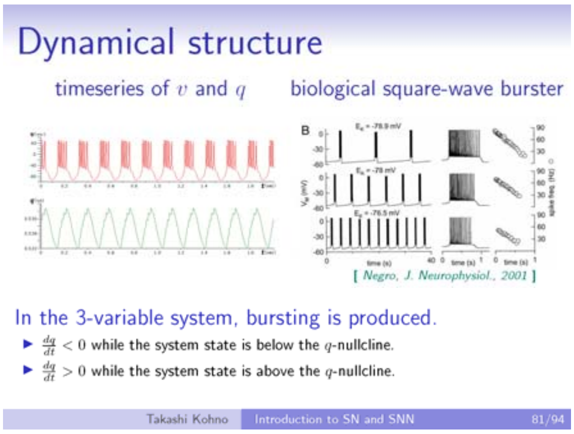
Dynamical structure
timeseries of v and q
biological square-wave burster
[Negro, J. Neurophysiol., 2001]
In the 3-variable system, bursting is produced.
$\frac{dq}{dt} < 0$ while the system state is below the q-nullcline.
$\frac{dq}{dt} > 0$ while the system state is above the q-nullcline.
Takashi Kohno
Introduction to SN and SNN
81/94

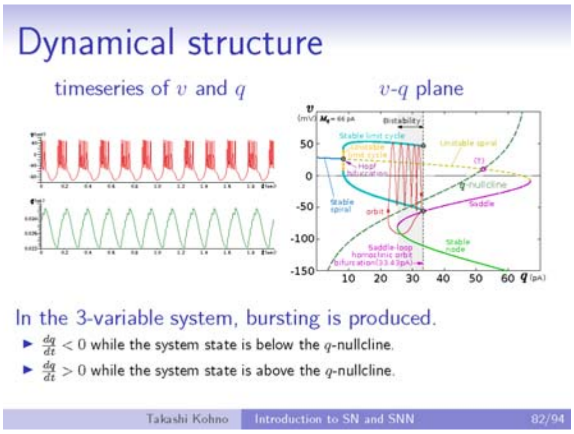
Dynamical structure
timeseries of v and q
v-q plane
Bistability
Stable limit cycle
Unstable spiral
Stable spiral
orbit
Saddle
Stable node
Saddle-loop homoclinic orbit bifurcation
In the 3-variable system, bursting is produced.
$\frac{dq}{dt} < 0$ while the system state is below the q-nullcline.
$\frac{dq}{dt} > 0$ while the system state is above the q-nullcline.
Takashi Kohno
Introduction to SN and SNN
82/94

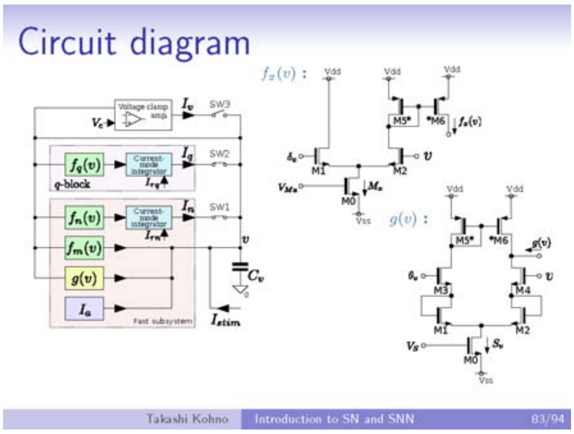
Circuit diagram
$f_x(v)$:
$g(v)$:
Voltage clamp amp.
Current-mode integrator
q-block
Fast subsystem
$f_q(v)$
$f_n(v)$
$f_m(v)$
$g(v)$
I_a
C_v
I_{stim}
SW1
SW2
SW3
Takashi Kohno
Introduction to SN and SNN
83/94

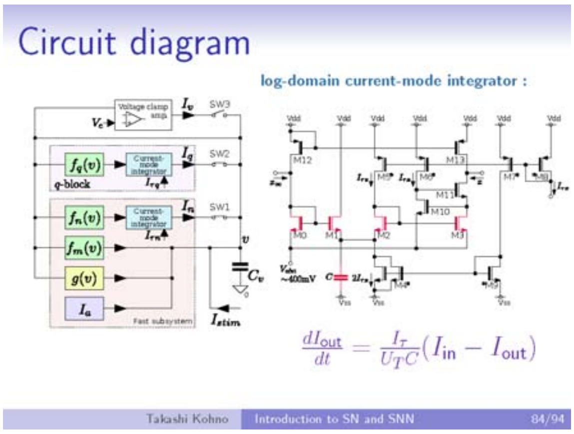
Circuit diagram
log-domain current-mode integrator :
$\frac{dI_{out}}{dt} = \frac{I_T}{U_T C}(I_{in} - I_{out})$
Voltage clamp amp.
Current-mode integrator
q-block
Fast subsystem
Takashi Kohno
Introduction to SN and SNN
84/94

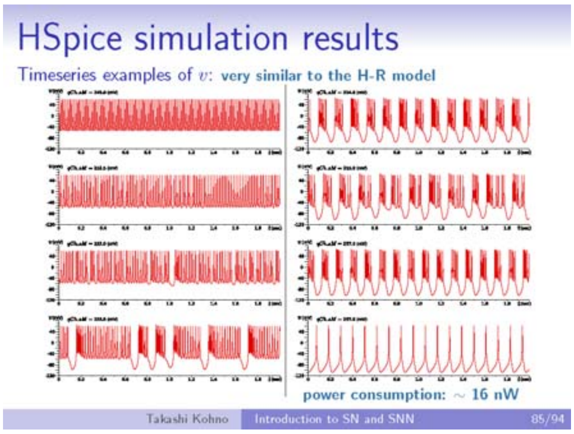
HSpice simulation results
Timeseries examples of v: very similar to the H-R model
power consumption: ~ 16 nW
Takashi Kohno
Introduction to SN and SNN
85/94

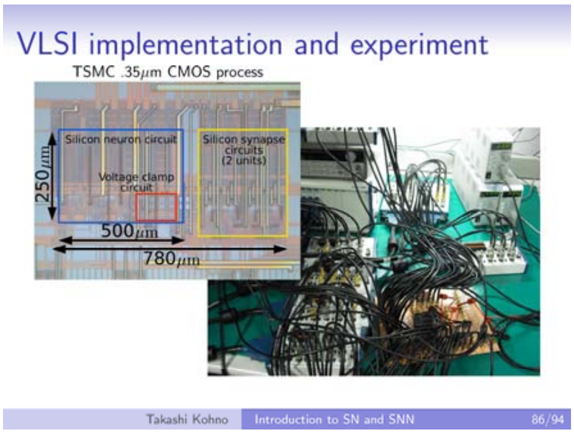
VLSI implementation and experiment
TSMC .35μm CMOS process
Silicon neuron circuit
Silicon synapse circuits (2 units)
Voltage clamp circuit
250μm
500μm
780μm
Takashi Kohno
Introduction to SN and SNN
86/94

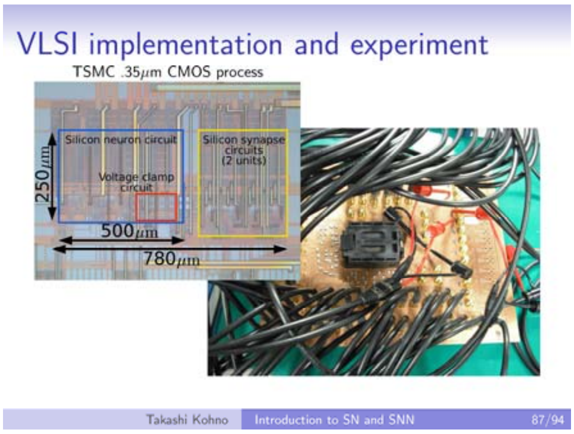
VLSI implementation and experiment
TSMC .35μm CMOS process
Silicon neuron circuit
Silicon synapse circuits (2 units)
Voltage clamp circuit
250μm
500μm
780μm
Takashi Kohno
Introduction to SN and SNN
87/94

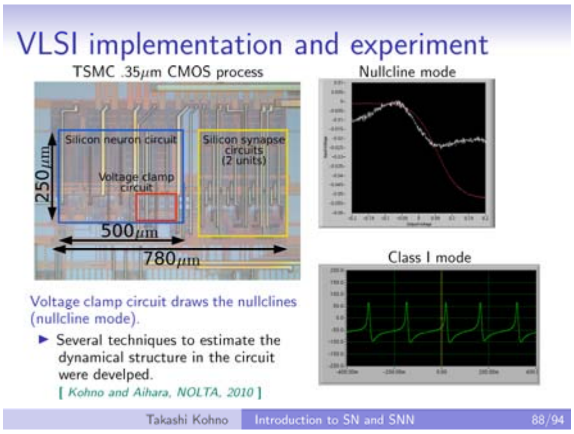
VLSI implementation and experiment
TSMC .35μm CMOS process
Nullcline mode
Silicon neuron circuit
Silicon synapse circuits (2 units)
Voltage clamp circuit
250μm
500μm
780μm
Class I mode
Voltage clamp circuit draws the nullclines (nullcline mode).
Several techniques to estimate the dynamical structure in the circuit were develped.
[Kohno and Aihara, NOLTA, 2010]
Takashi Kohno
Introduction to SN and SNN
88/94

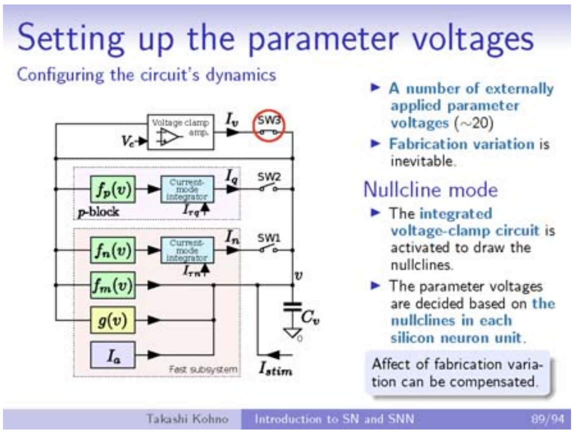
Setting up the parameter voltages
Configuring the circuit's dynamics
Voltage clamp amp.
SW3
SW2
SW1
p-block
Current-mode integrator
Fast subsystem
A number of externally applied parameter voltages (~20)
Fabrication variation is inevitable.
Nullcline mode
The integrated voltage-clamp circuit is activated to draw the nullclines.
The parameter voltages are decided based on the nullclines in each silicon neuron unit.
Affect of fabrication variation can be compensated.
Takashi Kohno
Introduction to SN and SNN
89/94

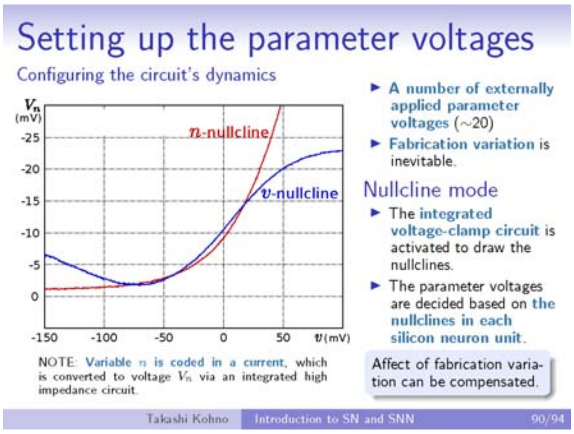
Setting up the parameter voltages
Configuring the circuit's dynamics
n-nullcline
v-nullcline
NOTE: Variable n is coded in a current, which is converted to voltage Vn via an integrated high impedance circuit.
A number of externally applied parameter voltages (~20)
Fabrication variation is inevitable.
Nullcline mode
The integrated voltage-clamp circuit is activated to draw the nullclines.
The parameter voltages are decided based on the nullclines in each silicon neuron unit.
Affect of fabrication variation can be compensated.
Takashi Kohno
Introduction to SN and SNN
90/94

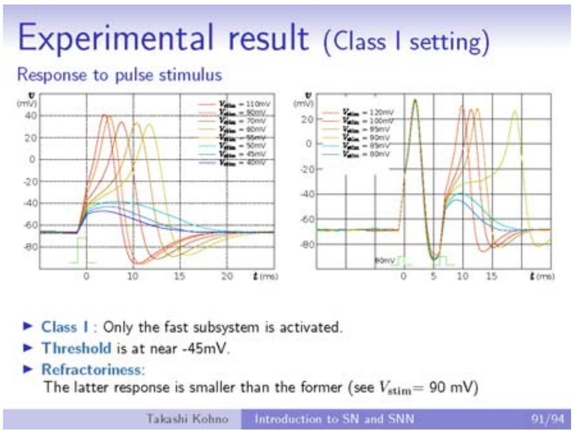
Experimental result (Class I setting)
Response to pulse stimulus
Class I : Only the fast subsystem is activated.
Threshold is at near -45mV.
Refractoriness:
The latter response is smaller than the former (see Vstim = 90 mV)
Takashi Kohno
Introduction to SN and SNN
91/94

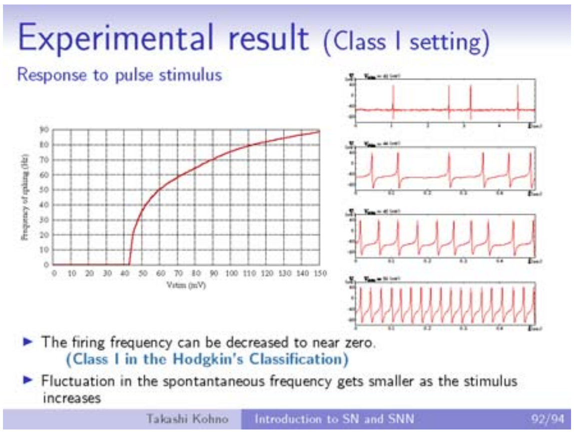
Experimental result (Class I setting)
Response to pulse stimulus
The firing frequency can be decreased to near zero.
(Class I in the Hodgkin's Classification)
Fluctuation in the spontaneous frequency gets smaller as the stimulus increases
Takashi Kohno
Introduction to SN and SNN
92/94

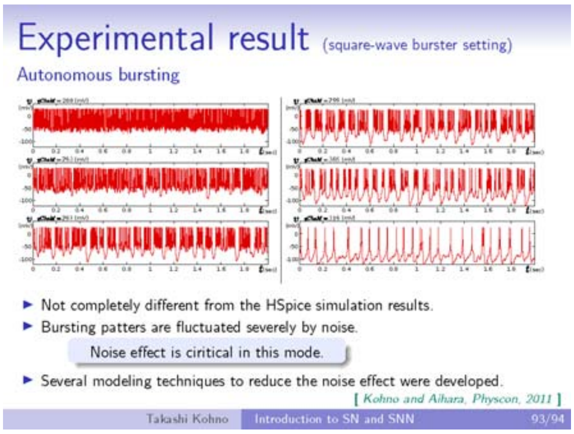
Experimental result (square-wave burster setting)
Autonomous bursting
Not completely different from the HSpice simulation results.
Bursting patters are fluctuated severely by noise.
Noise effect is ciritical in this mode.
Several modeling techniques to reduce the noise effect were developed.
[Kohno and Aihara, Physcon, 2011]
Takashi Kohno
Introduction to SN and SNN
93/94

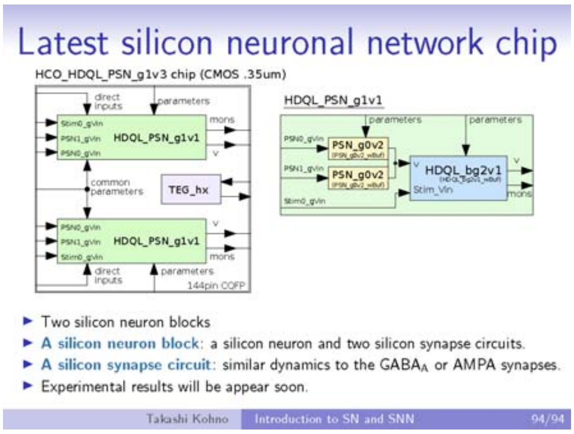
Latest silicon neuronal network chip
HCO_HDQL_PSN_g1v3 chip (CMOS .35um)
HDQL_PSN_g1v1
HDQL_PSN_g1v1
TEG_hx
PSN_g0v2
HDQL_bg2v1
144pin CQFP
Two silicon neuron blocks
A silicon neuron block: a silicon neuron and two silicon synapse circuits.
A silicon synapse circuit: similar dynamics to the GABAA or AMPA synapses.
Experimental results will be appear soon.
Takashi Kohno
Introduction to SN and SNN
94/94

The Seventeenth International Symposium on Artificial Life and Robotics 2012 (AROB 17th '12),
B-Con Plaza, Beppu, Oita, Japan, January 19-21, 2012

Flight guidance and control of a winged rocket

Tomoaki Shimozawa Shinichi Sagara Tomohiro Narumi Koichi Yonemoto
Department of Mechanical and Control Engineering, Kyushu Institute of Technology
Tobata, Kitakyushu 804-8550, Japan
E-mail: sagara@cntl.kyutech.ac.jp

Abstract: Since Reusable Launch Vehicles (RLVs) operate in a wide range of flight conditions, the values of the parameters of the RLVs' dynamic equations are not constant. Therefore, some adaptive control methods for RLVs have been proposed. We have proposed a digital adaptive feedback linearization control method with time-scale separation to a winged rocket. In this paper, we propose a digital adaptive feedback linearization control method using unscented Kalman filter. The simulation results with a guidance using genetic algorithm show the effectiveness of the proposed control systems.
Keywords:Adaptive Control, Flight Control

1 Introduction

In late years space development is performed lively all over the world, and the research of space transportation systems to enable them is performed. Especially, Reusable Launch Vehicles (RLVs) are expected for the systems because the RLVs are the low-cost and highly reliable transport system instead of the conventional disposable rockets.

Since the RLVs have wide range flight conditions, the values of parameters of the dynamic model of the RLVs are not constant. Therefore, gain scheduling control method has been applied for the RLVs [1]. However, when the air traffic window expands, the number of required gains to be designed becomes very large and the method can only correspondence to the known change; the control performance becomes worse for the unpredictable change in the flight condition such as the abort flight.

For the change of the flight conditions, adaptive control methods using approximated linear dynamic equation of the RLVs have been researched [2–5]. However, the control performance decreases when the nonlinearity strengthens though a linear adaptive control has an excellent performance when the nonlinearity of the controlled system can be disregarded. Then, a feedback linearization method for deleting the nonlinear term by the state feedback for the nonlinear equation of motion of the RLV have been researched [6]. In addition, the method for dividing time-scale by a fast motion and a slow motion is researched for the simplification of the structure of the control system [7]. We have also proposed a digital adaptive feedback linearization control method with time-scale separation to a winged rocket [8] which is one of the RLVs.

Here, the air data obtained from a pitot tube etc. contains many noises. Therefore, in order to guarantee the good control performance of RLVs, it is necessary to estimate the state variables. For estimation of the parameters and state variables of the nonlinear systems, Unscented Kalman Filter (UKF) is researched [9]. The UKF was developed as approximating a Gaussian distribution instead of linear approximating for a nonlinear system such as Extended Kalman Filter (EKF). Therefore, it is said that UKF is more effective than EKF for the estimation of a nonlinear system [10].

Fig. 1 Winged rocket

In this paper, we propose a digital adaptive feedback linearization control method using UKF to a winged rocket, and to validate the effectiveness of the control systems in wide range flight conditions, guidance and control simulations are done. The simulation results show that the control system has a good control performance.

2 Model of Winged Rocket

Fig. 1 shows an outline of a winged rocket [11] which is one of the RLVs. The body length is assumed to be 2.5[m] and the mass is 241[kg]. The rocket has two elevons and two rudders as aerodynamic control surfaces. Here, the equation of motion of the winged rocket divided into fast motion and slow motion is shown. Since the configuration of the winged rocket shown in Fig. 1 is similar for general airplanes [12]. Roll, pitch and yaw rotational rates with a fast response are assumed to be fast time scale variables $\boldsymbol{x} = [p,\ q,\ r]^T$, and angle of attack, sideslip angle and bank angle with a slow response are assumed to be slow time scale variables $\boldsymbol{y} = [\alpha,\ \beta,\ \phi]^T$. Therefore, equations of motion are expressed as follows:

$$\dot{\boldsymbol{x}}(t) = \boldsymbol{A}(\boldsymbol{x})\boldsymbol{x}(t) + \boldsymbol{B}(\boldsymbol{x})\boldsymbol{u}(t) + \boldsymbol{C}(\boldsymbol{x})\boldsymbol{w}(t), \quad (1)$$

$$\dot{\boldsymbol{y}}(t) = \boldsymbol{D}(\boldsymbol{y})\boldsymbol{x}(t) + \boldsymbol{E}(\boldsymbol{y})\boldsymbol{h}(t) + \boldsymbol{g}(t) \quad (2)$$

where

$$\boldsymbol{u}(t) = [\delta_{ac},\ \delta_{ec},\ \delta_{rc}]^T,$$

$$\boldsymbol{w}(t) = [pq,\ qr,\ rp,\ r^2 - p^2,\ \alpha,\ \beta]^T,$$

$$\boldsymbol{h}(t) = \left[\frac{1}{V_{TAS} C_\beta},\ \frac{1}{V_{TAS}}\right]^T,$$

$$\boldsymbol{g}(t) = \begin{bmatrix} \dfrac{g(C_\phi C_\alpha C_\theta + S_\alpha S_\theta)}{V_{TAS} C_\beta} \\ \dfrac{g(S_\theta\ C_\alpha S_\beta + C_\theta S_\phi C_\beta - C_\theta C_\phi S_\alpha S_\beta)}{V_{TAS}} \end{bmatrix},$$

$$\boldsymbol{A}(\boldsymbol{x}) = \boldsymbol{I}_d^{-1} \begin{bmatrix} L_p & 0 & L_r \\ 0 & M_q & 0 \\ N_p & 0 & N_r \end{bmatrix},\ \boldsymbol{B}(\boldsymbol{x}) = \boldsymbol{I}_d^{-1} \begin{bmatrix} L_{\delta_a} & 0 & L_{\delta_r} \\ 0 & M_{\delta_e} & 0 \\ N_{\delta_a} & 0 & N_{\delta_r} \end{bmatrix},$$

$$\boldsymbol{C}(\boldsymbol{x}) = \boldsymbol{I}_d^{-1} \begin{bmatrix} I_{xz} & I_{yy} - I_{zz} & 0 & 0 & 0 & L_\beta \\ 0 & 0 & I_{zz} - I_{xx} & I_{xz} & M_\alpha & 0 \\ I_{xx} - I_{yy} & -I_{zz} & 0 & 0 & 0 & N_\beta \end{bmatrix},$$

$$\boldsymbol{D}(\boldsymbol{y}) = \begin{bmatrix} -C_\alpha \tan\beta & 1 & -S_\alpha \tan\beta \\ S_\alpha & 0 & -C_\alpha \\ 1 & S_\phi \tan\theta & C_\phi \tan\theta \end{bmatrix},$$

$$\boldsymbol{E}(\boldsymbol{x}) = \begin{bmatrix} -\frac{L}{m} & 0 \\ 0 & \frac{Y}{m} \\ 0 & 0 \end{bmatrix},\ \boldsymbol{I}_d = \begin{bmatrix} I_{xx} & 0 & I_{xz} \\ 0 & I_{yy} & 0 \\ I_{xz} & 0 & I_{zz} \end{bmatrix}$$

and θ is pitch angle, m is mass, I_{ij} is moment/product of inertia, g is gravitational acceleration, V_{TAS} is true airspeed, L_*, M_* and N_* are aerodynamic rolling, pitching and yawing moments, δ_a, δ_e and δ_r are aileron, elevator and rudder deflection angles, and $S_* = \sin *,\ \ C_* = \cos *$.

When $\dot{\boldsymbol{x}}$ and $\dot{\boldsymbol{y}}$ are discretizaed for forward difference by a sampling period T, Eqs. (1) and (2) are expressed as follows:

$$\boldsymbol{x}(k+1) = \boldsymbol{A}_T(\boldsymbol{x})\boldsymbol{x}(k) + \boldsymbol{B}_T(\boldsymbol{x})\boldsymbol{u}(k) + \boldsymbol{C}_T(\boldsymbol{x})\boldsymbol{w}(k) \quad (3)$$

$$\boldsymbol{y}(k+1) = \boldsymbol{y}(k) + \boldsymbol{D}_T(\boldsymbol{y})\boldsymbol{x}(k) + \boldsymbol{E}_T\boldsymbol{h}(k) + T\boldsymbol{g}(k) \quad (4)$$

where $\boldsymbol{A}_T(\boldsymbol{x}) = \boldsymbol{I} + T\boldsymbol{A}(\boldsymbol{x})$, $\boldsymbol{B}_T(\boldsymbol{x}) = T\boldsymbol{B}(\boldsymbol{x})$, $\boldsymbol{C}_T(\boldsymbol{x}) = T\boldsymbol{C}(\boldsymbol{x})$, $\boldsymbol{D}_T(\boldsymbol{y}) = T\boldsymbol{D}(\boldsymbol{y})$, $\boldsymbol{E}_T = T\boldsymbol{E}$ and $\boldsymbol{I}$ is identity matrix.

3 Control System

In this section, the structure of a control system for Eqs. (3) and (4) in case the value of parameters are known is shown. Moreover, adaptive estimation using UKF which inhibits the suppress of a sensor noise and can respond to wide range flight environment flexibly is described.

3.1 Known parameter case

In the case that the value of parameters of Eqs. (3) and (4) are known the control commands for Eqs. (3) and (4) are defined as follows [8]. First, the rotational rate command for the slow state, i.e. control input to Eq. (4) is defined as

$$\begin{aligned} \boldsymbol{x}_c(k) = \boldsymbol{D}_T^{-1}\{&\boldsymbol{y}_d(k+1) - \boldsymbol{y}(k) - \boldsymbol{E}_T(\boldsymbol{y})\boldsymbol{h}(k) \\ &- T\boldsymbol{g}(k) - \boldsymbol{P}[\boldsymbol{y}_d(k) - \boldsymbol{y}(k)]\} \end{aligned} \quad (5)$$

where $\boldsymbol{P} = \mathrm{diag}\{p_i\}$ $(i = \alpha,\ \beta,\ \phi)$ is the gain matrix and $\boldsymbol{y}_d$ is the value which filtered $\boldsymbol{y}_c$ by a low pass filter. From Eqs. (4) and (5), the equation of the output error $\boldsymbol{e}_s(k) = \boldsymbol{y}_d(k) - \boldsymbol{y}(k)$ is

$$\boldsymbol{e}_s(k+1) = \boldsymbol{P}\boldsymbol{e}_s(k). \quad (6)$$

And if p_i is selected to satisfy $0 < p_i < 1$, the output error $\boldsymbol{e}_s(k)$ tends to zero as k tends to infinity.

Second, the control input for the fast state (Eq. (3)) is defined as

$$\begin{aligned} \boldsymbol{u}(k) = \boldsymbol{B}_T^{-1}\{&\boldsymbol{x}_d(k+1) - \boldsymbol{A}_T(\boldsymbol{x})\boldsymbol{x}(k) \\ &- \boldsymbol{C}_T(\boldsymbol{x})\boldsymbol{w}(k) - \boldsymbol{\Lambda}[\boldsymbol{x}_d(k) - \boldsymbol{x}(k)]\} \end{aligned} \quad (7)$$

where $\boldsymbol{\Lambda} = \mathrm{diag}\{\lambda_i\}$ $(i = p,\ q,\ r)$ is the gain matrix and $\boldsymbol{x}_d$ is the value which filtered $\boldsymbol{x}_c$ by a low pass filter. From Eqs. (3) and (7), the equation of the output error $\boldsymbol{e}_f(k) = \boldsymbol{x}_d(k) - \boldsymbol{x}(k)$ is

$$\boldsymbol{e}_f(k+1) = \boldsymbol{\Lambda}\boldsymbol{e}_f(k). \quad (8)$$

And if λ_i is selected to satisfy $0 < \lambda_i < 1$, the output error $\boldsymbol{e}_f(k)$ tends to zero as k tends to infinity.

3.2 Estimation by unscented Kalman filter

In the case of unknown parameters, we introduce the matrices $\hat{\boldsymbol{A}}_T(\boldsymbol{x})$, $\hat{\boldsymbol{B}}_T(\boldsymbol{x})$, $\hat{\boldsymbol{C}}_T(\boldsymbol{x})$, etc. those coefficients are estimated values of the coefficients in $\boldsymbol{A}_T(\boldsymbol{x})$, $\boldsymbol{B}_T(\boldsymbol{x})$, $\boldsymbol{C}_T(\boldsymbol{x})$, etc., respectively. Moreover, these matrices include the state variables. Therefore, states and parameters are estimated for the improvement of the control performance. For estimation of the parameters and state variables of nonlinear systems, UKF is used [9]. The UKF calculates the covariance of estimation by using the finite sample point that is called a sigma point around the mean. Then, sigma points are propagated through the nonlinear functions, and statistic is approximated, nonlinear system is estimated. Because the correction by the sample point is done, error margins are smaller than EKF. A detailed explanation of the UKF is omitted for want of space.

For Eqs. (5) and (7), the augmented state vector $\bar{\boldsymbol{x}}$ to estimate the parameters at the same time by

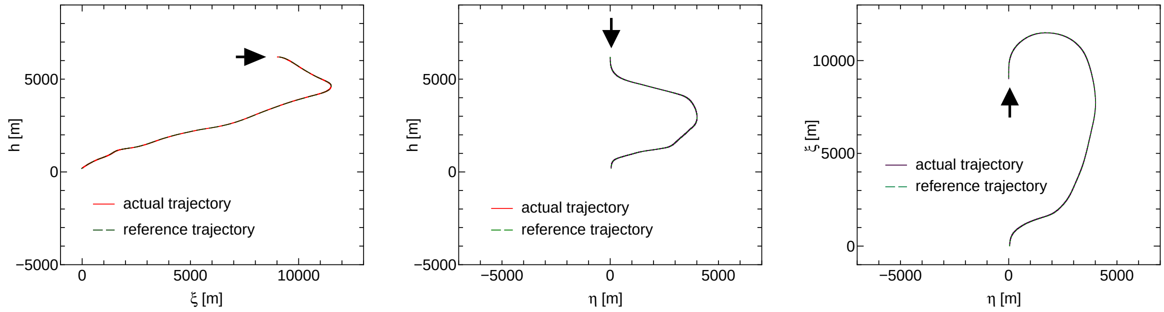

Fig. 2 Flight trajectory

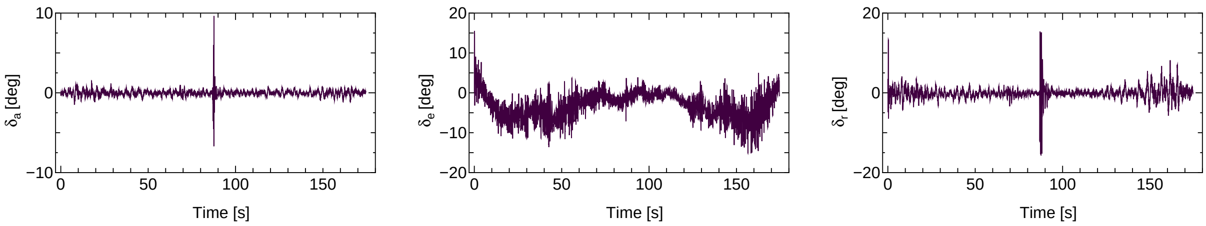

Fig. 3 Input

the UKF is introduced as follows:

$$\begin{aligned}\bar{\boldsymbol{x}}(k) =& [p\ q\ r\ \alpha\ \beta\ \phi\ \theta\ V_{TAS}\ I_{xx}\ I_{yy}\ I_{zz}\ I_{xz} \\ & L_p\ L_r\ M_q\ N_p\ N_r\ L_{\delta_a}\ L_{\delta_r}\ M_{\delta_e}\ N_{\delta_a}\ N_{\delta_r} \\ & L_\beta\ M_\alpha\ N_\beta\ \frac{X}{m}\ \frac{Y}{m}\ \frac{Z}{m}]^T \end{aligned} \tag{9}$$

And the augmented measurement vector is $\bar{\boldsymbol{y}}(k) = [p\ q\ r\ \alpha\ \beta\ \phi\ \theta\ V_{TAS}]^T$.

4 Simulation

To validate the adaptive control system described above, computer simulations for a 6-DOF nonlinear winged rocket model [13] considering the atmospheric fluctuation are performed.

The simulation condition is follows. When the winged rocket is in level flight those velocity is 93[m/s], the guidance is started at $h = 6200$[m], $\xi = 9000$[m] and $\eta = 0$[m] in altitude, downrange and crossrange, respectively. Moreover, the wind shear that the wind velocity in a downrange direction rapidly changes from -10[m/s] to 10[m/s] while flying was generated by about the 2500[m] in altitude. The guidance to the target point uses optimal trajectory generation using a genetic algorithm (GA) [14] which is a real-time guidance method. This method performs orbital optimization using GA, in order to suit flight environment without a preplanned reference trajectory and to generate a flexible trajectory, and it outputs an angle of attack command and a bank angle command required in order to realize the trajectory. The guidance is updated every 1[s]. The aerodynamic coefficient of the winged rocket uses the value obtained from the wind tunnel examination result. The actuators of elevons and rudders are used that the attenuation coefficient $\zeta = 0.7$ and the natural frequency $\omega_n = 72$[rad/s]. The sampling period of the control system is $T = 0.01$[s]. The gains are $\lambda_p = 0.94$, $\lambda_q = 0.92$, $\lambda_r = 0.94$, $p_\alpha = 0.95$, $p_\beta = 0.96$ and $p_\phi = 0.97$. The time constants of the low-pass filters for p, q, r, α and β are 0.2, 0.3, 0.5, 0.5 and 0.5[s], respectively. The UKF [9] is utilized for state and parameter estimation.

Fig. 2 shows the flight trajectory. From Fig. 2, we can see that the winged rocket can follows the reference trajectory. Fig. 3 shows the time history of the control input commands to the actuators. And Fig. 4 shows the time history of the output $\boldsymbol{y}$ and the estimated error $e_* = * - \bar{*}$. In Fig. 4 a dashed lines show the desired value obtained from the guidance. Since the wind shear is considered in this simulation, from Fig. 3 we can see that the input commands have vibrations with small amplitude. However, from Fig. 4, it can be seen that the estimation by the UKF is performed good and the output $\boldsymbol{y}$ follows the desired value. From the simulation result, it can be confirmed that the applied control method is effective for the flight control of the winged rocket.

5 Conclusion

In this paper, we propose a digital adaptive feedback linearization control method using UKF to a winged rocket. From the numerical simulation, we showed that the control system of the winged rocket has a good control performance.

References

[1] T. Tsukamoto *et al.*, "Guidance and control law design for high speed flight demonstration

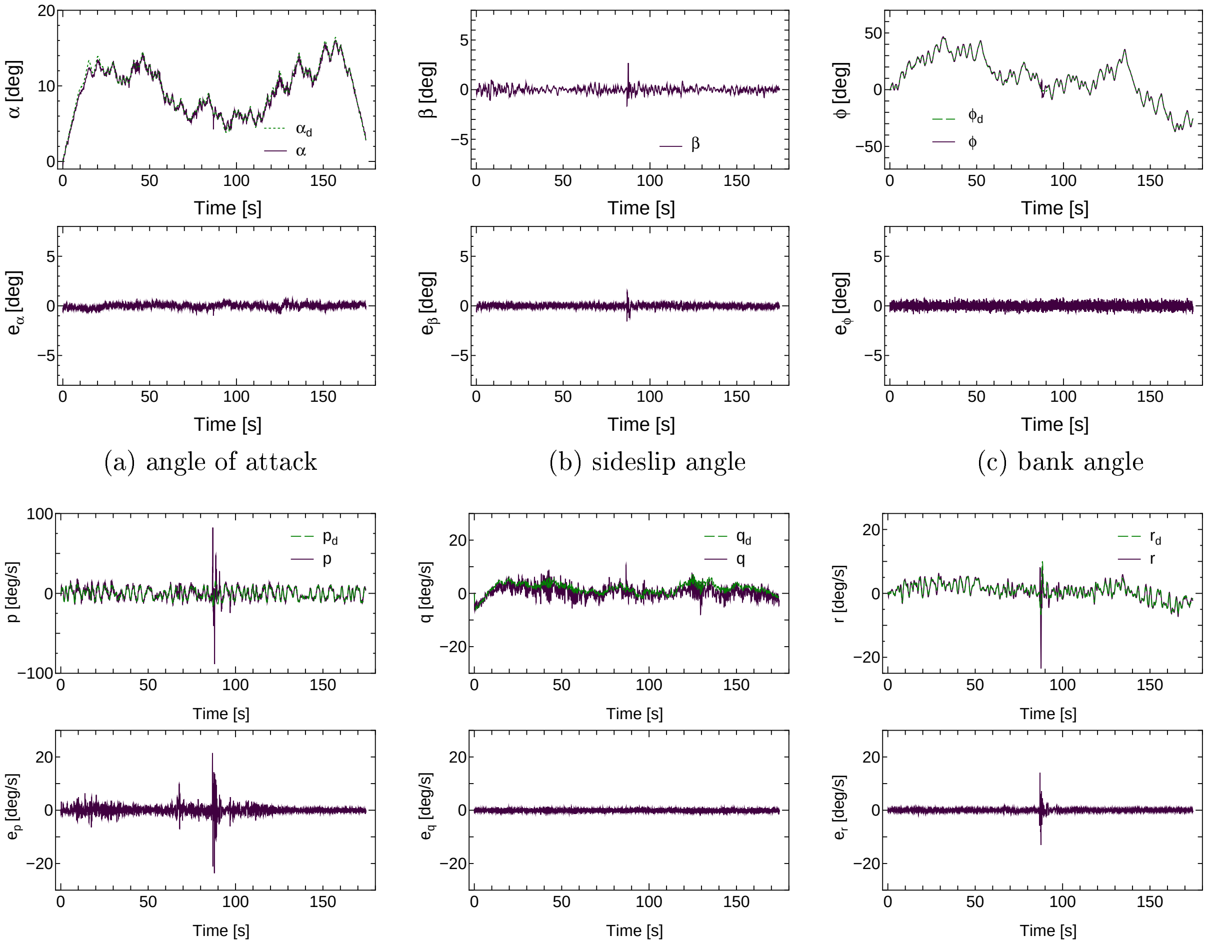

(a) angle of attack (b) sideslip angle (c) bank angle

(d) roll rate (e) pitch rate (f) yaw rate

Fig. 4 Output and estimated error

phase II",*JAXA Research and Development Report*, JAXA-RR-04-006, 2004 (in Japanese).

[2] J. Brinker, K. Wise, "Reconfigurable flight control for a tailless advanced fighter aircraft", *Proc. AIAA Guidance, Navigation and Control Conf.*, pp. 75–87, 1998.

[3] E. N. Johnson, A. J. Calise, "Pseudo-control hedging: a new method for adaptive control", *Advances in Navigation Guidance and Control Technology Workshop*, Alabama, 2000.

[4] E. N. Johnson, A. J. Calise, "Limited authority adaptive flight control for reusable launch vehicles", *J. Guidance, Control, and Dynamics*, Vol. 26, No. 6, pp. 906–913, 2003.

[5] M. Morimoto *et al.*, "Adaptive attitude control with reduced number of estimated parameters for automatic landing system", *Int. Conf. Control, Automation and Systems 2007*, pp. 2865–2870, 2007.

[6] E. N. Johnson, A. J. Calise, "A six degree of freedom adaptive flight control architecture for trajectory following", *Proc. AIAA Guidance, Navigation, and Control Conference*, Paper No. AIAA2002-4776, 2002.

[7] P. K. Menon *et al.*, "Nonlinear missile autopilot design using time-scale separation", *AIAA paper*, 97-3765-CP, pp. 1791-1803, 1997.

[8] T. Shimozawa, S. Sagara, "Digital adaptive control of a winged rocket applicable to abort flight", *Artif. Life Robotics*, Vol.16, pp.348–351, 2011.

[9] E. A. Wan, R. Van Der Merwe, "The unscented Kalman filter for nonlinear estimation", *Adaptive Systems for Signal Processing, Communications, and Control Symposium 2000*, pp. 153-158, 2000

[10] X. Wang, E. E. Yaz, "Improved chaotic communications using nonlinear filtering", *Int. J. Innovative Computing, Information and Control*, vol. 6, no 5, May, pp. 2127-2136, 2010

[11] K. Yonemoto *et al.*, "Development and flight test of winged rocket", *27th Int. Symp. Space Technology and Science*, 2009.

[12] B. Etkin, L. D. Reid, *Dynamics of flight: stability and control*, Wiley, New York, 1996.

[13] HIMES Research Group, "Conceptual design of HIMES (winged test rocket)", *Institute of Space and Astronautical Science, Ministry of Education*, March 19, 1987 (in Japanese).

[14] K. Okuda *et al.*, *Hybrid optimal trajectory generation using genetic algorithm and sequential quadratic programming*, Proc. ICCAS-SICE 2009, pp. 3233-3238, 2009.

The Seventeenth International Symposium on Artificial Life and Robotics 2012 (AROB 17th '12),
B-Con Plaza, Beppu, Oita, Japan, January 19-21, 2012

Position and attitude control of underwater vehicle-manipulator systems using a stereovision system

Akihito Shigetomi Shinichi Sagara Tomoaki Shimozawa
Department of Mechanical and Control Engineering, Kyushu Institute of Technology
Tobata, Kitakyushu 804-8550, Japan
E-mail: sagara@cntl.kyutech.ac.jp

Abstract: Underwater Vehicle-Manipulator Systems (UVMS) are expected to make important roles in ocean exploration. The manipulator operations in underwater need information of position between an object of capture and the vehicle. Therefore, sensors that measure position and attitude of the objects must be mounted on UVMS. We have been developing a stereovision system for UVMS. In this paper, to verify the effectiveness of the proposed stereovision system equipped to a floating UVMS, experiments on position and attitude control of the UVMS are done.

Keywords: Underwater Robot, Manipulator, Stereovision System

1 Introduction

Underwater robots are expected to make important roles in ocean exploration and many studies on Underwater Vehicle-Manipulator Systems (UVMS) are performed in recent years [1–5]. However there are only a few experimental studies. We have proposed digital Resolved Acceleration Control (RAC) methods for UVMS [6,7] and the effectiveness of the RAC methods has been demonstrated by using a floating underwater robot with vertical planar 2-link manipulator.

Here, underwater robots having small size manipulators have been used in real situations. Manipulator operations in underwater need information of position between object of capture and vehicle. Therefore, sensors that measure position and attitude of the objects must be mounted on UVMS.

We have been developing a stereovision system for UVMS. In this paper, to verify the effectiveness of the proposed stereovision system equipped to a floating UVMS, experiments on position and attitude control of the UVMS are done. The experimental results show the effectiveness of the stereovision system.

2 Configuration of Experimental System

2.1 UVMS

The underwater robot used in this paper is shown in Fig. 1. The robot has a robot base (vehicle) and a 2-link manipulator. By six thrusters equipped in the robot base, three-dimensional movement is possible. In addition, two waterproof cylinders has been equipped on front and rear of the robot. The one of cylinders is for a stereovision system and the other is for balance weights.

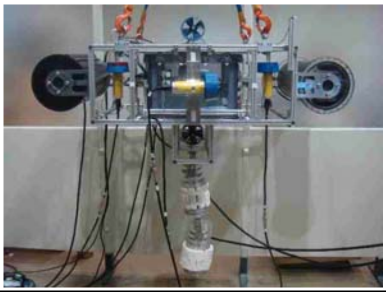

	Base	Link 1	Link 2
Mass [kg]	104.52	4.65	4.65
Volume [$\times 10^{-3}$ m^3]	108.04	3.3	3.1
Moment of inertia [kgm^2]	2.40	0.075	0.075
Link length (x axis) [m]	0.870	0.35	0.28
Link length (y axis) [m]	0.640	-	-
Link length (z axis) [m]	0.335	-	-
Link diameter[m]	-	0.13	0.13
Added mass(x) [kg]	73.19	0.35	0.35
Added mass(y) [kg]	30.57	3.31	3.31
Added mass(z) [kg]	99.54	3.31	3.31
Added moment of inertia [kgm^2]	1.28	0.06	0.06
Drag coefficient(x)	1.2	0	0
Drag coefficient(y)	1.2	1.0	1.0
Drag coefficient(z)	1.2	1.0	1.0

Fig. 1 2 link underwater robot

2.2 Stereovision system

Fig. 2 shows our developing stereovision system for UVMS. The size of the system is 540×140×136[mm] and the mass is 2.2[kg].

The stereovision system is equipped with two CCD cameras that can pan and tilt individually by

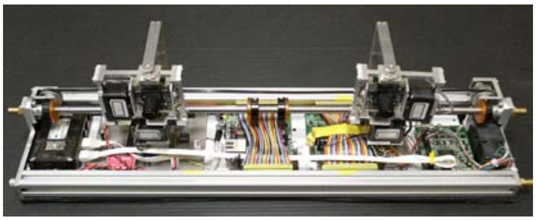

Fig. 2 Stereovision system

Table 1 Motor specification

Axis	Pan, Tilt	Slide
Gear ratio	-	1:10
Torque [kg·cm]	5.0	10
Resolution [deg]	0.2	0.072
Input signal	RS485	PWM

Table 2 Camera specification

Signal system	NTSC 30fps
Scanning system	2:1 interlaced
Picture elements	768(H)×494(V)[pixel]
Clock frequency	28.636[MHz]
Video output	1.0Vp-p/75Ω compositeVBS, digitalYUV

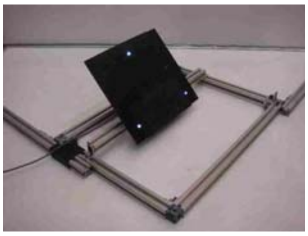

Fig. 3 LED marker

servo actuators. Moreover, the stereovision system has a slide mechanism by one stepping motor; it is possible to vary the distance between the cameras for avoiding occlusions. Table 1 shows specifications of the motors. Moving from side to side two cameras, the stereovision system control pan/tilt angle of the cameras to track the measurement object at the center of image surface. By doing this, the position and attitude can be obtained from that angles and measuring coordinates on the pixel surface of the cameras. the specification of the CCD camera to shoot object is shown in Table 2. In this paper, measurement object is flat object that has three radiants. Fig. 3 shows the LED marker for measurement. The cameras change of each pan/tilt angle to track the centroid of the three radiants.

3 Measurement Method

In this section, we explain the position and attitude measurement method using the stereovision system shown in Fig. 2.

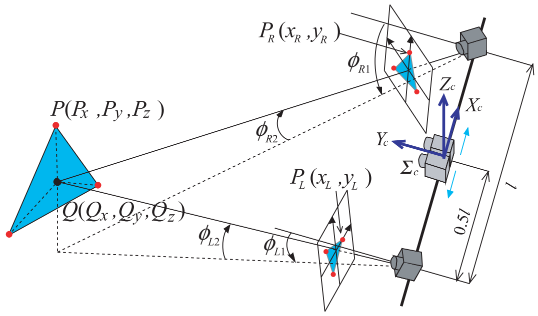

Fig. 4 Measurement model

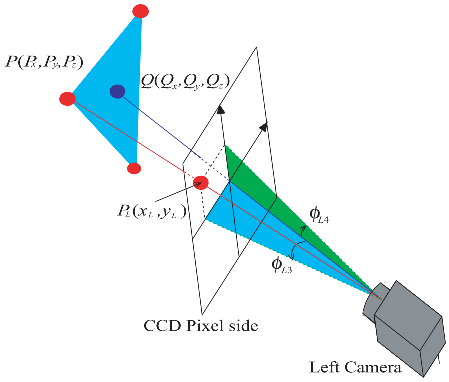

Fig. 5 Camera coordinate system

Fig. 4 shows the measurement model of Fig. 2. From Fig. 4, position of centroid of the object, $Q(q_x, q_y, q_z)$, can be calculated from the geometric relationship as follows:

$$\left.\begin{aligned} q_x &= 0.5l - k\sin\theta_{R_1}, \\ q_y &= k\cos\theta_{R_1}, \\ q_z &= k\tan\theta_{R_2} \end{aligned}\right\} \tag{1}$$

where

$$k = \frac{\cos\theta_{L_1}}{\sin(\theta_{R_1} - \theta_{L_1})}l, \quad \theta_{*_1} = \phi_{*_1}, \quad \theta_{*_2} = \phi_{*_2}.$$

Fig. 5 shows the camera coordinate system of the left camera. In Fig. 5, position of a radiant on the pixel surface is defined as $P_L(x_L, y_L)$. In the similar manner, $P_R(x_R, y_R)$ for the right camera is also defined. Positions of three radiants $P_i(x_i, y_i, z_i)$ $(i = 1, 2, 3)$ are similarly obtained by transforming Eq. (1) as follows:

$$\begin{gathered} \theta_{*_1} = \phi_{*_1} - \phi_{*_3}, \quad \theta_{*_2} = \phi_{*_2} + \phi_{*_4}, \\ \phi_{*_3} = \tan^{-1}\left(\frac{x_*}{f}\right), \quad \phi_{*_4} = \tan^{-1}\left(\frac{y_*}{f}\right) \end{gathered} \tag{2}$$

where f is the focal length. Using $P_i(x_i, y_i, z_i)$ the normal vector of the plane through three points, $\boldsymbol{m} = [u, v, w]^T$, can be obtained:

$$\boldsymbol{m} = \begin{bmatrix} (y_2 - y_1)(z_3 - z_1) - (y_3 - y_1)(z_2 - z_1) \\ (z_2 - z_1)(x_3 - x_1) - (z_3 - z_1)(x_2 - x_1) \\ (x_2 - x_1)(y_3 - y_1) - (x_3 - x_1)(y_2 - y_1) \end{bmatrix}. \tag{3}$$

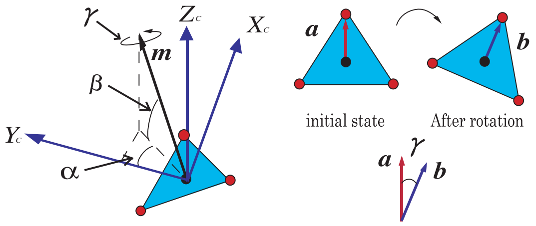

Fig. 6 Attitude

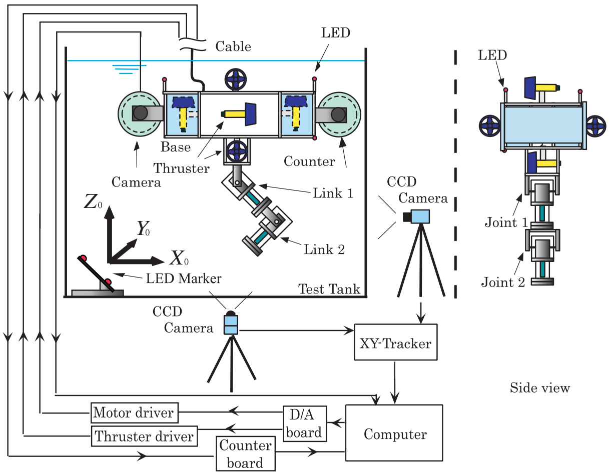

Fig. 7 Configuration of experimental system

The attitude of the measurement object is defined by the angle between the normal vector and the coordinate plane as shown in Fig 6. From Fig 6, attitude angles α and β are described as follows:

$$\alpha = -\text{atan2}\,(u,\ v)\,,\quad \beta = \text{atan2}\left(w,\ \sqrt{u^2+v^2}\right). \tag{4}$$

Moreover, in the initial state, $\boldsymbol{a}$ is defined as vector between Q and P_1, and $\boldsymbol{b}$ is defined as vector between Q and P_1 after rotation. From $\boldsymbol{a}$ and $\boldsymbol{b}$, the third attitude angle γ is described as follows:

$$\gamma = \cos^{-1}\left(\frac{\boldsymbol{a}^T\boldsymbol{b}}{||\boldsymbol{a}||||\boldsymbol{b}||}\right). \tag{5}$$

4 Experiments

In this section, PI control experiments are done to verify the effectiveness of the stereovision system for control of UVMS using the experimental system shown in Fig. 7.

The origin of the inertial coordinate frame is defined to the center of gravity of the LED marker. The LED marker is fixed to the bottom of the water tank. Position and attitude of the UVMS are calculated by measured information of the LED marker obtained from the stereovision system. Also, the pose of UVMS can be obtained by two CCD cameras (XY-Tracker) have been located outside of the tank. We compare the experimental results that controlled by stereovision system with the other controlled by XY-Tracker.

The experiments are carried out under the following condition. Two experimental conditions are the same. The sampling period is T=1/30[s]. The initial position is set up $(X,\ Y,\ Z)$ = $(0.4,\ 0,\ 0.9)$[m] on the inertial coordinate frame and the desired position and attitude of the base is set up $(X,\ Y,\ Z)$ = $(0.4,\ 0,\ 0.75)$[m]. The proportional and integral gains of the controller are $(P_x,\ P_y,\ P_z,\ P_r,\ P_p,\ P_y)$ = $(1.0,\ 1.5,\ 3,\ 1,\ 2,\ 1)$ and $(I_x,\ I_y,\ I_z,\ I_r,\ I_p,\ I_y)$ = $(0.8,\ 0.8,\ 0.9,\ 0.6,\ 0.6,\ 0.4)$.

Fig. 8 and 9 show experimental results. From results, the stereovision system of the present work similar to XY-Tracker. Therefore, the use of stereovision system to UVMS is considered to be effective.

5 Conclusion

In this paper, we proposed a stereovision system for UVMS. The effectiveness of the proposed stereovision system was demonstrated by using a floating underwater robot. The experimental results show the effectiveness of the stereovision system.

References

[1] H. Maheshi *et al.*, "A Coordinated Control of an Underwater Vehicle and Robotic Manipulator", *J. Robotic Systems*, Vol. 8, No. 3, pp. 339 – 370, 1991.

[2] T. W. McLain *et al.*, "Experiments in the Coordinated Control of an Underwater Arm/Vehicle System", *Autonomous Robots 3*, Kluwer Academic Publishers, pp. 213 – 232, 1996.

[3] G. Antonelli *et al.*, "Tracking Control for Underwater Vehicle-Manipulator Systems with Velocity Estimation", *IEEE J. Oceanic Eng.*, Vol. 25, No. 3, pp. 399 – 413, 2000.

[4] N. Sarkar and T. K. Podder, "Coordinated Motion Planning and Control of Autonomous Underwater Vehicle-Manipulator Systems Subject to Drag Optimization", *IEEE J. Oceanic Eng.*, Vol. 26, No. 2, pp. 228 – 239, 2001.

[5] G. Antonelli, *Underwater Robotics*, Springer, pp. 1194–1206, 2003.

[6] S. Sagara *et al.*,"Digital RAC for Underwater Vehicle-Manipulator Systems Considering Singular Configuration", *J. Artificial Life and Robotics*, Vol. 10, No. 2, pp. 106 – 111, 2006.

[7] S. Sagara *et al.*,"Digital RAC with a Disturbance Observer for Underwater Vehicle-Manipulator Systems", *J. Artificial Life and Robotics*, Vol. 15, No. 3, pp. 270 – 274, 2010.

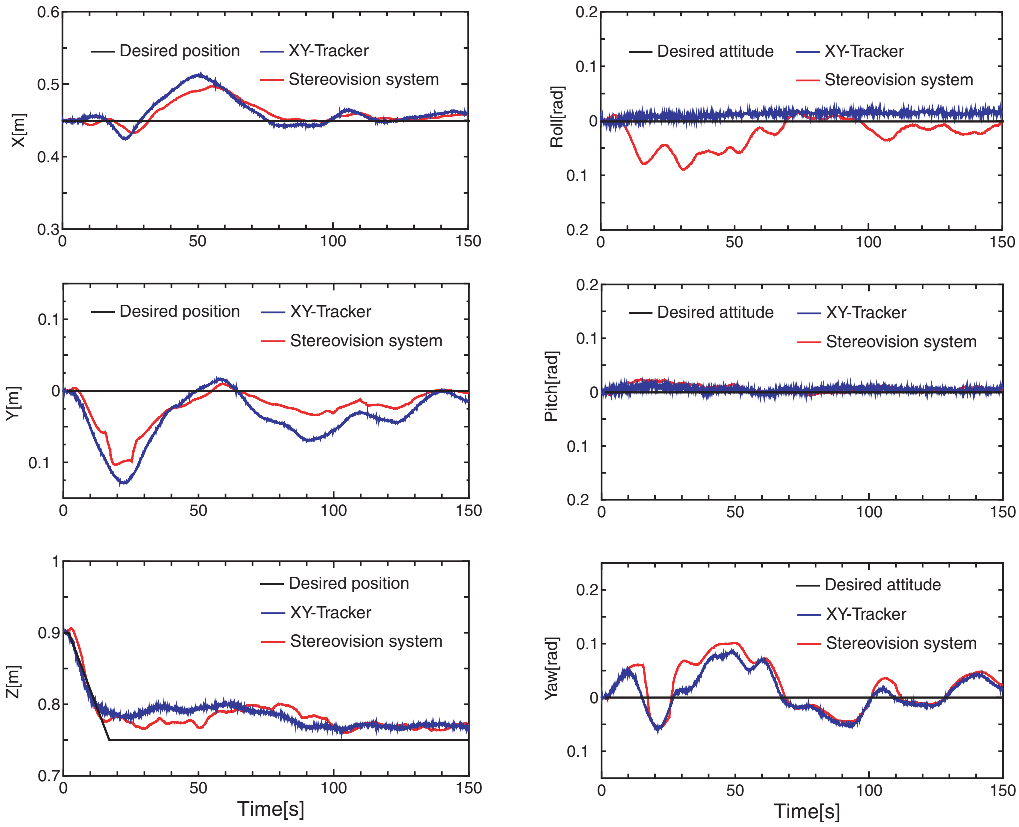

Fig. 8 Experimental result using stereovision system

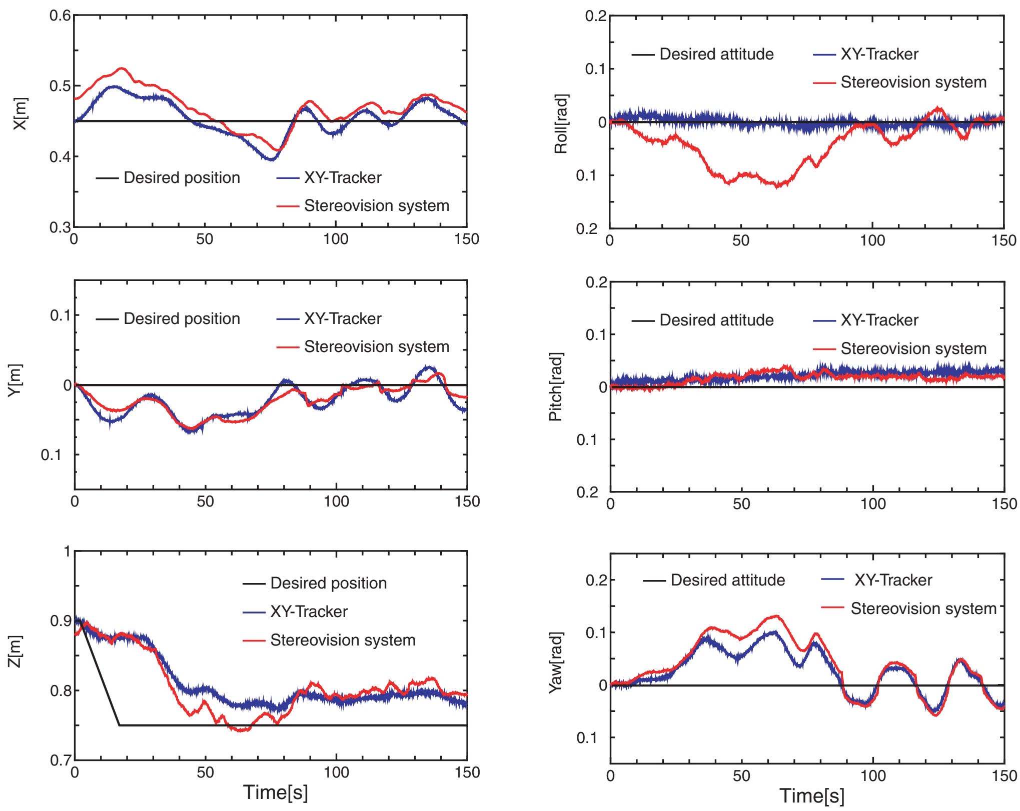

Fig. 9 Experimental result using XY-Tracker

The Seventeenth International Symposium on Artificial Life and Robotics 2012 (AROB 17th '12),
B-Con Plaza, Beppu, Oita, Japan, January 19-21, 2012

Adaptive control of underwater vehicle-manipulator systems using radial basis function networks

Yuichiro Taira[1], Masahiro Oya[2], and Shinichi Sagara[2]

[1] Dept. of Ocean Mechanical Engineering, National Fisheries University, Shimonoseki 759-6595, Japan
taira@fish-u.ac.jp

[2] Dept. of Mechanical and Control Engineering, Kyushu Institute of Technology, Kitakyushu 804-8550, Japan
oya@cntl.kyutech.ac.jp; sagara@cntl.kyutech.ac.jp

Abstract: This paper deals with a control scheme for underwater vehicle-manipulator systems with the dynamics of thrusters in the presence of uncertainties in system parameters. We have developed a regressor-based adaptive and a robust controller that overcome thruster nonlinearities, which cause an uncontrollable system. However, the structure of the adaptive controller is very complex due to the feedforward terms including the regressors of dynamic system models, and the error feedback gains of the robust controller with a good control performance are excessively high due to the lack of feedforward terms. In this paper we develop an adaptive controller that uses radial basis function networks instead of the feedforward terms. The replacement leads to a moderately high gain controller whose structure is simpler than that of the regressor-based adaptive controller.

Keywords: adaptive control, radial basis function network, thruster dynamics, underwater vehicle-manipulator system

1 INTRODUCTION

Adaptive or robust control schemes for autonomous underwater vehicles with manipulators, referred to as underwater vehicle-manipulator system (UVMS), have recently been developed in the presence of uncertainties in system parameters [1, 2]. In a general type of UVMS, the vehicle is propelled by marine thrusters, whereas the manipulator is driven by electrical motors. Despite such a different actuator system, the existing control schemes in [1, 2] were designed based on the dynamic system models without the thruster dynamics to obtain a simply structured controller. In each control scheme, furthermore, a high gain control system is constructed in order to achieve a good control performance. However, the vehicle propelled by marine thrusters generally has a considerably slower time response than the manipulator driven by electrical motors [2], and hence the high gains may excite the ignored thruster dynamics, which degrades a control performance and may even cause instability.

In order to overcome the problem, we have developed a regressor-based adaptive controller for UVMS with the thruster dynamics [3]. The adaptive control inputs are composed of adaptive feedforward signals including the regressors of the dynamic system models, and error feedback signals. Since the slow thruster dynamics is taken into consideration in the controller development, the control performance can be improved by the high gain feedback terms. However, the structure of the adaptive controller is very complex due to the regressors. On the other hand, we have developed a robust controller where the adaptive term is removed completely [4]. Although it has a much simpler structure than that of the adaptive controller, the removal leads to an excessively high gain controller, which may cause saturation or oscillations in the control inputs, to achieve a good control performance.

In this paper we develop an adaptive controller that uses radial basis function (RBF) networks, a type of neural network, instead of the adaptive terms including the regressors (see Fig. 1). The replacement leads to a moderately high gain controller whose structure is simpler than that of the regressor-based adaptive controller [3].

2 UVMS MODEL

Consider an underwater vehicle equipped with a Dm link manipulator with revolute joints. Let Dv and De be the numbers of dimensions for the vehicle's and the manipulator end-effector's motions, respectively. We assume without loss of generality that $Dm = De$.

As in [1, 5], the mathematical model of a UVMS with thruster dynamics is expressed as

$$\left.\begin{aligned} &M(\phi)\ddot{x}(t) + f(\phi, u) = J(\phi)^{-T}\begin{bmatrix} \bar{R}(\phi)\bar{K}D(v)v(t) \\ \tau_m(t) \end{bmatrix} \\ &\dot{v}(t) = -\frac{1}{2}AD(v)v(t) + \frac{1}{2}B\tau_b(t) \end{aligned}\right\} \quad (1)$$

$$\left.\begin{aligned} &M(\phi) = J(\phi)^{-T}\bar{M}(\phi)J(\phi)^{-1} \\ &f(\cdot) = J(\phi)^{-T}[\bar{f}(\phi, u) - \bar{M}(\phi)J(\phi)^{-1}\dot{J}(\phi, u)u(t)] \\ &D(v) = \mathrm{diag}\{|v_1|, \ldots, |v_{Dv}|\} \end{aligned}\right\} \quad (2)$$

where $D(\cdot) \in R^{Dv\times Dv}$, $v_i(t)$ is the ith element of $v(t)$, and the explanation of the main symbols is shown in Table 1.

In this paper, the backstepping control technology is used to develop an adaptive controller. To this end, the state $v(t)$ has to be replaced by the new one $z(t) = D(v)v(t)$. Rewriting the signal $D(v)v(t)$ as $z(t)$ in the model (1), we obtain the new representation

$$\left.\begin{aligned} &M(\phi)\ddot{x}(t) + f(\phi, u) = H(\phi)^T K\begin{bmatrix} z(t) \\ \tau_m(t) \end{bmatrix} \\ &\dot{z}(t) = -AD(v)z(t) + BD(v)\tau_b(t) \end{aligned}\right\} \quad (3)$$

$$\left.\begin{aligned} &H(\phi) = R(\phi)^T J(\phi)^{-1} \\ &R(\phi) = \begin{bmatrix} \bar{R}(\phi) & 0 \\ 0 & I_m \end{bmatrix}, \quad K = \begin{bmatrix} \bar{K} & 0 \\ 0 & I_m \end{bmatrix} \end{aligned}\right\} \quad (4)$$

where $R(\cdot),\ K \in R^{Dn\times Dn}$ and $I_m \in R^{Dm\times Dm}$ is an identity matrix.

The model (3) has the following properties useful for our controller development [1, 5]:

P1) The diagonal elements of A, B and $\bar{K}$ are positive constants, and there exists a positive constant c_B such that $c_B\|\bar{y}\|^2 \le \bar{y}^T B\bar{y}$ for any $\bar{y} \in R^{Dv}$.

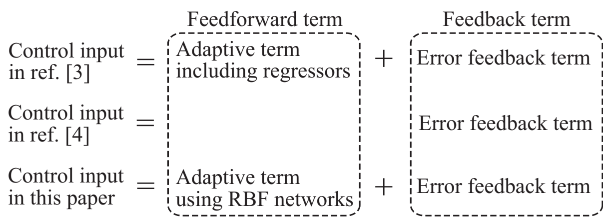

Fig. 1. Comparison of our controllers

Table 1. Symbols in the model (1)

Da	Number of dimensions for vehicle's orientation and manipulator's joint angles
Dn	Number of dimensions $Dv + De = Dv + Dm$
$x(t)$	Signal composed of vehicle's and manipulator end-effector's positions and orientations ($\in R^{Dn}$)
$\phi(t)$	Signal composed of vehicle's orientation and manipulator's joint angles ($\in R^{Da}$)
$u(t)$	Signal composed of vehicle's translational velocity and $\dot\phi(t)$ ($\in R^{Dn}$)
$\tau_m(t)$	Joint torques of manipulator ($\in R^{Dm}$)
$J(\phi)$	Jacobian matrix in the equation $\dot x(t) = J(\phi)u(t)$ ($\in R^{Dn\times Dn}$)
$\bar R(\phi)$	Transformation matrix from thrust forces to force and torque concerning inertial coordinate system ($\in R^{Dv\times Dv}$)
$\bar M(\phi)$	Inertia matrix ($\in R^{Dn\times Dn}$)
$\bar f(\cdot)$	Signal composed of centrifugal, Coriolis, gravitational and buoyant forces, and fluid drag ($\in R^{Dn}$)
$v(t)$	Shaft velocities of thruster's propellers ($\in R^{Dv}$)
$\tau_b(t)$	Shaft torques of thruster's propellers ($\in R^{Dv}$)
A, B, $\bar K$	Diagonal matrices composed of thruster's system parameters ($\in R^{Dv\times Dv}$)

P2) Each of $J(\phi)$ and $R(\phi)$ is composed of kinematic parameters and the functions of $\phi(t)$. Moreover, if each of $J(\phi)$ and $R(\phi)$ has a full rank, then there exists a positive constant c_{H2K} such that $c_{H2K}\|\bar x\|^2 \le \bar x^T H(\phi)^T K H(\phi)\bar x$ for any $\bar x \in R^{Dn}$.
P3) If $J(\phi)$ has a full rank, then $M(\phi)$ is symmetric and positive definite, and there exists a positive constant c_M such that $\|M(\phi)\| \le c_M$.

3 CONTROLLER DESIGN

The control objective is to develop a controller so that all the signals in the closed loop system can be bounded and the state $x(t)$ can track the desired trajectory $x_r(t)$ under the condition that the dynamic and hydrodynamic parameters (e.g., mass and a drag coefficient) are unknown constants.

In order to meet the objective, we make the following assumptions about the model (3) and the reference model (i.e., the desired trajectory $x_r(t)$):
A1) The signals $\phi(t)$, $x(t)$, $u(t)$ and $v(t)$ are available.
A2) The kinematic parameters in (3) (e.g., length) are known constants.
A3) Each of the matrices $J(\phi)$ and $R(\phi)$ in (3) has a full rank.
A4) The desired trajectory $x_r(t)$ and the derivatives $\dot x_r(t)$, $\ddot x_r(t)$ and $x_r^{(3)}(t)$ exist and are bounded.
It follows from the property P2 and the assumptions A1 and A2 that $J(\phi)$ and $R(\phi)$ are known matrices, and hence $\dot x(t)$ is available by using the equation $\dot x(t) = J(\phi)u(t)$.

In the following subsections we develop a controller that achieves the control objective by using a two-step backstepping procedure, as shown in Fig. 2. The first step is the design of an adaptive controller for the inputs $z(t)$ and $\tau_m(t)$, called Adaptive Controller I in this paper. The second step is the design of an adaptive controller for the input $\tau_b(t)$, called Adaptive Controller II in this paper. In this step we first replace $z(t)$, determined in the first step, by the desired trajectory $z_r(t)$, and then design the control input $\tau_b(t)$ so that $z(t)$ can track $z_r(t)$.

3.1 Adaptive Controller I

According to the design procedure shown in Fig. 2, we make the following assumption in the design of Adaptive Controller I:
A5) The control inputs are $z(t)$ for vehicle control and $\tau_m(t)$ for manipulator control.

In order to achieve the control objective described above, we use the tracking errors

$$\tilde s(t) = \dot{\tilde x}(t) + \alpha\tilde x(t), \quad \tilde x(t) = x(t) - x_r(t) \tag{5}$$

where $\alpha > 0$ is a constant design parameter. Using the first equations of (3) and (5), we have the error models

$$\left.\begin{aligned} M(\phi)\dot{\tilde s}(t) &= H(\phi)^T K\begin{bmatrix} z(t) \\ \tau_m(t)\end{bmatrix} - \frac{1}{2}\dot M(\cdot)\tilde s(t) \\ &\qquad - H(\phi)^T K f_x(n_x) - \tilde x(t) \\ \dot{\tilde x}(t) &= -\alpha\tilde x(t) + \tilde s(t) \end{aligned}\right\} \tag{6}$$

$$\begin{aligned} f_x(n_x) = K^{-1}H(\phi)^{-T}\{f(\cdot) - \frac{1}{2}\dot M(\cdot)\tilde s(t) \\ - M(\phi)[\alpha\dot{\tilde x}(t) - \ddot x_r(t)] - \tilde x(t)\} \end{aligned} \tag{7}$$

where $n_x(\cdot) \in R^{5Dn+Da}$ is composed of $\phi(t)$, $x(t)$, $x_r(t)$, $\dot x_r(t)$, $\ddot x_r(t)$ and $u(t)$. In a subsequent analysis, the control input $z(t)$ will contain $n_x(t)$. Moreover, the time derivative of $z(t)$ (i.e., the time derivative of $n_x(t)$) will have to be used in the control input $\tau_b(t)$ of Adaptive Controller II. However, the signal $n_x(t)$ includes $u(t)$ whose time derivative is not directly available, and hence we divide $n_x(t)$ into $u(t)$ and $n_{x1}(t)$ composed of $\phi(t)$, $x(t)$, $x_r(t)$, $\dot x_r(t)$ and $\ddot x_r(t)$ whose time derivatives are directly available.

In this paper, the nonlinear term $f_x(n_x)$ in the error model (6) is replaced by the following RBF network and compensated by Adaptive Controller I:

$$f_x(n_x) = \Theta_x\omega_x(n_x) + \delta_x(n_x) \tag{8}$$

where $\Theta_x \in R^{Dn\times Dx}$ is a constant parameter, $\delta_x(n_x)$ is an approximation error, and $\omega_x(\cdot) \in R^{Dx}$ is a signal whose ith element is given by

$$\omega_{xi}(n_x) = e^{-\|n_x(t)-\bar n_{x1i}\|^2/\bar n_{x2i}^2} \tag{9}$$

where $\bar n_{x1i} \in R^{5Dn+Da}$ and $\bar n_{x2i} \in R$ are constant design parameters. In order to obtain an adequate approximation accuracy, the network dimensions Dx is chosen to be sufficiently high so that the following assumption can be satisfied:
A6) There exists a positive constant $c_{\delta x}$ such that $\|\delta_x(n_x)\| \le c_{\delta x}$ for any $n_x(\cdot) \in \bar R_x$, where $\bar R_x$ is a compact subset of R^{5Dn+Da}.
The assumption A6 is a reasonable assumption because it is shown in [6] that an RBF network can approximate any continuous function on a compact set.

The adaptive control law for the error model (6) subject to the assumptions A1 to A6 is given by

$$\begin{bmatrix} z(t) \\ \tau_m(t)\end{bmatrix} = \hat\Theta_x(t)\omega_x(n_x) - \alpha H(\phi)\tilde s(t) \tag{10}$$

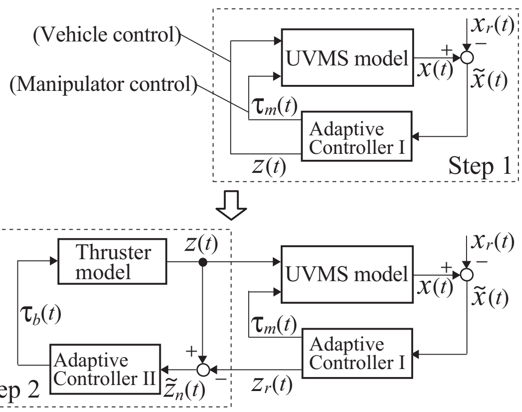

Fig. 2. Controller design procedure

where $\hat{\Theta}_x(t)$, the estimate of Θ_x, is generated by the adaptive law

$$\dot{\hat{\Theta}}_x(t) = -\sigma_{x1}\hat{\Theta}_x(t) - \sigma_{x2}H(\phi)\tilde{s}(t)\omega_x(n_x)^T \qquad (11)$$

where $\sigma_{x1},\,\sigma_{x2} > 0$ are constant design parameters. It can be shown that the adaptive controller (10) and (11) guarantees an ultimate boundedness of the tracking error $\tilde{x}(t)$.

3.2 Adaptive Controller II

According to the design procedure shown in Fig. 2, we make the following assumption instead of the assumption A5 in the design of Adaptive Controller II:

A7) The control inputs are $\tau_b(t)$ for vehicle control and $\tau_m(t)$ for manipulator control.

As shown in Fig. 2, we first replace the input $z(t)$ in (10) by the desired trajectory $z_r(t)$, i.e.,

$$\begin{bmatrix} z_r(t) \\ \tau_m(t) \end{bmatrix} = \hat{\Theta}_x(t)\omega_x(n_x) - \alpha H(\phi)\tilde{s}(t) \qquad (12)$$

and then design Adaptive Controller II by using the tracking error of $z(t)$. When we choose the error as the normal one $\tilde{z}_n(t) = z(t) - z_r(t)$, the error model is written as $\dot{\tilde{z}}_n(t) = -AD(v)z(t) - \dot{z}_r(t) + BD(v)\tau_b(t)$. This model has a situation where the system is uncontrollable due to the lack of the rank of $BD(v)$ when some of $v_i(t)$ equal zero. This situation is caused by the thruster nonlinearities. In order to avoid the situation, we propose the following error instead of the normal one $\tilde{z}_n(t)$:

$$\tilde{z}(t) = z(t) - z_r(t) + \frac{2}{\epsilon}\,l(v) \qquad (13)$$

$$\left.\begin{array}{l} l(v) = \{I_v - E(v)\}\,\bar{v}(v) \\ E(v) = \mathrm{diag}\left\{e^{-|v_1|}, \ldots, e^{-|v_{Dv}|}\right\} \\ \bar{v}(v) = [\mathrm{sgn}(v_1), \ldots, \mathrm{sgn}(v_{Dv})]^T \end{array}\right\} \qquad (14)$$

where $\bar{v}(\cdot) \in R^{Dv}$, $E(\cdot) \in R^{Dv\times Dv}$, $I_v \in R^{Dv\times Dv}$ is an identity matrix, and $\epsilon > 0$ is a design parameter. It should be noted that $l(v)$ is bounded for all $v(t)$. As a result of adding the term $l(v)$, the error model of $\tilde{z}(t)$ is expressed as

$$\dot{\tilde{z}}(t) = BL(v)\tau_b(t) - Bf_z(n_z) - \bar{I}^TKH(\phi)\tilde{s}(t) \qquad (15)$$

$$\left.\begin{array}{l} L(v) = D(v) + \frac{1}{\epsilon}E(v), \quad \bar{I} = \begin{bmatrix} I_v \\ 0 \end{bmatrix} \\ f_z(n_z) = B^{-1}[AL(v)z(t) - \bar{I}^TKH(\phi)\tilde{s}(t) + \xi(t) \\ \qquad + \bar{I}^T\{Y(\dot{u})y_2(t) - \alpha H(\phi)J(\phi)\dot{u}(t)\}] \\ \xi(t) = \bar{I}^T\{y_1(t) + \dot{\hat{\Theta}}_x(t)\omega_x(n_x) - \alpha\dot{H}(\cdot)\tilde{s}(t) \\ \qquad -\alpha H(\phi)[\dot{J}(\cdot)u(t) - \ddot{x}_r(t) + \alpha\dot{\tilde{x}}(t)]\} \\ y_1(t) = -2\,\hat{\Theta}_x(t)\bar{Y}_1(n_x)\dot{n}_{x1}(t) \\ y_2(t) = -2\begin{bmatrix} \bar{Y}_2(n_x)^T\hat{\theta}_{x1}(t) \\ \vdots \\ \bar{Y}_2(n_x)^T\hat{\theta}_{xDn}(t) \end{bmatrix} \\ \bar{Y}_1(n_x) = \begin{bmatrix} \bar{\omega}_1(n_x)[n_{x1}(t) - \bar{n}_{x111}]^T \\ \vdots \\ \bar{\omega}_{Dx}(n_x)[n_{x1}(t) - \bar{n}_{x11Dx}]^T \end{bmatrix} \\ \bar{Y}_2(n_x) = \begin{bmatrix} \bar{\omega}_1(n_x)[u(t) - \bar{n}_{x121}]^T \\ \vdots \\ \bar{\omega}_{Dx}(n_x)[u(t) - \bar{n}_{x12Dx}]^T \end{bmatrix} \\ Y(\dot{u}) = \begin{bmatrix} \dot{u}(t)^T & & 0 \\ & \ddots & \\ 0 & & \dot{u}(t)^T \end{bmatrix}, \; \bar{\omega}_i(n_x) = \dfrac{\omega_{xi}(n_x)}{\bar{n}_{x2i}^2} \end{array}\right\} \qquad (16)$$

$$\hat{\Theta}_x(t) = \begin{bmatrix} \hat{\theta}_{x1}(t)^T \\ \vdots \\ \hat{\theta}_{xDn}(t)^T \end{bmatrix}, \; \bar{n}_{x1i} = \begin{bmatrix} \bar{n}_{x11i} \\ \bar{n}_{x12i} \end{bmatrix} \qquad (17)$$

where $\bar{I} \in R^{Dn\times Dv}$, $Y(\cdot) \in R^{Dn\times(Dn)^2}$, $\bar{n}_{x11i} \in R^{4Dn+Da}$, $\bar{n}_{x12i} \in R^{Dn}$, $\bar{Y}_1(\cdot) \in R^{Dx\times(4Dn+Da)}$, $\bar{Y}_2(\cdot) \in R^{Dx\times Dn}$, $\hat{\theta}_{xi} \in R^{Dx}$, and $\bar{\omega}_i \in R$. In the derivation of (15), we use the equation

$$\hat{\Theta}_x(t)\dot{\omega}_x(n_x, \dot{n}_x) = y_1(t) + Y(\dot{u})y_2(t), \qquad (18)$$

which is modified so that $\hat{\Theta}_x(t)\dot{\omega}_x(\cdot)$ in $\dot{z}_r(t)$ can be separated into the unavailable signal $\dot{u}(t)$ and the available ones $y_1(t)$ and $y_2(t)$. It is noteworthy that the coefficient matrix $BL(v)$ of the input $\tau_b(t)$ in the error model (15) has a full rank for all $v(t)$, and hence the error model is controllable in spite of the thruster nonlinearities.

The nonlinear term $f_z(n_z)$ in the error model (15) is replaced by an RBF network in a way similar to the design of Adaptive Controller I. For the replacement of a function (e.g., $y = f(x)$) by an RBF network, it is necessary to identify not the structure but the arguments of a function replaced (i.e., x of $f(x)$). In view of the fact that the arguments of the unavailable signal $\dot{u}(t)$ are $\phi(t)$, $u(t)$, $v(t)$ and $\tau_m(t)$ (i.e., $\dot{u}(\phi, u, v, \tau_m)$), it can be seen from the third equation of (16) that the argument $n_z(t)$ of $f_z(n_z)$ is composed of $\phi(t)$, $u(t)$, $\tilde{s}(t)$, $v(t)$, $\tau_m(t)$, $y_2(t)$ and $\xi(t)$. The nonlinear term $f_z(n_z)$ is replaced by the following RBF network:

$$f_z(n_z) = \Theta_z\omega_z(n_z) + \delta_z(n_z) \qquad (19)$$

where $\Theta_z \in R^{Dv\times Dz}$ is a constant parameter, $\delta_z(n_z)$ is an approximation error, and $\omega_z(n_z) \in R^{Dz}$ is a signal whose ith element is given by

$$\omega_{zi}(n_z) = e^{-\|n_z(t) - \bar{n}_{z1i}\|^2/\bar{n}_{z2i}^2} \qquad (20)$$

where $\bar{n}_{z1i} \in R^{(Dn+3)Dn+Da+Dv}$ and $\bar{n}_{z2i} \in R$ are constant design parameters. We make the following assumption in common with the assumption A6:

A8) There exists a positive constant $c_{\delta z}$ such that $\|\delta_z(n_z)\| \le c_{\delta z}$ for any $n_z(\cdot) \in \bar{R}_z$, where $\bar{R}_z$ is a compact subset of $R^{(Dn+3)Dn+Da+Dv}$.

The adaptive control law for the error model (15) subject to the assumptions A1 to A4, A7 and A8 is given by

$$\tau_b(t) = L(v)^{-1}[\hat{\Theta}_z(t)\omega_z(n_z) - \alpha\tilde{z}(t)] \qquad (21)$$

where $\hat{\Theta}_z(t)$, the estimate of Θ_z, is generated by the adaptive law

$$\dot{\hat{\Theta}}_z(t) = -\sigma_{z1}\hat{\Theta}_z(t) - \sigma_{z2}\,\tilde{z}(t)\omega_z(n_z)^T \qquad (22)$$

where $\sigma_{z1},\,\sigma_{z2} > 0$ are constant design parameters.

For Adaptive Controller I and II, the following theorem holds:

Theorem 1 Consider the adaptive controller (11), (12), (21) and (22) for the error models (6) and (15) subject to the assumptions A1 to A4 and A6 to A8. This controller guarantees that signals in the closed loop system are bounded, and that the tracking error $\tilde{x}(t)$ satisfies the inequality

$$\|\tilde{x}(t)\|^2 \le \rho_1\,e^{-\gamma\alpha t} + \frac{\rho_2}{\alpha^2\bar{\epsilon}} \qquad (23)$$

where $\rho_1,\,\rho_2 > 0$ are positive constants, $\bar{\epsilon} = \min\{1, \epsilon^2\}$, and $\gamma = \min\{c_{H2K}/(2\,c_M),\,1,\,c_B\}$.

Proof: We can prove Theorem 1 in a way similar to the proofs of the main theorems in [3, 4].

4 SIMULATION EXAMPLE

In order to confirm the usefulness of the adaptive controller (11), (12), (21) and (22), we performed numerical simulations. Typical simulation results are presented in this paper. The UVMS simulated here was an underwater vehicle with a two-link manipulator, as shown in Fig. 3. The values of its system parameters (excepting thruster's parameters) were the same as those used in [3, 4]. In this figure, only the values of the main parameters are shown. The system parameters of the thrusters were given by $A = (1/T)I_3$, $B = (612.5/T)I_3$, $\bar{K} = 0.0408I_3$, where $I_3 \in R^{3\times 3}$ is an identity matrix and T is a positive constant. These values were determined so that the steady state responses could be roughly the same as those of the experimental results in [7], whereas the transient responses are changed by the parameter T. It should be noted that the time responses of the thrusters become slower with an increase in the parameter T. The design parameters of the proposed adaptive controller were chosen as $\alpha = 100$, $\sigma_{x1} = \sigma_{z1} = 0.01$, $\sigma_{x2} = \sigma_{z2} = 1$, $\epsilon = 10$, $Dx = Dz = 50$, $\bar{n}_{x2i} = \bar{n}_{z2j} = 3$, $\hat{\Theta}_{xki}(0) = \hat{\Theta}_{zhj}(0) = 0$ where $\hat{\Theta}_{xki}(\cdot)$ and $\hat{\Theta}_{zhj}(\cdot)$ are the (k, i)th and the (h, j)th element of $\hat{\Theta}_x(\cdot)$ and $\hat{\Theta}_z(\cdot)$, respectively. In addition, the design parameters $\bar{n}_{x1i}$ and $\bar{n}_{z1j}$ were set as points into which the interval of each variable corresponding to $n_x(t)$ and $n_z(t)$ is divided equally. Each of the desired trajectories of the vehicle's and the manipulator end-effector's position was set up along a straight path. Each of the velocities was given by a filtered trapezoidal function. In these simulations, the time at which each of the desired trajectories reaches a target point was about 15 seconds. On the other hand, the desired trajectory of the vehicle's orientation is selected to remain at the initial value.

In order to investigate an effect of thruster dynamics on a control performance, we performed simulations using a controller for UVMS without thruster dynamics, called Static Controller in this paper. Static Controller is composed of (11), (12) and the static model $\tau_b(t) = B^{-1}Az_r(t)$, which is obtained from the second equation of (3) when $\dot{z}(t) = 0$. Figure 4 shows the tracking errors of Static Controller for $T = 0.01, 0.1, 1$. It is worth noting that an unstable robot motion was observed when $T > 1$. It can be seen from this figure that the tracking error increases with an increase in the parameter T. This means that a slow thruster dynamics degrades a control performance when Static Controller is used. On the other hand, Fig. 5 shows the tracking errors of the adaptive controller (11), (12), (21) and (22) for $T = 1, 10, 100$. As shown in this figure, the tracking errors are roughly the same and remain small in the three cases, irrespective of the parameter T.

In order to compare the proposed adaptive controller with the robust controller developed in [4], we performed simulations using the robust controller. Figure 6 shows the tracking errors of the adaptive and the robust controller for $T = 1$. It can be seen from this figure that the tracking error of the proposed adaptive controller is smaller than that of the robust controller. It is noteworthy that the steady state error of the adaptive controller is considerably reduced, particularly after the desired trajectories reach the target points.

5 CONCLUSION

In this paper we developed an adaptive controller for underwater vehicle-manipulator systems with thruster dynamics. In the controller development we presented a new tracking error model that overcomes uncontrollability caused by the thruster dynamics, and then designed the adaptive controller with radial basis function networks. Furthermore, the usefulness of the proposed controller was demonstrated by the simulation results.

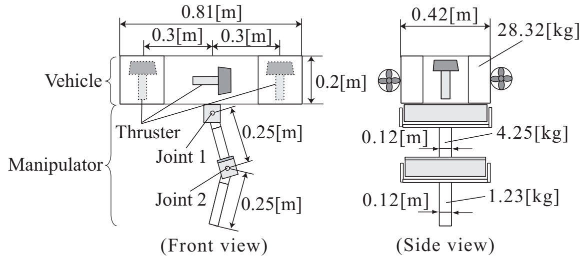

Fig. 3. UVMS for numerical simulation

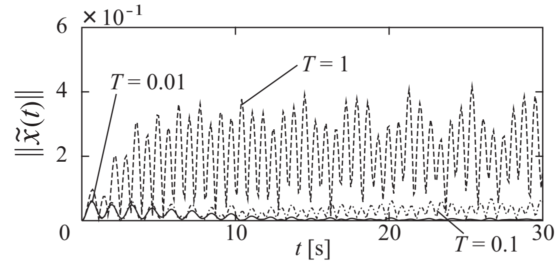

Fig. 4. Simulation results of Static Controller

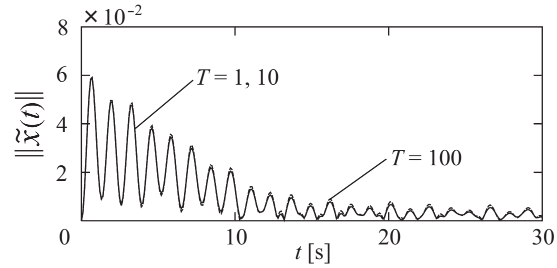

Fig. 5. Simulation results of proposed adaptive controller

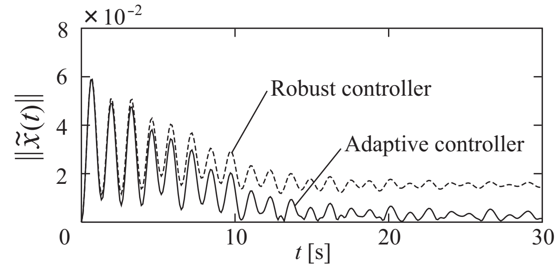

Fig. 6. Simulation results of controllers for $T = 1$

REFERENCES

[1] Antonelli G (2003), Underwater robots: motion and force control of vehicle-manipulator systems. Springer-Verlag

[2] Canudas de Wit C, Diaz EO, Perrier M (2000), Nonlinear control of an underwater vehicle/manipulator with composite dynamics. IEEE Trans Control Systems Technology 8(6): 948-960

[3] Taira Y, Oya M, Sagara S (2010), An adaptive controller for underwater vehicle-manipulator systems including thruster dynamics. Proc Int Conf Modelling, Identification and Control, pp.185-190

[4] Taira Y, Sugino J, Takagi N, Oya M (2011), Robust controller for underwater vehicle-manipulator systems including thruster dynamics. Proc Int Symposium Artificial Life and Robotics, pp.134-137

[5] Yoerger DR, Cooke JG, Slotine JJE (1990), The influence of thruster dynamics on underwater vehicle behavior and their incorporation into control system design. IEEE J Oceanic Engineering 15(3): 167-178

[6] Haykin S (1999), Neural networks: a comprehensive foundation (2nd edition). Prentice-Hall, pp.290-291

[7] Bachmayer R, Whitcomb LL, Grosenbaugh MA (2000), An accurate four-quadrant nonlinear dynamical model for marine thrusters: theory and experimental validation. IEEE J Oceanic Engineering 25(1): 146-159

The Seventeenth International Symposium on Artificial Life and Robotics 2012 (AROB 17th '12),
B-Con Plaza, Beppu, Oita, Japan, January 19-21, 2012

An improved adaptive controller in the presence of input saturation - In case of systems with available output derivatives up to the order of relative degree -

Natsuki Takagi[1] and Masahiro Oya[2]

[1] Miyakonojo National College of Technology, Miyakonojo, Miyazaki 885-8567, Japan
(Tel: 81-986-47-1179, Fax: 81-986-47-1184)
[2] Kyushu Institute of Technology, Kitakyushu, Fukuoka 804-8550, Japan

[1]takagi@cc.miyakonojo-nct.ac.jp

Abstract: We have proposed a model reference adaptive control scheme (conventional control scheme) for continuous time single-input single-output linear systems with an input saturation in which i-th derivatives of the output signal ($i = 1, \cdots$, relative degree) are available. In the conventional scheme, a condition for the initial states of the controlled object has to be satisfied. In this paper, the main attention is focused on the relaxation of the condition. To achieve the objective, we propose an improve adaptive control scheme. As a result of analyzing stability of the closed loop system using the improved adaptive control scheme, a new condition for the initial states is derived. It should be emphasized that we can apply the new control scheme in a larger region of initial states compared with the conventional one.

Keywords: adaptive control, input saturation, order of systems, improvement of control performance, relaxation of restrict condition

1 INTRODUCTION

In practice, the values of the system parameters, that are coefficients of dynamic equations describing behavior of physical systems, vary due to aged deterioration or environmental changes. For the systems, adaptive control schemes [1]-[3] were useful. However, input saturation was ignored in the early works. To overcome the problem, various adaptive control schemes have been developed for single-input single-output (SISO) linear systems [4]-[16]. These schemes guarantee boundedness of all signals in the closed loop systems. But most of them could not assure asymptotical stability of a tracking error between the output of the controlled object and a desired trajectory. Although there exist some schemes that can assure asymptotical stability of the tracking error, they have a problem that controlled objects are restricted to asymptotically stable systems. Moreover, in all proposed schemes, there exists a problem that a method to improve tracking performance have not been provided.

To struggle against these problems, for the first step, the authors proposed an adaptive output tracking control scheme for SISO linear systems with an input saturation in which full states can be measured [17]. The closed loop system using the proposed controller has the following properties: 1) Stability of all signals in the closed loop systems can be guaranteed; 2) Convergence of the tracking error to zero is assured even for unstable controlled objects; 3) Setting only one design parameter, the control performance can be easily improved. For the next step, to decrease measurement signals, for n-th degree systems with an input saturation and the relative degree n_r, we proposed an extended scheme satisfying 1)-3) in which i-th derivatives of output signal ($i = 1, \cdots, n_r$) are only required [18]. However, to achieve the good properties 1)-3), the condition for the initial states of the controlled object has to be satisfied.

In this paper, the main attention is to relax the condition for the initial states derived in [18]. We propose an improved adaptive controller for SISO linear systems with an input saturation in which the output derivatives up to the order of relative degree n_r are available. In the proposed adaptive controller, it is shown theoretically that the same good properties 1)-3) can be assured under a new condition for the initial states. Moreover, it can be shown theoretically that the improved adaptive controller can be utilized in a larger region of initial states compared with the adaptive control scheme proposed in [18].

2 PROBLEM STATEMENT

In this paper, we consider the controlled objects described by

$$\left.\begin{aligned} Y(s) &= \frac{b_m B_p(s)}{A_p(s)}F(s) + \frac{C_p(s)}{A_p(s)} \\ A_p(s) &= s^n + a_{n-1}s^{n-1} + \cdots + a_1 s + a_0 \\ B_p(s) &= s^m + b_{m-1}s^{m-1} + \cdots + b_1 s + b_0 \\ C_p(s) &= c_{n-1}s^{n-1} + \cdots + c_1 s + c_0 \end{aligned}\right\} \tag{1}$$

where $A_p(s)$ and $B_p(s)$ are coprime. $f(u) = \mathcal{L}[F(s)]^{-1} \in \mathbb{R}$ is a saturation function given by

$$f(u) = \begin{cases} \sigma & \text{for} \quad u(t) > \sigma \\ u(t) & \text{for} \quad |u(t)| \le \sigma \\ -\sigma & \text{for} \quad u(t) < -\sigma \end{cases} \tag{2}$$

where $u(t) \in \mathbb{R}$ is the control input and the positive constant σ is an amplitude saturation level of the actuator.

The reference model is given by

$$\left.\begin{aligned} Y_M(s) &= \frac{B_M(s)}{A_M(s)}R(s) \\ A_M(s) &= s^{n_M} + a_{M(n_M-1)}s^{n_M-1} + \cdots + a_{M1}s + a_{M0} \\ B_M(s) &= b_{Mm_M}s^{m_M} + \cdots + b_{M1}s + b_{M0} \end{aligned}\right\} \tag{3}$$

where $y_M(t) = \mathcal{L}^{-1}[Y_M(s)]$ is the reference output, $r(t) = \mathcal{L}^{-1}[R(s)]$ is the reference input, $A_M(s)$ is Hurwitz polynomia, and $n_M - m_M \ge n - m$. The reference input $r(t)$ is a deterministic signal given by

$$\left.\begin{aligned} R(s) &= \frac{B_R(s)}{A_R(s)} \\ A_R(s) &= s^{n_r} + a_{R(n_r-1)}s^{n_r-1} + \cdots + a_{R1}s + a_{R0} \\ B_R(s) &= b_{Rm_r}s^{m_r} + \cdots + b_{R1}s + b_{R0} \end{aligned}\right\} \tag{4}$$

where $A_R(s)$ and $B_R(s)$ are known polynomials, and $n_r - m_r \ge 0$.

The tracking error is defined as $y_e(t) = y(t) - y_M(t)$. Then, using the polynomials

$$\left.\begin{array}{l} A_p(s) = A_{pq}(s)B_p(s) + A_{pr}(s) \\ A_{pq}(s) = s^{n-m} + a_{q(n-m-1)}s^{n-m-1} + \cdots + a_{q1}s + a_{q0} \\ A_{pr}(s) = a_{r(m-1)}s^{m-1} + \cdots + a_{r1}s + a_{r0} \end{array}\right\}, \quad (5)$$

the following state space description can be derived [18].

$$\left.\begin{array}{l} \dot{\boldsymbol{x}}_e(t) = \boldsymbol{A}\boldsymbol{x}_e(t) + b_m\boldsymbol{b}\left(f(u) - \boldsymbol{c}_z^\top \boldsymbol{z}(t) - \boldsymbol{\theta}_r^\top \boldsymbol{x}_r(t) + \phi(t)\right) \\ \boldsymbol{x}_e(t) = \left[y_e(t),\ \dot{y}_e(t),\ \cdots,\ y_e(t)^{(n-m-1)}\right]^\top \\ \boldsymbol{A} = \overline{\boldsymbol{A}} - \boldsymbol{b}\boldsymbol{a}_q^\top,\ \boldsymbol{b}^\top = [0, \cdots, 0, 1] \\ \overline{\boldsymbol{A}} = \left[\begin{array}{c|c} \boldsymbol{0} & \boldsymbol{I} \\ \hline 0 & 0 \cdots 0 \end{array}\right],\ \boldsymbol{a}_q^\top = [a_{q0}, \cdots, a_{q(n-m-1)}] \\ \boldsymbol{c}_z^\top = [a_{r0}, \cdots, a_{r(m-1)}] \\ \dot{\boldsymbol{x}}_r(t) = \boldsymbol{A}_r\boldsymbol{x}_r(t),\ \boldsymbol{x}_r(0) = \boldsymbol{x}_{r0} \end{array}\right\} \quad (6)$$

$$\left.\begin{array}{l} \dot{\boldsymbol{z}}(t) = \boldsymbol{A}_z\boldsymbol{z}(t) + \boldsymbol{h}\boldsymbol{c}_x^\top \boldsymbol{x}_e(t),\ \boldsymbol{z}(0) = \boldsymbol{0} \\ \boldsymbol{A}_z = \left[\begin{array}{c|c} \boldsymbol{0} & \boldsymbol{I} \\ \hline -b_0 & -b_1 \cdots - b_{m-1} \end{array}\right] \\ \boldsymbol{h}^\top = [0, \cdots, 0, 1/b_m],\ \boldsymbol{c}_x^\top = [1, 0, \cdots, 0] \end{array}\right\} \quad (7)$$

Where $\phi(t)$ is an unknown bounded exponential damping function, $\boldsymbol{\theta}_r$ is an unknown parameter, $\boldsymbol{A}_r$ is known constant matrix, and $\boldsymbol{x}_r(t) \in \mathbb{R}^{n_M+n_r}$ is a known state with respect to the reference model.

Using a known constant vector $\boldsymbol{d} \in \mathbb{R}^{n-m}$, the Hurwitz matrix $\boldsymbol{A}_e$ is defined as $\boldsymbol{A}_e = \overline{\boldsymbol{A}} - \boldsymbol{b}\boldsymbol{d}^\top$. Then, defining the signal $\ell(t) = \boldsymbol{c}_z^\top \boldsymbol{z}(t)$, the tracking error system (6) can be rewritten as

$$\left.\begin{array}{l} \dot{\boldsymbol{x}}_e(t) = \boldsymbol{A}_e\boldsymbol{x}_e(t) + b_m\boldsymbol{b}\left(f(u) - q(t)\right) \\ q(t) = \boldsymbol{\theta}(t)^\top \boldsymbol{\omega}(t) + \ell(t),\ \ell(t) = \boldsymbol{c}_z^\top \boldsymbol{z}(t) \\ \boldsymbol{\theta}(t)^\top = \dfrac{1}{\varepsilon}\left[\phi(t),\ \boldsymbol{\theta}_e^\top,\ \boldsymbol{\theta}_r\right],\ \varepsilon \geq 1 \\ \boldsymbol{\omega}(t)^\top = \varepsilon\left[-1,\ \boldsymbol{x}_e(t),\ \boldsymbol{x}_r(t)\right] \\ \boldsymbol{\theta}_e = \dfrac{1}{b_m}(\boldsymbol{a}_q - \boldsymbol{d}) \end{array}\right\} \quad (8)$$

where $\boldsymbol{\theta}(t)$ and $\ell(t)$ are unknown signals. The design parameter ε is a positive constant. The design parameter ε is introduce to reduce the initial value $\|\boldsymbol{\theta}(0)\|$.

The controlled objective is that the tracking error becomes asymptotically stable even if a controlled object is not asymptotically stable. To achieve the controlled objective, the following assumptions are made:

A1 Coefficients of polynomials $A_p(s)$, $B_p(s)$ and $C_p(s)$ are unknown constants.
A2 The plant is minimal phase.
A3 Sign of b_m is known. It is assumed that the sign is positive hereafter.
A4 Relative degree $n - m$ is known.
A5 $y(t)^{(i)},\ i = 0, \cdots, n - m - 1$ are available.
A6 There exists a known positive constant δ_z such that $\overline{\boldsymbol{A}}_z = \boldsymbol{A}_z + \delta_z\boldsymbol{I}$ is Hurwitz matrix.
A7 There exists bounded positive constant $\overline{\rho}_{M1}$ and $\overline{\rho}_{M2}$ such that $|\boldsymbol{\theta}_r\boldsymbol{x}_r(t) - \phi(t)| \leq \overline{\rho}_{M1}$ and $\|\boldsymbol{x}_r(t)\| \leq \overline{\rho}_{M2}$.
A8 The relation $\sigma - \overline{\rho}_{M1} > 0$ holds.
A9 The saturation level σ is known.

The assumptions A1 ~ A4 are the same assumptions made in conventional adaptive control scheme. From the assumption A2, $\boldsymbol{A}_z$ becomes Hurwitz. Since $\phi(t)$ is bounded exponential damping function, it is also seen that there exist positive constants ρ_ϕ, δ_ϕ such that $\left\|\dot{\phi}(t)\right\| \leq \rho_\phi \exp(-\delta_\phi t)$. The assumptions A5 ~ A9 are introduced to develop the adaptive controller mentioned later. From the assumption A5, the signal $\boldsymbol{x}_e(t)$ is available.

3 DEVELOPMENT OF ADAPTIVE CONTROLLER

3.1 Conventional adaptive controller

In [18], the controller developed under the assumptions A1~A9 is given by

$$\left.\begin{array}{l} u(t) = \hat{q}(t) = \hat{\boldsymbol{\theta}}(t)^\top \boldsymbol{\omega}(t) + \hat{\ell}(t) \\ \hat{\boldsymbol{\theta}}(t) = \left[\hat{\theta}_\phi(t),\ \hat{\boldsymbol{\theta}}_e(t)^\top,\ \hat{\boldsymbol{\theta}}_r(t)\right]^\top \end{array}\right\}, \quad (9)$$

$$\left.\begin{array}{l} \dot{\hat{\boldsymbol{\theta}}}(t) = -\alpha^3 g(t)\tilde{\boldsymbol{x}}_e(t)^\top \boldsymbol{P}\boldsymbol{b}\boldsymbol{\Gamma}\boldsymbol{\omega}(t),\ \boldsymbol{\Gamma} > 0 \\ \dot{\hat{\ell}}(t) = -\delta_z\hat{\ell}(t) - \dfrac{1}{\rho_\ell}\alpha^3 g(t)\tilde{\boldsymbol{x}}_e(t)^\top \boldsymbol{P}\boldsymbol{b},\ \hat{\ell}(0) = 0 \\ \tilde{\boldsymbol{x}}_e(t) = \boldsymbol{x}_e(t) - \hat{\boldsymbol{x}}_e(t) \\ \dot{\hat{\boldsymbol{x}}}_e(t) = \boldsymbol{A}_e\hat{\boldsymbol{x}}_e(t) + \alpha^2\tilde{\boldsymbol{x}}_e(t),\ \hat{\boldsymbol{x}}_e(0) = \boldsymbol{x}_e(0) \\ g(t) = 1 - (1-\beta)(1 - \delta_{\tilde{e}f}(t)),\ 1 \geq \beta > 0 \\ \delta_{\tilde{e}f}(t) = \begin{cases} 1 & \text{for} \quad \tilde{\boldsymbol{x}}_e(t)^\top \boldsymbol{P}\boldsymbol{b}\tilde{f}(u) \leq 0 \\ 0 & \text{for} \quad \tilde{\boldsymbol{x}}_e(t)^\top \boldsymbol{P}\boldsymbol{b}\tilde{f}(u) > 0 \end{cases} \\ \tilde{f}(u) = f(u) - u(t) \end{array}\right\}, \quad (10)$$

where $\hat{\theta}_\phi(t)$, $\hat{\boldsymbol{\theta}}_e(t)$ and $\hat{\boldsymbol{\theta}}_r(t)$ are estimate values corresponding to the unknown signal $\phi(t)/\varepsilon$ and constants $\boldsymbol{\theta}_e/\varepsilon$ and $\boldsymbol{\theta}_r/\varepsilon$, respectively. $\hat{\boldsymbol{x}}_e(t)$ and $\hat{\ell}(t)$ are estimates of $\boldsymbol{x}_e(t)$ and $\ell(t)$, respectively. The design parameters α and β are positive constants, $\boldsymbol{\Gamma}$ is a positive definite matrix. The design parameter ρ_ℓ is a positive constant satisfying

$$\left.\begin{array}{l} \rho_\ell \leq \dfrac{\delta_z}{b_m}\left\{\left(\dfrac{4}{\underline{\alpha}} + \dfrac{6}{\rho_{\tilde{e}}}\right)\dfrac{\|\boldsymbol{c}_z^\top \boldsymbol{h}\boldsymbol{c}_x^\top\|^2}{\lambda_{\min}[\boldsymbol{Q}]} + \dfrac{4\|\boldsymbol{c}_z^\top \overline{\boldsymbol{A}}_z\|^2}{\rho_z\lambda_{\min}[\boldsymbol{Q}_z]}\right\}^{-1} \\ \rho_z = \left(\dfrac{4}{\underline{\alpha}} + \dfrac{6}{\rho_{\tilde{e}}}\right)^{-1}\dfrac{\lambda_{\min}[\boldsymbol{Q}_z]}{4}\dfrac{\lambda_{\min}[\boldsymbol{Q}]}{\|\boldsymbol{P}_z\boldsymbol{h}\boldsymbol{c}_x^\top\|^2} \\ \rho_{\tilde{e}} = \dfrac{\lambda_{\min}[\boldsymbol{Q}]}{6}\left(\dfrac{\|\boldsymbol{P}\|}{\underline{\alpha}}\right)^{-1} \end{array}\right\}, \quad (11)$$

where $\underline{\alpha}$ denotes a lower bound of the design parameter α such that $\alpha > \underline{\alpha} > 0$, design parameters $\boldsymbol{Q}$ and $\boldsymbol{Q}_z$ are positive definite matrices. $\boldsymbol{P}$ and $\boldsymbol{P}_z$ are the solutions of the following Lyapunov equations.

$$\left.\begin{array}{l} \boldsymbol{A}_e^\top \boldsymbol{P} + \boldsymbol{P}\boldsymbol{A}_e = -\boldsymbol{Q},\ \boldsymbol{Q} > 0 \\ \boldsymbol{A}_z^\top \boldsymbol{P}_z + \boldsymbol{P}_z\boldsymbol{A}_z = -\boldsymbol{Q}_z,\ \boldsymbol{Q}_z > 0 \end{array}\right\} \quad (12)$$

The estimated signal $\hat{\boldsymbol{x}}_e(t)$ and the design parameter α is introduced to improve performance of the estimators for $\hat{\boldsymbol{\theta}}(t)$ and $\hat{\ell}(t)$. The design parameter β is introduced to guarantee tracking performance between the control input signal $\hat{q}(t)$ and the ideal input signal $q_d(t) = \boldsymbol{\theta}(t)^\top \boldsymbol{\omega}(t) + \ell(t)$. The switch function $\delta_{\tilde{e}f}(t)$ is introduced to assure stability of the closed loop system with the input saturation.

To show the property of the closed loop system, we define the following Lyapunov function candidate

$$\left.\begin{array}{l} V(t) = V_1(t) + \rho_{v2}V_2(t) \\ V_1(t) = \alpha^3\tilde{\boldsymbol{x}}_e(t)^\top \boldsymbol{P}\tilde{\boldsymbol{x}}_e(t) + V_e(t) \\ \qquad + \rho_z\boldsymbol{z}(t)^\top \boldsymbol{P}_z\boldsymbol{z}(t) + b_m\rho_\ell\tilde{\ell}(t)^2 \\ \qquad + b_m\tilde{\boldsymbol{\theta}}(t)^\top \boldsymbol{\Gamma}^{-1}\tilde{\boldsymbol{\theta}}(t) \\ V_2(t) = \dfrac{2\rho_\phi\sqrt{b_m}\left\|\boldsymbol{\Gamma}^{-\frac{1}{2}}\right\|}{\varepsilon\delta_\phi}\exp(-\delta_\phi t) \\ \rho_{v2} = \dfrac{V_2(0) + \sqrt{V_2(0)^2 + 4V_1(0)}}{2} + \delta_v \\ \tilde{\ell}(t) = \ell(t) - \hat{\ell}(t),\ \tilde{\boldsymbol{\theta}}(t) = \boldsymbol{\theta}(t) - \hat{\boldsymbol{\theta}}(t) \end{array}\right\}, \quad (13)$$

$$V_e(t) = \rho_{\hat{e}} \hat{\boldsymbol{x}}_e(t)^\top \boldsymbol{P} \hat{\boldsymbol{x}}_e(t) \tag{14}$$

where $\tilde{\boldsymbol{\theta}}(t)$ and $\tilde{\ell}(t)$ are the parameter estimation errors, and δ_v is a design parameter of a positive constant.

Define a input estimation error $\tilde{q}(t)$ as $\tilde{q}(t) = q_d(t) - \hat{q}(t) = \tilde{\boldsymbol{\theta}}(t)^\top \boldsymbol{\omega}(t) + \tilde{\ell}(t)$. In the closed loop system using the conventional adaptive controller, the following theorem holds [18].

Theorem 1 If the initial states satisfy

$$\left.\begin{aligned}
&\rho_v^2 \geq V(0) \\
&\quad = \rho_{\hat{e}} \boldsymbol{x}_e(0)^\top \boldsymbol{P} \boldsymbol{x}_e(0) + b_m \tilde{\boldsymbol{\theta}}(0)^\top \boldsymbol{\Gamma}^{-1} \tilde{\boldsymbol{\theta}}(0) \\
&\qquad + \rho_{v2} V_2(0) \\
&\rho_v = \frac{1}{2\beta\rho_{u3}} \Big\{ -(\rho_{u1} + \beta\rho_{u2}) \\
&\qquad + \sqrt{(\rho_{u1} + \beta\rho_{u2})^2 + 4(\sigma - \bar{\rho}_{M1})\beta\rho_{u3}} \Big\} \\
&\rho_{u1} = \sqrt{2 \max\left\{ \frac{\|\boldsymbol{\theta}_e\|^2}{\rho_{\hat{e}} \lambda_{\min}[\boldsymbol{P}]}, \frac{\|\boldsymbol{c}_z\|^2}{\rho_z \lambda_{\min}[\boldsymbol{P}_z]} \right\}} \\
&\rho_{u2} = \sqrt{\frac{2}{b_m}} \max\left\{ \frac{\varepsilon \bar{\rho}_{M2}}{\lambda_{\min}\left[\boldsymbol{\Gamma}^{-\frac{1}{2}}\right]}, \frac{1}{\sqrt{\rho_\ell}} \right\} \\
&\qquad + \frac{\varepsilon}{\sqrt{b_m} \lambda_{\min}\left[\boldsymbol{\Gamma}^{-\frac{1}{2}}\right]} \\
&\rho_{u3} = \sqrt{\frac{2}{b_m \lambda_{\min}\left[\boldsymbol{\Gamma}^{-1}\right] \lambda_{\min}[\boldsymbol{P}]} \max\left\{ \frac{1}{\underline{\alpha}^3}, \frac{1}{\rho_{\hat{e}}} \right\}}
\end{aligned}\right\}, \tag{15}$$

in addition, the lower bound of the design parameter $\underline{\alpha}$ is given by

$$\underline{\alpha}^2 \geq 2 b_m \|\boldsymbol{\theta}_e\| \sqrt{\boldsymbol{b}^\top \boldsymbol{P} \boldsymbol{b} \lambda_{\min}[\boldsymbol{P}^{-1}]}, \tag{16}$$

the closed loop system using the controller (9) – (12) becomes stable, and the error signals $\boldsymbol{x}_e(t)$, $\tilde{\boldsymbol{x}}_e(t)$, $\boldsymbol{z}(t)$, $\tilde{\ell}(t)$ and $\tilde{q}(t)$ converge to zero. When the design parameters are fixed except for the design parameter α, the following relation holds.

$$\tilde{q}(t)^2 \leq \exp\left(-\alpha \bar{\rho}_{q1} t\right) \tilde{q}(0)^2 + \alpha^{-1} \bar{\rho}_{q2} \tag{17}$$

Where $\bar{\rho}_{qi},\ i = 1, 2$ are bounded positive constants independent of the design parameter α. ■

From Theorem 1, we have the following remarks.

Remark 1 It is seen from Theorem 1 that $\tilde{q}(t)$ converges to zero rapidly as the design parameter α increases. Then, the control input signal (9) becomes close to the ideal input $u(t) = q_d(t)$. Therefore, it can be expected that if the value of the design parameter α is large enough, the oscillations caused by the estimator of unknown parameters are hard to occur in the control input signal.

Remark 2 Consider the case when $\tilde{q}(t)$ converges to zero rapidly. Since $\boldsymbol{x}_e(t)$ converges to zero, from the assumption A8, it is seen that there exists $t_1 \geq 0$ such that $|q(t)| \leq \sigma,\ t_1 \geq t$. Then, for $t \geq t_1$, $\boldsymbol{x}_e(t)$ converges to zero at the convergent rate specified by the system matrix $\boldsymbol{A}_e$.

Remark 3 From (15), ρ_v becomes large as the desing parameter β decreases. The upper bound of ρ_v is

$$\lim_{\beta \to 0} \rho_v = \frac{\sigma - \bar{\rho}_{M1}}{\rho_{u1}}. \tag{18}$$

From this fact, it can be seen that if the condition

$$\left.\begin{aligned}
&\frac{(\sigma - \bar{\rho}_{M1})^2}{2} \min\left(\frac{\lambda_{\min}[\boldsymbol{P}]}{\|\boldsymbol{\theta}_e\|^2}, K_1 K_2 \right) > \boldsymbol{x}_e(0)^\top \boldsymbol{P} \boldsymbol{x}_e(0) \\
&K_1 = \frac{\lambda_{\min}[\boldsymbol{Q}_z] \lambda_{\min}[\boldsymbol{Q}] \lambda_{\min}[\boldsymbol{P}_z]}{16 \|\boldsymbol{P}_z \boldsymbol{h} \boldsymbol{c}_x^\top\|^2 \|\boldsymbol{c}_z\|^2} \\
&K_2 = \frac{6}{9 + \dfrac{\lambda_{\min}[\boldsymbol{Q}]}{\|\boldsymbol{P}\|}}
\end{aligned}\right\} \tag{19}$$

is satisfied, for any initial condition of the parameter estimation error $\tilde{\boldsymbol{\theta}}(0)$ and $V_2(0)$, there exist design parameters ε, $\boldsymbol{\Gamma}$, and β such that the first equation of (15) holds.

3.2 Improved adaptive controller

If the left side of the first equation in (19) can become large, the region of the initial states satisfying Theorem 1 can be expanded. To achieve this, the Lyapunov function candidate is redefined as (13) and

$$V_e(t) = \boldsymbol{x}_e(t)^\top \boldsymbol{P} \boldsymbol{x}_e(t). \tag{20}$$

Analyzing the derivative of (13) and (20), the improved adaptive controller is developed as (9) and

$$\left.\begin{aligned}
&\dot{\hat{\boldsymbol{\theta}}}(t) = -\alpha^3 g(t) \bar{\boldsymbol{x}}_e(t)^\top \boldsymbol{P} \boldsymbol{b} \boldsymbol{\Gamma} \omega(t),\ \boldsymbol{\Gamma} > 0 \\
&\dot{\hat{\ell}}(t) = -\delta_z \hat{\ell}(t) - \frac{1}{\rho_\ell} \alpha^3 g(t) \bar{\boldsymbol{x}}_e(t)^\top \boldsymbol{P} \boldsymbol{b},\ \hat{\ell}(0) = 0 \\
&\bar{\boldsymbol{x}}_e(t) = \tilde{\boldsymbol{x}}_e(t) + \frac{1}{\alpha^3} \boldsymbol{x}_e(t) \\
&\tilde{\boldsymbol{x}}_e(t) = \boldsymbol{x}_e(t) - \hat{\boldsymbol{x}}_e(t) \\
&\dot{\hat{\boldsymbol{x}}}_e(t) = \boldsymbol{A}_e \hat{\boldsymbol{x}}_e(t) + \alpha^2 \tilde{\boldsymbol{x}}_e(t),\ \hat{\boldsymbol{x}}_e(0) = \boldsymbol{x}_e(0) \\
&g(t) = 1 - (1 - \beta)(1 - \delta_{\tilde{e}f}(t)),\ 1 \geq \beta > 0 \\
&\delta_{\tilde{e}f}(t) = \begin{cases} 1 & \text{for} \quad \bar{\boldsymbol{x}}_e(t)^\top \boldsymbol{P} \boldsymbol{b} \tilde{f}(u) \leq 0 \\ 0 & \text{for} \quad \bar{\boldsymbol{x}}_e(t)^\top \boldsymbol{P} \boldsymbol{b} \tilde{f}(u) > 0 \end{cases} \\
&\tilde{f}(u) = f(u) - u(t)
\end{aligned}\right\}, \tag{21}$$

where the design parameter ρ_ℓ satisfies

$$\left.\begin{aligned}
&\rho_\ell \leq \frac{\delta_z}{4 b_m} \left\{ \frac{\|\boldsymbol{c}_z^\top \boldsymbol{h} \boldsymbol{c}_x^\top\|^2}{\lambda_{\min}[\boldsymbol{Q}]} + \frac{\|\boldsymbol{c}_z^\top \bar{\boldsymbol{A}}_z\|^2}{\rho_z \lambda_{\min}[\boldsymbol{Q}_z]} \right\}^{-1} \\
&\rho_z = \frac{\lambda_{\min}[\boldsymbol{Q}_z]}{16} \frac{\lambda_{\min}[\boldsymbol{Q}]}{\|\boldsymbol{P}_z \boldsymbol{h} \boldsymbol{c}_x^\top\|^2}
\end{aligned}\right\}. \tag{22}$$

Then, for the closed-loop system using the improved adaptive controller, the following theorem holds.

Theorem 2 If the initial states satisfy

$$\left.\begin{aligned}
&\rho_{v_m}^2 \geq V(0) \\
&\quad = \boldsymbol{x}_e(0)^\top \boldsymbol{P} \boldsymbol{x}_e(0) + b_m \tilde{\boldsymbol{\theta}}(0)^\top \boldsymbol{\Gamma}^{-1} \tilde{\boldsymbol{\theta}}(0) \\
&\qquad + \rho_{v2} V_2(0) \\
&\rho_{v_m} = \frac{1}{2\beta\rho_{u3}} \Big\{ -(\rho_{u1} + \beta\rho_{u2}) \\
&\qquad + \sqrt{(\rho_{u1} + \beta\rho_{u2})^2 + 4(\sigma - \bar{\rho}_{M1})\beta\rho_{u3}} \Big\} \\
&\rho_{m1} = \sqrt{\max\left\{ \frac{\|\boldsymbol{\theta}_e\|^2}{\lambda_{\min}[\boldsymbol{P}]}, \frac{\|\boldsymbol{c}_z\|^2}{\rho_z \lambda_{\min}[\boldsymbol{P}_z]} \right\}} \\
&\rho_{m2} = \frac{1}{\sqrt{b_m}} \max\left\{ \frac{\varepsilon(\bar{\rho}_{M2} + 1)}{\lambda_{\min}\left[\boldsymbol{\Gamma}^{-\frac{1}{2}}\right]}, \frac{1}{\sqrt{\rho_\ell}} \right\} \\
&\rho_{m3} = \frac{1}{\sqrt{b_m \lambda_{\min}\left[\boldsymbol{\Gamma}^{-1}\right] \lambda_{\min}[\boldsymbol{P}]}}
\end{aligned}\right\}, \tag{23}$$

the closed loop system using the controller (9), (12), (21), and (22) becomes stable, and the error signals $\boldsymbol{x}_e(t)$, $\tilde{\boldsymbol{x}}_e(t)$, $\boldsymbol{z}(t)$, $\tilde{\ell}(t)$ and $\tilde{q}(t)$ converge to zero. When the design parameters are fixed except for the design parameter α, there exist the bounded positive constant $\overline{\rho}_{qi}$, $i = 1, 2$ independent of the design parameter α satisfying (17). ■

For the lack of space, the proof is omitted. □

From Theorem 2, it can be ascertained that the properties stated in Remark 1 and Remark 2 hold. Moreover, we have the following remark for initial states.

Remark 4 From (23), ρ_{v_m} becomes large as the desing parameter β decreases. The upper bound of ρ_{v_m} is

$$\lim_{\beta\to 0}\rho_{v_m} = \frac{\sigma - \overline{\rho}_{M1}}{\rho_{m1}}. \tag{24}$$

From this fact, it can be seen that if the condition

$$(\sigma - \overline{\rho}_{M1})^2 \min\left(\frac{\lambda_{\min}[\boldsymbol{P}]}{\|\boldsymbol{\theta}_e\|^2},\ K_1\right) > \boldsymbol{x}_e(0)^{\mathrm{T}}\boldsymbol{P}\boldsymbol{x}_e(0) \tag{25}$$

is satisfied, for any initial condition of the parameter estimation error $\tilde{\boldsymbol{\theta}}(0)$ and $V_2(0)$, there exist design parameters $\varepsilon, \boldsymbol{\Gamma}$, and β such that the first equation of (23) holds.

From Remark 3 and Remark 4, we have following fact. Comparing with the value of (19) and (25), since the parameter K_2 becomes $K_2 < 1$, it can be easily ascertained that the value of the left hand side of (25) becomes at least two times larger than and equal to the value of the left side of (19). This means that the improved adaptive controller can be applied to the larger region of the initial states compared with the conventional one proposed in [18].

Therefore, it can be concluded that the improved adaptive controller can achieve good properties mentioned in Remark 1 and Remark 2 and the relaxation of the condition of the initial states.

4 CONCLUSION

In this paper, the main attention was to relax the condition for the initial states of the closed loop system using the conventional adaptive control scheme proposed in [18], we proposed the improved adaptive control scheme. Using the proposed adaptive controller, it is shown theoretically that the following properties can be achieved: 1) Stability of all signals i the closed loop systems can be guaranteed; 2) The tracking error can converges to zero even for unstable controlled objects; 3) Tracking performance can be improved by setting the only one design parameter α. Moreover, it was shown that we can apply the improved adaptive control scheme in the larger region of the initial states compared with the control scheme proposed in [18].

REFERENCES

[1] Narendra K. S. et al. (1986), Adaptive and learning system. Plenum Press, New York

[2] Krstic M., Kanellakopoulos I. and Kokotovic P. (1995), Nonlinear and adaptive control design, Wiley, New York

[3] P. A. Ioannou and Sun J. (1996), Robust adaptive control. Upper Saddle River, NJ

[4] Feng G., Zhang, C. and PalaniswamiM. (1991), Stability analysis of input constrained continuous time indirect adaptive control. Systems and Control Letters 17(3):209-215.

[5] Wang H. and SunJ. (1992), Modified model reference adaptive control with saturated inputs. In Proc. of the 31th IEEE CDC, Tucson, AZ, Dec 16-18, 1992, pp. 3255-3256

[6] Zhang C. and Evans R. J. (1994), Continuous direct adaptive control with saturation input constraint. IEEE trans. on Automatic Control 39(8):1718-1722

[7] Kárason S. P. and AnnaswamyA. M. (1994), Adaptive control in the presence of input constraints. IEEE trans. on Automatic Control 39(11):2325-2330

[8] Annaswamy A. M. and Wong J. -E. (1997), Adaptive control in the presence of saturation non-linearity. Int. J. Adaptive Control and Signal Processing 11(1):3-19

[9] De la Sen M. (2002), Adaptive Stabilization of Nonnecessarily Inversely Stable First-Order Continuous-Time Systems under Saturated Input. Nonlinear Dynamics 30:193-204

[10] Yang B.-J. Calise , A. J. and Craig J. I. (2003), Adaptive output feedback control with input saturation. In Proceedings of 2003 ACC, Denver, CO, June 4-6, 2003, pp. 1572-1577

[11] Lavretsky E. and HovakimyanN. (2004), Positive μ-modification for stable adaptation in the presence of input constraints. In Proc. of 2004 ACC, Boston, MA, June 30-July 2, 2004, pp. 2545-2550

[12] De la Sen M. (2004), Stabilization of continuous-time adaptive control systems with possible input saturation through a controllable modified estimation model. Nonlinear Analysis: Modelling and Control 9(1):3-37

[13] Tandale M. D. and Valasek J. (2005), Adaptive dynamic inversion control of a linear scalar plant with constrained control inputs. In Proc. of the 2005 ACC, Portland, OR, June 14-16, 2005, pp. 2064-2069

[14] Lavretsky E. and Hovakimyan N. (2005), Positive μ-modification for stable adaptation in dynamic inversion based adaptive control with input saturation. In Proc. of 2005 ACC, Portland, OR, June 14-16, 2005, pp. 3373-3378

[15] Zhong Y.-S. (2005), Globally stable adaptive system design for minimum phase SISO plants. Automatica 41(9):1539-1547

[16] Lavretsky E. and Hovakimyan N. (2007), Stable adaptation in the presence of input constraints. Systems and Control Letters 56(11-12):722–729

[17] Takagi N., Oya M. and Kobayashi T. (2010), Adaptive control scheme achieving smooth control input in the presence of input saturation. Int. J. Advanced Mechatronic Systems 2(4):225-235

[18] Takagi N. et al. (2011), Modification of an adaptive controller for systems with input saturation and available output derivatives up to the order of relative degree. Proc. of the 2011 4th International Symposium on Advanced Control of Industrial Processes Hangzhou, P.R. China, May 23-26, 2011, pp. 114-119

The Seventeenth International Symposium on Artificial Life and Robotics 2012 (AROB 17th '12),
B-Con Plaza, Beppu, Oita, Japan, January 19-21, 2012

Development of a Position Control Scheme for Rotating Sensor Unit Attached to In-pipe Robot

Hideki Wada[1], Masahiro Oya[2], and Katsuhiro Okumura[3]
[1]Shin-Nippon Nondestructive Inspection Co.,4-10-13 Ibori, Kokurakita-ku, Kitakyusyu-shi, Fukuoka, 803-8517 Japan
(Tel: 81-93-581-1256, Fax: 81-93-581-2232, E-mail: h-wada@shk-k.co.jp)
[2]Kyushu Institute of Technology, 1-1 Sensui-cho, Tobata-ku, Kitakyusyu-shi, Fukuoka, 804-8550 Japan
[3]Fukuoka Industrial Technology Center, Norimatu, Yahatanisi-ku, Kitakyusyu-shi, Fukuoka 807-0831 Japan

Abstract: In this paper, we propose a position control scheme for the rotation axis of a rotating ultrasonic sensor unit with a position adjustment mechanism. The control objective is that the position of the rotation axis can become equal to the center of a pipe. To realize the control objective, we provide a method to measure the vertical and horizontal position of the rotation axis. Using the measurements, we propose a position controller for the rotation axis. By carrying out experiments, we investigate the usefulness of the developed mechanism and the proposed position controller. As a result, it is shown that the proposed position control scheme has good performance.

Keywords: In-pipe Robot, Thickness measurement of the pipe, Ultrasonic sensor

1 INTRODUCTION

In the power generation plants, chemical plants and steel mills, the pipes may be deteriorated over time. Since these pipes have enormous length, it is a difficult task for human to inspect the deterioration state of the pipes [1]. Here, the deterioration state of the pipes means the decrease of the thickness of the pipes. To address the problem, we have developed inspection robots [2-8]. Those robots move on the outside of the pipes. Since most of such pipes are buried undergrounds or covered with the heat insulator, the high precision inspection can not be expected. For the reason, we have developed an in-pipe robot which can inspect the deterioration state from the inside of the pipes [9]. The robot has the inspection sensor unit in which ultrasonic sensors can be rotated in the circumferential direction of the pipe. However, there is a serious problem that the rotation axis in the inspection sensor unit may deviate from the center of the pipe while the in-pipe robot is moving inside the pipe. In such a case, the scanning speeds of the ultrasonic sensors are not constant and unknown. Then, the measurement precision of the thickness of the pipes may become worse.

To overcome this problem, we develop a new inspection sensor unit with a position adjustment mechanism for the rotation axis, and we propose a position control scheme. Namely, we provide a method to measure the vertical position and horizontal position of the rotation axis. Using the measurements, we propose a controller so that the position of the rotation axis can stay at the center of the pipe even if the in-pipe robot is moving inside the pipe.

2 OVERVIEW OF THE INSPECTION SYSTEM

Fig. 1 shows the overview of the in-pipe robot developed in [9]. The inspection sensor unit is attached to the front of the in-pipe robot (see the right hand side of Fig. 1). The inspection sensor unit has four inspection arms, and one ultrasonic sensor is attached on the top of the each inspection arm. Fig. 2 shows the details of the inspection arm. The inspection arm is composed of the holder part and the sliding part. Using a ball screw and a motor, the sliding

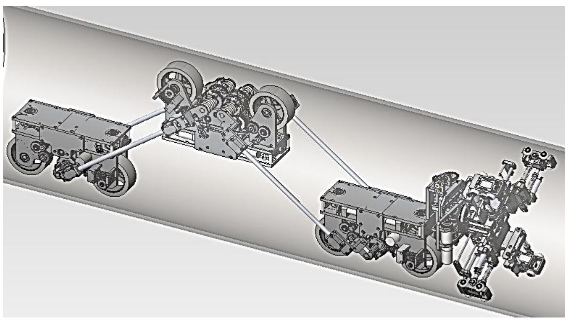

Fig. 1 Overview of the in-pipe robot.

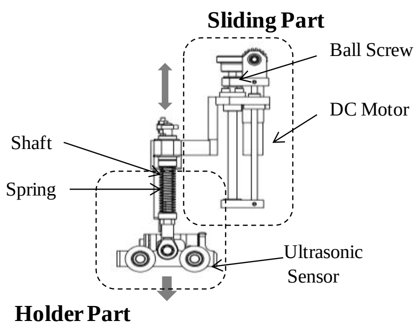

Fig. 2 Inspection arm.

part can move the holder part. There is a spring in the holder part. The ultrasonic sensor is pushed on the inner surface by the spring force. Moving the in-pipe robot and rotating the inspection arms, the all pipe thickness can be measured.

Fig. 3 shows the schematic of the initial configuration of the inspection sensor unit. The symbols l_{si} , i =1~4 are the spring strokes that are the distance from the rotation axis to the inner surface of the pipe. The symbol l_{sp} denotes the fixed stroke of the sliding part. In the initial configuration, the rotation axis corresponds to the center of the pipe. In this situation, all of the spring strokes l_{si} become same and the scanning speeds of the ultrasonic sensors become a known constant speed. Then, the high precision inspection can be expected. However, while the in-pipe robot is moving inside the pipe, the center of the in-pipe robot may move due to the influence of disturbances. In that case, the rotation axis of the inspection arms deviates from the center of the pipe. Fig. 4 shows the displacements x_p, y_p of the rotation axis. The scanning speeds of the ultrasonic sensors on the inner surface are not constant when the inspection arms are rotated. Furthermore, because of a lack of information of the position of the

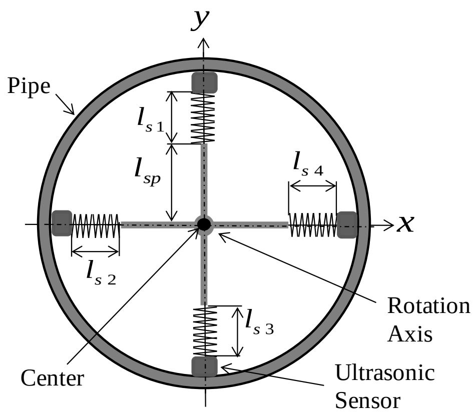

Fig. 3 Schematic of initial configuration.

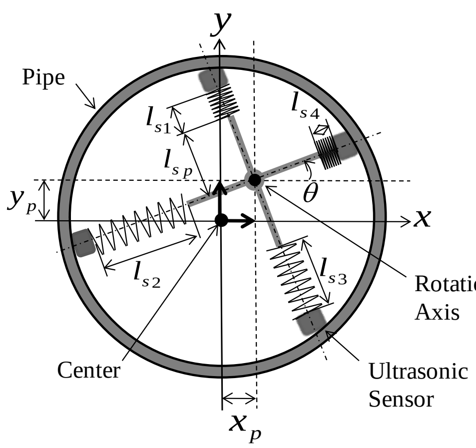

Fig. 4 Schematic in the presence of the deviation of the rotation axis.

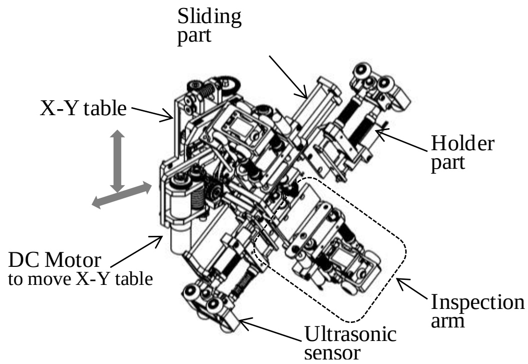

Fig. 5 Movable inspection unit.

rotation axis, the accurate location of the ultrasonic sensor cannot be obtained. Due to the influence, the measurement precision of the thickness may become worse.

3 MOVABLE INSPECTION SENSOR UNIT

To overcome the problem stated in the section 2, we develop an inspection sensor unit with a position adjustment mechanism for the rotation axis. Hereafter, the sensor unit is called the movable inspection unit. Fig. 5 shows the developed movable inspection unit. As shown in Fig. 5, the unit contains an adjustment mechanism (X-Y table) to move the rotation axis of the inspection arm. In order to make the position of the rotation axis be equal to the position of the center of the pipe, we require the displacement of the rotation axis from the center of the pipe.

3.1 Measurement of displacement of rotation axis

Fig. 6 shows the displacements x_p, y_p of the rotation axis. In Fig. 6, l_i , i =1~4 are the distances from the rotation axis to the inner surface of the pipe. The symbol θ is the rotation angle of the inspection arms. In Fig.6, x_θ and y_θ can be written by

$$x_\theta = \frac{l_4 - l_2}{2}, \quad y_\vartheta = \frac{l_3 - l_1}{2} \tag{1}$$

Using the equation (1), we have the following

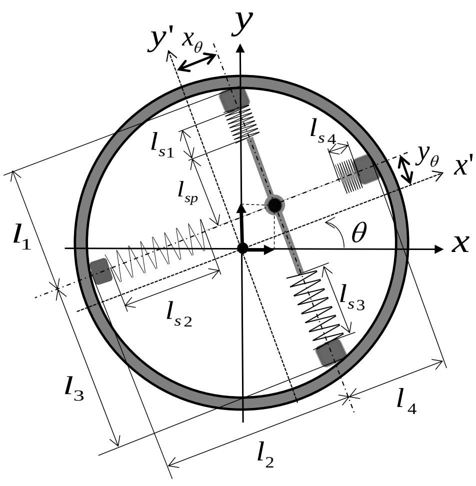

Fig. 6 The displacement of the rotation axis.

displacement of the rotation axis.

$$\begin{bmatrix} x_p \\ y_p \end{bmatrix} = \begin{bmatrix} \cos\theta & -\sin\theta \\ \sin\theta & \cos\theta \end{bmatrix} \begin{bmatrix} x_\theta \\ y_\theta \end{bmatrix} = \begin{bmatrix} \cos\theta & -\sin\theta \\ \sin\theta & \cos\theta \end{bmatrix} \begin{bmatrix} \frac{l_4 - l_2}{2} \\ \frac{l_3 - l_1}{2} \end{bmatrix} \quad (2)$$

Since the initial length of l_{sp} is fixed, the displacement of the rotation axis can be rewritten as

$$\begin{bmatrix} x_p \\ y_p \end{bmatrix} = \begin{bmatrix} \cos\theta & -\sin\theta \\ \sin\theta & \cos\theta \end{bmatrix} \begin{bmatrix} \frac{l_{s4} - l_{s2}}{2} \\ \frac{l_{s3} - l_{s1}}{2} \end{bmatrix} \quad (3)$$

In the developed movable inspection unite, the rotation angle θ and the spring strokes l_{si} can be measured. Using the measurements, we can calculate the displacements x_p, y_p of the rotation axis.

3.2 Position control of the rotation axis

To simplify the construction of the position controller, we derive a simplified model of the movable inspection sensor unit. Fig.7 shows the block diagram of the simplified model I for x axis direction. We can obtain the similar block diagram for y axis direction. In Fig. 7, u_x denotes the input signal (duty ratio ± 100%) added to DC motor to move the X-Y table, T_x is the equivalent time constant and K_x is the equivalent gain from the input to velocity $\dot{x}_p$ .The symbol d_x denotes the disturbance corresponding to the reaction force of springs which are attached to the holder parts in the inspection arms (see Fig.2). It is assumed that the equivalent time constant T_x is very short. Then, we propose a simplified model II shown in Fig. 8. Based on simplified model II, the following position controller is developed.

$$\begin{bmatrix} u_x \\ u_y \end{bmatrix} = -100 \begin{bmatrix} \operatorname{sgn} x_p \\ \operatorname{sgn} y_p \end{bmatrix} \quad (4)$$

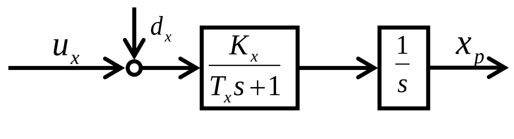

Fig. 7 Simplified model I.

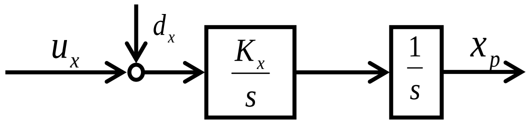

Fig. 8 Simplified model II.

4 EXAMINATIONS

4.1 Measurement of the displacement x_p, y_p

Fig. 9 shows the test equipment for the experiment of the position measurement of the rotation axis. The test equipment consists of ϕ350 acrylics pipe, the movable inspection sensor unit and the support base to fix the movable inspection sensor unit. The support base has the mechanism that the whole movable inspection sensor unit can be moved to top and bottom(y_M), right and left(x_M) by the handle operation. Using the mechanism, the position of the rotation axis can be moved from the center of pipe. The accurate displacements x_M , y_M of the rotation axis of the movable inspection unit is measured by using high precision encoders.

In the initial configuration, the position of the rotation axis and the center of the pipe are the same, and the rotation angle θ was fixed to be a certain angle. Then, the rotation axis is moved by using the handle attached to the support base, and the displacements x_p and y_p of the rotation axis are measured based on the equation (3).

The results of measurements of the displacements are shown in Figs 10-13. In Figs. 10 and 12, the horizontal axis denotes the accurate displacement x_M of the rotation axis which is moved by the handle operation. The accurate displacement y_M is fixed as $y_M = 0$. The vertical axis denotes the displacements x_p and y_p. In Figs. 11 and 13, the horizontal axis denotes the accurate displacement y_M of the rotation axis. The accurate displacement x_M is fixed as $x_M = 0$. The vertical axis denotes the displacement x_p and y_p.

As shown in Figs. 10-13, x_p and y_p are mostly same with the accurate displacements x_M and y_M . However, there exit small errors between the measurement displacements x_p , y_p and the accurate displacements x_M , y_M due to the low rigidity of the used acrylic pipe and the effect of gravity.

4.2 Position control position of the rotation axis

As with the measurement experiments of the displacement of the rotation axis, the test equipment shown

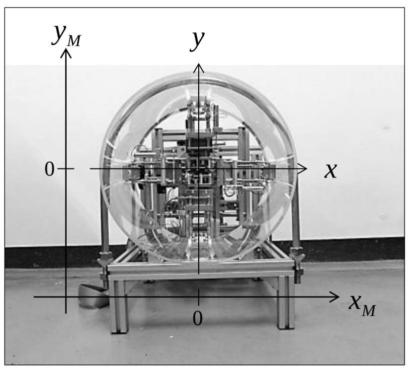

Fig. 9 The test equipment.

in Fig.9 is used in the position control experiments. In the initial configuration, the position of the rotation axis and the center of the pipe are the same, and the rotation angle θ was fixed to be zero. Next, the rotation axis is moved by the handle operation, and the inspection arms are rotated repeatedly within ±90[deg]. Then, the position control (4) is carried out.

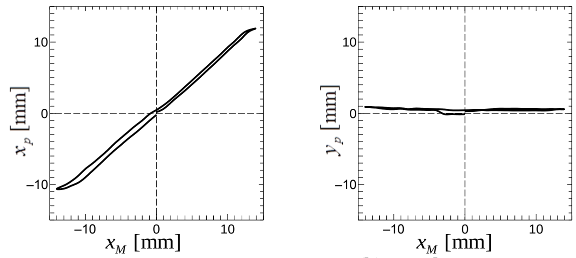

(a) Displacement x_p (b) Displacement y_p

Fig. 10 Displacement of the variation of x_M ($\theta = 0$).

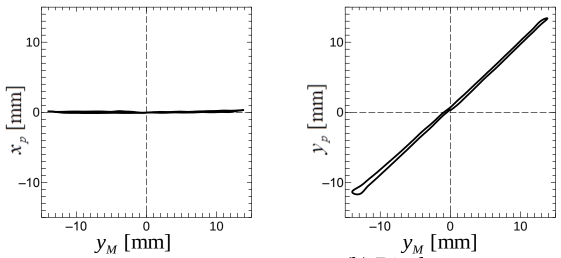

(a) Displacement x_p (b) Displacement y_p

Fig. 11 Displacement of the variation of y_M ($\theta = 0$).

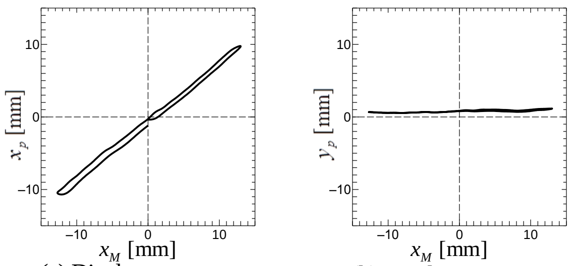

(a) Displacement x_p (b) Displacement y_p

Fig. 12 Displacement of the variation of x_M ($\theta = 30$).

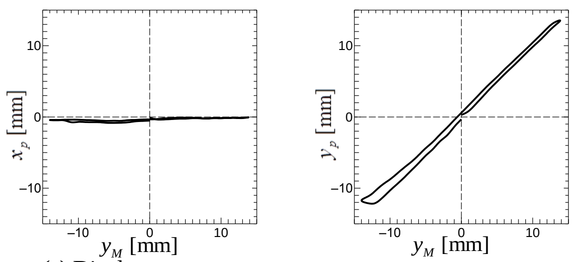

(a) Displacement x_p (b) Displacement y_p

Fig. 13 Displacement of the variation of y_M ($\theta = 30$).

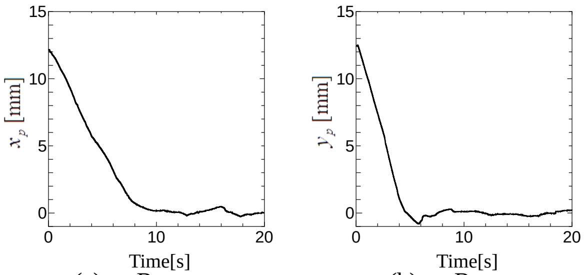

(a) x_p Response (b) y_p Response

Fig.14 Responses of the rotation axis.

Fig. 14 shows the responses of the displacements of the rotation axis. As shown in Fig. 14, the displacements x_p, y_p of the rotation axis converge to zero. Because of the effect of gravity, the convergence time of y_p becomes more quickly than that of x_p.

5 CONCLUSION

We develop an adjustment mechanism for the position of the rotation axis, and we propose the simple position controller for the adjustment mechanism. Carrying out experiments, it has been shown that the proposed position controller is very useful.

REFERENCES

[1] Y. Imagawa, H. Wada, Y. Wakibe, et al, Ultrasonic guided wave testing system for piping, Proc. of the ASME Pressure Vessels and Piping Conference, July 26-30, Prague Czech Republic, (in CD-ROM), (2009).

[2] T. Fukuda, H. Hosokai, and M. Otsuka, Autonomous pipeline inspection and maintenance robot with inch worm mobile mechanism, *Proc. of IEEE Int. Conf. on Robotics and Automation*, pp. 539-544, (1987).

[3] H. T. Roman and B. A. Pellegrino, "Pipe crawling inspection robot, An overview," *IEEE Trans. on Energy Conversion*, vol. 8 no. 3, pp. 576-583, (1993).

[4] H. B. Kuntze and H. Haffner, "Experiences with the development of a robot for smart multisensoric pipe inspection," *Proc. of IEEE Int. Conf. on Robotics and Automation*, pp. 1773-1778, (1998).

[5] S. G. Roh, S. M. Ryew, J. H. Yang, and H. R. Choi, Actively steerable in-pipe inspection robots for undergroung urban gas pipelines, *Proc. of IEEE Int. Conf. on Robotics and Automation*, pp. 761-766, (2001).

[6] M. Horodinca, I. Doroftei and E. Mignon : A Simple Architecture for In-Pipe Inspection Robots, Proceedings of the 2002 International Colloquium on Mobile and Autonomous Systems, pp.1-4, (2002).

[7] K. Suzumori, S. Wakimoto, and M. Takata, A miniature inspection robot negotiating pipes of widely varying diameter, *Proc. of IEEE Int. Conf. on Robotics and Automation*, pp. 2735-2740, (2003).

[8] H. Wada. (2010), Robotized for Nondestructive Testing (in Japanese), Proc. of The Japanese Society for Non-Destructive Inspection March 4-5, Tokyo, Japan, pp.17-20, (2010)

[9] k. Okumura, Y. Wtanabe, M. Oya, et al., Development of Inspection Robot Mechanism for Piping (in Japanese), Proceedings of Annual Conference of the Robotics Society of Japan, September 13-15, Chiba, Japan, (in CD-ROM), (2007).

The Seventeenth International Symposium on Artificial Life and Robotics 2012 (AROB 17th '12),
B-Con Plaza, Beppu, Oita, Japan, January 19-21, 2012

Adaptive Oscillation Control Scheme for a Wheeled Mobile Robot

Bo Zhou, Tasuku Eto, Hiroshi Shibata, Masahiro Oya
Department of Mechanical and Control Engineering, Kyushu Institute of Technology
1-1 Sensui-cho, Tobata-ku, Kitakyushu-shi, Fukuoka, Japan
(*Tel*: *+81-93-884-3186*; *Fax*: *+81-93-861-1159*)
(*E-mail*: *k344232s@tobata.isc.kyutech.ac.jp*)

Abstract: In the case when wheeled mobile robots run fast on rough terrain, due to the robot body acceleration and oscillation, sensors mounted on the robot body may be destroyed. In this paper, we propose a scheme to reduce the body acceleration at any specified location on the robot body. In the proposed scheme, a combined ideal model is designed so that the location where acceleration performance becomes best can be moved easily by setting only two design parameters. Then, an adaptive controller is developed so that the behavior of the actual mobile robot tracks that of the combined ideal model. It is ascertained by numerical simulations that the body acceleration at any specified location can be improved easily.

Key Words: Wheeled mobile robot, Oscillation, Adaptive control.

1. INTRODUCTION

In extreme environment, for example, disaster areas and minefields, there are many dangerous tasks for human. Recently, in the environment, mobile robots working instead of human have been developed [1]-[4]. In the case when robots go over steps, due to the vertical acceleration of the robot body, sensors mounted on the robot body may be destroyed or the measurement accuracy of sensors becomes worse. Nevertheless, the problem had not been considered yet. If the acceleration at each location on the robot body is controlled so as to be zero, that problem can be resolved. However, in such a case, the mobile robot cannot go over a slope. Therefore, the controllers are designed by using trial and error method so that the body acceleration can be suppressed at only one specified location on the robot body. In this case, well oscillation suppression of the acceleration can be realized for a sensor mounted on the robot body. If measurement accuracy is required for the other sensor, we have to redesign the controller. However, it will cost a lot of time.

To overcome the problem stated above, we proposed a robust oscillation control scheme [5] that can suppress the vertical acceleration at a specified location on the robot body without any redesigning of controllers. For uncertainties of the system parameters, the excellent robust performance can be also achieved. However, there is a problem that the scheme still requires accurate information of some parts of system parameters.

In this paper, we propose an adaptive oscillation control scheme. The controller does not require any information of system parameters. At first, a combined ideal model is designed based on the state space description containing the body acceleration. In the combined ideal robot model, the location where the acceleration becomes small can be moved easily by setting only two design parameters. Next, an adaptive tracking controller is developed so that the actual robot can track the behavior of the designed combined ideal robot model. In the proposed adaptive tracking control system, for any uncertainties of system parameters, it is shown that the tracking performance can be improved by setting design parameters. At last, the usefulness of the proposed controller is shown by carrying out numerical simulations.

2. WHEELED MOBILE ROBOT

The wheeled mobile robot is shown in Fig. 1, and Fig. 2 shows the simplified model of the wheeled mobile robot. To simplify the explanation below, each large wheel is labeled as 1, 2, and 3. Each large wheel has three small wheels. In the large wheels labeled 1 and 2, the small wheels are driving wheels. The wheeled mobile robot has the mechanism that each large wheel can be rotated by the motors set at the center axis of the large wheels 1, 2 and 3. The explanations of parameters are shown in Table 1.

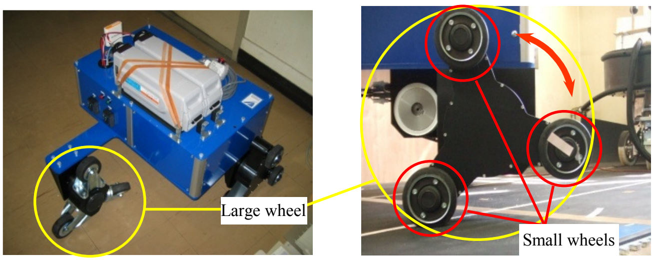

Fig. 1 Mobile robot and wheels.

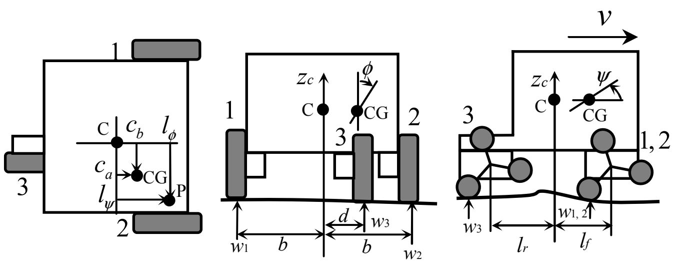

Fig. 2 Mobile robot model

Table. 1 Notation of wheeled mobile robot

C,CG	center and center of gravity of mobile robot body
z_c	vertical displacement at C
P	location on the robot body
ψ, ϕ	pitch and roll angle
x_1, x_2, x_3	vertical displacement at the center of large wheels
w_1, w_2, w_3	vertical displacement of road disturbance added to large wheels
v	longitudinal velocity of mobile robot
g	acceleration of gravity
m, i_ψ, i_ϕ	robot mass, pitch and roll moment of inertia of robot body
l_f, l_r, b, d	distance from C to large wheels
c_a, c_b	distance from C to CG
l_ψ, l_ϕ	distance from C to P
l_w	distance from the center of large wheel to the center of small wheel
k_a	voltage and torque conversion constant
r, k_G	reciprocal of armature resistance and gear ratio
j_{mL}, d_{mL}	moment of inertia and viscous damping constant between a motor and wheel center axis

It is assumed that the pitch angle ψ(t) and the roll angle ϕ(t) are small. Then, the dynamic equation of the wheeled mobile robot is given as follows.

$$\left.\begin{aligned} &M_p(t)\ddot{\boldsymbol{x}}(t) + K_d(t)\dot{\boldsymbol{x}}(t) = -K_b(t)\boldsymbol{u}(t) + D_p(t)\ddot{\boldsymbol{w}}(t) - \boldsymbol{g}_a \\ &\boldsymbol{x}(t) = \begin{bmatrix} x_1(t), & x_2(t), & x_3(t) \end{bmatrix}^T \\ &\boldsymbol{w}(t) = \begin{bmatrix} w_1(t), & w_2(t), & w_3(t) \end{bmatrix}^T \end{aligned}\right\} \quad (1)$$

$$\left.\begin{aligned} &M_c = \mathrm{diag}\begin{bmatrix} m, & i_\psi, & i_\phi \end{bmatrix} \\ &M_p(t) = \left(\left(HT_h\right)^T\right)^{-1} M_c \left(HT_h\right)^{-1} + K_j(t) \\ &D_p(t) = K_j(t) - M_p(t) \\ &H = \begin{bmatrix} 1 & l_f & -b \\ 1 & l_f & b \\ 1 & -l_r & d \end{bmatrix}, \quad T_h = \begin{bmatrix} 1 & -c_a & -c_b \\ 0 & 1 & 0 \\ 0 & 0 & 1 \end{bmatrix} \\ &K_d(t) = \theta_{kj} K_{j\theta}(t) \\ &K_j(t) = \theta_{kd1} K_{d\theta 1}(t) + \theta_{kd2} K_{d\theta 2}(t) \\ &K_b(t) = \theta_{kb} K_{d\theta}(t) \\ &\theta_{kj} = \frac{j_{mL}}{l_w^2}, \theta_{kd1} = \frac{j_{mL}}{l_w^3}, \theta_{kd2} = \frac{k_G^2 d_{mL} + r k_a^2}{k_G^2 l_w^2}, \theta_{kb} = \frac{r k_a}{k_G l_w} \\ &K_{j\theta}(t) = K_{d\theta 2}(t) = \mathrm{diag}[S_1^{-2}, S_2^{-2}, S_3^{-2}] \\ &K_{d\theta 1}(t) = \mathrm{diag}[C_1 S_1^{-4}\dot{x}_1(t), C_2 S_2^{-4}\dot{x}_2(t), C_3 S_3^{-4}\dot{x}_3(t)] \\ &K_{d\theta}(t) = \mathrm{diag}[S_1^{-1}, S_2^{-1}, S_3^{-1}] \\ &S_i = \sin(\theta_{wi}(t) + \cos^{-1}\frac{3}{4}) \\ &C_i = \cos(\theta_{wi}(t) + \cos^{-1}\frac{3}{4}) \\ &(i = 1,2,3) \end{aligned}\right\} \quad (2)$$

Where $\boldsymbol{g}_a$ is the constant vector including the gravity g and $\boldsymbol{u}(t)$ denotes an input voltage added to the motors set at the center axis of the large wheels 1, 2 and 3. In order to add a suspension characteristic to the wheeled mobile robot (1), the input voltage is given by

Table. 2 Nominal values of parameters

m	84.2	kg	i_ψ	1.72	kgm^2
i_ϕ	1.39	kgm^2	l_w	0.15	m
c_a	0.079	m	c_b	0.011	m
l_f	0.125	m	l_r	0.445	m
b	0.35	m	d	0.011	m
k_a	0.126	N/V	k_G	$1/160$	
j_m	0.21	kgm^2	d_m	1.72×10^{-4}	Nms/rad
r	0.226	1/Ω			

$$\left.\begin{aligned} &\boldsymbol{u}(t) = -\bar{K}_b^{-1}(t)(\boldsymbol{u}_a(t) - k_p \boldsymbol{x}(t) - \bar{K}_j(t)\ddot{\boldsymbol{w}}(t) + \bar{\boldsymbol{g}}_a) \\ &\bar{K}_b(t) = \bar{\theta}_{kb} K_{b\theta}(t), \bar{K}_j(t) = \bar{\theta}_{kj} K_{j\theta}(t) \end{aligned}\right\} \quad (3)$$

where $\boldsymbol{u}_a(t)$ is the new input signal introduced to control the acceleration of the robot body. The parameter $\bar{\bullet}$ denotes the parameters$\bullet$ in which the values of element are nominal values shown in table 2.

To develop a controller achieving a small acceleration of the robot body, the state space description including the acceleration of the robot body is introduced as follows. The symbols O_n, I_n used below denote $n\times n$ zero matrix and $n\times n$ unit matrix.

$$\left.\begin{aligned} &\dot{\xi}(t) = (\Gamma - B_\xi M_p^{-1}(t) F(t)^T)\xi(t) + B_\xi M_p^{-1}(t)\frac{\theta_{kb}}{\bar{\theta}_{kb}}\boldsymbol{\mu}(t) \\ &\quad + D_1(t)\ddot{\boldsymbol{w}}(t) + D_2(t)\dddot{\boldsymbol{w}}(t) - B_\xi M_p^{-1}(t)\left(\boldsymbol{g}_a - \frac{\theta_{kb}}{\bar{\theta}_{kb}}\bar{\boldsymbol{g}}_a\right) \\ &\boldsymbol{\mu}(t) = \dot{\boldsymbol{u}}_a(t) + \boldsymbol{u}_a(t), \\ &\xi(t) = \begin{bmatrix} \boldsymbol{x}(t)^T & \dot{\boldsymbol{x}}(t)^T & (H\ddot{\boldsymbol{q}}(t))^T \end{bmatrix}^T, \ddot{\boldsymbol{q}}(t) = \begin{bmatrix} \ddot{z}_c(t) & \ddot{\psi}(t) & \ddot{\phi}(t) \end{bmatrix}^T \end{aligned}\right\} \quad (4)$$

$$\left.\begin{aligned} &\Gamma = \begin{bmatrix} O_3 & I_3 & O_3 \\ O_3 & O_3 & I_3 \\ O_3 & O_3 & O_3 \end{bmatrix}, F(t) = \begin{bmatrix} k_p \frac{\theta_{kb}}{\bar{\theta}_{kb}} I_3 \\ \dot{K}_d(t) + K_a(t) + k_p \frac{\theta_{kb}}{\bar{\theta}_{kb}} I_3 \\ M_p(t) + \dot{K}_j(t) + K_d(t) \end{bmatrix} \\ &D_1(t) = \begin{bmatrix} O_3 \\ -I_3 \\ M_p^{-1}(t)(\dot{K}_j(t) + K_j(t) + K_d(t) - \frac{\theta_{kb}}{\bar{\theta}_{kb}}\left(\dot{\bar{K}}_j(t) - \bar{K}_j(t)\right) \end{bmatrix} \\ &D_2(t) = \begin{bmatrix} O_3 & O_3 & M_p^{-1}(t)\left(K_j(t) - \frac{\theta_{kb}}{\bar{\theta}_{kb}}\bar{K}_j(t)\right) \end{bmatrix}^T \\ &B_\xi = \begin{bmatrix} O_3 & O_3 & I_3 \end{bmatrix}^T \end{aligned}\right\} \quad (5)$$

Where $\boldsymbol{\mu}(t) = \dot{\boldsymbol{u}}_a(t) + \boldsymbol{u}_a(t)$ is the virtual input. The wheeled mobile robot with $\boldsymbol{\mu}(t) = 0$ is called the passive robot.

The control objective is to develop an adaptive controller so that the vertical acceleration at any specified location on the robot body can be reduced to a small value easily. To meet the objective, the following assumptions are made for the actual mobile robot (4).

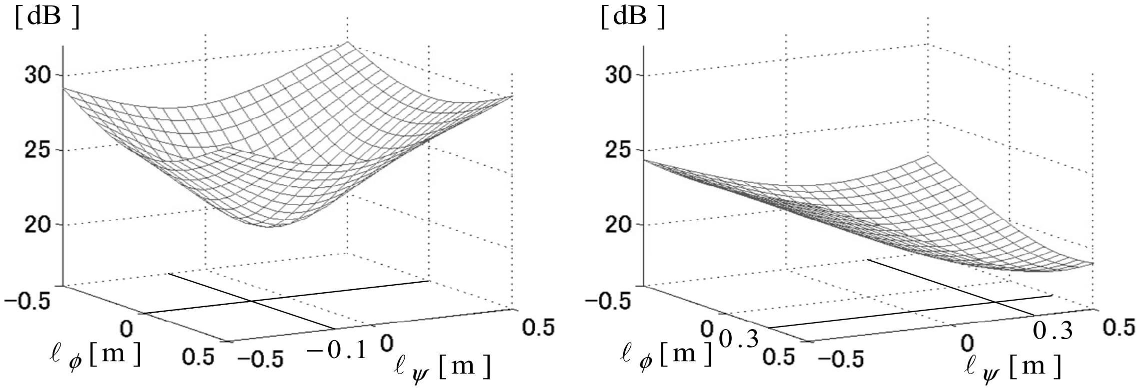

(a) Maximum gain surface of the passive robot (b) Maximum gain surface of the combined ideal robot model

Fig. 3 Properties of the passive robot and the combined ideal robot model

A1 The body acceleration $\ddot{\boldsymbol{q}}(t)$ can be measured.

A2 The vertical displacements $\boldsymbol{x}(t)$ at the center of large wheels and its velocity $\dot{\boldsymbol{x}}(t)$ can be measured.

A3 The acceleration $\ddot{w}(t)$ of road disturbance is bounded and can be measured

3. COMBINED IDEAL ROBOT MODEL

A combined ideal robot model that achieves the control objective is given by [5]

$$\left.\begin{aligned} &\dot{\boldsymbol{\xi}}_m(t) = \Gamma\boldsymbol{\xi}_m(t) - B_\xi \bar{M}_p^{-1} k_b \boldsymbol{f}_m(t) + \bar{D}\ddot{\boldsymbol{w}}(t) \\ &\boldsymbol{\xi}_m(t) = \left[\boldsymbol{x}_m(t)^T,\ \ \dot{\boldsymbol{x}}_m(t)^T,\ \ (H\ddot{\boldsymbol{q}}_m(t))^T\right]^T \end{aligned}\right\} \quad (6)$$

$$\left.\begin{aligned} &\bar{D}(t) = \left[O_3,\ \ -I_3,\ \ \bar{M}_p^{-1}k_d\right]^T \\ &f_m(t) = \sum_{i=1}^{2}\gamma_{\phi i}\sum_{j=1}^{2}\gamma_{\psi j}F_{m(2i+j-2)}(t)\boldsymbol{\xi}_{m(2i+j-2)}(t) \\ &\gamma_{\phi i} = \frac{(-1)^i l_{\phi p} + l_{\phi m}}{2l_{\phi m}},\ \gamma_{\psi i} = \frac{(-1)^{i-1} l_{\psi p} + l_{\psi m}}{2l_{\psi m}},\ i = 1,2 \\ &\boldsymbol{\xi}_{mi}(t) = \Omega_i\boldsymbol{\xi}_{di}(t),\ i = 1,2,3,4 \\ &F_{mi}(t) = \bar{M}_p H T_i H^{-1}\bar{M}_p^{-1}(\bar{F} - G_i)\Omega_i^{-1},\ i = 1,2,3,4 \\ &\Omega_i = \mathrm{diag}\left[HT_iH^{-1},\ \ HT_iH^{-1},\ \ HT_iH^{-1}\right],\ \ i = 1,2,3,4 \\ &T_i = I_3 - \boldsymbol{b}\left[0,\ \ l_{\psi p} - l_{\psi m},\ \ l_{\phi p} + (-1)^{i-1}l_{\phi m}\right],\ i = 1,2 \\ &T_i = I_3 - \boldsymbol{b}\left[0,\ \ l_{\psi p} + l_{\psi m},\ \ l_{\phi p} + (-1)^{i-1}l_{\phi m}\right],\ i = 3,4 \\ &\dot{\boldsymbol{\xi}}_{di}(t) = (\Gamma + \bar{B}(\bar{F} - G_i))\boldsymbol{\xi}_{di}(t) + \bar{D}_w\ddot{\boldsymbol{\omega}}(t) \\ &\boldsymbol{\xi}_{di}(t) = \left[\boldsymbol{x}_{di}(t)^T,\ \ \dot{\boldsymbol{x}}_{di}(t)^T,\ \ (H\ddot{\boldsymbol{q}}_{di}(t))^T\right]^T,\ \ i = 1,2,3,4 \end{aligned}\right\} \quad (7)$$

where the design parameters $l_\psi = l_{\psi p}, l_\phi = l_{\phi p}$ are introduced to the specified location where the vertical acceleration becomes minimum. Hereafter, the location where the vertical acceleration becomes minimum is called the best location. The feedback gains $G_i, i = 1 \sim 4$ are designed by using the optimal control theory so that the vertical acceleration of ideal robot models $\xi_{di}(t), i = 1 \sim 4$ become small at the specified locations $l_\psi = -l_{\psi m}, l_\phi = (-1)^i l_{\phi m}, i = 3,4$ and $l_\psi = l_{\psi m}$, $l_\phi = (-1)^i l_{\phi m}, i = 1,2,$ respectively. $\Omega_i, i = 1 \sim 4$ are transformation matrixes that are introduced to specified the best location.

Fig. 3 shows the properties of the passive robot and the designed combined ideal robot model. To show the gain characteristics relating to the vertical acceleration on the robot body, the maximum value of the norm of transfer function vector from the road disturbance $\dot{\boldsymbol{w}}(t)$ to the vertical acceleration at a location (l_ψ, l_ϕ) is plotted. Hereafter, the curve surface such as shown in Fig. 3 (a) is called the maximum gain surface. Fig.3 (a) shows the maximum gain surface of the passive robot and Fig. 3 (b) shows that of the combined ideal robot model. The two design parameters l_ψ, l_ϕ are set as $l_\psi = 0.3\mathrm{m}, l_\phi = 0.3\mathrm{m}$.

As shown in Fig. 3 (b), the combined ideal robot model has better performance in suppression of the vertical acceleration than the passive robot, and the best location is corresponding to the specified location $l_\psi = 0.3\mathrm{m}, l_\phi = 0.3\mathrm{m}$. From this fact, it can be concluded that the control objective can be achieved if the behavior of the actual mobile robot can track that of the combined ideal robot model.

4. ADAPTIVE TRACKING CONTROLLER

To develop a tracking controller, the tracking error between the actual mobile robot (4) and the combined ideal robot model (6) is defined as $\tilde{\xi}(t) = \xi(t) - \xi_m(t)$, and the new signal is defined by $\boldsymbol{\eta}(t) = [2I_3\ \ 3I_3\ \ I_3]\tilde{\xi}(t) = L^T\tilde{\xi}(t)$. Then, the error equation is given by

$$\begin{aligned} \dot{\boldsymbol{\eta}}(t) = &-d\boldsymbol{\eta}(t) - \frac{1}{2}M_p^{-1}(t)\dot{M}_p(t)\boldsymbol{\eta}(t) \\ &+ \frac{\theta_{kb}}{\bar{\theta}_{kb}}M_p^{-1}(t)\left\{\boldsymbol{\mu}(t) + \Theta\boldsymbol{\omega}_\eta(t) + \boldsymbol{\omega}_k(t) + \left(K_j(t) - \frac{\theta_{kb}}{\bar{\theta}_{kb}}\tilde{K}_j(t)\right)\ddot{\boldsymbol{w}}(t)\right\}, \end{aligned} \quad (8)$$

$$\left.\begin{array}{l}\Theta=\dfrac{1}{\theta_{kb}}\left[\left(\left(HT_h\right)^T\right)^{-1} M_c\left(HT_h\right)^{-1} \quad \theta_{kj}I_3 \quad \theta_{kd1}I_3 \quad \theta_{kd2}I_3 \quad \boldsymbol{g}_a\right] \\ \boldsymbol{\omega}_\eta(t)=\bar{\theta}_{kj}\left[\boldsymbol{\omega}_1(t)^T \quad \boldsymbol{\omega}_{j\theta}(t)^T \quad \boldsymbol{\omega}_{d\theta1}(t)^T \quad \boldsymbol{\omega}_{d\theta2}(t)^T \quad -1\right]^T \\ \boldsymbol{\omega}_{j\theta}(t)=K_{j\theta}(\boldsymbol{\omega}_1(t)+\boldsymbol{\omega}_2(t))+\dot{K}_{j\theta}\boldsymbol{\omega}_3(t) \\ \boldsymbol{\omega}_{d\theta1}(t)=K_{d\theta1}\boldsymbol{\omega}_4(t)+\dot{K}_{d\theta1}\boldsymbol{\omega}_5(t), \quad \boldsymbol{\omega}_{d\theta2}(t)=K_{d\theta2}\boldsymbol{\omega}_4(t)+\dot{K}_{d\theta2}\boldsymbol{\omega}_5(t) \\ \boldsymbol{\omega}_1(t)=L^T\Gamma\tilde{\boldsymbol{\xi}}(t)+d\boldsymbol{\eta}(t)-H\ddot{\boldsymbol{q}}(t)+\bar{M}_p^{-1}\left(\bar{K}_b\boldsymbol{f}_m-\bar{K}_d\ddot{\boldsymbol{w}}(t)\right) \\ \boldsymbol{\omega}_2(t)=\ddot{\boldsymbol{w}}(t), \boldsymbol{\omega}_3(t)=\ddot{\boldsymbol{w}}(t)-H\ddot{\boldsymbol{q}}(t)+\dfrac{1}{2}\dot{M}_p(t)\boldsymbol{\eta}(t) \\ \boldsymbol{\omega}_4=-\dot{\boldsymbol{x}}(t)+\ddot{\boldsymbol{w}}(t)-H\ddot{\boldsymbol{q}}(t), \boldsymbol{\omega}_5=-\dot{\boldsymbol{x}}(t) \\ \boldsymbol{\omega}_k(t)=-k_p\dot{\boldsymbol{x}}(t)-k_p\boldsymbol{x}(t)-\left(\dot{\bar{K}}_j(t)+\bar{K}_j(t)\right)\ddot{\boldsymbol{w}}(t)+\bar{\boldsymbol{g}}_a\end{array}\right\} \quad (9)$$

where Θ is unknown constant matrix, $\boldsymbol{\omega}_\eta(t)$ and $\boldsymbol{\omega}_k(t)$ are known signal vectors and d is design parameter.

We developed the following adaptive tracking controller based on the error equation (8).

$$\dot{\hat{\Theta}}(t)^T=\Gamma_\eta\boldsymbol{\omega}_\eta(t)\boldsymbol{\eta}(t)^T-\delta\hat{\Theta}^T(t), \qquad \delta>0 \quad \Gamma_\eta>0 \quad (10)$$

$$\boldsymbol{\mu}(t)=-\beta\boldsymbol{\eta}(t)-\hat{\Theta}(t)\boldsymbol{\omega}_\eta(t)-\boldsymbol{\omega}_k(t) \quad \beta>0 \quad (11)$$

Where $\hat{\Theta}(t)$ is the estimated matrix of the unknown matrix Θ . δandβ are positive design parameters and $\Gamma\eta$ is a positive definite matrix.

The following theorem holds in the mobile robot using controller (10) and (11).

Theorem 1

The adaptive wheeled mobile robot using the controller (10) and (11) becomes stable. In addition, there are positive values $\bar{\rho}_1, \bar{\rho}_2$ independent of β such that

$$\|\boldsymbol{\eta}(t)\|^2 \le \bar{\rho}_1 e^{-\beta t}+\frac{\bar{\rho}_2}{\beta^2}. \quad (12)$$

5. NUMERICAL SIMULATION

We show numerical simulation results to confirm the effectiveness of the proposed controller.

The mobile robot is running at the speed 0.5[m/s], and the left front wheel runs over the road disturbance with the amplitude 0.03m and the frequency 2Hz. The design parameters are set as $\beta=50^2$, $\Gamma_\eta=50^3 I_3$, $d=10$, δ=0.01 . The specified location was set as $l_\psi=0.3\text{m}, l_\phi=0.3\text{m}$. The initial value of $\hat{\Theta}(t)$ is set as $\hat{\Theta}(t)=0$.

Fig. 4 shows the responses at the specified location of $l_\psi=0.3\text{m}, l_\phi=0.3\text{m}$. Fig. 4 (a) is the vertical acceleration, (b) is the pitching angular acceleration, and (c) is the rolling angular acceleration. Dotted lines show the responses of the passive robot and thick solid lines are responses of the controlled mobile robot. The responses of the combined ideal model are shown by using thin lines. However since thin lines and thick solid lines are almost same, the thin lines disappeared.

6. CONCLUSION

We propose an adaptive oscillation controller for wheeled mobile robots. Carrying out numerical simulations, it has been shown that for any parameter uncertainties, the oscillation attenuation performance can be achieved.

REFERENCES

[1] Hoffmann. G. M., Tomlin. C. J. and Montebelo. M. et al (2007), Autonomous Automobile Trajectory Tracking for Off-Road Driving: Controller Design, Experimental Validation and Racing.American Control Conference, 2296-2301

[2] Terupally. C. R., Zhu. J. J. and Williams. R. L. (2007), Trajectory Tracking and Stair Climbing Capability Assessment for a Skid-Steered Mobile Robot, American Control Conference, 2861-2866

[3] Lhomme-Desages. D., Grand. C. and Guinot. J. -C. (2007), Trajectory Control of a Four-Wheel Skid Steering Vehicle over Soft Terrain using a Physical Interaction Model, Proc. IEEE Int. Conf. Robotics and Automation, 1164-1169

[4] Bugeja. M. K. and Fabri. S. G. (2007), Dual Adaptive Control for Trajectory Tracking of Mobile Robots, Proc. IEEE Int. Conf. Robotics and Automation, 2215-2220

[5] Yasutaka Tsuchida, Masahiro Oya, Natsuki Takagi and Qiang Wang (2009), Robust Oscillation Control of Wheeled Mobile Robots, International Journal of Artificial Life and Robotics,vol.14,pp.357-361,(2009)

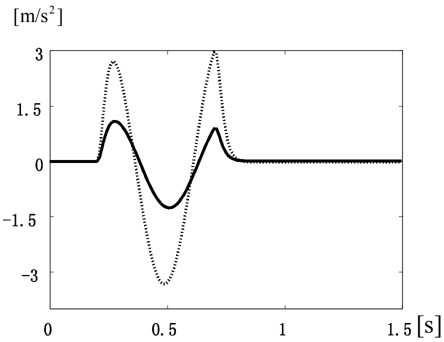

(a) Vertical acceleration

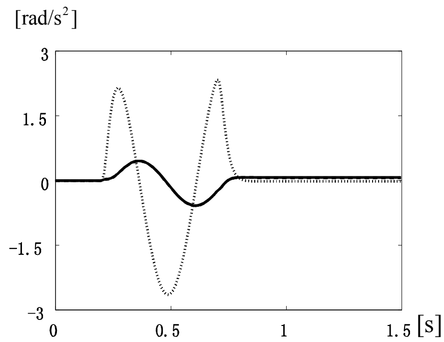

(b) Pitching angular acceleration

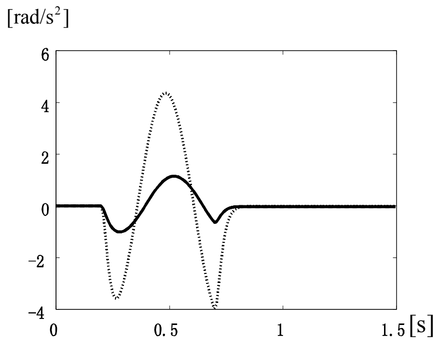

(c) Rolling angular acceleration

Fig. 4 Responses of the controlled mobile robot

The Seventeenth International Symposium on Artificial Life and Robotics 2012 (AROB 17th '12),
B-Con Plaza, Beppu, Oita, Japan, January 19-21, 2012

Visual chance discovery method of potential keys for innovations in tourism

Kiyota Hashimoto*, Kazuhiro Takeuchi**, Makoto Okada*, Sachio Hirokawa***

Osaka Prefecture University, 1-1 Gakuen-cho Naka-ku Sakai, 599-8531, Japan*
*Osaka Electro-Communication University**, 18-8, Hatsu-machi, Neyagawa, 572-8530, Japan*
*Kyushu University***, 6-19-1, Hakozaki, Higashi-ku, Fukuoka, 812-8581, Japan*
(Tel : 81-72-252-1161; Fax : 81-72-254-9944)
(hash@lc.osakafu-u.ac.jp)

Abstract: Online customer reviews have been variously employed for text mining and information retrieval in general. However, the result of those analyses has to be well visualized for prospective innovations of firms and enterprises that cannot afford a dedicated expert. In this study, we collected thousands of online customer reviews of hotels and restaurants, and divided them into a couple of groups according to customers' conditions to use those hotels and restaurants. We then made keygraphs of common keywords for each group and compared them visually. This method enables service providers with little knowledge of text mining to grasp different preferences of customers, and thus to improve their services in a more personified way.

***Keywords*: cultural influence, online customer review, distance-biased mi score, chance discovery**

I. INTRODUCTION

In order to sustainably enhance and advance tourism industries, it is important not only to maintain and improve existing resources and services but also to continuously increase tourism resources, which should be either invented or re-discovered. In so doing, it is necessary to investigate both the evaluations of those resources and services on the part of tourists with different preferences and those on the part of tourism industries, which are too often mismatched. For customization of services and information to be provided, there have been a number of studies[1-3], in particular those of collaborative filtering, and the ultimate personification is the ideal there. When a new product or service is devised, however, the ultimate personification is usually too minute to pursue. Based on the consideration above, this study proposes a method of chance discovery for future tourism resources by comparatively investigating various data obtained automatically on the Web. In particular, we focus on cultural preferences or backgrounds that are a basis of personal preferences.

This paper, as a first step of our study, tries to extract cultural biases in online customer reviews. For this purpose, we analyzed online customer reviews on the same targets written in different languages. We devised a distance-biased *mi*-scoring, and based on the scores, we visualized the results and investigated possible interpretations of the results.

II. EFFECTS OF CULTRUAL PREFERENCES

When we go somewhere, the destination as well as those during the path has a different culture and custom. Tourists always have some assumptions / expectations to the destination and the way they will be treated: some of their assumptions/expectations are confirmed while others turn out to be false Among them, some are happy surprises while others lead to dissatisfaction Their assumptions / expectations are affected by many factors: sex, personal backgrounds, personal preferences, and their cultural backgrounds / preferences. Cultural differences among peoples have long been investigated[4], and some computational studies have focused on their extraction [5]. The goal of our study is to propose a finer-grained way to computationally extract these relations, but, in this paper, we investigated the possibility to interpret our results from some stereotypical viewpoints on races/nationalities. Stereotypes on races/nationalities are expressed in various occasions, and some of them are invented by others and others by themselves. The formation of stereotypes is a difficult issue to discuss intensively and extensively, but, in this paper, we manually interpreted our results and checked their validity by making a simple questionnaire survey.

III. DATA

In order to capture cultural differences, it is useful to employ multiple sets of data that contain reviews and opinions that are written by people belonging to each culture. However, it is not a trivial matter to find such sets of data. In this study, we employed online customer reviews on *TripAdvisor.com*.[6] TripAdvisor is a website based on the idea that travelers rely on other travelers' reviews to plan their trips, or at least can be satisfactorily helped in their decisions by them. As of August 2011, TripAdvisor contains 50 million travel reviews and opinions and written by 20 million registered members and counts 50 million of unique visitors per month.[7]

There are some merits to employ online customer reviews on TripAdvisor.com for this study. First, TripAdvisor.com provides scores of, or even hundreds of, customer reviews of a hotel or of a restaurant. Second, it provides not only textual customer reviews but also the following features: overall rating, item-based ratings of price, room, location, cleanness, bed, and service, the date when the reviewer used the reviewed hotel or restaurant, and the purpose, together with reviewer's attributes, as shown in Table 1. So we can analyze them from various viewpoints. Third, and most importantly, it provides reviews written in different languages. Reviews in English or in Spanish can be written not only by their native speakers but also by those who can use them, but reviews in some language, in particular, Chinese, Japanese, and Korean, are highly likely to be written by their native speakers.

As a preliminary study, we gathered more than 5,000 online customer reviews on hotels written in Chinese and Japanese, as shown in Table 2. We then segmented textual data into words with morphological analyzers, MeCab[8] for Japanese and the Stanford Chinese Segmenter and Part-of-Speech Tagger[9].

Table 2 Data

	Japanese	Chinese
Reviews	2,512	2,504
Words	210,418	134,891

IV. METHOD FOR ANALYSIS

In this paper, we focused on relations between nouns and adjectives, since most of the evaluative expressions are combinations of nouns and adjectives. In order to

Table 1 Attributes in Reviews on TripAdvisor.com

	Attribute	Value
Review	Overall Rating	1-5
	Price	1-5
	Room	1-5
	Location	1-5
	Cleanness	1-5
	Bed	1-5
	Service	1-5
	Purpose	with family, in couple, for business, trip by himself, trip with friends
	Date	Year and Month
	Textual Review	Text
	Advice for room choice	Text
Reviewer	Age	Numerical
	Sex	Male/Female
	Living Place	City Name
	No. of his reviews	Numerical
	No. of visiting places	Numerical
	Evaluation by other users	Numerical
	Rating	Top Contributor, Advanced Contributor, Contributor
	Others	Photo and Self-Introduction

compare Japanese and Chinese data, we picked up the top two hundred nouns and the top fifty adjectives that appeared in Japanese and Chinese data, and we manually translated those words into English.

The strength of co-occurrence of two words can be expressed in various ways, including *mi*-score and dice score. In order to capture the effect of the distance of two words, we calculated the strength of co-occurrence of a noun and an adjective as follows:

$$db\text{-}mi(A_i,\ N_j) = \log_2 \frac{(\Sigma P_k(A_i,\ N_j)/k\ ) \times S}{P(A_i) \times P(N_j)} \quad (1)$$

where k is the distance of A_i and N_j, ($0<k<6$)
S is the sum of the words in the data,
A_i is an adjective,
N_j is a noun

The expression above is to calculate the *mi*-score that is sensitive to the distance between the two words, and we call this score a distance-biased *mi*-score, *db-mi*. We admit that *db-mi* is a very simple concept that reflects the distance between two words with *mi*-score, and a more intelligent way to measure the strength of co-occurrence is to be devised. However, as the interpretation below indicates, *db-mi* can offer an interpretable result. Note also that it is a small problem that we do not count negation. When we pursue a sentiment analysis, negation is a big issue, but in our analysis, the co-occurrence of a noun and an adjective indicates that the noun can be positively or negatively evaluated from the viewpoint of the meaning of the adjective.

We then plotted the results according to *db-mi*-scores by expressing the value with line weight, and by expressing the similarity of meaning between two words of ○ or ● with nearness. A sample of this visualization is shown in Fig.1, where ○ is a noun and ● is an adjective.

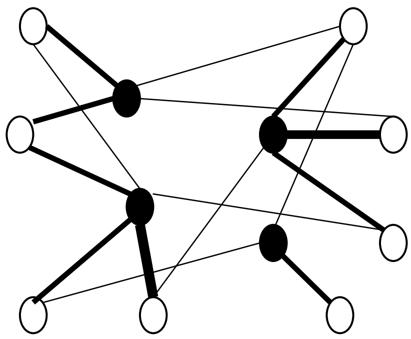

Fig.1 A sample visualization

V. INTERPRETATION

Based on the above method, we prototypically analyzed our data, and here we show some interpretations.

As related to "good evaluation", Japanese frequently use "good atmosphere" while Chinese frequently use "gorgeous," which is already well known, but Japanese's "good atmosphere" turns out to be well related to clerk's behavior, coloring of the room, ambient lighting. That means that Japanese are sensitive to those that are subtle, often invisible. At the same time, these target nouns are well related to "cozy."

On the other hand, Chinese's "gorgeous" is well related to bed, furniture, room bar, etc. That means that Chinese are more sensitive to those remarkably visible things, and these target nouns are also related to "great."

These tendencies are unanimously seen even when we focus on a particular segment of the corresponding Chinese and Japanese groups according to the purpose of the trip, reviewer's age, etc.

Another interesting tendency is that only Japanese are highly sensitive to cleanness. In fact, many Japanese reviewers put cleanness critically higher than other evaluative attributes while most Chinese reviewers do not.

We obtained eight tendencies including the above two that are seemingly culturally bound. Based on our interpretation, we made a simple questionnaire survey that asks if one thinks that the Chinese or the Japanese have a strong preference on X, where X is a tendency among the eight. Then we asked five Chinese, five Japanese, five Westerners including those who are British, Dutch, and French. Almost all of them, regardless of their nationality, answered affirmative to our interpretations, which, though quite intuitive, indicates that the tendencies we obtained are in fact culturally bound.

VI. CONCLUSION

We tried to extract cultural biases in online customer reviews. For this purpose, we employed online customer reviews on hotels on TripAdvisor.com that were written in Chinese and in Japanese. We devised a distance-biased *mi*-score, *db-mi*, to measure the degree of co-occurrence between nouns and adjectives, and visualized the results. We interpreted the visualization and obtained eight tendencies that are seemingly culturally bound, which is confirmed by a simple questionnaire survey. This study is quite a primitive one, but it shows that it is possible to extract culturally-bound characteristics from online customer reviews.

This method, though it should be extensively refined, can offer a seemingly valuable information on cultural differences behind various types of potential customers, and such a knowledge should be utilized for improvements and innovations of tourism industries as well as other industries.

REFERENCES

[1] Baeza-Yates, R., Ribeiro-Neto, B. eds. 2011,

Modern Information Retrieval, 2nd ed., ACM Press.
[2] Jannach, D., Zanker, M., Felfemig, A., and Friedrich, G., 2010, Recommender Systems: An Introduction, 2010, Cambridge UP.
[3] Ekstrand, M.D., Riedl, J.T., Konstan, J.A. 2011, Collaborative Filtering Recommender Systems, Now Publishers.
[4] Minkov, M. 2011, Cultural Differences in a Globalizing World, Emerald Group Publishing.
[5] Nakasaki, H., Kawaba, M., Utsuro T. and Fukuhara T. 2009, Mining Cross-Lingual/Cross-Cultural Differences in Concerns and Opinions in Blogs, in Computer Processing of Oriental Languages: Language Technology for the Knowledge-Based Economy, 213-224, Springer.
[6] http://www.tripadvisor.com/ (acessed on 2011/10/1)
[7] TripAdvisor Fact Sheet, http://www.tripadvisor.com/PressCenter-c4-Fact_Sheet.html
[8] http://mecab.sourceforge.net/
[9] Chang, P.-C., Galley, M. and Manning, C.D. 2008, Optimizing Chinese Word Segmentation for Machine Translation Performance, ACL 2008 Third Workshop on Statistical Machine Translation

.

The Seventeenth International Symposium on Artificial Life and Robotics 2012 (AROB 17th '12),
B-Con Plaza, Beppu, Oita, Japan, January 19-21, 2012

An improved method to extract landmarks information for the purpose of using maps and route

Shunichiro Sugimori[1], Yuki Murai[2], Makoto Okada[3], Kiyota Hashimoto[4]

[1234]Osaka Prefecture University, 1-1 Gakuen-cho, Naka Ward, Sakai, Osaka 599-8531, Japan
(Tel: +81-72-252-1161, Fax: +81-72-254-9944)
[1]ss301018@edu.osakafu-u.ac.jp, [3]okada@mi.s.osakafu-u.ac.jp, [4]hash@lc.osakafu-u.ac.jp

Abstract: When we want to go somewhere, we usually prepare maps, route and route descriptions. In that situation, we need these data to understand easy the map data and route descriptions, to contain appropriate information to reach to destinations from starting points, such as landmarks information and action points,, and not to contain ambiguous information. In this paper, we investigate difference between human route descriptions and those made automatically by Google Maps API in order to obtain the guidelines for good route descriptions.

Keywords: Automatic map construction, Landmark information, Route description.

1 INTRODUCTION

When we go somewhere, we usually proceed two tasks simultaneously. One is, as everyone knows, that we follow the dedicated route description or the map someone else made, and most of us think that we are just following them, but it is not the case. Actually, we reconstruct our own route description adding conspicuous landmarks in order to remember the route. In this sense, the navigation is an action to reach the destination by constructing and using our own route description [1]. The spatial knowledge acquired this way is called a cognitive map by Tolman [2]. From this viewpoint, the trouble with a given route description is caused by mismatches between it and what we expect to be included as landmarks. It is thus necessary to make the gap smaller in order to make a good, sufficient route description.

The aim of our study is to devise a better mechanism to improve route descriptions written by humans and to make route descriptions automatically from the relevant maps. For this purpose, an intense investigation is necessary to compare route descriptions written by humans and those automatically made with online maps. As a first approximation, we employ maps provided by Google Maps API, which we consider to have room to improve. With this investigation, the purpose of this paper is to make clear the guidelines for good route descriptions that is easy for us to understand.

The organization of this paper is as follows: Section 2 defines some important terms. Then section 3 describes our system that automatically generates a route description based on the information provided by Google Maps API and added some extra landmarks from our database of landmarks. Section 4 explains our evaluative experiment and discusses the result. Section 5 is the conclusion.

2 ACTION POINT AND LANDMARK IN ROUTE DESCRIPTIONS

Wherever we go, the route to the destination is not just straightforward. We have to cross a road or a river, turn right or left at a certain point, and so on. In other words, we are repeatedly forced to do actions at certain points, or *action points*. So it is quite important to recognize where the correct action point is for a certain action. Sometimes they are obvious enough to recognize it, but in many cases they are not so obvious and we need some extra key spots with which the action point is easily recognized and remembered. It is often difficult to distinguish between obvious action points and extra key spots for action points because they can be used interchangeably in different route descriptions. So Let us call obvious action points and extra key spots for action points *landmarks*.

Different types of spots can be landmarks. Some are natural and others are artifacts; some are small such as bulletin boards while others are big such as large buildings and rivers. As Lynch pointed out, even when an action point has its internal structure like buildings, it has little to do with its role of a landmark [3]. Whether a landmark is an action point or a key spot between action points that makes the next action point easier to detect, it should be conspicuous enough. Though different people have different preferences and viewpoints, and thus different people may regard different spots as their own landmarks, it is generally considered that there are still many potential landmarks that most people commonly regard as landmarks.

3 OUR ROUTING SYSTEM

In order to construct a more easily accessible navigation system, the current method to make a route description based on maps seems to have problems in adding and selecting the appropriate landmark information, though at the same time the mere addition of extra landmark information may not work. In order to the validity of landmark addition to route descriptions automatically made based on maps, we constructed an experimental routing system. The procedure is as follows:

1. Input of the source and the destination by a human

2. The system obtains the exact location of the source and destination using the prepared database.
3. The system obtains the route with necessary information and its route description from Google Maps API.
4. The system revises the obtained route description and the corresponding map by adding appropriate extra landmarks in the prepared landmark list.
5. The system shows the revised map and route description to the user.

We prepared tree different databases in advance for this sytem, which are described in 3.1.

3.1 Construction of Databases

The system we made has three databases: landmark's list, the list of the source locations like train stations, and the list of the destination locations that consists of restaurants' this time. All sources and destinations are located, for an experimental reason, in a small area, downtowns in Osaka, Japan. All databases are implemented with MySQL.

3.1.1 *The list of destination locations*

The list of destination locations is constructed as follows. First, we chose 1,200 restaurants in the targeted area from *Tabelog*, a famous online restaurant guide site with customer reviews. Second, we extracted the following information of each restaurants:

- Name
- Address
- Route description
- URL of the page of the restaurant in *Tabelog*

Third, the addresses above are modified in order to make them compatible to Google Maps API, using the following regular expression:

```
/(大阪府|京都府|北海道|東京都|[一-
龠]+[県]){1}([一-龠あ-
ケ]+[市区郡町村]){1}([一-龠あ-ケー]+([0-
9]+(\-|－|丁目|丁))*([0-9]+(\-
|－|番地|番))*([0-9]*[号]*))/
```

Fourth, we made queries to Google Geocoder API to obtain the exact location consisting of the latitude and longitude.

The prepared list of destination locations thus has eight fields shown in Table 1.

Table 1 Fields in the database of destination locations

field	description
id	unique id of the record
link	URL
name	the name of the restaurant
full_address	the address obtained from *Tabelog*
short_address	the address modified
lat	the latitude
lng	the longitude
description	the textual description of the restaurant

Lastly, we manually checked the information obtained and corrected errors and wrong data.

3.1.2 *The lists of the sources and landmarks*

As for the lists of the sources and landmarks, we first analyzed the route descriptions given by *Tabelog*, and manually selected the sources and landmarks frequently used in them. Then we obtained *name*, *lat*, and *lng* in the same way above, and the relevant map.

Red markers are landmarks and their information are appended to the route description in the right window. There are two *Green markers*, A is an original point, and B is a destination.
Blue line is a route calculated by our system.

Fig. 1. A screen shot of our system.

3.2 Method

Google Maps API provides maps and routes. The route is available in 3 types of travel modes, which is bicycling, driving, walking. Our purpose is to provide a better navigation for walkers and we chose walking, and add two types of modification to them.

3.2.1 Add Landmark Information

First, we insert pins on the map which means landmark. Landmark's information used for this method are registered in advance in the landmark's list described in section 3.2. The distance between a landmark and an action point is calculated, and if it is within 20m, then the landmark is inserted.

3.2.2 Clarify Directions

Route descriptions obtained from Google Maps API often lack the exact direction to be chosen at action points: e.g., to go straight or to turn left or right when crossing a road. So we manually added the exact direction for these cases.

4 EXPERIMENTS

We conducted two experiments to evaluate the accuracy and usability of the route that Google Maps API provides, and the usefulness of our system.

In the first experiment, in order to confirm that human route descriptions contain enough of information to arrive destinations from stating points and route on the map created by Google Maps API accord or not with human route descriptions, we compared them.

Next, we call it experiment 2, we compare the route's descriptions created by Google Maps API and the human route descriptions and discussed whether are according points and whether are difference in order to reveal what attributes are important for route descriptions to guide readers to destinations correctly.

4.1 Experimental data

We used the data of restaurants extracted from the web site "*tabelog*". Each restaurant data consists of maps, addresses of shops, route descriptions, starting points and destinations information. It turned out that many restaurants used the route description given by Google Maps API, and we extracted 41 data that contain route descriptions that are different from the corresponding route description obtained by Google Maps API and are seemingly described by a human with more than 60 characters.

4.2 Experiment 1: Comparison of route and route descriptions

In Experiment 1, we compared route descriptions by Google Maps API and by humans.

We assume two standard criteria of accordance with constructed routes and route descriptions as follows.

(1) *All actions on the action points of routes are consistent with human route descriptions.*

(2) *All landmarks are actually found from each action-point if the route descriptions contain some landmark information.*

We used Google Street View to confirm whether the criterion (2) is fulfilled or not.

As a result of this experiment 1, the correct route was constructed with 27 data and 14 wrong routes are created with the other data. There are three main reasons for wrong routes.

(i) Discrepancy between the shortest route and the com prehensible route

Route descriptions are supposedly used by a person who is going to the palce for the first time, and thus the most important feature of the route descprtion is comprehensibility. However, Google Maps API has a tendency to provide the shortest route, which is sometimes different from a comprehensible route. Eight of 14 route descriptions have different route between the two.

(ii) Multilayer type

If the starting point is above the subway station, Google Maps API would misunderstand that user is in the station. This type of error is shown only 1 of 14 data.

(iii) Double-sided type

Each destination, which is supposedly a building or a part of a building, is considerably large in size compared to a human, and there is no guarantee that the exact location of the *entrance* to the restaurant is obtained from Google Maps API. It might seem to be trivial, but it is not. Many restaurants face more than one street, and the choice of the correct street among them affects the decision of the total route.

4.3 Experiment 2: Comparison of modified route descriptions and human route descriptions

In this section, we compare human route descriptions with route descriptions obtained from Googe Maps API and modified by our proposed method. And we will show differences between these two types of route descriptions.

We investigated whether modified route descriptions accorded with human route descriptions at three points:

(1) whether all the same action points are contained

(2) whether the direction to chosse at each action point is described or not

(3) whether all the landmarks inserted are the same or not

Table.1 shows results of experiment 2. Experimental data is 27 data that accorded with their route descriptions and human route description in experiment 1.

Table 1. Results of experiment 2

Rate of landmark	Rates of action point	
	GMA⊃H	GMA⊂H
93.2%	60.3%	49.4%

In table 1, the rate of landmark shows the rate of the cases in which the same landmarks are used in both route descriptions. The rates of action point shows the rate of the cases in which the action points used in the route description obtained from one are used in the other. Average of action points of H was 3.4 times in one description, and average of action points of GMA was 5.5 times in them, so GMA is more redundant.

First, some of the landmarks were not contained in the route descriptions obtained from Google Maps API. The landmark information is found in only 1 data. Our proposed method considered landmarks information beside routes and it did not consider about landmarks in front of the routes. We will improve our method to search not only beside areas but also forward areas of routes.

Second, the proposed method cannot add streets and/or rivers as landmarks. Because these are inherently lines, not points, though they can be regarded as a point to be crossed in a route. In other words, if we add the information of relevant roads or rivers as landmarks, we need another method to specify the exact point that is to be regarded as a landmark in each case. 20 out of 27 wrong data contain this type of error, and we are devising some improvements else where.

Thirdly, 10 descriptions have a sentence like "*turn the left at the n-th corner*". The proposed method do not count the number of corners or signals from a particular action point, because it is a relative information to be computed separately.

Many description contained descriptions like "*cross over the ~ river*". Generally, names of rivers are more famous than bridges. Therefore there is not any description of "*cross over on ~ bridge*". Therefore sometimes we cannot obtain which road or bridge to be crossed. We suppose that action-points before rivers are important factors for correct information and we have to describe these information more clearly.

The proposed methods added information about walking time from the previous action point to the current one to route descriptions constructed by Google Maps API's. Human descriptors tend not to write these information, but it often concern people particularly in the case that two action points are rather remote.

Moreover, we also found the descriptions that show directions with compass points. However, we do not always have some devices to know directions like a compass. Because of it, we suppose that we should show direction by words "*right*" and "*left*" in route descriptions.

As the result shows, the rate in which the same landmarks are used in both description is rather high. Though we manually made the landmark list this time, but if the list can be constructed automatically, then we can apply our method to any locations, which is to be pursued else where. The result also shows the tendency that human descriptions contain fewer action points than descriptions obtained from Google Maps API, and the appropriate number of action points for human walkers should be investigated.

5 CONCLUSION

In this paper, we proposed a method to modify the maps, routes, and route descriptions obtained from Google Maps API, and discuss differences between map data by Google Maps API and human route descriptions. We obtained the results that they are often different, particularly in the usage of landmarks, and we proposed a method to add extra landmarks to route descriptions obtained from Google Maps API. The result is not still satisfactory and more refinements are needed, but the result indicates that this kind of improvements are necessary for a more comprehensible route description to be automatically constrcuted.

REFERENCES

[1] Shingaki N (2005), Internal and External Resources in Human Navigation (in Japanese). *Annual Bulletin of Graduate School of Innovation and Social Studies*, Seijo University 1(1): 61-78

[2] Tolman E. (1948), Cognitive maps in rats and men. *Psychological Review*, 55: 189-208.

[3] Lynch, K. (1960), *The Image of the City*. MIT Press.

The Seventeenth International Symposium on Artificial Life and Robotics 2012 (AROB 17th '12),
B-Con Plaza, Beppu, Oita, Japan, January 19-21, 2012

Automatic Generation of Tourism Quiz using Blogs

Jun Zeng[1], Toshihiko Sakai[1], Chengjiu Yin[2], Takahiko Suzuki[2], Sachio Hirokawa[2]

[1] Graduate School of Information Science, Kyushu University, Fukuoka 812-8581, Japan
[2]Research Institute for Information Technology, Kyushu University, Fukuoka 812-8581, Japan
(Tel: 81-92-642-2301, Fax: 81-92-642-2294)

[1](zeng.j.000, 2IE11060Y)@ s.kyushu-u.ac.jp
[2](yin, suzuki, hirokawa)@ cc.kyushu-u.ac.jp

Abstract: The one-way information provision can not impress the listeners well. As an efficient way, Question & Answer can help information provider understand the response of listeners. However, it is not easy for everyone to set a suitable question. In this paper, we propose an automatic quiz generation system using tourism blogs. The system can generate the quiz by extracting feature words of the topic keyword from the blogs. Our purpose is to help the tourism information providers to advertise their tourism events in an interactive way, in order to impress the tourists. By comparing with other method of quiz generation, we demonstrate that our method is more suitable for information provision.

Keywords: Quiz Generation, Tourism Blog, Feature Word, Information Provision.

1 INTRODUCTION

The traditional method of information provision is a one-way method from information providers to information recipients. There is no interaction between providers and recipients, so it is an inefficient method to provide information. You can image that when you are attending a philosophy class and listening to the virtually unintelligible theories, you may feel nothing but lethargic. But when the teacher says, “Who can answer this question?”, you may feel fresh instantly. Because you may want to know what the question is, and whether you will be asked to answer the question. If you are the one to answer the question unfortunately, you will be impressed by the question. Therefore, as an efficient way, Question & Answer (Q&A) can help information to provider understand the response of listeners. That is because Q&A changes the one-way into two-ways method. On the one hand, listeners not only just listen but also comprehend the content of information. On the other hand, the provider can also know how much the listeners have understood. As a typical form of Q&A, multiple choice questions require a short response time and with the possibility of covering a broad set of topics.

However, in order to set a question, user must quite understand the knowledge of the topic. Meanwhile, user has to read up a lot of literature to ensure the correction of answers. For helping user to set a multiple choice question easily, we propose a novel method to generate multiple choice questions automatically. In this paper, we mainly consider the automatic generation of quiz related to tourism event. Our purpose is to help the tourism information providers such as travel sites, tour guides and some other tour organizations to advertise their tourism events in an interactive way, in order to impress the tourists. The authors of this paper have been doing many researches on data mining of tourism data [1] [2]. In this paper we adopt tourism blogs as the experiment data. That is because the role of blogs became increasingly main stream in recent years. We collect the official blogs of Kyushu Tourism Promotion Organization[1] to generate quiz. Also, we develop a Automatic Quiz Generation System (AQGS) for realize the automatic generation of tourism quiz by using blogs.

2 RELATED WORKS

There is a large body of related work on automatic generation of multiple choice questions.

Tonoike et al [3] proposed an approach of answer validation based on the strengths of lexical association between the keywords extracted from a question sentence and each answer candidate. Tsumori and Kaijiri [4] generated the questions adapted to students' understanding based on the similarity of each word. Mitkov et al [5] distinguished the kind of problem sentences, and analyzed the structures (SVO, SVC, etc.) of the sentences. Moreover, the words that have the similar meaning with the correct answer in Wordnet are chosen as the distracters. Hoshino and Nakakawa [6] made a machine learn based on Naive Bayes and K-Nearest Neibors by using a collection of TOEIC question as training data. The blank in question was determined from the training result. The answers were random and chose from the same sentence.

However, all of these researches paid more attention to the difficulty of the questions. That is because these questions were generated for aims of education. In this

[1]http://www.welcomekyushu.jp/

paper, we focus on the interest of questions instead. Our purpose is make the listeners remember the information easily, not try to test the level of intelligence of listeners.

3 AUTOMATIC GENERATION OF QUIZ

3.1 Creation of Index

Before developing quiz generation system, we need to create an index. Index is design to optimize speed and performance in finding relevant documents for a search query. In this paper, we will not only build an index of full-text but also an index of each sentence.

For building a sentence index, we need to create a sentence-based frequency file. First of all, we divide every article into sentences. Next, we use "ChaSen" [7], which is a morphological parser for the Japanese language, to analyze morpheme of every word. After creating the frequency file, we use "GETA" [8], which is a generic engine for transposable association, to build an index of each sentence.

3.2 Extraction of Feature words

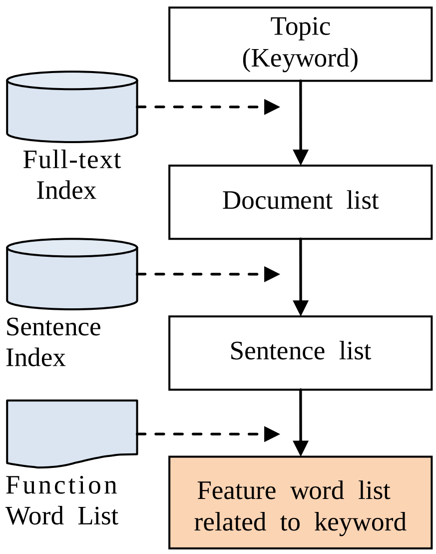

Fig. 1. Extraction of feature words

Typically, a multiple choice quiz contains two parts: a question and a group of suggested answers. In this paper, we generate the answers from a feature word list related to the user's keyword. A feature word is a word that appears in the same sentences with the user's keyword. In this section, we will introduce the extraction of feature words.

Fig. 1 shows the outline of the process for extracting the feature words. Firstly, the user must enter a topic (a keyword) of quiz. When user enters a keyword, the system searches all of the documents by using the full-text index, and generates a list of documents in which the keyword appears. Then, the system finds out all the sentences containing the keyword from the document list by using the sentence index. Finally, system extracts feature word list from the sentence list.

Table 1. Function words in Japanese

Category	Description and Examples
Pronoun	A pronoun is a pro-form that substitutes for a noun (or noun phrase) e.g. 私(I), 彼(he),これ(This), ここ(here)
Conjunction	A conjunction is a word that connects words, phrases, clauses, and sentences. e.g. しかし(but), また(or), そして(and)
Joshi	In Japanese grammar, particles are called joshi. e.g. に(in), で(at), は, を
Auxiliary verb	An auxiliary verb is a verb that gives further semantic or syntactic information about a main or full verb. e.g. できる(can), ない(not)

However, there are many function words in the feature word list. Function words express grammatical relationships with other words within a sentence. They have little lexical meaning or have ambiguous meaning. It is necessary to get rid of the function words from feature word list. Table 1 shows the category of the function words in Japanese. Fortunately, there are not many function words in Japanese, so we can manually create a function word file in advance. By using this file, we get rid of all the function words from feature word list effectively.

3.3 Generation of answers

The answers of a multiple choice quiz always contain a correct answer and a group of distracters. We consider the user's keyword as the topic of the quiz, so we can choose most relevant feature words as the answers. To some extent these feature words can describe the keyword.

In order to find out the most relevant feature words, we need to rank the feature words. In this paper, we use SMART (System for the Mechanical Analysis and Retrieval of Text) [9] to calculate the similarity between feature word and keyword. In other words, every feature word w_i will have $SMART(k, w_i)$, where $SMART(k, w_i)$ is the similarity between keyword k and w_i. If word w_i have a higher $SMART(k, w_i)$, it means that w_i is more similar with k.

Fortunately, GETA supports the computation of SMART, so we can get $SMART(k, w_i)$ of all the feature words as soon as we get the feature word list. According to $SMART(k, w_i)$, we sort the feature word list. If a word get a higher $SMART(k, w_i)$, it will appear at a higher rank. Finally, we choose the top 1 feature word as the correct answer, top 2 ~ 5 feature words as the distracters.

3.4 Generation of questions

As we mentioned above, before we extract the feature words, we have get all the sentences that contain the keyword. We will generate questions from the sentence list.

Table 2. An example of quiz

Question	(　)は、これを防ぐために、若者達が喊声をあげて、観音堂内の鬼の面箱を封じ直すという勇壮な裸絵巻。 現在では、「童子の舞」が(　)の中心となっていて、童子の舞や所作は一見の価値があります。
Answers	行事、イベント、公園、祭り、神社

Firstly, in order to avoid that the distracters appear in the questions, we need to get rid of the sentences that contain the distracters. And then we randomly choose a sentence from the sentence list as the question. Meanwhile, the correct answer will be replaced by brackets. Table 2 shows an example of quiz, where the red answer is the correct answer.

4 AUTOMATIC QUIZ GENERATION SYSTEM

4.1 Design goal

As we mentioned above, the goal of Automatic Quiz Generation System (AQGS) is to help the tourism information providers such as travel sites, tour guides and some other tour organizations to generate quiz easily. These quizzes can help them to advertise their tourism events in an interactive way, in order to impress and attract the tourists.

4.2 Outline of AQGS

We develop the AQGS based on the proposed method with PERL language. User can open the CGI file of AQGS by using any kind of browser. Fig. 2 shows the interface of AQGS. There is only a "topic textbox" and a "search button". When user enters a topic keyword and clicks the search button, the quiz will be displayed below.

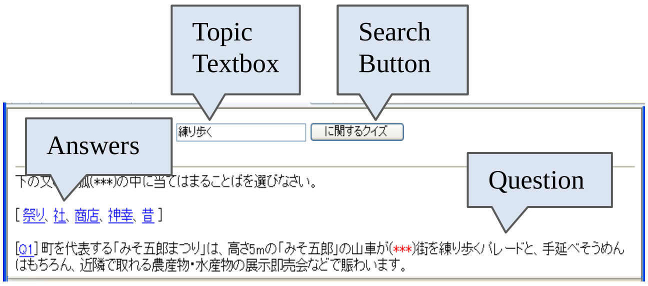

Fig. 2. The interface of AQGS

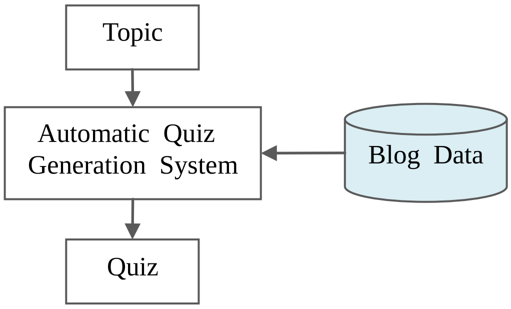

Fig. 3. The outline of AQGS

Fig. 3 shows the outline of AQGS. User only needs to enter a topic keyword. The system will automatically generate quizzes about the topic. It is not necessary for user to understand the topic well.

5 EXPERIMENT AND EVALUATION

5.1 Experiment Data

We collected the official blogs of Kyushu Tourism Promotion Organization to generate quiz. We focused on the events in the region, so we collected 906 events, at the first stage. However, some articles did not contain the date of event. So, we chose 316 articles that contain the date of the events. Some events are performed every year. So, we identified the articles of the same event in different years. As the result, we obtained 312 articles by which we generate quiz.

5.2 Methodology and procedure

To evaluate the usability of AQGS, we introduce a usability experiment. We developed two quiz generation system, one is proposed system by using feature word (F-System), and the other system generates the quiz by using Wordnet [5] (W-System). 5 participants joined in the experiment. Before the experiment, we did not introduce participants the purpose of this experiment. We design the task of usability experiment as follows:

(1) We generate the quizzes by F-System or W-System randomly. And the topic of quiz will also be determined randomly.

(2) We ask participants to answer these quizzes. They do not know whether the quizzes are generated by F-System or W-System.
(3) Participants evaluate each quiz they answered by 4 criterions, every criterion has 4 degrees. Table 3 shows the criterions and their degrees.

Table 3. Criterions of evaluation

Criterion	Degree
Interest	1 very boring, 2 boring, 3 Interesting, 4 very interesting
Difficulty	1 very difficult, 2 difficult, 3 easy, 4 very easy
Acquaintance	1 very well known, 2 well known, 3 known, 4 unknown
Impression	1 very impressed, 2 impressed, 3 unimpressed, 4 not impressed at all

5.3 Results and Analysis

Finally, we get 200 evaluation data: F-System 100 and W-System 100. We calculate the average degree of each criterion. Table 4 shows the result of evaluation, where the numbers in the arrow present the average degree of each criterion.

Table 4. Result of evaluation

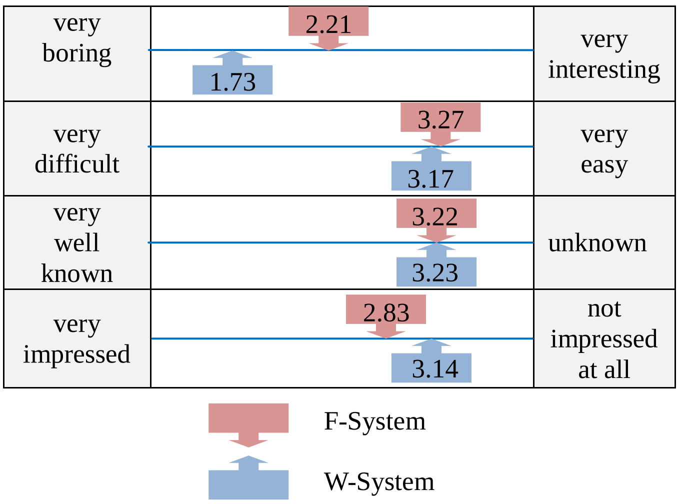

Although "Difficulty" and "Acquaintance" are not the most important criterions, the result shows that quizzes generated by two systems have the same difficulty and acquaintance. It proves that the quizzes are comparable.

The result also shows that the quizzes generated by F-System are considered more interesting than those of W-System. Because the distracters generated by W-System are chosen from similar words of Wordnet, such as ship, boat, vessel and watercraft. Participants consider that it is boring to tell the difference from the words. After all, the quizzes are not generated for intelligence test. Meanwhile, Participants consider the quizzes generated by F-System are more impressed than those of W-System. The result demonstrates that our method is more suitable for information provision instead of intelligence test.

6 CONCLUSION AND FUTURE WORK

In this paper, for providing an interactive way for the tourism information providers, we proposed a novel method to generate the tourism quiz automatically by extracting the feature words of topic keyword. We also developed a Automatic Quiz Generation System. By comparing with other method of quiz generation, we ensure that our method is more suitable for information provision instead of intelligence test. Because the quizzes are interesting, as well as they can impress the users.

In the future, we are planning to build a difficulty and interest model to modulate the quizzes automatically.

REFERENCES

[1] Jun Zeng, Sachio Hirokawa. Component Search Engine using Tree-View Interface for Tourist Blogs, 3rd International Conference on Awareness Science and Technology, Dalian, China.pp.327-331. 2011.
[2] Chengjiu Yin, Tetsuya Nakatoh, Sachio Hirokawa, Xiaobin Wu, Jun Zeng,A proposal of search engine "XYZ" for tourism events,JCAI2010 IEEE, pp.178-181, 2010.
[3] Masatsugu Tonoike,Satoshi Sato,Takehito Utsuro,Answer Validation by Keyword Association,Vol.2004 No.47, 2004-NL-161,pp.53-60, 2004.
[4] Shinichi Tsumori, Kenji Kaijiri, A Proposal for the Automatic Generation of Multiple-Choice Problems Adapted to Students' Understanding, Japanese Society for Information and Systems in Education,pp.26,2009.
[5] Mitkov, R., Ha, L.A., Karamanis, N.A computer-aided environment for generating multiple-choice test items Natural Language Engineering 12 (2), pp.177-194, 2006.
[6] Hoshino, A. and Nakagawa, H. A real-time multiple-choice question generation for language testing: a preliminary study, Proceedings of the second workshop on Building Educational Applications Using NLP, pp.17-20. 2005.
[7] http://chasen-legacy.sourceforge.jp/
[8] http://geta.ex.nii.ac.jp/
[9] G. Salton, The SMART Retrieval System—Experiments in Automatic Document Processing, Prentice-Hall, Inc. 1971.

Sharing Knowledge and Experience of Search with SNS

Xiaobin Wu[1], Jun Zeng[1], Chengjiu Yin[2], Sachio Hirokawa [2]

[1]Graduate School of Information Science and Electrical Engineering,
[2] Research Institute for Information Technology,
Kyushu University Hakozaki 6-10-1, Fukuoka, 812-8581, JAPAN

2ie10056y@s.kyushu-u.ac.jp, sousyun_kyusyu@yahoo.co.jp, {yin, hirokawa}@cc.kyushu-u.ac.jp

Abstract: The investigation activities using a search engine are indispensable to acquisition of new knowledge. When we investigate using a search engine, we leave a memo if needed, seeing the search results to an input keyword. Depending on the case, search refinement and search by a new related keyword are repeated. However, it is difficult to share the knowledge and the experience acquired under investigation activities with the others. On the other hand, SNS which promotes relation with people and a person attracts attention. This paper proposes a community type search platform which combines a search engine and SNS. By seamless use of various activities in search and the mutual comments, users can share a problem or new knowledge.

Keywords: SNS, Search, Community, Knowledge Share.

1 INTRODUCTION

With the development of internet, SNS (Social Network Service) plays a more and more important role on affecting interpersonal relationships. As typical SNS systems, Mixi has the largest number of members in Japan; GREE can support the mobile devices; Facebook is the most popular SNS in the world.

These SNS systems have become community Web sites that can broaden the relationship among person and person. Therefore, the researches on SNS have increased recent years. For instance, the authors of paper [1] take user's friend as a middleman, and proposed a chat system on circle of "user", "user's friend" and "friend of user's friend". The circle of "friends of friend" provides a chance to create new relationships, in order to sharing knowledge among all of friends.

In addition, when we try to investigate something, we always open a search engine, enter some keywords and click the "search" button. There is no doubt that search engine has become an indispensable tool for the current Internet users. Especially, with the increasing of the search engines which provide search service for documents of education and research, new issue or knowledge can be discovered in search activity. Sometimes we need to make a memo to record the discovery or our comment of search results. These memos may contain some important and valuable information. Therefore it is useful to share our memo and read others' memo.

Textbook is not the only way to obtain knowledge. We can also discover new knowledge during our search activity. In order to share the knowledge discovered in search activity, we propose a novel search engine called SNSearch (Social Network Search). It combines the SNS and search engine together. It help user to make memo easily and record user's search history automatically. It makes use of the relationship among persons, which was created through SNS, to share the knowledge to each other.

Our main purpose is to provide a new approach to help users share and obtain new knowledge expediently. In this paper, we consider the researchers as our chief users. The researchers can freely add new friends who may have similar interest. They can use the SNSearch to search papers and make memo. They can also read their friends' memos and search history. Thus the users can easily share and obtain new knowledge among their friends. By doing this research, we expect to affect the future prospects of the current search engines and SNS.

2 RELATED WORK

There are several researches in using access log of Web pages. Nakao et. al. [2] uses access log of a Web pages of each user to calculate the similarity of Web pages. They proposes a recommendation method of Web pages based on the similarity. They considered not only the similarity of Web pages but the similarity between sub-trees. They combined this similarity and the similarity by link structure.

Toda et. al.[3] paid attention to the Web pages visited often by many users to improve the efficiency of Web browsing routines and to discover new information at the same time. They analyzed the time and frequency of users visit to particular pages in their access log, to evaluate the importance of the pages for recommendation. They applied the collaborative filtering for Web page recommendation.

Liao et.al.[4] considered a mentoring system in WBT(Web Based Training) system. They analyzed the learning logs of students and formulated evaluation measures to capture the students feature. They constructed an "evaluation referential graph" to detect abnormal status of students. When such state is found, the system can alarm to keep students learning motivation.

So far qualitative analysis is attached great importance. Recently, the learning logs are attracting many researchers to help communication between users. Totoda et.al. [5] used the activity logs of runners in creating regional and focused communities of runners. Any member can read and comment the training plan of other members. So, participating member of the community can share and learn from others activity logs even if they have few experience.

Watanabe et.al. [6] used collaborative learning logs, where participants form a team to solve the same problem. They evaluated the number of users who made the same annotation in their utterance, and constructed a knowledge graph. They claimed that the graph is useful to point out the key issue for learners.

Anderson et.al. [7] designed and implemented the montage system to improve the experience for routine web browsing that users tend to repeat over and over in similar situations by providing a start page. The start page shows an ensemble of links and content based on a user's browsing history and preferences.

From these studies, we understand that users' logs are useful. However, there is no trial that connects search activity and SNS. The present paper seems to be the first one as far as authors know.

3 WHY SNSEARCH

3.1 Search and knowledge

Why do people search? A simple reason is that they want to know something that they do not know. Today, with the developing of internet, searching is a natural behavior like listening, speaking, reading or writing. There are many reasons for people to use search engine. Sometimes people use search engine to find something they are interested in. Sometime people use search engine to find some methods to solve some problems or do some studies. No matter why they search, people can learn some knowledge by their searching behavior. Different people use different keywords to search different things, and choose different results with different reasons. But, it is possible for different people to have the same characteristics such as interests, research, task, and purpose. In this kind of situation, sharing the experience of search can help people to learn something from other people who have some characteristics.

But, how to share the experience of search and the knowledge learned from search? In order to solve this problem we designed a system named SNSEARCH which combines search engine and a simple SNS system.

3.2 The main idea of SNSEARCH

In this paper, we designed a search engine of papers collected from IEICE technical report. By combining it and SNS communication ability, we provide the SNSEARCH system as a community portal to provide a platform with which people can share his knowledge and learn something from others'. As show in the Figure 1, the main idea of this system is that people can give something and take something by accumulating user's search record, and doing a memo of knowledge found from search behavior and some comments about the search behavior.

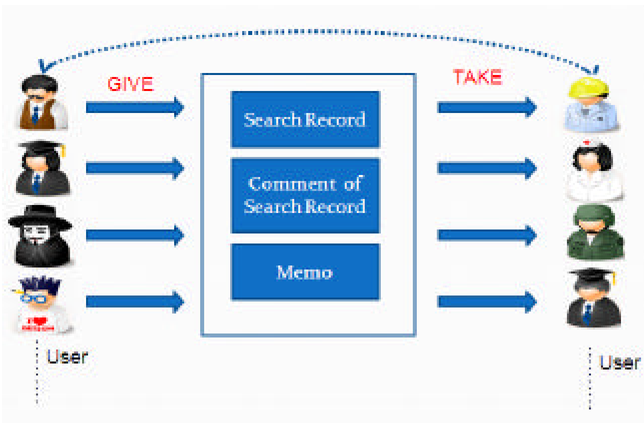

Fig. 1. The main idea of SNSEARCH

4 OUTLINE OF SYSTEM

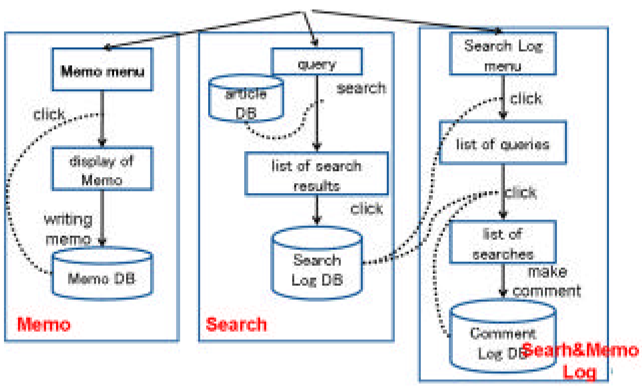

Fig. 2. System

Fig. 2 shows the outline of the system, which consists of three components -- Memo, Search and Comments Log. We used the abstracts of 42,921 articles of IEICE(the Institute of Electronics, Information and Communication Engineering) to create a search engine. The search engine can be substituted with other engine. We call the system as SNSearch, since it combines SNS and Search. The system keeps query logs of users in its database to help sharing the process of search between users. User can see, learn and comment on other search experience and on the search result. The system returns the search results for the query as an ordinary search engine does. When a user chose and clicked a result, the system keeps this behavior as users' preference. The queries and choices of one user can be used as knowledge for other users. Conventional SNS provides a communication environment to participants of the community. In SNSearch, user can give not only their opinion or comment, but also their experience of search. Moreover, they can comment on search process of other members.

5 FUNCTIONS OF SYSTEM

The present version of SNSearch has the following 8 functions.

(1) Writing memo
(2) Displaying the latest 10 memo
(3) Displaying memo of each member
(4) Search engine of articles
(5) Displaying memo according to date and time
(6) Displaying members' queries
(7) Displaying the action for the search result
(8) Making comments on members' search logs

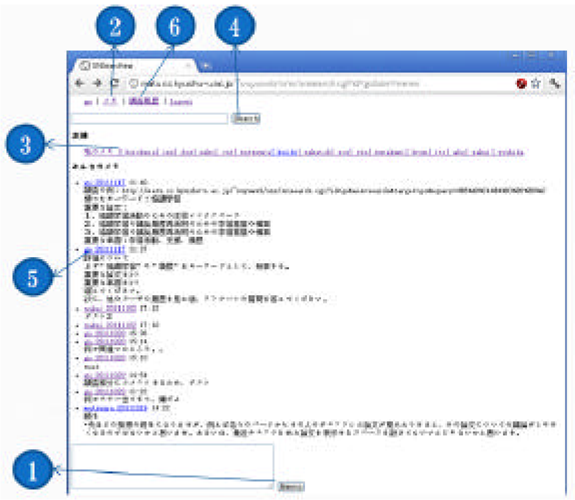

Fig.2 Listing of Memos

When a user logins to the system, he can choose the contents to be displayed from his own memo, the latest memo of all members and the search logs. When memo menu is chosen, the latest memos of all members are shown in order of time (Fig. 3). The list of fiends is always shown in all modes. When the own memo is selected, he can read and write the memo (Fig. 4). If a user wants to check the memo of his friend, he only has to click the name of the friend on the list. A simple click on a query (Fig. 5) can activate the search and re-display the result which his friend checked (Fig. 6).

Fig.3 A user's Memo

Fig.4 Listing of Queries

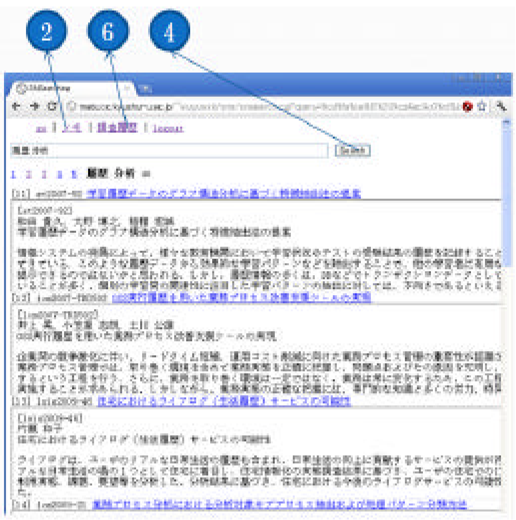

Fig.5 Search Interface

6 EVALUATION PLAN

The key feature of the proposed system is in the combination of a search engine and SNS. The interface of the system, however, influences whether the system is useful and convenient. In the rest of the paper, we analyzed the precedence studies to consider the frame work of evaluation. It turned out that there are two kinds of approaches, i.e., questionnaire by users and comparison of performance as search methods.

Specifically by the previous work, the following evaluations are performed. In [1], the questionnaire survey about an opinion and comment of a system was conducted to 11 users and was used for evaluation. In [2], the browsing logs of 11 users were used to recommend non-visited Web pages. The success ratio of arriving non-visited pages were used as the evaluation score for the method. Toda et. al. [3] used the decrease of users' clicks as the effectiveness of recommendation method for a user to reach the target Web page. In [4], the users are asked to use their system, and then answered the prepared question. Then the questionnaire survey was conducted to obtain the evaluation. In [5], two experiments were performed to compare their system with a conventional community site. In [4], four students were asked to solve three problems of Java programming, where students comprehension was formalized as "knowledge graph".

The authors made a brief hearing of users as preliminary evaluation. The main interests and reaction of users were convenience of an interface, flexibility of a system and whether users can share their knowledge which would be gained when they are actually using our system to explore their problems. We are planning the tasks to be solved by users in our experiment and the questionnaire to analyze these three points.

7 CONCLUSION

In this paper, we designed a search engine of data collected from IEICE technical report, which is different from traditional search engine. The difference is that the result of search if not only links of papers but also can save search log automatically. We combined it with a simple SNS system to provide a community portal, with which people can share their knowledge got from search behavior and learn something from others'. And we gave a detailed account of this system which has three components -- Memo, Search and Comment Log.

This time, we just gave an idea that people can share knowledge with each other by share combining SNS and Search. How to make it more available? How to make it more acceptable? In order to solve this kind of problem, some improvements of this system need to be considered.

As the next step of this study, we are planning to design an Information Recommendation Model to make it easy for people to find something they are intereste d in. By accumulating user's record of using the Infor mation Recommendation Model, we plan to conduct an experiment to evaluate the effectiveness of the system.

REFERENCES

[1] K. Kasuga (2007), Y. Saegusa, Y. FUrui, H. Hayami, SNS Chat : A Chat Function Integrated into SNS for Expanding Circles of Friends,Tech. Rep. IPSJ SIG-GN (32),pp.61-66,2007 (in Japanese)

[2] K. Nakao (2009), T. Mine, A Method for Relevance Calculation between Browsed Web Pages toward Personalized Recommendation System, Tech. Rep. IEICE SIG-AI 109(51), pp.31-36, 2009 (in Japanese)

[3] T. Toda (2007), T. Mine, M. Amamiya, Active Browsing : A Novel Personalized Web Browsing Support System,
Tech. Rep. IEICE SIG-KBSE 106(473), pp.1-6, 2007 (in Japanese)

[4] X. Liao (2004), K. Seki, T. Matsui, T. Okamoto, Development of the Mentoring System for WBT based on Learning Log Data, Tech. Rep. IEICE SIG-ET 104(222), pp.39-44, 2004 (in Japanese)

[5] N. Gotoda (2008), K. Matsuura, K. Kanenishi, Y. Yano, Support of the Running Motivation based on an ctivity Log, Tech. Rep. IEICE SIG-ET, 107(536), pp.65-68, 2008 (in Japanese)

[6] Y. Watanabe (2009), T. Kojiri, T. Watanabe, Knowledge Organization Framework from Discussion Records of Collaborative Learning, Tech. Rep. IEICE SIG-ET, 109(82),pp.21-26, 2009 (in Japanese)

[7] C. R. Anderson (2002), E. Horvitz, Web Montage: A Dynamic Personalized Start Page, WWW'02 :Proceedings of the 11th international conference on World Wide Web, pp.704-712,2002.

A method of sentiment analysis for online reviews containing values of multi-criteria evaluation

Takaya Nishikawa[1], Makoto Okada[2], and Kiyota Hashimoto[3]

[123]Osaka Prefecture University, 1-1 Gakuen-cho, Naka Ward, Sakai, Osaka 599-8531, Japan
(Tel: +81-72-252-1161, Fax: +81-72-254-9944)

[1]ss301018@edu.osakafu-u.ac.jp, [2]okada@mi.s.osakafu-u.ac.jp, [3]hash@lc.osakafu-u.ac.jp

Abstract: Online reviews of commercial sites are important sources for customers to obtain information and opinions. However, generally, these reviews contains several mixed information such as purpose and sentiments of reviewers. Therefore users need the method to separate these data and extract appropriate information from the reviews. In this paper, we investigated effectiveness of a method of machine learning *Support Vector Machine (SVM)* whether the method can classify reviews appropriately or not by using reviews of a travel information web site "*TripAdvisor*". We also investigate difference of precisions according to source textual data such as morpheme, bigram and trigram.

Keywords: Online reviews, Sentiment analysis, Support vector machine.

1 INTRODUCTION

The total size of the documents on the Internet has been more and more gigantic. Among them, many researchers and commercial enterprises have been paying more attention to online customer reviews found on various portal and purchase sites like Amazon.com and kakaku.com. These reviews contain a lot of personal opinions and they are considered to be very useful for other customers as well as enterprises. When a person wants to buy something, he can use others' reviews to know the product better from the customers' viewpoints. Enterprises can know better how their products are considered by customers by analysing those reviews. However, what is known with customers' reviews depends on the analytic method to be employed.

There have been many researches to analyze and utilize the reviews. Among them are two typical approaches. One is to search and extract all and only necessary information from the total data. Another approach is to classify reviews into several categories and to know the possible types of customers. For example, in some researches, weblog data are classified into two categories: *positive opinion* or *negative opinion*. In others, newspaper articles are classified into some categories based on various topics found in them.

In this paper, we adopt a different approach that classifies reviews considering not only sentiments and opinions of reviewers but also their personal information. This approach is obviously important because companies often obtain opinions classified based on generations and/or family structures of customers for market research. Therefore, it is very important for a better classification to investigate reviewers themselves together with what they write.

In this paper, we investigate effectiveness of a method to classify documents of reviews of a web site called *TripAdvisor* by experiments. The reviews there contains not only opinions but also other pieces of information such as the situation, the purpose of reviewers and themes for evaluation. For example, a keyword of "*with Friends*" or "*Solo*" are added to some reviews by reviewers. We constructed classifiers of *Support Vector Machine* (*SVM*). We constructed several classifiers by using different training data sets. We then investigate the effectiveness and the differences of each classifier based on different data sets by experimental results of review classification.

In section 2, we explain related works of our research. Next we will explain our data sets. In section 4, we explain techniques for our research, SVM. In section 5, we will show experimental results and discussion. Section 6 is the conclusion.

2 RELATED WORKS

There are two approaches to analyze a large scale document data in order to obtain useful information to human. One is a method to extract opinions, and another is a method to classify opinions.

The former approach considers components of opinions, defines the component and extracts them from text data. Sometimes the relationships of the components are used for the extraction of the opinions. Iida et al. [1] defined that an opinion can be represented as a tuple (Subject, Attribute, Value) and they extracted the pair of Attribute-value from text data.

On the other hand, the latter approach is to classify documents into some classes according to their characteristics. Hashimoto et al. [2] classified newspaper articles according to their topics or other viewpoints. In particular, *sentiment analysis* tries to classify textual data either as positive or as negative. For example, Ikeda et al. [3] classified weblogs into two classes of positive/negative.

Our research belongs to the latter approach and analyzed and classified the reviews that include much subjective information of reviewers such as feelings, reputations, and opinions of themselves. The subjective information depends on personal situations of reviewers. Therefore, in order to obtain the subjective information in the reviews considering personal data of reviewers appropriately, it is very important to classify the reviews firstly into some categories based on features or personal information of reviewers, for example single, married, have a family, and so on.

Therefore, we devised a method to classify reviews considering their personal information.

3 TripAdvisor

"*TripAdvisor*" is a review site that collects useful travel information around the world. This site contains information of hotels and restaurants in the world. And users of these facilities can add reviews to the web pages in the site. This site has more than 50 million reviews written by users in more than 20 different languages. For example, some foreign users of Japanese hotels and/or restaurants can write a review by his native language and add them to the relevant page of "*TripAdvisor*".

When users write reviews, they can add optional keywords called "Tags" that express categories of reviews. The tags show situations or purposes when writers used

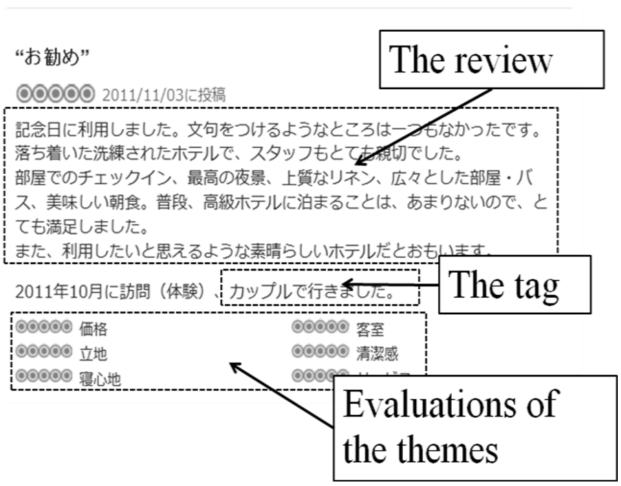

Fig.1. The example of a review in TripAdvisor

these hotels or restaurants. "*TripAdvisor*" provides five kinds of tags: "*Business*", "*Couples*", "*Family*", "*Friends*" and "*Solo*".

Users can also evaluate various themes by five grades. For example of the themes are "*Price*", "*Place*", "*Cleanliness*", "*Services*", and so on.

Fig.1 shows an example of reviews in this site. That shows a review text, tag data, and six themes. In later sections, we use 10,000 reviews automatically extracted from *TripAdvisor* as our data set.

4 PROPOSED TECHNIQUES

There are various methods of machine learning such as decision tree neural network and Support Vector Machine (SVM). In this study, we selected to use SVM because it fit for our purpose. We want to classify two classes: match or not match, and SVM classify data into binary.

4.1 Support Vector Machine

A support vector machine (SVM) is a supervised learning method for binary classification, originally proposed by Vapnik [4]. Fig.2 shows the basic concept of SVM.

The algorithm computes the hyperplane which divides two classes by analyzing the vector data of two classes as teacher data. With the hyperplane, the machine estimates the class of unknown data. Even if vector is high dimensional, the machine can analyze. Since the dimension of vector of documents data is often high, the machine is used for analyzing of natural language.

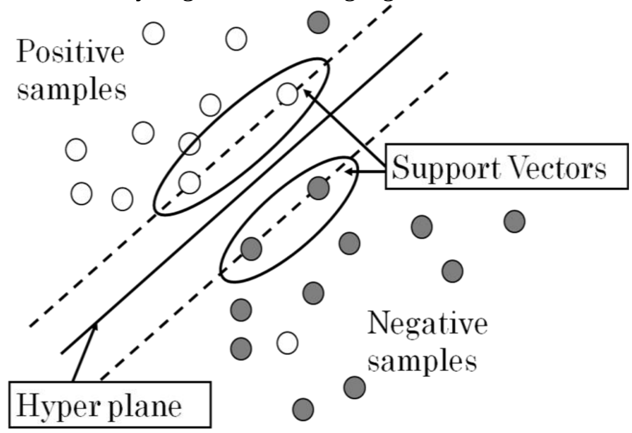

Fig.2 The illustration of SVM

4.2 Vectorization

We used ideas called "bag-of-words". For example, here are two texts S1 and S2:

S1: John likes to watch movies. Mary likes too.

S2: John also likes to watch football games.

Based on these two text documents, a dictionary is constructed as:

dictionary = {1:"John", 2:"likes", 3:"to", 4:"watch", 5: "movies", 6:"also", 7: "football", 8:"games", 9:"Mary", 10:"too"}

This dictionary has 10 distinct words. And using the indexes of the dictionary, each document is represented by a 10-entry vector as follows:

[1, 2, 1, 1, 1, 0, 0, 0, 1, 1]

[1, 1, 1, 1, 0, 1, 1, 1, 0, 0]

In English, there are spaces between each word. However, in Japanese, every words are attached each other. Therefore we need to separate them into pieces of word or other units. We used two major methods to make dictionaries and vectors of documents data.

The methods are as follows:

1. Using words segmented by a morphological analysis
2. Using character *n*-gram

We will explain each approach and their advantage and disadvantage.

4.2.1 Using words segmented by a morphological analysis

The first approach is to use words that are segmented from character strings using a morphological analyzer. We used Mecab[5], a Japanese morphological analyzer.

<u>Advantage</u>

This method can use words in an ordinary sense to make vectors. In addition, it is useful to decrease sizes of indice and dimensions of vectors.

For example, "begin", "began" and "begun" are different forms of the same word, "begin," in English, and using a morphological analyzer, we can easily put these different forms into a single word.

<u>Disadvantage</u>

If some words are not registered in the dictionary of the morphological analyzer employed, these words cannot be analyzed correctly. The information of words are lost.

4.2.2 Using *n*-gram

A character *n*-gram expression is a string of *n* characters. For example, if *n* is set to two, a word "nature" is separated to "na", "at", "tu", "ur", and "re" as 2-gram expressions.

<u>Advantage</u>

We can use this method in any written languages without complex preprocesses.

<u>Disadvantage</u>

An *n*-gram expression may not correpond to a meaningful unit in a usual sense. In addition, the dimension of the vector is very high by this method.

Online customer reviews usually contains expressions that are not registered in a dictionary for morphological analyzers. So if we take the first approach, there is a risk that expressions wrongly segmented badly affects our analysis. On the other hand, if we take the second approach, we need pruning many *n*-gram expressions of lower frequencies to enable a realistic computation. In other words, both approaches have some difficulties. So we compared these two approaces to know which is better for our purpose.

5 EXPERIMENTS AND DISCUSSIONS

5.1 Experiments and results

First, we collected the reviews of the accommodations in Japan from "TripAdvisor". We used only the data which have the tag of "Solo", "Couples", "Family" and "Friends". And we defined two classes that a class with the tag of "Solo" and another with the tags of "Couples", "Family" and "Friends".

We extracted 10,000 data at random from "TripAdvisor". These data are labeled by the two classes. And we divided those data into 5,000 training data and the 5,000 test data.

In the vectorization, vectors are constructed by three data set: morphological analysis, bigram, and trigram that are described in Chapter 4. Moreover we let vectors pass in the filters and made other data sets. The purposes of using filters are to reduce the element of an unnecessary vector and to raise the accuracy of analysis. We thought that heavily used words should have appeared in many reviews. On the other hand, the less frequency words are not special data. Therefore we expected that the accuracy of classification would go up if those words can be removed. We tried to use some simple filters that considered in the

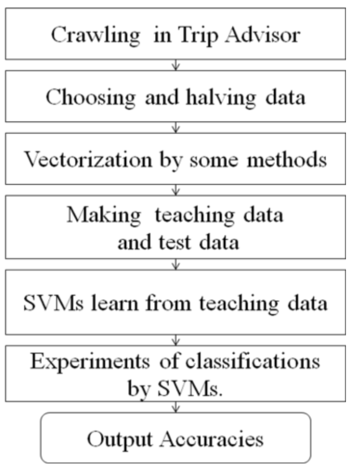

Fig.3. The flowchart of expriments

frequency of words. Seven data sets were made from each method.

- Data containing all the elements
- Data in which deleted the elements that frequency are top 10% , 20% and 30%
- Data in which deleted the elements that frequency are lower 10% , 20% and 30%

We used SVM as the method of machine learning. We used C-SVC of Soft margin classification among the kinds of SVM. Soft margin classification is the technique which allows some errors, loosens restrictions and raises accuracy.

Fig.3 shows the flow of the proposed method.

S1: crawling in Trip Advisor and gathered reviews and their options of tags.

S2: choosing the data of reviews that contain the tags, halving data and making data of teaching data and test data later

S3: making vector from data by the methods.

S4: reduceing elements of vector by the frequency, labeled vector from tag of reviews make teaching data and test data.

S5: SVMs learn from these teaching data.

S6: Experiments of classifications by SVMs using those test data.

Table.1 shows experimental results.

Table 1 Precision Rate of Experimental Results

			word	bigram	trigram
Without pruning			63.8	64.5	65.3
Pruning	top	10%	64.0	64.7	64.5
		20%	64.0	64.1	63.9
		30%	64.2	63.9	64.1
	bottom	10%	56.7	61.6	61.2
		20%	51.9	60.3	60.6
		30%	52.3	59.7	59.7

5.2 Discussions

Most accuracies rates were around 60%. When we use the data in which the top 10%, 20% and 30% of elements are pruned, there is not big difference in precision.

However, when we use the data in which The low 10%, 20% and 30% of elements are pruned, there is a small difference in precision. When we use the data made using word segmented by a morphological analyzer, the accuracy of an experimental result is worse than others. Especially, when the data in which the low 20% are pruned, the result is the worst of all results. It may be because the data whose atomic elements are words segmented by a morphological analyzer contain some important words in their low frequency words. Therefore we must not prune these data and we should give more weights to these data. Moreover, the big difference in accuracy was not observed by *n*-gram.

In this experiment, we cannot confirm the high effectiveness of filtering by the experimental results of the precisions. The precision rates of the data of morphological and bigram increased a little. And, in this experiment, precisions of the data of *n*-gram are not decreased very much. If the data of *n*-gram are used for construction of vectors, filtering technique may be useful for reducing computation times of vectors without decrease of precisions when using the data of *n*-gram.

Considering these experimental results, the experimental results are not of very high quality. We obtained two problems concerning these experiment results. Firstly, we should devise techniques to improve the accuracy rate higher. Next, we devise again techniques to make appropriate filters, especially for the data of morpheme. Filtering is necessary to reduce the computing times of vectors. However, if we apply the filters to the data, the accuracy tends to fall down. Therefore, we must increase the accuracy rate higher before applying the filters.

6 CONCLUSION

We devised a method to classify reviews by using features added by reviewers and we applied the machine learning method SVM to this problem. This work is a preliminary one, and we made a comparison of two data sets whose atomic units are different. Based on this result, we are planning to make an extensive analysis of online customer reviews to construct the best filter set for a certain purpose, and make a better analysis to obtain an intriguing result with online customer reviews.

REFERENCES

[1] Iida R, Kobayashi N, Inui K, Matsumoto Y, Tateishi K and Fukushima T (2005), A Machine Learning-Based Method to Extract Attribute-Value Pairs for Opinion Mining, IPSJ SIG Technical Report, 2005-165-4, pp21-28, 2005.

[2] Hashimoto T, Murakami K, Inui T, Utsumi K and Ishikawa M (2008), Topic Extraction And Social Problem Detection Based On Document Clustring, vol.5, pp216-226, 2008.

[3] Ikeda D, Takamura H and Okumura M (2008), Semi-supervised Learning for Blog Classification, IPSJ SIG Technical Report, 2008-4, pp.59-66, 2008

[4] V. N. Vapnik , The Nature of Statistical Learning Theory, 2nd ed., Springer-Verlag, New York,2000.

[5] http://mecab.sourceforge.net/

The Seventeenth International Symposium on Artificial Life and Robotics 2012 (AROB 17th '12),
B-Con Plaza, Beppu, Oita, Japan, January 19-21, 2012

Measurement System for Metal-Oxide Gas Sensors

Hideo Araki[1], Sigeru Omatu[2]

[1] Osaka Institute of Technology, 1-79-1 Kitayama, Hirakata, Osaka 573-0196, Japan
[2] Osaka Institute of Technology, 5-16-1 Omiya, Asahi-ku, Osaka 535-8585, Japan
(araki@is.oit.ac.jp) (omatu@rsh.oit.ac.jp)

Abstract: Study on smell sensing and classification has been developed for a long time by many ways. Most of these have been focused on bad smells, when factors of bad smells were known chemically. Many gas sensors have been developed to detect specific chemicals. Our purpose is to make a new measurement system of smell gases and to apply it to classification of many gases. The proposed system has many sensors in a chamber and detects some chemicals at the same time. Smells data are transmitted to an A/D converter in a host PC which can be used to analyze data to classify the smells. The system must classify not only kinds of smells but also densities of them. In this paper, we develop the measurement system for multi-channel sensors made of metal-oxide semiconductors with power supply circuits.

Keywords: metal-oxide gas sensor, smell measurement, multi-channel sensors

1 INTRODUCTION

Study on smell sensing and classification has been developed for a long time by many ways [1]. The olfactory have many receptors in a nose and these receptors can transform the smells to electrical signals. Those signals are transported to our brain to classify the kinds of smells. Much research has been focused on bad smells. Many of these reports on smells were discussed about bad smells when factors of bad smells were known chemically. Many gases sensors were developed to detect these chemicals. These sensors can detect a few chemicals. However, smells consist of many chemicals, and one sensor cannot classify the smells.

Our final goal is to make an artificial olfactory system which is called an electronic nose (e-nose) based on the knowledge of the human olfactory system and a neural network algorithm. To make an efficient e-nose, we must measure a precise smell data. Thus, we develop a high efficient measurement system for smells. For this purpose, it is difficult to realize the high efficient measurement system in which only one smell sensor is attached. In this paper we propose a many sensors array system instead of one smell sensor in a chamber of smell. The system must classify not only kinds of smells but also densities of them.

In this paper, we develop the measurement system for multi-channel sensors made of metal-oxide semiconductors with power supply circuits which satisfy the following conditions:

1. Power supplies for sensors are independently.
2. Power supplies for a sense and a heater are independently.
3. It must be connected with variable register loads as outputs of smell sensors.

Independence of power supply for sensors is to make the sensitivity of the each sensor variable and to change various sensors.

Many gas sensors have heaters in the sensor units. For stable detection, these sensors should be heated a few hour or days. However, only for the heating, the measurement circuit for a sensor is not use and the power of sensor circuit can be switched off. Furthermore, when temperature of a gas is changed, sensed data should be revised. This power system can change the heater power independently, and the revise is to be little.

Because sensors of characters are different, the measurement data should be normalized. However, an activity level of sensor is different. To apply high sensitivity level of sensors, it is necessary to adjust sensor output signal levels.

The proposed system has these features, and they are effective to realize an e-nose system. In this paper, we will consider the multi-channel system, and then the problems to realize it. Next, we will try to tune sensitivity of a sensor for the system, and we will show an evaluation system.

2 PROPOSED SYSTEM

2.1 Over view

Figure 1 shows our proposed system over view, and Figure2 shows a block diagram of the system. The system has 12 metal-oxide gas sensors. They have a 4 contacts for sensor power in, sensor out, heater power in, and GND, and are connected to power supply circuit each. A pair of the contacts is for a heater, and the other pair is for a sensor. Requirement of electric powers for the sensors are different, and there powers are supplied independently. Furthermore, the sensors heater voltage should be stable[2], the power system contribute the require. In our proposed system, a sensor have a 2 power supply system. One is for a heater, and the other is for a sensor circuit. Our evaluation system have 12 sensors. Hence, our system have 24 power supply circuits. In experiments section, we will show the way of tuning for these power supplies for setting sensitivity of a sensor.

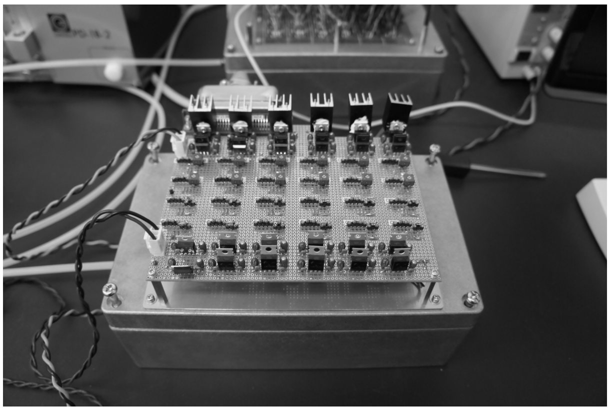

Fig. 1. evaluation system over view

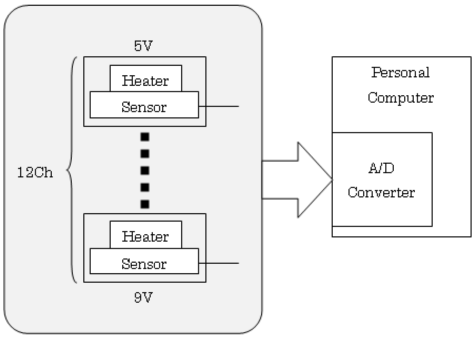

Fig. 2. system block diagram

3 EXPERIMENTS AND CONSIDERS

In this experiments, we evaluate the system using TGS 816 (Figaro Engineering) which is one of sensors in our system. TGS 816 is made for methane, propane and butane, and it can detect a ethanol [3]. An ethanol in a cup (3cm in diameter) and the sensor are in a chamber. Output signal of the sensor is observed by oscilloscope. Figure 3 shows a experiment circuit.

3.1 A transition of gas sens by heater voltage (Experiment 1)

At the first, we evaluate a transition by heater voltage changing. In this experiment, a voltage for VC is fixed, and a voltage for VH is changing. Figure 4 shows an output signal (VH=3V, VC=5V). We evaluate the experiment, we separate the waveform with a first section and a second section.

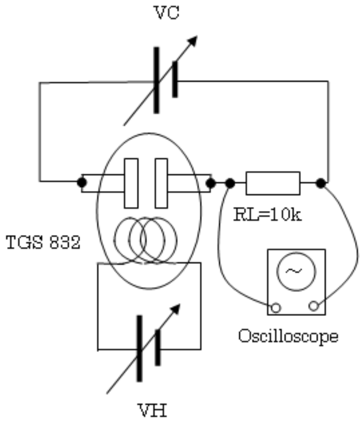

Fig. 3. Experiment circuit

The first section is started at about 38 second and finished at about 60 second in fig.4. The second section is started at about 60second and continue. Table 1 shows a calculation result from waveform. Rising rates of each sections are calculated by

$R = voltage/time$

By changing the heater voltage, the sensibility can be changed. The sensor output signals is different by changing VH. Furthermore, there are peaks of 1st section and 2nd section at different voltage. The result shows an ability to control a sensitivity of sensors. For example, we require a first response, we can select a VC at the peak on 1st section. When we require an result priority to an correct density, we can select a VC at the peak on 2nd section. The signal response in 1st section is too sensitive, and stable response appear in 2nd section. The sensitivity at the 1st section is shown on our next experiment result.

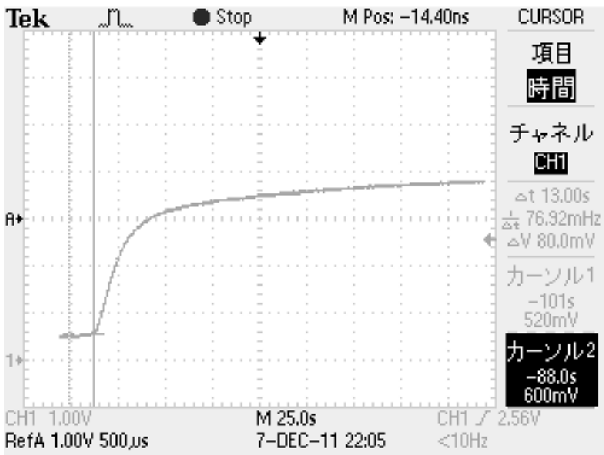

Fig. 4. sensor output signal waveform VH=3V VC=5V

Table 1. Experiment 1 result (VC=5V)

VH(V)	1st section rising rate (V/sec)	2nd section rising rate (V/sec)
2.0	0.013	0.0010
2.2	0.047	0.0021
2.4	0.072	0.0030
2.6	0.088	0.0024
2.8	0.084	0.0024
3.0	0.14	0.0024
3.5	0.30	0.0024
4.0	0.25	0.0048
4.5	0.092	0.0072
5.0	0.060	0.0056

Table 2. Experiment 2 result (VH=5V)

VC(V)	1st section rising rate (V/sec)	2nd section rising rate (V/sec)
5.0	0.026	0.0032
6.0	0.048	0.0052
7.0	0.078	0.0080
8.0	0.056	0.0090
9.0	0.052	0.0092
10.0	0.112	0.010
12.0	0.132	0.012
14.0	0.076	0.015
15.8	0.088	0.017

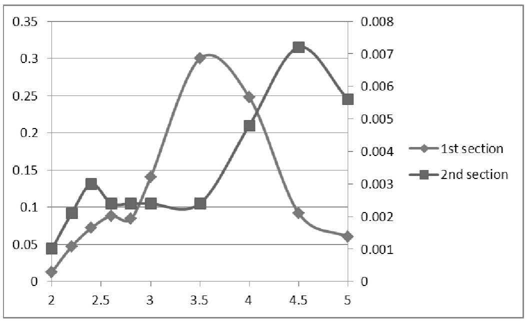

Fig. 5. Experiment 1 result (VC=5V)

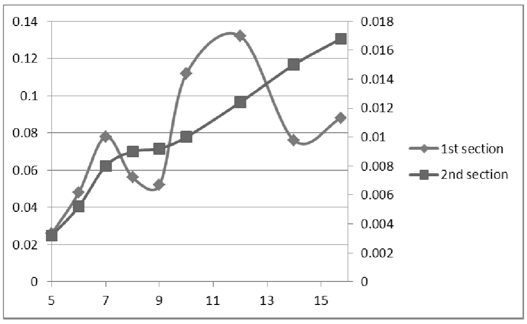

Fig. 6. Experiment 2 result (VH=5V)

3.2 A transition of gas sens by circuit voltage (Experiment 2)

Next experiments, we evaluate a transition by circuit voltage changing. In this experiment, a voltage for VH is fixed, and a voltage for VC is changing. Table 2 and Fig. 6 shows a experiment results. The result shows a fluctuation of 1st section response is large by changing VC. Moreover, we can see the 2nd section response is stable.

By comparing Table 1 and Table 2, the 2nd section rate is higher than experiment1. When we require the quick response on 2nd section, we set VC voltage to be high.

3.3 Evaluation system

Figure 7 shows sensors in our proposed system, and Table 3 is a list of the sensors. Power supply voltages of each sensors on the system were setting manually with check and try. Some sensors sense some gases. For example, methane will be sensed by TGS 816 and TGS 2611. Thus, the system detect balances of gases, and it is effective to realize a olfactory emulation. These sensors are connected through connectors, and any sensors could be changed other sensors. A chamber of the system is made by aluminum, and has a chemical durability. Signals of sensors are connected to A/D converter in a host PC, the signal voltage is matched by resisters on the system. The system has 2 power input inlets, one is for 5V power line and the other is for power line above 5V. The power line can be changed easily for experiments.

Figure 8 shows a graph of sampling data with 12Ch. This graph is illustrated by Microsoft excel from A/D converter sampling data. These 12 lines are 12 sensors output. They are detected data for ethanol. The result is shown that the sensors reaction are differed and could use an analyzing of gases.

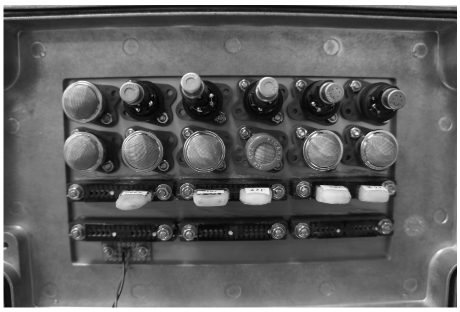

Fig. 7. sensors of evaluation system

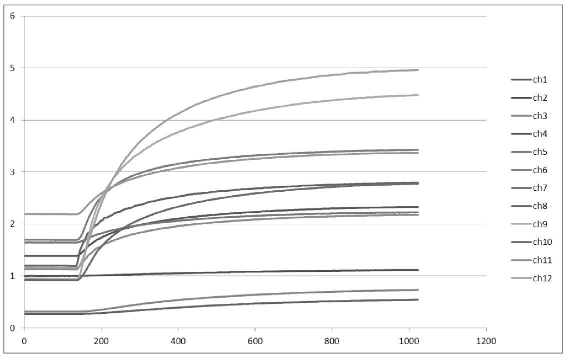

Fig. 8. Evaluation system output

Table 3. Sensors of the system

sensor	sense of gas	heater(V) VH	circuit(V) VC Max
TGS 816	methane propane butane	5	24
TGS 821	hydrogen	5	24
TGS 822	alcohol Solvent vapors	5	24
TGS 825	hydrogen sulfide	5	24
TGS 826	ammonia	5	5
TGS 830	fluorocarbons organochlorine	5	24
TGS 832	fluorocarbons organochlorine	5	24
TGS 2600	hydrogen alcohol	5	5
TGS 2602	alcohol ammonia VOC(volatile organic compounds	5	5
TGS 2610	propane butane	5	5
TGS 2611	methane LP gas	5	5
TGS 2620	alcohol Solvent vapors	5	5

4 CONCLUSION

In this paper, we have shown circuit design method for olfactory emulation system with multi-channel metal-oxide gas sensor. To use gas sensors whose electrical characters are different at the same time, it is necessary to tune the characters. We have realized a way to tune for sensitivity, and shown it. Furthermore, we have shown a evaluation system with 12Ch sensors.

The future research, to realize a automatic tuning, and to develop the system with intelligent signal processing.

Acknowledgement

This research has been supported by Grant-in-Aid for Challenging Exploratory Research No. 22656089 of Japan Society for the Promotion of Science and we wish to thank JSPS for their support.

REFERENCES

[1] Kiyoshi Tokou, The journal of IEICE. Vol.94 No.6,2011 pp.475-478

[2] Figaro Engineering General Information for TGS Sensors revised 03/05 http://www.figarosensor.com/products/common

[3] Figaro Engineering Data Sheet TGS 816 http://www.figaro.co.jp/data/pdf/20091110105219_25.pdf

Smell Classification by Using Metal Oxide Gas Sensors

Sigeru Omatu[+] and Hideo Araki[++]
[+]Osaka Institute of Technology, Asahi-ku, Osaka 535-8585, Japan
: omatu@rsh.oit.ac.jp
[++] Osaka Institute of Technology, Hirakata, Osaka, 573-0196, Japan
araki@is.oit.ac.jp

Abastract

In this paper, a reliable electronic nose (EN) system designed from the combination of various metal oxide gas sensors (MOGS) is applied to detect the early stage of fire from various sources. The time series signals of the same source of fire in every repetition data are highly correlated and each source of fire has a unique pattern of time series data. Therefore, the error back propagation (BP) method can classify the tested smell with 99.6% of correct classification by using only a single training data from each source of fire. The results of the k-means algorithms can be achieved 98.3% of correct classification which also show the high ability of the EN to detect the early stage of fire from various sources accurately.

1. Introduction

Every year the damage from the household fire disaster brings about not only severe loss to property assets, but also physical and psychological injuries of the people. Although most of the residences have installed the fire detectors system such as smoke detectors, those devices cannot detect the early stage of fire since their warning signals are triggered by the high smoke density or the high air temperature. In this paper, the reliability of a new electronic nose (EN) system developed from various metal oxide gas sensors (MOGSs) to specify the smell from various sources of fire is presented.

Jame A. Milke [1] has proved that two kinds of MOGSs have the ability to classify several sources of fire more precisely than conventional smoke detector. However, his results can be achieved only 85% of correct classification. In this paper, a new EN that has been successfully applied to classify not only the same smell from different brands, but also the same smell at different concentration levels [2] is applied to measure smells from various sources of fire such as household burning materials, cooking smells, the leakage from the liquid petroleum gas (LPG). The time series signals of the MOGSs from the beginning to the time until the MOGSs are fully absorbed the smell from each source of fire are recorded and analyzed by the error back propagation (BP) neural networks and the k-means algorithms. The average classification rate of 99.6% can be achieved by using the BP method with only a single training data from each source of fire. The results from the k-means algorithm can be achieved 98.3% of correct classification that also confirms the reliability of this new device to be able to detect various sources of fire in the early stage much better than the results of Jame A. Mike [1].

2. Metal Oxide Gas Sensors for EN

A commercial MOGS has been developed widely for more than thirty years.

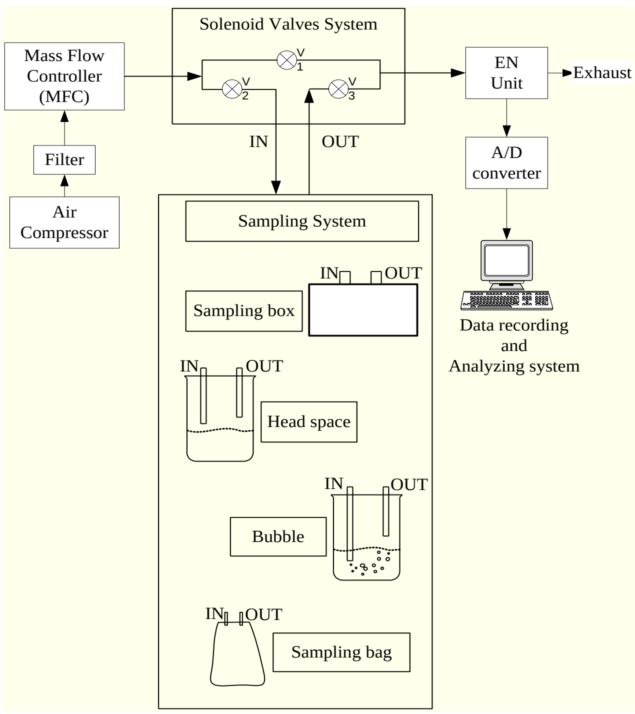

Fig. 1 Schematic diagram of the electronic nose system.

Generally, it is designed to detect some specific smell in electrical appliances such as an air purifier, a breath alcohol checker, and so on. Each type of MOGS has its own characteristics to response to different gases. When combining many MOGSs together, the ability to detect the smell is increased. An EN system shown in Fig. 1 has been developed based on the concept of human olfactory system by using the combination of MOGSs from FIS Inc. listed in Table I as the olfactory receptors in the human nose. The MOGSs unit is combined with the air flow system to flow the air and the tested smell into the MOGSs unit. The data logger converts the analog signals to digital signals and stores them in the data recording system before being analyzed by multivariate analytical methods, such as the BP method and the k-means algorithms.

The main part of the MOGS is the metal oxide element on the surface of the sensor. When this element is heated at a certain high temperature, the oxygen is absorbed on the crystal surface with the negative charge. The reaction between the negative charge of the metal oxide surface and deoxidizing gas makes the resistance of the sensor vary as the partial pressure of oxygen changes [3]. Based on this characteristic, we can measure the total voltage changes during the sensors absorbing the tested odor.

Table I List of MOGSs from the FIS Inc.

Sensor Model	Main Detection Gas
SP-53	Ammonia, Ethanol
SP-MW0	Alcohol, Hydrogen
SP-32	Alcohol
SP-42A	Freon
SP-31	Hydrocarbon
SP-19	Hydrogen
SP-11	Methane, Hydrocarbon
SP-MW1	Cooking vapor

Since the MOGS is sensitive to the temperature and the humidity, the MOGSs unit is put in a small chamber that has a heating system to increase the air temperature during winter season. The heating unit can also decrease the air humidity in the chamber. The clean water is manually sprayed into the chamber when the humidity drops lower than the control level. In this experiment the temperature in the chamber is kept between 20-30°C and the humidity is kept between 30-40%RH. The tested smell is sucked to mix with the fresh air before passing to the MOGSs unit. The distance from the tested smell to the MOGSs unit is approximately 1.5 m.

3. Experimental Data Collection

The smell from twelve sources of fire listed in Table II are measured by the EN system explained in previous section. Each source of fire has been tested with forty repetition data measured in different days in order to check the repeatability response of the MOGSs to the same smell.

For each data, the voltage signal of the normal air is measured every second for one minute and its average value, $\bar{v}_{air}$, is used as an air reference point. After that, the voltage signals of the sensors when absorbing tested smell, $v_{smell,t}$, are collected every two minutes for each smell sample. Finally, the total change in signals at each period, $V_{smell,t}$, is calculated by

$$V_{smell,t} = v_{smell,t} - \bar{v}_{air}$$

where t is the time from 1 to 120s.

After testing one smell the MOGSs need to be cleaned by removing the tested smell and supplying only the fresh air until the MOGSs return to stable point before testing the new sample. This process is just like the human nose which need to breath the fresh air before able to recognize the new smell accurately. Some time series data from the experiment in Fig.2 show that all smells approach the saturation stages within the measuring periods. The signals from the same source of fire in every repetition data are similar in most data sources. The results using the BP method and the k-means algorithm to analyze the time series data from each source of fire every two seconds and the average signals during the saturation stages(time 100-120s) are discussed in Section V.

Table II List of Burning Materials in the Experiment

Sources of fire	Abbreviation
Steam from boiling water	Steam
Burning joss stick	Joss
Burning mosquito coil	Mos
Aroma oil	Aroma
Aroma candle	Candle
Flame from liquid petroleum gas(LPG)	Flame
Leakage of LPG	LPG
Steam from Japanese soup called "oden"	Oden
Boiling vegetable oil	Oil
Toasted bread	Toast
Burning paper	Paper
Burning wood	Wood

4 Correlation of the Experimental Data

Before classifying each source of data, the correlation of each data source is investigated by using the similarity index (SI) and the principal components analysis (PCA).

4.1. similarity index

In the statistical application, the correlation value developed mainly by Karl Pearson is widely used to find the relationship between two random variables. In this paper, we call the correlation value as a similarity index

(SI). The SI value varies from -1 to 1. Two random variables with a SI of either 1 or 1 are highly correlated because knowledge of one provides precise knowledge of the other. However, the SI provides information only about linear relationships between random variables. Random variables could have a nonlinear relationship but still have a SI close to 0 [4]. Therefore, we make an assumption on this application that each data pattern has nearly linear relationship to the other data patterns. The SI value between two data is calculated by

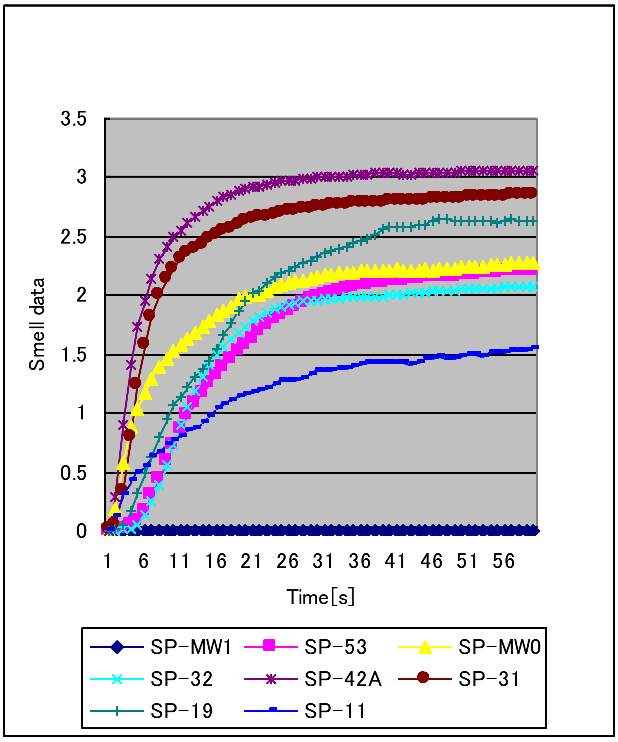

Fig.2 Time series data from some sources of fire in the experiment.

$$r_{xy} = \frac{\sum_{i=1}^{n} x_i y_i - n\bar{x}\bar{y}}{\sqrt{(\sum_{i=1}^{n} x_i^2 - \bar{x}^2)(\sum_{i=1}^{n} y_i^2 - \bar{y}^2)}}$$

where r_{xy} is the SI value, x and y are the comparing data, $\bar{x} = \frac{1}{n}\sum_{i=1}^{n} x_i$, $\bar{y} = \frac{1}{n}\sum_{i=1}^{n} y_i$, and n is the size of each data which equals 480 (60 periodsx8 sensors).

By using the SI to find the relationship between the repetition data of each data source, we found that all data sources except the paper and the wood have high average SI values above 0.99. During the experiment, the paper and the wood have inconsistent burning rates, therefore the signals from the repetition data of these sources are more fluctuated than the other sources that have better consistent burning rate.

4.2 principal components analysis

In this paper, the well known PCA is applied to analyze two cases of the experimental data. The full time series data case uses the data signals every two seconds, but the saturation stage data case uses only the average data from time 100 to 120s for analyzing.

The plots of two main components are shown in Fig.3. The distribution of the paper and the wood burning smell are more scattered than the other kinds of smells especially in the case of saturation stage data. Most of the tested data are separated into their own clusters with some overlap zones between different data source.

5. Experimental Results and Discussion

5.1 experimental result

Two case of data are analyzed by the BP method and k-means algorithm. The full time series data (TSD) case uses the data from all MOGSs every two seconds as the input data. The saturation stage data (SSD) case uses only the average value from time 100 to120s of all sensors as the input data.

The BP structure contains three layers. The input layer of the TSD case, and the SSD case consists of four hundred eighty nodes (8 sensors x 60 periods), and eight nodes(average signal from 8 sensors), respectively. For the hidden layer, we have tried with several values and the size that gives a good accuracy and a reasonable training time for both data cases is forty nodes. The output layer contains twelve nodes, each node represents one data source. The learning rate, the momentum rate, and the minimum mean square error (MSE) during the training period are set by trial and error method to 0.1, 0.001, and 0.0003, respectively.

Based on the information during investigating the correlation of the data, most data sources are highly correlated to their repetition data with high SI values. Therefore, only one data that has the highest average SI value to the other repetition data from each sources of fire are used as the training data for the BP and the rest of the data are used as the test data. We assume that a pattern is classified correctly if (output $\leq$ 0.7 and target=1) or (output $\leq$ 0.3 and target =0). For the k-means algorithm, the training data of the BP method are used as the initialize data and then assigns the data patterns to the nearest cluster center by calculating the Euclidean distance. After that, the new cluster center is recalculated. The process continues until the position of the cluster center is not changed. The final results of this experiment are shown in Table III.

The results using the TSD from both the BP method and the k-means algorithm are sufficiently effective. The data signals from the MOGSs are affected by many factors, such as the sampling condition, the inconsistency burning rate, the fluctuation from the standard air, and so on. Therefore, the saturation stages of the data are varied by those factors. By including the signal before approaching the saturation stage, the accuracy to classify all smell is increased.

5.2 Discussion

Although the distribution of PCA shown in Fig. 3 cannot clearly separate similar smell such as the aroma oil and the aroma candle, the BP method and the k-means algorithms are able to classify them perfectly as shown in Table III. The results of TSD using the BP method have only two incorrect classified data. These two data are not misclassified as the other smells. Only the output values of their paper node are not high enough to classify them as the paper. The output values of these two data on the paper node are only 0.4951, and 0.4799, respectively and the output of the others output nodes are nearly 0. The results are much better than the results from [1] which used two kinds of MOGSs to classify several sources of fire into three fire condition levels, flaming, smoldering, and nuisance, with only 85% of correct classification. The smoke density of the tested data is not high enough to trigger the alarm of the smoke detector. In case of unusual burning smells in the residences such as the wood burning, flaming from the LPG, or the leakage LPG, it is necessary to have a proper device to detect these sources before unable to stop the fire. We can conclude that the new EN system shown in this paper is a proper device for this application.

6. Conclusions

We have proposed a new EN system designed from various kinds of MOGSs. The EN has the ability to identify various sources of fire in the early stage with more than 99% of accuracy by using only a single training data in the BP case. The results from the k-means algorithm are also able to predict the sources of fire with more than 98% of accuracy. It can be concluded that the EN is suitable for detecting the early stage of fire.

References

[1] Jame A.Mike, "Applicaiton of Neural Networks for Discriminating Fire Detectors", International Conference on Automatic Fire Detection, AUBE'95, 10th, Duisburg, Germany, pp.213-222, April 4-6, 1995.

[2] Bancha Charumporn, Michifumi Yoshioka, Toru Fujinaka, and SigeruOmatu, "An Electronic Nose System Using Back Propagation Neural Networks with a Centroid Training Data Set", proceeding of the Eight International Symposium on Artificial Life and Robotics, Japan, pp.605-608, January 24-26, 2003

[3] General Information for TGS sensors, Figaro Engineering, available at www.figarosensor.com/products/general.pdf. M. Tanaka, "Modeling of Mixtures of Principal Component Analysis Model with Genetic Algorithm," Proc. 31st Int'l Symposium on Stochastic Systems Theory and Its Applications, pp. 157-162, Yokohama, Japan, 1999.

[4] William L. Carlson and Betty Thorne, Applied Statistical Methods, Prentice Hall International, 1997

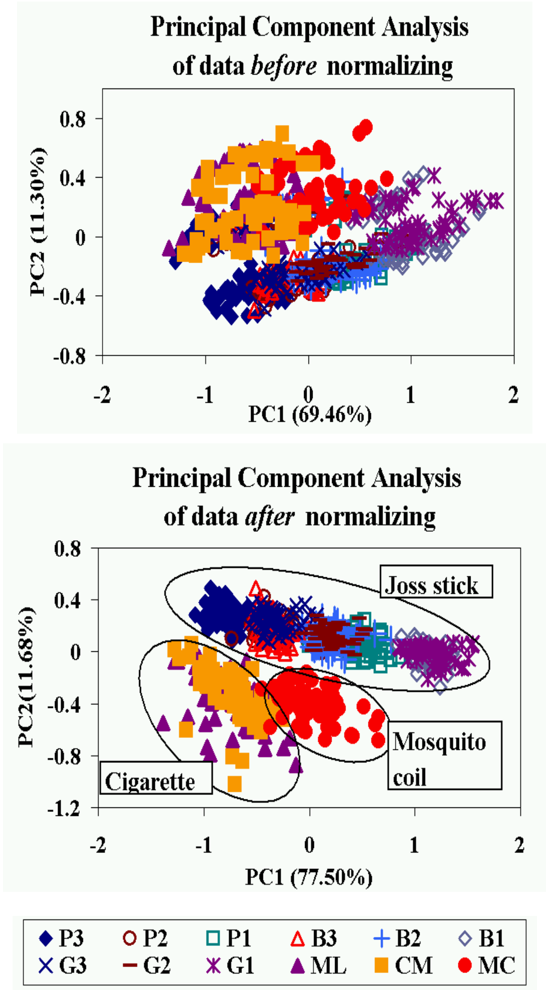

Fig.3. Two main components of the experimental data using the PCA.

Table III Experimental Results

Sources	TSD				SSD			
	BP		k-means					
	True	%	True	%	True	%	True	%
Steam	39/39	100	40/40	100	38/39	97	39/40	98
Joss	39/39	100	40/40	100	39/39	100	40/40	100
Mos	39/39	100	40/40	100	39/39	100	40/40	100
Aroma	39/39	100	40/40	100	39/39	100	40/40	100
Candle	39/39	100	40/40	100	39/39	100	40/40	100
Flame	39/39	100	40/40	100	39/39	100	40/40	100
LPG	39/39	100	40/40	100	39/39	100	40/40	100
Oden	39/39	100	40/40	100	39/39	100	40/40	100
Oil	39/39	100	40/40	100	39/39	100	40/40	100
Toast	39/39	100	40/40	100	38/39	97	37/40	93
Paper	39/39	100	40/40	100	38/39	97	40/40	100
Wood	38/39	95	35/40	88	31/39	80	28/40	70
	39/39	100	37/40	93	32/39	82	28/40	70
Average		99		98		96		94

The Seventeenth International Symposium on Artificial Life and Robotics 2012 (AROB 17th '12),
B-Con Plaza, Beppu, Oita, Japan, January 19-21, 2012

Measurement System for Quarts Crystal Microbalance Sensors

Hideo Araki[1], Sigeru Omatu[2]

[1] Osaka Institute of Technology, 1-79-1 Kitayama, Hirakata, Osaka 573-0196, Japan
[2] Osaka Institute of Technology, 5-16-1 Omiya, Asahi-ku, Osaka 535-8585, Japan
(araki@is.oit.ac.jp) (omatu@rsh.oit.ac.jp)

Abstract: Human olfactory is examined for a long time and many ways. Olfactory is studied based on gas chromatography technology. These studies have used gas sensors made of metal-oxide semiconductors. The semiconductor-sensors can detect gases as difference of resistance by oxidation or reduction of surface on the sensor. Human olfactory is organized by about 2,000 receptors of smell, and many sensors are used to emulate by electric sensors. We consider to apply multi-channel QCM for these sensors, and build an evaluation system.

Keywords: Olfactory, Multi-Channel-QCM, Oscillator

1 INTRODUCTION

Human senses are examined for long term and many ways and the olfactory of human senses has been examined. Olfactory is like a sense of gas and air, and is studied based on gas chromatography technology. These studies used sensors to detect gases by semiconductors. The semiconductor-sensor detects a gas as difference of resistance by oxidation or reduction of the surface on a sensor. Human olfactory is organized by about 2,000 receptors of smell, and many sensors are used to make an electric sensor[1]. We consider to apply QCM(Quartz Crystal Microbalance) sensors as these sensors.

QCM gas sensors are able to detect a small alternate of a mass on the crystal. By change a gas of air, the mass will change and it can be detected of difference of a frequency by the crystal oscillator. In usual, QCM is applied for measuring absolute alternation of the mass. However for the QCM sensor, we measure relative and differences of the mass. Usually, one QCM composes an instrument to measure the smell absolutely and correctly. In our system, 24 QCM sensors are attached in an instrument to detect differences of some gas in an air simultaneously. These QCM sensors consists of crystals which are coated in different chemical characteristics.

We realize the system to evaluate our proposal method. However, there are a lot of problem to build a stable system. When oscillators are built in a small area, they interfere each other. The interference disturbs oscillation frequencies and makes jams. QCM sensor needs a fine oscillation to detect a difference of an oscillation signal. However, the jams affects the precise measurement of oscillation signals. To realize our propose system, we take measures to the anti-jammers. These measures are as follows:

1. Measures to power supply and power line
2. Measures to signal lines from oscillator to voltage converter
3. Measures to signal lines from voltage converter to FPGA
4. FPGA logics for anti-jammers.

In this paper, we express these measures to realize an olfactory emulation system with QCM.

2 PROPOSED SYSTEM

2.1 Over view

Figures 1 and 2 are shown the block diagram and the proposed evaluation system.

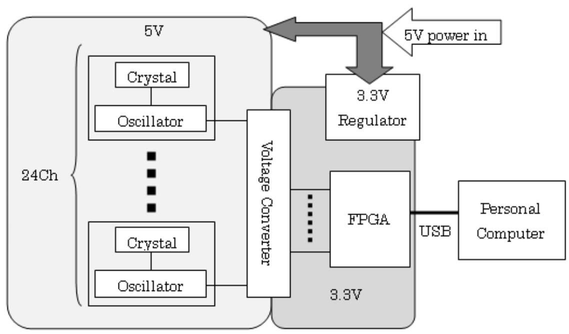

Fig. 1. Proposed system diagram

In Fig.1, the crystal oscillators are sensors of gas. These are connected to an oscillator circuit, and generate stable each pulses. Generated pulses are converted from 3.3V-level to 5V level in a level converter unit, and connected to the FPGA. In the FPGA, these pulses are used as clock signals for counters. These counters have 32bit length registers and count the number of the pulses for one second. The signal for one second is generated in an FPGA from 48MHz clock signal on the FPGA unit. The numbers of pulses are trans-

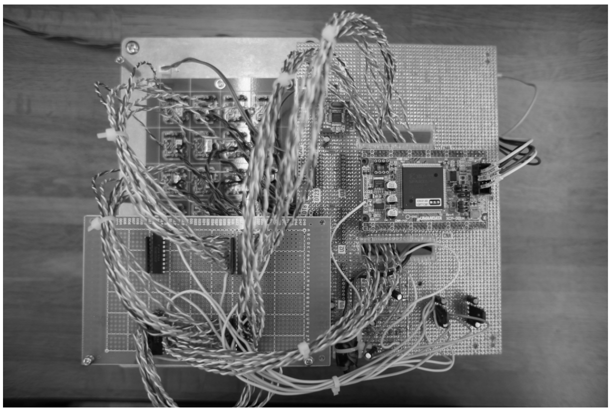

Fig. 2. Evaluation system

mitted to a host personal computer by the FPGA through USB(Universal Serial Bus), and are analyzed on it.

We consider to build a stable measurement system, and the crystals are not processed on their surface of QCM sensors on the evaluation system. Thus, we can get the pulses accurately. Figure 3 shows the crystals for an evaluation of the system.

The crystals are attached to each oscillation circuits which are built with a single inverter as like 74HCU04, CMOS inverter. An oscillator circuit schematic is in Fig. 4.

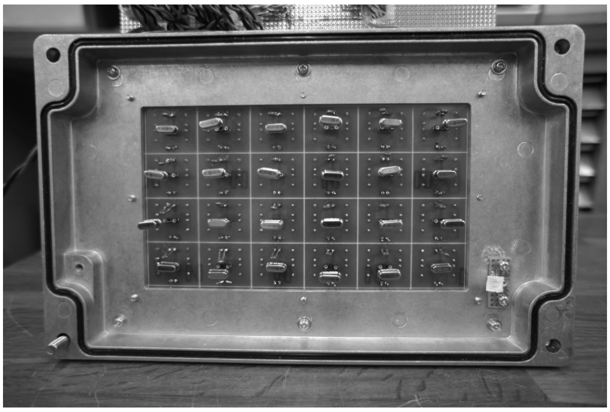

Fig. 3. Crystals for evaluating sensor system

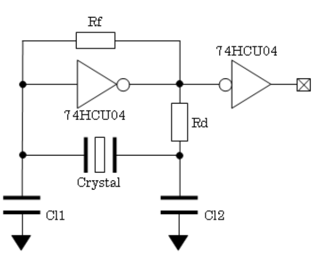

Fig. 4. An oscillator circuit for QCM sensor

2.2 Measure to power supply and power line

In our system, there are 4 power lines which are 5V, 3.3V, 1.2V. The system requires only 5V power. The voltages of 3.3V and 1.2V are generated by regulator circuits in the system. 3.3V power is supplied to the FPGA unit and voltage converter unit. 5V power is supplied to the oscillator circuit. In a conventional digital system, 5V power is generated from AC (100V) line by switching regulator circuit. However, this power is too noisy for the system, our system has direct current stabilized power supplies with series regulator.

3.3V power is delivered to voltage converter and the FPGA unit. In the FPGA, there are counter logics and communication logics. These logics are operated by 48MHz clock signal and there is jamming noise by them on power line. Voltage converter circuit is driven the same power line, convert 24 signals are 20MHz pulse signals from 5Vp-p to 3.3Vp-p. For cutting off the noises each, 3.3V power line is separated to the FPGA line and the voltage converter line. These power lines have 3.3V regulators circuit of each. In this way, a noise which is generated by FPGA logic can be reduced of effect to an oscillator circuit. Furthermore, the power line system can increase signal channels.

2.3 Measures to signal lines from oscillator to voltage converter

The oscillation circuit output is 5Vp-p signal and FPGA input should be lower than 3.3Vp-p, so it is necessary to change the voltage levels. To change the levels, TC74VHC9541[2] is used. This device has following characters.

1. 5V tolerant input (with 3.3V power)
2. Schmitt trigger input
3. Fast speed
4. Power-down protection

5V tolerance input is necessary function for this system. Usual CMOS IC device can not endure higher voltage signal input than VCC, and the device will break down. Schmitt trigger input has dual threshold and hysteresis, and realizes improvement of immunity against cross-talk. On this system, crystals for sensors have natural frequency as about 20MHz, and the device throughput is important. Power-down protection is able to do power control independently in each oscillator circuit and voltage converter circuit.

Signal lines between oscillator circuit to voltage converter are should be treated for emission and immunity of reciprocal action between each lines. These signal lines are connected line with side by side, and these lines have influences on each. By cross-talk which is one of influence, the pulse-signals are transmitted to other lines and it makes jamming to accuracy measurement. Furthermore these signal emissions influence signal lines between voltage converter to FPGA. The emission is to be large when over-shoot or under-shoot of the lines are large. A transmission-line impedance to be low, the emission by the signal can be reduced. For that, the signal lines are terminated at voltage converter input by capacitors and resisters. Next, for build a robust signal lines for immunity, we considered connection ways for the signal lines. The signal lines are 24 channels, and these are connected independently and need large space when using fat lines. To realize a small system, we should use a thin and robust line. An coaxial line is too fat and too hard for bending as small curve. Thin sealed line as like for microphone are weak to emission and immunity. And we selected a twisted-pair line for computer network(Ethernet:100Bast-T). This network line has 4 pairs. We disassembled the line and used a each pair of lines. They are thin and soft, and match the our requirement. Furthermore we can select the line length easily and change the distance the sensor unit and voltage converter unit. We are considering to apply our system for detection dog, the separation of these unit are advantage for the apply.

2.4 Measures to signal lines from voltage converter to FPGA

Converted signals to 3.3Vp-p are transmitted to FPGA input from voltage converter. These signal lines have same problems with signal lines from oscillator to voltage converter. Moreover the lines are weaker than lines from oscillator to voltage converter because of low voltage compared with them. These lines should be treated for immunity from other lines. The lines are connected by twist-pair cable, and are pulled down as 330ohm each. By keeping lower impedance than other lines, the lines immunity is robustly. However to connect the lines to ground line by capacitor, the signal is damped severely, and it makes more transmit error.

2.5 FPGA logics for anti-jammer

FPGA counts the signal pulse from oscillator for one second. the one second signal is generated from 48MHz clock on the FPGA unit. Oscillator signals are connected the FPGA as counters clock signal. These counters are reset by one second signal. Oscillator frequency fluctuation is appeared as counter number fluctuation. The number is transmitted to host PC through USB. When extreme noise influences to signals from oscillator to FPGA, the number will change on a grand scale. Usually in this system the number will be changed among about 1 to 10 for one second. The noise can be detected and canceled by a digital filter of the host PC.

3 EXPERIMENTS AND CONSIDERS

We build the system to evaluate these characters, and do the experiment using the system. In the experiment section, we show results for measured signal lines. Then we compared noise levels and jitters by wires and terminators, and evaluate differences of them. Figure 5 shows a circuit for the experiment. In this figure, 74HCU04 is a part of oscillator circuit for QCM. Other oscillators are oscillation units which are TOYOCOM TCO711A and TCO711A compatible MC0-1510A. Measurements are about each combinations of sealed wires and twisted pair wires. Measurement result is shown in table 1. In this table, QCM is a 74HCU04 output, and it is an equivalence of QCM sensor output. OSC1 and OSC2 are other oscillation unit's status of wirings and outputs. Fluctuation is a voltage at stable voltage region. Jitter is a voltage at voltage transition region.

Figure 6 is shown the measurement by an oscilloscope of condition No.1. In the experiments, this wave is a reference wave of best condition. Condition of No.4 is a changed line of QCM from sealed line to twisted pair line. However, other conditions are the same as No.1. In the conditions of No.1 and No.4, there are no differences of measurements. When other oscillator is no power, we can see there are not noise and jitters.

In conditions No.2 and 3, QCM, OSC1, and OSC2 are connected to 74VHC9541(Level converter) with sealed lines. Figure 7 showed a waveform in condition NO.3. There are

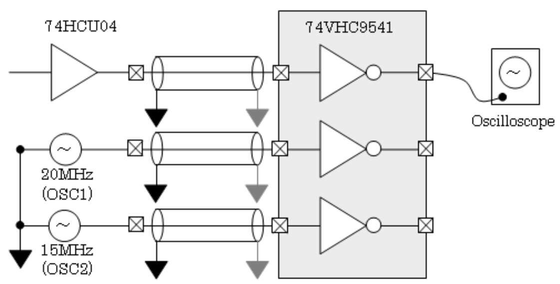

Fig. 5. Experiment circuit

Table 1. Measurements of experiments

combination				voltage measurement		
No.	QCM	OSC1	OSC2	fluctuations (mVp-p)	jitter (ns)	figure
1	S.L.	no	no	200	0.5	fig.6
2	S.L.	no	S.L.	680	2.0	
3	S.L.	S.L.	S.L.	720	2.0	fig.7
4	T.P.	no	no	200	0.5	
5	T.P.	S.L.	S.L.	680	2.6	
6	T.P.	T.P.	T.P.	680	1.4	Fig.8

S.L.: sealed line T.P.: twisted pair no: no signal

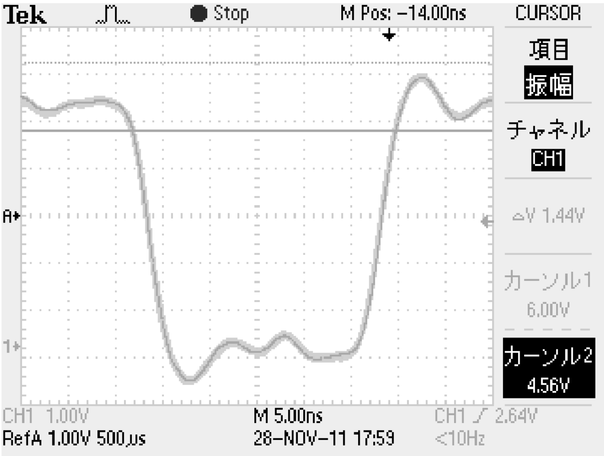

Fig. 6. Wave form of condition No.1

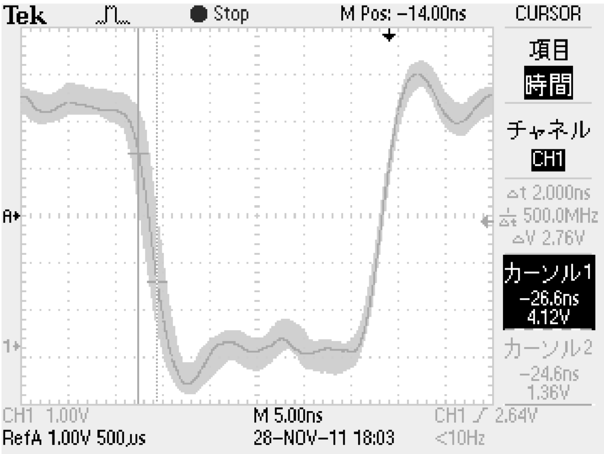

Fig. 7. Wave form of condition No.3

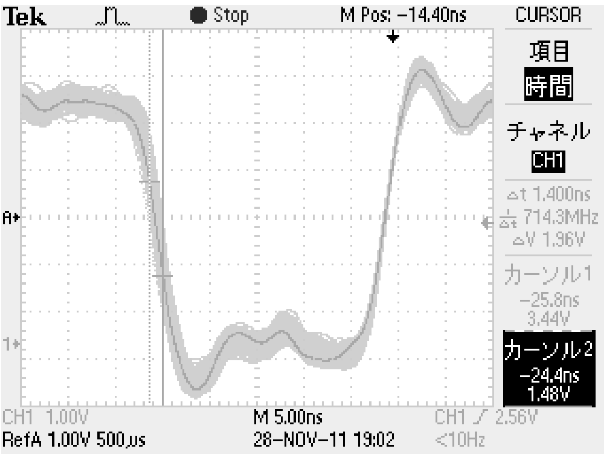

Fig. 8. Wave form of condition No.6

larger noises and jitters than No.1 results. Furthermore, there is no difference of jitters in condition No.2 and 3. The result shows an emission by OSC1 and OSC2 are strong in this condition.

In condition No.5, only QCM is connected by twisted pair wire. OSC1 and OSC2 are connected by sealed line wires. In this result, jitters are large and, fluctuations are the same as No.2 and 3. This result shows that strength of immunity by twisted pair line for QCM is not enough for emissions by OSC1 and OSC2.

Figure 8 is shown a result of condition No.6. In this condition, QCM, OSC1 and OSC2 are connected to 74VHC945 by twisted pair wires. This wave form shows that jitters are smaller than conditions No.2 or No.3. The result shows that an emission of OSC1 and OSC2 are reduced by the wires, and the twisted pair wires are effective for it.

From these experiments, by applying a twisted pare wire for the system, jitters become low. Ratio of jitter for the QCM output frequency is as follows:

$$(2.0 - 1.4)/50 = 0.012$$

$$QCMclock : 20MHz = 50nsec$$

The experiments show that the ratio is improved by 1.2%.

4 CONSOLUSION

In this paper, we show a building method for multi-channel QCM system. The multi-channel QCM can be realized by a small olfactory emulation system. Multi-channel QCM system requires a number of signal lines as channel numbers, and the system should use a thin wire to realize a compact system. Furthermore, jitters for these signals should be low for accuracy measurement. We considered wires to fit these requirements, and showed measured data with the wires. We will make a more flexible olfactory system by changing a number of channels and a stand-alone olfactory system without host PC.

Acknowledgement

This research has been supported by Grant-in-Aid for Challenging Exploratory Research No. 22656089 of Japan Society for the Promotion of Science and we wish to thank JSPS for their support.

REFERENCES

[1] Kiyoshi Tokou, The journal of IEICE. Vol.94 No.6,2011 pp.475-478

[2] Toshiba Data Sheet TC74VHC9541P/FT/FK 2009-06-01

The Seventeenth International Symposium on Artificial Life and Robotics 2012 (AROB 17th '12),
B-Con Plaza, Beppu, Oita, Japan, January 19-21, 2012

Clasification of Mixed Smells by Using Neural Networks

Toru Fujinaka[1], Sigeru Omatu[2], and Hideo Araki[3]

[1] Hiroshima University, Higashihiroshima, Hiroshima 870-0397, Japan
[2] Osaka Institute of Technology, Asahi-ku, Osaka 599-8531, Japan
[3] Osaka Institute of Technology, Hirakata, Osaka 573-0196, Japan
(Tel: 81-6-6954-4310, Fax: 81-6-6957-2136)
(omatu@rsh.oit.ac.jp)

Abstract: Compared with metal oxide semiconductor gas sensors, quarts crystal microbalance (QCM) sensors are sensitive for odors. Using an array of QCM sensors, we measure mixed odors and classify them into an original odor class before mixing based on neural networks. For simplicity, we consider the case where two kinds of odor are mixed since more than two become too complex to analize the classification results. We have used eight sensors and four kinds of odor are used as the original ones. The neural network used here is a conventional layered neural network. The classification is acceptable although the perfect classification could not been achieved.

Keywords: neural networks, separation of mixed gasses, odor classification

1 INTRODUCTION

Over the last decade, odor sensing systems (so-called electronic nose (EN) systems) have undergone important development from a technical and commercial point of view. The EN refers to the capability of reproducing human sense of smell using sensor arrays and pattern recognition systems [1].

We have presented a type of EN system to classify the various odors under the various densities of odors based on a competitive neural network by using the learning vector quantization (LVQ) method in [6]. The odor data were measured by an odor sensor array made of metal oxide gas (MOG) sensors. We used fourteen MOG sensors of Figaro Engineering Inc. [3] in Japan. We considered two types of data for classification in the experiment. The first type was a set of four kinds of teas and the second one was a set of five kinds of coffees of similar properties. The classification results of teas and coffees were about 96% and about 89%, respectively, which was much better than the results in [5].

In this paper, we will consider the classification of mixed odors based on the sensing data by using quarts crystal microbalance (QCM) sensors. QCM sensors are sensitive to odors and we can measure the odor data precisely. Using many QCM sensors, we will try to separate the odors being mixed with two kinds of odor into the original odors based on the neural network classifier.

2 PRINCIPLE OF QCM SENSORS

The QCM has been well-known to provide a very sensitive mass-measuring device in nanogram levels, since the resonance frequency will change sensitively upon the deposition of a given mass on the electrodes. Synthetic polymer-coated QCMs have been studied as sensors for various gasses since QCM coated with a sensing membrane works as a chemical sensor. The QCM sensors are made by covering the surface with several kinds of very thin membrane with about 1 μm as shown in Fig. 1.

Since the QCM oscillates with a specific frequency depending on the cross section corresponding to three axis of the crystal, the frequency will change according to the deviation of the weight due to the adsorbed odor molecular (odorant). The membrane coated on QCM has selective adsorption rate for a molecule and the frequency deviation show the existence of odorants and their densities. Odorants and membrane are in tight relation while it is not so clear whose materials could be adsorbed so much.

In this paper we have used the following materials as shown in Table **??**. The reason why fluorine compounds are used here is that the compounds repel water such that pure odorant molecules could be adsorbed on the surface of the membrane. To increase the amount of odorants to be adsorbed it is important to iron the thickness of the membrane. In Table **??**, we have tried to control the density of the solute in the organic solvent. The basic approach used here is a sol-gel method. The sol-gel process is a wet-chemical technique used for the fabrication of both glassy and ceramic materials. In this process, the sol (or solution) evolves gradually towards the formation of a gel-like network containing both a liquid phase and a solid phase. Typical precursors are metal alkoxides and metal chlorides, which undergo hydrolysis and polycondensation reactions to form a colloid. The basic structure or morphology of the solid phase can range anywhere from discrete colloidal particles to continuous chain-like polymer networks.

Table 1. Chemical materials used as the membrane

	materials of membrane
1	Triethoxymethylsilane, ethanol(4ml) dilute nitric acid, ethylacrylate(.043ml)
2	Triethoxymethylsilane, water(3.13ml), ethanol(4ml) dilute nitric acid, ethylacrylate(.043ml)
3	Triethoxymethylsilane, water(3.13ml), ethanol(4ml) water, dilute nitric acid, ethylacrylate(.014ml)
4	Triethoxymethylsilane, water(3.13ml), ethanol(4ml) dilute nitric acid, ethylacrylate(.015ml)
5	Triethoxymethylsilane, water(.30ml), ethanol(4ml) dilute nitric acid, ethylacrylate(.043ml)
6	Triethoxymethylsilane, water(.05ml), ethanol(3.0ml) dilute nitric acid, ethylacrylate(.043ml)
7	Triethoxymethylsilane, water(.30ml), ethanol(3.2ml) dilute nitric acid, ethylacrylate(.043ml)
8	no membrane

Table 2. Kinds of odors measured in this experimet.

Symbols	Kind of odors
A	Ethanol
B	Water
C	Methyl-salicylate
D	Triethylamine

3 ODOR SENSING SYSTEM

Generally, it is designed to detect some specific odor in electrical appliances such as an air purifier, a breath alcohol checker, and so on. Each of QCM membranes has its own characteristics in the response to different odors. When combining many QCM sensors together, the ability to detect the odor is increased. An EN system shown in Fig. 2 has been developed, based on the concept of human olfactory system. The combination of QCM sensors, listed in Table **??**, are used as the olfactory receptors in the human nose.

The odors used here are shown in Table 2. Note that the chemical properties of these odors are very similar and it has been difficult to separate them based on the measurement data by using MOGS sensors.

4 CLASSIFICATION METHOD OF ODOR DATA

In order to classify the odors we adopt a three-layered neural network based on the error back-propergation method as shown in Fig. 3.

The error back-propagation algorithm which is based on the gradient method is given by the following steps.

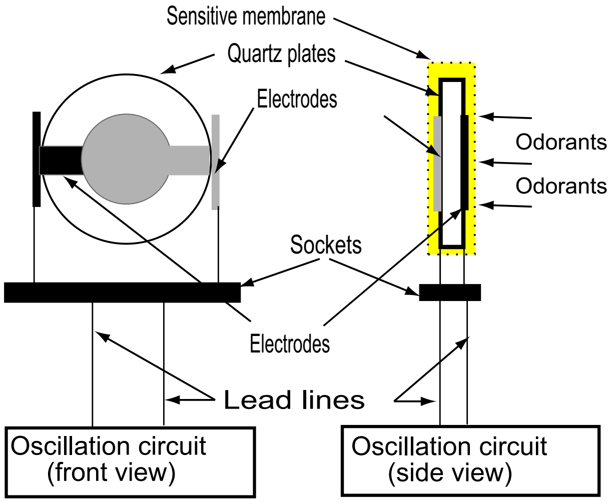

Fig. 1. Principle of QCM. The odorants attached on snsitive mambrane will make the weight of quartz plane. Thus, the original frequency of the crystal occilation will become smaller according to the density of odorants.

Step 1. Set the initial values of $w_{ji}, w_{kj}, \theta_j, \theta_k$,and $\eta (> 0)$.
Step 2. Specify the desired values of the output $d_k, k = 1, 2, \dots, K$ correspondint to the input data $x_i, i = 1, 2, \dots, I$ in the input layer.
Step 3. Calculate the outputs of the neurons in the hidden layer and output layer by

$$\begin{aligned} \text{net}_j &= \sum_{i=1}^{I} w_{ji} x_i - \theta_j, O_j = f(\text{net}_j), f(x) = \frac{1}{1+e^{-x}} \\ \text{net}_k &= \sum_{j=1}^{J} w_{kj} O_j - \theta_k, O_k = f(\text{net}_k). \end{aligned}$$

Step 4. Calculate the error e_n and generalised errors by

$$\begin{aligned} e_k &= d_k - O_k, \delta_k = e_k O_k (1 - O_k) \\ \delta_j &= \sum_{k=1}^{K} \delta_k w_{kj} O_j (1 - O_j). \end{aligned}$$

Step 5. If e_k is sufficiently small for all k, END and otherwise

$$\begin{aligned} \Delta w_{kj} &= \eta O_j \delta_k, w_{kj} \Leftarrow w_{kj} + \Delta w_{kj} \\ \Delta w_{ji} &= \eta O_i \delta_j, w_{ji} \Leftarrow w_{ji} + \Delta w_{ji}. \end{aligned}$$

Step 6. Go to *Step* 3.

Using the above recursive procedure, we can train the odor data. The measurement data is an eight-dimensional vector which are obtained with eight sensors stated in Table **??**.

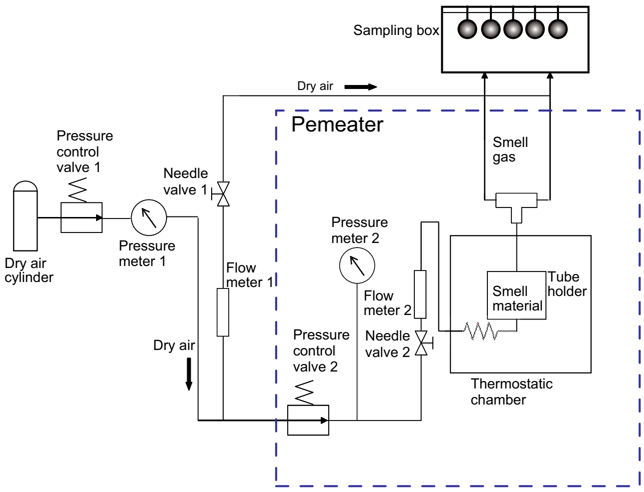

Fig. 2. Odor sensing systems. The air will be emitted from the dry air cylinder. Air flow is controlled by pressure control valves 1 and 2. By using the needle valve 2, more precise folow rate of the dry aircan be achieved and the thermostatic chamber in the pemeater can control the temperature of the dry air. Finally, the air is pull in the sampling box where the QCM sensors are attached on the ceiling of the box.

5 MEASUREMENT OF ODOR DATA

We have measured four types of odors as shown in Table 2. The sampling frequency is 1[Hz], the temperatures of odor gases are 24∼26 [$°C$], and the humidities of gases are 6∼8 [%]. To control the density of gases, we use the deffusion tubes. Odor data are measured for 600 [s]. They may include impulsive noises due to the typical phenomena of QCM sensors. To remove these impulsive noises we adopt a medean filter which replaces a value at a specific time by a median value among neighboring data around the specific time. In Fig. 4 we show the measurement data for the symbol A(ethanol) where the horizontal axis is the measurement time and the vertical axis is the frequency deviation from the standard value(9M[Hz]) after passing through a five-point medean filter.

6 TRAINING FOR CLASSIFICATION OF ODORS

In order to classify the feature vector, we allocate the desired output for the input feature vector where it is nine-dimensional vector as shown in Table 3since we have added the coefficient of variation to the usual feature vector to reduce the variations for odors. The training has been performed until the total error becomes less than or equal to .5 $\times 10^{-2}$ where η=.3.

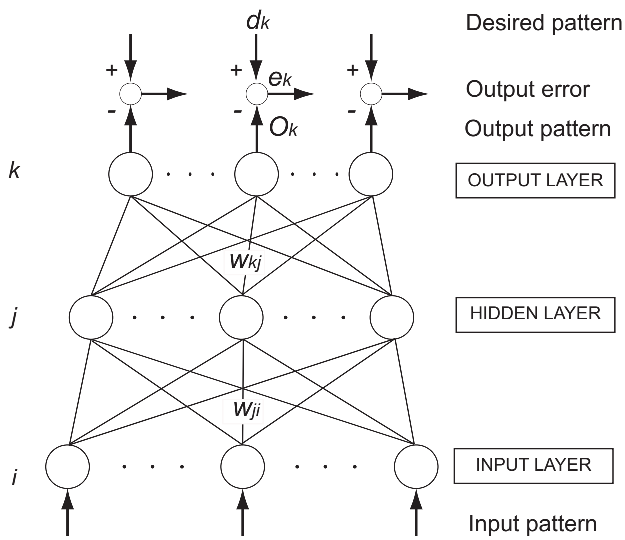

Fig. 3. Three layered neural network with the error back-propagation. The neural network consists of three layers, that is, an input layer i, a hidden layer j, and an output layer k. When the input data $x_i, i = 1, 2, \ldots, I$ are applied in the input layer, we can obtain the output O_k in the output layerwhich is compared with the desired value d_k which is assigned in advance. If the error $e_k = d_k - O_k$ occurs, then the weighting coefficients w_{ji}, w_{kj} are corrected such that the error becomes smaller based on the error back-propagation algorithm.

Table 3. Training data set for ethanol (A), water (B), methyl-salicylate (C), and triethylamine (D).

Symbols	Output A	Output B	Output C	Output D
A	1	0	0	0
B	0	1	0	0
C	0	0	1	0
D	0	0	0	1

7 TESTING FOR CLASSIFICATION OF ODORS

After training the data we have tested the other data sets such that two kinds of odors are mixed with the same rate. Then the classification results are shown in Table 4 where the underlined numerals dente the top case ahrere the maximum output values are achieved. The maximum values show one of the mixed odors. But some of them does not show the correct classification for the remaining odor. Thus, we have modefied the input features such that

$$z = x - 0.9y$$

where x is the feature, y denotes the top value of each row in Table 4, and z is new feature. Using the new feature vec-

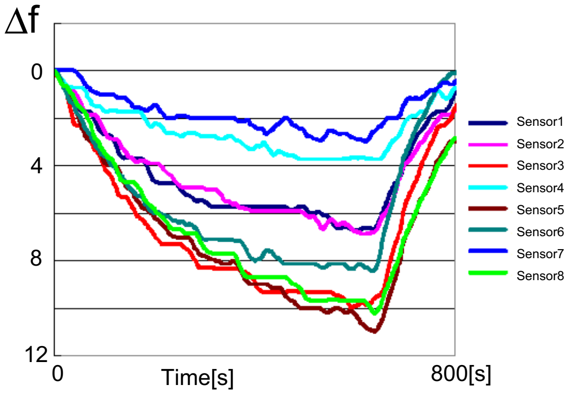

Fig. 4. Measurement data. Here, eight sensors are used and for six handred [s] the data were measured. The maximum value for each sensor among eight sensors is selected as a feature value for the sensor. Therefore, we have eight sensor values for an odor and they will be used for classification.

Table 4. Testing the mixed odors where the top and the second from the top are the classification results.

Symbols	Output A	Output B	Output C	Output D
A and B	.673	.322	.002	.001
B and C	.083	.696	.174	.001
C and D	.001	.004	.016	.992
D and A	.003	.003	.002	.995
A and C	.992	.006	.002	.000
B and D	.003	.003	.003	.995

tor, we have obtained the classification results as shown in Table 5. By changing the features according to the above rlation, better classification results have been obtained. But the coefficient .9 used the abouve equation is not considered so much. The value might be replaced by the partial correlation coefficient in multi-variate analysis.

8 CONCLUSIONS

We have presented the reliability of a new EN system designed from various kinds of QCM sensors. It has been sgown that after training the neural network for each odor, we can classify the original odor from the mixed odors in case of two odor case. More than two mixing case is open for the future research.

Table 5. Testing the mixed odors where except for the largest value the top is selected as the second odor among the mixed odors.

Symbols	Output A	Output B	Output C	Output D
A and B	.263	.290	.166	.066
B and C	.358	.029	.631	.008
C and D	.002	.071	.644	.163
D and A	.214	.004	.037	.230
A and C	.031	.020	.527	.026
B and D	.108	.010	.039	.325

Acknowledgement

This research has been supported by Grant-in-Aid for Challenging Exploratory Research No. 22656089 of Japan Society for the Promotion of Science and we wish to thank JSPS for their support.

REFERENCES

[1] Milke J. A. (1995), "Application of Neural Networks for discriminating Fire Detectors", *International Conference on Automatic Fire Detection*, AUBE'95, 10th, Duisburg, Germany, pp. 213–222

[2] Charumporn B. , Yoshioka M. , Fujinaka T. , and Omatu S. (2003), "An Electronic Nose System Using Back Propagation Neural Networks with a Centroid Training Data Set", *Proc. Eighth International Symposium on Artificial Life and Robotics, Japan*, pp. 605–608.

[3] General Information for TGS sensors, *Figaro Engineering*, available at www.figarosensor.com/products/general.pdf.

[4] W. L. Carlson and B. Thorne (1997), *Applied Statistical Methods*, Prentice Hall International.

[5] Fujinaka T. , Yoshioka M. , Omatu S. , and Kosaka T. (2008), "Intelligent Electronic Nose Systems for Fiore Detection Systems Based on Neural Networks", *The second International Conference on Advanced Engineering Computing and Applications in Sciences, Valencia, Spain*, pp. 73–76.

[6] Omatu S. and Yano M. (2011), "Intelligent Electronic Nose System Independent on Odor Concentration", *International Symposium on Distributed Cimputing and Artificial Intelligence, Salamanca, Spain*, pp. 1–9.

The Seventeenth International Symposium on Artificial Life and Robotics 2012 (AROB 17th '12),
B-Con Plaza, Beppu, Oita, Japan, January 19-21, 2012

Solving Sudoku with Bayesian Optimization Algorithm

Shinichi Shirakami[1], Yuji Sato[2]

[1,2]Hosei University, Tokyo 184-8584, Japan
(Tel: 81-042-387-6023, Fax: 81-042-387-6048)

[1]shinichi.shirakami.8c@stu.hosei.ac.jp
[2]yuji@k.hosei.ac.jp

Abstract: Recently, the Estimation of distribution algorithm (EDA) has been studied as a measure to solve the problem that the Genetic algorithm (GA) destroys effective building blocks. The Bayesian optimization algorithm (BOA) that is one of EDAs evolves a population of candidate solutions by building and sampling Bayesian networks. However, the BOA has some problems, for example the processing time is too longer. In this paper, we use the Sudoku puzzle that is one of the real problems, focusing on the problem of processing time and convergence to local solution. We propose the method defined chromosome combined nine candidate regions would make it possible to compress the search spaces. We evaluate this method by using two types of Sudoku puzzles and comparing result of the method that defines a one-dimensional chromosome that has a total length of at most 324 binary numbers and converts binary numbers into integer numbers to the result of our proposal method. In the result, our proposal method reduces processing time and amount of generations than the original program and performs as precision as the original program.

Keywords: Estimation of Distribution Algorithm, Bayesian Optimization Algorithm, Sudoku, Search domain reduction

1 INTRODUCTION

There is research into the solving several problems using GA, for example combinatorial optimization problems, NP-hard problems and so on. However, the GA operations are at risk for breaking building blocks. The Estimation of Distribution Algorithm (EDA) is a one of the way to mitigate risk. The EDAs are a statistical method using the probability distributions. In this research, we focus attention on small examples that typical the EDA, the Bayesian Optimization Algorithm (BOA) [1], is applied to the real problems because of the processing time of the BOA to generate networks using probabilistic models is too long, and study the method that solves the problems of the BOA applying the real problems. The Sudoku is a one of large scale combinatorial optimization problems, and is solved effectively by methods such as back-tracking and meta-heuristics approach, and GA with local search. As it stands now, it is difficult for the BOA that to solve effectively than back-tracking and GA. However, in this paper, we aim for getting a toehold in solving Sudoku with the BOA, and try new approach using candidate regions.

2 SUDOKU PUZZLE

General Sudoku puzzles consist of a 9 x 9 matrix of square cells, some of which already contain a numeral from 1 to 9. The arrangement of given numerals when the puzzle is presented is called the starting point. A Sudoku puzzle is completed by filling in all of the empty cells with numerals 1 to 9, but no row or column and no 3 x 3 sub-block may contain more than one of any numeral. For these basic puzzles, methods such as back-tracking and meta-heuristics approach are effective. Fig.1. shows an example of a Sudoku puzzle. In Sudoku puzzle, tandem 9 cells are called row, horizontal 9 cells are called column and 3 x 3 sub-block is called region.

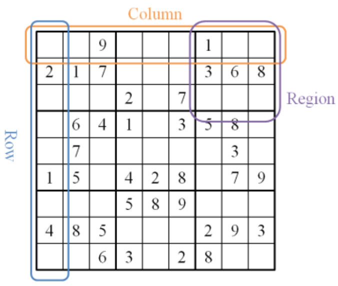

Fig.1. An example of Sudoku puzzle

3 SUDOKU SOLUTION DERIVED USING THE BOA

3.1 The original method using the BOA

3.1.1 The definition of the BOA chromosome

We must convert decimals to binary for the BOA is able to deal with a Sudoku puzzle in order to solve the Sudoku puzzles by using the BOA.Fig.2 and Fig.3 show the original method. Because of numerals 1 to 9 are used in a Sudoku puzzle, 4-bit binary is assigned to a cell. Therefore, to convert a Sudoku puzzle to binary needs at most 324-bit binary codes. When individuals are evaluated, there is a general way that converts binary to decimals to evaluate the individuals.

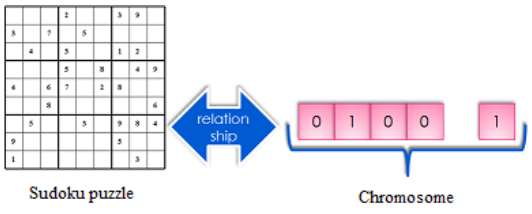

Fig. 2. Relationship between Sudoku puzzle and BOA Chromosome

Fig. 3. Conversion code

3.1.2 The evaluation of the BOA chromosome

We use the function to evaluate the BOA chromosome by

$$f(x) = \sum_{i=1}^{9}(r_i + c_i) \qquad (1)$$

where r_i is a number of different numbers in a row; and c_i is a number of different numbers in a column.

3.2 Problem and countermeasures

Because of a problem that length of chromosome is too long, it takes time to generate and extract the network. In addition, we consider a problem about an initial convergence. An important factor to minimize an initial convergence is the BOA parameter adjustment. Specifically, there are three parameters to minimize an initial convergence, to adjust a large population, to adjust at high rate of parents and to adjust rate of offspring. It creates population of diversity and reduces an initial convergence. However, ensuring population of diversity makes processing time of the BOA slowly. We propose the solution these problems below.

3.3 Proposed method using candidate region

In this paper, we propose definition of chromosome with candidate regions with the dual aims of reducing the processing time and accuracy improvement. Candidate regions compose of all types of regions. Each region has a 19-bit binary code and is referred to by code. We define the BOA chromosome as combination nine codes and enable to express a Sudoku puzzle in at most 171-bit binary codes. In this method, no region may contain more than one of any numeral. Thus, in evaluation term, the BOA doesn't have to evaluate all regions. As a result, we can compress the search space.

3.3.1 Candidate region

Fig.4 shows how to generate the candidate region. Candidate regions compose of all types of regions. Each region has a 19-bit binary code and is referred to by code in evaluation term.

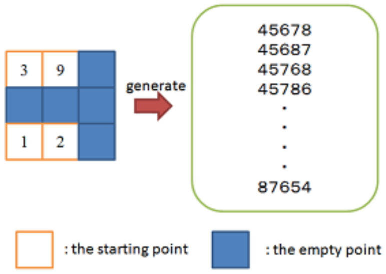

Fig. 4. Generate candidate region

3.3.2 Relationship of chromosome and candidate region

Fig.5 shows relationship of chromosome and the candidate region. There are 9! regions in candidate regions. A region code must express 2^{19} things in a binary code for relating candidate region to it. In other words, the length of region code is at most 19-bit. We define the BOA chromosome as combination nine codes and enable to express a Sudoku puzzle in at most 171-bit binary codes.

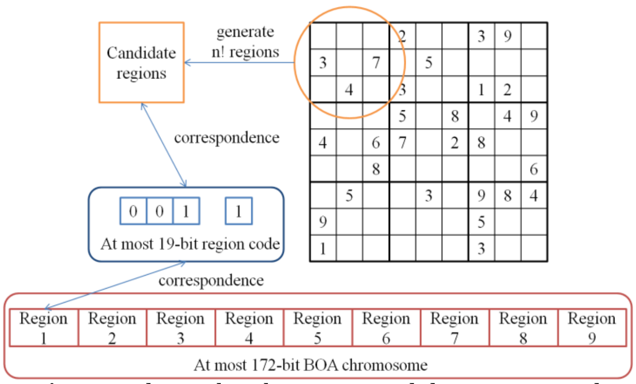

Fig. 5. Relationship between candidate region and chromosome

4 EXPERIMENT

4.1 Experimental methodology

In this research, we use two types of Sudoku puzzles. First one is 38 starting points and second one is 34 starting points. Fig.6 shows the Sudoku puzzle we use [2]. Original program (Original) and proposed method (Proposed) solve two Sudoku puzzles. We evaluate our method by parameter type.

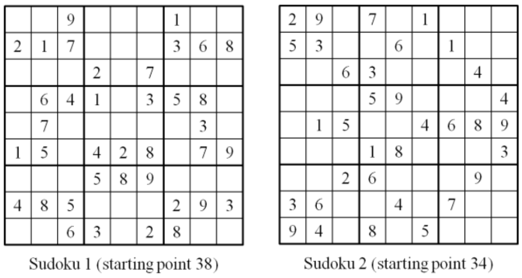

Fig. 6. Sudoku puzzles used in this experiment

4.2 BOA parameters

In this research, we use three types of parameters. Table.1 shows parameters in this research. Parameter group A has difference of population size. Parameter group B has difference of parents size. And parameter C has difference of offspring percentage. We evaluate proposed method by comparing accuracy and processing time with the original program. Additionally, maximal number of generations to perform is 100 generations.

Table. 1. BOA parameters

	Population size	Pearents size	Offspring percentage
Base	2500	50	50
A-1	1250	50	50
A-2	5000	50	50
B-1	2500	40	50
B-2	2500	60	50
C-1	2500	50	40
C-2	2500	50	60

4.3 Experimental result

4.3.1 Accuracy comparison in base parameter

Table.2 shows comparison result. Proposed surpass Original in accuracy rate. When it comes to Sudoku2, the result is that accuracy rate of Original is 12% and accuracy rate of Proposed is 56%. Also Proposed drastically lower Generation performed than Original. And average time required for Original to solve Sudoku1 is about 190 seconds and Sudoku2 is about 309 seconds. On the other hand, average time required for Proposed to solve Sudoku1 is about 9 seconds and Sudoku2 is about 19 seconds

.

Table.2. Comparison of base parameter

Correct Answer	Base(Original)	Base(Proposed)
Sudoku1	68	76
Sudoku2	12	56
Generation Performed	Base(Original)	Base(Proposed)
Sudoku1	63.04	44.92
Sudoku2	92.4	67.28

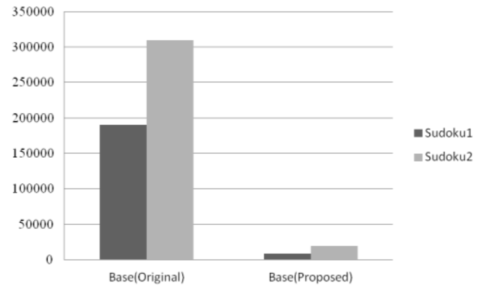

Fig.7. Processing time in base parameter

4.3.2 Accuracy comparison in parameter group A

Table.3 shows comparison result of parameter group A. Original is able to reduce the number of local solution by increasing population size. As a result, accuracy rate of Original becomes better. In contrast, we make sure of either improvement or not in Proposed by increasing population size. Fig.8 shows comparison of processing time in parameter group A. In parameter A-1, Proposed is twenty one times faster than Original in Sudoku1 and nine times faster than Original in Sudoku2. In parameter A-2, Proposed is sixteen times faster than Original in Sudoku1 and seventeen times faster than Original in Sudoku2.

Table.3. Comparison of parameter group A

Correct Answer (%)	A-1(Original)	A-1(Proposed)	A-2(Original)	A-2(Proposed)
Sudoku1	24	56	92	68
Sudoku2	0	36	44	88
Generation Performed	A-1(Original)	A-1(Proposed)	A-2(Original)	A-2(Proposed)
Sudoku1	80.36	60.84	49.72	49.68
Sudoku2	98.84	74.52	80.2	48.2

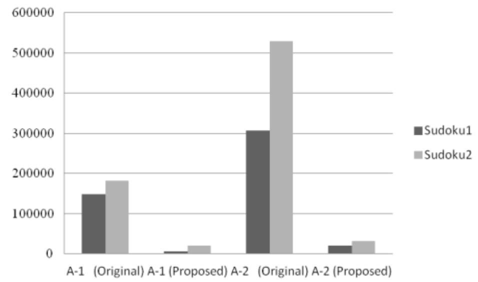

Fig.8. Processing time in parameter group A

4.3.3 Accuracy comparison in parameter group B

Table.4 shows comparison result of parameter group B. Original is able to reduce the number of local solution by increasing parents size. As a result, accuracy rate of original becomes better. In contrast, we make sure of either improvement or not in Proposed by increasing parents size. Fig.9 shows comparison of processing time in parameter group B. In parameter B-1, Proposed is twenty seven times faster than Original in Sudoku1 and sixteen times faster than original in Sudoku2. In parameter B-2, Proposed is eighteen times faster than Original in Sudoku1 and sixteen times faster than Original in Sudoku2.

Table.4. Comparison of parameter group B

Correct Answer (%)	B-1(Original)	B-1(Proposed)	B-2(Original)	B-2(Proposed)
Sudoku1	68	84	76	56
Sudoku2	12	52	28	72
Generation Performed	B-1(Original)	B-1(Proposed)	B-2(Original)	B-2(Proposed)
Sudoku1	59.24	35.8	63.72	61.24
Sudoku2	91.72	65.4	90.6	63.08

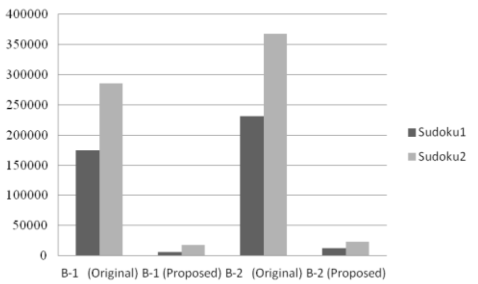

Fig.9. Processing time in parameter group B

4.3.2 Accuracy comparison in parameter group C

Table.5 shows comparison result of parameter group C. Original is able to reduce the number of local solution by increasing offspring percentage. As a result, accuracy rate of Original becomes slightly-improved. In contrast, we make sure of improvement in Proposed by decreasing offspring percentage. Fig.10 shows comparison of processing time in parameter group C. In parameter C-1, Proposed is eighteen times faster than Original in Sudoku1 and thirteen times faster than Original in Sudoku2. In parameter C-2, Proposed is twenty times faster than Original in Sudoku1 and sixteen times faster than Original in Sudoku2.

Table.5. Comparison of parameter group C

Correct Answer (%)	C-1(Original)	C-1(Proposed)	C-2(Original)	C-2(Proposed)
Sudoku1	68	68	76	60
Sudoku2	12	64	16	56
Generation Performed	C-1(Original)	C-1(Proposed)	C-2(Original)	C-2(Proposed)
Sudoku1	68.28	54.24	63.72	53.72
Sudoku2	95.6	67.88	89.6	64.44

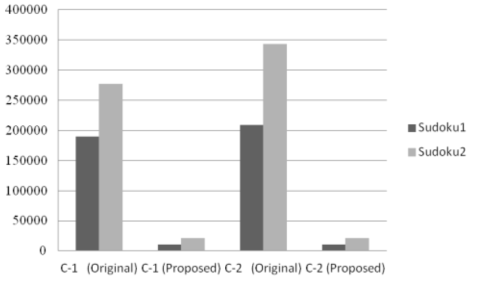

Fig.10. Processing time in parameter group C

5 DISCUSSION

From an examination of section 4, our proposal method surpasses Original in accuracy rate in most parameters. From these results, this is attributed to the fact that search domain reduction by using the candidate regions is effectively. However, Accuracy rate of Original becomes stricter and stricter with increasing population size. But we make sure of either improvement or not in Proposed by increasing population size. Thus, we surmise that when we ignore the processing time, Original surpasses Proposed in accuracy rate. Also generation performed, Proposed is few generations performed than Original. This is attributed to the BOA with candidate regions need not learn regions. Proposed has a large increase in speed of solving a Sudoku puzzles with the BOA. This is attributed to the fact that two factor involve this improve. One is the improving generation performed; the other is search domain reduction by using the candidate regions. In weak point of Proposed, we observe the case that Proposed converge a local solution. This is attributed to the BOA converge local solution once; the BOA is hard to get rid of local solution. We think one of the countermeasures is to add the local search to our approach.

6 CONCLUSIONS

To solve a Sudoku puzzle with the BOA, we propose a new approach with the candidate region. We evaluate our approach with two types of Sudoku puzzles. As a result, generation performed of the proposed method is more improved than generation performed of the original program. Also processing time of proposed method is more improved than processing time of the original program. And the proposed method surpasses the original program in accuracy rate. We showed new capability to solve a Sudoku puzzles with the BOA.

ACKNOWLEDGMENT

This research is partly supported by the collaborative research program 2011, Information Initiative Center, Hokkaido University.

REFERENCES

[1] Martin Pelikan, David E. Goldberg, Erick Cantu-Paz (1999), BOA: Bayesian Optimization Algorithm. Illigal Report, no.99003:

[2] COSMIC MOOK, The best 110 of number place part 15(in Japanese)

The Seventeenth International Symposium on Artificial Life and Robotics 2012 (AROB 17th '12),
B-Con Plaza, Beppu, Oita, Japan, January 19-21, 2012

Parallelization of Genetic Operations that Takes Building-Block Linkage into Account.

[1]Hazuki Inoue, [2]Naohiro Hasegawa, [3]Mikiko Sato and [4]Yuji Sato

[124]Hosei University, 3-7-2 Kajino-cho, Koganei-shi, Tokyo, Japan
(Tel: 81-42-387-6023, Fax: 81-42-387-6048)
[3]Tokyo University of Agriculture and Technology

[1]haduki.inoue.yw@stu.hosei.ac.jp
[4]yuji@k.hosei.ac.jp

Abstract: Previously, we proposed genetic operations that consider effective building blocks for using genetic algorithms (GA) to solve Sudoku puzzles, and proposed also a stronger local search function. In this paper, we propose performance enhancement by parallelization of genetic operations takes building-block linkage into account. In other words, parallelize sub-blocks (regions) of Sudoku puzzles. Valid parallelization of genetic operations becomes a strong method of speed-up in conjunction with parallelization of individuals, since parallelization of genetic operations is not competing with parallelization of individuals. We show using multi-core processors and OpenMp that parallelization of genetic operations have positive effect of for speeding up.

Keywords: Genetic Algorithms, Linkage, Parallelization, Sudoku.

1 INTRODUCTION

Sudoku puzzle that belong to constraint satisfaction problem is one of famous pencil puzzles. There are several conventional researches which applied GA to Sudoku, and it is demonstrated that be able to solve a Sudoku with GA. However, the execution time and number of steps leading to the optimum solution, particularly the difficult problem has become enormously large [1]. The presumed cause is that there are many local solutions, and the crossover that is the main operation of GA is more likely to destroy some of the valid solutions (building blocks) insofar as Sudoku puzzles. Therefore, in many cases conventional research have addressed the issue in conjunction with Grammatical Evolution [2] or Cultural Algorithm [3] to GA. Previously, we proposed a genetic operations considering the linkage of loci, and tried to improve the accuracy of the program. As a result, the conventional example of the difficulty in solving problems was able to derive a solution with half the number of runs [4]. However, in terms of Sudoku solving algorithms, and another algorithm that like a backtracking algorithm can be done faster than solving the proposed method. Parallel research using multi-core processors and GPU as a means to speed up the GA, many have been in recent years. Began to be popular in the general PC with multi-core processors and GPU, it became available relatively cheaply, was considered one of the reasons many examples of research.

2 THE RULES OF SUDOKU

The Sudoku rules are explained in Fig.1. General Sudoku puzzles consist of a 9 x 9 matrix of square cells, some of which already contain a numeral from 1 to 9. The arrangement of given numerals when the puzzle is presented is called the starting point. The degree of difficulty varies with the number of given numerals. In general, it will be difficult by increasing the number. A Sudoku puzzle is completed by filling in all of the empty cells with numerals 1 to 9, but no row or column and no 3 x 3 region (:the sub-blocks are bound by heavy lines in Fig.1) may contain more than one of any numeral.

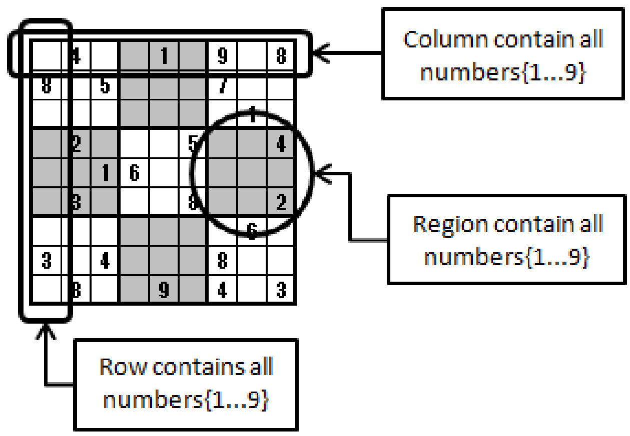

Fig.1 An example of Sudoku puzzles.

3 METHOD OF ACCURACY IMPROVEMENT OF SUDOKU SOLVING BY GA

GA is generally found to be useful for problems with a wide search range of solutions. However, the conventional example is applied to Sudoku to GA, has become a huge number of generations it takes to solve a problem with low number of initial placement [1]. The presumed cause is that the crossover that is the main operation of GA is more likely to destroy building blocks insofar as Sudoku puzzles, GA has a low performance of local search, and there are prone to local solution. In previous research, we have proposed genetic operations considering the linkage in order to improve these problems. Describe the proposed genetic operations below.

3.1 Genetic operation that consider linkage of genetic locus

3.1.1 Initial value setting

The initial value is determined by random numbers to fill in the blank mass other than initial placement. At that time, numbers do not overlap each region. Thereby, there meet conditions of Sudoku rules from the start that "No duplicate numbers in all regions". By performing the operations in each region, and continue meeting the above criteria, there are hardly disrupted the building blocks in the region.

3.1.2 Evaluation

As shown in Equation (1), evaluation value is sum of all evaluation value of row and column that is number of elements, with condition of "No duplicate number in each row and column". In addition, equation (2) and (3) as indicated, the numbers entering each row and column is limited to 1-9.

$$f(x) = \sum_{i=1}^{9} g_i(x) + \sum_{j=1}^{9} g_j(x) \tag{1}$$

$$g_i(x) = |x_i| \tag{2}$$

$$g_j(x) = |x_j| \tag{3}$$

3.1.3 Mutation

Mutation is performed for each region. As shown in Fig.2, randomly select two numbers in a region other than the initial placement, to replace the position for avoid duplicate numbers in the region.

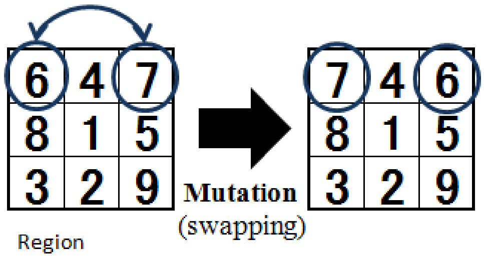

Fig.2 An example of mutation

3.1.4 Crossover

In the crossover, to generate two child individuals from two parent individuals. One is compares the evaluation value of each three rows, and child individuals inherit a higher parent individual. The other is compares of columns in a similar way with rows. Thus, compares have been six times by each three times with row-wise and column-wise comparison. Fig.3 shows the crossover.

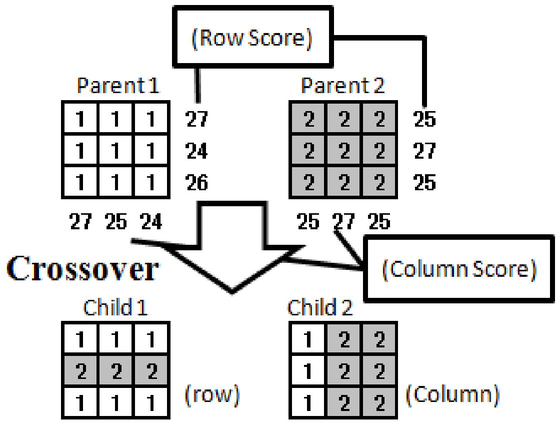

Fig.3 An example of crossover

3.2. Proposed method of improved local search

In general, local search is low performance than global search. Therefore, to improve the performance of local search, by means of population produces twice the number of child individuals produced by mutation, a wider range of child individuals is generated by selecting individuals from the high-evaluation-value.

4 PROPOSED METHOD OF PERFORMANCE INCREASE WITH PARALLELIZATION

There are various methods of the parallelization of the GA, in generally, most often do parallel by individuals, and has been successful in speed-up about solving Sudoku by GA [5]. In this paper, parallel operations by considering the linkage of genetic loci, aims to accelerate further, and we used the OpenMP about the implementation of parallelism.

4.1 Parallelization of genetic operation

4.1.1 Parallel mutation

In mutation, randomly select two numbers in a region other than the initial placement, to replace the position. Therefore, the number of times to replace by one individual is about nine times same by the number of the region. As Fig.4 shows, in parallelization, the parallel becomes 9-parallel by single thread to perform operations in one region.

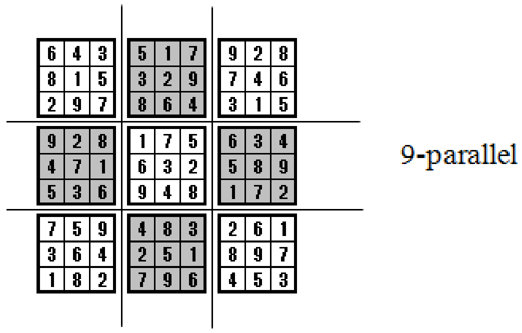

Fig.4 Parallelization of mutation

4.1.2 Parallel crossover

In the crossover, comparisons and inherited are six times as described in Section 3.1.4. As Fig.5 shows, in parallelization, the parallel becomes 3-parallel by performing the same thread with processing with row-wise and column-wise. Parallelized in one block has that calculation of evaluation value, comparison, and inherited to the child individuals.

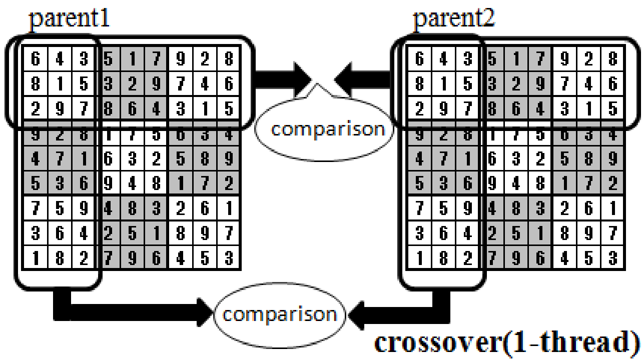

Fig.5 Parallelization of crossover

4.1.3 Parallel evaluation calculation

Evaluation calculation is performed in the same thread 1 by 1 evaluation calculations. As Fig.6 shows, Sudoku puzzles used in the experiment because it is a matrix with 9 rows 9 columns, the parallelization is 9-parallel.

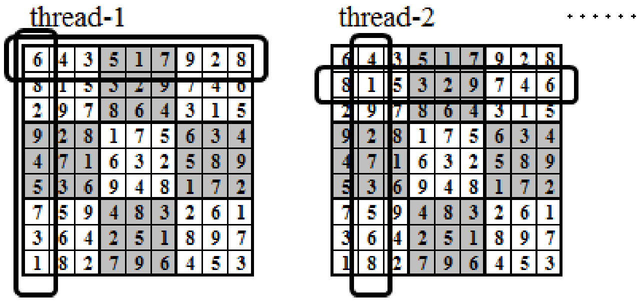

Fig.6 Parallelization of Evaluation Calculation

5 EVALUATION EXPERIMENTS

5.1 Experimental method

In this paper, the selection is used tournament selection. We used the Sudoku of workbook [6], and selected the 6 problems from the beginner, intermediate, and advanced problem each 2 problems.

5.2 Experiments about accuracy improvement

Fig.7 shows a graph of experimental results. If a solution was not obtained before 20,000 generations, the result was displayed as 20,000 generations. The tests were run 100 times and the averages of the results were compared. In Fig.7, direction x is the number of initial placement, and direction y is the number of generation.

In this paper, the method of described in Section 3.1 called Genetic Operation that consider Linkage (GOL). Random search, GOL, and proposed method compare, each method is proven to be effective.

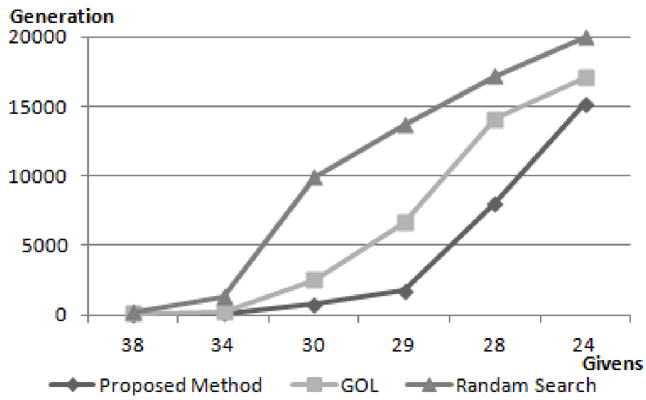

Fig.7 Relationship between givens and the average of generation

5.3 Experiments about performance increase

5.3.1 Basic specifications of a computer

Table.1 show the specifications of PC used in these experiments.

Table.1 Basic specifications of a computer

OS	Microsoft Windows 7 Enterprise
Processor	Intel Core i5 M520 @ 2.40GHz
Core	2/4 (logical / physical)
Memory	4.00GB

5.3.2 Result of experimentation

Table.2 and Fig.8 shows the experimental results. execution time is average of 50 times, and this is result of run of 10,000 generations. In Fig.8, direction x is the number of initial placement, and direction y is the execution time.

Parallelization of crossover is slower than no-parallelization. Parallelization of evaluation calculation and mutation succeeded in a speed-up. In the parallelization of mutation, many number of initial placement is more effective than less number of it.

Table.2 execution time

Gives	38	34	30	29	28	24
No-Parallel	32.11	31.57	28.93	31.21	28.48	28.43
P-Crossover	33.11	32.21	30.13	31.70	28.50	28.52
P-Evaluation(E)	31.05	30.33	27.80	29.61	26.79	26.10
P-Mutation(M)	28.67	27.86	26.10	27.19	26.51	26.69
P-E & M	24.61	24.70	23.46	24.05	23.13	23.22

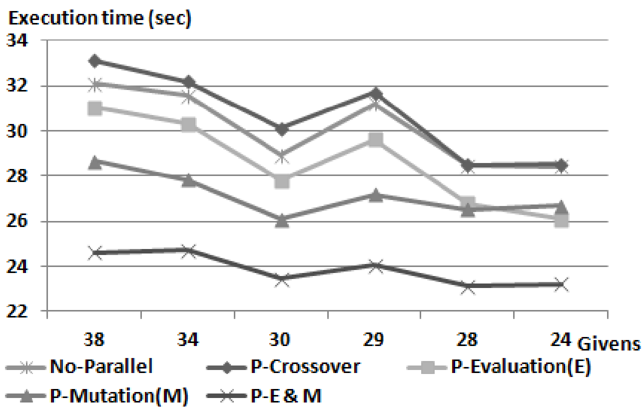

Fig.8 Relationship between givens and the execution time

5.4 Consideration

In the experiments about accuracy improvement, the proposed method finds optimum solution more than half within 20,000 generations. The proposed method has significantly improved accuracy compared with the conventional method [1] that is about 5% rate of solving within 100,000 generations. However, there is the high initial value dependence, and great variation in the number of generations to derive the optimum solution, and needs to consider, including how to escape from local solutions. In experiments about performance increase, together with parallelization of the evaluation calculation and the mutation, the effect of speed-up was obtained from 20 to 30%. And so the proposed method is parallelization of genetic operation, and we can use it in conjunction with parallelization of individuals. In consequence, the effect of each parallelization has been expected to be multiplied by the effect of both. The high-speed parallelization is less effective. This is attributed to that the small rate of each operation in the overall program, and creating threads and communication between threads is cost too much. And the future, reduced the cost of creating threads and communication, and we need a comparison with experiments using different ways such as a GPU.

6 CONCLUSION

In this paper, we propose speed-up of parallelization of genetic operations based on method of genetic operations that consider effective building blocks that previously we proposed. As a result, we succeeded in constant speedup and were able to improve performance. A proposed method which is parallelization of genetic operations becomes a strong method of speed-up in conjunction with parallelization of individuals, since parallelization of genetic operations is not competing with parallelization of individuals.

ACKNOWLEDGMENT

This research is partly supported by the collaborative research program 2011, Information Initiative Center, Hokkaido University, and a grant from 2011 the Institute for Sustainability Research and Education of Hosei University.

REFERENCES

[1] Timo Mantere and Janne Koljonen "Solving and Rating Sudoku Puzzles with Genetic Algorithms" New Developments in Artificial Intelligence and the Semantic Web Proceedings of the 12th Finnish Artificial Intelligence Conference STeP 2006

[2] Miguel Nicolau and Conor Ryan "Genetic Operators and Sequencing in the GAuGE System" 2006 IEEE Congress on Evolutionary Computation

[3] Timo Mantere and Janne Koljonen "Solving and Analyzing Sudokus with Cultural Algorithms" 2008 IEEE Congress on Evolutionary Computation

[4] Yuji Sato and Hazuki Inoue "Solving Sudoku with genetic operations that preserve building blocks" CIG, 2010 IEEE Symposium on

[5] Y.Sato, S.Kita, K.Takamine, and N.Hasegawa, " Speed up of Sudoku Solution with Genetic Operations by GPU", The Japanese Society for Evolutionary Computation 2010

[6] The best 110 of number place part 15, Cosmic Mook

The Seventeenth International Symposium on Artificial Life and Robotics 2012 (AROB 17th '12),
B-Con Plaza, Beppu, Oita, Japan, January 19-21, 2012

A detection method for intronic snoRNA genes using extended-weight-updating SOM with appearance probability of bases

Takuro MATSUO[1], Junichi IWAKIRI[2], Kunihito YAMAMORI[3], Naoya KENMOCHI[4],Ikuo YOSHIHARA[3]

[1] Graduate School of Engineering, University of Miyazaki
[2] Graduate School of Medicine, University of Miyazaki
[3] Faculty of Engineering, University of Miyazaki
[4] Frontier Science Research Center, University of Miyazaki
(Tel: +81 985 58 7589, Fax: +81 985 58 7589)
(matsuo@taurus.cs.miyazaki-u.ac.jp,yamamori@cs.miyazaki-u.ac.jp)

Abstract: Small nucleolar RNAs (snoRNAs) are known that they will participate with RNA modification. However, details of snoRNA's functions have not been clear still yet. In order to make clear functions of snoRNA, finding snoRNAs and studying their works in cells are required. In this paper, we propose a method to detect snoRNA genes using extended-weights-updating Self-organizing Map (eSOM). An input vector to eSOM consists of a feature vector and a target vector. A winner node for an input vector is decided by the feature vector, and all the weights around the winner node are updated to be close to the input vector. We employ base appearance probability and the complementary base pair ratio for feature vector only, and a flag for target vector. Experimental results showed our method achieved 91% and 93% detection ratio for boxC/D and boxH/ACA type snoRNA gene, respectively.

Keywords: Self-organizing Map (SOM), snoRNA, extended-weight-updating, eSOM

1 INTRODUCTION

Genome consists of two regions; one is the coding region which encodes information into protein, and the other is non-coding region. Non-coding regions have not been paid attention very much, but now we know non-coding regions include non-coding RNA (ncRNA) genes which play important roles such as gene expressions regulation or RNA modification, etc. Small nucleolar RNA (snoRNA) is a kind of ncRNA, and it will participate in RNA modifications such as methylation [1]. There are two types of snoRNAs; boxC/D type and boxH/ACA type. The functions of snoRNAs in detail have not been known still yet. In order to make clear functions of snoRNA, finding more snoRNAs and studying their works in cells are required.

As conventional snoRNA gene detecting method, Sakakibara *et al.* [2] has proposed to use support vector machine (SVM) with "stem kernel". It detects snoRNA gene based on characteristic structure of snoRNA called "stem". The SVM with stem kernel shows good performance for detecting boxC/D type snoRNA gene. However, detection accuracy for boxH/ACA type snoRNA gene is not enough still yet.

In this paper, we propose a method to decide whether a DNA sequence include a snoRNA gene or not using extended-weights-updating Self-organizing Map (eSOM) [3]. The eSOM is an extension of Kohonen's self-organizing map [4]. In the eSOM, an input vector is extended to consist of two parts; one is the conventional feature vector, the other is target vector. The dimension of a weight vector is the same of the input vector. A winner node for an input vector is decided by the feature vector part of the input vector, and all the weights in the winner node are updated to be close to the input vector. It means that the eSOM is self-organized based on the feature vector, and competitive nodes simultaneously obtain appropriate weight according to the target vector.

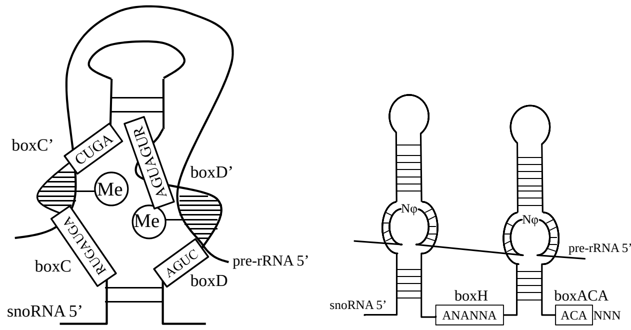

(a) Secondly structure of boxC/D type snoRNA.

(b) Secondly structure of boxH/ACA type snoRNA.

Fig. 1. Secondly structure of snoRNAs.

2 THE SNORNA

SnoRNA is a kind of ncRNA in nucleolus of cells. As shown Figure 1, there are two types snoRNAs based on their characteristic base sequences and secondary structure. BoxC/D type snoRNAs and boxH/ACA type snoRNAs con-

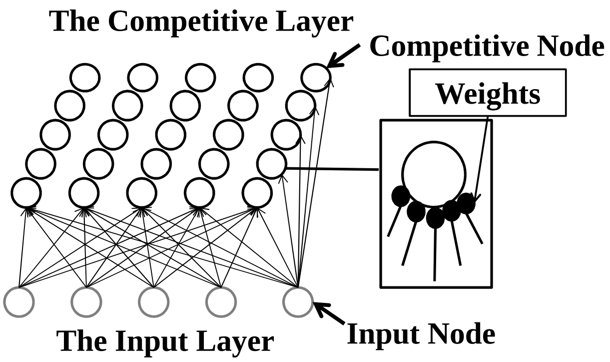

Fig. 2. Structure of SOM.

sist of 60-100 bases and 120-250 bases, respectively. The most of boxC/D type snoRNA genes have characteristic sequences called as "box C" and "box D", and they sometimes have other characteristic sequences called as "box C′" and "box D′". BoxH/ACA type snoRNA genes have characteristic sequences called as "box H" and "box ACA". Both types of snoRNAs also have characteristic secondary structure called as stem composed by complementary base pairs.

3 EXTENDED-WEIGHTS-UPDATING SELF-ORGANIZING MAP

3.1 Structure and learning algorithm of eSOM

Figure 2 illustrates the typical structure of SOM composed an input layer and a competitive layer. Competitive nodes are arranged as $N \times N$ mesh, and each of them has weights. The eSOM has the same structure of SOM.

Figure 3 shows the learning procedure of eSOM. When an input vector which consists of k-dimensional feature vector and 1-dimensional target vector is presented at the time $t (t = 1, 2, \cdots, T)$, the eSOM calculates distance $d^{ij}(t)$ between the input vector $\boldsymbol{x}(t) \in \Re^{k+1}$ and the weight vector $\boldsymbol{w}^{ij}(t) \in \Re^{k+1}$ of node $(i, j)(i, j = 1, 2, \cdots, N)$ according to Equation (1),

$$d^{ij}(t) = \sum_{m=1}^{k} \sqrt{(x_m(t) - w_m^{ij}(t))^2}. \quad (1)$$

Then, we decide the node with the smallest distance $d^{ij}(t)$ as a winner node C. After the winner node is decided, the neighboring nodes around the winner node update their all weights to be close to the input vector by Equation (2),

$$\boldsymbol{w}^{ij}(t+1) = \boldsymbol{w}^{ij}(t) + h_{cij}(t)[\boldsymbol{x}(t) - \boldsymbol{w}^{ij}(t)], \quad (2)$$

where $h_{cij}(t)$ is a neighborhood function defined by Equation (3),

$$h_{cij}(t) = \begin{cases} \alpha(t) & i, j \in N_c(t), \\ 0 & \text{otherwise}, \end{cases} \quad (3)$$

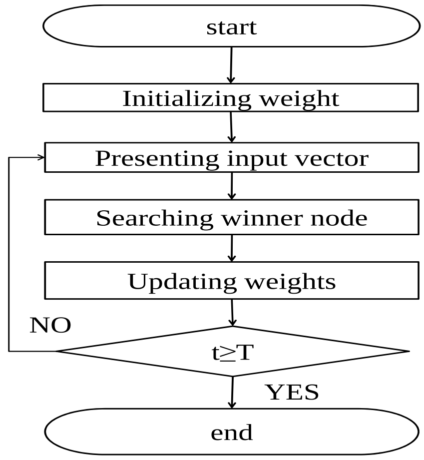

Fig. 3. Flow chart of eSOM.

where $\alpha(t)$ is a learning rate and $N_c(t)$ is a size of neighboring region around the winner node defined by Equation (4) and Equation (5), respectively. Both $\alpha(t)$ and $N_c(t)$ are gradually decreased as increasing of the t.

$$\alpha(t) = \alpha(0)\left(1 - \frac{t}{T}\right)\left(\frac{1}{d_c + 1}\right), \quad (4)$$

$$N_c(t) = N_c(0)\left(1 - \frac{t}{T}\right), \quad (5)$$

where d_c is the euclidian distance between the winner node (i_c, j_c) and the neighboring node (i_n, j_n).

In this paper, we give the information about base sequences to the elements of feature vector, and a real number flag that shows whether a snoRNA gene is included or not to the target vector. Thus, the eSOM is self-organized based on the similarity of the information about base sequences, and each competitive node simultaneously obtains appropriate flag value as a weight according to the similarity of feature vector.

3.2 Preparation of input vectors

We obtain the sequences including a snoRNA gene from the database "snOPY" [5]. They are used as positive samples. The negative samples without snoRNA gene are random base sequences whose length are the same as the positive samples. From these sequences, two kinds of information are extracted; the one is the base(s) appearance probabilities, and the other is complementary base pair ratio.

We employ the following three kinds of the base appearance probabilities;

- single-base appearance probabilities (eg. A, G, T, C),
- pair-base appearance probabilities (eg. AA, AG, $\cdots$, CC),
- triplet-base appearance probabilities (eg. AAA, AAG, $\cdots$, CCC).

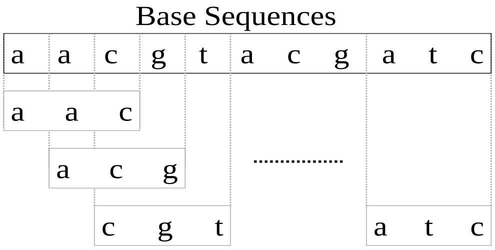

Fig. 4. An example for calculating triplet-base appearance probability.

Figure 4 shows how to count the triplet-base appearance frequencies. Each triplet-base appearance frequencies is divided by the sum of appearance frequencies. Since the number of combinations for single-base, pair-base and triplet-base is 4, 16 and 64 respectively, a part of the feature vector for the base(s) appearance probability has the same dimension of these combinations.

The complementary base pair ratio expresses the probability that the sequence forms the stem structure. We use CentroidFold [6] to calculate the complementary base pair ratio. This complementary base pair ratio is described as a scalar number. The concatenation of the base(s) appearance probability and the complementary base pair ratio becomes a feature vector of an input vector.

Finally we append the flag 1.0 to the input vector for positive samples, and 0.0 to that for negative samples. For the above three kinds of base(s) appearance probabilities, the total dimension of an input vector becomes 6, 18 and 66 respectively.

4 EXPERIMENTS AND DISCUSSIONS

4.1 Experimental conditions

We obtain 1,082 and 871 positive samples for boxC/D type snoRNA and boxH/ACA type snoRNA, respectively. As described in Section 3.2, the same number of negative samples are generated. These samples are divided into five groups, and we use four groups for learning and one group for validation as changing the combination of groups.

We use torus SOM to avoid discontinue on the edge of mesh. Experimental conditions are as follows:

- Competitive layer size : 100×100 nodes
- Initial neighboring region $N_c(0)$: 60×60 nodes
- Initial learning ratio $\alpha(0)$: 0.7
- Max learning iterations T : 100
- Numbers of positive (negative) samples for learning :

  boxC/D : 866 (866)

  boxH/ACA : 693 (693)

- Numbers of positive (negative) samples for validation :

  boxC/D : 216 (216)

  boxH/ACA : 174 (174)

- Number of trials : 10
- Initial weight range : 0.0∼1.0

We evaluate proposed method by the three indexes. The index "Accuracy" is a ratio of the correctly classified positive and negative samples to the total samples. The index "Sensitivity" is a ratio of the actual positive samples to the samples classified as positive samples. The index "Specificity" is a ratio of the actual negative samples to the samples classified as negative samples. If these are 1.0, perfect classification will be achieved.

4.2 Results and Discussions

We make eSOM learn on the condition described in Section 4.1. After learning, we present the validation samples to the learned eSOM, and decide winner node by Equation (1). If the weight of winner node corresponding to the target vector for a validation sample is more than 0.5, we decide this sample includes a snoRNA gene.

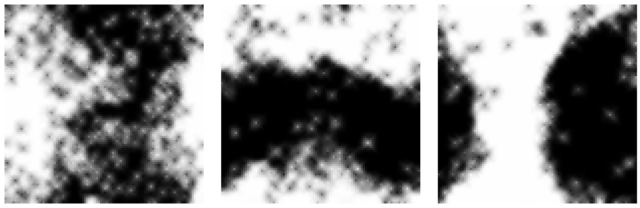

(a) Map of single-base appearance probability. (b) Map of pair-base appearance probability. (c) Map of triplet appearance probability

Fig. 5. Map for boxC/D type snoRNA gene.

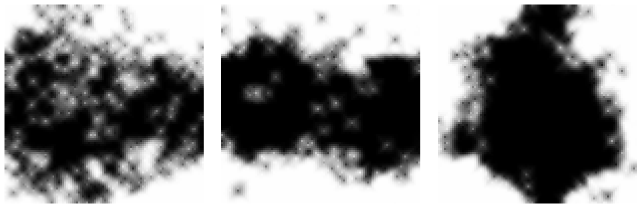

(a) Map of single-base appearance probability. (b) Map of pair-base appearance probability. (c) Map of triplet-base appearance probability.

Fig. 6. Map for boxH/ACA type snoRNA gene.

Table 1. Experimental results for boxC/D type snoRNA gene detection.

Data	Accuracy	Sensitivity	Specificity
single-base	0.780	0.772	0.788
pair-base	0.893	0.901	0.885
triplet-base	0.918	0.931	0.905

Table 2. Experimental results for boxH/ACA type snoRNA gene detection.

Data	Accuracy	Sensitivity	Specificity
single-base	0.789	0.770	0.806
pair-base	0.934	0.930	0.937
triplet-base	0.931	0.917	0.944

Figure 5 and Figure 6 show self organized map. The brightness of both figures denotes the value of weights corresponding to the target vector, it becomes more bright when the node has larger weight.

Fig. 5 and Fig. 6 said that increasing of the dimensions in the feature vector give us clear boundary between dark area and bright area. Especially, Fig. 5(c) is clearly divided between the dark areas and bright areas. We fill negative samples with randomly generated bases, so the base(s) appearance probabilities for the negative samples are almost the same. Meanwhile positive samples have characteristic sequences that compose Boxes or stems. Since eSOM can utilize this fluctuation among base(s) appearance probabilities and complementary base pair ratio, it clearly classifies positive samples and negative samples into two areas.

In Fig. 5(c) and Fig. 6(c), the bright nodes compose a cluster. It means that feature vectors of positive samples are similar each other. We try to utilize this similarity of feature vectors to detect snoRNA genes.

Table 1 and Table 2 show the average accuracy, sensitivity and specificity when we try to detect boxC/D type snoRNA genes and boxH/ACA type snoRNA genes, respectively.

Table 1 shows the experimental results for boxC/D type snoRNA gene detection. The best accuracy is 0.918 when we employ triplet-base appearance probability. Table 2 show the experimental results for boxH/ACA type snoRNA gene detection. The best accuracy is 0.934 when we employ pair-base appearance probability.

It is more desirable that the sensitivity is larger than the specificity to detect snoRNA genes. However, specificities for boxH/ACA type snoRNA gene detection are always better than sensitivities in our method. We guess it is no problem for practical use because sensitivities are high enough.

Sakakibara *et al.*[2] has reported that the accuracies to detect boxC/D type snoRNA genes and boxH/ACA type snoRNA genes by stem kernel method were 0.640 and 0.660, respectively. In comparison with these results, our method achieved much higher performance by using eSOM.

5 CONCLUSIONS

We proposed a new method to decide whether a DNA sequences include a snoRNA gene or not using eSOM. An input vector is compose of a feature vector and a target vector. A feature vector has information about base sequences, and a target vector has information about presence of absence of snoRNA gene. Our method organizes competitive nodes on eSOM based on the similarity of feature vectors, and each competitive node obtain an appropriate snoRNA existence probability as a weight.

We present the validation samples to the learned eSOM, and decide winner node. If the weight of winner node corresponding to the target vector for a validation sample is more than 0.5, we decide this sample includes a snoRNA gene. We discuss on detecting results and Maps.

Experimental results showed that the best accuracy for boxC/D type snoRNA gene detection was 91% when the triplet-base appearance probability was used, and it for boxH/ACA type snoRNA gene was 93% when the pair-base appearance probability was used. It was much superior than those of previous works. Those remain future works to make negative samples from real DNA sequences and to investigate the difference of sensitivity between pair-base and triplet-base for boxH/ACA type snoRNA gene detection.

REFERENCES

[1] Tran E, Brown J, Stuart Maxwell E (2004), Evolutionary origins of the RNA-guided nucleotide-modification complexes: from the primitive translation apparatus?. TRENDS in Biochemical Sciences, Vol.29, No.7, July, pp.343-350

[2] Sakakibara Y, Popendorf K, Ogawa N, Asai K, Sato K (2007), Stem kernels for RNA sequence analyses. J. Bioinform. Comput. Biol. 2007 Oct ;5(5):pp.1103-1122

[3] Fukushima T, Yamamori K, Yoshihara I, Nagahama K (2008), Feature extraction of protein expression levels based on classification of functional food with som. Proc. The 13th int'l. Symp. on AROB, pp.849-852

[4] Kohonen T (1996), SELF ORGANIZING MAPS. Springer Verlag Tokyo

[5] http://snoopy.med.miyazaki-u.ac.jp/

[6] Sato K, Hamada M, Asai K, Kiryu H, Mituyama T (2009), CENTROIDFOLD: a web server for RNA secondary structure prediction. Nucleic Acids Research, Vol. 37, Web Server issue, pp.277-280

The Seventeenth International Symposium on Artificial Life and Robotics 2012 (AROB 17th '12),
B-Con Plaza, Beppu, Oita, Japan, January 19-21, 2012

A method to detect intronic snoRNA genes using characteristic base patterns of DNA sequences

Chen XUE[1], Junichi IWAKIRI[2], Kunihito YAMAMORI[3], Naoya KENMOCHI[4], and Ikuo YOSHIHARA[3]

[1]Graduate School of Eng., Univ. of Miyazaki
[2]Graduate School of Med., Univ. of Miyazaki
[3]Faculty of Eng., Univ. of Miyazaki
[4]Frontier Science Research Center, Univ. of Miyazaki
(Tel: +81-985-58-7589; Fax: +81-985-58-7589)
(setsushin@taurus.cs.miyazaki-u.ac.jp, yamamori@cs.miyazaki-u.ac.jp)

Abstract: In recent researches of molecular cell biology and bioinformatics, it is one of the most important tasks to find and analyze functional RNAs, called as non-coding RNAs (ncRNAs) those do not carry any information to synthesize protein, but participate in post-translational modification. In this paper, we propose a method to detect intronic genes of small nucleolar RNA (snoRNA), it is a kind of functional RNA. SnoRNAs exist in the nucleolus, and contribute to the ribosomal RNA (rRNA) modification process. From their structure, snoRNAs can be classified into two types; the Box C/D type and the Box H/ACA type. Since each of them has some characteristic base sequences, we aim to detect snoRNA genes based on thes e characteristic base sequences and secondary structures. We evaluate proposed method by comparative experiments with other kernel function methods.

Keywords: snoRNA, box existence probability, stem appearance probability, secondary structure, functional RNA

1 INTRODUCTION

In recent researches of molecular cell biology and bioinformatics, it is one of the most important tasks to find and analyze functional RNAs, called as non-coding RNAs (ncRNAs) those do not carry any information to synthesize protein [1]. Many kinds of functional RNAs take part in various life phenomena such as basic metabolism, ontogeny and cell differentiation, etc. Researchers have reported that the defective functional RNA causes some kinds of diseases, so the progress of research on ncRNAs will give us significant advance in the field of drug discovery and regenerative medicine, etc.

In this paper, we propose a method to detect intronic genes of small nucleolar RNA (snoRNA) which is a kind of functional RNA. SnoRNAs exist in the nucleolus, and contribute to the ribosomal RNA (rRNA) modification process. From their structure, snoRNAs can be classified into two types; the Box C/D type snoRNA and the Box H/ACA type snoRNA. As shown in Figure 1, each of them has some characteristic base sequences and secondary structures. The Box C/D type snoRNAs have the Box C (AUGAUGA), the Box D (CUGA), the Box C' (UGAUGA) and the Box D' (CUGA). The Box H/ACA type snoRNAs have the Box H (ANANNA, N is an arbitrary base) and the Box ACA (ACA). Both types also have characteristic secondary structure called as stem. A stem consists of some complementary base pairs (A-U and C-G). We aim to detect snoRNA genes based on these characteristic base sequences and secondary structures.

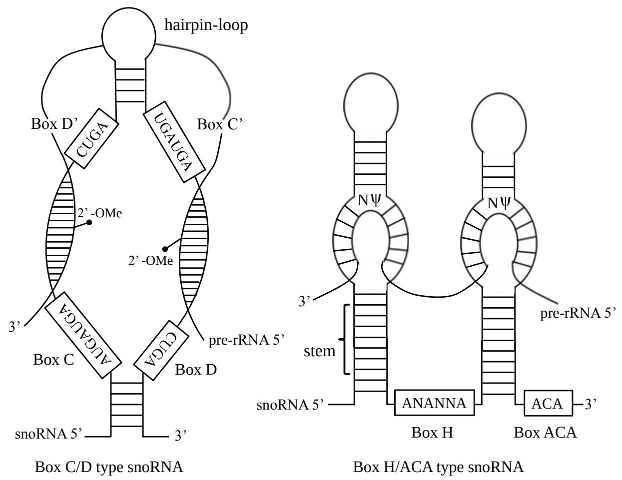

Fig. 1. Structure of the Box C/D type snoRNA and the Box H/ACA type snoRNA.

2 INTRONIC snoRNA GENE DETECTION

2.1 Small nucleolar RNA (snoRNA)

SnoRNAs exist in the nucleolus, and their length are about 60-250nt. SnoRNAs mainly work in biosynthesis process of ribosome, and they participate in modification of rRNA precursor. Until now, 236 and 75 kinds of snoRNAs are found in humans and in yeast, respectively. SnoRNAs are classified into the Box C/D type and the Box H/ACA type by their structural characteristic.

The length of Box C/D type snoRNAs is 60-100nt in general, a stem structure is composed by the complementary bases at the 3'end and the 5'end. The Box C/D type snoRNAs also have characteristic sequence AUGAUGA (Box C) and CUGA (Box D) adjacent the stem. Moreover, it sometimes has another similar sequences (Box C' and Box D') near the loop. Another stem is also found before the hairpin loop. Fig. 1 also says that the Box C/D type snoRNA has complementary sequences (9-20nt) to the targeted rRNA, the rRNA methylation occurs at the fifth nucleotide of the complementary domain as shown as the "2'-OMe" in Fig.1.

On the one hand, the length of the Box H/ACA type snoRNAs is 120-250nt, they consist of two hairpin loops as shown in Fig. 1. The Box H exists between stems, and the Box ACA exists in three nucleotides before from the 3' end. In the middle of stems, they have complementary sequences (6-20nt) to the targeted rRNAs. The rRNA is modified at the pseudouridine pocket in this domain.

Our proposed method utilizes these features to detect snoRNA genes.

2.2 Previous works

In this paper, we compare the performance of our method with the following two methods, the String Subsequence Kernel [2] and the Stem Kernel [3,4,5].

String subsequence kernel is a kernel for character strings, and it uses the appearance frequency of the string consisting of n characters as the coordinate of feature space. It counts the frequencies of the continuous or discontinuous strings in the sequence, and then these frequencies are weighted by λ^m where m is the length of partial string including gaps.

Stem kernel is a kernel for RNA sequences, and the feature space of this kernel considers the secondary structure of RNAs. The feature vector of this kernel consists of the appearance frequencies of arbitrary length continuous or discontinuous candidates for stem structures.

2.3 Proposed method

2.3.1 Flow of proposed method

Our method decides whether a peace of base sequence includes a snoRNA gene or not by the box existence probability and the stem appearance probability.

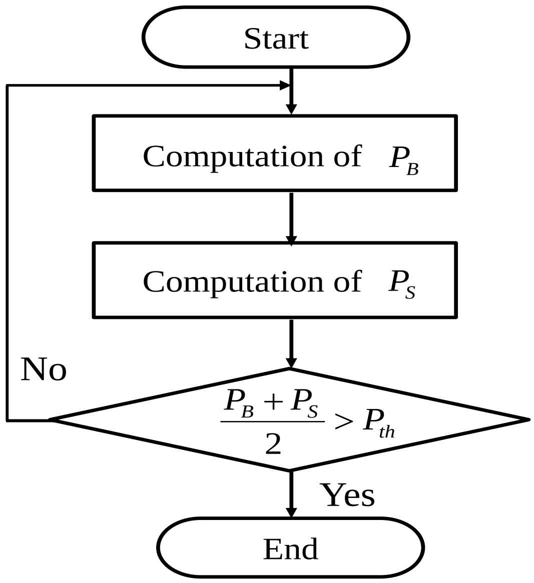

Fig. 2. Procedure of proposed method.

For this objective, we compare the target sequences with the box sequences and derive the similarity between these sequences. This similarity is denoted as box existence probability (P_B). Next, we also decide the target sequences have complementary base pairs that can organize stem structure. This is also denoted as Stem Appearance Probability (P_S). As shown in Figure 2, the average of the P_B and the P_S is more than the threshold value P_{th} , we decide the peace of base sequence include a snoRNA gene.

2.3.2 Box existence probability

Here explains how to calculate box existence probability in detail using an example case. Suppose we decide the sequence X [ACCUGAUGUAG] includes the Box D (CUGA) or not. As shown in Figure 3, the Box D consists of four bases, the first four bases [ACCU] of the X are compared with the Box D. In this case, no base is consistent with the Box D, so it gives us 0% as the box existence probability. Then the next four bases [CCUG] of the X are also compared with the Box D. In this case, only the first locus has the same base, so the box existence

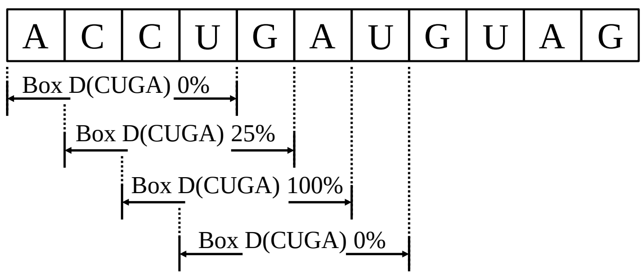

Fig. 3. A comparison of sequence X with the Box D, and calculation of the box existence probability.

probability becomes 1/4=25%. Hereafter, the same process is repeated until the end of the sequence X. The maximum probability is employed for the Box D existence probability for the sequence X. If the box existence probability will be less than 50%, we decide the sequence X does not have the Box D. The same process is repeated for the other Boxes.

2.3.3 Stem appearance probability

It is commonly known that the specific secondary structures in the cell are important features for modeling and detecting RNA sequences. The folding of an RNA sequence into a functional molecule is largely governed by the formation of the standard Watson-Crick base pairs A-U and C-G as well as the wobble pair G-U. Such base pairs constitute "biological palindrome" in the genome as shown in Figure 4. The secondary structures of RNAs are generally composed of stems, hairpins, bulges, interior loops, and multi-branches. A stem is a double stranded region of base-pair stacks. A hairpin loop occurs when RNA folds back on itself as shown in Fig. 4.

Here explains how to calculate the stem appearance probability between the Boxes. For this purpose, we calculate the appearance probability of the complementary base pairs (A-U and C-G). Suppose the sequence Y consists of eight bases [GUACGUAG]. Since the number of complementary pairs is three (U(A(CG)U)A) in the sequence Y as shown in Figure 5, the stem appearance probability becomes 6/8, 75%.

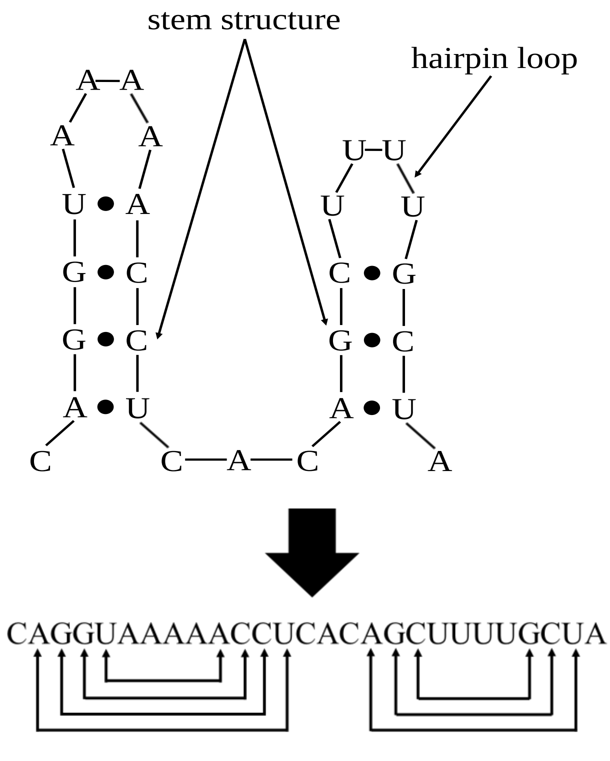

Fig. 4. Stem structure of an RNA sequence and its biological palindrome.

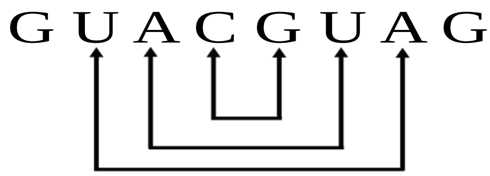

Fig. 5. Three complementary base pairs (U-A, A-U, C-G) are contained in the sequence Y.

3 EXPERIMENTS AND DISCUSSIONS

3.1 Data and conditions

We evaluate our method by actual snoRNA sequence data. All the positive examples that include a gene of a snoRNA are taken from the database "snOPY" [6]. We obtain 1,000 positive samples for Box C/D type snoRNAs and Box H/ACA type snoRNAs, respectively. For negative samples, we randomly shuffle the bases consisting of positive samples.

We use the following four indexes to evaluate proposed method. The sensitivity S_n is the ratio of the number of samples those are decided as including snoRNA gene to the positive samples. The specificity S_p is the ratio of the number of samples those are decided as not including snoRNA gene to the negative samples. The accuracy Acc is defined as the average of S_n and S_p in this paper. Figure 6 illustrates an example of ROC curve, where the x-axis is $1-S_p$ and the y-axis is S_n when the P_{th} is changed. The area under the ROC curve (AUC) means detection accuracy, $AUC=1.0$ denotes that all the positive and the negative samples are correctly identified.

3.2 Experimental results

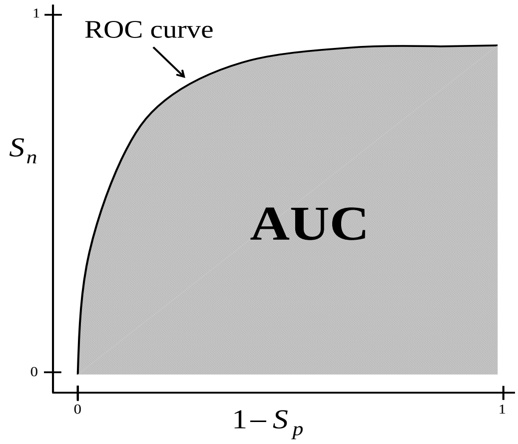

Fig. 6. Area under the ROC curve.

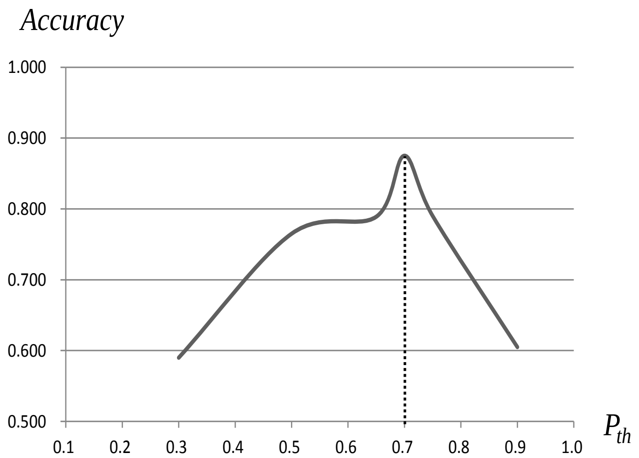

Fig. 7. The average accuracy in proportional to the P_{th}.

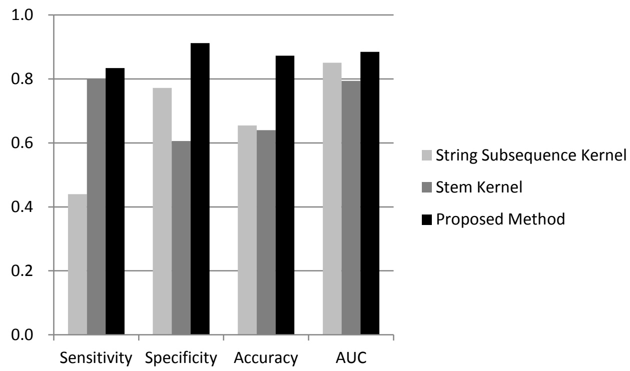

Fig. 8. Experimental results comparison with String Subsequence Kernel, Stem Kernel and proposed method.

We decide the sequence includes a snoRNA gene if the average of Box existence probabilities and stem appearance probability is more than P_{th}. It means that detection accuracy depends on the P_{th}, so we find appropriate P_{th} through preliminary experiments. Firstly we divide positive and negative samples into ten groups which have 100 positive and negative samples. Secondly we calculate accuracy described in Section 3.1 for each group as changing P_{th}, then derive the average accuracy among ten groups. Finally, we employ the P_{th} which shows the highest average accuracy. Figure 7 shows the average accuracy in proportional to the P_{th}. Fig.7 teaches us the highest accuracy is obtained when $P_{th} = 0.7$.

Here we compare proposed method with the string subsequence kernel method and the stem kernel method. As the same as the preliminary experiments, we execute cross-fold validation tests using above ten groups, and derive the average S_n, S_p, Acc and AUC. Experimental results showed that our method achieved the $S_n = 0.834$ and the $S_p = 0.912$ with 2,000 positive and negative samples when $P_{th} = 0.7$ as shown in Figure 8.

Fig.8 also said that our proposed method achieved more accurate snoRNA detection than that of the string subsequence kernel method and the stem kernel method. In Fig.8, the string subsequence kernel method showed poor S_n in comparison with the other methods. It means that the information about stems play an important role to detect the Box C/D type snoRNA genes. The stem kernel method showed inferior S_p than that of the other methods in Fig.8. It means that the using only information about stems cause miss classification of positive samples. To append the information about the Boxes contributed to improve specificity greatly. Since proposed method utilizes both the information about Boxes and Stems, it achieved the highest Accuracy.

4 CONCLUSIONS

In this paper, we proposed a method which is combined of the box existence probabilities with the stem appearance probability to detect the snoRNA genes, and it was evaluated by actual snoRNA base sequences. The detection accuracy for Box C/D type snoRNA was $Acc = 0.873$, however it for Box H/ACA type snoRNA was only $Acc = 0.547$. It is because the primary characteristic base sequence of the Box H/ACA type snoRNAs are uncertainty, detection accuracy stayed in low. Improvement of the detection accuracy for the Box H/ACA type snoRNA gene remains as a future work.

REFERENCES

[1] Eddy S (2001), Noncoding RNA genes and the moder n RNA world. Nature Reviews Genetics.2, pp.919-929

[2] Huma Lodhi, Craig Saunders, John Shawe-Taylor et al. (2002), Text Classification using String Kernels. Journal of Machine Learning Research, Vol.2, pp.419-444

[3] Sakakibara Y, Popendorf K, Ogawa N et al. (2007), Stem kernels for RNA sequence analyses. Bioinform Comput BIO V.5 No.5, pp.1103-1122

[4] Ogasawara K, Kobayashi S (2007), Stochastic Regular Approximation of Tree Grammars and Its Application to Faster ncRNA Family Annotation. Information Processing Society of Japan (IPSJ) 48 (SIG_17(TBIO_3)), pp.19-29

[5] Kin T, Tsuda K, Asai K (2002), Marginalized Kernels for RNA Sequence Data Analysis. Genome Informatics 13 , pp.112-122

[6] snoRNA Orthological Gene Database; http://snoop y.med.miyazaki-u.ac.jp/snorna_db.cgi

The Seventeenth International Symposium on Artificial Life and Robotics 2012 (AROB 17th '12),
B-Con Plaza, Beppu, Oita, Japan, January 19-21, 2012

Stochastic analysis of OneMax problem by using Markov chain

QingLian Ma[1], Yu-an Zhang[2], Kiminobu Koga[3],
Kunihito Yamamori[4], Makoto Sakamoto[4], and Hiroshi Furutani[4]

[1] Interdisciplinary Graduate School of Agriculture and Engineering, University of Miyazaki, Japan
[2] Department of Computer Science and Technology, Qinghai University, China
[3] Graduate School of Engineering, University of Miyazaki, Japan
[4] Faculty of Engineering, University of Miyazaki, Japan

Abstract: An experimental and analytical investigations are performed for OneMax problem using Wright-Fisher model. This study investigates the distribution of the first order schema frequency in the evolution process of Genetic Algorithm (GA). Effects of mutation in GA is analyzed for the standard mutation and asymmetric mutation models. If a population is in linkage equilibrium, it can be shown that OneMax problem is equivalent to the asymmetric mutation model. Thus we can apply theoretical results obtained in the asymmetric mutation model to OneMax problem, and investigate the convergence time within the framework of Wright-Fisher model.

Keywords: Genetic Algorithms, first order schema , asymmetric mutation , OneMax problem, Wrihgt-Fisher model

1 INTRODUCTION

Over the last decades, significant progress has been made in the theory, design and application of genetic and evolutionary algorithms. A decomposition design theory was proposed and several competent GAs have been developed [1]. Genetic algorithms are stochastic optimization techniques that apply three basic genetic operators; selection, crossover and mutation. Applying these genetic operators to a population of chromosomes, or individuals that represents possible solutions of the problem, forms new generations of the population [2]. Mutation plays an important role in computation of GAs. Doerr, B. et al. considered an asymmetric mutation operator for the Eulerian cycle problem and examine the effect of the asymmetric mutation on the runtime of the algorithms [3]. They showed that such an asymmetry of the mutation operator can speed up computations.

In this work, we study effects of mutation in the GA on OneMax problem. The analysis is made for standard mutation and asymmetric mutation models. The OneMax problem is a bit-counting problem where the fitness value of each binary string (individual) is equal to the number of bit 1's in it. The goal of OneMax problem is to maximize the number of 1's in the bit string.

We focus on the frequencies of the first order schemata, and calculate their changes in time by using the Wright-Fisher model of Markov chain. Furutani et al. calculated their changes in time by using the Wright-Fisher model [4]. We apply their stochastic approaches to the present problem, and consider the evolution of first order schema in the GA on OneMax problem with the finite population size.

2 MATHEMATICAL MODEL

As an evolution model, we use Simple Genetic Algorithm (SGA) proposed by Goldberg. For the case of OneMax problem, we derive the relation between standard mutation model and asymmetric mutation model. Individuals are represented by binary strings of fixed length ℓ, and there are $n = 2^\ell$ genotypes. The ith genotype is given by the binary representation of an integer i,

$$< i(\ell), \cdots, i(1) >, \quad (0 \le i \le n-1),$$

where $i(k)$ is a binary value of i at position k. We use the frequency $N_i(t)$ and relative frequency $x_i(t)$ of the ith genotype at generation t. The population size N is assumed to be time-independent, and

$$N = \sum_{i=0}^{n-1} N_i(t).$$

The relative frequency $x_i(t)$ is

$$x_i(t) = \frac{N_i(t)}{N}.$$

Fitness function f_i of OneMax problem for the ith genotype is defined as

$$f_i = \sum_{k=1}^{\ell} i(k).$$

The fitness is maximum when all bits are 1.

The linkage is an important notion to represent the status of population in genetics [5]. It also has a great influence on calculations of GA. Crossover and mutation make the linkage weak, and work to lead a population to linkage equilibrium [6]. If population is in linkage equilibrium, the distribution of individuals depends only on the frequencies of the first order schemata. We have the evolution equation for the first order schema [6]

$$h_1(t+1) \,=\, a h_1(t) + b, \tag{1}$$

where h_1 is the relative frequency for the first order schema of bit 1. The coefficients a and b are given by

$$a \,=\, (1-\frac{1}{\ell})\,(1-2p_m), \quad b \,=\, \frac{1}{\ell}(1-2p_m)+p_m.$$

In GA with asymmetric mutation, we assume mutation rate p_α for the mutation $1 \to 0$, and p_β for $0 \to 1$, respectively. We assume that all fitness values are $f_i = 1$. The deterministic evolution equation is given by

$$h_1(t+1) \,=\, (1-p_\alpha-p_\beta)h_1(t)+p_\beta. \tag{2}$$

Comparing this equation with equation (1), we have the following relations

$$p_\alpha \,=\, p_m, \quad p_\beta \,=\, p_m + \frac{1}{\ell}(1-2p_m). \tag{3}$$

3 WRIGHT-FISHER MODEL

Wright and Fisher put forward their evolution equation by considering the finite individuals [5]. The Wright-Fisher model treats chromosomes having one locus and two alleles, corresponding to the GA of $\ell = 1$ with genotypes $k \in \{0,1\}$ [7]. The number of the first genotype 1 takes the values of

$$N_1 \,=\, 0,1,\ldots,N,$$

and that of the genotype 0 is given by $N_0 = N - N_1$.

We analyze evolution processes by taking into account the effect of random sampling, and consider the fitness proportionate selection. If there are $N_1 = i$ copies of the genotype 1 at the current generation t, the probability $P(j|i)$ of N_1 taking the value of j at the next generation $t+1$ is given by the binomial distribution

$$P_{i,j} = P(j|i) = \binom{N}{j}\, p_i^j\,(1-p_i)^{N-j} \tag{4}$$

$$p_i \,=\, ay+b \,=\, a(\frac{i}{N})+b,$$

where i is the number of genotype 1 at the current generation t, and j is the number of genotype 1 at the next generation $t+1$.

The probability $P(j|i)$ specifies the process of random sampling, and the future behavior of the process only depends on its current frequencies [7]. Thus this process is a Markov chain. Let $\mu_i(t)$ be the probability that the population is in the state of $N_1 = i$ at generation t.

In the following, we use the vector notation

$$\mu^T \,=\, (\mu_0,\,\mu_1,\ldots,\mu_N),$$

with the normalization condition

$$\sum_{i=0}^{N} \mu_i(t) \,=\, 1. \tag{5}$$

Then the evolution process is described by

$$\mu_j(t+1) = \sum_{i=0}^{N} \mu_i(t)\,P_{i,j}. \tag{6}$$

The evolution equation is given in the vector form

$$\mu(t+1)^T \,=\, \mu(t)^T\,P, \tag{7}$$

where P is a matrix of the size $(N+1)\times(N+1)$. We know the eigenvalues of this matrix [8],

$$\lambda_0 \,=\, 1, \quad \lambda_1 \,=\, a, \quad \lambda_2 \,=\, a^2\,(1-1/N),\ldots. \tag{8}$$

It should be noted that the second largest eigenvalue λ_1 does not depend on the population size N. We denote the left and right eigenvectors

$$\mathbf{u}_i^T\,P \,=\, \lambda_i\,\mathbf{u}_i^T, \quad P\,\mathbf{v}_i \,=\, \lambda_i\,\mathbf{v}_i, \quad (0 \le i \le N).$$

These eigenvectors satisfy the orthogonality condition

$$\mathbf{u}_i^T \cdot \mathbf{v}_j \,=\, 0 \quad (i \ne j). \tag{9}$$

The explicit form of the right eigenvector $\mathbf{v}_0$ is given by

$$\mathbf{v}_0 \,=\, (1,1,\ldots,1)^T, \tag{10}$$

and all elements of the left eigenvector $\mathbf{u}_0$ are positive. We adopt the normalization conditions

$$\sum_{i=0}^{N} |u_i| \,=\, 1, \quad \mathbf{u}_i^T \cdot \mathbf{v}_i \,=\, 1.$$

We consider the GA under positive mutation rate $p_m > 0$. In this case, all elements of the transition matrix P are positive, and the Markov chain of schema evolution is irreducible and aperiodic. The Markov chain theory states that an irreducible and aperiodic Markov chain converges to the stationary distribution π

$$\lim_{t\to\infty} \mu(t) \,=\, \pi, \tag{11}$$

and all elements π_i are positive [8].

The initial distribution of the first order schema can be expanded in terms of the left eigenvectors

$$\mu(t=0)^T \,=\, \sum_{i=0}^{N} C_i\,\mathbf{u}_i^T. \tag{12}$$

Since $\mathbf{u}_i$ is eigenvector, and from equation (7), we have

$$\mu(t)^T \,=\, \sum_{i=0}^{N} \lambda_i^t\,C_i\,\mathbf{u}_i^T. \tag{13}$$

Multiplying the right eigenvector $\mathbf{v}_0$ from right side

$$\mu(t)^T \cdot \mathbf{v}_0 = \sum_{i=0}^{N} \lambda_i^t \, C_i \, \mathbf{u}_i^T \cdot \mathbf{v}_0 = \lambda_0^t \, C_0 = C_0,$$

and from equations(5) and (10), we have $C_0 = 1$. At large t, $\mu(t)$ is approximately given by

$$\mu(t) \approx \mathbf{u}_0 + a^t \, C_1 \, \mathbf{u}_1, \tag{14}$$

and $\mathbf{u}_0$ is the stationary distribution π.

In this study, we treat the convergence time T_c of Markov chain. To this end, the convergence time of the average fitness is defined as

$$T_c(\text{fitness}) \;=\; \min_t \{ \frac{\bar{f}(\infty) - \bar{f}(t)}{\bar{f}(\infty) - \bar{f}(0)} < 0.05 \}, \tag{15}$$

where $\bar{f}(t)$ is the average fitness at t, and $\bar{f}(\infty)$ is the average fitness in the stationary state. The theoretical estimation of the convergence time is given by

$$T_c(\text{eigenvalue}) \;=\; \min_t \{ a^t < 0.05 \}, \tag{16}$$

where a is the second largest eigenvalue of the transition matrix P.

4 NUMERICAL EXPERIMENTS

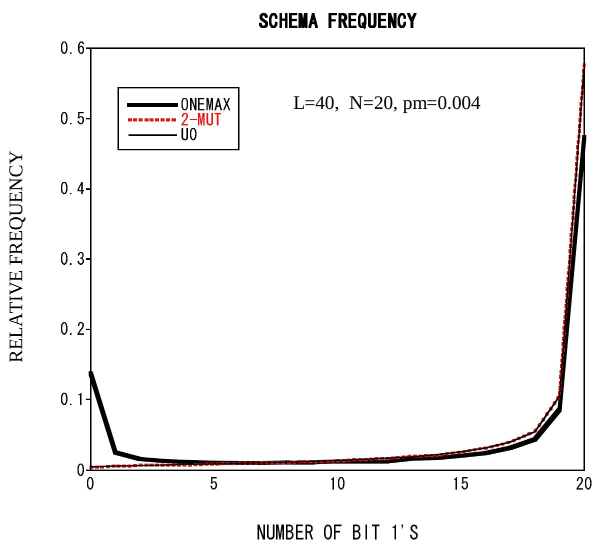

Fig. 1. The distribution of the number of bit 1's with $N = 20$ and $p_m = 0.004$. The thick solid line shows the result of OneMax GA calculation. The dotted line for asymmetric mutation model and the thin solid line for the left eigenvector $\mathbf{u}_0$, respectively.

Numerical experiments are performed in GA by standard mutation model on OneMax problem and asymmetric mutation model. They are compared with the theoretical results obtained by Wright-Fisher model. We carry out GA

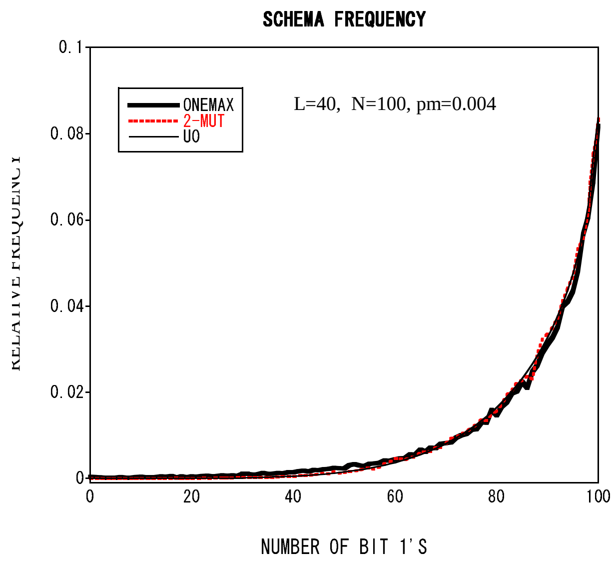

Fig. 2. The distribution of the number of bit 1's with $N = 100$ and $p_m = 0.004$.

with the fitness proportionate selection, and apply the uniform crossover with crossover rate $p_c = 1$. The string length is $\ell = 40$. The results are obtained by averaging 1000 repeated runs.

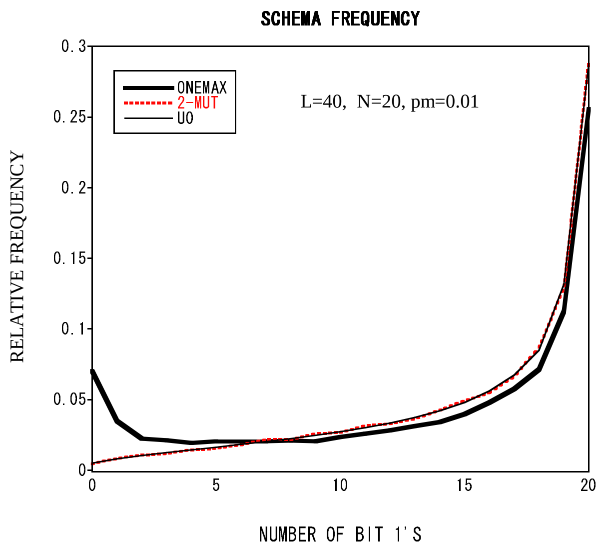

Fig. 3. The distribution of the number of bit 1's with $N = 20$ and $p_m = 0.01$.

Figure 1 shows the probability distribution of the first order schema with $N = 20$ and $p_m = 0.004$. The horizontal axis represents number of bit ones. The vertical axis represents the probability of the first order schema. The eigenvector $\mathbf{u}_0$ of Wright-Fisher model can reproduce the first order schema of the asymmetric mutation model almost com-

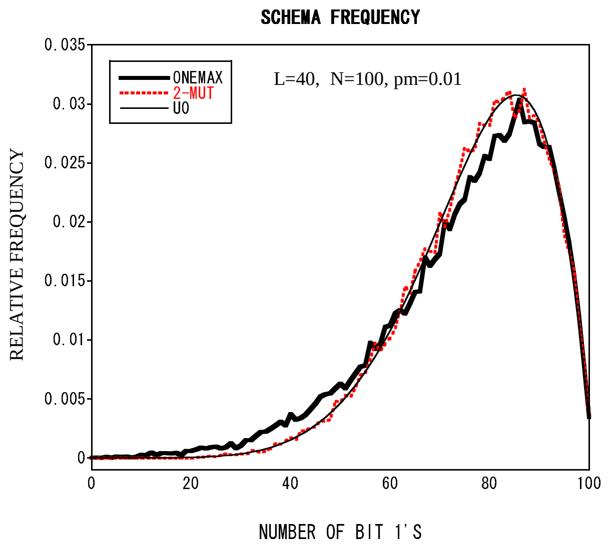

Fig. 4. The distribution of the number of bit 1's with $N = 100$ and $p_m = 0.01$.

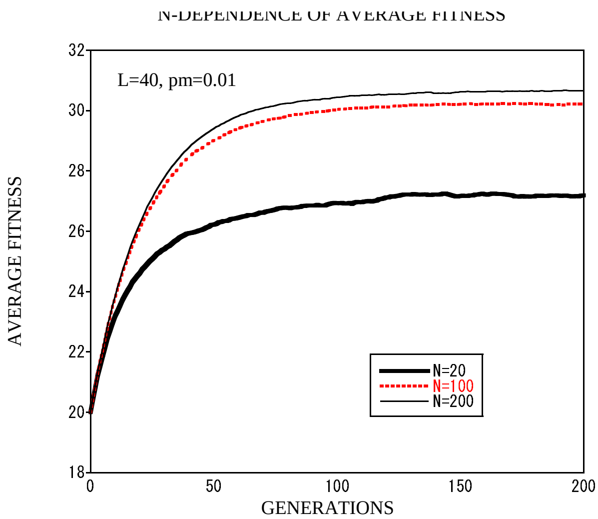

Fig. 5. Dependence of the average fitness on N. $pm = 0.01$. The horizontal axis represents generation.

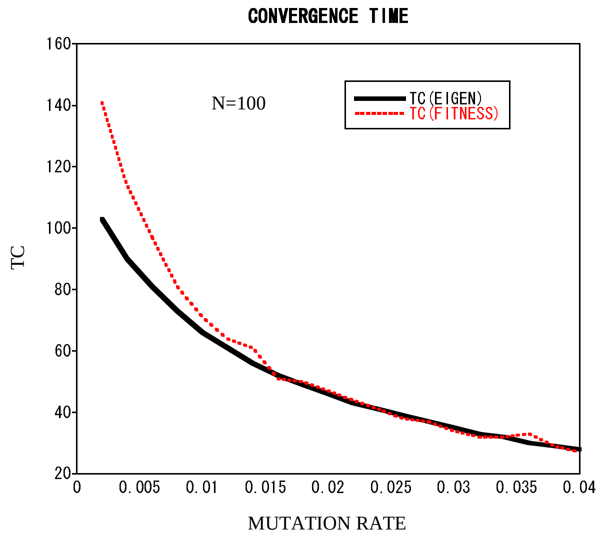

Fig. 6. The mutation rate dependence of the convergence times $T_c(\text{fitness})$ and $T_c(\text{eigenvalue})$ with $N = 100$.

pletely. However there are some discrepancies in the region of small i for OneMax GA calculation.

Figure 2 shows the probability distribution of the first order schema with $N = 100$ and $p_m = 0.004$. We used the same parameter as Fig.1 except for N. We notice that the difference between OneMax GA and asymmetric mutation model is small. The theory of Wright-Fisher model can reproduce both GA experiments.

Figure 3 and Figure 4 are the results with $N = 20$ and 100, respectively. For investigating the effects of mutation, we used the different mutation rate of $p_m = 0.01$ to compare $p_m = 0.004$ used in Figures 3 and 4. The form of schema distribution shows large difference in the comparison between Fig.2 and Fig.4.

Figure 5 shows the dependence of average fitness on N with $p_c = 1$ and $p_m = 0.01$ as function of generation t. We performed GA with $N = 20, 100, 200$. The dependence of average fitness $\bar{f}(t)$ on N is weak for large N, and $\bar{f}(t)$ shows almost the same behavior for large population size $N = 100$ and 200.

Figure 6 demonstrates the convergence times $T_c(\text{fitness})$ and $T_c(\text{eigenvalue})$ defined by equations (15) and (16), respectively. This figure gives the mutation rate p_m dependence of T_c. Theoretical estimation $T_c(\text{eigenvalue})$ well reproduces the the convergence time $T_c(\text{fitness})$ of GA calculation except for small p_m.

Figure 7 gives the population size N dependence of $T_c(\text{fitness})$. Since the second largest eigenvalue $\lambda_1 = a$ has no N dependence, it is concluded that the N dependence of $T_c(\text{fitness})$ is very weak. The figure supports this prediction.

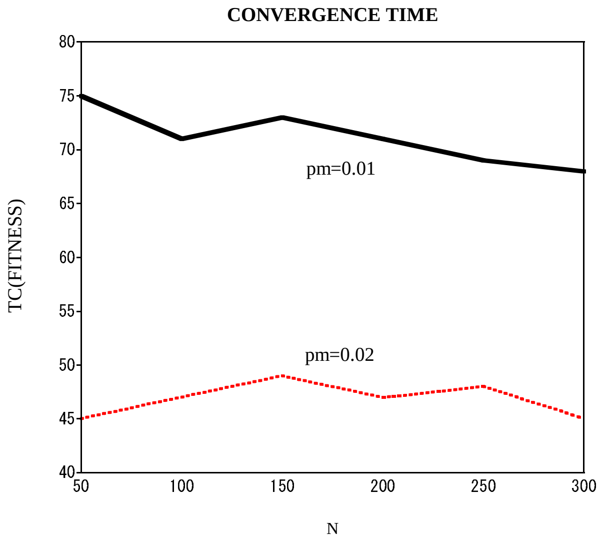

Fig. 7. The population size dependence of the convergence time $T_c(\mathrm{fitness})$ with $p_m = 0.01$ and 0.02.

5 SUMMARY

We report some results of probabilistic analysis of One-max problem in GA. The study of GA on OneMax problem demonstrates the effects of mutation on the performance of GA calculations. If the population is in linkage equilibrium, OneMax problem is equivalent to the asymmetric mutation model. We treat the distribution of the first order schema in the frame work of Markov chain, and Wright-Fisher model can give the distributions of the first order schema of One-Max problem and the asymmetric mutation model. The theoretical estimation of the convergence time is also given by using Wright-Fisher model, and can reproduce the convergence time of GA calculation.

There are many theoretical reports on asymmetric mutation model, and thus we can apply these findings to OneMax problem. Another interesting property of asymmetric mutation model is that this model leads to a considerable speed-up of GA calculation[3]. Further works have to be done for the application of the asymmetric mutation model.

REFERENCES

[1] D. E. Goldberg (1999), Lessons from genetic algorithms for the automation of design innovation and creativity. *Evolutionary Design by Computers*, Morgan Kaufmann, San Mateo, CA:105–118

[2] D. Dumitrescu, b. Lazzerini (2000), Evolutionary Computation. *CRC Press*, Boca Raton, FL.

[3] B. Doerr, N. Hebbinghaus and F. Neumann (2006), Speeding up Evolutionary Algorithms through Asymmetric Mutation Operators, *Evolutionary Computation*. 15(4): 401–410

[4] H. Furutani, S. Katayama, M. Sakamoto, M. Ito,(2007), Stochastic Analysis of Schema Distribution in a Multiplicative Landscape, Artificial Life and Robotics 11:101–104

[5] J. W. J. Ewens (2004), *Mathematical Population Genetics. I. Theoretical Introduction*, Second Edition. Springer-Verlag, New York.

[6] H. Furutani (2003), Schema Analysis of OneMax Problem –Evolution Equation for First Order Schemata. in Foundations of Genetic Algorithms 7, Morgan Kaufmann, San Francisco, 9–26

[7] J. F. Crow and M. Kimura (1970), *An Introduction to Population Genetics Theory*, Harper and Row, New York.

[8] W. Y. Tan (2002), *Stochastic Models with Applications to Genetics, Cancers, AIDS and Other Biomedical Systems*, World Scientific, Singapore.

High Signal and Power Integrity Design for VLSI Packaging Using Genetic Algorithms

Moritoshi Yasunaga [1], Hiroki Shimada [1], Shohei Akita [1], and Ikuo Yoshihara [2]

[1]Graduate School of Systems and Information Engineering, University of Tsukuba,
1-1-1 Tennodai, Tsukuba-shi, Ibaraki-ken, 305-8573, Japan
[2]Faculty of Engineering, Miyazaki University,
1-1, Gakuen-kibanadainishi, Miyazaki, Miyazaki, 889-2192, Japan

(Tel: 81-29-852-5323, Fax: 81-29-852-5323)

[1]yasunaga@cs.tsukuba.ac.jp

Abstract: Waveform distortion is one of serious problems in electronic packaging design in GHz-era because conventional impedance matching techniques for waveform improvement do not work anymore. In order to overcome this difficulty and to ensure the signal and power integrities (SI and PI), we have proposed a new techniques called segmental transmission line (STL) already. The STL does not adopt the impedance matching but impedance mismatching between the adjacent segments. We have applied the STL to some transmission systems and have showed its effectiveness in prototype measurements. In this paper, we apply the STL to another transmission system and show it effectiveness. Furthermore, we demonstrate the STL's high waveform learning capability changing the input signal.

Keywords: bus, genetic algorithms, memory module, signal integrity, transmission line

1 INTRODUCTION

One of tough problems in the electronic packaging in GHz-era is waveform distortion in digital signals on PCB traces. This is because the digital signals behave as "waves" and reflection occurs at every impedance mismatching point resulting serious waveform distortions. Furthermore, conventional impedance matching techniques cannot work in the GHz-era anymore.

In order to overcome this difficulty and to ensure the signal integrity (SI) and power integrity (PI), we have proposed a novel transmission line called "Segmental Transmission Line (STL)" already, which is designed based on the genetic algorithms (GAs) [1]. Furthermore, we have also shown its effectiveness using some prototypes already [2][3].Following the successful results in [2][3], in this paper, we demonstrate other experimental results that show high "waveform learning capability" in the STL.

2 SEGMENTAL TRANSMISSION LINE

No waveform distortion occurs in the PCB traces if nothing is connected to them. However, if some devices (e.g., VLSIs or Memory Modules), are connected to the traces (Fig. 1), their inputs, which can be regarded as load capacitances, cause characteristic impedance mismatching and dramatically distort the signals as shown in the lower figure in Fig. 1.

In the STL, a transmission line is divided into multiple (N) segments of individual characteristic impedance Z_i and length L_i as shown in Fig. 2. And each Z_i and L_i are adjusted to achieve an ideal digital waveform at target points such as input-points to the VLSIs on the line by superposing reflection waves generated at the interfaces between adjacent segments Z_i and Z_{i+1}. The adjustment of all Z_is however, results in a combinatorial-explosion-problem because the search-space expands to n^m, where n is the number of impedance and segment-length range candidates and m is the number of segments and it comes to 100^{10}-order usually. We have proposed to apply the genetic algorithms (GAs) to solve this problem and have already shown its effectiveness [1][2][3].

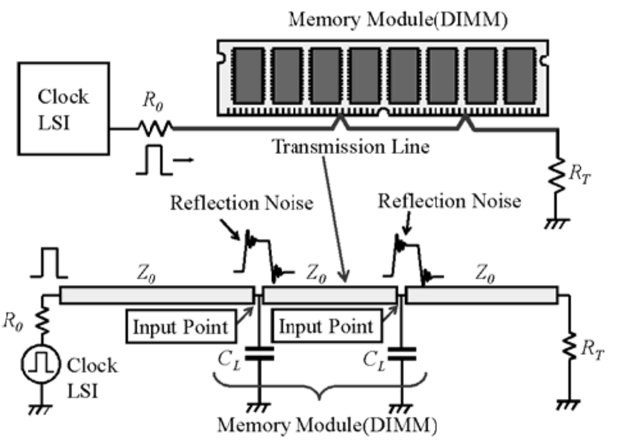

Fig. 1. Waveform distortion in bus-system

Figure 3 shows a bird-eye view and a cross-sectional view of STL in a PCB. Characteristic impedance Z is a function of trace width W, trace thickness T, and insulator thickness D. In the STL, Z is thus controlled easily by adjusting *W*.

The STL structure can be easily and well mapped onto the chromosome of one-dimensional array of genes as shown in the upper figure in Fig. 4. This chromosome is called "Simple Chromosome". In the STL, each segment-length L_i can be also used as a parameter, which expands the search-space more widely to include better solutions. The chromosome composed of both characteristic impedance Z_i and segment-length L_i is called "Hybrid Chromosome". In this variable-length-segment approach, however, we have to be careful not to produce fatal genes under the constraint that the total length is fixed.

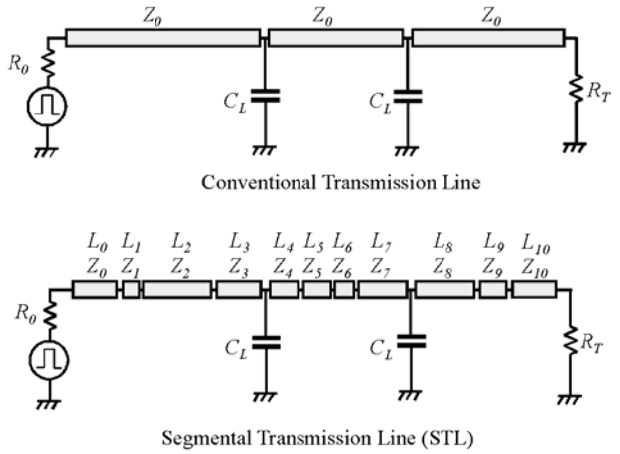

Fig. 2. Conventional transmission line and segmental transmission line (STL) for bus-system

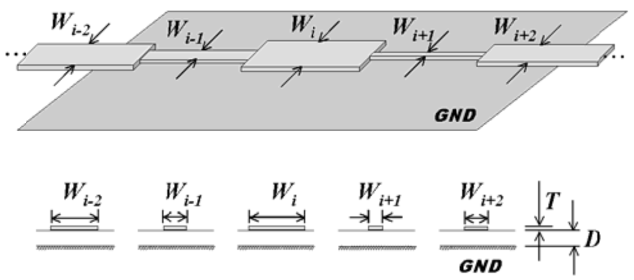

$$Z = f(W, T, D) = \frac{87}{\sqrt{\varepsilon_r + 1.41}} \ln \frac{5.98D}{0.8W + T}$$

Fig. 3. STL applied for PCBs

We have already developed an STL design system called STL Designer. Figure 5 shows outline of the STL Designer that is composed a GA-loop mainly. In the fitness evaluation, the STL Designer outputs the SPICE net list in which the genes, or characteristic impedances and segment lengths are embedded, and the circuit simulator SPICE is started up to simulate the net list. The resultant waveform is then fed back to the STL Designer and evaluated based on the area-difference between the calculated waveform (current waveform) and an ideal waveform as shown in Fig. 6: the difference area *Diff* between the ideal waveform *I*(t) and the current waveform *R*(t) is used for the fitness. The fitness is defined as the reciprocal of this difference area *Diff*.

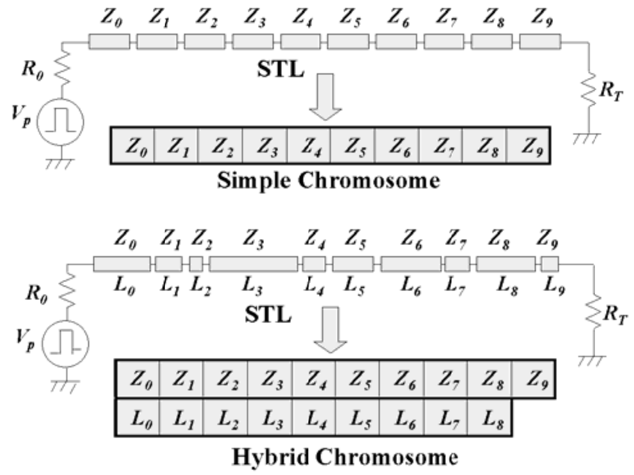

Fig. 4. STLs and their mapping onto chromosomes

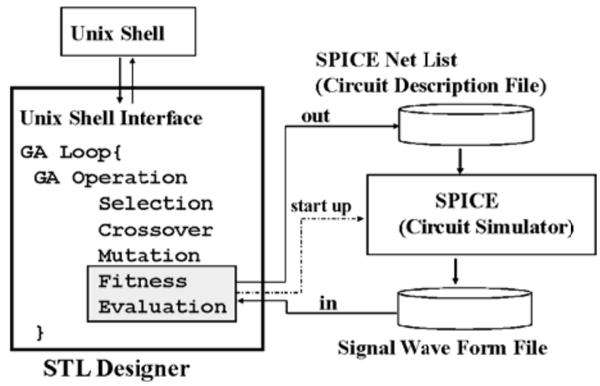

Fig. 5. Configuration of STL Designer

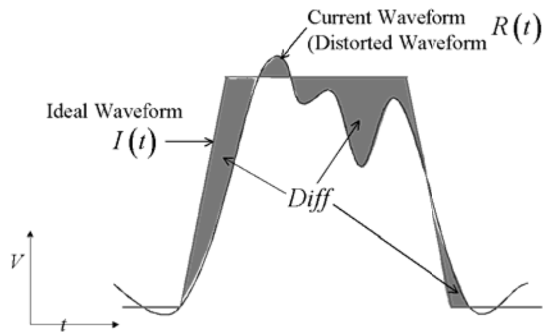

$$Diff = \int_{-\frac{T}{2}}^{\frac{T}{2}} |I(t) - R(t)| dt \qquad fitness = \frac{1}{Diff}$$

Fig. 6. Evaluation of waveforms (fitness used in the STL Designer for bus-system)

3 PROTOTYPE OF STL

3.1 Design Target

A design target for prototype is shown in Fig. 7, where a memory module (DIMM: Dual in-line Memory Module) of two inputs is connected to a 1GHz clock driver LSI through the STL (PCB trace) of 15cm long. Each input is equivalent to a load capacitance of 4pF, which causes the characteristic-impedance mismatch resulting in serious waveform distortion.

The 250MHz STL scale-up prototype is designed based on the 1GH DIMM (Fig. 7): The transmission line length L and the load capacitance C_L are designed to 60cm and 15pF, respectively from the scale-up ratio of 4, i.e., 250MHz to 1GHz. And the transmission line of 60cm is divided into 15 segments (T1 to T15), totally. P_O in the figure is the first input from the clock-driver-LSI to the DIMM and it is the waveform-observation-point in this paper.

3.2 STL Prototype and Its Evaluation

Table 1 shows the design result of characteristic impedance Z and length L of each segment (T1 to T15). We used a set of characteristic impedances from 30Ω to 120Ω at 5Ω intervals. As shown in the table, the lowest characteristic impedance of 30Ω to the highest of 115Ω are assigned in the design. This means many reflection waves are generated in each boundary between adjacent segments, and they are used to improve the distorted wave.

We have fabricated a 250MHz STL scale-up prototype based on the design result shown in Tab. 1. The lower photograph in Fig. 8 is the STL prototype while the upper one is the conventional-transmission-line of Z =50Ω uniformly.

The STL and the conventional-transmission-line both run in each board of 31cm long in U-turn way, where the line-space is designed widely enough to avoid cross-talk noises. Two chip-capacitors (C_L) of 15pF each are connected to the line, which represent the input-capacitances of the memory module (DIMM). In the waveform observation, we used a digital-storage oscilloscope of 2GHz bandwidth and 10GS/s sampling-rate (WR204Xi, LeCroy Ltd.).

Figure 9 shows waveforms observed at P_O in the conventional-transmission-line: the upper ones show simulation results of the input and observed (distorted) waveforms and the lower one shows the observed waveform in the prototype. The waveform in the prototype is dramatically distorted in its shape and amplitude: each pulse loses its sharpness in its rise and fall curves and has small jagged reflections on it. In addition, its amplitude is reduced to 1.06V from 1.8V of original input clock signal. As a result, the clock-signal in the conventional transmission line can be hardly used in the DIMM clock-signals.

Figure 10 shows waveforms observed at P_O in the STL: the upper ones show simulation results of the input and observed (distorted) waveforms and the lower one shows the observed waveform in the prototype. The distorted waveform in the conventional transmission line is well improved in the STL successfully: the reduced amplitude is restored to 1.6V, and jagged reflection noises disappear. The waveform is almost like a trapezoidal wave in its shape, which is close to the original clock-signal. The signal in the STL is thus enough for the clock-signal in its shape.

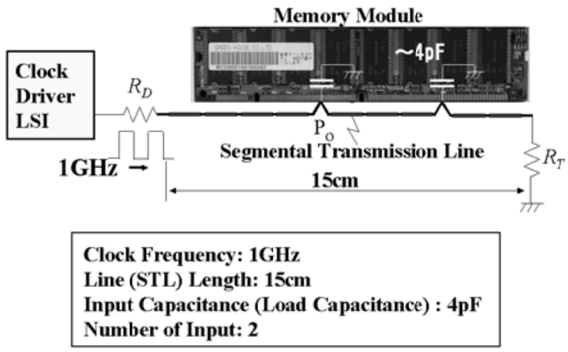

Fig. 7. Design target (1GHz memory-bus system for DIMM)

Table 1. Design result of STL

Seg.	T1	T2	T3	T4	T5	T6	T7	T8
Z(Ω)	35	50	30	35	120	105	45	85
L(mm)	37.5	36	37.5	39	69.5	38.5	40.5	41.5

Seg.	T9	T10	T11	T12	T13	T14	T15
Z(Ω)	115	75	55	105	50	120	76
L(mm)	40	39.5	38.5	42	32	32.5	35.5

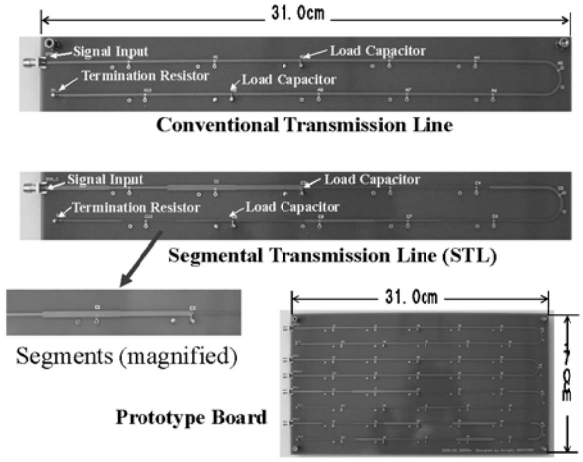

Fig. 8. Photograph of prototype

3.3 Waveform learning capability

In the design for Fig. 10, the input signal waveform outputted from the pulse generator, shown as "Input Signal", is used, and the STL learns it successfully. We have tried another STL design using an idealized trapezoid signal written in SPICE script as the input shown as "Input Signal (Ideal Waveform) in Fig. 11.

Figure 11 shows the STL waveforms designed for the idealized trapezoid signal and observed in the other prototype fabricated in this design, and Tab. 2 shows the STL design result of characteristic impedance and segment length, which can be compared with Tab. 1.

As shown in the results, the STL learns the idealized waveform successfully, and it is demonstrated in the prototype that the observed waveform is changed from the one in Fig. 10 and transforms into a trapezoid waveform closer to the ideal one. This result clearly shows the high waveform learning capability in the STL that can be applied widely to ensure the SI and PI.

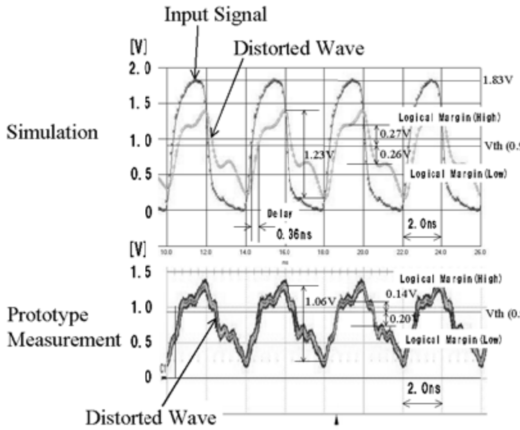

Fig. 9. Waveforms in conventional transmission line

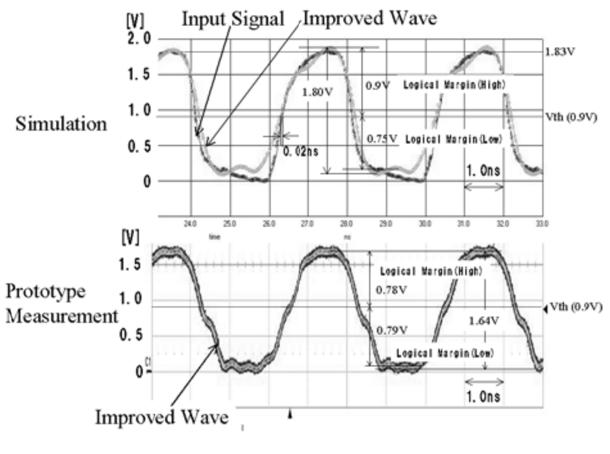

Fig. 10. Waveforms in STL

Table 2. Design result of STL for another input signal

Seg.	T1	T2	T3	T4	T5	T6	T7	T8
Z(Ω)	50	100	65	35	85	30	115	35
L(mm)	36.5	38.5	36.5	38.5	43.5	49.5	43	41.5
Seg.	**T9**	**T10**	**T11**	**T12**	**T13**	**T14**	**T15**	
Z(Ω)	90	30	110	65	40	85	90	
L(mm)	42	42.5	43	45	32.5	33	34.5	

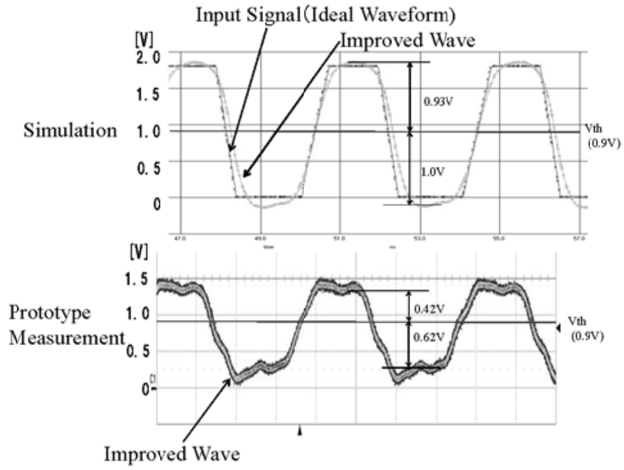

Fig. 11. Waveform in STL for another input signal

5 CONCLUSIONS

The segmental transmission line (STL) for a 1GHz memory bus connected with DIMM (Dual In-line Memory Module) was designed and its prototype was fabricated. The observation results showed that the distorted waveform in the conventional transmission line was restored almost completely in the STL prototype. The observed waveform in the prototype was also well matched the design result, or the simulation result. Effectiveness of the STL to restore the distorted waveform and to ensure the SI and PI was thus well demonstrated experimentally using the prototype. The STL for another input waveform was also designed, and the STL was able to learn the other waveform successfully, which showed the high waveform learning capability of the STL.

REFERENCES

[1] Moritoshi Yasunaga, Ikuo Yoshihara, and Jung, H. Kim, "The Design of Segmental-Transmission-Line for High-Speed Digital Signals Using Genetic Algorithms," Proc. IEEE Congress on Evolutionary Computation (CEC) 2003, Vol. 3. pp. 1748-1755, Canberra, Australia, 2003.

[2] Masami Ishiguro, Hiroshi Nakayama, Yuki Shimauchi, Noriyuki Aibe, Ikuo Yoshihara, and Moritoshi Yasunaga, "Signal-integrity improvement method and its robustness evaluation for VLSI and VLSI-packaging," Artificial Life and Robotics (Springer), Vol.15, No. 3, pp.325-329, 2010.

[3] Hiroki Shimada, Shohei Akita, Masami Ishiguro, Noriyuki Aibe, Ikuo Yoshihara, and Moritoshi Yasunaga, "Digital-signal-waveform improvement on VLSI packaging including inductances," Artificial Life and Robotics (Springer), Vol.16, No. 2, pp.194-197, 2011.

The Seventeenth International Symposium on Artificial Life and Robotics 2012 (AROB 17th '12),
B-Con Plaza, Beppu, Oita, Japan, January 19-21, 2012

Solving a Multi-Objective Constraint Satisfaction Problem with Genetic Algorithms - Making a Food Menu with GAs –

Hironori Fukamachi[1], Yuji Sato[2]

[1,2]Hosei University, Tokyo 184-8584, Japan
(Tel: 81-042-387-6023, Fax: 81-042-387-6048)

[1]hironori.fukamachi.rh@stu.hosei.ac.jp
[2]yuji@k.hosei.ac.jp

Abstract: Generally, it is difficult to make a food menu composed from many limitations. In this paper, we define the problem to make a menu of the one-week meal as a multi-objective constraint satisfaction problem with the upper and the lower limitations. We considered the nutritional composition and a composition of meals. Thereby, the composition of a menu which structured at one composition ought to compete with the nutritional composition. Additionally, we propose a method to apply Genetic Algorithm solving this making menu problem, thus we evaluate menus by applying multiple functions with GA. In conclusion, the results means that the composition of meals don't compete with the nutritive composition, moreover these are not correlation.

Keywords: Genetic Algorithm, Food Menu, Pareto optimal solution

1 INTRODUCTION

Generally, it is difficult to think about making a food menu. At first, a dietitian counsels a patient, next, the dietitian makes menu after defines the table of nutritional composition and the dietary composition list, at the last, examines the menu. Making menu, there are limitations which consist of the healthy situation, the salary dietary standard, the everyday nutrition situation, age, gender, taste, dietary habits and the activity level. According to food group selected for the menu, the dietitian makes the dietary composition list which determined the consumption to meet the table of nutritive composition. The dietitian makes a menu which considered the made dietary composition list, a season, colors and a pattern based on the set consisting of staple food, master greens, vice-greens, soup and dessert. In addition, the dietitian checks the menu. Because it is very serious that the dietitian makes a menu in this process and that the dietitian adjusts a menu fine, the menu is desirable to be made automatically. Furthermore, it is desirable for the best multiple solutions to be generated as the menu, because the only one menu should not be generated uniquely. Therefore, in this paper, we propose a menu making method using Genetic Algorithm; GA, thereby we discuss the method.

2 PROBLEMS IN MAKING MENU

In the menu making, at first, it becomes the problem whether the patient can take necessary nutritive value without over value. The index for nutritive values is determined with "Japanese nutrition standard" [1] in Japan. There are nutrients which are not applied the tolerable upper intake level, whereas a large quantity of intake is not recommended. Therefore, we determine a standard of intake in reference to recommended dietary allow or adequate intake. In addition, a combination of staple food, the main greens, vice-greens and soup is necessary to make menu. We suggest an application method of GA for the purpose of various menu making at next section.

3 Proposal of the GA application method

3.1. Structure of chromosome for various menu

At first, we define the individual. Fig. 1 illustrates an individual's chromosome of the menu. This chromosome has 21 lists. These lists have various number array from 1 to 5 length. The numbers mean a dish.

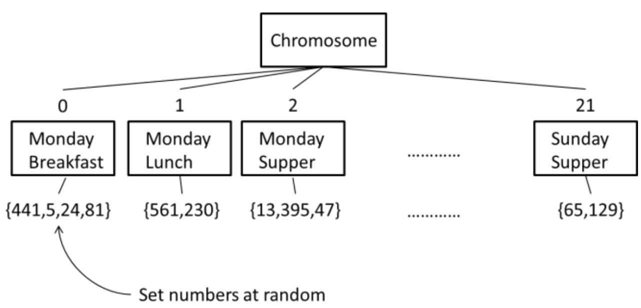

Fig. 1. The structure of a food menu's chromosome

3.2. Crossover method

We crossover the elements in 21 lists. The lists mean one meal, for example, breakfast, lunch, or supper. The number of dishes in the meal is various numbers. In addition, there is not numbers in the lists. Therefor, we crossover elements in the lists between same index of lists at random. If there is no number to crossover in the list, the number is changed to null.

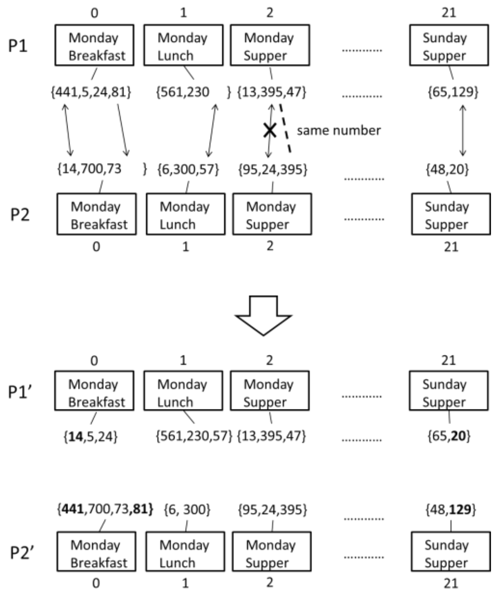

Fig.2. Crossover method for various length of gene

3.3. Method to evaluate the individual

3.3.1 Method to evaluate nutrient composition

We propose the method to evaluate balance of nutritive values. For example, when we evaluate value of total fat, we refer to “Japanese Nutrition Standard”[1]. Table. 1 shows the standard of fat intake. Additionally, We refer to “Nation health nourishment investigation”[2]. Table. 2 shows the distribution of fat intake. Therefore, we show an expression (1) using normal distribution. Fig.3 shows expression (1).

$$f(x) = N(\mu, \sigma^2)\cdot\sqrt{2\pi}\sigma = e^{-\frac{(x-\mu)^2}{2\sigma^2}} \qquad (1)$$

Consequently, the evaluation function of the lipid intake everyday is next expression (2) like Fig. 4.

$$f_{fat}(x) = \begin{cases} 1 & if\ \ 20 \le x < 30 \\ \frac{1}{2}\left(1 + erf\,\frac{x-20}{\sqrt{2}\sigma}\right) & if\ \ 0 \le x < 20 \\ \frac{1}{2}\left(1 - erf\,\frac{x-50}{\sqrt{2}\sigma}\right) & if\ \ x \ge 30 \end{cases} \qquad (2)$$

Table.1. The table of the fat intake standard

Age	Fat	
	Man	Woman
	DG(FPE*:%)	DG(FPE:%)
1~2 3~5 6~7 8~9 10~11 12~14 15~17 18~29	less than 30 more than 20	less than 30 more than 20
30~49 50~69 Over 70	less than 25 more than 20	less than 25 more than 20

* $FPE = Total\ Fat(g)\cdot 9(kcal/g)/Total\ Energy(kcal)\cdot 100$

Table.2. Distributions of fat intake

	people	μ	σ
The whole country	8,762	25.3	7.5

Percentile								
1	5	10	25	50	75	90	95	99
8.2	13.3	15.8	20.3	25.3	30.2	34.9	37.5	43.3

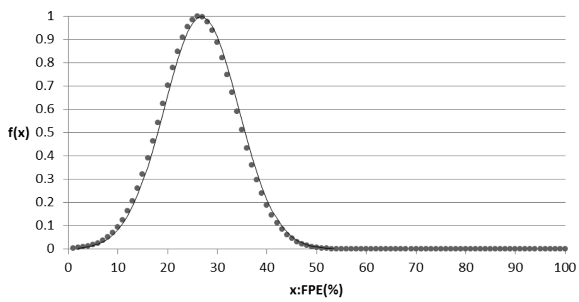

Fig.3. Normal distribution of fat intake

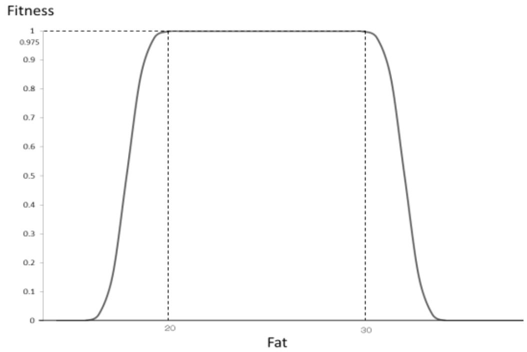

Fig.4. Fitness of fat intake

As a result, we show the function (3) which evaluates the nutritive intake every day. The number of nutrients is N.

$$f_{Nutritive} = \frac{1}{N}\sum_{k=1}^{N} f_k \tag{3}$$

3.3.2 Method to evaluate composition of dishes

The Japanese general menu structured with the mod el; soup, three side dishes and rice." The three dishes consisted of two vegetable dishes and one meat or fish dish. We make the menu which applied this model.

We classify dishes in A: Staple food, in B: Meat or fish dish, in C: Vegetable dish, in D: Soup, in E: Others; likes a fruit. Additionally, we give a point to the dishes (4).

$$\begin{aligned} W &= \{\lambda_A, \lambda_B, \lambda_C, \lambda_D, \lambda_E\} \\ &= \{0.2, 0.2, 0.1, 0.2, 0.2\} \end{aligned} \tag{4}$$

For example, if the menu is consisted of dish1: curry and rice, dish2: salad, and dish3: soup, we express three equations (5), (6), (7). The dish1 includes A, B, and C. The dish2 is C. The dish3 is D. Therefore, these three dishes can be expressed with byte code like follow equations. Consequently, this menu can be expressed with an equation (8).

$$dish\ 1 = \{1, 1, 1, 0, 0\} \tag{5}$$

$$dish\ 2 = \{0, 0, 1, 0, 0\} \tag{6}$$

$$dish\ 3 = \{0, 0, 0, 1, 0\} \tag{7}$$

$$\begin{aligned} table &= dish\ 1 + dish\ 2 + dish\ 3 \\ &= \{1, 1, 2, 1, 0\} \end{aligned} \tag{8}$$

Consequently, we define the function (9) which evaluates composition of dishes applying equation (4) to the array of a menu like the equation (8).

$$f_{table} = 1 - \left| 1 - table\, W^t \right| \tag{9}$$

In the case of the equation (8), a fitness value is 0.8. Therefore, from an expression (9), we define a purpose function for the composition of the menu every day the next expression (10).

$$f_{Composition} = \frac{1}{3}\sum_{k=1}^{3} f_{table_k} \tag{10}$$

If we evaluate the composition of the example menu consisting of soup, three side dishes and rice, that menu's evaluate level is maximum 1.

3.3.3 Method to evaluate a food menu

Thereby we express equation (3) is f_0, and equation (10) is f_1, we define purpose function which evaluates composition of menu everyday (11).

$$f_{Day} = \lambda_0 \cdot f_0 + \lambda_1 \cdot f_1 \tag{11}$$

$$\text{subject to} \quad \lambda_0 + \lambda_1 = 1 \quad (\lambda_0 \geq 0,\ \lambda_1 \geq 0) \tag{12}$$

Consequently, we define the evaluation function of the one-week menu which is 1 individual applying the equation (11) with the next equation (13).

$$f_{week} = \frac{1}{7}\sum_{k=1}^{7} f_{Day_k} \tag{13}$$

4 EXPERIMENT

4.1. Experimental method

4.1.1 Input and output

We prepared 700 samples of the dish, and we used each nutritive value, and the sample referred to the thing of the recipe site [4].

About nutrients, we consider energy, protein, total lipid, cholesterol, carbohydrates, a dietary fiber, vitamin B_1, vitamin B_2, niacin, vitamin B_6, folic acid, vitamin B_{12}, pantothenic acid, vitamin C, vitamin A, vitamin E, vitamin D, vitamin K, magnesium, calcium, phosphorus, ferrum, manganese, copper, zincum, sodium, potassium.

We set 25 years old, life activity level with 2 at a man who is menu user. The program prints the last population and an elite individual.

4.1.2 Setting GA parameters

We use the roulette selection and uniform crossover, population size with 100, generation size with 1000, mutation rate with 0.02, crossover rate with 0.25, the number of the elite preservation with 1. We change weights of functions in equation (12) by 0.1.

4.2. Experimental Results

The results appear in Fig. 5, Fig. 6. The graph in Fig.5 illustrates the evaluation level of functions (3), (10), (13). The scatter diagram in Fig. 6 shows fitness values of the composition of dishes and of the nutritive values.

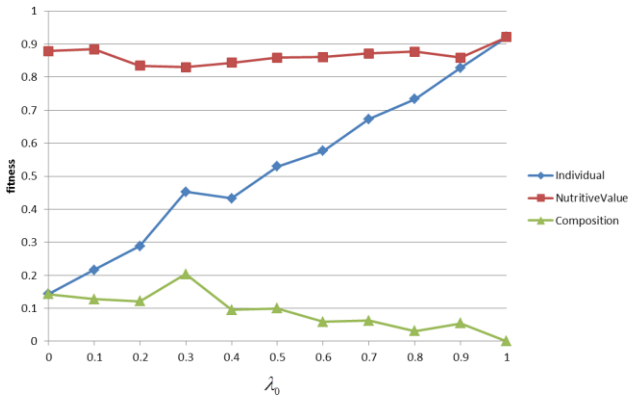

Fig.5. Diferrence of fitness about three functions

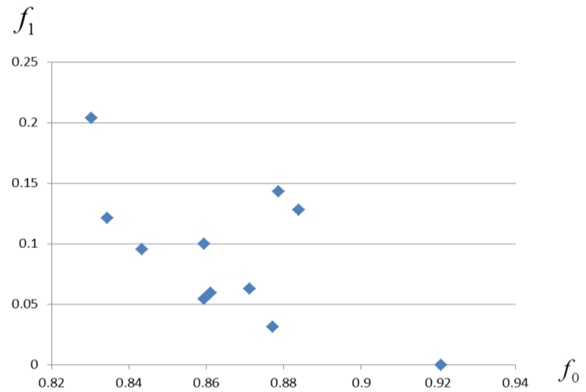

Fig.6. Scatter diagram with two functions

5 DISCUSSION

The nutritive values and the composition of dishes are seem not to have competetivity, moreover these are not correlation.in Fig.1 and Fig.2. It is easy to balance the nutritive values of the food menu, however, it is difficult to balance the composition of the dishes. When the composition of dishes decided strictly, the fitness of individual is very low. Therefore, the purpose function of the composition of dishes is necessary to be considered as important function. As the reason why an evaluation of the constitution of the dishes is low, the classification method of dishes is variable by a culture. For example, we classify the scone which is rich in carbohydrates as others this experiment and classify potato dishes as vice-greens. However, if we classify these meals as staple foods, the fitness value of individuals may be up. We change the classification of the dishes and the weight of the functions in the next research.

6 CONCLUSION

In this paper, we proposed an application method using GA for the menu making problem. The menu ought to be satisfying balance of the intake nutritive value and the composition of the meal consisting of soup, three side dishes and rice.

REFERENCES

[1] Ministry of Health, Labour and Welfare (2010), Japanese nutrition standard (in Japanese).

[2] Ministry of Health, Labour and Welfare (2003), Nation health nourishment investigation (in Japanese).

[3] Applied fuzzy system guide (1989) (in Japanese), pp.137-139

[4] Bob and Angie (in Japanese).
http://www.bob-an.com/

Improvement of the Reinforcement Learning Efficiency Using Individually Reward Value Allotment of the Soccer Video Game Agent

Daisuke Inami[1], Yuuki Sakaguchi[2], and Yuji Sato[1,2]

[1]Graduate School of Computer and Information Sciences, Hosei University, Tokyo 184-8584, Japan
[2]Facalty of Computer and Information Sciences, Hosei University, Tokyo 184-8584, Japan

(Tel: 81-042-387-6023, Fax: 81-042-387-6048)

[1]daisuke.inami.vy@stu.hosei.ac.jp

Abstract: Recently, soccer game algorithm has become shorter life cycle, due to complex game environment. We proposed hybrid classifier system for soccer video game simulation in recent paper and it indicated that hybrid classifier system is effective for online soccer strategy learning system. In this paper, we propose an individually role assignment for soccer game agent to reduce learning time and to achieve higher winning rate. We investigated individually role assignment by referring using real world soccer role assignment. Forwards agent's reward of shot should be high, and midfielder agent's should be separated into center and outer. We evaluated learning efficiency of our algorithm. As a result, it was found that winning rate of our algorithm with individually role assignment achieved greater than our former algorithm without individually role assignment.

Keywords: Classifier system, Reinforcement learning, Soccer game strategy

1 INTRODUCTION

Recently, it is common in the production of video games for human designers to explicitly specify the decision-making algorithms to be used by game agents. Meanwhile, video game environment has been changing offline to online in recent years. As a result, there are two problems in producing decision making algorithms. First, a single algorithm cannot possible satisfy all users, and as the number of users increase, differences in strategies is needed. Second, the appearance of users with advanced techniques has generated a need for decision-making algorithms under even more complicated environments. In additionally, as the Internet makes it easy for new users to appear one after another, it must be possible to provide and maintain bug-free programs that support such complex decision-making algorithms in a time frame much shorter than that in the past. As a means for addressing the above problem, taking a soccer game as an example of a video game. We have already proposed a hybrid learning classifier system [1] and we have also shown that we can automate the setting of reward values using genetic algorithms [2].

In this paper, we propose individually reward value allotment to soccer agents. Section 2 presents an overview of the conventional soccer game on which this study is based. In Section 3 we present soccer agent with individually role assignment. In Section 4 we present an evaluation method and the results of our tests, and we finally conclude with a summary.

2 CONVENTIONAL SOCCER VIDEO GAME AND ASSOCIATED PROBLEMS

The team of our soccer video game has 11 players each team. Two teams battle for the most points. Figure 1 shows a typical game scene targeting the area around the current position of the ball.

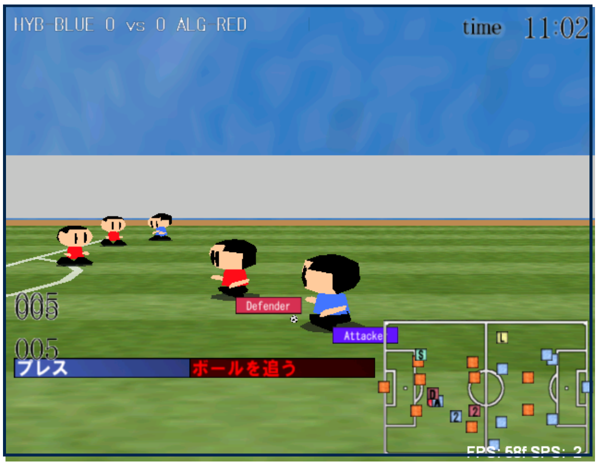

Fig. 1. Example of a typical game scene

We have studied the equipping of game programs with machine learning functions as an approach to solving the above problems. A number of techniques can be considered for implementing machine learning functions such as Q-learning [4] and genetic algorithms. We have decided on incorporating functions for acquiring rules based on classifier systems. We came to this decision considering the many examples of applying evolutionary computation to the acquisition of robot decision-making algorithms [5-8], learning classifier systems takes advantage of Gas and reinforcement learning to build adaptive rule-based systems that learn gradually via online experiences [4].

IF-THEN from learning methods is suitable for problem of selecting action under a situation such as game algorithm. As a result, IF-THEN learning methods can decreases bugs and increase mentenability.

Classifier system has rule set consist of condition part and consequents part. Rule held in IF-THEN form. Classifier system feedbacks selected action rules from rule set. It detects situation from environment by detector. Figure 2 is an overview of our hybrid classifier system. To improve learning efficiency, we proposed hybrid classifier system. Hybrid classifier system keeps privileged rules and learned rules from game. We succeeded learning time shorter by using hybrid classifier system. Figure 3

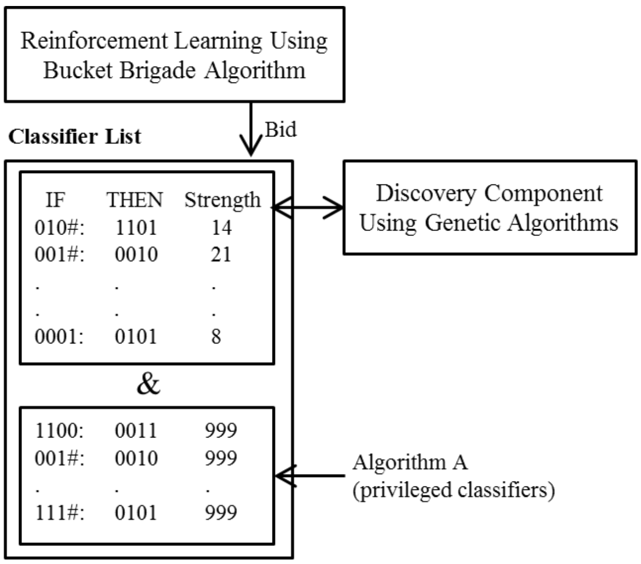

Fig.2. Overview of hybrid classifier system

Classifier system uses bucket brigade algorithm. System can learn continuous stream of action considering time series. In our previous study [3], we used 4-4-3 formation and FW, MF, DF. However, in real soccer game, FW can separated into side FW and center FW, DF can separated into center back and full back and required role is different. Separating position only FW, MF, DF can cause contradiction of role. For example, side MF should be more aggressive than center MF. Therefore, we can expect improve learning efficiency by defining player role more precisely.

3 INIDIVIDUALLY ROLE ALLOTMENT

We propose individually role allotment agent to solve these problems, and increase learning efficient, and set reward value based on real soccer game. Figure 3 shows overview of individually role allotment.

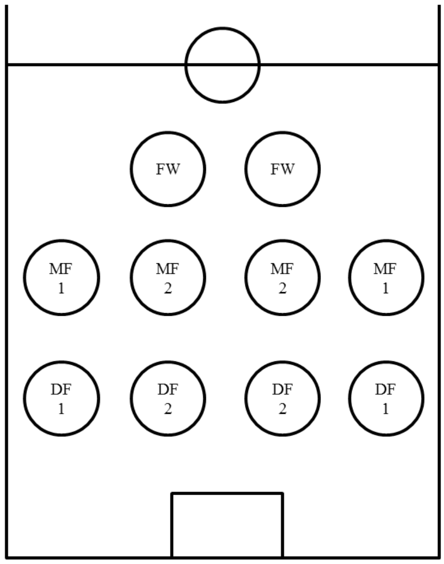

Fig.3. Individually role allotment agent

(I) FW

To get goal is priority role. Therefore we set get goal reward value high.

(II) MF (Center)

To pass ball to FW from DF is priority role. We expect pass route like DF2 to MF2 and forward from figure 3. Therefore we set dribble reward value and pass reward value high.

(III) MF (Side)

This position is relatively aggressive than (II). We expect pass route like DF1 to MF1 and forward from figure 3 this role also get goals if chance happen. We set dribble, pass, and get goal reward value high.

(IV) DF (Center)

To defend from opponent team is priority role. Therefore we set get ball reward value high.

(V) DF (Side)

This position is relatively required ability of pass than (IV), for example, we expect pass route like DF1 to MF1 or MF2, so we set dribble, pass, and get ball reward value high.

4 EXPERIMENT

4.1 Experimental method

Experiment conducts using 2 teams includes 22 agents. Conducts match with team using hybrid learning system and tem using only algorithm without learning system.

We define 200 matches as one learning and 30 learning is one set, and obtain winning rate. We use 4 reward settings such as Base, Position, Attack and Balance and conduct a match with algorithm A, B and C then investigate efficiency of individually role allotment.

There are three opponent algorithms with decision-making system A, B, and C. Algorithm A is a balanced team which attack and defense ability is balanced. Algorithm B is offensive team which attack ability is better than offence ability. Algorithm C is defensive team which defense ability is better than attack ability.

Table1 shows a Base reward. Base is designed to compare with a team which reward value is set by position. Therefore base team's reward value is set uniformly.

Table.1. Reward value of Base

Base	FW	MF	MF2	DF	DF2
GETGOAL	60	60	60	60	60
PASS	16	16	16	16	16
DRIBBLE	4	4	4	4	4
GETBALL	25	25	25	25	25
LOSTBALL	−50	−50	−50	−50	−50

Table2 shows a Position reward. Position is designed to compare with a team which reward value is set by individually. Therefore position team's reward value is set by position and do not separate reward value by MF1, MF2.

Table.2. Reward value of Position

Position	FW	MF	MF2	DF	DF2
GETGOAL	80	50	50	35	35
PASS	8	16	16	16	16
DRIBBLE	2	4	4	4	4
GETBALL	15	35	35	50	50
LOSTBALL	−50	−50	−50	−50	−50

Table3 shows a Balance reward. Balance's reward value is set by individually and this is our proposal. We set reward value individually like FW, MF1, MF2, DF1, DF2.

Table.3. Reward value of Balance

Balance	FW	MF	MF2	DF	DF2
GETGOAL	80	50	65	35	50
PASS	8	16	8	16	8
DRIBBLE	2	4	2	4	2
GETBALL	15	35	30	50	55
LOSTBALL	−50	−50	−50	−50	−50

Table4 is an Attack reward. Attack's reward value is set by individually like Balance, and we set relatively offensive than Balance team. We investigate winning rate with Balance team and Attack team, to find difference between two team.

Table.4. Reward value of Attack

Attack	FW	MF	MF2	DF	DF2
GETGOAL	80	50	60	35	45
PASS	8	16	12	16	12
DRIBBLE	2	4	3	4	3
GETBALL	15	35	30	50	45
LOSTBALL	−50	−50	−50	−50	−50

We use under formula (1) to calculate winning rate.

$$R_w = N_w / (N_t - N_c) \qquad (1)$$

Nt is a number of total match, *Nd* is a number of draw, *Nw* is a number of win. We define one set is 30 learning and one learning is 200 match.

4.2 Experimental result

4.2.1 Experimental result with algorithm A

Figure 4 is an experimental result of match with Base, Position, Attack and Balance to Algorithm A. Attack's winning rate is higher than Position from 3rd match and winning rate is 77% at 100th match. Balance's winning rate is higher than Position from 2nd match and winning rate is 78 % at 100th match.

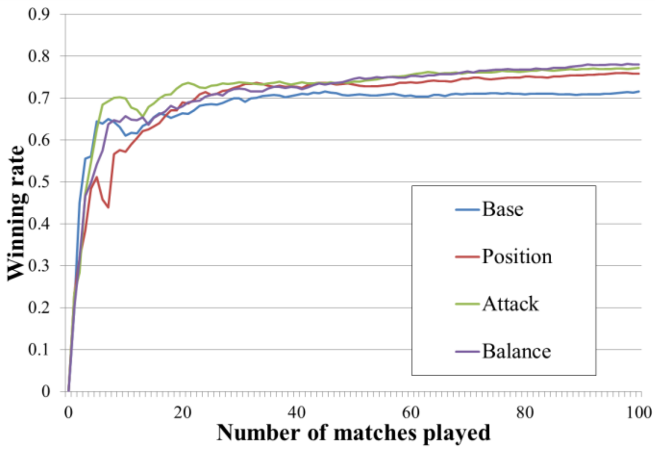

Fig.4. Winning rate with algorithm A

4.2.2 Experimental result with algorithm B

Figure 5 is an experimental result of match with Base, Position, Attack and Balance to Algorithm B. Balance's winning rate is 82% at 9th match and 84% at 100th match.

Balance's winning rate is 82% at 9th match while Position's winning rate is 69%.

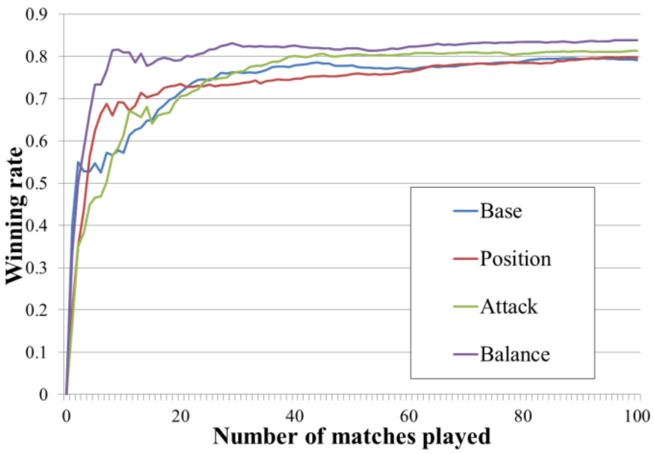

Fig.5. Winning rate with algorithm B

4.2.3 Experimental result with algorithm C

Figure 6 is an experimental result of match with Base, Position, Attack and Balance to Algorithm C. Balance's winning rate is 73% at 100th match while Position's winning rate is 69% at 100th match.

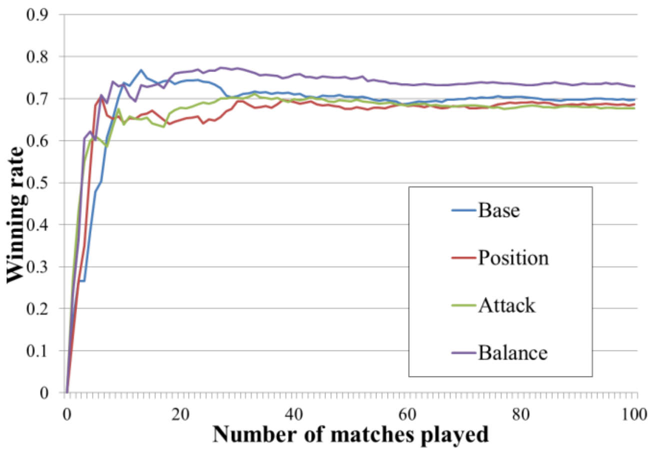

Fig.6. Winning rate with algorithm C

5.4 DISCUSSION

Compare individually role allotment agent with position agent, individually role allotment agent's winning rate average is higher than position agent with algorithm A at 2%, algorithm B at 7%, algorithm C at 7%. Balance team's winning rate is higher than Attack team's winning rate. Especially, this result is same with algorithm C which is defensive team. From this result, only raising offensive reward cannot cause raise of winning rate.

One reason of individually role allotment agent' winning rate is higher than position agent and offensive reward table does not always raise winning rate is we guess contradiction of rule set of classifier system decreased, because individually role allotment is more specific reward allotment than position role allotment. Second reason is the possibility of number of communication between players increased, so offensive reward table may interrupt communications between players and balanced reward table may assist increase of communications between players.

6 CONCLUSION

We proposed individually role allotment agent. From experimental result, individually role allotment agent obtained higher winning rate than position role allotment agent' winning rate, and offensive reward table do not always cause raise winning rate. Communications between players may one factor of winning rate. We continue to research about what factor is relate with winning rate.

REFERENCES

[1] J.H. Holland (1992), Adaptation in Natural and Artificial Systems. The MIT Press, Cambridge, MA

[2] Y. Sato, R. Kanno (2005), Event-driven Hybrid Learning Classifier System for Online Soccer Games. In Proceedings of the 2005 IEEE Congress on Evolutionary Computation, IEEE Press

[3] Y. Sato, Y. Inoue, Y. Akatsuka (2007), Applying GA to Self-allotment of Rewards in Event-driven Hybrid Learning Classifier Systems. In Proceedings of the 2007 IEEE Congress on Evolutionary Computation, IEEE Press, Singapore, pp. 1800-1807

[4] R.S. Sutton, A.G. Barto (1998), Reinforcement Learning: An Introduction. The MIT Press, Cambridge, MA

[5] S.M. Gustafson, W.H. Hsu (2001), Layered Learning in Genetic Programming for a Cooperative Robot Soccer Problem. In Proceedings of the Fourth European Conference on Genetic Programming, pp. 291-301

[6] S. Luke (1998), Genetic Programming Prodeced Competitive Soccer Softbot Teams for RoboCup 97. In Proceedings of the Third Annual Genetic Programming Conference, Morgan Kaufmann Publishers, San Francisco, CA, pp. 204-222

[7] A.D. Pietro, L. While, L. Barone (2002), Learning in RoboCup Keepaway using Evolutionary Algorithms. In Proceedings of the Fourth Annual Genetic and Evolutionary Computation Conference, Morgan Kaufmann Publishers, San Francisco, CA, pp.1065-1072

[8] T. Yamaguchi, Y. Nomura, Y. Tanaka, M. Yachida (1996), Acquiring Various Behaviours by Isomorphism of Actions in Reinforcement Learning. In Proceedings of IROS-96 Workshop on RoboCup, Osaka, pp. 40-46

Proposal and Implementation of CAM System for Industrial Robot RV1A

S. Yoshitake, F. Nagata and A. Otsuka
Tokyo University of Science, Yamaguchi
Sanyo-Onoda, Japan

K. Watanabe
Okayama University
Okayama, Japan

Maki K. Habib
American University in Cairo
Cairo, Egypt

Abstract

A CAM system for an articulated-type industrial robot RV1A is described from the viewpoint of robotic servo controller. It is defined here that the CAM system includes an important function that allows the industrial robot to move along cutter location data (CL data) consisting of position and orientation components. Another important point is that the proposed CAM system has a high applicability to other industrial robots whose servo systems are technically opened to end-user engineers. Our CAM system works as a straightforward interface without using any robot languages between CAD/CAM and industrial robots. Here, in order to raise the relationship between a conventional CAD/CAM and an industrial robot, a design and an implementation of CAM system are shown.

1 Introduction

Up to now, many studies focusing on the teaching of industrial robots have been conducted. Several promising teaching systems for industrial robots have been already developed according to each task. However, it seems that CAM system from the viewpoint of robotic servo system has not been sufficiently discussed yet.

In this paper, it is defined that CAM system includes an important function that enables an industrial robot to be accurately controlled along CL data consisting position and orientation components. Another important point is that the proposed CAM system has a high applicability to other industrial robots whose servo systems are technically opened to engineering users. At the present stage, the relationship between CAD/CAM and industrial robots is not deep, compared to NC machine tools widely spread in manufacturing industries. It seems that the CAM/CAM technology generating NC codes is technically matured for various NC machine tools. On the other hand, however, the CAM system for industrial robots has not been sufficiently considered and standardized yet, so that there still exist many kinds of robot languages. That is the reason why when an industrial robot is applied to a task, the required position and orientation data are acquired by on-line and/or off-line teaching system in almost all cases.

In this paper, a CAM system for an articulated-type industrial robot RV1A shown in **Fig. 1** is described from the viewpoint of robotic servo controller.

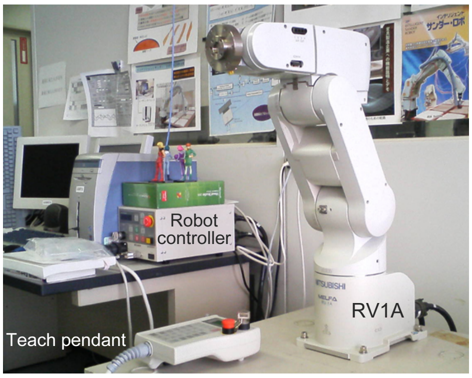

Figure 1: Desktop-size industrial robot RV1A.

The RV1A is one of the industrial robots provided by Mitsubishi Electric Corporation. In order to raise the relationship between a CAD/CAM and the industrial robot, a simple and straightforward CAM system is proposed. A basic design of the CAM system and experimental results are shown.

2 Desired Trajectory

2.1 Main-processor of CAM

Various kinds of CAD/CAM such as Catia, Unigraphics, Pro/Engineer, etc. are widely used in manufacturing industries. The main-processor of each CAM can generate CL data consisting of position and orientation components along a 3D model. In this section, how to calculate desired position and orientation for robotic servo system is described in detail.

For example, robotic sanding task needs a desired trajectory so that the sanding tool attached to the tip of the robot arm can follow the object's surface, keeping contact with the surface from the normal direction. If the object is fortunately designed by a CAD/CAM and manufactured by an NC machine tool, then CL data can be referred to as the desired trajectory consisting of position and orientation elements. It is important to show a guideline for raising the relationship between main-processor of CAD/CAM and industrial robot, which is the role of the CAM system proposed after this section.

2.2 Position and orientation for discrete-time control system

In order to realize non-taught operation, we have already proposed a generalized trajectory generator [1]

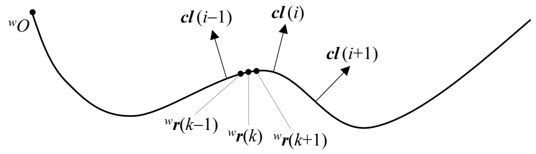

Figure 2: Relation between CL data $\boldsymbol{cl}(i)$ and desired trajectory ${}^w\boldsymbol{r}(k)$, in which ${}^wO$ is the origin of work coordinate system.

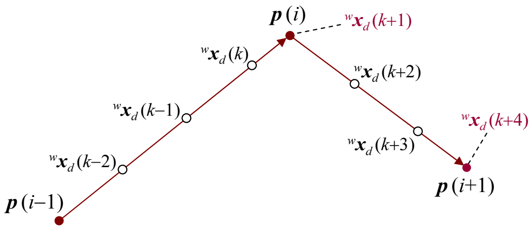

Figure 3: Relation between position component $\boldsymbol{p}(i)$ in CL data and desired position ${}^w\boldsymbol{x}_d(k)$, in which $\boldsymbol{p}(i) - {}^w\boldsymbol{x}_d(k)$ and $\boldsymbol{p}(i+1) - {}^w\boldsymbol{x}_d(k+3)$ are called the fraction vectors.

using CL data, that yields desired trajectory ${}^w\boldsymbol{r}(k)$ at the discrete time k given by

$$ {}^w\boldsymbol{r}(k) = \left[{}^w\boldsymbol{x}_d^T(k)\ {}^w\boldsymbol{o}_d^T(k)\right]^T \tag{1}$$

where the superscript w denotes the work coordinate system, ${}^w\boldsymbol{x}_d(k) = [{}^wx_d(k)\ {}^wy_d(k)\ {}^wz_d(k)]^T$ and ${}^w\boldsymbol{o}_d(k) = [{}^wo_{dx}(k)\ {}^wo_{dy}(k)\ {}^wo_{dz}(k)]^T$ are the position and orientation components, respectively. ${}^w\boldsymbol{o}_d(k)$ is the normal vector at the position ${}^w\boldsymbol{x}_d(k)$. In the following, we explain in detail how to make ${}^w\boldsymbol{r}(k)$ using the CL data.

A target workpiece with curved surface is generally designed by a 3D CAD/CAM, so that CL data can be calculated by the main-processor. The CL data consist of sequential points along the model surface given by a zigzag path or a whirl path. In this approach, the desired trajectory ${}^w\boldsymbol{r}(k)$ is generated along the CL data. The CL data are usually calculated with a linear approximation along the model surface. The i-th step is written by

$$\boldsymbol{cl}(i) = [p_x(i)\ p_y(i)\ p_z(i)\ n_x(i)\ n_y(i)\ n_z(i)]^T \tag{2}$$
$$\{n_x(i)\}^2 + \{n_y(i)\}^2 + \{n_z(i)\}^2 = 1 \tag{3}$$

where $\boldsymbol{p}(i) = [p_x(i)\ p_y(i)\ p_z(i)]^T$ and $\boldsymbol{n}(i) = [n_x(i)\ n_y(i)\ n_z(i)]^T$ are position and orientation vectors based on the origin ${}^wO$, respectively. ${}^w\boldsymbol{r}(k)$ is obtained by using both linear equations and a tangential velocity scalar v_t called feed rate.

A relation between $\boldsymbol{cl}(i)$ and ${}^w\boldsymbol{r}(k)$ is shown in **Fig. 2**. In this case, assuming ${}^w\boldsymbol{r}(k) \in [\boldsymbol{cl}(i-1), \boldsymbol{cl}(i)]$ we obtain ${}^w\boldsymbol{r}(k)$ through the following procedure. First, a direction vector $\boldsymbol{t}(i) = [t_x(i)\ t_y(i)\ t_z(i)]^T$ is given by

$$\boldsymbol{t}(i) = \boldsymbol{p}(i) - \boldsymbol{p}(i-1) \tag{4}$$

so that v_t is decomposed into x-, y- and z-components

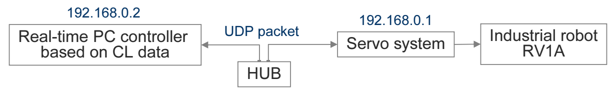

Figure 4: Block diagram of communication system by using UDP packet.

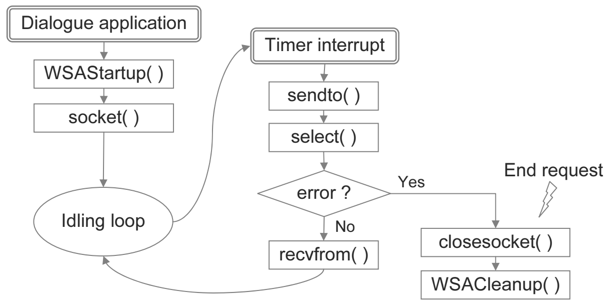

Figure 5: Communication scheme by using UDP packet between PC and Industrial robot RV1A, in which the sampling period Δt is set to 10 ms.

in work coordinate system as written by

$$v_{tj} = v_t \frac{t_j(i)}{\|\boldsymbol{t}(i)\|} \quad (j = x, y, z) \tag{5}$$

Using a sampling width Δt, each component of the desired position ${}^w\boldsymbol{x}_d(k)$ is represented by

$${}^wx_d(k) = {}^wx_d(k-1) + v_{tx}\Delta t \tag{6}$$
$${}^wy_d(k) = {}^wy_d(k-1) + v_{ty}\Delta t \tag{7}$$
$${}^wz_d(k) = {}^wz_d(k-1) + v_{tz}\Delta t \tag{8}$$

Next, how to calculate the desired orientation $\boldsymbol{o}_d(k)$ is considered. By using the orientation components of two adjacent steps in CL data, a rotational direction vector $\boldsymbol{t}_r(i) = [t_{rx}(i)\ t_{ry}(i)\ t_{rz}(i)]^T$ is defined as

$$\boldsymbol{t}_r(i) = \boldsymbol{n}(i) - \boldsymbol{n}(i-1) \tag{9}$$

Each component of desired orientation can be linearly calculated with $\boldsymbol{t}_r(i)$ as

$${}^wo_{dj}(k) = n_j(i-1) + t_{rj}(i)\frac{\|\boldsymbol{x}_d(k) - \boldsymbol{p}(i-1)\|}{\|\boldsymbol{t}(i)\|} \quad (j = x, y, z) \tag{10}$$

${}^w\boldsymbol{x}_d(k)$ and ${}^w\boldsymbol{o}_d(k)$ shown above are directly obtained from the CL data without either any conventional complicated teaching process or recently proposed off-line teaching methods. The desired position and orientation in the discrete time domain are very important to control the tip of an industrial robot in real time, i.e., to design a feedback control system.

If the linear approximation is applied when CL data are generated by the main-processor of CAD/CAM, CL data forming a curved line are composed of continuous minute lines such as $\|\boldsymbol{p}(i) - \boldsymbol{p}(i-1)\|$ and $\|\boldsymbol{p}(i+1) - \boldsymbol{p}(i)\|$ shown in **Fig. 3**. In this case, it should be noted that each position vector in CL data such as $\boldsymbol{p}(i)$ and $\boldsymbol{p}(i+1)$ shown in **Fig. 3** have to be carefully dealt with in order to be accurately followed along the CL data. For example, ${}^{w}\boldsymbol{x}_d(k+1)$ and ${}^{w}\boldsymbol{x}_d(k+4)$ are not calculated by using Eqs. (6), (7) and (8) but have to be directly set with $\boldsymbol{p}(i)$ and $\boldsymbol{p}(i+1)$, respectively, just before the feed direction changes. $\|\boldsymbol{p}(i) - {}^{w}\boldsymbol{x}_d(k)\|$ and $\|\boldsymbol{p}(i+1) - {}^{w}\boldsymbol{x}_d(k+3)\|$ are called the fraction.

3 Implementation to RV1A

3.1 Communication with robot controller

A Windows PC as a controller and the RV1A are connected with Ethernet as shown in **Fig. 4**. The servo system in Cartesian coordinate system of the RV1A is technically opened to users, so that absolute coordinate vectors of position and orientation can be given to the reference of the servo system. The servo rate of the robot is fixed to 7.1 ms. **Figure 5** illustrates the communication scheme by using UDP packet, in which sampling period is set to 10 ms. The data size in a UDP pachet is 196 bytes. The packet transmitted by 'sendto( )' includes values of desired position $\boldsymbol{X}_d(k) = [X_d(k)\ Y_d(k)\ Z_d(k)]^T$ [mm] and desired orientation $\boldsymbol{O}_d(k) = [\phi_d(k)\ \theta_d(k)\ \psi_d(k)]^T$ [rad] in robot absolute coordinate system. $\phi_d(k)$, $\theta_d(k)$, $\psi_d(k)$ are the rotational angles about x-, y- and z-axes, respectively, which are called X-Y-Z fixed angles or roll, pitch and yaw angles. The desired position and the desired orientation are set in a UDP packet as the reference of arm tip in the Cartesian servo system. Also, the packet received by 'recvfrom( )' includes values of current position $\boldsymbol{X}(k) = [X(k)\ Y(k)\ Z(k)]^T$ [mm] and current orientation $\boldsymbol{O}(k) = [\phi(k)\ \theta(k)\ \psi(k)]^T$ [rad] in robot absolute coordinate system, which can be used for feedback quantity.

3.2 Desired position and orientation

How to make $\boldsymbol{X}_d(k)$ and $\boldsymbol{O}_d(k)$ = based on the position and the orientation given by Eq. (1) is discussed in detail by using an example shown in **Fig. 2**, in which the tip of robot arm follows the trajectory keeping the orientation along normal direction to the surface. Each components of $\boldsymbol{X}_d(k)$ is represented with the initial position $\boldsymbol{X}_d(0)$ as

$$X_d(k) = X_d(0) + {}^{w}x_d(k) \tag{11}$$
$$Y_d(k) = Y_d(0) + {}^{w}y_d(k) \tag{12}$$
$$Z_d(k) = Z_d(0) + {}^{w}z_d(k) \tag{13}$$

where $\boldsymbol{X}_d(0)$ means the values of ${}^{w}O$ in robot absolute coordinate system.

Next, we consider the rotational components. Generally, rotational matrices R_X, R_Y and R_Z around x-, y- and z-axes are respectively given by

$$R_X = \begin{pmatrix} 1 & 0 & 0 \\ 0 & \cos\phi(k) & -\sin\phi(k) \\ 0 & \sin\phi(k) & \cos\phi(k) \end{pmatrix} \tag{14}$$

$$R_Y = \begin{pmatrix} \cos\theta(k) & 0 & \sin\theta(k) \\ 0 & 1 & 0 \\ -\sin\theta(k) & 0 & \cos\theta(k) \end{pmatrix} \tag{15}$$

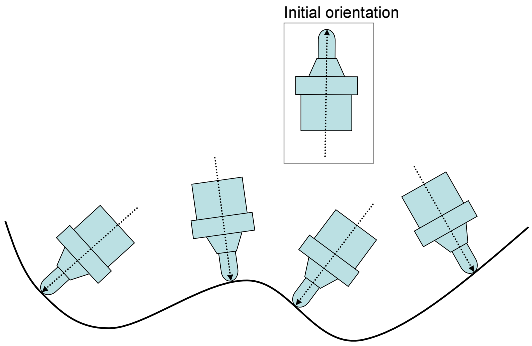

Figure 6: Orientation control of arm tip based on CL data shown in **Fig. 2**, in which the initial orientation is given with $[\phi(k)\ \theta(k)\ \psi(k)]^T = [0\ 0\ 0]^T$.

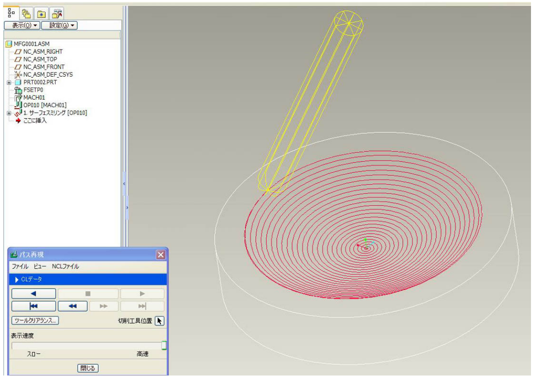

Figure 7: CL data $\boldsymbol{cl}(i) = [\boldsymbol{p}^T(i)\ \boldsymbol{n}^T(i)]^T$ consisting of position and orientation components, which is used for desired trajectory of the tip of robot arm.

$$R_Z = \begin{pmatrix} \cos\psi(k) & -\sin\psi(k) & 0 \\ \sin\psi(k) & \cos\psi(k) & 0 \\ 0 & 0 & 1 \end{pmatrix} \tag{16}$$

Accordingly, the rotational matrix $R_Z R_Y R_X$ with a roll angle $\phi(k)$, a pitch angle $\theta(k)$, and a yaw angle $\psi(k)$ is given by

$$\begin{pmatrix} C_\theta C_\psi & S_\phi S_\theta C_\psi - C_\phi S_\psi & C_\phi S_\theta C_\psi + S_\phi S_\psi \\ C_\theta S_\psi & S_\phi S_\theta S_\psi + C_\phi C_\psi & C_\phi S_\theta S_\psi - S_\phi C_\psi \\ -S_\theta & S_\phi C_\theta & C_\phi C_\theta \end{pmatrix} \tag{17}$$

where, for example, S_θ and C_θ means $\sin\theta(k)$ and $\cos\theta(k)$, respectively. **Figure 6** illustrates the trajectory following control along CL data shown in **Fig. 2**. As can be seen, the direction of ${}^{w}\boldsymbol{o}_d(k)$ is just inverse to the one of the arm tip. When referring the orientation components in CL data, the arm tip can be determined only with the roll angle and the pitch angle except for the yaw angle. That means $\psi(k)$ can be always fixed to 0 [rad]. Thus, the roll angle $\phi(k)$ and the pitch angle $\theta(k)$ at the discrete time k are obtained by solving

$$\begin{pmatrix} -{}^{w}o_{dx}(k) \\ -{}^{w}o_{dy}(k) \\ -{}^{w}o_{dz}(k) \end{pmatrix} = \begin{pmatrix} C_\theta & S_\phi S_\theta & C_\phi S_\theta \\ 0 & C_\phi & -S_\phi \\ -S_\theta & S_\phi C_\theta & C_\phi C_\theta \end{pmatrix} \begin{pmatrix} 0 \\ 0 \\ 1 \end{pmatrix} \tag{18}$$

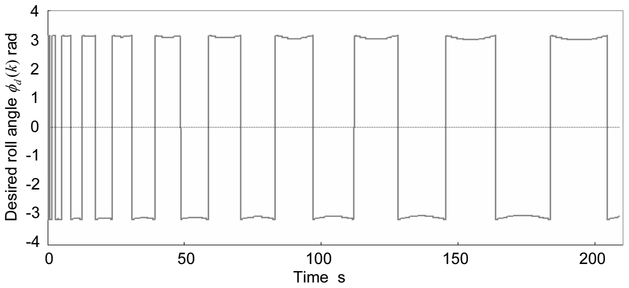

Figure 8: Initial part of desired roll angle $\phi_d(k)$ calculated from the desired trajectory shown in **Fig. 7**.

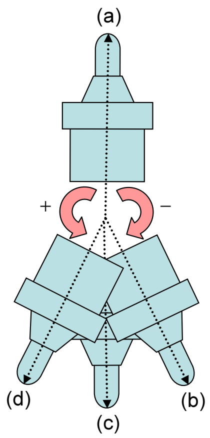

Figure 9: Roll angles around x-axis, in which (a) is the initial angle represented by $\phi(k) = 0$, (b) is the case of $-\pi \leq \phi(k) < 0$, (c) is the case of $\phi(k) = \pm\,\pi$, and (d) is the case of $0 < \phi(k) \leq\ \pi$.

where $[0\ 0\ 1]^T$ is the initial orientation vector in robot absolute coordinate system as shown in **Fig. 6**. Finally, $\phi(k)$ and $\theta(k)$ are calculated by using inverse trigonometric functions as

$$\phi(k) = \text{atan2}\{-{}^{w}o_{dx}(k),\ -{}^{w}o_{dz}(k)\} \quad (19)$$
$$\theta(k) = \text{asin}\{{}^{w}o_{dy}(k)\} \quad (20)$$

If the yaw angle is fixed to 0, then $\phi_d(k)$ and $\theta_d(k)$ can be calculated with Eqs. (19) and (20), respectively.

4 Experiment

In this section, an experiment of trajectory following control is conducted to evaluate the effectiveness of the proposed CAM system. **Figure 7** shows the desired trajectory generated by using the main-processor of 3D CAD/CAM Pro/Engineer, which consists of position and orientation components written by multi-lined "GOTO/" statements. It is tried that the arm tip is controlled so as to follow the position and orientation. The value of feed rate, i.e., tangent velocity, is set to 1 mm/s; the desired values composed of $\boldsymbol{X}_d(k)$ and $\boldsymbol{O}_d(k)$ are given to the references of the servo controller of RV1A every sampling period through UDP packets.

When the desired position $\boldsymbol{X}_d(k)$ and orientation $\boldsymbol{O}_d(k)$ is transmitted to the robotic servo system, the roll angle $\phi_d(k)$ has to be given within the range from $-\pi$ to π. **Figure 9** shows four examples of roll angle around x-axis, in which (a) is the initial angle represented by $\phi(k) = 0$, (b) is the case of $-\pi \leq \phi(k) < 0$, (c) is the case of $\phi(k) = \pm\,\pi$, and (d) is the case of $0 < \phi(k) \leq\ \pi$. It should be noted how to calculate the desired roll angle $\phi_d(k)$ as an manipulated value if the orientation changes as (b)→(c)→(d) or (d)→(c)→(b), i.e., in passing through the situation (c). In such cases, the sign of $\phi_d(k)$ has to be suddenly changed as shown in **Fig. 8**. In order to smoothly control the orientation of the arm tip , the following control rules were applied for the correction of roll angle.

if $\phi_d(k) > 0$ and $\phi(k) < 0$

$$\Delta\phi(k) = K_p\,\{\phi_d(k) - \phi(k) - 2\pi\} \quad (21)$$

else if $\phi_d(k) < 0$ and $\phi(k) > 0$

$$\Delta\phi(k) = K_p\,\{\phi_d(k) - \phi(k) + 2\pi\} \quad (22)$$

else if $\text{sgn}\{\phi_d(k)\} = \text{sgn}\{\phi(k)\}$

$$\Delta\phi(k) = K_p\,\{\phi_d(k) - \phi(k)\} \quad (23)$$

where $\phi_d(k)$ and $\phi(k)$ are the desired roll angle transmitted to the robotic servo controller and actual roll angle transmitted from the robotic servo controller, respectively. $\Delta\phi(k)$ is the output of proportional control action with a gain K_p. In fact, the desired roll angle $\phi_d(k+1)$ is generated as

$$\phi_d(k+1) = \phi(k) + \Delta\phi(k) \quad (24)$$

It was confirmed from the experiment that desirable control results of position and orientation could be obtained. The arm tip could gradually move up from the bottom center along the spiral path shown in **Fig. 7**. In this case, the orientation of the arm tip was simultaneously controlled so as to be normal direction to the surface. It was successfully demonstrated that the proposed CAM system allows the tip of the robot arm to desirably follow the desired trajectory given by multi-axis CL data without any complicated teaching tasks.

5 Conclusions

A CAM system for an articulated-type industrial robot RV1A has been proposed in order to raise the relationship between a design tool such as CAD/CAM and industrial robots spread to industrial manufacturing fields. The CAM system required for the industrial robot RV1A was realized as an integrated system including not only conventional main-processor of CAM but also robotic servo system and kinematics.

References

[1] F. Nagata, K. Watanabe and K. Izumi,"Furniture Polishing Robot Using a Trajectory Generator Based on Cutter Location Data, "*Procs. of 2001 IEEE International Conference on Robotics and Automation(IEEE ICRA 2001)*, pp. 319–324, 2001.

The Seventeenth International Symposium on Artificial Life and Robotics 2012 (AROB 17th '12),
B-Con Plaza, Beppu, Oita, Japan, January 19-21, 2012

The Adjustment of CPG Parameters to Realize Continuous Jumping Movements for a Six-legged Robot

Masaaki Ikeda[1], Keigo Watanabe[1], Kiyotaka Izumi[2]

[1] Okayama University, Okayama, Okayama 700-8530, Japan
[2] Saga University, Saga, Saga 840-8502, Japan
(Tel: 81-86-251-8064)
(ikeda-m@usm.sys.okayama-u.ac.jp)

Abstract: Central Pattern Generators (CPGs) as neural oscillators can determine a periodic motion state just like a walk. There exists a simple CPG for realizing the walk of an insect. It has been confirmed that a successive jump was able to be realized by applying such a simple structure. Furthermore, it was proved that different jumping appearances were generated according to the jumping-out posture, even if similar jumping generators were used. In this paper, for a CPG of a successive jumping six-legged robot, it is checked that parameters related to the CPG should be changed and optimized, depending on the jumping-out posture. A simple genetic algorithm is used as an optimization method. The simulation results that were obtained from a successive jumping simulation conducted by a dynamic simulator OpenHRP3, are used to evaluate the individuals in the GA.

Keywords: Six-legged robot, Jump robot, Central Pattern Generator, Genetic Algorithm

1 INTRODUCTION

Many wheels, crawlers, and legs are used as a locomotion mechanism of robots that move on the ground. Among them, since the locomotion using a leg can move on the rugged ground surface, it has some advantageous features[1]. Using such features, various legged robots are developed for explorations and work on irregular background. Now, the locomotion of legged robots is mainly based on a static walking. This is a natural selection in movement on the rugged ground surface for the legged robot whose mass becomes large comparatively to suppress an unexpected affection due to the changes of a ground surface, or to cope with such changes. However, a legged robot may move on the flat ground surface. In movement on the flat ground surface, the locomotion using wheels or crawlers has an advantage in speed.

Therefore, a dynamic walking is adopted for improving the locomotion speed of a legged mobile robot. The dynamic walking is a walk to which the time when a leg does not contact a ground surface exists in a walking cycle. A kind of dynamic walking has a jump. The successive jump can aim at improving a locomotion speed as a dynamic walking[2], [3]. Moreover, taking a jumping-out angle and an initial rate appropriately, a jump may be able to avoid a bigger obstacle than one that a static walking can do. This can extend the range of robot activities.

We have already set a jump mechanism in the leg-tip of a six-legged (or hexa-) robot, and have proposed how to generate the rhythm of a successive jump (hopping) using Central Pattern Generator (CPG)[4], [5]. Furthermore, it was confirmed that different jumping appearances were generated according to the jumping-out posture, even if similar jumping generators were used[6]. In this paper, for a CPG of a successive jumping six-legged robot, it is proved that parameters related to the CPG should be changed and optimized, depending on the jumping-out posture. A simple genetic algorithm (GA) is used as an optimization method. The simulation results that were obtained from a successive jumping simulation conducted by a dynamic simulator OpenHRP3, are used to evaluate the individuals in the GA.

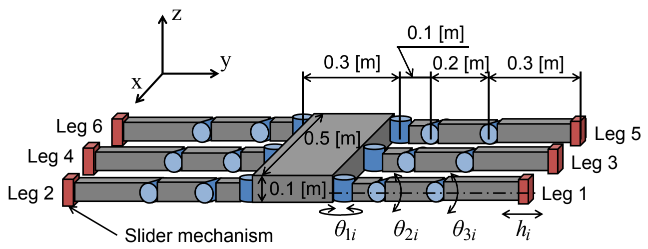

Fig. 1. Jumping six-legged robot

2 JUMPING SIX-LEGGED ROBOT

Although there are several legged robots that have different number of legs, in this paper, a six-legged robot is adopted because it is known that static stability nature is fully guaranteed during a walk. There are three joints in each leg of the robot to keep the posture and achieve walk movement. In addition, it has a prismatic mechanism at each leg-tip as a jump mechanism, which can slide to the leg-tip direction. Therefore, the six-legged jumping robot under study has 24 degrees of freedom in total because it has four degrees of freedom per each leg. The model for the six-legged jump-

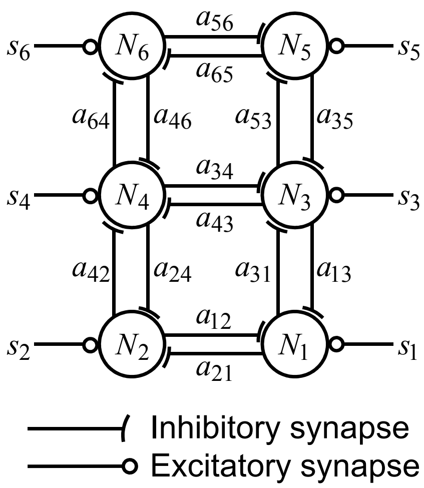

Fig. 2. Network for CPG

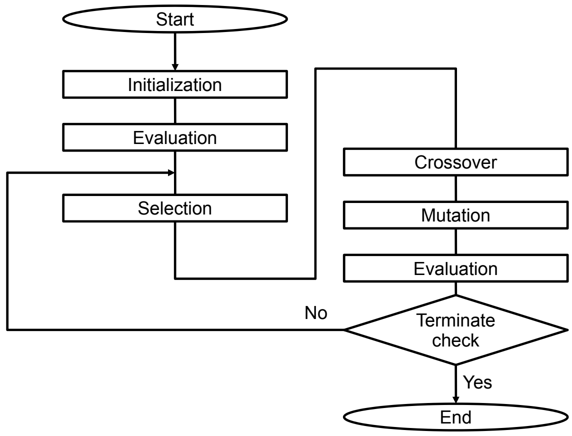

Fig. 3. GA flow chart

ing robot, the associated each link length and the leg number which were used in the dynamics simulator are shown in Fig. 1. The line extended above the robot in Fig. 1 denotes the perpendicular axis, which is regarded as z-axis, and the line extended to the front of the robot is viewed as x-axis. Furthermore, assume that y-axis makes a right-hand system, together with x- and z- axes. Let the field visible in front of Fig. 1 be a front face of the robot. When seeing the robot by him, odd numbers were assigned to the left legs and even numbers were assigned to the right legs, where the front leg of the left was set to Leg 1.

The total mass of the robot is 12.6 kg. For each leg, let joint angle be θ_{1i}, θ_{2i}, θ_{3i}, and h_i starting from the body, where i denotes the leg number. The length of each leg extending from each joint was 0.1 m, 0.2 m, and 0.3 m. The sliding mechanism for a jump can slide in $+0.05$ m and -0.05 m on the basis of the leg-tip. The other legs have the same mechanisms as stated above. In addition to the potentiometer to measure the joint displacement, the robot has a 3-axis accelerometer attached to the center of the fuselage. In the 3D model for the simulator, to overcome the contact calculations between parts of the robot, assume that a contact with the other leg and own body was not considered for the joint angle configuration. In the simulation, four cases will be prepared for the initial posture. The same controller will be used for all cases, and we examine how the jump behavior is changed due to each posture.

3 JUMPING RHYTHM GENERATOR

CPG is a kind of a neuron model and generates the periodic signal considered to be deeply related to the periodical activity of a living thing. When two or more CPG neurons exist, it is known that a phenomenon called an attraction is generated in the output periodic signal of each neuron with progress of time by suitably defining the coupling coefficients between neurons. Although there were some mathematical models proposed so far in CPG, in this paper, the Matsuoka oscillator with a comparatively simple relationship among parameters was used[7]. The Matsuoka model is formulated by

$$T_r \frac{\mathrm{d}u_i}{\mathrm{d}t} + u_i = -\sum_{j=1}^{n} a_{ij} y_j + s_i - b f_i \tag{1}$$

$$y_i = g(u_i) \quad (g(u_i) \triangleq \max(0, u_i)) \tag{2}$$

$$T_a \frac{\mathrm{d}f_i}{\mathrm{d}t} + f_i = y_i \tag{3}$$

where t is the time variable, i, j denote the neuron number. T_r is a rise time constant, u_i is the membrane potential of neuron body, a_{ij} (≥ 0 for $i \neq j$ and $= 0$ for $i = j$) is a weight of inhibitory synaptic connection from j-th neuron to the i-th neuron. y_i is a firing rate or an output of the neuron, s is an impulse rate of input. b is the parameter that determines the steady-state firing rate for a constant input. f is a fatigue state (or an adaptation variable), T_a is an adaptation time constant.

The composition of the CPG network by inhibited connections of six neurons used in this paper is shown in Fig. 2. The output value y from each neuron of the constituted CPG network is used as a next desired value of the sliding mechanism for a jump of the leg number i as shown by

$$h_{oi} = -y_i \tag{4}$$

However, it is assumed that if the accelerations in x- and y-directions of the robot center of gravity are less than a value and also z-directional acceleration approaches the gravitational acceleration enough, then the robot vibration is sufficiently settled down. Then, a CPG output is used as a desired value, as long as the robot vibration is fully settled down. The output of the sliding mechanism for a jump is calculated

Table 1. Joint angles of each leg for Case 1

i	θ_{1i}	θ_{2i}	θ_{3i}
1	$-\frac{\pi}{4}$	$\frac{\pi}{3}$	$-\frac{5\pi}{6}$
2	$\frac{\pi}{4}$	$\frac{\pi}{3}$	$-\frac{5\pi}{6}$
3	0	$\frac{\pi}{3}$	$-\frac{5\pi}{6}$
4	0	$\frac{\pi}{3}$	$-\frac{5\pi}{6}$
5	$\frac{\pi}{4}$	$\frac{\pi}{3}$	$-\frac{5\pi}{6}$
6	$-\frac{\pi}{4}$	$\frac{\pi}{3}$	$-\frac{5\pi}{6}$

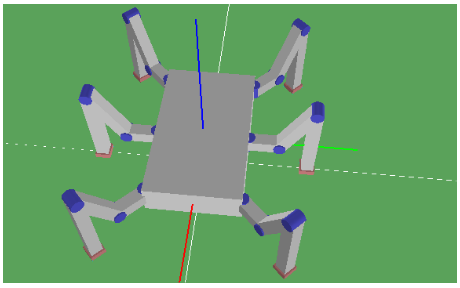

Fig. 4. Initial posture for Case 1

Table 2. Joint angles of each leg for Case 2

i	θ_{1i}	θ_{2i}	θ_{3i}
1	$-\frac{\pi}{2}$	$-\frac{\pi}{6}$	$-\frac{\pi}{3}$
2	$\frac{\pi}{2}$	$-\frac{\pi}{6}$	$-\frac{\pi}{3}$
3	$-\frac{\pi}{2}$	$-\frac{\pi}{6}$	$-\frac{\pi}{3}$
4	$\frac{\pi}{2}$	$-\frac{\pi}{6}$	$-\frac{\pi}{3}$
5	$\frac{\pi}{2}$	$-\frac{\pi}{6}$	$-\frac{\pi}{3}$
6	$-\frac{\pi}{2}$	$-\frac{\pi}{6}$	$-\frac{\pi}{3}$

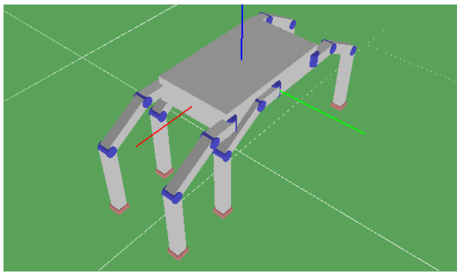

Fig. 5. Initial posture for Case 2

by using the desired value acquired from the CPG such that

$$T_i = P(h_{oi} - h_i) + D(v_{oi} - \dot{h}_i) \qquad (5)$$

where i denotes the leg number, h_i is the displacement of the slide joint, v_{oi} is an objective velocity (now, $v_{oi} = 0$). P is the proportional gain and D is the differential gain. Thus, the force for a jump is generated periodically.

4 GENETIC ALGORITHM

GA is an algorithm that imitates the evolution of a living thing, which was proposed by Holland and others late in the 1960s. The GA models the evolutionary mechanism of a living thing and is the algorithm in which an individual with the highest fitness against the environment is determined as the optimal solution to the objective function. The optimal solution in GA is searched by repeatedly applying the genetic operation of Selection, Crossover, and Mutation to the population. The fundamental flow of GA is shown in Fig. 3. A simple GA in which an individual is expressed by a binary number is adopted in this research, and parameters related to a CPG are explored optimally.

5 SIMULATION

5.1 Simulation Condition

Joint angles θ_{1i}, θ_{2i} and θ_{3i} of each leg prepared for the initial posture of the robot are shown in Table 1 to Table 2. The appearance when the robot actually becomes each initial posture by the dynamics simulation is shown in Fig. 4 to Fig. 5.

The total number of parameters is 35, which involve the CPG parameters. Each parameter is described by a binary number in 32 bits and put them in order to make one individual. A simulation is performed by using the parameters related to a certain individual, and the maximum jump height of the robot in each trial and continuous simulation time is used as a fitness of the individual. The design parameters related to this GA are as follows: the population size is 20 and the end of generation is 30; the individual length is 1120 bites because there are 35 parameters one of which is described by 32 bits; the Selection is a tournament selection by three individuals; the Crossover is one point crossover with the probability of 0.6; and the Mutation is produced with the rate of 1/1120.

PD gains are set to be constant in simulations. P and D gains at each joint are given in an order from the joint near the body; the 1st joint has P_{1i} = 50 and D_{1i} = 1; the 2nd joint has P_{2i} = 50 and D_{2i} = 0.8; and the 3rd joint has P_{3i} = 30 and D_{3i} = 1.

Each gain of a jump mechanism is set to P_{4i} = 10 and D_{4i} = 10. Note however that each leg is assumed to use the same gain. Furthermore, it is assumed that each gain is set by 100 times the above ones to generate a bigger power, when the

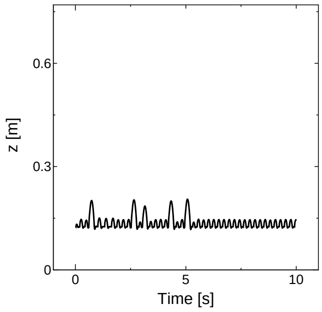

Fig. 6. Time history of the jump height for Case 1

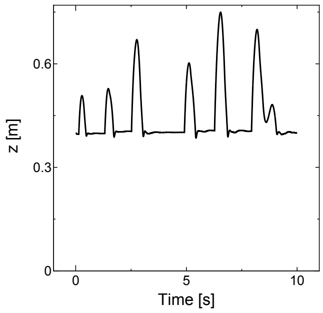

Fig. 7. Time history of the jump height for Case 2

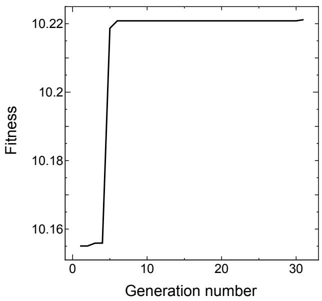

Fig. 8. Fitness history by generation for Case 1

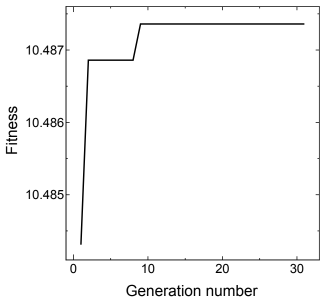

Fig. 9. Fitness history by generation for Case 2

robot jumps.

5.2 Simulation Result

By applying the CPG parameters decided by manual tuning in advance, the simulation results for cases 1 and 2 are shown in Fig. 6 and Fig. 7. These results prove that successive jumps have been realized using the outputs of CPG.

Furthermore, the simulation results of cases 1 and 2 optimized by GA are presented in Fig. 8 to Fig. 11. The best fitness values verses generations are shown in Fig. 8 and Fig. 9. It is found that the higher jump is gradually obtained as the GA search progresses.

Fig. 10 and Fig. 11 show the jump situations with the optimized parameters. Although the maximum jump height is not enough, compared to that tuned by any manual method, it seems that the robot can succeed a successive jump and there are less changes in jump.

6 CONCLUSION

In this paper, we have searched for the optimal CPG parameters to make a successive jump for a six-legged robot. In the simulation using the parameters optimized by GA, the six-legged robot was shown to realize a successive jump, whose amplitude change is less, compared to that tuned by any manual method. Thus, it is revealed a relationship between the initial jumping posture and the resultant jumping motion.

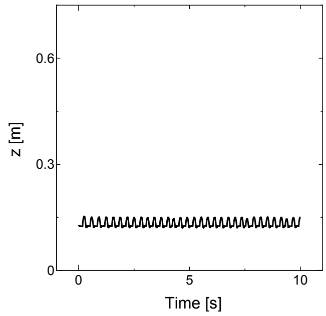

Fig. 10. The jump height with searched paremeter for Case 1

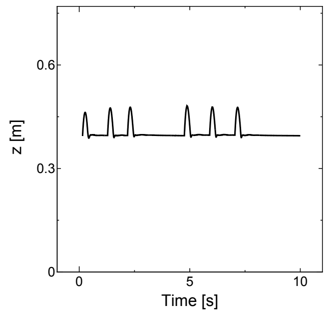

Fig. 11. The jump height with searched paremeter for Case 2

REFERENCES

[1] Arikawa K, Hirose S (1996), Development of quadruped walking robot *TITAN-VIII*. Proc. of IROS 96:208–214

[2] Najib S. M, Yusoh S, Yamashita Y, Kokubo N (2009), A study of a jumping one-leg robot with two degrees of freedom. Artificial Life and Robotics 13(2):442–446

[3] He G. P, Tan X. L, Zhang X. H, Lu Z (2008), Modiling, motion planning, and control of one-legged hopping robot actuated by two arms. Mechanism and Machine Theory 43:33–49

[4] Ijspreet A. J (2008), Central pattern generators for locomotion control in animals and robots: A review, Neural Networks 21:642–653

[5] Ikeda M, Izumi K, Watanabe K (2011), Jumping rhythm generator by CPG for a multi-legged robot. Proc. of AROB 16th '11 395–398

[6] Ikeda M, Watanabe K, Izumi K (2011), Motion Generation of Multi-legged Robot with a Slider Mechanism for Each Foot. Proc. of SICE Annual Conference 2011:1290–1293

[7] Matsuoka K (1987), Mechanisms of frequency and pattern control in the neural rhythm generators. Biological Cybernetics 56(5-6):345–353

The Seventeenth International Symposium on Artificial Life and Robotics 2012 (AROB 17th '12),
B-Con Plaza, Beppu, Oita, Japan, January 19-21, 2012

A Proposal of Experimental Education System of Mechatronics

N. Kitahara, F. Nagata and A. Otsuka
Tokyo University of Science, Yamaguchi
Sanyo-Onoda, Japan

K. Sakakibara
C-TASK Co., Ltd.
Tokyo Japan

K. Watanabe
Okayama University
Okayama, Japan

Maki K. Habib
American University in Cairo
Cairo, Egypt

Abstract

Recently, many studies on educational system are being conducted. In this manuscript, a unique education system is proposed for mechanical engineers to be able to efficiently learn basic mechatronics techniques. The system is composed of three subsystems. The first system is used to learn input/output port operations, periodically LED lights ON/OFF and a stepping motor control. The second system is effective to learn AD transformation for several sensor information, DA transformation for DC motor control and a PID control method. Further, the third system is multiple mobile robots system to learn the subsumption architecture for schooling behavior. The effectiveness of the proposed systems was confirmed through experimental instructions in Tokyo University of Science, Yamaguchi.

1 Introduction

Recently, many studies on educational system are being conducted. In this manuscript, a unique educational system is proposed for mechanical engineers to be able to efficiently learn basic techniques of mechatronics. Here, C++ of Microsoft Visual Studio is recommended as a software development environment, because which is one of the professional technical skills required from industrial fields. The system is composed of three subsystems. The first subsystem is used for second year students to learn input/output port operations with hexadecimal number, periodically LED lights ON/OFF by using Windows Timer, e.g., with a sampling period of 10 ms , and stepping motor controls built in a position control module and a mobile robot with two wheels. The second system is also used for third year students to learn AD transformation for several sensor information, DA transformation for DC motor control and PID control method. Further, the third system is multiple mobile robot system for the graduation study of fourth year students to learn the subsumption architecture for swarm intelligence. The effectiveness of the proposed systems is evaluated through experimental instructions in Tokyo University of Science, Yamaguchi.

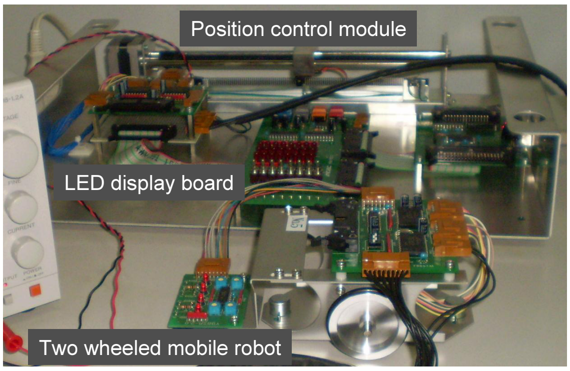

Figure 1: Mechatronics system consisting of an LED display board, a position control device and a mobile robot with two wheels.

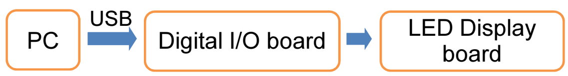

Figure 2: Block diagram of LED display experiment.

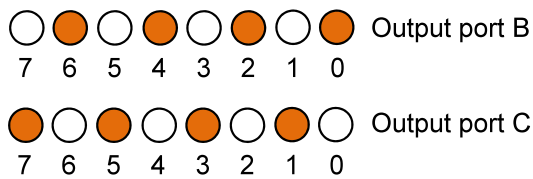

Figure 3: Relation between two-arrayed LEDs and output port B, C.

2 Mechatronics System I

Figure 1 shows the first mechatronics system consisting of an LED display board, a position control device and a mobile robot with two wheels. The system is used in the experimental lecture of "Experiments on Mechanical Engineering I" for the second year students. Figure 2 shows the block diagram of the LED display experiment. Sixteen LEDs are arrayed with two rows as shown in Fig. 3 and each row is related to output port B and C, respectively. In Fig. 3, hexadecimal number 0x55 and 0xAA are set to port B and port C, respectively. Lighting pattern can be designed by giving the hexadecimal number, also lighting period

Table 1: Binary number given to the lower four bits of port B and motion of stepping motor.

0110	Low level signal for clockwise motion
0111	High level signal for clockwise motion
0010	Low level signal for counterclockwise motion
0011	High level signal for counterclockwise motion
1000	Excitation of motor is OFF

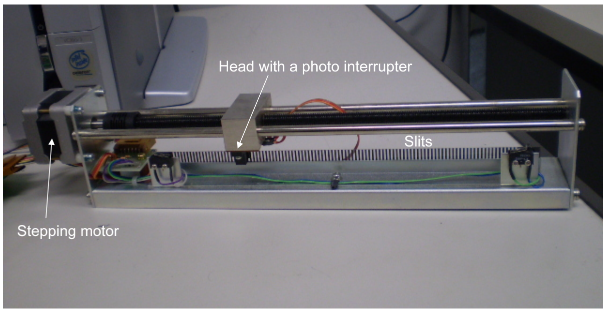

Figure 4: Position control device driven by a stepping motor.

can be changed by using Windows timer interrupt of 10 ms.

Figure 4 shows the position control device driven by a stepping motor. A photo interrupter is attached to the head to detect the position of the slit,i.e., black or transparent. The stepping motor is driven by pulse signals. One pulse signal rotates the stepping motor with 1.8 degrees, and this moves the head 6.25 μm. The pulse signal is generated by the lower four bits of output port B. Relation between binary number given to the port B and motion is as follows:

Figure 5 illustrates the mobile robot with two wheels and two photo reflectors. wheel 1 and 2 are driven by stepping motor 1 and 2, respectively. The stepping motor 1 and 2 are excited by the lower four bits of output port B and C, respectively. In. Fig. 5, v and ω are the translational velocity and the rotational velocity of the robot in robot coordinate system; $2L$ is the distance between the two wheels and R is the radius of each wheel. The robot can perform forward/backward motion or rotational motion. When forward/backward motion is applied, then the velocity of each wheel, v_1, v_2, are given by

$$v = v_1 = \omega_1 R = v_2 = -\omega_2 R \tag{1}$$

Also, when the rotational motion is conducted, the rotational velocity w is given by

$$\omega = \frac{\omega_1 R}{L} = \frac{\omega_2 R}{L} \tag{2}$$

where ω_1 and ω_2 are the rotational velocities of two wheels, respectively.

3 Mechatronics System II

Figure 6 shows the second mechatronics system consisting of three sensors for measuring temperature, dis-

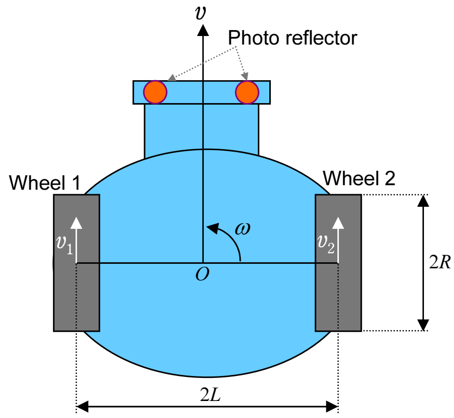

Figure 5: Top view of two-wheeled mobile robot with two photo reflectors.

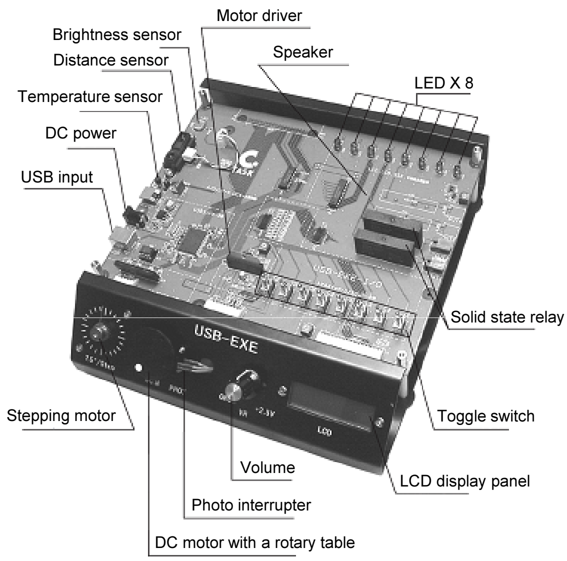

Figure 6: Mechatronics system consisting of of three sensors for measuring temperature, distance and brightness, AD/DA transformation interfaces, an LCD display panel and a DC motor with a photo interrupter.

tance and brightness, AD/DA transformation interfaces, an LCD display panel and a DC motor with a sensor of photo interrupter, which is provided by C-TASK Co., Ltd. The system is used in the experimental lecture of "Mechanical Engineering Experiment II" for the third year students.

Here, the basic software developed for velocity control of the DC motor is explained. A ladder type DA converter is connected to the output port 1, so that the voltage within the range from 0 to 3.3 V can be outputted with the resolution of 256 steps. The velocity control of the DC motor can be performed by changing the voltage. The velocity of the motor is controlled by a PI-action in the discrete time k given by

$$\tau(k+1) = \tau(k) + \Delta\tau(k) \tag{3}$$

$$\Delta\tau(k) = K_p\{v_d - v_s(k)\} + K_i \sum_{n=1}^{k} \{v_d - v_s(n)\} \quad (4)$$

where $\tau(k)$ is the output torque to the DC motor at the discrete time k; K_p and K_i are the P-gain and I-gain, respectively; v_d is the reference value of rotational velocity and $v_s(k)$ is the rotational velocity measured by using a photo interrupter shown in Fig. 7. A rotational wheel with a small hole is fixed to the DC motor. The pass of the hole can be counted by detecting the change of signal form the photo interrupter, i.e., from HIGH level to LOW level. The rotational velocity is defined as counted number of the hole per a constant time period.

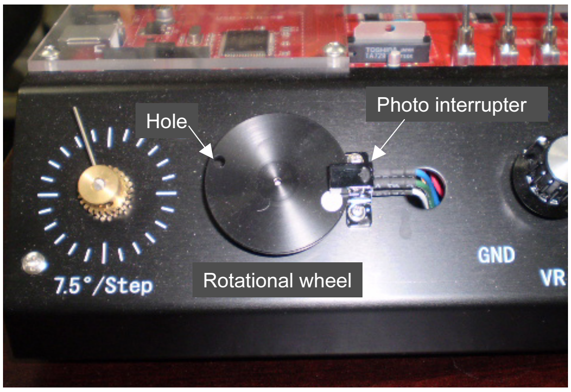

Figure 7: Rotational wheel fixed to a DC motor with a sensor of photo interrupter.

4 Basic Dialogues for Students' Experiment

In this section, basic dialogues developed for mechatronics experiments I and II are introduced. Students can effectively design a control program by using the dialogue and learn basic peripheral techniques concerning mechatronics.

4.1 Dialogue for Mechatronics Experiment I

Mechatronics Experiment I is considered for second year students in department of mechanical engineering, which is composed of three subjects, i.e., an LED lights ON/OFF experiment, a positioning experiment of a position control module and a line trace experiment of the two-wheeled mobile robot. As an example, Fig. 8 shows the windows dialogue designed for the line trace experiment using a mobile robot in mechatronics experiment I. At first, the students learn how to program important basic functions such as moving forward/backward, turning left/right and sensing two photo-reflectors through the dialogue developed by using Microsoft Visual C$^{\#}$. Then, students can make a program for a line trace by making use of the basic functions. Fifteen hours (five hours, three days) are allotted to Mechatronics Experiment I.

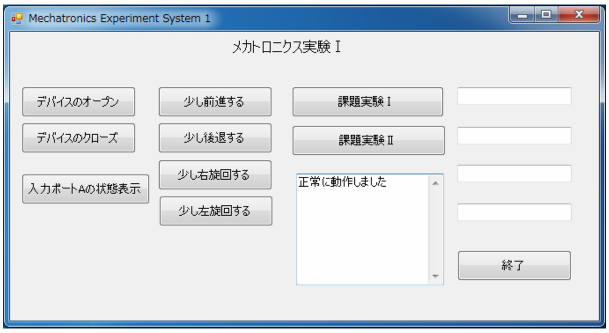

Figure 8: Windows dialogue designed for Mechatronics Experiment I.

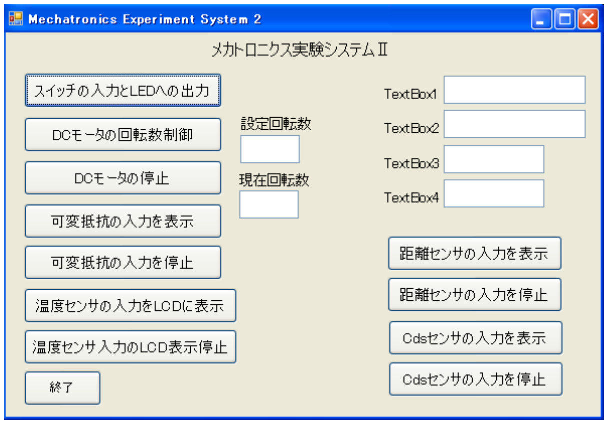

Figure 9: Windows dialogue designed for Mechatronics Experiment II.

4.2 Dialogue for Mechatronics Experiment II

Mechatronics Experiment II is considered for third year students, which is mainly composed of three subjects, i.e., AD transformation of several sensor signals such as distance, temperature and brightness, and DA transformation for velocity control of a DC motor. Students try to design a discrete-time PID controller for the velocity control of the DC motor. Figure 9 shows the windows dialogue designed for the Mechatronics Experiment II. Ten hours (five hours, two days) are allotted to Mechatronics Experiment II.

5 Multiple Mobile Robots System for Graduation Study

Students, who have gone through the experimental lectures Mechatronics I and II, can smoothly cope with the graduation study at fourth year. Finally, one of the student's graduation studies is introduced, in which multiple mobile robots with six sensuous sensors as shown in Fog. 10 are constructed for schooling behavior.

The third subsystem is designed with multiple mobile robots with three wheels and six PSD sensors [1], which is applied to the graduation study of fourth year students, e.g., to learn the subsumption architecture for schooling behavior. The subsumption architecture

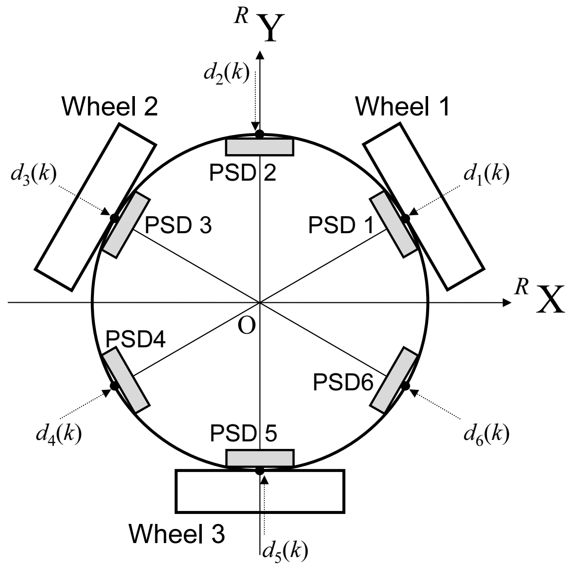

Figure 10: Positions of six PSD sensors fixed around a mobile robot.

is called Behavior-Based Artificial Intelligence, which was first proposed by Brooks [2]. Students can practically know the concept of subsumption architecture which provides a method for structuring reactive systems from lower level to higher level using layered sets of rules, i.e., reactive behaviors according to the change of environment.

Figure 11 shows an example of the controller based on the subsumtion atchitecture and Fig. 12 shows the experimental scene. If the schooling mode is set to all mobile robots, they try to regularly move along the inner of a circular fence keeping the distance to both the fence and other mobile robots. This mode allows the robots to behave like carps in a Japanese artificial circular pond. For example, when a robot moves counterclockwise along a circular fence, the following control law is basically applied by the task of "Move forward".

$$\dot{\boldsymbol{x}}_r = v\frac{\dot{\boldsymbol{x}}_{r2}}{\|\dot{\boldsymbol{x}}_{r2}\|} \tag{5}$$

where $\dot{\boldsymbol{x}}_r = [\dot{x}_r \ \dot{y}_r]^T$ is the translational velocity in robot coordinate system, $\dot{\boldsymbol{x}}_{r2} = [0 \ 1]^T$ is the normalized velocity for moving to PSD sensor 2. v is the scalar signifying the magnitude of the velocity. Also, the orientation is controlled by the task of "Turn to left or right" as

$$\dot{\phi}_r = K_\phi\{d_6(k) - d_1(k)\} \tag{6}$$

where $d_1(k)$ and $d_6(k)$ are the values measured by PSD sensors 1 and 6, respectively. K_ϕ is the gain which can control the orientation of the robot to be parallel to the inner of the circular fence. Further, the highest priority task "Avoid objects" actuates three wheels in order to avoid collisions to other robots.

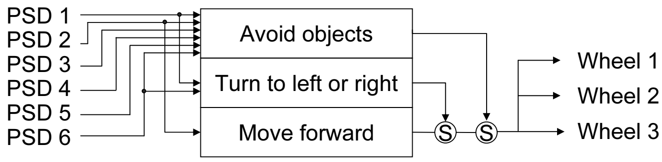

Figure 11: Controller designed based on subsumption architecture for schooling behavior.

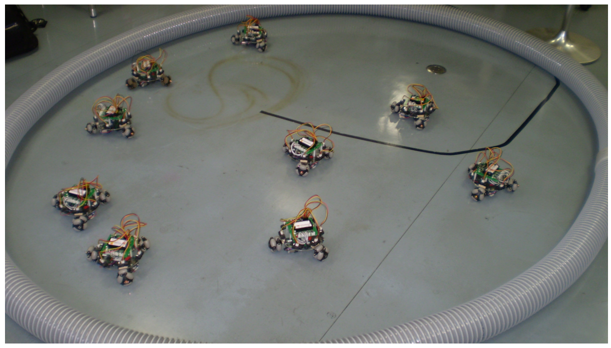

Figure 12: Experiment of schooling behavior based on subsumption architecture.

6 Conclusions

In this manuscript, a unique education system has been proposed for mechanical engineers to practically learn basic mechatronics techniques. The system is composed of three subsystems. The first system is used for second year students to mainly learn input/output port operations, periodically LED lights ON/OFF and a stepping motor control. The second system is effective for third year students to learn AD transformation for several sensor information, DA transformation for DC motor control and a design of a PID controller. Further, the third system is multiple mobile robots system as one of graduation studies so that the fourth year students can learn the subsumption architecture for schooling behavior. The effectiveness of the proposed mechatronics education system is evaluated through experimental instructions in Tokyo University of Science, Yamaguchi.

References

[1] F. Nagata, T. Yamashiro and K. Watanabe, "Cooperative Swarm Control for Multiple Mobile Robots Using Only Information from PSD Sensors," *Artificial Life and Robotics*, Vol. 16, No. 1, pp. 116–120, 2011.

[2] R. A. Brooks, "A robust layered control system for a mobile robot," *IEEE Journal of Robotics and Automation*, Vol. 2, No. 1, pp. 14–23, 1986.

The Seventeenth International Symposium on Artificial Life and Robotics 2012 (AROB 17th '12),
B-Con Plaza, Beppu, Oita, Japan, January 19-21, 2012

A Discontinuous Exponential Stabilization Law for an Underactuated X4-AUV

Zainah Md. Zain, Keigo Watanabe, Kiyotaka Izumi†, and Isaku Nagai

Department of Intelligent Mechanical Systems,
Division of Industrial Innovation Sciences,
Graduate School of Natural Science and Technology, Okayama University
3-1-1 Tsushima-naka, Kita-ku, Okayama 700-8530, Japan
Tel & Fax: +81-86-251-8064
E-mail: zainah@usm.sys.okayama-u.ac.jp, {watanabe, in}@sys.okayama-u.ac.jp
† Department of Mechanical Engineering,
Graduate School of Science and Engineering, Saga University
1-Honjomachi, Saga 840-8502, Japan
Tel: +81-952-28-8696, Fax: +81-952-28-8587
E-mail: izumi@me.saga-u.ac.jp

Abstract: In this paper, stabilization of a class of second-order nonholonomic systems for an underactuated X4-AUV is investigated. We present a model of the underactuated X4-AUV with six degrees-of-freedom (DOF) and four control inputs. Then the system is written in a control-affine form by applying a partial linearization technique and a dynamic controller based on Astolfi's discontinuous control is derived to stabilize all states of the system to the desired equilibrium point exponentially. A simulation is conducted to demostrate the effectiveness of the proposed controller.

Keywords: Discontinuous control, underactuated X4-AUV

I. INTRODUCTION

In the past few years, the problem of controlling nonholonomic systems has attracted much attention. These studies were primarily limited to first-order nonholonomic systems which undergo non-integrable kinematic constraints. However, there is still another type of nonholonomic systems called second-order nonholonomic systems, satisfying nonintegral relations involving not only generalized coordinates and velocities but also the generalized accelerations. Second-order and high-order nonholonomic systems arise in underactuated systems [1][2], where the numbers of available control inputs are less than the number of degrees of freedom. The lack of actuators introduces a set of nonholonomic constraints in the dynamic equations. These constraints are inherently at the acceleration level and generally not integral to velocity constraints, and hence are second-order nonholonomic. The studies of control issue of underactuated system with second-order nonholonomic constrains allow the design of fault-tolerant robots and the use of the energy resources more rationally while precisely controlling the system. Different from the first-order nonholonomic systems such as wheeled vehicles and free-floating space robot which have velocity constraints geometrically limiting the direction of mobility, second-order nonholonomic constraints, on the other hand, are the constraints that limit the generalized accelerations and cannot be integrated to first-order nonholonomic or holonomic constraints. These constraints make it difficult to directly apply the techniques so far developed for the first-order nonholonomic systems. It is known that certain mechanical systems can be converted to a second-order chained form, and more generally, a class of underactuated mechanical systems can be converted to a second-order chained form by constructing coordinate and input transformations. By converting the system to a second-order chained form, the dynamics are considerably simplified, and thus easy for controller design. The control problem of a second-order nonholonomic chained form has been studied by some researchers. Laiou and Astolfi [2] solved the stabilization problem for nonlinear systems in a generalized high-order chained form by means of discontinuous state feedback control law, yielding exponential converge of the states to the origin. Xu and Ma [3] converted a class of second-order nonholonomic systems to the second-order nonholonomic chained form, and proposed a discontinuous control law to stabilize states to the desired equilibrium point exponentially.

It has been proven that several classes of second-order nonholonomic systems are transformable into the following chained form by smooth state and input transformations

$$\begin{cases} \ddot{y}_1 &= u_1 \\ \ddot{y}_2 &= u_2 \\ \ddot{y}_3 &= y_2 u_1 \end{cases} \tag{1}$$

This paper is organized as follows: In section 2 the coordinate system of AUV is presented. The equations of motion of the system are presented in section 3. The discontinuous control law based on Astolfi's discontinuous control for an X4-AUV is constructed in section 4. The last section presents concluding remarks.

II. COORDINATE SYSTEMS OF AUV

Fig. 1 shows the coordinate systems of AUV, which consist of a right-hand inertial frame {E} in which the downward vertical direction is to be positive and a right-hand body frame {B}.

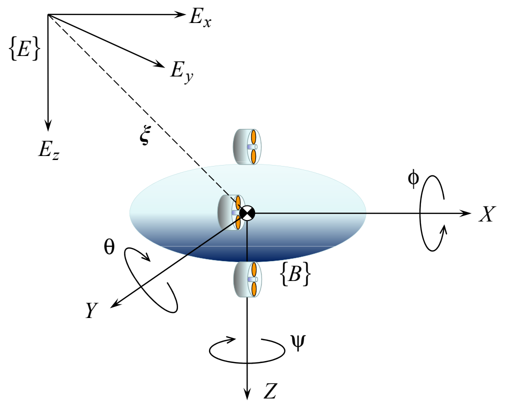

Fig. 1. Coordinate systems of AUV

Letting $\boldsymbol{\xi} = [x \quad y \quad z]$ denote the mass center of the body in the inertial frame, defining the rotational angles of X-, Y- and Z-axis as $\boldsymbol{\eta} = [\phi \quad \theta \quad \psi]^T$, the rotational matrix R from the body frame {B} to the inertial frame {E} can be reduced to:

$$R = \begin{bmatrix} c\theta c\psi & s\phi s\theta c\psi - c\phi s\psi & c\phi s\theta c\psi + s\phi s\psi \\ c\theta s\psi & s\phi s\theta s\psi + c\phi c\psi & c\phi s\theta s\psi - s\phi c\psi \\ -s\theta & s\phi c\theta & c\phi c\theta \end{bmatrix} \tag{2}$$

where $c\alpha$ denotes $\cos\,\alpha$ and $s\alpha$ is $\sin\,\alpha$.

III. DYNAMICAL MODEL

Defining $\boldsymbol{q} = [\boldsymbol{\xi}^T \quad \boldsymbol{\eta}^T]$, the dynamical model of an X4-AUV is described in the following matrix form [4]:

$$M(\mathbf{q})\ddot{\mathbf{q}} + V_m(\mathbf{q},\dot{\mathbf{q}})\dot{\mathbf{q}} + G(\mathbf{q}) = B(\mathbf{q})\boldsymbol{\tau} \tag{3}$$

where $M(\mathbf{q}) \in \Re^{6\times6}$ is the symmetric, positive definite inertia matrix, $V_m(\mathbf{q},\dot{\mathbf{q}}) \in \Re^{6\times6}$ is the centrifugal and Coriolis matrix, $G(\mathbf{q}) \in \Re^{6}$ is the gravitational vector, $B(\mathbf{q}) \in \Re^{6\times4}$ is the input transformation matrix, and $\boldsymbol{\tau} \in \Re^{4}$ is a generalized force vector consisting of force or torque components.

Note also that each matrix in the dynamical model can be reduced to

$$M(\mathbf{q}) = \begin{bmatrix} m_1 & 0 & 0 & 0 & 0 & 0 \\ 0 & m_2 & 0 & 0 & 0 & 0 \\ 0 & 0 & m_3 & 0 & 0 & 0 \\ 0 & 0 & 0 & I_x & 0 & 0 \\ 0 & 0 & 0 & 0 & I_y & 0 \\ 0 & 0 & 0 & 0 & 0 & I_z \end{bmatrix}$$

$$V_m(\mathbf{q},\dot{\mathbf{q}}) = \begin{bmatrix} 0 & 0 & 0 & 0 & 0 & 0 \\ 0 & 0 & 0 & 0 & 0 & 0 \\ 0 & 0 & 0 & 0 & 0 & 0 \\ 0 & 0 & 0 & 0 & I_z\dot{\psi} & -I_y\dot{\theta} \\ 0 & 0 & 0 & -I_z\dot{\psi} & 0 & J_t\Omega + I_x\dot{\phi} \\ 0 & 0 & 0 & I_y\dot{\theta} & -J_t\Omega - I_x\dot{\phi} & 0 \end{bmatrix}$$

$$B(\mathbf{q}) = \begin{bmatrix} c\theta c\psi & 0 & 0 & 0 \\ c\theta s\psi & 0 & 0 & 0 \\ -s\theta & 0 & 0 & 0 \\ 0 & 1 & 0 & 0 \\ 0 & 0 & l & 0 \\ 0 & 0 & 0 & l \end{bmatrix}$$

$$\mathrm{diag}(m_1, m_2, m_3) = m_b I + M_f$$
$$\mathrm{diag}(I_x, I_y, I_z) = J_b + J_f$$

Here, I denotes the unit matrix, M_f is an added mass matrix, and J_f is an added moment of inertia matrix. Assuming that the fluid density is ρ and the present AUV form is ellipsoid, it is found that suitable M_f and J_f are obtained [5]. Furthermore assume that the X4-AUV is in the state of neutral buoyancy to neglect the potential energy, so that $G(\mathbf{q}) = 0$.

From the rotational matrix (2), the kinematic equation for X4-AUV

$$\dot{\mathbf{q}} = S(\mathbf{q})v \tag{4}$$

can be reduce to

$$\begin{bmatrix} \dot{x} \\ \dot{y} \\ \dot{z} \\ \dot{\phi} \\ \dot{\theta} \\ \dot{\psi} \end{bmatrix} = \begin{bmatrix} c\theta c\psi & 0 & 0 & 0 \\ c\theta s\psi & 0 & 0 & 0 \\ -s\theta & 0 & 0 & 0 \\ 0 & 1 & 0 & 0 \\ 0 & 0 & 1 & 0 \\ 0 & 0 & 0 & 1 \end{bmatrix} \begin{bmatrix} \dot{x}_b \\ \dot{\phi} \\ \dot{\theta} \\ \dot{\psi} \end{bmatrix} \tag{5}$$

because the lateral type X4-AUV has only the total thrust in the X-direction, where v= $[\dot{x}_b \ \dot{\phi} \ \dot{\theta} \ \dot{\psi}]^T$, where $\dot{x}_b$ denotes the X-directional translational velocity and $[\dot{\phi} \ \dot{\theta} \ \dot{\psi}]^T$ is the rotational angular velocity vector in the body frame.

Applying a partial linearizing technique, it gives

$$\begin{aligned} \ddot{x} &= v_1 \\ \ddot{\phi} &= v_2 \\ \ddot{\theta} &= v_3 \\ \ddot{\psi} &= v_4 \\ \ddot{y} &= (m_1/m_2)\tan\psi v_1 \\ \ddot{z} &= (-m_1/m_3)\tan\theta\sec\psi v_1 \end{aligned} \tag{6}$$

where

$$\begin{aligned} v_1 &= \cos\theta\cos\psi\tau_1/m_1 \\ v_2 &= [\tau_2 - I_z\dot{\psi}\dot{\theta} + I_y\dot{\theta}\dot{\psi}]/I_x \\ v_3 &= [l\tau_3 + I_z\dot{\psi}\dot{\phi} - (J_t\Omega + I_x\dot{\phi})\dot{\psi}]/I_y \\ v_4 &= [l\tau_4 - I_y\dot{\theta}\dot{\phi} + (J_t\Omega + I_x\dot{\phi})\dot{\theta}]/I_z \end{aligned}$$

In the matrix form, Eq. (6) is described by

$$\begin{bmatrix} \ddot{x} \\ \ddot{y} \\ \ddot{z} \\ \ddot{\phi} \\ \ddot{\theta} \\ \ddot{\psi} \end{bmatrix} = \begin{bmatrix} 1 & 0 & 0 & 0 \\ \frac{m_1}{m_2}\tan\psi & 0 & 0 & 0 \\ -\frac{m_1}{m_3}\frac{\tan\theta}{\cos\psi} & 0 & 0 & 0 \\ 0 & 1 & 0 & 0 \\ 0 & 0 & 1 & 0 \\ 0 & 0 & 0 & 1 \end{bmatrix} \begin{bmatrix} v_1 \\ v_2 \\ v_3 \\ v_4 \end{bmatrix} \tag{7}$$

and

$$\begin{bmatrix} \tau_1 \\ \tau_2 \\ \tau_3 \\ \tau_4 \end{bmatrix} = \begin{bmatrix} \frac{m_1}{\cos\theta\cos\psi} & 0 & 0 & 0 \\ 0 & I_x & 0 & 0 \\ 0 & 0 & \frac{I_y}{l} & 0 \\ 0 & 0 & 0 & \frac{I_z}{l} \end{bmatrix} \begin{bmatrix} v_1 \\ v_2 \\ v_3 \\ v_4 \end{bmatrix}$$

$$+ \begin{bmatrix} 0 \\ -\dot{\theta}\dot{\psi}(I_y - I_z) \\ -\dot{\phi}\dot{\psi}\frac{I_z - I_x}{l} + J_t\dot{\psi}\Omega \\ -\dot{\phi}\dot{\theta}\frac{I_x - I_y}{l} - J_t\dot{\theta}\Omega \end{bmatrix} \tag{8}$$

IV. DISCONTINUOUS CONTROL

To facilitate the derivation of the stabilizing control law for the second-order form Eq. (6), the following proposition and lemma are needed[3].

Proposition 1. *For the nonlinear system*

$$\dot{x}_1 = x_2, \quad \dot{x}_2 = -s_1 s_2 x_1 - (s_1 + s_2)x_2,$$

if $s_2 > s_1 > 0$, *and the initial states* $(x_1(0), x_2(0))$ *satisfy* $x_1(0)(s_2 x_1(0) + x_2(0)) > 0$, *then*

$$x_1(t) \neq 0 \quad (\forall t \in (0, \infty)),$$

$$\lim_{t\to\infty} (\frac{x_2(t)}{x_1(t)} + s_1) = 0, \tag{9}$$

$$\int_0^\infty \left| \frac{x_2(t)}{x_1(t)} + s_1 \right| dt < \infty.$$

Lemma 1. *For the linear time-varying system*

$$\dot{x} = (A_1 + A_2(t))x, \tag{10}$$

where A_1 *is a constant Hurwitz matrix, and* $A_2(t)$ *a time-varying matrix. If* $A_2(t)$ *satisfies*

$$\lim_{t\to\infty} A_2(t) = 0, \quad \int_0^\infty \|A_2(t)\| \, dt < \infty, \tag{11}$$

then $\dot{x} = (A_1 + A_2(t))$ *is exponentially stable.*

In what follows, a discontinuous control law will be derived to stabilize the system to the origin exponentially based on the discontinuous coordinate transformation. Let $y_1 = x$, $y_2 = \dot{x}$, $y_3 = \phi$, $y_4 = \dot{\phi}$, $y_5 = \theta$, $y_6 = \dot{\theta}$, $y_7 = \psi$, $y_8 = \dot{\psi}$, $y_9 = y$, $y_{10} = \dot{y}$, $y_{11} = z$, and $y_{12} = \dot{z}$, the second-order form in Eq. (6) can be written as

$$\begin{aligned} \dot{y_1} &= y_2 \\ \dot{y_2} &= v_1 \\ \dot{y_3} &= y_4 \\ \dot{y_4} &= v_2 \\ \dot{y_5} &= y_6 \\ \dot{y_6} &= v_3 \\ \dot{y_7} &= y_8 \\ \dot{y_8} &= v_4 \\ \dot{y_9} &= y_{10} \\ \dot{y_{10}} &= (m_1/m_2)\tan y_7 v_1 \\ \dot{y_{11}} &= y_{12} \\ \dot{y_{12}} &= (-m_1/m_3)\tan y_5 \sec y_7 v_1 \end{aligned} \tag{12}$$

Designing control input

$$v_1 = -(k_1 + k_2)y_2 - k_1 k_2 y_1 \tag{13}$$

where $k_2 > k_1 > 0$ are constants, then $y_1 \neq 0$ $(\forall t \in (0, \infty))$ is guaranteed by Proposition 2 given in [3], and so the coordinate transformation

$$\begin{aligned} z_i &= y_i \quad (i = 1, \cdots, 8), \\ z_j &= \frac{y_j}{y_1} \quad (j = 9, \cdots, 12) \end{aligned} \tag{14}$$

is well defined. In the new coordinates z_i $(i = 1, \cdots, 12)$, Eq. (12) becomes

$$\begin{aligned} \dot{z_1} &= z_2 \\ \dot{z_2} &= -(k_1 + k_2)z_2 - k_1 k_2 z_1 \\ \dot{z_3} &= z_4 \\ \dot{z_4} &= v_2 \\ \dot{z_5} &= z_6 \\ \dot{z_6} &= v_3 \\ \dot{z_7} &= z_8 \\ \dot{z_8} &= v_4 \\ \dot{z_9} &= z_{10} + k_1 z_9 - (\frac{z_2}{z_1} + k_1)z_9 \\ \dot{z_{10}} &= (m_1/m_2){k_1}^2 z_7 + k_1 z_{10} \\ &\quad - (\frac{z_2}{z_1} + k_1)[\frac{m_1}{m_2}(k_1 + k_2)z_7 + z_{10}] \\ \dot{z_{11}} &= z_{12} + k_1 z_{11} - (\frac{z_2}{z_1} + k_1)z_{11} \\ \dot{z_{12}} &= -(m_1/m_3){k_1}^2 z_5 + k_1 z_{12} \\ &\quad + (\frac{z_2}{z_1} + k_1)[\frac{m_1}{m_3}(k_1 + k_2)z_5 - z_{12}] \end{aligned} \tag{15}$$

if $y_5 \simeq 0$ and $y_7 \simeq 0$.

The above Eq. (15) can be reorganized compactly as

$$\begin{aligned} \dot{z_1} &= z_2 \\ \dot{z_2} &= -(k_1 + k_2)z_2 - k_1 k_2 z_1 \\ \dot{Z}_{3-12} &= (A_1 + A_2(t))Z_{3-12} + B\mathbf{v} \end{aligned} \tag{16}$$

where $Z_{3-12} = [z_3 \quad z_4 \quad \cdots \quad z_{12}]^T$, $\mathbf{v} = [v_2 \quad v_3 \quad v_4]^T$ and

$$A_1 = \begin{bmatrix} 0 & 1 & 0 & 0 & 0 & 0 & 0 & 0 & 0 & 0 \\ 0 & 0 & 0 & 0 & 0 & 0 & 0 & 0 & 0 & 0 \\ 0 & 0 & 0 & 1 & 0 & 0 & 0 & 0 & 0 & 0 \\ 0 & 0 & 0 & 0 & 0 & 0 & 0 & 0 & 0 & 0 \\ 0 & 0 & 0 & 0 & 0 & 1 & 0 & 0 & 0 & 0 \\ 0 & 0 & 0 & 0 & 0 & 0 & 0 & 0 & 0 & 0 \\ 0 & 0 & 0 & 0 & 0 & 0 & k_1 & 1 & 0 & 0 \\ 0 & 0 & 0 & 0 & \frac{m_1}{m_2}k_1^2 & 0 & 0 & k_1 & 0 & 0 \\ 0 & 0 & 0 & 0 & 0 & 0 & 0 & 0 & k_1 & 1 \\ 0 & 0 & -\frac{m_1}{m_3}k_1^2 & 0 & 0 & 0 & 0 & 0 & 0 & 1 \end{bmatrix},$$

$$A_2(t) = (\frac{z_2}{z_1} + k_1) \begin{bmatrix} 0 & 0 & 0 & 0 & 0 & 0 & 0 & 0 & 0 & 0 \\ 0 & 0 & 0 & 0 & 0 & 0 & 0 & 0 & 0 & 0 \\ 0 & 0 & 0 & 0 & 0 & 0 & 0 & 0 & 0 & 0 \\ 0 & 0 & 0 & 0 & 0 & 0 & 0 & 0 & 0 & 0 \\ 0 & 0 & 0 & 0 & 0 & 0 & 0 & 0 & 0 & 0 \\ 0 & 0 & 0 & 0 & 0 & 0 & 0 & 0 & 0 & 0 \\ 0 & 0 & 0 & 0 & 0 & 0 & -1 & 0 & 0 & 0 \\ 0 & 0 & 0 & 0 & a & 0 & 0 & -1 & 0 & 0 \\ 0 & 0 & 0 & 0 & 0 & 0 & 0 & 0 & -1 & 0 \\ 0 & 0 & b & 0 & 0 & 0 & 0 & 0 & 0 & -1 \end{bmatrix}$$

where $a = -\frac{m_1}{m_2}(k_1 + k_2)$ and $b = \frac{m_1}{m_3}(k_1 + k_2)$.

$$B = \begin{bmatrix} 0 & 0 & 0 \\ 1 & 0 & 0 \\ 0 & 0 & 0 \\ 0 & 1 & 0 \\ 0 & 0 & 0 \\ 0 & 0 & 1 \\ 0 & 0 & 0 \\ 0 & 0 & 0 \\ 0 & 0 & 0 \\ 0 & 0 & 0 \end{bmatrix}$$

By Proposition 2 given in [3], we know

$$\lim_{t\to\infty}(\frac{z_2}{z_1} + k_1) = 0, \qquad \int_0^\infty \left|\frac{z_2}{z_1} + k_1\right| dt < \infty.$$

It follows that

$$\lim_{t\to\infty} A_2(t) = 0, \qquad \int_0^\infty \|A_2(t)\|\, dt < \infty.$$

Now let us check the controllability of $[A_1, B]$. Its controllability matrix can be calculated as $[B, A_1B, A_1^2B, A_1^3B, A_1^4B, A_1^5B, A_1^6B, A_1^7B, A_1^8B, A_1^9B]$, which is nonsingular because $k_1 > 0$. Therefore, $[A_1, B]$ is controllable and we can choose feedback gain matrix L as

$$L = \begin{bmatrix} l_1 & l_2 & l_3 & l_4 & l_5 & l_6 & l_7 & l_8 & l_9 & l_{10} \\ l_{11} & l_{12} & l_{13} & l_{14} & l_{15} & l_{16} & l_{17} & l_{18} & l_{19} & l_{20} \\ l_{21} & l_{22} & l_{23} & l_{24} & l_{25} & l_{26} & l_{27} & l_{28} & l_{29} & l_{30} \end{bmatrix},$$

so that the matrix $A_1 + BL$ is a Hurwitz matrix, i.e., control input

$$\mathbf{v} = LZ_{3-12}$$

can exponentially stabilize the linear system

$$\dot{Z}_{3-12} = A_1 Z_{3-12} + B\mathbf{v}$$

From Lemma 1, we can conclude that system

$$\dot{Z}_{3-12} = (A_1 + BL + A_2(t))Z_{3-12}$$

is exponentially stable, i.e., system

$$\dot{Z}_{3-12} = (A_1 + A_2(t))Z_{3-12} + B\mathbf{v}$$

can be exponentially stabilized to the origin by feedback control

$$\mathbf{v} = LZ_{3-12}$$

Since states z_1, z_2 are exponentially convergent to zeros, the whole states z_i (i=1, 2, $\cdots$, 12) converge to zeros exponentially. From $y_i = z_i$ (i = 1, $\cdots$, 8); $y_j = z_j z_1$ (j = 9, $\cdots$, 12), we can conclude that y_i (i = 1, 2, $\cdots$, 12) converge to zeros exponentially, and so do $(y, \dot{y})$. The above results are summarized in the following theorem.

Theorem 1. *If the initial states $(y_1(0), y_2(0))$ satisfy $y_1(0)(k_2 y_1(0) + y_2(0)) > 0$, $y_5 = y_7 \simeq 0$ and L is chosen such that $A_1 + BL$ is a Hurwitz matrix, then the second-order form in (6) can be exponentially stabilized to the origin by the following control law*:

$$\begin{aligned} v_1 &= -(k_1 + k_2)y_2 - k_1 k_2 y_1 \\ v_2 &= l_1 y_3 + l_2 y_4 + l_3 y_5 + l_4 y_6 + l_5 y_7 \\ &\quad + l_6 y_8 + l_7 \frac{y_9}{y_1} + l_8 \frac{y_{10}}{y_1} + l_9 \frac{y_{11}}{y_1} + l_{10} \frac{y_{12}}{y_1} \qquad (17) \\ v_3 &= l_{11} y_3 + l_{12} y_4 + l_{13} y_5 + l_{14} y_6 + l_{15} y_7 \\ &\quad + l_{16} y_8 + l_{17} \frac{y_9}{y_1} + l_{18} \frac{y_{10}}{y_1} + l_{19} \frac{y_{11}}{y_1} + l_{20} \frac{y_{12}}{y_1} \\ v_4 &= l_{21} y_3 + l_{22} y_4 + l_{23} y_5 + l_{24} y_6 + l_{25} y_7 \\ &\quad + l_{26} y_8 + l_{27} \frac{y_9}{y_1} + l_{28} \frac{y_{10}}{y_1} + l_{29} \frac{y_{11}}{y_1} + l_{30} \frac{y_{12}}{y_1} \end{aligned}$$

where $k_2 > k_1 > 0$ are two constants.

V. CONCLUSION

In this paper, we have converted the model of second-order nonholonomic systems of an underactuated X4-AUV to a certain second-order form by applying a partial linearization technique. A discontinuous time-invariant state feedback control law was derived to stabilize such a second-order form. It has been proved that the proposed control law was able to stabilize the second-order form exponentially, when the initial state is in or has been driven into certain regions of state space, and pitch and yaw angles are very small.

REFERENCES

[1] Oriolo G and Nakamura Y (1991), Control of mechanical systems with second-order nonholonomic constraints: Underactuated manipulators, in Proc. of 30th IEEE CDC, pp. 306–308

[2] Laiou M and Astolfi A (1999), Discontinuous control of high-order generalized chained systems, Systems Control Letters, 37(5), pp. 309–322

[3] Xu WL, Ma BL (2001), Stabilization of second-order nonholonomic systems in canonical chained form, Original Research Article Robotics and Autonomous Systems, 34(4), 223–233

[4] Okamura K (2009), Position and attitude control for an autonomous underwater robot using a manifold theory. Master Thesis, Saga University

[5] Zain ZM, Watanabe K, Danjo T, Izumi K and Nagai I (2010), Modeling an autonomous underwater vehicle with four-thrusters, Proc. of The Fifteenth International Symposium on Artificial Life and Robotics, (AROB 15th '10), 934–937

The Seventeenth International Symposium on Artificial Life and Robotics 2012 (AROB 17th '12),
B-Con Plaza, Beppu, Oita, Japan, January 19-21, 2012

Eye-Vergence Visual Servoing Enhancing Lyapunov-stable Trackability

Fujia Yu[1], Mamoru Minami[1], Wei Song[2], and Akira Yanou[1]

[1] Graduate School of Natural Science and Technology, Okayama University Tsushimanaka3-1-1 , Okayama, JAPAN.
[2] University of Shanghai

Abstract: Visual servoing methods for hand-eye configuration are vulnerable for hand's dynamical oscillation, since nonlinear dynamical effects of whole manipulator stand against the stable tracking ability (trackability). Our proposal to solve this problem is that the controller for visual servoing of the hand and the one for eye-vergence should be separated independently based on decoupling each other, where the trackablity is verified by Lyapunov analysis. Then the effectiveness of the decoupled hand & eye-vergence visual servoing method is evaluated through simulations incorporated with actual dynamics of 7-DoF robot with additional 3-DoF for eye-vergence mechanism by amplitude and phase frequency analysis.

Keywords: Visual servoing, Eye-vergence, trackability

1 INTRODUCTION

Recently much research attention has turned to focus on full DoF pose control of the robot end-effector toward a target object [1]. Full 3D Visual servoing requires simultaneously full 3D pose measurement and 3D motion control also. But researches so far seem to have tended to deal with these two problems separately as isolated issues. Different kinds of visual servoing – position-based, image-based or $2\frac{1}{2}$-D visual servoing [2] – usually discuss their methodologies based on an assumption that pose measurement is known or could be easily received from some other devices.

Eye-vergence function bears two fundamental fruits as kinematical merit and dynamical one. Firstly kinematical merit is described. Observing ability of a fixed-hand-eye configuration may be deteriorated by relative geometry of the camera and the target, as the robot cannot observe the object well when it is near the cameras (Fig. 1 (a)), small intersection of the possible sight space of the two cameras (Fig. 1 (b)), and the image of the object cannot appear in the center of both cameras, so we could not get clear image information of target reflected at its periphery, reducing the pose measurement accuracy (Fig. 1 (c)). To solve these problems, eye-vergence functions to rotate eye cameras orientation to see target object at center of the cameras' view, as shown in Fig. 2(a)-(c), enhancing the measurement accuracy in trigonometric calculation and avoiding aberration, i.e. peripheral distortion of camera lens. Moreover, recent researches on visual servoing are limited generally in a swath of tracking an object while keeping a certain constant distance, which are the researches based on different task scenarios from the approaching visual servoing discussed here.

The second merit is concerning dynamical effects to keep tracking a moving target in the camera's view. Needless to say in visual servoing application, keeping closed loop of visual feedback is vital from a view point of stability in control

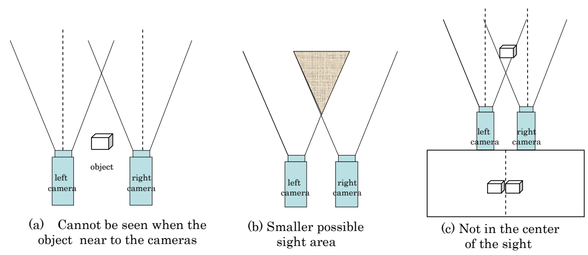

Fig. 1. Disadvantage of fix camera system

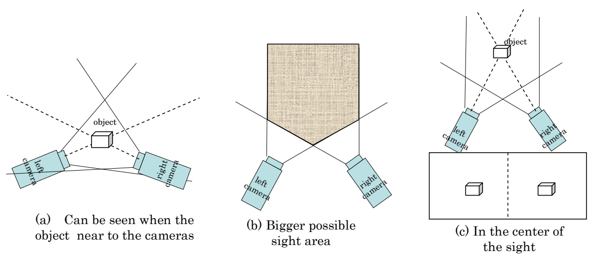

Fig. 2. Advantage of Eye-vergence system

theory. Cameras fixed at the hand of manipulator are keeping staring at the object at first, but when the target moves so fast that the manipulator cannot catch up the speed of the target because of whole manipulator's dynamics, resulting in the visual feedback cut , loosing feedback. To improve this pose tracking difficulty of fixed hand eye system, the eye-vergence function seems dynamically effective, because of small mass and inertia moment of the eye ball comparing those of full manipulator's structure. Therefore tracking ability of eye-vergence can be better than fixed, like animals tracks target with eye motion before rotate their heads to the target.

In this report, we propose a new control method of hand and eye-vergence dual visual servoing system with a stability analysis of Lyapunov method, guaranteeing that both the tracking pose errors of hand and eye-vergence orientation error converge to zero, providing target object stopping in work space. Further to evaluate the trackability through frequency response experiment we need a new measure to rate the eye's

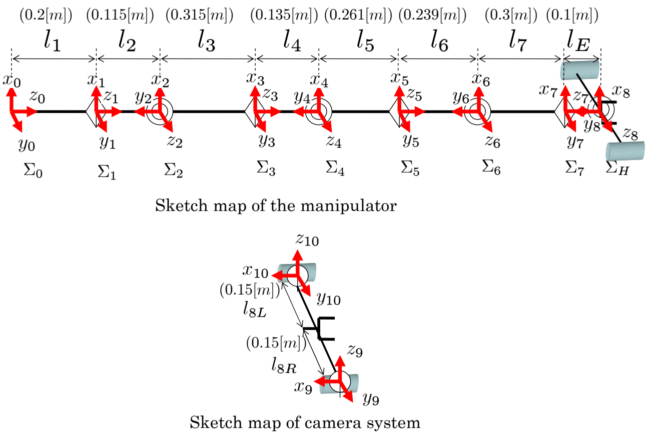

Fig. 3. Frame structure of manipulator

trackability to the target object oscillating with designated amplitude and angular velocity. We also come up with a yardstick to measure the eye's trackability.

2 SIMULATOR AND ROBOT DYNAMICS

The dynamics equation of the system is

$$\boldsymbol{M}(\boldsymbol{q})\ddot{\boldsymbol{q}} + \boldsymbol{h}(\boldsymbol{q}, \dot{\boldsymbol{q}}) + \boldsymbol{g}(\boldsymbol{q}) = \boldsymbol{\tau} \tag{1}$$

here $\boldsymbol{q}$ is a vector express the angle of each joint where $\boldsymbol{q}$ can be divided into $\boldsymbol{q} = [\boldsymbol{q}_E^T, \boldsymbol{q}_C^T]^T$, $\boldsymbol{\tau} = [\tau_1, \cdots, \tau_n]^T$ is the input torque, and $\boldsymbol{M}(\boldsymbol{q})$ is the inertia matrix, $\boldsymbol{h}(\boldsymbol{q}, \dot{\boldsymbol{q}})$is the vector representing the centrifugal and coriolis forces, $\boldsymbol{g}(\boldsymbol{q})$ is the vector representing the gravity load.

Our simulator is model PA-10 by using the actual physical parameters of the PA-10. Here, we install two cameras conclude 3 free degrees on the end-effector of PA-10.The structure of the system is shown in Fig. 3. The Homogeneous Transformation from coordinate static to the end-effector Σ_8 to the end-effector coordinate Σ_E is expressed by a constant matrix ${}^8\boldsymbol{T}_E$. In this paper we use $\boldsymbol{T}$ to express Homogeneous Transformation matrix. Σ_9 and Σ_{10} express the coordinate of the right and left camera separately, they will be written as Σ_R and Σ_L. While the two cameras are both installed on the end-effector, both the cameras share a same tilt angle, but each of them has an own pan angle, angular velocity $\boldsymbol{\omega}_i$, angular acceleration $\dot{\boldsymbol{\omega}}_i$, link acceleration $\ddot{\boldsymbol{p}}_i$ and the acceleration of the center of gravity $\ddot{\boldsymbol{s}}_i$ can be calculated by the method written in [3].

3 HAND & EYE VISUAL SERVOING

3.1 Desired-trajectory Generation

As shown in Fig. 4, the world coordinate frame is denoted by Σ_W, the target coordinate frame is denoted by Σ_M, and the desired and actual end-effector coordinate frame is denoted by Σ_{Ed}, Σ_E respectively. The desired relative relation between the target and the end-effector is given by Homogeneous Transformation as ${}^{Ed}\boldsymbol{T}_M$, the relation between the

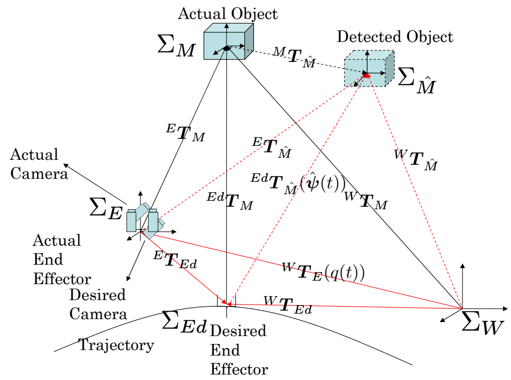

Fig. 4. Motion of the end-effector and object

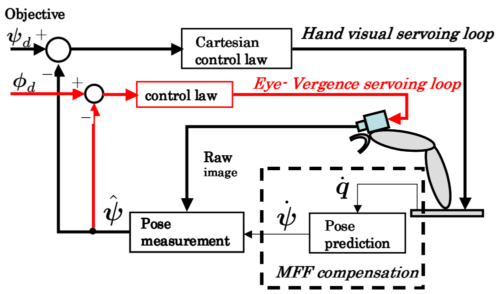

Fig. 5. Hand & Eye Visual servo system

target and the actual end-effector is given by ${}^E\boldsymbol{T}_M$, then the difference between the desired end-effector pose Σ_{Ed} and the actual end-effector pose Σ_E is denoted as ${}^E\boldsymbol{T}_{Ed}$, and calculated by:

$${}^E\boldsymbol{T}_{Ed}(t) = {}^E\boldsymbol{T}_M(t)\,{}^{Ed}\boldsymbol{T}_M^{-1}(t) \tag{2}$$

(2) is a general deduction that satisfies arbitrary object motion ${}^W\boldsymbol{T}_M(t)$ and arbitrary visual servoing objective ${}^{Ed}\boldsymbol{T}_M(t)$. However, the relation ${}^E\boldsymbol{T}_M(t)$ is only observed by cameras using the on-line model-based recognition method and 1-step GA [4]. Let $\Sigma_{\hat{M}}$ denote the detected object, there always exist an error between the actual object Σ_M and the detected one $\Sigma_{\hat{M}}$. However, in visual servoing we use different methods to decrease this error. for example, we can limit the error inside 5[mm] in [4]. So in visual servoing, (2) will be rewritten based on $\Sigma_{\hat{M}}$ that includes the error ${}^M\boldsymbol{T}_{\hat{M}}$, as

$${}^E\boldsymbol{T}_{Ed}(t) = {}^E\boldsymbol{T}_{\hat{M}}(t)\,{}^{Ed}\boldsymbol{T}_{\hat{M}}^{-1}(t), \tag{3}$$

where ${}^E\boldsymbol{T}_{\hat{M}} = {}^E\boldsymbol{T}_M$ determined by the given visual servoing objective. Differentiating Eq. (3) with respect by time twice,

$$\begin{aligned}{}^E\ddot{\boldsymbol{T}}_{Ed}(t) = {}^E\ddot{\boldsymbol{T}}_{\hat{M}}(t)\,{}^{\hat{M}}\boldsymbol{T}_{Ed}(t) + 2\,{}^E\dot{\boldsymbol{T}}_{\hat{M}}(t)\,{}^{\hat{M}}\dot{\boldsymbol{T}}_{Ed}(t) + \\ {}^E\boldsymbol{T}_{\hat{M}}(t)\,{}^{\hat{M}}\ddot{\boldsymbol{T}}_{Ed}(t),\end{aligned} \tag{4}$$

where ${}^{\hat{M}}\boldsymbol{T}_{Ed}$, ${}^{\hat{M}}\dot{\boldsymbol{T}}_{Ed}$, ${}^{\hat{M}}\ddot{\boldsymbol{T}}_{Ed}$ are given as the desired visual servoing objective. ${}^E\boldsymbol{T}_{\hat{M}}$, ${}^E\dot{\boldsymbol{T}}_{\hat{M}}$, ${}^E\ddot{\boldsymbol{T}}_{\hat{M}}$ can be observed by cameras. From these preparations, we can calculate the variables in the controllers of the system in the next subsection, such as $\Delta \boldsymbol{p}_E$ and so on, leaving detail explanation for next subsection. As shown in Fig. 4, there are two errors that we should decrease to the value as small as possible in the visual servoing process. First one is the error between the actual object and the detected one, ${}^M\boldsymbol{T}_{\hat{M}}$, and the other is the error between the desired end-effector and the actual one, ${}^E\boldsymbol{T}_{Ed}$. In our research, the error of ${}^M\boldsymbol{T}_{\hat{M}}$ is decreased by on-line recognition method of 1-step GA, MFF compensation method and the eye-vergence camera system, and the error of ${}^E\boldsymbol{T}_{Ed}$ can be decreased by the hand visual servoing controller.

3.2 Hand Desired Acceleration

The block diagram of our proposed hand & eye-vergence visual servoing controller is shown in Fig. 5. The hand-visual servoing is the outer loop. The controller used for hand-visual servoing is proposed by B.Siciliano [5]. First we will introduce the variables defined in the system:

$$\Delta \boldsymbol{p}_E = \boldsymbol{p}_d - \boldsymbol{p}_E \tag{5}$$

here d and E in the bottom right corner of the $\boldsymbol{p}$ means the desired position and actual position of the end-effector. There is no letter in the top left corner, it means the vector or the matrix is expressed in the world frame.

A special type of angle/axis representation of the orientation error is obtained with the quaternion, i.e

$$\begin{aligned} {}^E\eta &= cos\frac{\theta_{Ed}}{2} & (6)\\ \Delta {}^E\boldsymbol{\epsilon} &= sin\frac{\theta_{Ed}}{2}\ {}^E\boldsymbol{k}_{Ed} & (7)\end{aligned}$$

Here θ and $\boldsymbol{k}$ are the rotation angle and the rotation axis of the object. The letter in the top left corner express the coordinate where the vector or the rotation matrix is expressed in. While the angle velocity error between the desired and the actual angle velocity is defined as

$$\Delta \boldsymbol{\omega}_E = \boldsymbol{\omega}_d - \boldsymbol{\omega}_E \tag{8}$$

With the variables defined above, we just show main equations of the hand visual servoing controller that are used to calculate input torque $\boldsymbol{\tau}$.

$$\boldsymbol{a}_{pE} = \ddot{\boldsymbol{p}}_d + \boldsymbol{K}_{D_p}\Delta\dot{\boldsymbol{p}}_E + \boldsymbol{K}_{P_p}\Delta \boldsymbol{p}_E \tag{9}$$

$$\boldsymbol{a}_{oE} = \dot{\boldsymbol{\omega}}_d + \boldsymbol{K}_{D_o}\Delta\boldsymbol{\omega}_E + \boldsymbol{K}_{P_o}\boldsymbol{R}_E{}^E\Delta\boldsymbol{\epsilon} \tag{10}$$

$$\boldsymbol{s}_E = \boldsymbol{J}_E^+(\boldsymbol{q}_E)\{\boldsymbol{a}_E - \dot{\boldsymbol{J}}_E(\boldsymbol{q}_E, \dot{\boldsymbol{q}}_E)\dot{\boldsymbol{q}}_E)\} + \{\boldsymbol{I} - \boldsymbol{J}_E^+(\boldsymbol{q}_E)\boldsymbol{J}_E(\boldsymbol{q}_E)\}\{\boldsymbol{E}_p(\boldsymbol{q}_{Ed} - \boldsymbol{q}_E) + \boldsymbol{E}_d(\dot{\boldsymbol{q}}_{Ed} - \dot{\boldsymbol{q}}_E)\} \tag{11}$$

Here, $\ddot{\boldsymbol{q}}_E$ is a 7×1 vector representing the angular accelerations of the 7 links of the PA-10 manipulator. $\boldsymbol{a}$ can be written short for $[\boldsymbol{a}_p^T, \boldsymbol{a}_o^T]^T$. The quaternion error from the actual orientation to the desired orientation of the end effector ${}^E\Delta\boldsymbol{\epsilon}$ can be extracted from the transformation ${}^E\boldsymbol{T}_{Ed}$, and the other error variables in (9), (10) are described in Σ_W, which can be calculated by the transformation ${}^E\boldsymbol{T}_{Ed}$, ${}^E\dot{\boldsymbol{T}}_{Ed}$, ${}^E\ddot{\boldsymbol{T}}_{Ed}$ in (3), (4), using the rotational matrix ${}^W\boldsymbol{R}_E(\boldsymbol{q})$ through coordinate transformation.

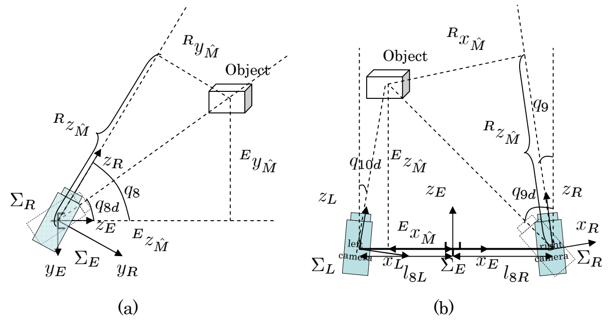

Fig. 6. Pan and Tilt Camera Angles Defined Based on Relation between Target object and Cameras

And $\boldsymbol{J}_E(\boldsymbol{q}_E)$ is the Jacobian matrix from the world coordinate to the end effector, which means that $\boldsymbol{\omega}_E = \boldsymbol{J}_E(\boldsymbol{q}_E)\dot{\boldsymbol{q}}_E$, and $\boldsymbol{J}_E^+(\boldsymbol{q}_E)$ in (11) is the pseudo-inverse of $\boldsymbol{J}_E(\boldsymbol{q}_E)$ given by $\boldsymbol{J}_E^+(\boldsymbol{q}_E) = \boldsymbol{J}_E^T(\boldsymbol{J}_E\boldsymbol{J}_E^T)^{-1}$. $\boldsymbol{K}_{D_p}$, $\boldsymbol{K}_{P_p}$, $\boldsymbol{K}_{D_o}$, $\boldsymbol{K}_{P_o}$ are positive control gains.

3.3 Eye-vergence Desired Acceleration

The eye-vergence visual servoing is the inner loop of the visual servoing system shown in Fig. 5. In this paper, we use two pan-tilt cameras for eye-vergence visual servoing. Here, the positions of cameras are supposed to be fixed on the end-effector. For camera system, q_8 is tilt angle, q_9 and q_{10} are pan angles, and q_8 is common for both cameras. As it is shown in Fig. 6, ${}^Ex_{\hat{M}}$, ${}^Ey_{\hat{M}}$, ${}^Ez_{\hat{M}}$ express position of the detected object in the end-effector coordinate. The desired angle of the camera joints $\boldsymbol{q}_{cd}^T = [q_{8d}, q_{9d}, q_{10d}]^T$ can be calculated by:

$$\begin{aligned} q_{8d} &= atan2({}^Ey_{\hat{M}}, {}^Ez_{\hat{M}}) & (12)\\ q_{9d} &= atan2(-l_{8R} + {}^Ex_{\hat{M}}, {}^Ez_{\hat{M}}) & (13)\\ q_{10d} &= atan2(l_{8L} + {}^Ex_{\hat{M}}, {}^Ez_{\hat{M}}), & (14)\end{aligned}$$

where $l_{8L} = l_{8R} = 150[mm]$ is the camera location. We set the center line of a camera as the z axis of each camera coordinate, so the object will be in the center of the sight of the right camera when ${}^Rx_{\hat{M}} = 0$ and ${}^Ry_{\hat{M}} = 0$. Here ${}^Rx_{\hat{M}}$, ${}^Ry_{\hat{M}}$, ${}^Rz_{\hat{M}}$ express the position of the detected object in the right camera coordinate.

$$\Delta \boldsymbol{q}_C = \boldsymbol{q}_{Cd} - \boldsymbol{q}_C \tag{15}$$

$$\boldsymbol{s}_C = \ddot{\boldsymbol{q}}_{Cd} + \boldsymbol{K}_{D_C}\Delta\dot{\boldsymbol{q}}_C + \boldsymbol{K}_{P_C}\Delta \boldsymbol{q}_C \tag{16}$$

here, $\boldsymbol{K}_{D_C}$, $\boldsymbol{K}_{P_C}$ are positive definite diagonal matrix.

3.4 Hand/Eye-vergence Controller

By the desired accelerations from (11) and (16), input $\boldsymbol{\tau}$ is calculated by:

$$\boldsymbol{s} = \begin{bmatrix} \boldsymbol{s}_E \\ \boldsymbol{s}_C \end{bmatrix} \tag{17}$$

$$\boldsymbol{\tau} = \boldsymbol{M}(\boldsymbol{q})\boldsymbol{s} + \boldsymbol{h}(\boldsymbol{q}, \dot{\boldsymbol{q}})\dot{\boldsymbol{q}} + \boldsymbol{g}(\boldsymbol{q}) \tag{18}$$

4 STABILITY OF HAND & EYE-VERGENCE MOTION

4.1 Manipulator Dynamics

First, we discuss about the convergence of our proposed hand visual servoing system. From the input torque of each joint in (18) and the dynamics equation of the system (1)

$$\ddot{\boldsymbol{q}} = \boldsymbol{s} \tag{19}$$

so

$$\ddot{\boldsymbol{q}}_E = \boldsymbol{s}_E. \tag{20}$$

Take (11) (here we do not consider the second item in the right side which is the controller of the redundance) into (20) we have

$$\boldsymbol{a}_E = \boldsymbol{J}_E(\boldsymbol{q}_E)\ddot{\boldsymbol{q}}_E + \dot{\boldsymbol{J}}_E(\boldsymbol{q}_E, \dot{\boldsymbol{q}}_E)\dot{\boldsymbol{q}}_E \tag{21}$$

so

$$\begin{bmatrix} \ddot{\boldsymbol{p}}_E \\ \dot{\boldsymbol{\omega}}_E \end{bmatrix} = \boldsymbol{J}_E(\boldsymbol{q}_E)\ddot{\boldsymbol{q}}_E + \dot{\boldsymbol{J}}_E(\boldsymbol{q}_E, \dot{\boldsymbol{q}}_E)\dot{\boldsymbol{q}}_E \tag{22}$$

which means:

$$\begin{bmatrix} \ddot{\boldsymbol{p}}_E \\ \dot{\boldsymbol{\omega}}_E \end{bmatrix} = \begin{bmatrix} \boldsymbol{a}_{pE} \\ \boldsymbol{a}_{oE} \end{bmatrix}. \tag{23}$$

Submit $\boldsymbol{a}_{pE}$, $\boldsymbol{a}_{oE}$ in (23) into (9) and (10),

$$\Delta\ddot{\boldsymbol{p}}_E + \boldsymbol{K}_{D_p}\Delta\dot{\boldsymbol{p}}_E + \boldsymbol{K}_{P_p}\Delta\boldsymbol{p}_E = \boldsymbol{0} \tag{24}$$

$$\Delta\dot{\boldsymbol{\omega}}_E + \boldsymbol{K}_{D_o}\Delta\boldsymbol{\omega}_E + \boldsymbol{K}_{P_o}\boldsymbol{R}_E\Delta^E\boldsymbol{\epsilon} = \boldsymbol{0} \tag{25}$$

4.2 Camera Dynamics

For the cameras, from (19),

$$\ddot{\boldsymbol{q}}_C = \boldsymbol{s}_C. \tag{26}$$

From (16), The close loop becomes:

$$\Delta\ddot{\boldsymbol{q}}_C + \boldsymbol{K}_{D_C}\Delta\dot{\boldsymbol{q}}_C + \boldsymbol{K}_{P_C}\Delta\boldsymbol{q}_C = \boldsymbol{0} \tag{27}$$

4.3 Stability Analysis

We invoke a Lyapunov argument, the feed back gains are taken as scalar matrices, i.e. $\boldsymbol{K}_{D_p} = K_{D_p}\boldsymbol{I}$, $\boldsymbol{K}_{P_p} = K_{P_p}\boldsymbol{I}$, $\boldsymbol{K}_{D_o} = K_{D_o}\boldsymbol{I}$ and $\boldsymbol{K}_{P_o} = K_{P_o}\boldsymbol{I}$. Here we assume that the feedback gains of the links are the same.

$$\begin{aligned} V &= \Delta\boldsymbol{p}_E^T\boldsymbol{K}_{P_p}\Delta\boldsymbol{p}_E + (\Delta\dot{\boldsymbol{p}}_E)^T\Delta\dot{\boldsymbol{p}}_E \\ &\quad + K_{P_o}\{(\eta-1)^2 + (\Delta\boldsymbol{\epsilon})^T\Delta\boldsymbol{\epsilon}\} + \frac{1}{2}(\Delta\boldsymbol{\omega}_E)^T\Delta\boldsymbol{\omega}_E \\ &\quad + \Delta\boldsymbol{q}_C^T\boldsymbol{K}_{P_C}\Delta\boldsymbol{q}_C + (\Delta\dot{\boldsymbol{q}}_C)^T\Delta\dot{\boldsymbol{q}}_C \\ &\geq 0 \end{aligned} \tag{28}$$

so

$$\begin{aligned} \dot{V} &= 2\Delta\dot{\boldsymbol{p}}_E^T(\Delta\ddot{\boldsymbol{p}}_E + \boldsymbol{K}_{P_p}\Delta\boldsymbol{p}_E) \\ &\quad + 2K_{P_o}\{(\eta-1)\dot{\eta} + \Delta\boldsymbol{\epsilon}^T\Delta\dot{\boldsymbol{\epsilon}}\} + \Delta\boldsymbol{\omega}_E^T\Delta\dot{\boldsymbol{\omega}}_E \\ &\quad + 2\Delta\dot{\boldsymbol{q}}_C^T(\Delta\ddot{\boldsymbol{q}}_C + \boldsymbol{K}_{P_C}\Delta\boldsymbol{q}_C) \end{aligned} \tag{29}$$

from (24) we can know that

$$\Delta\ddot{\boldsymbol{p}}_E + \boldsymbol{K}_{P_p}\Delta\boldsymbol{p}_E = -\boldsymbol{K}_{D_p}\Delta\dot{\boldsymbol{p}}_E \tag{30}$$

from the quaternion definition we can know that

$$\dot{\eta} = -\frac{1}{2}(\Delta\boldsymbol{\epsilon})^T\Delta\boldsymbol{\omega}_E \tag{31}$$

and

$$\Delta\dot{\boldsymbol{\epsilon}} = \frac{1}{2}\boldsymbol{E}(\eta, \Delta\boldsymbol{\epsilon})\Delta\boldsymbol{\omega}_E \tag{32}$$

where $\boldsymbol{E}(\eta, \boldsymbol{\epsilon}) = \eta\boldsymbol{I} - \boldsymbol{S}(\boldsymbol{\epsilon})$. $\boldsymbol{S}(\boldsymbol{a})$ is a antisymmetric matrix that satisfies $\boldsymbol{S}(\boldsymbol{a})\boldsymbol{b} = \boldsymbol{a} \times \boldsymbol{b}$.

From (27) we can get:

$$\Delta\ddot{\boldsymbol{q}}_C + \boldsymbol{K}_{D_C}\Delta\boldsymbol{q}_C = -\boldsymbol{K}_{D_C}\Delta\dot{\boldsymbol{q}}_C \tag{33}$$

Substitute (25), (30), (31), (32) and (33) into (29) we can get:

$$\begin{aligned} \dot{V} &= -2\Delta\dot{\boldsymbol{p}}_E^T\boldsymbol{K}_{D_p}\Delta\dot{\boldsymbol{p}}_E - \Delta\boldsymbol{\omega}_E^T\boldsymbol{K}_{D_o}\Delta\boldsymbol{\omega}_E \\ &\quad - 2\Delta\dot{\boldsymbol{q}}_C^T\boldsymbol{K}_{D_C}\Delta\dot{\boldsymbol{q}}_C \leq 0 \end{aligned} \tag{34}$$

here, because $\boldsymbol{K}_{D_p}$, $\boldsymbol{K}_{D_o}$ and $\boldsymbol{K}_{D_C}$ are positive definate, only if $\Delta\dot{\boldsymbol{p}}_E = \boldsymbol{0}$, $\Delta\boldsymbol{\omega}_E = \boldsymbol{0}$ and $\Delta\boldsymbol{q}_C = \boldsymbol{0}$, $\dot{V} = 0$. $\Delta\dot{\boldsymbol{p}}_E = \boldsymbol{0}$ and $\Delta\ddot{\boldsymbol{p}}_E = \boldsymbol{0}$, from (24),$\Delta\boldsymbol{p}_E = \boldsymbol{0}$. For the same reason, when $\Delta\dot{\boldsymbol{q}}_C = \boldsymbol{0}$, from (27), $\Delta\boldsymbol{q}_C = \boldsymbol{0}$. when $\Delta\boldsymbol{\omega}_E = \boldsymbol{0}$, $\Delta\dot{\boldsymbol{\omega}}_E = \boldsymbol{0}$. and from (25) $\Delta^E\boldsymbol{\epsilon} = \boldsymbol{0}$. The definition domain of θ is $(-\pi, \pi)$, so the manipulator and the cameras asymptotically converge to the invariant sets s.

$$\begin{aligned} s = \{&\Delta\boldsymbol{p}_E = \boldsymbol{0},\ \Delta\dot{\boldsymbol{p}}_E = \boldsymbol{0},{}^E\eta = 1,\ \Delta^E\boldsymbol{\epsilon} = \boldsymbol{0}, \\ &\Delta\boldsymbol{\omega}_E = \boldsymbol{0},\ \Delta\boldsymbol{q}_C = 0,\ \Delta\dot{\boldsymbol{q}}_C = 0\} \end{aligned} \tag{35}$$

so,

$$\lim_{t\to\infty} {}^E\boldsymbol{T}_{Ed} = \boldsymbol{I}, \quad \lim_{t\to\infty} {}^E\dot{\boldsymbol{T}}_{Ed} = \boldsymbol{0} \tag{36}$$

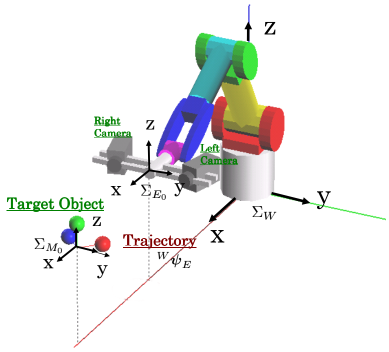

Fig. 7. Object and the visual-servoing system

substitute (36) to (3),

$$\lim_{t\to\infty} {}^E\boldsymbol{T}_{\hat{M}} = \lim_{t\to\infty} {}^{Ed}\boldsymbol{T}_{\hat{M}} \tag{37}$$

and from (12) to (14)

$$\lim_{t\to\infty} {}^R z_{\hat{M}} = 0,\ \lim_{t\to\infty} {}^R y_{\hat{M}} = 0,\ \lim_{t\to\infty} {}^L y_{\hat{M}} = 0 \tag{38}$$

which means the object will become on the center line of the cameras, which means that the object will always keep in the center of the sight of the cameras.

5 SIMULATION OF HAND & EYE-VERGENCE VISUAL SERVOING

To verify the effectiveness of the proposed hand & eye visual servoing system, we conduct the experiment of visual servoing to a 3D marker that is composed of a red ball, a green ball and a blue ball as Fig. 7. The radiuses of these three balls are set as 30[mm].

5.1 Simulation Condition

The recognition error does not affect the dynamic error, so we assume that ${}^M\boldsymbol{T}_{\hat{M}} = \boldsymbol{I}$, The position and orientation of the target object are given to the robot directly in the simulation. The initial hand pose is defined as Σ_{E_0}, while the initial object pose is defined as Σ_{M_0}, and the homogeneous transformation matrix from Σ_W to Σ_{M_0} is:

$${}^W\boldsymbol{T}_{M_0} = \begin{bmatrix} 0 & 0 & -1 & -1410[mm] \\ 1 & 0 & 0 & 0[mm] \\ 0 & -1 & 0 & 355[mm] \\ 0 & 0 & 0 & 1 \end{bmatrix}. \tag{39}$$

The target object move according to the following time function

$$\begin{aligned} {}^{M_0}\boldsymbol{\psi}_M &= [0, {}^{M_0}y_M(t), 0, 0, 0, 0]^T && (40)\\ {}^{M_0}y_M(t) &= 200\sin(\omega t)[mm] && (41) \end{aligned}$$

here, ω is the angular velocity of the motion of the object.

The relation between the object and the desired end-effector is set as:

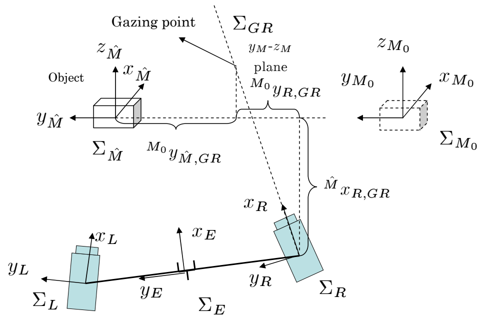

Fig. 8. Cameras' and End Effector's gazing point

$${}^{Ed}\boldsymbol{\psi}_M = [500[mm], 0, 0, 0, 0, 0] \tag{42}$$

The controller gain of the system $\boldsymbol{K}_{D_p}$, $\boldsymbol{K}_{P_p}$, $\boldsymbol{K}_{D_o}$, $\boldsymbol{K}_{P_o}$ are affected by the mass, initial moment, the amplifier output and many other conditions. From the common sense because the camera mass is smaller than the manipulator, $\boldsymbol{K}_{D_C}$ and $\boldsymbol{K}_{P_C}$ can be set bigger than $\boldsymbol{K}_{D_o}$ etc. Here $\boldsymbol{K}_{P_C} = diag\{5,5,5\}, \boldsymbol{K}_{D_C} = diag\{3,3,3\}, \boldsymbol{K}_{P_p} = \boldsymbol{K}_{P_o} = \boldsymbol{K}_{D_p} = \boldsymbol{K}_{D_o} = diag\{1,1,1\}$.

5.2 Definition of Trackability

5.2.1 Camera trackability

Here, to compare the trackability of the eye-vergence system and fixed camera system, we define a concept of gazing point. As it is shown in Fig. 8 the intersection of the gazing line of right camera and the y_{M_0}-z_{M_0} plane is defined as the gazing point. The relative relation between Σ_{M_0} and Σ_R is given by Homogeneous Transformation as ${}^{M_0}\boldsymbol{T}_R$, ${}^{M_0}\boldsymbol{T}_R$ conclude the rotation matrix ${}^{M_0}\boldsymbol{R}_R$ and the position vector ${}^{M_0}\boldsymbol{p}_R$, and the rotation matrix ${}^{M_0}\boldsymbol{R}_R$ can be written as $[{}^{M_0}\boldsymbol{x}_R, {}^{M_0}\boldsymbol{y}_R, {}^{M_0}\boldsymbol{z}_R]$. The direction of ${}^{M_0}\boldsymbol{l}_R$ in Fig. 8 is same to the direction of x_R, and ${}^{M_0}\boldsymbol{l}_R$ can be expressed as:

$${}^{M_0}\boldsymbol{l}_R = {}^{M_0}\boldsymbol{p}_R + k_R {}^{M_0}\boldsymbol{x}_R \tag{43}$$

here k_R is a scalar variable. The gazing point of the right camera expressed in Σ_{M_0} is ${}^{M_0}\boldsymbol{p}_{GR} = [0, {}^{M_0}y_{GR}, {}^{M_0}z_{GR}]^T$. For ${}^{M_0}\boldsymbol{l}_R = {}^{M_0}\boldsymbol{p}_{GR}$ in x direction, $({}^{M_0}\boldsymbol{p}_R)_x + k_R({}^{M_0}\boldsymbol{x}_R)_x = 0$. And usually $({}^{M_0}\boldsymbol{x}_R)_x \neq 0$, k_R can be calculated by $k_R = -({}^{M_0}\boldsymbol{p}_R)_x/({}^{M_0}\boldsymbol{x}_R)_x$, and the y, z coordinate of the gazing point in Σ_{M_0} can be calcated by:

$$\begin{aligned} {}^{M_0}y_{GR} &= ({}^{M_0}\boldsymbol{p}_R)_y + k_R({}^{M_0}\boldsymbol{x}_R)_y && (44)\\ {}^{M_0}z_{GR} &= ({}^{M_0}\boldsymbol{p}_R)_z + k_R({}^{M_0}\boldsymbol{x}_R)_z && (45) \end{aligned}$$

The target object's motion is given by (40), (41), because the motion of the target object M is parallel to the $\boldsymbol{y}_{M_0}$, we take ${}^{M_0}y_M(t)$ as the input, and the gazing point of the right camera ${}^{M_0}y_{GR}(t)$ as the response. And define the concept of trackability by the frequency response of ${}^{M_0}y_{GR}(t)$, the trackability of the left camera can be defined in the same way.

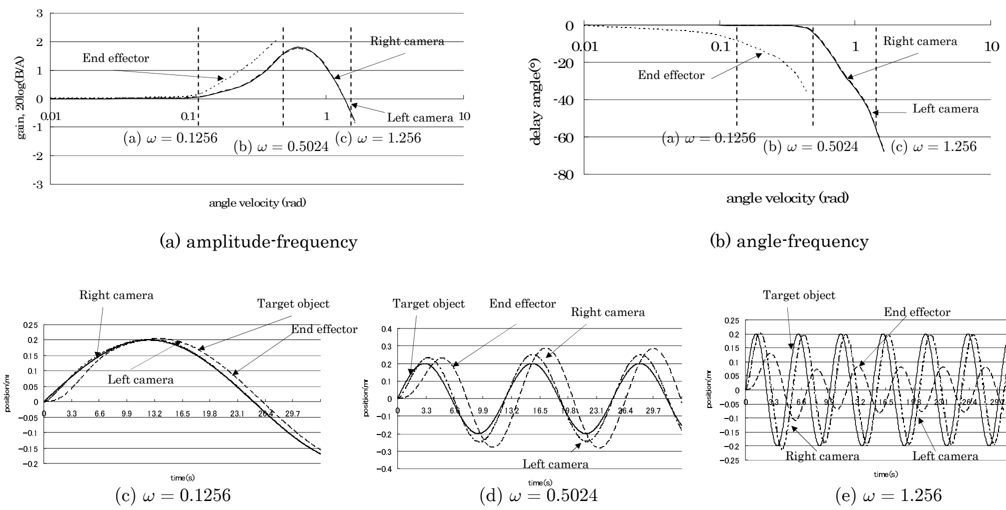

(a) amplitude-frequency (b) angle-frequency

(c) $\omega = 0.1256$ (d) $\omega = 0.5024$ (e) $\omega = 1.256$

Fig. 9. Comparison of Cameras' and End-effector's Trackabilities by Frequency Response

5.2.2 End-effector trackability

To compare with the trackability of the camera, it is necessary to define the End-effector trackability. Here the gazing line direction of normal static hand eye system is same to the x direction of Σ_E, so the gazing point of the static hand-eye system is same to the gazing point of the end-effector.

5.3 Simulation Results

The original position of the target object ${}^{W}\boldsymbol{T}_{M_0}$ is given by (39), the target object motion function is (40), the desired relation between the end-effector and the target object is given in (42). The ω in (40) changes from 0.01 to 2.00. In Fig. 9, we show the result of our experiment. The amplitude-frequence curve and the delay frequency curve are shown in Fig.9 (a) and Fig.9 (b). Here, for the fixed camera $A = {}^{M_0}y_M(t), B = {}^{M_0}y_{GE}(t)$. For the right camera of Eye-Vergence system $A = {}^{M_0}y_M(t), B = {}^{M_0}y_{GR}(t)$, for the left camera $A = {}^{M_0}y_M(t),\ \ B = {}^{M_0}y_{GL}(t)$. In this two figures the abscissa axes are logarithmic scalar of ω. In (a), (b), we sign the angular velocity when $\omega = 0.1256, 0.5024, 1.256$, and show the position of the gazing point of the cameras in eye-vergence simulation and the position of the gazing point of the end-effector in fixed camera experiment in (c), (d), (e). We can see that both the fixed-camera system and eye-vergence system can track the target object when $\omega = 0.1256$ while the fixed-camera system cannot track the target object when $\omega > 0.5024$ so in (e), and the eye-vergence system can track the target object even when $\omega = 1.256$.

From Fig. 9 (a) we can see the data of the cameras and the end-effector all become bigger as ω increases for the reason of resonance, but the curve of the fixed camera system is always below the curves of the cameras, we can see that the amplitude of the eye-vergence system is more closed to the target object than the fixed camera system, the fixed camera system cannot track the target object when $\omega > 0.5024$, so the point line dispear near $\omega = 0.5024$, while in eye-vergence system the fastest velocity of the target object under which the system can catch up with is 1.6956. From (b) the the curve of the fixed camera system is also below the curves of the cameras, which means that delay of the fixed camera system is bigger than the eye-vergence system, To be understood easily, we show the position of the gazing point of the cameras in eye-vergence experiment and the position of the gazing point of the end-effector in fixed camera experiment in (c), (d), (e). From the figures it is also easy to see that comparing with the fixed camera system, the eye-vergence system can track the target object better.

6 CONCLUSION

In this paper, we propose a concept of trackability to evaluate the observation ability on a moving object of visual servoing system. We get amplitud-frequency and phase-frequency curves of the cameras of the eye-vergence system and the fixed camera system under moving object with different angular velocity in simulation and get the conclusion that the trackability and stability of the eye-vergence system is better than that of the fixed-camera system.

REFERENCES

[1] S.Hutchinson, G.Hager, and P.Corke, "A Tutorial on Visual Servo Control", IEEE Trans. on Robotics and Automation, vol. 12, no. 5, pp. 651-670, 1996.

[2] E.Malis, F.Chaumentte and S.Boudet, *2-1/2-D Visual Servoing*, IEEE Trans. on Robotics and Automation, vol. 15, no. 2, pp. 238-250, 1999.

[3] Tsuneo Yoshikawa: *Foundations of Robotics: analysis and control*, ISBN 0-262-24028-9.

[4] W. Song, F. Yu, M. Minami, "3D Visual Servoing by Feedforward Evolutionary Recognition", Journal of Advanced Mechanical Design, Systems, and Manufacturing (JAMDSM) Vol. 4, No. 4 Page 739-755 (2010).

[5] B.Siciliano and L.Villani: *Robot Force Control*, ISBN 0-7923-7733-8, Jan, 2000.

The Seventeenth International Symposium on Artificial Life and Robotics 2012 (AROB 17th '12),
B-Con Plaza, Beppu, Oita, Japan, January 19-21, 2012

Image-based Fuzzy Trajectory Tracking Control for Four-Wheel Steered Mobile Robots

Tatsuya Kato, Keigo Watanabe, and Shoichi Maeyama

Department of Intelligent Mechanical Systems,
Division of Industrial Innovation Sciences,
Graduate School of Natural Science and Technology,
Okayama University,
3-1-1 Tsushima-naka, Kita-ku, Okayama 700-8530, Japan
E-mail: t.kato@usm.sys.okayama-u.ac.jp; {watanabe, maeyama}@sys.okayama-u.ac.jp
Tel&Fax: +81-86-251-8064

Abstract: A four-wheel steered mobile robot is fit for a higher power or improvement in the movement speed of a robot than a two-independent wheeled one. Since a steered mobile robot that slips very often cannot apply a popular dead-reckoning method by using rotary encoders, it is desirable to use external sensors such as cameras. This paper describes a method to trace a straight line for four-wheel steered mobile robots by using an image-based control method. Its controller is designed as a fuzzy controller and evaluated through some simulations and real robot experiments.

Keywords: Fuzzy control, Image-based control, Steered mobile robot, Trajectory tracking, Visual servo

1 INTRODUCTION

Although most of wheeled robots that are developed recently adopt a two-independent wheeled type which excels in simple mechanism and in turning-performance, steered mobile robots will be able to extend the field of robot applications, because it is fit for a higher power or improvement in the movement speed of a robot. Since a steered mobile robot that slips very often cannot apply a popular dead-reckoning method by using rotary encoders, it is desirable to use external sensors such as cameras.

Control methods using cameras are classified roughly into two methods[1, 2, 3, 4]. One is called "position-based" control method, which controls a robot by using the robot position that is estimated from matching previous knowledge of 3D environmental models with a captured image. The other is called "image-based" control method, which can operate a robot indirectly without using the robot position by controlling only image information on an image plane. This method seems to be similar to the processing that is performed by human, in fact that human behaviors are decided without using its own position. Thus, an image-based control method is studied in this research. As the earlier research of image-based control, Chen et al. [5] designed the fuzzy controller to stabilize an inverted pendulum by referring to images that is captured with a camera in front of the inverted pendulum. Kurashiki et al. [6] designed a controller to trace a curving line for two-wheel independent mobile robots by using a model based control method.

This paper describes a method to trace a straight line for four-wheel steered mobile robots by using an image-based control method. When designing the controller, it is hard to model the relationship between image information and robot states, so that a model-free fuzzy controller [7, 8] is adopted. The designed controller is evaluated through some simulations and real robot experiments.

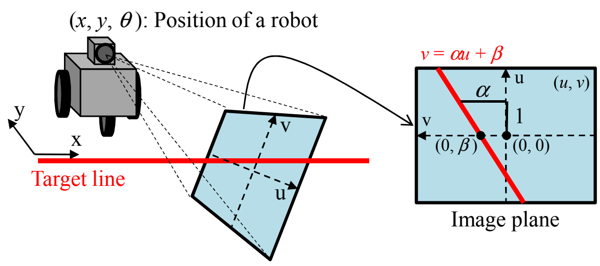

Fig. 1. World coordinate and image coordinate

2 PROBLEM SETTING

The goal of the present control is that a robot equipped with a camera tracks the target line drawn on the floor by image-based control. Fig. 1 shows the environmental overview and the definition of coordinates. Since the world coordinate is defined as x-axis to be along the target line, the function of the target line is $y = 0$. The image coordinate is represented by u-v coordinate with the direction of axes as shown in Fig. 1. On the image coordinate, the function of the target line is denoted as $v = \alpha u + \beta$, where α is the gradient and β is the intercept of the target line. The α and β can be obtained from an image processing.

The controlled object is a four-wheel steered mobile robot

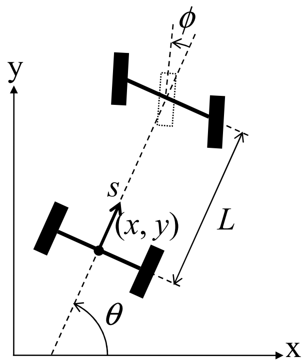

Fig. 2. Model of a mobile robot

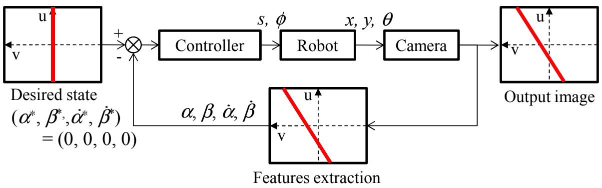

Fig. 3. Block diagram of the image-based control

as shown in Fig. 2. The robot state is denoted by the position and the direction such as (x, y, θ), and the steering angle is ϕ, the advanced speed is s, and the wheel base is L.

To track the target line, it can predict intuitively that α = 0 and β = 0 should be accomplished on the image coordinate instead of performing y = 0 and θ = 0 on the world coordinate. Therefore, the state variables are defined as (α, β, $\dot{\alpha}$, $\dot{\beta}$) and these desired values are (α^*, β^*, $\dot{\alpha}^*$, $\dot{\beta}^*$) = (0, 0, 0, 0). The controller is designed with the definition of control inputs as (s, ϕ). Fig. 3 shows the block diagram of this image-based control. In Fig. 3, the controller determines the control inputs, s and ϕ, from α, β, $\dot{\alpha}$, and $\dot{\beta}$ which are extracted by some image processing of a captured image. This block diagram shows that the robot is controlled without referring to its positions.

3 FUZZY CONTROLLER

The fuzzy controller determines the control inputs through mainly three steps:

1. Fuzzification of state variables
2. Calculation of grade of each rule
3. Defuzzification of input values

These are described below in detail.

3.1 Fuzzification of state variables

Fuzzification is to convert real numbers into fuzzy sets which are linguistic representations with grades which are given by membership functions. Fig. 4 shows the membership function of each state variable. Value of each state variable is fuzzified to linguistic representations (N: Negative, ZO: Zero, P: Positive) with grades which are given these membership functions. The membership functions are prepared from some preliminary experiments by heuristic method and depend on the properties of the camera and the robot.

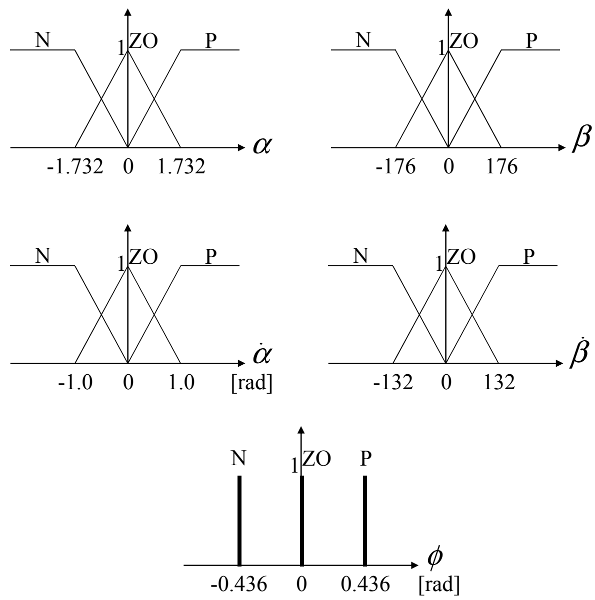

Fig. 4. Membership functions

3.2 Calculation of confidence of each rule

Table 1 shows fuzzy control rules for ϕ which are constructed based on the roughly separated positional relations with the fuzzified state variables, where s is assigned to be a constant. The interpretation of these rules is, for example, such that the rule No. 1 represents

$$\text{if } \alpha = \mathrm{N}, \beta = \mathrm{N} \text{ then } \phi = \mathrm{N} \tag{1}$$

The grade of each control rule is the same as the minimum value among the degrees of truth of the fuzzified state variables related to the rule. Although the degree of truth of each rule is adopted as the degree of truth of the control input, if other rules have the same values, then the maximum value among these degrees of truth is adopted (min-max algorithm).

3.3 Defuzzification of input values

Control inputs which are obtained as fuzzy sets should be defuzzified to provide control input values as real numbers. The defuzzification is the calculation of a weighted mean by a simplified fuzzy reasoning method with singletons as fol-

Table 1. Fuzzy rules for ϕ

No.	α	β	$\dot{\alpha}$	$\dot{\beta}$	ϕ
1	N	N	-	-	N
2	N	ZO	-	-	N
3	N	P	-	-	ZO
4	ZO	N	-	-	N
5	ZO	ZO	N	N	N
6	ZO	ZO	N	ZO	N
7	ZO	ZO	N	P	ZO
8	ZO	ZO	ZO	N	N
9	ZO	ZO	ZO	ZO	ZO
10	ZO	ZO	ZO	P	P
11	ZO	ZO	P	N	ZO
12	ZO	ZO	P	ZO	P
13	ZO	ZO	P	P	P
14	ZO	P	-	-	P
15	P	N	-	-	ZO
16	P	ZO	-	-	P
17	P	P	-	-	P

lows:

$$\phi = \frac{-0.436 \cdot h_{\phi,\mathrm{N}} + 0 \cdot h_{\phi,\mathrm{ZO}} + 0.436 \cdot h_{\phi,\mathrm{P}}}{h_{\phi,\mathrm{N}} + h_{\phi,\mathrm{ZO}} + h_{\phi,\mathrm{P}}} \tag{2}$$

where $h_{\phi,\mathrm{N}}$ denotes the grade of ϕ =N.

4 EXPERIMENTS

Simulations and real robot experiments were conducted to confirm that the designed image-based fuzzy controller can achieve the straight line tracking.

4.1 Simulation experiment

The initial state of the robot was assumed to be (x, y, θ) = (0.0 [m], -0.4 [m], $\pi/4$ [rad]) and the advanced speed of the robot s = 0.5 [m/s]. Maintaining of y = 0 was considered to be an accomplishment of the trajectory tracking. The working volume of steering angle was -0.436 [rad] $< \phi <$ 0.436 [rad] and its rate was -1.75 [rad] $< \dot{\phi} <$ 1.75 [rad]. The wheel base L was 0.26 [m]. The camera was attached on the robot, in which its height was 0.09 [m], the angle was 70 [deg] for forward from vertically downward, the focal length was 0.02 [m], the angle of view was 2.09 [rad], and the frame rate was 30 [fps]. The gradient of the target line on an image plane was represented as $-\infty < \alpha < \infty$ and the interception was to be $-\infty < \beta < \infty$. The time step of this simulation was set to 10 [ms].

Fig. 5 shows the movement trajectory of the robot on this simulation. Although the overshoot arose when the robot reached the target line at the first time, it was able to trace the line y = 0 without oscillations.

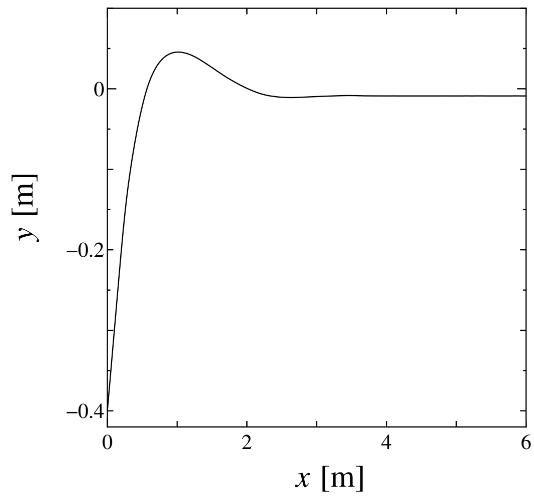

Fig. 5. Result of the simulation experiment

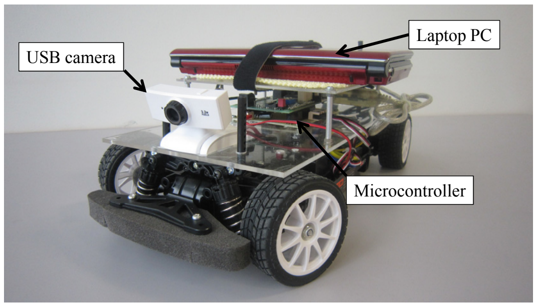

Fig. 6. Real robot for the experiment

4.2 Real robot experiment

The designed controller was tested on the real robot experiment, to check the usability on real environment. Fig. 6 shows the robot which was used for this experiment. This robot was a four-wheel steered mobile robot, which was made by modifying a commercially available radio controlled car to control it by a microcontroller. The USB camera attached on forefront gazes at floor to capture the target line. The laptop PC executes the image processing to extract α and β by using Hough transform from the captured image like as shown in Fig. 7. The rates, $\dot{\alpha}$ and $\dot{\beta}$, are to be the difference between current and previous extracted values. The initial state of the robot was assumed to be (x, y, θ) = (0.0 [m], -0.4 [m], $\pi/4$ [rad]) and the advanced speed was to be about 0.5 [m/s] as the same as the condition of the simulation.

Fig. 8 shows the result of this experiment. Although the robot moved along the target line y = 0 without both overshoots and oscillations, the residual error remained about -0.06 [m] for y-axis.

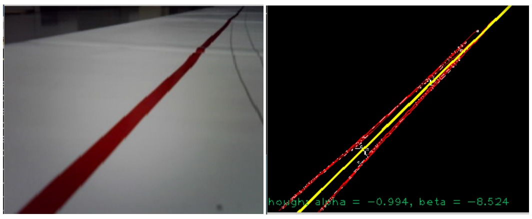

Fig. 7. Image processing

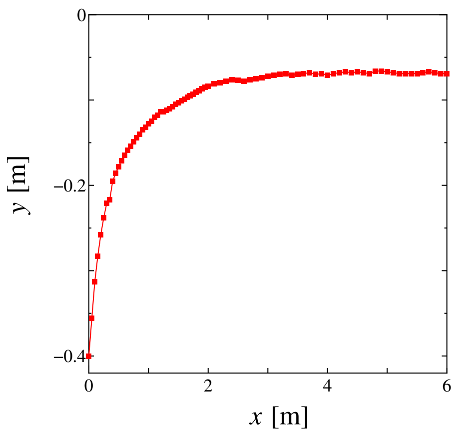

Fig. 8. Result of the real robot experiment

5 CONSIDERATION

The results of both simulations and real robot experiments show the usability of the designed controller. On the real robot experiment, the residual error remained about -0.06 [m] for y-axis. One of error causes is attributed to the fact that there is a robot property which turns right a little when it goes straight due to the difference of wheel diameters or the bias of center of gravity. Additionally, there is a little residual error in the result of the simulation. Thus, the error cause is coming from not only the robot property but also theoretical reasons. Fig. 9 shows a case where a robot exists along a target line with a little error for y-direction. In this case, since the state variables are α = N and β = P, the robot will advance because it believes the wrong situation such as shown in Fig. 10. Although one possible solution is to further refine the membership functions and the control rules in order to separate these similar situations, the tuning of the fuzzy controller will be very complicated. To adopt this solution, any optimization methods are required to automate the tuning process.

6 CONCLUSION

In this paper, an image-based control method which controls robots without referring to positions has been described. The objective was that a robot equipped with a camera was

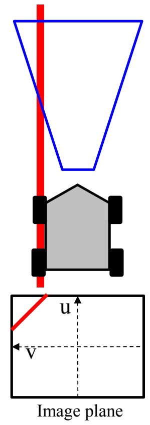

Fig. 9. Robot advancing along the target line

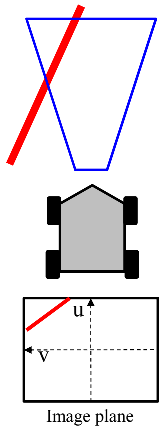

Fig. 10. Robot advancing toward the target line

to track a straight line drawn on a floor by image-based control, and a fuzzy controller was designed. The results of both simulations and real robot experiments showed the usability of the designed controller and it shed light on some problems. In the future, we have to consider a curvilinear trajectory tracking method and a speed control method to utilize characteristics of four-wheel steered mobile robots.

REFERENCES

[1] Hutchinson S, Hager G, and Corke P (1996), A tutorial on visual servo control. IEEE Trans. on Robotics and Automation 12(5):651–670

[2] Chaumette F, Hutchinson S (2006), Visual servo control part I: basic approaches. IEEE Robotics and Automation Magazine 13(4):82–90

[3] Chaumette F, Hutchinson S (2007), Visual servo control part II: advanced approaches. IEEE Robotics and Automation Magazine 14(1):109–118

[4] Malis E (2002), Survey of vision-based control. presented at the In European Naval Ship Design, Captain Computer IV Forum, ENSIETA, Brest, France

[5] Chen GM, Lin PZ, Wang WY, Lee TT, Wang CH (2008), Image-based fuzzy control system. IEEE Electronics Letters 44(7):461–462

[6] Kurashiki K, Takanori F (2011), Image-based robust arbitary path following of nonholonomic mobile robots (in Japanese). Trans. of the Society of Instrument and Control Engineers 47(5):238–246

[7] Zadeh LA (1968), Fuzzy algorithms. Information and Control 12:94–102

[8] Mamdani EH (1976), Advances in the linguistic synthesis of fuzzy controllers. International Journal of Man-Machine Studies 8(6):669–678

The Seventeenth International Symposium on Artificial Life and Robotics 2012 (AROB 17th '12),
B-Con Plaza, Beppu, Oita, Japan, January 19-21, 2012

Study on Mobile Mechanism of a Climbing Robot for Stair Cleaning - A Translational Locomotion Mechanism and Turning Motion to be Faced to a Stair -

Takahisa Kakudou, Keigo Watanabe, Isaku Nagai

Department of Intelligent Mechanical Systems,
Graduate School of Natural Sciences and Techology, Okayama University,
3-1-1 Tsushima-naka, Kita-ku, Okayama, 700-8530, Japan
(Tel & Fax: 81-86-251-8064)
t.kakudou@usm.sys.okayama-u.ac.jp, watanabe, in@sys,okayama-u,ac,jp

Abstract: In human living environments, it is often the case that the cleaning area is three-dimensional space such as a high-rise building. An autonomous cleaning robot is proposed so as to move on all floors including stairs in a building. The proposed robot has a body frame of a rectangular solid, which is equipped with L-shaped legs on the both sides and drive wheels on the top and bottom sides. The present robot climbs down stairs by rotating the body using L-shaped legs and it moves on smooth surfaces using wheels. In this paper, a mobile mechanism and a control method are described for translational locomotion. The operational check of the translational mechanism was conducted by facing the robot to the edge of stairs using the position sensitive detector (PSD).

Keywords: Cleaning robot, Climbing robot, Mechanism

1 INTRODUCTION

Recently, various robots that support and act for human work have been developed to be utilized in various fields. One of such robots is the autonomous cleaning robot [1]. The automation of cleaning by robots reduces labors and saves energy for a cleaning task, so that there is an increasing need for it in large areas such as stations and airports.

In human living environments, it is often the case that the cleaning area is a three-dimensional space such as a high-rise building. Considering cleaning in a three-dimensional space, the cleaning area includes the steps of stairs which lead from one level of a building to another. However, many of cleaning robots are not considered to move on places between floors. Tajima et al. [2][3] have developed a robotic system in which the cleaning robot cooperated with the elevator to clean floors in a high-rise building. However, this system did not consider the cleaning of stairs. As a result, a cleaning robot itself needs the ability to move on stairs for cleaning in a three-dimensional space. Also, the several types of climbing robot using crawlers, wheels and legs were proposed to move on stairs [4]-[6]. Those robots were developed to move on stairs only for improving transfer performance of them in uneven surfaces and transporting people or objects. Therefore, a cleaning robot for cleaning in a three-dimensional space needs to be able to turn itself and keep posture level on the tread board of stairs, as well as moving on stairs.

The objective of this study is to develop a climbing robot which can move on all floors including stairs in a building for autonomous cleaning in a three-dimensional space. A climbing robot has been already proposed, where its structure was divided into two mechanisms for climbing down stairs and translational movement [7][8]. In this paper, a mobile mechanism and a control method are described for translational locomotion. The operational check of the translational mechanism was conducted by facing the robot to the edge of stairs using the position sensitive detector (PSD).

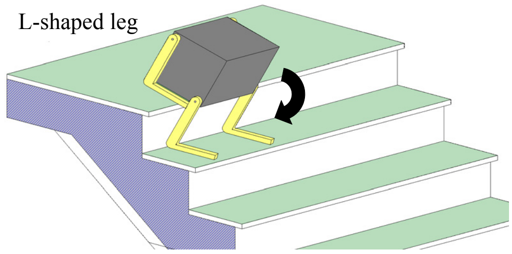

Fig. 1. Outline of a climbing robot for cleaning stairs

2 CONCEPT OF CLIMBING ROBOT

Fig. 1 shows the proposed robot whose structure is divided into two mechanisms for climbing down stairs and translational locomotion. The L-shaped legs which are equipped with on the both sides of a body are used as a climbing mechanism. The proposed robot climbs down stairs by rotating the body so that the top and bottom sides of body may be reversed using L-shaped legs with two degrees-of-

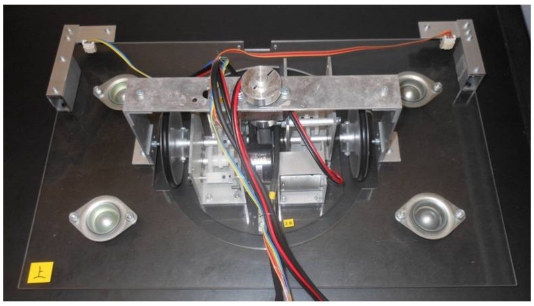

Fig. 2. Overview of translational mechanism

freedom. A translational locomotion mechanism is discussed in section 3.

3 MOBILE MECHANISM FOR TRANSLATIONAL LOCOMOTION

It is assumed that the cleaning robot is used in an indoor environment that is flat such as wooden floor or tile floor. The robot performs translational locomotion using wheels that have high transfer efficiency. However, the robot may be limited in motion by its corners colliding with the wall and the riser of stairs when turning around, because the robot shape is a rectangular solid as shown in previous sections. So omni directional mobility is adopted to move and turn around keeping a posture.

For some of omni directional mobile mechanisms with wheels, there are mechanisms with omni-wheel, mechanum wheels, etc. Since the robot climbs down stairs by rotating the body so that the upper and lower sides of body may be reversed, this mechanism is attached to the top and bottom of the robot. To reduce the robot weight, it is desirable to use the fewest possible actuators. Therefore, the mobile mechanism for translational mobility used an omni directional mobile mechanism of two-wheel-drive system in this study.

3.1 Mobile mechanism design

Fig. 2 shows the proposed mechanism for translating on stair treads. The size of the mechanism is as follows: the width is 400 mm, the length is 250 mm, and the vehicle height is 20 mm. Its mechanism consists of four ball-casters and two driving wheels that are attached on a circular plate with a joint.

Fig. 3 shows the layout of sensors mounted on a translational locomotion mechanism. The PSD as the range sensor is used for the robot to recognize stairs. Two PSDs are attached on both ends in the front side of mobile mechanism for translational locomotion. If the origin is set at the rotational axis, the positions of PSD 1 and PSD 2 are (x_{psd}, $-y_{\mathrm{psd}}$) and (x_{psd}, y_{psd}) as an x-y coordinate, respectively.

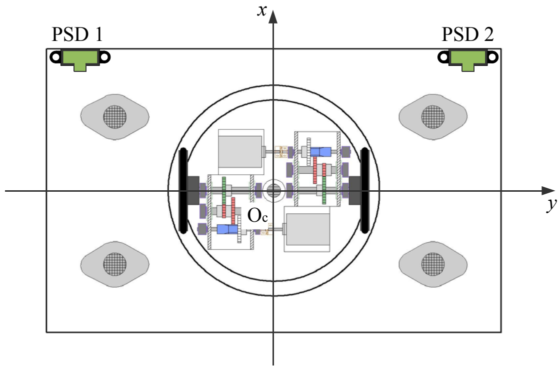

(a) Top view

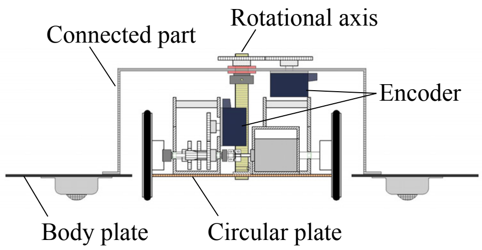

(b) Lateral view

Fig. 3. Design of a variety of sensors

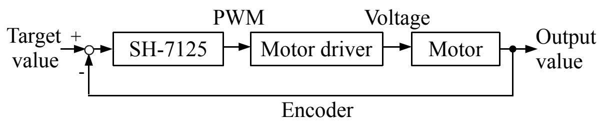

Fig. 4. Block diagram of velocity control

Also, the encoders are used to measure the forward velocity of the robot or the angle of the circular plate.

3.2 Controller design

Cleaning robots keep the quality of cleaning constant by velocity control. A velocity of the robot is controlled using a PD controller with encoders to measure the rotation of wheels. Fig. 4 shows the block diagram of velocity control. The motors for wheel can be controlled in normal and reverse rotations, stop and braking by sending the signal from the microcomputer SH7125 through a motor driver.

4 LOCOMOTION ON STAIRS

The locomotion of the robot on stairs assumes two motions, i.e., the cleaning motion and the recognition motion.

4.1 Cleaning motion

The locomotion of commonly-marketed cleaning robots is classified into four basic motions, while are parallel, spiral, wall-reflection and wall-following motions. the parallel motion which is a repeated motion combining advance and

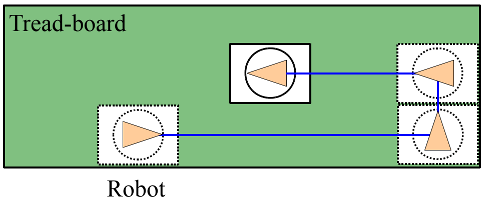

(a) Parallel motion to clean stairs

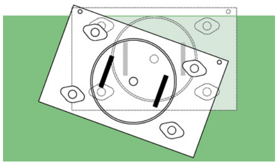

(b) Turning motion to be faced to stairs

Fig. 5. Translational locomotion on stairs

90-degree turns is one of more suitable motions for cleaning stairs, because the shape of step is a rectangular form which makes a path planning easy to make for cleaning evenly. In the cleaning motion based on the parallel motion, the robot repeats straight going and 90-degree turn, keeping the posture as shown in Fig. 5(a).

4.2 Recognition motion

When the robot changes from translational locomotion to climbing down motion, the robot might fall down stairs due to its posture. Whenever stairs are recognized, the robot turns to be faced to the edge of stair as shown in Fig. 5(b)

4.3 Kinematic model of mobile mechanism

The kinematic model of the mechanism for translational locomotion is given by

$$\begin{bmatrix} \dot{x} \\ \dot{y} \\ \dot{\theta}_c \end{bmatrix} = \begin{bmatrix} \frac{r}{2}\sin\theta_c & \frac{r}{2}\sin\theta_c \\ \frac{r}{2}\cos\theta_c & \frac{r}{2}\cos\theta_c \\ \frac{r}{2d} & -\frac{r}{2d} \end{bmatrix} \begin{bmatrix} \dot{\theta}_R \\ \dot{\theta}_L \end{bmatrix} \tag{1}$$

where x and y are the position coordinate of the robot, θ_c is the rotated angle of a circular plate, θ_R and θ_L are the rotational angles for the right and left wheels, r is the wheel radius, and $2d$ is the distance between wheels.

5 STAIR RECOGNITION USING PSD

The robot recognizes stairs by discriminating a difference between the vehicle height and the rise of stairs by using a PSD. The PSD outputs the value that converts a distance to an object into DC voltage. When a PSD value is less than or equal to a threshold for discriminating stair and floor, the robot recognizes it as a stair. On the other hand, the robot recognizes it as a floor.

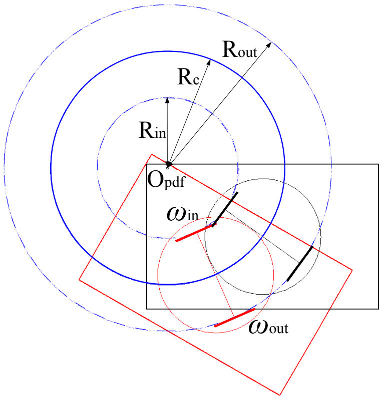

Fig. 6. Kinematic model of turning motion

The robot turns to be faced to the edge of stairs using two PSDs. If anyone of PSDs is recognizes a stair, a circular plate of the robot is rotated so that a reacted PSD is located on the wheel axis. Next the robot turns in direction, so the other PSD recognizes a stair. Finally, the robot stops if both PSDs recognizes stairs.

Also, the robot turns as shown in Fig. 6, if the angular velocities of inner and outer wheels have a relationship in their turning radii such as as follows:

$$\left|\frac{\omega_{\mathrm{in}}}{\omega_{\mathrm{out}}}\right| = \left|\frac{R_{\mathrm{in}}}{R_{\mathrm{out}}}\right| \tag{2}$$

where ω_{in} and ω_{out} are the angular velocities of the inner and outer wheels, and R_{in} and R_{out} are the turning radii of the inner and outer wheels.

5.1 Operational check

We had conducted an operational check to verify the accuracy of recognition motion using PSDs. The evaluation item is the posture of the robot after it was turned to be faced to stairs at a constant velocity of 150 mm/s from initial positions. Initial positions were assumed as 15 degrees, 30 degrees, 45 degrees, 60 degrees and 75 degrees. A threshold for recognizing a stair was decided as 300 in A/D converted value, because a rise is defined as 180 mm in this study. As a result, it is confirmed that the robot turned and stopped using PSDs. Fig. 7 shows the posture of the robot which was faced to the edge of stairs by initial postures. Table 1 shows the average and standard deviation (SD) of posture angles by initial postures.

5.2 Consideration

The error in the posture angle is within plus or minus five degrees through an operational check. This subsection states the error in posture angles.

A relationship between the angular velocity and the turning radius of wheel is $\omega_{\mathrm{in}} = 0.43\omega_{\mathrm{out}}$ defined by Eq. (2) in ideal condition. But in fact a relationship of them was

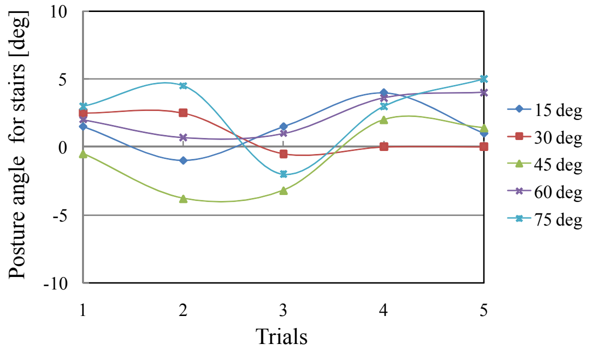

Fig. 7. Posture angle in faced to step

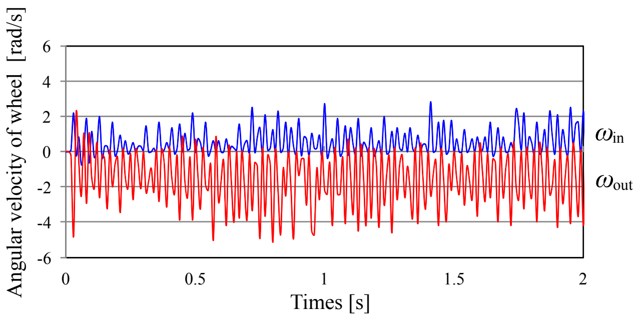

Fig. 8. Wheel velocity based on velosity control

Table 1. Average and SD of posture angles

Angle [deg]	Average [deg]	SD [deg]
15	1.40	1.59
30	0.90	1.32
45	–0.82	2.34
60	2.26	1.34
75	2.70	2.48

$\omega_{\text{in}} \simeq 0.28\omega_{\text{out}}$ as shown in Fig. 8. The inner wheel might stop, because ω_{in} was near zero. For a target of turning velocity of 150 mm/s, the motor was driven at duty cycle of 45 percents for inner wheel and 48 percents for outer wheel by the PWM signal. It is confirmed to be unstable at a low duty cycle by the PWM signal. Also, motors might give unstable behaviors due to the influence of the noise.

This problem will be overcome by reaalizing that the robot attains a velocity equal to a target at a high duty cycle by increasing gears reduction ratio.

6 CONCLUSION

A cleaning robot to climb down stairs has been developed for cleaning a three-dimension space. In particular, mobile mechanisms and a locomotion control method were proposed for the robot to clean and climb down stairs. The operational check of the robot was conducted for recognizing stairs. In the result, it was confirmed that it needs to change the high duty cycle. As future work, a stair cleaning robot will be developed to solve the above problem, together with making a real robot.

REFERENCES

[1] Tribelhoron B and Dodds Z (2007), Evaluating the roomba: a low-cost, ubiquitous platform for robotics research and educations. Proc. of the IEEE International Conference on Robotics and Automation, pp. 1393–1399

[2] Tajima S, Aoyama H, Seki T, Ishikawa K, Yokota K, Ozaki K and Yamamoto S (2004), Development of robotic floor cleaning system for high-rise buildings (in Japanese). Jour. of the Robotics Society of Japan 22(5):595–602

[3] Aoyama H, Ishimura S, Nishihara I, Ishikawa K, Seki J, Wadasako T, Satumi Y and Adachi Y (2009), The development of the cleaning device of the office building cleaning robot (in Japanese). Proc. of the JSME Conference on Robotics and Mechanics, pp. P1-B14(1)–P1-B14(2)

[4] Yuan J and Hirose S (2005), Actualization of safe and stable stair climbing and three-dimensional locomotion for wheelchair. Proc. of the IEEE/RSJ International Conference on Intelligent Robots and Systems, pp. 2391–2396

[5] Kashiki T, Koyanagi E, Yoshida T and Ikeda S (2005), A mobile robot which climbs stairs step by step turning two wheeled arms -configuration control system- (in Japanese). Proc. of the JSME Conference on Robotics and Mechanics, pp. 1P2-S-019(1)–1P2-S-019(4)

[6] Hirasawa J (2011), Traial production and analysi of a stair climbing robot that equips only one motor (in Japanese). Proc. of the JSME Conference on Robotics and Mechanics, pp. 2A2-L04(1)–2A2-L04(2)

[7] Kakudou T, Nagai I and Watanabe K (2010), A cleaning robot for stairs and the simulation of stair movement. Proc. of the 13th International Conference on Climbing and Walking Robots and the Support Techologies for Mobile Machines, pp. 1306–1313

[8] Kakudou T, Watanabe K and Nagai (2011), Study on mobile mechanism for a stair cleaning robot -Design of translational locomotion mechanism-. Proc. of the 11th International Conference on Control, Automation and Systems, pp. 1213–1216

The Seventeenth International Symposium on Artificial Life and Robotics 2012 (AROB 17th '12),
B-Con Plaza, Beppu, Oita, Japan, January 19-21, 2012

The Experiment of the Path Planning to Respect Human Movements Using a Human Frequency Map for a Mobile Robot

Kimiko Motonaka[1], Shoichi Maeyama[1], and Keigo Watanabe[1]

[1] Okayama University, Okayama, Okayama 700-8530 , Japan
(k.motonaka@usm.sys.okayama-u.ac.jp)

Abstract: A robot requires any path planning to respect human movements when the robot works with the person in an environment. Therefore, we use a Human Frequency Map (HFM) generated by using observed human positions. By applying the HFM, the robot can achieve the path planning that cares about the human movements and the pathway width. This paper describes the effectiveness of the HFM through some experiments in the real environment. The experimental results of navigation using a real mobile robot is also discussed.

Keywords: Mobile Robot, Path Planning, Human Observation, Environment Map

1 INTRODUCTION

Nowadays, a mobile robot has been expected to foray into home or office, and there exist many studies about path planning for these mobile robots[1][2]. However, it is often the case that path planning is studied for calculating the shortest distance to a goal[3]. Then, the mobile robot has to not only search the shortest path but also perform the path planning to respect human movement.

There are some approaches that several sensors are distributed in the environmental side for observing human positions and the data are used for path planning[4]. If the human's walking route is used, the robot can obtain the information on a safe route without searching on the whole environment[5][6]. Therefore, when implementing the safe operation of a robot in a real world, the robot should also consider the possibility for encountering human, and whether there is a wide aisle for path each other easily.

In this study, our path planning approach has a unique point so as to focuse the behavioral change of human in each time zone. Observed human positions are used for making a "Human Frequency Map (HFM)" , which is a grid map based on the observed human positions and frequency in each term. The pathway generated by the HFM contains the information on the passage width and the human frequency in the term. This research has a feature that the present path planning can minimize the possibility for encountering human by considering the human frequency of a certain time zone and the current position of human. Additionally, we conducted the experiment of navigation using a real mobile root by the path information generated from the HFM.

2 HUMAN FREQUENCY MAP

In this study, human positions are observed by sensors distributed in the environmental side. Then, the HFM is generated by the observed human positions. The HFM uses the grid map that has only the data of human frequency in each grid on the map (Fig. 1). Each grid keeps the data of human frequency in 4 levels (high, middle, low and zero) and the data can be referred to by an (i, j) element in the map. For more information about HFM, please refer to [7].

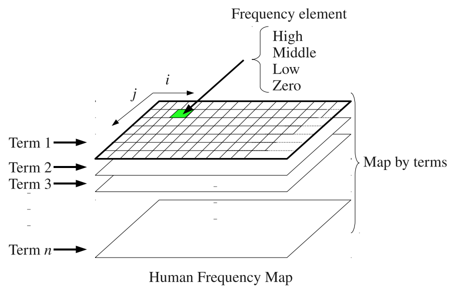

Fig. 1: Data structure of human frequency map

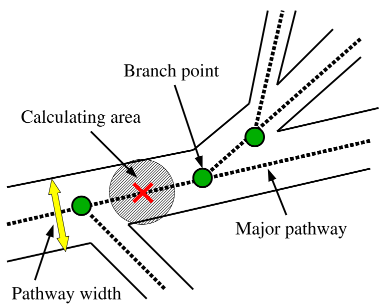

Fig. 2: Topological map of human's pathway

2.1 Generation of Pathway Information

The HFM has the information of human positions, but no information on the routes human which walked. Therefore, the pathway information should be reconstructed from the human positions. The pathway information means a passage

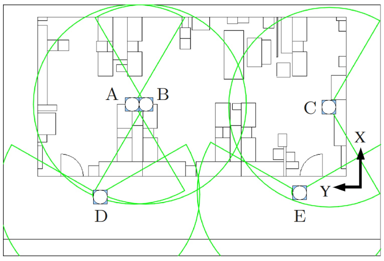

Fig. 3: Experimental environment

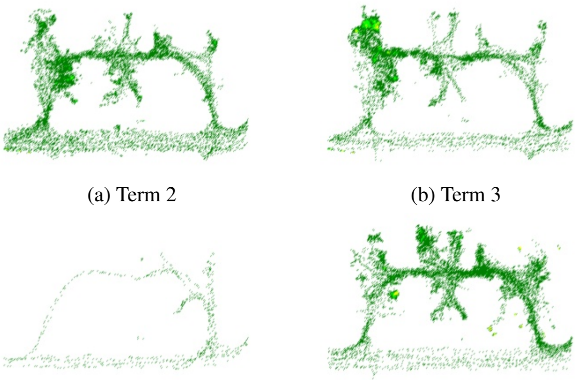

(a) Term 2 (b) Term 3

(c) Term 10 (d) Term 12

Fig. 4: Human frequency map

area, the passage width and human frequency(Fig. 2). These information could be calculated from the human positions data stored on HFM.

2.2 An Example of Generated Human Frequency Map

In this experiment, five laser range scanners were used to observe human positions in our office to generate the HFM. The size of the room is 12.6 $\times$ 6.6 [m^2]. Fig. 3 shows the layout chart of the room, the origin, the positions of sensors and the range of observations. Observed time was 24 hours from 18:00 to 18:00 on the next day. We call each observation duration every two hours (18:00–20:00,...,16:00–18:00) term 1 to term 12. The human frequency is the average number of times for the observed humans per grid. If observed more than one time in 5 minutes, it is set as High; if more than one time in 10 minutes, it is set as Middle; if observed only one time in the duration, it is set as Low; and if not observed at all, it is set as Zero. Note here that the door was released in this case.

Fig. 4 and Fig. 5 are the experimental results, in which Fig. 4 shows the HFM obtained in terms 2, 3, 10 and 12, whereas Fig. 5a depicts the human observed area through term 1 to term 12 with the room layout chart and Fig. 5b shows the major pathway generated by the HFM with the room layout chart.

The major pathway generated by the HFM was sufficiently close to the real passage (Fig. 5a). Additionally, the end-point node of the pathway reached the workspace such as doors or desks, so that the obtained pathway can be useful as an environmental map for the path planning of a robot. It was confirmed from the present method that the passage area and the major pathways were able to be calculated from the human positions.

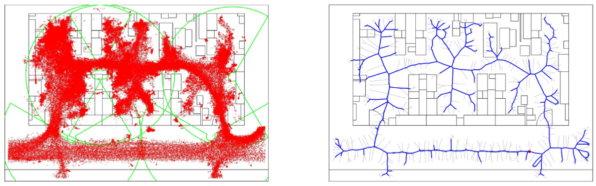

(a) Human observed area (b) Major pathway

Fig. 5: Generation of pathway information

3 PATH PLANNING

3.1 Evaluation of Path Candidates

In this method, a major pathway is stored as a non-directed graph. Here, the node of the graph is the branch point of the major path, and the edge of the graph is the major path. When the start and goal were set, all adjoining nodes are explored and all the pathways which reach the goal are saved as the path candidates.

Then, all candidates are evaluated and the best one is selected. In the evaluation, the pathway width and the traffic are considered. The evaluation function for the path selection V is give by

$$V = \sigma_a(l_p)\rho \tag{1}$$

Here,

$$\sigma_a(x) = \frac{K}{1 + e^{-a(x-b)}}$$

$$\rho = \begin{cases} \rho_m & \text{if } t_h \leq t_r \\ \rho_0 & \text{otherwise} \end{cases} \tag{2}$$

where ρ_m is the human frequency and l_p is the pathway width of the edge.

$\sigma_a(x)$ at $K = 1$ is called a sigmoid function, which is the threshold function and has the property of $(-\infty, \infty) \rightarrow (0, 1)$. In addition, a and b are constant, but note that a is a negative value in our case. t_h and t_r represent the minimum arrival time of human and robot, respectively. If $t_h > t_r$, then the robot doesn't encounter the human, otherwise the robot has possibilities to encounter the human. ρ_0 is sufficiently small compared to ρ_m. This is based on the idea that it is not necessary to care about the traffic if the robot doesn't encounter the human. V is increased when the pathway width is decreased or the human frequency ρ_m is increased. It means that V is more increased, if it is harder to pass the pathway.

3.2 Experimental Example of Path Planning

In this experiment, it is assumed that the robot runs in term 3 (Fig. 4b) and term 12 (Fig. 4d) of the HFM. V is calculated with $K = 1.0$, $a = \;\; 0.0367$, $b = l_r + l_h = 30.0 + 60.0$ [cm], $v_r = 30.0$ [cm/s] and $v_h = 105.0$ [cm/s], where l_r, l_h, v_r and v_h denote the robot width, the human width, the velocity of the robot and the velocity of the human, respectively.

The robot was given an order to start from the corridor and reach to the sink. Fig. 6 shows the room layout, start, goal and human positions.

All the paths from the start to the goal are shown in Fig. 7. The red line ($t_h \quad t_r$) and the blue line ($t_h > t_r$) are the major pathway.

Fig. 8 shows the graph of the evaluation value (V) of path 4 in term 3. The horizontal axis is a distance from the start point and the right endpoint of the graph is the goal point. The path having a minimum value of the sum of V is chosen as the best path in the term. Fig. 9 shows each sum of V of paths 1–4 in term 3 and term 12, and Fig. 10 shows the best path in each term with the room layout chart.

3.2.1 Considerations

It is found from Fig. 8 that V increases at the narrow or crowded passage. By comparing term 3 with term 12 as shown in Fig. 9, there is a difference in the sum of V even if they have the same path because the human frequency is different each other. Any pass is selected so as to have the minimum sum of V, because V increases in the point where it is hard to pass. The path length is also taken into account by using V.

According to this, path 2 is the best candidate for the robot in term 3, whereas path 4 is the best candidate in term 12. Thus, the path to be selected is changed depending on the time zone. It means that the path change can be achieved according to the human frequency every time zone. As seen in Fig. 10, the path is chosen so as to avoid the human crowded area. This is because the position of the current human movement is considered. There is a high possibility that human moves to the high human frequency area in each time zone.

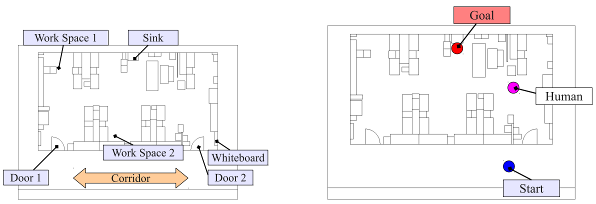

(a) Room map (b) Start and goal positions

Fig. 6: Room map and start and goal positions

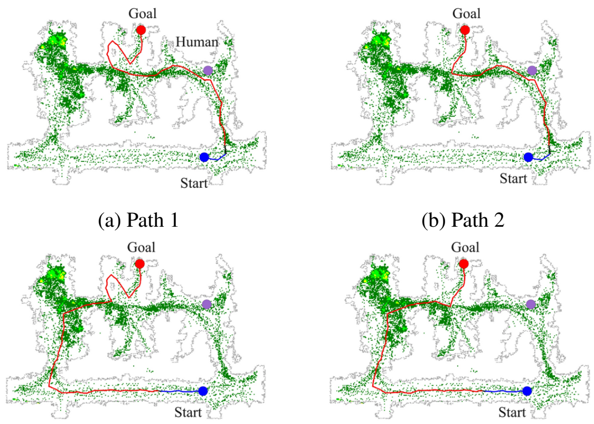

(a) Path 1 (b) Path 2

(c) Path 3 (d) Path 4

Fig. 7: Path candidates acquired in term 3

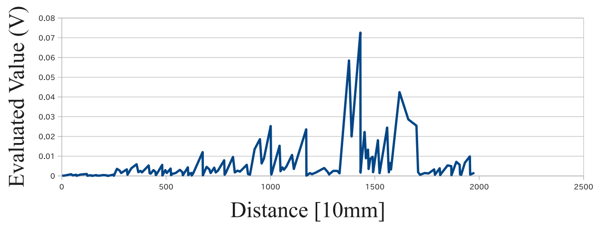

Fig. 8: Calculation result of path 4 in term 3

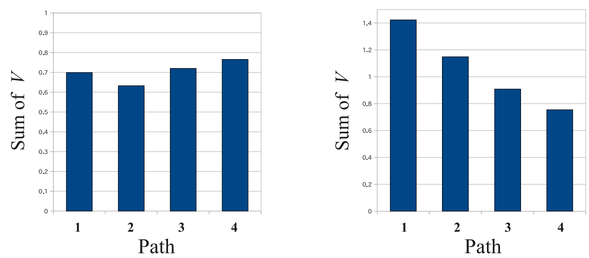

(a) Term 3 (b) Term 12

Fig. 9: Sum of V in term 3 and term 12

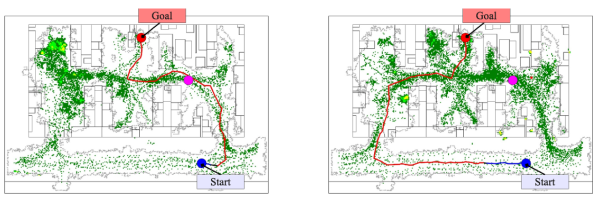

(a) The best path in term 3 (b) The best path in term 12

Fig. 10: The best path in term 3 and term 12

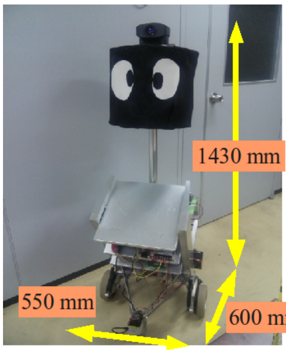

Fig. 11: Mobile robot used in the experiment

4 EXPERIMENTS USING MOBILE ROBOT

In this section, it is discussed about the navigation for the mobile robot by means of the path generated from HFM. For distant navigation, the only odometry is not enough for localization because of the cumulative error. Therefore, we need the additional information for localization. The system to generate the HFM has the function of the human position detection by the laser range sensors mounted on the environmental side. This system can be extended to estimate the robot position. The part of the robot body can be measured by these environment-side sensors. Then, we propose the localization method by fusion of odometry-based position and the robot position estimated by environment-side sensors. The proposed method makes it possible for the robot to keep own position over long distances.

4.1 Experiments

The experiment on the navigation of a mobile robot along a path generated by HFM is conducted. The objective of this experiment is to verify whether the proposed path can be used for the mobile robot navigation. Therefore, this experiment is done in the almost static environment in this instance. The experiment environment is the same as the environment shown in Fig. 3 and the size of the robot is 550 600 1430 [mm] shown in Fig. 11. In this experiments, 4 kinds of the path is provided to the mobile robot. The robot moves according to the path given by the branch point coordinates.

As the result of this experiment, the robot could reach the goal safely in four different routes. At this time, it confirmed that the robot could run through the narrow passage area like the entrance of the room. Therefore, it is confirmed that the path generated from the HFM is suitable for the navigation for the mobile robot.

Note however that, this experiment was conducted in the almost static environment with only a few human at only the one term. It is necessary to verify at various time zone with the view to usefulness of the HFM. Also, for the case where an unexpected obstacle is encountered, the robot should implement obstacle avoidance function as well.

5 CONCLUSION

In this paper, a path planning method has been proposed for mobile robots to respect human movements by using the HFM. First, the HFM based on the observed human position has been described with the sensors mounted on the environment. By using the HFM, the major pathway in the environment was calculated and the route from a start to the given goal was found. Then, the information of the human frequency and the pathway width were used as the evaluated value to select the best path. Finally, we confirmed that the robot can navigate according to four different paths given by the HFM at one time zone.

REFERENCES

[1] Uemura S, Szemes P, Lee J, Korondi P and Hashimoto H (2003), Path Planning of Mobile Platform with Haptic Interface (in Japanese). *Proc. of the 2003 JSME Conf. on Robitics and Mechatronics*, 1P1.2F.D8.

[2] Rennekamp T, Homeier K and Kroger T (2004), Distributed Sensing and Prediction of Obstacle Motions for Unknown Moving Obstacles, *Proc. of the 2004 IEEE Int. Conf. on Intelligent Robots and Systems*, 4833–4838.

[3] Kagami S and Thompson S(2006), Layered Architecture for Localization, Mapping, Path Planning and Control to Achieve Autonomy for Fast Mobility (in Japanese), *Proc. of the 24th Annual Conf. of the Robotics Society of Japan*, 24:1E13.

[4] Hashimoto H, niitsuma M and Sasaki T (2005), Intelligent Space, *The Robot Society Japan*, 23(6):674–677.

[5] Sasaki T, Szemes P and Hashimoto H (2005), Path Generation for Robot Based on Observation of Human Walking (in Japanese), *Proc. of the 23th Annual Conf. of the Robotics Society of Japan*, 23:2B24.

[6] Sasaki T and Hashimoto H (2008), Mobile Robot Navigation Based on Important Points Extracted from Human Observation, *Trans. of The Society of Instrument and Control Engineers*, 44(4):368–376.

[7] Motonaka K, Maeyama S and Watanabe K (2010), Path Planning to Respect Human Movements Based on Human Frequency Map for a Mobile Robot, *Proc. of Joint 5th Int. Conf. SCIS and ISIS*, 1121–1126.

The Seventeenth International Symposium on Artificial Life and Robotics 2012 (AROB 17th '12),
B-Con Plaza, Beppu, Oita, Japan, January 19-21, 2012

A Study of Tipping Stability for Omnidirectional Mobile Robot with Active Dual-wheel Caster Assemblies

M. Juhairi Aziz Safar, Keigo Watanabe, Shoichi Maeyama and Isaku Nagai

Department of Intelligent Mechanical Systems,
Graduate School of Natural Science and Technology, Okayama University,
3-1-1 Tsushima-naka, Kita-ku, Okayama 700-8530, Japan.
(Tel & Fax: +81-86-251-8064)
juhairi@sys.usm.okayama-u.ac.jp, {watanabe, maeyama, in}@sys.okayama-u.ac.jp

Abstract: A holonomic omnidirectional mobile robot is well known for a high mobility and capability in maneuvering. In our approach, the holonomic omnidirectional mobile robot was developed using two active dual-wheel caster assemblies with conventional tires. In this paper, we are focusing on the stability issues in the tipping problem that may occur in the existing of static and dynamic environments. We derive the dynamic model of the omnidirectional mobile robot to estimate the supporting force at each wheel and evaluate it through simulations.

Keywords: Tip-over, Roll-over, Stability, Balancing

1 INTRODUCTION

Tipping stability is an important concern for vehicles, especially for those related to a human driver or passenger. In most cases, the failure in instability monitoring and prevention could cause a catastrophic incident which leads to major injuries to the human and property losses. Most of the mobile robots constructed with more than two wheels configuration were statically stable. However, the mobile robots begin to be unstable when they are starting to operate in a high speed, making a sudden acceleration or deceleration (braking), turning in speed or operating in a slopped terrain. Mobile robots with higher center of gravity (CoG) and heavier mass possess higher possibility to tip-over or roll-over in a dynamic motion environment.

Most of the stability studies in wheeled mobile robotics were related to the two wheeled differential drive mobile robot [1] and four wheeled mobile robot [2]. There is also a few studies related to the omnidirectional mobile robots [3], but the study was mainly discussing on the conventional omnidirectional mechanism which uses some combination of the universal wheels. Most of these wheeled mobile robots also have a fixed wheel arrangements. Therefore, the shape of the support polygon was maintained all the time. In our approach, the supporting polygon will keep changing according to the trajectory path due to the changing of orientation for both active dual-wheel casters.

The existing study of stability focuses on the CoG projection [4, 5], static stability margin [6] and energy stability margin [7]. These stability studies belong to the class of quasi-static stability where in addition to the assumption of slow motion relative to the inertial frame, it was assumed that there were no inertial accelerations except for gravitational acceleration. However, in reality the inertial acceleration exists and it is possible to cause the mobile robot to tip-over. Therefore, in this paper a model of the omnidirectional mobile robot with active dual-wheel caster assemblies (ADWC) is presented to investigate both static and dynamic effects on the tipping stability. The model presented here is an extended one to the previous study of planar dynamics by Yamada et al [8]. Here, we derived the vertical dynamical model for the omnidirectional mobile robot with the existing of human passenger especially for the roll and pitch stability control. In our model, the omnidirectional mobile robot is assumed to be stable in a static condition due to the wide geometric footprint. The dynamics were derived using the Newtonian and D'Alembert principles to compute the instantaneous normal forces acting on the wheels, according to the current state of the caster's configuration.

2 OMNIDIRECTIONAL MOBILE ROBOT

The mobile robot used in this research is a holonomic omnidirectional mobile robot with active dual-wheel caster assemblies as shown in Fig. 1. A couple of active dual-wheel caster assemblies are arranged in a longitudinal direction. Each caster can generate velocity in the forward direction (X_i-axis) and sideway direction (Y_i-axis) of the passive steering axis which is caused by the differences in angular velocity of the right- and left-wheels. The existing of these velocities induces a holonomic motion to the center of the mobile robot, O where the velocity in X-axis, $\dot{x}$, velocity in Y-axis, $\dot{y}$ and the instantaneous rotation at Z-axis, ϕ were produced.

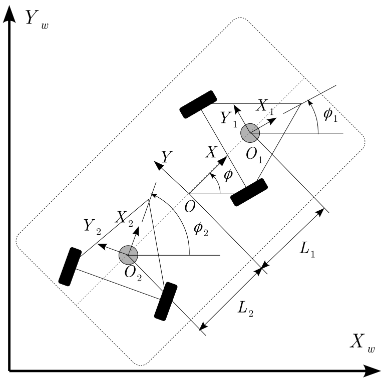

Fig. 1. Omnidirectional mobile robot with active dual-wheel caster assemblies

3 DERIVATION OF DYNAMICAL MODEL

The goal of this section is to derive a relationship between the dynamics of omnidirectional mobile robot and the normal forces acting on each wheel. In order to derive this relationship, we will make the following assumptions: (i) the mobile robot can operate in omnidirectional direction with the holonomic motion of $[\dot{x}\ \dot{y}\ \dot{\phi}]$, (ii) there is no additional motion in any direction; therefore, the mobile robot is kept in a stabilizing condition, i.e., equilibrium of moments.

3.1 Normal Forces Acting on Each Wheel

Let us consider the dynamical model as shown in Fig. 2 and Fig. 3 as our reference. Here, we assumed that the upper part of the vehicle includes the seat, passenger and the mobile platform as a single mass. We first calculate the normal forces at the steering axis of both dual-wheel casters and find its relationship to the supporting forces at each contact point of the wheel with the ground. The nomenclatures are as follows:

M_a	mass of the driver, seat and mobile platform, i.e., the total mass of upper vehicle
m_i	mass of the i-th dual-wheel caster
L_i	distance between i-th steering axis and CoG of the mass M_a
N_i	normal forces acting on steering axis
h_{M_a}	height of CoG of the mass M_a
h_{si}	height of steering axis
h_{mi}	height of CoG of the dual-wheel caster
$\ddot{x}, \ddot{y}$	accelerations at CoG of the mass M_a
$\ddot{x}_{gi}, \ddot{y}_{gi}$	accelerations at CoG of dual-wheel caster
g	gravitational acceleration
f_{xi}, f_{yi}	force acting on steering axis in Σ_w
${}^if_{xi}, {}^if_{yi}$	force acting on steering axis in Σ_i
f_{xri}, f_{xli}	driving forces of the wheel
f_{yri}, f_{yli}	sideway forces of the wheel
f_{zri}, f_{zli}	normal forces of the wheel
I	moment of inertia of the upper part of the vehicle

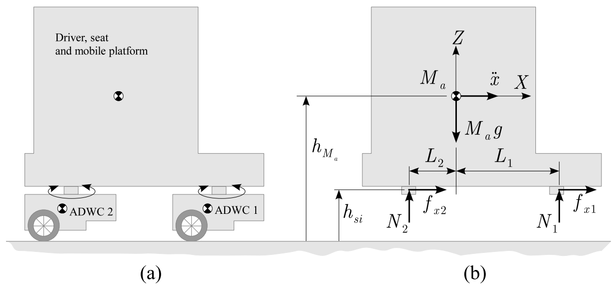

Fig. 2. Dynamical model of the omnidirectional mobile robot: (a) Single mass model, (b) Dynamics of upper part

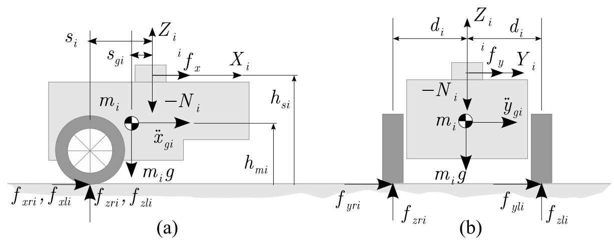

Fig. 3. Dynamical model of ADWC assemblies: (a) Side view (X_iZ_i-frame), (b) Front view (Y_iZ_i-frame)

Using the above mentioned assumptions, we can derive the following relation by applying Newton's motion of law for linear motion in x-, y- and z-direction and equilibrium of moments around x- and y-axis:

$$f_{zri} = \frac{1}{s_{ai}}H_{ai} - \frac{1}{2d_i}H_{bi} + \frac{1}{2s_{ai}}H_{ci} \tag{1}$$

$$f_{zri} = \frac{1}{s_{ai}}H_{ai} + \frac{1}{2d_i}H_{bi} + \frac{1}{2s_{ai}}H_{ci} \tag{2}$$

where,

$$\begin{aligned}
H_{ai} &= {}^if_x h_{ci} + m_i \ddot{x}_{gi} h_{mi} \\
H_{bi} &= {}^if_y h_{si} + m_i \ddot{y}_{gi} h_{mi} \\
H_{ci} &= N_i s_{bi} - m_i g s_{ai} \\
s_{ai} &= s_i - s_{gi} \\
s_{bi} &= s_i + s_{gi} \\
h_{ci} &= 2h_{mi} - h_{si}
\end{aligned}$$

Here, the value of N_i can be calculated from Fig. 2(b) as:

$$N_1 = \frac{1}{L}(M_a g L_2 - M_a \ddot{x} h_a) \tag{3}$$

$$N_2 = \frac{1}{L}(M_a g L_1 + M_a \ddot{x} h_a) \tag{4}$$

where, $L = L_1 + L_2$ and $h_a = h_{M_a} - h_{si}$.

Therefore, defining $\boldsymbol{f}_{zi} = [f_{zri}\ f_{zli}]^T$, ${}^i\boldsymbol{f} = [{}^if_x\ {}^if_y]^T$, ${}^i\ddot{\boldsymbol{x}}_{gi} = [\ddot{x}_{gi}\ \ddot{\phi}_i]^T$ and $\ddot{\boldsymbol{x}} = [\ddot{x}\ \ddot{y}\ \ddot{z}]^T$, the following equation is obtained by combining Eqs. (1)–(4) and replacing $\ddot{y}_{gi}$ with the time derivative of the non-holonomic constraint, $\ddot{y}_{gi} = s_{gi}\ddot{\phi}_i$.

$$\boldsymbol{f}_{zi} = \boldsymbol{A}_i {}^i\boldsymbol{f} + \boldsymbol{B}_i {}^i\ddot{\boldsymbol{x}}_{gi} + \boldsymbol{C}_i \ddot{\boldsymbol{x}} + \boldsymbol{D}_i \tag{5}$$

where,

$$\boldsymbol{A}_i = \begin{bmatrix} \frac{h_{ci}}{s_{ai}} & -\frac{h_{si}}{2d_i} \\ \frac{h_{ci}}{s_{ai}} & \frac{h_{si}}{2d_i} \end{bmatrix}, \boldsymbol{B}_i = m_i h_{mi} \begin{bmatrix} \frac{1}{s_{ai}} & -\frac{s_{gi}}{2d_i} \\ \frac{1}{s_{ai}} & \frac{s_{gi}}{2d_i} \end{bmatrix}$$

$$\boldsymbol{C}_1 = \begin{bmatrix} c_1 & 0 & 0 \\ c_1 & 0 & 0 \end{bmatrix}, \boldsymbol{C}_2 = \begin{bmatrix} -c_2 & 0 & 0 \\ -c_2 & 0 & 0 \end{bmatrix}, c_i = \frac{s_{bi} M_a h_a}{2 s_{ai} L}$$

$$\boldsymbol{D}_1 = \begin{bmatrix} \frac{s_{b1} M_a g L_2}{2 s_{a1} L} + \frac{m_1 g}{2} \\ \frac{s_{b1} M_a g L_2}{2 s_{a1} L} + \frac{m_1 g}{2} \end{bmatrix}, \boldsymbol{D}_2 = \begin{bmatrix} \frac{s_{b2} M_a g L_1}{2 s_{a2} L} + \frac{m_2 g}{2} \\ \frac{s_{b2} M_a g L_1}{2 s_{a1} L} + \frac{m_2 g}{2} \end{bmatrix}$$

Then, introducing the coordinate transformation matrix from Σ_i to Σ_w as ${}^w\boldsymbol{T}_i$, defining the normal force vector $\boldsymbol{f}_z = [\boldsymbol{f}_{z1}^T \ \boldsymbol{f}_{z2}^T]^T$ for the wheel, setting $\boldsymbol{f}_w = [\boldsymbol{f}_{w1}^T \ \boldsymbol{f}_{w2}^T]^T$, and $\ddot{\boldsymbol{x}}_g = [{}^1\ddot{\boldsymbol{x}}_{g1}^T \ {}^2\ddot{\boldsymbol{x}}_{g2}^T]^T$ gives

$$\boldsymbol{f}_z = \boldsymbol{A}\boldsymbol{f} + \boldsymbol{B}\ddot{\boldsymbol{x}}_g + \boldsymbol{C}\ddot{\boldsymbol{x}} + \boldsymbol{D} \tag{6}$$

where,

$$\boldsymbol{A} = \begin{bmatrix} \boldsymbol{A}_1 {}^w\boldsymbol{T}_1^T & \boldsymbol{0}_{2\times2} \\ \boldsymbol{0}_{2\times2} & \boldsymbol{A}_2 {}^w\boldsymbol{T}_2^T \end{bmatrix}, {}^w\boldsymbol{T}_i = \begin{bmatrix} \cos\phi_i & -\sin\phi_i \\ \sin\phi_i & \cos\phi_i \end{bmatrix}$$

$$\boldsymbol{B} = \begin{bmatrix} \boldsymbol{B}_1 & \boldsymbol{0}_{2\times2} \\ \boldsymbol{0}_{2\times2} & \boldsymbol{B}_2 \end{bmatrix}, \boldsymbol{C} = \begin{bmatrix} \boldsymbol{C}_1 \\ \boldsymbol{C}_2 \end{bmatrix}, \boldsymbol{D} = \begin{bmatrix} \boldsymbol{D}_1 \\ \boldsymbol{D}_2 \end{bmatrix}$$

Also the dynamic property for the omnidirectional mobile robot also can be described as:

$$\boldsymbol{M}\ddot{\boldsymbol{x}} = \boldsymbol{E}\boldsymbol{f} \tag{7}$$

where,

$$\boldsymbol{M} = \text{diag}(M_a, M_a, I)$$

$$\boldsymbol{E} = \begin{bmatrix} 1 & 0 & 1 & 0 \\ 0 & 1 & 0 & 1 \\ -L_1\sin\phi & L_1\cos\phi & L_2\sin\phi & -L_2\cos\phi \end{bmatrix}$$

Inserting the inverse equation of Eq. (7) into Eq. (6) yields

$$\boldsymbol{f}_z = \boldsymbol{A}\boldsymbol{E}^*\boldsymbol{M}\ddot{\boldsymbol{x}} + \boldsymbol{B}\ddot{\boldsymbol{x}}_g + \boldsymbol{C}\ddot{\boldsymbol{x}} + \boldsymbol{D} \tag{8}$$

where $\boldsymbol{E}^*$ denotes the pseudoinverse of matrix $\boldsymbol{E}$ as described by

$$\boldsymbol{E}^* = \frac{1}{L}\begin{bmatrix} L_2 + \alpha_{cc}(\phi) & \alpha_{sc}(\phi) & -\sin\phi \\ \alpha_{sc}(\phi) & L_2 + \alpha_{ss}(\phi) & \cos\phi \\ L_1 - \alpha_{cc}(\phi) & -\alpha_{sc}(\phi) & \sin\phi \\ -\alpha_{sc}(\phi) & L_1 - \alpha_{ss}(\phi) & -\cos\phi \end{bmatrix}$$

$$\alpha_{ss}(\phi) = \tfrac{1}{2}(L_1 - L_2)\sin^2\phi$$
$$\alpha_{sc}(\phi) = \tfrac{1}{2}(L_1 - L_2)\sin\phi\cos\phi$$
$$\alpha_{cc}(\phi) = \tfrac{1}{2}(L_1 - L_2)\cos^2\phi$$

Also the relationship between ${}^i\dot{\boldsymbol{x}}_{gi}$ and $\dot{\boldsymbol{x}}_i$ can be written as

$${}^i\dot{\boldsymbol{x}}_{gi} = \boldsymbol{F}_i\dot{\boldsymbol{x}}_i \tag{9}$$

where,

$$\boldsymbol{F}_i = \begin{bmatrix} \cos\phi_i & \sin\phi_i \\ -\frac{1}{s_i}\sin\phi_i & \frac{1}{s_i}\cos\phi_i \end{bmatrix}$$

Letting $\boldsymbol{x}_a = [\boldsymbol{x}_1^T \ \boldsymbol{x}_2^T]^T$ and referring to Eq. (9), the following equation is satisfied:

$$\dot{\boldsymbol{x}}_g = \boldsymbol{F}\dot{\boldsymbol{x}}_a \tag{10}$$

where,

$$\boldsymbol{F} = \begin{bmatrix} \boldsymbol{F}_1 & \boldsymbol{0}_{2\times2} \\ \boldsymbol{0}_{2\times2} & \boldsymbol{F}_2 \end{bmatrix}$$

Meanwhile, from the inverse kinematics equation [8] we obtained:

$$\dot{\boldsymbol{x}}_a = \boldsymbol{G}^*\dot{\boldsymbol{x}} \tag{11}$$

where,

$$\boldsymbol{G}^* = \begin{bmatrix} 1 & 0 & -L_1\sin\phi \\ 0 & 1 & L_1\cos\phi \\ 1 & 0 & L_2\sin\phi \\ 0 & 1 & -L_2\cos\phi \end{bmatrix}$$

Combining Eqs. (10) and (11) gives

$$\dot{\boldsymbol{x}}_g = \boldsymbol{F}\boldsymbol{G}^*\dot{\boldsymbol{x}} \tag{12}$$

Hence differentiating Eq. (12) with respect to time, we obtain

$$\ddot{\boldsymbol{x}}_g = (\dot{\boldsymbol{F}}\boldsymbol{G}^* + \boldsymbol{F}\dot{\boldsymbol{G}}^*)\dot{\boldsymbol{x}} + \boldsymbol{F}\boldsymbol{G}^*\ddot{\boldsymbol{x}} \tag{13}$$

Replacing Eq. (13) into Eq. (8) and rearranging the equation yields

$$\boldsymbol{f}_z = \boldsymbol{K}'\dot{\boldsymbol{x}} + \boldsymbol{K}''\ddot{\boldsymbol{x}} + \boldsymbol{D} \tag{14}$$

where,

$$\boldsymbol{K}' = \boldsymbol{B}(\dot{\boldsymbol{F}}\boldsymbol{G}^* + \boldsymbol{F}\dot{\boldsymbol{G}}^*)$$
$$\boldsymbol{K}'' = \boldsymbol{A}\boldsymbol{E}^*\boldsymbol{M} + \boldsymbol{B}\boldsymbol{F}\boldsymbol{G}^* + \boldsymbol{C}$$

4 SIMULATION RESULTS

The simulation time was 20 s, sampling period 20 ms, the initial pose of the omnidirectional mobile robot was $\boldsymbol{x} = [0 \ 0 \ 0]^T$ and the initial orientation of each dual-wheel caster is set to 0 rad. The reference trajectory was a straight line, whose gradient was 0 rad for the first 8 s, $\pi/4$ rad for 6 s and 0 rad for the rest. This simulation was conducted under the resolved velocity control [9]. The mobile robot is set to move from a stationary position to the velocity of 0.2 ms^{-1}, changing to 0.1 ms^{-1} after 14 s and stop at the time of 20 s. The purpose of this simulation was to estimate the supporting forces according to the given dynamics effect. Physical parameters are listed in Table 1.

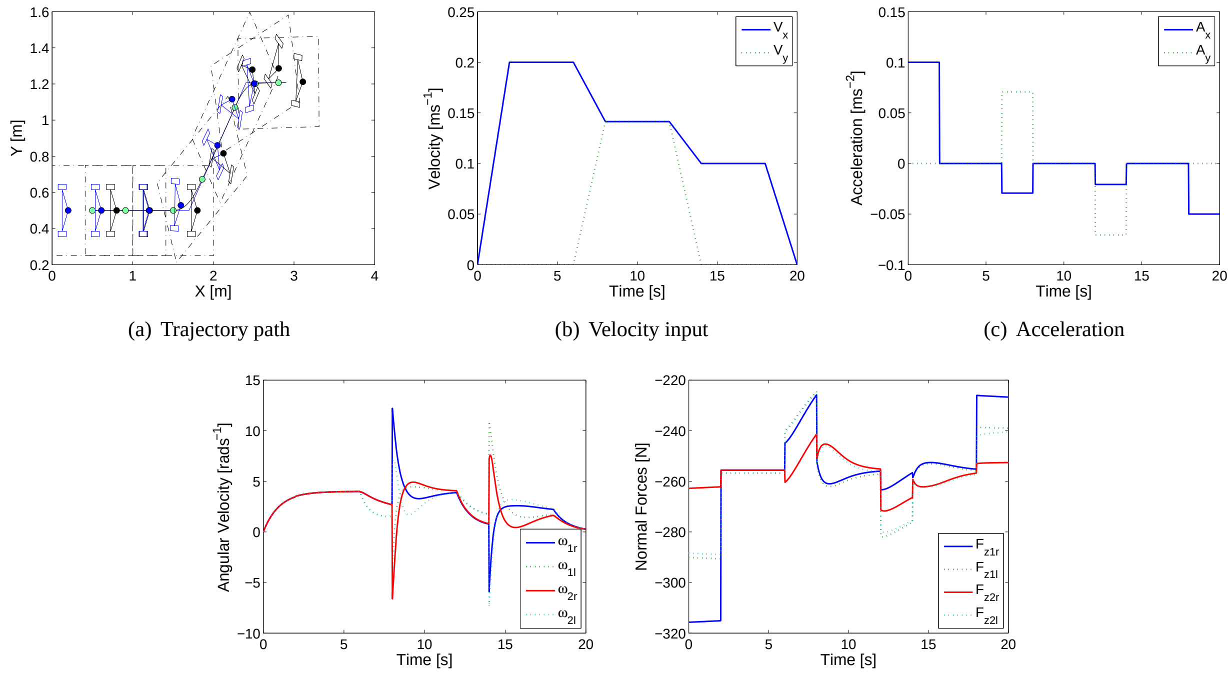

(a) Trajectory path (b) Velocity input (c) Acceleration

(d) Angular velocity of the wheel (e) Supporting forces

Fig. 4. Simulation results

Table 1. Physical parameters

d_1, d_2	0.13	[m]	r_1, r_2	0.05	[m]
s_1, s_2	0.075	[m]	s_{g1}, s_{g2}	0.0595	[m]
I_1, I_2	0.103	[kgm^2]	I	12.708	[kgm^2]
M_a	122	[kg]	m_1, m_2	6.5	[kg]
L_1, L_2	0.3	[m]	h_{M_a}	0.7	[m]
h_{s1}, h_{s2}	0.4	[m]	h_{m1}, h_{m2}	0.15	[m]

Presented in Fig. 4 is the result of the conducted simulation for estimating the supporting forces. The negative value of the force shows that the ground is supporting the load from the wheel with the same amount of force. Tipping instability may only occur when the value of the force is approaching zero which also increasing the tendency of the wheel to be lifted from the ground.

5 CONCLUSION AND FUTURE WORKS

In this paper, we have derived the vertical dynamics equation of the holonomic omnidirectional mobile robot with active dual-wheel caster assemblies. These equations have been verified through the MATLAB simulation but need to be compared with the real data. This study is the preliminary study which we would be implemented with higher techniques in the near future.

REFERENCES

[1] Lin SC, Tsai CC, Huang HC (2011), Adaptive robust self-balancing and steering of a two-wheeled human transportation vehicle. J. of Intelligent Robot System 62: 103–123

[2] Udengaard M, Iagnemma K (2009), Analysis, design, and control of an omnidirectional mobile robot in rough terrain. ASME J. of Mechanical Design 131(12)

[3] Wada M (2007), Omnidirectional and holonomic mobile platform with four-wheel-drive mechanism for wheelchairs. J. of Robotics and Mechatronics 19(3): 264–265

[4] Sardain P, Bessonnet G (2004), Forces acting on a biped robot. Center of pressure - Zero moment point. IEEE Trans. on Systems, Man and Cybernetics – Part A: Systems and Humans 34: 630–637

[5] Huang Q, Sugano S and Kato I (1994), Stability control for a mobile manipulator using a potential method. Proc. of IEEE/RSJ Int. Conf. on Intelligent Robots and Systems (IROS), pp. 839–846

[6] Messuri DA, Klein CA (1985), Automatic body regulation for maintaining stability of a legged vehicles during rough-terrain locomotion. IEEE J. Robotics and Automation 1: 132–141

[7] Hirose S, Tsukagoshi H and Yoneda K (2001), Normalized energy stability margin and its contour of walking vehicles on rough terrain. Proc. IEEE Int. Conf. Robotics and Automation, Vol. 1, pp. 181–186

[8] Yamada T, Watanabe K and Kiguchi K (2001), Dynamic model and control for a holonomic omnidirectional mobile robot. J. of Autonomous Robots 11: 173–189

[9] Han F, Yamada T, Watanabe K, Kiguchi K and Izumi K (2000), Construction of an omnidirectional mobile robot platform based on active dual-wheel caster mechanisms and development of a control simulator. J. of Intelligent and Robotic Systems 29: 257–275

The Seventeenth International Symposium on Artificial Life and Robotics 2012 (AROB 17th '12),
B-Con Plaza, Beppu, Oita, Japan, January 19-21, 2012

Unscented Transformation for a FastSLAM Framework

Saifudin Razali, Keigo Watanabe, and Shoichi Maeyama

Department of Intelligent Mechanical Systems,
Graduate School of Natural Science and Technology, Okayama University,
3-1-1 Tsushima-naka, Kita-ku, Okayama 700-8530, Japan
(Tel & Fax:+81-86-251-8064)
saifudin@usm.sys.okayama-u.ac.jp, {watanabe, maeyama}@sys.okayama-u.ac.jp

Abstract: This paper proposes an uscented transformation for a FastSLAM framework. The unscented transformation is used to estimate robot's poses in conjuction of generic particle filter used in standard FastSLAM framework. This method can estimate robot's poses more consistently and accurately than the use of single standard particle filters, especially when involving highly nonlinear models or non-Gaussian noises. In addition, our algorithm avoids the calculation of the Jacobian for motion model which could be extremely difficult for high order systems. Simulation results are shown to validate the performance goals.

Keywords: Unscented transformation, SLAM, FastSLAM.

1 INTRODUCTION

SLAM solves the problem of building a map and then recovering the robot pose with observations obtained from sensors mounted on the robot. The robot senses its own motion and at the same time identifies nearby landmarks. The SLAM problem can be presented as a probabilistic process known as a Markov process [5]. In particular, the robot motion is usually considered as a Markov process. The robot's pose at time t will be denoted by x_t. The robot's environment possesses N static landmarks. Each landmark is denoted by θ_k for $k = 1, \ldots, N$. The set of all landmarks will be denoted by θ.

SLAM algorithms calculate the posterior over the entire path along with the map such as

$$p\left(x^t, \theta \mid z^t, u^t, n^t\right) \tag{1}$$

where the path of the robot is denoted by $x^t = x_1, \ldots, x_t$, $z^t = z_1, \ldots, z_t$ is a sequence of measurements and $u^t = u_1, \ldots, u_t$ is a sequence of control inputs. The variables $n^t = n_1, \ldots, n_t$ are data association variables, in which each n_t specifies the identity of the landmark observed at time t. To compute the posterior in Eq. (1), the evolution of poses according to a probabilistic law is commonly referred to as a nonlinear motion model $p\left(x_t \mid x_{t-1}, u_t\right)$. The current pose x_t is a probabilistic function of the robot control u_t and the previous pose x_{t-1}. As the robot moves around, it takes measurements of its environment. Moreover, sensor measurements are governed by a probabilistic law referred to as a nonlinear measurement model $p\left(z_t \mid x_t, \theta, n_t\right)$.

In recent years, many research on SLAM was originated from a seminal paper by Smith and Cheesman [6], in which the use of the extended Kalman fillter (EKF) was proposed for solving SLAM and it was firstly implemented by [7].

However, there are two limitations of the EKF approach. One is the high computational cost to maintain a multivariate Gaussian vector which requires quadratic time in the dimension of the map. Therefore, it was proposed in [4, 8] to build a set of smaller maps and then combined them to build a large one. The other is related to the data association problem. It is critical to choose the correct data association hypotheses because different data association hypotheses lead to different maps. Maintaining posteriors over multiple data associations makes the SLAM algorithms more robust. Unfortunately, Gaussian distributions cannot represent multi-modal ones, so only the most likely data association can be incorporated. As a result, the approach tends to fail catastrophically when the incorporated data association is incorrect.

Another family of SLAM algorithms is called FastSLAM [2]. It was pointed out in [9] that the errors of the feature estimates would be independent if a robot path was given. This property is a base of FastSLAM algorithms to solve the SLAM problems. Particle filters are used to estimate the robot path. Conditioned on these particles, the mapping problem is factored into separate problems. Therefore, one EKF for each feature is used to update the feature estimate.

However, the standard FastSLAM frameworks used an EKF to improve the accuracy of a proposal distribution, but the EKF involves Jacobian matrices and the linear approximations of the nonlinear functions. Calculating the Jacobian is unwelcome effort, and inaccurate approximation to the posterior covariance deteriorates the estimate accuracy and the filter consistency. Therefore, in this paper we introduce an unscented transformation in the FastSLAM framework to eliminate the linearization as well as the Jacobian calculation.

The structure of this paper is as follows. In section 2 we generally describe about the FastSLAM framework and present the unscented transformation for the FastSLAM. A simulation setup for a SLAM problem is shown in section 3, as well as discussion on the simulation results. The paper is concluded in section 4.

2 FASTSLAM FRAMEWORK

2.1 Introduction to FastSLAM algorithm

The FastSLAM algorithm, introduced by Montemerlo et al. [1], is an efficient algorithm for the SLAM problem that is based on a straightforward factorization. This algorithm partitions the SLAM posterior in Eq. (1) into a localization problem and an independent landmark position estimation problem conditioned on the robot's pose estimate. It can be shown in the following form:

$$\begin{aligned} & p\left(x^t, \theta \mid z^t, u^t, n^t\right) \\ & = p\left(x^t \mid z^t, u^t, n^t\right) \prod_{k=1}^{N} p\left(\theta_k \mid x^t, z^t, u^t, n^t\right) \end{aligned} \tag{2}$$

This factorization is a fundamental idea behind the FastSLAM [9]. The FastSLAM uses a particle filter to approximate a recursive Bayesian filter for estimating the robot's poses. Each particle in the FastSLAM is formed as $X_t^{[m]} = \left\langle x_t^{[m]}, \mu_{1,t}^{[m]}, \Sigma_{1,t}^{[m]}, \ldots, \mu_{N,t}^{[m]}, \Sigma_{N,t}^{[m]} \right\rangle$ where the superscript $[m]$ indicates the index of the particle, $x_t^{[m]}$ is its path estimate, and $\mu_{k,t}^{[m]}$ and $\Sigma_{k,t}^{[m]}$ are the mean and covariance of the Gaussian vector, representing the kth landmark location attached to the mth particle.

There are two versions of FastSLAM, named as FastSLAM1.0 and FastSLAM2.0. In the FastSLAM2.0, the robot poses are sampled under the consideration of both the control u_t and the measurement z_t, while in the FastSLAM1.0, this consideration is based on only the motion control u_t. As a result, the FastSLAM2.0 is superior to the FastSLAM1.0 in all aspects [3]. The weight of each sample used in the resampling step is called the importance weight, which is denoted by $w_t^{[m]}$ and given by

$$\begin{aligned} w_t^{[m]} &= \frac{\text{target distribution}}{\text{proposal distribution}} \\ &= \frac{p\left(x^{t,[m]} | z^t, u^t, n^t\right)}{p\left(x^{t-1,[m]} | z^{t-1}, u^{t-1}, n^{t-1}\right) p\left(x_t^{[m]} | x^{t-1,[m]}, z^t, u^t, n^t\right)} \end{aligned}$$

For a complete derivation of the importance weight in the FastSLAM2.0, see [1] and [3].

Using a particle filter along with an EKF for robot pose estimation contains the linearization errors, and so that it may be prevented from a successful data association and cannot make an accurate map. To solve these problems, we propose the unscented transformation for robot's poses to the FastSLAM framework in the following section.

2.2 An unscented transformation for a FastSLAM framework

In general, the FastSLAM2.0 framework consists of three parts: the robot state estimation, the feature state estimation, and the importance weight calculation. In this section, the unscented transformation to the first part is discussed in detail. The last two parts still remain unchanged as applying to FastSLAM2.0. On our mind, the first part is crucial to develop accurate maps as well as to reduce overall computational cost.

Instead of linearinzing the nonlinear models through the 1st-order Taylor series expansion at the mean of the robot state, the proposed method introduces a set of deterministic points known as sigma points to propagate them through nonlinear model [11]. Since an observation is not always detected, constructing the proposal distribution and sampling from this prior have two steps. One is the prediction step and the other is the measurement update step. At first, the state vector is augmented with a control input and the observation

$$x_{t-1}^{a[m]} = \begin{bmatrix} x_{t-1}^{[m]} \\ 0 \\ 0 \end{bmatrix}, \quad P_{t-1}^{a[m]} = \begin{bmatrix} P_{t-1}^{[m]} & 0 & 0 \\ 0 & Q_t & 0 \\ 0 & 0 & R_t \end{bmatrix}$$

Here, $x_{t-1}^{a[m]}$ and $P_{t-1}^{a[m]}$ are the augmented vector for the state and related covariance, respectively. $x_{t-1}^{[m]}$ is the previous mean of the robot as well as it covariance, $P_{t-1}^{[m]}$. Q_t and R_t are the control noise covariance and the measurement noise covariance, respectively.

A symmetric set of $2L+1$ sigma points $\chi_{t-1}^{a[i][m]}$ for the augmented state vector can be calculated as

$$\chi_{t-1}^{a[i][m]} = \left[x_{t-1}^{a[m]} \ \cdots \ x_{t-1}^{a[m]}\right] + \gamma \left[0 \ \sqrt{P_{t-1}^{a[m]}} \ -\sqrt{P_{t-1}^{a[m]}} \right]$$

where $\gamma = \sqrt{L+\lambda}$ and L is the augmented state vector dimension. The $\lambda = \alpha^2 (L+\kappa) - L$ and α $(0 < \alpha < 1)$ should be a small number to avoid sampling nonlocal effects when the nonlinearities are strong. κ is a scaling parameter that determines how far the sigma points are separated from the mean and a good default choice is $\kappa = 0$ [11]. The set of sigma points $\chi_{t-1}^{a[i][m]}$ is then propagated through the motion model $\mathbf{f}(\cdot)$ given by

$$\bar{\chi}_t^{[i][m]} = \mathbf{f}\left(\chi_t^{[i][m]}, \chi_t^{u[i][m]}\right) \tag{3}$$

Here, $\bar{\chi}_t^{[i][m]}$ is the transformed sigma points of the robot state. $\chi_t^{[i][m]}$ and $\chi_t^{u[i][m]}$ are the part of augmented sigma points related to the robot poses and control component, respectively. The first two moments of the predicted robot state are computed by the following equations:

$$x_{t|t-1}^{[m]} = \sum_{i=0}^{2L} w_m^i \bar{\chi}_t^{[i][m]} \tag{4}$$

$$P_{t|t-1}^{[m]} = \sum_{i=0}^{2L} w_c^i \left(\bar{\chi}_t^{[i][m]} - x_{t|t-1}^{[i][m]}\right) \left(\bar{\chi}_t^{[i][m]} - x_{t|t-1}^{[i][m]}\right)^T \tag{5}$$

where the constant weights w_m^i and w_c^i are parameters related to computing mean and covariance given as follows [11]:

$$w_m^0 = \frac{\lambda}{(L+\lambda)}, \quad w_c^0 = w_m^0 + \left(1 - \alpha^2 + \beta\right)$$
$$w_m^i = w_c^i = \frac{1}{2(L+\lambda)}, \qquad i = 1, 2, \ldots, 2L$$

Here, the parameter β is used to incorporate the knowledge of the higher order moments of the posterior distribution.

As some features are observed, the data association provides their identities, and the updating step can be performed. The measurement sigma points $\bar{Z}_t^{[i][m]}$ are calculated using the observation model $\mathbf{h}(\cdot)$, function of sigma points of robot poses $\bar{\chi}_t^{[i][m]}$ and measurement noise $\chi_t^{z[i][m]}$ given belows:

$$\bar{Z}_t^{[i][m]} = \mathbf{h}\left(\bar{\chi}_t^{[i][m]}, \chi_t^{z[i][m]}\right) \tag{6}$$

Then, the measurement mean $\hat{\mu}_t^{[m]}$, covariance $S_t^{[m]}$, and cross covariance $\Sigma_t^{x,n[m]}$ as well as the Kalman gain $K_t^{[m]}$ can be computed as follows:

$$\hat{\mu}_t^{[m]} = \sum_{i=0}^{2L} w_m^{[i]} \bar{Z}_t^{[i][m]} \tag{7}$$

$$S_t^{[m]} = \sum_{i=0}^{2L} w_c^{[i]} \left(\bar{Z}_t^{[i][m]} - \hat{\mu}_t^{[m]}\right) \left(\bar{Z}_t^{[i][m]} - \hat{\mu}_t^{[m]}\right)^T \tag{8}$$

$$\Sigma_t^{x,n[m]} = \sum_{i=0}^{2L} w_c^{[i]} \left(\bar{\chi}_t^{[i][m]} - x_{t|t-1}^{[m]}\right) \left(\bar{Z}_t^{[i][m]} - \hat{\mu}_t^{[m]}\right)^T \tag{9}$$

$$K_t^{[m]} = \Sigma_t^{x,n[m]} \left(S_t^{[m]}\right)^{-1} \tag{10}$$

The estimated mean and its covariance of the robot state at time t are calculated by

$$x_t^{[m]} = x_{t|t-1}^{[m]} + K_t^{[m]} \left(z_t - \hat{\mu}_t^{[m]}\right) \tag{11}$$

$$P_t^{[m]} = P_{t|t-1}^{[m]} - K_t^{[m]} S_t^{[m]} \left(K_t^{[m]}\right)^T \tag{12}$$

3 EXPERIMENTS

In order to verify the performance of the proposed framework, some experiments were conducted using simulation data with 20 feature landmarks and known data association. The simulator was developed based on the work in [10]. The exploration area of the robot is 40 meters wide and 100 meters long, and the landmarks are randomly located in the area.

Fig. 1 shows the landmark and true robot trajectory setup for this simulation. The robot starts at the initial pose (0 m, 0 m, 0°) and travels with a nominal speed and a steering angle of 3 m/s and 30°, respectively. The nominal control values are corrupted with Gaussian noises with standard deviations 0.3 m/s and 3°, respectively for each 0.025 s sampling interval. The sensor takes measurements for each 0.2 s time interval and the nominal measurement values are also assumed to be corrupted with Gaussian noises with standard deviations 0.1 m and 1°, respectively. In this simulation, we set the number of particles equal to 100 for both estimators.

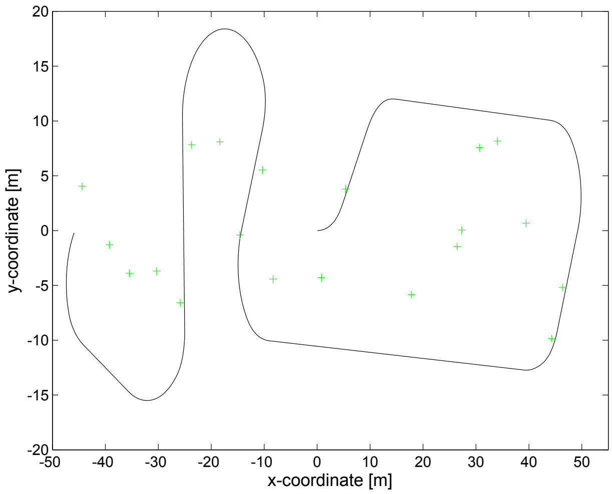

Fig. 1. True trajectory and landmark.

3.1 Motion Model and Observation Model

In our experiments, the motion model of the robot is assumed to be described as follows:

$$\begin{bmatrix} x_{t+1} \\ y_{t+1} \\ \phi_{t+1} \end{bmatrix} = \begin{bmatrix} x_t + V \cdot dt \cdot \cos(G + \phi_t) \\ y_t + V \cdot dt \cdot \sin(G + \phi_t) \\ \phi_t + \frac{V \cdot dt}{l} \cdot \sin(G) \end{bmatrix}$$

where x_t, y_t and ϕ_t are the vehicle position coordinates and its orientation in time step t, respectively. V is the vehicle velocity, and G is the vehicle steering angle. A parameter l is the vehicle wheel-base.

This vehicle is equipped with a range and bearing sensor. It can sense an object bounding in ± 30 degree semi-circle with the maximum range of 30 meter. The measurement equation is as follows:

$$\begin{aligned} \mathbf{z}_t &= \mathbf{h}(x_t, f_i) + \mathbf{w}_t \\ &= \begin{bmatrix} \sqrt{(f_{i,x} - x_t)^2 + (f_{i,y} - y_t)^2} \\ \tan^{-1}\left(\frac{f_{i,y} - y_t}{f_{i,x} - x_t}\right) - \phi_t \end{bmatrix} + \mathbf{w}_t \end{aligned}$$

where f_i is a landmark feature available at time when the sensor takes a measurement. This landmark feature is assumed to be static and represented as a Cartesian coordinate system as $(f_{i,x}, f_{i,y})$. $\mathbf{w}_t \sim \mathrm{N}(0, R_t)$ is a zero-mean Gaussian white measurement noise with $R_t = \text{diag}\left(0.1^2,\ 1^2\right)$.

3.2 Experimental Results

Fig. 2 shows the result of the FastSLAM2.0 and the proposed method. It is clear that the proposed method always follows the true trajectory with minimum error.

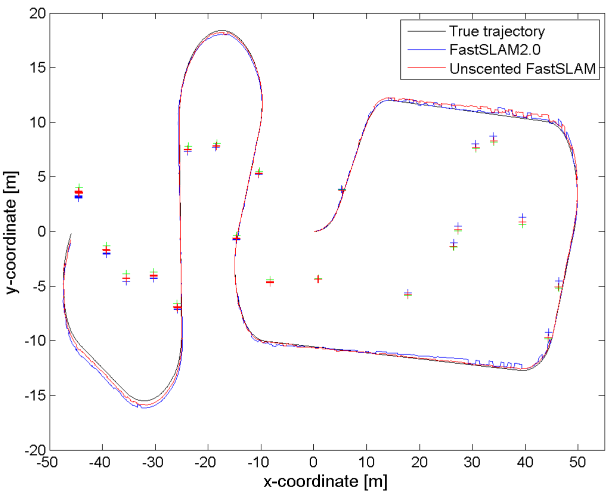

Fig. 2. Estimates by FastSLAM2.0 and unscented FastSLAM.

Furthermore, we then calculated the root mean square (rms) error of x-axis, y-axis, and orientation ϕ. The results of both filtering estimates are shown in Table 1 and it is proved that the unscented FastSLAM has better performance over the original FastSLAM2.0.

Table 1. RMS Errors

Method	x	y	ϕ
FastSLAM2.0	0.00685	0.74290	0.00009
Unscented FastSLAM	0.00357	0.33958	0.0014

4 CONCLUSION

In this paper, an unscented transformation for robot's pose estimation has been applied to a FastSLAM framework and its performance has been also evaluated. The simulation showed that the proposed method gave better estimation, compared to the previous FastSLAM2.0. It was demonstrated by comparing the actual robot trajectories with the FastSLAM2.0 and the unscented FastSLAM. The rms errors of x-axis, y-axis, and robot orientation ϕ proved that the proposed method had better performance over the FastSLAM2.0. In future work, we are focusing on investigating new sampling techniques of unscented transformation aiming for better performances and lowering computational cost.

REFERENCES

[1] Montemerlo M (2003), FastSLAM: A factored solution to the simultaneous localization and mapping problem with unknown data association. Ph.D. dissertation, Carnegie Mellon Univ., Pittsburgh, PA.

[2] Montemerlo M and Thrun S (2003), Simultaneous localization and mapping with unknown data association using FastSLAM. In Proc. of the IEEE Int. Conf. on Robotics and Automation (ICRA), 2: 1985–1991.

[3] Montemerlo M, Thrun S, Roller D and Wegbreit B (2003), FastSLAM2.0: an improved particle filter algorithm for simulteneous localization and mapping that provably converges. Proc. of the 18th Int. Joint Conf. on Artificial Intelligence, San Francisco, CA, USA: 1151–1156.

[4] Thrun S, Koller D, Ghahramani D, Durrant-Whyte H, and Ng AY(2004), Simultaneous mapping and localization with sparse extended information filters. Int. Journal of Robotics Research, 23(7-8): 693–716.

[5] Thrun S, Burgard W, and Fox D (2005), Probabilistic Robotics. Cambridge MA: MIT Press.

[6] Randall C. Smith and Peter Cheeseman (1986), On the representation and estimation of spatial uncertainty. Int. J. Robotics Research 5(4): 56–68.

[7] P. Moutarlier and R . C hatila (1989), Stochastic multisensory data fusion for mobile robot location and environment modeling. In 5th Int. Symposium on Robotics Research, Tokyo: 207–216.

[8] Leonard J J and Feder H J S (1999), A computationally efficient method for large-scale concurrent mapping and localization. In J. Hollerbach and D. Koditschek, editors, Proc. of the Ninth International Symp. on Robotics Research, Salt Lake City, Utah: 169–176.

[9] Murphy K (1999), Bayesian map learning in dynamic environments. Advances in Neural Information Processing Systems (NIPS), MIT Press.

[10] Bailey T (2002), Mobile robot localizatian and mapping in extensive outdoor environments. Ph.D. dissertation, University of Sydney, Australian Center for Field Robotics.

[11] van der Merwe R (2004), Sigma point Kalman filter for probabilistic inference in dynamic state-space models. Ph.D. dissertation, Oregon Health & Science University, Portland.

The Seventeenth International Symposium on Artificial Life and Robotics 2012 (AROB 17th '12),
B-Con Plaza, Beppu, Oita, Japan, January 19-21, 2012

Pedestrian detection and tracking in near infrared images

Masayoshi Tabuse[1] and Sayuri Kozawa[2]

[1]Kyoto Prefectural University, Kyoto 606-8522, Japan
[2]Sumitomo Forestry Archi Techno Co., Ltd., Chiba 261-0023, Japan
E-mail: tabuse@kpu.ac.jp

Abstract: We present a method for pedestrian detection applied to near infrared images. Near infrared ray is invisible, so that near infrared images are useful for surveillance systems day and night under near infrared light. In our method we use histograms of oriented gradient features and support vector machine. Furthermore, we present pedestrian trajectories using mean shift and nearest neighbor methods.

Keywords: surveillance system, pedestrian detection, pedestrian tracking, near infrared image

1 INTRODUCTION

Recently, research and development of surveillance systems are advanced as the heinous crimes increase. However, in present surveillance systems, it is necessary to monitor surveillance images 24 hours a day and a large load rests upon the person. It is very difficult to find crimes in real time. When the crime occurs, we often use the surveillance images later in the confirmatory purpose and the evidence purpose. Therefore, remote monitoring system that can inform us of the crime in the faraway place is needed even if we don't keep monitoring surveillance images. We also need that it records surveillance images and analyzes person action. The most important issue in surveillance systems is pedestrian detection [1], [2]. Pedestrian detection is a difficult task of a machine vision perspective because there is a wide range of possible pedestrian appearance, due to changing pose, clothing, lighting, and background. For pedestrian detection many features have been proposed (e.g. Haar-like features [3], histogram of oriented gradient (HOG) features [4], edgelet features [5]). In this paper, we present a method for pedestrian detection applied to near infrared images. Because near infrared light is invisible, near infrared images are useful for surveillance systems day and night under near infrared light. In this method we use HOG features and support vector machine (SVM). Furthermore, we present pedestrian trajectories using mean shift and nearest neighbor methods.

2 OUTLINE OF OUR APPROACH

Fig.1 shows the flowchart of our method. We use HOG features and a linear SVM classifier for pedestrian detection. We cluster detection windows using mean shift method [6]. Then we integrate the detection windows using nearest neighbor method and we determine pedestrian detection window which has 3 or more integrated detection windows. We track the pedestrian window based on probability of the same pedestrian in the previous image and the present image.

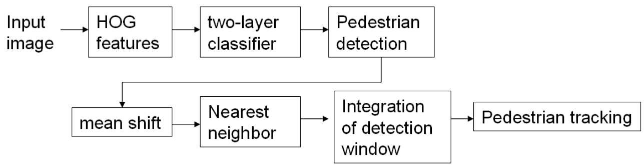

Fig. 1. The flowchart of our method

3 PEDESTRIAN DETECTION

3.1 Histograms of oriented gradients

Histograms of Oriented Gradients (HOG) feature [4] is a gray-level image feature based on a normalized local histograms of image gradient orientations. We divide each detection window in the image is divided into cells of size 8 $\times$ 8 pixels and accumulate a histogram of 9 gradient direction over pixels of the cell. 2$\times$2 cells are integrated into a block in a slide fashion, so that blocks overlap with each other. Thus each block is represented by a 36 dimensional normalized feature vector. Each detection window, which consists of 64$\times$128 pixels, is represented by 7$\times$15 blocks, giving 3780 dimensional feature vector. Then we train a linear SVM classifier using this feature vector. We use INRIA person dataset [7] as training data and test data.

3.2 Two-layer classifier

Pedestrian detection takes about 1 second per image (640$\times$480 pixels) using all the components of 3780 dimensional feature vector. Thus, we investigate amount of overlap between the probability distributions of classifier output values for each block of person and non-person images using Bhattacharyya coefficient. We select some blocks with lower Bhattacharyya coefficient, which have higher contribution to pedestrian detection and obtain lower dimensional feature vector from these blocks. Then we build two-layer classifier, in which the first layer consists of the selected lower dimensional feature vector and the second layer consists of 3780 dimensional feature vector, shown in Fig. 2.

Fig. 3 shows selected 3, 7, and 16 blocks, which means that the person area has higher contribution to pedestrian detection. Detection rates of pedestrian using two-layer classifier of 3 blocks and 105 blocks, 7 blocks and 105 blocks, and 16 blocks and 105 blocks are shown in Fig. 4.

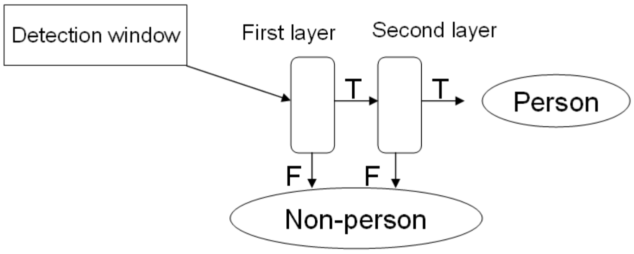

Fig. 2. Two-layer classifier

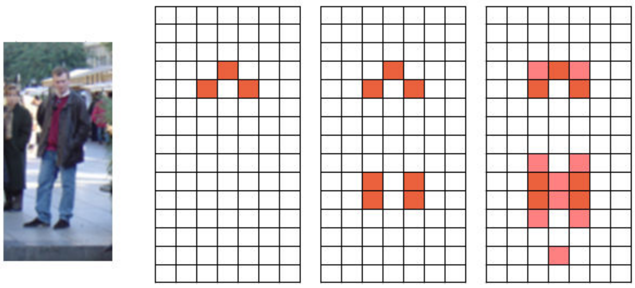

3 blocks 7 blocks 16 blocks

Fig. 3. Selected blocks

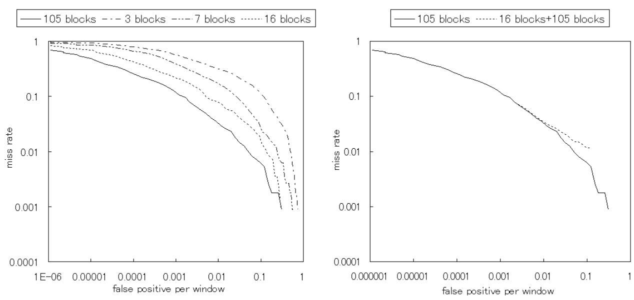

(a) (b)

Fig. 4. Detection performance in visible images
(a) 105 blocks, 3 blocks, 7 blocks and 16blocks
(b) 105 blocks and two-layer (16 and 105 blocks)

3.2 Near infrared images

Near infrared light is invisible so that near infrared images are useful for surveillance systems day and night under near infrared light. Furthermore a near infrared image is a image of reflection light like a visible image. Thus, we can detect pedestrians in the same method as pedestrian detection in visible images. However a near infrared image is a blurred one as compare with a visible image. Therefore detection rate of pedestrian in near infrared images is lower than that in visible images. Fig. 5 shows detection rate of pedestrian in near infrared images.

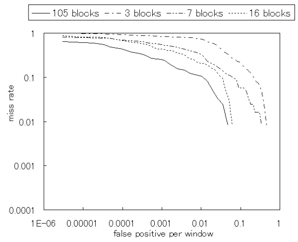

Fig. 5. Detection performance using 105, 3, 7, 16 blocks in near infrared images

4 INTEGRATION OF DETECTION WINDOWS

4.1 Mean shift method

We cluster detection windows using mean shift method [6]. Mean shift is a procedure for locating the maxima of a density of discrete data. We represent discrete data $\{x_i\}_{i=1,\dots,n}$ and use the Gaussian kernel. The mean shift vector Δx_i is weighted mean of the density determined by the kernel as follows:

$$\Delta x_i = \frac{\sum_j x_j \exp\left\{ (x_i - x_j)^2 / h^2 \right\}}{\sum_j \exp\left\{ (x_i - x_j)^2 / h^2 \right\}}$$

and $x_i \rightarrow x_i + \Delta x_i$ until $\Delta x_i <$ threshold.

4.2 Nearest neighbor method

We integrate the detection windows using nearest neighbor method and when the integrated window consists of three or more detection windows, it is considered as pedestrian detection window..

5 TRACKING

We track the pedestrian window based on probability of the same pedestrian in the previous image and the present image.

6 EXPERIMENTS

6.1 Experimental environment

We use a surveillance camera (SM-CKBE51AV, Wireless Tsukamoto Co.) which captures visible and near infrared images in daylight and in near infrared light, respectively. Near infrared floodlight is SM-140-850 (Wireless Tsukamoto Co.) emitting 850nm infrared light. The images are transformed into a digital signal by an A/D converter (ADVC-300, Thomson Canopus) and the signal was input into a computer with an IEEE 1394 interface board (1394-PCI3/DV6, IO Data Device). We used a computer (CPU: Intel Core i7 3.33GHz, main memory: 6 GB, and OS: Windows 7, Microsoft). For programming, we use Microsoft Visual C++ 2008 and Intel OpenCV 2.1 [7], SVM^{light} 6.02 [8].

The surveillance camera is setup at the window on the third floor of the lecture building on the campus of Kyoto Prefectural University and captures pedestrians walking out of door in visible light and near infrared light.

6.2 Condition

We find that there is much incorrect recognition when pedestrian detection is carried out in all the regions of images. Therefore, we setup pedestrian detection region and pedestrian tracking region in images shown in Fig. 6. In the pedestrian detection region, we detect pedestrians. Then we track these pedestrian in the pedestrian tracking region.

The experimental parameters of pedestrian detection are as follows:

(1) visible light images

Scanning step of detection window is 8 pixels in x-direction and 16 pixels in y-direction. SVM classifier thresholds of 105 and 16 blocks are 0.4 and 1.5, respectively.

(2) Near infrared images

Scanning step of detection window is 8 pixels in x-direction and 8 pixels in y-direction. SVM classifier thresholds of 105 and 16 blocks are 0.5 and 1.5, respectively.

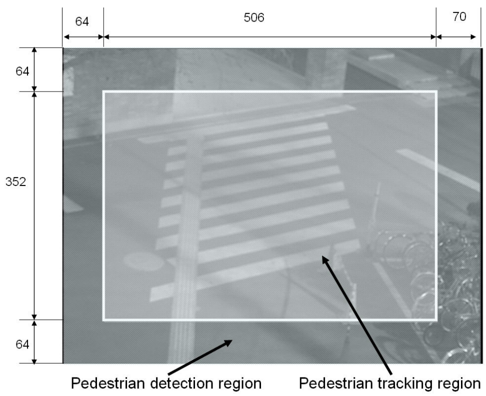

Fig. 6. Pedestrian detection and tracking regions

6.3 Results

The experimental results are shown in Fig. 7 and 8. A white rectangle indicates a pedestrian detection window and a white line indicates a pedestrian tracking. Pedestrian detection and tracking time is shown in Table 1.

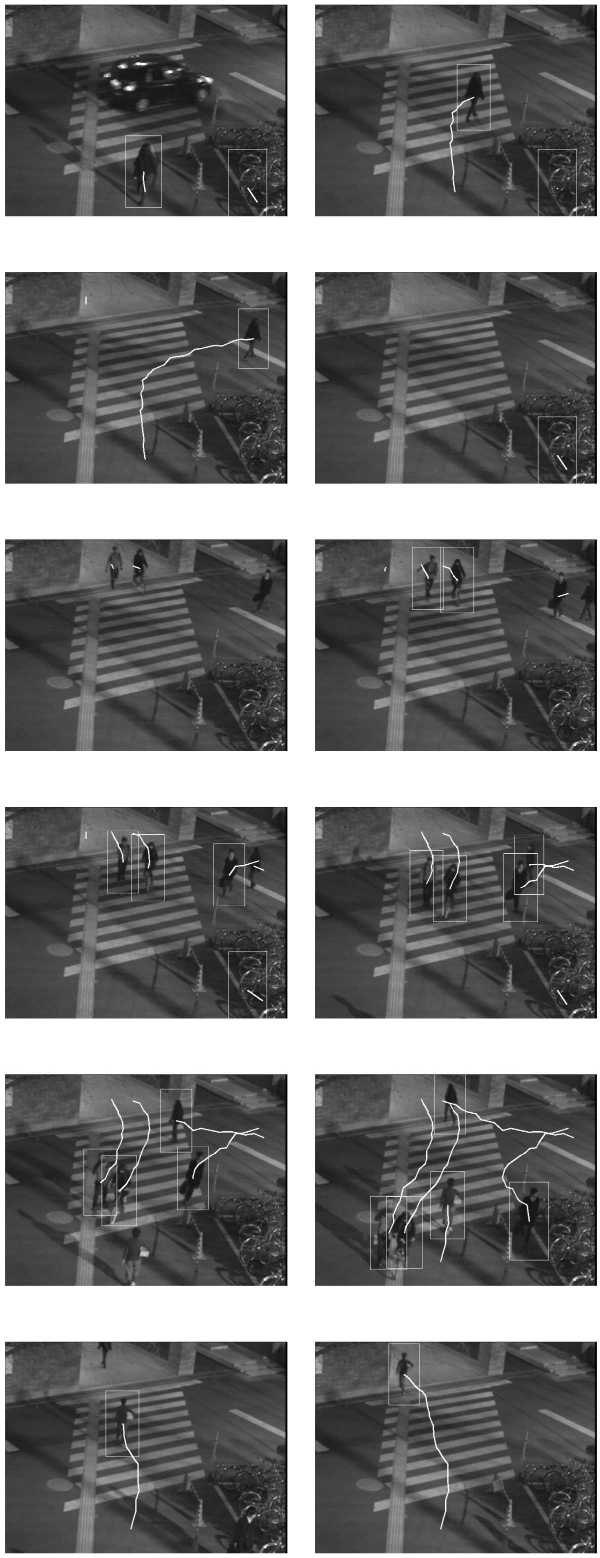

Fig. 7. Pedestrian tracking in visible images

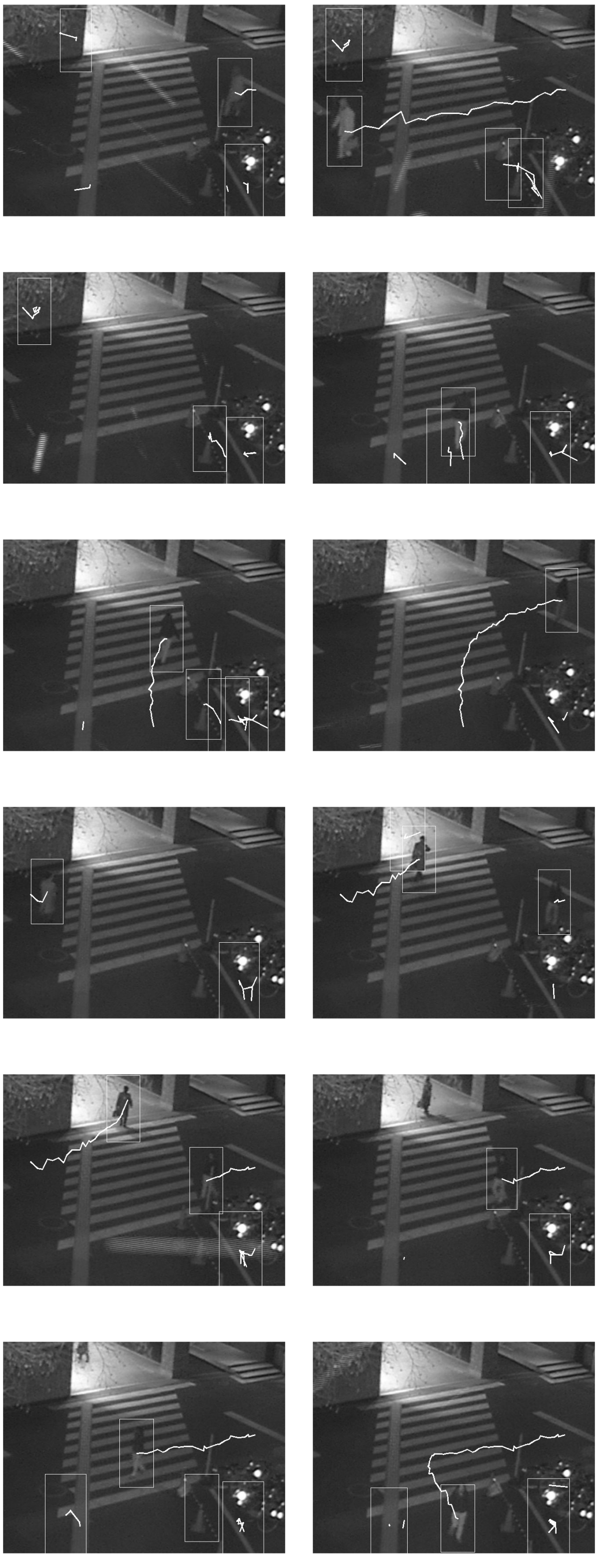

Fig. 8. Pedestrian tracking in near infrared images

Table 1. Pedestrian detection and tracking time in a visible image and in a near infrared image using 105 blocks and two-layer classifier (16 and 105 blocks)

	105 blocks	Two-layer classifier
Visible	453ms	413ms
NIR	960ms	833ms

7 CONCLUSION

In this paper, we present a method for pedestrian detection and tracking applied to visible and near infrared images. Pedestrian detection rates in visible images and near infrared images are 95.7 % and 92.2 %, respectively. In the future we want to reduce incorrect recognition of person detection by improving the person detection method, and to consider the application of those other than a surveillance system.

REFERENCES

[1] Enzweiler M, Gavrila DM (2009), Monocular Pedestrian Detection: Survey and Experiments, IEEE Trans. on PAMI, Vol.31, pp.2179-2195

[2] Dollar P, Wojek C, Schiele B, Perona P (2011), Pedestrian Detection: An Evaluation of the State of the Art, IEEE Trans. on PAMI Vol.33, pp.53-60

[3] Viola P, Jones MJ, Snow D (2005), Detecting Pedestrians Using Patterns of Motion and Appearance, Int. J. of Computer Vision, Vol.63, pp.153-161

[4] Dalal N, Triggs B (2005), Histograms of Oriented Gradients for Human Detection. ICCVPR, pp. 886-893

[5] Wu B, Nevatia R (2005), Detection of Multiple, Partially Occluded Humans in a Single Image by Bayesian Combination of Edgelet Part Detectors, ICCV, pp.90-97

[6] Cheng Y (1995), Mean Shift, Mode Seeking, and Clustering, IEEE Trans. PAMI Vol.17 pp.790–799

[7] INRIA Person Dataset, http://pascal.inrialpes.fr/data/human/

[8] Open Computer Vision Library, http://sourceforge.net/projects/opencvlibrary/

[9] Joachims T (1999), Making large-Scale SVM Learning Practical. In Advances in Kernel Methods - Support Vector Learning, MIT Press, http://svmlight.joachims.org/

The Seventeenth International Symposium on Artificial Life and Robotics 2012 (AROB 17th '12),
B-Con Plaza, Beppu, Oita, Japan, January 19-21, 2012

A system for facial expression recognition of a speaker using front-view face judgment, vowel judgment and thermal image processing

T. Asada, Y. Yoshitomi, and M. Tabuse

Graduate School of Life and Environmental Sciences, Kyoto Prefectural University,
1-5 Nakaragi-cho, Shimogamo, Sakyo-ku, Kyoto 606-8522, Japan
E-mail: t_asada@mei.kpu.ac.jp, yoshitomi@kpu.ac.jp, tabuse@kpu.ac.jp

Abstract: For facial expression recognition, we previously selected three images: (i) just before speaking and speaking (ii) the first vowel and (iii) the last vowel in an utterance. A frame of the front-view face in a dynamic image was selected by estimating the face direction. Based on our method, we have been developing an on-line system for recognizing the facial expression of a speaker using front-view face judgment, vowel judgment, and thermal image processing. In the proposed system, we used three personal computers connected by cables to form a local area network. As an initial investigation, we adopted the utterance of the Japanese name "Taro," which is semantically neutral. Using the proposed system, the facial expressions of one male subject were discriminable with 76% accuracy when he exhibited one of the intentional facial expressions of "angry," "happy," "neutral," "sad," and "surprised."

Keywords: facial expression recognition, on-line system, speech recognition, vowel judgment, thermal image processing, front-view face judgment

1 INTRODUCTION

To better integrate robots into our society, a robot should be able to interact in a friendly manner with humans. The goal of our research is to develop a robot that can perceive human feelings and mental states.

The first stage is to develop a method for integrating the information of human expression. The basic information for integration is the visible ray (VR) image, thermal image, and voice. In this first stage, an automatic, real-time, interactive system is not necessary. It is very difficult to equip a robot with a computer that can process information with the same efficiency as the human brain. Therefore, we chose to enable the robot to use a type of information, such as thermal imaging, that the human brain cannot process. Thermal imaging is a good example because it is impossible for a human to perceive heat via the naked eye.

The second stage is to develop an automatic, real-time, interactive system that has the information integration of human expression as a processing characteristic. The third stage is to develop a robot that has a function developed from the synthesis of the first and second stages for use in our daily lives.

The present investigation focuses on the first stage of development, in which a robot can visually detect human feelings or inner mental states. Although recognizing facial expressions has received considerable attention in the field of computer vision research, the mechanism of recognition still falls far short of human capability, especially from the viewpoint of robustness under widely varying lighting conditions. One of the reasons is that the nuances of shade, reflection, and local darkness influence the accuracy of facial expression recognition through the inevitable change of gray levels.

To avoid this problem and to develop a robust method for facial expression recognition applicable under widely varied lighting conditions, we did not use a VR image, as would be expected. Instead, we used an image produced by infrared rays (IR), which describe the thermal distribution of the face [1]–[11]. Although a human cannot detect IR, it is possible for a robot to process the information of the thermal images created by IR. Therefore, as a new mode of robot vision, thermal image processing is a practical method that is viable under natural conditions.

The timing of recognizing facial expressions is also important for a robot because the processing could be time-consuming. In a previous report, we adopted an utterance as the key to expressing human feelings or mental states because humans tend to speak when expressing a feeling [5]–[11].

In addition, we added a judgment function of a front-view face to our method for facial expression recognition [11]. A frame of the front-view face in a dynamic image was selected by estimating the face direction. The judgment function of a front-view face measures four feature parameters by thermal image processing.

In this paper, we propose an on-line system for recognizing the facial expression of a speaker using front-view face judgment, vowel judgment and thermal image processing, based on our method [10], [11].

2 IMAGE ACQUISITION

The principle behind thermal image generation is the Stefan–Boltzmann law, expressed as $W = \varepsilon\sigma T^4$, where ε is emissivity, σ is the Stefan–Boltzmann constant (=5.6705×10^{-12} W/cm^{2}K^4), and T is the temperature (K). For human skin, ε is estimated as 0.98 to 0.99 [12], [13]. In this study, the approximate value of 1 was used as ε for human skin because the value of ε for almost all substances is lower than that of human skin [12]. Consequently, the human face region is easily extracted from an image using the value of 1 for ε when a range of skin temperatures is selected to produce a thermal image [1]–[11], [14]. Fig. 1 shows examples of face images of a male, obtained by VR and IR. We can obtain a thermal image of the face without light, even at night. In principle, the temperature measurement by IR does not depend on skin color [13], darkness, or lighting condition. Therefore, the face region and its characteristics are easily extracted from the thermal image.

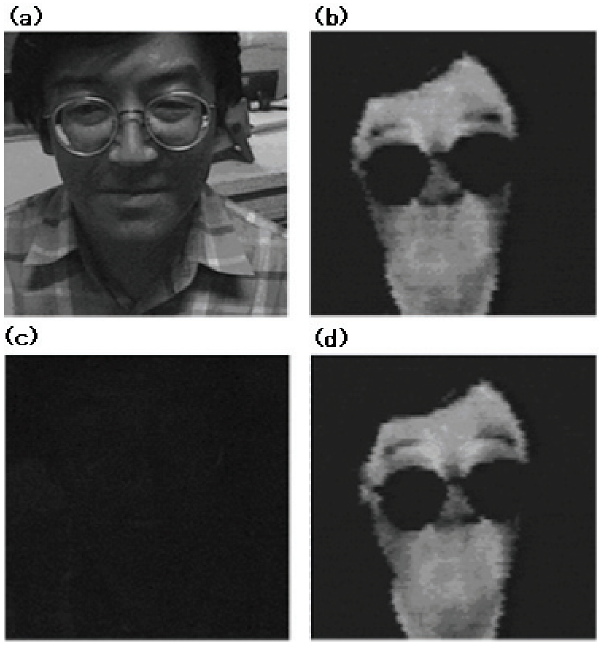

Fig. 1. Examples of a face image at night:
(a) VR with lighting, (b) IR with lighting,
(c) VR without lighting, (d) IR without lighting [3]

3 PROPOSED SYSTEM

In this study, as a pre-processing module, we added a judgment function [11] of a front-view face to our previously reported method [8] for facial expression recognition.

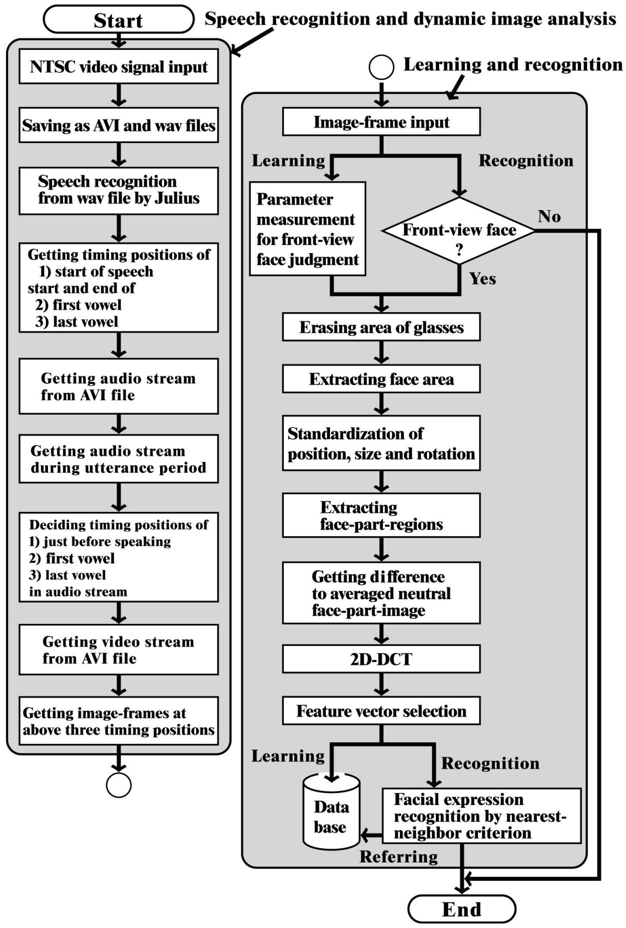

Fig. 2. Flowchart of our method [11]

Fig. 2 illustrates the flowchart of our method [11]. We have two modules in our system. The first is a module for speech recognition and dynamic image analysis, and the second is a module for learning and recognition. In the latter, we embedded the module for front-view face judgment.

3.1 Front-view face judgment

The training data is calculated from the images of a front-view face. We first define the face rotation around the X, Y, and Z axes. After normalizing the horizontal Feret's diameter of the segmented face image, the centerline of the face region is drawn as the first standard line. Each pixel point in the centerline has the same number of pixels on both the left and the right sides of the point. Then, a straight line as the second standard line is drawn from the upper to the lower edge points of the centerline. The two standard lines are used to estimate the deviation from the front-view face. To evaluate the face direction, we use four feature parameters (*nod*, *up*, *rotate*, *lean*), explained in detail in our previously reported paper [11].

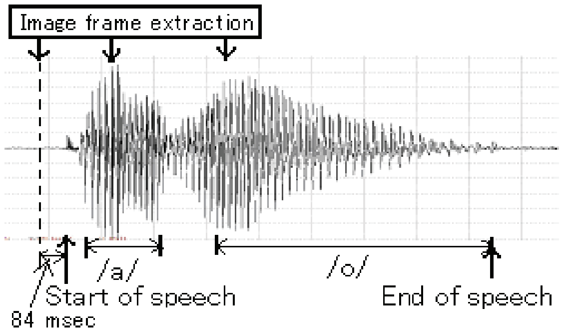

Fig. 3. Speech waveform of "Taro" and timing positions for image frame extraction [8]

3.2 Speech recognition and dynamic image analysis

We use a speech recognition system named Julius [15] to obtain the timing positions of the start of speech and the first and last vowels in a WAV file [8]–[11]. Fig. 3 shows an example of the waveform of the Japanese name "Taro"; the timing position of the start of speech and the timing ranges of the first vowel (/a/) and the last vowel (/o/) are decided by Julius. Using the timing position of the start of speech and the timing ranges of the first and last vowels obtained from the WAV file, three image frames are extracted from an AVI file at the three timing positions. For the timing position just before speaking, we use the timing position of 84 ms before the start of speech, as determined in our previously reported study [8]. For the timing position of the first vowel, we use the position where the absolute value of the amplitude of the waveform is the maximum while speaking the vowel. For the timing position of the last vowel, we apply the same procedure used for the first vowel.

3.3 Learning and recognition

For the static images obtained from the extracted image frames, the process of erasing the area of the glasses, extracting the face area and standardizing the position, size, and rotation of the face are performed according to the method described in our previously reported study [7]. Fig. 4 shows the blocks for extracting the face areas in a thermal image having 720 × 480 pixels. In the next step, we generate difference images between the averaged neutral face image and the target face image in the extracted face areas to perform a 2D discrete cosine transform (2D-DCT). The feature vector is generated from the 2D-DCT coefficients according to a heuristic rule [6], [7]. As stated above, we use the speech recognition system named Julius. Julius sometimes makes a mistake in recognizing the first and/or last vowel(s). For example, /a/ for the first vowel was misrecognized as /i/. In the training data, we correct the misrecognition. However, the test data cannot be corrected. The facial expression is recognized by the nearest-neighbor criterion in the feature vector space using the training data just before speaking and when speaking the phonemes of the first and last vowels. When we use the training data for all combinations of the first and last vowels [10], we can apply the proposed system to a speaker for any utterance.

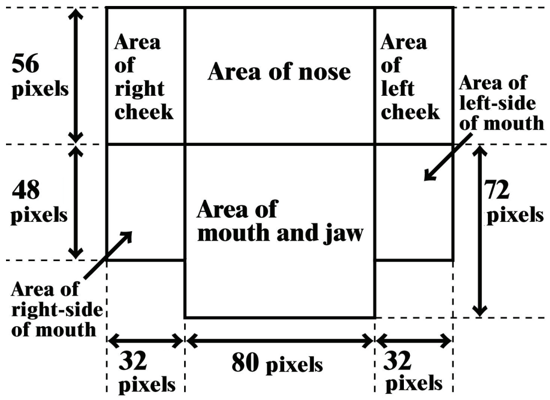

Fig. 4. Blocks for extracting face areas in the thermal image

3.4 Proposed system

Fig. 5 shows the structure of the proposed system. Figs. 6 and 7 show flow charts of the proposed system during facial expression learning and recognition, respectively. Figs. 6 and 7 demonstrate the processing shared by three computers (PC1, PC2, and PC3) connected by cables to

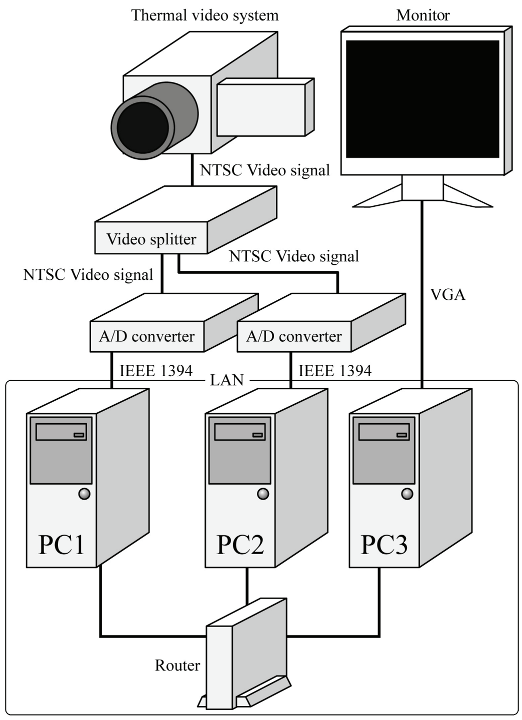

Fig. 5. Structure of the proposed system

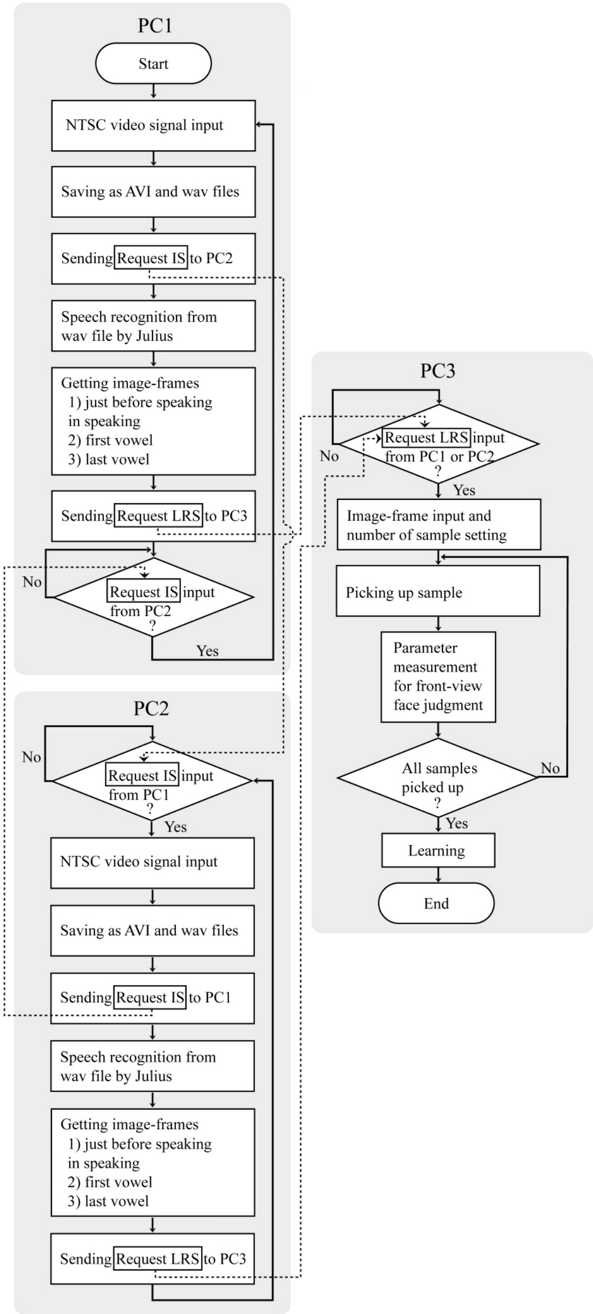

Fig. 6. Flow chart of the proposed system in learning for facial expression recognition

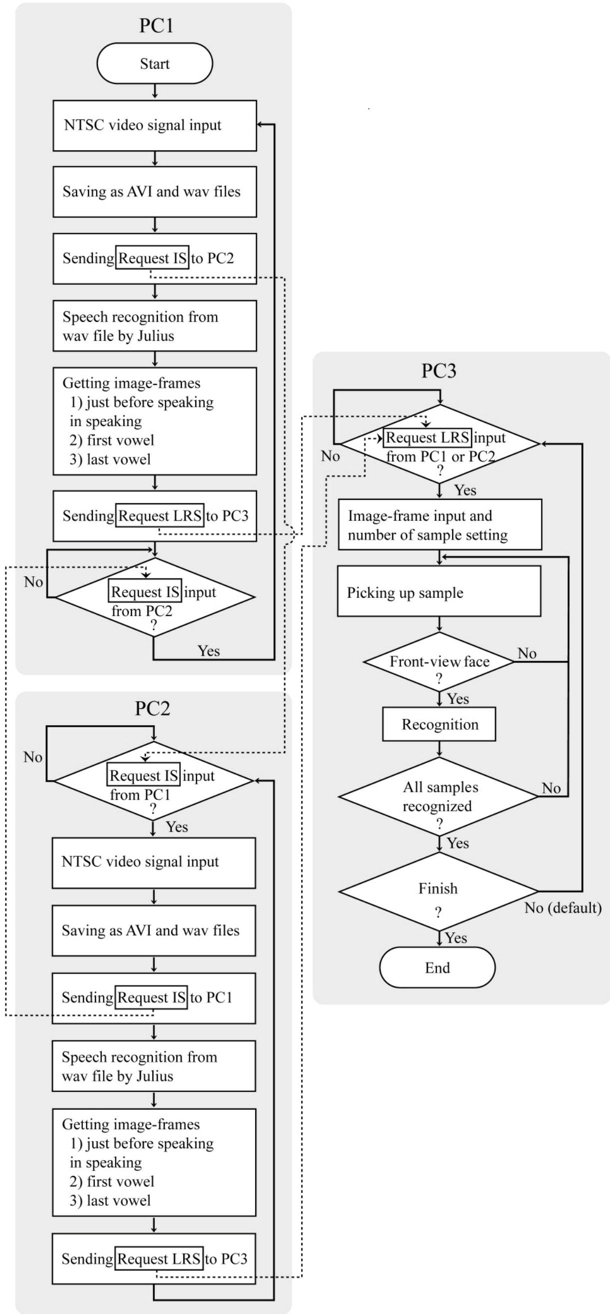

Fig. 7. Flow chart of the proposed system during facial expression recognition

form a local area network for performing the flow chart shown in Fig. 2. In Figs. 6 and 7, a line with an arrow attached denotes a process order, while a dotted line with an arrow attached denotes a communication from a PC to another PC in the local area network. The only difference between Figs. 6 and 7 is the processing in PC3. As shown in Figs. 6 and 7, an NTSC video signal from a thermal video system is successively inputted to either PC1 or PC2 to obtain image-frames: (i) just before speaking, and speaking (ii) the first vowel and (iii) the last vowel in an utterance. We use the proposed system for front-view face judgment using our previously reported method [11].

4 EXPERIMENTS

4.1 Condition

The thermal image produced by the thermal video system (Nippon Avionics TVS-700) and the sound captured from an Electret condenser microphone (Sony ECM-23F5), as amplified by a mixer (Audio-Technica AT-PMX5P), were transformed through an audio and video distribution amplifier (Maspro Denkoh VSP4) into a digital signal by two A/D converters (Thomson Canopus ADVC-100 for PC1 in Fig. 5 and Thomson Canopus ADVC-300 for PC2 in Fig. 5) and input into two computers (PC1 and PC2 in Fig. 5) with the same specification (Dell Optiplex 780, CPU: Intel Core 2 Duo E8400 3.00 GHz, main memory: 4.00 GB, OS: Windows 7 Professional (Microsoft) with an IEEE1394 interface board (I·O data device 1394-PCI3/DV6)). As PC3 in Fig. 5, we used a computer (Dell Precision T1600, CPU: Intel Xeon CPU E31225 3.10 GHz, main memory: 8.00 GB, OS: Windows 7 Professional (Microsoft)). The three computers (PC1, PC2, and PC3) were connected through a router (Buffalo WZR-HP-AG300H) with cables. We used Visual C++ 6.0 (Microsoft) as the programming language. To generate a thermal image, we set the condition that the thermal image had 256 gray levels for the detected temperature of 304 to 309 K. Therefore, one gray level corresponded to 1.95×10^{-2} K. The temperature range for generating a thermal image was decided to easily extract the face area on the image. We saved the visual and audio information in the computer as a Type 2 DV-AVI file, in which the video frame had a spatial resolution of 720×480 pixels and 8-bit gray levels, and the sound was saved in a stereo PCM format, 48 kHz and 16-bit levels.

Subject A exhibited in alphabetic order each of the intentional facial expressions of "angry," "happy," "neutral," "sad," and "surprised," while speaking the semantically neutral utterance "Taro." Fig. 8 shows examples of the thermal images of subject A. Subject A was a male wearing glasses.

In the experiment, subject A intentionally kept front-view faces in the AVI files saved as both the training and test data. We assembled 20 samples as training data and 10 samples as test data. From one sample, we obtained three images at the timing positions of just before speaking and just speaking the phonemes of the first and last vowels.

We obtained the feature parameter ranges for judging the front-view faces using the training data and the method stated in Section 3.1. The range was calculated as $a_i - min_i \le x_i \le a_i + max_i$ for all feature parameters in all other cases in the experiment, where x_1, x_2, x_3, x_4 were *nod*, *up*, *rotate*, and *lean* and a_1, a_2, a_3, a_4 were their

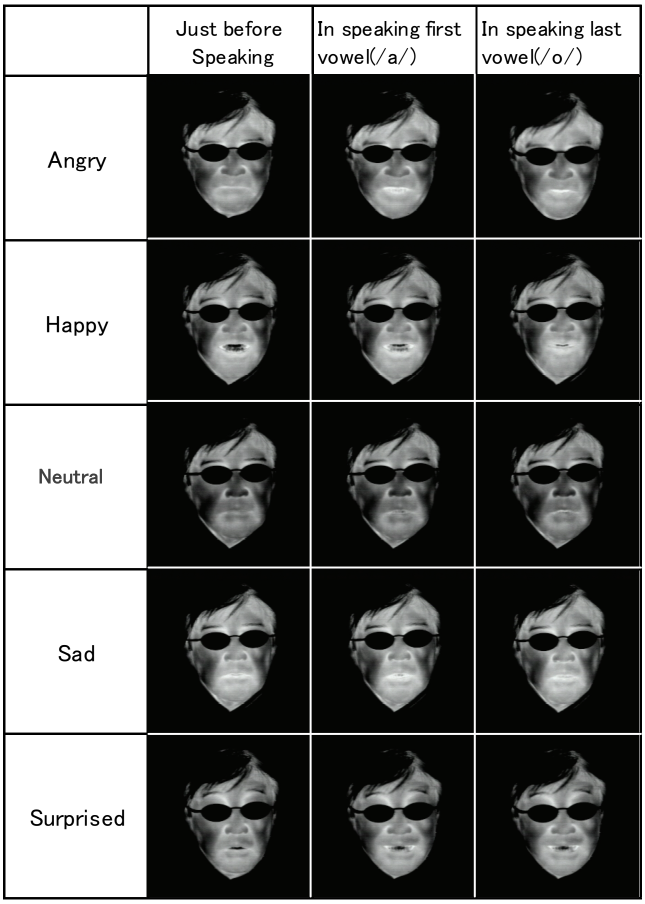

Fig. 8. Examples of thermal images of subject A having each facial expression in speaking

mean values, and $min_1, min_2, min_3, min_4$ were their minimum values and $max_1, max_2, max_3, max_4$ were their maximum values, respectively. We assembled twenty samples as training data and ten samples as test data for each facial expression. All facial expressions of test data for all subjects were judged as front-view faces by the method described in Section 3.1. For each sample, we obtained three images at the timing positions of just before speaking and while speaking the phonemes of the first and last vowels. If Julius misrecognized the vowel of the test sample, the corresponding image was not used for facial expression recognition. We had four cases of misrecognition for the vowel(s): (1) no misrecognition for the first and last vowels, (2) misrecognition only for the first vowel, (3) misrecognition only for the last vowel, (4) misrecognition for both the first and last vowels. We prepared feature vectors of the training data for each of the four cases.

4.2 Results and discussion

Table 1 shows the facial expression recognition accuracy for each facial expression. In the test data, only one thermal image just before speaking was judged as not having a front-view face, and thus the sample was removed and another sample, whose three thermal images were

Table 1. Recognition accuracy for subject A

		Input facial expression				
		Angry	Happy	Neutral	Sad	Surprised
Output	Angry	**90**	10			10
	Happy		**50**			10
	Neutral			**90**	10	10
	Sad		20	10	**90**	10
	Surprised	10	20			**60**

judged as having a front-view face, was added. The mean recognition accuracy was 76%. The facial expressions of "happy" and "surprised" were more difficult to recognize than those of "angry," "neutral," and "sad," which were almost perfectly recognized with 90% accuracy (Table 1).

In the present experiment, a subject spoke one word that was the semantically neutral utterance "Taro." The system recognized the facial expression in speaking each word. When we are ready to apply the proposed system for recognizing facial expressions in daily conversation, we should be able to recognize the facial expression during speaking for a certain interval, such as sentence by sentence. This is because we focus on human feeling through facial expression and it is difficult for humans to change their feeling while speaking word by word. When we use the training data for all combinations of the first and last vowels [10], we can apply the proposed system to a speaker for any utterance.

5 CONCLUSION

We propose an on-line system for recognizing the facial expression of a speaker using front-view face judgment, vowel judgment and thermal image processing, based on our previously reported method [10], [11]. Using the proposed system, the facial expressions of a subject were discriminable with 76% accuracy for the facial expressions of "happy," "neutral," and "others" when the subject exhibited one of the intentional facial expressions of "angry," "happy," "neutral," "sad," and "surprised." We expect the proposed system to be applicable for recognizing facial expressions in daily conversation.

Acknowledgment

This work was supported by KAKENHI (22300077).

REFERENCES

[1] Yoshitomi Y, Kimura S, Hira E, and Tomita S (1996), Facial expression recognition using infrared rays image processing. Proc. of the Annual Convention IPS Japan, 2:339-340

[2] Yoshitomi Y, Kimura S, Hira E, and Tomita S (1997), Facial expression recognition using thermal image processing. IPSJ SIG Notes, CVIM103-3:17-24

[3] Yoshitomi Y, Miyawaki N, Tomita S, and Kimura S (1997), Facial expression recognition using thermal image processing and neural network. Proc. of 6th IEEE Int. Workshop on Robot and Human Communication pp.380-385

[4] Sugimoto Y, Yoshitomi Y, and Tomita S (2000), A method for detecting transitions of emotional states using a thermal face image based on a synthesis of facial expressions. J. Robotics and Autonomous Systems 31:147-160

[5] Yoshitomi Y, Kim SIll, Kawano T, and Kitazoe T (2000), Effect of sensor fusion for recognition of emotional states using voice, face image and thermal image of face. Proc. of 6th IEEE Int. Workshop on Robot and Human Interactive Communication pp.178-183

[6] Ikezoe F, Ko R, Tanijiri T, and Yoshitomi Y (2004), Facial expression recognition for speaker using thermal image processing (in Japanese). Trans. Human Interface Society 6(1):19-27

[7] Nakano M, Ikezoe F, Tabuse M, and Yoshitomi Y (2009), A study on the efficient facial expression using thermal face image in speaking and the influence of individual variations on its performance (in Japanese). J. IEEJ 38(2):156-163

[8] Koda Y, Yoshitomi Y, Nakano M, and Tabuse M (2009), Facial expression recognition for a speaker of a phoneme of vowel using thermal image processing and a speech recognition system. Proc. of 18th IEEE Int. Symp. on Robot and Human Interactive Communication pp.955-960

[9] Yoshitomi Y (2010), Facial expression recognition for speaker using thermal image processing and speech recognition system. Proc. of 10th WSEAS Int. Conf. on Applied Computer Science pp.182-186

[10]Yoshitomi Y, Asada T, Shimada K, and Tabuse M (2011), Facial expression recognition of a speaker using vowel judgment and thermal image processing. J. Artificial Life and Robotics, 16(3):318–323

[11]Fujimura T, Yoshitomi Y, Asada T, and Tabuse M (2011), Facial expression recognition of a speaker using front-view face judgment, vowel judgment, and thermal image processing. J. Artificial Life and Robotics, 16(3):411-417

[12]Kuno H (1994), Infrared rays engineering (in Japanese). Tokyo, IEICE 22

[13]Kuno H (1994), Infrared rays engineering (in Japanese). Tokyo, IEICE 45

[14]Yoshitomi Y, Tsuchiya A, and Tomita S (1998), Face recognition using dynamic thermal image processing. Proc. of 7th IEEE Int. Workshop on Robot and Human Communication pp.443-448

[15]http://julius.sourceforge.jp/

Robust facial expression recognition of a speaker using thermal image processing and updating of fundamental training-data

Y. Nakanishi, Y. Yoshitomi, T. Asada, and M. Tabuse

Graduate School of Life and Environmental Sciences, Kyoto Prefectural University,
1-5 Nakaragi-cho, Shimogamo, Sakyo-ku, Kyoto 606-8522, Japan,
E-mail: y_nakanishi@mei.kpu.ac.jp, yoshitomi@kpu.ac.jp, t_asada@mei.kpu.ac.jp, tabuse@kpu.ac.jp

Abstract: We previously developed a method for the facial expression recognition of a speaker. For facial expression recognition, we selected three static images: (i) just before speaking and speaking (ii) the first vowel and (iii) the last vowel in an utterance. Then, only the static image of the front-view face was used for facial expression recognition. However, frequent updates of the training data were time-consuming. To reduce the time for updates, we found that the classifications of "neutral," "happy," and "others" were efficient and accurate for facial expression recognition. Using the proposed method with updated training data of "happy" and "neutral" after an interval such as approximately three and a half years, the facial expressions of two subjects were discriminable with 87.0% accuracy for the facial expressions of "happy," "neutral," and "others" when exhibiting the intentional facial expressions of "angry," "happy," "neutral," "sad," and "surprised."

Keywords: facial expression recognition, speech recognition, vowel judgment, thermal image processing, front-view face judgment

1 INTRODUCTION

The present investigation concerns the first stage of the development of a robot that has the ability to visually detect human feelings or mental states. Although the mechanism for recognizing facial expressions has received considerable attention in the field of computer vision research, it still falls far short of human capability, especially from the viewpoint of robustness under widely varying lighting conditions. One of the reasons for this lack of robustness is that nuances of shade, reflection, and local darkness influence the accuracy of facial expression recognition through the inevitable change of gray levels.

To avoid this problem and to develop a method for facial expression recognition applicable under widely varied lighting conditions, we did not use visible ray images. Instead, we used images produced by infrared rays (IR), which show the thermal distribution of the face [1]-[11]. Although a human cannot detect IR, it is possible for a robot to process the information in IR thermal images. Therefore, as a new mode of robot vision, thermal image processing is a practical method that is viable under natural conditions.

The timing of recognizing facial expressions is important for a robot because the processing can be time-consuming. We adopted an utterance as the key to expressing human feelings or mental states because humans tend to express feelings vocally [5]-[11].

In addition, we added a judgment function of a front-view face to our method for facial expression recognition [10]. A frame of the front-view face in a dynamic image was selected by estimating the face direction. The judgment function of a front-view face measures four feature parameters by thermal image processing.

In the present study, we have been investigating a method for efficiently updating the training data because frequent updates are time-consuming. Through experiments, we concluded that updating the training data corresponding to the facial expressions of "happy" and "neutral" is practical. These two facial expressions are not only very common in our daily lives, but are also easier to express than other facial expressions. Furthermore, the classifications of "neutral," "happy," and "others" are efficient for facial expression recognition under the condition that updating the training data of facial expressions is not often performed. The proposed method with updated training data of "happy" and "neutral" after an interval such as approximately three and a half years is applied to recognition of the facial expressions of two subjects when exhibiting the intentional facial expressions of "angry," "happy," "neutral," "sad," and "surprised."

2 IMAGE ACQUISITION

The principle behind thermal image generation is the Stefan–Boltzmann law, expressed as $W = \varepsilon\sigma T^4$, where ε is emissivity, σ is the Stefan–Boltzmann constant (=5.6705×10^{-12} W/cm^{2}K^4), and T is the temperature (K). For human skin, ε is estimated as 0.98 to 0.99 [12], [13]. In this study, the approximate value of 1 was used as ε

for human skin because the value of ε for almost all substances is lower than that of human skin [12]. Consequently, the human face region is easily extracted from an image by using the value of 1 for ε [1]–[11]. In principle, the temperature measurements by IR do not depend on skin color [13], darkness, or lighting condition, and so the face region and its characteristics are easily extracted from a thermal image.

3 PROPOSED METHOD

In this study, as a pre-processing module, we added a judgment function [10] of a front-view face to our previously reported method [8] for facial expression recognition.

Fig. 1 illustrates the flowchart of our method [10]. We have two modules in our system. The first is a module for speech recognition and dynamic image analysis, and the second is a module for learning and recognition. In the module for learning and recognition, we embedded the module for front-view face judgment.

3.1 Front-view face judgment

The training data is calculated from the images of a front-view face. We first define the face rotation around the *X*, *Y*, and *Z* axes. After normalizing the horizontal Feret's diameter of the segmented face image, the centerline of the face region is drawn as the first standard line. Each pixel point in the centerline has the same number of pixels on both the left and the right sides of the point. Then, a straight line as the second standard line is drawn from the upper to the lower edge points of the centerline. The two standard lines are used to estimate the deviation from the front-view face. To evaluate the face direction, we use four feature parameters (*nod*, *up*, *rotate*, *lean*), explained in detail in our previously reported paper [10].

3.2 Speech recognition and dynamic image analysis

We use a speech recognition system named Julius [14] to obtain the timing positions of the start of speech and the first and last vowels in a WAV file [8]–[10]. Fig. 2 shows an example of the waveform of the Japanese name "Taro"; the timing position of the start of speech and the timing ranges of the first vowel (/a/) and the last vowel (/o/) are decided by Julius. By using the timing position of the start of speech and the timing ranges of the first and last vowels obtained from the WAV file, three image frames are extracted from an AVI file at the three timing positions. For the timing position just before speaking, we use the timing position of 84 ms before the start of speech, as determined in our

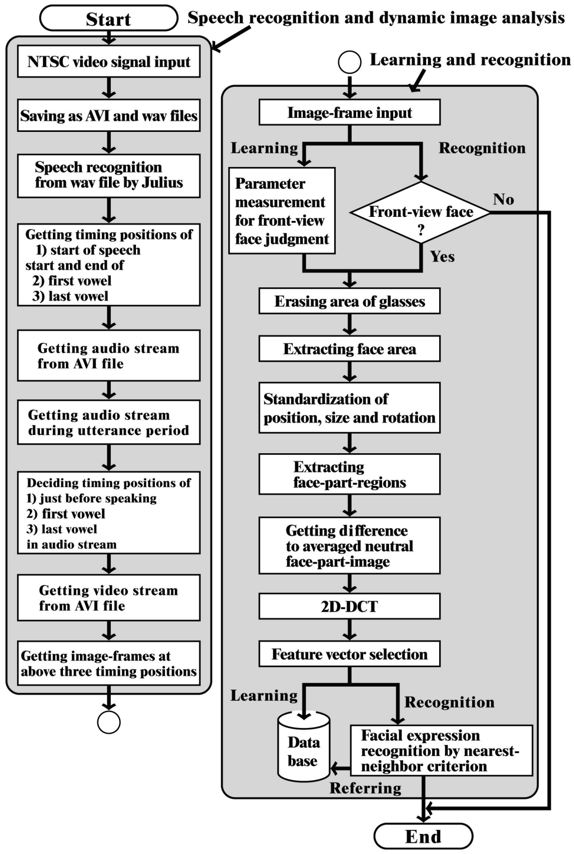

Fig. 1. Flowchart of our method [10]

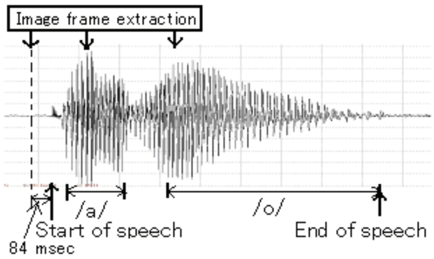

Fig. 2. Speech waveform of "Taro" and timing positions for image frame extraction [8]

previously reported study [7]. For the timing position of the first vowel, we use the position where the absolute value of the amplitude of the waveform is the maximum while speaking the vowel. For the timing position of the last vowel, we apply the same procedure used for the first vowel.

3.3. Learning and recognition

For the static images obtained from the extracted image frames, the process of erasing the area of the glasses, extracting the face area, and standardizing the position, size, and rotation of the face are performed according to the method described in our previously reported study [7]. In the next step, we generate difference images between the averaged neutral face image and the target face image in the extracted face areas to perform a 2D discrete cosine transform (2D-DCT). The feature vector is generated from the 2D-DCT coefficients according to a heuristic rule [6], [7]. As stated above, we use the speech recognition system named Julius. Julius sometimes makes a mistake in recognizing the first and/or last vowel(s). For example, /a/ for the first vowel might be misrecognized as /i/. In the training data, we correct the misrecognition. However, the test data cannot be corrected. The facial expression is recognized by the nearest-neighbor criterion in the feature vector space by using the training data just before speaking and when speaking the phonemes of the first and last vowels. After preparing the training data for all combinations of the first and last vowels, we could apply our method [8] to a speaker for any utterance [11].

4 EXPERIMENTS

4.1 Condition

The thermal image produced by the thermal video system (Nippon Avionics TVS-700) and the sound captured from an Electret condenser microphone (Sony ECM-23F5), as amplified by a mixer (Audio-Technica AT-PMX5P), were transformed into a digital signal by an A/D converter (Thomson Canopus ADVC-300) and input into a computer (DELL Optiplex 780, CPU: Intel Core 2 Duo E8400 3.00 GHz, main memory: 3.21 GB, and OS: Windows 7 Professional (Microsoft) with an IEEE1394 interface board (I·O Data Device 1394-PCI3/DV6)). We used Visual C++ 6.0 (Microsoft) as the programming language. To generate a thermal image, we set the condition that the thermal image had 256 gray levels for the detected temperature range of 5 to 12.9 K. Therefore, one gray level corresponded to 1.95×10^{-2} to 5.04×10^{-2} K. The temperature range for generating a thermal image was decided for each subject to easily extract the face area on the image. We saved the visual and audio information in the computer as a Type 2 DV-AVI file, in which the video frame had a spatial resolution of 720×480 pixels and 8-bit gray levels, and the sound was saved in a stereo PCM format, 48 kHz and 16-bit levels.

Two subjects exhibited in alphabetic order each of the intentional facial expressions of “angry,” “happy,” “neutral,” “sad,” and “surprised,” while speaking the semantically neutral utterance “Taro.” In this study, we categorized all of “angry,” “sad,” and “surprise” expressions as “others” in making the recognition results. Figs. 3 to 7 show examples of the thermal images of each subject. Subjects A and B were males with glasses. We captured the thermal images on June 20, 2006 (hereinafter referred to as First_period_A) (Fig. 3), at approximately 3 pm on January 22, 2010 (hereinafter referred to as Second_period_A) (Fig. 4), and at approximately 5 pm on January 22, 2010 (hereinafter referred to as Third_period_A) (Fig. 5) for subject A, and on June 20, 2006 (hereinafter referred to as First_period_B) (Fig. 6) and January 25, 2010 (hereinafter referred to as Second_period_B) (Fig. 7) for subject B.

In this study, we investigated several combinations of training and test data for each subject as listed in Tables 1, 2, and 3 in Section 4.2. Case-A-1-2 for subject A consisted of the following cases: (1) thermal images for both training and test data captured on First_period_A, (2) thermal images for both training and test data captured on Second_period_A, (3) thermal images for training and test data captured on First_period_A and Second_period_A, respectively, and (4) thermal images of training data of the facial expressions of “happy” and “neutral” captured on Second_period_A, thermal images of training data of the facial expressions of “others” captured on First_period_A, and the test data were captured on Second_period_A. In addition, Case-A-2-3 for subject A consisted of four cases decided by changing the data of First_period_A and Second_period_A in Case-A-1-2 to those of Second_period_A and Third_period_A, respectively. Case-B-1-2 for subject B consisted of the four cases defined in the same manner described above as Case-A-1-2 for subject A.

For Case-A-1-2, Case-A-2-3, and Case-B-1-2, we compared (3) and (4) for investigating the effects of updating the training data of the facial expressions of “happy” and “neutral”, whereas (1) and (2) were added for reference of thermal images for the training and the test data captured without intentional intervals.

Subjects A and B intentionally kept front-view faces during the capturing of thermal images for the training data in all cases, and subject A did so during the capturing of thermal images for the test data on First_period_A and Third_period_A. In addition, subject B intentionally kept front-view faces during the capturing of thermal images for the test data on First_period_B. Subjects A and B freely changed their face direction during the capturing of thermal images for the test data on Second_period_A and Second_period_B, respectively. We obtained the feature parameter ranges for judging the front-view faces by using the training data and the method mentioned in Section 3.1. The range was calculated as $a_i - 3\sigma_i < x_i < a_i + 3\sigma_i$ for all parameters of Case-A-2-3 (3), and $a_i - 2\sigma_i < x_i < a_i + 2\sigma_i$ for all feature parameters in all other cases in the experiment,

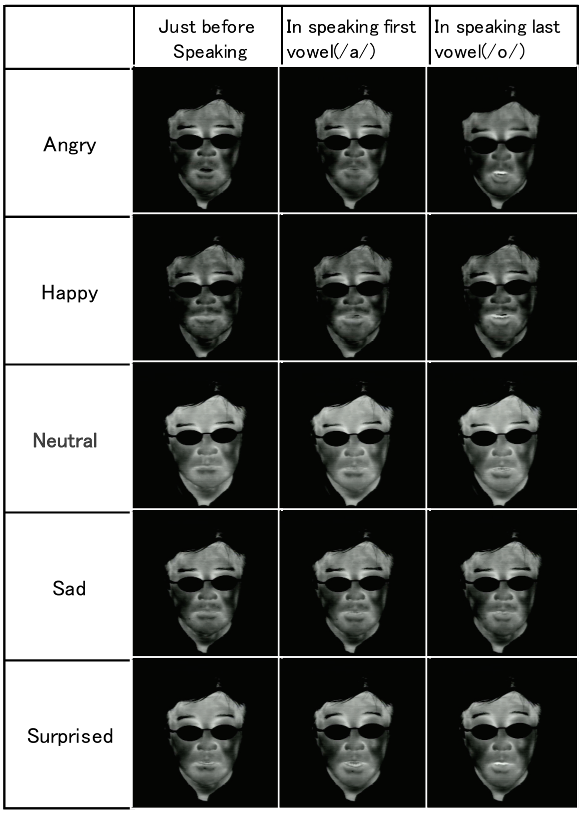

Fig. 3. Examples of thermal images of subject A captured on First_period_A and having each facial expression

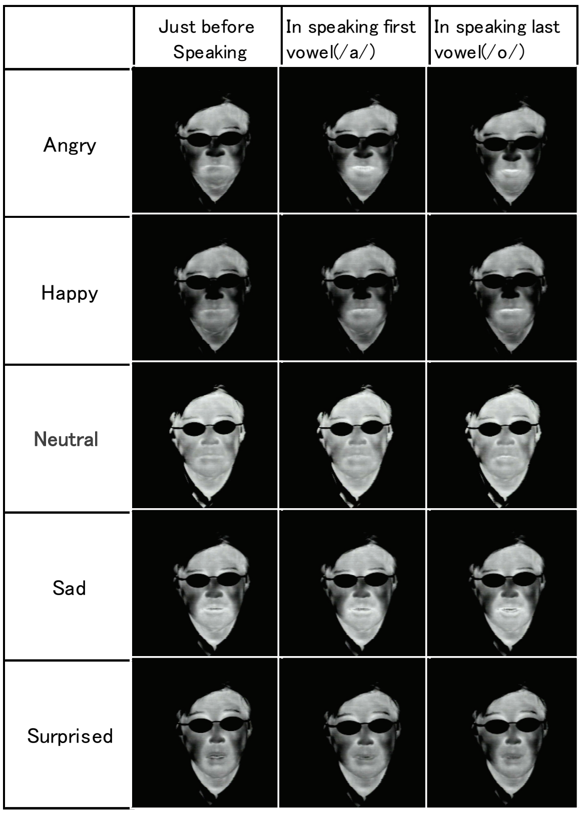

Fig. 4. Examples of thermal images of subject A captured on Second_period_A and having each facial expression

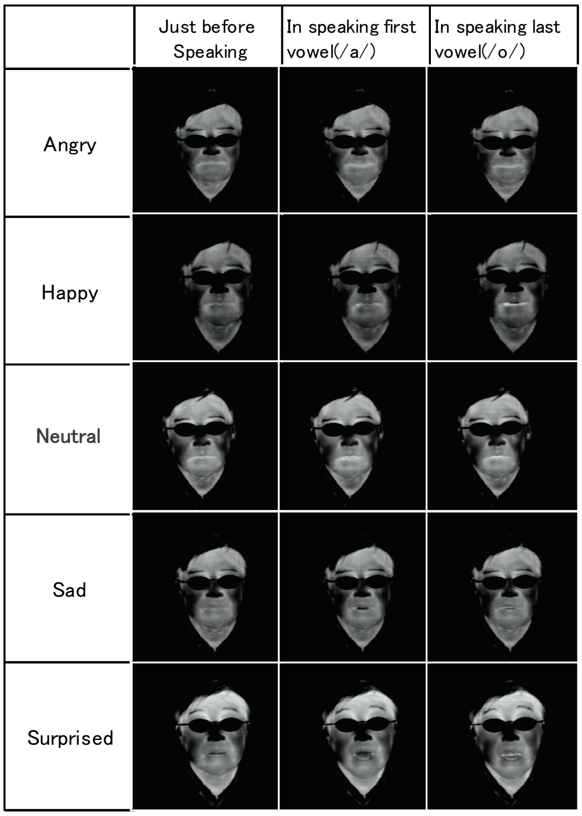

Fig. 5. Examples of thermal images of subject A captured on Third_period_A and having each facial expression

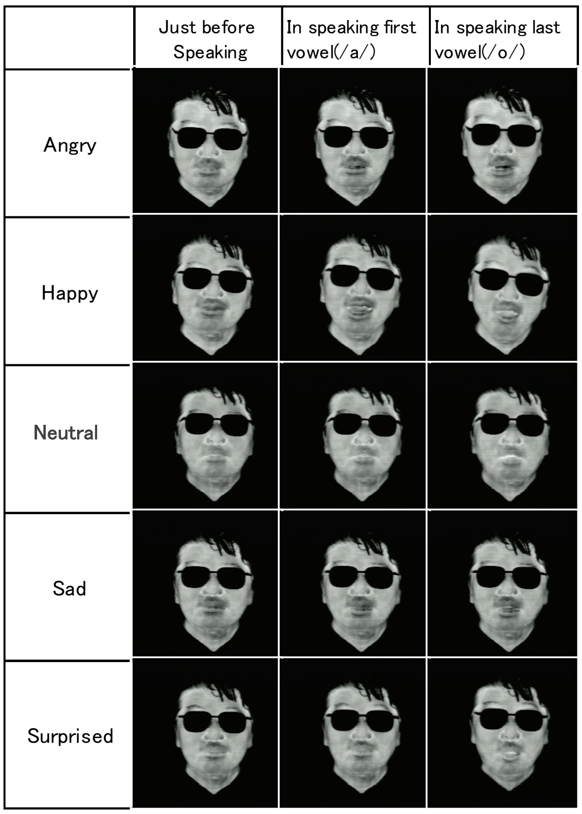

Fig. 6. Examples of thermal images of subject B captured on First_period_B and having each facial expression

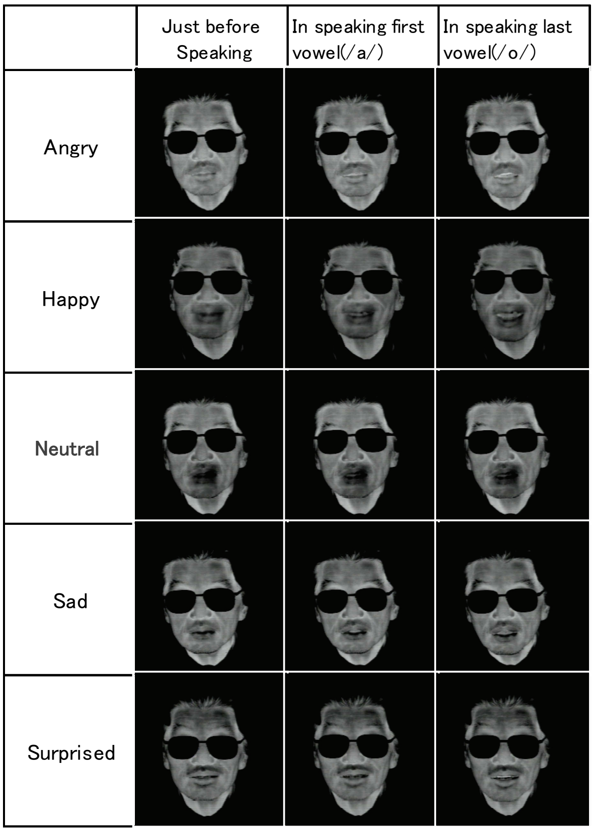

Fig. 7. Examples of thermal images of subject B captured on Second_period_B and having each facial expression

where x_1, x_2, x_3, x_4 were *nod*, *up*, *rotate*, and *lean*, and a_1, a_2, a_3, a_4 were their mean values, and $\sigma_1, \sigma_2, \sigma_3, \sigma_4$ were their standard deviation values, respectively. In Case-A-2-3 (3), the difference between the feature parameters obtained on Second_period_A and Third_period_A was so large that the feature parameter ranges for judging the front-view face were set to be wider than the ranges for the other cases. We assembled twenty samples as training data and ten or fewer samples as test data for each facial expression in each case, in which all facial expressions of test data for all subjects were judged as being exhibited on front-view faces by the method mentioned in Section 3.1. As one sample, we obtained three images at the timing positions of just before speaking and while speaking the phonemes of the first and last vowels. If Julius misrecognized the vowel of the test sample, the corresponding image was not used for facial expression recognition. We had four cases of misrecognition for the vowel(s): (1) no misrecognition for the first and last vowels, (2) misrecognition only for the first vowel, (3) misrecognition only for the last vowel, (4) misrecognition for both the first and last vowels. We prepared feature vectors of the training data in each of the four cases.

Table 1. Recognition accuracy of Case-A-1-2

(1) Training and test data: First_period_A

		Input facial expression		
		Happy	Neutral	Others
Output	Happy	100		23.3
	Neutral		90	
	Others		10	76.7

(2) Training and test data: Second_period_A

		Input facial expression		
		Happy	Neutral	Others
Output	Happy	80	10	
	Neutral		90	
	Others	20		100

(3) Training data: First_period_A,
Test data: Second_period_A

		Input facial expression		
		Happy	Neutral	Others
Output	Happy	100	10	86.7
	Neutral		90	
	Others			13

(4) Training data:
"happy" and "neutral"; Second_period_A,
"others"; First_period_A,
Test data: Second_period_A

		Input facial expression		
		Happy	Neutral	Others
Output	Happy	100		6.7
	Neutral		90	
	Others		10	93.3

Table 2. Recognition accuracy of Case-A-2-3

(1) Training and test data: Second_period_A

		Input facial expression		
		Happy	Neutral	Others
Output	Happy	80	10	
	Neutral		90	
	Others	20		100

(2) Training and test data: Third_period_A

		Input facial expression		
		Happy	Neutral	Others
Output	Happy	100		
	Neutral		50	
	Others		50	100

(3) Training data: Second_period_A,
Test data: Third_period_A

		Input facial expression		
		Happy	Neutral	Others
Output	Happy	0		
	Neutral		100	
	Others	100		100

(4) Training data:
"happy" and "neutral"; Third_period_A,
"others"; Second_period_A,
Test data: Third_period_A

		Input facial expression		
		Happy	Neutral	Others
Output	Happy	100		
	Neutral		100	
	Others			100

Table 3. Recognition accuracy of Case-B-1-2

(1) Training and test data: First_period_B

		Input facial expression		
		Happy	Neutral	Others
Output	Happy	100		
	Neutral		100	
	Others			100

(2) Training and test data: Second_period_B

		Input facial expression		
		Happy	Neutral	Others
Output	Happy	90		16.7
	Neutral		100	
	Others	10		83.3

(3) Training data: First_period_B,
Test data: Second_period_B

		Input facial expression		
		Happy	Neutral	Others
Output	Happy	100	70	100
	Neutral		20	
	Others		10	0

(4) Training data:
"happy" and "neutral"; Second_period_B,
"others"; First_period_B,
Test data: Second_period_B

		Input facial expression		
		Happy	Neutral	Others
Output	Happy	100		73.3
	Neutral		90	16.7
	Others		10	10

4.2 Results and discussion

Tables 1, 2, and 3 show the facial expression recognition accuracy for each case. The mean recognition accuracy on the condition of (3) in Tables 1, 2, and 3 was 58.1%, whereas that on the condition of (4) in Tables 1, 2, and 3 was 87.0%, which was slightly lower than the 90.7% obtained on the condition of (1) and (2) in Tables 1, 2, and 3. Updating the training data for the facial expressions of "happy" and "neutral" improved the accuracy of facial expression recognition by 28.9 % as the mean value.

5 CONCLUSION

We previously developed a method for facial expression recognition of a speaker using thermal image processing and a speech recognition system. In this paper, we propose a method for efficiently updating training data, such that the training data of only the facial expressions of "happy" and "neutral" were updated after an interval such as approximately three and a half years. By using the proposed method, the facial expressions of two subjects were discriminable with 87.0% accuracy for the facial expressions of "happy," "neutral," and "others" when they exhibited one of the intentional facial expressions of "angry," "happy," "neutral," "sad," and "surprised."

Acknowledgment

This work was supported by KAKENHI (22300077).

REFERENCES

[1] Yoshitomi Y, Kimura S, Hira E, and Tomita S (1996), Facial expression recognition using infrared rays image processing. Proc. of the Annual Convention IPS Japan, 2:339-340

[2] Yoshitomi Y, Kimura S, Hira E, and Tomita S (1997), Facial expression recognition using thermal image processing. IPSJ SIG Notes, CVIM103-3:17-24

[3] Yoshitomi Y, Miyawaki N, Tomita S, and Kimura S (1997), Facial expression recognition using thermal image processing and neural network. Proc. of 6th IEEE Int. Workshop on Robot and Human Communication pp.380-385

[4] Sugimoto Y, Yoshitomi Y, and Tomita S (2000), A method for detecting transitions of emotional states using a thermal face image based on a synthesis of facial expressions. J. Robotics and Autonomous Systems 31:147-160

[5] Yoshitomi Y, Kim SIll, Kawano T, and Kitazoe T (2000), Effect of sensor fusion for recognition of emotional states using voice, face image and thermal image of face. Proc. of 6th IEEE Int. Workshop on Robot and Human Interactive Communication pp.178-183

[6] Ikezoe F, Ko R, Tanijiri T, and Yoshitomi Y (2004), Facial expression recognition for speaker using thermal image processing (in Japanese). Trans. Human Interface Society 6(1):19-27

[7] Nakano M, Ikezoe F, Tabuse M, and Yoshitomi Y (2009), A study on the efficient facial expression using thermal face image in speaking and the influence of individual variations on its performance (in Japanese). J. IEEJ 38(2):156-163

[8] Koda Y, Yoshitomi Y, Nakano M, and Tabuse M (2009), Facial expression recognition for a speaker of a phoneme of vowel using thermal image processing and a speech recognition system. Proc. of 18th IEEE Int. Symp. on Robot and Human Interactive Communication pp.955-960

[9] Yoshitomi Y (2010), Facial expression recognition for speaker using thermal image processing and speech recognition system. Proc. of 10th WSEAS Int. Conf. on Applied Computer Science pp.182-186

[10]Fujimura T, Yoshitomi Y, Asada T, and Tabuse M (2011), Facial expression recognition of a speaker using front-view face judgment, vowel judgment, and thermal image processing. J. Artificial Life and Robotics, 16 in press

[11]Yoshitomi Y, Asada T, Shimada K, and Tabuse M (2011), Facial expression recognition of a speaker using vowel judgment and thermal image processing. J. Artificial Life and Robotics, 16 in press

[12]Kuno H (1994), Infrared rays engineering (in Japanese). Tokyo, IEICE 22

[13]Kuno H (1994), Infrared rays engineering (in Japanese). Tokyo, IEICE 45

[14]http://julius.sourceforge.jp/

The Seventeenth International Symposium on Artificial Life and Robotics 2012 (AROB 17th '12),
B-Con Plaza, Beppu, Oita, Japan, January 19-21, 2012

A system for synchronizing nods of a computer-generated character and a speaker using thermal image processing

Y. Yoshitomi, R. Kato, T. Asada and M. Tabuse

Graduate School of Life and Environmental Sciences, Kyoto Prefectural University,
1-5 Nakaragi-cho, Shimogamo, Sakyo-ku, Kyoto 606-8522, Japan,
E-mail: yoshitomi@kpu.ac.jp, t_asada@mei.kpu.ac.jp, tabuse@kpu.ac.jp

Abstract: The purpose of our study was to develop a system for communication between a speaker and a computer-generated (CG) character for making the speaker feel more peaceful and cheerful. In our system, the CG character can synchronize its nodding with a speaker's nodding by predicting the speaker's nodding angle. The CG character starts predicting it for nodding just after a human begins to speak, and the CG character stops nodding while maintaining a front-view face when the human maintains a front-view face and is silent. The CG character starts predicting it again for nodding when the human begins to speak again. The measured feature parameter is the input to a fuzzy algorithm system to obtain the nodding angle of the speaker in front of an infrared ray camera, and then a moving-average model is used to predict the nodding angle of the speaker.

Keywords: computer generated character, human computer interaction, sound analysis, thermal image.

1 INTRODUCTION

Nonverbal communication, such as a facial expression, a nod, or a hand gesture, is very important for reciprocal communication between humans. The realization of suitable communication between a human and a computer will help the development of computers, networking, and robots for people living alone. In an aging society such as that in Japan, the opportunity to talk diminishes for older people living alone. Embodied communication technologies have been developed using the relationship between speech and nodding [1]-[4]. In addition, several studies have investigated head gesture recognition [5]-[9]. However, in our daily lives, it is more difficult to take visual information from a person's head movements to synchronize the nod of a computer generated (CG) character compared with using audio information for the same purpose. The main reason for this difficulty is that the nuances of shade, reflection, and local darkness strongly influence the accuracy of head gesture recognition because of the inevitable changes in gray levels. In this study, an image registered by infrared rays, which display the thermal pattern of the face and neck, was used to develop a system of communication between a speaker and a CG character. To make the communication between the speaker and the CG character more natural, we have added some modules to detect the utterance of a human to our reported system [10].

2 BASIC PROCESSING FLOW

Fig. 1 shows the flow chart of our method. We use the fuzzy rules of the ratio of the horizontal length to the vertical length of the face region on the thermal image (hereinafter referred to as nod) and the face direction vector having a norm of 1 (hereinafter referred to as $\boldsymbol{n}$) [10]. Using the fuzzy algorithm [10] and the input of the nod , $\boldsymbol{n}$ is output as three estimated values of the elements of the vector and used for expressing the nodding of the CG character.

First, we obtain a pair of thermal images of the frontal and downward face directions of a subject to normalize the value of the nod as 1 in the case of the frontal direction, and to transform the value of the nod of the subject to that of a typical subject [10]. The normalization and the transformation of the value of the nod have been explained in detail in our previously reported paper [10]. Then, after capturing sound data to obtain constant thresholds, the sound data are judged by the thresholds to determine whether the subject has spoken an utterance. The preprocessing operation for measuring the nod includes segmentation with another constant threshold, erasing the isolated points, extracting the face area, standardizing the size of the face, and automatic segmentation [11], which are all performed for the thermal image [10]. Then, the nod is measured. To predict the nod of a human, we use the moving-average model [10]. Then, if the subject maintains a frontal face for longer than approximately 0.7 second, the CG character maintains a frontal face until the sound is judged to indicate an utterance. When the sound is judged as an utterance, the processing is restarted from the thermal image input. Otherwise, the processing is set back to the sound input and judgment of the utterance. The processing of utterance-driven nodding of the CG character is explained in detail in Section 3.

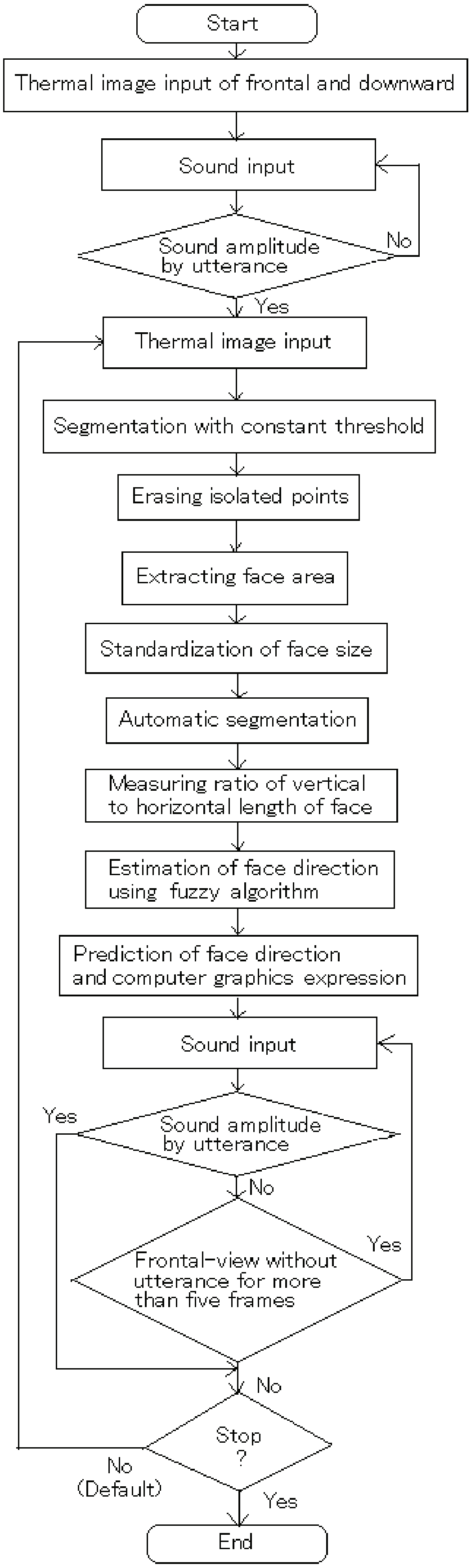

Fig. 1. Flow chart of our method

3 UTTERANCE-DRIVEN NODDING OF THE CG CHARACTER

The thresholds for the sound data value are set as $\bar{x}_s - 5\sigma_s$ and $\bar{x}_s + 5\sigma_s$, where $\bar{x}_s$ and σ_s express the average and the standard deviation, respectively, of the sound data value for one second under the condition of no utterance. The sound data for 0.5 second with an interval of approximately 0.2 second are performed to erase noises and then two series of samplings with an interval of 0.084 second are performed by using the method reported in [12]-[14]. Then, it is determined whether every sampled data fall within $[\bar{x}_s - 5\sigma_s, \bar{x}_s + 5\sigma_s]$, which is considered to be the range of no utterance. When at least one sampled datum has a value outside $[\bar{x}_s - 5\sigma_s, \bar{x}_s + 5\sigma_s]$, our system judges that the sound data contain an utterance. Once the sound data are judged as containing an utterance, the preprocessing operation for measuring the *nod* is started. When the subject maintains a frontal face for longer than approximately 0.7 second, the CG character maintains a frontal face until the sound is judged as an utterance. When the sound is judged as an utterance, the processing is restarted from the thermal image input. Otherwise, the processing is set back to the step of the sound input and the judgment of the utterance.

4 PREDICTION OF NODDING ANGLE

Fig. 2 shows the three-dimensional coordinate system used in this study. Here, $\boldsymbol{n} = (0,0,1)$ corresponds to the face direction when the face is facing the front. The three elements of $\boldsymbol{n} = (\alpha, \beta, \gamma)$ are used as consequent parameters in the fuzzy rules. Fig. 3 shows the downward rotation of the face. The *nod*, which is used as an antecedent parameter in the fuzzy rules, is measured as the ratio of the vertical length to the horizontal length of the face. To reduce the influence of hair style and throat region on the binary image, some image processing is performed [10].

The fuzzy rules are described in (1) [10]. The fuzzy algorithm is described in (2)–(5) [10].

$$\text{If } X = A_i \text{ then } Y_1 = B_{i1}, Y_2 = B_{i2}, Y_3 = B_{i3}, \quad (i = 1, 2, 3) \tag{1}$$

$$\mu^*_{B_{ij}}(Y_j) = W_i \mu_{B_{ij}}(Y_j), \ (i = 1, 2, 3, \ j = 1, 2, 3) \tag{2}$$

$$W_i = \mu_{A_i}(X^*), \ (i = 1, 2, 3) \tag{3}$$

$$B^0_j = \bigcup_{i=1}^{3} B^*_{ij}, \ (j = 1, 2, 3) \tag{4}$$

$$Y^*_j = \frac{\int \mu_{B^0_j}(Y_j) Y_j dY_j}{\int \mu_{B^0_j}(Y_j) dY_j}, (j = 1, 2, 3), \tag{5}$$

where X denotes the antecedent parameter; Y_1, Y_2, and Y_3 denote consequent parameters; A_i, B_{i1}, B_{i2}, and B_{i3} denote the corresponding fuzzy labels for X, Y_1, Y_2, and

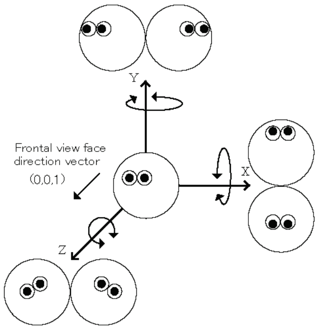

Fig. 2. Three-dimensional coordinate system [10]

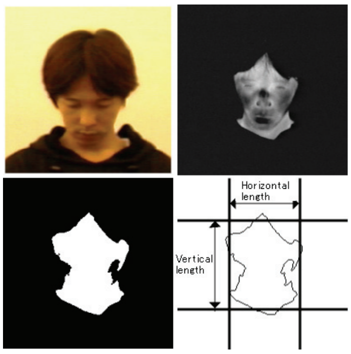

Fig. 3. Downward rotation [15]
Upper left: visible image, Upper right: thermal image, Lower left: binary image, Lower right: schematic diagram for explaining parameter *nod*

Y_3, respectively; W_i denotes the fitness value of the *i*-th rule to the input X^* for X; $Y_j{}^*$ denotes the output for Y_j. The integral in (5) is performed for the whole range of Y_j. In this study, X=*nod* , $Y_1=\alpha$, $Y_2=\beta$, $Y_3=\gamma$. We use three fuzzy rules to describe "frontal," "somewhat downward," and "downward." To determine the actual shape of each membership function, we use the measured values for the corresponding parameter [10]. For each measured value, we use an average for six people [10]. In addition, the value of *nod* is normalized by dividing by the value in the case of "frontal." We use a fuzzy algorithm for outputting $\boldsymbol{n}$ with the three fuzzy rules and the value of *nod* as the input. For integrating outputs from all the rules, we use (4) and (5). The nodding angle θ (°) which is calculated with γ and using the value of (6), where θ (°) is defined as follows.

$$\theta = 57.3\cos^{-1}\gamma \tag{6}$$

In this study, θ is positive in the case of downward rotation. Also in this study, we use (7), which was given in our previous study [10].

$$\begin{aligned}\hat{\theta}(i) = {} & 1.39\hat{\theta}(i-1) - 0.19\theta(i-2) - 0.24\theta(i-3) - 0.11\theta(i-4) \\ & + 0.053\theta(i-5) + 0.032\theta(i-6) - 0.043\theta(i-7) - 0.028\theta(i-8) \\ & + 0.024\theta(i-11) + 0.03\theta(i-10) + 0.12\theta(i-11) - 0.15\theta(i-12) \\ & - 0.005\theta(i-13) + 0.0073\theta(i-14) + 0.11\theta(i-15) \\ & + 0.031\theta(i-16) - 0.14\theta(i-17) - 0.041\theta(i-18) + 0.18\theta(i-19) \\ & - 0.056\theta(i-20) + 0.052\theta(i-21) - 0.18\theta(i-22) - 0.14\theta(i-23)\end{aligned} \tag{7}$$

where $\hat{\theta}(i)$ is the predicted value for $\theta(i)$, which is the nodding angle of the subject. We do not know the value of $\theta(i-1)$ at the timing position of $i-1$ because it took approximately 0.13 s to obtain $\theta(i-1)$ [10]. Accordingly, we used $\hat{\theta}(i-1)$ instead of $\theta(i-1)$, as described in (7).

5 FACE DIRECTION EXPRESSION USING COMPUTER GRAPHICS

We use the virtual reality modeling language (VRML) and Java for expressing the CG character. Fig. 4 shows examples of the CG character expressions of nodding. When $\hat{\theta}(i) < 5°$ in (7), $\hat{\theta}(i)$ is converted to 0° because the CG character having $\hat{\theta}(i) < 0°$ throws its head back and the character having the small value of $\hat{\theta}(i)$ fluctuating near 0° displays an unnaturally shaking attitude. Therefore, in this study, all nodding values of CG character are restricted to be above 5°.

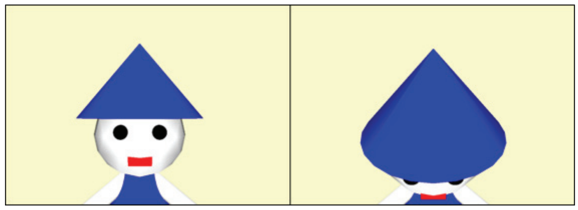

Fig. 4. CG expression of nodding [10]
Left: frontal view, Right: nodding at 30°

6 EXPERIMENT AND DISCUSSION

6.1 Experimental environment

The thermal image produced by a thermal video system (Thermo Shot F30, NEC Avio Infrared Technologies Co.) was transformed into a digital signal by an A/D converter (ADVC-300, Thomson Canopus) and the signal was input into a computer with an IEEE 1394 interface board (1394-PCI3/DV6, IO Data Device). We used a computer (Dell Optiplex 745, CPU: Intel Core 2 Duo 6600 2.4 GHz, main memory: 2 GB, and OS: Windows XP, Microsoft) (hereinafter referred to as PC1). For programming, we used Visual C++ 6.0 (Microsoft) and Java 2 SDK standard edition version 1.3, and VRML 2.0. The thermal image to be processed in the computer had a spatial resolution of 240 × 160 pixels and an 8-bit gray level at each pixel. The sound data captured by a wireless microphone (WM-1320, TOA Corporation) and a wireless tuner (WT-750B, TOA Corporation), were amplified by a blender (AT-PMX5P, Audio-technica) and transformed into a digital signal by the A/D converter, and the signal was input into a computer with the IEEE 1394 interface board (1394-PCI3/DV6, IO

Data Device). We used a second computer (Dell Optiplex GX620, CPU: Intel Premium 4 3.4 GHz, main memory: 1.99 GB, and OS: Windows XP, Microsoft) (hereinafter referred to as PC2). The CG character was expressed on PC2, which used Microsoft Internet Explorer 7.0 and Parallel Graphics Cortona VRML client Version 3.1.

PC1 was connected to PC2 by a cable to form a local area network. The thresholds for sound amplitude were decided in PC2. When the sound data were judged to be above the threshold as coming from the utterance, PC1 started a series of processing for measuring the *nod* just after receiving the signal from PC2 through the cable. Moreover, when the signal indicated that the subject was judged to have maintained a frontal face for longer than approximately 0.7 second, the signal was sent from PC1 to PC2 through the cable. Then, the CG character on PC2 maintained a frontal face until the sound was judged in PC2 as an utterance. When the sound was judged as an utterance in PC2, PC1 restarted the series of processing for measuring the *nod* from the thermal image input, just after receiving the signal from PC2 through the cable.

6.2 Conditions

The 11 subjects participating in the experiments consisted of the following: 2 males in their 20s, Subjects A and B; 3 females in their 20s, Subjects C, D, and E; 1 male in his 30s: Subject F; 1 female in her 30s, Subject G; 1 male in his 40s, Subject H; 1 female in her 50s, Subject I; 1 male in his 60s, Subject J; and 1 female in her 60s, Subject K. When the CG character synchronized its nodding to that of the subject during speaking, the subject's impression of the CG character's reaction was investigated with two kinds of experiments. The first experiment (hereinafter referred to as Experiment No. 1) was as follows. After watching a video digesting the soccer finals of the 2011 FIFA Women's World Cup for approximately five minutes, each subject verbally gave a summary and an impression of the video while in front of the computer monitor on which the CG character of our system was shown. The CG character synchronized its nodding to that of the subject.

The second experiment (hereinafter referred to as Experiment No. 2) was as follows. Each subject watched a video for approximately two minutes. The video was a comic skit by the Sandwich Man, a Japanese comedy duo. The subject sat in front of the computer monitor, on which the CG character of our system was shown. The CG character synchronized its nodding to that of the subject.

Fig. 5 shows a scene of Experiments No. 1 and No. 2. These two experiments were performed to investigate the

Experiment No.1 No.2

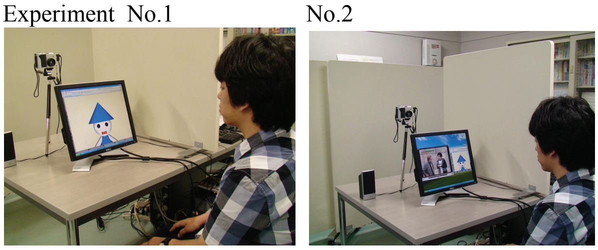

Fig. 5. Scenes of Experiments No.1 and No. 2

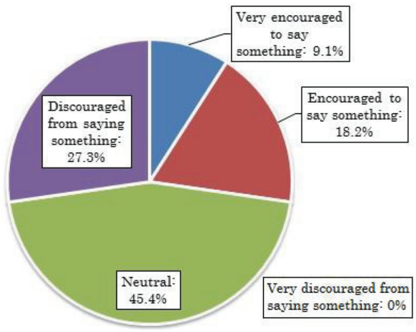

Fig. 6. Total impression of a CG character

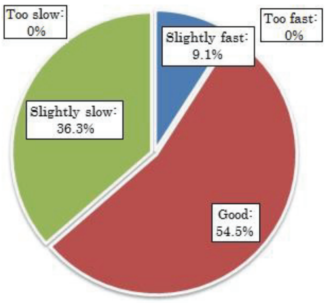

Fig. 7. Impression on speed of a CG character

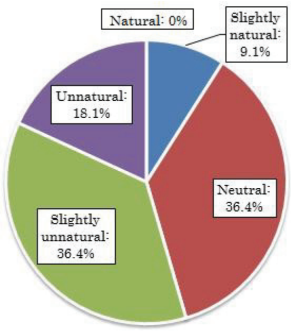

Fig. 8. Impression on reaction of a CG character

effect and the challenges of our system. After the two experiments, all subjects answered a questionnaire.

6.3 Results and discussion

Figs. 6-8 show the results of the questionnaire for Experiment No. 1. In the questionnaire, 27.3% (9.1% + 18.2%) of the subjects were encouraged to say something to our system, whereas an equal number (27.3%) were discouraged from saying anything to our system (Fig. 6). The movement speeds of the CG character were considered to be slightly low by approximately one-third of the subjects, as shown in Fig. 7. One of the reasons why the reaction of the CG character was considered to be unnatural or slightly unnatural by 54.5% of subjects, as shown in Fig. 8, was that the CG character only nodded and did not change its facial expression. Furthermore, when the hand of a subject appeared in the thermal image, the CG character nodded. This reaction could give the subject an unnatural impression of the CG character. At the initial stages of Experiments No. 1 and No. 2, the thermal images of the frontal and downward faces of each subject were captured for calculating the feature parameter *nod* of the subject. In our system, the degree of nodding of the CG character was obtained with the thermal images and the technique for converting the feature parameter *nod* of the subject to that of a standard subject [10]. Therefore, when the degree of nodding of the CG character was overly large for the initial downward face of the subject, the nodding of the downward face in the experiments became greater than that of the nodding of the subject. In the case of Subject I, this situation happened, resulting in the highest nodding angle (157.2°) of the CG character in Experiment No. 1. In contrast, the nodding angle of the CG character in Experiment No. 1 was within 60° for the other subjects. A ratio of the nodding angle that is more than 5° was assumed to express degree on communication between a subject and the CG character. The ratio seemed to depend on the subject. As shown in Table 1, the ratio was in the range of 0 to 53.4. Subjects B, D, I, and K, who had relatively small ratios of the nodding angle that is more than 5°, had the impression that the CG character moved slowly, and subjects B, D, and K had the impression that the total expression of the CG character was neutral. These impressions might be caused by the fact that the CG character could nod only when the subject nodded. However, subjects C, E, H, and J, who had relatively large ratios of the nodding angle that is more than 5°, had the impression that the CG character moved well, and subjects C, H, and J had the impression that the reaction of the CG character was unnatural or slightly unnatural. According to the comments of some subjects, the appearance and the static facial expression of the CG character did not give a natural impression.

Figs. 9-11 show the results of the questionnaire for Experiment No. 2. Because the sound from the loudspeakers of PC2 could influence the judgment of the utterance of a subject, the volume of the loudspeakers was kept at a low level. Therefore, some subjects commented that the voice of the video was not easy to hear. Most subjects concentrated their attention on the video of the comic skit while sitting still, so that the CG character maintained a frontal face. The ratio of the nodding angle that is more than 5° seemed to depend on the subject's personality and fell in the range of 0.9 to 78.7, as shown in Table 2. Subjects C, H, J, and K, who had a relatively large value of the ratio of the nodding angle that is more than 5°, had the impression that their attention was drawn to the CG character. According to the comments by some subjects, the CG character needed more kinds of appearances, reactions, facial expressions, and voices, so that their attention might be more drawn to the CG character, resulting in less attention to the video.

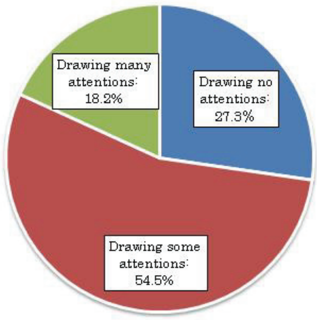

Fig. 9. Attention level to a CG Character

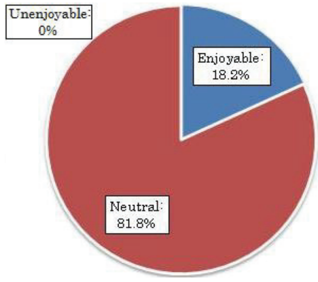

Fig. 10. Mental influence by a CG character

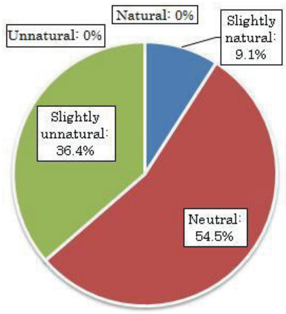

Fig. 11. Impression on movement of a CG character

Table 1. Ratio r of nodding angles above 5°

Subject	A	B	C	D	E	
r (%)	20.4	0.0	53.4	9.3	38.4	
Subject	F	G	H	I	J	K
r (%)	10.6	16.5	45.8	2.9	42.9	1.7

Table 2. The ratio r of nodding angle above 5°

Subject	A	B	C	D	E	
r (%)	18.1	9.8	51.0	35.1	19.6	
Subject	F	G	H	I	J	K
r (%)	16.8	29.2	46.2	0.9	41.0	78.7

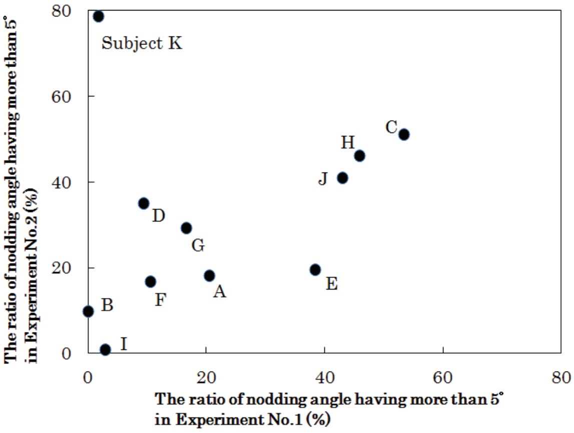

Fig. 12. Subject's personality expressed by the nodding of the CG character.

Fig. 12 shows subject's personality expressed by the nodding of the CG character. In the case of Subject K, she concentrated her attention on the video and sat almost still through Experiment No. 1, while she sat nodding to some extent in Experiment No. 2. In the cases of the other subjects, we found that the easiness of the interaction between the subject and the CG character depended on the subject's personality.

7 CONCLUSIONS

We developed a system for communication between a speaker and a CG character by using thermal image processing. The CG character synchronized its nodding with a speaker's nodding by predicting the speaker's nodding angle. The CG character itself had a great influence on the impressions of the user. In future work, we need to improve the CG character by considering the use of the system and the individual user's taste.

Acknowledgments

We would like to thank all the participants who cooperated with us in the experiments.

REFERENCES

[1] Watanabe T, and Yuuki N (1989), A voice reaction system with a visualized response equivalent nodding. Advances in Human Factors/Ergonomics, 12A:396-403

[2] Watanabe T, Okubo M, and Ogawa H (2000), An embodied interaction robots system based on speech. J. Robotics and Mechatronics, 12(2):126-134

[3] Watanabe T, Danbara R, and Okubo M (2002), InterActor: speech-driven embodied interactive actor. Proc. of 11th IEEE Int. Workshop on Robot and Human Interactive Communication, pp.430-435

[4] Watanabe T, Okubo M, Nakashige M, and Danbara R (2004), InterActor: speech driven embodied interactive actor. Int. J. Human-Computer Interaction, 17(1):43-58

[5] Zelinsky A, and Heinzmann J (1998), A novel visual interface for human-robot communication. Advanced Robotics, 11(8):827-852

[6] Choi HI, and Rhee PK (1999), Head gesture recognition using HMMs. Expert Systems with Applications, 17(3):213-221

[7] Nonaka H (2003), Communication interface with eye-gaze and head gesture using successive DP matching and fuzzy inference. J. Intelligent Information Systems, 21(2):105-112

[8] Lin CS, Ho CW, Chang KC, Hung SS, Shei HJ, and Yehd MS (2006), A novel device for head gesture measurement system in combination with eye-controlled human-machine interface. Optics and Lasers in Engineering, 44(6):597-614

[9] Jia P, Hu HH, Lu T, and Yuan K (2007), Head gesture recognition for hands-free control of an intelligent wheelchair. Industrial Robot Int. J., 34(1):60-68

[10] Kato R, Yoshitomi Y, Asada T, and Tabuse M (2010), A system for synchronizing the nods of a CG character and a human using thermal image processing and a moving-average model. J. of Artificial Life and Robotics, 15(1):10-16

[11] Yoshitomi Y, and Tanijiri T (2002), A machine for automatic segmentation of image and its method (in Japanese). Japan patent application 2002-344185

[12] Ikezoe F, Nakano M, Yoshitomi Y, and Tabuse M (2005), Facial expression recognition using thermal face image automatically acquired in speaking (in Japanese). Proc. of Human Interface Symposium 2005, pp.7-12

[13] Nakano M, Yoshitomi Y, and Tabuse M (2006), Efficient facial expression recognition using thermal face image in speaking and its application to analysis of individual variations (in Japanese). Proc. of Human Interface Symposium 2006, pp.1151-1156

[14] Nakano M (2008), (in Japanese). Robust facial expression recognition for various speakers, Master's thesis, Dept. of Environmental Information Graduate School of Human Environmental Sciences Kyoto Prefectural University, pp.1-70

[15] Yoshitomi Y, Tsuchiya A, and Tomita S (1998), Face recognition using dynamic thermal image processing. Proc. of 7th IEEE Int. Workshop on Robot and Human Communication, pp.443-448

The Seventeenth International Symposium on Artificial Life and Robotics 2012 (AROB 17th '12),
B-Con Plaza, Beppu, Oita, Japan, January 19-21, 2012

Music recommendation aimed at improving recognition ability using collaborative filtering and impression words

C. Koro[1], Y. Yoshitomi[2], T. Asada[2] and S. Yoshizaki[3]

[1]ISI Software Corp., 4-6-17 Honmachi, Chuo-ku, Osaka 541-0053, Japan
[2]Graduate School of Life and Environmental Sciences Kyoto Prefectural University,
[3]Faculty of Life and Environmental Sciences Kyoto Prefectural University,
[2,3]1-5 Nakaragi-cho, Shimogamo, Sakyo-ku, Kyoto 606-8522, Japan,
E-mail: yoshitomi@kpu.ac.jp, t_asada@mei.kpu.ac.jp

Abstract: Music therapy to improve recognition ability may be more effective when the favorite music of each person is adopted. A method is proposed that combines collaborative filtering and music recommendation based on impression words. In the proposed method, once the recommendation process using collaborative filtering is terminated because the number of users is zero in the reference user list of users with the same preference of recommended music, the second recommendation process finds the most similar music from the scores of impression words, so that music is successfully recommended from music not previously recommended. In experiments, 12 users rated 52 songs in a textbook database of songs for elementary schools. The number of recommended songs by the proposed method was 10 per user, whereas that of collaborative filtering was 6.25 per user. The recommendation accuracy of the proposed method was 68.3%, whereas that of collaborative filtering was 66.9%.

Keywords: Recognition ability, Music therapy, Collaborative filtering, Impression word, and Music recommendation.

1 INTRODUCTION

In Japan, the average age of the population has been increasing, and this trend is expected to continue. Recently, music therapy has been used for improving the recognition ability of people, particularly older people. Music therapy may be more effective when the favorite music of each person is adopted. We have been developing the technology of music recommendation aimed at improving recognition ability [1]. When using the reported method [1], it is not easy to recommend much music to a user. To overcome this difficulty in the present study, we propose a music recommendation method that combines collaborative filtering and our music recommendation process based on impression words. We evaluate the proposed method by using children's songs, which tend to be familiar to older people.

2 MUSIC RECOMMENDATION METHOD USING IMPRESSION WORDS

We use ten pairs of impression words (Table 1). Table 2 shows an example of user scores for one pair of impression words (quiet - busy). The original user scores consisted of seven levels, which are transformed to those having three levels, as shown in Table 2. In a music database, 52 songs are assigned scores $i\,(-3 \le i \le 3)$ for each pair of impression words evaluated by subjects. Fig. 1 shows a flowchart of the music recommendation based on impression words. When music not recommended to a user has the same values except "0" as that for at least one recommended music having a high evaluation on the three-

Table 1. Pairs of impression words [2]

quiet - busy
bracing - heavy
easy - uneasy
cheerful - gloomy
refreshing - depressing
happy - sad
comforting - harmful
calm - elevating
clean - dirty
magnificent - superficial

Table 2. Scores for pairs of impression words quiet – busy

Score	Three-level score	impression
3	-1	very busy
2		busy
1	0	slightly busy
0		neutral
-1		slightly quiet
-2	1	quiet
-3		very quiet

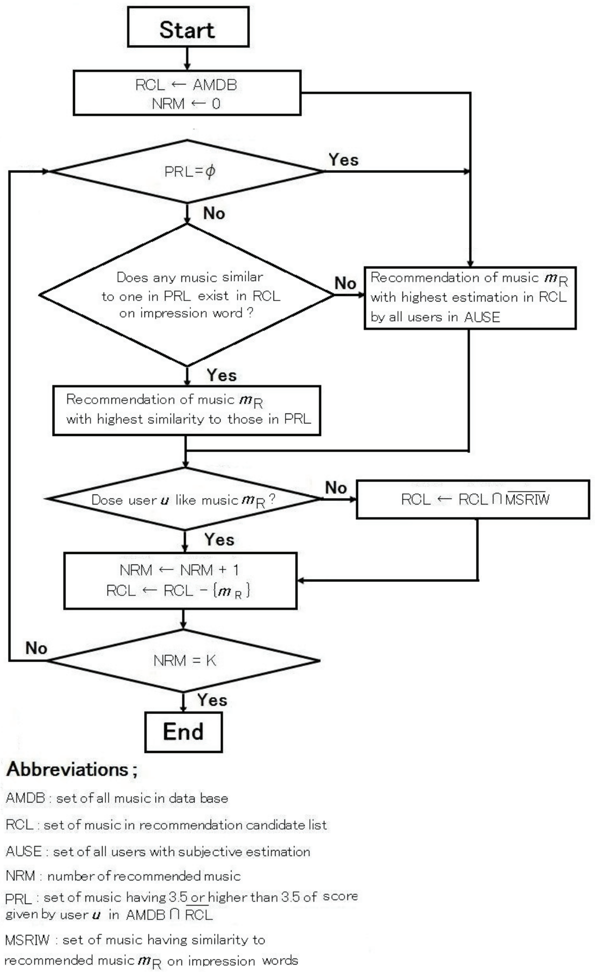

Fig. 1. Flowchart of music recommendation by using impression words

level score for at least five impression words, the music is treated as having a positive evaluation by the user. In contrast, when music not recommended to the user has the same scores except "0" as that for another music just recommended to the user and having a low evaluation on the three-level score for at least seven impression words, the music is assumed as having a negative evaluation by the user. In Fig. 1, when none of the music not recommended receives a positive evaluation by the user, another recommendation is performed by using the estimations of all users whose subjective estimations are stored in the database. It is expressed by "with highest similarity" in Fig. 1 that the music has the highest ratio of the same three-level scores except "0" as that of other music recommended to the user and having a positive evaluation among the music not recommended to the user. In Fig. 1, the "set of music with a similarity to the recommended music based on impression words" (MSRIW) is decided by using at least seven impression words in the case of a negative evaluation.

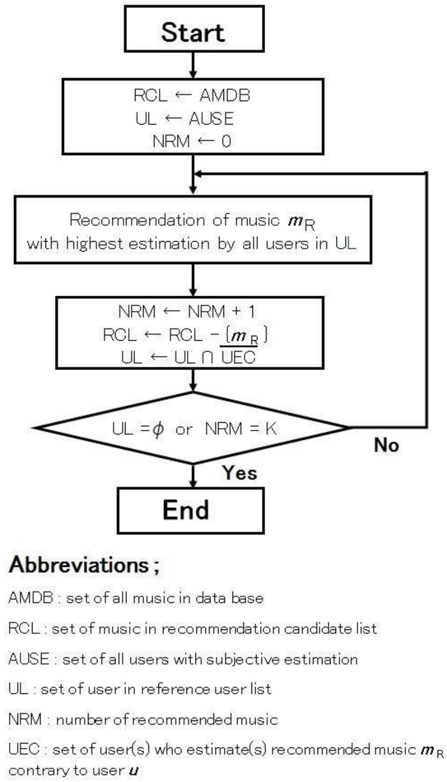

Fig. 2. Flowchart of music recommendation by collaborative filtering

3 PROPOSED METHOD

Figs. 2 and 3 show two music recommendation methods, Method 1 and Method 2, respectively. Method 1 (Fig. 2) is collaborative filtering only and it is compared with Method 2 (Fig. 3), which is the proposed method that combines collaborative filtering and our music recommendation process based on impression words (Fig. 1). In the proposed method, the recommendation process using collaborative filtering is terminated when the number of users is zero in the reference user list of users showing exactly the same evaluation for the recommended music as that of the subject up to that moment. Then, the recommendation process performs by finding out the most similar music, from the viewpoints of three-level scores except "0" on impression words, to that successfully recommended among music not yet recommended. Our system recommends music stored in the database to user u, as shown in Fig. 3. Both the recommendation process using collaborative filtering and that using the proposed method are terminated when the number of recommended music reaches the upper limit K, which was decided previously.

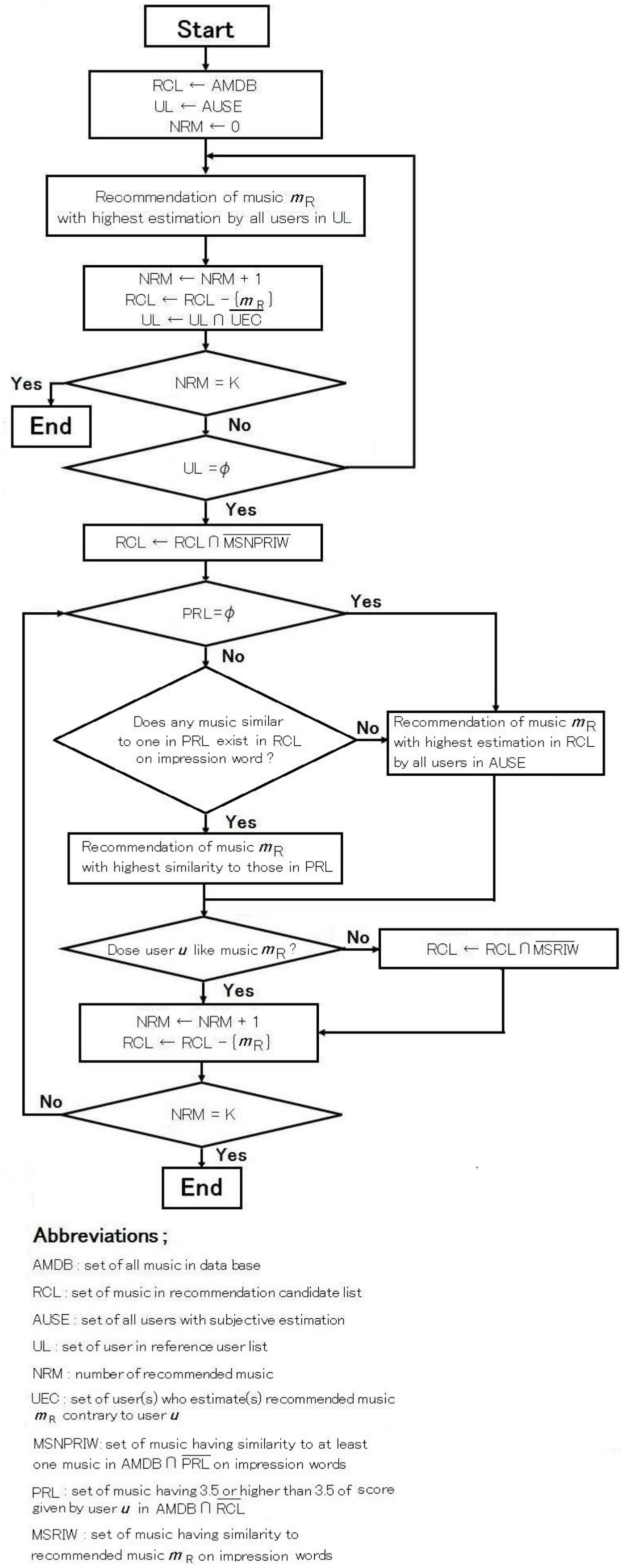

Fig. 3. Flowchart of music recommendation of the proposed method

In the flowcharts of Method 1 and Method 2, shown in Figs. 2 and 3, the estimation of user u for music m_R is set as 1 when the score of user u for music m_R is 4 or 5 ("slightly favorite" or "favorite"), and it is set as 0 when the score is 1 to 3 ("dislike," "slightly dislike," or "neutral").

4 PERFORMANCE EVALUATION

4.1 Conditions

Because older people tend to prefer children's songs [3], we selected a CD described as an anthology of older songs enjoyed by older people with dementia [4], and then we selected 52 songs on the CD that were also included in a music textbook database for elementary schools [5]. To evaluate the music recommendation methods, all 52 of the selected songs in the database were assigned scores s $(1 \le s \le 5)$ by 12 users of the following ages: teens: 1, twenties: 6, fifties: 5. We used 10 as the value of K in Figs. 2 and 3. For evaluating the two music recommendation methods described in Section 3, we chose each of the 12 users as user u and put the remaining users in the reference user list UL described in Figs. 2 and 3. Each user was user u one time and in the reference list 11 times. In addition, all 52 of the selected songs in the database were assigned scores i $(-3 \le i \le 3)$ for each pair of impression words by five subjects of the following ages: twenties: 3, forties: 1, fifties: 1. Of the five subjects, one, who was in his fifties, was the same as the user who assigned scores s . The average of scores i obtained by the five subjects for each pair of impression words was used as scores i for the performance evaluation. The 15 songs having the values except "0" as the three-level score for one impression word at most were not recommended in the process of recommendation based on impression words because they did not have distinct characteristics from the viewpoints of impression words. Then, we obtained the result of the music recommendation for each user for each method described in Section 3.

4.2 Results and discussions

As an example, Table 3 shows the process of the music recommendation for user 3. As shown in Table 3, Method 2 tended to recommend more music than did Method 1. Fig. 4 shows the performance of the two methods. The number of recommended songs by the proposed method (Method 2) was 10 per user, whereas that of only collaborative filtering (Method 1) was 6.25 per user. The recommendation accuracy of the proposed method was 68.3%, whereas that of only collaborative filtering was 66.9%. In the collaborative filtering (Method 1), the recommendation process was terminated at the rate of 10/12, because the number of users staying in the UL became zero (Fig.4(b)).

In contrast, in the proposed method (Method 2), the recommendation process was performed until the number of recommended songs reached the upper limit K decided previously. As a result, as compared with only using the collaborative filtering (Method 1), we could increase the number of recommended songs while keeping the accuracy of the recommendation by joining the recommendation based on the impression words to the collaborative filtering.

Table 3. Music recommendation process for user 3

[Method 1]

Order	Recommended music No.	Acceptance	User No. in UL
1	52	○	1,2,4,5,7,8,9,10,11,12
2	41	○	1,2,4,5,7,8,9,10,11,12
3	17	×	4
4	50	○	4
5	49	○	4
6	44	×	none

[Method 2]

Order	Recommended music No.	Acceptance	User No. in UL
1～6	Same as Method 1		
7	26	○	
8	21	○	
9	36	×	
10	5	○	

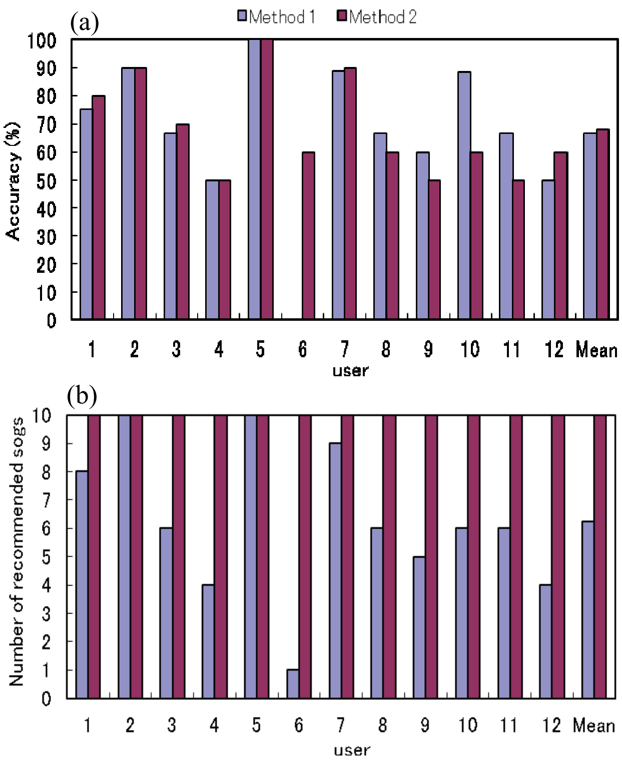

Fig. 4. Performance of music recommendation methods: (a) recommendation accuracy, (b) number of recommended songs

5 CONCLUSION

We propose a music recommendation method that combines collaborative filtering and music recommendation based on impression words. We showed that the proposed method was more effective for music recommendation than the method of only collaborative filtering when used on a music database composed of children's songs. In future work, we will increase the number of users who evaluate the music in the database and apply the proposed method to people who are much older and/or have a cognitive impairment.

Acknowledgments

We would like to thank Associate Professor M. Tabuse of Kyoto Prefectural University for his valuable advice and support. We would also like to thank all the participants who cooperated with us in the experiments.

REFERENCES

[1] Konishi H and Yoshitomi Y (2011), Music recommendation system aimed at improving recognition ability. Proc. of 16th Int. Symposium on Artificial Life and Robotics. pp.241-244

[2] Ohta K and Kumamoto T (2002), A design of music adjective pairs based on linguistic knowledge (in Japanese) IPSJ SIG Notes 40:97-102

[3] Takahashi T (1997), Research report on songs familiar to people advanced in years (in Japanese) Journal of Japanese music therapy associate 15(1):68-75

[4] Akahoshi T (2009), Good old anthology enjoyable for people advanced in years and troubled with dementia. Kirara shobo (in Japanese)

[5] Music textbook database for elementary school by Kanagawa prefectural education center (in Japanese); http://kjd.edu-ctr.pref.kanagawa.jp/daizai_music/

The Seventeenth International Symposium on Artificial Life and Robotics 2012 (AROB 17th '12),
B-Con Plaza, Beppu, Oita, Japan, January 19-21, 2012

The PSP Low Layer Practice Support used on The Android Personal Digital Assistant

Daisuke Yamaguchi[1], Ayahiko Niimi[2]

1:Toin University of Yokohama, 1614 Kurogane-cho, Aoba-ku, Yokohama, JAPAN
2:Future University-Hakodate, 116-2 Kamedanakano-cho, Hakodate, Hokkaido, JAPAN
yamaguti@intlab.toin.ac.jp

***Abstract*: In this paper, we propose the PSP Practice Support System that we realize record-keeping sup port of flame work performing data acquisition of process flow offered in PSP in other Android carry ing end with a software development environment using based on the Multiagent technologies. It is th ought that we can tie that we come true with an Android mobile terminal when we perform the conv enience that we don't affect to a software development environment and reference of a document if d ated consciousness of flow. So, We can be conscious of process flow in every environment with develo pment by this system can transmit programming to specific human among many software processes us ing Agent's technology. Applying the proposed method to a personal process remove task, a flexible pr ogramming for quality of software.**

Keywords: Personal Software Process, Agent System, Personal Digital Assistant, Android Platform support

I. INTRODUCTION

Software architecture has emerged as an important sub discipline of software engineering [1]. PSP support system is built using this. Moreover, We think that the data inputted can acquire software development process by sorting out using a user action record table [2].

In this paper, the Personal Software Process (PSP) practice support system that we realize record-keeping support of flame work performing data acquisition of process flow offered in PSP in other Android carrying end with a software development environment using based on the Multiagent technologies [3]. It is thought that we can tie that we come true with an Android mobile terminal when we perform the convenience that we don't affect to a software development environment and reference of a document if dated consciousness of flow. So, We can be conscious of process flow in every environment with development by this system can transmit programming to specific human among many software processes using Agent's technology. Intelligent agents and multiagent systems are one of the most important emerging technologies in computer science today [4]. Multiagent systems deal with coordinating intelligent behavior among a collection of autonomous agents. Emphasis is placed on how the agents coordinate their knowledge, goals, skills, and plans jointly to take action or to solve problems. Constructing the multiagent systems is difficult [5,6].

Applying the proposed method to a personal process remove task, a flexible programming for quality of software.

II. Android Personal Digital Assistant

The PSP data has record on the framework prescribed by the aforementioned individual specific exercise in support system. Therefore, Record time has been take many form to conducts based on the PSP base-line framework. Support System should be record processes by different development, quality control and large forms. So, it will be not very worried about an activity recording a process form that dealt in an experienced developer of the PSP and working-out of software for a long time. However, it increases that kept record of a form about becomes vague of that still pressed by everyday various works. In order to perform accurate record, their needs for support system automate and reduce the work measurement process.

It content is missing records, which it does not exactly the plan. Therefore, support systems is to record all the work, record and share information, and record information with other differences between them, what do you consider that characterize the individual.

This will be an important resource to support the ability to provide the information necessary to improve the process. However, to be commissioned to present the contents of any process improvement is not help from the Android devices. The recorded information itself, are working will consider process to improvement. An important aspect of this device, by allowing all times and there is early detection of leaks of personal records.

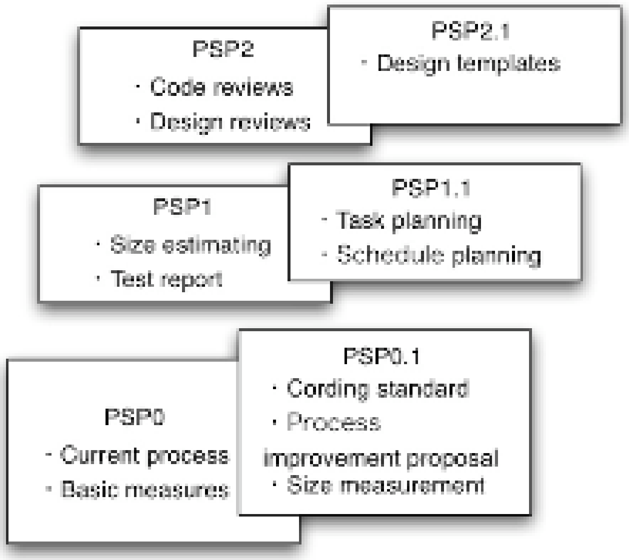

Fig.1. PSP Process Evolution

III. PSP (Personal Software Process)

The PSP is a self-improvement process that helps you to control, manage, and improve the way you work. It is a structured framework of forms, guidelines, and procedures for developing software [2]. Properly used, the PSP provides the data you need to make and meet commitments, and it makes the routine elements of your job more predictable and efficient.

The PSP's sole purpose is to help you improve your software engineering skills. It is a powerful tool that you can use in many ways. Rather than using one approach for every job, you need an array of tools and methods and the practiced skills to use them properly. The PSP provides the data and analysis techniques you need to determine which technologies and methods work best for you. PSP write several program using the evolving process shown Figure 1.

The PSP is not a magical answer to all of your software engineering problems, but it can help you identify where and how you can improve. However, you must make the improvements yourself. PSP0 and PSP0.1 hierarchy include introduces process discipline and measurement. PSP1 and PSP1.1 hierarchy include introduces estimating and planning. PSP2 and PSP2.1 hierarchy include Introduces quality management and design. Team Software Process exists over the PSP hierarchies.

So, This any measure record to support agent consider with using this Agent Learner expanded of PSP support. A person engaging in a person who experienced PSP and software development for many years is not very worried about a form record-keeping work.

Record keeping is vague, and what is performed of a person pressed by a work still increases. Necessity to perform automatically is important in a soldier, remission of an activity and process assay to record an activity precisely.

IV. Digital Assistant for Android mobile tools at Software Estimate Efficiency based on Agent Techniques

In this section, explain assistant of Software Estimate used to the Android Digital Assistant based on internal Agent Learner for Intelligent Agent. Intelligent Agent techniques give connects in other Intelligent Agent record data on PSP. Hence, that Intelligent Agent put the Agent Learner on necessary thoughts in Multi-agent [7].

In the PSP, engineers use the time recording log to measure the time spent in each process phase. In this log, they note the time they started working on a task, the time when they stopped the task, and any interruption time. For example, an interruption would be a phone call, a brief break, or someone interrupting to ask a question. By tracking time precisely, engineers track the effort actually spent on the project tasks. Since interruption time is essentially random, ignoring these times would add a large random error into the time data and reduce estimating accuracy.

Since the time it takes to develop a product is largely determined by the size of that product, when using the PSP, engineers first estimate the sizes of the products they plan to develop. Then, when they are done, they measure the sizes of the products they produced. This provides the engineers with the size data they need to make accurate size estimates. However, for these data to be useful, the size measure must correlate with the development time for the product. While a line of code (LOC) is the principal PSP size measure, any size measure can be used that provides a reasonable correlation between development time and product size. It should also permit automated measurement of actual product size.

1. Software Estimate Design of Agent Learner

The Software Design Estimate kept in Intelligent Agent. Figure 2 shows the Agent internal Data, PSP database and user logs connection modules in other communication method. In this case, Intelligent Agent supports the PSP time and size (LOC: Line of Code) measures record to user manipulation data. Intelligent Agent used to learning Control on internal database for AiD.

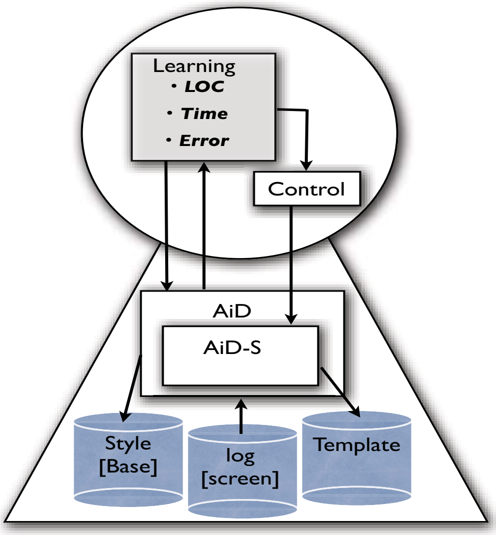

Fig.2. The AiD Data transferred from Agent Learner to action logs

2. The Estimating Probe Method of Agent Software Design

The Probe Method guides user in using historical data to make estimates. With estimated proxy size *E*, Intelligent Agent can calculate the projected program size *P* and did total estimate development time. The parameters β_0 and β_1 are used in the following equation to calculate projected added modified size:

Projected Added & Modfied size $P = \beta_0 + \beta_1 \cdot E$ (1)

When two sets of data are strongly related, Intelligent Agent can use the linear regression method to represent that relationship. This means that linear regression is often appropriate. The parameters β_0 and β_1 are calculated from user historical data.

3. The Android Digital Assistant Interface of Intelligent Agent Software Design

As for the Android terminal unit, it process take possible for archiving to convey the information that it is necessary in the PSP activity through a screen to an internal intelligent agent. Information to convey has memorized the time that activity content in form archiving was really performed.

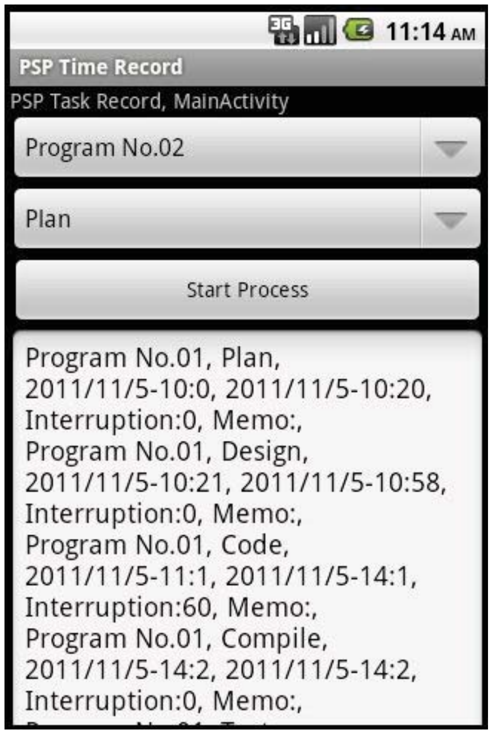

Fig.3. The Android Terminal Unit for first phase on the Agent Interface

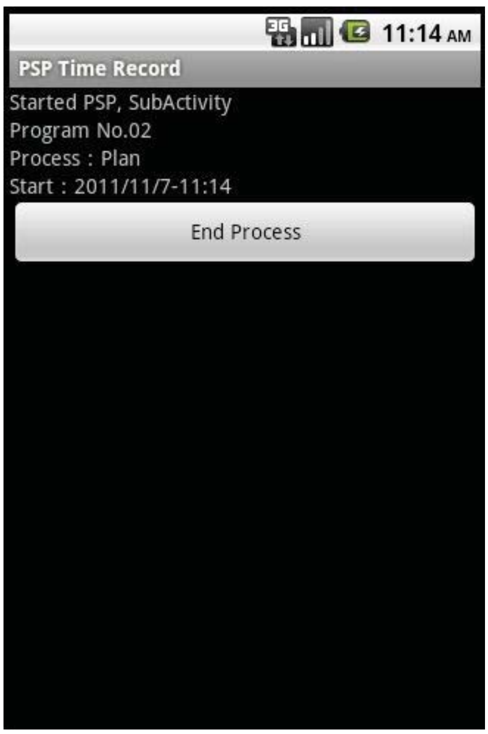

Fig.4. The Android Terminal Unit for second phase on the Agent Interface

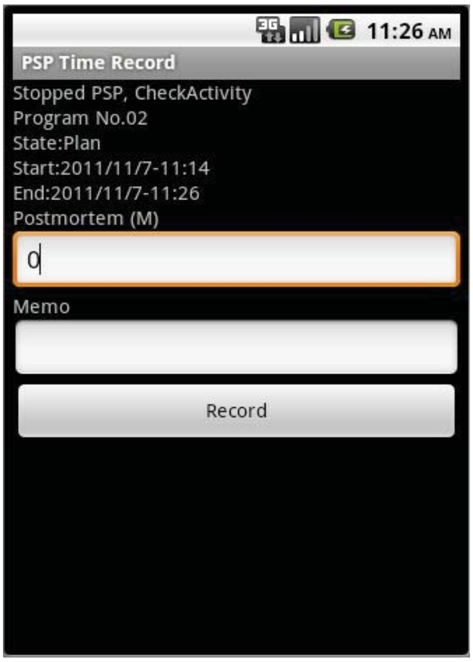

Fig.5. The Android Terminal Unit for third phase on the Agent Interface

When "Record" button be push the Android terminal unit Screen, in order of Figure 3, Figure 4, Figure 5, and activity changes screen design. Because a screen design changes, button of a new context format appears. Agent express current activity contents sequentially whether it has been work-in-process hereby whether it is activity record keeping.

An optional category have take the problems number, work-in-process practicing now. This work-in-process consists of all seven items that the Agent put activity break in as well as six items established in PSP. About activity cutoff, I step over a day and can record an activity.

Actually, I am recordable like Figure 4 when the Agent stepped over a day. A work to perform in this interface, work-in-process is recorded by the operation that it is easy only pushing it in button sequentially.

VI. CONCLUSION

In this research we were analyses PSP Practice Support System used to of flame work performing data acquisition of process flow offered in PSP by the Android terminal unit Interface. We were able to evidence user software working process data. We create agent learner data in real time work data beside with agent running and wrote PSP Practice process type and problem number.

For future works, we will consider methods used on record time data for agent learner in machine learning and user experience. It is necessary for us to consider only a clock through this system about the cause that a description error to be generated by human error.

Future versions of PSP Practice Support System based on Android Terminal Unit record of error type code or fact process from error message of compiler and executer to test pattern data. But, This model will show at the system in a more natural, unscripted scenario, involving multiple parts in addition to other forms of process and error type phenomenon. Now, This system Interface cannot edit by the record data that evidence and work in a process task on Agent Learning data. We consider to support system by what cannot edit record data activity archiving be able to offer the usability as evidence to the intelligent agent techniques.

REFERENCES

[1] Paul Clements, Felix Bachmann, Len Bass, David Garlan, James Ivers, Reed Little, Paulo Merson, Robert Nord, Judith Stafford (2010), Documenting Software Architectures SECOUND WDITION, Addison-Wesley
[2] Watts S. Humphrey (2005), PSP - A Self Improvement Process for Software Engineers, Addison-Wesley
[3] Daisuke Yamaguchi, Ayahiko Niimi and Muneo Takahashi (2010), Improvement of a Software Estimate Efficiency Centered PSP Practice Support System Using Multiagent Techniques, The Fifteenth International Symposium on Artificial Life and Robotics 2010, pp.857-860
[4] Weiss, G. (1999), Multiagent Systems, A Modern Approach to Distributed Artificial Intelligence, the MIT Press
[5] Abul, O., Polat, F., and Alhajj, R. (2000), Multiagent Reinforcement Learning Using Function Approximation, IEEE Transaction on systems, man, and cybernetics-part c: application and reviews, Vol. 30, No. 4, pp. 485-497.
[6] Khosla, R., and Dillon, T. (1997), Engineering Intelligent Hybrid Multi-Agent Systems, Kluwer Academic Publishers
[7] Carles Sierra, JohnThangarajah, Lin Padgham and Michael Winikoff (2007), Designing Institutional Multi-Agent Systems, AOSE 2006, LNCS 4405, PP.84-103

The Seventeenth International Symposium on Artificial Life and Robotics 2012 (AROB 17th '12),
B-Con Plaza, Beppu, Oita, Japan, January 19-21, 2012

Development of Game Based Learning Features in Programming Learning Support System

Eiji Nunohiro, Kotaro Matsushita, Kenneth J. Mackin, and Masanori Ohshiro

Tokyo University of Information Sciences, 4-1 Onaridai, Wakaba-ku, Chiba 265-8501, Japan
(Tel: 81-43-236-1292; Fax : 81-43-236-1292)
nunohiro@rsch.tuis.ac.jp

Abstract: In this research, a programming learning support system incorporating game based learning is proposed. The aim of the game based learning approach is to stimulate and sustain the motivation of the learner during programming training. In the developed system, a puzzle solving interface to programming training and a competitive scoring system was implemented to incorporate game based learning. The proposed system was applied to an actual college programming course to verify the effectiveness of the proposed system. Finally, future works based on the results are discussed.

Keywords: E-learning, Programming, Game Based learning.

1 Introduction

The field of study of students choosing to take courses in educational institution of computer and information sciences has broadened, to include not only computer science fields but also the arts fields including Web design, game, and multi-media. In such learning environments where students with different backgrounds take the same course, one method is to divide the course into classes depending on the initial skill or experience of the students. Even in such cases, depending on the teaching staff resources, each classroom may have as many as 50 students. In larger classes, it becomes more difficult to care for each individual student, and slower students fall behind, while advanced students become dissatisfied with the slow speed of progress. In either case, the student's motivation to study deteriorates. This has lead to the increased interest in improving the motivational aspects of learning in computer related courses.

For previous research on programming learning systems, a method which automatically creates fill-in-the-blanks style program source code problems from instructions embedded in the program code has been reported[1]. On the other hand, research on motivational learning methods for programming education based on the ARCS model[2] has also been reported[3]. But there have been no previous reports on implementation and evaluation of a motivational learning model in an actual e-learning system for programming training.

In this research, we proposed a game-based learning feature for a programming learning support system, in order to realize a learning environment which stimulates and sustains the learning motivation.

In this paper, we describe the overview of the proposed game-based programming learning support system and the features of game-based learning. The proposed system was applied to an actual college programming course to verify the effectiveness of the proposed system, and future works based on the results are discussed.

2 Purpose of the programming learning support system

From past experience, the low motivation of learners who have difficulty in programming is strongly related to stumbling in the early stages of programming training. We considered that a game-based programming learning environment that focuses on program structure recognition and training would stimulate and sustain the learning motivation as well as improve programming skill. From this, we proposed a programming training system with game based learning features to stimulate and sustain motivation for beginners and slow learners in programming. We aimed at developing a learning environment that can expect the following learning effects.

(a) To introduce programming training through a gaming experience in order to stimulate interest in programming.

(b) To improve understanding of programming structures and control flow through a gaming experience, instead of focusing on the language syntax or particular algorithms.

In order to provide a learning environment to achieve both (a) and (b), we proposed the following development goals to realize game-based programming learning features;

(1) Puzzle-based interface to realize a gaming experience programming environment.

(2) Building confidence in learners by presenting exercises that matches the learner's proficiency.
(3) Visual stimulation and effective breaks can be introduced in the learning process by displaying animation and illustrations.
(4) Sense of accomplishment can be given to the learner by displaying the study history and the acquired training contents.
(5) Implement a competing environment to strengthen the gaming experience in programming problem solving.
(6) Improve the satisfaction of learners by providing real-time progress monitor to teachers, allowing teachers to quickly find and support learners who fall behind or repeatedly error on particular problems.

3 Feature of the programming learning support system

We have already reported [4][5][6] about CAPTAIN (Computer Aided Programming Training And Instruction), a puzzle-based programming training system with motivational learning methods, in which learners create programs similarly to solving a puzzle game. In this research, we developed programming learning functions described in Section 2 and implemented these functions in CAPTAIN ver.3 (CAPTAIN3), based on the previous version of CAPTAIN. The main features of CAPTAIN3 are shown in Table 1 and the content of each function is described below.

3.1 Puzzle style program exercise function

This function implements puzzle-based interface in order to introduce programming training through a gaming experience. Programming training from the viewpoint of program structure comprehension and program flow comprehension can be compared to solving a 2-dimensional puzzle by logically laying out the puzzle pieces. From this standpoint, this function breaks up a program into puzzle pieces, and the user must reconstruct the program by selecting the correct program puzzle pieces in the correct order. Fig.1 shows a screenshot of the puzzle interface of CAPTAIN3 during programming exercise.

3.2 Automatic generation of programming exercise function

This function automatically creates puzzle pieces from the problem source code according to the progress and comprehension level of the learner using genetic algorithm. In CAPTAIN3, new functions to automatically insert incorrect and unnecessary puzzle pieces were added.

Table 1 main function of CAPTAIN3

No	main function	contents
1	Puzzle style program exercise function	This function offers the puzzle based interface for program exercise.
2	Automatic generation of programming exercise function	This function automatically creates puzzle pieces from the problem source code according to the progress and comprehension level of the learner.
3	Animation display function	This function displays animation and the illustration.
4	Learning history display function	This function displays individual learning history with the progress report and the accuracy rate.
5	Competitive learning function	This function displays the learner's relative level compared to other learners in the same group.
6	Learning progress monitoring function	This function displays every learner's progress status for the instructor.

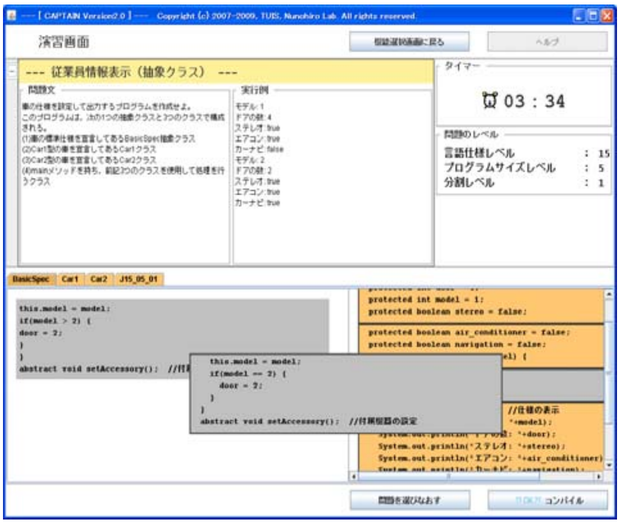

Fig.1 Programming training screenshot

3.3 Animation display function

This function aims to give effective breaks and to keep the motivation by using the visual stimulus such as display of the animation depending on the learner's exercise result and progress report in the programming training.

3.4 Learning history display function

This function aims to give the sense of accomplishment to the learner. The learner can confirm the exercise which were answered correctly and correct answer rate on the progress monitoring screen.

3.5 Competitive learning function

This function visually shows the learner's progress and the learner's relative level compared to other learners in the same group, in order to stimulate the learner's attention and motivation.

3.6 Learning progress monitoring function

This function displays the learning progress status of each learner in real-time. The instructor can monitor the progress of each learner in the classes using this information. Fig.2 shows the instructor's monitoring screen displayed as a Web application. The monitoring program retrieves updated progress status of all learners from the database on a short time interval, and displays the progress visually on a Web browser.

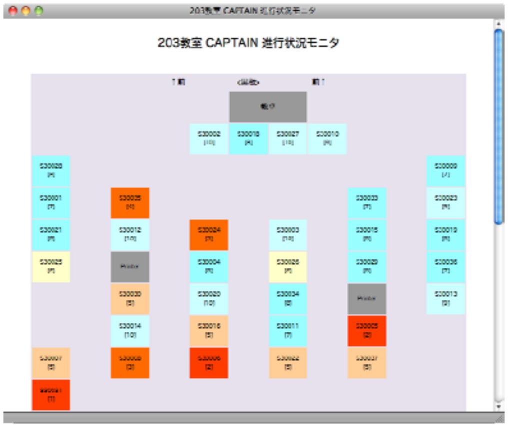

Fig.2 Progress monitoring Web application

4 Application and evaluation of Captain system

4.1 Application

CAPTAIN3 was applied in a Java programming course for 2nd year students in the Department of Information Systems, Tokyo University of Information Sciences. In this course, the students were divided into 3 classes (advanced, intermediate, introductory) according to the results of a preliminary test. CAPTAIN3 was applied in the introductory class. The applied programming course is a full year course consisting of 90 minutes lecture and 90 minutes lab per week.

4.2 Evaluation

In order to evaluate the learning effect by using CAPTAIN3, we executed the same progress evaluation test (5 mid-term exams and 1 final exam) for 3 classes (advanced, intermediate, introductory) and evaluated the results. An anonymous questionnaire was taken in the introductory class. The evaluation period is from April in 2010 to January in 2011 and the evaluation was applied to student data (20 students in the advanced, 28 students in the intermediate and 15 students in the introductory classes) who had attended all mid-term and final exams.

The test problems were classified into the following five skill groups, and the maximum total points for each test were 35 points.

(a)Basic knowledge for Java programming
(b)Program creation (fill in the blanks without answer group)
(c)Program analysis (execution results analysis without answer group)
(d)Program creation (fill in the blanks with answer group)
(e)Program reconstruction (program reconstruction using program pieces with answer group)

One of the main goals of CAPTAIN3 is to assist the learner in understanding programming structures and flow control through a base based interface. Therefore, we expected that the effect of training using CAPTAIN3 will be most visible in skill group (e). Following this expectation, we evaluated the effect of CAPTAIN3 for the following two cases.

case 1: total point for evaluation test (skill group (a) to (e)) : maximum 35 points
case 2: points for problems in skill group (e) : maximum 5 points

Table 2 shows statistical test results for case1. Table 2 shows that a significant difference was noted at 5% significance level between the advanced/intermediate and introductory classes in both the confirmation test 1 and the final test, meaning that there is still a significant difference in skill between the advanced/intermediate class and introductory class after the final exam. However, Fig.3 shows the difference of average score for these tests between the advanced/intermediate and introductory classes has become smaller.

Table 3 shows statistical test results for case2. Table 3 shows that for test 1, the difference of the average score between advanced/intermediate and introductory classes was also large and a significant difference between classes was shown by the t-test. But for the final exam, the difference of the average score between classes became smaller and a significant difference could not be seen in the result by the t-test. Fig.4 also shows that the difference of the average score between classes has become smaller.

These results showed that the introductory class using CAPTAIN3 was able to narrow the skill difference between the more advanced 2 classes.

Table 2 Comparison of advanced/ intermediate and introductory classes (case 1)

class		confirmation test 1 (6/2)	final test (1/26)
advanced/intermediate (CAPTAIN3 not used)	Average	29.7	29.1
introductory (CAPTAIN3 used)	Average	15.6	21.1
t-test between classes	*t* value	8.80	4.33
	significance	P<0.05	P<0.05

Table 3 Comparison of advanced/ intermediate and introductory classes (case 2)

class		confirmation test 1 (6/2)	final test (1/26)
advanced/intermediate (CAPTAIN3 not used)	Average	4.0	4.3
introductory (CAPTAIN3 used)	Average	1.7	3.8
t-test between classes	*t* value	6.03	1.59
	significance	P<0.05	none

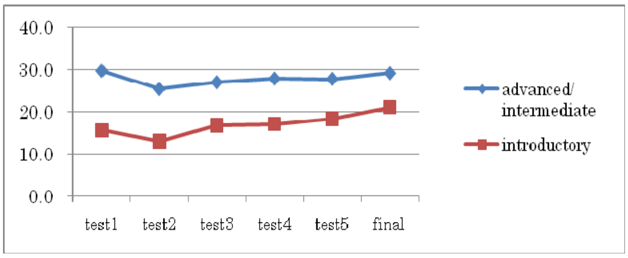

Fig.3 Transition of average for case1

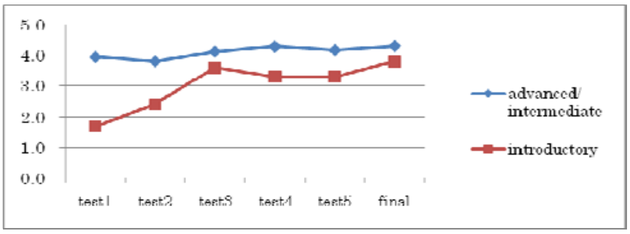

Fig.4 Transition of average for case2

5 Conclusion and future works

In this paper, we developed game based learning features in a programming learning support system, to offer a learning environment that stimulates and sustains the motivation of the learner during programming training. The proposed system was applied to an actual college programming course to verify the effectiveness of the proposed system.

From the result of transition of the average score for mid-term and final exams, we concluded that the developed CAPTAIN system was effective in the viewpoint that the student showed interested in programming. Moreover, from the result of case 2, it can be seen that this system was effective for the purpose of understanding the structure and processing flow of the program. However, from the result of t-test for case 1, it could not be established that the proposed method had a positive effect in improvement of the programming skill, and improvement of the learning features and revision on method of applying the proposed system in the programming course is necessary.

Acknowledgments

This research was supported by The Ministry of Education, Culture, Sports, Science and Technology (MEXT), Grant-in-Aid for Scientific Research(C) (21500953).

References

[1] Sugumura Akira, Mine Tsunenori, Shoudai Takayoshi "Automatic Exercise Generating System That Dynamically Evaluates both Students' and Questions' Levels(Learning Support)", IPSJ Journal, Vol.46, No.7, pp.1810-1818 (2005)

[2] Principles of Instructional Design (2005), Robert M. Gagne, Walter W. Wager, Katharine C. Golas, John M. Keller, Wadsworth Pub Co.

[3] Wenyong WANG, Mitsuru IKEDA, Fengrong LI (2007), Proposal and Evaluation of the "Motivation-Oriented" Teaching Method in Programming Education, *Japan Society for Educational Technology, Vol.31, No.3, pp.349-357 (in Japanese).*

[4] E.Nunohiro, K.J.Mackin, M.Ohshiro, K.Matsushita, K.Yamasaki (2007), Implementation of a GA driven programming training support system, *The 12th International symposium artificial life and robotics, pp.517-522*.

[5] E.Nunohiro, K.Matsushita, K.J.Mackin, M.Ohshiro, K.Yamasaki (2008), Design and development of a puzzle based programming learning support system with genetic algorithm, *Transactions of Japanese society for information and system in education, vol.25, No.2, pp.207-213 (in Japanese).*

[6] Yuji Yoneyama, Kotaro Matsushita, Kenneth J. Mackin, Masanori Ohshiro, Kazuko Yamasaki, Eiji Nunohiro (2008), Puzzle Based Programming Learning Support System with Learning History Management, *The 16th International Conference on Computers in Education (ICCE2008), pp. 623-627*

The Seventeenth International Symposium on Artificial Life and Robotics 2012 (AROB 17th '12),
B-Con Plaza, Beppu, Oita, Japan, January 19-21, 2012

Visualization of Satellite Data for Educational Use

Kotaro Matsushita, Shun Koshikawa, Taito Endoh, Jong G. Park
Takashi Yamaguchi, Kenneth J. Mackin and Eiji Nunohiro
Tokyo University of Information Sciences, Chiba 265-8501, Japan
(Tel: 81-43-236-1349, Fax: 81-43-236-1349)

matusita@rsch.tuis.ac.jp

Abstract: Tokyo University of Information Sciences maintains and distributes MODIS (Moderate Resolution Imaging Spectroradiometer) data as part of the research output for Frontier project. We have published many studies using MODIS data and many other researchers use them for their researches. On other hand, it is possible to use MODIS satellite data, especially NDVI (Normalized Difference Vegetation Index) for education. But it is necessary to visualize the data clearly for many users. In this research, we proposed a method to visualize satellite data for education and processed real MODIS data using the proposed method.

Keywords: MODIS, NDVI, Visualization, Education

1 INTRODUCTION

The Moderate Resolution Imaging Spectroradiometer (MODIS) is a scientific instrument aboard Terra satellite and Aqua satellite launched by NASA. MODIS data are used for various environmental researches.

Tokyo University of Information Sciences receives MODIS data and provides the processed data to university and research institutes. We have reported various researches [1][2][3][4][5] using MODIS data. Furthermore, it is possible to use satellite data for education. But in this case, satellite data should be displayed in the form that is easy to understand.

Recently, there has been more computer graphics (CG) teaching materials employed in classes for elementary and secondary education than in the past [6][7][8]. Applying CG teaching material in class can stimulate the interest of the students through visual effects, and improve the comprehension and learning experience.

In this research, we investigate a method to visualize satellite data for education, especially junior high school and high school students. Using proposed method, MODIS data, especially NDVI (Normalized Difference Vegetation Index), can be displayed simple 3D CG. Furthermore, we processed real NDVI by proposed method.

2 MODIS data and NDVI

2.1 MODIS data

The moderate resolution imaging spectroradiometer (MODIS) is a scientific instrument launched into Earth orbit by NASA in 1999 on board the Terra Satellite, and in 2002 on board the Aqua satellite. Terra's orbit around the Earth is timed so that it passes from north to south across the equator in the morning, while Aqua passes south to north over the equator in the afternoon. Terra MODIS and Aqua MODIS allow the viewing of the entire Earth surface every 1-2days. MODIS capture data in 36 spectral bands, or group of wavelengths. Moderate-resolution remote sensing allows the quantifying of land-surface type and extent, which can be used to monitor changes in land cover and land use for extended periods of time. These data are used to monitor and understand global dynamics and the processes occurring on the land, and in the oceans and the lower atmosphere.

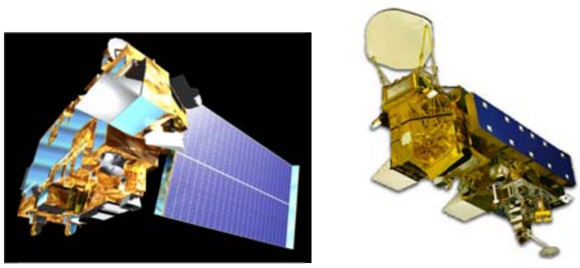

(a) Terra (b) Aqua

Fig. 1. Terra and Aqua satellites

2.2 NDVI

The normalized difference vegetation index (NDVI) is an index that provides a standardized method of comparing vegetation greenness between satellite images. NDVI is defined as follows,

$$NDVI = (RED - NIR) / (RED + NIR) \qquad (1)$$

where RED is visible red reflectance, and NIR is near infrared reflectance.

3 Visualization of NDVI

3.1 Development environment

In this research, we developed a simple system to change NDVI data to simulated color NDVI images and 3-D NDVI images. The system configuration is shown in Fig.2. Data used for visualization are read from the satellite database. The system was developed using Java language and Java 3-D for the 3-D API. Processing results of the system is output on the display and written to files.

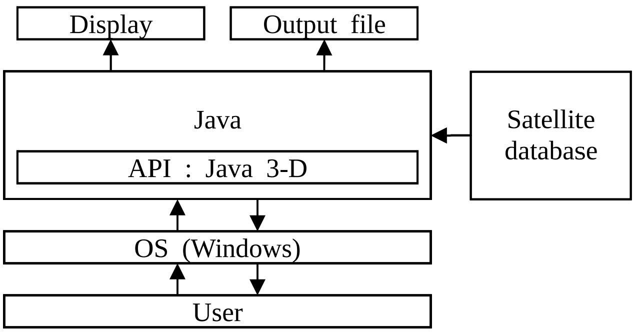

Fig. 2. System Configuration

3.2 Visualization Procedure

Visualization procedure is shown in Fig.3.

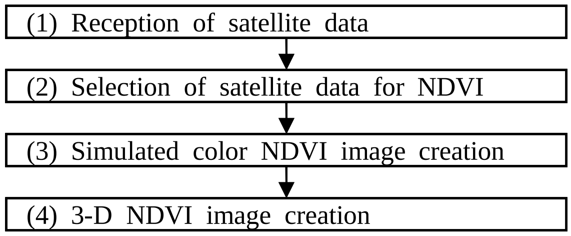

Fig. 3**.** Visualization procedure

(1) Reception of satellite data

Satellite data are received by the satellite data reception system at Tokyo University of Information Sciences. The satellite data are stored to the satellite database.

(2) Selection of satellite data for NDVI

Data necessary for calculation of NDVI are selected from the received MODIS data. The NDVI value can be calculated by formula (1). The satellite data reception system developed at the authors' university already supports NDVI creation, and NDVI values can be retrieved directly as a grayscale NDVI image. Examples of grayscale NDVI images are shown in Fig.4.

(a) Hokkaido region

(b) Kyusyu region

Fig. 4**.** Examples of grayscale NDVI images

(3) Simulated color NDVI image creation

The system changes grayscale NDVI images into simulated color NDVI images. The system maps high NDVI values to gradations of green to visualize vegetation areas, maps low NDVI values to gradations of brown to visualize non-vegetation areas, and maps extremely low NDVI values close to 0 to blue to visualize water covered areas. Examples of simulated color images are shown in Fig.5.

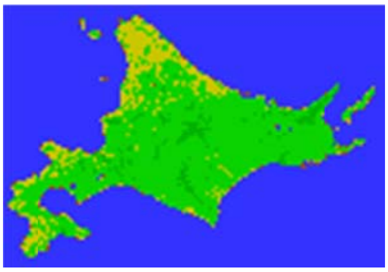

(a) Hokkaido region

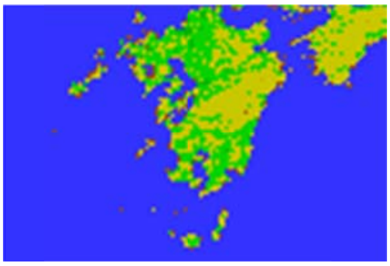

(b) Kyusyu region

Fig. 5. Examples of simulated color NDVI images

(4) 3-D NDVI image creation

3-D NDVI image is generated by treating NDVI values as height to the z-axis direction. Furthermore, the viewpoint can be changed by dragging the mouse so that it is easy to understand the results. Examples of 3-D NDVI images with different viewpoints are shown in Fig.6.

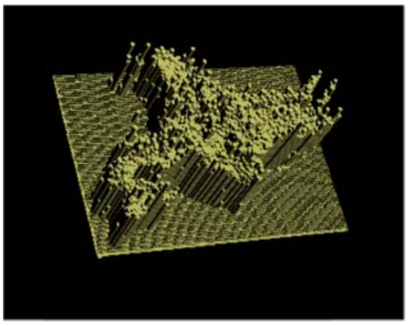

(a) Hokkaido region

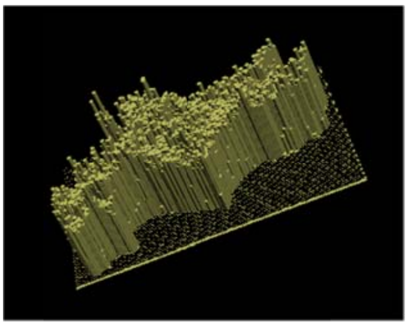

(b) Hokkaido region

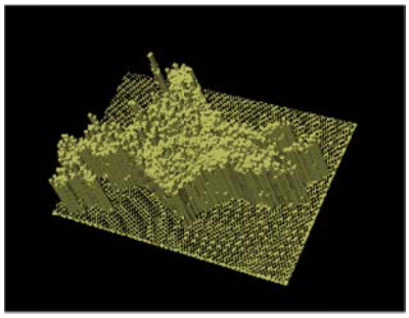

(c) Hokkaido region

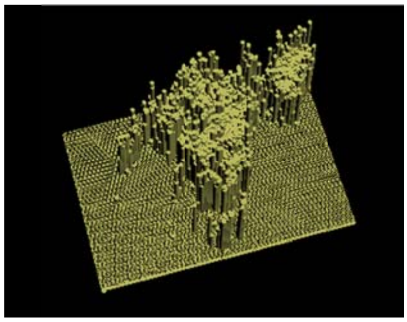

(d) Kyusyu region

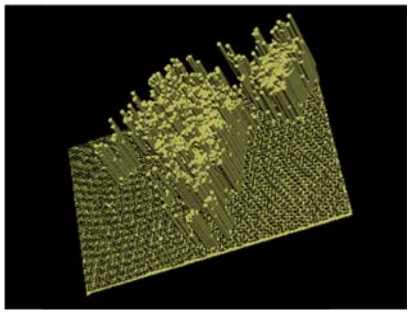

(e) Kyusyu region

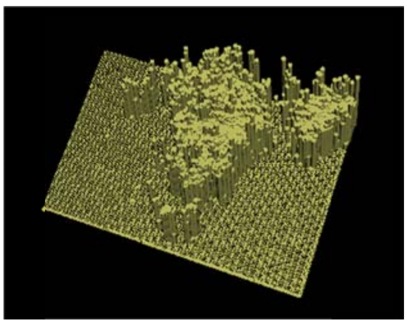

(f) Kyusyu region 3

Fig. 5. Examples of 3-D NDVI images

4 Educational use

We developed a prototype system to be used as educational material in science or social studies classes. The system allows a simplified visual presentation of complex satellite data, assisting the learner to understand the subject matter visually, improving the educational effect.

But to support various educational uses, it is necessary to display color 3-D NDVI images, as well as to support views for displaying representative values for given areas or districts and regions.

5 CONCLUSION

In this paper, the authors presented a visualization method of satellite data for educational use. In this research, we developed a system which simplifies the display of complex satellite data for junior high school and high school students.

The system is still a prototype, so we need to investigate necessary functions and implement them in the system. The system is scheduled to be implemented as a Web application to facilitate deployment in educational environments.

For future works, the authors plan to improve display of 3-D NDVI image and man machine interface, and evaluate the learning effect.

ACKNOWLEDGEMENTS

The authors wish to thank Dr. Yukio Yanagisawa, Dr. Masao Igarashi of Nihon University, Dr. Keitaro Hara and Dr. Ichio Asanuma of Tokyo University of Information Sciences for their valuable advice and collaboration.

This research was supported by the Research project of Tokyo University of Information Sciences for the sustainable development of economic and social structure dependent on the environment in eastern Asia.

REFERENCES

[1] J. G. Park, M. Saito, K. Hara, et al. (2011), Effective Band Combination for Landcover Classification Accuracy using MODIS Data, Journal of International Information Institute, vol.13, no.3(A), pp.709-717

[2] A. Nakamura, J. G. Park, K. Matsushita, et al. (2011), Development and evaluation of satellite image data analysis infrastructure, Proceedings of the 16th Artificial Life and Robotics, pp.439-442

[3] T. Yamaguchi, K. Kishida, Eiji Nunohiro, et al. (2010), Application of Artificial Neural Network for Paddy Field Classification using Spatiotemporal Information, Journal of International Information Institute, vol.13, no.3(B), pp.967-974

[4] T. Yamaguchi, K. Kishida, E Nunohiro, et al. (2010), Artificial Neural Network Paddy Field Classifier using Spatiotemporal Remote Sensing Data, Journal of Artificial Life and Robotics, Springer Japan, vol.15, no.2, pp.221-224

[5] E. Nunohiro, J. G. Park, J. Mackin, et al. (2009), Development of satellite data analysis system, Proceedings of the 5th International Conference on Information, pp.143-146

[6] K. Matsushita, T. Fukuda, K. J. Mackin, et.al (2010), Development of Teaching Materials Using 3D Computer Graphics in Mathematics Classes, Proceedings of the 15th World Conference on E-Learning in Corporate, Government, Healthcare, and Higher Education, pp.2649-2653

[7] K. Matsushita, H. Nishida, S. Furuya, et al. (2008), Development of Teaching Materials using 3-Dimensional Computer Graphics Animation in Elementary Education, Proceedings of the 19th International Conference on Society for Information Technology and Teacher Education, pp.3489-3493ngs of the 16th Artificial Life and Robotics, pp.439-442

[8] K. Mouri, M. Suzuki, T. Yasuda, et al. (2002), Production and Practical Use of Teaching Materials based on 3-dimensional Computer-graphics Technology with Collaboration in Education of Astronomy, The journal of Information and Systems in Education , vol.1, no.1, pp.3513-3516

The Seventeenth International Symposium on Artificial Life and Robotics 2012 (AROB 17th '12),
B-Con Plaza, Beppu, Oita, Japan, January 19-21, 2012

Programming Learning Support System with Competitive Gaming Using Monitoring and Nicknames

Masanori Ohshiro[1], Kotaro Matsushita[1], Kenneth J Mackin[1], and Eiji Nunohiro[1]

[1]Tokyo University of Information Sciences, 4-1 Onaridai, Wakaba-ku, Chiba, Chiba, 265-8501, Japan
(Tel: +81-43-236-4667, Fax: +81-43-236-4667)
(ohshiro@rsch.tuis.ac.jp)

Abstract: The authors have developed a programming training system CAPTAIN (Computer Aided Programming Training And INstruction) and have applied the system in an actual programming course. In this training system, learners create programs similarly to solving a puzzle game as follows. Each complete runnable program is fragmented randomly into a few lines by the system. Users must sort the lines as an original source program. The system compile the source program sorted by the user and check the correctness of it. In such a learning support system, it is important that the learner can view one's learning progress objectively. Furthermore, if the learning progress could be compared with those of other learners, competition will occur to stimulate the learner's motivation. In our previous paper, we proposed and implemented the real-time monitoring feature for the support system. The new system monitors the statuses of all students' progresses and evaluates their degrees of achievement and ranks them in real time and continuously. The proposed features allow the learner to view one's own progress ranking compared to the whole class, and also enables the teacher to monitor each individual learner, in order to quickly spot and support learners having difficulty. In this paper, we propose a new feature for the system using nicknames. The system assigns different nicknames to each student individually and randomly in the beginning of every class. The system displays ranking using nicknames to all students and teachers in public. Therefore, each student can know his or her absolute and relative rank in their community because they may tell his and her own nickname to their friends. In this situation, nickname makes learners ' rank public and protects their privacy. Every community seems to consist of members with similar comprehension degree. Furthermore, the ranking display is updated automatically at intervals of thirteen seconds. Therefore, learners can observe dynamic transition of his or her rank in real time. It seems that the feature improves students' motivation much more similarly to competitive games. We attached the feature to our programming learning support system and applied actual classes.

Keywords: programming, learning, game, java, nickname

1 INTRODUCTION

We have developed a programming training system CAPTAIN (Computer Aided Programming Training And INstruction) written by java. Fig.1 is a login window of CAPTAIN[1, 2, 3, 4, 5]. We have applied the system in an actual programming course. In the system, learners create programs similarly to solving a puzzle game as follows. Each complete runnable program is fragmented randomly into a few lines by the system. Users must sort the lines as an original source program. The system compile the source program sorted by the user and check the correctness of it. If the answer is correct, user can run it and observe it's behavior (Fig.2).

In such a learning support system, it is important that the learner can view one's learning progress objectively. Furthermore, if the learning progress could be compared with those of other learners, competition will occur to stimulate the learner's motivation. Therefore, we introduced a feature, an index-value for comprehension of each user and a ranking view using the index-value in the previous version of the system[5] as shown in Fig.3.

Fig. 1. CAPTAIN

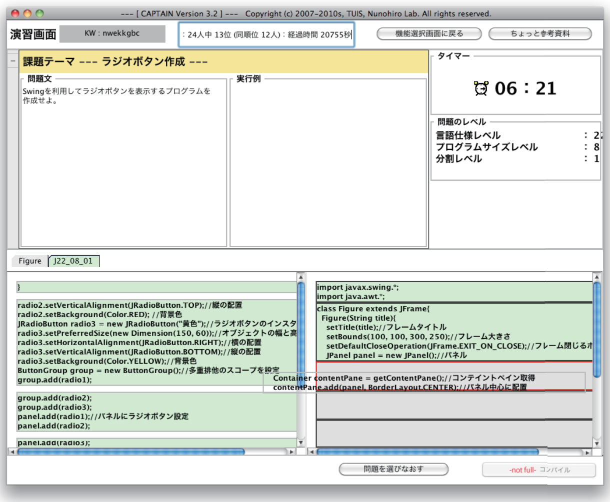

Fig. 2. Each learner must sort fragmented and randomly listed parts of a program into the correct order.

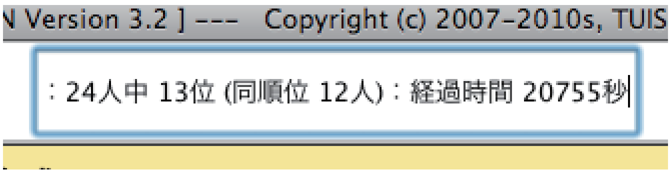

Fig. 3. A ranking display shows the ranking of the learner. For this example, the ranking of this learner is the 13th among 24 users and there are 12 learners in the same ranking). This ranking view is displayed in top of the main window and updated every 20 seconds by a thread.

In this paper, we update this ranking feature using nickname to improve learners' motivation using nicknames more efficiently.

2 PROBLEMS OF SIMPLE RANKING SYSTEM

We have noticed some problems of the simple ranking system for a competitive game.

2.1 Problems of a large group ranking

Can you keep your motivation for playing a competitive game in a large group? Every game player wants to see it's own rank rising by some efforts. Perhaps, in such a large group, your rank will not rise rapidly in spite of your efforts, therefore you may be tired of studying using the system. If your rank is very low in a large group, it seems that you will give up easily. We assumed that appropriate population is important for keeping and improve learners' motivation in such a competitive game. It can be considered that the best size of population for a learner depends on the comprehension degree of the learner. For example, the learner with the high degree of comprehension may not lose one's motivation even in a large group. On the other hand, the learner with the low degree of comprehension may be able to keep one's motivation only in a small group that consists of the people with similar degree of that. Fig.4 shows this problem schematically.

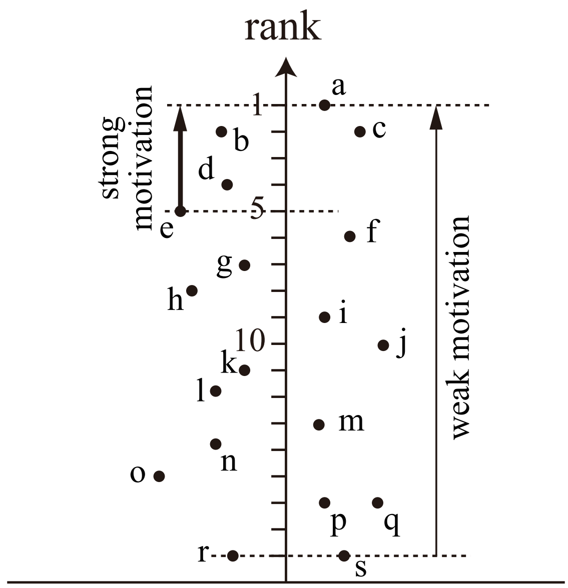

Fig. 4. Strength of each learner's motivation. The length and the thickness of each arrow toward to the apparent goal (i.e., the 1st rank) describe the strength of motivation of each learner. As thick and short arrows represent the motivation is strong. For example, the learner 'e' has strong motivation. On the other hand, the learner 's' has only weak motivation. The horizontal axis has no role in this figure.

2.2 Problems of a real name ranking

In the previous version of the system, each learner can know only their own rank, so every learner can't know other's rank and who their competitors are. In a typical competitive game, obvious competitors stir the player up and make him or her grow up. A game player often wants to know the ranks of their friends because people want to be not inferior to their friends, if possible, be superior to them. We considered whether to add the feature that real names of learners are displayed with their ranks or not. Finally, we gave up the real name display because if the real names of learners are displayed with the ranks, it violates their privacy as a result.

3 NICKNAME RANKING

We paid attention to the fact that students are divided and organized into some small groups of their own accord. It seems that these groups, their own communities, consist of their own friends with similar degree of comprehension. They often tell their results of tests each other in the small community. We tried to resolve the problems mentioned in the prior section by a nickname ranking system using the characteristic of such a small community of students. In the newest version of CAPTAIN, enough fictional nicknames are stored in our database and every learner is reassigned a unique nickname when the learner logs in the system everyday as shown in Fig.5. We adopted the names of famous heroes and heroines as nickname to attract the attention of the learners. The ranking list using nicknames (Fig.6) is displayed in an extra window as shown in Fig.7.

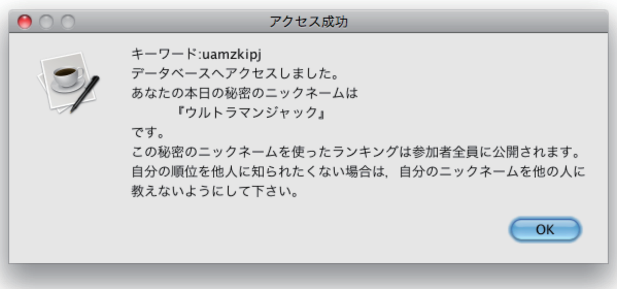

Fig. 5. Nickname assignment dialog window. This dialog is displayed after loggin in the system. It shows the today's nickname of the learner.

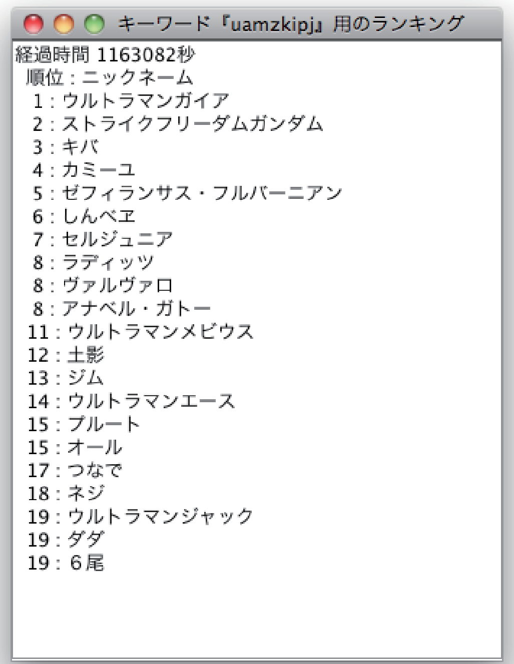

Fig. 6. A ranking list using nicknames. The list is updated every 20 seconds by a thread.

The comments of the nickname assignment dialog describe as follows "It is a today's your secret nickname. The ranking list using these secret nicknames will be displayed to every learner. Therefore, don't tell your nickname to other leaners if you want protect your privacy." It is expected that the learners tell their own secret nickname to his or her friends in the community for playing and enjoying a competition game in the system. It seems that the nickname system can protect learners' privacy and let the learners know who the competitors are only in his or her own community. Fig.8 schematically shows such a situation. In the case, there are many strong motivations in each community.

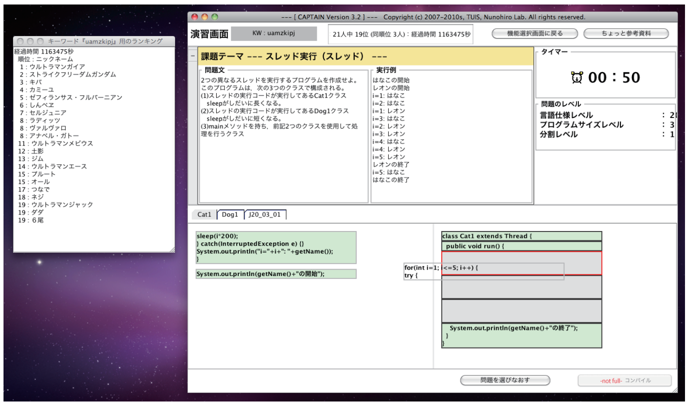

Fig. 7. A window configuration of the system. The ranking list using nicknames is displayed as an extra window during the lesson using the system.

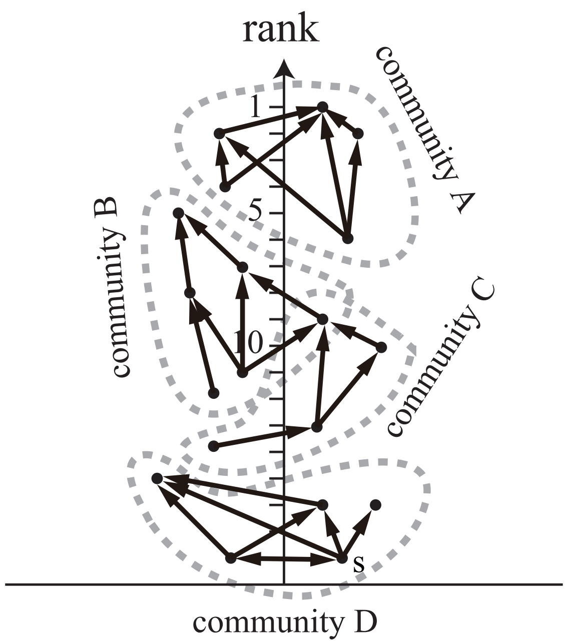

Fig. 8. An ideal situation under nickname ranking method. The horizontal axis represents some relationship between learners.

As for the learners in the community with low degree of comprehension, e.g. D in Fig.8, it seems that they can keep their motivation because they needn't mind the absolute rank and have only to compete with other members of their own community for the present.

4 CONCLUSION

It is expected that the nickname ranking can resolve the problems of the ranking in a large group and the learners' privacy. We are using the nickname ranking system in CAPTAIN for learners during actual class. We need to examine the effect of the experiment by analyzing the records of the learners' degree of comprehension and results of a questionnaire survey.

ACKNOWLEDGMENTS

This research was supported by The Ministry of Education, Culture, Sports, Science and Technology (MEXT), Grant-in-Aid for Scientific Research(C) (21500953).

REFERENCES

[1] Nunohiro E, Mackin K, Ohshiro M, Matsushita K, Yamasaki K (2007), Implementation of a GA driven programming training support system, The 12th International symposium artificial life and robotics, pp.517-522.

[2] Nunohiro E, Matsushita K, Mackin K, Ohshiro M, Yamasaki K (2008), Design and development of a puzzle based programming learning support system with genetic algorithm (in Japanese), Transactions of Japanese society for information and system in education, vol.25, No.2, pp.207-213.

[3] Yoneyama Y, Matsushita K, Mackin K, Ohshiro M, Yamasaki K, Nunohiro E (2008), Puzzle Based Programming Learning Support System with Learning History Management, The 16th International Conference on Computers in Education (ICCE2008), pp. 623-627

[4] Yamakawa Y, Ohshiro M, Matsushita K, Mackin K, Nunohiro E (2010), Programming Learning Support System 'CAPTAIN' with Motivational Study Model, The 18th International Conference on Computers in Education (ICCE2010), pp. 171-175

[5] Ohshiro M, Mackin K, Matsushita K, Nunohiro E, Yamakawa Y (2010), Programming Learning Support System with Learning Progress Monitoring Feature, Joint 5rd International Conference on Soft Computing and Intelligent Systems and 11th International Symposium on Advanced Intelligent Systems (SCISISIS 2010), pp.1465-1468

The Seventeenth International Symposium on Artificial Life and Robotics 2012 (AROB 17th '12),
B-Con Plaza, Beppu, Oita, Japan, January 19-21, 2012

Educational Effectiveness of the Lecture using Animated Figures for Beginner's Programming Course in the University

Yorinori KISHIMOTO[1], Kazuhisa KITAKAZE[1]

[1]Tokyo University of Information Sciences, Chiba 265-8501, Japan
(Tel: 81-43-236-4642)

[1]kisimoto@rsch.tuis.ac.jp

Abstract: In education, lecture is required to use computer software such as PowerPoint, flash, and so on. One of the utilization purposes of this is education effect improvement. Usually, showing animated figures is said to be good for education. So, many education systems using animated figures have been proposed. However, only few attempts have so far been made at discussion of these effects. Especially, it has not been comparing the education system using animated figures with the chalk talk. So, we research effects of a lecture using animated figures. This is a comparative research of a lecture using animated figures and a chalk talk lecture in a beginner's programming education course of university. Students of beginner's programming education course have been divided into three groups. We focus on only two groups of these. One of the groups is shown program behavior by Microsoft PowerPoint animations and follows the program statements step-by-step and show changing values of program variables by abstraction figures. Another group is a chalk talk lecture. Each group is the same syllabus, same assignments, same practical training, same final examination and same impressions questionnaire of lecture. So, difference of each group is only representation method. Thus, the proficiency effect of using animated figures is appears in a final examination. And, other effects (such as the desire to learn, satisfaction and so on) appear in the impressions questionnaire. We shows check fiver year's worth of the final examination and the impression questionnaire. As a result, this research has a little advantage of the lecture using animated figures in the representation method in this example. However, it does not show definite advantages of the lecture using animated figures.

Keywords: Computer aided education, E-Learning, Programming Education, Education Impression, Animated Figure

1 INTRODUCTION

In education, lectures are required to use computer software such as PowerPoint, flash, and so on. Usually, showing animated figures is said to be good for education in physics and geometry. Animated figures using computer can visualize an invisible motion of the physical laws like tiny or huge object motion. So, learners can understand invisible motions.

Usually, an execution of computer program just only shows results of program. Therefore, a behavior of computer by the program is invisible. Nevertheless, computer programming learner is required to understand behavior of computer by a program.

So, some system which shows a computer behavior by a program has been proposed. For example, one of the proposed systems is “Proposal of Program Text Markup Language through Program Visualization Tool” and “Effective IT Learning Method Using Schematic Diagram Approach”, which shows a behavior of a program [1][2]. And, VisuSim has been proposed, which is a visual computer simulator for education [3]. In addition, many teachers have made one-of-a-kind animated figures which show the behavior of computer by a program for education. However, many education systems using animated figures have been proposed. However, only few attempts have so far been made about the effectiveness of this method.

So, we researched effectiveness of a lecture using animated figures for the programming education. This class is teaching JAVA programming for beginner. Students of this class divide into three groups and each class are same syllabus, same practical exercise and same final examination. One of the group's lectures is using animated figure of program behavior. Other group's lecture is chalk-talk (using blackboard). So, we checked differences of each class.

The proficiency effect appears in evaluations of learning result. And, other effects (such as the desire to learn, satisfaction and so on) appear in impression questionnaire. Therefore, differences of the evaluations of learning result and the impression questionnaire are effects of a lecture showing animated figure for programming education.

In this paper, we report a comparison of evaluations of learning results and impression questionnaires in a JAVA programming education class for beginner in our university for five years for checking effects of lecture using animated figure.

2 BASIC IDEA

Checking effectiveness of animated figures for a lecture requires several divided groups of students which have same syllabus but just only presentation method is different. So, we focused on a beginner programming education course in our university. The exercise lesson (such as the programming exercise) requires tutorial process. In this case, too many students in a classroom make it difficult to program tutorial exercise. Thus, the exercise lesson consists of a small group of students.

However, even if these are several groups of students in class, usually these have same syllabus in our university. Therefore, an exercise lesson in our university is same lesson content, same exercise program, same final examination and same grade point assessment criterion of the academic achievement commonly. In this case, the difference of each group is just only the method of lecture by teachers. If one of the teacher using animated figures and another teacher using only blackboard in lecture, checking the academic achievement and the impression questionnaire is appearing differences of each other. These differences mean the effectiveness of a lecture using animated figures.

3 SURVEYED COURSES

We researched a class of the programming training course for beginners in our university. This class is teaching JAVA programming for beginner. The process of this class lesson is showed as follows;

1st: Teacher teaches today's content of a lecture.
2nd: Students take practical studies to JAVA programming assignments.

Students of this class divide into three groups and each class are same syllabus, same practical exercise and same final examination. One of the group's lectures is using animated figures of a program behavior. Other group's lecture is chalk-talk (using blackboard). And these classes have same lesson content, same exercise program, same final examination and same grade point assessment criterion of the academic achievement commonly. An image of the surveyed course is shown in Fig 1.

So, we focused on the two groups. Group A is using the power point animated figures. But Group B is using only black-board (Static figure). The difference of final result of Group A and Group B means effectiveness of the lecture using animated figures. In addition, this course has the impression questionnaire at the day of the final lecture. Thus, effects of the desire to learn, satisfaction and so on appear in impression questionnaire. So, we have checked the final result and the impression questionnaire of these classes for five years.

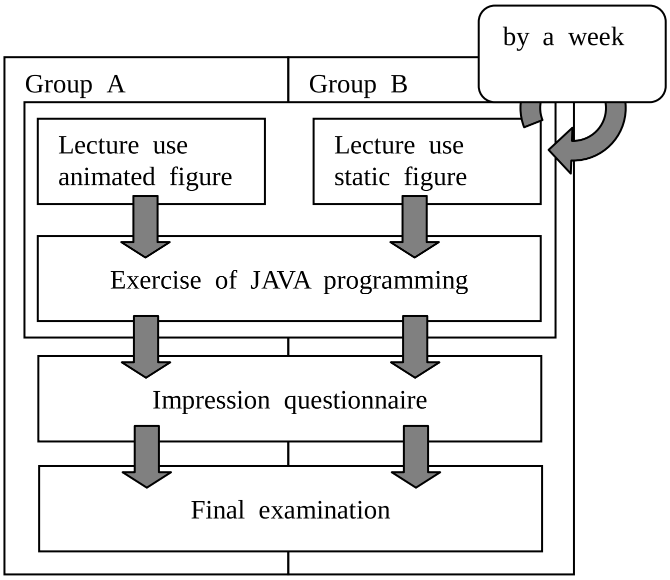

Fig. 1. An image of surveyed course

4 RESULTS

Table 1 shows the highest point, the lowest point, the standard deviation and the average of the final result of two groups for each five years. The maximum of this final result points is 113 and minimum of this points is 0. Table 1 shows Group A and Group B were similar result points.

Table 1. Final result of two groups for each five years

Year	Group	Average	Highest point	Lowest point	Standard deviation	Number of Sample
2007	A	88.6	112	8	17.2	46
	B	82.3	110	5	21.4	45
2008	A	83.0	112	0	22.3	62
	B	83.6	111	0	22.9	30
2009	A	72.3	102	0	21.3	64
	B	83.3	111	0	19.8	66
2010	A	89.6	108	0	19.2	63
	B	82.3	112	0	25.7	65
2011	A	85.0	111	0	22.0	46
	B	83.6	112	0	22.9	43

Table 2. Impression questionnaire of two groups for each five years

Questions	Were you able to understand lecture contents?		Were you able to learn new knowledge?		Was the speech skill of a teacher good for you?		Was the expression method plain for you?		Was the class executed according to syllabus?	
Group	A	B	A	B	A	B	A	B	A	B
2007	4.1	4.1	4.6	4.5	4.4	4.4	4.1	4.1	4.2	4.2
2008	4.1	4.1	4.3	4.5	4.4	4.3	4.1	4.2	4.1	4.3
2009	4.1	4.1	4.4	4.4	4.4	4.1	4.3	4.0	4.2	4.0
2010	4.1	3.9	4.6	4.4	4.6	4.1	4.2	3.8	4.3	4.0
2011	3.9	4.2	4.3	4.3	4.1	4.4	3.9	4.2	4.1	4.4

Questions	Was the volume of a lecture appropriate for you?		Were enthusiasm and good faith of a teacher felt for you?		Did the teacher deal with a question of a student faithfully?		Was it a valuable class for you?		As for you, did learning will increase by having attended this class?	
Group	A	B	A	B	A	B	A	B	A	B
2007	4.3	4.0	4.4	4.3	4.6	4.3	4.5	4.4	4.4	4.3
2008	4.0	4.3	4.3	4.2	4.4	4.5	4.4	4.5	4.3	4.2
2009	4.2	4.1	4.4	4.2	4.5	4.3	4.5	4.2	4.4	4.1
2010	4.3	4.1	4.5	4.2	4.7	4.0	4.6	4.4	4.3	4.1
2011	4.1	4.4	3.9	4.4	4.0	4.4	4.2	4.4	3.9	4.1

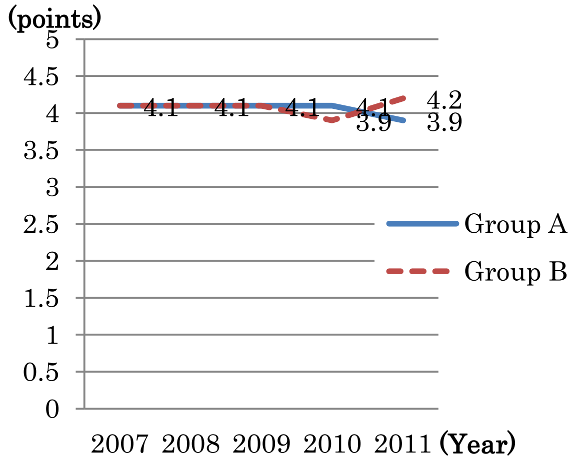

Fig. 2. Answer of question "Were you able to understand lecture contents?"

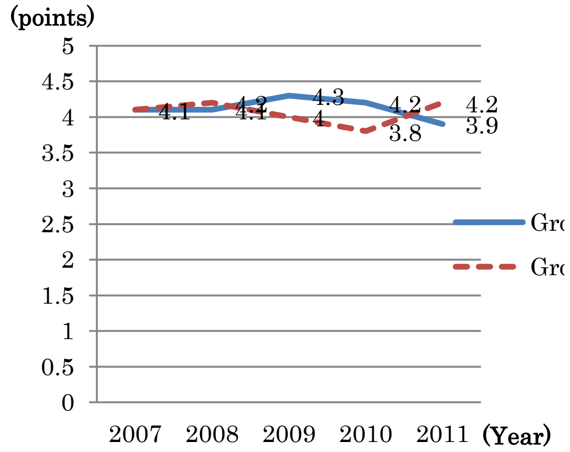

Fig. 3. Answer of question "Was the expression method plain for you?"

Table 2 shows the average of the impression questionnaire of two groups for each five years. This questionnaire is written in Japanese. The maximum of this point is 5 and minimum of this point is 0. Table 2 shows Group A and Group B were similar points.

The educational effectiveness of understanding appears as answers of the question "Were you able to understand lecture contents?" of a questionnaire. So, we show this answer of questionnaire in Fig.2.

The educational effectiveness of using animated figures appears as answers of the question "Was the expression method plain for you?" of a questionnaire. So, we show this answer of questionnaire in Fig.3.

5 CONSIDERATIONS

From Fig. 1 and Fig. 2, the understanding of learning fluctuates by each year. However, it is almost the same in the Group A and the Group B.

And, from Fig. 3, the expression method of Group A was a little higher. However, it has not shown definite advantages of lecture using animated figures.

In this research, the final result and the impression questionnaire of Group A and Group B are similar. This result means an educational effectiveness of a lecture using animated figures and a lecture using static figures is similar.

We consider a reason of this result is the effect of practical exercises. The practical exercise is more effective in this research. Therefore, more effective programming education requires an improvement of a practical exercise.

6 CONCLUSION

In this paper, we report a comparison of evaluations of learning results and impression questionnaires in a JAVA programming education class for beginners in our university for five years for checking effects of a lecture using animated figures.

In this research, an education effect of a lecture using animated figure and a lecture using static figure is similar. So, it has not shown the definite advantage of lecture using animated figures.

REFERENCES

[1] OHKI Mikio, "A Proposal of Program Text Markup Language through Program Visualization Tool", The Special Interest Group Notes of IPSJ 2003(60), 1-8, 2003-05-30

[2] Harada Noriyuki, Hamana Takahiro, Satou Tadamasa, "A Study of Effective IT Learning Method Using Schematic Diagram Approach", The Institute of Electronics, Information and Communication Engineering, Technical Report of Software Science 105(229), 1-5, 2005-07-29

[3] Imai Yoshiro, Imai Yoshiro, Tomita Shinji, Niimi Haruo, Inomo Hitoshi, Shiraki Wataru, Ishikawa Hiroshi, Inomo Hitoshi, "Practical Applications of Visual Simulator VisuSim and Reports of its Evaulation", The Institute of Electronics, Information and Communication Engineering, Technical Report of Education Technology, 102(455), 25-30, 2002-11-09 (in Japanese)

The Seventeenth International Symposium on Artificial Life and Robotics 2012 (AROB 17th '12),
B-Con Plaza, Beppu, Oita, Japan, January 19-21, 2012

Self-Learning Support System to Increase Motivation for Learning

Kei Ito[1], Tomoki Sato[1], and Ayahiko Niimi[1]

[1] Future University Hakodate, Hakodate, Hokkaido 041-8655, Japan
(Tel: 81-138-34-6228, Fax: 81-138-34-6301)
(kei@fun.ac.jp)

Abstract: In higher education, a decline in the academic abilities of students has become a serious problem. In this paper, we propose a system to increase learning motivation with the ultimate aim to increase the academic ability of students. To achieve this aim, we provide an environment for students to facilitate self-e-learning system in classes using blended learning. We report the development of this environment and the results obtained.

Keywords: Motivation for Learning, Self-Learning, Support System, Academic Ability

1 INTRODUCTION

With the development of information technology (IT), the number of learning options is continually increasing for students in IT-related course studies (both in universities or other institutions). However, due to reduction in the enrollment of students and increases in the advancement rate from high schools to universities, students' motivation for learning decreases. As a result, many universities are facing the problem of students with low academic abilities[1].

For effective learning and efficient operation of courses, blended learning, which is a combination of face-to-face lectures and e-learning, is widely used[2].

This research aims to increase learning motivation and consequently the academic abilities of students by developing an environment that facilitates a self-e-learning system for classes using blended learning. students'

2 APPROACH

For blended learning using face-to-face lectures and a course or learning management system, we propose to facilitate self-learning by students by providing a self-learning environment in a course management system and applying it to an existing class framework. This paper shows an experimental application for basic programming using Moodle, which is an open-source course management system.

3 REQUIREMENTS

Self-learning involves scheduled reviews of materials presented in a previous class or preparation of materials for the next class.

What is needed to promote self-learning, particularly preparation, in students? In programing classes involving the use of exercise, it is important that students acquire or review the prerequisite knowledge and skills while preparing for the class.

To assist students in self-learning using a course management system, short questions and quizzes are believed to be necessary. However, if the order and the contents of quizzes is same for every time or for every students, it can lower willingness to study. Therefore, it is required that the order and the contents of of the same quiz will be changed for every time by preparing many questions for the same difficulty and for the same learning item and by random selection of them.

4 SYSTEM

To achieve the requirements described in section 3, we implemented new functions using Moodle, an open-source course management system. In section 4.1, we introduce Moodle functions related to our requirements, such as quizzes, question banks and random questions. In section 4.2, we describe the design of the newly implemented function.

4.1 Moodle functions: Quizzes and Questions

In Moodle, a *quiz* is constructed using *questions* registered in a *question bank*. Categories are used to create hierarchy of questions in a question bank. To provide quizzes to students, teachers are required to create questions into the question bank and create quiz pages using them. Students can therefore take a quiz created by their teacher.

Moodle has a feature named *random question* which is used to create a quiz by randomly selecting a specific number of unique questions from a particular category. For example, if a category has 20 questions and a teacher specifies that four questions should be selected from the category, they will be randomly selected when each student takes the quiz. Each attempt of a student will result in a new selection of questions. This feature is therefore useful for both preparation and reviews of materials already learnt. This feature also decreases the probability that a student may hear correct answers from other students who have already completed the quiz. However, to ensure that the difficulty level is consistent for each attempt, teachers should develop sufficient number of questions with the same difficulty level in each category. Moreover, if a teacher wants to create a quiz with questions from different categories, many categories and many questions for each category should be created. Such situations cause inefficient maintenance and/or operation of the question bank.

4.2 Extended Random Question

To solve the problem mentioned in section 4.1, we have developed the feature of *extended random question* that allows *random questions* to be more easily managed and maintained. Random questions are selected according to question categories, whereas in extended random questions are selected according to a question category and the specified question tag. Extended random questions are as useful as random questions, and this feature allows maintenance of question banks.

Extended random questions also contain another feature. If a teacher wants to use random questions for a class examination instead of self-learning, the feature gives students belonging to a specific group the same selection of questions instead of giving different selections to each student. Hence, extended random questions allow question selection not only when each student attempts a quiz but also when a teacher creates a quiz. That is, all students who attempt the quiz get the same questions that were randomly selected when the teacher created the quiz.

To implement extended random questions, we add a *tags* field into the question table in the quiz module, in which teachers can specify a *tag* for each question. By using this extension, when a teacher creates a quiz, he/she can select an extended random question in the same manner as a random question and specify a tag for the qualified selection. Unless a teacher specifies a tag for an extended random question, questions are selected from the entire question bank of a specific question category, as in the case of the original random questions.

5 USAGE EXAMPLE

Moodle is used to implement the functions described previously in a real classroom.

5.1 Use case for basic programming

Basic programming classes do not usually involve classroom lectures and contain only practical session. Assume that there are six classes each containing 40 students. Normally, a class consists of seven practical sessions and one examination. We applied our system with the self-study quiz in a class comprising only repeater (35 students, 2 classes). Because the exercises in the class had already been implemented in the previous year, the students were graded on the basis of only three examination results.

Table 1. Category of quizzes

category
variable type and operator
array
input and output
conditional branch
loop
function
structure
string
file i/o

It was optional for the students to take a quiz and there were no restrictions on the number of attempts. Quizzes contained questions belonging to each of the nine categories listed in Table 1. Each quiz contained four questions: the question for confirming materials, the basic question, and the applied questions for each category. For example, a quiz covering the category "structure" contained four questions randomly chosen from each of the following categories: a set of questions for confirming materials covering the category "structure", a set of questions related to definitions of data structures and data access, a set of questions related to data structures and functions, and a set of questions related to data arrays.

Detailed explanations of answers are provided for all questions. The explanation for each question is displayed after the exam irrespective of whether a student's answer to the question is correct. Our aim is to ensure that even if students do not understand the topic covered by a question, they can obtain a sufficiently high score in the next attempt by understanding the explanation.

6 EVALUATION AND CONSIDERATION

6.1 Usage Results of Quizzes

We prepared a quiz for each of the categories described in section 5. A total of nine quizzes were prepared. Table 2 shows the total number of attempts for all nine quizzes for 70 repeaters. Thirteen students had never used quizzes and the total number of attempts for nine students was less than five, even though there were nine quizzes. In contrast, more than half the students had attempted the quizzes 15 or more times. In particular, the top seven high scorers had attempted 40 times or more.

6.2 Results of Certification Exams

Certification examinations are held three times per semester. Each examination is worth 30 points, with a total of 90 points. At the time of writing this paper, the scoring of all examinations was not completed. Table 3 shows the temporary scores by autoscoring. Although the scores are

Table 2. Distribution of number of attempts in all nine quizzes

number of attempts	head-count
40+	7
35 - 39	1
30 - 34	4
25 - 29	8
20 - 24	6
15 - 19	4
10 - 14	8
5 - 9	10
1 - 4	9
0	13

Table 3. Distribution of temporary score in certification exams

total score	head-count
70	1
60	2
50	8
40	7
30	11
20	14
10	14
0	13

generally low, they are considered to be satisfactory given that all the subjects failed this course in the previous year.

6.3 Questionnaire Survey

After the third certification exam, we carried out a survey pertaining to the quizzes. Responses were received from 59 out of the 70 students.

In the questionnaire, we asked "How often do you use quizzes for preparation?" The results indicate that over 70% students used the quizzes often (Table 4).

Because each quiz has randomly selected questions for each attempt, it is expected that each student would have taken the same quiz more than once. Hence, we asked "How many times did you take the same quiz?" The results obtained indicated that over 70% students had taken the same quiz more than once (Table 5).

We also asked the usefulness of the quizzes for preparation, reviews, and exams (Tables 6, 7, and 8, respectively). The results indicated that approximately 80% students found them to be very useful or useful for preparation, reviews and exams (Tables 6, 7, and 8). These results shows the usefulness of quizzes for the entire course.

We also asked the students about the usefulness of random selection of questions provided by extended random questions. Many students answered that it was very useful or useful (Table 9).

To increase understanding of a topic, we prepared explanations for each question. The explanations were displayed after each student took a quiz. In our survey, we asked about the ease of understanding of these explanations, and 70% of students indicate that they were very easy to understand or comprehensible (Table 10).

A free-description question asked students for ideas concerning how the quizzes could be improved. Three students suggested that the number of questions be increased, four students suggested that the difficulty level be changed, seven students suggested that more practical questions than fill in the blank questions be included, two students suggested other

Table 4. Result of "How often do you use quizzes for preparation?"

head-count		answer
17	(29%)	usually
26	(44%)	often
15	(25%)	sometimes
1	(2%)	never
0	(0%)	I don't know

Table 5. Distribution of the results of "How many times did you take the same quiz?"

head-count		answer
17	(29%)	4+
14	(24%)	3
10	(17%)	twice
15	(25%)	once
3	(5%)	I don't know

Table 6. Results of "How useful are the quizzes for preparation?"

head-count		answer
18	(31%)	very useful
28	(47%)	useful
3	(5%)	less helpful
3	(5%)	useless
7	(12%)	I don't know

Table 7. Results of "How useful are the quizzes for reviews?"

head-count		answer
22	(37%)	very useful
28	(47%)	useful
5	(8%)	less helpful
1	(2%)	useless
3	(5%)	I don't know

Table 8. Results of "How useful are the quizzes for exams?"

head-count	answer
16 (27%)	very useful
30 (51%)	useful
5 (8%)	less helpful
3 (5%)	useless
5 (8%)	I don't know

Table 9. Results of "How useful is the random selection of questions?"

head-count	answer
26 (44%)	very useful
23 (39%)	useful
7 (12%)	less helpful
1 (2%)	useless
2 (3%)	I don't know

Table 10. Results of "How comprehensible are the explanations?"

head-count	answer
18 (31%)	very easy to understand
23 (39%)	comprehensible
12 (20%)	somewhat cofusing
4 (7%)	difficult to understand
2 (3%)	I don't know

Table 11. Relationship between quiz attempts and temporary score of exam

total attempts	head-count	average score	max score	min score
30+	12	22.5	40	10
20-29	14	36.4	60	10
10-19	12	31.7	60	10
1-9	19	20.5	70	0
0	13	5.4	20	0

ideas, and the remaining 43 students did not provide any answer or saw no need to improve the quizzes.

We also asked for ideas to improve the explanations for each questions. Seven students wanted the explanation to be more comprehensible, five students wanted the answer for each question, as opposed to its explanation, two students had other ideas, and the remaining 45 students did not provide any answer or saw no need to improve the explanations.

The general feedback received in our survey was that the responses had high subjective evaluation.

6.4 Consideration of motivation for learning

The results of the usage of the quizzes and the accompanying survey show that many students took these quizzes although it was optional to take them.

It is believed that continued use of the quizzes will provide an environment that will assist students in maintaining their motivation for learning. However, a fair evaluation could not be achieved because all subjects were repeaters.

Furthermore, students who attempt the quizzes many times without reading and understanding explanations displayed after their attempts may continue to repeat their course until they earn full points. A detailed analysis of quiz attempts may be required.

6.5 Consideration of academic ability

Table 11 shows the distribution of then number of quiz attempts and the average temporary score of the certification exam for each distribution range. These results show that students who attempt quizzes multiple times may not necessarily obtain a good score on exams. It is therefore difficult to infer whether the introduction of quizzes for self-learning directly increases the academic ability of students. As already mentioned in section 6.4, students who attempt quizzes many times do not always read the explanation displayed. It is estimated that after taking a quiz two or three times, students who read and understand the explanations comprehend the contents in each category. It is thought that the advisable maximum number of quiz attempts is two or three for each quiz, that is, the total number of attempts for all quizzes ranges 18-27. As shown in Table 11, students who attempted the quiz 20-29 times had the highest average score.

Table 12. Relationship between quiz score and temporary score of exam

quiz score	head-count	average score	max score	min score
100	5	22.00	30	10
90-99	5	34.00	50	20
80-89	8	35.00	60	10
70-79	11	33.64	70	0
60-69	11	24.55	60	0
50-59	4	30.00	50	10
40-49	4	30.00	30	30
30-39	2	15.00	20	10
20-29	4	10.00	20	0
10-19	2	15.00	20	10
0-9	14	5.71	20	0

Table 12 shows the distribution of the score of quizzes and the average of temporary score of the certification exam for each distribution range Quiz score is the average of the highest scores in each quiz for each student. One hundred indicates that the student continues to take the quiz until he/she attains a score 100. This result also shows that students who achieve high quiz scores do not always achieve high certification exam scores. It has already been mentioned that some students repeatedly take quizzes without understanding the explanations displayed after quiz attempts. Because the number of prepared questions is limited, it is possible that some students who memorize correct answers after frequent quiz attempts without understanding the concepts involved get high quiz scores despite the random selection of questions.

7 CONCLUSION

We analyzed the required features of course management systems for increasing learning motivation and facilitating self-learning. On the basis of our analysis, we developed the required feature using Moodle, which is an open-source course management system. We introduced the feature into an actual course for learning programming and evaluated the use of the feature by a survey. We provided an environment that assists students in maintaining their motivation for learning by providing interesting system features and developing educational materials that utilize this feature. However, the features and materials do not always have the effect of increasing the academic ability of students. Therefore, a detailed analysis of the results and improvement of both features and educational materials is required. Finally, we express sincerely thank Version2, Inc. for its cooperation in the development of the Moodle feature.

REFERENCES

[1] Ui Tetsuo, "Problem on Decreasing Academic Ability of University Students and Its Solutions (in Japanese)", Operations Research, 54(5), pp243-248, Operations Research Society of Japan, 2009

[2] Miyaji Isao, Adachi Kazuhisa, Uchida Minoru et al., "Toward Blended Learning from E-learning (in Japanese)", Kyoritsu Shuppan, 2009

The Seventeenth International Symposium on Artificial Life and Robotics 2012 (AROB 17th '12),
B-Con Plaza, Beppu, Oita, Japan, January 19-21, 2012

A Proposal of Web-Com API for E-learning Contents Creation Services

Yoshihiro Kawano[1], Chao Zhou[2], and Tatsuhiro Yonekura[2]

[1]Tokyo University of Information Sciences, Chiba 265-8501, Japan
[2]Ibaraki University, Ibaraki 316-8511, Japan
(Tel: 81-43-236-1149, Fax: 81-43-236-1149)

[1]ykawano@rsch.tuis.ac.jp, [2]{10nm729r@hcs.ibaraki.ac.jp, yone@mx.ibaraki.ac.jp}

Abstract: This paper proposes Web-Com Service and Web-Com API. Web-Com Service enables to create/share easily multimedia learning contents on the Web. And, Web-Com API enable to access to the functions of Web-Com Service from other web sites by some program. Web-Com API provides as a web API for the usability. Web-Com API aims at the improvement in convenience of Web-Com service. The requirements of Web-Com API are "functions of Web-Com Service are available from other web sites", and "generation of a code for embedding the functions to other web sites". By realization of Web-Com API, the improvement in convenience of Web-Com service is expectable.

Keywords: e-learning, Web-Com Service, Web-Com API, multimedia learning content

1 INTRODUCTION

Recently, e-learning is introduced by the training in educational facilities and several companies. The main stream about e-learning is use of WBT (Web Based Training) because of the convenience in introduction or an aspect of practical use. There are authoring tool for e-learning contents [1][2] and LMS (Learning Management System) by using web browser [3][4]. However, problem of authoring tool is that it is difficult to share the learning contents, because shared mechanism of the contents is not provided. On the other hand, in LMS, while a learner can learn only by a web browser, the complicated work for which the contents creator used dedicated software is needed in many cases. The short supply of the learning contents is a problem. Thus, there are merits and demerits in authoring tool and LMS.

Then, the authors have proposed a learning contents creation service named Web-Com Service. Web-Com Service is a web service which users can create/share the multimedia contents including annotations of voice, free line, and etc. Web-Com Service has two functions. These are web authoring tool for learning content (as a web page), and creation/sharing function of Web-Com content on the web. Therefore, the learner can learn preparation and review of a class. On the other hand, the contents creator can create the learning contents with a workload comparable as an actual class.

In this paper, the authors propose Web-Com API (Application Programming Interface) to access to the functions of Web-Com from other web sites by some program. Web-Com API provides as a web API for the usability. Web-Com API aims at the improvement in convenience of Web-Com service. The requirements of Web-Com API are "functions of Web-Com Service are available from other web sites", and "generation of a code for embedding the functions to other web sites". By realization of Web-Com API, the improvement in convenience of Web-Com service is expectable.

2 WEB-COM SERVICE

2.1 Overview

The Web-Com Service had been developed as the Web service. Specifically, the service has two functions, which are web authoring tool for learning content (as a web page), and creation/sharing function of Web-Com content on the web [5].

The features of the service are below.

(1) Creation, edit, and use of the Web-Com contents on the web.
(2) Upload of the Web-Com contents created on the other computer.
(3) The creation of the web contents without technical knowledge, such as HTML and Flash.
(4) Expression of contents including a science-and-engineering system.
(5) The creation of the secondary contents using the primary contents created by the service.
(6) The mutual link between Web-Com contents.
(7) Embedding Web-Com contents to the web page.

The users of this service are an upload user, a creation user, an inspection user, and an embedding user. The upload user uploads the Web-Com contents created by existing Web-Com [1]. Then, the existing Web-Com contents are converted into Flash contents, and it can be browsed on the Web. The creation user is a user who creates the primary contents and secondary contents. The inspection user inspects the contents, and the embedding user embeds contents to Web pages. When the secondary contents are created, the iframe tag for embedding is generated automatically, and then the contents can be embedded at an external site.

The flow chart of contents creation is shown in Fig.1. On the upper part of the Fig.1, the user creates the primary contents, and inputs required information using the authoring tool. When the continuation page over two pages is created, each pages are mutually linked automatically. The creation of secondary contents is also continuously possible after the creation of primary contents. In creation of the secondary contents shown in the lower part of Fig.1, the user specifies URL of the created primary contents or a website, and adds notes information, including a sound, a free line, etc. Then, required information is inputted by the same way as the primary contents. In addition, the continuous secondary contents can be also created.

As mentioned above, the user can create the flexible and variegated contents on a web browser easily without technical knowledge. Furthermore, accumulation and sharing of various contents which the user created are attained by the Web Service.

Currently, this service is launched on the intramural server and the unregistered user can use only the function of an inspection and embedding. Use of the function of all above is permitted by registering as a user. In addition, Fig.2 is a top page of this service.

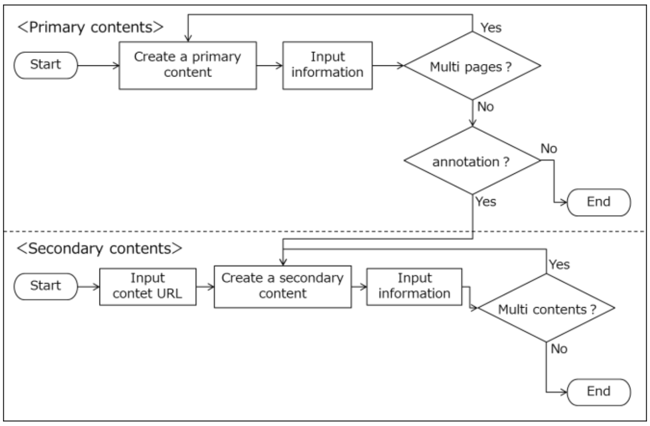

Fig. 1. Flowchart of creation of content

Fig. 2. Top page of Web-Com Service

Table 1. Functions of Web-Com API

No.	Function	API	Provide
1	Login	signin	JavaScript
2	Logout	signout	JavaScript
3	User registration	Signup	iframe tag
4	User deletion	deleteuser	JavaScript
5	Create a primary contents	createpage	iframe tag
6	Create a secondary contents	createcontent	iframe tag
7	Play	view	iframe tag
8	Search	search	iframe tag

2.2 Issue of Web-Com Service

By the launch of this service, the subject about the Web-Com has been solved basically. For the accumulation of contents, it is important to be recognized by more users and to be used for them. However, it is not used by many users although there is contents shared structure in this service.

Then, if the function of this service is available from the external site as API, the service would be recognized by more users, and the improvement in convenience of this service is also expected by cooperation with other services. This leads to accumulation of contents.

3 WEB-COM API

3.1 Purpose

Web-Com API was developed for the purpose of the improvement in convenience of the Web-Com Service. The requirements for Web-Com API are two points, "the function of this service can be used from the external site", and "the function is generated as a code, which can be embedded on a Web page."

3.2. Overview

In Web-Com API, eight functions shown in Table 1 are offered. Since each function is offered in the form of JavaScript or an iframe tag, a user without technical knowledge can also embed it easily at a Web page. The available URL is as follows. In addition, the API name corresponds with Table 1. Then, each function of API is explained. Detailed explanation is available on a reference page [6].

URL : http://yonyx1.cis.ibaraki.ac.jp/webcomcgm/api/[API name]

3.3. Functions

3.3.1 User Authentication

Here, the user management function of login, logout, user's registration, and user deletion is explained. The screen transition diagram of login, logout, and user deletion is shown in Fig.3. After the completion of login, the login button changes to logout, and the withdrawal button is displayed. This function can be used by embedding the code offered by JavaScript in the source code of the Web page.

The registration to this service is available by inputting registration information in the function of user's registration. This function is offered with an iframe tag.

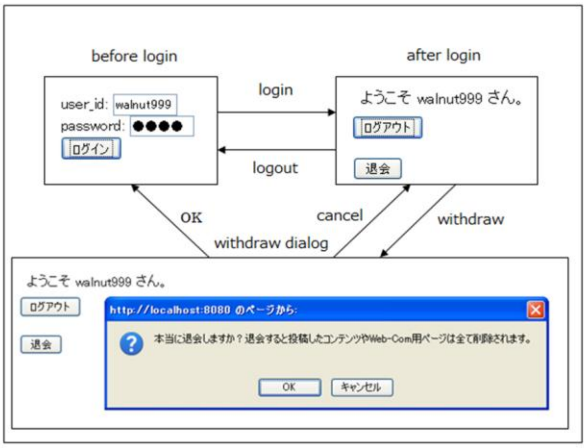

Fig. 3. Screen transition diagram of login process

3.3.2 Primary Contents

Fig.4 shows the creation screen of primary contents. In Fig.4, the Web authoring tool of this service is used from an external site. After contents creation, the screen changes to an information input screen and the user inputs required information. At this time, the user can choose disclosure or nondisclosure of contents. If disclosure is chosen, the contents are registered to this service as primary contents, and if nondisclosure is chosen, it can be downloaded as a html file, without being registered to this service.

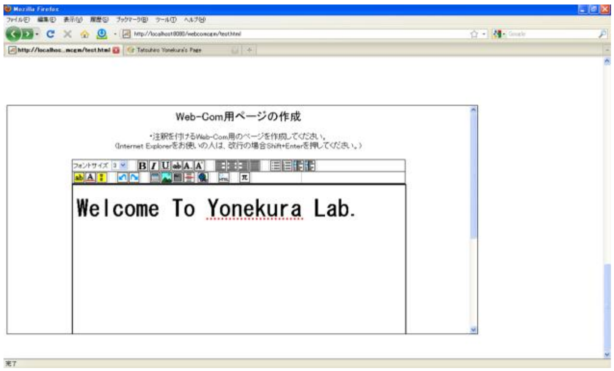

Fig. 4. Creation of primary content

3.3.3 Secondary Contents

Fig.5 is the creation screen of secondary contents. In Fig.5, the secondary contents creation function of this service is used from an external site. After contents creation, the screen changes to an information input screen and the user inputs required information. At this time, the user can choose disclosure or nondisclosure of contents as the same as primary contents. It can download as a swf file renewable by Flash Player, without registering to this service as secondary contents, if nondisclosure is chosen. And it is registered to this service, if disclosure is chosen (Fig.6).

For creation of primary contents and secondary contents, the user needs to log in to this service. However the user does not need to log in to use Web-Com API. This is for reducing the barrier of this service use in consideration of the use from an external site. In addition, when using without logging in, the user name should be specified as "Anonymous".

Fig. 5. Creation of Web-Com content

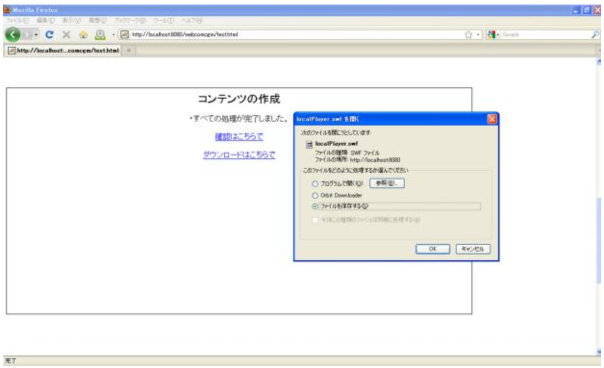

Fig. 6. Download of Web-Com content

3.3.4 Play

Fig.7 is the play screen of secondary contents. These contents can be played on the web browser in which FlashPlayer was installed.

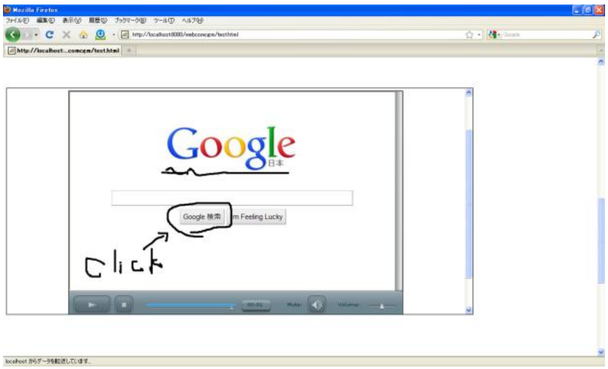

Fig. 7. Play of Web-Com content

3.3.5 Search

It is available to search of the secondary contents registered into this service from the external site. By specifying a keyword into the search window in iframe, the contents which correspond with the keyword are displayed.

3.4 Discussions

Almost all the functions of the Web-Com service were provided as API. And each function can be used from the external site. By having developed API which can be used only by the embedding of a code, the user without technical knowledge can use them easily. Thereby, the requirements shown with Section 3.1 have been satisfied.

However, contents creation and search have some subjects t o be solved. Now, it cannot respond to addition of the notes to a continuation page. On the other hand, the search functi on corresponds only to secondary contents. These are future subjects.

3.5 Use Scene

As a usage scene, cooperation with Learning Management System (LMS) can be considered. By providing of API, the function of the Web-Com Service can be used from the LMS site, and creation of the multimedia teaching-materials contents on LMS is enabled.

Furthermore, the application to the SCORM (Sharable Content Object Reference) [7] which is the e-learning standards designed by U.S. ADL (Advanced Distributed Learning Initiative) is also an important issue. Since the SCORM contents and LMS can be employed mutually, the present e-learning product employs SCORM.

By adoption to the SCORM of the secondary contents cre ated with this service, usage of multimedia learning contents are supposed to be available to many LMSs.

4 CONCLUSION

In this paper, the Web-Com Service and the Web-Com API were proposed. The Web-Com Service enables to create the e-learning teaching-materials. And the Web-Com API provides functions of the Web-Com Service. These realized the creation and the sharing of the multimedia teaching-materials contents on Web. By API, the improvement in convenience of Web-Com service is expectable.

In the future, the correction of the function of Web-Com API, the application of SCORM to secondary contents, the cooperation with LMS, and evaluations of those are due to be performed. And the enhancement of the contents of the Web-Com Service is needed. In addition, as internationalization, the provision by English and Chinese is being planned.

REFERENCES

[1] K. Hiraki, T. Yonekura, and S. Shibusawa, ""Web-Com": Interactive Browser for Web-Based Education", The Institute of Electronics, Information and Communication Engineers Transactions on Information and Systems, vol.E88-D, no.5, pp.912-918, May 2005.

[2] Adobe Systems Incorporated., "Adobe Captivate" , 2010, http://www.adobe.com/jp/products/captivate/.

[3] Japan Science and Technology Agency, "Web learnin g plaza", http://weblearningplaza.jst.go.jp/

[4] Commlife, "TOEIC online Learning", http://www.commlife.net/toeic/

[5] Y. Furukawa, T. Yonekura, M. Niibori, "Web-Com CGM: Integrated Environment for Producing e-lecture contents", IEICE Technical Report, 2009.

[6] Yonekura Labs. "Web-Com API reference", http://yonyx1.cis.ibaraki.ac.jp/webcomcgm/api/reference.html.

[7] ADL (Advanced Distributed Learning), "SCORM (Sh arable Content Object Reference Model)", http://www.adlne t.gov/Technologies/scorm/default.aspx.

The Seventeenth International Symposium on Artificial Life and Robotics 2012 (AROB 17th '12),
B-Con Plaza, Beppu, Oita, Japan, January 19-21, 2012

Using Smartphones in Sports Education

Shinya Iwasaki[1], Kenneth J. Mackin[1], and Masahiro Ishii[1]

[1]Tokyo University of Information Sciences, Chiba 265-8501, Japan
(Tel: 81-43-236-1329, Fax: 81-43-236-1329)

mackin@rsch.tuis.ac.jp

Abstract: Applying e-learning to hands-on education such as physical education has been difficult due to hardware and network restrictions in an out-of-classroom environment. In this research we propose using smartphones for sports education to improve the learning curve of athletes. There has been previous research reported on using carrier specific cellular phone applications for sports education. While the previous approach reported effectiveness on using mobile devices for education assistance, the carrier specific cellular phone approach had functional and interface limitations due to the hardware restrictions. For this research, we developed a Google Android application for sports education, namely track and field use, to support both the learner (athlete) and the educator (trainer). For the proposed application, we made use of the touch panel feature of Android hardware to facilitate data entry for the users. Validity of the proposed system was verified through experiment.

Keywords: Smartphones, Google Android application, sports education, e-learning

1 INTRODUCTION

Applying e-learning to hands-on education such as physical education has been difficult due to hardware and network restrictions in an out-of-classroom environment. In this research we propose using smartphones for sports education to improve the learning curve of athletes. There has been previous research reported on using carrier specific cellular phone applications for sports education. While the previous approach reported effectiveness on using mobile devices for education assistance[1], the carrier specific cellular phone approach had functional and interface limitations due to the hardware restictions. For this research, we developed a Google Android application for sports education, namely track and field use, to support both the learner (athlete) and the educator (trainer). The developed application targets men's decathlon and female's heptathlon, and calculates the points achieved for each event, and displays the current total score. The decathlon and heptathlon event is a 2 day competition, with decathlon athletes competing in 10 different events, and heptathlon athletes competing in 8 different events. It is important for each athlete to manage how much energy and strength should be spent on each event, in order to complete the 2 day competition. The calculating program is used by the athlete to check current performance, but more importantly used to simulate target records for coming events, in order to set a goal for each individual event performance. The same use applies to the trainer, where the trainer will simulate possible performances and give advice to each athlete based on the simulation results.

Capability for managing multiple records was implemented, so that the learner can compare previous and current performance. The feature is also used by the educator to manage multiple students at the same time.

Effective user interface for sport education was taken in consideration. For the previous research using standard cellular phones, data input was through number buttons only. For the proposed application, we made use of the touch panel feature of Android hardware to facilitate data entry for the users.

Validity of the proposed system was verified through experiment.

2 SMARTPHONE PLATFORM

In order to promote the use of e-learning for sports education, there are several barriers that must be overcome. Firstly, e-learning for sports education requires that each participant has access to the e-learning system, so expensive hardware or limited hardware support will be against the motivation. Secondly, the e-learning system must be easily carried outdoors where sports education will take place, so the size of the hardware should be able to fit in a pocket. Thirdly, the hardware should have enough computing power and features to run complicated sport education support applications.

To clear the above requirements, smartphones were selected as the target hardware for this research. In particular, Google Android was selected for the smart phone platform. Android is a free and open source operating system for mobile devices, mainly smartphones and tablet computers. The first commercial version, Android 1.0, was released in September 2008. By the end of 2011, Android had grown to become the largest smartphone platform in many markets. In this light, Google Android was selected for the research platform to provide the large client base, and easy development environment.

Important features of Android utilized in this research are Java programming language development support, touch panel user interface support, sandbox memory access for application memory, and file read/write capability.

3 SPORTS EDUCATION APPLICATION

In this research, a sports education support application was developed with the following specifications.

Supported OS: Android

Supported version: 1.6 or newer

Supported screen size: HVGA or better

Supported installation: Download via Google Android Market

Android OS is currently the largest smartphone platform on the market, and while the latest Android version for smartphones is version 2.3, support for version 1.6 or newer was targeted to allow close to all of the current Android smartphones to be covered. For the same reason, minimum supported screen size is HVGA, in order to allow a large range of supported hardware.

Android applications can be distributed easily over the web, but for this research, the developed Android application was distributed through the Android Market, Google's official online software store for Android applications, to facilitate installation into client devices. The Android Market was also used to collect feedback and comments from users.

For this research, we developed a Google Android application for sports education, namely track and field use, to support both the learner (athlete) and the educator (trainer). The developed application supports the following 2 track and field events:

1) men's decathlon event and

2) female's heptathlon event.

The developed application calculates the points achieved for each event, and displays the current total score. Fig.1 shows a snapshot of the application running the men's decathlon score calculation.

Fig. 1. Decathlon score calculation application

For the calculation program for both events, the following supporting features were implemented.

1) Simultaneous score calculation during user record entry.

2) Multiple file support for saving record and score status.

Simultaneous score calculation during user record entry was implemented to minimize user operation. By this feature, users do not have to select a separate button to initiate calculation, and also does not require unnecessary zeros after the decimal point.

Multiple file support of score tables allows a single user to keep records of previous records of the same athlete, as well as keep records of multiple athletes for the same event. Fig.2 shows the multiple file selection for the developed application. Multiple file support enables athletes to compare their current record and progress with past records on previous decathlon/heptathlon events. Athletes can estimate their final score, and motivate themselves to improve their record, as well as allow the athlete to simulate how much effort must be put in the individual events still left, in order to keep ahead of the competition or improve personal records. For the coaches (or educators), multiple file support allows the coach to keep track and compare the individual scores for each athlete competing in the same event, including scores of the competition. The coach can compare the scores of each athlete and their previous records, to give more precise advice on strategy on which individual events to save stamina and which events to give extra tries.

Fig. 2. Multiple file selection screen

4 EXPERIMENT RESULTS

The developed Android application was registered in Google Android Market as "Track and Field Combined Event Calculation Tool" for public access, as a free application. Fig. 3 shows the registered application as seen on Android Market. The developed application was the first registered Android Market application for track and field combined event (decathlon and heptathlon) score calculation to support Japanese. We also asked the Tokyo University of Information Sciences track and field team coach to use the application and asked for feedback regarding the effectiveness of the application for sports education.

On the Android Market, as of November 30, 2011, there has been over 500 downloads of the developed application, and the overall rating of the application is 4.4 from a maximum 5.0 . There had been 1 report on a program error, which was immediately fixed and the fixed program uploaded. Another comment gave positive feedback on requested features for user interface.

From the track and field coach, positive comments on the effectiveness of the application on sports education were received. Further enhancements on the user interface were also requested, such as being able to show multiple athletes' records on 1 screen, or a 1-click feature for quickly switching multiple athletes' records.

Currently, the effectiveness of the developed application has not yet been evaluated statistically, but from user reviews on the Android Market and direct feedback from the track and field coach, the developed application running on a smartphone was shown to be effective in sports education support. Compared to previous reports using mobile phone applications, the developed application using smartphones enabled multiple file support as well as touch screen user interface, and greatly improved on accessibility and operability.

Fig. 3. Application registered in Android Market

5 CONCLUSION

In this research we propose using smartphones for sports education to improve the learning curve of athletes. In order to promote the use of e-learning for sports education, smartphones were selected as the target hardware for this research. In particular, Google Android was selected for the smart phone platform for the large client base and ease of development. We developed a Google Android application for sports education, namely track and field use, to support both the learner (athlete) and the educator (trainer). The developed application targets men's decathlon and female's heptathlon, and calculates the points achieved for each event, and displays the current total score. In the developed application, features for 1) simultaneous score calculation during user record entry, and 2) multiple file support for saving records and scores were implemented.

From user reviews and comments from an active track and field coach, positive feedback on the effectiveness of the proposed application for sports education were received.

For future works, improvements on user interface based on user requests will be implemented. Further, we plan to create a client-server model for sports education to allow data sharing between learners and trainers, and support real-time educational feedback from trainers to learners.

REFERENCES

[1] Kenneth J. Mackin, Masahiro Ishii (2007), Using Mobile Computers in Sports Education (in Japanese). Tokyo University of Information Sciences Journal, Vol.10 No.1 pp.1-9

The Seventeenth International Symposium on Artificial Life and Robotics 2012 (AROB 17th '12),
B-Con Plaza, Beppu, Oita, Japan, January 19-21, 2012

A vision-based motion-speed instruction method. Application to motion learning of underarm throw.

Akinobu Morikawa [1], Ryota Sakamoto [2] and Yoshihiko Nomura [1]

[1] Mie-University, Tsu, Japan
[2] Mie University Hospital, Tsu, Japan

Abstract: When we learn our body motions with the physical exercises such as dances and sports, The learner, by him/herself, shall evaluate the correctness of the imitation in his/her movements. Therefore, we have developed a human-interface for instructing motions instead of instructors. The system was implemented with two functions. The first function is to evaluate the learner's movements. The second function is to correct the learner's motion using visual information. With these two functions, the learner can learn highly skilled motions in sports and dances by oneself. However, when instructing dynamic motions, we have to take into considerations not only postures but also speeds and accelerations. In this paper, aiming at providing a solution for the kind of motion speed instruction tasks, we proposed a vision-based system that is specifically designed for showing motion speed information to learner, and applied to an underarm ball throwing action. That is, while throwing before release, based on the online motion information, i.e., the velocity and position, the system predicts the after-release ball trajectory, and shows the trajectory to the learner in real-time. It is expected that, with the help of the predicted trajectory shown in real-time, the learner becomes to be able to adjust his/her motion in accelerative or declarative ways, and, thus, he/she masters the appropriate motion speed for hitting the reference. As a result of the instruction experiment, the proposed motion instruction system has feasibility as a practical tool for on-line motion speed

1. INTRODUCTION

How do we learn our body motions with the physical exercises such as dances and sports? While visually observing the expert's movements, we repeatedly practice in order to imitate expert's movements. Thus, vision-based motion learning methods, so-called, teach-by-showing, conversely learn-by-observing methods, would be typical ways of learning human boy motions. However, this process contains a fatal flaw in learning quality. It is that the learner, by him/herself, shall evaluate the correctness of the imitation in his/her movements. Even if the learner judged the movements correct, it may be actually incorrect movements. The misunderstanding may falls into a wrong motion acquirement. Thus, instructors who observe and correct the learners' movements are very important for learners to avoid such misleading. Therefore, we have developed a human-interface for instructing motions instead of instructors. The system was implemented with two functions. The first function is to evaluate the learner's movements. The second function is to correct the learner's motion using visual information. With these two functions, the learner can learn highly skilled motions in sports and dances by oneself.

In previous studies, we had developed a motion instructing system that visually teaches static postures using a motion-capturing suit and a head-mounted display. By using this system, we had instructed static poses of yoga [1] and pantomime [2].

However, when instructing dynamic motions, we have to take into considerations not only postures but also speeds and accelerations. For example, to enhance the correctness in ball throw toward a goal position (see Fig.1).Can you predict the trajectory of a ball from this picture? It must be impossible because, for the prediction, we need the ball velocity vector information together with the position at the release time.

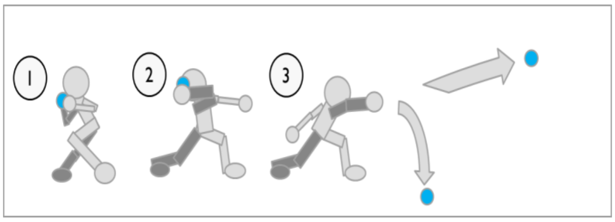

Figure 1 Ball throw toward a goal position

In previous studies, [3] and [4] utilized muscular power representation together with the postures . In this system, learners are assumed to align with the muscular power of reference motions. However, this system has a problem that we cannot perceive and control muscular powers quantitatively. In this sense, the muscular powers are not necessarily an effective way in motion monitoring.

Therefore, we recognized the importance of direct monitoring of the speed information. As for the speed information monitoring, there were various studies .

One of the systems has an off-line learning function that the learner can compare reference speed with his speed after operation [5]. Another system provides the motion correction information to learners so that learners adjust their motion speed either more or less faster in real-time [6]. However, there has not been seen any research on a systems that shows learners the difference of the present speed from the reference one. In this paper, aiming at providing a solution for the kind of motion speed instruction tasks, we proposed a vision-based system that is specifically designed for showing motion speed information to a learner. That is, while throwing before release, based on the online motion information, i.e., the velocity and position, the system predicts the after-release ball trajectory, and shows the trajectory to the learner in real-time. It is expected that, with the help of the predicted trajectory being shown in real-time, the learner becomes to be able to adjust his/her motion in accelerative or declarative ways, and, thus, he/she masters the appropriate motion speed for hitting the goal.

2. PROPOSED METHOD

2.1 Reference motion

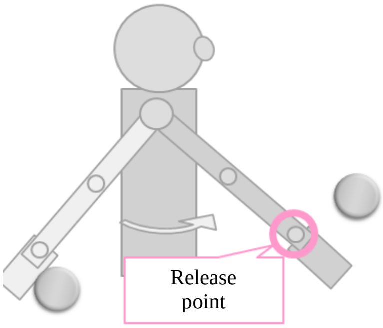

Figure 2 Example of a simple underarm throw motion

In this paper,, a simple underarm throw operation was examined. The underarm throw motion is a 1-DOF shoulder joint inward rotation, i.e., the flexion, where both an elbow and wrist joints were fixed so as not to bend.

2.2 Proposed display systems

Next, we considered the ways of presenting the velocity differential to a learner. We took the following points into considerations.

・The learner can react in real time.
・The learner can perceive the velocity differential.

Then, we thought up the following four presentation methods.

a. Ghost display
b. Speed meter display
c. Color display
d. Trajectory display

For all the display systems, the velocity difference is calculated by the following formulas, and is represented in either a desktop-PC monitor or a HMD by the ways to be described in the followings.

$$v_{e(t)} = v_{l(t)} - v_{r(t)} \dots\dots\dots\dots (1)$$

v_e : Velocity difference
v_r: Reference velocity
v_l: Learner's velocity
t : Present time ($t = 0$ at the motion start time)

a. Ghost display

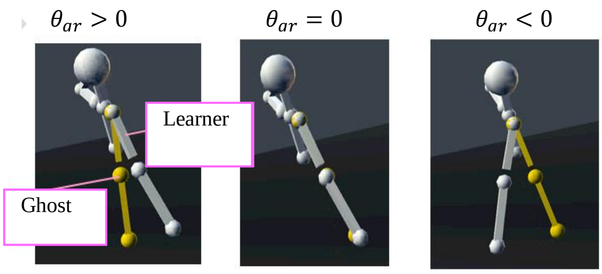

Figure 3 Ghost display system

While the learner's arm graphic being displayed, a ghost arm graphic is additionally displayed in proportion to the velocity difference of a ghost representing the reference motion, from a learner. The displayed ghost's shoulder joint rotation angle, θ_{gr}, is given by

$$\theta_{gr(t+1)} = \theta_{l(t)} - k_g e_{v(t)} \dots\dots\dots\dots\dots\dots (2)$$

θ_{gr} : Ghost's shoulder joint rotation angle (reference)
θ_l : Learner's shoulder joint rotation angle
k_g : Feedback gain for ghost display

The learner can learn a reference velocity by controlling his/her muscles so that the learner's arm graphic may lie on top of a ghost one.

b. Speed meter display

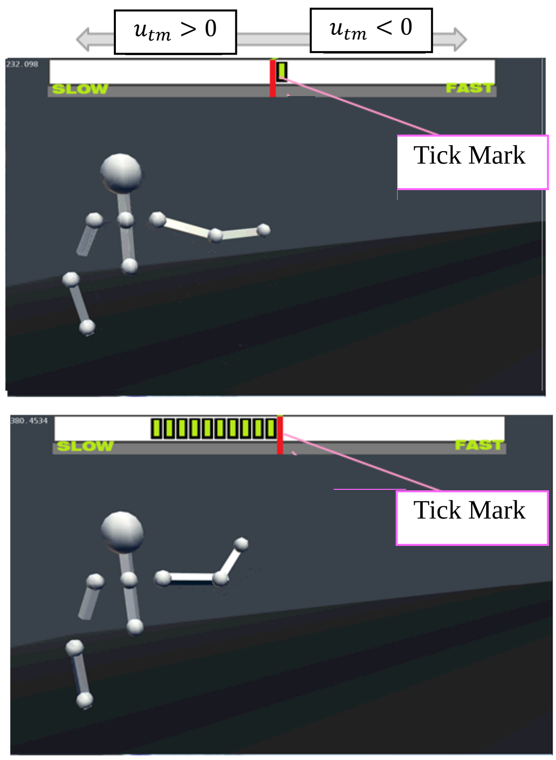

Figure 4 Speed meter display system

In the meter display system, a velocity differential is represented in the quantity of the tick marks. The quantity of the tick marks, u_{tm}, is given by

If the learner's motion is too fast, the tick marks increase to the right, which suggests the learner to move his/her arm more slowly., On the contrary, if, vice versa, the tick marks increase to the left, this system suggests the learner to move his/her arm faster.

c. Color display system

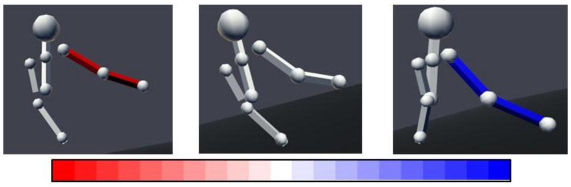

Figure 5 Color display system

The color display system represents the velocity difference by color. If the brightness of the color shows deep, the velocity difference is large. The RGB color intensites, *r*, *g*, *b*, are given by

If $v_{e(t)} > 0$

$$\begin{cases} r_{(t+1)} = 255 \\ g_{(t+1),} b_{(t+1),} = 255 - k_c v_{e(t)} \end{cases} \cdots\cdots\cdots(4)$$

If $v_{e(t)} < 0$

$$\begin{cases} b_{(t+1)} = 255 \\ r_{(t+1),} g_{(t+1),} = 255 - k_c v_{e(t)} \end{cases} \cdots\cdots\cdots(5)$$

k_c
: Feedback gain for color dispay
r, g, b : RGB intensity values

If model's arm changes its color to red, this system informs the learner to move his/her arm faster. While, if the model's arm color is blue, this system inform learner to move his/her arm more slowly.

d. Trajectory display system

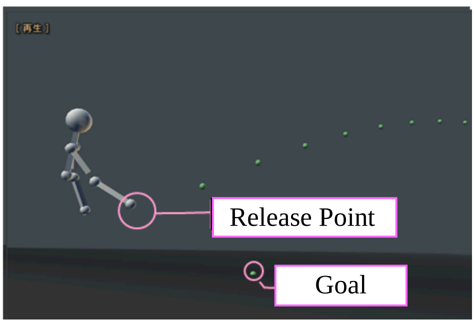

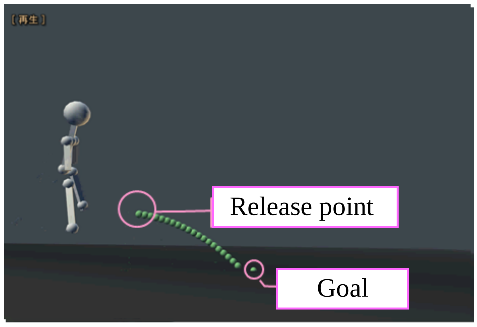

Figure 6 Trajectory display system

While throwing before release, based on the online motion information, i.e., the velocity $v_{l(t)}$ and position$\theta_{l(t)}$, the velocity vector $\vec{v}_{(t_{RP})}$ at the release point t_{RP} is assumed: in this paper, the magnitude of the velocity vector $\vec{v}_{(t_{RP})}$ at the release point t_{RP} is assumed to be identical to the present velocity $v_{l(t)}$, and the throwing direction is assumed to be given as a known unit vector $\vec{n}_{(t_{RP})}$. That is,

$$\vec{v}_{(t_{RP})} = \vec{n}_{(t_{RP})} v_{l(t)} \quad \cdots\cdots\cdots\cdots\cdots\cdots\cdots(6)$$

Next, assuming a free-fall motion with the initial velocity $\vec{v}_{(t_{RP})}$, the trajectory display system calculates the after-release ball trajectory and shows the trajectory to the learner in real-time.

It is expected that, with the help of the predicted trajectory shown in real-time. The learner becomes to be able to adjust his/her motion in accelerative or declarative ways, and, thus, he/she masters the appropriate motion speed for hitting the goal.

3. EXPERIMENTS

3.1 Discussing issues

We carried out some psychophysical experiments to evaluate the effectiveness of the proposed display systems. In this experiment, we ask for examinees to answer their subjective rating values with respect to the following issues.

1. Has the presentation been easy to perceive how much your motion velocities are deviated from the reference ones?
2. Have you enjoyed yourself when using the displaying method?
3. Haven't you felt stress?

3.2 Experimental devices

We used a binocular-type 3-D range finder, i.e., XtionPro which was made by Asus Corp (see Fig.7).

Figure 7 Xtion Pro: appearance (left), a captured range image (right)

3.3 Visual presentation program

An example of the visual presentation is shown in Fig.8. In the experiments, the upper-half- body model was employed.

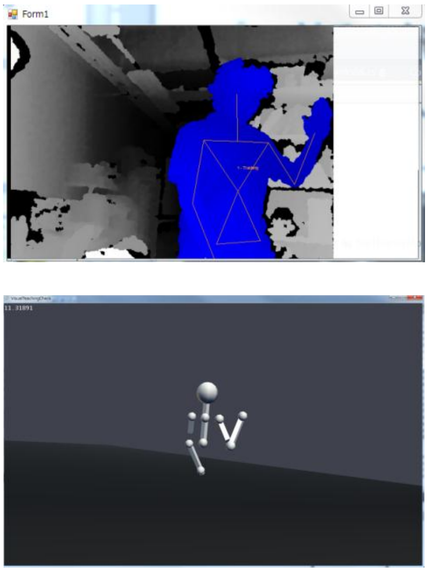

Figure 8 Visual presentation: an extracted human skeleton (top), created CG image based on the extracted human skeleton 3-D information (bottom)

3.4 Experimental result

The comments answered by the subjects with respect to the display systems were as follows.

Ghost display

・The CG images were just shown by the rectangular parallelepiped, and, therefore, I felt unclear in the discrimination of whether ghost model has overlapped or not.

. I felt disturbed in deciding an action of either acceleration or deceleration because the ghost responded to learner's motion too sensitively.

Speed meter display

・I felt disturbed in deciding an action of either acceleration or deceleration because the scale either increased or decreased too frequency.

・I suffered much stress in decreasing the quantity of the tick marks, i.e., in adjusting my arm velocity to the reference one .

Color display

・It was hard to notice the color change.

・I didn't feel much fun in this system because the color representation was too low-keyed.

・I feel tired in my eye when trying to detect the change in color.

Trajectory display

・ It was easy to perceive the appropriateness of my arm-motion speed by observing the predicted after-release trajectory.

・I felt fun in aiming at the goal position while changing trajectory.

As a result, almost all the people approved the trajectory display system among the four display systems. Two reasons are considered for the approval as in the followings. One reason is that the learners were able to learn as if they played a game. The other reason is that the learners were able to know in advance about what is going to happen.

4. CONCLUSIONS

We had thought up four kinds of motion display systems. Next, we had evaluated their performance through some psychophysical experiments, and confirmed that the trajectory display system was best performing among them, and it is considered to have a potential ability to meet our objective.

In the future, we are directed to evaluate the display system in learning under throw motion

This work was supported by KAKENHI (Grant-in-Aid for Scientific Research (B), No. 21300307) from Japan Society for the Promotion of Science (JSPS).

REFERENCES

[1]Yuki Yoshimura, Yoshihiko Nomura, Tokuhiro Sugiura, "An Upper-Limb Exoskeletal Motion Measurement System for Conservative Motion Instruction" JSME annual meeting 2008(5), 205-206, 2008-08-02

[2]Akinobu Morikawa, Yuki Yoshimura, Ryota Sakamoto, Yoshihiko Nomura, Tokuhiro Sugiura, "An Assistive System for Learning Human Motions and Anatomies", JSME annual meeting 2010(7), 141-142

[3] INABA Hiroshi, TAKI Tsuyoshi, TAKI Tsuyoshi , HASEGAWA Junichi, KOEDA Mitsuhiro, KITAGAWA Kaoru "Visualization of Human Body Sensing for Sports Training", The Journal of the Society for art and Science vol.2 No.3 pp.94-100

[4] Koji Ur awaki, Yasushi Masuda, Yoshihiro Yasumuro, Yoshitsugu Manabe and Kunihiro Chihara "Development of the Learning environment for Sport-form Education with the Visualization of Biophysical Information" , International Conference on Artificial Reality and Telexistence 576-579 (2004)

[5]Chan, J.C.P, Leung, H, Tang, J.K.T., Komura, T. "A Virtual Reality Dance Training System Using Motion Capture Technology", IEEE Transaction On Learning Technologies vol.4 (2011)

[6] Kazuki Ishii, Mastato Soga, Hirokazu Taki,"Reversal Motion Skill Learning Support Environment by Using A Wearable Motion Capture System", Information Processing Society of Japan Interaction2011

The Seventeenth International Symposium on Artificial Life and Robotics 2012 (AROB 17th '12),
B-Con Plaza, Beppu, Oita, Japan, January 19-21, 2012

Acquisition of Rules for Selecting Suppliers of Raw Materials in Distributed Production Systems by means of Reinforcement Learning

Hisaaki Yamaba[1], Kayoko Takatsuka[1], and Shigeyuki Tomita[1]

[1] University of Miyazaki, Miyazaki, Miyazaki 889-2192, Japan
(Tel: 81-985-58-7425, Fax: 81-985-58-7425)
(yamaba@cs.miyazaki-u.ac.jp)

Abstract: In these days, many production systems are consist of several factories. Such factories are dispersed in wide area and form "production networks". In such networks, each factory produces intermediate materials for other factories. In order to operate production networks efficiently, some rational and sound operational strategy is needed for realizing cooperative operation. In the previous work, "Behavior Model" of scheduling activities in decentralized production networks was developed and the validity was confirmed. Also, an attempt was made to obtain proper scheduling rules by means of reinforcement learning. Concretely, Profit Sharing was adopted in order to obtain rules for selecting suppliers of intermediate materials under the proposed operational model. In this work, improvement of the representation of states used in the rule learning was attempted. A series of experiments was carried out in order to examine the performances of the rules obtained under the new representations.

Keywords: Production System, Supply Chain, Reinforcement Learning

1 INTRODUCTION

In these days, many production systems are composed of several factories. Such factories are dispersed in wide area and form "production networks". In such networks each factory produces intermediate materials for other factories. In such networks, decision-making in each factory is currently carried out independently of other factories, and this causes low performance of the whole system. In order to operate production networks efficiently, some rational and sound operational strategy is needed for realizing cooperative operation among such networks. In order to manage such a production network soundly, negotiations among factories are very important. In the previous work, "Behavior Model" of scheduling activities in decentralized production networks was developed (Yamaba [1]). Also, an attempt was made to obtain proper scheduling rules by means of reinforcement learning (Yamaba [2]). Concretely, Profit Sharing was adopted in order to obtain rules for selecting suppliers of intermediate materials under the proposed operational model.

In this work, improvement of the representation of states used in the rule learning was attempted. A series of experiments was carried out in order to examine the performances of the rules obtained under the new representations.

2 CHARACTERISTICS OF TARGET PRODUCTION SYSTEM NETWORK

The target production system network in this work is composed of a single business department and several factories. Locations of them are widely dispersed.

Each order from customers is completed through multi-stage manufacturing processes. For example, plastic film manufacturing companies with an upper process of raw plastic film creation and several lower processes of chemical treatment of plastic films are assumed. Each stage of manufacturing of an order is allowed to be performed at different factories. Some factories have facilities only to create raw plastic film, some factories have facilities to perform chemical treatment of plastic film, and others have both of the facilities.

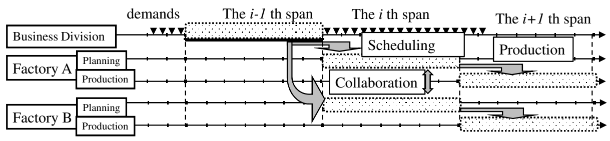

Fig. 1. An example of a timetable of the target production system

Orders from customers are concentrated to the single business department. The business department selects a factory for manufacturing processes of each order periodically (e.g., every one month). Each factory makes out production schedules of given orders together with procurement plans of intermediate materials at the same time. "Procurement plans" mean selection of factories for each intermediate material.

An example of a timetable of the production system is shown in Fig. 1. In general, schedules of orders given in the i 1 th span are made in the i th span and bases produce them in the $i+1$ th span.

In such a production network, if "Factory A" makes an order of its intermediate material needed to produce an order given in i 1 th span to "Factory B" in the i the span, "Factory A" cannot finish making out its schedule until it will be determined that "Factory B" will accept the order or not. Since "Factory B" makes out its own schedule for orders given in i 1 th span in the same span, "Factory B" cannot reply whether it can accept the order or not until the schedule is fixed. In general, "Factory B" also makes orders of its intermediate materials to other factories. This causes longer time until the whole scheduling process is finished. In particular, if "Factory B" also made an order to "Factory A", the scheduling process never finishes because of a deadlock. So it is indispensable to realize a scheduling algorithm which is equipped collaboration mechanism among factories.

3 BEHAVIOR MODEL OF DECENTRALIZED SCHEDULING

In order to realize the sound scheduling method, the concept of "behavior model" was introduced (Yamaba [1]).

Receiving orders of intermediate materials from other factories, each factory create several schedule candidates. However, it could be happened that no schedule candidate can satisfy all of the limitations of production (due date) of the given requirements in case that much workload which exceeds the productive ability of the factory is given. In this work, it is assumed that factories are allowed to reject some requirements on such occasions. But factories have to reply to the orderer that the requirements are rejected within the designated time span.

Receiving a reply of rejection ("reject messages"), production bases select another factory and make an order to the selected factory again. It is assumed that there is a limitation for the number of attempts of re-selection of factories. When the number of the re-selecton for the N 1th process exceeds the limitation, the orderer factory abandon the request of N th process given to the factory itself. Such factories reply the "reject message" to the orderer factory of the N th process.

4 LEARNING OF SUPPLIER SELECTION RULES

4.1 Supplier Selection Rules

There are several factors affecting the performance of schedules of production networks discussed here. In Yamaba [2], an acquisition method of rules for selecting proper factories for intermediate materials was proposed. Reinforcement learning was adopted in the method. Profit Sharing is one of the most promising methods of reinforcement learning. The method was used in order to obtain operational rules of engineering systems (Arai[3], Yamaba [4], Yamaba [5]).

The target production systems are plastic films factories. It is assumed that there are three processes in the production system: the film creation and two stages of chemical treatment of film processes (Fig. **??**.). Also, there are 3 types of factories in the target production system.

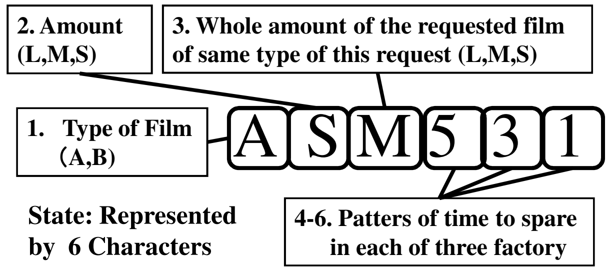

Fig. 2. Representation of states of an intermediate material requirement

Type 1: factories which has facilities for film creation processes only.

Type 2: factories which has facilities for chemical treatment processes only.

Type 3: factories which has all facilities.

It is assumed that there is one factory of Type 1 (factory 1), two factories of Type 2 (factory 2 and 5) and two factories of Type 3 (factory 3 and 4).

The target production systems deal with two types of films α and β. Each type of films is produced by fixed type of machines: machine type A and B. And in this work, it is assumed that requests of intermediate materials are limited to be required from Type 2 to Type 1 and 3. As for the factories of Type 3, intermediate materials required for the final products are processed the factory itself.

4.2 States of a production system

In this work, proper selection of factory for each of intermediate material requirement according to the conditions of the whole production network and the feature of the requirements is intended. Basically, next two points are concerned in representation of the states.

1. Vacant time in the current schedule (This means a time to spare for new requirements.)
2. Whole amount of requests

Concretely, a state of each intermediate material requirement is described as a string composed of six characters (See Fig. 2.).

1 The first character is one of "A" or "B". It represents the type of machine for film creation.

Table 1. The concrete values of L, M, S

	2	3 (α)	3 (β)	4-6
L	25	90	70	40
M	15 – 25	50 - 90	40 - 70	20 - 40
S	< 15	< 50	< 40	< 20

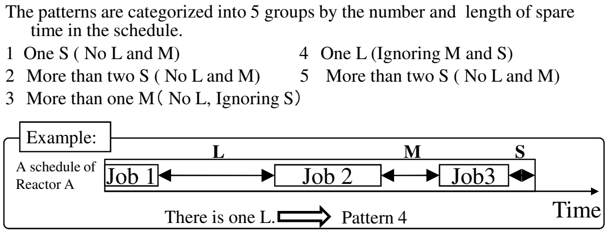

Fig. 3. Representation of vacant time in schedules

2 The second character is one of "S", "M" or "L". It represents the amount of the requested film. The first column in TABLE 1 shows the correspondence of an concrete amount and the three characters.

3 The third character is one of "S", "M" or "L". It represents the whole amount of the requested film which is the same type with the requests. Besides, requirements which are accepted already by some factory are ignored. The second and the third column in TABLE 1 shows the correspondence of an amount and the three characters.

4 – 6 Each of the 4 th , 5 th and 6th characters is one of "1", "2", "3", "4" or "5". They represent the pattern of vacant time in the factory 1, 3, and 4.

The 5 patterns used in from 4th to 6th characters are categorized by the number and the length of vacant time in the schedule of the corresponding factory (Fig. 3.). The length of vacant time is represented by "S", "M" or "L". The 4th column in TABLE 1 shows the correspondence of amounts and the three characters. Patterns are categorized by the number of each type of vacant time:

Pattern 1 There is only one S. (No M ,L).

Pattern 2 There are more than two S. (No M, L).

Pattern 3 There are more than one M. (No L).

Pattern 4 There is one L.

Pattern 5 There are more than two L.

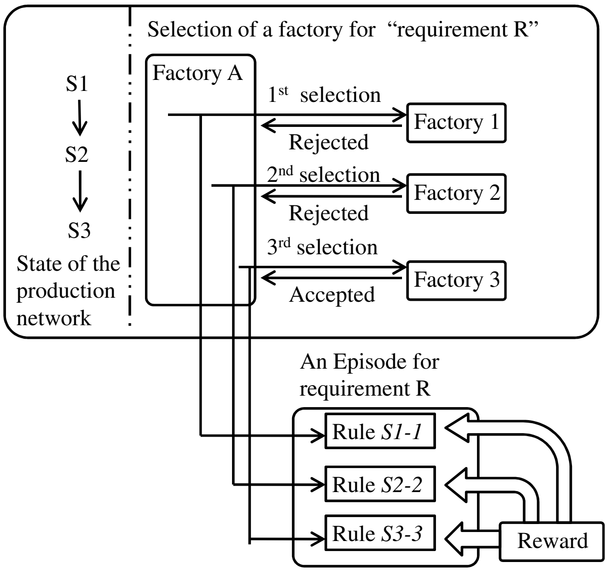

Fig. 4. The process of learning of rules

4.3 Process of Learning Rules

There are three actions (selection of factory 1, 3 or 4) for each state. A combination of each of the three actions and a state form "rules". The module of reinforcement learning observes the target production system and obtains data about current condition of the system. Next, the reinforcement learning module identifies the state of each intermediate material requirement. Then, the module selects a rule from three rules of the identified state.

Episodes of Profit Sharing start when requirement of intermediate materials are generated (See Fig.4.). A rule is selected from rules which are corresponding to the state of the requirement and the production network at that time. The selected rules are added to the episode of the requirement. The request of intermediate material is sent to the factory which is indicated by the selected rule. If the selected factory accepts the requests, a reward is given to the rules in the episode. On the other hand, in case that the request is not accepted, another factory is selected and the request is sent to the new factory. Since some requirements may be accepted, the state of each intermediate will be changed at each "re-scheduling".

5 IMPROVEMENT OF STATES REPRESENTATION

5.1 Introduction of new representation

First, preliminary experiments were carried out in order to examine the performance of the original representation. From the results of the experiments, several problems below were found.

- There are 2250 states under the proposed "6 characters"

Table 2. New ranges of spare times

Set No.	original	1	New 2
L	> 40	> 3000	> 5000
M	20 40	1500 3000	3000 3000
S	< 20	< 1500	< 3000

Table 3. Appearance of states

Set No.	original	1	2
Appeared states	307	1301	1349

representation, but the number of states which appeared frequently was almost 300 in the experiments.

- Appearance of states with Type 3 (including M size spare time) was very rare.
- 95% of appearedd states were type 4 or 5 (including L size spare time).

These results show that the ranges of a spare time used in the previous work did not match time length of production jobs. Concretely, the ranges of L and M have to be expanded.

So, new several candidates of ranges to represent spare time of machines were introduced. Table 2 shows two examples of the range sets used in the experiments below.

5.2 Experiments

A series of experiments was carried out in order to confirm that factory selection rules obtained under the new spare time ranges had ability to separate states of production networks properly keeping a performance of the rules. Since the model production network are same with the one used in the previous work (Yamaba [2]), the details is omitted here.

The numbers of appeared states are shown in Table 3. This result shows that the new ranges seems separate states of a production network more adequet then original one.

Table 4 shows the number of whole orders and rejected orders in the simulation experiments operated using the supplier selection rules obtained under the each spare time ranges. The column of "random" is the result of the experiment under the condition that supplier selection was carried out at random. Percentages of a rejected order ratio to the one when random selection was used are also shown in Table 4. The percentages show that the obtained rules can select proper factories.

6 CONCLUSION

An attempt was made to obtain operation rules by reinforcement learning in order to manage production network effectively.

Table 4. Comparison of performance

Set No.	original	1	2	random
Whole orders	170098	171556	172070	171234
Rejected orders	22216	22907	23327	26192
Rejected ratio	13.06	13.35	13.56	15.30
Percentage to random	85.39	87.29	88.63	100

The new candidates of ranges were proposed and it was confirmed that the new ranges separated the sates of the target production networks more adequate keeping the performance of the obtained supplier selection rules.

REFERENCES

[1] Yamaba H and Tomita S (2006), Network-based Support System for Decentralized Scheduling of Distributed Production Systems through Man-Machine Collaboration. Proceedings of 2006 IEEE International Conference on Indeutirial Informatics:1285-1290

[2] Yamaba H, Matsumoto S and Tomita S (2008), An Attempt to Obtain Scheduling Rules of Network-based Support System for Decentralized Scheduling of Distributed Production Systems. Proceedings of 2008 IEEE International Conference on Indeutirial Informatics:506-511

[3] Arai S, Miyazaki K and Kobayashi S (1998), Cranes Control Using Multi-Agent Reinforcement Learning. International Conference on Intelligent Autonomous System(5):335-342

[4] Yamaba H, Yoshioka H and Tomita S (2004), Acquisition of AGV Control Rules Using Profit Sharing Method and Evaluation of the Rules. Knowledge-Based Intelligent Information Engineering Systems & Allied Technologies(2):405-411

[5] Yamaba H and Tomita S (2010), A Design Support System for Discrete Production Systems with AGVs – Object-Oriented Simulator Generator and Acquisition of AGV Control Rules Using Reinforcement Learning– . Kagaku Kogaku Ronbunshu 36:127-135

The Seventeenth International Symposium on Artificial Life and Robotics 2012 (AROB 17th '12),
B-Con Plaza, Beppu, Oita, Japan, January 19-21, 2012

Analysis of Manipulator in Consideration of Impact Absorption between Link and Object

Asaji SATO[1] , Osamu SATO[2] , Nobuya TAKAHASHI[2] and Masahiro YOKOMICHI[2]

[1]*Dept. of Mechanical Engineering, Miyakonojo National college of Technology, Miyakonojo 885-8567, Japan.*
[2]*Dept. of Computer Science and Systems Engineering, Faculty of Engineering, University of Miyazaki, Miyazaki 889-219, Japan.*

Abstract: In this paper, equations of motion of a manipulator are derived in consideration of characteristics of driving source. By considering impact force absorption between a link and an object, trajectories for saving energy are calculated by the iterative dynamic programming (IDP) method. And, the dynamic characteristics of manipulator controlled based on the trajectory for saving energy are analyzed theoretically and investigated experimentally.

Keywords: Manipulator, Trajectory, Dynamic Programming, Impact force, Minimum Energy.

1 Introduction

For the purpose of enlarging the work space in carriage work, it is necessary to study the throwing motion of a manipulator. In a previous report [1], a casting manipulator is introduced, and it has large work space compared with its simple mechanism. However, considerations of energy consumption are not enough. Evaluations of robotic mechanisms subjected to impact load are investigated [2], but energy consumption is not considered.

In previous report [3], trajectories for saving energy about the throwing motion of manipulator were easily calculated by IDP method. And, dynamic characteristics of the system were analyzed. In previous report [4], considering the collision between the link and the object, and considering the active motion which absorbs kinetic energy from the object, the trajectories for saving energy are calculated by the IDP method.

In this paper, equations of motion of a manipulator are derived in consideration of the characteristics of DC servomotors, and a performance criterion for saving energy is defined in consideration of energy consumption of the driving source. When the manipulator is operated in a vertical plane, the system is highly non-linear due to gravity, and an analytical solution can not be found. Then, a numerical approach is necessary. By considering impact force absorption between a link and an object, trajectories for saving energy are calculated by IDP method. The dynamic characteristics of manipulator controlled based on above-mentioned trajectory are analyzed theoretically and investigated experimentally.

2 Modeling of manipulator

The dynamic equations of the manipulator with two degrees of freedom, as shown in Fig. 1, which is able to move in a vertical plane, are as follows.

$$\begin{bmatrix} A_{11} & A_{12} \\ A_{21} & A_{22} \end{bmatrix} \begin{bmatrix} \ddot{\theta}_1 \\ \ddot{\theta}_2 \end{bmatrix} = \begin{bmatrix} A_{13} \\ A_{23} \end{bmatrix} \tag{1}$$

where

$$A_{11} = a_1 \,, A_{12} = a_3 \cos(\theta_1 - \theta_2) \,, A_{21} = A_{12} \,, A_{22} = a_2$$

$$A_{13} = \tau_1 - a_3 \dot{\theta}_2^2 \sin(\theta_1 - \theta_2) - a_4 \cos\theta_1 - F l_1 \cos\theta_1$$

$$A_{23} = \tau_2 + a_3 \dot{\theta}_1^2 \sin(\theta_1 - \theta_2) - a_5 \cos\theta_2 - F l_c$$

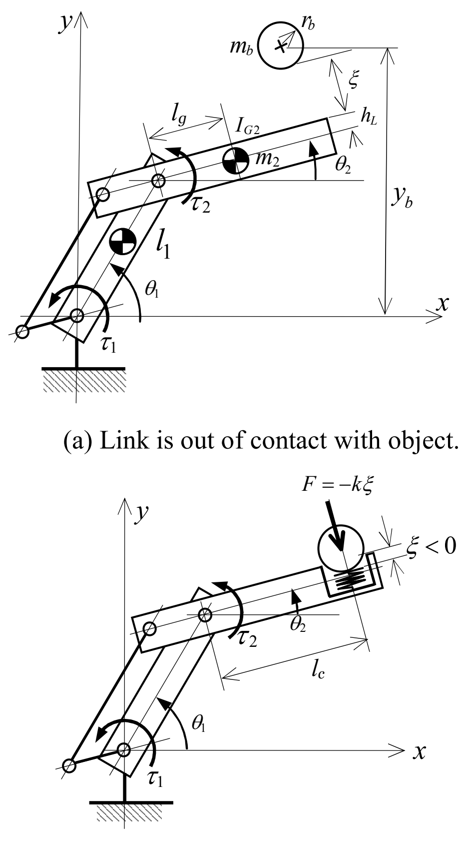

(a) Link is out of contact with object.

(b) Link is in contact with object.

Fig.1 Mechanism of manipulator

$$a_1 = m_1 l_{g1}{}^2 + I_{G1} + m_2 l_1^2 \ , a_2 = I_{G2} + m_2 l_{g2}{}^2$$
$$a_3 = m_2 l_1 l_{g2} \ , a_4 = \left(m_1 l_{g1} + m_2 l_1\right) g \ , a_5 = m_2 g l_{g2} \ .$$

When the link is in contact with an object, the contact force is

$$F = -k\xi \quad , \quad (\xi < 0) \quad . \tag{2}$$

Where ξ is displacement of spring, and

$$\xi = \frac{y_b - (l_1 \sin\theta_1 + l_c \sin\theta_2)}{\cos\theta_2} - (h_L + r_b) \quad . \tag{3}$$

The applied voltage of the servomotor is

$$e_j = b_{1j}\dot{\theta}_j + b_{2j}\ddot{\theta}_j + b_{3j}\tau_j + b_{3j}\tau_{f_j}\ \mathrm{sign}(\dot{\theta}_j) \tag{4}$$
$$(j = 1, 2) \quad ,$$

where

$b_{1j} = k_{vj} + (R_{aj}/k_{tj})D_{mj}$, $b_{2j} = (R_{aj}/k_{tj})\mathrm{I}_{mj}$, $b_{3j} = R_{aj}/k_{tj}$,

i_{aj} : electric current of the armature ,

R_{aj} : resistance of armature ,

I_{mj} : moment of inertia of armature,

D_{mj} : coefficient of viscous damping.

Then, the electric current is

$$i_{aj} = (e_j - k_{vj}\dot{\theta}_j)/R_{aj} \ . \tag{5}$$

And, the consumed energy is

$$E_j = \int (e_j \cdot i_{aj}) dt \ . \tag{6}$$

3 Simulation of the manipulator

We shall take the parameters of the system as shown in Table 1.

Figure 2 shows a flow chart for iterative dynamic programming method. In frame (A), the trajectory for saving energy is searched by IDP method [3]. In frame (B), the searching region is shifted to minimize the consumed energy, and width of the region is changed smaller.

Figure 3 shows the trajectory for searching, and initial trajectory for searching is expressed as

$$\theta_j = \theta_{ji} + \frac{(\theta_{jf} - \theta_{ji})}{2}\left\{1 - \cos\left(\frac{\pi}{t_f} t\right)\right\} \quad . \tag{7}$$

The performance criterion is

$$E' = \int (e \cdot i_a) dt + C_1 \int |F| \cdot dt + C_2 |y_b'| \quad . \tag{8}$$

The simulations of the system are done as follows.

Figure 4 and 5 show the response of the manipulator. The motion of an object is free-fall from initial height y_b=0.18(m). When t=0.206(s), the object is in contact with the link. And then, position and velocity are y_b'=0.03 (m), $\dot{y}_b$=–1.75 (m/s). Under the condition that $\theta_{2i} = \theta_{2f}$ =0, an optimal trajectory is calculated by IDP method.

Table 1 Parameters of the manipulator

Parameter	Value	Parameter	Value
l_2 (m)	0.10	I_{G2} (kgm^2)	4.8×10^{-5}
l_{g2} (m)	0.057	I_{m2} (kgm^2)	8.5×10^{-5}
m_2 (kg)	0.045	D_{m2} (Nms/rad)	7.9×10^{-5}
m_b (kg)	0.017	k_{t2} (Nm/A)	0.046
R_{a2} (Ω)	3.5	k_{v2} (Vs/rad)	0.046
k (N/m)	9000	τ_{f2} (Nm)	0.013
c (Ns/m)	2.0		

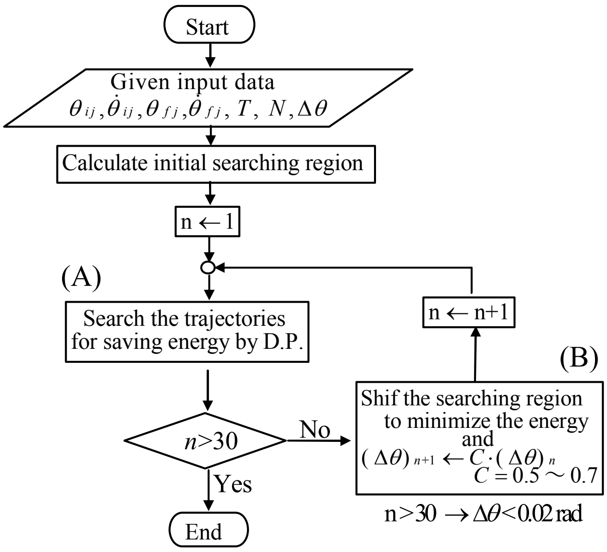

Fig.2 Flow chart for simulation

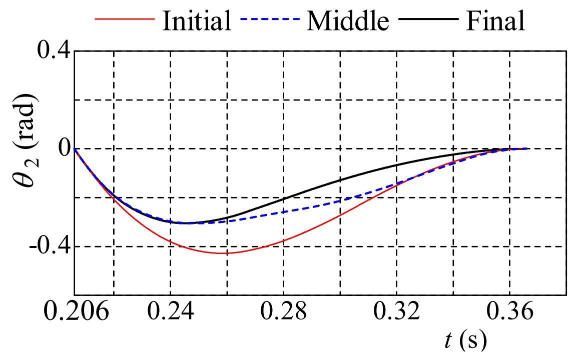

Fig.3 Trajectory for searching

In Figure 4, under the condition that $\dot{\theta}_{1i}$ =0, $\dot{\theta}_{2i}$ =–17.5 (rad/s), the solid lines show the response of manipulator which is actuated along the optimal trajectory. And broken lines show the response of manipulator which is fixed at the initial position. Impact force F about actuated case (solid line) becomes smaller than one of fixed case (broken line). And, consumed energy of motor is increases gradually.

In Figure 5, under the condition that $\dot{\theta}_{1i} = \dot{\theta}_{2i}$ =0, the solid lines show the response of manipulator which is actuated along the optimal trajectory. But, the impact force is not reduced.

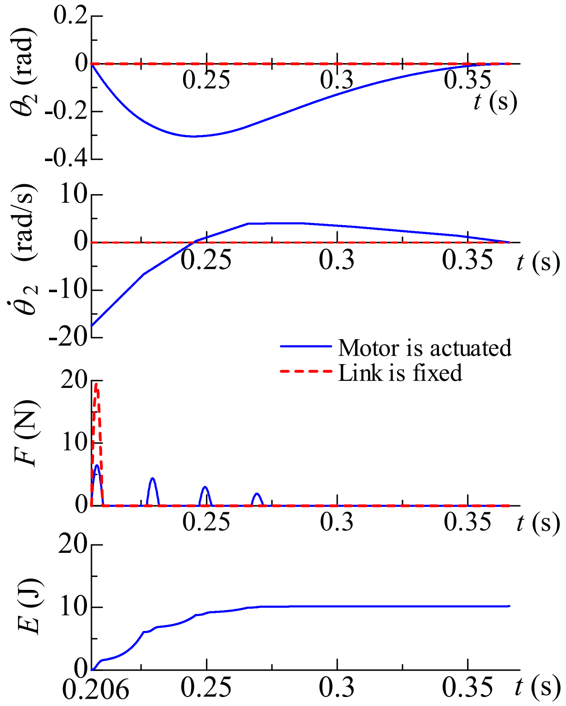

Fig.4 Theoretical results ($\dot{\theta}_{2i} = -17.5$ rad/s)

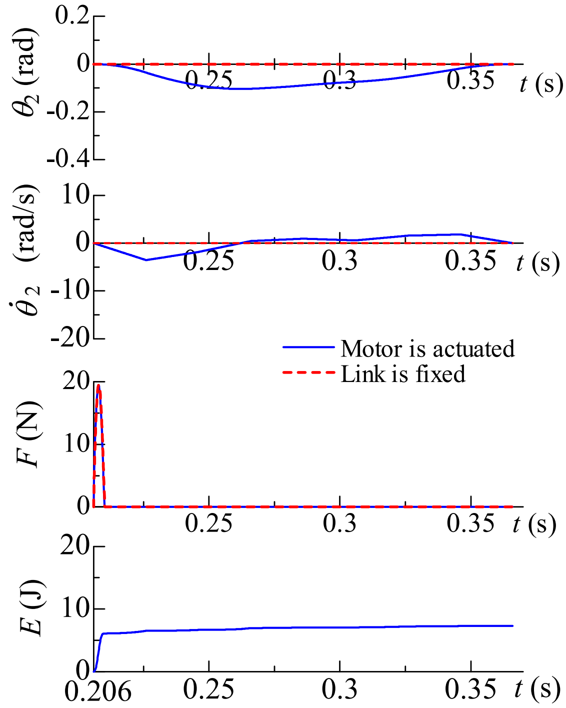

Fig.5 Theoretical results ($\dot{\theta}_{2i} = 0$)

5 Experimental results

In this section, the results of fundamental experiment are shown to examine the effectiveness of modeling for the simulations.

Figure 7 shows an experimental apparatus. Slide board is tilted ($\pi/3$) measured from the level surface. And, two Laser displacement meters are installed for measuring the passing time of the object.

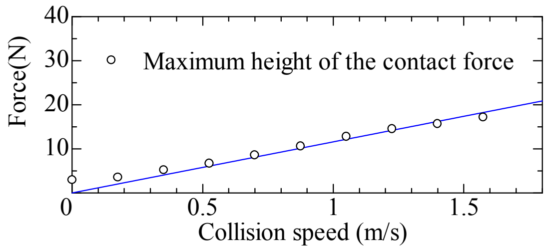

(a) Relation between collision speed and impact force

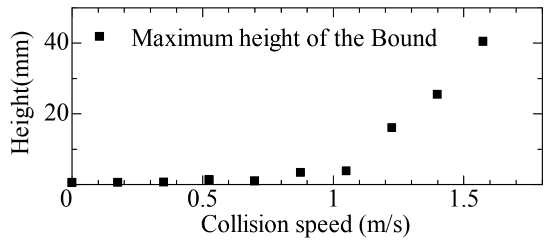

(b)Relation between collision speed and height of bound

Fig.6 Impact force and height of bound

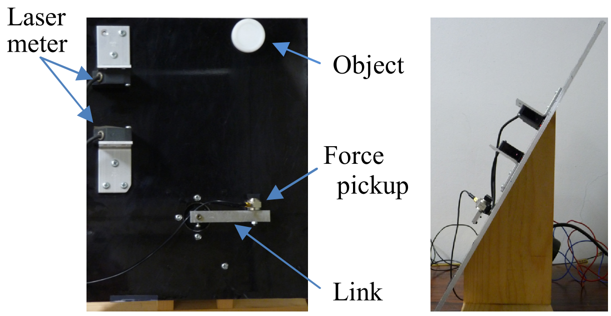

(a) Front view (b) Side view

Fig.7 Experimental apparatus

The parameter of the link and the motor are shown in Table 1, and the motor (rated 24 V, 60W) are on the frame, and sampling time of the control is 0.002 s. The feedback gain for angular displacement is 100 V/rad, and the feedback gain for angular velocity is 1.0 Vs/rad.

Figure 8 (a) and (b) show experimental results about motion of the link and object. In Figure (a), the link is fixed at initial position, and the object bounds high. In Figure (b), the link is actuated along the trajectory calculated by IDP method, and the object bounds low.

Figure 9 shows the experimental results about the response of the link and motor after the passing time of Laser meter. Impact force F about optimal case (b) becomes smaller than one of supported case (a). The experimental results (solid line) are similar to the theoretical results (broken line).

From these results, it is considered that modeling for simulation is effective.

6 Conclusions

The results obtained in this paper are summarized as follows.

(1) It is considered that the active motion to absorb the impact force is possible by analyzing the relative motion about the collision between the link and object.

(2) From experimental results, it is considered that modeling for simulation is effective.

References

[1] H.Arisumi, K.Yokoi, T.Kotoku et al (2002), Casting manipulation (Experiments of swing and gripper throwing control), International Journal of JSME, Vol.45, No.1 C, 267-274.

[2] H.Tachiya, K.Urano et al (1996), Characteristics evaluation and comparisons of robotic mechanisms (2nd report, Evaluation of robotic mechanisms subjected to impact load, Journal of JSME (in Japanese), Vol.62 No.598, 2395-2402.

[3] A.Sato, O.Sato, N.Takahashi and M.Kono (2006), Trajectory for saving energy of direct-drive manipulator in throwing motion, Artificial Life Robotics, 11:61-66

[4] A.Sato, O.Sato, N.Takahashi and M.Yokomichi (2011), Analysis of a manipulator in relation to collision between a link and an object, Artificial Life Robotics, 16: 169-173

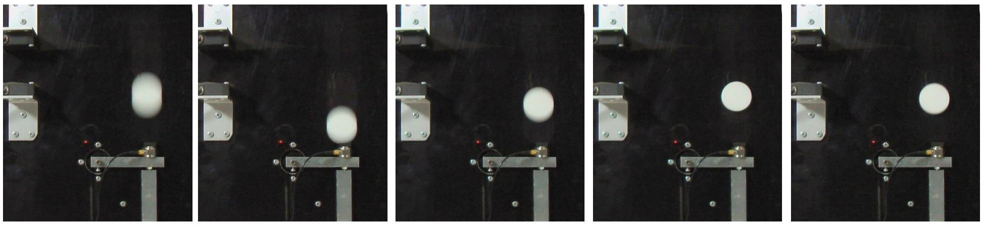

(a) Link is fixed at initial position.

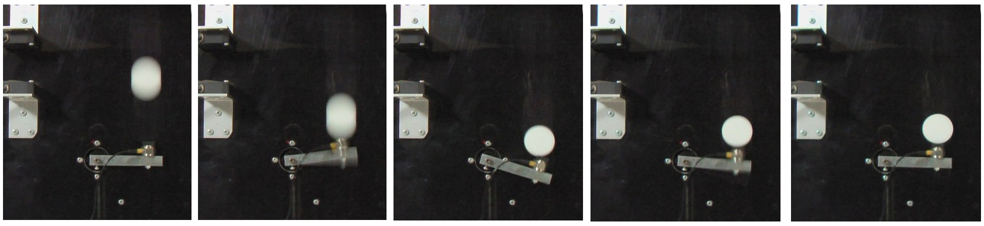

(b) Link is actuated along the trajectory calculated by IDP method.

Fig.8 Experimental results (motion about the link and object)

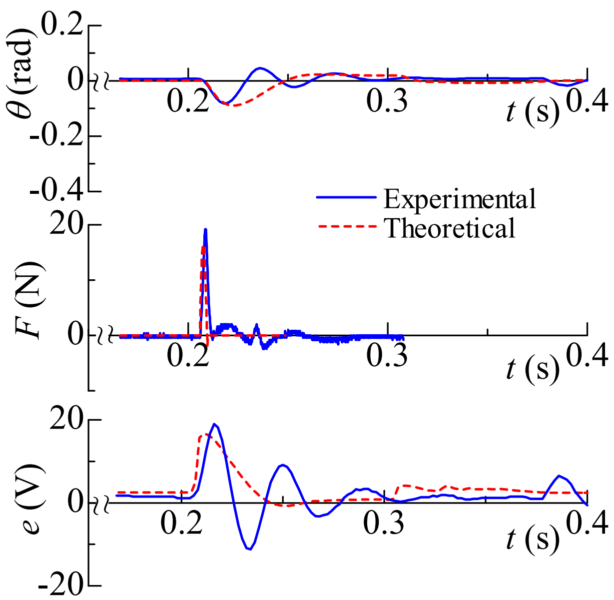

(a) Link is supported at horizontal.

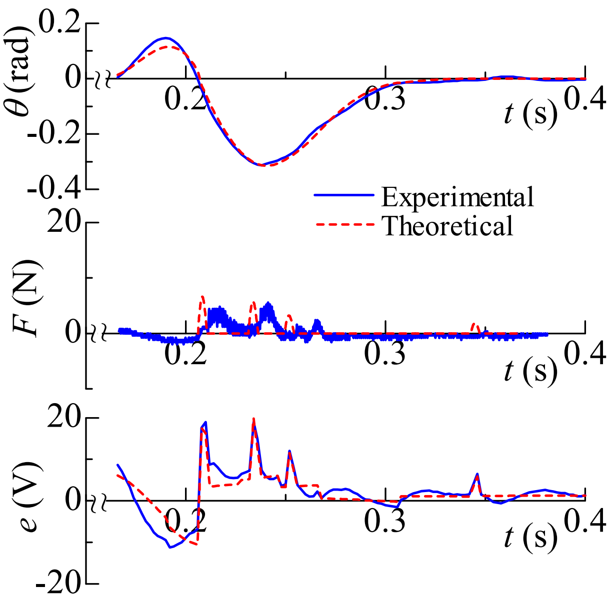

(b) Link is controlled by the optimal trajectory.

Fig.9 Experimental results (response of link and motor)

The Seventeenth International Symposium on Artificial Life and Robotics 2012 (AROB 17th '12),
B-Con Plaza, Beppu, Oita, Japan, January 19-21, 2012

An application of guaranteed cost control to a 3-DOF model helicopter

Erwin Susanto*, Tatsuhiro Tamura, Mitsuaki Ishitobi and Sadaaki Kunimatsu

Department of Mechanical Systems Engineering, Kumamoto University, Kumamoto 850-8555, Japan
(Tel: +81-96-342-3866, *e-mail: 095d9213@st.kumamoto-u.ac.jp)

Abstract: This paper deals with guaranteed cost control for a model helicopter which has 3-DOF (degree of freedom): the elevation, pitch, and travel angles. One of main difficulties in designing a feedback controller for the helicopter is that the model includes nonlinearities. In this paper, these nonlinearities are considered as the uncertainty terms. Guaranteed cost control is applied not only to achieve the closed-loop stability but also to guarantee an adequate level of performance of the nonlinear 3-DOF model helicopter. A numerical example is shown to illustrate the effectiveness of the proposed method.

Keywords: guaranteed cost control, 3-DOF model helicopter, LMI

1 INTRODUCTION

This paper deals with guaranteed cost control for a model helicopter which has 3-DOF (degree of freedom): the elevation, pitch, and travel angles [1], [2]. One of main difficulties in designing a feedback controller for the helicopter is that the dynamics include nonlinearities.

Although single-input single-output approaches have advantages in simple structure, straightforward and so on, these methods are difficult to consider uncertainties. Therefore, development of multi-input multi-output control approaches are widely applied, see e.g. [3], [4]. Moreover, avoiding difficulties in measurement of system state due to uncertainties, an observer can be applied to reconstruct the system dynamics [5].

In this paper, these nonlinearities are considered as the uncertainty terms. By using Taylor's expansion, the state equation of a nonlinear 3-DOF model helicopter is changed to the form of a continuous-time uncertain system. Because the presence of the uncertainties may cause instability and bad performance on a controlled system, then guaranteed cost control method is applied.

The objective of this paper is to propose a design method of guaranteed cost control with a minimal order observer for a 3-DOF model helicopter via linear matrix inequalities (LMIs) feasible solutions.

Finally, a numerical example is given to illustrate the effectiveness of the proposed method and it is shown that a 3-DOF nonlinear model helicopter can be stabilized by the guaranteed cost control method.

2 MODEL HELICOPTER

The dynamics of a 3-DOF model helicopter shown in Fig. 1. are described [1] as

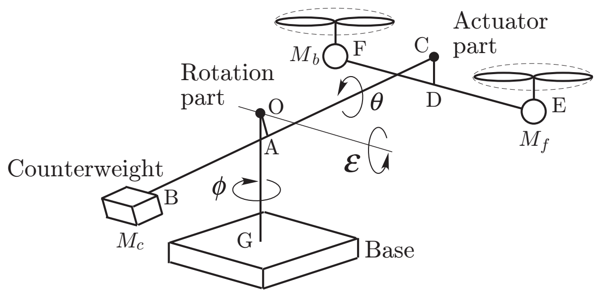

Fig. 1. A 3-DOF model helicopter

$$\dot{\boldsymbol{x}}_p = \begin{bmatrix} p_1\cos\varepsilon + p_2\sin\varepsilon + p_3\dot{\varepsilon} + p_4\cos\theta v_1 \\ p_5\cos\theta + p_6\sin\theta + p_7\dot{\theta} + p_8 v_2 \\ p_9\dot{\phi} + p_{10}\sin\theta v_1 \\ \dot{\varepsilon} \\ \dot{\theta} \\ \dot{\phi} \end{bmatrix} \tag{1}$$

where p_i, (i=1,...,10) are model helicopter constants; ε, θ, ϕ are the elevation, pitch and travel angles and

$$\boldsymbol{x}_p = \begin{bmatrix} \dot{\varepsilon}, \dot{\theta}, \dot{\phi}, \varepsilon, \theta, \phi \end{bmatrix}^T,$$
$$v_1 = V_f + V_b,\ v_2 = V_f - V_b,$$

V_f and V_b are voltages applied to the front and rear motor, respectively.

3 PROBLEM STATEMENT

By using Taylor's expansion, a 3-DOF nonlinear model helicopter (1) can be expressed by the form

$$\dot{\boldsymbol{x}}(t) = (A + \Delta A(t))\boldsymbol{x}(t) + (B + \Delta B(t))\boldsymbol{u}(t) \tag{2}$$
$$\boldsymbol{y}(t) = C\boldsymbol{x}(t),\ C = [O \ \ I_3] \tag{3}$$

$$\boldsymbol{u}(t) = \begin{bmatrix} u_1 \\ u_2 \end{bmatrix},\ u_1 = v_1 + \frac{p_1}{p_4},\ u_2 = v_2 + \frac{p_5}{p_8} \tag{4}$$

where

$$\begin{aligned}
A &= [a_{ij}],\ (i,j = 1,...,6),\\
a_{11} &= p_3,\ a_{14} = p_2,\ a_{22} = p_7,\ a_{25} = p_6,\\
a_{33} &= -\frac{p_1 p_{10}}{p_4},\ a_{41} = a_{52} = a_{63} = 1,\\
B &= [b_{ij}],\ (i = 1,...,6,\ j = 1,2),\\
b_{11} &= p_4,\ b_{21} = p_8,\\
\Delta A &= [\delta a_{ij}],\ (i,j = 1,...,6),\\
\delta a_{11} &= \Delta A_{11},\ \delta a_{14} = \Delta A_{14},\ \delta a_{15} = \Delta A_{15},\\
\delta a_{22} &= \Delta A_{22},\ \delta a_{25} = \Delta A_{25},\ \delta a_{33} = \Delta A_{33},\\
\delta a_{35} &= \Delta A_{35},\\
\Delta B &= [\delta b_{ij}],\ (i = 1,...,6,\ j = 1,2),\\
\delta b_{11} &= \Delta B_{11},\ \delta b_{22} = \Delta B_{22},\ \delta b_{31} = \Delta B_{31},\\
\Delta A_{11} &= \Delta p_3,\\
\Delta A_{14} &= p_2(-\frac{1}{3!}x_4^2 + O(x_4^4)) + p_1(-\frac{1}{2}x_4 + O(x_4^3)) + \Delta p_2,\\
\Delta A_{15} &= p_1(-\frac{1}{2}x_5 + O(x_5^3)),\ \Delta A_{22} = \Delta p_7,\\
\Delta A_{25} &= p_5(-\frac{1}{2}x_5 + O(x_5^3)) + p_6(-\frac{1}{3!}x_6^2 + O(x_6^4)) + \Delta p_6,\\
\Delta A_{33} &= \Delta p_9,\\
\Delta A_{35} &= -\frac{p_1 p_{10}}{p_4}(-\frac{1}{3!}x_5^2 + O(x_5^4)) - \Delta(p_1 p_{10}/p_4),\\
\Delta B_{11} &= p_4(-\frac{1}{2}x_5 + O(x_5^4)) + \Delta p_4,\\
\Delta B_{22} &= \Delta p_8,\ \Delta B_{31} = p_{10}(x_5 - \frac{1}{3!}x_5^3 + O(x_5^5)),
\end{aligned}$$

while other elements are zero, and $\boldsymbol{x}(t) \in \Re^n$ is the state vector, $\boldsymbol{u}(t) \in \Re^r$ is the control input vector, $\boldsymbol{y}(t) \in \Re^m$ is the measured output vector, Δp_i denote uncertain terms of p_i, A, B, C are known constant real-valued matrices with appropriate dimensions. Due to the system constraint, we have the bounds of $|\varepsilon|$, $|\theta|$ and $|\phi|$ as $\varepsilon_{max}(= 0.3)$, $\theta_{max}(= 0.3)$ and $\phi_{max}(= 0.8)$.

Under the limitations of $|\varepsilon|$, $|\theta|$ and $|\phi|$, matrices $\Delta A(t)$ and $\Delta B(t)$ can be represented as

$$\Delta A(t) = D_A F_A(t) E_A,\ \Delta B(t) = D_B F_B(t) E_B \tag{5}$$

with

$$F_A^T(t) F_A(t) \leq I,\ F_B^T(t) F_B(t) \leq I$$

where D_A, D_B, E_A, E_B are constant real-valued known matrices with appropriate dimensions, and $F_A(t)$ and $F_B(t)$ are real time-varying unknown continuous and deterministic matrices.

We assume that the initial state variable $\boldsymbol{x}(0)$ is unknown, but their mean and covariance are known

$$E[\boldsymbol{x}(0)] = \boldsymbol{m}_0 \tag{6}$$

$$E\left[(\boldsymbol{x}(0) - \boldsymbol{m}_0)(\boldsymbol{x}(0) - \boldsymbol{m}_0)^T\right] = \Sigma_0 > O \tag{7}$$

where $E[\cdot]$ denotes the expected value operator.

The problem considered here is to design a guaranteed cost controller with a minimal order observer so as to achieve an upper bound on the following quadratic performance index

$$E[J] = E\left[\int_0^\infty (\boldsymbol{x}^T(t) Q \boldsymbol{x}(t) + \boldsymbol{u}^T(t) R \boldsymbol{u}(t)) dt\right] < E[J^*] \tag{8}$$

associated with the uncertain system (2) where Q and R are given symmetric positive-definite matrices.

4 GUARANTEED COST CONTROLLER DESIGN

Design of a guaranteed cost controller is described in the following equations. Here, a minimal order observer is given by

$$\dot{\boldsymbol{z}}(t) = D\boldsymbol{z}(t) + E\boldsymbol{y}(t) + F\boldsymbol{u}(t) \tag{9}$$

$$\hat{\boldsymbol{x}}(t) = P\boldsymbol{z}(t) + W\boldsymbol{y}(t) \tag{10}$$

with

$$\begin{aligned}
&D = A_{11} + LA_{21},\ PT + WC = I_6,\\
&F = TB,\ TA - DT = EC,\ A = \left[\begin{array}{c|c} A_{11} & A_{12} \\ \hline A_{21} & A_{22} \end{array}\right],\\
&P = \begin{bmatrix} I_3 & \boldsymbol{0} \end{bmatrix}^T,\ T = \begin{bmatrix} I_3 & L \end{bmatrix}
\end{aligned}$$

and a controller is assumed to have a form of

$$\boldsymbol{u}(t) = K\hat{\boldsymbol{x}}(t),\ K = -R^{-1}B^T S_1 \tag{11}$$

where S_1 is a symmetric positive definite matrix.

Then, the following Theorem gives a design method of guaranteed cost control to the 3-DOF model helicopter (2)-(3).

Theorem 1. If the following matrix inequalities optimization problem; $\min\{\gamma_0 + \gamma_1 + \gamma_2 + \gamma_3 + \gamma_4\}$ subject to

$$\begin{bmatrix} \Lambda_0 & X^T & XE_A & XE_A \\ * & -Q^{-1} & 0 & 0 \\ * & 0 & -\alpha_1 I & 0 \\ * & 0 & 0 & -\alpha_4 I \end{bmatrix} < 0 \tag{12}$$

$$\begin{bmatrix} \bar{\Lambda}_0 & G_1 & G_2 & G_2 & G_3 & G_3 & G_4 \\ * & -R & 0 & 0 & 0 & 0 & 0 \\ * & 0 & -\alpha_{5,inv}I & 0 & 0 & 0 & 0 \\ * & 0 & 0 & -\alpha_{6,inv}I & 0 & 0 & 0 \\ * & 0 & 0 & 0 & -\alpha_3 I & 0 & 0 \\ * & 0 & 0 & 0 & 0 & -\alpha_6 I & 0 \\ * & 0 & 0 & 0 & 0 & 0 & -\alpha_{4,inv}I \end{bmatrix} < 0 \tag{13}$$

$$\sum_{k=1}^{6} \boldsymbol{e}_{6k}^T \Theta_0 \boldsymbol{e}_{6k} < \gamma_0,\ \sum_{k=1}^{3} \boldsymbol{e}_{3k}^T \Theta_1 \boldsymbol{e}_{3k} < \gamma_1,$$
$$\sum_{k=1}^{3} \boldsymbol{e}_{3k}^T \Theta_2 \boldsymbol{e}_{3k} < \gamma_2,\ \sum_{k=1}^{3} \boldsymbol{e}_{3k}^T \Theta_3 \boldsymbol{e}_{3k} < \gamma_3 \tag{14}$$

$$\begin{bmatrix} -\gamma_4 & \boldsymbol{v}_1^T Y^T & \boldsymbol{v}_2^T Y^T & \boldsymbol{v}_3^T Y^T \\ Y\boldsymbol{v}_1 & -S_2 & & \\ Y\boldsymbol{v}_2 & & -S_2 & \\ Y\boldsymbol{v}_3 & & & -S_2 \end{bmatrix} < 0 \tag{15}$$

where

$$\begin{aligned}
\Lambda_0 &= AX + XA^T - BR^{-1}B^T + (\alpha_2+\alpha_3)D_B D_B^T \\
&\quad + \alpha_1 D_A D_A^T + (\alpha_{2,inv}+\alpha_{5,inv})BR^{-1}E_B^T E_B R^{-1}B^T, \\
\bar{\Lambda}_0 &= S_2 A_{11} + A_{11}^T S_2 + YA_{21} + A_{21}^T Y^T, \\
Y &= S_2 L,\ Z = [S_2\ \ Y],\ G_1 = P^T S_1 B, \\
G_2 &= ZD_B,\ G_3 = P^T S_1 B R^{-1} E_B^T,\ G_4 = ZD_A, \\
\Theta_0 &= \frac{1}{2}(S_1(\Sigma_0 + \boldsymbol{m}_0\boldsymbol{m}_0^T) + (\Sigma_0 + \boldsymbol{m}_0\boldsymbol{m}_0^T)^T S_1), \\
\Theta_1 &= \frac{1}{2}(S_2\Sigma_{11} + \Sigma_{11}S_2),\ \Theta_2 = \frac{1}{2}(Y\Sigma_{21} + \Sigma_{21}^T Y^T), \\
\Theta_3 &= \frac{1}{2}(Y^T\Sigma_{12} + \Sigma_{12}^T Y),\ \boldsymbol{e}_{ik} = \ \ \mathbf{0}_{k-1}^T\ 1\ \mathbf{0}_{i-k}^T\ \ ^T, \\
\Sigma_0 &= \begin{bmatrix} \Sigma_{11} & \Sigma_{12} \\ \Sigma_{21} & \Sigma_{22} \end{bmatrix},\ \Sigma_{22}^{1/2} = [\boldsymbol{v}_1, \boldsymbol{v}_2, \boldsymbol{v}_3]
\end{aligned}$$

has a solution $S_1 > 0$, $S_2 > 0$, $X > 0$, Y, Z, $\alpha_1 > 0$, $\alpha_2 > 0$, $\alpha_{2,inv} > 0$, $\alpha_3 > 0$, $\alpha_4 > 0$, $\alpha_{4,inv} > 0$, $\alpha_{5,inv} > 0$, $\alpha_6 > 0$, $\alpha_{6,inv} > 0$, γ_0, γ_1, γ_2, γ_3, γ_4 which satisfy the relation $\alpha_2^{-1} = \alpha_{2,inv}$, $\alpha_4^{-1} = \alpha_{4,inv}$, $\alpha_6^{-1} = \alpha_{6,inv}$ and $S_1^{-1} = X$, then the minimal order observer-based control law (9)-(11) is a guaranteed cost controller which gives the minimum expected value of the guaranteed cost

$$E[J^*] = E\left[\boldsymbol{x}^T(0)S_1\boldsymbol{x}(0) + \boldsymbol{\xi}^T(0)S_2\boldsymbol{\xi}(0)\right] \tag{16}$$

where $\boldsymbol{\xi}(t) = \boldsymbol{z}(t) - T\boldsymbol{x}(t)$ is the estimated error of the minimal order observer.

Remark 1: Since inequalities in (12) and (13) contain scalars and matrices that satisfy inverse relations $S_1^{-1} = X$, $\alpha_2^{-1} = \alpha_{2,inv}$, $\alpha_4^{-1} = \alpha_{4,inv}$, and $\alpha_6^{-1} = \alpha_{6,inv}$. then an iterative LMI algorithm is adopted to solve [6],[7].

5 A NUMERICAL EXAMPLE

The nominal values of the model helicopter are as follows:

$$\begin{aligned}
p_1 &= [-(M_f + M_b)gL_a + M_c g L_c]/J_\varepsilon, \\
p_2 &= [-(M_f + M_b)gL_a \tan\delta_a + M_c g L_c \tan\delta_c]/J_\varepsilon, \\
p_3 &= \eta_\varepsilon/J_\varepsilon,\ p_4 = K_m L_a/J_\varepsilon,\ p_5 = (-M_f + M_b)gL_h/J_\theta, \\
p_6 &= -(M_f + M_b)gL_h \tan\delta_h/J_\theta,\ p_7 = -\eta_\theta/J_\theta, \\
p_8 &= K_m L_h/J_\theta,\ \ p_9 = -\eta_\phi/J_\phi, p_{10} = -K_m L_a/J_\phi, \\
\delta_a &= \tan^{-1}[(L_d + L_e)/L_a],\ \delta_c = \tan^{-1}(L_d/L_c), \\
\delta_h &= \tan^{-1}(L_e/L_h),\ J_\varepsilon = 0.86 \text{ kg m}^2, J_\theta = 0.044 \text{ kg m}^2, \\
J_\phi &= 0.82 \text{ kg m}^2, L_a = 0.62 \text{ m},\ L_c = 0.44 \text{ m}, \\
L_d &= 0.05 \text{ m},\ L_e = 0.02 \text{ m},\ L_h = 0.177 \text{ m}, \\
M_f &= 0.69 \text{ kg}, M_b = 0.69 \text{ kg},\ M_c = 1.67 \text{ kg}, \\
K_m &= 0.5 \text{ N/V},\ g = 9.81 \text{ m/s}^2, \\
\eta_\varepsilon &= 0.001 \text{ kg m}^2\text{/s},\ \eta_\theta = 0.001 \text{ kg m}^2\text{/s}, \\
\eta_\phi &= 0.005 \text{ kg m}^2\text{/s},
\end{aligned}$$

and the uncertain parameters Δp_2, Δp_3, Δp_4, Δp_5, Δp_6, Δp_7, Δp_8, Δp_9 $\Delta(p_1 p_{10}/p_4)$ are 5% of each p_2,p_3, p_4, p_5, p_6, p_7, p_8, p_9 and $(p_1 p_{10}/p_4)$, respectively. Next, D_A, E_A, D_B, E_B, $\boldsymbol{m}_0$, Σ_0, R, Q are given as

$$\begin{aligned}
D_A &= \ \ d_{A_{ij}}\ \ ,(i,j = 1,...,6) \\
d_{A_{11}} &= \sqrt{|\ \Delta A_{11}\ |}, d_{A_{14}} = \sqrt{|\ \Delta A_{14}\ |}, \\
d_{A_{15}} &= \sqrt{|\ \Delta A_{15}\ |}, d_{A_{22}} = \sqrt{|\ \Delta A_{22}\ |}, \\
d_{A_{26}} &= -\sqrt{|\ \Delta A_{25}\ |}, d_{A_{33}} = -\sqrt{|\ \Delta A_{35}\ |}, \\
F_A(t) &= I_6,\ E_A = \ \ e_{A_{ij}}\ \ ,(i,j = 1,...,6) \\
e_{A_{11}} &= \sqrt{|\ \Delta A_{11}\ |}, e_{A_{22}} = \sqrt{|\ \Delta A_{22}\ |}, \\
e_{A_{33}} &= \frac{\Delta A_{33}}{\sqrt{|\ \Delta A_{35}\ |}}, e_{A_{35}} = \sqrt{|\ \Delta A_{35}\ |}, \\
e_{A_{44}} &= \sqrt{|\ \Delta A_{14}\ |}, e_{A_{55}} = \sqrt{|\ \Delta A_{15}\ |}, \\
e_{A_{65}} &= \sqrt{|\ \Delta A_{25}\ |} \\
D_B &= \ \ d_{B_{ij}}\ \ ,(i = 1,...,6; j = 1,2) \\
d_{B_{12}} &= \frac{-\Delta B_{11}}{\sqrt{|\ \Delta B_{31}\ |}}, d_{B_{21}} = \sqrt{|\ \Delta B_{22}\ |}, \\
d_{B_{22}} &= -\frac{\sqrt{|\ \Delta B_{22}\ |} \times \sqrt{|\ \Delta B_{11}\ |}}{\sqrt{|\ \Delta B_{31}\ |}}, d_{B_{32}} = \sqrt{|\ \Delta B_{31}\ |} \\
F_B(t) &= I_2,\ E_B = \begin{bmatrix} -\sqrt{|\ \Delta B_{11}\ |} & \sqrt{|\ \Delta B_{22}\ |} \\ -\sqrt{|\ \Delta B_{31}\ |} & 0 \end{bmatrix}, \\
\boldsymbol{m}_0 &= \mathbf{0}_6,\ \Sigma_0 = 0.036 I_6, R = I_2, \\
Q &= \text{diag}(0.1, 0.1, 0.1, 1, 1, 1),
\end{aligned}$$

while other elements of $d_{A_{ij}}$, $e_{A_{ij}}$, and $d_{B_{ij}}$ are zero.

Results of the controller gain K, the observer gain L and the expected guaranteed cost $E[J^*]$ are obtained below

$$K = \begin{bmatrix} -2.4649 & 0.0078 & 0.0112 & -0.1667 & -0.0467 & -0.0033 \\ 0.0433 & -2.4787 & 7.2135 & -0.1399 & -3.0527 & 2.3029 \end{bmatrix},$$

$$L = \begin{bmatrix} -2.9302 & 0.0574 & -0.1278 \\ 0.0574 & -2.3582 & 2.6908 \\ -0.1278 & 2.6908 & -7.6101 \end{bmatrix}, \; E[J^*] = 28.9098.$$

Figure 2 shows the transition of the guaranteed cost, and Fig. 3-5 show the trajectories of elevation, pitch and travel angles with $\boldsymbol{x}(0) = [0\ 0\ 0\ 0.2\ 0.2\ 0.1]^T$.

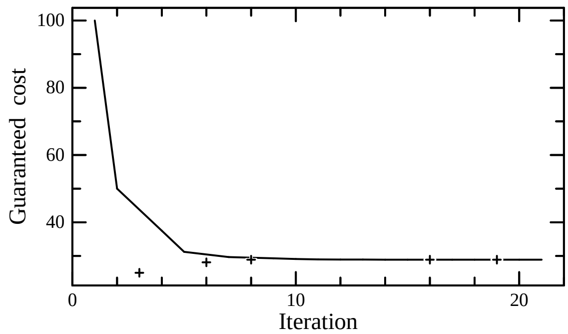

Fig. 2. Transition of the guaranteed cost

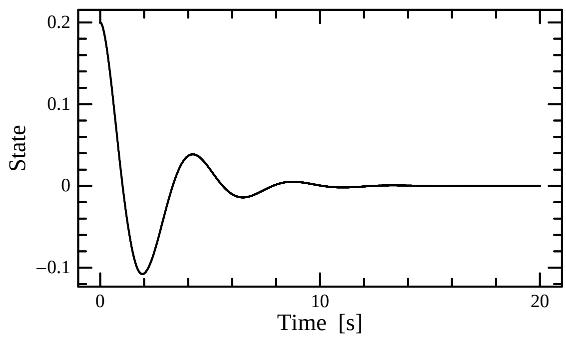

Fig. 3. Trajectory of elevation angle ε

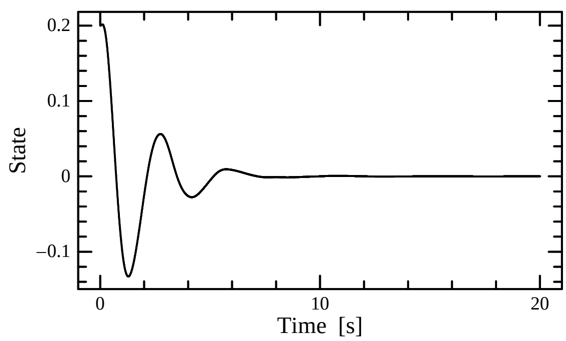

Fig. 4. Trajectory of pitch angle θ

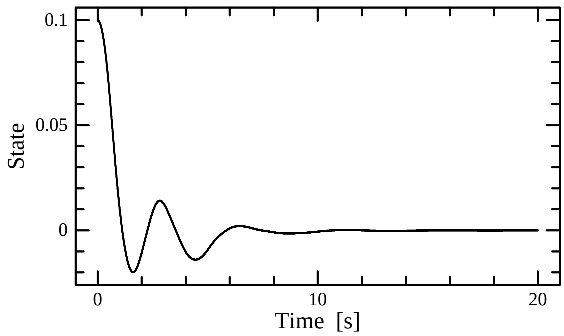

Fig. 5. Trajectory of travel angle ϕ

6 CONCLUSION

This paper discusses a design method of guaranteed cost control with a minimal order observer for a 3-DOF nonlinear model helicopter via linear matrix inequalities (LMIs). The results show the effectiveness of the proposed method.

REFERENCES

[1] Ishitobi M, Nishi M, Nakasaki K (2010), Nonlinear adaptive model following control for a 3-DOF tandem-rotor model helicopter. *Control Eng. Practice* 18(8):936-943

[2] Kutay AT, Calise AJ, Idan M, Hovakimyan N (2005), Experimental results on adaptive output feedback control using a laboratory model helicopter. *IEEE Trans. on Control Syst. Technology* 13(2):196-202

[3] Mahony R, Hamel T (2004), Robust trajectory tracking for a scale model autonomous helicopter. *Int. J. Robust & Nonlinear Control* 14(2):1035-1059

[4] Marconi L, Naldi R (2007), Robust full degree-of-freedom tracking control of a helicopter. *Automatica* 43(11):1909-1920

[5] Lien CH (2005), Guaranteed cost observer-based controls for a class of uncertain neutral time-delay systems. *J. Optim. Theory & Appl.* 126(1):137-156

[6] Matsunaga D, Ishitobi M, Kunimatsu S (2009), An ILMI approach to guaranteed cost controllers with a minimal order observer. *Proc. ICROS-SICE International Joint Conference*:583-588

[7] Susanto E, Ishitobi M, Kunimatsu S, Matsunaga D (2011), A minimal order observer-based guaranteed cost controller for uncertain time-varying delay systems. *IMA J. Math. Control Inf.*, to appear

The Seventeenth International Symposium on Artificial Life and Robotics 2012 (AROB 17th '12),
B-Con Plaza, Beppu, Oita, Japan, January 19-21, 2012

Robust Control of a three-link RRR Manipulator with Structured Uncertainty

Nobuya TAKAHASHI[1], Yoshiaki NAKAMURA[1], Osamu SATO[1]

[1] Faculty of Engineering, University of Miyazaki
1-1 Gakuenkibanadai-Nishi, Miyazaki, 889-2192, JAPAN
(Tel & Fax : +81-985-58-7419)
(ntakahasi@cc.miyazaki-u.ac.jp)

Abstract: In this paper, we propose a modeling method for an uncertain system of a three-link RRR manipulator. We consider that each rotation joint of this manipulator consists a nominal joint angle and uncertain joint angle. Though, the uncertainty is treated as disturbance in the system that is maximum possible value of the uncertain joint angle. A relationship between disturbance and the system structure in a state equation is clarified. Through the numerical example, we show the effectiveness of our proposed method. It can apply our result to the general method of the robust control with structured uncertainty, such as guaranteed cost control.

Keywords: Linear control system, Robust control, Guaranteed cost control

1 INTRODUCTION

In the framework of the linear control system theory, the design procedure for the controller is archived by a model based method. But the numerical model only contains a nominal characteristic of the plant. Thus, it is important problem to obtain the representation of the effect of the uncertainty, and use this information for the design of robust controller. Chang et al. proposed the design method to guarantee the existence of upper bound of performance index, which called guaranteed cost control (GCC) [1]. Sato et al. consider the trajectory generation problem for energy saving of the manipulator [2, 3]. Authors proposed a modeling method of a linear time invariant system which includes an uncertainty of the plant [4, 5]. And apply the uncertain system to GCC problem. In [6], authors consider GCC problem in the case with the system includes parameter variation in an output matrix. The parameter setting of the free variable $_i$ in the linear upper bound is available for adjustment of the closed-loop system's characteristic. In [7], authors consider a two-link RR manipulator model case. Such a higher-dimensional system, the effect of uncertainty to the disturbance becomes larger bad influence than smaller dimension one, so that it is not a negligible problem. The observer based method is effective to reduce the effects of disturbance.

In this paper, we apply our modeling method to the three-link RRR manipulator. In such a high dimensional system, the effect of nonlinear element is larger than the lower dimensional system. It is important the robustness of the controller.

2 DERIVATION OF THE UNCERTAIN SYSTEM

The dynamics of a three-link RRR manipulator is illustrated as a following second ordinary differential equation.

$$H(\boldsymbol{\theta})\boldsymbol{\theta} + D\dot{\boldsymbol{\theta}} + \boldsymbol{\eta}(\dot{\boldsymbol{\theta}},\boldsymbol{\theta}) + g\boldsymbol{\gamma}(\boldsymbol{\theta}) = \qquad (1)$$

where the inertia term is

$$H(\boldsymbol{\theta}) = \begin{bmatrix} h_{11}(\boldsymbol{\theta}) & h_{12}(\boldsymbol{\theta}) & h_{13}(\boldsymbol{\theta}) \\ h_{12}(\boldsymbol{\theta}) & h_{22}(\boldsymbol{\theta}) & h_{23}(\boldsymbol{\theta}) \\ h_{13}(\boldsymbol{\theta}) & h_{23}(\boldsymbol{\theta}) & h_{33}(\boldsymbol{\theta}) \end{bmatrix},$$

the nonlinear term is

$$\boldsymbol{\eta}(\boldsymbol{\theta},\dot{\boldsymbol{\theta}}) = \begin{bmatrix} & {}_{11}(\dot{\boldsymbol{\theta}},\boldsymbol{\theta}) & \\ {}_{21}(\dot{\boldsymbol{\theta}},\boldsymbol{\theta}) & & {}_{22}(\dot{\boldsymbol{\theta}},\boldsymbol{\theta}) \\ {}_{31}(\dot{\boldsymbol{\theta}},\boldsymbol{\theta}) & & {}_{32}(\dot{\boldsymbol{\theta}},\boldsymbol{\theta}) \end{bmatrix},$$

the dumping term is

$$D = \mathrm{diag}(d_1, d_2, d_3),$$

the gravity term and the input term are

$$\boldsymbol{\gamma}(\boldsymbol{\theta}) = \begin{bmatrix} {}_{1}(\boldsymbol{\theta}) \\ {}_{2}(\boldsymbol{\theta}) \\ {}_{3}(\boldsymbol{\theta}) \end{bmatrix}, \quad = \begin{bmatrix} {}_{1} \\ {}_{2} \\ {}_{3} \end{bmatrix}.$$

Here we derive the LTI system with structured uncertainty for the above dynamics. In this system, the relationship between an uncertainty of the system and system structure is expressed in the additional system matrix. Let us assume that the each rotation joints include an angle of the nominal element and an uncertain element. The possible value of the uncertain joint angle is unknown, therefore we use the maximum value of the uncertain angle as a disturbance of the system to derive an uncertain system. The nominal system structure is derived from the nominal joint angle, and the uncertain system structure is derived corresponding to the uncertain joint angle. The system uncertainty is only used to derive the uncertain system, though in the later section of numerical example, the simulation result is calculated by using nominal LTI system.

2.1 Introduce of uncertainty

In this section, we introduce an uncertain angle in the each joint to express the effect to the system structure. Here we consider that the rotation angle $\bar{\ }_i(t)$ of joint$_i$, $(i = 1, 2, 3)$ is constructed from an nominal joint angle $\ _i(t)$ and uncertain joint angle $\Delta\ _i$.

$$\bar{\ }_i \;=\; \ _i + \Delta\ _i, \quad (i = 1, 2, 3) \tag{2}$$

where the uncertain joint angle $\Delta\ _i$ takes very small value, it can be approximate sinusoidal functions $\sin, \cos$ as

$$\begin{aligned} \sin\Delta\ _i &\rightarrow 0 \\ \cos\Delta\ _i &\rightarrow \varDelta c_i \end{aligned}$$

Then, from the consideration of uncertainty of $\bar{\ }_i$, from the sinusoidal fundamental formulae, we have

$$\begin{aligned} \sin\bar{\ }_i &= \sin\ _i\cos\Delta\ _i + \cos\ _i\sin\Delta\ _i \\ & \quad \varDelta c_i\sin\ _i \end{aligned} \tag{3}$$

$$\begin{aligned} \cos\bar{\ }_i &= \cos\ _i\cos\Delta\ _i \quad \sin\ _i\sin\Delta\ _i \\ & \quad \varDelta c_i\cos\ _i \end{aligned} \tag{4}$$

In the term of $\bar{\ }_1 + \bar{\ }_2$, sin is becomes:

$$\begin{aligned} \sin(\bar{\ }_1 + \bar{\ }_2) &= \sin\bar{\ }_1\cos\bar{\ }_2 + \cos\bar{\ }_1\sin\bar{\ }_2 \\ & \quad \varDelta c_1\varDelta c_2(\sin\ _1\cos\ _2 + \cos\ _1\sin\ _2) \end{aligned} \tag{5}$$

We consider the approximation of cos as follows

$$\cos(\bar{\ }_1 + \bar{\ }_2) \quad \frac{1}{2}(\varDelta c_1 + \varDelta c_2)\cos(\ _1 + \ _2) \tag{6}$$

Then, the term of $\bar{\ }_1(t) + \bar{\ }_2(t) + \bar{\ }_3(t)$ becomes

$$\begin{aligned} &\sin(\bar{\ }_1 + \bar{\ }_2 + \bar{\ }_3) \\ &\quad \varDelta c_1\varDelta c_2\varDelta c_3(\sin\ _1\cos\ _2 + \cos\ _1\sin\ _2)\cos\ _3 \\ &\quad + \frac{1}{2}(\varDelta c_1 + \varDelta c_2)\varDelta c_3\cos(\ _1 + \ _2)\sin\ _3 \end{aligned} \tag{7}$$

The Taylor series expansion of Eqs. (3), (4), (5), (6) and (7) near $\ _i(t) = 0$, $(i = 1, 2, 3)$ up to the first-order are express as follows:

$$\begin{aligned} \sin\bar{\ }_1 &\quad \varDelta c_1\ _1 \\ \cos\bar{\ }_1 &\quad \varDelta c_1 \\ \sin\bar{\ }_2 &\quad \varDelta c_2\ _2 \\ \cos\bar{\ }_2 &\quad \varDelta c_2 \\ \sin\bar{\ }_3 &\quad \varDelta c_3\ _3 \\ \cos\bar{\ }_3 &\quad \varDelta c_3 \\ \sin(\bar{\ }_1 + \bar{\ }_2) &\quad \varDelta c_1\varDelta c_2(\ _1 + \ _2) \\ \cos(\bar{\ }_1 + \bar{\ }_2) &\quad \frac{1}{2}(\varDelta c_1 + \varDelta c_2) \\ \sin(\bar{\ }_1 + \bar{\ }_2 + \bar{\ }_3) &\quad \varDelta c_1\varDelta c_2\varDelta c_3(\ _1 + \ _2) \\ &\quad + \frac{1}{2}(\varDelta c_1 + \varDelta c_2)\varDelta c_3\ _3 \end{aligned}$$

By substituting these approximation terms into each elements h_{ij}, $(i = 1, 2, 3,\ j = 1, 2, 3)$ of the inertia term $H(\boldsymbol{\theta})$, The first row elements are:

$$\begin{aligned} \tilde{h}_{11} &= I_1 + m_1 l_{G1}^2 + I_2 + m_2(l_1^2 + l_{G2}^2 + 2\varDelta c_2 l_1 l_{G2}) \\ &\quad + I_3 + m_3\big(l_1^2 + l_{G2}^2 + l_{G3}^2 + 2\varDelta c_2 l_1 l_2 \\ &\quad + 2\varDelta c_3 l_2 l_{G3} + (\varDelta c_2 + \varDelta c_3) l_1 l_{G3}\big) \\ \tilde{h}_{12} &= I_2 + m_2\big(l_{G2}^2 + \varDelta c_2 l_1 l_{G2}\big) \\ &\quad + I_3 + m_3\big(l_2^2 + l_{G3}^2 + \varDelta c_2 l_1 l_2 + 2\varDelta c_3 l_2 l_{G3} \\ &\quad + \frac{1}{2}(\varDelta c_2 + \varDelta c_3) l_1 l_{G3}\big) \\ \tilde{h}_{13} &= I_3 + m_3\big(l_{G3}^2 + \varDelta c_3 l_2 l_{G3} + \frac{1}{2}(\varDelta c_2 + \varDelta c_3) l_1 l_{G3}\big) \end{aligned}$$

The second-row elements are:

$$\begin{aligned} \tilde{h}_{21} &= \tilde{h}_{12} \\ \tilde{h}_{22} &= I_2 + m_2 l_{G2}^2 + I_3 + m_3(l_2^2 + l_{G3}^2 + 2\varDelta c_3 l_2 l_{G3}) \\ \tilde{h}_{23} &= I_3 + m_3(l_{G3}^2 + \varDelta c_3 l_2 l_{G3}) \end{aligned}$$

The third-row elements are:

$$\begin{aligned} \tilde{h}_{31} &= \tilde{h}_{13} \\ \tilde{h}_{32} &= \tilde{h}_{23} \\ \tilde{h}_{33} &= I_3 + m_3 l_{G3}^2 \end{aligned}$$

As these results, the inertia term $H(\boldsymbol{\theta})$ is described as symmetric matrix with constant elements.

Table 1. Parameters of the Manipulator

Parameter	**Mean** [unit]
m_i	Mass of Link [kg]
I_i	Inertia moment of Link [kg·m^2]
l_i	length of Link [m]
l_{Gi}	Distance from the Joint to the center of gravity of the Link [m]
g	Gravity [m/sec^2]

$$H(\boldsymbol{\theta}) \quad \tilde{H} = \begin{bmatrix} \tilde{h}_{11} & \tilde{h}_{12} & \tilde{h}_{13} \\ \tilde{h}_{21} & \tilde{h}_{22} & \tilde{h}_{23} \\ \tilde{h}_{31} & \tilde{h}_{32} & \tilde{h}_{33} \end{bmatrix} \tag{8}$$

Next, we shall consider of the linearization of the gravity term. The elements in the first-row are:

$$\begin{aligned}\tilde{}_1 &= \Delta c_1\Big(m_1 l_{G1} + m_2(l_1 + \Delta c_2 l_{G2}) \\ &\quad + m_3(l_1 + \Delta c_2 l_2 + \Delta c_2\Delta c_3 l_{G3})\Big)\ {}_1 \\ &\quad \Delta c_1\Delta c_2\Big(m_2 l_{G2} + m_3(l_2 + \Delta c_3 l_{G3})\Big)\ {}_2 \\ &\quad \frac{1}{2}(\Delta c_1 + \Delta c_2)\Delta c_3 m_3 l_{G3}\ {}_3 \\ &= \Big[\ \tilde{}_{11}\ \ \tilde{}_{12}\ \ \tilde{}_{13}\Big]\boldsymbol{\theta} \qquad (9)\end{aligned}$$

where

$$\begin{aligned}\tilde{}_{11} &= \Delta c_1\big(m_1 l_{G1} + m_2(l_1 + \Delta c_2 l_{G2}) \\ &\quad + m_3(l_1 + \Delta c_2 l_2 + \Delta c_2\Delta c_3 l_{G3})\big) \\ \tilde{}_{12} &= \Delta c_1\Delta c_2\big(m_2 l_{G2} + m_3(l_2 + \Delta c_3 l_{G3})\big) \\ \tilde{}_{13} &= \frac{1}{2}(\Delta c_1 + \Delta c_2)\Delta c_3 m_3 l_{G3}\end{aligned}$$

The second-row elements are:

$$\begin{aligned}\tilde{}_2 &= \Delta c_1\Delta c_2\Big((m_2 l_{G2} + m_3 l_2) + \Delta c_3 m_3 l_{G3}\Big)\ {}_1 \\ &\quad \Delta c_1\Delta c_2\Big((m_2 l_{G2} + m_3 l_2) + \Delta c_3 m_3 l_{G3}\Big)\ {}_2 \\ &\quad \frac{1}{2}(\Delta c_1 + \Delta c_2)\Delta c_3 m_3 l_{G3}\ {}_3 \\ &= \Big[\ \tilde{}_{21}\ \ \tilde{}_{22}\ \ \tilde{}_{23}\Big]\boldsymbol{\theta} \qquad (10)\end{aligned}$$

where

$$\begin{aligned}\tilde{}_{21} &= \Delta c_1\Delta c_2\big(m_2 l_{G2} + m_3(l_2 + \Delta c_3 l_{G3})\big) \\ \tilde{}_{22} &= \Delta c_1\Delta c_2\big(m_2 l_{G2} + m_3(l_2 + \Delta c_3 l_{G3})\big) \\ \tilde{}_{23} &= \frac{1}{2}(\Delta c_1 + \Delta c_2)\Delta c_3 m_3 l_{G3}\end{aligned}$$

The third-row elements are:

$$\begin{aligned}\tilde{}_3 &= \Delta c_1\Delta c_2\Delta c_3 m_3 l_{G3}\ {}_1 \\ &\quad \Delta c_1\Delta c_2\Delta c_3 m_3 l_{G3}\ {}_2 \\ &\quad \frac{1}{2}(\Delta c_1 + \Delta c_2)\Delta c_3 m_3 l_{G3}\ {}_3 \\ &= \Big[\ \tilde{}_{31}\ \ \tilde{}_{32}\ \ \tilde{}_{33}\Big]\boldsymbol{\theta} \qquad (11)\end{aligned}$$

where

$$\begin{aligned}\tilde{}_{31} &= \Delta c_1\Delta c_2\Delta c_3 m_3 l_{G3} \\ \tilde{}_{32} &= \Delta c_1\Delta c_2\Delta c_3 m_3 l_{G3} = \tilde{}_{31} \\ \tilde{}_{33} &= \frac{1}{2}(\Delta c_1 + \Delta c_2)\Delta c_3 m_3 l_{G3} = \tilde{}_{13}\end{aligned}$$

From Eqs. (9), (10) and (11), the linearized gravity term is obtained as:

$$g\gamma(\boldsymbol{\theta}) \quad \tilde{\Gamma}\boldsymbol{\theta}(t),\ \ \tilde{\Gamma} = g\begin{bmatrix}\tilde{}_{11} & \tilde{}_{12} & \tilde{}_{13} \\ \tilde{}_{21} & \tilde{}_{22} & \tilde{}_{23} \\ \tilde{}_{31} & \tilde{}_{32} & \tilde{}_{33}\end{bmatrix}$$

2.2 Formulation of the uncertain system

Here we us assume that the derivative of the angle $\dot{}_i$ takes vary small value, the product term becomes $\dot{}_i\dot{}_j \to 0,\ (i = 1,2,3,\ j = 1,2,3)$. Thus, it can ignore the nonlinear term in Eq. (1). Let $\boldsymbol{\eta}(\boldsymbol{\theta},\dot{\boldsymbol{\theta}}) = \mathbf{0}$

$$H(\boldsymbol{\theta})\boldsymbol{\theta}(t) + D\dot{\boldsymbol{\theta}}(t) + g\boldsymbol{\gamma}(\boldsymbol{\theta}) = \qquad (12)$$

Let us substitute Eqs. (8), (12), then

$$\tilde{H}\boldsymbol{\theta}(t) + D\dot{\boldsymbol{\theta}}(t) + \tilde{\Gamma}\boldsymbol{\theta}(t) = \qquad (13)$$

By multiplying $\tilde{H}\ ^1$ from the left side to Eq.(13),

$$\boldsymbol{\theta}(t) = \ \tilde{H}\ ^1 D\dot{\boldsymbol{\theta}}(t)\ \ \ \tilde{H}\ ^1\tilde{\Gamma}\boldsymbol{\theta}(t) + \tilde{H}\ ^1 \qquad (14)$$

From the above equation, we can compose the augmented system as:

$$\begin{matrix}\dot{\boldsymbol{\theta}}(t) \\ \boldsymbol{\theta}(t)\end{matrix} = \begin{matrix}\mathrm{O} & \mathrm{I} \\ \tilde{H}\ ^1\tilde{\Gamma} & \tilde{H}\ ^1 D\end{matrix}\ \begin{matrix}\boldsymbol{\theta}(t) \\ \dot{\boldsymbol{\theta}}(t)\end{matrix} + \begin{matrix}\mathrm{O} \\ \tilde{H}\ ^1\end{matrix}$$

By the definition of the state vector $\boldsymbol{x}(t)$ and the input vector $\boldsymbol{u}(t)$ as:

$$\boldsymbol{x}(t) = \begin{matrix}\boldsymbol{\theta}(t) \\ \dot{\boldsymbol{\theta}}(t)\end{matrix} = \begin{bmatrix}{}_1(t) \\ {}_2(t) \\ {}_3(t) \\ \dot{}_1(t) \\ \dot{}_2(t) \\ \dot{}_3(t)\end{bmatrix},\ \boldsymbol{u}(t) = \begin{bmatrix}{}_1(t) \\ {}_2(t) \\ {}_3(t)\end{bmatrix}$$

We can obtain the uncertain LTI system.

$$\dot{\boldsymbol{x}}(t) = A(\boldsymbol{\xi})\boldsymbol{x}(t) + B(\boldsymbol{\zeta})\boldsymbol{u}(t)$$

where state matrix $A(\ )$ and intput matrix $B(\ )$ are:

$$A(\boldsymbol{\xi}) = \begin{matrix}\mathrm{O} & \mathrm{I} \\ \tilde{H}\ ^1\tilde{\Gamma} & \tilde{H}\ ^1 D\end{matrix},\ B(\boldsymbol{\zeta}) = \begin{matrix}\mathrm{O} \\ \tilde{H}\ ^1\end{matrix}$$

The uncertain system is express as $A(\boldsymbol{\xi})$ and $B(\boldsymbol{\zeta})$. This matrix is separates to a nominal elements A_0, B_0 and an uncertain elements $\Delta A, \Delta B$.

$$\begin{aligned}A(\boldsymbol{\xi}) &= A_0 + \Delta A \qquad (15) \\ B(\boldsymbol{\zeta}) &= B_0 + \Delta B \qquad (16)\end{aligned}$$

The structure of the nominal elements is express as A_0, B_0. The structure of the uncertain elements A_i and B_i is defined by uncertainty $\Delta\ \ _i$ where $i = 1,2,3$.

$$\Delta A = \sum_{i=1}^{3}\ {}_i A_i,\ |\ {}_i|\ \ 1 \qquad (17)$$

$$\Delta B = \sum_{j=1}^{3}\zeta_j B_j,\ |\zeta_j|\ \ 1 \qquad (18)$$

where $\ _i$ and ζ_j are scalar values which express a scale of uncertainty. A_i and B_j are matrices which expressed a structure of the uncertainty.

3 NUMERICAL RESULT

In this section, we show the numerical example that is modeling method of the state and input matrix with structured uncertainty in the state equation. Each parameters takes as in the table 2. The nominal system structure is obtained as follows:

Table 2. Parameters ($i = 1, 2, 3$)

Parameter	value	Parameter	value
m_i	1.00	l_{Gi}	0.15
I_i	0.30	g	9.80
Δc_i	0.03	d_i	0.03

$$A_0 = \begin{bmatrix} 0.00 & 0.00 & 0.00 & 1.00 & 0.00 & 0.00 \\ 0.00 & 0.00 & 0.00 & 0.00 & 1.00 & 0.00 \\ 0.00 & 0.00 & 0.00 & 0.00 & 0.00 & 1.00 \\ 74.34 & 81.94 & 14.42 & 0.64 & 1.10 & 0.16 \\ 104.35 & 164.46 & 24.81 & 1.10 & 2.05 & 0.44 \\ 10.77 & 29.62 & 11.35 & 0.16 & 0.44 & 0.51 \end{bmatrix}$$

$$B_0 = \begin{bmatrix} 0.00 & 0.00 & 0.00 & 21.26 & 36.57 & 5.50 \end{bmatrix}^{\mathrm{T}}$$

State matrix and input matrix of the structured uncertainty are:

$$A_1 = 10^{\ 7} \begin{bmatrix} 0.00 & 0.00 & 0.00 & 0.00 & 0.00 & 0.00 \\ 0.00 & 0.00 & 0.00 & 0.00 & 0.00 & 0.00 \\ 0.00 & 0.00 & 0.00 & 0.00 & 0.00 & 0.00 \\ 3.72 & 4.09 & 0.36 & 0.00 & 0.00 & 0.00 \\ 5.22 & 8.22 & 0.62 & 0.00 & 0.00 & 0.00 \\ 0.54 & 1.48 & 0.28 & 0.00 & 0.00 & 0.00 \end{bmatrix}$$

$$A_2 = 10^{\ 7} \begin{bmatrix} 0.00 & 0.00 & 0.00 & 0.00 & 0.00 & 0.00 \\ 0.00 & 0.00 & 0.00 & 0.00 & 0.00 & 0.00 \\ 0.00 & 0.00 & 0.00 & 0.00 & 0.00 & 0.00 \\ 9.1726 & 26.54 & 4.02 & 0.15 & 0.27 & 0.06 \\ 17.277 & 49.84 & 7.44 & 0.27 & 0.51 & 0.10 \\ 3.7671 & 9.30 & 1.02 & 0.05 & 0.10 & 0.02 \end{bmatrix}$$

$$A_3 = 10^{\ 7} \begin{bmatrix} 0.00 & 0.00 & 0.00 & 0.00 & 0.00 & 0.00 \\ 0.00 & 0.00 & 0.00 & 0.00 & 0.00 & 0.00 \\ 0.00 & 0.00 & 0.00 & 0.00 & 0.00 & 0.00 \\ 0.90 & 1.12 & 0.56 & 0.01 & 0.02 & 0.01 \\ 1.91 & 2.92 & 0.84 & 0.02 & 0.05 & 0.02 \\ 0.25 & 1.76 & 0.40 & 0.01 & 0.02 & 0.01 \end{bmatrix}$$

$$\begin{aligned} B_1 &= \mathbf{0}_{6\times 1} \\ B_2 &= 10^{\ 7} \begin{bmatrix} 0.00 & 0.00 & 0.00 & 4.86 & 9.13 & 1.78 \end{bmatrix}^{\mathrm{T}} \\ B_3 &= 10^{\ 7} \begin{bmatrix} 0.00 & 0.00 & 0.00 & 0.27 & 0.66 & 0.27 \end{bmatrix}^{\mathrm{T}} \end{aligned}$$

4 CONCLUSION

In this paper, we proposed the design method of uncertain system of three-link RRR manipulator with parameter variation in each joint angle. The relationship between an uncertainty and system structure is clarified in the structured uncertainty in the state matrix and input matrix of the state differential equation. The numerical example will be shown that the effectiveness of our method. Future study is to apply GCC to our method to design a robust controller.

REFERENCES

[1] S. S. Chang and T. K. C. Peng (1972), Adaptive guaranteed cost control of system with uncertain parameters, IEEE Transactions on AC 17(4):474-473

[2] A. Sato, O. Sato, N. Takahashi and M. Kono (2008), A study of manipulator with passive revolute joint, Artificial Life and Robotics 13:31-35

[3] A. Sato, O. Sato, N. Takahashi and M. Yokomichi (2011), Analysis of a manipulator in relation to collision between a link and an object, Artificial Life and Robotics 16(2):169-173

[4] N. Takahashi, O. Sato, M. Kono (2009), Robust control method for the inverted pendulum system with structured uncertainty caused by measurement error, Artificial Life and Robotics, 14(4):574-577

[5] N. Takahashi, O. Sato, M. Kono (2010), A study of guaranteed cost control of a manipulator with a passive revolute joint, Artificial Life and Robotics 15(4):482-485

[6] N. Takahashi, M. Kono and O. Sato (2009), Guaranteed cost control of the uncertain system with parameter variations in an output matrix, Proceedings of the 1st Japan-Korea Joint Symposium on Dynamics & Control 139-142

[7] N. Takahashi, M. Yokomichi, O. Sato and M. Kono (2011), Observer-based control of a manipulator system with structured uncertainty, Artificial Life and Robotics 16(2):234-238

The Seventeenth International Symposium on Artificial Life and Robotics 2012 (AROB 17th '12),
B-Con Plaza, Beppu, Oita, Japan, January 19-21, 2012

Obstacle Avoidance of Snake Robot by Switching Control Constraint

Yasunobu Hitaka[1] and Toshikazu Yoshitake[1]

[1]Kitakyushu National College of Technology, Fukuoka 802-0985, Japan
(Tel: 81-93-964-7244, Fax: 81-93-964-7298)

[1]hitaka@kct.ac.jp

Abstract: In this paper, we propose an obstacle avoidance strategy for the autonomous locomotion control of a snake robot with passive wheels. By using a general pass planning method for the head position control, it will be a complicated problem and the robot will have to take a circuitous path because any parts of the robot (from head to tail) must avoid contact with the obstacle. Our strategy is transformation of a periodic undulate gliding form for the robot to keep go straight without any collision with the obstacle. It is actualized by switching a control constraint imposed on the head of the robot. In this paper, we denote the detail of our strategy and investigate the effectiveness of our strategy by numerical simulations.

Keywords: snake-like robot, obstacle avoidance, control constraint

1 INTRODUCTION

As a control strategy of the n-link snake robot with passive wheel, Mita and Prautsch et al [1] proposed an autonomous locomotion control of the head's position based on Lyapnov function method. They also proposed another control strategy which restricts the motion of the snake robot to some kind of a serpenoid curve to minimize the energy needed for motion of the snake robot. The serpenoid curve has proposed by Hirose [2], he is a pioneer of the field of the snake robot, to describe the undulation of natural snakes. This is based on an assumption that natural snakes have developed an efficient way of creeping. As other approaches, Hoshi et al [3] proposed an autonomous control strategy with consideration of the dynamic manipulability. Sato et al [4] proposed a method that they removed passive wheels of some links, and introduce the shape controllable points in the snake robot's body.

Considering the autonomous locomotion control of the snake-like robot in real environment, obstacle avoidance is one of the important tasks. However, there are few reports about it. Therefore, in this paper, the obstacle avoidance is considered under following assumptions; a snake robot is going straight, this robot consists of some rigid links with passive wheels, there is one obstacle in the direction of forward movement of the robot, and the length of robot is long enough for the width and depth of the obstacle. For above assumption, a general path planning method for the head position control will be figured out immediately. However, the path must be designed to that any parts of the robot (from head to tail) avoid contact with the obstacle. Therefore, the path planning will be complicated problem and robot will have to take a circuitous path. Moreover, if the robot must go straight through the area where is narrow width, enclosed with walls (for example, pipe line or air duct) and assigned one obstacle, the robot might not be able to pass the area without any touch with the obstacle or walls.

For these problems, we propose a different approach of the obstacle avoidance. Note that the robot moves with periodic undulant gliding form. If the length of robot is long enough for the width and depth of the obstacle, and the amplitude and cycle length of the gliding form can be chosen appropriately when the snake robot closes the distance from the obstacle, the robot will be able to keep go straight without any collision with the obstacle. To control the snake locomotion with an arbitrary gliding form, we introduce zeroing method [1]. It constrains the motion of the snake robot to an arbitrary serpenoid curve. This constraint is imposed on the first link of the robot. The serpenoid curve can be calculated by numerical integration and the snake robot traces the curve exactly. Therefore, switching the control constraint, the gliding form is transformed and the snake robot traces the changed serpenoid curve. In this paper, we denote the detail of our strategy and investigate the effectiveness of our strategy by numerical simulations.

2 Dynamic model of the Snake Robot

In this research, we deal with the dynamical model of the snake-like robot consisting of n-links as shown in Figure 1. Length $2l$ and weight m are the same for each link and distribution of the weight is assumed to be uniform. Therefore, the COM (center of mass) of each link is placed at the middle of the link. (x, y) is the position of the head in $x-y$ coordinates on a ground. For each link, (x_i, y_i) and θ_i $(i=1,\ldots,n)$ represent the position of its COM and absolute angle measured clockwise from y axis. $p_i\,(i=1,\ldots,n-1)$ is the relative angle which is controlled by input torques $u \in R^{n-1}$.

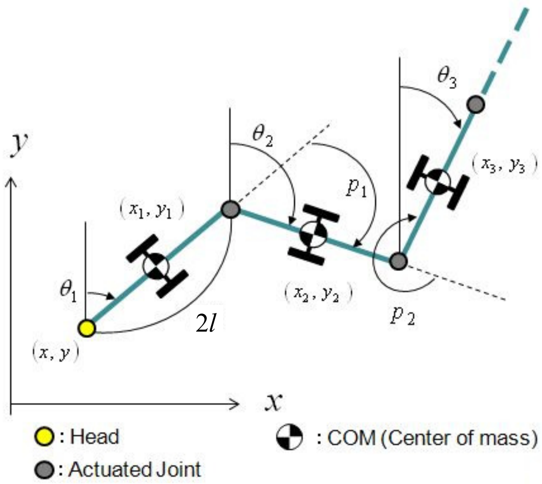

Fig. 1. n-link model of the snake robot

Each link has a passive wheel at the middle which does not slip in direction perpendicular to the body. From the condition, the equation of motion of the snake-like robot can be written as

$$\tilde{M}(\theta)\ddot{w} + \tilde{C}(\theta,\dot{\theta})\dot{w} + \tilde{D}(\theta)\dot{w} = F^T(\theta)Eu$$

$$w = \begin{bmatrix} x \\ y \end{bmatrix}, \theta = \begin{bmatrix} \theta_1 \\ \vdots \\ \theta_n \end{bmatrix} \qquad (1)$$

where $\tilde{M}$, $\tilde{C}$ and $\tilde{D}$ are matrices which are relevant to inertia, centrifugal force and friction, respectively. $E \in R^{n \times n-1}$ is a matrix satisfying $\theta = Ep$. F is a matrix which expresses the velocity constraint of each links is as $\dot{\theta} = F(\theta)\dot{w}$. In our research, we use another reduced order model using a different set of coordinate in order to control the robot motion with an arbitrary gliding form. Rewriting Eq.(1) with respect to the absolute angle of the 1st link θ_1 and the length of the trace of the 1st link η_1, the following system is obtained.

$$\bar{M}\begin{bmatrix} l\ddot{\theta}_1 \\ \ddot{\eta}_1 \end{bmatrix} + \bar{C}\begin{bmatrix} l\dot{\theta}_1 \\ \dot{\eta}_1 \end{bmatrix} + \bar{D}\begin{bmatrix} l\dot{\theta}_1 \\ \dot{\eta}_1 \end{bmatrix} = GF^T Eu \qquad (2)$$

Where, G is a transformation matrix, and $\bar{M}$, $\bar{C}$ and $\bar{D}$ are transformed matrices from $\tilde{M}$, $\tilde{C}$ and $\tilde{D}$ by the change of coordinate, respectively. The detail of the derivation of Eq. (1) or Eq (2) is introduced in [1].

3 Obstacle avoidance strategy

Here, let consider an obstacle avoidance problem for the snake robot modeled as Fig.1 under following assumptions; a snake robot is going straight, there is one obstacle in the direction of forward movement of the robot, and the length of robot is long enough for the width and depth of the obstacle. In the case, a general path planning method for the head position control will be figured out immediately. However, the path must be designed to that any parts of the robot (from head to tail) avoid contact with the obstacle as shown in Figure 2. Therefore, the path planning will be complicated problem and robot will have to take a circuitous path.

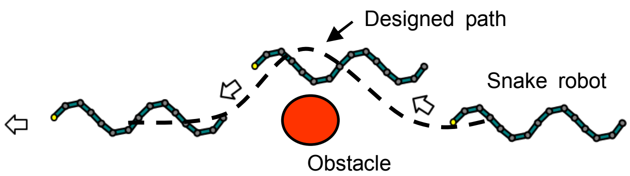

Fig. 2. Obstacle avoidance by the path planning

Moreover, as shown in Figure 3, the robot must go straight through the area where is narrow width, enclosed with walls (for example, pipe line or air duct) and assigned one obstacle, the robot might not be able to pass the area without any touch with the obstacle or walls.

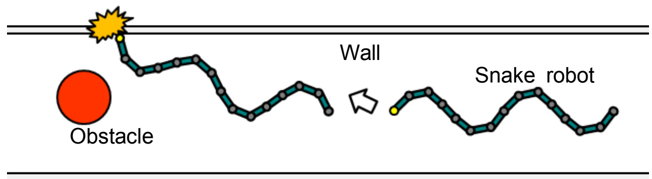

Fig. 3. Obstacle avoidance in the narrow width space

For these problems, if the robot can move with a periodic undulate gliding form, and the amplitude and cycle length of the gliding form can be chosen appropriately when the snake robot closes the distance from the obstacle, the robot will be able to keep go straight without any collision with the obstacle. Furthermore the robot will be able to pass the narrow width space without any touch with the obstacle or walls (See Figure 4).

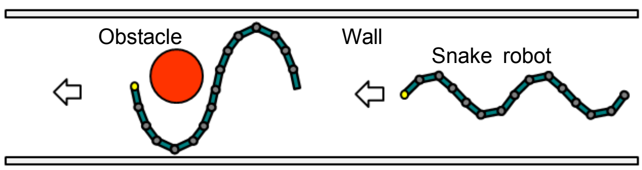

Fig. 4. Obstacle avoidance changing the gliding form

To control the snake locomotion with an arbitrary gliding form, we introduce zeroing method [1]. It constrains the motion of the snake robot to an arbitrary serpenoid curve.

3.1 Serpenoid Curve

The serpenoid curve has proposed by Hirose [2] to describe the undulation of natural snakes. An arbitrary curve can be described by its length η and the direction angle $\theta(\eta)$, as shown in Fig.5.

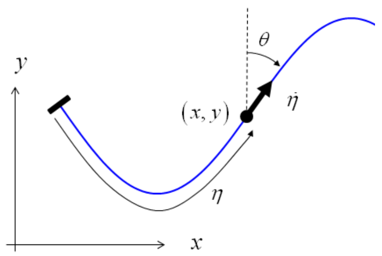

Fig. 5. Length and direction angle of a curve

Following Hirose[2], the serpenoid curve is defined as

$$\frac{dx}{d\eta} = \sin\left(w\sin(k\eta)\right), \frac{dy}{d\eta} = \cos\left(w\sin(k\eta)\right) \tag{3}$$

From this definition and relations $dx = \sin\theta d\eta$, $dy = \cos\theta d\eta$, it can be see that

$$\theta = w\sin\left(k\eta\right) = w\sin\left(\frac{\pi}{2L}\eta\right). \tag{4}$$

Therefore, the serpenoid function is a curve whose direction angle varies sinusoidally along the distance and shape of the curve depends on the w or k . Where, w is a maximum angle of gliding form and L is body length of 1/4 cycle of gliding form. The position of any point on the curve is obtained by integrating (3).

3.2 Restrict motion to the serpenoid curve

To restrict the motion of the robot to an arbitrary serpenoid curve, we use zeroing method [1]. For the control constraint to the serpenoid curve (4) and distance control with a reference distance along the curve γ expressed as

$$\begin{aligned} F_1 &= l\theta_1 - lw\sin(k\eta_1) = 0 \\ F_2 &= \eta_1 - \gamma = 0 \end{aligned} , \tag{5}$$

following differential equations are defined.

$$\begin{aligned} &\ddot{F}_1 + \alpha\dot{F}_1 + \beta F_1 = 0 \\ &\ddot{\eta}_1 + \vartheta\dot{\eta}_1 + \xi\left(\eta_1 - \gamma\right) = 0 \end{aligned} \tag{6}$$

where,

$$\begin{aligned} &\dot{F}_1 = l\dot{\theta}_1 - lwk\cos\left(k\eta_1\right)\dot{\eta}_1 \\ &\ddot{F}_2 = l\ddot{\theta}_1 - lwk\cos\left(k\eta_1\right)\ddot{\eta}_1 + lwk^2\sin\left(k\eta_1\right)\dot{\eta}_1^2 \end{aligned} \tag{7}$$

and $\alpha, \beta, \vartheta, \xi$ are positive coefficients. Define a nonsingular transformation matrix

$$P = \begin{bmatrix} 1 & -lwk\cos\left(k\eta_1\right) \\ 0 & 1 \end{bmatrix} \tag{8}$$

and multiply the vector $\begin{bmatrix} l\ddot{\theta}_1 \\ \ddot{\eta}_1 \end{bmatrix}$ by P from the left to get

$$P\begin{bmatrix} l\ddot{\theta}_1 \\ \ddot{\eta}_1 \end{bmatrix} = \begin{bmatrix} l\ddot{\theta}_1 - lwk\cos\left(k\eta_1\right)\ddot{\eta}_1 \\ \ddot{\eta}_1 \end{bmatrix} := K. \tag{9}$$

Substituting from (7) and (6) into (9) yields

$$\begin{bmatrix} l\ddot{\theta}_1 \\ \ddot{\eta}_1 \end{bmatrix} = P^{-1}\begin{bmatrix} -lwk^2\sin\left(k\eta_1\right)\dot{\eta}_1^2 - \alpha\dot{F}_1 - \beta F_1 \\ -\vartheta\dot{\eta}_1 - \xi\left(\eta_1 - \gamma\right) \end{bmatrix} \tag{10}$$

And then, substituting (10) into the system (2), the controller

$$\mathbf{u} = \left(GF^T E\right)^{\dagger}\left[\left(\bar{C} + \bar{D}\right)\begin{bmatrix} l\dot{\theta}_1 \\ \dot{\eta}_1 \end{bmatrix} + \bar{M}P^{-1}K\right] \tag{11}$$

are obtained. This ensure that $F_1 \to 0, F_2 \to 0$.

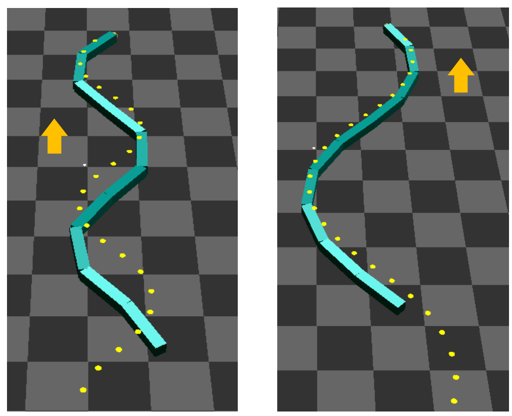

(a) $4L = 5.0[m]$ (b) $4L = 10.0[m]$

Fig. 6. Simulation of motion of a 10 link snake robot

Figure 6 shows two motions of the snake robot. These simulations are applied the controller (11) to the system (2). The robot has 10 links and each length is 1.0[m], yellow dot-lines denote the serpenoid trace, and the robot go straight to the upper direction. In the left figure (a), parameter w is set $\pi/4$ [rad] and $4L = 5.0[m]$ (It means that the robot moves with two cycle undulate motion). As a result, the robot shows a periodic undulate gliding form. However, the gap between the Serpenoid curve and link position is increased as the distance from the head. On the other hand, in the right figure (b), parameter w is set $\pi/4$ [rad] and $4L = 10.0[m]$. In this case, the gap is very small compared to (a). We simulated various patterns changing w, $4L$, the link length or the number of links. As a result, we confirmed that the number of links is larger or the cycle length of the serpenoid curve is longer, the gap tends to be decreased. Therefore, this control method is useful for the obstacle avoidance if the length of robot is long enough and has appropriate amount of links for the width and depth of the obstacle.

3.3 Switching control constraint

For the snake locomotion, there is an energy-efficient gliding form. Therefore, it is reasonable that under normal conditions, the robot moves with the energy-efficient gliding form, and when the robot confronts the obstacle, the gliding form is transformed to avoid collision with the obstacle. The transformation of the gliding form is actualized by switching the control constraint. Namely, change the values of w or k. However, at the switching point, the angle of the changed serpenoid curve must be coincided with the angle of the former serpenoid curve. If it is omitted, the trace of the 1st link strays far from the serpenoid trace after the switching point as shown in Fig.7.

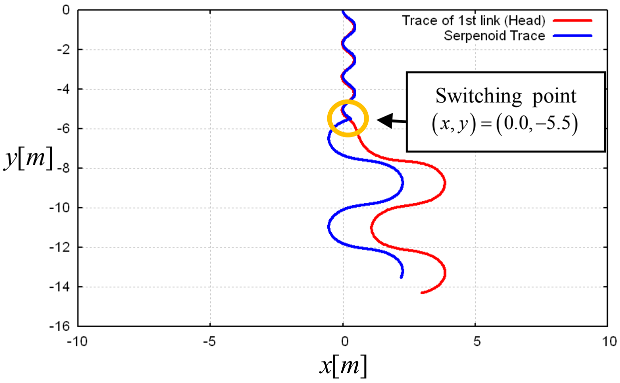

Fig. 7. Simulation result of switching control constraint

Moreover, about the connection of serpenoid functions, two cases are considered as shown in Fig.8. In Case1, the curve is non-smooth and it cause rapid variations of input torques. Therefore, Case2 should be chosen. To achieve the connection as Case2, the serpenoid function after the switching is designed as follows.

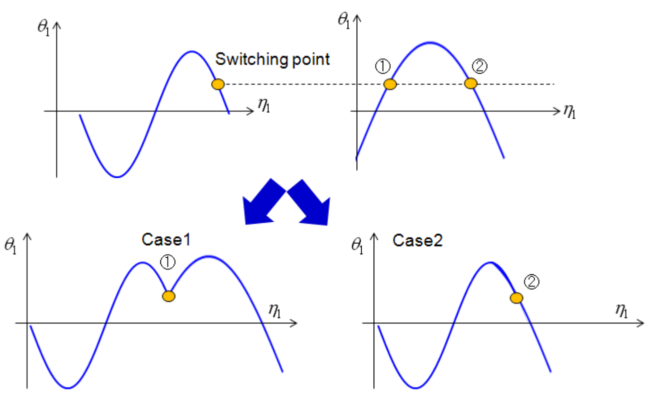

Fig. 8. Connection of the serpenoid function

$$\theta_1(\eta_1)=\begin{cases} w_\beta \sin\left(k_\beta \eta_1+\phi\right) & \dot{\theta}_1(\eta_{sw})\ge 0 \\ w_\beta \sin\left(k_\beta \eta_1+\pi-\phi\right) & \dot{\theta}_1(\eta_{sw})<0 \end{cases}, \qquad (12)$$
$$\phi = k_\beta \eta_{sw}+\sin^{-1}\left(\frac{\theta_1(\eta_{sw})}{w_\beta}\right)$$

where $w_\beta, k_\beta, L_\beta$ are parameters of the serpenoid function after the switching and η_{sw} is a constant of the length of the trace of the 1st link at the switching point. In Fig.9, it is shown that the trace of the1st link is well coincided with the serpenoid trace after the switching point.

From the result, it is known that designing a serpenoid curve to avoid an obstacle with the proposed technique, the snake robot achieve the obstacle avoidance because the robot can trace the designed trace exactly.

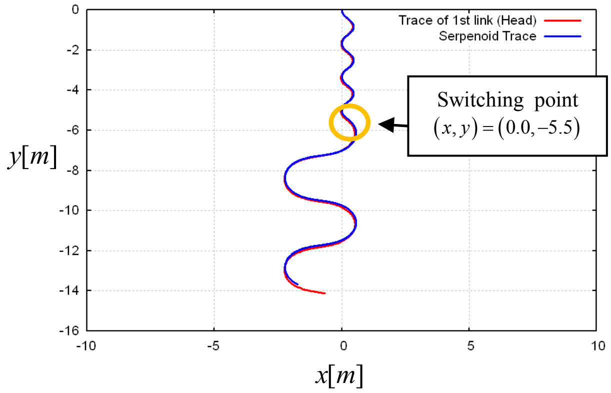

Fig. 9. Simulation result (using serpenoid function (12))

4 CONCLUSION

In this paper, we detailed the obstacle avoidance strategy for the snake robot. By the results of the numerical simulations, we were convinced that the design of the serpenoid curve with the switching control constraint is effective to the obstacle avoidance of the snake robot.

In our future works, we will construct an algorism which designs a serpenoid trace to avoid an obstacle automatically.

REFERENCES

[1] P. Prautsch, T. Mita and T. Iwasaki: Analysis and Control of a Gait of Snake Robot, T.IEE Japan, Vol. 120-D, No3, 2000, pp.372-381.

[2] S. Hirose: Biologically Inspired Robots, Oxford University Press, 1993.

[3] Y. Hoshi, M. Sampei and M. Koga: An Autonomous Locomotion Control of a Multi-Joint Snake-Like Robot with Consideration of the Dynamic Manipulability, Journal of the Robotics Society of Japan, Vol.18, No.8, 2000, pp.1133-1140.

[4] H. Sato, M. Tanaka and F. Matsuno: Trajectory Tracking Control of Snake Robots Based on Dynamic Model, Journal of the Society of Instrument and Control Rngineers, Vol.42, No.6, 2006, pp.651-658.

The Seventeenth International Symposium on Artificial Life and Robotics 2012 (AROB 17th '12),
B-Con Plaza, Beppu, Oita, Japan, January 19-21, 2012

Propose of the use to Alternative Gramian for the Controller Order Reduction

Shota Usui [1], Tsutomu Nagado [2], and Michio Kono[3]

[1] Miyakonojo National College of Technology. Miyakonojo, Miyazaki 885-8567, Japan
[2] University of the Ryukyus. Nishihara, Okinawa 903-0213, Japan
[3] University of Miyazaki. Miyazaki, Miyazaki 889-2192, Japan

Abstract: Robust controllers have feature of corresponding to the model error and the disturbance. However, obtained controller is generally high-order. The controller order is desirable in small from a standpoint of cost and reliability. The purpose of our work is to propose of effective controller order reduction method. In this paper, we propose a controller order reduction method using alternative Gramian. We were applied this method to conventional methods. Further, we confirmed effect using the numerical example. As a result, our proposed method found some efficacy in stability and performance degradation of a closed loop system. However, when applied to other controlled objects, these was relatively-ineffective. Therefore, this method admit of improvement. As one of these improvements, we are thinking that to use Genetic Algorithm (GA) for optimal solution derivation of the riccati inequality.

Keywords: controller order reduction, gramian, H_∞ controller

1 INTRODUCTION

Traditional modern control theory had a gap by between theory and reality, because it was not considering the model error. For resolve this problem, the robust control theory was corresponding to the model error and disturbance. However, the robust controller such as H_∞ controller is generally high-order. Generally, the controller order is desirable in small from a standpoint of cost and reliability. Therefore, it is necessary obtaining low-order controller that could be suppress to performance degradation. In this paper, we focus attention on the balanced realization truncation method.

The balanced realization truncation method is one of the controller reduction. In addition, the blocked balanced realization truncation method is also one of the controller reduction method, this method is considering the characteristics of the closed-loop system input-output. In these methods, we obtain controllability Gramian and observability Gramian from Lyapunov equations. When the Gramian replaced by a solution of stringent condition, we think that could effective coordinate transformation. We replaced the Gramian by the solution of stringent condition, it will be referred to as "Alternative Gramian".

In this paper, we propose a controller order reduction method using Alternative Gramian. Alternative Gramians were used a solution of three kinds, Lyapunov inequations, Riccati equations and Riccati inequations. Moreover, controller order reduction methods were applied to the balanced realization truncation method and the block balanced realization truncation method. We confirmed the effectiveness of the proposed method by numerical examples.

2 METHOD

2.1 Controllability and Observability Gramian

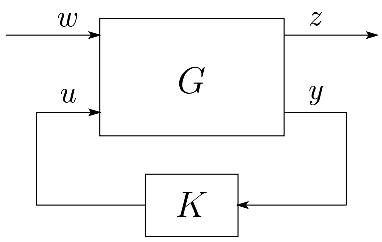

Fig. 1. The closed-loop system

Consider the closed-loop system shown in Fig.1. In the figure, w has shown the external input, z has shown the controlled output, u has shown the control input, and y has shown the measured input. Let, system G is the generalized plant, and K is the controller. G and K are represented as following.

$$G = \left[\begin{array}{c|c} A & B \\ \hline C & D \end{array}\right] = C(sI - A)^{-1}B + D \tag{1}$$

$$K = \left[\begin{array}{c|c} A_k & B_k \\ \hline C_k & D_k \end{array}\right] \tag{2}$$

where, the matrix A_k assumed to be stable. Solution Q of the following Lyapunov equation is called the "observability Gramian".

$$A_k^T Q + Q A_k + C_k^T C_k = 0 \tag{3}$$

In the same way, solution P of the following Lyapunov equation is called the "controllability Gramian".

$$A_kP + PA_k^T + B_kB_k^T = 0 \tag{4}$$

The eigenvalues size of the controllability Gramian and observability Gramian shows ease of the control and observation for corresponding states. However, the Gramian of alone cannot accurately assess effect of input-output relation. In order to solve this problem, we introduce a special realization of the controllability Gramian and observability Gramian.

2.2 Balanced realization truncation method

When controller K, controllability Gramian P and observability Gramian Q are shown in equation (2)-(4), we assume $P \geq 0$ and $Q \geq 0$. Here, we convert to $\hat{y} = Ty$ using the nonsingular matrix T. At this time, K is

$$K = \left[\begin{array}{c|c} \hat{A}_k & \hat{B}_k \\ \hline \hat{C}_k & \hat{D}_k \end{array}\right] = \left[\begin{array}{c|c} TA_kT^{-1} & TB_k \\ \hline C_kT^{-1} & D_k \end{array}\right] \tag{5}$$

Furthermore, Gramians will change as follows:

$$\hat{P} = TPT^T \tag{6}$$

$$\hat{Q} = (T^{-1})^T QT^{-1} \tag{7}$$

In particular, when these are the minimal realization, can be the following:

$$TPT^T = (T^{-1})^T QT^{-1} = \Sigma \tag{8}$$

$$\Sigma = \mathrm{diag}(\sigma_1, \sigma_2, \dots, \sigma_n) \tag{9}$$

This is called a balanced realization. And, $\sigma_1 \geq \sigma_2 \geq \cdots \geq \sigma_n \geq 0$ are called Hankel singular values. Corresponding state to the zero eigenvalue of P and Q can eliminate from the transfer function matrix. When the new realization of K is split as follows

$$K = \left[\begin{array}{c|c} TA_kT^{-1} & TB_k \\ \hline C_kT^{-1} & D_k \end{array}\right] = \left[\begin{array}{ccc|c} A_{11} & \cdots & A_{1j} & B_1 \\ \vdots & & \vdots & \vdots \\ A_{i1} & \cdots & A_{ij} & B_i \\ \hline C_1 & \cdots & C_j & D \end{array}\right] \tag{10}$$

We obtain the low-order system K_r by truncation of low-impact parts from the high-order system K. The obtained low-order system K_r is following.

$$K_r = \left[\begin{array}{c|c} A_{11} & B_1 \\ \hline C_1 & D \end{array}\right] \tag{11}$$

This method called the balanced realization truncation method. This is one of the famous model reduction method. The controller order reduction methods had been proposed various methods such as proposed of the frequency weight based on the balanced realization method. When using the balanced realization method to the controller order reduction, it is considering the input-output characteristics. However, it was not consider stability of the closed-loop system. Wherein, the blocked balanced realization was proposed for considering the input-output characteristics of the closed-loop system. The blocked balanced realization has been considered by the input-output characteristics of the closed-loop system by to think about overall the closed-loop system.

2.3 Proposed Method 1

As previously explained, controllability and observability Gramian are solution of Lyapunov equations (2) and (3). The balanced realization using these gramians have been considered for the mutual similarity with the original system. However, it has not considered for the performance degradation of low-order system. In addition, the traditional balanced realization was not consider stability of the closed-loop system. Here, in order to consider the H_∞ characteristics, we propose to use Riccati equations as alternative of controllability and observability Gramian. For example, when this method is applied by the block balanced realization, used Riccati equations are as following.

$$\begin{aligned}(A + BR^{-1}D^TC)^TQ + Q(A + BR^{-1}D^TC) \\ + QBR^{-1}B^TQ + C^T(I + DR^{-1}D^T)C = 0\end{aligned} \tag{12}$$

$$\begin{aligned}(A + BR^{-1}D^TC)P + P(A + BR^{-1}D^TC)^T \\ + PC^TR^{-1}CP + B(I + D^TR^{-1}D)B^T = 0\end{aligned} \tag{13}$$

Where, R is

$$R = \gamma^2 I - D^TD$$

or

$$R = \gamma^2 I - DD^T$$

To exist solutions of equation (12) ,(13) and to be less than γ to the H_∞ norm of the system are equivalent. Therefore, when the block balanced realization is applied by these solution,the H_∞ norm of the closed-loop system will can be expected to less than γ.

2.4 Proposed Method 2

Secondly, to further reduce the performance degradation, we propose to use solution of the Lyapunov inequality on alternative of gramian. For example, when this method is applied by the block balanced realization, used Lyapunov inequality are as following.

$$AP + PA^T + BB^T \leq 0 \tag{14}$$

$$A^TQ + QA + C^TC \leq 0 \tag{15}$$

Lyapunov equation has a unique solution exists, but there is no unique solution in the Lyapunov inequality. We give the guidepost for minimization of solution. When make the Trace(P) and Trace(Q) smaller, it is expected that truncation part of the Hankel singular values can be smaller. Therefore, when we find P and Q to minimize Trace(P) and Trace(Q) , the closed-loop system performance degradation will can reduce.

2.5 Proposed Method 3

Section 2.3 proposed that we use solution of the Riccati equation as alternative for the controllability and observability Gramian for to consider of the H_∞ characteristic. Moreover, Section 2.4 proposed also that we use solution of the Lyapunov inequality for to reduce the performance degradation of the closed-loop system used the low-order controller. In this section, we propose that we use solution of Riccati inequality for to reduce the performance degradation and to consider of the H_∞ characteristic. For example, when this method is applied by the block balanced realization, used Riccati inequality are as following.

$$\begin{bmatrix} AP+PA^T & PC^T & B \\ CP & -\gamma I & D \\ B^T & D^T & -\gamma I \end{bmatrix} < 0 \qquad (16)$$

$$\begin{bmatrix} A^TQ+QA & QB & C^T \\ B^TQ & -\gamma I & D^T \\ C & D & -\gamma I \end{bmatrix} < 0 \qquad (17)$$

To exist solutions of equation (16) ,(17) and to be less than γ to the H_∞ norm of the system are equivalent. Therefore, when this solutions are applied to the block balanced realization, the H_∞ norm of the closed-loop system will can be expected to less than γ. Also, the closed-loop system performance degradation will can reduce.

3 RESULT

As a numerical example, we treat the four-disk controller system. The state-space realization of generalized plant is at the left. In this paper, we design the H_∞ controller set at design specification γ=1.2. The obtained controller is the 8th-order, and this controller meets the specifications as follows:

$$\begin{aligned}\|F_l(G,K)\|_\infty &= \|G_{11}+G_{12}K(I-G_{22}K)^{-1}G_{21}\|_\infty \\ &= 1.1963 < 1.2\end{aligned}$$

We reduce order of this controller from 7th-order to 1st-order. We showing in Table 1-3 the H_∞ norm of the closed-loop system that is including by reduced-order controller. Where, in Table 1-3, "BT" has shown the balanced realization truncation method, "WBT" has shown the balanced realization truncation method with frequency weight($W = G(I+KG)^{-1}$), "BBT" has shown the block balanced realization truncation method. Moreover, "no mark" has shown a method using Lyapunov equations (conventionally method), "Ric(eq)" has shown a method using Riccati equations (Proposed method 1), "Lyap (ineq)" has shown a method using Lyapunov inequalities(Proposed method 2), "Ric(ineq)" has shown a method using Riccati inequalities(Proposed method 3). "U" has shown unstable system.

$$A = \begin{bmatrix} -0.161 & -6.004 & -0.58215 & -9.9835 & -0.40727 & -3.982 & 0 & 0 \\ 1 & 0 & 0 & 0 & 0 & 0 & 0 & 0 \\ 0 & 1 & 0 & 0 & 0 & 0 & 0 & 0 \\ 0 & 0 & 1 & 0 & 0 & 0 & 0 & 0 \\ 0 & 0 & 0 & 1 & 0 & 0 & 0 & 0 \\ 0 & 0 & 0 & 0 & 1 & 0 & 0 & 0 \\ 0 & 0 & 0 & 0 & 0 & 1 & 0 & 0 \\ 0 & 0 & 0 & 0 & 0 & 0 & 1 & 0 \end{bmatrix},$$

$$B_1 = \begin{bmatrix} 1 & 0 \\ 0 & 0 \\ 0 & 0 \\ 0 & 0 \\ 0 & 0 \\ 0 & 0 \\ 0 & 0 \\ 0 & 0 \end{bmatrix}, \quad B_2 = \begin{bmatrix} 1 \\ 0 \\ 0 \\ 0 \\ 0 \\ 0 \\ 0 \\ 0 \end{bmatrix},$$

$$C_1 = \begin{bmatrix} 0 & 0 & 0 & 0 & 0.00055 & 0.011 & 0.00132 & 0.018 \\ 0 & 0 & 0 & 0 & 0 & 0 & 0 & 0 \end{bmatrix}$$

$$C_2 = \begin{bmatrix} 0 & 0 & 6.4432\times10^{-3} & 2.3196\times10^{-3} & 7.1252\times10^{-2} & 1.0002 & 0.10455 & 0.99551 \end{bmatrix}$$

$$D_{11} = \begin{bmatrix} 0 & 0 \\ 0 & 0 \end{bmatrix}, \quad D_{12} = \begin{bmatrix} 0 \\ 1 \end{bmatrix}$$

$$D_{21} = \begin{bmatrix} 0 & 1 \end{bmatrix}, \quad D_{22} = 0$$

Table 1. H_∞ norm of $F_l(G, K_r)$

Order of K_r	BT	BT+Lyap(ineq)	BT+Ric(eq)	BT+Ric(ineq)
7	1.3211	U	1.3183	1.3240
6	1.2072	U	1.2055	1.2089
5	U	U	U	U
4	U	U	U	U
3	U	U	U	U
2	U	20.305	U	U
1	U	U	U	U

Table 2. H_∞ norm of $F_l(G, K_r)$

Order of K_r	WBT	WBT+Lyap(ineq)	WBT+Ric(eq)	WBT+Ric(ineq)
7	1.2482	7.9282	1.2548	1.2415
6	1.2015	2.4321	1.2029	1.1979
5	1.3018	13.613	1.3576	1.5902
4	1.3205	15.825	1.3354	1.2444
3	U	U	U	4.0781
2	U	U	U	2.3907
1	U	U	U	U

Table 3. H_∞ norm of $F_l(G, K_r)$

Order of K_r	BBT	BBT+Lyap(ineq)	BBT+Ric(eq)	BBT+Ric(ineq)
7	1.2462	12.684	1.2623	1.2038
6	1.2018	2.3397	1.2029	1.1959
5	U	145.07	U	1.4605
4	1.2336	7.7959	1.2412	1.1989
3	U	U	U	U
2	U	U	U	2.3056
1	U	U	U	U

From the Table 1, the method using Lyapunov inequality can be the most reduced order. However, the H_∞ norm of 2nd order by Lyapunov inequality is over 20, system performance degradation can not reduced in this method. In addition, when it used the balanced realization truncation method by alternative gramian that is solution of Riccati equations or Ricacati inequality, those are almost no variation by original balanced realization. Therefore, an alternative gramian unfitted for the balanced realization truncation method.

Next, from the Tabale 2, the method using Riccati inequality can be the most reduced order. Especially, when it was used Riccati inequality in 6th order, the H_∞ norm of the closed-loop system including the low-order controller is under γ. From this, we find that performance degradation is suppressed.

Finally, from the Table 3, the method using Riccati inequality can be the most reduced order. When the controller order is 7th, 6th and 4th, the H_∞ norm is under γ. In addition, In the 2nd order, closed-loop is stable, and performance degradation is most small. Therefore, we found significant effect by applying the solution of Riccati inequality to the block balanced realization from these results.

4 CONCLUSION

In this paper, we have proposed the controller order reduction method which used solution of the Riccati inequality etc. as substitute for the controllability grammian and the observability grammian. Moreover, this paper applied a proposed method to the block balanced realization etc, and looked at an effect of a proposed method by numerical examples. As a result, We were found that our proposed method obtained some efficacy in stability and performance degradation of a closed loop system. However, when applied to other controlled objects, these was relatively-ineffective. Therefore, this method admit of improvement. As one of these improvements, we are thinking that to use Genetic Algorithm (GA) for optimal solution derivation of the Riccati inequality.

REFERENCES

[1] G.Wang,V.Sreeram and W.Q.Liu,"Balanced performance preserving controller reduction",System and Control Letters 46,pp99-110 (2002).

[2] T.Mita,"H_∞ Seigyo-[H_∞ Control]",Tokyo,Japan :Shokodo (1994).

[3] K.Z.Liu,"Senkei Robust Seigyo-[Linear Robust Control]",Tokyo,Japan :Corona Publishing (2002).

[4] K.Zhou,J.C.Doyle and K.Glover,"Robust and optimal control, Prentice-Hall",Englewood Cliffs, NJ (1996).

The Seventeenth International Symposium on Artificial Life and Robotics 2012 (AROB 17th '12),
B-Con Plaza, Beppu, Oita, Japan, January 19-21, 2012

Classes of linear systems of difference equations with bounded solutions

Naoharu Ito[1], Reinhold Küstner[2], and Harald K. Wimmer[3]

[1] Nara University of Education, Nara 630-8528, Japan
(naoharu@nara-edu.ac.jp)
[2] Universität Hannover, D-30167 Hannover, Germany
[3] Universität Würzburg, D-97074 Würzburg, Germany

Abstract: In this paper we investigate higher order systems of linear difference equations where the associated characteristic matrix polynomial is self-inversive. We consider classes of equations with bounded solutions. It is known that stability properties of higher order systems of linear difference equations are determined by the characteristic values of the corresponding matrix polynomials. All solutions are bounded (in both time directions) if the spectrum of the corresponding matrix polynomial lies on the unit circle, and moreover if the characteristic values of modulus one are semisimple. If the corresponding matrix polynomial is self-inversive then one can use the inner radius of the numerical range to obtain a criterion for boundedness of solutions. We show that all solutions are bounded if the inner radius is greater than 1. In the case of matrix polynomials with positve definite coefficient matrices we derive a computable lower bound for the inner radius.

Keywords: linear difference equations, matrix polynomials, bounded solutions, self-inversive, inner radius, numerical range

1 INTRODUCTION

In this paper we investigate higher order systems of linear difference equations where the associated characteristic matrix polynomial is self-inversive. We consider classes of equations with bounded solutions.

Self-inversive polynomials and matrix polynomials have been studied in the literature under various names including reciprocal, self-reciprocal, palindromic and conjugate-symmetric (see [1], [3], [8], [12]). There are applications in numerous areas of engineering, for example, optimal design of problems governed by hyperbolic field equations [12], the study of line spectral pairs in speech coding [11], and kernel representations of time-reversible systems [9]. Moreover, such polynomials are used in applied mathematics to deal with stability of periodic orbits of autonomous Hamiltonian systems [10], and to investigate Lie algebras for semisimple hypersurface singularities [7].

Only recently self-inversive matrix polynomials and corresponding linear differential and difference equations appeared in the solution of discrete time linear quadratic optimal control problems [2], in the study of discretization schemes for cubic Schrödinger equations [4] and in vibration analysis of railway tracks for high-speed trains [5].

It is known that stability properties of higher order systems of linear difference equations are determined by the characteristic values of the corresponding matrix polynomials.

All solutions are bounded (in both time directions) if the spectrum of the corresponding matrix polynomial lies on the unit circle, and moreover if the characteristic values of modulus one are semisimple (that is the corresponding elementary divisors are linear). If the corresponding matrix polynomial is self-inversive then one can use the inner radius of the numerical range to obtain a criterion for boundedness of solutions. We show that all solutions are bounded if the inner radius is greater than 1. In the case of matrix polynomials with positve definite coefficient matrices we derive a computable lower bound for the inner radius. We illustrate our results by examples.

2 PRELIMINARIES

Let γ be complex number with $|\gamma| = 1$ and $F_0, F_1, \ldots, F_m$ complex hermitian $n \times n$ matrices satisfying

$$F_j^* = \gamma F_{m-j},\ j = 0, 1, \ldots, m, \qquad \det F_0 \neq 0,\ \det F_m \neq 0. \quad (1)$$

Consider the following higher order systems of linear difference equation:

$$F_m x(t+m) + F_{m-1} x(t+m-1) + \cdots + F_0 x(t) = 0, \quad (2)$$

where $\{x(t)\}_{t=-\infty}^{\infty}$ is a sequence of vectors in $\mathbb{C}^n$ to be determined. The associated characteristic matrix polynomial is as follows:

$$F(z) = F_0 + F_1 z + \cdots + F_m z^m \in \mathbb{C}^{n \times n}[z]. \quad (3)$$

The conjugate-reverse matrix polynomial of $F(z)$ in (3) is defined by

$$\hat{F}(z) = F_m^* + \cdots + F_1^* z^{m-1} + F_0^* z^m.$$

Then it follows form (1) that $F(z) = \gamma \hat{F}(z)$ and thus $F(z)$ is γ-self-inversive.

We use the following notation. If $P(z) \in \mathbb{C}^{n\times n}[z]$ then the set of characteristic values of $P(z)$ is denoted by $\sigma(P) = \{\lambda \in \mathbb{C}; \det P(z) = 0\}$. A characteristic value λ of $P(z)$ is said to be normal if for any $v \in \mathbb{C}^n$,

$$P(\lambda)v = 0 \Longleftrightarrow v^* P(\lambda) = 0.$$

A characteristic value λ of $P(z)$ is said to be semisimple if the corresponding elementary divisors are linear.

Let $W(P) = \{\lambda \in \mathbb{C}; v^* P(\lambda)v = 0 \text{ for some } v \in \mathbb{C}^n, v \neq 0\}$ be the numerical range of $P(z)$. It is obvious that $\sigma(P) \subset W(P)$. We call $r_i(P) = \min\{|\lambda|; \lambda \in W(P)\}$ the inner radius of $P(z)$. If H is hermitian then $\lambda_{\min}(H)$ and $\lambda_{\max}(H)$ shall denote the smallest and the largest eigenvalue of H, respectively. Let $\|H\|$ be the spectral norm of H. Then $\|H\| = \max\{|\lambda_{\min}(H)|, |\lambda_{\max}(H)|\}$ and

$$\|H\| \geq -|\lambda_{\min}(H)|.$$

3 BOUNDEDNESS

In this section we deal with the boundedness for the difference equation (2). The equation (2) is said to be bounded if any solution $x(t)$ of (2) with initial conditions $x(0) = x_0, x(1) = x_1, \ldots, x(m-1) = x_{m-1}$ is bounded for $t \to \infty$ and $t \to -\infty$.

In the rest of this paper we assume that the associated characteristic matrix polynomial $F(z)$ to (2) has the form

$$F(z) = P(z) + \gamma z^r \hat{P}(z) \tag{4}$$

for some $r \geq 0$ and some $P(z) = \sum_{j=0}^{k} A_j z^j \in \mathbb{C}^{n\times n}[z]$. Then $F(z)$ is γ-self-inversive. Note that for any $P(z) = \sum_{j=0}^{k} A_j z^j \in \mathbb{C}^{n\times n}[z]$ and any $r \in \mathbb{Z}, r \geq 0$, $P(z) + \gamma z^r \hat{P}(z)$ is γ-self-inversive.

We have the following fact (see [6]).

Proposition 1. *Let $F(z)$ be a self-inversive matrix polynomial of the form* (4) *and suppose $r_i(P) > 1$. Then the characteristic values of $F(z)$ lie on the unit circle, and they are normal and semisimple.*

An immediate consequence of the preceding proposition is the following.

Theorem 2. *Let $F(z)$ be a self-inversive matrix polynomial of the form* (4) *and suppose $r_i(P) > 1$. Then, the difference equation* (2) *is bounded.*

The following theorem provides a computable lower bound for the inner radius.

Theorem 3. *Let the coefficients A_j, $j = 0, \ldots, k$, of $P(z) = \sum_{j=0}^{k} A_j z^j$ be hermitian and positive definite. Set*

$$\mu(P) = \min\left\{\lambda_{\min}(A_j A_{j+1}^{-1});\ j = 0, \ldots, k-1\right\}.$$

Then $r_i(P) \geq \mu(P)$.

Corollary 4. *If $A_0 > A_1 > \cdots > A_k > 0$ then $\mu(P) > 1$.*

4 ROBUST BOUNDEDNESS

The difference equation (2) is said to be robustly bounded if there exists $\varepsilon > 0$ such that for any hermitian matrices $\tilde{F}_0, \tilde{F}_1, \ldots, \tilde{F}_m$ satisfying

$$\|\tilde{F}_j - F_j\| < \varepsilon,\ F_j^* = \gamma F_{m-j},\ j = 0, 1, \ldots, m,$$

and for any initial conditions $x(0) = x_0, x(1) = x_1, \ldots, x(m-1) = x_{m-1} \in \mathbb{C}^n$, the solution of the difference equation

$$\tilde{F}_m x(t+m) + \tilde{F}_{m-1} x(t+m-1) + \cdots + \tilde{F}_0 x(t) = 0$$

is bounded for $t \to \infty$ and $t \to -\infty$.

First, we consider the following difference equation in the case of $n = 1$:

$$\begin{aligned} a_0 x(t+m) &+ a_1 x(t+m-1) + \cdots \\ &+ a_k x(t+m-k) + a_k x(t+k) + \cdots \\ &+ a_1 x(t+1) + a_0 x(t) = 0,\ m > 2k, \end{aligned} \tag{5}$$

where $a_0, a_1, \ldots, a_k \in \mathbb{R}$ $(a_0 \neq 0)$ are given and $\{x(t)\}_{t=0}^{\infty}$ is a sequence in $\mathbb{R}$ to be determined.

Assume $a_0 > a_1 > \cdots > a_k > 0$. Set

$$\varepsilon = \min\{a_i - a_{i+1} \mid 0 \leq i \leq k-1\}. \tag{6}$$

Suppose that $\tilde{a}_0, \tilde{a}_1, \ldots, \tilde{a}_k \in \mathbb{R}$ satisfy

$$|\tilde{a}_i - a_i| < \frac{1}{2}\varepsilon,\ i = 0, 1, \ldots, k, \tag{7}$$

and consider the difference equation

$$\begin{aligned} \tilde{a}_0 x(t+m) &+ \tilde{a}_1 x(t+m-1) + \cdots + \\ &\tilde{a}_k x(t+m-k) + \tilde{a}_k x(t+k) + \cdots + \\ &\tilde{a}_1 x(t+1) + \tilde{a}_0 x(t) = 0 \end{aligned} \tag{8}$$

and the associated characteristic matrix polynomial

$$\begin{aligned} f(z) = \tilde{a}_0 &+ \tilde{a}_1 z + \cdots + \tilde{a}_k z^k + \\ &\tilde{a}_k z^{m-k} + \cdots + \tilde{a}_1 z^{m-1} + \tilde{a}_0 z^m. \end{aligned} \tag{9}$$

The condition (7) implies $\tilde{a}_0 > \tilde{a}_1 > \cdots > \tilde{a}_k$. Thus by Theorem 3.2 in [6] all zeros of f in (9) lie on the unit circle and simple, and hence for any initial conditions $x(0) = x_0, x(1) = x_1, \ldots, x(m-1) = x_{m-1} \in \mathbb{R}$ the solution of the equation (8) is bounded. Therefore the equation (5) is robustly bounded.

Next, we consider the equation (2) with $n \times n$ matrices. Suppose the matrices $M_i = A_{i-1} - A_i$, $i = 1, 2, \ldots, k$, are positive definite. Set $\mu_i = \lambda_{\min}(M_i)$, $i = 1, 2, \ldots, k$ and define $\mu = \min\{\mu_i; i = 1, 2, \ldots, k\}$. Then $M_i \geq \mu I > 0$, $i = 1, 2, \ldots, k$.

Lemma 5. *Suppose $A_0 > A_1 > \cdots > A_k > 0$. Let $\tilde{A}_0, \tilde{A}_1, \ldots, \tilde{A}_k$ be hermitian $n \times n$ matrices satisfying*

$$\|\tilde{A}_i - A_i\| < \frac{\mu}{2},\ i = 0, 1, \ldots, k.$$

Set $\tilde{A}_{k+1} = 0$. Then

$$\tilde{A}_{i-1} > \tilde{A}_i,\ i = 0, 1, \ldots, k+1.$$

Proof. Set $\Delta_i = \tilde{A}_i - A_i$. Then

$$\begin{aligned}\tilde{A}_{i-1} - \tilde{A}_i &= (A_{i-1} - A_i) + (\Delta_{i-1} - \Delta_i)\\ &\geq \mu I + (\Delta_{i-1} - \Delta_i).\end{aligned}$$

We have

$$(\Delta_{i-1} - \Delta_i) \geq \lambda_{\min}(\Delta_{i-1} - \Delta_i) I \geq -\|\Delta_{i-1} - \Delta_i\| I.$$

Moreover,

$$\|\Delta_{i-1} - \Delta_i\| \leq \|\Delta_{i-1}\| + \|\Delta_i\| < \mu.$$

Hence

$$(\Delta_{i-1} - \Delta_i) > \mu I,$$

and we obtain $\tilde{A}_{i-1} - \tilde{A}_i > 0$. □

Using the preceding lemma and Proposition 2 we obtain the following result.

Theorem 6. *Let $F(z)$ be a self-inversive matrix polynomial of the form* (4) *and suppose that $A_0, A_1, \ldots, A_k$ are hermitian with*

$$A_0 > A_1 > \cdots > A_k > 0. \quad (10)$$

Then the difference equation (2) *is robustly bounded.*

5 EXAMPLE

Example 1. Consider the following difference equation with $n = 2$:

$$\begin{aligned}&\begin{pmatrix} 2 & i \\ -i & 3 \end{pmatrix} x(t+3) + \begin{pmatrix} 1 & 0 \\ 0 & 1 \end{pmatrix} x(t+2)\\ &\quad + \begin{pmatrix} 1 & 0 \\ 0 & 1 \end{pmatrix} x(t+1) + \begin{pmatrix} 2 & i \\ -i & 3 \end{pmatrix} x(t) = 0 \quad (11)\end{aligned}$$

The associated characteristic matrix polynomial $F(z)$ is as follows:

$$\begin{aligned}F(z) = &\begin{pmatrix} 2 & i \\ -i & 3 \end{pmatrix} + \begin{pmatrix} 1 & 0 \\ 0 & 1 \end{pmatrix} z\\ &+ \begin{pmatrix} 1 & 0 \\ 0 & 1 \end{pmatrix} z^2 + \begin{pmatrix} 2 & i \\ -i & 3 \end{pmatrix} z^3 \quad (12)\end{aligned}$$

Setting

$$P(z) = \begin{pmatrix} 2 & i \\ -i & 3 \end{pmatrix} + \begin{pmatrix} 1 & 0 \\ 0 & 1 \end{pmatrix} z,$$

$F(z)$ has the form (4) with $\gamma = 1$ and $r = 2$. Thus $F(z)$ is self-inversive. It is easy to see that the coefficients of $F(z)$ are hermitian matrices satisfying

$$\begin{pmatrix} 2 & i \\ -i & 3 \end{pmatrix} > \begin{pmatrix} 1 & 0 \\ 0 & 1 \end{pmatrix} > 0.$$

Therefore, it follows from Theorem 6 that the equation (11) is robustly bounded.

We obtain that the spectrum of $F(z)$ lies on the unit circle and all characteristic values of $F(z)$ are normal and semisimple. In fact, one has

$$\begin{aligned}\det F(z) = (z+1)^2 &\left(z^2 - \left(\frac{1}{2} - \frac{\sqrt{5}}{10}\right) z + 1\right)\\ &\left(z^2 - \left(\frac{1}{2} + \frac{\sqrt{5}}{10}\right) z + 1\right)\end{aligned}$$

and all zeros of $\det F(z)$ lie on the unit circle (see Fig.1).

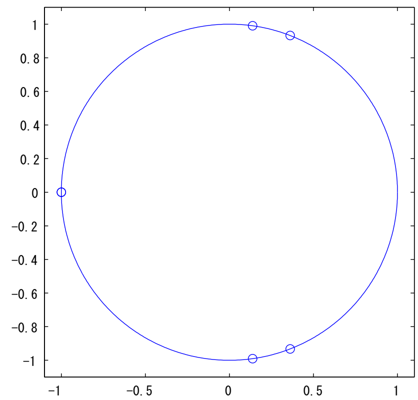

Fig. 1. Characteristic values of (12)

Computing the Smith form $S(z)$ of $F(z)$, we obtain

$$S(z) = \begin{pmatrix} z+1 & 0 \\ 0 & (z+1)p(z) \end{pmatrix}$$

where

$$\begin{aligned}p(z) = &\left(z^2 - \left(\frac{1}{2} - \frac{\sqrt{5}}{10}\right) z + 1\right)\\ &\left(z^2 - \left(\frac{1}{2} + \frac{\sqrt{5}}{10}\right) z + 1\right).\end{aligned}$$

Hence, it can be seen that all characteristic values of $F(z)$ are normal and semisimple.

Example 2. Consider the following diffrence equation with $n = 3$:

$$\begin{aligned}&A_0 x(t+3) + A_1 x(t+2)\\ &\quad + A_1 x(t+1) + A_0 x(t) = 0 \quad (13)\end{aligned}$$

where

$$A_0 = \begin{pmatrix} 2 & i & -i \\ -i & 3 & 0 \\ i & 0 & 3 \end{pmatrix}, \ A_1 = \begin{pmatrix} 1 & 0 & 0 \\ 0 & 1 & 0 \\ 0 & 0 & 1 \end{pmatrix}.$$

The associated characteristic matrix polynomial $F(z)$ is given by

$$F(z) = P(z) + z^2 \hat{P}(z), \ P(z) = A_0 + A_1 z. \qquad (14)$$

Then, it is easy to see that A_0 and A_1 are positive definite hermitian matrices. Moreover, one has $A_0 \not> A_1$, but $A_0 \geq A_1$ because of $\det(zI - (A_0 - A_1)) = z(z-2)(z-3)$.

We compute the inner radius $r_i(P)$. To do so, set $v \in \mathbb{C}, v \neq 0$. Then,

$$v^* P(\lambda) v = \begin{pmatrix} \bar{a} & \bar{b} & \bar{c} \end{pmatrix} P(\lambda) \begin{pmatrix} a \\ b \\ c \end{pmatrix} = \lambda |v|^2 + v^* A_0 v.$$

Thus $r_i(P) = 1$ because of $\det(zI - A_0) = (z-1)(z-3)(z-4)$.

We obtain

$$\begin{aligned} \det F(z) &= 12 + 19z + 27z^2 + 53z^3 + 49z^4 \\ &\qquad + 49z^5 + 53z^6 + 27z^7 + 19z^8 + 12z^9 \\ &= (z+1)^3 (z^2+1) \\ &\qquad (3z^2 - 2z + 3)(4z^2 - 3z + 4) \end{aligned}$$

and thus it can be seen that all zeros of $\det F(z)$ lie on the unit circle (see Fig.2).

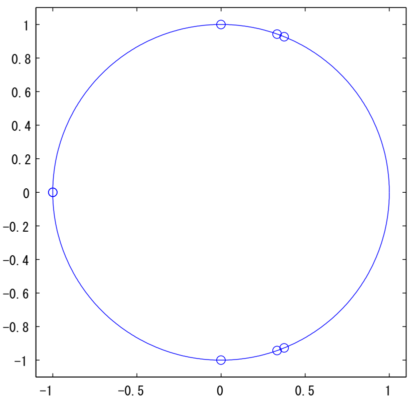

Fig. 2. Characteristic values of (14)

Computing the Smith form $S(z)$ of $F(z)$, we obtain

$$S(z) = \begin{pmatrix} z+1 & 0 & 0 \\ 0 & (z+1) & 0 \\ 0 & 0 & \frac{1}{12}(z+1)p(z) \end{pmatrix}$$

where $p(z) = (z^2+1)(3z^2-2z+3)(4z^2-3z+4)$. Hence, the spectrum of $F(z)$ lies on the unit circle and all characteristic values of $F(z)$ are normal and semisimple. Therefore, (10) is not nessesary for robust boundedness.

REFERENCES

[1] Y. Bistritz, A circular stability test for general polynomials, Systems Control Lett. 7 (1986) 89–97.

[2] R. Byers, D. S. Mackey, V. Mehrmann, and H. Xu, Symplectic, BVD, and palindromic approaches to discrete-time control problems, in P. Petkov and N. Christov, editors, A Collection of Papers Dedicated to the 60th Anniversary of Mihail Konstantinov, pp. 81–102, Sofia, 2009, Publ. House Rodina.

[3] K. Chinen, An abundance of polynomials satisfying the Riemann hypothesis, Discrete Math. 308 (2008), 6426–6440.

[4] M. Dahlby and B. Owren, Plane wave stability of some conservative schemes for the cubic Schrödinger equation, ESAIM: M2AN 43 (2009), 677–687.

[5] A. Hilliges Numerische Lösung von quadratischen Eigenwertproblemen mit Anwendung in der Schienendynamik, Diplomarbeit, TU Berlin, Institut f. Mathematik, 2004.

[6] N. Ito, R. Küstner and H. K. Wimmer, Self-inversive matrix polynomials with semisimple spectrum on the unit circle, Operators and Matrices, 5-3 (2011) 495–503.

[7] M. Jibladze and D. Novikov, Unimodularity of Poincaré polynomials of Lie algebras for semisimple singularities, Moscow Math. J. 7 (2007), 481–487.

[8] P. Lakatos, On polynomials with zeros on the unit circle, C. R. Math. Acad. Sci. Soc. R. Can. 24 (2002), 91–96.

[9] I. Markovsky and S. Rao, Palindromic polynomials, time-reversible systems, and conserved quantities, in: 16th Mediterranean Conference on Control and Automation, 2008, Ajaccio. `http://eprints.ecs.soton.ac.uk/16592/1/Med08.pdf`

[10] Ch. Skokos, On the stability of periodic orbits of high dimensional autonomous Hamiltonian systems, Physica D 159 (2001), 155–179.

[11] J. Y. Stein, Digital Signal Processing: A Computer Science Perspective, Wiley Series in Telecommunications and Signal Processing, Wiley, 2000.

[12] A. P. Velo, G. A. Gazonas, and T. Ameya, z-Transform methods for the optimal design of one-dimensional layered elastic media, SIAM J. Appl. Math. 70 (2009), 762–788.

The Seventeenth International Symposium on Artificial Life and Robotics 2012 (AROB 17th '12),
B-Con Plaza, Beppu, Oita, Japan, January 19-21, 2012

Dynamic Window-based Obstacle Avoidance in the Presence of Moving Obstacles

H. Harada[1], M. Yokomichi[2], and O. Sato[2]

[1] Graduate School of Enginnering, University of Miyazaki, Miyazaki 889-2155, Japan
[2] Faculty of Engineering, University of Miyazaki, Miyazaki 889-2155, Japan
(yokomich@cs.miyazaki-u.ac.jp)

Abstract: This paper proposes a reactive control method for mobile robots in the presence of moving obstacles. The method is based on the dynamic window algorithm and extends it in order to avoid moving obstacles efficiently. Firstly, the future collision is detected based on the generalized velocity obstacles. Secondly, input value can be varied within the prediction horizon. This means that better input can be selected such that the robot starts passing maneuver ealier. However, this causes the dimension of the search space larger. In order to reduce the computation time, GDS (gradually dense-sparse) discretization and randomized sampling method similar to RRT is adopted. By means of these extensions, the robot can avoid moving obstacles with simpler cost function and reasonable computation time. Performance of the proposed method is evaluated by numerical simulations.

Keywords: Dynamic Window, Receding Horizon Control, Randomized MPC GDS discretization

1 INTRODUCTION

The problems of path-planning and collision avoidance are computing a collision-free path for a robot moving among obstacles and are crucial tasks for mobile robots. The application area has been spread to wide areas such as, automated transportation systems, automated factories, and robot human interactions. In many cases, the environment is uncertain and dynamic, thus, the path-planning and obstacle avoidance system should perform in such environments. When restricted to the collision avoidance, there have been proposed many reactive approaches in the last thirty years. Originally, these approaches have been applied to the static environment, then, some of them have been extended to the dynamic case recently.

The dynamic window approach, which was originally proposed by Fox et al in [1], is one of the most popular reactive collision avoidance methods. The original algorithm was extended by Brock and Kathib [2] such that the global path planning such as A* is integrated in the cost function. Furthermore, Seder and Petrović [4] applied the FD* search algorithm in order to consider the dynamically changing environment. However, in the case where the obstacles are moving, the planning should be time-dependent especially in the predicting phase, thus, more complicated computation for path planning is needed.

On the other hand, because of its *look ahead* nature, the dynamic window approach can be thought as one of the *Receding Horizon Control* problem (RHC, for short) in the model predicted control. This point has been pointed out by Ogren and Leonard [3]. In the general RHC problem, it is assumed that the input may change within the predicting horizon when the optimal input is searched.

But, in many works on the dynamic window approach, the use of constant input value is assumed in order to reduce the dimension of search space and decrease the computation time. Recently, Kiss and Tecesz [7] applied the RHC approach to dynamic window and they permitted piecewise constant input in the prediction phase, however, they did not show the concrete method to compute the optimal input sequence and, in addition, considered only static problem.

In this paper, the authors propose a method to extend the dynamic window approach to the moving obstacle avoidance with piecewise constant input. In the proposed method, the obstacles are divided to two classes; static and dynamic. The goal-intended term in the cost function is calculated by path planning method only for static obstacles. The collision to the dynamic obstacles are evaluated by computing the generalized velocity obstacles which is proposed by Wilkie et al [5]. In order to reduce the computation time, a randomized planning method with the gradually dense-sparse discretization is applied. The randomized planning method used in this work is proposed by Brooks et al [9] for the static path planning problem and the authors modify it in order to fit to the dynamic obstacle avoidance. The gradually dense-sparse discretization [10] is one of the methods to discritize the time horizon in the RHC problem and can reduce the search space without the loss of control performance. By applying these methods, the robot can avoid the obstacles with better behavior and with admissible computation time. The effectiveness of the proposed approach is evaluated by numerical simulations.

2 PRELIMINARIES

In this paper, it is supposed that the robot moves on a horizontal plane and its kinematics is nonholonomic differential-drive type. The shape of the robot and the obstacles are assumed to be approximated by circles. The state vector of the robot is given by $p(t) := (x(t), y(t), \theta(t))^T$, where $q := (x, y)$ and θ are the position and the orientation of the robot. The continuous time kinematics of the robot is described as

$$\begin{aligned} \dot{x} &= \cos(\theta)v \\ \dot{y} &= \sin(\theta)v \\ \dot{\theta} &= w \end{aligned} \tag{1}$$

where the input $u = (v, w)$ consists of the translational and the angular velocities. The solution of (1) for $p(t_0) = p_0$ and $u(t); t \in [t_0, t_1]$ is denoted as $p(t_1; t_0, p_0, u)$. Furthermore, it is assumed that the values and instantaneous variations of these inputs are limited. It is also supposed that the static map of the environment and the movement of the temporally obstacles is known.

2.1 Dynamic Window Approach

The dynamic window approach, proposed by Fox et al. [1] is a velocity space based local reactive avoidance technique where the optimal control command is searched in the subspace of the velocity space. The search space is reduced by kinematic and dynamic constraint of the robot and the constraint that the robot with the input does not collide with the obstacles, and the reduced search space is called *Dynamic Window* and denoted as V.

Suppose that the time is discretized at equal intervals Δt and the input is constant within each interval. In addition, the predicting time horizon T is set as $T = n\Delta t$ for some integer $n > 1$ and it is assumed that the input is constant with in the predicting horizon in evaluating the input.

the cost function in [1] is defined as a linear combination of *heading* term, *distance* term, and *velocity* term. If the position trajectory by the input is directed towards the goal, then the heading term takes high value. The distance term is the smallest distance to the obstacles within the horizon, and the velocity term is simply the value of v.

2.2 Extensions of Dynamic Window

Using the original dynamic window approach proposed in [1], robust obstacle avoidance is achieved in many cases, but there exist several shortcomings. These are summarized as :

- The heading function may cause local minima when the shape of the free space is complicated .
- It does not consider the dynamic environment.

To overcome the first problem, Brock and Khatib modified the cost function such that the free space connectivity information is taken into account [2]. They used a navigating function (NF) which is a local minima-free function defined on the discretized configuration space. NF is computed by the global path planning algorithm such as A* or wavefront propagation, so their approach is called *global* dynamic window (GDW, for short). Suppose that NF is denoted as $N(q)$ and the current state p_0, input $u \in V$, and the corresponding trajectory $p(t; t_0, p_0, u)$, $t \in [t_0 : t_0 + T]$ is given. Then, the modified cost function in [2] has the following form:

$$\begin{aligned} \Omega_g(p, u) &= \alpha \cdot n_1(p, u) + \beta \cdot vel(u) \\ &\quad + \gamma \cdot goal(p, u) + \delta \cdot n_2(p, u), \end{aligned} \tag{2}$$

where n_1 takes high value when the difference between $\theta(t_0 + T; t_0, p_0, u)$ and the direction of $\nabla N(q(t_0 + T; t_0, p_0, u))$ is large, *goal* is a binary function (1 if the trajectory $q(t; t_0, p_0, u)$ pass through the goal area), and

$$n_2(p, u) = N(q_0) - N(q(t_0 + T; t_0, p_0, u)).$$

Because the original heading term is replaced with NF, the resulting maneuvers can avoid local minima so that the robot can move along the optimal path.

It should be noted that, in (2), the *distance* term is deleted. This is because the local minima may caused by the trade-off between *heading* term and this term.

The second problem is more serious. The framework in [1] can be easily extended to the dynamic environment by means of the velocity obstacles[8], or its generalizations [5]. However, if the moving obstacles is not considered in the path planning phase, trade-off problem may occurs. On the other hand, the method in [2] needs the global free-space information. this means, for all time instances, the position and shape of all obstacles should be known. When the environment is static, it is sufficient that the path planning is made at the first phase only. However, when the environment is dynamic, on-line re-planning is needed. Furthermore, when the obstacles move, the path planning problem should be time-dependent, such that, the search space is extended to $\mathscr{C}\mathscr{T}$-space[6].

In [4], FD* algorithm is applied to GDW and its effectiveness are shown. But, even if the FD* is used, the replanning needs large computation time, thus it is not easy to apply this method to the case where the moving obstacles are large, or when the obstacles move fast.

2.3 Optimality issue

Many of the previous researches about DW assume that through the predicting time horizon, the input should be constant. As mentioned above, this is because the search space can be reduced so that the computation time becomes small. In the case where the environment is static and where GDW is used, this yields satisfactory results in many cases because the optimal path is already given by path planning phase, thus the time horizon can be made rather short. However, especially in the dynamic environment without re-planning, this assumption causes not only non-optimal but also dangerous behaviors.

The Seventeenth International Symposium on Artificial Life and Robotics 2012 (AROB 17th '12),
B-Con Plaza, Beppu, Oita, Japan, January 19-21, 2012

3 EXTENSION TO PIECEWISE CONSTANT INPUTS

Based on the discussions in the previous section, it is preferred to use piecewise constant inputs for search instead of constant input throughout the predicting time horizon. As mentioned above, this extension causes the increase of the dimension of the search space such that the computation time increases exponentially. Therefore, some kind of computationally efficient solver is required.

It has been reported in [3], DW can be regarded as a special kind of *Receding Horizon Control* approach in the model predictive control (MPC), and several real-time solvers has been proposed for some problems including the trajectory generation problem for mobile robots. In this paper, Randomized MPC approach in [9] and GDS (Gradual Dense-Sparse) discretization are applied to DW for moving obstacle avoidance.

The randomized MPC is a kind of input space-based tree search for RHC, which is similar to RRT for path planning problem. For a system

$$\dot{x} = f(x,u) \tag{3}$$

with state variable $x \in X \subset \Re^n$ and input $u \in U \subset \Re^m$.

For given time horizon $[t_0 : t_0 + t']$, suppose that its discretization

$$t_0, t_1, t_2, \ldots, t_{r-1}, t_r = t_0 + t'$$

is given. We suppose that the input is piecewise constant and let $u_{t_0:t_r} = \{u_0, u_1, \ldots, u_{r-1}\}$ denotes a input sequence. Let $c(x(t_0), u_{t_0:t_r})$ denotes a cost function for initial condition and control sequence. The task is to find the control sequence $u^*_{t_0:t_r}$ which maximize (minimize) $c(x(t_0), u^*_{t_0:t_r})$. The basic ideas of the randomized MPC is similar to an RRT. A tree T is grown in which each node q consists of the tuple $< x_q, t_i, u_q >$: a state, a time, and a control input. This means, for the parent node $q' =< x_{q'}, t_{i-1}, u_{q'} >$, x_q is a solution of (3) at $t = t_i$ whose initial position is $x_{q'}$, and to which input u_q is applied. Thus, algorithm iteratively expands the tree by selecting an existing node q' and a control input u_q, then adding new nodes by integrating (3) forwards in time until t_q. Let $c_T(q_f)$ denotes a cost of the control input $u_{t_0:t_r}$ from the root node to a final leaf q_f at $t = t_0 + t'$. The basic procedure in [9] is summarized in Algorithm 1. Furthermore, in the next time, the previous optimal control sequence is used for the initial tree for effective search.

In the Algorithm 1, some subroutines should be specified. The usual RRT implementations of **SELECT_NODE** and **SELECT_CONTROL** sample a point in state space at first, select the nearest node as parent, then select the control which grows the tree from the node toward the sampled point. By means of these procedures, uniformly sampling or exploring the state space is achieved, however, these requires high computational time especially when the nearest neighbor node is found. In [9], parent node is selected uniformly from the existing nodes, and input is also selected uniformly from U. In addition, the method to discritize the time horizon is not addressed. These simplifications yields the low computational cost, but, may causes biased search in the state space. In order to achieve wider searching region with small number of node, Gradual Dense-Sparse discretization (GDS discretization) for predicting time horizon [10] is effective. In GDS discretization, the discretization time interval is made short in the early phase, and is made larger incrementally.

Algorithm 1 Tree Expansion for Randomized MPC

initialize: $T \leftarrow q_{root} =< x(t_0), t_0, u_0 >$, $c_{max} \leftarrow 0$;
for $i = 1, \ldots, N$ **do**
  $q \leftarrow$ SELECT_NODE(T);
  $u \leftarrow$ SELECT_CONTROL(T, q);
  $t \leftarrow t_i$, $x \leftarrow x_q$;
  while $t < t_0 + t'$ **do**
    $x \leftarrow x + \int_{t_i}^{t_{i+1}} f(x,u)dt$;
    $t \leftarrow t_{i+1}$;
    if $x \notin X$ **then**
      break;
    end if
    add $q_{new} =< x, t, u >$ to T;
    if $t = t_0 + t'$ **then**
      $c_q \leftarrow c_T(q_{new})$;
      if $c_q > c_{max}$ **then**
        $c_{max} \leftarrow c_q$, $q_{best} \leftarrow q_{new}$;
      end if
    end if
  end while
end for

4 SIMULATION RESULTS

The proposed algorithms have been implemented in *Player/Stage* software tools. In order to illustrate the effectiveness of the proposed algorithm, a result of a test is presented in Fig. 1. In Fig. 1 red rectangle is the controlled

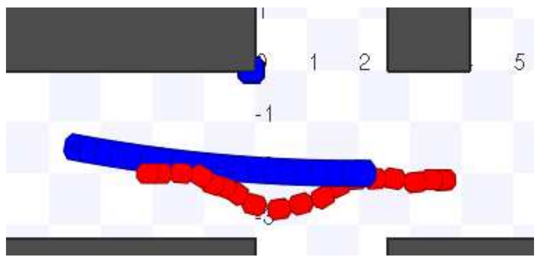

Fig. 1. Trajectories of the robot and the obstacle.

robot and blue one is the obstacle. The obstacle is also governed by the kinematic model (1) and the input is supposed to be constant $(v,w) = (0.3(m/s), -0.01(rad/s))$. The sampling interval and the prediction horizon are set to 0.1(s) and 3.2(s), respectively. The discretization intervals for GDS are set to 0.2, 0.2, 0.2, 0.2, 0.8, 1.6(s) and the number of nodes for randomized MPC is set to 4,200. In this case, the average computation time for about 16(s) execution was 0.012(s) by core i5 2.3GHz processor. The navigating function $N(q)$ for static environment was a L_1-based distance to the goal point, which was obtained by wavefront propagation algorithm a priori. It should be noted that, in the situation depicted in Fig. 1, the navigating function for the static map is the same as the simple L_1 distance. The cost function used at simulation is

$$\Omega_g(p,u) = \alpha \cdot n_1(p,u) + \gamma \cdot goal(p,u) + \delta \cdot n_2(p,u),$$

that is. less terms than (2) are used. This means that the parameter tuning becomes easier than GDW. In addition, the result is compared with those that the constant inputs are selected in Fig. 2, where additional *distance* term is added to the cost function. In Fig. 2, the line "single T=2" means

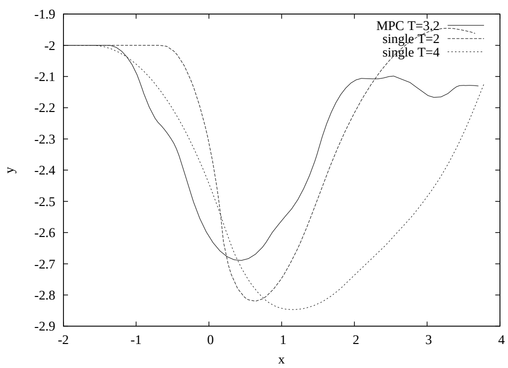

Fig. 2. Trajectories of the robot and the obstacle.

that the optimal constant input is searched in each time with prediction horizon $T = 2$. From the Fig. 2, the robot based on the proposed method starts avoiding maneuver as early as $T = 4$, and pass the obstacle more quickly than others.

5 CONCLUSIONS

In this paper, an extension of Dynamic Window approach is proposed for dynamic environment, and its effectiveness is examind by numerical simulations. By admitting piecewise constant input in the predicting and searching step, better performances are obtained. In addition, by means of randomized searching with GDS discretization, real-time calculation is also possible. However, the obtained trajectory seems to be nonsmooth and its modification is one of the future issues.

REFERENCES

[1] D.Fox, W.Burgard, and S. Thrun, "The dynamic window approach to collision avoidance," *IEEE Robotics Automation Magazine*, Vol. 4(1), 23-33, 1997.

[2] O.Broch and O.Khatib, "High-speed navigation using the global dynamic window approach," *Proc. of the Int. Conf. on Robotics and Automation*, 341-346, 1999.

[3] P.Ögren and N.E.Leonard, "A convergent dynamic window approach to obstacle avoidance," *IEEE Trans. Robot.*, Vol.21, 188-195, 2005.

[4] M.Seder and I.Petrovic, "Dynamic window based approach to mobile robot motion control in the presence of moving obstaecles," *Proc. of the Int. Conf. on Robotics and Automation*, 1986-1991, 2007.

[5] D.Wilkie, J.v.d.Berg, and D.Manocha, "Generalized velocity obstacles," *Proc. IEEE/RSJ int. Conf. Intelligent Robots and Systems*, 5573-5578, 2009.

[6] J. Latombe, *Robot motion planning*, Kluwer Academic Publishers, 1991.

[7] D.Kiss and G.Tevesz, "A receding horizon control approach to obstacle avoidance," *Proc. IEEE Int. Symp. on Applied Computational Intelligence and Infomatics*, 397-402, 2011.

[8] P.Fiorini and Z.Shiller, "Motion planning in a dynamic environments using velocity obstacles," *Int. J. of Robotics Research*, Vol.17(7), 760-772, 1998.

[9] A.Brooks, T.Kaupp, and A.Makarenko, "Randomised MPC-based motion-planning for mobile robot obstacle avoidance," *Proc. Int. Conf. on Robotics and Automation*, 3962-3967, 2009.

[10] P.Ögren and J.W.C.Robinson, "Receding horizon control of UAVs using gradual dense-sparse discretizations," *Proc. AIAA Guidance, Navigation and Control Conf.*, 2010.

The Seventeenth International Symposium on Artificial Life and Robotics 2012 (AROB 17th '12),
B-Con Plaza, Beppu, Oita, Japan, January 19-21, 2012

Multimodal MSEPF for visual tracking

Masahiro Yokomichi and Yuki Nakagama

University of Miyazaki, Miyazaki 889-2155, Japan
(Tel: 81-985-58-7420, Fax: 81-985-58-7420)

yokomich@cs.miyazaki-u.ac.jp

Abstract: Recently, particle filter has been applied to many visual tracking problems and it has been modified in order to reduce the computation time or memory usage. The one of them is the Mean-Shift embedded particle filter (MSEPF, for short) and Randomized MSEPF. These methods can decrease the number of the particles without the loss of tracking accuracy. However, the accuracy may depend on the definition of the likelihood function (observation model) and of the prediction model. In this paper, the authors propose an extension of these models in order to increase the tracking accuracy. Furthermore, the expansion resetting method, which was proposed for mobile robot localization, and the changing the size of the window in Mean-Shift search are also selectively applied in order to treat the occlusion or rapid change of the movement.

Keywords: Expansion Resetting, Mean-Shift, Multiple Model, Particle Filter, and Visual Tracking.

1 INTRODUCTION

Visual tracking is the process of locating a moving object (or multiple objects) over time using a camera. It has a variety of application areas, such as robot vision, human-computer interaction, security and surveillance, video communication, and so on. Visual tracking requires high accuracy tracking and real-time processing. To achieve high accuracy tracking, many approaches have been studied. Particle filter [1-3] is one of the robust tracking approaches in visual tracking, which has recently been developed. It performs a random search guided by a stochastic motion model to obtain an estimate of the posterior distribution describing the object's configuration. However, it is known that the degeneracy is one of the difficult problems inherent in particle filter. The degeneracy problem is a phenomenon of the tracking accuracy's decreasing because most particles may have very low likelihood. One of approaches that deal with it is to use very large number of particles, but it is hard to implement it to real-time systems because it requires a lot of computation times and resources. Shan and coworkers proposed the Mean-Shift embedded particle filter (MSEPF) in order to keep the accuracy with small number of particles [4]. In their approach, the state of each particle moves to the point in the window with the highest likelihood value.

In general, MSEPF overcomes the degeneration problem because each particle has higher likelihood. In addition, the accuracy of estimation depends on the size of the window, but the larger window size makes the computation slower. In the previous work [5], the authors modified the mean value calculation part of MSEPF by Monte-Carlo approximation and the likelihood function by adding the term about frame difference. It was shown that the computation time can be reduced without the loss of tracking accuracy.

In this paper, the authors extend the method in [5] such that the tracking accuracy can be improved. The first is application of the multiple prediction models for the case where the precise model for the movement of the tracked object cannot be obtained. The second is adaptation to the case where the tracked object is occluded or its velocity changes suddenly. In order to track the object robustly, two methods are switched according to the mean value of the likelihood function. The effectiveness of the proposed approach is examined by real video examples.

2 MEAN-SHIFT EMBEDDED PARTICLE FILT ER

2.1 Particle Filter

Particle filter is an approach for Bayes Estimation by Random Sampling. A continuous state vector of a target object and the observed feature vector at time step t are denoted by x_t and z_t, respectively. The dynamic model is assumed to be represented as a temporal Markov chain

$$p(x_t|x_1,\dots,x_t) = p(x_t|x_{t-1}), \qquad (1)$$

and the observation model is denoted as

$$p(z_1,\dots,z_t|x_1,\dots,x_t) = \prod_{i=1}^{t} p(z_i|x_i). \qquad (2)$$

Particle filter aims to estimate the sequence of hidden parameters x_t based only on the observed data $\{z_1,\dots,z_t\}$. According to the Bayes rule, the prior and the posterior are given by

$$p(x_t|z_1,\dots,z_{t-1}) = \int p(x_t|x_{t-1})p(x_{t-1}|z_1,\dots,z_{t-1})dx_{t-1} \quad (3)$$

$$p(x_t|z_1,\dots,z_t) = k_t p(x_t|z_1,\dots,z_{t-1}), \quad (4)$$

where k_t is the normalization term.

In the particle filter, by using a set of samples and the corresponding weights $S_t \coloneqq \{(s_t^n,\pi_t^n)\}_{n=1}^N$ at time step t (where N is the number of particles), the posterior is approximated as

$$p(x_t|z_1,\dots,z_t) \approx \sum_{n=1}^N \pi_t^n \delta(x_t - s_t^n), \quad (5)$$

where $\delta(\cdot)$ is the Dirac's delta function. Then, the prior can be approximated as

$$p(x_t|z_1,\dots,z_{t-1}) \approx \sum_{n=1}^N \pi_{t-1}^n p(x_t|s_{t-1}^n). \quad (6)$$

The weights π_t^n are determined such that $\pi_t^n \propto p(z_t|s_t^n) =: w_t^n$ (this probability is called as *likelihood*) and $\sum_{n=1}^N \pi_t^n = 1$. If sufficiently large number of particles can be prepared, Eq. (5) and (6) are accurate. In reality, however, using an infinite number of particles is not allowed, especially for real-time processing.

2.2 MSEPF

MSEPF is proposed in [4] which incorporates Mean-Shift into particle filter. Mean-Shift is another approach for visual tracking that climbs the gradient of a probability distribution to find the nearest dominant mode (peak). In the search window, the mean position of the target object is computed and the search window is centered at that position. Position of the target object is tracked by iterating this mean position calculation until the shift length converges.

In MSEPF, Mean-Shift analysis is applied to each particle based on observation density, after each particle was measured by likelihood function. MSEPF can keep the accuracy using fewer particles because particles converge to the local maximum. Therefore, MSEPF can reduce particles than particle filter. It is known that the accuracy of estimation depends on the size of the window. However, the larger window size requires additional computation time.

It was pointed out in [6] that the computational cost for mean value calculation is $O(n^2)$, where n denotes the window size. This shortcoming can be improved by replacing the mean value calculation by its Monte-Carlo approximation [5]. It is called as Randomized MSEPF (RMSEPF, for short). By means of this approximation, it was shown that the cost can be reduced to $O(n)$. Furthermore, in [5], the likelihood function for MSEPF was also modified using the edge detection and the frame difference.

3. EXTENSION OF RMSEPF

3.1 Multiple prediction models

In the particle filter-based state estimation, the state of each particle is updated by the prediction model Eq. (1). This is based on the property of the kinematics of the object to be tracked. However, many objects in the real world may not obey a simple kinematics, so precise modeling by single model is difficult. If insufficient prediction model is used, the tracking accuracy may decrease. Thus, in this paper, multiple prediction models are used in order to adapt to the various movement of the object.

3.1.1 Three types of prediction models

In this paper, three types of prediction models are adopted. They are *Static model*, *Drift model*, and *Statistical model*. The state of each model is (x, y) coordinates of the object on the image plane. These models are defined as follows:

1. Static model

$$\begin{aligned} x_t &= x_{t-1} + l_u \cos\theta_u, \\ y_t &= y_{t-1} + l_u \sin\theta_u. \end{aligned} \quad (7)$$

2. Drift model

$$\begin{aligned} x_t &= x_{t-1} + (x_{t-1} - x_{t-2}) + l_u \cos\theta_u, \\ y_t &= y_{t-1} + (y_{t-1} - y_{t-2}) + l_u \sin\theta_u. \end{aligned} \quad (8)$$

3. Statistical model

$$\begin{aligned} x_t &= x_{t-1} + \hat{x}_{t-1}, \\ y_t &= y_{t-1} + \rho_{t-1}\hat{x}_{t-1} + \sqrt{1-\rho_{t-1}^2}\,\hat{y}_{t-1}, \end{aligned} \quad (9)$$

where $\hat{x}_t \sim N(\mu_t^x, (\sigma_t^x)^2)$ and $\hat{y}_t \sim N(\mu_{t-1}^y, (\sigma_{t-1}^y)^2)$.In Eq. (7), $l_u \sim \mathcal{U}(0, l_{max})$ and $\theta_u \sim \mathcal{U}(0, 2\pi)$ are random variables with some positive l_{max}. In Eq. (9), μ_t^x and $(\sigma_t^x)^2$denote the median and the variation of the estimated velocity of the object in the x-direction up to time t. In addition, ρ_{t-1} denotes the correlation efficient of estimated velocity in the image plane.

The static model is based on the random walk movement. This model corresponds to the case where the object suddenly changes the direction. The drift model is used to describe the movement of the object with linear velocity. Finally, the statistical model predicts the nonlinear movement of the object by learning the change of the velocity and the direction from the sequence of the estimated state.

3.1.2 Model selection

One approach to use the multiple prediction model for the particle filter is applying the interacting multiple models (IMM, for short) [7, 8]. In this approach, each particle possesses additional information about which model is applied to it. However, the transition probability between models should be determined in advance. In this paper, a simple adaptive model selection algorithm is proposed. In this algorithm, the probability that each model is selected is proportional to their median of likelihood function. Suppose that the number of the models and the particles are $M > 0$ and $N > 0$ respectively. Furthermore, the models are denoted as $F^1, \ldots, F^M$. For any particle, the probability that it adopts the prediction model F^i at time t is denoted as n_t^i. The algorithm is summarized as follows:

0. Initialize the time as $t = 0$ and the model selection probabilities $\mathcal{N}_t := \{n_t^1, \ldots, n_t^M\}$ such that $\forall i \in \{1, \ldots, M\}, n_t^i > 0$, $\sum_{i=1}^{M} n_t^i = 1$.
1. For each particle, select a model according to $\mathcal{N}_t$ and update its state. For each model, define the group of particles X_t^i whose elements use F^i.
2. Compute the likelihood for all particles and obtain the median of likelihood $\widehat{W}_t^i =: med_{s_t^n \in X_t^i}(w_t^n)$.
3. For each group X_t^i. For some small positive constant ε, define $W_t^i := \widehat{W}_t^i + \varepsilon$.
4. Resample the particles and calculate each n_{t+1}^i such as $n_{t+1}^i = W_t^i / \sum_{j=1}^{M} W_t^j$.
5. Set $t \leftarrow t + 1$ and back to Step 1.

In the above algorithm, small constant ε should be added in order to avoid the case where certain models are not selected.

3.2 Escape from the Kidnapped state

Particle filters can approximate the probability of the existence of the object by means of many particles. However, if the particles lost the object by some reasons, the accuracy becomes very low. In this paper, the authors call such a situation as *kidnapped state*. The kidnapped state may occur when the object moves with very large velocity or the object is occluded by other objects (Fig. 1).

Fig. 1. Example of kidnapped state.

In this paper, two methods are selectively used in order to escape the particles from kidnapped state. The former is Expansion Resetting method [9] (ER method, for short) which was proposed for mobile robot localization problem. The latter is making the window size in the Mean-Shift search variable.

3.2.1 ER method

In the ER method, the particles are re-configured when they lost the object to be tracked. If the target was lost again, the particles are diffused to larger region (see Fig. 2). The decision whether particles lost the target or not is based on the mean $\bar{W}_t$ of likelihood. Suppose that the estimate of the position of the object by particles S_t is given by $\tilde{s}_t$. In addition, a PDF $p_0(x; \mu_x, \sigma_i^2)$ on the image plane, whose increasing variances are given by $\sigma_i^2, \forall j > i, \sigma_j^2 > \sigma_i^2$, is

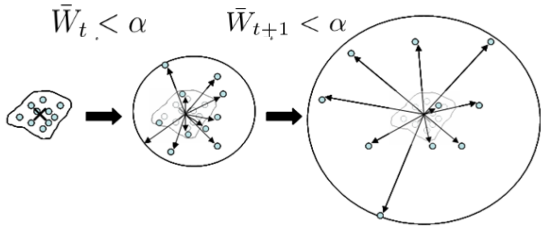

Fig. 2. Expansion resetting in 2D space.

also given. If $\bar{W}_t$ is smaller than a pre-defined threshold $\alpha > 0$ at certain time step t, then the particles are resampled based on $p_0(x; \tilde{s}_t, \sigma_0^2)$. Next, if $\bar{W}_{t+1}$ is also smaller than α, the particles are resampled again based on $p_0(x; \tilde{s}_{t+1}, \beta\sigma_1^2)$.

3.2.2 Changing the window size for Mean-Shift

In the visual tracking by only Mean-Shift search, large size of searching window is preferred because it is possible to robustly track the object even if it moves rapidly. However, in MSEPF, if large window in Mean-Shift search step is used, the particles may gather in local maxima. This weakens the variety of the particles, which is one of the important features of particle filter. Thus, small size of search window should be used, and we can see that there exists a trade-off.

To overcome this difficulty, the variable size of search window is adopted. When tracking is succeeded, it is made small. On the other and, if the object is lost, it becomes large.

3.2.3 Switching two methods

The ER method described in 3.2.1 can re-capture the object even if the object is occluded temporary. However, while this method is being used, tracking accuracy decreases. In contrast, changing the window size for Mean-Shift cannot track the object when the object is occluded, but it can track accurately, if the kidnapped state is rather weak. Thus, in this paper, two methods are switched according to the severity of the kidnapped state.

At first, two thresholds $0 < \alpha_0 < \gamma$ and the minimal (maximal) window sizes $W_{min}(W_{max})$ should be chosen. If $\bar{W}_t < \alpha_0$, then ER method is applied. Else if $\alpha_0 \leq \bar{W}_t < \gamma$, change the window size for Mean-Shift as

$$\frac{W_{min} - W_{max}}{\alpha_0 - \gamma}(\bar{W}_t - \alpha_0) + W_{max}.$$

4. EXPERIMENTS

This section illustrates the performance of proposed algorithm by real video sequences in lab environment. Tracked object is a pink toy shown in the left of Fig. 4 and the environment is shown in the left of Fig. 3.

Fig. 3. Tracked object (left) and lab environme nt with an occluding object

In Fig. 3 (left), there exists an object (yellow bottle) by which the tracked object may be occluded. Furthermore, there exists another object (tree) in the left side of image, which has decollations with several colors. In each video sequence, the object moves from the left to the right in the image plane. The image size is 320x240 (pixel) and the flame rate is 15(fps).

In the ER method, the particles are resampled on circle region whose center is $\tilde{s}_t$ and the radius is $5.18m + 0.5$, where m denotes how many times the heavily kidnapped state has been continue. The window size foe Mean-Shift varies in the range $[10 \times 10 : 30 \times 30]$. The threshold values are set as $(\alpha_0,\ \gamma) = (2.8, 20.6)$. On each experiment, the number of the particles is set to 50, and that of the samples in Mean-Shift search is also set to 50.

Fig. 4. Escape from the occluded state.

Fig. 5. Escape from the light kidnapped state (top: fixed window size; bottom: variable window size).

At first, Fig. 4 shows the results for the case where the object is occluded and this case corresponds to the heavily kidnapped state. We can see that,after diffusing, the particles can catch the object, and then track it.

Next, Fig. 5 shows results for the case where the object moves rapidly. When the constant (small) size of search window is used (top), the particles lose the object and they are caught by decollated tree which has similar color feature. On the other hand, the proposed method can track the object successfully.

5. CONCLUSIONS

In this paper, some extensions for Mean-Shift embedded particle filter are proposed. In order to improve the tracking performance when the tracked object changes the velocity rapidly or is occluded, two methods are selectively applied. In addition, multiple prediction models are used to take the complex and unpredictable movement of the object into account. Their effectiveness was examined by experiment with real video sequence and it was shown that the filter does not lose the object even when the object was occluded.

Evaluating the validity of the prediction models and finding more suitable models for each application are some of the future issues.

REFERENCES

[1] G. Kitagawa, "Monte-Carlo filter and smoother for non-Gaussian nonlinear state space models," Journal of Computational and Graphical Statistics, Vol. 5, No. 1, pp.1–25, 1996.

[2] N. J. Gordon, D. Salmond, and A. F. M. Smith, "Novel approach to nonlinear/non-Gaussian Bayesian state estimation, "IEEE Proc. F, Vol.140, No.2, pp.107-113, 1993.

[3] M. Isard and A. Blake, "CONDENSATION: condi tional density propagation for visual tracking," Int. J. Computer Vision, Vol. 29, No. 1, pp.5-28, 199 8.

[4] C. Shan, "Real time hand tracking by combining particle filter and mean shift," IEEE, Vol.88, No.12, pp.989-994, 2005.

[5] Y. Nakagama and M. Yokomichi, An improvemen t of MSEPF for visual tracking," Int. J. Artificial Life and Robotics, Vol. 15, No. 4, pp.534-538, 2 011.

[6] C. Yang, et al., "Efficient Mean-Shift tracking via a new similarity measure," Proc. of IEEE Comp uter Society Conference on Computer Vision and Pattern Recognition (CVPR'05) Vol. 1, pp.176-183, 2005.

[7] Y. Boers, J. N. Driessen, "Interacting multiple model particle filter," IEEE Proc. Radar, Sonar and Navigation, Vol. 150, No. 5, pp.344-349, 2003.

[8] J. Wang, D. Zhao, and W. Gao, and S. Shan, "Interacting multiple model particle filter to adaptive visual tracking," Proc. Int. Conference on Image and Graphics, pp.568-571, 2004.

[9] R. Ueda, T. Arai, K. Sakamoto, T. Kikuchi, a nd S. Kamiya, "Expansion resetting for recovery from fatal error in Monte Carlo localization - co mparison with sensor resetting methods," Proc. of IROS 2004, Vol. 3, pp.2481-2486. 2004.

The Seventeenth International Symposium on Artificial Life and Robotics 2012 (AROB 17th '12),
B-Con Plaza, Beppu, Oita, Japan, January 19-21, 2012

An analysis of spatial patterns in a spatial prisoner's dilemma

Yuji Katsumata[1], and Yoshiteru Ishida[2]

[1]Department of Electronic and Information Engineering,
[2]Department of Computer Science and Engineering,
Toyohashi University of Technology,
Tempaku, Toyohashi, Aichi, 441-8580, Japan
(Tel: +81-532-44-6868)

[1]katsumata@sys.cs.tut.ac.jp

Abstract: In the natural world, cooperative behavior emerges and assumes the crucial roles. Cooperative behavior means altruistic behavior and non-cooperative behavior (defection) means selfish behavior. Although cooperators emerge in the society, cooperation has not any advantage as compared to defection in rational terms. Earlier studies proposed many mechanisms to fill a gap between theoretical prediction and experimental evidence. As previous works, the authors studied the SPD that is spatial-temporal version of the Prisoner's Dilemma to investigate the maintenance mechanisms of cooperators. Then we observed a membrane formation as a mechanism that protects cooperation from invasion of defectors. The authors consider the effects of the interaction distance on the game payoff. In the present model, interacting with distant individuals pays a higher cost than interacting with adjacent individuals. In the SPD simulation, this paper shows that cooperators emerge easier by considering the effects of the interaction distance.

Keywords: cooperation, membrane formation, spatial generosity, spatial prisoner's dilemma

1 INTRODUCTION

In the natural world, cooperative behavior emerges and assumes the crucial roles. Cooperative behavior means altruistic behavior and non-cooperative behavior (defection) means selfish behavior. A cooperator pays a cost for someone's benefit. On the other hand, a defector does not pay a cost. Although cooperators emerge in the society, cooperation has not any advantage as compared to defection in rational terms. Instead of cooperating, each individual or player should defect pursing their benefit. Natural selection obviously favors defection over cooperation and prevents evolution of cooperation unless it has mechanisms. Earlier researchers proposed many mechanisms to fill a gap between theoretical prediction and experimental evidence. Some of them are based on the game theory, especially the Prisoner's Dilemma (PD) game.

The PD has been widely studied not only in international politics but also in the evolutionary biology [1]. Nowak and May invented a spatiotemporal version of the PD named Spatial Prisoner's Dilemma (SPD) [2, 3]. The SPD also is the model as to discuss cooperative behavior. In the SPD, the effects of a spatial structure that protects cooperators and sustains are well-known results. After the invention of the SPD, many types of the SPD that are more realistic than the conventional model have engendered. They have considered the realistic factors such as Tit-for-tat (direct reciprocity), indirect reciprocity, random graph networks, scale-free networks, heredity effects and social generosity effects [4 - 6].

As previous works, we studied the SPD that treats the spatial generosity, to investigate the effects of the social generosity on cooperation. Then the authors observed a membrane formation as a mechanism that protects cooperation from invasion of defectors and maintains cooperators in the SPD model with the spatial generosity.

The membrane works as a mechanism for protects cooperators from invasion from defectors. Moreover the membrane emerges even if the lattice structure (e.g., square lattice, hexagonal lattice) and neighborhood radius change.

The robustness of the membrane for the lattice topology and the neighborhood is already shown [7]. This investigation, however, was conducted on the SPD under the ideal conditions in which all of the neighbors have equivalent value. In the realistic interaction between individuals, to interact with distant individuals has a higher cost than adjacent individuals.

In the present work, we use the SPD model that takes into account the interaction distance and the spatial generosity to investigate the effects of the distance between individuals. In the previous studies, the interaction distance has not considered. Thus, the player profits whether it is playing with the adjacent players or the distant players. In the real situation, however, playing with the distant players requires the high costs than the adjacent players. We assume that the payoffs which the players receive by playing mutual interaction are affected and discounted as the interaction distance increases.

This paper shows that cooperators emerge easier by considering the effects of the interaction distance.

This paper is organized as follows. In the next section, we explain the games models. In the section 3, we describe the membrane formation. Subsequently, we show the main results of our simulations. In the last section, we conclude and summarize this paper.

2 MODEL

2.1 Prisoner's Dilemma

The Prisoner's Dilemma (PD) is a one of fundamental models of the game theory. It is played just once by two players with two actions (Cooperation, C, or Defection, D). The players decide action simultaneously whether to cooperate or to defect. If both players cooperate, players receive payoff *R* (Reward), whereas if both players defect, players receive payoff *P* (Punishment). If one player cooperates and one player defects, the cooperator receives payoff *S* (Sucker) and the defector receives payoff *T* (Temptation). In the PD game, the payoffs must satisfy the equation $T > R > P > S$. In this model, whatever the opponent player chooses, the defection is the optimal choice for individuals clearly.

Therefore, both players always choose defection and receive payoff *P*, which is lower than that received when both choose cooperation.

The Iterated Prisoner's Dilemma (IPD) is temporal extension of the PD. In IPD, the PD is carried out repeatedly where $2R > T + S$. For IPD, some earlier researches proposed the temporal strategy. Axelrod reported a tit-for-tat (TFT) strategy is the best strategy among other temporal strategies [1]. The TFT strategy consists of playing C in the first round and from then on copying the opponent's action of the previous round. The TFT strategy contains temporal generosity as an element.

2.2 Spatial Prisoner's Dilemma

The Spatial Prisoner's Dilemma (SPD) is a spatio-temporal version of the PD. Our model generalized SPD by introducing a spatial strategy. Each player takes over the each site of a two-dimensional lattice. There have an action and a spatial strategy, and receive a score. The spatial strategy determines the next action according to the spatial pattern of action of their neighbor. A player plays the PD game with its neighbors (eight adjacent players when *Moore* neighborhood and neighborhood radius is one), and changes its strategy to the strategy that earns the highest total score among the neighbors'. Table 1 shows the payoff matrix of the PD. In our simulations, *R*, *S*, *T* and *P* are set to 1, 0, *b* and 0, respectively, below following the Nowak-May's simulations.

Table 1. The Payoff Matrix of the Prisoner's Dilemma Game. *R*, *S*, *T* and *P* are payoff for the player 1. A single parameter *b* is used following the Nowak-May's simulation.

		Player 2	
		C	D
Player 1	C	*R*(1)	*S*(0)
	D	*T*(*b*)	*P*(0)

The SPD is conducted in the following way with *N* players simultaneously.

1. Initial arrangement phase: an action and a strategy of each player are determined randomly with equal probability.
2. Action renewal phase: the next action of player will be determined by its strategy based on the neighbors' action (excluding the player itself).
3. Interaction phase: the players play the PD game with the neighbors and player itself, and then receive the payoff according to the payoff matrix in Table 1. However, the receiving payoff is discounted by an effect of the interaction distance. The score for each player is calculated by summing up all the scores and add the sum to the current score of the player.
4. Strategy renewal phase: after (2-3) is repeated *q* (strategy update cycle) times, the strategy will be chosen from the strategy with the highest score among the neighbors and the player itself.

2.2.1 Weight of the Interaction Distance

We weight the payoff that the player receives from the PD game to incorporate the effects of the interaction distance. The weight *w* ($0 < w \leqq 1$) discounts the player's payoff according to the decreasing function of the interaction distance. Hence, as distance between players increases, the weight decreases and a discount factor increases. The net payoffs of player *x* is given by

$$P_x = w \times \textit{game payoffs}.$$

In this paper, we proposed the two types of the decreasing function of the interaction distance. One is,

$$w = -\frac{d}{r+1} + 1, \tag{1}$$

where *d* is a interaction distance and *r* is a neighborhood radius. The other one is,

$$w = \frac{1}{(d+1)^2}. \tag{2}$$

For both definitions, the payoff's weight is one, when only the player plays the PD game with itself.

2.2.2 Spatial Strategy and Spatial Generosity

We conduct the SPD simulation with the spatial strategy and spatial generosity. The player decides next action according to its strategy and the pattern of the neighbors' action.

The spatial strategy determines player's action only based on the pattern of the neighbors' action. However, the patterns of the neighbors' action make an enormous amount. For example, in *Moore* neighborhood and its radius is 1, the patterns of the neighbors' action amount to 2^9 patterns. Hence, the 2^9 rules are required. For simplicity, we consider only "totalistic spatial strategy" that depends on the number of defectors in the neighbors, not on their positions. To represent a strategy, let l be number of the D actions of the neighbors excluding the player itself.

As a typical totalistic spatial strategy, we define k-D strategy. The player chooses D if $l \geqq k$, otherwise chooses C (Fig. 1). For instance, All-C (always cooperate) corresponds to the 9-D strategy, whereas All-D (always defect) corresponds to the 0-D strategy.

The k-D strategy can be regarded as a spatial version of the TFT where k indicates the spatial version of generosity.

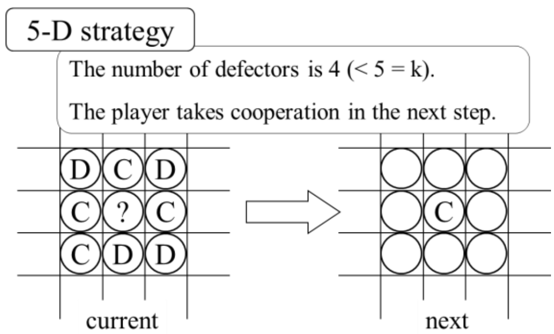

Fig. 1. An example of the spatial strategy. When k (spatial generosity) is five, the player tolerates to four defectors in the neighbors. Therefore, the center player will be cooperator in this situation.

3 MEMBRANE FORMATION

We already simulated the interaction between All-D (always D) vs. k-D instead of All-D vs. All-C (Nowak-May's simulation). In All-D vs. k-D interaction, we already observed the membrane as a mechanism for protects cooperation from invasion of defectors of All-D.

The membrane is composed of only the k-D defectors. Fig 2 shows an example of the membrane formation in *Moore* neighborhood.

In this paper, we also argue the effects of the weight of the interaction distance on the membrane formation.

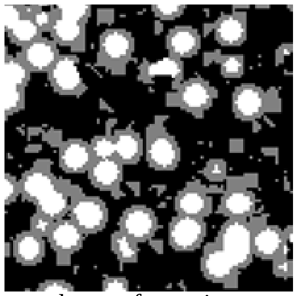

Fig. 2. The membrane formation generated by SPD simulation. *Black cells* indicate All-D players. *White and gray cells* indicate C and D players of k-D. In this snapshot, k is 6. The cooperators are covered by the membrane (*gray*).

4 SIMULATION

We carried out a SPD simulation in order to investigate the effects of the incorporating of the interaction distance with the parameter list in Table 2.

Table 2. Parameter list for the simulations

Parameter name	Description	Value		
$L \times L$	Size of lattice	700×700		
N	Number of players	490,000		
T	Number of steps	1,000		
r	Neighborhood radius	1	2	3
b	Bias of defectors of the payoff matrix in Table 1	1.8001, 2.0001	1.5625, 2.0001	1.4849, 2.0001

In a certain neighborhood radius, we carried out the two types of the simulation. In these simulations, we set a different parameter b (bias for defectors of the parameter matrix in Table 1).

1. The parameter b is set to be a minimum value that allows All-D to expand in the sea of cooperators from a single All-D player following the earlier study
2. The parameter b is set to be 2.0001. It does not satisfy the condition of the IPD ($2R > T + S$). This value favors a situation that defectors drive out cooperators in the IPD. Thus, it is favorable situation for the defector.

As a result, we observed the membrane formation whether the payoff is weighted (Fig. 3). Fig. 4 plots the time evolution of the cooperators when r = 1 and (1). In 6-D simulation, most players cooperate. This is because the All-D player could not invade and take over the cooperators

(Fig. 5). The cooperators receive higher payoff than defectors by an impact of self-interaction increasing.

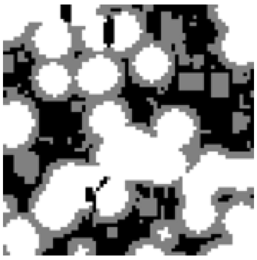

Fig. 3. The membrane formations emerge when k = 6, step t = 10, and the expression (1).

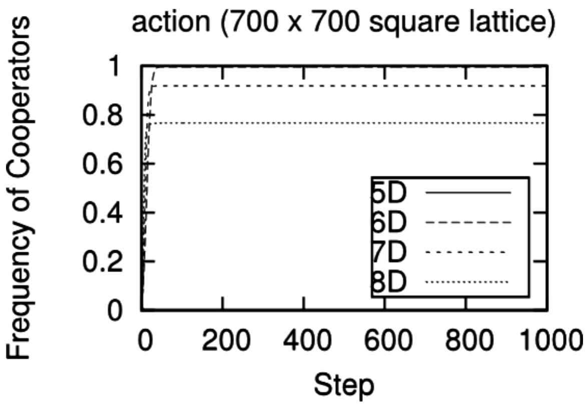

Fig. 4. The time evolution of the frequency of the cooperators. In the 6-D simulation, most players cooperate.

Fig. 5. This snapshots show step t = 100 of Fig. 3 simulation. The color code is same as in Fig. 3. The cooperators are not invaded by the defectors and remain.

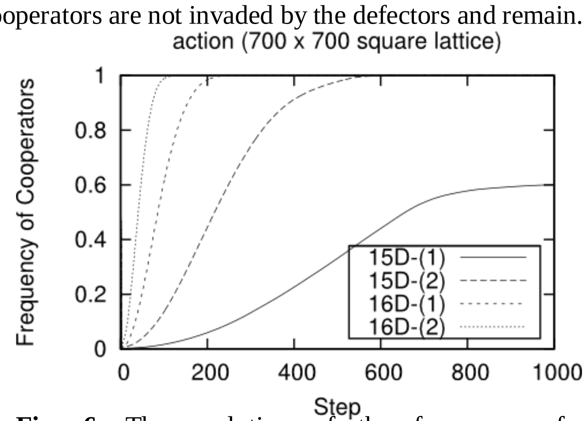

Fig. 6. The evolution of the frequency of the cooperators when r = 2. as the effect of the interaction distance increasing, the promotion of cooperation is preferred to defection.

Fig. 6 shows the time evolution of the cooperators when neighborhood radius r = 2. The cooperators easily emerge when (2). The interaction distance strongly influences a payoff weight when (2) than (1). Thus, as the effect of the interaction distance increasing, the promotion of cooperation is preferred to defection.

4 CONCLUSION

In conclusion, we have investigated the effect of the interaction distance on cooperation. In order to investigate this effect, we assumed that interacting with the distant individuals requires the high costs than the adjacent individuals. The payoff is discounted as the interaction distance increases.

In our model, cooperation easily emerges by incorporating the payoff's weight. The impact of the self-interaction increases by the introducing the payoff weight.

Moreover, we observed the membrane formation whether the payoff weight is introduced.

ACKNOWLIDGEMENTS

This work was supported in part by the Global COE Program "Frontiers of Intelligent Sensing" from the Ministry of Education, Culture, Sports, Science and Technology, Japan.

REFERENCES

[1] Axelod, R (1984), The Evolution of Cooperation, Basic Books, New York

[2] Nowak, MA, May, RM (1992), Evolutionary ga mes and chaos, Nature, vol.359:826-829

[3] Nowak, MA, May, RM (1993), The spatial dile mmas of evolution, Int. J. Bufurc. Chaos, vol.3:35-78

[4] Nowak, M.A.: Five Rules for the Evolution of Cooperation, Science, vol. 314, pp. 1560—1563 (2006)

[5] Ohtsuki, H, Hauert, C, Lieberman, E, Nowak, MA (2006) A simple rule for the evolution of cooperation on graphs and social networks, Nature, vol.441:502-505

[6] Run-Ran Liu, Chun-Xiao Jia, Bing-Hong Wang (2010), Effects of heritability on evolutionary cooperati on in spatial prisoner's dilemma games, Physics Proced ia, vol.3:1853-1858

[7] Katsumata Y., Ishida Y (2010) Robustness of Me mbrane Formation in a Spatial Prisoner's Dilemma wit h a Spatial Generosity, KES 2010

The Seventeenth International Symposium on Artificial Life and Robotics 2012 (AROB 17th '12),
B-Con Plaza, Beppu, Oita, Japan, January 19-21, 2012

Identifying Cellular Automata Rules Using Local Rule Network From Spatiotemporal Patterns

Takuya Ueda[1], Yoshiteru Ishida[1]

[1] Toyohashi University of Technology, Aichi, Toyohashi 441-8580, Japan
(Tel: 81-532-44-6868)
(ueda@sys.cs.tut.ac.jp)

Abstract: There are some methods of Identifying rules of cellular automata (CA) from their spatiotemporal patterns. But these methods do not consider relations of local rules. The relations include spatial ones and temporal ones. For example, a rule which satisfy the mass conservation law has spatial constraints for how to apply local rules to each cells. A local rule network represents spatial or temporal associations between local rules which are identified from spatiotemporal patterns. This paper address to construct local rule networks from spatiotemporal pattern and propose rule identification methods using the networks.

Keywords: Cellular Automata (CA), Rule Identification, Graphical Model

1 INTRODUCTION

Visualizations are used extensively for understanding behaviors of various phenomena. For example, Bayesian networks which are visualized causal associations by graphs (networks), apply to various area such as image recognition [1, 2]. Meanwhile, Wolfram classified 256 elemental rule of one dimensional cellular automata (CA) [3] into four classes by their behaviors [4]. Wolfram found differences between global behaviors of 256 rules by constructing directed graphs. The graphs represent transitions between possible configurations in certain space size. A Wolfram's graph can represent global behaviors of a rule but we cannot know local behaviors from the graph. Therefore we propose *local rule network* which consists of local rules as nodes and their transitions as arcs. A local rule network can represent associations between local rules. A rule of CA consists of local rules and each cell changes own state by applying a local rule. A local rule describes local a behavior which determine next state of a cell in a certain neighborhood pattern.

CA are known as which can generate various complex patterns from simple rules and uses for modeling of phenomena which generate spatiotemporal patterns. For example, ASEP[5] which is known as a traffic model is one of the one dimensional probabilistic cellular automata (PCA).

On the other hand, some researches deal with identifying cellular automata rules from analyzing their spatiotemporal patterns[6, 7]. Ichise proposed a method which identify a one dimensional deterministic and probabilistic cellular automaton rule from a spatiotemporal pattern generated by a computer simulation. Authors also applied the identifying method to actual phenomena and spatial prisoner's dilemma[8, 9]. The identifying method is simple which identifies local rules by scanning spatiotemporal patterns. The method can identify rules when spatiotemporal patterns are sufficiently big and simple such as patterns of Wolfram's 256 elemental rules. But the method cannot completely identify some rules which have hidden (embedded) rule such as ASEP's mass conservation law[10]. Because the method does not consider association between local rules. Therefore this paper propose local rules network which are constructed from spatiotemporal patterns and visualize local behaviors of these spatiotemporal patterns.

Section 2 explains cellular automata. Then local rule network is defined in section 3. Section 4 shows a example of patterns which the method cannot completely identify rules and discusses using local rule network.

2 CELLULAR AUTOMATA

Cellular automaton (CA) consists of cells which arranged on a lattice. Each cell has certain states and changes next own state following current neighborhood pattern. In this paper we restrict ourselves a case of one dimensional cellular automata. A time evolution of a cell is described by formula (1). Where n_i^t is a neighborhood pattern of cell i and r is neighborhood radius. When $r = 1$ current left, right and own three neighborhood determine the next state. A mapping $f : N \to S$ is a rule of CA where S is space of possible states and $N(= S^{r+1})$ is a set of possible neighborhood patterns. In a elemental CA (ECA) which is two states, three neighborhood and one dimensional CA has eight local rules because the number of possible neighborhood patterns is 2^3. Then there are $2^8 = 256$ rules in ECA.

$$\begin{array}{rcl} s_{i+1}^t & = & f(n_i^t) \\ n_i^t & = & s_{i-r}^t, \cdots, s_i^t, \cdots, s_{i+r}^t \end{array} \qquad (1)$$

Wolfram numbered these 256 ECA rules. The numbers are defined by formula (2). Where $c_j (\in S)$ is a state after applying local rule j such as table 1. The formula (2) also can consider that below of table 1 is binary string. Table 2 shows an example of rule 90.

$$R = \sum_{j=0}^{8} c_j 2^j \tag{2}$$

Table 1. A rule of 2-states,3-neighbors,one dimensional cellular automata (ECA). The rule consists of eight local rules.

n_i^t	111	110	101	100	011	010	001	000
s_i^{t+1}	c_7	c_6	c_5	c_4	c_3	c_2	c_1	c_0

Table 2. An example of rule90. When we consider the bottom column to binary number, it corresponds to $(01011010)_2 = 90$

n_i^t	111	110	101	100	011	010	001	000
s_i^{t+1}	0	1	0	1	1	0	1	0

Fig. 1 shows a spatiotemporal pattern generated by computer simulation of rule 90. Where white cells indicate 0 and black are 1. Space size is 100 and simulation time steps are 100. Initial condition is given by random.

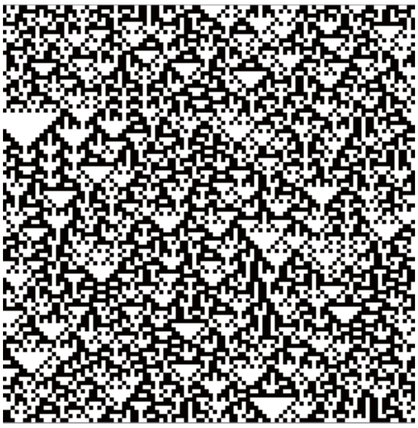

Fig. 1. A spatiotemporal pattern which is generated by rule90. White cells indicate 0 and black is 1. Space size is 100 and simulation time steps are 100. Initial condition is given by random.

3 LOCAL RULE NETWORK

Formula (3) defines a local rule network $G = (V, E)$. Fig. 2 shows a small example of local rule network. V is a set of nodes which are local rules and E is a set of arcs which are transitions (l_j, l_k) from local rule l_j to l_k. Where n_j is jth neighborhood pattern. For example, n_7 corresponds to $(1, 1, 1)$ in Table 1. When the neighborhood pattern of cell i at time step t is $(0, 0, 0)$, time step $t + 1$ is $(0, 1, 0)$ and the state of cell i at time step $t + 2$ is 0, there is a transition from local rule $((0, 0, 0), 1)$ to $((0, 1, 0), 0)$. Each arc has transition frequency $w(j, k)$ as weight. Then transition frequencies satisfy condition (4).

$$\begin{aligned} V &= \{l_j | l = (n_j, c_j), n_j \in N\} \\ E &= \{(l_j, l_k) | l_j, l_k \in V\} \end{aligned} \tag{3}$$

$$\sum_{l_k \in V} w(l_j, l_k) = 1 \quad \forall l_j \in V \tag{4}$$

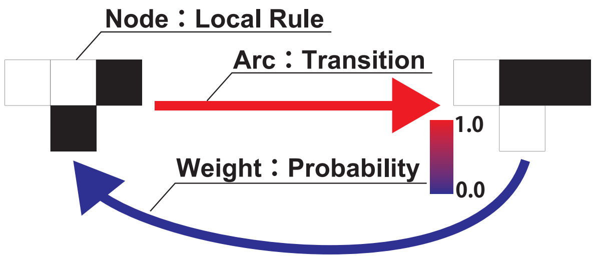

Fig. 2. An example of local rule network. Nodes correspond to local rules and arcs correspond to transitions between local rules. Each arc has transition frequency as a weight.

A local rule network is generated by scanning given a spatiotemporal pattern and finding local rules and their transitions. Then a transition frequency is obtained from the number of appearance. Fig. 3 shows a local rule network generated by a spatiotemporal pattern of rule 90 when space size is 1000, simulation time steps is 1000 and initial condition is random. Rule 90 is classified as class 3 which behaves chaos by Wolfram. Therefore rule 90 generates complex fractal patterns. Then the local rule network visualizes that there are many transitions and the rule is complex. Meanwhile, Fig. 4 shows a local rule generated by rule 5. This network has some hub local rules and it shows rule 5 is simple rule. Actually a spatiotemporal pattern of rule 5 is monotonous such as Fig. 5.

4 APPLICATION TO ASEP

ASEP is a traffic model and two states, three neighbors and one dimensional probabilistic CA. Each cell has a state, existing a car on the cell $(= 1)$or not existing $(= 0)$. Each car on the cell moves to front cell in probability p when front cell is empty. The number of cars is constant. Thus cars suddenly appears or disappears. It means that ASEP satisfies the mass

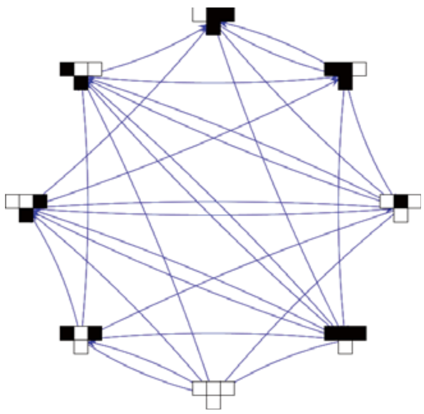

Fig. 3. A local rule generated from a spatiotemporal pattern of rule90. Each node indicates a two states and three neighbors local rule. White cells indicate 0 and black is 1.

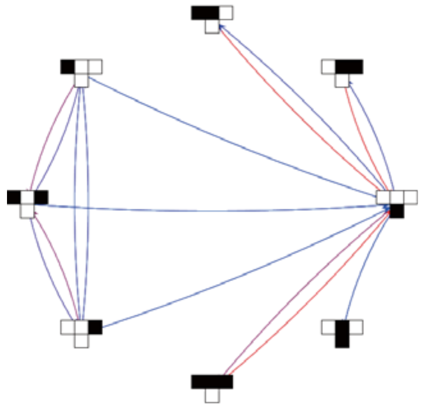

Fig. 4. A local rule generated from a spatiotemporal pattern of rule5. Each node indicates a two states and three neighbors local rule. White cells indicate 0 and black is 1. A spatiotemporal pattern is generated with 1000 space size and 1000 simulation time steps.

conservation law. But the mass conservation law cannot find a identified rule by the identifying method. While the method identify same rules from a pattern of satisfying the mass conservation law and not satisfying one [10]. Therefore we estimate whether spatiotemporal patterns satisfy the mass conservation law using local rule networks. Fig. 6 is generated by ASEP simulation and Fig. 7 is generated by a similar rule to ASEP but it does not satisfy the mass conservation law. These patterns shows major differences by comparison.

Fig. 8 is a local rule network generated from Fig. 6 and Fig. 9 is generated from Fig. 7. Fig. 9 shows that it has some transitions which do not appear in Fig. 8. These transitions break the mass conservation law. Thus local rule network can bring out differences between rules which identified as same rules by the identifying method.

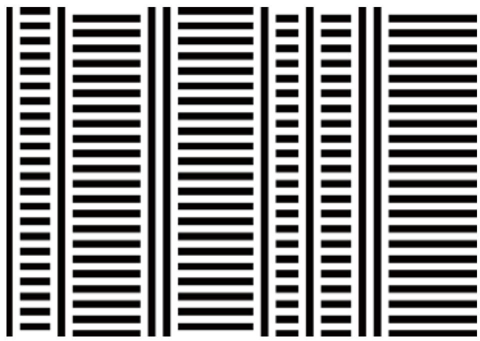

Fig. 5. A part of spatiotemporal pattern which is used for generating Fig. 4. White cells indicate 0 and black is 1.

5 CONCLUSIONS

This paper proposed a visualization of cellular automata rules from spatiotemporal patterns. A local rule network visualizes associations between local rules. Then we also shows an example of analysis in ASEP using local rule networks. Local rule network can bring out differences between rules which identified as same rules by the identifying method.

6 ACKNOWLEDGMENTS

This work was supported in part by Global COE Program “Frontiers of Intelligent Sensing” from the Ministry of Education, Culture, Sports, Science and Technology, Japan.

This work was partly supported by Grants-in-Aid for Scientific Research (B):“ Foundation on Immunity-Based Complex Systems and Sensor Agents ”(23300057) 2011.

REFERENCES

[1] Pearl J (1988) Probabilistic reasoning in intelligent systems: networks of plausible inference. Morgan Kaufmann.

[2] Jensen F (1996) An introduction to Bayesian networks, volume 210. UCL press London.

[3] Von Neumann J, Burks A, et al. (1966) Theory of self-reproducing automata. Univ. of Illinois Press Urbana, IL.

[4] Wolfram S (1983) Cellular automata. Los Alamos Science 9: 2–27.

[5] Rajewsky N, Santen L, Schadschneider A, Schreckenberg M (1998) The asymmetric exclusion process: Comparison of update procedures. Journal of statistical physics 92: 151–194.

[6] Richards F, Meyerb T, Packard N (1990) Extracting cellular automaton rules directly from experimental data. Physica D: Nonlinear Phenomena 45: 189–202.

Fig. 6. A spatiotemporal pattern of ASEP with $p = 0.8$, 100 space size and 100 simulation time steps. White cells indicate 0 and black is 1.

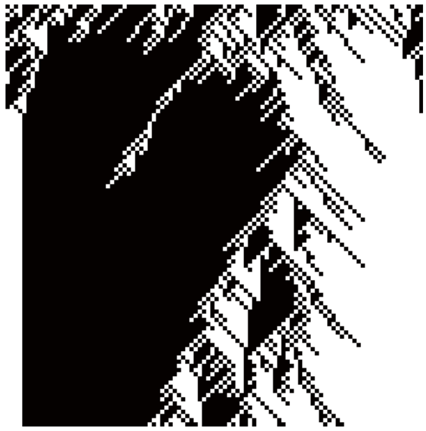

Fig. 7. A spatiotemporal pattern of general PCA with 100 space size and 100 simulation time steps. Its result of identification similar to Fig. 6 one. White cells indicate 0 and black is 1.

[7] Ichise Y, Ishida Y (2008) Reverse engineering spatial patterns in cellular automata. Artificial Life and Robotics 13: 172–175.

[8] Ueda T, Ishida Y (2011) Identifying generative mechanisms from spatiotemporal patterns in diffusion phenomena. Lecture Notes in Computer Science .

[9] Ueda T, Ishida Y (2009) Reverse engineering of spatio patterns in spatial prisoner 's dilemma. Artificial Life and Robotics 14: 498–501.

[10] Ueda T, Ishida Y (2011 to appear) Extracting probabilistic cellular automata rules from spatio-temporal patterns and analyzing features of these rules. Artificial Life and Robotics 16.

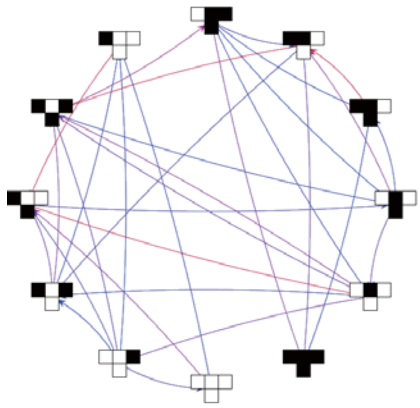

Fig. 8. A local rule network generated from Fig. 6.

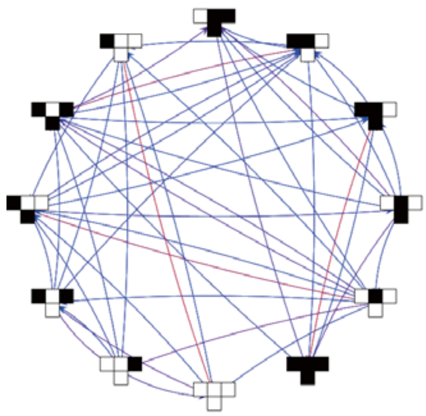

Fig. 9. A local rule network generated from Fig. 7.

The Seventeenth International Symposium on Artificial Life and Robotics 2012 (AROB 17th '12),
B-Con Plaza, Beppu, Oita, Japan, January 19-21, 2012

Performance evaluations of adaptive strategies in self-repairing network

Masahiro Tokumitsu[1,3] and Yoshiteru Ishida[1,2]

[1] Department of Electrical and Information Engineering,
[2] Department of Computer Science and Engineering,
Toyohashi University of Technology, Tempaku, Toyohashi, Aichi, 441-8580, Japan
[3] Research Fellow of the Japan Society for the Promotion of Science (DC2)
(Tel: +81-53-244-6895, Fax: 81-53-244-6873)
([1]tokumitsu@sys.cs.tut.ac.jp, [2]ishida@cs.tut.ac.jp)

Abstract: This paper studies a relationship between an adaptive strategy and its payoff. In a recent study, the adaptive strategy has already proposed to evaluate how much the strategy obtains a payoff on average against not only itself but also other strategies. We study the adaptive strategy in two examples: a prisoner's dilemma and self-repairing network. We study the prisoner's dilemma by focusing on two parameters: benefit and cost. We reveal a condition when the strategy gets the highest adaptive measure against other strategies in the prisoner's dilemma game. Further, we apply the analysis to the self-repairing network with spatial strategies. We investigate the adaptive strategy in the self-repairing network by simulations. We revealed that the adaptive strategies get the high payoff which minimize the standard deviations in the simulations.

Keywords: self-repairing network, adaptive strategies, spatial strategies, game theory, dynamic environments

1 INTRODUCTION

Autonomous distributed systems composed of agents need to adapt changes of environments. In the autonomous distributed systems, the agents pursue their own profits to achieve assigned their own goals. The agents need to change their behavior to adapt conditions in the dynamic environments. The agents determine next actions based on their own strategies. However, decision makings of the agents will affect each other. The policy of the agent behavior is represented as a strategy in game theory. The agents need to choose the strategy that earns the high profits as much as possible and determine their next actions based on their strategies.

There are various kinds of agents in information networks. The agents, connected each other with a network structure, interact with other agents based on their own strategies. The agents will encounter other ones having not only same strategies but also different strategies. For the agents, to choose the strategies earning the high payoff to specific strategies is risky, since, the agents face with a lot kind of the other agents selecting different strategies. The neighbor agents of the agent also will affect itself as the environment. The environments dynamically change according to interactions among them. Therefore, the agents need to have the strategies that obtain the high profits on average against other strategies.

An earlier study has already proposed a concept of an adaptive strategy [1] of which how well the strategies perform against other strategies. The performance of the strategies is evaluated as adaptive measures based on interaction results of the payoffs. In the study, the authors introduced two models as calculation examples: prisoner's dilemma [2] and self-repairing network [3, 1]. The evaluation results of the strategies from the viewpoint of the adaptive strategy showed that the strategies earning the highest payoff do not correspond to that ones getting the highest adaptive measures. The study has reported that the adaptive strategies would perform well against other strategies although they do not obtain the highest payoffs.

The related works on the adaptive strategies are fault-tolerant strategies [4] and evolutionary stable strategies [5, 6]. However, both notions aim to investigate robust strategies against other strategies. Other related studies aim to construct a good strategy (strong strategy) than other strategies. Further, they compared with the proposed and other strategies by simulations [7, 8, 9, 10]. However, the focus of the adaptive strategies is to investigate adaptiveness of the strategies that earn the high payoff on average against other strategies.

An aim of this paper is to investigate two issues on the adaptive strategies. Firstly, we analyze the iterated prisoner's dilemma game as a typical example. We reveal a certain condition in which an adaptive measure of a trigger strategy exceeds that one of always defection strategy. Secondly, we study relationships between the adaptive measures and variances of the payoffs earned by the strategies. The earlier study [1] showed the strategies earning the highest adaptive measures obtains the high payoffs on average against other strategies. For this issue, we consider a self-repairing network as another example in the autonomous distributed systems. We study the self-repairing network composed of the agents choosing spatial strategies by numerical simulations.

In Section 2, we give a formal definition of adaptive strategies, and we consider parameter conditions on the adaptive strategies in the iterated prisoner's dilemma with three simple strategies. In Section 3, we introduce and define the self-repairing network for simulations. In Section 4, we evaluate the self-repairing network from the viewpoint of the adaptive strategies by simulations. In Section 5, we discuss the significance of the adaptive strategies on the basis of the simulation results. In Section 6, finally, we state our conclusions in this paper.

2 ADAPTIVE STRATEGY

2.1 Definition

The concept of adaptive strategies and its formal definition has already introduced in the former paper [1]. The concept of the adaptive strategies is proposed in order to construct the autonomous distributed systems which work well on average in uncertain environments. The concept of the adaptive strategies incorporates fundamental two factors: (a) cooperative and (b) self-tolerance. Cooperative means that the strategies need to behave cooperative to maintain their performance against the opponents because the agents would encounter various kinds of strategies in information networks. Self-tolerance means that the agents need to cooperate with their neighboring agents because if they defect from others who have the same strategies, they would lose future opportunities to get a higher payoff. These two fundamental factors require agents to cooperate with not only themselves but also other agents.

For designing the strategies, performance of the strategies how much they behave well agains other strategies is evaluated as an adaptive measure. This measurement is defined by payoffs and strategies. Let S denote a set of strategies. Let N denote the cardinality of the strategy set S. Let i, j, and k denote natural numbers used for numbering the strategies in the strategy set. Strategy s_i is expressed as one strategy in the set S numbered as i. Let $E_p[s_i|s_j]$ denote the expected payoff of strategy s_i against s_j. Let $E_m[s_i]$ be the expected payoff of the strategy s_i for all strategies.

Let denote the adaptive measure $E[s_i]$ of a strategy s_i its strength. The adaptive measure is represented as follows:

$$E[s_i] = \frac{1}{NM} \sum_{s_j \in S} E_p[s_i|s_j] E_m[s_j] \tag{1}$$

$E_m[s_j]$ is expressed as follows:

$$E_m[s_j] = \frac{1}{NM} \sum_{s_k \in S} E_p[s_j|s_k] \tag{2}$$

The symbol M represents the maximum total payoff in the payoff matrix of the game. Formula (2) represents the averaged performance of strategy s_j for all strategies. The adaptive measure in Formula (1) is expressed as the product of $E_p[s_i|s_j]$ and $E_m[s_j]$ to evaluate whether strategy s_i achieves the higher payoff against strategy s_j even if s_j achieves a high payoff for other strategies. The adaptive measure will decrease when strategy s_i achieves the smaller payoff and even if strategy s_j achieves the higher averaged payoff. In contrast, the adaptive measure will increase when strategy s_i gets the larger payoff and strategy s_j obtains the higher averaged payoff. The range of the measure can be normalized from zero to one. The strategy is adaptive if the measure is close to one, and it is not adaptive if the measure is close to zero. The adaptiveness of the strategies can be evaluated by comparing with the measures.

2.2 Example of adaptive strategy analysis

We present a calculation example of the adaptive measures of the adaptive strategies in the iterated prisoner's dilemma (IPD). This example uses simple three strategies: All-C (always cooperate), All-D (alway defect) and Trigger (it cooperates until an opponent defects in a previous round, otherwise defects). We reveal a condition in which the adaptive measure of Trigger strategy exceeds All-D strategy's one where a discount rate is a variable parameter. The IPD is a temporal extension of the prisoner's dilemma. The prisoner's dilemma [2] is a one-shot game whereas the IPD is a repeated game. We consider a two-player game in the infinite IPD. The players determine their actions of cooperation or defection simultaneously without prior consultation before the game. The payoff for each player is determined by combinations of moves among the players.

The payoff matrix is shown in Table 1. The payoff matrix is defined with two parameters b (benefit) and c (cost). Each symbolic value in the table satisfies the conditions $T > R > P > S$ and $2R > T + S$. We assume a discount rate w of the payoff for every round. The discount rate can be used for calculating the discounted payoff regarded as the future payoff.

The expected payoffs of the infinite IPD for the three strategies can be calculated theoretically [2]. The theoretical results shown in Table 2 are calculated from the payoff matrix shown in Table 1.

Table 1. Payoff matrix for the proponent in the prisoner's dilemma with two parameters

		Player 2	
		C	D
Player 1	C	$R = b \quad c$	$S = \quad c$
	D	$T = b$	$P = 0$

Table 2. Expected payoff for the proponent in the infinite IPD with two parameters

		Opponent		
		All-D	Trigger	All-C
Proponent	All-D	0	b	$\frac{b}{1-w}$
	Trigger	c	$\frac{b-c}{1-w}$	$\frac{b-c}{1-w}$
	All-C	$\frac{-c}{1-w}$	$\frac{b-c}{1-w}$	$\frac{b-c}{1-w}$

From Table 2, we simply obtain the averaged payoffs for all strategies.

$$E_m[All \quad D] = \frac{2b \quad 3c}{3b} \tag{3}$$

$$E_m[Trigger] = \frac{1 \quad w}{3b}\left(\quad c + \frac{2(b \quad c)}{1 \quad w}\right) \tag{4}$$

$$E_m[All \quad C] = \frac{2 \quad w}{3} \tag{5}$$

We focus on the two strategies of Trigger and All-D. The adaptive measures of these two strategies can be calculated by the definitions. Therefore, we obtain adaptive measures of both strategies as follows:

$$E[All \quad D] = \frac{1}{9b}\Big(\quad cw^2 + 4cw \quad 2bw \quad 6c + 4b\Big) \tag{6}$$

$$E[Trigger] = \frac{1}{9b}\Big(\quad bcw^2 + (4bc \quad c^2)w + 6c^2 \quad 12bc + 4b^2\Big) \tag{7}$$

We calculate the condition of the discount rate which leads the adaptive measure of Trigger to be the highest value.

$$\begin{aligned} E[Trigger] &> E[All \quad D] \\ 2b^2w + c^2w &> 6c^2 \quad 6bc \end{aligned} \tag{8}$$

We replace the term c/b with r. Then, we obtain

$$w > \frac{6r(r \quad 1)}{(\sqrt{2} \quad r)(\sqrt{2} + r)} \tag{9}$$

According to the above result, the adaptive measure of Trigger exceeds the adaptive measure of All-D when the discount rate exceeds the threshold. Fig. 1 shows a curve of discount rate against the cost-benefit ratio calculated by Formula

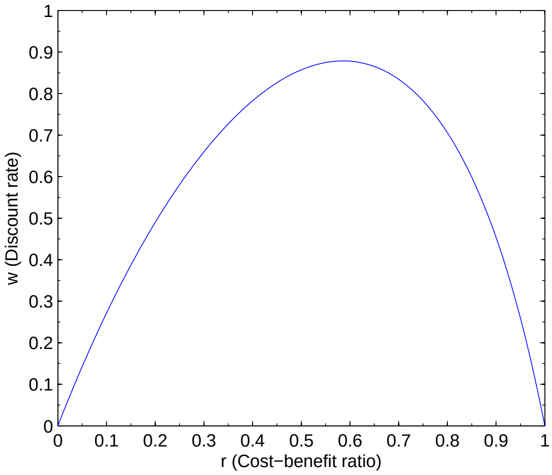

Fig. 1. Discount rate curve against cost-benefit ratio in Eq. (9).

(9). The highest discount rate is 0.88 when the cost-benefit ratio is 0.69. The discount rate increases as the cost-benefit ratio grows because the defective strategy dominates the cooperative strategies where the the discount rate is smaller than its highest value. On the other hand, the discount rate decreases as the cost-benefit ratio grows to be larger than 0.69 because the benefit is small due to the cost to be large.

3 SELF-REPAIRING NETWORK

In order to consider the relationship between the highest adaptive measures and the payoffs, we apply the adaptive strategy analysis to the self-repairing network with spatial strategies [11]. The self-repairing network is a network model in which agents repair other agents by copying their contents mutually. We consider the self-repairing network by game-theoretic approach model [3, 12]. We adopt the proposed former model defined by replicator dynamics and master equations.

For simplicity, we assume the network large, well-mixed population. Each agent has a state either normal or abnormal. We denote the frequency of normal agents (abnormal agents) by ρ_N (ρ_A). Each agent determines the next action: *repair* (C, cooperation) or *not repair* (D, defection). We denote the frequency of repair agents (not repair agents) in the network by ρ_C (ρ_D). The agents determine their actions based on their strategies.

The repairing is done between the two agents. The two agents are randomly chosen from the network, then they repair each other based on their decisions. The repair success rate is different by the state of the agent. We denote the repair success rate of the normal and abnormal agents by α and β respectively. We assume to simplify the model that the repair by the normal agents is always successful ($\alpha = 1$). The repaired agent becomes normal if the repairing is successful, otherwise the repaired agent becomes abnormal. We assume that the normal agents become abnormal by spontaneous failure. We denote the failure rate by λ.

From above definitions, the repairing dynamics is expressed as follows:

$$\begin{aligned}\frac{d\rho_N}{dt} &= \alpha\rho_N\rho_A\rho_C + \beta\rho_A^2\rho_C \quad (1 \quad \alpha)\rho_N^2\rho_C \\ &\quad (1 \quad \beta)\rho_A\rho_N\rho_C \quad \lambda\rho_N \end{aligned} \tag{10}$$

Each term represents the repair interactions between the two agents. The first and second terms express the increase of normal agents while the third and forth terms represent the decrease of the abnormal agents.

The agents have their own resources consumed by repairing. The normal agents (abnormal agents) have the maximum resources b_N (b_A). If the normal agents (abnormal agents) do the repairing, then the agents consume their resources only c_N (c_A). The agents deal with the remained resources as the available resources. The resources of the agents are filled in the beginning of the step.

The agents determine their next actions based on the strategies. We introduce spatial strategies [11] to the agents. The spatial strategies determine the actions involving the effects of neighborhood decision making. Especially, kC strategy of the spatial strategies is introduced into the agents. In an original definition of kC strategy, it determines the next action *repair* if the number of defeaters exceed the threshold k. We modify the strategy from the original one to the strategy one that determine the next actions based on the frequency of silent agents ρ_D in the previous step. The range of the threshold k is from 0 to 1. We denote the frequency of the kC strategy by ρ_k.

For calculating the payoff of each strategy, we define a function $\rho_C^k(\rho_C^p)$ that returns a binary value 0 or 1 according to the frequency ρ_C^p of the repair agents in the previous step. The function $\rho_C^k(\rho_C^p)$ is defined as follows:

$$\rho_C^k(\rho_C^p) = \begin{cases} 0 & (\rho_C^p > k) \\ 1 & (\rho_C^p \quad k) \end{cases} \tag{11}$$

Let denote $W(kC)$ the expected payoff of the strategy kC. The $W(kC)$ is expressed as follows:

$$\begin{aligned} W(kC) &= \rho_k(\rho_N((b_n \quad c_n)\rho_C^k(\rho_C^p) + b_n(1 \quad \rho_C^k(\rho_C^p))) \\ &\quad + \rho_A((b_a \quad c_a)\rho_C^k(\rho_C^p) \\ &\quad + b_a(1 \quad \rho_C^k(\rho_C^p)))) \end{aligned} \tag{12}$$

Let denote $\overline{W}$ expected payoff of the whole network. The expected payoff $\overline{W}$ is expressed as follows:

$$\overline{W} = \rho_{k_1}W(k_1C) + \rho_{k_2}W(k_2C) \tag{13}$$

We consider the self-repairing network with the agents implementing two different strategies. The strategies are denoted as k_1C and k_2C. Therefore, the dynamics of the competition among the strategies is expressed as follows:

$$\frac{d\rho_{k_1}}{dt} = (W(k_1C) \quad \overline{W})\rho_{k_1} \tag{14}$$

Therefore, the dynamics of the self-repairing network with the spatial strategies are expressed by the two equations (10) and (14) are expressed.

4 SIMULATIONS

We make a round-robin tournament of the self-repairing network with spatial strategies. We evaluate the spatial strategies in the self-repairing network from the viewpoint of the adaptive strategy. We choose two strategies from the strategy set and run the simulations with the two strategies. Parameters for simulations are shown in Table 3. After simulations, we calculate the adaptive measure for each strategy.

Table 4 shows the round-robin tournament results for the failure rate $\lambda = 0.01$. According to the result, the $0.6C$ strategy obtains the highest averaged payoff among the strategies, while the $1C$ strategy gets the highest adaptive measure and smallest standard deviation. The $0.6C$ strategy gets the high payoff against other strategies except the $1C$ strategy. The $1C$ strategy obtains the high payoff against not only itself but also other strategies although $1C$ strategy agents are repaired by other strategy agents. This difference makes the $1C$ strategy get the highest adaptive measure.

Table 5 shows the round-robin tournament result for the failure rate $\lambda = 0.04$. According to the result, the $0.6C$ strategy obtains the highest averaged payoff among the strategies, while the $0.6C$ strategy gets the highest adaptive measure and smallest standard deviation. This result is contrary to the round-robin tournament one where the failure rate $\lambda = 0.01$. For both cases, 0.6 strategy obtains the higher payoff than $0.6C$. Unfortunately, the $0.6C$ strategy causes the decrease of the payoff when it repairs itself. The $1C$ strategy makes its standard deviation the smallest. In other words, the strategy obtaining the highest adaptive measure also gets the smallest standard deviation.

According to two cases, the standard deviations of the adaptive strategies become the smallest values. The adaptive strategies earn the high payoff on average and make the standard deviations he smallest.

5 DISCUSSION

In the previous section, we compared the two results where the different failure rates are used. The round-robin

Table 3. Parameters for numerical simulations

Parameter	Name	Value
T	Step	500
α	Repair success rate by normal agents	1.0
β	Repair success rate by abnormal agents	0.1
b_N	Available resources of normal agents	1.0
c_N	Repair cost of normal agents	0.25
b_A	Available resources of abnormal agents	0.5
c_A	Repair cost of abnormal agents	0.25
λ	Failure rate	0.01, 0.04
k	k value for kC strategy	0.0-1.0 (0.2 step)
$\rho_k(0)$	Initial frequency of kC strategy	0.5
$\rho_C(0)$	Initial frequency of cooperators	0.5

Table 4. Adaptive measure and statistical values (The failure rate λ = 0.01)

	0.0	0.2	0.4	0.6	0.8	1.0	Averaged payoff	Standard deviation	Adaptive measure
0.0	0.424	0.424	0.424	0.002	0.002	0.002	0.213	0.211	0.046
0.2	0.424	0.424	0.424	0.002	0.002	0.002	0.213	0.211	0.046
0.4	0.424	0.424	0.424	0.002	0.002	0.002	0.213	0.211	0.046
0.6	0.845	0.845	0.845	0.358	0.358	0.003	0.542	0.325	0.151
0.8	0.714	0.714	0.714	0.358	0.358	0.003	0.477	0.265	0.137
1.0	0.534	0.534	0.534	0.531	0.528	0.260	0.487	0.102	0.168

Table 5. Adaptive measure and statistical values (The failure rate λ = 0.04)

	0.0	0.2	0.4	0.6	0.8	1.0	Averaged payoff	Standard deviation	Adaptive measure
0.0	0.357	0.357	0.357	0.002	0.002	0.002	0.180	0.178	0.033
0.2	0.357	0.357	0.357	0.002	0.002	0.002	0.180	0.178	0.033
0.4	0.357	0.357	0.357	0.002	0.002	0.002	0.180	0.178	0.033
0.6	0.712	0.712	0.712	0.292	0.292	0.003	0.454	0.276	0.105
0.8	0.582	0.582	0.582	0.292	0.292	0.003	0.389	0.216	0.093
1.0	0.507	0.507	0.507	0.505	0.504	0.252	0.464	0.094	0.136

tournaments demonstrated the considerable results. The standard deviations of the strategy obtaining the highest adaptive measure are the smallest values among the strategies. In one of the two cases, the strategy does not correspond to that one obtaining the highest averaged payoff. On the other hand, the strategy obtaining the highest adaptive measure correspond to that one obtaining the highest averaged payoff. However, the adaptive strategies could get the high payoff on average against given strategies set and make its standard deviation the smallest in them.

In information network, the agents encounter various kinds of agents implementing different strategies. The agents need to adapt behavior of the other agents in order to pursue their goals. According to the simulation results, the adaptive strategies could obtain high payoffs on average against other strategies. Further, their lack of the payoffs compared with the averaged payoffs would be the smallest or small values. The neighborhood of the one agent can be regarded as its environment. For the agents, to adapt for a specific environment is not reasonable because of they would face and need to follow the changes of the environments. The adaptive strategies would adapt to different environments by the simulation results.

6 CONCLUSIONS

We studied a relationship between an adaptive strategy and its payoff in both examples of a prisoner's dilemma and self-repairing network. In the prisoner's dilemma, we considered on the adaptive strategies what conditions make the strategies get the highest adaptive measure. We analyze the adaptive strategies in the prisoner's dilemma game with simple three strategies and certain parameters. For the analysis, this paper focused on the two parameters: benefit and cost. We revealed the condition of which the strategy gets the highest adaptive measure against other strategies in the prisoner's dilemma.

Further, we considered the adaptive strategies in the self-repairing network with spatial strategies. The dynamics of the self-repairing network involve interactions on a mutual repairing and strategy update. We investigated the adaptive strategy in the self-repairing network by numerical simulations. In the results, we showed that the standard deviations of the strategies obtaining the highest adaptive measures are the smallest values among the strategies even the strategies do not earn the highest averaged payoffs. We revealed that the adaptive strategies would get the high payoff which minimize the standard deviations.

ACKNOWLEDGEMENTS

This work was supported by the Global COE Program "Frontiers of Intelligent Sensing," from the ministry of Education, Culture, Sports, Science and Technology. This work was also supported by Grant-in-Aid for JSPS Fellows. This work was also partly supported by Grants-in-Aid for Scientific Research (B): "Foundation on Immunity-Based Complex Systems and Sensor Agents" (23300057) 2011.

REFERENCES

[1] Tokumitsu M (2011) Adaptive strategies: Toward a design of adaptive systems for dynamic environments. In: Proceedings of the International Conference on Management of Emergent Digital EcoSystems. New York, NY, USA: ACM, MEDES '11.

[2] Axelrod R (1984) The Evolution of Cooperation, Basic Books. New York.

[3] Ishida Y, Tokumitsu M (2008) Asymmetric interactions between cooperators and defectors for controlling self-repairing. Lecture Notes in Computer Science 5179: 440–447.

[4] Pelc A (2010) Fault-tolerant strategies in the iterated prisoner's dilemma. Information Processing Letters 110: 389–395.

[5] Weibull JW (1997) Evolutionary Game Theory. The MIT. Press.

[6] Smith JM (1982) Evolution and the Theory of Games. Cambridge, UK: Cambridge University Press.

[7] Beaufils B, Delahaye J, Mathieu P (1996) Our meeting with gradual, a good strategy for the iterated prisoner's dilemm. In: Artificial Life V: Proceedings of the Fifth International Workshop on the Synthesis and Simulation of Living Systems.

[8] Beaufils B, Delahaye JP, Mathieu P (1998) Complete classes of strategies for the classical iterated prisoner's dilemma. In: Porto VW, Saravanan N, Waagen D, Eiben AE, editors, Evolutionary Programming VII. Berlin: Springer, pp. 33–41.

[9] Nowak M, Sigmund K (1993) A strategy of win-stay, lose-shift that outperforms tit-for-tat in the Prisoner's Dilemma game. Nature 364: 56–58.

[10] Tzafestas E (2000) Spatial games with adaptive tit-for-tats. In: Proceedings of the 6th International Conference on Parallel Problem Solving from Nature. London, UK: Springer-Verlag, PPSN VI, pp. 507–516.

[11] Ishida Y, Mori T (2005) Spatial strategies in a generalized spatial prisoner ' s dilemma. Artificial Life and Robotics 9: 139–143.

[12] Tokumitsu M, Ishida Y (2011) An adaptive control technique for a connection weight of agents in a self-repairing network. Lecture Notes in Computer Science 6557: 44–55.

The Seventeenth International Symposium on Artificial Life and Robotics 2012 (AROB 17th '12),
B-Con Plaza, Beppu, Oita, Japan, January 19-21, 2012

Solar Insolation Simulation by Cellular Automata and Applications to Smart Home

Ken Matsuka, Yoshiteru Ishida

Toyohashi University of Technology
Aichi 441-8580, Japan

matsuka@sys.cs.tut.ac.jp

Abstract: Solar insolation influences important factors such as the indoor sunshine and room temperature. For a smart house, the amount of power generation of a photovoltaic generation depend on the solar insolation. However, knowledge required to evaluate the influences may not be readily available. We aim to build a solar insolation simulator that can be used without professional knowledge and detailed information. The simulator has simplicity and flexibility of a computational model of cellular automata. The advantage of this simulator is in an easy setup. Since this simulator needs only a floor plan diagram, its detailed knowledge is unnecessary. Moreover, the merit of the application by having created by the cellular automaton is also an advantage of this simulator.

Keywords: cellular automata, living climate, insolation

1 INTRODUCTION

Solar insolation influences important factors in designing a smart home such as the indoor sunshine, room temperature and the amount of power generated by a photovoltaic generation for the house installed. Many simulators of solar insolation have been already developed [1][2].

However, professional knowledge such as architectonics is required for those simulators, and it would be difficult to use those simulators for novices. For example, when Daysim [1] performs a simulation, it requires the three-dimensional model by CAD (Computer Aided Design). Therefore, a simulation cannot be performed without the knowledge of CAD. Further, information required to use those simulators described above (such as the quality of the material of a wall, the form of a roof, and information on the surrounding residence) may not readily be available.

We aim to develop a simulator which requires a floor plan diagram but neither professional knowledge nor detailed information. By performing a simulation only from a floor plan diagram, the time and effort for model creation is reduced.

Section 2 explains a definition of cellular automaton modified to simulate a light ray.

Section 3 presents the outline of the simulator.

Section 4 deals with the application of the simulator. The function and simulation result are also presented.

2 CELLULAR AUTOMATON MODEL

2.1 Cellular Automata

Cellular automata are a computational model composed of homogeneous cells each of which has the same number of states and the same set of rules to change the state. These cells are arranged in a regular lattice such as a square lattice and a hexagonal lattice. We use a two dimensional square lattice. In discrete time progresses, each cell determines the own state by an interaction from the state of itself and its neighborhood [3].

The cellular automaton can express a complicated phenomenon easily only by applying the same transition rule as all the cells. Moreover, it also has the pliability which can express another new phenomenon by adding a transition rule. For simplicity we used cellular automata to build solar insolation simulator.

2.2 Cellular Automata for the Simulation of Solar Insolation

The outline of cellular automata for the simulation of solar insolation is shown below.

The state s of a cell is a collection of states (as in the formula (1)): c is a type of a cell; a is the degree of incidence angle; x and y are the movements to the direction of x and y from an incidence position, respectively; and d is a direction of movement.

$$s = (c, a, x, y, d) \tag{1}$$

The type of a cell c is air, a wall, or light. Furthermore, when c is light, a cell has the information on the degree of incidence angle a, the amount of movements x and y, and a direction of movement d.

The degree of incidence angle a is the degree of incidence angle of sunlight. The position of the sun changes with time. Therefore, it is necessary to change the degree of incidence angle according to the date and time.

The amount of movements x and y are value used when determining a direction of movement, and x and y takes both of positive.

A direction of movement d is a direction where light actually progresses, and there are eight directions as shown in Fig.1. There is the degree of incidence angle to a range of 0 to 360 degrees, but the light cannot move to the direction of this angle correctly on grid-like space. Therefore, by choosing a direction of movement appropriately, light moves the degree of incidence angle approximately.

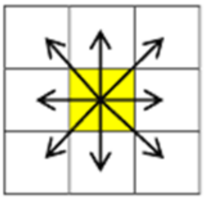

Fig. 1. The direction of movement of light

Each cell determines the next state by applying the transition rule f to determine the next state $s_{i,j}^{t+1}$ based on the state of the own cell and neighbor cell as in the following update rule (2). The symbol $s_{i,j}^{t}$ indicates the state of the cell in the coordinate (i, j) at the time t.

$$s_{i,j}^{t+1} = f(s_{i-1,j-1}^{t}, s_{i-1,j}^{t}, \cdots, s_{i,j}^{t}, \cdots, s_{i+1,j+1}^{t}) \qquad (2)$$

3 THE OUTLINE OF THE SIMULATOR

3.1 The Outline of the Simulator

A floor plan diagram is used for a simulation, and 1 pixel is set up as one cell. The state of each cell is distinguished by the color of a pixel when a floor plan diagram is read.

There are three kinds of sunlight: direct sunlight, skylight and catoptric light from the ground. But, for simplification of a setup, only direct sunlight with the largest amount of solar insolation is considered in this simulator.

The simulation is performed in two dimensions. And a floor plan top is set up north.

3.2 The Procedure of the Simulation

Operation of the simulator consists of arrangement of light, movements of light, and those repetitions. The details of three operations are shown below.

3.2.1 Arrangement of Light

If the type of a cell is air and the cell is on the edge of the screen, the type of the cell is made to change light. For example, sunlight is incident from the right and under of the screen at 9:00 (refer to Fig. 2). Moreover, light sets up the degree of incidence angle which suits at time (refer to Fig. 3).

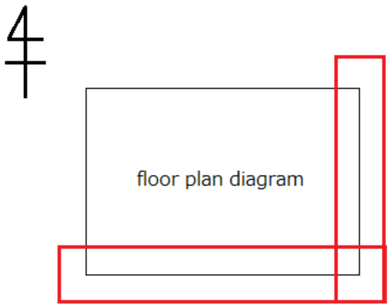

Fig. 2. The incidence position of light at 9:00

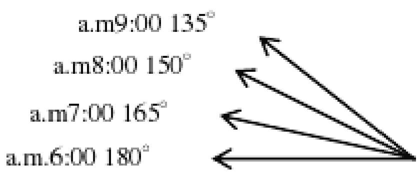

Fig. 3. The degree of incidence angle

3.2.2 Movements of Light

If there is the light whose the direction of movement turned to the own cell at neighborhood and the type of own cell is air, the type of the own cell changes to light. Moreover, if a type of a cell is light, the cell changes to air. And other cells do not change. This transition rule expresses movement of light.

Further, when changing in light, the degree of incidence angle a succeeds the same angle and the amount of movements increases according to a direction of movement.

A direction of movement is determined by the following formula (3).

$$d^{t+1} = \begin{Bmatrix} d_p : if \ |a - \theta_p| < |a - \theta_q| \ then \\ d_q : if \ |a - \theta_p| > |a - \theta_q| \ then \end{Bmatrix} \qquad (3)$$

The direction of movement of light is chosen from two directions of movement assumed, d_p and d_q (If it is 180 degrees to 135 degrees, they are the left or the upper left: refer to Fig.4). Angles θ_p and θ_q are calculated and the angle θ near the degree of incidence angle is chosen as a direction of movement. θ is determined by the formula (4).

$$\theta = sin^{-1} \frac{y}{\sqrt{x^2+y^2}} \tag{4}$$

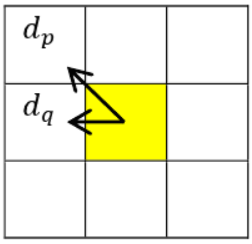

Fig. 4. The example of a direction of movement

3.2.2 Repetitions

If the cell which exists in the move direction of light is a wall or the edge of the screen, another cell is made to change to light and light is moved.

When changing and moving a cell of all the incidence positions to light, the degree of incidence angle is reduced by 1 degree and the simulation is repeated till finish time.

4 APPLICATION OF THE SIMULATOR

4.1 Simulation of Daylight of a Residence

Fig. 5 shows a simulation result of the snapshot daylight at 9:00 a.m. A dark portion expresses a wall and a bright portion expresses a sunshine portion. If a cell has changed to light at the time, the simulator expresses the cell as a sunshine portion.

Moreover, Fig. 6 shows daylight through the daytime. A cell with long time of type of light is expressed more brightly.

These two simulation result (Fig. 5 and Fig. 6) demonstrate that the simulator can be used to evaluate the indoor condition of daylight both at a specific time and during a daytime.

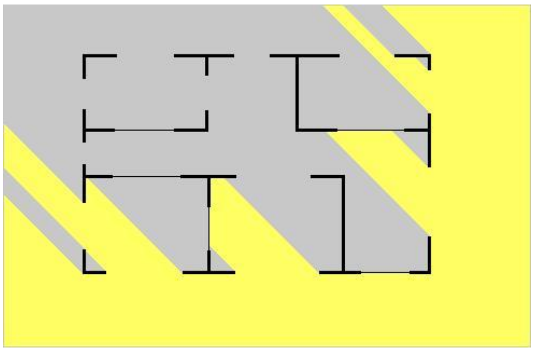

Fig. 5. Daylight of a residence at 9:00

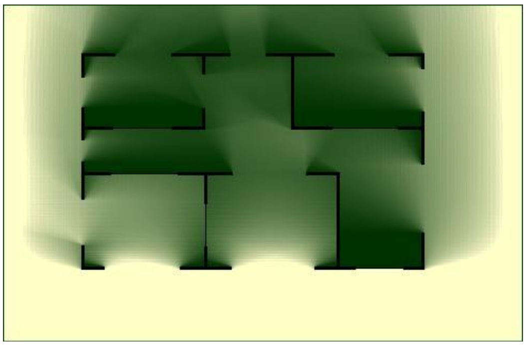

Fig. 6. Daylight of a residence through the daytime

4.2 Simulation of Daylight of a Roof

The amount of insolation of a roof can be checked by applying this simulator.

A roof and the hip of a roof are newly added to the type of a cell. Furthermore, the information on an amount of insolation is added to the state of a cell. The amount of insolation refers to METPV-3 [4].

METPV-3 is a database of insolation in Japan. It has data of various amounts of insolation (such as amount of global solar radiation (the sum of direct sunlight and skylight), the amount of insolation which enters into a slope) in each area.

Fig.7 is the example of a roof used for the simulation. Since an amount of insolation changes with the angles of direction of a roof, it changes a color. The roof on which a color is different is considered that the type of a cell is also different.

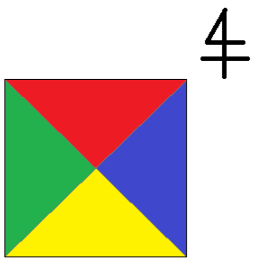

Fig. 7. The example of a roof

Light goes straight on until it strikes upon the hip of a roof. In the roof through which light passed, the amount of global solar radiation is added to the cell which light passed. Moreover, the amount of insolation of skylight is added to the roof through which light did not pass.

Fig. 8 is the simulation result of the amount of insolation of a roof. Table 1 is a setup of a simulation. This figure shows the place with many amounts of insolation more brightly.

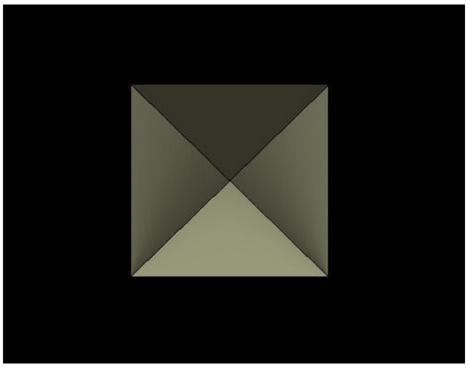

Fig. 8. The amount of insolation of a roof

Table 1. Setup of a simulation

Area	Tokyo
Date	Mid-March
Weather	Shine
A Cell Size	0.01 [m^2]
The angle of gradient of a roof	30°

The fault of this simulation is that the amount of insolation of the top of a roof is smaller than the actual condition. It is necessary to improve by setting up the information such as height.

Fig. 9 is a calculation result of the amount of insolation of the roof of each time. Since the amount of insolation of the roof facing east and west become the maximum around 10:00 and 14:00, respectively, that influence appears in this graph.

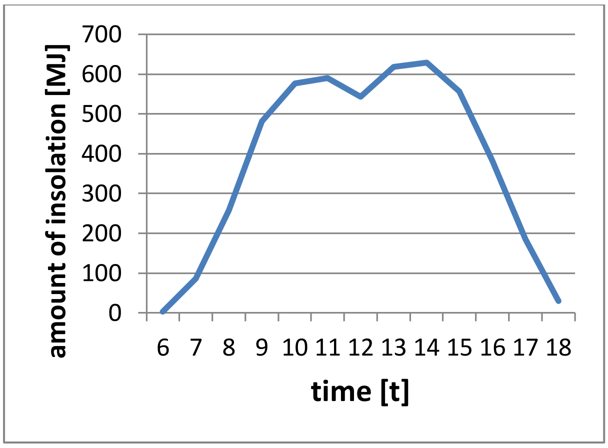

Fig. 9. The amount of insolation of each time

If a part with many amounts of insolation is known, it will be made to reference when performing the simulation such as a photovoltaic generation.

5 DISCUSSIONS

A conventional simulator needs the detailed information on a residence to calculate internal brightness. However, this simulator requires only a floor plan diagram because it does not calculate brightness.

Additional advantage of the simulator comes from the cellular automata model. Because cellular automata can express another new phenomenon easily by adding a new transition rule, the simulator in principle could estimate the room temperature. Since the current simulator could not involve air circulation, it cannot estimate the temperature.

We consider the simulation of a photovoltaic generation as an application of this simulator. The electricity generated of photovoltaic generation is calculable if an amount of insolation is known. If the electricity generated can be predicted only from one image, the advantage of not needing special knowledge will be made. Moreover, a simulation including an atmospheric state (for example, the simulation in the situation where snow lies on the roof) is also considered by using cellular automata.

6 CONCLUSION

A solar insolation simulator is introduced incorporating cellular automata. Simulations demonstrated that the simulator can estimate daylight of a residence using a floor plan diagram.

The simulator could also estimate the amount of insolation of a roof.

REFERENCE

[1] Dr. Christoph F. Reinhart (2010), Tutorial on the Use of Daysim Simulations for Sustainable Design. http://www.daysim.com/pub/Daysim3.0.Tutorial.pdf

[2] Kamata. T (2010), The sunshine simulation method for residences, and a display thing (in Japanese). Japanese Patent 4401377

[3] S. Wolfram (1983), Cellular Automata. Los Alamos Science

[4] NEDO: application (in Japanese) http://www.nedo.go.jp/library/shiryou_application.html

Toward Development of a Strategy to Drive HIV-1 into Self-Extinction through the Error Catastrophe

Kouji Harada[1], Yoshiteru Ishida[2]

[1,2]Toyohashi University of Technology
1-1, Tenpaku, Toyohashi, Aichi 441-8585, Japan
(Tel: 81-532-44-6885; Fax: 81-532-44-6873)

[1]harada,[2]ishida@cs.tut.ac.jp

Abstract: The present study examines a possibility of new AIDS treatment without using anti-HIV-1 drugs to avoid drug resistance. Our idea originated in Eigen [1] is by inducing excess mutations to HIV-1 genome, to drive HIV-1 population to destruction. Namely, we use the high mutation rate of HIV-1 as an underhanded way.

Our study proposes a novel HIV-1 mathematical model considered viral kinetic processes such as mutation, replication, infection and an action of a mutagen to control HIV-1 mutation rate. Through some model simulations by computer it reports to drive HIV-1 population to the error catastrophe by increasing HIV-1 mutation rate.

Keywords: HIV-1, AIDS, Mathematical model, Error catastrophe, Mutagen

1 INTRODUCTION

HIV-1 is the causal virus for AIDS (Acquired Immune Deficiency Syndrome). AIDS treatment mainly depends on drug therapy and now four different types of drugs are used for the therapy. However troublingly all types of drugs easily develop drug resistance if they are used as the sole regimen. In order not to evolve drug resistance, highly active antiretroviral therapy (HAART) based on the administration of at least three different drugs has been executing. However HAART also is somewhat less than perfect in terms of drug adherence because AIDS patients suffer in adverse effects with long-term use. From these reasons, the present study examines a possibility of new AIDS treatment without using drugs. Our idea is by inducing excess mutations to HIV-1 genome, to lead HIV-1 population to destruction. Namely, this study uses the high mutation rate of HIV-1 as an underhanded way.

There were some experimental studies which reported that destruction of a viral population by inducing excess of mutations was achieved. Crotty's group demonstrated inducing excess mutations to poliovirus population by mutagenic action of ribavirin drives poliovirus to error catastrophe, thereby turning a productive infection into an abortive one [2]. Domingo's group reported a similar result on foot-and-mouth disease virus (FMDV) [3].

Meanwhile in the theoretical point of view, quasispecies theory built by Eigen provided a motivation for our study. A viral population structured and maintained by various mutants transiting each other through mutations is called quasispecies [4]. Quasispecies theory suggests when viral mutation rate is crossed a threshold value (called error threshold), viral population formed by the wild type as the primary member changes drastically into a different population dominated by only low fitness mutants This change means that wild type disappears and viral population loses its identity. In terms of HIV-1, it was reported that an estimated HIV-1 mutation rate is near the error threshold value predicted by quasispecies theory, thus HIV-1 barely might keep its identity [5].

Taking the above mentioned background into consideration, the present study proposes a HIV-1 mathematical model considered viral kinetic processes such as mutation, replication, infection and an action of a mutagen to control HIV-1 mutation rate. Through some model simulations by computer it reports it is possible to drive HIV-1 population to the error catastrophe by increasing HIV-1 mutation rate.

2 MODEL

This section proposes a mathematical model to simulate HIV-1 reproduction process. The reproduction process is divided into two phases: (1) replication and mutation process in infected CD4+Tcells and (2) budding and infectious process. First, we introduce a model to simulate HIV-1 replication and mutation process. We consider a quasi-species of HIV-1 population classified into four types: fast or low replication type and viable or defective type referring to [6]. We assume the viable type maintain an ability to permit replication and infection; the defective one can permit replication but has a deficiency of an ability for infection. In the viable (defective) type, we denote fast replicators to *V** (*D**); slow ones *v** (*d**) where infected state be denoted by an asterisk. The fast replicators have an average of *R* (greater than one) offspring; slow ones have *r* (less than one).

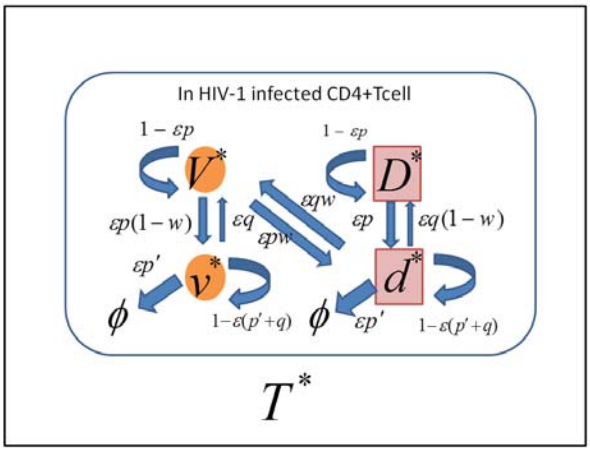

Fig. 1: HIV-1 kinetic processes of viral replication and mutation in HIV-1 infected CD4+T cell.

We assume mutational events occur between the four types. Fig. 1 is a schematic representation of possible mutations between them. This model assumes that (1) a fast replicator mutates a slow one with a mutation rate *p*; the inverse mutation which is called "backward mutation" occurs with a rate *q*, whose value is known very small and (2) small ratio (*w*) of mutated viable HIV-1 population mutates the defective type; the inverse mutation occurs at the same ratio. The replication and mutation process in Fig. 1 is formulated as a population dynamics:

$$\frac{dP_{V^*}}{dt} = F_{V^*}(P_{V^*}, P_{v^*}, P_{d^*}) \equiv R(1-\varepsilon p)P_{V^*} + r\varepsilon qP_{v^*} + r\varepsilon qwP_{d^*}$$

$$\frac{dP_{v^*}}{dt} = F_{v^*}(P_{V^*}, P_{v^*}) \equiv R\varepsilon(1-w)P_{V^*} + r(1-\varepsilon(p'+q))P_{v^*}$$

$$\frac{dP_{D^*}}{dt} = F_{D^*}(P_{D^*}, P_{d^*}) \equiv R(1-\varepsilon p)P_{D^*} + r\varepsilon q(1-w)P_{d^*}$$

$$\frac{dP_{d^*}}{dt} = F_{d^*}(P_{V^*}, P_{d^*}) \equiv R\varepsilon pwP_{V^*} + r(1-\varepsilon(p'+q))P_{d^*}$$

We next formulate HIV-1 infection and budding process represented schematically in Fig. 2. A role model of the process was proposed by Perelson[7] and Wei[8]. Our formulation is based on the role model. *T* and *T** denote uninfected and infected CD+4 T cells respectively. The four types of "free" HIV-1 are denoted by the previously given symbol without asterisk which means infected state. Uninfected CD+4 T cells are recruited at a birth rate λ and killed at a death rate *d*; infected ones are killed at δ. Viable and defective HIV-1 is released at a rate γ and s respectively from infected CD4+Tcells.

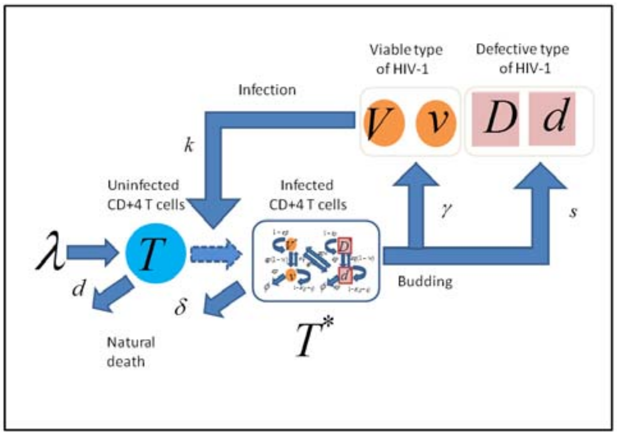

Fig. 2: HIV-1 infection and budding processes

The mutation and replication process of HIV-1 in infected CD4+Tcells and an infection and budding process of free HIV-1 are described by the following equations:

$$\frac{dP_T}{dt} = \lambda - dP_T - k(P_V + P_v)P_T$$

$$\frac{dP_{T^*}}{dt} = k(P_V + P_v)P_T - \delta P_{T^*}$$

$$\frac{dP_{V^*}}{dt} = F_{V^*}(P_{V^*}, P_{v^*}, P_{d^*}) + kvP_T - \delta P_{V^*} - \gamma P_{V^*}$$

$$\frac{dP_{v^*}}{dt} = F_{v^*}(P_{V^*}, P_{v^*}) + kvP_T - \delta P_{T^*} - sP_{d^*}$$

$$\frac{dP_{D^*}}{dt} = F_{D^*}(P_{D^*}, P_{d^*}) - \delta P_{T^*} - sP_{D^*}$$

$$\frac{dP_{d^*}}{dt} = F_{d^*}(P_{V^*}, P_{d^*}) - \delta P_{T^*} - sP_{d^*}$$

$$\frac{dP_V}{dt} = \gamma P_{V^*} - cP_V$$

$$\frac{dP_v}{dt} = \gamma P_{v^*} - cP_v$$

$$\frac{dP_D}{dt} = \gamma P_{D^*} - cP_D$$

$$\frac{dP_d}{dt} = \gamma P_{d^*} - cP_d$$

3 RESULTS AND DISCUSSIONS

3.1 A Mutagen's Action

Our scenario for AIDS treatment is to drive HIV-1 population to destruction due to the increase of the viral mutation rate by a mutagen. We examined feasibility of the scenario in simulations by controlling the parameter ε representing mutagen's action. Fig. 3 shows time series of viral load of free HIV-1 (V) when ε is 0.3, 0.6 and 0.9. The values of parameters except ε are $\lambda=10^4$ ml/day k=8x10^{-7} ml/day c=13 day^{-1} δ=0.7 day^{-1}, d=0.01 day^{-1}, R=1.3, r=0.1, p=0.5, q=0.09, w=0.2, p'=0.8 [9]. When a mutagen's action is relatively weak (ε=0.3), after a viral load once decreases, it continues to increase and finally leads to developing AIDS; when the mutagen's action is relatively strong (ε=0.9), a viral load continue to decrease slowly and viral eradication is achieved. This case indicates our scenario is feasible. Fig. 3 also clarifies the threshold value of ε of when the downward trend of the viral load changes into the upward trend is 0.8.

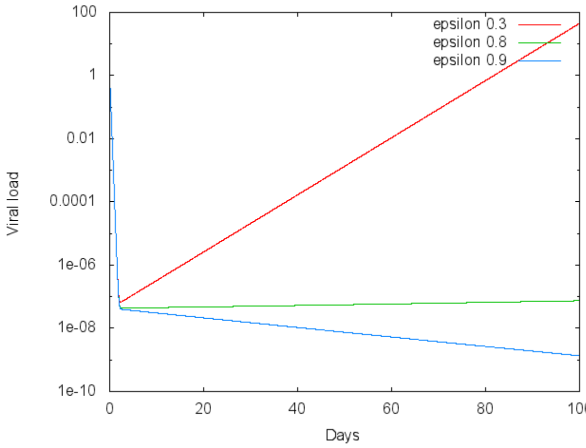

Fig. 3: The changes of time series of viral load over three cases of epsilon value

3.2 The Relationship between the Threshold Value of ε and a Replication Rate, R

We estimated threshold values of ε over the change of the parameter R. Fig. 4 shows the result. The figure indicates the threshold value of ε monotonically increases as parameter R increases. This means that if HIV-1 produces more offspring per replication, destructing HIV-1 population requires intensifying the mutagen's action ε.

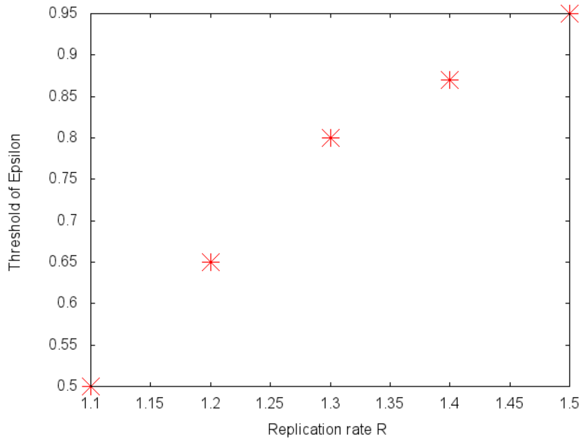

Fig.4: Threshold of the parameter ε versus viral replication rate R

3.3 Mutational Meltdown

The quasi-species theory proposes one scenario of viral extinction that when viral mutation rate is over the threshold value, the wild type disappears from the population and low fitness mutants dominate the population. This type of viral extinction means to lose the identity of the population.

This scenario in the case of our model is interpreted as the following condition:

$$P_V, P_{V*} = 0;\ P_v, P_{v*}, P_D, P_{D*}, P_d, P_{d*} \neq 0 (t \to +\infty).$$

Now we are studying whether this type of viral extinction occurs.

As another scenario of viral extinction, "mutational meltdown" is known. This scenario mentions all genotypes in the quasi-species disappear simultaneously. In the case of our model, this scenario is described as the followings:

$$P_V, P_{V*}, P_v, P_{v*}, P_D, P_{D*}, P_d, P_{d*} = 0\ (t \to +\infty).$$

The viral extinction observed in Fig. 3 corresponds to this type of extinction because the sum of four types of HIV-1 population decreases toward zero as displayed in Fig. 5

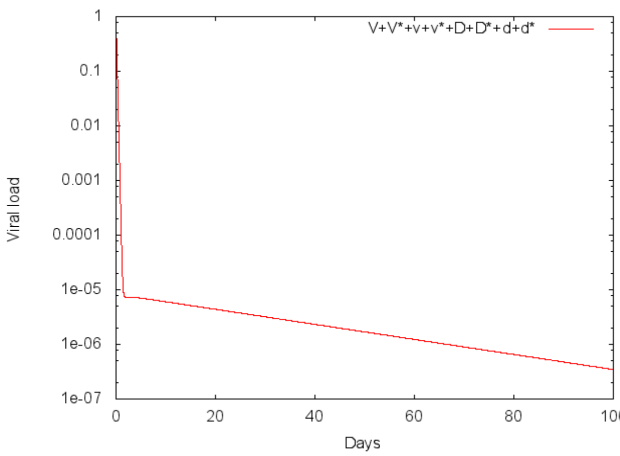

Fig. 5: A time series of the total viral population.

ACKNOWLEGEMENTS

This study was supported by Grant-in-Aid for Scientific Research(C) No.22500273 of Japan Society for the Promotion of Science (JSPS) from 2010 to 2011. We are grateful for their support.

REFERENCES

[1] Eigen M (2002), Error catastrophe and antiviral strategy. PNAS 49(21):13374-13376

[2] Crotty S, Cameron CE, Audino R (2001), RNA virus error catastrophe: Direct molecular test by using ribavirin. PNAS 98: 6895-6900

[3] Domingo E (2000), Viruses at the edge of adaptation. Virology 270:251-253

[4] Nowak MA (1992), What is a Quasispecies? Trends Ecol. Evol. 7(4):118-121

[5]Nowak MA (1990), HIV mutation rate. Nature 347:522

[6] Iranzo J, Manrubia SC (2009), Stochastic extinction of viral infectivity through the action of defectors. EPL 85:18001

[7] Perelson AS, Neumann AU, Narkowitz M, et al (1996), HIV-1 dynamics in vivo: virion clearance rate, infected cell life-span, and viral generation time. Science 271:1582-1586

[8] Wei X, Ghosh SK, Taylor ME, et al (1995), Viral dynamics in human-immunodeficiency-virus type-1 infection. Nature 373:117-122

[9] Callaway DS, Perelson AS (2002), HIV-1 infection and low steady state viral loads. Bull.Math.Biol. 64:29-64

The Seventeenth International Symposium on Artificial Life and Robotics 2012 (AROB 17th '12),
B-Con Plaza, Beppu, Oita, Japan, January 19-21, 2012

A Pattern Formation Mechanism of a Cellular Automaton Evolving on a Mutual Determination Rule of Variables and a Dynamics

Kouji Harada[1], Yoshiteru Ishida[2]

[1,2]Toyohashi University of Technology
1-1, Tenpaku, Toyohashi, Aichi 441-8585, Japan
(Tel: 81-532-44-6885; Fax: 81-532-44-6873)

[1]harada,[2]ishida@cs.tut.ac.jp

Abstract: The present study has an interest on complexity produced by removing the original boundary between different classes of concepts and it removes a boundary between a state variable and its dynamics by interacting them circularly on a two dimensional cellular automaton. It clarifies that removing the boundary creates the complexity of changing simple periodic orbits into attractive ones and proves a theorem about a period which characterizes periodic behaviors observed in simulations.

Keywords: Cellular automaton, Boundary, Complexity, Periodic attractor

1 INTRODUCTION

The cellular automaton is a computation model driven by a simple rule which describes the time evolution of a state of each cell on a lattice space. Despite its simplicity, it is much applied to simulating from life phenomena to physical ones such as crystal growth, turbulence and so on. As a typical example of cellular automaton, "life game" invented by Conway is very popular [1]. His model is thought to be able to simulate various growth patterns of living systems therefore it is called Life game. Life game's rule is quiet simple: a state of a cell at the next time is determined by the total number of active cells in its neighborhood. Namely the future states are directly determined by the past ones (the state is driven by itself); the dynamics is invariant on time. Namely there is a boundary to discriminate the state variable and its dynamics. Most of the cellular automata are modeled by the same formulation.

Meanwhile, the present study has an interest on complexity produced by removing the boundary between different class of concepts. In immunology, Jerne removed the discrimination between antibody (recognizer) and antigen (recognized entity) whereby built a new immunological theory called idiotype network theory [2]. In computer science, Lisp computer language opened a possibility of new calculation called λ calculation by removing the boundary between function (rulers) and dummy arguments (subject) [3]. In game theory, we tried to remove a boundary between player's move and its strategy by introducing a meta-rule to interact them circularly [4][5]. Masumoto and Ikegami achieved openness of a strategy space by rebuilding a framework of the game by λ calculus [6].

This study focuses on removing a boundary between a state variable and its dynamics by introducing a circular interaction between them.

This paper is composed of six sections. The second section proposes a standard two dimensional cellular automaton driven by a basic rule without interaction between state variables and its dynamics and discusses its behaviors. This standard model provides a control against a new model considered the interaction. The third section proposes new two dimensional cellular automaton, which introduces a reciprocal determination process between a state variable and its dynamics. The firth section discusses an analogous relationship between the new model and a spatial game model. In the fifth section, considering the fact that the space-temporal patterns of the new model has some 1-,3-,6- and 9-period attractors, it proves two lemma and one theorem about a period of these attractors. The last section discusses how difference introducing the reciprocal determination process makes on the dynamical behaviors.

2 ONE WAY DETERMINATION FROM A DYAMICS TO ITS VARIABLES

We consider a two dimensional square lattice with a size of its side, N. To designate a site of each cell, we prepare a horizontal and vertical axis with a suffix *i*, *j* respectively and place the origin at the top left of the lattice. The suffixes *i* and *j* take an integer value from 0 to *N*-1. We let a symbol $A^r_{i,j}$ to denote a state variable of a lattice cell (*i*, *j*) at the time *r* and the variable takes which of the two states:0 and 1. As a dynamical system of state variable $A^r_{i,j}$, we consider a linear system as the followings:

$$A^{r+1}_{i,j} = F(\vec{b}, \vec{A}^r_{i,j}) \equiv \vec{b} \cdot \vec{A}^r_{i,j}, \tag{1}$$

where $\vec{b}$ is a vector of coefficient parameters and is defined as $\vec{b} = (b_0, b_1, b_2, b_3, b_4, b_5, b_6, b_7, b_8)$ but $b_k = 1, b_i = 0 (i \neq k)$; $\vec{A}^{r+1}_{i,j}$ is defined as $(A^r_{i-1,j-1}, A^r_{i,j-1}, A^r_{i+1,j-1}, A^r_{i+1,j}, A^r_{i+1,j+1}, A^r_{i,j+1}, A^r_{i-1,j+1}, A^r_{i,j})$. As shown in Fig. 1, each component of the vector $\vec{A}^r_{i,j}$ arranges in a clockwise fashion from the upper left of the site (*i*,*j*)

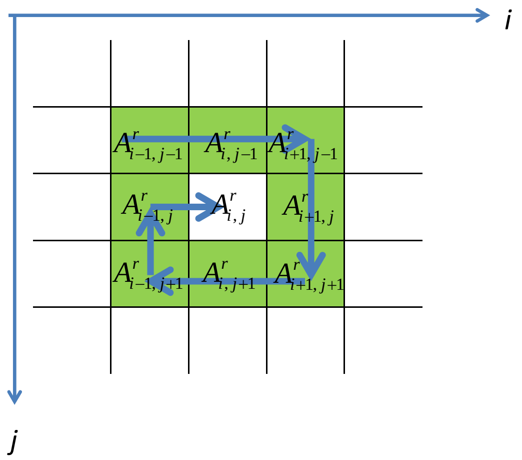

Fig.1. Arrangement of each component of the vector $\vec{A}^r_{i,j}$

2.2 Dynamic behaviors

Assuming the periodic boundary, a time evolution of spatial-temporal pattern of state variables is easily imagined from the model's definition. Only periodic motions in one direction which is determined by the vector $\vec{b}$ are observed. For example, when *k* is one, any spatial-temporal pattern moves downwards. In another case of *k* is three, any pattern moves leftwards. A period *T* is determined by *N* and is given as divisor of *N*. For example, *N* is four, *T* is one, two and four.

3 RECIPROCAL DETERMINATION BETWEEN VARIABLES AND ITS DYNAMICS

This study interests a reciprocal determination process between the state variables and its dynamics thus considers to update the parameter $\vec{b}$ through the time evolution of the state variables $\vec{A}^r_{i,j}$.We define a function $g(\vec{A}^r_{i,j})$ to calculate the sum of all cells' state in the Moore neighborhood of the cell (*i*,*j*) as

$$g(\vec{A}^r_{i,j}) = \sum_{i'=i-1}^{i+1} \sum_{j'=j-1}^{j+1} A^r_{i',j'} \quad . \tag{2}$$

Then through the value of $g(\vec{A}^r_{i,j})$ we update the parameter $\vec{b}$ as following:

When $g(\vec{A}^r_{i,j})$ is equal with *k*,

$$b^r_i = \begin{cases} 1 & (i = k) \\ 0 & (i \neq k) \end{cases} \tag{3}$$

After all, Eq.(1) results in

$$A^{r+1}_{i,j} = F(\vec{b}^r, \vec{A}^r_{i,j}) \equiv \vec{b}^r \cdot \vec{A}^r_{i,j}. \tag{4}$$

Fig.2 shows a situation that the state variable and its dynamics determine circularly.

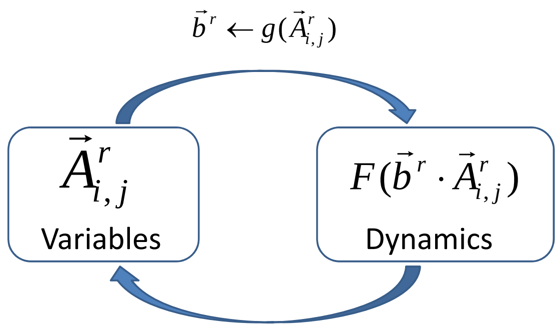

Fig.2 Reciprocal determination process between variables and its dynamics

4 A VIEW FROM SPATIAL GAME MODELS

Our proposed model is a particular kind of spatial game systems. In the common spatial games, a player has a game with each of its neighborhood players and in the next round uses the move of the highest scoring player among them.

We mention the correspondence relationship between the common spatial game model and our proposed model. We let the state variable $A^r_{i,j}$ to represent a move of a player at the site (*i*,*j*) at a certain time *r* thus a player's move is 0 or 1.

When the player (*i*,*j*) has a game with each of its Moore neighborhood players, our model determines the highest scoring player by the function $g(\vec{A}^{r}_{i,j})$. Concretely speaking, when the value of g is k, our model let the highest scoring player to be the one in the k-th site in the clockwise fashion from the top-left of the site (i,j). Fig. 3 shows a case of k is 4. Meanwhile, we can construe determining $A^{r+1}_{i,j}$ by Eq. (4) as for the player (i,j) to copy the highest scoring player's move as its own move at the next round, which is known as the copy strategy in the common spatial games.

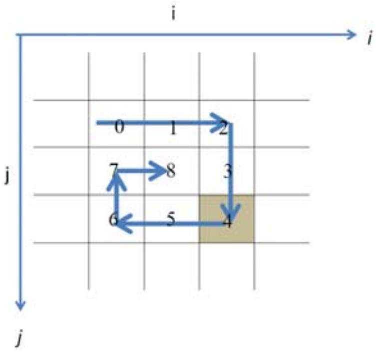

Fig. 3 A rule to assign k to each site. When k is 4, gray colored cell is selected as the highest scoring player's site.

In the present game, what sort of game situation must be established for a player to win? Only when not only the player but also all of the neighborhood players choose the same move 1, the player can be the winner.

The uniform state of all players taking the specific move 0 or 1 is unstable. Because when one player takes a opposite move in the uniform state, the system unable to return the original state.

5 THEOREMS ABOUT PERIODIC BEHAVIORS

We examined all of spatial temporal patterns observed in the case of the system size is 3 and clarified the emerged patterns are periodic and they are classified into 1, 3, 6 and 9 period. Fig. 4 is a typical example of the observed periodic behaviors. This section discusses why the observed period is limited to multiples of 3. We first mention a lemma on determination of the period. For the proof, we define two symbols: P^r and $S_{L,L'}$. Let P^r to be a configuration pattern of all players' action at the round r. Let $S_{L,L'}$ to be a translation to shift a configuration pattern P by L and L' in a vertical and horizontal direction respectively.

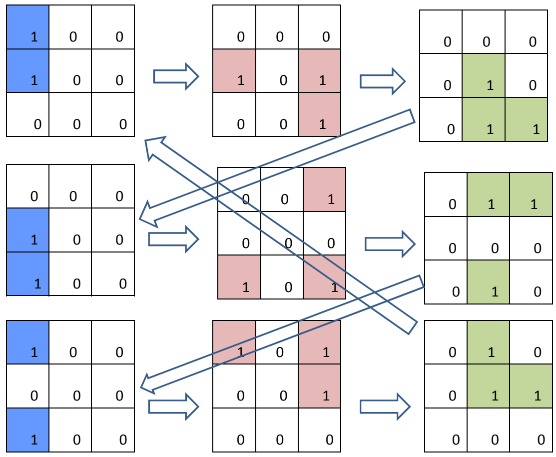

Fig. 3 Period-9 behavior

Lemma 1

Assume L, L' and n such that $S_{L,L'}P^1 = P^{n+1}$ exist, then $S_{L,L'}P^r = P^{n+r}$ for any r succeeds.

Proof

The assumption $S_{L,L'}P^1 = P^{n+1}$ succeeds thus for any i, j,

$$A^1_{i,j} = A^{n+1}_{i+L,j+L'}. \tag{5}$$

Eq. (5) leads to

$$\vec{A}^1_{i,j} = \vec{A}^{n+1}_{i+L,j+L'}. \tag{6}$$

And from Eq. (6),

$$g(\vec{A}^1_{i,j}) = g(\vec{A}^{n+1}_{i+L,j+L'}) \tag{7}$$

Due to Eqs. (6) and (7), for any i, j

$$A^2_{i,j} = A^{n+2}_{i+L,j+L'} \tag{8}$$

Therefore,

$$S_{L,L'}P^2 = P^{n+2} \tag{9}$$

Through the same discussions, for any r,

$$S_{L,L'}P^r = P^{n+r} \tag{10}$$

On the basis of lemma 1, we prove a theorem on the period of the dynamics.

Theorem

Assume $S_{L,L'}P^k = P^{n+k}$ and $S^r_{L,L'}P^1 = P^1$ then the period T is given as $n \times r$.

Proof

By the first assumption,

$$P^{2n+1} = S_{L,L'}P^{n+1} = S^2_{L,L'}P^1 \tag{11}$$

Applying S to Eq. (11) for r-2 times,

$$P^{r\times n+1} = S^r_{L,L'}P^1 \tag{12}$$

By the second assamption and Eq. (1),

$$P^{r\times n+1} = P^1 \tag{13}$$

So that

$$T = r \times n. \tag{14}$$

The following lemma answers how r is determined.

Lemma 2

Assume $S^{r}_{L,L'}P^{1} = P^{1}$, $L \neq 0$ and $L' \neq 0$ then

$$r = L.C.M\left(L.C.M(N,|L|)/|L|,\ L.C.M(N,|L'|)/|L'|\right).$$

But if $L(L') = 0$ then

$$r = L.C.M(N,|L|)/|L| \ \ (L.C.M(N,|L'|)/|L'|)$$

where $L.C.M(x,y)$ represents least common multiple of x and y.

Referring to lemma 2, we try to answer why the period is the multiple of 3 when the system size N=3.

All possibilities of (L,L') on the parallel translation $S^{r}_{L,L'}$ is (1,0),(0,1),(1,1),(2,0),(0,2),(2,1),(1,2) and (2,2).

1. $(L,L') = (1{,}0),(01)$
   $r = L.C.M(3{,}1) = 3.$
2. $(L,L') = (1{,}1)$
   $r = L.C.M\left(L.C.M(3{,}1), L.C.M(3{,}1)\right)$
   $= L.C.M(3{,}3) = 3$
3. $(L,L') = (2{,}0),(0{,}2)$
   $r = L.C.M(3{,}2)/2 = 6/2 = 3.$
4. $(L,L') = (2{,}1),(1{,}2)$
   $r = L.C.M\left(L.C.M(3{,}2)/2, L.C.M(3{,}1)/1\right)$
   $= L.C.M(3{,}3) = 3$
5. $(L,L') = (2{,}2)$
   $r = L.C.M\left(L.C.M(3{,}2)/2, L.C.M(3{,}2)/2\right)$
   $= L.C.M(3{,}3) = 3$

In all the cases, r is 3 thus based on the theorem the period is limited to the multiple of 3. This result is consistent with the fact that the observed period is 3, 6 and 9.

6 DISCUSSIONS

The main interest of the present study is what is the characteristic behaviors created by the reciprocal determination process between the variable and its dynamics. To clarify this question, we prepared two models: the former is not taken the reciprocal determination process between the variable and its dynamics into consideration and the latter is done, and examined the difference of behaviors between the former and the latter. The both models have periodic orbits but only the latter's periodic orbit is "attractive". Fig. 5 displays 3-period attractor and some part of its basin structure and shows the process of 6 different spatial patterns suctioned into the 3-periodic orbit.

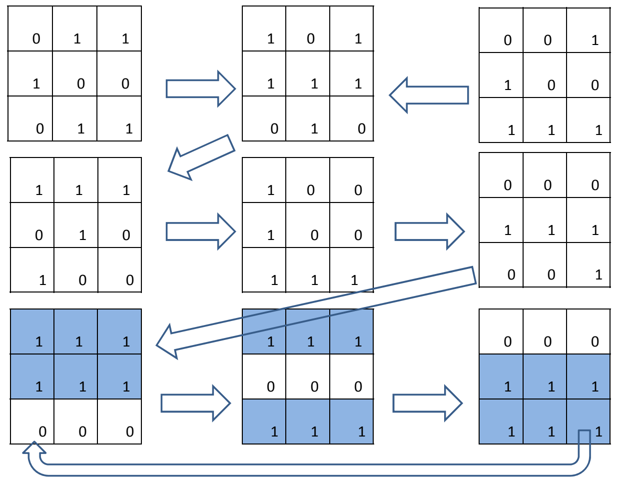

Fig. 5 3-periodic attractor

As a future work, we will clarify why non attractive periodic orbits transmutes into attractive ones by introducing the reciprocal determination process between the variable and its dynamics.

ACKNOWLEGEMENTS

This study was supported by Grant-in-Aid for Scientific Research(C) No.22500273 of Japan Society for the Promotion of Science (JSPS) from 2010 to 2011. We are grateful for their support.

REFERENCES

[1]Mertin G (1970). Mathematical games. Scientific American 223:120-123

[2]Jerne NK. (1974) Towards a network theory of the immune system. Ann Immunol. 125C(1-2): 373-89

[3]McCarthy J (1960) Recursive functions of symbolic expressions and their computation by machine, Part I. Comm. ACM. 3(4): 184–195

[4]Harada K, Ishida Y (2010) A Note on Dynamical Behaviors of a Spatial Game Operated on Intercrossed Rules. Lecture Notes in Computer Science 6278: 637-644

[5]Harada K, Ishida Y (2011) Emergence of observable rules in a spatial game system. Artificial Life and Robotics, in press.

[6]Masumoto G, Ikegami T. (2005) A New formalization of a meta-game using the lambda calculus. BioSystems. 80:219-231.

The Seventeenth International Symposium on Artificial Life and Robotics 2012 (AROB 17th '12),
B-Con Plaza, Beppu, Oita, Japan, January 19-21, 2012

Network Rewiring in Self-Repairing Network: from Node Repair to Link Rewire

Y. Ishida, K. Tanabe

Toyohashi University of Technology,
1-1 Hibarigaoka Tenpaku-cho, Toyohashi, Aichi 441-8580, Japan
(Tel.: +81-532-44-6895; Fax: +81-532-44-6895)
E-mail: ishida@cs.tut.ac.jp

Abstract: Among self-action networks: self-recognition network and self-repairing networks, the self-repairing network allows the state change of nodes as a result of action (repair). The self-repair network is extended to allow network change as a result of action (rewire). Self-rewiring algorithm is also extended from the self-repairing algorithm. The extended algorithm can be applied to several problems such as stable marriage problem and distance adjustment problem. Comparison between node repair and link rewire as well as further extension will be discussed.

Keywords: Network rewiring, self-action network, self-repairing network, probabilistic algorithm.

1 INTRODUCTION

Dynamic network has been attracting attention for large-scale systems such as genetic network, collaboration network. Preferential attachment of link has been studied extensively after pioneering work by Barabási, Albert and Jeong [1]. In contrast to such dynamic and growing networks, rewiring networks, which assumes preferential rewiring (of existing links) [2] rather than attachment also have been studied. The model and algorithm proposed here belongs to the latter class: network rewiring models. The self-rewiring algorithm proposed can also be understood as a generalization of Gale-Shapley algorithm [3, 4].

We have been studying self-action networks where the actions by nodes through arcs mutually affect the state of nodes, and the state of nodes in turn affects the result of the actions. As self-action networks, two networks (i.e., self-recognition network [5, 6, 7] and self-repairing network [8]) has already been proposed. The remarkable feature of self-action networks is that each agent (expressed as a node in the network) not only acts on other agents that are connected (expressed by an arc in the network) but also being acted from other agents connected. This paper proposes yet another self-action network: a self-rewiring network as an extension of self-repairing network. In the self-rewiring network, each agent indirectly acts on other agents through reconfiguration of arcs (or edges).

Self-recognition network assumes recognition of other agents as the self-action. Expressed by a graph, agents correspond to nodes; recognition to arcs; and results of the recognition to sign associated to the arc.

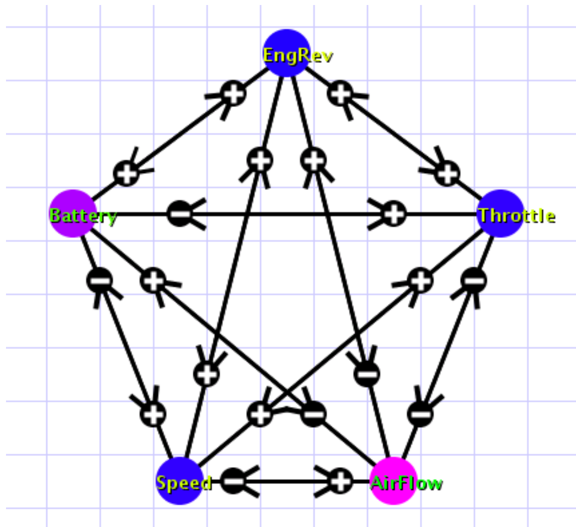

Fig.1 An example of self-recognition netwo rk for automobile engine diagnosis.
EngRev: Engine revolutions; Battery: Batt ery voltage. Gray level in the nodes indicat es credibility. Dark nodes correspond to hig h credibility, while light nodes to low credi bility (i.e. evaluated as faulty) [6].

Fig. 1 shows an example of self-recognition network expressed by a graph. The self-recognition network and technology to build the network have been extensively studied to apply to automobile engine [6], home security [9], motherboard [10], and information security [11]. The self-recognition network can be technique to recon ciliate and unify the observed data and inference, similarly to data reconciliation and can be related to data assimilation [12]. The self-recognition network where the recognition is based on the physical relation is also comparable to on-line simulation [13] where missing data will be inter- or extrapolated based on the observed data.

Self-repairing network, on the other hand, assumes repairing on other agents as the self-action. It can be expressed by a graph similarly to the self-recognition network. However, to derive significant results such as critical phenomena for a network cleaning problem [6], regular graph (as is often the case in cellular automata) is often assumed. While the self-recognition network assumes sensor networks as a potential application area, the self-repairing network assumes actuator network for applications. Both self-recognition and self-repairing network can be applied to a computer network where recognition as well as (software) repair are possible.

Section 2 briefly reviews the self-repairing network. Section 3 proposes a self-rewiring network and self-rewiring algorithm based on the self-repairing network. Section 4 presents possible applications to stable marriage problem and distance adjustment problem that intrinsically require network rewiring.

2 SELF-REPAIRING NETWORKS

A self-repairing network consists of agents capable of repairing other agents connected. In this study, each agent is placed at each node of one-dimensional lattice (Fig. 1) with a periodic boundary condition (leftmost

Fig.2 Cellular automaton with one-dimensional lattice and two states: normal (0) and abnormal (1) [6]

agent and rightmost agent are connected). Each agent has two states: normal (0) and abnormal (1).

Each agent tries to repair its neighbor agents. However, since the repairing is done possibly by abnormal agents, the repair could damage the neighbor agents rather than repair. Frequency of the repair trial is controlled by a parameter: repair rate ***Pr***. As shown in Fig. 3, the repair will be successful with a rate ***Prn*** (the repair success rate by normal agents) when the repair is done by a normal agent, and with a rate ***Pra*** (the repair success rate by abnormal agents) when it is done by an abnormal agent.

Self-repairing network consists of three elements (***U***, ***T***, ***R***) where ***U*** is a set of nodes, ***T*** is a topology connecting the nodes, and ***R*** is a set of rules of the interaction among nodes. A set of nodes is a finite set with ***N*** nodes, and the topology could be n-dimensional

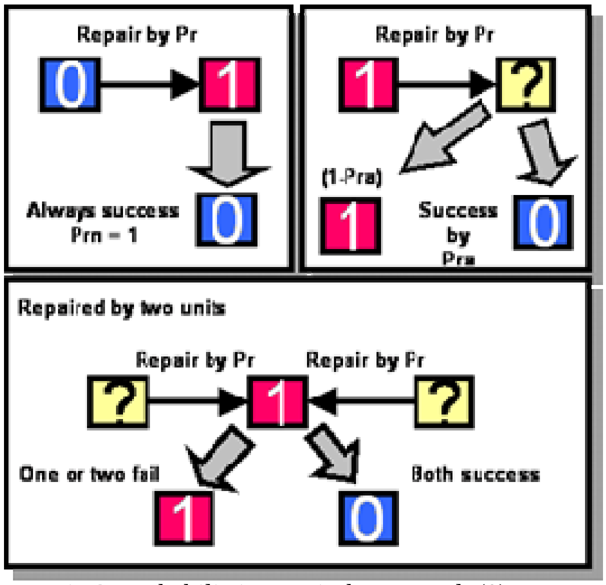

Fig.3 Probabilistic repair by normal (0) agents (*above left*) and by abnormal (1) agents (*above right*). Repair by two agents (*below*) [6].

array, complete graph, random graph, or even scale-free network where each node could have *S* neighbors for each nodes with a boundary condition, i.e. the structure of the array is a ring with node 1 adjacent to the node *N*. Also, we restrict the case where each node has a binary state: normal (0) and abnormal (1). Each node tries to repair the adjacent nodes in a synchronous fashion with a probability $\boldsymbol{P_r}$. The repairing will be successful with the probability $\boldsymbol{P_{rn}}$ when it is done by a normal node, but with the probability $\boldsymbol{P_{ra}}$ when by an abnormal node ($\boldsymbol{P_{ra}} < \boldsymbol{P_{rn}}$). The repaired nodes will be normal when all the repairing is successful. Thus, when repairing is done by the two adjacent nodes, all these two repairing must be successful in order for the repaired node to be normal.

3 SELF-REWIRING NETWORKS

Self-repairing network and its probabilistic repairing algorithm have been extended to include not only node repair but also link rewiring. The extended model and algorithm can deal with a wide variety of problems that require link rewiring to be solved. Such problems range from a naïve matching problem of Stable Marriage Problem (that requires link rewiring in bipartite graph) to a practical adjustment problem of inter satellites distance in the system of autonomous networked satellites.

In the extension, each node will evaluate the current link and rewire it from the current target node to other target node by conditions specific to the problem. Since

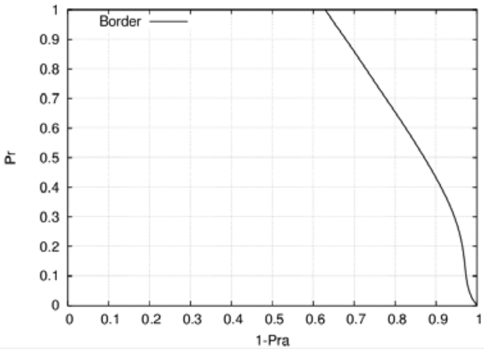

Fig.4 Frozen Phase (*left region* where all the agents are normal) and Active Phase (*right region* where some units remain to be abnormal) [6].

the evaluation will be done by a node with limited information, the evaluation could be wrong, hence the "double edged sward" would take place similarly to the original self-repairing network.

Self-repairing network with the probabilistic repairing algorithm is known to have a specific threshold in model parameters to eradicate all the abnormal nodes. This paper investigates if such specific threshold exists for the extended Self-repairing network in the network rewiring. If the threshold exists, engineering should be carried out in the close vicinity of the threshold, for the phase may be critically changed across the threshold, while the parameter regions far from the threshold need not be carefully managed.

Although the self-repairing networks assume a fixed network, the self-rewiring networks allow the network to change the connection. The state of nodes: normal or abnormal depends on the connection of the node. Normal state should be understood as the state that the agent cannot be better by changing the links incident to the node, while abnormal state as the state that agent can improve by changing the links. The self-rewiring algorithm can be similarly defined to the self-repairing algorithm.

[Step 1] Each agent will be activated with a probability *Pr*.

[Step 2] For the activated agent, try to activate the link with a probability proportional to the preference.

[Step 3] The other agent connected by the activated agent will accept the connection, if the connection improves the agent.

With this algorithm, all the agents become normal state, and this all normal state is a probabilistically stable. That is, once all nodes become normal state with a certain configuration, then transition probability to other configuration is smaller than the transition probability to the attained configuration.

4 APPLICATIONS OF THE SELF-REWIRING NETWORK

4.1 Stable Marriage Problem

The Stable Marriage Problem (SMP) assumes n women and n men each of them has an ordered preference list (or a rank) without tie to the opposite sex. As in the example shown in Fig. 5, the men m_2 has an ordered preference list (w_2, w_3, w_1) or a rank (2, 3, 1), which means m_2 likes w_2 best, and he prefers w_3 to w_1.

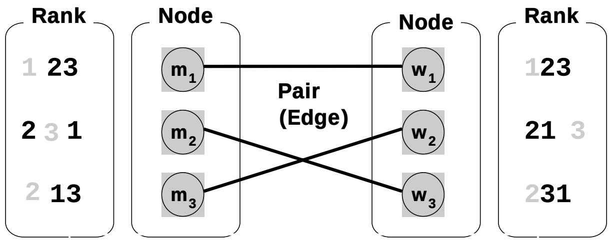

Fig. 5. An illustration of Stable Marriage Problem with size three.

Under the above assumptions, SMP seeks for the complete matching between n women and n men, which satisfies stability. The stability requires the concept of blocking pair. Two pairs (m_i, w_p) and (m_j, w_q) are blocked by the pair (m_i, w_q) if m_i, prefers w_q to w_p and w_q prefers m_i to m_j. For example, a pair (m_2, w_3) and (m_3, w_2) will be blocked by the pair (m_2,w_2). A complete matching without being blocked is called *stable* matching.

Self-rewiring algorithm applied to SMP may be summarized as follows:

[Step 1] For each agent, activate the agent with a probability *Pr*.

[Step 2] For the activated agent, try to find a higher rank with a probability proportional to the preference.

[Step 3] For the new partner agent being proposed in the previous step, accept the proposal if the new partner agent does not have the current partner, or the new partner agent has a higher rank on the proposing agent than the current partner.

In selecting agent in the step 1, the agents can be selected from male (female, or don't care) agent if the algorithm assumes male (female-optimal, or gender does not matter) as the proposing side (Fig. 6).

4.2 Simulation Result

We consider an instance of SMP with size 3 where every man has a fixed ordered preference list (w_0, w_1,

w_2) and every woman also has a fixed ordered preference list (m_0, m_1, m_2). In the simulation below, male is set to be the proposing side. In the Gale-Shapley algorithm, male-optimal solution will be obtained when the proposing side is fixed to the male side. In the self-rewiring algorithm, however, female side can attain optimal solution with a certain probability (Fig. 6).

In each plots of Fig. 6, horizontal axis is time step and vertical axis the rank attained for each individual shown line type. Figures left are the attained rank for male; and those right are the rank for female. Upper figures are when *Pr* =0.3 and those lower are when *Pr* =0.9. As *Pr* increases, female side attains happier matching (closer to female-optimal). This is because higher *Pr* would lead to more simultaneous proposals to a woman, which will give the woman a chance to select her preferred proposal.

Additional difference from the Gale-Shapley algorithm is on the concept of stability. Although Gale-Shapley algorithm obtain a stable matching, the network rewiring algorithm would obtain the distribution of matchings including all the stable matchings as well as the unstable ones with blocking pairs with a smaller probability than the ones for stable matchings (Fig. 6).

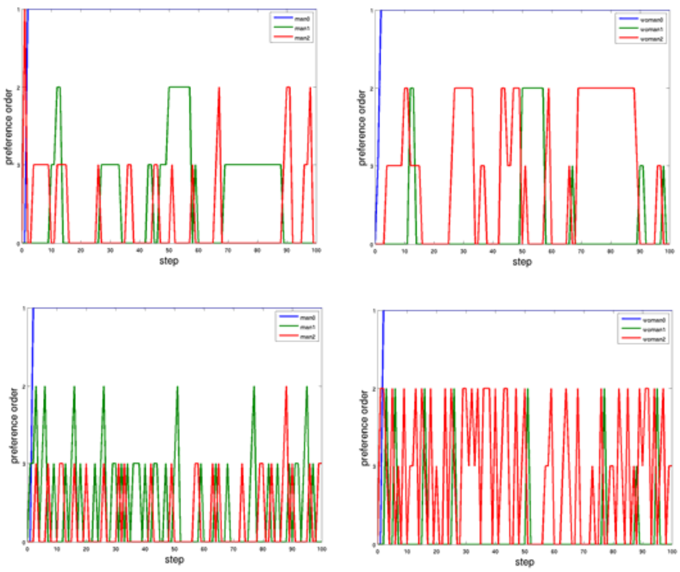

Fig. 6 Probabilistic rewiring applied to the Stable Marriage Problem with size three.

5 DISCUSSIONS

Since the self-rewiring network and algorithm are extension of the self-repairing network and algorithm, they share some commonalities. If we regard the normal state of agents as favorable state of agents (as in the Stable Marriage Problem above) defined similarly to the Nash equilibrium that any rewiring would not improve the satisfaction of agents, then self-rewiring algorithm also allows the normal state to spread.

Although simple and naïve problem of Stable Marriage Problem is used for illustrative purpose, the self-rewiring algorithm could be used for many other problems such as a distance adjustment problem (agents placed in a space will adjust their relative positions to meet a given constraint); and dynamic reconfiguration for embedded systems.

REFERENCES

[1] Barabási AL, Albert R, and Jeong H, (1999) Mean-field theory for scale-free random networks *Physica* A 272, 173.

[2] Ohkubo J, Horiguchi T (2005) Complex Networks by Non-growing Model with Preferential Rewiring Process, *J. Phys. Soc. Jpn*. 74, 1334

[3] Gale D, Shapley LS (1962), College admissions and the stability of marriage, *American Mathematical Monthly*, 69:9-15

[4] Gusfield D, Irving RW (1989) *The Stable Marriage Problem: Structure and Algorithm*, MIT Press, London

[5] Ishida Y (2004) *Immunity-Based Systems: A Design Perspective*, Springer

[6] Ishida Y (2006) Designing an Immunity-Based Sensor Network for Sensor-Based Diagnosis of Automobile Engines, *Lecture Notes in Computer Science* 4252, 146-153

[7] Ishida Y, Tokumitsu M (2009) Adaptive Sensing Based on Profiles for Sensor Systems Sensors, *Sensors*, 9(7)8422-8437

[8] Ishida Y (2005) A Critical Phenomenon in a Self-repair Network by Mutual Copying, *Lecture Notes in Computer Science* 3682 86-92 Springer

[9] Tokumitsu M, et. al. (2011) An adaptive sensor network for home intrusion detection by human activity profiling, *J. of Artificial Life and Robotics* 16(1)36-39

[10] Shida H, et. al. (2011) Immunity-Based Diagnosis for a Motherboard, *Sensors* 11(4), 4462-4473

[11] Okamoto T, Ishida Y (2009) An Immunity-Based Anomaly Detection System with Sensor Agents, *Sensors*, 9(11) 9175-9195

[12] Ide K., et. al. (1997) Unified Notation for Data Assimilation: Operational, Sequential and Variational, *Journal of the Meteorologcial Society of Japan*, 75(1B) 181–189

[13] Traffic Information System autobahn.NRW http://www.autobahn.nrw.de/

The Seventeenth International Symposium on Artificial Life and Robotics 2012 (AROB 17th '12),
B-Con Plaza, Beppu, Oita, Japan, January 19-21, 2012

A Multipath Immunity-based Statistical En-route Filtering in Wireless Sensor Networks

Yuji Watanabe and Tomotsugu Tamura

Nagoya City University, Nagoya 467-8501, Japan
(Tel: 81-52-872-5037, Fax: 81-52-872-5037)

yuji@nsc.nagoya-cu.ac.jp

Abstract: In our previous studies, we have proposed an immunity-based statistical en-route filtering (ImSEF) to not only eliminate false data injection attack in wireless sensor networks but also identify compromised nodes which are injecting false data. Some simulation results showed that ImSEF outperformed the original SEF. However, ImSEF does not deal with false negative attack where a compromised node can block legitimate reports from forwarding through it. In addition, ImSEF mistakenly filter out legitimate reports en-route with low probability (mistaken filter). In this paper, we propose a multipath immunity-based statistical en-route filtering (ImMEF) to combat both the false negative attack and the mistaken filter. Like a multipath en-route filtering method (MEF) proposed by Kim and Cho, ImMEF exploits a multipath routing technique and a random key pre-distribution scheme for key assignment. We carry out some simulations to evaluate the performance of ImMEF.

Keywords: Wireless sensor networks, Statistical en-route filtering, Immunity-based approach, Multipath routing

1 INTRODUCTION

Wireless sensor networks consisting of many small and cheap sensor nodes may be deployed in a potentially adverse environment where an attacker can launch various kinds of threats. *False data injection attack*, which is also called *false positive attack*, is that sensor nodes compromised by an attacker can inject false reports of non-existing or bogus events. The attack may cause not only false alarms but also the waste of the limited energy of the nodes forwarding these reports. A *statistical en-route filtering* (SEF) [1] and several revised schemes [2-4] have been proposed to combat the attack.

In our previous studies [5-7], we also have proposed an *immunity-based statistical en-route filtering* (ImSEF) to identify compromised nodes and achieve earlier detection of false reports. In ImSEF, each node assigns *credibility* to its neighboring nodes and updates the credibility based on the success or failure of filtering and transmission. And then each node uses the updated credibility as the probability of the next communication. Both simulation results and mathematical analyses [6,7] showed that ImSEF outperformed the original SEF. However, SEF and ImSEF do not deal with *false negative attack* where a compromised node can block legitimate reports from forwarding through it. As a result, users cannot receive the legitimate reports and cannot take appropriate countermeasures. In addition, ImSEF mistakenly filters out legitimate reports en-route with low probability (*mistaken filter*) in the environment where both legitimate and fake reports exist.

In this paper, we propose a *multipath immunity-based statistical en-route filtering* (ImMEF) to deal with not only false negative attack but also mistaken filter. Like a *multipath en-route filtering method* (MEF) proposed by Kim and Cho [3], ImMEF also exploits a multipath routing technique and a random key pre-distribution scheme for key assignment. We carry out some preliminary simulations to evaluate the performance of ImMEF.

2 SENSOR NETWORK MODEL

Following the previous studies on SEF, we consider a large-sized sensor network composed of a lot of sensor nodes and a base station (BS) which is a data collection center. We further assume that the nodes are deployed at a high density, so that an event (sensing target) can be detected by multiple surrounding nodes. It is unnecessary for each of the detecting nodes to send the event report (e.g., the location, the time, and the type of event) to the BS, so that one of them is elected as cluster head (CH). The CH collects all the event reports from all the detecting nodes and forwards a synthesized report to the BS. The report potentially traverses a large number of hops.

We assume that an attacker can compromise some nodes to obtain the security information installed in the nodes. Once compromised, the nodes can be used to inject false data reports of bogus events. Such an attack is called a *false data injection attack* (*false positive attack*). This paper also focuses on *false negative attacks* where a compromised node can block legitimate reports from forwarding through it. However, we consider that the attacker cannot defeat the BS because the BS has powerful security.

3 IMMUNITY-BASED STATISTICAL EN-ROUTE FILTERING (ImSEF) [5-7]

SEF and ImSEF can probabilistically filter out false reports en-route. They exploit collective decision-making by multiple detecting nodes and collective false detection by multiple forwarding nodes. They consist of three major components: (1) key assignment and report generation, (2) en-route filtering, and (3) base station verification. In addition, ImSEF has the credibility update and the communication based on the updated credibility.

3.1 Key Assignment and Report Generation

The process of key assignment and report generation in ImSEF is as follows.

1) The BS maintains a global key pool of N secret keys $\{K_i, 0 \leq i \leq N-1\}$, divided into n non-overlapping partitions $\{P_j, 0 \leq j \leq n-1\}$. Each partition has m keys (i.e., $N = m\ n$). A simple way to partition the key pool is $P_j = \{K_i | jm \leq i \leq (j+1)m - 1\}$.
2) Before each sensor node is deployed, it stores randomly chosen k ($k < m$) keys from a randomly selected partition in the key pool.
3) After all the nodes are deployed, they broadcast their indexes to their neighboring nodes within one-hop distance. Every node receives the message from each of its neighbors, establishes a list of neighboring nodes, and then assigns a state variable $R(t) \in [0, 1]$ indicating the *credibility of neighbor* to each neighboring node. The initial value of credibility $R(0)$ is set to 1.
4) When an event appears, multiple surrounding nodes can detect the event. A CH is elected from the detecting nodes for creating the synthesized event report.
5) Each of the nodes that detected the event generates a keyed message authentication code (MAC) M_i using the event report E and a randomly selected K_i, one of its k stored keys. Each detecting node then sends the key index and the MAC, $\{i, M_i\}$, to the CH. K_i is secret while M_i is public.
6) The CH collects all the $\{i, M_i\}$s from the detecting nodes and randomly chooses T MACs from distinct partitions. This set of multiple MACs acts as the proof that the report is legitimate. Then the CH sends the final report with T attached key indices and T MACs, e.g. $\{E, i_1, M_{i1}, i_2, M_{i2}, \ldots, i_T, M_{iT}\}$, toward the BS.

Fig. 1 depicts an example of the key assignment and report generation in ImSEF. In this figure, the BS has a global key pool of N = 12 keys divided into n = 4 partitions, each of which has m = 3 keys. Each node randomly picks k = 2 secret keys from one partition of the key pool. After each detecting node endorses the event report by producing a keyed MAC using one of its 2 stored keys, the CH collects all the MACs from the detecting nodes and attaches randomly selected T = 3 MACs, that is, M_2, M_9, and M_{10}, to the event report E.

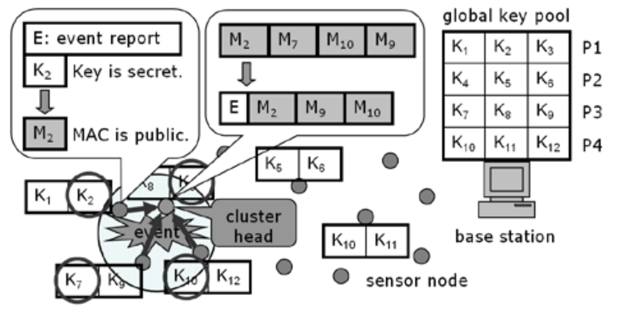

Fig. 1. An example of the key assignment and report generation in ImSEF [5].

3.2 En-Route Filtering and Credibility Update

In the en-route filtering component of SEF and ImSEF, intermediate forwarding nodes verify the correctness of the MACs probabilistically, and drop a report with forged MACs en-route. ImSEF also performs the credibility update and the communication based on the updated credibility. The process of en-route filtering in ImSEF is as follows.

1) Forwarding node j receives a report from the previous neighboring node i in proportion to the credibility $R_{ji}(t)$ of node i. In other words, node j drops a report from node i with the probability (1 - $R_{ji}(t)$) unconditionally and finishes the filtering process.
2) Since a legitimate report carries exactly T MACs produced by T keys of distinct partitions, a report with fewer than T MACs or more than one MAC in the same partition is dropped. Node j decreases the credibility $R_{ji}(t)$ of the previous node i and finishes the filtering process.
3) For the randomized key assignment, node j has a certain probability of possessing one of the keys that are used to produce the T MACs. If node j finds out that it has one of the T keys in the report, then it reproduces the MAC using its stored key and compares the result with the corresponding MAC attached to the report. If the reproduced MAC is different from the attached one, then the report is

dropped, the credibility $R_{ji}(t)$ of the previous node i decreases, and the filtering process is finished.

4) If node j verifies the reproduced MAC is the same as the attached one or if node j does not have any of the T keys, then it forwards the report to the next neighboring node k and replies an acceptance message to the previous node i to inform that the validation of the report is successful. Note that node j does not reply to node i if it discards the report.

5) Node j waits a reply from the next node k for a certain time. If node j can receive the reply from the next node k, it increases the credibility $R_{ji}(t)$ of the previous node i. Otherwise it decreases $R_{ji}(t)$.

To sum up the credibility update, node j updates the credibility $R_{ji}(t)$ of the previous node i based on its filtering result or the reply from the next node k as follows:

$$R_{ji}(t+1) = \begin{cases} R_{ji}(t) + \Delta_s & \text{if node } j \text{ receives the reply from next node } k \\ R_{ji}(t) - \Delta_f & \text{if node } j \text{ does not receives the reply from next node } k \\ R_{ji}(t) - \Delta_d & \text{if node } j \text{ drops the report} \end{cases}$$

For example, in Fig. 2, node i increases the credibility R_{ih} of the previous node h because the reply from the next node j can be received. However, node j decreases the credibility R_{ji} of the previous node i because the next node k drops the report and does not reply to node j. Since node k discards the report by itself, the credibility R_{kj} of the previous node j also decreases. To achieve the identification of compromised nodes, ImSEF not only updates the credibility but also uses the updated credibility as the receiving probability as mentioned in process 1) of the en-route filtering. In the same example, assuming that node h is compromised. Node i has an adversely higher probability of receiving the report from compromised node h because of the increase in the credibility R_{ih}. However, since node j has a lower probability of receiving a report from node i, node i may fail to send a next report to node j, and then the credibility R_{ih} of the previous node h in the neighborhood list of node i decreases. Although the credibility R_{kj} of the previous node j in the neighborhood list of node k decreases at first, if node j sends legitimate reports received from other previous nodes to node k, the credibility R_{kj} can be recovered. By iterating the credibility update and the communication based on the updated credibility, ImSEF is expected to inhibit neighboring nodes of compromised nodes from forwarding false reports.

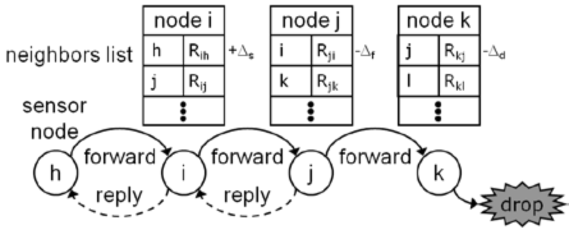

Fig. 2. An example of the credibility update in the en-route filtering process of ImSEF [5].

3.3 Base Station Verification

Owing to the statistical nature of the detection mechanism, a few bogus reports with invalid MACs may escape en-route filtering and reach the BS. In the base station verification process, the BS further verifies the correctness of all MACs and eliminates false reports that elude en-route filtering.

4 PROPOSED MULTIPATH ImSEF (ImMEF)

SEF and ImSEF do not address *false negative attacks* such as blocking legitimate reports or selective forwarding attacks by a compromised intermediate node. Furthermore, ImSEF may mistakenly drop legitimate reports in process 1) of the en-route filtering with low probability (*mistaken filter*). Kim and Cho [3] have proposed a *multipath en-route filtering method* (MEF) to tackle false negative attacks, and shown that MEF is more resilient to the attacks up to a certain number of compromised nodes than SEF.

In this paper, we propose a *multipath immunity-based statistical en-route filtering* (ImMEF) to deal with not only false negative attack but also mistaken filter. Like MEF, ImMEF exploits a multipath routing technique and a random key pre-distribution scheme for key assignment. Specifically speaking, the process 6) of report generation is changed as follows:

6') The CH collects all the $\{i, M_i\}$s from the detecting nodes and classifies the MACs into P separate groups, hashed as a function of key partition number, j of P_j. The CH allocates each of P different hash groups onto each path toward the BS. From each hash group, the CH randomly chooses S MACs and attaches them to the event report on the path. The CH sends P event reports of different hash group to the BS via multiple disjoint paths. The number of transmitted MACs per path is S ($S \leq T$) because the CH aggregates as least T MACs. The BS previously sets values for T and S.

The en-route filtering component in ImMEF is also slightly changed from T MACs to S MACs. In addition, a forwarding node verifies the group of received reports in process 2) of the en-route filtering. If a key index does not belong to the key group in the report, the report is dropped.

Fig. 3 shows an example of event reports of different hash group on multiple disjoint paths where $P = 2$ and $S = 2$. There are 2 event reports which have 2 MACs, M_6 and M_{10} and M_2 and M_9, of the hash group for "group 0 mod 2" and for "group 1 mod 2", respectively. Even if a compromised node can stall forwarding a legitimate report on a path as shown in Fig. 3, or a normal forwarding node mistakenly drops a report, the BS can receive the other reports.

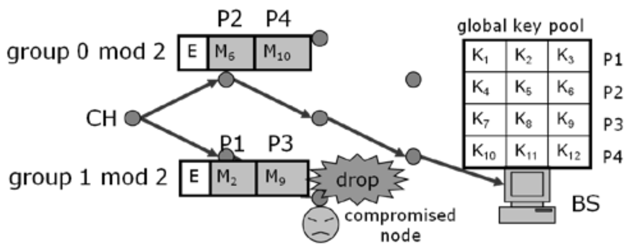

Fig. 3. An example of event reports of different hash group on multiple disjoint paths where $P = 2$ and $S = 2$.

5 SIMULATION

We perform some preliminary simulations to evaluate the performance of ImMEF on the following conditions: 9×100 sensor nodes are located in a two-dimensional lattice field. 9 source nodes sit at the left side of the field, and a base station is at opposite ends, with 100 hops between the sources and the base station. One of the source nodes is compromised and sends 1000 bogus reports, while the remaining sources transmit 1000 legitimate reports. A global key pool consists of $N = 1000$ keys, divided into $n = 10$ partitions, each of which has $m = 100$ keys. Each node has $k = 50$ keys. When $T = 5$, the number of transmitted MACs S per path and the number of disjoint paths P are varied as satisfying the inequality $P \cdot S \leq T$. All the values of the parameters Δ_s, Δ_f, and Δ_d are set to 0.02.

Fig. 4 illustrates the percentage of mistakenly dropped legitimate reports as a function of the number of paths P for ImMEF. ImSEF corresponds to ImMEF where $P = 0$. The result shows that as the number of paths increases, the percentage of mistakenly dropped legitimate reports decreases. By using multiple disjoint paths, ImMEF has been shown to deal with mistaken filter. We are now carrying out additional simulations for false negative attacks comparing with MEF, so that we will show the results at conference site.

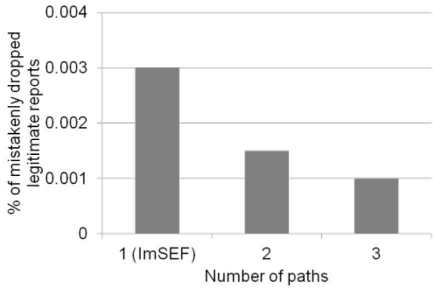

Fig. 4. Percentage of mistakenly dropped legitimate reports as a function of the number of paths P for ImMEF.

6 CONCLUSION

In this paper, we proposed a multipath immunity-based statistical en-route filtering (ImMEF) to deal with not only false negative attack but also mistaken filter. We performed some preliminary simulation to evaluate the performance of ImMEF. In future, the proposed scheme will be combined with the other revised SEFs for a higher security level.

ACKNOWLEDGEMENTS

This work was partly supported by a Grant-in-Aid for Scientific Research (C) (22500063) from the Japan Society for the Promotion of Science.

REFERENCES

[1] Ye F, Luo H, Lu S, Zhang L (2005), Statistical En-Route Filtering of Injected False Data in Sensor Ne tworks. IEEE Journal on Selected Areas in Communica tions 23(4):839-850

[2] Yu Z, Guan Y (2006), A Dynamic En-route Sch eme for Filtering False Data Injection in Wireless Sens or Networks. Proceedings of the 25th IEEE Conference on Computer Communications, 1-12

[3] Kim MS, Cho TH (2007), A Multipath En-Route Filtering Method for Dropping Reports in Sensor Net works. IEICE Transactions on Information and Systems E90-D(12):2108-2109

[4] Krauß C, Schneider M, Bayarou K, Eckert C (2 007), STEF: A Secure Ticket-Based En-route Filtering Scheme for Wireless Sensor Networks. 2nd IEEE Inter national Conference on Availability, Reliability and Sec urity, 310-317

[5] Watanabe Y (2010), An Immunity-based Scheme for Statistical En-route Filtering in Wireless Sensor N etworks. LNCS 6278, 660-665

[6] Watanabe Y (2011), Performance Evaluation of I mmunity-based Statistical En-route Filtering in Wireless Sensor Networks. Artificial Life and Robotics, 16(3):4 22-425

[7] Watanabe Y (2011), An Analysis of Immunity-ba sed Statistical En-route Filtering in Wireless Sensor Ne tworks. 3rd International Conference on Management of Emergent Digital EcoSystems, 250-256

Extraction of Operational Behavior for User Identification on Smart Phone

Yuji Watanabe and Shunta Ichikawa

Nagoya City University, Nagoya 467-8501, Japan
(Tel: 81-52-872-5037, Fax: 81-52-872-5037)

yuji@nsc.nagoya-cu.ac.jp

Abstract: A smart phone has a large amount of private information, so that user authentication and identification are important to prevent attacks by illegal users who are not the owner of the smart phone. Both password authentication and biometrics can be applied only at the beginning of use. After the authentication is passed, not only the legal owner but also illegal users freely use the phone. For the second protection, the behavior-based user identification can continuously check the user activities after login. In this paper, we investigate operational behaviors at the first stage for user identification on smart phone. We make a text browsing application to record fingers history on smart phone. From the recorded fingers history, we extract and compare characteristic operational behaviors, for instance, the speed and the acceleration of fingers, the distance between fingers, and the distribution of touched region.

Keywords: Smart phone, Behavior-based user identification, Operational behavior, Security

1 INTRODUCTION

In recent years, smart phones have been exponentially popularized for many convenient applications. Because a smart phone has as a large amount of private information as a personal computer, user authentication and/or user identification are important to prevent attacks by illegal users who are not the owner of the smart phone. At first, user authentication can be classified into two types, namely *password authentication* and *biometrics*. Although the password authentication requires that the owner only memorizes a short password and inputs the password for login, the password is probably lost or forgotten and then it is illegally shared and used by attackers. On the other hand, the biometrics verifies the owner based on the intrinsic physiological characteristics, for example, fingerprint, face and voice [1]. The biometric characteristics cannot be lost or forgotten, so that it is hard to copy and share them. However, the user authentication of both password authentication and biometrics can be applied only at the beginning of use. After the authentication is passed, not only the legal owner but also illegal users freely use the computer or the phone.

For the second protection, many user identification systems based on *user behavior* have been proposed since the 1990s in personal computer environment. As user behavior which is difficult to be imitated, commands sequence [2-4], keystroke pattern [5-9], or mouse operation [10] has been employed. The identification systems initially create normal profiles of a legitimate user behavior. If the systems observe the remarkable difference between the profiles and the current user activities, then they give an alarm. The behavior-based user identification can continuously check the user activities after login.

Isohara et al [11] have proposed a simple and easy-to-use user identification system on mobile phone environment for the first time. The system records keystrokes in the background process, calculates the frequency of keys or key groups from the recorded keystrokes to make a normal user profile, and then estimates a similarity score by comparing the frequency-based profile with the latest keystrokes to detect illegal users. A prototype system was implemented on the BREW emulator and error rates were evaluated. Because the system was proposed for mobile phone with severely limited calculation resources, it used only the key frequency for user identification. However, since smart phone has more powerful calculation resources than mobile phone, identification systems based on other complicated characteristics such intervals of time between keys can be applied on smart phone. In addition, unlike mobile phone where only key buttons are pushed, there are also operational behaviors peculiar to smart phone with touch-screen panel, for example, *swipe*, *tap*, *flick*, and *pinch*.

In this paper, we investigate operational behaviors at the first stage for user identification on smart phone. We make a simple text browsing application to record fingers history on smart phone, that is, iPhone, iPod touch and iPad. From the recorded fingers history, we extract and compare characteristic operational behaviors, for instance, the speed and the acceleration of fingers, the distance between fingers, and the distribution of touched region. From the experiment results, the distribution of region touched by fingers for each subject is interestingly different.

2 HISTORY RECORD APPLICATION

2.1 Platform for Development

To create an application to record fingers history on smart phone, we should firstly select a platform for developing the application. Although Google's Android became the world's leading smart phone platform in the last quarter of 2010 [12] (also in Japan [13]), we have developed some applications on iOS for a year (as a matter of course we start to develop on Android OS). iOS is Apple's mobile operating system for iPhone, iPod touch, iPad and Apple TV [14]. The user interface of iOS is based on the concept of direct manipulation, using multi-touch gestures. As interface control elements, there are sliders, switches, and buttons. Interaction with the OS includes gestures such as *swipe*, *tap*, *flick*, and *pinch*, all of which have specific definitions within the context of iOS and its multi-touch interface.

The iOS SDK (Software Development Kit) allows developers to make native applications for iPhone, iPod touch and iPad, as well as test them in an iPhone simulator. Xcode is the integrated development environment for the iOS SDK. Like iOS and Mac OS X, iPhone applications are written in Objective-C. iOS has four abstraction layers: the Core OS layer, the Core Services layer, the Media layer, and the Cocoa Touch layer. The developers mainly use the Cocoa Touch layer at the highest level because many sophisticated services and technologies can be implemented easily. However, lower level layers may still be accessed by the developer when needed.

2.2 Text Browsing Application

Like the previous studies on behavior-based user identification such as mouse operation [10] and mobile phone keystrokes [11], it is preferable that user behavior is recorded in the background process. Because multitasking is supported for iOS through only seven background APIs: background audio, voice over IP, background location, push notifications, local notifications, task completion, and fast app switching [14], it is difficult to store operational behaviors in the background process on iOS.

Because browsing is one of basic functions equipped with many applications on smart phone, as the first stage for user identification on smart phone, we make a simple text browsing application to record fingers history on iPhone and iPod touch as shown in Fig.1 (a). The display size is 480 pixels high by 320 pixels wide (iPhone 4 and 4th generation iPod touch has 960 x 640 pixels, and iPad has 1024 x 768 pixels). So the text browser has only vertical scroll. A text is scrolled by the following fingers operations.

- *Flick*: users place a finger on the screen and quickly swipe it in the desired direction.
- *Drag*: users place a finger on the screen and move it in the desired direction without lifting it from the screen.

Fig. 1 (b) illustrates that the origin is located at the top left corner of the screen, and the X and Y coordinates are specified. The UITextView Class which implements the behavior for a scrollable, multiline text region is used to display multiple lines of text, such as when displaying the body of a large text document. The class can get touched points not on screen but on text, so that the range of Y varies depending on the text document while the range of X is from 0 to 320. The Japanese text document in Fig. 1 (b) has Y ranging from 0 to 20000.

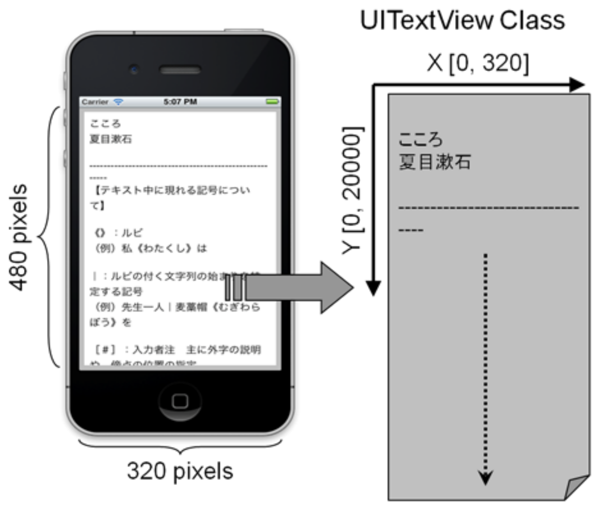

(a) (b)

Fig. 1. (a) screenshot of the simple text browsing appli cation to record fingers history on iPhone and iPod to uch. (b) the origin and the X and Y coordinates on U ITextView Class

2.3 Characteristic Operational Behaviors

The fingers history continuously recorded by the text browsing application is in the form of $\{(x, y), t, event\}$, where (x, y) is the coordinates of point touched by fingers, t is the touch event time. And *event* means one of 3 touch events as follows.

1. A finger is placed on the text.
2. The finger is moving without lifting from the text.
3. The finger is released.

From the recorded fingers history, we should extract characteristic operational behaviors suitable for user identification. This study is propably closer to the previous research on mouse operation [10] than on mobile phone keystrokes [11]. The research on mouse operation [10] has checked the following features and then used the last one for user identification.

1. The region of mouse used by each user
2. The moving route of mouse from the starting point to the ending point
3. The velocity of mouse
4. The acceleration of mouse
5. The movement direction near the starting point and the ending point
6. The pattern of mouse movement

We also extract the same features, that is, the distribution of region touched by fingers, the speed and the acceleration of fingers, the movement direction, and the operations pattern of fingers.

3 EXPERIMENTAL RESULTS

We carried out experiments using the text browsing application on iPod touch to extract characteristic operational behaviors. 5 subjects participated in this experiment. After the subjects were explained how to use iPod touch and the application, they were free to read the text document. When they finished reading, they returned iPod touch. We can get each recorded fingers history through iTunes.

Fig. 2 shows the distribution of region touched by fingers for 3 subjects, A, B, and C. From the results, subject A and C are accustomed to operation on smart phone while subject B may be not used to reading the text document on smart phone. The distribution can be one of promising characteristic operational behaviors suitable for user identification. Table 3 depicts average, minimum and maximum speeds of fingers for 3 subjects. The speed is calculated by dividing the distance between *event* 1 and the corresponding *event* 3 by the taken time. Although subject C can manipulate smart phone more quickly than the others, the feature is invalid for user identification because the minimum and maximum speeds are overlapped. The acceleration of fingers is also inappropriate. We are now extracting the other features for all the subjects including the remaining subjects, so that we will show the results at conference site.

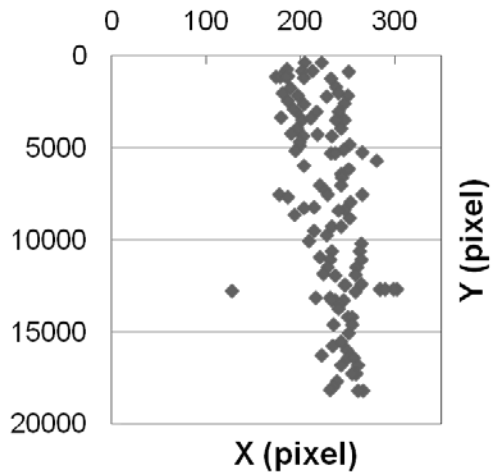

(a) subject A

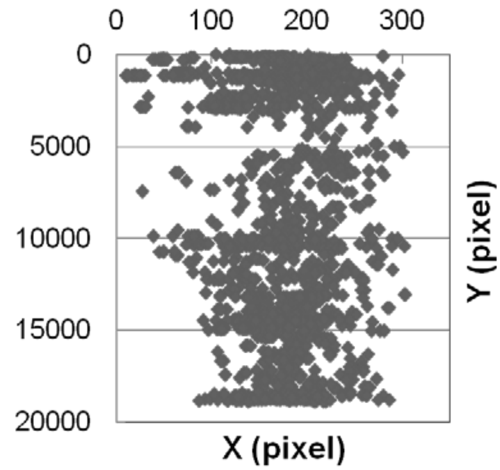

(b) subject B

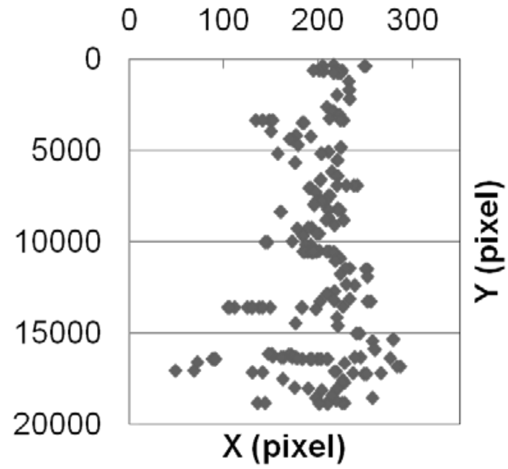

(c) subject C

Fig. 2. The distribution of region touched by fingers for 3 subjects

Table 1. Average, minimum and maximum speeds of fingers for 3 subjects

	A	B	C
Ave. speed	104.0	119.4	86.9
Min. speed	8.2	0	0
Max. speed	307.7	9749.3	608

4 CONCLUSION

In this paper, we made a text browsing application to record fingers history on smart phone and then extracted characteristic operational behaviors for user identification on smart phone. From the experiment results, the distribution of region touched by fingers for each subject was interestingly different. In future work, we will continue to extract and compare characteristic operational behaviors. We then plan to construct user identification system on smart phone based operational behavior.

REFERENCES

[1] Jain A, Bolle R, Panakanti S (1999), Biometrics: Personal Identification in Network Society. Kluwer Academic Publishers

[2] Shirai H, Nishino J, Odaka T, Ogura H (1999), An Intrusion Detection Technique Using Characteristics of Command Chains in an Interactive Computer Environment. IEICE Transactions on Fundamentals of Electronics, Communications and Computer Sciences, J82-A (10):1602-1611

[3] Schonlau M, DuMouchel W, Ju W, Karr A, Theus M, Vardi Y (2001), Computer Intrusion: Detecting Masquerades. Statistical Science, 16(1):58-74

[4] Okamoto T, Ishida Y (2009), An Immunity-Based Anomaly Detection System with Sensor Agents. Sensors, 9(11): 9175-9195

[5] Joyce R, Gupta G (1990), Identity Authentication Based on Keystroke Latencies. Communications of the ACM, 33(2):168-176

[6] Leggett J, Williams G, Usnick M, Longnecker M (1991), Dynamic Identity Verification via Keystroke Characteristics. International Journal of Man-Machine Studies, 35(6):859-870

[7] Monrose F, Rubin A (1997), Authentication via Keystroke Dynamics. Proceedings of the 4th ACM conference on Computer and communications security, 48-56

[8] Cho S, Han C, Han D, Kim H (2000), Web-Based Keystroke Dynamics Identity Verification Using Neural Network. Journal of Organizational Computing and Electronic Commerce, 10(4):295-307

[9] Bergadano F, Gunetti D, Picardi C (2002), User Authentication through Keystroke Dynamics. ACM Transactions on Information and System Security, 5(4):367-397

[10] Izumi M, Nagao W, Miyamoto T, Fukunaga K (2004), User Identification System Using Feature of Mouse Operation. IEICE Transactions on Communications, J87-B(2):305-308

[11] Isohara T, Takemori K, Sasase I (2008), Anomaly Detection on Mobile Phone Based Operational Behavior. IPSJ Journal, 49(1):436-444

[12] Alto P (2011), Google's Android Becomes the World's Leading Smart Phone Platform. Canalys research release 2011/013, http://www.canalys.com/static/press_release/2011/r2011013.pdf

[13] http://www.m2ri.jp/newsreleases/main.php?id=010120110510500

[14] iOS: http://en.wikipedia.org/wiki/IOS

Continuous review model of mutual support supply system for disaster responses

Nur Budi Mulyono[1], Yoshiteru Ishida[2]

[1 2]Toyohashi University of Technology, Toyohashi 441-8580, Japan
[1]nurbudi@gmail.com

Abstract: Mutual support of supply is needed to leverage number of stock between shelters during disaster response time. The goal of this research is to develop reactive lateral stock transshipment between shelters based on traditional continuous review inventory model in which demand and delivery lead time information are greatly biased. This paper presents self-repair framework that provide an emergency relief strategy after natural disaster events. In addition, supply system buffer analysis also presented to enrich model development. A case study focused on volcanic eruption disaster at Merapi Mountain Indonesia, illustrate application of the model.

Keywords: Mutual support supply network, continuous order review model, lateral transshipment, disaster relief supply, self-repair network, buffer analysis.

1 INTRODUCTION

Due to increasing number of natural disaster occurrence recently, disaster relief is extremely important activity today (EMDAT, 2010) [1]. The need to respond to human need in the event of disaster is not diminishing and may even be increasing. Government, NGO, and other related parties should provide life support items such as food, clothes, and medicine; in timely manner.

Planning and management of logistic and inventory activities is needed for better relief supplies. Inventory or supply system play critical role in this emergency situation, in which they system has to manage all the needed items, store it, and provide it to the victim whenever they need.

The role of logistic and inventory for famine relief is explicitly mentioned by (Long & Wood, 1995) [2] that describe complex environment in which disaster relief logistic and inventory system must operate.

The traditional design of an inventory system is hierarchical where transportation flows from one echelon to the next, i.e. from suppliers to manufacturers, from manufacturers to retailers, and from retailers to customers. This inventory system tends to have less flexibility since each supply point cannot communicate or help each other to get a better performance. The more flexible inventory system allows lateral transshipment within same or adjacent echelon, i.e. between wholesalers or retailers (Paterson, et al, 2010) [3].

At disaster recovery situation, lateral transshipments between inventories at each shelter points are allowed to minimize number of run out stock or stock out in each shelter point. Lateral transshipment is one of the alternative ways to leverage number of stock between shelter points and reduce stock out.

Simple lateral transshipment inventory system for a disaster situation is graphically illustrated in Figure 1 with single central warehouse supplies three inventory shelter points. Lateral transshipment in an inventory system is stock movements between locations of the same echelon (Paterson, et al, 2010) [3]. These transshipments can be conducted periodically at predetermined points in time to proactively redistribute stock, or they can be used reactively as a method of meeting demand, which cannot be satisfied from stock on hand.

In proactive transshipment models, lateral transshipments are used to redistribute stock amongst all stocking points in an echelon at predetermined moments in time. Reactive transshipments respond to situations where one of the stocking points faces a stock out or risk of a stock out.

Lateral transshipment is suitable to use in disaster situation since cost consideration is less important than saving life. By stock transfer from one surplus location into needed location, average stock out of all location will significantly reduce.

After occurrence of disaster, needed item's demand is usually fluctuate drastically and arrive at extremely irregular time. In most disaster-relief practices, demand information for emergency resources is mainly collected at the operational level and then flow upward to the higher level (Turoff, 2004) [4]. In addition, transportation time for the item to each shelter point becomes extremely vary due to infrastructure damages.

Lateral transshipment is suitable to use in disaster situation since cost consideration is less important than saving life. By stock transfer from one surplus location into needed location, average stock out of all location will significantly reduce.

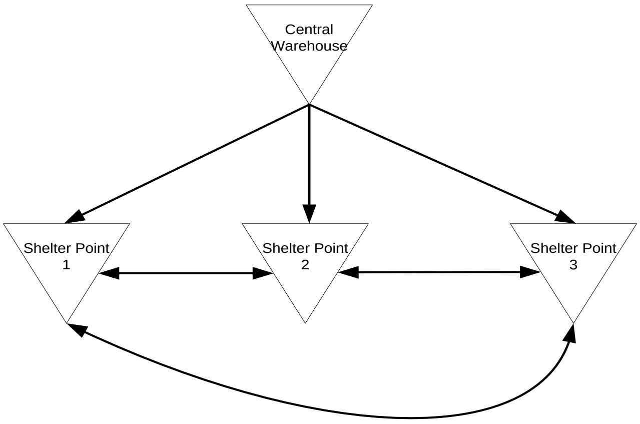

Fig. 1: Lateral transshipments between stock points

Self-repair network model in computer network application is one collaboration model of computer network where each computer tries to repair each other by mutual copying. Repairing process of self-repair network doesn't require resources while repairing process of lateral transshipment sacrifices resources.

This paper propose framework of lateral transshipment of supply system after occurrence of natural disaster with continuous review inventory model and self-repair network as reference model.

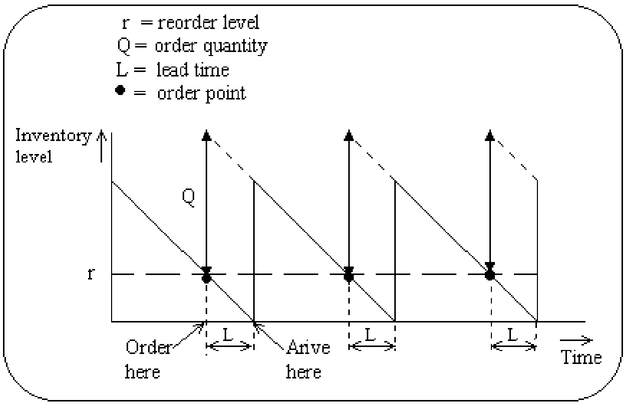

Fig. 2: Continuous review model of inventory

3 MUTUAL SUPPORT MODEL

There are differences between the enterprise and disaster-relief inventory models. These differences are found in the environment and characteristics of disaster-relief inventories in all area from acquisition through storage and distribution (Whybark,2007) [5]. Even though different, fundamental enterprise inventory model can be adopt for modeling inventory at disaster situation.

Continuous order review inventory model or known as economic order quantity (EOQ) model, state that there is optimum order quantity (Q) based on tradeoff between predetermined setup cost (SC) and holding cost (HC) (Heizer & Render, 2008) [6]. Figure 2 illustrate basic model of continuous order review inventory. Another variable necessary for calculating order quantity is overall demand along planning horizon (D). Equation 1 show the calculation of optimum order quantity based on this model.

$$\mathrm{Q} = \sqrt{\frac{2.D.SC}{HC}} \qquad (1)$$

This model used reorder point (R) formula which is derived from interaction of demand rate (d), delivery lead time (L), and safety stock (SS). Equation 2 shows calculation of reorder point while safety stock calculation of continuous order review is shown at equation 3.

$$R = d.L + SS \qquad (2)$$

$$\mathrm{SS} = z\sigma_{RP+L} \qquad (3)$$

We formulate the lateral transshipment problem into simple mathematical formulation. The model consists of three elements (U, T, R) where U is a set of shelter points, T is a topology connecting the units, and R is a set of rules of interaction among shelter points. A set of shelter point U is a finite set number of shelter points. The topology for the lateral transshipment inventory system is scale free network. We restrict the case where each shelter point has a state: normal (0), abnormal (1) and need help (-1). Each shelter point tries to help the other shelter points in a synchronous fashion with probability **Pr**. The helping will be successful with probability **Ps** and the shelter point states will increase if the current inventory level plus the proportion shared by another shelter point is greater than the standard normal threshold (N). Proportion shared by normal shelter point is Pn while the proportion shared by abnormal shelter point is Pa in which Pa<Pn. In this model, it is assume that *need help* shelter point cannot behave as helping unit. N and A is the proportion threshold of the normal and abnormal unit state, while I represent a proportion of current inventory level. There are several assumption used in this model

1. Only one shelter point can help another shelter point for one period of time.
2. Number of shelter point remains same during periodical review.
3. Each shelter point has dedicated transportation vehicle and common use transportation vehicle.

4. Logistic decision parameter such as vehicle capacity and route is neglected.

Our model has several similar characteristics with the self-repairing network model (SRN) where the network of computer repairs each other by mutual copying (Ishida, 2005) [7]. The following lists are characteristic of our model, which also exists in SRN model:

1. Set of units
2. Topology connecting the units
3. Set of rules of the interaction among units
4. Probability of repairing other units
5. There is possibility of disturbance occurs during interaction of the units

The definition of unit in both models is the smallest entity having an ability to interact, repair, and being repaired by other units. In SRN model, unit is a computer while in our model, unit is shelter points. Even though both models having a great number of similarity, there are also several differences between them as shown at Table 1

Table 1. Differences of SRN and our model

	SRN	Our Model
Repairing action	Mutual copying	Transfer stock
Sacrifices resource	No	Yes
Success rate	Probability (Prn, Pra)	Probability of success Ps and Proportion shared (Pn, Pa) and proportion of current inventory level (I)

Success rate of repairing is depending on the two factor ssuch as probability of success (Ps) and proportion shared (Pn and Pa). Probability Ps represents delivery success of items transported from one place to another during after occurrence of disaster event. Due to infrastructure damage, there is possibility transportation vehicle not able to reach destination or able to reach destination but the item carried has been damaged or deteriorated.

Transition rules for the state changes by helper unit are as followed:

$$0 \rightarrow 0 : (I\text{-}Pn) \geq N \tag{4}$$

$$0 \rightarrow 1 : A \leq (I\text{-}Pn) < N \tag{5}$$

$$0 \rightarrow \text{-}1 : (I\text{-}Pn) < A \tag{6}$$

$$1 \rightarrow 1 : A \leq (I\text{-}Pa) < N \tag{7}$$

$$1 \rightarrow \text{-}1 : (I\text{-}Pa) < A \tag{8}$$

Transition rules for the state changes by helped unit if help by normal unit are as followed:

$$0 \rightarrow 0 : (I+Pn) \geq N \tag{9}$$

$$1 \rightarrow 0 : (I+Pn) \geq N \tag{10}$$

$$1 \rightarrow 1 : A \leq (I+Pn) < N \tag{11}$$

$$\text{-}1 \rightarrow 1 : A \leq (I+Pn) < N \tag{12}$$

$$\text{-}1 \rightarrow 0 : (I+Pn) \geq N \tag{13}$$

Transition rules for the state changes by helped unit if help by abnormal unit are as followed:

$$0 \rightarrow 0 : (I+Pa) \geq N \tag{14}$$

$$1 \rightarrow 0 : (I+Pa) \geq N \tag{15}$$

$$1 \rightarrow 1 : A \leq (I+Pa) < N \tag{16}$$

$$\text{-}1 \rightarrow 1 : A \leq (I+Pa) < N \tag{17}$$

$$\text{-}1 \rightarrow 0 : (I+Pa) \geq N \tag{18}$$

4 NUMERICAL SIMULATION

Numerical simulation conducted using real disaster data of volcanic eruption in Indonesia. In November 2010, one of the active volcanoes in Indonesia, Merapi Mountain, located at Yogyakarta province erupted. During one month, government and other NGO trying to support their life at each shelter point, which spread all over the city. Data of evacuees and shelter points gathered from Indonesia National Disaster Management Agency for two provinces during one-month evaluation is shown at Table 2 (Indonesia National Disaster Management Agency, 2010) [8].

In numerical simulation, two options will be evaluated such as:

1. No transshipment
2. Transshipment

Table 2. Disaster evacuees and shelter point

Sub area	Areas (km2)	Evacuees	Shelter points	Evacuees/shelter	Shelter density
Sleman	574.82	109193	74	1476	7.77
Kulon Progo	586.28	4753	16	297	36.64
Yogyakarta city	32.5	5118	14	366	2.32
Bantul	506.85	20516	17	1207	29.81
Gunung Kidul	1485.35	12162	13	936	114.26
Total	*3185.8*	*151742*	*134*	*4282*	*190.8*

Table 3. Simulation setting

Simulation setting	
Evacuees/shelter	4282
Total demand	385380
Total period (hours)	720
demand rate (/hour)	535
Lead time (hours)	1
Safety stock	318
Order quantity (Q)	6207
Number of pool truck	268
Number of shelter truck/shelter	2
Pn	0.2
Pa	0.1
Pr	0.9
Ps	0.5
Normal threshold (N)	0.7
Abnormal threshold (A)	0.3

First option is the basic inventory model which not allowed any transfer items from any shelter points. This option made for performance reference of a transshipment system proposed. Second option allows transfer items between shelter points.

Number of truck for delivering item is assumed static throughout the time which is 268 trucks at pool or central warehouse and 2 trucks for each shelter. The other simulation setting can be seen at Table 3.

The result of numerical simulation as shown at Figure 3 that number of need help unit decreasing when success delivery rate is increasing and with transshipment option, number of need help unit decrease even bigger. Based on that fact, performance of transshipment system can be measured up to 60% as shown at Figure 4. In transshipment option, number of need help unit also sensitive to probability of helping where number of need help unit decrease significantly as probability of helping increase as shown at Figure 5.

5 BUFFER ANALYSIS

The purpose of buffer or safety stock is to reduce an effect of demand and lead time fluctuation. The prediction of the buffer is relied on the known distribution of the demand and lead time during a planning period.

We propose an analysis of buffer inventory for lateral transshipment system with the goal of getting percentage of expected reduce of stock out and also addition of expected over stock. The benefit of that action is reduction of stock out for certain amount but there is a side effect of increasing possibility of excessive stock.

Consider M as a percentage of additional buffers for current inventory level. Stock out occurs if a current level below abnormal threshold.

$$I \leq A \quad (19)$$

$$TI - d - Pr \cdot Pa \cdot TI \leq A \cdot TI \quad (20)$$

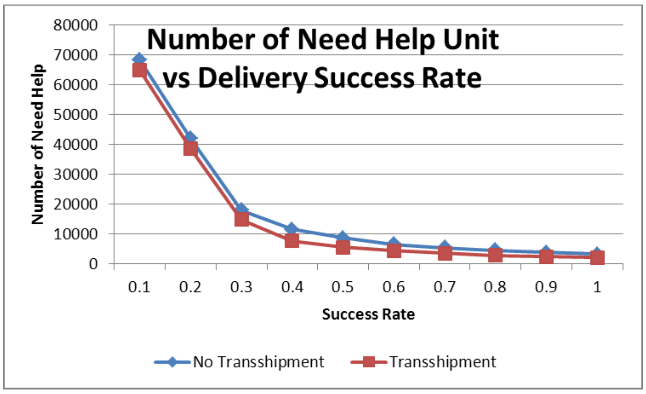

Fig 3. Number of need help unit vs delivery success rate

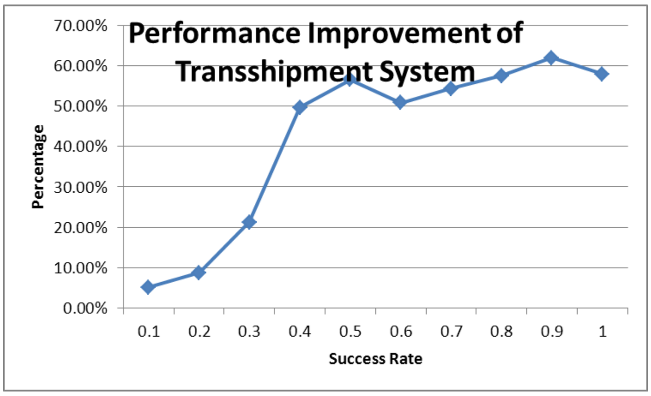

Fig 4. Performance improvement of transshipment

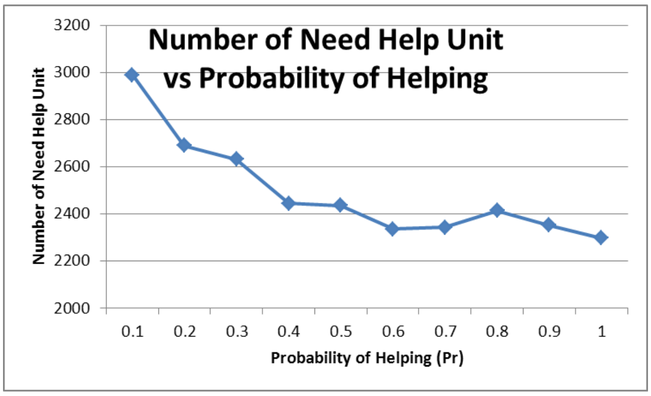

Fig 5. Number of need help unit vs probability of helping

If a proportion amount of M added to the current inventory stock the equation becomes as follows:

$$TI(1+M) \quad - d - Pr \cdot Pa \cdot TI(1+M) \le A \cdot TI \qquad (21)$$

$$TI - d - Pr \cdot Pa \cdot TI + M(1-Pr \cdot Pa) \le A \cdot TI \qquad (22)$$

From equation (22), we can conclude that buffer addition of M, cause the possibility of stock out reduced at maximum M(1 – Pr · Pa). On the other hand, if a proportion amount of M added to the current inventory stock, excess stock will add maximum as much as M(1 + Pr · Pn). The equation (25) shows the calculation of that excess stock.

$$I \quad \ge TI \qquad (23)$$

$$TI - d + Pr \cdot Pn \cdot TI \ge TI \qquad (24)$$

If a proportion amount of M added to the current inventory stock the equation become as follows:

$$TI(1+M) \quad - d + Pr \cdot Pn \cdot TI(1+M) \ge TI \qquad (25)$$

$$TI - d + Pr \cdot Pn \cdot TI + M(1+Pr \cdot Pn) \ge TI \qquad (26)$$

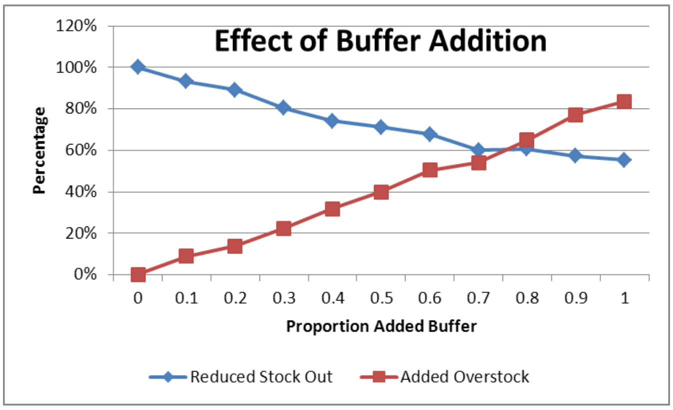

Fig 6. Effect of buffer addition

Based on numerical simulation data, if 10%, buffer is added to the current stock, then maximum stock out will be reduced as much as 9.1 % and maximum excess inventory will be added as much as 11.8 %. Figure 6 show the numerical simulation of proportion of need help unit after buffer M is added. Amount of stock out is reduced about 6.8% comparing the situation without buffer addition but expected maximum over stock increase as much as 8.7%. The result of numerical simulation is consistent with mathematical formulation where buffer addition will have greater effect to the expected over stock rather than expected stock out.

6 CONCLUSION

Lateral transshipment has demonstrated a positive impact to the performance improvement of the inventory system during a disaster where demand and lead time information are greatly biased. It can reduce number of stock out level for all shelter points. The performance of the system is greatly affected by success rate and probability of helping. Even with low delivery success rate and probability of helping, lateral transshipment supply system show significant improvement in inventory performance. It can be noted that the greater success rate and probability of helping the greater also inventory performance as measured by number of need help units.

Future research can be directed to the study on the dynamic of number of shelter points during planning horizon and also characteristic interaction between shelter points. Integration with logistic decision planning can also be one of the major concerns for future development such as truck capacity and routing problems.

7 ACKNOWLEDGEMENT

This works was supported by Global COE "Frontiers of Intelligent Sensing" from Ministry of Education, Culture, Sports, Science and Technology Japan. In addition, this works was supported by Scholarship from Nishijima corp. Not to mention, this works was also partly supported by Grants-in-Aid for Scientific Research (B): "Foundation on Immunity Based Complex Systems and Sensor Agents" (23300057) 2011.

REFERENCES

[1] EMDAT, (2010). Natural Disaster Reported 1900-2010., http://www.emdat.be.

[2] Long, D.C., Wood, D.F. (1995). The logistics of famine relief. Journal of Business Logistics 16 (1), 213.

[3] Paterson, Colin., Kiesmuller, Gudrun., Teunter, Ruud., Glazebrook., Kevin. (2010). Inventory model with lateral transshipments: a review. European Journal of Operation Research. 210. 125-136.

[4] Turoff, M., Chumer, M., Van de Walle, B., Yao, X. (2004). The design of a dynamic emergency response management information system (DERMIS). Journal of Information Technology Theory and Application. 5 (4), 1.

[5] Whybark, Clay.D. (2007). Issues in managing disaster relief inventories. Int. J. Production Economics 108, 228-235.

[6] Heizer, Jay H., Render, Barry., (2008). Operations Management 9th Edition., Prentice Hall.

[7] Ishida, Y. (2005). A critical phenomenon in a self-repair network by mutual copying, Lecture Notes in Artificial Intelligence (LNAI 3682) 86-92.

[8] Indonesia National Disaster Management Agency. (2010). Laporan Harian Tanggap Darurat Gunung Merapi 15 November 2010.

Network Rewiring by Matching Automaton: from Unit Reliability to Collective Survivability

Y. Ishida, M. Tokumitsu

Toyohashi University of Technology,
1-1 Hibarigaoka Tenpaku-cho, Toyohashi, Aichi 441-8580, Japan
(Tel.: +81-532-44-6895; Fax: +81-532-44-6895)
E-mail: ishida@cs.tut.ac.jp

Abstract: Collective intelligence of a group of intelligent robots can be realized as autonomous distributed robots with an advent of sensor network. Collective survivability can also be regarded as a subject of group problem solving, and realized by a framework of network rewiring (dynamic configuration) of systems. To realize the network rewiring, separation of physical systems and information systems is proposed to apply the self-rewiring network as well as self-repairing and self-recognition networks. Self-rewiring algorithm can be formalized as a matching automaton. An application to autonomous distributed satellites will be discussed.

Keywords: Network rewiring, rearrangement system, collective survivability, matching problem, dynamic configu ration.

1 INTRODUCTION

Network rewiring has been studied extensively in the new field of network science (e.g. [1, 2, 3]). Indeed, we can find network rewiring in many large-scale networks in nature: biological networks such as genetic networks; artificial networks such as the Internet; and social networks such as relation by birth or marriage.

On the other hand, current technology realizes highly reliable systems based on system reliability engineering using redundant components. However, the reliabilities of artificial systems are far behind from that of biological systems due to the different design principle. Biological systems involve rearrangement of similar and replaceable components when some important components fails or are missing.

As target areas for applications, group robotics where autonomous robots (agents) cooperate with each other in a framework of autonomous distributed network would be a potential area, since collective survivability is a sort of a group problem solving. The similar approach can be used for group satellite systems where small-sized but autonomous satellites cooperate with each other to increase the collective survivability for a given mission.

This paper proposes a design for autonomous distributed systems that allows rearrangement of autonomous components (agents) thus realizing high survivability rather than high reliability. The design incorporates network rewiring by matching automaton [4, 5].

Section 2 briefly surveys matching problems including stable marriage problem and stable roommate problems. Section 3 defines matching automaton based on the matching problems. Section 4 presents a design principle of separating physical and information systems to attain rearrangement system by network rewiring. A paradigm shift from unit reliability to group survivability will be discussed in several potential applications.

2 MATCHING PROBLEMS

The *Stable Roommates Problem* (*SRP*) [6] assumes 2*N* participants, each of whom has a strict (without tie) ordered preference over the other 2*N-1* participants. The *SRP* seeks complete matching consisting of *N* pairs without being blocked. A matching is said to be blocked if a participant A prefer the participant C to the current roommate B in the matching and that preferred participant C also prefers A to the current partner D in the matching. The pair A-C is called as blocking pair.

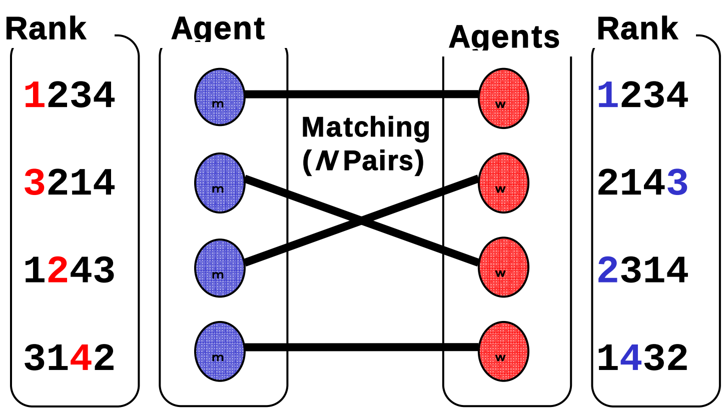

Fig. 1. An example of *SMP* instance specified by ordered preferences of men (left) and women (right) over the subscript of the member of the opposite sex. A bipartite graph shows a matching of *SMP* consisting of four pairs [9].

The *Stable Marriage Problem* (*SMP*) [7, 8, 9] assumes N women and N men, each of whom has a strict (without tie) ordered preference over the opposite sex. As in the example shown in Fig. 1, the man m_2 has a ranking (3, 2, 1, 4), which means that m_2 likes w_3 best, and prefers w_3 to w_2, w_2 to w_1, and w_1 to w_4.

The *SMP* seeks complete matching which satisfies *stability*. The stability requires the concept of *blocking pairs*. Two pairs (m_i, w_p) and (m_j, w_q) are blocked by the pair (m_i, w_q) if m_i prefers w_q to w_p and w_q prefers m_i to m_j. A complete matching without being blocked is called *stable* matching.

3 MATCHING AUTOMATON

Structure functions [10] to express the structure of system reliability and survival functions to evaluate a time to failure [11] have been used in system reliability theory for design and assessment of reliable systems. Similarly to the structural function used in system reliability, matching automaton [4, 5] will be used in collective survivability for design and assessment of survivable systems.

The matching automaton consists of two parts of N agents (automata) corresponding to men and women in the SMP. The preference is considered to be the input to the automata, and the resulting matching. In the interactive mode, the already determined pairs as well as the preference can be input to the agents whose pairs are to be determined, and that determined pair in turn can be the input to the rest of the agents, and so on.

The preference of each agent is expressed by a preference matrix $\{ a_{ij} \}$ where the element a_{ij} in the i^{th} row and j^{th} column is defined to be $R(m_i, w_j)/R(w_j, m_i)$ where $R(m_i, w_j)$ is the rank of m_i to w_j.

We will use the affinity matrix $\{A(m_i, w_j)/A(w_j, m_i)\}$ to specify the matching automaton. $A(m_i, w_j)$ is the man m_i's affinity for the woman w_j, and $A(w_j, m_i)$ is the woman w_j's affinity for the man m_i. The affinity is defined by the rank as: $A(m_i, w_j) = N + 1 - R(m_i, w_j)$, varying from N to 1 as the rank changes from 1 to N. In the following, the left matrix is the preference matrix and the right one is the affinity matrix of the example shown in Fig. 1. We will use the affinity matrix in the rest of the paper.

4/4,3/3,2/3,1/4	1/1,2/2,3/2,4/1
2/3,3/4,4/2,1/1	3/2,2/1,1/3,4/4
4/2,3/1,1/4,2/2	1/3,2/4,4/1,3/3
2/1,4/2,1/1,3/3	3/4,1/3,4/4,2/2

The cyclic preference can be generated by shifting one digit in the ordered list of 1, 2, 3, ..., N where N is the number of agents for one part.

For convenience of visualizing asymmetry and symmetry, the diagram is expressed on a coordinate system where women's satisfaction H_w and men's satisfaction H_m are defined as follows:

$$H_w(\mu) = \sum_{(w_j, m_i) \in \mu} A(w_j, m_i)$$

$$H_m(\mu) = \sum_{(w_j, m_i) \in \mu} A(m_i, w_j),$$

$A(w_j, m_i)$ is the woman w_j's affinity when the mating (w_j, m_i) is attained in a matching μ. All the possible matchings are plotted in the coordinate system of H_w on the vertical axis and H_m on the horizontal axis.

The matching automaton can be regarded as a discrete analog of a continuous dynamical model. In fact, Fig. 2 is called as *affinity space diagram*, and is similar to a *phase space diagram* which is often drawn for the continuous dynamical model where a stable matching (red node) corresponds to a stable equilibrium point (or an *attractor*) and the state proceeds to the stable matching as the exchange proceeds from an initial matching.

Since the matching automaton is a collection of automatons (similarly to cellular automatons) by identifying each agent as an automaton, the diagram of course can be regarded as a *state-transition diagram* where each node (corresponding to matching) represents a state and each edge represents a transition to and from by exchanging partners in two pairs.

As an illustration, let us explain the simplest matching automaton of a switching gate. The gate consists of two by two agents (*SMP* with size 2) and each agent in a set has a distinct preference to avoid symmetry; furthermore, each pair of agents has no first rank assignment (no *mutual infatuation*) to avoid fixation of the pair in matching. These restrictions lead to the following affinity matrix: 2/1, 1/2
1/2, 2/1.

With this preference as input, the behavior of the matching automaton is grasped by the affinity space diagram (Fig. 2). Note that only two matchings exist and both of them are stable. When the automaton seeks the women-optimal solution, then the matching will be the one on the upper left. On the other hand, if the automaton seeks the men-optimal solution, the matching will be switched to the one on the lower right.

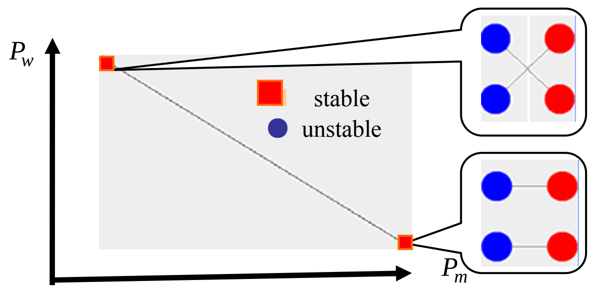

Fig. 2. An example of a switching gate realized by the matching automaton of 2 by 2 agents. Two squares indicate stable matchings. The matchings will be switched among one another by changing the mode of automaton, i.e., women-optimal or men-optimal [4].

4 NETWORK REWIRING BY MATCHING AUTOMATON

4.1 Separation of Physical Systems and Information Systems

Network-rewiring or rearrangement studied by matching automaton [4, 5] may be comparable to the network-rewiring by preferential rewiring in bipartite graph [12].

Network rewiring system by Matching Automaton can be applied to autonomous distributed systems such as a group of swarm robots and a group of networked satellites. Each robot (called $\boldsymbol{A_i}$, for the abbreviation of an agent i), for example, may be divided into two subsystems: physical system (called $\boldsymbol{P_i}$ for the agent i) including mechanical system, sensor system, and actuator system; and information system (called $\boldsymbol{I_i}$ for the agent i) including control and communication system from and to the sensor and actuator system.

Usually, in each agent $\boldsymbol{A_i}$, the information system $\boldsymbol{I_i}$ takes care of its own physical system $\boldsymbol{P_i}$, thus forming a disconnected independent nodes of $\boldsymbol{A_i}$. However, the remarkable feature of the network rewiring system is that $\boldsymbol{I_i}$ can take care of $\boldsymbol{P_j}$ ($i \neq j$), thus the network topology can be connected nodes of $\boldsymbol{A_i}$. In case of the failure of $\boldsymbol{P_i}$, $\boldsymbol{P_j}$ ($i \neq j$) can be used instead, and likewise in case of the failure of $\boldsymbol{I_i}$, $\boldsymbol{I_j}$ ($i \neq j$) can be used, thus attaining high survivability for the target tasks or the target missions. The rewiring can be used not only for collective survivability but also high robustness and high space/time resolution in sensory functions. The rewiring can be done by the Matching Automata if the preference between two sets $\{\boldsymbol{P_i}\}$ and $\{\boldsymbol{I_i}\}$ is determined considering the factors such as distances between the agents and the affinity among agents.

Matching automata is also used to evaluate the survivability of a given systems: two sets $\{\boldsymbol{P_i}\}$ and $\{\boldsymbol{I_i}\}$, and the preference between these two sets. If physical components $\boldsymbol{P_i}$ are equally important for the given mission, the preference (or affinity) from $\{\boldsymbol{I_i}\}$ should be distributed over all the $\boldsymbol{P_i}$ equally, otherwise (if the preference is biased toward one or few physical components) missing or malfunction of the preferred components would cause low preference (affinity) pair in any of rearrangements.

4.2 Application to Autonomous Networked Satellites

Recent advances in sensor network technology as well as collective intelligence robotics technology allows that these agents can be realized and used in the Space, that is "Sensor Net on the Space" and "Collective Intelligence on the Space" is technologically possible by small sized but ICT intensive satellites.

The framework of network rewiring by MA may be used in AntSat (AntSats, Autonomous Networked Tiny Satellites) project that aims a group of small satellites of mutually cooperative and controllable. Although sensing capability a single satellite may be limited, the space-time resolution of sensing will be greatly enhanced when a group of satellites cooperates with each other. Importantly, the survivability of a group of satellites will exceed that (reliability) of a single satellite when mutual repair and control are possible. This is true for a long term and a long distance mission demonstrated by Hayabusa [13]. Although CubeSat [14] also uses small size satellites, it does not assume Inter-satellites Corporation.

Whenever, some of the functions are disabled or failed, equal or similar functions will be enabled by rearrangement of the physical systems or the information systems. Again, the separation of physical systems and information systems will make the rearrangement possible.

Separation of physical systems and information systems allows not only rearrangement for collective survivability but also mutual repair and mutual recognition among autonomous satellites using a self-repairing network [15] and a self-recognition network [16]. For example, the self-recognition network formed by three sensors possibly from three satellites allows higher reliable prediction of High-energy Electron Flux at Geostationary Orbit [17] (Fig. 3).

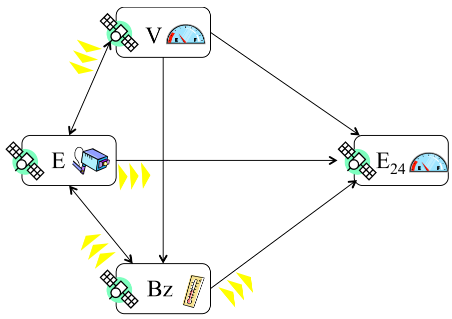

Fig.3. Mutual recognition network to predict High-energy Electron Flux at Geostationary Orbit [17]

The mutual recognition can be formed in a hierarchical system involving intra-satellite sensor systems as well as inter-satellite sensor systems (Fig. 4).

Similarly to the mutual recognition network, a mutual repair network can be formed among information systems (for the repair of information systems where repair may be carried out by mutual copying [14]) and among physical systems involving actuators that physically repair physical systems.

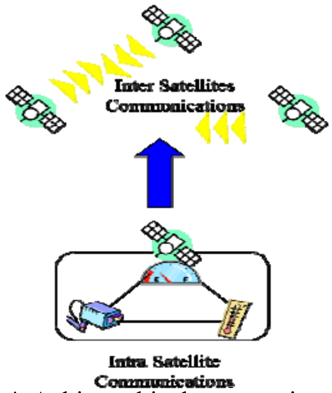

Fig. 4. A hierarchical system involving intra-satellite sensor systems as well as inter-satellite sensor systems.

4.3 Application to Formation of Sister Cities

As another avenue of network-rewiring application, disaster management may be worth mentioning. The following is basically a pairing, and matching automaton based on SRP as well as SMP can be used. First, we notice that the pairing of cities (or local governments) to provide mutual support in the case of natural disaster turned out to be effective as demonstrated after the Sichuan earthquake on 12 May, 2008 in China, and it is suggested that the policy could be implemented to support the recovery of the area damaged by the Tohoku earthquake on 11 March, 2011 in Japan. To set up the situation as a matching problem, preference may be carefully designed for disaster management and support. For, example, two cities close to each other would be damaged simultaneously by a large-scale natural disaster. To support and temporarily substitute the local industry specific to the city, the paired city should have a similar industrial structure. Thus, if we first want to separate cities that could be damaged by a disaster, we use MA of bipartite structure (as in SMP), as the west part and the east part in Japan. This is similar to separation of physical systems and information systems, but differs from it that a set of agents is divided into two, rather than dividing each agent.

If are separation is neither necessary nor inadequate, MA of single connected structure (as in SRM) may be used. The preference information required for each agent will be almost doubled though.

5 SUMMARY

Self-rewiring network is proposed to realize dynamic and functional rearrangement of components for collective survivability as well as collective sensing.

To realize self-active networks (self-rewiring, self-repairing, and self-recognition), a design principle of a separation of information systems from physical systems in each agent is adopted. Since the collective survivability may be applied to severe missions demonstrated by the Hayabusa project, an application to autonomous networked satellites has been briefly mentioned.

"Sensor network in the space" and "collective intelligence in the space" would be a technologically sound first step.

REFERENCES

[1] Barabási AL (2002). *Linked：The New Science of Networks*, Perseus Books Group
[2] Watts DJ (1999) *Small Worlds: The Dynamics of Networks Between Order and Randomness*, Princeton Univ Press
[3] Pastor-Satorras R, Diaz-Guilera A, *Statistical Mechanics of Complex Networks*, Springer (2003),
[4] Ishida Y, Hayashi T (2009) Asymmetric Phenomena of Segregation and Integration in Biological Systems: A Matching Automaton, *Lecture Notes in Computer Science* 5712, 789-796
[5] Ishida Y, Sasaki K (2011) Asymmetric Structure between Two Sets of Adaptive Agents: An Approach Using a Matching Automaton, *Lecture Notes in Computer Science* 6884, 362-371
[6] Irving RW (1985) An efficient algorithm for the "stable roommates" problem, *Journal of Algorithms* 6 (4)577–595
[7] Gale D and Shapley LS (1962), College admissions and the stability of marriage, *American Mathematical Monthly*, 69:9-15
[8] Gusfield D and Irving RW (1989), *The Stable Marriage Problem: Structure and Algorithm*, MIT Press
[9] Morizumi Y, et. al. (2011) A network visualization of stable matching in the stable marriage problem, *J. of Artificial Life and Robotics* 16(1)40-43.
[10] Tillman FA, Hwang CH, Kuo W (1980) *Optimization of Systems Reliability*, Marcel Dekker
[11] Elandt-Johnson R, Johnson N (1980). *Survival Models and Data Analysis*, John Wiley & Sons
[12] Ohkubo J, et. al. (2005) Generation of complex bipartite graphs by using a preferential rewiring process, *Physical Review* E 72, 036120
[13] Yano H, et. al., (2006) Touchdown of the Hayabusa Spacecraft at the Muses Sea on Itokawa *Science* 2 June, 1350-1353
[14] CubeSat Program official website http://www.cubesat.org/
[15] Ishida Y (2005) A Critical Phenomenon in a Self-repair Network by Mutual Copying, *Lecture Notes in Computer Science* 3682 86-92 Springer
[16] Ishida Y (2004) *Immunity-Based Systems: A Design Perspective*, Springer
[17] Tokumitsu M, et. al. Prediction of space weather by adaptive information processing, *J. of Artificial Life and Robotics*, 16-1, pp. 32-35, 2011

The Seventeenth International Symposium on Artificial Life and Robotics 2012 (AROB 17th '12),
B-Con Plaza, Beppu, Oita, Japan, January 19-21, 2012

Network Analysis of Ecologocal Footprint & CO2 Emission based on Input-Output Table for East Asia

X. Gao, T. Fujiwara, N. Sakurai, K. Yoshizawa, S. Miyake, Z. Zheng, K. Yamasaki

Tokyo University of Information Sciences, 4-1 Onaridai, Wakaba-ku, Chiba,Japan
(Tel&Fax : 81-43-236-4653)
(g11002sk@edu.tuis.ac.jp)

Abstract: We study the Input-Output table for East Asia as complex networks. The 50%~95% of sum of the off-diagonal elements is included in several percent of the big off-diagonal elements of the Input-Output table. This makes the network representation useful. We make the extracted networks with these big off-diagonal elements. The distributions of these off-diagonal elements (edge values) are power law shape with exponents of 2.56(money base), 2.07(EF base) and 2.00(CO2 emission base) on the average. EF base and CO2 base inter-dependences between industry sections are more unequal than money base, so from environmental point of view, a fewer inter-dependences are important. We can see the differences of the maximum 'degree', 'closeness' and 'the sum of elements (edge values)' in developed nations and in developing nations.

Keywords: Ecological Footprint, CO2 Emission, Input-Output table, Induced analysis, Complex Networks

I. INTRODUCTION

How production in each industry causes environmental impacts becomes more important for reducing these impacts and sustaining the earth for future. One of the methods to research this problem is to use environmental extension of Input-Output table. For decades, Input-Output table has been studied for analyzing the nation or regional economy on the basis of the inter-industry relations of how much production in one section is induced by the production in other sections. Generally, inter-industry relations are complicated, so it is not easy to extract the useful information to appeal to intuition. On the other hand, lots of studies on the topic of complex networks have been done recently and applied to various fields. Network representation is suitable to appeal to intuition and various analytical methods in this area help our deep understanding of the problems. And the Input-Output table can be thought as network matrix, but few studies of the complex networks have been applied to Input-Output table. [1][2][3] Moreover it is interesting to compare the economy (money) base inter-industry relations and the environmental impact base ones.

There are a lot of representations of environmental impact. One of them is Ecological Footprint (**EF**)[4] and other is CO2 emission. EF is one of the sustainable indexes, which converts nation's or regional basic consumption to the nation's or regional virtual area which is necessary to produce it. For example, we consume agricultural products to keep our life. These consumptions are converted to cropland area. Finally the virtual area caused by our total consumption is compared to bio capacity of the earth. The CO2 emission is most severe environmental impact which has to be reduced.

So in this paper, we compare inter-industry relations of money base , EF base and CO2 emission base.

II. INDUCED ANALYSIS OF ENVIRONMENTAL IMPACT

EF is represented by total area of six land types, "Cropland", "Forest", "Grazing land", "Fishing ground" , "Carbon uptake land" and "Built-up land". Each area is calculated to reproduce our final consumption as necessity area for "the supplies of crop", "the supplies of wood", "the supplies of livestock feed", "the supplies of fish", "absorption of CO2 emission" and "house, factory, road etc.". And it is compared to the real area (bio capacity) on the earth. Actually Japan needs 2.5 times as much area as real Japan area to keep our lifestyle. Whole world people need more area than whole area of the earth.

EF is calculated for an area on the basis of consumption in the area. That is, EF of the imported product does not belong to the nation in which the product is produced but it belongs to the nation in which the product is consumed.

$$EF_N = \sum_{\alpha,i,j\ldots k,\Omega} \frac{1}{y_{N,\alpha}} \varepsilon_{l(\alpha)} \psi_{N,l(\alpha)} \chi_{\alpha i} \chi_{ij} \cdots\cdots \chi_{k\Omega} C_\Omega \quad (1)$$

Here C_Ω is the weight of the consumed product Ω of which we want to know the effect, χ_{ij} is the weight of the product i to produce unit weight of product j, $\varepsilon_{l(\alpha)}$ is the equivalence factor of land type $l(\alpha)$ for the product α *, $\psi_{N,l(\alpha)}$ is yield factor of nation N and land type $l(\alpha)$, $y_{N,\alpha}$ is the average weight of the product from unit area in the nation N. And the sums are executed in all paths from product Ω to product α through intermediate products *i*, *j*... Using the matrix representation, $\{1+\chi+\chi\chi+\chi\chi\chi+\quad\}=[1-\chi]^{-1}$, and

$$EF = \vec{\lambda}[\mathbf{1}-\boldsymbol{\chi}]^{-1}\vec{C} \tag{2}$$

here $\vec{\lambda}$, $\vec{C}$ is vector representation of $\varepsilon_{l(\alpha)}\psi_{N,l(\alpha)} / y_{N,\alpha}$ and C_{Ω}, $\boldsymbol{\chi}$ is the matrix representation of χ_{ij} and $\mathbf{1}$ is unit matrix and we omit the nation's suffix N in *EF* and $\vec{\lambda}$.But usually it is difficult to know χ_{ij} of all products' pairs [*i*, *j*] without double counting. Sometimes we want to measure the effect of consumption toward other industrial sectors or toward other nations, not only on economic impact but also on environmental impact. Input-Output table enables us to calculate such impacts by induced analysis.

$$EF = \vec{\lambda}[\mathbf{1}-\boldsymbol{\chi}]^{-1}\vec{C} + \vec{\lambda}^{fuel}\vec{C} \tag{3}$$

In eq.(3), $\vec{C}$ is a demand vector of sectors expressed by amount of money, $\boldsymbol{\chi}$ is the coefficient matrix and $[\mathbf{1}-\boldsymbol{\chi}]^{-1}$ is the Leontief Inverse Matrix of the Input-Output table. $\vec{\lambda}$ is a kind of induced value added vector which shows environmental impacts. Additional term $\vec{\lambda}^{fuel}\vec{C}$ represents CO2 emission from the direct fuel use of final consumption. For example, in case of agriculture sector, $y_{N,\alpha}$ is the total amount of agricultural product divided by the total area of the Cropland of the considering region N. $\varepsilon_{l(\alpha)}$ is the equivalence factor of Cropland, $\psi_{N,l(\alpha)}$ is yield factor of the region N and Cropland .

There is another method to calculate the vector $\vec{\lambda}$. Global Footprint Network (GFN) calculates nation's EF_l of each land type l every year and these EF_l s represent the area after considering the productivity.

If EF_l s were distributed to each sector α (They are called direct EFs), $\vec{\lambda}$ is able to replace by them. The merit of this method is that induced EFs are able to compare to other nations' EFs through EFs calculated by GFN.

III. NETWORK REPRESENTATION

Our purpose of this paper is to study inter-industry relation on the economy (money) base and environmental impact base by network representation. So we rewrite the vectors $\vec{\lambda}$ and $\vec{C}$ to the diagonal matrix $\boldsymbol{\lambda}$ and $\mathbf{C}$. Then we get the basic matrix.

$$\mathbf{W} = [\mathbf{1}-\boldsymbol{\chi}]^{-1}\mathbf{C} \tag{4}$$

$$\mathbf{EF} = \boldsymbol{\lambda}[\mathbf{1}-\boldsymbol{\chi}]^{-1}\mathbf{C} + \boldsymbol{\lambda}^{fuel}\mathbf{C} \tag{5}$$

$$\mathbf{EF}_C = \boldsymbol{\lambda}_C[\mathbf{1}-\boldsymbol{\chi}]^{-1}\mathbf{C} + \boldsymbol{\lambda}_C^{fuel}\mathbf{C} \tag{6}$$

Here eq.(4), eq.(5) and eq.(6) are the matrix representations of normal induced analysis, of EF base (eq(3)) and of CO2 emission EF base. $\boldsymbol{\lambda}_C$ is one part of $\boldsymbol{\lambda}$ calculated by EF of Carbon uptake land.

$\mathbf{W}$, $\mathbf{EF}$ and $\mathbf{EF}_C$ are no symmetric matrix with diagonal elements, so they can be thought as the adjacency matrix of the directed multi-weighted networks.

IV. Input-Output Table for East Asia

We use "Input-Output table for East Asia" of 2000 [5]. This Input-Output table includes the data of 8 nations in East Asia (China, Indonesia, Japan, Korea, Malaysia, Philippines, Singapore, Thailand) and the data of USA. In this paper, we split this table into each nation's table with 76 industry sections.

1. To calculate the matrix $\boldsymbol{\lambda}, \boldsymbol{\lambda}^{fuel}, \boldsymbol{\lambda}_C, \boldsymbol{\lambda}_C^{fuel}$, we allocate the EF calculated by GFN to each sector of each nation. EFs are allocated in proportion to the total of each sector according to the Table 1. We reallocate the CO2 emission data provided by International Energy Agency(IEA) into the 76 sectors of Input-Output table. Next we allocate the Carbon uptake land EF into 76 sectors in proportion to these CO2 emission data.

Table 1. Land types and corresponding sectors

1	EF of Cropland	Agriculture sectors
2	EF of Forest	Forestry sectors
3	EF of Grazing land	Agriculture sectors
4	EF of Fishing ground	Fishery sectors
5	EF of Carbon uptake land	All sectors Final consumption
6	EF of Built-up land	All sectors

2. Using the Input-Output table, we calculate eq.(4), eq.(5) and eq.(6).
3. The networks represented by the adjacency matrixes $\mathbf{W}$, $\mathbf{EF}$ and $\mathbf{EF}_C$ are directed multi-weighted networks. But the analytical tools for directed multi-weighted networks have not been developed well, so in this paper we extract directed un-weighted networks as follows.

Extraction of the network

1. We make complete network of all industry sections as nodes being connected each other by edges.
2. We remove edges from the complete network in order from the smaller corresponding matrix elements until the number of nodes of largest connected network becomes 38(half of the number of all nodes).

V. RESULT

Figure 1 shows extracted network of **EF** in Japan, which includes 38 nodes. Figure 2 shows the distribution of off-diagonal elements (edge values) of the matrix **EF** of Japan. The edges (log(edge values) >

31, right side of the dotted line) remain in extracted network. Log-log plot of the cumulative distribution of extracted network is shown in Figure 3. It shows power law with exponent -2.12+1. For example in Japan, Table 2 shows that only 2.13%(money base), 1.83%(EF base) and 2.17%(CO2 base) of all edges remain in extracted network, but the sum of these edge values reaches 51.9% , 77.2% and 80.8% of the sum of all edge values. In EF base network, the smaller number of edges have more edge values than money base network. In CO2 base network, the smaller number of edges have more edge values than EF base network. The power law exponents in 27 extracted networks are summarized in Table 3. In Japan, power law exponents are 2.79, 2.12 and 2.08 on money, EF and CO2 base. Table 4 shows industry sections (nodes) of maximum degree, of maximum closeness and of maximum sum of elements (edge values), being calculated by out-edge and in-edge separately. In developed nations (USA, Japan, Korea, Singapore), on money base, Building construction sector has maximum connection and gives large influence to other sectors. On EF base and CO2 emission base, Wholesale and retail trade sector has maximum connection to inward direction. On money, EF and CO2 emission base, Other services sector has maximum connections to inward direction and gets large influence from other sections.

In developing nations (China, Malaysia, Philipines, Thailand, Indonesia), on money base, Wholesale and retail trade sector has maximum connection to inward direction from other sections. On EF base, Livestock and poultry/ Fishery/ Food crops have maximum connection to the outward direction to other sections. But on CO2 emission base, Wholesale and retail trade sector has maximum connection to the outward direction to other sections.

V. CONCLUSION

We study the Input-Output table for East Asia as complex networks. We show that 'the complex networks' is suitable method for these studies. We find the basic characteristics of the inter-connection between industry sections. Although we have not studied the international relations, it is expected that these studies will be able to make clear the way on which nations have developed with inter-nations connection if we study the Input-Output table of other years.

Acknowledgements

The study was supported by research project for a sustainable development of economic and social structure dependent on the environment of the eastern coast of Asia. We thank for not only financial support but also helpful discussion of the project members.

REFERENCES

[1]Wang H. et al, Multi-Weighted Monetary Transaction Network, Advances in Complex Systems, Vol. 14, No. 5 (2011) 691–710

[2] Yoshizawa K., T. Fujiwara, Z. Zheng , R. Shiba, N. Sakurai, K. Yamasaki(2010), Network Analysis of Japanese Ecological Footprint based on Input-Output Table for the 47 Prefectures in Japan, Proceedings of FOOT PRINT FORUN 2010

[3] Fujiwara T., K. Yoshizawa, N. Sakurai, K. Yamasaki (2010), The Analysis of Ecological Footprint using Multi-regional Input Output Table for 47 Prefectures in Japan, Proceedings of 38th Annual Meeting of Environmental Systems Research 2010, pp.239-243. (in Japanese)

[4]Ewing B. et al, Calculation Methodology for the National Footprint Accounts, 2010 Edition

[5] JETRO http://www.ide.go.jp/Japanese/Publish/Books/Tokei/material.html

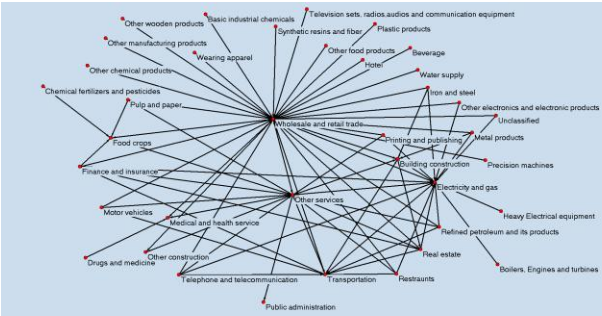

Fig. 1 Extracted network made by matrix **EF** in Japan, which includes 38 edges.

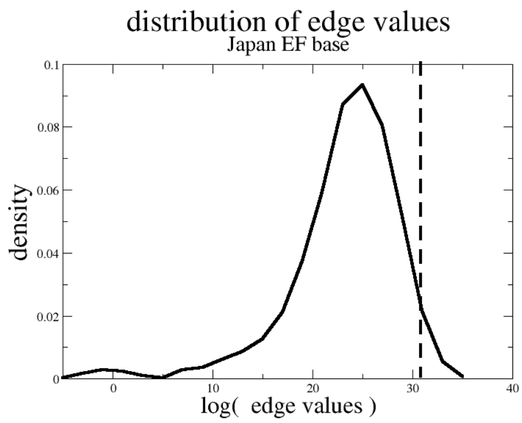

Fig. 2 Distribution of off-diagonal elements (edge values) of the matrix **EF** of Japan. The edges, log(edge values) > 31, remain in extracted network.

Table 4 Industry sections (nodes) of maximum degree, of maximum closeness and of maximum sum of elements (edge values), being calculated by out-edge and in-edge separately.

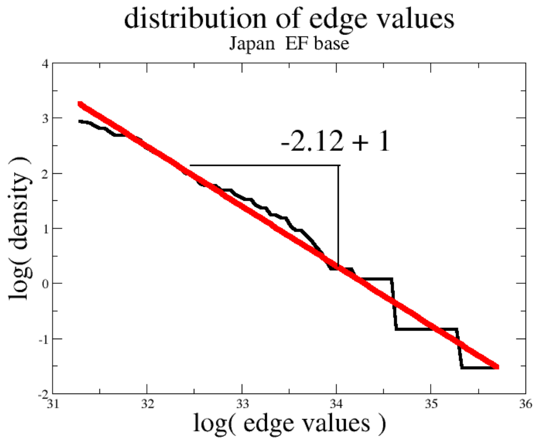

Fig. 3 Log-log plot of cumulative distribution of off-diagonal elements (edge values) of remaining in extracted network. Straight line is the least-squares approximation of the distribution. It shows power law with exponent -2.12+1.

Table 2 Percentage of the number of edges included in extracted network per the number of edges in complete network. And percentage of the sum of edge values included in extracted network per the sum of edge values in complete network.

	money		EF		CO2	
matrixes	**W**		**EF**		$\mathbf{EF}_C$	
Indonesia	1.28	54.90	2.22	81.90	1.48	82.30
Malaysia	1.85	59.30	2.30	81.60	6.98	91.00
Philippines	3.02	80.10	2.44	89.50	2.21	93.20
Singapore	5.13	83.20	2.21	97.60	23.90	99.00
Thailand	1.42	55.80	1.79	81.00	2.00	85.80
China	1.29	38.20	2.68	71.60	1.47	58.00
Korea	2.2	51.10	2.47	71.60	2.37	76.00
Japan	2.13	51.90	1.83	77.20	2.17	80.80
USA	2.2	60.40	1.29	86.10	1.43	88.80
average	2.28	59.43	2.14	82.01	4.89	83.88

Table 3 Power law exponents of distribution of off-diagonal elements in 27 extracted networks

	money	EF	CO2
matrixes	**W**	**EF**	$\mathbf{EF}_C$
Indonesia	2.69	2.17	2.03
Malaysia	2.69	2.10	1.99
Philippines	2.33	1.94	1.80
Singapore	2.14	1.70	1.65
Thailand	2.60	2.06	1.88
China	2.65	2.38	2.52
Korea	2.59	2.16	2.06
Japan	2.79	2.12	2.08
USA	2.56	1.97	1.96
average	2.56	2.07	2.00

BC Building construction
OS Other services
WR Wholesale and retail trade

Table 4

money base		USA		Japan		Korea		Singapore		China		Malaysia		Philipines		Thailand		Indonesia	
out	hub	BC	[19,2]	BC	[16,3]	BC	[16,1]	BC	[24,2]	BC	[23,0]	BC	[18,0]	Other food products	[16,7]	Public administration Restraunts	[11,0]		
	closeness	Public administration	0.50	BC	0.46	BC	0.44	BC	0.69	BC	0.63	BC	0.51	Public administration	0.52	Public administration	0.34	Other construction	0.35
	sum of edge [US$1000]	Public administration	7E+08	BC	3E+08	BC	4E+07	BC	7E+06	BC	3E+08	BC	4E+06	Other food products	4E+06	Public administration	1E+07	Other construction	1E+07
in	authority	OS	[7,16]	OS	[9,16]	OS	[7,11]	OS	[13,22]	WR	[0,5]	WR	[0,10]	WR	[8,18]	WR	[8,11]	WR	[2,16]
	closeness	OS	0.45	OS	0.45	OS	0.32	WR	0.74	WR	0.18	WR	0.37	WR	0.5	WR	0.32	WR	0.45
	sum of edge [US$1000]	OS	1E+09	OS	4E+08	OS	3E+07	OS	6E+06	Iron and steel	8E+07	WR	2E+06	OS	3E+06	WR	7E+06	WR	1E+07

EF base		USA		Japan		Korea		Singapore		China		Malaysia		Philipines		Thailand		Indonesia	
out	hub	WR	[34,2]	WR	[29,7]	WR	[22,6]	WR	[35,4]	Livestock and poultry	[29,0]	Fishery	[17,0]	Fishery	[20,0]	WR	[28,5]	Food crops	[22,3]
	closeness	WR	0.92	WR	0.79	WR	0.62	WR	0.95	Livestock and poultry	0.79	Fishery	0.55	Fishery	0.61	WR	0.78	Food crops	0.68
	sum of edge [gha][US$1000]	WR	2E+17	WR	1E+16	WR	3E+14	WR	7E+12	Livestock and poultry	1E+16	Fishery	5E+12	WR	1E+13	WR	5E+13	Food crops	6E+13
in	authority	OS	[4,8]	OS	[12,10]	OS	[10,11]	OS Finance and insurance	[0,5]	Chemical fertilizers and pesticides	[0,6]	WR	[12,9]	OS	[0,11]	Refined petroleum and its products	[1,5]	OS	[0,8]
	closeness	OS	0.24	OS	0.29	OS	0.32	Finance and insurance	0.16	Refined petroleum and its products	0.26	OS	0.27	OS	0.32	Crude petroleum and natural gas	0.16	WR	0.32
	sum of edge [gha][US$1000]	OS	1E+17	OS	5E+15	Refined petroleum and its products	8E+13	OS	2E+12	Chemical fertilizers and pesticides	4E+15	Refined petroleum and its products	4E+12	Refined petroleum and its products	8E+12	Refined petroleum and its products	2E+13	WR	3E+13

CO2 base		USA		Japan		Korea		Singapore		China		Malaysia		Philipines		Thailand		Indonesia	
out	hub	WR	[35,2]	WR	[30,6]	WR	[30,5]	WR	[37,2]	WR	[22,3]	Electricity and gas	[24,7]	WR	[28,7]	WR	[33,3]	WR	[28,7]
	closeness	WR	0.95	WR	0.82	WR	0.82	WR	1	WR	0.63	WR	0.76	WR	0.79	WR	0.902	WR	0.77
	sum of edge [gha][US$1000]	WR	2E+17	WR	1E+16	WR	3E+14	WR	7E+12	Electricity and gas	3E+15	Electricity and gas	3E+12	WR	1E+13	WR	4E+13	WR	3E+13
in	authority	OS	[4,7]	OS	[12,9]	OS	[10,7]	OS Finance and insurance	[0,3]	Crude petroleum and natural gas Refined petroleum and its products	[0,4]	Crude petroleum and natural gas	[1,5]	Refined petroleum and its products	[3,6]	Refined petroleum and its products	[1,3]	Crude petroleum and natural gas	[0,4]
	closeness	OS	0.21	OS	0.26	Iron and steel	0.23	Refined petroleum and its products	0.11	Crude petroleum and natural gas	0.14	OS	0.24	OS	0.24	Crude petroleum and natural gas	0.13	WR	0.21
	sum of edge [gha][US$1000]	OS	1E+17	OS	5E+15	Refined petroleum and its products	7E+13	OS	2E+12	Refined petroleum and its products	8E+14	Crude petroleum and natural gas	2E+12	Refined petroleum and its products	4E+12	Refined petroleum and its products	1E+13	Crude petroleum and natural gas	1E+13

[7,16] = [7 out edges, 16 in-edges]

The Seventeenth International Symposium on Artificial Life and Robotics 2012 (AROB 17th '12),
B-Con Plaza, Beppu, Oita, Japan, January 19-21, 2012

The fluctuation in Carbon emission trading Market

Zeyu Zheng[1], Naoko Sakurai[1], Takeshi Fujiwara[1] Kousuke Yoshizawa[1] and Kazuko Yamasaki[1]

[1]Tokyo University of information sciences, Wakaba-ku,Chiba 265-8501 Japan

(Tel: 81-43-236-4652, Fax: 81-43-236-4652)

[1]zhengzy@edu.tuis.ac.jp

Abstract: As an emerging financial market, the trading value of Carbon emission trading Market are definitely increased in recent years. The carbon emission is not only trading in Carbon emitters but also become an important investment target. For reveal the mechanism of this growing market, we analyzed the EU allowances (EUA) price series in European Climate Exchange (ECX), that is the leading European emissions futures market. As other financial market, the absolute value of price change (volatility) in Carbon emission trading Market also shows long-term power-law correlations. Our analysis shows that definite cross correlations exist between EUA and many other markets. These cross correlation exist in wild-range fields, stock market index, futures of crude, sugar, cocoa, etc. it suggest that in this new carbon emission trading market the speculation behavior had already become a main factor that can affect the price change.

Keywords: carbon emission, emerging financial market, Minimal-spanning trees,long-term power-law correlations

1 INTRODUCTION

Many social systems are characterized by complex int eractions between a large numbers of individual compo nents, which manifest in power-law Correlations. For e xample, in financial field, several stylized facts have b een found for the equity price data in temporal field, s uch as 1, the distribution of the stock price changes (r eturn) has a power-law tail. 2, the absolute value of st ock price change (volatility) is long-term power-law co rrelated. 3. The spectral density of stock price is well described by power-law function. Such as 1, the distrib ution of the stock price changes (return) has a power-l aw tail. 2, the absolute value of stock price change (v olatility) is long-term power-law correlated. 3. The spe ctral density of stock price is well described by power -law function [3-5].

In the field of physics and economy, not only the c haracter of a single asset (time series) is important, bu t also the cross-correlations between pairs of assets pla y a key role in the financial analysis. The taxonomy a nalysis for a stock portfolio is considered as a useful method. The investigation of correlation distance of dif ferent stocks can extract economic information stored i n the stock-price time series, and define the metric of the relative distance between the stocks included in po rtfolio. In this study we investigate the relative distanc es based on daily price time series of EU allowances (EUA) and with other stock and futures markets. The Minimal-spanning trees (MST) are determined by the r elative distances.

2 TAXONOMY OF EUA AND SOME OTHER MARKET

A method of determining a distance between time seri es (usually stock price time series) i and j evolving in time in a synchronous fashion is the following.

$$\tilde{S} \equiv \frac{S_i - \langle S_i \rangle}{\sqrt{\langle S_i^2 \rangle - \langle S_i \rangle^2}} \qquad (1)$$

Where S_i the logarithmic price difference of time seri es i, is given by equation (2).

$$S_i \equiv \ln Y_i(t) - \ln Y_i(t-1) \qquad (2)$$

Here is the daily closure price of time series i at tim e t, and S_i is the daily change of the logarithm of t he price of stock i.

The Euclidean distance d_{ij} between vectors $\tilde{S}_i$ and $\tilde{S}_j$ is obtainable from the Pythagorean relation. If th ere have n time series of $\tilde{S}_i$ present in the same tim e interval. The distance of time series i and j can b e described as equation (3)

$$d_{ij} = \| \tilde{S}_i - \tilde{S}_j \|^2 = \sum_{k=1}^{n} (\tilde{S}_{ik} - \tilde{S}_{jk})^2 \qquad (3)$$

The d_{ij} can also be described by correlation coefficie nt ρ_{ij}, as following function, the correlation coefficien t assume values ranging from -1 to 1.[1]

$$d_{ij} = \sqrt{2(1-\rho_{ij})} \qquad (4)$$

Because Equation (3) defines a Euclidean distance the following three properties must hold:

$$d_{ij} = 0 \Leftrightarrow i = j$$

$$d_{ij} = d_{ji}$$

$$d_{ij} \le d_{ik} + d_{kj}$$

Thus the quantity d_{ij} fulfills all three properties that must be satisfied by a metric distance. In the presence of a metric space in which n objects are linked toget her, the subdominant ultrametric can be obtained by de termining the minimal spanning tree (MST) connecting n objects. The MST is a concept in graph theory [2]. In a connected weighted graph of n objects, the MST is a tree having n-1 edges that minimize the sum of the edge distances.

In our study, we select 22 worldwide financial price time series from 2007 to 2010, which include 6 stoc ks indicates and 16 future options that include EU all owances (EUA). The data are download from finance yahoo and European Climate Exchange ECX market. All financial daily price time series that used in our study are list in Table 1.

Table 1. The list of financial products used in our stu dy

Name	***Description***
NYdow	indicator of NYDOW stock excha nge
FTSE100	Financial Times Stock Exchange 1 00 Index
BSE30	Bombay Stock Exchange Sensitive Index
BVSP	indicator of Sao Paulo Stock Exch ange
Nikkei	indicator of Tokyo stock Exchange
SSEindex	indicator of Shanghai stock Excha nge
Treasury30	U.S. 30-year bonds
UKgilt_all	Average UK gilt
EUA	EU allowances future price
WTI	West Texas Intermediate
RIchard_bay_Coal	Future price of coal loading at Ri chards Bay in South Africa
EUR_Index	Index of Euro
UK_Nature_Gas	Future price of UK nature gas
UK_Base_Electrici ty	Future price of UK base Electricit y
Coffee_C	Future price of Coffee in ECX
Sugar_No_11	Future price of Sugar No. 11
FCOJ-A	Future price of FCOJ A
Cotton_No_2	Future price of Cotton No.2
US_Dollar_Index	Index of US Dollar
Western_Barley	Future price of Western Barley
Canola_Futures	Future price of Canola of Canada
RJ/CRB_Index	Reuters Jefferies/CRB Index, benc hmark indicator of overall commo dity price

We calculate the relative distance of each two price time series from 2007 to 2010 by using equation (3). Next the MST can be produced by these relative dista nces. It is shown in Figure 1.

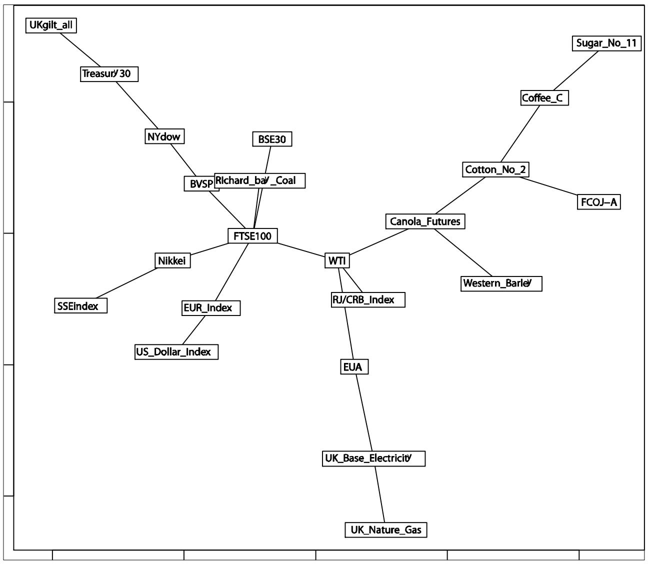

Fig. 1. The structure of minimal spanning tree (MST) for the time period 2007 to 2010.

From Figure 1, we can find that all stocks indicate b ecome a group, and EUA are strong correlated with ga s and electricity futures. In this graph we also find tha t WTI and FTSE100 are two key financial products, th e two connect the stocks and futures. Moreover, we fi nd that the same type financial productions are closer than different type. For example debt future Treasury30 and UKgilt are connected, EUR and Dollar futures ar e also connected.

3 STABILITY OF MST

In chapter 2, we investigate the relative distance of our selected worldwide financial products. Next we want to know how stable a minimal spanning tree structure can be. So we showed the minimal spanning tree obtained in the calendar years from 2007 to 2010 for the 22 financial products.

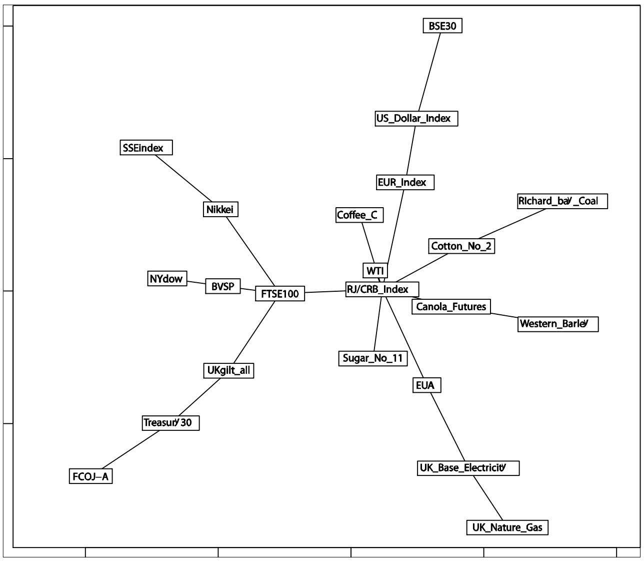

Fig. 2. The minimal spanning tree of 2007

In Figure 2, we show the MST during the calendar year 2007. From this graph we also find that the stock indicates and futures are grouped into two sides. The WTI and FTSE100 also show important characters. Different with figure 1, RJ/CRB index become Central node instead of WTI. Next, the FCOJ-A is moved to stock and debt side, BSE30 is connected with US dollar index. EUA are also correlated with nature gas and electricity futures.

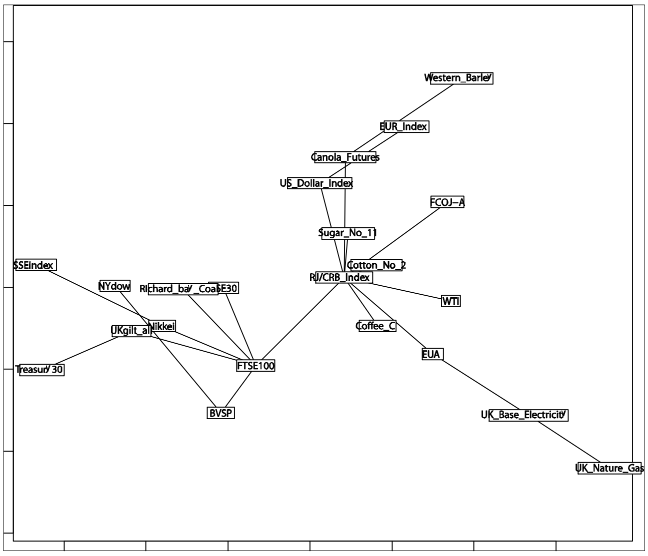

Fig. 3. The MST minimal spanning tree of 2008

Figure 3, shows the MST during the calendar year 2008. Compare with Figure 2 that is from 2007, the structure of MST is more similar with figure 1. The EUA connections with gas and electricity futures are still existed.

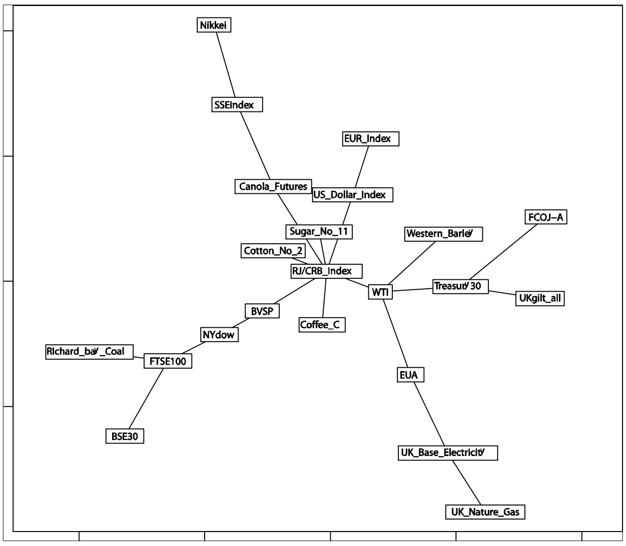

Fig. 4. The MST minimal spanning tree of 2009.

Figure 4, shows the MST during the calendar year 2009. The structure of MST is changed a lot, it look likes a one center tree, the center is RJ/CRB index. But the basic links are not changed, the stocks are connected as one group, debt future and currency index are connected too.

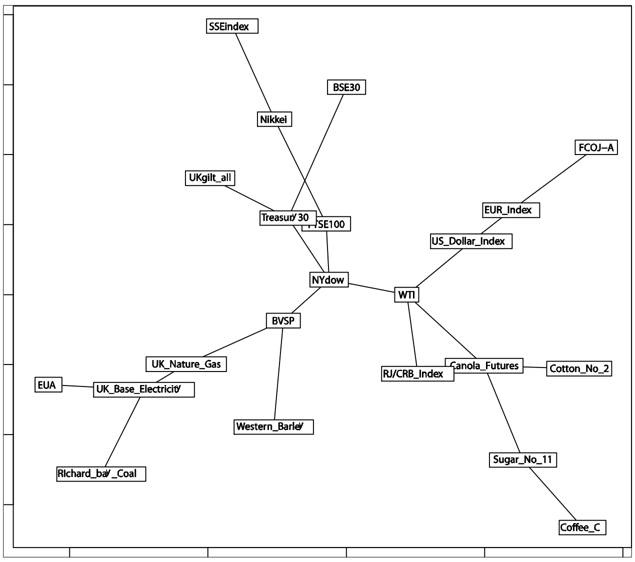

Fig. 5. The MST minimal spanning tree of 2010

Figure 5, shows the MST during the calendar year 2010. EUA are correlated with nature gas and electricity futures, and the base electricity future is connected with Coal. WTI and NYdow are two key financial products which connect the stocks and futures.

In these figures, the correlations of EUA and gas and electricity futures are observed in all years. It indicates that the stable correlation of EUA, nature gas and electricity futures. In all financial produces we may find that the center nodes of the structures are always included in next four products, WTI, RJ/CRB index, NYdow and FTSE100.

In summary, the Figure 2 to Figure 5 show that the MST is time dependent, but maintains on a time scale of years a basic structure that exhibits some meaningful economic correlations.

4 SUMMARY

In our study we have seen that is possible to devise strategies that allow us to obtain meaningful structure of taxonomies if we start from the synchronous analysis of more than one price time series. We find that compare with other links the links of EUA and Nature gas and base electricity price. It indicates d that the Carbon emission are more depended on nature gas and base electricity than other elements. Our study also show that the MST is time dependent, and it maintains on a long time scale a basic structure. The structure may exhibits some meaningful economic correlations.

5 ACKNOWLEDGEMENT

We thank JSPS for grant of "Research project for a s ustainable development of economic and social structur e dependent on the environment of the eastern coast o f Asia" that made it possible to complete this study.

REFERENCES

[1] Mantegna Rosario N, Stanley H Eugene (2000), Econophysics. Cambridge University Press New York.
[2] Mantegna RN (1999), Hierarchical structure in Financial Markets, Eur. Phys. J. B. 11, 193-197.
[3] Yamasaki K, Gozolchiani A, Havlin S, et al (2008), Climate Networks around the Globe are Significantly Affected by El Nino, Physics Review Letter 228501.
[4] Yamasaki K, Muchnik L, Havlin S, et al (2005), Scaling and Memory in Volatility Return Intervals in F inancial Markets, Proceeding of National Academy of Sciences, 9424.
[5] Wang F, Yamasaki K, Havlin S, et al (2006),Scalin g and memory of intraday volatility return intervals in stock markets, Physics Review E, 26117.

The Seventeenth International Symposium on Artificial Life and Robotics 2012 (AROB 17th '12),
B-Con Plaza, Beppu, Oita, Japan, January 19-21, 2012

Development of Stream Data Platform in Satellite Image Data Analysis System

Eiji Nunohiro[1], Hayao Mori[2], Masaki Hanada[1], Kenneth J. Mackin[1] ,and Jong Geol Park[1]

[1] Tokyo University of Information Sciences, 4-1 Onaridai, Wakaba-ku, Chiba 265-8501, Japan
[2] Graduate School of Tokyo University of Information Sciences, 4-1 Onaridai, Wakaba-ku, Chiba 265-8501, Japan
(Tel: 81-43-236-1292; Fax : 81-43-236-1292)

[1] nunohiro@rsch.tuis.ac.jp

Abstract: Tokyo University of Information Sciences receives MODIS (Moderate Resolution Imaging Spectroradiometer) data, one of the sensors equipped by NASA's Terra and Aqua satellites, and researches of the analysis on change of environment as part of the academic frontier project. For the information infrastructure of this frontier research, we are currently developing a satellite image data analysis system (SIDAS) implemented as a web system, with parallel distributed system configuration using multiple PC clusters, database for MODIS data, and applications to analyze the environmental changes. SIDAS is used to open the research results and MODIS data for public use. In this research, we are developing SIDAS 1.2 using the previously developed SIDAS 1.1 as the basic system. The main feature of SIDAS1.2 is the function of stream data processing, used to analyze the influence of the East Japan Earthquake and the monitor the regrowth of vegetation for the tsunami-stricken area in Tohoku region.This paper presents the overview of system configuration, the stream data processing and analysis functions of SIDAS 1.2.

Keywords: Satellite image data, MODIS, Stream Data Platform.

1 Introduction

Tokyo University of Information Sciences (TUIS) receives MODIS (Moderate Resolution Imaging Spectroradiometer) data, one of the sensors on NASA's Terra and Aqua satellites, and provides the processed data to universities and research institutes as part of the academic frontier project. The main research theme of this project is on “the sustainable development of economic and social structure dependent on the environment in eastern Asia”. One of the major fields of research using MODIS data is the analysis of change in the environment. In this research, we are developing satellite image data analysis system (SIDAS) to support the frontier research such as weather change and environmental changes. In order to improve the accuracy of the analysis, we have developed SIDAS 1.1 which is implemented as a web system, with a parallel distributed system configuration using multiple PC clusters and a database system. SIDAS 1.1 has already supported several applications to analyze the satellite data such as “search system for fire regions in forests and fields” and “search system for similar satellite image data”.

The purpose of our present study is to support the recovery from the East Japan Earthquake. In the research, we examined methods to observe the reconstruction of northeastern Japan after the East Japan Earthquake of March 11, 2011 by using the MODIS data. From these results, we are developing SIDAS 1.2 in order to provide the change of vegetation in time series of the north eastern regions, using the previously developed SIDAS 1.1 as the basic system. The main feature of the updated system is the addition of time series data processing to allow the analysis of the influence of the East Japan Earthquake and the revival of vegetation in the tsunami stricken area in north eastern regions. This paper presents the overview of system configuration, the stream data processing and analysis features of SIDAS V1.2 enhancements for the observation of the reconstruction from the East Japan Earthquake in the north eastern regions.

2 Overview of satellite data analysis system (SIDAS)

In this section, we describe the satellite data analysis system (SIDAS) to support the research environment and open the research results for public use. Figure 1 shows the overview of SIDAS 1.1. SIDAS 1.1 consists of a web server, an application server consisting of multiple PC clusters, and a database server. The application server schedules the execution of applications, manages the satellite data, and controls PC clusters which execute applications. The user can access the system, request data analysis and check the results over the network via a Web browser or other web applications, and the user can also download satellite image data through the system.

The processing flow of SIDAS1.1 is shown as follows.

(1) The Web server accepts request of the user and submits processing of the request to the application server.
(2) The application server transmits the MODIS data used by the processing from the MODIS database to the local disk in the application server.
(3) The application server executes application for the request and returns the results to Web server.

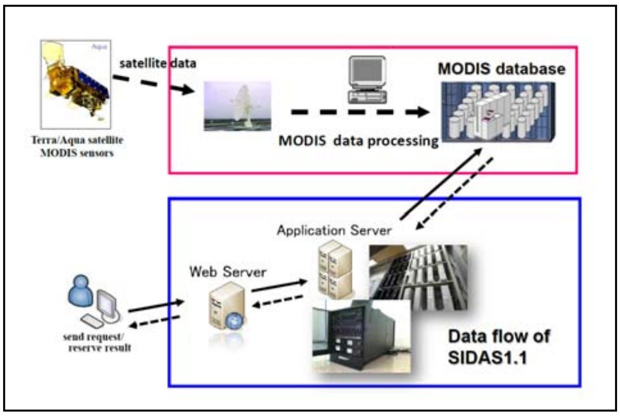

Fig. 1 Overview of SIDAS1.1

3 Overview of Satellite data analysis system 1.2

The purpose of our present study is to support the recovery from East Japan Earthquake. SIDAS 1.2 is being developed for this purpose, and the main feature of this updated system is the stream data processing, to enable the analysis of the influence of East Japan Earthquake and to monitor the regrowth of vegetation for the tsunami stricken area in Tohoku region. The analyzed results are automatically produced for open public access.

The information that we have planned to provide are the next 4 items to identify the reconstruction of land in the tsunami stricken area in the north eastern region from March 11, 2011.

(a) Image information from March, 2010 to the end of February, 2011 (Twice a month: In the first half and the latter half of each month).
(b) Image information after March 1, 2011 (Every day).
(c) Visible information of Normalized Difference Vegetation Index (NDVI), Sea Surface Temperature (SST) and Land Surface Temperature (LST) after March 1, 2011 (Every day).
(d) Visible information of difference between NDVI after March 1, 2011 and NDVI on the same day for one year ago (Every day).

Figure 2 shows the overview of SIDAS 1.2. SIDAS 1.2 executes the following processes every day.

(1) The application server receives the MODIS data stored in the MODIS database, and analyzes the information described in the above (a) ~ (d).
(2) The application server stores the analytical result in the database server.
(3) The Web server retrieves the analysis results from the database server and provides the data for open public access.

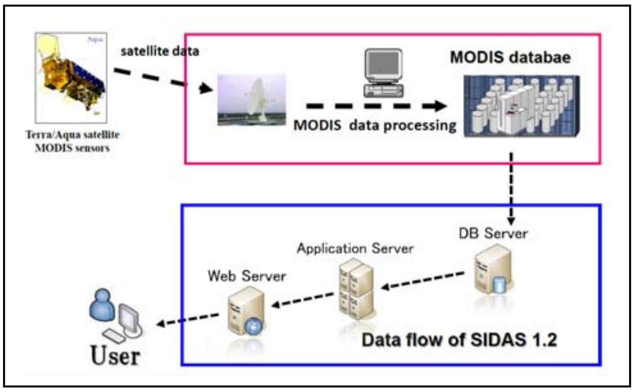

Fig. 2 Overview of SIDAS1.2

4 Summary of MODIS data in SIDAS

MODIS is a multiple band radiometric sensor instrument aboard Terra (NASA launched on December 18, 1999, at local time 10:30AM) and Aqua (NASA launched on May 4, 2002, at local time 1:30PM) satellites to monitor the environment of a large region of the earth covering a width of 2,330 km. It measures 36 spectral bands between 0.405 and 14.385 μm with three spatial resolutions (250m, 500m, 1,000m).

Tokyo University of Information Sciences (TUIS) is receiving MODIS data from three places in Hokkaido, Tokyo and Okinawa, and received the data 3 or 4 times in the daytime and 3 or 4 times in the nighttime from each place. The observing areas from the three places are from 100 degrees to 180 degrees of east longitude and from 10 degrees to 70 degrees of north latitude.

In this research, we use the following standard MODIS data products, MOD02 (MODIS calibrated radiances product: spatial resolution), MOD03 (geological location product), MOD11 (land surface temperature), MOD13 (vegetation index), MOD28 (Sea Surface Temperature), MOD35 (cloud mask) from MODIS products. Table 1 shows the band information of MODIS data.

Table 1 Relationship between the feature of the wavelength and the resolution of the bands

BAND	WAVELENGTH(nm)	SPATIAL RESOLUTIONS	KEY USE
1	620 ~ 670	250m	Absolute Land Cover change, Vegetation Chlorophyll
2	841 ~ 876	250m	Cloud Amount, Vegetation Land Cover change
3	459 ~ 479	500m	Soil/ Vegetation Differences
4	545 ~ 565	500m	Green Vegetation
5	1230 ~ 1250	500m	Leaf/Canopy Differences
6	1628 ~ 1652	500m	Snow/Cloud Differences
7	2105 ~ 2155	500m	Cloud Properties, Land Properties
21	3929 ~ 3989	1000m	Forest Fires & Volcanoes
22	3929 ~ 3989	1000m	Cloud Temperature, Surface Temperature
31	10780 ~ 11280	1000m	Cloud Temperature, Forest Fires & Volcanoes, Surface Temperature
32	11770 ~ 12270	1000m	Cloud High, Forest Fires & Volcanoes, Surface Temperature

5 Process of function in Stream Data Platform

In this research, we examined the observation method for the reconstruction of land in the Tohoku region from the East Japan Earthquake that had occurred on March 11, 2011 by using the MODIS data. The developed analysis functions of SIDAS1.1 is used to open the satellite data described in Chapter 3 for public retrieval. SIDAS1.1 that is base system of this research receives MODIS data, and this system executes application according the request of user such as "Search for fire regions in forests and fields" or "Search for similar image data" by using the MODIS data. Fig. 3 shows the configuration of SIDAS1.1.

In this research, we are examining stream data processing function that analyze reconstruction of the tsunami stricken areas in the Tohoku region, and are developing SIDAS1.2 to open the analytical result in real time by using the satellite data received every day.

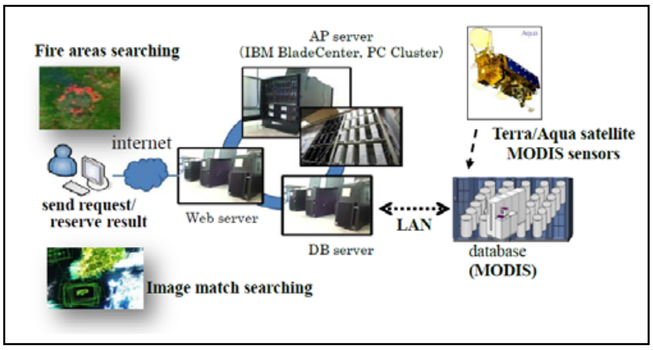

Fig. 3 Configuration of SIDAS1.1

Fig. 4 shows the configuration of SIDAS1.2. We used the stream data processing model for the data processing in SIDAS1.2. In this model, data processing scenarios are registered in the system beforehand, and the system receives and processes huge satellite data in real-time according to the predefined process scenario.

In the stream data processing function of SIDAS1.2, the analysis and web publishing function for the following item were implemented.

(a) Analysis from March in 2010 to the end of February in 2011

(b) Analysis after March 1, 2011

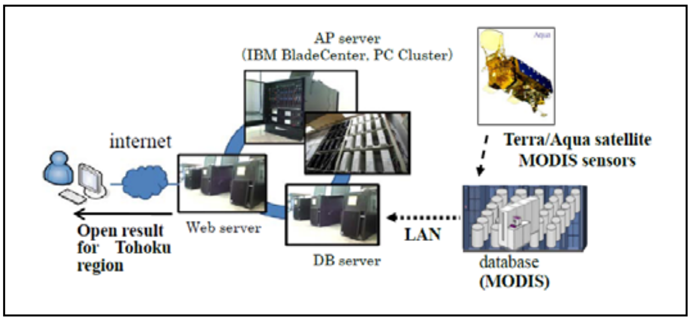

Fig. 4 Configuration of SIDAS1.2

MODIS data is analyzed beforehand and stored into the database for (a). We developed the data stream function to execute the reception, analysis and web data release of the satellite data in real time for (b). The process in the application server and Web server for (a) and (b) is shown as follows.

(a) Create analytical information from March, 2010 to the end of February, 2011

(a1) Application server

The following image data are created by using the MODIS data from March in 2010 to the end of February in 2011, and the image data are stored into the database.

(a1.1) RGB image data (GIF image : true color image)

The color image data in the Tohoku region is created by using radiance data (Band 1: Red and band 4: Green and band 3: Blue) of MOD02 (spatial resolution: 500m). The created data is GIF image data for 1- day composite data (received every day), 15- day composite data (removed cloud effects of 15-days) and Monthly composite data (removed cloud effects of 30-days). Fig. 5 shows example of display for RGB image data.

(a1.2) Visualized data of NDVI,SST and LST (GIF image : pseudo color image)

NDVI, SST and LST are single band data and thus the image data is normally shown as a grayscale image. In order allow make the data more intuitive to non-experts, the vegetation indexes and temperature values were mapped to color values to create pseudo color images.

(a2) Web server

The Web server publishes data (a), (b) from March, 2010 to February, 2011.

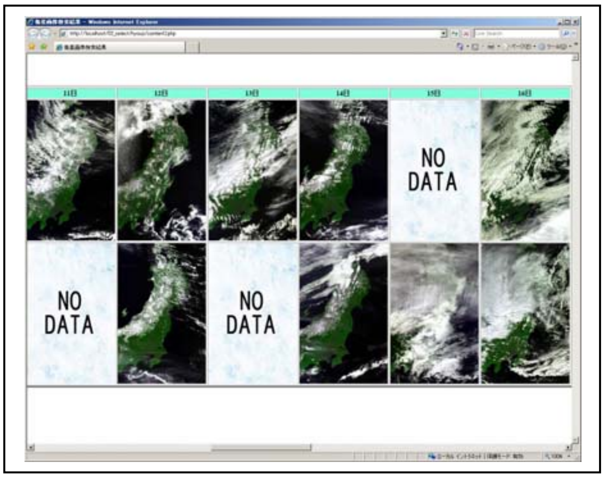

Fig. 5 Example of display for RGB image data

(b) Publish of analytical information after March 1, 2011 (The following process is executed once a day).

(b1) Application server

(b1.1) The application server retrieves the satellite data containing the Tohoku region for a single day. The number of reception from MODIS satellites is three or four times a day.

(b1.2) From the data received in (b1.1), the Tohoku region (north latitude 34°00' - 42°00' and longitude 138°00' - 43°00') is selected, and converts the HDF (Hierarchical Data Format) data to BSQ(binary Band SeQuential) data.

(b1.3) 1-day composite process is executed for the BSQ data created in (b1.2). 1-day composite processing combines the BSQ data with the best reception status (low cloud interface) from among the several MODIS data received that day and synthesizes them to one BSQ data for the selected day.

(b1.4) Create RGB image data from BSQ data (MOD02) and visualized data of NDVI, SST and LST from BSQ data (MOD11, MOS13, MOD28) created in (b1.3), and stores them into the database.

(b1.5) Execute the 15-days composite process once in the first half and once in the latter half of month, and the execute 30-days composite process once a month for BSQ data from (b1.3).

(b1.6) Create RGB image data from BSQ data (MOD02) from (b1.5).

(b1.7) Calculate the difference between the BSQ data (for LST, NDVI, and SST) of the selected observation date and the BSQ data (for LST, NDVI, and SST) created in (a) for exactly one year previous to the selected observation date, and create visualized data from the calculation results and store them into database.

(b2) Web server

Take out image data and visualization data that created in (1.4), (1.6), (1.7) from database and publish these data on the web server.

6 Conclusion and future works

In this research, we examined what information could be used to support the recovery from the East Japan Earthquake, and developed satellite data analysis system (SIDAS1.2) for this purpose. We developed SIDAS 1.2 to implement stream data processing in order to automatically publish up-to-date information on the influence of the East Japan Earthquake and to monitor the regrowth of vegetation in the tsunami stricken areas.

In future works, we intend to support the functions so that the user can acquire necessary information on demand, such as improved features to select analytical region and analytical information arbitrarily. Moreover, we plan to publish visual information incorporating other information sources such as aerial photographs, to examine the situation of the disaster and the reconstruction situation.

Acknowledgments

This research was supported by the Research project of Tokyo University of Information Sciences for the sustainable development of economic and social structure dependent on the environment in eastern Asia.

References

[1] Akihiro Nakamura, Jong Geol Park, Kenneth J. Mackin, Eiji Nunohiro, et al, "Development and Evaluation of Satellite Image Data Analysis Infrastructure", The Sixteenth International Symposium on Artificial Life and Robotics, Proceeding Index OS18-3, (AROB 16th, 2011)

[2] Eiji Nunohiro, Jong Geol Park, Kenneth J. Mackin, et al, "Development of satellite data analysis system", Proceedings of the 5th International Conference on Information (2009), pp.143-146

[3] Eiji Nunohiro, Kei Katayama, Kenneth J. Mackin, Jong Geol Park, "Forest and Field Fire Search System using MODIS Data", Journal of Advanced Computational Intelligence and Intelligent Informatics (JAC 3, 2007), vol.11 No.8, pp.1043 ~ 1048

[4] National Aeronautics and Space Administration (NASA), MODIS Web, http://modis.gsfc.nasa.gov/

The Seventeenth International Symposium on Artificial Life and Robotics 2012 (AROB 17th '12),
B-Con Plaza, Beppu, Oita, Japan, January 19-21, 2012

Flood risk assessment using MLSWI by MODIS Time Series data

Jonggeol Park[1], Youngjoo Kwak[2], and Nunohiro Eiji[1]

[1]Tokyo University of Information Sciences, Chiba 265-8501, Japan

[2] International Center for Water Hazard and Risk Management, Tukuba 305-8516, Japan

(Tel: 81-43-236-4644, Fax: 81-23-236-4644)

amon@rsch.tuis.ac.jp

Abstract: The principal purpose of this study is to describe the development and validation of an algorithm to estimate the fraction of water area within 500-m of the Moderate Resolution Imaging Spectroradiometer (MODIS) operating on the Earth Observation System Terra spacecraft. The result of this study is shown to be effective in determine the flood areas accurately in emergency response efforts as soon as possible. Estimation of a flood periphery is important to determine a fundamental hazard for risk management. This study was to accurately extract the spatial distribution of nation-wide flood risk using MODIS time series images and estimate simple algorithm for computing the flood inundation depth using Digital Elevation Model(DEM), flow direction and river network. The authors improved the accuracy of the water extent boundary using flood inundation depth (FID) data from a one year time-series of MODIS data.

Keywords: Flood risk, flood inundation depth (FID), DEM, MODIS, time-series.

1. INTRODUCTION

Floods are of increasing public concern world-wide due to increasing damages and unacceptably high numbers of injuries. Previous approaches of flood protection led to limited success especially during recent extreme events. Therefore, an integrated flood risk management is required which takes into consideration both the hydrometeorogical and the societal processes.

Real-time determination of flood inundation has been limited to large-scale events such as nationwide inundation. The geographic information system (GIS) including satellite images is an effective method to interpret and analyze a nation-wide flood risk assessment. Moreover, satellite images are also necessary to analyze flood disasters. Remote-sensing images are an effective tool to determine flood inundation areas. Estimation of a flood periphery is important to determine a fundamental hazard for water risk management. Many studies have been conducted by using remote-sensing data to detect spatial and temporal changes in the extent of flood inundation, including the delineation of wetlands [1][2]. The Normalized Difference Water Index (NDWI), a satellite-derived index from near-infrared (NIR) and short wave infrared (SWIR) channels [3], is used to derive water fraction and a flood map from MODIS data. The SWIR reflectance reflects changes in both the vegetation water content and the spongy mesophyll structure in vegetation canopies, while the NIR reflectance is affected by leaf internal structure and leaf dry matter content but not by water content. The combination of the NIR with the SWIR removes variations induced by leaf internal structure and leaf dry matter content, improving the accuracy in retrieving the vegetation water content [4].

The land surface water index (LSWI) use a red channel in place of NIR [1][5][6] used enhanced vegetation index (EVI), LSWI and DVEL (difference value of EVI and LSWI). However, it can be difficult to discriminate water body from clouds in the visual part of the spectrum. Also, it was not easy to extract the river width accurately because of a resolution problem in each a pixel. In this study, the proposed method was applied to extract water body from a channel reflectance by using MODIS time-series images and flood inundation depth (FID). This simple approach was to determine nation-wide inundation areas from a geomorphologic point of view, rather than a hydrological model.

The purpose of this study was to accurately estimate an inundation area based on the spatial distribution of flood hazard for nation-wide flood risk assessment using GIS data and MODIS time-series images. To determine the water extent boundary more accurately, the authors aimed to improve an extraction method of surface water with a simplified decision tree method using MODIS channel 6 reflectance (CH6) and channel 7 reflectance (CH7) acquired from a regional flooding. The improved method was then applied to the Indus River basin in Pakistan, which was selected as the prime research focus area. The selected area suffered from a huge, severe flood caused by abnormally heavy rainfall from late July to early August 2010.

2. DATA

2.1 MODIS MYD09A1

The MODIS Surface Reflectance products provide an estimate of the surface spectral reflectance as it would be measured at ground level in the absence of atmospheric scattering or absorption. MYD09A1 provides channels 1-7 at 500-meter resolution in an 8-day gridded level-3 product in the Sinusoidal projection. Each MYD09A1 pixel contains the best possible L2G observation during an 8-day period as selected on the basis of high observation coverage, low view angle, the absence of clouds or cloud shadow, and aerosol loading. Science datasets provided for this product include reflectance values for channels 1-7, quality assessment, and the day of the year for the pixel along with solar, view, and zenith angles[7].

2.2 Flood inundation depth

Topography is an essential factor for hydrologic models to simulate flooding and runoff. One of the most obvious factors controlling stream flow is the gradient, or slope, of the stream channel. The definition of FID is the accumulated level index overflowing the banks of a main river. It is clear that FID indicates the depth due to overflowing the banks of a river and can be defined as the accumulated level index. Kwak & Kondoh [8] developed and proposed FID for basin-wide flood risk assessment at the national level. Actual calculation of FID required a dataset composed of DEM, flow direction and river network. FID was determined based on DEM and the highest water level (HWL) of the main stream, as shown in equation (1) below:

$$H\_{ij}\ FID = H\_{ij}(DEM) - H\_{ij}(HWL\ of\ river) \qquad (1)$$

where, H is the height of surface, i is the number of pixels, and j is the number of lines.

3. Methodology

3.1 Extraction of water body

MODIS channels were strongly absorbed by water, providing information on the inundation pattern. Fig. 1 illustrates that the reflectance rate of clean water was the lowest among the classification of soil, vegetation, snow, cloud and clean water (up of Fig. 1). Particularly, the authors found that the reflectance rates of CH6 and CH7 were the lowest than the other channels in the case of surface water such as clean water, muddy water, and flooded water (down of Fig. 1). Flood hazard assessment was performed by using MODIS dataset with FIL, population and land-cover data. The developed approach was to determine inundation areas nation-wide from a geomorphologic point of view, rather than based on a hydrological model. First of all, to identity spatial inundation distribution, a decision tree was used to associate each pixel with one of the two categories: water body or land surface.

For flood risk assessment, the quantitative assessment was divided into three steps. To estimate flood areas, two categories of the MODIS images, water and non-water areas, are combined to obtain the maximum water area. The water areas were considered to be normal water such as river, lake, pond, and so on, and the non-water areas are considered to be non-flood areas. The main stream in the Indus River basin and the water areas were extracted to composite images derived from 46 image dataset in 2009.

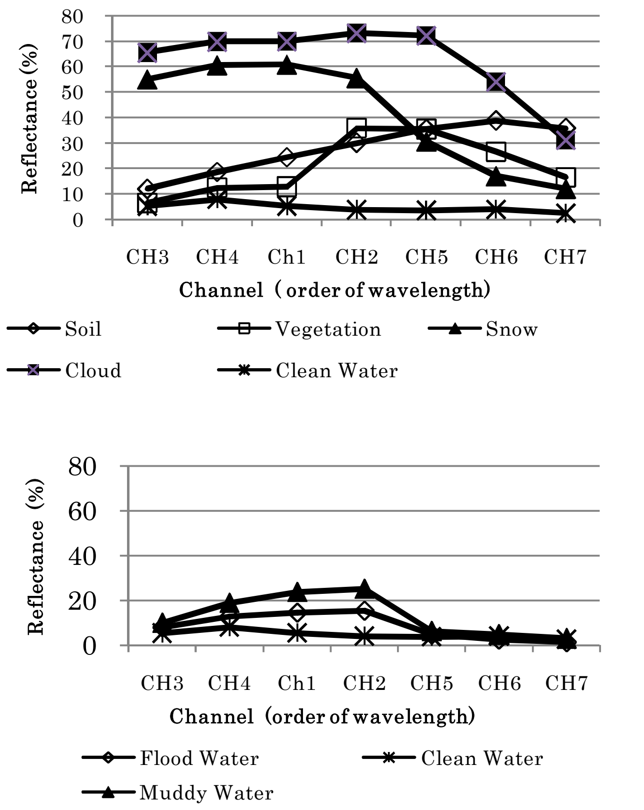

Fig. 1. Surface reflectance of MODIS land channels (up) and reflectance rate in case of surface water (down)

The MODIS channels were strongly absorbed by water, providing information on inundation patterns using Normalized Difference Index (NDI). However, the NDWI and LSWI have some weaknesses and errors to extract water bodies. For instance, the spectral reflectance rate of water is higher than that of a forest (e.g., forest = 0.14, clean water = 0.1). To assess a flood area, MLSWI was used an absorption ration instead of a reflection ration as follow; Absorption ration (A) = 1 – Reflection ration (R). The new approach also worked well to differentiate water from land under three conditions: CH7 < 10%, CH1+10% > CH2 and CH3 < 20%, where MODIS MYD09A1 land channels.

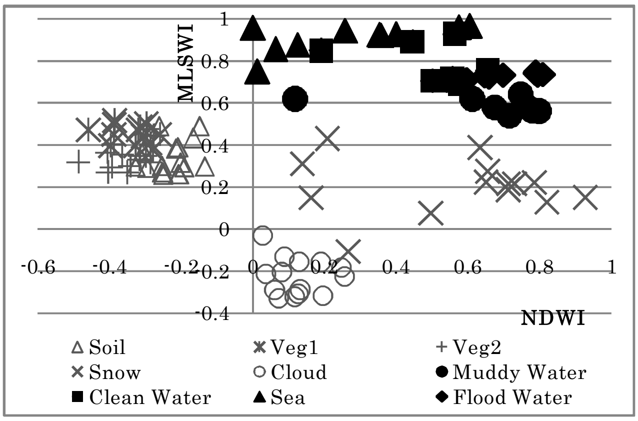

Fig.2. The index comparison of a land classification between MLSWI and NDWI for extracting flood areas

Equation (2) is a simple algorithm for identifying inundation areas by using combination of the NIR (841-875mm) with the SWIR (1628-1652mm).

$$MLSWI = \frac{A_{SWIR} - R_{NIR}}{A_{SWIR} + R_{NIR}} \quad (2)$$

As shown in Fig. 2, MLSWI can detect flood areas better than NDWI. MLSWI shows indices over 0.5 when detecting bodies of water, clean water and muddy water in flood areas. On the other hand, NDWI cannot distinguish water from land especially when the area contains snow cover, which shows indices of over 0.5. Second, the authors overlaid the FIL data and the extracted water areas which are covered two water areas (stream and flood areas) derived by MLSWI. It was considered as a major influencing factor on flood areas. The accumulated FIL of the target pixel was raised at 1 meter intervals. The calculated FIL provided a basis to estimate the flood extent areas of flood levels and inundation line in lowlands and near-zero gradients along the stream per 500 m-mesh. Potential FIL was conducted to identify flood inundation height and inundation probability. Finally, the flooded-area data obtained based on MODIS images and FIL are coupled with population and land cover datasets to estimate disaster damage. For each scenarios of the damage, the respective inundation depth and areas were obtained by extreme flood event, because FIL was a extreme analysis to the calculated results. Therefore, each exposed object can be linked to a distribution risk map related to potential FIL. FIL improved the simulation to clearly show that people living in the lowlands are more affected than those in other places. The land-cover data also improved it to identify flood risk per classification and enable damage estimation per 500 m mesh. Population and land cover classification schemes were proven very useful to assess flood damage over lowlands.

4. Result

Based on the flood water extent results, the authors conducted to identify expected flood inundation depth per 250 m-mesh. The periphery of flooded areas is directly correlated with an inundation depth around the river. Therefore, it was clear that flood inundation depth (FID) indicated the depth due to overflowing the banks of a river and can be defined as the accumulated level index. From Fig. 2 (Indus River basin), it can be concluded that, the FID of inundation area has a value ranging from -1 m to 9 m. Examining the relationship between FID ranges and MODIS images under the flooding, it was found that the inundation area was extracted 70253 pixels, 4390.8 km2 in the Indus River basin from late July to early August in 2010. For instance, the inundation area under the condition of FID = 0 m was estimated to be 31444 pixels, about 4390.8 km2. The inundation area under the condition of FID = 1 m was also estimated to be 8622 pixels, about 538.9 km2. The inundation area under the condition of FID = 2 m was also estimated to be 6468 pixels, about 404.3 km2. In detail, the right of Fig. 2 shows the enlarged view of a partial Punjab Province, Pakistan.

5. CONCLUSION

This is a case study considering the independence of the data sources and the resolution of the data available at the national level. Although flood is controlled by various risk factors, the flood vulnerable area was extracted from GIS-derived data such as FID and satellite images. To conclude flood risk assessment, the authors focused on improvement of the accuracy in determining a vulnerable inundation area using a simplified decision tree method based on MODIS time-series images in the Indus River basin, Pakistan. This new approach can be a very useful tool in emergency response efforts since it can conduct extreme value analysis and predict when and in what size a flooding event may occur. The water extent area can be classified a category of land cover for flood risk assessment affecting nation-wide flood damage based on FID. In the future, the authors are planning to improve the proposed assessment to be applicable on a national, as well as, global level.

ACKNOWLEDGEMENTS

This research was supported by the Research project of Tokyo University of Information Sciences for the sustainable development of economic and social structure dependent on the environment in eastern Asia. And the framework of the "assessment of the impact of climate change on flood disaster risk and its reduction measures over the globe and specific vulnerable areas (C-09)" under the "projection of the change in future weather extremes using super-highresolution atmospheric models" (PI: Akio Kitoh) supported by the Innovative Program of Climate Change Projection for the 21st Century (KAKUSHIN) of the Ministry of Education, Culture, Sports, Science, and Technology (MEXT).

REFERENCES

[1] Islam A.S., Bala. S.K. and Haque. M.A. (2010) Flood inundation map of Bangladesh using MODIS time-series image, J. Flood Risk Management 99(4), 333–339.

[2] Martineza J.M. & Toanb T. (2007) Mapping of flood dynamics and spatial distribution of vegetation in the Amazon floodplain using multitemporal SAR data. Remote Sens Environ, 108(3), 209–223.

[3] Gao, bo-cai (1996) NDWI a normalized difference water index for remote Sensing of Vegetation Liquid water from space, REMOTE SENS.ENVIRON. 58, 257-266

[4]Ceccato, P., Flasse, S., Tarantola, S., Jacquemond, S., and Gregoire, J.M. 2001. Detecting vegetation water content using reflectance in the optical domain. Remote Sensing of Environment 77: 22–33.

[5] Xiao X., Boles S., Frolking S., Li C., Bau J.Y. & Salas W. (2006) Mapping paddy rice agriculture in South and Southeast Asia using multitemporal MODIS images. Remote Sens Environ, 100, 95–113.

[6]Xiao X., Boles S., Liu J., Zuang D., Frolking S. & Li C. (2005) Mapping paddy rice agriculture in southern China using multitemporal MODIS images. Remote Sens Environ, 95, 480–492.

[7] USGS, The United States Geological Survey, access: Jan.2011https://lpdaac.usgs.gov/lpdaac/products/modis_products_table/surface_reflectance/8_day_l3_global_500m/myd09a1

[8] Kwak, Y.J. & A. Kondoh. (2010) A Study on the Assessment of Multi-Factors Affecting Urban Floods Using Satellite Image: A Case Study in Nakdong Basin, S. Korea, Advances in Geoscience. 17: Hydrological Science (HS), 265-278.

The Seventeenth International Symposium on Artificial Life and Robotics 2012 (AROB 17th '12),
B-Con Plaza, Beppu, Oita, Japan, January 19-21, 2012

Application of Transfer Learning to PSO for Similar Image Search

Kazuma Mori[1], Takashi Yamaguchi[1], Kenneth J. Mackin[1] and Yasuo Nagai[1]

[1] Department of Information Systems, Tokyo University of Information Sciences,
4-1Onaridai, Wakaba-ku, Chiba, 265-8501 Japan
(Tel:81-43-236-1329; Fax:81-43-236-1329)
g11007km@edu.tuis.ac.jp, {tyamagu, mackin, nagai}@rsch.tuis.ac.jp

Abstract: Remote sensing of the earth surface using satellite monitored sensor data is one of the most important methods for global environmental monitoring. For satellite monitored sensor data, MODIS (Moderate Resolution Imaging Spectoradiometer) satellite data is actively used for the remote sensing data. In remote sensing fields, similar image search which extracts local area images from a given global map image is often required. Similar image search is important because physical changes to the earth's surface caused by human or nature can be monitored. However, long calculation time is required for similar image search in MODIS data due to the very large search space. In our previous research, an effective result was yielded using genetic algorithm on the similar image search from the satellite image. Based on this result, we proposed a particle swarm optimization based search method that globally searches for the problem space using particle groups.

Keywords: particle swarm optimization, transfer learning, similar image search, remote sensing

1. INTRODUCTION

Remote sensing of the earth surface using satellite monitored sensor data is one of the most important methods for global environmental monitoring. For satellite monitored sensor data, MODIS (Moderate Resolution Imaging Spectoradiometer) satellite data is actively used for the remote sensing data. Moderate resolution remote sensing allows to quantify landscape and extent, which can be used to monitor changes in land cover and land use for extended periods of time.

Similar image search is an important problem in the remote sensing using moderate resolution satellite images. Similar image search extracts local area images from a given global image. Similar image search is important because physical changes to the earth's surface are caused by human or nature can be monitored. However, the search space size of the similar image search using MODIS data is very large since MODIS data consists of approximately 1TByte image data per a day. Thus the search process requires long calculation time. In previous research, higher fitness value was yielded using genetic algorithm (GA) on the similar image search from the satellite image. However, the GA depends on improving the solution through a probabilistic learning process, and requires relatively long calculation time. For this result, we proposed a particle swarm optimization (PSO) based method [1] that globally searches for the problem space using particle groups. PSO has advantage in fast conversion rate by comparison with other evolutionary computation algorithm.

Recently, the transfer learning is actively researched [2]. The transfer learning is the meta learning methods that uses the knowledge and data in an domain in order to solve the problem in the another domain. In transfer learning, it is expected that the improvement of the learning efficiency and the compensation for the lack of knowledge and data is performed when the problem is solved. There exists the similarity of pixel data in similar image search. Therefore, more effectively learning can be performed using transfer learning when an image similar to the previous learned image was given. The proposed method can use the learning result for a previous input image in order to learn to another input image. By this characteristic, it is expected that the similar image search is performed effectively. In this paper, we investigated the effectiveness of proposed method.

2. METHOD

In PSO [3], a i-th particle is defined by the d-dimensional position vector $\mathbf{x}_i = \{x^1{}_i, x^2{}_i, \ldots, x^d{}_i\}$ and velocity vector $\mathbf{v}_i = \{v^1{}_i, v^2{}_i, \ldots, v^d{}_i\}$ for the d-dimensional search space. A velocity is defined by the local best position $\mathbf{p}_i$ that is own best fitness position at the i-th particle and the global best position $\mathbf{p}_g$ that is best fitness position in the whole particle. Each particle moves according to velocity vector for search.

The proposed method divides the particles to the plural groups. Each group is composed of the N/K particles where N is the number of all particles and K is the number of groups. A velocity is defined by the local best position $\mathbf{p}_i$, the global best position $\mathbf{p}_g$, and the group best position $\mathbf{p}_k$ that is best fitness position in a group k. The particles are divided into the group by order of fitness value. Moreover, a velocity is defined to leave from the centroid of each group of the particles and the centroid of all groups of the particles in addition to the local best position, the global best position and the group best position. The particles of high ordered group search in the global best neighborhood and the particles of low ordered group searches around the location to leave for the centroid of each group and the centroid of all groups. In the proposed velocity determination method, the particles of high ordered group fall into local minimum and the particles of low ordered group are searched globally. In addition, the order of each group is changed by the fitness value at generation interval T. Behavior of the proposed method is shown in Figure 1 and a flow of the proposed method is shown in Figure 2.

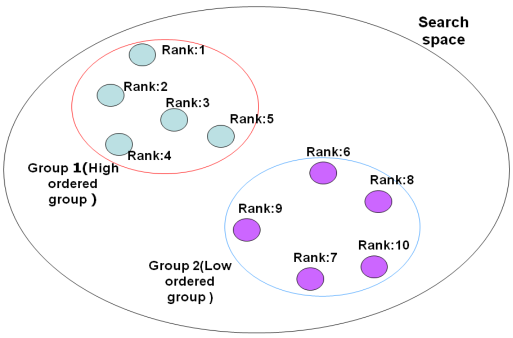

(a) Grouping of the particle by the order

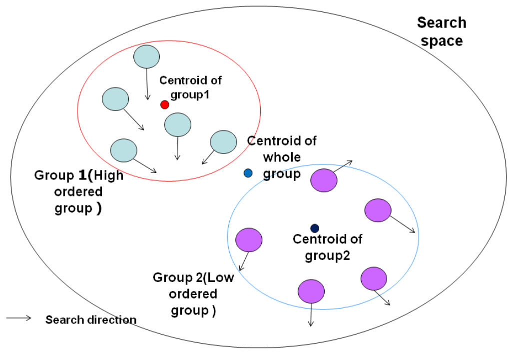

(b) Determination of search direction at every group

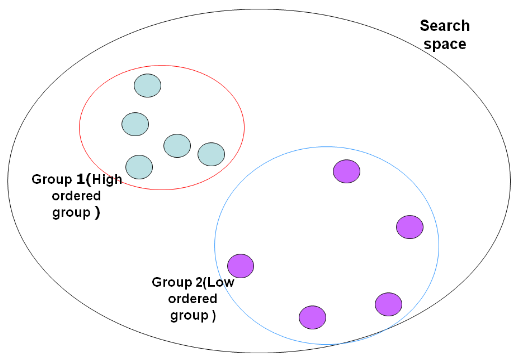

(c) Search of every group

Figure 1. Outline of the proposed method

Step1. A position $\mathbf{x}_i$ and a velocity $\mathbf{v}_i$ of each particle are initialized. Each particle is assigned to each group in random.

Step2. A fitness value of each particle is calculated by fitness function $f(\mathbf{x}_i)$.

Step3. The local best position $\mathbf{p}_i$ of the each particle, the global best position $\mathbf{p}_g$ and the group best position $\mathbf{p}_k$ of each group are updated.

Step4. The order $q_i = \{1,2,\ldots,N\}$ is defined by fitness value $f(\mathbf{x}_i)$ to each particle. The particle which got a best fitness value becomes rank 1 and the particle which got a worst fitness value becomes rank N. Each particle has total of the rank value R_i. R_i is calculated by q_i using equation (1)

$$R_i(t+1) = R_i(t) + q_i(t) \quad (1)$$

where t is a generation.

Step5. The position $\mathbf{x}_i$ and the velocity $\mathbf{v}_i$ of each particle are updated by equation (2) and equation (3)

$$\begin{aligned}\mathbf{v}_i(t+1) &= w_k \cdot \mathbf{v}_i(t) + c_1 \cdot \mathbf{r}_1 \cdot (\mathbf{p}_i(t) - \mathbf{x}_i(t)) \\ &+ c_2 \cdot \mathbf{r}_2 \cdot (\mathbf{p}_g(t) - \mathbf{x}_i(t)) + c_3 \cdot \mathbf{r}_3 \cdot (\mathbf{p}_k(t) - \mathbf{x}_i(t)) + h(t)\end{aligned} \quad (2)$$

$$\mathbf{x}_i(t+1) = \mathbf{x}_i(t) + \mathbf{v}_i(t+1) \quad (3)$$

where w_k is momentum rate for group k, $c_1,\ldots,c_5$ is the heaviness for each vector, $\mathbf{r}_1,\ldots,\mathbf{r}_5$ is a vector of random values from 0 to 1 and $h(t)$ is a function that updates the centroid of each group and the centroid of the whole groups. The function $h(t)$ is defined by equation (4)

$$h(t) = c_4 \cdot a(k) \cdot \mathbf{r}_4 \cdot \left\| \mathbf{x}_i(t) - \bar{\mathbf{x}}_k(t) \right\| + c_5 \cdot b(k) \cdot \mathbf{r}_5 \cdot \left\| \mathbf{x}_i(t) - \bar{\mathbf{x}}_g(t) \right\| \quad (4)$$

where $\bar{\mathbf{x}}_k$ is a centroid of group k and $\bar{\mathbf{x}}_g$ is a centroid of whole group. In addition, $a(k)$ and $b(k)$ are values of the functions to increase monotonically in [0,1].

Step6. If a generation is group reordering, go to Step7. If a generation is not group reordering and termination condition is not satisfied, return to Step2.

Step7. Based on total rank of each particle R_i, the affiliation of the particle of each group is changed. For example, the best fitness group is composed of the particles from the rank 1 to rank N/K in the low order of R_i. Each particle is assigned to the low order of R_i in each group. If termination condition is not satisfied, return to Step2.

From this characteristic, the proposed method can use the learning result of a previous input image in order to learn for another input image as transfer learning. Therefore, the proposed method has advantage in the calculation cost reduction and the finding of solution with higher fitness value when another input image is given.

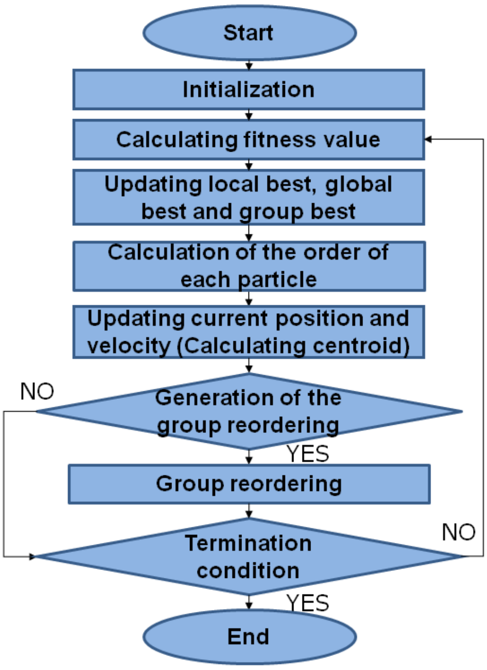

Figure 2. Flow chart of the proposed method

3. EXPERIMENT

3.1 Similar Image Search

A similar image search is a problem that extracts local area images for a given image from global map image. The similar image search is derived by information included in image (ex. a pattern of pixel data and the color). In this experiment, the new input image is given after defining an initial value through the learning of a different satellite image. Therefore, a previous learning result has an influence on the search of a new satellite image. Figure 3 shows a global image, a target image that is new input image, an image1, an image2 and an image3 that are previous input image in this experiment.

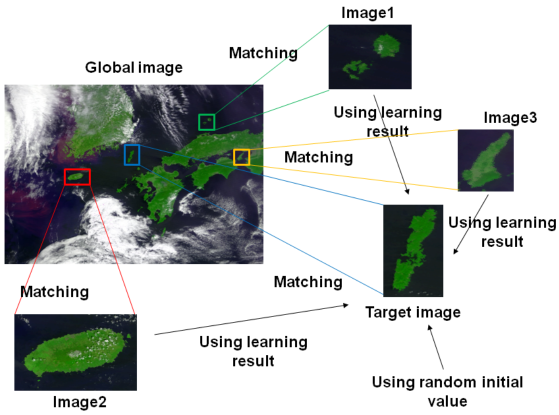

Figure 3. Similar image search in this experiment

In this experiment, the fitness value is calculated by the matching rate of the selected image pixel data specified by the search parameters. The parameters consist of translation, scale rate and rotation angle. The separation (absolute difference) of the values for each color from the compared pixel is calculated, and the sum of the separation is defined as the matching rate for the compared pixel. The fitness value fv is defined by equation (5)

$$fv = 1.0 - \left(\sum_{j}^{y}\sum_{l}^{z}\left|img1_{jl} - img2_{jl}\right|\right) / y \cdot z \cdot 255 \quad (5)$$

where $img1$ is the pixel data for the target MODIS data region, $img2$ is the pixel data for the image data modified by the search parameters and '255' is max value of each color. In addition, each pixel of the RGB color image is converted to gray-scale image using the equation (6)

$$gray = 0.299 \cdot R + 0.587 \cdot G + 0.114 \cdot B \quad (6)$$

where $gray$ is the image pixel of the gray-scale image, R, G and B are the respective red, green, blue pixel data of the color image at the same pixel location, and '0.299', '0.587', '0.114' are a coefficient for each color established in [4].

In this experiment, initial values are set to random value, learning result of image1, learning result of image2, and learning result of image3. Moreover, we evaluated the proposed PSO using the final fitness value of the global best and the conversion rate for the 50 trials. The generation of proposed PSO and GA are set to 500 in each initial value. In addition, the parameters in the proposed method were defined as follows. The number of all particles N is set to 200, the number of groups K is set to 10, the generation interval of the group reordering T is set to 20, the heaviness for each vector $c_1,\ldots,c_5$ are set to 1.5, 1.5, 1.8, 0.9, 0.9, the moment rate for each group w_k is set to from 0.4 to 0.9. GA was used for comparison with this experiment. The parameters in the GA were defined as follows. The population is set to 200, the crossover type is set to 1 point, the crossover rate is set to 0.9, the mutation rate is set to 0.05 and the strategy of selection is set to the roulette strategy and the elite strategy.

3.2 Experiment Result

Table 1 shows the average fitness value of global best position using each initial value in GA and the proposed PSO for target image. Table 1 shows that the proposed PSO yielded the fitness value higher than GA for each condition. Figure 4 shows the fitness value changes in calculation time of GA and proposed PSO when random initial value was used. The proposed PSO yielded the higher fitness value in calculation time less than GA. From this result, the proposed PSO is more effective than GA in similar image search. The search efficiency is improved by this characteristic that the particles of high order group fall into a local minimum and the particles of low ordered group are searched globally. Figure 5 shows that fitness value of a target image using each initial value in proposed PSO. In particular, the higher fitness value is yielded using a learning result of image2 in earlier generation than using random initial value. From this result, a learning result of image2 has a good influence to the search for a new input image. The proposed PSO can perform more effective search by this good influence.

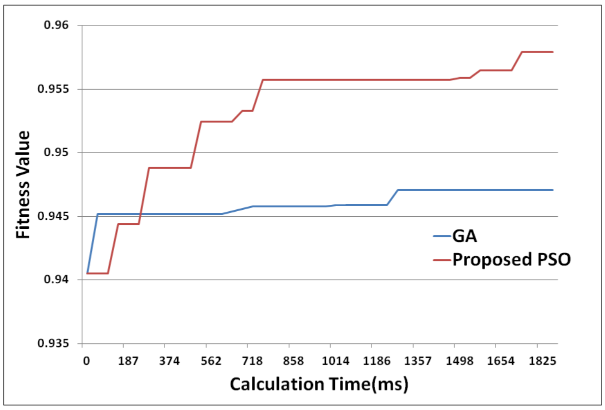

Figure 4. Fitness value changes in calculation time

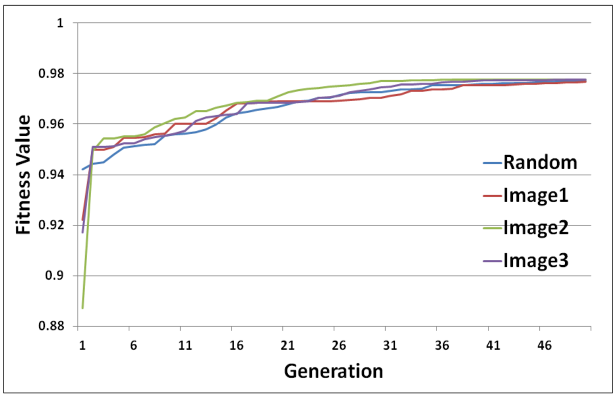

Figure 5. Fitness value of targeted image by each initial value in proposed PSO

Table 1. The average fitness value of global best using each initial value

	Random	Image1	Image2	Image3
GA	0.9609	0.9609	0.9604	0.9601
Proposed PSO	0.9775	0.9775	0.9775	0.9775

4. CONCLUSION

In this research, we proposed the particle swarm optimization based search method that searches for problem space globally by the particle groups and that applies similar image search for investigating the effectiveness of the proposed method. In this experiment, this result showed that the proposed PSO yielded the fitness value is higher than GA. In addition, the proposed PSO yielded the higher fitness value in calculation time less than GA. From this result, the effectiveness of the proposed PSO for similar image search using previous learned image is shown.

In this experiment, we compare the proposed PSO with GA. The distributed genetic algorithm (DGA) that is parallel model of GA has been applied to the similar image search using parallel processing in our previous research [5]. DGA yielded an effective result of calculation time in the similar image search using the parallel processing. For this result, we will plan to implement and evaluate the proposed method using the parallel processing as future works.

ACKNOWLEDGMENTS

This research was supported by the Research project of Tokyo University of Information Sciences for the sustainable development of economic and social structure dependent on the environment in eastern Asia.

REFERENCES

[1] K.Mori, T.Yamaguchi, K.J.Mackin, Y.Nagai (2011), Symbiosis Model in Particle Swarm Optimization for Dynamic Problems (in Japanese), Proceedings of the Forum on Information Technology 2011, vol.10, pp.469-470

[2] S.J.Pan and Q.Yang (2010), A Survey on Transfer Learning, IEEE Transactions on Knowledge and Data Engineering, vol.22, no.10, pp.1345-1359

[3] R.Poli, J.Kennedy and T.Blackwell (2007), Particle swarm optimization An overview. Swarm Intelligence, vol.1, no.1, pp.33-57, Springer

[4] K.Kashino, T.Kurozumi, H.Murase (2000),Quick AND/OR Search for Multimedia Signals Based on Histogram Feartures, The transactions of the institute of electronics, information and communication engineers D-II, vol.J83- D-II, no.12, pp.2735-2744

[5] E.Nunohiro, K.Katayama, K.J.Mackin, M.Ohiro, K.Yamasaki (2006), Image Match Search System using Distributed Genetic Algorithm, SCIS&ISIS 2006, pp.1536-1541

The Seventeenth International Symposium on Artificial Life and Robotics 2012 (AROB 17th '12),
B-Con Plaza, Beppu, Oita, Japan, January 19-21, 2012

The maximum and minimum temperature trends in Oita

Masao Igarashi[1], Takahiro Yamazaki[2] and Eiji Nunohiro[3]

[1] College of Bioresource Sciences Nihon University, Kanagawa, Fujisawa 252-0880, Japan (Tel 0466-84-3715)
[2] Graduate School of Bioresource Sciences Nihon University, Kanagawa, Fujisawa 252-0880, Japan
[3] Tokyo University of Information Sciences, Chiba, Wakaba-ku, 265-8501 Japan

Abstract: Japan Meteorological Agency has provided various kinds of historical temperature data of local meteorological station, such as Oita since February 1887. The provided temperature data contain the maximum, the minimum and the mean records on 17 leading and 57 local meteorological stations. We apply a nonlinear curve to the datasets and estimate the trends of the maximum, the minimum and the mean temperature, especially in Oita, by a numerical iteration method.

Keywords: Nonlinear fitting, Temperature, Warmth trend, Least square method, Newton method,

1 INTRODUCTION

There are many reports concerning to the global or local trends of temperature, such as the warmth is increasing or not. In many cases, the huge datasets and a super computer are applied to the estimations. Hence the practical model and the tuning method of parameters are hardly provided, because of the complexity. We propose a simple method to conform the local temperature trends, such as local warming or not, using the Oita temperature data since January 1888.

The temperature data in Oita is provided at the following URL: `http://www.data.jma.go.jp/obd/stats/etrn/index.php`

We apply a nonlinear model $f(x)$, the variable x is month, to the data. $f(x)$ consists of two terms, that is the year trend and the month trend. Mathematica `FindFit` function is applied to determine the parameters of the model[1]. Providing a fitness criterion to the model, the parameters of $f(x)$ are practically evaluated.

Applying $f(x)$, we are able to estimate an increasing trend of the maximum and minimum temperature respectively. The program to evaluate the parameters of $f(x)$ is at most 20-line as shown in this article. The year change trend is described by a linear term of $f(x)$ and the month change trend is also described by the periodical term of $f(x)$. The results clearly show the increasing trend of the temperature and the trend is similar the report provided by NASA [2] and JMA [3]. We remark that the proposed method does not need a statistics procedure, such as Annual Mean, 5-year Running Mean or regression analysis to evaluate $f(x)$.

2 MATERIAL AND METHOD

We apply the Oita local station data from 1888 to 2010 and denote the maximum and minimum temperature data obtained from the previous URL as follows ($^\circ$C) :

max={11.2, 8.5, 14.3, 17.2, 21.4, 24.3, 28.8, 30.4, 26.3, 21.5, 17.9, 13.7, $\cdots\cdots$, 11.4, 12.9, 14.7, 17.6, 23.6, 26.6, 31.3, 34.6, 30.7, 23.1, 17.6, 13.1 }

min={1.3, -0.1, 4.6, 9.7, 12.9, 16.4, 22.0, 22.7, 18.3, 11.6, 9.4, 4.5 , $\cdots\cdots$, 2.1, 5.1, 6.8, 9.6, 13.9, 19.3, 23.8, 25.6, 22.3, 16.5, 8.2, 4.7}

For example, the first record 11.2 and the last record 13.1 in the sequence "max" are the maximum temperature of January 1888 and December 2010 respectively. And also the first record 1.3 and the last record 4.7 in the sequence "min" are the minimum temperature of January 1888 and December 2010 respectively. Both data size are $k = (2011 - 1888) \times 12 = 1476$.

We apply the following nonlinear curve to the data

$$y = f(x) = a_1 + a_2 x + a_3 \sin(\pi x/n + a_4) \qquad (1)$$

where a_1,a_2,a_3,a_4 and n are the unknown parameters. This model is simplified compared with that of NDVI [1].

We apply the least square method and the Newton iteration method to determine these parameters. For simplicity, we use Mathematic's `FindFit` function for the fixed integer n and iterate n from $n = 1$ to $n = 100$. To find the best n between them, we apply the following CR$_n$ criterion [2] to terminate the iteration.

$$\mathrm{CR}_n = \frac{\sum_{i=1}^{k} \dfrac{|y_i - \widehat{y_i}|}{\max\left(|y_i|, |\widehat{y_i}|\right)}}{k} \qquad (2)$$

where y_i and $\widehat{y_i}$, $i = 1, 2, \cdots, \cdots, k$ are the estimated and the observed temperatures respectively. This CR$_n$ is similar to the mean value of the relative errors between the observed temperatures and the estimated temperatures

If CR$_n$ is small, $y_i = f(x_i)$ of (1) corresponds well to the observed temperatures $\widehat{y_i}$. On the other hand, if CR$_n$ is large,

[1] Mathematica Ver.8 built in function
[2] `http://data.giss.nasa.gov/gistemp/graphs/`
[3] `http://ds.data.jma.go.jp/gmd/tcc/tcc/products/gwp/temp/ann_wld.html`

y_i does not correspond well to the observed temperatures. Hence the integer n, $1 \leqq n \leqq 100$, is chosen so as to give the smallest value CR_n.

For the max data, a program to find the best fit nonlinear curve is as follows:

```
Clear[CR, p, q, s];
q = max; k = Length[q];
Do[{Clear[f], f[x_]
= a1*Sin[(π x)/n + a2] + a3 + a4 x /.
FindFit[q,
a1*Sin[(π x)/n + a2] + a3 + a4 x,
{a1, a2, a3, a4}, {x}],
y[n, x_] = f[x],
p = Table[f[x], {x, 1, k}],
s = Abs[p - q]/Max[Abs[p], Abs[q]],
CR[n] = Sum[s[[i]], {i, 1, k}]/k},
{n, 1, 100}];
r0 = Table[CR[i], {i, 1, 100}];
n = First[Position[r0, Min[r0]][[1]]];
r1 = Table[i, {i, 1, 100}];
r2 = Transpose[{r1, r0}];
Print["y = " y[n, x]]
fig1 = ListPlot[q, PlotStyle -> {Blue},
AxesLabel -> {Month, °C}]
fig2 = Plot[y[n, x], {x, 0, k},
PlotStyle -> {Thickness[0.0001], Green},
AxesLabel -> {Month, °C}]
Show[fig1, fig2]
ListPlot[r2, PlotRange -> {0.0, 0.25},
AxesLabel -> {"n", CR}]
```

3 RESULTS

We have the following best fit function using the criterion (2) for the maximum temperature

$$f(x) = 19.16 + 0.00116x + 10.0\sin(3.93 + \pi x/6) \quad (3)$$

where $\mathrm{CR}_6 = 0.028$.

For the case of minimum temperature we have

$$g(x) = 10.23 + 0.00139x + 10.7\sin(3.92 + \pi x/6) \quad (4)$$

where $\mathrm{CR}_6 = 0.044$.

Figure 1 shows the maximum temperature data (blue dots) and $f(x)$ (red curve). Figure 2 shows the minimum case.

We consider the 12 trends of decade's periods, such as 01/1890 to 12/2010, 01/1900 to 12/2010, $\cdots\cdots$ and 01/2000 to 12/2010. Figures 3 and 4 show the maximum and the minimum trends of each decade.

Figures 5, 6 and 7 show the trends evaluated by 57 (maximum and minimum temperature), and the mean temperature trend of 17 leading stations.

The temperature up trend from 1880 to 1980 and down trend from 1980 to 2010 are similar to the Figures 3, 4 and 5.

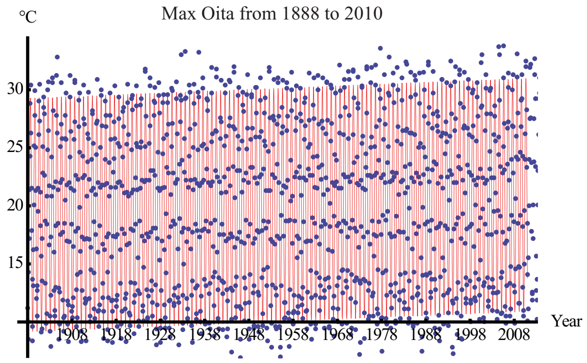

Fig. 1. The maximum data (dots) and the fitting curve

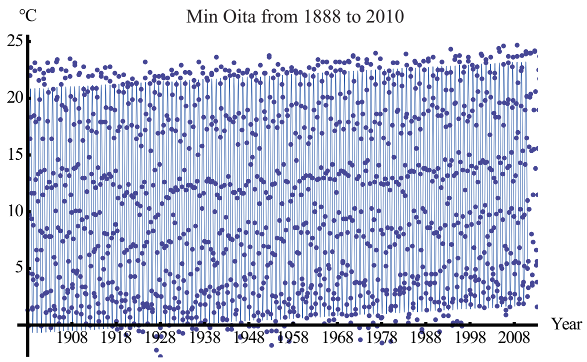

Fig. 2. The minimum data (dots) and the fitting curve

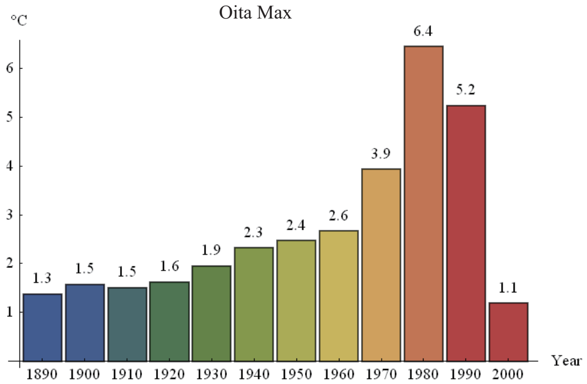

Fig. 3. The maximum trends of each decade

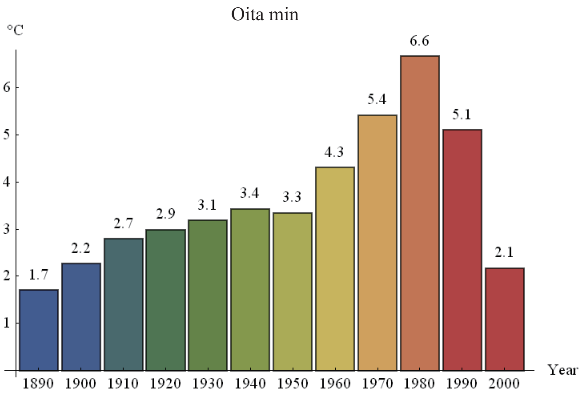

Fig. 4. The Minimum trends of each decade

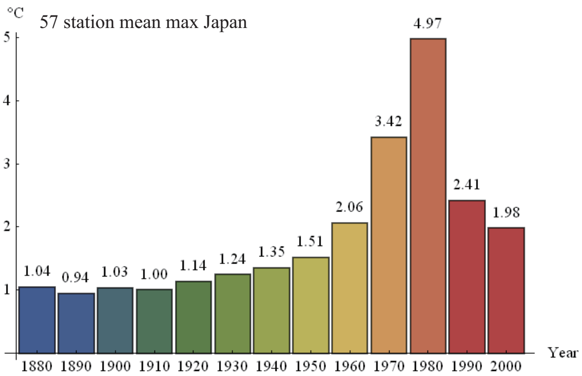

Fig. 5. The mean of maximum of 57 local stations

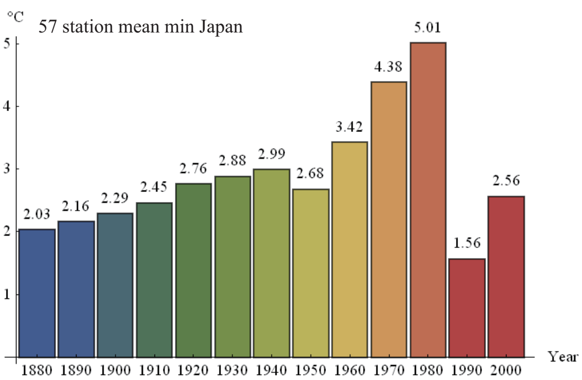

Fig. 6. The mean of minimum trend of 57 local stations

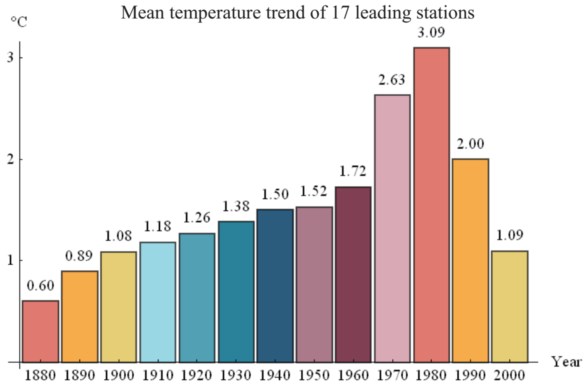

Fig. 7. The mean trend of 17 leading stations

4 DISCUSSION

The proposed criterion (2) gives $n = 6$ as the best parameter more than 200 examples. For the case of maximum temperature (3)

$$-\log_{10} \mathrm{CR}_6 = -\log_1 0.028 = 1.55$$

hence the coincident digits of y_i and $\widehat{y_i}$ are estimated more than 1.5 decimal digits in the mean for any i [3].

For the case of minimum temperature (4)

$$-\log_{10} \mathrm{CR}_6 = -\log_1 0.044 = 1.35$$

hence the coincident digits of y_i and $\widehat{y_i}$ are estimated more than 1.3 decimal digits in the mean for any i.

4.1 Year trend of max temp.

Separate f_{max} as follows:

$$f(x) = \underbrace{19.16 + 0.00116x}_{\text{Year Trend}} + \underbrace{10.0\sin(3.93 + \pi x/6)}_{\text{Month Trend}} \quad (5)$$

Ignore the Month Trend of (5), we have a following year trend

$$f_{max}(x) = 19.16 + 0.00116x$$

From

$$f_{max}(1) = 19.16 \quad \text{and} \quad f_{max}(1476) = 20.87$$

the maximum temperature increases 1.71 °C since 1888. Actually, the mean of maximum temperature from 1890 to 1894 is 19.86 °C and that of from 2006 to 2010 is 21.38 °C. Hence the difference is 1.52 °C. This shows that the estimated temperature and the actual temperature well agree and the difference is only 0.19 °C among 123 years.

4.2 Year trend of min temp.

For the case of minimum, we have followings:

$$g(x) = \underbrace{10.23 + 0.00138x}_{\text{Year Trend}} + \underbrace{10.7\sin(3.92 + \pi x/6)}_{\text{Month Trend}} \quad (6)$$

$$g_{min}(x) = 10.23 + 0.00138x$$
$$g_{min}(1) = 10.23$$
$$g_{min}(1476) = 12.26$$

Hence the minimum temperature is 2.03°C up since 1888 and the actual temperature is $13.14 - 11.36 = 1.76$(°C) up. The difference is only 0.27°C among 123 year.

4.3 Month trend of max temp.

The red dots in Figure 8 shows the mean of maximum values of each month from January 1888 to December 2010. The blue curve shows the "Month Trend" of (5) and the green curve shows the same trend from January 1998 to December 2010. Figuer 8 shows the increasing of warmth related to the maximum temperature in Oita.

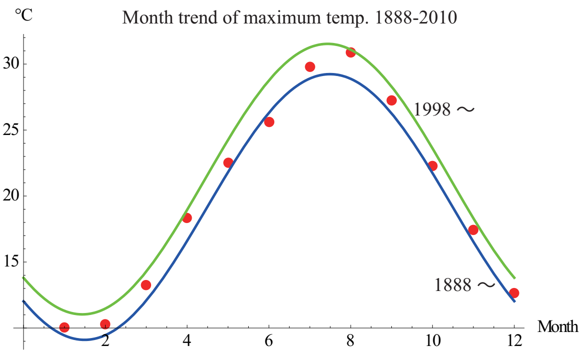

Fig. 8. The month trends of maximum temperature, the blue (green) curve is the trend since 1888 (1998)

4.4 Month trend of min temp.

The red dots in Figure 9 shows the mean of minimum values of each month from January 1888 to December 2010. The blue curve shows the "Month Trend" of (6) and the green curve shows the same trend from January 1998 to December 2010. Figure 9 also shows the increasing of warmth related to the minimum temperature in Oita.

5 CONCLUSION

The proposed model (1) is well fit the maximum and minimum temperature of Oita, because of the iteration always terminates at $n = 6$ and this means that the fundamental period of temperature change is 12 (months).

We also derive the trends of year concerning the maximum and the minimum temperature, and that the trends are described by a linear curve. The difference between the estimation and the actual temperature are 0.19 °C (maximum temperature) and 0.27 °C (minimum temperature) among 123 years.

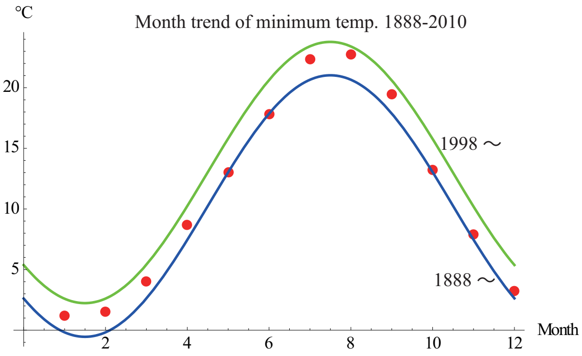

Fig. 9. The month trends of minimum temperature, the blue (green) curve is the trend since 1888 (1998)

The month trends of the maximum and minimum temperatures are increasing with the increasing decade.

The estimated results of Oita are something high compared with the 17 leading [4] and 57 [5] local meteorological stations trends of Japan.

REFERENCES

[1] Masao IGARASHI, Eiji NUNOHIRO and Jong Geol PARK(2009), A Method to Fit a Nonlinear Curve to NDVI, SST and LST, International Journal of Geology, **3**: 97-100.

[2] Masao IGARASHI, Jong Geol PARK, Chen Yen Tsai, Eiji NUNOHIRO and Yukio YANAGISAWA(2010), A Fitness Criterion on Finding Nonlinear Curve for the NDVI Data, INFORMATION **13**: 601-606

[3] S. D. Conte and Carl de Boor(1972), Elementary Numerical Analysis, McGraw-Hill Book Company

[4] 1) Abashiri 2) Nemuro 3) Suttu 4) Yamagata 5) Ishinomaki 6) Fushiki 7) Nagano 8) Mito 9) Iida 10) Chousi 11) Sakai 12) Hamada 13) Hikone 14) Miyazaki 15) Tadotsu16) Nase 17) Ishigakijima.

[5] 1) Abashiri 2) Akita 3) Aomori 4) Asahikawa 5) Choshi 6) Fukushima 7) Fukui 8) Fukuoka 9) Gifu 10) Hakodate 11) Hikone 12) Hiroshima 13) Ishigakijima 14) Kagoshima 15) Kanazawa 16) Kouchi 17) Koufu 18) Koube 19) Kumagaya 20) Kumamoto 21) Kushiro 22) Kyoto 23) Maebashi 24) Maizuru 25) Matsuyama 26) Matsue 27) Minamidaitoujima 28) Mito 29) Miyakojima 30) Miyazaki 31) Morioka 32) Muroran 33) Nagano 34)Nagasaki 35) Nagoya 36) Nara 37) Niigata 38) Oita 39) Okayama 40) Okinawa 41) Osaka 42) Saga43) Sapporo 44) Sendai 45) Shimonoseki 46) Shizuoka 47) Takamatsu 48) Tokushima 49) Tokyo 50) Tottori 51) Toyama 52) Tsu 53) Utsunomiya 54) Wakayama 55) Yamagata 57) Yokohama.

The Seventeenth International Symposium on Artificial Life and Robotics 2012 (AROB 17th '12),
B-Con Plaza, Beppu, Oita, Japan, January 19-21, 2012

H_∞ consensus control for high-order multi-agent systems with disturbances

Ping Wang[1], Yingmin Jia[1,2], Junping Du[3] and Fashan Yu[4]

[1] The Seventh Research Division and the Department of Systems and Control, Beihang University (BUAA), Beijing 100191, China (e-mail: wplh@ss.buaa.edu.cn).
[2] Key Laboratory of Mathematics Informatics and Behavioral Semantics (LIMB), SMSS, Beihang University (BUAA), Beijing 100191, China (e-mail: ymjia@buaa.edu.cn).
[3] Beijing Key Laboratory of Intelligent Telecommunications Software and Multimedia, School of Computer Science and Technology, Beijing University of Posts and Telecommunications, Beijing 100876, China (e-mail: junpingdu@126.com).
[4] School of Electrical Engineering and Automation, Henan Polytechnic University, Jiaozuo 454000, Henan, China (e-mail: yufs@hpu.edu.cn).

Abstract: This paper is devoted to consensus problems in directed networks of high-order agents with disturbances. A new distributed protocol is proposed with the consideration of model uncertainty, which only depends on the agent's own information and it's neighbors' first state, an auxiliary variable is included to describe the effects of all-order derivatives' relative information. Based on Lyapunov theory, for three cases: (a) network with fixed topology and zero time-delay; (b) network with switching topology and zero time-delay; (c) network with fixed topology and non-zero time-delay, sufficient conditions are derived correspondingly to make all agents reach H_∞ consensus. Especially, the approach used in this paper does not need any model transformation. Finally, numerical simulations are provided to show the effectiveness of the obtained results.

Keywords: Consensus, directed graph, H_∞ control, high-order multi-agent systems

1 INTRODUCTION

Recently, consensus problems of multi-agent systems have attracted researchers from a wide range of disciplines, and numerous significant theoretical results have been obtained [1-9]. In engineering practice, multi-agent systems are often subjected to various disturbances such as time-delay, model uncertainty, and the variation of network topology. As we all know, these disturbances might degrade the system performance and even cause the network system to diverge or oscillate. Therefore, it is of great significance to improve the robustness of the multi-agent systems. However, to the best of our knowledge, little work has been done to consider high-order consensus problem with disturbances.

With this background, we investigate consensus problems in directed networks of high-order agents with disturbances. Firstly, a new distributed protocol is proposed with the consideration of model uncertainty. Then, based on Lyapunov theory, sufficient conditions are derived to make all agents reach consensus while satisfying desired H_∞ performance for three cases. Especially, the approach used in this paper does not need any model transformation.

2 GRAPH THEORY

Let $\mathscr{G}(\mathscr{V},\varepsilon,\mathscr{A})$ be a directed graph of order n with the set of nodes $\mathscr{V}=\{s_1,\cdots,s_n\}$, set of edges $\varepsilon\subseteq\mathscr{V}\times\mathscr{V}$, and a weighted adjacency matrix $\mathscr{A}=[a_{ij}]$. The node indexes belong to a finite index set $I=\{1,2,\cdots,n\}$. An edge of $\mathscr{G}$ is denoted by $e_{ij}=(s_i,s_j)$. The adjacency elements associated with the edges are positive, i.e. $e_{ij}\in\varepsilon\Leftrightarrow a_{ij}>0$. Moreover, we assume that $a_{ii}=0$ for all $i\in I$. The set of neighbors of node s_i is denoted by $N_i=\{s_j\in\mathscr{V}:(s_i,s_j)\in\varepsilon\}$. A diagonal matrix $D=diag\{d_1,\cdots,d_n\}$ is a degree matrix of $\mathscr{G}$, with $d_i=\sum_{j=1}^{n}a_{ij}$ for $i\in I$. Then the Laplacian of the weighted graph $\mathscr{G}$ is defined as $L=D-\mathscr{A}\in\mathscr{R}^{n\times n}$. A directed path is a sequence of ordered edges of the form $(s_{i_1},s_{i_2}),(s_{i_2},s_{i_3}),\cdots$, where $s_{i_j}\in\mathscr{V}$. A directed graph is said to have a spanning tree, if there exists a node such that there is a directed path from every other node to this node[10]. If the graph $\mathscr{G}$ has a spanning tree, then its Laplacian L satisfies: zero is a simple eigenvalue of L, and $\mathbf{1}_n$ is the corresponding eigenvector [4].

3 PROBLEM STATEMENT

Consider the multi-agent system consisting of n identical agents, each agent is regarded as a node in a directed graph $\mathscr{G}$. Suppose the ith agent has the dynamics as follows:

$$\begin{array}{rcl}\dot{x}_i^{(0)}(t) & = & x_i^{(1)}(t)\\ & \vdots & \\ \dot{x}_i^{(l-2)}(t) & = & x_i^{(l-1)}(t)\\ \dot{x}_i^{(l-1)}(t) & = & u_i(t)+\omega_i(t)\\ y_i(t) & = & x_i^{(0)}(t)\end{array}\qquad(1)$$

where $x_i=[x_i^{(0)},x_i^{(1)},\cdots,x_i^{(l-1)}]^\top\in\mathbb{R}^l$ is the state of the ith agent, $u_i\in\mathbb{R}$ is the protocol, $\omega_i(t)\in L_2[0,\infty)$ is the external disturbance, $y_i(t)$ is the measured output that can be observed by its neighbors.

A protocol u_i is said to asymptotically solve consensus problem, if for any initial state, the states of all the agents satisfy

$$\lim_{t\to+\infty}[x_i(t)-x_j(t)]=0 \tag{2}$$

for all $i,j\in I$.

In order to solve the consensus problem of high-order multi-agent system (1), we propose the following consensus protocol

$$\begin{aligned} u_i &= k_0\sum_{s_j\in N_i}(a_{ij}+\Delta a_{ij}(t))(x_j^{(0)}(t-\tau)-x_i^{(0)}(t-\tau)) \\ &\quad -\sum_{j=1}^{l-1}k_jx_i^{(j)}(t)+p_i \\ \dot{p}_i &= -\gamma_1 p_i-k_l\sum_{s_j\in N_i}(a_{ij}+\Delta a_{ij}(t))(x_j^{(0)}(t-\tau)-x_i^{(0)}(t-\tau)) \end{aligned} \tag{3}$$

where $k_i>0, i=0,1,\cdots,l,\ \gamma_1>0$ are protocol parameters to be designed, p_i is an auxiliary variable to describe the effects of all-order derivatives' relative information. τ denotes communication delay, $\Delta a_{ij}(t)$ denotes the uncertainty of a_{ij}.

A controlled output function

$$z_i(t)=[z_{i1}(t),z_{i2}(t),\cdots,z_{il}(t)]^\top\in\mathbb{R}^l \quad i\in I$$

is defined as an average of the relative displacements of all agents as follows

$$\begin{aligned} z_{i1}(t) &= x_i^{(0)}(t)-\frac{1}{n}\sum_{j=1}^{n}x_j^{(0)}(t) \\ z_{i2}(t) &= x_i^{(1)}(t)-\frac{1}{n}\sum_{j=1}^{n}x_j^{(1)}(t) \\ &\ \,\vdots \\ z_{il}(t) &= x_i^{(l-1)}(t)-\frac{1}{n}\sum_{j=1}^{n}x_j^{(l-1)}(t) \end{aligned} \tag{4}$$

Obviously, the multi-agent system (1) achieves consensus if and only if

$$\lim_{t\to+\infty}z_i(t)=0 \qquad i\in I \tag{5}$$

Let

$$A=\begin{bmatrix} 0 & 1 & 0 & \cdots & 0 & 0 \\ 0 & 0 & 1 & \cdots & 0 & 0 \\ \vdots & \vdots & \vdots & \ddots & \vdots & \vdots \\ 0 & -k_1 & -k_2 & \cdots & -k_{l-1} & 1 \\ 0 & 0 & 0 & \cdots & 0 & -\gamma_1 \end{bmatrix}$$

$$B=\begin{bmatrix} 0_{l-1} & 0_{(l-1)\times l} \\ k_0 & 0_{1\times l} \\ -k_l & 0_{1\times l} \end{bmatrix} \quad B_1=\begin{bmatrix} 0_{l-1} \\ 1 \\ 0 \end{bmatrix}$$

$$B_2=\begin{bmatrix} I_l & 0_l \end{bmatrix}$$

$$C=\begin{bmatrix} \frac{n-1}{n} & -\frac{1}{n} & \cdots & -\frac{1}{n} \\ -\frac{1}{n} & \frac{n-1}{n} & \cdots & -\frac{1}{n} \\ \vdots & \vdots & \ddots & \vdots \\ -\frac{1}{n} & -\frac{1}{n} & \cdots & \frac{n-1}{n} \end{bmatrix}$$

Under the protocol (3), the network dynamics of the multi-agent system is

$$\begin{aligned} \dot{\varphi}(t) &= (I_n\otimes A)\varphi(t)-((L+\Delta L)\otimes B)\varphi(t-\tau) \\ &\quad +(I_n\otimes B_1)\omega(t) \\ z(t) &= (C\otimes B_2)\varphi(t) \end{aligned} \tag{6}$$

where $\varphi=[x_1^\top,p_1,\ \cdots\ x_n^\top,p_n]^\top,\ \omega=[\omega_1,\cdots,\omega_n]^\top,\ z=[z_1^\top,\cdots,z_n^\top]^\top$, L is the Laplacian of the graph $\mathscr{G}$, ΔL denotes the uncertainty Laplacian satisfying $\Delta L=E_1\Sigma(t)E_2$, where $E_1\in\mathbb{R}^{n\times|\varepsilon|}$, $E_2\in\mathbb{R}^{|\varepsilon|\times n}$ are specified constant matrices and $\Sigma(t)$ is a diagonal matrix satisfying $\Sigma^\top(t)\Sigma(t)\le I$.

Define the following H_∞ performance index

$$J=\int_0^\infty[z^\top(t)z(t)-\gamma^2\omega^\top(t)\omega(t)]dt<0 \tag{7}$$

where γ is a given positive constant.

Based on the above discussion, the H_∞ consensus problem to be addressed is stated as follows.

H_∞ **consensus problem**: For a given protocol u_i, we say the multi-agent systems reach H_∞ consensus if the following two conditions are satisfied simultaneously:
1). when $\omega(t)=0$, the multi-agent systems achieve consensus, i.e. $\lim_{t\to+\infty}z(t)=0$;
2). if $z_0=0$, the inequality (7) is satisfied.

4 MAIN RESULTS

In this section, we will give conditions to make all agents achieve H_∞ consensus. Before presenting the main results, we first introduce a lemma.

Lemma 1 [7]. Consider the matrix C. Then there exists an orthogonal matrix $U=[U_1\ \ \overline{U}_1]$ with $\overline{U}_1=\frac{1}{\sqrt{n}}\mathbf{1}_n$, such that

$$U^\top CU=\begin{bmatrix} I_{n-1} & \mathbf{0}_{(n-1)\times 1} \\ \mathbf{0}_{1\times(n-1)} & 0 \end{bmatrix}$$

holds.

Theorem 1. Consider a directed network with fixed topology and zero time-delay. The multi-agent system (6) reaches H_∞ consensus, if there exist a symmetric positive-definite matrix $\overline{P}\in\mathbb{R}^{(l+1)(n-1)\times(l+1)(n-1)}$, and a scalar $\mu>0$ satisfying

$$M=\begin{bmatrix} M_{11} & M_{12} & M_{13} \\ * & -\mu I & \mathbf{0} \\ * & * & -\gamma^2 I \end{bmatrix}<0 \tag{8}$$

where $M_{11}=\overline{P}(I_{n-1}\otimes A-\overline{L}\otimes B)+(I_{n-1}\otimes A-\overline{L}\otimes B)^\top\overline{P}+\mu\overline{E}+I_{n-1}\otimes B_2^\top B_2$, $M_{12}=\overline{P}(U_1^\top E_1\otimes B)$, $M_{13}=\overline{P}(U_1^\top\otimes B_1)$, $\overline{L}=U_1^\top LU_1$, $\overline{E}=(U_1^\top E_2^\top E_2U_1)\otimes I_{l+1}$.

Proof. Let

$$\begin{aligned} \delta(t) &= (U_1\otimes I_{l+1})^\top\varphi(t) \\ \overline{\delta}(t) &= (\overline{U}_1\otimes I_{l+1})^\top\varphi(t) \end{aligned} \tag{9}$$

where $\overline{\delta}(t)$ and $\delta(t)$ describe the average and disagreement states of all agents, respectively.

Define a Lyapunov function for system (6) as follows

$$V(t) = \varphi^\top(t)P\varphi(t)$$

where $P = P^\top \geq 0$ satisfies $P(\mathbf{1}_n \otimes I_{l+1}) = 0$ and $rank(P) = (l+1)n-(l+1)$.

Let $\overline{P} = (U_1 \otimes I_{l+1})^\top P(U_1 \otimes I_{l+1})$, then $V(t)$ can be rewritten as

$$\begin{aligned} V(t) &= \varphi^\top(t)P\varphi(t) \\ &= \begin{bmatrix} \delta(t) \\ \overline{\delta}(t) \end{bmatrix}^\top \begin{bmatrix} \overline{P} & 0 \\ 0 & 0 \end{bmatrix} \begin{bmatrix} \delta(t) \\ \overline{\delta}(t) \end{bmatrix} \\ &= \delta^\top(t)\overline{P}\delta(t) > 0 \end{aligned} \tag{10}$$

Differentiating $V(t)$ along the trajectory of (6), we have

$$\begin{aligned} \dot{V}(t) &= 2\delta^\top(t)\overline{P}\dot{\delta}(t) \\ &= 2\delta^\top(t)\overline{P}[I_{n-1} \otimes A - \overline{L} \otimes B]\delta(t) \\ &\quad - 2\delta^\top(t)\overline{P}(\overline{\Delta L} \otimes B)\delta(t) + 2\delta^\top(t)\overline{P}(U_1^\top \otimes B_1)\omega(t) \end{aligned}$$

where $\overline{L} = U_1^\top L U_1$, $\overline{\Delta L} = U_1^\top \Delta L U_1 = U_1^\top E_1 \Sigma(t) E_2 U_1$.

And since $\Sigma^\top(t)\Sigma(t) \leq I$, we can obtain

$$\begin{aligned} &-2\delta^\top(t)\overline{P}(\overline{\Delta L} \otimes B)\delta(t) \\ &= -2\delta^\top(t)\overline{P}(U_1^\top E_1 \otimes B)(\Sigma(t)E_2U_1 \otimes I_{l+1})\delta(t) \\ &\leq \tfrac{1}{\mu}\delta^\top(t)\overline{P}(U_1^\top E_1 \otimes B)(U_1^\top E_1 \otimes B)^\top \overline{P}\delta(t) \\ &\quad + \mu\delta^\top(t)\overline{E}\delta(t) \end{aligned}$$

where $\mu > 0$, $\overline{E} = (U_1^\top E_2^\top E_2 U_1) \otimes I_{l+1}$.

By Lemma 1, we have

$$\begin{aligned} z(t) &= (C \otimes B_2)(U \otimes I_{l+1})(U \otimes I_{l+1})^\top \varphi(t) \\ &= (CU \otimes B_2)\begin{bmatrix} \delta(t) \\ \overline{\delta}(t) \end{bmatrix} \\ &= (U_1 \otimes B_2)\delta(t) \end{aligned}$$

we have $\lim_{t\to+\infty} z(t) = 0$ if $\lim_{t\to+\infty} \delta(t) = 0$. Thus whether the system (6) can reach consensus is only related to the component $\delta(t)$.

Denote

$$\begin{aligned} N &= \overline{P}(I_{n-1} \otimes A - \overline{L} \otimes B) + (I_{n-1} \otimes A - \overline{L} \otimes B)^\top \overline{P} \\ &\quad + \mu\overline{E} + \tfrac{1}{\mu}\overline{P}(U_1^\top E_1 \otimes B)(U_1^\top E_1 \otimes B)^\top \overline{P} \end{aligned}$$

when $\omega(t) = 0$, we can obtain

$$\dot{V}(t) \leq \delta^\top(t)N\delta(t) \tag{11}$$

$N < 0$ holds when $M < 0$, it follows from (10) and (11) that consensus can be achieved asymptotically.

To study the H_∞ performance for the multi-agent system, assume zero initial condition, that is $V(0) = 0$. Therefore, we have

$$\begin{aligned} J &= \textstyle\int_0^\infty [z^\top(t)z(t) - \gamma^2\omega^\top(t)\omega(t) + \dot{V}(t)]dt - V(\infty) + V(0) \\ &\leq \textstyle\int_0^\infty [z^\top(t)z(t) - \gamma^2\omega^\top(t)\omega(t) + \dot{V}(t)]dt \\ &\leq \textstyle\int_0^\infty \xi^\top(t)\overline{M}\xi(t)dt \end{aligned}$$

where

$$\begin{aligned} &\xi(t) = [\delta^\top(t) \;\; \omega^\top(t)]^\top \\ &\overline{M} = \begin{bmatrix} \overline{M}_{11} & \overline{P}(U_1^\top \otimes B_1) \\ * & -\gamma^2 I \end{bmatrix} \\ &\overline{M}_{11} = M_{11} + \tfrac{1}{\mu}\overline{P}(U_1^\top E_1 \otimes B)(U_1^\top E_1 \otimes B)^\top \overline{P} \end{aligned}$$

By Schur complement, $M < 0$ is equivalent to $\overline{M} < 0$. That is, (8) guarantees $J < 0$. Therefore, under the condition $M < 0$, all agents reach H_∞ consensus.

Remark 1. The approach used in Theorem 1 does not need to perform any model transformation.

Remark 2. It is worth pointing out that a necessary condition for (8) is that the graph $\mathscr{G}$ has a spanning tree.

Theorem 2. Consider a directed network with switching topology $\mathscr{G}_\sigma$ and zero time-delay. The multi-agent system (6) reaches H_∞ consensus, if there exist a common symmetric positive-definite matrix $\overline{P} \in \mathbb{R}^{(l+1)(n-1)\times(l+1)(n-1)}$, and positive scalars μ_σ for each possible communication graph $\mathscr{G}_\sigma$ satisfying

$$\hat{M}_\sigma = \begin{bmatrix} \hat{M}_{11} & \hat{M}_{12} & \hat{M}_{13} \\ * & -\mu_\sigma I & \mathbf{0} \\ * & * & -\gamma^2 I \end{bmatrix} < 0 \tag{12}$$

where $\hat{M}_{11} = \overline{P}(I_{n-1} \otimes A - \overline{L}_\sigma \otimes B) + (I_{n-1} \otimes A - \overline{L}_\sigma \otimes B)^\top \overline{P} + \mu_\sigma \overline{E}_\sigma + I_{n-1} \otimes B_2^\top B_2$, $\hat{M}_{12} = \overline{P}(U_1^\top E_{1\sigma} \otimes B)$, $\hat{M}_{13} = \overline{P}(U_1^\top \otimes B_1)$, $\overline{L}_\sigma = U_1^\top L_\sigma U_1$, $\overline{E}_\sigma = (U_1^\top E_{2\sigma}^\top E_{2\sigma} U_1) \otimes I_{l+1}$, and σ denotes the switching signal that determines the topology.

Theorem 3. Consider a directed network with fixed topology and non-zero time-delay. The multi-agent system (6) reaches H_∞ consensus, if there exist symmetric positive-definite matrices $\overline{P}, \overline{Q}, \overline{R} \in \mathbb{R}^{(l+1)(n-1)\times(l+1)(n-1)}$, and positive scalars $\mu_1, \mu_2, \mu_3, \mu_4, \mu_5$ satisfying

$$\Gamma = \begin{bmatrix} \Gamma_{11} & \Gamma_{12} \\ * & \Gamma_{22} \end{bmatrix} < 0 \tag{13}$$

where Γ_{11}, Γ_{12} and Γ_{22} are defined in (14), $\psi_1 = \overline{P}(I_{n-1} \otimes A - \overline{L} \otimes B) + (I_{n-1} \otimes A - \overline{L} \otimes B)^\top \overline{P} + \overline{Q}$, $\overline{E} = (U_1^\top E_2^\top E_2 U_1) \otimes I_{l+1}$, and $\hat{E} = (U_1^\top E_2^\top E_2 U_1) \otimes BB^\top$.

Proof. This theorem can be proved following the lines of the proof of Theorem 1 and hence omitted. It deserves pointing out that the Lyapunov function adopted here is as follows

$$\begin{aligned} V(t) &= \varphi^\top(t)P\varphi(t) + \textstyle\int_{t-\tau}^t \varphi^\top(s)Q\varphi(s)ds \\ &\quad + \textstyle\int_{-\tau}^0 \int_{t+\theta}^t \dot{\varphi}^\top(s)R\dot{\varphi}(s)dsd\theta \end{aligned}$$

5 SIMULATIONS

The simulation is given to illustrate the effectiveness of the obtained results. Fig.1. shows a directed graph with 0-1 weights. Each agent has three-order dynamics. Suppose that the uncertainty of each edge satisfies $|a_{ij}| \leq 0.01$, the communication delay $\tau = 0.1s$, and the initial conditions $\varphi(0) = [0.5\; 0\; 0\; 0\; 1\; 0\; 0\; 0\; -0.5\; 0\; 0\; 0\; -1\; 0\; 0\; 0]^\top$.

$$\Gamma_{11}=\begin{bmatrix}\psi_1+I_{n-1}\otimes B_2^{\top}B_2 & -\tau(I_{n-1}\otimes A)^{\top}\overline{R}(\overline{L}\otimes B) & \overline{P}(U_1^{\top}\otimes B_1)+\tau(I_{n-1}\otimes A)^{\top}\overline{R}(U_1^{\top}\otimes B_1)\\ * & -\overline{Q}+\mu_1\overline{E}+\tau(\mu_2+\mu_3+\mu_5)\overline{E}+\tau\mu_4\hat{E} & -\tau(\overline{L}\otimes B)^{\top}\overline{R}(U_1^{\top}\otimes B_1)\\ * & * & -\gamma^2 I\end{bmatrix}$$

$$\Gamma_{12}=\begin{bmatrix}\overline{P}(\overline{L}\otimes B) & \overline{P}(U_1^{\top}E_1\otimes B) & \tau(I_{n-1}\otimes A)^{\top}\overline{R} & (I_{n-1}\otimes A)^{\top}\overline{R}(U_1^{\top}E_1\otimes B) & \mathbf{0} & \mathbf{0} & \mathbf{0} & \mathbf{0} & \mathbf{0} & \mathbf{0}\\ \mathbf{0} & \mathbf{0} & \mathbf{0} & \mathbf{0} & \tau(\overline{L}\otimes B)^{\top}\overline{R} & (\overline{L}\otimes B)^{\top}\overline{R}(U_1^{\top}E_1\otimes B) & \mathbf{0} & \mathbf{0} & \mathbf{0} & \mathbf{0}\\ \mathbf{0} & \mathbf{0} & \mathbf{0} & \mathbf{0} & \mathbf{0} & \mathbf{0} & \mathbf{0} & \mathbf{0} & \tau(U_1^{\top}\otimes B_1)^{\top}\overline{R} & (U_1^{\top}\otimes B_1)^{\top}\overline{R}(U_1^{\top}E_1\otimes B)\end{bmatrix} \quad (14)$$

$$\Gamma_{22}=diag\{-\frac{\overline{R}}{\tau},-\mu_1 I,-\tau\overline{R},-\frac{\mu_2}{\tau}I,-\tau\overline{R},-\frac{\mu_3}{\tau}I,\begin{bmatrix}-\tau\overline{R} & \overline{R}(U_1^{\top}E_1\otimes I)\\ * & -\frac{\mu_4}{\tau}I\end{bmatrix},-\tau\overline{R},-\frac{\mu_5}{\tau}I\}$$

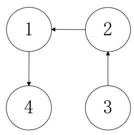

Fig. 1. A directed graph

Take $k_0=3, k_1=7, k_2=3, k_3=1, \gamma_1=1, \gamma=1$, and the external disturbance as $\omega(t)=[2\ -3\ 2.5\ -1]^{\top}\overline{\omega}(t)$, where

$$\overline{\omega}(t)=\begin{cases}1 & 0\le t\le 1\\ 0 & otherwise\end{cases}$$

is a pulse signal.

Fig.2. and Fig.3. give the state trajectories of the network, and energy trajectories of $z(t)$ and the disturbance $\omega(t)$.

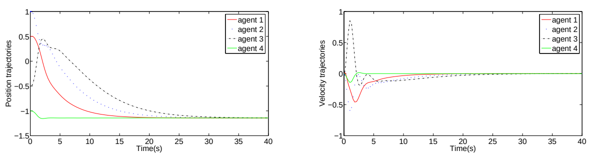

Fig. 2. Left: Position trajectories of the network
Right: Velocity trajectories of the network

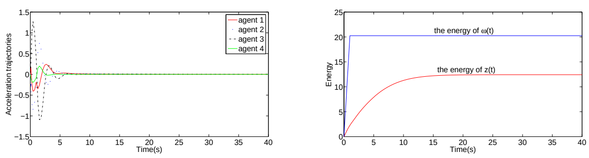

Fig. 3. Left: Acceleration trajectories of the network
Right: Energy trajectories of $z(t)$ and $\omega(t)$

Clearly, we can see that all agents achieve consensus while satisfying desired H_∞ performance.

6 CONLUSIONS

In this paper, we investigate the consensus problems in directed networks of high-order agents with disturbances. A new protocol is proposed with the consideration of model uncertainty. Sufficient conditions are derived to make all agents reach H_∞ consensus for three cases. Especially, the approach used in this paper does not need any model transformation. Finally, simulations are provided to show the effectiveness of the obtained results.

7 ACKNOWLEDGMENTS

This work was supported by the National 973 Program (2012CB821200) and the NSFC (61134005, 60921001, 90916024, 91116016).

REFERENCES

[1] Vicsek T, Czirok A, and Ben-Jacob E, et al (1995), Novel Type of Phase Transition in a System of Self-driven Particles, Physical Review Letters, 75(6):1226-1229

[2] Jadbabaie A, Lin J, and Morse AS (2001), Coordination of Groups of Mobile Autonomous Agents Using Nearest Neighbor Rules, IEEE Trans. Automatic Control, 48(6):988-1001

[3] Olfati-Saber R and Murray RM (2004), Consensus Problems in Networks of Agents with Switching Topology and Time-delays, IEEE Trans. Automatic Control, 49(9):1520-1533

[4] Ren W and Atkins E (2005), Consensus Seeking in Multi-agent Systems under Dynamically Changing Interaction Topologies, *IEEE Trans. Automatic Control*, 50(5):655-661

[5] Ren W, Moore K and Chen Y (2006), High-order Consensus Algorithms in Cooperative Vehicle Systems, Int.Conf. on Networking, Sensing and Control, 457-462

[6] Jiang F, Wang L and Xie G (2010), Consensus of High-order Dynamic Multi-agent Systems with Switching Topology and Time-varying Delays, J Control Theory Appl, 8(1):52-60

[7] Lin P and Jia Y (2009), Further Results on Decentralised Coordination in Networks of Agents with Second-order Dynamics. IET Control Theory and Applications, 3(7):957-970

[8] Lin P, Jia Y and Li L (2008), Distributed Robust H_∞ Consensus Control in Directed Networks of Agents with Time-delay. System & control letters, 57(8):643-653

[9] Lin P and Jia Y (2010), Robust H_∞ Consensus Analysis of a Class of Second-order Multi-agent Systems with Uncertainty. IET Control Theory and Applications, 4(3):487-498

[10] Godsil C and Royle G (2001), Algebraic Graph Theory. New York: Springer-Verlag

The Seventeenth International Symposium on Artificial Life and Robotics 2012 (AROB 17th '12),
B-Con Plaza, Beppu, Oita, Japan, January 19-21, 2012

Lane keeping control for 4WS4WD vehicles subject to wheel slip constraint

Changfang Chen[1], Yingmin Jia[1,2], Junping Du[3], and Fashan Yu[4]

[1] The Seventh Research Division and the Department of Systems and Control, Beihang University (BUAA), Beijing 100191, China (e-mail: chenchangfang012@163.com)

[2] Key Laboratory of Mathematics Informatics and Behavioral Semantics (LIMB), SMSS, Beihang University (BUAA), Beijing 100191, China (e-mail: ymjia@buaa.edu.cn)

[3] Beijing Key Laboratory of Intelligent Telecommunications Software and Multimedia, School of Computer Science and Technology, Beijing University of Posts and Telecommunications, Beijing 100876, China (e-mail: junpingdu@126.com)

[4] School of Electrical Engineering and Automation, Henan Polytechnic University, Jiaozuo 454000, Henan, China (e-mail: yufs@hpu.edu.cn)

Abstract: This paper proposes a lane keeping control scheme that prevents an autonomous 4WS4WD vehicle from wheel skidding in presence of road curvature and aerodynamic drag. The control objectives can be specified as various closed-loop specifications, such as lane departure avoidance, wheel slip constraint and disturbance attenuation. An LMI approach is used to deal with these objectives simultaneously, which combines the quadratic stabilization technique with constraints on inputs. Simulations show that the proposed controller effectively limits the combined wheel slip and improves lane keeping performance.

Keywords: Combined wheel slip, lane keeping, linear matrix inequality(LMI), wheel skidding

1 INTRODUCTION

Lane departure is one of the most important causes of car accidents. NHTSA estimated that running off the road caused about 28% of the fatal crashes in the United States in 2005. Most research on lane keeping system has focused on pure lateral control [1], [2]. However, it is known that the vehicle dynamics are not completely independent in both directions. The coupling effects become increasingly significant as maneuvers involve higher accelerations, larger tire forces, or reduced road friction [3], [4]. So many efforts have been made to merge the two control tasks into a single problem.

To avoid lane departure, the strategy of controlling the vehicle's worst displacement/offset to the guideline beneath the safety requirement in [5], [6]. The combined wheel slip can be used to characterize the vector of tire/road, particularly for the situation of path following [7], [8]. In this paper, we consider an issue of guiding an autonomous vehicle to follow the curve without wheel skidding in the presence of aerodynamic drag. The design task is synthesized as a multi-objective problem, which specifies the closed-loop objectives in terms of a common Lyapunov function. This still guarantees the desired specifications at the expense of conservation. As a benefit, controller design can be reduced to a convex optimization problem.

2 PROBLEM FORMULATION

2.1 Vehicle model

As shown in Fig. 1., the model considered here for simulation consists of 7 degrees of freedom (DOF), which includes longitudinal, lateral and yaw motion of the vehicle as well as the rotational dynamics of the four wheels. The vehicle body-fixed coordinate system is used to set up the model. The governing equations of motion for the vehicle can be expressed as follows:

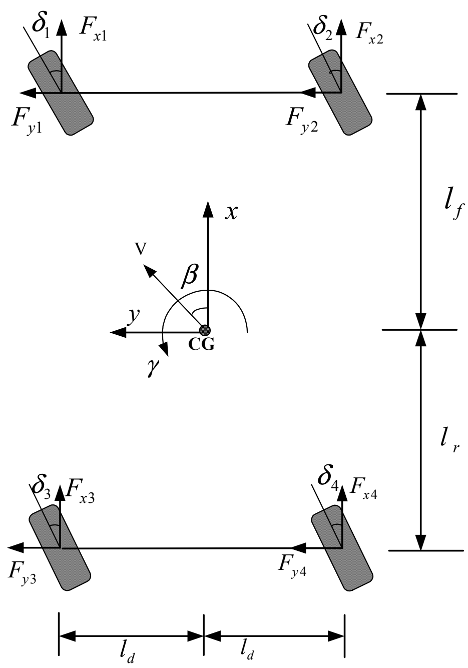

Fig. 1: Vehicle model

Longitudinal motion:

$$m(\dot{v}_x - \gamma v_y) = \sum F_x - C_{aero} v_x^2. \tag{1}$$

Lateral motion:

$$m(\dot{v}_y + \gamma) = \sum F_y. \tag{2}$$

Yaw motion:

$$J_z\dot{\gamma} = \sum M_z. \tag{3}$$

Wheel rotational equations of motion for wheels are as follows:

$$I_{wj}\dot{w}_j = T_j - r_j\begin{bmatrix}\cos\delta_j & \sin\delta_j\end{bmatrix}\begin{bmatrix}F_{xj}\\ F_{yj}\end{bmatrix}. \tag{4}$$

where m and J_z are the mass of vehicle and the inertia about z axis, respectively. F_{xj}, F_{yj}, and M_{zj} (j = 1, 2, 3, 4), defined in the body fixed $x-y-z$ coordinate system, are the external forces and yaw moments mainly resulting from tire/road friction. v_x and v_y stand for the longitudinal and lateral vehicle velocity, v the vehicle velocity, γ the yaw rate and β the vehicle side slip angle. $\sum F_x$, $\sum F_y$, $\sum M_z$ are the sum of the external forces and moments acting on the vehicle.

$$\begin{aligned}\sum F_x &= F_{x1}+F_{x2}+F_{x3}+F_{x4}\\ \sum F_y &= F_{y1}+F_{y2}+F_{y3}+F_{y4}\\ \sum M_z &= l_f(F_{y1}+F_{y2}) - l_r(F_{y3}+F_{y4})\\ &\quad + l_d(F_{x2}-F_{x1}) + l_d(F_{x4}-F_{x3}).\end{aligned}$$

where l_f and l_r and l_d are the distances from the center of gravity to to the front, the rear axles, and to the wheel side. I_{wj} and r_j represent respectively the moment of inertia and the radius of wheel j; T_j and δ_j are the wheel torque and wheel steering angle used for the control scheme.

Because the sensors that measure the lateral deviation are not normally fixed on the vertical line through CG. Moreover, feedback based on error measured at the CG leads to bad ride comfort. Hence, it is natural to describe the vehicle dynamics in terms of the lateral displacement at the sensor y_l. The dynamics of path tracking can be expressed as

$$\begin{aligned}\dot{\phi}_l &= \gamma - \rho v_x\\ \dot{y}_l &= v_x(\beta+\phi_l) + l_s(\gamma - \rho v_x).\end{aligned} \tag{5}$$

Let ϕ_l be the angle between the road centerline and the vehicle longitudinal axis in radians, ρ the road curvature.

Because the wheel subsystem converges much faster, singular perturbation theory is used for model reduction. By linearizing the above nonlinear vehicle system around the operating point:

$$\rho_{ref}=0,\ v_x=v_0,\ \beta=0,\ \gamma=0,\ y_l=0,$$
$$\phi_l=0,\ \delta_j=0,\ T_j=0,\ j=1,2,3,4,$$

we finally arrive at the following design model:

$$\begin{aligned}\frac{d}{dt}\begin{bmatrix}\partial v\\ \beta\\ \gamma\\ \phi_l\\ y_l\end{bmatrix} &= \begin{bmatrix}-2C_{aero}v_0/m & 0 & 0 & 0 & 0\\ 0 & 0 & -1 & 0 & 0\\ 0 & 0 & 0 & 0 & 0\\ 0 & 0 & 1 & 0 & 0\\ 0 & v_0 & l_s & v_0 & 0\end{bmatrix}\begin{bmatrix}\partial v\\ \beta\\ \gamma\\ \phi_l\\ y_l\end{bmatrix}\\ &+ \begin{bmatrix}1/m & 0 & 0\\ 0 & 1/(mv_0) & 0\\ 0 & 0 & 1/J_z\\ 0 & 0 & 0\\ 0 & 0 & 0\end{bmatrix}\begin{bmatrix}\sum F_x\\ \sum F_y\\ \sum M_z\end{bmatrix}\\ &+ \begin{bmatrix}-C_{aero}v_0^2/m\\ 0\\ 0\\ -v_0\rho_{ref}\\ -l_s v_0\rho_{ref}\end{bmatrix}.\end{aligned} \tag{6}$$

2.2 The combined wheel slip and friction forces

The combined wheel slip contains longitudinal and lateral components. The longitudinal slip S_L is defined in the direction of the wheel ground contact point velocity $v_j, j = 1,2,3,4$, and the lateral slip S_S at right angles to this.
When braking $(v_{Rj}\cos\alpha_j \le v_{Wj})$, the combined wheel slip is given by :

$$S_j = \begin{bmatrix}(v_{Rj}\cos\alpha_j - v_{Wj})/v_{Wj}\\ v_{Rj}\sin\alpha_j/v_{Wj}\end{bmatrix}. \tag{7}$$

When driving $(v_{Rj}\cos\alpha_j > v_{Wj})$, the combined wheel slip is given by:

$$S_j = \begin{bmatrix}(v_{Rj}\cos\alpha_j - v_{Wj})/v_{Rj}\cos\alpha_j\\ \tan\alpha_j\end{bmatrix}, \tag{8}$$

where the tire side slip angle α_j is the angle between the wheel plane and the velocity of the wheel ground contact point

$$\alpha_j = \delta_j - \beta_j,\ \beta_j = \arctan(v_{yj}/v_{xj}), \tag{9}$$

and

$$\begin{aligned}v_{W1} &= (v_x - l_d\gamma)\vec{e}_x + (v_y + l_f\gamma)\vec{e}_y\\ v_{W2} &= (v_x + l_d\gamma)\vec{e}_x + (v_y + l_f\gamma)\vec{e}_y\\ v_{W3} &= (v_x - l_d\gamma)\vec{e}_x + (v_y - l_r\gamma)\vec{e}_y\\ v_{W4} &= (v_x + l_d\gamma)\vec{e}_x + (v_y - l_r\gamma)\vec{e}_y.\end{aligned}$$

The resultant wheel slip is the geometrical sum of the longitudinal and lateral slip $S_{Res} = \sqrt{S_L^2 + S_S^2}$, and the resultant slip S_{Res} must always be between -1 and 1.

The friction forces in the body co-ordinate system (x,y) are given by

$$\begin{bmatrix}F_{xj}\\ F_{yj}\end{bmatrix} = F_{zj}\frac{\mu_{Res}(\|S_j\|,\chi)}{\|S_j\|}\begin{bmatrix}\cos\beta_j & \sin\beta_j\\ -\sin\beta_j & \cos\beta_j\end{bmatrix}\begin{bmatrix}1 & 0\\ 0 & k_s\end{bmatrix}\begin{bmatrix}S_{Lj}\\ S_{Sj}\end{bmatrix}$$

$\mu_{Res}(\|S_j\|,\chi)$ is the resultant friction co-efficient. It is a scalar saturation function depending on the magnitude of resultant slip $\|S_j\|$ and road condition χ. Define

$$k_j \triangleq \frac{\partial \mu_{Res}}{\partial S_{Res}} \tag{10}$$

where the slope k_j in equation (10) depends mainly on road conditions. A better road condition gives a larger slope k_j and in turn provides a larger friction force. Then

$$\begin{bmatrix} F_{xj} \\ F_{yj} \end{bmatrix} = F_{zj} \begin{bmatrix} \cos\beta_j & \sin\beta_j \\ -\sin\beta_j & \cos\beta_j \end{bmatrix} \begin{bmatrix} k_j & 0 \\ 0 & k_S k_j \end{bmatrix} \begin{bmatrix} S_{Lj} \\ S_{Sj} \end{bmatrix}. \tag{11}$$

In this paper, we assume that the vehicle runs on a uniform road condition, more specifically, k_j has the same value as k.

Consider yaw rate γ, lateral derivation y_l as the outputs, and $z_\infty = x$, $z_1 = y_l$ the variable to be regulated. By combining (6) and (11), we can arrive at

$$\begin{aligned} \dot{x} &= Ax + B_1 w + B_2 u \\ z_\infty &= C_\infty x \\ z_1 &= C_1 x \\ y &= C_2 x \end{aligned} \tag{12}$$

where

$$\begin{aligned} x &= \begin{bmatrix} \partial v & \beta & \gamma & \phi_l & y_l \end{bmatrix}^T, \\ u &= \begin{bmatrix} S_{L1} & S_{S1} & S_{L2} & S_{S2} \end{bmatrix}^T, \\ w &= \begin{bmatrix} f_w & \rho_{ref} \end{bmatrix}^T, f_w = C_{aero} v_0^2/m. \end{aligned}$$

The design objective is to design control laws to achieve the following objectives: 1) minimize the H_∞ norm of the transfer function matrix from w to z_∞ so as to reject disturbance; 2) keep the resultant wheel slip $S_{Res} \le s_{limi}$ to avoid wheel skidding; 3) keep z_1 bounded to satisfy the displacement constraints.

3 CONTROL LAW DESIGN

Theorem 1. *Consider system (12) with $S_j = C_u^i u$ for $i = 1,2$. Given some desired level of performance $\gamma_\infty > 0$, $\gamma_1 > 0$ and $\gamma_* = s_{limi}/w_{max}$ associated with each input, if there exist a constant matrix $Q > 0$ and a scalar $\nu > 0$ for some $\alpha > 0$ such that the following LMIs are feasible:*

$$\begin{aligned} \phi_S &\triangleq \begin{bmatrix} AQ + QA^T - \nu B_2 B_2^T & B_1 & QC_\infty \\ B_1^T & -\gamma_\infty^2 I_2 & 0 \\ C_\infty Q & 0 & -I_5 \end{bmatrix} < 0 \\ \Omega_S &\triangleq \begin{bmatrix} AQ + QA^T + \alpha Q - \nu B_2 B_2^T & B_1 \\ B_1^T & -\alpha I_2 \end{bmatrix} \le 0 \\ \theta_{Si} &\triangleq \begin{bmatrix} 4Q & \nu B_2 C_u^{iT} \\ \nu C_{ui} B_2 & \gamma_*^2 I_2 \end{bmatrix} > 0,\ i = 1,2 \\ \Pi_S &\triangleq \begin{bmatrix} Q & QC_1^T \\ C_1 Q & \gamma_1^2/w_{max}^2 \end{bmatrix} > 0. \end{aligned} \tag{13}$$

then the state feedback controller

$$u = -\frac{\nu}{2} B_2^T Q^{-1} x \tag{14}$$

guarantees quadratic stability with L_2-gain, from w to z_∞. Furthermore, within the ellipsoid $\xi_F = \{x : x^T Q^{-1} x \le w_{max}^2\}$ $\|S_j\|_\infty = \|-\frac{\nu}{2} C_u^i B_2^T Q^{-1} x\|_\infty \le s_{limi}$, $i = 1,2$.

Theorem 2. *For some desired level of performance $\gamma_\infty > 0$, $\gamma_1 > 0$ and $\gamma_* > 0$ associated with each input, assume there exist a constant matrix $P = Q^{-1} > 0$ and a scalar $\nu > 0$ for some $\alpha > 0$ such that the LMIs given in theorem 1 are satisfied. If there exist constant matrices $S > 0$ and W such that the following LMIs are feasible,*

$$\begin{aligned} \phi_L &\triangleq \begin{bmatrix} \Sigma_{11} & \frac{\nu}{2} P B_2 B_2^T P & PB_1 \\ * & \Sigma_{22} & SB_1 \\ * & * & -\gamma_\infty^2 I_2 \end{bmatrix} < 0 \\ \Omega_L &\triangleq \begin{bmatrix} \Sigma_{11}' & \frac{\nu}{2} P B_2 B_2^T P & PB_1 \\ * & \Sigma_{22} & SB_1 \\ * & * & -\alpha I_2 \end{bmatrix} \le 0 \\ \theta_{Li} &\triangleq \begin{bmatrix} P & 0 & -\frac{\nu}{2} P B_2 C_u^{iT} \\ 0 & S & \frac{\nu}{2} P B_2 C_u^{iT} \\ * & * & \gamma_*^2 I_2 \end{bmatrix} > 0 \\ \Pi_L &\triangleq \begin{bmatrix} P & C_1^T \\ C_1 & \gamma_1^2/w_{max}^2 \end{bmatrix} > 0. \end{aligned} \tag{15}$$

where $*$ represents a block matrix referred by symmetry.

$$\begin{aligned} \Sigma_{11} &= PA + A^T P - \nu P B_2 B_2^T P + C_\infty^T C_\infty \\ \Sigma_{22} &= SA + A^T S - WC_2 - C_2^T W^T \\ \Sigma_{11}' &= PA + A^T P + \alpha P - \nu P B_2 B_2^T P. \end{aligned}$$

then the observer-based output controller given by

$$\begin{aligned} \dot{\hat{x}} &= A\hat{x} + B_2 u + L(y - C_2 \hat{x}) \\ u &= -\frac{\nu}{2} B_2^T Q^{-1} \hat{x} \end{aligned} \tag{16}$$

with $L = S^{-1} W$ guarantees quadratic stability with L_2-gain, from w to z_∞. Furthermore, within the ellipsoid $\{\tilde{x} : \tilde{x}^T \hat{P} \tilde{x} <= w_{max}^2\}$, $\|\hat{S}_j\|_\infty = \|-\frac{\nu}{2} C_u^j B_2^T Q^{-1} \hat{x}\|_\infty <= s_{limi}$, $j = 1,2$, where $\hat{P} \triangleq blockdiag\{P,S\}$, $\tilde{x}^T = \begin{bmatrix} x^T & e^T \end{bmatrix}$.

Using the quasi-steady-state combined wheel slip, the wheel torque T_j and steering angle δ_j are derived

$$\begin{bmatrix} T_j \\ \delta_j \end{bmatrix} = \begin{bmatrix} 0 \\ \beta + l_j \gamma / v_0 \end{bmatrix} + \begin{bmatrix} F_{zj} r_j k & 0 \\ 0 & 1 \end{bmatrix} \begin{bmatrix} S_{Lj} \\ S_{Sj} \end{bmatrix},$$

where $l_1 = l_2 = l_f$, $l_3 = l_4 = -l_r$, $j = 1,2,3,4$. When the states of the system are unmeasurable, we substitute β_j, γ with their estimate.

4 SIMULATIONS

To examine the effectiveness of the control scheme, simulation tests are carried out as follows. The desired speed for traveling is set as $v_0 = 16.7\ m/sec$ and the reference path is assumed to be a circular path of curvature $\rho_{ref} = 1/100\ m^{-1}$. We employ the following tire model [7]

$$\mu_{Res}(\|S_j\|) = 1.1973(1 - exp(25.168\|S_j\|)) - 0.5373\|S_j\|$$

for simulating the dry concrete condition and thus obtain the related initial slope (10) as $k_j = k \simeq 30$. The data of the vehicle system is given as follows; $C_{aero} = 0.3743\ kg/m$, $m = 1480\ kg$, $J_z = 1950\ kgm^2$, $l_f = 1.421\ m$, $l_r = 1.029\ m$, $l_d = 0.751\ m$, $k_s = 0.9$, $g = 9.81\ m/s^2$. Based on the dry-concrete-covered road condition and the vehicle data, we choose the wheel slip constraint as $s_{limi} = 0.8$.

The vehicle control system is assumed to start with the following initial state: $V_0 = 16.7 m/sec$, $\beta(0) = 0\ deg$, $\gamma(0) = 0\ deg/sec$, $y_l(0) = 0.3\ m$, $\phi_l(0) = 0\ deg$. Fig. 2. and Fig. 3. illustrate the time responses of the lateral displacement and the longitudinal slip S_{L1} and lateral slip S_{S1} of the four wheels based on state feedback and output feedback. It can be seen that the maximum displacement can be kept less than 0.30 m, and the magnitudes of the resultant wheel slip S_{Res} are constrained below the pre-specified constraint $s_{limi} = 0.8$.

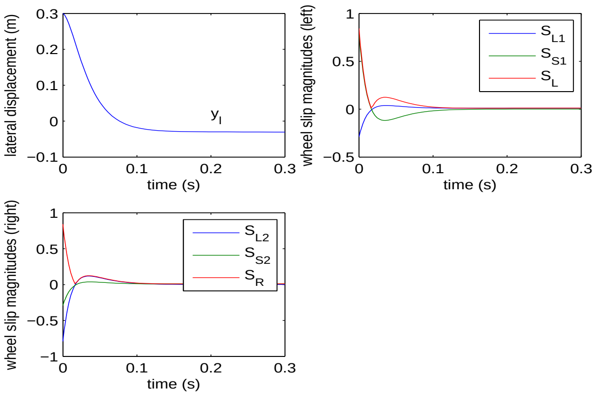

Fig. 2: displacement and magnitudes of the wheel slip

5 CONCLUSIONS

In this paper a robust controller is presented for an autonomous 4WS4WD vehicle to avoid lane departures and wheel skidding. The control strategy can be constructed as a multiobjective optimization problem. Simulation results are presented to validate the approach.

6 ACKNOWLEDGE

This work was supported by the National 973 Program (2012CB821200) and the NSFC (61134005, 60921001, 90916024, 91116016).

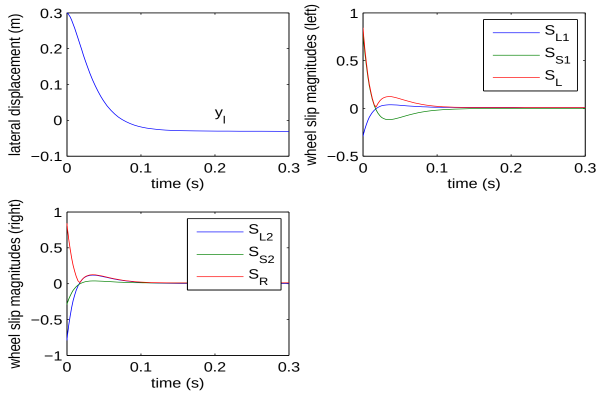

Fig. 3: displacement and magnitudes of the wheel slip based on observer

REFERENCES

[1] Vito Cerone, Mario Milanese, Diego Regruto (2009), Combined automatic lane-keeping and driver's steering through a 2-dof control strategy. IEEE Transactions on Control Systems Technology 17:135-142

[2] S. Mammar (2000), Two-degree-of-freedom H_∞ optimization and scheduling for robust vehicle lateral control. Vehicle System Dynamics 34:401-422

[3] Rajamani, R., Tan, H.S., Law, B.K. and Zhang, W.B. (2000), Demonstration of integrated longitudinal and lateral control for the operation of automated vehicles in platoons. IEEE Transaction on Control Systems Technology 8:695-708

[4] Sisil Kumarawadu, Tsu Tian Lee (2006), Neuroadaptive combined lateral and longitudinal control of highway vehicles using RBF networks. IEEE Transactions on Control Systems Technology 7:500-512

[5] N. MinoiuEnache, M.Netto, S. Mammar, B. Lusetti, James Lam (2009), Driver steering assistance for lane departure avoidance. Control Engineering Practice 17:642-651

[6] Nicoleta Minoiu Enache, S. Mammar, Mariana Netto, and Benoit Lusetti (2010), Driver steering assistance for lane-departure avoidance based on hybrid automata and composite Lyapunov function. IEEE Transactions on Intelligent Transportation Systems 11:28-39

[7] Uwe Kiencke, Lars Nielsen (2005), Automotive Control Systems For Engine, Driveline, and Vehicle, Springer-Verlag, Berlin

[8] Peng, S.T (2004), A control scheme for automatic path tracking of vehicles subject to wheel slip constraint. Proceedings of the American Control Conference 804-809

The Seventeenth International Symposium on Artificial Life and Robotics 2012 (AROB 17th '12),
B-Con Plaza, Beppu, Oita, Japan, January 19-21, 2012

Robust exponential stabilization criteria for uncertain linear systems with interval time-varying delay

Nan Xiao[1], Yingmin Jia[1,2], Junping Du[3], and Fashan Yu[4]

[1] The Seventh Research Division and the Department of Systems and Control, Beihang University(BUAA), Beijing 100191, China (e-mail: kgxn@yahoo.cn)

[2]Key Laboratory of Mathematics Informatics and Behavioral Semantics(LMIB), SMSS, Beihang University(BUAA), Beijing 100191, China (e-mail: ymjia@buaa.edu.cn)

[3] Beijing Key Laboratory of Intelligent Telecommunications Software and Multimedia, School of Computer Science and Technology, Beijing University of Posts and Telecommunications, Beijing 100876, China (e-mail: junpingdu@126.com)

[4] School of Electrical Engineering and Automation, Henan Polytechnic University, Jiaozuo 454000, Henan, China (e-mail: yufs@hpu.edu.cn)

Abstract: In this paper, we study the problem of robust exponential stabilization for uncertain linear systems with interval time-varying delay. We first rewrite the original system into a new form, then by dividing the delay intervals into two equal subintervals, we construct the Lyapunov-Krasovskii functional with augmented vectors. By appropriate enlarging some terms that appeared in the derivative of the Lyapunov-Krasovskii functional and using a new lower bounds lemma, delay-dependent robust exponential stabilization criteria are obtained based on Lyapunov stability theory and free weighting matrix technic. For getting the design of controller, we fix some formations of the introduced free-weighting matrices with given parameters, thus the obtained criteria are in terms of Linear Matrix Inequalities(LMIs). Finally numerical examples are given to show the effectiveness and less conservativeness of the proposed method.

Keywords: Delay-dependent, Interval time-varying delay, LMI, Robust exponential stabilization

1 INTRODUCTION

Interval time-varying delay system is a type of time-delay system in which the lower bound of delay needn't to be 0. Since the existence of time delay can make system instable and degrade its performance, much effort has been done to study the stability and stabilization problem for such systems in recent years. Wang [1] research the exponential stabilization problem for interval time-delay system by using free-weighting matrix method, but in the derivative of Lyapunov functional there are some terms are enlarged improperly, which will lead conservative results. Botmart [2] get criteria to design robust exponential stabilization controller for such system by assuming the controller have some formation and using convex combination method, which get less conservative results compared to some existing papers.

When considering this problem, we find that by choosing specific Lyapunov functional and appropriate enlarging some terms appeared in its derivative, less conservative stabilization criteria can be obtained. Motivated by the above ideals, we research the problem of delay-dependent robust exponential stabilization for uncertain time-delay systems with interval time-varying delay in this paper. We divide the delay intervals into two subintervals, and construct the corresponding Lyapunov functional by using the augmented vectors. Based on Lyapunov stability theory and free weighting matrix methods, delay-dependent robust stabilization criteria are obtained, and the controller can be obtained by solving LMIs. Finally, several numerical examples are given to show the effectiveness of the obtained criteria.

2 PROBLEM STATEMENT

Consider the following uncertain linear system with time-varying delay

$$\begin{aligned}\dot{x}(t) &= (A+\Delta A(t))x(t) + (A_d+\Delta A_d(t))x(t-h(t)) \\ &\quad + (B+\Delta B(t))u(t), \\ x(t) &= \phi(t),\ t\in[-h_2,0], \end{aligned} \tag{1}$$

where $x(t)\in R^n$ is the state vector, $u(t)\in R^m$ is the control input, the initial condition $\phi(t)$ is a continuously differentiable vector-valued function, A, A_d, and B are constant system matrices of appropriate dimensions, $\Delta A(t)$, $\Delta A_d(t)$ and $\Delta B(t)$ are unknown real matrices with appropriate dimensions representing the system's time-varying parameter uncertainties and satisfy

$$[\Delta A\ \Delta A_d\ \Delta B] = [E_1F_1(t)G_1\ E_2F_2(t)G_2\ E_3F_3(t)G_3] \tag{2}$$

with E_i, G_i $(i=1,2,3)$ are known real constant matrices. $F_i(t)$ is the time-varying nonlinear function which satisfies

$$F_i^T(t)F_i(t)\le I \quad \text{for } i=1,2,3,\ \forall t\ge 0. \tag{3}$$

$h(t)$ is a continuous time-varying function satisfying

$$0\le h_1\le h(t)\le h_2, \tag{4}$$

$$\dot{h}(t) \leq \mu, \tag{5}$$

where $h_1 < h_2$, and $\mu \geq 0$ are constants.

Definition 1 [3]**.** The original state $x^* = 0$ of time-delay system (1) with uncertainty and interval time-varying delay satisfying (2-5) is said to be robustly exponentially stabilizable if for given constants $\sigma \geq 1$ and $\rho > 0$, there exists state feedback controller such that the solution $x(t)$ to the resulting closed-loop of system (1) satisfies

$$\|x(t)\| \leq \sigma \|x(t_0)\|_\theta \mathrm{e}^{-\rho(t-t_0)}, \ \forall\, t \geq t_0, \tag{6}$$

where $\|x(t)\|_\theta$ is defined by

$$\|x(t)\|_\theta = \sup_{0\leq\theta\leq h_2}\{x(t-\theta),\ \dot{x}(t-\theta)\},$$

and ρ is called the exponential convergence rate.

The purpose of this paper is to study the robust exponential stabilization problem for system (1) with uncertainty and interval time-varying delay satisfying (2-5) under the state feedback controller

$$u(t) = Kx(t). \tag{7}$$

Lemma 1 [4]**.** For scalars $\alpha, \beta \in [0,1], \alpha + \beta = 1$, and vectors η_1, η_2 satisfy $\eta_1 = 0$ with $\alpha = 0$ and $\eta_2 = 0$ with $\beta = 0$, matrices $P > 0$, $Q > 0$, there exists matrix T, satisfies

$$\begin{bmatrix} P & T \\ T^T & Q \end{bmatrix} \geq 0,$$

such that the following inequality holds

$$\frac{1}{\alpha}\eta_1^T P \eta_1 + \frac{1}{\beta}\eta_2^T Q \eta_2 \geq \begin{bmatrix} \eta_1 \\ \eta_2 \end{bmatrix}^T \begin{bmatrix} P & T \\ T^T & Q \end{bmatrix} \begin{bmatrix} \eta_1 \\ \eta_2 \end{bmatrix}.$$

3 MAIN RESULTS

We rewrite the closed loop of system (1) as the following form

$$\dot{x}(t) = \bar{A}x(t) + A_d x(t-h(t)) + \bar{E}f(t,x), \tag{8}$$

with

$$\bar{A} = A + BK, \bar{E} = \begin{bmatrix} E_1 & E_2 & E_3 \end{bmatrix}, f(t,x) = \bar{F}(t)\bar{G}(x),$$

$$\bar{F}(t) = \mathrm{diag}\,\{F_1(t), F_2(t), F_3(t)\},$$

$$\bar{G}(x) = \begin{bmatrix} x^T(t)G_1^T & x^T(t-h(t))G_2^T & x^T(t)K^TG_3^T \end{bmatrix}^T.$$

Firstly we divide the delay intervals $[0, h_1]$ and $[h_1, h_2]$ into two subintervals separately, and denote $\delta_1 = \frac{h_1}{2}$, $\delta_2 = \frac{h_{12}}{2}$, $\delta = h_1 + \delta_2$, $\zeta_1(t) = \begin{bmatrix} x^T(t) & x^T(t-\delta_1) \end{bmatrix}^T$, $\zeta_2(t) = \begin{bmatrix} x^T(t) & x^T(t-\delta_2) \end{bmatrix}^T$. Then corresponding to the divisions and augmented vectors, we construct the following Lyapunov-Krasovskii functional

$$V(x_t) = V_1(x_t) + V_2(x_t) + V_3(x_t), \tag{9}$$

where

$$V_1(x_t) = x^T(t)Px(t),$$

$$\begin{aligned} V_2(x_t) &= \textstyle\int_{t-h(t)}^t x^T(s)\mathrm{e}^{\alpha(s-t)}Qx(s)\mathrm{d}s \\ &\quad + \textstyle\int_{t-\delta_1}^t \zeta_1^T(s)\mathrm{e}^{\alpha(s-t)}Q_1\zeta_1(s)\mathrm{d}s, \\ &\quad + \textstyle\int_{t-\delta}^{t-h_1} \zeta_2^T(s)\mathrm{e}^{\alpha(s-t)}Q_2\zeta_2(s)\mathrm{d}s, \end{aligned}$$

$$\begin{aligned} V_3(x_t) &= \delta_1 \textstyle\int_{-\delta_1}^0 \int_{t+\theta}^t \dot{x}^T(s)\mathrm{e}^{\alpha(s-t)}R_1\dot{x}(s)\mathrm{d}s\mathrm{d}\theta \\ &\quad + \delta_1 \textstyle\int_{-h_1}^{-\delta_1} \int_{t+\theta}^t \dot{x}^T(s)\mathrm{e}^{\alpha(s-t)}R_2\dot{x}(s)\mathrm{d}s\mathrm{d}\theta \\ &\quad + \delta_2 \textstyle\int_{-\delta}^{-h_1} \int_{t+\theta}^t \dot{x}^T(s)\mathrm{e}^{\alpha(s-t)}S_1\dot{x}(s)\mathrm{d}s\mathrm{d}\theta \\ &\quad + \delta_2 \textstyle\int_{-h_2}^{-\delta} \int_{t+\theta}^t \dot{x}^T(s)\mathrm{e}^{\alpha(s-t)}S_2\dot{x}(s)\mathrm{d}s\mathrm{d}\theta \end{aligned}$$

with P, Q, Q_i, R_i and S_i are symmetric positive matrices. Denote $\xi(t) = \begin{bmatrix} x^T(t) & x^T(t-\delta_1) & x^T(t-h_1) \end{bmatrix.$

$\begin{matrix} x^T(t-\delta) & x^T(t-h_2) & x^T(t-h(t)) & \dot{x}^T(t) & f^T(t,x) \end{bmatrix}^T$, and e_i $(i = 1, \cdots, 8)$ are block entry matrices such that $e_i\xi(t) = \xi_i(t)$.

Theorem 1. For given scalars $\alpha > 0$, $0 \leq h_1 < h_2$, $\mu \geq 0$, γ_1 and γ_2, the closed-loop system of (1) with uncertainty and time-delay satisfied (2-5) is robust exponential stabilization if there exist symmetric positive matrices $\bar{P}$, $\bar{Q}$, $\bar{Q}_i$, $\bar{R}_i$, $\bar{S}_i$, matrices $\bar{T}_i$ $(i = 1, 2)$, $\bar{N}$ and W, positive scalars $\bar{\epsilon}$ such that the following LMIs (10-11) hold for $i = 1, 2$, then the solution $x(t)$ of the closed-loop of system (1) satisfies (6) with convergence rate $\rho = \frac{\alpha}{2}$ and the robust stabilization controller is $K = W\bar{N}^{-1}$.

$$\begin{bmatrix} \bar{\Pi}(i) & \bar{\epsilon}\tilde{G} \\ \bar{\epsilon}\tilde{G}^T & -\bar{\epsilon}I \end{bmatrix} < 0, \tag{10}$$

$$\begin{bmatrix} \bar{S}_i & \bar{T}_i \\ \bar{T}_i^T & \bar{S}_i \end{bmatrix} \geq 0, \tag{11}$$

where

$$\bar{\Pi}(i) = \bar{\Pi}_0 + \bar{\Pi}_i + \bar{\Pi}_e,$$

$$\begin{aligned} \bar{\Pi}_0 &= e_1^T\bar{P}e_7 + e_7^T\bar{P}e_1 + \alpha e_1^T\bar{P}e_1 + e_1^T\bar{Q}e_1 + e_6^T\psi(\mu)\bar{Q}e_6 \\ &\quad + e_a^T\bar{Q}_1e_a - e_b^T\mathrm{e}^{-\alpha\delta_1}\bar{Q}_1e_b + e_c^T\mathrm{e}^{-\alpha h_1}\bar{Q}_2e_c - \bar{\epsilon}e_8^Te_8 \\ &\quad - e_d^T\mathrm{e}^{-\alpha\delta}\bar{Q}_2e_d + \textstyle\sum_{i=1}^2 e_7^T(\delta_1^2\bar{R}_i + \delta_2^2\bar{S}_i)e_7 \\ &\quad - (e_1 - e_2)^T\mathrm{e}^{-\alpha\delta_1}\bar{R}_1(e_1 - e_2) \\ &\quad - (e_2 - e_3)^T\mathrm{e}^{-\alpha h_1}\bar{R}_2(e_2 - e_3), \end{aligned}$$

$$\begin{aligned} \bar{\Pi}_1 &= -(e_4 - e_5)^T\mathrm{e}^{-\alpha h_2}\bar{S}_2(e_4 - e_5) \\ &\quad - \mathrm{e}^{-\alpha\delta}\begin{bmatrix} e_3 - e_6 \\ e_6 - e_4 \end{bmatrix}^T \begin{bmatrix} \bar{S}_1 & \bar{T}_1 \\ \bar{T}_1^T & \bar{S}_1 \end{bmatrix} \begin{bmatrix} e_3 - e_6 \\ e_6 - e_4 \end{bmatrix}, \end{aligned}$$

$$\begin{aligned} \bar{\Pi}_2 &= -(e_3 - e_4)^T\mathrm{e}^{-\alpha\delta}\bar{S}_1(e_3 - e_4) \\ &\quad - \mathrm{e}^{-\alpha h_2}\begin{bmatrix} e_4 - e_6 \\ e_6 - e_5 \end{bmatrix}^T \begin{bmatrix} \bar{S}_2 & \bar{T}_2 \\ \bar{T}_2^T & \bar{S}_2 \end{bmatrix} \begin{bmatrix} e_4 - e_6 \\ e_6 - e_5 \end{bmatrix}, \end{aligned}$$

$$\bar{\Pi}_e = \bar{\Omega} + \bar{\Omega}^T,$$

$$\bar{\Omega} = (e_1 + \gamma_1e_6 + \gamma_2e_7)^T(-\bar{N}e_7 + A\bar{N}e_1 + BWe_1$$

$$+ A_d\bar{N}e_6 + \bar{\epsilon}\bar{E}e_8),$$

$$\psi(\mu) = \begin{cases} (\mu-1)\mathrm{e}^{-\alpha h_1} \ (\mu \geq 1) \\ (\mu-1)\mathrm{e}^{-\alpha h_2} \ (\mu < 1), \end{cases}$$

$e_a = [e_1^T, e_2^T]^T$, $e_b = [e_2^T, e_3^T]^T$,

$e_c = [e_3^T, e_4^T]^T$, $e_d = [e_4^T, e_5^T]^T$,

$\tilde{G} = \bar{G}_1\bar{N}^{-1}e_1 + \bar{G}_2\bar{N}^{-1}e_6 + \bar{G}_3We_1$,

$\bar{G}_1 = \begin{bmatrix} G_1^T & 0 & 0 \end{bmatrix}^T$, $\bar{G}_2 = \begin{bmatrix} 0 & G_2^T & 0 \end{bmatrix}^T$,

$\bar{G}_3 = \begin{bmatrix} 0 & 0 & G_3^T \end{bmatrix}^T$, $\sigma = \sqrt{\frac{\bar{n}}{\bar{m}}}$, $\bar{N}_1 = \mathrm{diag}\{\bar{N}, \bar{N}\}$,

$\bar{m} = \lambda_{min}(\bar{N}^{-1}\bar{P}\bar{N}^{-T})$,

$$\begin{aligned}\bar{n} = {} & \lambda_{max}(\bar{N}^{-1}\bar{P}\bar{N}^{-T}) + (\tfrac{1-\mathrm{e}^{-\alpha h_2}}{\alpha})\lambda_{max}(\bar{N}^{-1}\bar{Q}\bar{N}^{-T}) \\ & + (\tfrac{1-\mathrm{e}^{-\alpha\delta_1}}{\alpha})\lambda_{max}(2\bar{N_1}^{-1}\bar{Q}_1\bar{N_1}^{-T}) \\ & + (\tfrac{\mathrm{e}^{-\alpha h_1}-\mathrm{e}^{-\alpha\delta}}{\alpha})\lambda_{max}(2\bar{N_1}^{-1}\bar{Q}_2\bar{N_1}^{-T}) \\ & + \delta_1(\tfrac{\mathrm{e}^{-\alpha\delta_1}+\alpha\delta_1-1}{\alpha^2})\lambda_{max}(\bar{N}^{-1}\bar{R}_1\bar{N}^{-T}) \\ & + \delta_1(\tfrac{\mathrm{e}^{-\alpha h_1}+\alpha h_1-\mathrm{e}^{-\alpha\delta_1}-\alpha\delta_1}{\alpha^2})\lambda_{max}(\bar{N}^{-1}\bar{R}_2\bar{N}^{-T}) \\ & + \delta_2(\tfrac{\mathrm{e}^{-\alpha\delta}+\alpha\delta-\mathrm{e}^{-\alpha h_1}-\alpha h_1}{\alpha^2})\lambda_{max}(\bar{N}^{-1}\bar{S}_1\bar{N}^{-T}) \\ & + \delta_2(\tfrac{\mathrm{e}^{-\alpha h_2}+\alpha h_2-\mathrm{e}^{-\alpha\delta}-\alpha\delta}{\alpha^2})\lambda_{max}(\bar{N}^{-1}\bar{S}_2\bar{N}^{-T}).\end{aligned}$$

Proof. Taking the time derivative of Lyapunov functional (9) along the trajectory of closed-loop of system (1), we have

$$\dot{V}_1(x_t) = 2x^T(t)P\dot{x}(t) + \alpha x^T(t)Px(t) - \alpha V_1(x_t),$$

$$\begin{aligned}\dot{V}_2(x_t) = {} & x^T(t)Qx(t) + \zeta_1^T(t)Q_1\zeta_1(t) - \alpha V_2(x_t) \\ & - (1-\dot{h}(t))x^T(t-h(t))\mathrm{e}^{-\alpha h(t)}Qx(t-h(t)) \\ & - \zeta_1^T(t-\delta_1)\mathrm{e}^{-\alpha\delta_1}Q_1\zeta_1(t-\delta_1) \\ & + \zeta_2^T(t-h_1)\mathrm{e}^{-\alpha h_1}Q_2\zeta_2(t-h_1) \\ & - \zeta_2^T(t-\delta)\mathrm{e}^{-\alpha\delta}Q_2\zeta(t-\delta),\end{aligned}$$

$$\begin{aligned}\dot{V}_3(x_t) = {} & \textstyle\sum_{i=1}^2 \dot{x}^T(t)(\delta_1^2R_i + \delta_2^2S_i)\dot{x}(t) - \alpha V_3(x_t) \\ & - \delta_1\textstyle\int_{t-\delta_1}^{t} \dot{x}^T(s)\mathrm{e}^{\alpha(s-t)}R_1\dot{x}(s)\mathrm{d}s \\ & - \delta_1\textstyle\int_{t-h_1}^{t-\delta_1} \dot{x}^T(s)\mathrm{e}^{\alpha(s-t)}R_2\dot{x}(s)\mathrm{d}s \\ & - \delta_2\textstyle\int_{t-\delta}^{t-h_1} \dot{x}^T(s)\mathrm{e}^{\alpha(s-t)}S_1\dot{x}(s)\mathrm{d}s \\ & - \delta_2\textstyle\int_{t-h_2}^{t-\delta} \dot{x}^T(s)\mathrm{e}^{\alpha(s-t)}S_2\dot{x}(s)\mathrm{d}s.\end{aligned}$$

Then by using Jensen inequality [5] and enlarging some terms appropriately, we get

$$(\dot{h}(t)-1)\mathrm{e}^{-\alpha h(t)} \leq \psi(\mu), \tag{12}$$

$$\begin{aligned}& -\delta_1\textstyle\int_{t-\delta_1}^{t} \dot{x}^T(s)\mathrm{e}^{\alpha(s-t)}R_1\dot{x}(s)\mathrm{d}s \\ & \leq -\delta_1\mathrm{e}^{-\alpha\delta_1}\textstyle\int_{t-\delta_1}^{t} \dot{x}^T(s)R_1\dot{x}(s)\mathrm{d}s \\ & \leq -(\textstyle\int_{t-\delta_1}^{t} \dot{x}(s)\,\mathrm{d}s)^T\mathrm{e}^{-\alpha\delta_1}R_1(\textstyle\int_{t-\delta_1}^{t} \dot{x}(s)\,\mathrm{d}s) \\ & = -\xi^T(t)(e_1-e_2)^T\mathrm{e}^{-\alpha\delta_1}R_1(e_1-e_2)\xi(t),\end{aligned} \tag{13}$$

$$\begin{aligned}& -\delta_1\textstyle\int_{t-h_1}^{t-\delta_1} \dot{x}^T(s)\mathrm{e}^{\alpha(s-t)}R_2\dot{x}(s)\mathrm{d}s \\ & \leq -\xi^T(t)(e_2-e_3)^T\mathrm{e}^{-\alpha h_1}R_2(e_2-e_3)\xi(t),\end{aligned} \tag{14}$$

for the case time delay $h(t) \in [h_1, \delta]$, by Lemma 1, there exists matrix T_1, such that

$$\begin{bmatrix} S_1 & T_1 \\ T_1^T & S_1 \end{bmatrix} \geq 0, \tag{15}$$

$$\begin{aligned}& -\delta_2\textstyle\int_{t-\delta}^{t-h_1} \dot{x}^T(s)\mathrm{e}^{\alpha(s-t)}S_1\dot{x}(s)\mathrm{d}s \\ & \leq -\delta_2\mathrm{e}^{-\alpha\delta}\textstyle\int_{t-d(t)}^{t-h_1} \dot{x}^T(s)S_1\dot{x}(s)\mathrm{d}s \\ & \quad - \delta_2\mathrm{e}^{-\alpha\delta}\textstyle\int_{t-\delta}^{t-d(t)} \dot{x}^T(s)S_1\dot{x}(s)\mathrm{d}s \\ & \leq -\mathrm{e}^{-\alpha\delta}\xi^T(t)\begin{bmatrix} e_3-e_6 \\ e_6-e_4 \end{bmatrix}^T \begin{bmatrix} S_1 & T_1 \\ T_1^T & S_1 \end{bmatrix} \begin{bmatrix} e_3-e_6 \\ e_6-e_4 \end{bmatrix}\xi(t).\end{aligned}$$

Similarly to above procedure, we can cope with the situation $h(t) \in [\delta, h_2]$.

According to (3), there exists scalar $\epsilon > 0$ such that

$$\epsilon f^T(t,x)f(t,x) \leq \epsilon\bar{G}^T(x)\bar{G}(x),$$

thus we have

$$\epsilon\xi^T(t)\bar{G}^T\bar{G}\xi(t) - \epsilon\xi^T(t)e_8^Te_8\xi(t) \geq 0 \tag{16}$$

with $\bar{G} = \bar{G}_1e_1 + \bar{G}_2e_6 + \bar{G}_3Ke_1$.

By using system's information we add the left side of following equation into the derivative of Lyapunov functional:

$$\begin{aligned}& 2(x^T(t)N_1 + x^T(t-h(t))N_2 + \dot{x}^T(t)N_3)(-\dot{x}(t) \\ & + \bar{A}x(t) + A_dx(t-h(t)) + \bar{E}f(t,x)) = 0,\end{aligned} \tag{17}$$

where N_i are matrices with appropriate dimensions.

For getting LMI criteria and obtaining the controller, we set $N_1 = N$, $N_2 = \gamma_1N$, $N_3 = \gamma_2N$ and assume N^{-1} exist, and from the above equations we can get

$$\dot{V}(x_t) + \alpha V(x_t) \leq \xi^T(t)(\Pi(i) + \bar{G}^T\bar{G})\xi(t), \tag{18}$$

with some transformation of the matrices. By Schur Complement, the negative of (18) imply

$$\begin{bmatrix} \Pi_i & \epsilon\bar{G} \\ \epsilon\bar{G}^T & -\epsilon I \end{bmatrix} < 0. \tag{19}$$

Pre-multiplying and post-multiplying both sides of (19) by $\mathrm{diag}\{\sum_{i=1}^7 e_i^TN^{-1}e_i + \epsilon^{-1}e_8^Te_8, \epsilon^{-1}I\}$ and its transpose, denoting $N_1 = \mathrm{diag}\{N, N\}$, $\bar{P} = N^{-1}PN^{-T}$, $\bar{Q} = N^{-1}QN^{-T}$, $\bar{Q}_i = N_1^{-1}Q_iN_1^{-T}$, $\bar{R}_i = N^{-1}R_iN^{-T}$ $\bar{S}_i = N^{-1}S_iN^{-T}$, $\bar{T}_i = N^{-1}T_iN^{-T}$ $(i = 1, 2)$, $\bar{N} = N^{-1}$, $W = K\bar{N}^T$ and $\bar{\epsilon} = \epsilon^{-1}$, then the hold of (19) is equivalent to (10). By applying the similar transformation to (15), and notice that from (9) and (18), we have

$$V(x_t) \geq \bar{m}\|x(t)\|^2, V(x_{t_0}) \leq \bar{n}\|x(t_0)\|_\theta^2, \tag{20}$$

$$V(x_t) < \mathrm{e}^{-\alpha(t-t_0)}V(x_{t_0}), \tag{21}$$

by some computation we can get Theorem 1, thus complete the proof.

Remark 1. The term $(\dot{h}(t)-1)\mathrm{e}^{-\alpha h(t)}$ appeared in the derivative of Lyapunov functional can be enlarged as $\mu e^{-\alpha h_1} - e^{-\alpha h_2}$, to reduce the conservativeness of the criteria, we consider the situations that $\mu \geq 1$ and $\mu < 1$, respectively, and enlarge it as $\psi(\mu)$, while the equation (24) in Wang [1] only holds when $\mu \geq 1$ but have some conservativeness when $\mu < 1$.

4 NUMERICAL EXAMPLES

In this section, we consider three examples to show the effectiveness of the obtained criteria.

We compare our methods to that of Botmart [2] in Example 1. The obtained results are listed in Table 1 below, which show the less conservativeness of our criteria.

Example 1. Consider the system (1) with

$$A = \begin{bmatrix} 0 & 0 \\ 0 & 1 \end{bmatrix}, A_d = \begin{bmatrix} -2 & -0.5 \\ 0 & -1 \end{bmatrix}, B = \begin{bmatrix} 0 \\ 1 \end{bmatrix}.$$

Table 1. Admissible upper bound h_2 for unknown μ and various (ρ, h_1) with $(\gamma_1, \gamma_2) = (0, 1.9)$.

	(ρ, h_1)	(0.1, 0)	(0.1, 0.5)	(0.2, 0)	(0.2, 0.5)
[2]	h_2	0.406	0.590	0.381	0.545
T1	h_2	1.2152	1.4650	1.0859	1.3172

Remark 2. Following the same method, we can get better results by dividing the time intervals into more subintervals while more computational burden will be taken.

Remark 3. To get the controller matrix K, we fix the formation of free-weighting matrices S_i, to get less conservative results the values of γ_1 and γ_2 need to be appropriate chosen, we will do further research to this problem.

In Example 2, we compare our method to that of Wang [1] with the robust exponential stabilization problem.

Example 2. Consider the uncertain system (1) with

$$A = \begin{bmatrix} -2 & 0 \\ 0 & -0.9 \end{bmatrix}, A_d = \begin{bmatrix} -1 & 0 \\ -1 & -1 \end{bmatrix}, B = \begin{bmatrix} 0 \\ 1 \end{bmatrix},$$

$$E_1 = \begin{bmatrix} \sqrt{0.2} & 0 \\ 0 & \sqrt{0.05} \end{bmatrix}, E_2 = \begin{bmatrix} \sqrt{0.1} & 0 \\ 0 & \sqrt{0.3} \end{bmatrix}, E_3 = \begin{bmatrix} \sqrt{0.01} & 0 \\ 0 & \sqrt{0.1} \end{bmatrix}, G_1 = E_1, G_2 = E_2, G_3 = \begin{bmatrix} 0.01 \\ 0 \end{bmatrix}.$$

For $\mu = 1.1$, $\rho = 0.1$, $h_1 = 0.3$, and $h_2 = 0.7$, in Wang [1] the state convergence rate is estimated as

$$\|x(t)\| \leq 2.0463 e^{-0.1(t-t_0)} \|x(t_0)\|_\theta,$$

while with $(\gamma_1, \gamma_2) = (0.1, 1)$, from Theorem 1 we get the stabilization controller is $K = [-0.2273, -3.0087]$, and with a smaller $\sigma = 1.5947$, the state convergence rate satisfy

$$\|x(t)\| \leq 1.5947 e^{-0.1(t-t_0)} \|x(t_0)\|_\theta.$$

Furthermore, by Theorem 1 we can get the allowable upper bound h_2 is 1.5815, and the stabilization controller is $K = [-49.5411, -157.8835]$ with $\sigma = 5.4790$. From Fig.1. we can see that the state of controlled closed-loop system is exponential stable under initial condition $\varphi(s) = [3, -1]$, interval time-varying delay $[h_1, h_2] = [0.3, 1.5815]$ and $\mu = 1.1$ with the convergence rate $\rho = 0.1$.

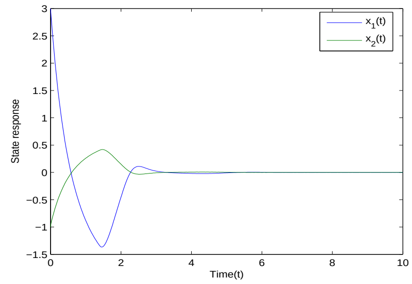

Fig.1. State response with controller $u(t)$

5 CONCLUSION

In this paper, the problem of robust exponential stabilization for interval time-varying delay systems have been investigated. By dividing the delay intervals into two equal subintervals and using free-weighting matrix technic, robust exponential stabilization criteria are obtained in terms of LMIs. Numerical examples are given to show the effectiveness and less conservativeness of our obtained criteria.

6 ACKNOWLEDGMENTS

This work was supported by the National 973 Program (2012CB821200) and the NSFC (61134005, 60921001, 90916024, 91116016).

REFERENCES

[1] Wang D, Wang W (2009), Delay-dependent robust exponential stabilization for uncertain systems with interval time-varying delays. Journal of Control Theory and Applications 7(3): 257-263

[2] Botmart T, Niamsup P, Phat VN (2011), Delay-dependent exponential stabilization for uncertain linear systems with interval non-differentiable time-varying delays. Applied Mathematics And Computation 217(21): 8236-8247

[3] Grammel G, Maizurna I (2007), Exponential stability of nonlinear defferential equations in the presence of pertubations or delays. Communications in Nonlinear Science and Numerical Simulation 12(6): 869-875

[4] Park PG, Ko JW, Jeong C (2011), Reciprocally convex approach to stability of systems with time-varying delays. Automatica 47: 235-238

[5] Gu K (2000), An integral inequality in the stability problem of time-delay systems. In proceedings of the 39th IEEE conference on decision and control, Sydney, Australia, Dec 12-15, 2000, 3: 2805-2810

The Seventeenth International Symposium on Artificial Life and Robotics 2012 (AROB 17th '12),
B-Con Plaza, Beppu, Oita, Japan, January 19-21, 2012

Improved Rao-Blackwellized particle filtering algorithms for multi-target tracking in clutter

Yazhao Wang[1], Yingmin Jia[1,2], Junping Du[3], Fashan Yu[4]

[1] The Seventh Research Division and the Department of Systems and Control, Beihang University (BUAA), Beijing 100191, China (e-mail: yzwang@ss.buaa.edu.cn)
[2] Key Laboratory of Mathematics, Informatics and Behavioral Semantics (LMIB), Ministry of Education, SMSS, Beihang University(BUAA), Beijing 100191, China (e-mail: ymjia@buaa.edu.cn)
[3] Beijing Key Laboratory of Intelligent Telecommunications Software and Multimedia, School of Computer Science and Technology, Beijing University of Posts and Telecommunications, Beijing 100876, China (e-mail: junpingdu@126.com)
[4] School of Electrical Engineering and Automation, Henan Polytechnic University, Jiaozuo 454000, Henan, China (e-mail: yufs@hpu.edu.cn)

Abstract: We consider the problem of multiple target tracking in the presence of clutter (false alarm) measurements. To improve the performance of the Rao-Blackwellized particle filter (RBPF) data association algorithms, some simple but effective strategies are implemented. We first present a sequential likelihood method, i.e., all measurements are used to update the particles more than one time in each time step. It is observed that the tracking performance of the algorithm is not severely loss with fewer particles. We then present a simple gating technique to reduce the validated measurements to a feasible level. It is worth mentioning that the association probabilities are not calculated by grouping targets into clusters as the joint probabilistic data association (JPDA), but only reserve the validated measurements in the joint validation region (gate) and ignore the measurements outside. Simulations are also presented to compare the performance of the proposed algorithms.

Keywords: Multiple target tracking, data association, Rao-Blackwellized particle filter, sequential likelihood

1 INTRODUCTION

In multi-target tracking, data association remains a challenge in cluttered environment [1]-[3]. As an important enhancement of the particle filter, Rao-blackwellized particle filter (RBPF) has also been used to solve this problem in recent years [4]-[6]. The idea of this approach is that the joint data association and target tracking problem can be solved by partly sequential Monte Carlo method instead of pure particle filter sampling [7], [8], so that the needed number of particles may be reduced to a low order of magnitude.

However, in the application of the RBPF multi-target tracking algorithms, we found that the success rate of data association could not be improved only by increasing the number of particles. To improve the ability of the algorithms but not increase the time cost, we present in this paper some simple but effective methods. The main contribution of this paper has two folders, one is the development of a sequential likelihood method in RBPF multi-target tracking algorithms, the other is the application of the simple gating technique, which restrict data association into validation regions.

The rest of this paper is organized as follows. In Section 2, we give a brief introduction of the RBPF data association algorithms. The sequential likelihood and simple gating methods are presented in Section 3. Finally, simulation results and conclusions are given in Section 4 and Section 5, respectively.

2 RAO-BLACKWELLIZED PARTICLE FILTER FOR MULTIPLE TARGET TRACKING

In this section we will give a brief introduction of the RBPF algorithms for multi-target tracking. The basic RBPF model is assumed to be time-varying system as follows:

$$x_k^2 = F_{k-1} x_{k-1}^2 + w_{k-1} \quad (1)$$

$$z_k = H_k x_k^2 + v_k \quad (2)$$

where, w_{k-1} and v_k are zero mean Gaussian random vectors, F_{k-1} and H_k are matrices with compatible dimensions. This type of system can be termed conditionally linear-Gaussian for the set of variables x_k^1, a RBPF algorithm can be applied to estimate the state $x_k = \{x_k^1; x_k^2\}$. The RBPF can be seen as a form of constrained PF (Particle Filter) applicable to a subclass of state-space models. By choosing N_p particles at time step k, a generic RBPF algorithm, applicable to problems of the form (1) and (2) is presented as follows [9].
Step 1. For every $i \in \{1, 2, ..., N_p\}$:

- Draw $x_k^{1(i)} \sim q(x_k^1 | x_{1:k-1}^{1(i)}, z_{1:k})$
- Set $x_{1:k}^{1(i)} = \{x_k^{1(i)}; x_{1:k-1}^{1(i)}\}$
- Compute the normalized weights:
$\tilde{w}_k^{(i)} \propto w_{k-1}^{(i)} \frac{p(z_k | x_{1:k}^{1(i)}, z_{1:k-1}) p(x_k^{1(i)} | x_{1:k-1}^{1(i)}, z_{1:k-1})}{q(x_k^{1(i)} | x_{1:k-1}^{1(i)}, z_{1:k})}$,

Step 2. For every $i \in \{1, 2, ..., N_p\}$:

- Update $p(x_k^2|x_{1:k}^{1(i)}, z_{1:k})$ using $p(x_{k-1}^2|x_{1:k-1}^{1(i)}, z_{1:k-1})$, $x_k^{1(i)}$, $x_{k-1}^{1(i)}$, and z_k.

Step 3. Resample the particles if needed.

In [5] it has been shown that the RBPF based data association algorithm can be obtained directly from the RBPF framework when the latent values x_k^1 are defined to contain the data association event indicators c_k,

$$x_k^1 = c_k \tag{3}$$

The advantage of RBPF is that only the index of data association needs to be sampled from the importance distribution so that the required number of particles can be greatly reduced. Nevertheless, it seems that the number of particles should still be large enough in dense clutter environment, because as data association becomes more difficult the importance distribution will be more complex. In experiments, it is found that only a few particles had unnegligible weights after a certain number of recursive steps, that is to say most of the particles are degenerated prematurely and we cannot improve the performance only by increasing the number of particles. Of course, the resampling strategy can be implemented when a significant degeneracy is observed, but the resampling threshold cannot be calculated analytically. Typically, the values of the threshold are selected ad hoc and degeneracy may possibly happen.

3 PROPOSED ALGORITHMS

In the following discussions, we will show two simple but effective methods to improve the performance of the RBPF algorithm in the application of multi-target tracking.

3.1 Sequential likelihood function based algorithms

we first present a sequential likelihood function based method to resolve the particle degeneracy problems, i.e., all validated measurements are used to update the state of particles more than one time in each time step. The proposed algorithm is derived based on an existing RBPF data association algorithm termed Rao-Blackwellized Monte Carlo data association (RBMCDA), in which the optimal importance distribution is used as the association sampling function. The main procedure of the proposed sequential likelihood technique based RBMCDA data association algorithm (S-RBMCDA) is presented as follows:

i. Calculation of the predicted measurement $\hat{z}_{j,k}$ and the related innovation $S_{j,k}$

$$\hat{z}_{j,k} = H_{j,k}\hat{x}_{j,k|k-1},\ S_{j,k} = H_{j,k}P_{j,k|k-1}H_{j,k}^T + R_{j,k} \tag{4}$$

where

$$\begin{cases} \hat{x}_{j,k|k-1} = \sum_{i=1}^{N_p} w^{(i)}\hat{x}_{j,k|k-1}^{(i)}, \\ P_{j,k|k-1} = \sum_{i=1}^{N_p} w^{(i)}P_{j,k|k-1}^{(i)}. \end{cases} \tag{5}$$

ii. Calculation of the association priors $p(c_k^{(i)}|c_{k-m:k-1}^{(i)})$ according to the Markov chain method introduced in [5].

iii. Calculation of the measurement likelihood for each data association hypothesis, $j = 1, \cdots, T$.

$$p(z_k|c_k = j, c_{1:k-1}^{(i)}, z_{1:k-1}) = \mathcal{N}(z_k|\hat{Z}_{j,k}^{(i)}, S_{j,k}^{(i)}) \tag{6}$$

and

$$p(z_k|c_k = 0, c_{1:k-1}^{(i)}, z_{1:k-1}) = V^{-1}, \tag{7}$$

where V is volume of the detection region.

iv. Calculation of the posterior distribution of $c_k^{(i)}$

$$\begin{aligned} &p(c_k^{(i)}|c_{1:k-1}^{(i)}, z_{1:k}) \\ &= p(z_k|c_k^{(i)}, c_{1:k-1}^{(i)}, z_{1:k-1})p(c_k^{(i)}|c_{k-m:k-1}^{(i)}), \end{aligned} \tag{8}$$

v. Sampling a new association $c_k^{(i)} = j$

vi. Calculation of the new weights for each particle

$$w_k^{(i)} \propto w_{k-1}^{(i)} \frac{p(z_k|c_k^{(i)}, c_{1:k-1}^{(i)}, z_{1:k-1})p(c_k^{(i)}|c_{k-m:k-1}^{(i)})}{p(c_k^{(i)}|c_{1:k-1}^{(i)}, z_{1:k})} \tag{9}$$

vii. Resampling the particles if needed.

In this procedure the target state priors can be represented as a weighted importance samples set

$$p(x_{j,0}) = \sum_{i=1}^{N_p} w_0^{(i)}\mathcal{N}(x_{j,0}|x_{j,0}^{(i)}, P_{j,0}^{(i)}) \tag{10}$$

where N_p is the number of particles. The dynamics and measurements for target j (j=1, $\cdots, T$) are assumed to be linear Gaussian

$$p(x_{j,k}|x_{j,k-1}) = \mathcal{N}(x_{j,k}|F_{j,k-1}\ x_{j,k-1}, Q_{j,k-1}) \tag{11}$$

$$p(z_k|x_{j,k}, c_k = j) = \mathcal{N}(z_k|H_{j,k}x_{j,k}, R_{j,k}). \tag{12}$$

Note that this algorithm is generally the same as the generic RBMCDA [4], [5] except the sequential likelihood procedure which is used to improve the ability of the data association. It just need to repeat from the procedure ii. to v. several times.

3.2 Simple gating

In the RBMCDA algorithms, gating techniques for selecting validated measurements are not introduced. For the known number of target version of the RBMCDA algorithm, it always deals with all measurements in the entire detection region, which is the same as the unknown number of target version. Obviously, too many clutter originated measurements are considered in data association and high computational complexity arises.

To overcome this difficulty, we then present a simple gating technique which can be incorporated into the known

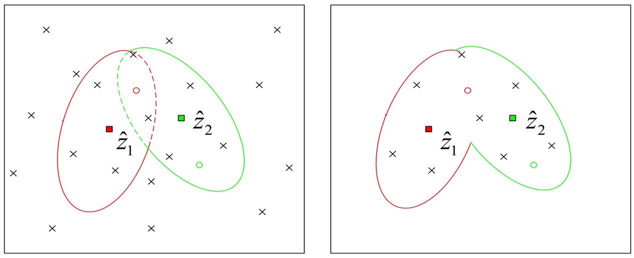

(a) (b)

Fig. 1: Example of the measurement validation. (a):Two targets tracking situation. (b): The equivalence simple gate.

number of target version of the RBMCDA algorithm for reducing the validated measurements to a feasible level. It is worth mentioning that the association probabilities are not calculated by grouping targets into clusters as the joint probabilistic data association (JPDA), but only reserve the validated measurements in the joint validation region (gate) and ignore the measurements outside. Following [10], the validation region is the elliptical region

$$\Gamma(k,\gamma) = \{z : [z - \hat{z}(k|k-1)]' S(k)^{-1} [z - \hat{z}(k|k-1)] \le \gamma\} \tag{13}$$

where γ is the gate threshold corresponding to the gate probability P_g, which is the probability that the gate contains the true measurement if detected, and $S(k)$ is the covariance of the innovation corresponding to the predicted measurement.

In Fig. 1, the target originated measurements "o" and clutter originated measurements "$\times$" are shown. A measurement is validated for target j if it falls inside the elliptical region centered at $\hat{Z}_j$ (the predicted measurement of target j), and only the validated measurements for a particular target are candidates to be association with that target. The simple gating technique can be easily incorporated into the framework of the algorithm in Section 3.1. In this gating based algorithm (G-RBMCDA), only the validated measurements are used to enumerate the data associations.

It should be noted that, the introduce simple gating technique can not be directly used in the sequential likelihood based algorithms. In fact, we found that the combinational algorithm may possibly be failed in experiments. An intuitive explanation of this problem is that the fixed validation regions should be changed even in one time step.

4 SIMULATIONS

The performance of S-RBMCDA and G-RBMCDA algorithms are compared with generic RBMCDA in this section. We model the two targets with near constant velocity model in 2-dimensional Cartesian coordinates and the discrete-time dynamic and measurement model of target j has the following form:

$$x_{j,k} = F x_{j,k-1} + w_{k-1} \tag{14}$$

$$z_{j,k} = H x_{j,k} + v_k \tag{15}$$

where

$$F = \begin{pmatrix} 1 & 0 & T & 0 \\ 0 & 1 & 0 & T \\ 0 & 0 & 1 & 0 \\ 0 & 0 & 0 & 1 \end{pmatrix}, H = \begin{pmatrix} 1 & 0 & 0 & 0 \\ 0 & 1 & 0 & 0 \end{pmatrix} \tag{16}$$

w_{k-1} and v_k are zero mean Gaussian process noise. The Process noise variance and the variance in the measurements are selected as 0.1. The sample interval $T = 0.1$ and the correct measurements returns with a know detection probability $P_d = 0.99$. The clutter are modeled as independent and identically distributed with uniform spatial distribution in a detection region of the coordinate plane $[0,\ 25] \times [0,\ 25]$, and the number of clutter measurements obeys a Poisson distribution with the Poisson random number λ. The gating region used is $P_g = 0.9997$ with $\gamma = 16$. The number of particles used in the three algorithms: 50 (RBMCDA), 20 (S-RBMCDA, repeat 2 times), 50 (G-RBMCDA). in All simulations are run on a PC with a 2.8-GHz Intel processor.

Fig. 2 and Fig. 3 show the position RMSE for tracking two crossing targets. The clutter rate $\lambda = 10$ and the experiments are repeated 100 times. It is observed that the RMSE of the S-RBMCDA algorithm is lower than the generic RBMCDA even with fewer particles. In fact, G-RBMCDA can further improve the ability of none-validation-region algorithms (RBMCDA and S-RBMCDA) mainly because only the validated measurements are considered in data association and the clutter measurements outside the validation regions are abandoned reasonably.

Fig. 4 gives the running time as a function of N_p, we can see that the S-RBMCDA and G-RBMCDA algorithms are computationally efficient than the generic RBMCDA as expected. The G-RBMCDA is the most efficient algorithms, but it can only be implemented in the known number version of target tracking. For each method we run the algorithms with the increasing number of particles and repeat each experiment 50 times to get an average results.

5 CONCLUSION

In this paper, the improved RBPF algorithms have been presented for multi-target tracking in clutter. The proposed sequential likelihood method can be used to improve the performance of the generic algorithm with less particles. If the number of targets is fixed, the simple gating based algorithm only consider validation regions where the true measurements are concentrated with high probability. The computational time is greatly decreased for less clutter needs to be considered. Moreover, the gating based algorithms can

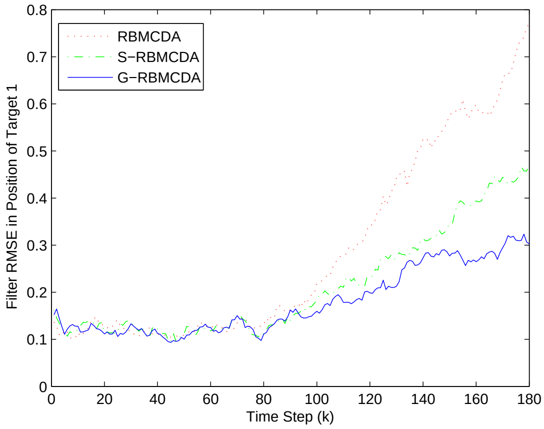

Fig. 2: Comparison of the average position estimation errors (RMSE) of target 1.

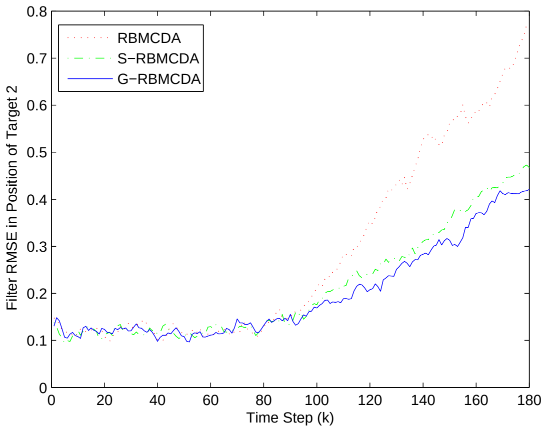

Fig. 3: Comparison of the average position estimation errors (RMSE) of target 2.

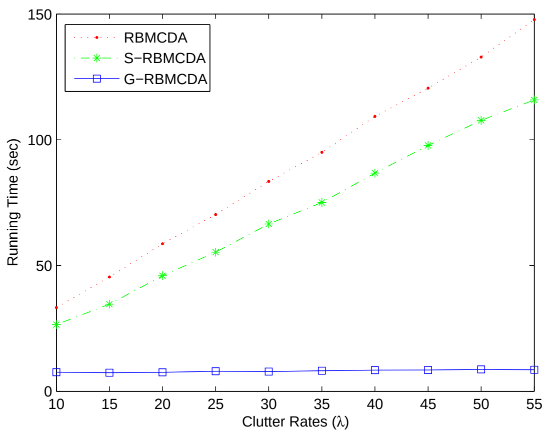

Fig. 4: Comparison of the average running time of the three algorithms.

improve the tracking ability of the algorithm without the disturbance of clutter outside the validation region. Future work should be done to intensively study the sequential likelihood method for the general particle filtering algorithms.

6 ACKNOWLEDGEMENT

This work was supported by the National 973 Program (2012CB821200) and the NSFC (61134005, 60921001, 90916024, 91116016).

REFERENCES

[1] Y. Bar-Shalom and X. R. Li, Multitarget-multisensor tracking: principles and techniques. Storrs, CT: YBS Publishing, 1995

[2] W. S. Wijesoma, L. D. L. Perera and M. D. Adams (2006), Toward multidimensional assignment data association in robot localization and mapping. IEEE Transactions on Robotics, 22(2): 365-365

[3] B. K. Habtemariam, R. Tharmarasa, T. Kirubarajan, D. Grimmett and C. Wakayama (2011), Multiple detection Probabilistic Data Association filter for multistatic target tracking. The 14th FUSION, 1-6

[4] S. Särkkä, A. Vehtari and J. Lampinen (2004), Rao-Blackwellized Monte Carlo data association for multiple targets tracking. Proceedings of the Seventh International Conference on Information Fusion, I: 583-590

[5] S. Särkkä, A. Vehtari and J. Lampinen (2007), Rao-Blackwellized particle filter for multiple target tracking. Information Fusion, 8(1): 2-15

[6] M. Vihola (2007), Rao-blackwellised particle filtering in random set multitarget tracking. IEEE Transactions on Aerospace and Electronic Systems, 43(2): 689-705

[7] O. Cappe, S. J. Godsill and E. Moulines (2007), An overview of existing methods and recent advances in sequential monte carlo. Proceedings of the IEEE, 95(5): 899-924

[8] P. M. Djurić, J. H. Kotecha, J. Zhang, Y. Huang, T. Ghirmai, M. F. Bugallo and J. Młguez (2003), Particle filtering. IEEE Signal Processing Magazine, 20(5): 19-38

[9] F. Mustiere, M. Bolic and M. Bouchard (2006), Rao-Blackwellised particle filters: examples of applications. IEEE CCECE/CCGEI (Ottawa), 1196-1200

[10] Y. Bar-Shalom, F. Daum and J. Huang (2009), The probabilistic data association filter : estimation in the presence of measurement origin uncertainty. IEEE Control Systems Magazine, 29: 82-100

System Development of an Artificial Assistant Suit

Jianling Bian[1, 2] Huailin Zhao(communication writer)[2] Xiaomin Liu[3] Masanori Sugisaka[4]

[1] College of Physical Science and Engineering, Zhengzhou University, China

[2] School of Electrical & Electronic Engineering, Shanghai Institute of Technology, China

[3] Dep. of Management & Economics, North China Univ. of Water Resources and Electric Power, China

[4] Mec. & Ele. Course, Nippon Bunri University, Japan

Abstract: The artificial assistant suit is a kind of assistant suit which can be put on the human upper body and help the actions of human's two arms. It is actuated by Mckibben pneumatic artificial muscles (simply call it Mckibben muscles later). This paper introduces the whole system and its structure. The configuration of the Mckibben muscles is discussed. The measurement and control system is introduced in detail. The electropneumatic valve's characteristics are analyzed. The detection of the motion intention of human arms by SEMG signals is discussed too.

Keywords: Artificial assistant suit, Mckibben muscle, electropneumatic valve, SEMG signal.

1. Introduction

The McKibben muscle has advantages such as small size, safe and compliance, great power/weight ratio. And it is simply constructed, easy-fixed, and cheap. Its force-length characteristic is similar to that of the biological muscle. Mainly it is used in robots. The robot joint actuated by it behaves a little like humen's or anminal's because of its similarity to the biological muscle. The robot actuated by McKibben muscles is much safer to human who interacts with it. Therefore, the McKibben muscle is a kind of very promising actuator in human recuperate field [1].

The world should be welfare. Developments of the robot capable of assisting elders, handicappeds, and patients are one of the main directions. Developing the devices capable of help getting well for patients is one of the main tasks of the modern technology. It's expectant for the McKibben muscle to play an important role in these fields. In some places such as Japan, china, America, and Europe, the artificial assisted suit made of McKibben muscles has come out. The suit is called as "dressable robot"[2]. Besides, the bipedal robot actuated by McKibben muscles has been developed. But to all of the developed artificial suit, Their structure is very complicated, and their weights are very large. Here what we are developing is a very light one, and its cost is very low.

2. Structure of the artificial assistant suit

To help the human arms act correctly, the Mckibben muscle actuators must be configured reasonably. Only one piece of the Mckibben muscle can't complete all the actions, because that the structure of the human arm is complicated and its actions are many and varied. Therefore, many pieces of the Mckibben muscles are required and they need to operate coordinately to achieve the required force. Based on the above analysis, we resolve the arm actions into the following basic ones：

①Shoulder's rising up and down (including to the front, to the back, and to the side)；

②Shoulder's swinging around the vertical axis；

③Elbow's bending and stretching；

④The forearm's rotating around the anatomic axis.

We think that all of the main arm actions can be realized based on the above four basic actions. The configuration of the Mckibben muscles can be done based on the requirement of the four basic actions. Let's analyze the anatomic structure of the human arm firstly. There are more than 20 pieces of muscles with the actions of both the shoulder joint and the elbow joint in the same arm[3]. All the actions of the shoulder and the elbow can be realized by these muscles' operating coordinately. Based on both the analysis to the anatomic structure and the dynamic requirement for the artificial assistant suit, 8 pieces of the Mckibben muscles are selected for the configuration of each arm of the suit, shown in Fig.1. They are corresponding to the functions of the following 8 muscles:

① Triceps brachii
② Brachioradialis
③ Biceps brachii short head
④ Biceps brachii long head
⑤ Deltoid anterior part
⑥ Deltoid middle part 1
⑦ Deltoid posterior part
⑧ Deltoid middle part 2

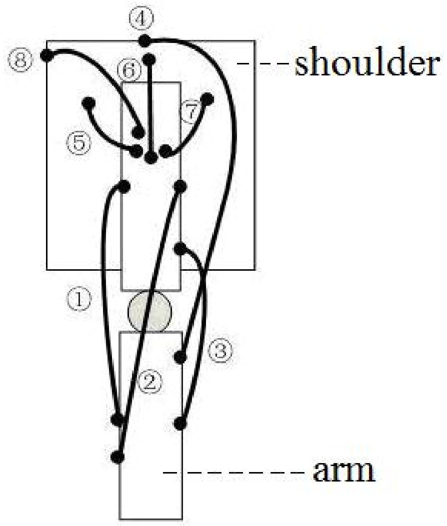

Fig.1 Configuration of the Mckibben mucles

3. Measurement and control system

The main characteristics of the artificial assistant suit are that it can sense the action intention of human arms and output forces to help the arm actions. To get the action intention of human arms exactly, the system uses both the SEMG signals and the gravity acceleration sensors to judge the action intention. Therefore the whole system should include at least the following parts:

① The compressor
② The electropneumatic volves
③ The artificial assistant suit actuated by pieces of Mckibben muscles
④ The SEMG signal detection device
⑤ The computer

The whole system is shown in Fig.2.

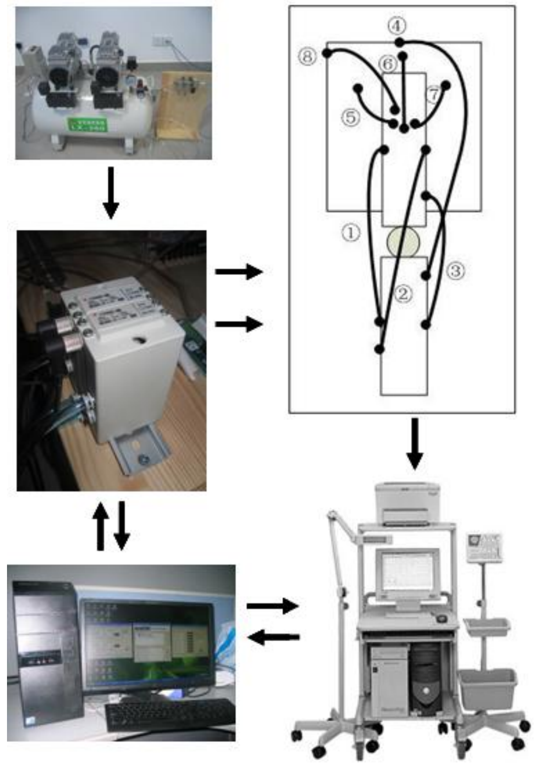

Fig.2 The whole system

The compressor is the source of the pressed gas. The Mckibben muscle needs pressed gas. Here the air is used. The electropneumatic valve is used to regulate the pressure of the air so that the Mckibben muscles can be input by the needed pressure of air. The SEMG signal device is used to detect the arm action by the SEMG signal of the arm. The computer is used as the center of measurement and control, which can control the electropneumatic valves to output the desired pressure of the air and sample the SEMG signals.

The compressor is a un-oil′s, the air from it must be passed through the air filter, the oil separator and the pressure-reducing valve, because that the air input into the electropneumatic valve have to be dry and pure. Otherwise the electropneumatic valve is easy to be damaged. The highest pressure of air must be lower than the highest pressure that the electropneumatic valve permits.

The electropneumatic valve in the system is made by SMC, Japan. The model is ITV0050-2ML. The permitted gas pressure varies from 0.1MPa-0.9MPa. So the highest output gas pressure of the compressor should be less than 0.9MPa. Its specification is DC24V/0.12A. So the max consumed power is 2.88W. The system has 16 valves. The whole power needed is 46.08W than which the source power of the electropneumatic valves should be larger. So we choice NES-200-24 made by Mingwei power source company as the electric power, shown in Fig.3. It can output 200W/24V, which can satisfy the requirement of the 16 valves. And the valve requires the input signal is DC0-5V. Its input impedance is about 10kΩ. Therefore, the max input power of the signal is about 2.5mW. The total input power of the signal is about 40mW. So the provided power from the signal input unit is larger than 40mW. Otherwise the voltage the valve got will be less than the required.

To satisfy the route number and the requirement for the input signal, The I/O card is selected as PCI-1724U which is 14-bit and has 32-channels' analog output, shown in Fig.4. Its output signal is DC0-10V. The required input signal voltage is 0-5V

Fig.3 The Power source (NES-200-24)

Fig.4 The I/O card (PCI-1724U)

To PCI-724U, the output current is 10mV, and if its output voltage is DC0-5V, the output power is 50mW. Fig.5 shows that the power requirement of the two valves can be satisfied by the I/O card.

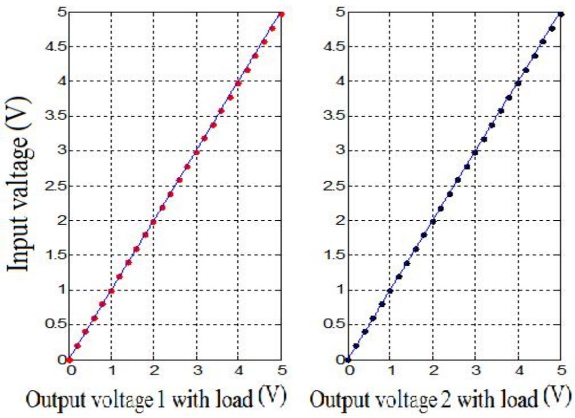

Fig.5 The voltage characteristics with loads

Fig 6 shows the good linearity of the electropenumatic valve. And Fig.6 indicates that the top voltage 5v is corresponds to the top pressure 0.9MPa. The highest pressure of air is 0.67MPa because that the compressor only provides the pressure 0.67MPa. It shows that the pressure gets its highest 0.67MPa when the input voltage is 3.8v. Therefore the input voltage 0-5v corresponds to the output pressure 0-0.9MPa instead of 0-0.67MPa.

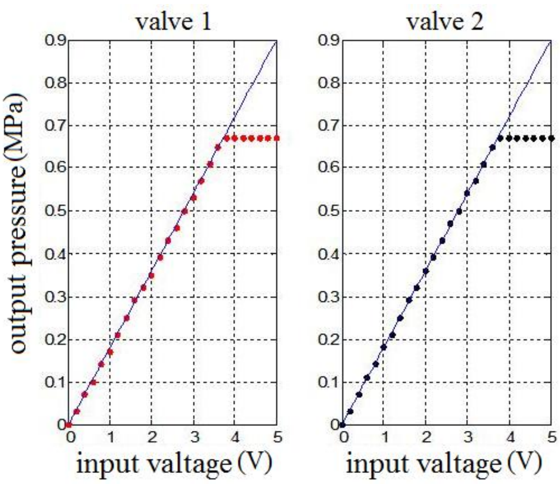

Fig.6 The linearity of the valve

The SEMG signal is used to detect the action intention because it can inform the muscle contraction[4]. We put six pairs of the SEMG signal electrodes on the arm, shown in Fig.7, which are used to detect the action intention of the related muscles. After analyzing, the computer can judge the action intention of the arm by the electrode distribution. A neural network is used to analyze the relationship between the SEMG signals and the action intention.

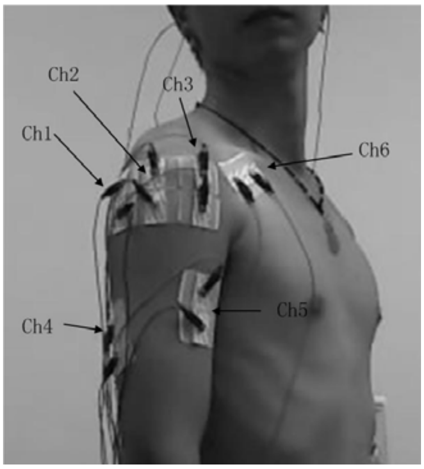

Fig.7 The distribution of the SEMG electrodes

4. conclusion

This paper introduced the whole system including the configuration of the Mckibben muscles in the artificial assistant suit, the integration of the system hardware, and the detection method of action intention of human arms. Of course some research still hasn't been finished including the software and the final experiments.

This study is supported by the project from Shanghai Committee of Science and Technology, China (Pujiang Plan: 10PJ1409200).

Reference

[1] N.Tsagarakis, Darwin G. Caldwell. Improved Modeling and Assessment of Pneumatic Muscle Actuators[J], Proceedings of 2000 IEEE International Conference on Robotics& Automatic, San Francis of CA. April 2000: 3641-3646

[2] Hiroshi Kobayashi, Takamitsu Aida, Takuya Hashimoto, Muscle suit development and factory application, Journal of Automation Technology, Vol.3(6), 2009，p209-213

[3] R. Nakamura, H. Saito, Fundamental kinesiology, 5th edition, Tokyo, Japan: Ishiyaku Publishers, 2000

[4] K. Nazarpour, A. Sharafat, S. Firoozabadi, Surface EMG Signal Classification Using a Selective Mix of Higher Order Statistics, 2005, p4208-4211

Fundamental research on the fuzzy control to the autonomous airship

Long Li [1], Yuan Li [1], Fengzhi Dai [1], Dejin Wang [1], Yutaka Fujihara [2]

[1]School of Electronic Information and Automation, Tianjin University of Science and Technology, China
[2]Department of Control Engineering, Matsue College of Technology, Japan

[1]daifz@tust.edu.cn

Abstract: The fuzzy control to the experimental autonomous airship is introduced in this paper. The fundamental development and research on the hardware and the program to control the airship navigating along the shortest flight path to the target point is executed. The fuzzy control is used because the airship system is nonlinear and it is difficult to describe the accurate motion equations of the system. At last, to compare the efficiency, the traditional PD control is also applied. The result of comparison shows the validity of the fuzzy control.

Keywords: autonomous airship, fuzzy control, side thruster

1 INTRODUCTION

Manned helicopters are used for aerial photography to obtain the geographical information. However, it results to the atmosphere pollution by the exhaust fumes. Also it will be very dangerous to navigate the region that is bearing the disaster or war.

To solve these problems, the unmanned autonomous green flying system is needed. Unmanned helicopter and airship have been developed for uses in the mine detecting, crop dusting and military surveillance. Aerosonde [1], Predetor [2], RQ-4A Global Hawk [3] and the unmanned helicopter developed by Nakamura et al. [4] are examples of these kinds of flying systems. Also Suzuki et al. [5] presented the research result of the control for the airship by reinforcement learning and adaptive control.

However, some of above systems have a little intelligent feature, and some of them have a few references and literature about the control unit because of the technology patents. Thus the detailed information cannot be gotten.

In this paper, the airship in our lab is introduced, which can remain stationary in the air and has low fuel consumption due to the usage of helium gas for buoyancy. Also the basic technology including the hardware and the control method by which the airship navigates along the shortest path to the target point is discussed.

2 STRUCTURE OF THE SYSTEM

To control the whole system, the mechanical control of the airship, determination of flight path to the target point and the flight technology along the flight path, real-time image recognition, and the telecommunication technology, is required.

2.1 Hardware

Fig. 1 shows the airship system. The balloon is elliptical with an overall length of 5.8 meters, its maximum diameter is 2.2 meters and the volume is 17.5m^3. Helium gas is used for buoyancy. The gondola under the balloon contains a microcomputer, a CCD camera, motors, batteries, a geomagnetic and a GPS sensor, a notebook computer and ballast, shown in Table 1 [6]. For navigation, the antenna for receiving GPS signals is fixed on the head of the balloon.

Table1 Specification of Equipment

	Equipment	Company
Notebook computer	Libretto L1/060TNCM	TOSHIBA
Micro computer	H8/3048F	HITACHI
Micro computer board	AKI-H8	AKIZUKIDENSHI
GPS receiver	GM-38	SANAV
DGPS receiver	NDIDEV003	Nippon Denso Industry
Earth magnetism sensor	3D motion sensor	NEC tokin

The notebook computer mounted on the system receives the latitude and longitude values of the airship from the GPS sensor, and obtains the direction for the airship to fly to by the geomagnetic sensor. The values of control variables are calculated and transmitted to the microcomputer. And then the microcomputer converts the values into the motor drive pulses and outputs them to each motor.

The power for the motion consists of a side thruster and two main fan ducts. The side thruster is used to rotate the airship around the vertical axis (yawing rotation). Two main fan ducts are used to control the airship flying up or down, and forward or backward.

Since the volume of the gondola can be negligible if it is compared with that of the envelope, it is reasonable to assume that the center of the volume lies on the axis of symmetry of the envelope. The airship is able to move in translation and rotate in three-dimensional spaces (rolling, pitching and yawing). In this paper the yawing rotation of the airship is mainly tested.

2.2 Control algorithm

The flow chart of the control algorithm is shown in Fig. 2. The airship goes up first. Next, the notebook computer that mounted in the gondola receives data from each sensor. Subsequently, the position of the airship compares with the target point. When it reaches the target, the program terminates and the airship hovers. Otherwise the notebook computer calculates the direction and distance to the target point shown in Fig. 3. Later the control is determined and outputted to each motor. Eventually by repeating these processes, the airship arrives at the target point.

2.3 Control of the side thruster

2.3.1 PD control

The side thruster is first controlled by the PD control as comparison. As shown in Fig. 3, the thrust S_t is determined by the angular difference θ_d (=$\varphi - \theta$), the angular velocity ω (=$d\theta_d/dt$) and the angular acceleration α (=$d^2\theta_d/dt^2$). Thus the thrust of the side thruster is expressed by

$$S_t = K_\theta(0-\theta_d) + K_\omega(0-\omega) + K_\alpha(0-\alpha) \qquad (1)$$

where K_θ, K_ω and K_α are constants and the target is set to (0, 0, 0). However, it is difficult to determine these constants because the airship is slow to respond and the characteristic of the airship is non-linear. Therefore, these constants are adjusted and determined by repeating the experiment.

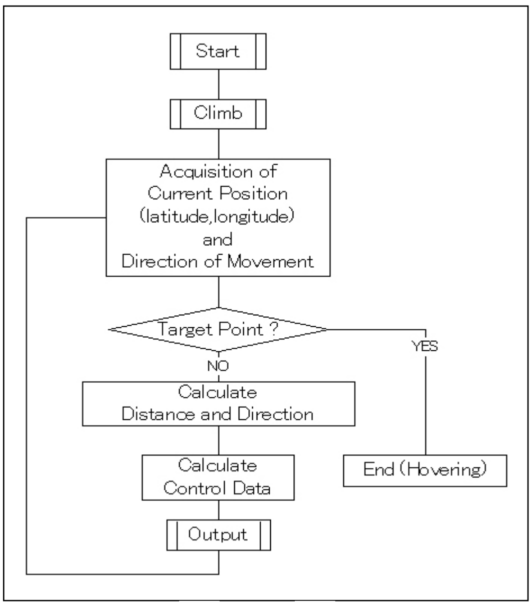

Fig. 2. Flow chart of the control algorithm

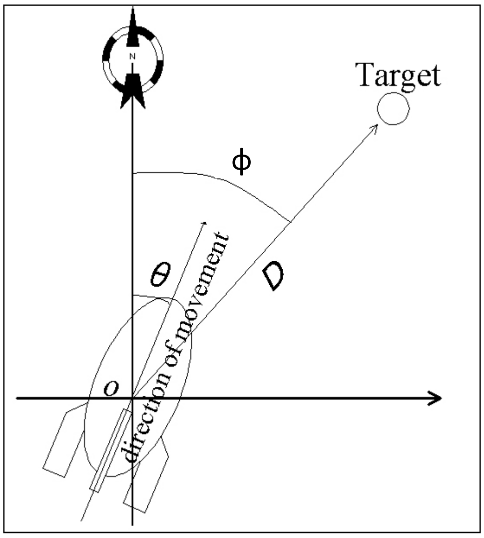

Fig. 3. Coordinate of the airship to target

2.3.2 Fuzzy control

Fig. 4 shows the fuzzy membership functions being used. Inputs are the angular difference θ_d and the angular velocity ω, output is S_t. The membership functions have triangular forms and seven vertices. Each set is labeled NL, NM, NS, ZR, PS, PM and PL, meaning negative or positive large, medium, small, and zero for each symbol. Fuzzy rules are

If θ_d is A_{11} and ω is A_{12} then S_t is B_1

If θ_d is A_{21} and ω is A_{22} then S_t is B_2 (2)

where A_{ij} and B_i are labels of each fuzzy set, and the fuzzy output set B_i is discrete, shown in Table 2.

Table 2. Rule Table S_t.

ω \ θ_d	NL	NM	NS	ZR	PS	PM	PL
NL	0	0.5	1	1	1	1	1
NM	0	0.4	0.7	0.3	1	1	1
NS	-0.7	0.3	0.5	0.1	0.3	1	1
ZR	-1	-0.5	-0.3	0	0.1	0.4	1
PS	-1	-1	-0.6	-0.4	-0.6	-0.4	0.6
PM	-1	-1	-1	-0.5	-0.8	-0.5	0
PL	-1	-1	-1	-1	-1	-0.6	0

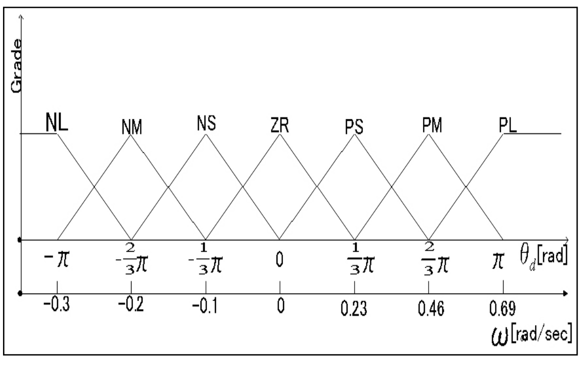

Fig. 4. Membership functions for inputs

2.4 Data Flow

Fig. 5 shows the block diagram of the data flow. Latitude and longitude values of the target point are set initially. In Fig. 3, D and φ are calculated as the difference between the positioning data of the target point and those obtained from the GPS. The angular difference θ_d ($=\varphi - \theta$) is the input variable to the side thruster controller, where the angle θ is the forward direction of the airship. D and θ_d are also inputs to the main fan duct controller [7].

3 EXPERIMENT

3.1 The task

The purpose of the experiment is to confirm that the airship navigates to the target point and to compare the two control methods for controlling the side thruster. It is desirable that the experiment is done indoors, where there is little influence to disturb the flight.

3.2 Result and analysis

The result is shown in Fig. 6. It gives two trajectories of the flight path, plotting longitude along the ordinate and latitude along the abscissa. By PD control, the airship flew changing the direction right and left before arriving at the target point. The main reason is that the gains K_θ, K_ω, K_α in equation (1) are not set properly. The adjustment is very

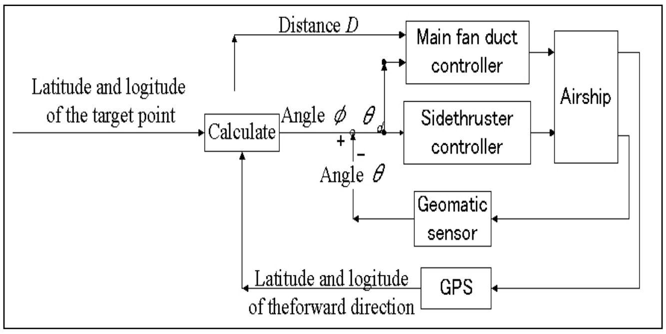

Fig. 5. Block diagram of data flow

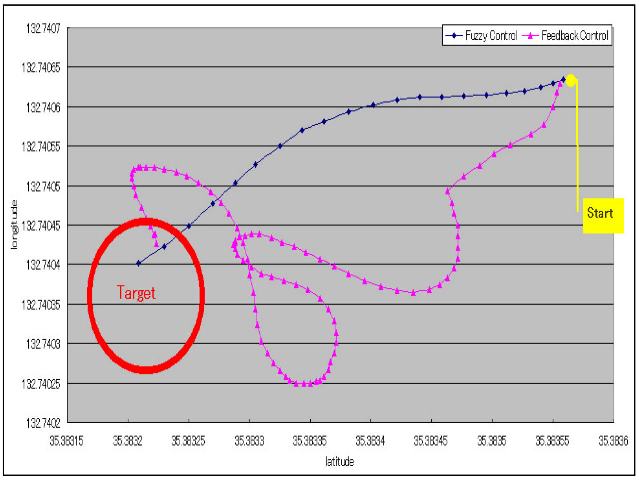

Fig. 6. Results of flight controlled by Fuzzy and PD

difficult without getting the perfect dynamic characteristics of the airship. By fuzzy control, the airship could autonomously navigate by almost the shortest flight path. The flight time is 1 minute and 27 second by PD control, and 20 second by the fuzzy control.

Fig. 7 shows another experiment controlled by the fuzzy algorithm. The airship starts from the "Start" point, and returns from the position "Target" to the "Goal" [8].

The results of the experiment show that the fuzzy control method is more effective than the PD control from the viewpoint of controlling an autonomous motion system, and the PD control is not suitable for the autonomous airship system in the present situation.

3.3 Landing stage

When the flying action is accomplished, it is time for the airship to land (or hover). The CCD camera on the airship searches the letter P or H (means parking point) on the land. Operation, such as image processing and segmentation, is done to find the letter P. And then automatically adjust the airship to land on the mark.

The question is how to make the airship recognize the mark rapidly. In practical application, the camera on the airship seldom sees the perfectly vertical P, always is italic or has random angle. Thus the recognition system needs to store a large number of templates for the letter P. In fact, moment invariance [9] can solve this problem. We can mapping the different angles to the few templates by invariant moment shown in Fig. 8.

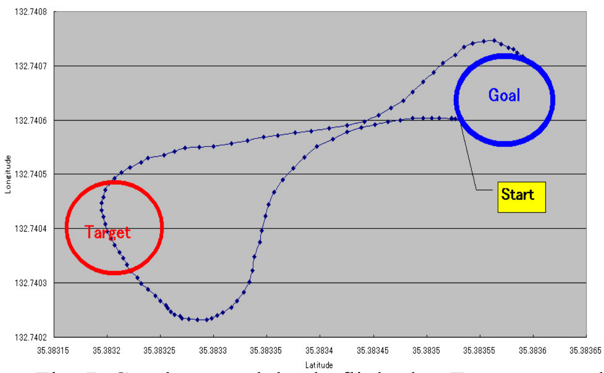

Fig. 7. Go there and back flight by Fuzzy control

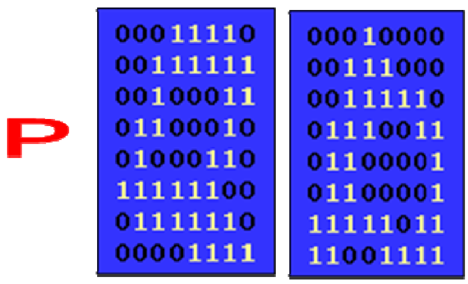

Fig. 8. Template of the letter P

4 CONCLUSION

In this paper, the simplified control system and the algorithm for the airship to navigate autonomously to the target point are proposed. To control the side thruster, the PD and the fuzzy control are applied respectively as comparison. As the result, it is clear that the fuzzy algorithm enables better control for the airship to reach the preset target point.

Of cause if the kinematics description of the airship's side thruster control and the PD parameters are set more accurate, the result for the PD control should be better than the proposed result in this paper. The contribution of this paper is to express that the fuzzy control is more suitable for the intelligent control system.

Further work of pattern recognition to a special object on the land by the single or stereo CCD cameras and the technology of telecommunication are being considered. Telecommunication technology is used to communicate mutually the data between the notebook computer mounted on the airship and the computer at the base station to establish the servo-client system. And the monitoring program by using wireless LAN should also be developed, which enables us to monitor the condition of the airship remotely.

ACKNOWLEDGMENT

This paper was supported in part by the National Natural Science Foundation of China under Grant 60874028, and the Laboratory Open Foundation of Tianjin University of Science and Technology under Grant 1102A204, and Tianjin Association for Science and Technology.

REFERENCES

[1] Aerosonde Robotic Aircraft Pty Ltd: http://www.aerosonde.com

[2] General Atomics Aeronautical systems, Inc: http://www.ga-asi.com/

[3] Northrop Grumman Corporation: http://www.northropgrumman.com/

[4] S. Nakamura, A. Sato, H. Shibata, et al (2000), A study on autonomous searching and tracking by an unmanned helicopter based on GPS and image information. Journal of the Robotics Society of Japan, vol. 18, no. 6, pp. 862-870.

[5] K. Suzuki, Y.Akisato, A Ohuchi (1999), Micro airship control based on reinforcement learning. Proceedings of 99th robotics and mechatronics conference on JSME, No. 99-9.

[6] M. Sugisaka, F. Dai, Y. Fujihara, et al (2005), Development of the fuzzy control for a GPS-located airship. Proceedings of the tenth International Symposium on Artificial Life and Robotics, pp. 436-439.

[7] Y. Fujihara, T. Kamioka, N. Takahashi, et al (2004), Development of the autonomous airship by fuzzy control. Proceedings of the Seventh International Conference on Industrial Management, pp. 183-190.

[8] F. Dai, W. Gao, N. Kushida, et al (2011), Fuzzy control for the autonomous airship. Proceedings of the 6th IEEE Conference on Industrial Electronics and Applications, pp. 778-782.

[9] F. Dai (2004): Development of Learning Methods on Control and Pattern Recognition for an Autonomous Mobile Vehicle. Ph. D Dissertation, Division of Materials Science and Production Engineering, Oita University, Japan.

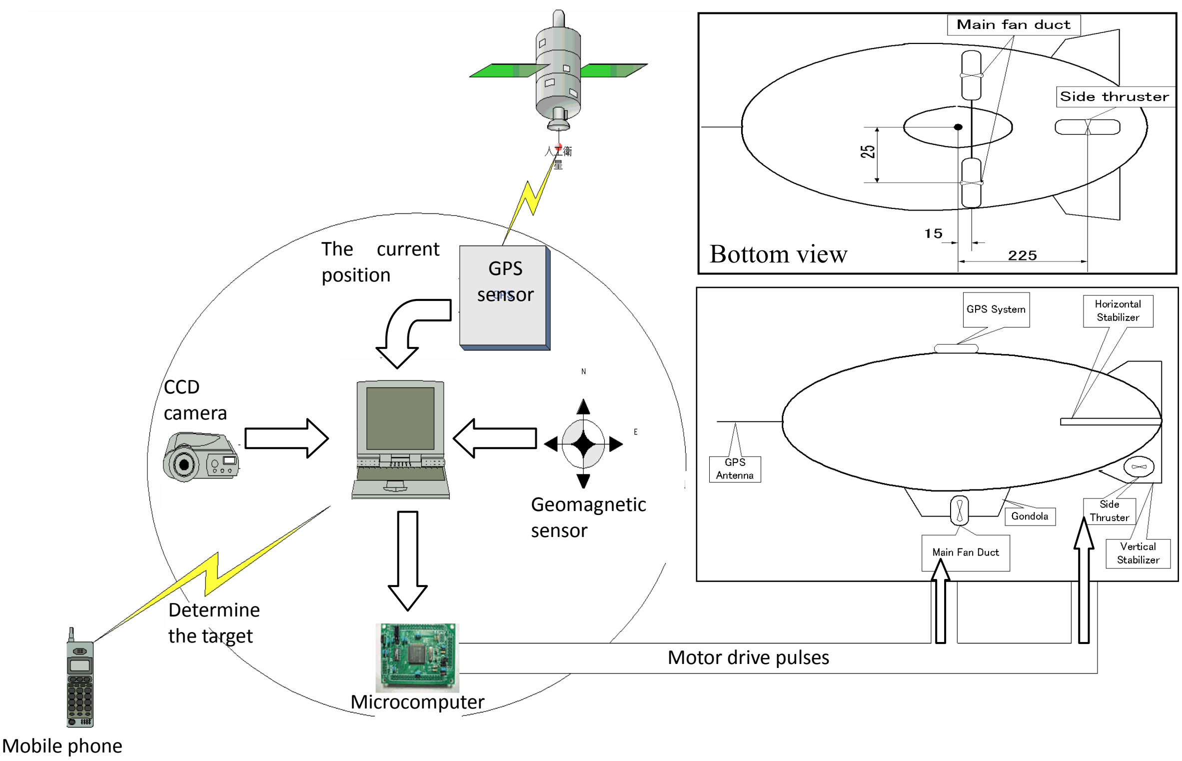

Fig. 1. The structure of the whole system

The Seventeenth International Symposium on Artificial Life and Robotics 2012 (AROB 17th '12),
B-Con Plaza, Beppu, Oita, Japan, January 19-21, 2012

Fundamental research on the fingerprint recognition algorithm

Binyao Li [1], Fengzhi Dai [1], Dejin Wang [1], Baolong Zhang [1], Naoki Kushida [2]

[1] School of Electronic Information and Automation, Tianjin University of Science and Technology, China
[2] Oshima National College of Maritime Technology, Japan

[1] daifz@tust.edu.cn

Abstract: With the further need for security, the fingerprint pattern recognition technology began to be used in various fields, from the theoretical field to practice. Digital fingerprint processing concerns the algorithms and processes of automated fingerprint image processing, feature measurement, detail description, pattern analysis, recognition and classification by the computer instead of manual. In this article, four modules for fingerprint identification are introduced: the modules for fingerprint image sampling, for image pre-processing algorithm, for feature extraction and for feature matching algorithm. Finally this article gives the completed procedure of the fingerprint image processing and feature extraction.

Keywords: fingerprint recognition, image processing, feature extraction, pattern recognition

1 INTRODUCTION

Fingerprint refers to the finger's end positive skin with uneven ridge, which is arranged in a regular formation of different texture. As the fingerprint has lots of characteristic (lifelong invariance, uniqueness, etc.) and convenience, it almost becomes synonymous with biometric identification [1].

At present, the solutions of security problems and the problem of identification method have been more and more important, it also has increasingly and widely application. Fingerprint characteristic is the inherently physiological feature and compared with traditional identification method, it has many advantages. Consequently the method of fingerprint identification has become one of the most important methods in the identification field.

Fingerprint identification is executed after fingerprint analysis. The purpose of fingerprint analysis is to extract the fingerprint features, in order to match the template of the special fingerprint. These features include the types of the texture (the arch, loop and whorl types), the shapes of the line (the straight line, arc or wavy lines), and the details in fingerprint (the end, the branch, the central point, the short line, etc.) [2].

There are three processes for the traditional manual fingerprint identification: establishing the fingerprint template card, sampling the fingerprint, and matching the sampled fingerprint to the templates. This method requires excessive personnel and needs many staffs. Thus it is gradually replaced by the digital fingerprint identification method.

Digital fingerprint identification method depends on the computer vision, and it can establish the electronic fingerprint templates automatically, sample the electronic fingerprint and match it with the templates.

The usage of the RFID technology, the embedded system, the communication and other technologies expands the application of fingerprint recognition. Further more, with the rapid development of the network information technology and E-Commerce, the research on the fingerprint pattern recognition becomes more important.

2 PREPROCESSING

2.1 Fingerprint mode conversion

There are six steps for the conversion of the fingerprint modes, from the real fingerprint to the final extracted features, which is shown in Fig. 1.

(1) Transfer the real fingerprint to the color image: scan the real fingerprint digitally by the fingerprint-sampling device using the proper resolution rate.

(2) Transfer the color image of fingerprint to the grayscale image: calculate all the pixels one by one by the color/gray conversion formula. The converted gray levels range from 0 to 255. The higher the value, the brighter the point is.

(3) Transfer the grayscale fingerprint image to the object mode: the fractal dimension of pixels between the background and fingerprint in the image is different. Thus we can extract the fingerprint object from the background.

(4) Transfer the fingerprint object to the fingerprint textural characteristic mode: by using the knowledge of the fingerprint analysis, we can mark each fingerprint feature point, so that we can obtain the information of the fingerprint texture and form the fingerprint feature pattern.

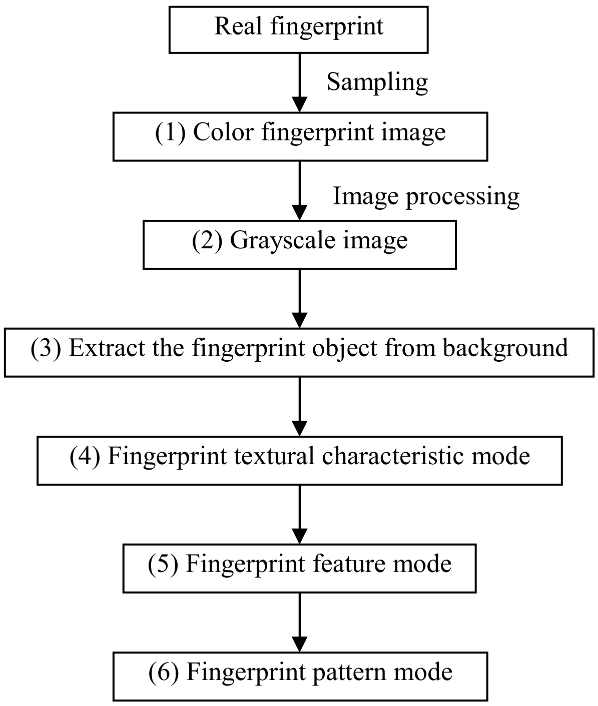

Fig.1. Fingerprint mode conversion

(5) Transfer the fingerprint textural characteristic mode to the fingerprint feature mode: using knowledge of topology, the fingerprint texture characteristic is classified according to the different characteristic branches. After transferring, the pattern can be recognized with high efficiency, and the recognition time can be decreased.

(6) Transfer the fingerprint feature mode to the fingerprint pattern mode: we form a template by combining the fingerprints and the holder's ID number, so that the database is established. Thus the pattern of the sampled fingerprint can be recognized.

2.2 Fingerprint recognition algorithm

There are four modules consist of the fingerprint pattern recognition algorithm [2], which is shown in Fig. 2:

(1) Fingerprint image acquisition module: the fingerprint image is sampled and the digital fingerprint data matrix is obtained.

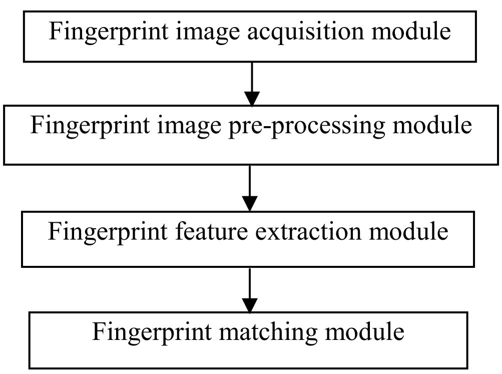

Fig.2. Four modules for fingerprint pattern recognition

(2) Fingerprint image pre-processing modules: restoration from the original fingerprint image. The process includes three steps, which are restoration, intelligent enhancement processing and thinning processing.

(3) Fingerprint feature extraction module: extract the features of the fingerprint.

(4) Fingerprint matching module: matching and comparison are included in this module.

3 DESIGN AND ANALYSIS

For the four modules discussed above, we need to make overall process planning and selection to each module respectively [1, 2].

First is the fingerprint image acquisition module: fingerprint image collector is used to sample the fingerprint image, but we need to judge its integrity and clarity. Here the difference-filtering algorithm is chosen for process, and then through the threshold to judge whether the image is qualified. If the result is zero, it means that none of the fingerprint data is collected, if it is more than the threshold, it means that the complete clear fingerprint image has been collected.

Secondly, the fingerprint image pre-processing module is executed: by using the aberration correction, segmentation, equilibrium, convergence, smooth, intelligent enhancement, binarization and thinning algorithms to get a clearer skeleton of the fingerprint image. The detailed algorithm is divided into the following seven steps, which is shown in Fig. 3 and Fig. 4.

(1) Distortional image correction processing includes geometrical optics and grayscale mapping.

(2) By calculating the distribution of intensity and gradient field to extract the fingerprint object: the fingerprint object has a higher value of both intensity and gradient fields than those of the background.

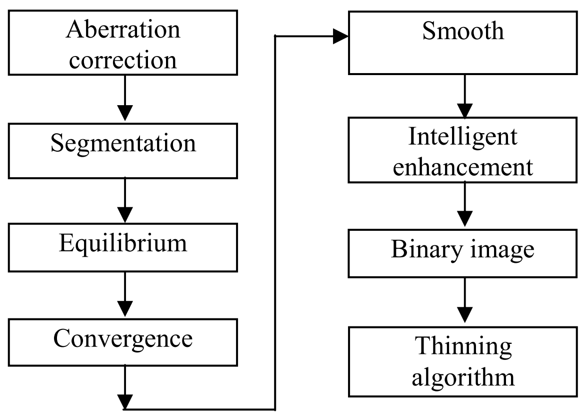

Fig.3. Fingerprint image pre-processing module

(3) The purpose of the gray level balance is to calculate the gray value of each pixel, and make images evenly distributed for each gray level.

The contrast processing for images is to solve the problem of balance. Because histogram is always used to describe the distribution of gray values, we need to establish a histogram distribution of the image and then make use of the grayscale algorithm to establish the mathematical model to balance the image.

(4) It exists objectively that the fingerprint image is divergent, and the convergence of overall picture is a micro process. Thus according to the chaotic divergent fingerprint physical model, the Gaussian function is used to do the image convergence.

(5) When the fingerprint image is sampled by the photoelectric sensor, it is easy to bring the surrounding dust and stain in the image, and this forms the noise points. In order to eliminate the noisy points in the fingerprint image, the average template for relevant pixels should be considered to smooth the image.

(6) Intelligence enhancement is the inherent ability of human eyes. To apply that ability to the computer, the Gabor physical model, which can do intelligence convergence and intelligence enhancement, is set up according to the fingerprint field of line direction.

(7) Threshold makes the gray value to be 255 at the valley line pixels in the fingerprint image, and 0 at the ridgeline pixels. There are two methods to realize binarization, which are the gray threshold segmentation method and the intelligent binary domain analysis method. If we want to extract the fingerprint skeleton, it's necessary to do the refined fingerprint image processing, and the common thinning algorithm and querying method are always used.

The third is the fingerprint feature extraction module: extracting all the fingerprint feature points from the preprocessing module, eliminating the false and retaining the true feature points, and saving to the database.

The last is the fingerprint pattern matching module: its main content is to match the fingerprint feature point topologically to the database precisely.

4 RESULT

Fig. 4 gives the completed procedure of fingerprint image processing and feature extracting. The gray level image Fig. 4(a) is used as the original image, at last the fingerprint feature points are extracted, which is shown in Fig. 4(k). And then, pattern matching and recognition [3] is used to find the fingerprint belongs to which person that is stored in the database.

5 CONCLUSION

In this article, the background and the basic content of the traditional and the digital fingerprint are described. And then the four modules for fingerprint identification are introduced: the modules for fingerprint image sampling, for image pre-processing algorithm, for feature extraction and for feature matching algorithm. After that, the detailed description for each module is expressed.

From the article, we see that the fingerprint recognition is not difficult unless the feature points can be defined and extracted by image processing, pattern matching and recognition.

In the future, the face recognition, voice recognition and signature recognition [4-6] are also considered for the security recognition system.

ACKNOWLEDGMENT

This paper was supported in part by the National Natural Science Foundation of China under Grant 60874028 and Tianjin Association for Science and Technology.

REFERENCES

[1] Davide Maloni, Dario Maio, Anil K. Jain, Salil Prabhaka: Handbook of fingerprint recognition. Springer-Verlag New York, 2003.

[2] Li Hao, Fu Xi: Mater the algorithms and realization of the fingerprint pattern recognigition system by Visual C++ (in Chinese). Posts & Telecom Press, 2008.

[3] Fengzhi Dai, Seiya Hamabe, Yutaka Fujihara: Research on autonomous mobile robot for visually handicapped persons by pattern recognition. Proceedings of the Thirteenth International Symposium on Artificial Life and Robotics, pp.819-822, 2008.

[4] Fengzhi Dai, Yutaka Fujihara, Naoki Kushida: A survey of face recognition by the genetic algorithm. Published by Nova Science Publishers, Inc. ISBN: 978-1-61324-597-2, 2011.

[5] Naoki Kushida, Junso Kimura, Fengzhi Dai: Research of clustering by self-organizing map of Chinese pronunciation. Proceedings of 2009 CACS International Automatic Control Conference, Nov. 27-29, 2009.

[6] Debnath Bhattacharyya, Samir Kumar Bandyopadhyay and Poulami Das: Handwritten signature extraction from watermarked images using genetic crossover. MUE' 07 IEEE CS Conference, Seoul, Korea, pp. 987-991, 2007.

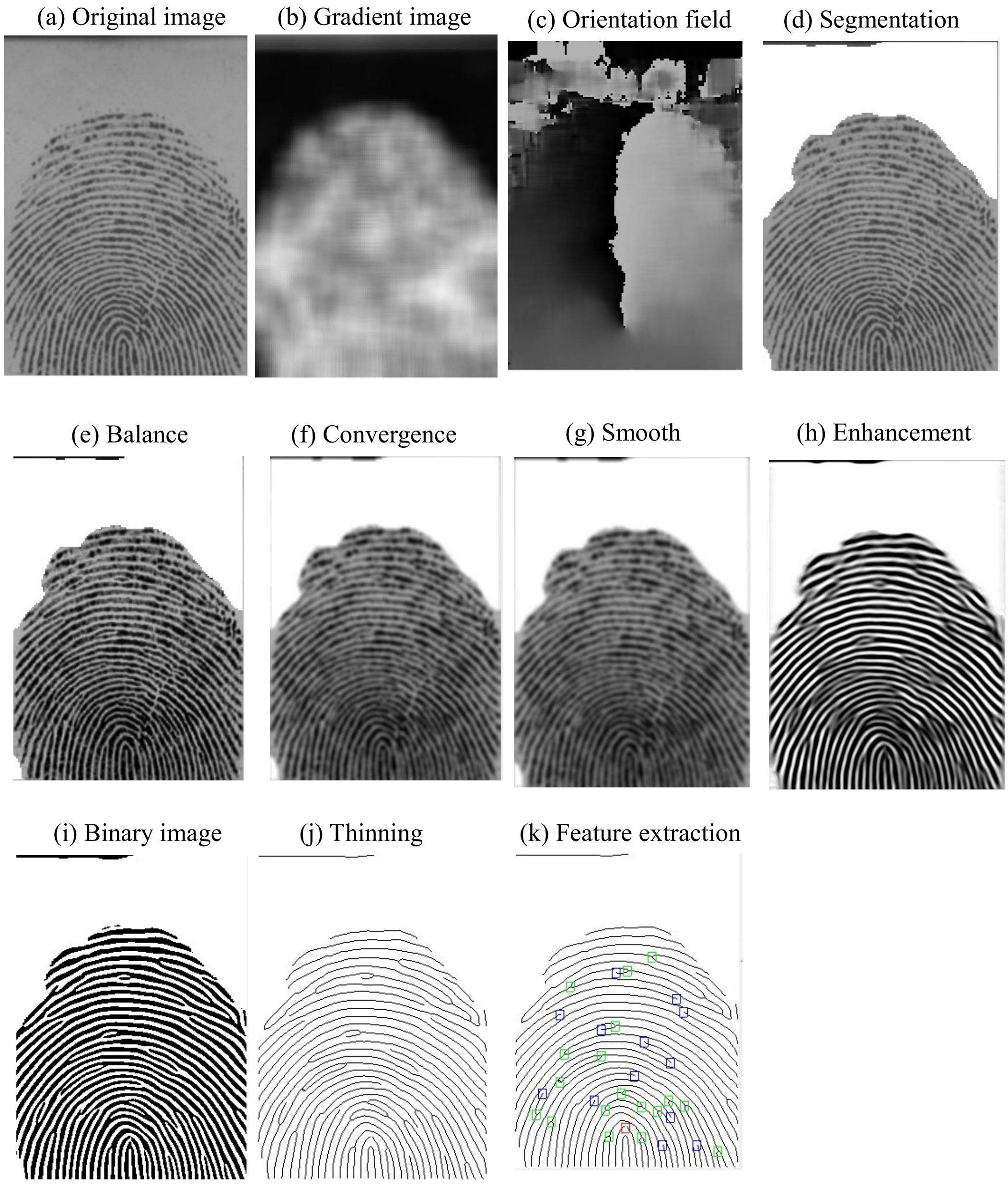

Fig.4. Image processing and feature point extraction

Configuration of the Mckibben Muscles and Action Intention Detection for the Artificial Assistant Suit

Xiaoqing Jia[1,2] Huailin Zhao(communication writter)[1] Lixia Wang[3] Masanori Sugisaka[4]
[1] School of Electrical & Electronic Engineering, Shanghai Institute of Technology, China
[2] College of Logistics Engineering, Shanghai Maritime University, China
[3] Library, Shanghai Institute of Technology, China
[4] Mec. & Ele. Course, Nippon Bunri University, Japan

Abstract: The artificial assistant suit is a kind of assistant equipment, which is actuated by Mckibben muscles and can be put on the human upper body, to help the upper limb act. It can detect the action intention of human's upper limb automatically and output definite force complying with the intention. The configuration of the Mckibben muscles is introduced in detail. How to detect the action intention by the surface electromyography signal is discussed deeply. The related experiments and their results are given.

Keywords: artificial assistant suit, Mckibben muscle, action intention, SEMG, classifier.

1. Introduction

Recently, our lab has been developing an artificial assistant suit actuated by the Mckibben muscles, which can be put on the human's upper body to help the two arms act. It can detect the action intention of human's two arms automatically and output definite force complying with the action intention (mainly including the actions of the shoulders and the elbows). Therefore it is a kind of action assistant equipment for human arms. To the ordinary or the old people, it can be used as the action assistant equipment to make them act easier. To patients, it can be used as the recuperate equipment to help them train their arms. To part of the disables, it can be used as the motive force equipment to help them to recovery their arm functions. Based on the functions and its characteristics of the artificial assistant suit, it must refer to the following problems. One, how many pieces of the Mckibben muscles are needed? How to distribute them and connect them with the artificial assistant suit? Two, how to detect the action intention of the human arms automatically? It should detect the action intention correctly in real time. Then it can output the corresponding force complying with the action intention correctly. Three, how will each of the Mckibben muscles operate after the action intention is got? Of course, only all of the Mckibben muscles must operate coordinately, the artificial assistant suit can output the required force and human feels comfortable. This paper mainly aims at the first two problems.

2. Configuration of the Mckibben muscles

To help the human arms act correctly, the Mckibben muscle actuators must be configured reasonably。Only one piece of the Mckibben muscle can't complete all the actions [1], because that the structure of the human arm is complicated and its actions are many and varied. Therefore, many pieces of the Mckibben muscles are required and they need to operate coordinately to achieve the required force. Based on the above analysis, we resolve the arm actions into the following basic ones：

①Shoulder's rising up and down (including to the front, to the back, and to the side), shown in Fig.1(a) and Fig.1(b)；

②Shoulder's swinging around the vertical axis, shown in Fig.1(c)；

③Elbow's bending and stretching, shown in Fig.1(d)；

④The forearm's rotating around the anatomic axis.

We think that all of the main arm actions can be realized based on the above four basic actions. The configuration of the Mckibben muscles can be done based on the requirement of the four basic actions. Let's analyze the anatomic structure of the human arm firstly. There are more than 20 pieces of muscles with the actions of both the shoulder joint and the elbow joint in the same arm[2]. All the actions of the shoulder and the elbow can be realized by these muscles' operating coordinately[3]. Based on both the analysis to the anatomic structure and the dynamic requirement for the artificial assistant suit, 8 pieces of the Mckibben muscles are selected for the configuration of one arm of the suit, shown in Fig.2. They are corresponding to the functions of the following 8 muscles:

① Triceps brachii
② Brachioradialis
③ Biceps brachii short head
④ Biceps brachii long head
⑤ Deltoid anterior part
⑥ Deltoid middle part 1
⑦ Deltoid posterior part
⑧ Deltoid middle part 2

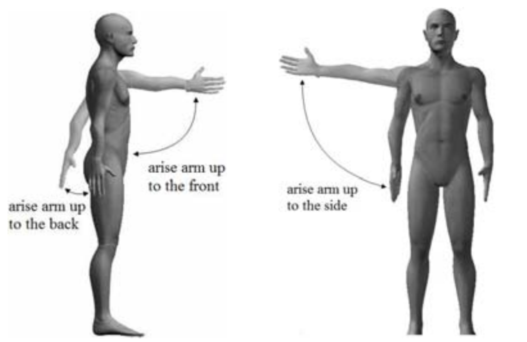

1(a) 1(b)

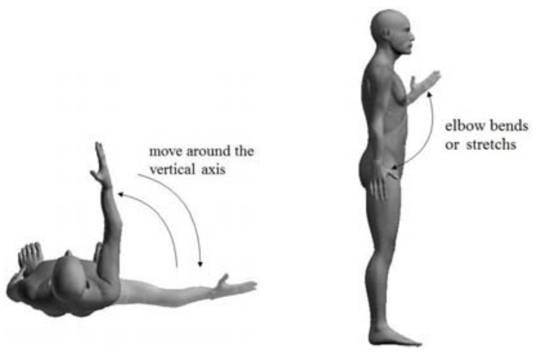

1(c) 1(d)

Fig.1 The basic actions

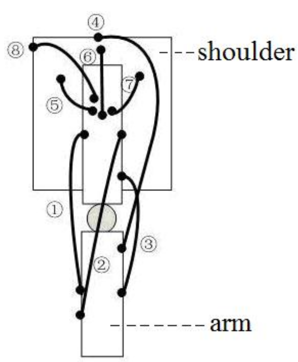

Fig.2 Configuration of the Mckibben muscles

3. The detection of the action intention of the human arm

To assist the actions of the human arm correctly, the artificial assistant suit should know the action intention of the person who is putting on it firstly. Then it calculates the quantity and the direction of the force. To the analysis of the motion intention of the human, the traditional way is getting it by analyzing the unbiological signals such as the angle, acceleration, force, or vision and hearing. All these unbiological signals are not direct to the motion intention. But the surface electromyography signal (SEMG) is generated directly by the muscles. Therefore, SEMG signals can express the motion intention more directly and more precisely [4], which is more suitable to be the control signal of the artificial assistant suit. This paper is right just to discuss how to detect the motion intention of both the human shoulder joint and the elbow joint by collecting the SEMG signals of the human.

On whole, we collect the data about the SEMG signal related with the given basic action. Then we establish the relationship between the motion intention and the SEMG signal by the classifier or BP neural network. We select the classifier in our research.

3.1 Design of the experiments

The motions of the human arm are very complicated. Here only the motions of both the shoulder and the elbow are considered. The experiments only referring to the four basic actions and their combination are done。Actually the first three actions are selected for the experiments. And they are divided into different degrees of freedom, which are degree 1 of freedom - shoulder's rising up and down, degree 2 of freedom – shoulder's swing around the vertical axis, degree 3 of freedom – elbow's bending and stretching.

The five motion states of the arm when human standing freely on the ground needs to be defined before experiment, shown in Fig.3. State 0 corresponds to when the arm is relaxing. State 1 corresponds to when the elbow is bending to almost its largest angle. State 2 corresponds to when the arm is rising up frontward to almost the same level with the shoulder and the elbow doesn't bend. State 3 is when the arm is rising up backward to the largest angle of the shoulder joint and the elbow doesn't bend. State 4 is when the arm rises up sideward to almost the same level with the shoulder.

Three healthy male master students took part in the experiments. The electroencephalogram apparatus, EEG1100 made by a Japan company is used, which's sampling frequency is set as 100Hz，sensitivity as 100μV, passband as 0.1~200Hz. A pair of electrodes, which locates 3cm apart from each other, are used and the distribution is consistent with the muscle fiber. The referential voltage is the average of the voltages of the two earlobes. To get the motion intention of human arm on every degree of freedom, the SEMG signals of Biceps brachii, Triceps brachii, Deltoid anterior part, Deltoid middle part, Deltoid posterior part and pectoralis major are detected.

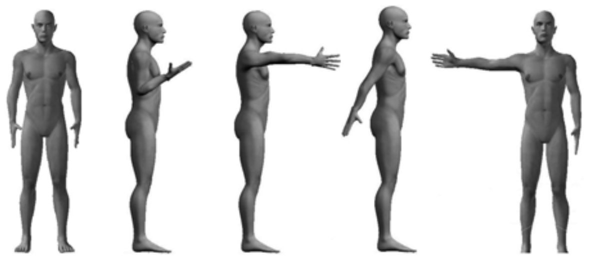

3(a 3(b) 3(c) 3(d) 3(e)

Fig.3 The different states of the upper limb

The experiments are divided into two stages which are training stage and test stage. In the training stage, the data of the SEMG signals of the four basic actions are sampled to establish and train the classifier. In the test stages, the classifier is tested to prove whether or not it can forecast the action intention correctly.

In the training stages, the experimenter's arm acts circularly as the following sequence（seeing Fig.3）: 0, 1, 0, 2, 0, 3, 0, 4, 2, 4, 0. The training is divided into two groups. Every group circulates this way ten times.

In the test stages, two complex actions are designed, shown in Fig.4. The classifier is used to forecast the action intention. The motions are recorded by a video camera so that it can be compared with the result calculated by the classifier.

4(a) 4(b)

Fig.4 The complex actions

3.2 Data process

In the training stages, the action between state 0 and state 1 is actually the motion on the degree 3 of freedom. The actions between state 0 and 2, state 0 and 3, state 0 and 4 actually are the motions on the degree 1 of freedom. The action between state 2 and 4 is actually the motion of the degree 2 of freedom. The task of the training stage is to train the three classifiers by the data of the SEMG signals to judge the motion intention on the three degrees of freedom. In the test stages, the experimenter does the complex actions. The complex action 1 includes the motions on all the three degrees of freedom, and the complex action 2 includes the motions of both degree1 of freedom and degree 3 of freedom.

To realize the judgment to the real-time motion intention of the human arm on the three degrees of freedom, the six pairs of SEMG signals are divided into three groups, shown in Table 1. Every group corresponds to one degree of freedom, which is used to judge the motion intention. The group 1, consisting of the SEMG signals of Deltoid anterior part, the middle part and the posterior part, is to judge the motion intention on degree 1 of freedom. Group 2, consisting of the SEMG signals of Pectorals Major, is to judge the motion intention of the degree 2 of freedom. The group 3, consisting of the SEMG signals of both Biceps brachia and Triceps brachia, is to judge the motion intention on degree 3 of freedom. The data processing of the three groups of SEMG signals are independent. For example of the group 1, affected by the weight on the vertical direction，the motion intention of the experimenter is to arise up when both the arm keeps the state 2, 3, 4 and it really rises up.

Like Fig.5, the three classifiers are designed and trained. Like Fig.6, the data in the test stage are used to check whether or not the classifiers work correctly. The output of the classifiers will be compared with the videos taken by video camera.

3.3 Experiment results

Fig.7 shows that the experimenter does the complex action 1. The former six figures show the relative SEMG signals, the later three figures show the analysis result of the motion intention which is clearly consistent with the real motion intention. Fig.8 is something with the complex action 2, and it shows the same situation with Fig.7

Table 1 Three signal groups and the corresponding degrees of freedom

Signal group	Related SEMG signals	Related degree of freedom	Motion intention
Group 1	SEMG of Deltoid anterior part, the middle part and the posterior part	Degree 1 of freedom	Rise up, put down
Group 2	SEMG of Pectorals major	Degree 2 of freedom	Swing forward, relaxed
Group 3	SEMG of Biceps brachia and Triceps brachia	Degree 3 of freedom	Bend forward, relaxed, stretch backward

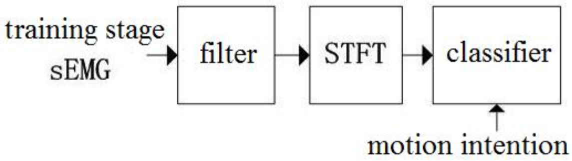

Fig. 5 data processing in the training stage

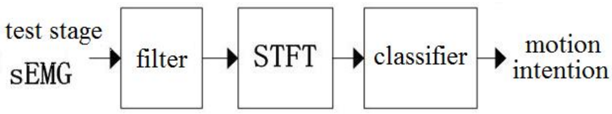

Fig. 6 data processing in the testing stage

4. Conclusion

Based on the requirement of the artificial assistant suit, the configuration of the Mckibben muscles is investigated. The detailed detecting methods of the action intention by SEMG signals are introduced. The experiment results show that the action intention detection is efficient and accurate. Of course, the research hasn't been completed. The third problem still hasn't been resolved. This is right just we are going to do in the next step.

This study is supported by the project from Shanghai Committee of Science and Technology, China (Pujiang Plan: 10PJ1409200).

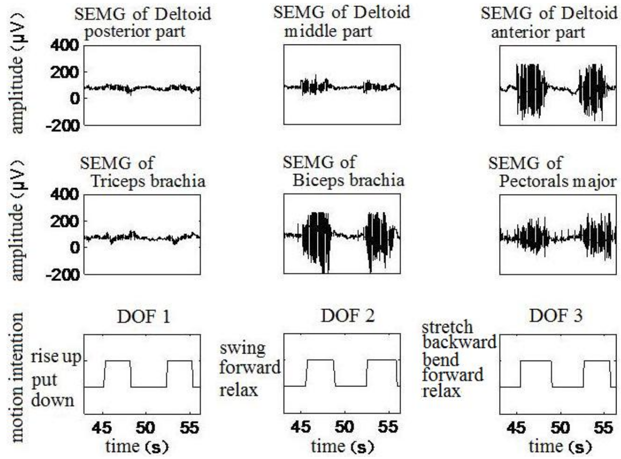

Fig. 7 Analysis of the complex action 1

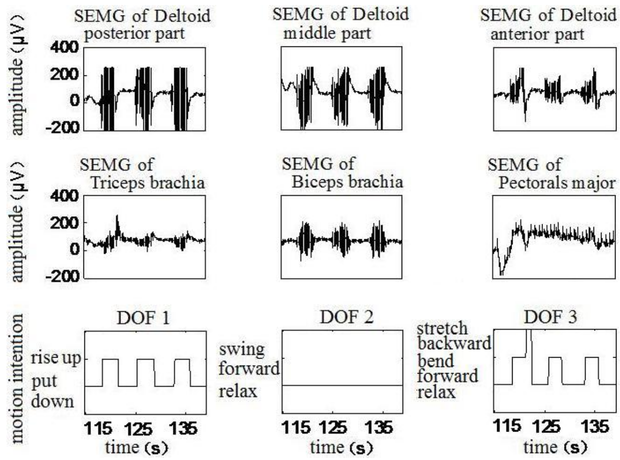

Fig. 8 Analysis of the complex action 2

References:

[1] Huailin Zhao, M.Sugisaka, A Model of the Mckibben muscle actuator based on experiment,Systems Science, Vol. 34, No. 2, p83-88

[2] T. Hujita, Primary human body anatomy, 4th edition, Tokyo, Japan: Nanedou Publisher, 2000

[3] R. Nakamura, H. Saito, Fundamental kinesiology, 5th edition, Tokyo, Japan: Ishiyaku Publishers, 2000

[4] Zhangyan Zhao, Research on some key technologies in the detection and process of SEMG, doctor dissertation, China Science and Technology University, University of Science and Technology of China, 2010

The Seventeenth International Symposium on Artificial Life and Robotics 2012 (AROB 17th '12),
B-Con Plaza, Beppu, Oita, Japan, January 19-21, 2012

Obstacle Avoidance Control of Indoor Patrol Robots Using Image-Sensing Techniques

Kuo-Hsien Hsia[1], Shao-Fan Lien[2], Juhng-Perng Su[3], and Wei-Cheng Lin[4]

[1]Department of Computer Science and Information Engineering, Far East University
No. 49, Chung Hua Rd., Hsin-Shih, Tainan 74448, Taiwan, R.O.C.
(Tel: 886-6-597-9566#7599, Fax: 886-6-597-7595)
(E-mail: khhsia@cc.feu.edu.tw)
[2]Graduate School of Engineering Science & Technology (Doctoral Program)
National Yunlin University of Science & Technology
No. 123, University Road, Section 3, Douliou, Yunlin 64002, Taiwan, R.O.C.
(E-mail: g9510801@yuntech.edu.tw)
[3,4]Department of Electrical Engineering, National Yunlin University of Science & Technology
No. 123, University Road, Section 3, Douliou, Yunlin 64002, Taiwan, R.O.C.
(E-mail: [3]sujp@yuntech.edu.tw, [4]pc7712@hotmail.com)

Abstract: The wheel robot is one of the very popular research topics. Applications of wheel robots include security, searching and rescue tasks in the indoor environment. In this paper, the image-sensing techniques, including an image system and a laser range finder, are used for obstacle avoidance and environment identification. The image system could provide 2D information of indoor environment, and the depth information is provided from the laser range finder. Therefore the 3D environment can be reconstructed and the position of the robot can be obtained. The moving paths of robot are automatically real-time regulated with 3D environment information. Moreover, a monitoring station is proposed for supervising the robot. The display of the station includes the laser range finder display and real-time video. In the experimental results, the 3D environment information is displayed on station and the robot can indeed avoid the obstacles in the indoor environment automatically.

Keywords: Patrol robots, Image processing, Obstacle avoidance**.**

1. INTRODUCTION

The developments of the robots are generally divided into two categories. They are service robots and industrial robots. In 90's, the mechatronic systems are extensively used for manufacturing and precision industry. In recent years, this technology is applied to robot systems. After years of researches, the functions of service robots are more and more comprehensive. For example, the home cleaning robots of Cyberhuis Company [1] are one kind of the service robots. Another application of wheel robots is security robot. Since the security robot has to take multiple tasks, the control of the security robot has to be more intelligent.

Chien et al [2] proposed the system architecture of security robot with multiple sensors. Obviously, designing functions of positioning and obstacle avoidance of a security robot is a difficult and important research problem. To achieve better performance, the dynamic of a robot system, which has been discussed in [3], [4] and [5], has to be considered. Yun et al described the wheeled mobile robot dynamic with physical analysis. The robot system used in this paper is s wheeled mobile robot. In this paper, we will propose a method for an indoor patrol robot to avoid obstacles automatically, based on the mobile robot model.

The planning of automatic obstacle avoidance includes "*Searching Mode*" and "*Obstacle Avoidance Mode*". The feedback of sensors will be the mode switching condition. From the experimental results, we will verify that the proposed method can achieve not only the obstacle avoidance but also basic navigation of robots. Moreover, the robot has been announced in robot competition conducted by SKS Co., Ltd., Taiwan, 2011.

2. OBSTACLE AVOIDANCE METHOD OF THE ROBOT

2.1. Modeling of robot system

Consider the mobile robot system with two fixed wheels as illustrated in Fig. 1. We define two coordinates, which are the inertial coordinate and the robot coordinate, for the robot system. In addition, the nonholonomic motion constraints [6] [7] are

$$\dot{X}_{cp}\cos\theta+\dot{Y}_{cp}\sin\theta-k\dot{\theta}-r\dot{\omega}=0 \qquad (1)$$

$$\dot{X}_{cp}\sin\theta-\dot{Y}_{cp}\cos\theta=0 \qquad (2)$$

where $Q(X_{cp}, Y_{cp})$ is the mass center of the robot, and ω is the wheel speed.

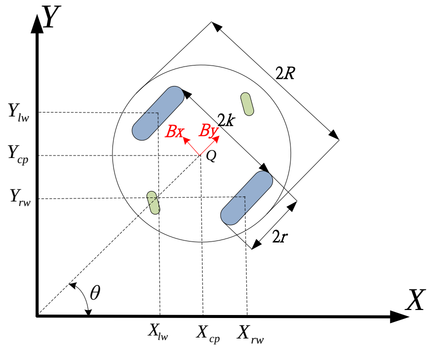

Fig. 1. The coordinate definitions of the robot.

Based on the Appell Equation, the dynamic equation of the robot system is

$$A(y)\ddot{y} + C(y,\dot{y})\dot{y} = B(y)\tau \tag{3}$$

where τ is the torque of the wheel, and

$$\begin{cases} \dot{y} = \mathrm{u} = \begin{bmatrix} \dot{\omega} & \dot{\theta} \end{bmatrix}^T \\ A(y) = \begin{bmatrix} \eta M_2 & M_1 \\ M_2 & \eta M_1 \end{bmatrix} \\ C(y,\dot{y}) = \begin{bmatrix} m_b r d_r \dot{\theta} & 0 \\ 0 & -m_b r d_r \dot{\theta} \end{bmatrix} \\ B(y) = \begin{bmatrix} 0 & 2\eta \\ 1 & 1 \end{bmatrix} \end{cases} \tag{4}$$

Moreover, in (4), M_1 and M_2 are

$$M_1 = m_b(d_r^2 + k^2) + U_p + 4m_w k^2 + 2U_w + 8\eta^2 U_w \tag{5}$$

$$M_2 = m_b r^2 + 2m_w r^2 + 4U_w \tag{6}$$

and the parameters in (4)-(6) are

$$U_p = \frac{1}{3} m_b \left(2R^2\right) \tag{7}$$

$$U_w = \frac{1}{2} m_w \left(r^2\right) \tag{8}$$

$$\eta = \frac{k}{r} \tag{9}$$

where U_p and U_w are the moments of inertia of the robot and wheels, respectively. The m_b and m_w are the mass of robot and wheels, respectively.

Equation (3) can be transformed into the state equation

$$\dot{\mathrm{x}} = \mathrm{f}(\mathrm{x}) + \mathrm{H}(\mathrm{x})\tau \tag{10}$$

where

$$\mathrm{x} = \begin{bmatrix} x_1 & x_2 & x_3 & x_4 \end{bmatrix}^T = \begin{bmatrix} \omega & \dot{\omega} & \theta & \dot{\theta} \end{bmatrix}^T, \tag{11}$$

$$\mathrm{f}(\mathrm{x}) = \begin{bmatrix} x_2 \\ -\eta\kappa J_s x_2 x_4 - \kappa J_v x_4^2 \\ x_4 \\ J_s \kappa\left(x_2 x_4 + \eta x_4^2\right) \end{bmatrix} \tag{12}$$

$$\mathrm{H}(\mathrm{x}) = \begin{bmatrix} 0 & 0 \\ -J_v & 2\eta^2 J_s - J_v \\ 0 & 0 \\ \eta J_s & -\eta J_s \end{bmatrix} \tag{13}$$

$$J_s = \frac{1}{\eta^2 M_2 - M_1} \tag{14}$$

$$J_v = \frac{M_1}{M_2} J_s, \kappa = m_b r d_r \tag{15}$$

Therefore the dynamic model of the robot system could be described by (10).

2.2. Image processing and image guiding method

Since it is possible that there is more than one room that the robot has to patrol, the area of door or corridor has to be computed. In this case, the image guiding method can be one solution to compute the area of doors or corridors and then label them. The image guiding method is illustrated as Fig. 2.

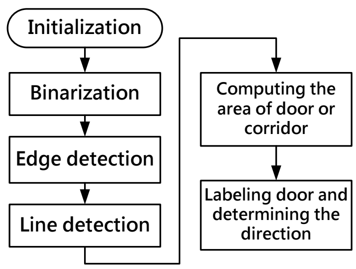

Fig. 2. Flowchart of the image guiding method.

There are three things that have to be considered in designing the algorithm. The first is the length and width of the room. The second is the dynamic restrictions of the robot. Finally, in order to prevent the collision with any obstacle near to the robot unexpectedly, the urgent distance is necessary. When there is any object entering the urgent area, the robot should stop immediately.

Hence, at first of the algorithm, the edges of the wall are detected [8] and the lines are extracted with Hough transform [9]. Then we compute the area of doors or corridors with information feedback from the laser range finder and the image information. The final step is labeling the door and determining the moving direction. The robot will turn toward the door with the image guiding method. Fig. 3 is a simulation of door labeling with the computer graphics (CG). Fig. 4 shows the real-time edge and line detecting results.

Since the robot may move in an unknown environment, two mission modes "***Searching Mode***" and "***Obstacle Avoidance Mode***", which constitute the automatic obstacle

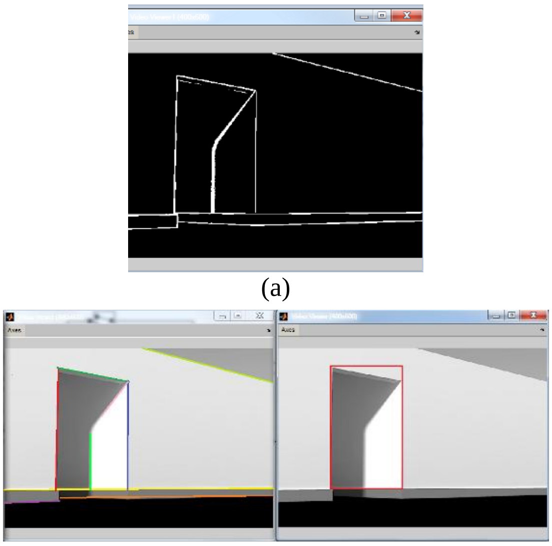

(a)

(b) (c)

Fig.3. Simulation of door labeling with the computer graphics (CG). (a) The detected edge. (b) The line detection. (c) The door labeling.

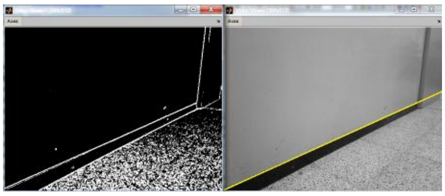

Fig.4. The real-time edge and line detecting results.

avoidance method, are defined in our setup. Two warning areas are defined by the distance from the robot for touching off the robot to run "*Searching Mode*" or "*Obstacle Avoidance Mode*".

Define an inner warning area W_2 which is the area with distance to the robot less than w_2, and an outer warning area W_1 which is the area with distance to the robot greater than w_2 but less than w_1. Base on these two warning area, there are three possible cases. Case 1 is the case if there is no obstacle located in region W_1. Case 2 is the situation that there are obstacles located in W_1. Case 3 occurs when any obstacle is located in W_2. The corresponding actions of the robot in each case are summarized in Table 1. The automatic obstacle avoidance method is illustrated as Fig. 5.

Table 1. The corresponding actions of robot in Case1~3.

Case	Robot actions
1	Running in "***Searching Mode***".
2	Warning and computing the distances of obstacles.
3	Running in "***Obstacle Avoidance Mode***".

All the orientation parameters are obtained by laser range finder in one scanning. The distance between the each edge points are

$$L_j = \sqrt{(x_j - x_{j+1})^2 + (y_j - y_{j+1})^2}, \quad j = 1,2,\cdots k. \qquad (16)$$

All possible passages are defined as "Candidate Passages". In order to select the correct passage, we further define the requirements of "Final Passage" and "Spurious Passages" are

$$\begin{cases} L_j \geq 2R + u, & \text{Final Passage} \\ \text{Otherwise}, & \text{Spurious Passage} \end{cases}. \qquad (17)$$

where R is the radius of the robot chassis and u is the urgent distance. Moreover the "Spurious Passages" will be regarded as obstacles. The automatic obstacle avoidance is illustrated as Fig. 6.

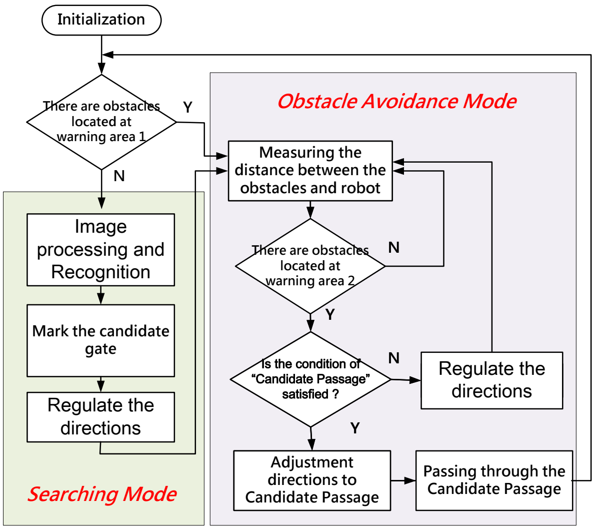

Fig.5. The automatic obstacle avoidance method.

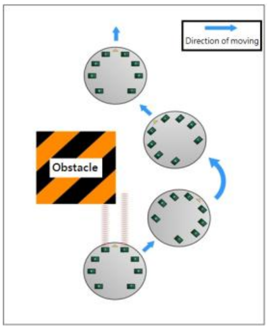

Fig.6. "*Obstacle avoidance mode*" of the robot.

3. SIMULATION RESULTS

There are two layers in the platform of the robot for the paper. The platform is constituted with aluminum panels. The maximum payload of the robot is 8 kg. The diameter and height of the mobile robot are 0.4 m and 0.44 m, respectively. The wheels are directly driven by the motors.

The design of the chassis is differential drive moving platform. The scanning laser finder used for the robot is UTM-30LX (Hokuyo Automatic Co., Ltd., Osaka, Japan), as shown in Fig. 7. The scanning angle and the guaranteed detection range are 0°~270° and 30 m, respectively. The interface of the robot system and the real-time image obtained from the robot are shown in Fig. 8.

Considering the experimental environment, the area W_1 is defined as the distance less than 3 m and the area W_2 is defined as the distance between 3 m and 0.75 m. The urgent distance is defined as 0.15 m. A tortuous corridor is designed for testing our method. Fig. 9 (a) (b) show the robot passing through the tortuous corridor successfully with "*Obstacle Avoidance Mode*". In addition, this testing example shows the obstacle avoidance performance of robot.

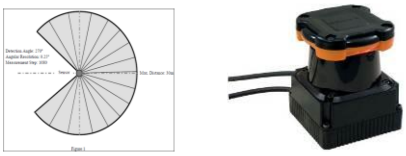

(a) (b)

Fig. 7. (a) The scanning range. (b) Appearance of UTM-30LX.

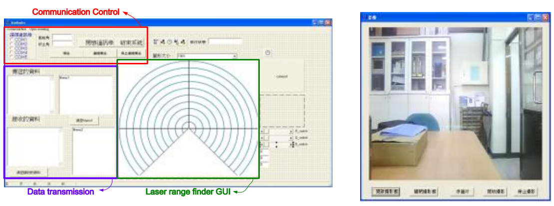

(a) (b)

Fig. 8. (a) The interface of the scanning laser finder. (b) The real-time image.

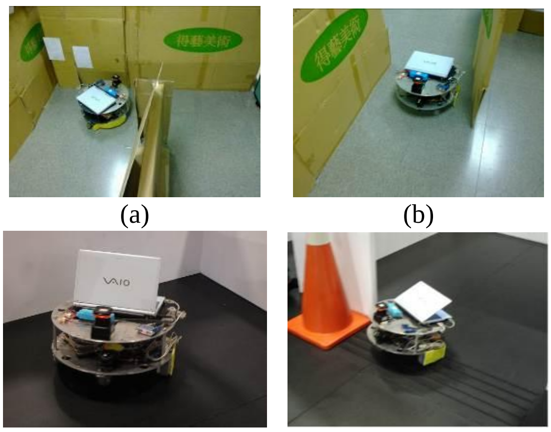

(a) (b) (c) (d)

Fig. 9. The robot passing through a corridor and patrolling in the room.

The next testing example is in the site of the SKS Company Robot Competition. In Fig. 9 (c) (d), the robot is patrolling in the room automatically. The algorithm can recognize the door and guide the robot passing through the door.

4. CONCLUSION

In this paper, we proposed a simple method for achieving autonomous obstacle avoidance and basic navigation of robot. Based on the feedback of the camera and laser range finder, the robot is more intelligent and sensitive. Moreover, the proposed algorithm is simple, therefore that could be used for real-time robot obstacle avoidance. In experimental results, we have shown that a robot with our algorithm could not only search rooms automatically but also pass through the narrow gallery in flexibility. It shows that the performance of the robot will be good for most indoor environments.

REFERENCES

[1] Cyberhuis, http://www.cyberhuis.nl/

[2] Chien TL, Su KL, Guo JH (2005), The multiple interface security robot - WFSR-II, IEEE International Workshop on Safety, Security and Rescue Robotics, Kobe, Japan, pp 47-52.

[3] Lee TC, Song KT, Lee CH et al (1999), Tracking control of mobile robots using saturation feedback controller, IEEE International Conference on Robotics & Automation, Detroit, Michigan, pp 2639-2644.

[4] Ciobanu L, Thirer N (2008), Modeling vechicles and mobile robots, IEEE Convention of Electrical and Electronics Engineers, Eilat, Israel, pp 246-249.

[5] Yun X, Yamamoto Y (1993), Internal dynamics of a wheeled mobile robot, IEEE/RSJ International Conference on Intelligent Robots and Systems, Yokohama, Japan, pp 1288-1294.

[6] Su CY, Stepanenko Y (1994), Robust motion/force control of mechanical systems with classical nonholonomic constraints, IEEE Transaction on Automatic Control, 39(3):609-614.

[7] Tsai PS, Wang LS, Chang FR (2006), Modeling and hierarchical tracking control of tri-wheeled mobile robots, IEEE Transaction on Robotics, 22(5):1055-1062.

[8] Hsia KH, Lien SF, Su JP (2011), Camera position estimation and feature extraction from incomplete image of landmark, International Journal of Artificial Life and Robotics, 16(2):152-156.

[9] Hartley R and Zisserman A (2003), Multiple view geometry in computer vision, Cambridge University Press.

The Seventeenth International Symposium on Artificial Life and Robotics 2012 (AROB 17th '12),
B-Con Plaza, Beppu, Oita, Japan, January 19-21, 2012

Twisting algorithm second order sliding mode control for a synchronous reluctance motor

Wen-Bin Lin[1], Huann-Keng Chiang[2], and Yi-Chang Chang[2]

[1] Graduate School of Engineering Science & Technology, National Yunlin University of Science & Technology, Yunlin 64002, Taiwan, R.O.C.
[2] Department of Electrical Engineering, National Yunlin University of Science & Technology, Yunlin 64002, Taiwan, R.O.C.
(Tel: 886-5- 5342601 ext: 4247, Fax: 886-5-5312065)
[2]chianghk@yuntech.edu.tw

Abstract: This paper shows the design of a twisting algorithm second order sliding mode controller (SOSMC) for a synchronous reluctance motor. The second order sliding mode control is an effective tool for the control of uncertain nonlinear systems since it conquers the main shortcomings of the conventional sliding mode control, namely, the large control effort and the chattering effect. Its theory implies simple control laws and assures an improvement of the sliding accuracy with respect to conventional sliding mode control. This paper proposes a novel scheme that based on the technique of twisting second order sliding mode control. First, the SOSMC is obtained by mathematics. Finally, the proposed method is verified by simulation. The proposed SOSMC shows the robustness for the motor parameters variation and the development of chattering effect.

Keywords: Twisting Algorithm, Second Order Sliding Modes, Synchronous Reluctance Motor, Chattering Effect.

1 INTRODUCTION

Fast accurate dynamic response is of primary importance in control systems. The motor control system with the high robustness is an important issue in research. Synchronous reluctance motor (SynRM) have a mechanically simple and robust structure. They can be used in high speed and high temperature environments. The rotor circuit of the SynRM is open circuit such that the flux linkage of SynRM is directly proportional to the stator currents. The torque of SynRM can be controlled by adjusting the stator currents. Therefore, there has been renewed interest in SynRM [1-3].

Sliding mode control (SMC) has attracted increasing attention in recent years because it is an effective and robust technology for parameter variation and external disturbance rejection. It has been applied to robot and motor control [3,4-6]. SMC is a robust control for nonlinear systems. However, sliding mode is a mode of motions on the discontinuity set of a discontinuous dynamic system. Therefore, reducing the chattering is very important for SMC. The second-order sliding mode technique has the same properties of robustness to uncertainties of model and external disturbances. Second-order SMC (SOSMC) [7] improves the chattering phenomenon. Due to few literatures about SOSMC in SynRM control application, therefore, it has valuable on investigation in SynRM control application for SOSMC.

Distinct from the conventional first order SMC, the SOSMC is belonging to the region of higher-order sliding mode (HOSM). Levant [7] had discussed the theory of HOSM. HOSM control have been applied to motor, and automatic docking [8-10].

There is no paper choosing twisting algorithm SOSMC in SynRM speed control so far. Therefore, this paper proposes a novel scheme that based on the technique of twisting algorithm SOSMC. Finally, the presentation of the proposed method is verified by simulation.

2 MODELING OF THE SYNRM

The d-q equivalent voltage equations of ideal SynRM model with a synchronously rotating rotor reference frame are shown in Fig. 1.

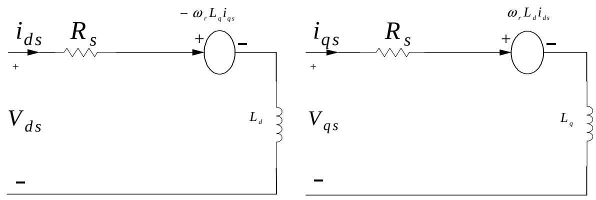

Fig.1. The d-q axis equivalent-circuit of SynRM

$$V_{ds} = R_s i_{ds} + L_d \frac{di_{ds}}{dt} - \omega_r L_q i_{qs} \tag{1}$$

$$V_{qs} = R_s i_{qs} + L_q \frac{di_{qs}}{dt} + \omega_r L_d i_{ds} \tag{2}$$

The corresponding electromagnetic torque T_e is:

$$T_e = \frac{3}{4} P_{ole} \left(L_d - L_q\right) i_{ds} i_{qs} \tag{3}$$

The corresponding motor dynamic equation is:

$$T_e - T_L = J_m \frac{d\omega_r}{dt} + B_m \omega_r \tag{4}$$

where V_{ds} and V_{qs} are direct and quadrature axis terminal voltages, respectively; i_{ds} and i_{qs} are, respectively, direct axis and quadrature axis terminal currents or the torque producing current; L_d and L_q are the direct and quadrature axis magnetizing inductances, respectively; R_s is the stator resistance; and ω_r is the speed of the rotor. P_{ole}, T_L, J_m, and B_m are the poles, the torque load, the inertia moment of the rotor, and the viscous friction coefficient, respectively. In this paper, the maximum torque control (MTC) strategy [3,4] is adopted. The torque current commands are shown in equations (5) and (6) [3]:

$$i_{ds}^{*} = \sqrt{\frac{|T_e|}{\frac{3}{8}P_{ole}\left(L_d - L_q\right)}}\cos\left(\frac{\pi}{4}\right) \tag{5}$$

$$i_{qs}^{*} = \operatorname{sgn}\left(T_e\right)\sqrt{\frac{|T_e|}{\frac{3}{8}P_{ole}\left(L_d - L_q\right)}}\sin\left(\frac{\pi}{4}\right) \tag{6}$$

3 INTEGRAL VARIABLE STRUCTURE SLIDING MODE CONTROLLER

We can rewrite the equation (4) as

$$\begin{aligned}\frac{d\omega_r}{dt} &= \left(-\frac{B_m}{J_m}\right)\omega_r + \frac{1}{J_m}\left(T_e - T_L\right)\\ &= a\omega_r + b\left(T_e - T_L\right)\\ &= \left(a_0 + \Delta a\right)\omega_r + \left(b_0 + \Delta b\right)\left(T_e - T_L\right)\\ &= a_0\omega_r + b_0\left(u(t) + f\right)\end{aligned} \tag{7}$$

where

$$a \equiv -\frac{B_m}{J_m} = a_0 + \Delta a$$

$$b \equiv \frac{1}{J_m} = b_0 + \Delta b$$

$$u \equiv T_e$$

$$f \equiv \frac{1}{b_0}\left(\Delta a\omega_r + \Delta b u(t) - bT_L\right)$$

$$J_m \equiv J_0 + \Delta J$$

$$B_m \equiv B_0 + \Delta B$$

The subscript index "o" indicates the nominal system value; "Δ" represents uncertainty, and f represents the lumped uncertainties.

Define the velocity error as $e(t) = \omega_r^{*} - \omega_r$, where ω_r^{*} is the velocity command. The velocity error differential equation of SynRM can be expressed as equation (8):

$$\frac{de(t)}{dt} = \dot{\omega}_r^{*} - a_0\omega - b_0\left[u(t) + f\right] \tag{8}$$

Let

$$S = e(t) + c\int_{-\infty}^{t} e(t)\,d\tau,\quad c > 0 \tag{9}$$

The input control $u(t)$ (the electromagnetic torque T_e) of (8) can be defined as equation (10).

$$u(t) = u_{eq}(t) + u_n(t) \tag{10}$$

where $u_{eq}(t)$ is used to control the overall behavior of the system and $u_n(t)$ is used to suppress parameter uncertainties and to reject disturbances. By making mathematical calculation, we get the overall control $u(t)$ as equation (10) [3].

$$u(t) = \frac{1}{b_0}\left[\dot{\omega}_r^{*} - a_0\omega_r + ce(t)\right] + (K + \frac{\eta}{b_o})\operatorname{sgn}(S) \tag{11}$$

where $|f| \le K$.

4 TWISTING SECOND-ORDER SLIDING MODE CONTROLLER

In conventional SMC design, the control target is let the system state move into sliding surfaces $S = 0$. But a second-order sliding mode controller aims for $S = \dot{S} = 0$. The system states converge to zero intersection of S and $\dot{S}$ in state space.

Twisting method mainly develops relative one order system for reducing chattering event [7]. The state trajectory of S and $\dot{S}$ phase plane is shown in Fig. 2. It converges to the origin of phase plane in finite time.

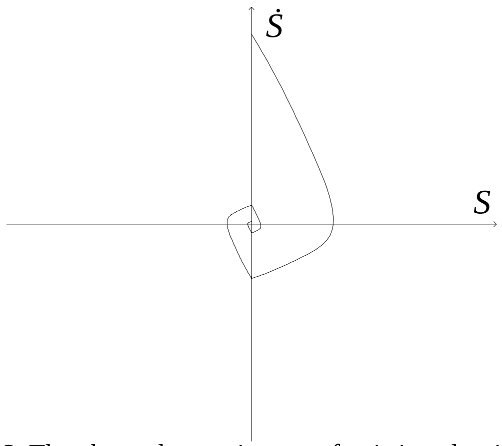

Fig.2. The phase plane trajectory of twisting algorithm

Now consider the following uncertain second order system:

$$\begin{cases}\dot{y}_1(t) = y_2(t))\\ \dot{y}_2(t) = \varphi\left(\mathbf{x}(t), \mathbf{y}(t), t\right) + \gamma\left(\mathbf{x}(t), \mathbf{y}(t), t\right)v(t)\end{cases} \tag{12}$$

in which $\varphi(\cdots)$ and $\gamma(\cdots)$ are uncertain functions with the upper and lower bounds of equation (13).

$$\begin{cases}\left|\varphi\left(\mathbf{x}(t), \mathbf{y}(t), t\right)\right| \le \Phi\\ 0 < \Gamma_m \le \gamma\left(\mathbf{x}(t), \mathbf{y}(t), t\right) \le \Gamma_M\end{cases} \tag{13}$$

By the control rule of equation (14), we can define this control method [8,9]:

$$v(t)=\begin{cases}-u\,, & if\quad |u|>U\\ -V_m\,\mathrm{sgn}(y_1)\,, & if\quad y_1y_2\le 0;|u|\le U\\ -V_M\,\mathrm{sgn}(y_1), & if\quad y_1y_2>0;|u|\le U\end{cases}\tag{14}$$

where U is control value boundary, and the sufficient condition of finite time converges to sliding situation as equation (15) [8].

$$\begin{cases}V_M>V_m\\ V_m>\dfrac{4\Gamma_M}{S_0}\\ V_m>\dfrac{\Phi}{\Gamma_m}\\ \Gamma_mV_M-\Phi>\Gamma_MV_m+\Phi\end{cases}\tag{15}$$

where S_0 is a boundary layer around the sliding surface S. Equation (4) can be rewritten as equation (16):

$$\frac{d\omega_r}{dt}=\frac{1}{J_m}(T_e-T_L-B_m\omega_r)\tag{16}$$

We define state variable as shown in equation (17):

$$\begin{cases}x_1(t)=\int_{-\infty}^{t}x_2(\tau)d\tau\\ x_2(t)=e(t)=\omega_r^*-\omega_r\end{cases}\tag{17}$$

We define sliding function y_1, and y_2 as

$$\begin{cases}y_1=x_2+cx_1\\ y_2=\dot{y}_1\end{cases}\tag{18}$$

Then, the system equation can be expressed as

$$\begin{cases}\dot{y}_1(t)=y_2(t)\\ \dot{y}_2(t)=\ddot{\omega}_r^*+\dfrac{B_m}{J_m}\dot{\omega}_r^*+\left(-\dfrac{B_m}{J_m}+c\right)\dot{x}_2+\dfrac{1}{J_m}\dot{T}_L+v(t)\end{cases}\tag{19}$$

where

$$\begin{cases}\varphi(\cdot)=\ddot{\omega}_r^*+\dfrac{B_m}{J_m}\dot{\omega}_r^*+\left(-\dfrac{B_m}{J_m}+c\right)\dot{x}_2+\dfrac{1}{J_m}\dot{T}_L\\ \gamma(\cdot)=1\\ v(t)=-\dfrac{1}{J_m}\dot{T}_e\end{cases}\tag{20}$$

According to (20), T_e is calculated from the integration of $v(t)$ which is a switching signal defined in (14), so improving the chattering problem in SOSMC control of SynRM.

5 SIMULATION RESULTS

A block diagram of the experimental SynRM drive and the super-twisting second-order sliding mode controller speed control block diagram of the SynRM servo drive are shown in Fig. 3. The synchronous reluctance motor modeled in this paper is a 0.37 kW, 2 pole, 230V, 4.7A, 60Hz, 3600rpm machine. The machine parameters are as follows: (1).Stator resistance Rs =4.2Ω, (2).Direct axis magnetizing inductance L_{dS} =328mH, (3).Quadrature axis magnetizing inductance L_{qS}=181mH, (4).Rotor inertia J_m = 0.00076Kg.m^2, and (5). Friction coefficient B_m =0.00012 Nt-m/rad/sec.

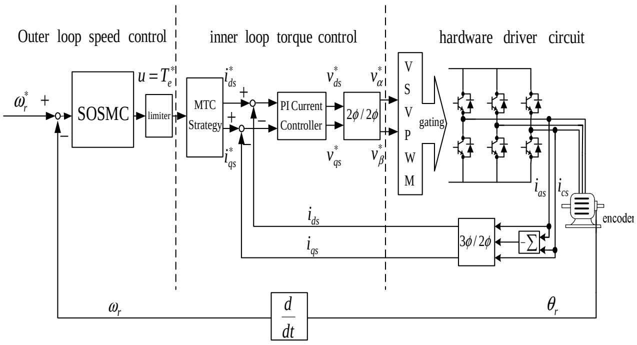

Fig.3. Twisting algorithm SOSMC speed control block diagram of SynRM servo drive

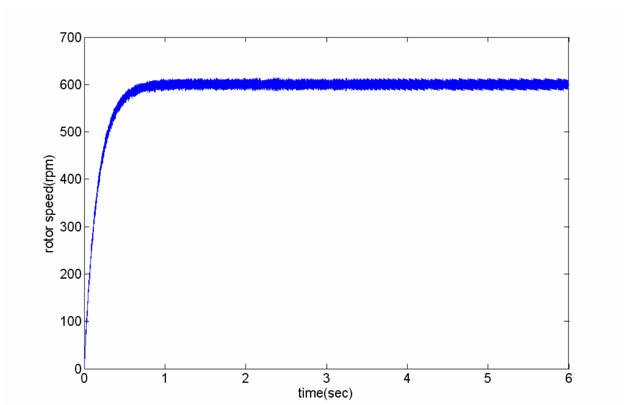

Fig.4. Simulation velocity response of the SMC due to $\omega_r^*=600$ rev/min without machine load in the nominal motor inertia and friction coefficient condition

In Fig.4, the simulation velocity response of the SMC due to $\omega_r^*=600$ rev/min without machine load in the nominal motor inertia and friction coefficient condition is depicted. In Fig.5, the simulation velocity response of the SOSMC due to $\omega_r^*=600$ rev/min without machine load in the nominal motor inertia and friction coefficient condition is depicted. The velocity response of SOSMC is smoother than the convention SMC.

In Fig.6, the simulation velocity response of the SOSMC due to $\omega_r^*=600$ rev/min under an 0.3 Nt-m machine load at the beginning and an 0.9 Nt-m machine load at 3seconds is added for the 2 times nominal case of the motor inertia and friction coefficient condition is presented. Hence, the SOSMC is a robust controller and improve the chattering phenomenon when the system has external disturbances and parameter variations.

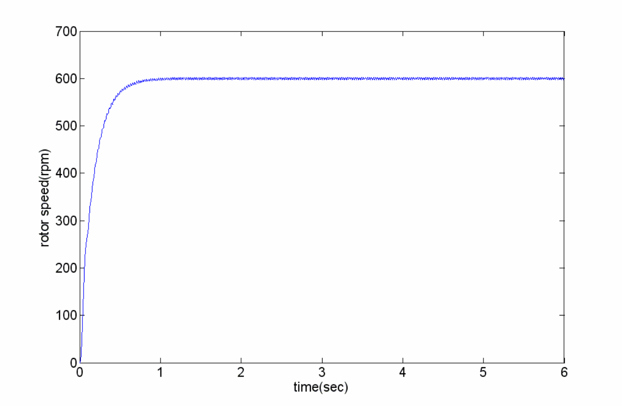

Fig.5. Simulation velocity response of the twisting algorithm SOSMC due to $\omega_r^* = 600$ rev/min without machine load in the nominal motor inertia and friction coefficient condition

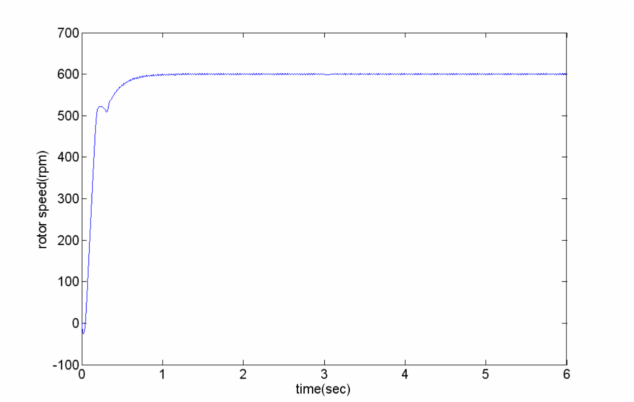

Fig.6. Simulation velocity response of the twisting algorithm SOSMC due to $\omega_r^* = 600$ rev/min under a 0.3 Nt-m machine load at the beginning and a 0.9Nt-m machine load at 3 seconds in the 2 times nominal case of the motor inertia and friction coefficient condition

6 CONCLUSION

In this paper, a twisting algorithm second-order sliding mode speed control design for robust stabilization and disturbance rejection of SynRM is presented. The simulation results show good performance of SOSMC under uncertain load subject to variaitons in inertia and system frcition. Also with SOSMC, there is no need for acceleration feedback. The proposed SOSMC law shows the advantage of continuous control signal which eliminates the chattering effect apparently and is more acceptable in application.

ACKNOWLEDGMENT

This work is supported by the National Science Council in Taiwan, Republic of China, through grant NSC100-2221-E-224-002.

REFERENCES

[1] Bianchi N., Bolognani S., Bon D., and Pre M. D. (2009), Rotor flux-barrier design for torque ripple reduction in synchronous reluctance and PM-assisted synchronous reluctance motors. IEEE Transactions on Industry Applications 45(3):921-928

[2] Kim W. H., Kim K. S., Kim S. J., Kang D. W., Go S. C., Chun Y. D., and Lee J. (2009), Optimal PM design of PMA-SynRM for wide constant-power operation and torque ripple reduction. IEEE Transactions on Magnetics 45(10):4660-4663

[3] Chen C. A., Lin W. B., and Chiang H. K. (2009), Design and implementation sliding mode controller based on radial basis function neural network for synchronous reluctance motor. Proceeding of 4th IEEE Conference on Industrial Electronics and Applications (ICIEA 2009), Xi'an, China, May 25-27, 2009, pp.281-286.

[4] Shyu K. K., and Lai C. K. (2002), Incremental motion control of synchronous reluctance motor via multisegment sliding mode control method. IEEE Transactions on Control Systems Technology 10(2): 169-176

[5] Huang Y. S., and Sung C. C. (2010), Implementation of sliding mode controller for linear synchronous motors based on direct thrust control theory. IET Proceedings on Control Theory & Applications 4(3):326-338

[6] Bartolini G., Ferrara A., Levant F., and Usai E. (1999), Variable Structure Systems, Sliding Mode and Nonlinear Control. Springer-Verlag

[7] Levant A. (1993), Sliding order and sliding accuracy in sliding mode control. International Journal of Control Automation and Systems 58(6):1247-1263

[8] Bartolini G., Ferrara A., Levant F., and Usai E. (1999), On second order sliding mode controllers, in Variable Structure Systems, Sliding Mode and Nonlinear Control, Lecture Notes in Control and Information Sciences K. D. Young and U. Ozguner, Eds., Springer-Verlag, London Ltd: 329-350

[9] Tournes C., and Shtessel Y. (2007), Automatic docking using second order sliding mode control. 2007 American Control Conference, New York City, USA, July 11-13, 2007 , pp.3455-3460

[10] Mohamadian M., Pedram M. M., and Ashrafzadeh F. (2004), Digital second order sliding mode control for a synchronous reluctance motor. Proceeding of 2004 IEEE Industry Applications Conference, Seattle, U.S., Oct 3-7, 2004, pp.1899-1902

The implementation of accelerometer and embedded system-based multi-functional pedometer

Yi-Yu Lu[1,2], Kuo-Sheng Cheng[1,3], Wen-Bin Lin[4,5] and Ji-Jer Huang[6]

[1] Department of Biomedical Engineering, National Cheng Kung University, Tainan 70101, Taiwan
[2] Department of Electrical Engineering, Far East University, Tainan 74448, Taiwan
[3] Medical Device Innovation Center, National Cheng Kung University, Tainan 70101, Taiwan
[4] Department of Optoelectronic Engineering, Far East University, Tainan 74448, Taiwan
[5] Graduate School of Engineering Sci. & Tech., National Yunlin University of Science & Technology, Yunlin 64002, Taiwan
[6] Department of Electrical Engineering, Southern Taiwan University of Technology, Tainan 71005, Taiwan
(Tel: 886-6-5979566 ext: 5408, Fax: 886-6-5977570)

[1,2]yiyu@cc.feu.edu.tw

Abstract: Pedometers are known to have steps estimation issues. This is mainly attributed to their innate acceleration based measuring sensory. In this work, purposes a novel implementation of microcontroller and accelerometer sensor- based for multi-function pedometer in calorie consumption calculation. To verify the output voltage stability of accelerometer sensor, the methods of statistics analysis is introduced to extract the useful features. Three kinds of different steps are employed to obtain the analytic data. The proposed pedometer dimension of a proto-type is 68 mm(L) X 42 mm(W) X 15 mm(H).

Keywords: Pedometers, Three-axis accelerometer, Calorie consumption, Microcontroller.

1 INTRODUCTION

Walking is one of the principle gaits of locomotion among legged animals. Walking motion is defined by an 'inverted pendulum' movement in which the body vaults over the stiff limb or limbs with each step. This applies regardless of the number of limbs – even to arthropods with six, eight, or more limbs [1]. In humans and other bipeds, walking is characterized by only one foot leaving the ground at any given time, resulting in a period of double-support. In contrast, running involves both feet leaving the ground with each step. This distinction assumes the status of a formal requirement in competitive walking events [1].

Sustained walking for a minimum of thirty to sixty min. a day, five days a week, with correct walking posture, [2-3] provides a variety of benefits in reducing health risks [4]. These benefits include a reduced chance of developing cancer, type 2 diabetes, heart disease, anxiety, and depression [1,5]. Walking can increase life expectancy, particularly among individuals suffering from obesity or high blood pressure. Walking enhances bone health, especially the hip bone, reduces harmful low-density lipoprotein (LDL), and increases useful high-density lipoprotein (HDL) cholesterol[6]. Studies have determined that walking can even prevent dementia and Alzheimer's.

Pedometers are often worn on the belt to record how many steps the wearer has taken, and thus determine the distance walked each day (distance = number of steps × step length) [5].

Some pedometers will also erroneously record movements other than walking, such as bending to tie one's shoes, or road bumps incurred while riding a vehicle, though the most advanced devices record fewer of these 'false steps'. Step counters provide encouragement by enabling the user to compete with oneself in getting fit and losing weight. A total of 10,000 steps per day, equivalent to 5 miles (8.0 km), are commonly recommended as a benchmark for an active lifestyle, although this remains an issue of debate among experts [5]. Step counters are increasingly being integrated into portable electronic devices such as music players and mobile phones.

Many pedometers erroneously record road bumps incurred while riding in vehicles or movements other than walking (such as bending over), although more advanced devices record fewer of these 'false steps'. Pedometers generally detect steps from vertical acceleration at the human trunk [7]. The technology for a pedometer includes a mechanical sensor and software to count steps. Today advanced step counters rely on MEMS inertial sensors and sophisticated software to detect steps. These MEMS sensors have either 1-, 2- or 3-axis detection of acceleration [5]. The use of MEMS inertial sensors permits more accurate detection of steps and fewer false positives. The software technology used to interpret the output of the inertial sensor and "make sense of accurate steps" varies widely [7-8].

This study develops the design and fabrication for an accelerometer and embedded system-based multi-functional pedometer in calorie consumption calculation.

2 MATHEMATICS MODEL & SYSTEM STRUCTURE

The system schematic diagram is shown in Fig. 1. The system is using PIC16F877A microcontroller [9] as the pedometer core, uses its embedded 10 bits A/D converter. The variation voltage value of exercise angles detected by MMA7260Q accelerometer [10] sends to the microcontroller for handling. When the angle is bigger the setting threshold value, it will start step-counting program for recording. Finically, the LCD displays the calorie consumption and the step counting during exercise by means of the calorie calculation formula. By means of the element of MAX232, this system also has an interface that links to the UART of personal computer for program initial debugging and development.

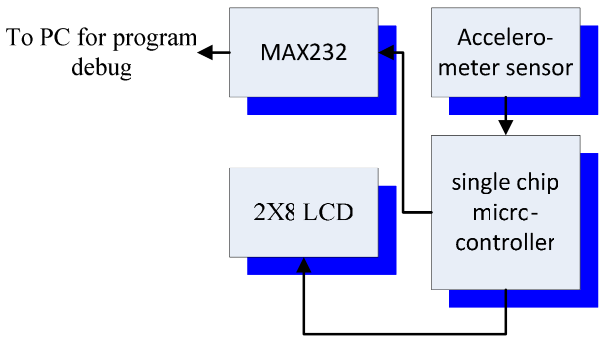

Fig. 1. Schematic diagram of proposed pedometer

The detected g value is hardly make mathematic analysis with the corresponding x axis voltage (V) in static acceleration mode of MMA7260Q. So these two values relationship is obtained from the measurement of the experimental data in table1. And the linear fit equation is expressed by

$$g = 1.25 \cdot V - 2.0625 \qquad (1)$$

where

$g \equiv$ The acceleration value after converting

$V \equiv$ The output voltage of x axis at three-axis accelerometer

Table 1. The experimental data in static acceleration mode

g value	+1	0	-1
x axis voltage (V)	2.45	1.65	+0.85

The correlation coefficient of curve fitting is 0.9999. From the food information websites in Department of Health at Taiwan [11], the relationship between speed and calorific capacity that can be a main reference issue about the calculation of exercise calorie is shown in Fig. 2.

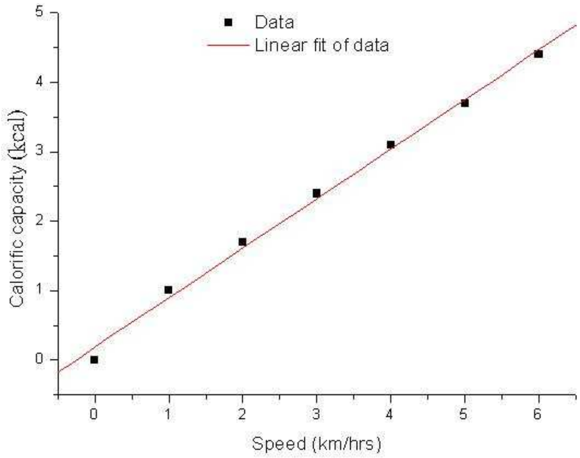

Fig. 2. The relationship between speed and calorific capacity [11]

We can get the Linear Fit equation is expressed as Equation (2). Where, $V(t)$ is the walking speed, and K is the Calorie consumption after converting. The correlation coefficient of curve fitting is 0.99761. Human weight is one of exercise calorie consumption factors, but we simplify the development of proto-type system. We make the human weight that is equals to 60kg as the basis, and leave the weight fitting as furthermore research in the future. Finally, the calorific capacity after converting displays in LCD module.

$$K = 0.71429 \cdot V(t) + 0.18571 \qquad (2)$$

3 WALKING STEP SIZE CONDITIONS

The system also can set three modes that include big step, middle step, and small step. Apart of the human weight factor, walking calorie consumption has the relationship of a linear equation with walking speed. In theory, the big step mode will take more calorie than others. But it has slower speed in big step mode and it results in the calorie consumption is smaller than others in per step.

After the practical pedometer calculation, the calorie consumption is shown in Table 2. Theoretically, on condition of uniform velocity, the paces are the greater to walk, the more its calorific consumed is. However, the speed would be slowdown in actual measurement when it walks in great paces. Thus, the calorie consumption of average in single paces consume will be reduced instead.

For calibration purpose between g value and voltage of x axis accelerometer, we take the voltage measurements at small step, middle step, and big step. Among these three modes, we take 10 points data and make statistical analysis respectively, for classifying these data sets. In the small and big step modes, there mean value

(Mean), variance (Var.) and coefficient of variance (CoefVar.) are nearly equal to each others. In Table 3, the mean value of small step is only smaller 0.003 than big step. Although the standard deviation (Std.) of small step is bigger than big step, but there is only 0.0125 difference between small step and big step. Find in the test, the average calorie consumption of steps in these two modes are nearly equal to each others. Besides, three parameters that described above have the same trend as shown in Fig. 3.

Table 2. The comparison of 3 modes for different step sizes

Steps mode	No. (steps)	Calorie (cal.)	Average cal./step
Small (40cm)	16	11	0.7
Middle (50cm)	10	14	1.4
Big (70cm)	20	16	0.8

Table 3. The statistics analysis for 3 steps modes

Steps	Mean	Std.	Var.	CoefVar.
Small (40cm)	1.754	0.27645	0.07643	0.15761
Middle (50cm)	1.858	0.23925	0.05724	0.12877
Big (70cm)	1.757	0.26395	0.06967	0.15023

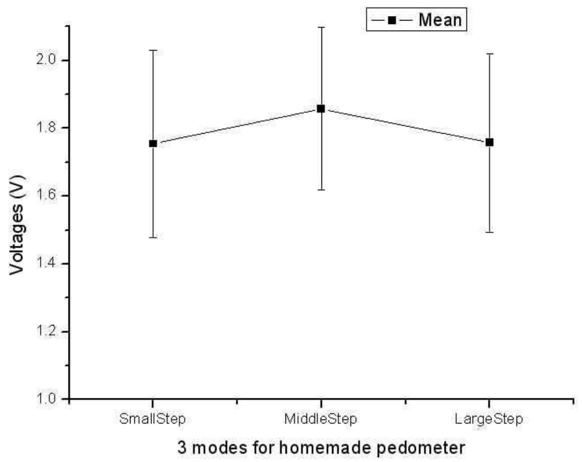

Fig. 3. The statistics data calculated at X axis in the pedo meter for 3 modes.

4 SYSTEM PROGRAMMING

Firstly, put the proposed pedometer on the shank. Then, turn on the power, it will display the words of Calorie (Calorie), st (step number), and se (setting) on LCD screen. Secondly, using push-button to select suitable step range by yourself. The region 1 is small step, and sensing range is from 0.25g to 0.05g. The region 2 is middle step, and sensing range is from 0.53g to 0.28g. The region 3 is big step, and sensing range is from 0.8g to 0.55g. If the user sets region 2 for walking step counting, then the setting location will display 2 on the screen of pedometer. After above procedures, the user pushes the "start" push-button for time counting, and then, it waiting the input signal.

By user walking, this action induces a signal to the X axis of accelerometer. This procedure contains the actions of step-counting plus one and time-counting during setting regions. By means of converting g value and formula (V=g • t) within software program setting, the program calculates the calorie consumption and displays the value on LCD screen. If the step span doesn't belong within setting sensing region, and then the program doesn't have step-counting action.

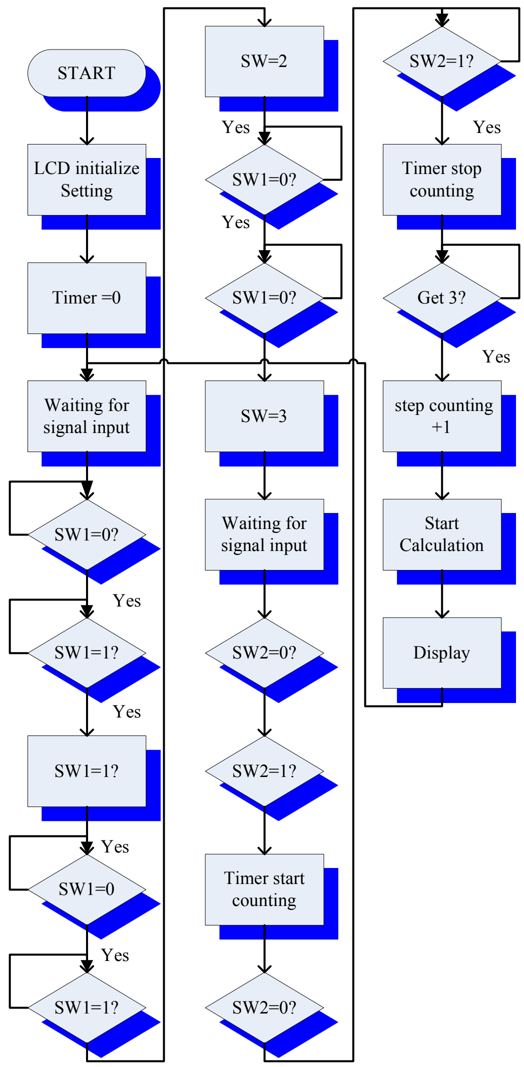

Fig. 4. The program flow chart of proposed pedometer [11]

After above procedures, the program will return last process. The setting procedures of region 1 and region 3 are the same as region 2. The user walk one step within setting sensing range, the program will plus one in step-counting procedure. After stop walking for one minute, it displays the data. And then, time counting, calculation, and display, the proposed pedometer will repeat the same actions again. The program flow chart of proposed pedometer is shown in Fig. 4.

5 CONCLUSION

The hardware pictures of this proposed pedometer are shown in Fig. 5 and Fig. 6. This study purposes a novel implementation of microcontroller and accelerometer sensor- based for multi-function pedometer with LCD display. It has the advantages with low power consumption, more robust and small dimension. Pedometer software is tested and showed 90% of step count accuracy. After verify the accuracy of the hardware design due to complete various function tests, the proposed hardware is realized that based on above concepts. The output voltage of accelerometer in three kind of different steps is employed to obtain the analytic data. The four parameters are calculated by statistics method. Finally, the three modes of hypothesis testing are verified for application. The 'mean' parameter is shown to be good to index the calorie consumption.

Fig. 5. The using picture of proposed pedometer

Fig. 6. The step-counting and Calorie consumption display of proposed pedometer

ACKNOWLEDGMENT

This work is supported by the National Science Council in Taiwan, Republic of China, through grant NSC 97-2622-E-269-013-CC3

REFERENCES

[1] http://en.wikipedia.org/wiki/Walking

[2] Frank L.D., Andresen M.A. and Schmid T.L. (2004), Obesity relationships with community design, physical activity and time spent in cars, American Journal of Preventive Medicine, 27(2), pp.87–96

[3] Michaud D.S., Giovannucci E., Willett W.C., Colditz G.A., Stampfer M.J. and Fuchs C.S. (2001), Physical activity, obesity, height, and the risk of pancreatic cancer, Journal of the American Medical Association, 286(8), pp.921–929

[4] Hatano Y. (1997), Prevalence and use of pedometer, Research Journal of Walking, 1(1), pp.45–54

[5] http://en.wikipedia.org/wiki/Pedometer

[6] Tudor-Locke C. and Bassett D.R. (2004), How many steps/day are enough?: Preliminary pedometer indices for public health, Sport Medicine, 34(1), pp.1–8

[7] Lim Y. P., Ian T., Joshua C.T. (2008),An accurate and robust gyroscope-gased pedometer, Proceeding of 30th Annual International IEEE EMBS Conference, Aug 20 - 24, 2008, Vancouver, Canada, pp.4587-4590

[8] Chae K.S., Park H.J. (2007), Evaluation of a 3D Motion Sensor including Accelerometer and Geomagnetic sensor, Proceeding of 16th IEEE International Symposium on Robot and Human interactive Communication, Aug 26-29, 2007. Jeju Island, Korea, pp.900 - 904

[9]http://ww1.microchip.com/downloads/en/DeviceDoc/39582b.pdf

[10]http://www.sparkfun.com/datasheets/accelerometers/MMA7260Q-Rev1.pdf

[11] http://www.mmh.org.tw/nutrition/ibw_doc.htm

An Efficient Three-Scan Approach for Mining High Utility Itemsets

Guo-Cheng Lan[1], Tzung-Pei Hong[2,3], and Vincent S. Tseng[1,4]

[1]Department of Computer Science and Information Engineering
National Cheng Kung University, 701, Taiwan
[2]Department of Computer Science and Information Engineering
National University of Kaohsiung, 811, Taiwan
[3]Department of Computer Science and Engineering
National Sun Yat-Sen University, 804, Taiwan
[4]Institute of Medical Informatics
National Cheng Kung University, 701, Taiwan

rrfoheiay@gmail.com, tphong@nuk.edu.tw, tsengsm@mail.ncku.edu.tw

Abstract: Utility mining finds out high utility itemsets by considering both the profits and quantities of items in transactions. In this paper, a three-scan mining approach is proposed to efficiently discover high utility itemsets from transaction databases. The proposed approach utilizes an itemset-generation mechanism to prune redundant candidates early and to systematically check the itemsets from transactions. Finally, the experimental results on a synthetic dataset show the superior performance of the proposed approach.

Keywords: Data mining, utility mining, high utility itemsets, the filtration mechanism.

1 INTRODUCTION

In the field of database knowledge, data mining techniques have been widely applied to various practical applications, such as supermarket promotions, biomedical data applications, multimedia data applications, and so forth. Association-rule mining [1] is one of the most important issues in data mining since the relationship among items in a database can be found by association-rule mining techniques. Traditional association rule mining [1], however, considers the occurrence of items in a transaction database but do not reflect any other factors, such as price or profit. Then, some product combinations with low-frequency but high-profit may not be found in association-rule mining. For example, assume there is a product combination like {DVD player, LCD TV}. The product combination may not have a high frequency in a transaction database, but may contribute a high utility in this database due to LCD TV. To handle this, a practical issue, namely utility mining, was thus proposed by Chan *et al.*, in 2003 [2]. In Chan *et al.*'s study [2], their proposed approach considered both the individual profits and quantities of products (items) in transactions, and used them to measure actual utility value for an itemset. The high utility itemsets, which had their utility values larger than or equal to a predefined minimum utility threshold, were then found as the desired.

However, since the downward-closure property in association-rule mining cannot directly be adopted to find high utility itemsets in utility mining. To deal with this, a new downward-closure property was designed by Liu *et al.*, in 2005 [6]. The property was called transaction-weighted utilization (abbreviated as *TWU*) model [6]. In addition, Liu *et al.* applied the model to their proposed two-phase utility mining algorithm (abbreviated as *TP*) [6] to complete the utility mining task. However, Liu *et al.*'s utility mining approach had to run level by level as the *Apriori* algorithm in association-rule mining, thus needing scanning database multiple times. As described above, it is quite urgent to efficiently complete the utility mining task.

In this study, we propose an efficient three-scan utility mining algorithm (abbreviated as *TSA*) for handling the problem of utility mining. Especially, a new filtration mechanism in the proposed algorithm is designed to effectively prune a large number of unpromising candidates for mining. Also, the proposed algorithm calculates both the transaction-weighted utility and the actual utility of each itemset at the same time. Finally, the experimental results show that the proposed *TSA* algorithm executes faster than the *TP* algorithm under various parameter settings.

The remaining parts of this paper are organized as follows. Some related works, the problem to be solved and related definitions are reviewed in Section 2. The proposed mining algorithm with a filtering strategy for finding high utility itemsets from a transaction database is stated in Section 3. The experimental results are shown in Section 4. Conclusions and future works are finally given in Section 5.

2 REVIEW OF RELATED WORKS

According to the principle of association-rule mining [1], only binary itemsets are considered. In practical applications, however, products bought in transactions usually contain both profits and quantities. Thus, for some high-profit products with low frequency, these items may not be found by the association-rule mining algorithms. For example, both jewel and diamond have high utility values but may not be a high frequency combination when compared to food and drink in a database. To deal with this, Chan *et al.* subsequently proposed utility mining to find high utility itemsets from a transaction database [2]. In this study [2], a utility itemset considers not only the quantities of the items in transactions, but also their individual profits.

However, traditional association-rule mining keep the downward-closure property, but utility mining does not. Liu *et al.* thus proposed a two-phase utility mining (*TP*) algorithm to handle this [6]. This approach used a new property, which was named as the transaction-weighted utilization (*TWU*) model, to find all high utility itemsets. It used the summation of utility values of all the items in a transaction as the upper bound of any itemset in that transaction to keep the downward-closure property. In Liu *et al.*'s study [6], their proposed algorithm could be divided into two phases. In the first phase, the possible candidates were found from a database by the *TWU* model. Then, in the second phase, an additional data scan was executed again to find the actual utility of each candidate, and then itemsets with actual utility values larger than or equal to a predefined minimum utility threshold were output. However, since the *TP* algorithm adopted the level-wise technique to find high utility itemsets from a database, the algorithm had to spend a great deal of time on data scan. Afterward, although some related studies about utility mining were published [3][5][7][8], but most of them were still based on the principle of the *TP* algorithm to find their desired interesting utility patterns. It is thus desirable to effectively find high utility itemsets from a database and reduce the number of candidate itemsets.

3 THE PROPOSED MINING ALGORITHM

In this section, the filtration mechanism in the proposed algorithm is first described below.

3.1 The Filtration Mechanism

In the proposed algorithm, we design an itemset-generation approach to reduce the number of database scans. In particular, a filtration mechanism in the itemset-generation approach is proposed to avoid producing a big number of unpromising candidate utility itemsets. The mechanism is based on the high transaction-weighted utilization (*HTWU*) *2*-itemsets and on Liu *et al.*'s approach to generate possible transaction-weighted utilization itemsets [6]. Thus, the high transaction-weighted utilization *2*-itemsets (abbreviated as $HTWU_2$) have to be first found, and then these itemsets are used to check a candidate itemset whether there exists at least a low transaction-weighted utilization *2*-itemset in the candidate itemset. If it does, the candidate itemset is identified as an unpromising candidate itemset, and then it is removed; otherwise, it is can be kept in the set of candidate itemsets. A simple example is first given below to illustrate the idea.

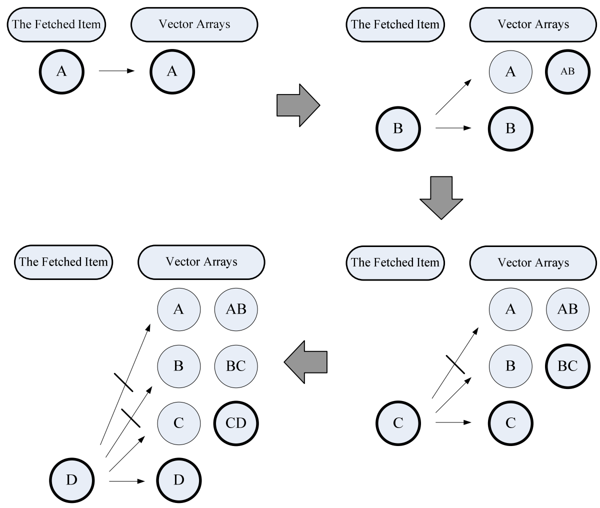

Fig. 1. The whole process of generating itemsets by using the filtration mechanism.

Example 1: Assume that a transaction *T* includes four items, 3*A*, 2*B*, 25*C* and 3*D*, where the numbers represent the quantities of the items. Also assume their profit values are 3, 10, 1 and 6, respectively, and the three itemsets {*AB*}, {*BC*}, and {*CD*} are all high transaction-weighted utilization *2*-itemsets, which have been found. Figure 1 shows the process of generating itemsets by using the filtration mechanism.

In Figure 1, the proposed algorithm first fetches the first item *A* in *T* and allocates it to the first row of the two dimensional vector array. The algorithm then fetches the second item *B* in *T* and allocates it to the second row of the vector array. Since there is only the item *A* in front of the fetched item *B*, the algorithm then checks whether items *A* and *B* have high transaction-weighted utilization relationship. In this example, {*AB*} is a high transaction-weighted utilization *2*-itemset. It is thus generated and put into the back of {*A*} in the first row because the first item in {*AB*} is *A*. The algorithm then continues to fetch the third item *C* and performs the same process. It puts {*C*} in the third row of the vector array, forms {*AC*}, and checks whether {*AC*} is a high transaction-weighted utilization *2*-itemset. In the example, {*AC*} is not, such that no combination of a subset in the first row with {*C*} is necessary. The algorithm then forms {*BC*} from the second row and finds it is a high transaction-weighted utilization *2*-itemset. {*BC*} is thus put in the back of {*B*} in the second row. Two new subsets {*BC*} and {*C*} are generated for the third item. Similarly, the fourth item *D* is fetched and the above process is repeated again. The two new subsets {*CD*} and {*D*} are derived and put into the suitable vector array.

As seen in this example, the filtering mechanism can be effectively adopted to reduce the number of unpromising candidate itemsets and speed up the execution efficiency.

3.2 The Three-scan Utility Mining Algorithm, *TSA*

The details of the algorithm are listed below.

INPUT: A set of items, each with a profit value; a transaction database, in which each transaction includes a subset of items with quantities; the minimum utility threshold.

OUTPUT: The final set of high utility itemsets (*HU*).

Scan 1:

STEP 1. For each y-th transaction $Trans_y$ in D, do the following substeps.

(a) Calculate the utility value u_{yz} of each z-th item i_{yz} in $Trans_y$ as:

$$u_{yz} = s_{yz} * q_{yz},$$

where s_{yz} is the profit of item i_{yz} and q_{yz} is the quantity of i_{yz} .

(b) Calculate the transaction utility tu_y of $Trans_y$ as:

$$tu_y = \sum_z u_{yz} .$$

STEP 2. For each item i in D, calculate the transaction-weighted utility twu_i of the item i as the summation of the transaction utility values of the transactions which include the item i. That is:

$$twu_i = \sum_{i \in Trans_y} tu_y .$$

STEP 3. For each item i in the set of candidate *1*-itemsets, if the transaction-weighted utility twu_i of i is larger than or equal to the minimum utility threshold, put it in the set of high transaction-weighted utilization *1*-itemsets, $HTWU_1$.

Scan 2:

STEP 4. For each $Trans_y$ in D, do the following substeps.

(a) Check each item in $Trans_y$ whether it is a member in the set of $HTWU_1$. If it is, put it in the modified transaction $Trans_{y'}$; Otherwise, it is omitted.

(b) Check the number of items in the modified transaction $Trans_{y'}$ whether its number of items is larger than or equal to 2. If it is, keep the transaction $Trans_{y'}$ in the set of the modified transactions, and do the next step; Otherwise, remove the transaction $Trans_{y'}$, and do substep (a).

(c) Generate all possible *2*-itemsets in $Trans_{y'}$, and then put them in the set of C_2.

(d) Add the transaction utility tu_y in the suitable transaction-weighted utility field values of the generated *2*-itemsets in the set of C_2.

STEP 5. Check whether the transaction-weighted utility twu_x of each *2*-itemset x in the set of C_2 is larger than or equal to the minimum utility threshold , put it in the set of high transaction-weighted utilization *2*-itemsets, $HTWU_2$.

Scan 3:

STEP 6. Initialize the temporary itemset table as an empty table, in which each tuple consists of two fields: itemset and actual utility.

STEP 7. For each transaction $Trans_{y'}$ in the set of the modified transactions, do the following substeps.

(a) Generate all possible itemset x in $Trans_{y'}$ by using the set of $HTWU_2$, where the relationship between any two items in an itemset has to be a high transaction-weighted utilization relationship.

(b) Find the utility values u_{yx} of the itemsets in $Trans_{y'}$, and then add in their actual utility field values in the temporary itemset table.

STEP 8. Check whether the actual utility au_x of each r-itemset x in the temporary itemset table is larger than or equal to the minimum utility threshold , put it in the set of high utility r-itemsets, HU_r.

STEP 9. Output the final set of high utility itemsets, *HU*.

4 EXPERIMENTAL EVALUATION

In the experiment, the public *IBM* data generator was used in our experiment to produce the dataset [4]. Since our purpose was to find out high utility itemsets, we thus developed a simulation model, which was similar to that used in Liu *et al*. [6], to generate the quantities of the items in the transactions. In addition, the parameters used in the *IBM* data generator [4] were *T*, *I*, *N* and *D*, which represented the average length of items per transaction, the average length of maximal potentially frequent itemsets, the total number of different items, and the total number of transactions, respectively. All the algorithms were implemented in J2SDK 1.5.0 and executed on a PC with 3.0 GHz CPU and 1 GB memory.

Figure 2 then showed the execution time comparisons of the two algorithms for the synthetic T10I4N4KD200K dataset with various minimum utility thresholds, *min_util*.

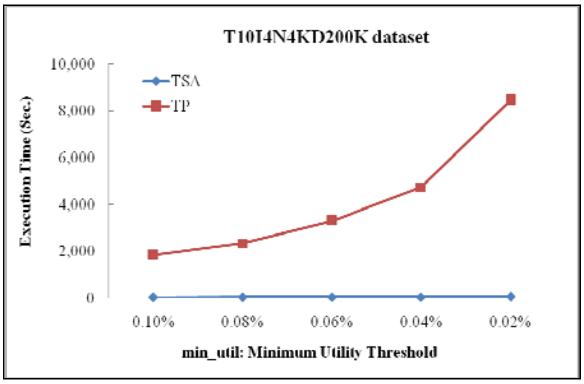

Fig. 2. Execution time of the two algorithms along with various minimum utility thresholds

It could be seen in the figure that the efficiency of the *TSA* algorithm was better than that of the *TP* algorithm, especially when the minimum utility threshold decreased. With the filtration mechanism, the *TSA* algorithm could thus effectively reduce a great number of unpromising candidates to achieve the goal of finding high utility itemsets. For the *TP* algorithm, since it adopted a level-wise technique to handle the problem of utility mining, a huge number of candidates had to be generated for mining. Thus, the candidate itemset requirement of the *TSA* algorithm was smaller than that needed by the *TP* algorithm.

5 CONCLUSIONS

In this paper, we have proposed an efficient three-scan utility mining approach (*TSA*) to find high utility itemsets from a transaction database. Especially, the proposed algorithm only needs three data scan to achieve the utility mining task. Also, the filtration mechanism adopts in this work can effectively skip unpromising candidate itemsets and thus further save time. The experimental result shows that the proposed mining algorithm is able to execute faster than the traditional *TP* algorithms for the synthetic datasets generated by the public *IBM* data generator.

REFERENCES

[1] R. Agrawal, T. Imielinksi, and A. Swami (1993), Mining association rules between sets of items in larg e database. The ACM SIGMOD International Conferen ce on Management of Data, pp. 207-216

[2] R. Chan, Q. Yang, and Y. Shen (2003), Mining high utility itemsets. The 3rd IEEE International Confe rence on Data Mining, pp. 19-26

[3] C. J. Chu, V. S. Tseng, and T. Liang (2008), Mi ning temporal rare utility itemsets in large databases us ing relative utility thresholds. International Journal of I nnovative Computing, Information and Control, 4(8):27 75-2792

[4] IBM Quest Data Mining Project, "Quest synthetic data generation code," Available at (http://www.almade n.ibm.com/cs/quest/syndata.html)

[5] G. C. Lan, T. P. Hong, and V. S. Tseng (2011), Discovery of high utility itemsets from on-shelf time p eriods of products. Expert Systems with Application, 3 8(5):5851-5857

[6] Y. Liu, W. Liao, and A. Choudhary (2005), A fa st high utility itemsets mining algorithm. The Utility-B ased Data Mining Workshop, pp. 90-99

[7] H. Yao and H. J. Hamilton (2006), Mining items et utilities from transaction databases. *Data & Knowled ge Engineering*, 59(3):603-626

[8] J. S. Yeh, C. Y. Chang, and Y. T. Wang (2008), Efficient algorithms for incremental utility mining. *The International Conference on Ubiquitous Information M anagement and Communication*, pp. 229-234

The Seventeenth International Symposium on Artificial Life and Robotics 2012 (AROB 17th '12),
B-Con Plaza, Beppu, Oita, Japan, January 19-21, 2012

Thermal Wave Effect for Living Tissue with Surface Heating Problems by Differential Transformation Method

Song-Yih Lin[1,2],Hsin-Yi Lai[1], Cha'o-Kuang Chen[1]

[1]Department of Mechanical Engineering, National Cheng Kung University
No.1, Daxue Rd., East Dist., Tainan City 70101, Taiwan, R.O.C.
[2]Department of Computer Application Engineering, Far East University
No. 49, Chung Hua Rd., Hsin-Shih, Tainan 74448, Taiwan, R.O.C.
(Tel: 886-6-597-9566#7233, Fax: 886-6-597-7115)
(E-mail: songyih@cc.feu.edu.tw)

Abstract: The Pennes' bio-heat conduction equation is common used to simulate temperature distribution for bio-heat transfer problems, it adopted the classical Fourier heat conduction law that is obviously incompatible with physical reality when research on microscopic heat transfer, low-pressure gases, cryogenic engineering, etc. Applying the concept of finite heat propagation speed, a thermal wave model of bi-heat transfer has developed. In order to analyze the thermal wave effect on temperature distributions, the different boundary heating conditions are considered with thermal wave model of bi-heat transfer and also compare to the Pennes'. The differential transform method combined with the finite difference scheme is proposed to simulate the temperature distributions. From results show it takes a period of time for the surface heating to propagate to a desired point inside the living tissue by the effect of thermal wave.

Keywords: Thermal wave, Thermal relaxation time, Differential transformation method**.**

1. INTRODUCTION

Temperature predictions for living tissues have attracted a lot of interesting in the processes of hyperthermia, thermal diagnostics, cryosurgery, thermal comfort analysis, and thermal parameter analysis. There were many models have been developed for describing bio-heat transfer behavior [1]. Among these models, the well known Pennes' model is the most commonly adopted [2]. It used the classic Fourier's law for its conduction term and was given as

$$q(\vec{r},t) = -\kappa\nabla T(\vec{r},t) \tag{1}$$

where κ is conductivity. The thermal signal propagates in infinite velocity in Eq. (1) that is obviously incompatible with physical reality when studies the processes of microscopic heat transfer, low-pressure gases, cryogenic engineering, etc. Thus, the concept of finite heat propagation wave velocity was proposed to apply for the bio-heat transfer processes [3-4]. Vernotte and Cattaneo [5] proposed a modified unsteady heat condition equation with the thermal relaxation time and was given as

$$q(\vec{r},t+\tau) = q(\vec{r},t) + \tau\frac{\partial\vec{q}(\vec{r},t)}{\partial t} = -\kappa\nabla T(\vec{r},t) \tag{2}$$

here $\tau = \alpha / V^2$ is defined as the thermal relaxation time, and α is the thermal diffusivity, V is denoted as the heat propagation velocity in the medium.

In homogeneous substances, τ is in the range of $10^{-8} \sim 10^{-10}$s as for gases, and $10^{-8} \sim 10^{-14}$s for liquids and dielectric solids [6]. The time of heating process is much longer than the thermal relaxation time scale in homogeneous substances, so the phenomenon of heat wave is relatively more difficult to observe. In non-homogeneous materials such as living tissues, τ is the characteristic time that needs to take time to accumulate the thermal energy in order to transfer to the nearest element. Kaminski [7] reported the value of τ is 20~30 s in meat product. Liu et al. [8] used the thermal wave model of bio-heat transfer (TWMBT) to analysis the thermal signal wave of bio-heat transfer. Liu [9] performed the Laplace transform method to investigate the thermal propagation behaviors. Liu and Lin [10] investigated physiological parameters by the hybrid numerical scheme. It is difficult to obtain the fundamental solution of the thermal propagation wave model of bio-heat transfer for living tissue [11]. In this article, a differential transform method is proposed to predict temperature distributions for living tissues with different boundary heating conditions. The effects of thermal wave on temperature distribution are also investigated.

2. THE DIFFERENTIAL TRANSFORMATION METHOD

Zhou [12] proposed the concept of the differential transform and can be summarized below.

$$X(k;t_0) = M(k)\left[\frac{d^k}{dt^k}(q(t)x(t))\right]_{t=t_0}, \quad k \in K \tag{3}$$

where k belongs to a set of non-negative integer denoted as K domain. $X(k;t_0)$ is the differential transformation of

$x(t)$ at $t = t_0$, *M(k)* ($M(k) \neq 0$) is called the weighting factor and *q(t)* ($q(t) \neq 0$)is a kernel corresponding to *x(t)*. Thus, if *q(t)x(t)* can be expressed in terms as Taylor's series, then *x(t)* can be presented by using the differential inverse transformation of $X(k;t_0)$ as

$$x(t) = \frac{1}{q(t)} \sum_{k=0}^{\infty} \frac{(t-t_0)^k}{k!} \frac{X(k;t_0)}{M(k)}, \quad \forall t \in T \tag{4}$$

If $M(k) = H^k / k!$ and $q(t) = 1$, then Eq. (3) and (4) become

$$X(k) = T[x(t)] = \frac{H^k}{k!} \left[\frac{d^k x(t)}{dt^k} \right]_{t=0}, \quad k \in K \tag{5}$$

$$x(t) = T^{-1}[x(t)] = \sum_{k=0}^{\infty} \left(\frac{t}{H} \right)^k X(k), \quad \forall t \in T \tag{6}$$

3. BIOHEAT TRANSFER PROBLEMS

The Pennes' bio-heat transfer equation is described as

$$-\nabla \cdot \vec{q} + W_b C_b (T_b - T) + q_m + q_r = \rho C \frac{\partial T}{\partial t} \tag{7}$$

where, ρ C, and T denote the density, specific heat, and temperature of living tissue, C_b is the specific heat of blood, W_b blood perfusion rate, q_m and q_r are the heat generation from metabolism and the spatial heat source respectively, T_b is the artery temperature. Liu et al. [13] introduced a general model of thermal wave form of the bio-heat transfer in living tissue from Eq. (2) and (7) as

$$\begin{aligned} &\nabla \cdot (\kappa \nabla T) + W_b C_b (T_b - T) + q_m + q_r \\ &+ \tau(-W_b C_b \frac{\partial T}{\partial t} + \frac{\partial q_m}{\partial t} + \frac{\partial q_r}{\partial t}) = \rho C (\tau \frac{\partial^2 T}{\partial t^2} + \frac{\partial T}{\partial t}) \end{aligned} \tag{8}$$

Equation (8) is a general form of TWMBT in living tissue. When heat mainly propagates in the perpendicular direction to the living tissue surface, one-dimensional heat transfer can be a good approximation. With constant thermal properties, $q_m =$ constant, and $q_r = 0$, Eq. (8) can be expressed as

$$\kappa \frac{\partial^2 T}{\partial x^2} + W_b C_b (T_b - T) + q_m - \tau W_b C_b \frac{\partial T}{\partial t} = \rho C (\tau \frac{\partial^2 T}{\partial t^2} + \frac{\partial T}{\partial t}) \tag{9}$$

By assuming $T_i(x,0)$ is the initial steady state temperature, then Eq. (9) is turned into a new form as

$$\kappa \frac{\partial^2 T_i}{\partial x^2} + W_b C_b (T_b - T_i) + q_m - \tau W_b C_b \frac{\partial T_i}{\partial t} = \rho C (\tau \frac{\partial^2 T_i}{\partial t^2} + \frac{\partial T_i}{\partial t}) \tag{10}$$

Define a transformation of $\theta(x,t) = T(x,t) - T_i(x,0)$ and combine Eq. (9) and (10), the final result becomes

$$\rho C \tau \frac{\partial^2 \theta}{\partial t^2} + (\rho C + \tau W_b C_b) \frac{\partial \theta}{\partial t} + W_b C_b \theta - \kappa \frac{\partial^2 \theta}{\partial x^2} = 0 \tag{11}$$

By taking differential transformation of Eq. (11), then

$$\begin{aligned} &\rho C \tau \frac{(k+1)(k+2)}{H^2} U(k+2) + (\rho C + \tau W_b C_b) \frac{(k+1)}{H} U(k+1) \\ &+ W_b C_b U(k) = \kappa \frac{\partial^2 U(k)}{\partial x^2} \end{aligned} \tag{12}$$

where $U(k) = U(x,t)$ is the differential transformation function at $\theta(x,t)$. By dividing the coordinate of x into N equal internals and taking the finite difference approximation to Eq. (12)

$$\begin{aligned} &\rho C \tau \frac{(k+1)(k+2)}{H^2} U_i(k+2) + (\rho C + \tau W_b C_b) \frac{(k+1)}{H} U_i(k+1) \\ &+ W_b C_b U_i(k) = \kappa \frac{U_{i+1}(k) - 2U_i(k) + U_{i-1}(k)}{(\Delta x)^2} \end{aligned} \tag{13}$$

3. NUMERICAL SIMULATION

When the surface of living tissue is heated by different boundary heating conditions, the bio-heat conduction equation and relative conditions are discussed.

3.1. Case 1：Constant surface temperature heating

The skin surface is heated for constant temperature and the temperature distributions have simulated.

$$\rho C \tau \frac{\partial^2 \theta}{\partial t^2} + (\rho C + \tau W_b C_b) \frac{\partial \theta}{\partial t} + W_b C_b \theta - \kappa \frac{\partial^2 \theta}{\partial x^2} = 0 \tag{14}$$

Assume there is no heat flux at x=L [8], then the initial and boundary conditions are described as

$$\theta(x,0) = 0 \tag{15}$$

$$\frac{\partial \theta(x,0)}{\partial t} = 0 \tag{16}$$

$$\theta(0,t) = \theta_0 \tag{17}$$

$$\frac{\partial \theta(L,t)}{\partial x} = 0 \tag{18}$$

The differential transformation of Eq. (15)-(18) are

$$U_i(0) = 0 \tag{19}$$

$$U_i(1) = 0 \tag{20}$$

$$U_1(0) = \theta_0 \quad , \quad U_1(k) = 0 \quad k \neq 0 \tag{21}$$

$$U_N(k) - U_{N-1}(k) = 0 \tag{22}$$

The differential transformation equation from Eq. (14) can be resulted in tow situations.

For $\tau = 0$

$$U_i(k+1) = \frac{H}{\rho C(k+1)} \left\{ \begin{aligned} &-W_b C_b U_i(k) \\ &+ \frac{\kappa}{(\Delta x)^2} \begin{bmatrix} U_{i+1}(k) - 2U_i(k) \\ + U_{i-1}(k) \end{bmatrix} \end{aligned} \right\} \tag{23}$$

For $\tau \neq 0$

$$U_i(k+2) = \frac{H^2}{\rho C \tau (k+1)(k+2)} \left\{ \begin{aligned} &-(\rho C + \tau W_b C_b) \frac{(k+1)}{H} U_i(k+1) \\ &- W_b C_b U_i(k) \\ &+ \frac{\kappa}{(\Delta x)^2} \begin{bmatrix} U_{i+1}(k) \\ -2U_i(k) + U_{i-1}(k) \end{bmatrix} \end{aligned} \right\} \tag{24}$$

3.2. Case 2：Constant surface flux heating

For a constant heat flux heat at the living surface, the corresponding boundary conditions typically can be described as

$$\begin{cases} -\kappa \dfrac{\partial\theta(0,t)}{\partial x} = q(t) \ \ 0 < t < t_s \\ -\kappa \dfrac{\partial\theta(0,t)}{\partial x} = 0 \ \ t > t_s \end{cases} \tag{25}$$

$$\frac{\partial\theta(L,t)}{\partial x} = 0 \tag{26}$$

Where t_s is defined as the duration of heating period and $q(t)$ denotes the heat flux that is time variable. Considering the heating time is short then the heat flux is approximately assumed as a constant, q_0. In the practices the heat flux is 83.2kw/m^2 as for the flash fire on the human skin surface.

3.3 Case 3：Constant temperature pulse surface heating

In the cases of eye surgery by using laser pulse or skin subjects to hot plate for a short period of time, the boundary conditions are expressed as

$$\begin{cases} \theta(0,t) = \theta_0 \ \ 0 \le t \le t_s \\ \theta(0,t) = 0 \ \ t > t_s \end{cases} \tag{27}$$

$$\frac{\partial\theta(L,t)}{\partial x} = 0 \tag{28}$$

4. RESULT AND DISCUSSION

The thermal property for homogeneous tissue are taken as $\rho = 1000 kg/m^3$, $C = C_b = 4200 J/kg°C$, $W_b = 0.5 kg/m^3$, $T_b = 32.5°C$, and $\kappa = 0.2 W/m$ [5]. As shows in Fig. 1, the computation domain is taken as L=0.01208m and the value of θ_0 is specified as 12℃ [5] and temperature distributions were analytically estimated at x=0.00208m inside the body.

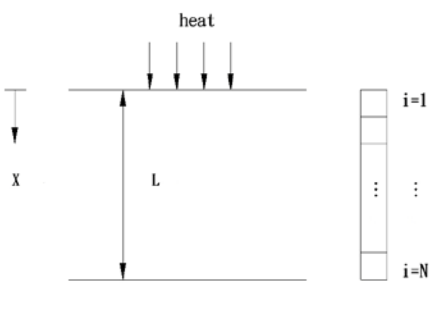

Fig. 1. The physical model

4.1. Case 1：Constant surface temperature heating

In Fig. 2, the temperature distributions predicted from Pennes' and TWMBT equation were different. As $\tau = 0$, the Pennes' bio-heat equation is used to characterize the thermal conduction, the thermal gradient has no jump discontinuity because of the infinite speed of thermal wave and the thermal signal can arrive the positions instantaneously. For $\tau \neq 0$, the influence of thermal relaxation time can result in a finite thermal wave propagation velocity and a travel time for thermal heat to distribute. The time for thermal heat to arrive at x=0.00208m is evaluated by using $t = L/\sqrt{\alpha/\tau}$. For $\tau = 20$ s and $\tau = 30$ s, the thermal wave reach x=0.00208m in $t = 0.00208/\sqrt{0.2/(1000 \times 4200 \times 20)} = 42.627(s)$ and $t = 0.00208/\sqrt{0.2/(1000 \times 4200 \times 30)} = 52.21(s)$, respectively.

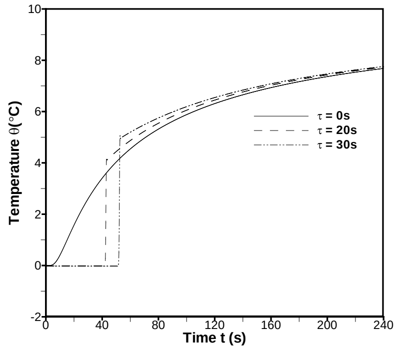

Fig. 2. Temperature distribution during constant surface temperature heating at x=0.00208m

4.2. Case 2：Constant surface flux heating

When there is a constant heat flux on the living skin surface for a period of heating time, as shows in Fig. 3. A substantial deviation was found between temperature predictions from the Pennes' and TWMBT equation. The temperature distributions predicted by the Pennes' equation increase at the initial then quickly decrease when the surface heat flux becomes zero. As in TWMBT equation, a period of time is needed for the thermal signal to travel from the surface to the particular position, the temperature distribution increase with a slope for the period of heating time then decrease. In Fig. 4, the different heat time were carried out to analyze the effect of thermal wave. The longer the heating time is the higher temperature is.

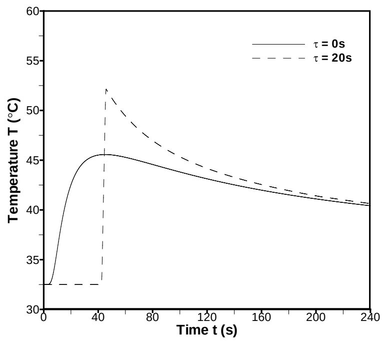

Fig. 3. Temperature distribution for t_s =3s during constant surface flux heating at x=0.00208m

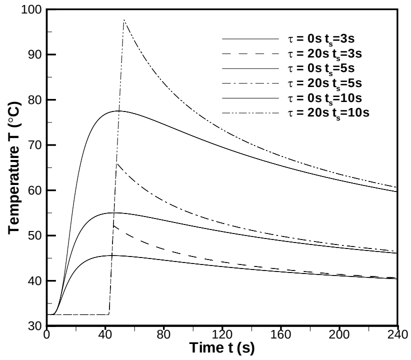

Fig. 4. Temperature distribution for various t_s during constant surface flux heating at x=0.00208m

4.3 Case 3：Constant temperature pulse surface heating

When the living tissues heat by the constant temperature pulse heating, such as eye surgery by laser irradiation or a flash fire on skin. As shows in Fig. 5, the temperature distributions predict by Pennes' and TWMBT equations for 3s, 5s, and 10s heating time. There is a travelling time for the thermal wave propagates from the heating living tissue surface to the particular and the temperature increase for the period of temperature pulse heating time. The longer heating time is, the higher temperature is. As for $\tau = 0$, the temperature increases at the period of temperature pulse heating time from begin, then gradually decreases at the end of heating.

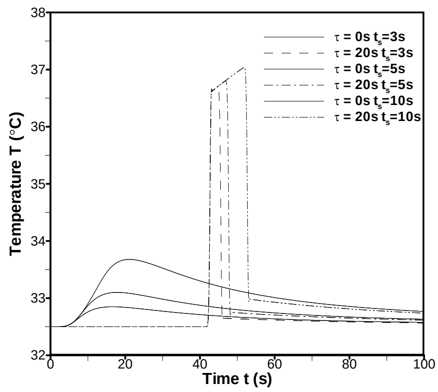

Fig. 5. Temperature distribution for various t_s, $\theta_0 = 12°C$ during constant temperature surface flux heating at x=0.00208m

5.CONCLUSION

The paper presents the effect of thermal wave in the living tissues for different surface heating problems. We simulate the bio-heat conduction problems with different values of the thermal relaxation time and also compares the results simulated by Pennes' and TWMBT equations. The results show that the heat wave speed under the effects of various thermal relaxation time and heat transfer wave propagation, can be expressed as $V = \sqrt{\alpha / \tau} = \sqrt{\kappa / \rho C \tau}$ and the travelling time also be calculated. In the non-homogeneous substance, the thermal wave propagates in a finite speed and cause a delay time to heat transfer compare with the temperature predicted by the Pennes' equation.

REFERENCES

[1] Arkin H, Xu LX, Holmes KR (1994), Recent developments in modeling heat transfer in blood perfused tissues, IEEE Transactions on Biomedical Engineering, 41:97-107.

[2] Liu KC (2008), Thermal propagation analysis for living tissue with surface heating, International Journal of Thermal Sciences, 47:507-513.

[3] Weymann HD (1967), Finite speed of propagation in heat conduction diffusion and viscous shear motion, American Journal of Physical, 35:217-229.

[4] Sobolev SL (1991), Transport processes and traveling waves in systems with local nonequilibrium, Soviet Physics Uspekhi, 34:217-229

[5] Liu J, Chen X, Xu LX (1999), New thermal wave aspects on burn evaluation of skin subjected to instantaneous heating, IEEE Transactions on Biomedical Engineering, 46:420-428.

[6] Sieniutycz S (1997), The variational principle of classical type for non-coupled non-stationary irreversible transport processes with convective motion and relaxation, International Journal of Heat and Mass Transfer, 20:1221–1231.

[7] Kaminski W (1990), Hyperbolic heat conduction equation for material with a nonhomogenous inner structure, ASME Journal of Heat Transfer,112: 555–560.

[8] Liu J, Chen X, Xu LX (1999), New thermal wave aspects on burn evaluation of skin subjected to instantaneous heating, IEEE Transactions on Biomedical Engineering, 46:420-428.

[9] Liu KC (2008), Thermal propagation analysis for living tissue with surface heating, international journal of thermal sciences, 47:507-513.

[10] Liu KC and Lin CN (2010), Temperature prediction for tumor hyperthermia with the behavior of thermal wave, Numerical Heat Transfer, Part A, 58:819-833.

[11] Lu WQ, Liu J, Zeng Y (1998), Simulation of the thermal wave propagation in biological tissues by the dual reciprocity boundary element method, Engineering Analysis with Boundary Elements, 22:167-174.

[12] Zhou X (1986), Differential transformation and its applications for electrical circuits, Zuazhong University Press, Wuhau.

[13] Liu J, Zhang X, Wang C et al (1997), Generalized time delay bioheat equation and preliminary analysis on its wave nature, Chinese Science Bulletin, 42:289-292.

The Forming Parameter Analysis of the Circular Plate by Using Computer-Aided Engineering

Yen-Liang Yeh[1], Kuo-Ying Chen[1], Chia-Hsing Shen[2]

[1]Far East University, Tainan 744, Taiwan
[2]Far East University, Tainan 744, Taiwan
(Tel:886-6-5979566#7275, Fax:886-6-597115)

[1]yehyl@cc.feu.edu.tw

Abstract: This paper is investigation of the effect of the large deformation on the forming parameter for the circular plate forming. This analysis tool of this paper is the ANSYS LS DYNA software. The forming parameter of the paper includes the punching velocity and die material property. From the analysis result, this can be known the variable result can be got under the differential parameter condition. When the punching velocity is increasing, the extrusive material will appear. When the die material strength increase, the forming thickness of the forming shape becomes small. When the deform velocity of the die material is increasing, the forming thickness of the forming shape becomes small. Therefore, the effect of the die material effect on the thickness of the forming shape is very clear. This analysis tool can effectively predict the forming shape.

Keywords: ANSYS LS DYNA , die material property, Oil Seal Cover, punching velocity,

1 INTRODUCTION

Now, the manufacturing velocity of the industry is very fast. So, the plastic injecting forming is used in many lifting field. But, the plastic structure strength is very weak. Therefore, the high structure product can not use the plastic material. The metal material is good material for the high structure product. The injecting forming method can not be used for the metal material. The fast forming method of the metal can use punching forming or deep drawing. This object of the punching forming is the forming shape for the beforehand plane plate or the undeveloped product. The forming shape include square, circular, rectangle, triangle …, etc. The punching forming action is by way of the mold interaction. The die material have the metal flow. This cause the die plate into the mold, then the die plate have pressured into the inside of the mold. In order to pressure the die plate forming, the die material cause metal flow.

In the process of the metal deep forming, the metal flows include the bending, stretching, friction and compressed. This can cause the deformation of the die plate. In general, the forming of the circular cup shape can cause the crack of the cup well in the place of the subjected force and transportation. When the plate material extend by using the force, the plate material thickness become thin. The thickness of the sheet plate on the place of the interaction between sheet plate and the corner of the punch pin become too thin. When the plate material is formed, the status of the forming force and transportation can be controlled. The forming shape can be get the best result.

From the literate, this can be known the parameter can be controlled to get the best forming result.[1] J.P.Fang etc [2] use the ABAQUS software to analyze the deep forming to understand the wrinkle of the plate material. This is closed compare between the experiment result and analysis result. Manabe etc [3] analyze the thickness variation of the plate material by using the 「LS-DYNA90」 soft ware. From the analysis result, this can be known that the LS-DYNA90 can be used to analyze the thickness variation. Natarajan and Venkataswamy[4] analyze the circular cap forming by using the finite element method. Compare the experiment result and analysis result, this can be found that the thickness of the plate material in the compressed plate and the flange of the mold become thin. This can be known that the finite element method can to analyze the forming process. In 2002, the Naval Kishor and Ravi Kumar[5] use the LSDYNA software to explore the forming shape optimization. This tool is used to reduce the ratio of the wrinkle shape. This result is close to the experiment result. In 2006, Yang [6] used the DEFORM software to analyze the semi circular deep. This simulate the thickness variation and the effect of the forming force. From the analysis result, this can be known that as the blank holder force and friction force become great, the forming force become great and the thickness of the plate become thin. Kirby and Wild[7] use the MARC software to analyze the deep forming. From the analysis result, this can be known that the effect of the friction coefficient and the blank holder gap on the principal strain of the blank material is very small. When the friction coefficient increase linearly, the maximum punch force increase linearly. When the blank holder gap increases, the blank hold force and punch force decrease. Therefore, this can be known that the effect of the friction coefficient on the maximum punch force is very clear. The effect of the blank holder gap on the maximum blank holder force is very clear. From the above literate, this can be known that the computation add engineer can be used to predict the forming shape.

2 Theory Analysis

In order to get the correct analysis result, the real material measurement is very important. The material test is satisfying the ASTM standard. The test material show in Fig. 1. The thickness of the blank plate material is 2.62mm. The test result show in Fig. 2. The test result is the displacement and force curve. In general, the analysis model property must is the real stress-strain curve. The relation of the engineering material property and the real material property can be get from equ. (1)-(4), shown in following:

$$\sigma = \frac{F}{A_0} \quad (1)$$

$$\varepsilon = \frac{l - l_0}{l_0} = \frac{\Delta l}{l_0} \quad (2)$$

$$\sigma_t = \frac{F}{A_0}(1+\varepsilon) \quad (3)$$

$$\varepsilon_t = \ln(1+\varepsilon) \quad (4)$$

Where σ is the engineering stress, σ_t is the real stress, ε is the engineering strain. ε_t is the real strain. F is the extend force. l_0 is the length of the test material. l is the length of the test material after extending. A_0 is the area.

Fig. 1. Flat sheet of material testing standard map

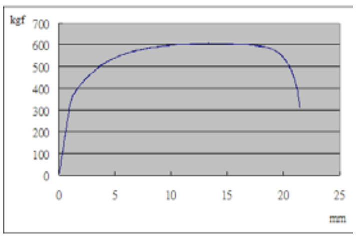

Fig. 2. Pull test of strength and displacement application diagram Flat sheet of material testing standard map

From the tensile test, the coefficient of elasticity is 593kgf/mm^2, yielding stress 168MPa limited strength is 273.5MPa, ratio of the extension 49.5%. The stress strain curve can be get, show in Fig 3. The relation of the punch forming velocity is shown in Fig.4.

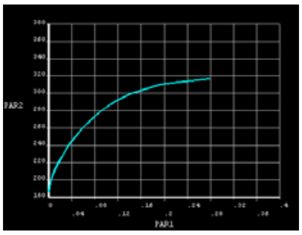

Fig. 3. Stress-strain diagram

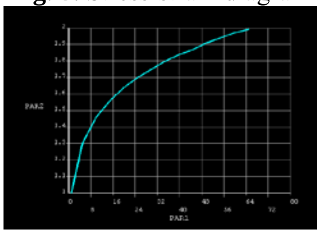

Fig. 4. Speed and strain rate graph

This paper uses the ANSYS/LS-DYNA software to build the solid modeling. This modeling includes the punch mold, draw die and blank plate. Due to, the analysis object is the thickness and Flange of the circular cup. The blank plate use the shell 163 element of the ANSYS, this element is show in Fig.5. The punch and die element is the solid 164 of the ANSYS, this shows in Fig.6.

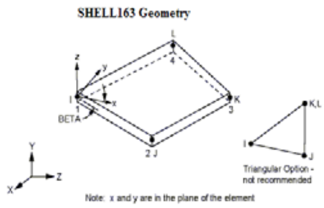

Fig. 5 shell163 of the ANSYS diagram [8]

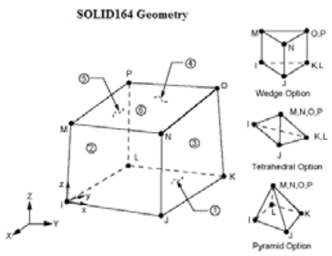

Fig. 6 solid164 of the ANSYS diagram[8]

3 Analysis Result

In order to understand the effect of the punching velocity on the forming shape, this consider the constant distant of the punching and die with the variation time. The trip of the punch from the top to down is 0.05m. These six times of the punching 0.05m trip include 0.05s、0.1s、 0.2s、0.3s、0.4s and 0.5s. These analysis results show in following:

. **(a) T=0.05** This consider the punching time is t=0.05s. The punching velocity is very fast. This analysis result shows in Fig.7. Fig. 7 show the deformation shape of the circular cup and the thickness contour of the circular cup. From the Fig. this can be found that the flange of the circular cup appear. The thickness of the circular cup become very thin (0.053mm). In order to understand the effect of the material strength on the deformation shape, the Fig.8 show the deformation shape curve of the circular cup with the differential multiplicand of the stain rate of the material (in Fig.4). From Fig.8, this can be found the effect of the strain rate of the material on the deformation shape curve is very small.

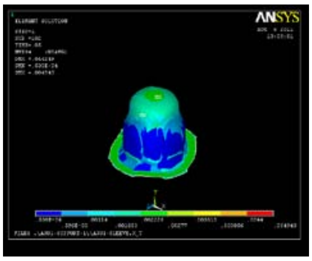

Fig. 7. The thickness contour and the forming shape diagram t=0.05s

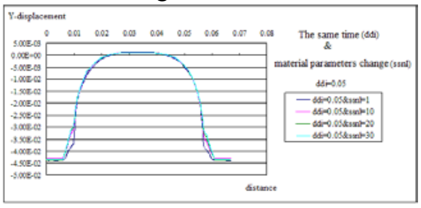

Fig. 8. The shape curve with variation strain ratio in t=0.05s

(b) T=0.1 The t=0.1s is applied in this system.

The analysis result show in Fig.9. From the Fig.9, this can be found that the flange of the circular cup appear. The flange of the punching time 0.1s is smaller than the punching time 0.05s. The thickness of the circular cup become very thin (0.225mm). In order to understand the effect of the material strength on the deformation shape, the Fig.10 show the deformation shape curve of the circular cup with the differential multiplicand of the stain rate of the material (in Fig.4). From Fig.10, this can be found the effect of the strain rate of the material on the deformation shape curve is not clear..

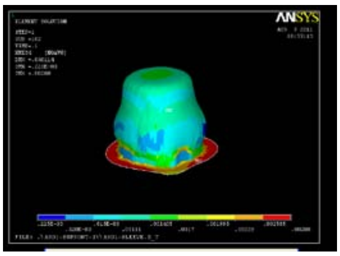

Fig. 9. The thickness contour and the forming shape diagram t=0.1s

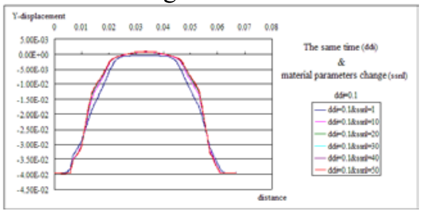

Fig. 10. The shape curve with variation strain ratio in t=0.1s

(c) T=0.2 The t=0.2s is applied in this system. The analysis result show in Fig.11. From the Fig.11, this can be found that the flange of the circular cup disappear. The thickness of the circular cup become very thin (0.915mm). The Fig.12 shows the deformation shape curve of the circular cup with the differential multiplicand of the stain rate of the material (in Fig.4). From Fig.12, this can be found the effect of the strain rate of the material on the deformation shape curve is not clear..

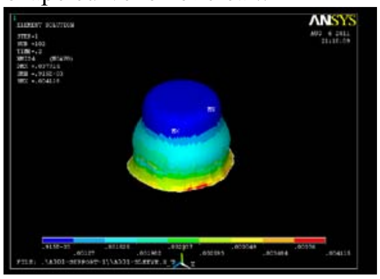

Fig. 11. The thickness contour and the forming shape diagram t=0.2s

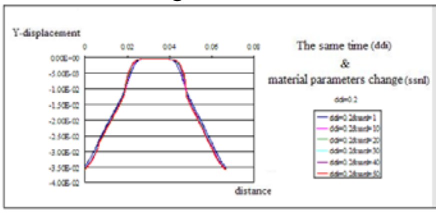

Fig. 12. The shape curve with variation strain ratio in t=0.2s

From the above analysis result, this can be known the effect of the train ratio of the material on the deformation shape is not clear. But, the thickness of the circular cup is too thin after the blank plate is formed, shown in Fig.13. From this can be found that the strain ratio of the material is great, the flow of the material is very difficult.

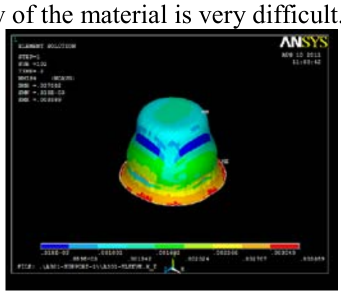

Fig.13. The thickness contour and the forming shape diagram t=0.2 with multiplicand of the strain ratio 50

(c) T=0.3 The t=0.3s is applied in this system. The analysis result show in Fig.14. From the Fig.14, this can be found that the flange of the circular cup disappears. The thickness of the circular cup becomes very thin (1.16mm). The Fig.15 shows the deformation shape curve of the circular cup with the differential multiplicand of the stain rate of the material (in Fig.4). From Fig.15, this can be found the effect of the strain rate of the material on the deformation shape curve is not clear.

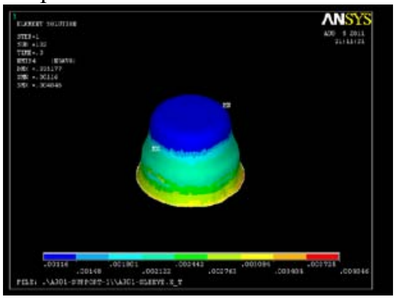

Fig.14. The thickness contour and the forming shape diagram t=0.3

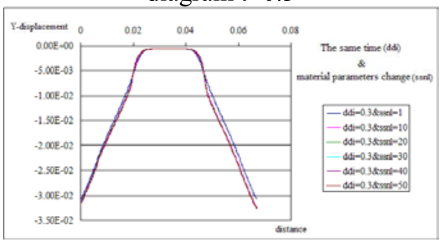

Fig.15. The shape curve with variation strain ratio in t=0.3s

(d) T=0.4 The t=0.4s is applied in this system.

The analysis result show in Fig.16. From the Fig.16, this can be found that the flange of the circular cup disappears. The thickness of the circular cup becomes very thin (1.395mm).

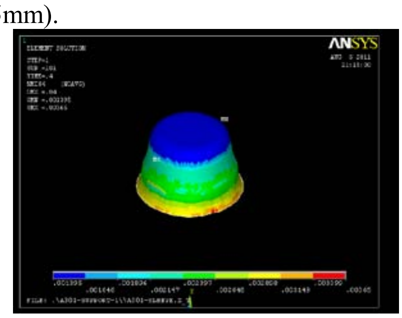

Fig.16. The thickness contour and the forming shape diagram t=0.4

(e) T=0.5 The t=0.5s is applied in this system. The analysis result show in Fig.17. From the Fig.17, this can be found that the flange of the circular cup disappears. The thickness of the circular cup becomes very thin (1.598mm).

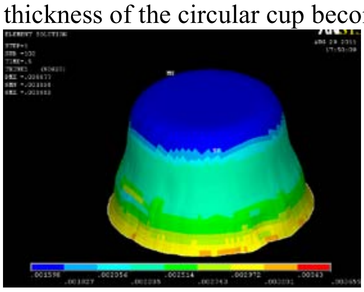

Fig.17. The thickness contour and the forming shape diagram t=0.5s

4 CONCLUSION

This object of the paper is analysis of the plate forming by using the CAE software. This uses the AN SYS LS-DYNA to analyze the circular cup forming. Fr om the above analysis result, this can be get this follo wing:

1. This can get the good analysis result by using the CAE.
2. From analysis result, this can be found that the differential result can be get as the differential forming parameter.
3. In the deformation shape, the effect of the punching velocity is very clear. As the punching time is smaller than 0.2s, the flange of the circular cup appers.
4. In the thickness of the forming product, the effect of the punching velocity is very clear.
5. When the stain ratio of the blank material is great, the thickness of the circular cup is thin. When the punching time is greater, the thickness of the circular cup become big.

REFERENCES

[1] Dai Yijie, Stamping and Die Design, New Land Book Co., Ltd., 1999

[2] J.P.Fana, CTTangb, C.P.Tauib, L.C. Chanb, T.C. Lee, 3D Finite element simulation of deep drawing with damage development, International Journal of Machine Tools & Manufacture, Vol.46, PP. 1035-1044,2006

[3] K.I Manabe, Y. YAMAUCHI and T. YADAMI, FE simulation on blank holder control using friction reducing algorithm in deep drawing process, JSME International Journal, Series Vol.48 No.4 pp.342-345, 2005

[4] S. Natarajan, and S. Venkataswamy, 2002, A Note on Deep Drawing Process:numerical Simulation and Experimental Validation, Journal of Materials Processing Technology. Vol. 127, pp. 64-67

[5] Naval Kishor, and D. Ravi Kumar, 2002, Optimization of Initial Blank Shape to Minimize Earing in Deep Drawing Using Finite Element Method, Journal of Materials Processing Technology, Vol. 130-131, pp. 20-30.

[6] T.S Yang, and Y.C Hsu, 2006, An Analysis of The Hemisphere Deep Drawing Process of Metal Sheet, Journal of the Chinese Society of Mechanical Engineers. Vol. 21, No.1, pp. 81-86.

[7]
D.S. Kirby and P.M Wild, 2000, Deep Drawing of Pressure Vessel End Closures: Finite Element Simulation and Validat ion, Journal of Materials Processing Technology, Vol. 103, pp. 247-260.

[8] Documentation for ANSYS

The Seventeenth International Symposium on Artificial Life and Robotics 2012 (AROB 17th '12),
B-Con Plaza, Beppu, Oita, Japan, January 19-21, 2012

Motion planning using memetic evolution algorithm for network robot systems

Chien-Chou Lin[1], Wei-Ju Chuang[2], and Kun-Cheng Chen[3]

Department of Computer Science and Information Engineering,
National Yunlin University of Science and Technology,
Douliou, Yunlin 64002, Taiwan, R.O.C.

{[1]linchien, [2]g9917709, [3]g9817704}@yuntech.edu.tw

Abstract: A hierarchical memetic algorithm (MA) is proposed for the path planning of swarm robots. The proposed algorithm consists of a global path planner (GPP) and a local motion planner (LMP). The GPP plans a trajectory within the Voronoi diagram (VD) of the free space. An MA with a non-random initial population plans a series of configurations along the path given by the former stage. The MA locally adjusts the robot positions to search for better fitness along the gradient direction of the distance between swarm robots and intermediate goals (IGs). Once the optimal configuration is obtained, the best chromosomes are reserved as the initial population for the next generation. Since the proposed MA has a non-random initial population and local searching, it is more efficient and the planned path is faster than the traditional genetic algorithm (GA).

Keywords: memetic algorithm, genetic algorithm, hierarchical, local motion planner, swarm robots, Voronoi diagram

1 INTRODUCTION

In recent years, an increasing number of multi-robot systems have been proposed. Swarm robotics [1][2][3] is an approach for coordinating multi-robot systems. The swarm shares information about the environment and individual members interact with each other. Cooperative behavior may be used to complete a task. Most studies on robot swarm cooperation have focused on formation control, which refers to the task of controlling a group of mobile robots to follow a predefined path or trajectory while maintaining the desired formation pattern. Numerous methods have been proposed for formation control, which can be roughly categorized into four basic approaches, namely behavioral, virtual structure, leader-follower, and potential field.

In virtual structure approaches, the robot swarm is considered as a single rigid robot. A rigid geometric relationship among group members is maintained [4]. Therefore, the path planning of a robot swarm can be simplified as the path planning of a rigid robot. The advantage of the virtual structure approach is ease of implementation. However, the approach has low path planning flexibility.

For behavior-based approaches, several desired behaviors, i.e., movement towards the goal, obstacle avoidance, collision avoidance, and keeping formation, are defined for each robot to create its trajectory. The planning of robots can be done concurrently. Since each robot is considered individually, it is difficult to guarantee precise formation control.

In leader-follower approaches, the ability of a robot depends on its job. In the swarm, one or a few robots act as leaders which move along predetermined trajectories and other robots in the group follow while maintaining the desired relative position with respect to the leader. Generally, leader-follower-based robot systems are implemented as centralized systems. However, most leader-follower approaches are not complete algorithms because the safe path, that which gives a robot sufficient distance from obstacles and other robots is difficult to derive.

In order to obtain a safe path for swarm robots, the present paper proposes a hierarchical path planning algorithm. The proposed algorithm consists of a global path planner (GPP) and a local motion planner (LMP).

The rest of this paper is organized as follows. The GPP and the LMP of the proposed hierarchical path planning algorithm for swarm robots are introduced in Section 2 and 3, respectively. In Section 4, simulation results are given. Finally, conclusions and suggestions for future work are given in Section 5.

2 GLOBAL PATH PLANNING

Global path planning can be considered as a planning problem for a point robot. In Fig. 1(a), a swarm of two robots moves to the goal configuration; the planned path is close to obstacles [5]. In order to obtain a safe path, a Voronoi diagram (VD) is adopted since it is easy to implement and has been shown to work well in many cases. There are many variants of VD [6][7][8]. In the present study, a VD consisting of line segments is considered. A VD shows a set of free points which are equidistant to two closest obstacles. In [9], the VD was constructed using

Voronoi vertices and Voronoi arcs. The Voronoi vertices are points equidistant to the closest features of three (or more) polygons. The vertices are connected by continuous chains of Voronoi arcs. An arc may be equidistant to two closest vertices or to two closest obstacle edges or to an obstacle vertex and an obstacle edge.

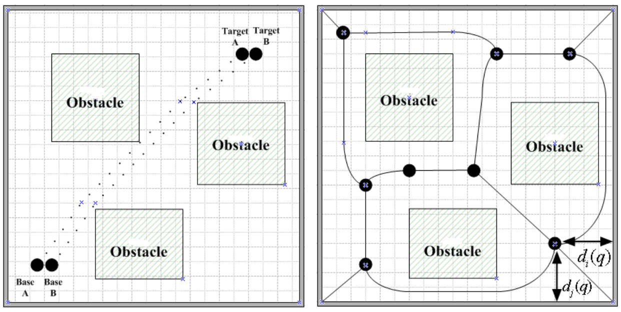

(a) (b)

Fig. 1. (a) Simple path of moving straight from start to goal. (b) Voronoi graph for Fig. 1(a).

As shown in Fig. 1(b), all edges and vertices of obstacles are used to construct the VD. The computation complexity is proportional to the total number of features of obstacles. Only a partial VD is used for global path planning for swarm robots. An efficient approach for constructing the partial VD is proposed in this paper.

Unlike approaches which construct the whole Voronoi diagram of the free space and then search for the path, the proposed scheme constructs a partial VD of the region of interest. As shown in Fig. 2(a), the proposed approach explores Voronoi vertices constructed from obstacles which are near the straight line from start to goal. Then, the Voronoi vertices are connected by a Voronoi arc which is formed by the nearest edges along the line, as shown in Fig. 2(b). The approach significantly reduces the computation complexity. Since a VD is the medial axis of the free space, the global path derived using a VD for swarm robots is the safest path.

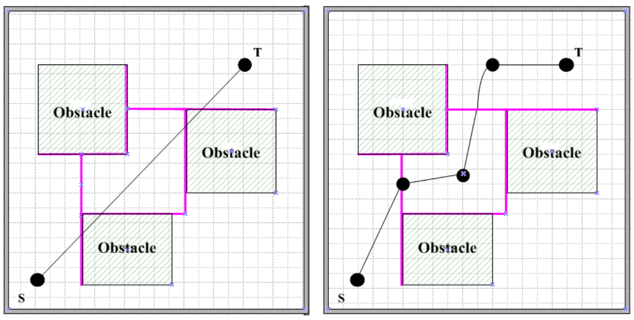

(a) (b)

Fig. 2. The Voronoi vertices are connected by a Voronoi arc which is formed by the nearest edges along the line.

3 LOCAL MOTION PLANNING

The global path obtained in the previous stage can be sampled as a series of positions, denoted as (q_1, q_2, q_3,…,q_n), which the center of the swarm robots should follow. These positions can be considered as the intermediate goals (IGs). For each position q_i, the memetic algorithm (MA)-based local motion planner plans a set of configurations for the robots to which the center of swarm is fixed at point, q_i. The proposed memetic algorithm is:

Potential-based Memetic Algorithm
Begin
***i* = 1; /* Initialize the first intermediate goal */**
***t* = 0; /* Initialize the evolutionary generations */**
  Randomly generate an initial population *Pi (t)*;
  fitness(*Pi(t)*);
    repeat until (reach the final goal *qn*) Do
    Pi+1(t)= Pi(t);
      repeat until (reach the intermediate goal *qi*)
      Do
        select *Pi(t+l)* from *Pi(t)*;
        crossover(*Pi(t+l)*);
        mutate (*Pi(t+l)*);
        fitness(*Pi(t+l)*);
        apply FT Local Search to *Pi(t+l)*
        t = t +1;
      end
    i= i +1;
  end
End

To apply an MA search for the optimal configurations, the coordinates of the robot swarm are encoded into one chromosome. The configuration of k robots is defined as their displacements, denoted as ((x_1, y_1), (x_2, y_2) ,…,(x_k, y_k)).

3.1 Initialization

The population, $P_1(0)$, of the first intermediate goal is generated randomly. The initial populations, ($P_i(0)$, i >1), of other intermediate goals are partially obtained from the last generation of the preceding intermediate goal and are partially randomly generated. Since these initial populations are eugenic and inherit from ancestors, the evolution time is reduced.

3.2 Natural selection

Natural selection is a genetic operator that chooses a chromosome from the current generation's population for inclusion in the next generation's population. Before making it into the next generation's population, selected chromosomes may undergo crossover and/or mutation (depending upon the probability of crossover and mutation) in which case the offspring chromosome(s) are actually the ones that make it into the next generation's population.

The aim of selection is to preserve optimal chromosomes and abandon suboptimal ones. In this study, the top percent scheme is adopted. The top 10 percent of the population is reserved as the next generation's population and the others are selected randomly.

3.3 Crossover and mutation operators

Selection alone cannot generate any new chromosomes for the population. The reproduction operators, crossover and mutation, are used to generate new offspring for the next generation. Crossover is performed between two selected chromosomes, called parents, by exchanging parts of their genomes to form two new chromosomes, called offspring. The most popular types of crossover operations are one-point, two-point, uniform, and blending. In this paper, since the *i-th* gene of a chromosome represents the position of robot *i*, the crossover operator exchanges similarly positioned genes of a pair of chromosomes.

For the mutation operator, an arbitrary bit in a genetic sequence is changed with a probability. The purpose of mutation in evolutionary algorithm (EA) is as a genetic operator used to maintain genetic diversity from one generation of a population of chromosomes to the next while attempting to avoid local minima.

3.4 Fitness function

Generally, selection is conducted according to the fitness of every chromosome, where the fitness evaluation of the GA is an objective function for chromosomes.

The fitness function can be rewritten [10] as:

$$V_q = f_{collide}(q)\times\left(\sum_{i=1}^{k} D^i{}_q + \rho U_{rep}\left(q\right)+\frac{1}{2}k\sum_{i=1}^{n} X_i^2\right) \tag{1}$$

where $D^i{}_q$ is the distance between robot i and the intermediate goal of the swarm center, q. The ρ is a constant and $U_{rep}(q)$ is the repulsive potential of swarm robots from obstacles. When a configuration collides with obstacles, the collision function, $f_{collide}(q)$, is equal to V_{max}, which is a penalty; otherwise, it is equal to 1. The potential $U_{rep}(q)$ can be calculated analytically as:

$$U_{rep}(q) = \sum_{i=1}^{k} U^i_{rep}(q) \tag{2}$$

where $U^i{}_{rep}(q)$ is the repulsive potential of robot i from the nearest obstacle.

$$U^i{}_{rep}(p) = \begin{cases} \frac{1}{2}\eta\left(\frac{1}{Dist(p)} - \frac{1}{Q^*}\right)^2, & Dist(p)\le Q^* \\ 0, & Dist(p) > Q^* \end{cases} \tag{3}$$

where Q^* is the minimum distance from obstacles and η is a gain of the repulsive gradient. *Disp (i)* is the distance between robot *i* and the closest obstacle. For swarm cohesion, a robot in the swarm should keep a certain distance from the swarm center and not stray far from other robots. In the proposed algorithm, a spring function is adopted as a repulsive/attractive potential function in the fitness function. In (1), X_i^2 is the difference between the distance between robot i and the nearest neighbor robot and the safe distance which should be kept between robots.

3.5 Local search of memetic algorithm using gradient between swarm robots and IGs

Conventional genetic algorithms (CGAs) don't have a fine-tuning (FT) process to get closer to optimal solutions. Unlike CGAs, an MA is an EA with a local search process to refine individuals. In this paper, the local research scheme is used to adjust the position of the center of the robot swarm moving toward the IG. The top 20 percent of chromosomes are reserved for the next generation. The chromosomes are fine-tuned before the next evolution. Consider the position of the swarm center of a chromosome as $R^c = (R^c_x, R^c_y)$ and the current intermediate goal as $IG_i = (IG_{ix}, IG_{iy})$. The best movement direction is defined as:

$$\vec{p} = IG_i - R^c = \left(IG_{ix} - R^c_x, IG_{iy} - R^c_y\right) \tag{4}$$

Therefore, the fine-tuning procedure of the genes of the chromosomes is defined as:

$$gene_i = \begin{cases} gene_i + p_i, & if \quad gene_i + p_i \le gene_{\max} \\ gene_{\max}, & if \quad gene_i + p_i > gene_{\max} \end{cases} \tag{5}$$

4 SIMULATION RESULTS

The proposed algorithm consists of the GPP and the LMP. The former was implemented using a modified Voronoi algorithm. The population was 100 and the maximum number of generations was set to 120. The probabilities of mutation and crossover were both 10%. The safe distances, *l* and Q^*, were set to 10 pixels and 2 pixels, respectively. The range of the genes was 30 to -30.

4.1 Swarm robot path planning by genetic algorithm and memetic algorithm

Case 1

The 3-robot swarm is shown in Fig. 3(a). There are 5 IGs and 3 obstacles in this case. The simulation took 8.609 seconds to plan a 10-configuration collision-free path. A similar simulation of the CGA is shown in Fig. 3(b). The CGA took 10.11 seconds to plan a 12-configuration path. The proposed algorithm is faster and more efficient.

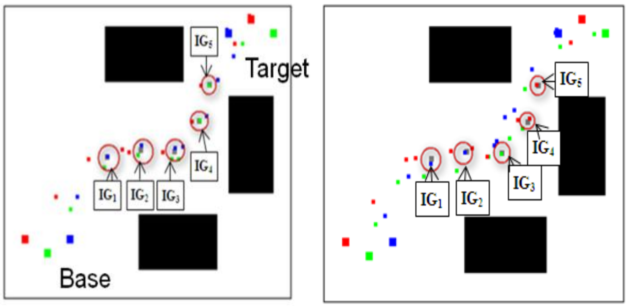

(a) (b)

Fig. 3. Three trajectories for 3-robot swarm example. Motion planning obtained using (a) MA and (b) CGA.

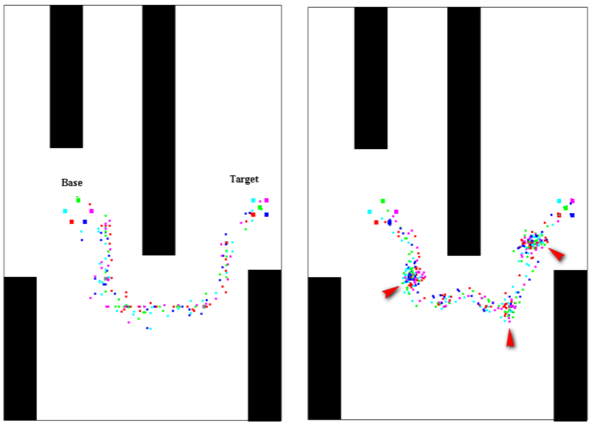

(a) (b)

Fig. 4. Five trajectories for 5-robot swarm example. Motion planning obtained using (a) MA and (b) CGA.

Case 2

The simulation of a 5-robot swarm is shown in Fig. 4(a). The planned path is smooth. There are 4 IGs and 4 obstacles in this case. The simulation took 56.094 seconds to plan a 39-configuration collision-free path. A similar simulation of the CGA is shown in Fig. 4(b). The simulation took 88.563 seconds to plan a 59-configuration path.

5 CONCLUSION

The proposed MA has a non-random initial population and fine-tuning based local searching, which make it more efficient and faster than the traditional CGA. The proposed hierarchical approach avoids becoming trapped in local minima. The path planning problem for swarm robots was considered for 2-D workspaces. The proposed algorithm can be extended to 3-D workspaces without significant modification. For example, the gene of a robot can be represented as (x, y, z). In future works, we will focus on smoothing the planned paths to reduce redundant movements. With this modification, the proposed algorithm should be more efficient.

Acknowledgment. This work was supported by the National Science Council of Taiwan under grants NSC 98-2220-E-224-003, NSC 99-2220-E-224-007 and NSC 100-2218-E-224-009-MY3.

REFERENCES

[1] Yogeswaran M and Ponnambalam SG (2010), Advanced knowledge application in practice. Intech, Croatia, pp. 259-279

[2] Samitha WE and Pubudu NP (2009), Formations of robotic swarm: An artificial force based approach. International Journal of Advanced Robotic Systems 6(1): 7-24

[3] Alan FTW, Jin Sa, Mari CFG, Clare D and Michael F (2008), On formal specification of emergent behaviours in swarm robotic systems. International Journal of Advanced Robotic Systems, 2(4):363–370

[4] Beard RW, Lawton J and Hadaegh FY (2001), A coordination architecture for spacecraft formation control. IEEE Transactions on Control Systems Technology 9:777-790

[5] Ahmad G and SMRS N (2011), Optimal trajectory planning for design of a crawling gait in a robot using genetic algorithm. International Journal of Advanced Robotic Systems 8(1):29-36

[6] Choset H, Lynch KM, Hutchinson S, kantor G, Burgard W, Kavraki LE and Thrun S (1989), Principles of robot motion: Theory, Algorithms, and Implementations.

[7] Erinc G and Carpin S (2007), A genetic algorithm for nonholonomic motion planning. Proceedings of IEEE International Conference on Robotics and Automation, pp. 1843-1849

[8] Kloetzer M and Belta C (2007), Temporal logic planning and control of robotic swarms by hierarchical abstractions. IEEE Transactions on Robotics, 23(2):320-330

[9] Wein R, van den Berg JP and Halperin D (2005), The visibility-voronoi complex and its applications. In: Proceedings of the Twenty-first Annual Symposium on Computational Geometry, ACM, Pisa, Italy, pp. 63-72

[10] Lin CC, Hsiao PY and Chen KC (2010), A motion planning of swarm robots using genetic algorithm. Proceedings of the 2010 International Conference on Broadband, Wireless Computing, Communication and Applications, IEEE Computer Society, pp. 538-543

A correction circuit of Hall sensor signal base speed measurement for BLDC motors

Chung-Wen Hung, Jhih-Han Chen, Ke-Cheng Huang

National Yunlin University of Science and Technology, Yunlin 640-02, R.O.C. Taiwan
(Tel: 886-5-534-2601)

wenhung@yuntech.edu.tw

Abstract: A speed correction circuit is proposed in this paper, the speed measurement is based on Hall sensor signal. Brushless DC (BLDC) motors are more and more popular, and the Hall sensors are usually built in for commutation. The Hall sensors and poles of the rotor are supposed to be placed in uniform distance and angle, then Hall sensor signal feedbacks are also used to measure motor speed. However, there is misalignment, and what will cause the error of measurement. A method is discussed to estimate the error of misalignment, and the inaccuracy could be corrected by the proposed circuit. This circuit is based on the hardware description language and implemented in FPGA, and then the synthesizing simulation results are presented to prove this circuit is workable.

Keywords: Hall sensor, FPGA, BLDC Motor, misalignment correction.

1 INTRODUCTION

The speed measurement of BLDC motors is usually based on the Hall sensor signals, but there are some errors have to be suppressed. Due to its high power density, easy maintenance and simple driving, BLDC motors are more popular. Although, an accurate rotor encoder is not necessary, to decide the commutation, the rotor position information is still important, and Hall sensors are a regular solution. Basically, the Hall sensor signal feedbacks could be used to measure motor speed, Hall sensors are supposed on uniform distance and the angles of rotor poles are considered as equal. However, there are misalignments for placement of Hall sensors and poles in consumer motors, and the inaccuracy will cause the speed measurement error. For example, for a four poles three phase BLDC motor, the Hall sensor should feedback a new signal in every 30 degree rotation, but the misalignment will cause that the feedback angle is not exactly 30 degree, and include the measurement error. A typical real experimental example is shown in Fig. 1, a motor runs in steady state and MCU clock is captured to calculate motor speed when Hall sensor signal is updated. Here, vertical axis is clock count between every two Hall sensor feedbacks and the waveform is similar to a periodic signal in 12Hz, then period should be caused by the misalignment. Author discussed this phenomenon in Chung-Wen Hung [1], and proposed dynamic moving average filter to get a trade-off between stable and fast response. Samoylenko [2] also proposed different filters and compared the performances. Chung-Wen Hung [1] and N. Samoylenko[2] treated the variation of Hall sensor feedback intervals caused by unbalance placement of Hall sensors and poles as noise, then designed a suitable filter to get correct signal. Neither required hardware circuit, but both took CPU calculation resource and induced phase delay.

P.B. Beccue [3] discussed a compensation method that implemented a Hall effect position observer to estimate the rotor position. This method used the angle and axes to define the rotor position and based on those to build a table. And it used the table to compute the error of the rotor angle and compensate the phase of the rotor.

S.-Y. Kim [4] intro- deuced a vector-tracking observer that used a feed forward input of the average rotor speed to calculate the rotor speed. And this observer is utilized to obtain the phase detector, which is used to estimate the angle error of the rotor. Using the observer to estimate the back-EMF and compare with the reference back-EMF to define the position and implement the compensation. Anno Yoo [5] used the d-q axis to define the phase and current, and utilized the dual observer to estimate rotor speed and position, respectively. Based on the rotor position to obtain the error value and implemented the compensation algorithm. Kuang-Yao Cheng [6] implemented a mixed mode integrated circuit (IC) of the sensorless commutation for BLDC motor. This circuit utilized the back-EMF and zero-crossing point to detect the phase error. Compensation the phase error by the rotor speed estimation depended on the changing phase lag due to the low-pass filtering of the terminal voltages. The said compensation methods have to implement the complex observer and the other Hall sensor detection circuit to perform the estimator.

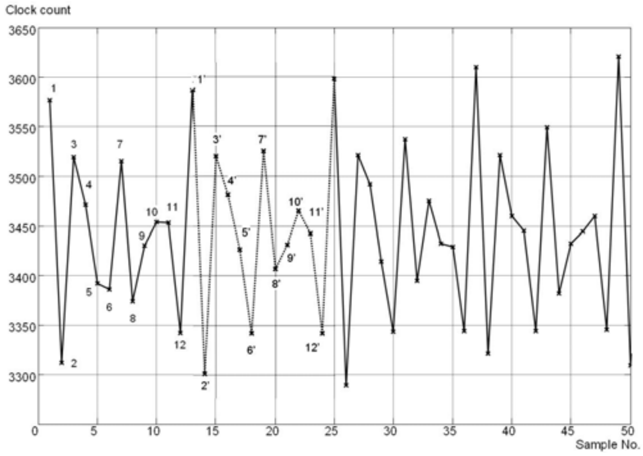

Fig. 1. The intervals of the Hall sensor updating

This paper presents a speed correction circuit for a HALL sensor signal base. This circuit is implemented in hardware description language and on filed programming gate array (FPGA), and it could calibrate the speed measurement what is caused by the misalignment of the poles of the rotor and Hall sensors. A method is discussed to estimate the error of misalignment, and the circuit structure will be introduced. Then, the synthesizing simulation results are presented to prove this circuit is workable

2 A CORRECTION OF HALL SENSOR SIGN AL BASE SPEED MEASUREMENT

Normally, the Hall sensor feedback will be used to measure motor speed if Hall sensors are build-in for commutation, and the sequence is depend on rotate direction as shown in Fig. 2. The change of the Hall sensor signal means that the rotor rotated 60 degree for 2-pole, or 60 degree for 4-pole motor. Next, the time interval between two signal changing could be measured to calculate motor speed. The speed correction method and circuit are also depended on the information of Hall sensor signals and time intervals.

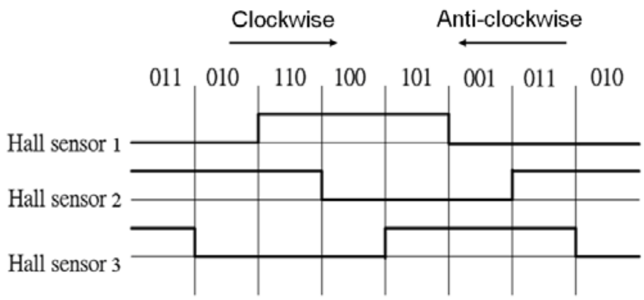

Fig. 2. The intervals of the Hall sensor updating

2.1 A calibration method of Hall sensor signal base speed measurement

A calibration method [1] is discussed to get more accurate speed estimation based on Hall sensors. To get the error ration of every sector caused by misalignments of Hall sensors and rotor poles, the motor could be driven by another constant speed motor or fixed PWM duty to free, and get every sectors average speed error ratios. The correction of speed would be based on these error ratios. As shown in Fig. 3, a zoom figure of Fig. 2, and the average clock count of a 3-phase 4-pole BLDC motor is about 3390, and the clock count samples is corrected by the error ratio and shows more accurate results. Note, in Fig. 3, the samples is a periodic signal with the period of twelve samples caused by the sensor and pole misalignments, however, the correction is indexed in only 6 Hall sensor signal and only 6 correction ratio could be used. The R.M.S. of error is reduced less than 40% of original's. If this method is used in a 2 pole BLDC motor, the effect should be better.

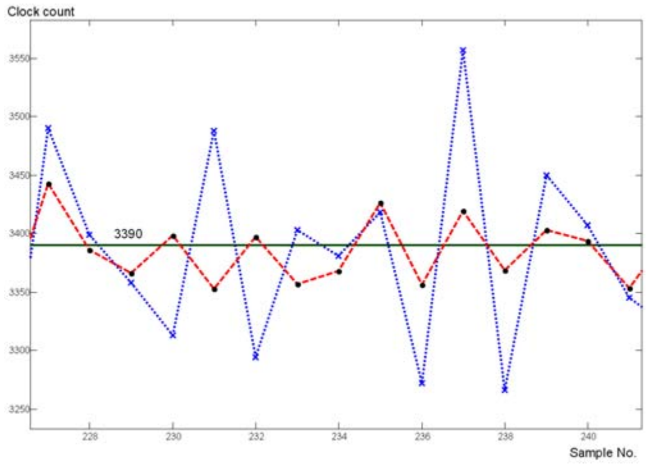

Fig. 3. The average (solid), sampling (dot) and correction (dash) clock count

2.2 A Correction circuit of Hall sensor signal base s peed measurement

Based on above discussion, a correction circuit is proposed to implement the algorithm. The system block diagram is shown in Fig. 4: there are three one-bit inputs for Hall sensor signals, six register inputs for correction ratios and clock; one output is the interrupt to inform the controller to read the new 16 bits corrected time interval and update the speed calculation.

The clock source is connected to the controller or MCU system clock, it is much faster than Hall sensor changing, and then the clock could be used to latch the Hall sensor signals. A previous Hall sensor capture is applied to latch the last the Hall sensor status, and the previous and current Hall sensor statuses are send to a compare block. When the Hall signals in two capture registers are different, an interrupt signal is declared to indicate that the rotor already rotes over a new sector, 30 or 60 degree, and the controller could get new speed measurement and change the commutation status. This interrupt signal is also used to latch the content of the clock counter into correction block, which counter is used to accumulate the clock in a sector, then the counter is reset to zero for next new sector. The signal of the previous Hall sensor capture register is employed to index the corresponding correction ratio from the six correction registers, which contents are got based on correction method what is discussed in last section. Note, to use the previous Hall sensor signal to select correction register is better than the current signal, and it could ignore the direction of a motor because it is the previous sector could be corrected. If the current Hall sensor signal is used to index, the direction should be consider in the structure and circuit would be more complicated.

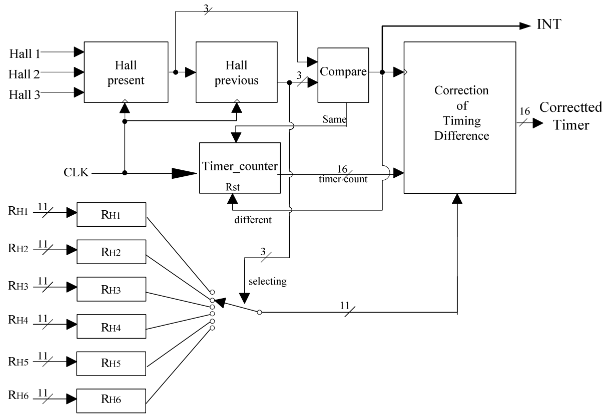

Fig. 4. The block diagram of HALL sensor signal base speed measurement

3 Hardware Implementation and Simulation Results

3.1 Hardware implementation

The structure is implemented in verilog HDL and on FPGA, Altera Cyclone II EP2C70: 176 logic elements, 63 registers and 2 embedded multiplier 9-bit elements are used. The bit width of timer counter is set to 16 bits, what is depend on clock source and lowest speed motor, means the clock number between two Hall sensor changes, and the correction ratio registers are set to 11 bits for the fraction format.

For reduction of circuit the complexity, the number format should be fixed pointed. The number correction ration is in the quasi positive I1Q10 mode, due to that the error ranges are about 15% which means correction ration is a fraction number from 0.85 to 1.15. Every correction number is multiplied with 1024 before written into the register. When interrupt occurs, the product of clock counting and correction ratio is right shifted by 10 bits, then fraction effect is achieved.

Table 1. Correction ratios

Hall sensor Index	Correction Ratio
100	1.00 = 10000000000 B
110	0.95 = 01111001100 B
010	1.05 = 10000110011 B
011	1.10 = 10001100110 B
001	0.97 = 01111000011 B
101	0.93 = 01101110101 B

3.2 Simulation Results

The simulation results are shown in this section to presented workability of the proposed structure. The values of correction ratios are list in table 1, what includes Hall sensor index, fraction mode ratios and I1Q10 mode ratios. The function is verified by Fig. 5. The clock is set on 100M Hz, 10 nS, and Hall sensor signal changes every 511 clock cycles. The output 485 is the product of 511 and correct ratio of a110, because the correction ration is indexed by previous Hall sensor signal "110", which ration is 0.95. Next out put is 511, due to previous index is 100. The simulation result shows the structure works well.

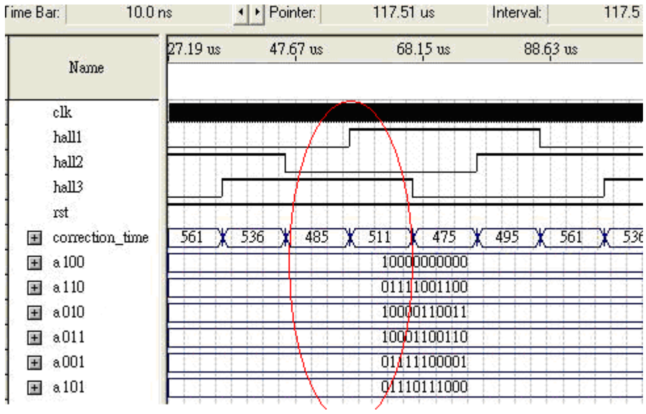

Fig. 5. The simulation results of fixed Hall sensor intervals

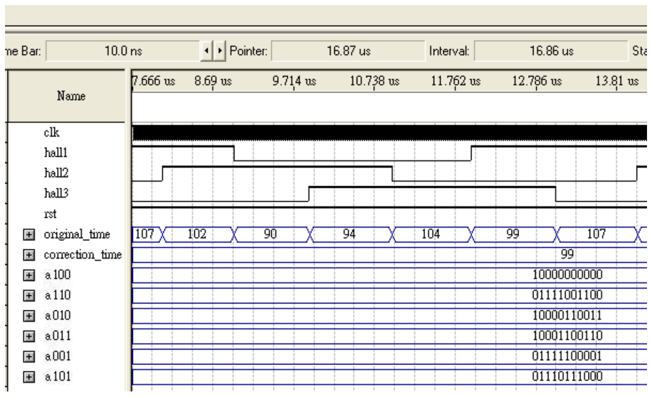

Fig. 6. The simulation results of variable Hall sensor intervals of misalignment

To get more detail simulation result, the Hall sensor intervals are set similar to real misalignments, and the counter will catch the different intervals corresponded with Hall sensor sectors. The result is present in Fig. 6, the timer counter before correction and correction output are probed. All of outputs are 99 cycles; no matter counter is capture 107 or 90. For example, when the content of counter is 90, the previous Hall sensor signal is "011", which indicates that correction ration is 1.10, and the corrected output is 99 cycles. Again, for the 107 output, the previous index is "101" and the ration is 0.93, so, the output should be 99. Note, to get more accurate result, 512 is added to product before shift to perform rounding.

4 CONCLUSION

A correction circuit of speed measurement what is based on Hall sensor signals for BLDC motors is proposed this paper. The Hall sensors are originally built in for commutation in BLDC motors, and normally there are misalignments in the placement of sensors and rotor poles in consumer motors due to cost issue. To get accurate speed, FPGA is used to implement a correction circuit, the correction ratios are prepared in the calibration processor, then a corresponding ratio what is index previous Hall sensor signal multiplier with the content of timer counter what is rest every Hall sensor changes. The simulation results show the structure is work successfully, and could provide more accurate speed measurement. Moreover, the resource requirement of the circuit is few and could be implemented easily to improve the performance of a BLDC motor system.

Acknowledgments: This work is partly supported by the National Science Council, Taiwan, under contract NSC 100-2622-E-224-006-CC3

REFERENCES

[1] Chung-Wen Hung, Cheng-Tsung Lin, Chih-Wen Liu, Jia-Yush Yen (2007), A Variable-Sampling Controller for Brushless DC Motor Drives With Low-Resolution Position Sensors, IEEE Transactions on Industrial Electronics, 54(5):2846 -2852

[2] N. Samoylenko, Qiang Han, J. Jatskevich (2008), Dynamic Performance of Brushless DC Motors With Unbalanced Hall Sensors, IEEE Transactions on Energy Conversion, 23(3):752 - 763.

[3] P.B. Beccue, S.D. Pekarek, B.J. Deken, A.C. Koenig (2007), Compensation for asymmetries and misalignment in a Hall-effect position observer used in PMSM torque-ripple control, IEEE Transactions on Industrial Electronics, 43(2): 560 - 570.

[4] S.-Y. Kim, C. Choi, K. Lee, W. Lee (2011), An Improved Rotor Position Estimation With Vector-Tracking Observer in PMSM Drives With Low-Resolution Hall-Effect Sensors, IEEE Transactions on Industrial Electronics, 58(9):4078- 4086.

[5] Anno Yoo, Seung-Ki Sul, Dong Cheol Lee, Cha Seung (2009), Novel Speed and Rotor Position Estimation Strategy Using a Dual Observer for Low-Resolution Position Sensors, IEEE Transactions on Power Electronics, 24(12):2897-2906

[6] Kuang-Yao Cheng, Ying-Tsan Lin, Chung-Hsien Tso, Ying-Yu Tzou (2002), Design of a sensorless commutation IC for BLDC motors, Power Electronics Specialists Conference, Cairns, Queensland, Australia, Jun 23-27, 2002, pp. 295-300.

An image sensor based virtual mouse including fingertip detection in face mask algorithm

Chung-Wen Hung, Hsuan T. Chang, and Cheng-Yang Chen

National Yunlin University of Science and Technology, Yunlin 640-02, Taiwan
(Tel: 886-5-534-2601)

wenhung@yuntech.edu.tw

Abstract: An image sensor based virtual mouse with fingertip detection in face mark (FDIFM) function is proposed in this paper. As the image sensors or webcams are more and more cheap and popular, the algorithms are developed to detect the fingertip location and its motions. The motion information could be used to define the mouse functions and perform a virtual mouse. When the fingertip locates in the face area, it is difficult to detected, due to similar skin colors. The FDIFM algorithm is developed to handle this exceptional situation, using the red component image of the face area, the fingertip could be detected successfully. In this paper, the algorithms and simulation results are described, and the experimental results are also presented to verify the virtual mouse workable.

Keywords: virtual mouse, image sensor, webcam, fingertip detection in face mask (FDIFM).

1 INTRODUCTION

Improving the efficiency of human computer interface (HCI) devices, such as keyboard and mouse, has been an important issue for a long time. Due to the development of new technologies and cost down, there are a lot of new HCI devices and methods are proposed, such as touch panel and its user friendly control. However, with the price reduction and popularity of a digital image capture sensor, another HCI technology which is based on image processing and detection made progress, and the Microsoft's Kinect is a good example[1], but the function focuses on TV games. Chen [2] proposed an interface method which is based on hand-gesture and facial expression, and Qzawa [3] utilized the data glove to control a robotic hand. These researches tacked a lot of CPU resource or needed some extra equipment.

A webcam based virtual mouse is proposed in this paper. As the price reduction of CMOS image sensors and the popularity of social communication software, the webcam became a regular peripheral. Based on such a low cost webcam, the simplified algorithms are development to perform the functions of a traditional mouse in this research. First, every single image frame is captured and processed with several operations, which include the background removal, the skin color detection, the background updating, and the fingertip detection. Then the fingertips are tracked, and the traveling direction and distance are measured. Furthermore, when the fingertip overlaps the user's face region, a special algorithm is proposed to detect. Finally, the specific fingertip motions are defined as to the corresponding functions of the virtual mouse. The algorithm will be discussed as following, and the experimental results also will be presented.

2 The algorithm

The algorithm includes several procedures: background removal, skin detection, hand detection, connected regions labeling, hand region extraction, fingertip detection, fingertip motion tracking, and fingertip extracting from overlapping facial region. The details and operations are described as following:

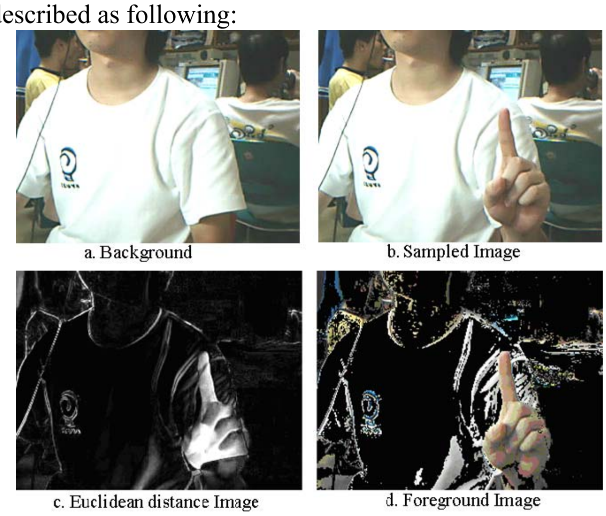

Fig. 1 The background, sampled and background-removed Images

2.1 Background Removal

First, take an image in advance as background, as shown in Fig. 1.a; then calculate the RGB Euclidean distance between sampled image, shown in Fig. 1.b, and background for every pixels as (1), Y. Cui [4]:

$$A = \sqrt{(I_{CR}(x,y) - I_{BR}(x,y))^2 + (I_{CG}(x,y) - I_{BG}(x,y))^2 + (I_{CB}(x,y) - I_{BB}(x,y))^2} \quad (1)$$

Here, I is the brightness, C and B show current sampled image and background, respectively, and R, G and B indicate red, green and blue, respectively. If the Euclidean distance of a pixel is greater than threshold, it means that this pixel is not similar to the background and will be retained. Finally, the background is removed, and the foreground is obtained, as shown in Fig. 1.c.

2.2 Skin Detection

Based on the database proposed by Maricor Sorian [5], [6], the skin detection processing is used to detect the skin region on the previous foreground image. The normalization values of red and green are determined from (2) and (3), respectively.

$$r = \frac{R}{R+G+B} \quad (2)$$

$$g = \frac{G}{R+G+B} \quad (3)$$

If the r and g values of a pixel are located in the skin region as shown in Fig. 2, in which the region is bound in a pair of 2nd order functions as (4)~(7), the pixel will be treated as the skin.

$$f_1(r) = -1.3767r^2 + 1.0743r + 0.1452 \quad (4)$$

$$f_2(r) = -0.776r^2 + 0.5601r + 0.1766 \quad (5)$$

$$W = (r - 0.33)^2 + (g - 0.33)^2 \quad (6)$$

$$s = \begin{cases} 1, & \text{if}\,(g < f_1(r))\,\&\,(g > f_2(r))\,\&\,(r > 0.2) \\ & \&\,(r < 0.6)\,\&\,(W > 0.0004) \\ 0, & \text{otherwise} \end{cases} \quad (7)$$

The S=1 marks the pixel as the skin. The result is shown in Fig. 3.

Fig. 3 The binary image of skin detection.

2.3 Hand Detection

The morphological erosion and dilation operators are used to detect the hand region in the above binary image, H. J. Lee [7]. The erosion is utilized to eliminate the small noise area, and then the dilation operation is applied to reconstruct the hand region which is shrunken and broken by the previous erosion operator. The result image of erosion and dilation operators is shown in Fig. 4, and the hand region is successfully detected with some noise blocks.

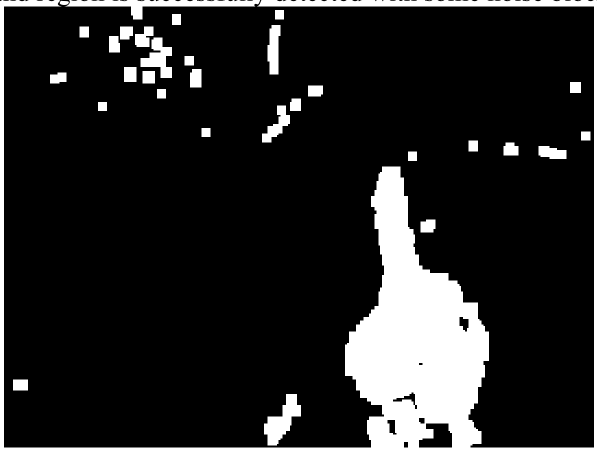

Fig. 4 The result image of hand detection.

2.4 Connected regions labeling

The result image of erosion and dilation operators would contain only few bigger skin regions. They will be labeled for every connected region for the calculation of the region size.

2.5 Hand Region Extraction

For all the connected skin labeled region, their sizes of regions are calculated. The maximum is treated as the hand region, because the user's hand is supposed to be closest to the webcam, and the other region is supposed to be noise or the region closed to the skin color. The extraction result is shown in Fig. 5, it proves that the extraction algorithm is workable.

Fig. 5 The extracted hand region.

2.6 Fingertip Detection

When the hand region is extracted, the edge detection is next processed. The Prewitt algorithm is employed to detect the edge boundary, and then the contour will be more obvious, D. Wang [8]. Next, the contour search criteria are proposed, H. Soltanian-Zadeh [9]: the lowest and leftest point of the hand region edge is the starting point; and the left-to-right and bottom-to-top search criteria are used to find the next connected pixel of edge; then the searching is repeated until back to the starting point.

When the contour of a hand is detected, the pixels are compared one-by-one to find the top point. Because the default command finger is fixed to the forefinger, and this point is treated as a candidate fingertip point. However, some other gestures would lead to a wrong detection.

To confirm this point is the fingertip point and filter out wrong hand gestures, a checking processing is necessary. Fist, based on this point, the next 10-points pair and next 15-points pair are located on the contour by forward and backward searching; then, the angles of a candidate fingertip point with the next 10-points pair and next 15-points are calculated. Based on the characteristic of a forefinger, the former angle should be bigger than latter's. Otherwise, the image will be treated as an invalid image. The fingertip detection result is shown in Fig. 6.

2.7 Fingertip Motion Tracking

If a fingertip is marked, the fingertip is tracked and the traveling direction and distance are measured. Then the direction and distance will be used to define the mouse action, like a left-key click. The Lucas-Kanade optical flow method is used to track the motions, which will be applied to measure the direction and distance, S. N. Tamgade [10].

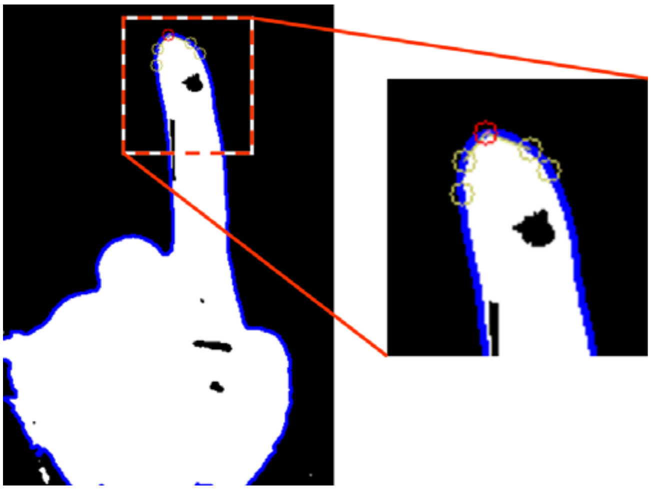

Fig. 6 The fingertip detection result.

2.8 Fingertip Motion Tracking

In normal cases, the mentioned procedures could successfully detect the fingertip and track the motions. However, some errors happen when the finger locates in the face region, because the face and finger have similar colors and the gesture region will be lost in above methods. The FDIFM algorithm is proposed to handle such situation.

First, the face mask sensing area is defined, which is based on a rectangular face mask with extended outward 50 pixels. It is used to decide that processing should fast switch to the FDIFM procedure. When the fingertip moves into the mask area, the mask area is extracted, names region of interest (ROI). Next, the negative image of the ROI is calculated, as shown in Fig. 7.a. Based on the red component of ROI negative image, the fingertip will be found, due to it is a obvious dark region in face area as shown in Fig. 7.b. Finally, the grayscale image is transformed into a binary image, and the fingertip will be detected more easily, as shown in Fig. 7.c.

a. Negative image b. Red component image c. Binary image

Fig. 7 The processed images in FDIFM algorithm.

2.8 The function definition of the virtual mouse

When the fingertip and its motion are tracking successfully, the functions of the virtual mouse could be defined by the motion of fingertip, such as the double click of fingertip indicates a click action of a mouse, and the angles of fingertips could be used to define other functions of a mouse.

To differentiate between the vertical movement and the click action, the mouse click should be defined as double click of the fingertip. If the locations of fingertip in several consecutive images show fingertip motion is in "up-down-up-down" moving, the mouse click message will be send to the PC system. Similarly, the angle of the line from the center of the minimal rectangular to the fingertip could be measurement, and then the clockwise and counterclockwise angles could be used defined as other function of a mouse. The detections are shown in Fig. 8.

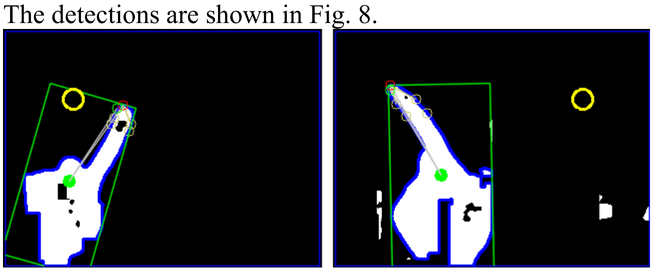

a.The fingertip move clockwise b. The fingertip moves counterclockwise

Fig. 8 The images of clockwise and counterclockwise motions detection.

3 Experimental Results

The above algorithms are developed in desktop or notebook personal computers. So the experiments are implemented on following specifications: the hardware specification is Intel Core 2 Quad 2.4GHz CPU with 3 GB DDR2 DRAM; software is programmed under Microsoft Visual Studio 2008 and program runs in Windows 7 professional 32bit OS; the image is captured by Logitech QuickCam which is set to 24bit RGB colors, 640×480 resolution, and 12 frames per second. The program occupies about 28% of CPU resource.

The fingertip detection is the base of the proposed algorithm, and the experimental result is shown in Table. 1, the average success rate is about 94.4%.

Table. 1 The correct fingertip detection rate

	Total frame	Correct fingertip frame	Success rate
User 1	600	575	95.8%
User 2	600	574	95.6%
User 3	600	540	90.0%
User 4	600	565	94.2%
User 5	600	567	94.5%
User 6	600	564	94.0%
User 7	600	573	95.5%
User 8	600	554	92.3%
User 9	600	570	95.0%
User 10	600	580	96.7%
Average			94.4%

The experimental results of the left-key click function for a virtual mouse are shown in Table. 2. Here, the rates of the User 1 and 2 are lower, which should be caused from too fast clicks. The average successful rate is about 83.5%. The other two functional experiments for clockwise- and counterclockwise-motion detections are respectively listed in Tables 3 and 4, in which the successful rates are about 95% and 100%, respectively. Due to distinct shapes, the detection rates are higher than other functions.

Table. 2 The successful click detection ratio

	Total frame	Correct fingertip frame	Success rate
User 1	20	15	75%
User 2	20	13	65%
User 3	20	18	90%
User 4	20	18	90%
User 5	20	16	80%
User 6	20	16	80%
User 7	20	18	90%
User 8	20	17	85%
User 9	20	18	90%
User 10	20	18	90%
Average			83.5%

Table. 3 The successful ratio of the clockwise motion detection

	Total frame	Correct fingertip frame	Success rate
User 1	20	19	95%
User 2	20	18	90%
User 3	20	19	95%
User 4	20	18	90%
User 5	20	18	90%
User 6	20	19	95%
User 7	20	20	100%
User 8	20	20	100%
User 9	20	19	95%
User 10	20	20	100%
Average			95%

Table. 4 The successful ratio of the counterclockwise motion detection

	Total frame	Correct fingertip frame	Success rate
User 1	20	20	100%
User 2	20	20	100%
User 3	20	20	100%
User 4	20	20	100%
User 5	20	20	100%
User 6	20	20	100%
User 7	20	20	100%
User 8	20	20	100%
User 9	20	20	100%
User 10	20	20	100%
Average			100%

4 CONCLUSION

An image sensor based virtual mouse including the FDIFM algorithm is proposed in this paper. Based on popular image sensors or webcams, the proposed algorithms could efficiently detect the fingertip locations and motions, which information could be used to replace the mouse and act as the virtual mouse. The FDIFM algorithm is also developed to handle the exceptional situation that the fingertip locates in the facial region. From the experimental results, the virtual mouse is workable, and the algorithms could be extended to other new HCI devices.

Acknowledgments: This work is partly supported by the National Science Council, Taiwan, under contract NSC 100-2622-E-224-006-CC3

REFERENCES

[1] T. Leyvand, C.Meekhof , Y.-C. Wei, J. Sun, B. Guo (2011), Kinect Identity: Technology and Experience, Computer, 44(4):94-96

[2] Q. Chen, M. D. Cordeal, E. M. Petriu, T. E. Whalen, I. J. Rudas, and A. Varkonyi-Koczy (2008), Hand-gesture and facial-expression human-computer interfaces for intelligent space applications, Proceedings of the IEEE International Workshop on Medical Measurements and Applications, Ottawa, Canada, May 9-10, 2008, pp. 1-6

[3] R. Ozawa, N. Ueda (2007), Supervisory control of a multi-fingered robotic hand system with data glove, IEEE/RSJ International Conference on Intelligent Robots and Systems, San Diego, California U.S.A, Oct. 29 - Nov. 2, 2007, pp.1606-1611
[4] Y. Cui and J. J. Weng (1996), Hand sign recognition from intensity image sequences with complex background, Proceedings of the Second International Conference on Automatic Face and Gesture Recognition, Killington, VT , USA, Oct. 14-16, 1996, pp.259–264
[5] E. Marszalec, B. Martinkauppi, M. Soriano, and M. Pietikäinen (2000), A physics-based face database for color research, Journal of Electronic Imaging, Zadar, Croatia, 9(1):32-38
[6] M. Soriano, B. Martinkauppi, S. Huovinen, and M. Laaksonen (2000), Using the Skin Locus to Cope with Changing Illumination Conditions in Color-Based Face Tracking, Proc. IEEE Nordic Signal Processing Symposium, Kolmården, Sweden, Jun. 13-15, 2000, pp.383-386
[7] H. J. Lee and J. H. Chung (1999), Hand gesture recognition using orientation histogram, Proceedings of the IEEE Region 10 Conference TENCON 99, Cheju Island, Korea, Sept 15-17, 1999, Vol. 2, pp.1355-1358
[8] D. Wang and S. Zhou (2008), Color Image Recognition Method Based on the Prewitt Operator, International Conference on Computer Science and Software Engineering, Wuhan, China, Dec. 12-14, 2008, pp.170-173
[9] H. Soltanian-Zadeh, J. P. Windham, and F. Chen (1994), Automated contour extraction using a multi-scale approach, 1994 IEEE Conference on Nuclear Science Symposium and Medical Imaging, Norfolk, VA , USA, Oct 30- Nov 5, 1994, vol. 4, pp.1797-1801
[10]S. N. Tamgade and V. R. Bora (2009), Motion Vector Estimation of Video Image by Pyramidal Implementation of Lucas Kanade Optical Flow, 2009 2nd International Conference on Emerging Trends in Engineering and Technology, Nagpur, India, Dec.16-18, 2009, pp.914-917

The modeling and implementation of tri-rotor flying robot

Jie-Tong Zou [1], Kuo-Lan Su [2], Haw Tso [1]
[1] Department of Aeronautical Engineering National Formosa University, Taiwan
[2] Graduate school Engineering Science and technology, National Yunlin University of Science & Technology
(Tel: +886-5-6315556, Fax: +886-5-6312415)

E-mail: scott@nfu.edu.tw, sukl@yuntech.edu.tw, alan29433973@yahoo.com.tw

Abstract: The objective of this study is going to develop a tri-rotor flying robot, which adopts the Y-shaped three-rotor structure. In order to balance the yaw torque produced by the three rotors, it installs the RC servo motor and linkage on the tail axis, so as to improve the angle of the rolling axis of the tail motor. Moreover, through the torque generated by the horizontal component of the lift from the inclined motor on the tail axis, it balances the yaw torque of the three rotors.

The dynamic equations of the tri-rotor flying robot were determined in this paper. The relationship between motor thrust, angular acceleration and voltage input were also studied in this research. In order to study the effect of control parameters on the flight stability completely, this study develops a universal stability experimental platform to help tuning the control parameters safely. Based on this, the tri-rotor flying robot can rapidly change flying gesture and avoid oscillation.

Finally, we made some indoor and outdoor flight tests. From the experimental results, the tri-rotor flying robot can fly and hover stably in the sky.

Keywords: tri-rotor, tricopter, flying robot, dynamic equations, stability experiment, hover

I. INTRODUCTION

The unmanned aerial vehicles (UAV) are widely applied in aerial photography, marine or air pollution detection, aerial security surveillance and disaster response. The lifting force of a rotorcraft is mainly the air reaction force produced by the rolling of one or multiple rotors. However, when the rotor provides lift, the fuselage will also tend to roll towards the opposite direction due to the effect of reaction torque. For the multi- rotor helicopter, it mostly uses the opposite rolling between the rotors to balance the effect of the reaction torque.

Fig. 1 is the real view of the tri-rotor flying robot. The yaw control in this study adopts the variable inclination angle mechanism of the back rotor. The rolling axis of the back rotor uses the RC servo motor and the linkage mechanism to control the variable declination angle. The rolling axis is fixed by using two pillow block ball bearings. Yaw angular speed is detected by a MEMS (Micro Electro Mechanical Systems) based Gyro, which is also used to adjust the inclination angle of the rolling axis of the back propeller. These are then taken as the compensation of the yaw torque produced by the three rotors.

Fig. 1 Real view of the tri-rotor flying robot

II. FLIGHT PRINCIPLE OF THE Y-SHAPED TRI-ROTOR FLYING ROBOT

The tri-rotor flying robot in this study adopts the Y-shaped three-rotor structure (as shown in Fig. 2). The three rotors are divided into two right-handed and one left-handed, one right-handed and two left-handed, or three right-handed. In order to balance the yaw torque produced by the three rotors, it installs the RC servo motor and linkage structure on the tail axis, so as to improve the angle of the rolling axis of the motor on the tail axis. Moreover, through the torque generated by the horizontal component of the lift from the inclined motor (motor 3) on the tail axis, it balances the yaw torque of the three rotors.

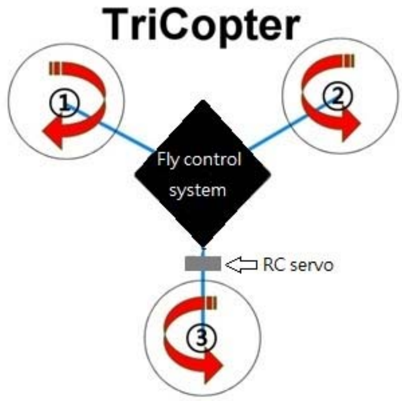

Fig. 2 Rolling directions of the propellers of the Y-shaped tri-rotor flying robot

Below will introduce the flight principle of the tri-rotor flying robot:

- *Fly forwards:*

When flying forwards, motor 1and 2 must decelerate, while motor 3 on the tail axis must accelerate. As a result, the fuselage of the tricopter is inclined forwards, so it flies towards the same direction. On the contrary, when flying backwards, motor 1and 2 must accelerate, while motor 3 must decelerate.

- *Fly to the right direction:*

When the tri-rotor flying robot flies to the right direction, motor 1 on the left side must accelerate, while motor 2 on the right side must decelerate, so as to allow the fuselage incline to the right side and make the tricopter fly to the right direction.

- *Clockwise yaw*

When the tri-rotor flying robot yaws in the clockwise direction, it needs to use the RC servo motor and linkage to drive the propeller of the motor 3 inclined in the left side. When the motor 3 rolls, it will generate the clockwise yaw torque, so as to make the tri-rotor flying robot yaw in the clockwise direction.

III. KK MULTICOPTER FLIGHT CONTROL SYSTEM

The KK multicopter controller (as shown in Fig. 3) is a kind of flight control system, which can be applied in the multi-rotor aircraft with different axes, including: single-axis, dual-axis, tri-axis, quad-axis, hex-axis, eight-axis, as well as the aircraft with fixed wings. The KK multicopter flight controller has an Atmega micro-processor, and tri-axis Gyro that can detect the angular velocity of roll, pitch and yaw directions, as well as 8-channel PWM signal output. It can control 8 motors or RC servos at most, so that the aircraft can fly stably.

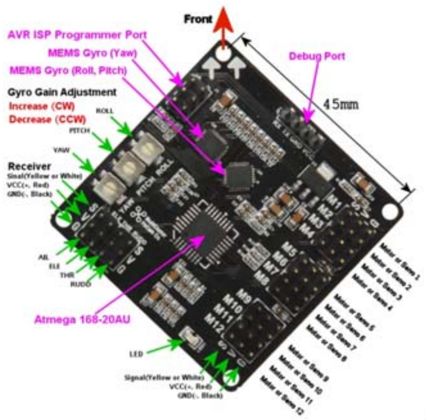

Fig. 3 KK multicopter flight controller

3.1 Basic functions of KK multicopter flight controller:

Tri-axis Gyro-stabilized system has contra-rotating Gyro chips, with the functions of electronic adjustment and calibration of the accelerator pedal and locking protection. Fig. 4 is the hardware architecture of the flight controller applied on the tricopter, in which the remote control receiver is used to receive the remote control signal sent from the radio controller. And the MEMS gyro can be used to detect the angular velocity of the directions of roll, pitch and yaw for the three rotors. The simulated voltage output by the gyro can be directly read by the single chip Atmega 168-20AU on the flight controller, based on which the axis declination angles of the three rotors are calculated. The single chip on the flight controller can control the speed difference between the three motors, and the declination angle of the RC servos, so as to maintain the balance gesture of the three rotors.

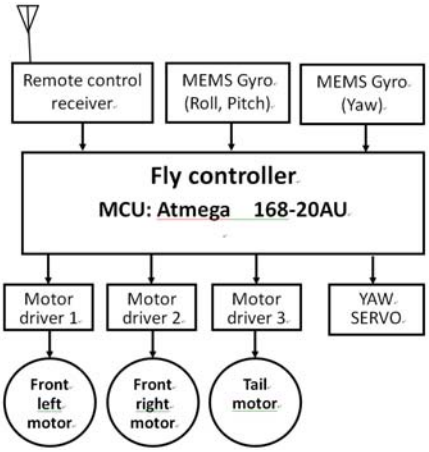

Fig. 4 Hardware architecture of the KK multicopter flight controller applied on the tri-rotor flying robot

IV. MATHEMATICAL MODEL

Fig. 5 is diagram of dynamic equation of the tricopter, in which the lower right side is the diagram of dynamic equation of the Yaw control. That is because in Yaw control, RC servo motor drives the tail axis to change the declination angle of the tail axis.

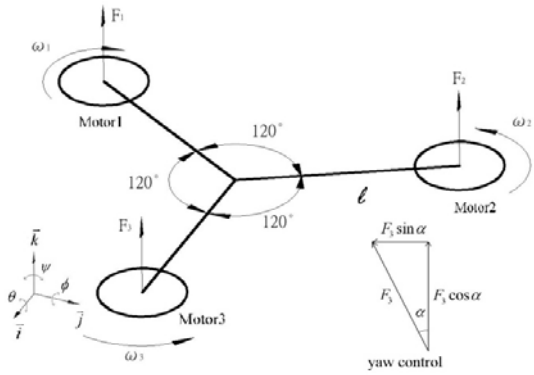

Fig. 5 Diagram of dynamic equation of the tri-rotor flying robot

4.1Moment of Inertia of tricopter

Fig. 6 is the diagram of the moment of inertia of the tri-rotor flying robot. When calculating the inertia torque of the tri-rotor flying robot, we assume the fuselage is rectangular shape, the three motors are cylinder shape, and moreover, the inertias of the round rods of the axes are neglected.

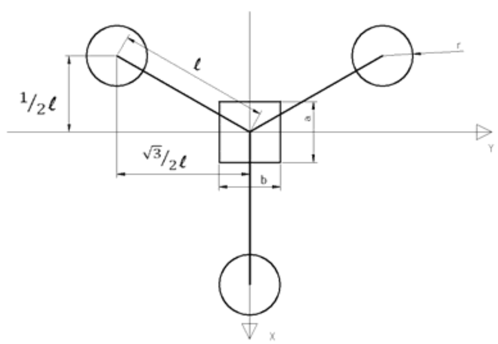

Fig. 6 moment of inertia of the tri-rotor flying robot

Moment of inertia of each axis:

- Moment of inertia about axis X:

The total moment of inertia about X-axis:

$$I_{xx} = \frac{3}{2}m\ell^2 + \frac{1}{12}m_0 b^2 + \frac{1}{12}m(3r^2 + h^2) \tag{1}$$

- Moment of inertia about axis Y:

The total moment of inertia about Y-axis:

$$I_{yy} = \frac{3}{2}m\ell^2 + \frac{1}{12}m_0 a^2 \tag{2}$$

- Moment of inertia about axis Z:

The total moment of inertia about Z-axis:

$$I_{zz} = \frac{1}{12}m_0(a^2 + b^2) + 3m\ell^2 \tag{3}$$

4.2 Relationship between motor thrust and voltage

The thrust of the motors on the rotorcraft is the most important variables to determine the load and lift of the entire craft. The pre-condition to select the suitable motor is the net weight and expected payload of the entire tricopter. After that, it needs to determine the cruising ability of the craft, namely, how long it can fly. Next, it will select the suitable battery based on the voltage and power consumption of the motor. Therefore, the relation between the motor and voltage needs to be discussed.

The air speed generated by the propeller:

$$V_h = \sqrt{\frac{F}{2A\rho_a}} \tag{4}$$

$$P_h = F\sqrt{\frac{F}{2A\rho_a}} \tag{5}$$

where: P_h:*the power induced in air*

F: thrust of the propeller

ρ_a:*air density*

A: area scanned when the properller spins

Motor torque:

$$\tau_m = K_t F \tag{6}$$

voltage input can be obtained as follows:

$$F = 2\rho_a A\left[\frac{f\eta K_t}{K_q}\right]^2 V^2 \tag{7}$$

where: K_t:*constant of torque*

4.3 Relationship between angular acceleration of the motor and the voltage

$$\mathrm{V} = \frac{\mathrm{JZ}\dot{\Omega}}{\mathrm{K_q}} + \mathrm{K_e}\Omega + \frac{ZD\Omega^2}{K_q} \tag{8}$$

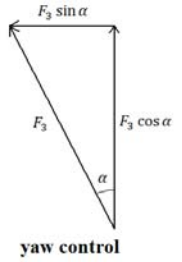

Fig. 7 Thrust force diagram of Yaw control

4.4 Relationship between the declination angle of the Yaw motor and the Yaw control

The yaw control of the tricopter is realized by the declination angle of the motor M_3. The declination angle is determined by a RC servo motor and a linkage. Assume the thrust force of the tail motor M_3 is F_3, and the declination angle is α, as shown in Fig. 7. The vertical component of F_3 is $F_3 \cos\alpha$, and the horizontal component of F_3 is $F_3 \sin\alpha$.

4.5 The principle of rotor torque

The torque rotors have a circular are profile. With this profile the torque forces increase as the angle of attack increases. While the rotor blades are fixed in place, they are quite flexible and probably change attack angle when they are accelerated.

$$F_{drag} = \frac{\rho C_d U^2 S}{2} = K_d \rho_{mp}^2 \tag{9}$$

Where :ρ is the fluid density, U is the flow velocity, C_d is the torque coefficient and $\mathrm{S} = \mathrm{span} \times \mathrm{chord}$

4.6 Relationship between the angular acceleration and voltage of the motors

When the tricopter rolls, pitches, yaws and moves vertically, it is directly related with the motor's angular velocity or voltage input. Rolling to axis X is called Roll, to axis Y is Pitch, to axis Z is Yaw, moving along the Z-axis is vertical motion.

Assume the rolling torque is τ_{xx}, angular acceleration is $\ddot{\theta}$, moment of inertia of axis X is I_{xx}, unit vector of axis X is $\hat{\imath}$, therefore, the rolling torque is:

$$\tau_{xx} = I_{xx}\ddot{\theta}\hat{\imath} \tag{10}$$

- Rolling about X-axis

The rolling motion equation finally:

$$\ddot{\theta} = \frac{\sqrt{3}\rho_a A\ell}{I_{xx}}\left[\frac{f\eta K_t}{K_q}\right]^2 ({V_2}^2 - {V_1}^2) \tag{11}$$

- Pitching about Y-axis

The pitching motion equation finally:

$$\ddot{\phi} = \frac{2\rho_a A\ell}{I_{yy}}\left[\frac{f\eta K_t}{K_q}\right]^2 [\frac{({V_1}^2 + {V_2}^2)}{2} - {V_3}^2\cos\alpha] \tag{12}$$

- Yawing about Z-axis

The yawing motion equation finally:

$$\ddot{\psi} = \frac{F_{drag}}{I_{zz}} - \frac{2\rho_a A\ell}{I_{zz}}\left[\frac{f\eta K_t}{K_q}\right]^2 {V_3}^2 \sin\alpha \tag{13}$$

- Vertical acceleration

The vertical lift is generated by the three propellers, in which the thrust of the vertical component force of motor M_3 is $F_3\cos\alpha$. The resultant force of three motors is vertical to the plane of three propellers. If the pitch angle (ϕ) and roll angle (θ) are not equal to zero. The Z-axis component of the resultant force is $F_{total}\cos\theta\cos\phi$, which is applied on the centroid of the tricopter.

The lift in the centroid is:

$$F_{all} = Ma_z = (F_1 + F_2 + F_3\cos\alpha)\cos\theta\cos\phi - Mg \tag{14}$$

Substitute it into equation (7) to get the relationship between the vertial acceleration and input voltage of motor:

$$a_z = \frac{2\rho_a A}{M}\left[\frac{f\eta K_t}{K_q}\right]^2 \left(V_1{}^2 + V_2{}^2 + V_3{}^2 \cos\alpha\right)\cos\theta\cos\phi - g \quad (15)$$

V. EXPERIEMENTS OF THE TRI-ROTOR AERIAL VEHICLE

5.1 The universal test platform:

The gains of the response parameters of pitch, roll and yaw on KK multicopter flight controller need to be slightly adjusted, so we made a universal test platform to adjust the gains of pitch, roll and yaw for the tri-rotor flying robot, with the expectation to rapidly return to the stable gesture without oscillation state. The universal test platform (as shown in Fig. 8) is designed to test the stability and balance of the tricopter. The biggest advantage of this test platform is to conduct the balance test of pitch, roll and yaw in all directions, and the error between the frictional force and the inertia of the test platform is the smallest.

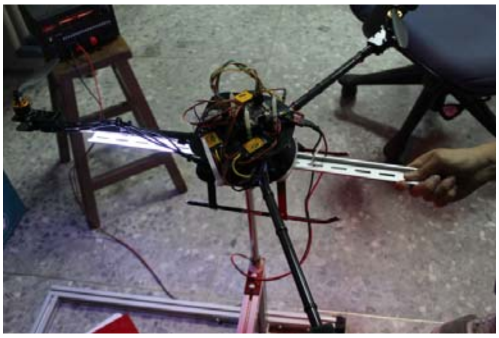

Fig. 8 Mount the tricopter on the universal test platform

5.2 Outdoor flight test

In terms of outdoor flight test, comparing the generation I tri-rotor flying robot (without KK multicopter installed) with the generation II tri-rotor flying robot with KK multicopter installed, it is found the latter one performs better than the former one in terms of auto-hovering and stability. Fig. 9 is the actual test of outdoor flight for the generation II tri-rotor flying robot with KK multicopter installed.

Fig. 9 Outdoor flight test of the tri-rotor flying robot with KK multicopter installed

VI. CONCLUSION

The rolling speed of the rotor on the fueling helicopter is not suitable for indoor flight, and there is potential injury risk of the operator in case of high rolling speed. Moreover, the waste gas produced by burning the fuel will cause environmental pollution. Therefore, using the brushless motor as the resource of driven force is safe and environmental-friendly.

At present, the stable hovering of the tri-rotor flying robot has been completed, which is quite good flight platform. When studying this copter, most cases are the application of chemical, biological and radioactive (C.B.R.) detection, reconnaissance combat, disaster prevention and criminal prevention. The purpose of this study expects the stability of the tri-rotor flying robot can reach some level, and the tri-rotor flying robot can fly indoor or outdoor with hovering in the fixed indoor point, so as to accomplish the assigned tasks.

ACKNOWLEDGMENT

This work is sponsored by the National Science Council, Taiwan, Republic of China under grant number NSC 99-2221-E-150 -063.

.

REFERENCE

[1] Wooseok Choi, Hyunsoo Koo, and Se-han Lee, "Stabilization Control of an Aerial vehicle by Experimental Setup", 2007.
[2] Marcelo H. ANG, JR. Vassilios D. Tourassis, "Singularities of Euler and Roll-Pitch-Yaw Representations",1987.
[3] Phillip Mc Kerrow, "Modeling the Draganflyer four-rotor helicopter", 2004.
[4] Haomiao Huang, Gabriel M. Hoffmann, Steven L. Waslander, Claire J. Tomlin , "Aerodynamics and Control of Autonomous Quadrotor Helicopters in Aggressive Maneuvering",2009.
[5] Atheer L. Salih, M. Moghavvemi, Haider A. F. Mohamed and Khalaf Sallom Gaeid , "Modeling and PID Controller Design for a Quadrotor Unmanned Air Vehicle".
[6] Matko Orsag, Marina Poropat, Stjepan Bogdan, "Hybrid fly-by-wire quadrotor controller".
[7] Engr. M. Yasir Amir, Dr. Valiuddin Abbass, "Modeling of Quadrotor Helicopter Dynamics", 2008.
[8] Chang, Hao-Chien, "Development and Test of Micro-quadrotor Helicopter" , master paper from Graduate Institute of Opto-Mechatronics of Department of Automation Engineering, Chienkuo Technology, 2007
[9] http://www.mikrokopter.de/ucwiki/en/MikroKopter/
[10] http://www.youtube.com/watch?v=pIBqzTtdpMg
[11] http://www.youtube.com/watch?v=PW9z61z9LC0&feature =related
[12] http://www.youtube.com/watch?v=wZJzFDYrzY0&feature =related
[13] http://www.rcexplorer.se/projects/tricopter/tricopter.html
[14] http://shrediquette.blogspot.com/
[15] http://www.mcselec.com/index.php?option=com_content& task=view&id=263&Itemid=57

The Seventeenth International Symposium on Artificial Life and Robotics 2012 (AROB 17th '12),
B-Con Plaza, Beppu, Oita, Japan, January 19-21, 2012

Path Planning of Fire Escaping System for Intelligent Building

Hsu-Shan Su[1], Kuo-Lan Su[2]

1. graduate school Engineering Science and technology, National Yunlin University of Science & Technology
2. Department of Electrical Engineering, National Yunlin University of Science & Technology, Taiwan
(Tel: +886-5-5342601, Fax: +886-5-5312065)

E-mail: sukl@yuntech.edu.tw

Abstract: We present the path planning techniques of the fire escaping system using multiple smart mobile robots for intelligent building. The fire escaping system contains a supervised computer, an experimental platform, some fire detection robots and some navigation robots. These mobile robots have the shape of cylinder and its diameter, height and weight is 10cm, 15cm and 1.5kg, and contain a controller module, two DC servomotors (including drivers), three IR sensor modules, a voice module and a wireless RF module, and acquire the detection signal from reflective IR sensor through I/O pins, and receive the command from the supervised computer via wireless RF interface. The fire detection robot carries the flame sensor to detect fire sources. The supervised computer controls the fire detection robots to detect fire source moving on the grid based experiment platform, and calculates the more safety escaping path using piecewise cubic Bezier curve on all probability escaping motion paths on the user interface. Then the system uses A* searching algorithm to program escaping motion paths to approach to Bezier curve. Then the navigation robot guard peoples moving to the safety area or exit door using the escaping motion path. In the experimental results, the supervised computer can programs the escaping paths using the proposed algorithms, and presents the scenario using the multiple smart robots on the platform. The user interface transmits the motion command to the mobile robots moving on the grid based platform, locates the positions of fire sources by the fire detection robots. The navigation robots guard peoples leaving the fire sources using the low risk escaping motion path, and moves to the exit door.

Keywords: path planning, fire escaping system, multiple smart robots, intelligent building, wireless RF module, piecewise cubic Bezier curve, A* searching algorithm

I. INTRODUCTION

Fire event is one of the great scourges on the human life. Thousands of people are injured each year by accidental fire event explosions on the known or unknown environment. There are approximately many thousand million dollars buried each year in many countries. Fire event is many risks to human life and property of societies which must be managed. How to develop a safety processing method to detect fire sources and guard peoples leaving the dangerous environment very quickly is a challenge problem.

In the past literatures, many experts research in the mobile robot. Wang et al [1] develops a multisensor fire detection algorithm using neural network. One temperature and one smoke density sensor signal are fused for ship fire alarm system. Healey et al. [2] presents a real-time fire detection system using color video input. The spectral, spatial, and temporal properties of fire were used to derive the fire-detection algorithm. Neubauer [3] apply genetic algorithms to an automatic fire detection system. The on-line identification of stochastic signal models for measured fire signals was presented. Ruser and Magori [4] described the fire detection with a combination of ultrasonic and microwave Doppler sensor. Luo and Su [5, 6] use two smoke sensors, two temperature sensors and two flame sensors to detect fire event, and diagnosis which sensor is failure using adaptive fusion method. These papers have not considered how to program the escaping paths on the fire environment on real-time, and reduce the risks of human life and property.

The paper considers the problems of the fire event, and uses the multiple robot system working together. Mobile robots are active detection modules to be more merits than passive detection modules, and are applied in fire source detection and escaping system. The multiple mobile robot system has more advantages than one single robot system [7]. First, the multiple mobile robots have the potential to finish some tasks faster than a single robot [8]. Furthermore, using several robots introduces redundancy. Multiple mobile robots therefore can be expected to be more fault tolerant than only one robot. Another advantage of multiple mobile robots is due to merging of overlapping information, which helps compensate for sensor uncertainty [9]. How to program the escaping motion path in the fire area is a important research problem. The paper uses piecewise cubic Bezier curve and A* searching algorithm to program the safety escaping path, and guards people leaving the fire area using navigation robots.

II. SYSTEM ARCHITECTURE

The system architecture of the fire escaping system is shown in Fig. 1, and contains a supervised computer, an experimental platform, some wireless RF modules, some fire detection robots and some navigation robots. The supervised computer transmits the command to control all mobile robots, and receives detection signal, and location, and orientation, and ID code of each mobile robot via wireless RF interface. The fire detection robot (FDR) detects fire sources using flame sensors moving along the experimental platform. The navigation robot (NR) guards people leaving the fire sources according to the programmed escaping motion path. The supervised computer transmits motion command to the mobile robots, and improves the mobile robot moving to the assigned location or not.

The mobile robot has the shape of cylinder, and is equipped with a microchip (MCS-51) as the main controller. Two DC servomotors transmit the pulse signals to the controller, and program orientation and displacement according to pulse numbers. The reflective IR sensors detect obstacles and cross points of the experimental platform, and decide the location of the mobile robot. The flame sensor is R2686 to detect fire sources on the front side of the mobile robot, and detection range is about 6m. The mobile robot can control two DC servomotors and voice module through I/O pins, and communicate with the supervised computer using wireless RF module. The core of the RF module is microprocessor (AT89C2051), and communicates with the controller via wire series interface (RS232).

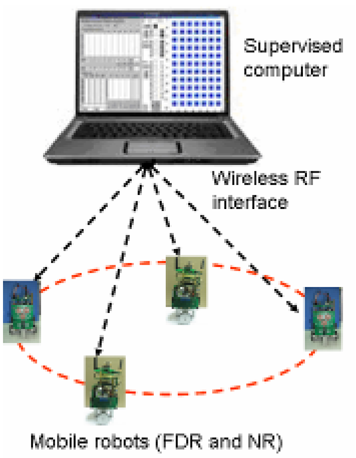

Fig. 1. System architecture

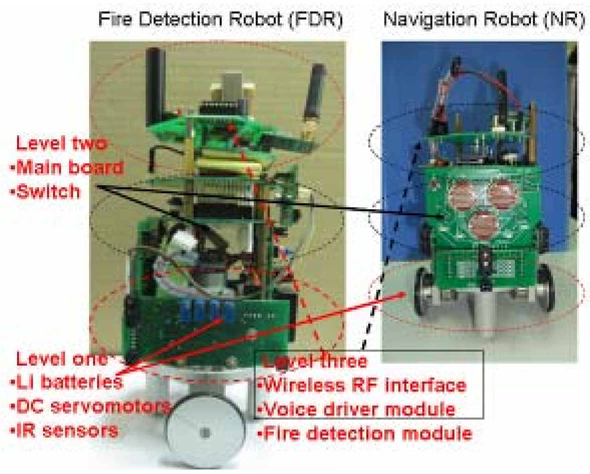

Fig. 2. The mobile robots (FDR and NR)

The structures of the two mobile robots are shown in Fig. 2. The two mobile robots contain some hardware circuits that are classified three levels. The level one of the mobile robot is two DC servomotors, three IR sensor modules and Li batteries. The three reflective IR sensors are embedded on the right side, left side and front side of the mobile robot. In general, the mobile robot moves on the aisle of the experimental platform, and detects obstacles using the three reflective IR sensors. Otherwise the mobile robot detects obstacles on the right side, left side and front side. The power of the mobile robot is three Li batteries to be connected with parallel arrangement. The level two of the mobile robot has main board. The controller of the mobile robot receives the status of the environment, and communicates with the supervised computer via wireless RF interface. The switch input can turn on the power of the mobile robot, and selects power input to be Li batteries or adapter. The level three contains a wireless RF module, a fire detection module and a voice driver module for the FDR. The NR has not fire detection module in the level.

The encoder module of the DC servomotor calculates the movement displacement on the experimental platform. We can set the pulse numbers for per revolution to be A, and the mobile robot moves total pulse numbers to be B. The controller of the mobile robot can calculates the movement displacement D on the platform as following

$$D = 4.25 \times \pi \frac{B}{P} (cm) \tag{1}$$

The diameter of the driver wheel is 4.25 cm. We can calculate per pulse number to be 0.0845cm displacement. Each grid of the platform is 30cm to be computed about 355 pulse numbers. Users can set the grid numbers for mobile robots moving on the platform. The controller of the mobile robots improves the motion trajectory to be right according to the pulse numbers.

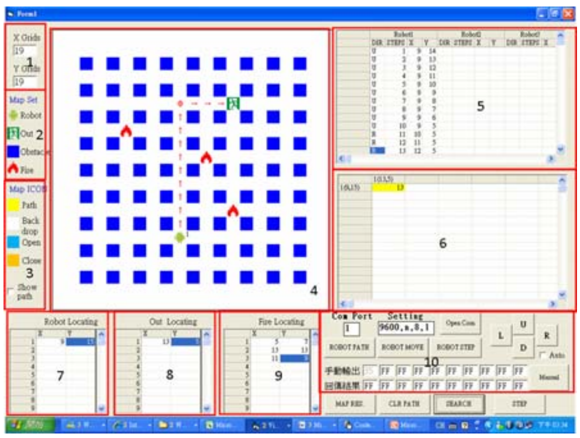

Fig. 3. The user interface

The user interface of the multiple mobile robot based escaping system has ten parts to be shown in Fig. 3. Users can set the size of the experimental platform in the part "1". The graphic labels of each function are listed in the part "2" and "3". Such as fire source, exit door, FDR and NR. The part "4" is the experimental platform to display the motion path that is computed by piecewise cubic Bezier curve and A* searching algorithm. The part "5" displays the searching processing of A* searching algorithm. The part "6" calculates the cost functions for navigation robot moving to the exit door. The supervised computer transmits the control command to the mobile robot, and receives the status of the mobile robot, and displays the position of the mobile robot moving on the platform simultaneously to be shown in the part "7". The parts "8" and "9" display locations of exit doors and fire sources. The part "10" sets the communication protocol between the user interface and mobile robots. The communication port of the user interface is 1, and sets baud-rate to be 9600.

III. PATH PLANNING

We use Piecewise cubic Bezier curve (PCBC) to program the escaping path of the intelligent building, and use A* searching algorithm to approach the programmed escaping path and decide the final escaping motion path to leave the fire sources using mobile robots. The piecewise cubic Bezier curve (PCBC) is used between each waypoint to connect with smooth curve. The equation of a cubic Bezier curve is listed as following [10].

$$\vec{p}(t) = \vec{a}t^3 + \vec{b}t^2 + \vec{c}t + \vec{p}_0 , \quad \text{For } 0 < t < 1$$
$$\text{where } \vec{p} = (x, y), \vec{c} = 3(\vec{p}_1 - \vec{p}_0) \tag{2}$$
$$\vec{b} = 3(\vec{p}_2 - \vec{p}_1) - \vec{c}, \vec{a} = \vec{p}_3 - \vec{p}_0 - \vec{b} - \vec{c}$$

Since the parameter of Bezier curve is not time or distance dependence, the curve trajectory cannot be used directly. Some researchers used a modification method of curves as a time variable [11]. Others used an approximation of curves by dividing the parameter t into n intervals [13].

We use numerical method to calculate parameter t of Bezier curves with respect to the distance s of curve. If the curve parameter t of the current position can be calculated, then the directional vector of the curve can be calculated at the position, too. Finally, we can fine the relation between the distance and the parameter t can be shown in equation (3). We can use a fourth order Runge-Kutta method to calculate the inverse of the equation as following.

$$\frac{ds}{dt} = \sqrt{\left(\frac{d}{dt}x(t)\right)^2 + \left(\frac{d}{dt}y(t)\right)^2} = S(t) \tag{3}$$

$$t_{n+1} = t_n + T(t_n, s_n)$$
$$\text{where } T(t_n, s_n) = \Delta s \frac{(f_1 + 2f_2 + 2_3 + f_4)}{6} \tag{4}$$
$$f_1 = \frac{1}{S(t_n)}, \ldots, f_4 = \frac{1}{S(t_n + \Delta s f_3)}$$

Finally, we can calculate the directional vector as following [12].

$$\vec{V} = \left(\frac{dx(t)}{dt}, \frac{dy(t)}{dt}\right) \tag{5}$$

We use the proposed method to program the escaping path to be a curve. The programmed curve is tuning by two control points that are fixed on the fire sources. Then we use A* searching algorithm to improve the curve to be applied in the grid based experimental platform. We select the minimum distance between the programmed Bezier curve and the improved escaping motion path. A* searching algorithm is explained in the reference [14].

IV. EXPERIMENTAL RESULTS

In the fire escaping system, we use multiple mobile robots to detect fire sources on the experimental platform to be shown in Fig. 4. The mobile robots transmit the location of fire source to the supervised computer, and detect the other fire source moving on the horizontal direction and vertical direction. We use candle to present fire source on the experimental platform. The mobile robot starts at the initial position is shown in Fig. 4(a). The mobile robot moves one grid, and turns right to face the aisle. Then the mobile robot finds the first fire source using flame sensor, and transmits the detection results to the supervised computer via wireless RF interface. The fire source is detected by the mobile robot, and is recoded the horizontal direction on the user interface. The fire detection robot moves over the horizontal direction to record the positions of the three flame sources. The supervised computer only knows the horizontal locations of the three fire sources, and can't appear the fire symbol on the user interface. The experimental results are shown in Fig. 4(b) - (d).

Then the mobile robot turns right 90^0 to detect the vertical direction of the platform. Finally, the robot (FDR) detects the vertical locations of the three flame sources to be shown in Fig. 6(e) - (g), and transmits vertical locations of the three fire sources on the user interface of the supervised computer. The supervised computer locates the coordinate locations of the three flame sources.

Next the supervised computer uses piecewise cubic Bezier curve to program the escaping curves from the people to the exit door to be shown in Fig. 5(a). The leaving people are the start position, and the exit door is the target position. The navigation robot can't moves according to the escaping curve. The supervised computer uses A* searching algorithm to decide the final escaping motion path that is approach to the escaping curve. The experimental result is shown in Fig. 5(b). We can see the final escaping motion path to be near the escaping curve. The final escaping motion path is plotted along the aisle of the experimental platform, and is implemented the movement scenario by the navigation robots. Finally, the navigation robot guards the people moving to the exit door, and leaves the three fire sources. The experimental results are shown in Fig. 5(c) – (h).

(a)

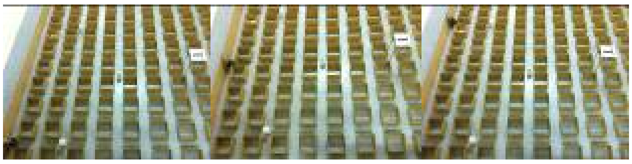

(b) (c) (d)

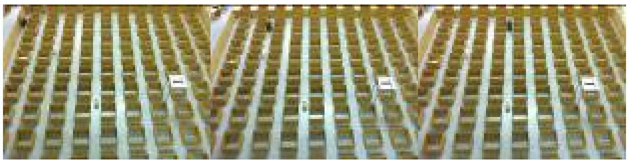

(e) (f) (g)

Fig. 4. FDR detects fire sources

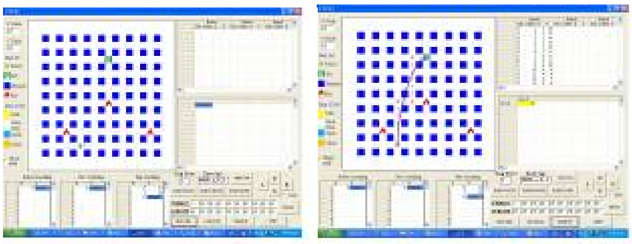

(a) (b)

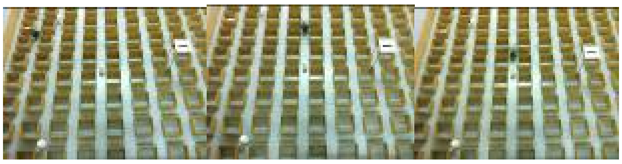

(c) (d) (e)

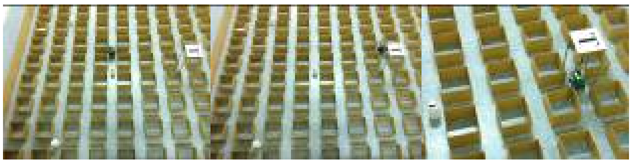

(f) (g) (h)

Fig. 5. NR guard people leaving fire sources

V. CONCLUSION

We have developed the fire escaping system to guard peoples leaving the dangerous area using some smart mobile robots. The system contains a supervised computer, some wireless RF modules, a experimental platform and some mobile robots. Mobile robots contain two types. One is fire detection robot; the other is navigation robot. In general, the intelligent mobile robot has huge size, and is not easily to implement the experimental scenario in the environment. We use some smart mobile robots to integrate the supervised computer to instead of the huge size based intelligent mobile robots. The supervised computer programs the escaping path using piecewise cubic Bezier curve and A* searching algorithm, and controls multiple mobile robots to present the movement scenario via wireless RF interface. In the future, we want to extend the escaping path programming algorithms using mobile robot, and develop more application fields of the multiple robots' system to be work cooperation in free space. The mobile robot can communicates with the other robots, and combines with the passive security modules in the intelligent building.

ACKNOWLEDGMENT

This work was supported by the National Science Council of Taiwan, (NSC 100- 2221- E-224-018)

.

REFERENCE

[1] Wang X .H., Xiao J. N., Bao M. Z. (2000), A ship fire alarm system based on fuzzy neural network,in Proceedings of the 3rd World Congress on Intelligent Control and Automation, Vol. 3, pp. 1734 -1736.

[2] Healey, G., Slater, D., Lin, T., Drda et al (1993), A system for real-time fire detection, in Proceedings of IEEE Computer Society Conference on Computer Vision and Pattern Recognition, pp. 605-606.

[3] Neubauer A. (1997), Genetic algorithms in automatic fire detection technology, Second International Conference On Genetic Algorithms in Engineering Systems: Innovations and Applications, pp. 180-185.

[4] Ruser H., Magori V. (1998), Fire detection with a combined ultrasonic-microwave Doppler sensor, in Proceedings of IEEE Ultrasonics Symposium, Vol.1, pp. 489-492.

[5] Luo R. C., Su K. L., Tsai K. H. (2002), Fire detection and Isolation for Intelligent Building System Using Adaptive Sensory Fusion Method, The IEEE International Conference on Robotics and Automation, pp.1777-1781.

[6] Luo R. C., Su K. L., Tsai K. H. (2001), Intelligent Security Robot Fire Detection System Using Adaptive Sensory Fusion Method, The IEEE International Conference on Industrial Electronics Society, pp.2663-2668.

[7] Cao Y. et al (1997), Cooperative mobile robotics: antecedents and directions, Autonomous Robots, 4(1), pp.7-27.

[8] Guzzoni D. et al (2006), Many Robots make short work, AI Mag., 18(1), pp 55-64.

[9] Burgard W., M. Moors et al (2005), Coordinated Multi-Robot Exploration, IEEE Transaction on Robotics, 21(3), pp.376-386.

[10] Newman P. Bosse M., Integrated Local Trajectory Planning and Avoidance, The Department of Ocean Engineering at MIT.

[11] Khatib M., Jaouni H., Chatila R.et al (1997), Dynamic Path Modification for Car-Like Nonholonomic Mobile Robot, IEEE International Conference on Robot, Autom., Albuquerque, New Mexico, pp.2920-2925.

[12] Hwang J. H., Arkin R. C. and Kwon D. (2003), Mobile Robots at Your Fingertip: Bezier Curve on-line Trajectory Generation for Supervisory Control, IEEE/RSJ International Conference Robots System, Las Vegas, NV, pp.1444-1449.

[13] Komoriya K. Tanie K.(1989), Trajectory Design and Control of a Wheel-type Mobile Robot Using B-Spline Curve, IEEE International Workshop on Intelligent Robots and Systems, pp.398-405.

[14] Su K. L., Chung C. Y., Tzou J. T. et al (2011), A* Searching Algorithm Applying in Chinese Chess Game, International Journal on Artificial Life and Robotics, 16(2), pp.132-136.

Speech Based Formation Control of multiple Mobile Robots

Kuo-Lan Su[1], Bo-Yi Li[2], Jr-Hung Guo[2], Chih-Hung Chang[2]

1. Department of Electrical Engineering, National Yunlin University of Science & Technology, Taiwan
2. graduate school Engineering Science and technology, National Yunlin University of Science & Technology
(Tel: +886-5-5342601, Fax: +886-5-5312065)

E-mail: sukl@yuntech.edu.tw, g9910813@yuntech.edu.tw, g9710801@yuntech.edu.tw

Abstract: The article presents multiple pattern formation control of the multi-robot system using A* searching algorithm, and avoids the collision points of motion paths. We use speech recognition algorithm to control the variety pattern formations exchange, and use mobile robots to present the movement scenario on the grid based motion platform. We have been developed some pattern formations according to game applications, such as long snake pattern formation, phalanx pattern formation, crane wing pattern formation, sword pattern formation, cone pattern formation and so on. The mobile robot contains a controller module, three IR sensor modules, a voice module, a wireless RF module, a compass module, and two DC servomotors. The mobile robot can acquires the detection signals from reflect IR sensor modules and compass module, and decides the cross points of the aisle, and receives the command from the supervised compute, and transmits the status of environment to the supervised computer via wireless RF interface. We develop the user interface of the multi-robot system to program motion paths for variety pattern formation exchange on the minimum displacement. Users can use speech to control the multiple mobile robots to executed pattern formation exchange on step by step or continuously. In the experimental results, mobile robots can receive the pattern formation command from the supervised computer, and change the pattern formation on the motion platform, and avoid other mobile robots.

Keywords: pattern formation exchange control, multi-robot system, A* searching algorithm, phalanx pattern formation, DC servomotors, wireless RF interface

I. INTRODUCTION

With the robotic technologies development with each passing day, mobile robot systems have been widely employed in many applications. Recently, more and more researchers are interest in the intelligent mobile robots which can help people in our daily life, such as entertaining robots, museum docent robots, educational robots, medical robots, service robots, office robots, security robots, home robots, and so on. In the future, we believe that intelligent robot will play an important role in our daily life. To design a big sized mobile robot to be equipped with many functions to become complex and huge, and the development period is too long. Thus, recently small-sized mobile robot systems have been investigated for a specific task, and program the optimal motion path on the dynamic environment [1].

There is a growing in multi-robot cooperation research in recent year. Compare to single mobile robot, cooperation multiple mobile robots can lead to faster task completion, higher quality solution, as well as increase robustness owing its ability adjust to robot failure [2]. Grabowski and Navapro-serment [3] suggested multiple mobile robots in which each mobile platform had a specific sensor for some purpose and therefore the system's task can be distributed to each mobile platform during surveillance. The feature of this system is that each mobile robot had a common motion platform, but had different sensors. Some papers consider the problem of the multiple robot system working together. The multiple mobile robot system has more advantages than one single robot system [4]. The multiple mobile robots have the potential to finish some tasks faster than a single robot using searching algorithm or ant colony algorithm [5].

Liu proposed a motion planning approach to coordinating multiple mobile robots moving along specified paths for minimizing formation errors [6]. The mobile robots are required to maintain the formation relationship, and are subject to the restrictions of velocity and acceleration bounds and collision avoidance [7]. Javier described work on multi-robot pattern formation. Arbitrary target patterns are represented with an optimal final formation [8]. The pattern formation is developed in ancient Chinese history. Sun Tzu and Zhuge Liang that are the symbol of resourcefulness and wisdom in Chinese Folklore proposed many pattern formations. The paper develops the multiple mobile robots to implement some pattern information.

II. SYSTEM ARCHITECTURE

The system architecture of the team robot system is shown in Fig 1. The system contains a supervised computer, a microphone, a motion platform, some wireless RF modules and five mobile robots. The supervised computer programs five pattern formations to be shown in Fig. 2. We name the pattern formations to be long snake pattern formation, wild goose pattern formation, sword pattern formation, cone pattern formation and crane wing pattern formation. Users can select each pattern formation using Chinese speech on the supervised computer. The supervised computer can programs the motion paths of the multiple mobile robots using minimum displacement method, and transfer change the pattern formation to the assigned pattern formation. The mobile robots move on the motion platform, and avoid collision with other robots. The supervised computer can transmits the command of the final locations to each mobile robot. The mobile robots can move to the final locations autonomous according to the programmed motion paths.

There are more merits in the mobile robots to use team robot cooperation capabilities to such a large fleet of robots. In general, the control structure of the large fleet mobile robots is classified centralized control and decentralized control. A centralized control requires robust and permanent communication capabilities between all mobile robots and the supervised system. A decentralized control only requires local communication between robots and the supervised system. Each mobile robot of the multiple robots' system will communicates with the other robots [9]. The paper uses the centralized control in the pattern formation arrangement. That is to say, the multiple mobile robots only communicate with the supervised computer via wireless RF interface. The mobile robot has been developed in my laboratory.

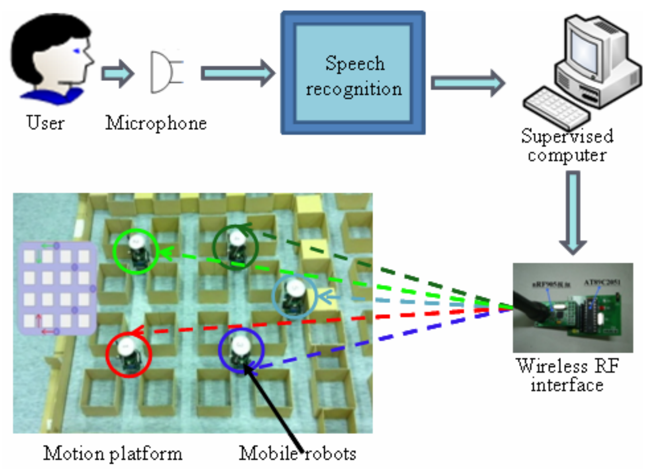

Fig. 1. The system architecture

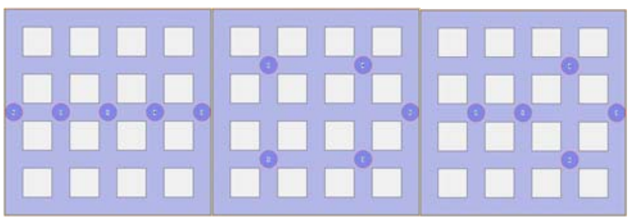

(a) Long snake pattern (b) Wild goose pattern (c) Sword pattern

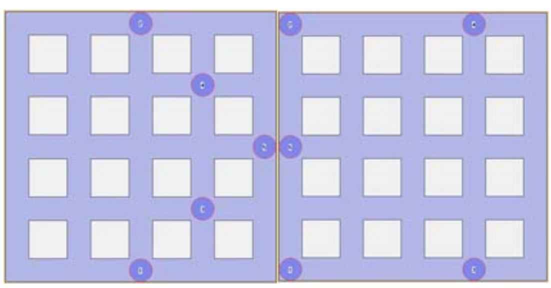

(d) Cone pattern (e) Crane wing

Fig. 2. The pattern formation model of multiple mobile robots

The core of the wireless RF module is microprocessor (AT89C2051), and communicates with the controller of the mobile robot or the supervised computer via series interface (RS232). The communication protocol of the system is 10 bytes. There are start byte (1 byte), data byte (8 bytes) and check byte (1 byte). The data bytes contain ID code (1 byte), robot code (1 byte) position and orientation data bytes. The ID code decides the transmitting direction between of the supervised computer and the multiple mobile robots.

III. Pattern Analysis

We program the shortest motion path of the pattern formation exchange using A* searching algorithm for each mobile robot, and locate the start position and final position of each mobile robot. The start position is the start point of the pattern formation, and the final position is the final point of the assigned pattern formation. The programmed motion paths have collision condition at the cross point of the programmed motion paths. The short displacement based mobile robot must stay at the original position to wait the long displacement based mobile robot moving through the point. Then the mobile robot moves through the point.

A^* searching algorithm solves the shortest path problem of multiple nodes travel system. The formula of A^* searching algorithm is following

$$f(n) = g(n) + h(n) \qquad (1)$$

The core part of an intelligent searching algorithm is the definition of a proper heuristic function $f(n)$. $g(n)$ is the exact cost at sample time n from start point to the target point. $h(n)$ is the minimum cost. In this study, n is reschedules as n' to generate an approximate minimum cost schedule for the next point. The equation (1) can be rewritten as follows:

$$f(n) = g(n) + h(n') \qquad (2)$$

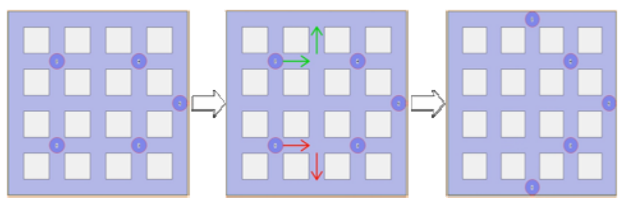

Fig 3. Wild goose pattern formation to cone formation

Now we make some examples to explain how to control pattern formation exchange using A* searching algorithm. The first example, the wild goose pattern formation transfers to the cone pattern formation to be shown in Fig. 3. The supervised computer programs the minimum robots to move on the assigned pattern formation, and can computes the shortest displacement of the selected robots moving to the assigned positions. We can see the only two mobile robots moving to the new assigned positions according to the cone pattern formation. Then the three mobile robots stay at the original positions. The total movement displacement is minimum value. The experimental results are shown in Fig. 3(b) and (c).

In the other example, is shown in Fig. 4. The long snake pattern formation transfers to the sword pattern formation. We program the motion paths of five mobile robots to exchange the formation, and use A* searching algorithm to program motion paths of moving robots, and uses the minimum moving robots on the pattern formation. Finally, we can see the only two mobile robots moving to the assigned positions. The others are stay at the original positions.

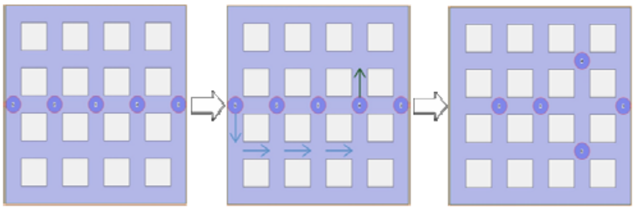

Fig 4. Long snake pattern formation to sword pattern formation

The structure of speech recognition is shown in Fig. 5. In speech signal processing, preemphasis, namely, the compression of the signal dynamic range by flattening the spectral tilt, preemphasis can also be accomplished after A/D conversion through differential calculation or through application of the first-order digital filter.

$$H(z) = 1 - a \times z^{-1} \quad (3)$$

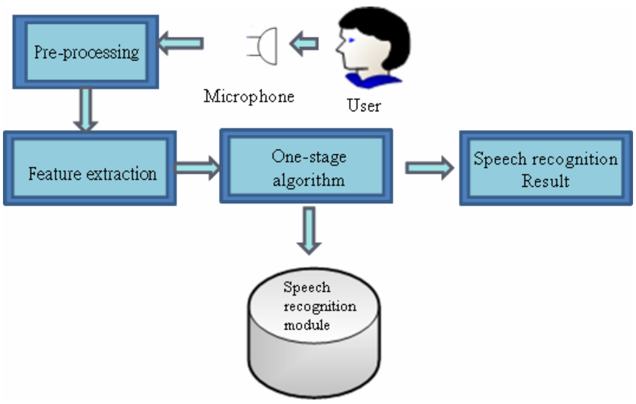

Fig 5. The structure of speech recognition

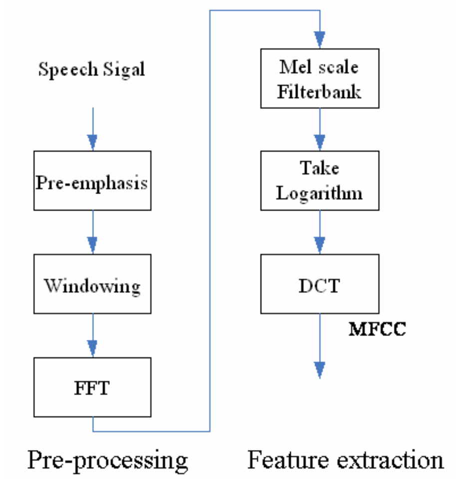

Fig. 6. The flow-chart of feature extraction

In the speech recognition, we want to extract the N-sample interval from the speech wave for calculating the autocorrelation function and spectrum. The speech wave must multiply by an appropriate time window. Thus several compromise window functions have been proposed. Among these, we use the Hamming window $W(n)$ as following [10]:

$$W(n,a) = (1-a) - a \times \cos(2\pi n/(N-1)), 0 \le n \le N-1 \quad (4)$$

We take $a = 0.46$ in the paper. We want to analyze the speech wave, and transfer the speech signals in the time domain to the frequency domain. The energy spectrum presents the phenomenon of variety speech signals. Then we can use Mel frequency to analyze the speech signals. The relation of Mel frequency and general frequency as following:

$$mel(f) = 2595 * \log 10(1 + f/700) \quad (5)$$

or

$$mel(f) = 1125 * \ln(1 + f/700) \quad (6)$$

Then we can find 12-level Mel-scale coefficients using discrete cosine transform (DFT) as following:

$$C_m = \sum_{k=1}^{M} E_k \cos[\left(k - \frac{1}{2}\right)\frac{\pi}{M}], m = 1, \ldots\ldots, L \quad (7)$$

Then we program the flow chart of feature extraction for speech recognition for variety pattern formation of the team robots to be shown in Fig. 6.

IV. EXPERIMENTAL RESULTS

We implement the pattern formation exchange control using five mobile robots, and presents the movement scenarios of the pattern formation exchanges on the grid based motion platform (One grid is 30 cm on the platform). The first formation exchange is the wild goose pattern formation transform to the cone pattern formation. The formation exchange only moves two robots, and uses A* searching algorithm and minimum movement displacement to program the motion paths that are plotted in Fig. 7, and transfers the wild goose pattern formation to the cone pattern formation.

In the experiment scenario, we use five mobile robots to arrange the wild goose pattern formation on the motion platform. The supervised computer transmits the cone pattern formation command to the five mobile robots via wireless RF interface, and assigns the new positions for five mobile robots. The experimental scenario of the first step is shown in Fig. 7(a). The two mobile robots move forward 30 cm (one grid) according to the programmed motion paths. Then one turns right 90^0 moving forward 30cm. The other turns left 90^0 moving for ward 30cm. The two mobile robots stop, and face the right side to be the same direction as the original direction for all mobile robots. The experimental scenarios are shown in Fig. 7(b) and (c). Finally, the five mobile robots leave the original location, and stay at the new positions to arrange cone pattern formation on the platform.

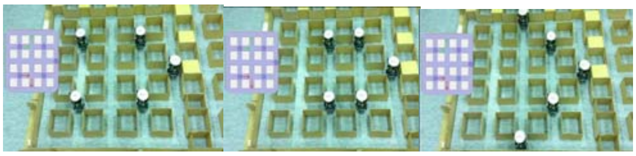

Fig. 7. The scenario of wild pattern to cone pattern

Next we implement the pattern formation exchange control using five mobile robots, and present the movement scenarios from the cone pattern formation to the wild goose pattern formation. The formation exchange only moves two robots, too. In the experiment scenario, the supervised computer transmits the wild goose pattern formation command to the five mobile robots via wireless RF interface, and transmits the new positions to the assigned two mobile robots. The experimental scenario of the first step is shown in Fig. 8(a). The two mobile robots turn 180^0 to move forward 30 cm (one grid). Then one turns right 90^0 moving forward 30cm. The other turns left 90^0 moving for ward 30cm. The two mobile robots stop, and face the right side. The experimental scenario of the first step is shown in Fig. 8(b) and (c).

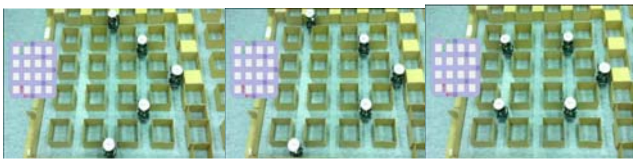

Fig. 8. The scenario of cone pattern to wild pattern

Finally we implement the pattern formation exchange control using five mobile robots, and present the movement scenarios from the long snake pattern formation to the sword pattern formation. The formation exchange only moves two robots, too. In the experiment scenario, the supervised computer transmits the sword pattern formation command to the five mobile robots via wireless RF interface, and transmits the new positions to the assigned two mobile robots. The experimental scenario of the first step is shown in Fig. 9(a). One mobile robot turn left 90^0 to move forward 30 cm (one grid), and turns right 90^0 to face right side. The tail of the snake (robot) turns right 90^0 moving for ward 30cm. Then the robot turns left 90^0 to move forward 90cm (3grids). The five mobile robots stop, and face the right side. The experimental scenario of the first step is shown in Fig. 9(b) and (c).

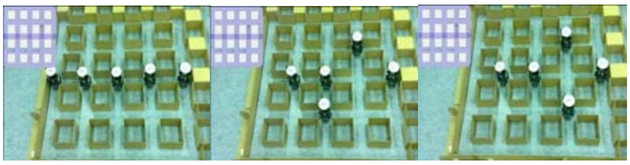

Fig. 9. The scenario of long snake pattern to sword pattern

V. CONCLUSION

We have developed five pattern formations' exchange control of the team robot system. The five pattern formations have long snake pattern formation, wild goose pattern formation, sword pattern formation, cone pattern formation and crane wing pattern formation. The formation control system contains a supervised computer, some wireless RF modules, a motion platform and five mobile robots. Users can use Chinese speech to control the multiple mobile robots to exchange pattern formation. The supervised computer can controls five mobile robots, and receives the status of the multiple mobile robots via wireless RF interface. The paper has been presented multiple pattern formation exchange control using five mobile robots. The experimental scenario of the four mobile robots moves on the motion platform, and obeys the programmed motion paths using A* searching algorithm. The five mobile robots can avoid the other mobile robots in the pattern formation control. In the future, we want to develop more complexity pattern formation using more and more mobile robots for war game, and develop the pattern formation programming according to the war laws of Sun Tzu or Zhuge Liang.

ACKNOWLEDGMENT

This work was supported by the National Science Council of Taiwan, (NSC 100- 2221- E-224-018)

.

REFERENCES

[1] Su K L, Chung C Y, Liao Y L et al (2011) A* searching algorithm based path planning of mobile robots, ICIC Express Letters, Part B: Applications, Vol. 2, No. 1, pp. 273-278.

[2] Song T, Yan X, Liang A et al (2009) A distributed bidirectional auction algorithm for multi-robot coordination, IEEE International Conference on Research Challenges in Computer Science, pp.145-148.

[3] Grabowski R and Navarro-Serment L, Paredis C et al (2000) Heterogeneous teams of modular robots for mapping and exploration, Autonomous Robots, Vol.8, No. 3, pp.293-308.

[4] Cao Y et al (1997) Cooperative mobile robotics: antecedents and directions, Autonomous Robots, Vol.4, No. 1, pp.7-27.

[5] Guo J H and Su K L (2011) Ant system based multi-robot path planning, ICIC Express Letters, Part B: Applications, Vol. 2, No. 2, pp. 493-498.

[6] Liu S, Sun D and Zhu C G (2010) Motion planning of multirobot formation", IEEE/RSJ International Conference on Intelligent Robots and Systems. October 18-22, Taipei, Taiwan, pp.3848-3853.

[7] Liu S, Sun D and Zhu C G (2010) Coordinated motion planning of multiple mobile robot in formation", Proceeding of the 8th World Congress on Intelligent Control and Automation, July, 6-9. Jinan, China, pp.1861-1811.

[8] Javier A M, Breitenmoser A, Rufli M. et al (2011) Multi-robot system for artistic pattern formation", IEEE International Conference on Robotics and Automation, May, 9-13, Shanhai, China, pp. 4512-4517.

[9] Alami R, Fleury S, Herrb M et al (1998) Multi-robot cooperation in the MARTHA project, IEEE Robotics & Automation Magazine, March, pp. 36-47.

[10] Sadaoki F (1989) Digital speech processing synthesis, and recognition, Marcel Dekker, INC.

The Seventeenth International Symposium on Artificial Life and Robotics 2012 (AROB 17th '12),
B-Con Plaza, Beppu, Oita, Japan, January 19-21, 2012

Development of the Residual Power Prediction System of Mobile Robots

Jr-Hung Guo[1], Jie-Tong Zou[2], Kuo-Lan Su[3], Cheng-Yun Chung[1]
1. graduate school Engineering Science and technology, National Yunlin University of Science & Technology
2. Department of Aeronautical Engineering National Formosa University, Taiwan
3. Department of Electrical Engineering, National Yunlin University of Science & Technology, Taiwan
(Tel: +886-5-5342601, Fax: +886-5-5312065)

E-mail: g9710801@yuntech.edu.tw, scott@nfu.edu.tw, sukl@yuntech.edu.tw

Abstract: The article presents a multiple residual power prediction system to be applied in mobile robots or automation fields. The system contains multiple power detection units to measure multiple on-line power values. Each power detection unit uses four current sensors to measure the current variety, and uses weighted average method and redundant management method to calculate the exact current value, and isolates faulty measurement values. We use the proposed algorithms to be applied in voltage detection of each power detection unit, too. Then we can calculate the real-time power values according to the current and voltage measurement values. The control core of the power detection unit is HOLTEK microchip, and communicates with the data integration unit via wire I2C interface. The power detection units transmit the measurement values of current and voltage to the controller of the system. The main controller of the power detection system is PC based system, and communicates with the data integration unit via wire RS232 interface. The main controller of the system can controls each power output ratio of the power sources, and predicts the power loading and the residual power for each power detection unit using auto-regression algorithm, and computes the residual time of mobile robots to work in the free-space, and arrange the residual power of the enough power source to the weakness power sources using sequential single-item auction algorithm. In experiment result, the residual power prediction system can adjusts the working time of the power sources to be the maximum value.

Keywords: multiple residual power prediction system, weighted average method, redundant management method, HOLTEK microchip, I2C interface, RS232 interface, auto-regression algorithm, sequential single-item auction algorithm.

I. INTRODUCTION

Intelligent power management system can provides convenience and high efficiency for human living in the 21st century, and allows effective management of power source with minimum life-time costs at the same time. In the recently, Intelligent system has been widely applied in many fields. The residual power of the intelligent system is under the critical power. The system can't work and shutdown. The power supply of the system must be stability. The power management system may knows the residual using time, and adjust the power output to improve the working time of the intelligent system to be maximum. We must detect power variety of the intelligent system all the time very carefully, and program each power output to supply all devices of the intelligent system in the limited total power condition.

We have been designed a power detection module applying in Chung Cheng I security robot using microprocessor (MCS51), and the on-line experimental results are very successful [1,2]. We are implemented the new power detection module applying in the fire fighting robot using HOLTEK microchip, too. The goals of the paper integrates many new power detection modules to extend the interface function, and transmits the measurement values to the controller of the intelligent power management system using series interface, and extends the function of the power detection module to isolate the faulty measurement values, and reduce detection error, and predict the residual time using multi-level multisensor fusion algorithms [3].

In the past literature, many researches have been proposed power detection and prediction algorithms. Levi was one of the first persons to comment upon the characteristics of CMOS technology which make it special amenable to I_{DD} Testing [4]. Malaiya and Su use I_{DD} testing to estimate the effects of increased integration on measurement resolution [5,6].Hawkins et al reported on numerous experiments where current measurements have forecast reliability problems in devices which had previously passed conventional test procedures [7,8]. Then, researches dedicated to improving the accuracy of measuring current [9,10]. Maly et al proposed a build-in current sensor which provides a pass/fail signal when the current exceeds a set threshold [11,12].

II. SYSTEM ARCHITECTURE

We develop the residual prediction system in the paper, and measure the exact power values to isolate the error measurement values, and calculate the residual time under the critical values to adjust working time to be maximum value. The system architecture of the residual power prediction system is shown in Fig. 1. There are many power detection units, many power sources, one data integration unit and a controller. The system measures the variety power outputs of the power sources respectively. These power detection units can detects multiple DC power sources.

Each detection unit assigns identification (ID) code to be classified the data sequence.

The data integration unit connects with many power detection units via I2C interface, and deals with the received measurement values according to ID code of each power detection unit, and transmits the measurement values to the controller of the residual power prediction system via RS232 interface. The prototype of the power detection unit is shown in Fig. 2. The controller unit of the power detection unit is HOLTEK microchip, and monitors each power variances of the power sources. The controller of the residual power prediction system is PC-based structure, and adjusts each power output of the power sources via wire series interface.

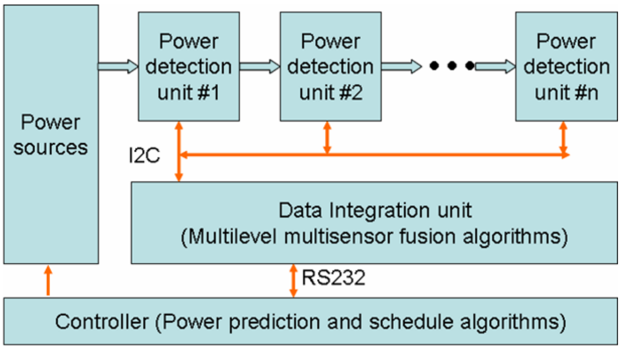

Fig. 1 The system architecture

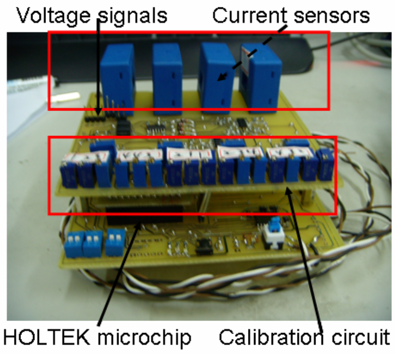

Fig. 2 The prototype of the power detection unit.

Each power detection unit contains four current sensors, a HOLTECK microchip, a calibration circuit and a series interface, and measures four current and four voltage signals. The control core is a HOLTEK microchip (HT46R25) to detect the power variance using four DC type current sensors, and measures four voltage values simultaneously. Users can adjust the sensitiveness of the measurement signal, and delete offset value, and select all measurement values are the same sensitiveness. The output signal contains safety switch, I2C interface, display and alarm. The safety switch may be used to turn on or off the supply power to the target devices. The current range tuning can be assigned the maximum measurement current up to about 50A.

The user interface of the residual power prediction system is shown in Fig. 3. Users can select any time point of these curves, and display these current and voltage measurement values on the upper side of the monitor to be shown in the part "1" and "2". Uses can select each power detection unit to display current measurement values and voltage measurement values, power estimated value, and plot the curves for these measurement values to be shown in the part "3". The part "4" of the user interface presents the color curve to display the variety detection power sources for each power detection unit. The part "5" can displays the real-time power, critical power, residual power, assigned power and residual time of each power detection unit. The part "6" displays the set residual time of the system to be 60 second, and calculates the power efficiency.

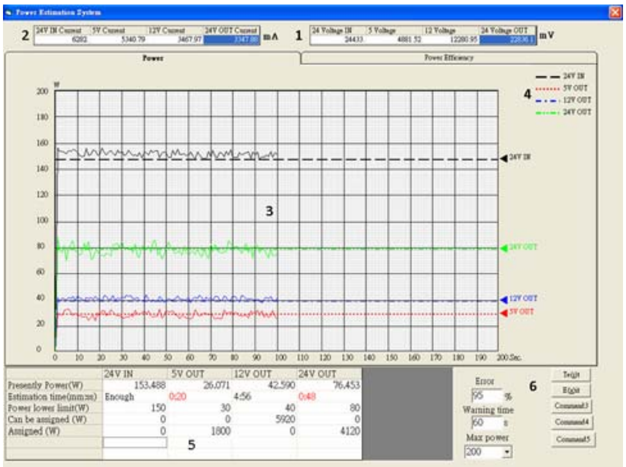

Fig. 3 The user interface

III. ALGORITHM ANALYSIS

In the power detection unit, we use weighted average method and redundant management method to compute power measurement values. The proposed methods are implemented in the HOLTEK microchip. The weighted value of the nth sensor measurements x_i is w_i with $0 \le w_i \le 1$. We can compute the weighted value according to the precious of the measurement value relation to the others; thus

$$I_i = \sum_{j=1}^{n} u_i, \quad i = 1,2,\ldots\ldots,n \tag{1}$$

$$u_i = \begin{cases} 1, & \text{if } |m_i - m_j| \le b_i \\ 0, & \text{if } |m_i - m_j| > b_i \end{cases} \tag{2}$$

$$w_i = \frac{I_i}{\sum_{j=1}^{n} I_j}, \quad i = 1,2,\ldots\ldots,n \tag{3}$$

The b_i is a threshold value for each measurement value m_i, and m_j is another measurement value. The maximum value of w_i is n, and the minimum value is zero. Then we can compute the estimated value $\overline{m}$ according to each weighted value to be

$$\overline{m} = \sum_{i=1}^{n} w_i m_i \tag{4}$$

Where $\sum_i w_i = 1$ and $w_i = 1$ if m_i is not within some specified thresholds. The weights can be used to account for the differences in accuracy between sensors, and a moving average can be used to fuse together a sequence of measurement values from a single sensor so that the more recent measurement values are given a greater weight.

Then we want to calculate the residual time under the critical power using power prediction algorithm for each power detection unit. The algorithm is based on ARIMA (p,d,0) model structure and least square method. It general form of model is as following.

$$\varphi(B)w(t) = a(t) \tag{5}$$

Where $a(t)$ is zero mean value white noise, B is backward operator, and

$$\varphi(B) = 1 - \varphi_1 B - \varphi_2 B^2 - \cdots - \varphi_p B^p \tag{7}$$

Then equation can be expressed in the vector form can be rewritten as

$$w(t) = u^T(t)\lambda + a(t) \tag{8}$$

$$\lambda = [\varphi_1, \varphi_2, \cdots, \varphi_p]^T \tag{9}$$

$$u^T(t) = [w(t-1), w(t-2), \cdots, w(t-p)] \tag{10}$$

Take the place of λ and u^T into recursive least square formula with forgetting factor. Given the original value, regressive parameters estimation can be found out on line.

Next we can compute each residual time of each power detection unit on the assigned critical power. If the power detection units measure the average powers of the n power sources to be $\overline{P_1}, \overline{P_2}, \ldots\ldots, \overline{P_n}$. We use sequential single-item auction algorithm in the paper. The weakness power source bides the enough power source. The goal of the proposed method wants to increase the working time in the fixed power condition. A formal definition of the auction algorithm is given a number of enough power sources $p_1, p_2, \ldots\ldots, p_m$, and a number of weakness power sources $s_1, s_2, \ldots\ldots, s_l$. The total power sources $n = m + l$, and subtasks are, $P = \{P_1, P_2, \ldots\ldots, P_n\}$. A subtask $P(s_i)$ is a set that contains some enough power sources that are bided by the weakness power sources s_i. A function $F(s_i, p_j)$ specifies the cost of using the enough power source p_j to provide to the weakness power sources s_i.

$F(s_i, P(s_i))$ specifies the cost of using power sources $P(s_i)$ by the weakness power source s_i. We have two performance function to compare the efficiently for the multiple target devices executing power sources' allocation. The residual time of the ith power detection unit is T_{pi} $i = 1,2,\ldots m$, T_{si} $i = 1,2,\ldots,l$. The kth power is under the critical power, and the residual time is smaller than the threshold time (60 second). The lth power source is enough to provide the lth target device. The part of the lth power source is assigned to provide the power to the ith target device using single-item auction algorithm. We define the maximum average working time to be T_M, and fine the balance relation s following:

$$\underset{T_M}{MAX}\left[\sum_{i=1}^{m} p_i (T_{pi} - T_M) = \sum_{j=1}^{l} s_j (T_M - T_{sj})\right] \tag{11}$$

IV. EXPERIMENTAL RESULTS

The residual power prediction system measures multiple power sources to display on the user interface. Users select the measurement range value of each power detection unit on the user interface to be shown in the upper side of Fig. 4. The user interface can plots four power curves and four prediction curves that are selected by users (5V, 12V 24V input and 24V output). The sample time is 1 second for the PC-based controller of the residual power prediction system.

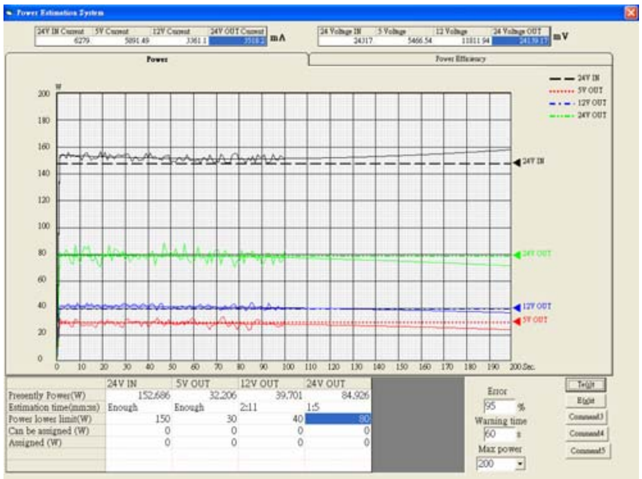

Fig. 4 The residual power prediction experimental result (I).

In the residual power prediction experiment, users can set the four critical powers and four residual times on the user interface of the system. We can select the critical power for 5V to be 30W, 24V (IN) to be 150W, 12V to be 40W and 24V (OUT) to be 80W, and the same critical time to be 60 second. The controller plots curve lines on the monitor of the interface according the real-time measurement value. First, the system can fits four second-order curves using polynomial regression algorithm for each assigned power sources. Then it computes the cross points of the critical power lines and the second-order curves. The cross points are the residual times (unit is second) for each detection power sources, Otherwise, the cross point is not exist, and the power source is enough. These cross point times displayed on the bottom of the interface. The user interface computes the residual times under the critical power to be 2 minute 11 second for 24V (output), and enough time for 12V and 24V (input) (no cross point). All residual times are bigger than the threshold time (60 seconds). The system can't execute the power assigned in the case.

In the other case, the residual power prediction system can knows the residual time to be 35 seconds. The 5V power source shutdowns on weakness power, and programs the enough power source 12V to provide the power to the weakness power source (5V) using single-item auction algorithm. Then we can compute the residual power until the critical power for each power source. The residual power output is about 2480W for 12V power source, and the residual time of 24V is about 1 minute 13 second. We can know the arrangement percent on each power source of the residual power prediction system, and program the 12V power source to provide 1000W to the 5V power source using the proposed algorithm. The experimental result is shown in Fig. 5.

The residual power prediction system can knows the residual time to be 49 seconds for the power source 24V (output), and the others are enough. The system programs the enough powers 5V and 12V to provide the power to the weakness power source (24V output) using single-item auction algorithm. Then we can compute the residual power until the critical power for each power source. The residual power output is about 1800W for 5V power source, and the residual power output is about 2400W for 12V. We can know the arrangement percent on each power source of the residual power prediction system, and program 5V and 12V power source to provide power to the 24V power source output using the proposed algorithm. The experimental result is shown in Fig. 6.

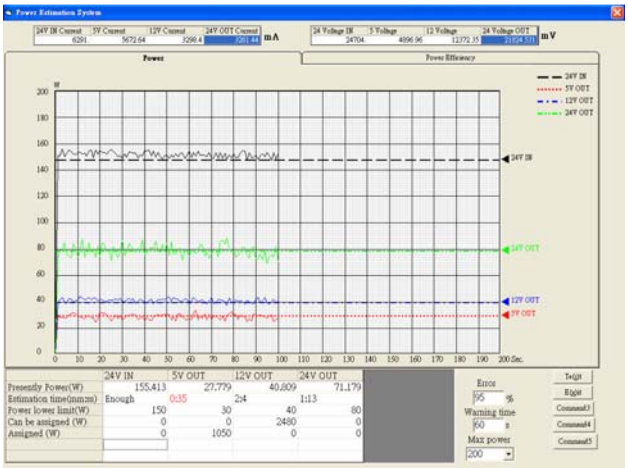

Fig. 5 The residual power prediction experimental result (II).

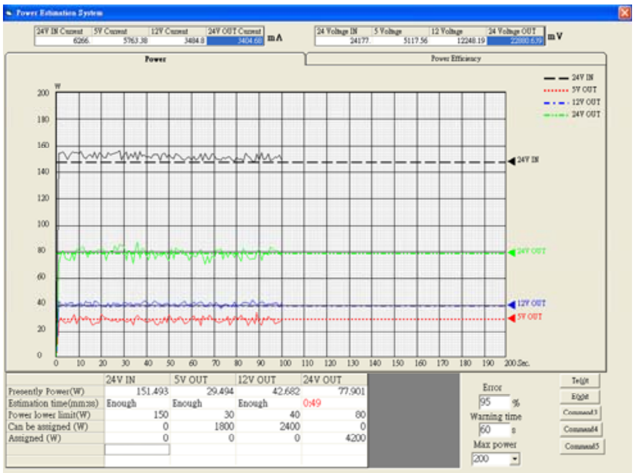

Fig. 6 The residual power prediction experimental result (III).

V. CONCLUSION

We have successful designed a residual power prediction system that has been applied in the multiple power source management. We developed the new power detection unit that used the HOLTEK microchip as controller to measure multiple power sources. The residual power prediction system used statistical signal detection algorithm and auto-regression algorithm to predict the residual times on the critical threshold power values for each power detection unit, and used single-item auction algorithm to adjust the power output ratio according the residual time. The system used the proposed algorithms to program the maximum working time of the target device before the weakness of the power source. We develop the user interface to integrate multiple power detection units to measure the power values. The power detection units can transmits the measurement values to the data integration unit via wire I2C interface. The PC based controller of the residual power prediction system communicates with the data integration unit via wire RS232 interface. In future, we want to adjust the more and more power sources of the system to increase the maximum working time of the target devices of the intelligent system, and implement the experimental results using the improved power detection unit.

ACKNOWLEDGMENT

This work was supported by the National Science Council of Taiwan, (NSC 100-2221-E-224-018).

.

REFERENCE

[1] Luo R C, Su K L, Deng C W (2003), Power Supply Diagnosis System Using Redundant Sensor for Intelligent Security Robot, IEEE International Conference on Industrial Electronic, Control, and Instrumentation, pp.2500-2506.

[2] Luo R C, Su K L (2008), Multi-level multisensor based intelligent recharging system for mobile robot, IEEE Transaction on Industry Electronic. 55(1), pp.270-279.

[3] Su K L, Guo J H, Tzou J H et al (2009), Develop an auto-recharging method for mobile robot," The International Conference on Service and Interactive Robotics, pp.13.

[4] Levi M W (1981), CMOS is most testable, Proceedings of International Test Conference, pp.217-220.

[5] Malaiya Y K, Su S Y H (1982), A new fault model and testing technique for CMOS devices, Proceedings of International Test Conference, pp.25-34.

[6] Frenzel J F (1994), Power-Supply CurrSent Diagnosis of VLSI Circuits, IEEE Transaction on reliability 43(1), pp.30-38.

[7] Horning L K (1987), Measurements of quiescent power supply current for CMOS ICs in production testing, Proceedings of International Test Conference, pp.300-309.

[8] Soden J M, Hawkins C F (1986), IEEE Design & Test. Considerations for Gate Oxide Shorts in CMOS ICs. 3(4).

[9] Crapuchettes C (1987), Testing CMOS I_{DD} on large devices, Proceedings of International Test Conference, pp.310-315.

[10] Keating M; Meyer D (1987), A new approach to dynamic I_{DD} testing, Proceedings of International Test Conference, pp.316-321.

[11] Carley L R, Maly W (1988), A circuit breaker for redundant IC systems, Proceedings of Custom Integrated Circuits Conference, pp.27.6.1-27.6.6.

[12] Feltham D B I (1988), Current sensing for built-in testing of CMOS circuits, Proceedings of International Conference on Computer Design, pp.454-457.

The Seventeenth International Symposium on Artificial Life and Robotics 2012 (AROB 17th '12),
B-Con Plaza, Beppu, Oita, Japan, January 19-21, 2012

Development of tactile sensing system and evaluation for the application to the intelligent robot using the microbending fiber optic sensors

Ju-Won Jeong[1], Heo-Jin Seok[2] Jung-Ju Lee[3]

[1, 3] Department of Mechanical Engineering, Korea Advanced Institute of Science and Technology, Daejeon, Korea
(Tel: 82-42-350-3033, Fax: 82-42-350-3210)
[2]Samsung Electronics company, San #16, Banwol-dong, Hwasung-city, Gyeonggi-do, 445-701 Korea

[3]*leejungju@kaist.ac.kr*

Abstract: This paper describes the system design and the structural design to evaluate the tactile sensor using the microbending fiber optic (MBFO) sensors. The small light emitted diode (LED) and charge coupled device (CCD) are used as a single light source and a light detector for the bundle of optical fibers respectively. And the structure of this type tactile sensor which is composed of crossed fibers in the silicone rubber is very simple. And the tactile sensor element using MBFO sensor is fabricated and the performance of this sensor is evaluated.

Keywords: 3-6 key words or phrases in alphabetical order, separated by commas.

1 INTRODUCTION

The tactile sensor is one of the essential means for interfacing between human and robots [1]. Some tactile sensors using the MEMS(Micro Electro Mechanical System) technology have been introduced [2-5]. Even though these sensors have several merits such as their small size, good spatial resolution, and so on, they still have some problems to apply the practical system: they don't have enough flexibility to attach on the curved surface and the more elements of sensor are connected, the more wires they need. To mimic human skin, a new design for a tactile sensor array that uses optical fiber both as sensing elements and as signal-transmission media is tried. Heo, Cheong and Lee [6] introduced an optical fiber tactile sensor using fiber Bragg grating sensors embedded in silicone rubber, which to a degree mimics the feeling of human skin. This type of tactile sensor has simple wiring for application of the wavelength division multiplexing method with a broadband light source and some fiber Bragg gratings, which have different Bragg wavelength in a given optical fiber. Nevertheless, the optical system, especially the broadband light source, is too expensive to be applied to a practical system. Therefore, in this paper, we designed the flexible tactile sensor using microbending optical fiber sensor with the structure of crossed fibers in the silicone rubber. And, we designed the tactile sensor system using a single light source and a detector for the bundle of optical fibers which are not expensive.

2 STRUCTURE AND SYSTEM OF THE TACTILE SENSOR

2.1 Structure of the tactile sensor

Using the taxel of this study, we designed the tactile sensor with the fabric structure of the optical fibers embedded in the silicone rubber like Fig. 1.

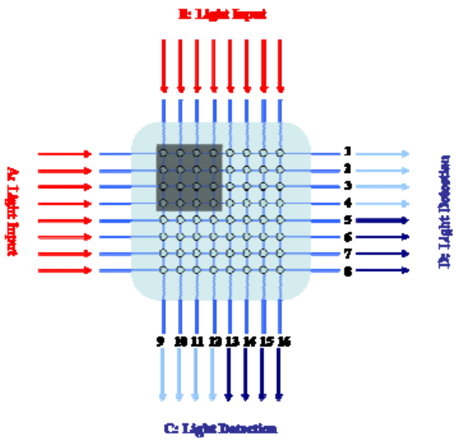

Fig. 1. Schematics of the tactile sensor using microbending optical fiber sensors with the fabric structure

If the some area is contacted by a wide material, the contact mesas make the microbending on the optical fibers in the silicone rubber which decreases the output of the light intensity of optical fiber. The numbers of the optical fiber contains the position information of the contact area, and the light intensity informs the change of the contact force. Hence, using this structure, the point contact load and distributed contact load can be measured.

The input light is incident to the optical fibers, which are located on sides A and B in Fig. 1. The output light is transmitted through optical fibers of sides C and D. If some area is pressed, as in Fig. 1, the intensities of the output light from the optical fibers, which are related to the pressed area, are decreased by the microbending loss. Based on the intensity changes and positions of the optical fibers, the quantity and the position of the applied force can be calculated at each taxel. And Fig. 2 shows the fabricated prototype tactile sensor using the microbending fiber optic sensors and its flexibility.

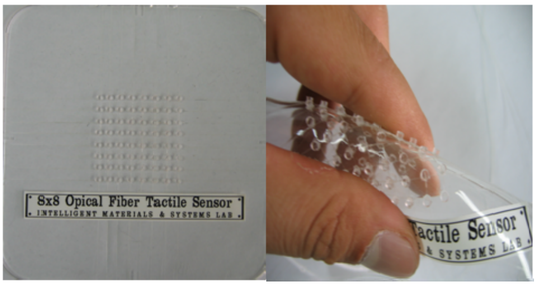

Fig. 2. Fabricated prototype tactile sensors and its flexibility.

2.2. Tactile sensor system

The Fig. 3 indicates the concept of the optical measurement system for the tactile sensor system using microbending optical fiber sensors. The wider distributed tactile sensor we fabricate, the more optical fibers are needed. To solve this problem, we use the optical fiber bundle as shown in Fig. 3. Many optical fibers can be united as one optical fiber bundle. Hence, using the optical fiber bundle, many fibers can be handled as one line.

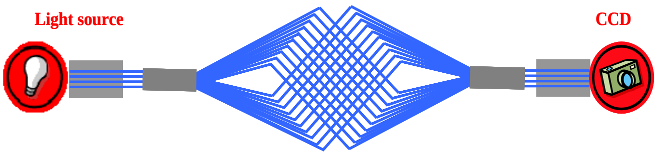

Fig. 3. Schematics for the tactile sensor system

As mentioned before, the optical measurement system of the intensity based optical fiber sensor is composed of a simple light source and a light detector. In this study, a small power LED(Light Emitted Diode) is used as the light source and a CCD(Charge Coupled Device) module is used for the light detector of this sensor system. The intensity changes of each optical fiber can be measured at once by the CCD module. This means that a CCD module makes the optical measurement system minimized. When the light intensity of the optical fiber is changed by contact force, the light intensity is evaluated from the output signal of the CCD. The gray scale value from the output signal of the CCD expresses the light intensity change of the optical fiber.

2.3. Light detection of multiple fibers using CCD

Using the prototype sensors, we can design artificial skin including the fabric-structured microbending optical fiber tactile sensors, as shown in Fig. 4. The fabric structure allows the implementation of simple and well arranged wiring. In addition, the fiber-cross area plays the role of a microbender, inducing light loss via perpendicular contact force.

Although this tactile type sensor needs many optical fibers compared with a FBG tactile sensor [6], they can be arranged as a bundle of optical fibers. In a general case, one light detector is used at one optical fiber when light intensity is measured. Thus, numerous detectors are required when the tactile sensor array is evaluated. However, by using a CCD as a light intensity detector, the intensity changes of all optical fibers can be measured at once. Thus, the CCD makes it possible to minimize the number of the optical measurement system and detect multiple light intensity changes from the optical fiber bundle.

In order to realize accurate and reliable measurement, a connector to a CCD must be designed to make intensities from all optical fibers similar at the same light input. An aligner, which is the main part of the connector, consists of four V-grooved plates to align the optical fibers on a plate a nd four dummy plates so that the space will not interfere with the neighboring lights, as illustrated in Fig. 4. The V-grooved plates and dummy plates are made of Si wafer and are fabricated by a wet etching process.

Using the plastic molding, the connector body can be made. Finally, the end of the connector needs to be polished to align all fibers on the bottom plate. Fig. 5 shows the fabricated fiber bundle connectors to align the optical fibers to the CCD.

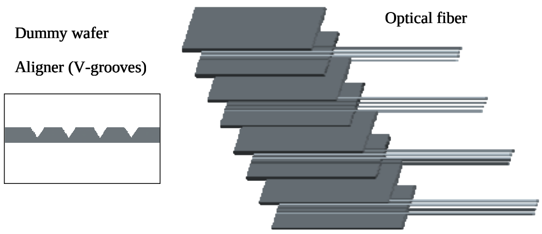

Fig. 4. Structure of the aligner

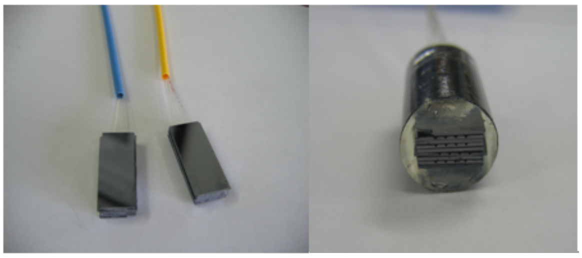

(a) (b)

Fig. 5. Fiber bundle connector: (a) fabricated aligner, and (b) connector

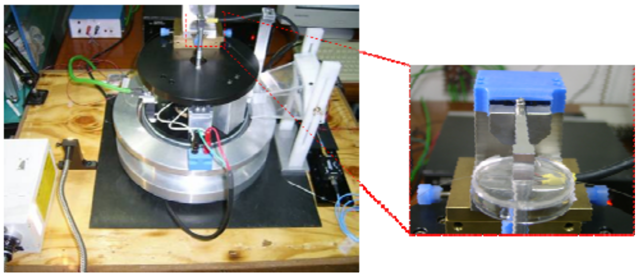

Fig. 6. Experimental setup for the evaluation of the taxel.

3 EXPERIMENTAL RESULTS

3.1. Evaluation of the tactile sensor element

The fabricated prototype taxel is evaluated by the verified experimental equipments composed of a uniaxial load-cell and a fatigue test system for small load as shown in Fig. 6.

This main device applies perpendicular load to the taxel which is placed on the top of this device. So, when the perpendicular load is applied to the taxel, the light intensity of the optical fiber is changed because of the low of action and reaction between the taxel and the load-cell. Also the load-cell detects the load. Therefore, through comparing the light intensity change of the optical fiber with load-cell load signal, the load information which is applied on the taxel is obtained.

The output signal of this prototype taxel is shown in Fig. 7. The light intensity of this taxel is decreased for its microbending light loss as the contact load is increased. The sensitivity of this sensor is -20 gray scale value / N and the resolution of this prototype sensor is 0.05N. And the exact load amount which is applied on the taxel is obtained by calibrating the sensitivity of the taxel.

The calibration process is very simple. By multiplying the sensitivity to the light intensity change, we can calculate the applied contact force as shown in Fig. 8. And the hysteresis error of this sensor is about 6.3% as shown in Fig. 9. This hysteresis error is caused by the characteristic of the silicone rubber which is the material of its transducer because the characteristic of silicone rubber is nonlinear. And the error of repeatability is about 2%.

Next, we verified the maximum capacity of this prototype taxel. The linearity between the light intensity change and the applied load is broken after 15N is applied. This phenomenon can be estimated as the abrupt stress change of the silicone rubber by the insertion of sensor is 15N which the linear response of the light intensity guarantees.

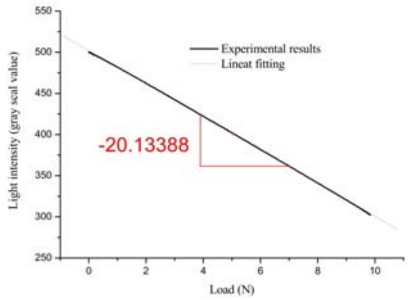

Fig. 7. Experimental verification of the prototype taxel.

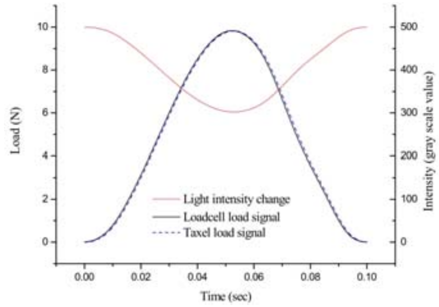

Fig. 8. Calibration of this prototype taxel.

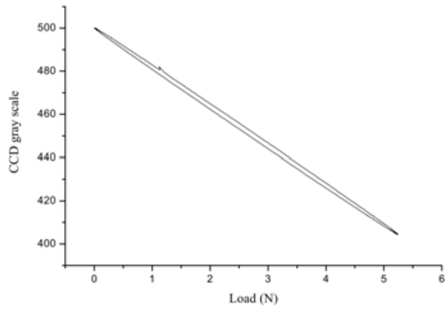

Fig. 9. Hysteresis of the prototype taxel.

3.2. Evaluation of the connector for the tactile sensor

To check the performance of the connector, the intensities changes from 16 optical fibers included in a bundle were tested, the results of which are graphically displayed in Fig. 10.

A single light input is incident to a bundle of 16 optical fibers and the light intensities measured from the output signal of the CCD. All light intensities indicate an approximately 500 gray scale value, and the difference between the maximum intensity value and the minimum inten sity value is about a 10 gray scale value. This indicates that all fibers in a bundle are well arranged and aligned to measure the light intensities changes. Point load and distributed load tests are conducted to check the proper output load from the fabricated tactile sensors. When a point load of 1.8N was applied to the pixel (6, 3) in the 5mm spatial resolution tactile array sensor, approximately 1.8N is indicated from the change of light intensity. When 5N is applied to nine taxels, as illustrated in Figure 12, each taxel that is pressed by the weight displays about 0.5×0.6 N. The small deviation of mesa depth and the relatively long spatial resolution result in differences in the output load from the taxels. A 8×8 tactile array sensors are fabricated using a molding process, as mentioned with regard to taxel fabrication. From the evaluation process, we confirmed that fabricated artificial skin by using microbending optical fiber sensor system showed us good performance during the demonstration for verification as shown Fig. 11.

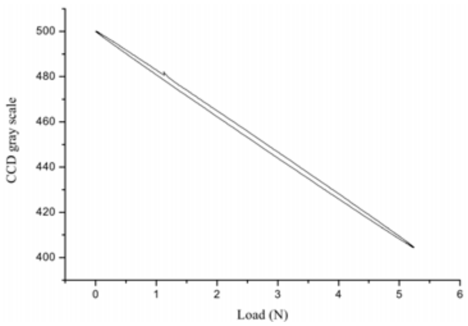

Fig. 10. Intensity change detection using CCD

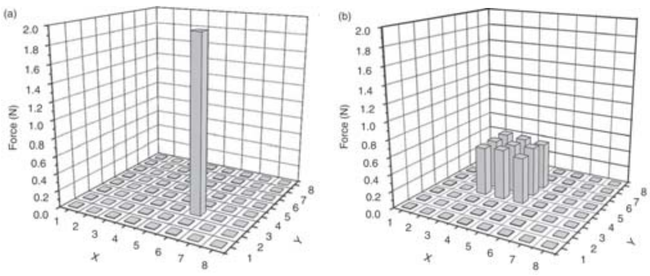

(a) (b)

Fig. 11. Experimental results of the tactile sensor (spatial resolution = 5mm): (a) point load detection, and (b) distributed load detection

4 CONCLUSION

In this paper, the force sensor using microbending light loss for the tactile sensor is newly designed and experimentally verified. The structure of this sensor with the crossed optical fibers embedded in the silicone rubber is very simple. The linear light intensity change by the applied load is verified by the experimental results. And this prototype sensor has a good performance: the resolution of this sensor is 0.05N and its maximum capacitance is 15N. However, a little hysteresis error exists due to the material of its transducer, silicone rubber. And we designed the tactile sensor with the fabric structure of the optical fibers based on the taxel. When the tactile sensor is fabricated, even though many optical fiber sensors are needed, they can be handled as one line by using the optical fiber bundle. This prototype sensor is sufficient for its application of the artificial skin which includes the tactile sensor. And, we introduce the tactile sensor system using a power LED and a CCD module which are used as a light source and a light detector respect ively. Especially, as a CCD can process hundreds of optical fibers' light output, this type of tactile sensor can be easily expanded maintaining the same optical systems. And, we design the connectors to align the cross sectional area of the optical fiber. A connector which contains 16 optical fibers shows the good performance and it is sufficient to align the optical fibers.

REFERENCES

[1] Nicholls and Lee "Tactile sensing for mechatronics – a state of the art survey", Mechatronics, Volume 9, Issue 1, 1 February 1999, Pages 1-31

[2] T. Mei, W. J. Li, Y. Ge, Y. Chen, L. Ni and M. H. Chan, "An integrated MEMS three dimensional tactile sensor with large force range", Sensors and Actuators (A), Vol. 80, pp155-162, 2000

[3] M. J. Yoon, K. H. Yu, G. Y. Jeong, S. C. Lee and T. G. Kwon, "Development of a Distributed Flexible Tactile Sensor System", J. of KSPE, Vol. 19, No. 1, pp. 212~218, 2002

[4] N. Futai, N, Futai, K. Matsumoto and I. Shimoyama, "A flexible micromachined planar spiral inductor for use as an artificial tactile mechanoreceptor", Sensors and Actuators (A), vol. 111, pp293~303, 2004

[5] U. Paschen, M. Leineweber, J. Amelung, M. Schmidt and G. Zimmer, "A novel tactile sensor system for heavy-load applications based on an integrated capacitive pressure sensor", Sensors and Actuators (A), vol. 68, pp294~298, 1998

[6] Jin-seok Heo, Jong-ha Cheung, and Jung-Ju Lee, "Tactile Sensor Arrays Using Fiber Bragg Grating Sensors", Sensors and Actuators, Vol.126, No.2, pp.312-327, 14 February, 2006.

The Seventeenth International Symposium on Artificial Life and Robotics 2012 (AROB 17th '12),
B-Con Plaza, Beppu, Oita, Japan, January 19-21, 2012

Gesture detection based on 3D tracking for multimodal communication with a life-supporting robot

Tetsushi Oka[1], Ryuichi Kibayashi[2], and Hirosato Matsumoto[2]

[1]Nihon University, Chiba 275-8575, Japan
(Tel/Fax: 81-47-474-9693)
[2]Graduate School of Industrial Technology, Nihon University, Chiba 275-8575, Japan
(Tel/Fax: 81-47-474-9693)

[1]oka.tetsushi@nihon-u.ac.jp

Abstract: This paper reports some recent results from a study on multimodal communication between life-supporting robots and their users. In the study, novice users understood how to use four types of hand gestures, raising, lowering, pushing, and pulling in a short period of time. They successfully conveyed their intensions to a robot using gestures, after watching a video for four minutes that explained how to use gestures and practicing for less than four minutes. The robot guided the users by displaying messages on its front screen and detected gestures by tracking the user's head and right hand based on depth and color information. The results show that novice users can learn quickly how to convey intentions to our robot and imply that it is easy for untrained users to combine hand gestures and spoken messages, in order to make a robot to turn to them, move forward to them, back away, approach them, and so on.

Keywords: communication, gesture detection, life-supporting, multimodal, robot

1 INTRODUCTION

These days, there are robots that work in various kinds of places. We predict that in near future, there will be more and more life-supporting robots, which are supposed to help non-experts, especially in aging societies, including Japan. Millions of robot cleaners are already in homes and offices all over the world and help people who do not have special knowledge or training experiences. However, many robots are still operated by experts and it is difficult for untrained people to command them.

This study focuses on communication between a life supporting robot and its user, in particular, commanding the robots to look at the user, come close to the user, and move forward and backward to keep appropriate distance from each other, which would be necessary before the user gives a task to the robot, receive help from it, or work on a cooperative task.

We believe that multimodal communication using spoken messages and three dimensional hand gestures is effective when we want a life-supporting robot to turn to us or come close to us. The robot can also send verbal and nonverbal messages on its screen and through its speakers.

We realized a 3D hand gesture detection system for life-supporting robots that understand multimodal commands and conducted a user study in order to verify hypotheses that novice users can convey their intensions through 3D hand gestures in a short period of time and that our system can recognize their gestures without errors. There have been studies in multimodal languages, combining speech and key input, speech and body touch, or speech and 2D gestures, for untrained users of home-use and life-supporting robots [1-4], which have shown that the languages are beginner friendly for some groups of tasks, such as moving the robot and moving an object. However, it is difficult to specify 3D positions and distances in the real world in those multimodal languages.

We have proposed a multimodal language in which one can command robots using a touch screen and a speech interface [5]. However, the language requires a hand-held device and it is difficult to let robots know one's own location or distance information. In this paper, we propose a multimodal language which combines speech and 3D gesture, which allows users to intuitively convey their own location, goals, and short distances. For example, one can raise the hand and say "turn to me" in order to turn a robot to the person. Without gestures, they would give a spoken command, say, "make a 73-degree right turn," which is not very natural and difficult for untrained users: they have to determine angles, distances, and other spatial quantities by eye. Without speech, it is also difficult to give robots a variety of commands: one needs to learn many types of gesture [6].

These days, it is possible to obtain depth images [7], find and track an object, and recognize spoken commands in real time using inexpensive computers and input devices. Therefore, one can develop and test robots that understand multimodal commands combining speech and 3D gesture.

Our gesture recognition system detects four types of 3D single-hand gestures: raising, lowering, pushing, and pulling, which we find important for communication between a life-supporting robot and its user. These types of gesture are useful when one wants to start communicating and collaborating with a robot and to maintain a comfortable distance during communication. Pushing and pulling gestures convey a 3D direction, forward or backward, and length information. A raising gesture can inform a robot of a 3D position. Finally, raising and lowering gestures can be used to start and stop robot actions.

In the rest of this paper, we describe our gesture detection system and a user study of it. Eleven novice users learned to use the four types of 3D gesture within ten minutes and all of their properly used gestures were classified correctly by our system. These facts and question sheets filled out by the users imply that our gesture detection system is of a great value for multimodal communication between life-supporting robots and their users, none the less because the system works well on a single laptop computer equipped with a microphone and an inexpensive motion input device to capture color and depth images.

2 GESTURE DETECTION SYSTEM

2.1 User detection

Our gesture detection system can find the nearest user sitting on a chair in the view in the following steps:

1. find every person in the view
2. mark each person's top of head
3. find the closest sitting person using 3D information

Our current system is built using OpenNI [8], a free SDK for Kinect motion sensor [9], and OpenCV [10] for image processing and GUI. OpenNI includes a function to obtain a depth map from a Kinect and a function to label image pixels by person. Both are incorporated into our system.

2.2 Hand detection and tracking

The system can find the right hand of the nearest sitting person, when the person moves the hand up close to the face. It traces the boundary of the sitting person's label looking for the right elbow, i.e. the lowest point, and then the right hand (see **Fig. 1**). If this does not work, the system assumes that the hand is near the label closest to the view

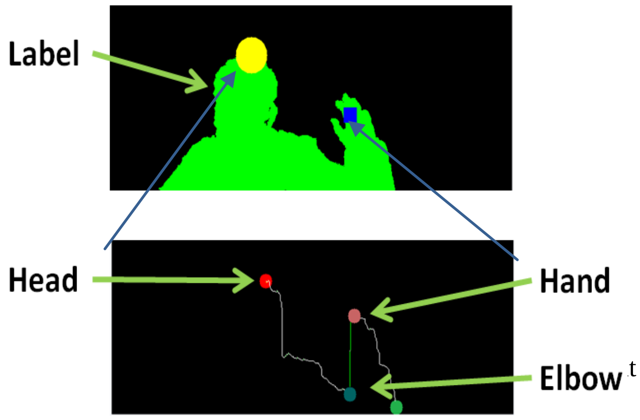

Fig. 1. Finding the right hand

2.3 3D gesture detection

Our system can detect raising, lowering, pushing, and pulling gestures based on the results of real-time 3D hand tracking described above. It looks for a 3D motion segment that fulfills several conditions of duration, speed, the location of the start/end point relative to the head position, distance between the start and end point, and direction. **Table 1** shows some of the criteria for each type of 3D gesture. For instance, to give a raising gesture, one must stop the right hand below the top of head ($y < 0$), move it fast and straight upward, and stop it above the top of head ($y > 0$).

Table 1. Gesture detection criteria

Gesture Type	raise	lower	push	pull
average speed [m/s]	0.3	0.3	0.15	0.15
top speed [m/s]	0.84	0.9	NA	NA
distance [m]	0.13	0.09	0.19	0.19
start point(x,y,z)[m]	y < 0	y > 0	z < 0.4	z < 0.4
end point (x,y,z)[m]	y > 0	y < 0	z > 0.4	z > 0.4
direction	+y	-y	-z	+z
	up	down	forth	back

2.4 Messages and images on the screen

Our system displays verbal messages, a face, and a hand on a PC screen (see **Fig. 2**). When the system finds a sitting person, a frontal face appears (bottom-left). When the right hand is successfully tracked, a hand and a "ready" sign are displayed near the face and up-left corner of the screen, respectively (top). The screen shows a verbal sign such as "up" and "back" and an image that depicts a gesture for two seconds after a gesture is detected (middle).

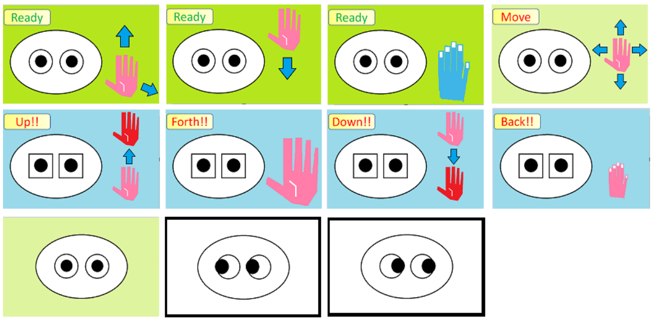

Fig. 2. Screen messages

3 USER STUDY

Fig. 3 shows Rocky, our life-supporting robot platform, which we used in the user study of our gesture detection system. It has a Kinect motion sensor on top, a 10 inch touch screen at front, and a laptop PC with an Intel Core i7 processor inside the body. The gesture detection system ran on the PC and the touch screen, connected with the PC via a USB cable, displayed messages and images to the users.

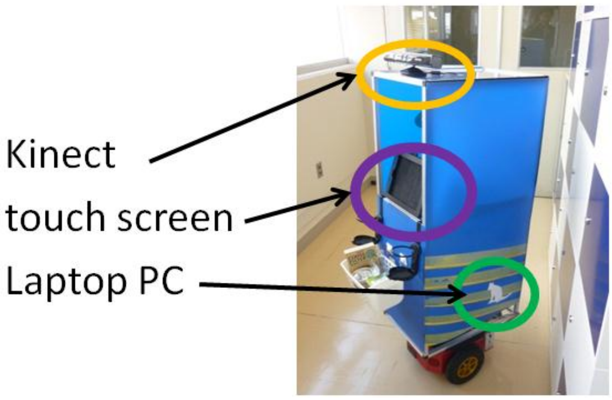

Fig. 3. Rocky, our life-supporting robot

We showed each of the eleven novice users a four-minute demonstration video, who then sat on a chair 2[m] away from the robot and moved the right hand as instructed.

The users were advised to move the right hand fast and straight when the screen displays a "ready" sign and let it down immediately after each gesture. We also suggested them to move the hand up or to the right when the system could not find it.

The first six users (Group A) practiced for two minutes after watching the demonstration video. Then, they were given pieces of advice described above and instructed to show the robot three gestures in a row for each type to test the system.

The other five users (Group B) practiced until we judged they learned the four gestures, since some of the former six users failed to practice all the types. We advised them during the practice and emphasized that they needed to wait for a "ready" sign. In the test phase, they were instructed to show gestures one by one rather than three in a row, in order to avoid unnecessary confusions.

Each of the eleven users filled out a question sheet which included eight questions (see **Table 2**).

4 RESULTS

Our system detected and correctly classified all the 3D gestures given properly by the eleven novice users. All of them moved their hand quickly and straight. However, some moved their hand when there was no "ready" sign on the screen, and also, there were three users, two in Group A and one in B, who did not put their hand down immediately after some of their pushing and pulling gestures. They told us that they had moved their hand "without thinking." In addition, some users moved their hand forward when our system happened to give a false alarm on the screen.

Table 3 shows the results of the first six questions in **Table 2**. A user (Group A) answered that the system failed to detect pulling and pushing gestures. Four in Group A thought that our system classified pulling as pushing and vice versa.

Six people found the screen messages comprehensible, and three thought they were slightly comprehensible. The other two's answers were neutral.

Table 2. Questions to the users

Id	Question
Q1	Do you understand how the four types of 3D gesture work?
Q2	Do you know exactly when to gesture?
Q3	Did our robot fail to detect your gesture during the final test?
Q4	Did our robot fail to classify your gesture?
Q5	During the final test, did the robot react to your unintended hand motion?
Q6	Have you mastered the four types of 3D gesture?
Q7	Were the pictures and signs on the screen comprehensible?
Q8	Any problems or comments?

Table 3. Answers to Q1-Q6

Id	Yes	No
Q1	11	0
Q2	10	1 (Group A)
Q3	1(Group A)	10
Q4	4 (Group A)	7
Q5	0	11
Q6	11	0

5 DISCUSSION

The results imply that our gesture detection system is of great value for multimodal communication between a life-supporting robot and its novice users. Even beginners can learn to use the four types of 3D gestures given some simple advice within less than ten minutes. Our system can detect 3D gestures properly given by beginners at a very high probability. It can be applied to understanding multimodal commands combining speech and 3D gesture. Our robot would be able to detect and classify multimodal commands at a high rate and reduce false alarms since it is unlikely that speech and gesture false alarms are given simultaneously.

Although our system ignored hand motions for two seconds after a gesture was detected, in multimodal communication it would not be necessary because only gestures that match spoken messages are in question. The users, mostly in Group A, who tried to give gestures when the screen was not displaying a ready message, were probably confused by images and messages that showed detected gestures (**Fig. 2**). Presumably, they tried to give a second gesture and our system detected a hand motion in the opposite direction as a gesture. We need to avoid such confusions when designing multimodal human-robot communication.

Users in Group B, who practiced given our advice, had better impression about our system, so it is important that novice users learn to wait for a ready message and give a gesture properly.

Although our current system is already highly reliable with respect to detection classification of four types of 3D gesture, we can improve it by reducing false positives and negatives. We presume that we can add more types without performance degradation. Finally, our 3D gestures are more intuitive than static hand gestures [11] for multimodal commands.

6 CONCLUSION AND FUTURE WORK

We built a 3D gesture detection system for multimodal communication with a life-supporting robot and conducted a user study. In the study, eleven novice users learned using 3D gestures properly within a short period of time, and our system correctly recognized the users' intentions when they moved their hand as instructed. The results show that our 3D gesture detection system can be readily applied to multimodal communication with life-supporting robots. We are currently developing a life-supporting robot one can command by combining spoken messages and 3D hand gestures.

ACKNOWLEDGMENT

This work was supported by KAKENHI Grant-in-Aid for Scientific Research (C) (22500179).

REFERENCES

[1] Oka T, Abe T, Shimoji M, Nakamura T, Sugita K, Yokota M (2008) Directing humanoids in a multi-modal command language. The 17th International Symposium on Robot and Human Interactive Communication

[2] Oka T, Abe T, Sugita K, Yokota M (2009) RUNA: a multi-modal command language for home robot users. Journal on Artificial Life and Robotics 13-2: 455-459

[3] Oka T, Sugita K, Yokota M (2010) Commanding a humanoid to move objects in a multimodal language. Journal on Artificial Life and Robotics 15-1:17-20

[4] Oka T, Abe T, Sugita K, Yokota M (2011) User study of a life supporting humanoid directed in a multimodal language. Journal on Artificial Life and Robotics 16-2:224-228

[5] Oka T, Matsumoto H, Kibayashi R (2011) A multimodal language to communicate with life-supporting robots through a touch screen and a speech interface. Journal on Artificial Life and Robotics 16-3:292-296

[6] Wachs JB, et.al. (2011) Vision-based hand-gesture applications. Communications of the ACM 54-2:60-71

[7] Goth G (2011) I, domestic robot. Communications of the ACM 54-5:16-17

[8] OpenNI: http://www.openni.org/

[9] Kinect: http://www.xbox.com/en-US/Kinect

[10]OpenCV: http://sourceforge.net/projects/opencvlibrary/files/

[11] Wang K, Wang L, Li R, Zhao L (2010) Real-time hand gesture recognition for service robot. Proc. of 2010 International Conf. on Intelligent Computation Technology and Automation

Evaluation of Some User Interfaces for Elderly Persons

Shinichi Inenaga[1], Kaoru Sugita[2], and Masao Yokota[2]

[1]Graduate School of Fukuoka Institute of Technology, 3-30-1, Wajiro-Higashi, Higashi-ku, Fukuoka, 811-0295, Japan
[2]Fukuoka Institute of Technology, 3-30-1, Wajiro-Higashi, Higashi-ku, Fukuoka, 811-0295, Japan
(Tel: 81-92-606-4965, Fax: 81-92-606-4965)

[1]mgm08004@bene.fit.ac.jp, [2]{sugita, yokota}@fit.ac.jp

Abstract: We have already proposed a new concept of 'universal multimedia access' intended to narrow the digital divide by providing appropriate multimedia expressions according to users' (mental and physical) abilities, computer facilities, and network environments. Our previous work has evaluated some types of multimedia user interfaces only for younger persons who can utilize keyword search functions. In this paper, we describe several multimedia contents particularly for elderly persons' aid and evaluate them based on a questionnaire survey.

Keywords: Multimedia, User Interface, Digital Divide.

1 INTRODUCTION

Recently, immense multimedia information has come to be exchanged on the Internet, where 3DCG, video, image, sound, and text are involved in various circumstances with terminal devices, networks and users different in their competences and performances. This fact may easily lead to 'digital divide' so called unless any special support is given to the weaker.

The universal design concept is proposed to support handicapped people in their social activities [1]. In the computer science field, the universal web [2] has been proposed to evolve this concept. However, this does not support to switch the contents, media or its quality of service (QoS) function to work the devices and network environments in their full performances. On the other hand, many studies about QoS function proposed to optimize video quality for priorities on users' requests [3]. These studies focused on performances of devices and network environments but neither users' abilities nor contents. Of course, there were also several studies on 'universal multimedia access (UMA)' but they could not narrow the digital divide because they concerned 'content switching' only [4].

Considering this fact, we have already proposed a new concept of UMA and its switching functions [5] intended to narrow the digital divide by providing appropriate multimedia expressions according to users' (mental and physical) abilities, computer facilities and network environments. In this paper, we introduce some multimedia contents for user switching function and evaluate a questionnaire survey conducted for elderly persons.

2 UNIVERSAL MULTIMEDIA ACCESS

The digital divide is caused by the differences in users' personal competences, computer facilities and network environments with such detailed items as follows.

(1) Personal competence: Physical abilities for seeing, hearing and manipulating; linguistic literacy; computer skill and cultural background,

(2) Computer facility: Processing power, resolution, color quality, sound quality and battery life,

(3) Network environment: Bandwidth availability, specification and transfer mode.

Therefore, multimedia information is necessarily accompanied by switching user interface, media and QoS parameters reflecting these differences. Here, we present a new approach to UMA for elderly people with handicap in working their devices and network environments in full performances based on such a concept as shown in Fig.1.

3 SWITCHING FUNCTIONS

UMA is to selectively provide three kinds of switching function, namely, user interface switching (UIS), media switching (MS) and QoS switching (QS). Fig.2 shows these switching functions working as follows:

(SF1) UIS: Switch to user interfaces (UI) appropriate for users' competences and display devices,

(SF2) MS: Switch to media appropriate for users' competences, performances of terminal devices and networks,

(SF3) QS: Control media qualities appropriate for users' competences and terminal devices.

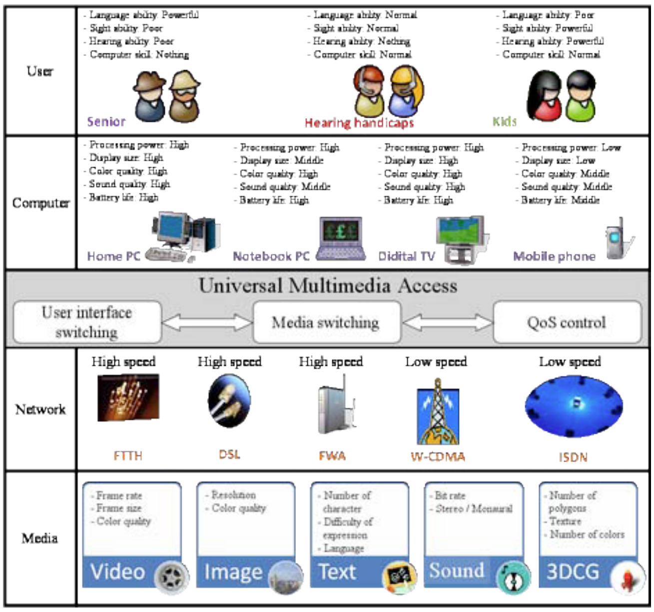

Fig. 1. UMA.

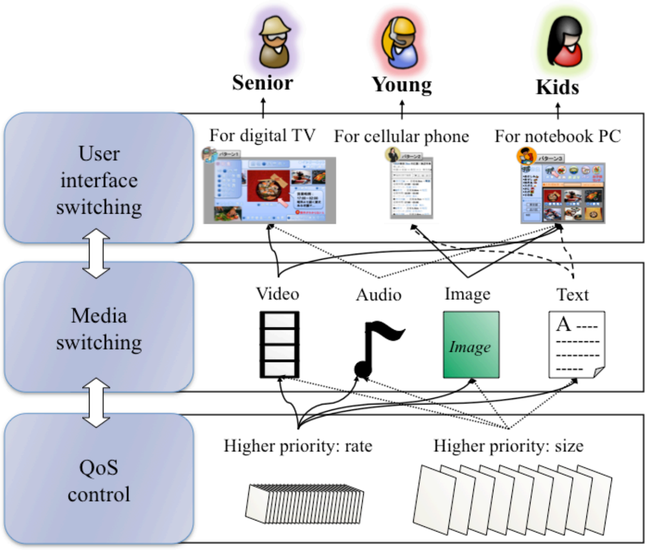

Fig. 2. Switching functions

These functions are applied in the ascending order (from SF1 to SF3) at beginning to play multimedia information or in the descending order at playing.

4 USER INTERFACE SWITCHING

UI provides users with appropriate operations and media according to their computer skill and computer facilities.

Computer skill is graded in such a way as follows.

(G0) No Knowledge about Computer: Unable to operate any computer functions.

(G1) Computer Beginner: Able to start up an application software such as Web browser and play media.

(G2) General Web User: Able to operate general Web pages and select to play a media.

(G3) Internet Expert: Able to use efficiently interactive online applications such as a search engine.

On the other hand, computer facilities are rated from several viewpoints and classified into 4 levels (None, Low, Middle, High) to setup media.

UI is provided differently according to computer skills and facilities. Table.1 shows 12 types of UI expressed in a matrix.

Computer beginners are supposed to select Broadcast Operation (BO) so as to play media according to the program without complicated operations. The user can get information just like watching TV because it is not necessary to operate any application software fundamentally. Choice Operation (CO) is intended for general Web users so as to select media only. But it takes user much time to select one from a lot of media. Search Operation (SO) is supposed to support Internet experts by providing a keyword search function.

Low power terminals are supported to play AA and text with only low graphics power and narrow bandwidth of network. Middle power terminals are to display contents such as combinations of still image and text. High power terminals play video requiring not only high power CPU but also high power Graphic device.

A layout is used to put media on UI and to specify the display region, display size and number of media for resolutions of the terminal device and the media. These relations enable a layout to specify the display position according to the display size and the number of media.

In order to introduce UIS, we focused on CO because willing users are supposed to perform this operation driven by necessity. On the other hand, they will not use any operation without CO. From this point of view, CO is applied to UIS switching from a current UI to desired one and controlling types of UI with buttons just like TV remote control.

Table 1. User interface according to user's operation a nd types of media

Operation	Media			
	AA (Ascii Art)	Text	Image&Text	Video
Broadcast	- No operation - Displaying a AA according to the program	- No operation - Displaying a text according to the program	- No operation - Displaying images and text according to the program	- No operation - Playing a video according to the program
Choice	- Selection - Displaying a AA according to the program	- Selection - Displaying a text according to the program	- Selection - Displaying selected images and text	- Selection - Playing a selected video
Search	- Keyword search - Displaying a AA according to the program	- Keyword search - Displaying a text according to the program	- Keyword search - Playing searched images and text	- Keyword search - Playing a searched video

5 IMPLEMENTATION

Our ideas were implemented as Flash applications running on a web browser as shown in Fig.3. These applications introduce the sightseeing area called the 'Keishouchi (=Splendid scenery)' contents providing the 12 UIs mentioned above. These UIs can be switched to a desired one using 'software remote controller (SRC)' as shown in Fig.4. SRC is supposed for general Web users and over so as to select a UI with simple button operation because other users would not like complicated operations.

6 EVALUATION

In order for evaluation, the web-based questionnaire survey system has been used to correct for the results of questionnaire sheets and to support following functions:

(ES1) Make a new questionnaire,
(ES2) Perform a questionnaire survey,
(ES3) Output the results of survey.

The system published contents [8] as shown in Fig.5 and was constructed on the following 4 types of software:

(FW1) Web server: apache 2.2.14 [10],
(FW2) Web Survey System: LimeSurvey 1.90 [11],
(FW3) Script language: PHP 5.3.1 [12],
(FW4) Database: MySQL 5.1.41 [13].

A questionnaire survey has been carried out for 5 elderly persons (over 70 years old) using the questionnaire sheet as shown in Fig.6. In the survey, the graduate student instructs them to operate the UI and fill out to the sheet. For this reason, none of them can do any computer operation. The results are shown in Fig.7. From the evaluation, we find that they can only use BO in order not to operate a general PC, but CO is preferred to BO using a tablet PC. Also, the information can be understood easily by video content regardless of its operation. But both of text and ascii art content are more difficult than other contents.

7 CONCLUSION

In this paper, we discussed the UI appropriate for low computer skills and facilities. Especially, we evaluated the 12 types of UIs for elderly persons. From the evaluation, elderly persons can only use BO in order not to operate a general PC, but CO is preferred to BO on a tablet PC. Currently, we are evaluating SRC and its UI for more persons. In near future, we will construct some types of content for evaluating UIS and other switching functions for UMA.

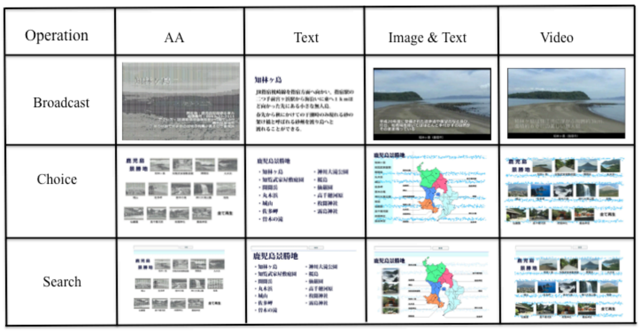

Fig. 3. 'Keishouchi' contents

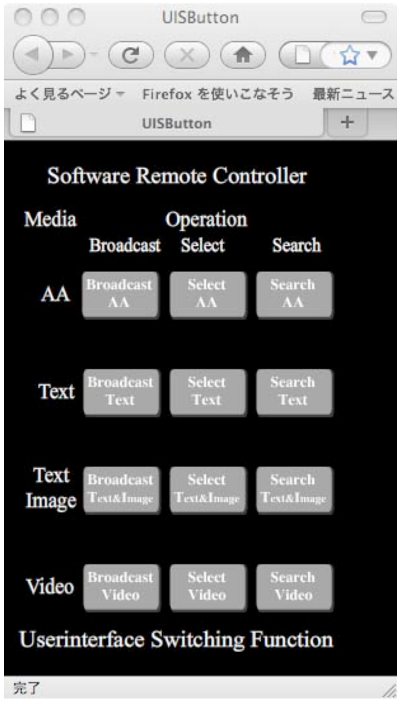

Fig. 4. SRC.

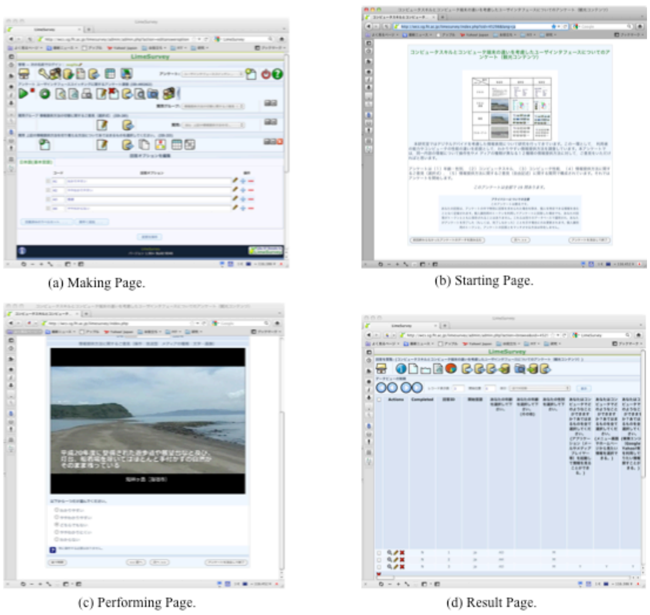

Fig. 5. The evaluation system

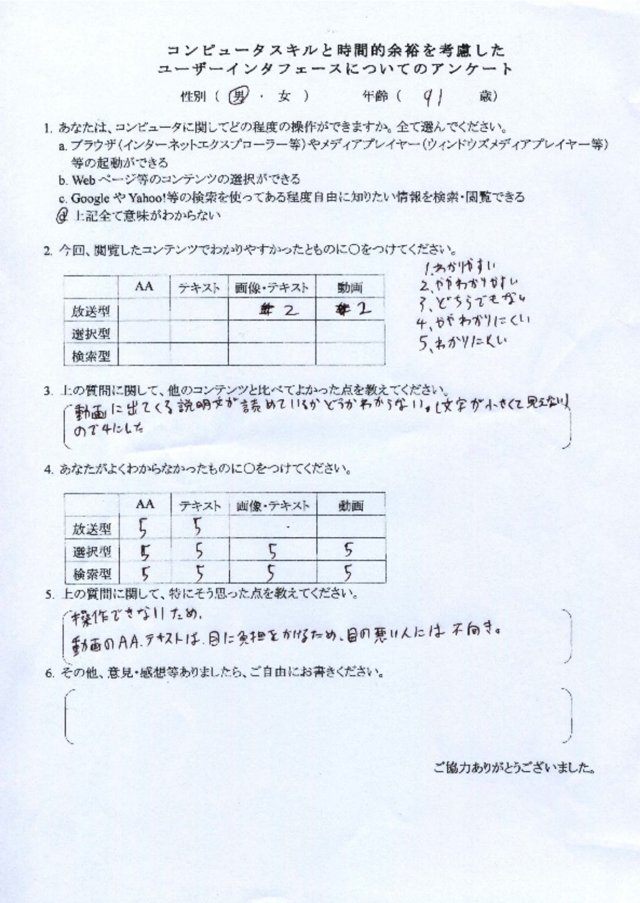

コンピュータスキルと時間的余裕を考慮した
ユーザーインタフェースについてのアンケート

性別（男・女）　　年齢（ 91 歳）

1. あなたは、コンピュータに関してどの程度の操作ができますか。全て選んでください。
a. ブラウザ（インターネットエクスプローラー等）やメディアプレイヤー（ウィンドウズメディアプレイヤー等）等の起動ができる
b. Web ページ等のコンテンツの選択ができる
c. Google や Yahoo!等の検索を使ってある程度自由に知りたい情報を検索・閲覧できる
d. 上記全て意味がわからない

2. 今回、閲覧したコンテンツでわかりやすかったとものに○をつけてください。

	AA	テキスト	画像・テキスト	動画
放送型			2	2
選択型				
検索型				

1.わかりやすい
2.ややわかりやすい
3.どちらでもない
4.ややわかりにくい
5.わかりにくい

3. 上の質問に関して、他のコンテンツと比べてよかった点を教えてください。
動画に出てくる説明文が読めているかどうかわからない。(文字が小さくて見えない)ので4にした

4. あなたがよくわからなかったものに○をつけてください。

	AA	テキスト	画像・テキスト	動画
放送型	5	5		
選択型	5	5	5	5
検索型	5	5	5	5

5. 上の質問に関して、特にそう思った点を教えてください。
操作できないため。
動画のAA.テキストは.目に負担をかけるため、目の悪い人には不向き。

6. その他、意見・感想等ありましたら、ご自由にお書きください。

ご協力ありがとうございました。

Fig. 6. The questionnaire sheet

REFERENCES

[1] Ronald L. Mace, Graeme J. Hardie, and Jaine P. Place (1991), Accessible Environments: Toward Universal Design, The Center for Universal Design, North Carolina State University, USA

[2] Kazuhiko Yamazaki (2001), Achievement of universal Web (1) (in Japanese). Design study research 48:330-331

[3] Mohan, R, Smith, J.R and Chung-Sheng Li (1999), Adapting multimedia Internet content uni versal access, IEEE Multimedia Transcations 1(1):104-114

[4] Fernando Pereira and Ian Burnett (2003), Universal Multimedia Experience for tomorrow, IEEE Signal Procces ing Magazine, IEEE 20(2): 63-73

[5] Y. Maeda, K. Sugita, T. Oka, and M. Yokota (2008), Proposal of a New Concept of Universal Multimedia Acces s, Proc. 13th International symposium on ARTIFICIAL LIF E AND ROBOTICS (AROB 13th '08), OS7-6

[6] Y. Maeda, E. Tsujimura, K. Sugita, T. Oka, and M. Y okota (2009), Some consideration on user adaptive interfac e for universal multimedia access, Proc. 13th International s ymposium on ARTIFICIAL LIFE AND ROBOTICS (ARO B 14th '09), OS13-5

[7] Y.Maeda, K.Sugita, T.Oka, M.Yokota (2009), Evaluation of sume user interfaces for universal multimedia access, Proc. the 19Th Intelligent System Symposium (FAN2009), F3-3:120-124

[8] Tourist Information of 'Keishouchi' in Kagoshima Pr efecture, (in Japanese), "http://wcs.sg.fit.ac.jp/limesurvey/in dex.php?sid=45298& lang=ja"

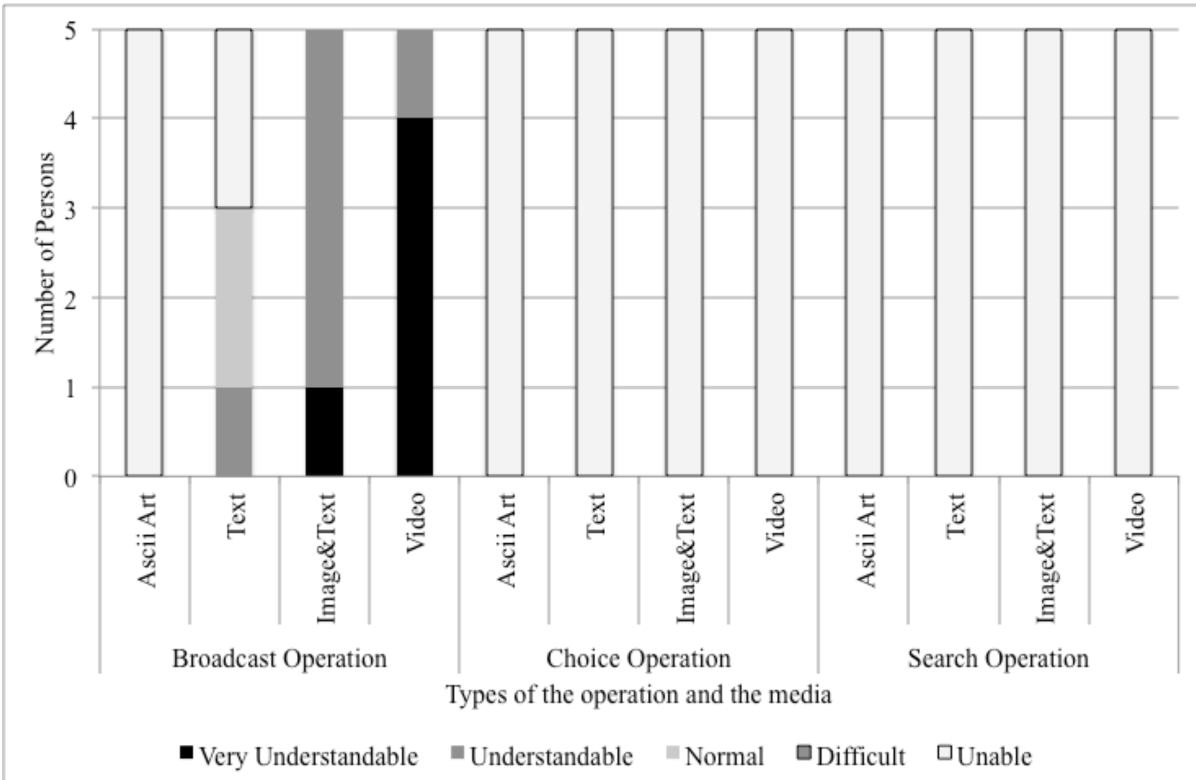

Fig. 7. The result of questionnaire survey

The Seventeenth International Symposium on Artificial Life and Robotics 2012 (AROB 17th '12),
B-Con Plaza, Beppu, Oita, Japan, January 19-21, 2012

Toward Artificial Kansei Based on Mental Image Directed Semantic Theory

Tzu-Hsuan Huang Kaoru Sugita Masao Yokota
Fukuoka Institute of Technology
yokota@fit.ac.jp

Abstract

The authors have proposed a human mind model of human mind consisting of Stimulus, Knowledge, Emotion and Response Processing Agents and simulated human-robot communication based on it. This paper proposes 'Artificial *Kansei* (AK)', namely, *Kansei* for a robot as tight collaboration of Knowledge and Emotion Processing Agents of our mind model, and considers its application to a *Kansei* information system for Buddhism statues made to order.

1. Introduction

In recent years, there have been developed various types of robots in Japan. However, they are to play their roles according to programmed actions to stimuli and have not yet come to understand such a mental function of their human partners as is called *Kansei*. The authors have proposed a human mind model of human mind consisting of Stimulus, Knowledge, Emotion and Response Processing Agents (see Fig.1) and simulated human-robot communication based on it [1]. Besides this, we have tried to describe the meanings of *Kansei* expressions such as 'heart-calming', 'fantastic', 'soft', 'thick', 'grotesque', etc related to visual images of crafts and to retrieve them by these expressions as queries [4-6]. In this paper, we describe 'Artificial *Kansei* (AK)', namely, *Kansei* for a robot as tight collaboration of Knowledge and Emotion Processing Agents of our mind model, and verbalization of *Kansei* information so called '*Kansei* expression' by Response Processing Agent in the view of artificial or robotic individuality.

2. Multi-agent mind model

Figure 1 shows the multi-agent mind model proposed by the authors [1]. This is a functional model of human central nervous system consisting of the brain and the spine. The basic performances of its agents are as follows.

(1) **Stimulus Processing Agent** (**St**) receives stimuli from the world (**W**) and encodes them into mental images (i.e. encoded sensations) such as *"I sensed something oily."* (if verbalized in English.)
(2) **Knowledge Processing Agent** (**Kn**) evaluates mental images received from the other agents based on its memory (e.g. knowledge), producing other mental images such as *"It is false that the earth is flat."*
(3) **Emotion Processing Agent** (**Em**) evaluates mental images received from the other agents based on its memory (e.g. instincts), producing other mental images such as *"I like the food."*
(4) **Response Processing Agent** (**Re**) converts mental images (i.e. encoded physical actions such as *"I'll walk slowly."*) received from the other agents into real physical actions against **W**.

A *performance* ***P*** for a *stimulus* X with a *result* Y at each agent can be formalized as a function by the expression (1).

$$Y=\boldsymbol{P}(X), \tag{1}$$

where

P: a combination of ***atomic performances*** described later,
X: a spatio-temporal distribution of stimuli from **W** to **St** or a mental image for another agent, and
Y : a series of signals to drive an actuator for **Re** or a mental image for another agent.

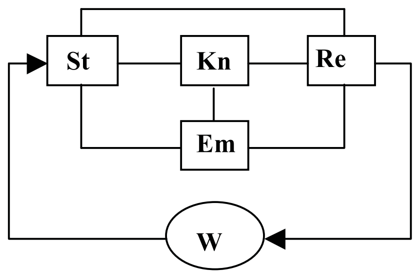

St: Stimulus Processing Agent.
Kn: Knowledge Processing Agent.
Em: Emotion Processing Agent.
Re: Response Processing Agent.
W: World surrounding human mind, including his/her body.

Fig.1. Multi-agent model of human mind.

A performance ***P*** is assumed as a function formed either consciously or unconsciously. In a conscious case, a set of atomic performances are to be chosen and combined according to X by a meta-function, so called, '***Performance Selector*** (PS)' assumed as '***Conscience***'. On the contrary, in an unconscious case, such a performance as associated most strongly with X is to be applied automatically [8]

3. Mental image description

Mental Image Directed Semantic Theory (MIDST) has modeled mental images as "Loci in Attribute spaces" [3], [7]. An attribute space corresponds with a certain measuring instrument just like a thermometer, map measurer or so and the loci represent the movements of its indicator. The performance of 'Attribute space' is the model of '***Atomic performance***' introduced in Section 2.

A general locus is to be articulated by "Atomic locus" formalized as the expression (2) in first-order logic, where "L" is a predicate constant.

$$L(x,y,p,q,a,g,k) \quad (2)$$

The expression (2) is called "Atomic locus formula" whose arguments are referred to as 'Event Causer', 'Attribute Carrier', 'Initial Attribute Value', 'Final Attribute Value', 'Attribute Kind', 'Event Kind' and 'Standard Attribute Value', respectively.

The interpretation of (2) is as follows, where "matter" refers to "object" or "event".

"Matter 'x' causes Attribute 'a' of Matter 'y' to keep (p=q) or change (p ≠ q) its values temporally ($g=G_t$) or spatially ($g=G_s$) over a time-interval, where the values 'p' and 'q' are relative to the standard 'k'."

When $g=G_t$ and $g=G_s$, the locus indicates monotonic change or constancy of the attribute in time domain and in space domain, respectively. The former is called 'temporal event' and the latter, 'spatial event'.

For example, the motion of the 'bus' represented by S1 is a temporal event and the ranging or extension of the 'road' by S2 is a spatial event whose meanings or concepts are formalized as expressions (3) and (4), respectively, where the attribute is "physical location" denoted as A_{12}. We think that the verb 'run' used in S2 must reflect the motion of the observer's attention [4].

(S1) The bus runs from Tokyo to Osaka.

$$(\exists x,y,k)L(x,y,Tokyo,Osaka,A_{12},G_t,k)\wedge bus(y) \quad (3)$$

(S2) The road runs from Tokyo to Osaka.

$$(\exists x,y,k)L(x,y,Tokyo,Osaka,A_{12},G_s,k)\wedge road(y) \quad (4)$$

The expression (5) is the conceptual description of the English word "fetch", implying such a temporal event that 'x_1' goes for 'x_2' and then comes back with it, where 'Π' and '•' are instances of the tempo-logical connectives, 'SAND' and 'CAND', standing for "Simultaneous AND" and "Consecutive AND", respectively.

In general, a series of atomic locus formulas with such connectives is called simply 'Locus formula'.

$$(\exists x_1,x_2,p_1,p_2,k)\ L(x_1,x_1,p_1,p_2,A_{12},G_t,k)$$
$$\bullet (L(x_1,x_1,p_2,p_1,A_{12},G_t,k)\Pi L(x_1,x_2,p_2,p_1,A_{12},G_t,k))$$
$$\wedge x_1 \neq x_2 \wedge p_1 \neq p_2 \quad (5)$$

4. Artificial *Kansei*

It is well known that emotion in a human can be affected by his/her world, namely, ***W*** in Fig.1. For example, a person's evaluation of live image of an object (i.e. image output from **St**) expressed by such words as 'favorite', 'beautiful', 'tasty', etc can vary depending on his/her emotional bias such as 'hungry', 'depressed', etc.

Kansei is one of mental functions with emotion involved but has a more complicated phase than pure emotion originated from instincts or imprinting. For example, sweet jam may be nice on toast but not on pizza for certain people knowledgeable about these foods. For another example, people can be affected on their evaluation of an art by its creator's name, for example, 'Picasso'. These are good examples of *Kansei* processing as emotional performance affected by knowledge in humans.

Therefore, *Kansei* can be defined as human emotion toward an object affected by its information, so called, 'concept', including his/her intellectual pursuits, traditions, cultures, etc concerning it. In this sense, *Kansei* is assumed to be reasonable among the people sharing such concepts unlike pure emotion. These hypothetic considerations are formalized as (7) and (8).

$$I_P(x)= \boldsymbol{P_E}(S(x)) \quad (7)$$

$$I_K(x) =\boldsymbol{P_E}(S(x)\wedge O(x)) = \boldsymbol{P_E}(S'(x)) \quad (8)$$

where

$\boldsymbol{P_E}$(X): Performance of **Em** for mental image 'X',
I_P(x): Mental image as pure emotion for object 'x',
I_K(x): Mental image as *Kansei* for object 'x',
S(x): Live image of object 'x' from **St**,
O(x): Concept of object 'x' from **Kn**,
S'(x): Unified image of live image and concept.

Figure 3 shows an example of *Kansei* processing in our mind model, where perceived, induced and inspired images correspond to S(x), S'(x) and I_K(x), respectively, while Fig.2 is for pure emotion with I_P(x) as the inspired image.

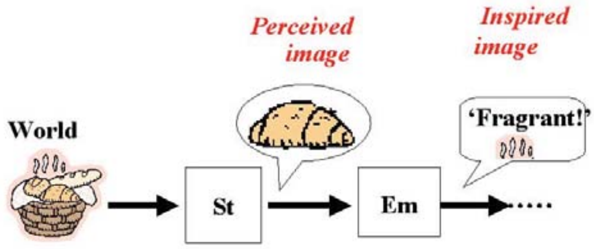

Fig.2. Example of pure emotion

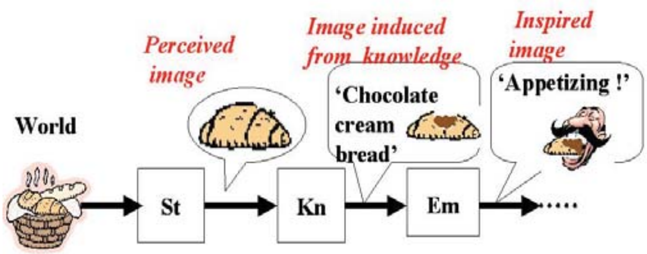

Fig.3. Example of *Kansei* processing

These two inspired images are to be verbalized in **Re** as 'Fragrant!' and 'Appetizing!', labeled in Fig.2, respectively. The essential difference between them is assumed to reside in whether or not they are affected by O(x), namely, the concept of 'chocolate cream bread', inferred by **Kn** from the shape and the smell. Whereas, pure emotion for an object can be a special case of *Kansei* processing without knowing or recognizing what it is.

In MIDST, the concept of an object 'x' is given as an integrated omnisensory mental image of its properties and its relations with other objects involved. For example, the concept of 'chocolate cream bread' can be given by (9), reading that x is bread, sweet due to chocolate cream, fragrant of itself, etc, where A_{29} and A_{30} refer to 'Taste' and 'Odour', respectively.

$$(\lambda x)chocolate\_cream\_bread(x) \Leftrightarrow (\lambda x\exists y,k_1,k_2)L(y,x,Sweet,Sweet,A_{29},G_t,k_1)\Pi\, L(x,x,Fragrant,Fragrant,A_{30},G_t,k_2) \wedge bread(x) \wedge chocolate\_cream(y) \wedge \ldots \quad (9)$$

5. Human language understanding in robots

For comprehensible communication with humans, robots must understand natural language *semantically* and *pragmatically*. Here, semantic understanding means connecting symbols to conceptual images of objects and pragmatic understanding means connecting symbols to real objects by unifying conceptual images with perceptual images. However, humans and robots can be equipped with sensors, actuators and brains of different performances and their vocabularies may well be grounded on quite different sensations, physical actions or mental actions. And in turn such a situation may bring inevitably different kinds of semantics to them, so called, "Natural Semantics (NS)" for humans and "Artificial Semantics (AS)" for robots.

For example, consider such a scenario as follows.

...A human 'Kate' and a humanoid robot 'Robbie' encounter at the terrace in front of the room where a Christmas party is going on merrymaking. Kate says "Robbie, please fetch me some nice food from the gaudy room." Robbie replies "OK, Kate."….

For a happy end of this dialog, Robbie must have a good knowledge of Kate's NS for *Kansei* and translate it into its AS appropriately enough to find out the real objects referred to by her words. In this case, Robbie needs at least to interpret Kate's statement as the expression (10) reading "If <u>*Robbie* fetches *Kate* some food nice ***for her*** from the room noisy ***for her*** (***E1***),</u> then consecutively <u>it makes *Kate* happier (***E2***)</u>". It is notable that (10) is the canonical form of the meaning of an imperative sentence.

$$\boldsymbol{E_1} \rightarrow_c \boldsymbol{E_2} \quad (10)$$

where

$$\boldsymbol{E_1} \Leftrightarrow (\exists x_1,x_2,k_1,k_2,k_3,k_4)\ (L(R,R,K,x_2,A_{12},G_t,k_1)\bullet (L(R,R,x_2,K,A_{12},G_t,k_1)\Pi L(R,x_1,x_2,K,A_{12},G_t,k_1))) \Pi(L(K,x_1,Nice,Nice,B_{08},G_t,k_2) \Pi\, L(K,x_2,Gaudy,Gaudy,B_{08},G_t,k_4) \wedge food(x1) \wedge room(x2)$$

$$\boldsymbol{E_2} \Leftrightarrow (\exists e_1,e_2,k_7)\ L(\boldsymbol{E_1},K,e_1,e_2,B_{04},G_t,k_7) \wedge e_2>e_1.$$

The special symbols and their meanings in the expressions above are:

'$X \rightarrow_c Y$' ='If X then consecutively Y', R='Robbie', K='Kate', B_{08}='*Kansei*' and B_{04}= 'Happiness (=degree of happiness)'.

As easily imagined, these values of the attribute *Kansei* (B_{08}) greatly depend on their standards (i.e. k_2 and k_4) that are most closely related to 'Individual' or 'Purposive' standard shown in Table 1 (see APPENDIX).

By the way, Robbie's task is only to make ***E1*** come true where each atomic locus formula is associated with his actuators/sensors. Of course, Robbie believes that he will become happier to help Kate, given by expression (11) where 'B_{03}' is 'trueness (=degree of truth)'and 'K_B' is a certain standard of 'believability'. That is *emotionally* to say, Robbie likes Kate. Therefore, this example is also very significant for intentional sensing and action of a robot driven by logical description of its belief.

$$(\exists p)L(R,\boldsymbol{E},p,p,B_{03},G_t,K_B) \wedge p>K_B \wedge \boldsymbol{E} = \boldsymbol{E_1} \rightarrow_c \boldsymbol{E_2} \quad (11)$$

6. Affective analysis of Buddhism statues

Many psychologists have claimed that certain emotions are more basic than others (Ortony & Turner, 1990). We have assumed that human emotion consists of 5 primitives representing the degrees of 1) Anger, 2) Disgust, 3) Anxiety, 4) Happiness, and 5) Superiority. For example, the degree of Happiness is measured by using such a word set as {anguish, distress, sorrow, gloom, content, joy, ecstasy}, whose each element is possibly arranged on a coordinate axis and fuzzified with a certain characteristic function. Therefore, we have assumed Kansei as a certain function to evaluate totally the loci in the attribute spaces of these primitives. Based on the 5 primitive emotional parameters, we have been analysing Buddhism statues as shown in Fig.4 in order to plot them in the attribute space of Kansei (B_{08}) with some purposive standard of Buddhism. Table 1 shows an example of such analysis, where H, M and L denote high, middle, and low in degree, respectively. These results are to be associated with Kansei words such as divine, gentle, reverential, noble, valiant, etc. analyzed in the same way and to be applied to the customer servicing interface of a Buddhism statue ordering system.

a) Dainichi-nyorai (DN) b) Fudo-myo-o (FM)

Fig.4. Samples of Buddhism statues

Table 1 Affective analysis of Buddhism statues

Sample	anger	disgust	anxiety	happiness	superiority
DN	L	L	L	H	H
FM	H	M	H	L	H

7. Discussion and conclusion

Our mind model is much simpler than Minsky's [2] but the locus formula representation can work for representing and computing mental phenomena fairly well [1, 3]. For realizing a plausible *Kansei*, it is most essential to find out functional features of **Em** and to deduce from them such laws that rule $\boldsymbol{P_E}$. The most important problems to be solved are how to realize the attribute space of *Kansei* and how to build its corresponding atomic performance. In order to solve these problems, focusing on Buddhism statues, we will consider the application of soft computing theories such as neural network, genetic algorithm, fuzzy logic, etc. in near future.

References

[1] Yokota,M., Shiraishi,M. and Capi,G.: "Human-robot communication through a mind model based on the Mental Image Directed Semantic Theory," Proc. of the 10th International Symposium on Artificial Life and Robotics (AROB '05), pp.695-698, 2005.
[2] Minsky, M: The society of mind, Simon and Schuster, New York, 1986.
[3] Yokota, M. & Capi,G.: "Cross-media Operations between Text and Picture Based on Mental Image Directed Semantic theory," WSEAS Trans. on INFORMATION SCIENCE and APPLICATIONS, Issue 10, 2, pp.1541-1550, Oct. 2005.
[4] M.Fukuda, K.Sugita and Y.Shibata, "Perceptional Retrieving Method for Distributed Design Image Database System," IPSJ Journal, Vol.39, No.2, pp.158-169, 1998.
[5] K.Sugita, A.Miyakawa and Y.Shibata, "Relation Between Kansei Words and the Room Space in Digital Traditional Japanese Crafting System," The International Conference on Advanced Information Networking and Applications (AINA), 159-162, 2003.
[6] K.Sugita, T.Ishida, A.Miyakawa, Y.Shibata, "Kansei Retrieval Method using the Quantitative Feature of Traditional Japanese Crafting Object," Proc. of The 6th International Workshop on Multimedia Network Systems and Applications (MNSA'2004), 112-117, 2004.
[7] Prinz, W.: "A common coding approach to perception and action", In *Relationships between perception and action* (Neumann, O. and Prinz, W. eds.), pp.167-201, Springer-Verlag, 1990.
[8] Brooks, R. A.: "A robust layered control system for a mobile robot", IEEE Journal of Robotics and Automation, RA-2, pp.14-23, 1986.
[9] Ortony,A. and Turner,T.J.: "What's basic about basic emotions?", Psychological Review, Vol.97, pp.315-331,1990.

APPENDIX

Table 2 Examples of standards.

Categories of standards	Remarks
Rigid Standard	Objective standards such as denoted by measuring *units* (meter, gram, etc.).
Species Standard	The *attribute value ordinary* for a species. A *short train* is ordinarily longer than a *long pencil*.
Proportional Standard	'*Oblong*' means that the width is greater than the height at a physical object.
Individual Standard	*Delicious* food for one person can be too *poor* for another.
Purposive Standard	One room *comfortable* enough for a person's *sleeping* may be *uncomfortable* for his *jogging*.
Declarative Standard	The origin of an order such as 'next' must be declared explicitly just as 'next *to him*'.

The Seventeenth International Symposium on Artificial Life and Robotics 2012 (AROB 17th '12),
B-Con Plaza, Beppu, Oita, Japan, January 19-21, 2012

A high-sensitivity 3-D shape measurement method with microscope

Xueli Zhang[1], Kazuhiro Tsujino, and Cunwei Lu[2]

Fukuoka Institute of Technology,
3-30-1 Wajiro-higashi, Higashi-ku, Fukuoka, 811-0295 Japan
(Tel: +81-92-606-3578, Fax: +81-92-606-0726)

[1] bd11003@bene.fit.ac.jp, [2] lu@fit.ac.jp

Abstract: An optical microscope commonly has the magnification from tens times to thousands times, and is often used for the observation of a micro specimen. The three-dimensional (3-D) form measurement of the specimen surface is broadly demanded of fields, such as medical treatment, pharmacy, life science, and materials science. On the conventional methods, the focus distance is regulated with great precision or the system is complex and the operation and observation is simply by the skilled personnel. In order to solve these problems, we propose a high-sensitivity 3-D shape measurement method with microscope. The measurement system is consisted of a normal microscope, a line laser, and a computer can obtain the high precision of target. The method is unnecessary to regulate the focus distance with great precision, simply project the laser source onto the surface of target and obtain the reflection image with the camera of microscope, and by using the image processing to obtain the center point of waveform of the intensity distribution of reflection image, finally calculate the 3-D shape information based on the triangulation method. The experimental results show the proposal method is available.

Keywords: Laser, 3-D measurement, Microscope.

1 INTRODUCTION

An optical microscope commonly has the magnification from tens times to thousands times, and is often used for the observation of a micro specimen. The three-dimensional (3-D) shape measurement of the specimen surface is broadly demanded of fields, such as medical treatment, pharmacy, life science, and materials science and so on.

The methods of 3-D shape measurement with microscope are various. For instance, laser-scanning confocal optical microscopy[9], strength is spatial resolution is high; weakness is the focus distance is regulated with great precision, and it cost time and observation is simply by the skilled personnel. AOD-based two-photon microscopy[10], strength is high-speed in vivo; weakness is the system is complex and the operation and observation is simply by the skilled personnel. Laser-induced fluorescence (LIF) detection system[5], strength is to provide effective high-throughput flow cytometry measurements; weakness is simply available for the direction. Shape from focus[1], strength is the system is simple and inexpensive; weakness is not available for the non-uniform spatial resolution, and the observation view is limited and performance affected by ambient light. And holographic optical element[6], strength is the calculation method is simple; weakness is the system is complex that the various mirror and microscope are used, the operation is difficult.

In order to solve these problems described on above methods, we propose a high-sensitivity 3-D shape measurement method with microscope.

The papers are formed with 5 sections as the following:

Section 2 introduces the composition, principle and methods of the 3-D measurement system we presented.

Section 3 shows the experimental results by using the method we proposed.

Section 4 introduces the conclusion for the method we proposed.

2 COMPOSITION, PRINCIPLE AND METHODS

The composition, principle and methods of the 3-D measurement system we presented is shown as following.

2.1 System composition

The measurement system on our proposal method is consisted of a microscope, a line laser, and a computer. It is shown as Figure. 1.

The operation of the method we proposed is as the following. At first, the line laser source is projected onto the surface of the micro target by the line laser. And next,

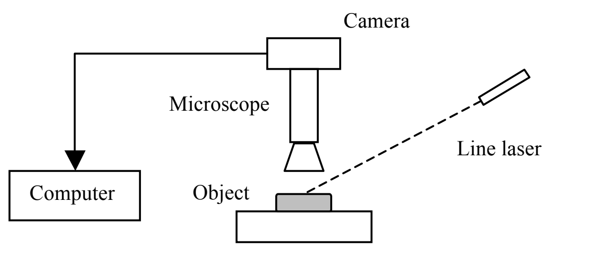

Fig. 1 Microscope 3-D measurement system

we regulate the microscope to observe the reflection image of target, and then, the camera of the microscope photographs the reflection image, and the image is inputted into the computer. Finally, the measurement image is obtained through the image processing on the computer, and the 3-D shape information of the target is calculated from the measurement image by using the triangulation.

2.2 Measurement principle

The measurement method is based on an optical principle - the intensity distribution of a reflection light likes a cosine waveform. For the cosine waveform, we can simply detect the top point of it. (On our research "Accuracy Improvement for Projection Patterns in 3-D Measurement" (Ref. [4], [5]), the top-point analysis method is introduced on detail.)

On the basis of the principle, when the microscope observes the reflection image, the focus distance can be regulated within great precision. It means the observation time and operation degree are reduced. It's the prominent strength of proposal method.

The cause is for the reflection image at any station, we can use the image processing to process the image, and obtain the ideal the cosine waveform of the intensity distribution of it. For the cosine waveform, we can easily detect the top point – the real center point of the waveform. And then, we can calculate the correct 3-D shape information of the observation point.

2.3 Measurement methods

2.3.1 Microscope observation

At first, in order to observe the target clearly, we put the specimen on the microscope stage, and move location of the stage to make the target on the center of the visual field of the microscope. And then, we regulate the focal distance of the objective of microscope to obtain the distinct image of the target, and regulate the light source of the microscope to obtain the primitive image of the target.

2.3.2 Laser projection

Second, we regulate the distance and rotation angle of the laser to make the line laser project onto the surface of the target and the reflection image on the visual field of the microscope. And then, we can obtain the reflection image intermix with the reflection light of laser source and light source of the microscope. The image is called the laser and light source image.

2.3.3 Camera photographs

And then, we close the light source of the microscope, and obtain the reflection image of the laser source by using the camera of the microscope. The image is called the laser source image.

2.3.4 Image processing

Be aimed at the laser source image, we will use the image processing to obtain the measurement image.

In order to obtain the channel had the maximum value of R, G, B, we use the method choose the measurement channel and generate a measurement image (Ref. [2], [3]).

In every pixel of the extracted object image, the color and intensity distributions are detected. The channel of the initial observation pattern image intensity maximum is chosen to be the measurement channel of the pixel by

$$\bar{I}(x,y) = \max\{\bar{I}_R(x,y), \bar{I}_G(x,y), \bar{I}_B(x,y)\} \qquad (1)$$

where the (x,y) is the image coordinate of current pixel, $\bar{I}(x,y)$ is intensity of the (x,y), $\bar{I}_R(x,y)$, $\bar{I}_G(x,y)$, $\bar{I}_B(x,y)$ is respectively intensity of the Red, Green channel of the (x,y), Blue of (x,y).

The result image is called the monochrome image.

2.3.5 Center point detection

Through using the moving average method, we can obtain the cosine waveform of the intensity distribution of the reflection light.

For the cosine waveform, we can easily detect the top point of it. The result is shown as Fig. 2.

Where the yellow line on the Intensity distribution figure is the top point position of reflection light on the red line of the measurement light.

2.3.6 3-D information calculation

Fig. 3 is the diagram used the proposal method based on the triangulation method. On the basis of the diagram, we obtain the equations calculated the 3-D information of the target, they are shown as the (2), (3) and (4)

$$X = Z \times \frac{x}{f} \qquad (2)$$

$$Y = X \times \frac{y}{x} \qquad (3)$$

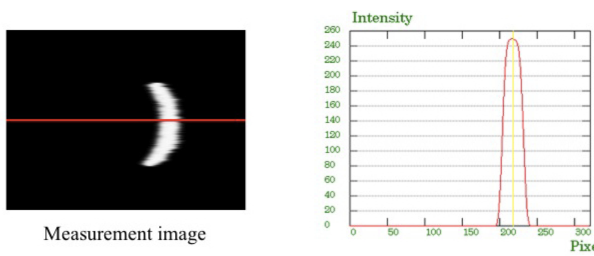

Measurement image

Intensity distribution figure

Fig. 2 Detection results of the object

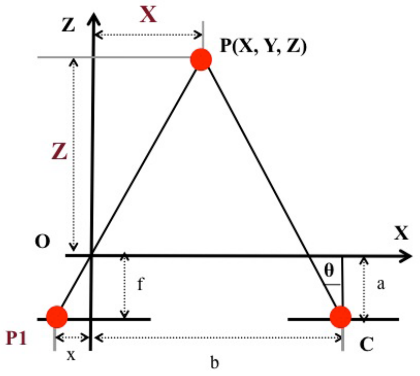

Fig. 3 The principle of triangulation method

$$Z = \frac{b - a\tan\theta}{\tan\theta \pm x/f} \tag{4}$$

Where P is the observation point on the target, C is the projection point from the laser, and P1 is the reflection point of the projection point from the target to the camera. X is the horizontal distance from P to the mid-perpendicular line of camera. Y is the vertical distance from P to the mid-perpendicular line of camera. Z is the depth distance from P to the image plane of camera. x is the horizontal distance from P1 to the mid-perpendicular line of camera. y is the vertical distance from P1 to the mid-perpendicular line of camera. b is the distance between the laser and camera. a is the distance from the laser to the lens of the microscope. tan θ is the angle between the projection laser source and the vertical line. f is the focal distance of camera.

By using the equations (2), (3) and (4), we can calculate the 3-D information of each top point on the reflection light.

3 EXPERIMENTAL RESULTS

The experimental conditions: The microscope is the pinhole confocal optical system; the magnification is from 25 to 175. The spatial resolution of the camera of the microscope is 320 × 240, the CCD is the ½ type 900,000 pixel CCD series. The laser is the semiconductor line laser.

For test the proposal method, we make a series experiments for various specimens. The experimental results are shown as following. (Because the time is not enough on the deadline of the manuscript, the experiment from 3.2 to 3.4, we only obtain the analysis result and can't calculate the depth distance.)

3.1 Pine needle

The experiment is on the pine needle; the specimen is the section of a pine needle. For the case, the magnification of microscope is 175. The result is shown as the Fig. 4.

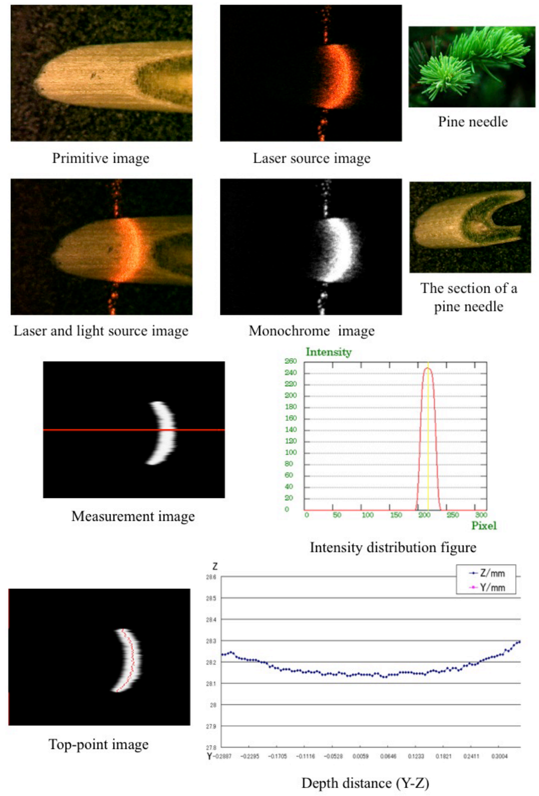

Fig. 4 Measurement results of a Pine needle

Where, the red point on the Top-point image is the top point position of each line of the reflection light.

3.2. Drawing pin

The experiment is on the pine needle; the size of the specimen is shown as the "Drawing pin". For the case, the magnification of microscope is 25. The result is shown as

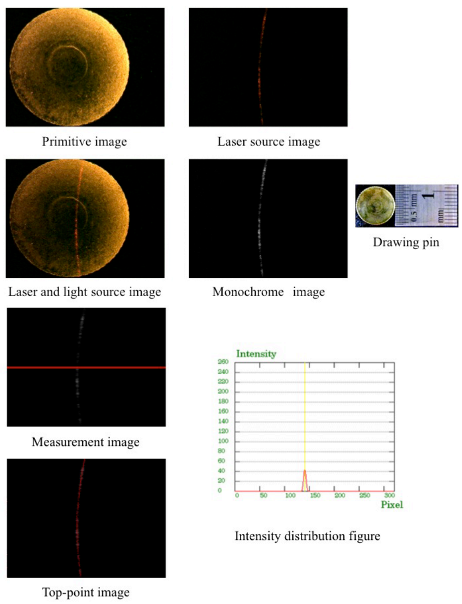

Fig. 5 Measurement results of a Drawing pin

the Fig. 5.

On the case, for the smooth surface of target, the results are very well.

3.3 Flat head tapping screw

The experiment is on the flat head tapping screw; the size of the specimen is shown as the "Flat head tapping screw". For the case, the magnification of microscope is 25. The result is shown as the Fig. 6.

On the "Section image", we can see the problem for the concave surface, the reflection light has the loss, and the 3-D information of the loss can be not measured in reality.

3.4 Self-tapping screw

The experiment is on the self-tapping screw; the size of the specimen is shown as the "Self tapping screw". For the case, the magnification of microscope is 25. The result is shown as the Fig. 7.

On the "Analysis image", we can see the problem for the concave-convex surface, the reflection light not only has the loss, but also has the two waveform, the case become more complex, to calculate the 3-D information is too difficult in reality.

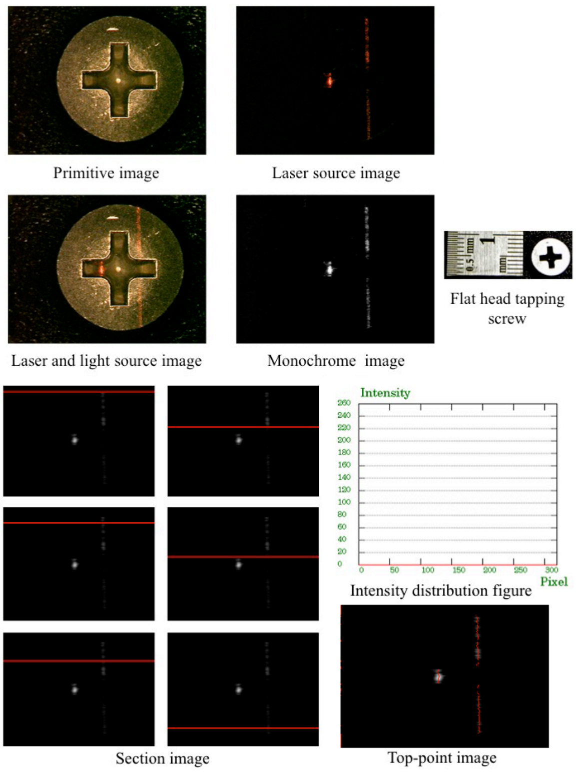

Fig. 6 Measurement results of a Flat head tapping screw

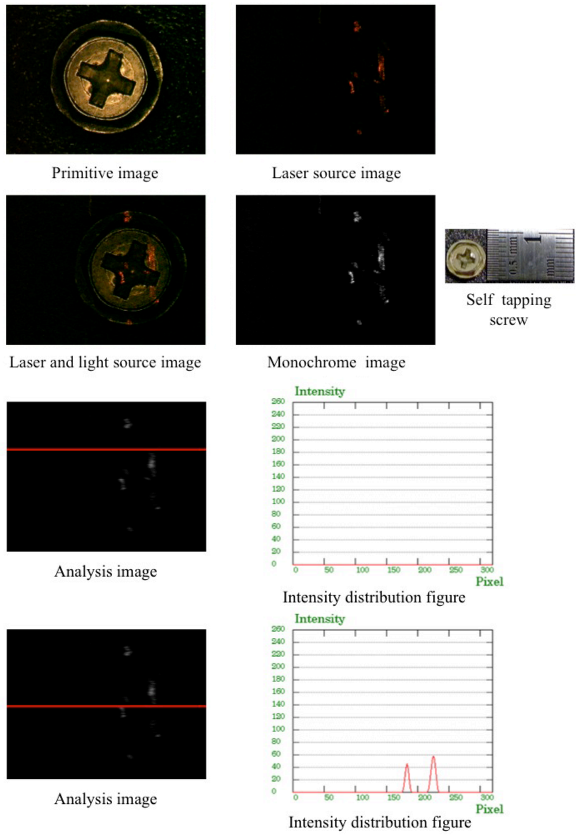

Fig. 7 Measurement results of a Self-tapping screw

4 CONCLUSION

On the research, we combine a simple, inexpensive and easy operation system, and lead the top-point analysis method for the system.

At present, through a series experiments, we can prove the method is available for the system. And from the experiment 3.2, 3.3 and 3.4, we can see: for the uniform, smooth surface shape, the method is well. For the free-form shapes, the reflection light has loss. For the complex shapes, the reflection light becomes too complex to detect the top-point of the intensity distribution.

And at the further, we will be aimed at these problems to perfect the proposal method.

REFERENCES

[1] S.K. Nayar, Y. Nakagawa, "Shape from Focus", IEEE Transactions on Pattern Analysis and Machine Intelligence, vol. 16, no. 8, pp. 824-831, Aug. 1994

[2] C. Lu, G. Cho and J. Zhao, "Practical 3-D Image Measurement System using Monochrome-Projection Color-Analysis Technique", Proc. of the 7th IASTED International Conference on Computer graphics and

imaging (CGIM 2004), pp.254-259, Kauai, Hawaii, USA, August, 2004

[3] Genki Cho, "Practical research for projection patterns in 3-D measurement", Dissertation, 2006

[4] C. Lu, G. Cho, "3-D Image Measurement by Combination of Monochrome-Projection Color-Analysis and OIMP Technique", The Institute of Systems Control and Information Engineers, Vol.19, No. 6, pp.1-8, 2006

[5] Xiaole Mao, Sz-Chin Steven Lin, Cheng Dong, Tony Jun Huang, "Single-layer planar on-chip flow cytometer using microfluidic drifting based three-dimensional (3D) hydrodynamic focusing", The Royal Society of Chemistry 2009, 9, 1583–1589

[6] Thomas D. Ditto, Jim Knapp, Shoshana Biro, "3D inspection microscope using holographic primary objective", SPIE 7432, 74320V (2009)

[7] Xueli Zhang, Kazuhiro Tsujino, Cunwei Lu, "Accuracy Improvement for Projection Patterns in 3-D Measurement", Proceedings of the 2010 IEICE General Conference, Vol.2010, Information·System-2, pp.31, 2010.03.02

[8] Xueli Zhang, "An Accuracy Improvement Method for 3-D Image Measurement", Dissertation, 2010

[9] Karthik Kumar, Rony Avritscher, Youmin Wang, Nancy Lane, David C. Madoff, Tse-Kuan Yu, Jonathan W. Uhr, Xiaojing Zhang, "Handheld histology-equivalent sectioning laser-scanning confocal optical microscope for interventional imaging", Biomed Microdevices (2010) 12:223–233 DOI 10.1007/s10544-009-9377-6

[10] Benjamin F Grewe, Dominik Langer, Hansjörg Kasper, Björn M Kampa, Fritjof Helmchen, "high-speed in vivo calcium imaging reveals neuronal network activity with near-millisecond precision", Nature methods, Vol.7, No.5, MAY 2010, Nature America, Inc

[11] Seiji Inokuchi, Kosuke Sato, "3-D imaging techniques for measurement", ISBN: 4-7856-9036-4

[12] Max Born, Emil Wolf, "Principles of Optics: electromagnetic theory of propagation, interference and diffraction of light", Cambridge University Press, ISBN-13 978-0-521-64222-4

[13] Tsutomu Inoue, "All the microscopes", ISBN: 4-8052-0565-2

The Seventeenth International Symposium on Artificial Life and Robotics 2012 (AROB 17th '12),
B-Con Plaza, Beppu, Oita, Japan, January 19-21, 2012

Tele-immersive Environment with Tiled Display Wall for Intuitive Operation and Understanding in Remote Collaborative Work

Yasuo Ebara

Osaka University, Ibaraki, Osaka 567-0047, Japan
(Tel: 81-6-6879-4481, Fax: 81-6-6879-8988)
(eba@cmc.osaka-u.ac.jp)

Abstract: In remote collaborative work via WAN, share various high-quality visual contents such as photography, visualization image, and real video streaming, and recognizing these contents clearly is extremely important. Supporting a high-quality display of these contents on a large-scale display system is necessary to support intellectual remote collaborative work. However, these contents are currently magnified in low resolution on a general projector using large-sized display equipment, and a sufficient quality of the contents is not obtained. In this paper, we focus on a tiled display wall using two or more LCD panels on a large-sized display system to display realistic high-resolution visual contents to solve these issues. We have constructed a tele-immersive environment with a tiled display wall, and have studied the availability for intuitive operation and understanding in remote collaborative work by implementing various collaborative applications for the effective display of high-resolution contents as well as developing interaction techniques for enormous visual contents in this environment. As a result, we have showed that the practical use of a tiled display wall is useful in the construction of intellectual remote collaborative environment.

Keywords: Tele-immersion, Tiled display wall, Remote collaborative work

1 INTRODUCTION

Remote collaborative work utilizing enormous quantity of data between multi-field researchers is very useful, and supports new intellectual discovery and knowledge-creation in many research fields. To realize intellectual remote collaborative work with participants at remote sites via WAN, sharing various high-quality visual contents is important, in addition to the existence of remote participants using video streaming to promote remote communication with high realistic sensation [1].

The use of large-scale display system with tele-immersion technology [2] is effective in order to realize the sharing of high-quality enormous quantity of visual contents with video-conference system and it is considered to use display equipment such as projectors and large-sized monitors. However, the display of video streaming and these contents with sufficient quality is difficult because the specification of a commercial projector and large-sized display equipment is low-resolution.

We have focused on the tiled display wall by two or more LCD and tried to display realistic high-resolution visual contents as effective large-sized display system in order to solve these issues. In this paper, we construct a tele-immersive environment with a tiled display wall to display realistic high-resolution video streaming and visual contents on the tiled display wall. In addition, we study the possibility of realizing intuitive operation and understanding in remote collaborative work by implementation of various collaborative applications for this environment.

2 RELATED WORKS

2.1 Tele-immersion Technique

Tele-immersion is defined as a new type of telecommunication media in which virtual reality has been incorporated into video-conference systems. In the 3D tele-immersion system, a user wears polarized glasses and a head tracker and a view-dependent scene is rendered in real-time on a large stereoscopic display in 3D [5].

Recently, Immersive Projection Technology (IPT) such as the CAVE system has become popular, and tele-immersive virtual environments have been constructed by several IPT environments [6]. Video avatar technology has been studied to realize real-world-oriented 3D human images for remote communication with high-presence tools between remote places [7]. The video avatar is a technique that represents a human image with a high-presence by integrating live video images of humans into the 3D virtual world. However, remote collaborative works in an IPT environment require deflection glasses and HMD. Under such conditions, carrying out smooth remote communication between participants is usually difficult.

Therefore, we use a tiled display wall to display higher quality visual contents which realize remote collaborative work with highly realistic sensation. In this research, we construct tele-immersive collaborative environment with tiled display wall to realize intuitive operation and understanding in remote collaborative work, and implement various applications for remote collaborative work in the environment.

2.2 Tiled Display Wall

Tiled display wall is a technology to display high-resolution visual contents on a large-sized screen with two or more LCD panels in order to construct effective large-sized display system. Much research has been done on tiled display walls and remote displays by using a distributed rendering technique for virtual walls.

For example, Chromium has designed and built a system that provides a generic mechanism for manipulating streams of graphic API commands [8]. This system can be used as the underlying mechanism for any cluster graphics algorithm by having the algorithm use OpenGL to move geometry and imagery across a network as required. In addition, Chromium's DMX extension allows execution of multiple applications and window control. However, it has a single source, and its design is not suitable for data streaming over a long-distance network.

In this research, we apply a Scalable Adaptive Graphics Environment (SAGE) developed by EVL at the University of Illinois [3]. SAGE is a graphics streaming architecture for supporting collaborative scientific visualization environments with potentially hundreds of mega-pixels of contiguous display resolution. In collaborative scientific visualization, it is crucial to share high-resolution visualization image as well as high-quality video streaming between participants at local or remote sites. The network-centered architecture of SAGE allows collaborators to simultaneously run various applications on local or remote clusters, and share them by streaming.

We constructed a tiled display wall environment consisting of 1 master node, 8 display nodes, and 16 LCD panels (17inch, SXGA). The tiled display wall's LCDs are located at 4x4 arrays as shown in Fig. 1. Master node and all display nodes are connected by gigabit Ethernet network, and 2 LCDs are connected to 1 display node with DVI cables.

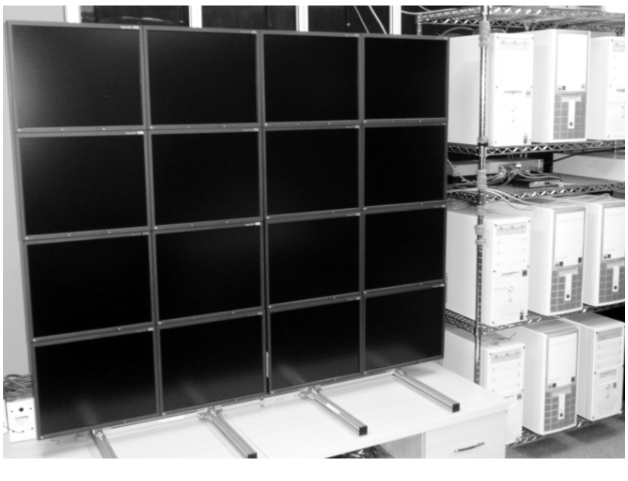

Fig. 1. Tiled display wall in this research.

3 MULTI-VIDEO STREAMING ON TILED DISPLAY WALL

We have implemented an application of high-resolution real video streaming by adding the API code of the SAGE Application Interface Library (SAIL) in a source program of application. In the application, pixel information obtained from a small camera is rendered as a video image by glDrawPixels on the tiled display wall. The video image captured by a camera located at frame of the LCDs on the tiled display wall is transmitted to remote sites, and its video image is displayed on the tiled display wall in a remote site.

We believe the display of the workspace in remote site with real video streaming by applying the ultra high-resolution display technique is an advantage of tiled display wall. We have showed that an ultra high-resolution video streaming with tiled display wall is effective to display the existence of participant and ambiance in remote place as a result from current experiments [9]. However, the video image captured by a single small camera is difficult to display with realistic high-resolution on a tiled display wall, because there is a limit in the display resolution of the video image captured by a single small camera. In addition, the magnified view of original video image on tiled display wall causes to degrade the quality of video image.

In this research, we have constructed an environment to display realistic high-resolution video streaming on a tiled display wall. In this environment, each piece of video image data captured by multiple cameras is transmitted to display nodes of the tiled display wall in remote sites from each application node. In addition, a high-resolution video which is generated by compositing these transmission video images are displayed on the tiled display wall. Fig. 2 shows that transmission multi-video streaming captured by 2 sets of small cameras (Pointgray Flea: XGA, 30fps) located at remote site in LAN. The display resolution of each video is set at 2048 1536 pixels. From this result, we showed to display a clear video image of a remote site over a wide range. As future work, we will study the technique to display more high-quality video image of workspace in remote site on tiled display wall by increasing number of captured camera.

In addition, we have measured the network throughput performance for each transmission video in the environment. The measured results, shown in Fig. 3, are the network throughput of the transmission video about for 20 minutes, and we plot the average value for measurement results for every 2 seconds. From the measurement results, the steady throughput of about 500 Mbps on average, which is considered a full performance of the camera, is gained in each video streaming. Moreover, the transmission delay between each video image is not seen in the observation of each display video on the tiled display wall.

Fig. 2. Multi-video streaming on tiled display wall.

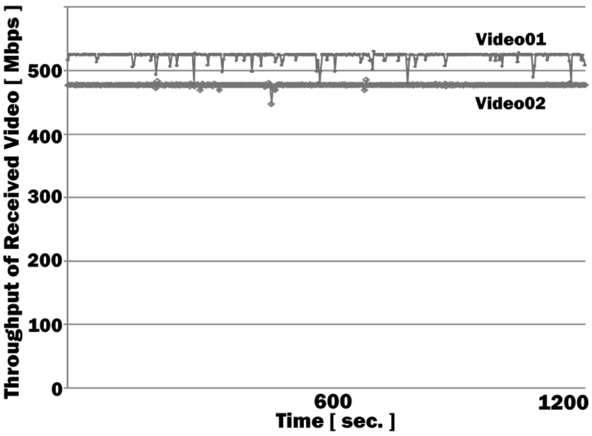

Fig. 3. Network throughput of each video streaming.

4 REALISTIC DISPLAY OF HIGH-RESOLUTION OBSERVATION DATA

We have applied this environment with tiled display wall to the field of astronomy as an effective application to realize a realistic high-resolution display of observation image data on a tiled display wall. Recently, Space Weather Forecast research has been able to predict flares, which occur on the sun's surface and influence the environment globally. In order to establish a high-precision forecast model, it is necessary to analyze a large amount of phenomena with high-resolution observation image data. We have executed realistic display processing of high-resolution astronomical observation image data.

In general, the Flexible Image Transport System (FITS) is used as standard image format for astronomical observation images. FITS is now used as an universal image format which can handle ordinary data in the field of astronomy. In this research, the observation data (resolution of image: 4,096 4,096 pixels) by the Solar Magnetic Activity Research Telescope (SMART), located in Kwasan and Hida Observatories, Kyoto University, is used as image data. The astronomical observation data saved in the local site is transmitted via WAN, and displayed on the tiled display wall in remote sites. An example of observation data by realistic resolution on a tiled display wall is shown in Fig. 4.

These results allow to observe the entire image of the high-resolution observation data on the tiled display wall. It may possible to promote new discoveries from the observation data through remote collaborative work because the data can be observed by multiple users at the same time in this environment. In addition, this environment can display a large amount of observation data that can be expanded and reduced in scale at free positions on the tiled display wall. Therefore, an analysis for these observation images by various techniques can be expected. The construction of a new environment according to user requirements will be examined in the future work.

5 COLLBORATIVE LEARNING USING TILED DISPLAY WALL IN GROUPWORK

As an example of practical use for a remote collaborative environment with the tiled display wall in this paper, we have executed collaborative learning using multi LCDs , and the tiled display wall in discussions to display student materials (Fig. 5:(top)). In addition, distance learning with the tiled display wall has been used in cooperation with classes given at the same time in other buildings, as shown in Fig. 5:(bottom).

From this approach, we understood that additional study on an effective display method for visual contents such as video streaming and presentation materials is important, even though each student used it effectively for the presentation and the discussion through the collaborative environment. In addition, we recognized that the demands for effective tech-

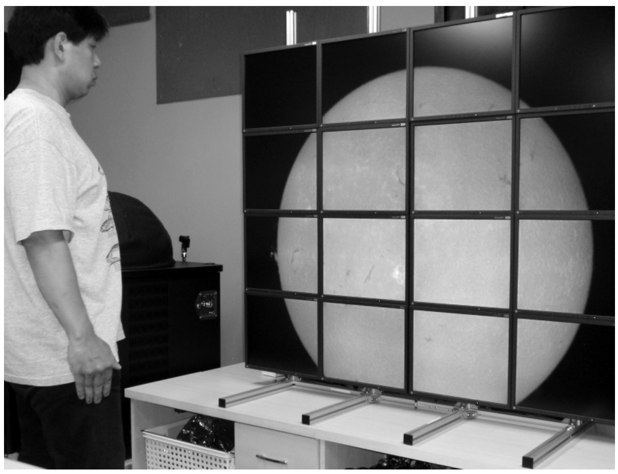

Fig. 4. Realistic display of astronomical observation image (4,096 4,096 pixels).

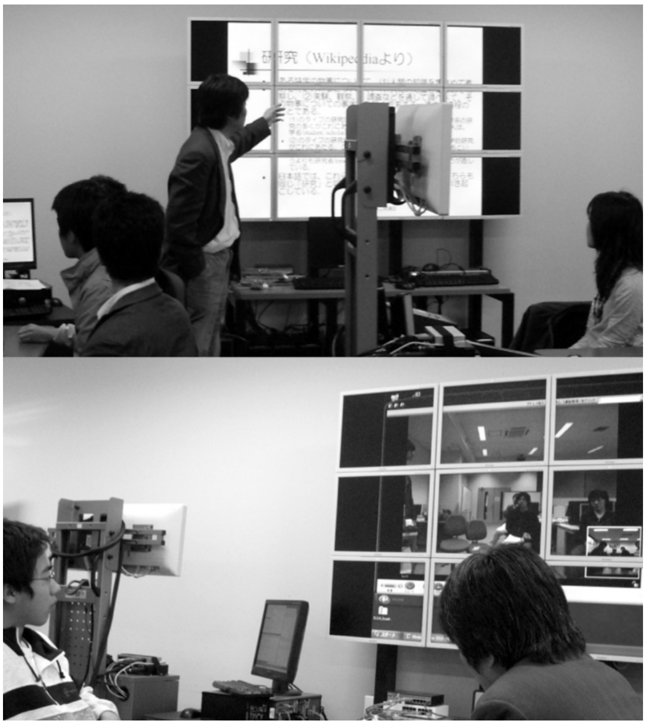

Fig. 5. Collaborative learning using tiled display wall in group work.

niques to display enormous quantity of experimental data and visualization images simultaneously to realize more intelligent collaborative work has risen from the collaborative learning approaches.

On the other hands, an advantage of tiled display wall is that multiple users can look at information at the same time. To utilize the advantage, we have developed a Graphical User Interface (GUI) for a mobile PC to control the enormous quantity of visualization contents on the tiled display wall by multiple users at the same time [10]. However, the GUI is difficult to execute while viewing various contents data on the tiled display wall when users operate the interactive control with a mobile PC. As a result, the use of GUI is expected to interfere by confusing the operation in collaborative works while viewing contents data on tiled display wall among some users.

Therefore, we need to develop a new user interface system to operate interactively with enormous amounts of content on the tiled display wall by some users while viewing the screen of the tiled display wall. An example of the user interface system that allows users to control for each piece of content on tiled display wall are functions such as movement of display location, scaling of window size, and hand-written annotation for each contents by holding or wearing the user interface in a natural state. For the future work, we propose an implement a mechanism to achieve these functions to support intellectual collaborative work using the tiled display wall.

6 CONCLUSION

In this paper, we have constructed tele-immersive environment with tiled display wall, and have studied the possibility of realizing intuitive operation and understanding in remote collaborative work by implementation of various collaborative applications such as the effective display of high-resolution visual contents and the interaction techniques for enormous contents in the environment. As a result, we have showed that the practical use of tiled display wall is useful in the construction of intellectual remote collaborative environment.

REFERENCES

[1] Finn, K. E., Sellen, A. J., Wilbur, S. B. (1997), Video-mediated communication. Lawrence Erlbaum Assoc Inc

[2] Sadagic, A., Towles, H., Holden, L., et al (2001), Tele-immersion portal:Towards an ultimate synthesis of computer graphics and computer vision systems, 4th Annual International Workshop on Presence, 21-23

[3] Renambot, L., Rao, A., Singh, R., et al (2004), SAGE: The Scalable Adaptive Graphics Environment. Workshop on Advanced Collaborative Environments

[4] Nirnimesh, H. P., Narayanan, P. J. (2007), Garuda: A scalable tiled display wall using commodity PCs. IEEE Transactions on Visualization and Computer Graphics, 13(5):864-877

[5] Gibbs, S. J., Arapis, C., Breitender, C. J. (1999), TELEPORT-towards immersive copresence, Multimedia Systems, 7:214-22

[6] Kukimoto, N., Nonaka, J., Ebara Y., et al, (2005), Scientific visualization in collaborative virtual environment with PDA-based control and 3D annotation, JSME International Journal Series B, 48(2):252-258

[7] Ogi, T., Sakai, M. (2006), Communication in the networked immersive environment. ASIAGRAPH 2006, 67-72

[8] Humphreys, G., Houston, M., Ng, Y., et al, (2002), Chromium: A stream-processing framework for interactive rendering on clusters. The 29th Annual Conference on Computer Graphics and Interactive Techniques SIGGRAPH '02, 693-702

[9] Ebara, Y., Kukimoto, N., Leigh, J. et al, (2007), Tele-immersive collaboration using high-resolution video in tiled displays environment, IEEE 21st International Conference on Advanced Information Networking and Applications, 2:953-958

[10] Ebara, Y., Kukimoto, N., Koyamada, K., (2008), Tele-immersive environment with tiled displays wall system for remote collaborative work. ASIAGRAPH 2008 in Tokyo, 2(2):130-133

The Seventeenth International Symposium on Artificial Life and Robotics 2012 (AROB 17th '12),
B-Con Plaza, Beppu, Oita, Japan, January 19-21, 2012

How does the network structure of standard-setters affect its standard-setting activity?

Kensuke Ogata[1]

[1]University of Nagasaki, 123 Kawashimo, Sasebo, 858-8580, Japan
(Tel: 81-956-47-6831)
[1]ogata@sun.ac.jp

Abstract: This article aims to explain the following question: how does the network structure of standard-setters affect their performance? This paper focuses on the activities and structures of FASB and IASB. It presumes that the standard-setters strategically alter the organizational structure and consequently change the activities. To identify the structures, this paper uses coreness analysis in network theory. According to the analyses, it follows as below. First, the FASB has recognized the survival-crisis due to the rise of IASB. Preventing from the crisis, the Board has sought to take alliances with the users and attempted to set lots of innovative standards. Second, to reinforce its position as a global ruler, the IASB has needed to acquire the trust of global and local regulators as well as the businesses. Then, the IASB has had to play as a coordinator with the preferences of broad constituencies and adopted the compromised standards slowly.

Keywords: accounting standard-setting, FASB, IASB, network theory

1 INTRODUCTION

The U. S. financial reporting standards setter, the Financial Accounting Standards Board (FASB) and the international counterpart, the International Accounting Standards Board (IASB) agreed upon the Norwalk Agreement, which both Boards decided to develop big projects, for examples, financial presentation, revenue recognition, financial instruments, fair value measurement, post-retirement benefits, lease, and business combinations, on September 2002. However, these projects except for business combinations project have been still under deliberation; furthermore each Board made different decisions in the business combinations project. The reason why both Boards couldn't obtain their consensus in developing these projects is thought that they should respectively have different preferences and ideas of accounting methods, and different standard-setting activities. How can we explain difference of the activities between FASB and IASB?

Throughout the history of FASB (Zeff [1]), it is founded that standard-setters could strategically alter the organizational structure by means of the shift of the member composition and the selection of members, in order to take care of problems which the Board faces. With this concept, it is thought that the difference of standard-setting activities between the FASB and the IASB could be explained on the difference of the facing issues and/or organizational structures. That is, the scheme is shown as follows: the facing issues affect the strategies of standard-setters; the strategies alter the organizational structures of the setters; and the structures change the activities of the setters. Following the premise, this paper aims to make clear what kinds of problems each Board face and what kinds of strategies they have respectively.

2 THE BEHABIOR MODEL OF THE STANDARD-SETTERS

2.1 The Characteristics of the Accounting Standard-Setting

Financial reporting standards are originally rules or guidelines which have to be followed when the management would prepare their financial statements for providing to various stakeholders and when the accountants audit these statements. Most importantly, these standards are thought to be necessary for the users of financial statements to help their making decisions on investment or credit. Therefore, the creation of new standards and the revisions or removals of existing standards can alter the quality and quantity of the accounting information; such information consequently make some kinds of stakeholders change their decision-makings and behaviors. Among these actors, the following two ones are significant: the public regulator and the business community.

2.2 The Behaviors of the Regulatory Agency and the Business Community

The regulatory agency delegates the authority of setting the standards to a specific standard-setter instead of providing them *per se*. In delegating the authority to the setter, the agency might usually be trust to the setters considerably; at the same time, the setter would develop the standards which are consistent with the agency's policy targets for the purpose of establishing its credibility. This mutual confidence consequently gives the setters discretion of setting standards (Büthe [2]). Obtaining the discretion, the setter comes to give considerations to the business community unduly and to establish the standards which are undesirable to the original policy targets and aims. With the frequent occurrence of such cases, the agency might make a judgment that the current setter could no longer fulfill their tasks, and decide to crate a new setter.

The accounting regulations are essentially meant to reduce discretion of companies on selecting accounting techniques in preparing their financial statements in order to increase the comparability among companies and to improve the companies' transparency. The business community is thus inclined to become opponents against the standard-setters. However, excessive opponents could not be rational to the business community, because these consequences replace the existing private-sector regulation with the public-sector to which the community can't easily access in developing standards (Kelly-Newton [3]; Mattli and Büthe [4]).

2.3 The Regulatory Behavioral Model of the Accounting Standard-Setter

Recognizing needs of certain standards, the setters would initially set the standards based on the fundamental theory or thought, i.e. the conceptual framework. In a large proportion of cases where the setters would establish significant standards, they face heavy oppositions from constituencies. Suppose that the setters would strategically take the most suitable action under every situation, it seems that they could change their behaviors depending on how they recognize the positions in which they are (see Figure 1).

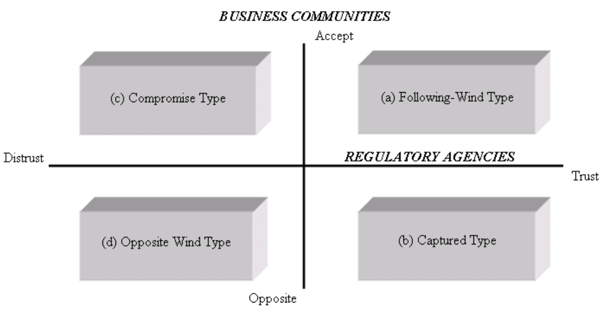

Figure 1: Behavioral Model of the Accounting Standard-Setters

Table 1 shows the behavioral model of standard-setter. This model illustrate as below: the setter at first recognizes the situation surrounding to it; based on the recognition, the setter prescribes its regulatory motivation; corresponding to the motivation, the setter strategically constructs the network; finally following the network, the setter sets the standards. Additionally, Figure 2 illustrates each network type in the behavioral model.

3. THE PERFORMANCES OF BOTH BOARDS

Table 2 shows the number of standards which each Board has respectively issued during 1991 to 2010. The FASB had issued 93 publications and the IASB had issued 98 standards during this term. The FASB had set less than 5 standards every year from 1991 to 2008; and thus it is hard to describe that the Board was the activist for setting accounting standards during this term. In contrast, the IASB had had two significant periods for actively issuing the standards: (a) from 1998 to 2000, for making ready to the completion of Core Standards, and (b) from 2003 to 2004, for providing the adoption of IASs/IFRSs in the EU jurisdiction.

Table 1: The Behavioral Model of Accounting Standard-Setter

	Following-Wind Type	Captured Type	Compromise Type	Opposite Wind Type
Situation	Regulatory agency trusts; Business community accepts.	Regulatory agency trusts; Business community opposites.	Regulatory agency distrusts; Business community accepts.	Regulatory agency distrusts; Business community opposites.
Regulatory Motivation	The setter would establish the standards, which it believes valid, based on the idea of investors' protection, because of growing its legitimacy. For the same reason, it would collect voices from some kinds of interested parties.	The setter would recover the acceptance from business leaders.	The setter would recover the trust from the regulatory agency. At the same time, it takes account of the business community for preserving the support from the community. Without its support, it might not set the standards.	The setter pursues to closely and directly formulate a new alliance with investors for keeping them on its side.
Network Structure	The setter attempts to build up the open network in order to easily gather the voices and ideas of various constituencies.	The setter would form the network with closer relations to business communities comparative to other stakeholders.	The setter would form the network with close relationship to business community as well as regulatory agency and investors.	The setter would form the network with closer and more directly relationships to investors rather than other stakeholders.
Activity of Setting Standards	The number of standards issued by the setter might be almost as same as the necessary number. Also, the contents can be similar to what it originally proposed to.	The number of standards issued by the setter would be less than what the setters need to establish. Also, in the case of being heavily criticized from the business leaders, the setter decides to cancel or postpone the projects or sets the standards which should have no real impacts.	The setter would establish the compromise standards which are incorporated into both preferences of the regulatory agency and the community at the same time. Also, the number of standards issued by the setter would be less than what the setter need to set because of spending considerable time and efforts for coordinating with some kinds of the interested parties.	The setter should establish the standards which it believes true. Therefore, the setter would establish standards as much as possible.

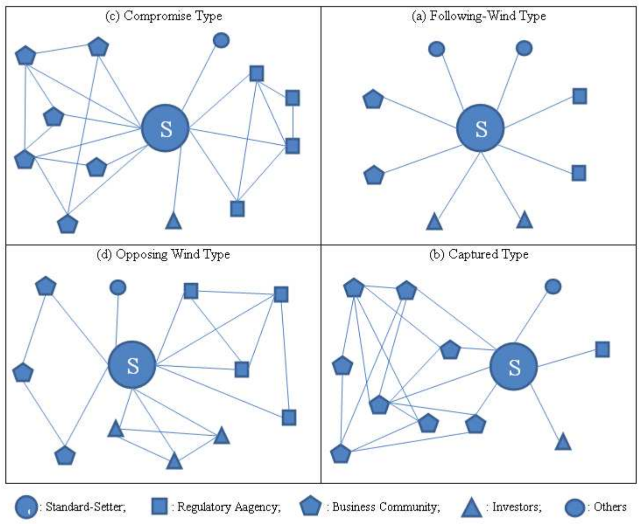

Figure 2: Four Types of Network Structures

Focus on the activity of each Board in the last two years, 2009 and 2010. While the FASB had issued 21 standards and published the most number of standards in last 20 years, the IASB had set mere seven standards and hardly published the ones. The composition is drawn that the FASB actively attempts to set the standards; on the other hand, the IASB takes a passive stance for setting standards

Table 2: The Number of the Standards Issued by FASB and IASB

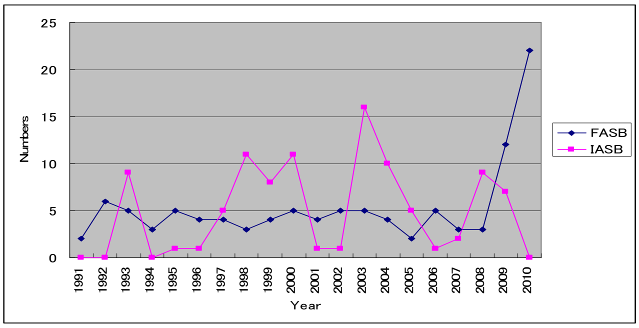

Next, turn to the preference of each Board in the standard-setting. According to some projects which have already completed recent years and has deliberated at this moment, it is noted that the FASB strongly aims to adopt the innovative standards which have been rarely used at present or never done by now; in contrast, the IASB takes negative attitude for setting these standards and thus has a tendency for permitting the current practices as alternatives with the innovative techniques.

4. METHODOLOGY AND DATA

4.1 Analytical Method

To illustrate the network structure of standard-setters, this article uses graph theory or network theory for specifying the structure of standard-setters. The researches applying the network theory to the accounting arena are listed as below: Perry and Nöelke [5], Richardson [6], and Ogata [7]. Network theory usually quantifies the relations measured among actors in the network and provides descriptions of structural properties of actors, subgroups of actors, or groups (Wasserman and Faust [8]). In addition, the theory attempts to describe the network structure and the relationship using a graph shown by nodes and edges.

This paper applies the continuous coreness analysis to identify the network structure of each Board. Here, the "coreness" mentions that who have a high density of ties within the network by many events in common. The coreness analysis can capture a density continuously (Borgatti and Everett [9]).

4.2 Using Data

In analyzing the network structure respectively, this article focuses on the "career path" which means that each member who belongs to any organizations of each Board would arrive at the organization with his/her backgrounds on the basis of their previous jobs and extracts the organization-to-organization relationship from such a data. By manifesting such relationships, it could seem to be clear that what organizations could take on the central positions of and establish their influence on each Board.

As of January 2011, the FASB had four main organizations (FAF, FASB, FASAC, and EITF) and six advisory groups (ITF, ITAC, NAC, PCFRC, SBAC, and VRG); the IASB had four organizations (IFRS Foundation, IASB, Advisory Council, and Interpretations Committee) and five groups (ARG, GPF, EBWG, IWG, and FIWG); and both Boards had some joint advisory groups (FCAG, LAWG, JIG, and FIAG). This research traced the careers of all members in these organizations and groups through their curriculum vitae disclosed in their belonging organizations as of January 2011. As a result, this article could gain the following data: on the FASB, 208 members had gotten engaged in 540 organizations; for the IASB, 233 members had related to 496 organizations.

5. ANALYTICAL RESULTS

5.1 The Results on FASB

Table 3 shows the result of coreness analysis on FASB. The shaded parts on this table indicate organizations and groups relating to the FASB. Also, Graph 1 depicts the network of FASB.

Table 3: The Result of Coreness Analysis on FASB

1	AICPA	0.506	24	Not-for-Profit Advisory Committee (NAC)	0.067	47	Loews Corporation	0.027
2	FAF/FASB	0.412	25	Board member	0.066	48	LoopNet	0.027
3	IFRSF/IASB	0.282	26	JP Morgan	0.058	49	MacDonald Dettwiler	0.027
4	FASAC member	0.255	27	Goldman Sachs Group, Inc.	0.057	50	Maryland Association of CPAs	0.027
5	EITF member	0.219	28	Grant Thornton	0.055	51	Public Oversight Board (POB)	0.027
6	PwC	0.192	29	Financial Crisis Advisory Group (FCAG)	0.054	52	R.G. Associates, Inc.	0.027
7	FEI	0.167	30	Standard & Poor's	0.050	53	Sapient Corporation	0.027
8	Valuation Resource Group(VRG)	0.163	31	McGladrey & Pullen	0.049	54	Thomson Reuters	0.027
9	Arthur Andersen & Co	0.149	32	American Society of Appraisers (ASA)	0.048	55	American Arbitration Association	0.026
10	PCAOB	0.147	33	International Swaps and Derivatives Association	0.042	56	Appraisal Foundation	0.026
11	Ernst & Young	0.140	34	EFRAG	0.041	57	CitiGroup	0.026
12	SEC	0.133	35	U.S. Government Accountability Office (GAO)	0.041	58	Financial Consulting Group (FCG)	0.026
13	KPMG	0.130	36	Corporate Reporting Users' Forum (CRUF)	0.040	59	Financial Valuation Group	0.026
14	Deloitte	0.128	37	BDO International	0.036	60	Financial Valuation Group of Florida, Inc	0.026
15	IMA	0.124	38	Stanley Black & Decker	0.035	61	Florida Bar,	0.026
16	Trustee	0.105	39	A.C. Sondhi & Associates, LLC	0.034	62	Florida Institute of CPAs	0.026
17	Investors Technical Advisory Committee(ITAC)	0.103	40	UBS	0.034	63	Intellectual Property Owners Association	0.026
18	Joint International Group on Financial Statement Presentation(JIG)	0.100	41	Healthcare Financial Management Association	0.028	64	Licensing Executive Society	0.026
19	Small Business Advisory Committee(SBAC)	0.096	42	Career Education Corporation	0.027	65	Bank of America Corporation	0.025
20	CFA Institute	0.087	43	Chicago Mercantile Exchange	0.027	66	Deutsche Bank	0.025
21	Lease Accounting Working Group(LAWG)	0.086	44	GE Company	0.027	67	Duff & Phelps	0.025
22	Moody's Investors Service	0.076	45	IBM	0.027	68	University of North Carolina	0.025
23	Private Company Financial Reporting Committee(PCFRC)	0.072	46	Insweb Corporation	0.027			

Graph 1: The Network of FASB as of January 2011

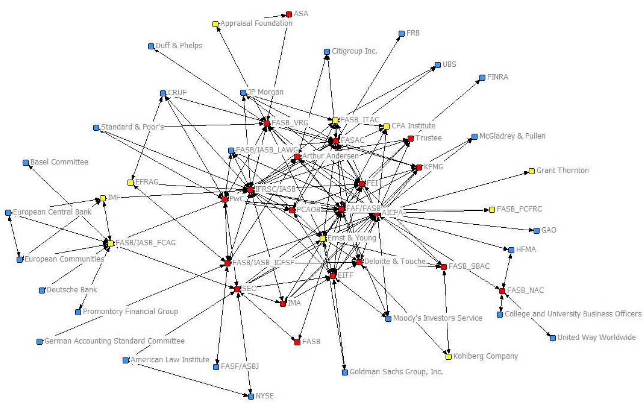

According to the analysis and the graph, it follows that (1) the accounting professions like AICPA, PwC, Deloitte, KPMG and E &

Y are core actors; (2) the domestic actors like SEC, PCAOB, AICPA, FRB, and NYSE stand on core positions within the network; (3) the business community actors like FEI are core, while its range of network is restricted; and (4) although the user actors composed of (a) analyst groups like CFA Institute and CRUF, (b) the financial institutes, and (c) the credit rating agencies are less core, its range is broad.

5.2 The Results on IASB

Table 4 shows the result of coreness analysis on IASB. The shaded parts on this table indicate organizations and groups within the IASB. Also, Graph 2 depicts the network of IASB at the same point.

Table 4: The Result of Coreness Analysis on IASB

1	SAC member	0.449	29	Financial Crisis Advisory Group (FCAG)	0.068	57	Goldman Sachs Group Inc.,	0.034
2	IFRSF/IASB	0.392	30	Australian Accounting Standards Board	0.066	58	International Swaps and Derivatives Association	0.034
3	PwC	0.313	31	World Bank Group	0.065	59	XL Capital Ltd.	0.034
4	EFRAG	0.232	32	Arthur Andersen & Co.	0.064	60	Australian Public Sector Accounting Standards Board	0.033
5	FAF/FASB	0.226	33	International Actuarial Association	0.062	61	Basel Committee on Banking Supervision	0.033
6	KPMG	0.185	34	Global Preparers Forum (GPF)	0.061	62	CICA	0.033
7	Insurance Working Group (IWG)	0.172	35	UBS	0.061	63	AIG	0.032
8	Deloitte	0.151	36	Standard & Poor's	0.060	64	Equitable Companies	0.032
9	Board member	0.149	37	IMF	0.056	65	Hudson International	0.032
10	Analyst Representative Group (ARG)	0.147	38	CFA Institute	0.055	66	Aviva	0.030
11	FRC/ASB (UK)	0.131	39	European Commission	0.051	67	IMA	0.030
12	IOSCO	0.124	40	CESR	0.050	68	CitiGroup	0.029
13	SEC	0.114	41	BUSINESSEUROPE	0.049	69	GE Company	0.028
14	Financial Institution Advisory Group on Financial Statement Presentation (FIAG)	0.112	42	FASF/ASBJ	0.049	70	Institutes of Chartered Accountants of Alberta and Ontario	0.028
15	Joint International Group on Financial Statement Presentation (JIG)	0.109	43	ACTEO (France)	0.046	71	Inter-American Investment Corporation	0.028
16	Corporate Reporting Users' Forum (CRUF)	0.106	44	Group of North American Insurance Enterprises (GNAIE)	0.045	72	Nippon Keidanren	0.028
17	IFAC	0.098	45	American Academy of Actuaries	0.041	73	Association of British Insurers	0.027
18	Financial Instruments Working Group (FIWG)	0.093	46	Merrill Lynch	0.041	74	Business Accounting Deliberation Council	0.027
19	Interpretations member	0.092	47	Australian Securities and Investments Commission	0.039	75	Institute of International Finance	0.026
20	JPMorgan Chase & Co.	0.092	48	CNC (France)	0.039	76	International Corporate Governance Network	0.026
21	AICPA	0.089	49	European Round Table of Industrialists	0.039	77	Ministry of Economy, Trade and Industry(Japan)	0.026
22	Ernst & Young	0.089	50	Trustees	0.038	78	Ceylon Electricity Board	0.025
23	AMF (Financial Market Authority, France)	0.084	51	ASOC/AcSB (Canada)	0.037	79	Independent Television Network (Sri Lanka)	0.025
24	FEI	0.084	52	Bear Stearns & Co	0.037	80	Institute of Chartered Accountants of Sri Lanka	0.025
25	Lease Accounting Working Group (LAWG)	0.080	53	Mazars	0.037	81	Post Graduate Institute of Management (Sri Lanka)	0.025
26	DRSC e.V.(German Accounting Standard Committee)	0.078	54	South African APB/South African ICA	0.037	82	South Asian Federation of Accountants	0.025
27	Employee Benefits Working Group (EBWG)	0.076	55	PCAOB	0.036	83	Sumitomo Corporation	0.025
28	ICAEW	0.072	56	Credit Suisse First Boston	0.035	84	UK Financial Services Authority	0.025

By the analysis of the IASB, it follows that (1) similar to the case of FASB, the accounting professions are core actors within the IASB network; (2) the international authority actors like IOSCO, IMF, World Bank, and the Basel Committee naturally stand on core positions; (3) European actors comprised of (a) the administrative agencies and the corresponding bodies like EC, CESR, EFRAG,, and European Central Bank, and (b) the national standard-setters in the EU like ASB (U. K.), CNC (France), and DRSC (Germany); (4) the business community actors including FEI, BusinessEurope, European Round Table, and Nippon Keidanren construct a broad network; and (5) the user actors are not so core and shouldn't build up a broad network.

Graph 2: The Network of IASB as of January 2011

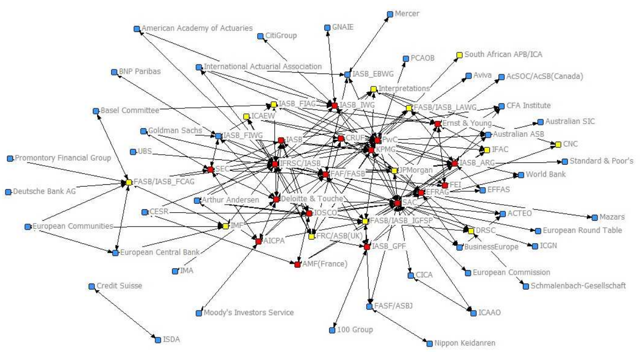

6. DISCUSSION

Above results suggests some following points. First, both Boards are in close contact with accounting professions. It means that, in the case of standard-setting called for high degree of expertise, accounting professions could play key roles. Second, the FASB of course makes tight relationship with the national actors; by contrast, the IASB establishes close ties to the European actors. It is generally predicted that local actors applying a specific set of standards which are endorsed in the jurisdiction stand on the central stances. In that case, with respect to the IASB, it is noted that European actors would be responsible for actively setting standards. Third, the IASB comes to formulate the tight relations with the international organizations, especially the international financial agencies. In fact, the IASB includes the representatives of IOSCO and Basel Committee as observers in the FIWG (IFRS Foundation 2011). Fourth, each Board constructs discrete relationship between the business community actors and the user actors. For the FASB, though being core, the business community actors have a closed network; being not so core, the user actors are created a broad network. For the IASB, the business community actors, especially European industrial associations establish a broad and close network; the user actors build up a coreless and closed network. From the viewpoint of the range of network, it can be stated as follows: the FASB seeks to formulate a more friendly relationship with investor actors in comparison with the business community actors; the IASB attempts to construct a more comfortable network for the business community actors than the user actors.

Such a structural outline is consistent with the description of performance of each Board from the quantitative and qualitative perspectives, as mentioned above: the FASB strongly proposes to adopt innovative techniques; the IASB develops a negative attitude for establishing such techniques. Although causing the businesses to impose heavy burdens including the increment of the amount of liabilities, the extreme volatility of earnings or losses, and the increasing costs of preparing for their financial statements, these techniques could provide the users with transparent and useful information.

In sum, it is noted as follows: for the FASB, putting weight on the user actors rather than the business community actors; the Board stands on the stage that it would issue a lot of innovative standards; in the case of the IASB, coordinating with the preferences of the European and the international actors as well as the business community actors, the Board couldn't positively develop so many standards and adopted the compromised standards allowing either the current practices or the innovative methods.

7. CONCLUSION

From the viewpoint of the behavioral model in this paper, the story of each Board is presumed as described below. First, the

FASB has recognized the crisis of its survival by itself due to the rise of IASB in the U. S. and global accounting standard-setting. To prevent from the survival-crisis, the Board has sought to take a new alliance with the users and consequently has tried to set lots of innovative standards. Second, having faced the endorsement problem, the IASB has needed to reinforce its position as a global ruler by means of acquiring the trust of international regulators and national and jurisdictional administrative agencies. In addition, on conducting its tasks, the Board can't afford to lose the support from the businesses, because the lost of their supports possibly causes these agencies to evaluate the inadequacy against the Board. Therefore, the IASB has had to play as a coordinator with the preferences of various kinds of the constituencies and has adopted the compromised standards at a slow pace.

There seem to be some implications of this paper. First, the behaviors of the accounting standard-setters have a possibility to depend on their network structures. Second, the networks have prospects of being strategically constructed by the standard-setters. And third, the strategies might be dependent on the situations with which the setters are facing. However, it is necessary to furthermore consider the validity of the model developed in this paper. To do so, we attempt to focus on the time-series transition of the network on the same organization.

REFERENCES

[1] Zeff, S. (2005), The Evolution of U. S. GAAP, The Political Forces behind Professional Standards, Part II. The CPA Journal 75(2): 19-29.
[2] Büthe, T. (2010), The Dynamics of Principals and Agents: Institutional Persistence and Change in U. S. Financial Regulation, 1934-2003. unpublished. 1-46.
[3] Kelly-Newton, L. (1980), Accounting Policy Formulation: The Role of Corporate Management. Addison-Wesley Publishing.
[4] Mattli, W. and Büthe, T. (2005), Accountability in Accounting? The Politics of Private Rule-Making in the Public Interest. Governance: An International Journal of Policy, Administration, and Institutions 18(3): 399-429.
[5] Perry, J. and Nöelke, A. (2005), International Accounting Standards Setting: A Network Approach. Business and Politics 7(3: 5): 1-32.
[6] Richardson, A. J. (2009), Regulatory Networks for Accounting and Auditing Standards: A Social Network Analysis of Canadian and International Standard-Setting. Accounting, Organizations and Society 34: 571-588.
[7] Ogata, K. (2010), A Study of Accounting Standard-Setting Using Graph Theory. Artificial Life and Robotics 15: 279-283.
[8] Wasserman, S. and Faust, K. (1994), Social Network Analysis: Methods and Applications. Cambridge University Press.
[9] Borgattei, S. P. and Everett, M. G. (1999), Models of Core/Periphery Structures. Social Networks 21: 375-395.

Simple Model of Economic Stability and Control

S. Lu[1] and T. Ito[2]

1 Management School, Fudan University, Shanghai, & Shandong University in Weihai, China
(Tel : 86-631-5688389; Fax : 86-631-5688389)
(*lushuquan2000@yahoo.com*)
2 Dept. of Business Administration, Ube National College of Technology, Yamaguchi, Japan
(Tel : 81-836-35-7115; Fax : 81-836-35-7115)
(ito@ube-k.ac.jp,)

Abstract: Stability is one of the important issues in the system studies of economic structures, investment's decisions, and government expenditures. We simplify the model of the stability and control of economic systems in this paper. Two important variables, the GDP and investment, are included in economic systems. We build a model to identify the stability in economic systems including these two variables. The stable control shows that the control should have inverse relation to the state of the systems. A system will be exploded if an immense control shock makes it reach an unstable equilibrium state. It indicates that the government investments or expenditures should decrease but not increase when the economic or government expenditure continues increasing.

Keywords: Government Investment or Expenditure, Euler Equation, Approximate Control

I. INTRODUCTION

Stability is very crucial for the system studies, such as economic structures, investment's decisions, and government expenditures.

Only recently has performance, which is based on graph theory, been extended and analyzed to assess structural change of network organizations.

Intuitively speaking, the stability is that the systems will keep some characteristics of its structure when its form or initial value varies in different ways. Hence, it is necessary to control the systems in order to keep it stable. In other words, the stability is to design a control such that a small perturbation does not have a great influence on the system [1].

Many researchers suggest different perturbation techniques in mathematics, physics and engineering. How should we, however, consider the stability to design a control in the economic systems?

Two very important variables, the GDP and investment, are included in the economic systems. Considering a system at any time *t*, its state can be described as a differential equation,

$$\frac{du}{dt} = g(u,v), u(0) = c \qquad (1)$$

where $u(t)$ represents a function for the GDP, du/dt=u', that is the derivative of $u(t)$, can be thought of as the investment, *v* is a control variable, and *c* is the initial state of $u(t)$. Since the function *g* is undetermined, this gives us a few troubles for analytically dealing with the stability and control. Therefore, we may let the function *g* be a simple form, for example, $g(u,v) = v$. Although this simple form can not quite illustrate the complex of the real economic systems, this is enough for our purpose of research

The main contribution of this paper is to suggest that for stability of the above simple form, the control is $u' = -u$, that is, the investment (for example, the government investment to rescue the market) should have inverse relation to the state of the GDP. The second contribution shows that the simple economic structure would become unstable when a big control perturbation (say, the government investment) happened.

The structure of this paper is as follows. In section 2, we build a new model and show the solution of the stability in economic systems. Section 3 analyzes stability of control. In section 4, we make a brief discussion about economic systems including government investment and expenditures. Section 5 contains some concluding remarks.

II. MODEL, SET-UP, SOLUTION and APPROXIMATE CONTROL

1. Model

Assume an economic system is described as equation (1), where we make $du/dt = g(u,v) = v$. We choose control variable $v(t)$ such that the variations of u and u' are very small on average. For instance, we want to determine a $v(t)$ such that

$$\min_{u'}\left\{\int_0^T [u^2+(u')^2]dt\right\} \qquad (2)$$

We may denote the functional $J(u)$ by $J(u):=\int_0^T [u^2+(u')^2]dt$.

2. Set-up

The basic problem is to determine the functional $J(u)$ well-defined. Our set-up here is $u'(t)\in L^2[0,T]$.

To make equation (2) have solution u, it is necessary to satisfy the Euler equation

$$-u''+u=0,\ u(0)=c,\ u'(T)=0 \qquad (3)$$

We see that this variation problem (2) becomes the Euler equation.

3. Solution and approximate control

Solute equation (3) and get the analytical solution

$$u=c\left(\frac{e^{t-T}+e^{-(t-T)}}{e^{-T}+e^{T}}\right)=c\frac{ch(t-T)}{chT} \qquad (4)$$

What we sometimes want to know is the characteristics of the control v (or u') when $T\to\infty$.

By equation (4), we obtain

$$u'=c\frac{sh(t-T)}{shT} \qquad (5)$$

After algebraic calculation, we further have $|u'+ce^{-t}|\le 2|c|e^{-T}$. In equations (4) and (5), we may explain the parameter c as the initial value of the equation system, that is, c is also the constraint or initial endowment for the system. If T is very large, we can get the approximate control $u'=-u$ [2].

III. MSTABILITY of CONTROL

C To illustrate the stability of control, we consider the following equation of pendulum

$$u''+au'+\sin u=g(t) \qquad (6)$$

where $g(t)$ is a control variable. In fact, the behavior of economic is somewhat similar to the motivation of pendulum. We know that $u(t)=0$ is one of its solutions, which correspond to its equilibrium if $g(t)=0$.

Could this system keep stable when a large control perturbation $g(t)$ is imposed on the system such that the system even reaches another equilibrium state, $u(t)=\pi$. After $g(t)$ disappears, then the new equation becomes

$$u''+au'+\sin(\pi+u)=0 \qquad (7)$$

In addition, assume that $u(0)=e_1$ and $u'(0)=e_2$.

$\sin(\pi+u)=-\sin u\approx -u$ when u is small. Therefore, we approximately have

$$u''+au'-u=0,\ u(0)=e_1,\ u'(0)=e_2 \qquad (8)$$

Characteristic roots of this differential equation is

$$\lambda_1,\lambda_2=\frac{-a\pm(a^2+4)^{0.5}}{2}$$

One of characteristic roots is positive and the other negative for whatever value of a. Hence $u(t)$ will explode when $t\to\infty$, that is, the system is unstable at $u(t)=\pi$ [3].

IV. DISCUSSION

In order to get a stable control, Section 2 shows that approximate control, for example, the government investment, should have inverse relation to the state of the GDP. Section 3 suggests that the system likely becomes more volatile if imposing an immense shock on it.

As a national GDP always continue highly increasing, decreasing instead of increasing government investment may stabilize the economic systems. There is surprisingly increasing in Chinese economic system in last decade as we know. 4 trillion Chinese Yuen (?) of economic stimulus plans, however, launched out into business in various government investments from 2008 to 2011. Does this stabilize or rescue the market? The answer seems to be obvious because high inflation, which could destroy the stability of economic systems, had occurred in 2011 in China.

Another example is London riots in 2011. Between 6 and 10 August 2011, many London districts and some other cities and towns in England suffered widespread rioting, looting and arson. Possible causes for the riots of many, however, it is not to be neglected that while a great deal of domestic expenditures had to pay, England government has paid a lot of war bills, such as Afghan, Iraq, and Libya wars. This violates the rule of stable control, which means that the control should have inverse relation to the state of the system, $u'=-u$.

V. CONCLUSION

We simply model the stability and control for economic systems. By Euler equation of variation method, we obtain the analytical solution for this system and the approximate control rule for stability. The stable control shows that the control should have inverse relation to the state of the system. Furthermore, by the analysis of pendulum's motivation, we see that a system will explode after an immense control shock makes the system reach an unstable equilibrium state.

These indicate that the government investments or expenditures should decrease but not increase when the economic or government expenditure continues increasing.

REFERENCES

[1] Brockett R. W., 1966, The status of stability theory for deterministic system, *IEEE Trans. Automatic Control*, *11 (3)*; 596-606
[2] Bellman R., 1967, *Introduction to the mathematical theory of control processes*, New York: Academic Press
[3] Bellman R., 1964, Perturbation techniques in mathematics physics and engineering, Holt, New York: Dover Publications Inc

An Efficiency Analysis using the ICB Model in Mazda's Keiretsu

S. Matsuno[1], T. Ito[1], M. Hasama[1], R. Mehta[2], and M. Sakamoto[3]

[1] Dept. of Business Administration, Ube National College of Technology, Yamaguchi, Japan
(Tel : 81-836-35-7115; Fax : 81-836-35-7115)
matsuno@ube-k.ac.jp, ito@ube-k.ac.jp, hasama@ube-k.ac.jp
[2] School of Management, New Jersey Institute of Technology, USA
(Tel : 1-973-596-6419; Fax : 1-973-596-3074)
Mehta@njit.edu
[3] Dept. of Computer Science and Systems Engineering, University of Miyazaki, Japan
(Tel : 81-985-58-7392; Fax : 81-985-58-7392)
sakamoto@cs.miyazaki-u.ac.jp

Abstract: Performance—an indicant of corporate efficient and effectiveness—is determined by many different factors, such as economic environment and coordination of managerial resources. Only recently has performance, which is based on graph theory, been extended and analyzed to assess structural change of network organizations. Only a few indexes based on graph theory have applied and analyzed in most recent research to measure the structural changes of network organizations. In order to develop a rational model, this empirical research attempts to establish the inter-relational linkages among multiple corporate performance indices. Specially, this paper seeks to assess corporate efficiency using the DEA analysis. Accordingly, the contribution of this research is to propose a new way to build a quantitative model that identifies the efficiency of each individual firm in Mazda's Yokokai Keiretsu.

Keywords: Degree, Closeness, Influence, Efficiency, the DEA

1 INTRODUCTION

Performance—an indicant of corporate efficient and effectiveness—is determined by many different factors, such as economic environment and coordination of managerial resources. Only recently has performance, which is based on graph theory, been extended and analyzed to assess structural change of network organizations. Only a few indexes based on graph theory have applied and analyzed in most recent research to measure the structural changes of network organizations. One of the important issues is to improve the efficiency in corporate management. The position of each individual firm in the Keiretsu instead of the input is calculated using graph theory in this paper. The contribution of this research is to propose a new way to build a quantitative model that identifies the efficiency of each individual firm in Mazda's Yokokai Keiretsu.

2 BACKGROUND

Recently most of the research on network analysis focused on a few indices to determine the position of each individual firm in the Keiretsu. Single index usually express only one aspect of the position. Much more indexes should be used to determine the precise position. Therefore, the authors selected the relevant indexes based on the previous research, and built a quantitative model called ICB (In-degree, Closeness and By-influence) model under the measurement results of the correlation coefficient in this paper.

Many useful indexes to identify the factors of the position have been developed recently.

Centrality index is one of the useful indexes. Basically it includes degree, closeness and betweenness. Degree is one of the centrality indexes to express a firm's potential communication activity. In transaction network, degree includes two categories: in-degree and out-degree, because transaction network is an asymmetric network organization. In-degree means a firm purchases the parts from other firms, and out-degree means a firm sells the parts to other firms. Closeness is another centrality index to express the distance from a firm to all other firms linking with it direct and indirectly. Two indexes are included in transaction networks. They are in-closeness and out-closeness. In-closeness is the summation of the length from a firm to all other reachable firms, and out-closeness is summation of the length from all other reachable firms to it. In transaction network, the firm is located at an easy position if its closeness value is low.

Table 1. Matrix of correlation coefficients between network indexes and corporate performance

		Out-degree	In-degree	Betweenness	Closeness	Influence	By-influence	Sales	Profit
Out-degree	Pearson’ correlation coefficient	1							
	Significant Probability (Two side)								
	N	89							
In-degree	Pearson’ correlation coefficient	-0.433**	1						
	Significant Probability (Two sid	0							
	N	89	89						
Betweenness	Pearson’ correlation coefficient	0.112	0.035	1					
	Significant Probability (Two sid	0.295	0.746						
	N	89	89	89					
Closeness	Pearson’ correlation coefficient	-0.329**	-0.389**	-0.194	1				
	Significant Probability (Two sid	0.002	0	0.068					
	N	89	89	89	89				
Influence	Pearson’ correlation coefficient	0.977**	-0.420**	0.101	-0.328**	1			
	Significant Probability (Two sid	0	0	0.348	0.002				
	N	89	89	89	89	89			
By-influence	Pearson’ correlation coefficient	-0.433**	0.999**	0.03	-0.386**	-0.419**	1		
	Significant Probability (Two sid	0	0	0.778	0	0			
	N	89	89	89	89	89	89		
Sales	Pearson’ correlation coefficient	-0.468**	0.766**	-0.018	-0.325**	-0.449**	0.794**	1	
	Significant Probability (Two sid	0	0	0.873	0.003	0	0		
	N	80	80	80	80	80	80	80	
Profit	Pearson’ correlation coefficient	-0.302**	0.676**	0.025	-0.345**	-0.288*	0.706**	0.916**	1
	Significant Probability (Two sid	0.009	0	0.834	0.003	0.013	0	0	
	N	74	74	74	74	74	74	74	74

Betweenness is another useful as an index of the potential of a firm to control communication, and it is also useful as an index of the network structure. Ito et al once measured centrality index including degree, closeness and betweenness to determine the positions of each individual firm [1]-[3].

Influence is a power to have impact on other firms. The power is called by-influence when the firm is affected by other firms. Therefore, influence will be divided into two parts: influence and by–influence in transaction networks. Kimura et al once proposed and calculated the influence in 2007 [4][5].

3 METHOD

3.1 Variables selection

Corporate performance index plays important roles in strategy formation. Not only labor productivity and return on investment, but also sales and profit are considered as the index of corporate performance. In this paper, the authors use sales and profit to express the corporate performance.

The following step is needed to build up an effective model.

1. Select the relevant variables which have potential effect on position-determination.
2. Calculate the correlation coefficients between the selected variables and corporate performance.
3. Determine framework of the model.

In this paper, all of these indexes are used as the input factor to determine sales and profit, the output of each firm.

The authors selected the degree, closeness and influence, and calculated the correlation coefficients between the selected variables and corporate performance.

3.2 Data collection

In order to measure all member firms’ capacity in networks, transaction data in the Yokokai Keiretsu was collected from personal interviews with senior managers as well as publications of the Japan Auto Parts Industries Association and Automotive Parts Publishing Company [6][7]. In addition, corporate performance as measured by Mazda’s revenues and profits for fiscal year 2004 was obtained.

In 2004, 177 component-parts suppliers were members of Mazda’s Yokokai Keiretsu. Seventy-two parts suppliers and Mazda have reciprocal transactional relationships, whereas 105 parts suppliers are singletons. A singleton means a firm which has no relationship with other firms in the network. Furthermore, a singleton is an isolate company whose in-degree and out-degree are both zero.

3.3 Outline of the ICB model

The transactional relationships among the companies were identified through graph modeling. A tie shows the percentage of the transaction between each pair of firms. We collected directed and weighted data to measure the selected indexes of each firm.

Table 2. Top ten firms of the selected firms in Yokokai

		In-degree (rank)		Closeness (rank)		By-influence (rank)	
1	Mazda Motor Corporation	774.277	(1)	0.0076	(1)	7.8296	(1)
2	Toyota Motor Corporation	648.605	(2)	0.0065	(3)	7.3868	(2)
3	Nissan Motor Co., Ltd.	541.188	(3)	0.0061	(7)	5.5561	(3)
4	Mitsubishi Motors	508.601	(4)	0.0068	(2)	5.1719	(4)
5	Honda Motor Co., Ltd.	487.596	(5)	0.0065	(4)	5.0799	(5)
6	Suzuki Motor Corporation	231.424	(6)	0.0058	(11)	2.4179	(6)
7	Denso Corporation	190.379	(7)	0.0061	(6)	1.9112	(7)
8	Fuji Heavy Industries Ltd.	172.414	(8)	0.0055	(35)	1.7821	(8)
9	Daihatsu Motor Co., Ltd.	129.521	(9)	0.0051	(60)	1.3638	(9)
10	Hino Motors Ltd.	52.446	(10)	0.0047	(66)	0.547	(10)
17	NSK Ltd.	4.026	(17)	0.0062	(15)	0.0403	(17)
12	Calsonic Kansei Corporation	12.278	(12)	0.0058	(8)	0.1233	(12)
40	Nisshinbo Industries, Inc.	0	(*)	0.0058	(9)	0	(*)
11	Hitachi, Ltd.	13.474	(11)	0.0058	(10)	0.1356	(11)

*: less than 21

All of the selected indexes are calculated as follows.

1) Degree

$$C_D(p_k) = \sum_{i=1}^{n} a(p_i, p_k); \quad k = 1, 2, \cdots, n$$

where

$a(p_i, p_k) = 1$; if and only if p_i and p_k are connected by a line

$= 0$; otherwise

2) Closeness

$$C_C(p_k)^{-1} = \sum_{i=1}^{n} (p_i, p_k); \quad k = 1, 2, \cdots, n$$

where

d(pi,pj): the number of edges in the geodesic linking p_i and p_j

3) Betweenness

$$C_B(p_k) = \sum_{i}^{n}\sum_{j}^{n} \frac{g_{ij}(p_k)}{g_{ij}} = \sum_{i}^{n}\sum_{j}^{n} b_{ij}(p_k)$$

where

$i>j$; $i \neq j \neq k$;

$g_{ij}(p_k)$: the geodesics linking p_i and p_j that contains p_k

g_{ij}: the geodesics linking p_i and p_k

4) Influence

$$T = A + R = A(I - A)^{-1}$$

where

A: direct influence

I: Identity matrix

In order to determine a significant relationship between input and output, then matrix of correlation coefficients is shown as Table 1. In-closeness and out-closeness cannot be calculated technically because the distance between two firms is infinity even when they are connected separately. For instance, Sumino sells the parts to NSK Co., Ltd, and NSK sells parts to Mazda, but Mazda sells nothing to Sumino. In this case, the distance between Sumino and Mazda is not computable because the distance is infinity. Therefore, the authors modified the transaction network as symmetric organization, and then calculated closeness.

It is easy to find that in-degree or by-influence has positive strong impact when out-degree or influence has negative impact on sales and profit in Table 1. Betweenness means a firm purchase parts from other firms and sells its products to other firms. Thus betweenness should have impact on sales and profit. Unfortunately no significance could be found between betweenness and sales, profit. It is obviously that sales

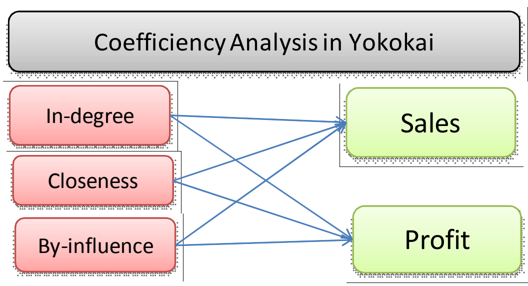

Fig. 1. Framework of the efficiency analysis

and profit are affected by degree, closeness and influence. In this paper, in-degree, closeness and by-influence is used as the input of efficiency. The framework is shown as follows.

4 RESULTS AND DISCUSSIONS

All of the selected indexes are measured based upon on the collected data. Top ten firms of the selected indexes are shown in Table 2. Figure 2 shows the position of all firms including the Yokokai.

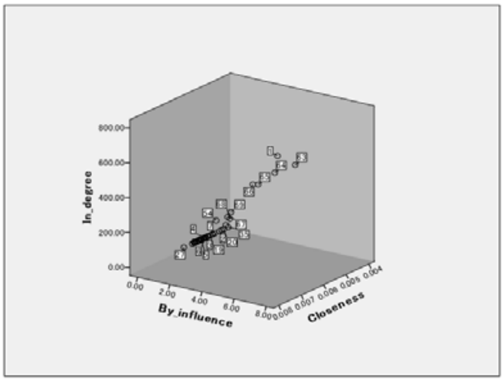

Fig. 2. Efficiency of the firms in Mazda's Keiretsu

The efficiencies of all the firms including parts makers and 11 car-makers are shown in Figure 3.

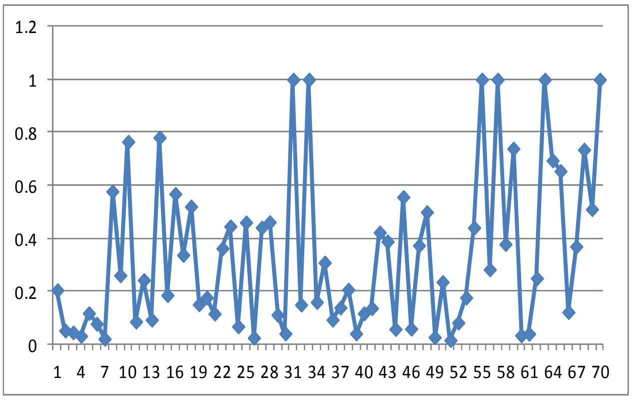

Fig. 3. Efficiency of each firm in Yokokai

In Figure 3, 6 firm's efficiency is 1. They are Pioneer Corporation (31), Hitachi, Ltd. (33), Tokai Rika Co., Ltd. (55), Toyota Gosei Co., Ltd. (57), Toyota Motor Corporation (64), and Hino Motors Ltd. (71). All of these companies are belong to the Toyota group. It is considered as the evidence that Keiretsu is no more centralized or integrated as it was before 1990. It is called loosening of Keiretsu alliance.

Ten firms with lowest value of efficiency are Kokusan Parts Industry Co., Ltd. (0.017), Nippon Thermostat Co., Ltd. (0.022), Ring Techs Hiroshima Co., Ltd. (0.023), Owari Precise Products Co., Ltd. (0.026), Hanshin Electric Co., Ltd.(0.031), Meiwa Industry Co., Ltd. (0.036), Sumino Kogyo Co., Ltd. (0.038), Hikari Seiko Co., Ltd. (0.043), and Kurashiki Kako Co., Ltd. (0.048). In order to improve the efficiency, the detailed relationship between the selected network indices and corporate performance should be analyzed.

5 CONCLUSION AND FUTURE WORKS

In this paper, the authors proposed a new model of efficiency analysis based upon the calculation of the position of each individual firm, such as degree, betweenness, closeness and influence. And the efficiency of all individual firms in the Yokokai is calculated. Further studies such as the solution to improve the input indices, the relationship between selected network indices and corporate performance are considered as the future works of this research.

Acknowledgment: This research was partially supported by the Ministry of Education, Culture, Sports, Science, and Technology, Grant-in-Aid for Exploratory Research, 21510171, 2009.

REFERENCES

[1]Fukuoka S., Ito T., Passerini K. and Sakamoto M. (2006) An Analysis between Transaction and Cross Shareholdings in the Keiretsu of Nissan, *Managing Information in the Digital Economy Issues & Solutions*, 163-169, IBIMA International Conference, Bonn Germany

[2]Ito T., Passerini K., Sakamoto M. (2008) Structure Analysis of Keiretsu of Toyota, Encyclopedia of Networked and Virtual Organizations, pp.1542-1548, Idea Group Publishing

[3]Ito T., Medlin C., Passerini K., Sakamoto M. (2009) Influence Trust and Trade in the Keiretsu of Toyota: A Centrality *Analysis*, *Trust, Globalisation and Market Expansion*, Chapter 8, pp.101-118, Nova Science

[4] Kimura H., Ito T., and Xia Z. (2009) Module production, centrality, and M&A in the Keiretsu of Mazda, Artificial Life and Robotics, Volume 14, pp.332-336, Springer Japan

[5]Ito T., Matsuno S., Xia Z., Sakamoto M., and Rajiv Mehta (2010) An Analysis of Interactive Influence in Mazda's Yokokai Keiretsu, Artificial Life and Robotics, Volume 15, Number 3, 249-252, Springer Japan

[6]JAPIA&APPC (2004) *Japanese Automotive Parts Industry*, Automotive Parts Publishing Company, (Japanese Edition)

[7]JAPIA&APPC (2005) *Japanese Automotive Parts Industry*, Automotive Parts Publishing Company, (Japanese Edition)

The Seventeenth International Symposium on Artificial Life and Robotics 2012 (AROB 17th '12),
B-Con Plaza, Beppu, Oita, Japan, January 19-21, 2012

A Note on Three-Dimensional Probabilistic Finite Automata

M. Sakamoto[1], T. Ito[2], X. Qingquan[3], Y. Uchida[2], ,
T. Yoshinaga[4], M. Yokomichi[1], S. Ikeda[1], and H. Furutani[1]

[1] University of Miyazaki, Miyazaki, Miyazaki 889-2192, Japan
[2] Ube National College of Technology, Ube, Yamaguchi 755-8555, Japan
[3] Harbin Institute of Technology, Harbin, Heilongjiang 150001, China
[4] Tokuyama College of Technology, Shunan, Yamaguchi 745-8585, JAPAN
(Tel: 81-985-58-7392, Fax: 81-985-58-7392)
(sakamoto@cs.miyazaki-u.ac.jp)

Abstract: We think that recently, due to the advances in many application areas such as computer graphics, computer vision, image processing, robotics, and so on, it is useful for analyzing computation of three-dimensional information processing to explicate the properties of three-dimensional automata. From this point of view, we have investigated many properties of three-dimensional automata and computational complexity. On the other hand, the class of sets accepted by probabilistic machines have been studied extensively. As far as we know, however, there is no results concerned with three-dimensional probabilistic machines. In this paper, we introduce three-dimensional probabilistic finite automata, and investigate some accepting powers of them.

Keywords: Accepting power, Alternation, Chunk, Probabilistic finite automaton, Three-dimensional input tape

1 INTRODUCTION

Computer science is the systematized field of knowledge and technology concerning computation. Its realistic beginnings can be traced back to the formalization of the concept of an effective procedure and the advent of excellent digital computers. In theoretical computer science, the Turing machine has played a number of important roles in understanding and exploiting basic concepts and mechanisms in computing and information processing. It is a simple mathematical model of computers which was introduced by Turing [17] in 1936 to answer fundamental problems of computer — 'What kind of logical work can we effectively perform ?' If the restrictions in its structure and move are placed on the Turing machine, the restricted Turing machine is less powerful than the original one. However, it has become increasingly apparent that the characterization and classification of powers of the restricted Turing machines should be of great important. Such a study was active in 1950's and 1960's. On the other hand, many researchers have been making their effects to investigate another fundamental problems of computer science — 'How complicated is it to perform a given logical work ?' The concept of computational complexity is a formalization of such difficulty of logical works. In the study of computational complexity, the complexity measures are of great importance. In general, it is well known that the computational complexity has originated in a study of considering how the computational powers of various types of automata are characterized by the complexity measures such as space complexity, time complexity, or some other related measures. After that, the growth of the processing of pictorial information by computer was rapid in those days. Therefore, the problem of computational complexity was also arisen in the two-dimensional information processing. Blum and Hewitt first proposed two-dimensional automata — two-dimensional finite automata and marker automata, and investigated their pattern recognition abilities in 1967 [1]. Since then, many researchers in this field have been investigating a lot of properties about automata on a two-dimensional tape [17]. By the way, the question of whether processing three-dimensional digital patterns is much difficult than two-dimensional ones is of great interest from the theoretical and practical standpoints. In recent years, due to the advances in many application areas such as computer graphics, computer-aided design / manufacturing, computer vision, image processing, robotics, and so on, the study of three-dimensional pattern processing has been of crucial importance. Thus, the study three-dimensional automata as the computational model of three-dimensional pattern processing has been meaningful. However, it is conjectured that the three-dimensional pattern processing has its own difficulties not arising in two-dimensional case. One of these difficulties occurs in recognizing topological properties of three-dimensional patterns because the three-dimensional neighborhood is more complicated than two-dimensional case. Generally speaking, a property or relationship is topological only if it is preserved when an arbitrary 'rubber-sheet' distortion is applied to the pictures. For example, adjacency and connectedness are topological; area, elongatedness, convexity, straightness, etc. are not. During the past thirty years, automata on a three-dimensional tape have been proposed and several properties of such automata have been obtained. We have also studied about three-dimensional automata, and introduced many computational models on three-dimensional input tapes. On the other hand, the classes of sets recognized by one- or two-dimensional probabilistic finite automata and probabilistic Turing machines have been studied extensively [2-15, 18-22]. As far as we know, however, there is no results concerning with three-dimensional probabilistic machines. In this paper, we introduce three-dimensional probabilistic finite automata, and investigate some their accepting powers.

2 PRELIMINARIES

Let Σ be a finite set of symbols. A *three-dimensional tape* over Σ is a three-dimensional array of elements of Σ. The set of all three-dimensional tapes over Σ is denoted by $\Sigma^{(3)}$. Given a tape $x \in \Sigma^{(3)}$, for each integer $j(1 \leq j \leq 3)$, we let $l_j(x)$ be the length of x along the jth axis. The set of all $x \in \Sigma^{(3)}$ with $l_1(x)$=n_1, $l_2(x)$=n_2, and $l_3(x)$=n_3 is denoted by $\Sigma^{(n_1,n_2,n_3)}$. When $1 \leq i_j \leq l_j(x)$ for each $j(1 \leq j \leq 3)$, let $x(i_1,i_2,i_3)$ denote the symbol in x with coordinates (i_1,i_2,i_3). Furthermore, we define x [(i_1,i_2,i_3), (i'_1,i'_2,i'_3)], when $1 \leq i_j \leq i'_j \leq l_j(x)$ for each integer $j(1 \leq j \leq 3)$, as the three-dimensional input tape y satisfying the following conditions : (i) for each $j(1 \leq j \leq 3)$, $l_j(y) = i'_j - i_j + 1$; (ii) for each r_1, r_2, r_3, $(1 \leq r_1 \leq l_1(y)$, $1 \leq r_2 \leq l_2(y)$, $1 \leq r_3 \leq l_3(y)$, $y(r_1, r_2, r_3) = x(r_1 + i_1 - 1, r_2 + i_2 - 1, r_3 + i_3 - 1)$.

A *three-dimensional probabilistic finite automata* (denoted by 3-*PFA*) is a 6-tuple $M = (Q, \Sigma, \delta, q_0, q_a, q_r)$, where Q is a finite set of *states*, Σ is a finite set of *input symbols*, δ is a *transition function*, $q_0 \in Q$ is the *initial state*, $q_a \in Q$ is the *accepting state*, and $q_r \in Q$ is the *rejecting state*. An *input tape* for M is a three-dimensional tape over Σ surrounded by the *boundary symbols* $\#$'s (not in Σ). The transition function δ is defined on $(Q - \{q_a, q_r\}) \times (\Sigma \cup \{\#\})$ such that for each $q \in Q - \{q_a, q_r\}$ and each $\sigma \in \Sigma \cup \{\#\}$, $\delta[q, \sigma]$ is a *coin-tossing distribution* on $Q \times$ { East, West, South, North, Up, Down, Stay }, where East means ' moving east ', West ' moving west ', South ' moving south ', North ' moving north ', Up ' moving up ', Down ' moving down ', and Stay ' staying there '. The meaning of δ is that if M is in state q with the input head scanning the symbol σ, then with probability $\delta[q, \sigma]$ (q', d) the machine enters state q' and either moves the input head one symbol in direction d if $d \in$ { East, West, South, North, Up, Down } or does not move the input head if $d =$ Stay. Given an input tape $x \in \Sigma^{(3)}$ M starts in state q_0 with the input head on the upper northwest corner of x. The computation of M either accepts by entering the accepting state q_a or rejects by entering the rejecting state q_r. We assume that δ is denoted so that the input head never falls off an input tape out of the boundary symbols $\#$'s. M halts when it enters state q_a or q_r.

A *three-dimensional alternating finite automaton* (denoted by 3-*AFA*) is an alternating version of a three-dimensional finite automaton. See [1, 6, 7] for the formal definition of 3-*AFA*'s [16, 17].

Let $\mathcal{L}$[3-*PFA*] = $\{T \mid T = T(M)$ for some 3-*PFA* M $\}$. $\mathcal{L}$[3-*AFA*] is defined in the same way as $\mathcal{L}$[3-*PFA*].

3 RESULTS

This section shows that the 3-*PFA* is incomparable with 3-*AFA*. We first give several preliminaries to get our desired results. Let M be a 3-*PFA* and Σ be the input alphabet of M. For each $l, m, n \geq 1$, a three-dimensional type in $\Sigma^{l \times m \times n}$ is called an $(l, m, n) - chunk$ over Σ. For any (l, m, n)-chunk v with $l \geq 1$, $m \geq 1$, and $n \geq 2$, we denote by v($\#$) the pattern obtained from v by attaching the boundary symbols $\#$'s to v. Below, we assume without loss of generality that M enters or exits the pattern v($\#$). Thus, the number of the entrance points to v($\#$) (or the exit points from v($\#$)) for M is $4m + 8$. Let PT(v($\#$)) be the set of these entrance points (or exit points). .

Lemma 3.1. *Let* $L_1 = \{x \in \{0,1\}^{(3)} | \; l_3(x) \geq 2$ $\exists \; k \; (2 \leq k \leq l_3(x)) \; [x[(1,1,1),(l_1(x),l_2(x),1)] = x[(1,1,k),(l_1(x),l_2(x),k)]]$ *(i.e., the top plane of* x *is identical with some another plane of* x)]. *Then,* $L_1 \in$ 3-*AFA* — 3-*PFA*.

Proof: L_1 is accepted by the 3-*AFA* M with acts as follows. Given an input tape x with $l_3(x) \geq 2$, M existentially tries to check that, for each $i, j (1 \leq i \leq l_1(x)$, $1 \leq j \leq l_1(x)$ $x(i,j,k) = x(i,j,1)$. That is, ont the kth plane of $x(1 \leq i \leq l_1(x)$, $1 \leq j \leq l_2(x)$, $1 \leq k \leq l_3(x)$, M enters a universal statoe to choose one of two further actions. One action is to pick up the symbol $x(i,j,k)$, move up the symbol store in the finite control, compare the stored with the symbol $x(i,j,1)$, and enter an accepting state if both symbols are identical. The other action is to continue to move next tape cell (in order to pick up the symbol $x(i+1,j+1,k)$ and compare it with the symbol $x(i+1,j+1,k)$ and compare it with the symbol $x(i+1,j+1,1)$. It will be obvious that M accepts L_1.

We next show that $L_1 \notin$ 3-*PFA*. Suppose to the contrary that there exsts a 3-*PFA* M' recognizing L_1 with error probability $\epsilon < \frac{1}{2}$. For large m, let V(n) be the set of all the (2^n, 2^n, n)-chunks over $\{0, 1\}$. We shall below consider the computations of M' on the input tapes x with $l_1(x) = l_2(x) = 2^n$ and $l_3(x) = n$. Let c be the number of states of M'. Consider the chunk probabilities p(v, σ, τ) defined above. For each (2^n, 2^n, n)-chunk v in V(n), there are a table of

$$d(n) = c \times | \text{PT(v(}\#\text{))} | \times (c \times | \text{PT(v(}\#\text{))} | + 5) = O(n^2)$$

chunk probabilities, where fo any S, $\mid S \mid$ denotes the number of elements of S. Fix some ordering of the pairs (σ, τ) of starting and stopping conditions and let **p**(v) be the vector of these d(n) probabilities according to this ordering. By using the counting argument and reduction to absurdity, we can derive the following lemma. □

Lemma 3.2. *Let* $L_2 = \{x \in \{0,1\}^{(3)} \mid l_3(x) = 1\&$ (x *is of the form* 0^n1^n *for some* $n \geq 1$) $\}$. *Then,* $L_2 \in$ 3-*PFA* — 3-*AFA*.

Proof: It is showed the L_2 is recognized by a two-way probabilistic finite automaton with error probability ϵ for any $\epsilon < \frac{1}{2}$ [1, 3]. On the other hand, it is showed that alternating finite automata accept only regular sets. Thus $L_2 \in \mathcal{L}$[3-*PFA* — 3-*AFA*] by using the same technique. □

From Lemmas 3.1 and 3.2, we have the following theorem.

Theorem 3.1. 3-*PFA is incomparable with* 3-*AFA*.

4 CONCLUSION

It was introduced three-dimensional probabilistic finite automata 3-*PFA*^{c}'s and shown their some properties in this paper. We conclude this paper by giving the following open problems.

(1) Let 3-*PFA*^{c} (resp. 3-*AFA*^{c}) be the class of sets of cubic tapes recognized by 3-*PFA*^{c}'s with error probability less than $\frac{1}{2}$ (resp., accepted by 3-*AFA*^{c}'s). Is 3-*PFA*^{c} incomparable with 3-*AFA*^{c} ?

(2) Let T^c be all the three-dimensional connected tapes. Is Tc recognized by 3-*PFA*^{c}'s ?

(3) It will be interesting to investigate the properties of various three-dimensional probabilistic Turing machines.

(4) It will be also interesting to deal with the closure properties of 3-*PFA*^{c}'s.

REFERENCES

[1] Blum M and Hewitt C (1967), Automata on a twodomensional tape. IEEE Symposium on Switching and Automata Theory:155-160

[2] Chandra AK, Kozen DC, and Stockmeyer LJ (1981), Alternation. Journal of the ACM 28(1):114-133

[3] Dwork C and Stockmeyer LJ (1992), Finite state verifier I : the power of interaction. Journal of the ACM 39(4):800-828

[4] Freivalds R (1981), Probabilistic two-way machines. Proceedings of the International Symposium on Mathematical Foundations of Computer Science, Lecture Notes in Computer Science 118, Springer, New York

[5] Gill J (1977), Computational complexity of probabilistic Turing machines. Journal of the SIAM, Comput 6(4):675-695

[6] Greenberg AG and Weiss A (1986), A lower bound for probabilistic algorithms for finite state macines. Journal of Computer and System Sciences 33:88-105

[7] Inoue K, Takanami I, and Nakamura A (1978), A note on two-dimensional finite automata. Information Processing Letters 7(1):49-52

[8] Inoue K, Takanami I, and Taniguchi H (1983), Two-dimensional alternating Turing machines. Theoretical Computer Science 27:61-83

[9] Ito A, Inoue K, and Wang Y (1997), Nonclosure properties of two-dimensional one-marker automata. International Journal of Pattern Recognition and Artificial Intelligence 11(7):1025-1050

[10] Kaneps J (1991), Regulality of one-letter languages acceptable by 2-way finite probabilistic automata. In:Proceedings of the Fundamentals of Computation Theory, Lecture Notes in Computer Science 529:287-296, Springer, New York

[11] Karpinski M and Verbeek R (1987), On the Monte Carlo space constructible functions and separation results for probabilistic complexity classes. Information and Computation 75:178-189

[12] Macarie II (1997), Multihead two-way probabilistic finite automata. Thoretical Computer Science 30:91-109

[13] Okazaki T, Inoue K, Ito A, and Wang Y (1999), Closure properties of the classes of sets recognized by space-bounded two-dimensional probabilistic Turing machines. Information Sciences 115:61-81

[14] Rabin MO (1963), Probablistic automata. Information and Control 6:230-245

[15] Rosenfeld A (1979), Picture Language (Formal Models for Picture Recognition). Academic Press, New York

[16] Sakamoto M (1999), Three-dimensional alternating Turing macines. Ph.D. Thesis, Yamaguchi University

[17] Sakamoto M, Tomozoe N, Furutani H, Kono M, Ito T, Uchida Y, and Okabe H (2008), A Survey of Automata on Three-Dimensional Input Tapes. WSEAS TRANSACTIONS on COMPUTERS 10(7):1638-1647

[18] Seneta E (1981), Non-negative matrices and Markov Chains. 2nd ed., Springer, New York

[19] Siromoney G, Siromoney R, and Krithivasan K (1973), Picture languages with array rewriting rules. Information and Control 22:447-470

[20] Wang J (1992), A note on two-way probabilistic automata. Information Processing Letters 43:321-326

[21] Yamamoto Y and Noguchi S (1985), Time- and -leaf bounded 1-tape alternating Turing machines (in Japanese). The Transactions of the IECE J68-D(10):1719-1726

[22] Yamamoto Y, Morita K, and Sugata K (1979), Space complexity for recognizing connected patterns in a three-dimensional tape (in Japanese). Technical Report of the IECE AL79-104:pp.91-96

The Seventeenth International Symposium on Artificial Life and Robotics 2012 (AROB 17th '12),
B-Con Plaza, Beppu, Oita, Japan, January 19-21, 2012

A Study on Factors Affecting the Degree of Bullwhip Effect and Inventory Cost to an Optimal Management Strategy for Information Sharing in Supply Chains

Masayoshi HASAMA[1], Seigo.MATSUNO[1], Takao ITO[1], Koichi SAEKI[1], and Yu SONG[2]

[1]Dept. of Business Administration, Ube National College of Technology, Yamaguchi, Japan
(Tel: 81-836-35-7199, Fax: 81-836-35-7199)
[2]Dept. of System Management, Fukuoka Institute of Technology, Fukuoka, Japan
(Tel: 81-92-606-5919, Fax: 81-92-606-0756)

[1]hasama@ube-k.ac.jp

Abstract: *To compete successfully in today's marketplace, it has become that success cannot rely solely on improving the efficiency of internal operations, and that collaboration with trading partners can build the foundation for a competitive advantage and substantially improve the bottom line. Companies need to efficiently manage the activities of design, manufacturing, distribution, service and recycling of their products, and services to their customers. The coordination and integration of these flows within and across companies are critical in effective supply chain management (SCM). In this paper, we define a two-stage supply chain model (a retailer and supplier). Based on results of simulations, we identify the factors*

Keywords: Supply Chain Management, Bullwhip Effect, Information sharing.

1 INTRODUCTION

Supply Chain Management deal with the management methods in World-Wide. For example, it is known as s uccess in DELL, Wal-Mart and so on. According to success auto-mobile industry in Japan, the company can be reduction cost by information exchange from phases of development to a close rate in many *keiretsu* companies.

In the auto-mobile industry of Japan, it is a group in the pr operties such as the system, and the subsidiary company succeeded in cost reduction by information exchange being performed frequently from phases of development to sales stage. We share management resources and information as one of the process in supply chain, and this is because, it is possible to reduce "waste" by optimizing the supply chain.

Based on the case study of the supply chain management, there are many theoretical studies in the bullwhip effect. Th e Supply Chain subjected to information distortion as demand information is processed and passed on from one part of the chain to another.

Information sharing among companies in a supply chain is regarded as an effective measure, the relations of WIN-WIN and the management strategy to relieve the Bullwhip Effect. In previous study, there are effective with the information sharing as measures to control Bullwhip Effect. However, it may be hard to do information sharing because there is not a clear standard and does not succeed in particular with the thing such as the profit allocation.

In this paper, we perform analysis about the effectiveness of the information sharing with the factor of inventory control. Moreover, using Excel Statistical software, we approach order policy and inventory cost with information sharing in management for decision making.

In Section2, we consider the study of Bullwhip Effect. We define the model for simulation in Section3.

In finally, we describe the inspection of information s haring with numerical analysis.

2 LITERATURE

The previous studies of Supply Chain Management co nsider two points. There are the cause and existence o f Bullwhip Effect, the reduction of Bullwhip Effect.

It was recognized that the inventory in the company played a role as the buffer which controlled uncertain demand conventionally. Therefore, it was thought that degree should be smaller than a change of the demand as for the change of the quantity of ordering of the company by holding extends stock.

In contrast, Forrester (1961) showed that width was rather bigger than a change of the demand to the company to the change of the quantity of ordering of the company using empirical evidence in American energy industry [3]. This phenomenon was called "Forrester phenomenon" using his name. These were pointed out in the TV production industry by Holt, Modigliani and Shelton (1968) and the auto-mobile industry by Blanchard (1983) [2], [4].

In a phenomenon to contradict it for such a previous way, Caplin (1985) [5] and Blinder (1986) [6] performed theoretical inspection and proved the existence. For example, it was considered that the model of the ordering (S, s) policy [5]. As a result, the fluctuation of the ordering by the retail proved the thing that was bigger than fluctuation of the demand when demand to retail was independent each other.

As an advanced study for Supply Chain became popular, it was cleared that the phenomenon occurred in an individual type of industry. This phenomenon was named "Bullwhip phenomenon" in American P&G Corporation.

In the cause study of Bullwhip phenomenon, we showed that the optimal stock quantities of the retail were correlation to demand in a period, and Kahn (1987) [7] derived that raise Bullwhip phenomenon by a backlog in the excessive demand. Sterman (1989) [8] considered the cause of Bullwhip phenomenon using a production distribution game (i.e. beer game). This game noted that fluctuation of the ordering is appeared; one of the causes in Bullwhip phenomenon is an information distortion. There were four mains. That is the error in demand forecasting, failure of supplies and the device of leadtime, price fluctuation.

Chen et al. (1998)[11] considered the influence of the Bullwhip phenomenon using two forecasting models in the moving average and exponential smoothing method. Moreover, Cheung and Zhang (1999) [12] described the cancellation of the customer ordering with being a cause of Bullwhip phenomenon. It is because that the canceled demand is similar with dummy demand. The customer and the Supply Chain partner considered it what kind of factor damaged retail and an upstream (wholesale, maker and so on).

Therefore, Chen et al. (2000) examined the influence of the demand forecasting to become the factor to cause Bullwhip phenomenon in the Supply Chain model consisting of one stage (retail) or two stages (e.g.between retail and manufacturer) in [14].

3 MODEL

In this section, we define three information sharing m ethods: demand information, demand forecasting and or der information (See Fig.1, 2 and 3).

3.1 The method of Information Sharing

The models of study consist of three information sharing methods. First, DIS is to approach for ordering in Stage 2 using a data of demand in Stage 1. Second, FIS is to use moving average method in the order of Stage 2 based on the trend of demand. Third, OIS is to approach ordering using the data of order in Stage1.

Therefore, If Stage2 exists out of stock, approach for using the data of order in Stage1. If not, used for Stage 2 directly as a data of order in Stage1.

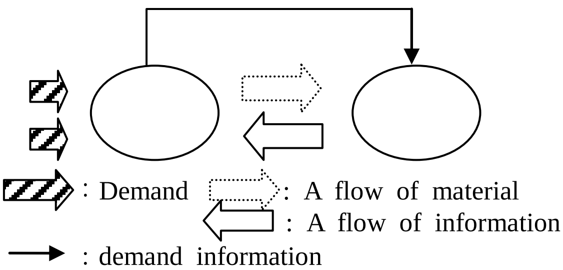

Fig1. DIS（Model 1）

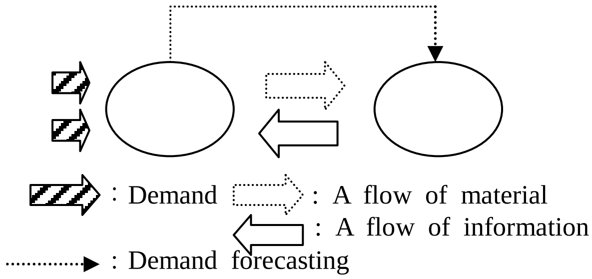

Fig2. FIS（Model 2）

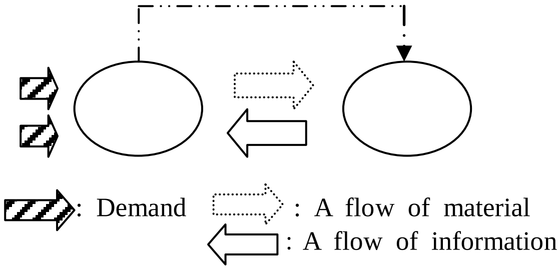

Fig3. OIS（Model 3）

3.2 Simulation

Using the model from Figure 1 to 3, we demonstrate simulation. The design of simulation is as follows.

Definition:

1. The simulation software use Microsoft Excel.
2. The number of trying simulation is fifty.
3. The data use average of simulation until fifty.

4 NUMERICAL ANALYSIS

In this section, we discuss inspection about the information sharing. At first, we inspect the Bullwhip Effect about three information sharing models.

In next sections, it considers the inventory cost and short age cost and inspects the elements of which inventory control are influenced by management strategy using the correlation.

Table1. The degree of phase1 until phase5

level / PA	phase1	phase2	phase3	phase4	phase5
MAP	3	5	10	15	20
LE	2	3	4	5	6
DA	55	60	65	70	75
DV	9	12	15	18	21
SS	1.65	1.76	1.89	2.05	2.33
OC	1	2	3	4	5

e.g) parameter stand for "PA", the moving average peri od stand for "MAP", the leadtime stand for "LE", the demand average stand for "DA", the demand variance stand for "DV", the safety stock stand for "SS", the o rdering cycle stand for "OC".

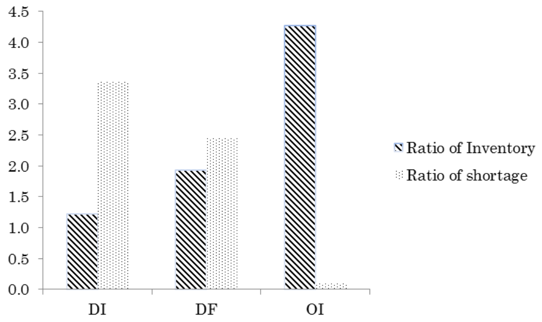

Fig4. Inspection of Information Sharing

4.1 Inspection of Bullwhip Effect

At first we discuss the inspection of the Bullwhip Effect. The inspection method uses the value that divided standard deviation of the quantity of ordering of Stage1 by standard deviation of the quantity of ordering of Stage2. It understands that an ordering information sharing is more effective to protect the degree of Bullwhip (See Fig.4).

4.2 Inspection of inventory and Shortage Cost

The inventory ratio consists of inventory cost ratio in Stage1 and Stage2. At first, the demand information sharing understands that the ratios out of stock increase. This can control the inventory to use information of the final demand for an ordering policy of Stage2, however, trend of the quantity of demand changes increases out of inventory cost. As the demand forecasts see the cost of the inventory and shortage inventory, we can understand balance.

4.3 Inspection of management

We consider the amount of change from phase1 to phase2 in three information sharing models.

The case of demand information is to optimal the moving average period parameter in ratio of inventory, ratio of standard deviation and ratio of shortage. Moreover, in the case of demand forecast and ordering information, the ratio of inventory and standard deviation optimal the moving average period parameter and ordering cycle parameter, respectively.

Finally, the correlation describes the higher significant relation in demand information and demand forecast sharing.

5 CONCLUSION

In this study, we performed inspection of the information sharing from three models. When demand forecasting and ordering information sharing were the same tendencies and changed two factors.

It is understand that demand information sharing and demand forecasting should discuss about a strategy with the same tendency.

REFERENCES

[1] Holt, C. C., Modigliani, F., Muth, J. and Simon, H., "Planning Production, Inventories and the Work Force", Prentice-Hall, NJ (1960).

[2] Holt, C. C., Modigliani, F., and Shelton, J.P., "The Transmission of Demand Fluctuations through Distribution and Production Systems TV-set Industry", *Canadian J Economics* 14, 718-739 (1968).

[3] Forrester, J., "Industrial Dynamics", MIT Press Cambridge MA, and Wiley New York, (1961).

[4] Blanchard, O. J., "The Production and Inventory Behavior of The American Automobile Industry", *J. Political Economy* 91, 365-400 (1983).

[5] Caplin, A. S., "The Variability of Aggregate Demand with (S, s) Inventory Policies", *Econometrica* 53, 1396-1409 (1985).

[6] Blinder, A. S.,"Can the Production Smoothing Model of Inventory Behavior be saved" *Quarterly J. Economics* 101, 431-454 (1986).

[7] Kahn, J., "Inventories and The Volatility of Production", *Am Econ Rev*,77 ,667-679 (1987).

［8］ Sterman, J. D., "Modeling Managerial Behavior: Misperceptions of Feedback in a Dynamic Decision Making Experiment", *Management Science* 35, 321-339 (1989).

［9］ Lee, H, Padmanabhan, P, and Whang, S., "The Bullwhip Effect in Supply Chains", *Sloan Management Review* 38, 93-102 (1997a).

［10］ Lee, H, Padmanabhan, P, and Whang, S., "Information Distortion in a Supply Chain the Bullwhip Effect", *Management Science*, 43,546-558 (1997b).

[11] Chen, F, Ryan, J. K, and Simchi-Levi, D.,"The impact of exponential smoothing forecasts on the bullwhip effect", *Working Paper, Decision Sciences Department,* National University of Singapore (1998).

［12］ Cheung, K. L, and Zhang, A. X., "The Impact of Inventory Information Distortion due to Customer Order Cancellations", *Naval Res. Logistics* 46 (2), 213-231(1999).

[13] Baganha, M, Cohen, M, "The Stabilizing Effect of Inventory in Supply Chains", Operations *Research*, 46, 72-83 (1998).

［14］ Chen, F, Drezner, Z, Ryan, J. K., and Simchi-Levi, D., "Quantifying the Bullwhip Effect：The Impact of Forecasting, Lead time and Information", *Management Science,* 46, 436-443 (2000).

［15］ Zipkin, P.," Performance Analysis of a Multi-item production inventory system under alternative policies", *Management Science* 41/4 690-703 (1995).

[16] Lee, H, So, K, and Tang, C., "Supply Chain reengineering through information sharing and replenishment coordination", *Working Paper*, Department of Industrial Engineering Stanford University (1996).

[17] G, Cachon, and M, Fisher., "Supply Chain Inventory Management and The Value of Shared Information", *Working Paper*, Wharton School, University of Pennsylvania(2000).

[18] Yu, Zhenxin, Yan, Hong, and Edwin, T, Cheng, C., "Benefits of Information Sharing with Supply Chain Partnerships", *Industrial Management & Data System*, 101(3) , 114-119 (2001).

[19] Zhao, Xiande, Xie, Jinxing, Leung, Janny., " The Impact of Forecasting Model Selection on the Value of Information Sharing in a Supply Chain", *European Journal of Operational Research* ,142 , 321-344 (2002).

[20] Srinivasan, Raghunathan., " Impact of Demand Correlation on the Value of and Incentives for Information Sharing in a Supply Chain", *European Journal of Operational Research*, 146,634-649 (2003).

[21] Dejonckheere, J, Disney, S. M, Lambrecht, M. R, Towill, D. R, "The Impact of Information Enrichment on the Bullwhip Effect in Supply Chains: A Control Engineering Perspective", *European Journal of Operational Research* 153,727-750 (2004).

[22] Ralph, D. Snyder, Anne, B. Koehler, Rob, J. Hyndman., J, Keith, Ord., "Exponential Smoothing Models: Mean and Variances for Lead-time Demand", *European Journal of Operational Research 158,444-455* (2004).

[23]Per, J. Agrell, Robert, Lindroth, Andreas, Norrman, "Risk, Information and Incentives in Telecom Supply Chains", *Int. J. Production Economics* 90,1-16 (2004).

[24] Pablo, A, Miranda, Rodrigo, A, Garrido, "Incorporating Inventory Control Decisions into a Strategic Distribution Network Design Model with Stochastic Demand", *Transportation Rearch Part E* 40,183-207 (2004).

[25] Nikolaos, A. Panayiotou, Sotiris, P. Gayialis, Ilias, P. Tatsiopoulos., "An E-Procurement System for Governmental Purchasing" *Production Economics* 90, 79-102, (2004).

[26] Vicky, Manthou, Maro, Vlachopoulou, Dimitris, Folinas., "Virtual e-Chain (VeC) Model for Supply Chain Collaboration", Int. J. *Production Economics 87*, 241-250 (2004).

[27] Zheng, Y, and Zipkin, P., "A queuing model to analyze the value of centralized inventory information", *Oper. Res* 38,296-307 (1990).

[28] Bourland, K, Powell, S, and Pyke, D,, "Exploring timely demand information to reduce inventories", *European Journal Oper. Res*, 92, 239-253 (1996).

Modified Local Gaussian Process Regression for Inverse Dynamics Learning

Seung-Yoon Cho[1], Sung-Soon Yim[2], and Ju-Jang Lee[3]

[1,2,3] KAIST, Daejeon, 305-701, Korea
(Tel: 82-42-350-8032, Fax: 82-42-350-5342)
[1]jove@kaist.ac.kr
[2]matssam@kaist.ac.kr
[3]jjlee@ee.kaist.ac.kr

Abstract: Robots have been playing an important roles on our life. In various field such as entertainment, military, space and medical fields, the precise control is required according to the increase of the importance on robot. In robot manipulator position control problem, modeling robot inverse dynamics is important because it can allow accurate robot control using computed torque control and PD control with computed feedback. However, modeling rigid-body inverse dynamics is not simple and not accurate in some case, because of unmodeled nonlinearities such as hydraulic cable dynamics, complex friction or actuator dynamics. Instead of rigid-body dynamics, nonparametric regression such as Locally Weighted Projection Regression (LWPR), Gaussian Process Regression (GPR) is proposed as alternative. Locally Weighted Projection Regression is fast, but it is difficult to tune because of many user-parameters. Gaussian Process Regression has high accuracy but low computation speed. In other word, high complexity of computation is drawback of Gaussian process regression. In Gaussian Process Regression, the inverse of Gram matrix is a significant problem and it dominates the computation time. To improve the low computation speed, there are many methods such as approximation method and Local Gaussian Process Regression (LGPR). In approximation method, the approximation of inverse of Gram matrix is proposed and in local Gaussian Process Regression, the training data is divided into local training data using Gaussian kernel. It generates M local models. After partitioned the training data, the local model is trained. When test data is given, each local model predicts the local prediction. The total prediction value is weighted average of M local prediction values. The weight is a similarity measure and it can be calculated by Gaussian kernel. Local Gaussian Process Regression In this paper, Modified Local Gaussian Process Regression (MLGPR) is suggested for improving accuracy and computation time of Local Gaussian Process Regression. Modified Local Gaussian Process Regression is used adaptive method for partitioning the training data. Modified Local Gaussian Process Regression uses multiple model generation threshold w_{gen} values depending on the local target variance. Proposed method is demonstrated by 2-dimension regression example and learning inverse dynamics of SARCOS arm. The result of simulations will be compared with other method such as Gaussian Process Regression, Local Gaussian Process Regression. As a result, the accuracy of Modified Local Gaussian Process Regression is improved and computation cost is reduced. The result represent Modified Local Gaussian Process Regression has low computation cost as compared with Local Gaussian Process Regression.

Keywords: inverse dynamics, machine learning, Gaussian Process Regression, Local Gaussian Process Regression

1 INTRODUCTION

Robots have been studied and applied in various field such as entertainment, military, space and medical fields. The precise control is required according to the increase of the importance on robot. For more precise control, more precise models of inverse dynamics is needed. In other word, precise models of inverse dynamics allow the effective control [1] [2]. However, finding precise models of inverse dynamics is difficult in some cases because of unmodeled nonlinearity. This modeling error comes from hydraulic cable dynamics, complex friction or actuator dynamics [3]. To solve this problem, the alternative method which is using nonparametric regression method is proposed. The nonparametric regression method is a kind of supervised learning, and it is more flexible than parametric regression. This method predicts inverse dynamics model from pre-measured data [6]. The most common used nonparametric regression methods are Locally Weighted Projection Regression (LWPR) [4], Gaussian Process Regression (GPR) [5] and Support Vector Regression (SVR). Although LWPR is fast ,accurate and incremental learning is possible, it is hard to tune due to many user parameters. GPR has high accuracy but its computation cost is increased when the data is large. To overcome the high computation cost, Local Gaussian Process Regression (LGPR) [3][7][8][9] is proposed. LGPR is an algorithm which combines the accuracy of GPR method on one region with the good capability of LWPR to split the input domain into regions [6]. The more detail regression methods are well organized and summarized in [6].

In this paper, Modified Local Gaussian Process Regression (MLGPR) is suggested for improving accuracy and computation time of LGPR. In section 2, Gaussian Process Regression and Local Gaussian Process Regression are presented in detail. I propose Modified Local Gaussian Process Regression (MLGPR) in section 3. MLGPR is used adaptive method for partitioning the training data. In section 4, the simulation of modified local Gaussian Process Regression is demonstrated. The result of simulation will be compared with other method such as Gaussian Process Regression, Local Gaussian Process Regression. In section 5, we suggest conclusion.

2 LOCAL GAUSSIAN PROCESS REGRESSION

2.1 Gaussian Process Regression

A Gaussian Process is completely specified its mean function and covariance function. The covariance function $k(\mathbf{x}, \mathbf{x}')$ can be any positive semi-definite functions. The square exponential(SE) covariance function is frequently used and are given by:

$$k(\mathbf{x}_p, \mathbf{x}_q) = \sigma_f^2 \exp(-\frac{1}{2}(\mathbf{x}_p - \mathbf{x}_q)^T \mathbf{M}(\mathbf{x_p} - \mathbf{x_q})) \tag{1}$$

where σ_f^2 is data variance and $\mathbf{M}$ is the symmetric matrix and it represent distance measure. $\theta = [\sigma_f^2, \{\mathbf{M}\}]^\mathbf{T}$ is the hyperparameters of a Gaussian Process.

Consider a set of *n* training data $\mathbf{X} = [\mathbf{x}_1, \mathbf{x}_2, ..., \mathbf{x}_n]$ and $\mathbf{y} = [y_1, y_2, ..., y_n]$. Using the training data $(\mathbf{X}, \mathbf{y})$ and a new data point $\mathbf{x}_*$, we want to know the predictive distribution of the corresponding $\mathbf{y}_*$. The joint distribution of the training outputs, $\mathbf{y}$ and the test outputs, $\mathbf{y}_*$ is

$$\begin{bmatrix} \mathbf{y} \\ \mathbf{y}_* \end{bmatrix} \sim N\left(\mathbf{0}, \begin{bmatrix} K(\mathbf{X},\mathbf{X}) & K(\mathbf{X},\mathbf{x}_*) \\ K(\mathbf{x}_*,\mathbf{X}) & K(\mathbf{x}_*,\mathbf{x}_*) \end{bmatrix}\right) \tag{2}$$

From the joint distribution, the predictive distribution is

$$\begin{aligned} &\mathbf{y}_*|\mathbf{x}_*, \mathbf{X}, \mathbf{y} \sim N(\bar{\mathbf{y}}_*, \mathrm{cov}(\bar{\mathbf{y}}_*)) \\ &\bar{\mathbf{y}}_* = K(\mathbf{x}_*, \mathbf{X})K(\mathbf{X}, \mathbf{X})^{-1}\mathbf{y} = k_*{}^T \boldsymbol{\alpha} \\ &\mathrm{cov}(\bar{\mathbf{y}}_*) = K(\mathbf{x}_*, \mathbf{x}_*) - K(\mathbf{x}_*, \mathbf{X})K(\mathbf{X}, \mathbf{X})^{-1}K(\mathbf{X}, \mathbf{x}_*) \end{aligned} \tag{3}$$

The computation cost for predictition is dominated by inverse of K^{-1}. It is about $O(n^3)$, where n is the number of training data. For large problem, computation cost increases rapidly. This is main weakness in Gaussian Process Regression. For solving this problem, Local Gaussian Process Regression [3] is suggested.

2.2 Local Gaussian Process Regression

A Local Gaussian Process Regression(LGPR) proposed for reducing computation cost of GPR is inspired by local weighted regression and Gaussian Process Regression. The procedure of LGPR is as follows: Firstly, the training data is partitioned into M local training data. here, the weight w_i which is similarity measure can be used for partitioning the training data. After local Gaussian Process model is partitioned, for each test data $\mathbf{x}_*$ the prediction of local model $\bar{y}_i(\mathbf{x}_*)$ can be calculated by using eq(3). Finally, the prediction of entire model $\hat{y}(\mathbf{x}_*)$ is given by weighted mean of all local model predictions.

$$\hat{y}(\mathbf{x}_*) = \frac{\sum_{i=1}^M w_i(\mathbf{x}, \mathbf{c_i})\bar{y}_i(\mathbf{x}_*)}{\sum_{i=1}^M w_i(\mathbf{x}, \mathbf{c_i})} \tag{4}$$

where, i is the number of local models. The partitioning algorithm of LGPR is represented in Algorithm 1 and the prediction algorithm of LGPR is represented Algorithm 2. The method for updating Cholesky matrix $\mathbf{L}$ and prediction vector $\boldsymbol{\alpha}$ is presented in [3].

Using LGP regression the computation cost can be reduced from $O(n^3)$ to $O(n_1^3 + n_2^3 + ... + n_k^3)$ where k is the number of local model, $n_1 + n_2 + ... + n_k = n$.

3 MODIFIED LOCAL GAUSSIAN PROCESS REGRESSION

3.1 Issue of Local Gaussian Process Regression

In the preceding sections the computation cost which is the problem of GPR can be reduced by using local weighted regression. But now the problem of LGPR is how to choose the number of local model, in other word, how to divide the training data. According to determination of local training data, the computation cost and accuracy of LGPR can be changed. This represents the importance for dividing of local model. In LGPR algorithm, the training data is partitioned by using similarity measure w, and model generation threshold value w_{gen}. The w_{gen} is open parameter and there's no rule to choose w_{gen}. If w_{gen} is too large, many local model will be generated and the number of training data in each local model is too small. Although it takes small computation cost, the local model with small data makes a ill distribution, i.e. accuracy of LGPR is decreased. If w_{gen} is too small, small local model with large training data is generated. Accuracy of LGPR will be increased but the computation cost will be high. LGPR loses the advantage of computation cost.

3.2 Adaptive method for partitioning of Training Data

In LGPR, every local model has only one fixed model generation threshold w_{gen}. Because the accuracy and computa-

Algorithm 1 Partitioning the training data with incremental model learning(Modified)

Input: new data point $\{\mathbf{x}_{new}, y_{new}\}$
for $i = 1$ to number of local models **do**
  Compute proximity to the ith local model:
    $w_i = k(\mathbf{x}_{new}, \mathbf{c}_i)$
end for
Take the nearest local model: $v(i) = \max_i w_i$
if $v(i) < w_{gen}(i)$ **then**
  Insert $\{\mathbf{x}_{new}, y_{new}\}$ into the nearest local model:
    $\mathbf{X}_{new} = [\mathbf{X}_i, \mathbf{x}_{new}]$, $\mathbf{y}_{new} = [\mathbf{y}_i, y_{new}]$
  Update the corresponding center: $\mathbf{c}_{new} = mean(\mathbf{X}_{new})$
  Update the Cholesky matrix, $\mathbf{L}_{new}$ and the prediction vector, $\boldsymbol{\alpha}_{new}$ of local model
  if the maximum number of data point is reached **then**
    delete another point randomly
  end if
  Compute $\boldsymbol{\alpha}_{new}$ by back-substitution
  Update w_{gen} {This is the new part of MLGP}
  if $\mathrm{Var}(\mathbf{y}_{new}) > \mathrm{E}(\mathrm{Var}(\mathbf{y}))$ **then**
    $w_{gen}(i) = w_{gen}(i) - \delta$
  else
    $w_{gen}(i) = w_{gen}(i) + \delta$
  end if
else
  Create new model:
    $\mathbf{c}_{i+1} = \mathbf{x}_{new}$, $\mathbf{X}_{i+1} = [\mathbf{x}_{new}]$, $\mathbf{y}_{i+1} = [y_{new}]$
  Initialize of new Cholesky matrix $\mathbf{L}$ and new prediction vector $\boldsymbol{\alpha}$
end if

Algorithm 2 Prediction for a query point

Input:query data point $\mathbf{x}_*$, M
Determine M local models closest to $\mathbf{x}_*$
for $i = 1$ to M **do**
  Compute proximity to the ith local model:
    $w_i = k(\mathbf{x}_*, \mathbf{c}_i)$
  Compute local prediction using kth local model:
  $\bar{y}_i(\mathbf{x}_*) = \mathbf{k}(\mathbf{X_i}, \mathbf{x}_*)^T \boldsymbol{\alpha}_i$
end for
Compute weighted prediction using M local models:
$\hat{y}(\mathbf{x}_*) = \frac{\sum_{i=1}^{M} w_i \bar{y}_i(\mathbf{x}_*)}{\sum_{i=1}^{M} w_i}$

tion cost of LGPR are changed depending on w_{gen}, using same w_{gen} on all local model is inefficient. When a local target variance $\mathrm{Var}(\mathbf{y}_{new})$ is large, the result of LGPR can't predict the original distribution. To use small w_{gen} for improving accuracy of LGPR makes the number of local training data large and makes computation cost high. On the other hand, when a local target variance $\mathrm{Var}(\mathbf{y}_{new})$ is small, the result of LGPR is good, even use of large w_{gen}. So it is required change of w_{gen} depending on local target variance $\mathrm{Var}(\mathbf{y}_{new})$ and use different w_{gen} for local models. Therefore it makes a sense to set large w_{gen} to reduce computation cost, when local target variance is small. When local target variance is large, small w_{gen} is used for improving accuracy of prediction. This is a key idea of MLGPR. Now every model has own w_{gen} values and it can be changed according to local target variance. If the w_{gen} of ith local model is bigger than mean of local target variance $\mathrm{E}(\mathrm{Var}(\mathbf{y_i}))$, w_{gen} is decreased as much as δ. It means that accuracy of LGPR is increased using more training data, when the target variance is high. If the w_{gen} of ith local model smaller than mean of local target variance $\mathrm{E}(\mathrm{Var}(\mathbf{y_i}))$, w_{gen} is increased as much as δ. It means that computation cost of LGPR is decreased by reducing the number of training data, when the target variance is low. Modified method for partitioning training data is included in Algorithm1.

3.3 Accuracy and Computation Cost of MLGP

Table.1 shows a comparison of computation cost GPR, LGPR and MLGPR. In GPR, computation cost for calculation of K^{-1} is about $O(n^3)$. In LGPR, the computation cost can be reduced from $O(n^3)$ to $O(n_1^3 + n_2^3 + ... + n_M^3)$ due to using a local prediction, where n is the number of training data, M is the number of local model and n_i the number of local training data. In MLGP, the computation cost for calculation of K^{-1} is $O(n_{m1}^3 + n_{m2}^3 + +n_{mM}^3)$ where n_{mi} the number of local training data , mM is the number of MLGPR local model. The computation cost for prediction is $O(n)$ in GPR, $O(n_iM)$ in LGPR and $O(n_{mi}M)$ in MLGPR. Here, n_{mi} is bigger than n_i, when the variance of ith model is bigger than variance of target. Otherwise n_{mi} is smaller than n_i. Thus the computation cost of MLGPR is usually lower than one of LGPR.

Table 1: The table of computation cost

Method	For calculation of K^{-1}	For prediction
GPR	$O(n^3)$	$O(n)$
LGPR	$O(n_1^3 + n_2^3 + ... + n_M^3)$	$O(n_iM)$
MLGPR	$O(n_{m1}^3 + n_{m2}^3 + +n_{mM}^3)$	$O(n_{mi}M)$

4 SIMULATION

In this section, simulation of Modified Local Gaussian Process Regression is demonstrated by 2-

dimension regression example and learning inverse dynamics of SARCOS arm. 500 noisy training data comes from the two dimensional function[4]: $y = \max\left[\exp(-10{x_1}^2), \exp(-50{x_2}^2), 125\exp(-5({x_1}^2 + {x_2}^2))\right] + N(0, 005)$. Fig.1 shows the result of regression using MLGPR. Its nMSE is 0.012 and it is lower than the LPGR one.

Fig.2 shows the result for inverse dynamics learning of SARCOS arm. The data set consists of 45,000 training data and 5,000 test data[1]. Fig.2(a) shows the nMSE of each link of robot. Fig.2(b) is Computation cost of MLGPR and LGPR. nMSE of MLGPR is lower than one of LGPR,

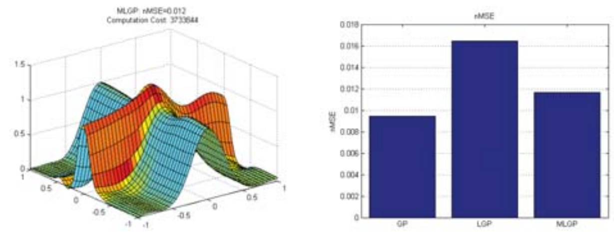

(a) Result of regression using MLGPR (b) nMSE of GPR, LGPR, MLGPR

Fig. 1: 2-dimension regression example

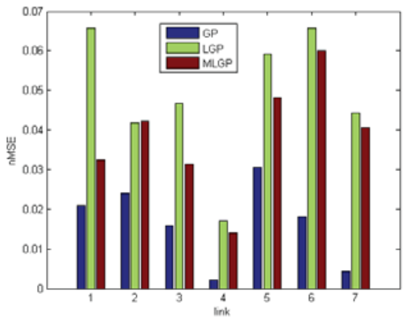

(a) nMSE of each link of robot

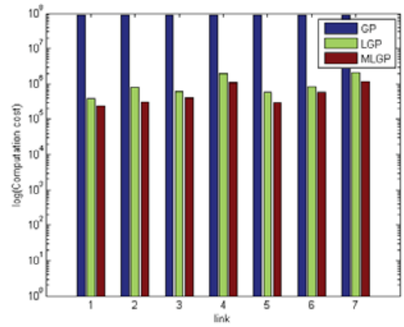

(b) Computation cost of MLGPR and LGPR

Fig. 2: Learning inverse dynamics of SARCOS arm

5 CONCLUSION

Modified Local Gaussian Process Regression(MLGPR) uses multiple model generation threshold w_{gen} values depending on the local target variance. It means each local model has own w_{gen}. If the w_{gen} of ith local model is bigger than mean of local target variance , w_{gen} is decreased for improving the accuracy. Otherwise, w_{gen} is increased for reducing computation cost. MLGPR is compared with GPR and LGPR. As a result, the accuracy of MLGP is improved and computation cost is reduced in simulation results.

REFERENCES

[1] R. M. Murray(2006), A Mathematical Introduction to ROBOTIC MANIPULATION. CRC Press, pp.191-195

[2] Rafael Kelly, Ricardo Salgado (1994), PD control with Computed Feedforward of Robot manipulators:A Design Procedure, IEEE Transactions on Robotics and Automation, voulum.10 pp.566-571.

[3] D. Nguyen-Tuong, M. Seeger, J. Peters (2009), Model Learning with Local Gaussian Process Regression. Advanced Robotics, Volume 23, Number 15, pp. 2015-2034(20)

[4] S. Vijayakumar, S. Schaal (2000), Locally Weighted Projection Regression: An O(n) Algorithm for Incremental Real Time Learning in High Dimensional Space, Proceeding of Seventeenth International Conference on Machine Learning, pp.1079-1086

[5] C. E. Rasmussen, C. K. I. Williams (2006), Gaussian Processes for Machine Learning. MIT Press

[6] O. Sigaud, C. Salaun, V. Padois (2011), On-line regression algorithms for learning mechanical models of robots: A survey, Robotics and Autonomous Systems 59, pp.1115-1129

[7] D. Nguyen-Tuong, J. Peters, M. Seeger (2008) Local Gaussian Process Regression for Real Time Online Model Learning and Control. In Advances in Neural Information Processing Systems, pp. 1193-1200

[8] D. Nguyen-Tuong, J. Peters (2008) Local Gaussian process regression for real-time model-based robot control. Intelligent Robots and Systems, 2008. IROS 2008. IEEE/RSJ International Conference on , pp. 380 - 385

[9] D. Nguyen-Tuong, M. Seeger, J. Peters (2008), Computed Torque Control with Nonparametric Regression Models. American Control Conference, pp. 212 - 217

[1]This dataset is available at 'http://www.gaussianprocess.org/gpml/data'

The Seventeenth International Symposium on Artificial Life and Robotics 2012 (AROB 17th '12),
B-Con Plaza, Beppu, Oita, Japan, January 19-21, 2012

Bioinspiration and Modern Actuators

Maki K Habib[1], Keigo Watanabe[2], and Fusaomi Nagata[3]

[1]The American University in Cairo, New Cairo, Egypt
[2]Okayama University, Okayama, Japan
[3]Tokyo University of Science, Yamaguchi, Japan

[1]maki@aucegypt.edu

Abstract: Biological systems in nature went through long evolution process that led to highly effective and efficient systems with excellent performance. Biomimetics is an interdisciplinary scientific research focuses on making nature as new sources of inspiration to study, analyze and design of creative and efficient engineering systems supported by innovative technologies. Smart materials are the foundation supporting the development of creative bioinpiration. Wide range of biologically inspired systems have been developed. However, engineering such biomimetic intelligent creatures were hampered by physical and technological constraints, and it is still a challenge. Actuators are essential elements within Mechatronical systems due to their important role in motion control systems and hence the development of modern actuators can be inspired from biological actuation systems in nature associated with different level of control. Making intelligent creatures that are actuated by biologically inspired modern actuators and artificial muscles would create new reality with great potentials. This paper provides the concept of Biomimetic as an interdisciplinary field, discusses the enabling technologies, and presents the development of biologically inspired actuators.

Keywords: Bioinspiration, Biomimetic, Intelligent creature, Modern actuators, and Artificial muscles.

I. INTRODUCTION

The evolution of nature led to the introduction of highly effective and power efficient biological systems in general and mechanisms in specific. Nature tested every field of science and engineering leading to inventions that work well, can adapt and last. Biological systems exhibit remarkable physical properties and have been a source of inspiration. Adopting mechanisms and capabilities from nature and the use of scientific approaches led to effective materials, structures, tools, mechanisms, processes, algorithms, methods, systems and many other benefits. Nature has always served as a model for mimicking and inspiration to humans in their efforts to improve their life. Humans throughout history have always sought to mimic the appearance, mobility, functionality, intelligent operation, and thinking process of biological creatures [1].

Maturing conventional technologies are associated with constraints and inadequate performance and this foster the demand for new solutions to maximize functionality while minimizing costs in energy and materials. The need to seek for new solutions is driving science to consider nature as biologically inspired model. The driving force behind attempting to merge biological principles and physics applications stems from the recognition that there are a number of areas where biological methods are more efficient, environmentally and ecologically friendly, and overall superior to current technology. Hence, understanding biological systems presents unique opportunities for wide range development of innovative ideas, paradigms, concepts and methods for engineering solutions, and helps to create new generations of smart materials, novel advanced structures, intelligent devices and technologies. Engineers are increasingly turning to biologists to understand and learn how living organisms function and solve problems. This leads to fuse the best solutions from nature with artificially engineered components to develop systems that are better in functions and efficiency than existing conventional approaches, and this science and technology became known as "Biomimetics" or the 'Mimicry of Nature'. Researchers diverge in precisely how they define biomimetics [2]. However, the use of inspiration instead of mimics is a more accurate description since mimicry is neither possible nor desirable.

Biomimetics can be defined as a new interdisciplinary scientific field featured by technology outcome (hardware and software), and it lies at the interface between biology, physics, chemistry, information, and engineering sciences [3]. Biomimetics focuses on making nature as a model of inspiration that would immensely help conscious abstraction of new principles and ideas, foster innovative design collections, find out new techniques and functionalities, seek new paradigms and methods, develop new materials, and design new streams of intelligent machines, robots, systems, devices, algorithms, etc. Biomimetics incorporates building novel materials at nature's scale and techniques drawn from naturally made substances, and resembles biological systems in structure and/or function as necessary. In the field of sensing and actuations, biomimetics devices can provide an efficient way of converting mechanical energy into electrical or chemical forms and vice versa. Scientists hope this blending may one day lead to stronger, cost- and energy-efficient, and intelligent products that are attractive ecologically.

Making creatures that look and behave like biological models, such as robots and toys that are greatly inspired by science fiction, have established perceptions and expectations that are far beyond the reach of current engineering capabilities, which are constrained by laws of physics and current state-of-the-art. The accelerating pace of the advancements in the field of biomimetics seems to make evident that the emergence of machines as our peers is imminent. Further advancement and the actual realization of these possibilities depends on a number of factors, including local acceptance of technological change, levels of technology and infrastructure investments, market drivers and limitations, and technology breakthroughs and advancements.

II. Biologically inspired Actuation

Actuation presents constraints to novel designs of intelligent mechanisms. Different types of actuators have been developed and used. Three types of conventional actuation are considered as the core of motion and force power for all motion based systems: Hydraulic, Pneumatic, and Electromagnetic actuators. These three come from two main types of power conversion. The first two are considered fluid machines in that they use fluid to create mechanical motion whereas the electric motor converts electrical energy into mechanical energy. Electromagnetic actuators are considered as practical solution for some applications, but these actuators are not ideal in providing the necessary and comparatively high torque and their overall power density is typically low. In addition, most electromagnetic devices cannot supply sufficient energy in a single stroke. Hence various complex transmissions means such as gear boxes, pulleys, etc. are required. However, heavy and inefficient electromagnetic actuation and mechanisms remain the convention not only for robots but also for other motion devices in general. The challenges of energy inefficiency, flexibility, stability and maneuverability, robustness and other technical motivations have been many in getting robots to perform bio-inspired motion, such as that of human, animal, insect, etc (The properties of the muscles vary by species). Hence, there are demands to develop technologies that would drive robots with efficient, high power density actuation, stability and speed in a variety of natural environment to achieve lifelike motion performance. The most significant difficulty in achieving lifelike performance or appearance is the lack of actuator technology that can truly mimic natural muscles even at its most basic performance.

Natural muscles are essential to the mobility and manipulation capabilities of biological creatures. Skeletal muscle accounts for nearly half of the total mass of the average adult human and is unique in its ability to actively modify its mechanical properties within tens of milliseconds to allow human and animals to rapidly react to different environment needs. Muscle is a linear actuator technology whose properties are very well suited to provide intermittent displacements and variable stiffness in organisms ranging from micrometers to meters in length. In addition, muscle is a multifunctional and a 3D nanofabricated element with integrated circulation system (delivers energy (fuel) and removes heat and waste), good work density, act as energy absorber and repair mechanisms. The efficiency and plasticity that characterize muscles arise from the properties of biomolecular motors. Muscle cells serve to self-organize, maintain, repair, and control the mechanical actions of large arrays of biomolecular motors. Tendon tissue is an extension of the extracellular matrix muscle (ECM) and muscle tendon junctions at the ends of each muscle fiber. The mechanical structures that make up this transition from muscle to tendon are critical for the transduction of force, work, and power between muscle tissue and the external environment [4]. In order to achieve desirable bio-inspired motion, such as human, animal, insect, etc. like motions, actuators must be able to reproduce the important features of natural muscle such as adaptable stiffness, high energy, moderate stress and large strain, response speed, efficiency, controllability and high cycle life. Although tremendous technological progress has been made and some artificial actuator technologies are already matching or exceeding muscle in strain, stress, and specific power they cannot yet perform as well as their biological counterparts, whether in terms of stability, fatigue-life or speed [5]. Biomimetics is not limited in mimicking the appearance of natural organisms and surpass the general properties of natural muscles, rather to achieve natural superior behavior and performance. The hope is to develop intelligent robots and machines that are independent, flexible, light in weight, high level of autonomy with capability to learn and adjust their behavior within their dynamic environment. This highlights the need and the necessity to develop actuators that emulate and supersede the behavior and performance of natural muscles. The potential to make such actuators is increasingly becoming feasible with the emergence of new development and technologies.

Many new types of actuators and materials have been used or currently under development to provide the necessary motion and force input. Examples of these actuators are Shape Memory Alloys, Electro-Rheological Fluids, Magneto-Active Transducers, single Crystal Piezoelectric ceramics, Carbon nanotubes, Electrostatic, and Electroactive Polymers. Although natural muscle is not the best in many individual categories of performance, such as strain, actuation power/stress, density, efficiency, actuation speeds, etc, they are still superior in their behavioral performance. This leads to the observation that conventional technologies fail to achieve lifelike motion not because they cannot match or exceed natural muscle performance in any given performance measure, but rather they fall short because their overall performance is not yet comparable to that of natural muscle [6]. In addition, the comparison between the available technologies shows that the electrostatic actuators meet all the stated individual categories of performance requirements for an artificial muscle except in actuation stress. The same comparison shows that dielectric elastomers (DE) can also achieve good overall performance compared to that of natural muscles. Elastomers are sufficiently compliant that large strains are induced and there is efficient coupling between the electrical energy input and mechanical energy output. Electroactive polymers artificial muscles (EPAM), and dielectric elastomers, electro-elastromers are two terms used to indicate to electroactive polymers. Hence, it would be possible to view dielectric elastomer technology as a way to increase actuation stress in electrostatic actuators or as a muscle-like actuator technology in its own right. Research into natural muscle shows that muscle has a number of important passive properties, such as passive elasticity, damping, braking functions (actively absorbing mechanical energy beyond simple damping), and even integrated sensing [7, 8], which help organisms achieve remarkable dynamic performance in the presence of obstacles and unexpected perturbations. While probably not all these functions are needed simultaneously to achieve lifelike motion and/or performance in many cases, the biomimetic actuator designer must consider the range of natural muscle capabilities and how they relate to the capabilities of a given actuator technology. While dielectric elastomers are not an exact analogue of natural muscle, they capture many of the important general features of natural muscle such as stress, high fracture toughness, damage tolerance, inherent vibration damping, large actuation strains, and elasticity. Dielectric elastomers have been operated successfully between 250 ^{o}C, and at -100 ^{o}C for silicones and -10 ^{o}C and 90 ^{o}C for acrylic [9]. However, there are still some of the limitations associated with this technology such as, the need to convert line or battery voltages, which adds cost and consumes volume. Also, pre-stretching mechanisms currently add substantial mass and volume. In addition, the dielectric breakdown can limit actuator yield especially when imperfections exist within films [9].

Synthetic and tissue based technologies of smart materials, such as the category of electroactive polymers (EAP), which includes EPAM, and the electrostrictive polymers [10-12] which, change its dielectric constant as part of the actuation mechanism. These technologies are rapidly emerging as quantitatively functional equivalents to muscle tissue. Electrostrictive polymers have comparable performance to many types of EPAM, but they are typically stiffer and have lower strains. EPAM has demonstrated promise for a variety of applications since it represents a significant difference not only from the conventional electromagnetic actuators but also from other emerging technologies like piezoelectric crystals and shape memory alloys (SMA). Piezoelectric polymers, such as PVDF material have found some non-robotic applications, but for robots, it has relatively low power and energy density. More recently, other types of polymers have been investigated, such as electrochemically actuated conducting polymers and gels (sometimes referred as ionic polymers) that are actuated through the use of chemical changes driven by low voltage signal [10]. In spite of the attractive features of these polymers in terms of low voltage operation and good actuation pressure, they have limited performance in relation to robotic applications because of their relatively slow speeds and low efficiency. Nickel Titanium (NiTi or Nitinol) are the most extensively studied SMA and used as artificial muscles because of their relative nontoxicity, reasonable cost and an electrical resistivity [13, 14]. Martensitic transformations are at the heart of the shape memory effect. Shape memory alloys can exert very large forces per unit area, operate at very high strain rates and undergo relatively large deformations [13, 14]. One of the difficulties that limit the use of SMA as impede their use as muscle-like actuators is the difficulty of controlling the length of NiTi fibers as they undergo a phase transformation (usually run between fully contracted and fully extended but not between). In addition, NiTi actuators have a limited cycle life and their shape memory effect degrades significantly at very large strains.

The most significant advantage EPAM has over electromagnetic actuators is energy density, i.e., more energy created per unit mass of the actuator itself. EPAM demonstrated energy density of 3.4 [J/g] and this density is about 21 times that of single crystal piezoelectric. The energy density gains from EPAM will bring mobility and flexibility to robots and other intelligent machines. In addition, with regards to shape memory alloy and piezoelectric technology, EPAM has a significant direct displacement advantage. While shape memory alloy and piezoelectric technology might get a 1 per-cent direct displacement, EPAM actuators can reach 20-30 per cent levels over long life cycles. With respect to conventional electromagnetic motors, EPAM has a significant advantage in power density. EPAM will provide the same level of power as an EM motor device but with a much smaller and lower weight form factor, much like the human muscle [15]. Furthermore, one can have multi layer of EPAM to get additional displacement or stroke as well as getting higher exerted forces. These layers can be constructed in multiple planar configurations or in linear rolls. In addition, EPAM can be patterned to pinpoint actuation in multiple locations. The overall displacement is a function of the area of EPAM, and the force exerted is a function of the number of layers of EPAM. These layers can be constructed in multiple planar configurations. The electrode layer of the EPAM can be patterned to achieve specific envelopes of motion. Further work will undoubtedly improve the match of EPAM to natural muscle.

Most of the presented newly developed actuator technologies require electrical energy and will generally rely on batteries when used in autonomous systems such as autonomous mobile robots. Cost, energy density and cycle life of fuel cells will alleviate this issue in systems on ground and space. Submersible use is challenging as both fuel cells and chemical oxidation reactions require the harvesting of dissolved oxygen and of air bubbles. Though batteries can be used for autonomous robots, current battery technology store too little energy and deliver it at too low a rate for prolonged or intense activity. The most advanced battery can only store about one-thirtieth of the energy that is stored chemically in fuels such as methanol. To solve these problems, new muscle fibers have been developed just like real muscles [6]. They can power themselves instead of relying on external electrical power. Among the developed artificial muscles of this type is a nickel-titanium alloy coated with platinum, which causes the fuel, currently methanol (hydrogen or alcohol could work, too) to react with oxygen, producing heat. The metal shrinks; the muscle flexes. The artificial muscle can apply 100 times as much force as real muscle. The other artificial muscle, currently less powerful, is made of a sheet of carbon nanotubes, tiny but super strong cylindrical molecules of carbon. Carbon nanotubes are hollow cylinders that are typically 1.2 nm in diameter or larger. Their structure is that of a single rolled sheet of graphite that can have lengths on the micrometer scale [16, 17]. The reaction of fuel and oxygen releases electrical charges that repel each other and cause the nanotube sheet to expand. In order to put such artificial muscles into robots will require solving other problems, like how to control the amount of fuel going to the muscles. In addition, the small to moderate strains characterizing current carbon nanotube actuators require some mechanical amplification, while the electromechanical coupling is poor and require energy recovery to achieve better efficiency. It is expected to overcome many of these issues and promise to provide better performance [17].

III. Biomimetics: challenges and Innovations

None of the available intelligent systems and mechanisms has yet reached the flexibility, adaptability and performance of biological systems, such as human, cheetah, bees, ants, birds, fish, etc. This has motivated researchers to look further into biological systems, navigation mechanisms and sensing capabilities that can be inspired and lead to better ways in the design and implementation of intelligent and autonomous system. Systems synthesis must guarantee an eventual consensus and coherence between behavioral and structural domains, as well as ensure descriptive and integrative features in the design. These can be achieved by applying the evolutionary biological systems developments. A highlight for some of the challenges may include the following,

a) Deep understanding of the diversity and efficiency of structure-function relationships in natural/biological systems at the element/component, subsystems and system levels. The interest lies not just in the abstraction of new and useful ideas from nature but also in the process by which this is done,
b) It is important to understand that nature may evolve different biological mechanisms to solve real world problems in different environments and circumstances,
c) Biological inspiration does not mean that the weaknesses of biology must be adopted along with the strengths,
d) Biological adaptation to a given environment emerge from a natural selection and evolving process that depends on the environment and the entire historical evolution,
e) It is necessary to keep in mind that the relation between understanding of biological organisms and developing engineered solutions is cyclic. Solutions arrived at by natural selection are often a good starting point in the search for answers to problems. The use of a biological metaphor to inspire new approaches does not necessarily imply that the biological side is well understood,
f) When seeking for an effective solution, it is important to identify the needs from engineering side and then try to match them with most effective biologically inspired solution(s) and find-out how best to implement them,
g) Biological systems are multifunctional and they cannot be optimized for any individual function separately. Hence, successful implementation of a particular biological function requires the ability to isolate irrelevant parts that do not contribute to the desired function.
h) Innovative solutions may require to consider the possibility of combining functions from different biological systems,
i) Biomimetic and bioinspiration demand to integrate biological materials and elements with man-made components/modules through bio-interfacing.

.

IV. Conclusions

By studying and analyzing biological systems, one may be able to derive or understand the relevant principles and use them to help solve engineering problems. However, the main challenge facing the development of biologically inspired actuators is the available technology, materials and the methods of fabrication as it is still in their infancy compared to nature's evolution. Biomaterials are expected to become the dominant focus of materials research, as it would lead to down-sizing of engineered components and the up-scaling incorporation of biomimetic concepts and processes. Finally, in order to achieve desirable lifelike motion, actuators must be able to reproduce the important features of natural muscle.

References

[1] Y. Bar-Cohen, "Biologically Inspired Intelligent Robotics", In Proceedings of the SPIE Smart Structures Conference, March 2003. Paper 5051-02,
[2] L. D. Paulson, "Biomimetic Robots", IEEE Computer, 2004, pp. 48-53.
[3] M. K. Habib, K. Watanabe, and K. Izumi, ""Biomimetics Intelligent Robots and Biological Inspiration", Int. Conf. on Control, Instrumentation and Mechatronics 'CIM'2007', Johor-Malaysia, 2007, pp. 824-832.
[4] R. G. Dennis and H. Hugh Herr, "Engineered Muscle Actuators: Cells and Tissues," In Biomimetics: Biologically Inspired Technologies Edited by Bar-Cohen, CRC Publisher, 2005, pp. 243-266.
[5] D. Popovic and T. Sinkjaer, "Control of movement for the physically disabled," Springer-Verlag, 2000.
[6] M. H. Dickinson, C.T. Farley, R.J. Full, M.A.R. Koehl, R. Kram, and S. Lehman. 2000. "How Animals Move: An Integrative View," *Science* 288, pp. 100–106.
[7] J. E. Clark, J. G. Cham, S. A. Bailey, E. M. Froehlich, P. K. Nahata, R. J. Full, and M. R. Cutkosky, "Biomimetic Design and Fabrication of a Hexapedal Running Robot," In Proceedings of IEEE ICRA'2001, Vol. 4, 2001, pp. 3643–3649.
[8] R. Pelrine, R. Kornbluh, Q. Pei, S. Stanford, S. Oh, J. Eckerle, R. Full, Ma. Rosenthal and K. Meijer, "Dielectric Elastomer Artificial Muscle Actuators: Toward Biomimetic Motion," In SPIE Conf. Proceedings, Smart Structures and Materials 2002, Vol. 4695, 2002, pp. 126-137.
[9] S. Ashley, "Artificial Muscles", Scientific American, 2003, pp. 52-59.
[10] A. M. Anderson, K. Streitlien, D. S. Barrett and M. S. Triantafyllou, "Oscillating Foils of High Propulsive Efficiency," Journal of Fluid Mech, Vol. 360, 1998, pp. 41-72.
[11] Unver, A. Uneri, A. Aydemir, and M. Sitti, "Geckobot: A Gecko inspired climbing robot using dry adhesives," In Proceedings of the IEEE ICRA'2006, 2006, pp. 2329-2335.
[12] Funakubo, H. (ed.) Shape Memory Alloys. Gordon and Breach: New York, 1987.
[13] I. W. Hunter, S. Lafontaine, J.M. Hollerbach and P.J. Hunter, "Fast reversible NiTi fibers for use in microrobotics," Proceedings IEEE Micro Electro Mechanical Systems, 1991, 2, 166-170.
[14] K. Ikuta, "Micro/miniature shape memory alloy actuator," Proceedings IEEE Micro Electro Mechanical Systems, 1990, 3, 2156-2161.
[15] T. M. Kubow and R. J. Full, "The Role of the Mechanical System in Control: A Hypothesis of Self-Stabilization in Hexapedal Runners," Philosophical Transactions of the Royal Society of London Series B-Biological Sciences, Vol. 354, No. 1385.1999, pp. 849–861.
[16] J.N. Barisci, G.M. Spinks, C.C. Wallace, J.D. Madden and R.H. Baughman, "Increased actuation rate of electromechanical carbon nanotube actuators using potential pulses with resistance compensation," Smart Materials and Structures, 2003, Vol. 12 , No. 4, pp. 549-555.
[17] G. Gu, M. Schmid, P.-W. Chiu, A. Minett, J. Fraysee, G.-T. Kim, S. Roth, M. Kozlov, E. Munoz & R. Baughman, "V2O5 nanofibre sheet actuators," Nature Materials, 2003, Vol. 2, pp. 316-319.

The Seventeenth International Symposium on Artificial Life and Robotics 2012 (AROB 17th '12),
B-Con Plaza, Beppu, Oita, Japan, January 19-21, 2012

Ubiquitous System and Application Networks

Young Im Cho

Dept. of Computer Science, The University of Suwon, Korea
(Tel: 82-31-229-8214, Fax: 82-31-229-8281)

ycho@suwon.ac.kr

Abstract: Many ubiquitous systems and technologies have been developed as of now. As known the goal of ubiquitous computing is to achieve the well-being life. There are four different aspects for achieving ubiquitous computing, namely, they are within the computing paradigm, technical principle, application domain and application space. Nowadays, ubiquitous city (U-City) is the most applicable domain in the world. Therefore, the talk will mainly introduce and discuss an overview of the U-City idea and the known ubiquitous computing systems as well as new trends in this field.

Keywords: Ubiquitous computing, intelligent system, smart computing, ubiquitous city

1 INTRODUCTION

Ubiquitous computing was started in 1984 by Mark Weiser in USA [1]. Ubiquitous computing is roughly the opposite of virtual reality**.** Usually, virtual reality puts people inside a computer-generated world, but ubiquitous computing forces the computer to live out here in the world with people. Virtual reality is primarily a horse power problem; ubiquitous computing is a very difficult integration of human factors, computer science, engineering, and social sciences. Ubiquitous computing is a post-desktop model of human-computer interaction in which information processing has been thoroughly integrated into everyday objects and activities.

The core technology of ubiquitous computing is an autonomic collaboration model for ubiquitous fusion services in ubiquitous computing environment. To do some action in ubiquitous computing, many elements coordinate to complete such action. Ubiquitous networking in ubiquitous computing is completed by the collaboration of many types of networks, city technologies, city sociology and governance.

Therefore, in this paper I will explain and the main technologies and applied services in ubiquitous computing, particularly within the developing aspect of ubiquitous cities. I will also give more details and explain in examples more about the new trends of ubiquitous computing at the present time and what is expected to take place in this area of research in the near future.

2 UBIQUITOUS COMPUTING PARADIGM

2.1 Ubiquitous essential elements

In Fig.1, in computerized generation, industrial society paradigm was popular. That means that making some products by industry was so important at that time.

After that as time goes by, in 'e' generation and 'u' generation, information society paradigm is more popular. That mans that information is very important thing.

Nowadays new paradigm is necessary. Smart society is dawning. If we disregard this changes or needs, we will degenerate from informatization ages. Smart paradigm is just an extension of ubiquitous paradigm, so called post-ubiquitous age.

Main keywords in new paradigm are the power of people, collective intelligence and new ecosystem. The power of people use Mobile device and social media increasing the power of people in life. Collective Intelligence is the creation of value by collective intelligence as well as collective power. New Ecosystem is the creation of additional value by new ecosystem using open as well as sharing.

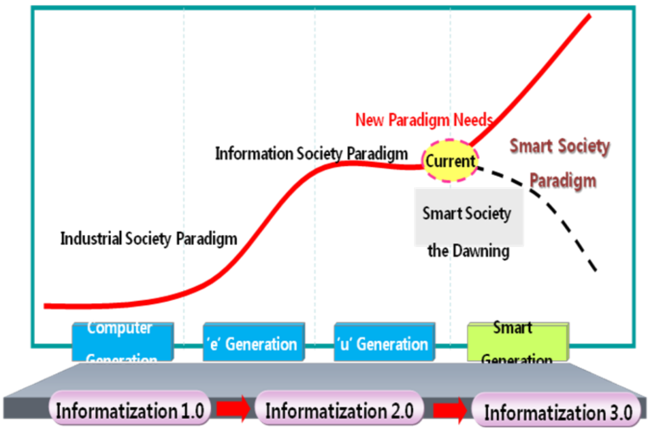

Fig.1. IT generation

Actually, the goal of ubiquitous computing is to make the safety, security and peace of mind society. The key technology to be a ubiquitous society is ubiquitous sensor network, in short USN. There are many application areas that use USN, such as home control, health medical care, welfare, hospital, school or education, traffic, culture, sports, environments, tracking of produce, anti-disaster, city security, etc.

Human will, in an ambient intelligent environment, be surrounded by intelligent interfaces supported by computing and networking technology that is embedded in everyday objects such as furniture, clothes, vehicles, roads and smart materials-even particles of decorative substances like paint. Ambient intelligent is the vision of the world in which different classes of smart players are proactively assisted by the environment [2].The environment is able to aware of the smart player's current situation and his interact within his environment and of its own current state. And then the interpretation of those occurrences into smart player's goals and accordingly into possible reactions is activated. The translation of the interpreted goal into strategies to adapt itself to the smart player's needs is performed in ubiquitous computing. Ubiquitous Space [2] is the space that objects collaborate seamlessly and automatically to achieve user's or community's goal for supporting u-Society and u-Life in Fig.2.

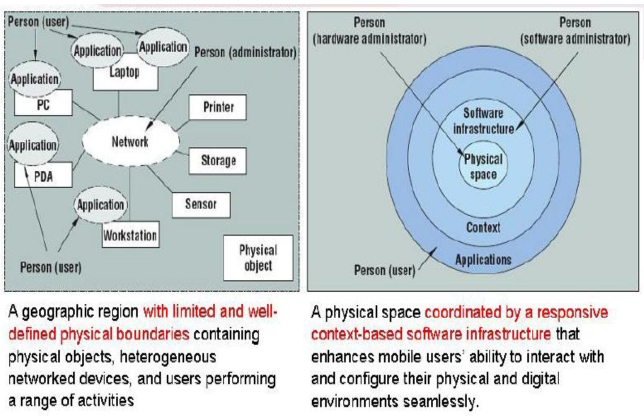

Fig. 2. Ubiquitous space

To be in intelligent ubiquitous system, there are three technical principles of ubiquitous space: infrastructure with situation-awareness, system with autonomic management, service with self-growing intelligence. Already, the mega trend goes with the ubiquitous scenario according to the suggestions given by Mark Weiser 20 years ago [1].

Before 21 the century, person-to-person is the mainstream of multimedia intelligence. After 2002, many devices using person-to-machine are developed for multimedia intelligence. Also many types of ubiquitous networked machine-to-machine devices are developed. Nowadays, in 4G, object-to-object mannered devices are developed for our convenience.

There are 4 types of viewpoints in ubiquitous computing in Fig.2. In the aspect of computing paradigm, the technology is changed from static community to automatic community. In the aspect of technical principle, the technology is changed from situation aware to self growing. However, in the aspect of application domain, the technology is changed from healthcare to environment preservation. The fourth aspect concerns the application space, the technology is changed from home or building to society.

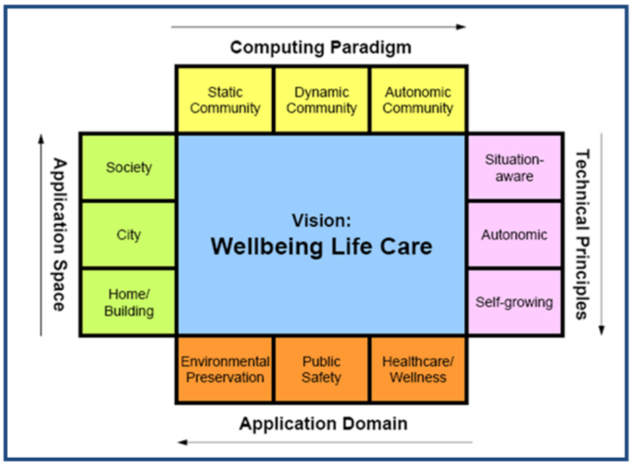

Fig.2. Ubiquitous goal

Recently, especially ubiquitous society, IT paradigm is shifting from hard tool to soft construction tool. Hard computing and soft computing have very different application areas. However, soft computing is more suited to ubiquitous computing than hard computing, because of the intelligent characteristics of ubiquitous computing.

2.2 Ubiquitous integrated control center and platform

All of organs or elements in a Human body are fully connected to compose a real Human. Likewise, from one building to a large building, every elements are connected to compose a city. If a man wants to do some action, many elements in a body coordinate to complete such action, even if we can see or not.

U-City is ubiquitous based City for service through City Integrated Center, for example u-transfortation, u-environment etc.

The main components of U-City are the integrated control center and platform.

Platform is the structure and law for easy transaction among groups. Usually U-City platform is as important as services. Platform is a system structure for information service of special area. The role of platform is like Fig.4. For communication between side A and side B, they have to have platform having architecture and some rule for protocol. If not, it is hard to communicate each other as well as share some information. The goal of U-City is for collaboration. To reach this goal, the platform should prepared first of all.

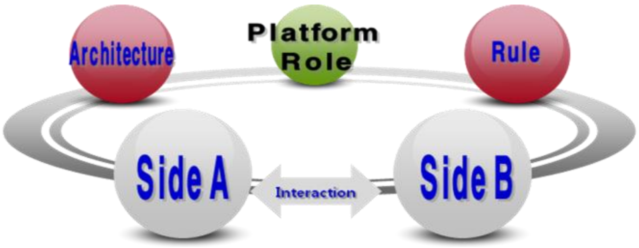

Fig.4. The role of U-City platform

The integrated control center is the place for providing the Integrated IT Infra environment by structuring of U-City IT elements. Definitely, the platform should prepare in the integrated control center.

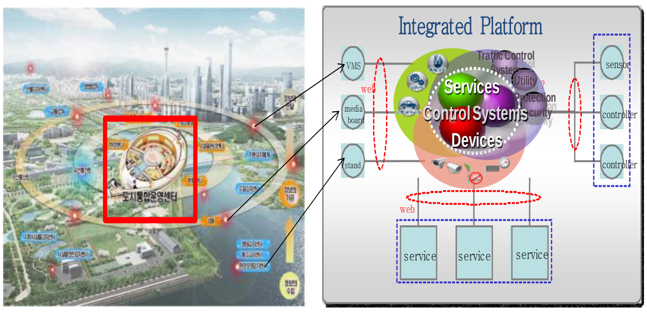

Fig.5. The U-City platform and integrated

What kind of services are provided or developed is as important as anything u-city construction. The row represents a classification by personal life in Fig.6, and the column represents a classification by land and facilities. From the list, you can choose U-city services for your purpose.

City Activities / City Spaces	1 Public Government	2 National Defense	3 Education	4 Medical & Health	5 Social Welfare	6 Culture & Sightseeing	7 Environment	8 Traffic	9 Agriculture	10 Manufacturing	11 Electrical equipment	12 Construction	13 Wholesale & retail	14 Lodging	15 Transportation	16 Network	17 Finance	18 Estate lease	19 Business service	20 Entertainment	21 Resort
A. Home	O	O	O	O		O		O	O	O	O			O			O		O		
B. Office	O	O	O	O				O		O						O		O	O		
C. Building		O									O					O			O		
D. Market & Store	O		O	O		O			O		O		O	O			O		O		
E. Park & green Zone			O		O	O	O	O													
F. Street	O			O	O	O		O					O		O					O	
G. School & Campus	O		O		O	O										O				O	
H. Hospital				O																	
I. Government & Public Offices	O	O					O									O					
J. Public Facilities	O	O	O	O	O	O	O				O	O				O					
K. Transportation	O	O	O	O	O	O	O	O	O			O	O	O	O						
L. Airport & Harbor	O	O		O	O			O	O	O				O	O		O				
M. Restaurant & Hotel				O		O															
N. Industrial Facilities	O	O		O		O	O	O		O		O	O						O		
O. Automobile								O							O						
P. Utility-Pipe Conduit	O																				
Q. Entertainment Facilities						O	O						O	O						O	
R. Land	O						O											O			
S. Agricultural District							O		O				O								

Fig.6. U-City services

The Fig.7 is about the comparison of the cost between with U-City and without U-City. In Fig.7(a), let the service construction cost of each building is 1million$ and service management cost is 1million$. Let 8 different services are here. In Fig.7, the circle typed numbers are specified U-City services.

If there are 4 buildings, the total cost will be 16million$(service construction cost is 8million$ + service management cost is 8million$).

However, if U-City integrated control center is used, the total cost will be reduced to 10.8million$(service construction cost is 6million$ + service management cost is 4.8million$). It makes about 32.5% reduction effect in U-City construction as well as management.

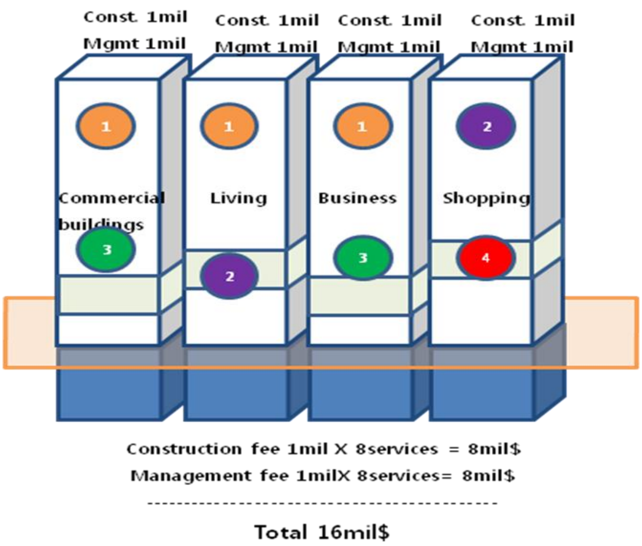

(a) Without U-City

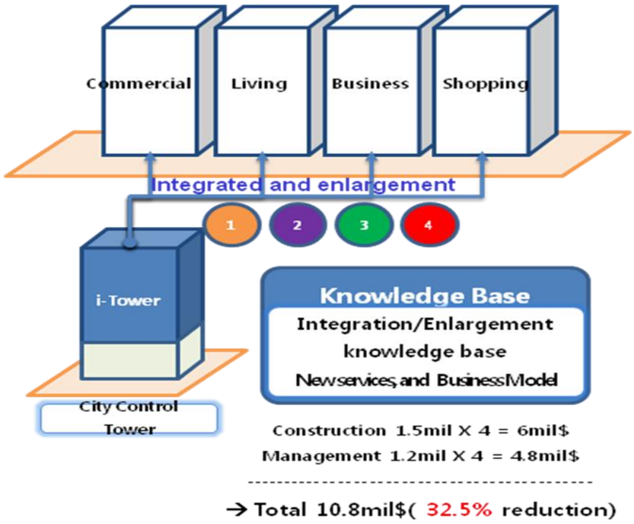

(b) With U-City

Fig.7. Comparison cost between with U-City and without U-City

3 UBIQUITOUS CITY AND FUTURE RESEARCH THEMES

Among many application areas, ubiquitous city, in short U-City, is the most applicable area. U-City is the constructed city by ubiquitous technologies and paradigm. To be the U-City, there are many ubiquitous services and hybrid technologies using RFID, USN, IPv6, sensing devices, monitoring, auto-control, real-time management etc. Usually, U-City is the same as smart city because smart has intelligent concept.

There are some examples of U-City like the media hub city and cool town in Singapore, cyber port in Hong Kong, Finland as well as Korea [3].

The U-City application service models are still being developed. I would suggest some matrix style service model according to the classification by personal life as well as the classification by land and facilities. The details will be given in my talk at the conference,

In the future we still need to develop what has already been done so far. The first theme is the research about the infra structure of U-City such as platform, security, pattern, service scenario etc. The second theme is the research about the paradigm of `U-City such as role play between government and local government to perform U-City etc. The third theme is the research about the consulting of U-City such as the best service model according to many types of organs, and business model, and so on.

As a result, ubiquitous society is a combination of safety and security for the sake of peaceful society. Now, many services of IT mobile devices are provided with personalized manners. For completion of real ubiquitous space through U-City, the standard model and some platforms should be a prerequisite condition for success.

4 CONCLUSION

Firstly, I explained about IT paradigm shift. Main keywords in IT changes are the power of people, collective intelligence, and new ecosystems.

Secondly, I explained is about ubiquitous society. Real as well as virtual world are combined to be the safe, security, peace of mind society

Finally, I explained about inevitable IT trend. For completion of real ubiquitous space through U-City, the standard model and some platforms should be a prerequisite condition.

Now we are going to cloud and computing. So we have to adopt to the changes and develop some appropriate services and paradigm.

References

1. Young Im Cho (2008), U-Society and U-Convergence Paradigm, 2008 Asia Pacific Woman Leaders Forum for Science & Technology, Sep.3, pp.183-204
2. Manuel Roman et al (2002), A Middleware Infrastructure for Active Spaces, IEEE pervasive computing
3. Young Im Cho (2008), Practical Approaches for Ubiquitous Convergence System, Joint 4th International Conference on Soft Computing and Intelligent Systems and 9th International symposium on Advanced Intelligent Systems, Sep.17-21

Simultaneous optimization of path planning and flow shop scheduling by bacterial memetic algorithm

János Botzheim[1,2], Yuichiro Toda[2], and Naoyuki Kubota[2]

[1] Department of Automation, Széchenyi István University, 1 Egyetem tér, H-9026 Győr, Hungary
[2] Graduate School of System Design, Tokyo Metropolitan University, 6-6 Asahigaoka, Hino, Tokyo, 191-0065 Japan
[1] botzheim@sze.hu

Abstract: The paper deals with simultaneous optimization of path planning of mobile robots and flow shop scheduling problem. The goal of the path planning problem is to determine an optimal collision-free path between a start and a target point for a mobile robot in an environment surrounded by obstacles. The objective is to minimize the path length without colliding with an obstacle. On the other hand, shop scheduling problems deal with processing a given set of jobs on a given number of machines. Each operation has an associated machine on which it has to be processed for a given length of time. The problem is to minimize the makespan, i.e., the overall time demand of the whole process. In this paper we deal with two robots carrying items between the machines. Bacterial memetic algorithm is proposed for solving the problem.

Keywords: path planning, flow shop scheduling, memetic algorithm

1 INTRODUCTION

Path planning is an essential task in mobile robotics. The goal is to find an optimal, collision-free path between a start and a target point for a mobile robot in an environment composed of walls and obstacles. The objective is to minimize the path length without colliding with an obstacle. Sometimes the optimization of the smoothness of the path (i.e., the number of robots turns) is also a goal of the path planning problem. For its practical importance many approaches have been suggested in the literature [1, 2].

In shop scheduling problems there are n jobs to be processed on m machines. There is a matrix specifying how much time needed for a job to be processed on a given machine. The processing times of operations of a job cannot overlap. Each machine can process at most one operation at a given time. In case of flow shop scheduling problems the number of operations of each job is the same as the number of machines (one operation per machine), and the order in which they must be processed is same for all the jobs [3, 4]. The problem is to minimize the makespan, i.e., the overall time demand of the whole process.

The above problems belong to the group of hard combinatorial optimization problems which can be approached by modern optimization techniques such as evolutionary algorithms. Evolutionary algorithms can explore large search spaces, however, their convergence speed is low. By incorporating problem domain knowledge the evolutionary process can be accelerated converging faster to the global optimum. Memetic algorithms combine evolutionary algorithms with local search heuristics in order to speed up the evolutionary process. In this paper the Bacterial Memetic Algorithm (BMA) is proposed for solving the path planning and flow shop scheduling problem simultaneously. We apply two robots making the optimization problem even more complicated.

In the next section we describe the problem. Section 3 presents our proposed algorithm. Simulation experiments are shown in section 4. Section 5 draws the conclusions of the paper.

2 PROBLEM STATEMENT

In case of flow shop problems there is more than one machine and each job must be processed on each of the machines. The number of operations for each job is equal to the number of machines. The processing order of the operations of the job is predefined and it is the same for each job. In case of permutation flow shop problems the machines process the jobs in the same order, so the order of the jobs on each machine is the same. The task here is to find a permutation of the jobs which permutation will fit on every machine. There are n jobs, m machines and two robots. The inputs of the problem are the map with obstacles and machines, and a matrix containing the processing time for each job on each machine. There are three subproblems:

- Finding the permutation of jobs
- Task assignment for the robots
- Path planning for the robots with collision avoidance

The machines are processing the jobs, while the robots are carrying the items between the machines. After a job is finished on a machine the job will be carried to the next machine by one of the two robots. The job can be processed on this next machine only after the robot is reached the machine with the job related items and the previous job according to the schedule on the machine is already finished. Thus the results of the problem will be the schedule of the jobs, the task assignment for the robots explaining which job (item) has to be carried by which robot between two given machines, and the paths for the robots in order they can find an optimal, collision-free way between the machines.

The goal is to minimize the makespan, i.e., the completion time of the whole process. The time consists of the jobs' processing time on the machines and the time needed for the robots for carrying items from one machine to another one. We use cell decomposition based map for the path planning and we assume that the time needed for the robot from one cell to a neighboring cell is one unit, and the processing times in the processing time matrix are in the same unit. A collision means that the two robots occupy the same cell on the map except the positions of the machines where we assume that the two robots can be together at the same time. In order to calculate the makespan considering the difficulty of the whole scenario we need state matrices describing the states of the machines, the current job times on the machines and the states of the robots. We also developed a visualization software to illustrate the scenario.

3 THE PROPOSED ALGORITHM

Nature inspired evolutionary optimization algorithms are often suitable for global optimization of even non-linear, high-dimensional, multi-modal, and discontinuous problems. Bacterial Evolutionary Algorithm (BEA) [5] is one of these techniques. BEA uses two operators, the bacterial mutation and the gene transfer operation which are based on the microbial evolution phenomenon. The bacterial mutation operation optimizes the chromosome of one bacterium; the gene transfer operation allows the transfer of information between the bacteria in the population. Each bacterium represents a solution for the original problem.

Evolutionary algorithms are global searchers, however in most cases they give only a quasi-optimal solution to the problem, because their convergence speed is low. Local search approaches can give a more accurate solution, however they are searching for the solution only in the neighborhood of the search space. Local search approaches might be useful in improving the performance of the basic evolutionary algorithm, which may find the global optimum with sufficient precision in this combined way. Combinations of evolutionary and local-search methods are usually referred to as memetic algorithms [6]. A new kind of memetic algorithm based on the bacterial approach is the bacterial memetic algorithm (BMA) proposed in [7]. The method can be applied for path planning problem of mobile robots [8] and for the traveling salesman problem [9] which is similar to the flow shop scheduling problem.

The algorithm consists of four steps. First, a random initial population with N_{ind} individuals has to be created. Then, bacterial mutation, local search and gene transfer are applied, until a stopping criterion (number of generations, N_{gen}) is fulfilled.

3.1 Encoding method and evaluation

When applying evolutionary type algorithms first of all the encoding method must be defined. The evaluation of the individuals (bacteria) has to be discussed, too. The operations of the algorithm have to be adapted to the given problem. The evaluation of a solution can be done by state matrices as mentioned above. The encoding of the problem is illustrated in Fig. 1.

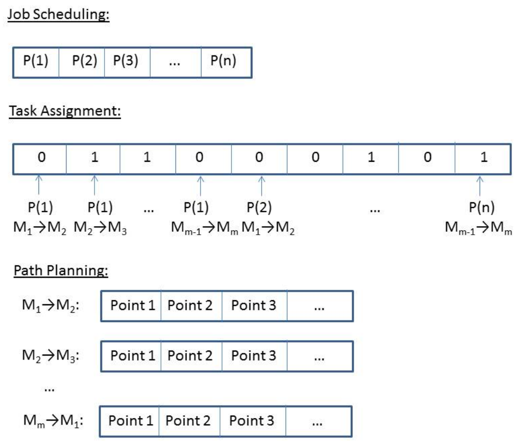

Fig. 1. Encoding

In Fig. 1 we can see the three different subproblems. In the permutation flow shop scheduling problem one individual corresponds to one job permutation. $P(1), P(2) \ldots P(n)$ in Fig. 1 means a possible permutation of the jobs. In the task assignment problem the transportation tasks are assigned to the robots. There are n jobs and $m-1$ transportation tasks for each job (from the first machine to the second, from the second to the third etc.), so $n \cdot (m-1)$ is the chromosome length in case of task assignment problem. The zeros in the chromosome refer to one of the robots while the ones refer to the other robot. In case of path planning there are lots of different path planning tasks. The robots can move not only from machine i to machine $i+1$ because the robots also have to come back empty for starting their next task. The total number of possible path planning tasks is $(m-1) \cdot (m+2)/2$. In case of three machines, the following five paths have to be planned: $M1 \to M2$, $M2 \to M3$, $M2 \to M1$, $M3 \to M1$, $M3 \to M2$. In the path planning problems the chromosome contains intermediate points between the start and target points. The length of the chromosome of the path planning subproblem can change during the evolutionary process. Not every neighboring points are stored in the chromosome, only some intermediate points, and between this intermediate points the path is linearly approximated based on the cells on the map [8]. The paths can be evaluated independently from each other and from the other two chromosome parts related to the job permutation and task assignment. The evaluation of a path is based on the number of neighboring cells the path covers from the start point to the target point, on the number of collisions with obstacles and on the number of turns, i.e., number of direction change of the robot [8]. This evaluation gives an idea about how good is the path alone, however the different chromosome types have to be used together in order to evaluate a solution for the whole problem.

3.2 Bacterial mutation

To find a global optimum, it is necessary to explore new regions of the search space not yet covered by the current population. This is achieved by adding new, randomly generated information to the bacteria using bacterial mutation.

Bacterial mutation is applied to all bacteria one by one. First, N_{clones} copies (clones) of the bacterium are created. Then, a random segment of length l_{bm} is mutated in each clone except one clone which is left unmutated. After mutating the same segment in the clones, each clone is evaluated. The clone with the best evaluation result transfers the mutated segment to the other clones. These three steps operations (mutation of the clones, selection of the best clone, transfer of the mutated segment) are repeated until each segment of the bacterium has been mutated once. When a clone is mutated the other kinds of chromosomes are left unchanged. For example if the chromosome related to the job permutation is mutated in a job permutation type clone, then the other kinds of chromosomes do not change during this time. In case of the path planning subproblem the mutation may not only change the content, but also the length. The length of the new elements is chosen randomly as $l_{bm} \in \{l_{bm}-l^\star, \ldots, l_{bm}+l^\star\}$, where $l^\star \geq 0$ is a parameter specifying the maximal change in length. At the end, the best clone is kept as the new bacterium and the other clones are deleted. The mutation in a permutation type individual alters the segment of the individual by producing a random permutation on the segment. The segment do not need to consist of consecutive elements [9]. The mutation in the binary type individual randomly changes the bits in the mutated segment. In the integer type individual the numbers are changed in the possible interval (positions in the map) and when changing a segment of a clone, we must take care that the new segment is unique within the clone.

3.3 Local search

Local search is performed between the bacterial mutation and the gene transfer operators. The local search has a probability, which is a parameter reflecting the chance for a bacterium to be local searched in a given generation. Too frequent local search can drive the population into local optimum, but if its probability is too small then it will not sufficiently accelerate the evolutionary process.

In case of path planning type chromosome four different local search strategy is proposed [8]. The insertion inserts a new point between those two intermediate points where the insertion has the biggest benefit. The deletion deletes that point from the individual which removal's has the biggest benefit. The swap operation tries to swap each pair of consecutive points in the individual's chromosome. The local improvement tries to improve each point in the chromosome in a given radius, which is a parameter of the algorithm.

In case of the job permutation and task assignment type chromosomes the swap operation is applied.

3.4 Gene transfer

The bacterial mutation operator optimizes the bacteria in the population individually. To ensure the information flow in the population, gene transfer is applied.

First, the population must be sorted and divided into two halves according to their evaluation results. The bacteria with better result are called superior half, the bacteria with worse result are referred to as inferior half. Then, one bacterium is randomly chosen from the superior half and another from the inferior half. These two bacteria are called the source bacterium, and the destination bacterium, respectively. A segment of length l_{gt} from the source bacterium is randomly chosen and this segment overwrites a random segment of the destination bacterium. The above steps (sorting the population, selection of the source and destination bacteria, transfer the segment) are repeated N_{inf} times, where N_{inf} is the number of "infections" per generation.

In contrast with the bacterial mutation, in the gene transfer in case of the permutation problem, the segment can contain only consecutive elements within the bacterium. The reason for that is the segment containing consecutive elements representing sub-scheduling in the bacterium, and transferring good sub-scheduling is the main goal of the gene transfer operation.

4 SIMULATION RESULTS

In the simulation experiment we used 10 jobs and 3 machines with the processing time matrix presented in Table 1.

The map size is 20×20 and can be seen in Fig. 2, where the optimal solution is illustrated with the simulator program.

In Fig. 2 the black cells are obstacles or walls, the blue cells are the machines, and the red and orange cells are the robots. We can also see the current job time matrix and the state matrix used for the evaluation. In the simulation we

Table 1. Processing time

	M1	M2	M3
J1	17	23	18
J2	16	18	25
J3	21	19	23
J4	19	27	26
J5	28	17	21
J6	18	26	19
J7	26	20	22
J8	24	24	24
J9	20	21	22
J10	19	22	20

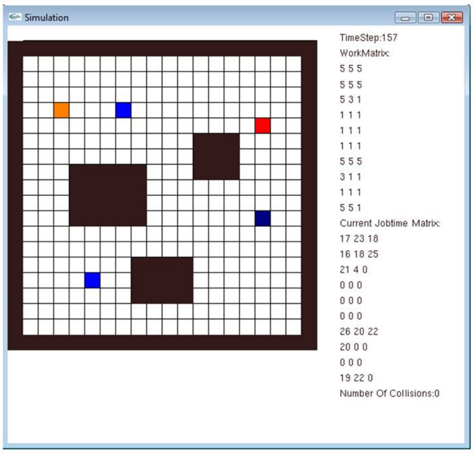

Fig. 2. Simulation

applied 25 generations, 25 bacteria, 5 clones and 5 infections in case of path plannings and 3 clones and 5 infections in case of job permutation and task assignment. The mutation and infection segment lengths are 2 in case of path plannings and 3 for the other two types. The local search probability is 20%. The collision penalty between robots is 10, which means that for every collision of the robots 10 time unit is added to the solution as penalty. The average of best solutions based on 10 simulations for the makespan is 379.7, the best is 376, the worst is 383. In the best solution the job permutation is (2,1,6,8,4,3,10,9,7,5) and the task assignment is 00101010101100101011. The path lengths are 19,18,19,17,18, respectively.

5 CONCLUSION

In this paper the bacterial memetic algorithm was proposed for simultaneous optimization of path planning and flow shop scheduling in case of two robots. The algorithm effectively combines the bacterial operators with local search heuristics and can speed up the evolutionary process in this way. The operators can handle different type of encodings at the same time, like permutation type chromosome, binary, and integer encoding.

Our future work is to extend the technique for more than two robots and for other kind of shop scheduling problems, too.

Acknowledgements – The research was supported by Universitas-Győr Foundation in the framework of TÁMOP 4.1.1/A-10/1/KONV-2010-0005 Programme.

REFERENCES

[1] Amir Hosseinzadeh and Habib Izadkhah. Evolutionary approach for mobile robot path planning in complex environment. *International Journal of Computer Science Issues*, 7(8), 2010.

[2] Jing Xiao, Zbigniew Michalewicz, Lixin Zhang, and Krzysztof Trojanowski. Adaptive evolutionary planner/navigator for mobile robots. *IEEE Transactions on Evolutionary Computation*, 1(1):18–28, 1997.

[3] J. Grabowski and J. Pempera. The permutation flowshop problem with blocking. A tabu search approach. *The International Journal of Management Science*, 35:302–311, 2007.

[4] M. Mirabi and M. D. Ashkezari. Application of hybrid meta-heuristic approach to solve flow-shop scheduling problem. *Australian Journal of Basic and Applied Sciences*, 5(10):93–98, 2011.

[5] N. E. Nawa and T. Furuhashi. Fuzzy system parameters discovery by bacterial evolutionary algorithm. *IEEE Transactions on Fuzzy Systems*, 7(5):608–616, Oct. 1999.

[6] P. Moscato. On evolution, search, optimization, genetic algorithms and martial arts: Towards memetic algorithms. Technical Report Caltech, Pasadena, California, USA, 1989.

[7] J. Botzheim, C. Cabrita, L. T. Kóczy, and A. E. Ruano. Fuzzy rule extraction by bacterial memetic algorithms. In *Proceedings of IFSA 2005*, pages 1563–1568, Beijing, China, 2005.

[8] J. Botzheim, Yuichiro Toda, and Naoyuki Kubota. Path planning for mobile robots by bacterial memetic algorithm. In *Proceedings of IEEE SSCI 2011*, pages 107–112, Paris, France, 2011.

[9] P. Földesi, J. Botzheim, and L. T. Kóczy. Eugenic bacterial memetic algorithm for fuzzy road transport traveling salesman problem. *International Journal of Innovative Computing, Information and Control*, 7(5(B)):2775–2798, 2011.

The Seventeenth International Symposium on Artificial Life and Robotics 2012 (AROB 17th '12),
B-Con Plaza, Beppu, Oita, Japan, January 19-21, 2012

Lateral Controller Design for an Unmanned Vehicle via Kalman Filtering

Man Hyung Lee[1], Hyung Gyu Park[1], Kil Soo Lee[1], Young Chul Cha[1], Dong Jin Kim[1], Byung Il Kim[2], Sinpyo Hong[3], Ho Hwan Chun[3], Bong Jin Lee[4] and Yun Ja Lee[4]

[1]Graduate School of Mechanical Engineering, Pusan National University, Busan, 609-735, Korea
[2]Powertrain CAE Team, Powertrain Center, Hyundai Motor Company, Korea
[3]Advanced Ship Engineering Research Center, Pusan National University, 609-735, Busan, Korea
[4]Department of Dance, Pusan National University, Busan, 609-735, Korea

[1]mahlee@pusan.ac.kr, gyunious@pusan.ac.kr, melgibsoo@pusan.ac.kr, mecha-cha@pusan.ac.kr, tntno9@nate.com
[2]taranis@hanmail.net,
[3]sinpyo59@paran.com, chunahh@pusan.ac.kr,
[4]bongbong486@hanmail.net, leeyj@pusan.ac.kr

Abstract: This paper proposes a lateral control system for an unmanned vehicle to improve the responsiveness of the system with a PD control. Heading error can be stabilized and the transient response characteristics can be improved with the controller. In this paper, a mathematical modeling of the vehicle dynamics using two degrees of freedom is used for the controller design. Waypoint tracking method of autonomous navigation was done with the Point to Point algorithm with position and heading measurements from GPS receivers via Kalman filtering. Performance of the designed controller was verified through experiment with a real vehicle**.**

Keywords: Lateral control, PD controller, Unmanned vehicle, P to P algorithm, Kalman filtering.

1 INTRODUCTION

Even though societies have become more convenient with the rapid development of transportation, traffic congestion and accidents are increasing the seriousness of the traffic problems. The cause of most accidents is considered to be the carelessness of an individual. So safety-devices to prevent accidents are being developed [1], [6]. Research and development of unmanned vehicles are also being conducted in many countries [2], [3], [5], [7].

In this paper, a lateral control method using a proportional-derivative (PD) controller for point to point (P to P) driving is studied. In proportional controllers for P to P navigation, the heading angle error is used to determine the steering value. However, stable driving is not guaranteed with this controller due to the rapid changes of the steering value near the waypoints which are renewed along the path.

PD controller can stabilize steering motions and reliable driving can be expected with it. In the main part of this paper, two wheel steering (2WS) model and PD-controller design is described. PD-controller and P-controller are applied to unmanned waypoint tracking experiments and test results are analyzed and compared.

Due to the excellent navigation results of the designed PD controller, this system was used to compare the existing GPS and Kalman filtering systems. To improve the precision of the unmanned vehicle navigation, results of GPS signals reception and results of the signal reception combined with Kalman filtering were analyzed.

2 2WS MODEL

In 2WS model, the car has two front steering wheels while the rear wheels are fixed. According to general steering characteristics of the car when driving [4] a linear model of two degrees of freedom can be used to obtain accurate results if the lateral acceleration is less than 0.4G. The linear model uses lateral displacement and yaw to describe the mechanical system. Since a 2WS vehicle model is used in this study, the roll and pitch motions and the difference between the yaw directions of the wheels are ignored in the controller design.

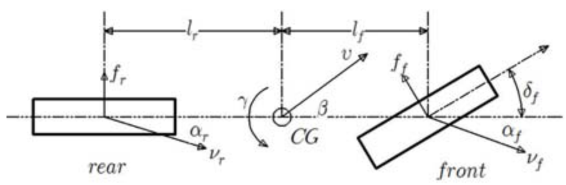

Fig. 1. 2WS bicycle model

Slip angles α_f and α_r can be calculated with the speed of vehicle υ, distances of the front-wheel and rear-wheel from the center of gravity l_f and l_r, yaw rate γ, lateral velocity of the center of gravity ν, rear-wheel steering angle δ_r, and front-wheel steering angle δ_f as shown in Fig. 1 such that

$$\alpha_f = \delta_f - \frac{\nu + \gamma l_f}{\upsilon} \tag{1}$$

$$\alpha_r = \delta_r - \frac{\nu + \gamma l_r}{\upsilon} \tag{2}$$

Since a linear tire model is used, the cornering forces f_f and f_r acting on the front tire and rear tire can be calculated as

$$f_f = c_f \cdot \alpha_f \tag{3}$$

$$f_r = c_r \cdot \alpha_r \tag{4}$$

where c_f and c_r are the cornering stiffnesses. Therefore, using equations (3) and (4), the equations of vehicle motion can be derived from the equilibrium conditions of the vehicle's lateral and yaw moment as follows:

$$m(\dot{\nu} \quad \cdots \quad {}_f \cdot \alpha_f + c_r \cdot \alpha_r \tag{5}$$

$$J\dot{\gamma} \quad \cdots \quad \alpha_f - c_r \cdot l_r \cdot \alpha_r \tag{6}$$

where m is the mass of the vehicle and is the vehicle's yaw moment of inertia. From equations (1), (2), (5), and (6), linear equations of motion can be expressed as follows:

$$\dot{} \quad \cdots \quad t) + Bu(t)$$

$$x(t) = \left\{ \frac{\nu}{\gamma} \right\}, \qquad u(t) = \left\{ \frac{\delta_f}{\delta_r} \right\}$$

$$A = \begin{bmatrix} a_{11} & a_{12} \\ a_{21} & a_{22} \end{bmatrix}, \qquad B = \begin{bmatrix} b_{11} & b_{12} \\ b_{21} & b_{22} \end{bmatrix} \tag{7}$$

$$\begin{bmatrix} \dot{\nu} \\ \dot{\gamma} \end{bmatrix} = \begin{bmatrix} \cdots & a_{12} \\ \cdots & a_{22} \end{bmatrix} \begin{bmatrix} \nu \\ \gamma \end{bmatrix} + \begin{bmatrix} b_{11} & b_{12} \\ b_{21} & b_{22} \end{bmatrix} \begin{bmatrix} \delta_f \\ \delta_r \end{bmatrix} \tag{8}$$

with

$$b_{11} = -\frac{(c_r + c_f)}{m\upsilon}, \quad b_{12} = -\frac{(c_r l_f + c_r l_r)}{m\upsilon} - \upsilon$$
$$b_{21} = -\frac{(c_r l_f + c_r l_r)}{J\upsilon}, \quad b_{22} = -\frac{(c_r l_f^2 + c_r l_r^2)}{J\upsilon} - \upsilon \tag{9}$$

$$b_{11} = \frac{c_f}{m}, \qquad b_{12} = \frac{c_r}{m}$$
$$b_{21} = \frac{c_r l_f}{J}, \qquad b_{22} = -\frac{c_r l_r}{J} \tag{10}$$

In the four wheel steering system, to increase the response during fast speed driving, the rear wheel is steered in-phase with the front wheel. During low speed, to increase the maneuverability, the rear wheel is steered anti-phase of the front wheel.

In this study, when the vehicle navigates at low or equal speed, the revolving radius is reduced and to increase the maneuverability, the anti-phase steering system is used. The equivalent of the front wheel steering value is the anti-phase of rear wheel steering. The multi-input multi-output (MIMO) system, Eq. (8), where input values of δ_f, are entered independently, can be simplified into single input single output(SISO) system of Eq. (11). Where δ_{fr} is $\delta_f - \delta_r$ because of assuming to the anti-phase steering system. In this study to obtain the position of vehicle, θ is gained with Eq. (12) and output $y(t)$ is given by Eq. (14).

$$\begin{bmatrix} \dot{\nu} \\ \dot{\gamma} \end{bmatrix} = \begin{bmatrix} \cdots & a_{12} \\ \cdots & a_{22} \end{bmatrix} \begin{bmatrix} \nu \\ \gamma \end{bmatrix} + \begin{bmatrix} b_{11} - b_{12} \\ b_{21} - b_{22} \end{bmatrix} \begin{bmatrix} \delta_{fr} \end{bmatrix} \tag{11}$$

$$\dot{\theta} \quad \cdots \tag{12}$$

$$\begin{bmatrix} \dot{\nu} \\ \dot{\gamma} \\ \dot{\theta} \end{bmatrix} = \begin{bmatrix} \cdots & a_{12} & 0 \\ \cdots & a_{22} & 0 \\ \cdots & 1 & 0 \end{bmatrix} \begin{bmatrix} \nu \\ \gamma \\ \theta \end{bmatrix} + \begin{bmatrix} b_{11} - b_{12} \\ b_{21} - b_{22} \\ 0 \end{bmatrix} \begin{bmatrix} \delta_{fr} \end{bmatrix} \tag{13}$$

$$y(t) = [0 \quad 0 \quad 1][\upsilon \quad r \quad \theta]' + \nu(t) \tag{14}$$

Here $\nu(t)$ is (0, R) and R is 5cm.

3 PD-CONTROLLER DESIGN AND IMPLEM ENTATION OF KALMAN FILTERING

PD-Controller reduces controller errors effectively since the error rate is taken into account in the controller. As a result, the damping ratio is increased and the overshoot is suppressed. Considering the effect of these differential controls in the controller design, the system can improve the transient response characteristics. Transfer function $K(s)$ of controller is

$$K(s) = K_p(1 + T_d s) \tag{15}$$

The Table 1 shows the dynamic parameters of the unmanned vehicle.

Table 1. Unmanned Vehicle Parameters

Parameter	Value
$m(kg)$	2,055
$\upsilon(m/s)$	2.78~8.33

$J(kgm^2)$	2568.75
$c_f(kN/rad)$	74.1
$c_r(kN/rad)$	62.2
$l_f(m)$	1.158
$l_r(m)$	1.737
$L(m)$	2.895

4 EXPERIMENTS

In this study, a PD-controller is applied to a two-wheel steering unmanned vehicle. P to P driving algorithms using P and PD controllers are experimentally compared. A general vehicle can run on curved paths with the speed of 20km/h without exceeding the lateral acceleration of 0.4G if the maximum steering angle is less than 20 degrees.

Fig. 2 shows the vehicle used in the experiment, and driving tests were carried out with it at the speeds of 10km/h and 20km/h. The vehicle used in the experiments was a Hyundai-Kia MOHAVE. The experiments were conducted in the school field. GPS measurements were obtained in the experiments in which the vehicle was running on an elliptical course.

Fig. 2. Equipment used in the experiment

The waypoints to be passed by the vehicle were prepared with DGPS. Tests were conducted with various driving speeds from 10km/h to 20km/h. The resulting vehicle traces were compared with the waypoints.

Table 2. Error values of unmanned vehicle to reference path

Test Controller / Velocity	P Controller		PD Controller	
	Maximum Error	RMS Error	Maximum Error	RMS Error
10km/h	0.56 m	0.54 m	0.47 m	0.38 m
20km/h	1.94 m	1.06 m	0.94 m	0.51 m

Table 3. Specifications of gyro Sensor.

Specification	Value
Range: Yaw(°/sec)	±100
Bias: Yaw (°/sec)	< ±1.0
Scale Factor Accuracy(%)	< 1
Non-Linearity(% FS)	< 0.3
Resolution (°/sec)	< 0.025
Bandwidth (Hz)	> 25
Random Walk (º $/hr^{1/2}$)	< 2.25
Operating Temperature(º C)	-40 to +70
Non-Operating Vibration (g rms)	6
Non-Operating Shock (g)	1000

The last test is executed with the IMU and position is calculated with dead-reckoning. Fig. 3 shows the results of the path positioning tests along the reference path.

Table 4 represents the maximum error and the root mean square (RMS) error values of path tracking tests using GPS and Kalman filtering in the test area shown in Fig. 4 with the speed of 30km/h. Kalman filtering method has improved the maximum error by 400% and the RMS error by 20% compared to those of using GPS.

Table 4. Tracking errors of tests using GPS and kalman filtering to unmanned vehicle at 30km/h, respectively

Test / Velocity	GPS		Kalman Filtering	
	Maximum Error	RMS Error	Maximum Error	RMS Error
30km/h	3.93 m	0.64 m	0.77 m	0.54 m

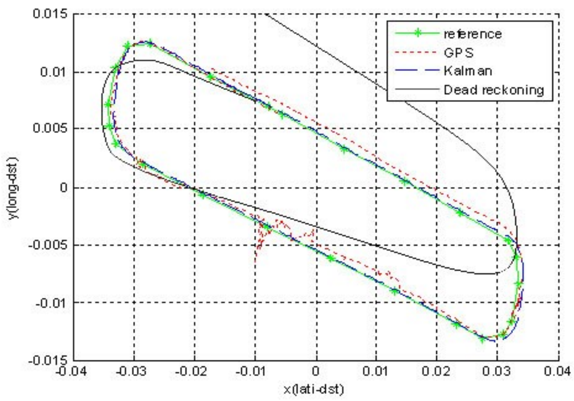

Fig. 3. Experimental results of positioning tests

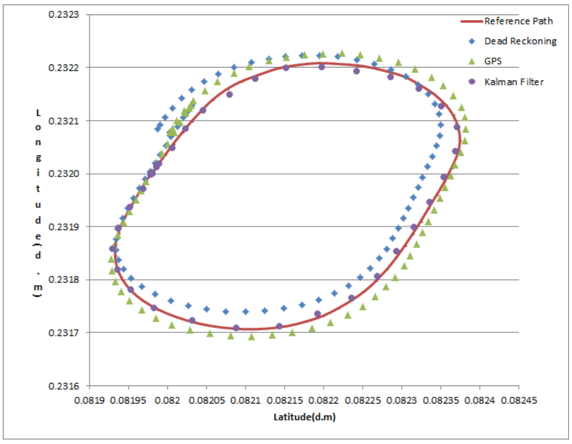

Fig. 4. Experimental results of the downtown in busan

Table 5. Tracking errors of rest using dead reckoning, GPS and kalman filtering to unmanned vehicle 30km/h at downtown, respectively

Test / Velocity	Dead Reckoning		GPS		Kalman Filtering	
	Maximum Error	**RMS Error**	**Maximum Error**	**RMS Error**	**Maximum Error**	**RMS Error**
30km/h	9.75 m	5.78 m	3.85 m	1.5 m	0.42 m	0.25 m

In navigations using only dead reckoning, the errors increased in the recognition of the standard path as time passed. Comparing the navigation trail when using only the GPS and that of the Kalman filter, the Kalman filter trail was found to be closer to the standard path in Table 5. When the allowable error was established to be 0.45m half radius, which considered the width of the vehicle(1.915m), the Kalman filter navigated the path within the acceptable error range of test results in Table 5.

5 CONCLUSION

When the waypoints and the traces of the vehicle obtained from the tests were compared, the turning radii of the traces were larger than those of waypoints. This error seemed to occur because the dynamic elements of the vehicle were not properly considered. In the future research the dynamic elements of the vehicle need to be reflected in the controller design so that reliable path tracking can be performed with various vehicle velocities.

In this paper, we suggest an autonomous vehicle's positioning method for navigation system. To get successful operation, the position and heading angle measurements are necessary. Positioning with GPS or dead reckoning with does not guarantee successful operation. GPS and dead reckoning both have error elements. GPS measurements are sensitive to environment conditions. Dead reckoning produces error that increases with time due to sensor errors.

For successful operation of navigation system, a Kalman filtering of positioning sensor measurements is suggested in this paper. Positioning with Kalman filter is more accurate than that using GPS or IMU dead reckoning. GPS can compensate the error accumulation of dead reckoning. Test results indicate good performances with the Kalman filter.

At 30km/h of unmanned driving, the Kalman filtering method reduces the error by 20% compared to the existing GPS method. Based on this study, unmanned drive testing at 50km/h has been successful in the test area (Hyundai Kia Motors Namyang Institute, Jangdeok-dong, Hwaseong-si, Gyeonggi-do, Korea) and is now being tested around downtown in the Busan area.

REFERENCES

[1] Choi, J. H. (2006). Wheel Slip Control of ABS Using Adaptive Control Method, Journal of the Korean Society of Manufacturing Process Engineers, 5, 3, 71~79.

[2] Lee, M. H., Lee, K. S., Park, H. G., Chun, H. H. and Ryu, J. H. (2010). Robust Lateral Controller for an Unmanned Vehicle via a System Identification Method, Journal of Mechanical Systems for Transportation and Logistics, 3, 3, 504~520.

[3] Lee, Y. H., Kim, S. I., Suh, M. W., Son, H. S. and Kim, S. H. (1994). Linearized Dynamic Analysis of a Four-wheel Steering Vehicle, The Korean Society of Automotive Engineers, 2, 5, 101~109.

[4] Lee, M. H., Bae, J. I., Yoon, K. S. and F. Harashima (2000). Real Time and an In-Process Measuring System for the Grinding Process Cylindrical Workpieces Using Kalman Filtering, IEEE Transactions on Industrial Electronics, 47, 6, 1326-1333.

[5] Moon, H. C., Kim, C. M. and Kim, S. G. (2001). The Research for the Vision System of Tele-operated Unmanned Vehicle, The Korean Society of Automotive Engineers, 2, 1316~1323.

[6] Oh, Y. R., Lee, H. J. and Park, Y. P. (2007). A Study on Validation of Braking Performance Considered ABS Friction Characteristics, The Korean Society of Automotive Engineers, 2, 884~889.

[7] Um, J. Y. and Lee, I. S. (2004). A Study for DGPS Navigation System for an Autonomous Vehicle, The Korean Society of Automotive Engineers, 3, 1179~1188.

Unmanned Container Transporter via Pseudolite Ultrasonic System

Man Hyung Lee[1], Kil Soo Lee[1], Young Chul Cha[1], Dong Jin Kim[1], Jung Hyun Moon[2], Fumio Harashima[3], Bong Jin Lee[4], Sung Mi Kim[4] and Yun Ja Lee[4]

[1]Graduate School of Mechanical Engineering, Pusan National University, Busan, 609-735, Korea
[2]Aztechs Co.,Ltd, Chilgok-gun, Gyeongbuk, Korea
[3]Tokyo Metropolitan University, Tokyo, Japan
[4]Department of Dance, Pusan National University, Busan, 609-735, Korea

[1]mahlee@pusan.ac.kr, melgibsoo@pusan.ac.kr, mecha-cha@pusan.ac.kr, tntno9@nate.com
[2]aztechs@kornet.net
[3]harashima-fumio@tmu.ac.jp
[4]bongbong486@hanmail.net, sungmi4881@lycos.co.kr, leeyj@pusan.ac.kr

Abstract: This paper presents studies on the Kalman filtering of yaw angle and vehicle position in the integration of an inertial measurement unit(IMU) with a new accurate real-time ultrasonic distance measurement system on a unmanned container transporter(UCT). Experimental tests conducted with a very low grade IMU and pseudolite ultrasonic system(PUS) measurement system showed that a moving vehicle's position can be estimated with a few centimeters accuracy. The test results confirmed that angular motions and vehicle positions improve the estimates of yaw angle and angular velocity, respectively.

Keywords: Kalman filtering, unmanned container transporter (UCT), pseudolite ultrasonic system (PUS), angular motions, ve hicle positions

1 INTRODUCTION

Research on the issue of the position acquisition of moving vehicles has been actively progressing in the field of navigation of which global positioning system(GPS) and inertial navigation system(INS) are widely known [1]. INS provides accurate positional information during brief periods, however, the fault of accumulating errors during prolonged periods still needs to be resolved. On the other hand, GPS gives greater errors during short time periods and has location limitations depending on the use but provides more stable positional information during longer periods of time. Since the two systems complement each other's faults, the combination of the two systems will lead to more accurate positioning information. Active research is being done to combine the two systems. Pseudolite(pseudo satellite) Ultrasonic System(PUS), which can operate indoors where GPS can't and are adaptable in ports, are also being studied for location positioning and control of moving vehicles and for calculating distance. Recently, studies to apply accurate estimated positioning into mobile robots and/or unmanned vehicles have increased [2].

In general, ultrasonic waves are used in mobile robots to detect objects and measure distances, in vehicle rear sensing, in vehicle traffic detection, in speed systems, in invasion detecting security systems, in accurate processing and measurements.

In the distance measurement systems using ultrasonic waves, there are two types of transmitter-receiver systems. The integrated type uses reflecting waves while the separated type uses direct waves. The integrated type is simple and easy to operate but precision target is difficult due to the wide angle. The separated type does not have this problem, but the transmitter and receiver require wireless synchronization. The basic method of distance measurement of the two types is measuring the time of flight it takes for the transmitted ultrasonic frequency to be received.

The threshold method is the most commonly used method to measure the flight time. However, the threshold method is affected by temperature, distance, the absorption of the ultrasonic waves by the object, the medium change in the air, and noise. To supplement these drawbacks, methods to control the various threshold levels are applied. Various calculation methods, such as measuring the initial point of the reception wave from the maximum amplitude point of the sound wave envelope, the time of flight acquired using the maximum time in the cross correlation of signals, or using the topology of the reception waves from the converted transmission waves [3]. Also, the topology difference of a wave using discrete fourier transform is used with the threshold method [4].

Another purpose of the study is to evaluate estimator performance in the integrated system of a pseudolite ultrasonic system(PUS) and low-grade inertial measurement unit(IMU). The experiments were conducted for the estimation of errors in the integrated system of PUS and IMU. A PUS receiver for position estimation and IMU were mounted on a plate so that the relative position between the ultrasonic receiver and IMU could be accurately measured.

2 IMPLEMENTATION OF THE PSEUDOLITE ULTRASONIC SYSTEM(PUS)

2.1 Period detecting method

2.1.1 Basic time of flight detecting method

The time it takes for the transmitted ultrasonic frequency to reach the receiver is defined by the difference of the transmitted time T_t and the received time T_r. The distance d between the transmitter and receiver using direct frequencies of the separated transmitter and receiver are shown in Eq. (1).

$$d = c \times T_f + d_0 \quad (1)$$

Here, $T_f = T_r - T_t = TOF$ (Time of Flight), d_0 is the offset distance due to the position error of the diaphragm, and c is the speed of the ultrasonic frequency according to the air temperature in Celsius (T).

$$c = 331.5 + 0.60714 \times T \quad (2)$$

The precision ultrasonic distance measurement is directly influenced by the precision measurement of flight time, that is the recognition accuracy of the transmitted ultrasonic frequency time T_r .

2.2 Accurate ultrasonic distance measuring system via the PUS

2.2.1 The organization of the accurate ultrasonic distance measuring system

The ultrasonic sensor 40kHz MA40BR/S was used in the accurate ultrasonic distance measuring system. This sensor is widely used to detect obstacles. The sensor sensitivity is highest around 40 kHz and the direction angle is about 70 degrees. The long distance accurate ultrasonic distance measuring system is shown in Fig. 1. The transmitter and receiver are separated and synchronized using RF to transmit the initial transmission point to the receiver. The time delay of RF is minute and so ignored. The transmitter transmits the ultrasonic frequency in certain cycles and the receiver receives the ultrasonic frequency and RF signal. The receiver measures the flight time using the period detection method and with this the final distance information is calculated. The calculated distance information is sent via wireless communication at 115200bps to a PC for confirmation.

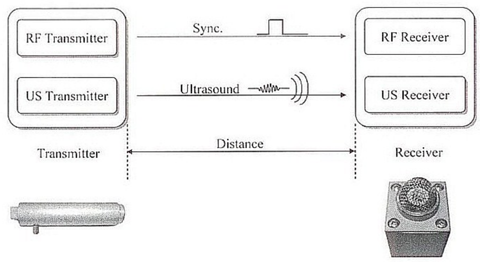

Fig. 1. Configuration of ultrasonic distance measurement system

2.2.2 Ultrasonic distance measurement test

The proposed ultrasonic distance measurement test was done with one transmitter and one receiver. The transmission distance was from 1m to 30m. The experiment started with the transmitter and receiver facing each other at 0m. The distance offset d_0 due to the diaphragm position error of the transmitter and receiver was measured and applied to the distance information.

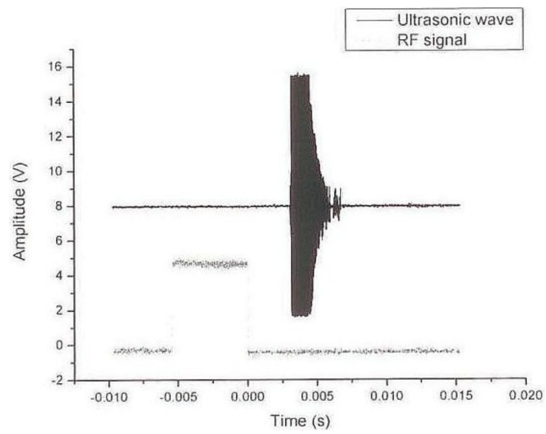

Fig. 2. Received ultrasonic waves at 1m

Fig. 2 show the measured reception frequency and RF synchronized signal at 1m and 20m, respectively. The wave form at the upper part of the figure is unprocessed signal while the lower part of the square wave form is the synchronized RF signal. The declining edge section corresponds to the ultrasonic transmission point.

The main reason of the distance error in the period detection method was examined. The ultrasound can react sensitively to the external environment. The velocity changes depending on the temperature and the frequency is stronger at close range so external disturbances matter less. However, in long distances, external disturbances greatly affected the results even in indoors testing. To determine the reception point of the ultrasonic frequency, repeating cycles were examined and the initial point was located.

Table 1. Distance errors by using threshold method and period detecting method

Distance (mm)	Threshold method (mm)		Period detecting method (mm)	
	mean	STD	mean	STD
1000	9.959	1.011	3.584	0.459
3000	12.698	1.455	5.611	0.681
5000	13.655	1.713	4.113	0.905
10000	11.180	3.589	4.879	1.280
15000	10.377	6.684	3.600	1.981
20000	10.241	9.139	6.715	5.417
25000	45.808	10.982	5.291	7.138
30000	97.166	24.853	14.602	16.559

2.3 Precision position sensing system using the PUS

The ultrasonic position sensing system uses the trilateration to calculate the position of the measuring object and the distance between three or more standard points. This method is the basis of GPS which recognizes the object's position by measuring the reception time of the signal from the satellite.

The ultrasonic positioning system is largely divided into two types according to the position of the transmitter and receiver [3]. The first type is the infrastructure transmitting type where the transmitter is positioned as the basis on the measurement object. Cricket [3] and global ultrasonic sensing system are the applied examples. The second type is the infrastructure receiving type where the receiver is the basis and the transmitter is located on the measurement object. Applied examples are Active Bat and similar method using infrared light is Active Badge.

The infrastructure transmitting type calculates the position information from the moving object, so it is more favorable in mobile robots during position prognosis. The infrastructure receiving type calculates the position information from the infrastructure so used to track moving objects.

Cricket transmitted RF that includes transmitter coordinates at the same time as the transmitting signals. The difference of the arrival time was obtained with the envelope detection method and the distance and location was calculated. The advantage is that the cover range expansion is simple. However, the disadvantages are the inference among the numerous transmitters is unavoidable so the position cannot be obtained in constant time intervals and the inference evaluation algorithm is very complicated. The restrictions of the direction angle range are difficult to overcome so the transmitters are placed within 5m range intervals.

3. Navigation Experiment of UCT

3.1 Location Positioning System and Navigation Algorithm

Four 40kHz ultrasonic transmitters are placed at high locations or indoor ceilings and synchronized to receive one RF signal. A built-in timer transmits the ultrasound every specific time(0.4 sec). The time of flight(TOF) value is calculated and the distance between the transmitter and receiver is estimated. Generally, it can consist of one or two receivers. In the case of one receiver, the local coordinates x, y, z are acquired. When two receivers are used, the direction angle can also be measured. In unmanned navigation, the absolute position and the direction angle of the UCT are needed and so two receivers were used in our experiment.

3.2 Unmanned Driving Test and Performance Evaluation of Model Car on UCT

The UCT speed of 0.36m/s, the control cycle of 0.4 sec when the Kalman filtering was not applied and the control cycle of 0.1 sec when Kalman filtering was applied were tested, respectively.

The dotted line represents without Kalman filtering and the solid line shows the data after it has been filtered through every 0.1 sec and measurement noise is (0.16)

3.3 Implementation to PUS of North Harbor in Busan, Korea

Fig. 3 shows the position recognition system of the vehicle using PUS in the harbor yard. Under the assumption that the height of the vehicle is constant, only two distances of the PUS transmitter needs to be measured for accurate x, y value. Therefore, placing the PUS transmitters in a row as shown in Fig. 4, and successively transmitting 300ms three times from the 1st transmitter to minimize the interference of the transmitters. The overall positions are shown in Fig. 21. ①, ②, ③ transmit the same identification signals successively and different identification signals are transmitted in different areas according to color. Each ultrasonic signal includes a different identification signal. Based on this, the receiver calculates position from the identification signal and distance from the transmitter.

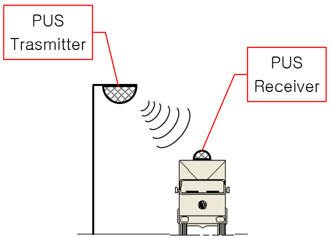

Fig. 3. The distance calculation of PUS transmitter and receiver

Fig. 4 shows the actual installation positions of the PUS transmitters, and Fig. 5 shows the ①, ②, ③ array of the transmitter groupings installed for the experiment. The experimental results of a vehicle installed with Kalman filter verifies accurate position recognition is possible even when applied in the real environment. During 10km/h forward and backward movements, ±100mm of error occurred. However, the efficiency can be increased with the accurate compensation of the ultrasonic transmitter. And also with the use of multiple transmitters, the efficiency will increase.

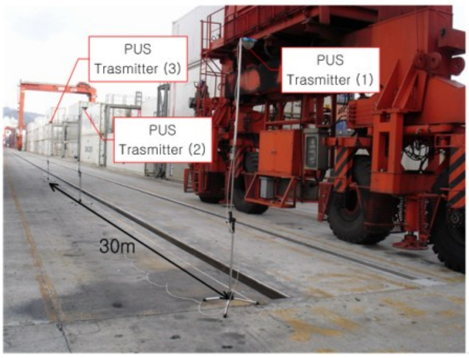

Fig. 4. The calculation of the receiver's coordinates using two PUS transmitters

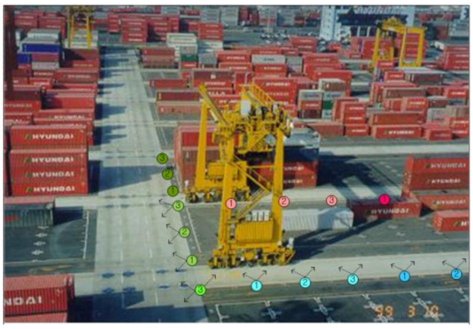

Fig. 5. The position of PUS in the yard

4. Conclusion

A precision position detecting system for indoors and/or designated areas was proposed, its practicality was demonstrated, and the following was concluded.

To satisfy the recognition range and the measurement precision at the same time, period detection method was proposed and test results confirmed its performance efficiency to be outstanding.

Pseudolite Ultrasonic Satellite (PUS) was proposed to enable position detection of multiple moving objects. The system demonstrated superior performance efficiency in precision and recognition. The proposed 3D ultrasonic position detecting system uses a low cost 8 bit microprocessor and is practical in design, power, and weight.

For application in mobile robots or ports that require precise positioning systems, Kalman filtering position estimation algorithm was applied and analyzed.

Test results show that this system can be applied in various ways such as position recognition of mobile robots, in production lines, or in large distribution centers. And also in AGV autonomous driving position detection, motion detection, and 3D precise coordination detection.

The Kalman Filtering method was adopted into the PUS to improve the vehicle's various operation performances. Especially, the proposed PUS was built into the real vehicle and basic experiments showed that the control of the vehicle was possible in centimeters error range. With these results, we confirmed that this system can be applied to actual port UCT.

Actual testing was applied to two transporter cranes at the Hutchison Terminal, Jasungdae Port, Busan Harbor.

REFERENCES

[1] I. Y. Bar-Itzhack and B. Porat, "Azimuth Observability Enhancement During Inertial Navigation System In-flight Alignment," J. Guid. Control, Vol. 3, No. 4, pp. 337-344, Jul./Aug. 1980.

[2] D. H. Lee, S. Y. Kim, K. S .Yoon, and M. H. Lee, "A Long Range Accurate Ultrasonic Distance Measurement System by Using Period Detecting Method," Journal of the Korean Society of Precision Engineering, Vol. 24, No. 8, pp. 41-49, 2007.

[3] A. Smith, H. Balakrishnan, M. Goraczko, and N. Priyantha, "Tracking Moving Devices with the Cricket Location System," The 2nd International Conference on Mobile Systems, Applications, and Services, Boston, USA, June 2004.

[4] F. E. Gueuning M. Varlan, C. E. Eugene, and P. Dupuis, "Accurate Distance Measurement by an Autonomous Ultrasonic System Combining Time-of-flight and Phase-shift Methods," IEEE Tans. on instrumentation and Measurement, Vol. 46, No. 6, pp. 1236-1240, 1997.

The Seventeenth International Symposium on Artificial Life and Robotics 2012 (AROB 17th '12),
B-Con Plaza, Beppu, Oita, Japan, January 19-21, 2012

Hyper-gourd theory: solving simultaneously the mysteries in particle physics, biology, oncology, neurology, economics, and cosmology.

Ken Naitoh[1]

[1]Waseda University, 3-4-1 Ookubo, Shinjuku, Tokyo 169-8555, Japan
(Tel: 81-3-5286-3265)
[1]k-naito@waseda.jp

Abstract: The inevitability of various particle masses for hadrons, quarks, leptons, atoms, biological molecules, droplets of fossil fuel and water, living cells including microorganisms and cancers, multi-cellar systems such as organs, neural systems, and the brain, stars, galaxies, and the cosmos is synthetically revealed. This is possible because each flexible particle is commonly generated by a mode in which a larger particle breaks up into two smaller ones through a gourd shape with two lumps. These masses, sizes, frequencies, and diversity dominated by super-magic numbers including the silver ratio, in fractal nature can be derived by the fusion of the quasi-stability principle defined between absolute instability and neutral stability, the indeterminacy principle extended for quantum, statistical, and continuum mechanics, and the spherical Lie group theory. The analyses also result in a new mathematical definition of living beings and non-living systems and further explain the standard network patterns of various particles and also the relation between information, structure, and function, because the proposed theory based on gourds posits a new hyper-interdisciplinary physics that explains a very wide range of scales, while the Newton, Schrodinger, and Boltzmann equations describe only a narrow range of scales.

Keywords: Biological, cosmic, hyper-interdisciplinary, subatomic, quark.

1. INTRODUCTION

There are still so many mysteries about non-living and living systems from subatomic to cosmic scales, which are related to the masses of subatomic particles, quantum entanglement, the magic numbers, morphogenetic processes, the standard circuit pattern of the neural network in the brain, overall mechanism of cancer, fusion of left-right symmetric and asymmetric organs, the definition of life, side effects, functions of introns and junk, economic systems generated by the human brain, dark matter, and super-cosmos outside our universe.

The reason why so many mysteries have not been explained is related to the fact that the traditional Newton, Schrodinger, and Boltzmann equations can reveal only a narrow range of scales, although each equation describes several classes of conservation of mass, momentum, moment, and energy. Super- interdisciplinary and supermulti-scale physics, which synthesizes the whole span from the pico- to the peta-scale, is necessary to go further.

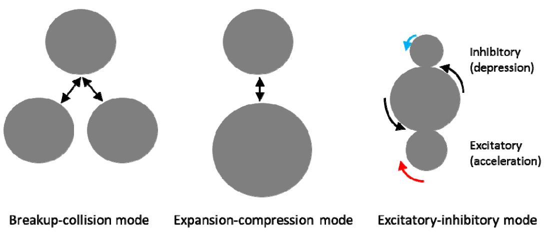

Fig. 1 Three modes.

Fig. 2 Gourd shapes.

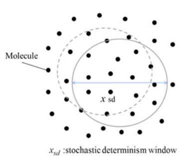

Fig.3 Window for averaging

Our previous researches [1, 2] offered some hypotheses and predictions regarding these mysteries. Later, some experimental researches done by other people verified our hypotheses and predictions [3, 4]. One concerns the function of introns and junk. Another concerns the left-right asymmetric part inside the brain system, which brings feelings of comfort.

Here, we will reveal the mysteries above more intensively and extensively. First, we will classify the natural processes into three modes: breakup-collision, expansion-compression, and excitatory-inhibitory process (acceleration-depression). (Fig.1) We name the modes of breakup-collision, expansion-compression, and excitatory-inhibitory process (acceleration-depression), as Gourds I, II, and III, respectively. This is because each one of the three modes has shape of gourd. (Fig. 2) Nature is dominated by gourds, rather than by strings or spheres. In short, we propose here a physical theory that explains the fractal nature in the gourds of the three models, although the fractal concept has only been used in mathematics so far.

2.METHODOLOGY

2.1 Quasi-stability principle [2, 5-7]

Natural systems are essentially discontinuous in three-dimensional space but relatively continuous in time, because from the subatomic to the cosmic scale they consist of particles such as quarks, hadrons, atoms, molecules, fluid particles, cells, and stars. Accordingly, various natural processes for non-living and living systems can approximately be described by the following momentum equation systems:

$$\frac{d^{(n)}}{dt^{(n)}} y_i(t) = \sum_j f_{ij}(y_i, y_j) + \varphi_i \text{ or } \frac{\partial^{(n)}}{\partial t^{(n)}} y_i(t, x_k) = \sum_j f_{ij}(y_i, y_j) + \varphi_i \quad (1)$$

where y_i, x_k, t, n, f_{ij}, and φ_i denote physical quantities such as velocity, particle deformation rate, and pressure, spatial coordinates, time, order of derivative, function of y_i and y_j, and random disturbance related to indeterminacy coming from the small number of particles, respectively. [2, 5-7] Quasi-stability is defined as a principle in which one part on the right-hand side of Eq. 1 is zero, when disturbance of φ_i enters the system. When at least one of the various terms of i or j for f_{ij} is zero, the system is quasi-stable against the disturbance. Quasi-stability as it is used here lies between neutral stability and an absolutely unstable condition. The quasi-stability is different from meta-stability denoted in thermo-physics, because this quasi-stability for momentum is weaker than the meta-stability for energy conservation. [One example of evidence is that the elimination of only one term among various numerical error ones in a finite difference equation derived with the Taylor series yields an approximate solution for a physical phenomenon such as the transition to turbulence [8].]

It is emphasized here that traditional stability analyses based on a mathematical variable transformation for matrix diagonalization is meaningless for revealing the nature of living beings, because life is not in mathematical space.

2.2 Indeterminacy level:

As shown above, various natural phenomena consist of particles, i.e., discontinuity in space. This discontinuity of particles leads to indeterminacy (stochasticity) for several stages of phenomena, such as electron particles described by the Schrodinger equation. An important point is that the level of indeterminacy, i.e., degree of variation, varies according to length scales and the number of particles. As an example, when the system being analyzed consists of a smaller number of particles, the level of indeterminacy increases. (Fig. 3)

Statistical mechanics based on the Liouville and Boltzmann equations tells us that a very large window for averaging the aggregation of a huge number of particles brings deterministic continuum mechanics, whereas a small window for a small number of particles leads to a stochastic differential equation. When a small window for averaging is used, physical quantities such as mass, size, and velocity are defined with indeterminacy, i.e., vagueness. [9]

The baryons and mesons are constructed of only three and two quarks, respectively. There are only two electrons inside the smallest orbit around an atom. The number of carbon, oxygen, and nitrogen particles inside a nitrogenous base is not enough for continuum, because of the order of ten. These small numbers of particles lead indeterminacy in the governing equations. On the other hand, a biological cell or a liquid droplet of over one millimeter in size includes a lot of molecular particles that result in deterministic governing equations. The most important point is that a system of only one particle is deterministic, although such systems are of an infinitely small number.

3. BREAKUP PHENOMENA (Gourd Ia)

3.1 Size and weight

The breakup phenomena on various spatial scales commonly show the shape of a gourd having two lumps at the time of breakup (Fig. 2). Thus, we can model the gourd having two lumps using two flexible spheroids connected as an approximation. [2, 5] Here, we define a parcel as a flexible spheroid (lump) having two long and short radii *a(t)* and *b(t)* dependent on time *t*, for the aggregation of some quarks or leptons generated by a high energy experiment, the aggregation of neutrons and protons in each child atom resulting from the fission of a large atom such as a uranium 235, a nitrogenous base in biological base pairs of nucleic acids hydrated with a lot of water molecules, a biological cell just before division, a liquid droplet at breakup, and a star (or dark matter) at breakup in the cosmos. The parcel becomes a sphere of the radius r_d ($=[ab^2]^{2/3}$) under an equilibrium condition. The deformation rate γ (t) is defined as *a(t)/b(t)*, while a sphere without deformation corresponds to $\gamma = 1$. Next, we derive a theory for describing the deformation and motions of the two connected spheroid parcels having two radii of r_{d1} and r_{d2} under equilibrium conditions and two deformation rates of $\gamma_k\ [k=1,2]$, while the size ratio of the two parcels is defined by $\varepsilon = r_{d1}/r_{d2}$.

We model the relative motion between the two parcels, nonlinear convections inside the parcels, and the interfacial force at the parcel surface. The interfacial force is evaluated in the form of σ / r^m where *m* and σ are constants and *r* is the curvature of the parcel surface. Several types of forces such as nuclear force, van der Waals force, surface tension, coulomb force, and the force of gravity can be explained by varying *m*. The relation *m* = 1 implies the surface tension of liquid. Mean density of the parcels is ρ_L.

We assume that the convection flow inside a flexible parcel is irrotational, i.e., potentially one. This potential flow is applicable, because fluctuations entering the parcels such as bases, cells, and atoms will be those of thermal fluctuations with very high speeds, which are less dissipative (fluctuation dissipation theorem). The potential assumption is also valid for star breakups, because of their large size and high speed. Moreover, we must consider that a parcel is not often a continuum, because the number of nucleons and water molecules inside the parcels of atom and nitrogenous bases will be fewer than 1,000. Thus, this leads to a weak indeterminacy of physical quantities such as deformation and density.

Here, we derive the relation between the dimensionless deformation rate $\gamma_k (\equiv a_k / b_k\ [k=1,2])$ of each parcel dependent on dimensionless time $\bar{t}$ and the size ratio of two parcels of $\varepsilon = r_{d1}/r_{d2}$.

The stochastic governing equation having indeterminacy can be written for momentum as

$$\frac{d^2}{d\bar{t}_i^{\,2}}\gamma_i = \{m_{ci}(\frac{d}{d\bar{t}_i}\gamma_i)^2 + m_{cj}(\frac{d}{d\bar{t}_j}\gamma_j)^2 + m_{si}\ \gamma_i^{\frac{5}{3}-\frac{2}{3}m} + m_{sj}\ \gamma_j^{\frac{5}{3}-\frac{2}{3}m}\} / Det + \delta_{st}$$
$$[\text{for } i = 1, 2.\ j = 1, 2.\ i \neq j] \qquad (2)$$

with $m_{ci}, m_{cj}, m_{si}, m_{sj}\ Det,\ B_{0k}\ , C_{0k}$, and E_{0k} [for $k = 1, 2$] defined in Refs. 2,5,6, and 7,

where the parameter δ_{st} denotes random fluctuation.

Next, we also define $y_i = \gamma_i - 1$ as deviation from a sphere.

The momentum equation is

$$\frac{d^2 y_i}{d\bar{t}_i^{\,2}} = [-\frac{2}{3}(3-\varepsilon^3-2\varepsilon^{2+m})\left(\frac{dy_i}{d\bar{t}_i}\right)^2 + 3(3-\varepsilon^3)my_i - 4\varepsilon^{1+m}\left(\frac{dy_j}{d\bar{t}_j}\right)^2 + 12\varepsilon^{1+m}my_j]/[3(\varepsilon^3+1)]$$
$$+\delta'_{st}, \qquad (3)$$

which is approximated by the first order of the Taylor series [2, 5-7].

For each *m*, the quasi-stable size ratios of 1.0 and about 1.44 appear in Eq. 3, i.e., in the 1st-order term of the Taylor series. It is stressed that a deformation disturbance entering a particle, i.e., that for y_i, leads to an asymmetric size ratio around $\varepsilon = 1.44$, while a disturbance of deformation speed, $dy_i / d\bar{t}_i$, brings a symmetric ratio of 1.0.

The higher-order of the Taylor series for parcel 1 results in

$$\frac{d^2 y_1}{d\tau_1^2} = \left(\sum_{k=1}^{\infty} b_k(\varepsilon,m) y_1^{k-1}\right)\left(\frac{dy_1}{d\tau_1}\right)^2 + \sum_{k=1}^{\infty} a_k(\varepsilon,m) y_1^k + \zeta \qquad (4)$$

where the third term on the right-hand side includes influences from parcel 2.

The higher order of terms of the Taylor series obtained with the statistical fluid dynamics model also reveals the various super-magic numbers for the size ratios of (Table 1). It is stressed that the ratios are desultory or discontinuous. We should recall that various values of *m* bring the same quasi-stable ratios of 1.0 and about 1.44 for the first order of the Taylor series, whereas the higher-order terms lead to various other ratios.

Table 1 Super-magic numbers

m=-3	m= -1	m=1	m=1.04	m= 1.3	m= 1.5	m=2	m=3
conv.							
1	1	1	1	1	1	1	1
1.23	1.34	1.27	1.27	1.26	1.25	1.24	1.21
1.39	1.4	1.35	1.35	1.34	1.34	1.32	1.29
3.51	1.42	1.39	1.27×10^{30}	10321	256	16.1	4.36
1.42	1.43	1.4	1.38	1.38	1.37	1.36	1.33
4.22		1.41	9.08×10^{22}	1151	68.7	8.33	3.07
1.43		1.42	1.4	1.4	1.4	1.39	1.36
4.44		1.43	4.06×10^{22}	1033	64.4	8.02	2.86
1.44			1.41	1.41	1.41	1.4	1.38
4.5			2.82×10^{25}	2472	108.7	10.4	2.99
4.52			1.42	1.42	1.42	1.41	1.39
4.53			1.95×10^{34}	37325	553.6	23.5	4.25
			1.43	1.43	1.43	1.42	1.4
surface							
1.44	1.44	1.44	1.44	1.44	1.44	1.44	1.44
	1.8	3.58	4.57				3.14
	1.7	2.47	1.99				
	1.63	2.1	1.84				
	1.59	1.79	1.74				
	6.11	1.71	4.42				
		4.54	1.68				
			2.97				

The size and weight ratios of purines and pyrimidines in DNA are around 1.45, which is close to 1.44 in Table 1, while the size ratios of identical bases in RNA is 1.0. Heavy chains in immune globulins (IgX) have size ratios of about 1.5, while the frequency ratio of small and large types of IgXs is also 1.5: two types of large immune globulines (IgM and IgE) and three small ones (IgG, IgD, and IgA).
The largest amino acid is about three times larger than the smallest one, which corresponds to 3.58 in the higher order of the Taylor series for m=1. The ratios of chromosomes in human beings are about six times at maximum, which may be seen as 4.54 in the higher order of the Taylor series for m=1 or 6.11 in the higher order of the Taylor series for m=-1. [This is because the values of m may be 1.0 or less for van der Waals and coulomb forces.]
Equations 2-4 and Table 1 may also explain the mysterious electron orbits such as 4f, because quasi-stable ratios do not increase monotonously according to increasing of the orders of the Taylor series related to the energy levels of orbits. For examples, the 3rd and 8th orders of terms bring the relatively large quasi-stable size ratios of about 3.58 and 4.54, whereas the 4th and 5th orders lead to the relatively small ones of about 2.47 and 2.10.
The constant m will often have values larger than 1.0 or 1.0 for nuclear force. Table 1 also reveals the magic numbers appearing in the weight ratios in various atoms generated by cold fusion: about 3.9, 2.1, and1.8 [5, 10].
When m has a value between 1.3 and 3.0, the ratios of ε are between 1.0 and about 105, which may correspond to the mass ratios in small particles including quarks and leptons or those in the hadron classes of baryons and mesons. [It is stressed that a weight ratio of about 2:3 is also observed in dark matter [10]. The fractional Taylor series also show quasi-stable ratios including about 1.44 and 1.0 in Table 1.]

3.2 Permanent and tentative components inside parcels

Parcels can essentially include two types of components, which are permanent and tentative ones. The permanent part exists both before and after the breakup process, while the tentative part appears and shows important features only at the time of breakup. In several cases of natural phenomena, the permanent part is a one-dimensional string or ring, having a mass proportional to the parcel size ε. Parcels including both tentative and permanent parts have a mass proportional to ε^3. Some natural phenomena have no tentative part, in which case only the permanent part is proportional to ε^3.
Let us examine the following examples. In biological systems, these magic numbers of ε explain those for biological molecules of one-dimensional strings and rings such as nitrogenous bases, amino acids, and proteins, whereas the values of ε^3.correspond to biological molecules hydrated by water molecules. In subatomic processes, the aggregation of baryons is one-dimensional, while the total mass including baryons, gluons, and the quark condensation effect is three-dimensional. The tentative part is similar to the immersed mass in fluid dynamics. Pure droplets of water or fuel and stars are three-dimensional because they only have the permanent part.
The group theory shows that one- and three-dimensional spheres are in a group. This may support the idea that ε and ε^3 repeatedly appear in various natural particles (parcels), while nature is relatively obviative to two-dimension, ε^2.

3.3 Discontinuity around m =1

Let us think about the reason why discontinuous jumps in size ratios can appear around m = 1. When the curvature is $1/r$, we define the surface force as one proportional to $1/r^m$. We can employ the simple form of $1/r^m$, because we consider only the breakup timing of the gourd having two lumps. Taking the r-integral of $1/r^m$ as the potential, the integral forms are discontinuous for m around 1.0. This is the reason why values of m a little larger than 1.0 discontinuously induce extremely large size ratios.
There are extremely large size ratios over 10^{30} in Table 1 for $1.0 < m < 1.1$. These very large ratios might possibly correspond to the size ratios of vapor molecules and water droplets produced at breakup and also to those of subatomic particles and stars, or the very large or infinite ratios for $1.0 < m < 1.1$ may explain interaction between particles at a infinite distance, i.e., the quantum entanglement.
The potential flow assumption, irrortaional flow one without viscosity, is applicable even for very small subatomic and molecular systems, because very high energy, ie., very high speed, is put for the particle. Actually, energy at the level of sound speed is put into the molecular system, while energy at the level of light speed is put into the subatomic experiment.

3.4 Number of particle types and frequencies

The size asymmetry of around 3:2 of the main rings in purines and pyrimidines naturally leads us to an asymmetric number of types, i.e., "two" types of purines and "three" types of pyrimidines, [6, 7] The multiplicative inverse of the asymmetric number of types is the size asymmetry. This can be easily understood from the mass conservation law, that is, from the fact that the main rings of purines have "nine" molecules of carbon and nitrogen, while "six" molecules of carbon and nitrogen form the main rings of pyrimidines. Accordingly, the number of base types is proportional to the frequency of bases inside RNA [6, 7]. In qualitative terms, the sizes and molecular weights of the twenty types of amino acids are also inversely proportional to the frequencies.

4. STRINGS AND RINGS PRODUCED BY COALESCENCE (Gourd Ib)

4.1 Clover structure

An extremely large frequency ratio for purines and pyrimdines in tRNA, say, far larger than 1.5, cannot produce the stem in tRNA, because purine and pyrimidine pairs do not easily form in the presence of only one type of base [6, 7]. It is also known that, as purines and pyrimidines in DNA have the same density, they form a pair at each locus due to hydrogen bonding. Thus, this frequency ratio of 1.0 for purines and pyrimidines cannot generate loops in tRNA [6, 7]. This is the reason why a frequency ratio between 1.0 and 1.5 for purines and pyrimidines promotes clover structures having stems and loops (Fig. 4). More complex structures such as rRNA can also be explained by the above-mentioned dynamical mechanism. [6, 7] Concavity and convexity, like thumbs in RNAs, play an important function for grasping objects, including nucleic acids and proteins.

During differentiation and proliferation of the morphogenetic process, repeats of symmetrical and asymmetrical cell sizes also induce the structures of concavity and convexity in multi-cellar systems, thereby leading to functional parts such as arms and legs.

Chromosomes in multi-cellar systems also have three-dimensional repeat structures of concavity and convexity. It is known that introns and junk are concave in shape, while exons having the clear function of producing proteins are convex in shape.

[Several sequence data in the world-wide databases show a tendency of purines richer than pyrimidines in RNA, which is contradict to the principle that smaller bases are more. Non-coding RNA reported recently solves this contradiction. There may also be other unknown RNAs which are rich with pyrimidines.]

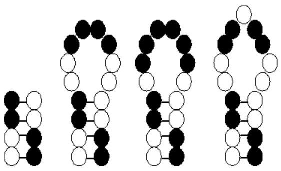

Fig. 4. Schematic diagram of symmetric and asymmetric density ratios in DNA and one leaf of tRNA

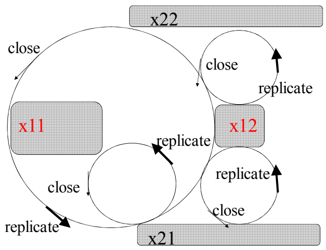

Fig. 5 Four-stroke molecular engine

4.2 Comfort

Human brain feels the golden and silver ratios of around 2:3 to be comfortable. Thus, our previous reports predicted that there will be about 2:3 ratios in the aggregations of neural cells of the brain. [2] Recently, some researchers found the left-right asymmetric part inside the habenular nucleus of the zebrafish brain, which has size ratios between 1:1 and 1:2 [4]. It is known that the habenular nucleus is related to fear, which is the opposite feeling of comfort. Thus, the asymmetric size ratios of neurons and networks inside the brain, which may be induced by some different neurons such as GnRH neurons and glia cells, also have sympathetic vibration with the asymmetric ratios in picture images entering from the outside into the eyes. The sympathetic vibration brings comfort.

Next, let us think about the musical scale inducing comfortable music. Musical scale Perfect 5 uses the ratio of 2:3 for the sound frequencies, while perfect 4 employs 3:4. Music also uses the magic numbers shown above. Then, perfect 5 consists of "seven" half tones, while perfect 4 is with "five" half tones. It is also stressed that the magic numbers of 2:3 (1.5) and 3:4 (1.33) mentioned above result in the ratio of 7:5 close to the silver ratio, which is the rhythm used for Japanese poems such as "haiku" and "tanka".

5. AGGREGATIONS GENERATED BY MORE COALESCENCES (Gourd Ic)

5.1 Inner-asymmetry in cells and morphogenesis

Symmetric and asymmetric size ratios are also observed at the cell level of microorganisms. [6, 7]

There are terminal cells and basal cells of different sizes in the morphogenetic processes. This difference in cell size also shows asymmetry [6, 7]. Embryo stem (ES) cells also show asymmetric cell divisions (differentiation) such as a division to glial cells and neurons.

The left-right symmetric distribution of arms and legs is observed in outward appearance, although the inner body, including the heart and liver, is asymmetric. Outer cells close to the surface move relatively easily in relation to the absolute origin on the earth, because one part of the cell is free without any connection to other cells. However, inner cells receive forces from many directions due to the presence of other cells in a homogeneous field, making it difficult for them to move relative to the origin on the earth. Therefore, inner cells deform relatively easily without any translational motion of the gravity center.

Equations 3 and 4 explain this important characteristic of the asymmetric division of inner cells and the symmetric division of outer cells. This is because the asymmetric size ratio of cells (the size ratio of about 1.45) is relatively quasi-stable against the disturbance of deformation that easily affects inner cells and also because the second term on the right-hand side of Eqs. 3 and 4 implies cell deformation. Outer cells divide into identical sizes of cells, because the first term corresponds to the translational motion of a cell.

5.2 Protons and neutrons in atoms

It is also well known that several atoms in nature have number ratios of protons and neutrons between 1:1 and 2:3. Here, let us examine the reason why larger atoms have larger number ratios close to 2:3.

As shown above, the inner and outer parcels of baryons determine whether the number ratio of neutrons and protons are asymmetric or symmetric, respectively [5, 6].

Larger aggregations of parcels such as thorium (Th), which contains more baryons than helium (He), have more inner baryons, because the surface/volume ratio of the aggregation becomes smaller as the size increases. More inner baryons for larger atoms bring more asymmetric number ratios of protons and neutrons.

Mysteriously, the masses of stable protons and neutrons are almost the same, while child atoms generated by fission of uranium 235 and nitrogenous bases (pyrimidines and purines) have a different weight ratio around 2:3. Some reasons are shown [5, 6]. There is the other analogical evidence supporting the inevitability of the ratio close to 1:1 for proton and neutron, that the Watson-Crick pair of nitrogenous bases has the asymmetric weight ratio of about 2:3, whereas the weight ratio of the pair including sugars inside DNA and RNA is close to 1:1 because of addition of sugar for each base.

6. REPEATS OF BREAKUP AND COALESCENCE (Gourd Id)

As shown above, one particle alone is deterministic without indeterminacy, whereas systems of two particles interacting can have indeterminacy, because the continuum assumption is impossible when there are only two flexible particles. Of course, systems having a number of particles from three to several hundred can also be indeterminant. Systems having more particles may be approximated as a continuum, i.e., deterministic, if the representative scale in space for averaging is very large. Aggregation of a lot of small particles results in a large particle at the next scale, which is close to a sphere or a spheroid. The new large particle is deterministic again, because it is only one.

As an example, let us look at the biological system. Only one DNA existing inside a cell is deterministic, because DNA must accurately determine the structures and functions of living beings. Two male and female DNAs for mating can produce diversity with indeterminacy by crossing over. There are extremely large numbers of genes, proteins, and water molecules inside a cell, which leads to a continuum, i.e., the next deterministic behaviors and sustainability during the cell's life time. Compartment due

to cell membrane leads to the determinacy as sustainability. The loss of many molecules during the aging process results in indeterminacy and also instability or death. Therefore, further thought experiments based on the indeterminacy level mentioned above may reveal the total numbers and groups of bio-molecules inside human beings, including presently unknown ones. The death rate of children will be between 10% and 0.1%, although the rate depends on economical situation of each country. This may imply that the total number of molecular groups inside healthy human beings is between 10 and 1,000.
Moreover, if the total numbers and types of molecules (or molecular groups) are revealed, the probability of survival after developing cancer can also be clarified by the indeterminacy level analysis. [It is known that a few electron orbits around atomic cores are indeterminant. Stars are nearly deterministic, because weak gravity forces lead to individual motion for each star.]

7. EXPANSION AND COMPRESSION (Gourd II)

Other natural phenomena such as the morphogenetic and aging process are in the topological mode of expansion and compression. This mode is like a gourd expanding, which has two spherical parts and a duct for suction.
Our three-dimensional unsteady flow simulations obtained by solving the stochastic Navier-Stokes equation revealed the three-dimensional structure of the morphogenetic processes of human beings, including organs and the brain [11]. The morphogenetic process of the main blood vessels inside the brain was also simulated [12]. The computational simulations demonstrate left-right asymmetric organs in the inner region of the body, while symmetric organs and parts are relatively outside the body. The simulation results showing the principle of inner asymmetry and outer symmetry also correspond to the analytical results obtained in the foregoing sections by the quasi-stability principle (Eq. 3). Moreover, the simulation results also show another principle of early symmetry and later asymmetry [10]. [Compression will correspond to death, because compression process is very unstable as seen in turbulence increase during the compression stage of piston engine.]
Our universe may also be expanding. If there are no super-universes outside our universe, our one is symmetric.

8. EXCITATORY AND INHIBITORY MODE (Gourd III)

8.1 Self-replication
Our previous reports clarified the minimum excitatory network of chemical reactions necessary for self-replication. [7] The minimum system has four types of molecules (molecular groups): two information groups x11 and x12 and two functional molecular groups x21 and x22. (Fig. 5) [7] This four-cycle system in Fig. 5 works as a closed loop. Microorganisms including bacteria and archaea and cancer cells basically employ this network of the four molecular groups, because of a monotonic increase without any depression. Emphasis is placed on the fact that Fig. 5 shows a new, concrete, mathematical definition of life at a higher level. We can topologically see the symmetric and asymmetric circles of reaction networks in Fig.5, which also have gourd shapes connected with symmetric and asymmetric lumps. These gourds commonly appear because both parcels in a base-pair and those in network have connection at the rate-determining stage.
It is also clear that the fusion of asymmetric and symmetric size ratios of molecules (bipolarity of sizes) also naturally results in the fusion of asymmetrical and symmetrical network patterns (bipolarity of topology).
Complementary pairs of RNA such as double-strand RNA (dsRNA) may form the simplest cycle. However, information and a catalytic function are undetached in this type of system, because each strand of dsRNA has both of them. This leads to the fact that the dsRNA and DNA suitable for stabilizing information is not conducive to the production of various functions for inducing multi-cellar systems having complex geometries. Thus, living beings select the detachment of information and function.
8.2 Morphogenetic and economic processes
The main temporal mystery is the basic molecular instrument regulating the biological rhythm common to the cell cycle, proliferation and differentiation induced by the stem cell cycle, neural pulse, neural network, and circadian clock. At least two more inhibitory molecules (molecular groups) of information and function should be added to depress a monotonous increase in DNA. [13].
Here, we define x13 and x23 as the other molecular groups for inhibitory factors repressing reactions. These two groups are incorporated in the four groups of x11, x12, x21, and x22, because today's cells and the morphogenetic processes of multi-cellar systems use negative controllers such as Oct-4 and SOX2 for producing tissues and organs [14]. This leads to a macroscopic model having six types of molecular groups, or in other words, a six-stroke engine (Fig. 6a). We can describe the densities of the six groups at generation N after the mother cell generation by the following equations.

$$x_{1i}^{N+1} - x_{1i}^{N} = \alpha_{i1} x_{1i}^{N} \otimes x_{21}^{N} \quad ,(i = 1,2,3)$$
$$x_{2i}^{N+1} - x_{2i}^{N} = \alpha_{i2} \delta(x_{1i}^{N} - \xi_i x_{23}^{N}) \otimes x_{22}^{N} \quad ,(i = 1,2,3) \tag{5}$$

where $x_{ij} \otimes x_{km}$ denotes the smaller value among x_{ij} and x_{km} and also where $\delta(x)$ denotes the larger value of x or 0, i.e., max (x, 0). [13] Statistical mechanics inevitably leads to the mathematical form on the right-hand side in Eq. 5, because of collision probability.
Numerical solutions for Eq. 5 show about a sevenfold beat cycle of densities for molecular groups on average, while varying the parameters in Eq. 5 results in four- to ten- fold beat cycles.

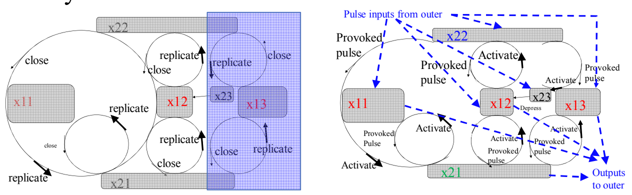

(a) (b)

Fig. 6 Six-stroke engines for morphogenetic process and neural systems.

An important point is that the actual morphogenetic processes show about seven-beat cycles of molecular densities [13, 15]. Another example is that, in the morphogenetic processes, both human beings and giraffes have "seven" neck bones. These facts provide substantiating evidence for Eq. 5.
8.3 Neural network
Equation 5 also reveals the standard topology of the cortical neural circuit (network), the integration mechanism of brain functions, the neural system for muscle control, and the chemical reaction network inside a neuron [15].
Figure 6b shows the standard pattern for neural networks, which includes inputs and outputs. For the network, six variables of xij (i=1-2, j=1-3) are redefined as the activation level of neurons, related to the density of molecules and amount of total energy inside the neurons.
There are two sides in Fig. 6b, one for inputs and one for outputs, which correspond to information and functional molecules in Eq. 5 and Fig. 6a. The upside-down topology of inputs and outputs in Fig. 6b is also possible.
The most important point is that the present equation (Eq. 5) and Fig. 6 describe the essential physics underlying the

network of neural cells and the molecular network inside a neuron, whereas the Hodgkin-Huxley (H-H) model describes only the outer electrical quantities such as electron flow and voltage for a single neuron. It should be added that some variations modified from the network pattern in Fig. 6 and Eq. 5 are also possible, by varying the arbitrary constants and also by adding more molecular types except for x13 and x23.

It is stressed that the equation generated by the six groups for describing the seven-beat cycle on average (Eq. 5) also shows a quasi-stable feature for healthy conditions, whereas an unstable condition will be for sickness.

Equation 5 is an ordinary differential one that eliminates spatial variations of quantities, because the spatial diffusion of molecules and cells is relatively fast in comparison with temporal oscillations and also because a lot of molecules move between cells. However, spatial variations of quantities should be included for a detailed analysis.

Circadian clock of about 24-25 hours are also seven times the fundamental temperature oscillation of about 3.5 hours. [13, 15]It is interesting that these beat cycles from four to ten include those of five and seven for musical scales of Perfects 4 and 5, which are shown in the foregoing section.

Moreover, emphasis is placed on the fact that the cycles of boom and bust appearing in economic and social systems are also the seven-beat on average, because economic systems are produced by human brains. Flux and reflux of companies and capital can also be clarified by the present analysis.

[For standard neural network systems, the initial conditions or inputs may be inputs from outside networks. The initial inputs can be included on the right-hand side of Eqs. 5 and 6 by the Delta function.]

8.4 Total energy limit

The model (Eq. 5) in the previous sections was derived under the assumption of an infinite energy supply. However, energy supplied for molecular networks, cell colonies, organs, neural networks, or economic systems is limited, because the surface-to-volume ratio of each system decreases according to an increase in the number of molecules, cells, neurons, or populations, leading to a condition of insufficient energy. Thus, a new energy restriction term should be added to Eq. 5, which results in Eq. 6 [15].

$$x_{ij}^{\;N+1} - x_{ij}^{\;N} = \alpha_{ij}\,(x_{1j}^{\;N} - \beta_{ij}\,x_{23}^{\;N}) \otimes x_{2i}^{\;N} - \varepsilon_{ij}\,[x_{ij}^{\;N}]^{q},$$

$$x_{ij} \ge 0, \quad x_{1j}^{\;N} - \beta_{ij}\,x_{23}^{\;N} \ge 0. \; (i = 1-2, j = 1,-3) \qquad (6)$$

If the symbol $\otimes$ implies product, q > 2. If the symbol $\otimes$ means smaller value among two, q > 1

Numerical solutions for the equation extended with total energy limit show a transition to sick situation such as cancer in the aging process of the human beings including the brain, i.e., a mysterious transition from chaotic oscillation at 2nd stage to periodic one at 3rd stage, while the vibration amplitude keeps a constant level. (Fig. 7)

This limitation on the total mass and energy is also evident in today's economic systems, because a huge amount of information travels at the very high speed of light through the worldwide internet, whereas the speed of cargo shipment is still at the sonic level. This supply unbalance between information and objects may induce very complex oscillations and economic crisis, which do not have the sevenfold beat mentioned above.

8.5 Higher pressure for evolution and self-organization

The scenario described above for a universal network pattern in fractal nature can reveal the reason why living beings from the pre-biotic process to multi-cellar systems can be induced stably in a self-organizing manner. Random processes cannot generate the present living system having complex chemical reaction processes.

9. CONCLUSION

This approach solves mysterious problems concerning the origin of life, evolution, molecular biology, microbiology, system biology, morphogenesis, economics, medicine, brain science, subatomic theories, and cosmology.

Equation 5 may indicate that countries with excessive use of alcohol as depression factor now result in strong economic oscillations and low economic growth. Then, Eq. 6 shows that countries with less domestic and oversea transport lead to stop of economic growth in earlier time, while weak compartments such as national border and different current money are necessary.

Acknowledgement

This article is part of the outcome of research performed under a Waseda university Grant for special research project (2009B-206). This research was partially supported by the CREST project of Japan Science and Technology Agency. The author thanks Mr. Hiromi Inoue and Mr. Kenji Hashimoto of Waseda University for their help on this study.

References

[1]Naitoh K (1998) Introns for Accelerating Quasi-macroevolution, JSME International Journal, Series C, Vol.41, No.3: 398-405.
[2] Naitoh K (2001) Cyto-fluid dynamic theory. Japan J. of Industrial and Applied Mathematics, 18-1, pp75-105.
[3] Hirotsune S, Yoshida N, Chen A, Garrett L, Sugiyama F, Takahashi S, Yagami K, Wynshaw-Boris A, Yoshiki A. Addendum: (2003) An Expressed Pseudogene Regulates the messenger-RNA Stability of Its Homologous Coding Gene. Nature 423. 91-96.
[4] H.Aizawa, Isaac H. Bianco, T.Hamaoka, T. Miyashita, O.Uemura, Miguel L. Concha, C. Russell, S.W. Wilson and H. Okamoto:(2005) Current Biology Vol.15, 8, Pp 238-243.
[5] Naitoh K (2011) A force theory. RIMS Kokyuroku 1724, pp176-185.(also accepted in J. of Physics.)
[6] Naitoh K (2010) Onto-biology. Artificial Life and Robotics, 15, pp117-127.
[7] Naitoh K Stochastic Determinism. Artificial Life and Robotics, 13, pp10-17. 2008.
[8] Naitoh and Kuwahara (1992) J. of Fluid Dyn. Res.
[9] Naitoh K and Shimiya H (2011) Japan J. Indust. Appli ed Mathematics.
[10] Naitoh K (2011) Proc. of 15th Nordic and Baltic Conf. on Biomedical Engineering and Biophysics, Denmark.
[11] Naitoh K (2008) Engine for cerebral development. Artificial Life Robotics, Springer, 13 pp 18.
[12] Naitoh K and Kawanobe H (2011), Artificial Life Robotics.
[13] Naitoh K (2011) Morphogenic economics. Japan J. of Industrial and Applied Mathematics, Vol. 28, No.1.
[14] Takahashi K, Yamanaka S (2006) Cell 126, pp663-676.
[15] Naitoh K (2011) Onto-neurology. Proc. of JSST2011, Int. Conf. Modeling and Simulation Technology, Tokyo, pp.322-327.

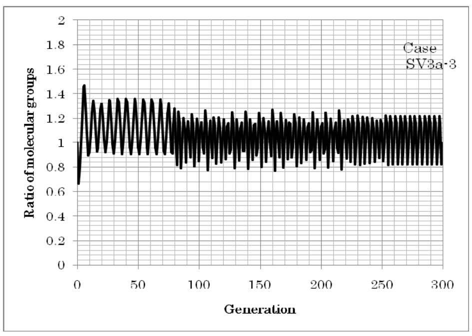

Fig. 7 Transition to sick condition as the 3rd stage in the aging process of the human being including the brain.

The Seventeenth International Symposium on Artificial Life and Robotics 2012 (AROB 17th '12),
B-Con Plaza, Beppu, Oita, Japan, January 19-21, 2012

Quasi-stability: Revealing the inevitability of biological molecules

H.Inoue, K.Hashimoto, K.Naitoh,
Waseda University, Faculty of Science and Engineering, 3-4-1 Ookubo, Shinjuku, Tokyo, 169-8555 Japan
(Tel : 81-3-5286-3265)
(Email address:k-naitoh@waseda.jp)

Abstract: Living beings meta-stable between unstable and neutral-stable conditions use only five types of nitrogenous bases and twenty amino acids selected naturally. The quasi-stability principle derived for spheroid particles [Naitoh, JJIAM 2001, Artificial Life Robotics 2010, Naitoh et al. Artificial Life Robotics 2011] reveals the reason why the molecular weight of purines and pyrimidines among nitrogenous bases varies by only about 1.5 times, whereas the threefold variation for the molecular weights of amino acids. Here, the theoretical model extended for the various levels of van der Waals force, surface tension, and coulomb force reveals the inevitability of proteins having the size ratios over 3.0. Moreover, we will also show the theoretical considerations for the other shapes of particles except for spheroids.

***Keywords*: Asymmetry, Size, Cyto-fluid dynamic theory, Nitrogenous base, Amino acids, Inevitability**

I. INTRODUCTION

Lots of types of amino acids and bases are possible in the artificial pools of molecules, but living beings use only five types of nitrogenous bases and twenty amino acids selected naturally. [1-5]

Meta-stable living systems can exist only when fully surrounded by water molecules. Thus, the quasi-stability of biological molecules such as nitrogenous bases, nucleic acids, amino acids, and proteins in living beings should be analyzed by considering the flows of water molecules.

Our previous model based on statistical fluid dynamic [6-10] has revealed the reason why living beings employ only five nitrogenous bases, i.e., two purines of A and G and three pyrimidines of T, C, and U, and also why purines and pyrimidines have a size ratio of about 1.5. In addition, the model has revealed the reason why the molecular weights of the twenty types of amino acids show a threefold variation between 240 of cysteine as the maximum and 75 of glycine as the minimum by taking a higher order of the Taylor series for the unified momentum equation describing the deformation motions of biological molecules. Then, the model extended [10, 14] also reveal the inevitability of proteins having the size ratios over 3.0.

In this report, we will show that the momentum theory extended for the various levels of van der Waals force, surface tension, and coulomb force qualitatively [10, 14] reveals the inevitability of proteins having the size ratios over 3.0 in details. Moreover, we also show the theoretical considerations for the other shapes of particles except for spheroids.

II.CYTO-FLUID DYNAMIC THEORY BASED ON the γ-ε EQUATION[6-11]

First, we define a parcel as a flexible spheroid having two long and short radii of $a(t)$ and $b(t)$ dependent on time t and constructed of a bio-molecule such as a base, an amino acid or a protein that is surrounded by water molecules. (A parcel consists of a bio-molecule such as nitrogenous base, amino acid, or protein, water molecules hydrated with the bio-molecule, and the immerse mass due to adding mass effect while impulsive start and stop of deformations occur [8, 9].) It is assumed that the parcel size is proportional to that of biological molecules such as nitrogenous base, amino acid, or protein.

The parcel becomes a sphere of the radius $r_d(=[ab^2]^{1/3})$ under an equilibrium condition. The deformation rate $\gamma(t)$ is defined as $a(t)/b(t)$, while a sphere without deformation corresponds to $\gamma = 1$. We assume that the flow field inside the parcel is the potential flow.

We derive a theory for describing the deformation and motions of two connected spheroid parcels having two equilibrium radii of r_{d1} and r_{d2} and two deformation rates of γ_k $[k = 1, 2]$, while the size ratio of the two parcels is defined by $\varepsilon = r_{d1}/r_{d2}$.(Fig. 1) We model the one-dimensional relative motion between the two parcels, nonlinear convections inside the parcels, the interfacial force at the parcel surface due to forces interacting between molecules, and collisions with water molecules outside the parcels. The interfacial force is evaluated in the form of σ / r^m where m and σ are constants and r is the curvature of parcel surface. Several types of forces such as van der Waals force, coulomb force, and surface tension can be explained by varying m. Here, the relation m = 1 implies the surface tension of liquid. The mean density of the parcels is ρ_L.

Moreover, the scale for averaging, i.e., the minimum scale representing the phenomenon, will be smaller than that in continuum mechanics and will be between the atomic scale and the size of the bio-molecule. Thus, this small averaging window applied to the Boltzmann equation leads to a weak indeterminacy of physical quantities such as deformation and density because of molecular discontinuity. [9, 10, 11]

Next, we derive the momentum equation describing the relation between a dimensionless deformation rate $\gamma_k (\equiv a_k / b_k\ [k=1,2])$ of each parcel dependent on dimensionless time $\bar{t}_k = \sqrt{\dfrac{8\sigma}{\rho_L r_{dk}^{2+m}}}t \quad [k=1,2]$ and the size ratio of the two parcels of $\varepsilon = r_{d1}/r_{d2}$. The stochastic governing equation having indeterminacy can be described as

$$
\begin{aligned}
\frac{d^2}{d\bar{t}_i^{\,2}}\gamma_i = \{ & [(-\varepsilon-\varepsilon^4+\frac{2}{3}\varepsilon E_{0j}\gamma_j^{-1/3})B_{0i}+\frac{2}{9}\varepsilon^{2+m}E_{0i}\varepsilon\gamma_i^{-4/3}](\frac{d}{d\bar{t}_i}\gamma_i)^2 \\
& +[\frac{2}{3}\varepsilon^{2+m}E_{0i}\gamma_j^{-1/3}B_{0j}-\frac{2}{9}\varepsilon^{2+m}E_{0i}\gamma_j^{-4/3}](\frac{d}{d\bar{t}_j}\gamma_j)^2 \\
& +(-\varepsilon-\varepsilon^4+\frac{2}{3}\varepsilon E_{0j}\gamma_j^{-1/3})C_{0i}\,\gamma_i^{\frac{5}{3}-\frac{2}{3}m}+\frac{2}{3}\varepsilon^{2+m}E_{0i}\gamma_j^{-1/3}C_{0j}\,\gamma_j^{\frac{5}{3}-\frac{2}{3}m}\}/Det \\
& +\delta_{st}
\end{aligned}
$$

$$[\text{for } i=1,2.\ j=1,2.\ i\neq j] \tag{1}$$

with

$$Det=-\varepsilon-\varepsilon^4+\frac{2}{3}\varepsilon^4 E_{0i}\gamma_i^{-1/3}+\frac{2}{3}\varepsilon\ E_{0j}\gamma_j^{-1/3},\ B_{0k}=\frac{1}{3\gamma_k}\frac{\gamma_k^{\,2}-2}{\gamma_k^{\,2}-1/2},$$

$$C_{0k}=\frac{3}{8}\frac{2\gamma_k^{\,2m}-1/\gamma_k^{\,m}-\gamma_k^{\,m}}{\gamma_k^{\,2}-1/2},\ \text{and } E_{0k}=3\frac{\gamma_k^{\,7/3}}{\gamma_k^{\,2}-1/2}[\text{for } k=1,2]$$

where the parameter δ_{st} denotes random fluctuation.

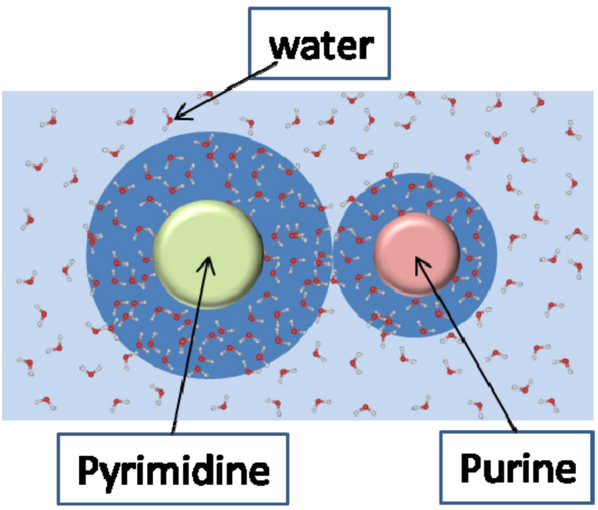

Fig.1. Two parcels connecting

III. FIRST ORDER OF ANALYSIS [6-9]

We then define the deviation from a sphere as y_i, which is equal to $\gamma_i - 1$. Taking the first order of approximation in the Taylor series leads to

$$
\begin{aligned}
\frac{d^2 y_i}{d\bar{t}_i^{\,2}} = [& -\frac{2}{3}(3-\varepsilon^3-2\varepsilon^{2+m})\left(\frac{dy_i}{d\bar{t}_i}\right)^2+3(3-\varepsilon^3)my_i \\
& -4\varepsilon^{1+m}\left(\frac{dy_j}{d\bar{t}_j}\right)^2+12\varepsilon^{1+m}my_j]/[3(\varepsilon^3+1)] \\
& +\delta'_{st},
\end{aligned} \tag{2}
$$

where the parameter δ'_{st} denotes random fluctuation.

A symmetric ratio of 1.0 (ε=1) makes the first term on the right-hand side of the equation zero, while an asymmetric ratio of $\sqrt[3]{3}$ around 1.44 (ε^3=3) makes the second term zero. The size ratios of 1.00 and approximately 1.44 can be described by the unified number of the n-th root of n.

We define a system as being quasi-stable when only one term on the right-hand side of the differential equation system governing the phenomenon (Eq. (2)) is zero. Life is relatively quasi-stable because d^2y_i/dt^2 becomes smaller when the size ratio of connected parcels takes the values of ε=1 or ε^3=3. An important clue for clarifying the inevitability and variety of biological molecules is the concept of quasi-stability (meta-stability) weaker than neutral stability. This is because biological systems are essentially neither neutrally stable nor absolutely stable owing to the potential for a brush with death and also since people can live over 50 years while maintaining the mysterious shape of the body. Thus, a new stability concept between the neutrally stable and unstable conditions is necessary for a meta-stable system of life, i.e., quasi-stability. [6-9]

Free nitrogenous bases in water often seem to be a column of two identical bases such as adenine-adenine, which are not in a two-dimensional plane. There are also multimeric complexes such as that of guanines. Then, it is well known that identical base pairs of $\varepsilon=1$ are often in RNA, while asymmetric base pairs such as the Watson-Crick type of about $\varepsilon^3=1$ are used in DNA.

IV. HIGHER-ORDER OF ANALYSIS [10, 11]

Higher order of the Taylor series

$$
\begin{aligned}
f(y) = & f(0)+\frac{f^{(1)}(0)}{1!}y+\frac{f^{(2)}(0)}{2!}y^2+\frac{f^{(3)}(0)}{3!}y^3 \\
& +.\frac{f^{(4)}(0)}{4!}y^4+\frac{f^{(5)}(0)}{5!}y^5+\frac{f^{(6)}(0)}{6!}y^6+\frac{f^{(7)}(0)}{7!}y^7 \\
& +\frac{f^{(8)}(0)}{8!}y^8+\frac{f^{(9)}(0)}{9!}y^9+......
\end{aligned} \tag{3}
$$

can be applied to Eq. (1).The ninth order of the Taylor series for parcel 1 brings

$$\frac{d^2y_1}{d\tau_1^2}=\left\{\begin{array}{l}\displaystyle\sum_{k=1}^{9}a_{9k}y_1^k+\sum_{k=0}^{8}\sum_{l=1}^{9-k}a'_{9\left\{l+k(19-k)/2\right\}}y_1^k y_2^l\\ \displaystyle+\left(\sum_{k=1}^{9}b_{9k}y_1^{k-1}+\sum_{k=0}^{7}\sum_{l=1}^{8-k}b'_{9\left\{l+k(19-k)/2\right\}}y_1^k y_2^l\right)\left(\frac{dy_1}{d\tau_1}\right)^2\\ \displaystyle+\left(\sum_{k=1}^{9}c_{9k}y_1^{k-1}+\sum_{k=0}^{7}\sum_{l=1}^{8-k}c'_{9\left\{l+k(19-k)/2\right\}}y_1^k y_2^l\right)\left(\frac{dy_2}{d\tau_2}\right)^2\end{array}\right\} \tag{4}$$

with

$\sum_{k=1}^{9}a_{9k}$, $\sum_{k=0}^{8}\sum_{l=1}^{9-k}a'_{9\{l+k(19-k)/2\}}$, $\sum_{k=1}^{9}b_{9k}$, $\sum_{k=0}^{7}\sum_{l=1}^{8-k}b'_{9\{l+k(19-k)/2\}}$, $\sum_{k=1}^{9}c_{9k}$, $\sum_{k=0}^{7}\sum_{l=1}^{8-k}c'_{9\{l+k(19-k)/2\}}$

are coefficients which include ε .

V. QUASI-STABILITY EXTENDED [7, 10, 11]

We can consider only the disturbance for parcel1, because the system of two parcels is mathematically symmetric. Then, we get

$$\frac{d^2y_1}{d\tau_1^2}=\left\{\sum_{k=1}^{9}a_{9k}y_1^k+\left(\sum_{k=1}^{9}b_{9k}y_1^{k-1}\right)\left(\frac{dy_1}{d\tau_1}\right)^2\right\} \tag{5}$$

as the ninth order of approximation, when the terms related to parcels 2 are eliminated.

The nine terms of $a_{91}y_1, a_{92}y_1^2, \cdots, a_{99}y_1^9$ come from interfacial force such as van der Waals force, coulomb force, and surface tension, whereas the later terms of $b_{91}, b_{92}y_1, \cdots, b_{99}y$ come from convection.

Here, we define

$a_{91}=0\ or\ b_{91}=0$

as the quasi-stable condition, while

$a_{92}=0,\ a_{93}=0,\ a_{94}=0,\ a_{95}=0,\ a_{96}=0,\ a_{97}=0,\ a_{98}=0,\ a_{99}=0,$
$b_{92}=0,\ b_{93}=0,\ b_{94}=0,\ b_{95}=0,\ b_{96}=0,\ b_{97}=0,\ b_{98}=0,\ or\ b_{99}=0$

is semi quasi-stable.

Table 1 shows the size ratios of parcels, which bring quasi-stable and semi quasi-stable conditions.

An important point is the numbers such as 4.25, 4.36, 4.54, 6.11, 8.02, 8.33, 10.4, 16.1, and 23.5. These numbers over 3.0 for size ratio will correspond to those of proteins.

VI. QUASI-STABILITY FOR THE OTHER SHAPES OF PARTICLES

We define a parcel as a spheroid shape in the cyto-fluid dynamic theory shown above, but biological molecules have various shapes. Thus, we redefine a parcel as that of a rice ball shape axi-symmetric for the x, which is formed by using spherical surface harmonics (Fig.2).

Assumptions different from the cyto-fluid dynamic theory are three. We first redefine $a(t)$ and $b(t)$ as lengths on the x axis, although $\gamma=(a/b)$ is same as that for the cyto-fluid dynamic theory. Secondly, the parcel becomes a sphere of the constant radius $r_d(=(a+b)/2)$ under equilibrium. Thirdly, the volume is shown by

$V=(\beta^3+4\pi/3)r_d^3$.

where β is defined as follows.

The rice ball shape axi-symmetric for the x axis is shown by

$$R(\theta,\varphi)=r_d\{1+\beta\cdot Y(\theta,\varphi)\} \tag{6}$$

With

$$Y(\theta,\varphi)=1/4\sqrt{7/\pi}\left(5Cos^3[\theta]-3Cos[\theta]\right)$$
$$\beta=2\sqrt{\pi/7}(\gamma-1)/(\gamma+1)$$

where the parameters θ and ϕ denote angle between *R* and the x axis and arbitrary rotation angle around the x axis, respectively.

In the case of m=1 the stochastic governing equation having indeterminacy can be described as

$$\begin{aligned}d^2\gamma_1/d\bar{t}_1^2=&-\Big[E_1F_1(1+\gamma_1)^2(1+\gamma_2)^2\Big(\big(-4H_1\varepsilon^3/(1+\gamma_1)^3\\&+B_1\big((-2E_2F_2+(1+\gamma_2)^2)H_2+(1+\gamma_2)^2H_1\varepsilon^3\big)\big/E_1(1+\gamma_2)^2\big)(d\gamma_1/d\bar{t}_1)^2\\&+\Big((1+\gamma_2)\big(-2C_2E_1F_2\gamma_2H_2\varepsilon^2+C_1\gamma_1\big((-2E_2F_2+(1+\gamma_2)^2)H_2+(1+\gamma_2)^2H_1\varepsilon^3\big)\big)\\&-2E_1(-2+B_2F_2(1+\gamma_2))H_2\varepsilon^2(d\gamma_2/d\bar{t}_2)^2\Big)\Big/E_1(1+\gamma_2)^3\Big)\Big]\Big/Det+\delta''_{st}\end{aligned} \tag{7}$$

With

$$Det=(1+\gamma_1)^2\left(2E_2F_2-(1+\gamma_2)^2\right)H_2+\left(2E_1F_1-(1+\gamma_1)^2\right)(1+\gamma_2)^2H_1\varepsilon^3,$$
$$B_k=-5\gamma_k^{-1}+8+\gamma_k^2,\ C_k=15/4(\gamma_k-1)(\gamma_k+1),\ E_k=3\gamma_k(1+\gamma_k)^2,$$
$$F_k=\left[2(-1+4\gamma_k-\gamma_k^2)\right]^{-1}$$
and $H_k=\left(49+6\sqrt{7\pi}(-1+\gamma_k)^3\right)/(1+\gamma_k)^3$ [for $k=1,2$]

where the parameter δ''_{st} denotes random fluctuation. Taking the first order of approximation in the Taylor series leads to

$$\frac{d^2y_1}{d\bar{t}_1^2}=\left[(1+\varepsilon^3)\left(\frac{dy_1}{d\bar{t}_1}\right)^2+\frac{15}{4}\left(\frac{1}{2}-\varepsilon^3\right)y_1+\frac{45\varepsilon^2}{8}y_2\right]/(\varepsilon^3+1)+\delta'''_{st,} \tag{8}$$

where the parameter δ'''_{st} denotes random fluctuation. A new ratio of about 1.26 makes the second term zero. This quasi-stability may correspond to base pairs of A-T.

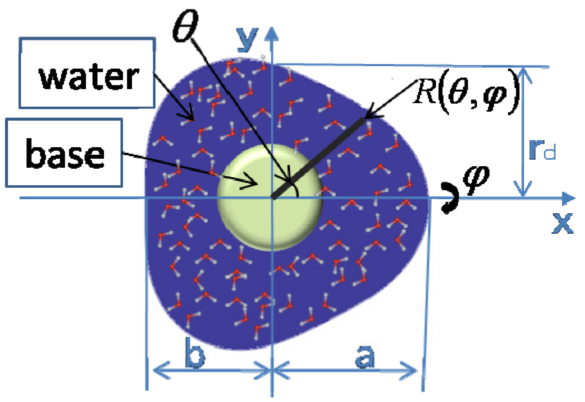

Fig.2. parcel of rice ball shape

Ⅶ. CONCLUSION

The theoretical model extended for the various levels of van der Waals force, surface tension, and coulomb force qualitatively reveals the inevitability of proteins having the size ratios over 3.0. Moreover, analysis based on a rice ball shape for parcel reveals the new quasi-stable ratio, which may correspond to base pairs of A-T.

REFERENCES

[1] S. L. Miller, A production of amino acids under possible primitive earth conditions. Science, 117: 528-529, 1953.
[2] J. Oro and A.P. Kimball, Synthesis of Purines Under Possible Primitive Earth Conditions. I. Adenine from Hydrogen Cyanide, Arch. Biochem. Biophys. 94: 217–227, 1961.
[3] H. Yanagawa, How Life Originated. TBS Britannica. 1-466, 1991.
[4] A. Ricardo and J.W. Szostak, Origin of Life on Earth. Scientific American, 2009.
[5] J.D. Watson, N.H. Hopkins, J.W. Roberts, et al. Molecular Biology of the Gene, Fourth edition: The Benjamin/Cummings Publishing Company, 1987.
[6] K. Naitoh, Cyto-fluid Dynamic Theory, Japan Journal of Industrial and Applied Mathematics, 18-1: 75-105, 2001.
[7] K. Naitoh, Macroscopic kinetic model on the origins of biological information. Trans. of JIAM: 115-137, 2003.
[8] K. Naitoh, Stochastic Determinism underlying Life, Artificial Life and Robotics, Springer, 13: 10-17, 2008.
[9] K. Naitoh, Onto-biology: clarifying the spatiotemporal structure, Artificial Life and Robotics, Springer, 15: 117-127, 2010.
[10] K. Naitoh, A force theory. RIMS Koukyuroku, Kyoto University, 2011. (to be published in J. of Physics.)
[11] K. Naitoh, K. Hashimoto, H. Inoue, to be pubshed in Artificial Life and Robotics, 2011.
[12] H. Lamb, Hydrodynamics, 6th ed. New York: Dover, 1945.
[13] K. Naitoh, Morphologic Economics. Proceedings of the conference in honor of Murray Gell-mann's 80th Birthday. Pp. 673- 680. World Scientific Publishing Co. Ltd, 2011.
[14] K. Naitoh, Proceedings of 15th Nordic and Baltic Conference on Biomedical Engineering and Medical Physics, Denmark, 2011.

Table1. Size ratios of parcels (The ninth order of approximation type)

	m=-2		m=-1		m=1		m=2		m=3	
Stability	Interfacial force term	Convective term	Interfacial force term	Convective term	Interfacial force term	Convective term	Interfacial force term	Convective term	Interfacial force term	Convective term
quasistable	1.44	1.00	1.44	1.00	1.44	1.00	1.44	1.00	1.44	1.00
	1.44	1.37	1.44	1.34	1.44	1.27	1.44	1.24	1.44,3.14	1.21
	1.44	1.41	1.44	1.40	1.44,3.58	1.35	1.44	1.32,16.1	1.44	1.29,4.36
	1.44	1.42	1.44,2.55	1.42	1.44,2.47	1.39	1.44	1.36,8.33	1.44	1.33,3.07
	1.44	1.43	1.44,2.01	1.42	1.44,2.10	1.40	1.44	1.39,8.02	1.44	1.36,2.86
Semi-quasistable	1.44	1.43	1.44,1.80	1.43	1.44,1.90	1.41	1.44	1.40,10.4	1.44	1.38,2.99
	1.44	1.44	1.44,1.70	1.43	1.44,1.79	1.42	1.44	1.41,23.5	1.44	1.39,4.25
	1.44	1.44	1.44,1.64	1.44	1.44,1.71 4.54	1.43	1.44	1.42	1.44	1.40
	1.44	1.44	1.44,1.59 6.11	1.44	1.44,1.65 2.93	1.43	1.44	1.42	1.44	1.41

The Seventeenth International Symposium on Artificial Life and Robotics 2012 (AROB 17th '12),
B-Con Plaza, Beppu, Oita, Japan, January 19-21, 2012

BioCell Print Utilizing PELID (Patterning with Electrostatically-Injected Droplet) Method

Shinjiro Umezu[1,2]

[1]Tokai University, Kanagawa 259-1292, Japan
[2]Riken, Saitama 351-0198, Japan
(Tel: 81-463-58-1211, Fax: 81-463-59-2207)

[1]umezu@tokai-u.jp

Abstract: The object of this study is to fabricate three Dimensional cell structures utilizing PELID (Patterning with ELectrostatically-Injected Droplet) method. Because it is preferable to perform laboratory experiments with 3D cell structures in tissue engineering and artificial organ. However, it is difficult to fabricate 3D cell structures because own weight of cell is above the bonding force between cells. In this paper, we printed MDCK cells and collagen as scaffolds utilizing the PELID method. We investigated growth of printed cells. Number of printed cells was increased day by day. We investigated fundamental characteristics on patterning collagen. The printed collagen was thick when the time to print was increased. These results indicated that it is possible to fabricate 3D cell structure.

Keywords: Inkjet, PELID, Scaffolds, Cell

1 INTRODUCTION

The goal of this study is to fabricate precision 3-Dimensional cell structures utilizing PELID (Patterning with ELectrostatically-Injected Droplet) method. It is preferable to perform laboratory experiments with 3D cell structures in tissue engineering and artificial organ. However it is difficult to fabricate 3D cell structures because own weight of cell is above the bonding force between cells. Commercial piezo inkjet technology was applied for 3D positioning of calcium alginate which contained living cells [1, 2]. Calcium alginate was used as scaffolds instead of gelatin liquid or collagen liquid because these were difficult to eject due to high viscosity. Because calcium alginate was easy to stick each other, 3D positioning of cells was succeeded. However cells could not contact each other by the wall of the calcium alginate. To clear this problem, inkjet technology should be more developed to eject highly viscous liquid. Our inkjet technology, PELID method, had two merits; those were high resolution and ability to eject highly viscous liquid. These merits were suitable to print cells precisely and eject highly viscous scaffolds. We reported that living cells were printed and 3D structures which contained living cells were fabricated utilizing the PELID method [3] with born stem cells. In this paper, we print MDCK cells because we are now applying the PELID method for fabrication of 3D cell structures.

2 EXPERIMENTAL SET-UP

Merits of the PELID method were suitable to print living cells and to fabricate 3D cell structures because cell structures should be precise and liquid with scaffolds was relatively highly viscous. However, voltage of the PELID method is about several kV. Sometimes people are killed by electric shock through consent. Household voltage is about several hundred V. We should investigate effect on the cells ejected by the PELID method.

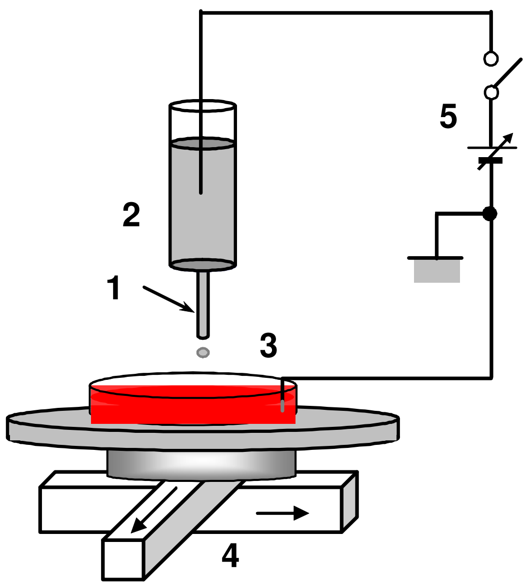

Figure 1 Experimental set-up of cell patterning utilizi ng PELID method. (1: water pin electrode, insulative c apillary tube was mounted at tip of syringe, 2: tank, fi lled with liquid of cells, 3: dish, filled with medium, 4: xyz linear stages, 5: DC high voltage power supply)

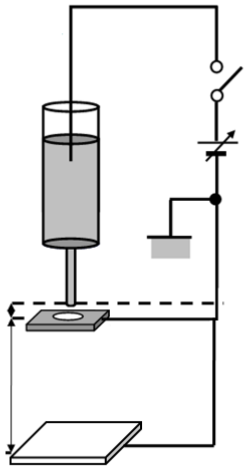

Figure 2: Experimental set-up to pattern collagen utilizing PELID. (plate electrode with hole is installed between nozzle and target)

An experimental set-up shown in Fig.1 was constructed to investigate characteristics to print living cells utilizing the PELID method. MDCK cells were used in this experiment. The tube filled with the liquid which contained the cells was hanged down perpendicular to a dish filled with medium. Voltage was applied between the syringes and the dish by a power supply (voltage range: -5kV ~ +5kV, Matsusada Precision Inc, Tokyo, HVR-10P). The air gap was adjusted by a z-stage and the dish was moved in x and y directions with two linear motors. Voltage application and motion of the linear stages were controlled by a PC.

In this paper, collagen was used as scaffolds between cells to fabricate 3D cell structures. An experimental set-up illustrated in Fig. 2 was constructed to investigate fundamental characteristics to print collagen. A tube filled with liquid that contained collagen was mounted perpendicular to a plate electrode made of stainless steel or dish that was filled with medium.

3 RESULTS

3.1 Cell ejection

Figure 3 and 4 show photos of printed cells when one day has passed after ejection of MDCK cells utilizing the ELID method. Figure 5 shows the enlarged view of living cells. Living cells were attached to the dish and spread. Dead cells were not attached to the dish and floating in the medium. Most cells were living in spite of high voltage application because current did not flow inside cells but around cells. Cells were living in case that the diameter of the tube was over 100 micron meters. In case that the diameter of the tube was less than 50 micron meters, it is difficult to eject continuously because cell attachment took place inside the tube. These results indicated that it was possible to print cells utilizing the PELID method.

3.2 Collagen patterning

Scaffolds are necessary to fabricate 3D cell structure because own weight of cell is above the bonding force between cells. In this paper, collagen is used as scaffolds. We investigate fundamental characteristics on patterning collagen. Figure 6 shows the line width in case that applied voltage is changed. When applied voltage is increased, line is fine. When applied voltage is further increased, line is wide. In case that applied voltage is the threshold of droplet mode

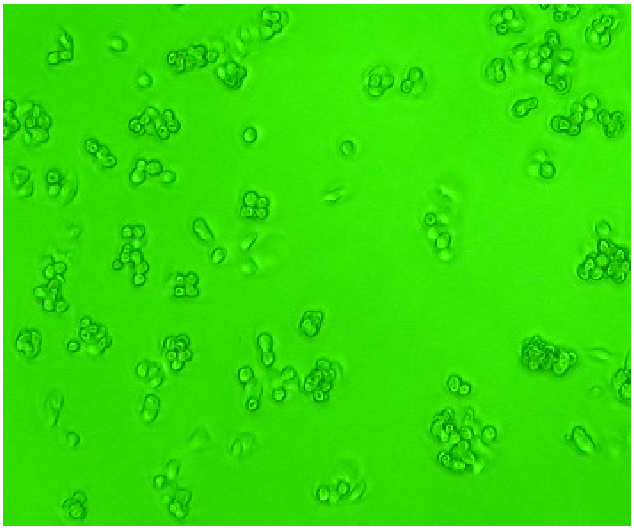

Figure 3 Picture of printed cells. (applied voltage: 2.9 kV)

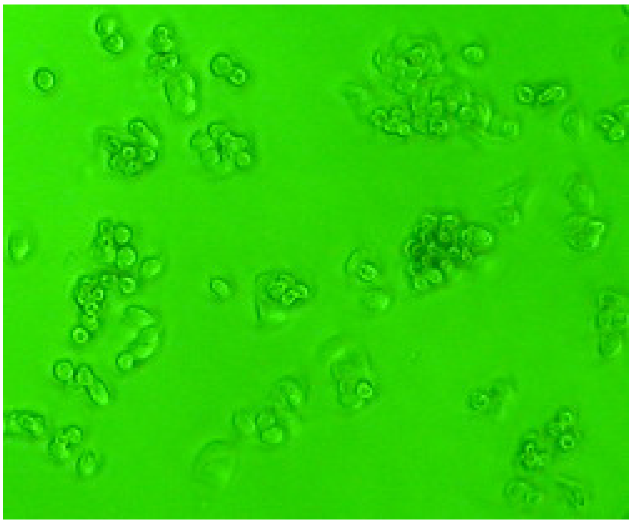

Figure 4 Picture of printed cells. (applied voltage: 3.9 kV)

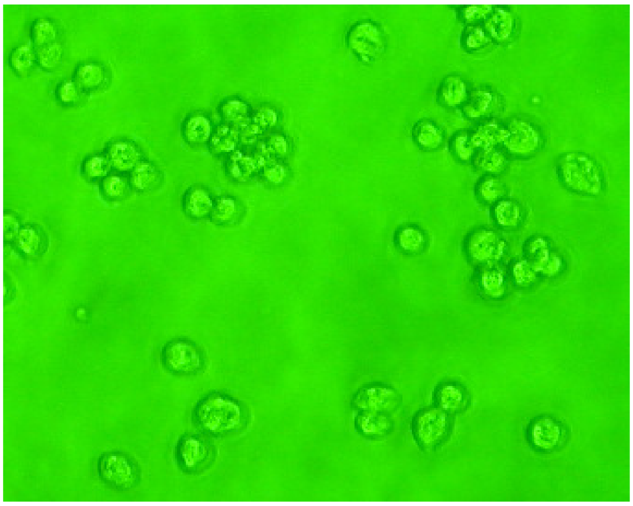

Figure 5 Enlarged view of printed cells.

[3], printed line is finest because ejected droplet is very small.

Figure 7 shows the thickness of printed collagen when the time to print is changed. Figure 8 shows photo of printed collagen. We measure height in center of printed collagen. The thickness is linearly increased when the time to print is increased. When the printed collagen is thick, the air gap is short. However, electric field around tip of nozzle is constant because plate electrode with hole is installed between the nozzle and target shown in Fig. 2. This result indicates that thickness of collagen is easy to control and it is possible to fabricate 3D cell structures.

Transportation of nutrient in 3D cell structure is most important issue. We fabricate 3D cell structure that collagen is printed on printed MDCK cells. This structure is fabricated in 96 well plates. Medium with nutrient is set on this structure. Figure 9 shows fabricated cell structures when 1 day has passed after print. Figure 10 shows fabricated cell structures when 2 days has passed after print. Figure 11 shows fabricated cell structures when 3 days has passed af-

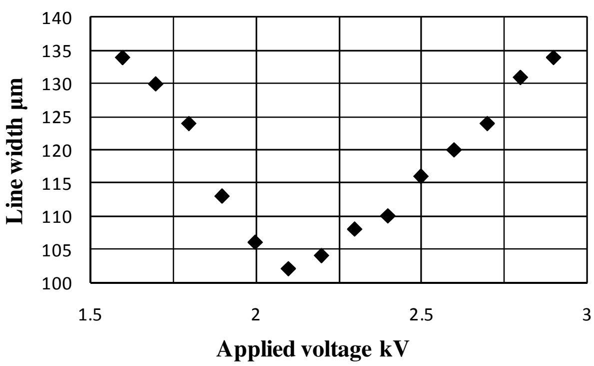

Figure 6 Line width of printed collagen.

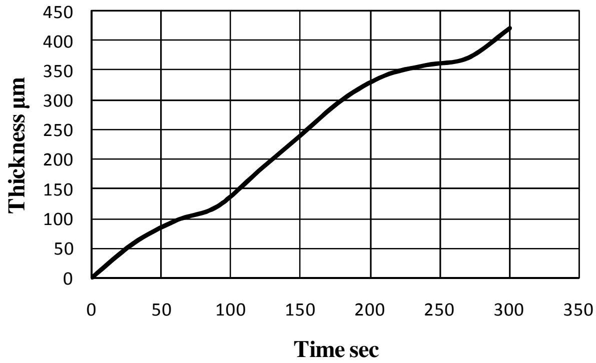

Figure 7 Thickness of printed collagen when the time to print was changed.

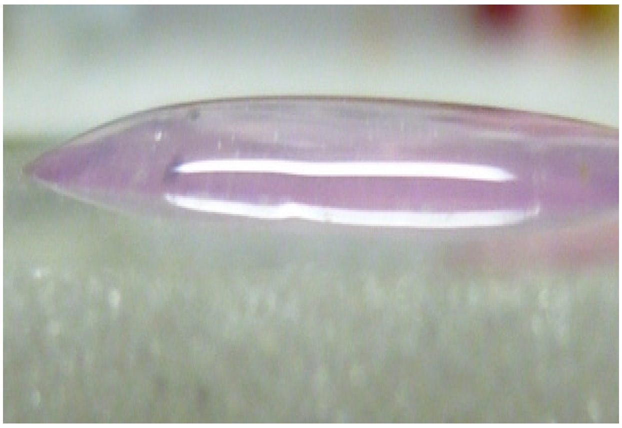

Figure 8 Photo of printed collagen.

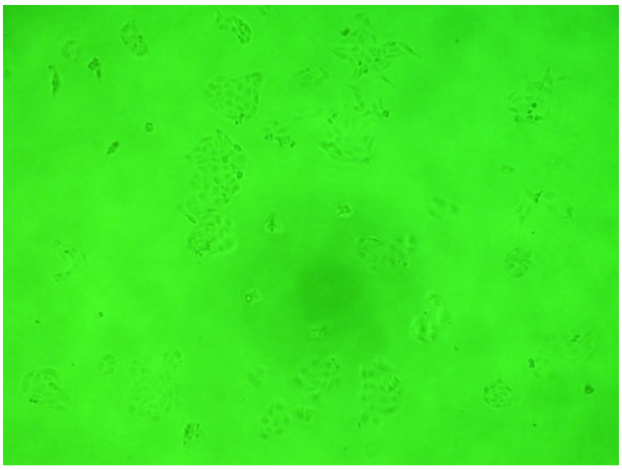

Figure 9 Photo of printed structure of collagen layer on MDCK cells when 1day has passed after print.

ter print. In spite that thickness of collagen is changed, nutrient reaches cells because collagen layer has cavit y. This result indicates that 3D cell structure is fabrica ted by PELID method and fabricated cell structure is l iving.

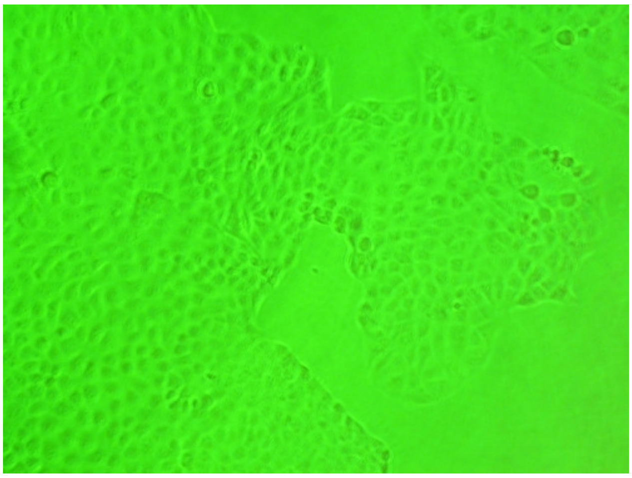

Figure 10 Photo of printed structure of collagen layer on MDCK cells when 2days has passed after print.

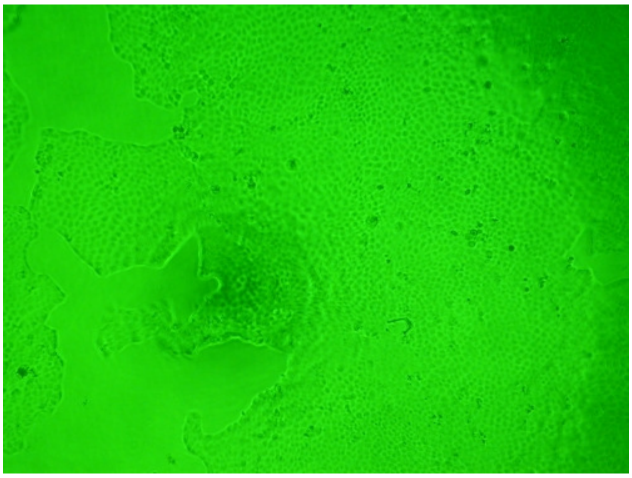

Figure 11 Photo of printed structure of collagen layer on MDCK cells when 3days has passed after print.

4 CONCLUSION

We fabricate 3D cell structure by using PELID method. The fabricated 3D cell is living and number of cells is increased day by day.

REFERENCES

[1] C. Henmi, etal., AATEX, 14, Special Issue, pp. 689-692 (2007)
[2] P. Calvert, science, 318, 5848, pp. 208-209 (2007).
[3] S. Umezu, etal., Proc. of DF2009, pp. 407-410 (2009).
[4] H. Kawamoto, etal., JIST, 49, 1, pp. 19-27 (2005).
[5] S. Umezu, etal., Proc. Euspen int'l conf. 2008, pp. 443-447 (2008).
[6] KH Choi, etal., Proc. of 1st Joint Workshop 2009 on Printed Electronics, pp. 45-49 (2009).

The Seventeenth International Symposium on Artificial Life and Robotics 2012 (AROB 17th '12),
B-Con Plaza, Beppu, Oita, Japan, January 19-21, 2012

Collective Motions of Chases and Escapes

Toru Ohira[1]

[1] Sony Computer Science Laboratories, Inc. Shinagawa, Tokyo 141-0022, Japan
(Tel: 81-3-5448-4380, Fax: 81-3-5448-4283)
(ohira@csl.sony.co.jp)

Abstract: We discuss a new take on an old mathematical problem of chase and escape. We consider one group chases another, called "group chase and escape", by presenting simple models. We have found that even a simple model can exhibit rich and complex behavior. The model has been extended to investigate the effects of (1) fluctuations in chasing and escaping movements, (2) reaction delays when chasing, and (3) the conversion of caught escapees to new chasers. We show that these effects can add further complexity and result in unexpected behaviors.

Keywords: Collective Motion, Chase and Escape, Delay, fluctuation

1 INTRODUCTION

"Chases and Escapes" (or "Pursuit and Evasion") is a traditional mathematical problem[1]. Typical questions include "How much time is needed for a chaser to catch a target?" and "What is the best escaping strategy?" There has been much mathematical interest in obtaining analytical results, so the majority of the questions have dealt with cases in which one chaser is pursuing a single escapee.

We recently proposed a simple extended model called "Group Chase and Escape"[2] in which one group chases another group. This extension connects the traditional problem of "Chases and Escapes" with current interest in the collective motions of self-driven particles such as animals, insects, cars, etc[3, 4, 5].

In this paper, we briefly present our basic model and its rather complex behaviors. Each chaser approaches its nearest escapee while each escapee moves away from its nearest chaser. Although there is no communications within groups, aggregate formations are observed both for both chasers and escapees. How these behaviors appear as a function of parameters, such as densities will be discussed.

In addition, we have extended our models in three main ways. First, we introduced a fluctuation. Players now make errors in which direction they step with some probability. It turns out that some levels of fluctuations work better for more effective capturing. Second, we introduced a reaction delay in a chaser who is pursuing an escapee that is moving with a uniform speed in a circular path. We did not observe a complex chaser's trajectory with constant reaction delay, but distance–dependent reaction delays can cause quite complex behaviors. Finally, we report briefly on the effect of the probabilistic conversion of the captured escapees into new chasers.

2 BASIC MODEL OF "GROUP CHASE AND ESCAPE"

Here, we describe our basic "Group Chase and Escape" model[2]. Essentially, it is a chase and escape problem in which one group chases another. In order to keep our extension simple, we made each chaser in a chasing group take one step toward its nearest escapee, while each escapee takes one step away from its nearest chaser. They do this independently of each other, meaning there is no communication or direct interaction among members within either the chasing or the escaping groups. We also decreed that a caught escapees be removed from the field, so that gradually the number of escapees decreases. The chase and escape finishes when all the escapees are caught and removed from the field ("complete capture").

There are various possible implementations of this conceptual model. To start with, we considered a square lattice with a periodic boundary condition and discrete step and time movements of the players. We also introduced an exclusion volume property: they cannot move if another of the same type (chaser or escapee) occupies the next location of intended motion. Also, when there are multiple choices (typically only two, due to the square lattice) for the next step, one of them is chosen with equal probability.

We have simulated the above model under various conditions[2, 6]. One of the interesting qualitative behaviors observed is a formation of aggregates by both chasers and escapees in spite of the fact that there is no direct interaction among the members of each group. In a related matter, given the initial size of the number of escapees, there exists an optimal number of chasers for effective capture. This can be seen by increasing the number of chasers with a given number of escapee, and noting the time taken to finish capturing all of the escapees. This complete capture time will decrease at a rather fast pace until it reaches the optimal number of chasers, after which it changes at a much slower rate. One of the reasons for this is the excluding volume effect (mentioned above): chasers get in each other's way. However, this is not the only cause – the very act of chasing and escaping is also a crucial factor, as such an effect is not seen if we set both chasers and escapees as groups of random walkers.

3 EFFECTS OF FLUCTUATION

We have extended our study to examine the effects of fluctuation in the above basic model[2, 7, 8, 9]. Specifically, we introduced errors in taking steps by players of both sides. With some probability, a chaser now takes a step in the wrong direction, thus increasing its distance from the nearest escapee. This error probability, which is also introduced in the steps of the escapees, is designed so that with the maximal error both sides become groups of random walkers, while with zero errors the model is reduced to the basic model described in the previous section.

We simulated the model with the above fluctuation error with varying probabilities and different ratios of the numbers of chasers and escapees. Increasing the error rate naturally led to a longer time for complete capture, and this is what happened when the number of chasers was relatively large. However, a rather interesting situation was observed when there were small number of chasers and escapees compared to the size of the square grid field. In this case, there exists the optimal level of fluctuation with which the time for complete capture became minimal – indeed less than not only the case in which both sides were randomly walking, but also in the case of the basic model mentioned above.

Cases that exhibit an appropriate level of fluctuation leading to "better" effects are being studied in various fields, including biology, material science, engineering and so on, under the name of "stochastic resonance"[10, 11, 12]. Our observation here can be considered as one of such examples.

4 EFFECTS OF DELAY

Next, we consider the effects of delayed reaction time on the part of the chasers[13, 14]. To examine this, we go back to one of the original one-to-one chase and escape problems in which the escapee moves in a circular path at a constant speed while the chaser moves with its velocity vector pointing to the current position of the escapee. We know that if the speed of the chaser is not as fast as the escapee, the capture is not possible, and the path of the chaser will approach to a "limit circle". The center of the two circles is the same and the ratio of the radii is the same as the ratio of the speeds of the chaser and the escapee.

Now let us consider a case in which the speeds of the chaser and escapee are the same. In this case, the chaser moves behind the escapee with the same uniform distance on the same circle. We now introduce a delay to the reaction time of the chaser. Specifically, the velocity vector of the chaser points to the past position of the escapee. We can immediately see that if we introduce this reaction time as fixed constant (fixed delay), the qualitative behavior of the chaser's motion does not change: the effect is merely an increase of the distance between the chaser and the escapee on the same circle.

However, if we set the reaction time to be proportional to the distance between the chaser and the escapee (distant dependent delay: the longer the distance, the longer the delay), the path of the chaser deviates from the circle. As we increase the rate of this proportionality, the path will become quite complex.

Delay–induced complex behaviors have been studied in various contexts. The most notable examples are the dynamical trajectories given by delay differential equations, such as the MacKay – Glass model[15]. In this model, a very simple first order differential equation with an external force term, which is a function of the delayed past state of the dynamical variable, can show various dynamics from a stable fixed point, limit cycles, and further create complex chaotic trajectories as we increase the value of the delay. Our observation here can be considered another example of delay–induced complexities.

5 EFFECTS OF CONVERSION

Finally, we briefly discuss the effect of conversions[16]. We extend the basic model in such a way that the caught escapee becomes a new chaser with a certain probability, while escapees can proliferate with some probability as well. The balance between these two factors again produces a non-monotonic change in the time it takes for complete capture with varying parameters. For example, if we fix the number of chasers and escapees and change the proliferation probability, there exists an optimal value to have the longest time for complete capture for a smaller value range of conversion probabilities. This finding has also been reported in a separate publication[16].

Using our model with this extension has potential for application to studies on the spread of certain epidemics such as rabies.

6 DISCUSSION

We have described our recent proposal and investigation of group–based chases and escapes and are faced with the following tasks. First, we should make our model more realistically by including communication within groups or more complex chasing and escaping strategies. They reflect such cases of one group of animals chasing another, e.g., wolves hunting deer[17]. Second, we need to consider a possible application to distributed robotics or other engineering systems. For example, the human immune system includes neutrophil granulocytes that chase foreign external viruses or chemicals. Could we implement such a defense system against attacks in cyberspace by adapting the concept of chase and escape included? Finally, this type of chase and escape interactions among the constituents in groups has not been addressed in studies of physical theories. Extension of many-body theories of statistical physics for the purpose of adapting them to chase and escape–type interactions will likely pose interesting challenges in the future.

The author would like to thank A. Kamimura, S. Matsumoto, and R. Nishi for their collaborative works. Thanks also go to T. Nogawa, N. Ito, K. Nishinari and J. Milton for their fruitful discussions.

REFERENCES

[1] P. J. Nahin, *Chases and Escapes: The Mathematics of Pursuit and Evasion*, Princeton: Princeton University Press, Princeton, New Jersey, 2007.

[2] A. Kamimura and T. Ohira, *New Journal of Physics*, vol. 12, 053013, 2010.

[3] T. Vicsek and A. Zafiris, "Collective Motion", *ArXiv.*, cond-mat:1010.5017, 2010.

[4] D. Chowdhury, L. Santen and A. Schadschneider, Phys. Rep., 329, 2000.

[5] D. Helbing, Rev. Mod. Phys., 73, 1067, 2001.

[6] S. Matsumoto, T. Nogawa, A. Kamimura, N. Ito and T. Ohira, in *Nonequilibrium Statistical Physics Today: Proceedings of the 11th Granada Seminar on Computational and Statistical Physics* (La Herradura, Spain, September 2010), P. L. Garrido, J. Marro, and F. Santos (Eds.) AIP Conf. Proc. 1332, 226-227, 2011.

[7] A. Kamimura, S. Matsumoto, N. Ito and T. Ohira, in *Proceedings of the International Conference on Cellular Automata for Research and Industry* (Ascoli Piceno, Italy, September, 2010), S. Bandini, S. Manzoni, H. Umeno, G. Vizzari (Eds.) Lecture Notes in Computer Sciences, vol. 6350, 570-579, 2010.

[8] A. Kamimura, S. Matsumoto, T. Nogawa, N. Ito and T. Ohira, in *NOISE AND FLUCTUATIONS: 21st International Conference on Noise and Fluctuations; ICNF 2011* (Toronto, Canada, September, 2011.)

[9] S. Matsumoto, T. Nogawa, A. Kamimura, N. Ito and T. Ohira, in *Proceedings of the 16th Symposium on Simulations of Traffic Flow* (Nagoya, Japan, Nov.25, 2010.), vol. 16, 1, 2010.

[10] K. Wiesenfeld, and F. Moss, *Nature*, vol. 373, 33, 1995.

[11] A. R. Bulsara and L. Gammaitoni, *Physics Today*, vol.49, 39, 1996.

[12] L. Gammaitoni, P. Hänggi, P. Jung, and F. Marchesoni, *Rev. Mod. Phys.*, vol.70, 223, 1998.

[13] T. Ohira, A. Kamimura, J. Milton, in *Proc. 7th European Nonlinear Dynamics Conference*(Rome, July,2011)

[14] J. Milton, J.Lippai, R. Bellows, A. Blomberg, A. Kamimura, T. Ohira, in *Proc. ASEM2010 Int.Design Engng. Tech. Conf.*(Washington DC, August,2011)

[15] M. Mackey, L. Glass, Science, vol.197, 287–289, 1977.

[16] R. Nishi, A. Kamimura, K. Nishinari, T. Ohira, Physica A, vol. 391, 337-342, 2012.

[17] T. Vicsek, *Nature*, vol. 466, 43, 2010.

Form and function of arterial bifurcations in the various parts of animal body

Takashi Matsuo[1], Shin-ichi Watanabe[1], Masato Nakakubo[1], Hidenobu Takao[1], and Tatsuhisa Takahashi[2]

[1]Kanagawa Institute of Technology, Atsugi, Kanagawa 243-0292, Japan
[2]Asahikawa Medical University, Asahikawa, Hokkaido 078-8510, Japan
(Tel: 81-46-291-3279, Fax: 81-46-291-3262)

matuo@rm.kanagawa-it.ac.jp

Abstract: Arterial casts from animal brain, kidney, and ear as well as chorioallantonic arteries of chick embryo were subjected to the microscopic measurement of arterial geometry. According to the optimization principle known as Murray's law, the blood vessel geometry at a bifurcation satisfies the relation $D_0^m = D_1^m + D_2^m$ $(m=3)$, where D_0, D_1, and D_2 are the diameters of the parent and two daughter vessels, respectively. The values of diameter exponent m were found to be 2.59 for brain, 2.54 for kidney, 2.58 for earlobe, and 2.49 for chick embryo, showing significant deviation from the Murray's law. Physiological implication of m values is discussed.

Keywords: Arterial geometry, Blood flow, Murray's law, Optimal theory,

1 INTRODUCTION

Understanding the physiological significance of organization and structure of the vascular system has been the major subject of vascular physiology. Murray [1] has applied minimum work concept to a theoretical analysis of blood flow through cylindrical segment of blood vessel. This principle, which stipulates that the total energy required to drive and maintain the blood to be minimal, predicts an expression that the diameters D of blood vessels are proportional to the cube root of the flow Q which they convey,

$$D \sim Q^{1/m}, \quad \text{or} \quad Q \sim D^m \quad (m=3). \qquad (1)$$

With similar consideration, the angle of vascular branching has been predicted to be a function of relative sizes of the parent trunk and its branch vessels [2]. Considering the mass flow continuity at arterial bifurcation, we obtain the relation among vessel diameters at a bifurcation ,

$$D_0^m = D_1^m + D_2^m, \qquad (2)$$

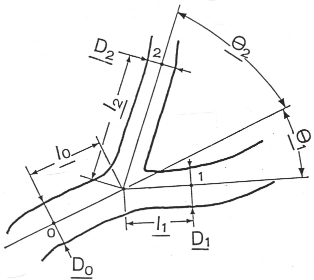

Fig. 1. Scheme of arterial bufurcation

where Do, D_1 , and D_2 are the respective lumen diameters of the parent vessel and the two daughter vessels (Fig. 1.).

Murray's law has been tested in the cardiovascular systems of several different animals including man [3][4]. It has been generally accepted that the arterial bifurcation geometries are understandable in terms of optimization with respect to the energy expenditure required for the fluid conducting system. However, some authors, who measured arterial geometries, reported significant deviation from the Murray's law. For example, Suwa et el. [5] reported that the diameter exponent m is different in organ to organ, and average value for various organs in human body is to be 2.7.

In this study, we made arterial casts from several parts of animal body such as brain, kidney and ear, and measured parent and branch vessel diameters and branching angles at arterial bifurcations. We also measured geometries of living arteries growing around chick embryo. Based on the geometrical data of arteries, we derived m values and compared them with those from the theory and other experiments.

2. METHOD

2.1 Preparation of arterial casts

Arteries in the cat brain, kidney and earlobe were visualized by casting procedure using a silicone compound or a aclilic resin. For the casting procedure, after death of animals due to excess dose of an anesthetic, a cannula was inserted into the ascending aorta through the left ventricle of the heart. Then the animal was perfused with a normal saline solution, and then a fixative solution under physiological pressure. After that, the casting medium was injected through the cannula. After few hours of medium polymerization, the organs were removed, and subsequently immersed in a glycerin solution to clear the tissue. Then, the photographs of the cleared organs were taken using a photomicroscope. Finally, the tissue surrounding the cast was corroded away by using a KOH solution. Microscopic examination readily allowed three dimensional visualization of the vascular bed. The present animal experiment has been approved by the Tokyo Medical and Dental University Institutional Review Board.

2.2 Visualization of arteries in chick embryo

Chick eggs incubated at a temperature of 311 K to 5-12 days of a 21-day incubation period were used for the present measurement. The shell and inner membrane were removed carefully and the avian chorioallantonic membrane (CAM) were exposed, which were subjected to the present measurement. The chorioallantonic artery is the largest extra embryonic and the major respiratory organ in the chick embryo.

(A)

(B)

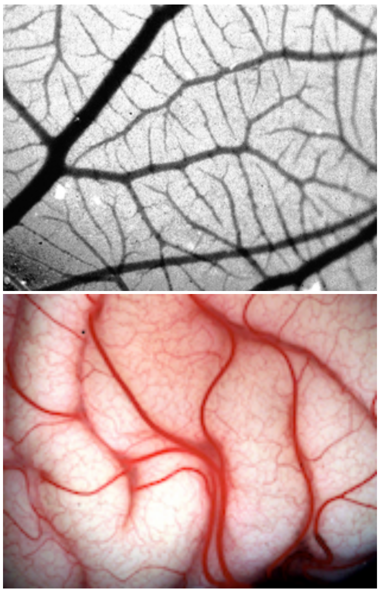

Fig.2 (A) Blood vessels (arteries and veins) in the CAM of chick embryo. (B) Arteries distributing on the cortical surface of the brain.

2.3 Measurement of vessel geometry

The vessel patterns obtained were magnified and recorded with a disecting microscope coupled with a video imaging system and a digital camera. Measurements were made manually on frame-grabbed images using an image analysis software.

Figure 2 (A) shows an example of the photograph of blood vessels in the CAM, and (B) arteries distributing on the cortical surface of the cat brain. Arteries in the CAM grow in a topologically two-dimensional and both arteries and veins show comparatively simple layered structure with little overlapping among them. The patterns are clear and the geometric measurements could be dome easily. We classified the vessels as arteries, if the blood flowed from the parent to the daughter vessels, otherwise, classified them as veins.

The diameter was measured at three locations near the bifurcation (see Fig. 1). Then, the average diameters D_0, D_1 and D_2 were computed for the parent the larger daughter, and the smaller daughter vessel, respectively.

3. RESULTS

3.1 Determination of diameter exponent

In order to obtain diameter exponent m from measured lumen diameters of the parent vessel and the two daughter vessels at arterial bifurcation, we rearrange equation (2) into following equations [6];

$$\frac{D_1}{D_0} = \left[1 + \left(\frac{D_2}{D_1}\right)^m\right]^{-1/m} , \quad (3)$$

and

$$\frac{D_2}{D_0} = \frac{D_2}{D_1}\left[1 + \left(\frac{D_2}{D_1}\right)^m\right]^{-1/m} . \quad (4)$$

We obtained diameter exponent m by nonlinear regression analysis of measured diameter ratios.

3.2 Measured diameter exponent

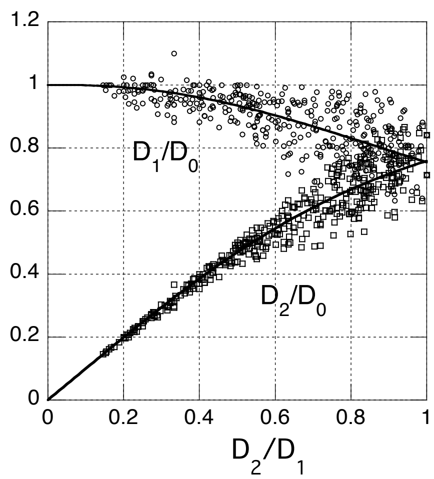

Fig.3. CAM arteries

In Fig. 3, normalized diameters of larger and smaller daughter branches (D_1/D_0 and D_2/D_0, respectively) are plotted as functions of the diameter ratio of the daughter branches (D_2/D_1) in the CAM arteries of chick embryo. In Fig. 3, also plotted are nonlinear regression fits to Eqs. (3) and (4) with *m* taken as the regression parameter. The regression analysis resulted in *m*= 2.46 for (D_1/D_0) and 2.51 for (D_2/D_0).

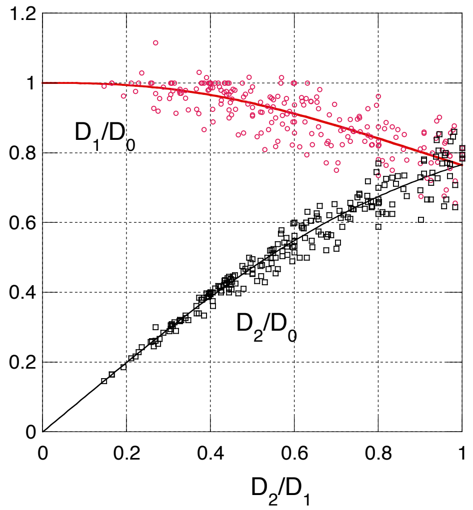

Fig. 4. Cortical surface of the brain

Figure 4 shows normalized diameters (D_1/D_0 and D_2/D_0, respectively) as functions of the diameter ratio (D_2/D_1) in the arteries distributed over the cortical surface of the cat brain. The regression analysis yielded *m*= 2.58 for (D_1/D_0) and 2.60 for (D_2/D_0).

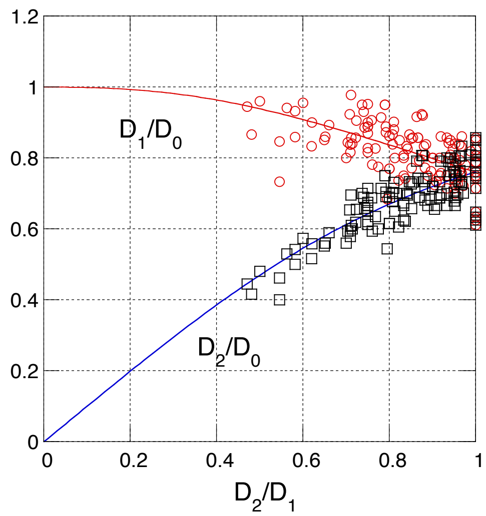

Fig. 5. Kidney

Figure 5 shows the results for arteries in the kidney. The regression analysis showed *m*= 2.53 for (D_1/D_0) and 2.54 for (D_2/D_0)in this case.

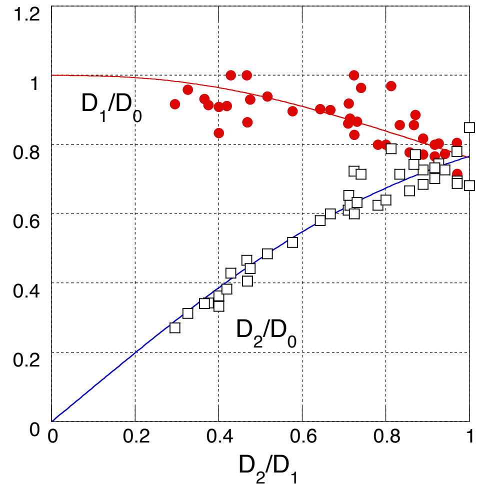

Fig. 6. Earlobe

Figure 6 shows the results for arteries in the earlobe. The regression analysis showed *m*= 2.56 for (D_1/D_0) and 2.61 for (D_2/D_0).

4. DISCUSSION

4.1 Statistical error

As can be noted in Figs. 3-6, the relationships between diameter ratios show considerable scattering. The degree of scatter is similar to that found by other researchers [6]. Human error is considered to be the main source of error in the present study. Selection of vessels to be measured was highly subjective, and choosing the proper locations of diameter measurements required some judgment. We tried to minimize such errors by averaging measurements at three positions for one artery. Moreover, the reliability of the data is supported by the fact that four people participated in the measurement at different times obtained similar results. The scattering of the geometry data is ascribable to the essential nature of blood vessels.

4.2 Determination of diameter exponent

In several reports [6][7], the validity of Murray's law was confirmed based on the regression analysis for α (= $(D_1^m + D_2^m)/ D_0^m$) with assuming *m*=3 a priori. This way assuming *m*=3 a priori could, however, yield misleading results. In Figs. 7 (a)(b), are plotted the present $(D_1^m + D_2^m)$ versus D_0^m relationships in CAM arteries with linear regression analysis; panel (a) : *m*=3 and panel (b) : *m*=2. In both cases, the slopes of regression lines are around unity with correlation coefficient R of nearly 1. These indicate that the linear regression analysis for ($D_1^3 + D_2^3$) versus D_0^3 relationships is not satisfactory for determination of diameter exponent m. This is because we calculated m values using equations (3) and (4).

(a)

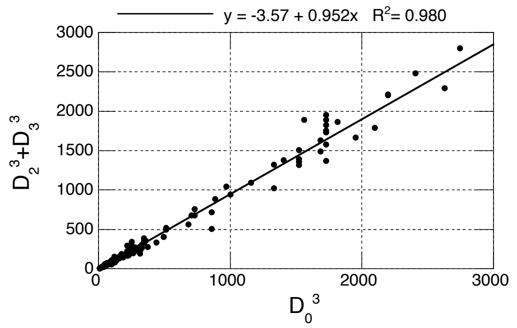

(b)

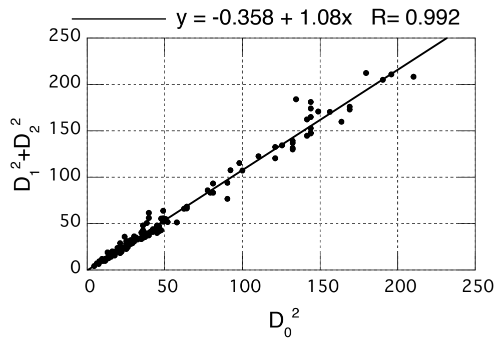

Fig.7. Relationships between ($D_1^{\mathrm{m}} + D_2^{\mathrm{m}}$) and D_0^{m}

4.3 Comparison of diameter exponent

Taber et al. [6] have reported diameter exponent for living organisms. They measured vessel diameters in yolk arteries of chick embryo, and reported the diameter exponent to be 2.88, which is markedly larger than the present m=2.49 for CAM arteries. The difference is significant, and in part ascribed to the difference of tissues, to which the arteries are belonging. In the present study, yolk arteries around chick embryo were visualized as well as CAM arteries. However, we exclude yolk arteries from the measurement, since they were frequently overlapped by yolk veins and tended to subduct in the yolk, and thereby geometric measurement for them were rather difficult. In fact, Taber et al. obtained m values using data from both arteries and veins. This can be another reason for the difference in m.

4.4 Physiological implication of diameter exponent

From equation (1), the averaged velocity (over cross sectional area) Va of blood flow through a vessel of diameter D is given by:

$$Va \sim D^{m-2}. \qquad (5)$$

Diameter exponent m=3 means that the velocity Va is linearly proportional to D. When m=2, Va is constant irrespective of diameter. Differences in m in different organs indicate that diameter-velocity relationships are different in organ to organ and connected to the function of organ.

It is remarkable that in the animal body, m could take a value smaller than 2, where the blood velocity increases as vessel diameter decreases. Bennett et al. [8] have found that m values for the perinatal pulmonary arteries were 1.74-1.82. They concluded that compared with an adult, the increased velocity is necessary to yield a very high flow resistance that serves to shunt blood flow away from the lung to other organs prior to birth. Thus, the diameter exponent m is considered to be an important index characterizing the blood circulation of organ.

5. CONCLUSION

The presently measured values for diameter exponent were considerably smaller than 3, which Murray' law predicts. It should be noted that the Murray' low was derived from several assumptions; Poiseuille flow for blood flow and simplified assumption for energy expenditure of blood. The physiological importance of diameter exponent is that it is closely related to blood flow properties in organs. In this sense, more sophisticated measurements of m for various organs would be necessary.

REFERENCES

[1] Murray C D (1926), The physiological principle of minimum work I. Proc. Natl. Acad. Sci., 12:207-214.

[2] Murray C D (1926), The physiological principle of minimum work applied to the angle of branching of arteries. J. Gen. Physiol., 9:835-841.

[3] Zamir M (1978), Nonsymmetrical bifurcations in arterial branching. J. Gen. Physiol. 72:837-845.

[4] Zamir M, Medeiros A and Cunningham K (1979), Arterial bifurcation in the human retina. J. Gen. Physiol.74: 537-548.

[5] Suwa N (1963), Estimation of intravascular blood pressure gradient by mathematical analysis of arterial casts. Tohoku J Exp. Med, 79:168-198.

[6] Taber L, Ng S, Alicia M. et al. (2001), Investigating Murray's law in the chick embryo, J. of Biomechanics 34:121- 124.

[7] LaBarbela L (1990), Principles of design of fluid transport systems in zoology. Science, 249:992-1000.

[8] Bennett S, Eldridge M, Zaghi D et al. (2000), Form and functions of fetal and neonatal pulmonary arterial bifurcations. Am. J. Physiol. 279:H3047-3057.

The Seventeenth International Symposium on Artificial Life and Robotics 2012 (AROB 17th '12),
B-Con Plaza, Beppu, Oita, Japan, January 19-21, 2012

Analytical approach to synchrony between populations of neurons with modulatory effects

Yoichiro Hashizume[1], Osamu Araki[2]

Department of Applied Physics, Tokyo University of Science,
1-3 Kagurazaka, Shinjuku-ku, Tokyo 162-8601, Japan
[1] hashizume@rs.tus.ac.jp, [2] brainics@rs.kagu.tus.ac.jp

Abstract: We have analyzed the synchrony of neurons using the effective input theory. First, the dependence of intra-regional synchrony on the strength of synaptic connections is clarified. When the synaptic connections are weaker than thresholds of neurons, spontaneous firings do not exist. Second, we have studied the inter-regional synchrony of two regions connected by modulatory common noises. As a result, under the appropriate modulatory-effects there exist nontrivial sets of synchronized states of regions. Furthermore, at least one of these two regions satisfies the condition of intra-regional synchrony. When both regions do not satisfy the condition of intra-regional synchrony, these two regions should have the same structure of synaptic connections in order to synchronize inter-regionally.

Keywords: Populations of neurons, Effective input theory, Synchronized firing, Synchrony between regions, Analytical approach

1 INTRODUCTION

Up to now, the input trains to a neuron are mainly described as stochastic processes in such as Ricciardi[1], Stein[2], and others. Because the properties of the stochastic processes with random Langevin forces are well known (Uhlenbeck and Ornstein[3]), we can easily obtain a lot of essential properties of neurons with applying the stochastic theories. However, methods of stochastic theories approximate the neurons to a single neuron framework which corresponds to the mean-field theory or the phenomenological theory. Essentially these approximations do not include synaptic connections directly. On the other hand, Chen and Jasnow[4] formulate the "effective input theory", which includes one or more synaptic connections using "effective inputs". Here, the "effective inputs" denote the mean value of inputs to populations of several neurons, namely "cluster", from outside neurons through the synaptic connections. Thus the effective input theory is useful to clarify the effects of synaptic connections on synchronies of neurons.

Using the effective input theory, we have studied the conditions of the synchrony in two typical cases as follows:

(1) When neurons are firing spontaneously (and periodically) without external inputs from outside the system, there assumes to exist only effective inputs. First, we obtain the frequency of synchronous firing of neurons under effective inputs. Then we require the condition that the effective inputs corresponds to the frequency of synchronous firings. From this condition, namely "self-consistency", we obtain the frequency of the synchronous firing. If the self-consistency is not fulfilled by any frequency, the synchronous firing does not occur. From the above discussion, we have shown that high frequency is obtained for strong synaptic connections, while low frequency is obtained for weak synaptic connections.

(2) When the neurons additionally receive modulatory effects, we have examined the effects on synchronies of neurons. We have introduced two independent clusters of neurons and obtained the self-consistency using the effective input theory. Here the synaptic connections and external inputs have changed under the modulatory effects. If we assume that modulatory effects are global, two independent clusters receiving the same modulatory effects correlate each other. Then we analyzed the condition of synchrony between the independent areas.

In section 2, we make a brief review of the effective input theory and discuss synchronized firings of neurons in a cluster. Then we obtain the conditions between synaptic connections and thresholds for the spontaneous synchronized firings. In Section 3, we apply the effective input theory for synchronization between different regions with modulatory common noises. In Section 4, we summarize the results of our studies.

2 EFFECTIVE INPUT THEORY

In this section, we make a brief review of the effective input theory[4] for discussing a periodic synchronized firing of neurons located in the same cortex region, namely "spontaneous firings", using our formulation.

At first, we approximate the neuron connections as shown in Fig.1. Because the neurons are connected very complexly, we approximate the cluster neurons i and j whose membrane potentials are denoted as $V_i(t)$ and $V_j(t)$, respectively, with the effective input $I_{\rm eff}$. The effective input $I_{\rm eff}$ includes large numbers of inputs from outside of the cluster.

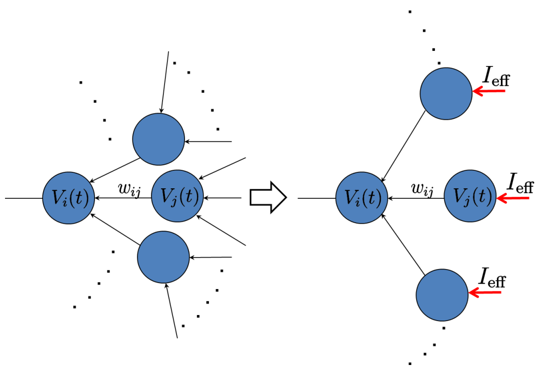

Fig. 1. Approximation of the cluster neurons: The neurons are connected each other as shown in the left-side figure. We approximate the neuron connections to the cluster including the neurons i and j and the effective input as shown in the right-side figure.

Then we obtain the effective equations of motion about the membrane potentials $V_i(t)$ and $V_j(t)$ as follows:

$$\tau\frac{d}{dt}V_j(t) = -V_j(t) + I_{\rm eff} \tag{1}$$

and

$$\tau\frac{d}{dt}V_i(t) = -V_i(t) + \sum_{j=1}^{c}\tau w_{ij}\sum_{k}\delta(t - t_j^k), \tag{2}$$

where the parameters τ, w_{ij}, c, and t_j^k denote time-constants, synaptic weights, connection numbers, and the k-th firing time of neuron j, respectively.

From Eq.(1), the membrane potential $V_j(t)$ is obtained as

$$V_j(t) = I_{\rm eff}(1 - e^{-t/\tau}). \tag{3}$$

Then we obtain the firing time $t_j^k = kT_j$ using the effective input $I_{\rm eff}$ as

$$T_j = -\tau\log\frac{I_{\rm eff} - \theta}{I_{\rm eff}} \tag{4}$$

with the threshold potential θ. Here, for convenience of calculations, we use a simple condition that the resting potential and the reset potential after firing take the same value of 0.

The time dependence of $V_i(t)$ is derived from Eq.(2) under the firing of j-neuron satisfying Eq.(4) as follows:

$$\begin{aligned} V_i(t) &= \frac{1}{\tau}e^{-t/\tau}\int_0^t ds e^{s/\tau}\sum_{j=1}^{c}\tau w_{ij}\sum_{k}\delta(s - t_j^k) \\ &= W\frac{1 - e^{-t/\tau}}{1 - e^{-T_j/\tau}}, \end{aligned} \tag{5}$$

where the parameter $W = \sum_j w_{ij}$ means the total synaptic weight. Then, we obtain the cycle-time T_i of i-neuron's firings as

$$T_i = -\tau\log\left[1 - \frac{\theta}{W}(1 - e^{-T_j/\tau})\right]. \tag{6}$$

Now, we consider the self-consistency

$$\begin{aligned} I_{\rm eff} &= \frac{1}{T}\int_0^T ds\sum_{j=1}^{c}\tau w_{ij}\sum_{k(<t)}\delta(s - t_i^k) \\ &\simeq \frac{\tau}{T}\sum_{j=1}^{c}w_{ij}\sum_{k=1}^{T/T_i}\int_0^T ds\delta(s - kT_i) \\ &= \frac{\tau}{T_i}W. \end{aligned} \tag{7}$$

This consistency means a periodic synchronized firing of neurons what we call "spontaneous firing". Then, from Eqs.(4), (6), and (7), we obtain the self-consistent equation as

$$\frac{\tau}{T}(1 - e^{-T/\tau}) = \left(\frac{\theta}{W}\right)^2, \tag{8}$$

where we have redefined $T = T_i$. The cycle-time T of spontaneous firing of the cluster neurons is given as a solution of Eq.(8). The function $f(T/\tau)$ defined as the left-side of Eq(8), namely $f(T/\tau) = (\tau/T)(1 - e^{-T/\tau})$, is plotted in Fig.2. As is shown in Fig.2, the function $f(T/\tau)$ has the asymptotic value 1 in the case of $T \to 0$ (namely the frequency $\nu = 1/T \to \infty$). Consequently, in the case of $\theta > W$, there does not exist the spontaneous firing. On the other hand, in the case of $\theta < W$, there exists the spontaneous firing. This result is supported by the following physical phenomena, that is, the firing frequency of neurons are enhanced by effective inputs (from neighbor neurons) exceeding the threshold potential. Meanwhile the spontaneous firing does not occur under the weak effective inputs.

3 SYNCHRONY OF DIFFERENT REGIONS

We apply the above effective input theory to analyze the modulatory effects for synchronization between different regions. Membrane potentials of neurons are modulated by diffuse modulatory systems, for example, norepinephrine, 5-hydroxytryptamine, dopamine, and others. These transmitters cause diffusive effects to neurons, and modulate the neuron's behaviors (especially the acceptance of noise effect). Thus we introduce a model which has two neural clusters and the common random input trains from modulators, as shown in Fig.3.

At first, we analyze the membrane potentials $V_i(t)$ and $V_j(t)$ in the region R1. The equations of motion of neurons in the region R1 are defined as follows:

$$\tau\frac{d}{dt}V_j(t) = -V_j(t) + I_{\rm eff} + \eta(t) \tag{9}$$

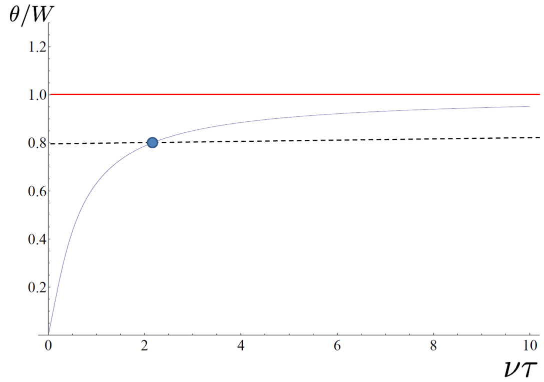

Fig. 2. Condition of spontaneous firings: The vertical axis expresses the rate θ/W while the horizontal axis expresses the firing frequency. The condition has the asymptotic value 1 with respect to θ/W. Then, in the case of $\theta > W$, spontaneous firing never occurs.

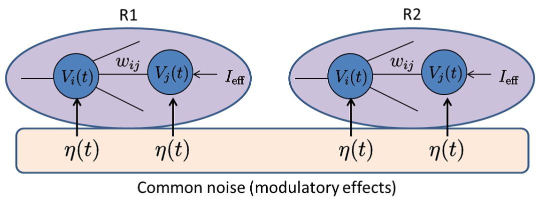

Fig. 3. Modulating effects for populations of neurons: Neurons in the two different regions (R1 and R2) receive the common noise from the diffuse modulatory systems. The regions R1 and R2 synchronize through the common noise.

and

$$\tau \frac{d}{dt} V_i(t) = -V_i(t) + \sum_{j=1}^{c} \tau w_{ij} \sum_{k(<t)} \delta(t - t_j^k) + \eta(t), \quad (10)$$

using the effective input $I_{\rm eff}$ and the common random input $\eta(t)$. Here the random input assumes to be a stochastic input train with the average $\langle \eta(t) \rangle = \lambda$.

From Eq.(9), the average potential $\langle V_j(t) \rangle$ is obtained as

$$\langle V_j(t) \rangle = (I_{\rm eff} + \lambda)(1 - e^{-t/\tau}). \quad (11)$$

Then, the condition $\langle V_j(T_j) \rangle = \theta$ yields the cycle-time T_j as

$$T_j = -\tau \log \frac{I_{\rm eff} + \lambda - \theta}{I_{\rm eff} + \lambda}. \quad (12)$$

Similarly to the derivation of Eq.(5), we obtain the time dependence of $V_i(t)$ from Eq.(10) as

$$\begin{aligned} V_i(t) &= \frac{1}{\tau} e^{-t/\tau} \int_0^t ds e^{s/\tau} \left[\sum_{j=1}^{c} \tau w_{ij} \sum_{k(<t)} \delta(s - kT_j) + \eta(s) \right] \\ &= W e^{-t/\tau} \frac{e^{T_j/\tau}(e^{t/\tau} - 1)}{e^{T_j/\tau} - 1} + \frac{1}{\tau} e^{-t/\tau} \int_0^t e^{s/\tau} \eta(s) ds. \end{aligned} \quad (13)$$

Then, the random average of Eq.(13) yields

$$\langle V_i(t) \rangle = \sum_{j=1}^{c} w_{ij} e^{-t/\tau} \frac{e^{T_j/\tau}(e^{t/\tau} - 1)}{e^{T_j/\tau} - 1} + \lambda(1 - e^{-T_i/\tau}). \quad (14)$$

From Eq.(14), we obtain the mean value of cycle-time T_i as the solution of the following equation:

$$\theta = e^{-T_i/\tau} \sum_{j=1}^{c} w_{ij} \frac{e^{T_j/\tau}(e^{T_i/\tau} - 1)}{e^{T_j/\tau} - 1} + \lambda(1 - e^{-T_i/\tau}). \quad (15)$$

Using the self-consistency Eq.(7), and Eqs.(12) and (15), we obtain the self-consistent condition

$$1 = \left[\alpha \left(\frac{\alpha}{x} + \bar{\lambda} \right) + \bar{\lambda} \right] (1 - e^{-x}), \quad (16)$$

with the dimensionless parameters $\bar{\lambda} = \lambda/\theta$, $\alpha = W/\theta$, and $x = T/\tau$, where we redefine the cycle-time as $T = T_i$.

The self-consistent condition in the region R2 is obtained similarly as

$$1 = \left[\alpha' \left(\frac{\alpha'}{x} + \bar{\lambda} \right) + \bar{\lambda} \right] (1 - e^{-x}), \quad (17)$$

where the parameter α' reflects the construction of synaptic connections $\{w'_{ij}\}$ in R2, namely $\alpha' = \sum_j w'_{ij}/\theta$.

When the synchronized firing occurs between the regions R1 and R2, the firing cycle T takes the same value in each region. Consequently, we obtain the relation between α and α' under synchrony as

$$\bar{\lambda} = \frac{x - \alpha^2(1 - e^{-x})}{x(1 - e^{-x})(\alpha + 1)} = \frac{x - \alpha'^2(1 - e^{-x})}{x(1 - e^{-x})(\alpha' + 1)} \quad (18)$$

The second equation of Eq.(18) has nontrivial solution

$$\alpha' = \frac{\alpha - e^x(\alpha + x)}{(e^x - 1)(\alpha + 1)}. \quad (19)$$

The solutions $\alpha = \alpha'$ and Eq.(19) are shown in Fig.4. From the discussion in Section 2, in the case of $|\alpha| > 1$, R1 shows the spontaneous firing, while, in the case of $|\alpha| < 1$, R1 does not show the spontaneous firing. Similar relation is shown in R2 with respect to $|\alpha'|$. Then, from Fig.4, it is necessary to lead the nontrivial synchrony that the parameters $|\alpha|$ and $|\alpha'|$ take $(|\alpha| > 1, |\alpha'| > 1), (|\alpha| > 1, |\alpha'| < 1)$ or $(|\alpha| < 1, |\alpha'| > 1)$. That is, there exists nontrivial synchrony of two regions only in such cases that at least one region takes conditions of spontaneous firings.

The strength of modulating effects $\bar{\lambda}$ is shown in Fig.5 using Eq.(18). Especially, when the parameters α and α' take the value $|\alpha| < 1$ and $|\alpha'| < 1$ (namely both R1 and R2 do not show the spontaneous firing), there exists only trivial relation $\alpha = \alpha'$ for synchrony. Then, from Eq.(18), the limiting behavior of $\bar{\lambda}$ for $x \to \infty$ and $x \to 0$ is obtained as

$$\bar{\lambda}_\infty \equiv \lim_{x \to \infty} \bar{\lambda} = \frac{1}{1 + \alpha} \quad (20)$$

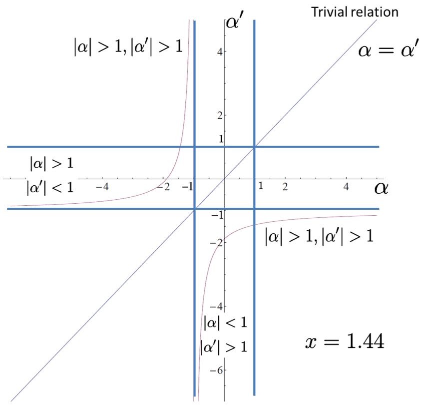

Fig. 4. Relation of α and α' where $x = 1.44$: The vertical axis express the parameter α' while the horizontal axis expresses α. Parameters α and α' means W/θ and W'/θ, respectively. These parameters mean the characters of each region (R1 (α) or R2 (α')). Of course, this graph has a symmetry between α and α'. We find the non-trivial relation as shown in Eq.(19) only in the cases of $(|\alpha| > 1, |\alpha'| > 1), (|\alpha| > 1, |\alpha'| < 1)$ and $(|\alpha| < 1, |\alpha'| > 1)$.

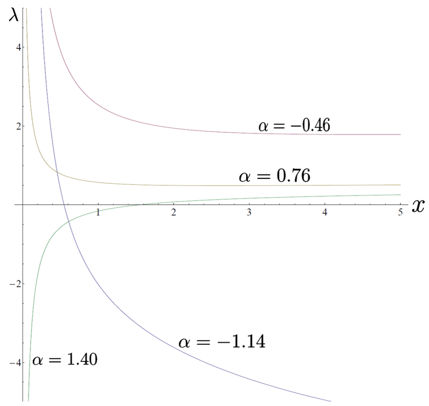

Fig. 5. Dependence of common noise on the synchrony frequency: The vertical axis expresses the parameter $\bar{\lambda}$ while the horizontal axis expresses the parameter x. The parameter $\bar{\lambda}$ means the strength of common noises, and the parameter x means the cycle-time of a synchrony. We chose the parameters $\alpha = -1.14, -0.46, 0.76$ and 1.40. These cases are corresponds to each region of Fig.4.

and

$$\bar{\lambda}_0 \equiv \lim_{x \to 0} \bar{\lambda} \sim \frac{1-\alpha}{x}. \tag{21}$$

Consequently, under the condition $|\alpha|, |\alpha'| < 1$, $\bar{\lambda}$ satisfies the conditions $\bar{\lambda}_\infty > 0$ and $\bar{\lambda}_0 \to +\infty$, that is, the parameter $\bar{\lambda}(x)$ takes positive value for all x. This result shows the following plausible physics: The modulatory effects should enhance the firings of neurons in both regions when the spontaneous firing does not occur in each regions R1 and R2 (Fig.5). Additionally, the R1 and R2 should be constructed by the same configuration (Fig.4). Conditions for synchrony between the regions which do not show the spontaneous firing are very strict.

4 CONCLUSION

We have studied the synchrony firings of neurons in typical two cases.

First, using the effective input theory, we have analyzed the inner region synchrony of neurons (spontaneous firing) using the effective input theory within the region. We have clarified that the inner region synchrony depend on the strength of synaptic connections. When the synaptic connections are weaker than thresholds of neurons, there do not exist spontaneous firings.

Second, we consider the synchrony between two regions connected by modulatory common noises. The synchrony of different regions through the modulators occurs in two typical cases as follows:

(1) At least one of two regions takes the state for spontaneous firings and receiving appropriate modulation.

(2) When both two regions do not take the state for spontaneous firings, these two regions should be constructed by the same synaptic connections for synchrony. Additionally, modulatory effects enhance the firing of neurons in both regions.

The second condition is very strict, and may be very rare.

We have considered the two regions for inter region synchrony. If these regions assumed to be two of many regions in brain, the parameters α and α' can be treated as continuous parameters. Then this model of synchrony may change depending on the region of the brain.

This method is generally applicable to other complicated dynamical systems. Although we have used the integrate-and-fire neuron model in this study, any other neuron models can be analyzed generally in the same way.

REFERENCES

[1] Ricciardi LM (1976), Diffusion approximation for a multi-input model neuron, Biol Cybern 24:237-240

[2] Stein RB (1965), A theoretical analysis of neuronal variability. Biophys J 5:173-194

[3] Uhlenbeck GE, Ornstein LS (1930), On the theory of Brownian motion. Phys Rev 36:823-841

[4] Chen CC, Jasnow D (2010) Mean-field theory of a plastic network of integrate-and-fire neurons, Phys. Rev.E 81: 011907(1-12)

The Seventeenth International Symposium on Artificial Life and Robotics 2012 (AROB 17th '12),
B-Con Plaza, Beppu, Oita, Japan, January 19-21, 2012

A Computational Model for Multiple Potential Actions for Inferred Movement Goals

Takuro Fujimura[1], Yuta Kakimoto[2] and Osamu Araki[3]

Department of Applied Physics, Tokyo University of Science
1-3 Kagurazaka, Shinjuku-ku Tokyo 162-8601, Japan

[1]j1510632@ed.kagu.tus.ac.jp, [2]ykaki@rs.kagu.tus.ac.jp, [3]brainics@rs.kagu.tus.ac.jp

Abstract: Klaes et al. showed that multiple potential actions could be generated only single spatial cue according to task rule. Also they reported that population activities of the PPC neurons which represent two different motor goals might be biased. The motivation of this paper is to make a computational model which can reproduce Klaes's experimental results. We have proposed a decision making model which has the PFC layers encoding the rule informations and showed that the potential action for the inferred goal was observed in the PPC layer, and the balance of the potential actions in the PPC layer varied depending on the connection strength from PFC to PMd. These results suggest that the observed biased potential actions during the memory periods were the result of "trade-off" for achieving the balanced multiple potential actions while the spatial cue was presented.

Keywords: action choice, computational model, parietal cortex, potential actions, premotor cortex, rule selection task

1 INTRODUCTION

Recent studies have demonstrated that when animals are presented multiple action goals, they compute multiple potential goals (multiple potential actions) based on visual inputs simultaneously and choice an action from them [1][2][3]. These studies have also reported that frontparietal cortex, specifically PPC (Posterior Parietal Cortex), PMd (Premotor Dosal), and PFC (Prefrontal Cortex) relate to information processing on generating potential actions[1][3].

Cisek et al. [1] observed neural responses corresponding to potential actions in primate motor area. In this experiment, two reaching goals (spatial cues) were presented to monkeys and successive cue (color cue) indicated the correct goal which monkeys had to select. Although the spatial cues generated two potential actions in PMd, one of the potential actions was specified by color cue presentation. [1]. Cisek and his colleagues also demonstrated that a computational model composed of frontoparietal stream simulated the process of generation and selection of potential actions as short term memory of visual inputs [2].

On the other hand, Klaes et al. showed that multiple potential actions could be generated even when only single spatial cue was visually presented. In this experiment, monkeys were trained to reach in the same or opposite direction to the presented spatial cue depending on the rule cue which are successively presented. Neurons in the primate PPC simultaneously represented two distinct potential actions corresponding to direct and opposite (inferred) movement goals[3]. This result means that the potential actions are not only the short term memory of the presented spatial cues, but the representation of the movement goals internally generated by the neural processes using information of the presented cues.

In the Klaes's rule-selection task, it is also reported that the population tuned activities of the PPC neurons which represent two different motor goals might be biased. Interestingly, trained monkeys showed a preference to reach the opposite direction of the spatial cue, and neural activities correspond to the inferred direction in the PPC become strong during the spatial cue period. This biased neural activity was balanced only if the probabilities of the rewards were adjusted to reinforce balanced choice behavior.

In this paper, we propose a computational model which generates multiple potential actions and decides appropriate one according to the task rules in the

Klaes's task. We also show that this model also exhibits the biased or balanced potential actions depending on parameter values and consider the mechanisms of the biased potential actions observed in the Klaes's task.

2 METHODS

2.1 Process of the Psychological Experiment

First, we show the potential motor-goal task[3] (Fig.1) which we simulate in this study. This paradigm is the fundamental framework of Klaes's experiments.

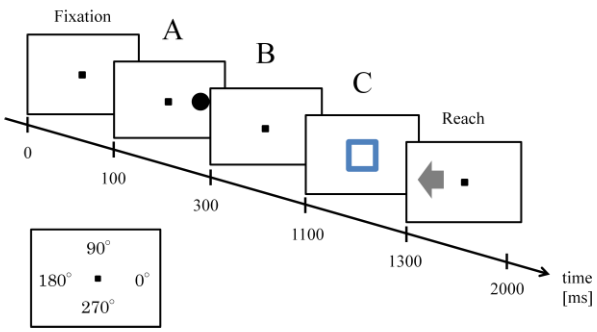

Fig. 1. Rule selection task. The inset shows directions of the spatial cue.

At stage A in Fig.1, a spatial cue (one of the four positions: 0, 90, 180, 270 degree) is provided for 200ms. Then, the subject should keep this memory at least for 800ms. At stage C, after the rule cue (direct or inferred rule) is provided, the subject is required to the same direction as the spatial cue (direct rule) or the opposite direction (inferred rule) alternatively. The direct (or the inferred) rule is instructed by a green (or blue) square on the fix point.

2.2 Framework of Model

In this study, we expand the Cisek's computational model to go through with the potential motor-goal task. Our model neurons, neural connections within layers and inter-layers, and the basic structure of the network are almost the same as Cisek's model. Two main differences are as follows: (1) We introduced two prefrontal layers that are responsive to direct and inferred rules (PFC_D and PFC_I), (2) There are synaptic connections from PFC_D and PFC_I to corresponding neurons in the first PMd layer.

Visual inputs include spatial cues and rule cues (Fig.2). The information of position of a spatial cue is provided to PPC, PFC_D and PFC_I neurons. In case of a rule cue, rule information is given to PFC_D or PFC_I alternatively. Each neuron in PPC, PMd, and M1 has directional preference to reach, and its neighboring neurons represent close directions. The arrow in Fig.2 shows the direction of each projection of synaptic connection. To generate two neural activities representing potential plans from a spatial cue, the PFC_I neuron should excite PMd layer neurons which represent the direction opposite from the spatial cue.

On the other hand, within each of the frontparietal layers except PFC, neurons with similar directional preferences excite each other, whereas neurons with different preference mutually inhibit each other.

Since some neurons are excited and others are suppressed in this competitive neural field, some groups of activated neurons usually appear. We regard the activated group represents a potential action (potential action plan). Neural activities generated in PPC, PFC_D, PFC_I layers are integrated in PMd1 layer.

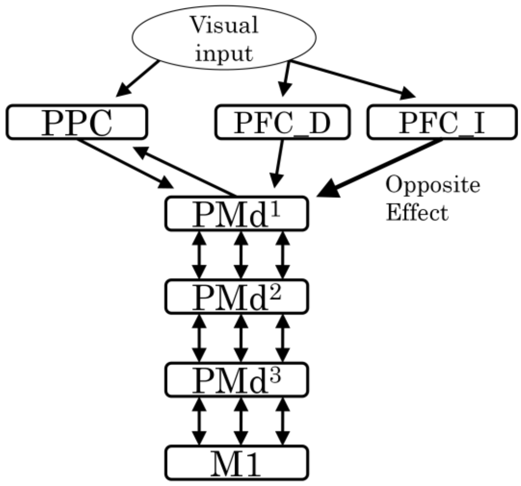

Fig. 2. Framework of this model [2]

2.3 Neuron Model

We use the "mean-rate leaky-integrator" neurons model. The mean firing rate of *i* th neuron at layer N follows this differential equation [2]:

$$\frac{dx_i^N}{dt} = -\alpha X_i^N + (\beta - X_i^N)\cdot\gamma\cdot E_i^N - X_i^N \cdot I_i^N + \Theta, \quad (1)$$

where X_i^N is the activity of the *i* th neuron in layer *N*, E_i^N is the excitatory input to the neuron, I_i^N is the inhibitory input to the neuron, α is the decay rate, β is the neuron's maximum activity, and γ is the excitatory gain. Θ is a Gaussian noise. Each parameter value follows Cisek's numerical experiments[2].

2.4 Neural Connections between Layers

To excite two neurons in different layers each other if they insist similar directions, the synaptic weight from *j* th neuron in layer N to *i* th neuron in layer M depends on the difference of neuron index (*i* – *j*) as follows:

$$\begin{cases} W_{ji}^{N\to M} = 0.4 - 0.2(i-j) & \text{if} \quad i-j \geq 0 \\ W_{ji}^{N\to M} = 0.4 + 0.2(i-j) & \text{if} \quad i-j < 0 \end{cases} \quad (2)$$

The synaptic weights from PFC_I to PMd1, however, should be relatively so strong that the neural activity representing direct direction supported by PPC and PFC_D competes with that of inferred direction by PFC_I only. Otherwise, the potential action in an inferred direction will be suppressed away. Thus we introduced an amplitude parameter κ to examine the effects of synaptic weights from PFC as follows:

$$\begin{cases} W_{ji}^{PFC\to PMd1} = \kappa\cdot\{0.15 - 0.015(i-j)\} & \text{if } d \geq 0 \\ W_{ji}^{PFC\to PMd1} = \kappa\cdot\{0.15 + 0.015(i-j)\} & \text{if } d < 0 \end{cases} \quad (3)$$

When we think of PFC_D (PFC_I), we regard κ as κ_D (κ_I).

3 RESULTS

3.1. Balanced Potential actions in Memory Period

Figure 3 shows activity of the model network at $\kappa_D = \kappa_I = 1.0$.

The cue direction neurons in the PFC_D and the inferred direction neurons in the PFC_I were activated by the visual input. During the cue period, neural populations encoding the cue direction in the PPC and PMd layers were strongly activated.

The potential actions in the PPC were balanced during the memory period (Fig.1 B) because the connection strength from the PFC_D and the PFC_I were same value. On the other hand, PPC neurons showed biased potential actions during the cue period because of the additional visual input to the PPC population tuning to the cue direction.

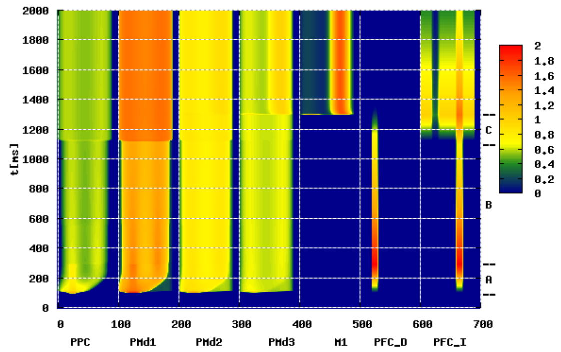

Fig. 3. Population result for the balanced data set (0 degree cue, Inferred rule, $\kappa_D = \kappa_I = 1.0$). A is the spatial cue period, B is the memory period, and C is the rule cue period.

3.2 Biased Potential actions in Memory Period

Figure 4 shows activity of the model network at $\kappa_D = 1.0$, $\kappa_I = 5.3$. In the situation of larger KI, the projections from PFC_I to PMd excites the neural population to encode opposite goal more than direct goal in PPC. Simulated biased potential actions during the memory periods require at least a condition that $\kappa_D < \kappa_I$. This means that the connections from the PFC_I to the PMd is stronger than that from the PFC_D.

In the PPC layer, neural population encoding the direct cue direction was strongly activated during the spatial cue period. In contrast, neural population encoding the opposite cue direction was strongly activated during the memory period. The cause of inversion in active groups is due to the disappearance of the spatial cue during the memory period. Therefore, "direct" population became weaker, and "inferred" population became stronger relatively.

However, despite biased activities in PPC, this model chose appropriate an action according to the displayed rule, on the rule cue period. As a result, under the conform to the biased data set and choose the action comfortable to rule cue which are consistent with the experimental data[3].

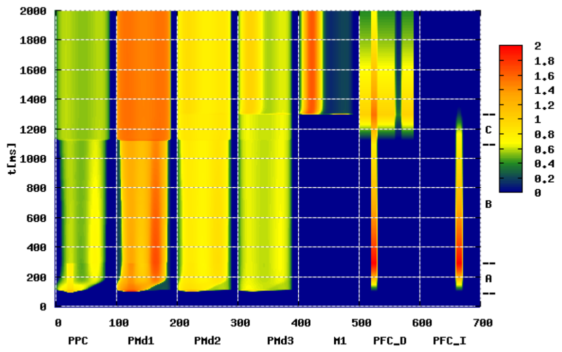

Fig. 4. Population result for the biased data set (0 degree cue, Direct rule, κ_D =1.0, κ_I =5.3).

3.3 Mechanism for bias of potential actions

Klaes et al. reported that, for the well trained monkeys, the potential actions in the PPC were biased during the memory periods. Two types of the rule cue (indicating the direct motor goal and the inferred motor goal) were equally presented in their experiment. So the biases of the potential actions may not be reasonable.

Figure 5 shows a population activities when the spatial cue was presented for a prolonged time (κ_D =1.0, κ_I =5.3). In this situation, the potential actions during the prolonged cue period seemed balanced. The time lag of the potential actions for the direct and the inferred goal is caused by the parameters β and γ which are different between PFC and PPC neurons. This time lag was responsible for the switching of the potential actions in the PPC for the short-lasting cue presentation (200-400 ms in Fig.4).

This result implied that the balance of the cue period may make it inevitable that the potential actions during the memory periods become biased. That is, although the bias of the potential actions (and the behavioral performance) of the trained monkeys is apparently unreasonable, this bias can be reasonably interpreted as the "trade-off" for the balanced activities of the potential actions when the spatial cue is continuously presented. We also insist that this hypothesis will be confirmable by the physiological experiment that the cue stimulus will be continuously presented to the monkeys while this hypothesis is a matter of speculation at the current moment.

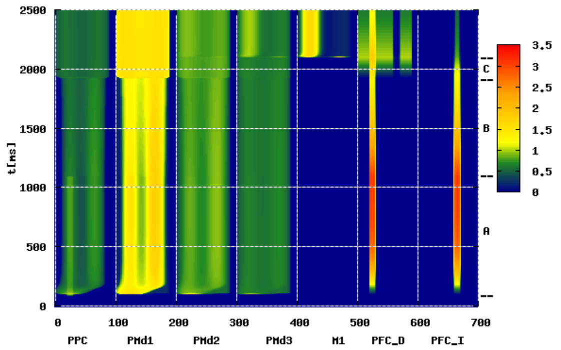

Fig. 5. Population result with longer spatial cue (0 degree cue, Direct rule, κ_D =1.0, κ_I =5.3).

4 CONCLUSION

In this paper, we proposed a decision making model with PFC layers which encodes the rule information of the task. This model generates the multiple potential actions which correspond to the candidates of the movement goals even when the single spatial cue was presented in the task.

We also demonstrated that the proposed model shows both the biased and balanced potential actions. This result suggests that the observed biased potential actions (and biased behaviors) during the memory periods were the results of "trade-off"s for achieving the balanced multiple potential actions while the spatial cue was presented.

REFERENCES

[1] Cisek, P. , & Kalaska, J. F. (2005), Neural correlates of reaching decisions in dorsal premotor cortex: specification of multiple direction choices and final selection of action. Neuron 45:801–814
[2] Cisek, P. (2006), Integrated neural processes for defining potential actions and deciding between them: a computational model. J Neurosci 26:9761–9770
[3] Klaes, C. , Westendorff, S. , Chakrabarti, S. , & Gail, A. (2011), Choosing goals, not rules: deciding among rule-based action plans. Neuron, 70: 382-384

The Seventeenth International Symposium on Artificial Life and Robotics 2012 (AROB 17th '12),
B-Con Plaza, Beppu, Oita, Japan, January 19-21, 2012

An action planning model using short-term and long-term memory information during learning of sequential procedures

Nao Tomoda, Yuta Kakimoto, and Osamu Araki

Department of Applied Physics, Tokyo University of Science
1-3 Kagurazaka, Shinjuku-ku, Tokyo 162-8601, Japan

Abstract: To make an action plan, it is thought that the brain uses memory systems. Thus, we propose an action plan model, which deals with the physiological experiments to push buttons in the correct order. In the model, there are two independent action-planning systems of long-term memory and working memory. When the stimulus set is input, they propose action plans, and the selection is decided in a competitive way via the value of estimation parameters. As a result, the model reproduces similar behaviors to the biological data. Especially our model make errors at first but it gradually learns correct responses by trial and error utilizing the memory systems as the monkey did in the physiological experiment. The results suggest that SMA and pre-SMA may have close relationships to the entries to long-term memory and working memory systems in the brain.

Keywords: action plan, long-term memory, Pre-SMA, sequential procedure, short-term memory, SMA

1. INTRODUCTION

In the physiological experiments of Hikosaka et al., 2 of 16 (4 by 4 matrix) buttons were illuminated (this matrix is called a "set") simultaneously and the monkey had to push them in a predetermined order. The monkey was required to push the buttons in 5 consecutive sets (called a "hyperset") [1]. When a hyperset which the subject has already learned is the stimulus, the task is called a "learned task". And when a hyperset consists of only novel sets, it is called a "new task". It is reported that SMA and pre-SMA are specifically activated by the case of the learned task and new task, respectively [1][3][4]. When a hyperset of which a few sets in a learned hyperset are replaced by novel sets, the task is called "modified task". Although monkey made mistakes in the early trials in the modified task, it gradually became to push the buttons correctly. Intriguingly, in the early trials, the monkey sometimes pushes unilluminated buttons in response to a novel set [1]. We think that this is because it may associate the previous stimulus sets with an action to be done next from the learned memory of a series of actions even if it actually encounters a novel stimulus.

Additionally, in the modified task, the neurons in pre-SMA become activated in response to the learned sets as well as the novel sets [1]. This implies that the activation in pre-SMA in response to the learned sets increases while the monkey is learning the modified task.

On the other hand, Nakahara et al. reproduced the behaviors and neural activities using a neural network model of the basal ganglia and the cortices in the reinforcement learning framework [2]. But the model does not attend the kinds of monkey's errors, where all of them are treated as learning errors. Thus, we pay attention to the error that is sometimes observed in the modified task, which makes the monkey to push an unilluminated buttons. From a new viewpoint to explain this error behavior, the

purpose of this study is to propose the simple functional model, which reproduces this error as well as the other behaviors observed in the previous experiments.

2. OUTLINE OF THE MODEL

2.1 Task for computer simulations

According to the previous experiments, we assume a task as follows: the subject is required to push the buttons in the correct order in 5 sets, treated as a sequential procedure, in a trial. Since 2 of 16 (4 × 4 matrix) square buttons are illuminated evenly on a set, the subject has to learn the order from the visual pattern of illuminated positions by trial and error. If it makes a mistake, the trial returns back to the first stage, but the pattern of five stimuli do not change within the same task. Thus five consecutive sets (hyperset) are presented in a fixed order. The task is repeated until the subject completed the hyperset successfully for a total of 10 trials.

2.2 Structure of the model

Fig.1 shows the outline of our proposed model. The model mainly consists of three systems as follows: short-term memory system (STMS), long-term memory system (LTMS), and decision system of strategy (DSS). STMS proposes an action plan based on the short-term memory especially dealing with stimuli in the current task, while LTMS tries to retrieve an action sequence in the long-term memory over tasks. These systems work in parallel and independently. Actually only one action plan should be selected to execute in DSS. For each stimulus set, DSS stochastically and alternatively selects one of LTMS or STMS. The probability of the selection is updated depending on the estimate of decisions and their results in response to the stimulus sets.

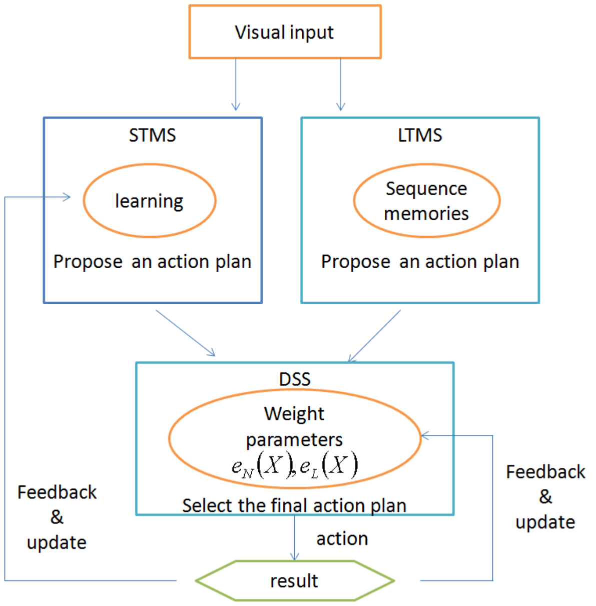

Fig.1. Outline of the model

2.3 Short-term memory system

STMS proposes one action plan from two options of action orders based on the short-term memory for the current stimulus (illuminated two buttons). In response to a novel stimulus, the probability of selection is even. As the monkey learns stimulus-response relationships, the probability to press the buttons correctly becomes higher. The probability will be influenced by how many times it has received the stimulus so far. Thus, we assume that the probability of proposal of the correct action plan for a set in STMS is updated by the short-term experience as follow

$$p_{\text{set}}(n+1) = p_{\text{set}}(n) + \gamma \ (\alpha_{\text{MAX}} - p_{\text{set}}(n)) \qquad (1)$$

where n is the number of input of the stimulus sets, α_{MAX} is the maximum value of the probability, and γ is a learning rate.

2.4 long-term memory system

LTMS also proposes one action plan from the two options based on the long-term sequential memory. When the model recognizes that the first set is a learned stimulus, we assume that this memory system recalls 5 series of actions responsive to current and succeeded stimuli. Therefore, LTMS is completely different from the STMS in that LTMS suggests plans for supposed stimuli in the near future.

Additionally, this memory has been constructed for a long time such as a year or two years. Thus, the probability to suggest the correct order for the learned hyperset is assumed to be very high rate. Thus, we let this higher probability be P_l. When the hyperset of stimuli includes a few new sets after the first set (i.e. modified task), however, LTMS at first proposes to push an unilluminated button and the panel does not respond. For this error, LTMS is temporarily suspended and STMS is driven to deal with this stimulus.

2.5 decision system of strategy

DSS selected the final action plan to execute from the plans proposed by STMS and LTMS. We assume two weight parameters $e_S(X)$ and $e_L(X)$ to represent the reliability of STMS and LTMS, respectively. The strategy with a large value of this parameter assumes to be more reliable. If the stimulus is a learned one and the result of LTMS strategy is correct, $e_L(X+1) = e_L(X) + u_1$. But, if it was wrong, $e_L(X+1) = e_L(X) - u_2$. If LTMS is suspended in case of modified hyperset as shown above, $e_L(X+1) = e_L(X) - u_3$.If STMS strategy is selected and the result is correct, $e_S(X+1) = e_S(X) + u_4$, otherwise $e_S(X+1) = e_S(X) - u_5$.

Initially, $e_S(0) = e_L(0) = 0$. u_1, u_2, u_3, u_4,and u_5 are positive constant parameters. According to the physiological experiment [1][3], the monkey seemed to infer whether the current task is a new or learned one when it watched the first stimulus set. We think that this influence strongly biases the monkey's behavior to coming stimuli. Thus, we assume that $e_L(1) = e_L(0) - b$ if the first set is new, and $e_L(1) = e_L(0) + b$ if it is already learned.

The larger the value of $e_S(X)$ or $e_L(X)$ is, the more the probability of selection of corresponding plan is. Because of sigmoidal shape and the range, we assume that the probability to adopt one from two systems depends on the sine of difference of $e_S(X)$ and $e_L(X)$ as follows :

$$p_L(X) = 0.5\{\sin(e_L(X) - e_S(X)) + 1\}, \qquad (2)$$

$$p_S(X) = 0.5\{1 - \sin(e_L(X) - e_S(X))\}. \qquad (3)$$

The difference of $e_L(X)$ and $e_S(X)$ is limited to the range [$-\pi/2, \pi/2$]. These values are updated within this range.

3. COMPUTER SIMULATIONS

We show the results of computer simulations of the model in the new task, the learned task, and the modified task, respectively. The parameter values are selected to field results correspondent to physiological data as follow: $p_{\text{set}}(0) = 0.5$, $\gamma = 0.4$, $\alpha_{\text{MAX}} = 0.91$, $P_l = 0.99$, $u_1 = 0.01$, $u_2 = 0.1$, $u_3 = 0.5$, $u_4 = 0.1$, $u_5 = 0.01$, $b = \dfrac{\pi}{2}$.

3.1 New task

During this task, no stimulus set is assumed to be memorized in LTMS. As the learning proceeds, it gradually becomes to act correctly because of the role of STMS. **Fig.2** shows a typical example of temporal change of the number of successful sets. The average number of mistakes until 10 trials successful is 10.2±6.0 (which is close to 10.3±5.9 from experimental data [1]). In this task, STMS was almost selected in DSS because novelty of the first stimulus decreases e_L . This activated STMS may correspond to higher activities in Pre-SMA in this task of experimental data [1][4][5].

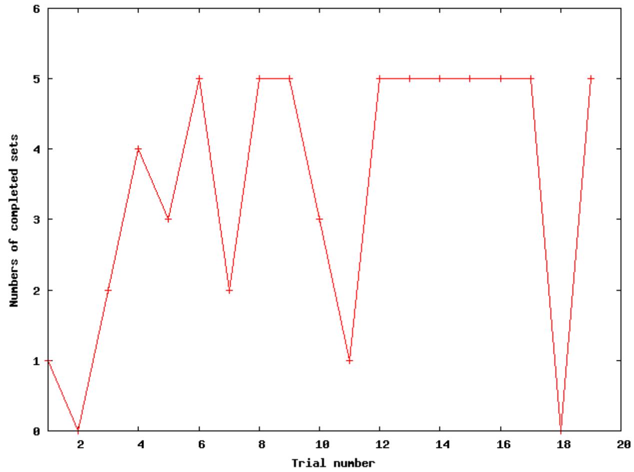

(a)

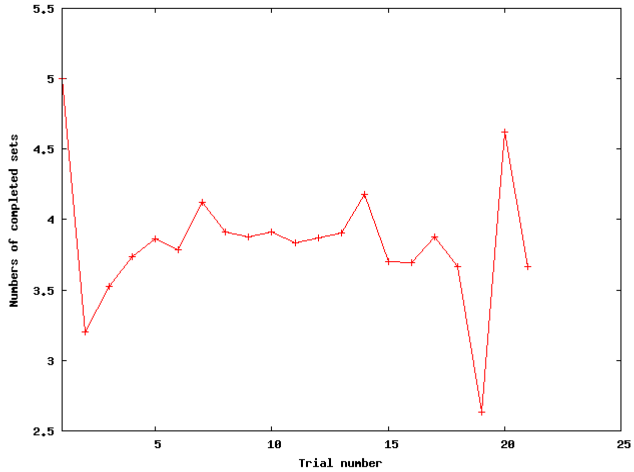

(b)

Fig.2. Simulation results in the new task: (a): Numbers of completed sets. (b): Numbers of completed sets from the first successful trial averaged over 100 tasks.

3.2. Learned task

In this task, the familiar stimulus in the first set increases e_L greatly and immediately. The probability of selection of STMS has been kept small, because the probability for success by STMS is much lower than that by LTMS. Fig.3 shows the examples of numbers of successful sets in the learned task. It is shown that the model performed perfectly for already learned hyperset. The average number of mistakes until 10 trials successful is 0.48±0.72, (which is close to 0.5±1.2 from experimental data [1]). In this task, almost all plans proposed by LTMS were adopted by DSS.

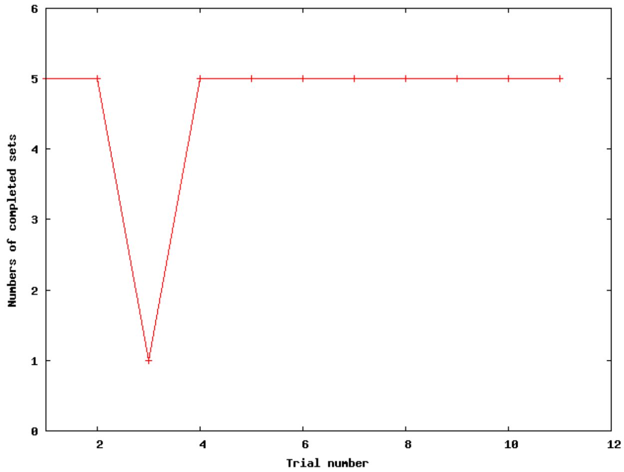

Fig.3. Simulation results in the learned task: Numbers of completed sets.

3.3. Modified task

In this task, second and third stimulus sets in hyperset are modified. Table2. shows the actions and results for each stimulus set. The meaning of abbreviations in table2. are as follows. SC: correct result by STMS plan, SW: wrong result by STMS plan, LC: correct result by LTMS, and rC/rW: correct or wrong result by retried STMS plan after ineffective LTMS action. In the early trials of the task, DSS selected the plan from LTMS because the first set is a learned one. In table2., trial #1 and set #2, trial #3 and set #2, and trial # 4 and set #2 indicate the case, when the subject pushed an unilluminated button in vain and retry another strategy of STMS. When the errors in response to the modified sets occur, the selected plan in DSS will be replaced by STMS with decreased e_L . At the same time, the correct rate of the plan from STMS gradually increases following eq.(1) from 50% as the learning proceeds. If the correct probability increases, its estimate increases e_S . Fig.4 shows temporal change of the values of e_L and e_S . Finally the performance was improved with high accuracy rate adopting the STMS plan for all of the sets.

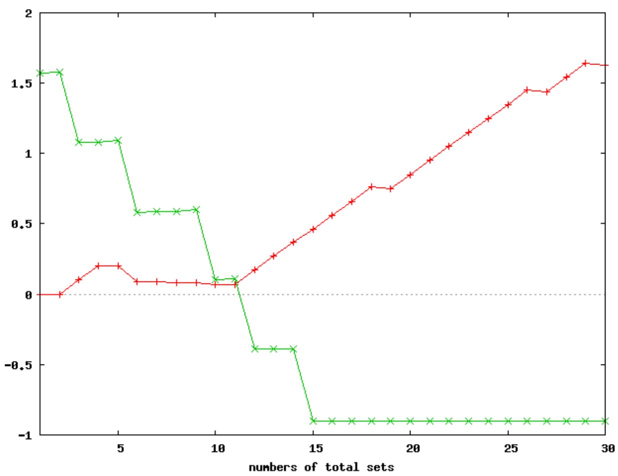

(a)

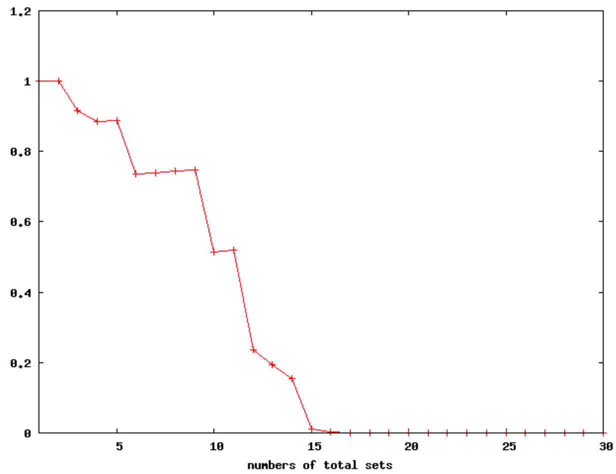

(b)

Fig. 4. (a):The temporal change of weight parameters. (Green line denotes e_L and red line denotes e_S) (b):The temporal change of the probability of selection of LTMS

Table2. Actions and results in the modified task

Trial number	Set number 1	2	3	4	5
1	LC	rC	SC	LC	LC
2	LC	SW			
3	LC	rW			
4	LC	rC	SC	SC	SW
5	SC	SC	SC	SW	
6	SC	SC	SC	SC	SC
7	SC	SC	SW		
8	SC	SC	SW		
9	SC	SC	SW		
10	SW				
11	SC	SW			
12	SC	SC	SC	SC	SC
13	SC	SC	SC	SC	SC
14	SC	SC	SC	SW	
15	SC	SC	SC	SC	SC
16	SC	SC	SC	SC	SC
17	SC	SW			
18	SW				
19	SC	SC	SW		
20	SC	SC	SC	SC	SC
21	SC	SC	SC	SC	SC
22	SC	SC	SC	SC	SC
23	SW				
24	SC	SC	SC	SC	SC

4. CONCLUSIONS

We propose a simple action selection model in the brain, which deals with pushing two illuminated buttons in the correct order. In this model, there are two independent action-planning systems using either of long-term memory or short-term memory (working memory), respectively. When the stimulus set is input, they propose action plans, and the selection is decided in a competitive way via the value of estimation parameters. The results show that our model could make a few errors to push an unilluminated buttons following long-term memory at first but it gradually learns correct responses by trial and error using working memory in the modified task, as the monkey did in the physiological experiment. In addition, the model also reproduces similar behaviors to the biological data in the new and learned task.

On the other hand, the value of the reliability parameter e_L and e_S show common tendencies with the neuronal activities of SMA or pre-SMA in the previous experiments [1][3], in that some neurons in the SMA are relatively activated in the learned task and some pre-SMA neurons are activated in the modified task, respectively. In the modified task, the value of e_S increases not only for the novel stimulus but also for the learned stimulus as the observed pre-SMA neurons. If the distinctive memory system in our model actually works in the brain, SMA and pre-SMA may have close relations to the entries to long-term memory and working memory systems in the brain, respectively.

To confirm this hypothesis, more refinements of the model plausible to biological data and computer experiments are needed in our future works. Other issues include how to implement interactions between decision system of strategy and memory systems, and memory consolidation from the short-term memory to long-term memory.

REFERENCES

[1] Nakamura K, Sakai K, Hikosaka O (1998), Neuronal activity in medial cortex during learning of sequential procedures.*J.Neurophysiol*.80, 2671-2687

[2] Nakahara H, Doya K, Hikosaka O (2001), Parallel cortico-basal ganglia mechanisms for acquisition and execution of visuomotor sequences - a computational approach. *Journal of Cognitive Neuroscience,* 626-647

[3] Sakai K, Kitaguchi K, Hikosaka O (2003), Chunking during human visuomotor sequence learning. *Exp Brain Res* 152, 229–242

[4] Nakamura K, Sakai K, Hikosaka O (1999), Effects of local inactivation of monkey medial frontal cortex in learning of sequential procedures. *J. Neurophysiol*.82, 1063-1068

[5] Hikosaka O, Nakamura K, Sakai K et al(2002),Central mechanisms of motor skill learning. *Current Opinion in Neurobiology*.12, 217-222

The Seventeenth International Symposium on Artificial Life and Robotics 2012 (AROB 17th '12),
B-Con Plaza, Beppu, Oita, Japan, January 19-21, 2012

Coherence patterns in neural fields at criticality

Teerasit Termsaithong[1,3], Makito Oku[2], and Kazuyuki Aihara[2]

[1] Department of Mathematical Informatics, Graduate School of Information Science and Technology, University of Tokyo, 7-3-1 Hongo, Bunkyo-ku, Tokyo 113-8656, Japan
[2] Institute of Industrial Science, University of Tokyo, 4-6-1 Komaba, Meguro-ku, Tokyo 153-8505, Japan
[3] teerasit@sat.t.u-tokyo.ac.jp

Abstract: Phase synchronization is a mechanism that plays a crucial role for information processing in the brain, and coherence is one of methods that are used to evaluate pairwise degree of phase synchronization. Coherence is also an important measure for examining brain functions because it can indicate communication and cooperation among neurons. In this work, we study the coherence patterns of spontaneous activity in the neural field model at criticality, which is a region where a second order phase transition occurs. The results are summarized as follows. First, at high frequency bands, the system outside the critical regime cannot communicate via phase synchronization at all. Second, the dynamical coherence patterns in the critical regime show switching between high and low coherent states. Finally, we found that in a very brief period of time, there is the high broadband coherence between some pairs of spatial points. This phenomenon can be observed only in the critical regime.

Keywords: criticality, neural fields, coherence, synchronization, brain spontaneous activity

1 INTRODUCTION

Critical phenomena occur at a second order or continuous phase transition (a critical point). This point is at the boundary between a stable and ordered state and a disordered state. Critical phenomena can be found frequently in various natural systems, such as earthquakes and avalanches. This kind of systems is characterized by scale invariance, which is a power-law distribution of some variables, and by the divergence of both spatial and temporal correlation scales.

Recently, there is a proposal by many authors suggesting that neuronal networks probably operate on the critical regime [1]. Some researches also show that at the critical point, the dynamic range [2], memory capacity [3], and computational power [4] are optimal in neural network simulations. The critical neural network also provides important factors for learning, such as flexible response and adaptation to input [5]. Furthermore, there are some evidences from experimental data pointing that criticality might underlie neural network behaviour, such as neuronal avalanches *in vitro* [6], $1/f$ type power spectrum of local field potential in visual neocortex [7] implying long-range correlations, and $1/f^{\beta}$ power spectrum of electroencephalograms (EEG) [8] and functional magnetic resonance imaging (fMRI) [9]. In addition, functional brain networks exhibit a power-law degree distribution [10].

Even when someone receives no explicit sensory stimulus and does not perform any task, which is called a resting state, his brain is still active. This activity is brain spontaneous activity or so-called ongoing activity. In the most brain experiments, spontaneous activity is filtered or averaged out and treated as a baseline activity or noise because experimenters are interested only activity induced by performing tasks or given stimuli. However, it was found that this spontaneous activity is not random noise but specifically organized [11]. Until now, the function which spontaneous activity in the brain serves for is still unclear. After all, the importance of spontaneous activity is stressed by the fact that most of the energy consumed by the brain is accounted for this activity, and task-induced activity increases only a small portion ($< 5\%$) of brain energy consumption [11].

Phase synchronization plays a crucial role for brain information processing. It is one of the methods the brain uses to code information and to allow distributed neural populations to communicate. Phase synchronization occurs not only when external stimuli are presented but can also occur in spontaneous activity of the brain during the resting state [12]. Coherence is one of methods that are used to evaluate pairwise degree of phase synchronization and is an important measure for examining brain functions and structures. It can indicate communication and cooperation between neurons.

Here, we use the neural field model tuned to the critical region and regions outside to simulate the brain spontaneous activity and studied some dynamical aspects of coherence by adopting the analysis using a moving time window. The results from the field at criticality are compared with those from the fields far from critical point.

2 METHODS

2.1 Neural field model

Neural fields are the mesoscopic models used to describe spatio-temporal dynamics of neural activity in the brain at a tissue level, where there are many neural populations interacting with each other. Because a brain cortex tissue is composed of a large number of neurons, we can take the continuum limit and characterize activity of neural populations as a field [13]. Here, we use this model to describe activity in the brain's cortex tissue.

In neural field models, the dynamics of each point in a field depends on its internal dynamics, activity of other points, and an external stimulus. A common form of neural field equation [14] is the integro-differential equation

$$\frac{1}{\ }\frac{\partial u(x,t)}{\partial t} = -u(x,t) + \int_{-\infty}^{\infty} w(x-y) f(u(y,t))dy, \quad (1)$$

where $u(x,t)$ is the neural activity at point x and time t. It corresponds to the local potential in this work.   is the decay rate of activity. $w(x)$ is the weight function, which describes the strength of connections between points in the field. $f(x)$ is the firing rate function, which determines firing rate output transmitted to postsynaptic neurons. The first term in the right-hand side of equation (1) represents neurons' internal dynamics, while the second term is a convolution between $w(x)$ and $f(x)$ representing influence of output from other neurons weighted by synaptic efficacy between points.

There are many choices of proper $w(x)$ and $f(x)$. In this research, we choose

$$w(x) = (2-|x|)\frac{e^{-|x|}}{2}. \quad (2)$$

It is called a Mexican hat function because its shape looks like a Mexican hat. The lateral-inhibition connectivity used by Amari [14] is the function of this type, too. The shape of this weight function displays local (short-range) excitation and distant (long-range) inhibition, which are typical cortical connections. It is also assumed that this neural field is homogeneous and isotropic, i.e., the weight function is identical for all neurons and depends only on distance between interacting neurons. For the firing rate function $f(x)$, we use a half sigmoidal function,

$$f(x) = \frac{2}{1+e^{-ax\Theta(x)}} - 1, \quad (3)$$

where $\Theta(x)$ is the Heaviside step function. The negative input cannot send out the output at all. Here, a is a parameter controlling steepness of the function when $x > 0$.

The real brain tissue is noisy and also has spontaneous activity, so we add a noise term ξ and small external field h representing spontaneous activity to the equation (1). Now, we have a neural field model of the form

$$\begin{aligned} \frac{1}{\ }\frac{\partial u(x,t)}{\partial t} &= -u(x,t) + \int_{-\infty}^{\infty} w(x-y) f(u(y,t))dy \\ &\quad +h(x,t) + \xi(x,t). \quad (4) \end{aligned}$$

ξ is a multiplicative white noise with $\langle \xi(x,t)\xi(x',t')\rangle = \ u(x,t)\delta(x-x')\delta(t-t')$, and   is noise intensity. For the spontaneous activity, we use a constant $h(x,t) = h$.

2.2 Critical point

Our neural field model (equation (1), (2), and (3)) can feature second order phase transition and a critical point. The steepness variable a in equation (3) works as a control parameter. To identify a critical point, we want to know at which value of a, a uniform stationary solution $u(x) = 0$ for all x begins to be unstable, or the order parameter $\langle u\rangle = \frac{1}{2L}\int_{-L}^{L} u(x)dx$, where L is a half size of the neural field, becomes nonzero.

Then, we did simulations of one dimensional neural field and consider the model's bifurcation graph between the order parameter $\langle u\rangle$ versus the control parameter a (Fig. 1.). According to the diagram, we can see that many possible neural activity patterns can emerge. However, the point that a non-uniform stationary solution begins to appear is $a_c \approx 1.782$, which is the position of a critical point. From now, we will call the left side of the critical point ($a < a_c$) a subcritical region and the right side of the critical point ($a > a_c$) a supercritical region, while a critical region is placed in the vicinity of a_c.

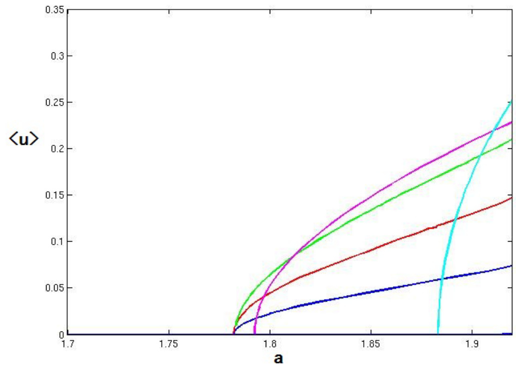

Fig. 1. A bifurcation diagram of the neural field model. A blue, red, green, pink, and light blue lines represent a pattern of 1, 2, 3, 4, and no bump, respectively.

In our simulation, we used $a = 1.782$, 1.982, and 1.582 to represent critical, supercritical, and subcritical region, respectively. We used $L = 20$ and applied periodic boundary condition to the field. Other parameters were set as follows: decay rate, $= 0.2$; noise intensity, $= 1$; and spontaneous activity, $h = 0.00001$.

2.3 Dynamical coherence

The coherence or magnitude-squared coherence is used in spectral analysis for measuring of the phase consistency and one of methods to determine a degree of phase synchronization between a pair of signals. It does not only determine the dependency between simultaneous values of two time series but also considers leading and lagging relationships. The coherence between signals $x(t)$ and $y(t)$ at given frequency f

is defined by

$$C_{xy}(f) = \frac{|P_{xy}(f)|^2}{P_{xx}(f)P_{yy}(f)}, \tag{5}$$

where P_{xy} is the cross power spectral density (CPSD) between $x(t)$ and $y(t)$, which is the Fourier transform of cross correlation, and P_{xx} and P_{yy} are power spectral densities of $x(t)$ and $y(t)$, which are the Fourier transform of autocorrelation. Also, note that the coherence is a function of frequency f, and signals are regarded as the superposition of each frequency component.

The coherence value ranges from 0 to 1. The coherence value of 1 or perfectly coherent signals indicate that the phase difference between two signals is fixed with time, while the value of 0 means that the two signals are completely unrelated. However, noise in the systems can contribute to the coherence greater than zero.

We were interested in dynamical coherence patterns, which mean that coherence values can change in time. We begin with defining the time window Δt as a length of time series at each time step (here, $\Delta t = 2000$). Then, move this frame forward by 1 step in each time step until it reaches the terminal time point. Consequently, dynamical time window is constructed, and we obtain a set of time series at each time step in which we can measure dynamical quantities of our interest, coherence in this case.

3 RESULTS

The spatial averages of dynamical coherence between the point $x = 0$ and all other points in the field for four frequency bands (f_0, $2f_0$, $3f_0$, and $4f_0$) from one sample of simulations are shown in Fig. 2 (Here, $f_0 = 5$ Hz, and the sampling rate determined from the time constant (decay rate) is 2000 points). The dynamical coherence of random noise is also shown for being a reference of insignificant coherence level. It is apparent that the highest coherence appears in the critical region at all frequency bands. In the other regions, the coherence is very low, particularly in higher frequency bands. Actually, at higher frequencies ($\geq 2f_0$), only coherence values in the critical region are significantly higher than the coherence level of noise, though, sometimes the coherence level in supercritical region can be little higher than noise's but still lower than the critical region's. However, there are some periods of time where the coherence in the critical region drops to the same level with or lower than noise's.

Another interesting phenomenon observed only in the critical region is broadband coherence. For the coherence of some pairs of spatial points, there are some short periods of time where high coherence appears in many frequency bands. For example, Fig. 3. shows dynamical coherence in all frequencies between the point $x = 0$ and $x = -20$ at the critical region in the same simulation of Fig. 2.

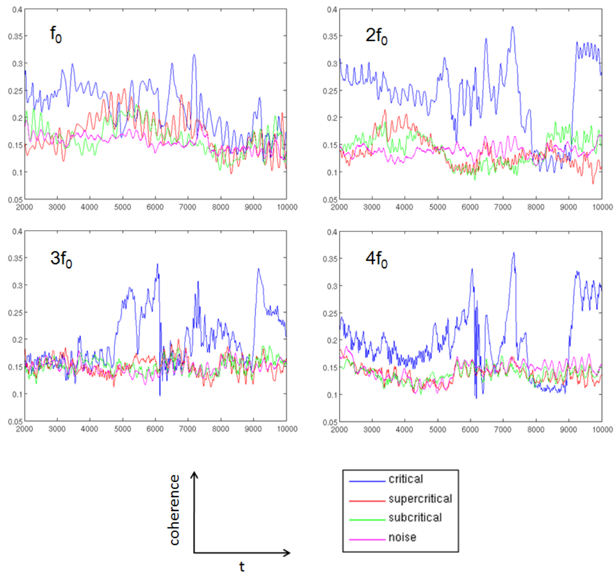

Fig. 2. Spatially average values of dynamical coherence between the point $x = 0$ and the others of the three regions in f_0, $2f_0$, $3f_0$, and $4f_0$ frequency bands including that of random noise.

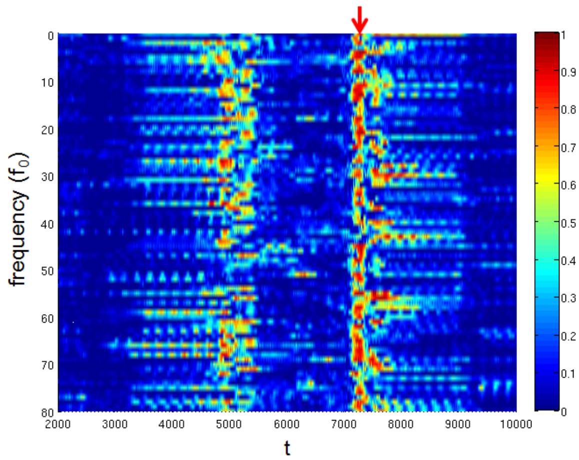

Fig. 3. The pairwise dynamical coherence between points $x = 0$ and $x = -20$. The arrow points the brief periods of high broadband coherence.

4 DISCUSSION & CONCLUSION

The dynamical coherence is highest in the critical region. Actually, at frequencies higher than $2f_0$, only coherence in the critical region is significantly higher than coherence of noise. This result shows that outside the critical region, neurons in the field communicate to each other by high frequency bands much less efficiently than those at criticality. Also, it is at criticality that neurons can communicate most efficiently by any frequency, although there are some periods that the coherence level drops to a value of a non-coherent state. The rise and drop of coherence can be regarded as coherence switching. Archerman and Borbély demonstrated the similar switching in human EEG during NREM-REM (non-rapid eye movement and rapid eye movement) sleep cycles [15].

Furthermore, we found that only at criticality, there are some periods in time that the coherence of some pairs become broadband, i.e., coherence occurs in almost all frequencies at the same time. One reason for this phenomenon is that power spectral density and squared CPSD's cross-frequency correlations are very high in the critical region (the results are not shown). However, its origination and functions still need further investigation. Gervasoni and his colleagues found the high transient broadband coherence occurring at global brain state transitions in rats' LFP (local field potential) [16]. They also suggested that this transient coherence may construct distributed structures of functional connectivity and allow information flow between neurons.

In summary, we used the neural field model to simulate spatio-temporal evolution of spontaneous neural activity in the critical regime, namely, the region around a critical point. Then, dynamical coherence patterns were studied in the critical region compared with regions outside. Our study suggests that communication between neurons in the field is optimized in the critical region. Also, in this region, we observed many phenomena that are consistent with the empirical experiments of the brain.

ACKNOWLEDGEMENTS

This research is partially supported by Grant-in-Aid for Scientific Research (A) (20246026) from MEXT of Japan.

REFERENCES

[1] Beggs JM (2008), The criticality hypothesis: how local cortical networks might optimize information processing. Phil Trans R Soc A 366:329-343

[2] Kinouchi O, Copelli M (2006), Optimal dynamical range of excitable networks at criticality. Nat Phys 2:348-351

[3] Haldeman C, Beggs JM (2005), Critical branching captures activity in living neural networks and maximizes the number of metastable states. Phys Rev Lett 94(5):058101

[4] Bertschinger N, Natschläger T (2004), Real-time computation at the edge of chaos in recurrent neural networks. Neural Comput 16(7):1413-1436

[5] de Arcangelis L, Herrmann HJ (2010), Learning as a phenomenon occurring in a critical state. Proc Nat Acad Sci USA 107(9):3977-3981

[6] Beggs JM, Plenz D (2003), Neuronal avalanches in neocortical circuits. J Neurosci 23(35):11167-11177

[7] Henrie JA, Shapley R (2005), LFP power spectra in V1 cortex: the graded effect of stimulus contrast. J Neurophysiol 94:479-490

[8] Freeman WJ, Rogers LJ, Holmes MD et al (2000), Spatial spectral analysis of human electrocorticograms including the alpha and gamma bands. J Neurosci Methods 95:111-121

[9] Thurner S, Windischberger C, Moser E et al (2003), Scaling laws and persistence in human brain activity. Physica A 326:511-521

[10] Eguíluz VM, Chialvo DR, Cecchi GA et al (2005), Scale free brain functional networks. Phys Rev Lett 94(1):018102

[11] Fox MD, Raichle ME (2007), Spontaneous fluctuations in brain activity observed with functional magnetic resonance imaging. Nat Rev Neurosci 8(9):700-711

[12] Ito J, Nikolaev AR, van Leeuwen C (2005), Spatial and temporal structure of phase synchronization of spontaneous alpha EEG activity. Biol Cybern 92(1):54-60

[13] Coombes S (2006), Neural fields. Scholarpedia 1(6):1373

[14] Amari S (1977), Dynamics of pattern formation in lateral-inhibition type neural fields. Biol Cybern 27(2):77-87

[15] Achermann P, Borbély AA (1998), Temporal evolution of coherence and power in the human sleep electroencephalogram. J Sleep Res 7(S1):36-41

[16] Gervasoni D, Lin SC, Ribeiro S et al (2004), Global forebrain dynamics predict rat behavioral states and their transitions. J Neurosci 24(49):11137-11147

The Seventeenth International Symposium on Artificial Life and Robotics 2012 (AROB 17th '12),
B-Con Plaza, Beppu, Oita, Japan, January 19-21, 2012

A network consisting of phase adjusting units

Masanori Shiro[1 2], Syotaro Akaho[1],
Kazuyuki Aihara[2]

[1] AIST Human Technology Research Institute, Tsukuba 305-8563, Japan
[2] IIS, University of Tokyo, Meguro-ku Tokyo 153-8505, Japan

Abstract: We propose a one-step prediction method by using a simple network consisting phase adjusting units. The network is for learning a continuous time series. Each unit have a function of amplitude and phase adjusting. We tried to predict a point for nonlinear time series like as a logistic map by using the lasso algorithm.

Keywords: Network, Phase, Chaos, time series

1 INTRODUCTION

It is important to make a mathematical model for an observed time series which is complicated such as a deterministic chaos. Although some methods are proposed[1, 2, 3], it is still difficult problem to make a mathematical model for the deterministic chaos yet. As a preliminary step, we propose a method to predict the next point of a given time series by using the lasso algorithm[4]. Our method will be very fast for one-step prediction of complicated time series.

2 PROPOSAL METHOD

First, we prepare k units each of which outputs d dimensional polynomial equation $f(x) = \sum_{j=0}^{d} a_j x^j$. The given parameter k corresponds to the dimension of delay coordinates. This scheme can express many types of complicated time series including chaos.

The dimension of given time series is usually estimated by false nearest neighbor method. In future, we will consider about some types of networks consisted of these units. However in this report, we put the units linearly as shown in Fig. 1.

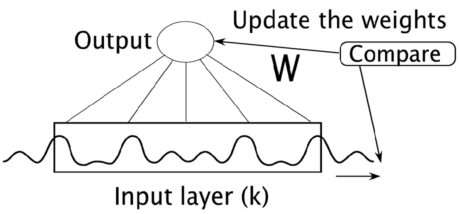

Fig. 1: Schematic diagram of inputs and output.

Next, we minimize the following error value E in Eq. (1) for an applicable prediction. We consider a decaying weight for using late x values.

$$E = \mathrm{E}_t \left(x_{t+1} - \sum_{i=0}^{k} \sum_{j=0}^{d} a_{ij} {x_{t-i}}^j \right)^2 + \lambda \sum_{i=0}^{k} \sum_{j=0}^{d} w_{ij} |a_{ij}|, \quad (1)$$

where x_i is i th data point of given time series, λ is the regularization parameter for the lasso, the weights w_{ij} means $\exp(\gamma_i)$ representing decaying weight, and γ is given value from 1.01 to 1.1. By using the lasso, we expect to get a sparse representation of the polynomial equation which is useful for checking a behavior of the dynamics.

Actually, we split the given time series by k th, and pack up into the following matrix X in Eq. (2).

$$\begin{cases} X = \begin{pmatrix} x_1, ..., x_k, x_1^2, ..., x_k^2, x_1^d, ..., x_k^d \\ x_2, ..., x_{k+1}, x_2^2, ..., x_{k+1}^2, x_2^d, ..., x_{k+1}^d \\ \vdots \\ x_{z-k}, ..., x_{z-1}, x_{z-k}^2, ..., x_{z-1}^2, x_{z-k}^d, ..., x_{z-1}^d \end{pmatrix} \\ Y = (x_{k+1} \cdots x_z)^T \end{cases} \quad (2)$$

We obtain the parameter sets satisfied the map $X \mapsto Y$ by using the lasso.

3 RESULTS

We used a logistic map which is generated a following equation (3) as a tested time series.

$$x_{n+1} = a x_n (1 - x_n), \quad (3)$$

where a characterized parameter a is fixed to 3.8, an initial value x_0 is set to 0.1, and the data size is 5000 points. The dimension of delay coordinates k is assumed to 2. The polynomial dimension of a model d is given to 2. We use the glmnet package[5] under the R system. A parameter in this package s corresponding to λ is set to 0.001. The results will be diverged when the parameter s is very small.

As the results, we obtained an estimated polynomial equation shown in Eq. (4). We completed the calculation within 1 sec.

$$x_{n+1} = 3.4911(x_n)^2 - 0.0160(x_{n-1}) - 3.5508(x_{n-1})^2 + 0.0881 \quad (4)$$

The convergence in a number of parameters and mean squared errors are shown in Figs. 2 and 3. We confirmed that the regularization parameter λ is an effective of the sparse representation. The results of one step prediction using obtained parameters are shown in Fig. 4. We confirmed that our method is effective for one step prediction of complicated time series. However, our method is inability for free-run with parameters fixed. The difference between given time series and obtained model are shown in Fig. 5.

We also checked the effects with an assumed dimension d and an assumed delay dimension k. The results in case of the dimension d assumed 3, are shown in Figs. 6, 7, and 8. The results in case of the delay k assumed 3, are shown in Figs. 9, 10, and 11.

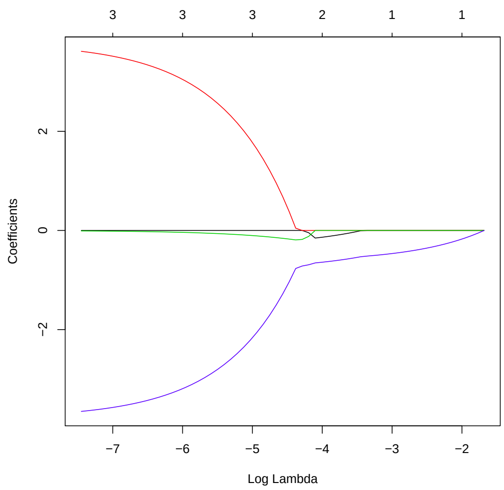

Fig. 2: The convergence in a number of parameters with lasso strength λ.

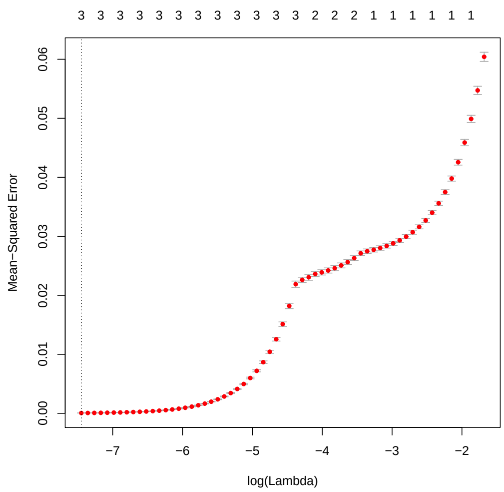

Fig. 3: MSE with the λ.

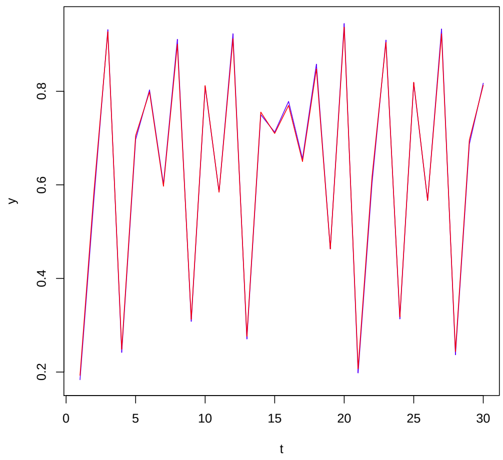

Fig. 4: Results of one step prediction.

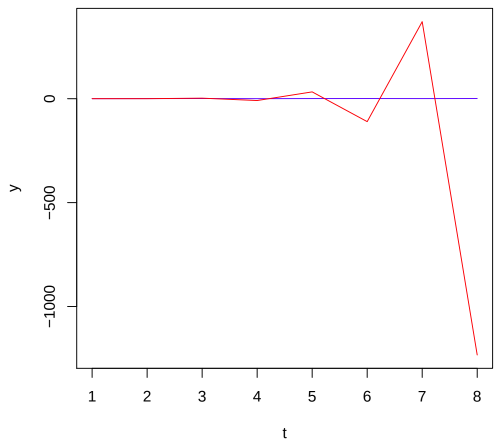

Fig. 5: Results of free run.

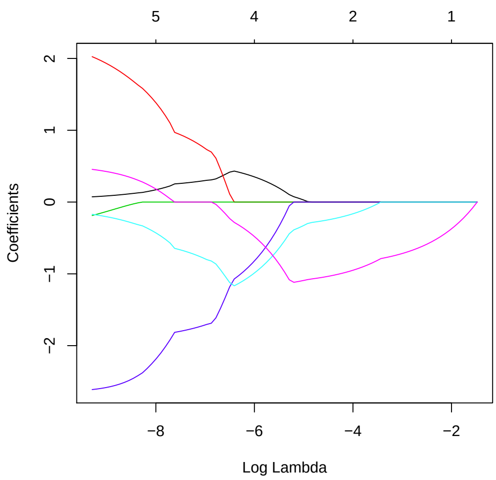

Fig. 6: The convergence in a number of parameters with the λ in case of $d = 3$.

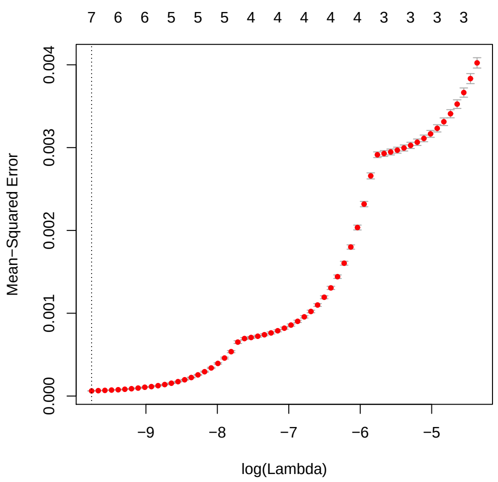

Fig. 7: MSE with the λ in case of $d = 3$.

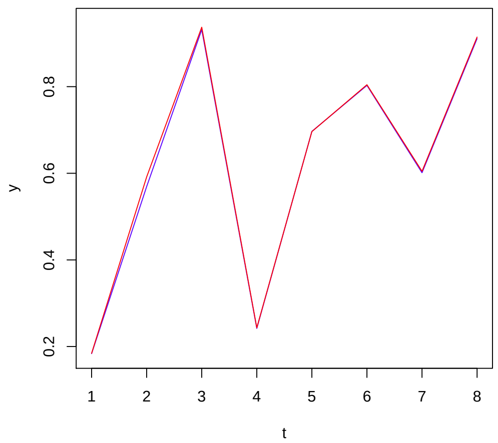

Fig. 8: Results of one step prediction in case of $d = 3$.

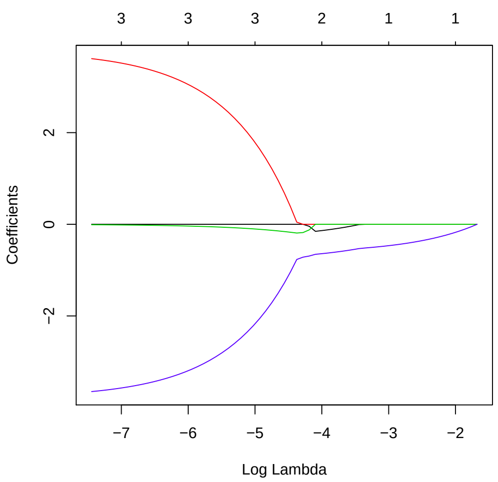

Fig. 9: The convergence in a number of parameters with the λ in case of $k = 3$.

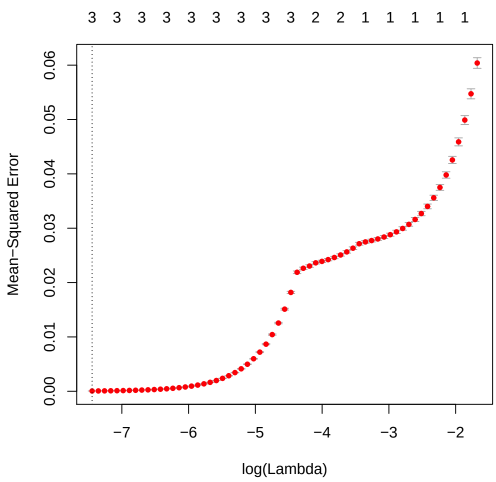

Fig. 10: MSE with the λ in case of $k = 3$.

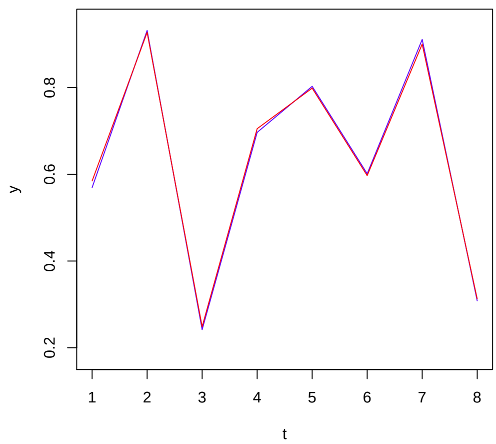

Fig. 11: Results of one step prediction in case of $k = 3$.

4 CONCLUSION

We proposed a one-step prediction method for chaotic time series using the lasso. As the results, we got good predictions for the logistic map. In future we will try to make a mathematical model which is capable of free run, based on this method.

ACKNOWLEDGEMENT

This work was supported by KAKENHI (23240043).

REFERENCES

[1] L. Jaeger and H. Kantz, Chaos 6 pp.440 (1996)

[2] H. Kantz and L. Jaeger, Physica D109 pp.59 (1997)

[3] M. Shiro, Y. Hirata and K. Aihara, SIAM DS09 Abstracts pp. 197 (2009)

[4] R. Tibshirani, J. Royal. Statist. Soc B., 58, pp. 267 (1996).

[5] J. Friedman, T. Hastie, and R. Tibshirani, J. Statistical Software, 33 pp. 1 (2010).

The Seventeenth International Symposium on Artificial Life and Robotics 2012 (AROB 17th '12),
B-Con Plaza, Beppu, Oita, Japan, January 19-21, 2012

Modeling of potential- and noise-induced intracellular dynamics with cell-cell communication

Tomoyuki Yamada[1,2,†], Atsushi Kamimura[1], Tetsuya J. Kobayashi[1,2,3,4]

[1] Institute of Industrial Science, the University of Tokyo, Tokyo, 153-8505, Japan
[2] Department of Electrical Engineering and Information Systems, Graduate School of Engineering, the University of Tokyo
[3] PREST, Japan Science and Technology Agency (JST), Saitama 332-0012, Japan
[4] Department of Mathematical Informatics, Graduate School of Information Science and Technology, the University of Tokyo
†yamada@sat.t.u-tokyo.ac.jp

Abstract: In cellular systems, complicated intracellular reaction circuits implement various types of information processing in response to external stimuli such as decision-making. These processes involve stochastic fluctuations owing to low copy numbers of molecules per cell and uncertainty of environmental signals. Major mechanisms that can cope with such noise, known currently, are potential-induced bistability at the single-cell level, or mutual communication at the population level. Another mechanism, noise-induced bistability, is recently demonstrated to be connected to optimal noise-filtering dynamics from external stimuli. In this work, we focus on the difference of potential-induced and noise-induced dynamics in terms of their information processing ability. Furthermore, we investigate the effect of mutual communication to the noise-induced dynamics. To address these problems, we propose a mathematical model of an intracellular network that combines both bistablility. In addition, we also investigate the impact of intercellular communication.

Keywords: Cellular dynamics, Decision making, Stochastic process, Cell-cell communication

1 INTRODUCTION

Information processing in response to external stimuli is a fundamental function of all living systems. In cellular systems, for example, various types of information processing such as decision-making are implemented by complicated intracellular reaction circuits. However, all components of the circuits such as transcriptional control, alternative splicing, translation, diffusion and chemical modification reactions of transcriptional factors, involve stochastic fluctuations owing to low copy numbers of molecules per cell and uncertainty of an external environment. These intrinsic and extrinsic noise in the building components can inevitably disturb the cellular information processing [1].

Two mechanisms are mainly known that can cope with such noise: one is single-cell level, and the other is the population level. At the single-cell level, a cell may have intracellular circuits that can resist to noise. For example, a bistable potential system implemented by mutually inhibitory reactions can sustain its state against noise if the deterministic force exerted by the potential is sufficiently strong. At the population level, cells can also employ mutual communication to realize coordinated behavior out of noisy single-cell level behavior [2, 3, 4]. While these mechanisms are prevalently observed within intracellular circuits, they may be insufficient to explain all the biological phenomena because such strong deterministic potential or communication may reduce not only the noise but also the flexibility and variability of the cells to the external stimuli.

On this issue, one of the authors has recently demonstrated that intracellular networks that can optimally filter out noise in external stimuli have ability to show noise-induced bistability [5, 6], suggesting that noise-induced as well as deterministic potential-induced dynamics can also efficiently cope with noise. Furthermore, it is also suggested that such dynamics can optimally balance the suppression of noise and sensitivity to external stimuli. Nonetheless, the difference between potential-induced and noise-induced dynamics in terms of their information processing ability has not yet been clarified. Furthermore, even though mutual communication of potential-induced dynamics has been intensively investigated [3, 7, 8], almost nothing is known on the effect of mutual communication to the noise-induced dynamics.

In this study, we tackle this problem using a mathematical approach, and propose a model of an intracellular network that combines both potential-induced and noise-induced bistablility. First, we analyze deterministic and stochastic properties of this model by calculating null-clines and bifurcation diagram. Next, by numerical simulations, we confirm that this model exhibits bimodal histograms produced by the potential-induced and noise-induced bistability in case of constant external stimuli. We also examine the response of the model to a step-like external stimuli. Finally, we introduce intercellular communication that enables each cell to detect the state of the other cells and react together with them. We investigate the responses to external stimuli for different strength of communication to clarify the impact.

2 COMBINED MODEL OF POTENTIAL- AND NOISE-INDUCED BISTABILITY

2.1 Derivation of equation

In [5], it was demonstrated that the following autophosphorylation and autodephosphorylation reaction as an intracellular network is approximately equivalent to an optimal dynamics to infer the state of environment from noisy receptor signal. Its Gaussian approximation was derived subsequently in [6] to further clarify the noise-induced bistability in that cycle. We extend this model such that a new model can have potential-induced bistability as well as noise-induced bistability that the original model has.

The model is described as follows:

$$\frac{\mathrm{d}Z_i}{\mathrm{d}t} = \quad Z_i\tilde{Z}_i I(t) + r_{\mathrm{on}} H(\tilde{Z}_i)\tilde{Z}_i \quad r_{\mathrm{off}} H(Z_i) Z_i, \tag{1}$$

where $Z_i \in [0,1]$ and $\tilde{Z}_i := 1 \quad Z_i$ are the state of the system in i-th cell, such as ratios of phosphorylated and un-phosphorylated molecules in a cell. Under this interpretation, $r_{\mathrm{on}}H(\tilde{Z}_i)$ and $r_{\mathrm{off}}H(Z_i)$ are respectively the rate of input-independent phosphorylation and dephosphorylation reactions that occur spontaneously where $H(Z) := p + 2(1 \quad p)/(K_0^n + Z^n)$. When $p = 1$, Eq. (1) is equivalent to the model derived in [6]. When $p = 0$, $r_{\mathrm{on}}H(\tilde{Z}_i)\tilde{Z}_i \quad r_{\mathrm{off}}H(Z_i)Z_i$ has a bistable potential by the inhibition of state transition between Z_i and $\tilde{Z}_i$ introduced by the Hill's kinetics. Thus, $p \in [0,1]$ controls the extent to override bistable potential onto the original model. The external input $I(t)$ with extrinsic noise is described as the following:

$$I(t) = \alpha(\ _0 U dt + \sigma \circ \mathrm{d}W_t), \tag{2}$$

where $\circ$ represents Stratonovich interpretation [9]. $\ _0U$ is the signal that the cell have to detect. $\sigma W_t$is the noise that cell receives. $\ _0$ is introduced to control the strength of the signal with respect to noise. The signal noise ratio (SNR) $\ _0/\sigma$ determines the ambiguity of the signal. α is the amplification factor of both signal and noise that a cell can control. For notational simplicity, we define the following functions:

$$F(Z,U) = \alpha\ _0 U Z\tilde{Z} + r_{\mathrm{on}}H(\tilde{Z}) \quad r_{\mathrm{off}} Z H(Z),$$
$$G(Z) = \alpha\sigma Z\tilde{Z}.$$

2.2 Deterministic properties of Eq. (1)

Firstly, we analyze deterministic properties of our model. The equilibrium state of Eq. (1) satisfies $F(Z,U) = 0$. By solving this equation with respect to U, we obtain

$$U_{null}^{det}(Z) = \frac{1}{\alpha\ _0} \quad \frac{r_{\mathrm{on}}}{Z}H(\tilde{Z}) + \frac{r_{\mathrm{off}}}{\tilde{Z}}H(Z) \ ,$$

which is the analytic expression of the null-cline of Eq. (1). For a given U, the equilibrium state of Z may have more than one state. In other words, the system can have multi-stable states. While the condition for multi-stable state is not generally expressed analytically, we can derive it for a symmetric condition such that $K_0 = 1/2$, $r_{\mathrm{on}} = r_{\mathrm{off}} = r_0$. Fig. 1. (a) and (b) show the null-clines of this system with respect to the parameters n and p, respectively. Given these conditions, Eq. (1) becomes symmetric with respect to the exchange of Z and $\tilde{Z}$. Thus, when $U = 0$, $Z = 1/2$ is always one of the equilibrium state. Therefore, the derivative of $U_{null}^{det}(Z)$ with respect to Z can be used as the condition for the transition from monostable to bistable state. More specifically, $\left.\frac{\mathrm{d}U_{null}^{det}(Z)}{\mathrm{d}Z}\right|_{Z=1/2} = 0$ is the condition of changing the number of the equilibrium states. By rearranging this equation, we have

$$p = \frac{2^n(n \quad 2)}{2 \quad 2^{1+n} + 2^n n} \qquad (n \neq 1),$$

which is depicted by the solid line in Fig. 2.

2.3 Stochastic properties of Eq. (1)

Next we clarify the properties of Eq. (1) when noise is introduced. Let consider the situation such that U and σ are constant and that $\mathrm{d}W_t$ is the white Gaussian process. Then,

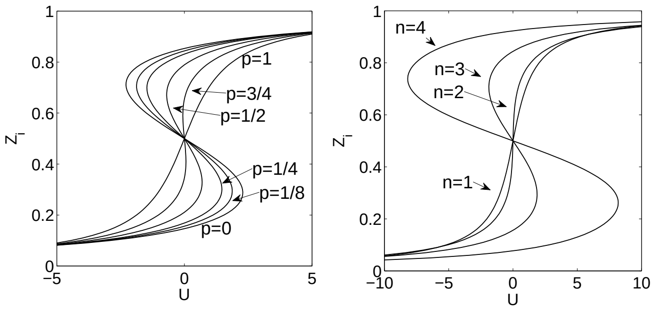

(a) Null-clines for different values of p (b) Null-clines for different values of n

Fig. 1. Null-clines of Eq. (1)

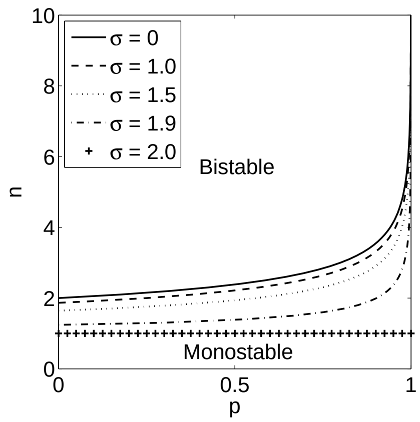

Fig. 2. Bifurcation Diagram. The upper (lower) side area of each curve correspond to bimodal (unimodal) distribution.

Eq. (1) can be described by a stochastic differential equation as

$$\mathrm{d}Z_i = F(Z,U)\mathrm{d}t + G(Z) \circ \mathrm{d}W_t. \tag{3}$$

We here use Stratonovich interpretation as the original work did[6].

The probability distribution $\mathbb{P}(t,Z)$ of Eq. (3) then satisfies the corresponding Fokker-Planck equation [9] as

$$\frac{\partial \mathbb{P}(t,Z)}{\partial t} = \quad \frac{\partial \left[F_{Ito}(Z,U)\mathbb{P}(t,Z)\right]}{\partial Z} + \frac{1}{2}\frac{\partial^2 \left[G(Z)^2\mathbb{P}(t,Z)\right]}{\partial Z^2},$$

where $F_{Ito}(Z,U) := F(Z,U) + \alpha\sigma G(Z)(1/2 \quad Z)$. The stationary state of Eq. (3) can be represented [9] as

$$\mathbb{P}_{st}(Z) = \frac{N}{G(Z)^2}\exp\left[2\int^Z \frac{F_{Ito}(Z',U)}{G(Z')^2}dZ'\right].$$

This equation can be solved analytically when $p = 1$ as

$$\mathbb{P}_{st}(Z) \propto \frac{1}{Z\tilde{Z}}\left(\frac{Z}{\tilde{Z}}\right)^{\bar{U}} \exp\left[\quad \frac{2}{(\alpha\sigma)^2\left(\frac{r_{\mathrm{on}}}{Z} + \frac{r_{\mathrm{off}}}{\tilde{Z}}\right)}\right],$$

where $\bar{U} = \frac{2(\alpha\mu_0 U + r_{\mathrm{on}} \quad r_{\mathrm{off}})}{(\alpha\sigma)^2}$.

For $p < 1$, this equation cannot be analytically solved. Nevertheless, some properties, especially stochastic bifurcation, can be analytically derived. Let identify the peak positions of stationary distribution of Eq. (3) with the deterministic equilibrium points considered in the previous section. Then, the change of the number of peaks can be regarded as the bifurcation of the stochastic system, which is known as phenomenological bifurcation [10]. The peak positions of $\mathbb{P}_{st}(Z)$ satisfies $\frac{\partial \mathbb{P}_{st}(Z)}{\partial Z} = 0$. This equation can be solved with respect to U as

$$U_{null}^{st}(Z) = U_{null}^{det}(Z) + \frac{(\alpha\sigma)^2}{\alpha \quad _0}(1/2 \quad Z).$$

Similarly to the deterministic case, $U_{null}^{st}(z)$ becomes symmetric around $Z = 1/2$ when $r_{\mathrm{on}} = r_{\mathrm{off}} = r_0$. In addition, $Z = 1/2$ and $U = 0$ is always the equilibrium state under the symmetric condition. Thus, the bifurcation points from unimodal to bimodal distribution satisfy

$$\left.\frac{\mathrm{d}U_{null}^{st}(Z)}{\mathrm{d}Z}\right|_{Z=1/2} = \left.\frac{\mathrm{d}U_{null}^{det}(Z)}{\mathrm{d}Z}\right|_{Z=1/2} \quad \frac{(\alpha\sigma)^2}{\alpha \quad _0} = 0,$$

which is also the condition for the change of the number of peaks when $\left.\frac{\mathrm{d}^2 U_{null}^{st}(Z)}{\mathrm{d}Z^2}\right|_{Z=1/2} \neq 0$. Then we have

$$\begin{cases} p = \frac{2^n(n \quad 2)}{2 \quad 2^{1+n}+2^n n} + \frac{(\alpha\sigma)^2/(4r_0)}{2 \quad 2^{1+n}+2^n n} & (n \neq 1) \\ \sigma = 2 & (n = 1), \end{cases}$$

which is depicted in Fig.2.

2.4 Simulation results

We compare monostable and bistable potential cases for external input signal $\quad = 0$. We choose $p = 1$ for monostable potential case and $p = 1/8$ for bistable potential case. We set parameter of Hill function $n = 3$ to have bistable potential for $p = 1/8$, and noise intensity $\sigma = 7$ to realize noise-induced bistability for $p = 1$. We simulate Eq. (1) for $\quad t = 0.001$ and $N = 2000$ by using Milstein scheme [9]. Fig. 3. (a) and (b) show the results of monostable potential case whereas Fig. 3. (c) and (d) show those of bistable potential case.

Then we simulate the response of cells to step-wise change of external signal $\quad _0U$ from $\quad$ to $+ \quad$. Now $\quad = 21$, and time of step-wise change is at $t = 0.1$. Fig. 4. (a) and (b) show responses of populations to the inputs. Both figures show similar Z_i trajectories and mean trajectory of Z_i.

3 CELL-CELL COMMUNICATION MODEL

We modify Eq. (3) to have cell-cell communication by adding the term for diffusive cell-cell communication. The equation is described as follows:

$$\begin{aligned} \mathrm{d}Z_i = {} & F(Z_i,U)\mathrm{d}t + G(Z_i) \circ \mathrm{d}W_t \\ & \frac{D}{N \quad 1}\sum_{j\neq i}(Z_i \quad Z_j)\mathrm{d}t, \end{aligned} \tag{4}$$

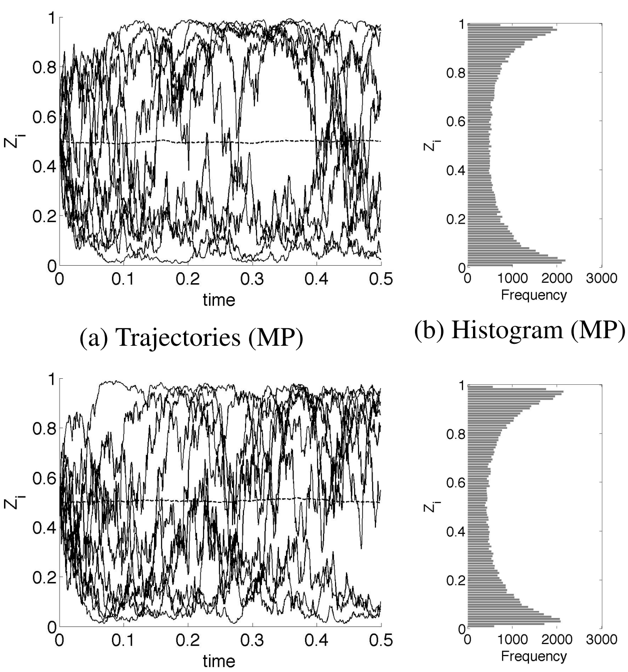

(a) Trajectories (MP) (b) Histogram (MP)

(c) Trajectories (BP) (d) Histogram (BP)

Fig. 3. Response to constant input. MP and BP represent monostable and bistable potentials, respectively. (a) and (c) show the trajectories of Z_i. Solid curves are the trajectories of Z_i (We plot trajectories of only 10 cells). Dashed curve is the trajectory of mean of Z_i. (b) and (d) are the histogram.

where D is the diffusion constant controlling the strength of communication, and N is the total number of cells.

Fig. 4. (c) and (d) show the simulation results of the response of cells to step-wise change of external signal $_0U$ from to $+$. Now $= 21$, $D = 10$, rising time of step input is $t = 0.1$.

Comparison of Fig. 4. (a) (b) and Fig. 4. (c) (d) show that fluctuation of Z_i by noise is moderated by communication, which means that intercellular communication made the transitions of cellular populations more adequate.

To confirm the effect of diffusion constant D, we conduct simulation for various D. Fig. 5. (a) and (b) are the results of monostable and bistable potential cases, respectively. We plot the trajectories of mean of Z_i for various D. The larger D becomes, the faster the reaction of cellular population is in both monostable and bistable potential cases.

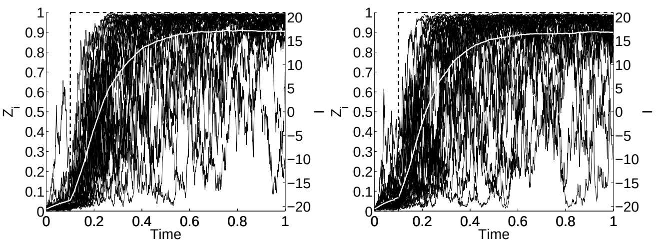

(a) Without coupling (MP) (b) Without coupling (BP)

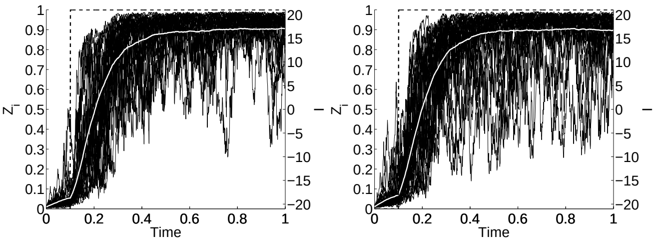

(c) With coupling (MP) (d) With coupling (BP)

Fig. 4. (a) and (b) are the response to step-wise input without coupling. Solid curves are trajectories of Z_i (We plot trajectories of only 30 cells) and correspond to left axis. White curve is trajectory of mean of Z_i, correspond to left axis. Dashed curve is external signal and correspond to right axis. (c) and (d) are the response to step-wise input with coupling. The meaning of curves are the same as (a) and (b).

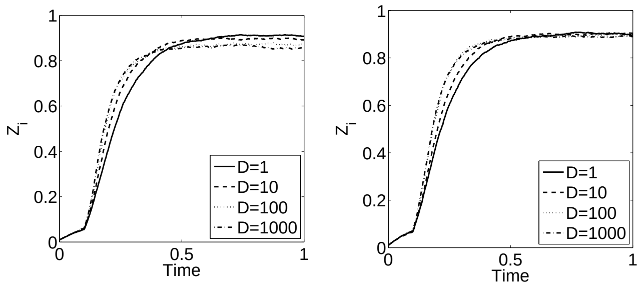

[1] Monostable potential [2] Bistable potential

Fig. 5. Average Z_i in switching at various diffusion constant

4 DISCUSSION

In this study, we have examined the difference of potential-induced and noise-induced bistability with respect to their response to external stimuli with and without intercellular communication. However, their difference is not clearly observed. The reason of this small difference may be attributed to the property of our model; bistable potential is overridden onto the noise-induced bistability, indicating that two mechanisms are not clearly separated. In order to reach firm conclusion, we need further investigation and/or modification of our models.

ACKNOWLEDGMENT

We thank Dr. Md. Khayrul Bashar, Mr. Ryo Yokota and Mr. Tomoyuki Itagaki for their valuable comments. This work was supported by KAKENHI.

REFERENCES

[1] Elowitz MB, Levine AJ, Siggia ED et al. (2002), Stochastic gene expression in a single cell. Science 297(5584):1183-1186

[2] Perbal B (2003), Cell communication and signaling communication is the key. Cell Communication and Signaling 1:3

[3] Taga ME, Bassler BL (2003) Chemical communication among bacteria. Proc. Natl. Acad. Sci. U.S.A. 100:14549-54

[4] De Monte S, d'Ovidio F, Dano S et al. (2007), Dynamical quorum sensing: Population density encoded in cellular dynamics. Proc. Natl. Acad. Sci. U.S.A. 104(47):18377-81

[5] Kobayashi TJ (2010), Implementation of dynamic bayesian decision making by intracellular kinetics. Phys. Rev. Lett. 104:228104

[6] Kobayashi TJ (2011), Connection between noise-induced symmetry breaking and an information-decoding function for intracellular networks. Phys. Rev. Lett. 106:228101

[7] Lindner B, Garcia-Ojalvo J, A. Neiman et al. (2004), Effects of noise in excitable systems. Physics Reports 392(6):321-424

[8] Tanouchi Y, Tu D, Kim J et al. (2008), Noise reduction by diffusional dissipation in a minimal quorum sensing motif. PLoS Comput. Biol. 4(8):e1000167

[9] Gardiner C (2009), Stochastic methods: a handbook for the natural and social sciences. Springer,Verlag; 4th ed.

[10] Horsthemke W, Lefever R (2006), Noise-induced transitions: theory and applications in physics, chemistry, and biology. Springer,Verlag; 2nd printing ed.

The Seventeenth International Symposium on Artificial Life and Robotics 2012 (AROB 17th '12),
B-Con Plaza, Beppu, Oita, Japan, January 19-21, 2012

Cholinergic top-down modulation based on the free-energy principle

Masaaki Takada[1,†], and Kazuyuki Aihara[1,2,‡]

[1] Department of Mathematical Informatics, The University of Tokyo, Meguro-ku, Tokyo 153-8505, Japan
[2] Institute of Industrial Science, The University of Tokyo, Meguro-ku, Tokyo 153-8505, Japan
([†]takada@sat.t.u-tokyo.ac.jp, [‡]aihara@sat.t.u-tokyo.ac.jp)

Abstract: Acetylcholine (ACh) has a key role in the cortex in perception. Although cholinergic modulations have been revealed in recent experimental studies, it remains unclear what is the essential role of ACh. In order to clarify the crucial computational function of ACh in perceptual inference, we propose a model of cholinergic top-down modulation based on the free-energy principle in this paper. We made the only assumption that ACh modulates the magnitude of top-down processing. Then, dynamics of the ACh level is derived by the free-energy principle. Our model suggests that ACh reports uncertainty of top-down information and reduces noise of top-down input. Thus, ACh can contribute to precise perception.

Keywords: neuromodulation, acetylcholine, free-energy principle, perception

1 INTRODUCTION

Acetylcholine (ACh) is one of the neuromodulators such as dopamine, serotonin, and noradrenaline. ACh is synthesized in the basal forebrain including medial septum, diagonal band of Broca, and nucleus basalis. Then, it is delivered to large areas of the cortex. Delivered ACh acts various functions in the cortex [3], [4]. First, recurrent intracortical connections and top-down processing are suppressed via muscarinic receptors. Second, afferent input is facilitated via nicotinic receptors. These cholinergic modulations relate to perception.

In theoretical studies, Yu and Dayan have suggested that the ACh level represents the uncertainty associated with top-down information [6], [7]. They proposed an ACh model by means of hidden Markov model, showing that cholinergic modulation leads to efficient perceptual inference. On the other hand, Friston has recently suggested that perception is realized by the free-energy principle. The free-energy principle has strong impacts because we can uniformly deal with neuronal activity, synaptic plasticity, and neuromodulation.

Although cholinergic modulation is well studied in recent studies, the relationship between cholinergic modulation and the free-energy principle is not clear. Furthermore, the crucial computational role of ACh is poorly understood. Here, we propose a model of cholinergic modulation based on the free-energy principle in this paper. We assume that ACh modulates the efficacy of top-down processing, showing that the ACh level changes in response to uncertainty of top-down information and ACh yields better perceptual inference.

2 MODELING OF PERCEPTION

Before we introduce cholinergic modulation, we review the perception model derived by the free-energy principle proposed by Friston [1] in this section. See [1] and [2] for details.

2.1 Generative model

Consider the following state-space model,

$$\dot{x} = Ax + Bv + z_x, \tag{1}$$

$$y = Cx + z_y, \tag{2}$$

where $v, x,$ and y denote input, state, and output, respectively. State equation (1) demonstrates the transition of state x in terms of input v, state itself x, and noise z_x. Output equation (2) defines output y by state x and noise z_y. $A, B,$ and C are time-invariant matrices. This linear state-space model generates observable consequence y by causes x and v. In this sense, this state-space model is called a generative model.

Next, generalized coordinates are introduced under the smoothness assumptions. We assume that all variables are smooth enough to differentiate infinitely. We use the notations, tildes, in the sense of generalized coordinates, e.g., $\tilde{x} := [x^T, \dot{x}^T, \ddot{x}^T, \dots]^T$. Then, the state-space model can be written by

$$D\tilde{x} = \tilde{A}\tilde{x} + \tilde{B}\tilde{v} + \tilde{z}_x, \tag{3}$$

$$\tilde{y} = \tilde{C}\tilde{x} + \tilde{z}_y, \tag{4}$$

$$\tilde{A} := I \otimes A,\ \tilde{B} := I \otimes B,\ \tilde{C} := I \otimes C, \tag{5}$$

$$D := \begin{bmatrix} 0 & 1 & 0 & \cdots \\ 0 & 0 & 1 & \cdots \\ \vdots & \vdots & & \ddots \end{bmatrix} \otimes I, \tag{6}$$

where I is the identity matrix and $\otimes$ is Kronecker product.

Moreover, if we assume that noises $\tilde{z}_x$ and $\tilde{z}_y$ obey Gaussian distributions $\mathcal{N}(0, \Sigma_x)$ and $\mathcal{N}(0, \Sigma_y)$, we can rewrite the state-space model to the probabilistic model as follows

$$p(\tilde{y}, \tilde{x}, \tilde{v}) = p(\tilde{y}|\tilde{x}, \tilde{v})p(\tilde{x}|\tilde{v})p(\tilde{v}), \quad (7)$$

$$p(\tilde{y}|\tilde{x}, \tilde{v}) = \mathcal{N}(\tilde{y} : \tilde{C}\tilde{x}, \Sigma_y), \quad (8)$$

$$p(\tilde{x}|\tilde{v}) = \mathcal{N}(D\tilde{x} : \tilde{A}\tilde{x} + \tilde{B}\tilde{v}, \Sigma_x). \quad (9)$$

We solve the inversion of this generative model in the following section.

2.2 Perception model

In the perception model, the brain estimates states $\tilde{x}$ and $\tilde{v}$ by observing $\tilde{y}$ and using prior knowledge $\tilde{v}_{\mathrm{pr}}$. Under the ergodic assumptions, given model m, the entropy of sensory state is

$$H(\tilde{y}|m) = -\int p(\tilde{y}|m) \ln p(\tilde{y}|m) d\tilde{y} \quad (10)$$

$$= -\int \ln p(\tilde{y}|m) dt \quad (11)$$

$$\leq \int \left(-\ln p(\tilde{y}|m) + D_{\mathrm{KL}}(q(\vartheta)||p(\vartheta|\tilde{y}, m))\right) dt \quad (12)$$

$$= \int \left(\langle -\ln p(\tilde{y}, \vartheta|m)\rangle_q - \langle -\ln q(\vartheta)\rangle_q\right) dt, \quad (13)$$

where ϑ is internal parameter including causes $\tilde{x}$ and $\tilde{v}$. Distribution q is (arbitrary) recognition density. Here, we define the free-energy $\mathcal{F}$ as

$$\mathcal{F} := -\ln p(\tilde{y}|m) + D_{\mathrm{KL}}(q(\vartheta)||p(\vartheta|\tilde{y}, m)) \quad (14)$$

$$= \langle -\ln p(\tilde{y}, \vartheta|m)\rangle_q - \langle -\ln q(\vartheta)\rangle_q. \quad (15)$$

The free-energy is an upper bound of sensory entropy. The free-energy principle says that recognition is realized by minimizing this free-energy.

Here, we assume that the recognition density $q(\tilde{x}, \tilde{v})$ can be factorized into $q(\tilde{x})$ and $q(\tilde{v})$ (mean field approximation), and has a Gaussian form with means $\tilde{\mu}_x$ and $\tilde{\mu}_v$ (Laplace assumption). We also assume that noise $\tilde{z}_v$ obeys $\mathcal{N}(0, \Sigma_v)$, where $\tilde{\mu}_v = \tilde{v}_{\mathrm{pr}} + \tilde{z}_v$. Then, the free-energy can be written by (ignoring constant)

$$\mathcal{F} = \frac{1}{2}\varepsilon_y^T \Pi_y \varepsilon_y + \frac{1}{2}\varepsilon_x^T \Pi_x \varepsilon_x + \frac{1}{2}\varepsilon_v^T \Pi_v \varepsilon_v - \frac{1}{2}\ln|\Pi_y| - \frac{1}{2}\ln|\Pi_x| - \frac{1}{2}\ln|\Pi_v|, \quad (16)$$

$$\varepsilon_y = \tilde{y} - \tilde{C}\tilde{\mu}_x, \quad (17)$$

$$\varepsilon_x = D\tilde{\mu}_x - \tilde{A}\tilde{\mu}_x - \tilde{B}\tilde{\mu}_v, \quad (18)$$

$$\varepsilon_v = \tilde{\mu}_v - \tilde{v}_{\mathrm{pr}}, \quad (19)$$

where precision matrices Π_y, Π_x, and Π_v are defined as the inverse of covariance matrices Σ_y, Σ_x, and Σ_v.

Thus, we can obtain the inversion (perception) model by gradient descent of minimizing free-energy as follows

$$\dot{\tilde{\mu}}_x = D\tilde{\mu}_x - k_1(-\tilde{C}\Pi_y\varepsilon_y + (D - \tilde{A})\Pi_x\varepsilon_x), \quad (20)$$

$$\dot{\tilde{\mu}}_v = D\tilde{\mu}_v - k_1(-\tilde{B}\Pi_x\varepsilon_x + \Pi_v\varepsilon_v). \quad (21)$$

Note that $\tilde{\mu}_x$ and $\tilde{\mu}_v$ are estimated values of $\tilde{x}$ and $\tilde{v}$.

One of the advantages of this perception model is that the equations (20) and (21) reflect cortical circuitry as shown in Fig. 1. It consists of thalamus, lower cortex, and higher cortex. Sensory input enters from environment through thalamus to the lower cortex, while prior knowledge enters from the higher cortex to the lower cortex. The cortical circuit estimates states in deep layers and conveys estimation to the lower area, while it also calculates estimation errors in superficial layers and conveys errors to the higher area.

3 MODELING OF ACETYLCHOLINE

In this section, we introduce ACh effects in the above perception model proposed by Friston [1]. Then, ACh dynamics is derived by the free-energy principle.

3.1 Introduction of acetylcholine effects

Yu and Dayan have proposed ACh model in a framework of hidden Markov model, suggesting that ACh represents uncertainty of top-down information, and controls the balance between bottom-up and top-down input [6], [7]. So, we also start with the following assumption.

Assumption: Let α denote the ACh level. Then, ACh controls the magnitude of top-down input as follows

$$\Pi_v = \pi_v \exp(-\lambda_v \alpha), \quad (22)$$

where π_v is prior precision matrix, and λ_v is positive constant.

The high ACh level decreases the magnitude of precision matrix Π_v, resulting in decreasing the contribution of ε_v to estimation in (21). In other words, ACh suppresses top-down processing. It corresponds to muscarinic feedback suppression by ACh released from the basal forebrain as shown in Fig. 1.

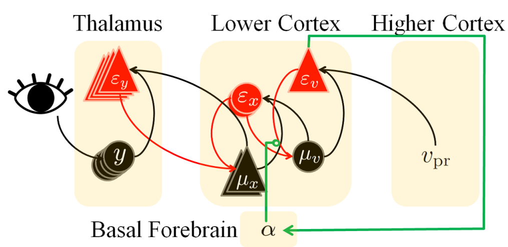

Fig. 1. Neuronal implementation of perception model with cholinergic modulation

3.2 Derivation of acetylcholine dynamics

Since we defined cholinergic modulation, we next derive dynamics of ACh level by the free-energy principle. Assuming that α obeys prior distribution $\mathcal{N}(\alpha_{\mathrm{pr}}, \Pi_\alpha)$, the free-energy is given by

$$\mathcal{F} = \frac{1}{2}\varepsilon_y^T \Pi_y \varepsilon_y + \frac{1}{2}\varepsilon_x^T \Pi_x \varepsilon_x + \frac{1}{2}\varepsilon_v^T \pi_v \varepsilon_v \exp(-\lambda_v \alpha) - \frac{1}{2}\ln|\Pi_y| - \frac{1}{2}\ln|\Pi_x| - \frac{1}{2}\ln|\pi_v| + \frac{1}{2}\lambda_v \alpha + \frac{1}{2}\varepsilon_\alpha^T \Pi_\alpha \varepsilon_\alpha - \frac{1}{2}\ln|\Pi_\alpha|, \tag{23}$$

where $\varepsilon_\alpha = \alpha - \alpha_{pr}$. Because the ACh level changes slower than state estimation, ACh minimizes the time integral of the free-energy by gradient descent as follows

$$\dot{\alpha} = -k_2 \partial_\alpha \int \mathcal{F} dt \tag{24}$$

$$= -k_2 \int (\frac{1}{2}\lambda_v - \frac{1}{2}\lambda_v \varepsilon_v^T \pi_v \varepsilon_v \exp(-\lambda_v \alpha) + \Pi_\alpha \varepsilon_\alpha) dt. \tag{25}$$

By time differentiating of both sides, we obtain ACh dynamics.

Derived dynamics: ACh level changes according to

$$\ddot{\alpha} = -k_2(\frac{1}{2}\lambda_v - \frac{1}{2}\lambda_v \varepsilon_v^T \pi_v \varepsilon_v \exp(-\lambda_v \alpha) + \Pi_\alpha \varepsilon_\alpha). \tag{26}$$

Instead of using gradient descent, the optimal ACh level that minimizes the free-energy at each time can be written analytically by solving $\partial_\alpha \mathcal{F} = 0$ and assuming that Π_α is close to zero. The optimal ACh level can be written by

$$\alpha = \frac{1}{\lambda_v} \ln \varepsilon_v \pi_v \varepsilon_v. \tag{27}$$

This equation shows that the ACh level varies proportional to the square of the estimation error ε_v. In other words, the ACh level represents the magnitude of estimation errors associated with top-down information in perception. Released ACh affects the efficacy of top-down modulation.

4 SIMULATION

We first simulate the generative model to create observed data, and then simulate the perception model with cholinergic modulation using sensory data given by the generative model. We use time step $\Delta t = 0.01$ in both the generative and perception model.

4.1 Generative model

In our simulation, the generative model creates 2 dimensional state x and 4 dimensional output y according to the equations (3) and (4) with scholar input v, given by

$$v(t) = \tanh(t-70) - \tanh(t-130) + \tanh(t-270) - \tanh(t-330) + \tanh(t-470) - \tanh(t-530) + z_v. \tag{28}$$

Embedded order of generalized coordinates is $n = 3$. We used the following constant parameters

$$A = \begin{bmatrix} -0.25 & 1.00 \\ -0.50 & -0.25 \end{bmatrix}, B = \begin{bmatrix} 1 \\ 0 \end{bmatrix}, \quad C = \begin{bmatrix} 0.1250 & 0.1633 \\ 0.1250 & 0.0676 \\ 0.1250 & -0.0676 \\ 0.1250 & -0.1633 \end{bmatrix}, \tag{29}$$

and precision matrices

$$\Pi_y = S \otimes I_4 \exp(10), \quad \Pi_x = S \otimes I_2 \exp(4), \quad \Pi_v = S \exp(6), \quad S = \begin{bmatrix} 1 & 0 & -\frac{1}{2}\gamma & \cdots \\ 0 & \frac{1}{2}\gamma & 0 & \\ -\frac{1}{2}\gamma & 0 & \frac{3}{4}\gamma^2 & \\ \vdots & & & \ddots \end{bmatrix}^{-1}, \tag{30}$$

with a roughness parameter $\gamma = 4$. These parameterizations are similar to [1].

Simulation results of the generative model are shown in Fig. 2. Input v becomes high at time $t = 70\sim130$, $270\sim330$, and $470\sim530$. State x and output y vary depending on the input v. In our simulation, we raise the noise level to $\Pi_y = S \otimes I_4 \exp(8)$ at time $t = 200\sim400$.

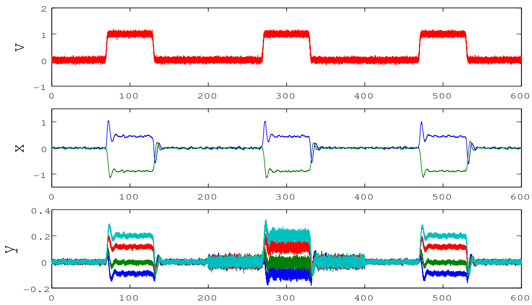

Fig. 2. Generative model

4.2 Perception model with cholinergic modulation

Next, we simulate the perception model (20) and (21) with ACh effects (22) and (26). We used parameters

$$\Pi_\alpha = 1, \alpha_{pr} = 0, \tag{31}$$

$$\pi_v = S \exp(6). \tag{32}$$

A, B, C, Π_y, and Π_x are the same as those of the generative model. Afferent input y is noisy at time $t = 200 \sim 400$, while prior knowledge v_{pr} is noisy at time $t = 400 \sim 600$.

Simulation results are shown in Fig. 3. Cortical circuitry estimates states μ_x and μ_v, changing the ACh level α in response to estimation errors at the same time. Estimated states μ_x and μ_v are similar to true dynamics in the generative model in Fig. 2. The ACh level α has oscillatory behavior after afferent input comes in. When prior knowledge is noisy, the ACh level becomes high. This means that ACh reports uncertainty of top-down information. The lower two figures show the free-energy $\mathcal{F}$ in the case of proper cholinergic modulation (above) and cholinergic deficit in which α is always zero (bottom). Although the free-energy level increases when afferent input as well as prior knowledge is noisy regardless of cholinergic modulation, ACh suppresses the rise of the free-energy in the case of noisy prior knowledge. As a result, ACh yields better perception.

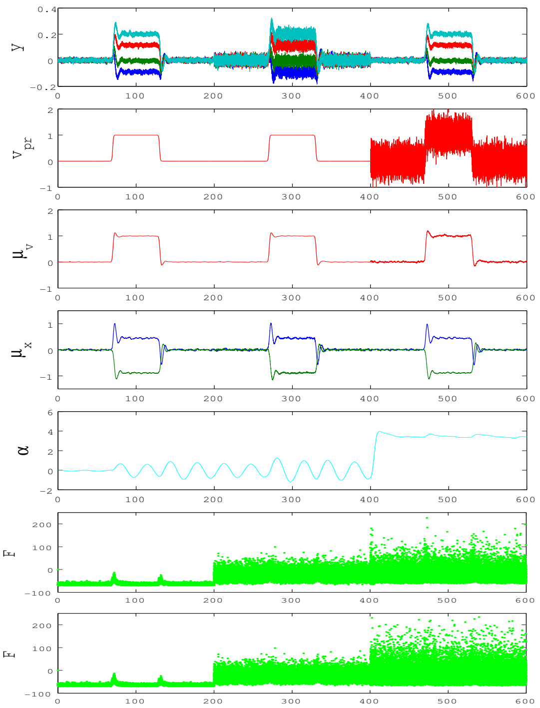

Fig. 3. Perception model with cholinergic modulation (above) and without cholinergic modulation (the lowest)

5 DISCUSSION

The role of ACh in this study is similar to that of [6] and [7], which is based on hidden Markov model, because both suggest that ACh reports uncertainty associated with top-down information. The biggest difference is that ACh contributes to efficient calculation in [6] and [7], whereas it contributes to estimation precision in our model, which is thought to be more realistic.

In addition to changing the ACh level depending on the noise level, ACh has oscillatory behavior. This is because the ACh level is defined by the "time integral" of the free-energy and thus its dynamics is written by quadratic differential equation. This fact indicates the possibility that oscillations in the brain can occur by minimizing the time integral of the free-energy.

Besides inserting cholinergic modulation effects in Σ_v, we can also introduce ACh effects in Σ_y and Σ_x [5]. These effects correspond to nicotinic thalamo-cortical facilitation and muscarinic intracortical suppression [3], [4]. We consider that the effects on Σ_v, Σ_y, and Σ_x result in noise reduction of prior knowledge, noise reduction of afferent input, and detection of mismatch of prior knowledge and afferent input, respectively.

6 CONCLUSION

In this paper, we introduce cholinergic modulation effects in a perception model based on the free-energy principle. The effects correspond to muscarinic top-down suppression. Then, we derive ACh dynamics by the free-energy principle. Our model suggests that the ACh level increases when top-down input is noisy, that is, ACh represents uncertainty of top-down information. Precise perception can be realized by cholinergic top-down modulation.

ACKNOWLEDGEMENTS

This research is supported by the Aihara Project, the FIRST program from JSPS, initiated by CSTP.

REFERENCES

[1] Friston K (2008), Hierarchical models in the brain. PLoS Comput Biol 4(11):e1000211

[2] Friston K (2010), The free-energy principle: a unified brain theory? Nat Rev Neurosci 11: 127–138

[3] Gil Z, Connors BW, Amitai Y (1997), Differential regulation of neocortical synapses by neuromodulators and activity. 19(3):679–686

[4] Hasselmo ME (2006), The role of acetylcholine in learning and memory. Current Opinion in Neurobiology 16(6):710–715

[5] Takada M, Aihara K (2012), A mathematical model of cholinergic function based on the free-energy principle. Cosyne Abstracts, Salt Lake City USA (submitted).

[6] Yu AJ, Dayan P (2002), Acetylcholine in cortical inference. Neural Networks 15:719–730

[7] Yu AJ, Dayan P (2005), Uncertainty, neuromodulation, and attention. Neuron 46:681–692

The Seventeenth International Symposium on Artificial Life and Robotics 2012 (AROB 17th '12),
B-Con Plaza, Beppu, Oita, Japan, January 19-21, 2012

Dynamics of associative memory network with self-oscillatory and non-self-oscillatory oscillators

Yusuke Okada[1], Yuichi Katori[2,3], Kazuyuki Aihara[1,3] and Hideyuki Suzuki[1,3]

[1] Graduate School of Information Science and Technology, The University of Tokyo, Meguro-ku, Tokyo 153-8505, Japan
[2] FIRST, Aihara Innovative Mathematical Modelling Project, JST, Meguro-ku, Tokyo 153-8505, Japan
[3] Institute of Industrial Science, The University of Tokyo, Meguro-ku, Tokyo 153-8505, Japan
(Tel: 81-3-5452-6697, Fax: 81-3-5452-6694)
(okada@sat.t.u-tokyo.ac.jp)

Abstract: We investigate an associative memory model consisting of both self-oscillatory and non-self-oscillatory oscillators that store temporal patterns on relative phase differences between the oscillators. We numerically simulate this model and show that the speed of memory retrieval is enhanced with increase in the proportion of number of non-self-oscillatory elements. These results imply, from a viewpoint of neuroscience, that the presence of resting or down state of neurons facilitates an ability of memory retrieval.

Keywords: associative memory, aging transition, coupled oscillators, up-down state transition.

1 INTRODUCTION

There have been many associative memory models composed of various elements that store various types of patterns. Aoyagi proposed an associative memory network, each element of which is an oscillator, and represents patterns in their relative phase difference [1]. In this model, the Stuart-Landau equation is used as the model of oscillator. The oscillators are connected with Hopfield-like weight matrix [2].

Dynamics of coupled oscillators are well studied independently of the associative memory models. Daido and Nakanishi studied globally coupled oscillators which are composed of two types of oscillators: namely, active and inactive oscillators [3, 4]. The active oscillator shows oscillation without an external driving force (self oscillatory) and its underlying mechanism is characterized by a stable limit cycle. The inactive oscillator requires external driving forces to oscillate (non-self oscillatory) and is characterized by a stable equilibrium point. If the proportion of number of inactive oscillators in the coupled oscillator system is sufficiently small, all the oscillators show synchronous oscillation; the active oscillators oscillate around the limit cycle and the inactive ones oscillate around the stable equilibrium with small amplitude. If the proportion of number of inactive oscillators becomes large, on the other hand, the system shows a phase transition and stops the oscillation. This phase transition is called an aging transition [3, 4].

In the present study, we investigate an associative network model which stores phase information and is composed of both active and inactive oscillators. We first model the associative network model. Then, we analyze the dynamics of the system while the system retrieves stored pattern, i.e., how the increase in the proportion of number of inactive oscillators contributes to the initial quickness of retrieving the stored patterns. Finally, we discuss the underlying mechanism of this initial quick memory retrieval and an interpretation of the model from a viewpoint of neuroscience.

2 MODEL

Our model is based on the associative memory model proposed by Aoyagi [1], which is a coupled oscillator system that stores phase patterns in the coupling connections.

The coupled oscillator system is described by

$$\frac{\mathrm{d}z_i}{\mathrm{d}t} = f_i(z_i) + K(\sum_{j=1}^{N} C_{ij}z_j - z_i), \tag{1}$$

where z_i is the complex state variable of the ith element. The interactions between the elements are represented by the complex weight matrix C_{ij} and the coupling strength $K \geq 0$. As for the oscillation dynamics f_i, we follow Aoyagi [1] and use the Stuart-Landau equation as follows:

$$f_i(z_i) = (\alpha_i + \mathrm{i}\Omega - |z_i^2|)z_i, \tag{2}$$

where the parameter α_i determines the dynamical characteristics of the ith element; the ith oscillator is active if $\alpha_i > 0$ and inactive if $\alpha_i < 0$.

This coupled oscillator system is an associative memory model that stores relative phase differences between the elements. The μth phase pattern is represented by a complex vector $Z^\mu = (Z_1^\mu, \dots, Z_N^\mu)$, where each element Z_i^μ with $|Z_i^\mu| = 1$ represents the phase of the ith element in the pattern. Note that multiplying by $e^{\mathrm{i}\theta}$ does not alter the embedded pattern, since only the phase differences are stored. Here, we assume the phase patterns $Z^1, \dots, Z^P$ are orthogonal. The complex weight matrix C is determined from the

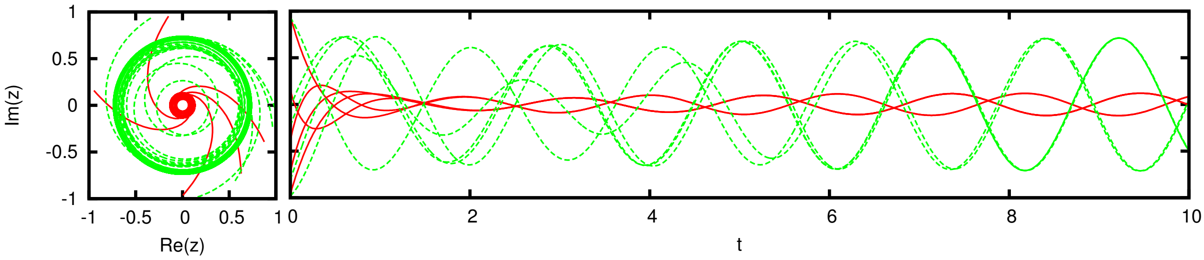

Fig. 1. Dynamics of the coupled oscillator system with $p = 0.6$. The trajectries of z_i in the complex plane (left) and the time evolutions of the imaginary part $\mathrm{Im} z_i$ (right) of five active oscillators (dashed lines) and five inactive oscillators (solid lines) are shown.

phase patterns $Z^1, \ldots, Z^P$ as follows:

$$C_{ij} = \frac{1}{N} \sum_{\mu} Z_i^{\mu} \cdot \overline{Z_j^{\mu}}. \tag{3}$$

Using the model whose all the elements are identical ($\alpha_i = 1$), Aoyagi [1] showed that the coupled oscillator system recalls the embedded phase patterns.

In this paper, we consider a network consisting of both active ($\alpha_i = 1$) and inactive ($\alpha_i = -2$) oscillators. This kind of network with active and inactive oscillators has been investigated by Daido and Nakanishi [3, 4], though their model is not for associative memory. Specifically, they studied the system with uniform connection weights $C_{ij} = 1/N$ as follows:

$$\frac{\mathrm{d}z_i}{\mathrm{d}t} = f_i(z_i) + K\left(\frac{1}{N} \sum_{j=1}^{N} z_j - z_i\right). \tag{4}$$

If the proportion of inactive oscillator p is small, inactive elements oscillate by effect of oscillation of active elements. If p is increased, the oscillation stops at the critical value $p = p_c$, which is given by

$$p_c = \frac{K+2}{3K}. \tag{5}$$

This phase transition is called an aging transition.

Retrieval of the μth pattern embedded in the system is evaluated by the overlap M_μ with pattern Z^μ defined by

$$M_\mu = \frac{1}{N} \left| \sum_i \overline{Z_i^{\mu}} \cdot \frac{z_i}{|z_i|} \right|. \tag{6}$$

This value shows a concordance rate between the state of the system and the stored pattern Z_μ. The larger M is, the more accurately the pattern is retrieved.

3 SIMULATION RESULTS

We performed numerical simulations of the associative memory model composed of $N = 100$ elements with $\Omega = 3$. For simplicity, the number $P = 3$ of orthogonal patterns are chosen from $\{\pm 1\}^N$ and embedded in the weight matrix C_{ij}. The coupling strength is set to $K = 1$.

From N elements, pN elements are randomly chosen as inactive elements, and the rest $(1-p)N$ elements are set as active elements.

We set initial states close to a certain embedded pattern $Z^\mu \in \{\pm 1\}^N$. Specifically, we obtained initial phases from the chosen pattern by adding perturbations $\Delta\theta$ that follow the von Mises distribution, whose probability density function is given by

$$\mathrm{P}(\Delta\theta|\kappa) = \frac{1}{2\pi \mathrm{I}_0(\kappa)} \exp(\kappa \cos \Delta\theta), \tag{7}$$

with the measure of concentration $\kappa = 1$

Figure 1 shows the dynamics of the system with $p = 0.6$ in the simulation. Active oscillators and inactive oscillators show oscillations with large and small amplitude, respectively. Inactive oscillators converge to the corresponding limit cycle more quickly than active oscillators.

In the following, we calculate the overlap M_μ with the chosen pattern Z^μ averaged over 3000 realizations.

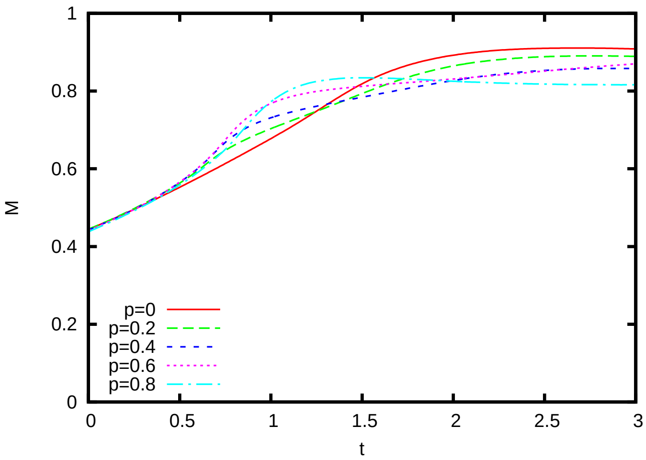

Fig. 2. The overlap M as a function of time t.

Figure 2 shows the overlap M as functions of time t for each value of p. We find that M is an increasing function in most of the time region. While the value of M for $p = 0$

is the smallest at time $t = 1$, it becomes the largest at time $t = 2$.

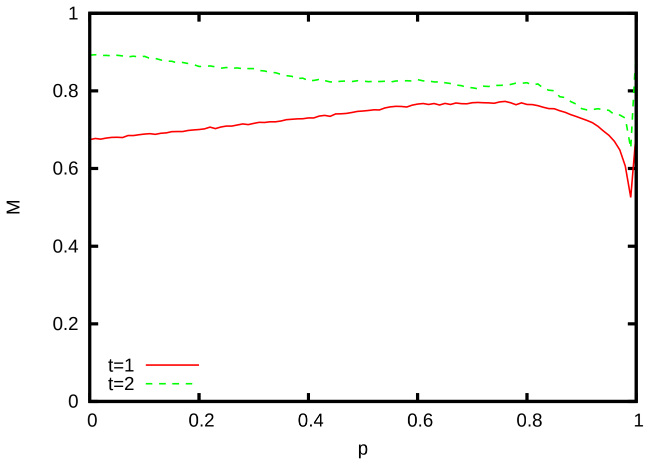

Fig. 3. The overlap M as a function of p at $t = 1$ and 2. In the range $0 \leq p \leq 0.8$, it is almost increasing for $t = 1$ (solid line) and almost decreasing for $t = 2$ (dashed line).

The dependence of the overlap on p is shown in Fig. 3. The solid and dashed lines correspond to $t = 1$ and $t = 2$, respectively. At $t = 1$, M is an almost increasing function in the range between $p = 0$ and $p = 0.8$. At $t = 2$, M is an almost decreasing function in the range.

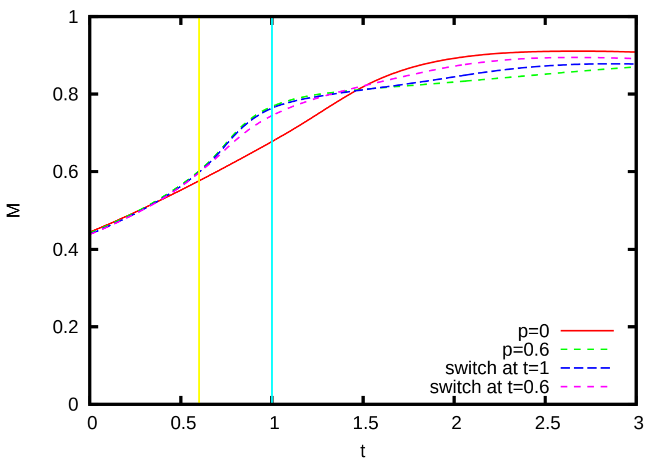

Fig. 4. The overlap M as a function of time t. The value of p is changed from 0.6 to 0 at time $t = 0.6$ and $t = 1$. The cases of $p = 0$ and $p = 0.6$ without the change are also shown.

These result show that small p enhances speed of retrieving and decrease the value M after certain period of time. We investigate the case in which the value of p is changed at a certain time. Figure 4 shows the overlap M as functions of t when the value of p changes from 0.6 to 0 at $t = 0.6, 1$. The value of M at time $t = 2$ in the cases with the change are larger than the case of $p = 0.6$ without the change. While the value of M at $t = 1$ in the case with the change at $t = 0.6$ is smaller than the case without the change, it becomes larger at $t = 2$.

4 DISCUSSION

In the previous section, we observed that the system with inactive oscillators shows quicker initial responses than without inactive oscillators. This can be intuitively explained as follows. Let r_i and θ_i be the amplitude and the phase of the state z_i of the ith element, respectively; i.e., $z_i = r_i \exp \mathrm{i}\theta_i$. Then the dynamics of θ_i is given by

$$\frac{\mathrm{d}\theta_i}{\mathrm{d}t} = \Omega + K\frac{r_i^\star}{r_i}\sin(\theta_i^\star - \theta_i), \tag{8}$$

where $r_i^\star$ and $\theta_i^\star$ are the amplitude and the phase of the input to the ith element through C_{ij}, respectively, as follows:

$$\sum_j C_{ij} z_j = r_i^\star \exp \mathrm{i}\theta_i^\star. \tag{9}$$

The second term of Eq. (8) describes the effect that attracts θ_i to $\theta_i^\star$. Thus its strength is inversely proportional to r_i. Since the amplitude r_i is large for active elements and small for inactive elements, the phases of inactive elements move more quickly to an embedded pattern than active elements.

In the context of neuroscience, temporal aspects of neural activities have been considered to be important [6]. In a neural network, spikes (action potentials) are responsible for the mutual interaction and communication between neurons. Multi-channel recording of neural activities often shows a repetition of certain temporal patterns of spike train, which may be caused by interactions among neurons. Such temporal aspects of neural activities are often modeled with coupled oscillators as shown in the present paper. In Aoyagi's model, temporal patterns are represented as the phase differences among oscillators and embedded in the complex weight matrix.

Another intriguing observation of neural activities is about the two-state dynamics [7], which is a characteristic switching of the membrane potential between two preferred levels, namely the more polarized level (down state) and the more depolarized level (up state). Similarly, the transition between the resting state and the sustained oscillatory state is observed and is modeled as a bistable system with a stable equilibrium and a stable limit cycle [8]. Such a model is closely related to Daido's model in the sense that active and inactive element coexist.

In the present study, to elucidate the contribution of coexistence of active and inactive elements in the associative network, we consider non-uniformity of the elements instead of the bistability. We found that the proportion of inactive oscillator is important for speed of retrieving a temporal pattern. This indicates that the increase in proportion of neurons in resting state facilitates retrieval process of memories. Although the proportion of inactive oscillators is fixed or time-invariant in the present network model, real neurons dynamically switch their state between up and down state. Contribution of this dynamical aspect of switching to the ability of memory retrieval should be evaluated in future.

5 CONCLUSION

We investigated the dynamics of pattern embedded oscillatory networks which include non-self-oscillatory elements. The property of non-self-oscillatory element determines the speed of retrieving stored patterns. This mechanism may play some functional role in neural networks of the brain.

ACKNOWLEDGEMENT

This research is partially supported by the Aihara Innovative Mathematical Modelling Project, the Japan Society for the Promotion of Science (JSPS) through the "Funding Program for World-Leading Innovative R&D on Science and Technology (FIRST Program)," initiated by the Council for Science and Technology Policy (CSTP).

REFERENCES

[1] Aoyagi T (1995), Network of Neural Oscillators for Retrieving Phase Information, Phys. Rev. Lett. 74(20):4075-4078.

[2] Hopfield J J (1982), Neural Networks and Physical Systems with Emergent Collective Computational Abilities, Proc. Natl. Acad. Sci. 79:2554-2558.

[3] Daido H and Nakanishi K (2004), Aging Transition and Universal Scaling in Oscillator Networks, Phys. Rev. Lett. 93(10):104101.

[4] Daido H and Nakanishi K (2007), Aging and Clustering in Globally Coupled Oscillators, Phys. Rev. E 75(5):056206.

[5] Bishop C M (2006), Pattern Recognition and Machine Leaning, Springer.

[6] Theunissen F and Miller J P (1995), Temporal Encoding in Nervous Systems: a Rigorous Definition, J. Comput. Neurosci. 2(2):149-162.

[7] Wilson C J and Kawaguchi Y (1996), The Origins of Two-State Spontaneous Membrane Potential Fluctuations of Neostriatal Spiny Neurons, J Neurosci. 16(7):2397-2410.

[8] Katori Y, Lang E, Onizuka M, Kawato M and Aihara K (2010), Quantitative modeling of Spatio-temporal Dynamics of Inferior Olive Neurons with a Simple Conductance-based Model, Int. J. Bifurcation Chaos 20(3):583-603.

The evaluation of the emotion by NIRS

Hirotoshi ASANO. Author[1], Takanori SAGAMI. Author[2], and Hideto IDE[1,2]

[1]Aoyama Gakuin University, Kanagawa 252-5258, Japan
(Tel: 81-42-759-6419, Fax: 81-42-759-6528)

[1]hirotoshi.asano@gmail.com

Abstract: We experimented for the purpose of development of the objective evaluation technology of emotions. Persons requiring care will also increase in number with the increase in this population. In the case of the person requiring care who lost the function to convey an intention especially, the objective judgment to a physical and mental pain is required. Specifically, we gave subjects stimulus of a comfortable or an uncomfortable sound and measured concentration of the oxygenated hemoglobin of a frontal lobe part by Near-Infared Spectroscopy. Based on the experimental result, a comfortable state or an uncomfortable state was distinguished concentration of the oxygenated hemoglobin using the bayesian network. As a result, we were able to estimate the subject's psychological condition.

Keywords: objective evaluation, Near-Infared Spectroscopy, bayesian network, emotion.

1 INTRODUCTION

In Japan, low birthrate and longevity are progressing quickly. According to National Institute of Population and Social Security Research, the rate of population aged 65 and over will reach to 35.7% in 2050. Persons requiring care will also increase in number with the increase in this population. In the case of the person requiring care who lost the function to convey an intention especially, the objective judgment to a physical and mental pain is required. In the past, the objective evaluation of the intention by brain waves (the sensitivity-spectrum analyzing method and the sensitivity fractal dimension analyzing method) has been proposed. Moreover, the machine which operates an electronic device using brain waves is developed. The interface which applies cerebral activity to control or support is called Brain Machine Interface. BMI is expected as a machine which supports transfer of a human intention [1][2].

By the way, functional Magnetic Resonance Imaging (fMRI) and Near-Infared Spectroscopy (NIRS) are the methods of measuring cerebral activity. When oxygenated hemoglobin changes to deoxygenated hemoglobin, the method of measuring brain activity indirectly using the increase in a magnetic resonance signal is fMRI [3][4]. Generally restriction by the environment and the conditions of measurement is strong. Moreover, the influence of the motion with the body is strong. On the other hand, NIRS is equipment which measures the amount of change of oxyHb and deoxyHb in blood using near-infrared light. In process of cerebral information processing, the system of the communication of information which nerve activity bears and the system of the energy supply supporting nerve activity are related [5]. If nerve activity takes place, the blood vessel in the circumference will be extended. The mechanism of the adjustment for supplying the arterial blood containing oxygen and glucose occurs [6]. The quantity of a blood flow increases in the tissue of a nearby nerve. The oxidation state (ratio of oxyHb and deoxyHb) of blood changes. Based on assumption that the relation between nerve activity and a blood flow exists, NIRS measures the oxygenated hemoglobin within a brain. In short, this index is not the nerve activity which is actually processing information. However, it is an index of an indirect brain function. Moreover, the measurement by NIRS uses the two characteristics [7]. The 1st is the high permeability of the organism in near-infrared light (700-900 nm). The 2nd is the permeability of the light from which oxyHb and deoxyHb in blood differ. When the head is irradiated with near-infrared light, the ingredient of the light is diffused in cerebral tissue by high permeability. And the cerebral cortex which is in a depth of about 20-30 mm flatly is reached. When light is measured in about 3-cm distance from a glaring point, the optic element which has returned by diffused reflection can be detected [8]. NIRS calculates change of oxyHb and deoxyHb of the cerebral cortex using this detection light. NIRS is inferior to fMRI in the point of visualization of structure and the range of measurement. However, the restriction to a motion of the body is small. Moreover, it can experiment in the more natural state. Therefore, NIRS has high practicality as a means for transmitting an intention.

We experimented for the purpose of development of the objective evaluation technology of emotions. There are some researches on the emotions using NIRS. For example, there is research on change of a cerebral blood flow when a vision stimulus and a sense-of-smell stimulus are given. But, there are still few examples. Moreover, there is almost no example studied about objective evaluation of a comfortable sound or an uncomfortable sound. A sound stimulus is one of the important stimuli which evoke the emotions of those dependent on care. A sound stimulus is one of the important stimuli which evoke the emotions of a person requiring care [9]. Therefore, we set up the sound stimulus as a candidate for evaluation. Specifically, we gave subjects stimulus of a comfortable or an uncomfortable sound and measured concentration change (⊿oxyHb) of the oxygenated hemoglobin of a frontal lobe part by NIRS. Be based on the measured data, we evaluated quantitatively the difference in brain activity. By developing the technology of objective evaluation, it may be applicable to evaluation of the brain activity under various environments. It is shown that the result of an experiment has relation nature between the psychological amount by a comfortable or an uncomfortable sound and ⊿oxyHb in a part of frontal lobe. Based on the experimental result, a comfortable state or an uncomfortable state was distinguished ⊿oxyHb using the bayesian network (BN). As a result, we were able to distinguish the subject's psychological condition.

2 EXPERIMENT METHOD

2.1 Experimental environment

It experimented within electromagnetism shield room. Room temperature was 22.0±1.0 [℃]. Illumination was about 200 [lx]. The interior of a room was calm. Fig.1 showed the counting system. The shimadzu FOIRE-3000 was installed next to the subject and we measured ⊿oxyHb. Fig.2 shows the position of the measured channel and measurement. The position of measurement serves as the middle point of the position of irradiation, and the position of detection. First of all, the channel 9 of the holder for measurement was united with Fpz. In the next step, the subject was equipped with the holder using the fixed belt. The interval of the probe for irradiation and the probe for detection was set to about 30 [mm].The number of the measured channels was 32. Sampling time was 175 [ms].

2.2 Experimental conditions

The number of subjects was 5 (21-25 age, healthy subjects). We experimented after the subject rose and 4 hours or more had passed. The subject's previous day sleeping hours were about 8 hours. 2 hours before beginning an experiment, ingestion of a meal, smoking and a caffeine was forbidden. Excessive movement on the day was forbidden. This experiment was conducted by ethical consideration based on Declaration of Helsinki (1964). The subject's human rights were considered in the experiment. We fully explained and got consent by signature. Fig. 3 shows a measurement schedule. The subject which hears sound was performed in Task. The subject was made to hear white noise within a rest time. The comfortable sound used the album (music gentle to autonomic nerves). The uncomfortable sound used scratch sound. It is clear that these tasks give a subject comfortable or uncomfortable emotions in a preliminary experiment. Time to hear these tasks was set to 60 [sec]. Moreover, Visual Analogue Scale questionnaire was written 20 seconds after the start of rest time.

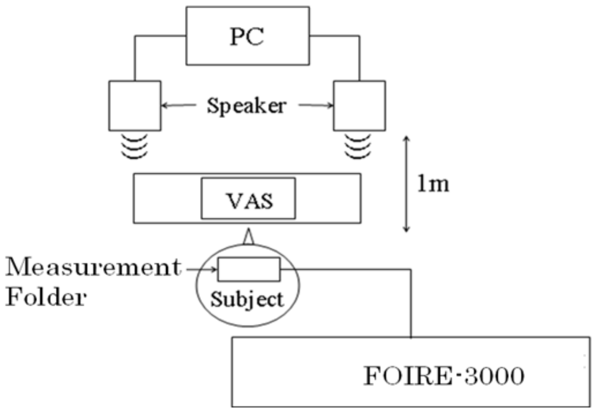

Fig.1. Measurement System

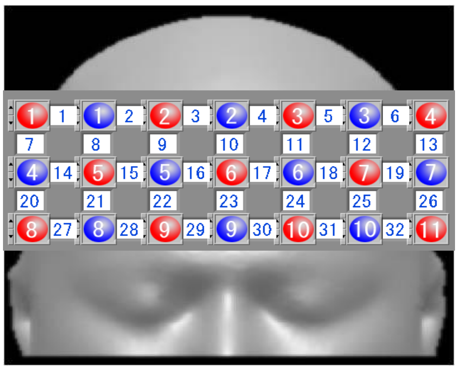

Fig.2. Measurement position

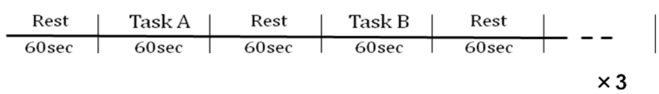

Fig.3. Measurement Schedule

3 EVALUATION METHOD

3.1 Psychological index

The Visual Analogue Scale questionnaire was used for the psychological index [10]. Fig.3 shows an example about how to write a Visual Analog Scale questionnaire. Visual Analog Scale is a tool used to help a person rate the intensity of certain sensations and feelings. The rate (0% - 100%) of the length from a left end to a check position was measured to the length of a line segment. This experiment estimated uncomfortable (0%) - comfortable (100%).

3.2 Physiological index

⊿oxyHb in a frontal lobe part was measured. Baseline compensation was performed in order to extract only a changed part to a stimulus (Fig.4). Task for 3 times was added and averaged. The following is the method of compensation. ⊿oxyHb of the channel measured at the TASK time T and the REST time R is made into the following.

$$h(t),(-R<t<T+R) \qquad (1)$$

Compensation data is hC(t). The data at the time of a Task start is h(0).

$$h_C(t)=h(t)-h(0) \qquad (2)$$

Moreover, the average amount of change of oxygenated hemoglobin concentration is defined as ⊿oxyHbave. It is considered as a physiological index.

$$\Delta oxyHb-abe=\frac{1}{T}\sum_{t=0}^{T}h_C(t) \qquad (3)$$

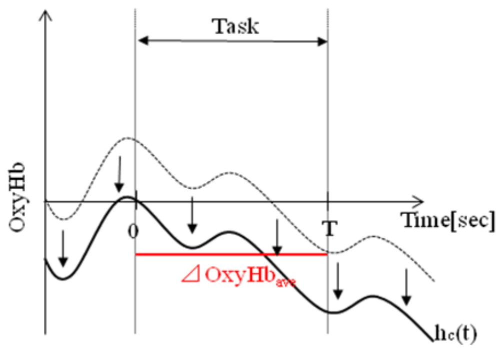

Fig.4. Baseline compensation

4 EVALUATION METHOD

When a comfortable stimulus was given, ⊿oxyHb decreased in a part of measured part (Fig.5). On the other hand, when an uncomfortable stimulus was given, ⊿oxyHb decreased slightly (Fig.6). However, the parts which reacted to each stimulus differed. Comfortable and uncomfortable emotions are related to a limbic system. It is closely related to especially an amygdaloid body. Control and rise of frontal lobe activity are affected. In short, reduction of ⊿oxyHb is considered that rise of activity of a limbic system has influenced. Under the influence through which blood flowed into the nearby part, it is thought that reduction of ⊿oxyHb occurred in a part of frontal lobe part. Based on the result of Fig.5 and Fig.6, the difference in ⊿oxyHb in two stimuli was evaluated. T test was performed for every Channel using ⊿oxyHbave. As a result, there was a significant difference in Channel 2 and Channel 28 (Fig.7). Fig.8 is a time change of ⊿oxyHb in Channel 2. ⊿oxyHb at the time of giving a comfortable stimulus showed the tendency higher than ⊿oxyHb at the time of giving an uncomfortable stimulus. The relation between ⊿oxyHbave of channel and VAS was considered. Fig.9 is a relation of ⊿oxyHbave and VAS in Channel 2. In the case of Channel 2, the correlation coefficient of VAS and ⊿oxyHbave was 0.55. In the case of Channel 28, it was 0.66. Both of channels were positive correlation. It inquired in the similar way also to other subjects. Channels which were a significant difference and positive correlation were examined. It was a result as shown in Table 1. These results show a possibility that NIRS can estimate emotions objective.

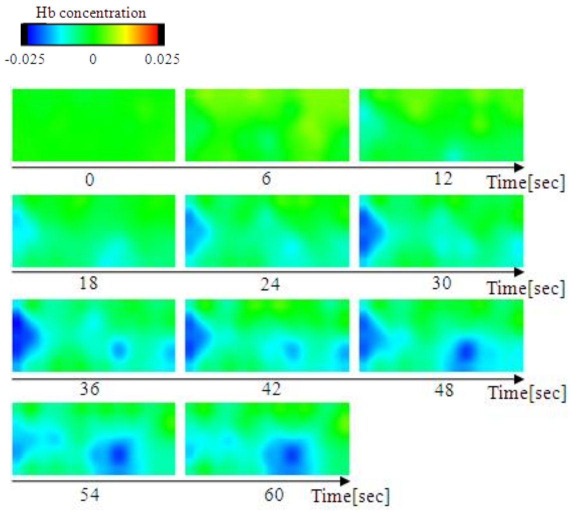

Fig.5. Topographical observation
(When a subject hears a comfortable sound)

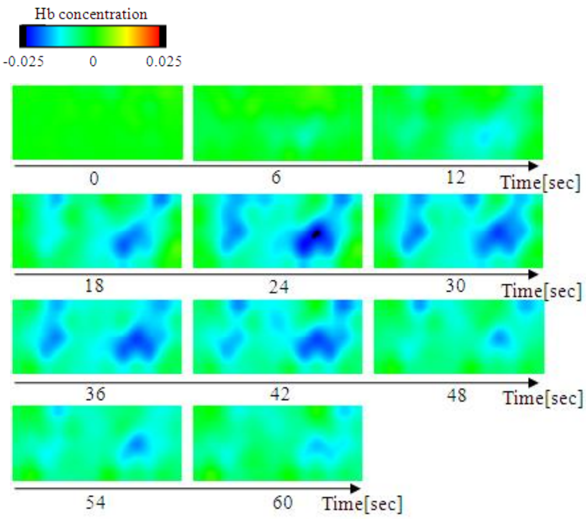

Fig.6. Topographical observation
(When a subject hears an uncomfortable sound)

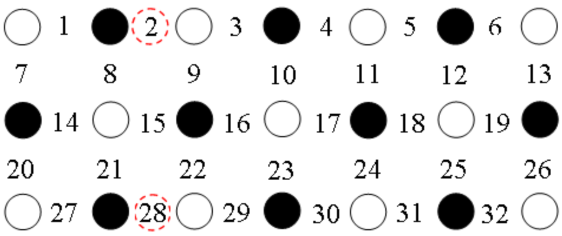

Fig.7. Channels with a significant difference

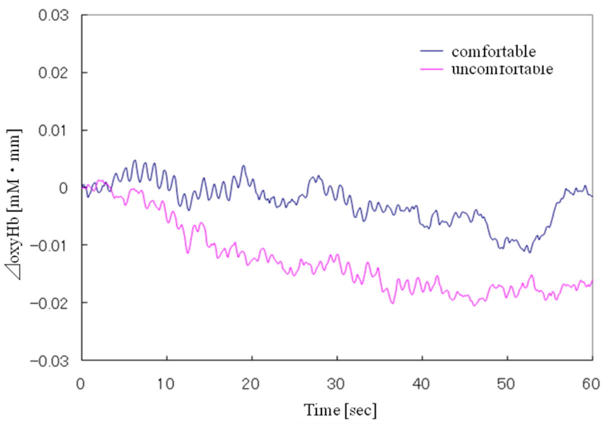

Fig.8. Time series graph of ⊿oxyHb (channel 2)

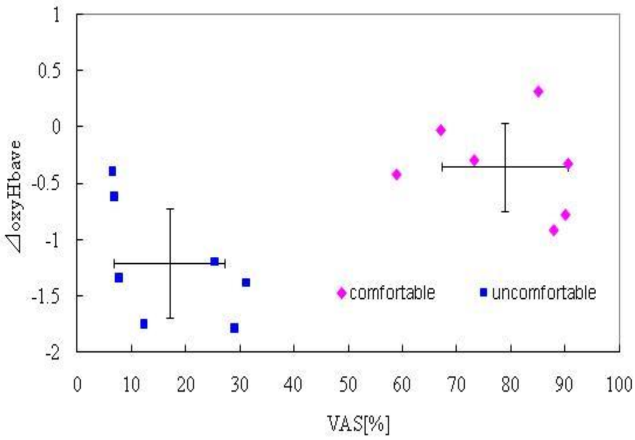

Fig.9. Relation between ⊿oxyHb-ave and VAS (channel 2)

Table.1. Channels with a significant difference (All subjects)

	Channel				
Subject A	2	28			
Subject B	3				
Subject C	2	6	9		
Subject D	2	4	9	15	18

5 ESTIMATION MODEL

Based on the experimental result, we built the estimation model of emotions using BN. A figure is the estimation model of emotions. Visual Analog Scale performed t official approval by each channel. The data used for the construction was data of the channel which had a significant difference in ⊿oxyHb. A physiological quantity used the average value (⊿oxyHb-ave) of ⊿oxyHb of task. A psychological quantity classified the value of Visual Analog Scale into three states. Three states were "uncomfortable (0-33%)", "normal (34-66%)", and "comfortable (67-100%)." The frequency of each state was computed from reference data. Graph structure and the conditional probability in each state were calculated. BN was built using the data. The following is a formula of graph structure. The following is a formula of graph structure. The amount-of-information standard AIC was used for the judgment of the dependency between nodes. The number of times of trial was performed 10 times per person. The amount of seven trials was the reference data for model construction. The amount of three trials was the data for evaluation for presumption.

6 RESULT AND CONSIDERATION

Bayesian estimation was performed from the built model to the data for evaluation. The presumed result was compared with actually measured VAS and the presumed rate was calculated from the number of coincidence. Fig.10 is presumed accuracy. The presumed rate became 67% on the average as a result of the experiment. This result shows a possibility that emotions can be presumed by BN.

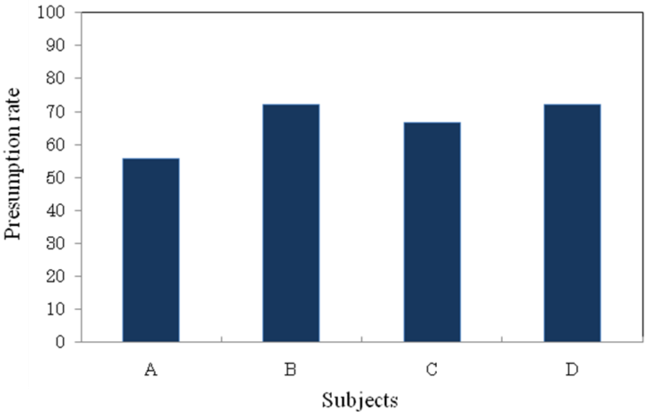

Fig.10. Estimation rate

7 CONCLUSION

We proposed the technique of objective evaluation of the emotions by NIRS. If this research develops, we may be able to develop the system by which a care worker can understand the emotions of a person requiring care easily. Specifically, we gave subjects stimulus of a comfortable or an uncomfortable sound and ⊿oxyHb of a frontal lobe part by NIRS. Be based on the measured data, we evaluated objectively the difference in brain activity. It is shown that the result of an experiment has relation nature between the psychological amount by a comfortable or an uncomfortable sound and ⊿oxyHb in a part of frontal lobe. Based on the experimental result, a comfortable state or an uncomfortable state was distinguished ⊿oxyHb using BN. The presumed rate became 67% on the average as a result of the experiment. This result shows a possibility that emotions can be presumed by BN. As a result, we were able to estimate the subject's psychological condition by BN.

REFERENCES

[1] T.Musya (1996), Heart is measured (in Japanese). Nikkei science, 126(4):20-29

[2] T.Sato, M.Nakagawa (2002), Quantification of Emotions using Fractal Dimension Analysis Emotion Fractal-dimension Analysis Method (in Japanese). The Institute of Electronics, Information and Communication Engineers, 102(534):13-18

[3] M.Tashiro (2005), Development of neuroimaging research on human emotion (in Japanese). The Japanese Pharmacological Society, 125(2):88-96

[4] T.Sato (2005), Imaging of brain function with light: optical topography (in Japanese). The Japanese Pharmacological Society, 12(3):296-307

[5] G.Maehara (2006), Neural Activation during the Shape Matching Task Measured by Near-Infrared Spectroscopy, The Institute of Electronics (in Japanese). Information and Communication Engineers, 106(328):53-56

[6] S.Hoshi (2005), Functional Near-infrared Spectroscopy: Limitations and Potential (in Japanese). Japanese College of Angiology, 45(2):61-67

[7] T.Yamamoto (2009), The outline of the optical topographical observation method, and examination to the improvement in space decomposition (in Japanese). JSLSM, 26(3):257-265

[8] A.Sato (1998), Nerve nature regulation of a brain blood flow is revolved (in Japanese). The Japanese Pharmacological Society, 112:5-9

[9] T.Kitamura (2007), A moral disease and brain imaging research (in Japanese). Nikkei science, 24:132-136

[10] Independent corporation industrial technical research institute (2003), Human measurement handbook, Asakura Publishing Co. Ltd.

The Seventeenth International Symposium on Artificial Life and Robotics 2012 (AROB 17th '12),
B-Con Plaza, Beppu, Oita, Japan, January 19-21, 2012

A Reward Allocation Method for Reinforcement Learning in Stabilizing Control Tasks

Shu Hosokawa[1], Joji Kato[2], and Kazushi Nakano[12]

[1] Dept. of Electronic Eng. , The University of Electro-Communications, Chofu, Tokyo 182-8585, Japan
[2] Dept. of Mechanical Eng. and Intelligent Systems, The University of Electro-Communications, Chofu, Tokyo 182-8585, Japan
(Tel : 81-42-443-5190; Fax : 81-42-443-5183)
(hosokawa@francis.ee.uec.ac.jp)

Abstract: Reinforcement learning is a machine learning method that does not require a detailed teaching signal by a human, which is expected to be applied to real robots. In its application to real robots, the learning processes are required to be finished in a short learning period of time. A reinforcement learning method of non-bootstrap type has fast convergence speeds in the tasks such as Sutton's maze problem that aim to reach the target state in a minimum time. However, these methods are difficult to learn either task to keep a stable state as long as possible. In this study, we improve the reward allocation method for stabilizing control tasks. The validity of our method is demonstrated through simulation for stabilizing control of an inverted pendulum. Our proposed method can acquire a policy in order to keep a stable state within a short learning period of time.

Keywords: Reinforcement Learning, Stabilizing Control Tasks, Profit Sharing, SMDP

1 INTRODUCTION

The machine learning methods have attracted a lot of attention by a characteristic that robot's adaptive actions are able to get from action results of itself. Reinforcement learning is a method of machine learning, which does not require a detailed teaching signals by a human. Reinforcement learning can be divided into two types of bootstrap and non-bootstrap. As well-known non-bootstrap methods, there are Profit sharing [1] , Adaptive immunity - based reinforcement learning [2] and so on. Those types of learning methods are faster than famous reinforcement learning methods such as Q-learning [3] in learning convergence speeds, when applying to the problem of minimizing the amount of time to achieve the goal (e.g., maze searching, swing-up control for an invert pendulum and so on). Those methods are not able to get the optimal policy, but they can get the policy that achieves to the goal state by satisfying the rationality theorem proposed by Miyazaki et al [4].

However, when applying that method to stabilizing control tasks, we cannot acquire a policy to achieve the goals. The bootstrap methods can acquire the policy of the stabilizing control by giving a negative reward at a change from a stable state to an unstable state [5]. On the other hand, since the non-bootstrap learning method cannot deal with negative a reward value, the reward value has to take a positive value [6]. In this case, there is a great risk of learning an undesirable behavior of changing from a stable state to an unstable state according to reward values.

In this study, we improve the reward allocation method for the stabilizing control tasks. In the stabilizing control tasks, we need to model an environment by Semi-Markov decision process (SMDP) because a time of doing actions is not constant by each state. The validity of our method is demonstrated through simulation for stabilizing control of an inverted pendulum.

2 PROFIT SHARING

Reinforcement learning method is for learning by updating to the Q-value that is an estimated value of action in a state. The reinforcement learning method of non-bootstrap type does not require Q-values of other states in Q-value updating process. The following equation shows how to update the Q-values of the Profit Sharing.

$$Q(s_t, a_t) \leftarrow Q(s_t, a_t) + \alpha\left[r(t) - Q(s_t, a_t)\right] \tag{1}$$

where t is the time, s_t is the state in time t, a_t is the selected action in time t, $\alpha(0 < \alpha < 1)$ is the learning rate and $r(t)$ is the reward function. The Q-value is updated based on the reward function of the actions that has been selected before receiving a reward. Following equation is generally to use as a reward function that satisfied the rational theorem [4], when applying to the problem of minimizing the amount of time to achieve the goal.

$$r(t) = R\left(\frac{1}{S}\right)^{T-t} \tag{2}$$

where, $S(\geq L+1)$ is the constant value, L is the number of selectable actions, T is the episode time and R is received reward.

In many cases, action selection methods in Profit Sharing use the roulette selection, which is based on the probability

$P(s,a)$ with weight of the Q-values.

$$P(s,a) = \frac{Q(s,a)}{\sum_{a \in A} Q(s,a)} \tag{3}$$

Here, since Eq. (3) cannot take zero or negative Q-values, the Q-values must be greater than zero in updating process.

3 REWARD FUNCTIONS IN STABILIZING CONTROL TASKS

In this section, we discuss about the method of non-bootstrap reinforcement learning for applying it to the stabilizing control tasks. We considered about conditions of the reward allocations for obtaining the policy of the stabilizing control tasks. In addition, we propose a reward allocation method by use of those conditions.

3.1 Semi-Markov Decision Process

The problem of minimizing amount of time to achieve the goal dose not need to deal with the actions of keeping same state. On the other hand, there are no problems that deal with actions of keeping the same state in the stabilizing control tasks. However, Markov decision process (MDP) must to select an action at the each time of the constant control cycles. If the state is divided roughly, each action selection may include multiple effective action or illegal actions in the same state. It can be resolved by dividing the state into smaller pieces, but it requires longer time to learning.

In this study, we model an environment by SMDP. SMDP selects an action after the state transition has occurred. It cannot completely resolve the trade-off for the state space division, but there is no need to handle the autoregressive action to the same state. Therefore, it is possible to make a relatively rough state division.

3.2 Reward allocation

The non-bootstrap method updates all estimate values of state and action when receive a reward. Therefore, we can use the duration of actions in the episode unlike bootstrap methods such as Q-learning. However, if using the duration of episode as the reward, we have a very large reward. Overflow may occur when performing the actual calculation, or if the estimated value has a very small initial one, there is a risk that state solution search is not performed sufficiently. Therefore, we give the reward of constant value (R=1), which is allocated from duration time of action. In addition, we assume that each episode starts from the stable region, and discuss about a reward allocation method in stabilizing control tasks by using an example shown in Fig. 1.

First of all, we give an example of the state transition in Fig. 1.

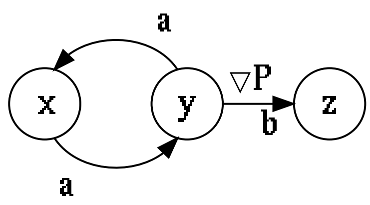

Fig. 1. An example of state transition

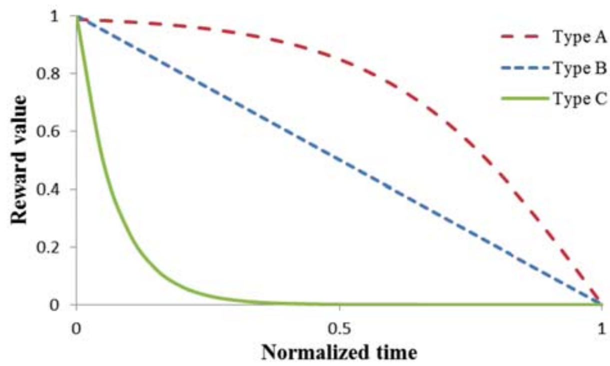

Fig. 2. An example of reward allocation

State transition example(1)

$x_a \rightarrow y_b \rightarrow z$

State transition example(2)

$x_a \rightarrow y_a \rightarrow x_a \rightarrow y_b \rightarrow z$

where x and y are the stable states, and z is the unstable state their subscripts is show selected actions. The above example means to suppress the action b of under going a transition from the state y to the state z. For the stabilizing control tasks, the reward allocation value should be zero or small value because action taken just before receiving the reward should not be selected. On the other hand, the reward allocation value may be higher values because actions taken long before receiving the reward one useful for stabilization. Therefore, the reward of actions allocates higher value around the initial time (t_a), and does lower values around the episode end time (t_b).

$$r(t_a) > r(t_b)$$

Figure 2 shows three types of functions. The horizontal axis in this figure shows the normalized time duration episode, the vertical axis does the value of reward allocation. In initial learning is short, it is better to reduce the action selections for changing to unstable state as soon as possible. We want to assign a small reward for it. The type C function is not suitable from the above view. And also, the episode duration time becomes longer on the way of learning. In this case, since it may also contribute on the way of learning, it is better allocate the reward equivalent to that in the initial episode. The type A functions allocates a small reward to actions just before Stabilization state end, and dose a small discounted reward to actions in the initial-middle stage of the episode. The following equation is an example of the type A functions shown in Fig. 2.

$$r(t) = 2\left(0.5 - \frac{1}{1+\exp(-(t-1)/T_a)}\right) \quad (4)$$

where t is the normalized time by episode time and T_a is the constant value for decide to functions gradient.

As the duration of episode becomes to be longer with learning, action selection is to be performed multiple times in the same state. However, the type A function cannot make an evaluation of difference between actions for moving to unstable state and others. Because each evaluation is decided by normalized time of action, and each value has only small difference. Here, we consider about the number of selected actions when transitions among some states are undergone periodically. We set that the action for keeping stable state is a_{loop}, and the action for moving to unstable state is a_{open}. It is clear that the number of action selection for keeping stable state is longer than that of the action for moving to unstable state ($Num(a_{loop}) \geq Num(a_{open})$, $Num()$ is action selected numbers). And also, the actions for keeping stable state are made earlier than the actions for moving to unstable state. From those considerations, we can make a difference in the update process by use of the sum of the reward. Therefore, the update formula of Profit Sharing method for stabilizing control task is shown as.

$$Q(s_i,a_i) \leftarrow Q(s_i,a_i) + \alpha\left[\sum_t r(t|s_i,a_i) - Q(s_i,a_i)\right] \quad (5)$$

The reward function $r(t)$ is defined in the range $[0,1)$, the initial Q-values have to set 1 and more. This provides a searching in the environments is performed well by Boltzmann and roulette selection.

4 SIMULATION

This section shows a simulation result of our proposed method applying to stabilizing control of the inverted pendulum (Fig. 3). The motion equation of the inverted pendulum is expressed as

$$(M+m)\ddot{x} + ml\cos\theta\ddot{\theta} + D_x\dot{x} + ml\sin\theta\dot{\theta} = a \quad (6)$$

$$-ml\cos\theta\ddot{x} + I\ddot{\theta} + D_\theta\dot{\theta} - mgl\sin\theta = 0 \quad (7)$$

where, M is the mass of the cart, m is the weight of the pendulum, l is the length of the pendulum to the gravity center,

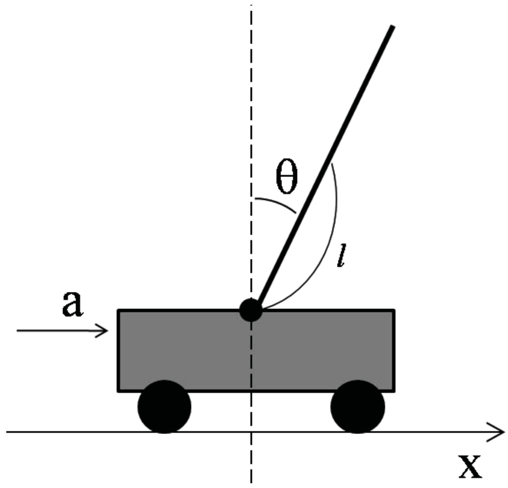

Fig. 3. Inverted pendulum

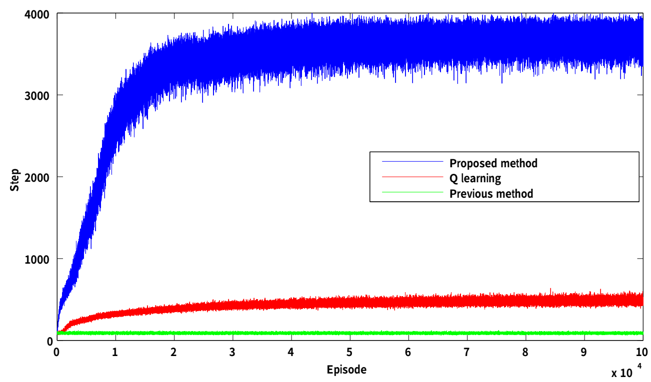

Fig. 4. Results of convergence speeds

D_x is the frictional coefficient on the cart, D_θ is the friction of the pendulum rotation, I is the moment of inertia of the pendulum. The states $x, \dot{x}, \theta$ and $\dot{\theta}$ are inputted to the learning module, whose values are observed with the normalized random values ($N(\mu,\sigma^2), \mu = 0, \sigma = 0.0001$) added. And also, we divide the states as 10 for x, 10 for $\dot{x}$, 50 for θ and 50 for $\dot{\theta}$. In this simulation, we perform a learning of the stabilizing control of the inverted pendulum according to action list $\boldsymbol{A} = [-10, -1, -0.1, 0, -0.1, 1, 10]$. If the pendulum is not around the upright position ($|\theta| > 0.1$[rad]), or the cart position is out of the range ($|x| > 3$[m]), we give the reward, and restart and proceed to the next episode. Also, if we can reach to 4,000 simulation steps, we deemed that it was possible to get the stabilizing control policy; we give the reward and end the episode.

Figure 4 shows the results of convergence speeds in learning by using our proposed reward allocation method, the previous reward allocation method (Eq. (2)) and the Q-learning method. In the case of the Q-learning, we give the penalty reward ($R = -10$), when the pendulum is not around upright position, or the cart position is out of the range. The previous reward allocation method was not able to give the policy of the stabilizing control. It was able to give the policy that the pendulum fall down as soon as possible instead. On the other hand, the Q-learning was able to give the stabilizing control policy, but only in a short time this success was made. Our method was able to produce the stabilizing control policy with a shorter convergence time than other methods.

5 CONCLUSION

In this paper, we improved the reward allocation method in the non-bootstrap reinforcement learning through the stabilizing control tasks. We showed the conditions of reward allocation for the stabilizing control tasks, and introduced an example of reward allocate function for it. Since the reward is allocated only from the duration time of action, we do not need to change the reward value according to environments.

In our future works, we are to build a learning method that can deal with combined problems such as swing-up and stabilizing controls of the inverted pendulum. And also, we have studied on the reinforcement learning method imitating the human adaptive immunity [2][7]. Those methods have fast convergence speed in the problems of minimizing the amount of time to achieve the goal with a very few configuration parameters. It is possible to construct a learning method with fast convergence speed by integrating those methods.

REFERENCES

[1] J. J. Grefenstette. Credit assignment in rule discovery systems based on genetic algorithms. In J. W. Shavlik and T. G. Dietterich, editors, *Readings in Machine Learning*, pp. 524–534. Kaufmann, San Mateo, CA, 1988.

[2] Jungo Ito, Kazushi Nakano, Kazunori Sakurama, and Shu Hosokawa. Adaptive immunity based reinforcement learning. *Artificial Life and Robotics*, Vol. 13, No. 1, pp. 188–193, 2008.

[3] Christopher J. C. H. Watkins and Peter Dayan. Technical note: q-learning. *Mach. Learn.*, Vol. 8, No. 3-4, pp. 279–292, 1992.

[4] Miyazaki Kazuteru, Yamamura Masayuki, and Kobayashi Shigenobu. A theory of profit sharing in reinforcement learning. *Journal of Japanese Society for Artificial Intelligence*, Vol. 9, No. 4, pp. 580–587, 1994-07-01. (in japanese).

[5] Yu Zheng, Siwei Luo, and Ziang Lv. Control double inverted pendulum by reinforcement learning with double cmac network. In *Proceedings of the 18th International Conference on Pattern Recognition*, Vol. 04 of *ICPR '06*, 2006.

[6] Atsushi Suzuki, Tohgoroh Matui, and Hirohisa Seki. Profit sharing considering penalty. *The 17th Annual Conference of the Japanese Society for Artifical Intelligence*, pp. 3F4–02, 2003. (in japanese).

[7] Shu Hosokawa, Kazushi Nakano, and Kazunori Sakurama. A consideration of human immunity-based reinforcement learning with continuous states. *Artifical Life and Robotics*, Vol. 15, No. 4, pp. 560–564, 2010.

Acquisition of Stationary Behavior Based on Multiagent Enforced SubPopulations

Joji Kato[1], Shu Hosokawa[2], and Kazushi Nakano[1,2]

[1]Dept. of Mechanical Eng. and Intelligent Systems, The University of Electro-Communications, Japan
[2]Dept. of Electronic Eng. , The University of Electro-Communications, Japan
(Tel: 81-42-443-5190, Fax: 81-42-443-5183)
(kato@francis.ee.uec.ac.jp)

Abstract: This paper presents a solution for the problems of state representation as well as a variety of optimal solutions in multiagent systems. These problems cannot be solved by traditional reinforcement learning methods such as Sarsa(λ). We apply a method of Multiagent Enforced SubPopulations to the task of stationary behavior acquisition. The stationary behavior acquisition task means that the agents continue to select behavior in order to keep the stationary state. The behaviors of acquired agents are not uniquely determined in those tasks. In addition, there is a state representation problem in multiagent systems due to the complexity of the system. Furthermore, there is no example of the Multiagent Enforced SubPopulations applied to these types of tasks, in which the design policy of the fitness function is unclear. We demonstrate the validity of our proposed method through comparison with a Keepaway task in RoboCup Soccer as a stationary behavior acquisition task.

Keywords: Multiagent system, Multiagent Enforced SubPopulations, Fitness function, Keepaway

1 INTRODUCTION

The researches on multiagent systems aim to solve more complex problems with the cooperation of multi-robots. However, the multiagent systems are difficult to control agents by top-down methods which enumerate all behaviors, because it is necessary for us to consider mutual behaviors between agents. Therefore, bottom-up methods teaching with fitness in each behavior should be proposed.

There are unsupervised reinforcement learning methods, for example, Q-learning [6], Sarsa(λ) [7] as bottom-up methods. These methods achieve the desired state by selecting a behavior to maximize an expected reward which will be received in each decision. The Q-learning guarantees convergence to an optimal value in the Markov decision process, and there are many examples in its application. However, these applications need to properly divide the state to satisfy the Markov property. In general, the amount of state divisions increases exponentially because the number of states in multiagent systems increases over that of single-agent systems. There are traditional research studies about state division methods such as tile-coding, but they cannot fundamentally resolve the problems. In addition, the optimal solution is not uniquely determined in multiagent systems, and these methods do not consider about a variety of optimal solutions.

There is the Multiagent Enforced SubPopulations (ESP) method as an evolutionary neural network method which is different from Q-learning or Sarsa(λ). The Multiagent ESP method is expected to solve the problems of state representation and of a variety of solutions which cannot be solved by traditional reinforcement learning methods, due to a combined advantage of neural networks and genetic algorithms. However, the Multiagent ESP is applied only to a prey catch task scheme, and also there is no discussion about the design of fitness functions.

In this research, the Multiagent ESP apply to a Keepaway task which is a sub-task of the RoboCup Soccer Simulation League. The aim of this task is to keep a ball as long as possible against 2 "Takers" by cooperating with 3 "Keepers". The existing research uses traditional reinforcement learning methods such as Sarsa(λ). So, the methods and accuracy of state division influence learned behavior. In addition, this task continues to select behavior in order to keep a stationary state while controlling the ball. We call these behaviors as stationary behavior. It is natural that there are more than one solution in the achieved stationary behavior. Therefore it is difficult to get a unique solution. We demonstrate the validity of our proposed method by applying the Multiagent ESP to the Keepaway task. Our proposed method is better than traditional reinforcement learning methods in multiagent tasks beyond the prey catch task. Lastly, we summarize an experimental consideration on fitness function design in the case where the Multiagent ESP is applied to the acquisition of a stationary behavior as in the case of Keepaway task.

2 BACKGROUND AND RELATED WORKS

We describe Multiagent ESP method underlies bases for our proposed method, and describe Keepaway task which is an application of our proposed method.

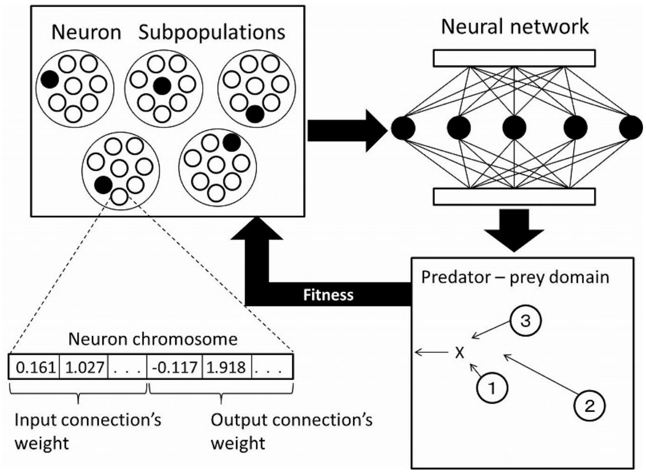

Fig. 1. ESP method applying to prey catch task

2.1 Multiagent ESP method in prey catch task

Multiagent ESP method is a coevolution method in multiagent systems, which is proposed by C. H. Yong, R. Miikkulainen [3]. Next, Multiagent ESP method is of ESP method expanded to multiagent systems. ESP method is proposed by F. Gomes, R. Miikulaiinen [4], [5]. So, we explain ESP method and Multiagent ESP method through the prey catch task [3].

The prey catch task is a task that “Takers” chase and catch the “Prey”. One task is finished when Takers catch a Prey, or time is over. The symbols ①, ②, ③ are Takers, and X is Prey in Fig. 1 showing ESP method's framework. One of Taker's policy is coordinated with learning in ESP method. The controller for learning Taker is 3 layered neural network. The input of this neural network is a difference between my current position and Prey. The output is moving direction for Taker. Hidden layer neuron has a weight of network. We define neuron subpopulations which have some different connection weights in each hidden neuron. The agent controller is constructed by random-selected neuron from neuron subpopulations in each task. If the agents catch a Prey in limited time by using this controller, it gets a constant fitness. In contrast, if the agents miss catch a Prey by using this controller, it gets more lower fitness based on average distance between Takers and a Prey. The fitness is accumulated in neuron subpopulations by repeating this task. As a result, high fitness neurons are selected by genetic algorithm, then neuron subpopulations are constructed by high fitness neuron. Lastly, we can get the controller to solve the task.

Next, we explain Multiagent ESP method which is one expansion of ESP method. All takers learn at one time to solve the task in Multiagent ESP method. Figure 2 shows a structure in which Multiagent ESP is applied to the prey catch task. The controller of each agent is of the same structure with ESP method, and is prepared with the same number as learning agents. Each controller is coordinated independently by ESP method. The calculation of fitness is same as ESP method, and there are no difference between agents.

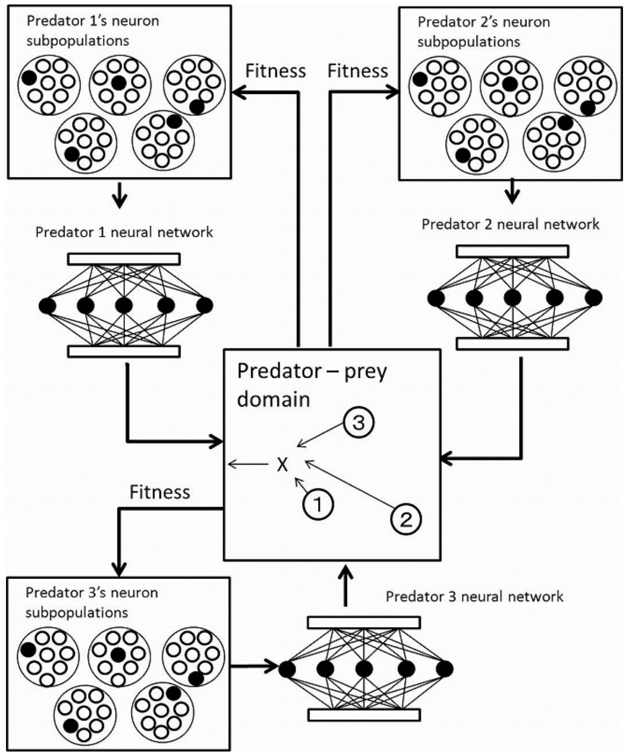

Fig. 2. Multiagent ESP method applying to prey catch task

As a property of ESP method, the input of controller can take continuous value. It is different from Q-learning or Sarsa(λ) which need state division. So, it can be expected to solve the state representation problems essentially. And also, ESP method has more than one optimal solutions in the form of neuron subpopulations after learning. As a result, it can be expected to get a class of optimal solutions in the task that the optimal solution cannot be determined.

In the existing researches which apply to prey catch task, the aim of all Takers is to go around the Prey as quickly as in order to achieve the task. This task easily determines the aim of each agent to achieve the task. And also, it is proper to hypothesize that there are a unique optimal solution. However, there are some tasks which cannot determine clearly the aim of each agent for achieving the task, and cannot determine a unique optimal solution in multiagent systems. In this research, multiagent ESP method will be applied to Keepaway task as an example of a task that cannot determine the aim of each agent and a unique optimal policy. So, we discuss about the design of fitness function.

Table 1. Agent selectable macro behaviors

Agent Role	**Selectable Macro Behavior**
Passer	Hold Ball, Pass Ball K_2, Pass Ball K_3
Receivers	Get Open, Go To Ball
Takers	Go To Ball, Block Pass K_2, Block Pass K_3

2.2 Keepaway task

Keepaway task is a testbed of reinforcement learning which is used in RoboCup Soccer Simulation League. This task is proposed by P. Stone, R. S. Sutton, G. Kuhlmann [1]. The aim of this task is that 3 Keepers keep a ball against 2 Takers as long as possible. Keepers are numbered K_1, K_2, K_3 in order of the distance to ball. Takers are numbered T_1, T_2 in order of the distance to K_1. And each agent have a specific ID such as K^1, K^2, K^3, T^1, T^2. K_1 is called "Passer", and he can actively control a ball. The other Keepers are called "Receiver". Task start position of Passer is top-left, and the positions of Receivers are top-right and bottom-right, and the positions of Takers are bottom-left. The task continues until fail in ball keeping. One task called one episode.

Keepers and Takers select a macro behavior once every 100 milliseconds. Here, we summarize macro behavior which each agents can select as shown in Table 1. Hold Ball behavior means to keep a ball at the current position. Pass Ball behavior means to pass a ball to a Receiver. Get Open behavior means to go to an open space. Go To Ball behavior means to go near to the ball. Block Pass behavior means to cut a pass course of the target (Keepers).

Learning objects in this task is Passer's policy. Passer is one of the Keepers who nearest to the ball, and is changed off in this task. Each Keeper has a controller learning independently, so he needs a coevolution with the others. The policies of agents without Passer are designed by human. First, Fig. 3 shows a Receiver's policy. Receivers select Get Open when friends have a ball, or friends is nearer to ball than me. They select Go To Ball in the other state. We prepare two types of Taker's policies. The first type policy is that all Takers select Go To Ball. This policy is often used in many existing researches. The second policy is that one agent selects Go To Ball, the other agent selects Block Pass. There are few researches on the second policy, which is more difficult than the first.

The lines in Fig. 4 shows a state variable which Passer can know during the episode.

Existing researches on Keepaway task uses traditional reinforcement learning method such as Sarsa(λ) [1], [2]. Sarsa(λ) algorithm needs to divide environment, but it cannot get enough state representation due to the limit of methods

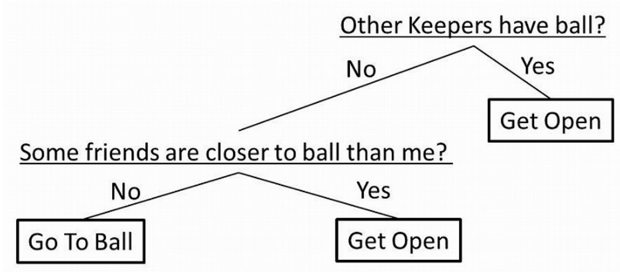

Fig. 3. Receiver's policy

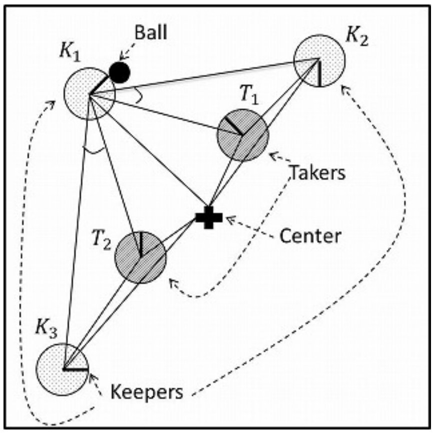

Fig. 4. State variable in Keepaway task

and accuracy of discretization in multiagent systems. The optimal solution is unique according to Sarsa(λ), but it is natural that there are more than one optimal solutions in the task which needs to continue to select stationary behavior such as this task. We think that these problems are occurred by Sarsa(λ) algorithm. In this research, Multiagent ESP method is applied to Keepaway task to improve the episode duration time.

3 MULTIAGENT ESP APPLY TO KEEPAWAY TASK

In this section, we explain how to apply the Multiagent ESP method to a Keepaway task. First, we explain configuration of our system, and next explain the design of fitness function in the Keepaway task. Finally, we explain about process of generation change in the Multiagent ESP method.

3.1 Multiagent ESP method in Keepaway task

Figure 5 shows a configuration of the Multiagent ESP method applying to the Keepaway task. Each Keeper have an independent controller, and they independently evolve according to received fitness value.

Each agent controller is in the form of three layered neural network. Its input takes 13 state values, the output does 3

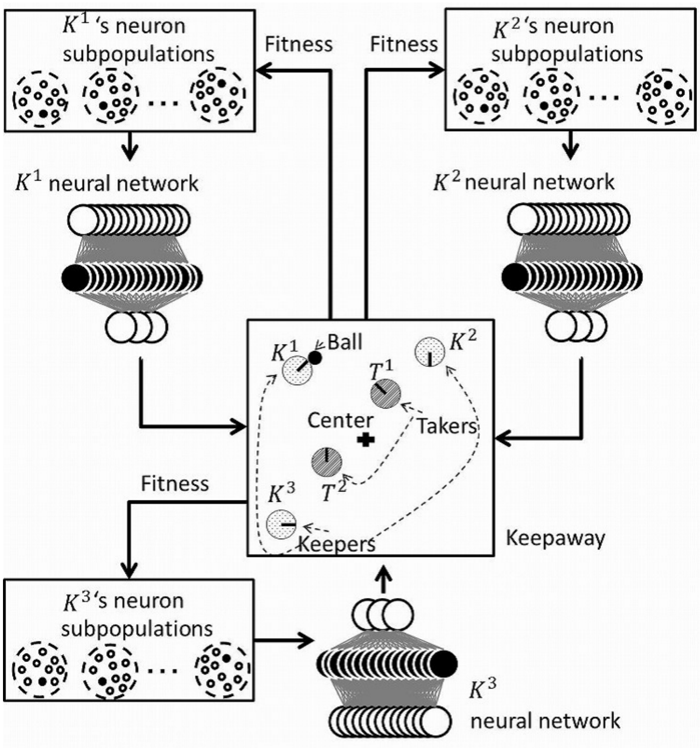

Fig. 5. Multiagent ESP method applying to Keepaway task

macro behaviors, and the number of hidden layer's neuron is 16. The calculation of activation of hidden and output neurons is made by use of the sigmoid function. Passer chooses the behavior of the highest activating neuron. The number of neuron belonging to neuron subpopulations in each agent is 100. These neurons are received fitness values calculated by the fitness function as shown in 3.2. The connection weights of controller are renewed to fit the task through the process of generation change as shown in 3.3.

3.2 Design of fitness function

In this section, we describe the design of fitness functions in the Multiagent ESP method applied to a Keepaway task. The fitness function shows how much the controller constructed by selected neurons in each episode fit to the aim of the task. Existing researches such as Sarsa(λ) give reward when Passer decides his own behavior. However, Passer's strategy can evaluate correctly at the end of task in the endless task such as the Keepaway task. The reward on the way of task is sub goal. But, it is difficult to correctly decide sub goals to achieve the aim of task. Furthermore, the research by Arai et al. shows that it is effective to combine reward and penalty to achieve the aim of task [2]. That is concluded that appropriate setting of some sub goals is effective to achieve the aim of the task. But this approach is reduced to a multipurpose optimal problem, and sometimes shows the inferior performance based on the combination of sub goals due to mutual actions.

Table 2. Sub goals and fitness functions

No.	Sub goal	Fitness
1	The purpose of making a ball to each agent as long as possible time to pass	Eq. (1)
2	The purpose of not relating with task failure	Eq. (2)
3	Our purpose to keep 5m distance from Passer to the nearest Taker	Eq. (3)

First of all, this research shows the difficulty to set some sub goals. Table 2 shows sub goals and fitness functions in own interests. Sub goal 1 is proposed by Stone et al. and has the purpose of making a ball to each agent as long as possible time to pass [1]. Sub goal 2 is proposed by Arai et al. and has the purpose of not relating with task failure [2]. Arai et al. shows the validity to combine sub goal 1 and 2 through experiments. Sub goal 3 is introduced to show the difficulty to set the sub goal by us. It is our purpose to keep 5m distance from Passer to the nearest Taker.

$$fitness = T_C - T_A \tag{1}$$

$$fitness = \begin{cases} -\frac{1}{T_E - T_A} & \text{(failure)} \\ 0 & \text{(otherwise)} \end{cases} \tag{2}$$

$$fitness = \begin{cases} \frac{dist}{5} & (0 \leq dist \leq 5) \\ \frac{4}{3} - \frac{dist}{15} & \text{(oherwise)} \end{cases} \tag{3}$$

Here, T_C is the current time, T_A is the last time for action selection, T_E is task end time, $dist$ is a distance to the nearest Takers. Figures 6, 7 show the result of preliminary experiment which shows the difficulty to set some sub goals. These experiments are made by Multiagent ESP method. Figure 6 shows the Taker's policy is Go To Ball, and Figure 7 shows the Taker's policy is Go To Ball and Pass Cut. The broken line shows the result of the combination of sub goals 1 and 2, the solid line shows the result of the combination of sub goals 2 and 3, the 1-dot dashed line shows the result of sub goal 3. Each pattern is simulated three-times. The combination of sub goals 2 and 3 shows a bad result from these figures. This fact demonstrates the difficulty in a sub goal design.

It is possible to give the rewards based on episode duration time in Multiagent ESP method, but not in Sarsa(λ) algorithm. So, our method gives fitness based on episode duration time(T_D) given by Eq. (4). Existing methods need a design of sub goals to achieve the aim of the task, but our proposed method does not need a sub goal design.

$$fitness = T_D \tag{4}$$

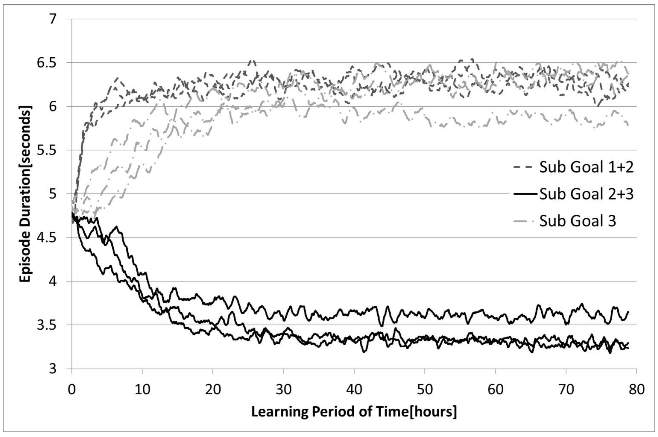

Fig. 6. Taker's policy: Go To Ball

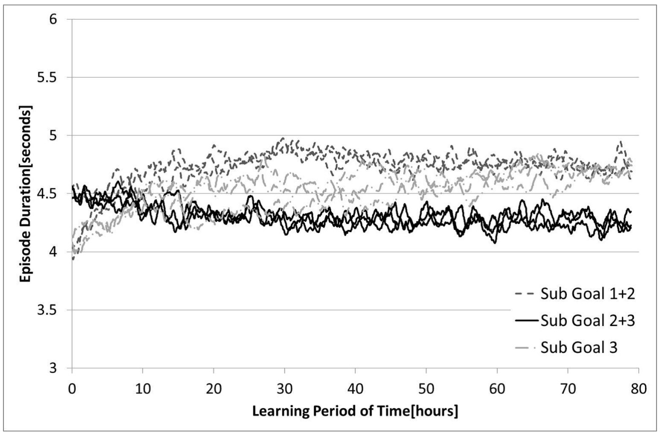

Fig. 7. Taker's policy: Go To Ball and Pass Cut

3.3 Process of generation change

In this section, we describe about the process of generation change in the Multiagent ESP method. The generation changing process is performed through three steps, which is selection, crossover, and mutation. The first selection is a process to bring down high fitness neurons to the next generation, and in our method roulette selection is used. The fitness is updated by windowing which subtract a minimum fitness value in neuron subpopulation from the fitness, and is performed by the power-law scaling which raises the fitness. The second step is one point crossover whose probability is 60 %. The third step is mutation whose probability is 10 % .

This process has to be performed just when all the neurons in neuron subpopulations have been evaluated enough. In this research, the process of generation change are performed every 1000 episodes. That is, one neuron is evaluated 10 times because there are 100 neurons in each neuron subpopulations. Finally, Fig. 8 summarized the process of generation change under these conditions.

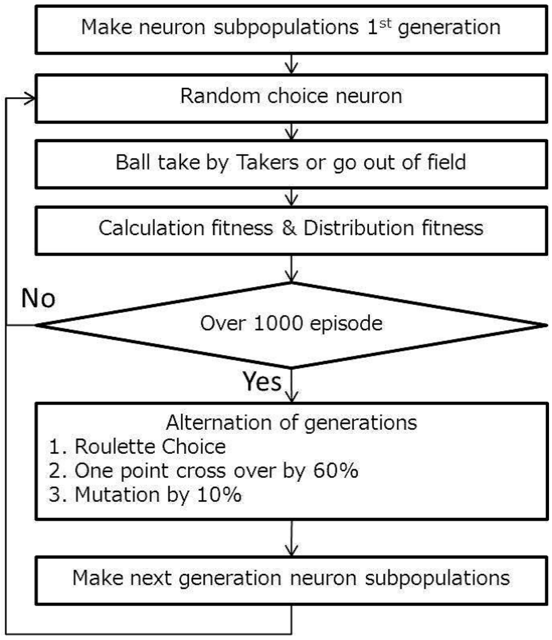

Fig. 8. Process of generation change in Multiagent ESP

4 SIMULATION RESULT

To demonstrate the validity of our proposed method, Figs. 9, 10 show the results of three-times learning of 80 hours in the Keepaway task. Our proposed method which uses the episode duration time as a fitness value is compared with the Sarsa(λ) method proposed by Stone et al. [1], and with the Multiagent ESP method which uses sub goal combination as the fitness value proposed by Arai et al. [2]. Figure 9 shows that the Taker's policy is Go To Ball. Figure 10 shows that the Taker's policy is Go To Ball and Pass Cut. The solid line shows the result of our proposed method, the 1-dot dashed line shows the result of the Sarsa(λ), the broken line shows the result of the Multiagent ESP by Arai's sub goal. The horizontal axis is the learning period of time, and the vertical axis is the episode duration time.

In both of Taker's policies, our proposed method using the episode duration time as a fitness value can give the longest episode duration time. This is because the aim of the task reflect clearly the fitness by using the Multiagent ESP. And, if Taker's policy becomes more difficult, our method can get a better solution than the existing researches by advantages of that it can take continuous state values and can have a set of the optimal solutions. We concluded that the problems in traditional reinforcement learning methods' (such as Sarsa(λ)) : the state representation problem and a variety of the optimal solutions can be solved by using our proposed Multiagent ESP method.

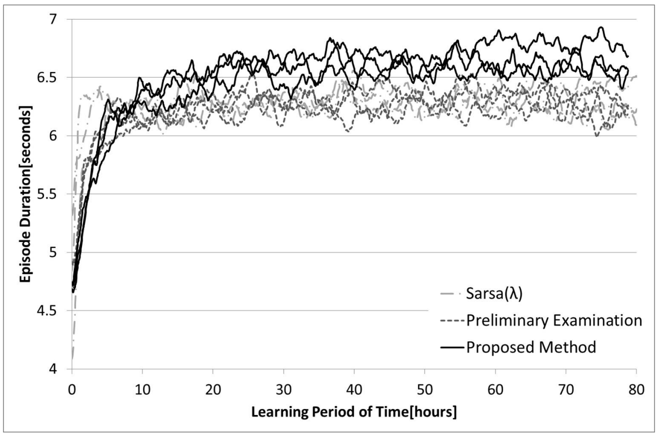

Fig. 9. Taker's policy: Go To Ball

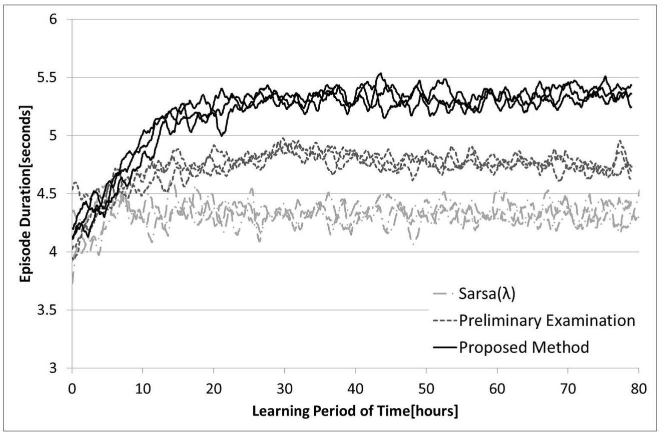

Fig. 10. Taker's policy: Go To Ball and Pass Cut

5 CONCLUSION

In this research, we proposed that the problems of state representation and a variety of optimal solutions can be solved by using our proposed Multiagent ESP method through Keepaway task. And also, we demonstrated that it produced a good learning result to calculate the fitness based on the task duration time at the end of task in order to apply the Multiagent ESP to acquisition of stationary behavior task.

REFERENCES

[1] Peter Stone, Richard S. Sutton, Gregory Kuhlmann: Reinforcement Learning for RoboCup Soccer Keepaway: International Society for Adaptive Behavior, Vol. 13, No. 3, 2005

[2] Sachiyo Arai, Nobuyuki Tanaka: Experimental Analysis of Reward Design for Continuing Task in Multiagent Domains - RoboCup Soccer Keepaway -: The Japanese Society for Artificial Intelligence, Vol. 21, No. 6, 2006

[3] Chern Han Yong and Risto Miikkulainen: Coevolution of Role-Based Cooperation in Multiagent Systems: IEEE TRANSACTIONS ON AUTONOMOUS MENTAL DEVELOPMENT, VOL. 1, NO. 3, 2009

[4] Faustino Gomez and Risto Miikkulainen: Incremental evolution of complex general behavior: Adapt. Behav., vol. 5, 1997

[5] Fasutino Gomez and Risto Miikkulainen: Solving non-Markovian control tasks with neuroevolutio: in Proc. 16th Int. Joint Conf. Artif. Intell., San Francisco, CA, 1999

[6] Watkins, C. J. C. H. and Dayan, P.: Technical Note Q-Learning: Machine Learning, Vol. 8, 1992

[7] Singh, S. P. and Sutton, R. S.: Reinforcement Learning with Replacing Eligibility Traces: Machine Learning, Vol. 22, No. 1-3, 1996

The Seventeenth International Symposium on Artificial Life and Robotics 2012 (AROB 17th '12),
B-Con Plaza, Beppu, Oita, Japan, January 19-21, 2012

Robust Digital Control of DC-DC Buck Converter with Low Frequency Samplings

Yuji Fukaishi[1], Yoshihiro Ohta[1], Kohji Higuchi[1], Eiji Takegami[2], Satoshi Tomioka[2], and Kosin Chamnongthai[3]

[1] Dept. of Electronic Engineering, The University of Electro-Communications, Chofu, Tokyo 182-8585, Japan
[2] TDK-LAMBDA K.K., 2701 Togawa, Settaya, Nagaoka 940-1195, Japan
[3] King Mongkut's University of Technology Thonburi, 126 Pracha-utid Road Bangmod, Toongkru, Bangkok, Thailand
(Email:[1] fukaishi@francis.ee.uec.ac.jp, [2] e.takegami@jp.tdk-lambda.com, [3] kosin.cha@gmail.com)

Abstract: Robust DC-DC converter which can covers extensive load change and also input voltage changes with one controller is needed. Then demand to suppress output voltage change becomes still severer, We propose an approximate 2 DOF digital controller which realized the startup response and dynamic load response independently. Controller make the control bandwidth wider, and at the same time make variations of the output voltage small at sudden changes of load and input voltage. In this paper a new approximate 2DOF digital control system with additional zeros is proposed. Using additional zeros second-order differential transfer characteristics between equivalent disturbances and output voltage are realized. Therefore the new controller makes variations of the output voltage smaller and sudden changes of load and input voltage. These controller is actually implement on a DSP and is connected to DC-DC converter. Experimental results demonstrate that this type of digital controller can satisfy given severe specifications with low frequensy sampling.

Keywords: DC-DC converter, Approximate 2DOF, Second-order differential, Digital Robust control

1 INTRODUCTION

In many applications of DC-DC converters, loads cannot be specified in advance, i.e., their amplitudes are suddenly changed from the zeros to the maximum rating. Generally, design conditions are changed for each load and then each controller is re-designed. Then, a so-called robust DC-DC converter which can cover such extensive load changes and also input voltage changes with one controller is needed. Analog control IC is used usually for control of DC-DC converter. Simple integral control etc. are performed with the analog control IC. Moreover, the application of the digital controller to DC-DC converters designed by the PID or root locus method etc. has been recently considered [1]. However, it is difficult to retain sufficient robustness of DC-DC converter by these techniques. Various robust control methods [2] for improving start-up characteristics and load sudden changes characteristics of DC-DC converters. However, they take tens [ms] for the rising time of the startup response, and hundreds [mV] output voltage regulations, have arisen in the load sudden changes. The demand for suppressing output voltage changes becomes still severer, and the further improvements to startup characteristics and load sudden changes characteristics are required. In this paper, we propose a new approximate 2DOF digital controller which realizes second-order differential transfer characteristics. These characteristics are realized by introducing additional zeros into transfer functions between equivalent disturbances and the output. The new controller make the variations of the output voltage the almost same as the former controller [3] at sudden changes of resistive loads and input voltages with low sampling frequensy. A new DC-DC converter equipped with the proposed controller in DSP is actually manufactured. Some simulations and experiments show that this new DC-DC converter can satisfy given severe specifications.

2 DESIGN METHOD

2.1 DC-DC converter

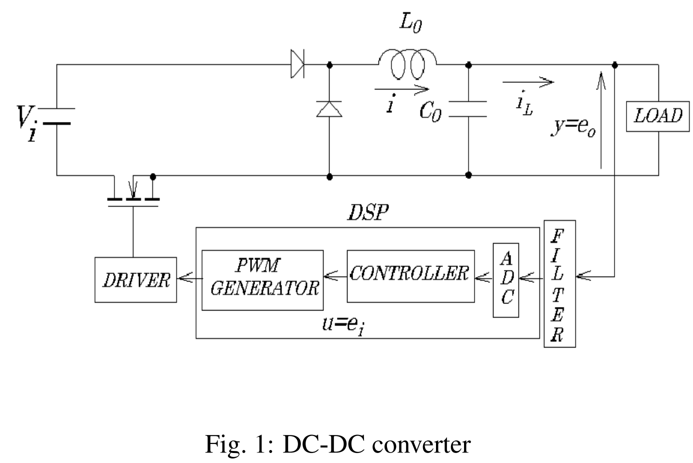

Fig. 1: DC-DC converter

The DC-DC converter are shown in Fig.1 has been manufactured. In order to realize the approximate 2DOF digital controller which satisfies given specifications, we use the DSP (TMS320F28335). This DSP has a builtin AD converter and a PWM switching signal generating part. The triangular wave carrier is adopted for the PWM switching signal. The switching frequency is set at 100[KHz]. The LC circuit is a filter for removing carrier and switching noises. Where Co is 235[μF] and Lo is 0.55[μH]. If the frequency of control signal u is smaller enough than that of the carrier, the state equation of the DC-DC converter at a resistive load in Fig.1 except for the controller in DSP can be expressed from the state equalizing method as follows:

$$\begin{cases} \dot{x} = A_c x + B_c u + B_{cq} u \\ y = C_x + q_y \end{cases} \tag{1}$$

where

$$x = \begin{bmatrix} e_0 \\ i \end{bmatrix} A_c = \begin{bmatrix} -\frac{1}{C_0 R_L} & \frac{1}{C_0} \\ -\frac{1}{L_0} & \frac{R_L}{L_0} \end{bmatrix} B_c = \begin{bmatrix} 0 \\ \frac{k_p}{L_0} \end{bmatrix} c = \begin{bmatrix} 1 & 0 \end{bmatrix}$$

$$u = e_i, y = e_o, k_p = -\frac{V_i}{C_m L_0}, G_p = \frac{R_L}{R_0 + R_L} \times \frac{V_{in}}{TBPRD}$$

and R_0 the total resistance of coil and ON resistance of FET, etc., whose value is 0.015[Ω]. Then the discrete-time state equation of the system eq.(1) with a zero-order hold is express as

$$\begin{cases} x(k+1) = A_d x(k) + B_d u(k) + B_{dq} u(k) \\ y(k) = Cx(k) + q_y(k) \end{cases} \tag{2}$$

where

$$A_c = \begin{bmatrix} a_{11} & a_{12} \\ a_{21} & a_{22} \end{bmatrix} = e^{A_c T}$$

$$B_c = \begin{bmatrix} b_{11} \\ b_{21} \end{bmatrix} = \int_0^T e^{A_c T} B_c d_t$$

2.2 Additional zeros method

The following equation is obtained by repeating the difference of the output of eq.(2):

$$Y = O^* xd(k) + U\bar{u}(k) + U\bar{q_u} + \bar{q_y} \tag{3}$$

where

$$Y = \begin{bmatrix} y(k) \\ y(k+1) \\ y(k+2) \end{bmatrix} O^* = \begin{bmatrix} C \\ CA_d \\ CA_d^2 \end{bmatrix} U = \begin{bmatrix} 0 & 0 \\ CB_d & 0 \\ CA_d B_d & CB_d \end{bmatrix}$$

$$\bar{u} = \begin{bmatrix} u(k) \\ u(k+1) \end{bmatrix} \bar{q_u} = \begin{bmatrix} q_u(k) \\ q_u(k+1) \end{bmatrix} \bar{q_y} = \begin{bmatrix} q_y(k) \\ q_y(k+1) \\ q_y(k+1) \end{bmatrix}$$

If both sides of eq.(3) are multiplied by $\bar{I}_2$from the left, x_d is obtained by the following equation:

$$\begin{aligned} x_d(k) &= (\bar{I}_2 O^*)^{-1} \bar{I}_2 Y - (\bar{I}_2 O^*)^{-1} \bar{I}_2 U \bar{u}(k) \\ &- (\bar{I}_2 O^*)^{-1} \bar{I}_2 U \bar{q_u} - (\bar{I}_2 O^*)^{-1} \bar{I}_2 \bar{q_y} \end{aligned} \tag{4}$$

where

$$\bar{I_2} = \begin{bmatrix} 1 & 0 & 0 \\ 0 & 1 & 0 \end{bmatrix}$$

By substituting the above equation into eq.(3), the following equation is obtained:

$$(I_3 - (\bar{I}_2 O^*)^{-1} \bar{I}_2) U \bar{q_u} + (I_3 - (\bar{I}_2 O^*)^{-1} \bar{I}_2) \tag{5}$$

where I3 is a 3 $\times$ 3 unit matrix. That is, $\bar{q_u}$ and $\bar{q_y}$ can bbe replaceed to Y and $\bar{u}(k)$. Eq.(5) is transformed as

$$\begin{aligned} &- \quad (l_2 z + l_1) q_u(k) + (z^2 + m_2 z + m_1) q_y(k) \\ &= \quad (l_2 z + l_1) u(k) + (z^2 + m_2 z + m_1) y(k) \end{aligned} \tag{6}$$

where

$$\begin{bmatrix} l_1 & l_2 \end{bmatrix} = -(I_3 - O^*(\bar{I}_2 O^*)^{-1} \bar{I}_2) U$$

$$\begin{bmatrix} m_1 & m_2 & m_3 \end{bmatrix} = (I_3 - O^*(\bar{I}_2 O^*)^{-1} \bar{I}_2) \tag{7}$$

The delay time for AD convertion time etc., replacing current feedback and zeros addition are connected to input of system(2). The state equation of a new controlled object connecting can be expressed as

$$\begin{aligned} &x_{dw}(k+1) = A_{dw} x_{dw}(k) + B_{dw} v(k) \\ &y(k) = C_{dw} x_{dw}(k) \end{aligned} \tag{8}$$

where

$$x_{dw}(k) = \begin{bmatrix} x_d(k) \\ \xi_1(k) \\ \xi_2(k) \\ \xi_3(k) \end{bmatrix} \quad A_{dw} = \begin{bmatrix} A_d & B_d & 0 & 0 \\ 0 & 0 & 1 & 0 \\ 0 & 0 & 0 & 1 \\ 0 & 0 & 0 & 0 \end{bmatrix}$$

$$B_{dw} = \begin{bmatrix} 0 \\ 0 \\ 0 \\ 1 \end{bmatrix} \quad C_{dw} = \begin{bmatrix} C & 0 & 0 & 0 \end{bmatrix} \; \xi_1(k) = u(k)$$

Applying the following feedforwards from q_u, q_y and r, and state feedback from x_{dw} for model matching to the system in eq.(8), the system shown in Fig.2 is obtained. From Fig.2.

$$\begin{aligned} v(k) = &-k_q(l_2 z + l_1) q_u(k) + k_q(z^2 + m_2 z + m_1) q_y(k) \\ &+(z^2 + g_2 z + g_1) r(k) + [f_1 \; f_2 \; f_3 \; f_4 \; f_5] x_{dw}(k) \end{aligned} \tag{9}$$

In Fig.2, the parts surrounded by dotted lines are the feedforward coefficients from q_u and q_y and the part surrounded by a chain line is the estimated part of current. From eq.(6), the feedforwards of eq.(9) are changed as

$$\begin{aligned} &v(k) = k_q(l_2 z + l_1) u(k) + k_q(z^2 + m_2 z + m_1) y(k) + \\ &(z^2 + g_2 z + g_1) r(k) + [f_1 \; f_2 \; f_3 \; f_4 \; f_5] x_{dw}(k) \end{aligned} \tag{10}$$

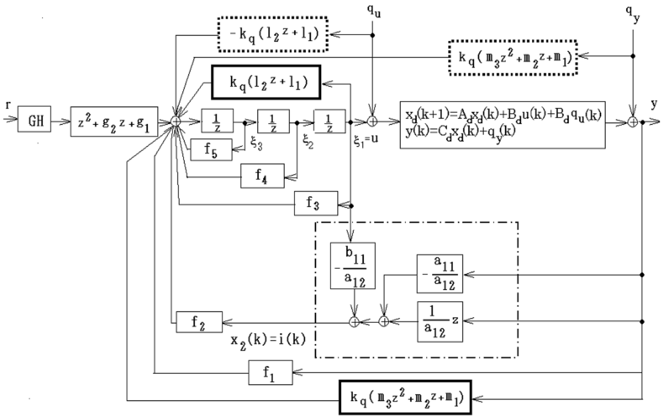

Fig. 2: Feedforword from equivalent disturbances q_u and q_y, and model matching with state feedback

That is, the parts surrounded by the dotted lines are replaced by the parts surrounded by solid lines from u and y. The system expect for the parts surrounded by the dotted lines in Fig.2 can be transformed equivalently as shown in Fig.3. In Fig.3,

$$\begin{aligned}
ff_1 &= f_1 - f_2(a_{11}/a_{12}) + k_q m_1 + f_5(k_q m_2 + f_2/a_{12}) \\
&+ f_5^2 k_q m_3 + (f_4 + k_q l_2) k_q m_3 \\
ff_2 &= k_q m_2 + f_2/a_{12} + f_5 k_q m_3 \\
ff_3 &= f_3 - f_2(b_{11}/a_{12}) + k_q l_1 \\
ff_4 &= f_4 + k_q l_2 \\
ff_5 &= f_5 \\
ff_6 &= k_q m_3 \\
gg_1 &= f_5^2 + f_5 g_2 + k_q l_2 + f_4 + g_1 \\
gg_2 &= f_5 + g_2 \qquad (11)
\end{aligned}$$

The transfer function between r and y, q_u and y, and q_y and

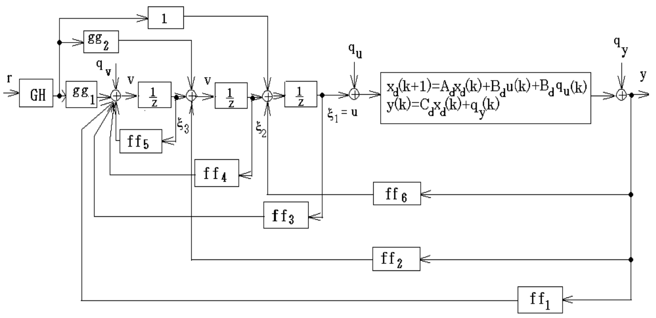

Fig. 3: Model matching system using only voltage (output) feedback

y in Fig.3 are descrived as

$$\begin{aligned}
W_{ry}(z) &= N_{ry}(z)/D(z) \qquad (12) \\
W_{q_u y}(z) &= N_{q_u y}(z)/D(z) \qquad (13) \\
W_{q_y y}(z) &= N_{q_y y}(z)/D(z) \qquad (14)
\end{aligned}$$

where

$$\begin{aligned}
N_{ry}(z) &= GH(z^2 + g_1 z + g_0)(b_{11}z + b_{21}a_{12} - a_{22}b_{11}) \\
N_{q_u y}(z) &= N_{qz} N_p \\
N_{q_y y}(z) &= N_{qz} D_p \\
N_{qz} &= (a_{12}z^3 - a_{12}f_5 z^2 + (a_{12}b_{11}k_q - a_{12}f_4)z \\
&- f_3 a_{12} + f_2 b_{11} - a_{12}a_{22}b_{11}k_q + a_{12}^2 b_{21} k_q) \\
D(z) &= z^5 + (-f_5 - a_{22} - a_{11})z^4 + (a_{11}f_5 \\
&+ a_{11}a_{22} - a_{21}a_{12} + a_{22}f_5 - f_4)z^3 \\
&+ (a_{21}a_{12}f_5 - f_3 + a_{11}f_4 - a_{11}a_{22}f_5 \\
&+ a_{22}^2 2f_4)z^2 + (a_{22}f_3 + a_{21}a_{12}f_4 + a_{11}f_3 \\
&- b_{11}f_1 - f_2 b_{21} - a_{11}a_{22}f_4)z + f_2 a_{11} b_{21} \\
&- a_{21}f_2 b_{11} + a_{21}a_{12}f_3 + f_1 a_{22} b_{11} \\
&- f_1 a_{12} b_{21} - a_{11}a_{22}f_3
\end{aligned}$$

From $D(z)$, the poles of the overall system can be arranged arbirarily by f_1, f_2, f_3, f_4 and f_5. From $N_{ry}(z)$, two zeros of r-y can be arranged arbitrarily by g_0 and g_1. Moreover, from common N_{qz} in $N_{qz}(s)$ and $N_{q_y y}(s)$, one zeros of $q_u - y$ and $q_y - y$ can be arranged arbitrarily at the same place by k_q. That is, one zeros can be added arbitrarily to W_q.

2.3 Design of the model matching system

We consider transfer function between the reference input r and the output y specified as below.

$$W_{ry}(z) = \frac{(1+H_1)(1+H_2)(1+H_3)(z-n_1)(z+n_2)(z+n_4)(z+n_5)}{(1-n_1)(1-n_2)(1+H_1)(z+H_2)(z+H_3)(z+H_4)(z+H_5)} \qquad (15)$$

This transfer function is realized by the model matching system shown in Fig.5. The robust system is constructed as shown in Fig.4. The transfer function r to y and q of Fig.5 are as follows

$$y \approx \frac{1+H_2}{z+H_2} \quad y \approx \frac{(z-1)^2}{z-1+k_z}\bar{W_{Qy}}Q \qquad (16)$$

From eqs. (16) it turn out that the characteristics from r to y can be specified with H_2, and the characteristics from qu and q_y to y can be independently specified with k_z. That is, the system in Fig.4 is an approximate 2DOF, and its sensitivity against disturbances becomes lower with the increase of k_z. If an equivalent conversion of the controller in Fig.4 is carried out, the approximate 2DOF digital integral-type control system will be obtained as shown in Fig.5.

3 SIMULATION AND EXPERIMENTAL RESULTS

The sampling period T are set 10[μs].The nominal value of R_L is 0.33[Ω]. We design a control system so that H_1,

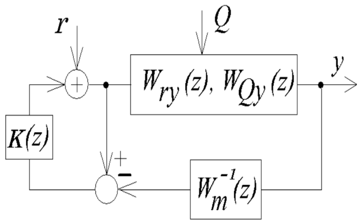

Fig. 4: System reconstituted with inverse system and filter

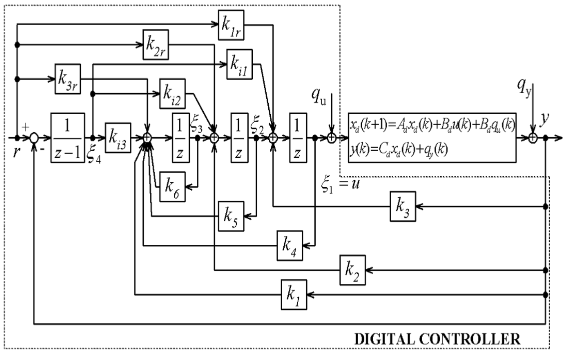

Fig. 5: Approximate 2DOF digital integral-type control system

H_2, H_3, H_4, and H_5 are specified as

$$H_1 = -0.2 + 0.2i \qquad H_2 = -0.9 \qquad H_3 = -0.2 - 0.2i$$
$$H_4 = -0.4 + 0.3i \quad H_5 = -0.4 - 0.3i$$

The simulations results of the dynamic load responses is smaller than 50[mV] as shown in Fig.6 Experimental results are shown in Fig.7,8. Experimental results of dynamic load response by the first order differentiation with sampling frequency 300[KHz] is shown in Fig.8. The output voltage change is suppressed within about 50[mV]. This is almost the same results by the second order differentiation with sampling frequency 100[KHz] as shown in Fig.7. We can get almost the same performance with low sampling fregeuncy.

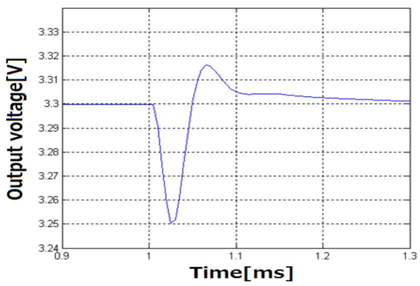

Fig. 6: Dynamic load response

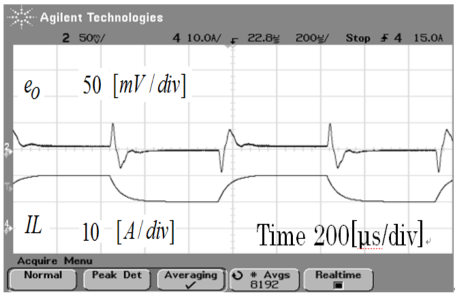

Fig. 7: Experimental results of using the second order differential characteristic with Fs = 100[kHz]

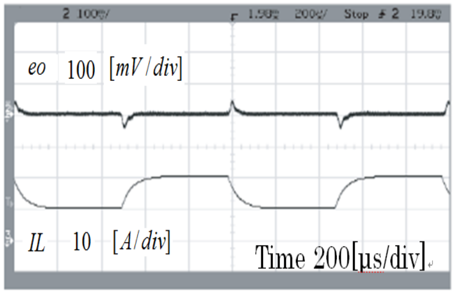

Fig. 8: Experimental results of the first order differential with Fs = 300[kHz]

4 CONCLUSION

In this paper, the concept of controller of DC-DC converter to attain good robustness against extensive load changes and input voltage changes was given. The proposed digital controller was implemented on the DSP. It was shown from experiment that the sufficiently robust digital controller is realizable. The characteristics of dynamic load response and output response were improved by using low sampling frequency approximate 2DOF digital controller with additional zeros.

REFERENCES

[1] H. Guo, Y. Shiroishi and O. Ichinokura, Digital PI controller for High Freguency Switching DC-DC Converters Based on FPGA, IEEE INTELEC03,536/541 (2003).

[2] L. Corradini, P. Mattavelli and D. Maksimovic, Robust relay-Feedback Based Autotuning for DC-DC converters, IEEE PESC2008, 2196/2202(2007).

[3] E. Takegami, K. Higuchi, K. Nakano, K. Watanabe, S. Tomioka, The Method For Determined Parameters of Approximate 2DOF Digital controller for Robust Control of DC-DC Converter ECTI-CON2005,pp.593-596, 2005.

EMG Analysis Accompanied by Tactile Apparent Movement

Ali Mokhtari*, Masafumi Uchida**

*The Graduate School of Electro-Communications, The University of Electro-Communications
**The Graduate School of Informatics and Engineering, The University of Electro-Communications
1-5-1, Chofugaoka, Chofu, Tokyo, Japan
Tel: 81-42-443-5173 Fax: 81-42-443-5173
alim@zidane.ee.uec.ac.jp

Abstract: Tactile apparent movement recognition is normally considered as a subjective sense of human. Applying the tactile apparent movement to an engineering system, a quantitative evaluation study becomes necessary. In previous studies, finding the body-sway caused by the tactile apparent movement in a fixed experimental condition became possible. However, characteristic of the body-sway was not thoroughly investigated. In this study, investigating the body-sway caused by tactile apparent movement in a fixed experimental condition was aimed. Therefore, we focused on biological information, the body-sway and the comparison between the apparent movement recognized trials and the non-recognized trials. The findings of this research will be conducive to optimize the performance of the systems that are using the tactile apparent movement.

Keywords: Tactile Apparent Movement, EMG (Electromyography), Discrete Wavelet Packet Transforms

I) INTRODUCTION

Tactile sense as one of the five senses of human body has always been considered as an efficient substitution for the other senses of body such as sight and hearing. For example, a tactile interface system is able to transfer the required information by using the tactile sense instead of visual sense. Today we can see the various applications of this substitution in different interface and display systems that are helping people specially the physically challenged persons to perform many tasks despite of a loss in one of their sensory organs. [1]

In this study, the term *apparent movement* (AM) refers to the illusory perception of a movement on skin that is created by the discrete stimulations of a number of points on skin of a part of body that are appropriately separated in space and time. [2]

In previous studies the evaluation of the apparent movement recognition was particularly based on the statistical techniques instead of the quantitative evaluations. As a result of our previous studies, the sway of the subjects' arm during a tactile apparent movement experiment under a specified experimental condition was reported. [3] It has been expected that the quantitative evaluation of the body-sway that in our study refers to the sway of the testing arm, will make the tactile apparent movement evaluation possible.

The characteristics of the body-sway were analyzed by studying the EMG (electromyography) waveforms recorded during the apparent movement recognition time. The analysis was performed by using the various frequency analysis methods and tools such as the Wavelet packet transform. [4]

II) MEASURMENT AND EXPERIMENT

The experiments of our study take place on two different days. Figure 1 shows the experiment system of the first day. By using a PC different stimulations can be applied to the 4 skin stimulators (vibrators) randomly through a D/A convertor and an Op-amp amplifier.

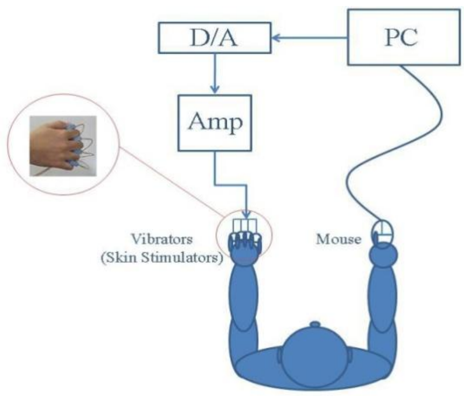

Figure 1: AM recognition experiment system.

During the measurement, the subject (in this report, three 23 years old male student) sits on a chair while the arm (which the vibrators are between its fingers) is open and making a 90 degree angle with upper body. The eyes will be closed and ears will be covered by a voice proof cover. The mouse clicks will be recorded as the subjects' reaction when recognizing the apparent movement.

Figure 2 shows the experiment system that has been used on the second day's experiment. There are two PCs in the experiment system that the first one (PC1) is responsible for applying the stimulations to the stimulators and also recording the real-time tracing data (CCD camera). The second PC (PC2), after amplification and A/D conversion, records the EMG data and the signals from a three-axis acceleration sensor attached to the wrist of the subject`s testing arm. In this experiment, EMG waveforms will be recorded by means of 12 electrodes and 18 channels resulting from the electrode combination.

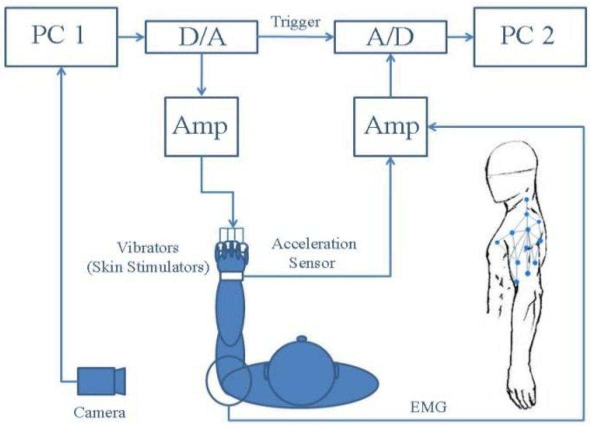

Figure 2: EMG measurement system and electrode combination.

The stimuli are controlled by the two parameters of T and τ that will be applied to the stimulators randomly in 10 cycles (repetitions). The period of applying the stimulation is represented by T and τ is for the interval between the starting (trigger) points of the stimulation in the 4 vibrators (see Figure 3).

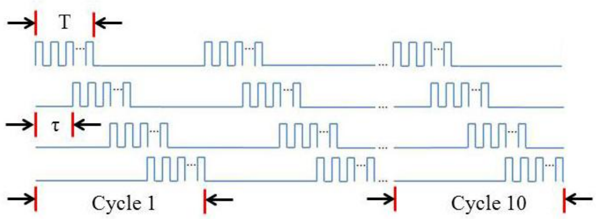

Figure 3: T and τ.

Table 1 shows the of T and τ values which will be selected randomly to make the different types of stimulations.

Table 1: Values of T and τ.

Parameter	[ms.]					
T	300	500	700	900	1100	1300
τ	100	200	300	400	500	600

III) DATA ANALYSIS AND RESULTS

Figure 4 shows the result of the first day`s experiment on one of the subjects. The area with higher values shows the AM recognition area, where the subject has reacted to the stimuli by a mouse click. The center of gravity of the recognition area is named as the (TM, τM) point. In this stage, the experiment will be repeated with the constant value of the T=TM in order to see the precise values (thresholds) of τ at the recognition area which the lower threshold will be represented by τL and the higher threshold will be represented by τH (see Figure 5).

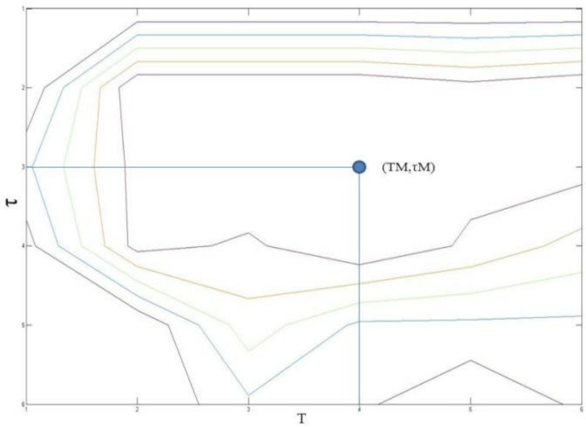

Figure 4: Results of the AM recognition experiment

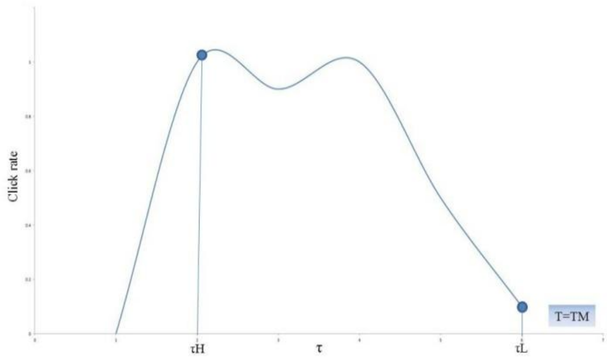

Figure 5: Results of the AM recognition experiment with the constant value of T=TM.

The obtain values of TM, τ0 (the lowest τ value in the first experiment's result), τL, τM, τH will be used as the variables of the second day's (EMG) experiment.

In our study, two periods of the EMG data are in the center of attention: the period before applying the stimulations (pre-stimulation data) and the period after applying the stimulations (post-stimulation data).

In order to study the frequency characteristics of the EMG data (since it has a vast frequency range from 50Hz to 200Hz) discrete Wavelet packet transform was tried. The Wavelet packet transformation is performed in 8 levels by using the Doubachese-3 mother wavelet. As a result of wavelet packet decomposition in 8 levels, 256 packets appeared. Additionally, in order to compare the data of wavelet packets of different channels and different subjects *Fisher`s ratio* is used. Fisher's ratio (FR) is a measure for (linear) discriminating power of some variable that is defined as below: [5]

$$FR = \frac{\sum_{i=1}^{c} \frac{n_i}{n} \left\| \bar{x}_i - \bar{x} \right\|^2}{\sum_{i=1}^{c} \frac{n_i}{n} \bar{\bar{x}}_i} \tag{2}$$

when:

$$\bar{\bar{x}}_i = \frac{1}{n_i} \sum_{i=1}^{c} \left\| x_i - \bar{x}_i \right\|^2 \tag{3}$$

The EMG results recorded with (TM,τ0) parameters will be considered as class 1 and the EMG results recorded with (TM,τL) or (TM, τM) or (TM,τH) parameters will be considered as class 2. In these equations *i* is the index of wavelet packets, $\bar{x}$ is the average values and $\bar{\bar{x}}$ represents the variance values.

Since the EMG data recorded before applying the stimulations can be considered as the default behavior of the subject, the results of data analysis will be presented as the variance between the post-stimulation data and pre-stimulation EMG data (*V*) as:

$$V = (Post\ Stimulation - Pre\ Stimulation) \tag{4}$$

The calculated FR of the 12^{th} EMG recording channel of all subjects owns the maximum value of FR among the other 18 channels. Thus, the 12^{th} channel`s results will be presented as the final results for each subject.

After obtaining Fisher`s ratio in the mentioned 3 types of class selection (τ0-τL, τ0-τM andτ0-τH), we tried to find the packets (frequency ranges) which Fisher`s ratio is maximum when the selected 2 classes, regarding to the definition of τM, are τ0 and τM .

Different ranges of Fisher`s ratio were tried and compared. In order to find the range that owns the maximum FR values, variance between the 3 types of FR class selection was calculated. Figures 6 and 7 show the variance between the summations of FR values that have been calculated in 3 different types of class selection. In figure 6 variances between FR summations of two different class selection groups (τ0-τM and τ0-τL) for 3 subjects is depicted. Figure 7 depicts the variances of FR summations in two different class selection groups of τ0-τM and τ0-τH (3 Subjects).

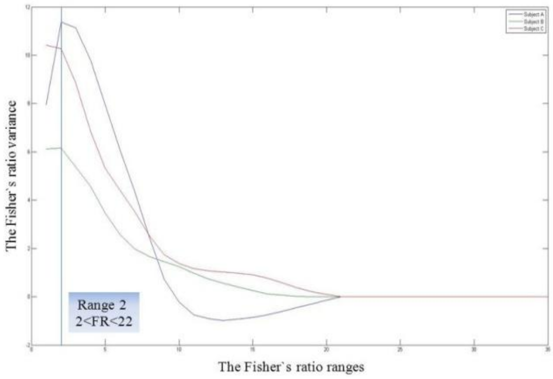

Figure 6: Subject A

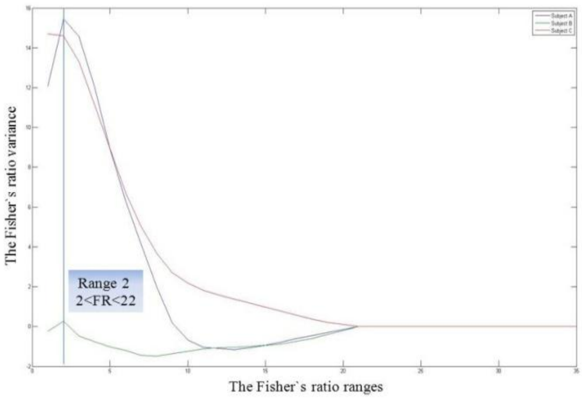

Figure 7: Subject B

Comparing the different FR ranges, we came to this conclusion that Fisher`s ratio is maximum in the $2^{nd}$ range that belongs to the range between FR=2 and FR=22. Figures 8, 9 and 10 show the Fisher`s ratio values (calculated with the two classes of τ0/τM) in the mentioned range of 2~22 for all the 256 packets of the 8^{th} level of DWPT.

In order to present the most results in the most understandable form, the results of the figures 8, 9 and 10 are depicted after applying a low-pass filtration in frequency domain. In these figures, the higher areas show the bigger values of FRs that has been calculated between the two classes of data recorded with τ0 and τM.

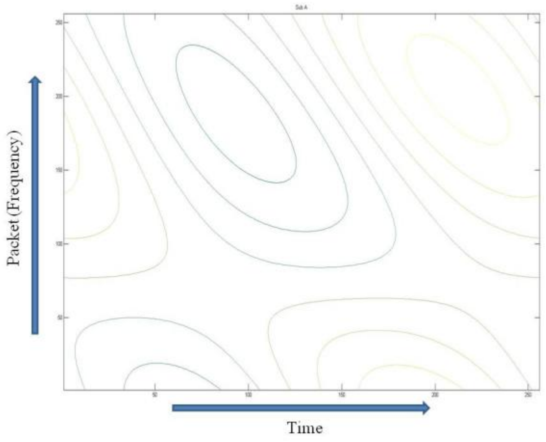

Figure 8: Subject A

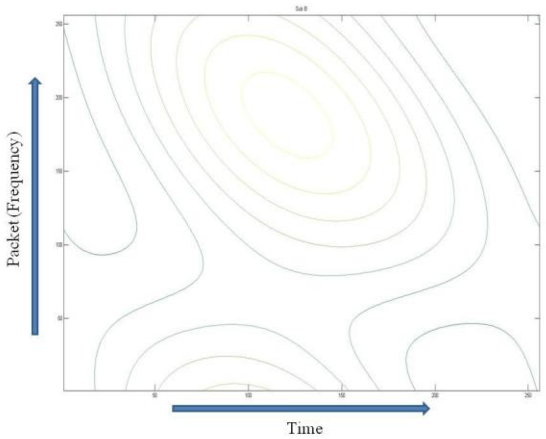

Figure 9: Subject B

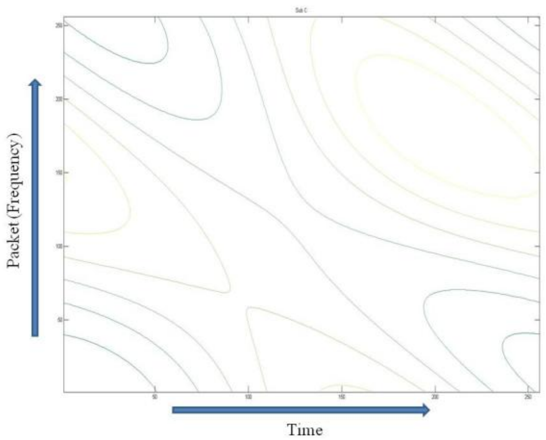

Figure 10: Subject C

Comparing the results of the recorded EMG data analysis for the 3 subjects of A, B and C, basically, two significant areas own the maximum ranges of FR with a similar shape and formation. It can be understood that the results of the subjects A and C are quite similar from the formation of the maximum areas point of view while the result of subject B is still obeying the same form with a down-ward shifting.

IV) CONCLUSION

In this study, the sway of the subjects' arm caused by individual tactile stimulations and tactile apparent movement recognition as its result was investigated. By focusing more on the frequency characteristics of the body-sway, the expected quantitative evaluation of the body-sway became possible. The results of this study show the possibility of the periodic movements of the testing part of the body which occur during the apparent movement recognition.

REFRENCES

[1] S. Ueda, M. Uchida, A. Nozawa, and H. Ide (2007), A Tactile Display Used Phantom Sensation with Apparent Movement Together (in Japanese), IEEJ Trans. FM, Vol. 127, No. 6, pp. 227-284

[2] J.H. Kirman (1974), Tactile apparent movement: The effects of interstimulus onset interval and stimulus duration, Perception & Phychophysics, Vol. 15, pp. 1-6

[3] Y. I. Park and M. Uchida (2010), Swing Analysis of Body-parts Motion Accompanied by Apparent Movement, The International Symposium on Artificial Life and Robotics 2010 (AROB 15th), OS1-4

[4] M. B. I. Reaz, M. S. Hussain, F. Mohd-Yasin (2006), EMG Analysis Using Wavelet Functions to Determine Muscle Contraction, HEALTHCOM International Conference, pp. 132-134

[5] Tran Huy Dat, Cuntai Guan (2007), Feature Selection Based on Fisher Ratio and Mutual Iinformation Analysis for Robust Brain Computer Interface, ICASSP International Conference, pp. I-337 - I-340

Estimation of Hazardous Area with Surveillance UAV

Hiroshi Sato[1], Masao Kubo[1], and Akira Namatame[1]

[1] National Defense Academy of Japan, Yokosuka, Kanagawa 239-8686, Japan
(Tel: 81-46-841-3810, Fax: +81-46-844-5911)
(hsato@nda.ac.jp)

Abstract: Unmanned Aerial Vehicle (UAV) is becoming useful tool for the surveillance of the area where man can't go in. Ideally, UAV should fly fully automatically and some of them are becoming to be able to do this. Autonomous flying UAV can use large amount of data for posture control and navigation during its flight. This paper proposes the method which recycles these data for the purpose of environment recognition. In order to achieve this, we adopt machine learning techniques. Support Vector Machine (SVM) is chosen because it is faster and lighter than other machine learning technique. We demonstrate the method using the UAV made by Hitachi Ltd. and Kawada Industries, Inc. It can fly autonomously using GPS, motion sensor, magnetic sensor. From the flight log obtained by these sensors, SVM can not only classify the space into safe and dangerous area, but also predict undiscovered dangerous area. These areas coincident with the impression of operator who flied the radio control airplane in the same airspace.

Keywords: UAV, Automatic Surveillance, Machine Learning, Data mining, Support Vector Machine

1 INTRODUCTION

There is a growing demands for surveillance using UAV (Unmanned Aerial Vehicle) in disaster area[1][2][3]. For example, at the early stage of the nuclear crisis in Fukushima Daiichi Nuclear Power Station which is caused by Tsunami of 2011 Tohoku earthquake, US military's global hawk flied around and collected valuable data[4].

Ideally, the UAV should fly autonomously, but there are many difficulties for autonomous flight. Compared with the automatic flight of large passenger plane, the status of the flight airspace of UAV is usually unknown because when it is expected to fly above disaster area, the previous information wii be useless.

This paper proposes a method that enables the UAV to recognize the environment using machine learning technique. This method recycles the information from GPS, motion sensor, and so on which is observed originally for flight control.

The following is the contents of this paper. Section 2 introduce the UAV which is used in this research. Section 3 explains our proposed method environment recognition. Section 4 show the results of the recognition from real data. Section 5 concludes this paper.

2 EXPERIMENTAL APPARATUS

The UAV used in this study is made by Hitachi Ltd. and Kawada Industries, Inc. Fig. 1 shows the appearance of the UAV and Table 1 show the specs of the UAV.

The significant feature of the UAV is that it can fly fully autonomously using the hybrid navigation of GPS and INS. In order to achieve that, the UAV equipped various sensors. The following is the information that can be observed.

Table 1. The specs of the UAV used in this research

size	600 x 503 x 163 (mm)
weight	720g
air speed	45 – 70 km/h
duration of flight	15 min
propulsion	propeller propulsion
power	lithium polymer battery
control of flight	autonomous / radio control
camera	1280 x 1024
record	flight data and photo data
takeoff / landing	hand throw / belly-landing

- GPS (position, time)
- acceleration sensor (3-axis acceleration)
- angular velocity sensor (3-axis angular velocity)
- magnetic sensor (direction)
- anemometer (air speed)
- digital camera (photo)

The UAV can send the status to and receive the com-

Fig. 1. The micro UAV used in this research.

mand from the ground station with wireless communication. The flight plan consist of the sequence of waypoints. Hand thrown take off and belly landing enable us to operate the UAV without a runway. It can fly about 15 minutes by the power of lithium-polymer batteries. In autonomous flight, the UAV can't recognize obstacle. Therefore human operator can override the control by radio-control.

3 THE RECOGNITION OF ENVIRONMENT

This section proposes the environment recognition method using support vector machine[6]. SVM is one of the supervised learning method and is used for binary classification.

3.1 Support Vector Machine

SVM has linear separator but the separation is done in the feature space which is produced by kernel function. SVM shows a good performance in non-linear separation problem.

Let the mapping to feature space $\Phi : X \rightarrow H$. Kernel function k can be represented by the inner product of them as $< \Phi(x), \Phi(x') >$.

$$k(x, x') =< \Phi(x), \Phi(x') > \tag{1}$$

In classification problem, SVM divide the hyperplane into two class by

$$< \mathbf{w}, \Phi(x) > +b = 0. \tag{2}$$

Decision function f is

$$f(x) = \mathrm{sign}(< \mathbf{w}, \Phi(x) > +b). \tag{3}$$

The performance of separation is maximum when the margin which is made by hyperplane is maximum.

This problem result in solving constrained quadratic programming. For many kernel functions, the weight can be written as $\mathbf{w} = \sum_i \alpha_i \Phi(x_i)$.

This classification only depends on the data on the margin. These data are called support vectors.

In an attempt to meet the overlapped data, soft margin term ξ can be introduced:

$$\begin{aligned} \text{minimize} \quad & t(\mathbf{w}, \xi) = \tfrac{1}{2}||\mathbf{w}||^2 + \tfrac{C}{m} \textstyle\sum_{i=1}^{m} \xi_i \\ \text{subject to} \quad & y_i(< \Phi(x_i), \mathbf{w} > +b) \geq 1 - \xi_i \\ & \xi_i \geq 0 \;\; (i = 1, \ldots, m) \end{aligned} \tag{4}$$

Here, m is a number of training data and $y_i = \pm 1$.

Solution of SVM $\mathbf{w}$ can be represented as follows:

$$\mathbf{w} = \sum_{i=1}^{m} \alpha_i y_i \Phi(x_i) \tag{5}$$

α_i can be obtained by solving the following duality problem.

$$\begin{aligned} \text{maximize} \quad & W(\alpha) = \textstyle\sum_{i=1}^{m} \alpha_i \\ & -\tfrac{1}{2} \textstyle\sum_{i,j=1}^{m} \alpha_i \alpha_j y_i y_j k(x_i, x_j) \\ \text{subject to} \quad & 0 \leq \alpha_i \leq \tfrac{C}{m} \\ & \textstyle\sum_{i}^{m} \alpha_i y_i = 0 \\ & \xi_i \geq 0 \;\; (i = 1, \ldots, m) \end{aligned} \tag{6}$$

Using duality theorem $\mathbf{w}$ and b can be disappeared and the problem becomes to the maximization problem only for α.

3.2 Data to be Classified

During the flight of our UAV, various kinds of data which is explained in Section 2 is observed and stored in the form of CSV file. The sampling rate is 0.1 sec.

4 EXPERIMENTS

In order to demonstrate our method, some experimental flights have been done. The flight area is the above of the baseball ground in our campus (Fig. 2).

The purpose of this experiment is to find dangerous airspace to flight. Knowing the dangerous airspace is very important for this UAV because it flies fully autonomous.

We set the criteria of dangerous airspace as follows:

- The airspace where large acceleration is observed.
- The airspace where the difference between ground speed and air speed is large.

As we explained in Section 3.2, the UAV gathers a data every 100 msec. Each sampling point checked and marked as "danger" when the above criteria is hold. SVM learned and classify the airspace from these data. Table 2 is a summary of the parameters and results.

The results of estimation are shown from Fig. 3 to Fig. 6. In these figures, each point shows the observation point. Circle is judged as "normal" airspace and triangle is judges as "danger." Black circles and triangles are support vectors.

From the top view (Fig. 3 and Fig. 5), we can see the dangerous airspace is slightly different. This means acceleration based dangerous airspace and speed difference based dangerous airspace is not the same, however the overlapping zone is quite dangerous.

From the side view (Fig. 4 and Fig. 6), we can see the middle of the height is more dangerous than other heights. This result coincidents with the impression of human pilot of radio controlled airplane which flied just before the experiments. This can be thought that there are some air flow around the middle height above the ground. This wind comes from the sea and make a turbulence above the ground because the ground is located on the top of the hill very near from the sea. You can see the location from Fig. 2.

Table 2. Setting parameters and results of support vector machine

experiment	cost parameter	hyperplane parameter	number of support vector	error
Fig. 3	4	4.69	1431	0.336
Fig. 4	8	16.31	1400	0.320
Fig. 5	7	8.96	482	0.059
Fig. 6	7	11.65	424	0.065

5 CONCLUSION

This study proposes a machine learning based method of environment recognition for small UAV in disaster area. This method recycles the information that is obtained originally for autonomous flight into the environment recognition. This method estimates air status of whole airspace from the very little airspace where the UAV fly. As a demonstration, we flied the UAV above the ground of our campus and made the hazard map of the air. The results coincident with the human expert impression. For future works, we need an extension of this method to the realtime estimation (on-flight estimation) and to the coordinated estimation by multiple UAV.

Fig. 2. Map of the experimental field — upper: entire field, lower: zoom up

REFERENCES

[1] Bertuccelli LF and How JP (2005), Robust UAV Search for Environments with Imprecise Probability Map, Proc. 44th IEEE Conference on Decision and Control, 5680-5686

[2] Doherty P and Rudol P (2007), A UAV Search and Rescue Scenario with Human Body Detection and Geolocalization, LNCS 4830: 1-13

[3] Suzuki T, Meguro J, et. al. (2008), Development of Information Collection System using a Small Unmanned Aerial Vehicle for Disaster Prevention and Mitigation (in Japanese), Journal of Robotics Socieity of Japan 26(6): 553-560

[4] M. Sugisaka (2011) , Working Robots for Nuclear Power Plant Disasters, Proceedings of The 5th IEEE International Conference on Digital Ecosystems and Technologies Conference, 358-361

[5] Y. Tanabe, T. Furukawa, T. Akasaka, H. Kushida (2004), Colugo — a New Mini Aerial Vehicle Developed by Kawada and Hitachi, UAV 2004, Paris, UVSI,

[6] C. Cortes, V. Vapnik (1995), Support-vector network, Machine Learning, 20(3): 273-239

[7] R project, http://www.r-project.org

[8] A. Karazoglou, D. Meyer, K. Hornik (2006), Support Vector Machine in R, Journal of Statistical Software, 15(9): 1-28

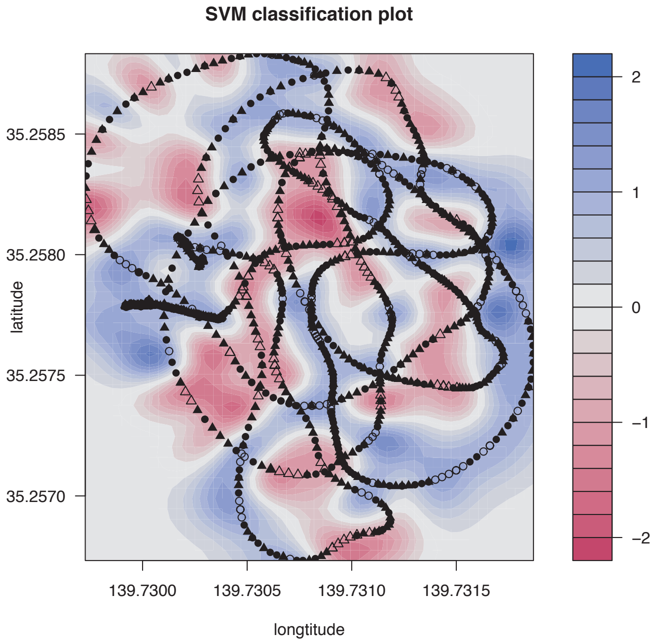

Fig. 3. Classification of the airspace by support vector machine: Classification criteria: large acceleration, View: top view, Date: 27, Aug.

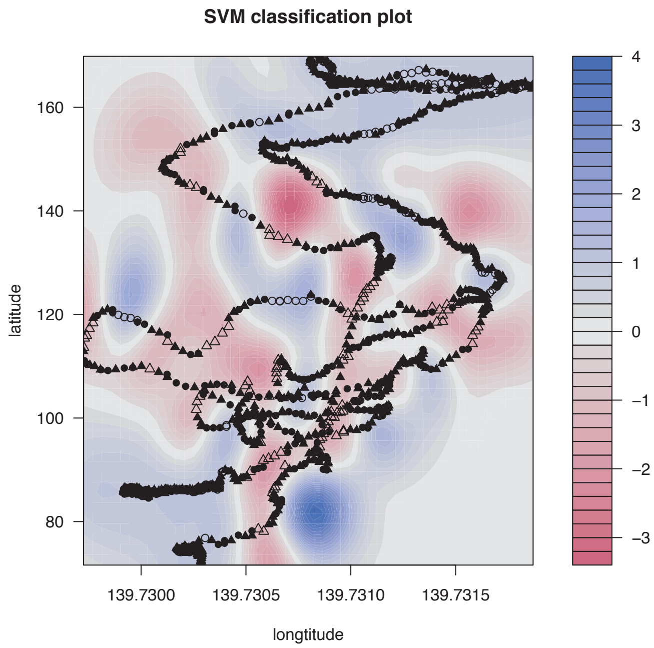

Fig. 4. Classification of the airspace by support vector machine: Classification criteria: large acceleration, View: side view, Date: 27, Aug.

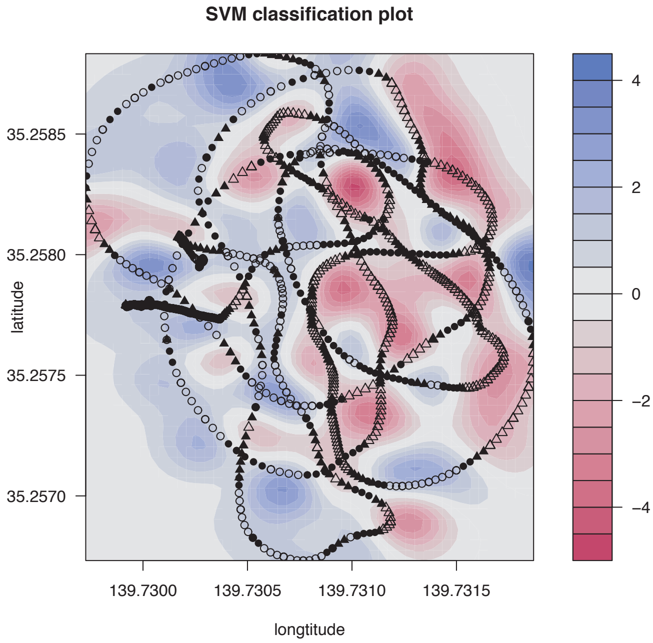

Fig. 5. Classification of the airspace by support vector machine: Classification criteria: large difference between ground speed and air speed, View: top view, Date: 27, Aug.

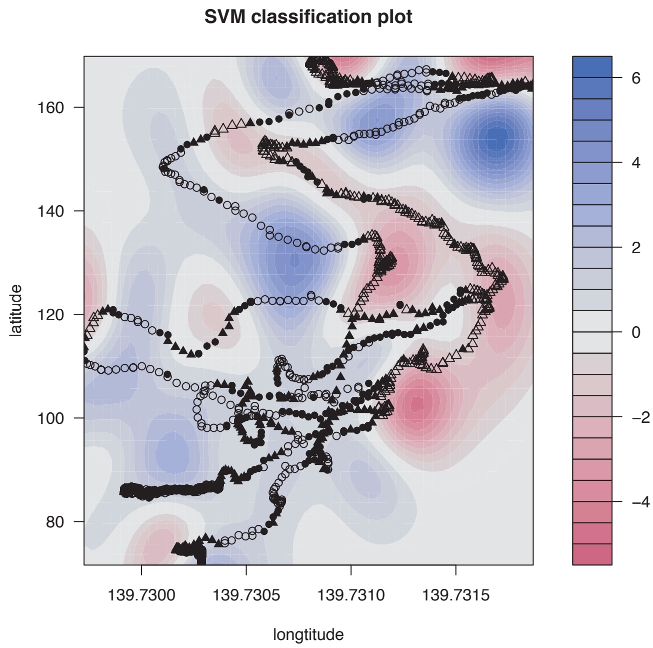

Fig. 6. Classification of the airspace by support vector machine: Classification criteria: large difference between ground speed and air speed, View: side view, Date: 27, Aug.

Safety of ships evacuation from Tsunami
- Survey Unit about the Great East Japan Earthquake -

Saori Iwanaga[1] and Yoshinori Matsuura[1]

[1]Japan Coast Guard Academy, Kure, Hiroshima 737-0832, Japan
(Tel: 81-823-21-4961 (ext.373), Fax: 81-823-21-8105)

[1]s-iwanaga@jcga.ac.jp

Abstract: The Great East Japan Earthquake occurred at 14:46 on Friday, 11 March 2011. It was the most powerful known earthquake to have hit Japan, and one of the five most powerful earthquakes in the world overall since modern record-keeping began in 1900. The earthquake triggered extremely destructive tsunami waves of up to 40.5 meters in Miyako, Iwate. Over 20,000 people dead and the missed.

International Research Center for Marine Policy is think tank of Japan Coast Guard and is belong to Japan Coast Guard Academy. Research unit was organized to survey and research of The Great East Japan Earthquake in particular about ocean. This unit collects the information about it and analyzes and synthesizes collected information from a professional viewpoint respectively. Then, the unit study about damage by TSUNAMI, damage of ships, urgent refuge and search rescue to pick new actual explication and various lessons out.

Keywords: the Great East Japan Earthquake, TSUNAMI, evacuation, multi-agent simulation.

1 INTRODUCTION

The earthquake off the Pacific coast of Tohoku, also known as the 2011 Tohoku earthquake, or the Great East Japan Earthquake, was a magnitude 9.0 undersea megathrust earthquake off the coast of Japan that occurred at 14:46 on Friday, 11 March 2011. It was the most powerful known earthquake to have hit Japan, and one of the five most powerful earthquakes in the world overall since modern record-keeping began in 1900. The earthquake triggered extremely destructive tsunami waves of up to 40.5 meters in Miyako, Iwate. In some cases it traveled up to 10 km inland. In addition to loss of life and destruction of infrastructure, the tsunami caused a number of nuclear accidents in the Fukushima I Nuclear Power Plant complex.

Over 20,000 people dead and the missed and over 125,000 buildings damaged or destroyed by the earthquake. The earthquake and tsunami caused extensive and severe structural damage in Japan, including heavy damage to roads and railways as well as fires in many areas, and a dam collapse. Around 4.4 million households in northeastern Japan were left without electricity and 1.5 million without water. Many electrical generators were taken down, and at least three nuclear reactors suffered explosions due to hydrogen gas that had built up within their outer containment buildings after cooling system failure.

International Research Center for Marine Policy is think tank of Japan Coast Guard and is belong to Japan Coast Guard Academy. Research unit was organized to survey and research of Tohoku - Pacific Ocean Earthquake in particular about ocean. This unit collects the information about it and analyzes and synthesizes collected information from a professional viewpoint respectively. Then, the unit study about damage by TSUNAMI, damage of ships, urgent refuge and search rescue to pick new actual explication and various lessons out.

In our viewpoint, we focus on the evacuation from TSUNAMI. Then, we analyze about ships evacuation from TSUNAMI using multi-agent simulation and we want to prepare for a coming earthquake. When considering evacuation, we often stick to only refuge to a hill and a shelter to get it. But, as seen on TV news, some ships run aground on land by TSUNAMI. And staffs of local public bodies lead refuge or staffs of peace or rescue organization go to the office urgently. Then, there occur very traffic jam and it is difficult to reach the destination. We investigate the evacuation to shelter from TSUNAMI of refugees and perform the own mission of staffs.

2 RESERCH UNIT

Research unit was organized to survey and research of the Great East Japan Earthquake in particular about ocean this summer. And they collect and the public or non-public information about the earthquake and analyzes and synthesizes collected information from a professional viewpoint respectively. Then, the unit study about damage by TSUNAMI, shipping damage, urgent refuge and search rescue to pick new actual explication and various lessons out.

The research unit is classified into six groups. The groups is for stering and perform a ship, traffic on the sea, estimation of floatage, rescue and disaster prevention, technique of search in the sea, and the engine of ship.

Our study belongs to group about traffic on the sea. We can deal with Automatic Identification System data what is called AIS [1] data, Marine Traffic Information service[2], what is called MARTIS radar data, record of communication by VHF, directions such as taking shelter of ships, ebb and flow data, tide data, and so on. The research group has three sub groups. First sub group is to analyze the actual taking shelter of ships when a seismic sea-wave warning alarmed and TSUNAMI came. Second sub group is to survey the control in the port and sea route control when a seismic sea-wave warning alarmed and TSUNAMI came. And last sub group is to study of simulation when ships take shelter, which is we belong to.

3 BEHAVIOR OF SHIPS AFTER EARTHQUAKE

Fig. 1 is plotting figure of the real AIS data of ships after the earthquake around port of Sendai-Shiogama.

With the AIS installed, vessels are able to monitor the movement of a multiple number of vessels simultaneously regardless of visibility, thereby dramatically reducing the danger of ship collision. Furthermore, ground facilities can obtain the ship-specific information necessary for automatic, real-time maritime traffic control. AIS will play an important role in ensuring navigational and operational efficiency in congested waterways [1].

In Japan, passenger ships of less than 300 tons of gross tonnage and all ships of more than 300 tons of gross tonnage for international sailing, and all ships of more than 500 tons of gross tonnage for non-international sailing have to be equipped AIS equipment[3].

Because AIS data was recorded, we can review the behavior big ships by AIS data in Japan.

In Fig.1, there are several banks at offshore of port. And in Fig. 1(a), there were some ships with AIS in the bay at the time of earthquake. Ship is described by an isosceles triangle and the heading is shown by the top. Speed and the heading of the ship are described by a bar, that is, length of the bar means the speed and the direction of bar means the heading of ship. And light lines mean the traits of ships.

Then, from Fig. 1(b), we found that many ships started to go offshore to evacuate at 30 minutes after the earthquake. Fig.1 (c) shows the behavior of ships at one and half hour after earthquake, it looks like that many ships were push by TSUNAMI. It is reported that TSUMAMI reach to this area around 4 pm, which is about between 1 hour and 1.5 hours after earthquake. Then, many ships could escape TSUNAMI, but several ships, which started go offshore lately, could not evacuate and were repelled from TSUMANI to bay.

Fig.1 (d) shows the behavior of ships at three hours after earthquake. We found that several ship remain the bay because they fail to escape.

Then, we found that ship started go offshore early could escape the TSUNAMI. Japan Coast Guard also recommends going away off the port for safety of ships in case of TSUNAMI. And this is the cope with the TSUNAMI. But, sailors are not always on ship and many sailors are on the ground when the ship is anchoring. So, to go offshore the ship, the sailors must rerun the ship quickly. But, the roads to the port on the ground are crowded because many people evacuate from TSUNAMI for the hill. Then, it will be done to confront the crowded for the port.

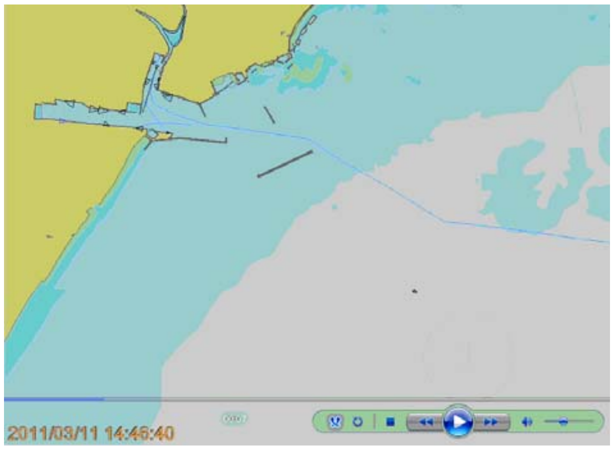

(a) At that time of earthquake

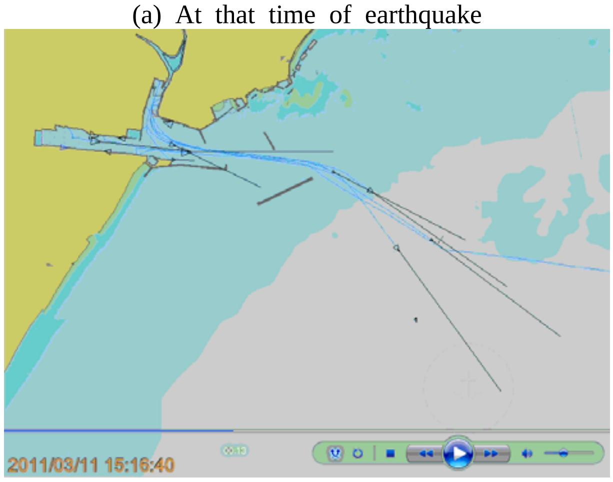

(b) after 30 minutes

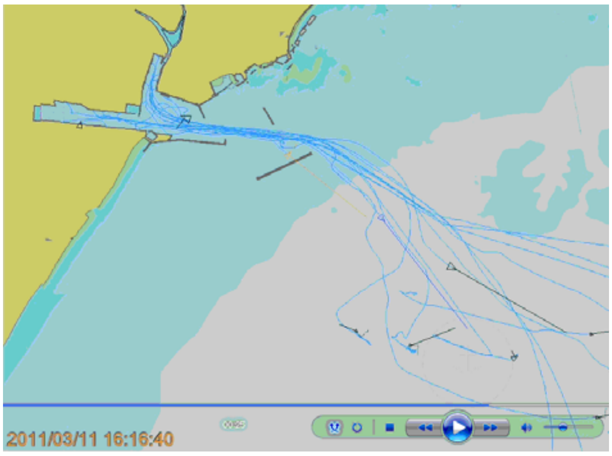

(c) After 1.5 hour

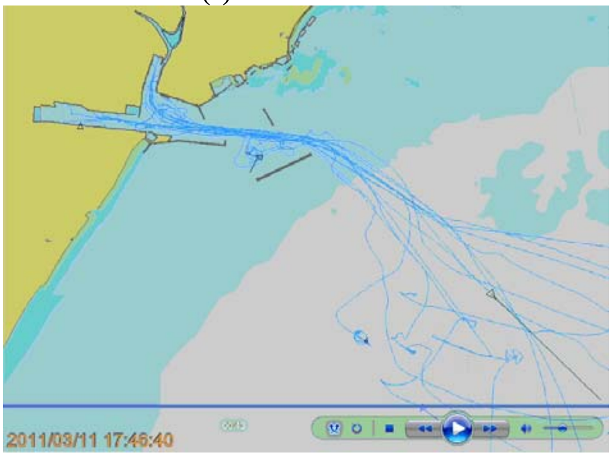

(d) After 3 hours

Fig. 1. Traits of large big ships

After the earthquake, many people will move to get away. And staffs of local public bodies lead refuge or staffs of peace or rescue organization, such as policemen, firemen or coast guard staffs, go to the office urgently. Then, there occur very traffic jam and it is difficult to arrive at the destination. We investigate the evacuation to shelter from TSUNAMI of refugees and perform the own mission of staffs.

Indeed, staffs of local public bodies or city worker have to lead refuge or broadcast for going away to hills. Staffs of Japan Coast Guard have to go to work, that is, he has to go port after the big earthquake immediately. And some fire brigades have to go to shut the floodgate in case of TSUNAMI.

At the beginning, we thought about on the sea to escape the ships. But, the ships could not launch because the sailor could not gather the ship in time in many cases. So, we expand the research area not only on the sea but also on the land. Moreover, when we think about disaster prevention, we tend to focus on the refuge of people. On the other hands, there are many people to support the refugee. And they want to complete the mission, safety. But, there occur very traffic jam and it is difficult to arrive at the destination.

Then, we investigate the evacuation to shelter from TSUNAMI of refugees and action to perform the own mission using multi-agent simulation.

4 MODEL

We have an idea of simulation of earthquake and TSUNAMI. We denote briefly as follows.

4.1 Space

We deal with land and ocean. The sample is shown Fig.2 using Google Map (http://www.google.co.jp). In land, there are many roads and almost people move on the roads to get away. And people want to get away in time to survive. So, behaviors of people are restricted by space and time. But, there might be traffic jam or the road might cut by earthquake. Then, there need to control traffic. On the other hand, sailors gather to port to launch the ship to offshore. If sailor is in town, he will be done to confront the crowded for the port to go back to port.

Then, when the sailors gather to the ship, the ship will launch to offshore. On the sea, ship can move freely because there are not specified road. But, if ship move freely, ships can corrupt each other or ship can go aground. Then, it becomes difficult for ships to go away. Especially after earthquake, almost all are in hurry. Then, we design the sea route for simplify the simulation.

In fact, the performers on the sea is very few, comparing with on land because only few people have ship, such as fisher, ferry company, Japan Coast Guard. That is why multi-agent simulation on the sea is few and agent in the sea such as fish often moved freely on the sea. And agents move shortsightedly, such as fish go to the nearest plankton and eat it. So, if there is obstacles in front of the fish, it cannot eat the over the obstacle. But, ship is clever because sailors ride on. And they have a map and they know the land and the obstacles. To realize the ships as agent, it is simple to design the ocean route similar on land.

Fig. 2. Image of simulation

4.2 Agent

We define the agents as Table 1. Refugee agent evacuate from TSUNAMI shelter or hill immediately. City worker agent of local public bodies broadcasts the information about TSUNAMI and leads refuge or patrol the town immediately. And policeman agent goes to point of traffic jam or traffic accident immediately. Fireman agent leads refuge. Sailor agent in town goes to the port. If sailors of ship are gathered, the ship agent leaves the port t to offshore.

Table 1. Agents in simulation

	Behavior	Destination	Start time
Refugee	Move	Hills	Immediately
City worker	Stay building		Immediately
	patrol		Immediately
policeman	Move	Traffic jam point	Immediately
fireman	patrol		Immediately
Sailor	Move	Port	Immediately
ship	move	offshore	when sailors gather

4.3 Behavior of agent

4.3 Simulation

We are now programming using multi-agent simulator Artisoc [4]. Artisoc allows us to easily and quickly reproduced on a computer interactions between humans, is a multi-agent simulator to analyze social phenomena alive dynamically changing.

Artisoc, the five-year plan implemented in fiscal 2003 Scientific Creation Project "social order change research by the multi-agent simulator," which was developed as part of copyright, Ltd. Kozo Keikaku belong to both the Graduate School of Arts and Sciences, Professor, University of Tokyo Susumu Yamakage.

Using this simulator, some disaster or accident are dealt with such as TSUNAMI in Okushiri in 1993, accident on Akashi footbridge in 2001.

4 CONCLUSION

Now, we are discussing and programming the simulation. We analyze about ships evacuation from TSUNAMI using multi-agent simulation and we want to prepare for a coming earthquake. When considering evacuation, we often stick to only refuge to a hill and a shelter to get it. And staffs of local public bodies lead refuge or staffs of peace or rescue organization go to the office urgently. Then, there occur very traffic jam and it is difficult to reach the destination. We investigate the evacuation to shelter from TSUNAMI of refugees and perform the own mission of staffs.

REFERENCES

[1] Ministry of Internal Affairs and Communications http://www.tele.soumu.go.jp/e/adm/system/satellit/ais/index.htm

[2] Japan Coast Guard (2009), Report of Japan Coast Guard (in Japanese).
http://www.kaiho.mlit.go.jp/info/books/report2009/Degital/tokushu/p019.html

[3] Japan Cost Guard (2005), TSUNAMI measure of Japan Coast Guard (in Japanese).
www.kaiho.mlit.go.jp/info/tsunami/tsunami-shiryo.pdf

[4] Aritisoc http://mas.kke.co.jp/index.php

Individual Recognition-Free Target Enclosure Model

Masao Kubo[1], Tatsurou Yoshimura[1], Akihiro Yamaguchi[2], and Hiroshi Sato[1]

[1] National Defense Academy of Japan, Yokosuka, Kanagawa239-8686, Japan
[2] Fukuoka Institute of Technology, Fukuoka, Fukuoka 811-0295, Japan

Abstract: Target enclosure by autonomous robots is useful for many practical applications, for example, surveillance of disaster sites. Scalability is important for autonomous robots because a larger group is more robust against breakdown, accidents, and failure. However, it is more difficult to operate a larger group of robots because their individual capacity for recognizing teammates should be higher. In this paper, to achieve a highly scalable target enclosure model, we demonstrate a new condition for Takayama's enclosure model. The original model requires a static relationship between agents. However, robots can form an enclosure even under a dynamic topology on the basis of a nearest neighbor graph; hence, they do not require recognition capability. We confirm this by an analytical discussion of switched systems and a series of computer simulations.

Keywords: Collective Intelligence, Distributed robotics, Formation, Cyclic pursuit, robot swarm

1 INTRODUCTION

In this paper, we propose a new condition for Takayama's target enclosure model [10] that can allocate robots to an unspecified number of targets.

Target enclosure, which is useful for monitoring disaster sites and unknown vehicles, has recently become an important goal for multiple robots. Robots can operate in dangerous circumstances, replacing human presence.

Disaster sites are usually far from an operator. In this case, a group of robots examines the exact number of sites to be observed and their locations. Therefore, it is desirable that more robots than necessary are employed, which enables them to accept a larger number of targets . For this purpose, the tasks of target allocation and target enclosure must be performed simultaneously.

However, it seems difficult for most target enclosure models proposed so far to realize this requirement.

Several related studies deal with target enclosure[12][5][4][10]. Except for the study of Kobayashi et al.[5], all other studies require that a particular physical arrangement of the robots be maintained in order to build a target enclosure. For example, Yamaguchi[12] discussed a target capturing task in which the robots must maintain a chain structure. Kim et al.[4] discussed the target enclosure problem; in their solution, each robot needs information on the relative speed of one robot and relative geographical relation to its target to determine its behavior. If the relationship between a robot and its reference robot is considered as a link in graph theory, the graph of the group of robots must follow a Hamiltonian cycle.

When a robot changes the target to be enclosed, the following two events should be considered: withdrawal and accedence of the robot. In the former, the remaining robots in the group must maintain the constraint of the Hamiltonian cycle without the removed robot. In the latter, a group that satisfies the Hamiltonian cycle condition and the new member must form a new Hamiltonian cycle. As far as we know, discussion of these events is inadequate when there are no restrictions on the timing of withdrawal and accedence of robots.

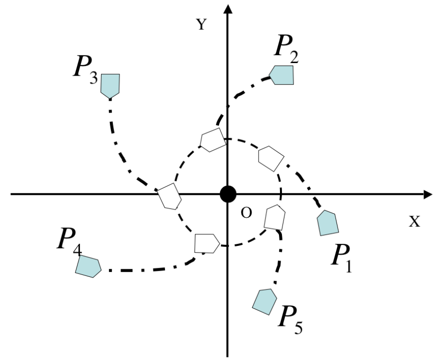

Fig. 1. Process of target enclosure using five robots.

Therefore, we investigated the relaxation of the condition of maintaining a Hamiltonian cycle to achieve target enclosure. In particular, we focused on the study of Takayama et al.[10]. In their model, each robot needs information of one neighbor and its target. As in other studies, this model also requires the Hamiltonian cycle constraint. However, in this paper, we show that this model can realize target enclosure without this constraint when each robot bases its behavior on information from its nearest neighboring robot. Therefore, in this model, robots can change targets without considering the above two events.

Note that the reference relationships among more than four robots in the proposed nearest neighbor model are often unconnected in the graph theory sense. Therefore, it is not

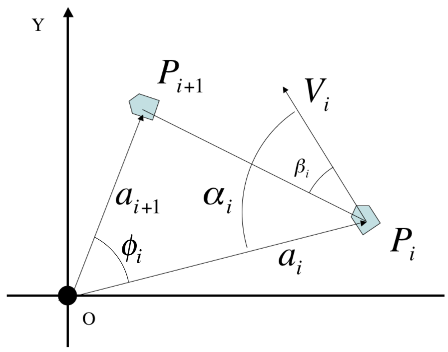

Fig. 2. Model of Takyama's target enclosure: α, β.

easy to discuss this issue using a graph Laplacian, which is the primary analytical approach used for multirobot systems. In this paper, the theory of switched systems[7] is adopted for analyzing groups of less than five robots. A series of computer simulations is used for larger groups.

This paper is organized as follows. First, Takayama's model is introduced. Next the proposed method based on using the nearest neighbor as a reference is presented, and the problems in verifying its ability to form a target enclosure are discussed. In section 4, the practical asymptotic stability of a small group is proven analytically. In addition, we use computer simulations to demonstrate the ability of a larger group to achieve target enclosure.

2 TAKAYAMA'S TARGET ENCLOSURE MODEL

Firstly, Takayama's target enclosure model is explained.

2.1 Takayama's target enclosure model

In this section, we assume that all robots choose the same target. We assume that on a two-dimensional (2D) plane, there is only one target O at the origin and n robots. Fig.1 illustrates the case of $n = 5$. Robots are numbered counterclockwise as $P_1, \ldots, P_n$, and r_i is the position vector of the robot P_i. In the target enclosure task, each robot moves to the corresponding white marker.

To achieve this task, Takayama et al.[10] proposed the following model. Each robot determines its control input, speed v_i, and angular velocity ω_i using two aspects of angular information: relative angles with respect to the target and an anterior neighboring robot,denoted as α_i and β_i, respectively. As a result, rotational movement occurs with a central focus on the target.

$$v_i = f\beta_i \tag{1}$$

$$\omega_i = v_i/\bar{r} \quad k\cos\alpha_i, \tag{2}$$

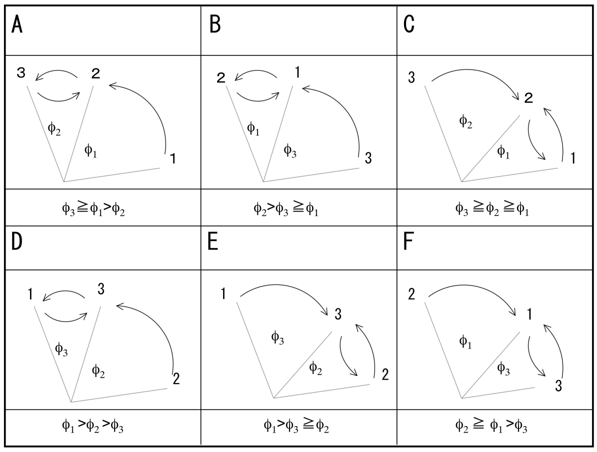

Fig. 3. Patterns of reference relationships among robots in a three-robot group.

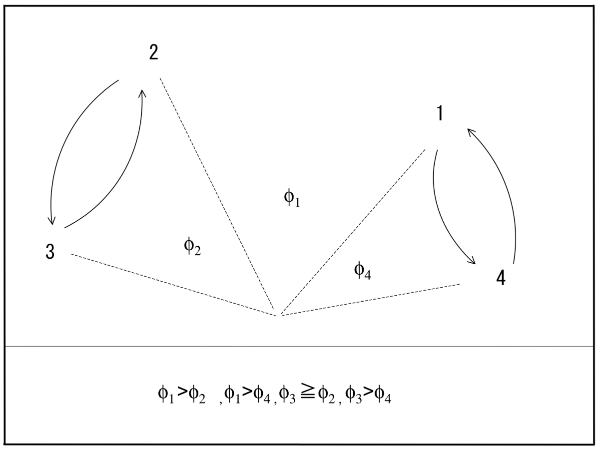

Fig. 4. Unconnected pattern of reference relationships in a four-robot group.

where the parameters $\bar{r}, k$, and $f > 0$ specified beforehand. P_{i+1} is the robot to which P_i refers, and $\bar{r}$ is the expected distance to the target. In Takayama's model, the i-th robot refers to the $i+1$-th robot, and the n-th robot refers to the first robot P_1. That is, if the relationship between a robot and its reference robot is considered as a link in graph theory, the graph of the group of robots must be a Hamiltonian cycle. The authors proved the convergence to the goal state of the target enclosure under this constraint.

Takayama et al. reported the following three characteristics of their model. (E1) The distance between the target and each robot converges to $\bar{r}$. (E2) The speed vector V_i and the vector $(O \quad P_i)$ are orthogonal. (E3) The gaps between a robot and its neighbors are equalized, i.e., $\ _i = \frac{2\pi}{n}$.

3 NEW REFERENCE RULE PROPOSAL OF TAKAYAMA'S MODEL

3.1 Takayama's model considering the nearest neighboring robot as the reference

In this paper, the robots observed by the i-th robot are considered to be its reference robots. In the original Takayama's model, the i-th robot P_i's reference robot is the $i+1$-th robot P_{i+1}. This relationship forms a Hamiltonian cycle. As mentioned above, this constraint makes target allocation behavior difficult. It also causes the scalability problem. Furthermore, each robot must identify its reference robot from the group of robots. This typically becomes difficult as the group size increases.

Therefore, we examine a new reference robot scheme in which each robot considers its anterior neighboring robot as its reference robot. Each robot controls itself as described in equations 1 and 2, but it chooses its nearest neighbor as its reference robot. If possible, the robots can change their target during the target allocation task. Such a system also has higher scalability because individual robots need not be identified to observe the nearest robot.

3.2 Problems in verification of the proposed reference model

In the work of Takayama et al.[10], the model was proven analytically by two approaches: convergence of the distance from the target and convergence of the distance between robots. The former convergence holds true for our proposed model.

In contrast, the result of the latter approach in which the angle between each adjacent robot converges to 2 $/n$ does not apply in our proposed model because Takayama's proof assumes that the relationship between the robot and its reference robot is static and robots are connected in the graph theory sense, as in references [8], [8], [9], and [10]. However, this assumption is inadequate for the following reasons.

1. The reference relationship in the proposed model changes dynamically. For example, there are six graphical patterns for the three-robot group (see Fig.3.).

2. The graph is not connected when $n > 3$. If $n \quad 3$, the graph is dynamic but connected (at least, it is weakly connected as a digraph). However, when $n > 3$, unconnected patterns appear, as shown in Fig.4.

Because of these two differences, alternative approaches of verifying the proposed model are required.

4 VERIFICATION OF THE PROPOSED NEAREST NEIGHBOR REFERENCE MODEL

In this section, switched systems theory is adopted to verify the convergence of the angle between a pair of neighboring robots in the three- and four-robot groups.

First, the target enclosure problem is defined.

4.1 Definition of enclosure task

In this paper, the target enclosure task for an n-robot group is defined as follows. The task consists of determining the distance to the target and equalizing the gap angle.

The distance task is

$$E_d = \sum_{i=1}^{n} (r_i \quad \bar{r})^2. \tag{3}$$

The angle equalization task is

$$E_a = \sum_{i=1}^{n} (\;_i \quad \frac{2}{n})^2. \tag{4}$$

Because of these two requirements, the robots are deployed evenly on a circle having a radius of $\bar{r}$.

4.2 Verification using switched system

The results of the switched system are used here. Instead of the graph Laplacian, the Poincaré-Bendixson theorem[3] can be used, but this theorem is generally applicable only to systems with two variables. In contrast, the results of the switched system adopted here can be used to examine the convergence property of a small group of robots.

4.3 Switched systems

A switched system is defined as[7, 11]

$$\dot{x} = f_s(x), \tag{5}$$

where $x \in R^n$ is a continuous state variable, and $\dot{x}$ is its derivative. Furthermore, S is a set of discrete values s, and s is static even if t and/or x change. In this case, reference [11] proves the sufficient condition for the practical asymptotic stability of the switched system. Let $V(x)$ be a continuous differentiable positive definite function. In addition, we assume that a set of positive values $\Omega_\rho = \{x \in R^n : V(x) \quad \rho\}$ is bounded. In this case, the switched system exhibits practical asymptotic stability for any $D \subset \Omega_\rho$ when the following conditions are satisfied.

$$a) \quad \min_{s \in S} \frac{\partial V}{\partial x} f_s(x) < 0, \;\; \forall x \in \Omega_\rho \quad \{0\} \tag{6}$$

$$b) \quad 0 \in Int(C), \tag{7}$$

where $Int(C)$ is the interior of (C). C is given as

$$\begin{aligned} C &= conv(\{f_s(0) : s \in S\}) \\ &= \{\sum_{s\in S} \lambda_s f_s(0) : \lambda s \quad 0, \sum_{s\in S} \lambda_s = 1\}. \end{aligned} \tag{8}$$

We assume that a sufficient time has passed so that all the robots are near their common target. Furthermore, we assume that the distance between the robots and the target is $\bar{r}$, and each robot determines its nearest neighbor using only the angle with respect to its neighbor. In this case, the angle $_i$ between the i-th robot and its reference robot is expressed as follows.

Case 1: $_{i+1} \quad _i, \; _i \quad _{i\ 1}$

$$\frac{d \ _i}{dt} = \frac{b}{2}(\quad _i + \ _{i\ 1}) \tag{9}$$

Case 2: $_{i+1} < \ _i, \; _i \quad _{i\ 1}$

$$\frac{d \ _i}{dt} = \frac{b}{2}(\ _{i+1} + \ _{i\ 1} \quad 2 \ ) \tag{10}$$

Case 3: $_{i+1} \quad _i, \; _i < \ _{i\ 1}$

$$\frac{d \ _i}{dt} = b(\quad _i) \tag{11}$$

Case 4: $_{i+1} < \ _i, \; _i < \ _{i\ 1}$

$$\frac{d \ _i}{dt} = \frac{b}{2}(\ _{i+1} \quad _i) \tag{12}$$

where $b = f/\bar{r}$. In this case, the dynamics of their angles is considered to represent a switched system according to each robot's three angles $_{i\ 1}, \ _i, and \ _{i+1}$.The heading direction d_i of the i-th robot can be described by $_{i\ 1}$ and $_i$ as follows.

$$d_i = \begin{cases} 1 & (\ _i \quad _{i\ 1}) \\ 0 & (otherwise) \end{cases} \tag{13}$$

where "0" and "1" indicate a counterclockwise and clockwise heading direction, respectively. By using equation 13, equations 9-ref(84) are written as follows.

$$\dot{} = A_s \quad + B_s \tag{14}$$

$$= [\ _1 \cdots \ _i \cdots \ _n]^T \tag{15}$$

$$A_{s,i,j} = \begin{cases} \frac{b}{2} d_i & (j = i \quad 1) \\ \frac{b}{2}(d_{i+1} \quad d_i + 1) & (j = i) \\ \frac{b}{2}(1 \quad d_{i+1}) & (j = i + 1) \\ 0 & (otherwise)) \end{cases} \tag{16}$$

$$B_i = \ (d_{i+1} \quad d_i) \tag{17}$$

$$s = \{d_1, \ldots, d_i, \ldots, d_n\} \in \{0, 1\}^n \tag{18}$$

where $_n = 2 \quad \sum_{i=1}^{n\ 1} \ _i$. For simplicity, let $b = 1$ in the remainder of this paper. In the next subsection, we prove the practical asymptotic stability of the system represented by equation 14.

4.4 A four-robot group

In this section, we discuss the practical asymptotic stability of a four-robot system. A four-robot group has 14 control inputs, $s = \{1, 0, 1, 0\}$, $\{1, 0, 0, 1\}$, $\{0, 1, 1, 0\}$, $\{0, 1, 0, 1\}$, $\{0, 0, 1, 1\}$,
$\{1, 1, 1, 0\}$, $\{1, 1, 0, 1\}$, $\{1, 0, 1, 1\}$, and $\{0, 1, 1, 1\}\}$.

When $s = \{1, 0, 0, 0\}$, the result of the left of equation 6 in this case by using equation 16 is $w(\ ) = \ 4 \ ^2 \quad 3 \ _1^2 \ 4 \ _1 \ _2 \quad 3 \ _2^2 + 6 \ (\ _1 + \ _2) + 8 \ _3 \quad 6 \ _1 \ _3 \quad 4 \ _2 \ _3 \ 4 \ _3^2$. Therefore, the maximum of $w(\ )$ in the given range is calculated by a Lagrange multiplier. We rewrite $z(\ ) = \ w(\ )$ as a minimization problem.

The set of constraints representing the control input $s = \{1, 0, 0, 0\}$ is $_1 > \ _4 \wedge \ _2 < \ _1 \wedge \ _3 < \ _2 \wedge \ _4 < \ _3 \wedge \ _1, \ _2, \ _3 > 0, \ _4 > 0$. We define the following functions from this condition by adding equal conditions for convenience.

$$\begin{aligned} g_1(\ ) = 2 \quad 2 \ _1 \quad _2 \quad _3 \quad 0 \\ g_2(\ ) = \ _2 \quad _1 \quad 0 \\ g_3(\ ) = \ _3 \quad _2 \quad 0 \\ g_4(\ ) = \ _1 \quad 0 \\ g_5(\ ) = \ _2 \quad 0 \\ g_6(\ ) = \ _3 \quad 0 \\ g_7(\ ) = \ 2 \ + \ _1 + \ _2 + \ _3 \quad 0 \end{aligned} \tag{19}$$

$$\begin{aligned} \nabla g_1 = [\ 2 \quad 1 \quad 1]^T, \nabla g_2 = [\ 1\ 1\ 0]^T \\ \nabla g_3 = [0 \quad 1\ 1]^T, \nabla g_4 = [\ 1\ 0\ 0]^T \\ \nabla g_5 = [0 \quad 1\ 0]^T, \nabla g_6 = [0\ 0 \quad 1]^T \\ \nabla g_7 = [1\ 1\ 1]^T \end{aligned} \tag{20}$$

Then, the following Karush-Kuhn-Tucker conditions are obtained from $\nabla z(\ ) + \sum_i^7 \nabla g_i(\ ) = 0$.

$$\begin{aligned} 6 \ _1 + 4 \ _2 \quad 6 \ + 6 \ _3 \quad 2u_1 \quad u_2 \quad u_4 + u_8 = 0 \\ 4 \ _1 + 6 \ _2 \quad 6 \ + 4 \ _3 \quad u_1 + u_2 \quad u_3 \quad u_5 + u_7 = 0 \\ 6 \ _1 + 4 \ _2 \quad 8 \ + 8 \ _3 \quad u_1 + u_3 \quad u_6 + u_7 = 0 \\ u_1(2 \quad 2 \ _1 \quad _2 \quad _3) = 0, \ u_1 \quad 0 \\ u_2(\ _2 \quad _1) = 0, \ u_2 \quad 0 \\ u_3(\ _3 \quad _2) = 0, \ u_3 \quad 0 \\ u_4(\quad _1) = 0, \ u_4 \quad 0 \\ u_5(\quad _2) = 0, \ u_5 \quad 0 \\ u_6(\quad _3) = 0, \ u_6 \quad 0 \\ u_7(\ 2 \ + \ _1 + \ _2 + \ _3) = 0, \ u_7 \quad 0 \end{aligned} \tag{21}$$

This equation reveals that the maximum of $w(\ )$ in the given range is $w(\ ) = 0$ at $_1 = \ _2 = \ _3 = \ _4 = \frac{\pi}{2}$.

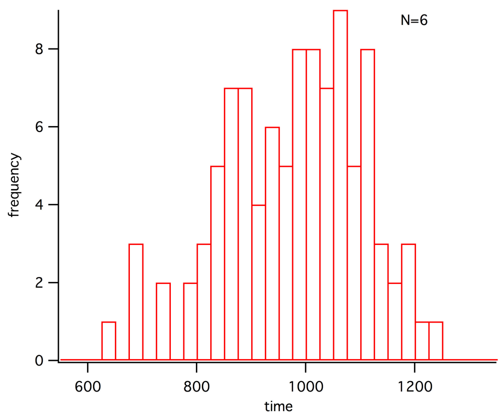

Fig. 5. Time to achieve enclosure task by 6 robots group

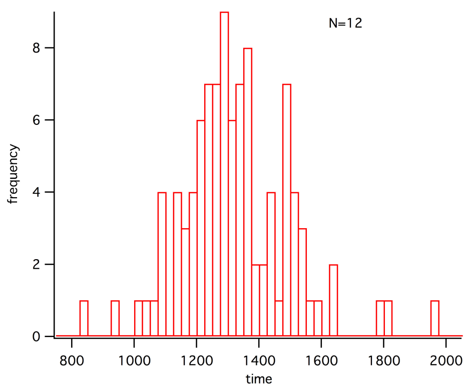

Fig. 6. Time to achieve enclosure for 12-robot group.

Therefore, equation 6 is satisfied when this control signal s is activated.

We verify the maximum of $w(\ )$ for all other s values in a similar manner.

When $s = \{0, 1, 0, 0\}$, $w(\ ) = \ \ 4 \ ^2 \ \ \ 4 \ ^2_1 \ \ \ \ ^2_2$ $2 \ _2 \ _3 \ \ \ 3 \ ^2_3 \ \ \ 2 \ _1(\ _2 + 2 \ _3) + 2 \ (4 \ _1 + \ _2 + 2 \ _3)$. The maximum of $w(\ )$ is 0 at $(\ _1, \ _2, \ _3) = (\frac{\pi}{2}, \frac{\pi}{2}, \frac{\pi}{2})$.

In the same manner as these cases, the maximum of $w(\ )$ in all of the remaining cases, is 0.

Therefore, equation 6 is satisfied for any control input s. Furthermore, $C = \{0\}$ satisfies $0 \in Int(C)$ because $\ _1 = \ _2 = \ _3 = \ _4 = \frac{\pi}{2}$ is a fixed point for which $f_s(\ ) = 0$ for all f_s. Therefore, equation 7 is satisfied.

4.5 Verification of target enclosure task for larger groups

The above discussion shows that the proposed model can achieve angle equalization for a small group. However, we did not provide the proof of the distance task represented by equation 3. In addition, we did not verify the performance for groups of more than four robots. Therefore, in this section, we discuss the ability to achieve target enclosure by using computer simulations.

We examined 3-, 4-, 6-, and 12-robot groups. There was only one target at the origin, and it was assumed that $\bar{r} = 20$. The initial position of a robot was specified inside a 100 100 rectangular region by a 2D uniform random number generator. We counted the time to achieve target enclosure as the time until $E_d + E_a < 0.5$ in equations 3 and 4. This simulation was repeated 100 times for each group size.

Fig.5,6 show the results for the 3-, 4-, 6-, and 12-robot groups, respectively. The x-axis of each graph indicates the time required to achieve enclosure, and the y-axis denotes the frequency. For the three-robot system, the average time required for enclosure is 813.123, and the standard deviation is 125.737. For the four-robot system, the average time is 813.123 and the standard deviation is 125.737. For the six-robot system, the average time is 874.143 and the standard deviation is 96.921. For the 12-robot system, the average time is 1044.371 and the standard deviation is 115.408.

Thus, as the number of robots increases, the time required to achieve target enclosure increases. However, in all the simulations, groups of any size can achieve this task. Therefore, we conclude that any group of fewer than 13 robots can achieve target enclosure.

5 CONCLUSION

In this paper, to achieve a highly scalable target enclosure model, we examined a new reference model based on that of Takayama et al., in which each robot determines its actions according to its nearest neighboring robot. We demonstrated the model's performance using an analytical discussion and a set of computer simulations. Conventional research on target enclosure assumes that a robot can recognize predefined team-mates from among many robots. However, this recognition becomes difficult as the group size increases. In the proposed model, a robot does not need this recognition capability. The results of switched systems theory were applied instead of the graph Laplacian to prove the convergence to an enclosure state because the connectivity of the reference relationship among robots is not maintained. We analytically proved that a group containing fewer than five robots can enclose a target. Computer simulations with n = 3, 4, 6, and 12 suggest that a group of 12 or fewer robots can enclose a target.

REFERENCES

[1] H. Kopka and P. W. Daly, *A Guide to LaTeX*, 3rd ed. Harlow, England: Addison-Wesley, 1999

[2] D. Eppstein, M. S. Paterson and F. F. Yao, On Nearest-Neighbor Graphs, Discrete & Computational Geometry, vol. 17, no. 3, 263-282 (1997)

[3] E.Atlee Jackson, Perspectives of Nonlinear Dynamics 1,Cambridge University Press(1995)

[4] T. Kim and T. Sugie, Cooperative control for target capturing task based on a cyclic pursuit strategy, Automatica, vol. 43, pp. 1426-1431(2007)

[5] Kobayashi Y., Otsubo K. , Hosoe S., Autonomous Decentralized Control of Capturing Behavior by Multiple Mobile Robots,Transactions of the Society of Instrument and Control Engineers, 43(8), 663-671(2007)

[6] Kawakami H., Numerikawa T.,Network-topology Independent Cooperative Target-enclosing Behavior by Swarms of Vehicle,Transactions of the Society of Instrument and Control Engineers,5(12), 688-695(2009)

[8] J. A. Marshall,M. E. Brouvke and B. A. Francis, Formations of Vehicles in Cyclic Pursuit, IEEE Transactions on Automatic Control, vol. 49, no. 11 (2004)

[7] Masubuchi I., Zhai G.,Control of Hybrid Systems-V : Analysis and Control of Switched Systems,Systems, Control and Information,52(1), 25-31(2008)

[8] R. Olfati-Saber, Flocking for Multi-Agent Dynamic Systems: Algorithms and Theory, IEEE Transactions on Automatic Control, vol. 51(3), pp. 401-420, Mar. (2006)

[9] R. Olfati-Saber, J. A. Fax and R. M. Murray, Consensus and Cooperation in Networked Multi-Agent Systems, Proceedings of the IEEE, vol. 95, no. 1, pp. 215-233, Jan. (2007).

[10] Takayama Y., Yamamoto S., Takimoto T., Distributed Formation Control of a Nonholonomic Multi-agent System for Target-enclosing Operations, Proceedings of 9th SICE System Integration Division Annual Conference (2008)

[11] X. Xu and G. Zhai,Some Results on Practical Asymptotic Stabilizability of Switched Systems, 44th IEEE Conference on Decision and Control, 2005 and 2005 European Control Conference. CDC-ECC '05, 3998-4003(2005)

[12] Yamaguchi H., A Cooperative Hunting Behavior by Nonholonomic Mobile Robot Troops,Transactions of the Japan Society of Mechanical Engineers. C, 69(688), 3285-3292(2003)

The Seventeenth International Symposium on Artificial Life and Robotics 2012 (AROB 17th '12),
B-Con Plaza, Beppu, Oita, Japan, January 19-21, 2012

Binary MEMS optically reconfigurable gate array for an artificial brain system

Yuichiro Yamaji and Minoru Watanabe

Electrical and Electronic Engineering
Shizuoka University
3-5-1 Johoku, Hamamatsu, Shizuoka 432-8561, Japan
Email: tmwatan@ipc.shizuoka.ac.jp

Abstract: Optically reconfigurable gate arrays (ORGAs) consisting of a holographic memory, a laser diode array, and a programmable gate array were developed to realize an artificial brain system for robots. In the ORGA, much information or many reconfiguration contexts can be stored in a volume-type holographic memory and can be programmed dynamically onto a programmable gate array at nanosecond-order perfectly in parallel. Therefore, by exploiting the huge storage capacity of the holographic memory and large parallel operations on a programmable gate array, huge parallel brain operations can be executed quickly on an ORGA. This paper presents a proposal of a binary MEMS-interleaving reconfiguration operation on an optically reconfigurable gate array for an artificial brain system.

Keywords: Field programmable gate arrays, optically reconfigurable gate arrays, programmable logic devices.

1 INTRODUCTION

An adult human brain holds more than 100 billion neurons and more numerous synapses connecting them [1]–[3]. To realize an artificial neural network system that can provide performance similar to that of a human brain, a huge number of parallel operations must be executed on an embedded system. In this case, a three-dimensional very large scale integration (VLSI) technology is one candidate.

However, fortunately, the response time of each neuron of a human brain is about 1,000,000 times slower than that of the currently available VLSIs. Therefore, for emulation of a human brain, one neuron circuit can serve 1,000,000 neuron operations. Despite that rapid performance, since the storage capacity and bandwidth of synaptic connections of a human brain are extremely large and broad, respectively, the capabilities of current silicon memories remain insufficient to emulate synaptic weights.

Holographic storage systems are excellent candidates for such human brain systems since three-dimensional holographic memories can easily provide large storage capacity. The density potential reaches V/λ^3, where V denotes the recording volume and λ is the wavelength of the recording light source [4][5]. For example, photorefractive crystal holographic memories $LiNb0_3$ can store 100 bits/μm^2 [6] and can achieve 100 Gbit/in^2 [7]. The area densities are superior to even the latest 32 nm process dynamic random access memory (DRAM) cell with area of 0.039 μm^2 [8].

To date, optically reconfigurable gate arrays (ORGAs) have been developed to realize next-generation large-virtual gate count programmable VLSIs [9]–[12]. An ORGA typically comprises an ORGA-VLSI, a holographic memory, and a laser array. The ORGA-VLSI is a fine-grained gate array, as are field-programmable gate arrays (FPGAs)[13],[14]. Its function is the same as those of currently available FPGAs, but the ORGA-VLSI configuration procedure is executed optically. In an ORGA, many configuration contexts can be stored on a holographic memory that is addressed by a laser array, and which can be implemented dynamically onto the ORGA-VLSI in a very short time [11]. By virtue of those features, the ORGA can achieve numerous virtual gates along with a high-speed nanosecond-order context switching capability. Using these features, vastly numerous synaptic weight operations and neuron operations can be executed. However, although the ORGA architecture presents such advantages, an important issue is its future mass production. The salient cost problem is posed by the laser array. For example, to implement a million reconfiguration contexts onto an ORGA, a million lasers must be implemented onto the ORGA, but a laser array with numerous lasers is invariably expensive. In contrast, other components such as photopolymer holographic memory materials and a standard process ORGA-VLSI are cheap. Therefore, the number of lasers presents an important concern in developing ORGAs.

Recently, a useful microelectromechanical system (MEMS) technology, a digital micromirror device (DMD), was produced by Texas Instruments Inc. [15],[16]. The specifications of a DMD device are presented in Table 1. A photograph of the chip, which consists of 1,024 × 768 mirrors, is portrayed in Fig. 1. Potentially, it can address numerous reconfiguration contexts. Although the response time of the DMD device is slow, many interleaving methods have been proposed to increase the speed of slow response devices, particularly the speed of memory devices [17]–[20].

Therefore, this paper presents a proposal of a binary

Table 1. Specifications of a digital mirror array device.

	0.55 XGA
Resolution	1024 × 768 mirros
Mirror tilt angle	±12°
Mirror size	10.8 μm × 10.8 μm
Package size (inch)	1.6 × 1.25

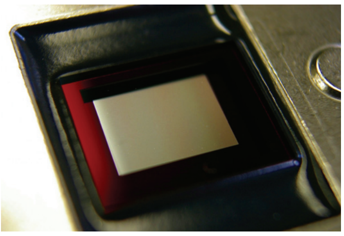

Fig. 1. Photograph of the digital mirror array device.

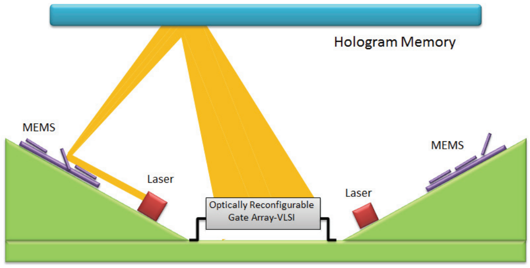

Fig. 2. Novel concept of a MEMS-interleaving optically reconfigurable gate array (ORGA).

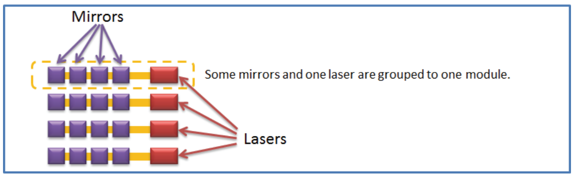

Fig. 3. Laser-MEMS module.

MEMS optically reconfigurable gate array for use in an artificial brain system based on a binary MEMS-interleaving method.

2 BINARY MEMS-INTERLEAVING METHOD

2.1 MEMS device

As explained previously, the MEMS device described in Table 1 and presented in Fig. 1 has 1,024 × 768 tiny mirrors, each having a size of 10.8 × 10.8 μm^2. For example, if the DMD device is implemented and each mirror is used for addressing one configuration context, then 786,432 configuration contexts can be addressed. Therefore, the MEMS is useful for addressing numerous reconfiguration contexts. However, the microsecond-order switching of the MEMS device is not sufficiently fast. In artificial brain operations on an ORGA, the gate array must be reconfigured at nanosecond-order. Therefore, microsecond-order switching speed is insufficient for an artificial brain system.

2.2 Interleaving method

This paper therefore presents a proposal of a binary MEMS-interleaving ORGA designed to achieve a higher reconfiguration frequency than the MEMS switching speed. Up to now, many interleaving methods have been proposed in earlier reports of the literature [17]–[20]. Based on them, the MEMS - laser addressing interleaving method concept was produced. A block diagram of a novel concept of a MEMS-interleaving ORGA is depicted in Fig. 2. In this method, some MEMS mirrors and a laser are grouped to a module, as shown in Fig. 3. In addition, many modules are implemented onto a MEMS-interleaving ORGA. When a certain reconfiguration request arises, firstly, a MEMS mirror angle is changed and then a laser in the same module turns on so that the laser beam is reflected on the MEMS mirror and is incident to a holographic memory. Then, an optical configuration context is read out from the holographic memory and finally, the configuration context is programmed onto an ORGA-VLSI, as shown in Fig. 2. This is a normal reconfiguration procedure. Of course, if a second configuration procedure is executed inside the same module, then the procedure must wait until the first mirror angle is changed to an off state, another mirror angle is changed to an on-state, and the laser turns on again. In this case, the wait period becomes the summation of the MEMS response time and the laser switching period. Consequently, the period of this reconfiguration procedure is longer than the MEMS switching period: no acceleration can be achieved.

However, using the interleaving method, in such a case, a laser of another module, for which the angles of mirrors have already been adjusted and a configuration procedure has been readied, turns on. Furthermore, the lasers on the third module, the fourth module, and so on turn on in sequence. While the other modules function, modules which have completed one configuration procedure start to prepare the next-configuration mirror position. For example, it is assumed that if the respective switching speeds of a laser and MEMS are 10 ns and 10 μs, and 1001 modules which have 1000 mirrors are implemented onto the ORGA, then the ORGA has a million configuration contexts. Each reconfiguration can be executed within 10 ns constantly because mirrors of the idle module can be changed for 10,000 ns while another 1000 modules work for a period 1000 × 10 ns. Therefore, using this method, even a million configuration contexts can be switched by only 1001 lasers.

Up to now, a MEMS-interleaving read operation of a holo-

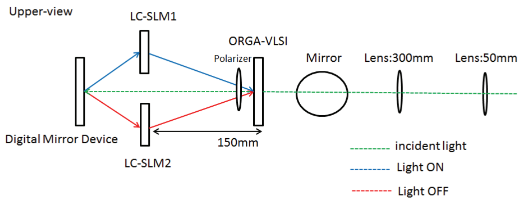

Fig. 4. Experimental system.

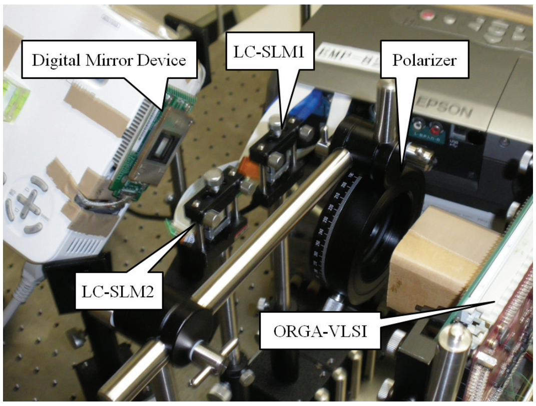

Fig. 5. Photograph of the experimental system.

graphic memory, which can control a MEMS mirror as an ON/OFF switch, has been proposed [21]. In this method, 1000 mirrors could only address 1000 configuration contexts. However, if we can use both angles of ON state and OFF state of each mirror for configurations, the number of mirrors can also be decreased. Therefore, this paper proposes a binary MEMS-interleaving method. In this method, a mirror is used to generate two beams instead of ON/OFF states. Therefore, 1000 mirrors address 2000 reconfiguration contexts. Results show that this system uses fewer lasers and fewer MEMS mirrors.

3 EXPERIMENTAL SYSTEM

For this study, a single-module implementation with two configuration contexts was conducted as the first step for binary MEMS-interleaving ORGA development. Figures 4 and 5 respectively portray a block diagram and a photograph of the binary MEMS-interleaving ORGA. The binary MEMS-interleaving ORGA was constructed by using a 532 nm, 300 mW laser (torus 532; Laser Quantum), a MEMS device, two liquid-crystal spatial light modulators (LC-SLMs), and an ORGA-VLSI. The 1.7-mm-diameter beam from the laser source was expanded six times to 10.2 mm using two lenses of 50 mm focal length and 300 mm focal length. The expanded beam is incident to a MEMS mirror device (Digital Mirror Device). In this case, the mirror state is controlled as with a binary state. If the MEMS mirror is +12°, then the reflected laser beam is incident to the LC-SLM1, which

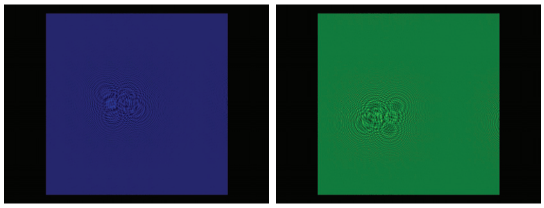

(a) OR circuit (b) AND circuit

Fig. 6. Holographic memory patterns calculated using a personal computer.

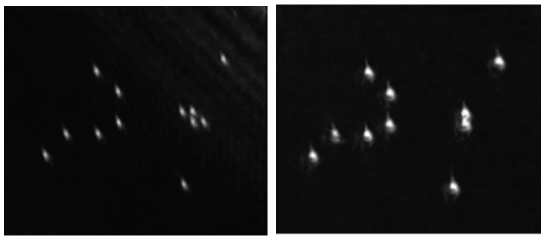

(a) OR circuit (b) AND circuit

Fig. 7. CCD-captured images of configuration context patterns of an OR circuit and an AND circuit.

functions as a holographic memory. However, the reflected laser beam is incident to the LC-SLM2 if the MEMS mirror is -12°. Two holographic memory patterns respectively recording an OR circuit and an AND circuit were calculated as shown in Figs. 6(a) and 6(b) and were displayed on LC-SLM1 and LC-SLM2, respectively. Holographic memory patterns comprised 700 × 700 pixels. The LC-SLMs are a 90° twisted nematic device with a thin film transistor. Each pixel is 12 μm × 12 μm. The first holographic memory pattern shown in Fig. 6(a) is used for +12°-state of a MEMS mirror and the second holographic memory pattern shown in Fig. 6(b) is used for -12°-state of the MEMS mirror. For this implementation, an ORGA was placed 150 mm distant from the LC-SLM. The ORGA had been fabricated using a 0.35 μm triple-metal CMOS process. Photodiodes were constructed between the N-well layer and the P-substrate. The photodiode size and distance between photodiodes were designed as 25.5 × 25.5 μm^2 and as 90 μm to facilitate the optical alignment. The gate array structure is fundamentally identical to that of typical FPGAs. The ORGA-VLSI chip includes 4 logic blocks, 5 switching matrices, and 12 I/O bits. In all, 340 photodiodes were used to program the gate array.

4 EXPERIMENTAL RESULTS

Using the optical system explained above, the binary MEMS-interleaving operation has been confirmed. First, the MEMS mirror angle was adjusted to +12°. Then a laser source was turned on. In this case, the laser beam is reflected on the MEMS mirror. It is then incident to the LC-

SLM1 including a holographic memory pattern of an OR circuit. Finally, the configuration context pattern generated from the holographic memory, as shown in Fig. 7(a), was programmed correctly onto an ORGA-VLSI. For the next experiment, the MEMS mirror angle was adjusted to -12°. Then a laser source was turned on. In this case, the laser beam is reflected on the MEMS mirror. It is incident to the LC-SLM2, including a holographic memory pattern of an AND circuit. Finally, the configuration context pattern generated from the holographic memory pattern shown in Fig. 7(b) was programmed correctly onto an ORGA-VLSI. Therefore, we have demonstrated that one MEMS mirror can address two configuration contexts.

5 CONCLUSION

Optically reconfigurable gate arrays (ORGAs) have been developed to realize artificial brain systems for robots. Nevertheless, conventional ORGAs require many lasers to address the configuration contexts stored on a holographic memory. Such laser arrays with numerous lasers are invariably expensive, which presents an extremely important concern related to their development. Therefore, to address numerous configuration contexts with fewer lasers, this paper has proposed a novel method using a binary MEMS-interleaving ORGA. If a 4,000 $\times$ 4,000 mirror array with 10 μs response time can be used along with about 1,000 lasers that can generate a 10 ns light pulse, then 32 million reconfiguration contexts can be achieved along with 10 ns reconfiguration speed, since two configuration contexts can be addressed by a MEMS mirror. This method can be expected to provide an addressing capability of a billion configuration contexts along with nanosecond-order high-speed configuration capability which is very suitable for emulation of an artificial neural network.

ACKNOWLEDGMENTS

This research was supported by the Accelerating Utilization of University Intellectual Property Program. The VLSI chip in this study was fabricated in the chip fabrication program of VLSI Design and Education Center (VDEC), the University of Tokyo in collaboration with Rohm Co. Ltd. and Toppan Printing Co. Ltd.

REFERENCES

[1] Antonio R. Damasio et al., "The Scientific American Book of the Brain," New York: Scientific American, 1999.

[2] A. L. Hodgkin, A. F. Huxley, "A quantitative description of membrane current and its application to conduction and excitation in nerve," Journal of Physiology, vol 117, pp. 500-544, 1952.

[3] R. H. Adrian, "Conduction Velocity and Gating Current in the Squid Giant Axon," Proceedings of the Royal Society B: Biological Sciences, vol. 189, pp. 81-86, 1975.

[4] P. J. van Heerden, "Theory of optical information storage in solids," Applied Optics, vol. 2, 393–400 (1963).

[5] T. Watanabe, M. Watanabe, "Robust holographic storage system design," Optics Express, Vol. 19, No. 24, pp. 24147-24158, Nov., 2011.

[6] A. Pu and D. Psaltis, "Holographic data storage with 100 bits/μm^2 density," Optical Data Storage Topical Meeting Conference Digest, 48–49 (1997).

[7] G. W. Burr, C. M. Jefferson, H. Coufal, C. Gollasch, M. Jurich, J. A. Hoffnagle, R. Macfarlane, and R. M. Shelby, "Volume holographic data storage at an areal density of 100 Gbit/in^2," Conference on Lasers and Electro-Optics, 188–189 (2000).

[8] N. Butt et al., "A 0.039 μm^2 High Performance eDRAM Cell based on 32nm High-K/Metal SOI Technology," IEEE International Electron Devices Meeting, 27.5.1 – 27.5.4 (2010).

[9] N. Yamaguchi, M. Watanabe, "Liquid crystal holographic configurations for ORGAs," Applied Optics, Vol. 47, No. 28, pp. 4692-4700, 2008.

[10] D. Seto, M. Watanabe, "A dynamic optically reconfigurable gate array - perfect emulation," IEEE Journal of Quantum Electronics, Vol. 44, Issue 5, pp. 493-500, 2008.

[11] M. Nakajima, M. Watanabe, "A four-context optically differential reconfigurable gate array," IEEE/OSA Journal of Lightwave Technology, Vol. 27, No 20, pp. 4460-4470, 2009.

[12] M. Nakajima, M. Watanabe, "A 100-Context Optically Reconfigurable Gate Array," IEEE International Symposium on Circuits and Systems, pp. 2884-2887, 2010.

[13] Altera Corporation, "Altera Devices," http://www. altera.com.

[14] Xilinx Inc., "Xilinx Product Data Sheets," http://www. xilinx.com.

[15] Texas Instruments, "DLP," http://www.ti.com/

[16] Texas Instruments, "Discovery 4000," http://www.ti.com/

[17] B. Khargharia, S. Hariri, M.S. Yousif, "An Adaptive Interleaving Technique for Memory Performance-per-Watt Management," IEEE Transactions on Parallel and Distributed Systems, Vol. 20, Issue 7, pp. 1011 - 1022, 2009.

[18] G.S. Sohi, "High-bandwidth interleaved memories for vector processors-a simulation study," IEEE Transactions on Computers, Vol. 42, Issue 1, pp. 34 - 44, 1993.

[19] C. Song; A. Postula, "Synthesis of custom interleaved memory systems," IEEE Transactions on Very Large Scale Integration (VLSI) Systems, Vol. 8, Issue 1, pp. 74 - 83, 2000.

[20] T. VanCourt, M.C. Herbordt, "Application-Specific Memory Interleaving Enables High Performance in FPGA-based Grid Computations," IEEE Symposium on Field-Programmable Custom Computing Machines, pp. 305-306, 2006.

[21] H. Morita, M. Watanabe, "MEMS interleaving read operation of a holographic memory for optically reconfigurable gate arrays," International Workshop on Applied Reconfigurable Computing, Lecture Notes in Computer Science, Vol. 6578, pp. 242-252, 2011.

Synaptic redistribution and variability of signal release probability at hebbian neurons in a dynamic stochastic neural network

Subha Fernando[1], Koichi Yamada[2]

Nagaoka University of Technology, Niigata 940-2188, Japan
(Tel: 81-258-47-3180, Fax: 81-258-47-9359)

[1]s085160@stn.nagaokaut.ac.jp, [2]yamada@kjs.nagaokaut.ac.jp

Abstract: This paper presents the finding of the research we conducted to evaluate the variability of signal release probability at Hebb's presynaptic neuron under different firing frequencies in a dynamic stochastic neural network. According to our results, synaptic redistribution has improved the signal transmission for the first few signals in the signal train by continuously increasing and decreasing the number of postsynaptic 'active receptors' and presynaptic 'active-transmitters' within a short time period. In long-run at low-firing frequency it has increased the steady state efficacy of the synaptic connection between Hebbian presynaptic and postsynaptic neuron in terms of the signal release probability of 'active-transmitters' in the presynaptic neuron. However, this 'low-firing' frequency of the presynaptic neuron has been identified by the network when compared it to the ongoing frequency oscillation of the network.

Keywords: Dynamic stochastic network, Hebbian neurons, Synaptic redistribution, Release probability

1 INTRODUCTION

As per recent biological findings a synaptic connection between two neurons is strengthened by increasing the number of postsynaptic receptor channels or by increasing the probability of neurotransmitter release at presynaptic neuron. This functional behavior at synapses is varied if long-term plasticity interacts with the short-term depression, Abbott and Nelson [1]. Short-term depression is an activity dependent reduction of neurotransmitters from the readily releasable pool at presynaptic neurons, Zucker [2]. When long-term plasticity interacts with the short-term depression, the effect is called synaptic redistribution. This synaptic redistribution increases the probability of neurotransmitter release at presynaptically; and subsequently increases the efficiency of signal transmission between neurons and decreases presynaptic readily releasable pool size, Abbott and Nelson [1]. Therefore, the high-frequency dependent increase in synaptic response for the first few spikes in the spike-train is caused because of the redistribution of the available synaptic efficacy and not because of the increase of synaptic efficacy at the steady-state. However, at low-firing-frequencies of presynaptic neuron such as < 10 Hz, an increase of synaptic efficacy at steady state has been observed. This increase of synaptic efficacy depends on the short-term plasticity factors such as probability of neurotransmitter release and time constant of recovery, Markram and Tsodyks [3]. Conversely Okatan and Grossberg [4] suggest that pairing of Hebbian neuron to reach the steady state, might be frequency-dependent and as a result the time taken to reach to the steady-state at high-firing-frequency of presynaptic neuron may be longer than at lower-presynaptic-firing frequencies; therefore even there is steady-state increase of the synaptic efficacy at high-firing frequency of presynaptic neuron, it is not well observed due to the effect of short-term synaptic plasticity factors on the synaptic efficacy. Lisman and Spruston [5] have further added that this increase or decrease of synaptic efficacy at steady state is not merely based on spike arriving time to the synapses but also on the level of postsynaptic depolarization, rate of synaptic inputs and the phase of synaptic input relative to the ongoing frequency oscillations.

2 METHOD

Our modeled neuron had thousands of artificial units, named 'transmitters' and 'receptors'. The 'transmitters' in a presynaptic neuron contacted the corresponding 'receptors' in postsynaptic neuron dynamically according to the presynaptic activity by forming an artificial synaptic connection between the two neurons. Therefore, one can presumes that synaptic connection between the presynaptic neuron and postsynaptic neuron in our network as a dynamic connection which mediates the intercommunication between the presynaptic 'transmitters' and the corresponding postsynaptic 'receptors'. Furthermore these artificial units were two-state stochastic computational units which stochastically updated their signal release probability at time t, i.e. $P(t)$, according to the history of their activity by adapting to the mathematical model of Maass and Zador [6] which describes the signal release probability as a function of spike arrival time and the effect of short-term plasticity. The active state of a given artificial unit at a specified time *t* was determined by the release probability at that time and a threshold value *theta* (θ). The threshold θ was updated according to the feedback of a stability promoting mechanism which sensed the neuronal local excitation and the corresponding postsynaptic excitation as defined in eq. (1) and eq. (2). Thus, an artificial unit was in *active state* at time *t* if $P(t) > \theta$ and was allowed to transmit/receive signals between neurons; otherwise it was in *inactive state*.

3 EXPERIMENT

An experiment was conducted on fully connected neural network which had four neurons namely *A*, *B*, *C* and *D*. The neuron *A* and neuron *B* were set to process similar to the long-term plasticity by setting time decay constants to 30 min while neuron *C* and *D* simulated the short-term effects on the network with time decay constants 100 sec and 15 min respectively. We have shown that with this setting of the network, the neurons *A* and *B* formed a Hebbian pairing and was capable of demonstrating the characteristics explained in fundamental learning theories; Hebb's postulate and Stent's anti-Hebbian postulate, see Fernando, Yamada and Marasinghe [7]. The experiment had three stages where each stage consisted of two phases; correlated and uncorrelated, and each phase consisted of two sessions, namely training and testing sessions. In between sessions, a random delay was introduced. Throughout the experiment, the firing frequency of neurons *B*, *C*, and *D* remained in a constant firing rate at 1 Hz while neuron *A* updated its firing frequency accordingly as it was moved from one stage to the other. At stage-1, the firing frequency of neuron *A* was at 1 Hz, at stage-2 it was 2 Hz and stage-3 it was 0.5 Hz. Therefore, comparatively neuron *A* was in high-firing frequency at stage-2 and was in low-firing frequency at stage-3. At stage-1 the network was allowed to stabilize its activity as a one unit because all the neurons were firing at 1 Hz. Signals in terms of sine waves were externally fed to the network through neuron *A* and neuron *B* based on the phase and the session they were in. The phases were named according to the frequency of the sine waves applied to neuron *B*. Throughout the experiment the frequency of the sine waves applied to neuron *A* was at $f'_A = 1\,\text{Hz}$ and the frequency of the sine waves applied to neuron B (f'_B) was randomly selected from interval (0.95, 1.05) Hz at the correlated phase. At the uncorrelated phase f'_B was randomly selected either from interval (0.5, 0.8) Hz or from interval (1.2, 1.5) Hz. At the training sessions, the external signals were fed to the both neurons but at the testing sessions signals were not externally fed to the neuron *B*. At testing sessions, threshold values of all the four neurons were not updated; the threshold values trained at the training sessions were taken as constants at the corresponding testing sessions. Each neuron had 60,000 artificial units which were uniformly distributed between 'receptors' and 'transmitters'; and subsequently 'receptors' were distributed uniformly between 'receptor-groups'. Initially 1% of the receptors in each receptor group and 1% of the 'transmitters' in each neuron were set to an active state. Fig.1 shows the architecture of the network in abstract.

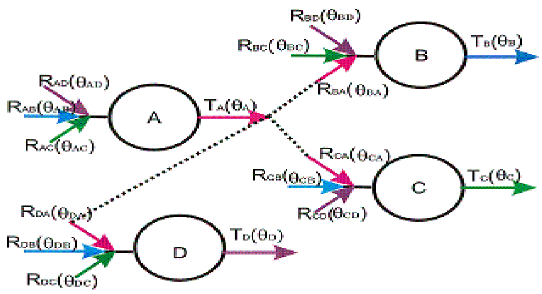

Fig.1. Architecture of the network with dynamic synaptic connections. The developed network had four neurons, each neurons had three 'receptor-groups', and set of 'transmitters'. $T_I(\theta_I)$ denotes the 'transmitters' in neuron *I* and its threshold value. Similarly, $R_{JI}(\theta_{JI})$ denotes the 'receptor-group' in neuron *J* that is contacted by the 'transmitters' in neuron *I*. For simplicity the figure illustrates the communication between the 'transmitters' in neuron *A* with relevant 'receptor-groups' of the postsynaptic neurons only. The dotted connecting lines in the network indicate the dynamicity of the synaptic connection between neurons since it depends on the number of 'active-transmitters' in neuron *A* and their signal release probability, and the number of 'active-receptors' in the relevant receptor-group of the corresponding postsynaptic neuron.

$$\theta_{JI}(t) = f\left(X_{JI}(t)/O_I(t)\right) \qquad (1)$$

$$\theta_I(t) = f\left(O_I(t).(X_{IJ_1}(t) + X_{IJ_2}(t) + X_{IJ_3}(t))\right) \qquad (2)$$

$f(x) = 1/\left(1 - e^{-x}\right)$, $X_{JI}(t) = \left|R_{JI}^{Act}(t)\right| / \left|R_{JI}\right|$, $O_I(t) = \left|T_I^{Act}(t)\right| / \left|T_I\right|$,
$|G|$ – number of components in G, and
$\left|G^{Act}(t)\right|$ - number of acitve components in G at time t

4 RESULTS

The distribution of the number of 'active-transmitters' in neuron *A* and their probability of signal release at each stage, and the distribution of the number of 'active-receptors' in the receptor group R_{BA} that is contacted by the 'transmitters' in neuron *A* through the artificial synaptic connection between neuron *A* and neuron *B* are shown from fig.2 to fig.5.

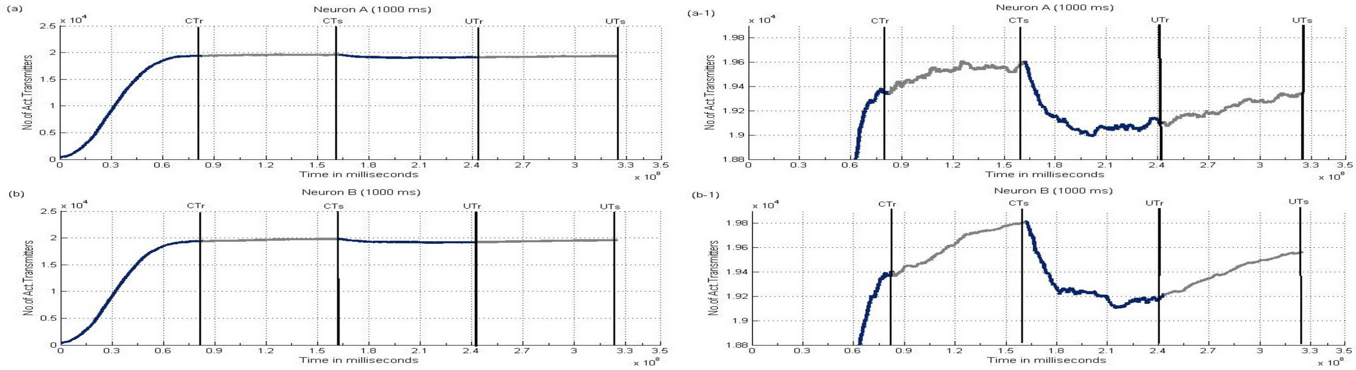

Fig.2. Distributions of 'active-transmitters' in neurons *A* and *B* at stage-1 over the time (a): 'active-transmitters' in neuron *A*, **(b):** 'active-transmitters' in neuron *B*, **(a-1):** Enlarged version of subfigure (a), and **(b-1):** Enlarged version of subfigure (b).

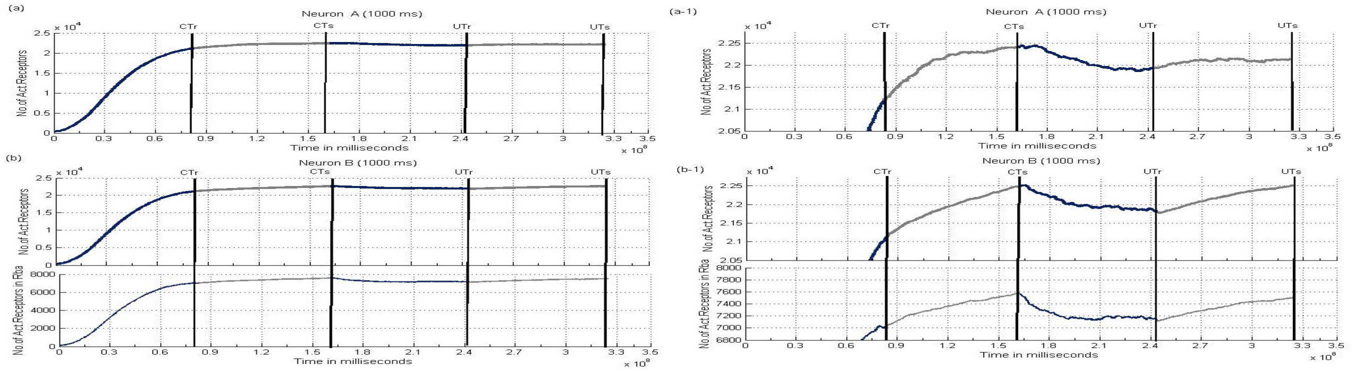

Fig.3. Distributions of 'active-receptors' in neurons *A* and *B* at stage-1 over the time (a): 'active-receptors' in neuron *A*, **(b):** 'active-receptors' in neuron *B* and in R_{BA} respectively, **(a-1):** Enlarged version of subfigure (a), and **(b-1):** Enlarged version of subfigure (b)

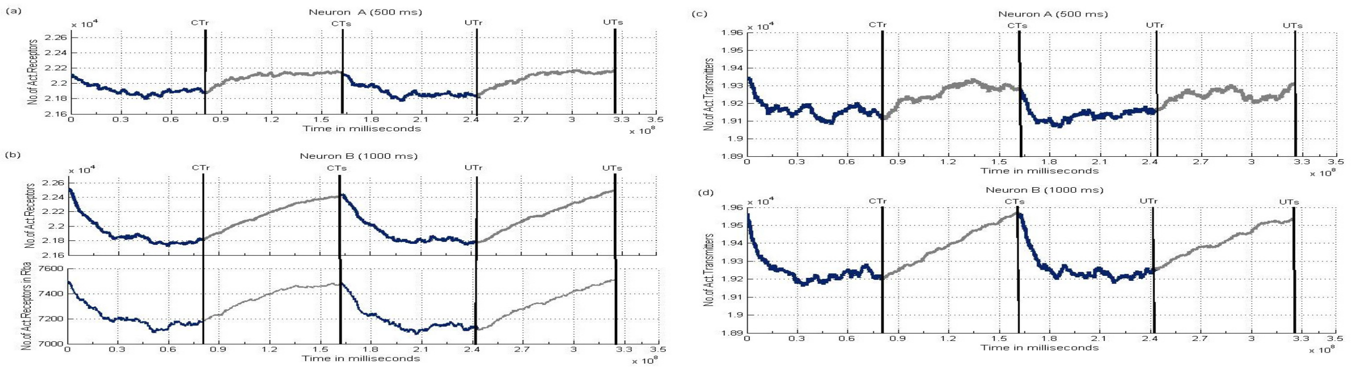

Fig.4. Distributions of active components in neurons *A* and *B* at stage-2 over the time (a): 'active-receptors' in neuron *A*, **(b):** 'active-receptors' in neuron *B* and in R_{BA} respectively, **(c):** 'active-transmitters in neuron *A*, **(d):** 'active-transmitters' in neuron *B*

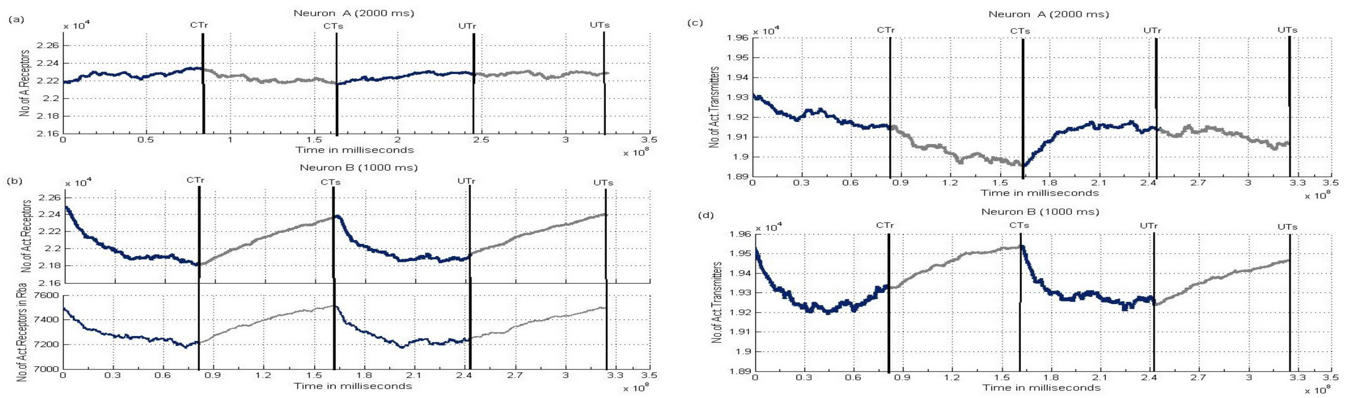

Fig.5. Distributions of active components in neurons *A* and *B* at stage-3 over the time (a): 'active-receptors' in neuron *A*, **(b):** 'active-receptors' in neuron *B* and in R_{BA} respectively, **(c):** 'active-transmitters in neuron *A*, **(d):** 'active-transmitters' in neuron *B*

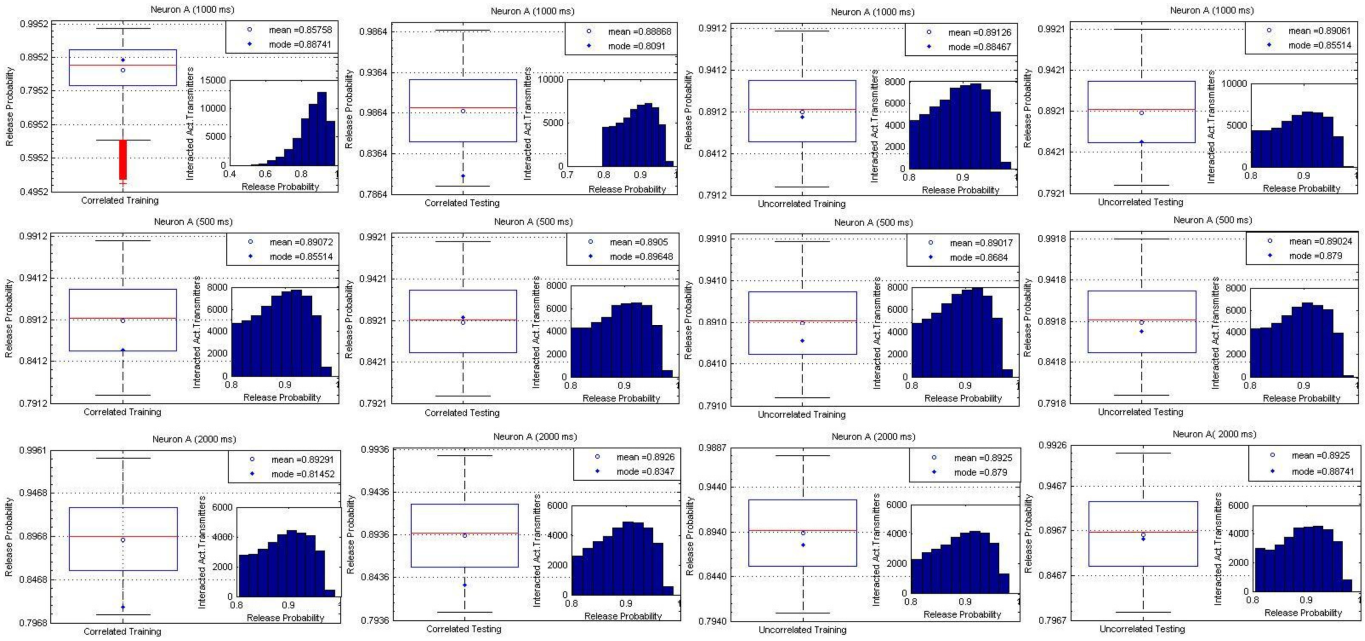

Fig.6. Box plot in each subfigure illustrates the variation of the release probability of the interacted 'active-transmitters' of neuron *A* (i.e., 'active-transmitters' that communicated with 'receptors' in R_{BA} receptor-group during the session). The inner histograms depict the variation of the number of interacted 'active-transmitters' in neuron *A* over the time against the signal release probability at the corresponding session of the stage.

5 DISCUSSION

According to the results of, from fig.2 to fig.5, the increase or decrease of the response of neuron *A* is a continuous insertion and deletion of the presynaptic 'active transmitters; and the redistribution of the number of 'active receptors' of the receptor group R_{BA} in the postsynaptic neuron *B*. Further this dynamic update to the number of presynaptic 'active transmitters' and the number of postsynaptic 'active receptors' in R_{BA} was remained in very short time period, and subsequently presynaptic neuron *A* attained to the steady state. However in long-run we could see that although neuron *A* at high-firing frequency (i.e. at 2Hz in stage-2) increased the number of 'active transmitters', it has not increased the average (mean) signal release probability at the steady state of the synaptic connection compared to when presynaptic neuron *A* fired at low-firing frequency(i.e. 0.5Hz in stage-3, see fig.6). In contrast, at the low-firing frequency of neuron *A,* even though the number of 'active-transmitters' in neuron *A* has decreased (compared to when *A* was at high-firing frequency), the average signal release probability of 'active transmitters' at the steady state has increased, see fig.6. Therefore, synaptic redistribution has improved the transmission for the first few signals in the signal train by dramatically increasing or decreasing the number of postsynaptic 'active receptors'. In long-term at low-firing frequency synaptic redistribution has increased the steady state synaptic efficacy of the synaptic connection (i.e. increase of the signal release probability of 'active-transmitters' in neuron *A*). Further, in our experiment the firing frequency of neuron *A* was always < 10 Hz. Therefore, according to Markram and Tsodyks [3] we were supposed to observe an increase in the efficacy at the synaptic connection between *A* and *B* at all the stages. But, we could observe an increase of the synaptic efficacy only at stage-3, i.e. when neuron *A* was in 0.5 Hz. Therefore the increase or decrease of synaptic efficacy at a steady state may not only base on rate of synaptic inputs but also on the phase of the synaptic input relative to the ongoing frequency oscillations of the network.

REFERENCES

[1] Abbott LF and Nelson SB (2000), Synaptic plasticity: taming the beast, Nature Neuroscience, 3:1178-1183.

[2] Zucker RS (1989), Short-term synaptic plasticity, Annual Reviews of Neuroscience, 12:13-31.

[3] Markram H and Tsodyks M (1996), Redistribution of synaptic efficacy between neocortical pyramidal neurons, Nature, 382:807-810.

[4] Okatan M and Grossberg S (2000), Frequency-dependent synaptic potentiation, depression and spike timing induced by Hebbian pairing in cortical pyramidal neurons, Neural Networks, 13(7): 699-708.

[5] Lisman J and Spruston N (2005), Postsynaptic depolarization requirements for LTP and LTD: a critique of spike timing-dependent plasticity, Nature Neuroscience, 8 (7): 839-841.

[6] Maass W and Zador AM (1999), Dynamic stochastic synapses as computational units, Neural Computation, 11(4): 903-917.

[7] Fernando SD, Yamada K and Marasinghe A (2011), Observed stent's anti-hebbian postulate on dynamic stochastic computational synapses, in Proceedings of International JCNN, pp-1336-1343.

The Seventeenth International Symposium on Artificial Life and Robotics 2012 (AROB 17th '12),
B-Con Plaza, Beppu, Oita, Japan, January 19-21, 2012

Properties of Hopfield model with the zero-order synaptic decay

Ryota Miyata[1], Jun Tsuzurugi[2], Toru Aonishi[1], and Koji Kurata[3]

[1] Interdisciplinary Graduate School of Science and Engineering, Tokyo Institute of Technology,
4259-G5-17, Nagatsuta-cho, Midori-ku, Yokohama-city, Kanagawa, 226-8502, Japan
[2] Faculty of Engineering, Okayama University of Science, 1-1, Ridai-cho, Kita-ku, Okayama-city, Okayama, 700-0005, Japan
[3] Faculty of Engineering, University of the Ryukyus, 1, Senbaru, Nishihara-cho, Nakagami-gun, Okinawa, 903-0213, Japan
(Tel: +81 45 924 5546, Fax: +81 45 924 5546, E-mail: miyata@acs.dis.titech.ac.jp)

Abstract: In this paper, we investigate the effect of synaptogenesis on memories in the brain, using the abstract associative memory model, Hopfield model with the zero-order synaptic decay. Using the numerical simulation, we demonstrate the possibility that synaptogenesis plays a role in maintaining recent memories embedded in the network while avoiding overloading. For the network consisting of 1000 units, it turned out that the minimum decay rate to avoid overloading is 0.02, and the optimal decay rate to maximize the storage capacity is 0.08. We also show that the average numbers of replacement synapses at each learning step corresponding to these two values are 1187 and 21024, respectively.

Keywords: synaptogenesis, zero-order synaptic decay, associative memory, Hopfield model, forgetting process, overloading

1 INTRODUCTION

Memory was considered to consist of three processes: (i) learning and (ii) keeping information in the network, and then, (iii) recalling it when needed. Hopfield model [1], the best-known associative memory model, could reproduce the form of memory in the brain. By changing the synaptic strengths, the model stored memory patterns in the network. Thereafter, this network could retrieve the stored pattern even if given its noisy version. The properties of the associative memory model have been investigated over several decades [1]-[4].

The ordinary Hopfield model has a critical number of memory patterns that can be stably stored, $0.138N$, where N is the system size. The additional learning of new patterns beyond the value overloads the network system, and makes no patterns retrievable [4].

As a matter of fact, the past associative memory model missed the fourth factor of memory, i.e., forgetting old information. If the dynamics of the synaptic strength in the network have decay or saturation, overloading does not occur. The forgetting model, an alternative associative memory model to avoid overloading, was proposed by Mézard et al. [5]. In the forgetting model, every time the network learns a new pattern, the synaptic strength decays in proportion to itself. In this scheme, the old memory traces are erased exponentially with time. However, as yet there is no conclusive experimental evidence for the existence of such a system in the brain.

Recently, it has been reported that synaptogenesis, birth of synapses, continues to take place in certain regions of the postnatal brain including the hippocampal regions [6],[7]. Synaptogenesis, i.e., replacement of old synapses with new ones, seems to be crucial for the formation of neural networks. Thus, it affects neural network functions, especially memory formation. Furthermore, according to the previous neurophysiological experiment, synapses with smaller strength tend to be replaced with higher probability [7]. This raises questions about how this synaptogenesis affects memories in the brain. Should synaptogenesis, which breaks the memory circuit, be a negative factor for memories embedded in the network?

In this paper, we investigate the effect of this synaptogenesis on memories, modeling it mathematically: Hopfield model with the zero-order synaptic decay. In our model, every time the network learns a new pattern, all the synaptic strengths decay a constant value , i.e., decay rate α. This decay process represents the characteristics of the synaptogenesis more exactly than the forgetting model: The smaller synaptic strength is, the more easily synaptogenesis occurs.

From a computational perspective, we demonstrate the possibility that synaptogenesis plays a role in maintaining recent memories embedded in the network while avoiding overloading. Moreover, we show that the storage capacity (maximal number of retrievable patterns in the network) of our model depends on the decay rate. For the network consisting of 1000 units, it turned out that the minimum decay rate to avoid overloading, $\alpha_{\rm min}$, is 0.02, and that the optimal decay rate to maximize the storage capacity, $\alpha_{\rm opt}$, is 0.08. Finally, we show how many synapses are replaced with new ones at each learning step when the decay rate takes these two critical values. For the network consisting of 1000 units, it turned out that the average number of replacement synapses corresponding to $\alpha_{\rm min}$ is 1187, and that corresponding to $\alpha_{\rm opt}$ is 21024.

The Seventeenth International Symposium on Artificial Life and Robotics 2012 (AROB 17th '12),
B-Con Plaza, Beppu, Oita, Japan, January 19-21, 2012

This paper is organized as follows: Section 2 gives a formulation of the zero-order synaptic decay process in the Hopfield model. Section 3 shows the numerical simulation results using our model. Section 4 gives our conclusions.

2 MODELING THE SYNAPTOGENESIS

2.1 Network dynamics

We begin by formulating a recurrent neural network with N units and $N(N-1)$ synapses. We assume that all the units work synchronously at discrete time $t = 1, 2, \cdots$. The network dynamics are determined by

$$s_i(t+1) = \mathrm{sgn}\Big(\sum_{j=1(\neq i)}^{N} J_{ij} s_j(t)\Big), \tag{1}$$

where $s_i(t)$ is the state of unit i at discrete time t. J_{ij} denotes the strength of the synapse connecting unit j to i, and it is symmetrical, i.e., $J_{ij} = J_{ji}$. We assume that the network is assumed to have no self-interaction, $J_{ii} = 0$. In Eq.(1), the sign function $\mathrm{sgn}(x)$ denotes the next state $s_i(t+1)$ of unit i as

$$\mathrm{sgn}(x) = \begin{cases} \;\;1 & x \geq 0, \\ -1 & \text{otherwise.} \end{cases} \tag{2}$$

According to Eqs.(1) and (2), when a weighted sum of its inputs $\sum_{j=1(\neq i)}^{N} J_{ij} s_j(t)$ exceeds 0 (threshold), the next state $s_i(t+1)$ becomes 1, representing the neuronal firing. On the other hand, $s(t+1) = -1$ represents that the unit is not firing at $t+1$. Equation (1) defines the time evolution of the system state. For any symmetric connection matrix $J_{ij}; J_{ij} = J_{ji}$, the network system has finite possible states. Starting from any arbitrary initial state, the system state of the Hopfield model always reaches an equilibrium or a periodic solution, and the period is known to be no more than 2.

2.2 Associative memory with the zero-order synaptic decay

Each element ξ_i^μ of the μ-th memory pattern $\boldsymbol{\xi}^\mu$, which is stored in the network, takes ± 1, and is generated independently with the probability,

$$\mathrm{Prob}[\xi_i^\mu = \pm 1] = \frac{1}{2}. \tag{3}$$

Here, we consider the following learning dynamics of the synaptic strength J_{ij}, reflecting the characteristics of the synaptogenesis. The synapse which has its small strength $\|J_{ij}\|$ tends to be replaced with new ones. We assume that if the synaptogenesis occurs, the new synapses rebuilds the connection to all the units except for self-coupling. We use the following synaptic decay process, which is equivalent to the above replacement procedure of synapses.

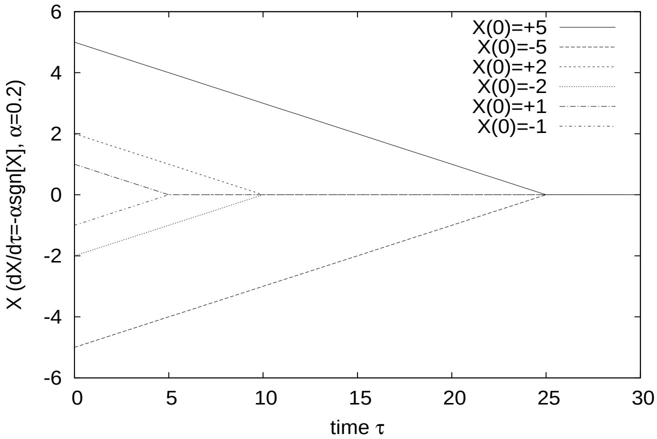

Fig.1: Dynamics of the zero-order synaptic decay process (the second term of the right-side Eq.(4), ordinate). The quantity τ (abscissa) denotes time. Convergence speed (i.e., decay rate $\alpha = 0.2$) is constant with the sign and the value of $X(\tau)$. Thus, the smaller the synaptic strength is, the faster it converges to zero.

$$\Delta J_{ij} = \xi_i^\mu \xi_j^\mu - \alpha \mathrm{sgn}[J_{ij}], \tag{4}$$

where α is the decay rate. The index μ of ξ_i^μ denotes the learning step. Note that $\mu = 1$ corresponds to the latest learning step. The larger serial number $\mu > 1$ signifies that pattern $\boldsymbol{\xi}^\mu$ was stored earlier than $\boldsymbol{\xi}^1$.

The first term of the right-side Eq.(4) denotes the Hebbian learning in the Hopfield model. Every time the network learns a new pattern $\boldsymbol{\xi}^\mu$, J_{ij} is increased by ξ_i^μ and ξ_j^μ, not depending on the global structure of the state.

On the other hand, the second term of Eq.(4) denotes the zero-order synaptic decay process, modeling the synaptogenesis. Every time the network learns a new pattern, J_{ij} decays at a constant rate α. Figure 1 illustrates the dynamics of the second term of Eq.(4). The smaller the synaptic strength is, the faster it converges to zero. On the other hand, the larger synaptic strength takes more time to converge to zero. If the sign of the synaptic strength inverts ($J_{ij} \geq 0$ and $J_{ij} + \Delta J_{ij} < 0$, or $J_{ij} \leq 0$ and $J_{ij} + \Delta J_{ij} > 0$), then the synaptic strength is reset ($J_{ij} = 0$). This procedure represents that the synapse with the small strength dies and the new one is born.

3 NUMERICAL SIMULATION

For simplicity, we assumed that neither number of units nor synapses does change over time in the following numerical simulation. The network consisting of 1000 neurons learned M memories, $\boldsymbol{\xi}^1, \cdots, \boldsymbol{\xi}^M$, one by one. The maximum value of M was set to 400 (i.e., $0.4N$), which was much larger than the critical value of the ordinary Hopfield model: $0.138N$. All of the initial synaptic strengths were set to zero, $\{J_{ij}\} = 0$. Every time the network learned a memory pattern, the synaptic strength $\|J_{ij}\|$ was weaken by the decay rate α. The smaller $\|J_{ij}\|$ is, the more frequently synaptogenesis occurs, i.e., $J_{ij} = 0$. Each stored pattern $\boldsymbol{\xi}^\mu$ ($\mu = 1, 2, \cdots, M$) was given as a initial state $\boldsymbol{s}(0)$ in the network dynamics. We assume that the system is forced to stop when the present state $s_i(t)$ equals the second to last one $s_i(t-2)$ in the network dynamics, considering the periodical solution of the network dynamics. Simulations were carried out on a computer by varying the decay rate α.

First, we investigate how many patterns are retrievable in the network with the zero-order synaptic decay. Because the synaptic decay process implies erasing the old memory traces gradually, a limit exists on the number of retrievable patterns. As the criterion of successful recall, we used the overlap m^μ between the μ-th memory pattern $\boldsymbol{\xi}^\mu$ and the stationary system state $\boldsymbol{s}$:

$$m^\mu = \frac{1}{N}\sum_{i=1}^{N} \xi_i^\mu s_i. \tag{5}$$

If $m^\mu \geq 0.8$, we regarded $\boldsymbol{\xi}^\mu$ as the retrievable pattern, and we counted it. The results are shown in Fig.2, which plots the number of retrievable patterns as a function of the number of stored ones, M. According to Fig.2, we see that the larger the decay rate α is, the earlier forgetting starts: for $\alpha = 0$, forgetting started at around $M = 140$; for $\alpha = 0.2$, it started at around $M = 30$; for $\alpha = 0.4$, it started at around $M = 10$. Our interest is in the properties of the network when the number of retrievable patterns is nearly saturated. The network for $\alpha = 0$, i.e., the ordinary Hopfield model could not recall any memory pattern when $M > 220$. On the other hand, for $\alpha \neq 0$, the Hopfield model with the zero-order synaptic decay could recall an almost constant number of memories when $M > 40$.

Second, we investigate how old stored patterns are retrievable in the network with the zero-order synaptic decay. Figure 3 plots the overlap m^μ as a function of the learning step μ for two values of the decay rate α. As shown in Fig.3, only the recent memories could be recalled correctly ($m^\mu \geq 0.8$). Moreover, Fig.3 predicts a phase transition phenomenon depending on the learning step μ: If the learning step is smaller than the storage capacity ($\mu < \psi$), the memory retrieval state ($m^\mu \approx 1$) is stable. On the other hand, if the learning step exceeds the storage capacity ($\mu > \psi$), the memory retrieval state becomes unstable, and the so-called spin-glass state ($m^\mu \approx 0$) appears.

Figures 2 and 3 show the number of retrievable patterns depends on the decay rate α. Thus, we investigate two critical decay rate: the minimum value to avoid overloading, $\alpha_{\min}$, and the optimal value to maximize the storage capacity, α_{opt}. Figure 4 illustrates the storage capacity ψ of the zero-order decay model as a function of the decay rate α. It turned out

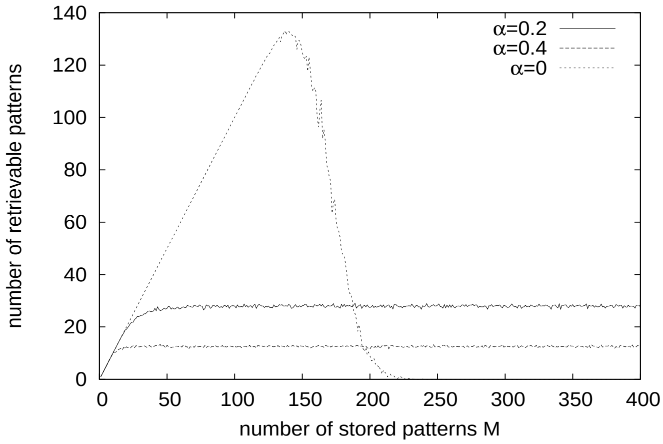

Fig.2: Relation between the number of stored patterns, M (abscissa) and that of retrievable patterns (ordinate). Each curve is the average of 10 samples ($N = 500$), illustrating how many memories so far learned were remembered. Solid curve is the result of the zero-order synaptic decay model with $\alpha = 0.2$, dashed one is that with $\alpha = 0.4$, and dotted one is that with $\alpha = 0$, i.e., the ordinary Hopfield model.

that for $N = 1000$, the minimum decay rate to avoid overloading ($\alpha_{\min}$, a point at the intersection of the abscissa with the solid curve in Fig.4) is 0.02. The optimal decay rate to maximize the storage capacity (α_{opt}, a point at the peak of the solid curve in Fig.4) is 0.08.

Finally, we approximate the number of replacement synapses at each learning step corresponding to these two critical decay rates. In other words, we investigate how many synapses should be replaced with new ones on average at each learning step to avoid overloading, or to maximize the storage capacity. Figure 5 plots the number of replacement synapses at each learning step for $\alpha_{\min}$ and α_{opt}, respectively. According to Fig.5, as time advances, the number of replacement synapses becomes nearly constant. Averaged by the number of stored patterns, M, the minimum number of replacement synapses at each learning step to avoid overloading is 1187, which corresponds to $\alpha_{\min}$. Moreover, the optimal one to maximize the storage capacity is 21024, which corresponds to α_{opt}.

4 CONCLUSION

In order to investigate the effect of synaptogenesis on memories embedded in the neural network, we proposed the Hopfield model with the zero-order synaptic decay. Using the numerical simulation, we demonstrated the possibility that synaptogenesis plays a role in maintaining recent memories while avoiding overloading. Moreover, it turned out that the storage capacity of this model depends on the decay rate α, which corresponds to the number of replacement

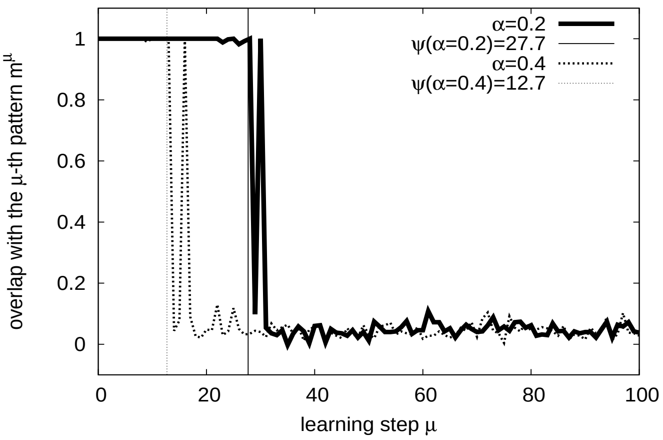

Fig.3: Overlap m^{μ} (ordinate) between the stationary system state $\boldsymbol{s}$ and the μ-th memory pattern $\boldsymbol{\xi}^{\mu}$ (abscissa). Note that $\mu = 1$ represents the most recently learned pattern, and that the larger μ is, the older $\boldsymbol{\xi}^{\mu}$ is. $N = 1000$, and $M = 400$. Heavy solid and dashed curves are the results when $\alpha = 0.2,\ 0.4$ (1 sample), respectively. Vertical solid and dashed curves are the storage capacity ψ when $\alpha = 0.2,\ 0.4$, respectively. Both values are taken from the results shown in Fig.4.

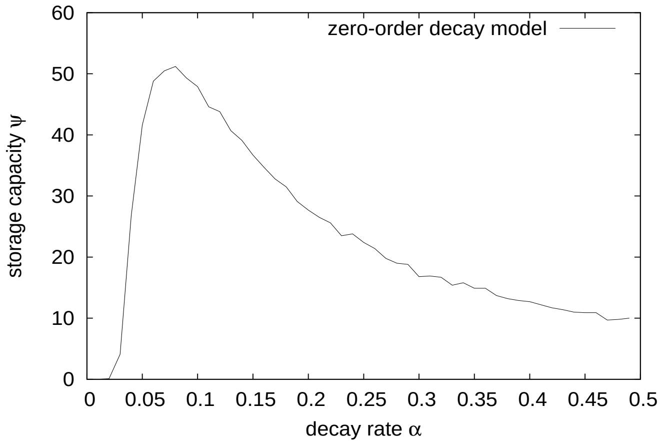

Fig.4: Storage capacity ψ of the zero-order decay model as a function of the decay rate α. Each curve shows the average of 10 samples ($N = 1000$, $M = 400$).

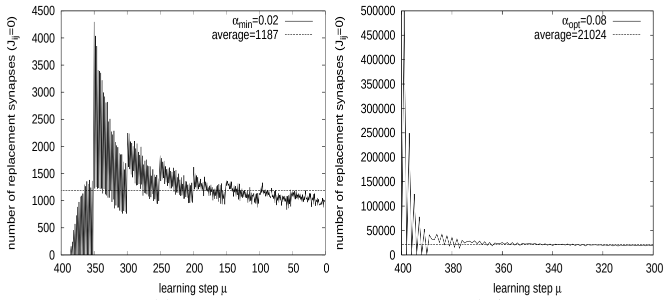

(I) (II)

Fig.5: Number of replacement synapses (ordinate) at each learning step μ (abscissa). Dashed line in each figure shows the averaged number of replacement synapses by the number of stored pattern M. $N = 1000$, and $M = 400$ (1 sample). (I) Minimum number of replacement synapses to avoid overloading corresponding to $\alpha_{\rm min}$. (II) Optimal number of replacement synapses to maximize the storage capacity corresponding to $\alpha_{\rm opt}$.

synapses. For $N = 1000$, the minimum decay rate to avoid overloading, $\alpha_{\rm min}$, is 0.02 and it is equivalent to an average of 1187 synapses replaced with new ones at each learning step. The optimal decay rate to maximize the storage capacity, $\alpha_{\rm opt}$, is 0.08 and it is equivalent to an average of 21024 synapses replaced with new ones.

The followings are our possible future works: (i) Since early times, it has also been reported that neurogenesis continues to take place in certain regions of the postnatal brain including the hippocampal regions[8],[9]. Moreover, it has been also demonstrated using numerical simulations that the Hopfield model with unit replacement, mathematically-modeled neurogenesis, avoids overloading and keeps the recent memories[10]. Thus, comparison of the properties between the synaptogenesis (zero-order synaptic decay model) and the neurogenesis (unit replacement model) should be done. (ii) Characteristics of the Hopfield model depend largely on how items are encoded in the pattern vectors to be stored. When most of the components of encoded patterns to be stored are inactivated and only a small share of the components are activated, the encoding scheme is said to be sparse[2],[3]. Investigation how synaptogenesis affects the sparsely encoded network will be done.

REFERENCES

[1] J. J. Hopfield, *Proceedings of the National Academy of Sciences*, 79:2554-2558, 1982.

[2] S. Amari, *Neural Networks*, 2:451-457, 1989.

[3] M. Okada, *Neural Networks*, 9(8):1429-1458, 1996.

[4] D. J. Amit, H. Gutfreund, and H. Sompolinsky, *Physical Review Letters*, 55(14):1530-1533, 1985.

[5] M. Mézard, J, P. Nadal, and G. Toulouse, *Journal of Physique*, 47:1457-1462, 1986.

[6] K. Tominaga-Yoshino, S. Kondo, S. Tamotsu, and A. Ogura, *Neuroscience Research*, 44:357-367, 2002.

[7] N. Yasumatsu, M. Matsuzaki, T. Miyazaki, J. Noguchi, and H. Kasai, *The Journal of Neuroscience*, 28(50):13592-13608, 2008.

[8] J. Altman, *Science*, 135:1127-1128, 1962.

[9] P.S. Eriksson, E. Perfilieva, and T. Bjork-Eriksson et al., *Nature Medicine*, 4(11):1313-1317, 1998.

[10] A. Date and K. Kurata, *Artificial Life and Robotics*, 12:291-294, 2008.

[11] M. Ishikawa, *Neural Networks*, 9(3):509-521, 1996.

The Seventeenth International Symposium on Artificial Life and Robotics 2012 (AROB 17th '12),
B-Con Plaza, Beppu, Oita, Japan, January 19-21, 2012

Pulse-type hardware neural networks circuit for PWM servo motor control

Ken Saito[1], Masahiko Kato, Minami Takato, Yoshifumi Sekine[2] and Fumio Uchikoba[3]

Nihon University, Chiba 274-8501, Japan
(Tel: +81-47-469-5343, Fax: +81-47-467-9504)

[1]kensaito@eme.cst.nihon-u.ac.jp
[2]ysekine@ecs.cst.nihon-u.ac.jp
[3]uchikoba@eme.cst.nihon-u.ac.jp

Abstract: This paper presents the pulse-type hardware neural networks circuit (P-HNNC) which could control pulse width modulation (PWM) servo motor of robots. Basic components of P-HNNC were pulse-type hardware neuron model (P-HNM). P-HNM generated oscillatory patterns of electrical activity such as living organisms. Basic components of the P-HNM corresponding to the cell body circuit, the axon circuit and the synaptic circuit. P-HNM had the same basic features of biological neurons such as threshold, refractory period, spatio-temporal summation characteristics and enabled the generation of continuous action potentials. P-HNM was constructed by MOSFETs without any inductors could be integrated by CMOS technology. As a result, we showed that P-HNNC could control the PWM servo motor from 0 to 180 degrees. Same as the living organisms, P-HNNC realized the control of PWM servo motor without using any software programs, or A/D converters.

Keywords: Pulse-type Hardware Neuron Model, Neural Networks, Servo Motor, Humanoid Robot.

1 INTRODUCTION

Programmed control by a microcomputer has been the dominant system among the robot control. However, some advanced studies of artificial neural networks have been paid attention for applying to the robot control. A lot of studies have reported both on software models and hardware models [1-3]. For example, oscillatory patterns of artificial neural networks have been used to operate movement of the robot. Oscillatory patterns of electrical activity are ubiquitous feature in nervous systems. Living organisms use several oscillatory patterns to operate movement, such as swallowing, heart rhythms, and so on [4]. To clarify oscillatory patterns, coupled neural oscillators are paid attention. Synchronization phenomena or bifurcation phenomena of coupled neural oscillators have been studied using the Hodgkin-Huxley model or the Bonhoeffer-van der Pol model. Therefore, the synchronization phenomenon of the coupled neural oscillators using mathematical neuron models has proposed for generating the oscillatory patterns of living organisms [5-7]. However, using the mathematical neuron models in large scale neural networks is difficult to process in continuous time because the computer simulation has been limited by the computer performance, such as the processing speed and memory capacity. In contrast, using the hardware neuron model is advantageous because even if a circuit scale becomes large, the nonlinear operation can perform at high speed and process in continuous time. Therefore, the construction of a hardware model that can generate oscillatory patterns is desired. The hardware ring coupled oscillators have already been studied as a system which can demonstrate the various oscillatory patterns and the synchronization phenomenon [8, 9]. The neural networks need various oscillatory patterns. For this reason, the ring coupled oscillators is expected to be a structural element of the cellular neural networks. However, most of the hardware models contain the inductor in circuit architecture [8-11]. If the system contains the inductor on the circuit system, it is difficult to implement the system to a CMOS IC chip.

We are studying about implementation of hardware neural networks controlling system to robot system. Previously, we proposed the pulse-type hardware neural networks which could generate the locomotion patterns to actuate the micro robot [12].

This paper presents the pulse-type hardware neural networks circuit (P-HNNC) which can control pulse width modulation (PWM) servo motor of robots. P-HNNC generates oscillatory patterns of electrical activity such as living organisms. P-HNNC is constructed by MOSFETs without inductor can be integrated by CMOS technology.

2 PWM SERVO MOTOR

Fig. 1. shows the example of pulse waveform to actuate the PWM servo motor. It is necessary to output the pulse waveform to control the servo motor.

Table 1. shows the pulse specifications of servo motor. The specifications were measured the control signal by oscilloscope.

It is shown that if the P-HNNC can output the waveform

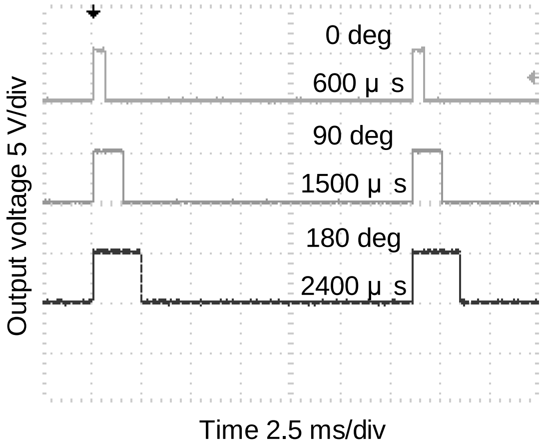

Fig. 1. Pulse waveform to actuate the servo motor

Table 1. Pulse specifications of servo motor (Hitec Multiplex Japan HSR-8498HB)

Pulse period	16040 μs
peak-to-peak voltage	5.04 V
motion range	0 to 180 degree
increase of pulse width per degree	10 μs
minimum pulse width (0 degree)	600 μs
maximum pulse width (180 degree)	2400 μs

such as shown in **Fig. 2.** satisfying the specifications of **Table 1.** the PWM servo motor can be control.

3 PULSE-TYPE HARDWARE NEURAL NETWORKS CIRCUIT

P-HNMs were used for the basic elements of the P-HNNC. P-HNMs consisted of a cell body model, synaptic model and axon model.

3.1 Neural networks

Fig. 2. shows the schematic diagram of P-HNNC. In the figure, C indicates cell body model, A indicates axon model and synapse indicates synaptic model. The cell body model were connected cascade, where n $(1 \le n \le 24)$ was number of cell body model. In addition, the axon model were connected cascade, where m $(1 \le m \le 136)$ was number of axon model. The cell body model and axon model were connected cascade such as ring neural networks. In the case of inputting the single external trigger pulse to C_1, the pulse propagated the ring neural networks with delay. If the delay of cell body model and axon model could set as 100 ms/number, 24 cell body model and 136 axon model could realize the pulse period (16040 μs) of PWM servo motor. In addition, n-th cell body model was connected to synaptic model. The synaptic model outputted the pulse waveform

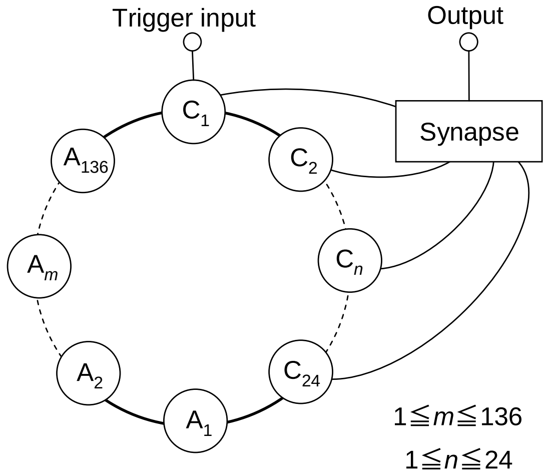

Fig. 2. Schematic diagram of pulse-type hardware neural networks circuit

which could control the PWM servo motor. The pulse width could vary from 600 μs to 2400 μs by switching the synaptic weights (1 or 0).

3.2. Pulse-type hardware neuron model

Fig. 3. shows the circuit diagram of n-th $(1 \le n \le 24)$ stage of cell body model. The cell body model consisted of a voltage control type negative resistance and an equivalent inductance, membrane capacitor C_{Mn}. The voltage control type negative resistance circuit with equivalent inductance consisted of n-channel enchantment-mode MOSFET M_{C1n}, p-channel enchantment-mode MOSFET M_{C2n}, and voltage source V_A, resistors R_{Mn}, R_{Gn}, and a capacitor C_{Gn}. The cell body model had the negative resistance property which changed with time like a biological neuron, and enabled the generation of a continuous action potential v_{Cn} by a self-excited oscillation and a separately-excited oscillation. Moreover, the cell body model could switch between both oscillations by changing V_A. The separately-excited oscillation occurred by direct-current voltage stimulus or pulse train stimulus. The circuit parameters of cell body model were as follows: C_{Mn}=1.8 nF, C_{Gn}=0.8 nF, R_{Mn}=10 kΩ, R_{Gn}=390 kΩ, R_{an}=20 kΩ, R_{bn}=15 kΩ, $M_{C3n}, M_{C4n}, M_{C5n}$: W/L=1. The voltage source were V_A=3.3 V, V_{DD}=5 V. The input current of n-th stage of cell body model was i_{cn-1} which was the output of (n-1)-th stage of cell body model. The output voltage n-th stage of cell body model was v_{cn}

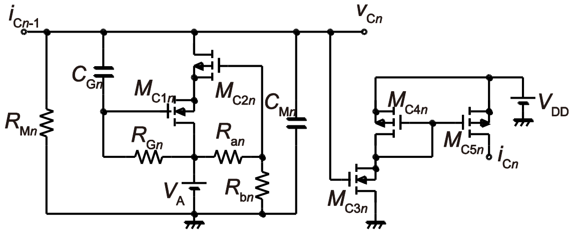

Fig. 3. Circuit diagram of cell body model

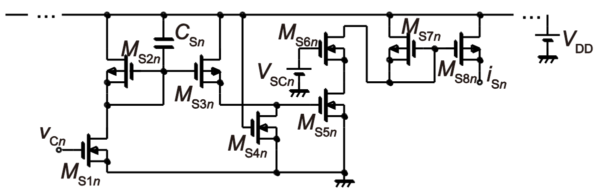

Fig. 4. Circuit diagram of synaptic model

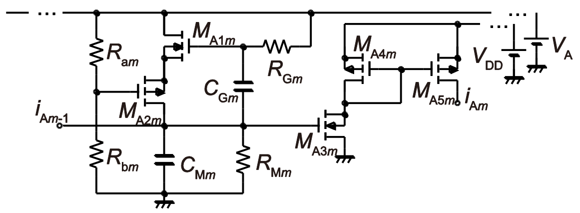

Fig. 5. Circuit diagram of axon model

which was the input voltage of synaptic model.

Fig. 4. shows the circuit diagram of n-th $(1 \le n \le 24)$ stage of synaptic model. The synaptic model spatio-temporal summated the outputs of cell body models according with synaptic weights. Synaptic weights were controlled by the voltage source V_{SCn}. In this paper, the synaptic weights were set as 1 or 0. The circuit parameters of synaptic model were as follows: C_{Sn}=1 pF, M_{S1n}:W/L=3, M_{S2n}, M_{S3n}, M_{S7n}, M_{S8n}:W/L=1, M_{S4n}:W/L=0.25, M_{S5n}:W/L=5, M_{S6n}:W/L=0.2. The voltage source was V_{DD}=5 V.

Fig. 5. shows the circuit diagram of m-th $(1 \le m \le 136)$ stage of axon model. The axon models were connected cascade. The axon model was active distributed constant line which had the threshold function and waveform shaping function. The input current of m-th stage of axon model was $i_{Am\text{-}1}$ which was the output of (m-1)-th stage of axon model. The circuit parameters of axon model were as follows: C_{Mm}=1.8 nF, C_{Gm}=0.8 nF, R_{Mm}=10 kΩ, R_{Gm}=390 kΩ, R_{am}=20 kΩ, R_{bm}=15 kΩ, M_{A3m}, M_{A4m}, M_{A5m}: W/L=1. The voltage sources were V_A=3.3 V, V_{DD}=5 V.

Fig. 6. shows the example of output waveform of P-HNNC. The simulation results of output waveform were given by PSpice. In the figure, angles of the PWN servo motor were 0, 90, 180 degree where pulse period was 630, 1490, 2390 μs, respectively. The output waveform was generated by waveform generator inputting the output waveform given by PSpice. It is shown that P-HNNC can output the waveform to actuate the PWM servo motor such as **Fig. 1.**

Fig. 7. shows number of neurons vs. pulse width and angle of servo motor. In the figure, solid circles indicate the pulse width, open circles indicate angle of servo motor and solid line indicates the theoretical line. This figure shows

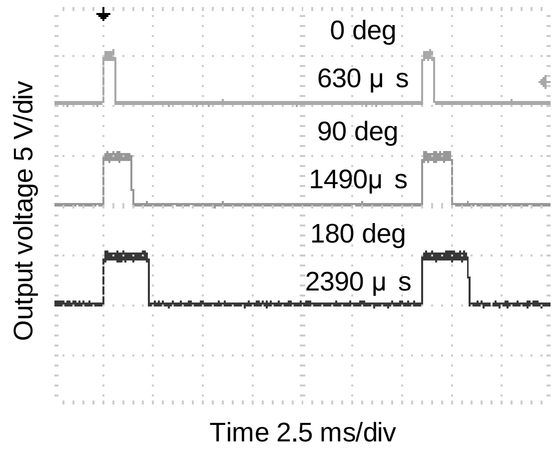

Fig. 6. Example of output waveform of P-HNNC

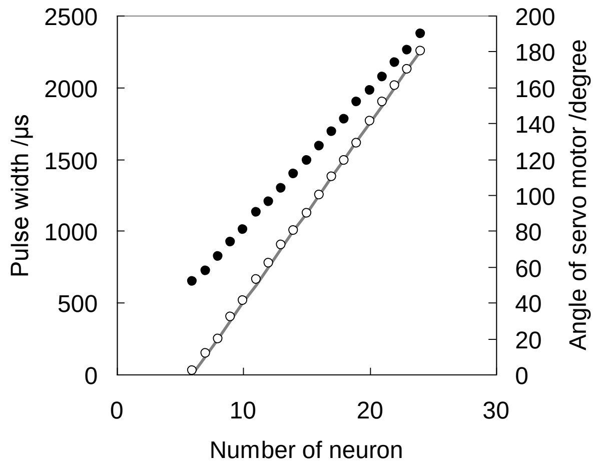

Fig. 7. Number of neuron vs. pulse width and angle of servo motor

that our P-HNNC can change the pulse width of output waveform by changing the number of neurons and controlled the PWM servo motor.

4 CONCLUSION

In this paper, we proposed pulse-type hardware neural networks circuit which could control pulse width modulation servo motor of robots. As a result, we showed that pulse-type hardware neural networks circuit could control the PWM servo motor. P-HNNC realized the PWM servo motor control without using any software programs, or A/D converters.

In the future, we will integrate pulse-type hardware neural networks circuit to the humanoid robot.

ACKNOWLEDGEMENTS

This study was supported by Nihon University Academic Research Grant (Total research, "11-002"), JSPS

KAKENHI (23760243). We appreciate the support.

REFERENCES

[1] Matsuoka K (1987), Mechanism of Frequency and Pattern Control in the Neural Rhythm Generators, Biological Cybernetics 56, pp. 345-353

[2] Ikemoto T, Nagashino H, Kinouchi Y, Yoshinaga T (1997), Oscillatory Mode Transitions in a Four Coupled Neural Oscillator Model, International Symposium on Nonlinear Theory and its Applications:561-564

[3] Nakada K, Asai T, Amemiya Y (2003), An Analog CMOS Central Pattern Generator for Interlimb Coordination in Quadruped Locomotion. IEEE Transaction on Neural Networks 14, pp.1356-1365

[4] Delcomyn F (1980), Neural basis of rhythmic behavior in animals, Science, vol.210, pp.492-498

[5] Tsumoto K, Yoshinaga T, Aihara K and Kawakami H (2003), Bifurcations in synaptically coupled Hodgkin-Huxley neurons with a periodic input, International Journal of Bifurcation and Chaos, vol.13, no.3, pp.653-666

[6] Tsuji S, Ueta T, Kawakami H and Aihara K (2007), Bifurcation analysis of current coupled BVP oscillators, International Journal of Bifurcation and Chaos, vol.17, no.3, pp.837-850

[7] Tsumoto K, Yoshinaga T, Iida H, Kawakami H and Aihara K (2006), Bifurcations in a mathematical model for circadian oscillations of clock genes, Journal of Theoretical Biology, vol.239, no.1, pp.101-122

[8] Endo T and Mori S (1978), Mode analysis of a ring of a large number of mutually coupled van del Pol oscillators, IEEE Trans. Circuits Syst., vol.25, no.1, pp.7-18

[9] Kitajima H, Yoshinaga T, Aihara K and Kawakami H (2001), Burst firing and bifurcation in chaotic neural networks with ring structure, International Journal of Bifurcation and Chaos, vol.11, no.6, pp.1631-1643

[10] Yamauchi M, Wada M, Nishino Y, and Ushida A (1999), Wave propagation phenomena of phase states in oscillators coupled by inductors as a ladder, IEICE Trans. Fundamentals, vol. E82-A, no.11, pp.2592-2598, Nov

[11] Yamauchi M, Okuda M, Nishino Y and Ushida A (2003), Analysis of Phase-Inversion Waves in Coupled Oscillators Synchronizing at In-and-Anti-Phase, IEICE Trans. Fundamentals, vol. E86-A, no.7, pp.1799-1806, July

[12] Okazaki K, Ogiwara T, Yang D, Sakata K, Saito K, Sekine Y, Uchikoba F (2011), Development of Pulse Control Type MEMS Micro Robot with Hardware Neural Network. Artificial Life and Robotics, vol16, pp.229-233,

The Seventeenth International Symposium on Artificial Life and Robotics 2012 (AROB 17th '12),
B-Con Plaza, Beppu, Oita, Japan, January 19-21, 2012

Power saving parameter learning for light power control in public space

Hiroaki Obana[1], Hirokazu Miura[1], Noriyuki Matsuda[1], Hirozumi Kaneko[1],
Fumitaka Uchio[1], Hirokazu Taki[1]

[1]Wakayama University, Wakayama 640-8510, Japan

[1]is-staff@sys.wakayama-u.ac.jp

Abstract: This paper describes a parameter learning system for light energy saving control. It is very important to control the light system efficiently because the large electric energy consumer is the light system. In the home light control, so far, the brightness sensor system which controls each light has been developed. However it controls each light independently, the multiple light control system doesn't work well. There are a lot of lights in even a single room of the office or the school. Furthermore, user requirements for lighting intensity are different according to user locations in the room. Therefore, in order to control each light properly, we must calculate optimal brightness pattern quickly. In this study, we propose the lighting system to determine the brightness of the lighting system using genetic algorithms in public spaces. This system solves the trade-off between the user satisfaction and the energy saving.

Keywords: lighting, energy conservation, usability, sensor network, genetic algorithm

1 INTRODUCTION

Recently, promotion of energy efficiency regulations for greenhouse gas emissions has become active to address global warming issues. Therefore, the saving energy is closely watched in the home and office. The targets of energy saving are the lighting, the air conditioning, and the consumer electronics etc. Among them, it is very important to control the light system efficiently because the large electric energy consumer is the light system [1]. So, the lighting energy saving is desirable. In the home light control, so far, the brightness sensor system which controls each light has been developed. However it controls each light independently, the multiple light control system doesn't work well in the home. In the public space, such as the office and the school, the light control is achieved by more simple way which is switched on-off by detecting a human or comparing the brightness sensor with the fixed threshold value. Several works on the lighting control system providing a comfortable space for the end user and reducing power consumption in public space has been studied[2], [3]. There are a lot of lights in even a single room of the office or the school. Furthermore, user requirements for lighting intensity are different according to user locations in the room or the purpose. Therefore, in order to control each light properly, we must calculate optimal brightness pattern quickly. This problem is combinational optimization problem.

In this study, we propose the lighting system to determine the brightness of the lighting system using genetic algorithms (GA) in public spaces. This system solves the trade-off problem between the user satisfaction and the energy saving. Considering the sunlight, the total of power and the user requirement simultaneously, the lighting intensity must be controlled adequately. The genetic algorithm can solve this combinational optimization problem that decides the brightness of all lightings. To apply GA to control the light system, the genetic code is defined as the power level and brightness for each light. We considered the total electric power in a room and the amount of the differences between current and desired brightness of each light, to select good genes. In our method, fitness function is defined as the sum of these values, and gene is selected so that the function is minimized.

2 LIGHT POWER CONTROL SYSTEM

2.1 System configuration

Fig. 1 shows the lighting system configuration in this study. This system consists of the illuminance sensor, dimmable lighting and management PC. The end users have mobile device and can send the user preference information on brightness to management PC. Then, the desired brightness of each illumination is determined by gathering the user preference information. This system adjusts the brightness of each illumination near the desired brightness and uses the genetic algorithm to determine the optimal lighting pattern. If the environment changes, the desired brightness of each illumination is changed and the optimum lighting pattern of each illumination is determined again.

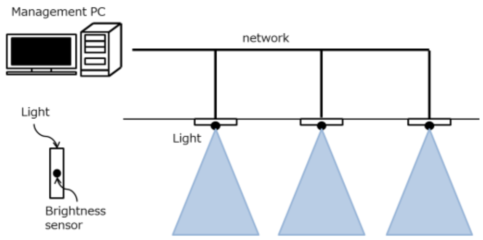

Fig. 1. Lighting system

2.2 Method to determine the optimal lighting pattern

This system uses the genetic algorithm to determine the optimal lighting pattern. The genetic algorithm is learning algorithm designed to model the biological mechanisms of genetic. This algorithm is superior to efficiently obtain the optimal solution. Therefore, the genetic algorithm has been shown to be effective systems for energy management plan [4], [5]. This section describes the flow of our system making use of genetic algorithm. Our system consists of the following 4 steps and repeats these steps to decide an adequate brightness. In the first step, we provide a plurality of individual. Fig. 2 shows the one example of an individual. The individual has a lot of gene. The gene has the value of power level and is prepared number of lighting in the room. The power level is divided by 8 intensities from level 1 to level 8 ,which is linked to the electric power and the brightness(in Table 1). In the second step, children's individuals are made with combination of the individuals. This process is called crossover. Then, in the third step, the outstanding individuals are selected from a collection of children's individuals. This process is called selection. The selection is used for the fitness function to evaluate whether the superior individual. This study used the following objective function,

$$F_n = W_{average} * Ld_{average} \qquad (1)$$

$$W_{average} = \frac{\sum_{i=0}^{L_{number}} w_i + 1}{L_{number}} \qquad (2)$$

$$Ld_{average} = \frac{\sum_{i=0}^{L_{number}} Ld_i}{L_{number}} \qquad (3)$$

$$Ld_i = \begin{cases} 0 & (Lc_i - Lt_i \geq 0 \quad and \quad Llv = 1) \\ |Lc_i - Lt_i| & (otherwise) \end{cases} \qquad (4)$$

where L_{number} is the number of lights. Fitness function F_n is defined as the multiplication of the total electric power in a room and the amount of the differences between current and desired brightness of each light, and the individual is selected so that the function is minimized. $W_{average}$ is the average of electric power to control all lighting(in eq.2). Ld_i represents the absolute value of the difference between current and desired brightness of each illumination. But, if the current brightness exceeds the desired brightness and the power level is level 1, this value is 0. In the final step, the selected individuals may mutate. This is mutation process.

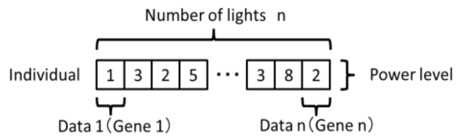

Fig. 2. One example of an individual

Table 1. Electric power and brightness

	Electric power	Brightness
Level 1	0 W	0 lx
Level 2	1 W	60 lx
Level 3	3 W	210 lx
Level 4	5 W	270 lx
Level 5	7 W	333 lx
Level 6	9 W	390 lx
Level 7	11 W	466 lx
Level 8	13 W	542 lx

3 PERFORMANCE EVALUATION

In order to verify the effectiveness of the proposed method in this study, we evaluated our system by computer simulation. This section shows our simulation environment and the results which is the brightness of each illumination and the number of generations created till the performance converges to the optimal solution.

3.1 Simulation Environment

Fig. 3 shows the simulation environment. The room of simulation environment has 12 lights which. Fig. 4 shows the coefficient representing the influence of the brightness from their neighbors. This coefficient is used to calculate the brightness considering indirect light. In this study, this coefficient calls the brightness coefficient. The brightness considering indirect light is calculated by summing up the multiplication of the brightness and the brightness coefficient. The specification of the PC performs simulation has a Core2Duo CPU, 3.0GHz memory and Windows7 OS. We evaluated our method in three environments where user requirement for lighting intensity are different. In the first environment, user requirements are uniformly distributed, in other words all requirements are equal. The second one is heterogeneous model, where the requirements are partially different. In the final environment, user requirement changes according to elapsed time.

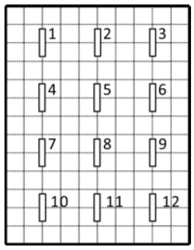

Fig. 3. Room of Simulation environment

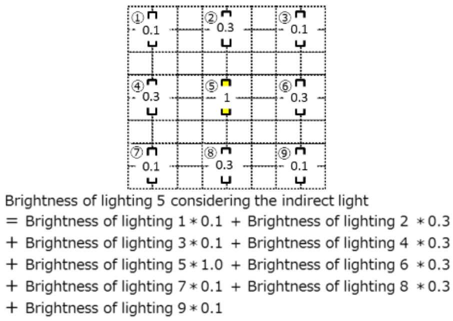

Fig. 4. Illuminance coefficient

Table 2. Parameters of Genetic Algorithm

	Number	Method
Initial individual	20	Random
Selection	10	Elitism
Crossover	20	Uniform crossover
Mutation probability	0.03	Random

3.2 SIMULATION RESULTS

3.2.1 Case 1: All requirements are equal

In the first environment, user requirement are uniformly distributed, in other words all requirements are equal. Table 3 shows the power level and brightness of each illumination. Table 4 shows the value of the optimal solution and the electric power. Fig. 5 shows the number of generations which is necessary to converge to the optimal solution. The simulation result shows that our method can satisfy the brightness of user requirements and reduce energy consumption. From table 3, the maximum difference among current brightness and desired brightness is about 37(lx). There is no problem because human eye cannot recognize such a difference. [6]. From Fig.5, the number of generations converges to the optimal solution in the first environment is the 158 generation and the convergence time is less than one second.

Table 3. Power level and brightness

Lighting Number	Power Level	Current Brightness	Desired Brightness
1	Level 4	402 lx	400 lx
2	Level 3	432 lx	400 lx
3	Level 4	402 lx	400 lx
4	Level 3	399 lx	400 lx
5	Level 2	363 lx	400 lx
6	Level 3	399 lx	400 lx
7	Level 3	399 lx	400 lx
8	Level 2	363 lx	400 lx
9	Level 3	399 lx	400 lx
10	Level 4	402 lx	400 lx
11	Level 3	432 lx	400 lx
12	Level 4	402 lx	400 lx

Table 4. Optimal solution and electric power

Optimal solution	Electric power
54.2	40 W

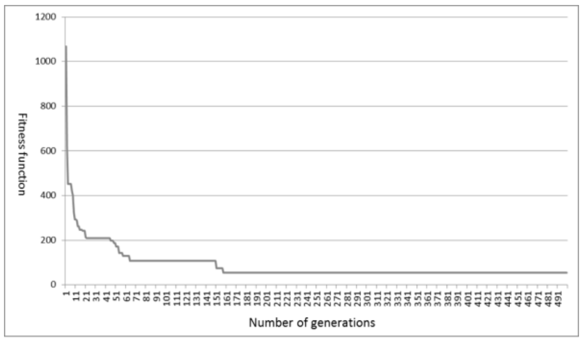

Fig. 5. Fitness function of generations

3.2.2 The requirements are partially different

The second environment is heterogeneous model, where the requirements are partially different. Table 5 shows the power level and brightness of each illumination. Table 6 shows the value of the optimal solution and the electric power. Fig. 6 shows the number of generations which is necessary to converge to the optimal solution. The simulation result also shows that our method can satisfy the brightness of user requirements and reduce energy consumption. But, there are great difference between current and desired brightness of lighting 9 and lighting 11. This is because the low desired brightness lighting is located next to the high desired brightness lighting. The number of generations converges to the optimal solution in the second environment is 3208 generation and the convergence time is less than one second, which is same as the case in the first environment.

Table 5. Power level and brightness

Lighting Number	Power Level	Current Brightness	Desired Brightness
1	Level 3	412 lx	400 lx
2	Level 3	427 lx	400 lx
3	Level 4	414 lx	400 lx
4	Level 7	595 lx	600 lx
5	Level 1	418 lx	400 lx
6	Level 4	399 lx	400 lx
7	Level 2	385 lx	400 lx
8	Level 4	445 lx	400 lx
9	Level 1	267 lx	200 lx
10	Level 5	396 lx	400 lx
11	Level 2	345 lx	400 lx
12	Level 5	378 lx	400 lx

Table 6. Optimal solution and electric power

Optimal solution	Electric power
111.2	44 W

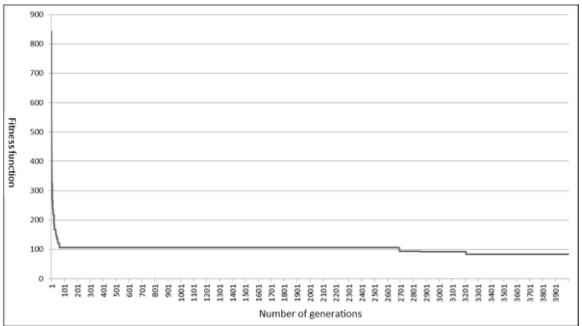

Fig. 6. Fitness function of generations

3.2.3 The end-user move in the room

In the third environment, user requirement changes according to elapsed time. One end-user moves as in Fig. 7 and requires 400[lx]. Fig. 8 shows the electric power of the user position. The simulation result shows that lighting intensities are adjusted adaptively according to varied demands.

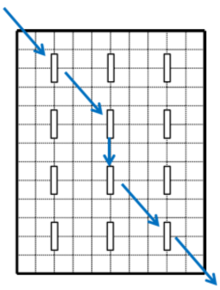

Fig. 7. Transfer pathway of the user in the room

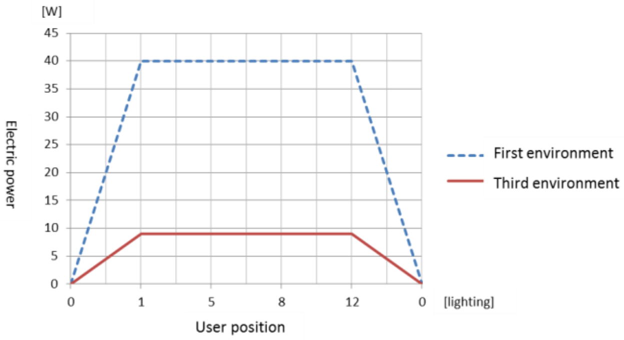

Fig. 8. Electric power of the user position

4 DISCUSSION

In summary, we propose the power saving control method for the lighting system to determine the brightness of the lighting system using genetic algorithms in public spaces. The simulation results in three environments show that the brightness provided by our method can satisfy the user requirements and reduce energy consumption. In the future, we would like to implement our method in a light power control system.

REFERENCES

[1] CHAN ALS LAM JC (1997), Energy audits and surveys of air-conditioned buildings. Proc.JSME International Symposium on Optimization and Innovative Desin(OPID97)

[2] Ono K, Miki M, Yonezawa M (2010), Autonomous Distributed Optimization Algorithm for Intelligent Lighting System (in Japanese). The transactions of the Institute of Electrical Engineers of Japan. C, A publication of Electronics, Information and System Society 130(5), 750-757

[3] Shimoda H, Obayashi F (2008), Energy Saving in Office Buildings and Productivity Lighting (in Japanes e). The transactions of the Institute of Electrical Engin eers of Japan. C, A publication of Electronics, Informa tion and System Society 128(1), 2-5

[4] W.Huang, H.N.Lam (1997), Using Genetic algorit hms to optimize controller parameters for HVAC syste ms. Energy and Buildings 26, 277-282

[5] Obara S, Kudo K (2003), Multiple-purpose Oper ational Planning of Fuel Cell and Heat Pump Compou nd System using Genetic Algorithm (in Japanese). The transactions of The Society of Heating, Air-Conditioni ng and Sanitary Engineers of Japan 91, 65-74

[6] Shikakura T, Morikawa H, Nakamura Y (2001), Research on the Perception of Lighting Fluctuation in a Luminous Offices Environment. J.Illum Engng Inst J pn 85(5), 346-351

The Seventeenth International Symposium on Artificial Life and Robotics 2012 (AROB 17th '12),
B-Con Plaza, Beppu, Oita, Japan, January 19-21, 2012

Control of flock behavior by using tau-margin -Obstacle avoidance and reformation-

Tatsuya Kon[1], Akira Yokokawa[2], and Kazuyuki Ito[3]

[1,3]Hosei University, Tokyo 184-8584, Japan
[2]SANYO Electric Co., Ltd., Osaka 574-8534, Japan
(Tel: 81-42-387-6093, Fax: 81-42-387-6381)

[1] 10r6114@stu.hosei.ac.jp, [2] akira.yokokawa@sanyo.com, [3] ito@hosei.ac.jp

Abstract: In this paper, we address the control of flock behavior using the time to contact called the tau-margin. Recently, swarm intelligence has attracted considerable attention, and it has been applied to control various agents. The Boid theory proposed by Craig Reynolds (1987) is one such application. In ecological psychology, it is considered that animals perceive the time to contact with an object, instead of the distance to the object. In this study, we developed a simulator that simulates the dynamics of mobile agents and their visual system. We embedded modified Boid rules in which the tau-margin is considered instead of the distance. Our simulation results show the realization of flock behavior. In addition, we observe separation to avoid obstacles and reformation to pass through a narrow space.

Keywords: tau-margin, boid, flock behavior

1 INTRODUCTION

Recently, swarm intelligence has attracted considerable attention, and it has been applied to control various agents [1-7].

The Boid theory proposed by Craig Reynolds [1] is one such application. In this theory, we can simulate flock behavior by using three simple rules: separation, alignment, and cohesion. Therefore, the Boid theory was used in various conventional areas.

However, Boids are significantly different from real creatures. Thus, we cannot explain the mechanism of flock behavior of real creatures by using this theory. The difference lies in the information utilized for realizing flock behavior. In the Boid theory, information about the distances among agents is employed. However, most animals have no distance sensor and hence cannot perceive precise distance. Thus, most animals cannot utilize the rules of Boid.

On the other hand, in ecological psychology, it is considered that animals perceive the time to contact with an object, instead of the distance to the object [8]. This time to contact is called the tau-margin and is obtained from the apparent size of the object and its temporal change.

In our previous work, we assumed that the flock behavior of animals was realized by using the tau-margin. Moreover, we tried to realize flock behavior using the tau-margin instead of the distance [9]. However, there were no obstacles and the size of all the agents was the same. Therefore, the discussion on the validity of control using the tau-margin was restricted.

In this paper, we propose modified Boid rules in which the tau-margin is employed instead of the distance. We discuss the validity and effectiveness of this method by using obstacles and many agents whose sizes are different from each other.

2 TAU-MARGIN

In ecological psychology, it is considered that animals perceive the time to contact with an object, instead of the distance to the object. This time to contact is called the tau-margin. Fig. 1 shows the tau-margin when an object is approaching.

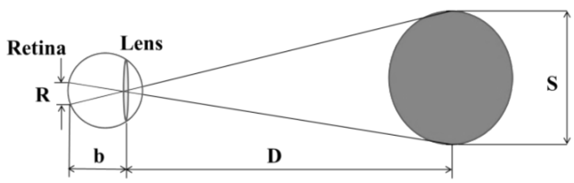

Fig. 1. Tau-margin

S is the diameter of the object, and D is the distance from the object to the crystalline lens. The distance from the crystalline lens to the retina is b.

In this case, the diameter of the retinal image of the object, R, is given by equation (1).

$$R = \frac{bS}{D} \tag{1}$$

By differentiating equation (1), we obtain equation (2).

$$\frac{d}{dt}R = \dot{R} = -\frac{bS}{D^2}\dot{D} \tag{2}$$

From equations (1) and (2), tau-margin τ is given by equation (3)

$$\frac{R}{\dot{R}} = \frac{\frac{bS}{D}}{-\frac{bS}{D^2}\dot{D}} = -\frac{D}{\dot{D}} = \tau \tag{3}$$

Equation (3) indicates that the time to contact $D/\dot{D}$ can be determined from the apparent size and its temporal change. In other words, the tau-margin is obtained from visual information instead of distance information.

3 FLOCK BEHAVIOR

In this section, we realize flock behavior by applying modified Boid rules using the tau-margin.

3.1 Model

We employ agents moving on the horizontal $x-y$ plane. To simulate the movement of the agents, we employ equation (4).

$$m\frac{d^2\mathbf{x}(t)}{dt^2} + C\frac{d\mathbf{x}(t)}{dt} = \mathbf{F} \tag{4}$$

m is the mass of an agent, and $\mathbf{x}$ is a position vector in the $x-y$ plane. C is the air resistance coefficient. $\mathbf{F}$ is the impellent force of the agent.

3.2 Modified Boid rules

We modify the conventional Boid rules by using the tau-margin instead of the distance. Boid theory consists of the three rules of separation, alignment, and cohesion. The modified rules are as follows:

<Separation>

Implement force to separate is given by equations (5) and (6), such that

$$F_x = -\cos\theta \cdot Kp \cdot \frac{1}{\tau} \tag{5}$$

$$F_y = -\sin\theta \cdot Kp \cdot \frac{1}{\tau} \tag{6}$$

where Kp is the proportional gain. F_x and F_y are impellent forces in the x and y directions, respectively. τ is the minimum tau-margin among neighboring objects. θ is the angle to the object that has the minimum tau-margin from the *x* axis, as shown in Fig. 2 (anticlockwise is positive).

When an object approaches the agent, τ converges to 0. Therefore, the implement force to avoid collision is generated by equations (5) and (6).

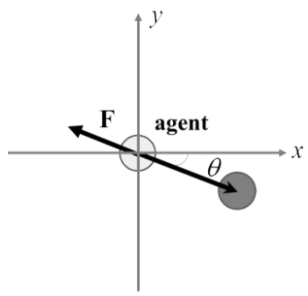

Fig. 2. Separation

<Alignment>

Implement force for alignment is given by equations (7) and (8).

$$F_x = -\cos\theta \cdot Kp \cdot \tau \tag{7}$$

$$F_y = -\sin\theta \cdot Kp \cdot \tau \tag{8}$$

When a neighbor object moves away from the agent, τ of the object has a negative value. Therefore, the behavior to follow the object is realized, as shown in Fig. 3.

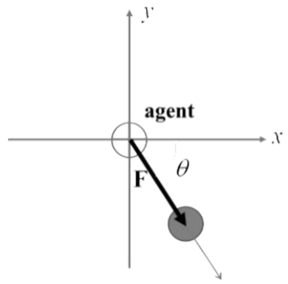

Fig. 3. Alignment

< Cohesion>

Implement force for cohesion is given by equation (9) and (10).

$$F_x = \cos\varphi \cdot Fc \tag{9}$$

$$F_y = \sin\varphi \cdot Fc \tag{10}$$

Fc is a positive constant. φ is an angle to the center of gravity of the apparent size of visible objects, as shown in Fig. 4. From equations (9) and (10), it can be found that the agent moves to the center of the flock by a constant force.

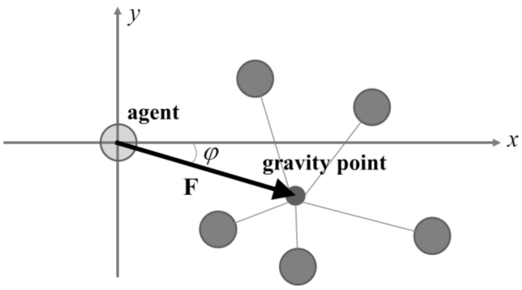

Fig. 4. Cohesion

<Selection of rule>

In the conventional Boid theory, a suitable rule is selected from separation, alignment, and cohesion, on the basis of distance. In contrast, in this study, we select a suitable rule on the basis of the tau-margin, details of which are provided in section 4.

4 SIMULATION

We employ one circular leader agent and nine circular follower agents. The leader agent has a radius of 0.5 m, and the followers' body size is set at random, with a radius within the range from 0.3 m to 2.5 m. Each agent has one eye, and its view angle ranges from -135° to +135°. The distance from the crystalline lens to the retina is 0.02 m. The mass of each body is 5 kg. The air resistance coefficient is $C = 1.8 \times 10^{-5}$. The proportional gain is 50, and Fc is 30.

In case of $0 < \tau \leq 5$, the rule for separation, in case of $-30 < \tau \leq 0$, the rule for alignment, and, in other cases, the rule for cohesion are selected.

4.1 Task 1: Avoiding an obstacle

4.1.1 Outline of simulation

We set agents on the left side of the field, a leader robot on the right side of the agents, and an obstacle (2.5m in radius) on the right of the leader robot. The task of the leader robot is to move to the right, avoiding the obstacle. The implement force of leader robot is applied to move to the right. The rule of separation is the only one employed; the rules of alignment and cohesion are not used. The other agents follow the leader by using modified Boid rules.

In this simulation, an agent is not aware of the positions and the actual sizes of the other agents; moreover, it cannot distinguish between the agents and the obstacles. Only the apparent size and its temporal change are employed for determining the tau-margin.

4.1.2 Simulation result

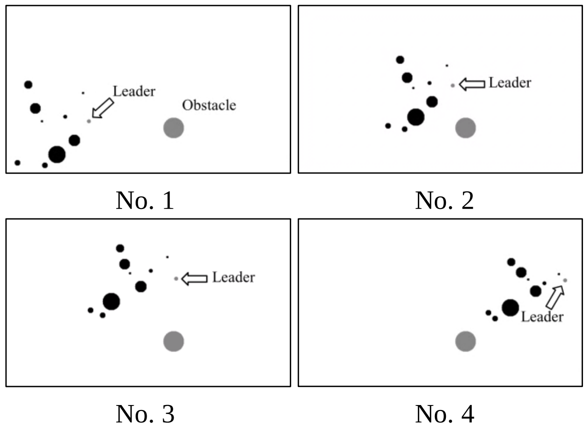

Fig. 5. Task 1

Fig. 5 shows the simulation result of Task 1. When the obstacle approaches the leader agent, the leader avoids the obstacle. Then, the follower agents follow the leader, avoiding collisions.

4.2 Task 2: Passing through narrow space

4.2.1 Outline of simulation

We set follower agents on the left side of the field, a leader agent on the right side of the other agents, and two obstacles on the right of the leader robot. The task of the leader robot is to move to the right. In this case, the leader robot does not have to avoid the obstacles. It can pass through the space between the obstacles. However, the space is so narrow that the flock should change its formation to pass through the space.

4.2.2 Simulation result

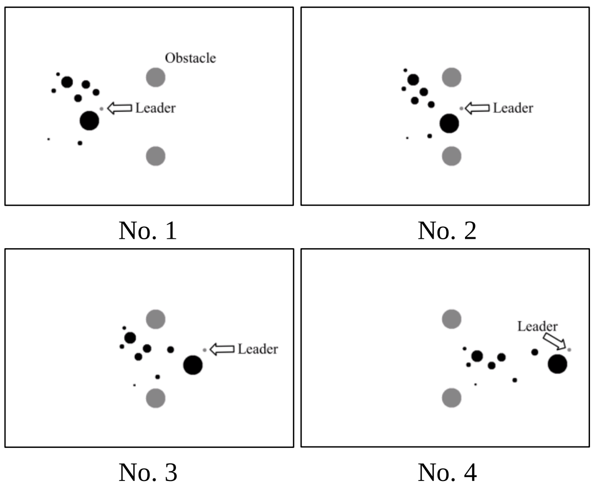

Fig. 6. Task 2

Fig. 6 shows the simulation result of Task 2. From the result, we observe that agents can pass through the space by changing their formation. In addition, we also find that they can avoid collisions with each other in spite of the fact that they are not aware of the distances between themselves.

4.3 Task 3: Avoiding obstacles and passing through narrow space

4.3.1 Outline of simulation

Task 3 is a combination of Task 1 and Task 2. We employ three obstacles, and the leader robot moves to the right, avoiding the obstacles. In this case, the movement of the leader agent is not straight and the other agents have to follow the leader, avoiding the obstacles.

4.3.2 Simulation result

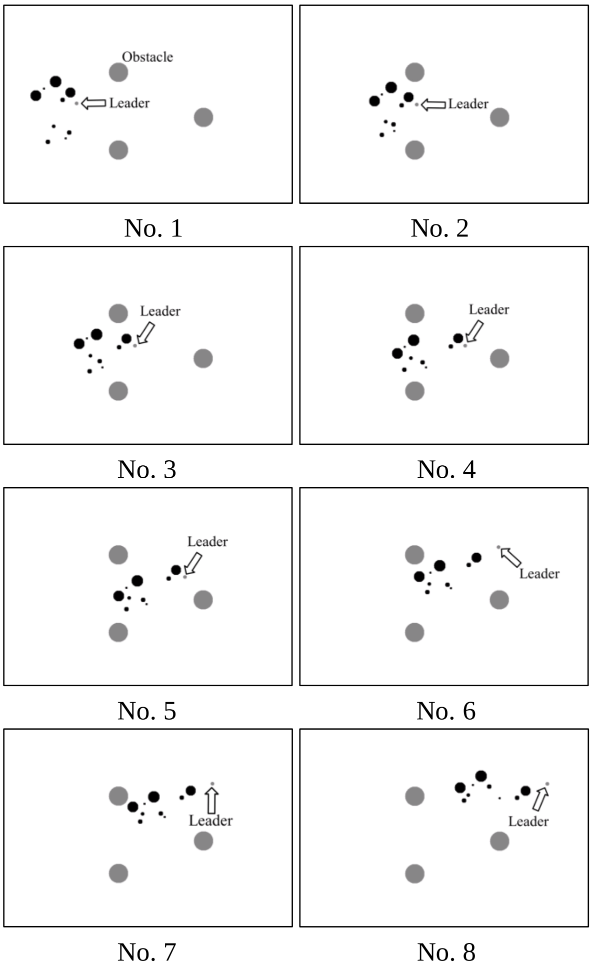

Fig. 7. Task 3

Fig. 7 shows the simulation result of Task 3. We observe that the rules of separation, alignment, and cohesion are suitably selected, and flock behavior to follow the leader agent, avoiding collisions, is realized.

5 CONCLUSION

In this paper, we addressed control of a flock behavior using the time to contact called the tau-margin. We proposed modified Boid rules in which the tau-margin is employed instead of the distance. To discuss the effectiveness of the modified Boid rules, we conducted simulations. From the simulation results, we confirmed that in all cases, agents avoid collisions and follow the leader agent without distance information.

We can conclude that flock behavior can be realized by using only the tau-margin that is obtained from visual information.

ACKNOWLEDGMENT

This study was partially supported by the Suzuki Foundation.

REFERENCES

[1] Reynolds C. W. (1985), Flocks, herds, and schools: A Distributed Behavioral Model. Computer Graphics 21(4):25-35

[2] Spector L., Klein J., Perry C., Feinstein M. (2005), Emergence of Collective Behavior in Evolving Populations of Flying Agents. Genetic Programming and Evolvable Machines 6(1):111-125

[3] Kurabayashi D. (2007), Algorithms in Individuals to Behave as an Intelligent Swarm (in Japanese). Journal of the Society of Instrument and Control Engineers 46(11):829-834

[4] Brogan C. B., Hodgins J. K. (1997), Group Behaviors for Systems with Significant Dynamics. Autonomous Robots 4(1):137-153

[5] Reynolds C. W. (1999), Steering Behaviors for Autonomous Characters. Proceedings of the 1999 Game Developer's Conference:763-782

[6] Ronald C. K., Zhang H. (1997), Task Modelling In Collective Robotics. Autonomous Robots 4(1):53-72

[7] Shinchi T., Nishimura H., Kitazoe T. (2001), A Fractal Evaluation of School Movement Patterns Using Fish Behavior Models (in Japanese). IPSJ Journal 42(6):1592-1600

[8] Lee, D. N. (1985), Visual timing of interceptive action. Brain Mechanisms and Spatial Vision:137-139

[9] Yokokawa A., Ito K. (2008), Realization of flock behavior by using Tau-margin. Artificial Life and Robotics 113:259-263

The Seventeenth International Symposium on Artificial Life and Robotics 2012 (AROB 17th '12),
B-Con Plaza, Beppu, Oita, Japan, January 19-21, 2012

A proposition of adaptive state space partition in reinforcement learning with Voronoi Tessellation

Kathy Thi Aung[1], Takayasu Fuchida[2]

[1,2]Kagoshima University, Kagoshima 890-0065, Kohrimoto 1-21-40, Japan
[1,2]Graduate School of Science and Engineering, Department of System Information Science
(Tel: 81-99-285-3408, Fax: 81-99-285-8464)

[1]kathythiaung@gmail.com , [2]fuchida@ibe.kagoshima-u.ac.jp

Abstract: This paper presents a new adaptive segmentation of continuous state space based on vector quantization algorithm such as LBG (Linde-Buzo-Gray) for high-dimensional continuous state spaces. The objective of adaptive state space partitioning is to develop the efficiency of learning reward values with an accumulation of state transition vector (STV) in a single-agent environment. We constructed our single-agent model in continuous state and discrete actions spaces using Q-learning function. Moreover, the study of the resulting state space partition reveals in a Voronoi tessellation. In addition, the experimental results show that this proposed method can partition the continuous state space appropriately into Voronoi regions according to not only the number of actions, and achieve a good performance of reward based learning tasks compared with other approaches such as square partition lattice.

Keywords: Q-learning, LBG, new Vector quantization method, State space partitioning

1 Introduction

Reinforcement learning [1] is a type of active learning in which the autonomous agent interacts with its initially un-known environment, observes the results of its actions, and adapts its behavior appropriately. This type of learning has been widely studied as a learning method for determining the optimal actions. In particular, Q-learning [2] is a common reinforcement learning algorithm that is being investigated in a variety of applications.

In this paper, we develop an efficient algorithm for partitioning the state space in terms of computation. There are multiple ways of partitioning the state space such that Voronoi tessellation. Since we consider a single-agent RL problem in high-dimensional continuous state space and discrete actions, we built two experimental models A and B in different environments, and conduct two experiments to test the efficiency of reward learning. Our proposed method is based on the use of LBG for experimental model B, therefore, we use adaptive vector quantization method and the quality of a partitioning algorithm could also be estimated according to the number of non-overlapping regions of the partitioned state space. However, in order to increase the performance of learning efficiency, it is essential to achieve a good reward on the action space.

The following is a detailed description of our approach. First, a review of reinforcement learning and basic algorithm of Q-learning is presented in Section 2. And then, the adaptive partitioning of the state space and performance of the algorithm is described in detail in Section 3. The characteristics of proposed algorithm using vector quantization method and the efficiency of reward learning are investigated in Section 4. Finally, a conclusion is given in Section 5.

2 Reinforcement learning framework

In a typical reinforcement learning model, a learning agent is connected to achieve a reward or to reach a goal through interactions with its environment. In each time step, an autonomous agent observes the environmental state and makes a decision for a specific action, and selects an action in a current state according to a control policy. The control policy specifies each admissible action as a function of the observed state. At the next time step, a reward is generated according to the agent's environment after executing the action, and learns by that reward. It works much like human learning, and search for the optimal policy that maximizes the total expected reward. This is achieved by estimating the action value function, which is the total expected reward of taking action at a state.

2.1 Q-learning algorithm

Q-learning algorithm due to Watkins [2] is a policy for estimating the optimal state-action value function, denoted by $Q(s_t, a_t)$, as the value of Q. In general Q-learning, it discretizes the state and gives the Q-value that corresponds to each state and action pair. Q-value shows the value of action, and these Q-values are initialized to small random values and gradually change to the optimal values through learning process. In the state where the agent observed, the action with the highest Q-value is considered as the optimal action, and learns by adding the random action to it. Q-value is updated by this following equation.

$$Q(s_t,a_t) = Q(s_t,a_t) + \alpha(r_t + \gamma \max_a Q(s_{t+1},a) - Q(s_t,a_t))$$

In this equation, $0 \leq \gamma < 1$ is the discount factor, α is the learning factor, and r_t is the reward given in current state s_t, $Q(s_t,a_t)$ is the Q-value of action a in state s at time t, $\max_a Q(s_{t+1},a)$ is a maximum Q-value of state at time $t+1$.

3 Experiments A

We experiment the implementation of the partitioning algorithm on 2-dimensional one state input and N-actions variables alternatively known as continuous state space and discrete actions. In this model A, the position of the agent is expressed as a state input, and the reward area is placed at the center of the action space as shown in Figure 1, and action space and state space completely coincide with each other. The aim of the learning agent is to develop an optimal control policy, in other words, to achieve a good reward within a short period of time.

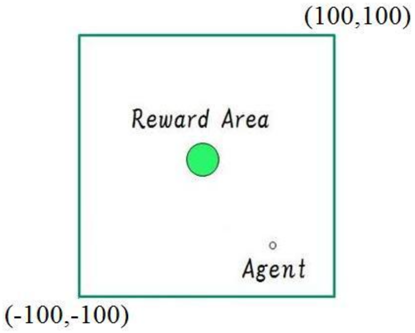

Fig.1. Experimental model A

We conducted a simple simulation experiment with a learning rate of 0.1, discount rate of 0.9 for Q-learning algorithm, and a random action rate was initialized to 0.3. A continuous action learning time is 20 thousand time for 1 episode and acts for 50 episodes, and perform 10 trials on each episode by changing the different initial seeds of random number. Furthermore, we examine the number of accumulated rewards by taking the average of each 10 trials for each episode.

3.1 Adaptive state space partitioning method (not use LBG method)

The idea of proposed partitioning algorithm is to group together states with similar action. In this way, the agent learns a suitable partitioning for a particular task and easily partition the state space using a clustering state transition vector (STV) or nearest-neighbor method. Our algorithm

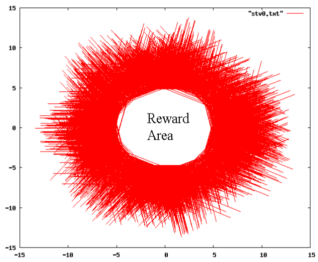

Fig.2.1. Collecting STV

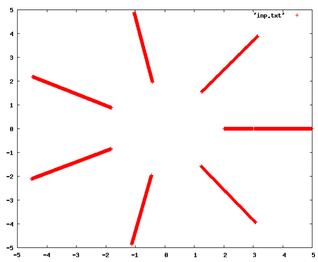

Fig.2.2. Seeking RV

for partitioning is performed on two steps. In the first step, we arrange the temporary points into lattice structure and collect the STV in regard to reward area that is a distance pointing from position of the agent to reward area that are described in Figure 2.1 when the agent enters the reward area. If the amount of rewards, in other words, the number of STV is accumulated 1000 or more, we group together STV by continuously taking the same actions, and seek those STV groups into representative vectors (RV) according to the number of actions are illustrated in Figure 2.2.

The accumulated STV with respect to a particular action is the sum of the total rewards received by taking the same actions. Then, the new Voronoi points are generated at the place of those representative vectors in relation to the reward area based on the number of actions, after all, we remove the temporary points in which the new Voronoi points are added. In essence, the continuous state space is partitioned into the number of N-actions subspaces as Voronoi regions shown on bottom of Figure 3.1.

In the second stage of partition formation, we collect the STV that come from temporary points to new Voronoi points of the quantized first-stage output, and group STV again which exceeds a threshold value by taking the same action. We do not take the STV that come from new Voronoi points to new Voronoi points. A threshold value is calculated dividing the number of accumulated STV 1000

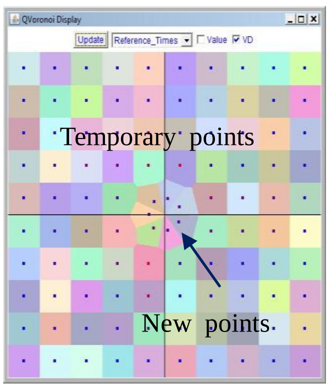

Fig.3.1. First stage of partition formation

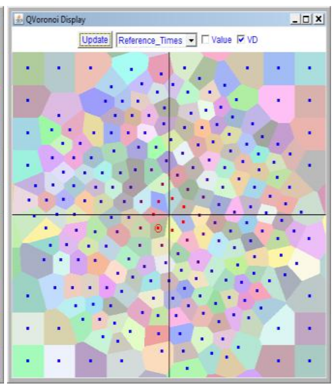

Fig.3.2. State space partition of 7-actions

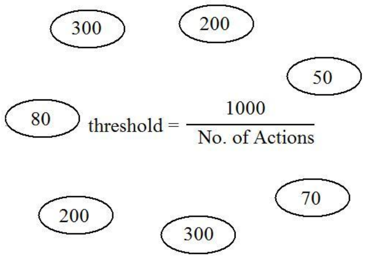

Fig.3.3. Calculation of threshold values for second stage formation

by the number of actions such that 7-actions, 6-actions. Figure 3.3 shows the formula quantization in order to make the group defined by threshold settings. Hence, the new Voronoi points are produced but it does not exactly the number of actions as new Voronoi points created in first stage formation (Fig.3.2). Moreover, we calculate the minimum distance between two new added Voronoi points to merge the points into one that are very close when we add the new Voronoi points of quantized second-stage process. If the distance between two new Voronoi points is less than the ratio of a minimum distance, we add the first entry Voronoi point. Furthermore, the reward numbers of state space partition are compared with square lattice partition.

3.2 Results

A summary of our experimental result is illustrated in Figure 3.4. It shows the comparison of two learning methods with the same number of Voronoi points. These two learning methods are partitioning of the state space using 7-actions on an experimental model A, and the regular arrangement of Voronoi points in a lattice structure are compared and discussed. As a result, adaptive partitioning the state space with N-actions has shown that

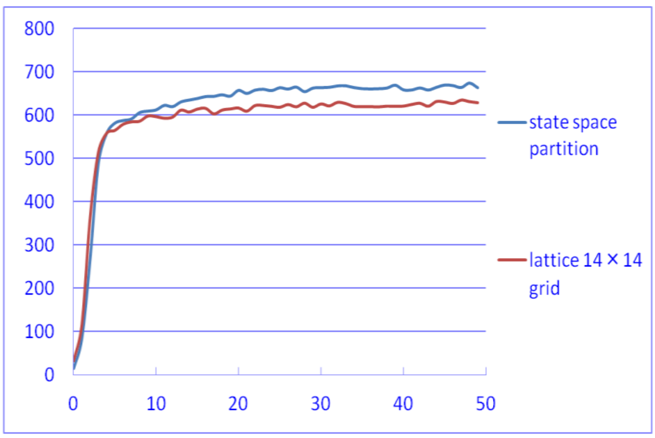

Fig.3.4. Comparison of learning performance using experimental model A for 7-actions
(X-axis: Episode number, Y-axis: Rewards number)

improved performance of reward learning, and it can accurately segment the state space as Voronoi tessellation with N-actions. However, the new points are not added if the ratio of the minimum distance is over 0.5 on the number of 3-actions and 4-actions.

4 LBG vector quantization algorithm

LBG (Linde-Buzo-Gray) is a typical technique of vector quantization algorithm. Modification of adaptive vector quantization method was introduced Enhanced LBG (Patane & Russo, 2001) [3], Adaptive incremental LBG (Shen & Hasegawa, 2006) [4]. Vector quantization method assumes that a set of input points is organized into a number of groups having approximately the same number of points closest to them. Each group is represented by its centroid point, as quantum vector (QV) idyllically known as representative vector. However, since the quantum vectors are not represented very well, we implemented the improved vector quantization algorithm as follow:

1. Collect the input vectors and tentatively place the QVs in random position.
2. Move the QVs in random directions by putting noise at the position of QVs.
3. Then, tentatively group the input vectors that are very close from the QVs, and move the QVs to the center position of input vectors.

We then repeated the above process until the number of QVs is -1, and reduce the amount of motion. Figure 4 describes an example of modified group vector quantization. Since the number of QV in clustering problem is not known a priori, we determines the number of QV by the index of their closest centroid which have smallest measurement error rates in group by changing the number of QV, and represents using that QV at a given time.

However, one group was represented with two QVs or two groups were represented with one QV. Therefore, we move the QVs of smallest measurement error to the

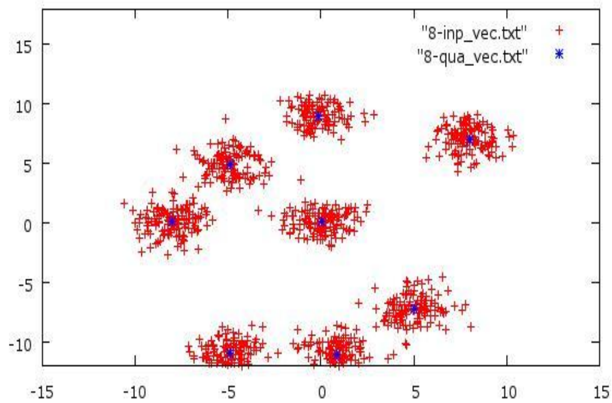

Fig.4. Input random vector quantization

position of the largest measurement error if the standard deviation is large. A standard deviation indicates that data are widely scatter condition of one group, and a small standard deviation is being able to represent as a representative vector, also known as quantum vector surely.

4.1 Experiments B

We test our approach by applying it in a continuous state space as shown in Figure 5. The agent learns to achieve optimal action, it means to arrive at a feeding area or reward area, and test its performance. If an agent reaches the goal, it receives a reward of +1, otherwise, if an agent collides into a border or wall, it was penalized by -1. For every reward, the agent is bounced to its new random position. The agent has 3 actions of straight forward, right rotation and left rotation, and observes the distance to a reward area and the angle between the direction of the agent forward movement and reward area, and learns by considering them as state inputs.

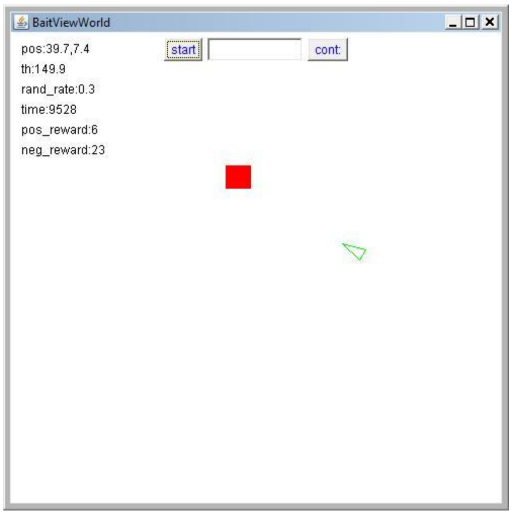

Fig.5. Experimental model B

Since the number of reward area is 1, these two state input values construct the 2-dimensional state space. The dimension of the state space goes up by two dimensions when one reward area is increased. We conducted experiments with one hundred thousand action learning times as 1 episode to 100 episodes and tested on 10 trials, and execute experiment as above.

4.2 Adaptive state space partitioning with LBG vector quantization algorithm

In this section, we do the same process of partitioning the state space that described in section 3.1 above. However, since the state input values and environments are different, the continuous state space is not partitioned into a number of N-actions subspaces. Further, we group together STV by using the LBG type of vector quantization algorithm and extract the representative vectors. We all take the STV (i.e, do not calculate a threshold value) for the second stage of partition formation.

4.3 Experimental results

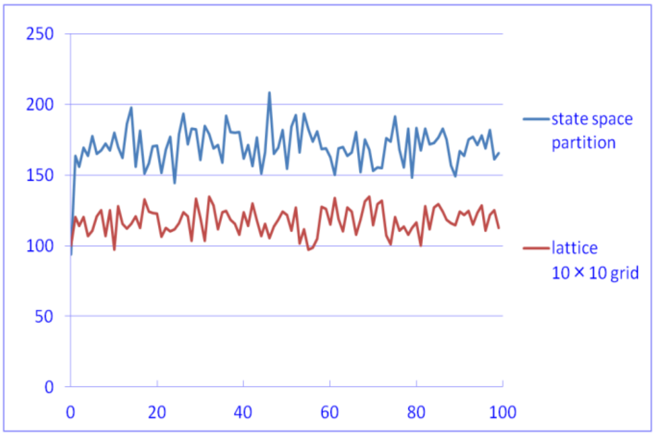

Fig.6. Comparison of learning performance using model B for 3-actions
(X-axis: Episode number, Y-axis: Rewards number)

The experimental results of Figure 6 show that our proposed approach raises the efficiency of the reward learning than the regular arrangement of lattice points.

5 Conclusions

This paper presented a new LBG vector quantization algorithm for partitioning the state space to Voronoi regions and adaptive continuous state space partition method. In our experiments, a simple experiment model by an agent was used in different environments with different state input values, and the effectiveness and efficiency of reward learning for two algorithms has been checked. When looking in terms of the reward, we see that our technique performs almost as good as square partition lattice and much better than its performance.

REFERENCES

1. Sutton RS, Barto AG (1998), Reinforcement learning an introduction, MIT Press, Cambridge.
2. Watkins CJCH, Dayan P. Technical notes: Q-learning. Machine Learning 1992;8:279-292.
3. G.Patane and M.Russo, The enhanced LBG algorithm, In proceedings of Neural Networks, 2001, pp.1219-1237.
4. F.Shen, O.Hasegawa, An adaptive incremental LBG for vector quantization, Neural Networks 19 (2006) 694-704.

The Seventeenth International Symposium on Artificial Life and Robotics 2012 (AROB 17th '12),
B-Con Plaza, Beppu, Oita, Japan, January 19-21, 2012

Universal Creativity Engine: Real-time Creation of Melody and Lyrics based on the Ant System

Kenta Nishio[1] and Takaya Arita[2]

[1,2]Graduate School of Information Science, Nagoya University
Furo-cho, Chikusa-ku, Nagoya, 464-8601, Japan
[1]kenta.nishio@gmail.com
[2]arita@nagoya-u.jp

Abstract: Creativity plays an important role in almost all human activities and has been investigated by many researchers in a wide variety of fields. However, it is difficult to design a methodology for generating highly creative artifacts mainly because previous researches tended to depend a little too much on human subjective evaluation. One idea to tackle with creativity is to leave out the value aspect from the definition of creativity for the moment at least. This paper proposes Universal Creativity Engine (UCE), a conceptual organization for reproducing the creative process in human brain on the basis of the idea. It is characterized by a real-time property, representation universality and creativity based on two types of deviation. This paper also describes the design of UCE-ANT, the initial prototype implementation of UCE, for creation of melody and Lyrics based on the Ant system.

Keywords: Creativity, Ant colony optimization, Artificial life

1 INTRODUCTION

Creativity plays an important role in almost all human activities, and therefore, has been investigated by many researchers in a wide variety of disciplines such as psychology, cognitive science, philosophy, artificial intelligence, and engineering. We usually assume that creativity has an inseparable connection with the concept of value. For example, Boden defined creativity as the ability to come up with ideas or artifacts that are 1) new, 2) surprising and 3) valuable [1]. Therefore, it is extremely difficult to provide an objective definition of creativity and a reliable method for its evaluation. In a sense, it is thus reasonable that previous researches tended to depend a little too much on human subjective evaluation. However, for automatic generation of highly creative artifacts, it is important to develop a methodology that does not depend on human evaluation.

One idea here for tackling with creativity might be to leave out the value aspect when considering creativity for the moment at least. Dorin et al. [2] presented a value-free account: Creativity is the introduction and use of a framework that has a relatively high probability of producing representations of patterns that can arise only with a smaller probability in previously existing frameworks. If we accept such a formal and systematic account, when a solution to a problem can be cast in terms of a computational representation to be found in some definable representation space, then the problem can be tackled by applying some search algorithm to that space.

We hypothesize that new frameworks in this context can continue to be created by the coupling of two types of deviations, and propose *Universal Creativity Engine* (*UCE*), a conceptual organization for continuously generating the creative property based on the hypothesis. It accepts data streams from real world, updates the internal model representation of the world, and at the same time, generates data streams on a real-time basis just like human brain. It has representation universality in the sense that it stores and updates the internal representations in abstract and unified forms, and can treat any discrete data sequences in principle.

This paper describes the concept of UCE, and then reports on the initial prototype implementation, *UCE-ANT*. It composes a song, in other words, creates melody and lyrics at the same time using the same process based on one of the simplest ant colony metaheuristics, Ant system [3].

2 CONCEPTUAL ORGANIZATION OF UNIVERSAL CREATIVITY ENGINE (UCE)

Creativity is defined by Dorin et al. as *the introduction and use of a framework that has a relatively high probability of producing representations of patterns that can arise only with a smaller probability in previously existing frameworks*. Here, *frameworks* are defined as stochastic generative procedures. Their idea is shown in Figure 1. In this figure, Distribution 1 and 2 represent the old and new frameworks, respectively. Both are probability distributions over a common design space (horizontal axis). It shows that the new framework produces representation patterns that can hardly be produced by the old framework. They consider that the use of Distribution 2 relative to the prior use of Distribution 1 to generate one of these points is therefore creative.

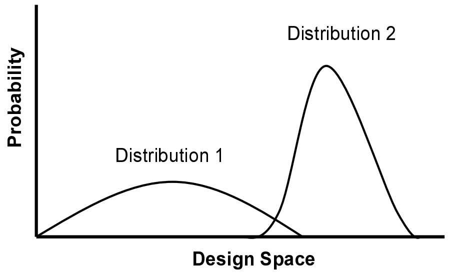

Fig. 1. The use of Distribution 2 relative to the prior use of Distribution 1 is creative.

We propose Universal Creativity Engine (UCE), a conceptual organization for reproducing the creative process in human brain (Fig. 1). UCE accepts data streams from real world, updates the internal model representation of the world, and at the same time, generates data-streams stochastically as the results of a creative process. The internal model is represented in a distributed manner, and the positive feedback loop is used to extract standard patterns inherent in the current data streams.

We considered the following requirements when designing UCE.

1. Real-time property
   UCE works on a real-time basis just like our brains. The world is changing every minute, and the existing frameworks captured in UCE should also change correspondingly to make the output streams creative. For example, timeline of Twitter can be used as an input data stream as described later.

2. Creativity based on two types of deviations
   We adopted the creativity concept proposed by Dorin, and embodied them in the following two types of deviation. Deviation from the frameworks that are updated by the input data streams from the world (I-deviation) and deviation from the frameworks of the output data streams themselves (O-deviation).

3. Representation Universality
   UCE stores and updates the internal model representations in abstract and unified forms, and can treat any discrete data sequences in principle. For example, melody and lyric are created using the same process based on two types of deviations in the prototype system.

3 PROTOTYPE IMPLEMENTATION (UCE-ANT)

We report on UCE-ANT, the initial prototype implementation of the UCE concept. It continues to compose a song: creates melody and lyrics at the same time representing the atmosphere of real world at the present moment, using the same process based on one of the simplest ant colony metaheuristics, Ant system [3][4].

UCE-ANT is composed of two layers: one for lyrics and the other for melody. Data streams (timeline) from Twitter and melody data from currently popular music scores are used as input for the melody and lyrics layers, respectively. Each layer has a directed network as an internal model of real world, in which each node represents a note or a word. Each link represents a connection from a node to the other with a pheromone value reflecting the strength of the connection. Two types of virtual ants: *Reflector* and *Performer* are moving from one node to another. The amount of the pheromone on link$_{ij}$ deposited by Reflector ants and Performer-ant$_n$ are described by T_{ij} and t^n_{ij}, respectively.

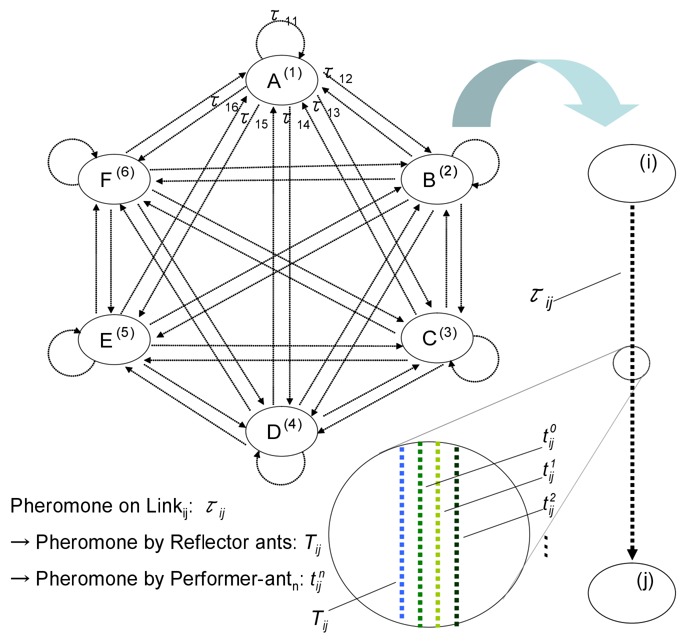

Fig. 3. Internal representation based on an ant colony metaheuristic.

While moving, they deposit pheromone on the links. The pheromone on the links evaporates slowly with time.

$$T_{ij} \leftarrow (1 - \rho_a) * T_{ij} \tag{1}$$

$$t^n_{ij} \leftarrow (1 - \rho_b) * t^n_{ij}, \tag{2}$$

where ρ is a parameter called evaporation ($0 \leq \rho \leq 1$).

UCE-ANT works as follows.

1) World representation by Reflector ants

Each reflector ant moves according to its input data stream (note or word sequence), and deposits their identical

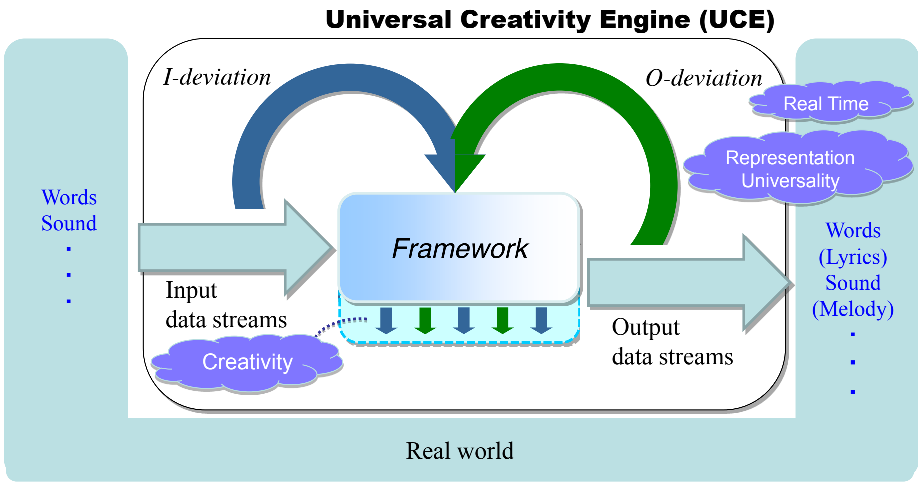

Fig. 2. Universal Creativity Engine (UCE).

pheromone on the link when moving. Each time a reflector ant moves from a node *i* to a node *j*, it deposits a pheromone quantity $T_{reflect}$ as follows:

$$T_{ij} \leftarrow T_{ij} + T_{reflect}. \tag{3}$$

The real world model is constructed and maintained actively as a pheromone distribution on the network on each layer through this process by Reflector ants and pheromone evaporation.

2) Exploration by Performer ants

Each Performer ant explores the network according to its pheromone distribution (deposited by itself and Reflector ants), creating melody or lyrics using an ant colony metaheuristic as follows.

When located at a node *i*, the probability for Performer-ant$_n$ to choose a node *j* is given by:

$$P_{ij}^n = \frac{T_{ij} + t_{ij}^n}{\sum_k (T_{ik} + t_{ik}^n)}(1 - \epsilon_n) + \epsilon_n, \tag{4}$$

where ε_n is a random selection rate for performer-ant$_n$ ($0 \leq \varepsilon_n \leq 1$). Each Performer ant has its own random selection rate, which affects the creative property of its output data stream as described later.

When moving from a node *i* to a node *j*, it deposits a pheromone quantity $t_{perform}$:

$$t_{ij}^n \leftarrow t_{ij}^n + t_{perform}. \tag{5}$$

Every when they reach a new node, the corresponding note or word is selected. The node sequences, melody and lyrics, selected by performer ants on both layers are combined to play a tune continuously.

3) Creativity control

We hypothesize that new framework can continue to be created dependent on the coupling of I-deviation and O-deviation in UCE. Furthermore, we assume that creativity would be optimized by letting both deviations to be certain values (I-deviation$_{opt}$ and O-deviation$_{opt}$), although it might be difficult to know the values a priori. In UCE-ANT, I-deviation$_n$ of Performer-ant$_n$ corresponds to the difference between pheromone distributions of Reflector ants and the pheromone distribution detected by Performer-ant$_n$ (pheromone deposit by itself and Reflector ants). O-deviation$_n$ corresponds to the difference between the current distribution and the past distribution (*N* steps ago) of pheromone detected by Performer-ant$_n$.

We defined these measures simply as follows.

I-deviation for a Performer-ant$_n$, I-d$_n$, is given by

$$I\text{-}d_n = \sqrt{\sum_i \sum_j (P_{ij}^n - \frac{T_{ij}}{\sum_k T_{ik}})^2}. \tag{6}$$

O-deviation for a Performer-ant$_n$, O-d$_n$, is given by

$$O\text{-}d_n = \sqrt{\sum_i \sum_j (P_{ij}^n - \frac{\sum_k P_{ijk}^n}{N})^2}, \tag{7}$$

where P_{ijk}^n is the past distribution (*k* steps ago) of pheromone detected by Performer-ant$_n$.

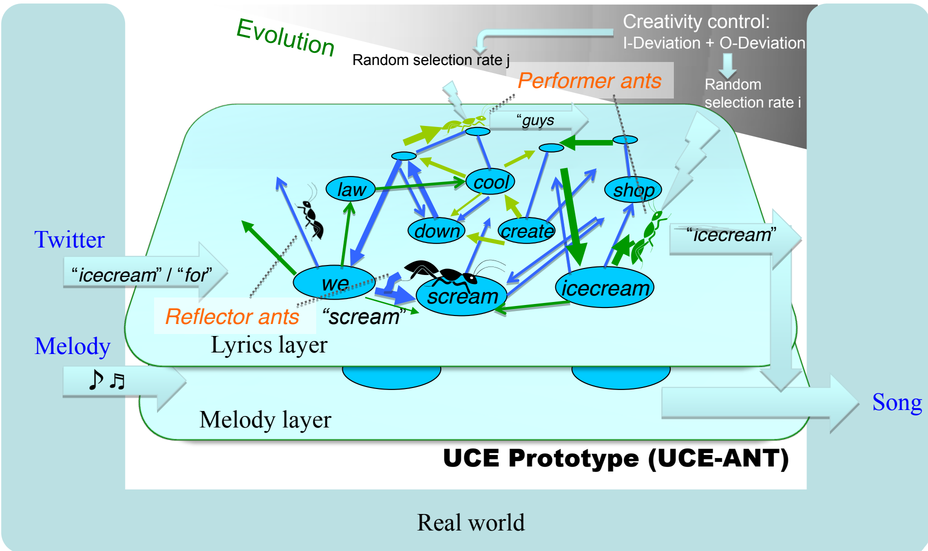

Fig. 4. Prototype Implementation of UCE (UCE-ANT).

Using these measures, Performer-ant$_n$ is evaluated as

$$E_n = \frac{1}{1 + |I\text{-}d_{opt} - I\text{-}d_n| + |O\text{-}d_{opt} - I\text{-}d_n|}, \quad (8)$$

where I-d$_{opt}$ and O-d$_{opt}$ are the values that are supposed to maximize the creativity.

Each Performer ant has its own random selection rate, which controls both deviations, I-deviation and O-deviation. Evolutionary processes are used to evolve Performer ants with the optimal random selection rate that maximizes E$_n$.

We are currently conducting some preliminary experiments to examine the basic behavior of UCE-ANT. We found that in terms of the balance between intensification (exploitation of the previous solutions) and diversification (exploration of the search solutions), the former due to the positive feedback loop provided by the pheromone-based metaheuristic [5] works stronger than expected. Therefore, sufficiently large values of I- deviation$_{opt}$ and O-deviation$_{opt}$ are necessary to work against it. However, it is also the case that excessively large random rates make the melody or lyrics generated by the Performer ant unattractive.

4 CONCLUSION

This paper hypothesizes that the creative process is dependent on the coupling of two types of deviations, and proposes Universal Creativity Engine, a conceptual organization based on the hypothesis. This paper also described UCE-ANT, the first prototype implementation of UCE based on an ant colony metaheuristic. We examined basic behavior of it and found some characteristic of its dynamics arising from the balance between intensification and diversification, although UCE-ANT is still under development.

We gave simple definitions of two types of deviations for UCE-ANT. The future work includes investigating the effects when changing the definition of the deviations. It might be also interesting to generate motion of dancing and singing robots by adding a Motion layer in which each node represents an action of a joint.

REFERENCES

[1] M. Boden, *"The Creative Mind: Myths and Mechanisms" (second edition)*, Routledge, London, 2004.

[2] A. Dorin and K. B. Korb, "A New Definition of Creativity", *Proc. 4th Australian Conference on Artificial Life (ACAL 2009) (Lecture Notes in Computer Science, Vol. 5865)*, pp. 11-21, 2009.

[3] M. Dorigo, V. Maniezzo and A. Colorni, "The Ant System: Optimization by a Colony of Cooperating Agents", *IEEE Transactions on Systems, Man, and Cybernetics - Part B*, Vol. 26, No. 1, pp. 29-41, 1996.

[4] C. Gueret, N. Monmarche and M. Slimane, "Ants Can Play Music", *Proc. of 4th International Workshop on Ant Colony Optimization and Swarm Intelligence (ANTS '2004) (Lecture Notes in Computer Science, Vol. 3172)*, pp. 310-317, 2004.

[5] Y. Nakamichi and T. Arita, "Diversity Control in Ant Colony Optimization", *Artificial Life and Robotics*, Vol. 7, No. 4, pp. 198-204, 2004.

The Seventeenth International Symposium on Artificial Life and Robotics 2012 (AROB 17th '12),
B-Con Plaza, Beppu, Oita, Japan, January 19-21, 2012

Simple system for detecting sound localization based on the biological auditory system

Takanori Tomibe[1] and Kimihiro Nishio[2]

[1,2]Tsuyama National College of Technology, 624-1, Numa, Tsuyama, Okayama, Japan, 708-8509
(Tel: 81-868-24-8266)

[1]e-t-t@tsuyama-ct.ac.jp
[2]nishio@tsuyama-ct.ac.jp

Abstract: In this study, we proposed and fabricated the simple system for detecting sound localization based on the biological auditory system. The proposed system is constructed with the simple circuit for detecting sound localization, two microphones, the photodiode, the motor and the rotation table. The test system was fabricated by the simple circuit for detecting sound localization by using the simple circuit constructed with discrete metal oxide semiconductor (MOS) transistors on the breadboard. The experimental results of the test system showed that the proposed system can detect the position of the sound of the target. We can realize novel target tracking system by applying the proposed system based on the biological auditory system.

Keywords: sound localization, auditory system, tracking system, analog circuit, digital circuit

1 INTRODUCTION

It is necessary for robotics vision, monitoring system and collision avoidance system to capture quickly the target in the visual field. However, it is difficult for the systems based on only the vision system to capture quickly the target in the visual field since the system cannot detect the position of the target when the target is not existed on the visual field. On the other hand, the animal can capture quickly the target in the visual field by using other functions such as the auditory system. The biological auditory system can process the sound information of the target and detects the position of the sound, even if the target is not existed on the visual field.

Recently, many researchers proposed and fabricated the simple system for target tracking based on the biological vision system [1]-[5]. These systems can track the target by using the motion signals. These systems are characterized by simple structure, low power consumption and high speed processing. However, these systems could not track the target when the target was not projected on the input parts since the systems were proposed by mimicking only the vision system. If the system based on the vision system is connected with the system based on the auditory system, it is able to track the target in various situations.

L. A. Jeffress proposed the model for detecting sound localization based on the biological auditory system [6]. Because the model is constructed with the delay line and the comparator, the model is simple structure. We proposed the simple analog-digital circuit for detecting sound localization based on the model by Jeffress [7]. The proposed circuits were constructed with the current mode delay line and the NOR circuits. The proposed unit circuit of delay line was constructed with 9 metal oxide semiconductor (MOS) transistors and 1 capacitor. The NOR circuit used as the comparator was constructed with 4 MOS transistors. Therefore, the proposed circuit is simple structure. We showed that the circuit can detect the position of the sound of the target. It is necessary to fabricate the system for detecting the position of the target (sound) by using the proposed simple circuit.

In this study, we tried to propose and fabricate the system for detecting sound localization. The proposed system is constructed with the circuit for detecting sound localization, two microphones, the photodiode, the motor and the rotation table. The test system was fabricated by using test circuit for detecting sound localization constructed with discrete MOS transistors on the breadboard. The experimental results of the test system showed that the proposed system can detect the position of the sound, and capture the target in the visual field.

2 MODEL AND CIRCUIT

2.1 A model

Figure 1 shows the model for detecting sound localization proposed by Jeffress [6]. The model is constructed with the delay line constructed with the delay neuron D and the comparator C. The Unit is constructed two delay neurons and one comparator, as shown in Fig.1.

I_{left} is input signal for delay line (left) generated by the left ear. I_{left} transmits the delay line (left) from D_1 to D_n. I_{right} is input signal for delay line (right) generated by the right ear. I_{right} transmits the delay line (right) from D_n to D_1. Therefore, delay neurons output the signal sequentially.

When the sound of the target is large, I_{right} and I_{left} become large. Inversely, I_{right} and I_{left} become small when the sound of the target is small. When I_{right} (I_{left}) is large, I_{right} (I_{left}) transmits the delay line quickly. When I_{right} (I_{left}) is small, the I_{right} (I_{left}) transmits the delay line slowly.

The output signals of delay neurons are input to the comparator. When both delay neurons in the Unit output the signal, the comparator outputs the signal.

When the sound of the target located on the right side, the Unit located on the left side outputs the signal. When the sound of the target located on the left side, the Unit located on the right side outputs the signal. When the positions of the sound of the target differ, the different comparator outputs the signal. Therefore, the Jeffress model can detect the position of the sound.

2.2 Circuits

Figure 2 shows the unit circuit of the delay line [5]. The unit circuit is constructed with 9 MOS transistors and 1 capacitor. The input current I_{in} flows into the capacitor C_n. Then, the voltage V_C is increased. The circuit transmits I_{in} to the neighboring unit circuit and outputs the output voltage V_o to the comparator.

When I_{in} is large, V_C is increased quickly. Then, the unit circuit outputs V_o quickly. When I_{in} is small, V_C is increased slowly. Then, the unit circuit outputs V_o slowly. The voltage V_{th} is the constant voltage. The voltage V_r is utilized to reset V_C.

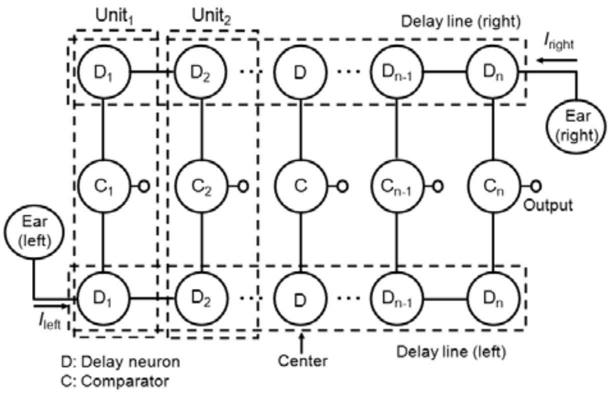

Fig. 1. The model for detecting sound localization

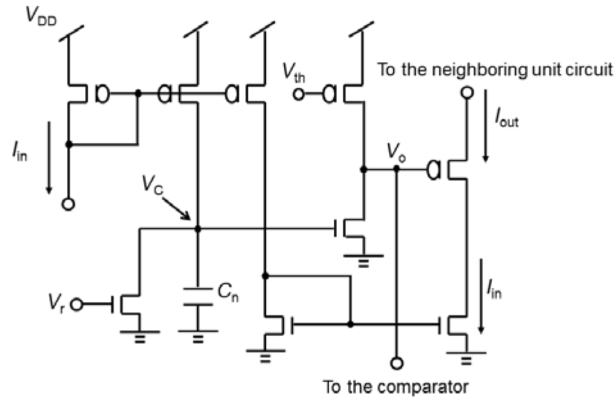

Fig. 2. The unit circuit of delay line

Figure 3 shows the NOR circuit used as the comparator. The NOR circuit is constructed with 4 MOS transistors. Therefore, the circuit is simple structure.

3 SYSTEM CONSTRUCTION

Figure 4 shows the proposed simple system for detecting sound localization. The proposed system is constructed with the simple circuit for detecting sound localization, two microphones, the photodiode, the motor and the rotation table. The output terminals of neighboring Units are connected each other. For example, the output terminals of Unit1 and Unit2 are connected, as shown in Fig.4. All of the terminals are connected with the capacitor and Reset line. The Reset line is connected with the terminals of V_r in Fig.2. When the voltage of the Reset line becomes supply voltage V_{DD}, the circuits are reset.

The voltage V_{right} is generated by connecting the output terminals of Units located on the left side. The voltage V_{left} is generated by connecting the output terminals of Units located on the right side. The output terminals of the Units located on the center are connected with the Reset line.

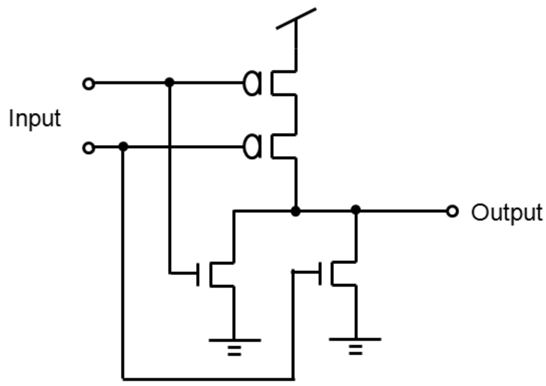

Fig. 3. The construction of NOR circuit

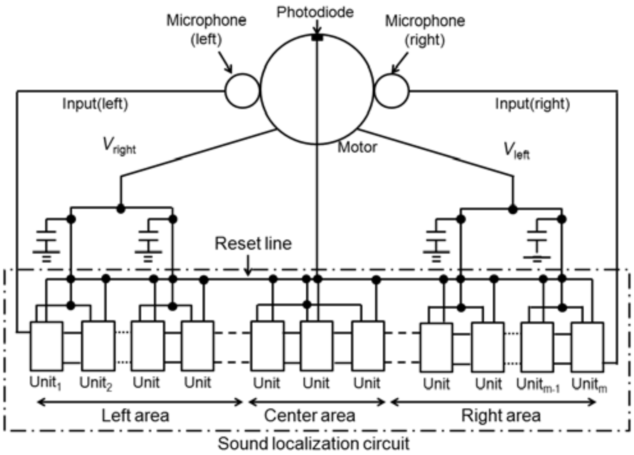

Fig. 4. Simple system for detecting sound localization

The microphones generate the input signal of the system. When the sound of the target is large, the signal of the microphone is large. When the sound of the target is small, the signal of the target is small.

The photodiode is connected with the Reset line. The photodiode is utilized as the visual sensor. When the target is projected on the photodiode, the signal of the photodiode becomes V_{DD}.

The terminal of V_{left} and V_{right} are connected to the motor driver. When V_{left} becomes V_{DD}, the motor rotates the rotation table from center to left. Inversely, the motor rotates the rotation table from center to right when V_{right} becomes V_{DD}. When both of the terminals of V_{left} and V_{right} are 0 V or V_{DD}, the motor does not rotate. The time of rotation was changed by the capacitance.

When the sound of the target is located on the right, the input signal of the right is larger than input signal of the left. Then, the output terminals of Units located on the left area becomes V_{DD}. V_{right} and the voltage of the Reset line become V_{DD}. Then, the motor rotates the rotation table from center to right. After that, the circuits were reset.

When the sound of the target is located on the left, the output terminals of the Units located on the right area becomes V_{DD}. Then, V_{left} and the voltage of the Reset line become V_{DD}. The motor rotates the rotation table from center to left.

When the sound of the target is located on the center, the terminal located on the center area becomes V_{DD}. Then, the system is reset by the voltage of the Reset line becomes V_{DD}.

When the target is projected on the photodiode, the system is reset by using the signal of the photodiode. Therefore, the proposed system can detect the position of the sound and can capture the target in the visual field.

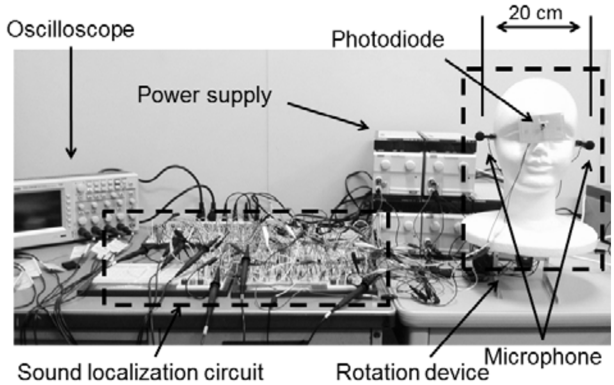

Fig. 5. The photograph of test system for detecting sound localization

4 EXPERIMENTAL RESULTS

We tried to fabricate the test system for detecting sound localization. Figure 5 shows the photograph of the fabricated test system for detecting sound localization. The test circuit was fabricated by discrete MOS transistors (nMOS: 2SK1398, pMOS: 2SJ184, NEC) on the breadboard. The test circuit for sound localization was constructed with 7 Units. Unit1 and Unit2 were connected

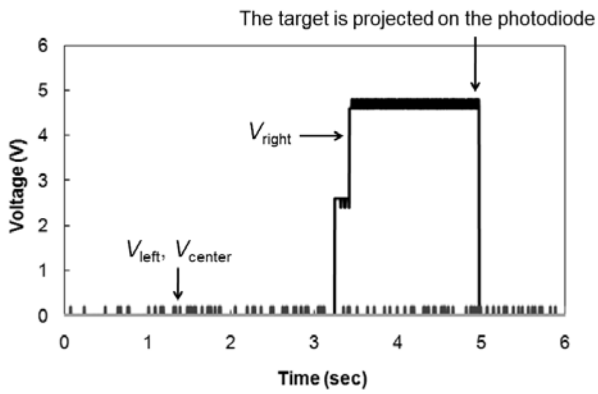

(a)

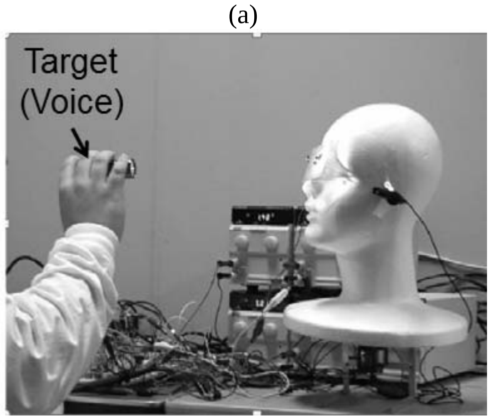

(b)

Fig. 6. The experimental result of the test system when the target located on the right side. (a) Output voltage of the test circuit. (b) The measured results of the test system when the system captures the target.

with the terminal of V_{right}. Unit3, Unit4 and Unit5 were connected with the terminal of V_{center}. Unit6 and Unit7 were connected with the terminal of V_{left}. The voice was utilized as the target. The microphones (ECM-C115, SONY) and the photodiode were attached to a mannequin.

Figure 6 shows the experimental results when the sound located on the right side. When the sound located on the right side, V_{right} become about 5 V, as shown in Fig.6 (a). Then, the motor was rotated from center to right. The motor stopped when the target was projected on the photodiode, as shown in Fig.6 (b).

Figure 7 shows the experimental results when the sound located on the left side. V_{left} become about 5 V, as shown in Fig.7 (a). The motor was rotated from center to left, as shown in Fig.7 (b). The motor stopped when the target was projected on the photodiode.

Therefore, the proposed system can detect the position of the sound of the target.

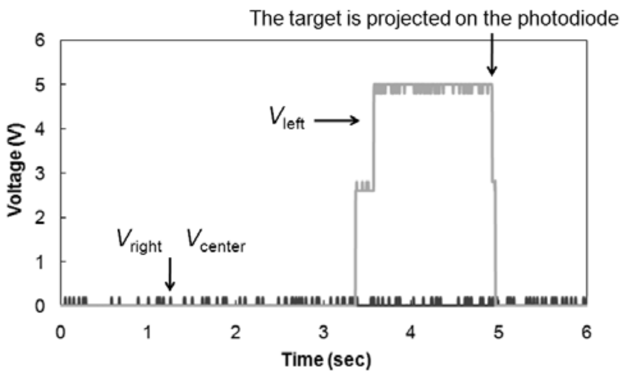

(a)

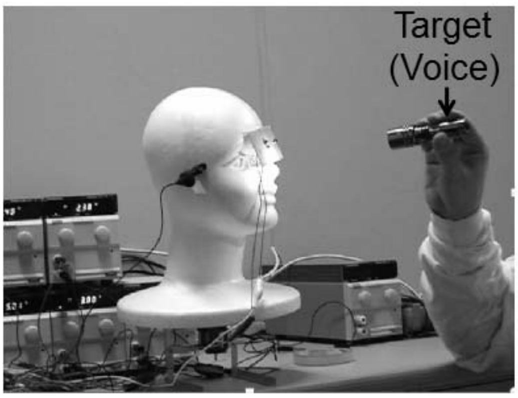

(b)

Fig. 7. The experimental result of the test system when the target located on the left side. (a) Output voltage of the test circuit. (b) The measured results of the test system when the system captures the target.

5 CONCLUSION

In this study, we proposed and fabricated the simple system for detecting sound localization based on the model by Jeffress. The system is constructed with the simple circuit for detecting sound localization, two microphones, the photodiode, the motor and the rotation table. The experimental results of the test system showed that the proposed system can detect the position of the sound of the target and can capture the target in the visual field. We can realize novel target tracking system by applying the proposed system based on the biological auditory system.

ACKNOWLEDGEMENT

This work was partially supported by Japan Society for the Promotion of Science, Grant-in-Aid for Young Scientists (B), 23700222.

REFERENCES

[1] Moini A (1999), Vision Chips. Kluwer Academic, Norwell, MA, 1999.

[2] Nishio K and Matsuzaka K (2008), Target Tracking System Using Analog Circuit for Motion Detection, Proc. of 2008 IEEE Int. Conf. on Mechatronics and Automation, TC3-5.

[3] Nishio K and Matsuzaka K (2009), Target Tracking System Using Analog Motion Detection Circuit Based on Biological Vision System. Far East Journal Electronics and Communications vol. 3, pp. 111-124.

[4] Yamamoto. T and Nishio. K (2011), Simple Analog-Digital Circuit for Motion Detection and Its Application to Target Tracking System. Proceedings of the 16th International Symposium on artificial life and robotics, pp.785-788.

[5] Nishio. K and Yamamoto. T (2011), Simple Analog-Digital Circuit and Its Application to Target Tracking System. Artificial Life Robotics vol. 16, pp. 57-60.

[6]Jeffres LA(1948), A Place Theory of Sound Localization, J.Comp. Physiol. Phychol. 41, 35-39.

[7] Nishio K and Tomibe T (2010), An analog-digital circuit for sound localization based on the biological auditory system. Artificial Life Robotics vol. 15, pp. 347-350.

The Seventeenth International Symposium on Artificial Life and Robotics 2012 (AROB 17th '12),
B-Con Plaza, Beppu, Oita, Japan, January 19-21, 2012

Two-dimensional cellular automata model of microorganism morphosis

Takeshi Ishida

Nippon Institute of Technology, 4-1, Gakuendai, Miyashiro, Minami-Saitama, Saitama, 345-8501 Japan
(Tel : 81-480-33-7719; Fax : 81-480-33-7663)

ishida06@ecoinfo.jp

Abstract: Living organism creates various shapes of the organ and the body by lamination of cells. An understanding of the generalized mechanism of biological morphosis is considered fundamental to applications in various fields, such as the mass-production of molecular machines in nanotechnology and artificial synthetics in biology. This study developed the model to simulate the morphogenetic mechanism of cells under the condition of two-dimensional cellular automata. Each cell is renewed by transition rules and the state of the next step was decided by the state of the cell and that of neighboring sites. The microbes such as protists create a variety of shapes by a single cell or a few cells. As trial simulation cases, we simulated the shape similar to various form of the microbe. Using our model, we confirmed that the variety of shapes was emerged with the slight changes of some parameters value..

Keywords: cellular automaton, self-organization, unicellular organism, morphosis

1 INTRODUCTION

Living organism creates various shapes of an organ and the body by lamination of cells. An understanding of the generalized mechanism of biological morphosis is considered fundamental to applications in various fields, such as the mass-production of molecular machines in nanotechnology and artificial synthetics in biology (synthetic biology). Furthermore, it is difficult to construct large, complex machine systems that exceed a certain size, using a top-down approach. Therefore, such complex machine systems must be constructed using a bottom-up approach based on the phenomenon of biological morphosis.

Historically, researchers have attempted to develop a mathematical model to simulate the morphosis of living matter. Studies on the reproductive models of a body surface design, namely, the Turing model (Turing, 1952), and those on the leaf vein pattern of a plant (Feugier, 2005) and mollusk shell patterns (Meinhardt, 2003) are examples of previous research. In addition, many researchers have used a cellular automaton model to study tissue or tumor growth. Although these models can simulate a number of features of biological morphosis on a computer, they cannot reproduce the entire body on the basis of unified equations and rules, such as cytodifferentiation by gene expression → morphosis of cells → organogenesis → emergence of function.

2 OBJECTIVE

This study developed the model to simulate the morphogenetic mechanism of cells under the condition of two-dimensional cellular automata. Each cell of the automaton model expresses cell organelle and holds an various states in each cell. We modeled the mechanism of gene expression by the information exchange between the adjacent cells of the automaton model. Furthermore, shapes emergence of various creature organs was simulated by the rules of cellular differentiation and rules of hierarchical formation of cells. Simultaneously we also simulated the possibility of the self-repair.

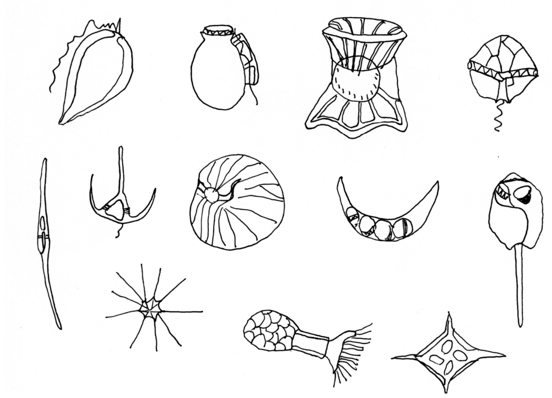

Fig. 1. Various shapes of the unicellular organism

With the real living organism, all forms are not described in DNA, and it is thought that the physical phenomena such as the diffusion of the chemical substance were used in living cells. For this reason, we considered not only the state transition rules but also the concentration diffusion of the field. Thus our model was able to simulate morphogenetic formation in few state transition rules and few parameters of concentration diffusion equations.

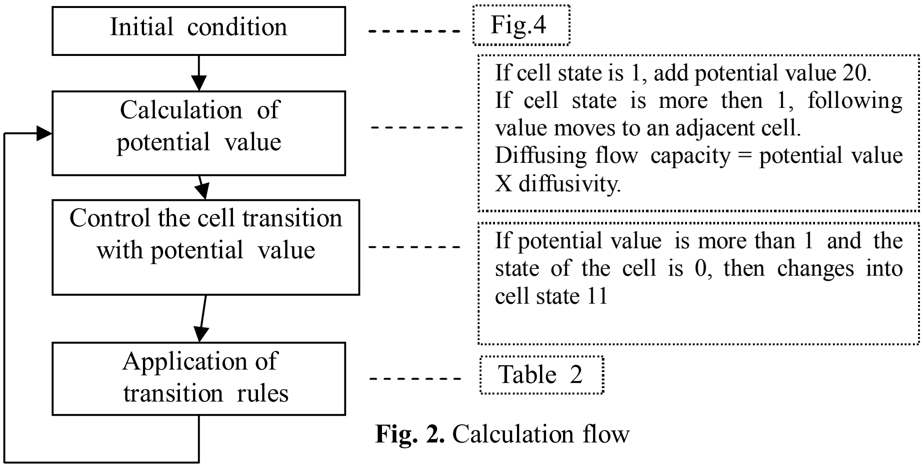

Fig. 2. Calculation flow

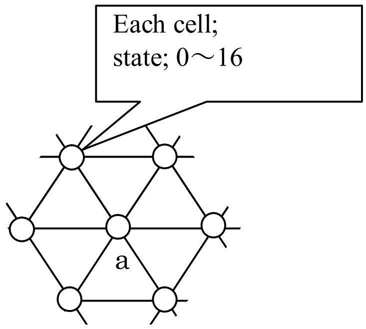

Fig. 3. Triangle grid model

The microbes such as protists create a variety of shapes by a single cell or a few cells (Fig.1). As trial simulation cases, we simulated the shape similar to various form of the microbe.

3 RESEARCH METHOD

3.1 Cellular automaton model

A two-dimensional hexagonal grid model was used in this study (Fig.3). The cell automaton was constructed according to the transition rules so that the state of the next step was determined by the state of the cell itself and the states of the six neighboring cells. Each cell had a state (0–16 states), Table 1 shows the content of 16 states.

Figure 2 shows the calculation flow. In a hexagonal grid, the calculations start from a certain initial condition. We calculates the potential value of gird fields, and control the cell transition with potential value. Then, we applied the transition rules, and settled the total states in all cells.

3.2 Transition rules

The transition rules are presented in Tables 2. We have not yet discovered a method with which to derive transition rules automatically according to a uniform law. Therefore, we constructed transition rules step-by-step according to the movements of the automaton.

3.3 Initial conditions

Figure 6 shows the notation of initial condition. Initial condition is consisted of 7 cells. Central cell is state 1 which has initial potential value. Around the central cell, we set 6 initial cells, which have state from 2 to 6, expressing by six columns of numerical value.

Table 1. States of cell

Cell state	Content	Color
①	cell nucleus	purple
②	cellular cytoplasm	maroon
③	cellular cytoplasm	olive
④	cellular cytoplasm	yellow
⑤	cellular cytoplasm	cream
⑥	cellular cytoplasm	white
⑦	cellular cytoplasm	skyblue
⑧	cellular cytoplasm	lime
⑨	cellular cytoplasm	green
⑩	cellular cytoplasm	pink
⑪	diffusion reaction place	gray
⑫	cell membrane	red
⑬	flagellar	dark blue
⑭	flagellar	peal
⑮	flagellar	aqua blue
⑯	flagellar	blue

Table 2. Transition Rule

	Central Cell	Conditions of six neighborhoods	Transition of central cell (state)	supplemental remarks
1	⑪	②～⑥＝1、⑧＝2	⑦	formation of cell cytoskeleton
2	⑪	②～⑥＝1、⑧＝0	⑦	〃
3	⑦	②～⑥≧2	⑪	〃
4	⑪	②～⑥＝2	⑧	〃
5	⑦	⑪≧3、m(m＝3～6)＝1	m-1	〃
6	⑦	⑦＝2、m(m＝3～6)＝1	m-1	〃
7	⑦	②≧1	⑧	〃
8	⑪	②≧1	⑧	〃
9	⑪	⑧＝2、⑪≧2	⑨	〃
10	⑪	⑧＝1、⑨＝1	⑨	〃
11	⑪	⑨≧2、⑪≧1	⑩	formation of cell membrane
12	⑪	⑨≧1、⑩≧2	⑫	〃
13	⑩	⑨≧1,⑪≧1、⑩＝0、⑫＝2	⑫	formation of cell membrane patterns
14	⑩	⑨≧1,⑪≧1、⑩＝1、⑫＝1	⑩	
15	⑩	⑨≧1,⑪≧1、⑩＝2、⑫＝0	⑫	〃
16	⑫	⑨≧1,⑪≧1、⑩＝0、⑫＝2	⑫	〃
17	⑫	⑨≧1,⑪≧1、⑩＝1、⑫＝1	⑫	〃
18	⑫	⑨≧1,⑪≧1、⑩＝2、⑫＝0	⑫	〃
19	⑪	⑩≧1、⑪≧4	⑬	formation of flagellar
20	⑪	⑫＝1、⑬＝1	⑭	〃
21	⑪	⑬＝1、⑭＝1	⑮	〃
22	⑪	⑭＝1、⑮＝1	⑯	〃
23	⑪	⑮＝1、⑯＝1	⑬	〃
24	⑪	⑬＝1、⑯＝1	⑭	〃
25	⑮	⑬＝2、⑯＝1	⑬	〃
26	⑯	⑬＝2、⑭＝2	⑭	〃

・The number with the circle shows the state of the cell.(ex. ◎ indicates state 0, ① indicates state 1)
・The description method of the condition ; For example, "①≧ 1" shows that there is more than one cell which is state 1 in six neighborhoods.

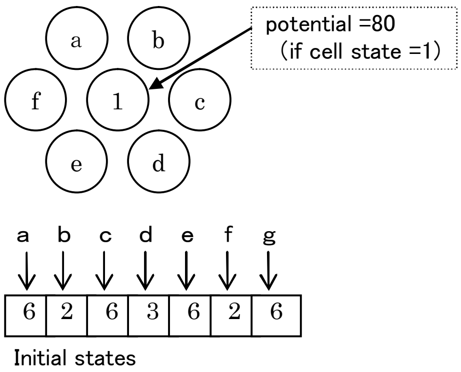

Fig. 4. Notation of initial condition

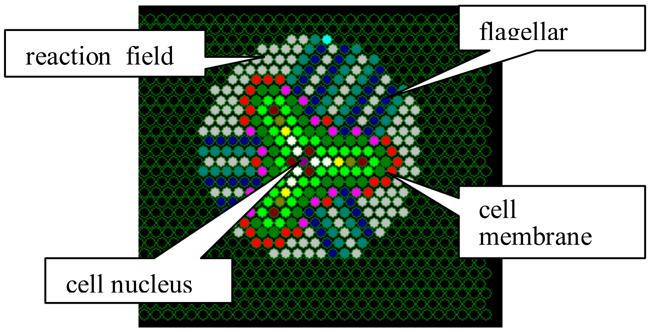

Fig. 5. Calculation result (initial condition 626262)

4 RESULTS

Figure 5 shows the calculation result in the initial case of 626262. A triangular cell is formed and some flagellars are formed. Figure 6 shows the process of cell membrane formation. Figure 7 is change of the result by the difference in initial condition. It is understand that various shapes were formed by the difference in initial condition. Figure 8 shows the change of the result by the difference in cell membrane condition from 13 to 18 in Table 2.

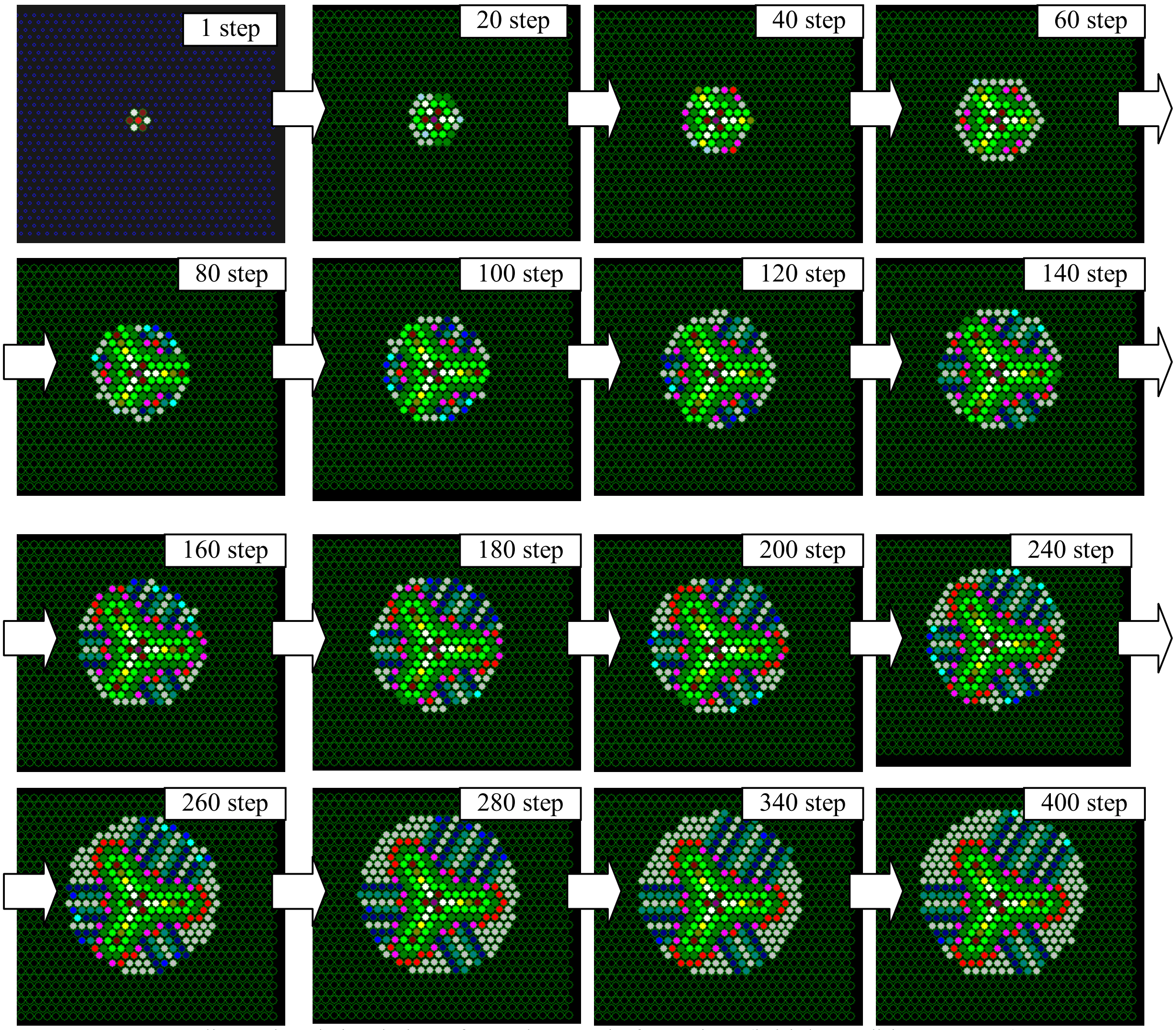

Fig. 6. Two-dimensional simulation of morphogenetic formation (initial condition 626626)

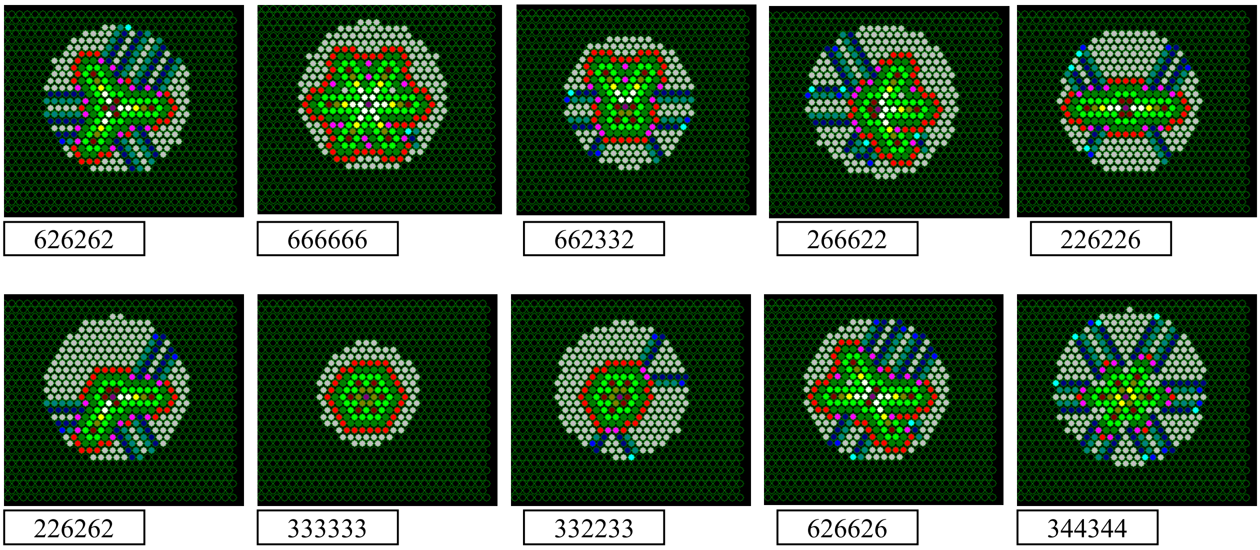

Fig. 7. Two-dimensional simulation of morphogenetic formation (Change of the result by the difference in initial condition)

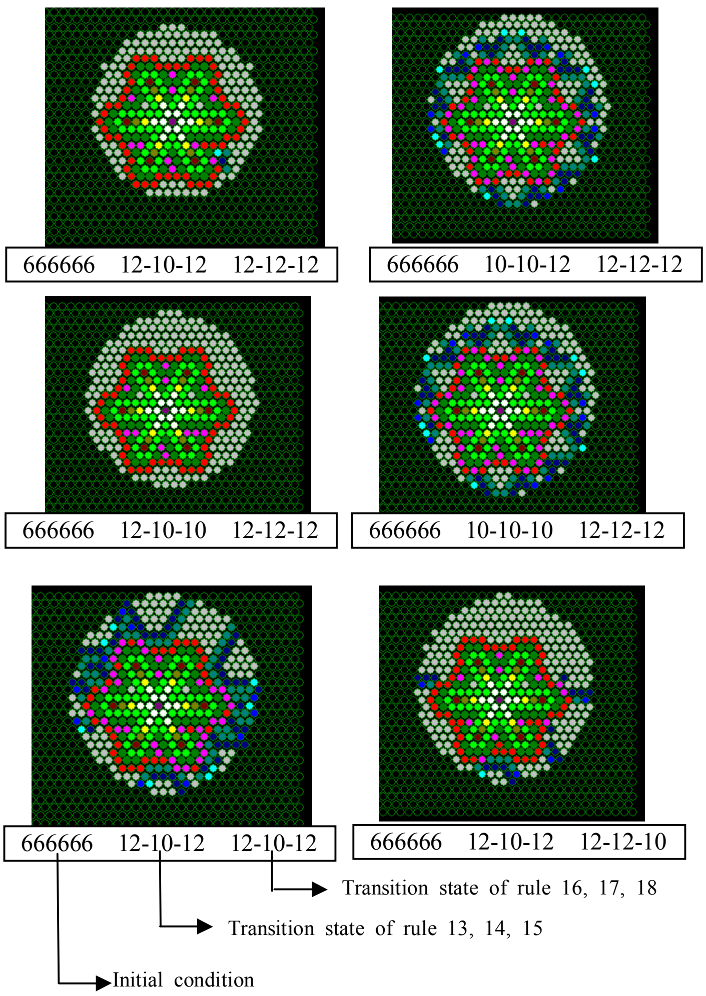

Fig. 8. Two-dimensional simulation of morphogenetic formation (Change of the result by the difference in cell membrane condition)

5 CONCLUSION

Using our model, we confirmed that the variety of shapes was emerged with the slight changes of some parameters value. Future directions are as follows:

- Find other transition rule sets.
- Find a way to automatically derive transition rules based on the uniformity law.
- Apply transition rules to chemical reaction system theoretically.

We believe that transition rules of this model can be applied to simulate self-organizing phenomena in real dynamic chemical reaction environment by applying transition rules determined in this study.

REFERENCES

[1] Turing, A. M., (1952). "The chemical basis of morphogenesis", Phil. Trans. Roy. Soc. Lond. B, Vol.237 No.641, pp.37-72

[2] F. G. Feugier, A. Mochizuki, Y. Iwasa; Self-organization of the vascular system in plant leaves: Inter-dependent dynamics of auxin flux and carrier proteins, Journal of Theoretical Biology 236, 366–375, 2005.

The Seventeenth International Symposium on Artificial Life and Robotics 2012 (AROB 17th '12),
B-Con Plaza, Beppu, Oita, Japan, January 19-21, 2012

Control of water flow to avoid twining of artificial seaweed

J. Ogawa[1], I. Suzuki[2], M. Yamamoto[2] and M. Furukawa[2]

[1] School of Engineering, Hokkaido University, Kita 14, Nishi 9, Kita-ku, Sapporo, Hokkaido, 060-0814, Japan
[2] Graduate School of Information Science and Technology, Hokkaido University,
Kita 14, Nishi 9, Kita-ku, Sapporo, Hokkaido, 060-0814, Japan
(Tel: 81-11-706-6445)
({ogawa, ikuo, masahito, mack}@complex.ist.hokudai.ac.jp)

Abstract: This study presents a control method for a water flow to avoid seaweed twining in a cultivation pool. The water flow in the pool is modeled by the lattice Boltzmann method (LBM). Morphology of the seaweed is determined by L-system. Physics Modeling (PM) represents its physical model. Three physical properties, gradual collision, adhesiveness, and tear phenomenon for the seaweed are artificially introduced into simulation. Motion of the seaweed is examined in the virtual underwater pool by PM simulation. A water flow pattern is realized by controlling particles distributed in lattices. We ascertained that some water flow pattern can avoid the seaweed twining phenomenon by changing the water flow pattern in the simulation.

Keywords: Physics modeling, Seaweed, L-system, Computational Fluid Dynamics, Lattice Boltzmann Method

1 INTRODUCTION

The technology of renewable energy is required for solving the global warming problem. In recent years, seaweed has been attracted for this purpose [1]. It absorbs CO_2 and emits O_2 in growing. The growth rate of the marine plant is 10 times faster than the terrestrial plant. Because the marine plant grows in a rich nutrition sea and the terrestrial one grows in soil. The grown seaweed is available as a material of bio-ethanol. Growing seaweed in seawater dissolving high concentration CO_2 can accelerate the growth rate of seaweed.

There arise some difficulties to introduce seaweed cultivation in large-scale bio factory. One of problems is to control a water flow for avoiding seaweed twining. Factors of the environment for effectively growing the seaweed are CO_2 assimilation of seawater and water temperature. Physical motion of seaweed with the growth process is also an important factor. Twining of seaweed causes depression of assimilation efficiency of CO_2 and death. It makes an adverse effect to effective growing. Therefore, the control of water flow is required for solving these problems.

Understanding physical motion of seaweed in fluid is important. Seaweed motion in fluid is flexible. This is one of biological properties and cause seaweed twining. Finding out conditions to generate twining has significant meaning.

This study aims at making a simulation model that examines water flow conditions causing seaweed twining. We make a physical model of seaweed and develop a virtual underwater pool where some water flow occurs. The motion of the seaweed is physically realized in the virtual underwater pool and verifies that our model can simulate suitable seaweed motion and fluid flow.

2 ARTIFICIAL SEAWEED

The physical model of seaweed is represented by connecting some small rigid spheres. It has three degrees of freedom and approximates soft motion of plants.

2.1 Physical model

The algorithm called L-system can represent the growth process in plants [2]. It was proposed by Hungarian theoretical biologist and botanist, Aristid Lindenmayer. We adopt L-system for modeling seaweed morphology and the grow process. L-system is shown in (1)-(4). Notations to make a growth model in fig.(1) are introduced as follow; V is the replaceable set of rigid bodies shown in fig.1, S is the invariable set of rigid bodies, ω is the initial state and P is the replacement rule.

$$V = \{A, B, C\} \quad (1)$$
$$S = \{E, D\} \quad (2)$$
$$\omega = A \quad (3)$$
$$P : (A \rightarrow EBA), (B \rightarrow C), (C \rightarrow D) \quad (4)$$

The seaweed grows by iteratively dividing branches. By applying L-system, the growth process of the artificial seaweed is represented in a natural form of plants.

A physical model is designed as shown in fig.3. It consists of 340 rigid bodies. Each rigid body has the same volume as the sphere one with 0.25 meters in radius.

2.2 Physical property

In order to mimic real seaweed as much as possible, we give physical properties to the artificial seaweed model. Such properties are gradual collision, adhesiveness and tear.

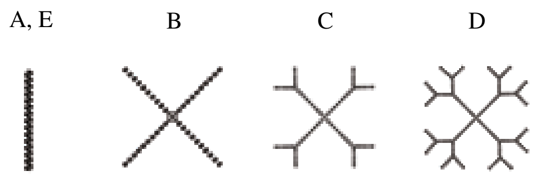

Fig. 1. The component of the physical model

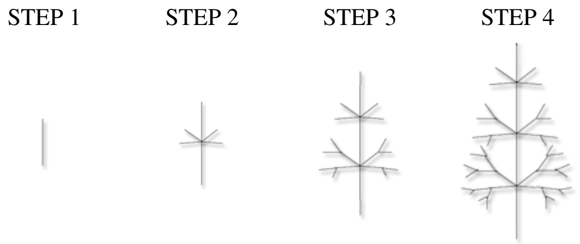

Fig. 2. The growth process of the physical model

2.2.1 Gradual collision

Gradual collision is observed among actual plants. An automatic calculation of collision by physical engine depends on a value of reflection coefficient. We set 0.05 to the value of reflection coefficient e. The gradual collision is realized by relatively reducing force in collision.

2.2.2 Adhesiveness

When some seaweeds colide each other, attractive forces among them appear. We model this phenomenon as adhesiveness. We add a small force similar to Coulomb one between two rigid bodies as the adhesiveness when a distance between two rigid bodies is less than the threshold r_t. This force is given by eq.(5),

$$F_A = k_a \frac{1}{r^2} \quad \text{for} \quad r < r_t \tag{5}$$

where k_a is an adhesive coefficient, r is a distance between two rigid bodies.

2.2.3 Tear

Seaweed is teared when a strong force works to it. In our model connection of rigid bodies is teared into two parts when receiving the external force larger than 10,000[N]. Teared parts cannot be reconnected any more.

3 VIRTUAL UNDERWATER ENVIRONMENT

A physical model for a virtual underwater pool is constructed by using PhysX that is the physical engine provided by NVIDIA cooperation. PhysX can do fast physical calculation and physical simulation on rigid bodies easily. However, functions for the buoyancy and drag forces in a fluid are not supported in the PhysX. We implement three forces as referred in [3].

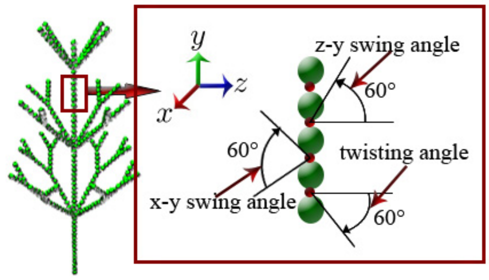

Fig. 3. The artificial seaweed model

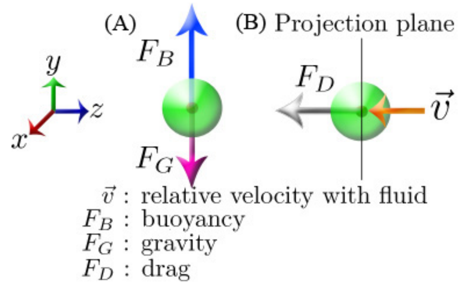

Fig. 4. Buoyancy and drag calculation

3.1 Buoyancy

In a fluid environment, the upward force called the buoyancy F_B works to the center of objects as shown in fig.4(A). A calculation of this force is given in eq.(6),

$$F_B = \rho V g \tag{6}$$

where ρ is a density of the water, V is a rigid volume, g is acceleration of gravity.

3.2 Drag force

Drag force F_D shown in fig.4(B) works to the rigid body in a fluid. This force that directs to opposite movement is proportional to a square of a relative velocity with a fluid. A calculation of this force based on fluid dynamics is given in eq.(7),

$$F_D = \frac{1}{2} \rho A C_D v^2 \tag{7}$$

where ρ is a density of the water, A is an area to which the drag works, C_D is a drag coefficient of inherent nature of rigid body, v is relative velocity of rigid with fluid.

4 WATER FLOW

In order to examine a pattern of water flow that makes avoiding seaweed twining, we require a realistic water flow model. Water is a fluid and its density is not changed by pressure. Therefore, the water flow can be treated as an incompressible fluid. In this study, it is modeled by the lattice Boltzmann method (LBM) [4].

4.1 Lattice Boltzmann Method

LBM is one of analytical techniques in computational fluid dynamics [5]. The method uniformly discretizes a simulating space into lattices and make it possible to simulate fluid movement as a continuum by use of particles distributed in the lattices. A particle distribution function is obtained by calculating ensemble average of a number of particles in each lattice. A fluid density and velocity is easily computed in this way. The number of particles is provided by real number. It can represent a high-precision flow without noise.

Particles have some velocities in LBM. In a discretizing time, they leave lattice or move to other lattice once at each time step $\quad t$. Some particles change the direction of velocity by collision. All particles are located in lattices at each time step. Particle collision appears in all lattices at the same moment.

4.2 Fluid model

We employ D3Q15 model as a particle distribution model in LBM [6]. The particles have velocities as shown in fig.5. The model only considers the mass conservation and momentum one.

4.2.1 Time evolution of particle distribution

To calculate a time evolution of particle distribution, we use the lattice Boltzmann equation defined by eq.(8).

$$f_i\left(x + e_i \quad t, t + \quad t\right) = \left(\frac{\lambda \quad 1}{\lambda}\right) f_i\left(x, t\right) + \frac{1}{\lambda} f_i^{eq}\left(x, t\right) \quad (8)$$

This equation is an evolution equation for the virtual particles. λ is a relaxation frequency. Particles move by iterating collision and they transit from a movement state to a equilibrium state at a constant rate. f_i^{eq} is a local equilibrium distribution. This particle equilibrium distribution function is given by eq.(9),

$$f_i^{eq}\left(x, t\right) = \omega_i \rho \left(1 \quad \frac{3}{2}\vec{u}^2 + 3\left(\vec{e_i} \quad \vec{u}\right) + \frac{9}{2}\left(\vec{e_i} \quad \vec{u}\right)^2\right) \quad (9)$$

$$\text{where, } \omega_i = \begin{cases} \frac{2}{9} & : \quad i = 0, \\ \frac{1}{9} & : \quad i = 1..6, \\ \frac{1}{72} & : \quad i = 7..14. \end{cases}$$

and ρ is a density of fluid, $\vec{u}$ is a velocity of fluid, $\vec{e_i}$ is a velocity of particle. By adding f_i^{eq} to the particle distribution function, eq.(8) guarantee a situation that fluid transit to the equilibrium state [6].

4.2.2 Boundary condition

In a lattice making a border as obstacles, the particle distribution function cannot give particles' direction to the fluid as obstacles. Therefore, we apply *bounce-back* to such lattices as a boundary condition. This condition rebounds particles into 180 degrees of direction from an obstacle shown in fig.6.

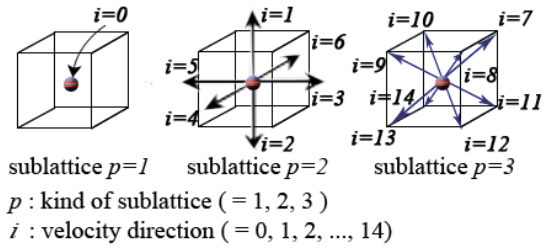

Fig. 5. D3Q15 Model

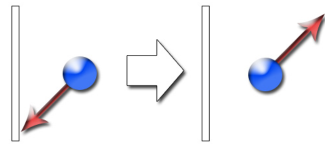

Fig. 6. This figure gives an overview of the translate and collide processes for a fluid lattice next to an obstacle.

5 NUMERICAL SIMULATION

In order to study the growth environment for avoiding seaweed twining, we examine two water flow patterns. We simulate physical motion of the artificial seaweeds in the virtual underwater pool considering in the water flow.

5.1 Conditions

Two patterns of water flow are experimented. The virtual underwater pool consists of 100 meters square cube and it is split up into 10^6 lattices. A central coordinate in the square cube is (0[m], 50[m], 0[m]).

We prepare two patterns of water flow as the forced convection. One of water flows is set by two spiral flows which are generated along y axis from 0[m] to 100[m] toward each other. The other is set by two spiral flows along z axis from -50[m] to 50[m] toward each other. The number of artificial seaweeds is four and initial positions of them are located at (10[m], 50[m], 10[m]), (-10[m], 50[m], 10[m]), (10[m], 50[m], -10[m]) and (-10[m], 50[m], -10[m]). A density of the model ρ_r equals to 1000.0[kg/m^3], a density of the water ρ 998.2[kg/m^3], drag coefficient C_D 1.0 and the project area A 0.25^2 . The initial state in the underwater is perfectly motionless. The simulation time is 20[sec]

5.2 Results of experiment

The results obtained from the computer simulation are shown in fig7. As for the pattern of water flow 1, the artificial seaweeds move outside in a spiral water flow from the upper surface. They move toward the position y=0 and are

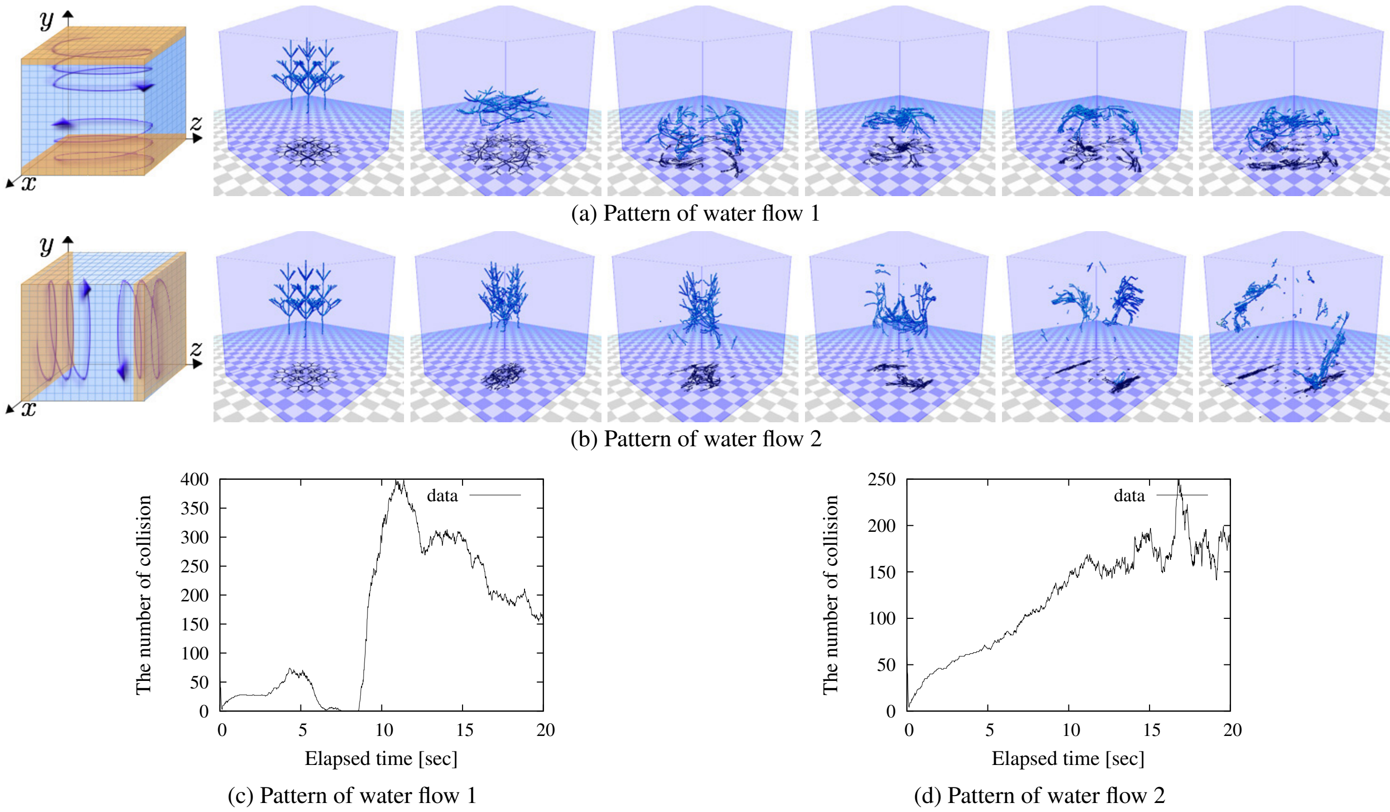

(a) Pattern of water flow 1

(b) Pattern of water flow 2

(c) Pattern of water flow 1

(d) Pattern of water flow 2

Fig. 7. Results of physical motion of artificial seaweed in underwater. (a) and (b) shows two patterns of water flow 1 and 2 respectively. Two graphs show the number of collision between rigid bodies at each time.

involved in a vortex generated by convection. Then the artificial seaweeds repeat to move upward and are involved in a vortex. Fig.7(c) shows the number of collision among rigids calculated by physical modelling rapidly increases up to 12 [sec] and them it decreases gradually. This shows that twining is generated and a part of the artificial seaweed teared is lost.

As for the pattern of water flow 2, the seaweed moves to right and left surfaces in the generated water flow when two artificial seaweeds keep in contact each other. Fig.7(d), the number of collision increases with the elapsed time and the moving range of artificial seaweeds is gradually partitioned into two ranges. Note that the number of collision does not decrease. In two separated regions twined artificial seaweeds cannot be observed but tear phenomenon.

6 CONCLUSION

We present a seaweed model having physical properties and realized seaweed twining phenomenon by physical simulations. High density of seaweed in the virtual underwater pool is one of conditions to generate twining. A tear occurs by adding forces in multiple directions into rigids. Water flows and circulating realize seaweed twining including tear. However, a water flow along a specific orbit cannot be introduced. We would like to find some patterns for avoiding the tear and seaweed twining.

REFERENCES

[1] Packer, 2009 M. Packer, Algal capture of carbon dioxide; biomass generation as a tool for greenhouse gas mitigation with reference to New Zealand energy strategy and policy. Energy Policy, 37 (2009), pp. 3428-3437.

[2] Corbit and Garbary, 1993 J.D. Corbit and D.J. Garbary, Computer simulation of the morphology and development of several species of seaweed using Lindenmayer systems. Comput. Graphics, 17 1 (1993), pp. 85-88.

[3] K.Nakamura, M.Morinaga, K.Iwadate, K.Yoneda, I.Suzuki, M.Yamamoto, and M.Furukawa, "Studies on Modeling Environment for Physics Modeling", *Conference Abstracts of Fourth International Symposium on Adaptive Motion of Animals and Machines*, pp.123-124, 2008.

[4] Shuling Hou, Qisu Zou, Shiyi Chen, Gary Doolen, Allen C. Cogley Simulation of Cavity Flow by the Lattice Boltzmann Method Journal of Computational Physics 118, 329-347 (1985)

[5] S. Chen and G. D. Doolen, Lattice Boltzmann Method for Fluid Flows, Annu. Rev. Fluid Mech. 30, pp.329-364 (1998)

[6] G. McNamara and G. Zanetti, Use of the Boltzmann equation to simulate lattice-gas automata, Phys. Rev. Lett. 61, Issue 11, pp.2332-2335 (1988)

Dealing with Rounding Error Problems in Evolutionary Physical Simulation

Marcin L. Pilat[1], Reiji Suzuki[1], Takaya Arita[1]

[1]Graduate School of Information Science, Nagoya University
Furo-cho, Chikusa-ku, Nagoya 464-8601, Japan
(pilat@alife.cs.is.nagoya-u.ac.jp)

Abstract: This paper introduces the problem of floating-point rounding errors in physical simulation. A simple virtual creature is simulated in a physical environment for a specified number of time steps. The effect of rounding errors is illustrated by varying the initial position of the creature which causes a change in the fitness value computed by a simple distance-based fitness function. With a large evaluation time, these rounding errors can produce significantly large differences in fitness. A discussion is provided on the importance of this finding for evolutionary simulations, including suggestions to alleviate the problem.

Keywords: physical simulation, floating point, rounding errors, evolutionary computation, artificial life

1 INTRODUCTION

Physical simulation is gaining popularity in the artificial life community. It enables experimentation with physical models which reflect the physical nature of biological organisms. Such experiments are vital in real-world applied robotics research. Furthermore, physical simulation allows for a complex simulation environment, important for the study of theoretical problems.

Physics engines are made for the video gaming market and are not meant to be used for accurate scientific simulation. However, they are valuable as they offer an approximation to more accurate physical simulation but at real-time speeds. We present and discuss problems that occur when using video game grade physics engines for scientific simulation, focusing on the problem of floating-point rounding errors. We simulate a simple virtual creature in a simple physical environment and demonstrate the rounding error problem on fitness evaluation by varying the creature's initial position.

We show that the fitness performance is highly sensitive to small variations in the creature's initial position producing significant variation in fitness values. These rounding errors occur after only a few simulation steps and increase drastically over simulation time. While not generally destructive, these errors can impact the performance of evolutionary algorithms that use fitness-proportional selection. Having identified the problem and presented evidence of its occurrence, we offer solutions that can alleviate it.

2 TEST MODEL AND ENVIRONMENT

Floating-point is the most common method to represent real numbers in computers. However, it is often poorly understood by software developers and researchers alike [1]. The most common floating-point representation currently used is defined by the IEEE 754 standard. There are mainly two sources of error when using floating-point representation: not all real numbers can be exactly represented and rounding error is inherent in floating-point computation.

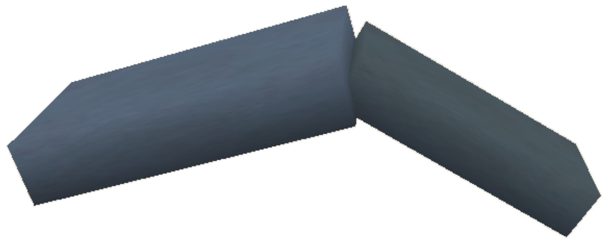

Fig. 1: Hand-crafted virtual creature used in the presented experiments composed of two bodies connected with a hinge joint. Neural network controller not shown.

The virtual creature model provides a simple yet powerful model for the study of evolution of morphologies and controllers for tasks such as locomotion [2] and light following [3]. We use a simple hand-crafted virtual creature, using the virtual creature model described in [2], composed of two blocks of different sizes joined with a hinge joint (shown in Fig. 1). The neural network consists of a sine wave generator neuron feeding into an effector allowing the smaller body part to rotate around the hinge joint.

The testing environment is composed of a simple plane simulation surface with friction. Virtual creatures are initially positioned above the surface and are allowed to drop due to the gravitational force. Once a creature rests on the ground surface and is stable from movement, the neural network of the creature is turned on which makes the creature move along the surface. We use a simple fitness function, measuring fitness as a simple displacement from the original resting position to the final resting position, to demonstrate the rounding error problem.

Physical simulation is performed using the Morphid

Academy software [2]. Morphid Academy is a virtual laboratory for the evolution of functional forms called Morphids. The software features physical simulation using the Open Dynamics Engine[1] (ODE) and NVIDIA PhysX[2] engines, graphical visualization through the OGRE graphics engine, and an ability to perform structured evolutionary experiments with a built-in genetic algorithm.

3 EXPERIMENTS AND RESULTS

We executed a suite of creature evaluation experiments to showcase the problem with physical simulation due to floating-point rounding errors. These experiments only performed creature simulation and fitness evaluation and did not have an evolutionary component. The position and evaluation time experiments were run using the NVIDIA PhysX engine while the precision experiments used ODE. The evaluated creature was recreated for each evaluation to prevent accumulation of internal state errors. For each evaluation, the creature was located at a certain (x,y) coordinate, along the simulation plane. The z-coordinate was kept constant.

3.1 Position

The initial creature position experimental results demonstrate the main problem of rounding errors in the floating-point representation producing unexpected behavior in physical simulations. Physics engines generally produce deterministic behavior (at least on the same hardware). When a fixed initial position is used (as in most virtual creature evolution systems), the behavior of a virtual creature is the same over a number of evaluations. However, modifying the initial position by a small amount can produce chaotic behavior with drastically different fitness values.

Fig. 2c illustrates this phenomenon showing the fitness values of the evaluated creature for 10000 initial positions centered around the origin and offset by multiples of a fixed position delta $\delta_x = 0.001$ along the x-axis. It is expected that the fitness will be independent of the initial x position value, producing a plot with a straight line. However, the fitness values vary greatly with a somewhat random distribution.

Additional experiments were performed varying the value of δ_x (not shown). Experiments with smaller values of δ_x have similar fitness behavior. With larger δ_x, somewhat periodic patterns of fitness values can be seen, which is likely due to the larger position values (in 100s). Similar results are observed varying δ_y along the y-axis.

3.2 Evaluation Time

Evaluation time is important for physical simulation since adequate evaluation time is required for the occurrence of certain behaviors. Evaluation time is expressed in terms of evaluation steps where each step is equal to one step of the physics engine. Fig. 2 shows the dependence of the evaluation time of 10, 1000, and 10000 on the error propagation in fitness values using $\delta_x = 0.001$.

These results indicate that the problem of rounding errors occurs quite early with only a few number of steps (10 evaluation steps in Fig. 2a). The rounding errors propagate over

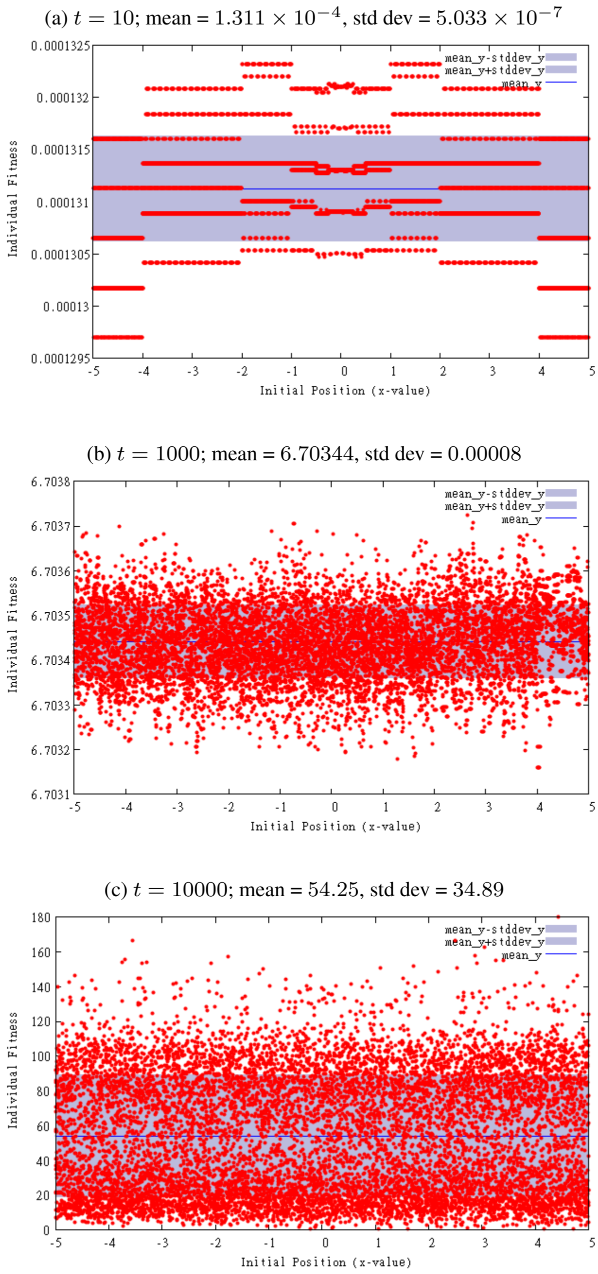

Fig. 2: Results of the evaluation time experiments with evaluation time t of 10 (a), 1000 (b), and 10000 (c). The x-coordinate of the initial creature position is plotted against the computed fitness value. Mean and standard deviation are displayed for each plot.

[1]ODE is available at `http://www.ode.org` under an open source license.

[2]The PhysX SDK is available for free from NVIDIA Corporation at `http://developer.nvidia.com/physx`.

evaluation time to a point where they produce a large range of results (as seen in Figs. 2b and 2c).

3.3 Precision

We run similar fitness evaluation experiments using the single and double precision versions of ODE with various evaluation time settings. ODE was used for these experiments since the NVIDIA PhysX SDK is only available in single precision. Selected results are shown in Fig. 3.

The results for smaller values of evaluation time (100 and 1000) show a larger dispersion of values using single precision. On the other hand, double precision produces more irregular fitness behavior within range $[-2, 2]$ (see Fig. 3a vs. Fig. 3b). With evaluation time of 10000, the single and double precision results are very similar with significantly large standard deviation values as demonstrated in Fig. 3c.

From these results, it is difficult to conclude whether the double precision fitness results are, in general, better than the ones with single precision, especially for a higher number of evaluation steps. It is interesting to note that while the mean fitness values for single and double precision are very similar with 100 and 1000 time steps, they are quite different with 10000 time steps (e.g., means of 96.434 vs. 69.447).

4 DISCUSSION

The floating-point rounding errors, presented by the examples in the previous section, are not necessarily a disadvantage of physics engines. The real world is inherently chaotic and capturing this behavior in simulations allows for results that appear more realistic and can be more suited to the real world. Artificial life simulations, especially involving a large number of interacting entities, are often criticized to be too orderly and thus not able to evolve novelty. Chaotic systems, such as physics engines, can be of benefit in this domain since they introduce inherent perturbations. Physically simulated ecosystems of evolving entities are a promising future for artificial life research.

The effect of this chaotic behavior has to be considered for each simulation since it can have a strong effect on the performance of the system and on the acquired results. In an evolutionary system where the fitness value decides on the reproductive strength of an individual, it needs to be calculated accurately for the algorithm to be effective. If the fitness of an individual significantly varies between different evaluations, the evolutionary algorithm might not select the individual for reproduction even though the individual is generally fit.

Fig. 4 illustrates the effect of the position-based rounding error problem on the performance of a genetic algorithm using the simple displacement fitness function. The variation in fitness values can be seen on the best of population line (in green). Furthermore, the evolutionary algorithm performance is decreased since good individuals can be eliminated from the population by worse performing individuals due to a significant variation in fitness values over different evaluations.

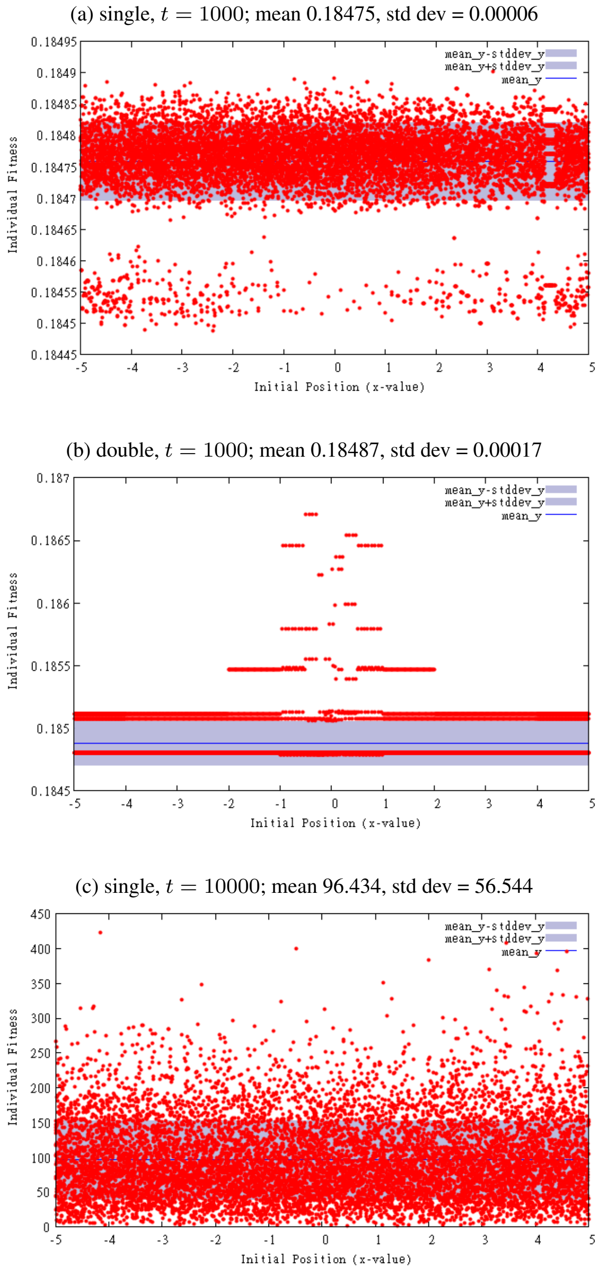

Fig. 3: Results of the precision experiments with single (a,c) and double (b) precision and evaluation time t of 1000 (a,b) and 10000 (c). The x-coordinate of the initial creature position is plotted against the computed fitness value. Mean and standard deviation are displayed for each plot.

The fitness values and their spread are greatly dependent on the fitness function used. Thus, care must be taken to craft a fitness function where the position-dependent fitness variation of a fit individual is still able to distinguish it from an unfit individual. The simple distance-based locomotion fitness

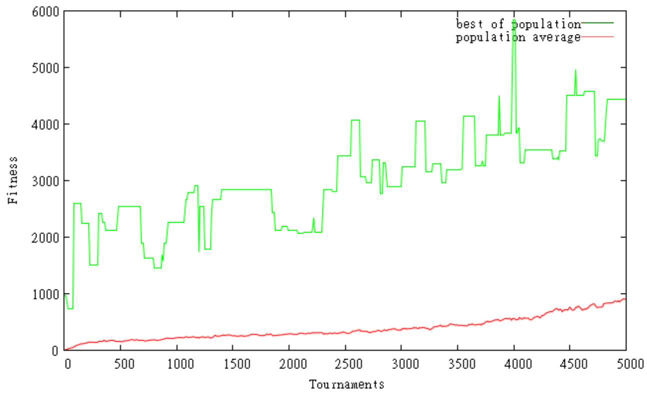

Fig. 4: Fitness plot of an evolutionary run with virtual creatures using the locomotion distance fitness function. The initial position of each evaluated creature is randomized. The best of population (in green) and population average (in red) are shown.

function used in the presented experiments was specifically chosen to demonstrate the rounding error and is not a good choice of a fitness function to alleviate the problem.

A simple solution to the initial position-based rounding error problem is to evaluate each individual at the same initial position. This idea works well with a simple evolutionary scenario where the evaluation of each virtual creature is separate. However, it is not well suited for co-evolutionary scenarios where multiple virtual creatures need to be evaluated in the same environment. Furthermore, a slight variation in initial position can prevent problems with the evolutionary system exploiting the position and can generally be beneficial if the effect of rounding errors can be minimized.

The floating-point precision setting can improve the results as we found the double precision performance in ODE more stable. However, with a large evaluation time, the problem is still significant. For closed source engines, such as NVIDIA PhysX, the precision is fixed and cannot be modified by the user. To alleviate the problem further, the floating-point representation can be replaced with a fixed-point representation if the range of required values does not need to be large. Fixed-point representation can provide more stable behavior but we are currently not aware of any free 3D physics engines that use a fixed-point representation.

A more important problem with floating-point arithmetic is that it is not guaranteed to produce the same results on different computer architectures and across different compilers or optimization settings as detailed in [4]. This can severely affect the reproducibility of results over different machines. The problem can be solved to an extent but solving it is considered to be very difficult [5].

5 CONCLUSIONS

We presented experimental results showing the effect of floating-point rounding errors on a sample fitness calculation of a virtual creature simulated using a physics engine. The variation of fitness values due to the difference in initial position of evaluation is evident and continues to increase with the evaluation time. The variation is significant on the time scale that is typically used for evolutionary experiments such as the virtual creature experiments presented.

This chaotic behavior can add beneficial randomness to the simulations but needs to be considered, especially for evolutionary experiments where the survival of an individual is directly related to its fitness value as compared with other individuals. In these evolutionary scenarios, a wrong choice of fitness function can have a negative effect on the evolutionary performance. We identified several possible methods of alleviating the floating-point rounding error problem.

The presented issue raises some important directions for future research. Can and should floating-point rounding errors be eliminated in physical simulations? Can evolutionary systems using well-crafted fitness functions harness the chaotic power of physics engines? How does this problem affect an evolutionary ecosystem simulated with a physics engine? The answers to these questions can situate physical simulation as a basis for future artificial life simulation systems studying open-ended evolution.

REFERENCES

[1] Goldberg, D., What Every Computer Scientist Should Know About Floating-Point Arithmetic. *ACM Computing Surveys*, 23 (1), pp. 5–48, March 1991.

[2] Pilat, M. L. and Jacob, C., Creature Academy: A System for Virtual Creature Evolution. In *Proceedings of the IEEE Congress on Evolutionary Computation (CEC 2008)*, pp. 3289–3297, IEEE, 2008.

[3] Pilat, M. L. and Jacob C., Evolution of Vision Capabilities in Embodied Virtual Creatures. In *Proceedings of the 12th annual Conference on Genetic and Evolutionary Computation Conference (GECCO 2010)*, pp. 95–102, ACM, 2010.

[4] Corden, M. J. and Kreitzer D., Consistency of Floating-Point Results using the Intel Compiler or Why doesnt my application always give the same answer? Published online: `http://software.intel.com/file/32018/`. Retrieved: September 2011.

[5] Fiedler, G., Floating Point Determinism. Published online: `http://gafferongames.com/networking-for-game-programmers/floating-point-determinism/`. Retrieved: September 2011.

The Seventeenth International Symposium on Artificial Life and Robotics 2012 (AROB 17th '12),
B-Con Plaza, Beppu, Oita, Japan, January 19-21, 2012

Adaptive Behavior to Environmental Changes: Emergence of Multi-generational Migration by Artificial Monarch Butterfly

Katsuya Suetsugu[1], Atsuko Mutoh[1], Shohei Kato[1], and Hidenori Itoh[1]

[1] Dept. of Computer Science and Engineering, Graduate School of Engineering, Nagoya Institute of Technology,
Gokiso-cho, Showa-ku, Nagoya 466–8555, Japan
(Tel:+81-52-735-5625 , Fax:+81-52-735-5625)
(suetsugu@juno.ics.nitech.ac.jp)

Abstract: The target of our study is the Monarch Butterfly, which is known for its multi-generational migration behavior: it migrates between southern Canada and Mexico over the course of one year within three to four generations. We approach this subject by using an evolutionary simulation that is an ecosystem consisting of artificial agents and five areas. We focus on the metamorphosis and the reproductive diapause, which are the ecological characteristics of the Monarch, and we design a model of agent which has the state as its inner parameter. We simulate under the environmental condition that the average annual temperature rises every year, which is modeled on the current global temperature rise. Our agents emerge the migration behavior similar to the multi-generational migration behavior of the actual Monarch. The migration process of the agents and their genetic factors are discussed, and our proposed model and the previous model are compared.

Keywords: Artificial Life, Adaptive Behavior, Monarch Butterfly, Evolutionary Simulation

1 INTRODUCTION

One academically valued of studying the behaviors of these organisms is evolutionary simulation based on models. Computer-simulated virtual ecosystems allow us to perform experiments rapidly and repeatedly, and the evolutionary processes of artificial organisms can be observed. Even if an agent has only a simple mechanism, if key aspects of behaviors are modeled, complex behaviors can be obtained through the evolutionary process [1].

The subject in our study is the Monarch Butterfly (*Danaus plexippus L., Nymphalidae, Lepidoptera*). This butterfly is known for its multi-generational migration behavior: it migrates between southern Canada and Mexico over the course of one year within three to four generations. Their life cycle has been detailed in reference [2] and our previous paper [3]. In spite of many reported studies [4], [5], [6], little is known about what influences their migration.

We have designed a model for the migration behavior of Monarchs by adaptiogenesis to environments with sensory agents in the previous research, but the previous model was incomplete because of many differences between the migration behavior emerged by agents and actual migration of Monarchs. In this paper, we focus on the metamorphosis and the reproductive diapause, which are the ecological characteristics of the Monarch, and we design a model of agent which has the state as its inner parameter. The agent changes its state depending on inner or outer information, and this changed state causes characteristic alterations. Additionally, we included the day length in the area models as an environmental factor because entomology shows that agent transformation depends on both temperature and day length. We show the advantage of our model by comparing the result with actual migration behavior of Monarchs and the previous model.

1.1 Area

The ecosystem has five areas that we label as $area_0$, $area_1$, ... , $area_4$ from south to north. Each area is modeled after the area of North and Central America (Table 1) where the migration of Monarchs actually occurs and consists of a two-dimensional 40×40 grid. $area_i$ has three environmental parameters, which are temperature, day length, and foods. These three environmental factors have significant effects on the migration of the Monarch. Each parameter is explained below.

Table 1. Five areas.

$area_i$	Model city
$area_4$	Minneapolis, U.S.A.
$area_3$	Kansas City, U.S.A.
$area_2$	Oklahoma City, U.S.A.
$area_1$	Austin, U.S.A.
$area_0$	Michoacan, Mexico

1.1.1 Temperature.

Temperature is decided by two kinds of environmental changes: long-term and short-term. A long-term change is an annual temperature rise and a short-term change is a daily change of temperature. To configure short-term change, we used real data from the past 20 years in each original area (collected by the National Climate Data Center [7]) and calculated the average annual data by trigonometric function. Thus, we define a temperature $tmpr_i(y,d)$ in $area_i$ at year y and day d as

$$tmpr_i(y,d) \quad = \quad short_i(d) + 0.01 \times y, \tag{1}$$

where $short_i(d)$ is short-term change in $area_i$. In this paper, the average annual temperatures of all areas rise $0.01°$ F every year.

1.1.2 Day Length.

In this paper, we newly focused on the day length as one of the environmental factors. The day length is defined as the time difference from sunrise to sunset. We can compute the time of sunrise and sunset using latitude, longitude, and altitude by the computation approach in reference [8]. We use real data to compute day length of each area.

1.1.3 Food

Each area has foods used as source of vital energy for the agents. The number of foods N_i in $area_i$ is determined by

$$N_i(t) = N_i(t-1) + \mathrm{M_F} \times incFood(\mathrm{S_F}, tmpr_i(t)), \tag{2}$$

where t is the number of steps ($t = \mathrm{DAY} \times y + d$, where DAY is a certain fixed number of days in one year), $\mathrm{M_F}$ is the maximum increment of foods in one day, and $\mathrm{S_F}$ is the most suitable temperature for increment of foods. $incFood()$ is the function which determines the increment of foods and outputs a real number while 0 to 1. The output of $incFood()$ is inversely proportional to the difference between $\mathrm{S_F}$ and $tmpr_i$. The life-span of the plant is $\mathrm{L_F}$. A food is removed from the simulation when it is eaten by the agent or reaches the end of its life-span.

1.2 Agent

An agent can sense internal information, and external information. By using sensory information, an agent decide its action and decide its state only once a day. In this paper, the behavioral strategy and the transformational strategy are expressed by n-output binary decision diagram (n-BDD) [9], which is an extension of BDD [10]. An agent $agent_j$ (j is identifier) has four genetic component and characterized as

$$agant_j(ea_j, cs_j, ast_j, sst_j), \tag{3}$$

where ea_j is a thermal sensitivity, cs_j is a cold resistance of the diapause agent, ast_j is the behavioral strategy, and sst_j is the transformational strategy. We describe ea_j and cs_j in Section 1.2.3, ast_j in Section 1.2.4, and sst_j in Section 1.2.5.

1.2.1 Action.

Five actions — W, E, R, Mn, and Ms — can be performed by the agent. An agent that selects W stays in the same grid of the same area for one day. An agent that selects E increase its energy by eating a food. If there is no food in its visual field, the agent moves at random looking for foods. An agent that selects R reproduces a new agent with another agent. If there is no agent in its visual field, the agent moves at random looking for agents. The Mn and Ms are the migration behavior. An agent that selects Mn migrates from $area_i$ to $area_{i+1}$ and that selects Ms migrates from $area_i$ to $area_{i-1}$ in 10 days. If there is no destination area, the agent changes their action to W.

1.2.2 State.

We newly focused on the "states" of the agents, which we neglected in the previous study. An agent has the state $state_j$ as its internal parameter. We defined three states — Cp, Dp, and Rp — which an agent can enter. The state determines which action an agent can select, if and when it can transition the state, and how long it can stay in the state.

The Cp state is the stage of an egg, a larva, or a pupa. An agent is in the Cp state, which is an initial state when it is first born. In the Cp state, only W and E are selectable actions and the agent can transition its state to either Dp or Rp. The Dp state is the reproductive diapause stage of an adult. An agent in the Dp state can select any action except R and can transition to Rp when the transition condition is met. The Rp state is an adult stage that can reproduce. All five actions are selectable in this state and can never transition back to the other two states. The age age_j, which is the maximum life-span of the agent in the state $state_j$, is initialized by L_{state_j} when the agent changes its states.

1.2.3 Sense.

All agents can sense the seven pieces of information. X_m has a truth-value, true or false. X_0 is information about whether the agent is in the diapause. X_1 is about whether the energy level is in the condition of "$in_j > \mathrm{I_B}$", where in_j is the amount of energy which agent stores and $\mathrm{I_B}$ is a specific energy level. An agent has a visual field (8-point neighborhood) and can sense the other agent and the food in its visual field. X_2 is information about whether other agents are in the visual field, and X_3 is information about whether foods are in the visual field. X_4 is information about the day length of the area; an agent can ask, "Are there more than 12 hours in this day?" X_5 and X_6 are information about the temperature of the area. To sense a temperature, each agent has up_lim_i and lo_lim_i, which are given by

$$lo\_lim_j = s_j - ea_j, \tag{4}$$

$$up\_lim_j = s_j + ea_j. \tag{5}$$

ea_j is an integer fulfilling $0 \leq ea_j \leq \mathrm{EA}$ (where EA is a constant) and represents the thermal sensitivity. An agent becomes sensitive to temperature changes when ea_j is small.

s_j is given by

$$s_j = \begin{cases} \mathrm{S_A}, & \text{if } state_j = \mathrm{Dp} \\ \mathrm{S_A} - cs_j, & \text{otherwise} \end{cases} \quad (6)$$

where $\mathrm{S_A}$ is the most suitable temperature of the agent and cs_j is an integer fulfilling $0 \leq cs_j \leq \mathrm{CS}$ (where CS is a constant). We observed that Monarchs in reproductive diapause pass the winter by reducing metabolic activity, so we set agents in the Dp state to be resistant to cold and agents in the Cp and Rp states to not be resistant. $X_5 = \mathrm{true}$ shows $tmpr_i < lo\_lim_j$, in which case the agent feels cold. $X_6 = \mathrm{true}$ shows $tmpr_i > up\_lim_j$, in which case the agent feels hot.

1.2.4 Action Decision Diagram.

The agent $agent_j$ decides which action $act_j(t)$ is performed every day by

$$act_j(t) = ast_j(X_0(t), \cdots, X_m(t)). \quad (7)$$

ast_j is expressed by 5-BDD with seven variables and five possible outputs: W, E, R, Mn and Ms.

1.2.5 State Decision Diagram.

The agent $agent_j$ decides to enter state $state_j$ by using counter $c_j(t)$, which is updated every day by

$$c_j(t) = c_j(t-1) + sst_j(X_0(t), \cdots, X_m(t)). \quad (8)$$

sst_j is expressed by 2-BDD with seven variables and two outputs: $+1$ or -1. The transition method of the two states is different. An agent, which reaches the end of its life in the Cp state ($age_j = 0 \wedge state_j = \mathrm{Cp}$), transitions a state. It can transition to Rp if $c_j(t) > 0$ or to Dp if $c_j(t) \leq 0$. In the Dp state, the agent can transition to Rp when $c_j(t) > 0$. In the Rp state, the agent cannot transition to another state.

1.2.6 Energy Level Update

After the action, the energy in_j is updated by

$$in_j(t) = in_j(t-1) + f(act_j(t), td), \quad (9)$$

$$td = |s_j - tmpr_i|, \quad (10)$$

where function f is the update function of the energy level. Increases or decreases to the energy level are directly determined by which action is selected and decreases are large if the value of td is also large. The E action is the only action by which an agent can increase its energy level and other actions decrease.

1.2.7 Reproduction.

An agent is generated from two agents by R action, which is the reproductive behavior. Four genetic parameters of a child agent are generated from that of both parents by crossover and mutation. We adopt two-point crossover for ea_j and cs_j, and uniform crossover for ast_j and sst_j. Let age_j, in_j, $state_j$, and c_j are each initialized by $\mathrm{L_{Cp}}$, $\mathrm{I_B}$, Cp, and 0, respectively.

1.2.8 Death.

If an agent suffers either one of the following conditions, it dies and is removed from the simulation.

$$in_j < 0 \quad \vee \quad age_j < 0, \quad (11)$$

Each condition means a starving and a natural death.

2 EXPERIMENTS AND DISCUSSION

In this section, we present the parameter settings and simulation results. We placed 200 agents with randomly generated genetic codes in $area_0$. Note that the experimental parameters in Table 2 are based on the actual biological features of the Monarch Butterfly and their habitat. We simulated 2000 years. All experimental results are the average of 30 trials.

Table 2. Parameters Setting.

DAY (1 year)	$\mathrm{S_F}$	$\mathrm{M_F}$	$\mathrm{L_F}$
365	65	30	30

$\mathrm{L_{Cp}}$	$\mathrm{L_{Dp}}$	$\mathrm{L_{Rp}}$
30	200	30

$\mathrm{S_A}$	EA	CS	$\mathrm{I_B}$
70	15	20	120

2.1 Experiment 1.

We simulated our proposed model. Fig. 1 shows the migration process from $area_0$ to the other areas that was obtained after 30 experimental runs. In the early simulations, many agents migrated to $area_1$ or $area_2$. Gradually, agents expanded their migration range with a temperature rise. In the later simulations, about 35 percent of the agents migrated to $area_4$. Our agents migrated from $area_0$ to $area_4$ within 3.76 generations on an average, which matches the fact that Monarchs migrate within 3 to 4 generations.

Fig. 2 shows the action decision diagram and the state decision diagram (variable nodes and outputs nodes appear in Section 1.2.1 and 1.2.2). X_0 is the next most significant information after X_1. The agent positively selects R and increases the number of agents because it can reproduce new agents only in the Rp state. The agent positively selects migration behavior, especially Ms, in the Dp state. It is clearly that the state is the agents, which we have newly focused on in this paper, is the essential factor for its behavioral decisions. On the other hand, X_5 and X_6 are the two most significant pieces of information for the agents in terms of deciding its states, while X_4 is third. This matches the behavior of actual Monarchs, which decide when to diapause and enter into a reproductive season on the basis of information about temperature and day length.

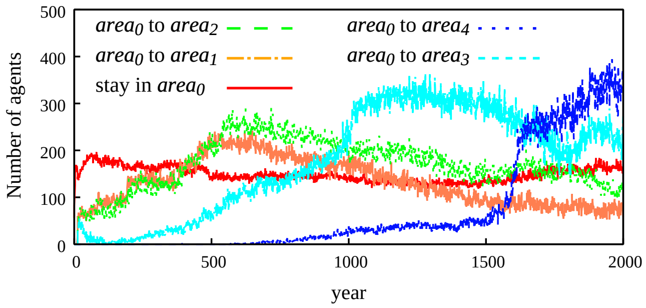

Fig. 1. The number of agents that stay in $area_0$ or migrate from $area_0$ to $area_n$ for 2000 years.

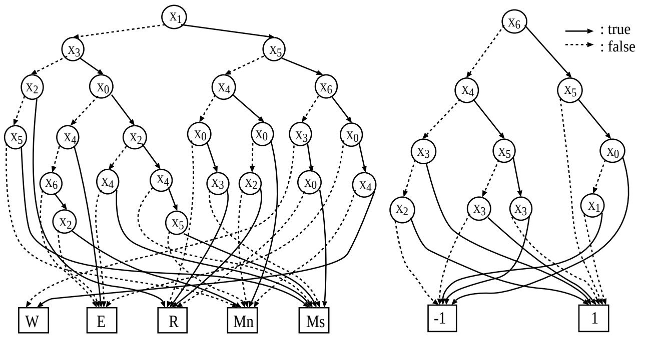

Fig. 2. Left: Action decision diagram (5-BDD), Right: State decision diagram (2-BDD).

2.2 Experiment 2.

We compared the annual migration of agents with that of actual Monarchs. Fig. 3 shows a time-line chart of migration. In the previous model, agents migrate from $area_0$ to $area_1$ between November and June of next year. Migrating toward colder areas in winter is completely different from the actual migration of Monarchs, which migrate south in fall and stay in wintering places to survive the cold winter. In contrast, agents proposed in this paper stay in $area_0$ from mid-December to February of next year. In spite of some differences in beginning and ending periods of migration, the migration cycle is similar to real one: the agents migrate north from spring to summer, migrate south from fall, and stay in $area_0$ from winter to next spring. We conclude that our proposed model extracts more significant key aspects of Monarchs' migration behavior than the previous model.

3 CONCLUSION

We presented an evolutionary model to simulate the multi-generational migration of the Monarch Butterfly. We build the model considering with the metamorphosis and the reproductive diapause. Agents emerged migration behavior similar to the multi-generational migration behavior of the actual Monarch. We show the advantage of our model by comparing with the result of the previous model.

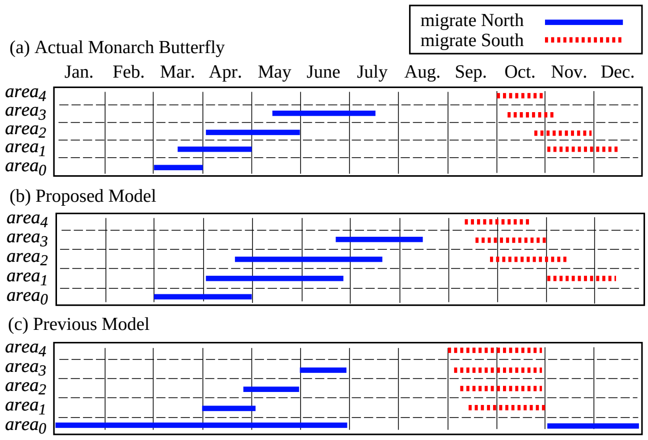

Fig. 3. Time-line chart of migration.

REFERENCES

[1] Langton C. G. (1986), Studying artificial life with cellular automata. *Physica. D*, 2, pp.135–149.

[2] The University of Kansas Entomology Program. Monarch Watch. `http://www.monarchwatch.org`.

[3] Hashizume H, Mutoh A, Kato S, Itoh H, and Kunitachi T. (2008), Evolution of migration behavior with multi-agent simulation. *Lecture Notes in Artificial Intelligence*, 5351, pp.685–667.

[4] Alerstam T, Hedenstrom A, and Akesson S. (2003), Long-distance migration: evolution and determinants. *Oikos*, 103(2), pp.247–260.

[5] Etheredge J. A, Perez S. M, Taylor O. R, and Jander R. November 1999, Monarch butterflies (danaus plexippus l.) use a magnetic compass for navigation. *National Academy of Sciences of the United States of America*, 96(24), pp.13845–13846.

[6] Walker T. J. (2001), Butterfly migrations in florida: Seasonal patterns and long-term changes. *Environmental Entomology*, 30(6), pp.1052–1060.

[7] National Climatic Data Center. NNDC Climate Data Online (Global Summary of the Day). `http://cdo.ncdc.noaa.gov/CDO/cdo`.

[8] Nagasawa K. (2000). *Computations of sunrise and sunset*. Chijin-Shoin, (in Japanese).

[9] Sawada T, Mutoh A, Kato S, and Itoh H. (2002), A model of biological differentiation in adaptiogenesis to the environment. *8th International Conference on the Simulation and Synthesis of Living Systems: Artificial Life VIII*, pp. 93–96.

[10] Akers S. B. (1978), Binary decision diagrams. *IEEE Transactions on Computers*, C-27(6), pp.509–516.

The Seventeenth International Symposium on Artificial Life and Robotics 2012 (AROB 17th '12),
B-Con Plaza, Beppu, Oita, Japan, January 19-21, 2012

Real-Time Generation of Prime Sequence by One-Dimensional Cellular Automaton with 8 States

K. Miyamoto [1], H. Umeo [2]

[1] Japan Advanced Institute of Science and Technology, Ishikawa 923-1292, Japan
[2] Univ. of Osaka Electro-Communication, Osaka 572-8530, Japan
(Tel: 0761-51-1111)
(k-miyamoto@jaist.ac.jp)

Abstract: In the present paper, we study a prime sequence generation problem on one-dimensional cellular automata. We show that an infinite prime sequence can be generated in real-time by a one-dimensional cellular automaton with 8 states. The algorithm that we propose is based on the well-known sieve of Eratosthenes, and its implementation is realized on an 8-state cellular automaton using 301 transition rules.

Keywords: one-dimensional cellular automaton, real-time prime generation algorithm, sieve of Eratosthenes

1 INTRODUCTION

Cellular automaton is considered to be a good model of complex systems in which an infinite one-dimensional array of finite state machines (cells) updates itself in a synchronous manner according to a uniform local rule. In the present paper, we study a prime sequence generation problem on one-dimensional cellular automata. The sequence generation problem has been studied for many years and a variety of interesting sequences has been shown to be generated in real-time by one-dimensional cellular automata [1-9].

Arisawa [1971], Fischer [1965], Korec [1997, 1998] and Mazoyer and Terrier [1999] have considered the sequence generation problem on the cellular automata model. Umeo and Kamikawa [2002] showed that infinite non-regular sequences such as $\{2^n | n = 1, 2, 3, ..\}$, $\{n^2 | n = 1, 2, 3, ..\}$ and Fibonacci sequences can be generated in real-time and the prime sequence in twice real-time by $\mathrm{CA}_{1-\mathrm{bit}}$. Umeo and Kamikawa [2003] showed that the prime sequence can be generated in real-time by a $\mathrm{CA}_{1-\mathrm{bit}}$ having 34 internal states and 107 transition rules. The cellular automaton model $\mathrm{CA}_{1-\mathrm{bit}}$ is a special subclass of *conventional* (i.e., *constant-bit-communication*) cellular automata. Each cell having the 1-bit inter-cell communication link can communicate with its nearest neighbor cells by sending and receiving a 1-bit information at each step.

Korec [1997] has shown that the prime sequence generation problem can be solved in real-time by using sieve of Eratosthenes. He also presented a one-dimensional cellular automaton with 11 states which can generate the prime sequence. Later, Korec [1998] gave a one-dimensional cellular automaton with 9 states generating the prime sequence in real-time.

In this paper we improve the implementation by presenting a smaller implementation on the same computational model. We show that an infinite prime sequence can be generated in real-time by a one-dimensional cellular automaton with 8 states.

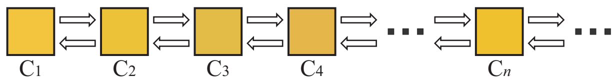

Fig. 1. One-dimensional cellular automaton.

First, in Section 2 we introduce a one-dimensional cellular automaton and define the sequence generation problem on the cellular automaton. In Section 3, we give a real-time prime sequence generation algorithm on a one-dimensional cellular automaton. The algorithm is based on the well-known sieve of Eratosthenes, and its implementation will be made on a one-dimensional cellular automaton with 8 states. The number of states implemented is the smallest one, known at present.

2 SEQUENCE GENERATION PROBLEM ON ONE-DIMENSIONAL CELLULAR AUTOMATON

A one-dimensional constant-bit-communication cellular automaton consists of an infinite array of identical finite state automata, each located at a positive integer point. See Fig. 1. Each automaton is referred to as a cell. A cell at point i is denoted by C_i, where $i \geq 1$. Each C_i, except for C_1, is connected to its left- and right-neighbor cells by a communication link.

A cellular automaton $\mathcal{A} = (\mathcal{Q}, \delta, \mathcal{F})$, where

1. $\mathcal{Q}$ is a finite set of internal states.

2. $\delta : \mathcal{Q}^3 \rightarrow \mathcal{Q}$ is a transition function. A quiescent state $q \in \mathcal{Q}$ has a property such that $\delta(q, q, q) = q$.

3. $\mathcal{F}$ is a special subset of internal states $\mathcal{Q}$.

The set $\mathcal{F}$ is used to specify a designated state of C_1 in the definition of the sequence generation.

We now define the sequence generation problem on the cellular automaton. Let M be a cellular automaton and $\{t_n | \, n = 1, 2, 3, ...\}$ be an infinite monotonically increasing positive integer sequence defined on natural numbers such that $t_n \geq n$ for any $n \geq 1$. We then have a semi-infinite array of cells, as shown in Fig. 1, and all cells, except for C_1, are in the quiescent state at time $t = 0$. The communication cell C_1 assumes a special state "0" (zero) in Q and starts its operation at time $t = 0$ for initiation of the sequence generator. We say that M generates a sequence $\{t_n | \, n = 1, 2, 3, ...\}$ in k *linear-time* if and only if the leftmost end cell of M falls into a special state "1" (one) in Q at time $t = kt_n$, where k is a positive integer. We call M a *real-time* generator when $k = 1$.

In designing algorithms for a cellular automaton, for ease of understanding and description of algorithms on cellular automata, we often use *signals* or *waves*, instead of transition tables. A signal (wave) is an information flow that is described as a straight line in the space-time diagram. Note that any signal cannot propagate at speed more than one cell per one step due to the definition of the transition function.

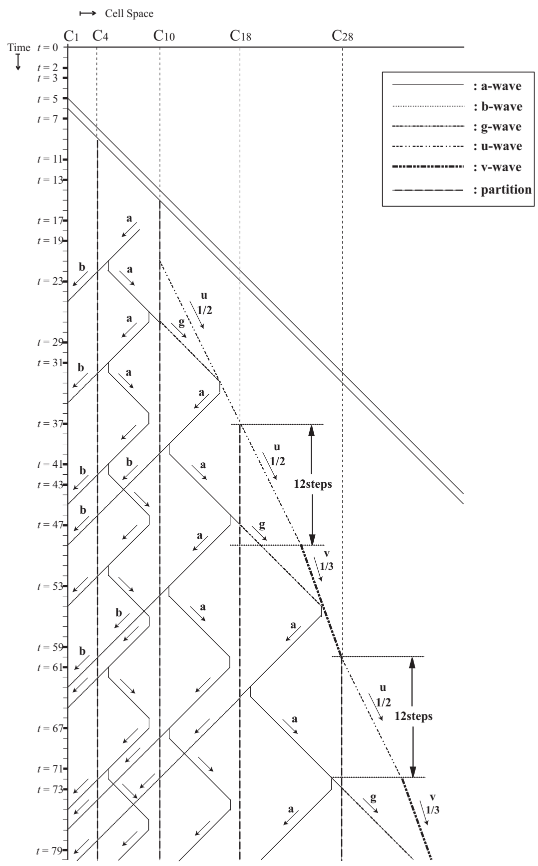

Fig. 2. Space-time diagram for real-time generation of prime sequence.

3 REAL-TIME GENERATION OF PRIME SEQUENCE ALGORITHM

In this section, we present a real-time generation algorithm for prime sequence on cellular automaton. The algorithm is implemented on an 8 state cellular automaton using 301 transition rules. Our prime generation algorithm is based on the classical sieve of Eratosthenes. Its cross out technique in the sieve of Eratosthenes is as follows. Imagine a list of all integers greater than 2. The first member, 2, becomes a prime and every second member of the list is crossed out. Then, the next member of the remainder of the list, 3, is a prime and every third member is crossed out. In Eratosthenes' sieve, the procedure continues with 5, 7, 11, and so on. In our procedure, given below, for any odd integer $k \geq 3$, every $2k$-th member of the list beginning with k^2 will be crossed out, since the k-th members less than k^2 (that is, $\{i \cdot k | \, 2 \leq i \leq k-1\}$) and $2k$-th members beginning with $k^2 + k$ (that is, it is an even number such that $\{(k+2i-1) \cdot k | i = 1, 2, 3, ...\}$) should have been crossed out in the previous stages. Thus, every k-th member beginning with k^2 is successfully crossed out in our procedure. Those integers never being crossed out are the primes. Figure 2 is a space-time diagram that shows a real-time detection of odd multiples of odds.

Our implementation that C_1 translate for state 0 when b-wave arriving C_1 and C_1 translate for state 1 when b-wave don't arriving C_1. The b-wave is generated by three ways. First, b-wave is generated when C_2 translate for state L. Second, b-wave is generated when C_3 translate for state L. Finally, b-wave is generated when a-wave collides with left partition.

3.1 Removing multiples of 2 and 3

In this section, we present a cross-out operation for multiples of 2 and 3. In the case of multiples of 2, the array repeats two states: R and L, alternatively on C_3. As for the case of multiples of 3, it repeats a state R, V and L on C_2 at each step. The cells C_2 and C_3 generate a b-wave, then they fall into the state L. A state transition into the state L on C_2 is done at time $t = 3k - 1 (k \geq 2)$ and the state transition into L on C_3 is done at time $t = 2k (k \geq 2)$. In this way the multiples of 2 and 3 can be removed.

We implemente Removing multiples of 2 and 3 algorithm.

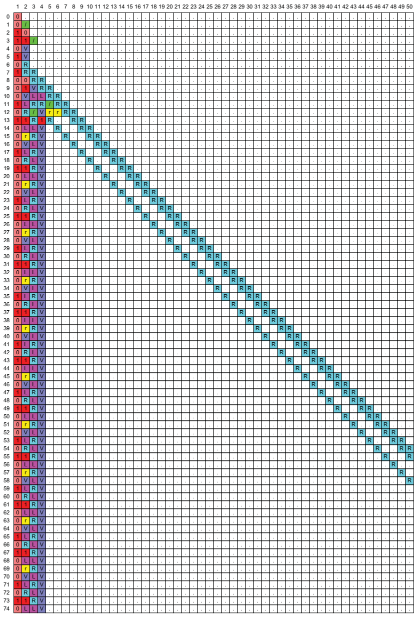

Fig. 3. Implementation of removing multiples of 2 and 3.

See the Figure 3 for implementation of removing multiples of 2 and 3. This figure is first partition generation on C_4, but this partition isn't need removing multiples of 2 and 3 algorithm. We generate first partition that it is easy to look.

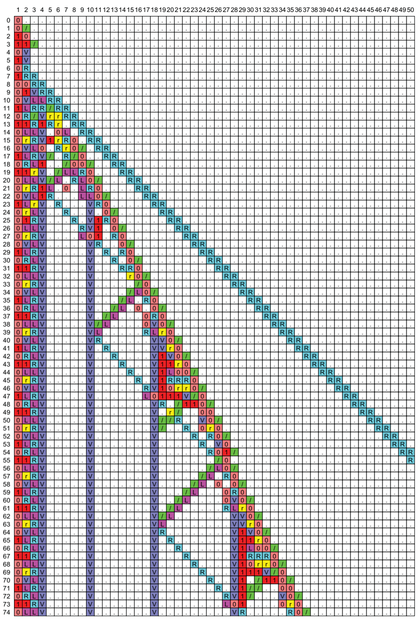

Fig. 4. Generation of partition.

3.2 Removing algorithm for odd multiple numbers greater than 5

In this section, we present a removing algorithm for odd multiples greater than 5. Those cross-out operations are done by a signal which moves around between partitions generated by the cellular automaton. The CA generates partitions, denoted by the state V on $C_{i^2+3i}(i \geq 1)$. We define the subspace $S_i, i \geq 1, i \in \mathcal{N}$, as the ith cellular space delimited by the consecutive partitions. The length of the space of S_i is $|S_i| = 2i+3$. The subspace $S_i, i \geq 1$ is used to generate a signal for removing odd multiples greater than 5, that is, $(2i+3)k, i \geq 1, k \geq 1$. The a-wave goes left and right between those partitions at a unit speed, one cell per one step. It changes into the b-wave, then it collides with the left partition. Those odd multiples greater than 5 are crossed out by the b-wave that goes through the partition in the left direction. The first partition is generated on C_4. See the Figure 4 for the real-time generation of those partitions.

We must generate the a-wave in each S_i. The a-wave generation in each partition is as follows: Thus the a-wave in S_2 is generated at $t = 34$ on C_{16} and the a-wave in S_3 is generated at $t = 56$ on C_{26}. The a-wave in S_1 is specially described in terms of finite states. At $t = 34$ the cell C_{16} generates a-wave which arrives on C_1 at $t = 49(= 7^2)$, and the a-wave generated on C_{26} at $t = 56$ arrives on C_1 at $t = 81(= 9^2)$. We use these a-waves to remove odd multiples greater than 5. The implementation of the generation of partitions can be done shown in Figure 4.

3.3 Real-time generation of prime sequence

In this section, we present a real-time generation of prime sequence algorithm. The algorithm is combination by "Removing multiples of 2 and 3" and "Removing algorithm for odd multiple numbers greater than 5". Those algorithms are implemented follows: section 3.1 and 3.2. Space-time diagram is shown in Figure 2. Figure 5 shows the transition table consisting of the 8 states and 301 transition rules where state '*' is a wall state of the left neighbor of C_1. Figure 6 shows some snapshots of the prime generation on 50 cells. Now we have:

Theorem There exists a cellular automaton having 8-states and 301-rules that can generate prime sequence in real-time.

4 CONCLUSIONS

We have studied a real-time prime sequence generation problem on a cellular automaton. The proposed real-time prime generator, based on the classical sieve of Eratosthenes, is implemented on a cellular automaton using 8 states and 301 transition rules. The implementation is the smallest one known at present.

.	Right State								
Left State	.	0	1	V	R	L	r	/	*
.	.	.	/	.	.	L	/	/	.
0	/	0			/	.			
1	.	.			.	L	/	/	
V	.	1			.	L	/	/	
R	R	R	r	R	R	R		r	
L	.	.	/	.	0			/	
r					L			r	
/	.		/	.	.	L		/	
*									

0	Right State								
Left State	.	0	1	V	R	L	r	/	*
.	.	V	0	R	0	r	.	R	
0	0				1			R	
1	1						1	0	
V	1							r	
R	0		/					V	
L	V	R	V					R	
r	0							/	
/	0	L							
*	0	0	0	1	1	0	0	1	

V	Right State								
Left State	.	0	1	V	R	L	r	/	*
.	V	0	V	V	V	1		1	
0	V	L				L			
1	R	1			L			1	
V		V					1		
R	V		0			1		1	
L	V					1		1	
r	V					1		1	
/	V					1	1	1	
*									

R	Right State								
Left State	.	0	1	V	R	L	r	/	*
.	.	.	L	L	.	.	.	/	
0	R	V			V	1		1	
1	.	.	L	L	0		.	/	
V	.	.			L				
R	R	r			r			V	
L		L	L	L	/				
r		r	L	L	.				
/	.		L	L	r			/	
*									

r	Right State								
Left State	.	0	1	V	R	L	r	/	*
.		.	L					/	
0		R			V	1	1		
1	.	0	L	L	R			/	
V		V					R		
R	0	R							
L		V	L	L					
r		V	L	L	r				
/			L					/	
*									

/	Right State								
Left State	.	0	1	V	R	L	r	/	*
.	.	L	/	.	.	L	/	/	
0	0				V				
1	.				.	L		/	
V	.	1			.	L	/	/	
R	R	0	r	R	r			r	
L	.		/	.				/	
r	R			R					
/	.		/	.	.	L		/	
*									

1	Right State								
Left State	.	0	1	V	R	L	r	/	*
.	V				V	1	1	1	
0	R		R	V	L	L	L	0	
1		.	.	/	L		L	V	
V	1	1	1	1	1	1	.	1	
R	V				V	1		1	
L	V				V	1	1	1	
r	V				V	1		1	
/	V		.		V	1		1	
*		1	0	0	0	0			

L	Right State								
Left State	.	0	1	V	R	L	r	/	*
.	.	.	/	.	L	.		/	
0	R				R	r	r		
1	R	R	r	R	R		r		
V	R	R	r	R		R		r	
R		L	r	R			V		
L		V	r	R	R				
r			r	R					
/	.	.		.		.			
*									

Fig. 5. Transition table for the 8-state real-time prime generator.

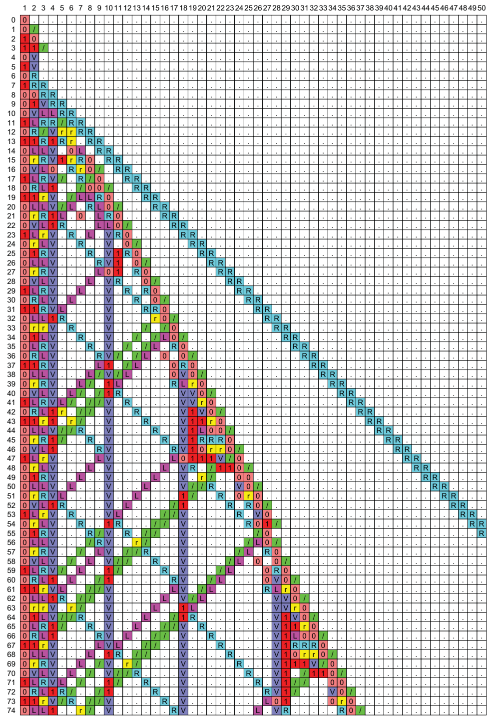

Fig. 6. Snapshots for the real-time generation of prime sequence on 50 cells.

ACKNOWLEDGEMENTS

A part of this work of the second author is supported by Grant-in-Aid for Scientific Research (C) 21500023.

REFERENCES

[1] M. Arisawa: On the generation of integer series by the one-dimensional iterative arrays of finite state machines (in Japanese). *Trans. of IECE*, 71/8 Vol.54-C, No.8, pp.759-766, (1971).

[2] C. R. Dyer: One-way bounded cellular automata. *Information and Control*, Vol.44, pp.261-281, (1980).

[3] P. C. Fischer: Generation of primes by a one-dimensional real-time iterative array. *J. of ACM*, Vol.12, No.3, pp.388-394, (1965).

[4] I. Korec: Real-time generation of primes by a one-dimensional cellular automaton with 11 states. *Proc. of 22nd Intern. Symp. on MFCS '97*, *LNCS*, 1295, pp.358-367, (1997).

[5] I. Korec: Real-time generation of primes by a one-dimensional cellular automaton with 9 states. *Proc. of MCU'98*, pp.101-116, (1998).

[6] J. Mazoyer and V. Terrier: Signals in one-dimensional cellular automata. *Theoretical Computer Science*, 217, pp.53-80, (1999).

[7] A. R. Smith: Real-time language recognition by one-dimensional cellular automata. *J. of Computer and System Sciences*, 6, pp.233-253, (1972).

[8] H. Umeo and N. Kamikawa: A design of real-time non-regular sequence generation algorithms and their implementations on cellular automata with 1-bit inter-cell communications. *Fundamenta Informaticae*, 52, No.1-3, pp.255-273, (2002).

[9] H. Umeo and N. Kamikawa: Real-time generation of primes by a 1-bit-communication cellular automaton. *Fundamenta Informaticae*, 58(3, 4)421-435, (2003).

The Seventeenth International Symposium on Artificial Life and Robotics 2012 (AROB 17th '12),
B-Con Plaza, Beppu, Oita, Japan, January 19-21, 2012

AGVs' Control in Autonomous Decentralized FMS (AGVs' Mind with Neural Networks)

Hidehiko Yamamoto[1], Hiroaki Tashiro[2] and Takayoshi Yamada[3]

[1]Department of Human and Information Systems, Gifu University, Japan
[2]Graduate School of Engineering, Gifu University, Japan
[3]Department of Human and Information Systems, Gifu University, Japan
(Tel: 81-52-293-2550)

[1]yam-h@gifu-u.ac.jp

Abstract: This paper describes control of the moving robots in an autonomous decentralized Flexible Manufacturing System (FMS) by moving robots according to its mind change. We propose Experience based Stimulation Adjustment by NN (ESAN) that is the method of efficiently changing the mind of the automated guided vehicles. The mind changes by various stimulation. In ESAN, the stimulation sent to the mind is adjusted to an appropriate value by using the neural network. The effectiveness of ESAN is evaluated with production simulations in an autonomous decentralized FMS virtual factory.

Keywords: Autonomous decentralized FMS, Mind, AGV

1. INTRODUCTION

The purpose of our research is to improve the productivity of the Autonomous Decentralized Flexible Manufacturing System (FMS) factory. In Autonomous decentralized FMS, many moving robots called Automated Guided Vehicles (AGVs) are operated. In this research, we focused on the action control of AGVs.

In a past research as a method of evading the interference with the route of AGV, the mind of AGV is modeled and the action control that gave AGVs was tried. [1][2] As a result, each AGVs could perform various actions according to the change of mind.

However, in Autonomous Decentralized FMS that has many AGVs, it took much time to evade the route interference, and because of this, we had many cases that the productive efficiency of Autonomous Decentralized FMS dropped. Then we thought the change of mind cannot always correspond to various situations.

To solve this problem, we propose Experience based Stimulation Adjustment by Neural network (ESAN). ESAN stimulates the mind to efficiently change the mind of AGVs.

2. ESAN AND MODEL OF MIND

2.1. Past method and ESAN

Fig.1 shows the comparison between the method of stimulating the mind in a past research and the method by ESAN. In a past research, when AGV failed in the action, the mind of the AGV had been stimulated directly. In ESAN newly proposes this time, stimulation is adjusted by NN according to the situation at that time, and the mind of AGV is stimulated afterwards when AGV fails in the action.

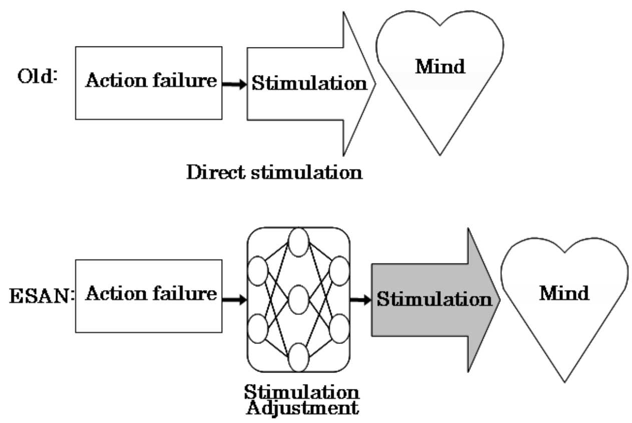

Fig.1 Comparisons between past method and ESAN

2.2. Element of mind

The mind is defined to have combined three elements which are the unit, the stimulation vector, and the load. (Shown in Fig.2-Fig.4.) The stimulation vector is an element that is tied to unit the load. The unit is composed of two numerical values of excited degree [E] and threshold [T]. [E] is able to increase and decrease by the value of the load. [T] is an upper bound of [E]. [E] is lowered to [T] when [E] exceeds [T], and it makes a signal to the stimulation vector. The unit for [E] of the unit to reach [T] is called excited and the unit that excited, and doesn't reach [T] is called calm. The state of mind is decided by combining units that have been excited

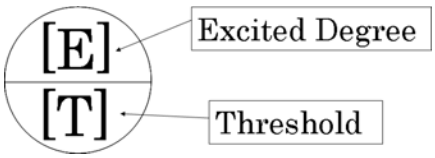

Fig.2 Unit

Fig.3 Stimulation vector

Fig.4 Load

2.3. Model of mind that uses ESAN

Fig.5 shows the model of the mind that uses ESAN. This model is a model to unite the load α, β, and γ with two units A and B by the stimulation vector. This model is divided into two parts. It is in the part where stimulation is received from the outside of the part, β, and γ that decides the state of the mind of A, B, and α.

There are two states of mind, which are an arrogant mind and a modest mind. AGV acts while doing these two minds in switches.

When A gets excited, AGV becomes modest, and takes a modest action that transfers the load to others. Moreover, when A is calm, AGV becomes arrogant, and takes an action that advances forcibly on the load and is arrogant. When the action rails because the mind of AGV is arrogant, the mind is received as stimulation through β. Then, this increases A[E]. Unit A gets excited when A[E] reaches A[T]. When the action fails because the mind of AGV is modesty, the mind is received as stimulation through γ. Then, this increases B[E]. Unit B gets excited when B[E] reaches B[T].

2.4. Generation of NN and its working in ESAN

The new function of ESAN includes the stimulation adjustment function that is caused by the NN after some AGVs experiences. The NN in ESAN uses Backpropagation method (BP method). The instruction signal used for this is made by performing the FMS production simulation beforehand, and using the result.

At first, the FMS production simulation is made visible, and animation on the FMS factory is made. Next, the action of AGVs in the animation is analyzed. The analysis is to understand whether the route interference is generated easily under what situation in the animation.

That is, look for the case with route interference to which the route interference is quickly evaded and time-consuming route interference. The states of mind of AGVs in these cases request either arrogance or modesty. The result of such an analysis is used as a instruction signal of NN.

The BP method is done based on this instruction signal and NN is generated. The generated NN stimulates two values of the mind of AGVs. Whenever AGV causes route interferences, the NN of ESAN receives five kinds of information. The five kinds of information are the destination of the AGV, previous destination, other nearby AGV number, other AGV number in goal direction, own current location as shown in Fig.5. In other words, these are the input information of NN. And, NN decides the two values in the model of the mind as an output. The mind of AGVs receive the value of β and γ from NN every time AGVs causes route interference. There are two states of mind. One is arrogant mind and the other is modest mind. The arrogant AGV forcibly moves, and the modest AGV makes way for other AGVs. AGV moves while in these two states of mind by switching one after another. One of the AGV acts while in these two minds in switches. When A has gotten excited, the state of mind is modest. At this time, AGV takes a modest action that transfers the load to others. Moreover, when A is calm, the state of the mind is arrogant. AGV takes an arrogant action that advances forcibly on the load. If AGV failed action in arrogant, the mind receives stimulation by β. Then, mind's A[E] is increased by the value of β. A gets excited when A[E] reaches A[T]. If AGV failed action in modesty, the mind receives stimulation by γ. Then, mind's B[E]is increased by the value of γ.

3. SIMULATION RESLUTS

Fig.6 shows CG of applied Autonomous Decentralized FMS. The model of the mind that used the above-mentioned ESAN for each AGV was transplanted. At this time, the value of β and γ was set to the numerical value of 1～4. And, the production simulation that operated this Autonomous Decentralized FMS for eight hours was done.

The production simulation was performed for eight hours with the Autonomous Decentralized FMS. The production simulations of the number of AGV 3, 5, 7, and 9 were carried out 20 times respectively.

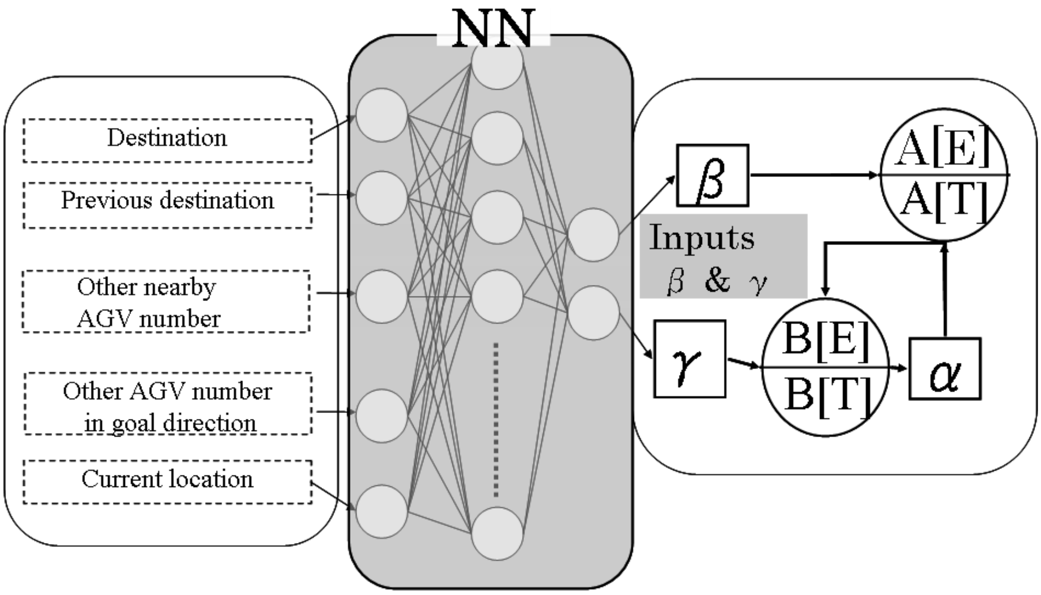

Fig.5 Model of AGVs' mind for ESAN

Table. 1 Average outputs and their increased rates

Methods \ Number of AGVs	3	5	7	9
past research methods outputs	111.7	162.15	199.65	228.6
ESAN outputs	115.3	171.2	215.25	249.4
Increased rate (%)	+3.22	+5.58	+7.81	+9.1

Table. 2 Route interference number and its increased

Methods \ Number of AGVs	3	5	7	9
past research methods	943.2	2715.0	5034.1	7643.8
ESAN	735.7	2412.2	4671.3	7178.2
Increased rate (%)	-22.0	-11.15	-7.2	-6.1

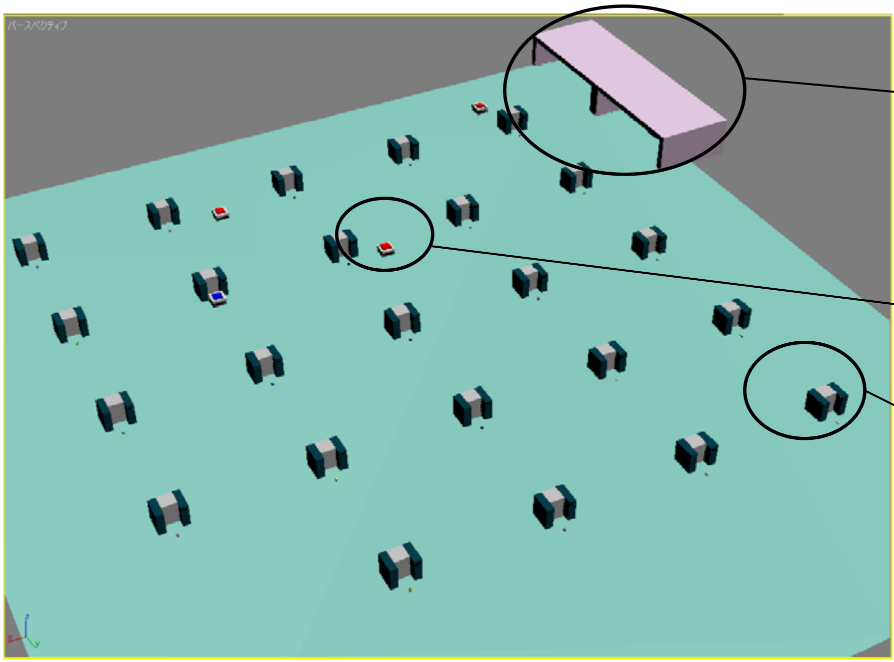

Fig.6 Autonomous decentralized FMS

The average outputs are shown in Table.1 and the number of route interference is shown in Table.2. The simulation result under this condition of old methods is shown for comparison. The increasing rate of the average production based on earlier methods and the increasing rate of the number of route interference are shown respectively.

For example, when the number of AGV is 3, the average outputs were 111.7 in the case where the past research method was used. On the other hand, the average outputs are 115.3 in the case where ESAN is used, and the average outputs increased by 3.22%. Route interference number decreased by 22% in ESAN compared with the past research method. Moreover when ESAN was used, the average production increased in any conditions. Especially, if the number of operating AGVs increases, average outputs are increasing more and more. In the same way, the number of route interference decreases by 22% in ESAN compared with earlier methods when the number of AGVs is three. (as shown in table.2) When ESAN is used, the number of route interference decreases in other conditions.

Based on the above-mentioned, it has been understood that the productive efficiency of the factory improves by using ESAN.

4. CONCLUSIONS

In this thesis, ESAN is proposed as the method of adjusting the stimulation sent to the mind to an appropriate value as a method of changing the mind of AGVs more efficiently. The method of using ESAN as the method of adjusting stimulation to mind by NN is compared with the simulation result of the old method.

Under all conditions, it was achievable that the mind was changed more efficiently. Thus, ESAN was proven to be more effective than earlier methods..

REFERENCES

[1]Hidehiko Yamamoto, Kikuchi Hiroyuki, Takayoshi Yamada and M. Anouar Jamali, Moving Robots' Mind of Autonomous Decentralized FMS and Mind Change Control, The Journal of Artificial Life and Robotics, Vol. 14, No.1, 34-38(2009), Springer

[2]Hidehiko YAMAMOTO, Takayoshi YAMADA and Shinsuke KATO, AGV Mind Model and its Usage for Autonomous Decentralized FMS by Change of Mind, Proceeding of Third KES International Symposium, KES-AMSTA 2009, Agent and Multi-Agent Systems : Technologies and Applications, Lecture Notes in Artificial Intelligence, Edited by Anne Hakansson, Ngoc Thanh Nguyen etc. , ISSN 0302-9743, Uppsala, Sweden, pp.744-753, June(2009), Springer.

The Seventeenth International Symposium on Artificial Life and Robotics 2012 (AROB 17th '12),
B-Con Plaza, Beppu, Oita, Japan, January 19-21, 2012

Modelling mental representation as evolved second order learning

Solvi Arnold[1*], Reiji Suzuki[1], and Arita Takaya[1]

[1]Graduate School of Information Science, Nagoya University, Aichi 464-8601, Japan
(Tel: 81-52-789-4716, Fax: 81-52-789-4800)

[*]solvi@alife.cs.is.nagoya-u.ac.jp

Abstract: Mental representation is a fundamental aspect of advanced cognition. An understanding of the evolution of mental representation is essential to an understanding of the evolution of mind. However, being a decidedly mental phenomenon, its evolution is difficult to study. This research addresses the question of how representation ability may emerge from non-representational cognition. We reformulate cognitive map ability, a paradigm case of mental representation, in terms of second order learning. We provide a neural network species with neural mechanisms for second order change and evolve them in an environment of randomly generated Tolman mazes, known to require mental representation. Some runs of this model evolve near-optimal performance, providing support for the hypothesis that mental representation is evolved second order learning.

Keywords: artificial life, cognitive map, evolution of mind, learning, mental representation, neural networks.

1 INTRODUCTION

Mental representation (MR for short) is, abstractly put, the ability to simulate or reconstruct in the mind aspects of the environment that lie outside the scope of one's current perception. The type of MR we focus on in this paper is the ability to navigate using "cognitive maps": mental representations of the layout of an environment (see Tolman [1]). Much of an environment may lie outside one's view, but mental representation of these parts makes it possible to take those parts into account nonetheless. Other types of MR are "mental time-travel" and "theory of mind" (see Takano & Arita [2], Minoya, Arita & Omori [3] for computational approaches to the latter). There too, inaccessible aspects of the environment (respectively: future and past, other minds) are mentally simulated or reconstructed.

The evolution of MR is not well-understood. MR is a highly structured and organized form of cognition, and already in the early decades of connectionism, it has become clear (contrary to common intuition) that adaptive processes such as evolution or learning do not, in general, produce such structured or organized AI (see e.g. Fodor & Pylyshyn [4]). This raises the question how MR can have evolved in biological cognitions. We propose that the representational nature of MR emerged from the interaction between adaptation processes, specifically: first and second order learning. We provide a proof of concept for this hypothesis in the form of a computational model in which a neural network species with the basic elements for second order change is evolved in an environment composed of maze tasks generally believed to demand cognitive map ability. If second order learning can be evolved into MR, this may improve our understanding of the evolutionary transition from non-representational to representational cognition.

2 TOLMAN MAZES

In experimental psychology, MR ability in biological species is often studied using Tolman mazes [1]. A Tolman maze has multiple paths from its start to its goal. Exploring the maze, subjects latently learn to take the shortest path. Subsequently, the shortest path is blocked, meaning they have to switch to a different path. However, the maze is set up so that after blockage of the shortest path, the new optimal choice of path depends on the location of the blockage (Fig. 1). Many species need to re-learn on the altered layout, while some species find the new optimal path without additional exploration (needing merely to observe the position of the blockage). The standard explanation is that the former category of species does not acquire a mental representation (cognitive map) of the maze during initial exploration, while the latter does. Animals that have acquired a representation of the maze can exploit that representation to infer the new optimal path without additional exploration.

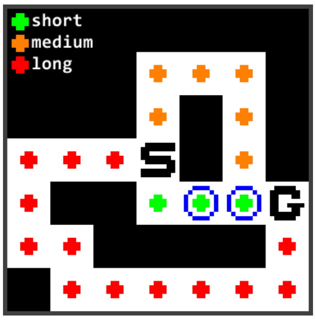

Fig. 1. Generated Tolman maze on 7x7 grid. S: Start G: Goal. Dot colours indicate path lengths. Blue circles indicate possible locations for the blockage. Blockage on the left blue ring obstructs only the short path, while blockage on the right blue ring blocks both the short and medium path.

3 HYPOTHESIS

Here we propose a different explanation, in terms of second order learning. MR can be viewed as acquired isomorphism between a mind's content and its environment. It has previously been established that innate isomorphism can emerge from interactions between evolution and learning (Arnold [5]). Acquired isomorphism might similarly emerge from interactions between first and second order learning.

Let us first give a working definition of first order learning: "advantageous change in behaviour, caused by exposure to pertinent information". Second order learning, then, must be advantageous change in (first-order) learning, caused by exposure to pertinent information. When after blockage of the shortest path in a Tolman maze a subject infers the new optimal path without additional exploration, we can view this inference as a split-second learning process: exposure to pertinent information (observation of the location of the blockage) produced an advantageous change in behaviour (the subject abandons the blocked path and switches to the new optimal path). Viewing it as such requires that we explain how this (first order) learning process can produce such a fast and effective behaviour-update (the information in the observation alone does not suffice to explain the update). Our explanation is that during exploration, not just the animal's behaviour has adapted to the maze (via a learning process), but that that learning process itself has been adapted to the maze as well. In other words, a second-order learning process optimized the (first-order) learning process to the current environment: the optimal change in behaviour (from selecting the blocked path to selecting the optimal path) has come to be causable by minimal information: mere observation of the location of the blockage has come to trigger this behaviour-update.

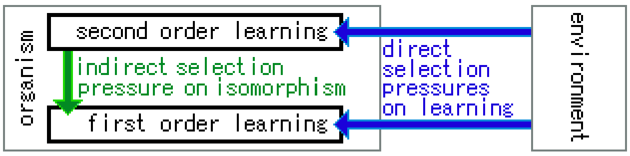

Fig. 2. Learning and isomorphism (MR).

A second order learning process associates possible future observations with suitable behaviour updates. This may sound infeasible, and for almost all first order learning schemes, it is. But if the first order learning scheme produces behaviour-implementations that are isomorphic with the environment, then second order learning suddenly becomes quite feasible: simply keeping the behaviour-implementation isomorphic with the environment (i.e. updating it continuously with present perception) keeps the behaviour optimal with respect to that environment. So when there is selection pressure on second order learning, then indirectly there is selection pressure on isomorphism-based first order learning schemes. Mental representation, then, could be this isomorphism.

The proposed reformulation might seem highly specific to the case of Tolman mazes, but equivalent reformulations can be given for many or all other situations that involve MR. We omit detailed examples here, but the general form is as follows. Consider an environmental object X to be represented. We (should) perceive our subject as representing X if and only if it can pre-emptively adjusts its behaviour so as to avoid or bring about specific unseen situations involving X after some period of observation of X. In all such cases, observation affects future changes in behaviour. To the extent such pre-emptive adaptation characterizes MR, explanation in terms of second-order learning should be applicable. In the focal case of cognitive maps, X is the maze, but the general scheme may equally well describe a scenario of spontaneous novel tool use (a scenario generally recognized as involving MR), with X being the tool.

4 MODEL

We test the hypothesis using a model in which neural nets with the basic elements for second order neural change are evolved in an environment composed of Tolman mazes.

Each individual's fitness is assessed on multiple Tolman mazes (randomly generated continuously over the course of the experiment). In each maze, the agent first gets 150 time steps to explore the maze (exploration phase), is then placed back at the start position and given exactly enough time steps to reach the target over the shortest path (exploitation phase). On a portion of the mazes, the shortest path is blocked at the start of the exploitation phase. When the agent arrives at the blockage, its remaining time steps are again set so as to make it only just possible to reach the target. Fitness is awarded for reaching the target. A population of size 100 is evolved, using a genetic algorithm with mutation but no crossover.

In addition to standard (activatory) connections, the network species has connection types that can be wired up to create second order changes in behaviour. These connection types are (1) activatory connections with lag, and (2) neuromodulatory connections. That two mechanisms are provided is merely to improve flexibility so as to facilitate evolution. Theoretically, one mechanism should suffice.

(1) Activatory connections with lag. These transmit activation signals much like standard connections, except with a short delay. This makes it possible for the nets to retain activation patterns over time. This sort of connection is common in recurrent neural networks. Retention of activation makes it possible for perception of a stimulus to af-

fect behaviour at some later point in time. For long-term change, one needs loops (in the simplest case, a single reflexive connection). Trivially, second order behaviour change can be construed too: if a retained local activation pattern A somewhere in a net affects behaviour, and another retained local activation pattern B affects A, then B has a second order effect on behaviour.

(2) Neuromodulatory connections. These connections convert activation into "modulation": the pre-synaptic neuron's activation arrives at the post-synaptic neuron as modulation. Typically, a neuron's modulation determines its connections' plasticity, in a simple (e.g. Hebbian) weight update rule (see Soltoggio et al. [6]). We let a gene pick from among a number of update rules (various combinations of pre- and post-synaptic activation and modulation values). Connection weight changes can change behaviour, and again quite trivially, they can change change in behaviour, too. Say change in connection X affects behaviour. Then weight change in connections that control change in X has a second order effect on behaviour.

Naturally these mechanisms can also be combined to create second order dynamics. Fig. 3 gives a schematic representation of the four possible circuits that produce second order dynamics (provided the connections are non-zero).

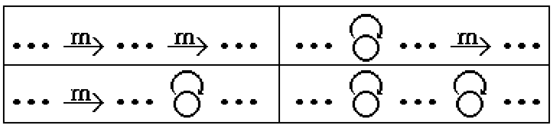

Fig. 3. Genotypic circuits for second order change. Any of these combinations occurring along a path from input to output neurons can cause second order changes. Arrows marked with M are modulatory connections. The lagged reflexive connections may produce local instead of reflexive connectivity in the phenotype, but either can support sustained change.

Informed by what's known about the neurology of spatial representation (See Moser et al. [7] for a review), we let the genotype encode not simple neurons, but neuron grids. We use square grids of three sizes: 1x1, 3x3, and WxW, where W is the size of the world (7 for our 7x7 world). Given the setup of the model, sizes larger than W offer no additional functionality (i.e. WxW is functionally equivalent to an infinite grid). The peculiar 3x3 size is included because it can concisely encode directional information. Connectivity is defined on two levels: inter-grid and intra-grid.

Intra-grid all connections are of the lagged activatory type. They can be reflexive or local. If a grid has a reflexive connection to itself, this means that all neurons in the grid get a reflexive connection to themselves. A local connection means that each neuron has connections to its four neighbours in the grid. So, connectivity within a grid is uniform (the genotype essentially defines connectivity for a single neuron, and the number of copies to make of that neuron). Propagation within a grid runs at a faster (24x) timescale than propagation among grids. Observe that reflexive connections allow retention of an activation pattern on a grid, while local connections lead to diffusion of activation patterns over time.

Grids can be connected by any connection type other than lagged activatory connections. If the genotype defines a connection between two grids, then the phenotype gets uniform connectivity between the neurons in the two grids. If the grids are equal in size, connectivity is one-to-one, otherwise all-to-all. This leads to a highly symmetrical connectivity, which by itself would cause the activation within a grid to remain uniform and redundant. This symmetry is broken by our neurotransmitter logic.

There are two global "neurotransmitter" values, nt-Bx and nt-By. These dynamically control (in two dimensions, as the neuron grids are 2D) which connection subsets of an all-to-all projection can transmit activation. When both are zero, then this set comprises connections linking corresponding neurons in the grids (e.g. the centre neuron in the pre-synaptic grid to the centre neuron in the post-synaptic grid). Non-zero nt-B values cause simple offsets, as illustrated in Fig. 4. Currently, nt-Bx and nt-By values are hardwired to reflect the agent's current x-coordinate and y-coordinate, so signal transfer can shift along with position in space. This makes it relatively easy for evolution to devise nets that store information in different locations in a grid depending on their own position in space: if a smaller grid projects to a larger grid, then the activation pattern on the smaller grid affects only a sub-region of the larger grid. We will call this sub-region the *focal area* of the smaller grid on the larger grid. Nt-B does not correspond directly to any biological neurotransmitter, but can be reduced to a biologically plausible neurotransmitter via a trivial network transformation (which increases network size dramatically).

Inclusion of coordinates in the input is unnatural, but preliminary experiments with a simple spatial memory task have shown it quite possible with our model to evolve agents that keep track of their own coordinates. Cognitively interpreted, the coordinates in the input and their linkage to the nt-B values make it trivially easy to evolve an innate sense of space as an extended medium in which movement predictably changes one's position. Construction of the ability to represent the volatile and non-uniform *contents* of space, however, is left to evolution.

The nets have one 3x3 grid and a number of 1x1 grids (i.e. single neurons) receiving input. The 3x3 grid encodes for each of the four cardinal directions whether there is a wall in that direction (on the 4 neurons adjacent to the middle neuron). The 1x1 grids encode whether the current position is the start position, whether the current position is the goal position, and the current phase (exploration or exploitation). Additionally, there are input neurons for bias (always 1.0) and noise (random real numbers from [0,1]). Output is read from two 3x3 grids. From the four neurons corresponding to the cardinal directions, the one with the highest activation is selected, and movement in that direction is performed (if possible). One set is read during exploration and the other during exploitation (so that the nets can easily evolve specialized behaviour per phase).

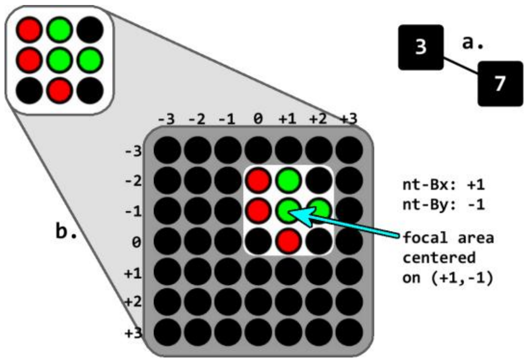

Fig. 4. Neural grids and nt-B. **a.** Genotype encoding a 3x3 grid, a 7x7 grid, and their connection. **b.** The corresponding phenotype. The 3x3 grid projects into the focal area of the 7x7 grid. The position of focal areas for projections between unequally sized grids is dynamically controlled by the global neurotransmitter values nt-Bx and nt-By. This mechanism lets the nets conveniently allocate neurons to spatial locations.

5 RESULTS

While success rates are very low, the model does occasionally produce networks with optimal performance on our Tolman mazes. We concisely describe an evolved solution here.

As the agent moves through the maze, the 3x3 input grid projects onto different regions of a 7x7 grid. Modulation working on the 7x7 grid records the paths travelled into the connectivity of this grid, replicating the maze layout. Activation diffusion in the grid then comes to follow this layout. The T-splits in the layout receive high activation due to their high connectivity, and consequently activation in other neurons on the grid comes to depend on proximity (along the replicated paths) to these T-splits. Effectively, local activation levels in the 7x7 grid come to indicate path length, and can thus be used to select the shortest path. Blockages are handled simply by updating (weakening) the connectivity in the grid at the position corresponding to the blockage. The activation pattern then settles into a new state with low activation on the blocked paths, as positions on these paths lose their proximity to one of the T-splits.

This solution is representational in nature: the connectivity pattern that forms on the grid during exploration is isomorphic with the maze, and the activation pattern on it identifies the paths and orders them by length. Also, the solution shows second order dynamics on the neural level. The neural circuit are of the bottom-left type in Fig. 3: a modulatory connection projects to a grid with activation retention (in the form of local connectivity). This second order circuit is crucial to the ability to solve the Tolman mazes (breaking either connection removes this ability).

6 CONCLUSION & FUTURE WORK

We proposed the hypothesis that mental representation is evolved second order learning, and tested this hypothesis using an artificial life model in which cognitive map ability, a paradigm case of mental representation, is evolved from the neural elements for second order neural change. Although success rates are very low, successful runs provide a proof of principle for our hypothesis. Future directions for our research are extension of this approach to other domains of representation, such as temporal or social forms.

REFERENCES

[1] Tolman E C (1948), Cognitive maps in rats and men, Psychological Review 55(4):189–208
doi: 10.1037/h0061626

[2] Takano M, Arita T (2006), Asymmetry between Even and Odd Levels of Recursion in a Theory of Mind, Proceedings of ALIFE X, 2006, pp.405-411

[3] Minoya K, Arita T, Omori T (2011), An artificial life approach for investigating the emergence of a Theory of Mind based on a functional model of the brain, Proceedings of the 2011 IEEE Symposium on Artificial Life, 2011, pp.108-115

[4] Fodor J, Pylyshyn Z (1988), Connectionism and Cognitive Architecture: a Critical Analysis. Cognition, 28(1988):3-71

[5] Arnold S (2011), Neuro-cognitive Organization as a Side-effect of the Evolution of Learning Ability, Proceedings of the IEEE Symposium on Artificial Life, 2011, pp.100-107

[6] Soltoggio A, Bullinaria J A, Mattiussi C et al. (2008), Evolutionary Advantages of Neuromodulated Plasticity in Dynamic, Reward-based Scenarios, Proceedings of Artificial Life XI, MIT Press, 2008.

[7] Moser E I, Kropff E, Moser M (2008), Place Cells, Grid Cells, and the Brain's Spatial Representation System Annual Review of Neuroscience 31:69-89
doi: 10.1146/annurev.neuro.31.061307.09072

The Seventeenth International Symposium on Artificial Life and Robotics 2012 (AROB 17th '12),
B-Con Plaza, Beppu, Oita, Japan, January 19-21, 2012

How equity norms evolve?
- An evolutionary game theory approach to distributive justice

Kazuaki Kojima[1], Takaya Arita[2]

Nagoya University, Furo-cho, Chikusa-ku, Nagoya 464-8601, Japan
(Tel: 81-52-789-4266, Fax: 81-52-789-3503)
([1]k-kojima@alife.cs.is.nagoya-u.ac.jp, [2]arita@nagoya-u.jp)

Abstract: A Nash demand game (NDG) has been applied to explain moral norms of distributive justice. In NDG, two players simultaneously make demands and receive them unless the sum of the demands exceeds the amount of the resource. Otherwise, they obtain nothing. This paper proposes the demand-intensity game (D-I game), which adds an "intensity" dimension to NDG in order to discuss various scenarios for the evolution of norms concerning distributive justice. We show basic analyses of the D-I game in game theory and then evolutionary simulations. Descriptive/evolutionary approaches show that three types of norms could evolve mainly dependent on the conflict cost in the game: egalitarianism, "wimpy" libertarianism and libertarianism in decreasing order of the cost. Although the wimpy libertarianism is classified as the libertarianism in the sense of claiming the full resource, it can achieve an egalitarian division without conflict cost as a result.

Keywords: Distributive justice, Evolutionary game theory, Nash demand game

1 INTRODUCTION

Game theoretic models have been successfully used in the studies on the evolution of moral norms which promote cooperation mainly in humans. Classical game theory is based on a normative theory of rational choice and prescribes what people ought rationally to choose ("normative approach"). Recently, researchers in various fields have tried a different approach based on evolutionary game theory that dispenses with strong assumption about rationality. Rather than asking what moral norms ought to be, they aim at describing how people will in fact choose or how can the existing norms have evolved ("descriptive/evolutionary approach") [1].

The Nash Demand Game (NDG) [2] has been widely employed to explain the emergence of moral norms, especially the evolutionary bases of *distributive justice* [3], [4], [5], etc. In NDG, each player simultaneously makes a demand and each obtains the claimed demand if the aggregated demand between both is no less than the full amount of resource. Otherwise, they obtain nothing. Every pair of the claimed demands that total 100% of the resource is a strict Nash equilibrium; however, people intuitively make the 50% demand [6]. Skyrms provided a game theoretic account of how norms of fair division might have evolved using replicator dynamics as a descriptive/explanatory approach [4]. With a finer step size of the demand than 0.1 and a higher probability of playing between similar strategies, the population always evolved into the fair division equilibrium. However, the assumption of correlated interactions of strategies have been criticized for the reason that it has no actual grounding in reality [7]. Instead, fair division has been achieved by spacial models [5] and two-population models [8].

Skyrmsian approach is evolutionary generalist as it entirely omits the psychological mechanisms, in contrast to evolutionary psychology, which emphasizes particular psychological factors of human behaviors [7]. This paper proposes the demand-intensity game (D-I game), which adds an "intensity" dimension related to some psychological factor (e.g. *bold* or *timid*) to NDG in order to discuss various scenarios for the evolution of norms concerning distributive justice, while keeping such simplicity that it can be analyzed by the concepts and tools of game theory. In NDG, if the sum of the demands exceeds the amount of resource, they obtain nothing. This rigidity in evaluation of the conflict cost is weakened depending on the intensity values of the players.

2 D-I GAME

Similar to NDG, the D-I game is a two-player one-shot game and deals with the problem of allocating a limited resource between two players as shown in Fig. 1, in which d_0, i_0, d_1 and i_1 represent self demand, self intensity, the other's demand and the other's intensity, respectively.

Each player has a strategy $S(d, i)$ noted as a set of parameters d and i $(0 \leq d, i \leq 1)$. The parameter d represents the demand, which is an demanding amount in supposing a total amount of the resource is 1. If the total demand between the two players is not over 1 (the full amount of resource), each player gains the demand as a reward, which equates to NDG.

Otherwise, the conflicted part of the resource $(d_0 + d_1 - 1)$ is divided according to the newly introduced parameter i, the intensity of the demand, as $1/2 + (i_0 - i_1)/2 : 1/2 + (i_1 - i_0)/2$. For example, $(i_0, i_1) = (0, 0)$, $(0.5, 0.5)$, $(1, 0.5)$ or $(1, 0)$ makes the conflicted part divided as $1:1$, $1:1$,

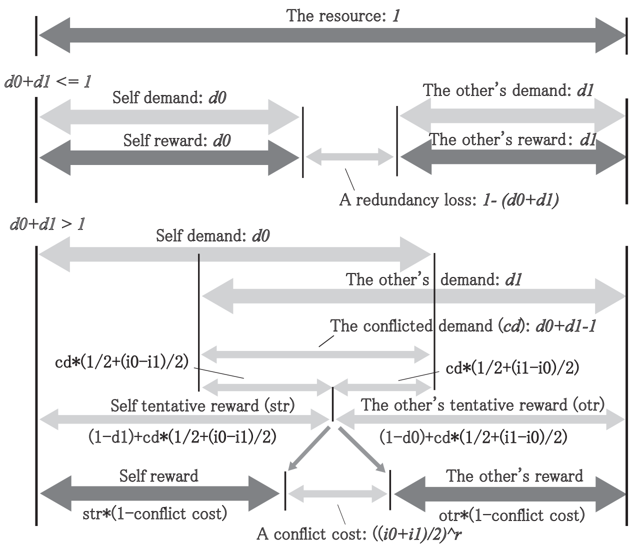

Fig. 1. Rewards in the D-I game.

$0.75 : 0.25$ or $1 : 0$, respectively. Finally, divided resources are reduced in reversely proportional to the sum of i_0 and i_1 as conflict cost. The larger the combined intensity between the players, the smaller rewards both gain. If the sum is maximum ($i_0 = i_1 = 1$), no reward is gained, as is the case with NDG. On the other hand, both share the resource without a loss of a conflict when the combined intensity is minimum ($i_0 = i_1 = 0$). Therefore, the game features two dilemmas: demand and intensity. Each player wants to receive more reward than the other and at the same time wants to avoid the conflict cost for the demand and the intensity.

The reward in the D-I game is shown as Eq. 1. (Fig. 1).

$$R(d_0, i_0, d_1, i_1) = \begin{cases} d_0 & (d_0 + d_1 \leq 1) \\ \{(1 - d_1) + (d_0 + d_1 - 1)(\frac{1}{2} + \frac{i_0 - i_1}{2})\}(1 - cost) & \\ & (else) \end{cases} \quad (1)$$

$$cost = \left(\frac{i_0 + i_1}{2}\right)^r \quad (2)$$

r specifies the game structure in terms of the conflict cost as shown in Eq. 2. At $r = 0$, the conflict cost is maximized and the game is equivalent to NDG.

We refer to a strategy of d below 0.5 as "generous" and above 0.5 as "greedy." Specifically, the cases that d is 0, 0.5 and 1 are defined as "unselfish," "even" and "selfish," respectively. The parameter i, the intensity of the demand, represents how strong people claim their own demand in a conflict. The strategy is referred to as "timid" if i is less than 0.5, and "bold" if i is more than 0.5. Specifically, the intensities i of 0, 0.5 and 1 are defined as "wimpy," "moderate" and "belligerent, " respectively.

Regarding d, there are two typical strategies: $d = 0.5$ and $d = 1$. Although debatable, we simply associate the former with egalitarianism and the latter with libertarianism. When $r = 0$, all strategies with $d = 0.5$ are ESS independently of i. Previous studies on a descriptive/evolutionary approach intended to describe how people could evolve this egalitarian norm. However, the strategies with $d = 0.5$ are not ESS except $r = 0$ and the norm becomes weaker as r increases. This is because a decrease of conflict cost (an increase of r) makes greed attractive.

When both players use the same greed strategy ($d_0 = d_1 > 0.5$), the reward is 0.5 at $i_0 = 0$ and decreases monotonically as i_0 increases when $r > 0$. Therefore, it is notable that ideal society in the sense of equality and efficiency can be achieved by not only a pure egalitarianism norm ($S(0.5, *)$) but also an eventual equality norm based on libertarianism ($S(1, 0)$) in the D-I game as shown later.

3 GAME THEORETIC ANALYSES

There are many efficient strategies in the D-I game according to a Nash equilibrium analysis as in NDG. An ESS (Evolutionary Stable Strategy) analysis leads to only three types of norms in these efficient strategies. The three norms (ESS) are egalitarianism (Norm A: $S(0.5, *)$, when $r = 0$), libertarianism (Norm B: $S(1, i^*)$ (i^* depends on r as shown in Fig. 3), when $r \geq 0.5$) and "wimpy" libertarianism (Norm C: $S(1, 0)$, when $0 < r < 0.773$). Fig. 2 shows the three norms in two dimensions of strategy: demand and intensity. The left, middle and right panels illustrate the cases of $r = 0$, $0 < r \leq 1$ and $r = 1$, respectively.

Norm A is represented as an ESS group of even strategies ($d = 0.5$) with any intensity value only when $r = 0$ (NDG setting) as shown in the left panel of Fig. 3. When $r > 0$, the egalitarian strategies are divided into two groups according to the the value of the intensity (X and Y in the middle and right panels of Fig. 3). The "bolder" egalitarian strategies (X) can be invaded only by all the egalitarian strategies (X+Y), while the "timider" strategies (Y) can be invaded not only by all the egalitarian strategies (X+Y) but also by other strategies. As r grows from 0 to 1, the range of bolder strategies (X) narrows from $0 \leq i \leq 1$ to $0.438 < i \leq 1$, and it finally vanishes when $r = 4.67$.

Although both Norm B and Norm C have a selfish property ($d = 1$, libertarianism), Norm B exists as an ESS under lower-cost conditions ($r \geq 0.5$) while Norm C exists as an ESS under higher-cost conditions ($0 < r < 0.773$) as shown in Fig. 3. Norm B bifurcates into two ESS at $r = 0.5$, $i = 0.25$. One of the bifurcated ESS becomes "timider" along with increased r, and the other "bolder." The "timider" ESS exists in $0.5 \leq r < 0.571$, whereas the "bolder" ESS exists till infinity. It should be noted that a society with Norm C is ideal from the aspect of equality and efficiency as in

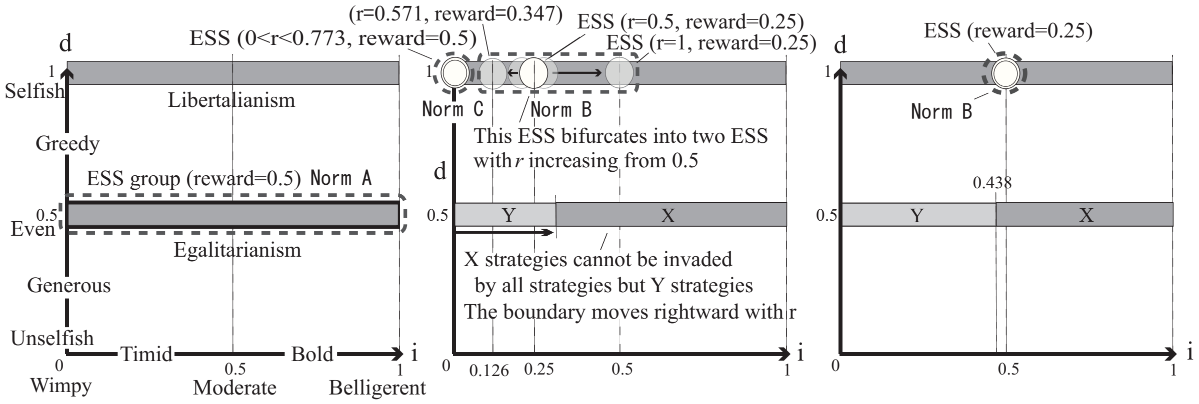

Fig. 2. Three types of norms in strategy space (Norm A: egalitarianism, Norm B: libertarianism, Norm C: "wimpy" libertarianism). The left, middle and right panels correspond to the cases of $r = 0$, $0 < r \leq 1$ and $r = 1$, respectively.

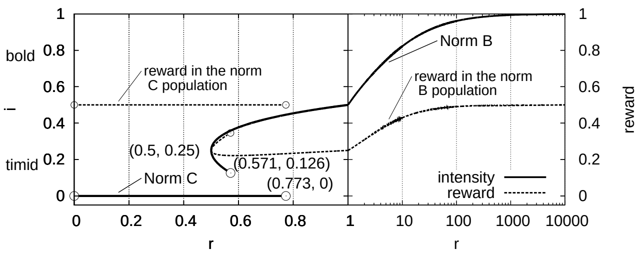

Fig. 3. Intensity i of two types of ESS (Norm B and Norm C). $d = 1$ (libertarianism). Rewards in the ESS population.

the case with Norm A, in the sense that each obtains the maximum reward (0.5) in the ESS population of selfish and wimpy strategies ($d = 1$ and $i = 0$). On the other hand, a society with Norm B is inefficient in the sense that each obtains less than 0.5 in the ESS population of "greed" and "bolder" strategies. The reward each obtains approaches 0.5 as r approaches infinity, in other words, the conflict cost approaches 0.

4 EVOLUTIONARY SIMULATIONS

We performed evolutionary simulations using a genetic algorithm. The population was composed of N individuals represented as the strategy parameters, d and i. The fitness of each individual was defined proportional to the total amount of rewards in playing the D-I game with all other members in the population. The strategy parameters d and i were and discretized into steps of size S_d and S_i in the range of $[0, 1]$, respectively. The initial populations consisted of N individuals with randomly selected d and i.

New individuals were generated by the three genetic operations: fitness-proportionate selection, crossover with a rate R_c, which simply exchanged the parent's intensity values, and mutation with a rate R_m, which selected another value for d or i, keeping them in the range of $[0, 1]$. We show

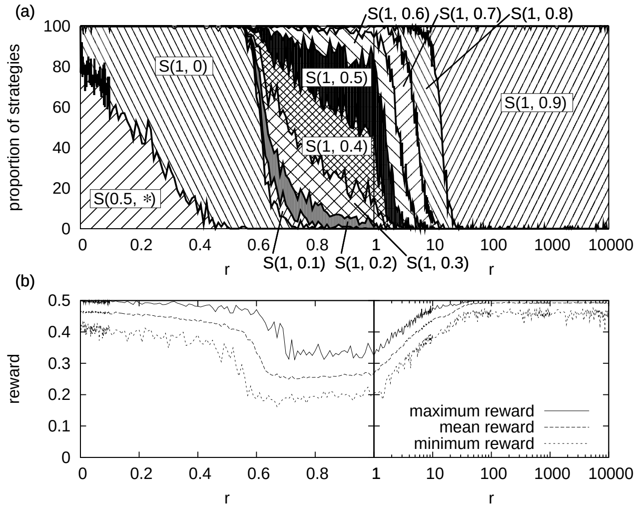

Fig. 4. (a) Proportion of the most common strategy in a population at the last generation over all 100 trials. (b) Average reward in the population. The graphs are the maximum, the mean and the minimum of the rewards over all 100 trials.

the result with $N = 100$, $S_d = S_i = 0.1$, $R_c = 0.5$, and $R_m = 0.05$.

Fig. 4 (a) illustrates a proportion of the most popular strategy at the last generation (1500th generation) over all 100 trials. For small r, the egalitarian strategies ($d = 0.5$) remained as the most common strategies until the last generation in many trials. While the proportion over all 100 trials decreased along with a growth of r, libertarian strategies ($d = 1$) became the most common strategies in more trials. The intensity of the libertarian strategies became larger as r increases.

The egalitarian ESS prevailed at $r = 0$ with 100% trials and the "wimpy" libertarian ESS prevailed for $0 < r < 0.773$ with the percentage of trials as shown in Fig. 4 (a). The egalitarian strategies remained until the last generation

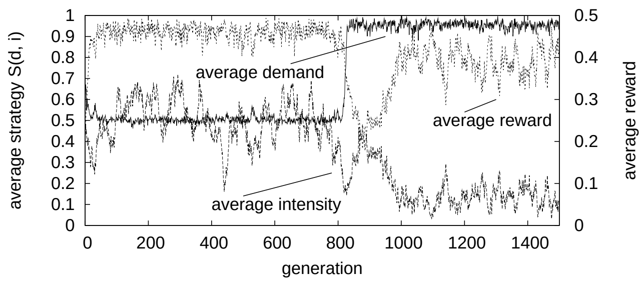

Fig. 5. Average demand, average intensity and average reward in a population through an evolutionary simulation for $r = 0.6$.

in some evolutionary simulations for $r > 0$. Fig. 5 shows the average demand, the average intensity and the average reward in a population for $r = 0.6$. Some trials kept egalitarian strategies until certain generation even when $r = 0.6$. The egalitarian strategies can be stabilized for $r > 0$ because a strategy distribution in a population is diverse through evolutionary simulations and thus the bolder egalitarian strategies (X in Fig. 2) can obtain a stability for some situations.

On the other hand, there was no coexistence between egalitarian strategies and libertarian strategies. Here we consider the reason of it. The generation in Fig. 5 sees a quick transition from an egalitarian to a libertarian population at about 800th generation. It is possible reason that a libertarian strategy obtains three times as much as an egalitarian strategy's reward when they play the game with each other under the same intensity. The difference is lager when i is smaller. Once libertarian strategies, especially the wimpy libertarian strategy, invade in a population, egalitarian strategies obtain the lower reward and can not remain in the population.

The most common strategy was various for around $0.6 < r < 10$ with a low reward in a population as shown in Fig. 4. The various strategies include not only the libertarian ESS but also other libertarian strategies. Furthermore, libertarian strategies coexisted with other libertarian strategies in trials for the range of r. It might be due to a little difference in the rewards between similar libertarian strategies.

For $0 \leq r < 0.6$, an ideal society was achieved with the successful reward in the population (0.5) by egalitarian strategies or the "wimpy" libertarian strategy. Fig. 4 (b) illustrates the average reward in a population at the last generation. The most successful trial for $0 \leq r < 0.6$ achieved the reward of around 0.5 ("maximum reward" in Fig. 4 (b)). When r approaches infinity (no conflict cost), an ideal society was also achieved, as a matter of course.

5 CONCLUSION

We proposed the D-I game, which adds an "intensity" dimension to NDG in order to discuss various scenarios for the evolution of norms concerning distributive justice. We did game theoretic analyses of the D-I game and performed evolutionary simulations. Descriptive/evolutionary approaches (an ESS analysis and evolutionary simulations) show evolution into three types of norms: egalitarianism, libertarianism and wimpy libertarianism. While the wimpy libertarianism is classified as the libertarianism for claiming the full resource, it can also achieve an egalitarian division in a population without conflict cost as a result.

A level of conflict cost has a large influence on what kind of norms emerge: the egalitarianism, the wimpy libertarianism and the libertarianism in decreasing order of the cost (which could be interpreted as a psychological cost). People may not feel conflict cost pressure so much when we share sweets among family members. We may act like a libertarian in this case and we may demand the whole sweets strongly. If the members are friends, we may feel more cost pressure. Then, we may act like a wimpy libertarian. If the share resource is money, we may feel more cost pressure than sharing the sweets and we may make an equal demand strictly as an egalitarian.

We believe that the D-I game provides us with a useful framework to study dynamics of distributive justice from an emergence perspective, beyond the question of whether strategies demanding equal share can dominate the population or not.

REFERENCES

[1] G. Mar. Evolutionary game theory, morality, and darwinism. In D. Katz, editor, *Evolutionary Origins of Morality*. 322–326, Imprint Academic, 2000.

[2] J. F. Nash. The bargaining problem. *Econometrica*, 18:155–162, 1950.

[3] R. Sugden. *The Economics of Rights, Co-operation and Welfare*. Basil Blackwell, Oxford, 1986.

[4] B. Skyrms. *Evolution of the Social Contract*. Cambridge University Press, Cambridge, 1996.

[5] J. M. Alexander. Evolutoinary explanations of distributive justice. *Philosophy of Science*, 67(3):490–516, 2000.

[6] C. T. Dawes, J. H. Fowler, T. Johnson, R. McElreath, and O. Smirnov. Egalitarian motives in humans. *Nature*, 446:794–796, 2007.

[7] J. D'Arms, R. Batterman, and K. Górny. Game theoretic explanations and the evolution of justice. *Philosophy of Science*, 65(1):76–102, 1998.

[8] H. Ohtsuki. Evolutionary dynamics of the nash demand game: A diffusion approach. *Dynamic Games and Applications*, in press.

The Seventeenth International Symposium on Artificial Life and Robotics 2012 (AROB 17th '12),
B-Con Plaza, Beppu, Oita, Japan, January 19-21, 2012

Dynamics of rules internalized in dynamic cognitive agents playing a multi-game

Takashi Sato

Okinawa National College of Technology, Henoko, Nago, Okinawa 905-2192, Japan
(Tel: 81-980-55-4179, Fax: 81-980-55-4012)
stakashi@okinawa-ct.ac.jp

Abstract: Rules such as laws, institutions, and norms can be changed dynamically in our society, because they are shaped by interactions among social members who are affected by them. However, there are also some stable rules enhanced by interactions among rules. In this article, we discuss whether or not rules can be stabilized by interactions among the rules. To investigate this, we propose a multi-game model in which different games are played simultaneously by the dynamic cognitive agents. A minority game (MG) and an *n*-person iterated prisoners' dilemma game (NIPDG) are adopted. In our simulation, we found that the agents internalize the complex rules expressed as intricate geometrical shapes like strange attractors on the phase spaces, when the complex macro dynamics emerged. Furthermore, it showed that the macro dynamics shaped by the macro rules in the MG can be stabilized by interaction between the MG and the NIPDG rules internalized in the agents.

Keywords: Dynamic cognitive agent, Internal dynamics, Minority game (MG), Multi-game, N-person iterated prisoners' dilemma game (NIPDG), Simple recurrent network with self-influential connections (SRN-SIC)

1 INTRODUCTION

There are many behavioral guidelines that have an influence on determination of our actions in our society. Rules such as laws, institutions, and norms can be regarded as the guidelines. We focus here on the institutions as the rules. North[1] claims that the institutions establish stabilities of themselves by making complex aggregates of them. Many institutions mutually support each other, and their functions are enhanced by other institutions. Aoki[2] defines this enhancing effect as institutional complementarity.

On the other hand, Nishibe[3] proposes an institutional ecology. This institutional ecology is defined as a dynamical system in which many institutions can be shaped and fluctuated through changes of human cognitions and behaviors by interactions among the institutions. He claims that the institutional ecology becomes a complex system, and diversity of the institutions is maintained, because the interactions among them are nonlinear.

The purpose of this article is to discuss whether or not rules can be stabilized through interactions between the rules actually. According to North's interpretation[1], the institutions are distinguished between formal and informal institutions. We refer to the formal institutions as global rules and the informal institutions as local rules. In this study, we assume that the local rules are the global rules internalized in the individuals and play an important role to stabilize the global rules and the macro dynamics based on the global rules, because their actions are affected by each internalized rules, and the global rules are shaped by the actions of all individuals.

In order to investigate what effects the interactions between the local rules of the individuals have on the stabilization of the global rules and the macro dynamics, we propose a multi-game model in which different games are played simultaneously by the dynamic cognitive agents who can internalize the rules through the learning process.

2 MULTI-GAME AND DYNAMIC COGNITIVE AGENT AS ITS PLAYER

2.1 Multi-game

We propose a multi-game model in which players play many types of games simultaneously. This is a game theoretical model to investigate what kind of the macro dynamics of the games the interactions between the rules internalized in the players form, and what rules for forming the dynamics the agents internalize through the learning process. The minority game (MG)[4] and the *n*-person iterated prisoners' dilemma game (NIPDG)[5] are adopted here.

The MG is a simple game, where n (odd) players must select one out of two actions (e.g., -1 or 1, like buy or sell) independently, and those who are on the minority side win. The NIPDG is a version of the IPDG with many players. In this study, we define the NIPDG as follows: each player has to choose one of two actions, defection (D) and cooperation (C) individually; the players who chose D always win if there is one or more player who chose C; namely, when all players select D, they lose. In the multi-game, the actions D and C in the NIPDG are expressed as -1 and 1, respectively.

2.2 Dynamic cognitive agent as its game player

We adopt a model of the dynamic cognitive agent with internal dynamics represented by a simple recurrent network with a self-influential connection (SRN-SIC), as proposed in our previous work[6] and illustrated in Fig.1. The internal states of humans change even in the situations in which the same external stimulus is constantly given or when no external stimulus is given. We refer to this autonomous change of the internal states as the internal dynamics.

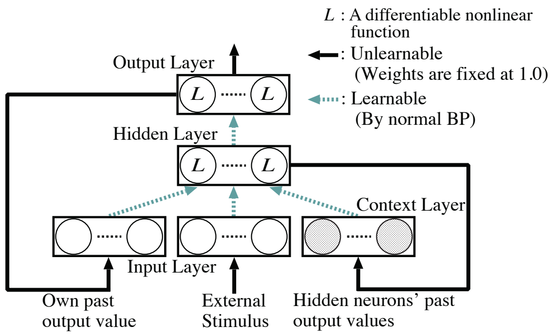

Fig. 1. The SRN-SIC proposed in our previous work as an architecture of a dynamic cognitive agent with internal dynamics.

The SRN-SIC is an Elman-type network[7] modified by adding recurrent connections between the output and input layers so that the agent can determine his/her own action based on his/her own past action, and the internal dynamics is produced by the recurrent connections.

2.3 The procedure of the multi-game

The procedure of the multi-game is as follows:

1. Except for initial time step, each agent independently decides their actions for the games based on their own past actions, internal states, and the results of the games at the last play.
2. A current game results, namely, winners' actions, are determined from all agents' actions.
3. The step is given an increment and goes to 1.

The procedure from 1 to 3 is called *one step*. By error back-propagatkon (BP) learning algorithm, all agents learn a time-series of the winners' actions in the games every 10,000 steps. A teacher's signal is the sequence of the actions at the last 100 steps immediately before the learning. We refer to the 10,000 steps as *one turn* between the learning processes.

3 SIMULATION RESULTS

Before describing the results, let's give the specification of the simulations[1]. The games are played until 10,000,000 steps; namely, 1,000 turns. The population size of the agents is 101.

[1]The settings and mathematical expressions of the SRN-SIC are omitted due to space constraints and for details to Sato and Hashimoto[6, 8].

3.1 Occurrence frequency of complex macro dynamics

First, we observe the macro dynamics expressed by a time-series of winners' actions in the games. Most of the macro dynamics have short period numbers, but sometimes complex macro dynamics represented as aperiodic motions are shaped, as illustrated in Fig.3 to be hereafter described. Fig.2 shows the average numbers of occurrences of the complex macro dynamics emerged in the games.

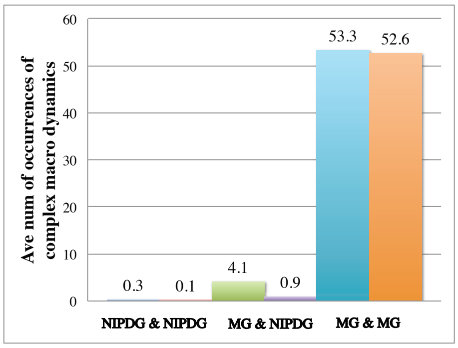

Fig. 2. Average numbers of occurrences of the complex macro dynamics in each game.

The two bar graphs on the left-hand side of Fig.2 indicate that the complex macro dynamics hardly emerge when the agents played the NIPDG and the NIPDG simultaneously. The middle two bar graphs of Fig.2 depict the results of the combination between the MG and the NIPDG. In this case, the complex macro dynamics in the MG is suppressed, although the MG is easy to shape such dynamics. The last two bars on the right-hand side of Fig.2 show the results in case that the agents played two MGs coinstantaneously. As can be seen, the number of occurrences of the complex macro dynamics is the highest of three types of game combinations. Also note that, in case of playing the MG by one group independently, the average number of occurrences of the complex macro dynamics is twenty and it was confirmed in our previous work[9]. Therefore, these results suggest that the rules shaped in the NIPDG hold enormous potential to stabilize the macro dynamics strongly, although the MG has a possibility to destabilize macro dynamics of the other game. However, the combination between the MG and the MG generates a synergistic effect to raise the frequency of occurrences of the complex macro dynamics.

3.2 Differences between the MG and the NIPDG

Second, we confirm the differences of the MG and the NIPDG from the viewpoint of the macro dynamics and the rules internalized in the agents.

Fig.3 show the examples of the complex macro dynamics[2] that emerged in the both of combined games simultaneously. Fig.3(a) illustrates the macro dynamics shaped in the MG

[2]The x-axis and the y-axis of each figure are the steps and the time-series of winners' actions converted to real numbers, respectively.

(a) Macro dynamics shaped in the MG and the NIPDG (b) Macro dynamics shaped in the MG and the MG

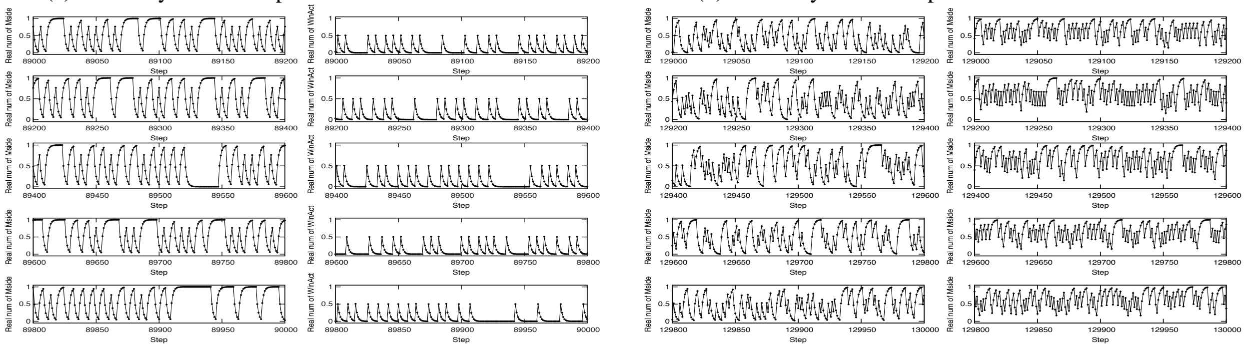

Fig. 3. Examples of complex macro dynamics.

(a) Internalized rules in the MG and the NIPDG (b) Internalized rules in the MG and the MG

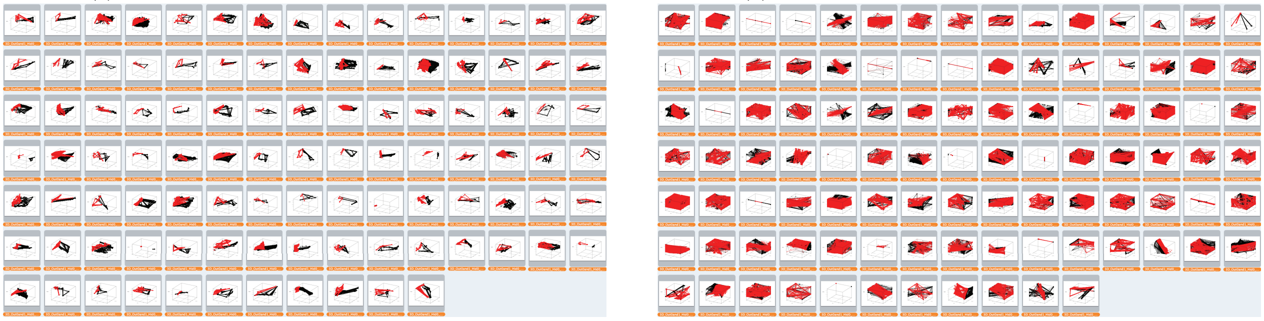

Fig. 4. Examples of rules internalized in the all agents through the learning process.

(left column) and the NIPDG (right column). Both of the dynamics are aperiodic, but change pattern of winners' actions in the NIPDG (right column) is relatively-monotonous than that of the MG (left column). In contrast, both the macro dynamics shaped by all agents who play two MGs simultaneously are very complex, as illustrated in Fig.3(b).

Fig.4 depicts the rules internalized in all agents who form the complex macro dynamics as illustrated in Fig.3. These rules are expressed as intricate geometrical shapes like strange attractors on the phase spaces which represent the relationship among two output and two hidden values[3]. The black and the red trajectories in Fig.4(a) are the internalized rules in the MG and the NIPDG, and that in Fig.4(b) are both the internalized rules in the MG, respectively.

As can be seen, each agent has two different rules to decide thier actions for the games. Furthermore, the points on the phase space of most of internalized rules illustrated in Fig.4(b) are so dense obviously. Most of these rules creates a one-to-many relationship from an input to the agent's actions, because the points on the phase space ranges over almost the entire area of the output (the x-axis on the phase space). That is to say: the rules internalized in the agents who play two MGs simultaneously, as illustrated in Fig.4(b), is more complex than that of the combination between the MG and the NIPDG, as illustrated in Fig.4(a).

[3]The x, y and z-axes of each figure are the values of the output neurons, the 1st and the 2nd hidden neurons, respectively.

3.3 Complex structures of internalized rules

In the previous section, we confirmed that the agents can internalize with different complex rules for each game through the learning process. Fig.5 gives the examples of the complex rules internalized in the agents in detail.

(a) (b)

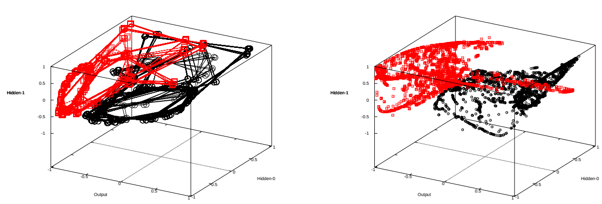

Fig. 5. Examples of complex internalized rules like combination between limit cycles and finite automaton with many states (a) and strange attractors (b).

Fig.5(a) shows the complex rules expressed by two combinations of limit cycle and finite automaton with many states. This means that the agent has the rules that can switch two action sequences with short and long periods according to the external stimuli.

Fig.5(b) can be easily imagined that the agent having this rule can output apperiodic actions. The aperiodic action may be chaotic dynamics. Chaotic dynamics has orbital instability, which expands small differences in the trajectories of agents' actions. Therefore, even a small displacement in an agents' group can induce a change in the macro level dynamics, if the number of agents with the rule that can generate the time-series of chaotic actions is much larger than that of agents without it. However, in case of playing two different games that can stabilize and destabilize the macro dynamics easily, it is considered that the agents are difficult to acquire the rules that can generate chaotic actions.

3.4 Degree of concordance of internalized rules

Finally, we analyze whether or not there is a difference between the internalized rules for the MG and the NIPDG and the ones for the two MGs. In comparison with the rules for the two MGs, it is often the case that both the rules for the MG and the NIPDG have similar or symmetric structures, as illustrated in Fig.4. This suggests that both actions decided by the rules for the MG and the NIPDG depend on the values of the same hidden neurons.

Fig.6 shows the degree of concordance of the internalized rules that are observed in the combination of the MG and the NIPDG and in the combination of the two MGs. The degree of concordance of the internalized rules is calculated as follows: correlation coefficients between each value of the output and the hidden neurons are calculated; the numbers of combinations between such neurons with strong coefficients (0.7 and more) are counted every the agents; the numbers are averaged for 1,000 turns; the averaged numbers are also averaged by the number of the agents.

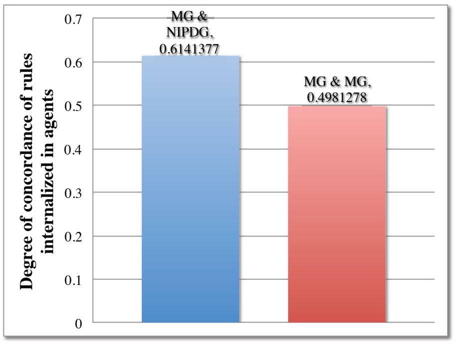

Fig. 6. Degree of concordance of rules internalized in agents

We found that there is subtle but important difference. The results in Fig.6 mean that the actions decided by both of the rules for the MG and the NIPDG are dependent on the values of the same hidden neurons than the ones determined by the rules of the two MGs. This can be interpreted that both the rules for the MG and the NIPDG have the same partial structures, and such structures can be internalized at an early stage of the games, because the agents shape only simple macro dynamics at the early stage even though they play the MG.

4 SUMMARY AND CONCLUSION

We proposed a multi-game model in order to investigate whether or not the interactions between the rules internalized in the individuals have an influence on the stabilization of the rules and the macro dynamics shaped by the rules. In this model, different games are played simultaneously by the dynamic cognitive agents who can internalize the rules through the learning process.

The simulation results showed that the agents can internalize different complex rules represented as strange attractors, but the agents are difficult to acquire the rules that can generate chaotic actions when playing simultaneously both two different games, where the macro dynamics can be stabilized easily in at least one of the games. Furthermore, we confirmed that both the rules for the MG and the NIPDG have the same partial structures, and it was suggested that such structures can be internalized at an early stage of the games, because the agents shape only simple macro dynamics at the early stage even though they play the MG.

From these results, we conclude that the followings are the important to stabilize the macro dynamics; the agents internalize different rules for each game in which at least one of the games has a feature to stabilize the macro dynamics easily, and the ones have the common partial structures between the different rules at an early stage of the games.

ACKNOWLEDGMENT

The author thanks Takashi Hashimoto and Zacharie Mbaitiga for their fruitful discussions. This work was supported by a Grant-in-Aid for Young Scientists (B) No. 22700242 from the Japan Society for Promotion of Science (JSPS).

REFERENCES

[1] North DC (1990), Institutions, institutional change and economic performance. Cambridge University Press, Cambridge
[2] Aoki M (2001) Toward a comparative institutional analysis. MIT Press, Cambridge
[3] Nishibe M (2006), Rules and institutions in evolutionist institutional design (in Japanese). Economic Studies, Hokkaido University, 56(2):133-146
[4] Challet D, Zhang YC (1997), Emergence of cooperation and organization in an evolutionary game. Physica A 246:407-418
[5] Colman AM (1982), Game theory and experimental games. Pergamon Press, Oxford
[6] Sato T, Hashimoto T (2007), Dynamic social simulation with multiagents having internal dynamics. In: Sakurai A (ed) New frontiers in artificial intelligence. Joint Proceeding of the 17th and 18th Annual Conferences of the Japanese Society for Artificial Intelligence. Springer, pp.237-251
[7] Elman JL (1990), Finding structure in time. Cognitive Sci 14(2):179-211
[8] Sato T, Hashimoto T (2005), Effect of internal dynamics and micro-macro loop on dynamics of social structures (in Japanese). Trans Math Modeling Appl (TOM) 46:81-92
[9] Sato T (2012), Effect of interaction between rules on rule dynamics in a multi-group minority game. Artificial Life and Robotics 16 (in press)

The Seventeenth International Symposium on Artificial Life and Robotics 2012 (AROB 17th '12),
B-Con Plaza, Beppu, Oita, Japan, January 19-21, 2012

On classification of interview sheets for ophthalmic examinations using self-organizing maps

Naotake Kamiura[1], Ayumu Saitoh[1], Teijiro Isokawa[1], Nobuyuki Matsui[1], and Hitoshi Tabuchi[2]

[1]Graduate School of Engineering, University of Hyogo, Himeji 671-2280, Japan
(Tel: 81-79-267-4918, Fax: 81-79-266-8868)
[2]Tsukazaki Hospital, Himeji 671-1227, Japan

[1]{kamiura, saitoh, isokawa, matsui}@eng.u-hyogo.ac.jp

Abstract: In this paper, a method of determining examination groups for new patients is presented, using self-organizing maps. Assuming that interview sheets are divided into four classes, the method copes with the examination determination as the classification of the sheets. The data are generated from handwriting sentences in the sheets. Some nouns in them are picked up as elements of the data. After map learning is complete, its neurons are labeled. The class of the sheet corresponding to the data to be checked is specified by the label of the winner neuron for the data. It is established that the multiple-map-based scheme achieves favorable classification accuracy.

Keywords: data classification, interview sheets, self-organizing maps, waiting time problems

1 INTRODUCTION

In Japan, long waiting time has been considered to be one of the major reasons that prevent chronic patients from going to hospitals. The condition of chronic patients keeps on worsening, and the fatal damage tends to suddenly befall to such patients. In Ji, Yanagawa, and Miyazaki [1], an event-driven network approach using queuing theory is presented to reduce the waiting time. The dispatching rules are suggested based on patients' expected visitation time and expected service time, and they are used to schedule the patients. The advisability of applying the rules is sometimes restricted by situations associated with the numbers of clinical testing equipments, medical doctors, nurses, medical technologists and so forth.

Managing the waiting time as part of the examination time is also a promising approach. Before consultation, a doctor first reads an interview sheet filled out by a new patient. The doctor then determines a set of examinations for the new patient, whereas the patient must wait for a while before the doctor make a determination. This medical protocol also prevents the doctor from allotting enough time to see the patient. The doctors are therefore anxious for the system that automatically checks the interview sheets and determines a set of the examinations.

In this paper, the determination of examination groups for new patients is presented, using self-organizing maps (SOM's). SOM's are applied as useful classification tools. In Kurosawa et al [2] and Ohtsuka et al [3], [4], SOM's have strong research interest as a means of expressing and/or processing clinical examination results. The proposed method assumes that each of the interview sheets filled out by new patients belongs to one of the four classes. It therefore copes with the examination determination as the classification of data corresponding to the sheets. An open source engine developed for Japanese language morphological analysis is applied to handwriting sentences in the sheets, and some nouns in them are picked up as elements of the data presented to the maps. After general SOM learning is complete, neurons in the maps are labeled. The class of the data to be checked is specified by the label of the winner neuron. The scheme using a single map for all of the patients and that dividing patients into five age groups and preparing a map for each of the groups are discussed. It is revealed that the latter scheme is useful in achieving favorable classification accuracy, compared with the former scheme.

2 PRELIMINARIES

A map consists of neurons, and a neuron has a reference vector with M element values if the M-dimensional data is presented to the map. General SOM learning is conducted using the following formulas.

$$NF(t) = r_0\left(1 - t/T\right), \quad (1)$$

$$\tau_i(t) = \tau_0\left(1 - t/T\right), \quad (2)$$

$$W_i(t) \leftarrow W_i(t) + \tau_i(t)\left(X^l(t) - W_i(t)\right). \quad (3)$$

$X^l(t)$ means the l-th training data. The neighborhood function around the winner neuron for the data presented at time t is defined by Eq. (1). $W_i(t)$ is the reference vector of the i-th neuron, C_i. If C_i is located inside the area specified by $NF(t)$, $W_i(t)$ is modified according to Eqs. (2)

and (3). $\tau_i(t)$ is the learning rate. T is the epoch number employed as the learning-termination condition.

This paper focuses on sentences handwritten in Japanese by new patients visiting the department of ophthalmology. They appear in interview sheets. It is probable that patients contracting different diseases undergo same examinations. According to common characteristics in terms of the examinations for the diseases, this paper divides examinations into the following four classes: Class 1 associated with fundus examinations, Class 2 associated with glaucoma tests, Class 3 associated with slit lamp tests, and Class 4 associated with oculomotor tests. Class 1 is strongly linked to cataract, diabetes, retinal disease, uveitis, and pediatric ophthalmology. Class 3 is strongly linked to corneal and/or conjunctival disease, lacrimal apparatus, and ametropia. A similar relationsip holds between Class 4 and each of strabismus, neuro-ophthalmologic disease, and trauma. Since a new patient undergoes the examinations belonging to one of the four classes, the interview sheets can also be divided into such four classes. The proposed method then copes with determination of examinations as classification of data corresponding to interview sheets with the four classes.

3 DATA GENERATION FROM INTERVIEW SHEETS

Handwriting sentences in interview sheets are first electronically registered from the keyboard. MeCab, which is the open source engine developed for Japanese language morphological analysis by Kudo, Yamamoto, and Matsumoto [5], is then applied to divide the words in them into some parts of speech. Several of the nouns are picked up per sentence by consulting the list of prohibited words. Table 1 shows examples of the prohibited words.

The proposed method next generates a matrix. Let us assume that N interview sheets whose classes are perfectly known are available. Let d denote the total number of nouns picked up in the above manner. The matrix then has N rows and d columns. In other words, the nouns are assigned to the columns, and each of the sentences (i.e., the interview sheets) corresponds to a row. Frequencies of appearance are initially given as follows: if the p-th noun appears in the l-th sentence m_{lp} times, the element specified by the l-th row and p-th column is set to m_{lp}, where $1 \le l \le N$ and $1 \le p \le d$. Fig. 1 depicts an example of the first matrix. In the following discussions, m_{lp} means the value given to the element specified by the l-th row and p-th column.

Table 1. Examples of prohibited words

Types of prohibited words	Examples
Numbers	1, 2, 0, 100, 36.5
Symbols associated with SI base units	m, mm, cm, kg
Geographical names	姫路/ Himeji, 佐用/ Sayoh
Words associated with time	週/ week, 金曜日/ Friday, 去年/ last year, 先月/ last month

Weighting element values adequately is useful in emphasizing the significance of the words corresponding to such values. The proposed method weights some values, based on the probability of words appearing. Let us assume that the p-th noun appear NA_p^q times in the set of registered sentences (i.e., the interview sheets) belonging to Class q, where $1 \le p \le d$ and $1 \le q \le 4$. In addition, let R_p^q denote the ratio of the number of the p-th nouns appearing in the sentences belonging to Class q, compared to the total number of the sentences belonging to Class q. Assuming that the latter number is denoted by NS^q, R_p^q is as follows.

$$R_p{}^q = NA_p{}^q / NS^q . \quad (4)$$

It is considered that nouns with comparatively high R_p^q's are of importance in specifying attributes of Class q. The threshold value associated with R_p^q is set to 0.055 when the noun is checked whether its element values are weighted.

The p-th noun is defined as a powerful word, if the value calculated by Eq. (4) is more than 0.055 for Class k solely, where $k \in \{1, 2, 3, 4\}$. We then have $R_p^k \ge 0.055$ and $R_p^q < 0.055$ for any q, where $q \in \{1, 2, 3, 4\}$ and $k \ne q$. If Eq. (4) calculates the value more than 0.055 for two classes, the noun is defined as a special word. In the case where the p-th noun is the special word, $R_p^q < 0.055$, $R_p^{k1} \ge 0.055$ and $R_p^{k2} \ge 0.055$ hold for $k1$, $k2$, and any q, where $k1$, $k2 \in \{1, 2, 3, 4\}$, $k1 \ne k2$, $k1 \ne q$, and $k2 \ne q$. The first matrix is modified as follows. Each of the element values on the columns corresponding to the powerful (or special) words is multiplied by 4 (or 2). For example, if Word 2 in Fig. 1 is the powerful word, element values on the second column are weighted and change from $(m_{12}, m_{22}, m_{32}, \ldots, m_{N2})=(0, 2, 0, \ldots, 1)$ to $(0, 8, 0, \ldots, 4)$. Besides, if Word 3 is the special word, we have $(m_{13}, m_{23}, m_{33}, \ldots, m_{N3})=(4, 0, 2, \ldots, 2)$ as weighted values.

It is difficult to specify the attribute of a unique class, using a noun that equally appears in the numerous sentences belonging to arbitrary classes. This is why targets of weighting are restricted to the nouns, each of which has the value calculated by Eq. (4) exceeding the threshold for at most two classes.

	Word 1	Word 2	Word 3	…	Word d
	検査 "Examination"	白内障 "Cataract"	眼鏡 "Glasses"	…	網膜 "Retina"
Sheet 1	0	0	2	…	1
Sheet 2	1	2	0	…	0
Sheet 3	1	0	1	…	0
⋮	⋮	⋮	⋮	⋱	⋮
Sheet N	0	1	1	…	0

Fig. 1. Example of first matrix

4 EXAMINATION DETERMINATION USING SELF-ORGANAIZING MAPS

For the use of SOM's, two schemes are available. The first scheme is based on using a single map, whereas the other prepares a map for each age group. The maps are constructed in the general manner using Eqs. (1)-(3). The general manner is also adopted in Ohtsuka et al [3], [4]. Note that a row in a matrix generated by the method in Sect. 3 is presented to a map as a member of the training data set.

Let us discuss the single-map-based determination. The information associated with age is added as the rightmost (i.e., the (d+1)-th) column to the matrix. One of the three-level values is given to each element in the (d+1)-th column. If the patient filling out the l-th sheet is younger than 11 years old, 0 is given as m_{ld+1}. If the age of the patient is more than 10 and less than 46, we have m_{ld+1}=6. If it is larger than or equal to 46, m_{ld+1}=12 holds.

Once general SOM learning is complete, neurons in the map are labeled as follows.

<Neuron labeling>

[Step 1] Let $F_q^{\,i}$ denote the frequency of the i-th neuron (C_i) firing for the training data belonging to Class q, where $1 \le q \le 4$. Set four $F_q^{\,i}$'s to 0, and set l to 1.

[Step 2] The l-th training data is presented, and $F_q^{\,i}$'s of the winner are updated. The value of l is incremented by 1.

[Step 3] If $l \le N$, go to Step 2; otherwise, go to Step 4. Note that N is the total number of training data.

[Step 4] Let LN^i denote the label of C_i. It is as follows.

$$LN^i = \arg\left\{ \max_q \left(F_q^{\,i} \right) \right\}. \tag{5}$$

Labels are assigned to the other neurons, using Eq. (5).

In this paper, each of the data unused for SOM learning is referred to as pilot data. The set of pilot data is also generated in the manner described in Sect.3. When one of the pilot data is examined, it is presented to the map with labeled neurons. The class of the data is considered to be that specified by the label of the winner for it.

Let us next explain the determination employing multiple maps. The following five age groups are defined: Group 1 with patients whose age is less than 31, Group 2 with patients whose age is more than 30 and less than 56, Group 3 with patients whose age is more than 55 and less than 66, Group 4 with patients whose age is more than 65 and less than 76, and Group 5 with patients whose age is more than 75. A training data set with four classes is generated for each group, and a map intended for exclusive use with a group is constructed by using it. The (d+1)-th column associated with age is ignored for learning, labeling, and data classification. The above labeling method is also adopted. Classifying the pilot data is also similar to that applied for the first scheme, except that the map used depends on age of the patient corresponding to the data.

5 EXPERIMENTAL RESULTS

The proposed method was applied to interview sheets provided from Tsukazaki hospital in Japan. A map with ten rows and ten columns is prepared. It is trained, subject to T=1000 in Eqs. (1) and (2). Besides, r_0=20 and τ_0=1.0 hold for initial values of in Eqs. (1) and (2).

Let $IS_q^{\,k}$ denote the number of pilot data, each of which is judged as Class q while its actual class is Class k, where k, $q \in \{1, 2, 3, 4\}$. The percentage of the number of pilot data whose classes are judged as Class q, compared to the total number of pilot data actually belonging to Class k, is calculated. The following value is referred to as the percentage of concordance associated with Class k, PC_k.

$$PC_k = 100 \times IS_k^{\,k} \,/\, \left(\sum_{q=1}^{4} IS_q^{\,k} \right). \tag{6}$$

The experimental results for the scheme using a single map are first shown. A set of data generated from interview sheets for 580 patients is used. The sheets were filled out from May through November 2010. The correspondence between a sheet and its class is perfectly known in advance. The sheets for hundred patients are randomly chosen, and a set of pilot data is generated from them. A set of training data is then generated from the remaining sheets, and a map is constructed by presenting members in the training data set. The classification capability of the resultant map is evaluated, using the pilot data set. A trial consisting of the above is repeated ten times, and mean values of PC_k's are obtained. The results are tabulated in Table 2. Note that unfavorable values associated with the percentages of discordance also appear in it. We have PC_1=82.0, PC_2=48.8, PC_3=62.8, and PC_4=48.8. PC_1 is the highest value of four PC_k's, and the proposed method achieves favorable PC_3. Both of PC_2 and PC_4, however, are less than fifty percent. This is due to the fact that the data actually belonging either to Class 2 or to Class 4 tend to be misjudged as the data of Class 1. Inhibiting misjudgment from Class 2 (or 4) to Class 1 is especially crucial in improving capability of the single-map-based classification.

Let us next show the experimental results for the five-map-based classification. The number of interview sheets is 2407. They were filled out from May through November 2010. The classes of data generated from them are perfectly known in advance. The data of fifty patients are randomly chosen as pilot data for each of the age groups (Groups 1 through 5). The remaining data are used as training data. Recall that a map is constructed for each group. The five-map-based method is evaluated by classifying the pilot data. A trial consisting of the above is repeated ten times, and the following value, PC_{ave}, is calculated for each group from averaged PC_k's.

$$PC_{ave} = \left(\sum_{q=1}^{4} PC_q\right)/4. \quad (8)$$

PC_{ave}'s are tabulated in Table 3. Patients in Group 3 suffer from a wide range of diseases compared with patients in any other group. This is why PC_{ave} is somewhat disappointing for Group 3. The method, however, achieves favorable PC_{ave}'s for other groups. It is thus established that the classification should be conducted for each age group.

6 CONCLUSIONS

This paper proposed the SOM-based method of determining examination groups for new patients from their interview sheets. MeCab is applied to handwriting sentences in the sheets, and several of the nouns are picked up per sentence. A matrix in which the sheets (or nouns) are related with the rows (or columns) is then generated. Frequencies of the nouns appearing in the sentences are basically given as element values in the matrix, and its row is presented to a map as a member of a training data set. The proposed method determines the examination group for some patient by classifying the data generated from the interview sheet filled out by the patient. The class of data is specified by the label assigned to the winner neuron for the data. From experimental results, it has been revealed that the scheme using maps for five age groups is superior in classification accuracy to the single-map-based scheme.

In future studies, the proposed method will be modified to improve the classification accuracy.

Table 2. Classification results achieved by single-map-based method

		Classification results (%)			
		Class 1	Class 2	Class 3	Class 4
Actualities	Class 1	82.0	4.0	12.0	2.0
	Class 2	42.4	48.8	8.4	0.4
	Class 3	21.6	0.0	62.8	15.6
	Class 4	36.8	1.6	12.8	48.8

Table 3. Classification results achieved by five-map-based method

Age groups	PC_{ave}'s (%)
Group 1	75.2
Group 2	65.2
Group 3	59.6
Group 4	72.2
Group 5	78.0

REFERENCES

[1] Ji Y, Yanagawa Y, and Miyazaki S (2010), Reducing outpatient waiting times for hospital using queuing theory (in Japanese). Journal of Japan Industrial Management Association, Vol. 60, No. 6, Feb., pp. 297-305

[2] Kurosawa H, Maniwa Y, Fujimura K, Tokutaka H, and Ohkita M (2003), Construction of checkup system by self-organizing maps, Proc. of Workshop on Self-Organizeing Maps, Kitakyushu, Japan, Sept.11-14, pp.144-149

[3] Ohtsuka A, Kamiura N, Isokawa T, Okamoto M, Koeda N, and Matsui N (2005), A self-organizing map approach for detecting confusion between block samples, SICE Trans., vol.41, no.7, July, pp.587-595

[4] Ohtsuka A, Tanii H, Kamiura N, Isokawa T, and Matsui N (2007), Self-organizing map based data detection of hematopoietic tumors, IEICE Transaction on Fundamentals of Electronics, Communications and Computer Sciences, vol. E90-A, no.6, June, pp.1170-1179

[5] Kudo T, Yamamoto K, and Matsumoto Y (2004), Applying conditional random fields to Japanese morphological analysis, Proc. of Conference on Empirical Methods in Natural Language Processing, Barcelona, Spain, July 25-26, pp. 230-237

The Seventeenth International Symposium on Artificial Life and Robotics 2012 (AROB 17th '12),
B-Con Plaza, Beppu, Oita, Japan, January 19-21, 2012

An electrophysiological model of the pharyngeal muscle in *Caenorhabditis elegans*

Yuya Hattori[1,2], Michiyo Suzuki[2], Zu Soh[3], Yasuhiko Kobayashi[2], and Toshio Tsuji[4]

[1] Department of System Cybernetics, Graduate School of Engineering, Hiroshima University, Hiroshima 739-8527, Japan
[2] Quantum Beam Science Directorate, Japan Atomic Energy Agency, Gunma 370-1292, Japan.
[3] Department of Biotechnology, Graduate School of Engineering, Osaka University, Osaka 565-0871, Japan.
[4] Department of Electrical, Systems and Mathematical Engineering, Faculty of Engineering, Hiroshima University, Hiroshima 739-8527, Japan
(Tel: 81-27-346-9542, Fax: 81-27-346-9688)
[1] hattori@bsys.hiroshima-u.ac.jp (Hattori, Y.)

Abstract: The pharyngeal pumping motion to send food to the bowel is a rhythmic movement in *Caenorhabditis elegans*. We proposed a computer simulation of the pumping motion to investigate the mechanisms of rhythm phenomena in living organisms. To conduct the simulations we developed an electrophysiological model of the pharyngeal muscle that corresponds to the actual structure at a muscular level, and which generates the pumping rhythms. Each of 29 cells was modeled as a membrane potential model to simulate the internal response. The electrophysiological responses of the pharyngeal muscular cells were measured as an electropharyngeogram (EPG) that records the activities of the pharynx as a signal pattern, including the membrane potentials in multiple cells. We also developed an EPG model that calculated EPG based on the outputs of individual membrane-potential models. We confirmed that our model of the pharynx could generate rhythms similar to the EPG measured from *C. elegans*.

Keywords: *C. elegans*, electropharyngeogram, electrophysiological model, pharyngeal muscle, pumping motion

1 INTRODUCTION

Living organisms exhibit various rhythmic movements such as walking and myocardial pulsation, which are important for their survival. The mechanisms of generation and control of these rhythmic movements remain largely unknown. Further understanding of these mechanisms may help in the treatment of diseases caused by defects in rhythmic control. Further, if the mechanisms can be modeled, they can be applied to engineering systems including developing novel control methods of humanoid robots.

The nematode *Caenorhabditis elegans* is a well-studied model organism with a simple nervous system, and shows several rhythmic movements including the pumping motion for chewing and swallowing involving the pharyngeal muscle. The pharyngeal muscle is composed of only 20 muscular cells and 9 marginal cells. Various biological signals including membrane potentials have been measured in pharyngeal muscular cells using the electropharyngeogram (EPG), and there is evidence that the pumping rhythms are generated by the pharyngeal muscular cells and controlled by pharyngeal neuronal cells (neurons) [1]. In addition, we recently reported that the pumping rhythms temporarily change after ionizing irradiation [2]. Thus, the pumping motion in *C. elegans* is considered a useful system to investigate the mechanisms of rhythmic phenomena in living organisms. However, it is difficult to measure the membrane potentials of individual pharyngeal muscular cells by electrophysiological techniques, and as such the mechanisms of rhythm generation and control in pharyngeal muscular cells are not well understood.

In the present study, we propose a computer simulation with a mathematical model that is constructed based on the actual structure of the *C. elegans* pharynx, and which corresponds to the biological response at an individual cellular level. A previous study superficially simulated the pharyngeal motion sending food to bowel [3] and is impossible to represent the cell-level responses. Therefore, we propose a structure-based pharyngeal model that can be used for the cell-level analysis and simulation of rhythmic phenomena. The first step of these simulations involves developing a mathematical model of the pharyngeal muscle of *C. elegans* to reproduce the pumping rhythms.

In section 2, we give an outline of the pharyngeal pumping motion and introduce the EPG, which is caused by the electrophysiological responses of muscular cells. In section 3, we model individual cells in the pharynx at the membrane-potential level, and propose a method to tune multiple parameters included in the model comprised of individual muscular-cell models using a genetic algorithm. In section 4, we confirm that an appropriate set of parameters is obtained by our parameter-tuning method and that the model can generate rhythms similar to the EPG measured from *C. elegans*. In section 5, we provide a conclusion to our study and discuss future research.

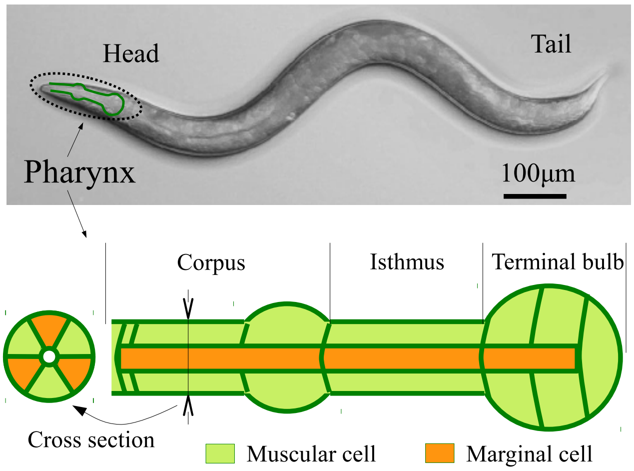

Fig. 1. Structure of the pharyngeal muscle in *C. elegans*.

2 PHARYNGEAL MUSCLE IN *C. ELEGANS*

2.1 Structure of the pharyngeal muscle

C. elegans has a simple cylindrical body approximately 1 [mm] in length (Fig.1, upper panel), and the body is composed of 959 cells. Neuronal networks consisting of 302 neurons include approximately 5,000 chemical synapse connections, approximately 600 gap junctions and approximately 2,000 connections between neurons and muscles [1]. The pumping motion (chewing and swallowing) is a rhythmic movement that is generated by the pharyngeal muscle and is required to send food (bacterial cells) to the bowel. The pharyngeal muscle alternatively contracts and relaxes 0.3 [sec]. It is structurally divided into the corpus, the isthmus and the terminal bulb (Fig.1, lower panel). The corpus is composed of four different types of 10 muscular cells (pm1, pm2VL, pm2VR, pm2D, pm3VL, pm3VR, pm3D, pm4VL, pm4VR and pm4D) and three marginal cells (mc1V, mc1DL and mc1DR). The isthmus is composed of one type of three muscular cells (pm5VL, pm5VR and pm5D) and three marginal cells (mc3V, mc3DL, and mc3DR). The terminal bulb is composed of three different types of seven muscular cells (pm6VL, pm6VR, pm6D, pm7VL, pm7VR, pm7D and pm8) and three marginal cells (mc3V, mc3DL and mc3DR). Muscular cells and marginal cells are alternately arranged in a radial manner (Fig 1, cross-section view). Each marginal cell connects with the adjacent pharyngeal muscular cells by gap junctions and does not contract and relax.

The functions of some pharyngeal neurons in the pumping motion have been elucidated, including the control of the interval between contraction and relaxation of the pharyngeal muscle and control of the pumping cycle. In addition, cell ablation studies have demonstrated that the rhythm of the pumping motion is generated by only pharyngeal muscular cells, as the pumping motion continues after all pharyngeal neurons are killed. Furthermore, the activity of muscular cells in the pharynx is synchronized by signal transduction via gap junctions between muscular cells, as mutants with a defect in the function of the gap junctions in the isthmus show disrupted synchronization between the muscular cell in the corpus and those in the terminal bulb.

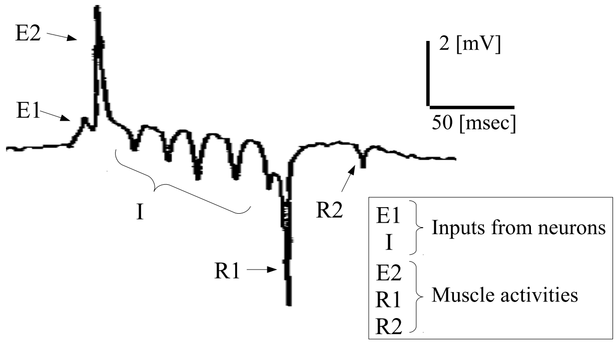

Fig. 2. The EPG recorded by Raizen et al. (revised Fig. 6A in the literature [5]).

2.2 Electropharyngeogram (EPG)

Several methods to measure activities of muscular cells in the pharynx have been developed, including membrane-potential recording [4], myoelectric-potential recording [5] and cell imaging [6]. In particularly, the myoelectric-potential recording is a popular method that can record the activities of pharyngeal cells as a signal pattern, including the membrane potentials, in the multiple pharyngeal muscular cells. The myoelectric potential in *C. elegans* is termed the electropharyngeogram (EPG). The EPG is measured by fitting a glass electrode into head of a fixed *C. elegans*, and is calculated as the difference of voltages between recordings with and without the pharynx. The EPG is composed of the time derivative of membrane potentials summed over all pharyngeal muscles and the input signals from neurons. Thus, each rapid positive change in membrane potential is observed as a positive spike in the EPG, and vice versa. However, the activity of the peristaltic motion present in the isthmus is not shown in the EPG. Each spike observed in the EPG is termed E1, E2, I, R1 and R2 (Fig. 2). E1 corresponds to the inputs by MC neurons, E2 corresponds to the contraction of the corpus and terminal bulb, I corresponds to the inputs by M3 neurons, R1 corresponds to the relaxation of the corpus and R2 corresponds to the relaxation of the terminal bulb. There is individual variability in the voltage level of the spikes depending on the electrical property of the membrane and/or the measurement environments. Therefore, we focused on the qualitative properties of the EPG including the spiking intervals that are largely independent of individual variance.

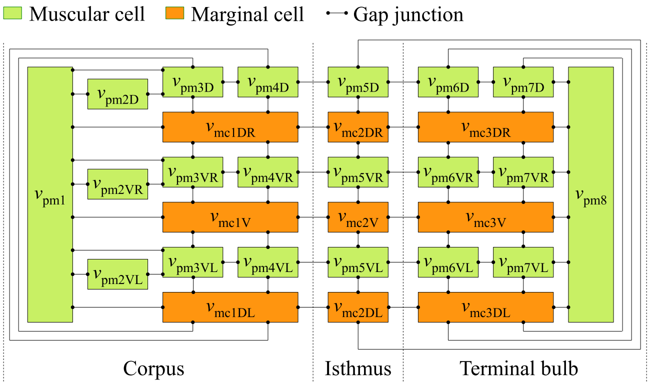

Fig. 3. Electrophysiological model of the pharyngeal muscle.

3 ELECTROPHYSIOLOGICAL MODEL OF THE PHARYNGEAL MUSCLE

In this next section, we propose an electrophysiological model of the pharyngeal muscle, which can reproduce the membrane potential of each cell and the EPG of the pharynx. This model is composed of two parts; a membrane potential model of individual cells in the pharynx (cell-level model) and an EPG model to reproduce the EPG based on the outputs of membrane potential models. The parameters of the membrane-potential models are then tuned to reproduce the actual EPG.

3.1 Membrane potential model (cell-level model)

The membrane potential of each pharyngeal muscular cell in the pharynx is important for the rhythm generation and synchronization in the pumping motion [7]. Therefore, we developed a mathematical model of each cell that shows the cell response at the membrane-potential level. Based on the actual structure of *C. elegans* [1], [8], we utilized all 29 cells in the pharynx (i.e., 20 muscular cells and 9 marginal cells), and modeled each of them individually. In the model of the cell $n(\in \mathrm{pm1}, \mathrm{pm2VL}, \cdots, \mathrm{mc3DR})$, the membrane potential is represented by v_n (Fig. 3). To describe the behavior of v_n, we introduced the FitzHugh-Nagumo model [9], [10], which is used for heart muscle modeling and analyses of various rhythmic phenomena. Cells, n and m, are connected by gap junctions based on the actual structure [8], and the connection weight is represented by $w_{n,m}$. Note that $w_{m,n} = w_{n,m}$. The electrical current from m to n is given by $w_{n,m}(v_m - v_n)$ using $w_{n,m}$ and the difference of potential between v_m and v_n. Therefore, the membrane potential, v_n, is represented by:

$$T_n \frac{dv_n}{dt} = c_n\{v_n - \frac{v_n^3}{3} - u_n + \sum_m w_{n,m}(v_m - v_n)\}, \quad (1)$$

$$T_n \frac{du_n}{dt} = \frac{1}{c_n}(a_n + v_n - b_n u_n), \quad (2)$$

where T_n is a time constant to account for the rapid change of the membrane potential in the pumping motion. a_n, b_n, and c_n are constants used in the FitzHugh-Nagumo model. u_n is a recovery variable. These parameters determine the cycle and the response rate of v_n, and should be tuned to generate rhythms in the pumping motion. This is the first model to reproduce the activities of individual cells in the pharynx at the membrane potential level.

Since the EPG can be used to directly observe the rhythms generated in the pharynx, we used the EPG to compare the rhythm of v_n with that of the pumping motion itself. For this purpose, we developed the EPG model to calculate the EPG based on the individual membrane potential models.

3.2 EPG model

We calculated the EPG based on the membrane potential, v_n, of each cell model in **3.1**. The EPG is measured as the time derivative of the membrane potentials summed over all pharyngeal muscular cells because there is a capacitance between the electrode and the head of the *C. elegans*. Therefore, the EPG, $V^{\mathrm{EPG}}_{\mathrm{model}}$, generated by $v_n(n \in \mathrm{pm1}, \mathrm{pm2D}, \cdots, \mathrm{mc3V})$ is represented by:

$$V^{\mathrm{EPG}}_{\mathrm{model}} = \sum_n R_n C \frac{dv_n^{\mathrm{act}}}{dt}, \quad (3)$$

$$v_n^{\mathrm{act}} = \max(v_n, 0), \quad (4)$$

where $v_n^{\mathrm{act}}(n \in \mathrm{pm1}, \mathrm{pm2D}, \cdots, \mathrm{mc3V})$ is an action potential, R_n is a resistance depending on the distance between the electrode and the cell body, and C is a capacitance. We can compare the rhythm of v_n with that of the pumping motion by using the EPG model.

3.3 Parameter tuning method for the pharyngeal muscle model

The parameters should be well tuned in order to reproduce the actual EPG using the model. To tune parameters included in the membrane potential model of each cell in **3.1**, we compared the actual EPG recorded from a *C. elegans* with the EPG calculated by the model in **3.2**. As the recorded EPG is affected by electrical properties of the membrane and/or measurement environments, there is individual variability in the voltage level of the spikes. Therefore, we used qualitative properties, in particular spiking intervals, which are largely independent of individual variability, for the parameter tuning. The spikes that correspond to muscular activities are E2, R1, and R2 (Fig. 2). Positive and negative membrane potentials in the corpus cells generate E2 and R1 spikes, respectively, while positive and negative membrane potentials in the terminal-bulb cells generate E2 and R2 spikes, respectively. Therefore, we tuned the membrane potential models

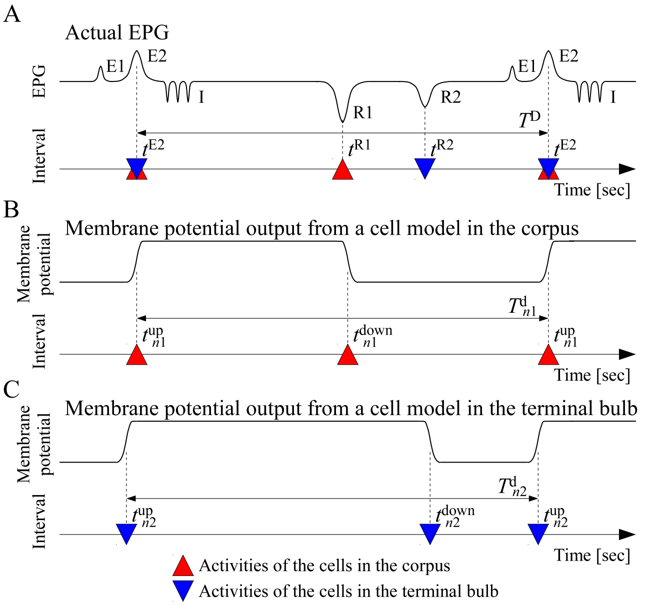

Fig. 4. Intervals of the activities of the corpus and the terminal bulb.

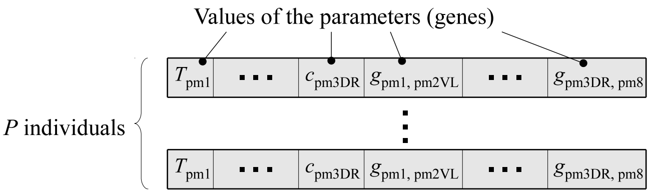

Fig. 5. The GA string.

to reflect the positive and negative membrane potential properties and the spiking intervals between each spike in the actual EPG.

t^{E2}, t^{R1}, and t^{R2} represent the intervals of E2, R1, and R2 (Fig. 4A), and are calculated as the peak value of each spike. In addition, the pumping cycle measured from the actual EPG is represented by T^{D}. The positive and negative intervals in the outputs of the membrane potential models in the corpus are represented by t^{up}_{n1} and t^{down}_{n1} (Fig. 4B), where $n1$ is the cell name (pm1, pm2VL, pm2VR, pm2D, pm3VL, pm3VR, pm3D, pm4VL, pm4VR, pm4D, mc1V, mc1DL, and mc1DR). The positive and negative intervals in the outputs of the membrane potential models in the terminal bulb are represented by t^{up}_{n2} and t^{down}_{n2} (Fig. 4C), where $n2$ is the cell name (pm6VL, pm6VR, pm6D, pm7VL, pm7VR, pm7D, pm8, mc3V, mc3DL, and mc3DR). These parameters are calculated as the maximum/minimum values of the time derivative of each membrane potential model. In addition, the output cycles of the membrane potential models of the corpus and the terminal bulb are represented by T^{d}_{n1} and T^{d}_{n2}, respectively.

To evaluate the fitness of the positive and negative intervals calculated by the individual membrane potential models of the pharyngeal cells, we defined the following error judgment standard that compares the intervals of membrane potentials output from individual cell models to the actual EPG in the pharynx:

$$E = \frac{E^{c} + E^{t}}{23}, \tag{5}$$

$$E^{c} = \sum_{n_1} \frac{|t^{E2} - t^{up}_{n_1}| + |t^{R1} - t^{down}_{n_1}| + |T^{D} - T^{d}_{n_1}|}{3}, \tag{6}$$

$$E^{t} = \sum_{n_2} \frac{|t^{E2} - t^{up}_{n_2}| + |t^{R2} - t^{down}_{n_2}| + |T^{D} - T^{d}_{n_2}|}{3}, \tag{7}$$

where E^{c} is an integrating error of the corpus cells, and E^{t} is an integrating error of the terminal bulb cells. As the activity of the isthmus cells is not shown in the actual EPG, we evaluated the fitness of 23 membrane potential models in the isthmus (6 membrane potential models were not used). The smaller the E, the more the EPG model reproduces the actual EPG. We employed a learning and evolutionary genetic algorithm (GA) to suitably tune the parameters included in the membrane potential models on the basis of E.

First, all the parameters included in the membrane potential models are represented as individual genes in a GA string (Fig. 5). A string arranging all the parameters (genes) is treated as an individual in the GA. P individuals are produced, where the initial value for each gene is given as a uniform random number. Next, all individuals of the current generation (the repeat number of calculation for the GA tuning) are evaluated by equation (5), which are used to produce the next generation. The elite R_{elite} [%] individuals with the superior error value, E, remain as a part of the next generation. $(100 - R_{elite})$ [%] of the population of the next generation is produced by the three operations of a GA; i.e., crossover for $R_{crossover}$ [%] of the population, mutation for $R_{mutation}$ [%] of the population, and copying for $R_{copying}$ [%] of the population. These procedures (evaluation, crossover, mutation, copying) are repeated every generation until the generation g reaches G. We essentially follow the procedures of GA operations we previously reported [11].

4 REPRODUCTION OF PUMPING RHYTHMS IN A WILD TYPE *C. ELEGANS*

We evaluated the effectiveness of our proposed pharyngeal muscle model. To generate the actual pumping rhythms in our model, we tuned the parameters included in the membrane potential models by the GA-based tuning method. As an example to reproduce the actual EPG, we used the EPG of a wild type *C. elegans* in which neurons except for the M4 neuron were ablated.

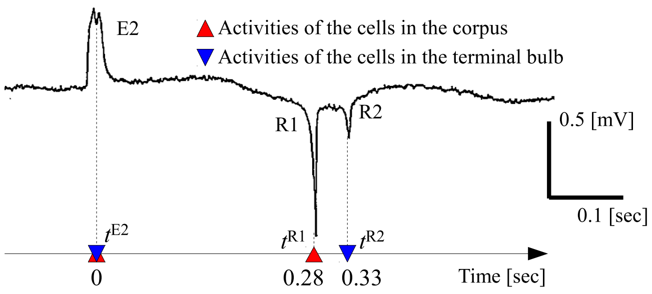

Fig. 6. EPG measured by Raizen et al. (revised Fig. 6A in the literature [5]).

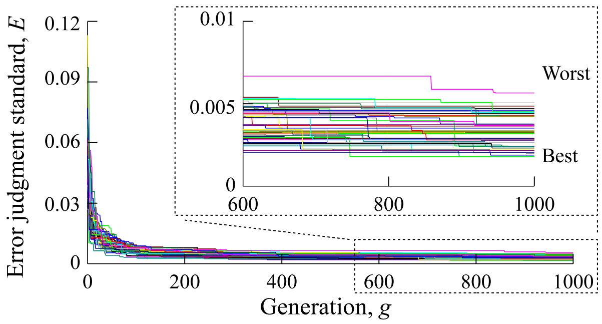

Fig. 7. Evolution of the error judgment standard, E.

4.1 Methods

The EPG includes E1 and I spikes corresponding to neuronal activity and E2, R1, while R2 spikes correspond to muscular activity. As the proposed electrophysiological model targets only muscular activity, we employed the EPG measured from a wild type *C. elegans* in which all neurons but the M4 neuron were ablated [5]. As shown in Fig.6, the EPG includes only E2, R1, and R2 spikes. Although the M4 neuron controls the peristaltic motion of the isthmus, the input from the M4 neuron to the pharyngeal muscle and the peristaltic motion are not shown in the EPG. Therefore, the spikes observed in Fig.6 can be treated as muscular activity only.

The data of the spiking intervals used for the parameter-tuning were derived from the EPG in Fig.6, where we defined the spiking interval of E2 as a standard time ($t^{\mathrm{E2}} = 0$ [sec]) and the spiking intervals of R1 and R2 were given by $t^{\mathrm{R1}} = 0.28$ [sec] and $t^{\mathrm{R2}} = 0.33$ [sec], respectively. The pumping cycle was given by $T^{\mathrm{D}} = 1.2$ [sec]. The spiking intervals calculated by the membrane potential models, t_n^{up} and t_n^{down}, were normalized by those generated by a cell near the glass electrode, pm4D ($t_{\mathrm{pm4D}}^{\mathrm{up}} = 0$ [sec]). The range of parameters used in this simulation were $T_n = [0, 0.1]$, $a_n = [0, 1]$, $b_n = [0, 1]$, $c_n = [0, 10]$, and $w_{n,m} = [0, 1]$. Parameters included in the models of the same types of cells are tuned as the same value. The condition settings of the GA were set to $P = 20$, $R_{\mathrm{elite}} = 5$, $R_{\mathrm{crossover}} = 76$ [%], $R_{\mathrm{mutation}} = 9.5$ [%], $R_{\mathrm{copying}} = 9.5$ [%], and the at-end generation was set to $G = 1,000$.

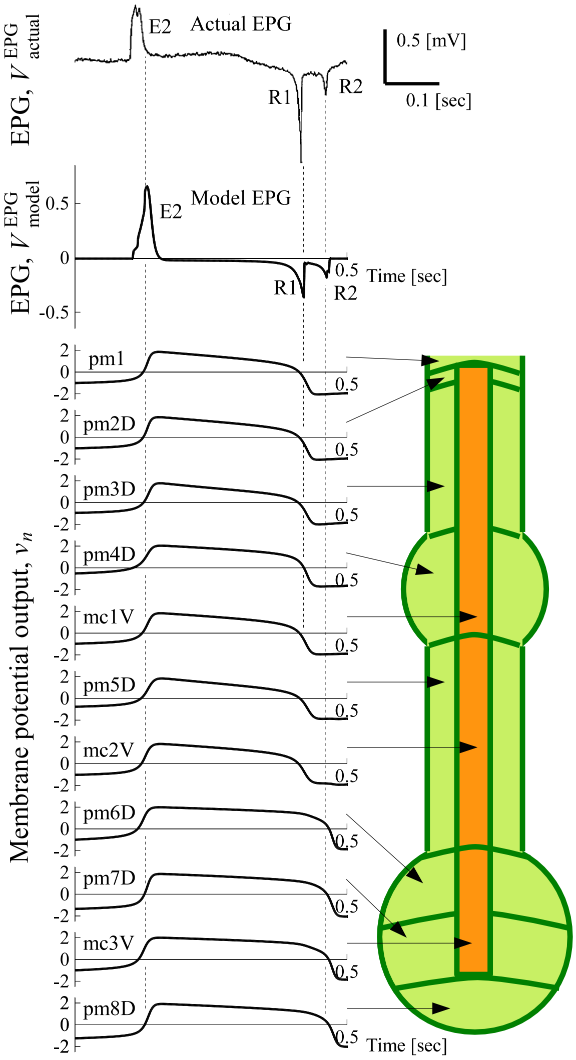

Fig. 8. Reproduction of pumping rhythms of a wild type *C. elegans* at the EPG level.

4.2 Results

We conducted 50 trials using different initial values for the GA-based tuning method. Evolution of the error judgment standard, E, in a top individual at each GA generation among 50 trials is shown in Fig. 7. Values of E among all trials decreased rapidly until $g = 100$, and were less than $E = 0.015$ at $g \leq 200$. After $g = 200$, values of E among all trials decreased slowly, and at $g = 1,000$ the maximal and minimal values reached $E = 0.0056$ and $E = 0.0018$, respectively (worst and best trials in Fig. 7).

The membrane potential output of individual cell models, v_n, employing a set of the parameters obtained at $g = 1,000$ and the EPG, $V_{\mathrm{model}}^{\mathrm{EPG}}$, calculated from v_n are shown in Fig. 8.

The output EPGs from the actual *C. elegans* and the proposed model, $V^{\mathrm{EPG}}_{\mathrm{actual}}$ and $V^{\mathrm{EPG}}_{\mathrm{model}}$, are shown on the top panel. $V^{\mathrm{EPG}}_{\mathrm{actual}}$ is a replot of Fig. 6. The EPG of the model was calculated based on v_n of the membrane potential models of 23 cells (equations (3) and (4)). Since the cells in the pharynx are divided into 11 types based on the function, a single example of output of each is shown on the bottom panel. The right panel shows the position of each cell in the pharynx. The capacitance included in equation (3) was set to $C = 276$ [pF] based on a previous report [4]. The resistances included in equation (3) were set to $R_{\mathrm{pm4VL}} = R_{\mathrm{pm4VR}} = R_{\mathrm{pm4D}} = 1$ [MΩ] and $R_{\mathrm{pm6VL}} = R_{\mathrm{pm6VR}} = R_{\mathrm{pm7D}} = R_{\mathrm{pm7VR}} = R_{\mathrm{pm7D}} = 0.3$ [MΩ]. The resistances corresponding to the isthmus were set to $R_n = 0$ [MΩ] as the activity of the cells in the isthmus is not shown in the actual EPG. Other resistances were set to $R_n = 0.01$ [MΩ]. From Fig. 8, we confirmed that the shapes of the membrane potential, v_n, were similar in all cells. In the membrane potential models of all cells, the rising time of v_n is the same as that of the spike E2 in the actual EPG. v_n in the corpus decreased corresponding to the decrease of the spike R1, and v_n in the terminal bulb decreased at the same time as R2 in the actual EPG. Furthermore, the EPG of the proposed model, $V^{\mathrm{EPG}}_{\mathrm{model}}$, calculated based on v_n, was similar to the actual EPG, $V^{\mathrm{EPG}}_{\mathrm{actual}}$. As such, the proposed electrophysiological model of the pharyngeal muscle composed of the membrane potential models accurately reproduced the pumping rhythms (i.e., spiking intervals of the actual EPG).

5 CONCLUSION

In this paper, we developed a membrane potential model of individual muscular cells in the pharynx based on the actual structure of the *C. elegans* to investigate the mechanisms of rhythm generation and control in living organisms. In addition, we proposed an EPG-level model that calculates the electropharyngeogram (EPG) based on outputs of individual membrane potential models. In the parameter tuning for the membrane potential models, we focused on the spiking intervals in the actual EPG and tuned the parameters so as to reproduce the intervals rather than the EPG itself. In our numerical experiment of rhythm generation, the proposed model successfully generated similar pumping rhythms to those observed in a wild type *C. elegans*.

As our model was based on the actual structure of cell connections and each cell corresponds to the actual cell in the *C. elegans*, by ablating each connection included in this model virtually, we can investigate the role of the gap junctions on the rhythmic phenomena. In pilot experiments, we virtually ablated gap junctions in the isthmus, as seen in the *eat-5* mutant that exhibits functional gap junctions deficits in the isthmus and shows disrupted synchronization between the muscular cells in the corpus and those in the terminal bulb. Similarly, we found that the membrane potential models generated rhythms that were not synchronized between the corpus and the terminal bulb (data not shown). Thus, this model will be useful for further studies examining mechanisms of rhythmic phenomena in *C. elegans*.

ACKNOWLEDGMENT

This study was partially supported by a Grant-in-Aid for Scientific Research on Innovative Areas from MEXT to T.T. (No. 20115010).

REFERENCES

[1] White, J.G., Southgate, E., Thomson, J.N., and Brenner, S. (1986), The structure of the nervous system of the nematode *Caenorhabditis elegans*. Philos. Trans. R. Soc. Lond. B. Biol. Sci. 314, pp. 1-340.

[2] Suzuki, M., Sakashita, T., Hattori, Y., Tsuji, T., and Kobayashi, Y. (2011), Effects of ionizing radiation on pharyngeal pumping in *Caenorhabditis elegans*. 18th Int. *C. elegans* Meeting, Full Abstracts, pp. 158-159.

[3] Avery, L. and Shtonda, B.B. (2003), Food transport in the *C. elegans* pharynx. J. Exp. Biol., 206, pp. 2441-2457.

[4] Shtonda, B. and Avery, L. (2005), CCA-1, EGL-19 and EXP-2 currents shape action potentials in the *Caenorhabditis elegans* pharynx. J. Exp. Biol., 208, pp. 2177-2190.

[5] Raizen, D.M. and Avery, L. (1994), Electrical activity and behavior in the pharynx of *Caenorhabditis elegans*. Neuron, 12, pp. 483-495.

[6] Kerr, R., Lev-Ram, V., Baird, G., Vincent, P., Tsien, R.Y., and Schafer, W.R. (2000), Optical imaging of calcium transients in neurons and pharyngeal muscle of *C. elegans*. Neuron, 26, pp. 583-594.

[7] Starich, T.A., Lee, R.Y.N., Panzarella, C., Avery, L., and Shaw, J.E. (1996), *eat-5* and *unc-7* represent a multigene family in *Caenorhabditis elegans* involved in cell-cell coupling. J. Cell Biol., 134, pp. 537-548.

[8] Albertson, D.G. and Thomson J.N. (1976), The pharynx of *Caenorhabditis elegans*. Phil. Trans. Roy. Soc. B, 275, pp. 299-325.

[9] Fitzhugh, R. (1961), Impulses and physiological states in theoretical models of nerve membrane. Biophys. J., 1, pp. 445-466.

[10] Nagumo, J., Arimoto, S., and Yoshizawa, S. (1961), An active pulse transmission line simulating nerve axon. Proceedings of the IRE, 50, pp. 2061-2070.

[11] Hattori, Y., Suzuki, M., Soh, Z., Kobayashi, Y., and Tsuji, T. (2012), Theoretical and evolutionary parameter tuning of neural oscillators with a double-chain structure for generating rhythmic signals. Neural Comp., 24, in press.

The Seventeenth International Symposium on Artificial Life and Robotics 2012 (AROB 17th '12),
B-Con Plaza, Beppu, Oita, Japan, January 19-21, 2012

Origin of the Chukchee−Kamchatkan language familyfrom the Paiwan language in Formosa: Evidenced by Swadesh basic vocabulary comparison, providing basicknowledge for understanding DNA haplotype distributions

Koji Ohnishi[1]

[1]Faculty of Science, Niigata University, Niigata 950-2181, Japan

(Tel: 81-25-262-5237, Fax: 81-25-262-5237)

[1]ohnishi@bio.sc.niigata-u.ac.jp

Abstract: Chukchee-Kamchatkan (ChKm) basic body-part name words (BBPs) in Swadesh 200 basic word vocabulary. were compared with ca. 1,300 basic words of 80 different Austronesian (AN) languages, which has resulted in finding 13 cognates of ChKm BBPs. Out of the 13 ChKm BBP word-items, 5.3 items were found to have cognate in Formosan, and 3.5 items in Paiwan. Chi-squared statistical test concluded that ChKm have evolved from the Paiwan language or its close kin language. The results were compared with the results from similar analyses of Formosan-related non-AN languages and Gilyak (Nivkh). Results were also discussed from aspects of mitochondrial and Y-chromosomal DNA-haplotype distributions.

Keywords: 3-6 key words or phrases in alphabetical order, separated by commas.

1 INTRODUCTION

The Origin of Chukchee-Kamchatkan (ChKm) language family is unknown. ChKm is divided into Chukchee-Koryak branch (Chukchee, Koryak, Alutor) and Itelmen (Itel) branch, the latter consisting of Northern and Southern dialects (N.Itel, S.Itel) of Western Itelmen (W.Itel = Western Kamchadal) and distinct Eastern Itel and Southern Itel (Kurebito [1]). The aim of this paper is to elucidate phylogenetic position of ChKm language family by basic word (BW)-comparison method, and to provide basic knowledge for analyzing recently accumulating data of mitochondrial, Y-chromosomal and HLA haplotype distribution in Eurasia, Oceania, and Americas.

2 METHODS, RESULT and DISCUSSIONS

BBP comparison: Basic body-part name words (BBPs) (ca.32 word items for human and animals, See [2]), defined as body-part name words included in Swadesh 200 basic words (Sw200W), were taken from ChKm vocabulary in the references, Kure* (Kurebito [1]), Worth*, and Bogo*, listed in Table 1, and compared with ca. 1,300 Austronesian (AN) basic words listed in Tryon's "Comparative Austronesian Dictionary" (CAD* in Table 1), and with representative Eurasian languages. AN cognates of ChKm BBPs thus found are listed in Table 2, where BBP items are classified to 5 AN subgroups (FORM, W.MP, C.MP, SHWNG, and OC in Table 1) to which AN cognates most similar to the corresponding ChKm BBPs belong. Cognates found in Niger-Kordofanian are also given in Table 2. Abbreviations used in Tables 2-6 are listed in Table 1.

Closest similarity analysis (CSA): CSA (Ohnishi [3]) was revised and employed to this study. Cognates most similar (= closest) to these ChKm BBPs were found in the frequencies as below. Cognates were found in 13 ChKm BBP items, out of which 11.2 BBP items are found in AN, and 1.8 items are in non-AN languages. The 11.2 items consists of (**Formosan 5.3** (**Paiwan 3.5**, Tsou 1, Atayal 0.8), Western Malayo-Polynesian(=W.MP) 3 (Philippines 1 / Borneo 0 / Sundic 2/ Sulawesi 0), CentralMP= 0.5, Oceanic = 2), as shown in Table 3. These values, which we call here "closest similarity (CS)-scores", are calculated by the method shown detailedly in Table 3, using the cognate data in Table 2. The CS-scores, thus calculated for each of the 5 AN subgroups, tell us the subgroup to which ChKm would be most closely related. In the case of Table 3, Formosan seems to be most closely kin to ChKm.

Chi-squared test: In order to statistically evaluate the result of CSA in Table 3 and Table 4, χ^2-test for the degree 2 of freedom was employed as below (Snedecor [4]).

χ^2 is given by

$$\chi_X{}^2 = \Sigma_i\, (Observed_i - Expected_i\,)^2 /(Expected_i)$$
$$= (O_X - E_X\,)^2 /E_X + (O_{non\text{-}X} - E_{non\text{-}X}\,)^2 /E_{non\text{-}X} \qquad \text{[Eq.1]}$$

By letting

Number of AN languages listed in CAD*: $N_{AN} = 80$.

Number of languages in a subgroup X of AN family: n_X

Number of languages in the remaining subgroup (non-X) of AN family: $n_{non\text{-}X} = N_{AN} - n_X$

Number of word items whose closest cognate is observed in subgroup X: O_X

Number of word items whose closest cognate is observed in subgroup $non\text{-}X$: $O_{non\text{-}X}$

Number of total number of word items whose closest cognates are found in AN: $O_{AN} = O_X + O_{non\text{-}X}$,

we have

$E_x = O_{AN}\ (n_x / N_{AN}),\ E_{non\text{-}X} = O_{AN}\ (n_{non\text{-}X}/N_{AN})$. [Eqs 2]

From Eqs 2 and Eq.1, we obtain the value of $\chi_X{}^2$ for subgroup X.

For $O_{FORM} = 5.3\ (O_{AN} = 10.8)$, and $O_{Paiwan} = 3.5\ (O_{AN} = 10.8)$, in Table 4, we can conclude $P < 0.05$ for both cases, as is shown in Table 4..

Thus we can conclude thast ChKm is most kin to Formosan, especially to Paiwan language. It is very plausible that ChKm have evolved from an ancient Paiwan language or its kin language. Results of similar CSA and χ^2-test for other possibly Formosan-related languages, Mayan, Eskimo, and Mongolic, taken from Ohnishi [3], are also given in Table 4, for the sake of compasison with ChKm. Further relationship among these possibly Formosan-related languages needs to be analyzed in future.

AN cognates of ChKm non-BBP vocabulary are also searched in CAD*, and listed in Table 5.

In order to know whether or not the Nivkh (= Gilyak) language is related or not related to ChKm, CSA and χ^2-test were similarly done for analyzing AN cognates of Nivkh BBPs, and the result is given in Table 6 and Table 3. Nivkh is now concluded to be closely kin to Oceanic (P < 0.005), and is therefore unrelated to Nivkh.

Relationship to DNA haplotype distribution: Chukchee and Eskimo share some haplotypes such as Q and N3 haplotypes of Y chromosome, A2 and D2 haplotypes of mitochondrial DNA (Sakitani, 2008[5], p.13, p.p.31; Adachi *et al.*[6]). It seems to be interesting to answer the question whether or not these and/or some other haplotypse might be shared by some different language groups of possible Formosan origins.

3 CONCLUSION

ChKm is a language derived from ancient Formosan, most plausibly from a Paiwan-like language. Eskimo seems to be considerably kin to ChKm, but seem to have been derived from different branches of Formosan or Formosan-related AN languages. Closest similarity analysis and chi-squared test concerning the distribution of basic body-part word cognates in AN subgroups was found to be an efficient method for finding phylogenical relationship to various subgroups of Austronesian.

Table 1: Abbreviations used in Tables 2 -5.

§ **General:** A < B, B > A: "A has/had been derived from B"; A < > B: "A is genetically (phylogenetically) related to B" (= "A cognates with B") ; A << B, B >> A: "A has/had been borrowed from B"., pX = protoX (e.g., pJp = proto-Japanese); dial. = dialect, N.=North(ern), S.=South(ern), E.= East(ern), W.=West(ern), C.= Central, wr.= Written, mid./Mid.= Middle, mod= Modern

§ **Language names:** **ChukKm** = Chukchee-Kamchatkan, Chuk.= Chukchee, Itel.= Itelmen ▌**Esk** = Eskimo ▌**AN** = Austronesian, FORM= Formosan, MP=Malayo-Polynesian, W.MP= Western MP {PHIL= Philippines, SND= Sundic, SLW=Sulawesi },C.MP=Central MP, SHWNG= S.Halmahera and W.New Guinea), OC = Oceanic {ADM= Admiralties, W.OC = Western OC, S.E.Solom.= S.E.Solomons, ReOC= Remote OC {MicN= Micronesian, NCal= New Caledonian, Vanu.= Vanuatu, C.Pacif.= C.Pacific, PolyN= Polynesian} ▌**NiKord** = Niger-Kordofanian, Jxxx (J26, J145, etc.) = language number #xxx in John* (see below), where J1~ J226 belong to Bantu.

References: ▌Bogo*= Bogoras, W.(1917) Koryak Texts (Publication of the American Ethnological Society, Vol.5), Leiden ▌CAD*= Tryon, D.T.(1995) *Comparative Austronesian Dictionary Parts 1-4*, Mouton de Gruyter, Berlin/New York. ▌CED*= Fortesque, M. *et al.* (1994) *Comparative Eskimo Dictionary*, Alaska Native Language Center, Fairbanks. ▌John* = Johnston, H.H.,Sir (1919, 1922) A Commparative Study of the Bantu and Semi-Bantu Languages, Volumes I, II, Clarendon Press, Oxford. ▌Kure* = Kurebito [1] ▌MTFNT-App* = Appendix in Ogawa (1935) *The Mytths and Traditions of the Native Tribes (Texts and Notes)* (In Japanese), Inst. of Linguistics, Taihoku Imperial University, Taipei. (2nd printing in 1996) ▌Savel'eva*= Savel'eva, V. N. and Taksami, Ch.M. (1970): *Nivkhsko-Russkiĭ Slovar'*, Moskva. ▌Tak*= Takahashi, M. (1942): *Karafuto Giryaaku-go (Sakhalin Gilyak Language)* (In Japanese), Osaka Asahi-Shinbunsha, Osaka. ▌Worth*= Worth, D.S. (1969) Dictionary of Western Kamchadal (Univ. of California Publications in Linguistics), Berkley and and Los Angeles. ▌YH* = Yasumoto,B. and Honda,M. (1978) *Nihongo no Tan'jyou* (The Birth of the Japanese Language), Taishukan Shoten, Tokyo.

Table 2. Distribution of Austronesian and non-Austronesian cognates of Chukchee-Kamchatkhan basic body-part name words (BBPs), shown together with the method of closest similarity analysis (CSA) using CS-scores

§§ 1. Cognate distribution and CS-scores

§ Most similar to Formosan (FORM):

4 items (Paiwan) = [FORM (Paiwan) = 3, Tsou 1]

(Tsou-like: 1 item)

BLOOD: Koryak muL (Bogo*) //N.Itel. młəm /S.Itel. młim (Kure*) /W.Itel. młim "blood" (< *muḷi- ~ *muL < *xmul u ~ *xmuju "blood"); Chuk. *mułłəmuł* /Alutor *mulləmul* /Ko ryak mulləmul (Kure*) ||| **FORM: Tsou** *xmuru* (CAD*), hu mulu, humuju (MTFNT-App*,p.7) "blood"

(Paiwan-like) 3 items

EYE: N.Itel *ḷʸaŋocχ* (< **ḷʸaŋocχ*) ||| **FORM: Paiwan** *ḷʸ-əm-əŋ-ḷʸəŋ* (=*ḷʸəŋ-ḷʸəŋ* + -əm-) (< **ḷʸəŋ*)

HEAD: N.Itel *kəmtqol, k'əmtqol* "head" <**kəmt-qol* "hair of head" < **kəm-* "hair" + **-t* "?" + **qol* "head", where **qol* < FORM: **qoḷo* "head"), S.Itel *caqol* "head" (< **ca-qol* < **ca-* "?" + **qol* "head") ||| **FORM: Paiwan** *qoḷo, ʔoḷo* (MTFNT-App*, p.2), *quḷu (CAD*) "head" (< *pAN *quluH "head") ||| Es k: pEsk **qulə-* "area above" ||| NiKord: (Bantu) [J140] *-gul u* /[J153] li-gulu /[J155] li-kolo "above, up"

TONGUE: Chk *jiłił* (< *jiłəjił) /Koryak *jiləjil* "tongue, language , speech", Autor *jiləjil* "tongue" (< **jilə-jilə ~~ *jiłə-jiłə* < *jilə ~ *jilə < *ǰila ~ *ǰiła < W.MP *dila "tongue" < $*d_3$íla "t o lick") ||| **FORM: Paiwan** *ɟ-im-iḷaḳ* (= *ɟiḷaq* + *-im-*) (< **dilaq*) || W.MP: (SLW) Da'a *ǰila* /Uma ǰilaʔ// (SND) Madure se *ǰʰila* //Batak Toba dila /Aceh dilah // (Borneo) Murut dilaʔ //(P HIL) Tagalog, Aklanon *dīlaʔ* "tongue" (< $*d_3$ila "to lick") ; (SND) Batak Toba dilat /Minangkabau ǰilat /IndoN mən-ǰilat / Javanese *n-dilat* /Madurese *ǰʰilat* /Sasak *delaʔ* "to lick" (*dila ~ *dela < *dela < NiKord: *deda "tongue") ||| NiKord: [J151 a] [J244] **deda* /[J242] *lelā* "tongue" (< **deda*)

§ Most similar to FORM/Oceanic(OC)/Turkic :

1 item = [FORM(Atayal) 0.3, OC 0.3, Turkic 0.3]

LIP: Alutor, Koryak *waməlkalŋən* "lip" (Kure*) (< **waməl -kalŋən*, where **-kalŋən* <**kalŋa-(n)*< >OC:*kalŋa-*"language") |||OC: **(W.OC) Mbula** *kalŋa-* "language" (< **kal-ŋa* < **kal-* "to speak"), (NCal) A'jie *kãřãwã* "lip" (< **kala-wã*) || **FOR M: Atayal** *k-um-ał* "to speak" (<**kał* + *-um-*) ||| Turkic:Chu vash *kal-* "to speak"

§ Most similar to FORM/Eskimo(Esk):

1 item = [FORM(Paiwan)= 0.5, Esk= 0.5]

FAT: S.Itel *qalk'* "fat, grease" (< **qal-k'*, where *qal- < > FORM: **qaḷum* "fat") ||| **FORM: Paiwan** *ḳaḷum* (= *qaḷum*) "fat, grease" ||| **Eskimo**: pEsk **qalunəq ~*qaluniq* "grease floating on stew", Gleenlandic Inuit *qaluniq* "fat, lard" (< **qalu-niq*) ||| Mongolic: Written Mongolian *qalim* "fat, skin cut off with remaining fat" ||| NiKord:(?)[J193] *(a-)gali* "fat,oil"

§ Most similar to FORM/Quechuan(Que.):

1 item = [FORM(Atayal)= 0.5, Que.= 0.5]

to BREATHE: Chuk, Koryak wəjentok /Alutor wəjisʔtək "to bre athe" (< *wəj- < *waj-) ||| **Quechuan:** wayra (= huayra) "to breathe" (< *way-ra) ||| **Atayal** βayhu "wind" (< *βay-), vāyu- "wind" (Borrowed from IE: Sanskrit.); Paiwan vaḷi "air, wind" (< *bāli ~ *bali "wind"), v-ən-aḷi "to blow" (= vaḷi + -ən-) (vaḷi > *vay < > Koryak wəj- "to breahe" || W.MP: (PHIL) Bangingi Sāma *baliyu* "wind, air", Kalinga Limos *bāli* "monsoon wind".

§ Most similar to W.MP:

3 items = [W.MP= 3(PHIL 1, SND 2)]

BACK(anatomical): N.Itel. *k'aac* /S.Itel. *k'awac* (< pItel. **k'awac* < **kawa-c, where *kawa-* < (pAN ?) **kawa* < **kuwa* < NiKord **kua "back"*) ||| W.MP: **(PHIL) Molbog** *kaʔay likud* "behind" (< *kaway likud (Molbog *kaʔay* < *ka way < > pItel. *k'awac*),Cf. Aklanon, Palawan *likud* "back, be hind") ||| Note: Might cognate with; (FORM): Paiwan *qavan* "shoulder" (< **kava-n = *kawa-n*) ||| NiKord: J200, J220 *-k oan, -kuan* "back" (< **-kuan*)||| Note: Unrelated to: (W.MP: PHIL) Molbog *awak* //Esk (W.Greenlandic) *avaq* "back"

FAT: Chukchee *esʔən* /Alutor *asʔən* /Koryak *acʔən* "fat, grease" (<**asʔən*) ||| W.MP: **(SND) Aceh** *asəə* "flesh"

FLESH: N.Itel., S.Itel. *tχaltχal* "flesh" (< *tχal < *dgal < *dagal*) ||| W.MP: **(SND) Batak Toba** *ǰagal* "meat" (< *Dagal ~*dagal < Nijer-Kordofanian **dagala*) ||| Nijer-Kordofanian: (Bantu) Lu-ganda *-dagala* "meat" (John*, vol.II, p.344)

§ Most similar to Central MP(C.MP)/Esk:

1 item = [C.MP= 0.5, Esk= 0.5]

NOSE: S.Itel *qŋasəŋ* "nose" (< **qəŋa-səŋ* < **qəŋa* "to smell ~ nose" + **səŋ(u)* "to sniff, to smell")||| **Esk: pEsk** **qəŋaʀ* "no se" (< pAN **qaŋ* "to smell") (< pAN **qaŋ* "to smell")||| OC: Kwaio *gʷaŋo(-na) "*nose"|| W.MP: (SND) Batak Toba *aŋgo* "to smell" (<**aŋ-go* <**aŋ-* < pAN **qaŋ*)|| **C.MP: Ngada** *səŋu* "to smell, to smell"|| W.MP:(PHIL) Kagayanen *siŋŋu'tan* "to smell (v.t.)"

§ Most similar to OC: 2 items

HAIR: N.Itel *k'əmkəm* "hair of head, hair", S.Itel *k'mki'm* "hair of head" (< **k'əmk'əm ~ * k'imk ' im < *k'imk'im < *kum(i)kumi* "beard") ||| MP: (W.MP: PHIL) Salangani Blaan *kum i* // (C.MP) Ngada *kumi* /Sika *ʔumi-ŋ* "beard" || OC:(W.OC) Roviana *ɣumi* //(North & Central Vanuatu) Raga *ɣumʷi-* // (Central OC) **Rotuman** *kumkumi* /Tahitian *ʔmi ʔmi* "beard"

HEAD:Alutor *lawət* /Koryak *lewət* /Chuk. *łewət* "head"(< proto- Chukchee-Koryak **ławət ~ *lawət* "head" < *ław-(ət) ~ *law-(ət) "feather ~ leaf (of head)" <**llau* ~ *lau "feather ~ leaf" < *lalau "feather" ~ *dau "hair of head (= leaf (of head) ~ feather" < **dau* < pMP *$*d_2ahun$* "leaf") ||| OC:**(W. OC) Manam** *lalau* //(N.C.Vanuatu) Raga *lalau* "feather" (< **la-lau* <**lau* "leaf" < **dau* "leaf") ; **(C.Pacif.) E.Fijian** *dʳau-ni-ulu* "hair-of-head" (< "leaf of head", Tongan lau-ʔulu "hair of head" (< *lau* "leaf" + *ʔulu* "head") ; Manam dau / Raga, Rotuman *rau* /Samoan *lau* "leaf" || W.MP: Sasak dauŋ /Aklanon dāhun /Bangingi Sama dahun "leaf" ||| Chinese: C antonese *t'au*[21] "head" (< **dau* "leaf")

§ Similar to many subgroups (Not counted in Table 3) **:**

SKIN: W.Itel. qułxi (Worth*)/Koryak qɪḷh "skin" (<**gul(i)-xi ~ *kuli(-xi)*) ||| OC: **(W.OC) Maringe** guli "skin" |||Note: Possibly further cognates with; (FORM) Puyuma koḷiṭ "skin of fluit" //OC: (W.OC) Mbula *-kuli* // W.MP: (PHIL)Yami ko lot /Molbog kulit //(SND)Sundanese kulit //(SLW) Wolio kuli "skin" ; NiKord: (Bantu) [J25][J26] -kuli "skin". ||| Note 2: S.Itel. *kilwiłχ* "skin, hide" (Kure*) (<**kil-wiłχ <*kil-* "skin" < **kul-* ?) | OC: (MicN) Marshallese *kil* "skin" (< *kul ?)

Table 3. Closest similarity analysis of the cognates found in Table 2. Method of calculating Closest similarity (CS) -scores for each language group or subgroup

§§ 1. CS-scores found in Table 2.

§ Most similar to Formosan (FORM):
4 items (Paiwan) = [FORM (Paiwan) = 3, Tsou 1]
§ Most similar to FORM/ OC/Turkic :
1 item = [FORM(Atayal) 0.3, OC 0.3, Turkic 0.3]
§ Most similar to FORM/Eskimo(Esk):
1 item = [FORM(Paiwan)= 0.5, Esk= 0.5]
§ Most similar to FORM/Quechuan(Que.):
1 item = [FORM(Atayal)= 0.5, Que.= 0.5]
§ Most similar to W.MP:
3 items = [W.MP= 3(PHIL 1, SND 2)]
§ Most similar to Central MP(C.MP)/Esk:
1 item = [C.MP= 0.5, Esk= 0.5]
§ Most similar to OC: 2 items

§§ 1. CS-scores for each language group or subgroup

§ **Sum of scores**:
SC-scores for each language groups or subgroups obtained in §§ 1 above are summed up as follows;

(i)AN= **11.2** (= 5.3 + 3 + 0.5 + 2.3)
FORM= 4(Paiwan 3,Tsou 1) + 0.3 (Atayal) + 0.5(Paiwan) + 0.5(Atayal)
= **5.3 (Paiwan 3.5, Tsou 1, Atayal 0.8)**
W.MP = 3 (PHIL 1, SND 2)
C.MP = **0.5**
OC = 2 + 0.3 = **2.3**
(ii)Non-AN: 1.8 (= 1 + 0.5 + 0.3)
Esk = 0.5 + 0.5 = **1**
Quechuan = 0.5
Turkic = 0.3
Total sum = 13 items

§ Result :
AN 11.2 = (**FORM 5.3**(**Paiwan 3.5**,Tsou 1,Atayal 0.8), W.MP 3(PHIL 1 /Borneo 0/SND 2/SLW 0)), C.MP=0.5,OC=2)
Non-AN 1.8 = (Esk 1, Que.= 0.5, Turkic 0.3)

Total = 11.2 + 1.8 = **13 BBP items**

Table 4. Occuring frequencies of Austronesian cognates of Chukchee Kamchatkan and Nivkh languages shown together with other possibly Formosan-derived language groups and with Nivkh.
(Results of χ^2-test are indicated by: #, P<0.1, +, P< 0.05; ++, P< 0.025; *, P< 0.01; **, P< 0.005)

Subgroups of AN	FORM	W.MP (PHIL/Borneo/SND/SLW)	C.MP	SHWNG	OC (ADM/W.OC/ SE.Sol/ReOC)	Non-AN languages	Number of word items whose closest cognates are found in AN
Number of languages in CAD*	4	26 (11/ 2/ 9/ 5)	6	2	41 (1 /15/ 2/ 23)		
§ 1. Formosan (FORM)-like							
Chukchee-Kamchatkan (BBP)	**<u>5.3</u> (Paiwan:**3.5)	3 (1/ 0/ 2/ 0)	0.5	0	2	Esk.1,Quechuan 0.5,Turkic 0.3	10.8
Mayan (BBP)	**<u>7</u>	2(0/0/1/1)	0	0	3(0/2/0/1)	Mongolic 1?	12
§ 2. FORM-W.MP-like							
Eskimo (BBP)	**<u>4.5</u>	<u>7.5</u> (#<u>5</u>/ 0 /<u>2.5</u> /0)	2	1	4.3(0/ 1.5/ 0.3/ 0.5)	Itelmen 0.3/Mong. 0.3	18.3
Mongolic (BBP)	**3.5	++<u>8.5</u> (1/ 0 /**<u>5</u> / 0)	0	0	2 (0/1.5 /0/0.5)	Esk. 1.5, TRKc 2	14
§ 3. Oceanic-like							
Nivkh (=Gilyak)(BBP)	0	1	0.5	0	**<u>13.5</u>(0 /6.5 /1 /6)		15

REFERENCES

[1] Kurebito M (ed.) (2001), *Comparative Basic Vocabulary of the Chukchee-Kamchatkan Language Family:1* (ELPR Publication Series A2-011).

[2] Ohnishi K (2012) Prehistorical multiple moveme nts of modern humans from Od World to Americas: E vidence based on comparing basic body part-name wor ds with Austronesiasn. In: *These Proceedings*.

[3] Ohnishi K (1999), Evolution of Mongoroid Languages. Shokado, Kyoto.

[4] Snedecor GW (1956), Statistical Method (Fifth ed.), Iowa State Univ. Press, Ames.

[5] Sakitani M(2008), A New History vof Hokkaido, as viewed from Interdisciplinary Researches of the sciences of DNA, Archeology, and language. (In Japanese), Bensei Shupp an, Tokyo.

[6] Adachi N, et al.(2011), Mitochondrial DNA analysis of Hokkaido Jomon skeletons. Am. J. Phys. Anthropol. 146:34 6-360.

Table 5. AN and non-AN cognates of Chukchi-Kamchatkan vocabulary other than basic body-part names

§ Most similar to AN:

\# BODY: Chuk əwik /Alutor, Koryak uvik /S.Itel uwik (< *əwik ~ *əvik < W.MP: *awek ~ *avek) ||| W.MP: **(SND)** Sundanese, Balinese, Sasak awak /Javanese awaʔ (< *awak < *pMP *hawak "body") || **OC: Paamese** avek ||| NiKord: J254 -aba "body"

\# COLD: N.Itel ləqlaχ /S.Itel lqlaχ (< pItel *ləqlaχ) ||| **FORM: Paiwan** *ɭʸa-ɭʸəḳəɭ* "cold" (< *ɭʸəḳəɭ)*

\# to GO: Koryak jeləŋ təlek "to go" (jeləŋ < *ǰalan < pAN * Zalan "road") ; S.Itel łalekas "to go" (< *dalekas < *dale-kas, where *dale- < *Zalan) ||| **FORM: Paiwan** ɟaḷan / Rukai ka-daḷan-anə "road"

\# GOOD: S.Itel melaχ ||| W.MP: (SND) Balinese məlah

\# GRASS: N.Itel, S.Itel *isi* "grass" (< **işi*) ||| **FORM: Bunun** işimo:t "grass" (< *işi-mo:t), ??Paiwan *tsimiɭ* "grass" (< *itsi-muɭ ?)

\# LEAF: N.Itel. plapl /S.Itel. pəlapəl (< *pəla-) ||| O C: (MicN) Marshallese pʷələk (< *pəlak ~ bəlak ?) ||| Note: Cf. (FORM) Atayal *pałi* "leaf"

\# LOUSE: N. Itel, S.Itel məlməl /Chuk. məməł /Alutor mə məl "louse" (< *mə(l)məl < *məl "louse ~ flea") ||| C.MP: Manggarai, Ngada məla "flea"

\# ONE: Chuk., Koryak ənnen /Alutor ənnan "one" (< *ənnan < *hənnan < *hannan only" < > Indonesian haña "only") ||| W.MP: (SND) Indonesian haña "only" (CAD*, #13.330), **(SLW) Bugis** ánnəŋ, ɨnnɨŋ /Konjo annaŋ "six" (< *ənnaŋ-mələŋin "6" < *ənnaŋ- "one" + * mələŋin "5", where **ənnaŋ- ~ *annaŋ-* < > Indonesian *haña* "only".) || C.MP: Manggarai *hanaŋ* "alone, only" ||| KOR: Middle Korean *hŏna(h)* "one" (< > Indonesian *haña* "only".) ||| Note: pMP *h- > ChKm *Ø- (zero).

§ Most similar to non-AN

\# ELBOW: N.Itel. lot'eŋ /S.Itel. lot'əl "elbow" ||| Comecrudo lot "arm"

\# FOUR: Chuk ŋeraq /Alutor ŋəraqqə /Koryak ŋəjaq "four" (< pChukchee *ŋərjaq ~ *ŋerjaq < > Finnish *ńeljä* "four") ||| Korean: Mid.Korean nə̄i(h) "four" (< *nəri < *nərj < > pChukchee *ŋərjaq //Finnish *ńeljä* "four") ||| Uralic: Finnish *ńeljä* "four" (< *ŋelj(a))

\# GRANDFATHER:S.Itel *mitix* "grandfather", *mitiχ* "grand -mother" (<< Ainu ?) ||| Ainu *miti* "father"(<< ChKm ?)

Table 6. Distribution of Austronesian and non-Austronesian cognates of Nivkh (= Gilyak)* basic body-part name words (BBPs).

§ 1. W.MP-like: 1 item

\# SALIVA: (Amur) *lils* "saliva" ||| W.MP: (PHIL) Yami *lila* "tongue"

§ 2. C.MP/W.OC(Yabem)-like: 1 item (0.5, 0.5)

\# LIP: *əvləx* (< **ə(ᵐ)veləx < *ə(ᵐ)velař < *abelar ~ *iᵐbela-*) ||| **C.MP: Dobel** *ʔabelar* "tongue" || OC: (W.OC) Yabem *iᵐbela* "his/her tongue", *iᵐbela-m* "your tongue" (CAD*)

§ 3. OC-like: 13 items = (0, 6, 1, 6)

§ 3.1. W.OC-like: 6 items

\# ARM: *tot* ||| OC: **(W.OC) Takia** to-n "arm"

\# BELLY: (Sakh.) nauf, ŋaur "belly" ||| OC: **(W.OC) Maringe** *naũafa* "heart" (< *naü- ~ *naüa- ?)

\# FEATHER: *tupr* (< **dup-r*) ||| OC: **(W.OC) Adzera** <u>dzuf</u>- "to fly" (< **dup-*), <u>dza</u>ᵑʔ*-dzuf* "bird", Tawala *lupa* "to fly" (< **dup-a* ?) ||| ?Jpn: *tubasa* "wing" (< **duba-sa* ?)

(Yabem-like) 3 items

\# EAR: (Amur) nos "ear" (< **no-s < *ŋo-*"to hear"), (Sakh.) noχo- "to smell badly, to smell), *noχjai-* "to smell badly" ||| OC: **Yabem** *-ŋò* /Kiribati *oŋo* /Kwaio *loŋo-a* "to hear", Tawala *nonoil* /Maringe *noŋo* "to hear"

\# HEART/LIVER: (Amur) *ŋif* /(Sakh.) Trambaus dial., Tyk dial. *ŋif* (Murasaki*), *ŋif, nif* (Tak*) "liver" (< *ŋip ~ *nip) ||| OC: **(W.OC) Yabem** *(ŋa-)nip-kaləp* "heart"

\# NECK: (Amur) q'os (YH*) //(Sakh.) kŏř (Tak*) (< **ko-ř* ?) ||| OC: **(W.OC)Yabem** *kɔʔ-labɛŋ* "throat" || ?W.MP: (Sundic) Sasak korok "neck". ||| Note: Cf. (OC:NCal) Nengone ko den "nape of neck" | (PHIL) Sarangani Blaan kolloŋ "neck".

§ 3.2. S.E.Vanuatu-like: 1 item

\# TOOTH: (Amur) *ŋəɣs* , (Sakh.) Tyk dial. *ŋuɣzur,* Trambaus dial. *ŋaɣzuʃ* "tooth" (< **ŋaɣ-zur*) ||| **OC: Kwaio** *nago* "gums". Cf. Roviana *ŋaŋadolo* "gums".

§ 3.3. ReOC-like: 6 items

\# BELLY: (Sakh.) *komk* (Tak*) //(Amur) *q'oχ* "belly" (Tak*) (< *kom-k) ||| **OC: Rapanui** *kokoma* "intestines, guts" (< *koma) || W.MP: (SLW) koᵐpo "stomach"

\# BLOOD: (Sakh.) *soχ, tʃof, tʃoχ* (Tak*) ||| OC: **(MicN) Woleaian** *cɔ̄*

\# EGG: (Amur) *ŋoiq* "egg"(< **ŋoi-q*), (Sakh.) *ŋoi* "penis" (Tak*) (< **ŋoi* "testis, egg") ||| OC: **Port Sandwitch** *ŋovüč* "yolk" (< **ŋo-vüč* ?), Cf. Mbula *ŋonōno* "fruit" (< **ŋo-nōno*) ||| C.MP: Buru *oŋo-n* "sphere, ball"

\# FOOT: ŋəcx ||| OC: **Kwamera** nəsu- "leg", Marshallese ne "leg, foot", Ponapean nē "leg" || W.MP: Sasak nae "leg, foot" ||| Jpn: Old Jpn *-ne* "leg" (in compounds)

\# LIVER: (Sakh.) ŋɯlf (< *ŋɯl-f < *ŋol(u)-) ||| OC:(MicN) ŋoluŋol (< *ŋolu-ŋol < *ŋol(u)-)

\# TAIL: (Amur) ŋəki //(Sakh.) ŋaki, ŋakki (Tak*) "tail" (< *ŋa-ki < Nivkh *ŋa* "beast, animal" + **-ki* "tail", where **-ki* < > OC: Xaracuu *kʷi* "tail".) ||| OC: (NCal) Xaracuu *kʷi* "tail"

* Nivkh vocabulaly is obtained from YH* for Amur dialect (from Savel'eva*) and from Tak* for Sakhalin dialect.

The Seventeenth International Symposium on Artificial Life and Robotics 2012 (AROB 17th '12),
B-Con Plaza, Beppu, Oita, Japan, January 19-21, 2012

A study on line length and direction perception via cutaneous sensation

Syed Muammar Najib Syed Yusoh[1], Nomura Yoshihiko[1], Sakamoto Ryota[1] and Iwabu Kazuki[1]

[1]Mie University, Tsu Mie 514-8507, Japan
(Tel: 059-231-9895, Fax: 059-231-9895)

[1]najib@robot.mach.mie-u.ac.jp

Abstract: In this paper, we studied the contribution of the cutaneous sensation in the perception of the line segment's length and direction through psychophysical experiments where a mechatronic stage was utilized to express virtual line segments. The perceived lengths and directions were compared to the true values, and the mean errors, the standard deviations, and RMSE (Root Mean Square Error) were examined. As the results of the examinations, it was found as for the mean error of the perceived length that the more the length is increased from 10 to 90 mm, the more the subjects perceived decreased length from about 0 to 30%. As for the mean error of the perceived direction, another finding was that the subjects can recognize the direction with less than errors of about 10 degrees in the counter-clock wise direction.

Keywords: haptic display, length perception, direction perception, cutaneous sensation.

1 INTRODUCTION

Support systems have been developed to improve communication and quality of life for the people in need. Human can accept objects' geometrical information such as the lengths and directions of the line segments as the results of physical contacts [1]. Therefore, as an alternative for visually impaired persons, to create mental images of the objects, researchers have been studying human haptic sensational characteristics in the object perception. As for the objects, the representative ones are line segments, and they were provided as the raised dots and edges, rods, and ditches [2, 3, 4, 5], and, nowadays, by virtue of the development of robotic technologies [6, 7], the objects can be virtually represented by a feedback force as in this paper.

Here, the perceptual processes with the contacts can be categorized from the two viewpoints. The first is the sense organs; (1) the cutaneous sense on a fingertip abdomen (where the index finger is often used) (2) the proprioceptive sense such as the joint rotation and the kinematic/force sense relating to muscle expansions and contractions, and (3) the combination of both the cutaneous and the proprioceptive.

The second sense, i.e., the proprioceptive sense is with the movements of his/her hand, and it works only when his/her hand moves. Here, the person can take initiative against the outside world in the perceptual process, and the person moves his/her hand voluntarily: the mode of movement is called "active" in this paper [19, 20]. On the other hand, the outside world, vice versa, can take initiative against the person in the perceptual process, and his/her hand is forcibly moved by external actuators: the mode of movement is called passive movement [19, 20]. That is, as for the proprioceptive sense, we should consider the two modes: (1) the passive movement when the person has his/her hand motion activated by actuators, and (2) the active movement when the person voluntarily activates his/her hand to gain some haptic information about the outside world. Therefore, relating to the proprioceptive sense, both active and passive movements should be considered, which results in the following four modes: (1) PrPa mode (proprioceptive passive), (2) CoPa mode (combined passive), (3) PrAc mode (proprioceptive active), and (4) CoAc mode (combined active) [8, 9, 10, 11, 12, 13, 14, 15, 16, 17, 18, 21]. As a result, five modes would be considered in the haptic perception, and these five modes is considered to be important in practical situations.

As for the sense, i.e., the cutaneous sense itself, even though his/her hand is stationary or not, the cutaneous sense works if the touched object moves relatively to his/her fingertip, and causes slip to the fingertip abdomens. Thus, we can consider a mode, i.e., (5) CuPa mode (cutaneous passive): the person keeps his/her hand stationary while the outside object moves, and he/she passively gets information through the physical interactions between the fingertips and the outside object.

The cutaneous sense is considered to enhance the performance of the proprioceptive sense in the combination, and, therefore, the CuPa mode must be a key issue in considering the performances of the above mentioned five modes since the CoPa mode is an integration of CuPa and PrPa, and the CoAc mode is an integration of CuPa and PrAc.

In this paper, we studied the contribution of the cutaneous sensation in the perception of the line segment's length and direction through psychophysical experiments where a mechatronic stage was utilized to express virtual line segments.

2 EXPERIMENTAL METHOD

2.1 Apparatus

Fig.1. shows the experimental apparatus. The length, width and height of table base are 510 × 500 × 610 mm, respectively. It consisted of a power supply, a controller, an acrylic plate with a hole, a flat plate, a linear actuator and a rotation board. The acrylic plate was mounted on top of the flat plate. The hole was at the center of the acrylic plate. The gap between the two plates was set at 6 mm. The flat plate was attached on the top of the linear actuator (IAI-ICSA series) and it could be moved in the left and right direction in 300 mm range. The linear actuator was mounted to the top of the rotation board so that it could be rotated 360 degrees.

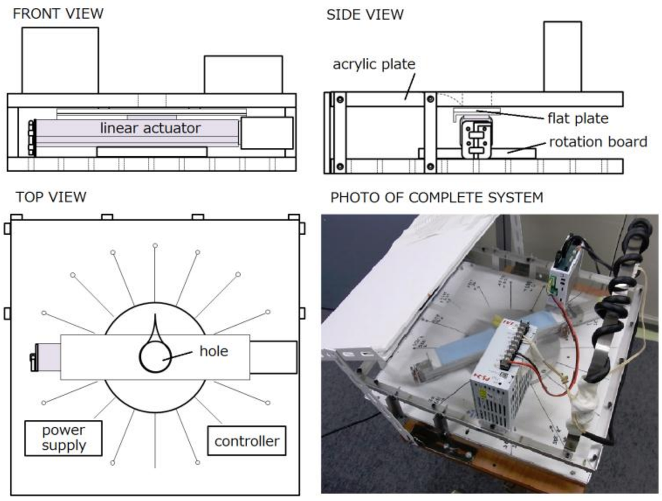

Fig.1. Experimental apparatus

2.2 Subjects

Eight right-handed subjects (male students, aged 22 to 35 years) volunteered for their participation. None of the subjects had a neurological disorder affecting the hands and fingers. None of subjects had any previous experience with the stimuli or tasks used in this study.

2.3 Task

The line lengths presented were 10, 30, 50, 70, 90 mm and the directions were 0 to 360 degrees with the interval of 22.5 degrees: the number of pieces of the presented lengths is five and that of the directions is 16. Subjects were asked to choose which line segment corresponded to the tested one among the multiple solutions presented on the answer board. This answer board consisted of a reference pattern as shown in **Fig.2.,** that was composed of concentric circles of which radiuses were 5 to 125 mm with the interval of 5 mm. All the patterns of 80 line segments with 5 lengths by 16 directions were presented in pseudo random order. All the experiments were carried out with a speed of 50, 100,141 and 200 mm/s.

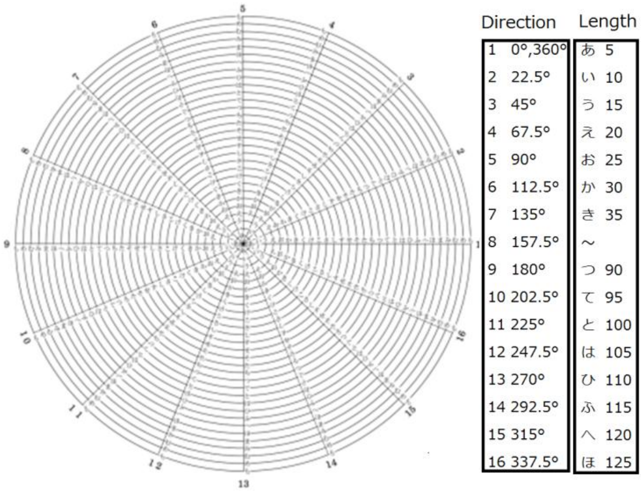

Fig.2. Answer board

2.4 Procedure

Fig.3. shows the experimental views. The subjects were comfortably seated in a chair (**Fig.3.(b)**) with their right hand on the acrylic plate (**Fig.3.(a)**). During experiment, subjects were instructed to relax, close their eyes, and focus on the perception of the length and direction of the presented line segment through the cutaneous sensation of his/her index finger. The subjects put their index fingertip abdomen on the surface of the flat plate (**Fig.3.(a)**), at that same time the subjects arm angle was positioned at 90 degrees or horizontal to table base (**Fig.3.(c)**). The subject shoulder was on the mid-sagittal axis, aligned with the hole in the acrylic plate (**Fig.3.(d)**). Headphones with white noise were provided to the subject to prevent hearing the sound generated by linear actuator. The white noise was played at a volume just below the irritation threshold to mask any remaining sound cues and avoid any side effects on the spatial perception. Stimulation starts when fingertip is at an end of the line stimulus and stops when it reaches the other end. The velocity is generated by the linear actuator controlled with a computer and the software X-SEL. It should be noted that the speed of movement is driven with a rectangular velocity pattern. The direction of the linear actuator was set by manual operation each time. The velocity and angle were pseudo-randomly assigned for each subject. After the experiment, subjects open their eyes

and, by looking at the answer board, they give their perceived direction and length by stating a number between 1 and 16 and a letter between A and HO (**Fig.3.(b)**). The whole experiment took 25-35 minutes per subject.

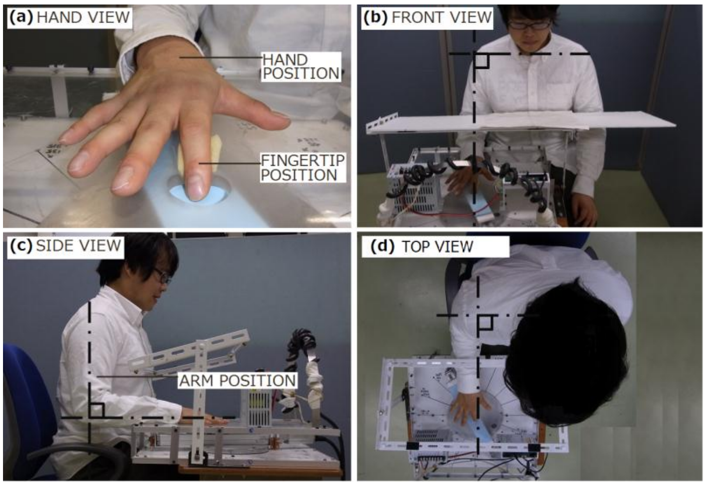

Fig.3. Experimental view

3 RESULTS AND DISCUSSION

3.1 Analysis of length

Fig.4. shows the experimental results with the length perceptual error characteristics.

(1) **Fig.4.(a)** shows the actual-perceptual length relationship. Form this data, the errors were obtained and plotted in **Fig.4.(b)**.

(2) **Fig.4.(b)** shows the length-caused foreshortening effect with the length perceptual error.

The systematic errors: in the case of the actual length of 10 mm, the perceptual length mean error was positive with less than 5 %. On the other hand, the longer the actual length was than 30 mm, the more the magnitude of the perceptual length mean error increased in the negative value up to 30 % at 90 mm of actual length.

The random errors: for all the variations of the actual lengths, the longer the actual length was, the more the

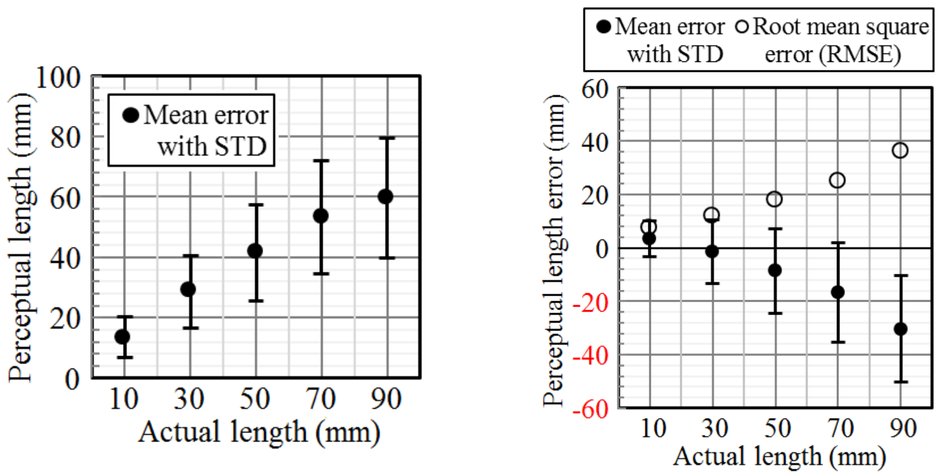

(a) Actual-perceptual length relationship **(b)**Length-caused foreshortening effect

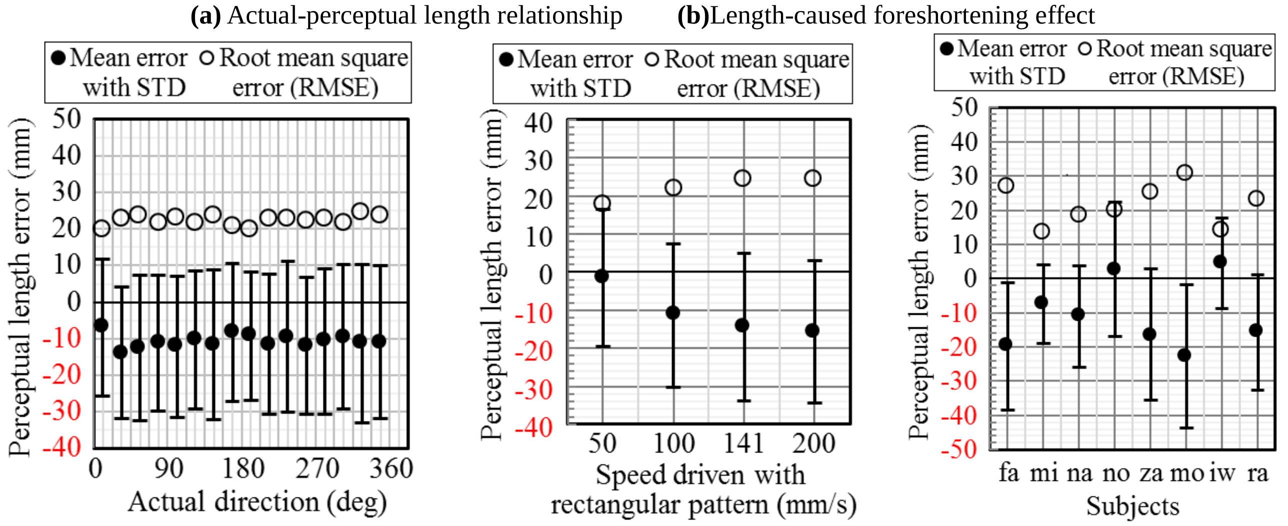

(c) Directionally isotropic characteristic **(d)** Speed-caused foreshortening effect **(e)** Individual variation with subjects

Fig.4. Experimental results with the length perceptual error characteristics

STD of the perceptual length deviations increased, Therefore, RMSE (Root Mean Square Error) was raised up.

(3) **Fig.4.(c)** shows the directionally isotropic characteristic with the length perceptual error. The direction of subjects shows RMSE stayed constant at approximately 20 degree.

(4) **Fig.4.(d)** shows the speed-caused foreshortening effect with the length perceptual error. Perceptual the length was perceived shorter as velocity increased more than 100 mm/s and this became significant as the length became longer.

(5) **Fig.4.(e)** shows the subjects with the length perceptual error. Individual variation with the eight subjects was observed, and its STD was given by 10 mm.
For six out of the eight subjects, a more or less beneficial effect was found of having perceptual length.

3.2. Analysis of direction

Fig.5. shows the experimental results with direction perceptual error characteristics.

(1) **Fig.5.(a)** shows the actual-perceptual direction relationship. Form this data, the errors were obtained and plotted in **Fig.5.(b)**.

(2) **Fig.5.(b)** shows direction-related rotating effect: the subjects perceived the direction with the additional value of about 0 to 15 degrees in the counter-clock wise direction. The rotating effect of the mean error shows greater by about 15 degrees in the upper-left direction (in the region of actual direction between 112.5 and 202.5 degrees where the rightward direction is defined as zero degree), meanwhile, it shows less by about 0 to 5 degrees in the remaining direction. As for the STD, they are almost identical over the whole direction.

(3) **Fig.5.(c)** shows the length invariant characteristics with the directional perceptual error. The mean errors and RMSE shows no significant change against the actual length variation.

(4) **Fig.5.(d)** shows the speed invariant characteristics with the directional perceptual error. The mean errors and

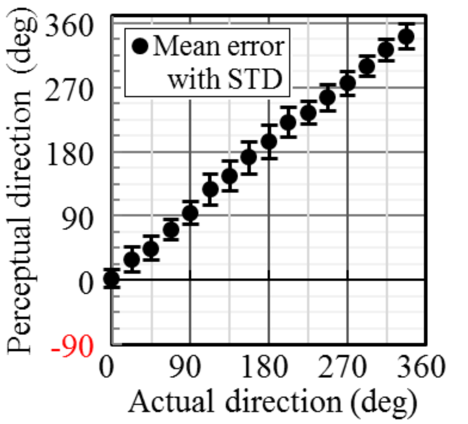

(a) Actual-perceptual direction relationship

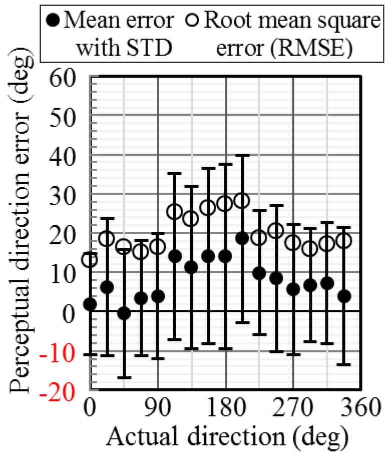

(b) Direction-related rotating effect

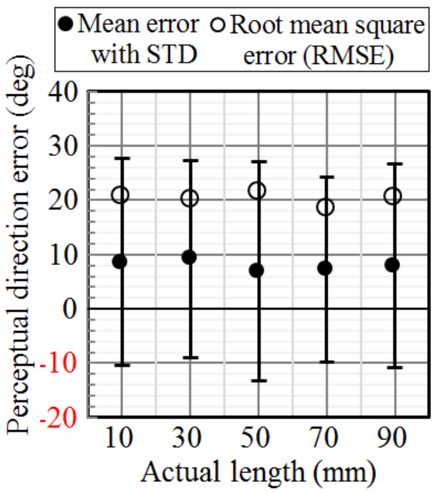

(c) Length invariant characteristic

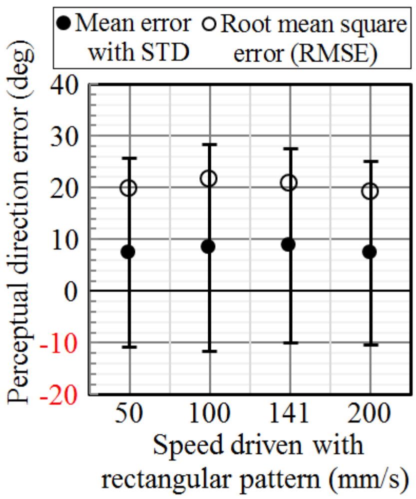

(d) Speed invariant characteristics

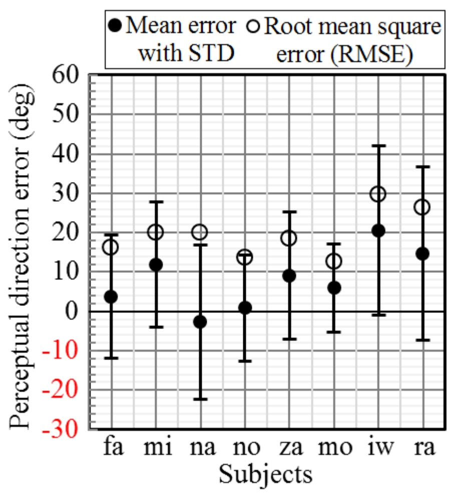

(e) Individual variation with subjects

Fig.5. Experimental results with the directional perceptual error characteristics

RMSE shows that no significant change was found when changing the speed.

(5) **Fig.5.(e)** shows the between-subjects individual variation with the directional perceptual error. The mean error with the directional perception shows that all the subjects have different sensitivity between 0 and 20 degrees in the counter-clock wise direction.

4 CONCLUSIONS

The perceived lengths and directions were compared to the true values, and the mean errors, the standard deviations, and RMSE were examined. The results are

(1) As for length perception, the more the length is increased from 10 to 90 mm, the more the subjects perceived decreased length from about 0 to 30% .

(2) As for the direction perception, another finding was that the subjects can recognize the direction with the mean errors of about 10 degrees in the counter-clock wise direction.

ACKNOWLEDGEMENTS
This work was supported by KAKENHI (Grant-in-Aid for Scientific Research (B), No. 21300307) from Japan Society for the Promotion of Science (JSPS).

REFERENCES

[1] Robert S. Davidon and Mei-Fang Hsieh Cheng (1964), Apparent distance in a horizontal plane with tactile-kinesthetic stimuli. The Quarterly Journal of Experimental Psychology, 16(3), pp.277-281.

[2] Mei-Fang Cheng (1968), Tactile-Kinesthetic Perception of Length, The American Journal of Psychology, 81(1), pp.74-82.

[3] R.H. Day and G.C. Avery (1970), Absence of the horizontal-vertical illusion in haptic space. Journal of Experimental Psychology , 83(1-1), Jan, pp.172-173

[4] R.H. Day, T.S. Wong and Charles I. Brooks (1971), Radial and tangential movement directions as determinants of the haptic illusion in an L figure. Journal of Experimental Psychology, 90(2), Oct, pp.344

[5] J. Deregowski and Hadyn D. Ellis (1972), Effect of stimulus orientation upon haptic perception of the horizontal-vertical illusion. Journal of Experimental Psychology, 95(1), Sep, pp.14-19.

[6] Paul Bach-y-Rita (1972), Brain mechanisms in sensory substitution Academic Press(New York)Text book.

[7] Paul Bach-y-Rita, L. Scadden and C.C. Collins (1975), Tactile television system. SRS Final Report (Res. Grant NP 55282) San Francisco: Smith Kettlewell Institute of Visual Sciences, Division of Research and Demonstration Grants, Social and Rehabilitation Service. Text book.

[8] Arthur S. Schwartz, Alan J. Perey and Alan Azulay (1975), Further analysis of active and passive touch in pattern discrimination. Bulletin of the Psychonomic Society, 6(1), Jul, pp. 7-9.

[9] Tong S. Wong (1977), Dynamic properties of radial and tangential movements as determinants of the Haptic Horizontal-Vertical Illusion with an 'L' figure. Journal of Experimental Psychology: Human Perception and Performance, 3(1), Feb, pp. 151-164.

[10] Lochlan E. Magee and John M. Kennedy (1980), Exploring pictures tactually, Nature (London), 283, Jan, pp.287-288.

[11] Susan J. Lederman, Roberta L. Klatzky and Paul O. Barber (1985), Spatial and movement-based heuristics for encoding pattern information through touch. Journal of Experimental Psychology: General, 114(1), Mar, pp.33-49.

[12] B. L. Whitsel, O. Franzen, D. A. Dreyer, M. Hollins, M. Young, G. K. Essick and C. Wong (1986), Dependence of Subjective Traverse Length on Velocity of Moving Tactile Stimuli. Somatosensory & Motor Research, 3(3), Jan, pp.185-196.

[13] Mark Hollins and Alan K. Goble (1988), Perception of the length of voluntary movements. Somatosensory & Motor Research, 5(4), Jan, pp.335-348.

[14] F. Vega-Bermudez, K. O. Johnson and S. S. Hsiao (1991), Human tactile pattern recognition: active versus passive touch, velocity effects, and patterns of confusion. Journal of Neurophysiology, 65(3), March, pp.531-546.

[15] Laura Armstrong and Lawrence E. Marks (1999), Haptic perception of linear extent. Perception & Psychophysics, 61(6), pp.1211-1226.

[16] Patrick Haggard, Chris Newman, Justine Blundell and Holly Andrew (2000), The perceived position of the hand in space. Perception & Psychophysics, 68(2), pp.363-377.

[17] Pierre Wydoodt, Edouard Gentaz and Arlette Streri (2006), Role of force cues in the haptic estimations of a virtual length. Experimental Brain Research, 171(4), pp.481-489.

[18] Kazunori Terada, Akinori Kumazaki, Daisuke Miyata and Akira Ito (2006), Haptic Length Display Based on Cutaneous-Proprioceptive Integration. Journal of Robotics and Mechatronics, 18(4), pp.489-498.

[19] Yoshihiko Nomura, Yuki Yagi, Tokuhiro Sugiura, Hirokazu Matsui and Norihiko Kato (2006), Fingertip Guiding Manipulator: Haptic Graphic Display for Mental Image Creation. Proceedings of the Computers Helping People with Special Needs (ICCHP), 4061, pp.1131-1138.

[20] Syed Muammar Najib Syed Yusoh, Yoshihiko Nomura, Naomi Kokubo, Tokuhiro Sugiura, Hirokazu Matsui and Norihiko Kato (2008), Dual Mode Fingertip Guiding Manipulator for Blind Persons Enabling Passive/Active Line-Drawing Explorations. Proceedings of the Computers Helping People with Special Needs (ICCHP), 5105, pp.851-858.

[21] Wouter M. Bergmann Tiest, L. Martijn A. van der Hoff and Astrid M. L. Kappers (2011), Cutaneous and kinaesthetic perception of traversed distance. Proceedings of the World Haptics Conference (IEEE), June, pp.593-597.

The Seventeenth International Symposium on Artificial Life and Robotics 2012 (AROB 17th '12),
B-Con Plaza, Beppu, Oita, Japan, January 19-21, 2012

Correlation-based competition regulated by nonlinear interspike interaction in STDP

Shigeru Kubota

Graduate School of Science and Engineering, Yamagata University,
4-3-16 Jonan, Yonezawa, Yamagata, 992-8510, Japan
(Tel: +81-238-26-3585, Fax: +81-238-26-3240)

kubota@yz.yamagata-u.ac.jp

Abstract: The development of visual cortical circuits is strongly influenced by the sensory experience during a restricted critical period, as demonstrated by the loss of neural responses to the eye that has been briefly deprived of vision. It has been suggested that to reflect the sensory experience into the pattern of synaptic weights, the competition between groups of correlated inputs to an identical postsynaptic cell is essential and that spike-timing-dependent plasticity (STDP) may provide the basis of this type of correlation-based competition. To predict the consequences of competition by STDP in natural physiological conditions, I here investigate the effects of nonlinear interspike interaction in STDP that is experimentally observed in the visual cortical cells. The simulations show that the interspike interaction can prevent the induction of competition and counteract the effect of activity-dependent feedback (ADFB) that facilitates competitive functions. However, once the competition occurs, the level of competition is not affected by the interspike interaction. These results may suggest that the interspike interaction in STDP acts to delay the induction of experience-dependent plasticity through suppressing synaptic competition, thereby leading to a delay in the onset of critical period plasticity in the visual cortex.

Keywords: Critical period, Visual cortex, STDP, Activity-dependent feedback.

1 INTRODUCTION

Neural circuits are developed through reflecting sensory experience during a critical period in postnatal development [1]. A representative example is an ocular dominance plasticity observed in visual cortical cells [1-3]: if either one eye is briefly deprived of vision within a critical period, the response of many visual cortical neurons is dominated by the non-deprived eye following deprivation; in contrast, the monocular deprivation before or after the critical period does not significantly affect the cell responses.

Both experimental and theoretical studies have suggested that the ocular dominance plasticity may involve the competition between different groups of inputs that originate from each eye and are correlated within each group [1, 4-6]. In the presence of correlation-based competition, the strengthening of the inputs from one eye leads to the weakening of those from the other eye. Therefore, the neural response can be dominated by one eye, as observed experimentally, and which group becomes dominant depends on the sensory experience, thereby inducing experience-dependent plasticity [4]. Furthermore, recent modeling studies have shown that spike-timing-dependent plasticity (STDP), wherein the magnitude and direction of plasticity depends on the precise timing of pre- and postsynaptic spikes, may provide a physiological mechanism that underlies correlation-based competition [4, 7].

To investigate the consequences of correlation-based competition by STDP in natural physiological conditions, I examine in this study the effects of interspike interaction in STDP [8], which is experimentally observed in the visual cortex, on the dynamics of synaptic population. The interspike interaction in STDP has been suggested to exert a suppressive effect on synaptic modifications such that the occurrence of a spike weakens the level of plasticity caused by a successive spike in the same neuron. The level of the suppressive effect of the preceding spike on the present spike follows an exponential function of the time interval between the two spikes, suggesting that the interspike interaction nonlinearly affects STDP [8]. In this study, I construct a conductance-based pyramidal neuron that receives many random inputs from synapses following STDP, as in *in vivo* conditions, and demonstrate that the interspike interaction in STDP tends to prevent the occurrence of competition between two groups of correlated inputs. This may suggest that the interspike interaction functions to suppress the ability of neurons to embed the correlation structure to synapses during early development and can contribute to delaying the onset of the critical period of ocular dominance plasticity in the visual cortex.

2 METHODS

2.1 Conductance-based neuron model

I constructed a two-compartment conductance-based pyramidal neuron, which comprises a soma and a dendrite, and is described by the following equation [4]:

$$C_m \frac{dV_s}{dt} = -I_{leak} - I_{Na} - I_K + \frac{g_c}{p}(V_d - V_s) + I_{inj}, \qquad (1)$$

$$C_m \frac{dV_d}{dt} = -I_{leak} - I_{Na} - I_K - I_{Ca,V} - I_{AHP} + \frac{g_c}{1-p}(V_s - V_d) - I_{syn}. \qquad (2)$$

Here, V_s and V_d are the membrane potentials of the somatic and dendritic compartments, respectively. Both the compartments contain leak (I_{leak}) and voltage-dependent Na^+/K^+ currents (I_{Na}/I_K). The voltage-dependent calcium currents ($I_{Ca,V}$) and calcium-dependent K^+ currents (I_{AHP}) are included in the dendrite to reproduce spike frequency adaptation observed in pyramidal cells [9]. g_c is a coupling conductance between the two compartments, and I_{inj} and I_{syn} are the injected and synaptic currents, respectively.

2.2 Synaptic inputs

The dendritic compartment receives random inputs, which are activated by Poisson processes, from 4000 excitatory (mediated by AMPA and NMDA receptors) and 800 inhibitory (GABAergic) inputs [10]. To explore the influences of input correlation, I divided excitatory inputs into two equally sized groups and introduced the same magnitude of correlation into each input group [11]. Any two inputs that belong to different groups are uncorrelated. All the inhibitory inputs are uncorrelated and activated by random homogeneous Poisson processes. Mean input frequencies are 3 Hz for all the synapses. Taking into account the low success rate (around 10 %) of synaptic transmission observed in central synapses [12], the input frequency of 3 Hz corresponds to the presynaptic firing rate of 30 Hz. This firing rate can be considered physiologically relevant as the sensory-evoked response of neocortical cells [9]. To quantify the level of the competition between the two groups of excitatory inputs, I introduced synaptic competition index (SCI) defined as $|\bar{w}_1 - \bar{w}_2| / (\bar{w}_1 + \bar{w}_2)$ with the average weight $\bar{w}_i$ for group i [4]. SCI of 0 means that the two groups have the same average weight, whereas SCI of 1 means that synaptic weighs of either one group converges to 0 and only one group contributes to the postsynaptic activity.

2.3 Biophysical STDP model

A previously proposed biophysical STDP model [13] was applied to all the excitatory synapses. In this model, plasticity induced by each pre- and postsynaptic spike pair is determined based on an STDP map $\Delta w(\Delta t,\ \tau_{NMDA},\ g_{NMDA})$, which was constructed by using an *in vitro* pairing protocol simulation based on intracellular Ca^{2+}-dependent plasticity, and decides the magnitude of plasticity Δw as a function of an interspike interval between pre- and postsynaptic spikes Δt, NMDA receptor (NMDAR) peak conductance g_{NMDA}, and NMDAR decay time constant τ_{NMDA} [13]. Theoretical studies suggest that an approximate balance between LTP and LTD is required to activate competitive function of STDP [4, 7]. To attain the balanced state, I introduced activity-dependent feedback (ADFB) mechanism, in which the NMDAR peak conductance and decay time are dynamically regulated as a function of postsynaptic firing rate f_{post}:

$$\tau_{decay} = (1-\rho)\tau_1 + \rho\tau_2 - k_1 \rho f_{post}, \qquad (3)$$

$$g_{NMDA} = g^0_{NMDA} - k_2 \rho f_{post}. \qquad (4)$$

The parameter ρ represents the expression level of NR2A subunits in NMDARs, which considerably increases during early development [14-16]. In this model, the increase in ρ values functions to strength the ADFB modulation. ρ = 0 corresponds to a state where the ADFB function is absent because of very low level of NR2A subunits, whereas ρ = 1 corresponds to a state where the ADFB modulation is sufficiently strong due to a large number of NR2A-containing NMDARs. The first two terms in the right-hand side of Eq. 3 describes the alteration in the decay kinetics of single NMDAR currents by the increase in the NR2A-containing receptors [17, 18]. The ADFB model of STDP describes the activity- and subunit-dependent desensitization of NMDARs based on experimental observations and can contribute to facilitating the correlation-based competition [4, 19, 20].

2.4 Interspike interaction in STDP

I introduced the nonlinear interspike interaction observed in visual cortical STDP [8]. To incorporate the interspike interaction, each spike is assigned an efficacy, which is determined as a function of the time interval from a preceding spike in an identical neuron:

$$\varepsilon^f_K = 1 - \exp[-(t^f_K - t^{f-1}_K)/\tau_K], \ (K = \text{pre or post}) \qquad (5)$$

where the subscript K denotes the pre- or postsynaptic activity, ε^f_K is the efficacy assigned to the *f*th spike, t^f_K and t^{f-1}_K are the *f*th and (*f*−1)th spike timing of the K neuron, τ_{pre} = 28 ms and τ_{post} = 88 ms are the time constants by which the influence of a prior spike decays exponentially for the pre- and postsynaptic cells, respectively [8]. The change in the synaptic weights induced by the pair of the *f*th presynaptic spike and *f'*th postsynaptic spike is described as $\varepsilon^f_K \varepsilon^{f'}_K \Delta w(\Delta t, \tau_{NMDA}, g_{NMDA})$. The weight updating rule is assumed to be additive [21] and the effect of all the spike pair on STDP is taken into account.

3 RESULTS

To explore the influence of interspike interaction in STDP on its competitive property, I have examined dynamics of synaptic population when a neuron receives correlated inputs from two groups of STDP synapses. As shown in the previous study [4], in the absence of interspike interaction, STDP elicited strong competition where one group dominates over the other in the equilibrium state (Fig. 1a). However, in the presence of the interspike interaction, competition disappeared and the two input groups were shown to converge to the same average weights (Fig. 1b). The interspike interaction did not significantly alter the average weight of all the synapses (Fig. 1a, gray).

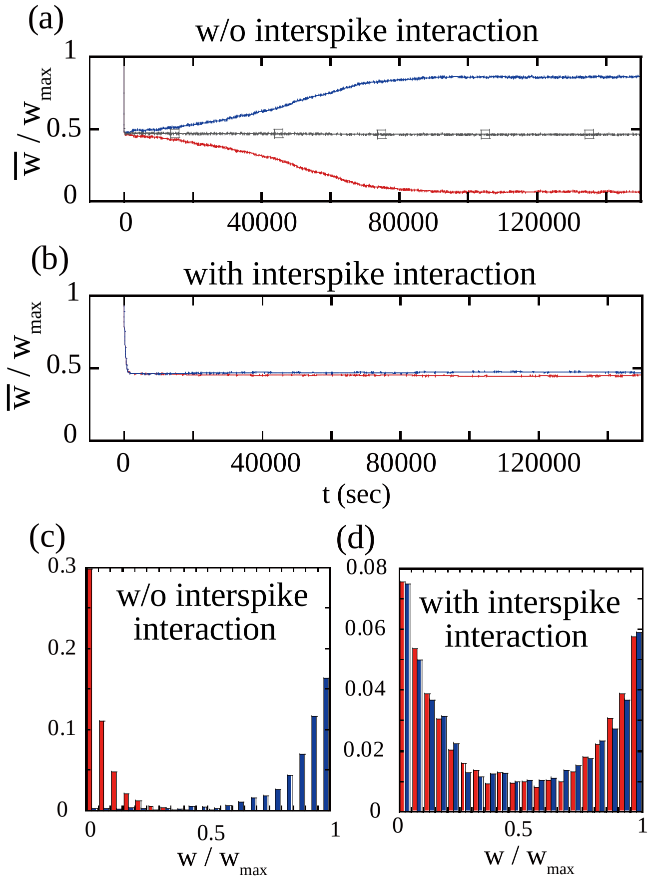

Fig. 1. The predicted effects of nonlinear interspike interaction in STDP on the correlation-based competition. (a and b) The time courses of weight averages for the two groups are shown by red and blue lines. The gray line in (a) denotes the average weight of all the inputs. (a) and (b) show the cases without and with the interspike interaction, respectively. (c and d) The final weight distributions of the two input groups are depicted by red and blue bars for the cases without (c) and with (d) interspike interaction.

These results have been clarified by examining the weight distribution at the equilibrium state (Fig. 1c and 1d). The figures show that without the interspike interaction, the weight distribution differs between the correlated groups such that the synaptic weights of one group accumulates near 0 whereas those of the other group tends to be pushed toward the maximum weight (Fig. 1c). However, without the nonlinear interaction, the weight distribution is nearly the same for the two groups, implying the lack of correlation-based competition.

To examine physiological significance of interspike interaction, I calculated the weight averages of the two groups with changing ρ, a parameter representing the level of NR2A subunit expression in NMDAR channels (Fig. 2a). The result shows that the interspike interaction significantly increases a threshold value of ρ required to induce the between-group competition. Accordingly, a threshold ρ value, above which SCI becomes positive, is significantly larger in the presence of interspike interaction (Fig. 2b). Interestingly, once the competition occurs for sufficiently larger ρ values, the level of competition is nearly the same independent of whether the interspike interaction is incorporated. These results suggest that the interspike interaction in STDP in the visual cortex can contribute to regulating the induction of competition and the resulting occurrence of critical period such that the nonlinear suppression delays the timing of the critical period, but does not affect the level of plasticity once it occurs.

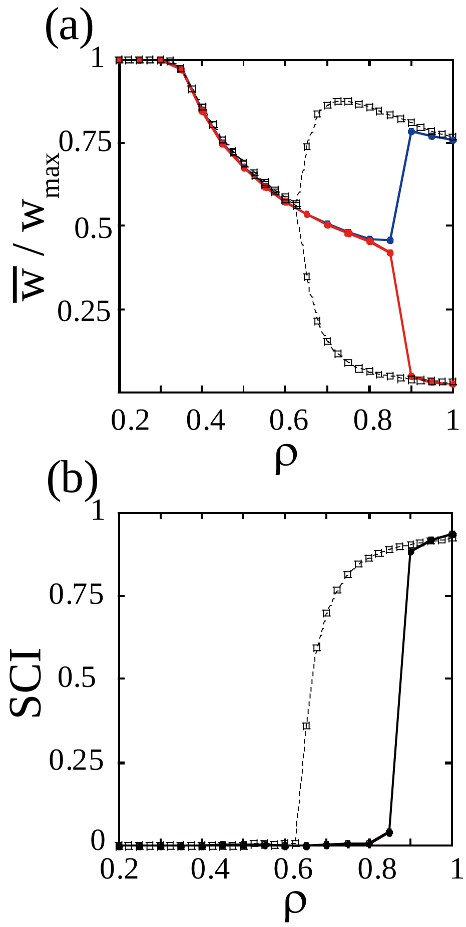

Fig. 2. The weight averages of the two groups (a) and synaptic competition index (SCI) (b) are plotted as a function of the strength of ADFB modulation ρ. Solid lines show the case of introducing nonlinear interspike interaction in STDP, whereas dashed lines show the case of not incorporating interspike interaction.

4 DISCUSSION

In this report, I have studied the effects of nonlinear interspike interaction in STDP on the competition between inputs based on their correlation structure, and have found that this interaction may function to prevent the occurrence of competition. This effect could be attributable to the net decrease in the correlation between the pre- and postsynaptic activity, because the nonlinear interaction would tend to weaken the actual influence of presynaptic inputs on the postsynaptic spike, particularly when the postsynaptic spikes occurs repetitively within a short time interval. The variance of the level of ocular dominance plasticity within the visual cortical cells might be partly explained by the variance in the level of the interspike interaction, although additional experiments would be clearly required to sort out how the effects of nonlinear interaction are physiologically regulated in individual neurons.

ACKNOWLEDGMENTS

This study is partially supported by Grant-in-Aid for Scientific Research (KAKENHI(19700281), Young Scientists (B)) from the Japanese government.

REFERENCES

[1] Wiesel TN (1982), Postnatal development of the visual cortex and the influence of environment. Nature 299:583–591

[2] Hensch TK (2005), Critical period plasticity in loca l cortical circuits. Nature Reviews Neuroscience 6: 8 77–888.

[3] Gordon JA, Stryker MP (1996), Experience-dependent plasticity of binocular responses in the primary visual cortex of the mouse. Journal of Neuroscience 16: 3274–3286.

[4] Kubota S, Kitajima T (2010), Possible role of cooperative action of NMDA receptor and GABA function in developmental plasticity. Journal of Computational Neuroscience, 28:347-359

[5] Shatz, CJ (1990), Impulse activity and the patternin g of connections during CNS development. Neuron, 5:745–756.

[6] Rauschecker JP, Singer W (1979), Changes in the circuitry of the kitten visual cortex are gated by pos tsynaptic activity. Nature, 280:58–60.

[7] Song S, Miller KD, Abbott LF (2000), Competitive Hebbian learning through spike-timing-dependent sy naptic plasticity. Nature Neuroscience, 3: 919–926.

[8] Froemke RC, & Dan Y (2002), Spike-timing-depen dent synaptic modification induced by natural spike trains. Nature, 416: 433–438.

[9] Ahmed B., Anderson JC, Douglas RJ, Martin KAC, Whitteridge D (1998), Estimates of the net excitato ry currents evoked by visual stimulation of identifie d neurons in cat visual cortex. Cerebral Cortex, 8: 462–476.

[10] Kubota S, Kitajima T (2008), A model for synapt ic development regulated by NMDA receptor subunit expression. Journal of Computational Neuroscience, 24: 1–20.

[11] Song S, Abbott LF (2001), Cortical development and remapping through spike timing-dependent plasti city. Neuron, 32: 339–350.

[12] Hessler NA, Shirke AM, Malinow R (1993), The probability of transmitter release at a mammalian ce ntral synapse. Nature, 366: 569–572.

[13] Kubota S (in press), Biophysical mechanisms underlying the critical period of visual cortical plasticity: A modeling study. In Harris and Sccott (eds) Visual cortex: Anatomy, functions and injuries, Nova Science Publishers.

[14] Kubota S, Rubin J, Kitajima T (2009), Modulatio n of LTP/LTD balance in STDP by an activity-depe ndent feedback mechanism. Neural Networks, 22, 5 2:7–535.

[15] Quinlan EM, Olstein DH, Bear MF (1999), Bidire ctional, experience-dependent regulation of N-methyl-D-aspartate receptor subunit composition in the rat v isual cortex during postnatal development. Proceedin gs of the National Academy of Sciences of the Unit ed States of America, 96: 12876–12880.

[16] Quinlan EM, Philpot BD, Huganir RL, Bear MF (1999), Rapid, experience-dependent expression of sy naptic NMDA receptors in visual cortex in vivo. Na ture Neuroscience, 2: 352–357.

[17] Flint AC, Maisch US, Weishaupt JH, Kriegstein AR, Monyer H (1997), NR2A subunit expression sh ortens NMDA receptor synaptic currents in developi ng neocortex. Journal of Neuroscience, 17: 2469–24 76.

[18] Monyer, H, Burnashev N, Laurie DJ, Sakmann B, Seeburg PH (1994), Developmental and regional expression in the rat brain and functional properties of f our NMDA receptors. Neuron, 12: 529–540.

[19] Medina I, Leinekugel X, Ben-Ari Y (1999), Calci um-dependent inactivation of the monosynaptic NM DA EPSCs in rat hippocampal neurons in culture. European Journal of Neuroscience, 11: 2422–2430.

[20] Krupp JJ, Vissel B, Heinemann SF, Westbrook G L (1996), Calcium-dependent inactivation of recombi nant N-methyl-D-aspartate receptors is NR2 subunit s pecific. Molecular Pharmacology, 50: 1680–1688.

[21] Kepecs A, van Rossum MCW, Song S, Tegner J (2002), Spike-timing-dependent plasticity: Common t hemes and divergent vistas. Biological Cybernetics, 87: 446–458.

The Seventeenth International Symposium on Artificial Life and Robotics 2012 (AROB 17th '12),
B-Con Plaza, Beppu, Oita, Japan, January 19-21, 2012

Density map of attentional capacity allocation

Satoshi Kambara[1,3], Shigeyuki Oba[1,2]

[1] Graduate School of Informatics, Kyoto University, Gokasyo, Uji-city, Kyoto 611-0011, Japan
[2] PRESTO, Japan Science and Technology Agency
(Tel: 81-774-38-3938)

[3] kanbara-s@sys.i.kyoto-u.ac.jp

Abstract: Allocation of attentional capacity is an important consequence of visual attention, but its psychophysical mechanism has not been understood very well. We, in this study, investigate a procedure to estimate a high-resolution density map of the attentional capacity allocation on a visual field by analyzing a set of cognition performances on randomly located tasks. We propose a logistic regression model with multi-scale basis functions in order to achieve high-resolution density map, and an experimental scheme with different sizes of square shaped regions of attractors. Our preliminary results on two subjects showed that the corresponding shapes of attentional capacity allocation were different from those of the attractors which may reflect a hidden allocation mechanism of computational resource in brain.

Keywords: visual attention, attentional capacity, logistic regression

1 INTRODUCTION

Attention is a function of human or mammals brain, to select objective information from sensory organ. We must quickly and efficiently detect and distinguish important information in the environment such as food and predators, otherwise probability to survive can decrease. However, limited computational resource of brain does not allow us to process all of sensory input information simultaneously with high accuracy. Therefore, we concentrate computational resources to a selected set of important objects. This selection process is called *allocation of attentional capacity*. A large resource to a specific area enhances quickness and accuracy of the corresponding information processing.

Visual attention, especially, concentrates information processing resources to specific visual items; namely positions, objects, and features[11]. A large resource to a specific visual item enhances corresponding cognition performances, such as sensitivity to subtle differences in colors, directions, and shapes[8]. Several experiments had proven that the enhancement in human-subject's cognition performances in visual tasks, shortened reaction times and improvement in cognition accuracies[9].

Although we have not fully understood the mechanism of attentional capacity allocation yet, we can indirectly observe the amount of attentional resource allocation via a fluctuation of cognition performance. Thus, attentional capacity allocation is regarded as one of important topics in recent studies on visual attention. Deep relationship has been found between attentional capacity and various problems, processing of bottom-up information (ex. saliency) and top-down information (ex. intention, goal, and preferences)[1], serial and parallel search of objects with visual attention[3, 10], and problems in a relationship between visual attention and eye movement (ex. premotor theory of attention)[2, 4].

In this study, we investigate spatial resolution of attentional capacity allocation. When a human subject put an attention to a region of interest with a certain size and shape, how does the corresponding resource allocation reflect the size and shape? How can we estimate the detail shape of allocation from an observed change in cognition performance? We apply logistic regression model to represent a density map of cognition performance as a set of multi-resolution spatial bases. According to our model, spatial distribution of visual attention itself is estimated by removing background factors coming from direction of gaze effect which directly affects cognitive performances. We have conducted experiments in which subjects have to direct attention to a specific region and assign cognition tasks whose accuracy depends on attentional capacity allocation at specific location in visual field. We construct density maps of attentional capacity allocation based on the logistic regression model and investigated differences between conditions.

There have been many recent works that constructed density maps on visual field. Famous examples are saliency map[6] and Bayesian surprise[5], which predicted direction of gaze. In general, however, directions of gaze and visual attention are not always consistent, and density map of spatial attention itself should be constructed by subtracting gaze effect. There have a few attempt (ex. [7]) to estimate the attention map, however, the estimated shape of a density map is limited to several candidate patterns and did not represent general spatial patterns. We, in this study, extended these studies to investigate general shape of density map of visual attention capacity allocation with subtracting gaze effect.

2 MODEL

We applied following logistic regression model that represents spatial allocation of attentional capacity. In this model, an accuracy of a visual task is represented as a function of target position $\boldsymbol{x}$ at which the visual task appeared. The odds ratio of the accuracy is regarded as a sum of attentional capacity term and background term. The background term reflects a difference in cognition accuracy between fovea and peripheral vision that is believed to be task independent, which should be subtracted in order for the attentional capacity term to reflect the effect of task dependent allocation of attentional capacity. The parameters of each terms are determined to fit the experimental data.

2.1 Logistic Regression Model

The odds ratio of accuracy in trial j, is written as a function of the corresponding target position $\boldsymbol{x}_j$ as follows:

$$\begin{aligned}\ln\left(\frac{p(\boldsymbol{x}_j)}{1-p(\boldsymbol{x}_j)}\right) &= \beta^{(0)} + \beta^{(g)} f^{(g)}(\boldsymbol{x}_j) + \sum_{k=1}^{K} \beta_k^{(a)} f_k^{(a)}(\boldsymbol{x}_j) \\ &= \boldsymbol{\beta}^T \boldsymbol{f}(\boldsymbol{x}_j) \qquad (1)\end{aligned}$$

$$f^{(g)}(\boldsymbol{x}_j) = \exp\left(-\frac{(\boldsymbol{x}_j - \boldsymbol{x}^{(\text{fix})})\Sigma^{-1}(\boldsymbol{x}_j - \boldsymbol{x}^{(\text{fix})})}{2}\right)$$

$$f_k^{(a)}(\boldsymbol{x}_j) = \begin{cases} 1 & (\text{if } \boldsymbol{x}_j \text{ in } k \text{ th grid}) \\ 0 & (\text{otherwise}) \end{cases}$$

where $\boldsymbol{x}_j$ and $\boldsymbol{x}^{(\text{fix})}$ denotes 2-d coordinates of the target position at the jth trial and the fixation point of eye-gaze in the experiment, respectively. $p(\boldsymbol{x})$ is a true probability of correct answer that is a function of the target position. $\beta^{(0)}$, $\beta^{(g)}$, and $\beta_k^{(a)}$ are parameters corresponding to bias term, fixation term, and attentional effect at the kth grid, respectively. The kth grid is defined by the basis function $f_k^{(a)}(\boldsymbol{x}_j)$ which takes value of either one or zero if a position $\boldsymbol{x}_j$ is included in the kth region of interest or not, respectively. $f^{(g)}$ denotes background effect determined as a Gauss function peaked at the fixation point $\boldsymbol{x}^{(\text{fix})}$.

In a set of experiment, we observe a corresponding set of results $t_n \in \{0, 1\}$, where $t_n = 1$ and 0 denote correct and incorrect answer at the nth task trial, respectively. The nth task links to the nth position $\boldsymbol{x}_n$. Thus, total log-likelihood of the unknown parameters based on the set of experimental results is given as,

$$L(\boldsymbol{\beta}) = \sum_{n=1}^{N} \{t_n \ln p_n + (1 \quad t_n) \ln(1 \quad p_n)\} \qquad (2)$$

$$p_n = \frac{1}{1 + \exp(\quad \boldsymbol{\beta}^T \boldsymbol{f}(\boldsymbol{x}_n))}. \qquad (3)$$

We estimate the parameters $\beta^{(0)}, \beta^{(g)}$, and $\beta_k^{(a)}$ that fit the observed data by maximum likelihood estimation with regularization term. Using the estimated parameters, we achieve corresponding density map of attentional capacity by $\text{MAP}(\boldsymbol{x}) = \sum_{k=1}^{K} \beta_k^{(a)} f_k^{(a)}(\boldsymbol{x})$ that reflects a level of correspondence of attentional capacity to the odds ratio of task performance with subtracting the other factors, bias and gaze effect.

2.2 Designing basis functions $f_k^{(a)}$

$f^{(a)}(\boldsymbol{x})$ in eq. (1) denotes a basis function that determines spatial extension in the visual field, where we considered multiple layers of base sets corresponding to multiple scales of unit bases. The first scale consists 20 32 grids of bases whose size are 1 1 as like in the left panel in the fig. 1. And, the second scale is made by picking all 2 2 grid in the first scale as in the right panel in the fig. 1. Similarly, we repeated the same procedure until the sixth scale which has all 6 6 size of grid in the first scale.

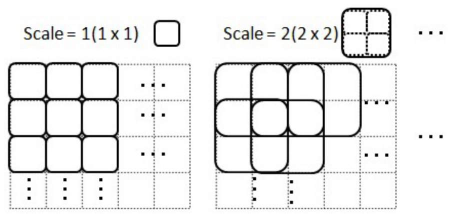

Fig. 1. Determination of multi-scale square grid. The k-th scale grid is made from all possible $k \quad k$ patches that are overlapped each other.

2.3 Ridge Regularlized Maximum Likelihood Estimation

This model is highly redundant because of overlap between the six scales, which makes it impossible to solve without regularization. We calculate parameters that maximizes likelihood function with a Ridge regularization term.

$$\hat{\boldsymbol{\beta}}_{ML \quad R(\lambda)} = \arg\max L(\boldsymbol{\beta}) \quad \lambda||\boldsymbol{\beta}||^2 \qquad (4)$$

where $L()$ is the log-likelihood function and λ is a regularization parameter. We calculated $\boldsymbol{\beta}$ in (4) by Newton-Raphson method. The regularization parameter is determined in a cross-validation procedure.

3 EXPERIMENT

In order to investigate spatial allocation of attentional capacity of human subjects, we conducted the following experiment.

The experiment consists of hundreds of unit tasks for each condition. A single unit task includes the following steps.

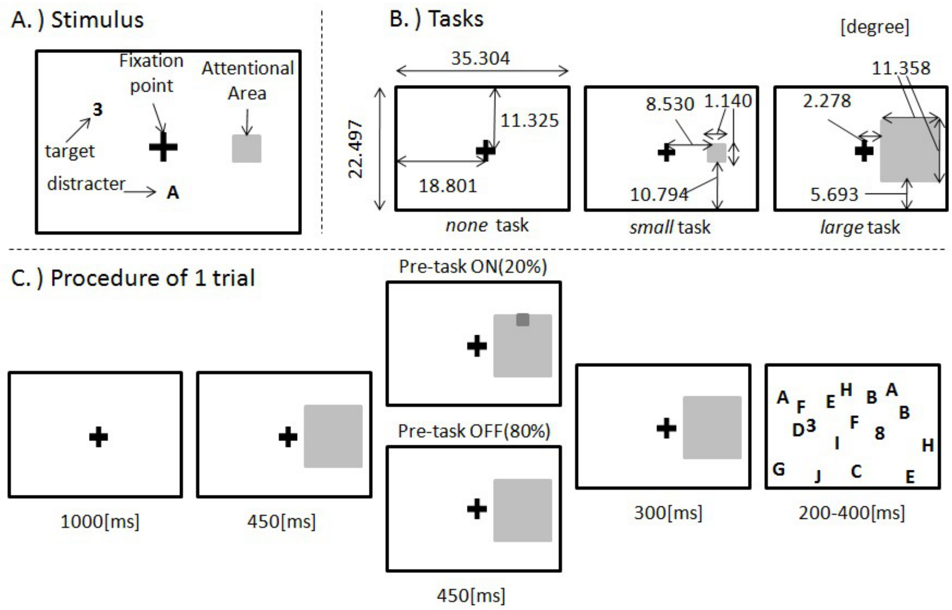

Fig. 2. A.) Stimulus in our experiment. Size of targets and distractors is 1.424 degree. B.) Position and size of pre-cue. C.) Procedure of 1 trial. *None* task do not have pre-task.

First, a pre-cue that specifies a certain region of a screen panel is shown for a subject to draw attention. Then, 10-15 alphabet and two digit letters are displayed simultaneously in a screen panel. The subject is asked to detect the two digit letters and answer them with fixing eye-gaze on the fixation point at the center of the screen. Since there are alphabet letters as distractors and all the letters disappears in a short while, the subject cannot answer correctly if the digit letters are displayed in the area where attentional capacity is not payed enough. (See Fig. 2(a), (c) for detail.)

We compared three types of pre-cue settings; they are (1) large square (2) small square, and (3) none. (See Fig 2(b) for detail.) The duration time to show the letters is set at a value from 200msec to 400msec depending on individual subject so that the task is not too easy nor difficult and the accuracy at a location takes a value from 10 to 90 percent.

In order to confirm that the subject really payed attention to the pre-cued area, a sub-task is asked; color of a small square in the pre-cued area is slightly changed with a certain probability and the subject is asked if the change occured after the main task. In order to confirm that the subjects fixed their eye gaze to the fixation point, the eye movement is observed by an eye-tracker device, EYE-LINK.

Two healthy adult male subjects conducted 360 trials of the unit task for each of three pre-cue settings with 5 minutes rest in less than every 120 trials. The resultant performance data, set of record of correct/wrong answers with the locations of digit letters, is integrated to form a density map of attentional capacity allocation in each condition.

In order to obtain the density maps of attentional capacity allocation in the *small* and *large* tasks, we treated the *none* task as an origin of common background factor. And, since there were statistical variance in the estimated background factor, we estimated a null standard deviation σ of odds ratio of the *none* task by calculating 4-fold cross-validation. We normalized the estimated odds ratio of the *small* and *large* tasks by using the estimated mean and standard deviation of the common background factor. Regularization factor was set at $\lambda = 400$ at which cross-validation likelihood was maximized.

$$\ln\left(\frac{p(\boldsymbol{x}_j)}{1 \quad p(\boldsymbol{x}_j)}\right) = {}^{(0)} + \sum_{k=1}^{K} {}^{(a)}_{k} f_k^{(a)}(\boldsymbol{x}_j) + \mathrm{MAP}^{none}(\boldsymbol{x}_j) \quad (5)$$

$\mathrm{MAP}^{none}(\boldsymbol{x}_j)$: $\mathrm{MAP}(\boldsymbol{x})$ learned by data of *none* task.

The result is shown in Fig. 3. Strong allocation of attentional capacity was observed around the center of pre-cued attractor region for both of small and large square tasks. But, detail size and shape of the allocated regions were different between the two conditions. Attentional capacity allocation in small task was concentrated at smaller area than those in large square task, which suggested that total resource of the subject was limited and had to distribute it when a large area was attracted. In detail, however, the size of the region of allocated attentional capacity did not seem proportional to those of the corresponding region of attractors. The shape were also different between the attention allocation and the region of attractors; in small task, significant enhancement of attentional capacity was observed even in the regions around the small attractors; in large task, the enhanced region did not fill all the corners of the large square shaped region of attractors. These differences suggested a kind of limitation in spatial resolution of attentional capacity allocation.

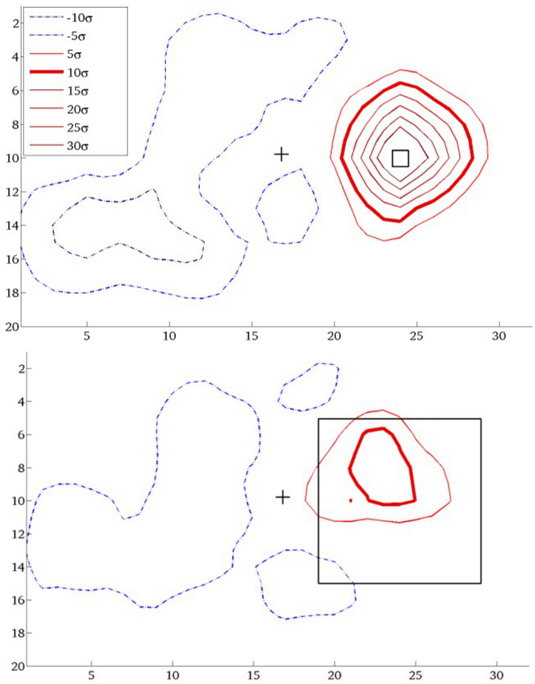

Fig. 3. Estimated density maps of *small* and *large* tasks are shown in top and bottom panels, respectively. Maps of a single subject in two subjects are shown. Contour lines denotes normalized odds ratios whose values are normalized by an estimated standard deviation σ of *none* task. Black square indicates pre-cued region of attention attractor. Black cross indicates fixation point.

4 DISCUSSION

We have constructed spatial density map of attentional capacity allocation by using a logistic regression model with multi-scale basis functions. Based on this model, we have investigated spatial resolution of the attentional capacity allocation. For different settings of pre-cued region of attractors, small and large squares, we found different results in size and strength of attentional capacity allocation, however, the shape of the attentional capacity did not obviously reflect the square shape of pre-cued region of attractor, which suggested a limited spatial resolution of attentional capacity allocation.

Our final goal is to understand mechanism of allocation of attentional capacity. We will increase the number of subjects and unit tasks of experiment, and establish the model of allocation of attentional capacity. In this paper, we have confirmed that allocation of attentional capacity is done as the shape of area where subjects attend and added some modification. In the future, we aim to discover the factors and mechanism related to the model of allocation of attentional capacity.

In addition, we will improve logistic regression model. For example, we change the designing basis functions $f_k^{(a)}$ to that has more biological validity. Furthermore, we add the factors which affect cognition performance(ex. saliency, Bayesian surprise) to our model in addition to attentional term and fixation term. By these improvement, we aim to represent density of attentional capacity more accurately.

REFERENCES

[1] Belopolsky AV, Zwaan L, Theeuwes J, et al (2007), The size of an attentional window modulates attentional capture by color singletons, Psychonomic Bulletin and Review 16(5):934-938.

[2] Hunt AR, Kingstone A (2003), Covert and overt voluntary attention: Linked or independent?, Acognitive Brain Research 18(1):102-105.

[3] Awh E, Pashler H (2000), Evidence for split attentional foci, Journal of Experimental Psychology Human Perception and Performance 26(2):834-846.

[4] Klein RM (1980), Does Oculomotor Readiness Mediate Cognitive Control Of Visual Attention?, Attention and performance 8:259-276.

[5] Itti L, Baldi P (2009), Bayesian Surprise Attracts Human Attention, Vision Research 49(10):1295-1306.

[6] Itti L, Koch C, Niebur E (1998), A Model of Saliency-Based Visual Attention for Rapid Scene Analysis, Pattern Analysis and Machine Intelligence, IEEE Transactions on 20(11):1254-1259 .

[7] Gobell JL, Tseng C, Sperling G (2004), The Spatial Distribution of Visual Attention, Vision Research 44(12):1273-1296.

[8] Huang L, Pashler H (2005), Attention Capacity and Task Difficulty in Visual Search, Cognition 94(3):B101-B109.

[9] Carrasco M, Ling S, Read S (2004), Attention Alters Appearance , Nature Neuroscience 7(3), 308-313.

[10] VanRullen R, Carlson T, Cavanagh P (2007), The Blinking Spotlight of Attention, Proceedings of the National Academy of Sciences 104(49):19204-19209.

[11] Luck SJ, Hillyard SA, Mouloua M, et al (1996), Mechanisms of Visual-spatial Attention: Resource Allocation or Uncertainty Reduciton?, Journal of Experimental Psychology: Human Perception and Performance 22(3):725-737.

The Seventeenth International Symposium on Artificial Life and Robotics 2012 (AROB 17th '12),
B-Con Plaza, Beppu, Oita, Japan, January 19-21, 2012

Development of a brain computer interface using inexpensive commercial EEG sensor with one-channel

M.Obayashi*, K.Watanabe*, T.Kuremoto*, and K.Kobayashi*

*Graduate School of Science and Engineering, Yamaguchi Univ.
,2-16-2 Tokiwadai, Ube, Yamaguchi,755-8611, Japan
(Tel : 81-836-85-9518, Fax : 81-836-85-9501)
(Email: {m.obayas,r051vk,wu,koba}@yamaguchi-u.ac.jp)

Abstract: Brain Computer Interface (BCI) is a system to connect brain of human and computer in order to realize a though of human. In recent years, many such interfaces have been researched and applied for practical applications. Up to now, BCI systems, which have already applied practically, use expensive and large devices to measure the electroencephalographs(EEG). They are for almost all of users to be used for medical treatments. As a result, the BCI systems can't get the popularization to use easily. So, subjects of this study are construction of a BCI system using inexpensive commercial EEG sensor with one-channel, and investigation of the ability to apply it for utilization in various way. In this paper, using the methods of analyses for EEG that have already existed or have improved, we show that the BCI system using inexpensive commercial EEG sensor with one-channel is also useful.

Keywords: robust, reinforcement learning, actor-critic, sliding mode control, inverted pendulum

I. INTRODUCTION

In recent years, Brain Machine Interfaces (BMIs) to operate devices using electrical signals generate during brain activity have been researched extensively. In particular, Brain Computer Interfaces (BCIs) to operate computer applications using the electroencephalograph (EEG) have many fruitful achievements.

These technologies are applied to support patients with paralysis, such a Amyotrophic Lateral Sclerosis (ALS) and spinal cord injury patients, etc. who are difficult to communicate others by means of gesture and speech [1]. By use of techniques of BCIs, improving of QOL (Quality of Life) is expected

However, these techniques are low awareness except some prevalent hospitals. Therefore, this study aims at creating a computer application using commercial EEG sensors at cheap and readily available. To realize that, we intend to improve conventional feature extraction methods, validation method. We use the single-channel EEG sensor called "MindSet" manufactured by NeuroSky Corp. [2].

In this research, BCI system using neural network classifiers with Fourier transform, averaging and feature extraction by nonlinear normalization [8] is used. First, to improve the above-mentioned conventional method, we propose to adopt 1) restricting the frequency bands within the scope seemed to be effective in identifying, 2) introducing the support vector machine classifiers. Second, performance verification of the proposed classifier is carried out using benchmark data. Finally, we also study the usefulness of the proposed BCI system with single channel EEG, that is, using the MindSet through the computer simulation of distinguishing color information on display.

II. Feature extraction and Identification technique

In this section, we explain the basic method [8] and the proposal technique based on [8].

2.1. The basic method

In this paper, we use the method using Self Organization Map (SOM) and Multi Layer Perceptron (MLP) [8]. This method uses the Fourier transform (Eq. (1)), the averaging and nonlinear normalization (Eq. (2)) in the feature extraction, and use SOM and MLP in the feature discrimination.

$$F(\omega) = \int_{t=0}^{T} f(t)\big(\cos(\omega t) - i\sin(\omega t)\big)dt \tag{1}$$

$$f(x) = \frac{\log(x-\min+1)}{\log(\max-\min+1)} \tag{2}$$

Examples of above mentioned each processing and the figu re of discriminator are shown in Figs. 1 and 2, respectively. In Fig.2, X means input vector, W means connecting weights between SOM and MLP

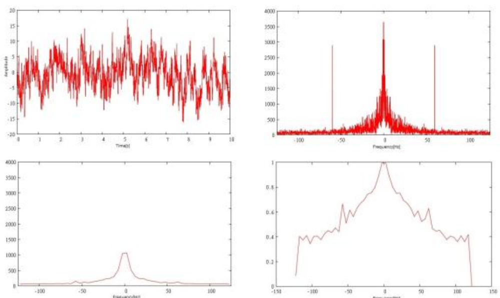

Fig. 1. Upper left: Electroencephalographic data. Upper right: Fourier Transform. Lower left: Equaliz ation. Lower right: Nonlinear normalization

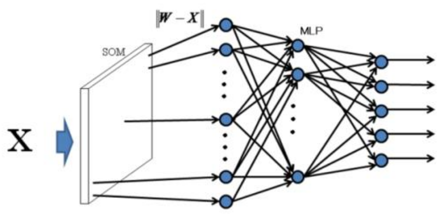

Fig. 2. Discrimination circuit by SOM and MLP

2.2 Improved method

Jie. Li, et al. [10] verified relation between frequency bands of EEG and the brain activity, that is, what frequency bands different stimulus and brain activities are related to. But, such things aren't considered in [8]. So, we intend to enhance the ability of feature extraction by changing the averaging used in [8] for restricting the frequency bands within the scope validated by [10].

Furthermore, in the feature discrimination, we intend to improve the ability of the feature discrimination by using Support Vector Machine (SVM) that is known to the model with the higher generalization performance for unlearned data rather MLP used in [8].

2.3 Multiple classification by SVM

SVM can't discriminate over 3 classes of data, because of the method of discrimination. Therefore, in this paper, in order to discriminate the multiclass of data using the SVM, we set multi SVMs.

For example, we have the data of 3 class labeled A, B and C . Then, a SVM can't correspond to discriminate of these dat a. So, we set any combination of the two among these three classes. Final judge is done by majority of each winner of t he two. In the case of Fig. 3, we decide that input data X belongs to the class A. If the number of majority is the sa me, we judge it "No Decision".

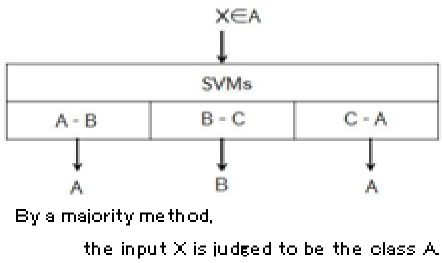

Fig. 3. Multi-class discrimination circuit by SVM

III. Simulation

In section 2, we showed the methods of EEG analysis. In section 3, we verify the performance of each methods through computer simulation using benchmark EEG data.

3.1 The Benchmark EEG data

The benchmark EEG data we used in the simulation is open ed in web sites of Colorado University [3]. The data are ta ken at 250Hz on sampling ratio for 10 seconds on measure ment time. And, these data have been measured using 6 EE G sensors and a EOG sensor to measure the electromyogra m of eye movements as shown in Fig. 4. The number of the subjects to measure these signals is seven healthy young me n. Furthermore, kinds of the mental tasks measured are sho wn to Table 1.

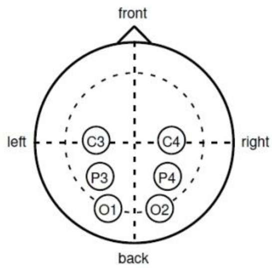

Fig. 4. Brain-waves measurement positions

Table. 1. Contents of mental tasks

Mental task	Contents
Baseline	It relaxes as much as possible.
Multiplication	It calculates multiplication mentally.
Letter-composing	It considers the contents of the letter.
Rotation	It imagines rotation of a three-dimensional object.
Counting	It imagines writing a number in order.

3.2 Term of simulation

The term of this simulation is shown in Table 2.

Table. 2. Simulation conditions

The simulation conditions of a feature extraction method	
The number of data samples after equalization	20
The restriction range of a frequency band	4～45[Hz]
The simulation conditions of SOM	
Initial connection weights	-0.1～0.1
Form of a map layer	Tetragonal-lattice type
The number of nodes of one side of a map layer	50
The number of times of study	30,000
Distance with the input vector of a map layer	Euclid distance
The simulation conditions of MLP	
Initial joint load	-0.1～0.1
The number of the units of a hidden layer	20
Activating function	Sigmoid function
Learning rate	10^{-2}
The number of times of learning	30,000
The simulation conditions of SVM	
The initial value of a Lagrange multiplier	0.0～1.0
Learning rate	10^{-3}

A kernel function and the parameters of each function	Polynomial kernel $K(x_1, x_2) = (a{x_1}^T x_2 - b)^p$ $a = 0.1, b = 0.5, p = 1$ Sigmoid kernel $K(x_1, x_2) = \tanh(a x_1^T x_2 - b)$ $a = 0.1, b = 0.5$ Gauss kernel $K(x_1, x_2) = \exp\left(\frac{-\lVert x_1 - x_2 \rVert^2}{2\sigma^2}\right)$ $\sigma = 2$
the number of SVM	10
The discernment determination method	Majority method

3.3 The process of simulation

In the simulation, we perform the following stems:

① Provide N sets of T kinds of Mental task data .
② Perform feature extraction on each of input sample N.
③ As training data, take n samples out of each mental tasks randomly, the rest of samples (N-T × n) are treated as test data.
④ Execute training for classifier by using the training data.
⑤ Determine the type of mental tasks of the test data using the learned classifier.
⑥ Repeat any times from ② to ⑤.

3.4 Simulation results

The case of seven channels EEG data for all subjects

The number of samples of EEG signals measured at each subject is 60 for each of 5 mental tasks, 12 samples is for test data in it, and the rest is for training data. Changing the test samples, repeat the above experiment five times.

Results of discrimination using each of the methods have been shown in Table 3.

In the results, the best result is the discrimination ratio of 75% of the improved method using Gaussian Kernel. This result is 4% better than the result of the conventional method with 71%. This improved result may be due to improvements of restricting the frequency bands in Feature Extraction and introduction of SVM. It can be seen that the Gaussian kernel is the most appropriate in the kernel trick used in this study.

Table 1 Discernment results by each method in the case of seven-channel electroencephalographic data for seven subjects

		B	M	L	R	C	Average
SOM + MLP	SOM 50	58	76	63	87	70	71
SVM	Alignment	50	62	58	70	60	60
	Polynomial	50	60	63	72	65	62
	Gauss	60	64	82	85	78	75
	Sigmoid	52	70	66	73	59	64

In the case of one channel using EEG data for one subject

Excluding EEG, Data are measured by 6-channel EOG electrodes and discernment of the data is carried out. The EEG data of the subject 1 is used. The data of subject 1 are measured 10 times per each of the five mental tasks, a total is 50 samples. Two samples for each 5 mental tasks, that is, 10 samples are taken as test data, and the remaining 40 samples are used as training data. Discernment testing is executed five times changing test samples.

In addition, the improved method uses the Gaussian kernel in SVM showing high recognition rate in Section 3.3 and 3.4.

Table 4 shows the discernment results of each method.

In this simulation, overall, the improved method with the Gaussian kernel shows better results. From this one channel used results, it is said that the improved method is effective even for a single-channel EEG data, like the case of multi-channel.

Table 2 Discernment result by each method in the case of one-channel electroencephalographic data for one subject

		B	M	L	R	C	Ave.	All the averages
SOM 50	C3	30	0	10	20	40	20	19
	C4	0	0	20	20	20	12	
	P3	20	10	20	0	70	22	
	P4	20	20	0	10	50	20	
	O3	0	0	0	0	90	18	
	O4	20	0	0	0	80	20	
SVM & Gauss kernel	C3	20	30	30	10	20	22	24
	C4	10	0	40	20	20	18	
	P3	30	30	0	0	60	24	
	P4	50	20	10	20	50	30	
	O3	0	40	30	0	80	30	
	O4	0	0	20	10	60	18	

IV. Experiment

Next, using a Gaussian kernel SVM showed good results in the simulation, discernment testing for EEG data obtained f rom single-channel EEG sensors, MindSet, is executed.

4.1 Inexpensive commercial EEG sensor with one-ch annel

The MindSet has two electrodes which are attached to left ear and forehead. It measures a potential difference between before-mentioned two electrodes. The sampling rate for measurement is 512Hz.

In addition, the MindSet has no recording equipment of EEG data, it only has the ability to measure EEG data. Therefore MindSetRearchTool, a research tool MindSet (MRT), is used to compensates for their function. The MRT has various functions: the EEG recording, saving features, which is also equipped with connectors for use with software such as MATLAB, numerical analysis software.

Fig. 5. MindSet made by NeuroSky Ltd.

4.2 Measuring method

The subjects is one healthy male in his 20s. Brain waves of the subject with the MindSet on the head sitting in a chair are measured. Mental task is looking the blinking image, changing black, red and blue, every two seconds and the EEG data are measured when viewing.

The measurement time is 10 seconds and the measurement is made for three colors each, then set in the one-minute break before the next measurement.

As described above, measurement is done 10 times for each mental task. The total number of data is 30. The subsequent experiments are done using these 30 data set.

4.3 Experimental conditions of Feature Extraction

Restricting range of frequency bands for feature extraction method in an improved process is 4-125 [Hz]. These EEG and EEG data are the different benchmarks such as intellectual thought during the simulation. Therefore the restricting range of frequency bands are set arbitrarily.

4.4 Experimental conditions of Support Vector Machines

Table 5 shows the condition of the SVM in this experiment.

Table 3. Experimental condition of SVM

The initial value of a Lagrange multiplier	0.0～1.0
Learning rate	10^{-3}
A kernel function and the parameter of each function	Gauss kernel $\sigma = 2$
The number of SVM	3
The discernment determination method	Majority method

4.5 Experimental procedure

Discernment test of experiments was carried out as same as in the simulation.

4.6 Experimental results

Under the experimental conditions described above, the results of discernment test are shown in Table 6. In this experiment, the lowest diecerment rate of 60%, the highest recognition rate of 80%, 70% were discerned on average. This is not said that very high recognition rate. However, it is said that the one channel EEG sensors "MindSet" EEG data can be discerned, this may show that 1 channel commercial EEG sensor are applicable to the engineering fields .

Table 4. Experimental result

	Black	Red	Blue	Average
Gauss kernel	60	70	80	70

5. Conclusions

By incorporating the existing proposal as the basis of the BCI system, BCI system with high generalization performance as shown in this simulation and experiment was able to be constructed. It is also found that mental tasks can be identified in single-channel EEG sensors.

However, results of this research are only shown to be useful for identifying a simple mental task. We don't have practical applications yet. Therefore, the goal of future studies are

① Seeking viable mental tasks can be identified by MindSet,

② Development of real-time BCI system that can be Identified.

The construction of viable applications using the MindSet is remained.

REFERENCES

[1]J.R.Wolpaw, N.Birbaumer, D.McFarland, G.Pfurtscheller, T.Vaughan, "Brain-computer interfaces for communication and control", Clinical Neurophysiology, vol.113, pp.767-691, 2002

[2]http://www.neurosky.jp/

[3] http://www.cs.solostate.edu/eeg/

[4]Teruo Ohkuma , Clinical Neuroscience , Igakushoin, 5th Edition, 1999 (in jaoanese)

[5]Kiyoot Inagaki, kouji Nakayama, "Classification of mental tasks by using neural networks based on brain waves" , Information and Comunication Enjineers, Vol.105 No.174 pp.25-30, SIP2005.07

[6]K.Nakayama and K.Inagaki, "A brain computer interface based on neural network with efficient preprocessing" , Proc.IEEE , ISPACS2006 , Yonago , Japan , pp.673-676 , Dec.2006

[7]Hiroya Saito, Kenji Nakayama, Akihiro Hirano, "On future extraction from multi-channel brain waves used for brain computer interface", 24th signal processing symposium, pp.384-38, 2009 (in Japanese)

[8]Jie Li, Liqing Zhang , "Regularized tensor discriminant analysis for single trial EEG classification in BCI", Elsevier Science Direct Complete, vol.31,pp.619,2010

[9]Takio Kurita, "In troduction to support vector machine", http://www.neurosci.aist.go.jp/%kurita/lecture/svm.pdf,2003

[10] V.Vapnik, "Statistical Learning Theory", Johon Wiley Sons, 1998

The Seventeenth International Symposium on Artificial Life and Robotics 2012 (AROB 17th '12),
B-Con Plaza, Beppu, Oita, Japan, January 19-21, 2012

A sparse regression method to estimate neuronal structure from spike sequence

Syunsuke Aki[1], Shigeyuki Oba[1,2], Ken Nakae[1], and Shin Ishii[2]

[1] Graduate School of Informatics, Kyoto University, Kyoto, Japan
[2] PRESTO, Japan Science and Technology Agency
(Tel: 0774-38-3938, Fax: 0774-38-3941)
(aki-s@sys.i.kyoto-u.ac.jp)

Abstract: Recent imaging techniques enable us to observe activities of hundreds of neurons simultaneously as spike sequences. The objective of this study is to estimate the network structure based on such spike sequences. Our method is an extension of existing sparse regression technique, in which we have implemented the following three ideas: (1) Each spike time-series obeys a non-stationary Poisson process whose Poisson intensity is given by an auto-regression model. (2) Spike response functions are represented by a linear summation of smooth basis functions. (3) A group-LASSO regularization is applied to obtain a sparse regression solution. When applied to simulation datasets, our method showed a better estimation performance than that by an existing state-of-the-art method.

Keywords: Computational neuroscience, network estimation, sparse estimation, generalized linear model

1 INTRODUCTION

To estimate underlying structures of networks is one big challenge not only in the field of data mining but also in various biological fields. A typical application in the field of neuroscience is to estimate the network structure from neurons' spike sequences. Recently, a variety of high-throughput measurement systems of neural networks have been proposed; for example, multi-electrode array (MEA) [1] measures neurons' action potential by inserting an electrode array into a specific brain region. Another way is a high-throughput Calcium imaging, which is now available with as much as 1000 Hz. Not only these new technologies but also the development of sophisticated statistical methods have enabled us to estimate the network structure based on a rather limited data amount. Granger causal modeling (GCM) [2] and dynamic causal modeling (DCM) [3] are such innovative statistical methods. GCM estimates causal connections between neurons based on the predictability. According to DCM, on the other hand, we assume a dynamic equation between neurons, and the total dynamical system is identified by means of, say, Bayesian statistical method. In this study, we aim to present a robust network estimation method based on modification of existing generalized linear modeling (DCM). Since this is a simple sparse regression technique, it may work especially when the available data amount is rather small (Fig.1). Here, estimation of spike response functions has an important role.

The estimation of spike response functions has been done by hierarchical Bayesian modeling [4, 5], but it has some concerns on the stability of computation and appropriate setting of priors. In many applications of structure estimation methods, the target network is partially observable, i.e., there are some hidden structures which cannot be directly observed. In such cases, the structure estimation may be affected by indirect relationship between observable elements through unobservable structures. Even in such hard situations, there may be a way to separate observable elements into clusters based on their spike response functions. This is one advantage of network estimation via the estimation of spike response functions. Therefore, we put our focus on network estimation methods based on the estimation of spike response functions in this study.

2 GENERALIZED LINEAR MODEL

Our method is based on the generalized linear model (GLM) presented formerly by Stevenson et al. [4]. After briefly introducing GLM, we describe our extensions.

2.1 Poisson process with an auto-regression model

Let $N_i(t)$ be a random variable denoting a spike event; when $N_i(t) = 1$, the i-th neuron emits a spike once in the t-th frame, and when $N_i(t) = 0$, it does not emit a spike in the frame.

Following the formulation by Stevenson et al., each spike event of neuron i obeys a non-stationary Poisson process with the time-variant Poisson intensity $\lambda_i(t)$. Here, the continuous time axis is segmented into frames with a fixed interval $\Delta t > 0$, which is small enough to make each segmented time frame (with a center at t and a width of Δt) to include at most one spike event. With these notations, the binary random variable $N_i(t)$ obeys a Bernoulli distribution: $P(N_i(t) = 1|\lambda_i(t)) = 1 - \exp(-\lambda_i(t)\Delta t)$.

Stevenson et al. assumed the Poisson intensity is given by

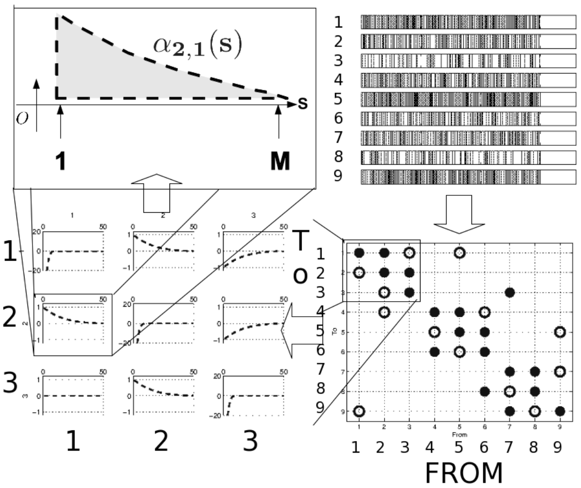

Fig. 1. Our objective is to estimate the network structure (right lower panel) from spike sequences over constituent neurons (right upper panel). In the right-lower matrix, a symbol ○ (●) denotes there is an excitatory (inhibitory) connection from neuron 'From' to neuron 'To'. No circle means no connection. The left lower panel shows the spike response functions of nine connections in the right lower panel (inset). The left upper panel shows a spike response function $\alpha_{2,1}(s)$, connectivity from neuron 1 to neuron 2.

the following auto-regression model:

$$\begin{aligned}\lambda_i(t) &= \lambda_i(t;\boldsymbol{\alpha}_i) \\ &= \exp\left(\alpha_{i,0} + \sum_{c=1}^{C}\sum_{s=1}^{M}\alpha_{i,c}(s)N_c(t-s)\right), \quad (1)\end{aligned}$$

where $\boldsymbol{\alpha}_i \equiv \{\alpha_{i,0}, \alpha_{i,c}(s) | i = 1, \cdots, C, c = 1, \cdots, C, s = 1, \cdots, M\}$ are coefficients of the auto-regression model. Since the vector $\boldsymbol{\alpha}_{i,c} \equiv (\alpha_{i,c}(s))$ represents the connection from a pre-neuron c to a post-neuron i, it is called a spike response function.

2.2 Introduction of basis functions

According to the model (1), the spike response function for a neuron pair (i, c), $\boldsymbol{\alpha}_{i,c}$, may take an independent value for each time-delay s, i.e., M-dimensional. Since the spike response function is determined based on data, this large degree of freedom may be disadvantageous especially when the delay time is long (M is large). Moreover, since the spike response function is represented biophysically in reality, it should be smooth; that is, the difference between $\alpha_{i,c}(s)$ and $\alpha_{i,c}(s+1)$ is not very large. In order to reduce the effective dimensionality whereas allowing long time delay of the spike response function, we assume it to be represented by a linear summation of temporally smooth basis functions:

$$\begin{aligned}\lambda_i(t) &= \lambda_i(t;\boldsymbol{\alpha}_i) \quad (2)\\ &= \exp\left(w_{i,0} + \sum_{c=1}^{C}\sum_{s=1}^{M}\sum_{k=1}^{K} w_{i,c,k}b_k(s)N_c(t-s)\right),\end{aligned}$$

where $b_k(s), k = 1, \cdots, K$ are K pre-fixed basis functions, and $\boldsymbol{z}_i \equiv \{w_{i,0}, w_{i,c,k}, i = 1, \cdots, C, c = 1, \cdots, C, k = 1, \cdots, K\}$ are their linear coefficients (parameters). When $K \ll M$, the effective dimensionality of the spike response function is much reduced from the original M-dimensional one, thus the estimation variance from a fixed amount of data and computational cost are both reduced. Determining the parameters $\boldsymbol{z}_i$, we have the spike response function $\boldsymbol{\alpha}_i$, because $\alpha_{i,0} = w_{i,0}$ and $\alpha_{i,c}(s) = \sum_{k=1}^{K} w_{i,c,k}b_k(s)$. When $K = M$ and $b_k(s) = I(k = s)$, the model (2) becomes identical to the original GLM (1). Here, $I(A)$ is an indicator function, which takes 1 if the condition A is true and 0 otherwise. From this observation, the model with basis functions (2) is one extension of GLM.

We in particular used logarithmic cosine functions for the basis functions $b_k(s)(k = 1, 2, \cdots, K)$:

$$b_k(s) \equiv \begin{cases} \cos^2(D_1\log(1+(s-1)D_2)\pi/2 - (k-2)\pi/4) \\ (\text{if } D_1\log(1+(s-1)D_2)\pi/2 \in \\ [-\pi/2+(k-2)\pi/4, \pi/2+(k-2)\pi/4]) \\ 0 \\ (\text{else}) \end{cases}.$$

Here, D_1, D_2 denotes the scale parameter and is set arbitrarily. These basis functions have fine and coarse temporal resolutions when the corresponding delay times are short and long, respectively. This setting allows the resultant spike response function to represent well the rapid change of postsynaptic membrane potential after the spike input but to reduce the effective dimensionality simultaneously.

2.3 Optimization problem

We estimate the linear coefficients of the basis functions, $\boldsymbol{z}_i$, such to minimize the following loss function with a regularization term:

$$\boldsymbol{z}_i^* = \mathrm{argmin}_{\boldsymbol{z}_i}\mathcal{L}_i(\boldsymbol{z}_i) + \Lambda\mathcal{G}(\boldsymbol{z}_i), \quad (3)$$

where $\mathcal{L}_i(\boldsymbol{z}_i)$ is the loss function for the i-th neuron, and $\mathcal{G}(\boldsymbol{z}_i)$ is the regularization term that is explained in the section 2.4. $\Lambda > 0$ is a balancing factor between the loss function and the regularization term, whose value is determined by a cross-validation method such to show a good generalization performance.

Since we assume that the random variable $N_i(t) \in \{0, 1\}$, $i = 1, \cdots, C$, $t = 1, \cdots, T$ obeys an independent

Bernoulli process, the log likelihood is given by

$$\sum_{t=1}^{T} \log P(N_i(t)|\lambda_i(t)). \tag{4}$$

Since the Poisson intensity $\lambda_i(t)$ is determined by the parameter vector $\boldsymbol{z}_i$ (equation (2)), the log likelihood is a function of the parameter vector. Then, the maximum likelihood estimation of the parameter vector is equivalent to the minimization of the following loss function with the auto-regression model (2) in terms of the parameter vector $\boldsymbol{z}_i$:

$$\mathcal{L}(\boldsymbol{z}_i) \quad = \quad -\sum_{t=1}^{T} \left(N_i(t) \log \lambda_i(t) - \lambda_i(t)\right), \tag{5}$$

where we have used the likelihood of the Bernoulli process.

2.4 Group-LASSO regularization

The regularization term in equation (3) is given by

$$\mathcal{G}_i(\boldsymbol{z}_i) = \sum_{c=1}^{C} \sqrt{\sum_{k=1}^{K} w_{i,c,k}^2} \quad , \tag{6}$$

which is a kind of group-LASSO regularizer. A linear regression method employing an L^1 regularizer $\mathcal{G}_i^{(\mathrm{L}^1)} = \sum_{c=1}^{C} \sum_{k=1}^{K} |w_{i,c,k}|$ is called LASSO and tends to produce a sparse solution whose linear coefficient is likely to be zero. A group-LASSO is an extension such that the sparseness works in each group of linear coefficients. According to the regularization term (6), $\{w_{i,c,k}|k = 1, \cdots, K\}$ constitutes a group, and the variables in a single group are often estimated as zero simultaneously. In our particular application, $w_{i,c,k}, k = 1, \cdots, K$, should be simultaneously zero if a neuron pair (i, c) has no connection. When applying to estimation of neuronal network structure, therefore, a group-LASSO-based regularization method would work well.

3 SIMULATION

The proposed method was applied to simulation spike datasets.

3.1 Simulation setting

Simulation 1 Kim et al. [2] prepared a network model consisting of nine neurons (Fig. 2), and produced a spike dataset by introducing specific spike response functions to the connected neuron pairs. Although the spike response functions are not presented, the simulated spike sequence is open for public[1]. The spike sequence with a frame rate of 1,000 Hz is for 100,000 frames (100 seconds).

[1]http://www.neurostat.mit.edu/gcpp

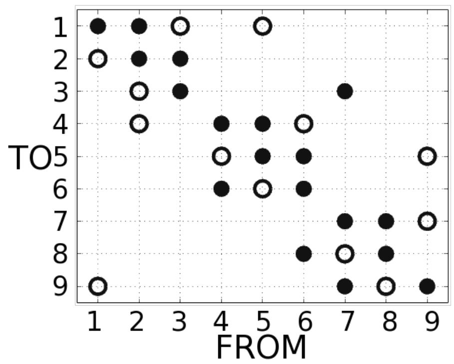

Fig. 2. The connection matrix showing the true network structure in simulation 1

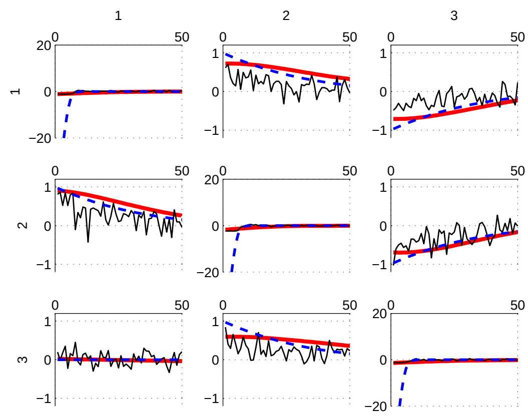

Fig. 3. The true spike response function and its estimation in simulation 2. The figure shows spike response functions between three neurons out of nine neurons. A dotted line is the true one. A thick solid line and a thin solid line show the estimated response functions with and without the logarithmic cosine basis functions, respectively.

Simulation 2 Since the true spike response functions are unknown in the Kim et al.'s dataset, we did a simulation by applying our own spike response functions (therefore, we know the truth) to the same network structure as that used by Kim et al.

3.2 Estimation of spike response functions

Fig. 3 shows the spike response functions obtained by applying the proposed method to the dataset in simulation 2. In particular, this figure shows the performance of the logarithmic cosine bases, which can be seen by comparing the group-LASSO regression with (thick solid line) and without (thin solid line) logarithmic cosine basis functions. In both cases, the regularization coefficient Λ was set at 10. We can see that the smoothness constraints due to the logarithmic cosine functions worked well to obtain smooth and hence biologically natural response functions.

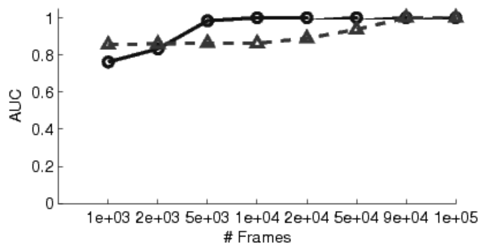

Fig. 4. Network estimation when applied to the dataset of simulation 1. A dotted line and a solid line show the AUC values by Kim et al. and our method, respectively.

3.3 Estimation of network structure

Based on the estimated spike response functions, we can estimate the network structure.

We say there is an excitatory (inhibitory) connection from a pre-neuron c to a post-neuron i if the auto-regression coefficient $\alpha_{i,c}(s)$ is consistently positive (negative) for all delay times $s = 1, \cdots, M$. We also say there is no connection from c to i if $\alpha_{i,c}(s)$ is consistently zero. However, it may be the case of estimation that $\alpha_{i,c}(s)$ is positive with some delay times but negative with other delay times. Such an estimation result may be obtained due to the estimation variation and/or to the mixture of direct effects and indirect (i.e., multi-synaptic) effects. In order to extract a reasonable structure from such ambiguous spike response functions, we needed a heuristic criterion; by defining the connectivity strength: $Q_{i,c} = \sqrt{\sum_{s=1}^{M} \alpha_{i,c}^2(s)}$ and the connectivity polarity: $R_{i,c} = \text{sign}(\sum_{s=1}^{\tilde{M}} \alpha_{i,c}(s)), \tilde{M} < M$ we determined as follows, either excitatory, inhibitory or no connection from pre-neuron c to post-neuron i.

- If $Q_{i,c} > h$ and $R_{i,c} = 1$, an excitatory connection.
- If $Q_{i,c} > h$ and $R_{i,c} = -1$, an inhibitory connection.
- If $Q_{i,c} < h$, there is no connection.

In the above criterion, h is a positive threshold to be pre-tuned. Although we tuned it heuristically in this experiment, it should be determined by controlling the false positive rate in more realistic applications [2].

In our method, we obtained spike response functions from the given spike dataset, and then the network structure was determined by applying the above criterion to the estimated spike response functions. We also applied the network estimation method by Kim et al. to the same dataset. Here, we examined the estimation performance by varying the number of frames (i.e., sequence length).

From Fig. 4, we can say that the proposed method shows a good performance for network estimation over a wide range of available number of frames. Here, AUC (area under the receiver-operator curve) shows the general accuracy by integrating both of the false positive rate and false negative rate; the larger it is, the better the classifier is.

4 CONCLUSION AND DISCUSSION

In this study, we presented a GLM-based network estimation method employing smooth basis functions such to reduce the effective dimensionality whereas maintaining the representation capability of the model. In addition, the group-LASSO-type regularization introduced an effective and biophysically natural sparseness into the estimation, and hence was effective for stabilizing the estimation.

There are some remaining issues in our network estimation method. First, performance of network estimation will be deteriorated when the target network receives structured inputs from external networks. One possible solution is to incorporate location information of each network element into our model. Second, we have not established a good criterion to extract the network structure from the estimated spike response functions. We have applied a cross-validation technique to determine the threshold value in the criterion, but also found its result behaves unstably especially when the data amount is not sufficient. There are some remaining issues like above, and we will cope with them in our future study.

REFERENCES

[1] Heuschkel MO, Fejtl M, Ragenbass M, et al (2002), A three-dimensional multi-electrode array for multi-site stimulation and recording in acute brain slices. *Journal of Neuroscience Methods*, 114(2):135 – 148

[2] Kim S, Putrino D, Ghosh S, et al (2011), A granger causality measure for point process models of ensemble neural spiking activity. *PLoS Computational Biology*, 7(3):e1001110

[3] Penny ND, Stephanand KE, Moran RJ, et al (2010), Ten simple rules for dynamic causal modeling. *NeuroImage*, 49(4):3099–3109

[4] Stevenson IH, Rebesco JM, Hatsopoulos NG, et al (2009), Bayesian inference of functional connectivity and network structure from spikes. *Neural Systems and Rehabilitation Engineering*, 17(3):203–213,

[5] Yoshimoto J, Doya K (2011), Model-based identification of synaptic connectivity from multi-neuronal spike train data (in Japanese). *IPSJ SIG Technical Report*, 2011-BIO-25(4)

ACKNOWLEDGMENT

This study was supported by Grant-in-Aid for Scientific Research on Innovative Areas: " Mesoscopic neurocircitry towards understanding of the functional and structural basis of brain information processing " from MEXT, Japan.

The Seventeenth International Symposium on Artificial Life and Robotics 2012 (AROB 17th '12),
B-Con Plaza, Beppu, Oita, Japan, January 19-21, 2012

A potential model pruning in Monte-Carlo *go*

Makoto oshima[1], Koji yamada[2], and Satoshi endo[2]

[1]The Graduate School of Engineering and Science, University of the Ryukyus, Okinawa 903-0213, Japan
[2]The Department of Information Engineering, Faculty of Engineering, University of the Ryukyus,
Okinawa 903-0213, Japan
(Tel: 81-98-895-8724, Fax: 81-98-895-8727)

[1]mako10@eva.ie.u-ryukyu.ac.jp

Abstract: In this study, we tackled the reduction of computational complexity by pruning the *igo* game tree using the potential model based on the knowledge expression of *igo*. The potential model considers *go* stones as potentials. Specific potential distributions on the *go* board result from each arrangement of the stones on the *go* board. Pruning using the potential model categorizes the legal moves into effective and ineffective moves in accordance with the threshold of the potential. In this experiment, 5 kinds of pruning strategies were evaluated. The best pruning strategy resulted in an 18% reduction of the computational complexity, and the proper combination of two pruning methods resulted in a 23% reduction of the computational complexity. In this research we have successfully demonstrated pruning using the potential model for reducing computational complexity of the *go* game.

Keywords: Monte-Carlo *go*, Potential, Pruning, Range search

1 INTRODUCTION

Monte-Carlo *go* [1] is the computer *igo* which satisfy the strength without the knowledge expressions of *igo*. Monte-Carlo *go* is very computationally intensive. However, reduction of the computational complexity is possible by properly pruning the *igo* game tree. In this study, we tackled the reduction of computational complexity by the pruning the *igo* game tree using the potential model.

2 PROPOSED METHOD

The proposed method in this research is consists of Monte-Carlo *go* and potential model.

2.1 Monte-Carlo *go*

Monte-Carlo *go* evaluates legal moves at each phase to choose the next move by simulation based on the Monte-Carlo search. Monte-Carlo search consists of many moves of a simulation. This simulation is called "Play Out." Play Out involves both sides constantly choosing the next move alternately and randomly from the current phase to the end game. Play Out calculates an estimation ($\overline{X_\iota}$) for each legal move (i). (s_i) is the number of times of Play Out. (X_i) is the total considerations of Play Out. In Play Out, if the offensive wins, the consideration is 1, and if it loses, the consideration is 0. As a result, the move which has the best estimation is selected as next move.

$$\overline{X_\iota} = \frac{X_i}{s_i} \tag{1}$$

2.2 Potential model

Stones influence the possibility of the surrounding intersection becoming their territory. The potential model is to quantify these influences by assuming *go* stones as potentials following earlier studies [2-4].

2.2.1 Definition of potential

The definition of potential in this experiment is shown in Formula (2-4) and Table 1. The plus and minus of Formula (3) is switched by the setting of proposed method. A potential gradient are calculated by Geographical Information Systems [5].

$$r = \sqrt{(X - x_i)^2 + (Y - y_i)^2} \tag{2}$$

$$P_i = \pm \frac{1}{2^r} \tag{3}$$

$$P_{all} = \sum_{\mathrm{k}=1}^{\mathrm{n}} P_i(X, Y) \tag{4}$$

Table 1. Mathematical expression

r	Euclidean distance
x_i, y_i	Intersection of $Stone_i$
$P_k(X, Y)$	Potential to intersection (X, Y) from $Stone_k$
n	Total number of stone on the *go* board
$P_{all}(X, Y)$	Total potential to
$PG(X, Y)$	A potential gradient at an intersection.

2.2.2 Pruning using potential model

Potential Filters

Potential Filters are pruning instruments in this experiment. At each phase to choose the next move, these Filters pruned legal moves according to the following procedures:

i. Calculate potential distribution result from arrangement of go stones on the *go* board.
ii. Rank legal moves by each magnitude of potential (or potential gradient.)
iii. Categorize the ranked legal moves into effective and ineffective moves in accordance with thresholds for the ranking. (Each Potential Filter has unique threshold levels.)
iv. Eliminate the ineffective moves from candidates for the next move. (Run Monte-Carlo search only on effective moves.)

In accordance with the number of eliminated legal moves, the computation load of Monte-Carlo search is reduced. Said differently, the Potential Filters reduce the range of search spaces on the *go* board.

Configurations of Potential Filters

Table 2 shows the threshold conditions of the 5 kinds of Filters. Each Potential Filter ranked legal moves in descending order of potential or potential gradient values, and categorized in accordance with each threshold condition for the ranking. All Filters mutually reduced by half the number of legal moves. Thus all Filters reduced by half the computational load at each phase to choose the next move.

On and Off Switch of Potential Filter

Potential Filters had a switching point, which switched their states ON and OFF. This switching point was within a range of legal intersection numbers on the *go* board. A switching point was selectable from 2 to 81 when the board size was 9 x 9 (= 81), or from 2 to 169 when the board size was 13 x 13 (= 169).

During the course of a game, in the case a remaining legal move number on the *go* board was above a switching point, the Potential Filters were ON. If a remaining legal move number was under a switching point, the Potential Filters were OFF. In this experiment, boundaries where Potential Filters became ineffective from effective were measured by changing the switching point. The boundaries were the points where winning percentages crossed an average winning percentage between two normal Monte-Carlo *go*.

Monte-Carlo search has higher performance when a game tree is small. In contrast, Monte-Carlo search has low performance when a game tree is large. Thus, pruning is effective in the opening game. However, afterwards, pruning gradually becomes ineffective.

3 STRENGTH OF MONTE-CARLO *GO* WITH POTENTIAL FILTERS

The strength of Monte-Carlo *go* with Potential Filters was indicated by its winning percentage against normal Monte-Carlo *go*. Monte-Carlo *go* with Potential Filters used the initiative move while normal Monte-Carlo *go* used the passive move. In a match-up between two normal Monte-Carlo *go*, the winning percentage of the initiative move was 57% when board size was 9 x 9, or 51% when board size was 13 x 13. (The winning percentage of initiative exceeded 50% because the initiative move was advantageous.) Therefore, 57% or 51% is considered the average level of normal strength.

4 RESULTS AND OBSERVATION

The strength of Monte-Carlo *go* with Potential Filters is shown in Fig. 1, upper (board size: 9 x 9) and lower (board size: 13 x 13) graphs, left axis. Strength transitioned with Filters and switching points. A winning percentage of 57% or 51% and calculating the results of the Random Filter were important for comparing and evaluating the effects and tendency of Potential Filters. Total Play Out numbers needed in one game are shown in Fig. 1, upper and lower graphs, right scale. Total Play Out numbers transitioned with these Filters and switching points.

In theory, when the Random Filter was used, the next move became the best move by Monte-Carlo search 50% of the time and the second or several moves thereafter by Monte-Carlo search the other 50% of the time.

In the case that the number of legal moves was large, Monte-Carlo search had low precision. Thus, there was no big decrease of strength, because there was no defining difference between the best move and the second or several moves thereafter by Monte-Carlo search. The precision of Monte-Carlo search increased with a decrease in the number of legal moves. The strength of the Random Filter decreased gradually with a decrease in the number of legal moves.

Potential Filter 1 became the bias around which black stones gathered. In the opening game, these collective black stones effectively strengthened initiative territory. However, in the middle game, the initiative move could not expand its territory. As a result, the passive move acquired more territory than the initiative move on the *go* board. When strength exceeded average (57% or 51%), Potential Filter 1 properly pruned ineffective moves that Monte-Carlo search was unable to do. Thereafter, the strength of the Potential Filter 1 decreased gradually with a decrease in the number of legal moves and an increase in the precision of Monte-Carlo search. In fact, the pruning of Potential Filter 1had encumbered the precision of Monte-Carlo search.

Potential Filter 2 became the bias where black stones were attracted around white stones. In the opening game, black stones effectively suppressed white stones. However, in the middle game, black stones were removed easily by collective white stones. As a result, the passive move acquired more territory than the initiative move on the *go* board. When strength exceeded average (57% or 51%), Potential Filter 2 properly pruned ineffective moves.

Potential Filter 3 became the bias where black stones were scattered on the *go* board. These black stones were removed easily by collective white stones. As a result, the passive move acquired more territory than the initiative move on the *go* board. In the opening game, Potential Filter 3 barely pruned ineffective moves. However, Potential Filter 3 decreased the strength in comparison with other Filters more gently.

Potential Filter 4 became the bias where black stones were attracted around black and white stones, and areas between black and white stones were closed. This is important in *igo*. Potential Filter 4 could prune more properly than the other Filters, but decreased the strength in comparison with other Filters more drastically in the middle game.

Potential Filter 5 became the bias where stones were attracted around black and white stones. Potential Filter 5 could prune more properly than the other Filters, but decreased the strength in comparison with other Filters more drastically in the middle game as well as Potential Filter 5.

As for Combination, Potential Filter 5 and Potential Filter 3 combined pruned a game tree more properly than Potential Filter 5 alone. In the opening game, Potential Filter 5 was effective and this initiative had high strength. However, in the middle game, Potential Filter 5 decreased the strength in comparison with other Filters more drastically. On the other hand Potential Filter 3 decreased the strength in comparison with other Filters more gently. So the strength keeps the average for a longer time by switching Potential Filter 5 to Potential Filter 3 at the point where the strength of Potential Filter 5 began to decline (switching point 68 or 145).

4 CONCLUSION

In this study, we tackled the reduction of computational complexity by pruning the *igo* game tree using the potential model based on the knowledge expression of *igo*. In our experiments, 5 kinds of pruning strategies (Potential Filters) were evaluated for their removal effect. Maintaining normal strength of Monte-Carlo *go*, Potential Filter 4 or 5, based on potential gradient distribution or homopolarity potential distribution, could reduce up to 18% of total Play Out numbers needed in one game. Potential gradient and homopolarity potential could identify important areas around black and white stones as well as close areas between black and white stones. In addition, combining Potential Filter 5 and Potential Filter 3 could reduce up to 23% of total Play Out numbers by switching Potential Filter 5 to Potential Filter 3 at the point where the strength of Potential Filter 5 began to decline (switching point 68 or 145). This shows the tendency of *igo* transition as the game progresses.

In this research we successfully demonstrated pruning using the potential model for reducing computational complexity of the *go* game. However, our experiments were limited as the Play Out number was set at 100 and the board size was set at 9 x 9 or 13 x 13. For our future research, we intend to expand the proposed strategy to tackle more complex games with larger Play Out numbers and *go* board size.

REFERENCES

[1] Brügmann B (1993), Monte Carlo *Go*. Physics Department, Syracuse University

[2] Zobrist AL (1969), A model of visual organization for the game of *GO*. AFIPS '69 (Spring) Proceedings of the May 14-16, 1969, spring joint computer conference, pp.103--112

[3] Nakamura K, Syuhei K, Analyzing Go Board Patterns Based on Numerical Features. IPSJ Journal (The Information Processing Society of Japan) 43, no. 10 (10 2002):3021-3029.

[4] Yajima T, Effect of Stone and Effect of Table. SIG Technical Reports, Surugadai, Kanda, Chiyoda: The Information Processing Society of Japan, 2009, pp. 41-46

[5] Burrough PA and McDonnell RA (1998), Principles of Geographical Information Systems, Oxford University Press, p.190

Table 2. Types of Potential Filters

Method	1	2	3	4	5
Ranking	Potential	Potential	Potential	Gradient	Potential
Black/White	+/−	+/−	+/−	+/−	+/+
Filtering	Low 50%	Top 50%	Above 25% and below 75%	Low 50%	Low 50%
Overhead	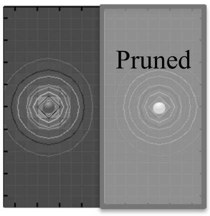	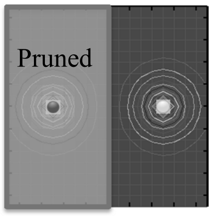	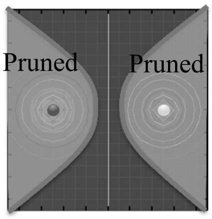	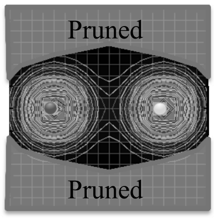	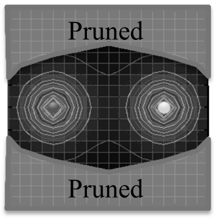
Landscape	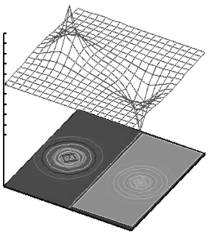	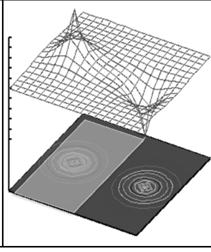	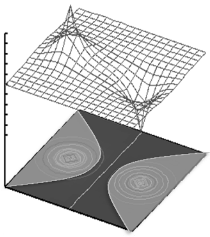	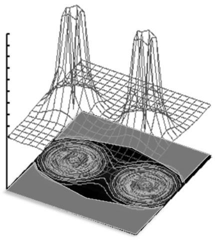	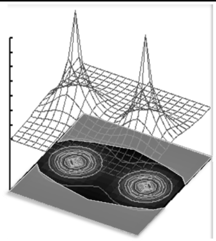

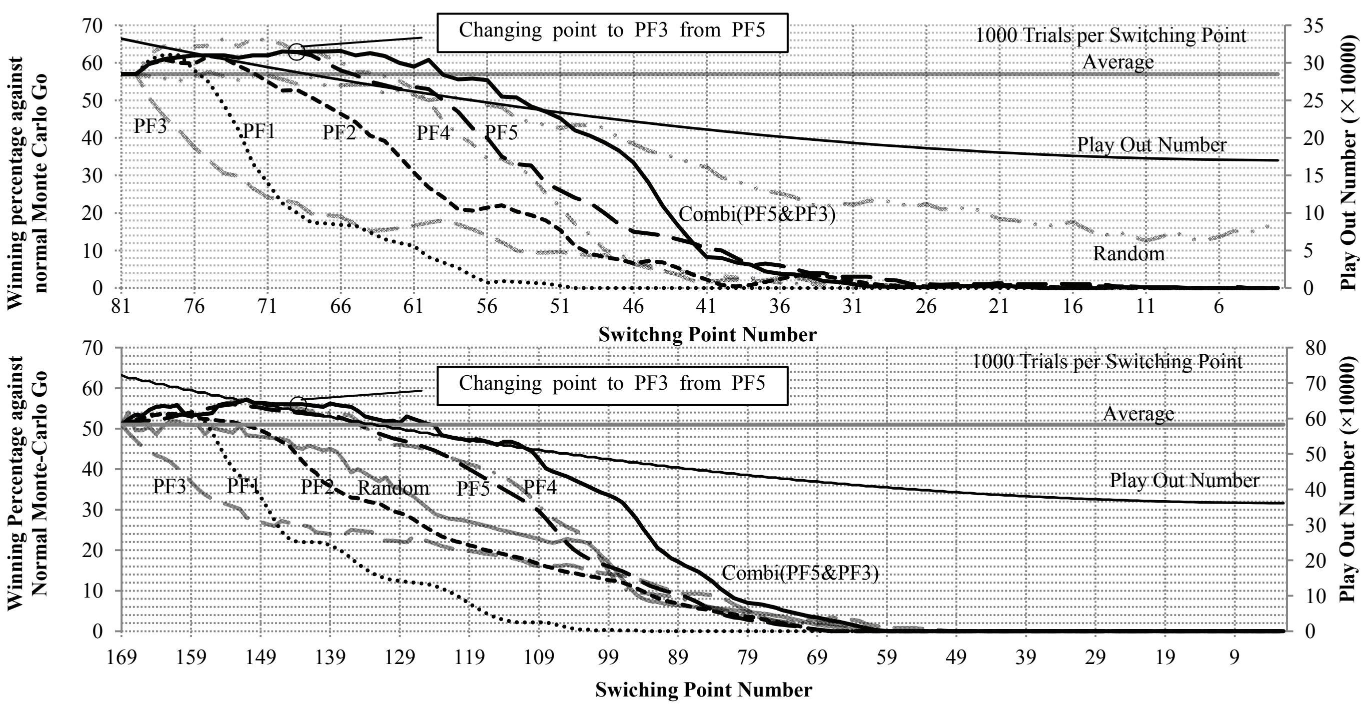

	9 x 9			13 x 13		
	Border	Play Out Number	Reduction Rate	Border	Play Out Number	Reduction Rate
Random	–	332000	00.0	–	722400	00.0
Potential Filter 1	77	316300	04.7	157	673200	06.8
Potential Filter 2	73	301400	09.2	152	649950	10.2
Potential Filter 3	–	332000	00.0	–	722400	00.0
Potential Filter 4	64	270800	18.4	135	592350	18.0
Potential Filter 5	64	270800	18.4	135	592350	18.0
Combination	59	255500	23.0	125	559600	22.5

Fig. 1. Strengths of Monte-Carlo *go* with Potential Filters

The Seventeenth International Symposium on Artificial Life and Robotics 2012 (AROB 17th '12),
B-Con Plaza, Beppu, Oita, Japan, January 19-21, 2012

Emergence of autocatalytic reaction in a meme propagation model based on particle motion

Kengo Kobayashi[1], Reiji Suzuki[1] and Takaya Arita[1]

[1] Graduate School of Information Science, Nagoya University
Furo-cho, Chikusa-ku, Nagoya 464-8601, Japan
Tel, Fax: +81-52-789-4258
kengo@alife.cs.is.nagoya-u.ac.jp

Abstract: Meme refers to a unit of human cultural transmission, analogous to gene in biological evolution. Meme propagation has an autocatalytic property in the sense that it increases its reproductive rate by duplicating the source of propagation. The purpose of this study is to gain general knowledge about dynamics of meme propagation. This paper presents a minimal model based on physical movement of particles for investigating the relationship between the behavior of the hosts (velocity of particles) and the autocatalytic property of the meme. It is demonstrated that two extreme memes, the fastest and the slowest ones, have a strong tendency to survive by autocatalytic properties at individual and aggregate levels, respectively, although all memes seem neutral in terms of fitness in the model definition.

Keywords: Agent-based model, Artificial life, Autocatalytic reaction, Meme

1 INTRODUCTION

Meme [1] refers to a unit of human cultural transmission, analogous to gene in biological evolution. A meme parasitizes a human brain and propagates from one brain to another mainly by imitation. For a meme to be successful, it has to have "fecundity", "longevity" and "accuracy of replication", which are recognized as the main components of the fitness of memes.

In principle, meme propagation has an autocatalytic property in the sense that it increases its reproductive rate by duplicating the source of propagation. When comparing it with chemical autocatalytic reactions, we see a big difference arising from the difference between duplication of materials and information. This autocatalytic property of memes will be more strengthened if the meme has a greater fecundity, in other words, a greater tendency to make the host behave for propagating the meme. Bura [2] successfully demonstrated that this type of autocatalytic process could evolve memes which are detrimental to their hosts. In his model MINIMEME, the interaction between the memes and the host animals are modeled, and the following autocatalytic phenomenon was found: memes provoked the gathering of their hosts, which led to a situation in which they reinforced each other and their replication was made easier. Thus, memes that kill their hosts by overcrowding could survive and even become dominant.

The purpose of this study is to gain general knowledge about dynamics of meme propagation. Specifically, this paper presents a minimal model based on physical movement of particles for investigating the relationship between the behavior of the hosts (velocity of particles) and the autocatalytic property of the meme. It is demonstrated that two extreme memes, the fastest and the slowest ones, have a strong tendency to survive by autocatalytic properties at individual and aggregate levels, respectively, although all memes seem neutral in terms of fitness in the model definition.

2 MODEL

Particles move around on a two-dimensional square field with boundaries in the model. Memes inhabit the particles and decide the velocity of the hosts. There are seven kinds of memes, each corresponding to a different velocity: "meme0", "meme1", ..., "meme6" in ascending order of velocity. Fig. 1 shows the relationship between an agent and memes. A meme is represented as an arrow of which length corresponds to its velocity. Each particle has four memes (allowing duplication of kinds), and moves forward with the velocity specified by one of these memes at each step. In-use meme is represented as a solid arrow and the others are represented as a dashed arrow in this figure. The velocity of each particle is switched according to a randomly selected meme from these four memes with a fixed probability at each time step. Each particle keeps its moving direction unless it switches its in-use meme or collides with other particles or boundaries.

Fig. 2 shows an example of meme transmission. Each particle has an interaction area represented as a circle (all particles have the same radius in this paper). While two interaction areas overlap, both particles send their in-use meme to the other at the same time at each step. When receiving a meme, a randomly chosen meme is replaced by the received meme. The thick and solid arrows represent the transmitted

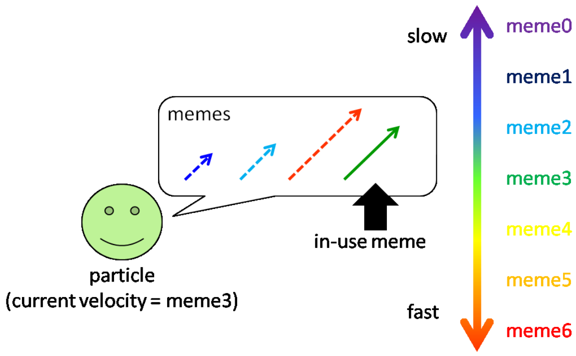

Fig. 1. Relationship between a particle and memes.

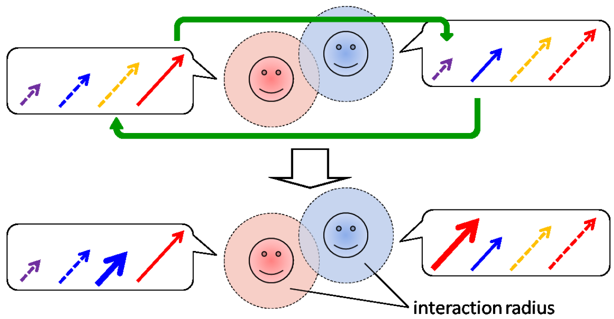

Fig. 2. Meme transmission.

Table 1. Parameters.

Size of field	510 × 510
Number of particles	100
Velocity of meme0	3
Velocity of meme1	6
Velocity of meme2	12
Velocity of meme3	24
Velocity of meme4	48
Velocity of meme5	96
Velocity of meme6	192
Particle radius	5.0
Interaction radius	[5.0, 7.0]

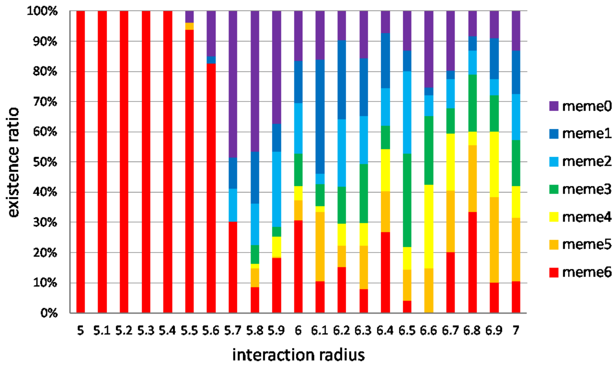

Fig. 3. Existence ratio after convergence.

memes in this figure. Therefore, through each meme transmission, the number of the in-use memes is increased by one unless they are replaced by the meme transmitted by the other particle or they replace the same meme of the other particle.

3 EXPERIMENTS

In the initial population of memes, we put particles at random in the field and allocated memes to each particle randomly. We ran the model until the time step reached 50,000. Table 1 shows the parameters to be used. We conducted experiments by changing the value of the interaction radius from 5.0 to 7.0.

Fig. 3 shows the existence ratio of each meme in the population during the last 100 time steps in the different cases of the interaction radius. Each value is the average over 10 trials.

We see that the behavior of the population is strongly dependent on the interaction radius. When the interaction radius was small, 5.4 or less, the population converged to the fastest meme (meme6) in all trials. As the interaction radius increased until around 5.7, the existence ratio of the slowest meme (meme0) increased, and thus the fastest and the slowest memes tended to coexist. As the interaction radius got larger, we observe that memes with intermediate velocity survived and tended to coexist but their ratio fluctuated significantly.

Fig. 4 shows examples of the transition of the number of memes in the population with three typical settings of interaction radius (a: 5.4, b: 5.6 and c: 6.0). In order to analyze the actual behavior of particles in each case, we visualized example snapshots of the model in Fig. 5. Particles are represented as small circles and their color represent their in-use meme.

In the case (a), the population was quickly dominated by the meme6, which had the highest velocity. When two particles interact, the in-use meme of a particle is guaranteed to overwrite one of four memes of the other particle. On the other hand, the probability that the in-use meme of a particle is overwritten by the in-use meme of the other particle is 1/4. Therefore, in general, in-use memes can replicate itself in the population by an interaction because of this asymmetric property in probability of meme propagation. In other words, the more a particle interacts, the more frequent opportunities it has to increase the ratio of its in-use meme. Therefore, whether memes increase or not is dependent on the frequency of the propagation of memes. If the interaction radius is small, memes with higher velocity can invade into the population because they enable particles to interact

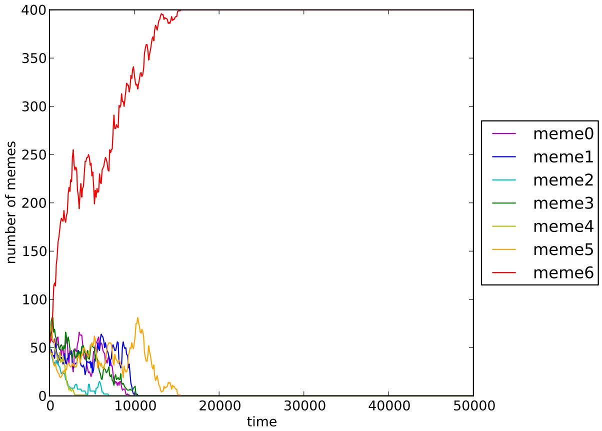

(a) Interaction radius: 5.4.

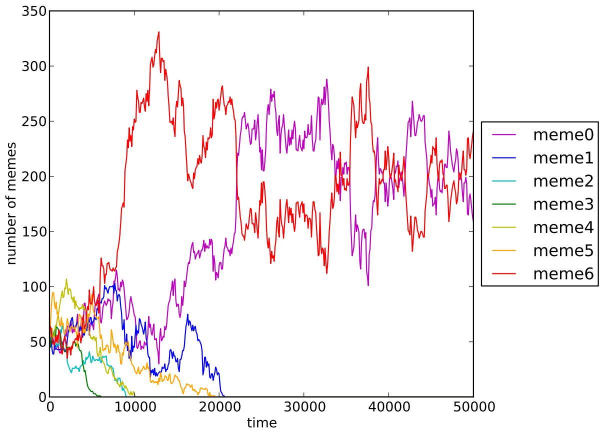

(b) Interaction radius: 5.6.

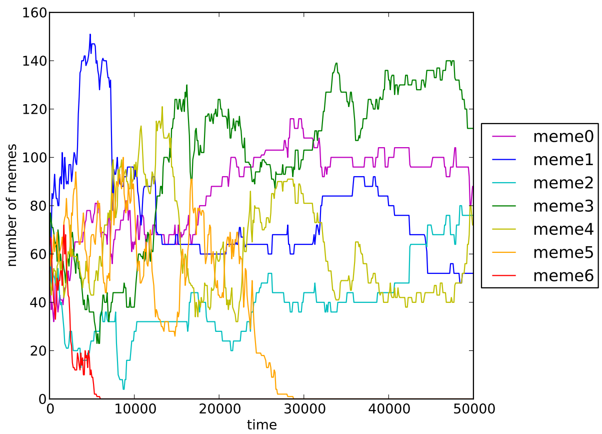

(c) Interaction radius: 6.0.

Fig. 4. Examples of the transition of the population.

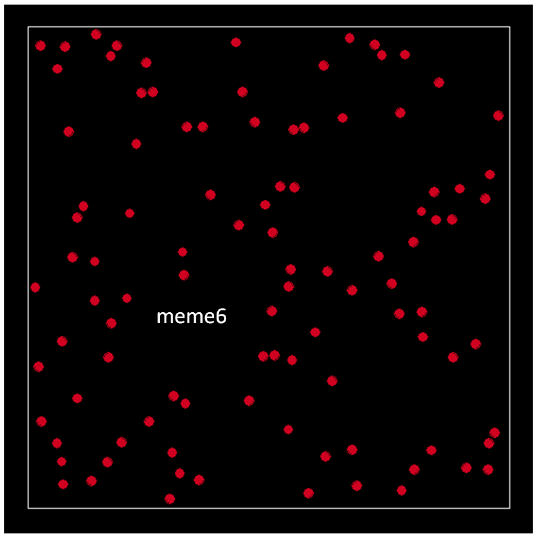

(a) Every particle has four meme6 (interaction radius: 5.4).

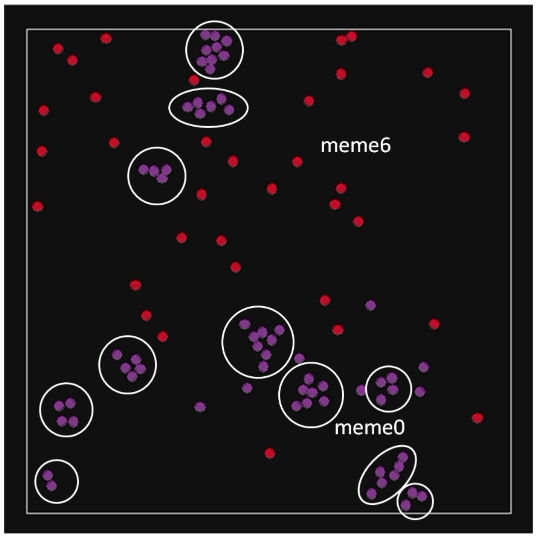

(b) Particles with meme0 gather in the moving particles with meme6 (interaction radius: 5.6).

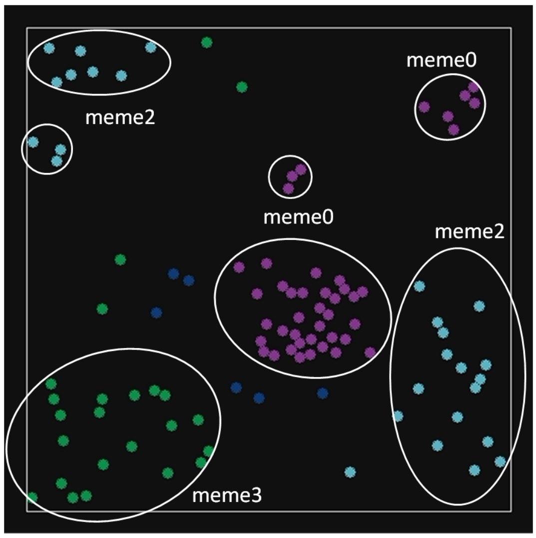

(c) Particles with each kind of meme gather (interaction radius: 6.0).

Fig. 5. Example snapshots of the population (almost every particle has one kind of meme).

with many other particles by moving around the field. Thus, we can say that meme6 is dominant due to this autocatalytic property at individual level.

In the case (b), the population converged to the state with meme0 and meme6. We can observe the clusters of the meme0 in Fig. 5(b). Note that the white and open circles in Fig. 5 represent the clusters of each meme. The detailed analyses of the behaviors of particles showed that the particles with the meme0 maintained their clusters by trapping incoming particles with the meme6, while they were scattering very slowly. Fig. 6 shows the transition of the proportion of interaction events when a particle received the same kind of meme as the one it sent to the other particle among events when a particle sent the focal kind of meme (the interaction radius = 5.6). Because the percentage of meme0 is large, we can say that the meme0 replicated and increased their frequency via interactions among particles in their clusters due to the larger interaction radius. This makes incoming particles into the clusters receive the meme0 very frequently, and thus they tend to become a part of the clusters. From these facts, despite meme0 has the lowest autocatalytic property at individual level, we can say that meme0 was dominant because of this autocatalytic property at aggregate level.

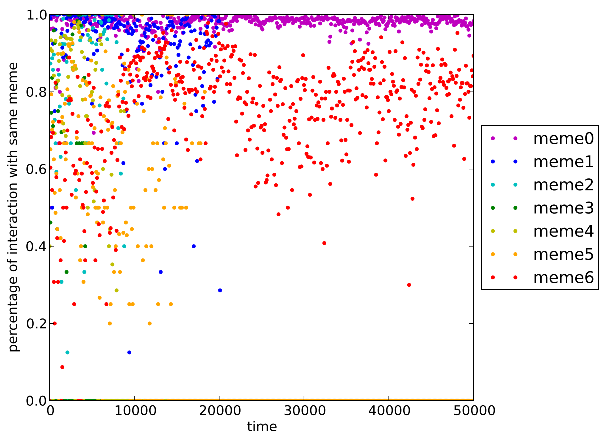

Fig. 6. Transition of the proportion of the interactions between the particles with the same kind of in-use memes.

However, as the interaction radius increased further, such as case (c), the population converged to the state with more kinds of memes as shown in this example. We did not observe dominant memes because of large variations in each trial within the limited number of the time step 50,000. It is expected to be due to the fact that the larger interaction radius makes effects of the difference in the velocity of memes on the behavior of particles less significant, by making interaction events frequent and global. Thus, we did not observe emergence of autocatalytic behaviors at both individual and aggregate level, which are based on the two extreme properties of memes.

4 CONCLUSION

We presented a minimal model based on physical movement of particles for investigating the relationship between the behavior of the hosts and the autocatalytic property of the meme. The simulation results showed that two types of autocatalytic processes could emerge at individual and aggregate levels, which evolve two extreme memes, the fastest and the slowest ones, respectively. It is a noticeable fact that the evolution was not based on the explicit fitness definition. If we consider the model describes religious propagation, the fastest meme and the slowest meme might correspond to a popular religion and a cult, respectively.

Our model assumes a direct relationship between a meme and the movement of its hosts. It would be interesting to associate the assumption with the recent experimental finding by Hommel et al. that religious practice can not only affect spatial and temporal characteristics of stimulus selection but also control processes devoted to action regulation [3].

Sayama is developing the Swarm Chemistry model [4], which is an artificial chemistry framework that can demonstrate self-organization of dynamic patterns of kinetically interacting heterogeneous particles. One of the promising directions would be to enhance our model towards Sayama's model to aim to make our model capable of open-ended evolution while keeping neutrality of memes in terms of fitness in the model definition.

REFERENCES

[1] Dawkins, R. (1976), *The selfish gene.* Oxford University Press.

[2] Bura, S. (1994), MINIMEME: Of Life and Death in the Noosphere. *From Animals to Animats* 3:479-486.

[3] Hommel, B. *et al.* (2011), Religion and action control: Faith-specific modulation of the Simon effect but not Stop-Signal performance. *Cognition* 120(2):177-185.

[4] Sayama, H. (2011), Robust Morphogenesis of Robotic Swarms. *Computational Intelligence Magazine* 5(3):43-49.

The Seventeenth International Symposium on Artificial Life and Robotics 2012 (AROB 17th '12),
B-Con Plaza, Beppu, Oita, Japan, January 19-21, 2012

Pre-historical multiple movements of modern humans from Old World to Americas: Evidence based on comparing basic body part-name words with Austronesian

Koji Ohnishi[1,2]

[1]Faculty of Science, Niigata University, Niigata 950-2181, Japan
(Tel: 81-25-262-5237, Fax: 81-25-262-5237)
[1]ohnishi@bio.sc.niigata-u.ac.jp

Abstract: Basic body-part name vocabulary of representative Native American languages (NAmLs) and Eurasian languages was compared with ca. 1300 Austronesian (AN) basic words and with basic words of Eurasian languages. By applying closest similarity analysis of occurring frequencies of thus found AN cognates (of non-AN vocabulary) in subgroups of AN, NAmLs are concluded to have been derived from various branches of AN family, by human movements not only via Behring land-bridge but also via trans-Pacific sailing rout (as represented by Maipuran language in Amazonian area). Such independent human movements to Americas are concluded to be much more frequent than has been generally considered.

Keywords: basic Austronesian origins, body-part names, closest similarity analysis, trans-Pacific movement to America

1 INTRODUCTION

Origins of Native American languages (NAmLs) and peoples are generally considered to be yet unknown [1]. However, most of representative language families/groups in Eurasia have been strongly suggested by Ohnishi [2,3,4] to share many cognate basic words with Austronesian (AN) language (Lg) family, and therefore, seem to have been derived from AN Lgs. This paper aims to find multiple origins of NAmLs by basic word comparison, and present a new classification of modern human Lgs.

2 METHODS, RESULTS AND CONCLUTION

Basic body-part name words (BBP) (for 30 ~ 32 word items) in Swadesh' 200 basic words (SW200W) (See Ref. YH* in Table 1) or body part names (BP) of representative NAmLs were extensively compared with vocabulary of Eurasian and Pacific Lgs, especially with ca. 1,300 AN basic words listed in "Comparative Austronesian Dictionary (CAD*)" (See CAD* in Table 1). CAD* lists basic vocabulary for 80 AN Lgs consisted of 4 Formosan (FORM), 26 Western Malayo-Polynesian (W.MP), 6 Central MP (C.MP), 2 South Halmahera-West New Guinean (SHWNG), and 41 Oceanic (OC) Lgs, as is given in the uppermost lines in Table 3.

The 30~32 meanings of BBPs in Sw200W are as follows:

(i) [in Swadesh basic 100 words (Sw100W)] 25 ~ 26 word-meanings: belly (or bowels), blood, bone, breast(s), (egg), ear, eye, fat (or grease), feather, foot, hair, hand, head, heart, horn, knee, liver, meat (or flesh), mouth, neck, nose, saliva (or spit), skin, tail, tongue, tooth.

(ii) [in Sw200W other than Sw100W] 5~6 word-meanings: arm, back, (breath, to breathe), leg, lip, wing

When two or more different words have the same meaning of a Swadesh basic word, AN and Eurasian cognates of the two or more words were also searched and analyzed. Cognates having different meanings, whether ancestral meanings or derived/converted meanings, were also considered to be cognates of the (B)BPs. Searching such cognates having converted meanings is very important in increasing sensitivity of finding distantly relationship between different language families.

Closest similarity analysis (CSA): Based on thus found AN cognates of vocabulary in NAmLs and Eurasian Lgs listed in Table 2, every basic word item of non-AN Lg(s) (or Lg groups) were analyzed by CSA described in Ohnishi [6]. CSA determines the AN subgroup (in the above five) to which the morphologically most similar AN cognate word belongs. Cognates having different meanings, whether ancestral meanings or derived meanings, were also considered to be cognates of (B)BPs. Thus found cognates of BBPs or BPs, or of general (basic) words are listed in Table 2, as classified by most similar subgroup out of the five AN language groups. When two or more different basic words have the same meaning of a Swadesh basic words, cognates of the two or more words were also searched and analyzed. After such detailed analyses, occurring frequencies of most similar cognates of ca.30 BBPs in the 5 AN subgroups were counted and listed in Table 3, and statistically tested (by χ^2-test, as described in [5]) for finding an AN subgroup which is most closely kin to the "query" language (e.g. Quechuan, Yahgan, Mongolic, etc.) ?". Results of χ^2-test are indicated in Table 3 by #, +, ++, *, and **, for significant levels $P < 0.1$, < 0.05, < 0.025, < 0.01, and < 0.005, respectively.

Table 1: Abbreviations used in Table 2 and Table 3.

§ **General:** A < B, B > A: "A has/had been derived from B"; A < > B: "A is genetically (phylogenetically) related to B" (= "A cognates with B") ; A << B, B >> A: "A has/had been borrowed from B"., pX = protoX (e.g., pJp = proto-Japanese); dial. = dialect, N.=North(ern), S.=South(ern),E.= East(ern),W.=West(ern),C.= Central, wr.=Written, mid./Mid.=Middle, mod=Modern, BP=body part names, BBP=basic BP

§ **Language names:** **AN** = Austronesian, FORM= Formosan, MP=Malayo-Polynesian, W.MP= Western MP {PHIL= Philippines, SND= Sundic (Minang.= Minangkabau, IndoN= Indonesian), SLW=Sulawesi },C.MP=Central MP, SHWNG= S.Halmahera and W.New Guinea), OC = Oceanic {ADM= Admiralties, W.OC = Western OC, S.E.Solom.= S.E.Solomons, ReOC= Remote OC {MicN= Micronesian, NCal= New Caledonian, Vanu.= Vanuatu, C.Pacif.= C.Pacific (Fiji.= Fijian), PolyN= Polynesian} ▌**Eurasia:** Jpn, Jp = Japanese {O.Jpn = Old Jpn., Ml.Jpn = Mainland Jpn, RYU=Ryukyuan (Hate.= Hateruma dial.)}; KOR= Korean, Chin.= Chinese, TNG= Tungus {Manchu.= (Literaly) Manchurian.}, MNG = Mongolic, Mong.= Mongolian, TbB= Tibeto-Burman {Tb= Tibetan}, DRAV = Dravidian, URA = Uralic { Finn.= Finnish, Hung.= Hungarian, FU= Finno-Ugric},ChukKam= Chukchee- Kamchatkhan}, IE = Indo-European {Skr. = Sanskrit}, Yns = Yeniseian ▌**Nat.AmL** = Native American Languages: Esk = Eskimo, KoaAla. = Koasati-Alabaman, Comec.= Comecrudo, MxZq= Mixe-Zoquean (Mx= Mixean, Zq= Zoquean), Maip= Maipuran, Que. = Quechua(n)

§ **References:** ADD*= Hattori, S. (1964) *Ainu Dialect Dictionary*, Iwanami Shoten, Tokyo. ▌Bene*72 = Benedict, P.K. (1972) Sino-Tibetan. A Conspectus, Cambridge Univ. Press,Cambridge, U.K. ▌Brick*= Bricker,V. et al. (1998) A Dctionary of the Maya Language as spoken in Hocabá, Yucatan. Univ. of Utah Press, Salt Lake City. ▌Brinton*= Brinton, D.G (1892) Proc. Amer. Philos. Soc. 30: 83-90. ▌CAD*= Tryon, D.T.(1995) *Comparative Austronesian Dictionary Parts 1-4*, Mouton de Gruyter, Berlin/New York. ▌CED*= Fortesque, M. *et al.* (1994) *Comparative Eskimo Dictionary*, Alaska Native Language Center, Fairbanks. ▌DAlaL*= Sylestine, C. et al. (993) *Dictionary of the Alabama Language*.Univ. Texas Press, Austin. ▌DED*= Burrow, T. and Emeneau, M.B. (1984) Dravidian Etymological Dictionary, 2nd ed., larendon Press, Oxford. ▌DMaoL*= Williams, H.W. (1978) *Dictionary of the Maori Language, 7th ed.* (Reprinted, Wellington, 1992) ▌DQEQ* = *Diccionario Quechua-Español-Quechua, Simi Taqe.* Qosqo, 1995. ▌DTrkL*= Öztopçu, K. et al. (1996) Dictionary of the Turkic Languages, Routledge, London /New York. ▌EDAL*= Starostin, S. *et al.* (2003) *Etymol. Dict. of the Altaic Languages*, Brill, Leiden-Boston. ▌GrCoc*= Faust, M.(2008) *Gramatica Cocama, Tercera ed.,* Instituto Lingüistico de Verano, Lima. ▌Hashi*76= Hashimoto, M. (1976) The Wênch'ang dialect of the Hainan Language (In Japanese), *Journal of Asian and African Studies* 11:65-86. ▌Hofl*= Hofling, C.A.(1997) *Itzaj Maya-Spanish-English Dictionary*, Univ. of Utah Press, Salt Lake City. ▌IKJ*= Ohno, S. (1990) *Iwanami Kogo Jiten, Zoutei-ban.* Iwanami-Shoten, Tokyo. ▌Kawachi* = Kawachi, Y. (1996) M*ansyu-go Bungo Bunten* (In Jpn.), Kyoto Univ. Press, Kyoto. ▌KoaD*= Kimball, G.D.(1994) *Koasati Dictionary*, Univ. of Nebraska Press, Lincoln & London. ▌Kauf*= Kaufman, T.(2003) Introduction to "A Ppreliminary Mayan Etymological Dictionary", FAMSI. (http://www.famsi.org/reports/01051/ index.html) ▌LAm*= Greenberg, J.H. (1987) Lqanguages in Americas, Stanford Univ.Press, Stanford. ▌MTFNT-App* = Appendix in Ogawa (1935) *The Mytths and Traditions of the Native Tribes (Texts and Notes)* (In Japanese), Inst. of Linguistics, Taihoku Imperial University, Taipei. (2nd printing in 1996) ▌OrL*= Ruhren, M. (1994) Origin of Language, Stanford Univ. Press, Stanford. ▌Ozawa*94= Ozawa, S. (1994) Gendai Mongoru-go Jiten, Daigaku-Shorin , Revised and Enlarged ed., Tokyo. ▌Payne*91= Payne, D.L. (1991) A classification of Maipuran (Arawakan) languages Based on Sharedlexical retentions. pp.355-499, In: Delbyshire,D.C. and Pullum, G.K. (eds.) *Handbook of Amazonian Languages, Vol. 3*, Mouton de Gruyter, Berlin/New York. ▌RHJ*=Nakamatsu, T.(1987) Ryukyuu Hogen Jiten (The Dictionary of the Ryukyu Language),Naha Shuppan-sha, Hayebaru-chou (Okinawa). ▌Schu* =Schuessler, A.(2007): ABC Etymol. Doict. of Old Chinese. Univ. of Hawai'i Press, Honolulu. ▌Swad*54 = Swadesh, M. (1954) *Word* 10: 306-332. ▌SwadLfTp*= Swadesh lists for the Tupi-Guarani languages, Tupinamba and Modern Guarani.(http://www.geocities.jp/ikoh12/honnronn5/00503/AppendixSwadesh-Wiktionary.htm) ▌Swan*40=Swanton,J.R.(1940): Linguistic Material from the Tribes of Southern Texas and Northeastern Mexoco. *Smithonian Institution Bureau of American ethnology Bulltin 127*. Washington. ▌Tam* = Tamura, S.(1996) *The Ainu-Japanese Dictionary. Saru dialect (English by I.R.L.McDonnel)* (In Japanese), Sofukan, Tokyo. ▌UEW* = Redéi, K. (1991) *Uralisches etymologisches Wöterbuch I-III,* Harrassowitz, Wiesbaden. ▌Wat*= Watkins, C. (2000) *The American Heritage Dictionary of Indo-European Roots*, 2nd ed., Houghton Mifflin Co., Boston/New York. ▌Witch*= Witchmann (1995) The Relationship among the Mixe-Zoquean Languages in Mexico. Univ.of Utah Press, Salt Lake City. ▌YH* = Yasumoto,B. and Honda,M. (1978) *Nihongo no Tan'jyou* (The Birth of the Japanese Language), Taishukan Shoten, Tokyo.

Conclusion: From Table 3, we conclude that: (1) Native American and Eurasian Lgs and language families listed here are have been derived directly or indirectly from various branches of AN Lg family. (2) Maipuran has derived from Maori, via ancient trans-Pacific sailing to South America (See "Hah-Vah-Ee-Kay" (=Hawaikii) story in [6] (Jpn. trnsl. ed. p.163, p.515) and [2], p.115.). (3) Comecrudo, Aymara, Yamanan, and Mixe-Zoquean are also (directly or indirectly) of OC-origin, some of which might have moved via trans-Pacific rout. (4) Koasati-Alabaman is Philippines-derived. (5) Multiple movements to Americas are evident. (6) Further details will be published elsewhere.

REFERENCES

[1] Campbell L (1997), *American Indian Languages*, Oxford University Press, Oxford/New York.

[2] Ohnishi K(1999), *Evolution of Mongoloid Languages. Macrocomparative and etymological analyses.* Shokado, Kyoto,(http://www.nacos.com/shokado/Site01/mokuroku09 1203.pdf).

[3] Ohnishi K (2009), Sound-correspondence laws of word-initial consonants between proto-Indo-European and Austronesian languages. *Artif. Life Robotics* 14(4):567- 573.

[4] Ohnishi K (2009), Origin of the word-initial consonant system of the Japanese-Ryukyuan (JR) language from Oceanic constant system: Elucidation by JR-Oceanic consonant-corresponding laws. *Artif. Life Robotics* 14(4): 545-550.

[5] Ohnishi, K (2012), Origin of the Chukchee-Kamchatkan language family from the Paiwan language in Formosa. In: *These Proceedings*.

[6] Underwood,P (1993): *The Walking People: A Native American Oral History*,TheLearningWayCo.(See [2],p.115)

Table 2. Most similar Austronesian cognates (in CAD*) of basic words in Native American and Eurasian languages.

§§ **Mayan-FORM** (Mayan data from: Swad*54, Kauf*, Hofl*,Brick*) ▌# BONE: pMaya **b'aaq (= bak)* / Yuc. *bak*, /Hocabá *b'àak* /Itzaj *b'aq* (< **βaq*) ||| **FORM: Atayal** *βaqniʔ* "bone" (< **βaq-niʔ* < **baq-*) ▌# FOOT/LEG: Yuc. *ok* "foot, leg" (< **ʔok(o)* < **ʔoko* "foot" < **kokoˀ* "leg ~ foot" < > FORM: *ʔoʔoʔ, kokoˀ* "leg ~ foot") ||| **FORM: Ami** (dialects: 馬蘭社, 奇密社) *ʔoʔoʔ* /(dialect: 荳蘭社) *kokoˀ* "leg ~ foot" (< proto-Ami **kokoˀ*) (From MTFNT-App*, p.6) || W.MP: Gorontaro *ʔoʔoato* "foot" (< *ʔoʔo-ato < *ʔoʔo- "leg ~ foot") ▌# HAND: pMaya **q'ab' (= qab)* /Yuc. *k'ab' (< *qhabh- ~ *ghabh- < *qabh- ~ *qaβ-)* ||| **FORM: Atayal** *qaβaʔ* "arm" || OC: (S.E.Solomons) Lau *ʔab* "hand, arm", (C.Pacif.) Rotuman *ʔu-hapa* "hand" (< **-hapa* < **qaba*) ||| URA: pFV **käppä* /Finnish *käppä* /Estonian *käpp* "hand, paw"; Mordvin *kepe, käpä*, "barfuss" ||| IE: pIE **ghabh-* "to give, to receive, to seize" (< MP: **qab-*) ||| Quechuan: Que. *ccapa* "hand" (= *k'apa* < **qaba* "hand") █ §§ **Eskimo-FORM :** (CED*) ▌# EYE: pEsk **əðə* "eye" (< *əði- < **edɨ* < > AN: **edɨ* "to find"), (AAY= Alutiiq Alaskan Yupik)(CAY= C. Siberian Y.) *ii* /(CAY) *iya* /(Sirenik) *aca* /(NAI= North Alaskan Inuit) *iži* /(WCI= W.Canadian Inu.) (ECI= E.CI) *iyi* /(GRI= Greenlandic Inu.) *iši* "eye" (< *iðə < *ida ?) ; pEsk **əðəkə-* "to watch" (< **əðə-kə-*). ||| **FORM: Tsou** *edɨ* "to find" (< **idu*) ▌# FAT /GREASE: pEsk **qalunəq ~ *qaluniq* "grease floating on stew" (< **qalu-niq* < **qalu-* "grease, fat"), (ECI) q*aluniq* "melting grease floating on meat stew", (GRI) *qaluniq* "fat, lard" ||| **FORM: Paiwan** *ḳaḷum* (= *qaḷum*) "grease,fat" ▌# NECK: Eskimo-Aleut: (Esk) pEsk **uya* "non-anatomical neck" || Aleut **uyu-X* "neck" (*uyu-* < > AN: *uɥun* "backbone of neck"), *uyaʀ-* "sprout, muzzle, neck of bottle" (< **uyuaʀ-* < **uyu-aʀ-* "thing resembling neck" < **uyu-* "neck" + pEsk **-aʀ-* (postbase) "thing resembling something") ||| **FORM: Paiwan** *uɥun* "backbone of neck" (< **uyu-n* < > Aleut *uyu-X* "neck" /Aleut *uyaʀ* "neck of bottle" (< **uyu-aʀ*) █ §§ **Mongolic (MNG)**: (EDAL*, Ozawa*94, YH*) ▌▌§ **MNG-FORM** ▌# FOOT: wr. Mong. *köl* /mid. Mong. *kul* /Buryat *xül* /Dagur *kul* "foot" (< pMNG **kul-*) ||| FORM: **Paiwan** *kuḷa* "foot" || W.MP: **(SND) Madurese** *čiŋkul (< *čiŋ-kul) //*(SLW) Konjo *'siŋkulu* "elbow" (< **-kulu* "arm") ; Konjo *kulantuʔ* "knee" ▌# HAIR: pMNG **hüsü ~ *füsü* /wr.Mong. *üsü* /mid.MNG *xüsun* /Mongor *fuʒə* "hair" (< **fʔusü*) ||| FORM: Tsou *fʔisɨ* (dialects: *fuʔusʉ, fʉʔʉsʉ*) "hair" (< **fuʔu-si* < **fulu-si* "hair, feather" < **bulu-siw ~ *buu(n)* < **bulu* "hair, feather" ~ **buun, *buuk* "hair (of head)" + **siwi* "feather, bird") || OC: Dami *siwi* "feather" ||| Note: W.MP: (SND) Madurese, Balinese *bulu* "feather", (PHIL) Kalinga Limos *buʔūk* /Aklanon b*uhuk* /Kagayanen *buuk* /Bangingi Sama *buʔun* "hair (of head)" ▌# SKIN/ BARK: **Wr.Mong.** *qalisu* "bark, skin" (< **qaLi-su*) ||| FORM: **Paiwan** *ḳaḷʸi¢(= *qaḷʸiC*) /Atayal *ḳaɬiʔ* (< pAN **qaLiC* "bark, skin") ▌▌§ **MNG-Sundic (SND):** ▌# NECK: wr.Mong. *küǰüdgü* /modern Mong. *kudu* (< **kudu(d)-gü ~ *kudu-dgü*) ||| AN: **(SND) Minangkabau** *kuduᵊʔ* "neck" █ §§ **Quechuan-W.MP (PHIL/ SND):** (DQEQ*) ▌# BONE: Cuzco Que. *tullu* "bone, stem of plants" (< W.MP: **tulu-*)||| W.MP: **(SND) Aceh** *tuluəŋ* /Sundanese *tulaŋ* //(PHIL) Kalinga Limos *tulʔaŋ* (< **tulu-aŋ*) ▌# MOUTH: Cuzco Que. *simi* "mouth, language, word" (< **simi ~ *sim-i* "mouth ~ beak") ||| W.MP: **(PHIL) Isnag** *simtu* "beak" (< **sim-tu*) ▌# NAIL:Cuzco Que. sillu || Aymara *sillu* ||| W.MP: **(PHIL) Kagayanen** *sulu* (< **silu* ?) ▌# EYE: Cuzco Que. *ñawi* "eye" (< **njə-ɯ-i* < **niəŋ* "to see" + **ɯ- ~ *u-* "to see" + *-i (nominal suffix)) ||| W.MP: **(SND) Aceh** *niəŋ* "to see", *ɯ-* "to see" █ §§ **Na-Dene-W.MP(PHIL, SND):** **(OrL*)** ▌# SKIN: Haida *q'ał* "skin" || Ath.: Sarsi *-kàł* "hide" ||| **FORM: Paiwan** *ḳaḷʸi¢* (= *qaḷʸiC*) "skin" ▌# GUTS: Haida *qasan-ts'ang* "brains" (= "head-guts") (*ts'ang* < **tsiaŋ ~ *tsian < *tian* "stomach, guts") || Athabaskan.: Sarsi *čá(n)* "guts"/ Inglik *-čání* "guts" (< **čán-(í)* < **tsiʸan* < **tiyan*) ||| **W.MP:** (PHIL)Tagalog, Aklanon tiyan //**(SND) Sasak** tian "stomach" ▌# FEATHER: Haida *taw* "feather" || Athabaskan: Tlingit *t'áw* "feather, leaf" ||| W.MP: **(SLW) Wolio** *tawa* / Da'a *tava* "leaf" █ §§ **Yeniseian(Yns)-W.MP** (OrL*) #HEART: pYns **pu-* /Ket *hū* /Yug *fu* /Pumpokol *pfu* ||| W.MP: **(Borneo) Malagasi Merina** *fu* "heart" ||| TbB: **pu-k* "cave, belly", Kabui, Meithei *puk* /Lepcha *tafuk* (*-fuk* < **phu-k*) "belly", Lushei *pu-k* "cave" ▌# MEAT: pYns **īči ~ *īši* / Ket *īś* /Yug *īs* /**Kott** *īči* /Arin *is* "meat" ||| W.MP: **(SND) Bali** *isi* //**(PHIL) Bangingi Sama** *isi* /Yami aṣiṣi "flesh" (< pAN **Sisi* "meat) ▌# TAIL: Ket *hūt* /Yug *fūt* (< **pūt* < > W.MP: Isnag *īput* ~ Konjo *poti* ?) ||| W.MP: **(PHIL) Isnag** *īput* /Palawan, Molbog *iput* (< **īput* < **ii-put* ?, where *ii- < > OC: Kwaio *ʔiʔi-na* "tail") ; **(SLW) ?Konjo** *poti* (< **puti* ?) █ §§ **Koasati-Alabaman-PHIL:** (KoaD*, DAlaL*) ▌# BLOOD: Koasati,Alabama *łakhaní* (<**daga-ní* < pAN **daRaq*) "blood" ||| W.MP: **(PHIL) Isnag** *dāga* /Molbog *daha* /**Bangingi Sama** *lahaʔ* //(Sundic) Aceh, Miinangkabau *darah* "blood" < pAN **dáRaq* "blood" ||| JR: Ml.Jpn *aka* "redness" (< **raga* < **daRaq*) ▌# EYE: Koasati,Alabama *ittili* "eye" ||| W.MP: **(PHIL) Sarangani Blaan** *m-iti* **"**to see" ▌# to SAY: Koasati *mán-kan* "to tell someone something", Alabama *man-ka* "to say, to ask" (< *man- "to say") ||| **W.MP: (PHIL) Sarangani Blaan** *man* "to say", Yami *maniẓəŋ* "to speak, to talk" █ §§ **Tungus(TNG)-PHIL:** (EDAL*, YH*,Kawachi*) ▌# ARM: Literaly Manchu. *mayan* "arm" (< **may-* "to take" + -an) ||| W.MP: **(PHIL) Palawan** maya /**Kagayanen** *may* "to have" (= existential marker, "there is/are") ▌# BREAST: Lit. Manchu. *tuŋgen* "breast" (< **tuŋ-gen*) ||| W.MP: (PHIL) **Bangingi Sama** *tuŋay duduʔ* "nipple" ▌# to HEAR: pTNG **dōldī-* /Evenki *dōldī-* /Orok *dool-ǰi, dōlʒi* "to hear" (< **dool-dī-* < **doʔol-* < (W.MP: PHIL) **doŋol* "to hear") ||| W.MP: **(PHIL) Kagayanan** *doŋol* /Molbog, Murut *doŋog* "to hear" || OC: (W.OC) Manam *loŋo* /Takia *-loŋ* / Buang *ŋo*, (MicN) Woleaian *ṛoŋoṛoŋo* (< **ṛoŋo* < **loŋo< *doŋo*) "to hear" ||| Ainu: *nu* "to hear" (< OC:**ŋo* < **oŋo* < **loŋo* "to hear") █ §§ **Tupi:** (SwadLfTp*,GrCoc*) ▌▌§ **Tupi-TbB:** ▌# BLOOD (sangre): Coc. (= Cocama) *tsuɨ* / Guarani *tugui, tuguy* (= *tuwi* ?) /Tupinamba *ugûy(-t)* (< **tsuwi* < **šuwi ~ *šui* "blood") ||| TbB: **(W.Himal.) Bunan, Thedor** šui /Tinan sui /Manchad ši (< *šui) ||| Note: Possibly further cognates with; (TbB) wr.Burmese. *swêi²* /Spoken Burmese *θwêi* "blood". ▌# HEAD (cabeza): Coc. *yaquɨ* (= *yakɨ*), *yaquicuara* "head" ||| **TbB: Lepcha** *(a-)yăk* "top" ▌# WATER (agua): Coc. *uni* "water" ||| **Arawakan: Culimo** *unin* "river" ||| **TbB: Lepcha** *un̊* (= *uŋ*) "water" ▌▌§ **Tupi-SND** ▌#to COME (venir): Coc. *uri* "to come" (< **uliʔ* "to come back") ||| W.MP: **(PHIL) Molbog** *uliʔ* /Kalinga Limos ulin "to come

Table 2. (Continued.)

back" || C.MP: Buru *oli* "to come back" (< **uliʔ*) ▌# TREE (arbol): Coc. *ɨhuɨra* (= *ɨwɨra*) "tree" (< **lɨwɨ-ra*) ||| W.MP: **(SND) Sundanese** *lɨwɨŋ* "woods, forest" ■ §§ **Tibeto-Burman (TbB)-SND:** (Bene*72) ▌# BONE: pTbB:**rus* /Written Tibetan (= Tb) *rus ba*, *ruiba* /Lushai *ruʔ* /Tiddim *gùʔ* (< pTbB: *Rus ~ *grus) ||| W.MP: **(SND) Aceh** *rusoʔ* /Batak Toba *rusuk* //(PHIL) Kagayanen *gusuk* "rib" (< pMP **Rusuk* "rib" = **grusuk*) ▌# LEG: pTbB: **kaŋ* "leg" ||| W.MP: **(SND) Sasak** (Teewi dial.) pi-kaŋ, pu-kaŋ "thigh" ▌# MEAT: (W.Him.) Rampa *sya* /Thebor *sa* // Tb *sa* (< **sya*), pTbB **sya-n* ||| W.MP: **(SND) Aceh** *siə* ■ §§ **Aymara-OC:** (LAm*) ▌#TOOTH: Aym. *k'achi* "tooth"(< **gadi* "to bite") ||| OC: **(W.OC) Kilivila** *-gadi* "to bite", Cf. Takia *kasi-n* "gums" ||| Jpn: *kadi-ru* "to gnaw" ▌# NOSE: Aym. *nasa* "nose" (< **ŋasa* "good smelling") ||| OC: (MicN) Woleaian *ŋasa* "fragrant, good smelling" ▌# WATER: Aym. *uma* "water" ||| OC: (MicN) Woleaian *umak* "river" ■ §§ **Yamanan-OC:** (LAm*, Swad*54, Brinton*) ▌# HEAD: Yamana *lamina* (< **lami-na* < **lami-* "hair of head" + **-na* "nominal suffix") ||| OC: **(Admiralties) Nyindrou** *lami-n* "hair (of head)" ▌# ARM: Yamana *kamayn* (< **kamay-n*) ||| OC: **(W.OC) Maringe** *k^hame* "arm, hand" ▌# EYE: Yamana *tela* /Alakaluf *tel* /Ona tel /Mataco *te* "eye" (< **te(-la)* "eye" < **te* "to see") ||| OC: **(W.OC) Manam** *te* //**(NCal) Xaracuu** *tē* "to see" || C.MP: Ngada *tei* "to see" ■ §§ **Comecrudo** (Comec)**-Oceanic (Remote Oceanic) :** (Swan*) ▌# EYE: Comec. *u-i* (Swan*), *huy* (Swad*54) "eye" (< **(h)u-i* < **hu-ʔi*) ||| OC: **(PolyN) Rapanui** *uʔi* "to look, to look at" (< *ʔuʔi ~ *huʔi) ▌# FAECES: Comec. *kalet* ||| OC: **(NCal) Nengone** *kalet* ▌# SALIVA: Comec. *xatetis, xatatis* "saliva" (< **kate-tis* ~ **kata-tis*) ||| OC: **(C.Pacif.) West. Fijian** *katahiβi* "to spit" (< **kata-hiβi*) ■ §§ **Ainu-OC:** (ADD*) ▌# BELLY: Ainu: *hon* "belly" ||| OC: **(NCal) Nemi** *hōna* "intestines, guts" ▌# FAT (noun): Ainu Hokkaido *kírpu* / Sakhalin. *kirupu* "fat" (< **kir(u)-pu* < **kir(u)-* < **giru-*) ||| OC: **(W.OC) Dami** *gigiru* "grease, fat" (< **gi-giru* < **giru*) ||| Korean: mid. Korean *kirŭm* "fat" (YH*) (< **kirŭ-m* < **giru-*) ▌# HEART: Ainu *sanpé* "heart" (< **san-pe* < *san* "to go out" + Ainu *pe* "thing". From Tam*); *san* "to go downstream, to flow, to go from the inside of a house towards hearth" (Tam*) (< **san* "to go out ?") ||| OC: **(W.OC) Yabem** *-sa* "to go out" || SHWNG: Irarutu *ɸe* "thing" (< **pe*) ■ §§ **Proto-Indo-European** (pIE)**-OC:** (Wat*) ▌# to BREATHE: pIE **H_2enH_1-* (= **$henH_1$-* , or else, < **$henH_1$-*) "to breathe" (> pIE **H_2anH_1-*) (< > OC: **haŋ(u)* "to breathe") ; Middle Welsh *eneit* "soul" ||| OC:(S.Vanu.)**Kwamera** *-eiahaŋ* "to breathe" (< **-eia-haŋ*), (PolyN) **Rapanui** *haŋu-haŋu* "to breathe" (< **haŋu*) ▌# EYE: pIE **H_3ek^w-* /Sanskrit *ákṣi* "eye" (< pIE **H_3ak^wasi* < MP: **ʔagasi*), Old Norse *auga* /English eye /Armenian *akn* /Tocharian A *ak* "eye" (Pok*, pp.775-777) ||| OC: **(S.E.Solomons) Kwaio** *agasi* "eye" (< > pIE **H_3ak^wasi* "eye"), *agasi-a* "to see" ▌# HEAD: pIE **kaput* "head" (< **kapu-* ?), (> Eng. *head*) ||| OC: **(S.Vanu.)Kwamera** *kap^wa* "head" (< **kapu̯a* < **kapu-a*) ■ §§ **Mixe-Zoquean** (MxZq)**- OC:** (Witch*) ▌# FOOT: Zq *neʔŋ* "foot" (Sw*) (< **ŋeʔ-ŋ* ~**ne-ʔŋ* < OC: **ne(ʔ)-* "foot") ||| OC: **(MicN) Marshallese** *ne* "foot" (< **ŋe*) //(W,OC) Takia *ŋe-n* "foot" ||| JPN: Old Jpn **-ne* "foot" (in compound) (Found in; Old Jpn *sune* "fat of leg bone" (< **su-ne* < **su-* "fat" + **ne* "foot, leg". From IKJ*) ▌# MOUTH: pMZ **ʔaw* "mouth" (< OC:**au* ~ **aw(a)* "mouth") ||| OC: **(PolyN) Ponapean** *āu* //(W.OC) Manam *aua* / Takia *awa-n* / Dami *awa* / Yabem *àwa* "mouth" ▌# BLOOD: pMZ **niʔpin* "blood" (< **ni:ʔ-pin* "blood (= water-of-person)" < **ni:ʔ* "water" + pZq **pin* "person, man", where **ni:ʔ* < **nuiʔ* and **pin* < > Ainu *pin-ne* "a male".) ||| OC: **(S.Vanu.) Kwamera** *nui* "flesh water; spring, well" (< **nui* ~ **nu-i* ?) ||| **Ainu** *pinne* "a male" (< **pin-ne* "to be male" < **pin-* "male, man" + **-ne* "to be"), *numa* "swamp" (< **nu-* "water ?" + Ainu *ma* "spring, lake", where **nu-* < > OC: Kwaio *nui* "flesh water".) ||| Note: Most plausibly, Jpn *numa* "swamp" is a loan word borrowed from Ainu *numa*. ■ §§ **Japanese** (Jp)**-New Caledonian**(NCal): (IKJ*,RHJ*) ▌# BELLY/INSIDE: Modern Jp *naka* "inside, bowels, belly" (< **na-ka* < *na* "inside" + *-ka* "place"), Old Jp *na* "inside" ||| OC: **(NCal) Cemuhi** *nà* "stomach" ; (MicN) Ponapean *nan* "inside" (< *na-n) ▌# FOOT: Old Jp *a* ||| OC: **(NCal) Cemuhi** *à-n* //**(W.OC) Yabem** *a* ▌# TOOTH: Old Jp *pa* //Ryukyuan (Hateruma dial.) *pan* ||| OC: **(NCal) Xaracuu** *pã* ■ §§ **Turkic** (TRKc)**-OC:** (DTrkL*, EDAL*) ▌# ARM: TRKc: Uighur *biläk* "arm" (< **bilek* < MP: *bili-* "hand"); Chuvash *pilĕk* "five" (< **bilĕk-*), Tk *biş* /Old Turkic *biš* "five" (< **bīš* < **biiš* < **biliš* ~ **bilik* < **bilë-* ?) ||| OC: **(W.OC) Kaulong** *bili-n* "hand" ▌# HEAD: Kazakh *bas* /Tatar, Uighur *bash* /Turkish *baş "head"* (< **ba-ş* < **ba* ~ **b^wa*), ?Chuvash puś "head" ||| OC: **(NCal) Nemi** *b^wa-n* /Xaracuu *b^wa* "head" (*b^wa-* < **b^wat* < **b^watu* < **batu* "head") ; (Admiralties) Nyindrou *batu-n* //(W.OC)Roviana *batu* //Raga *b^watu-* ||| Note: Cf. (W.MP) Wolio *ɓaa* "head". ▌# SKIN: TRKc: Tatar *tire "skin" (< *dire* "fur" *)* ||| OC: **(NCal) Nengone** *dire-* "fur" ||| Note: Probably, (TRKc) Kaz, Kyrgm Uzbek *teri* / Uighur *terä* / Azerb *dəri* /Turkmen *deri* "skin" (< **deri* < TRKc **dire* "skin"). ■ §§ **Maipuran** (Maip)**-Maori:** (Payne*91, DMaoL*) ▌# ANIMAL: pMaip **pɨra* /Pir. *pɨra* /Apu.*-pɨra* /Ign. *-pera* /Pal. *pir* "animal" "animal (domesticate)" (**pɨra* < **pura* "bird") ||| OC: **(PolyN) Cook Island-Maori** *pura* "bird" ▌# BONE: Yuc. *-ip^hi* (< **ivi* ~ **ibi*) ||| OC: **(PolyN) Samoan, Tahitian, Rapanui** *ivi* /Maori *iwi* (< **ivi* ~ **ibi*) ▌# FEATHER: Amu. *peʔ-* ||| OC: **(MicN) Ponapean** *pē* "feather" ; **(PolyN) Cook Island-Maori** *pē-'au* "wing" ▌# SKIN: Pal. *-mági* "skin" ||| OC: **(PolyN) Maori** *mai* "clothing, garment" (DMaoL*) (< **maʔi* < **magi* "skin ~ cloth(es)" ?) ■ §§ **Chinese(Chin.)-Rotuman-Fijian:** (Hashi*76) ▌# HAND: Wen.(= Wên'cheng (= Bun-sio) dial. in Hainan language) *siu^3* /Taiwan *$ts'iu^3$* /Peking *$ʂəu^3$* //{Schu*: pMin **$tš^hiu^{B1}$* /Old Chin. *$śjəu^B$* (手)/ Literaly Han *$śu^B$* } "hand" (< pChin. **s'iu* ~ **śiu* < MP: **siʔu* "arm" < **siku* "elbow") ||| **OC: Rotuman** *siʔu* "hand, arm" (< **siku* "elbow") || W.MP: (SND) Sundanese *siku* /Uma *hiku* "elbow" ▌# HEAD: Wen. *hau^2* /**Taiwan** *$t'au^2$* /Cantonese *$t'au^{21}$* /[Mei-hsien *$t'eu^2$-na^2* /Peking *$t'əu^2$* (頭)|||OC:**(C.Pacif.) E.Fijian** *ɗau-ni-ulu* "hair (of head)" (= "leaf-of-head") (< *ɗau* "leaf" + *ni* "CONNECTIVE" + *ulu* "head"), Samoan *lau-ulu* "head" (< *dau-ulu "hair of head" (= "leaf-head") <*dau + ulu "head"), Mele-Fila *rauru* /Tahitian *rouru* "head" (< *rau-uru* < **lau-ulu* < **dau-ulu*) ▌# NECK: Wen.

Table 2. (Continued.)

Dau¹-kiaŋ¹ (-頚) /Min-hsien *-kiaŋ³-kin¹* (< pChin. **kiaŋ* (頚) "neck") ||| OC: **(C.Pacif.) Rotuman,Tongan** *kia* "neck" █ §§ **Dravidian** (DRAV)**-W. Oceanic** (W.OC)**:** (DED*) ▌**# CHEST:** Kui *ḍaki* "chest" (D#2976) (<**dagi*) ||| OC: **(W.OC) Yabem** *bo-dagi* "chest" (< **-dagi*) || W.MP: (PHIL) Bangingi Sama *dākan* /Kagayanen *dagʔaˈnan* "chest" ▌**# NOSTRIL:** Tamil *nāsi* "nostril" (< **nas-i* < **ŋas-* < *ŋasu* "bad smelling") ||| OC: **(W.OC) Yabem** *ŋasu* "striking, bad smelling" (CAD*, #15.260) (< **ŋas-u*) ;(MicN)Woleaian *ŋasa* /Marshallese *ŋac* "fragrant, good smelling" ||| Note: OC: Nemi *ŋa* "mucus", Maringe *ŋalu* "to sniff". ▌**# TOOTH:** Tamil *pal* "tooth" (< OC: *pəl-a-ŋie-* "tooth" < *pal- "skin") ||| OC: **(W.OC)Tolai** *pəl* "skin", *pə̊l-a-ŋie-* "tooth" (< *pəl-* "skin" + *-a-* "CONNECTIVE" + **ŋie*) ||| Note: Ohno (1981, p.264) wrongly compared Tamil *pal* with Old Jpn *ɸa* (< **pa*) "tooth". █ §§ **Uralic** (URA)**-W. OC:** ▌# HEAD: pURA *päŋe /Finnish *pää* /Hungarian *fej* ||| OC: **(W.OC) Manam** *peŋana, paŋana* "head" (< **peŋa-~*peŋa-* "head");(Cf. Kilivila *pʷaneta-*"skull") |||Ainu:*pen* "upper,above, source, upriver" (< *peŋ "head ?") ▌# BONE: pURA **tuwe* (K.O.*) ~**luwe* (UEW*,p.254)) /Finnish *luu* "bone,leg",Estonean *luu* "bone" (< **luw(e)*), Vogul *luw* /Ostyak (dialects) *lŏɣ, tŭw, lăw* "bone" (pURA **luwe /*tuwe* < *tuwiə-* < **duwi-a-*< **duwi-* "bone" < *dui < *duri < pAN **DuRiH* "bone") ||| OC: (W.OC) **Kaulong** *luu-n* "thigh" (< **luw-n* < **luw(i)-* "bone" + *-n*), Nyindrou *ⁿd'uwi-n* (<**duwi-*) /**Dami** *tuwa* /Motu *turia -na* (< **turi-a-(na)*) / Kwaio *suri(-na)* /Cemuhi *dû̂-n* /Nengone *dun* / Rotuman, E.Fijian *sui* "bone" (< **duwi(a)-* < pAN **DuRiH* "bone") ▌# HAIR: Finnish *hius* "hair" (< **hiu-s* < OC:**hiu-* "hair") ||| OC: **(W.OC) Motu** *hiu-na* "hair" (< **hilu-*) ; (N.C.Vanu.) Paamese *hiluk* "hair (of head)"

Table 3. Occuring frequencies of Austronesian cognates of Native American and Eurasian languages: Closest similarity analysis (χ^2-test: #, P<0.1; +, P<0.05; ++, P<0.025; *, P<0.01; ** P<0.001)

	FORM	W.MP (PHIL/BOR/SND/SLW)	C.MP	SHWNG	OC (ADM/W.OC/ SE.Sol/ReOC)	Non-AN languages	Number of word items whose closest cognates are found in AN
Number of languages in CAD*	4	26 (11/ 2/ 9/ 5)	6	2	41 (1 /15/ 2/ 23)		
§ 1. Formosan (FORM)-like							
Mayan (BBP)	**7	2(0/0/1/1)	0	0	3(0/2/0/1)	Mongolic 1?	12
§ 2. FORM-W.MP-like							
Eskimo (BBP)	****4.5**	7.5 (#5/ 0 /2.5 /0)	2	1	4.3(0/ 1.5/ 0.3/ 0.5)	Itelmen 0.3/Mong. 0.3	18.3
Mongolic (BBP)	****3.5**	++8.5 (1/ 0 /**5 / 0)	0	0	2 (0/1.5 /0/0.5)	Esk. 1.5, TRKc 2	14
§ 3. Western Malayo-Polynesian (W.MP)-like							
Quechuan (BBP)	2	**10 (5.5/ 1.5/ 3.0/ 0)	1.5	0	1.5 (0/ 1.5 / 0/ 0)		15
Na-Dene BP	1	++9 (3/ 0/4/ 2)	3	1	1	Yeniseian 3~4	15
Yeniseian BBP	0	+3.7(1.3/ 1 /1.3// 0)	0	0	1.3 (0 /1.3/ 0/ 0)	**Na-Dene 3~4,TbB 3**	5
§ 3.1. Philippines(PHIL)-like							
Koasati-Alabaman	5.5	*14.5 (**14.5 /0 /0 /0)	2	0	3 (0 /0 /0 /3)		23
Tungus (BBP)	0	**11 (**9.5/ 0.5 /1 /0)	1	0	3		15
§ 3.2. Sundic (& Tibeto-Burman (TbB))-like							
Tupi (Sw100)	0	#6.3(1 /0 /**4.3 /1)	0.3	1	2.8	**TbB 9.5**	10.5
TbB (BP)	0	**17(4 /1.5 /**7.7 /#3.8)	2	1	4		24
§4. Oceanic-like							
Aymara (B100W)	0	0	0	0	++6.8 (0 / 3.8 / 0 / 3)	Ainu 0.5,Tipula 0.3,Tamil 0.3	6.8
Yamanan	0.25	1.25	0	0	#7.5 (1 /3.75 /0 / 3)		9
Ainu (BBP)	1	2.5	2	0	+15.5(1 /#7 /0 /**8.5**)	Macro-Ge 2, Comecrudo 1	21
§ 4.1. Remote Oceanic-like)							
Comecrudo (BP)	0	0	1	0	++9 (0 /2 /1 /+6)	Itelmen 1, Ainu 1	10
IE (English) (BBP)	0	1	0	0	**14(0 /3 /1 /****10 (S.Vanu.:Kwamera.4)**)		15
§ 4.1,1. Micronesian (MicN)-like							
Mixe-Zoquean(BBP)	1	2 (0/0/0/2)	0.5	0.5	#12.3 (0 /4.5 /0 /#**7.8 (MicN **5**))	Ainu 1.3,Jpn 1,Hopi 0.3	16.3
§ 4.1.2. New Caledonian-like							
Japanese (BBP)	1	0	0	0.5	****27.5** (0/4/1 /****22.5 (NCal **15**, MicN 4))		29
Turkic (BBP)	1	2 (1.5 / 0 /0 /0.5)	0	0	**8** (0 /2.5 /0 /**5.5 (NCal **4)**)	Jpn 1, [wr.Mong. 1]	11
Turkic(Non-BP B100W)	0	2 (0 /0 /0 / 2)	1	0	+**11** (0 / 3 /0 / ***8**)	[wr. Mong. 1]	14
§ 4.1.3. Central Pacific(C.Pac.)-like [= Sino-Central Pacific Cluster ?]							
Maipuran (Arawakan)	0	0	0	1	****32** (0 /6.5 /0 /****25.5 (C.Pac. **16.5)**)	Ainu 1	33
		ReOC **25.5 = (NCal 4, MicN 4, Rotuman-Fijian 2, **PolyN **14.5 (Maori **7~9)**)					
Chinese	1	3(0 /0 /3 /0)	0	0	14 (0 /3 /0 /**10** (**C.Pac. 7**))	Bantu 1	15
		C.Pac. **7 = (**Rotuman-W.Fijian 4, E.Fijian 2.5**, Tongic 0.5, PolyN 0)					
§ 4.2. Western Oceanic (W.OC)-North New Guinea Cluster(NNG)-like							
Dravidian (BP):	0	1	2	0	****18** (0 /****11 (NNG **7**, Pap.Tip 4) /1 /6)		21
Finnish (BBP)	1	1(0 /0 /0 /1)	0	0	+**8.8** (0 /****7.8 (NNG **6.8**, Pap.Tip 1) /0/1)	Jpn 1,pIE 0.5,DRAV 0.3,TRKc 0.3	10.8

The Seventeenth International Symposium on Artificial Life and Robotics 2012 (AROB 17th '12),
B-Con Plaza, Beppu, Oita, Japan, January 19-21, 2012

Bifurcation analysis in a silicon neuron

F. Grassia[1], T. Levi[1], S. Saighi[1] and T. Kohno[2]

[1]Laboratoire IMS, UMR CNRS 5218, Université de Bordeaux, Talence, France
[2]IIS University of Tokyo, Japan

[1]filippo.grassia@ims-bordeaux.fr

Abstract: In this paper, we describe an analysis of the nonlinear dynamical phenomenon associated with a silicon neuron. Our silicon neuron integrates Hodgkin-Huxley (HH) model formalism, including the membrane voltage dependency of temporal dynamics. Analysis of the bifurcation conditions allow us to identify different regimes in the parameter space that are desirable for biasing our silicon neuron. This approach of studying bifurcations is useful because it is believed that computational properties of neurons are based on the bifurcations exhibited by these dynamical systems in response to some changing stimulus. We describe numerical simulations and measurements of the Hopf bifurcation which is characteristic of class 2 excitability in the HH model. We also show a phenomenon observed in biological neurons and termed excitation block. Hence, by showing that this silicon neuron has similar bifurcations to a certain class of biological neurons, we can claim that the silicon neuron can also perform similar computations.

Keywords: Silicon Neuron, Hopf bifurcation, Hodgkin-Huxley equations, neuromorphic engineering.

1 INTRODUCTION

Neuromorphic engineering is a research field where microelectronics meets biology. The link between both is done by computational neurosciences which model and emulate a part of brain activity. Neuromorphic systems emulate biological structures in the hope of retaining its remarkable computational efficiency. Analysis of the bifurcation is useful because it is believed that computational properties of neurons are based on the bifurcations exhibited by these dynamical systems in response to some changing stimulus [1] [2]. These artificial systems would be useful to neuroscientists for exploring neural computation. Contrarily to computer simulation, analog circuits are inherently suitable for simulating differential equations in real time and in parallel [3]. The hardware simulation further facilitates the building of a hybrid network connecting artificial and biological neurons to create a real-time loop or can be even used to replace nonfunctional neurons as a prosthesis.

Pioneering work in modeling the dynamics of a biological neuron was done by Hodgkin and Huxley (HH) [4]. In the most detailed family of neuron models, known as conductance-based models, ionic and synaptic currents charge and discharge a capacitor representing the neuron membrane. All of these models find their origins in the HH formalism. Each ionic channel (sodium, potassium, calcium, etc.) is represented by a time and voltage dependent conductance: this electrophysiological description makes these models particularly well-suited to an implementation involving analog electronics [5]. The main advantage of this formalism is that it relies on biophysically realistic parameters and describes individual ionic and synaptic conductances for each neuron in accordance with the dynamics of ionic channels.

Hodgkin classified biological neurons mainly into two classes according to their response properties to a sustained current stimulus [6]. The cells that show Class 1 neural excitability can fire with an arbitrarily low frequency by applying a sufficiently close-to-threshold current. The frequency increases monotonically as the current increase. The cells that show Class 2 neural excitability transitioned from silence to firing at an arbitrary nonzero frequency. Furthermore, the Class 1 characteristic is can be associated with a saddle-node bifurcation at the transition from silence to spiking. As shown by bifurcation analysis, the Class 2 excitability is observed when the resting state loses its stability via an Hopf-bifurcation.

The Hodgkin-Huxley model belongs to Class 2. Its dynamical properties with a constant stimulus have been studied extensively [7] [8], and these have shown that the Class 2 neural excitability of the HH model is generated by Hopf bifurcations.

Innovative work in modeling of a simplified silicon neuron that exhibits HH type dynamics was done in [9] and in [10]. On the other hand, some designs have faithfully replicated full Hodgkin-Huxley dynamics, resulting in large footprints for each neuron [5]. We implement in our chip the HH model with an approximation: we use a fixed time constant to reduce the silicon area required by the neuron implementation in the chip. In this paper we present an analysis of the nonlinear dynamical phenomenon associated with our silicon neuron. We show a Hopf bifurcation which is characteristic of class 2 excitability in the HH model in our approximated model. We also show a phenomenon observed in real neurons and termed excitation block.

2 HH MODEL IN VLSI

2.1 The Hodgkin-Huxley Formalism

We chose to implement neuron model following the Hodgkin-Huxley formalism. Electrical activity of a neuron is the consequence of the diffusion of different ionic species through its membrane. The HH formalism provides a set of equations and an equivalent electrical circuit which describes conductance phenomena.

The current flowing across the membrane is integrated on the membrane capacitance, according to expression (1):

$$C_M \frac{dV_M}{dt} = -\sum I_I + I_S \tag{1}$$

where V_M is the membrane potential, C_M is the membrane capacitance, and I_S is a stimulation or synaptic current. I_I is the current for a given channel type and its associated equation is:

$$I_I = g_I.m^p.h^q.(V_M - E_I) \tag{2}$$

where g_I is the maximum conductance; m and h represent the activation and inactivation terms, respectively. They are dynamic functions, which describe the permeability of membrane channels to its specific ion. E_I is the ion-specific reverse potential and p and q are integers.

According to the first order differential equation (3), m relaxes back towards its associated steady-state value m_∞, which is a sigmoid function of V_M (4). The time constant for convergence is τ_m which is also voltage dependent of the membrane voltage V_M.

$$\tau_m(V_M)\frac{dm}{dt} = m_\infty - m \tag{3}$$

$$m_\infty = \frac{1}{1+\exp\left(-\frac{V_M - V_{Offset,m}}{V_{Slope,m}}\right)} \tag{4}$$

In (4), $V_{Offset,m}$ and $V_{Slope,m}$ are the offset and the slope of the activation sigmoid respectively. The inactivation parameter h follows identical equations, except for the sign inside the brackets, which is positive.

The HH model describes sodium, potassium and leakage channels, with p = 3 and q = 1; p = 4 and q = 0; p = 0 and q = 0 respectively, in expression (2). These channels are responsible for action potential generation. For more complex activity patterns, such as bursting or the discharge of action potentials with adaptation phenomena, additional channels such as slow potassium (p=1 and q=0) and L-Type calcium for bursting (p=2 and q=1) have to be taken into account. Our chip has a large range of validity domains for the parameter to reproduce different kind of neurons like: Fast Spiking (FS), Regular Spiking (RS), Intrinsically Bursting (IB), and Low Threshold Spiking (LTS) [11]. Although these HH-type models sometimes exhibit much more complex dynamics than the original HH model, they share common nonlinear characteristics and dynamics with the HH in many aspects.

2.2 The model dedicated to our integrated circuit

Our system is composed of our most recent chip called Galway and the dedicated board named Ekerö. This chip includes analog operators for the computation of the HH formalism, and for the construction of neural networks, multi-synapses that consist of gathering all synaptic inputs in one electronic input. We implement in our chip the HH model with an approximation: we use a fixed time constant in (3). We made this choice to reduce the size of the chip. So the only difference between the model for the VLSI and the HH model presented in [12] is the approximation used for the gating variable.

2.3 Hopf bifurcation

The Hopf bifurcation theory [8] asserts that if a parameterized system possesses an equilibrium point and two of the eigenvalues of the Jacobian matrix of the system linearized around the equilibrium point are conjugate pure imaginary numbers and the others have negative real parts, one of the following bifurcations takes place as the parameter changes:

1) A bifurcation from a stable equilibrium point to an unstable equilibrium point with a stable limit cycle around it; or a bifurcation with the opposite direction. We refer to this bifurcation as supercritical.

2) A bifurcation from an unstable equilibrium point to a stable equilibrium point with an unstable limit cycle around it; or a bifurcation with the opposite direction. We refer to this bifurcation as subcritical.

2.3 Simulation

To validate our approximation we used continuation of solutions in AUTO, an open source mathematical package that can produce bifurcation curves for equilibria as well as for periodic orbits, to get the complete bifurcation diagram of the system. We compare the simulations between HH based model and our implemented HH model.

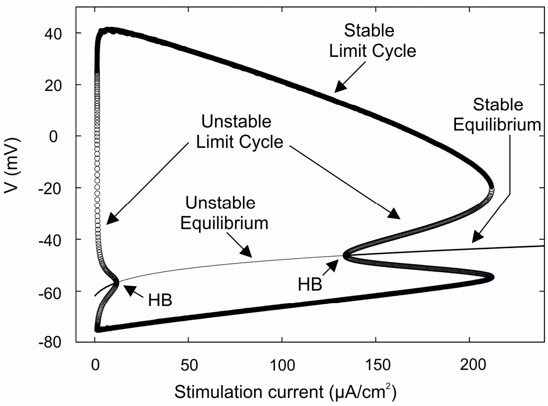

Fig. 1. Bifurcation diagram for our approximated model.

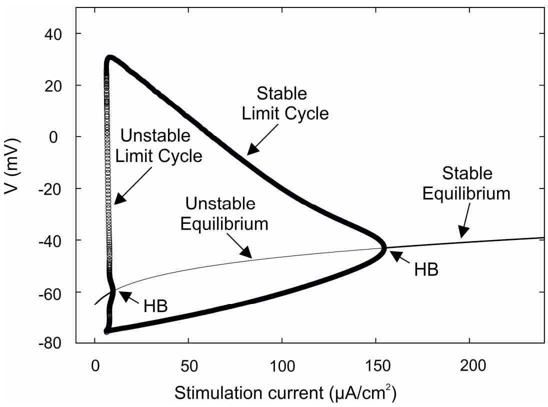

Fig. 2. Bifurcation diagram for HH model.

Fig. 1 shows the resulting bifurcation diagram of our HH approximated model where solid thick and solid thin curves represent stable and unstable equilibria respectively while solid and dashed circles denote stable and unstable limit cycles. It can be seen that the limit cycles are born initially through a fold bifurcation of cycles. Both the Hopf bifurcations are subcritical as they involve an unstable limit cycle. The amplitude of the stable limit cycle keeps on reducing until it coalesces with the unstable limit cycle in another fold bifurcation. The resting state loses stability via the subcritical Hopf bifurcation at the first point HB in Fig. 1. At the second point HB in Fig. 2, a stable limit cycle and an unstable one arise via the fold bifurcation. Bifurcation diagram in Fig. 1 illustrate how the repetitive firing emerges when we apply sustained stimulus current. Stable limit cycle corresponds to repetitive firing.

For a comparison with HH model, its bifurcation is also shown in Fig. 2. The Hopf bifurcation for smaller current is subcritical. The limit cycle appears by a fold bifurcation and disappears by a supercritical Hopf bifurcation. The reduction in amplitude before the subcritical Hopf bifurcation is similar to the Fig. 1. It can be seen in Fig. 2 that the limit cycle is born by a fold bifurcation but terminates in a supercritical Hopf bifurcation. The bifurcation diagrams shown in Fig. 1 and Fig. 2 share the topology in a biologically meaningful range of stimulus current. The qualitative nature of the plots (Fig. 1 and Fig. 2) is similar as the reduction in amplitude of the limit cycle before its disappearance is present in both pictures.

3 RESULTS IN VLSI

3.1 Firing rate

In Fig. 1, the system state jumps to the stable limit cycle when the stimulus current exceeds the Hopf bifurcation point. In this case the firing frequency cannot be zero at the bifurcation point for the Class 2. Steps of input current are important type of stimulus typically used to characterize the behavior of neuron models. The resulting spike frequencies for different values of stimulation current are plotted in Fig. 3. This figure shows a behavior typical of class 2 neurons where the spiking frequency does not tend zero upon reduction of the input current. In other word, the disappearance of the limit cycle is not associated with its frequency reducing to zero like in class 1 neurons.

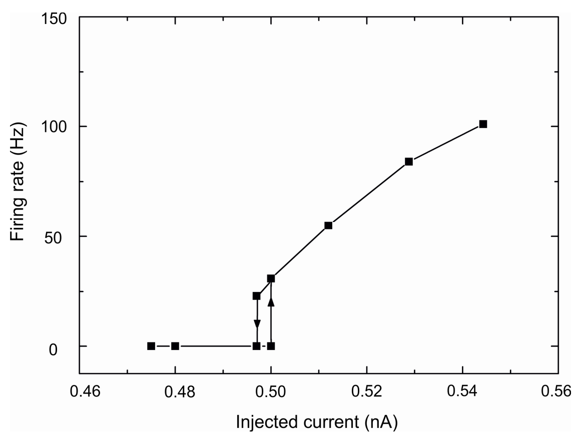

Fig. 3. Hardware measurements of the frequency versus stimulation current curves of our silicon neurons. Arrows describes the existence of bistability; onsets of firing are different when the stimulus increased or decreased.

3.2 Effect of current impulses

Fig. 4 shows the effect of current impulses of different values in our silicon neuron. Larger current pulses shifts the initial condition beyond the unstable limit cycle leading to spontaneous oscillations. We used four different current pulses of increasing amplitude to stimulate our silicon neuron. It can be seen in Fig. 4 that for the first two case the neuron come back to resting state and in the third and fourth case it start the oscillations. This demonstrates the existence of the threshold that in our silicon neuron is 0.5 nA.

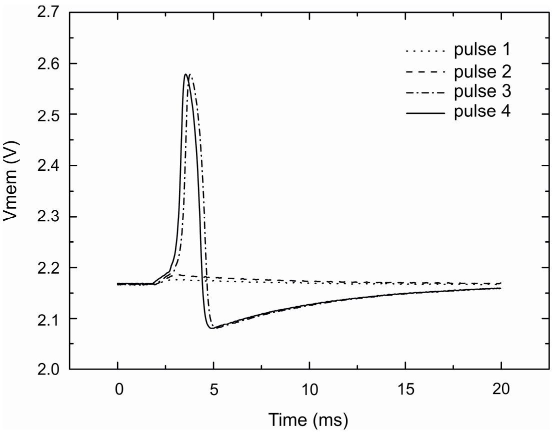

Fig. 4. Hardware neuron membrane voltage depending on current impulses.

3.3 Excitation block

To prove that the silicon neuron reproduces similar dynamical properties of biological neuron, we also explored the phenomenon known in biology and termed excitation block. In this case, there is the cessation of repetitive spiking as the amplitude of the stimulus current increases. The equilibrium regains stability through a Hopf bifurcation which may be subcritical or supercritical. To observe this phenomenon a slowly increasing ramp of current was injected. In Fig. 5 is showed that for much larger value of the stimulus the equilibrium becomes stables again.

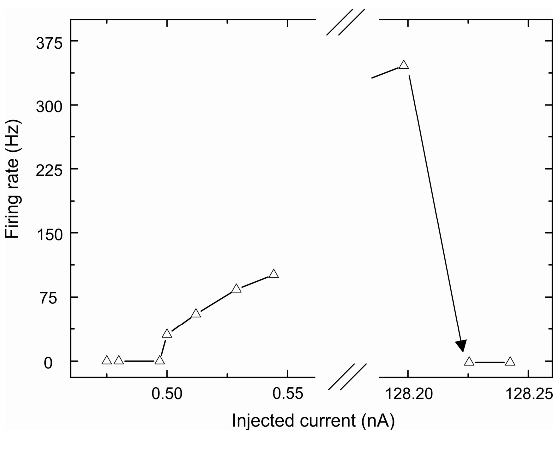

Fig. 5. Measured data of the excitation block where the input current is slowly increased.

4 CONCLUSION

In this paper, we described an analysis of the nonlinear dynamical phenomenon associated with a silicon neuron. We implemented an approximated HH model using fixed time constant. We showed numerical simulations of the Hopf bifurcation which is characteristic of Class 2 excitability in the HH model. We compared the results with the HH model showing that our model shares the dynamics with the full HH model. We also showed the firing rate and then the phenomenon observed in real neurons and termed excitation block. Hence, by showing that this silicon neuron has nonlinear dynamical phenomenon similar to a certain class of biological neurons, we can claim that the silicon neuron can also perform similar computations.

ACKNOWLEDGMENTS

This project was partly supported by the Seventh Research Framework Program of the European Union under the Grant n°237955 (FACETS-ITN).

REFERENCES

[1] Izhikevich EM (2000), Neural excitability, spiking and bursting. IJBC, vol.10, pp. 1171–1266.

[2] Rinzel J, Ermentrout GB (1989), Analysis of Neural excitability and oscillations. Methods in Neural Engineering, Koch C and Segev I, Eds, Cambridge.

[3] Chua LO, Roska T, Kozek et al (1996), CNN universal chips crank up the computing power.
IEEE Circuits Devices Mag., vol. 12, pp. 18–28.

[4] Hodgkin, AL, Huxley AF (1952). A quantitative description of membrane current and its application to conduction and excitation nerve. Journal of physiology,vol.117, pp. 500-544.

[5] Simoni MF, Cymbalyuk GS, Sorensen ME et al(2004), A multiconductance silicon neuron with biologically matched dynamics. IEEE Transactions on Biome-dical Engineering, vol. 51, pp. 342-354.

[6] Hodgkin AL (1948), The local electric changes associated with repetitive action in a non medullated axon. Journal of physiology, vol. 107, pp. 165-181.

[7] Hassard B (1978), Bifurcation of periodic soluti-ons of the Hodgkin-Huxley model of the squid giant axon. J. Theor. Biol., vol. 71, pp. 401–420.

[8] Hassard B, Kazarinoff ND, Wan YH (1981), Theory and Applications of Hopf Bifurcation. Cambrid-ge, U.K.: Cambridge Univ. Press.

[9] Kohno T, Aihara K (2005), A MOSFET - basedmodel of a class 2 nerve membrane. IEEE Transac. onNeural Networks, vol. 16, no. 3, pp. 754–773.

[10] Basu A, Petre C, Hasler P (2010), Dynamics and Bifurcations in a Silicon Neuron. IEEE Tr. on Biomedical Circuits and Systems vol. 4, pp. 320-328.

[11] Grassia F, Buhry L, Lévi T et al (2011), Tuna-ble neuromimetic integrated system for emulating corti-al neuron models. Front. Neurosci. 5:134.

[12] Hansel D, Mato G, Meunier C (1993), Phase dynamics for weakly coupled Hodgkin-Huxley neurons.Europhys. Lett, vol. 23, pp. 367-372.

The Seventeenth International Symposium on Artificial Life and Robotics 2012 (AROB 17th '12),
B-Con Plaza, Beppu, Oita, Japan, January 19-21, 2012

Attitude control of an airborne two wheeled robot

Huei Ee Yap[1] and Shuji Hashimoto[1]

[1] Graduate School of Advanced Science and Engineering, Waseda University
55N-4F-10A, 3-4-1 Okubo, Shinjuku-ku, Tokyo, 169-8555, Japan
huei@shalab.phys.waseda.ac.jp, shuji@waseda.jp

Abstract: The problem of balancing a two wheeled robotic platform has been intensively studied and well understood. However in such studies, the mathematical model of the robot is commonly derived under the assumption that the robot remains constant contact with the ground. This assumption limits the movement of the robot to continuous ground surface. In other words, any momentary airborne situation, such as traversing down a flight of stairs or falling off edges will render the control algorithm ineffective and cause the robot to fall upon landing. In this paper, the dynamics of a free falling two wheel robot are investigated and a novel attitude control scheme is proposed. We proposed using the wheel of the pendulum as a reaction wheel to provide control torque for correcting the robot's attitude in air and ensure a safe landing. The effectiveness of the proposed approach is demonstrated through both simulations and actual implementation.

Keywords: two-wheeled balancing robot, free fall, dynamic balancing, attitude control

1 INTRODUCTION

Mobile robots that are deployed into human environment will need to traverse through non-continuous terrains such as steps or stairs in order to navigate around certain area. Various kinds of robots have been designed to tackle this problem. Most notably biped type humanoid robot such as ASIMO [1] are able to traverse up and down stairs. However, due to its complexity and price of manufacturing, deployment of biped type humanoid robot is still uncommon and not economically practical. As for wheeled robots, maneuvering through non-continuous terrains remains a challenging open problem.

Various statically stable mobile wheeled robots have been developed for tackling such problem. For example the Sojourner [2] developed by NASA and the Shrimp robot [3] developed by EPFL uses a combination of adaptive legs with the efficiency of wheels to enable the robot to traverse through uneven terrain and steps. These approaches rely on the redundancy of static points of support on the base to provide stability to the robot during climbing up/down steps. Drawbacks on these robots are increased complexity in structure and control and increased size. In human environment where workspace is limited, their navigation ability may be restricted since they typically require a larger workspace.

In contrast, dynamically stable robots like JOE [4], Ballbot [5] which use active control to achieve balance possess greater flexibility in maneuvering and are more resistant to external disturbance. These robots also have a smaller footprints and possess a near-zero turn radius for moving in a limited space. Given the robustness against applied external forces, these robots prove to be more usable when deployed into human environment.

This paper explores the possibility of a two wheeled robot to traverse down a non-continuous ground step. The dynamics of the free falling motion are investigated and a novel attitude control scheme is proposed. The proposed approach extends the ability of the two wheeled robot to traverse through rough and edgy terrains. During free fall, a two wheel robot behaves similarly to a reaction wheel pendulum, with pivot point at the center of mass. Hence it is possible to use the momentum of the wheels to generate correction torque to alter the orientation of the robot and ensure a safe landing. Two separate feedback control schemes designed using the linear-quadratic controller (LQ) are employed for two phases of airborne falling and ground contact. A switching controller selects the adequate controller according to the situation. The effectiveness of the proposed approach is demonstrated through simulations and actual implementation.

2 RELATED WORK

IHop [6] developed by the Flow Control and Coordinated Robotics Labs, UCSD uses an interesting approach, similar to our proposed technique to balance a hopping robot. IHop demonstrated that it is possible to use the wheels as reaction wheels to alter the movement of the center of mass of the robot to achieve dynamic balancing. However in the case of IHop, dynamic balancing of the robot is demonstrated only on flat ground. Experiment on traversing through steps was not demonstrated. Kikuchi et al [7] proposed using vibration of a 2-DOF system as a hopping mechanism for the robot. The robot uses a moving mass and potential energy stored in springs to achieve soft landing through a vertical step. However, the robot presented is statically stable and exhibits drawbacks that were discussed earlier.

3 DYNAMIC MODEL

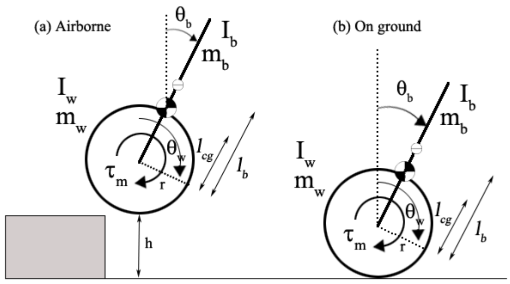

Fig. 1: The schematic of two wheeled robot

In this section, the dynamics of the robot is presented. To simplify the problem, a few assumptions are made. First, it is assumed that the orientation of the robot in roll direction remains constant during flight and hence attitude control in roll direction is negligible. Under this assumption, the problem can be simplified into a two dimensional pendulum problem. Second, the moment of inertia of the wheels is sufficiently large in order to be able to act as a reaction wheel to alter the momentum of the robot. This assumption ensures that the system is controllable without introducing additional actuating mechanism. Mathematical models of the robot during ground contact and airborne phases are derived according to the schematic shown in Fig.1 corresponded to the parameters in Table 1. On ground, the robot behaves just like an ordinary two wheeled pendulum robot whereas during airborne phase, the robot behaves like a reaction wheel pendulum with the pivot point on the center of mass of the robot. Due to large available literatures on derivation of the dynamic models of two wheeled pendulum and reaction wheel pendulum [8][9][10], detailed step-by-step derivation of the mathematical model is omitted.

Table 1: List of symbols

m_b	Mass of body
m_w	Mass of wheels
I_b	Inertia of body around center of mass
I_w	Inertia of wheels around center of mass
r	Wheel radius
l_b	Length of wheel axis to body's center of mass
l_{cg}	Length of wheel axis to robot's center of mass
g	Gravity
θ_b	Tilt angle of robot body
θ_w	Rotational angle of wheels
τ_m	Motor Torque

3.1 On ground

Using Lagrangian mechanics the equation of motion of the robot traveling on ground can be easily obtained [10]. The equations of motions are then linearized and put into the form of state-space representation for controller design as described in the next section,

$$\dot{x}_g = F(x, u) = A_g x_g + B_g u \tag{1}$$

where $x_g = \begin{bmatrix} x_{g1} & x_{g2} & x_{g3} & x_{g4} \end{bmatrix}^{\mathrm{T}}$ is the state vector and u is the scalar motor torque input. By choosing $x_{g1} = \theta_w$, $x_{g2} = \dot{\theta}_w$, $x_{g3} = \theta_b$, $x_{g4} = \dot{\theta}_b$, and $u = \tau_m$, we obtain

$$A_g = \begin{bmatrix} 0 & 1 & 0 & 0 \\ 0 & 0 & a_{g23} & 0 \\ 0 & 0 & 0 & a_{g34} \\ 0 & 0 & a_{g43} & 0 \end{bmatrix}, \quad B_g = \begin{bmatrix} 0 \\ b_{g2} \\ 0 \\ b_{g4} \end{bmatrix} \tag{2}$$

The values of a_{g23}, a_{g34}, a_{g43}, b_{g2} and b_{g4} are specific to actual robot configuration [10].

3.2 Airborne

Similarly, using Lagrangian mechanics, the equations of motions of the robot during airborne can be derived, linearized and put into state space form as shown below,

$$A_a = \begin{bmatrix} 0 & 1 & 0 \\ a_{a21} & 0 & 0 \\ 0 & 0 & 0 \end{bmatrix}, \quad B_a = \begin{bmatrix} 0 \\ b_{a2} \\ b_{a3} \end{bmatrix} \tag{3}$$

Here, only three of four available states are used to describe the motion of the robot, namely θ_b, $\dot{\theta}_b$ and $\dot{\theta}_w$. The rotational angle of the wheel are not controlled during airborne phase and hence not included into the motion model. Note that in the case of airborne, unlike conventional reaction wheel pendulum where the pivot lies on the base of the pendulum, the pivot point actually lies on the center of mass of the robot.

4 CONTROL

The control of the robot is divided into two phases. When the robot is moving on the ground, a linear quadratic(LQ) controller designed around equation (2) is employed. The feedback control torque τ_m is given by

$$\tau_{gm} = -K_g x_g + k_{g1}\theta_{wref} \tag{4}$$

where $K_g = [\ k_{g1} \quad k_{g2} \quad k_{g3} \quad k_{g4}\ ]$ is the feedback gain obtained from the LQ controller and θ_{wref} is the reference value for controlling the rotational angle of the wheel and hence the horizontal position of the robot.

When the robot falls off a step, a different LQ controller designed based on equation (3) is employed to control the attitude of the robot. The feedback control torque in this case can be written as

$$\tau_{am} = k_{a1}(\theta_{bref} - \theta_b) - k_{a2}\dot{\theta}_b - k_{a3}\dot{\theta}_w \tag{5}$$

where k_{a1}, k_{a2} and k_{a3} are feedback gains computed from LQ controller. θ_{bref} is the reference body tilt angle during airborne.

Additionally, a simple switching controller is used to select appropriate controller depending on the height of the robot above ground.

$$\tau_m = \begin{cases} \tau_{gm} & \text{for} \quad |h| \leqq h_{threshold} \\ \tau_{am} & \text{for} \quad |h| > h_{threshold} \end{cases} \tag{6}$$

where h is the height of the robot above ground and $h_{threshold}$ is the height threshold value determined experimentally.

5 SIMULATION RESULTS

Before building an actual experimental platform, computer simulation is carried out to test the viability of the proposed idea. Based on our assumptions made in section 3, our problem is simplified into a 2 dimensional problem and hence in simulating the problem, a 2 dimensional simulator, Box2D [11] physics engine is used. The simulation results show that

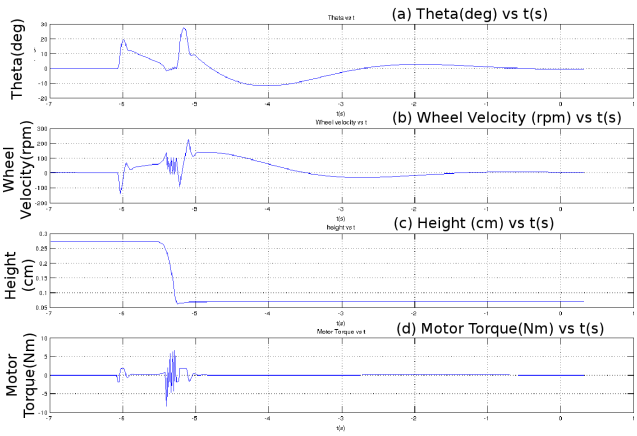

Fig. 2: Simulation results: freefall using attitude control

the robot is able to land and remain upright from a fall height of 0.25 meters. By actively controlling the rotation of the wheel, it is possible to generate sufficient torque to alter the angle of tilt of the robot body to ensure safe landing. However in this simulation, issues on motor torque limit versus motor size were not taken into consideration and hence simulation results might be biased.

6 EXPERIMENTAL PLATFORM

In addition to simulation results, an experimental two wheeled mobile robot platform (Fig.3) is constructed to evaluate the validity of the controllers. The robot is equipped with an inertia measurement unit (IMU) consists of a 3-axis accelerometer and a 2-axis gyroscope and a DC motor with encoder. Kalman filter is used to estimate the angle of tilt and angular velocity of the body. As for calculating the angular velocity of the wheel, instead of direct differentiating the measurements of encoder to obtain the angular velocity, an alpha-beta filter is used for estimation. This is due to the fact that direct

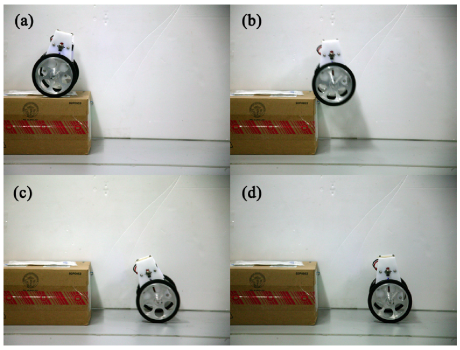

Fig. 3: Free fall of a 2 wheeled pendulum robot

differentiation of encoder measurements will introduce additional noises from non-linearities such as gear backlash. The alpha-beta filter is a simplified kalman filter with constant update gains. Values of α and β are experimentally chosen. An ultrasonic distance sensor is fitted onto the bottom of the robot to measure the height of the robot above ground. All the sensor information is measured and processed using a 32-bit ARM microcontroller running at a clock speed of 96MHz.

7 EXPERIMENT AND DISCUSSIONS

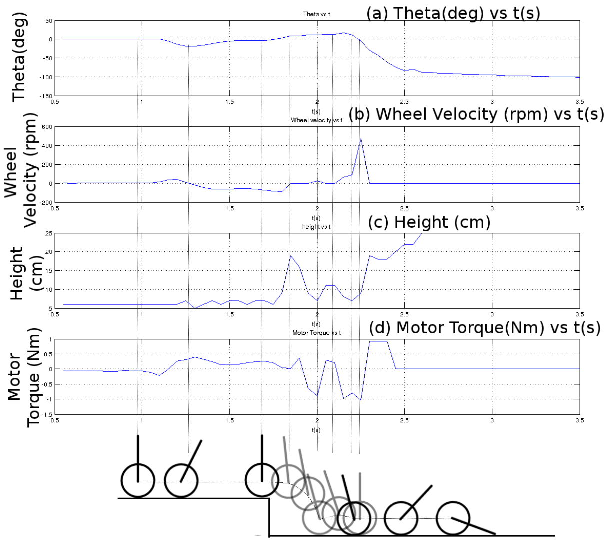

Fig. 4: Free fall using conventional feedback control

In our experiment, the robot is commanded to fall from a 20cm step (roughly same height as the robot). Figure 4 shows the experiment results of the free fall dynamics of the 2 wheel pendulum robot using conventional feedback controller. During free fall, the robot lost contact with the ground and is unable to generate balancing torque. This triggers the feedback controller to increase the feedback signal and spins the wheel faster. On landing with fast spinning wheels, large torque is applied on the robot and causes it to loose balance and fall. We have also experiment with turning off the motor

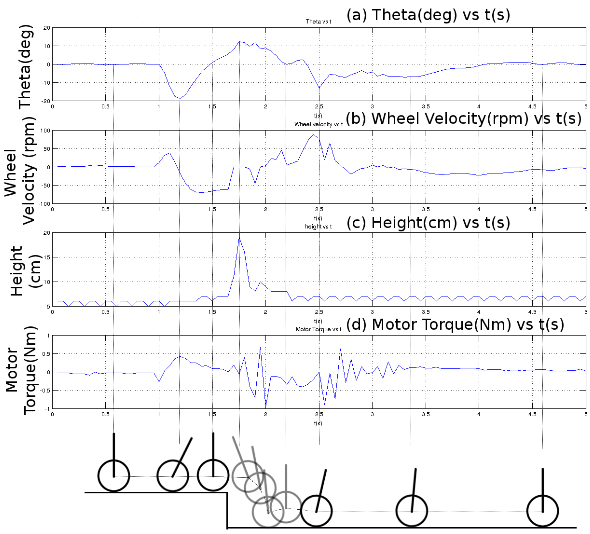

Fig. 5: Free fall with attitude control

during airborne. However, forward momentum from the fall is too large and the robot failed to recover. Figure 5 shows the experiment results of our proposed method. During the fall, the robot tilts backward in order to cope with the forward momentum during landing. Tilting control is achieved by spinning the wheels. Upon landing forward momentum neutralizes the tilt and brings the robot straight up. On-ground feedback controller take over and ensures the robot remains balance. The process of safe landing from a fall is illustrated in Fig.5.

8 CONCLUSION

In this paper we presented a unique solution enabling 2 wheeled pendulum robots to traverse down a non-continuous ground. During free fall, the 2 wheeled pendulum robot acts like a reaction wheel pendulum with pivot point at the center of mass. Hence, by actively controlling the spin of the wheels, it is possible to generate attitude controlling torque to ensure a safe landing. On ground and airborne dynamic models are presented along with two feedback controllers designed accordingly. The idea is simulated before an actual experimental platform is built. The experiment results show that the proposed method is viable and extends the maneuvering ability of 2 wheeled robots. Currently the airborne tilt angle are chosen experimentally. Future work will aim to automate airborne tilt angle control, as well as safe landing from increased height.

9 ACKNOWLEDGEMENT

This work was supported in part by the CREST project "Foundation of technology supporting the creation of digital media contents" of JST, and the Global Robot Academia, Grant-in-Aid for Global COE Program by the Ministry of Education, Culture, Sports, Science and Technology, Japan.

REFERENCES

[1] http://world.honda.com/ASIMO/

[2] Volpe, R., Balaram J., Ohm T., Ivlev T. (1996) The Rocky 7 Mars Rover Prototype. IEEE/RSJ International Conference on Intelligent Robots and Systems, November 4-8 1996, Osaka Japan

[3] Estier T., Crausaz Y., Merminod B., Lauria M., Piguet R., Siegwart R. (1994) An innovative Space Rover with Extended Climbing Alilities, Proceedings of Space and Robotics 2000, Albuquerque, USA, February 27-March 2, 2000.

[4] F. Grasser, A. D' Arrigo, S. Colombi, and A. Rufer, "JOE: a mobile,inverted pendulum," IEEE Transactions on industrial electronics, vol. 49, no. 1, pp. 107-114, 2002.

[5] T. Lauwers, G. Kantor, and R. Hollis, A dynamically stable single-wheeled mobile robot with inverse mouse-ball drive, in Robotics and Automation, 2006. ICRA 2006. Proceedings 2006 IEEE InternationalConference on, 2006, pp. 2884-2889.

[6] Schmidt-Wetekam, C., Zhang, D., Hughes, R., Bewley, T., "Design, optimization, and control of a new class of reconfigurable hopping rovers," Decision and Control, 2007 46th IEEE Conference on , vol., no., pp.5150-5155, 12-14 Dec. 2007

[7] K. Kikuchi, K. Sakaguchi, T. Sudo, N. Bushida, Y. Chiba, and Y. Asai, A study on wheel-based stair-climbing robot with hopping mechanism, Mechanical Systems and Signal Processing(MSSP), ELSEVIER, Vol.22, Issue 6, 1316-1326, (2008-8)

[8] K.J Astrom, D.J. Block, M.W. Spong, The Reaction Wheel Pendulum, Morgan and Claypool, 2007.

[9] M.W. Spong, P. Corke, R. Lozano, "Nonlinear Control of the Inertia Wheel Pendulum," Automatica, vol. 37, pp.1845-1851, 2001.

[10] Teeyapan, K., Jiuguang Wang, Kunz, T., Stilman, M., "Robot limbo: Optimized planning and control for dynamically stable robots under vertical obstacles," Robotics and Automation (ICRA), 2010 IEEE International Conference on , vol., no., pp.4519-4524, 3-7 May 2010

[11] http://box2d.org/

The Seventeenth International Symposium on Artificial Life and Robotics 2012 (AROB 17th '12),
B-Con Plaza, Beppu, Oita, Japan, January 19-21, 2012

A new adaptive and flexible communication protocol for long-term operation of ubiquitous sensor networks with multiple sinks and multiple sources

Satoshi Yasuda[1], Akihide Utani[1], and Hisao Yamamoto[1]

[1]Tokyo City University, Tokyo 158-8557, Japan
(Tel: 81-3-5707-0104)

[1]autani@tcu.ac.jp

Abstract: There is growing expectation for a wireless sensor network. A wireless sensor network has great potential as a means of realizing a wide range of applications, such as natural environmental monitoring and environmental control in residential spaces or plants. To facilitate a ubiquitous environment by a wireless sensor network, however, its control mechanism should be adapted to the variety of types of communication, i.e., one-to-one, one-to-many, many-to-one, and many-to-many, depending on application requirements and the context. This paper proposes a new adaptive communication protocol for the long-term operation of such a ubiquitous sensor network. We evaluate the proposed protocol using computer simulation experiments and discuss its development potential.

Keywords: Sensor Networks, Ubiquitous Environments, Adaptive Communication Protocol.

1 INTRODUCTION

Various network services have been provided. They include inter-vehicle communication, which is a network service in intelligent transport systems, environmental monitoring and control, and ad-hoc communication between mobile nodes in such emergent situations as disasters. As a means of realizing the above network services, autonomous decentralized networks, such as a mobile ad-hoc network, a wireless sensor network, and a mesh network, have been intensively researched with great interests. Especially, a wireless sensor network, which is a key network to facilitate ubiquitous information environments, has great potential as a means of realizing a wide range of applications, such as natural environmental monitoring, health monitoring, environmental control in residential spaces or plants, object tracking, and precision agriculture[1-4].

In a general wireless sensor network, hundreds or thousands of static micro sensor nodes, which are compact and inexpensive, are placed in a large scale observation area, and sensing data from each node is gathered to a sink node by inter-node wireless multi-hop communication. Each sensor node consists of a sensing function to measure the status (temperature, humidity, motion, etc.) of an observation point or object around it, a limited function of information processing, and a simplified wireless communication function, and it generally operates on a resource with a limited power supply capacity such as a battery. Therefore, a data gathering scheme capable of meeting the following two requirements is mainly needed to prolong the network lifetime.

(1) Efficiency of data gathering
(2) Balance of communication load among sensor nodes

As data gathering schemes for the long-term operation of a wireless sensor network, clustering-based data gathering[5,6], synchronization-based data gathering[7,8], gradient-based data gathering[9], and bio-inspired data gathering[10,11] are under study, but not all the above requirements are sufficiently satisfied. In a wireless sensor network, the communication load is generally concentrated on sensor nodes around a sink node during the operation process. In cases where sensor nodes are not placed evenly in an observation area, the communication load is concentrated on sensor nodes placed in an area of low node density. The above data gathering schemes[5-11] do not positively ease the communication load concentration to sensor nodes around a sink node, which is the source of problems in the long-term operation of a wireless sensor network. Intensive data transmission to specific nodes, such as sensor nodes around a sink node and sensor nodes placed in an area of low node density, results in concentrated energy consumption by them, and causes them to break away from the network early. This makes long-term observation by a wireless sensor network difficult. To solve this communication load concentration problem, data gathering schemes for a wireless sensor network with multiple sink nodes have been proposed[12,13]. In comparison with the case of a one-sink wireless sensor network, the communication load of sensor nodes around a sink node can be reduced. Especially, the scheme in Utani et al.[13] can actualize autonomous load-balancing data transmission to multiple sink nodes and can sufficiently reduces the load of load-concentrated sensor nodes. This balances the load of nodes autonomously.

To facilitate a ubiquitous environment by a wireless sensor network, however, its control mechanism should be adapted to the variety of types of communication, i.e., one-to-one, one-to-many, many-to-one, and many-to-many, depending on application requirements and the context. This paper proposes a new adaptive communication protocol for the long-term operation of such a ubiquitous sensor network. We evaluate the proposed protocol using computer simulation experiments and discuss its development potential. In simulation experiments performed, the effectiveness of the proposed protocol is investigated in detail. The rest of this paper is organized as follows. In Section 2, the existing representative protocol for adaptive communication in a wireless sensor network is outlined. In Section 3, the proposed protocol is described. In Section 4, the experimental results are reported, and the effectiveness of the proposed protocol is demonstrated by comparing its performances with those of existing protocols. Finally, we give our conclusions and ideas for further study in Section 5.

2 DIRECTED DIFFUSION

Recently, a few adaptive wireless sensor network protocols to facilitate ubiquitous information environments, which are directed diffusion[14] and rendezvous-based communication protocols[15,16] have been proposed. This paper focuses on directed diffusion that is a most representative protocol for adaptive communication in a wireless sensor network and applicable to various requirements from many sensor nodes constructing a network. The purpose of directed diffusion is to establish efficient *n*-way communication between one or more sink nodes and source nodes. Directed diffusion, which is also a data centric communication protocol, consists of the following protocol family,

(1) Two-phase pull diffusion and one-phase pull diffusion

(2) Push diffusion

where the above protocol family in directed diffusion are introduced by considering the types of communication.

In two-phase pull diffusion and one-phase pull diffusion, each sink node firstly broadcasts a message (a query) which specifies what it wants throughout the network, and afterward it gathers sensing data from each source node capable of meeting its query. In push diffusion, on the other hand each source node firstly broadcasts a message which specifies what it has measure and can provide throughout the network, and afterward it transmits sensing data to each sink node that wants sensor information included in its message. Pull types, which are two-phase pull diffusion and one-phase pull diffusion, adapt themselves to cases where the number of source nodes is more than the number of sink nodes, and push diffusion adapts itself to their contrary cases. In cases where communication between sink nodes and source nodes dynamically changes, therefore, it is difficult to use directed diffusion effectively. Directed diffusion includes the following problems.

1. Since flooding is frequently used for disseminating messages (or queries), each sensor node is loaded with loads of energy consumption.
2. Since the function for autonomously selecting the effective protocol from the above protocol family according to the situations of communication is not arranged, directed diffusion can not always achieve efficient communication in changing communication environments.
3. The communication load of each sensor node is not sufficiently balanced

3 PROPOSED PROTOCOL

The proposed protocol, which is an adaptive communication protocol for a ubiquitous sensor network, is devised for improving the above-mentioned problems included in directed diffusion. In the proposed protocol, the first node that disseminated a query in sink nodes, called *head sink*, functions for efficient data gathering, and the first node that disseminated a message, the contents of which is outlined in section 2, in source nodes, called *head source*, functions for efficient data providing in the same way. In addition, the mechanism of autonomous load-balancing communication[13] is introduced in the proposed protocol. By realizing efficient and load-balancing communication between sink nodes and source nodes, the proposed protocol can prolong the lifetime of a ubiquitous sensor network.

The proposed protocol is composed of two protocol family: sink-oriented communication protocol and source-oriented communication protocol. In the proposed protocol, each node has a connective value named *value to self*, which is not updated by transmitting and/or receiving messages or sensing data, and this is used for autonomous load-balancing communication between sink nodes and source nodes, where parts on autonomous load-balancing communication in the proposed protocol is outlined in the following subsections. The mechanism is detailed in Utani et al.[13].

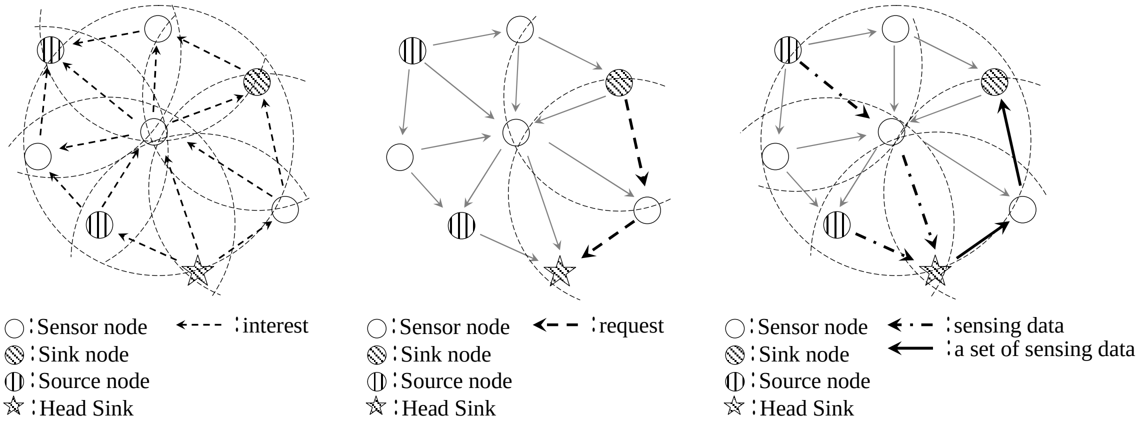

1) Interest propagation 2) Request transmission 3) Data delivery

Fig.1. Flow of communication based on sink-oriented communication protocol.

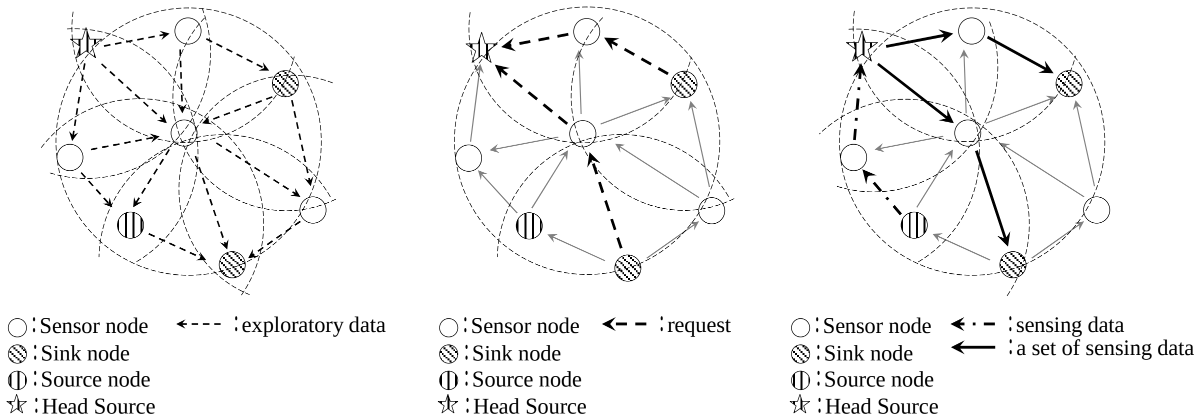

1) Exploratory data propagation 2) Request transmission 3) Data delivery

Fig.2. Flow of communication based on source-oriented communication protocol.

3.1. Sink-Oriented Communication Protocol

The flow of communication based on sink-oriented communication protocol consists of the following steps. In **Fig.1**, the communication flow is illustrated.

1) A sink node broadcasts a message (a query) which includes what it wants named *interest* and its own *value to self* throughout the network with hop counts updated, where this node, which is the first sink node that broadcast a query in sink nodes, becomes the head sink. Each node that repeatedly receives this message stores the connective values computed from *value to self*, "hop counts" and "residual energy" in the matching neighborhood node fields of its own routing table. In each node, the connective values updated by "residual energy" are used as the only index to evaluate the relay destination value of each neighborhood node.
2) Each sink node, which wants to gather the same sensing data (sensor information) as what the head sink wants, transmits a message named *request* to the head sink according to the above connective values which are the only route information. Therefore, the path between the head sink and each sink node is constructed.
3) Each source node, which has measure and can provide sensing data (sensor information) specified in *interest* that is propagated by the head sink, transmits sensing data to the head sink according to the above connective values, and then the head sink transmits a set of data consisting of sensing data gathered from source nodes to each sink node along the constructed path.

3.2 Source-Oriented Communication Protocol

Next, the flow of communication based on source-oriented communication protocol is described. In **Fig.2**, the communication flow is similarly illustrated.

1) A source node broadcasts a message which includes what it has measure and can provide named *exploratory data* and its own *value to self* throughout the network with hop counts updated, where this node, which is the first source node that broadcast a message in source

nodes, becomes the head source. Each node that repeatedly receives this message stores the connective values computed from *value to self*, "hop counts" and "residual energy" in the matching neighborhood node fields of its own routing table. As in the above-mentioned sink-oriented communication protocol, the connective values updated by "residual energy" are used as the only index to evaluate the relay destination value of each neighborhood node in each node.

2) Each sink node, which wants to gather sensing data (sensor information) specified in *exploratory data* that is propagated by the head source, transmits a message named *request* to the head source according to the above connective values which are the only route information. As in step 2) of sink-oriented communication protocol, therefore, the path between the head source and each sink node is constructed.

3) Each source node, which has measure the same sensing data (sensor information) as what the head source can provide, transmits sensing data to the head source according to the above connective values, and then the head source transmits a set of data consisting of its own sensing data and sensing data transmitted from the other source nodes to each sink node along the constructed path.

4 SIMULATION EXPERIMENT

Through simulation experiments on a large scale and dense ubiquitous sensor network, the performance of the proposed protocol, i.e., the adaptability of the proposed protocol in a changing communication environment, is investigated in detail to verify its effectiveness.

4.1. Conditions of Simulation

A ubiquitous sensor network composed of many static sensor nodes with global positioning system placed in a large scale square field was assumed. The conditions of the simulation which were used in the experiments performed are shown in **Table1**, where a thousand static sensor nodes were randomly arranged in the set simulation area as in **Fig.3**. The *value to self* of each node and the connective value attenuation factor accompanying hop[13] for autonomous load-balancing communication were set to 100.0 and 0.5 from a preliminary investigation, respectively. As in Intanagonwiwat et al.[14], messages which include *interest* were modeled as 36-byte packets, and messages which include *exploratory data* as 64-byte packets, where the size of sensing data of each node was set to 10 byte. The battery capacity of each node was modeled as 0.5J, and energy consumption was computed as in Heinzelman et al.[17]. In the following experimental results reported, the proposed protocol is evaluated through a comparison with "one-phase pull diffusion" and "push diffusion" in directed diffusion.

Table1. Conditions of simulation.

Simulation size	2,400[m]×2,400[m]
Operation time	1,000[s]
Number of sensor nodes	1,000
Range of ratio wave	150[m]
Value to self of each node	100.0
Connective value attenuation factor	0.5
Interest message	36-byte packet
Exploratory data message	64-byte packet
Size of sensing data	10[bytes]
Battery capacity of each node	0.5[J]

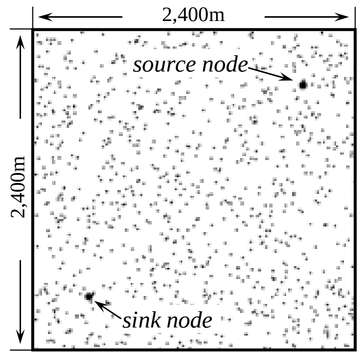

Fig.3. Arrangement of sensor nodes in the set simulation area.

4.2. Experimental Results

In the first experiment, it was assumed that the sink node marked in **Fig.3** transmitted the data packet with sensing data measured to the source node similarly marked in **Fig.3**, where the data packets were periodically transmitted every 10sec and the network operation duration was 1,000sec. The routes used by applying the proposed protocol are shown in **Fig.4**. Of the 100 data packets transmitted from the sink node, the routes used by the first 25 data packets are illustrated in **Fig.4**(1), those used by the 50 data packets are in **Fig.4**(2), and those used by a total of 100 data packets are in **Fig.4**(3). **Fig.4** indicates that the proposed protocol enables the autonomous load-balancing transmission of data packets using multiple routes. By this autonomous load-balancing communication, to prolong the network lifetime can be expected.

Next, the sustainability of the proposed protocol was evaluated in a changing communication environment. Here, it was assumed as a changing communication environment that sinks to sources was periodically transformed from *one-to-one* to *one-to-ten*, from *one-to-ten* to *ten-to-one*, and from *ten-to-one* to *ten-to-ten* every 250sec, where all sink nodes and all source nodes were randomly selected from a total of 1,000 nodes shown in **Fig.3**. In the same way as in the above experiment, all data packets were periodically transmitted every 10sec and the operation duration was 1,000sec. In **Figs.5** and **6**, the transition of total energy consumption of all nodes arranged in the set simulation area is shown, and total energy consumption in applying the proposed protocol is compared with it in directed diffusion. From **Figs.5** and **6**, it can be confirmed that the proposed protocol always realizes efficient communication between one or more sink nodes and source nodes accompanying the variety of types of communication. In **Figs.7** and **8**, the transition of the average data delivery ratio of fifty trials is shown, and the network lifetime in a changing communication environment is compared. From **Figs.7** and **8**, it can be confirmed that the proposed protocol achieves a longer-term operation of a ubiquitous sensor network than directed diffusion because it improves and balances the load of each node by the communication load reduction for network control and data gathering, and the load-balancing communication. Through simulation experiments, it was verified that the proposed protocol is substantially advantageous for the long-term operation of an ubiquitous sensor network.

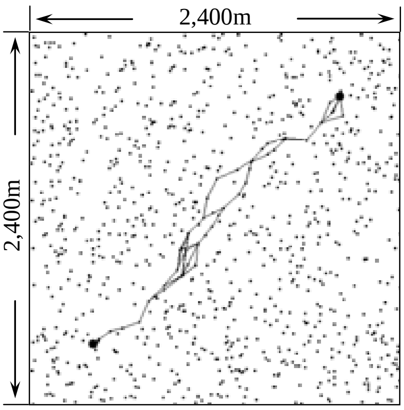

(1) 1 to 25 data packets.

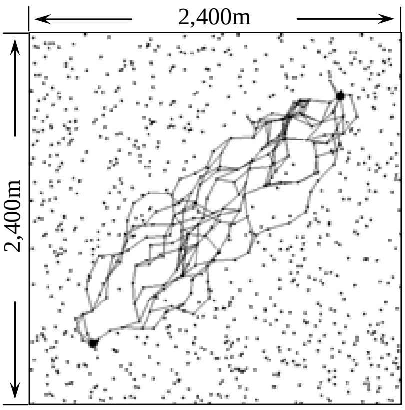

(2) 1 to 50 data packets.

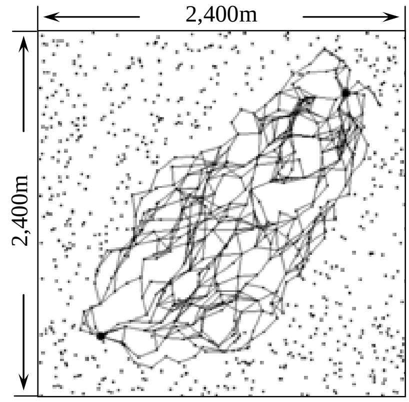

(3) 1 to 100 data packets.

Fig.4. Routes used by applying the proposed protocol.

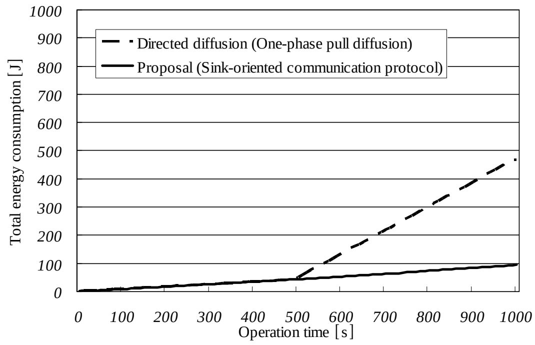

Fig.5. Transition of total energy consumption (Sink-oriented protocol).

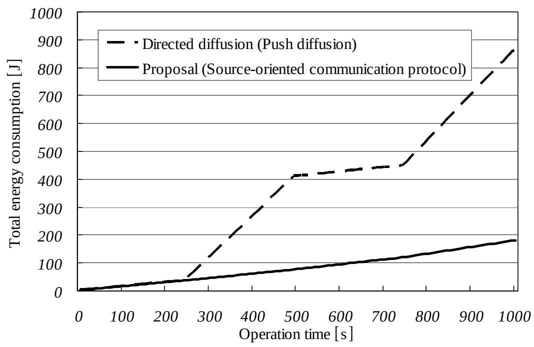

Fig.6. Transition of total energy consumption (Source-oriented protocol).

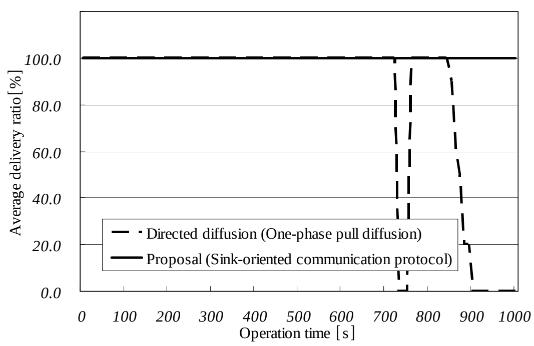

Fig.7. Transition of average data delivery ratio (Sink-oriented protocol).

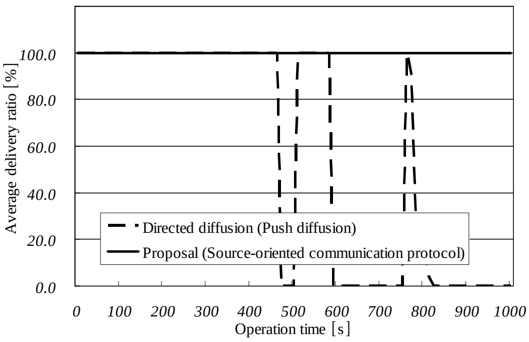

Fig.8. Transition of average data delivery ratio (Source-oriented protocol).

5. CONCLUSIONS

In this paper, a new adaptive communication protocol for a wireless sensor network, which adapts itself to the variety of types of communication, has been proposed. The proposed protocol can improve several problems in directed diffusion, which is the existing representative protocol for adaptive communication in a wireless sensor network. In simulation experiments performed, the performances of the proposed protocol were compared with those of directed diffusion. The experimental results indicate that the proposed protocol is superior to directed diffusion from the viewpoint of the long-term operation of a ubiquitous wireless sensor network, and has the development potential as a promising one. Future work includes a detailed evaluation of the adaptability of the proposed protocol in dramatically changing communication environments.

REFERENCES

[1] I. Akyildiz, W. Su, Y. Sankarasubramaniam and E. Cayirci, Wireless Sensor Networks: A Survey, *Computer Networks Journa*l, Vol. 38, No.4, pp.393-422, 2002.

[2] R. Rajagopalan and P. K. Varshney, Data Aggregation Techniques in Sensor Networks: A Survey, *IEEE Communications Surveys and Tutorials*, Vol.8, pp.48-63, 2006.

[3] W. Seah and Y. K. Tan, *Sustainable Wireless Sensor Networks*, InTech Open Access Publisher, 2010.

[4] W.Y. Chung and G. Walia, Query Driven Architecture in Wireless Sensor Network for Ubiquitous Health Monitoring, *Sensor Letters*, Vol.9, No.1, pp.384-392, 2011.

[5] K. Dasgupta, K. Kalpakis and P. Namjoshi, An Efficient Clustering-based Heuristic for Data Gathering and Aggregation in Sensor Networks, *Proc. of the IEEE Wireless Communication and Network Conference*, pp.16-20, 2003.

[6] M. Esnaashari and M. R. Meybodi, A Cellular Learning Automata Based Clustering Algorithm for Wireless Sensor Networks, *Sensor Letters*, Vol.6, No.5, pp.723-735, 2008.

[7] N. Wakamiya and M. Murata, Synchronization-based Data Gathering Scheme for Sensor Networks, *IEICE Trans on Communications*, Vol.E88-B, No.3, pp.873-881, 2005.

[8] H. Nakano, A. Utani, A. Miyauchi, and H. Yamamoto, Data Gathering Scheme using Chaotic Pulse-coupled Neural Networks for Wireless Sensor Networks, *IEICE Trans on Fundamentals*, Vol.E92-A, No.2, pp.459-466, 2009.

[9] L. Xia, X. Chen, and X. Guan, A New Gradient-based Routing protocol in Wireless Sensor Networks, *Lecture Notes in Computer Science*, Vol. 3605, pp.318-325, 2004.

[10] Y. Ohtaki, N. Wakamiya, M. Murata, and M. Imase, Scalable and Efficient Ant-based Routing Algorithm for Ad-hoc Networks, *IEICE Trans on Communications*, Vol.E89-B, No.4, pp.1231-1238, 2006.

[11] A. Utani, E. Orito, A. Kumamoto, and H. Yamamoto, An Advanced Ant-based Routing Algorithm for Large Scale Mobile Ad-hoc Sensor networks, *Trans on SICE*, Vol.44, No.4, pp.351-360, 2008.

[12] H. Dubois-Ferriere, D. Estrin and T. Stathopoulos, Efficient and Practical Query Scoping in Sensor Networks, *Proc. of the IEEE International Conference on Mobile Ad-Hoc and Sensor Systems*, pp.564-566, 2004.

[13] A.Utani and H. Yamamoto, Autonomous Load-balancing Data Transmission Scheme to Multiple Sinks for Long-term Operation of Wireless Sensor Networks, *IEICE Trans on Information and Systems*, Vol.J93-D, No.6, pp.1056-1060, 2010.

[14] C. Intanagonwiwat, R. Govindan, D. Estrin, J. Heidemann, and F. Silva, Directed Diffusion for Wireless Sensor Networking, *ACM/IEEE Trans on Networking*, Vol.11, pp.2-16, 2003.

[15] B. Krishnamachari and J. Heidemann, Application-Specific Modeling of Information Routing in Wireless Sensor Networks, *USC-ISI Technical Report*, ISI-TR-2003-576, 2003.

[16] M. Wakabayashi, H. Tada, N. Wakamiya, M. Murata, and M. Imase, Proposal and Evaluation of a Bio-inspired Adaptive Communication protocol for sensor networks, *IEICE Technical Report*, Vol.107, No.29-4, pp.89-94, 2007.

[17] W.R. Heinzelman, A. Chandrakasan, and H. Balakrishnan, Energy Efficient Communication Protocol for Wireless Microsensor Networks, *Proc. of the Hawaii International Conference on System Sciences*, pp.3005-3014, 2000.

The Seventeenth International Symposium on Artificial Life and Robotics 2012 (AROB 17th '12),
B-Con Plaza, Beppu, Oita, Japan, January 19-21, 2012

Data gathering scheme for area monitoring-based wireless sensor networks

Kosuke Ikeda[1], Akihide Utani[1], and Hisao Yamamoto[1]

[1]Tokyo City University, Tokyo 158-8557, Japan
(Tel: 81-3-5707-0104)

[1]autani@tcu.ac.jp

Abstract: Wireless sensor networks have great potential as a means of realizing a wide range of applications, such as natural environmental monitoring, environmental control in residential spaces or plants, and object tracking. As a frame to actualize these sensor applications, this study assumes a monitoring-oriented wireless sensor network, which periodically gathers their sensing data from all sensors placed in a service area. This paper proposes an autonomous decentralized control scheme with data aggregation technique to prolong the lifetime of monitoring-oriented wireless sensor networks. This is a novel scheme devised by considering the application environment of a wireless sensor network as a typical example of a complex system where the adaptive adjustment of the entire system is realized from the local interactions of components of the system. We evaluate our scheme using simulation experiments, and also discuss its development potential.

Keywords: Monitoring, Wireless sensor networks, Multiple sinks, Autonomous decentralized control, Data aggregation.

1 INTRODUCTION

Various communication services are currently considered. They include environmental monitoring or control by static sensors, ad-hoc communication between mobile nodes, and inter-vehicle communication in intelligent transport systems. As a means of facilitating these advanced communication services, autonomous decentralized networks, such as wireless sensor networks [1,2], mobile adhoc networks [3-6], and wireless LAN mesh networks [7], have been intensively studied with great interests. Especially, a wireless sensor network, which is a key network to construct ubiquitous information environments, has great potential as a means of realizing a wide range of applications, such as natural environmental monitoring, environmental control in residential spaces or plants, object tracking. Recently, there is growing expectation for a new network service by a novel wireless sensor network consisting of a lot of static sensors arranged in a service area and a few mobile robots as a result of the strong desire for the development of advanced systems that can flexibly function in dynamically changing environments [8].

As a frame to actualize the above-mentioned sensor applications, this study assumes a monitoring-oriented wireless sensor networks composed of many static sensors with global positioning system, which periodically gathers their sensing data from all sensors placed in a service area. In a general monitoring-oriented wireless sensor network, hundreds or thousands of sensors with limited resources, which are compact and inexpensive, are placed in a large scale service area, and the sensing data from each node is gathered to a sink node by inter-node wireless multi-hop communication. Each sensor node consists of a sensing function to measure the status of an observation point or object, a limited function of information processing and a simplified wireless communication function, and it generally operates on a resource with a limited power-supply capacity such as a battery. Therefore, a data gathering scheme and/or a routing protocol capable of meeting the following requirements is needed to prolong the lifetime of wireless sensor networks made up of hundreds or thousands of sensors with limited resources.

1. Efficiency of data gathering
2. Balance of communication load among sensor nodes
3. Adaptability to network topology changes

For the long-term operation of wireless sensor networks, clustering-based schemes [9,10], gradient-based routing protocol [11] and synchronization-based schemes [12-14] are under study, but not all the above requirements are sufficiently satisfied. Recently, bio-inspired routing algorithms, such as ant-based routing algorithms, have attracted a significant amount of interest from plural researchers. In ant-based routing algorithms [15,16], the routing table of each sensor node is updated by applying the process in which ants build routes between their nest and food by chemical substances (pheromones). The advanced ant-based routing algorithm proposed as an example that satisfies the three requirements above is an efficient route-learning algorithm which shares route information between ants (control messages) [17]. In contrast to conventional ant-based routing algorithms, this can suppress the communication load of each sensor node and adapt itself to network topology changes. However, this does not positively ease the communication load concentration on specific sensors, which is the source of problems in the long-term operation of sensor networks. Intensive data transmission to specific sensors results in concentrated energy consumption by them, and causes them to break away from the sensor network early. This makes long-term observation by a wireless sensor network difficult.

In wireless sensor networks, the communication load is concentrated on sensors around a sink node during the operation process. In cases where sensors are not evenly placed in a service area, the communication load is concentrated on sensor nodes placed in a range of low node density. To solve this communication load concentration problem, recent approaches have been to introduce multiple sinks in a wireless sensor network [18,19]. In the fundamental scheme [18], each sensor node sends the sensing data to the nearest sink node. In comparison with the case of one-sink wireless sensor networks, the communication load of sensors around a sink node is reduced. In each sensor node, however, the destination sink node cannot be selected autonomously and adaptively. Therefore, the load of load-concentrated nodes is not sufficiently balanced. The pheromone-oriented routing protocol, which belongs to the category of ant-based routing algorithms, achieves autonomous load-balancing data transmission to multiple sinks, but requires the periodical update of routing table of each sensor node by ants (control messages) dispersed in a wireless sensor network [19]. In monitoring-oriented wireless sensor networks, the nearest sink data transmission scheme in [18] achieves a longer-term operation of the network than the pheromone-oriented routing protocol in [19].

In the previous study [20], we devised a novel autonomous decentralized control scheme and evaluated its fundamental performance through simulation experiments. This scheme needs no special communication for network control, but enables autonomous load-balancing data transmission to multiple sinks. The load of each sensor node is autonomously balanced. In monitoring-oriented wireless sensor networks, however, the efficiency of data gathering should be improved. In this paper, we propose an autonomous decentralized control scheme with data aggregation technique for the long-term of monitoring-oriented wireless sensor networks, and evaluate the proposed scheme using simulation experiments in detail. The rest of this paper is organized as follows. First, in Sec.2, the proposed scheme is detailed, and its novelty and superiority are described. In Sec.3, the experimental results are reported in detail, and the effectiveness of the proposed scheme is demonstrated by comparing its performances with those of the existing scheme. Finally, we give the overall conclusion and future problem of this study in Sec.4.

2 PROPOSED SCHEME

To facilitate the long-term operation of an actual sensor network service, recent approaches have been to introduce multiple sinks in a wireless sensor network. In wireless sensor networks with multiple sinks, the sensing data of each node is generally allowed to gather at any of the available sinks. The proposed scheme devised by considering the application environment of a wireless sensor network as a typical example of a complex system where the adaptive adjustment of the entire system is realized from the local interactions of components of the system is a novel data gathering scheme based on this assumption, which can be expected to produce a remarkable effect in monitoring-oriented wireless sensor networks with multiple sinks.

2.1 Construction of a data gathering environment

Each sink node has a connective value named a "value to self", which is not updated by transmitting a control packet and receiving data packets. In the initial state of monitoring-oriented wireless sensor network with multiple sinks, each sink node broadcasts a control packet containing its own ID and "value to self", and hop counts ($=0$). This control packet is rebroadcast throughout the sensor network with hop counts updated. By receiving the control packet from each sink node, each sensor node can grasp the "value to self" of each sink node, and the IDs and the hop counts from each sink node of its own neighboring nodes.

Initial connective value of each sensor node, which is the connective value before starting data transmission, is generated by using the "value to self" of each sink node and the hop counts from each sink node. The procedure for computing initial connective value of a node (i) is as follows:

1. The value [$v_{ij}(0)$] on each sink node ($j = 1, \dots, S$) of node (i) is first computed according to the following equation

$$v_{ij}(0) = vo_j \times dr^{hops_{ij}} \qquad (j = 1,\dots,S) \tag{1}$$

   where vo_j ($j = 1, \dots, S$) is the "value to self" of sink node (j), $hops_{ij}$ is the hop counts from sink node (j) of node (i). dr represents the value attenuation factor accompanying the hop determined within the interval [0,1].

2. Then, the initial connective value $[v_i(0)]$ of node (i) is generated as follows

$$v_i(0) = \max v_{ij}(0) \qquad (j = 1, \ldots, S) \tag{2}$$

where this connective value $[v_i(0)]$ can be also conducted from the following equation

$$v_i(0) = vm_i(0) \times dr \tag{3}$$

In(3), $vm_i(0)$ represents the greatest connective value before starting data transmission in the neighborhood nodes of node (i).

Before starting data transmission, each sensor node computes the initial connective value of each neighborhood node according to the above (1) and (2), and stores the computed connective value, which is used as the only index to evaluate the relay destination value of each neighboring node, in each neighborhood node field of its own routing table. Therefore, the routing table of each sensor node, which is made up of the IDs and initial connective values before starting data transmission to neighboring nodes, is constructed.

2.2 Data transmission and connective value update

For data transmission, each sensor node selects the neighboring node with the greatest connective value from its own routing table as a relay node, and transmits the data packet to this selected node. In cases where more than one node shares the greatest connective value, however, the relay node is determined between them at random. The data packet in each sensor node is not sent to a specified sink node. By repetitive data transmission to the neighboring node with the greatest connective value, data gathering at any of the available sinks is completed. In the proposed scheme, the connective value of each sensor node is updated by considering residual node energy. Therefore, by repetitive data transmission to the neighboring node with the greatest connective value, the data transmission routes are not fixed.

To realize autonomous load-balancing data transmission, the data packet from each sensor node includes its own updated connective value. Here, we assume that a node (l) receives a data packet at time (t). Before node (l) relays the packet, it replaces the value in the connective value field of the data packet by its own renewal connective value computed according to the following connective value update equation

$$v_l(t) = vm_l(t) \times dr \times {e_l(t)}/{E_l} \tag{4}$$

where $vm_l(t)$ is the greatest connective value at time (t) in the routing table of node (l), and $e_l(t)$ and E_l represent the residual energy at time (t) of node (l) and the battery capacity of node (l), respectively.

In our scheme, the data packet addressed to the neighboring node with the greatest connective value is intercepted by all neighboring nodes. This packet includes the updated connective value of the source node based on (4). Each neighborhood node that intercepts this packet stores the updated connective value in the source node field of its own routing table. **Fig.1** shows an example of data packet transmission and its accompanying connective value update. In this example, node (l) refers to its own routing table and addresses the data packet to node (r), which has the greatest connective value $[vm_l(t)]$. When this data packet is intercepted, each neighboring node around node (l) stores the updated connective value $[v_l(t)]$ included in the data packet in the node (l) field of its own routing table.

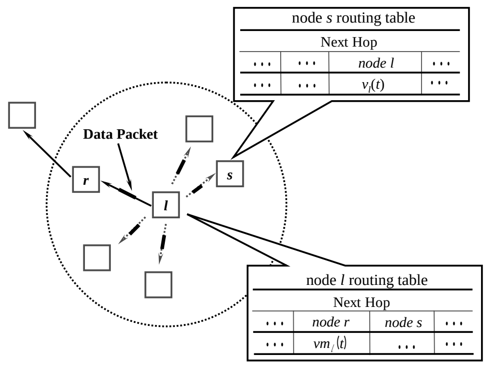

Fig.1. Data transmission and connective value update

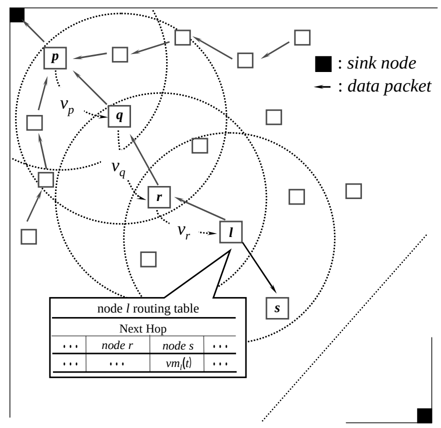

Fig.2. Autonomous load-balancing data transmission to multiple sinks

The proposed scheme requires the construction of a data gathering environment in the initial state of wireless sensor networks with multiple sinks, but needs no special communication for network control. The above-mentioned simple mechanism alone achieves autonomously adaptive load-balancing data transmission to multiple sinks, as in **Fig.2.** It can be expected that the lifetime of wireless sensor networks is extended by reducing the communication load for network control and solving the node load concentration problem.

2.3. Autonomous data aggregation technique

To improve the efficiency of data gathering, an autonomous data aggregation technique is newly introduced in our scheme. This data aggregation technique matches our autonomous decentralized control scheme. Generally, data aggregation-based schemes improve the efficiency of data gathering in a wireless sensor network, but some of them facilitate the communication load concentration on specific sensors and/or limited routes [2]. Since our scheme has the mechanism to realize autonomous load-balancing data transmission to multiple sinks using many routes, however, it can be considered that to introduce a data aggregation technique in our autonomous decentralized control scheme is effective.

The data aggregation to improve the efficiency of data gathering is autonomously actualized without special communication in the operation process of a wireless sensor network. In our data aggregation technique, the node that first transmits the original data packet or the data packet from the other sensor node to the neighboring node with the greatest connective value in the node itself and its own neighboring nodes becomes a data aggregation node called *head node*, and functions for efficient data gathering. Here, the neighboring node that intercepts the data packet from a head node becomes the member of the head node in cases where it is not the member of any of the other head nodes, and the connective value of the head node is greater than its own connective value. When the node that is the member of a head node transmits the data packet to any of its own neighboring nodes, it addresses the data packet to the head node. **Fig.3** shows an example of efficient data gathering by our data aggregation technique. In **Fig.3**, node (l) and node (r) are head nodes, and node (s) is the member of head node (l). In this example, node (l) transmits the data aggregation packet containing the sensing data from each member to the node (r) with the greatest connective value in its own neighboring nodes.

In addition, the function to ease the continuous communication load concentration to head nodes is introduced in our data aggregation technique. The node that is the member of a head node breaks away from the member when the connective value of the head node became less than its own connective value in the network operation process, and it becomes a new head node, and newly functions for efficient data gathering in cases where the other head node, the connective value of which is greater than its own connective value, does not exist in its own neighboring nodes. On the other hand, it becomes the member of the other head node with the greatest connective value in cases where the other head nodes, the connective values of which are greater than its own connective value, exist in its own neighboring nodes. **Fig.4** illustrates an example of this additional function. In **Fig.4**, node (l) and node (r) are head nodes, as in **Fig.3**. In this example, node (s) breaks away from the member of head node (l) because the connective value of head node (l) became less than its own connective value. Here, node (s) becomes a new head node when the connective value of head node (r) is less than its own connective value, as shown in **Fig.4**(a), and becomes the member of node (r) when the connective value of head node (r) is greater than its own connective value, as shown in **Fig.4**(b).

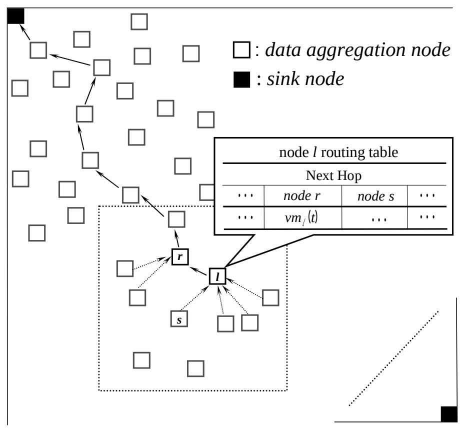

Fig.3. An example of data aggregation

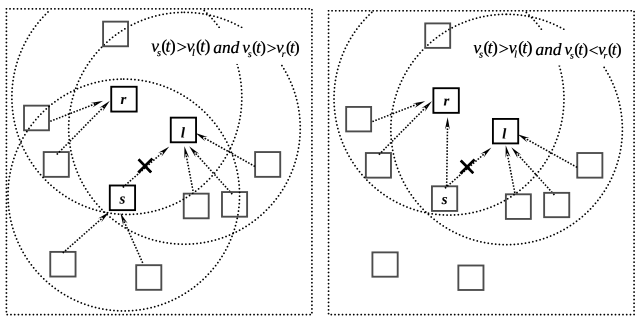

(a) Case1 (b) Case2

Fig.4. An example of additional function

3 SIMULATION EXPERIMENTS

Through simulation experiments on monitoring-oriented wireless sensor networks, the performances of our autonomous decentralized control scheme with data aggregation technique is investigated in detail to verify its effectiveness.

In a large scale and dense wireless sensor network with multiple sinks made up of many static sensors placed in a large scale square field, it is assumed that each sensor node constructing the network transmits the data packet with the measurement data periodically. The conditions of the simulation which were used in the experiments performed are shown in **Table1**. In the initial state of the simulation experiments, many static sensors are randomly arranged in the set experimental area, and two sinks are placed on the corners of this area. An example of the arrangement of sensors in the set experimental area is illustrated in **Fig.6**. In the experiments performed, the value attenuation factor accompanying hop (*dr*) and the "value to self" of each sink node introduced in the proposed scheme were set to 0.5 and 100.0, respectively. The sizes of the control packets were set to 36 bytes and the sizes of the data packets were set to $40+10\times n$ bytes, where the size of sensing data of each node was set to 10 bytes, and n represents the number of sensing data in each data packet. The battery capacity of each sensor node was modeled as 0.5J, and the energy consumption of each sensor node was computed as in [9].

Table 1. Conditions of simulation

Simulation size	*2,400 m × 2,400 m*
Number of sensor nodes	*1,000*
Range of radio wave	*150 m*
Number of sinks	*2*

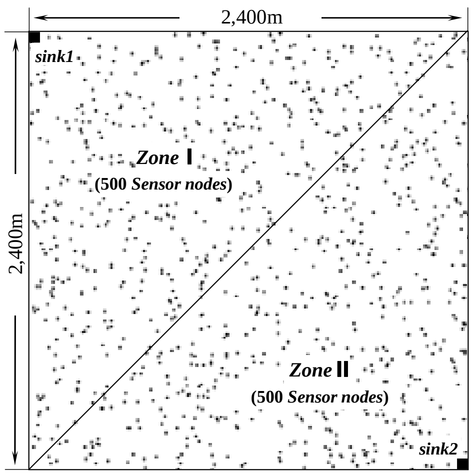

Fig.5. Arrangement of sensors in the set experimental area (Case1)

The proposed scheme is evaluated through a comparison with the existing one [18], which describes representative data gathering for wireless sensor networks with multiple sinks. In the experimental results reported, the scheme in [18] is denoted as "Nearest Sink". First, the experimental results on the arrangement of sensors (Case1) illustrated in **Fig.5** is shown. **Fig.6**(a) and (b) illustrate the routes used by applying Nearest Sink and the proposed scheme, where the bold lines in these figures indicate the routes frequently used. From **Fig.6**, it is confirmed that the proposed scheme can balance and improve the load of each sensor node by the autonomous load-balancing data transmission mechanism and the data aggregation technique newly introduced. **Fig.7** shows the transition of the delivery ratio of the total number of sensing data periodically transmitted from each sensor node. In **Fig.7**, our scheme without data aggregation is denoted as "Proposal A", and our scheme with data aggregation technique is as "Proposal B". From **Fig.7**, it can be confirmed that the proposed scheme achieves a longer-term operation of a monitoring-oriented wireless sensor network than Nearest Sink, and the effect of our scheme is facilitated by the autonomous data aggregation technique newly introduced in this study.

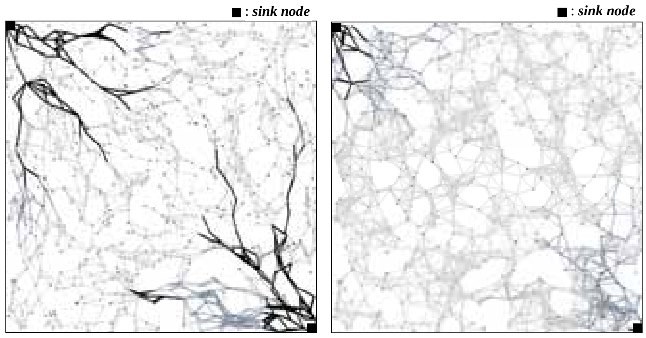

(a) Nearest Sink (b) Proposal

Fig.6. Routes used by applying Nearest Sink or the proposed scheme

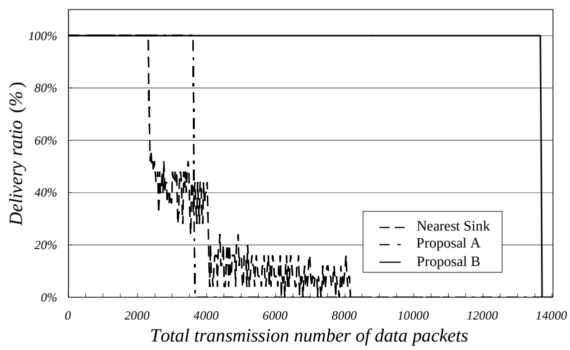

Fig.7. Delivery ratio (Case1)

Next, we assume the cases where sensors are not evenly placed in the set experimental area, as in **Figs.8**(Case2). **Fig.9** shows the transition of the delivery ratio of the total number of sensing data periodically transmitted from each sensor node, as in **Fig.7**. Through the experimental results, it can be also confirmed that our scheme with data aggregation technique is substantially advantageous for the long-term operation of monitoring-oriented wireless sensor networks with multiple sinks.

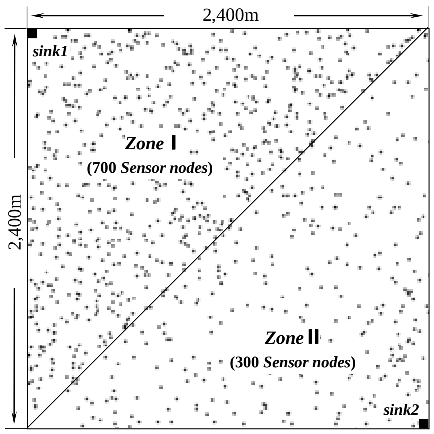

Fig.8. Arrangement of sensors（Case2）

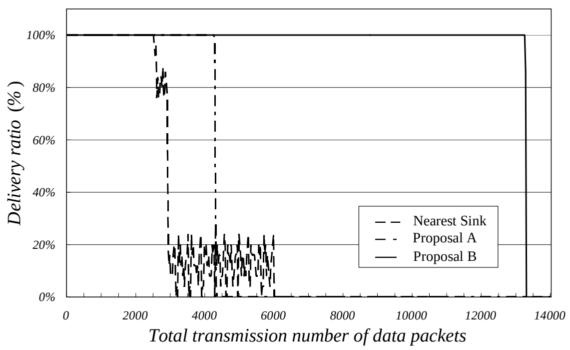

Fig.9. Delivery ratio（Case2）

4 CONCLUSION

In this paper, an autonomous decentralized control scheme with data aggregation technique that adaptively reduces the load of load-concentrated sensors and facilitates the long-term operation of monitoring-oriented wireless sensor networks with multiple sinks has been proposed. This is a novel scheme devised by considering the application environment of a wireless sensor network to be a typical example of a complex system where the adjustment of the entire system is adaptively realized from the local interactions of components of the system. In simulation experiments, the performances of the proposed scheme were compared with those of the existing one. The experimental results indicate that the proposed scheme is superior to the existing one from the viewpoint of the long-term operation of monitoring-oriented wireless sensor networks. Future work includes a detailed evaluation of the proposed scheme in various network environments.

REFERENCES

[1] I. Akyildiz, W. Su, Y. Sankarasubramaniam and E. Cayirci, Wireless sensor networks: A survey, *Computer Networks Journal*, Vol.38, No.4, pp.393-422, 2002.

[2] R. Rajagopalan and P. K. Varshney, Data aggregation techniques in sensor networks: A survey, *IEEE Communications Surveys and Tutorials*, Vol.8, pp.48-63, 2006.

[3] C. E. Perkins and E. M. Royer, Ad hoc on-demand distance vector routing, *Proc. of the 2nd IEEE Workshop on Mobile Computing Systems and Applications*, pp.90-100, 1999.

[4] D. B. Johnson, D. A. Maltz, Y. C. Hu and J. G. Jetcheva, The dynamic source routing protocol for mobile ad hoc networks, *IETF Internet Draft, draft-ietf-manet-dsr-09.txt*, 2003.

[5] T. Clausen and P. Jaquet, Optimized link state routing protocol, *Request for Comments 3626*, 2003.

[6] R. Ogier, M. Lewis and F. Templin, Topology dissemination based on reverse-path forwarding（TBRPF）, *IETF Internet Draft, draft-ietf-manet-tbrpf-10.txt*, 2003.

[7] S. Sakata, H. Aoki and K. Mase, Mobile ad hoc networks and wireless LAN mesh networks, *IEICE Trans. Commun.*, Vol.E89-B, No.6, pp.811-823, 2006.

[8] K. Matsumoto, A. Utani and H. Yamamoto, Adaptive and efficient routing algorithm for mobile ad-hoc sensor networks, *ICIC Express Letters*, Vol.3, No.3（B）, pp.825-832, 2009.

[9] W. R. Heinzelman, A. Chandrakasan and H. Balakrishnan, Energy-efficient communication protocol for wireless microsensor networks, *Proc. of the Hawaii International Conference on System Sciences*, pp.3005-3014, 2000.

[10] Y. Jin, J. Jo and Y. Kim, Energy-efficient multi-hop communication scheme in clustered sensor networks, *International Journal of Innovative Computing, Information and Control*, Vol.4, No.7, pp.1741-1749, 2008.

[11] L. Xia, X. Chen and X. Guan, A new gradient-based routing protocol in wireless sensor networks, *Lecture Notes in Computer Science*, Vol.3605, pp.318-325, 2004.

[12] N. Wakamiya and M. Murata, Synchronization-based data gathering scheme for sensor networks, *IEICE Trans. Commun.*, Vol.E88-B, No.3, pp.873-881, 2005.

[13] H. Nakano, A. Utani, A. Miyauchi and H. Yamamoto, Data gathering scheme using chaotic pulse-coupled neural networks for wireless sensor networks, *IEICE Trans. Fundamentals*, Vol.E92-A, No.2, pp.459-466, 2009.

[14] H. Nakano, A. Utani, A. Miyauchi and H. Yamamoto, Chaos synchronization-based data transmission scheme in multiple sink wireless sensor networks, *International Journal of Innovative Computing, Information and Control*, Vol.7, No.4, pp.1983-1994, 2011.

[15] D. Subramanian, P. Druschel and J. Chen, Ants and reinforcement learning: A case study in routing in dynamic networks, *Technical Report TR96-259*, Rice University, 1998.

[16] Y. Ohtaki, N. Wakamiya, M. Murata and M.Imase, Scalable and efficient ant-based routing algorithm for ad-hoc networks, *IEICE Trans. Commun.*, Vol.E89-B, No.4, pp.1231-1238, 2006.

[17] A. Utani, E. Orito, A. Kumamoto and H. Yamamoto, An advanced ant-based routing algorithm for large-scale mobile ad-hoc sensor networks, *Trans. SICE*, Vol.44, No.4, pp.351-360, 2008.

[18] E. I. Oyman and C. Ersoy, Multiple sink network design problem in large scale wireless sensor networks, *Proc. of the 2004 International Conference on Communications*, Vol.6, pp.3663-3667, 2004.

[19] E. Orito, A. Utani and H. Yamamoto, Pheromone-oriented routing protocol for load balancing of wireless sensor networks with multiple sinks, *Journal of SOFT*, Vol.21, No.1, pp.56-68, 2009.

[20] K. Matsumoto, A. Utani and H. Yamamoto, Bio-inspired data transmission scheme to multiple sinks for the long-term Operation of wireless sensor networks, *Int. J. Artificial Life and Robotics*, Vol.15, No.2, pp.189-194, 2010.

The Seventeenth International Symposium on Artificial Life and Robotics 2012 (AROB 17th '12),
B-Con Plaza, Beppu, Oita, Japan, January 19-21, 2012

A centralized control system for ecological vehicle platooning using linear quadratic regulator theory

Anan Kaku[1], Masakazu Mukai[2], and Taketoshi Kawabe[1]

[1] Graduate School of Integrated Frontier Sciences, Kyushu University, Fukuoka 819-0395, Japan
[2] Graduate School of Information Science and Electrical Engineering, Kyushu University, Fukuoka 819-0395, Japan
(Tel: 81-92-802-3675, Fax: 81-92-802-3692)

[1]kakuanan@cig.ees.kyushu-u.ac.jp

Abstract: This paper presents an ecological vehicle platooning control system that aims in reducing overall fuel consumption of the vehicles in a platoon. A centralized linear quadratic regulator system for controlling the vehicles in the platoon has been developed considering the aerodynamic characteristics of the vehicle and the resistance due to the road slope. The proposed control system is simulated on a highway with up-down slopes for high speed driving. Its fuel saving performance is compared with a conventional decentralized vehicle platooning control system. Computer simulation results reveal the significant improvement in fuel economy by the proposed control system.

Keywords: Aerodynamic characteristics, centralized control, ecological driving, linear quadratic regulator theory, platooning, road shape information.

1 INTRODUCTION

In recent years, global warming and ozone depletion have been gotten widespread international attention. Since the energy consumption of vehicles accounts for a substantial amount of all the energy consumption, it is considered that so-called "eco-driving" by vehicles is important to solve such environmental issues. Eco-driving can be characterized by a fuel-efficient driving style to match various road-traffic situations. The fuel consumption caused by the aerodynamic drag during high speed driving can be reduced by platooning. As shown in Fig.1, a number of vehicles run with short spacing in a line. The aerodynamic drag of each vehicle is reduced owing to the improved airflow profile around the platoon [1]. Therefore, fuel consumption of each vehicle caused by the aerodynamic drag can be reduced. Automated control of the vehicles has been introduced for such platooning. Various conventional methods mainly focused on the platoon formation and achievement of the string stability [2] [3] [4]. On the other hand, automated driving control system for energy saving of two vehicles has been proposed [5]. However, fuel saving by synchronized driving behavior of more vehicles was not considered. To build an ecological vehicle platooning (EVP) control system, it is considered that centralized controller is efficient in synchronizing motion of the vehicles by using driving information of all the vehicles in the platoon.

In this paper, a centralized linear quadratic regulator (LQR) system for the ecological vehicle platooning is proposed to reduce the overall fuel consumption of the vehicles in the platoon. The dynamical model of the platoon including the varying aerodynamic drag coefficient depending on vehicles' spacings and the road shape has been developed. This model is linearized around the target driving situation. The fuel consumption model based on the engine efficiency characteristics is constructed. Computer simulations considering high speed driving on a typical highway with up-down slopes were conducted. The fuel-saving performance of the proposed control system was compared with a conventional decentralized vehicle platooning control system (CVP). Significant improvement in fuel economy by the proposed control system was verified.

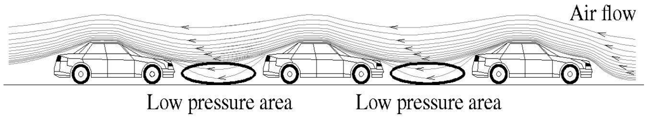

Fig. 1. Air flow profile around a platoon

This paper is structured as follows. In Section 2, control for an ecological vehicle platooning is proposed. In Section 3, computer simulation results demonstrate the effectiveness of the proposed control system. In Section 4, conclusions are discussed.

2 CONTROL METHOD FOR ECOLOGICAL VEHICLE PLATOONING

2.1 Vehicle model

A platoon consisting of three vehicles is shown in Fig.2. Longitudinal movement of a vehicle in the platoon can be

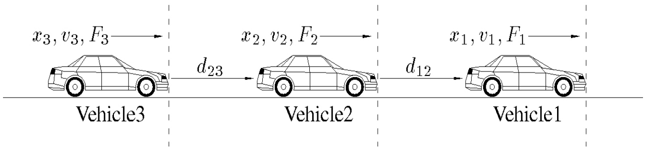

Fig. 2. A platoon consists of three vehicles

represented by the following equations:

$$\begin{aligned}
&\dot{x}_i(t) = v_i(t) \ , \\
&m_i \dot{v}_i(t) = F_i(t) - f_{ai}(t) - f_{gi}(t) - f_{\mu i} \ , \\
&f_{ai}(t) = \frac{1}{2}\rho A_i C_i(d_{12}(t), d_{23}(t)) v_i^2(t) \ , \\
&f_{gi}(t) = m_i g \sin\theta(x_i(t)) \ , \\
&f_{\mu i} = \mu_i m_i g \ , \\
&d_{12}(t) = x_1(t) - x_2(t) - l_1 \ , \\
&d_{23}(t) = x_2(t) - x_3(t) - l_2 \ , \qquad (1)
\end{aligned}$$

where, subscript i is an integer which indicates the i-th vehicle (i=1,2,3) counted from the leading vehicle in the platoon. Parameters ρ, g, m_i, A_i, μ_i, and l_i are the air density, the gravity acceleration, the mass, the projected frontal area, the coefficient of all the other friction resistances, and the length of the i-th vehicle, respectively. Variables x_i, v_i, F_i, d_{12}, and d_{23} are the position, the velocity, the traction force or the brake force of the i-th vehicle, and the spacing between the neighbor vehicles, respectively. Functions f_{ai}, f_{gi}, and $f_{\mu i}$ denote the aerodynamic drag, the grade resistance, and all the other friction resistances of the i-th vehicle, respectively. $C_i(d_{12}, d_{23})$ is the aerodynamic drag coefficient that depends on the spacing. $\theta(x_i)$ is the road gradient that depends on the position of each vehicle. The time delay from input command to the traction force or the brake force is assumed to be represented by the first order lag:

$$\dot{F}_i(t) = -\frac{1}{\tau_i}F_i(t) + \frac{1}{\tau_i}u_i(t) \ , \qquad (2)$$

where, τ_i and u_i are the time delay constant and the control input command of the traction force or the brake force of the i-th vehicle, respectively.

Around the target driving situation, the model of the vehicle' longitudinal equations are linearized. Each deviation of the velocity δv_i, the traction force or the brake force δF_i, the control input δu_i, and the spacings are represented by

$$\begin{aligned}
&\delta v_i(t) = v_i(t) - v^* \ , \\
&\delta F_i(t) = F_i(t) - f_{ai}^* - f_{gi}(t) - f_{\mu i} \ , \\
&\delta u_i(t) = u_i(t) - f_{ai}^* - f_{gi}(t) - f_{\mu i} \ , \\
&\delta d_{12}(t) = d_{12}(t) - d^* \ , \\
&\delta d_{23}(t) = d_{23}(t) - d^* \ , \\
&f_{ai}^* = \frac{1}{2}\rho A_i C_i(d^*, d^*) v^{*2} \ , \qquad (3)
\end{aligned}$$

where, v^* and d^* are the target velocity and the target spacing. A state equation used in the centralized LQR control system is represented as

$$\begin{aligned}
&\dot{x}(t) = Ax(t) + Bu(t) \ , \\
&x(t) = \left[\ \delta v_1\ \ \delta F_1\ \ \delta d_{12}\ \ \delta v_2\ \ \delta F_2\ \ \delta d_{23}\ \ \delta v_3\ \ \delta F_3\ \right]^T \ , \\
&u(t) = \left[\ \delta u_1\ \ \delta u_2\ \ \delta u_3\ \right]^T \ , \qquad (4)
\end{aligned}$$

$$A = \begin{bmatrix}
-\frac{\alpha_1}{m_1} & \frac{1}{m_1} & -\frac{\beta_1}{m_1} & 0 & 0 & -\frac{\gamma_1}{m_1} & 0 & 0 \\
0 & -\frac{1}{\tau_1} & 0 & 0 & 0 & 0 & 0 & 0 \\
1 & 0 & 0 & -1 & 0 & 0 & 0 & 0 \\
0 & 0 & -\frac{\beta_2}{m_2} & -\frac{\alpha_2}{m_2} & \frac{1}{m_2} & -\frac{\gamma_2}{m_2} & 0 & 0 \\
0 & 0 & 0 & 0 & -\frac{1}{\tau_2} & 0 & 0 & 0 \\
0 & 0 & 0 & 1 & 0 & 0 & -1 & 0 \\
0 & 0 & -\frac{\beta_3}{m_3} & 0 & 0 & -\frac{\gamma_3}{m_3} & -\frac{\alpha_3}{m_3} & \frac{1}{m_3} \\
0 & 0 & 0 & 0 & 0 & 0 & 0 & -\frac{1}{\tau_3}
\end{bmatrix}, B = \begin{bmatrix}
0 & 0 & 0 \\
\frac{1}{\tau_1} & 0 & 0 \\
0 & 0 & 0 \\
0 & 0 & 0 \\
0 & \frac{1}{\tau_2} & 0 \\
0 & 0 & 0 \\
0 & 0 & 0 \\
0 & 0 & \frac{1}{\tau_3}
\end{bmatrix} .$$

$$\begin{aligned}
&\alpha_i = \left.\frac{\partial f_{ai}}{\partial v_i}\right|_{v_i=v^*, d_{12}=d^*, d_{23}=d^*} \\
&\beta_i = \left.\frac{\partial f_{ai}}{\partial d_{12}}\right|_{v_i=v^*, d_{12}=d^*, d_{23}=d^*} \\
&\gamma_i = \left.\frac{\partial f_{ai}}{\partial d_{23}}\right|_{v_i=v^*, d_{12}=d^*, d_{23}=d^*} \ ,
\end{aligned}$$

where, α_i, β_i, and γ_i are parameters of Taylor expansion of f_{ai} that ignore the terms over second-order.

2.2 Centralized control system using LQR

The performance index using LQR is formulated as

$$J = \int_0^\infty \left(x^T Q x + u^T R u\right) dt \ , \qquad (5)$$

where, Q is positive semidefinite matrix, and R is positive definite matrix. The control input is calculated by

$$u_{LQR} = -R^{-1} B^T P x(t) \ , \qquad (6)$$

where, P is the solution of the following equation:

$$A^T P + PA - PBR^{-1}B^T P + Q = 0 \ . \qquad (7)$$

3 COMPUTER SIMULATION

In the computer simulations, a typical vehicle equipping continuously variable transmission (CVT) was selected. The parameters of the vehicles were $m_i = 1480$ [kg], $A_i = 2.87$ [m^2], $l_1 = l_2 = 4.3$ [m], and $\tau_i = 0.1$. The driving condition were $\rho = 1.2$ [kg/m^3] and $\mu = 0.01$. To construct the function C_i, a set of data that represents the relationship of C_i, d_{12}, and d_{23} obtained from wind tunnel experiments [1] was adopted. The approximation results of C_i are shown in Fig.3 and Fig.4. The fuel consumption of the vehicle was

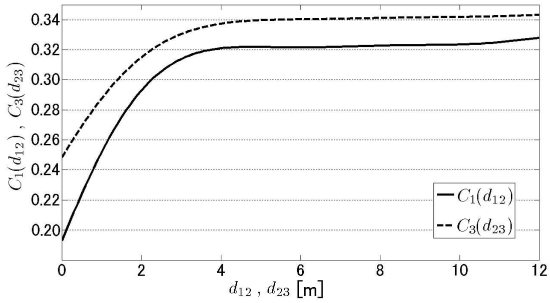

Fig. 3. Approximation results of C_1 and C_3

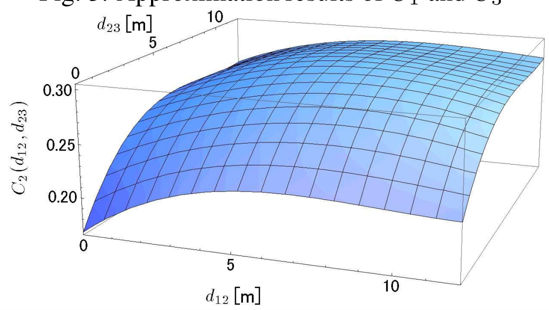

Fig. 4. Approximation result of C_2

estimated as

$$f_{uel\ i}(t) = \begin{cases} \dfrac{P_i(t)}{\eta_i(P_i(t))Q} & \text{for} \quad u_i \geq 0 \\ 0 & \text{for} \quad u_i < 0 \end{cases},$$

$$\begin{aligned} P_i(t) &= \big(m_i \dot{v}_i(t) + f_{ai}(t) + f_{gi}(t) + f_{\mu i}\big)v_i(t) + P_c \\ &= F_i(t)v_i(t) + P_c\ , \end{aligned} \tag{8}$$

where, f_i is the fuel consumption per unit time, P_i is the engine power output needed for driving a vehicle, η_i shown in Fig.5 is the maximum efficiency based on the engine characteristics map [6], $Q = 34.5$ [MJ/L] is the calorific value of gasoline, $P_c = 845.825$ [W] is the constant power required when the vehicle is idling. This equation was matched with the fuel consumption rate of the selected vehicle on the Japan 10-15 mode test.

At the initial time ($t = 0$), $v_1(0) = 95$ [km/h], $v_2(0) = 90$ [km/h], $v_3(0) = 85$ [km/h], $d_{12}(0) = d_{23}(0) = 10$ [m]. The desired driving situation was set as $v_i^* = 100$ [km/h] and $d_{12}^* = d_{23}^* = 2$ [m]. Altitude and slope of the road shapes used here are shown in Fig.6. $\sin\theta$ was approximated as $\sin\theta \approx \theta$ since the road slope is very small. The matrices Q and R are defined as

$$\begin{aligned} Q &= \text{diag}[\ 340 \quad 80 \quad 12 \quad 360 \quad 80 \quad 12 \quad 380 \quad 80\ ]\,, \\ R &= \text{diag}[\ 380 \quad 390 \quad 400\ ]\,. \end{aligned} \tag{9}$$

The sampling period was set as 0.01 [s]. To evaluate the performance of the proposed EVP control system, its computer simulation results were compared with a CVP control system. In the CVP control system [2], the control inputs of

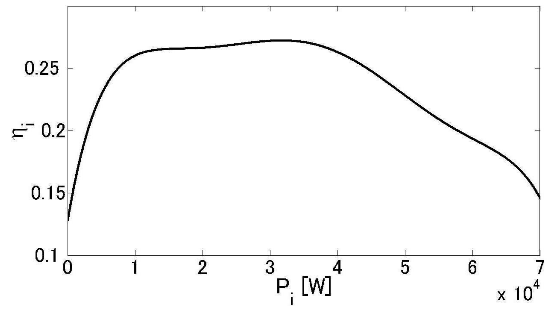

Fig. 5. Approximate engine efficiency η_i

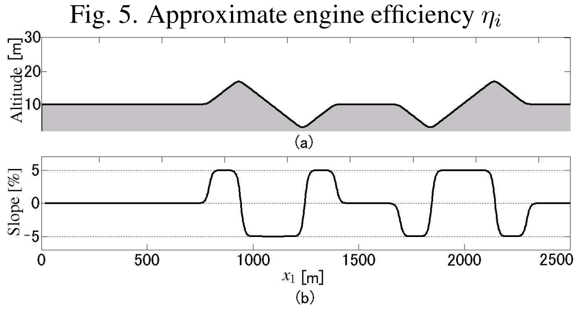

Fig. 6. Road shapes (a) altitude, (b) slope

the traction force or the brake force of the vehicles are represented as follows:

$$\begin{aligned} u_{CVP\ 1}(t) &= k_a\big(v^* - v_1(t)\big) + \int_0^t k_p\big(v^* - v_1(t')\big)dt', \\ u_{CVP\ 2}(t) &= k_1\big(v_1(t) - v_2(t)\big) \\ &\quad -k_2\big(hv_2(t) + \delta_{min} - d_{12}(t)\big), \\ u_{CVP\ 3}(t) &= k_1\big(v_2(t) - v_3(t)\big) \\ &\quad -k_2\big(hv_3(t) + \delta_{min} - d_{23}(t)\big), \end{aligned} \tag{10}$$

where, $k_a = 1184$, $k_p = 296$, $k_1 = 29600$, $k_2 = 2960$, $\delta_{min} = 0.5$, and $h = 0.05$ are constant parameters. To confirm the advantage of the platoon driving, the solitude driving (SOL) of a vehicle without the platooning ($u_{SOL} = u_{CVP\ 1}$) was also simulated. The initial velocity of this vehicle was the same as the velocity of the lead vehicle of the CVP.

The fuel consumption of the vehicles of the EVP, the CVP and the SOL at a distance of 2500 [m] are shown in Fig.7. Here, the improvement rates mean that the fuel consumption of the i-th vehicle of the EVP is compared with those of the CVP and the SOL. It is clear that the vehicles of the EVP further reduce the fuel than the CVP, and the platoon driving can save more fuel than the SOL.

The computer simulation results shown in Fig.8 and Fig.9 indicate that: During the early time period (0-25 [s]), the lead vehicle of the EVP accelerated slightly while the middle vehicle and the tail vehicle accelerated. This maneuver indicated that the EVP synchronously controlled the vehicles, the fast convergence in their spacings was achieved. The control inputs were small owing to the low acceleration of the vehicles. The vehicles of the CVP accelerated independently

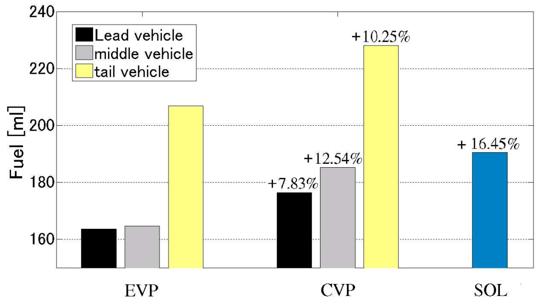

Fig. 7. Fuel consumption in 0–2500 [m]

since each vehicle of the CVP did not use the information of the other vehicles. By this maneuver, the slow convergence in their spacings was observed, and the control inputs were very large because of the high acceleration of the vehicles. During the uphill-downhill driving (25-90 [s]), the vehicles of the EVP tried to keep a low speed during uphill driving and a high speed during downhill driving. The amplitude of the control inputs was small owing to these driving policies. The vehicles of the CVP tried to keep the desired speed. This driving policy needed the large control inputs during the uphill driving, and wasted the kinetic energy of the vehicles during the downhill driving.

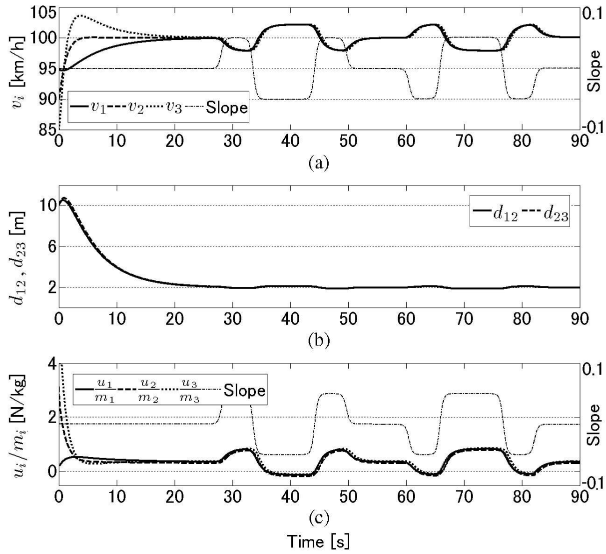

Fig. 8. The computer simulation results of the EVP

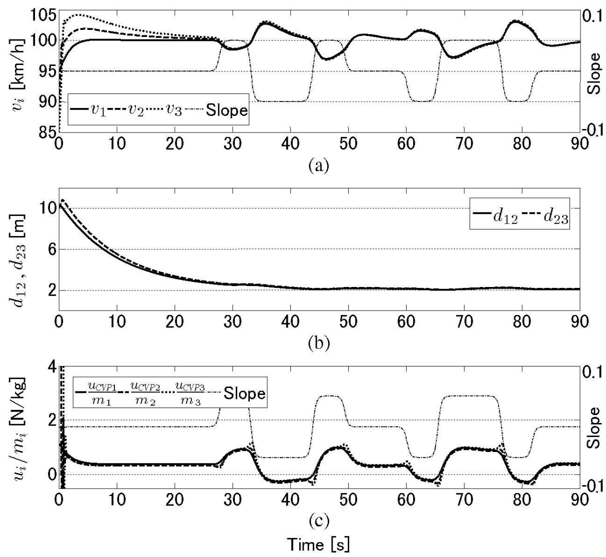

Fig. 9. The computer simulation results of the CVP

4 CONCLUSIONS

A centralized linear quadratic regulator system for ecological vehicle platooning considering the aerodynamic drag varied by the spacing and the road shape has been presented. The performance of the proposed control system was confirmed by the computer simulations. The synchronized driving obtained by the centralized control has provided the fast convergence of the spacings. The excessive acceleration and deceleration during the uphill and downhill driving have been avoided. The results revealed the significant improvement in fuel economy by using the proposed control system in comparison with those of a conventional vehicle platooning.

REFERENCES

[1] Marcu B, Browand F (1999), Aerodynamic forces experienced by a 3-vehicle platoon in a crosswind. SAE Paper 1999-01-1324

[2] Swaroop D, Hedrick J K, Chien C C et al (1994), Comparison of spacing and headway control laws for automatically controlled vehicles. Vehicle System Dynamics 23:597-625

[3] Zhang Y, Elias B, Kosmatopoulos et al (1999), Autonomous intelligent cruise control using front and back information for tight vehicle following maneuvers. IEEE Transactions on Vehicular Technology 48(1): 319–328

[4] Levine S W, Athans M (1966), On the optimal error regulation of a string of moving vehicles. IEEE Transactions on Automatic Control 11(3): 355–361

[5] Kaku A, Kamal M A S, Mukai M et al (2009), Model predictive control of a platoon for optimal fuel consumption based on vehicle aerodynamics (in Japanese). Proceedings of the 11th Symposium on Motion and Vibration Control (11^{th} MoViC), Fukuoka, Fukuoka Japan, Sep 2-4, 2009, pp. 234–237

[6] Kuroki M, Mukai M, Kawabe T et al (2009), Vehicular model predictive control for optimal fuel consumption based on engine map (in Japanese). Proceedings of the 28th Kyushu Annual Congresses of The Society of Instrument and Control Engineers, Fukuoka, Fukuoka Japan, Nov 28-29, 2009, pp. 29–30

The Seventeenth International Symposium on Artificial Life and Robotics 2012 (AROB 17th '12),
B-Con Plaza, Beppu, Oita, Japan, January 19-21, 2012

A feedback-trained robot task assignment system

Jeremy Straub[1, 2], Eunjin Kim[1]

[1]University of North Dakota, Grand Forks, ND 58202, USA
(Tel: 1-701-777-4107, Fax: 1-701-777-3330)

[2]jeremy.straub@und.edu

Abstract: Many applications (such as search and rescue or planetary exploration) require robots to characterize an environment that they have little or no initial information about. In this type of a scenario, a team of heterogeneous robots can be used to perform discovery and characterization activities. Unlike a collection of homogeneous robots which can be controlled without regards to the particular abilities possessed (e.g., using many common swarm techniques), the effective use of heterogeneous teams requires dynamic assignment based on constantly changing needs, available skills and robot locations. This paper discusses one such control technique that is demonstrated via a collection of small robots with very limited – but heterogeneous – sensing capabilities.

Keywords: heterogeneous robot team control, robot group communications, robotic control techniques.

1 INTRODUCTION

Task assignment to a collection of heterogeneous robots is an ill posed problem that also presents the complexity of continuous change. Assignment algorithms commonly consider distance from a target, closeness of fit for a given task and other metrics in considering which robot or robots to assign. Various assignment approaches are presented in the literature including self-assignment, central-assignment and swarm-based assignment. This paper proposes a feedback-trained task assignment mechanism which is demonstrated via a foraging application.

Obstacles of different heights were placed in the testing area; robots with sensors mounted at different height levels seek to generate a range measurement for the obstacles. A minimum of two robots is required to identify the height of an object (if it is taller than the highest sensor, for example). A second appropriately equipped robot must confirm each classification. Practically, several robots with different height measurement capabilities will be required to determine the lower and upper bound of the height. Then robots with corresponding height measurement capabilities will be required to confirm these findings. This experimental setup mirrors a variety of real-life conditions where alternate sensor types may be required (for example, sensors focusing on an adjacent range of light spectrum, etc.) to complete a task.

In this application, robots begin by searching for targets of interest and return to this when not assigned an alternate task. When a target is found the robot determines whether it is able to adequately assess it and then either issues a request for confirmation of its assessment or a request for an alternately equipped robot to be sent.

A central planner that runs on a selected robot (any robot with sufficient capabilities can potentially take this role) receives all confirmation or alternate robot requests and tasks a robot based on a combination of existing task-load, closeness to the target and closeness of task fit. The assigned robot receives the task and incorporates it into its task list based on path optimization. The central planner occasionally polls all of the robots for movement and task completion times. This data is used to update the controller's time-cost estimates via a weighted feedback incorporation technique. Updated estimates are sent out to all robots which incorporate the new data (weighed against local condition data) in to their internal costing values.

2 BACKGROUND

Collaborative robotic group control has a myriad of prospective applications. Three of these are particularly relevant to the research that has been conducted and the proposed control techniques: planetary exploration, reconnaissance and search-and-rescue.

It has been proposed, by Fink [1, 2, 3], to perform collaborative planetary exploration (inclusive of Earth science) through the use of a multi-tier robotic group. This concept presents an obvious collection of heterogeneous robots. They are differentiated by their movement type (orbital, flying or ground-based) and their particular function within the group. This mission architecture takes a top-down approach to task assignment. Orbital tier members (with great scope of coverage but limited resolution) identify targets of interest for exploration by aerial tier members which direct the efforts of (and may deploy) ground-based robots.

The multi-tier architecture presented for planetary exploration purposes is also highly relevant for reconnaissance. Work on sensornets [e.g., 4] is a demonstration of collaborative control of multiple heterogeneous robots. While many sensornets do not control the actual actions of their component sensors (robots), they do control the interaction between the data consumer and various sensors for the particular application. The sensornet concept can be looked at as a special case of the multi-tier mission architecture which may focus only on a particular subset of tiers and evidence only limited control.

Terrestrial search and rescue applications are also similar to the aforementioned applications. While this effort may be occurring in what was previously a well-known space, there is no guarantee that its configuration is as-previously-known and no guarantee that any particular infrastructure will be available. In fact, urban search and rescue presents a particular challenge as the environment may contain both physical and electromagnetic hazards to collaborative robotic operation. Robots deployed into search and rescue applications must be self-sufficient and be prepared to encounter electromagnetic interference to group communications and a changing array of hazards. They must also operate under a level of time pressure that is not present in many other robotic applications.

3 COLLABORATIVE CONTROL

To simulate the real-world conditions typical of the operation of heterogeneous group robot operations, each robot in the experimental group is controlled by a separate process that communicates with other robot control processes via message passing. Due to onboard processing limitations of the very basic robot hardware that was used for this experiment and the desire to capture performance information in real time, these processes were all physically located on a single computer that communicates with the robots via Bluetooth. This wireless protocol has limited range, but it was sufficient for the experimental environment used – specifically a small classroom-sized room. The experimental area was a rectangle approximately 10 feet by 20 feet. Three robots were operated concurrently in this area; they searched for and characterized pseudo-randomly placed obstacles.

The robots each begin in exploration mode, but will switch in to exploring traversal mode when another robot detects an object of interest and requests assistance to characterize it. When a robot is in close proximity to an object (or the believed position of an object) it switches into characterization mode. Once the robots have characterized the area completely (no area with a radius greater than a specified value remains unexplored) they switch in to terminal mode.

3.1 Exploration Mode

In exploration mode, the robot moves in a search pattern that is determined based on the presence of known and unknown areas surrounding it. The robot will avoid known obstacles, but prefers unknown (no pheromone) grid locations to those with known (positive pheromone) traverse-cost values. The robot will move will move to maximize its expected utility; however, in this mode, unknown grid locations will be treated as having +10 pheromone, impassible ones will be treated as having -100 and known locations will be treated has having -1 pheromone. The robot will continue in a utility maximizing search pattern until an uncharacterized obstacle is identified, the grid space is completely explored or another robot requests characterization assistance that it is well positioned to offer.

3.2 Exploring Traversal Mode

When a robot receives a suitable request, it evaluates the closeness and priority of the request relative to others that it is presently processing. If the new request has a lower combined (importance weighted against distance and current completion progress) selection value, it is queued; otherwise, the robot begins moving to the new location.

$$SEV = a\bullet I_t - b\bullet D_t - c\bullet C_{cur} \quad (1)$$

A robot that is in exploration mode will service any request that it is suitable to service (that is, it meets the instrumentation requirement and is not beyond the maximum traversal distance away from). Once a robot selects a request, it enters exploring traversal mode. In this mode, the robot selects the lowest-cost route. Unknown grid locations are assigned a cost of zero while those which slow movement (which was not a condition that was tested in this experiment) or contain an obstacle are considered based on their assigned negative utility value. The robot also continues its exploration activities along the path. If an object of interest is detected, it will compare the need to characterize this new object (that it is obviously in close proximity to) to the combined selection metric for its current task. Based on this, it may characterize this newly discovered object or queue it for later revisiting.

3.3 Characterization Mode

When the robot is in close proximity to an object that it has discovered and decided to characterize or one for which it has received a characterization or verification request, it will enter characterization mode. Characterization mode has two goals. First, the robot attempts to perform the characterization or verification activity required. Secondarily, it aims to align its grid with that of any previous robots that have visited this obstacle.

The robot moves around the obstacle and attempts to locate (trigger the bump sensor) from various directions. Through this, the robot characterizes the size of the object (i.e. how many and which grid squares it occupies). This is stored and transmitted to the central control process. If a previous robot has visited, the shape, size and location are compared and the correlation matrix between the grids of the robots are updated.

3.1 Terminal Mode

The robot enters terminal mode when it believes that its exploration area is completely characterized and there are no pending characterization assistance or verification requests remaining. In terminal mode, the robots return to their starting location and attempt to locate each other (through bump sensor triggering). This step is used to perform a final alignment on the grid correlation matrix between robots and once the robots locations are known to each other, they return to their ending formation.

4 COMMUNICATIONS

A simplified version of the communications architecture presented in [5] was used for message passing between the robot control processes and the central controller. Three message types (and their respective response) were used: object located, object characterized and request. Messages are processed by the central controller and forwarded out (containing the ID of the initiating robot, which is important for grid matching use) to the other robots to update their internal state database.

4.1 Object Located Message

The object located message is used to send a preliminary point obstacle to the central control process for distribution to the rest of the robots. This allows other robots to consider the presence of this obstacle when planning their routes during the characterization process. It also communicates that characterization of this object is in process and will prevent another robot that detects the same object during the characterization process from beginning to characterize it.

4.2 Object Characterized Message

When an object has been characterized (or verified) completely (i.e., from all directions), the object characterized message is sent to the central controller. This message contains all grid spaces that the object has been identified to occupy. When the central controller receives this message, it will send the preliminary data to all of the other robots and automatically generate characterization assistance or verification messages (depending on whether the characterization by the current robot was definitive – or simply determined that an alternately configured robot is required for further characterization).

4.3 Request Message

The request message is sent by the central controller once it receives an initial characterization completion notification (via the object characterized message). It will then, if this characterization was definitive (i.e., no other robot is required to characterize the object) issue a verification request; if further characterization is required it will issue a characterization request stating the required characterization capabilities (e.g., sensor above 2.2 cm, etc.). All request messages contain the grid location or locations of the object that requires the robot's characterization efforts and the reporting robot (for grid matching purposes).

4.3 Current State Message

The current state message is sent regularly by each robot to the central controller. The central controller distributes this message to any other robots that are operating in close proximity to the sending robot. This message is designed to allow robots to be aware of each other to prevent collisions.

Fig. 1. Picture of one of the robots that was used for testing the system. This robot has its second bump sensor set at the lowest setting (directly above the lower sensor). Other robots had their sensors at higher settings.

5 COMBINED SYSTEM OPERATIONS

The robotic control in this system is event driven. Once a path is selected for robot exploration or traversal, the control software will continue to execute the movement actions required to follow the designated route until interrupted by the detection of an obstacle, arrival in proximity to a characterization or verification target, receipt of a request that exceeds the selection value of the present task, or the determination that the entire exploration area has been completely explored.

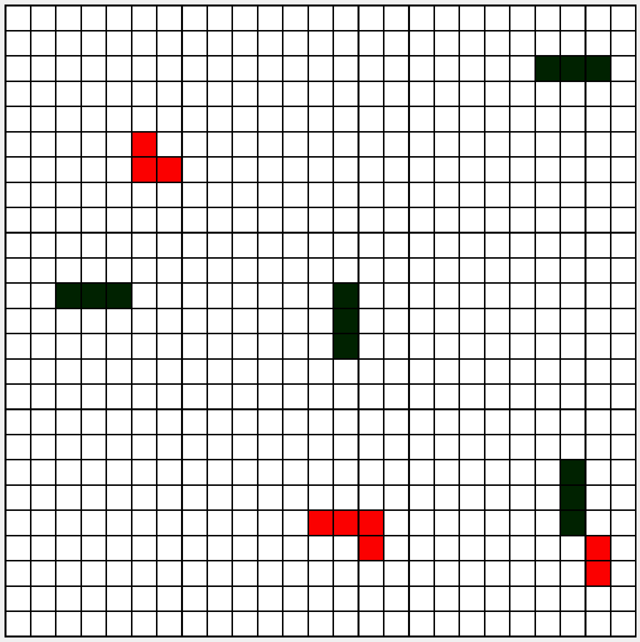

Fig. 2. Partial grid of exploration area showing obstacles (red / light) and demonstrated-traversable areas (green / dark)

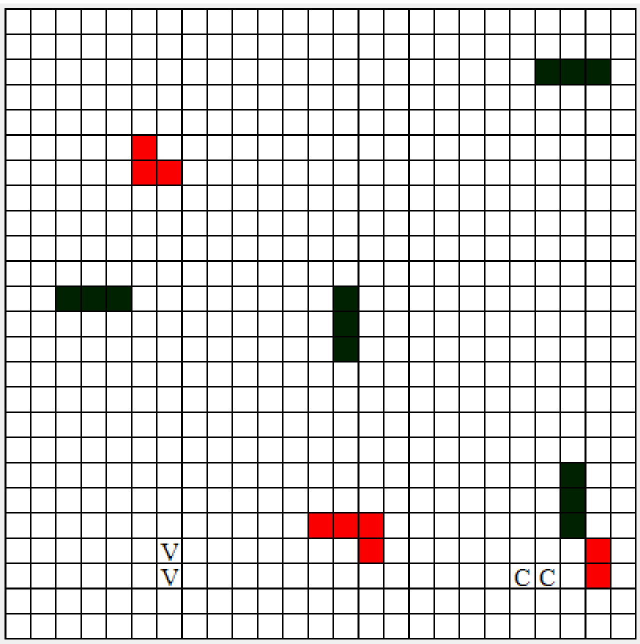

Fig. 3. Partial grid of exploration area showing obstacles, demonstrated-traversable areas and areas that need to be verified (V) or characterized (C)

The system determines the speed of robot movement based on the current mode that the robot is in and the nature of the grid locations that it is traversing. In exploring traversal mode, the robot will increase speed across regions of well-known (demonstrated-traversed) grid locations; however, it will slow when preparing to enter an unknown region or approaching the target to be characterized. The effect of different speed settings was not tested; however, this is an area that learning techniques (which will be discussed in the following section) could possibly be used to increase system performance in future research.

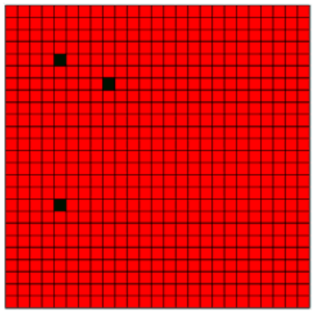

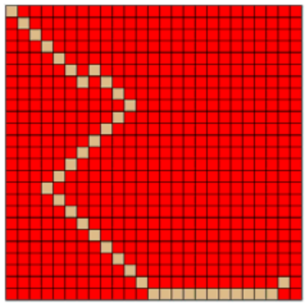

Fig. 4 & 5. Left: Partial grid of exploration area with initial -10 setting for all uncharacterized grid locations (red / light) and three characterized demonstrated-traversable locations (green / dark). Right: Partial grid of exploration area showing how high utility grid locations (as shown in Fig. 4.) impact routing

5.1 Path Planning

Path planning is utility and pheromone driven. The routing engine will make selections based on the lowest cost route that it perceives. Locations with known obstacles will have high negative utility values while those that have been demonstrated to be passable without issue on several occasions will have moderate positive utility values. A modified version of the A* path-finding algorithm is used. The route with the lowest total cost is selected.

6 LEARNING

The system relies on several constant values that are used to guide system operation. These values include the maximum target separation distance for accepting a task, the radius that determines when exploration is complete (when there is no region of this radius left unexplored, exploration is deemed complete) and the values that are used for positive and negative pheromone when regions are deemed impassible or well-traveled-enough to be demonstrated-traversable.

A learning algorithm based on testing incremental changes and evaluating their outcome has been developed and limited testing has been conducted. Minor changes to these values have been shown to have minimal effect; however, future research may focus on changing these values in conjunction. Additionally, correlation of particular value sets to preferential performance in various scenario types should be investigated.

7 EXPERIMENTAL SETUP

For testing, three robots were built which could be transformed into a variety of configurations. For characterization testing, the robots were set up with three different height levels for the upper bump sensor. For verification testing, two robots were assigned the same height level and the third was assigned a level that would only trigger characterization help requests (its upper sensor was shorter than the other group and also shorter than all obstacles).

A variety of obstacles were placed in the exploration area prior to each test; there location was measured so that the robotic results could be compared to the actual placement of obstacles. Obstacles were all heavy enough to avoid being moved by robot impact and no changes were made during each testing run.

The robots were placed in a central location facing in different directions. Once the test begun, the robots all moved off in their initial direction and begun random search activities.

Several scenarios were created which differed primarily in the density of obstacles present. The starting location of the robots was also varied as they were placed arbitrarily each time; however, the initial formation-placement of the robots was always very similar.

8 PERFORMANCE EVALUATION

The system was demonstrated to perform exceptionally well. In all test scenarios presented, the system identified all obstacles present in the exploration area. Additionally, this was done with virtually no manual involvement (in a few limited instances the robot dislodged one of its bump sensors requiring manual reattachment; however, this is a construction issue and not a control one). Despite having no mechanism for detecting side or rear impacts, the robots managed to successfully their exploration activities after rear collisions or side-swipes. Settings that allowed only short rearward movements for backing away from an obstacle worked as intended. The occasional non-bump-sensor-triggering collision (i.e., a collision with the front treads, etc.) or side swipe would temporarily cause a divergence of the robot's internal state believed-position and its actual position; however, this was generally resolved reasonably quickly by encountering an obstacle or wall and 'snapping' back to the grid based on this.

The small exploration area and high-traction carpet that it was covered with were undoubtedly factors in this performance. If the robot were more prone to slipping (or even could be spun by an impact) it is likely that re-snapping would have taken significantly longer or not occurred. The sensor configuration onboard the robots makes them have an exceptionally low tolerance for capture-and-place activities as they must physically explore a large area and encounter several known obstacles to reorient their internal position state.

9 CONCLUSION

The research conducted has demonstrated that limited communication and a set of well-defined behaviors are sufficient for characterizing an unknown environment. The robots in this experiment were purposefully simplistic in sensing capabilities and intentionally did not have any way to determine their true position (e.g., GPS). They demonstrated that with a reasonable level of relative movement knowledge, robots could assist each other in characterizing an environment that each could not sufficiently characterize on its own.

The control techniques demonstrated in this experiment are highly applicable to a variety of real world applications. Additional research, however, is required to validate their suitability and to identify required application-specific algorithm augmentations and constant values. A variety of general enhancements are also of research interest. These include adaptive learning (where constant values are updated based on performance in near-real-time by the evaluation system) and enhancements to deal with sensor data of varied levels of accuracy (i.e., visually sensed data versus bump-sensed data).

ACKNOLEDGEMENT

Thanks is given to the University of North Dakota Computer Science Department, especially Tom Stoke and Dr. Ronald Marsh, for providing the components that were used in this research.

REFERENCES

[1] Fink, W (2006), Generic Prioritization Framework for Target Selection and Instrument Usage for Reconnaissance Mission Autonomy, Proceedings of the International Joint Conference on Neural Networks, pp. 11116-11119.

[2] Fink, W, Dohm, JM, Tarbell, MA, Hare, TM, & Baker, VR (2005), Next-Generation Robotic Planetary Reconnaissance Missions: A Paradigm Shift, Planetary and Space Science, pp. 1419-1426.

[3] Fink, W, et. al. (2011), Robotic Test Bed for Autonomous Surface Exploration of Titan, Mars, and other Planetary Bodies, Proceedings of the IEEE Aerospace Conference, pp. 1-11.

[4] Tsatsoulis, C (2008), Sensor Webs as Multiagent, Negotiating Systems, *NASA Earth Science Technology Conference.* Adelphi: National Aeronautics and Space Administration.

[5] Straub, J (2011), A Modular, Application-Agnostic Distributed Control Framework for Robotic Applications, Accepted for publication in the Proceedings of the International Conference on Information and Communication Technologies and Appliations.

The Seventeenth International Symposium on Artificial Life and Robotics 2012 (AROB 17th '12),
B-Con Plaza, Beppu, Oita, Japan, January 19-21, 2012

A control method to suppress the rotational oscillation of a magnetic levitating system

Toshimasa Nishino[1,2], Yasuhiro Fujitani[2], Norihiko Kato[2], Naoaki Tsuda[3], Yoshihiko Nomura[2], Hirokazu Matsui[2]

[1]Toshiba industrial products manufacturing corporation, Mie-gun 510-8521, Japan
[2]Mie University, Tsu 514-8507, Japan
[3]Wakayama National College of Technology, Gobou 644-0023, Japan
(Tel: 059-376-6147, Fax: 059-376-6178)
[1]toshimasa.nishino@glb.toshiba.co.jp

Abstract: A magnetic levitation technique has a potential to realize a non-contact object manipulation. As a result, it is expected that a lot of problems caused by contacts can be evaded. Then, the authors developed a magnetic levitation system that was able to manipulate a magnetically levitated hand by non-contact. In this system, four electromagnets are assigned on a horizontal plane for 3-D positioning of the hand. However, it had been examined only about the movement of three directions so far.

In this paper, a new controller was presented which was developed to suppress the rotation around z axis, and its effectiveness was conformed through magnetic levitating experiments.

Keywords: Magnetic levitation, Adaptive Control, Positioning, Manipulation, Sensor

1 INTRODUCTION

Problems sometimes occur from the contacts between actuators and objects. Among various actuator systems, a magnetic levitation technique that levitates a hand by an electromagnetic force with no contact has a potential ability of achieving non-contact object manipulations. Therefore, the non-contact object manipulations would be a solution for the above described problems.

Thus, the magnetic levitation technologies have been in practical uses in some fields [1, 2, 3, 4] such as in a wind-tunnel test [5], and have been studied by applying various control theories such as the model reference adaptive control system (MRACS), H-infinity control [6, 7, 8, 9] to improve control characteristics. As for the multidegree-of-freedom systems, Fulford et al. [10] and Kim et al. [11] have studied on the magnetic levitation control where the air gap to the levitated object were very thin and the work spaces were restricted in very small range: the work spaces of translation was from nanometer to several millimeters, and that of rotation was from micro-radian to milliradian. Although Craig et al. [12] employed a magnetic levitation system that have as much wide work-spaces of several centimeters as our system, they studied only on the three-DOF positional control technique, but didn't take up the rotational control.

The authors have also developed a magnetic levitation system. In the system, four electromagnets are assigned on a horizontal plane for 3 dimensional (3-D) positioning of the hand as well as the work by Khamesee [13]. Yet we have also developed various 3-D positional control schemes such as the model reference adaptive control system (MRACS) heretofore [14], there has been remaining a problem of controlling orientations. Especially, unexpected rotational oscillation occurred around the vertical axis, which was a pressing issue for the system. Thus, we have studied on the oscillation-suppressing controller. The detail of the study for developing the controller was presented in this paper. Experimental apparatus including a sensor system to measure the rotational angle is described in Chapter2. Next, after showing a finding that the magnetic flux sum value has a dominant effect on the rotational oscillation, we present a way of designing oscillation-suppressing controller, i.e., a controller for stabilizing the magnetic-flux sum, in Chapter 3. Then, the effectiveness of the proposed method is confirmed by magnetic levitation experiments using a trial controller in Chapter 4. Finally, Chapter 5 concludes this paper.

2 EXPERIMENTAL APPARATUS

2.1 Magnetic levitation system

Schematic view of a magnetic levitation system used in this work is shown in Fig. 1and Fig. 2. In the system, as shown Fig. 3 and Fig. 4, four electromagnets are assigned on a horizontal plane for 3 dimensional (3-D) hand positioning. The electric circuits for the four electromagnets are independently controlled by FET amplifier circuits. The hand is levitated at an arbitrary position by controlling the currents flowing into the four electromagnets where the hand position is utilized as feedback information (Fig. 5). Fig. 6 shows an appearance of the levitated hand that is carrying a transistor. The permanent magnet in the driving unit is used to achieve the zero-power control: the zero-power control decreases the necessary power for the electromagnetic by compensating the hand gravity. As for the hand, the mass is approximately 6 g, and the weight capacity is approximately 1 g in the space of 20 mm × 20 mm × 20 mm cubic, and the spacing between the hand and the electromagnets is approximately 50 mm. The magnetic fluxes below the electromagnets are measured with the hall elements (THS119, Toshiba Corporation) that are attached at the electromagnets one-by-one.

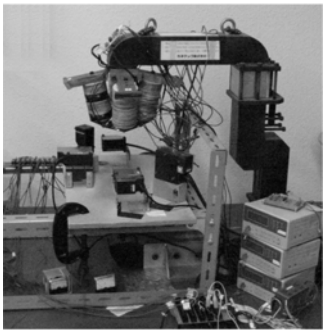

Fig. 1. Photograph of Magnetic levitation system

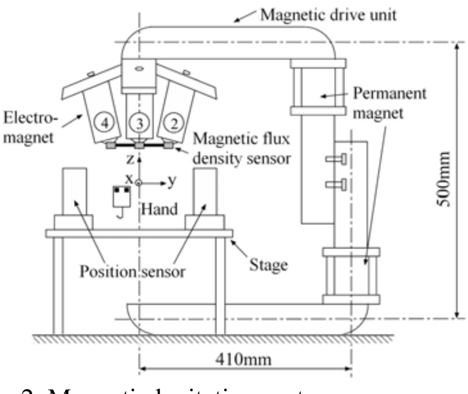

Fig. 2. Magnetic levitation system

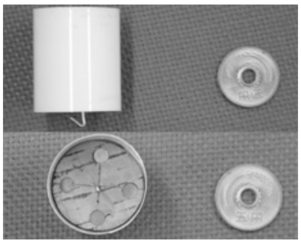

Fig. 3. Photograph of magnetically levitated hand

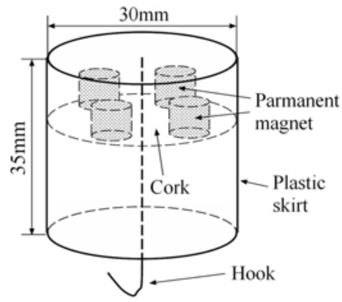

Fig. 4. Magnetically levitated hand

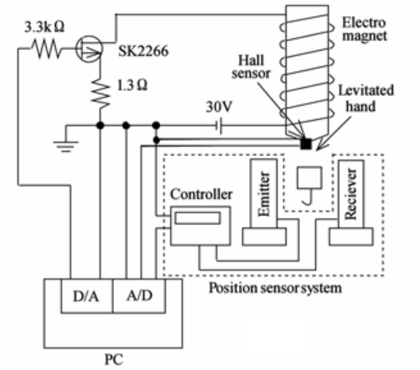

Fig. 5. Circuit diagram of magnetic levitation system

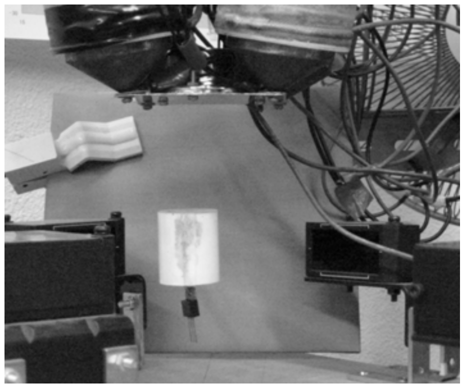

Fig. 6. Photograph of the levitated hand that is carrying a transistor

2.2 Rotation measurement system

This section describes a sensor system to measure the rotational angle around the axis in the longitudinal direction of the levitating hand.

As for a preparatory for developing the system, we had to examine the behavior of the levitated hand, and had to quantitatively evaluate the rotational oscillation. Here, since non-contact sensing system for measuring rotation to be applied to our levitation system was not available, we contrived a rotational measurement system. As shown in Fig. 8 and Fig. 9, by chipping off the lower part of the hand, we carved the bottom face into the spirally elevated slope. Then, the vertical distance between the slope and a distance sensor that was located down below varies with the rotation around the vertical axis as well as the 3-D positional change. As for the distance sensor, we employed a positional sensor (LB-040, Keyence): the measurable range is 35 to 45 mm, and the resolution is 2 μ m.

To confirm the effectiveness of the proposed rotation measurement system and to get an angle-distance conversion coefficient, rotational angle measurement experiments were carried out. While rotating the hand by a motor, the distance between the bottom of the hand and the positional sensor was measured.

Taking the medium height of the measured one as the origin, the averaged value of ten times of distance measurement is plotted along with the time in Fig. 10. While the hand rotating 360 ° in 0.8 seconds, the hand position decreased from 3.78 to -3.78. It gives the angle-to-distance conversion coefficient of 0.021mm/°. Here, note that, if the hand changes its 3-D position, the positional change causes an offset of the hand-sensor distance. Therefore, given the hand position, we should subtract the offset. Thus, the distance can be transformed into the rotation angle.

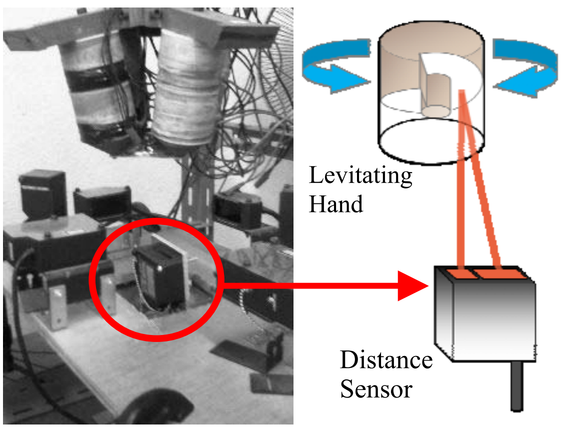

Fig. 7. Rotation measurement system using a distance sensor

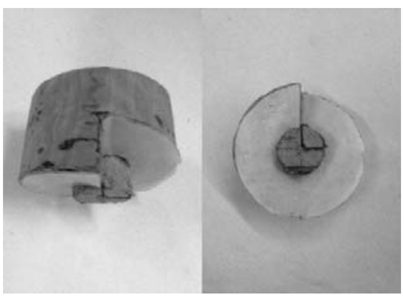

Fig. 8. Photograph of spirally carved hand: the left shows a side view, and the right, bottom view.

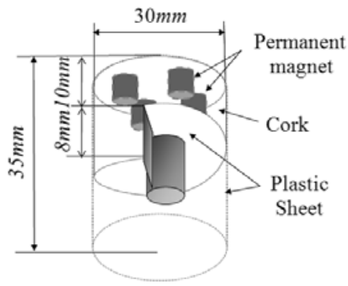

Fig. 9. Oblique projection of the hand with geometrical dimensional information

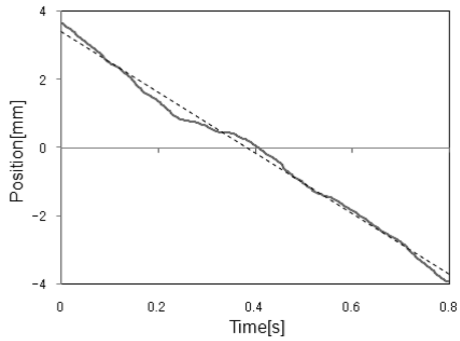

Fig. 10. Experimental result of rotational angle measurement

3 DESIGN OF CONTROLLER

3.1 Positional control of magnetically levitated hand

This section describes the positional control method of the magnetically levitated hand.

The 3-D position of the hand is controlled by manipulating the currents i_1, i_2, i_3,and i_4, each of which is to be input into the corresponding electromagnet: based on the following equations, we can determine i_1, i_2, i_3,and i_4 from $\boldsymbol{u_p} = [u_x, u_y, u_z]$ except that one of the four currents is determined arbitrarily.

$$\begin{aligned} &\Sigma_{j=1,4}\, i_j = u_z \\ &i_1 - i_3 = u_x, \\ &i_2 - i_4 = u_y \end{aligned} \tag{1}$$

Utilizing the positional sensor information as a feedback signal, we applied a feed-forward PID control to the hand position control. That is, the nonlinear compensators from the levitating position X, Y, Z to the manipulated variables $\boldsymbol{u_p} = [u_x, u_y, u_z]$ were represented by the second order approximate equations, and were utilized for feed-forward signals. The approximate equations had been obtained by a preparatory experiment: while changing the levitating position X, Y, Z, the relationships between the levitating position X, Y, Z and the manipulated variables $\boldsymbol{u_p} = [u_x, u_y, u_z]$ were measured.

Let $\boldsymbol{e}_p$ denote the deviation of the present position $\boldsymbol{p}_p = [p_{px}, p_{py}, p_{pz}]$ from the desired position $\boldsymbol{r}_p = [r_{px}, r_{py}, r_{pz}]$. If we denote the gains with respect to the position by K_{pp}, K_{ip}, and K_{dp}, and denote the nonlinear compensation with respect to the position by $\boldsymbol{u}_{fp} = [u_{fpx}, u_{fpy}, u_{fpz}]$, the manipulated variable in the horizontal direction, $\boldsymbol{u_p} = [u_x, u_y, u_z]$ is given by

$$\boldsymbol{u}_p = K_{pp}\boldsymbol{e}_p + K_{ip}\int \boldsymbol{e}_p dt + K_{dp}\dot{\boldsymbol{e}}_p + \boldsymbol{u}_{fp} \tag{2}$$

3.2 Magnetic flux control (MF control)

As for the hand's positional control in the horizontal plane, a magnetic flux control loop using hall elements was embedded into the inside of the positional control loop. Here, note that, because the electromagnets interfere with each other, it is difficult to control the magnetic fluxes independently. Therefore, as well as the horizontal positional control method described in the section 3.1, we took the differences between the fluxes emitted from the opposing electromagnets to control them.

We constituted a magnetic flux vector $\boldsymbol{p}_f = [p_{fx}, p_{fy}, 0]$ from the magnetic fluxes b_1, b_2, b_3, b_4: they are measured by the hall elements that are attached at the electromagnets. That is,

$$p_{fx} = b_1 - b_3$$
$$p_{fy} = b_2 - b_4 \tag{3}$$

As well as 3.1, let $\boldsymbol{e}_f$ denote the deviation of the present magnetic flux $\boldsymbol{p}_f$ from the desired magnetic flux $\boldsymbol{r}_f$. If we denote the gains with respect to the magnetic flux by K_{pf}, K_{if}, and K_{df}, and denote the nonlinear compensation with respect to the magnetic flux by $\boldsymbol{u}_{ff} = [u_{ffx}, u_{ffy}]$, the manipulated variable in the horizontal direction, $\boldsymbol{u}_f = [u_x, u_y, u_z]$ is given by

$$\boldsymbol{u}_f = K_{pf}\boldsymbol{e}_f + K_{if}\int \boldsymbol{e}_f dt + K_{df}\dot{\boldsymbol{e}}_f + \boldsymbol{u}_{ff} \tag{4}$$

where

$$\boldsymbol{e}_f = \boldsymbol{r}_f - \boldsymbol{p}_f$$
$$\boldsymbol{r}_f = K_{pp}\boldsymbol{e}_p + K_{ip}\int \boldsymbol{e}_p dt + K_{dp}\dot{\boldsymbol{e}}_p + \boldsymbol{u}_{fp}$$
$$\boldsymbol{e}_p = \boldsymbol{r}_p - \boldsymbol{p}_p$$

The nonlinear compensators are represented by approximate equations that were obtained by a preparatory experiment: while changing the manipulated variable values, that is, the levitating position X, Y, Z and the control currents i_1, i_2, i_3, i_4, we measured the magnetic fluxes $\boldsymbol{b} = [b_1, b_2, b_3, b_4]$.

The block diagram of the magnetic flux controller before-improvement is shown in Fig. 11. The block of [CONV2] in the block diagram represents the transformation from $\boldsymbol{b}$ into $\boldsymbol{p}_f$ by Eq.(3). And, the block of [CONV1] represents the transformation from $\boldsymbol{u}_f$ into i_1, i_2, i_3, i_4 as in the followings.

$$\Sigma_{j=1,4}\, i_j = u_z$$
$$i_1 - i_3 = u_x,$$
$$i_2 - i_4 = u_y \tag{5}$$

where $\boldsymbol{u}_f = [u_x, u_y, u_z]$

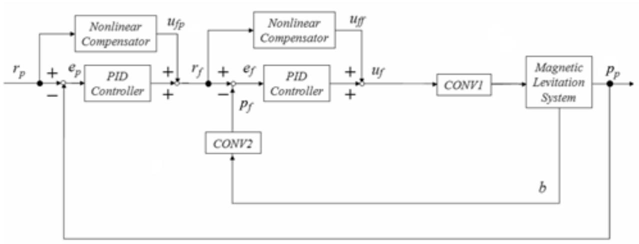

Fig. 11. Block diagram of MF control

3.3 Rotation suppressing control

The authors introduced a control method to suppress the unwilled rotational oscillation around the vertical axis in the magnetic levitating system.

We found an important behavior from experimental data: when hand suffering rotation oscillation, the rotational oscillation was in phase with the perturbation of the sum value of four pieces of the magnetic flux emitted from the four electromagnets. It means that the magnetic flux sum value has a dominant effect on the rotational oscillation, and it suggested us the necessity of suppressing the perturbation of the sum value. Taking sum of the magnetic fluxes in the X-direction, and that in the Y-direction, we apply a PID control for the rotation suppression: the desired value of the sum in the X-direction is denoted by r_{sx}, and that in the Y direction is by r_{sy}, and the measured value of the sum in the X-direction is denoted by p_{sx}, and that in the Y direction is p_{sy}. If the deviation of r_{sx} from r_{sy} is denoted by r_s and that of p_{sx} from p_{sy} is by p_s, they are shown by

$$r_s = r_{sx} - r_{sy}$$
$$p_s = p_{sx} - p_{sy}, \quad p_{sx} = b_1 + b_3, \quad p_{sx} = b_2 + b_4 \tag{6}$$

If the deviation of r_s from p_s is denoted by e_s, and if the gains with respect to the magnetic flux are K_{ps}, K_{is}, and K_{ds}, the manipulated variable in the horizontal direction, $\boldsymbol{u}_s = [u_x, u_y, u_z]$, is given by the following PID control.

$$\boldsymbol{u}_s = K_{ps}\, e_s + K_{is} \int e_s dt + K_{ds}\, \dot{e}_s \qquad (7)$$

By adding $\boldsymbol{u}_s$ of Eq. (7) to $\boldsymbol{u}_f$ of Eq. (4), the input for the [CONV1] in the block diagram, $\boldsymbol{u}_f'$ shown in Fig. 12 is given by

$$\boldsymbol{u}_f' = K_{pf}\boldsymbol{e}_f + K_{if} \int \boldsymbol{e}_f dt + K_{df}\dot{\boldsymbol{e}}_f + \boldsymbol{u}_{ff} + \boldsymbol{u}_s \qquad (8)$$

The block diagram of the proposed magnetic flux control is shown in Fig. 12 where the sampling time of the positional control loop was set at 4 ms, and that of the magnetic flux control loop 1 ms.

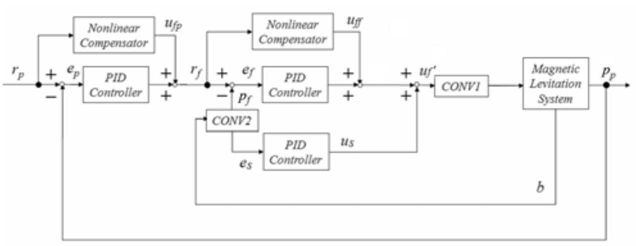

Fig. 12. Block diagram of proposed MF control with rotation suppressing control

4 EXPERIMENT

To confirm the effectiveness of the proposed method, the authors implemented the above-described controller, and carried out some magnetic levitation experiments.

First of all, to make clear the problem of the existing method that is represented by Eq. (4), a result of before-improvement p_s is shown in Fig. 13 where the hand was levitated at the height of Z=5 mm. Next, to make clear the effectiveness of the proposed rotational measurement system, the measured values after the hand's Z positional correction, the converted hand's rotational angles are shown in Fig. 14. Contrary to Fig.13 and Fig. 14, after-improvement result of p_s is shown in Fig. 15 where the proposed controller by Eq. (8) is implemented, and the corrected hand's rotational angle is also shown in Fig. 16.

As you can see from Fig. 13 and Fig. 14, they were found that the magnetic flux p_s has a strong correlation with the hand's rotational angle, and that the hand oscillates periodically within the range of -110 degree ~ +110 degree. The findings support the validity of the principle of the rotation-suppressing-control described in the section 3.3. Next, from Fig. 15 and Fig. 16, by virtue of the proposed controller, the periodic oscillation in the magnetic flux p_s has been markedly suppressed, and the consequently occurring periodic oscillation in the hand's rotational angle has also been effectively suppressed within the range of -15 degree ~ +15 degree.

As a result, it can be concluded that the proposed method effectively decreased the unwilled rotation around Z-axis much more than the existing method.

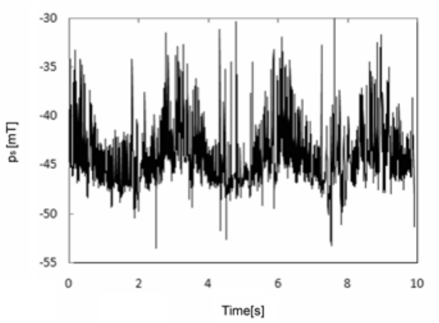

Fig. 13. Experimental result of p_s by MF controller

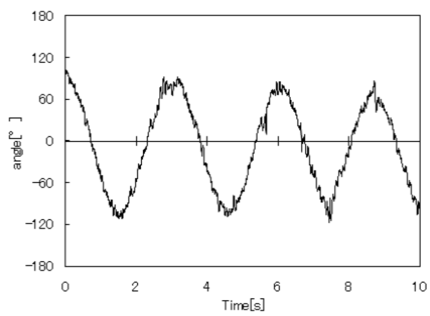

Fig. 14. Rotation angle by MF controller

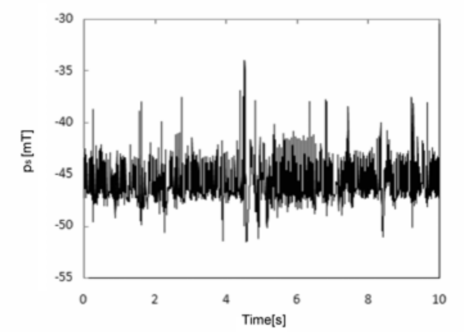

Fig. 15. Experimental result of p_s by proposed controller

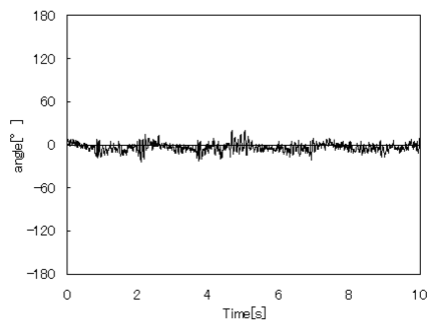

Fig. 16. Rotation angle by proposed controller

5 CONCLUSION

A controller to suppress the oscillation around the vertical axis was presented in this paper. The main points are as follows:

(1) Carrying out some magnetic levitating experiments, we have found an interesting behavior: the rotational oscillation was in phase with the perturbation of the sum value of four pieces of the magnetic flux respectively emitted from the four electromagnets. It means that the magnetic flux sum value has a dominant effect on the rotational oscillation, and it suggested us the necessity of suppressing the perturbation of the sum value.

(2) Considering this necessity, we designed a controller for stabilizing the magnetic-flux sum, and developed a trial system of the controller.

(3) We carried out some magnetic levitating experiments:the perturbation of the sum of four pieces of the magnetic flux was markedly decreased, and the ill rotational oscillation around the vertical axis was successfully suppressed. As a result, the effectiveness of the proposed method was confirmed.

In the future, based on the rotational oscillation suppression technique, we are directed to enhance the control characteristics of the magnetic levitating system: if we can arbitrarily control the rotation around the vertical axis, the system would be applied to more wide range of areas.

REFERENCES

[1] Higuchi T (1991), Applications of Magnetic Levitation and Magnetic Bearings in Robotics (in Japanese), J. of RSJ, 9, 4, pp.474-478

[2] Nagai M (1993), Recent Trends and Dynamical Issues in Magnetic Levitation Technology (in Japanese), Trans. of JSME, 96, 899, pp.876-879

[3] Magnetic levitation and Magnetic Bearing (in Japanese), IEEJ (1993), Corona Publishing Co.,Ltd, pp. 469-479

[4] Azukizawa T, Uemura K (1986), Magnetically Levitated Dust - free Transport System (in Japanese), J. of IEEJ, 106-7, pp.677-680

[5] Suda S, Sawada H, Kunimasu T (2004), Analysis on Control Characteristics of Magnetic Suspension and Balance System for High Subsonic Wind Tunnel (in Japanese), Dynamics and Design Conference 2004 CD-ROM

[6] Kojima H, Kimura J, Kobayashi T (1992), Magnetic Levitation Neuro-Adaptive Control of Body by Electromagnet Attached to Robot Arm (in Japanese), Trans. of JSME (C), 60, 571, pp.930-935

[7] Qi Run-de, et al (1994), H∞ Control Approach to a Magnetic Levitation System by 4 Points Attraction with Nonlinear Characteristics (in Japanese), Trans. of IEEJ D, 114, 6, pp.680-688

[8] Ando T, Iwatsubo K (1998), Adaptive Control for a Nonlinear Control System by Gain Self-tuning and It's Application to a Magnetic Levitation System (in Japanese), Trans. of SICE, 34 , 8, pp.1019-1024

[9] Oshinoya Y, Ishibashi K, Hekihara T (2002), Horizontal Uniaxial Noncontact Positioning Control for a Magnetically Levitated Steel Plate (in Japanese), J. of JSAEM, 10, 2, pp.200-207

[10] Fulford C, Maggiore M, Apkarian J (2009), Control of a 5DOF Magnetically Levitated Positioning Stage, IEEE Trans. on Control Systems Technology, 17, 4, pp.844-852

[11] Kim W, Verma S (2007), Multiaxis Maglev Positioner With Nanometer Resolution Over Extended Travel Range, J. of Dyn. Sys., Measurement, and Control, 129, pp.777-785

[12] Craig D, Khamesee M. B (2007), Motion control of a large gap magnetic suspension system for microrobotic manipulation, J. of Phys. D, 40, pp.3277-3285

[13] Khamesee M.B, et al (2002), Design and Control of a Microrobotic System Using Magnetic Levitation, IEEE/ASME Trans. on Mechatronics, 7, 1, pp.1-14

[14] Nishino T, Kato N, Nomura Y (2005), Magnetic Levitation in 3 Dimensional Space using 4 Different Electromagnets (in Japanese), Trans. of JSME (C) , 71, 706, pp.130-136

The Seventeenth International Symposium on Artificial Life and Robotics 2012 (AROB 17th '12),
B-Con Plaza, Beppu, Oita, Japan, January 19-21, 2012

Fuzzy Servo Control of an Inverted Pendulum System

Mohd Khairi Bin Mohamed Nor[1], Shigenori Okubo[1]

[1] Graduate School of Science and Engineering, Yamagata University, 4-3-16 Jonan, Yonezawa,Yamagata,992-8510, Japan
(Tel: 81-23-826-3245, Fax: 81-23-826-3245)
(khairimn@gmail.com)

Abstract: The studies of model based fuzzy control system are concentrating on regulator problem. But in real system, the output of the system needs to be regulated to the desired reference output which is not only zero. Servo system can regulate the output to desired reference output without steady state error against unknown disturbance. In this paper, application of fuzzy servo control for stabilizing inverted pendulum system will be discussed. The inverted pendulum system is a simple system consists of pendulum and cart but has strong nonlinearity and inherent instability. The simulations are done and the result shows that the proposed method can stabilize the system.

Keywords: Davison-Smith method, Fuzzy control, Inverted pendulum system, Nonlinear servo system

1 INTRODUCTION

The studies of model based fuzzy control system are concentrating on regulator problem, which is involved with the design of the controller that can drive all the initial condition to zero as required by the design specification. In real system, the output of the system needs to be regulated to the desired reference output which is not only zero. Servo system can regulate the output to desired reference output without steady state error against unknown disturbance. In this paper, application of fuzzy servo control for stabilizing inverted pendulum system will be discussed. The inverted pendulum system is a simple system consists of pendulum and cart but has strong nonlinearity and inherent instability. It is used as benchmark problem for study the performance and effectiveness of new control method. The idea behind of this control method is to divide the operating region of nonlinear system into small area, and to treat as a collection of local linear servo systems by using Davison-Smith method. The control rule of each local linear servo systems is calculated using pole assignment method proposed by Hikita. Fuzzy method is applied to each local linear servo system and combines it as new control rule. The simulations have been done and the results shown that proposed can stabilize the system. As shown in the result, the output of the system follows the reference given and converges to the reference value as desired.

2 SYSTEM DESCRIPTION

Let the original system S be a nonlinear system one as

$$\dot{x} = f(x,u) + d \tag{1}$$
$$y = g(x) + d_o \tag{2}$$

Where, $x \in R^n$ is state vector, $u \in R^m$ is control input, $y \in R^l$ is control output, $d \in R^n$ is state disturbance and $d_o \in R^l (m \geq l)$ is output disturbance. n, m and l are dimensions of state, input and output of the system. Assume the trajectory of nonlinear system around operating point of the system(x_i, u_i) as

$$\delta x = x - x_i \tag{3}$$
$$\delta u = u - u_i. \tag{4}$$

Where δx and δu represent the small quantity of state and input variable respectively.The system can be linearized by applying Taylor expansion to (1) and (2) around operating point (x_i, u_i), where

$$\begin{aligned} \delta\dot{x} &= \frac{\partial}{\partial x^T} f(x_i,u_i)\,\delta x + \frac{\partial}{\partial u^T} f(x_i,u_i)\,\delta u \\ &\quad + f(x_i,u_i) + d \end{aligned} \tag{5}$$
$$y = \frac{\partial}{\partial x^T} g(x_i)\,\delta x + g(x_i) + d_o. \tag{6}$$

The linear approximated system S_i can be represented as,

$$\dot{x} = A_i x + B_i u + d_{xi} \tag{7}$$
$$y = C_i x + d_{oi} \tag{8}$$

where,
$A_i = \frac{\partial}{\partial x^T} f(x_i,u_i), B_i = \frac{\partial}{\partial u^T} f(x_i,u_i), C_i = \frac{\partial}{\partial x^T} g(x_i), d_{xi} = f(x_i,u_i) - A_i x_i - B_i u_i + d, d_{oi} = g(x_i) - C_i x_i + d_o$.
Let error of the system be as following

$$\dot{v} = y - r. \tag{9}$$

Derive the augmented system from (7),(8) and (9).

$$\begin{aligned} \frac{d}{dt}\begin{bmatrix} x \\ v \end{bmatrix} &= \begin{bmatrix} A_i & 0 \\ C_i & 0 \end{bmatrix}\begin{bmatrix} x \\ v \end{bmatrix} + \begin{bmatrix} B_i \\ 0 \end{bmatrix} u \\ &\quad + \begin{bmatrix} d_{xi} \\ d_{oi} - r \end{bmatrix} \end{aligned} \tag{10}$$

Equation(10) can be re-written as

$$\dot{z} = A_{zi}z + B_{zi}u + d_{zi} \tag{11}$$

where,
$z = \begin{bmatrix} x \\ v \end{bmatrix}, A_{zi} = \begin{bmatrix} A_i & 0 \\ C_i & 0 \end{bmatrix}, B_{zi} = \begin{bmatrix} B_i \\ 0 \end{bmatrix},$
$d_{zi} = \begin{bmatrix} d_{xi} \\ d_{oi} - r \end{bmatrix}.$
The system that has ability to follow the given reference is called as servo system.This system in (11) is controllable if controlability condition satisfies.

$$rank \begin{bmatrix} B_{zi} & A_{zi}B_{zi} & A_{zi}^2 B_{zi} & \cdot\cdot & A_{zi}^{n+l-1} B_{zi} \end{bmatrix} = n+l. \tag{12}$$

This condition is equivalent to the next one.

$$rank \begin{bmatrix} B_i & A_iB_i & A_i^2 B_i & \cdots\cdot & A_i^{n-1}B_i \end{bmatrix} = n, \quad rank \begin{bmatrix} A_i & B_i \\ C_i & 0 \end{bmatrix} = n+l \tag{13}$$

3 FUZZY SERVO SYSTEM

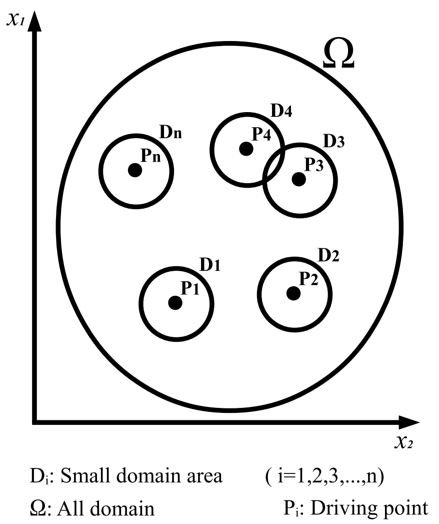

Fig. 1. Partition of driving domain Ω

In this section we apply fuzzy method to develop the control rule for the nonlinear system. First, nonlinear variable for system in (1) and (2) will be determined. Let, the element of nonlinear variable for x in funtion $f(x, u), g(x)$ as x_{ej} and can be determine as

$$\frac{\partial}{\partial x_{ej}} f\,(x, u) \neq const. \tag{14}$$

This definition also can be use for output equation u. The origin point $(0, 0)$ are used as linear driving point. Let, the vector of the set of nonlinear variable x and u for $f(x, u), g(x)$ as $x_n \in R^{n_{xn}}$ and $u_n \in R^{n_{un}}$. The relationship between x, u and x_n, u_n can be shown as

$$x_n = C_{xn}x \tag{15}$$
$$u_n = C_{un}u \tag{16}$$

$C_{xn} \in R^{n_{xn} \times n} and C_{un} \in R^{n_{un} \times m}$ are the matrix of which its elements are 1 or 0. Define the vector for all nonlinear variable as $z_n \in R^{n_{zn}}, n_{zn} = n_{xn} + n_{un}$, the relatioship between the variable can be represent as

$$z_n = \begin{bmatrix} x_n \\ u_n \end{bmatrix} = \begin{bmatrix} C_{xn} & 0 \\ 0 & C_{un} \end{bmatrix} \begin{bmatrix} x \\ u \end{bmatrix} = C_n \begin{bmatrix} x \\ u \end{bmatrix}. \tag{17}$$

Where $C_n \in R^{n_{zn} \times (n+m)}$. Next, we divide the region of nonlinear variable z_n,into small area D_i around driving point P_i. Fuzzy method has been apply to each local linear system and combines it and treated as a collection of local linear servo systems (Fig.1). The fuzzy rule R_i can be define as

$$R_i : \quad IF \;\; z_n \in D_i \;\; THEN \;\; S \;\; is \;\; S_i. \tag{18}$$

Where, the fuzzy rules are $-N \leq i \leq N$. Let ω_i define as Gaussian type fuzzy membership function (Fig.2) as following.

$$\omega_i = e^{-(z_n - z_{ni})^T Q_n (z_n - z_{ni})} \tag{19}$$
$$Q_n = {Q_n}^T > 0 \tag{20}$$

ρ_i can be define as,

$$\rho_i = \frac{\omega_i}{\sum_{i=-N}^{N} \omega_i}. \tag{21}$$

The Fuzzy Servo System can be re-write as,

$$\dot{z} = \sum_{i=-N}^{N} \rho_i \left(A_{zi}z + B_{zi}u + d_{zi} \right). \tag{22}$$

In order to stabilized the system in (22), the control input u can be defines as

$$u = -\sum_{i=-N}^{N} \rho_i K_i z. \tag{23}$$

K_i is the feedback coefficient matrix of the input for small area D_i. This matrix calculated using Hikita method [3] based on servo system proposed by Davison-Smith[2]. Let

$$\begin{aligned} f_{ij} &= -(\lambda_{ij}I - A_{zi})^{-1} B_{zi} g_{ij} \\ (j &= 1, 2, 3, ...n + l), \\ g_{ij} &\in R^m, f_{ij} \in R^{n+l}. \end{aligned} \tag{24}$$

λ_{ij} be the eigenvalues, g_{ij} be non-zero vector and f_{ij} be eigenvector of the system. The feedback co-efficient matrix can be represented as

$$K_i = \begin{bmatrix} g_{i1} & \ldots & g_{i(n+l)} \end{bmatrix} \begin{bmatrix} f_{i1} & \ldots & f_{i(n+l)} \end{bmatrix}^{-1} \quad (-N \leq i \leq N) \tag{25}$$

The input u in (23) are applied to system in (1) and (2).

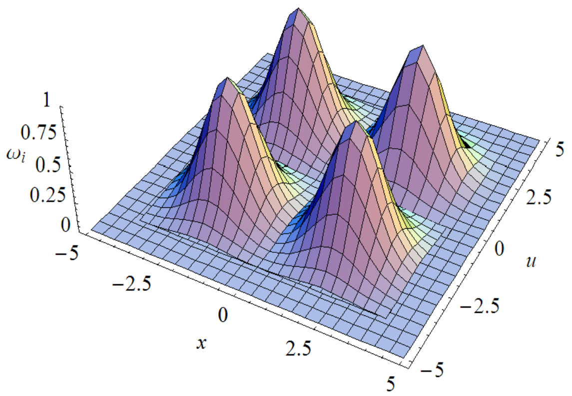

Fig. 2. Gaussian type fuzzy membership function ω_i

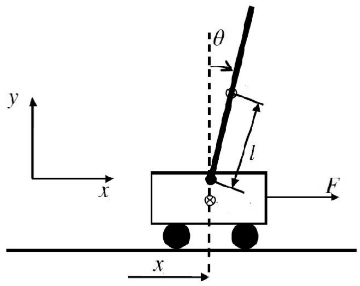

Fig. 3. Inverted Pendulum system

4 SIMULATION AND RESULTS

The inverted pendulum used in this simulation is shown in Fig.3. It consists of cart and a pendulum. The cart is free to move the horizontal direction when the force F applies to it. We assume that the mass of the pendulum and cart are homogenously distributed and concentrated in their center of the gravity and the friction of the cart is proportional only to the cart velocity and friction generating by the pivot axis is proportional to the angular velocity of the pendulum. The parameters used for simulation are shown in Table 1.The mathematical model of inverted pendulum system can be described as the following.

$$(M+m)\ddot{x}+mlcos\theta\ddot{\theta}+D\dot{x}-mlsin\theta\dot{\theta}^2=F \tag{26}$$

$$mlcos\theta\ddot{x}+\frac{4}{3}ml^2\ddot{\theta}-mglsin\theta+C\dot{\theta}=0 \tag{27}$$

With output as

$$y=x_1 \tag{28}$$

Define an error of the system as

$$\dot{v}=e=y-r. \tag{29}$$

Table 1. Parameters of Inverted Pendulum System

Parameter	Description	Value
Mass of the cart	M	0.165kg
Mass of the pendulum	m	$0.12kg$
Distance from pivot to center of mass of the pendulum	l	$0.25m$
Gravitational constant	g	$9.80m/s^2$
Co-efficient of friction for pivot	C	$0.01kgm/s$
Co-efficient of friction for cart	D	$4.0kg/s$

Re-arranged the equation in term of $x_1=x, x_2=\dot{x}, x_3=\theta, x_4=\dot{\theta}$ and $F=u$. The new equation for inverted pendulum are shown in (30), (31),(32) and (33).

$$\dot{x_1} = x_2 \tag{30}$$

$$\begin{aligned}\dot{x_2} = {} & 3cosx_3\,(mglsinx_3-Cx_4) \\ & -4l\left(u-Dx_2+mlsinx_3x_4^2\right)/ \\ & \left\{4l(m+M)+3mlcosx_3^2\right\}\end{aligned} \tag{31}$$

$$\dot{x_3} = x_4 \tag{32}$$

$$\begin{aligned}\dot{x_4} = {} & -3\,\{(m+M)(mglsinx_3-Cx_4) \\ & -mlcosx_3(u-Dx_2+mlsinx_3x_4^2)\}/ \\ & \left[ml^2\left\{-4(m+M)+3mcosx_3^2\right\}\right]\end{aligned} \tag{33}$$

The nonlinear variable for the system are calculated using (14). In this example the nonlinear variable are x_2, x_3, x_4 and u. The linearization has been done to mathematical model of the inverted pendulum system using Taylor expansion as shown in (5) and (6) around of the driving points for nonlinear variables x_2, x_3, x_4 and u. Where,

$$\delta x_2 = x_2 - x_{2i} \tag{34}$$

$$\delta x_3 = x_3 - x_{3i} \tag{35}$$

$$\delta x_4 = x_4 - x_{4i}. \tag{36}$$

$$\delta u = u - u_i. \tag{37}$$

The linearization has been done and the linear servo system can be represent as

$$\dot{z} = A_{zi}z + B_{zi}u + d_{zi}. \tag{38}$$

The controllability of the servo system of inverted pendulum system has been investigated using (12). In this case, the output of system has been setting as shown in (28) because of the controllability problem. Let,

$$Q_n = \begin{bmatrix} q_2 & 0 & 0 & 0 \\ 0 & q_3 & 0 & 0 \\ 0 & 0 & q_4 & 0 \\ 0 & 0 & 0 & q_5 \end{bmatrix} \tag{39}$$

and the nonlinear variables x_2, x_3, x_4 and u can be represent as

$$z_n = \begin{bmatrix} x_2 \\ x_3 \\ x_4 \\ u \end{bmatrix}, C_n = \begin{bmatrix} 0 & 1 & 0 & 0 & 0 \\ 0 & 0 & 1 & 0 & 0 \\ 0 & 0 & 0 & 1 & 0 \\ 0 & 0 & 0 & 0 & 1 \end{bmatrix} \quad (40)$$

The fuzzy membership function ω_i can be represent as

$$\begin{aligned} \omega_i &= e^{-(z_n - z_{ni})^T Q_n (z_n - z_{ni})} \\ &= e^{-q_2(x_2 - x_{2i})^2 - q_3(x_3 - x_{3i})^2 - q_4(x_4 - x_{4i})^2 - q_5(u - u_i)^2} \end{aligned} \quad (41)$$

So that,

$$\rho_i = \frac{\omega_i}{\sum\limits_{i=-N}^{N} \omega_i}. \quad (42)$$

The fuzzy servo system for inverted pendulum system is,

$$\dot{z} = \sum_{i=-N}^{N} \rho_i \left(A_{zi} z + B_{zi} u + d_{zi} \right). \quad (43)$$

The set of poles used is $\lambda = [-1.2 - 1.3 - 1.4 - 1.5 - 1.6]$ .The feedback coefficient matrices K_i are calculated using Hikita Method. The input of the system is

$$u = -\sum_{i=-N}^{N} \rho_i K_i z. \quad (44)$$

with $x_{2i} = h_2 i(-N_2 \leq i \leq N_2), x_{3i} = h_3 i(-N_3 \leq i \leq N_3), x_{4i} = h_4 i(-N_4 \leq i \leq N_4), u_i = h_5 i(-N_5 \leq i \leq N_5), N_2 = 5, N_3 = 5, N_4 = 5, N_5 = 5, N = (N_2) \times (N_3) \times (N_4) \times (N_5) = 625$, increment $h_2 = 0.1, h_3 = 0.01, h_4 = 0.1, h_5 = 0.1$. The initial condition is $z_0 = [0\ 0\ \theta\ 0\ 0]^T$ with value of angle, θ is 33^o.The simulation are done for three different values of Q_n. Where, in simulation 1: $q_2 = 1.0, q_3 = 1.0, q_4 = 1.0, q_5 = 1.0$, simulation 2: $q_2 = 14.0, q_3 = 14.0, q_4 = 14.0, q_5 = 14.0$ and simulation 3: $q_3 = 0.1, q_3 = 0.1, q_4 = 0.1, q_5 = 0.1$.

The graph in Fig.4 and Fig.5 are the results for the simulation. The result shows that not only the output of system $y = x_1 = x$, but the value of $x_3 = \theta$ also converges to zero. The effect of varying the value of matrix Q_n also can be observe in the result. The simulation shows that the fuzzy servo control can stabilize inverted pendulum system.

5 CONCLUSION

In this paper, we discuss about the application of the fuzzy servo control on inverted pendulum system. The theory used have been explained in detail and the simulations have been done. As shown in the result, the output of the system follows the reference given and converges to the reference value as desired. For future work, study of characteristic of the proposed method will be done by doing the simulation using other system together with the study of the stability issue.

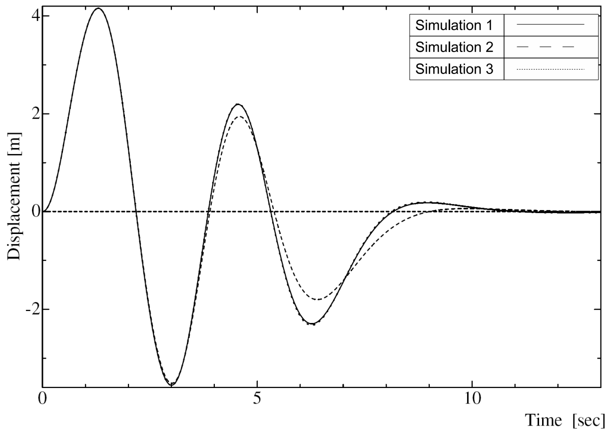

Fig. 4. Simulation result for $y = x_1 = x$

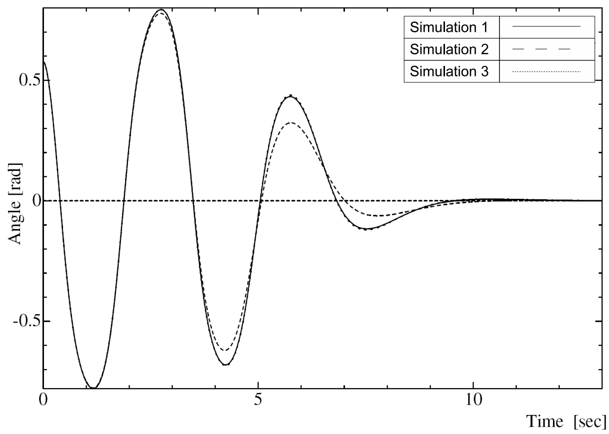

Fig. 5. Simulation result for $x_3 = \theta$

REFERENCES

[1] T.Takagi and M.Sugeno, Fuzzy Identification of systems and its application to modeling and control, IEEE Transactions on Systems, Man and Cybernetics, Vol.15, No.1, 116-132,1985.

[2] E.J.Davison and H.W.Smith, Pole Assignment in Linear Time-Invariant Multivariable System with Constant Disturbances, Automatica, Vol.7, 489-498, 1971.

[3] H.Hikita, S.Koyama and R.Miura, The Redundancy of Feedback Matrix and the Derivation of Low Feedback Gain Matrix in Pole Assignment, Transactions of the Society of Instrument and Control Engineers, Vol.11, No.5, 556-560, 1975. (in Japanese)

The Seventeenth International Symposium on Artificial Life and Robotics 2012 (AROB 17th '12),
B-Con Plaza, Beppu, Oita, Japan, January 19-21, 2012

A lightweight sensing method of tooth-touch sound for disabled person using remote controller

Akira Yamawaki[1] and Seiichi Serikawa[1]

[1] Kyushu Institute of Technology
1-1, Sensui, Tobata, Kitakyushu, Fukuoka 804-8550, Japan
yama@ecs.kyutech.ac.jp

Abstract: To support disabled people using remote controllers, biological signals have been applied to. We propose a lightweight sensing method extracting the tooth-touch without a sophisticated signal processing to eliminate the normal audio sound. Proposal uses a shock wave (i.e. ultrasonic wave) which is generated when the upper and lower tooth hit each other, instead of the sound wave of tooth-touch. By our method, the signal processing has only to perform a high-pass filter eliminating lower frequency domain than the ultrasonic domain. Through the preliminary experiment with a conventional microphone, we show that the tooth-touch has the larger power than the voice sounds in the ultrasonic region. Then, we design the filtering hardware to implement a small and cheap SoC. Through the implementation to the FPGA, and the simulation, we show that our hardware is small and has the enough performance for a real-time operation.

Keywords: Disable people, Supporting system, Remote control, Tooth-touch, Ultrasonic

1 INTRODUCTION

Since the remote controllers for the house appliances are becoming complex, a method supporting disabled people to use them is very important for providing more efficient social life. To tackle such problem, the biological signals such as voice, eye blinks, chin operated control sticks, mouth sticks [1], and brain computer interfaces [2, 3] have been applied to the supporting systems.

The tooth-touch sound is one of the simplest biological signals, i.e. the simplest human actions. It can be easily sensed by the trivial sensors such as electret condenser microphone. In general, to realize the remote controller by the tooth-touch sound, the sequences of the tooth-touch sounds are converted to the operation code sequences [4]. However, since the tooth-touch sound is mixed with the normal audio sound, the sophisticated signal processing to extract only the tooth-touch sound is needed [4]. In order to spread the supporting system using tooth-touch sound to many disabled people, the system must be very cheap, small and low-power consumption for the battery. That is, the signal processing has to be simple and mature enough to realize a low-cost hardware module which can be mounted to a cheap system-on-chip (SoC).

This paper proposes a lightweight sensing method extracting the "**tooth-touch**" that does not need a sophisticated signal processing to eliminate the normal audio sound. This method uses an shock wave (i.e. ultrasonic wave) which is generated when the upper tooth and the lower tooth hit each other, instead of the sound wave of tooth-touch. Conventional microphones such as electret condenser microphone have a sensitivity to the ultrasonic wave. By our proposed method, the the signal processing extracting the tooth-touch has only to perform a well-known filter eliminating lower frequency domain than the ultrasonic domain.

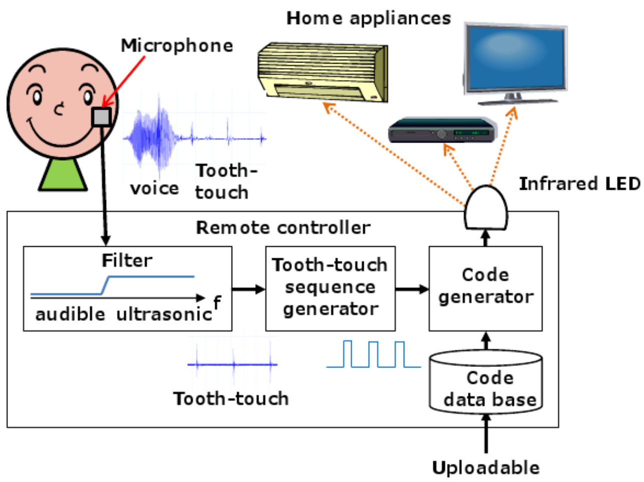

Fig. 1. System Overview.

The rest of this paper is organized as follows. Section 2 describes the system overview which employs our proposed method. Section 3 confirms that the ultrasonic wave can be detected by the conventional microphone, while hitting the upper tooth and the lower tooth. Section 4 designs the filtering hardware based on the above analysis by the conventional FFT and IFFT pair [5]. Then, Section 5 shows the performance and the hardware size of our filter hardware. Finally, Section 6 concludes this paper.

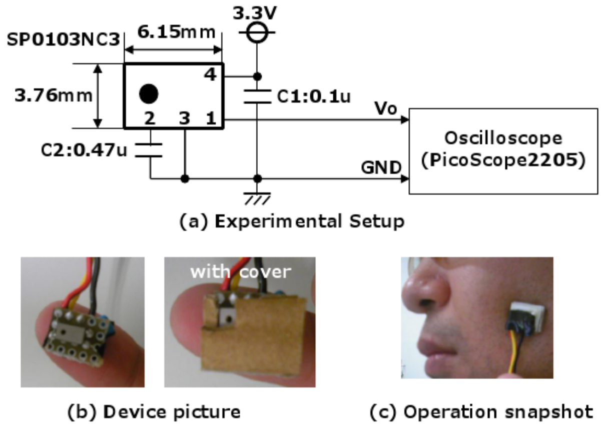

Fig. 2. Prototype Hardware.

2 SYSTEM OVERVIEW

Fig. 1 shows a system overview employing our proposed method. A microphone which has sensitivity to the ultrasonic region is attached to the cheek of the user. This is because if the microphone resides in front of the mouth, it may disturb the user's talking, eating, drinking and so on.

The shock wave is generated when one material strikes another material [8]. That is, when the upper tooth strikes the lower tooth, the ultrasonic wave that is equal to the shock wave may also be generated. However, this case would need to strike them rather strongly compared with the normal chewing. In general, many cheap and trivial microphones can generate some output to the ultrasonic wave [6, 7]. Thus, a special and expensive microphone is not needed to sense the ultrasonic wave.

The waveform from the microphone includes the voice and the tooth-touch. To leave only the ultrasonic wave of the tooth-touch from the waveform, it is input to a highpass filter with the cutoff frequency near the entrance of the ultrasonic region.

To make the command sequence from the tooth-touch sequence, the waveform including only the ultrasonic wave is rectified to the pulse wave. Considering of the number, the time duration and the time interval of pulses, the command sequence is generated [4]. Finally, the remote controlling code is generated by matching the generated command sequence with the registered it in the data base.

The data base can be updated arbitrarily. By using the data base, the differences among the makers and the products of the same maker can be hidden.

3 WAVEFORM ANALYSIS

3.1 Experimental Setup

To confirm that the ultrasonic wave can be detected by the conventional microphone, while hitting the upper tooth and the lower tooth, we have developed a prototype hardware shown in Fig. 2.

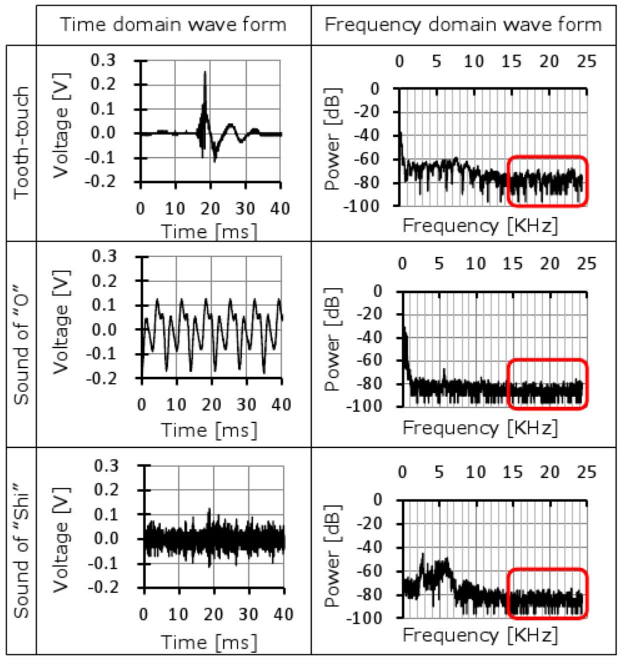

Fig. 3. Waveform Analysis.

The microphone used is the SP0103NC3 of Knowles Acoustics co. which has the wide sensitivity ranging from 100Hz to 10KHz or more [6]. The microphone is given 3.3V power. The capacitor of C1 in Fig. 2 (a) is a bipass condenser. This microphone includes an amplifier. The capacitor C2 is used to make its gain 10 times. Fig. 2 (b) is the pictures of the device we have developed. We also have made a cover of the corrugated cardboard so that the microphone does not contact directly to the cheek. When measuring, the microphone with the cover is attached to the user's cheek as shown in Fig. 2 (c).

We have probed the output voltage of the microphone by the oscilloscope, PicoScope2205 [9]. Via this oscilloscope, the waveform is acquired into the personal computer. The acquired waveforms are analyzed by the FFT we have developed by C language at the frequency domain. The rectangular window is used in this analysis. The time frame is about 42 ms and the number of data points is 2048. Thus, the sampling period is 20.5 us and the sampling frequency is 48 KHz. Consequently, the FFT can analyze the frequency ranging from 0 Hz to 24 KHz, with the resolution of about 23 Hz.

3.2 Result and Discussion

The waveforms of the time and frequency domains are shown in Fig. 3. As shown in Fig. 3, the tooth-touch has the larger power than that of the voice sounds, in the ultrasonic region from 15 KHz to 24 KHz. The difference between them reaches about 10 dB. This fact indicates that a conventional microphone can actually sense the shock wave generated by

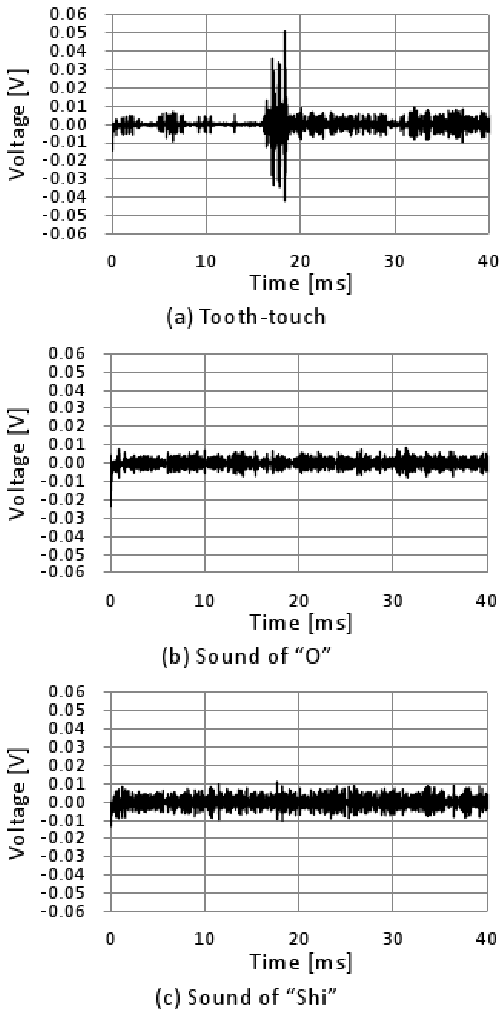

Fig. 4. Filtered Waveform by FFT–IFFT Pair.

the tooth-touch that the voice sounds never include.

Through the analysis mentioned above, the highpass filter with the cutoff frequency of 15 KHz is built by using FFT–IFFT pair [5]. This filter pads 0 from DC to 15 KHz on the waveform of the frequency domain generated by the FFT. Then, the filtered wavform of the time domain is regenerated by IFFT to this padded waveform of the frequency domain. This result is shown in Fig. 4. The waveform of the tooth-touch shows obviously larger peaks than those of the voice sounds. Thus, by the simple method setting the appropriate voltage threshold, the tooth-touch can be detected except for the voice sounds.

4 HARDWARE DESIGN

Fig. 5 is an FFT filter hardware we have designed. It has 6 pipelined stages. This hardware employs the decimation-in-frequency (DIF) radix-2 FFT. The width of the real number and the imaginary number is 16 respectively. That is, the value is the fixed-point number with 16bit width. The decimal point is set to the 1bit lower point from MSB. Thus, the input data must be normalized to [-1,1).

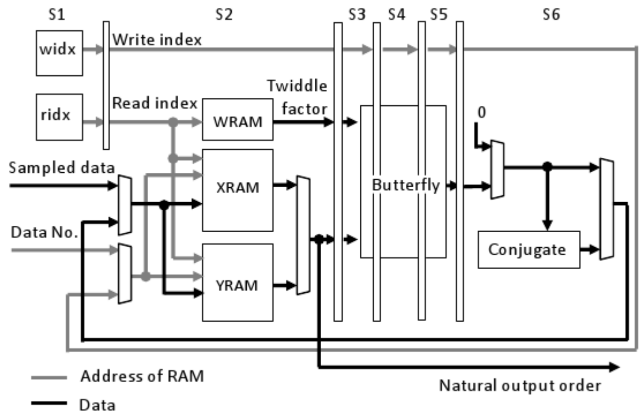

Fig. 5. Pipelined FFT Filter Hardware.

The sampled data comes from an AD converter to the data RAM (initially XRAM) according to the sampling rate used. Once the data RAM is filled with the sampled data, this hardware starts the pipelined execution. The FFT is constructed by log2(number of data points) stages. Our hardware executes the pipelined execution at each stage in the FFT. Thus, the continuous stages in the FFT are sequentially executed.

In each FFT stage, this hardware outputs the intermediate results calculated at the current stage to the temporary RAM (initially YRAM). Until the forward FFT finishes, this hardware uses the data RAM and temporary RAM, flipping their role per stage. In the final stage of the forward FFT, this hardware conjugates the complex number and stores the temporary RAM in order to execute the inverse FFT (IFFT) next. At the same time, the result with the index less than the index corresponding to the cutoff frequency is set to 0 in order to play the role of the highpass filter.

Once the forward FFT finishes, the IFFT starts immediately using the processed data in the internal RAM. Since all input data of IFFT has already been conjugated, the IFFT has only to perform the same execution as the FFT. After the IFFT, the filtered data in the data RAM are outputted sequentially to a DA converter according to the sampling rate.

This hardware consumes the $(6 + N)$ clocks in each FFT stage. The 6 clocks are for filling the pipeline with the data. The N is the number of data points. Thus, the forward and inverse FFT takes the $(2 \times log2(N) \times (6 + N))$ clocks for the completion of the FFT filter.

5 HARDWARE EVALUATION

5.1 Size and Clock Speed

To evaluate the amount of hardware and the achievable clock speed, we have implemented our hardware and the conventional FFT hardware to FPGA. The used tool is ISE13.2 and the used FPGA is spartan 6. The conventional hardware is generated by the Xilinx IP generation tool (Core-

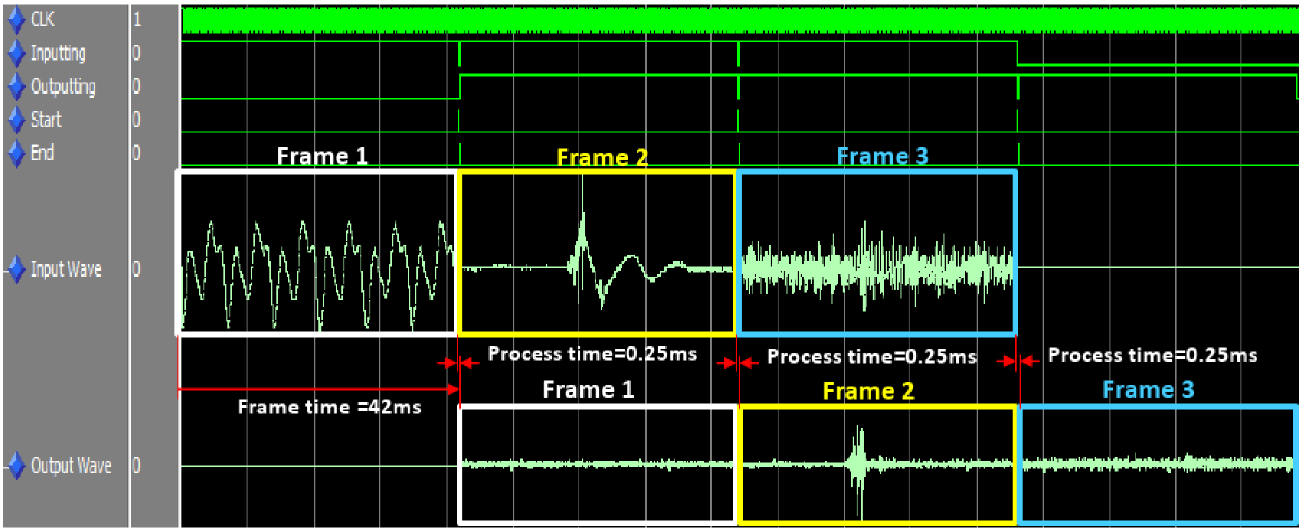

Fig. 8. Execution Snapshot.

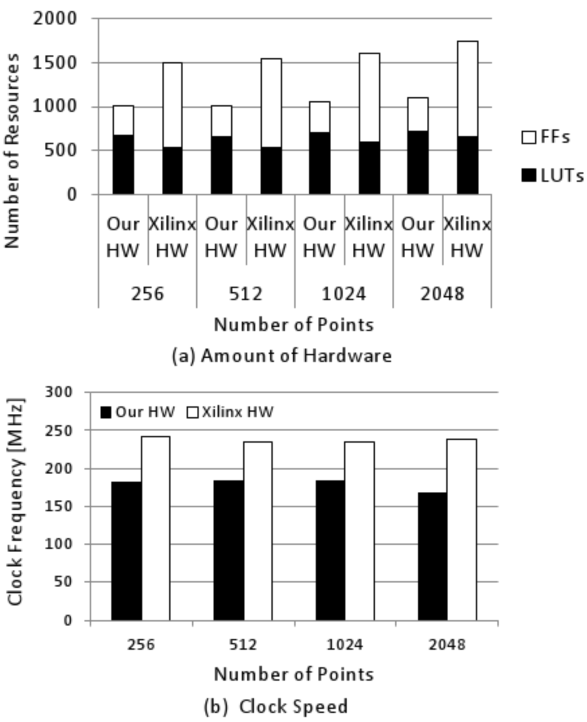

Fig. 6. Result of Hardware Evaluation.

Gen) [10]. The Xilinx FFT can switch the forward and reverse operations by the input signal. The parameters of the conventional FFT hardware generated by the CoreGen have been chosen where the hardware architecture of each other becomes equivalent.

Fig. 6 shows the result of implementation. Our hardware is smaller than the Xilinx FFT. However, the achievable clock speed of our hardware is less than the Xilinx FFT. This is because the Xilinx FFT may have deeper pipeline of the butterfly calculation than our hardware. That is, the Xilinx FFT consumes more flip-flops (FFs) than us to improve the

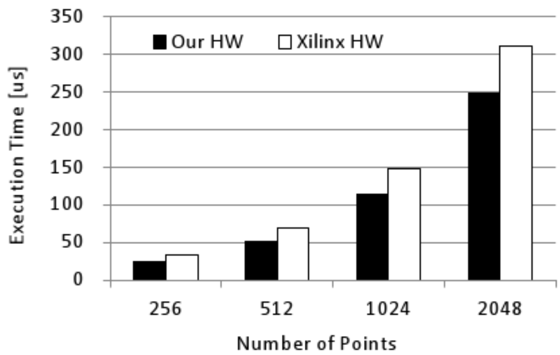

Fig. 7. Performance Evaluation.

clock speed. The hardware generated by the CoreGen is not the hardware description language (HDL) program but the netlist highly optimized to the target device. Thus, the Xilinx FFT cannot be ported to other FPGAs. In contrast, our hardware can be ported without any modification since it is described only by the generic features of HDL. In addition, the our hardware has room to optimize the pipeline structure to improve clock speed more.

5.2 Performance

Fig. 7 shows the result of the performance evaluation. We have used the ModelSim SE 10.0b as a logic simulator. The clock period is set to 10 ns; the clock frequency is 100MHz. Our hardware can improve the performance compared with the Xilixn FFT. In the Xilinx FFT, all data processed by the FFT have to be loaded from the internal output memory before IFFT. Then, the loaded data is re-inputted into the internal input memory for the Xilinx FFT setting the functionality to reverse operation. In contrast, our hardware immediately executes the IFFT using the processed data in the internal memory once the FFT finishes. The execution time that is less than 250us may be neglectable to the frame time of 42 ms as mentioned in Section 3.

Fig. 8 depicts the snapshot that our hardware actually operates in the environment that is same as Section 3. This result indicates that the execution time of our hardware is actually neglectable to the frame time. That is, our hardware has enough performance such as not to affect the realtime operation.

6 CONCLUSION

This paper has proposed a lightweight sensing method extracting the tooth-touch that does not need a sophisticated signal processing to eliminate the normal audio sound. This method uses an shock wave (i.e. ultrasonic wave) which is generated when the upper tooth and the lower tooth hit each other, instead of the sound wave of tooth-touch. By our proposed method, the the signal processing extracting the tooth-touch has only to perform a well-known filter eliminating lower frequency domain than the ultrasonic domain.

Through the preliminary experiment by using the prototype hardware with a conventional microphone, we have confirmed that the tooth-touch has the larger power than that of the voice sounds, in the ultrasonic region from 15 KHz to 24 KHz. Based on the above analysis, we have designed the filtering hardware by the conventional FFT and IFFT pair. Through the implementation to the FPGA, and the simulation near the actual environment, it has been confirmed that our hardware is small and has the enough performance for a realtime operation.

As future work, we will develop the total system as shown in Fig. 1. Then, we will perform the operation test by some testees.

REFERENCES

[1] Barnes MP (1994), Switching devices and independence of disabled people, British Medical Journal 309:1181-1182.

[2] Crag A, MaIsaac P et.al. (1997), Mind over matter: Brain signals and control of electrical devices, Today's Life Science 9:12-15.

[3] Kirkup L, Searle A, Craig A et. al. (1997), EEG system for rapid on-off switching without prior learning, Medical and Biological Engineering and Computing 35:504-509.

[4] Kuzume K, Morimoto T (2006), Hands-free man-machine interface device using tooth-touch sound for disabled persons, Proceedings of the 2010 ACM Symposium on Applied Computing:1159-1164.

[5] Press WH, Teukolsky SA, Vetterling WT, Flannery BP (2007), Numerical recipes third edition:667-668.

[6] Knowles Acoustics (2003), Product Specification: SP0103 Series with Integrated Amplifier.

[7] Panasonic (2004), Omnidirectional Back Electret Condenser Microphone Cartridge.

[8] Leighton TG (2007), What is ultrasound?, Progress in Biophysics and Molecular Biology 93:3-83.

[9] Pico Technology (2011), http://www.picotech.com.

[10] Xilinx (2011), LogiCORE IP Fast Fourier Transform v8.0 Product Specification DS808.

The Seventeenth International Symposium on Artificial Life and Robotics 2012 (AROB 17th '12),
B-Con Plaza, Beppu, Oita, Japan, January 19-21, 2012

Two-dimensional merging path generation using model predictive control

Wenjing Cao[1], Masakazu Mukai[2], and Taketoshi Kawabe[1]

[1] Graduate School of Integrated Frontier Sciences, Kyushu University, Motooka, Nishiku,Fukuoka, 819-0395, Japan
[2] Graduate School of Information Science and Electrical Engineering, Kyushu University, Motooka, Nishiku,Fukuoka, 819-0395, Japan
(Tel: 81-92-802-3691, Fax: 81-92-802-3692)

[1]bwiner@gmail.com

Abstract: In this research, the merging problem is considered in the two-dimensional space instead of the one-dimensional space. In this paper, we set up the mathematic model of the system, formulate the two-dimensional merging problem as an optimization problem and solve it by model predictive control (MPC). To compare the simulation results with the practical situation, three typical cases were researched. In order to be more practical, the initial conditions of the cases were set according to the data obtained through analyzing the helicopter-shot video. The results represent that the MPC-controlled merging maneuver carried out safely and smoothly, and the relative positions after merging is also the same with the practical results in all the three representative conditions considered in this research. The absolute values of the accelerations of the vehicles are all below 3m/s^2, which are quite practical as well. The simulation results also represented the importance of the adjustment in driving during merging. By adjusting these vehicles, this control algorithm would generate the merging path that could avoid merging accident even in the very severe condition.

Keywords: automotive control, merging, model predictive control, optimal control, path generation.

1 INTRODUCTION

As motorization grows, it is becoming more and more important to realize a safe and ecological driving. From Ohashi et al [1] and Takayama et al [2] we could know that one of the riskiest maneuvers that a driver has to perform is to merge into the traffic, especially for the beginners and the aged people. It would take a lot courage and attention for them to conduct the maneuver. Iguchi et al [3] tells that merging is also one of the reasons for traffic congestion at the same time. The traffic throughput is often reduced at the merging part.

As a result, many researchers are now working on this subject. Jula et al [4] worked on collision avoidance merging through calculating the safe region. However, this paper does not represent the exact merging way for the vehicles. It will still be a difficult problem for the driver to merge into the traffic. Lu et al [5] worked on automated vehicle merging, and provided the 'adaptive solution', but the ecological requirement was not considered.

This paper presents an algorithm for merging path generation, in which the two-dimensional merging problem was formulated as a nonlinear optimization problem. The initial conditions were set according to the helicopter-shot video data. The input constraints, and the performance function, which realizes ecology and safety, were also set realistically. With all these elements chosen, the optimization problem was solved by the C/GMRES method proposed in Otsuka [6]. To investigate the effectiveness of the control algorithm, three representative cases were researched. The computer simulation results show that in all the three conditions the algorithm could generate smooth merging and the relative positions of the two vehicles are also practical. The results of the case, which have a quite severe initial condition, also represent the function of trajectory adjustment of this algorithm, what we think is also the key point during merging. If a vehicle merges automatically under the control of this algorithm, the driver would not feel any pressure during the merging maneuver, and the ecological requirement could also be satisfied at the same time.

The rest part of this paper is arranged as follows. In the section 2 we describe the formulation of the merging problem. The simulation results and analysis are shown in the section 3. The section 4 gives some conclusions of the whole paper.

2 MERGING PROBLEM FORMULATION

Due to the difficulty of merging and the time varying nature of the traffic situation, it is essential to predict the future situation of the traffic. Taking these aspects into account, we choose nonlinear model predictive control to solve the merging problem. As shown in **Fig. 1.**, in this research, only one vehicle on the merging lane, and one vehicle on the main lane, are considered. The vehicle on the merging lane is denoted as Vehicle1, and the vehicle on the main lane is denoted as Vehicle2 in the following parts of this paper. The merging problem is formulated as the following optimization problem.

$$\min_{a} J = \int_{t}^{t+T} L(x(\tau), a(\tau), \tau) d\tau \quad (1)$$

subject to the input constraints and the vehicle dynamics.

Here, x denotes the state variables, and a denotes the input of the system, respectively. The expression of function L is described in Subsection 2.3.

The optimal control input is updated at each time step by solving the above optimal control problems during the prediction horizon T. Only the first element of the optimal control sequence is applied to the system as the actual input. The process is repeated at each time step.

2.1 Vehicle model

To save the calculation time, a simplified vehicle dynamics is used. Instead of the actual three-dimensional movement, only the horizontal motion is considered. In this paper it is assumed that the main lane can be approximated to be straight and the width of the main lane is quite a small number compared to the length of it. Then the lateral movement of Vehicle2 is omitted. We assume that Vehicle2 always moves on the middle line of the main lane. This means that the coordinate, the velocity and the acceleration of Vehicle2 in the Y-axis direction are all 0.

Under these assumptions, the state equation of the system is as follows.

$$\dot{x} = \begin{bmatrix} \dot{x}_{hx} \\ \dot{x}_{hy} \\ \dot{x}_m \\ \dot{v}_{hx} \\ \dot{v}_{hy} \\ \dot{v}_m \end{bmatrix} = \begin{bmatrix} v_{hx} \\ v_{hy} \\ v_m \\ 0 \\ 0 \\ 0 \end{bmatrix} + \begin{bmatrix} 0 \\ 0 \\ 0 \\ a_{hx} \\ a_{hy} \\ a_m \end{bmatrix} \quad (2)$$

where

$$x = [x_{hx} \;\; x_{hy} \;\; x_m \;\; v_{hx} \;\; v_{hy} \;\; v_m]^T$$
$$a = [a_{hx} \;\; a_{hy} \;\; a_m]^T$$

Here, x_{hx} and x_{hy} denote Vehicle1's coordinate in X-axis and Y-axis respectively. v_{hx} and v_{hy} denote the velocities, and a_{hx} and a_{hy} denote the accelerations of Vehicle1 in the X-axis and Y-axis respectively. The x_m, v_m and a_m denote the coordinate, the velocity and the acceleration of Vehicle2 in X-axis respectively.

During merging, the two vehicles have to adjust their velocities. Therefore the brake and the accelerator are involved. The acceleration and the deceleration have upper bounds. It is assumed that the system has the following input constraints.

$$\begin{cases} -a_{hxmax} \le a_{hx} \le a_{hxmax} \\ -a_{hymax} \le a_{hy} \le a_{hymax} \\ -a_{mmax} \le a_m \le a_{mmax} \end{cases} \quad (3)$$

Where a_{hxmax}, a_{hymax}, and a_{mmax} are the upper bounds of the absolute value of a_{hx}, a_{hy}, and a_m, respectively.

2.2 Expression of the road shape

Fig. 1. shows the figure of the merging part of the helicopter-shot roads and the initial position of the two vehicles. The ○ represents the initial position of Vehicle1 and the × represents the initial position of Vehicle2.

Fig. 1. The merging part of the roads

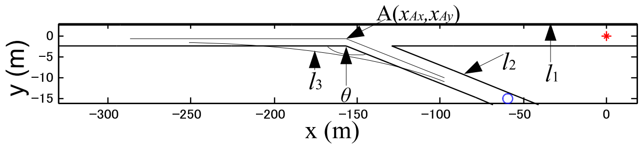

Fig. 2. The approximation results of the roads

To simplify the calculation we approximate this typical roads' figure with two straight lines and a hyperbola. The result is shown in **Fig.2.**. Choose the initial position of Vehicle2 as the origin of the coordinate system, the driving direction of Vehicle2 as the X-axis positive direction, the expressions of the lines are as follows:

$$l_1 = x_{hy} - \frac{1}{2}d = 0 \quad (4)$$

$$l_2 = kx_{hx} + x_{hy} + c = 0 \quad (5)$$

$$l_3 = 1 + \frac{(-\sin\frac{1}{2}\theta(x_{hy} - x_{Ax}) + \cos\frac{1}{2}\theta(x_{hy} - x_{Ay}))^2}{k_d(\tan\frac{1}{2}\theta)^2} - \frac{(\cos\frac{1}{2}\theta(x_{hx} - x_{Ax}) + \sin\frac{1}{2}\theta(x_{hy} - x_{Ay}))^2}{k_d} = 0 \quad (6)$$

The meanings of the variables are shown in Table 1. To keep safe, point A is set at the upper right side of the intersection point of the left side of the merging lane and the main lane.

Table 1. Variables in l_1, l_2, and l_3

d	the width of the main lane
k	the slope of the merging lane
c	a constant of the road shape
θ	the angle between the main lane and the merging lane
x_{Ax}	abscissa of the point A
x_{Ay}	ordinate of the point A
k_d	a constant of the shape of the hyperbola

2.3 Performance function

Subject to the input constrains, there are also many requirements which must be considered during the merging maneuver. These requirements are realized by the performance function as equation 1. The expression of function $L(x(\tau), a(\tau), \tau)$ is as follows.

$$\begin{aligned} L \;=\; & \frac{\omega_1}{r^2} - \omega_2 \log(l_1) - \omega_3 \log(l_2) - \omega_4 \log(l_3) \\ & + \omega_5 (v_{hx} - v_m)^2 + \omega_6 a_{hx}^2 + \omega_7 a_{hy}^2 + \omega_8 a_m^2 \\ & + \omega_9 (v_{hx} - v_i)^2 + \omega_{10} (v_m - v_i)^2 + \omega_{11} x_{hy}^2 \quad (7) \end{aligned}$$

Where ω_1, ω_2, ω_3, ω_4, ω_5, ω_5, ω_6, ω_7, ω_8, ω_9, ω_{10}, and ω_{11}, represent the weight of every term respectively, r is the relative distance of the two vehicles, defined in equation 8, and v_i is the desired value of the velocity.

$$r = ((x_{hx} - x_m)^2 + x_{hy}^2)^{\frac{1}{2}} \quad (8)$$

The cost function L consists of 11 terms. The first term is the cost due to the relative distance r. The second term, the third term and the forth term are the barrier functions to represent the road shape. Among them, the second term represents the restriction of the line l_1, which is shown in **Fig. 2.**, the third term represents the restriction of the line l_2, and the forth term represents the restriction of the line l_3. All the barrier functions are chosen as minus logarithm functions, because the restrictions of the road shape could never be violated, or there will be an accident. The fifth term describes the cost due to relative velocity, because running at the same speed would generate smooth merging. The terms from the sixth one to the eighth one describe the requirements of ecology. They minimize the accelerations and decelerations to save unnecessary fuel consumption. The ninth term and the tenth term make the two vehicles run as closely as possible at the desired value of the velocity v_i. The eleventh term is used to reduce the overshoot of Vehicle1.

3 SIMULATION RESULTS AND ANALYSIS

To investigate the effectiveness of the control algorithm, three representative cases are researched. The computer simulation was conducted with the time step $h = 0.01$s, and the prediction horizon is $T = 1$s. The values of the parameters are chosen suitably as follows: $\omega_1 = 4.0$, $\omega_2 = 0.01$, $\omega_3 = 0.01$, $\omega_4 = 0.01$, $\omega_5 = 0.01$, $\omega_6 = 0.03$, $\omega_7 = 0.01$, $\omega_8 = 0.01$, $\omega_9 = 0.01$, $\omega_1 0 = 0.01$, $\omega_1 1 = 0.01$, $d = 5$m, $k = -0.16$, $c = 24$, $\theta = 3.0$rad, $x_{Ax} = -160$m, $x_{Ay} = -2.0$m, $k_d = 0.01$, $v_i = -17$m/s (about 60km/h), $a_{hxmax} = a_{hymax} = a_{mmax} = 3$m/s^2.

3.1 Case 1

The initial conditions of the two involved vehicles in this case were set according to the data drawn from the helicopter-shot video. The obtained initial conditions are as follows: $(x_{hx}, x_{hy}) = (-59\text{m}, -15\text{m})$, $x_m = 0$m, $v_{hx} = -9.9$m/s, $v_{hy} = 1.6$m/s, $v_m = -20$m/s, $a_{hx} = 0$m/s^2, $a_{hy} = 0.03$m/s^2, $a_m = -0.05$m/s^2. The actual merging trajectories of this situation is shown in **Fig. 3.**, while the simulation result is shown in **Fig. 4.**. In **Fig. 3.** the ◯ represents the position of Vehicle1 and the × represents the position of Vehicle2 of every time respectively. In **Fig. 4.** The ∘ represents the position of Vehicle1 and the ∗ represents the position of Vehicle2 of every time respectively. The time in these two figures is: $t_0 = 0$s, $t_1 = 4$s, $t_2 = 8$s, $t_3 = 12$s, $t_4 = 16$s respectively. **Fig. 5.** shows the variation of the variables during the merging maneuver.

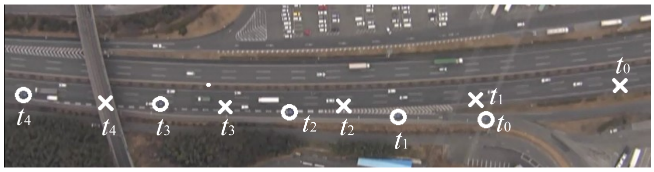

Fig. 3. The actual merging result of the case 1

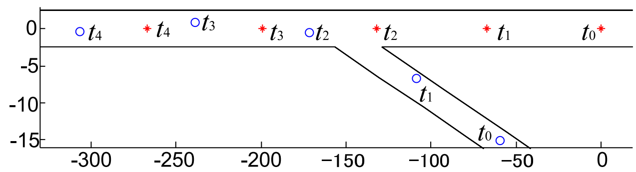

Fig. 4. Merging trajectories of the two vehicles of the case 1

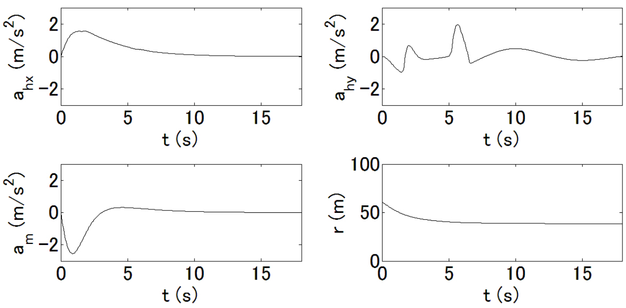

Fig. 5. Variation of the variables in the case1

We could see from **Fig. 4.** that Vehicle1 merged into the main lane without hitting any side of the main lane and the merging lane, and ran in front of Vehicle2 after merging. The time-history of r is shown in the second diagram in the second row of **Fig. 5.**. From it we could see that during the merging maneuver Vehicle1 kept an appropriate distance with Vehicle2. We could also see from **Fig. 5.** that all accelerations were kept below 3m/s^2.

3.2 Case 2

The initial condition of the two vehicles were set as follows: $(x_{hx}, x_{hy}) = (-59\text{m}, -15\text{m})$, $x_m = -59$m, $v_{hx} = -9.9$m/s, $v_{hy} = 1.6$m/s, $v_m = -20$m/s. Accelerations are all the same with the case 1. Since $x_{hx} = x_m$, $|v_{hx}| < |v_m|$, and accelerations are very small, without control, Vehicle1 would go to the behind of Vehicle2 and follow it. The simulation results, shown in **Fig. 6.** and **Fig. 7.**, represented that Vehicle1 merged to the behind of Vehicle2 successfully just as it was supposed to be.

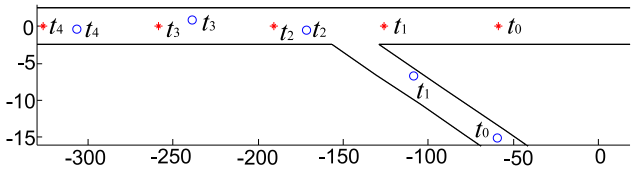

Fig. 6. Merging trajectories of the two vehicles of the case 2

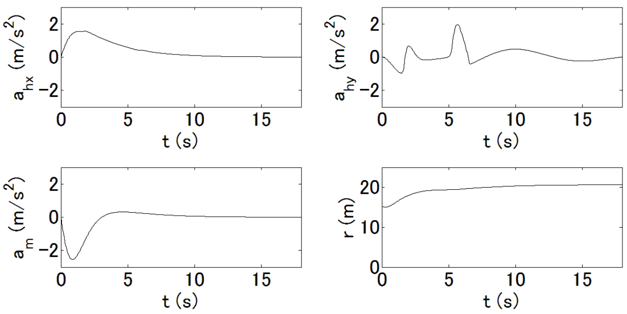

Fig. 7. Variation of the variables in the case 2

We could see from **Fig. 7.** that Vehicle1 kept an appropriate distance with Vehicle2 too. Accelerations are always below 3m/s^2 as well.

3.3 Case 3

As it was considered in the two dimensional space, x_{hy} could be involved in the calculation of r. This enables an extreme condition, that is: $(x_{hx}, x_{hy}) = (-59\text{m}, -15\text{m})$, $x_m = -59\text{m}$, $v_{hx} = -16\text{m/s}$, $v_{hy} = -1.6\text{m/s}$, $v_m = -16\text{m/s}$, $a_{hx} = 0\text{m/s}^2$, $a_{hy} = -0.03\text{m/s}^2$, $a_m = 0\text{m/s}^2$. Since $x_{hx} = x_m$, $v_{hx} = v_m$, $a_{hx} = a_m$, if no adjustment of trajectories is employed, the two vehicles will collide with each other. However the simulation results shown in **Fig. 8.** and **Fig. 9.** represented that Vehicle1 merged successfully to the behind of Vehicle2, and kept an appropriate distance. The accelerations were kept below 3m/s^2. The relative distance was more than 2m, hence the collision was avoided successfully.

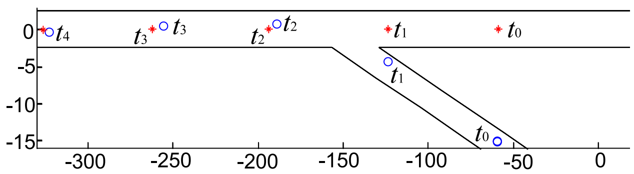

Fig. 8. Merging trajectories of the two vehicles of the case 3

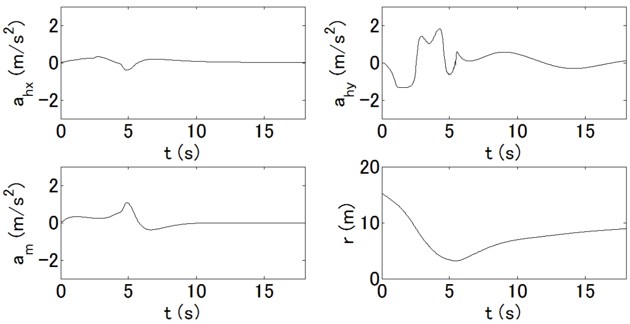

Fig. 9. Variation of the variables in the case 3

4 CONCLUSION

With the algorithm proposed in this paper, in all the three representative conditions the trajectories of the two vehicles showed that the merging vehicle merged successfully. The distance between the merging vehicle and the main lane vehicle is kept long enough during the merging maneuver as well. So the requirement of safety is satisfied. Besides, both the absolute values of the accelerations of the two vehicles can be kept below the specified value. Furthermore, the relative positions of the two vehicles in the simulation results are the same with the actual situations. That is, in the case 1 Vehicle1 became the preceding vehicle, which is the same with the helicopter-shot result, and in the case 2 Vehicle1 became the following vehicle as it should be. Remarkably, in the case 3 Vehicle1 slowed down a little to keep the safe distance between Vehicle2 and itself, instead of colliding with Vehicle2. This clearly shows the function of trajectory adjustment of this algorithm, which we think is also the key point of merging. The simulation results of the three cases show that the proposed algorithm enables smooth merging. Under the control of this algorithm, the two vehicles could merging smoothly by adjusting with each other.

REFERENCES

[1] Ohashi M, Uchida T, Yai T (2000), A study on the measurement of mental load and safety evaluation in the condition of driving on expressway(in Japanese). Journal of the City Planning institute of Japan 35:541 - 546
[2] Takayama J, Nakayama S, Uno N et al (2002), An analysis of the giveway behavior of vehicles around the joint department of arterial roads(in Japanese). Infrastructure Planning Review 19(4):847 - 852
[3] Iguchi T, Wakita Y, Shimizu H et al (2009), Improvement of traffic jam at merging point of roads by using multicar-following model(in Japanese). Transactions of the Japan Society of Mechanical Engineers. C 75(758):2695 - 2702
[4] Jula, H., Kosmatopoulos, E.B., Ioannou, P.A. (2000), Collision avoidance analysis for lane changing and merging. Vehicular Technology, IEEE Transactions on 49(6):2295 - 2308
[5] Lu X.-Y., Hedrick, J.K.(2003), Longitudinal control algorithm for automated vehicle merging. International Journal of Control 76(2):193-202
[6] Ohtsuka T (2004), A continuation/GMRES method for fast computation of nonlinear receding horizon control. Automatica 40(4):563-574

The Seventeenth International Symposium on Artificial Life and Robotics 2012 (AROB 17th '12),
B-Con Plaza, Beppu, Oita, Japan, January 19-21, 2012

Model predictive control of a power-split hybrid electric vehicle system

Kaijiang Yu[1], Masakazu Mukai[1], and Taketoshi Kawabe[1]

[1] Graduate School of Information Science and Electrical Engineering, Kyushu University, Fukuoka 819-0395, Japan
(Tel: 81-92-802-3691, Fax: 81-92-802-3692)

[1]yukaijiang@cig.ees.kyushu-u.ac.jp

Abstract: This paper presents a model predictive control (MPC) approach for the energy management problem of a power-split hybrid electric vehicle (HEV) system. The MPC is suggested to optimally share the road load to the engine and the battery. By analyzing the configuration of the power-split HEV system, we developed a simplified model for better implementation of MPC. The MPC problem is solved using numerical computation method: continuation and generalized minimum residual (C/GMRES) method. The computer simulation results showed that the fuel economy was improved using the MPC approach than the ADVISOR rule based approach over three driving cycles respectively. We conclude that the MPC approach is effective for the application of power-split HEV systems energy management and has the potential for real-time implementation. The simplified modeling method of the power-split HEV system configuration can be applied to other configurations of HEV.

Keywords: energy management, hybrid electric vehicle, model predictive control

1 INTRODUCTION

In recent years, HEV has become a research hotspot due to rising cost of fossil fuels and environmental problems. HEV has an electrical power source and it can downsize the engine, optimize the engine operating point and recuperate braking energy, which helps to improve fuel economy, and reduces emissions Serrao [1].

The key technology of HEV is its energy management. A lot of works have been published on the energy management problem of HEV systems. These approaches are typical in a family of optimal control techniques. And they can be subdivided into four categories: numerical optimization, analytical optimal control theory, instantaneous optimization, heuristic control techniques Serrao [1]. The most representative of numerical optimization is dynamic programming (DP) Serrao [1] and Liu et al [2] . However DP is based on known driving cycle which is impossible to get in reality. A kind of analytical optimal control techniques is Pontryagin's minimum principle Kim et al [3]. It gives necessary conditions that the optimal solution must satisfy. It also needs to know the entire driving cycle in prior. The instantaneous optimization includes the equivalent consumption minimization strategy (ECMS) Serrao [1]. It is based on instantaneous optimization and is easy to implement in real time. However it can not garantee the optimality over the whole driving cycle. Heuristic control techniques like rule based control strategies are robust but they are impossible to guarantee the optimality.

Although MPC Borhan et al [4] is also in numerical optimization class, its advantage is its predictive nature which can use vehicle-road-traffic information in the near future Deguchi et al [5] and Kamal et al [6] and be applicable to unknown driving cycles Kaku et al [7]. Based on a simple and accurate model of the system, MPC can provide real time control for the system.This paper examines energy management problem of a power-split HEV system over known and unknown driving cycles. Because the power-split HEV system has functionality of both series and parallel HEV systems, it has more modes to operate the energy management system for better fuel economy. The simplified modeling method by introducing contraints to reducing the system degrees of freedom is presented.

The rest of this paper is organized as follows: In Section 2, simplified model of the power-split HEV system and MPC algorithm are presented. Section 3 gives comparative simulation results between the MPC approach and the ADVISOR Wipke et al [8] rule based approach over three different driving cycles. Section 4 provides conclusions.

2 MODELING OF THE POWER-SPLIT HEV SYSTEM

The configuration of the power-split HEV system is shown in **Fig. 1.**. FD rerespents the final drive. The power split device (PSD) is the key component of the power-split HEV system and has both functionality of speed coupler and continuously variable transmission (CVT). There are five dynamic components: the engine, the battery, two motor/generators (M/G), and the wheels in this power-split HEV system, the only dynamic state to be considered in the optimal control problem based on known driving cycle is the battery state of charge (SOC) which can simplify the MPC algorithm for implementation. This simplification is possible because we introduce four constraints: the road load, the torque and speed relationship of the speed coupler, the power flow relationship among the five components, and the engine optimal operating line (OOL) using CVT. We divided the optimal control problem into two levels. The high level controller determines the optimal battery power and the low level controller determines the optimal torque and speed of the engine and the motor/generators. In this paper we focus on the high level controller.

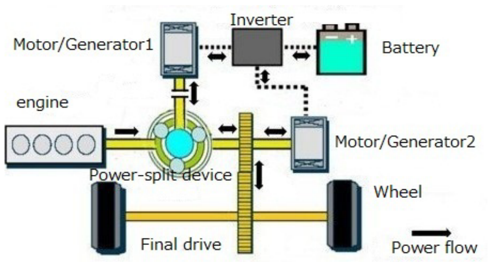

Fig. 1. Configuration of the power-split HEV system. Diagram adapted from Liu et al [2]

The torque and speed relationship of the speed coupler can be expressed as Ehsani et al [9]:

$$\begin{aligned} \tau_{eng}(t) &= -(1+\frac{R}{S})\tau_{M/G1}(t) \\ \tau_{eng}(t) &= -(1+\frac{S}{R})(\tau_{M/G2}(t) - \frac{\tau_{req}(t)}{g_f}) \\ S\omega_{M/G1}(t) &+ R\omega_{M/G2}(t) - (S+R)\omega_{eng}(t) = 0 \end{aligned} \tag{1}$$

where S and R are the number of sun gear and ring gear teeth respectively, $\tau_{M/G1}$, $\tau_{M/G2}$, τ_{req}, and τ_{eng} are the torques of the M/G1, M/G2, the road load and the engine respectively, $\omega_{M/G1}$, $\omega_{M/G2}$ and ω_{eng} are the angular speeds of the M/G1, the M/G2, and the engine respectively.

The power flow relationships among the five components at the inverter and the power split device in **Fig. 1.** are given as:

$$\begin{aligned} P_{batt}(t) &= P_{M/G1}(t) + P_{M/G2}(t) \\ P_{req}(t) &= P_{M/G1}(t) + P_{M/G2}(t) + P_{eng}(t) \end{aligned} \tag{2}$$

where P_{batt}, $P_{M/G1}$, $P_{M/G2}$, P_{eng}, and P_{req} are the power of the battery, the M/G1, the M/G2, the engine, and the road load.

We assume that the engine always works along its OOL using CVT which can also be considered as a constraint. When the engine power is known, by looking up the table of OOL, the engine speed and torque can be obtained.

We evaluate the fuel consumption using Willans line method to reduce the complexity of the engine fuel consumption model. It was found that good approximation are obtained using the Willans line method Serrao [1]. The fuel consumption can be expressed as:

$$\dot{m}_f(t) = \dot{m}_f(P_{req}(t) - P_{batt}(t)) \approx c_f(P_{req}(t) - P_{batt}(t)) \tag{3}$$

where c_f is a constant.

The road load which are the vehicle speed and the required power at the wheels is known when the driving cycle is known. From the configuration of the power-split HEV system, the M/G2 speed is also known as:

$$\omega_{M/G2}(t) = \frac{g_f}{r_w} v_{req}(t) \tag{4}$$

where $\omega_{M/G2}$ is the speed of the M/G2, g_f is the final drive gear ratio, r_w is the wheel radius, v_{req} is the required vehicle speed by the driving cycle.

When the drivng cycle is known, the system dynamics is reduced to the battery dynamics. The optimization objective is only the fuel economy. The only state variable is the battery SOC, x_{SOC}, and the control input is the battery power. The battery model can be expressed as Kim et al [3]:

$$\dot{x}_{SOC} = -\frac{V_{OC} - \sqrt{V_{OC}^2 - 4P_{batt}R_{batt}}}{2R_{batt}Q_{batt}} \tag{5}$$

where V_{OC}, R_{batt}, and Q_{batt} are the open circuit voltage, the internal resistance, and the capacity of the battery.

When the driving cycle is unknown, the system dynamics includes the battery and the vehicle dynamics. Both the fuel economy and the driving profile are optimized. The system model is then represented by

$$\dot{x} = \begin{bmatrix} v \\ w - \frac{1}{2}\rho C_D A v^2/m - g\mu - g\sin(\theta(p)) \\ k_p(u_1 - w) \\ -\frac{V_{OC} - \sqrt{V_{OC}^2 - 4P_{batt}R_{batt}}}{2R_{batt}Q_{batt}} \end{bmatrix} \tag{6}$$

$$\begin{aligned} x &= [p\ v\ w\ x_{SOC}]^T \\ u &= [u_1\ P_{batt}]^T \end{aligned} \tag{7}$$

where p, v, and w are the vehicle position, speed, and acceleration or deceleration converted from the traction force or brake force. ρ, C_D, A, m, g, μ, and $\theta(p)$ are the air density, the air drag coefficient, the frontal area of the vehicle, the vehicle mass, the gravity acceleration, the rolling resistance coefficient, and the road grade. u_1 and k_p are the vehicle acceleration or deceleration control input and the delay constant.

Due to the simplified modeling method derived from the power relationship among the engine, the battery and the road load which is general in the HEV configurations, it can be applied to other HEV configurations.

3 MODEL PREDICTIVE CONTROL

The optimal control problem based on known driving cycle is defined as:

$$\text{Min. } J_{known} = \int_t^{t+T} L_{known}(x_{SOC}(\tau|t), P_{batt}(\tau|t))d\tau \tag{8}$$

$$\begin{aligned} \text{Subject to:} \quad & SOC_{min} \le x_{SOC}(\tau|t) \le SOC_{max} \\ & P_{battmin} \le P_{batt}(\tau|t) \le P_{battmax} \end{aligned} \tag{9}$$

where T is the prediction horizon, $_{min}$ and $_{max}$ denote the minimum and maximum bounds of battery SOC and power.

The objectives of this optimal control problem is to minimize the fuel consumption, meanwhile, the battery SOC is maintained between the thresholds. This is achieved by minimizing the cost function L_{known} including three terms: the fuel use, the engine use and the mechanical brake use, and the deviation of battery SOC from the reference value. The cost function L_{known} is defined as follows:

$$\begin{aligned}L_{known} &= w_1 c_f (P_{req} - P_{batt})/(1 + e^{-\beta(P_{req} - P_{batt})}) \\ &+ w_2 (P_{req} - P_{batt})^2 + w_3 (x_{SOC} - SOC_d)^2 \\ &+ w_4 (-\ln(x_{SOC} - SOC_{min}) - \ln(SOC_{max} - x_{SOC})) \quad (10)\end{aligned}$$

where SOC_d is the desired SOC value. w_1, w_2, w_3 and w_4 are the weights.The sigmoid function is chosen to evaluate the vehicel brake fuel comsumption. The log barrier function is used as a penalizing term for violations of state contraints.

The optimal control problem based on unknown driving cycle is defined as:

$$\text{Min. } J_{unknown} = \int_t^{t+T} L_{unknown}(x(\tau|t), u(\tau|t)) d\tau \quad (11)$$

$$\begin{aligned}\text{Subject to: } \quad & SOC_{min} \le x_{SOC}(\tau|t) \le SOC_{max} \\ & P_{battmin} \le P_{batt}(\tau|t) \le P_{battmax} \\ & u_{1min} \le u_1(\tau|t) \le u_{1max} \quad (12)\end{aligned}$$

The cost function $L_{unknown}$ is defined as follows:

$$\begin{aligned}L_{unknown} &= w_x L_x + w_y L_y + w_z L_z + w_d L_d + w_e L_e + w_f L_f \\ L_x &= (w - \frac{1}{2}\rho C_D A v^2 / m - g\mu)^2 \\ L_y &= (v - v_d)^2 \\ L_z &= c_f (mwv - P_{batt})/(1 + e^{(-\beta(mwv - P_{batt}))}) \\ L_d &= (x_{SOC} - SOC_d)^2 \\ L_e &= (mwv - P_{batt})^2 \\ L_f &= -\ln(x_{SOC} - SOC_{min}) - \ln(SOC_{max} - x_{SOC}) \quad (13)\end{aligned}$$

where w_x, w_y, w_z, w_d, w_e, and w_f are the weights, v_d is the desired vehicle speed. The first term of $L_{unknown}$ indicates the acceleration and braking cost.

At each time t, the optimal control input is computed by solving the above optimal control problems during the prediction horizon T. Only the first element of the optimal control sequence is applied. At the next time step, the prediction horizon moves forward, and the process is repeated.

4 COMPUTER SIMULATION

4.1 Simulation conditons

In this simulation, vehicle parameters are obtained from ADVISOR 2002. **Fig. 2.** gives the engine OOL of the power-split HEV system. The vehicle parameters are m=1368 [kg], ρ=1.23 [kg/m³], C_D=0.3, A=1.746 [m³], g=9.8 [m/s²], μ=0.015, V_{OC}=307.85 [V], R_{batt}=1.004 [Ω] and Q_{batt}=6 [Ah], c_f=0.0874. The control parameters are β=0.5, SOC_d=0.7, SOC_{min}=0.6, SOC_{max}=0.8, k_p=10, $P_{battmin}$=-20 [kW], $P_{battmax}$=20 [kW], u_{1min}=-3 [m/s^2], u_{1max}=3 [m/s²], v_d=50 [km/h], w_1=4000, w_2=5000, $w_3 = 3.5 \times 10^7$ and $w_4 = 10^5$, w_x=10, w_y=20000, w_z=40000, $w_d = 9 \times 10^7$, w_e=2200 and w_f=100. The MPC problem is solved using a numerical computation method: continuation and generalized minimum residual (C/GMRES) method Ohtsuka et al [10].

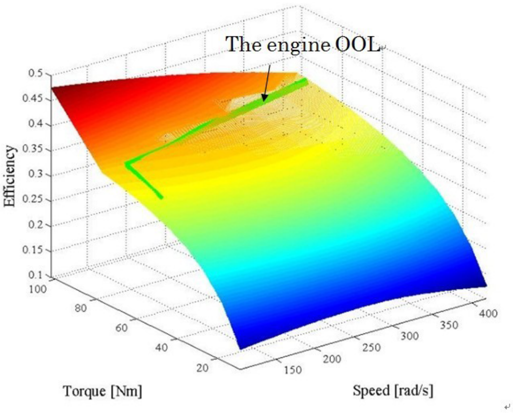

Fig. 2. The engine OOL of the power-split HEV system

Driving cycle 1 included acceleration, deceleration, and cruise scenario (see the first row of **Fig. 3.**). Driving cycle 2 was the standard driving cycle: Japan 10-15 (see the first row of **Fig. 4.**). Driving cycle 3 was an unknown driving cycle with road slopes (see the first and second row of **Fig. 5.**).

4.2 Simulation results

Driving cycle 1:

The simulation results of driving cycle 1 were presented in **Fig. 3.** using the ADVISOR simulation results as comparison. We observed from these results that the MPC algorithm performed better than the ADVISOR rule based algorithm. In the case of MPC, the battery assisted vehicle driving and recuperated vehicle braking power properly.

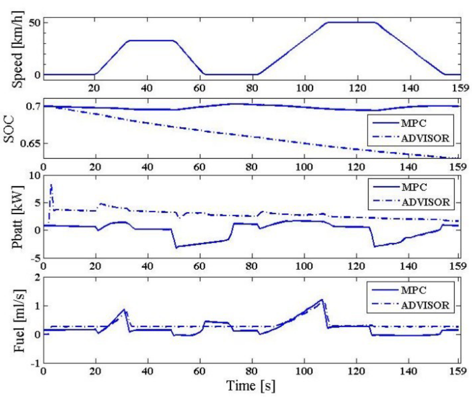

Fig. 3. Performance of the MPC algorithm and the ADVISOR rule based algorithm over driving cycle 1

Driving cycle 2:

Japan 10-15 simulation results (see **Fig. 4.**) showed that the MPC algorithm performed similarly as driving cycle 1.

Driving cycle 3:

The unknown driving cycle simulation results (see **Fig. 5.**) showed that the MPC algorithm could also use the road slope information well to reduce the fuel consumption. The vehicle accelerated before the upslope to make use of the kinetic energy. The battery recuperated vehicle braking power during the vehicle downslope driving. Since over this low road load

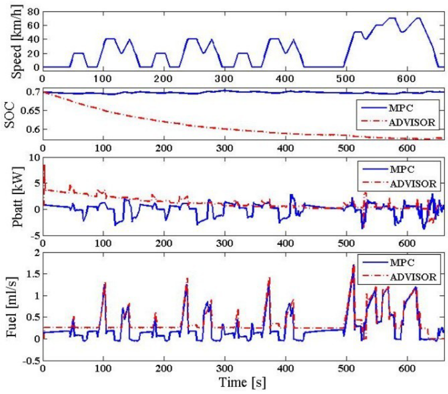

Fig. 4. Performance of the MPC algorithm and the ADVISOR rule based algorithm over driving cycle 2

driving cycle the ADVISOR rule-based algorithm used the motor assist driving mode, the fuel consumption reduction by MPC was not evident.

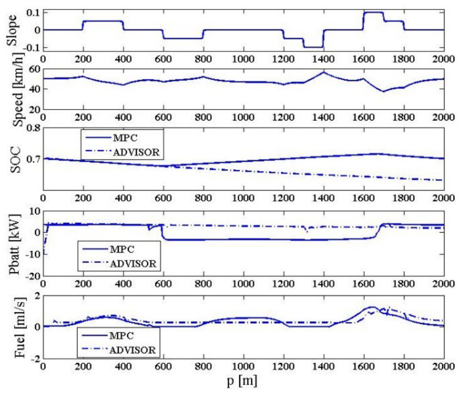

Fig. 5. Performance of the MPC algorithm and the ADVISOR rule based algorithm over driving cycle 3

The overall fuel economy results over the three driving cycles were presented in **Table. 1.**. We can see that the MPC approach can impove fuel economy significantly and keep the final SOC near the initial SOC compared to the ADVISOR approach over the three driving cycles. Although the ADVISOR approach considers the idling, accessories losses, battery efficiency and motor/generator efficiency, it performs poorly according to the road load, which results in the large deviation of the battery SOC. Therefore the MPC approach results are optimistic because of not considering those losses, but the results are still reasonablely better compared with the ADVISOR approach.

5 CONCLUSION

MPC of a power-split HEV system was presented. The simplified system model was developed. The simulation results of the MPC algorithm using known and unknown driving cycle revealed a significant improvement of the fuel economy compared to the ADVISOR rule based algorithm. Because the MPC algorithm uses simplified system model and can be applied to unknown driving cycle, it has the potential for the real-time implementation. The simplified modeling method of the power-split HEV system configuration can also be applied to other configurations of HEV.

Table 1. Fuel economy comparison results

Method	Cycle	Initial SOC	Final SOC	Fuel (km/l)
MPC(known)	Cycle1	0.7	0.6997	26.40(+33.64%)
ADVISOR	Cycle1	0.7	0.6302	17.52
MPC(known)	Cycle2	0.7	0.6995	23.97(+32.87%)
ADVISOR	Cycle2	0.7	0.5745	16.09
MPC(unknown)	Cycle3	0.7	0.7000	38.49(+16.19%)
ADVISOR	Cycle3	0.7	0.6312	32.26

REFERENCES

[1] Serrao L (2009), A comparative analysis of energy management strategies for hybrid electric vehicles. PhD thesis, The Ohio State University, pp.12-43

[2] Liu JM, Peng H (2008), Modeling and control of a power-split hybrid vehicle, IEEE Transactiosons on Control Systems Technology 16(6):1242-1251

[3] Kim N, Cha SW and Peng H (2011), Optimal control of hybrid electric vehicles based on Pontryagin's minimum principle. IEEE Transactions on Control Systems Technology 19(5):1279-1287

[4] Borhan HA, Vahidi A, Phillips AM, Kuang ML, Kolmanovsky IV (2009), Predictive energy management of a power-split hybrid electric vehicle. American Control Conference, St. Louis, MO, USA, June 10-12, 2009, pp.3970-3976

[5] Deguchi Y, Kawabe T (2004), HEV charge/discharge control system based on navigation information.SAE, 2004-21-0028

[6] Kamal MAS, Mukai M, Murata J, Kawabe T (2010), On board eco-driving system for varying road-traffic environments using model predictive control. Proc. of 2010 IEEE Multi-Conference on Systems and Control, Yokohama, Japan, Sep 8-10, 2010, pp.1636-1641

[7] Kaku A, Kamal MAS, Mukai M, Kawabe T, Model predictive control for ecological vehicle synchronized driving varying aerodynamic drag and road shape information. Accepted in the IEEE Transactions on Intelligent Transportation System

[8] Wipke K, Cuddy M, Burch S (1999), ADVISOR 2.1: A user-friendly advanced powertrain simulation using a combined bachward/forward approach. IEEE Transaction on Vehicular Technology 48(6):1751-1761

[9] Ehsani M, Gao Y, Emadi A (2009), Modern electric, hybrid electric, and fuel cell vehicles: fundamentals, theory, and design, second edition. CRC press, Boca Raton, London, New York, pp.138-144

[10] Ohtsuka T (2004), A continuation/GMRES method for fast computation of nonlinear receding horizon control. Automatica 40(4):563-574

The Seventeenth International Symposium on Artificial Life and Robotics 2012 (AROB 17th '12),
B-Con Plaza, Beppu, Oita, Japan, January 19-21, 2012

Web Search Support System for the Smartphone Using Call and Web Logs

Takuya Ito[1] and Hiroyuki Nishiyama[1]

[1] Graduate School of Science and Technology, Tokyo University of Science,
2641 Yamazaki, Noda-shi, Chiba-ken, Japan
(Tel:+81-47122-1106; Fax:+81-47122-1106)
(j7411606@ed.tus.ac.jp)

Abstract: In recent years, Web searching on mobile devices with a touchscreen has increased. However, a search query using a mobile phone is not easy as that using a PC. In this study, we propose a search support system that provides user search queries and Web pages to suit the user's situation. This system continually records the user's location, time, Web search log and call log. Since the system does not have a server, the user's mobile phone records everything and provides search assistance to the users based on the recorded information.

Keywords: Mobile Phone, Web Serch, Query, Search Intention

1 INTRODUCTION

The increase of smartphones with a Web Browser has resulted in an icreasing need to view Web pages created for a PC using a mobile terminal rather than for mobile phones. Nevertheless, the labor required for searching is a major issue for mobile devices using touchscreens, unlike PCs where data can be entered from the keyboard. In order to solve such problems, a method recommending useful search queries and web pages from the search history, Web page information recorded when the user searches the Web, has been proposed. Whereas, they are focused on activities in the user's web search. However, little research on Web page recommendations has focused on the user's behavior in the real world.

Our goal is to recommend appropriate Web pages to users and to determine their search intentions with mobile phones depending on their situation. Their search intentions are related to the content that they utilize on their mobile phones , not rather than being limited to their user's Web search history. Call and mail contents are rich with keywords of interest to the user. Recently, smartphones have becomes popular. Therefore, with the user's permission, it is easy to collect Web search history and call history beyond the user's location. However, the risk of leaking user's private information to others has increased. Also related to the issue of personal privacy is the fact that the proposed system uses call logs.

The purpose of this study is to recommend Web pages that users can easily visit and search queries that users are expected to use, in order to eliminate the need for user input and to allow quick access to the desired page. For this reason, this system recommends Web pages and search queries based on the user's situation e.g., latitude and longitude, time, call log, and Web search log from the mobile phone.

In this paper, Section 2 discusses the motivation for this study. Section 3 describes the design of the proposed syste. Section 4 describes the implementation of the proposed design. Section 5 concludes this paper.

2 MOTIVATION

Mobile phones are used in many different situations. Therefore, research has focused on gathering information that can be observed with mobile phones and added sensors, and the use of the collected information to suit the user 's situation. For example, Uesaka et al. observed actual daily mobile phone user operations with minimal interference for six months [1]. As a result, they demonstrated that Machine learning could be used predict operation from the collected information. Additionally, Uesaka et al. proposed a system to recommend applications, according to the situation, based on collected information and application usage [2]. In studies using sensors in mobile phones, Minamikawa et al. proposed a system that indicates calories burned by the user by estimating the user movement with an accelerometer in the phone [3]. Yamamoto et al. proposed to a system to recommend contents using a GPS sensor in a mobile phone[4]. The system in the present study searches for the overlap between context of the content to be recommended and context in the user's Web page by recording Web page browsing history, location information, and time. Moreover, the system recommend a wide range of information. The difference between the system and this system is to decide to delivery information and to recommend contents which Web pages are viewed by the user.

Mobile phones involve many physical constraints such as the difficulty of entering information as compared to a PC. It is studies on the support that has been searching for many studies. Letizia by Lieberman automatically recommends links based on the user's browsing behavior[5]. FIXIT by Hart et al. searches repair information from copier manuals, associating keywords related to the symptoms of the failure[6]. Uchiyama et al. proposed an information search system in the user's clearance time, by using mobile phones that recommend queries extracted from the browsing history on the user 's PC[7]. Y!Q by Kraft et al. searches related pages, analyzing the Web pages content[8, 9]. For example, when a user searches news articles related to browsing news articles, the system extracts only the keywords that the user selects the area of care from the area of interest. Hattori et al. proposed a system that presents queries that meets the user's search request by gestural manipulation after the user specifies a range of the word that would be[10]. Nishio et al. proposed a recommendation system that automatically extracts words that are likely to be used as a search query from Web pages that the users views[11]. Their studies recommend queries that are expected to be available to users within a Web page. In contrast, the present system recommends search queries based on the user's current location.

3 SYSTEM DESIGN

This section describes the processing flow and a system overview of search support that reduces input effort by reaching its goal of a user's page.

3.1 System overview

The purpose of the proposed system is to reduce the user's input in a search. Therefore, the user's input must not be inhibited when this system is collecting necessary information. This information must be collected automatically when the user acts (e.g., searches). Furthermore, the information collected and removed should be ready for utilization, and the user's privacy must be protected. Screens to help users find prepare recommended Web Page screen and recommended search query screen. A screen recommends Web pages in a list format, in descending order based on points assigned by this system. The information on each page includes the title, some excerpts from the text in the body, and frequently appearing keywords. In addition, each page has a related- view button. Thus, even if the desired page is not presented, the user can find some input by pressing the related-view button to close the related page. A screen also recommends search queries in a list format, in descending order based on points assigned by this system, and each query has a related-view button. Two screens were prepared for the following reasons. To reduce the user 's input, it is better to recommend Web pages than to recommend search queries. However, a Web page provides more information than a search query does. Therefore, the method of recommending a search query can be more widely applied than the method of recommending Web pages. Thus, the search query screen supplements the Web Page screen.

3.2 Processing flow

This section describes information processing (e.g., Web browsing history, call log and location).

Location information

The mobile device records position (latitude and longitude) information on a regular basis, and it guesses the user 's movement. Latitude and longitude information is based on GPS information when a GPS is available. When a GPS is not available, latitude and longitude information is received as a unit area of 300m by acquiring radio signals from the base station. We want to collect latitude and longitude information in short intervals in order to estimate the user 's movement. Here, latitude and longitude information is acquired every 600sec, due to battery power[12]. The user is classified as either stationary or moving, based on the speed calculated using latitude and longitude information obtained from the mobile phone. If the mobile terminal indicates lack of movement, Web search history and call history in the error range of latitude and longitude information from the current position are recognized in the same stationary period. If the mobile phone indicates movement, it refers to the Web search history on the move rather than the current position. In addition, the location information is also recorded in the Web browsing history and call history.

Web Browsing Logs

Each time the user searches, Web browsing logs are collected as follows. In general, the users who wants to search for information enters a query into a search engine and then presses the search button. The search results page appears, and the user selects the desired page.

This system detects that the page has changed and collects information about the user's location and the query that the user entered when the search button is pressed. No information about the page that appears in the search engine results list is extracted; this system collects information on the page that the user selects from the search results (e.g., the user 's start time of viewing that page, the URL of the page, keywords appearing on a page, and location information at that time). When the user closes the browser or moves to a different page, this system records the time just be-

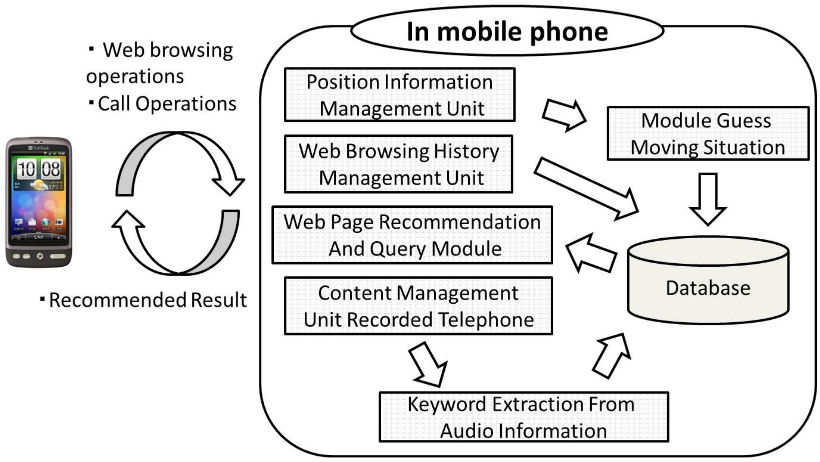

Fig. 1. System configuration

fore the page you were viewing. Thus, the time during which the user was looking at the page is recorded. This is one indicator of whether or not the user was interested in that page.

Call Logs

Each time the user calls, the call log is collected as follows. The system detects that the user's mobile phone is in initiating a call. At that time, this system collects current time and location information, as well as the content of the calls (e.g., what the user said during the call) and keywords from it. When the system detects that the call has ended, it stops grecording the content and extracting keywords. In this case, only the user's voice information is recorded since the called or calling party has not consented to the recording of his or her voice.

This system always records the user 's location information, Web browsing history, and call history. It weights Web pages and search queries using the information collected and recommends Web pages and search queries depending on the user's location and the time when the user starts the system.

4 IMPLEMENTATION

This system is implemented on an HTC Desire SoftBank X06HT equipped with Android 2.2. Getting location information uses locaton package(android.location) in AndroidSDK[13]. GPS that can be used outdoors is better than to obtain the signal strength from base station, so that this system primarily uses GPS. In case that this system does not use only GPS, it uses to obtain the signal strength from base station. Jump detection during Web browsing uses webkit package(android.webkit) in AndroidSDK. In feature extraction from Web Pages, JavaScript extracts HTML sources. The full text is extracted with tagsoup. Feature extraction from the full text of Web Pages uses WebAPI(e.g., Yahoo! keyphrase extraction). The process documenting of call of content uses speech package(android.speech) in AndroidSDK. Feature extraction from call contents is also performed. This system processing almost completely on a mobile phone to protect privacy. Fig. 1 depicts the configuration. From the same viewpoint, algorithm(e.g., Collaborative filtering) does not use, because others do not use the information recorded in the user's mobile phone.

5 CONCLUSION

This study proposes a search support system for a mobile phone with a touchscreen. This system records the user 's Web browsing history, call history, and location and automatically collects information based on the user's daily operations. By utilizing these information, A system to close to help users conduct searches implements. To protect the user's privacy, data is recorded in only the user's mobile device, and the user can view and remove the data. A system to help users conduct searches implements by varying the contents of Web pages and search queries recommendation to the user depending on the user's moving situation and location information.

Since evaluation indicates a time is delay for reading a Web page that users access on a daily basis, it is necessary to review the procession of keyword extraction. Specifically, it is necessary to reduce keyword extraction, or to perform keyword extraction when the user is' not operating his or her mobile phone.

Future tasks include reflecting the user's search, increasing the information collected in the PC Web Browsing History, reducing keyword extraction time, improving the relevancy of recommendations and processing when recording data is little.

REFERENCES

[1] Daisuke Kamisaka, Shigeki Muramatsu and Hiroyuki Yokoyama (2008), A Study on Situation-Adaptive Operation-Assisting Method for Mobile Phone. Information Processing Society of Japan SIG Technical Report 2008-UBI-20(110):33-38.

[2] Daisuke Kamisaka, Takeshi Iwamoto, Shigeki Muramatsu and Hiroyuki Yokoyama (2009), Long-term Data Analysis and Operation Prediction for Context-Aware UI of Mobile Phones. FIT2009 8(4):23-29.

[3] Atsunori Minamikawa, Arei Kobayashi and Hiroyuki Yokoyama (2011), Energy Expenditure Monitoring System on Mobile Phone Using Information Gain Based Locomotion Estimation Method. Information Processing Society of Japan Journal 52(2):866-876.

[4] Katsuaki Tanaka, Koichi Hori and Masao Yamamoto (2008), Development of a Recommender System based on Personal log. Transactions of the Japanese Society for Artificial Intelligence Journal 23(6):412-423.

[5] H. Liebermanm, (1995), Litizia: an agent that assists web browing. Proceedings of the 14th international Joint Conference on Artificial intelligence (IJCAI '05):924-929.

[6] P. E. Hart and J. Graham, (1997), Query-Free Information Retrieval. IEEE Expert, 12(5):32-37.

[7] Mitsumasa Kondo, Tetsushi Morita, Akimichi Tanaka and Tadasu Uchiyama (2008), Mobile Information Retrieval System using Query Extraction from Web Browsing log on PC. The 22nd Annual Conference of the Japanese Society for Artificial Intelligence (22):2P2-10.

[8] Kraft, R., Maghoul, F., and Chang, C. C. (2005), Y!Q: Contextual Search at the Point of Inspiration, Proc. the Int'l Conf. on Information and Knowledge Management(CIKM 2005):816-823.

[9] Kraft, R. and Chang, C. C. (2006), Searching with Context, Proc. Int'l Conf. on World Wide Web(WWW 2006):477-486.

[10] Masayuki Okamoto, Masaaki Kikuchi, Nayuko Watanabe, Takayuki Iida, Kenta Sasaki, and Masanori Hattori (2010), First Query Term Extraction from Current Browsed Webpage for Embedded Device (DEIM Forum 2011):F6-5.

[11] Daijiro Komaki, Yuki Arase, Takahiro Hara, Gen Hattori, Yasuhiro Takishima, and Shojiro Nishio (2010), An Interface for Supporting Web Search Query Input for Mobile Devices Equipped with Touch Panels. Forum on Data Engineering and Information Management (DEIM Forum 2010):A6-3.

[12] Hideki Yoshii, Hayato Shirai, Shunichiro Butsuen and Naohisa Komatsu (2009), A Study on analyzing GPS-based Location Data Using Segment Verocity Technique. The Institute of Electronics, Information and Communication Engineers (IEICE Technical Report LOIS2009-7):109-112.

[13] Android SDK Guide, http://www.android.com/

The Seventeenth International Symposium on Artificial Life and Robotics 2012 (AROB 17th '12),
B-Con Plaza, Beppu, Oita, Japan, January 19-21, 2012

Sentiment Analysis for Domain-Specific Texts

Hidekazu Yanagimoto[1], and Michifumi Yoshioka[1]

[1] Osaka Prefecture University, Sakai, Osaka 599-8531, Japan
(Tel: 81-72-254-9279, Fax: 81-72-254-9909)
{hidekazu, yoshioka}@cs.osakafu-u.ac.jp

Abstract: We develop a sentiment analysis system for domain-specific texts. The sentiment analysis estimates a polarity of a text, for example positive or negative. To develop such a system a dictionary, which consists of words and their polarities, is needed. The dictionary reflects specialists ' knowledge and affects a sentiment analysis precision. Hence, it is important to construct an appropriate dictionary. And making a dictionary needs much human cost generally. As a good dictionary is constructed, the human cost must be decreased. To achieve the goal our proposed approach uses a bootstrap method to decrease human cost and a χ^2 statistic to estimate a polarity of a word correctly. To evaluate a performance of the proposed approach we carried out an evaluation experiment using real stock market news, T&C news. We confirmed that the proposed approach could construct a dictionary but had some problems which were inappropriate words and that the dictionary did not have enough words.

Keywords: Sentiment Analysis, Bootstrap, Natural Language Processing

1 INTRODUCTION

Many reviews are posted in shopping sites and opinion sites and shared in the Internet. The reviews include opinions of users and are read by many users and affect a consumer activity. Hence, opinion mining and sentiment analysis is paid attention by many researchers. Turney[1] reported because there often were positive words around a positive word, a polarity of a word was determined using a cooccurrence frequency. Hatzivassiloglou et al[2] determined a polarity of a word using a conjunction. Nasukawa et al[3] estimated a polarity of a word using context coherence. Pan et al[4] focuses domain-specific words and domain-nonspecific words and developed a cross-domain sentiment classifier.

In the paper we focus a sentiment analysis for domain-specific texts. The domain-specific texts include a lot of technical terms because only users shared with the same interests read them. Hence, to develop the sentiment analysis system we must deal with the technical terms effectively. However, it is difficult to determine polarities for the terms because specialists for the specific domain need to determine them. This means that the specialists pay much effort to construct a dictionary that represents polarities of the technical terms. To solve the problems a dictionary construction approach must decrease human costs.

Previous works used a cooccurrence frequency to determine a polarity that a word has not attached yet. It is important what kind of evaluation criterion is used to evaluate how often the word occurs with positive words or negative words. The simple cooccurrence frequency includes much noise and is not a reliable criterion. Hence, a new evaluation method, which is hard to be disturbed by noise, must be proposed.

The χ^2 statistic is one of criteria that evaluates a bias of an occurrence probability. As the χ^2 statistic is big, it means that occurrence of the word has statistical significant. Hence, if words have the bigger χ^2 statistic than a threshold that is enough big, a pseudo cooccurrence can be neglected. Using the χ^2 statistic, we construct a dictionary that includes many words attaching correct polarities.

In the paper we presents a dictionary construction approach that uses a bootstrap method and a χ^2 statistic to evaluate the polarity of a word. The bootstrap method starts a dictionary construction from a small dictionary and expands it using predefined rules. Hence, the initial small dictionary must be constructed manually but human costs are decreased because of the small number of words in the initial dictionary.

Finally we check our proposed approach using real stock market news, T&C news. At first the polarity dictionary is constructed using all the articles in T&C news. We discuss the dictionary constructed with our proposed approach and found some characteristics.

1. The dictionary consists of the similar number of positive and negative words.

2. The dictionary includes words attaching correct polarities form the viewpoint of human judgment.

3. The dictionary includes some inappropriate words. For example, some words have opposite polarities.

4. The number of words in the dictionary is too small comparing with the number of all adjectives in all the articles.

In the next section we describe the proposed approach and the details of our approach are presented. In Section 3 we explain experiment and discuss the proposed approach. And we conclude our work in Section 4.

2 PROPOSED METHOD

We explain a dictionary construction method using a bootstrap method and χ^2 statistic for domain-specific texts. To determine a polarity for a domain-specific text it is important to use technical terms appropriately. For example, though "hooked" is often appeared in video game reviews[4] and is a positive word, it is a neutral word in some cases and a negative word in other cases. So it is important to construct a specific dictionary that assigns correct polarities with words.

In making the dictionary it is important to decrease human cost. Because a dictionary is constructed using a lot of specialists' knowledge generally, it denotes that making a dictionary needs a lot of human costs. Hence, we develop an automatic dictionary construction method using the least human costs.

To achieve our aim we use a bootstrap approach to construct a dictionary. The bootstrap approach stars from a small dictionary where some words are registered according to specialists' knowledge. A dictionary construct cost is very small because the initial dictionary is small. The approach expands the dictionary using rules that are used to select words that are assigned with polarities. In a proposed approach we use a cooccurrence frequency with words that have positive or negative polarities. We show a bootstrap flow below.

1. Select seed words and assign their correct polarities manually.
2. Count cooccurrence frequency with polarity-attached words.
3. Select words that polarities are estimated using the cooccurrence frequencies.
4. Retuen step 2 if a polarity is assigned with a new word in step3.

In the flow it is important what kind of criterion is used. Words that occur frequently with positive words are assigned with positive polarities. Hence, we must evaluate a bias of the cooccurrence frequency. The proposed approach uses a χ^2 statistic to evaluate the bias because a raw cooccurrence frequency is so noisy. Equation (1) shows how to calculate χ^2 statistic from cooccurrence frequencies.

$$\chi^2(w) = \sum_{w^s \in D_s} \frac{(\mathrm{freq}(w^s, w) \quad \frac{\mathrm{freq}(w^s)\mathrm{freq}(w)}{N})^2}{\frac{\mathrm{freq}(w^s)\mathrm{freq}(w)}{N}} \tag{1}$$

The $\mathrm{freq}(w_1, w_2)$ is cooccurrence frequency in a sentence and the $\mathrm{freq}(w)$ is occurrence frequency in a text corpus. The N denotes the number of all the sentences in the text corpus and the D_s denotes a set of seed words.

In this approach we use the χ^2 statistic to evaluate how often a word occurs with positive words or negative words. In constructing a dictionary the number of words attached with positive polarities are different from the number of words attached with negative polarities. Because the number of polarity-attached words have an affect on the χ^2 statistic, we must deny the affect in calculating the χ^2 statistic. The improved χ^2 statistics is defined below.

$$\chi_P^2(w) = \frac{1}{|D_S^P|} \sum_{w^s \in D_s^P} \frac{(\mathrm{freq}(w^s, w) \quad \frac{\mathrm{freq}(w^s)\mathrm{freq}(w)}{N})^2}{\frac{\mathrm{freq}(w^s)\mathrm{freq}(w)}{N}} \tag{2}$$

$$\chi_N^2(w) = \frac{1}{|D_S^N|} \sum_{w^s \in D_s^N} \frac{(\mathrm{freq}(w^s, w) \quad \frac{\mathrm{freq}(w^s)\mathrm{freq}(w)}{N})^2}{\frac{\mathrm{freq}(w^s)\mathrm{freq}(w)}{N}} \tag{3}$$

The D_S^P and the D_S^N are a set of words with positive polarities and a set of words with negative polarities respectively.

The bigger a χ^2 static of a word is, the more reliable a polarity of the word is. Hence, when the χ^2 static is over a threshold, which are defined previously, the word is registered in the dictionary.

$$w = \begin{cases} \text{positive} & (\chi_P^2(w) > \text{threshold}) \\ \text{negative} & (\chi_N^2(w) > \text{threshold}) \end{cases} \tag{4}$$

As the threshold is big, it is difficult to register new words in the dictionary and to expand the dictionary. On the other hand, as the threshold is small, new words are registered easily and the dictionary includes many meaningless words. Hence, because we must adopt the appropriate threshold.

We describe a sentiment analysis using the constructed dictionary. Because the dictionary consists of words and their polarities, a polarity of an article is determined according to how many positive or negative words are included. The above judgement uses a assumption that is that negative articles include many negative words and positive articles include many positive words. Hence, when an article includes more positive words than negative words, the article is estimated as a positive one. One the other hand, when an article includes more negative words than positive words, the article is estimated negative one. When there are the same number of positive words and negative words in a article or there are no polarity-attached word in a article, the article is estimated as neutral one.

The proposed approach does not consider negation and adversative conjunction at all. This decreases a performance of the proposed approach. This improvement is a future work.

3 EXPERIMENT

3.1 Data Set

In this experiments we used T&C news, which was one of stock market news delivery services, as data for dictionary construction. T&C news is written in Japanese and consists of 62,478 articles in 2010, which are stock price news, business performance reports, comments of specialists and so on.

We used all articles to construct a dictionary including word polarities. Using some articles to evaluate a performance of the proposed method is not a severe drawback, although the articles is shared in a construction step and an evaluation step. Because the proposed approach does not need labels of articles, which denotes whether the articles is positive or negative.

We extracted sentences from the all articles. The T&C news includes many tables and charts to explain a stock market situation for readers. The non-sentence elements tend to overestimate statistics to determine whether words are registered in a dictionary. After this preprocess we got 2,084,105 sentences from our data set. Hence, we made a polarity dictionary using all the sentences.

To construct the dictionary we used only adjectives in the sentences because adjective includes stronger polarity than other part of speech, for example, noun, verb, and adverb. In this experiment we used MeCab, which is a morphological anlyzer for Japanese, to extract adverbs from the sentences.

3.2 Dictionary Construction

We constructed a dictionary, which define words' polarities, using the all sentences, which are extracted from T&C news.

The proposed approach needs seed words to make the dictionary with a bootstrap method. Table 1 shows the seed words in this experiment. In this case we used 5 negative polarity words and 5 negative polarity words. Because the seed words are selected manually according to domain knowledge, they are correct polarities.

Table 1. Seed words to construct the dictionary

Positive polarity	Negative polarity
powerful	obscure
accessible	heavy
strong	low
successful	poor
positive	difficult

Using the seed words, we carried out the proposed method and constructed the dictionary. In this process we decreased the threshold, which was used to determine whether new words were registered in the dictionary. At first the registration criterion is so strict but the criterion is not strict finally. Because polarity-attached words are few At the beginning of the process, χ^2 statistic is not reliable, the threshold should be high. On the other hand after the polarity-attached words are enough, we can trust χ^2 statistic. So the threshold is small at the end of process. In this experiment the threshold was equal to 300.0 and is discounted at the rate of 0.95 times per loop.

Table 2 shows the number of words that are registered in the dictionary after executing the propose approach. Because there are 1,166 unique adjectives in T&C news, we think the number of words is so small. It is future work to increase the number of words that polarity we can estimate. The number of word with positive polarity is similar to the number of words with negative polarity. We found it was favorable that the number of positive words was similar to the number of negative words. If we use a dictionary that included more negative words, almost all articles are judged as negative article in a sentiment analysis step because negative words occurs in almost all articles easily. So the dictionary constructed in the experiment has a good feature.

Table 2. The number of positive polarity words and negative polarity words in the dictionary

Words with positive polarity	48
Words with negative polarity	47

We discuss the words that are registered in the dictionary using the propose method. Table 3 shows polarity-attached words in the dictionary. Some words, for example "appropriate" and "inappropriate", "necessary" and "unnecessary", "unstable" and "hard", and "thick" and "hard", has correct polarities. The "appropriate" and the "necessary" are common words and their polarities are estimated easily. The "thick" and "hard" is not common words but technical terms in stock market. It is difficult to estimate their polarities without using stock market news. Hence, the proposed approach is good because it can adapt easily using domain-specific texts and human load is small.

Table 3. The dictionary constructed with the proposed method

Words with positive polarity	Words with negative polarity
appropriate	inappropriate
necessary	unnecessary
unstalbe	stable
thick	hard
annoying	comfortable

The proposed approach has some drawbacks. In Table 3 some words are incorrect opposite to human judgement. The "annoying" is usually a negative word and the "comfortable" is usually a negative word. Because the proposed method does not consider negation and adversative conjunction in a sentence, the problems happen. It is a future work to improve the proposed method considering negation and adversative conjunction. Now we illustrate a problem on adversative conjunction. An article includes a sentence, "it is positive in C-duration and it is negative in D-duration." The sentence does not include adversative conjunction but the former clause is opposite to the latter clause. It is difficult to solve the problem from viewpoint of syntax level processing.

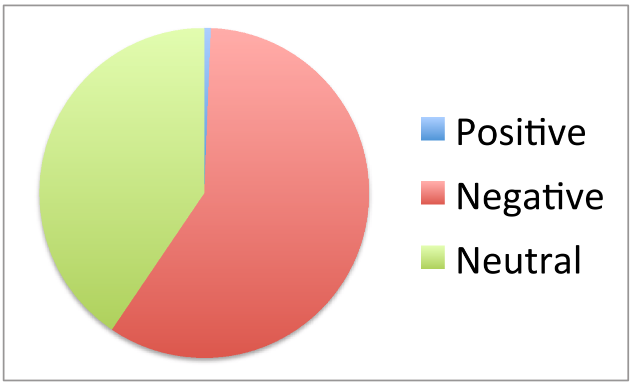

Fig. 1. The distribution of sentiment in all articles

Figure 1 shows the distribution of positive articles, negative ones, and neutral ones, which are not assigned with polarities. This figure shows negative articles occupy over half of articles. Because the articles are created after Lehman Shock, they include many negative articles. The number of positive articles, however, is too small in the result. Hence, the dictionary constructed with the proposed approach is difficult to capture sentiments of articles. There are many neutral articles in the result. This means that the number of words in the dictionary is too small.

4 CONCLUSION

We proposed a dictionary construction method to estimate correct polarities for domain-specific texts. The proposed approach has some features: (1)low human costs, and (2)easy adaptation for specific domain. The approach uses (1)a boostrap method and (2)a χ^2 statistic to construct the dictionary automatically. We confirmed that the proposed approach could make a dictionary in assign correct polarities with few words manually in an evaluation experiment.

The proposed approach, however, needs some improvements. The approach can not assign polarities with enough words in a data set. To improve the drawback we must discuss a χ^2 statistic and a criterion, which determine whether a word is registered in a dictionary or not. The approach assign incorrect polarities with some words. To improve the drawback we must consider negation and adversative conjunction in a sentence.

ACKNOWLEDGEMENT

We thank Centillion Co. for giving us data sets and many supports.

REFERENCES

[1] Peter D. (2002), Thumbs up? thumbs down? Semantic Orientation Applied to Unsupervised Classification of Reviews. Proceedings of the 40th Annual Meeting of the Association for Computational Linguistics, pp.417-424.

[2] Htzivassiloglou V. and McKeown K. R. (1997), Predicting the Semantic Orientation of Adjectives. Proceedings of the 35th Annual Meeting of the Association for Computational Linguistics, pp.174-181.

[3] Nasukawa T. and Kanayama H. (2004), Acquisition of Sentiment Lexicon by Using COntext Coherence (in Japanese). NL-162-16, pp.109-116.

[4] Pan S.J. et al. (2010), Cross-Domain Sentiment Classification via Spectral Feature Alignment. Proceedings of WWW2010, pp.751-760.

The Seventeenth International Symposium on Artificial Life and Robotics 2012 (AROB 17th '12),
B-Con Plaza, Beppu, Oita, Japan, January 19-21, 2012

A Localization Method for Smart Phones by Detection of Walking Using an Accelerometer in Indoor Environments

Kunioki Hayashi[1], Hiroyuki Nishiyama[1]

[1]Graduate School of Sci.and Tech, Tokyo University of Science
Yamazaki 2641, Noda-shi, CHIBA, 278-8510, Japan
(Tel: 81-47122-1106, Fax: 81-47122-1106)
(j7411624@ed.tus.ac.jp)

Abstract: This paper proposes a new localization method for smart phones using an accelerometer. Although the global positioning system (GPS) is applied in various fields, it has a disadvantage in that it cannot be used effectively in indoor environments. To overcome this problem, many localization methods in indoor environments exploiting Wireless LANs have been proposed, but few systems achieve high accuracy. On the other hand, the smart phones with many sensors and powerful CPUs are becoming wide spread. We examined a localization method specialized for smart phones, and evaluated our proposed method by implementing a prototype system and conducting experiments with it.

Keywords: localization, smart phone, accelerometer, Wireless LAN

1 INTRODUCTION

Currently, the Location-Based Services (LBS) are spreading widely. Using GPS is one way to obtain position information, and it is being used for variety of LBS, including car-navigation systems. However, this approach is difficult to use in indoor environments where electromagnetic waves cannot reach. Then, many systems utilizing variety of wireless equipment for indoors have been proposed[1][2], but they require constructing an infrastructure specifically for the service. Therefore, they may not be the best policy because of the cost. Some systems using existing Wireless LAN(WLAN) access points to solve that problem. If a WLAN is used for localization, a simple and widely used way to estimate distance is based on Received Signal Strength Indicator (RSSI), which do not require complex hardware. Unfortunately, RSSI is environment-dependent, and the wireless channel is very noisy in indoor environments. A radio frequency signal can suffer from reflection, diffraction, and multipath effects, making the signal strength a complex function of the distance. Therefore, the many existing methods exploiting RSSI cannot provide results high accuracy.

On the other hand, over the last few years, smart phones with many sensors have become widely distributed and are expected to increase in the future. Nevertheless, almost all existing localization methods for mobile phones are for non-smart phones, there are few or no methods specialized for smart phones.

Based on this background, we propose a localization method achieving greater accuracy with smart phones by making the best use of the its advantage. The smart phone has features such as usability, powerful computing ability and many sensors. We attempted to use the accelerometer in smart phone for localization. In this study, we exploit existing wireless access points for localization to avoid the cost of custom system.

2 LOCALIZATION METHOD

In this study, we use the RSSI received by a smart phone for position estimation using existing WLAN access points. Generally, the RSSI value will vary in the same place because the radio signal emanating from an access point is affected by shadowing and multipath fading. Therefore, it is hard to accurately estimate distance or position based on the RSSI . Assuming an office environment as the situation requiring the LBS, users will be stationary most of the time. If the user is not moving, it is reasonable to use all signals during the period the user remains stationary to estimate the position rather than using only the last signal. In general, the signal strength follows a Gaussian distribution, so we can improve overall accuracy by using the average value in our estimation.

2.1 Models for localization

The system estimates the user's position using the RSSI from WLAN access points. As the localization algorithm, we use least-squares approach, which is the most common and easiest using RSSI.

2.1.1 Distance estimation using RSSI

We assume a localization model comprising a set of access points as anchors $A \ni a_i$, which have well-known positions on the map and are identified by the pair (x_i, y_i), a smart phone designated as the target T and a localization server. Generally, a smart phone can obtain RSSI from WLAN access points. As mentioned above, though the RSSI value is very noisy, when defining d_i as the true distance between a_i

and T, the variation in RSSI can be well modeled with the following[3]:

$$\overline{P}_i = \alpha d_i \tag{1}$$

where $\overline{P}_i$ denotes the average signal power received at the ith access point, and α and β are two channel parameters representing the attenuation factor and the power decay factor, which are uniquely determined by the location estimation area.

2.1.2 Localization model

Generally, the localization model using least-squares approach is defined by the following[4]:

$find\ \varphi = (x, y)\ which\ minimizes$

$$E(\varphi) = \sum_{a_i \in A} w_i^2 \left(\hat{d}_i \quad d_i(\varphi)\right)^2 \tag{2}$$

where $\hat{d}_i$ is the estimated distance between a_i and T, or in other words between the ith access point and the smart phone using the model in Eq. (1), and $d_i(\varphi)$ is the distance between a_i and a coordinate (x, y). the w_i term represents the weight applied to each equation. For simplicity we assume that $w_i = 1$. This equation allows us to find a coordinate (x, y) that minimizes $E(\varphi)$ and exhibits a non-linear continuous function about φ. As a result, the localization problem can be viewed as a problem of minimizing a non-linear continuous function with no constraints.

However, in many cases, distance $\hat{d}_i$ estimated by RSSI is unreliable because of large amount of noise, made worse by using only a single RSSI measurement. Since $\overline{P}$ in the model of Eq. (1) denotes an average of RSSIs, we need to measure many times and calculate the average for a proper estimation. Clearly the more measurement made the more accurate $\hat{d}_i$ will be. The best approach is to have the system calculate the average from all RSSIs during periods the user does not move.

2.2 Movement detection

In order to detect whether or not user is moving, specifically whether or not the user is walking in this study, we utilize information from the accelerometer in the smart phone. The accelerometer must always be running while the position is being estimated, raising the issue of battery drain. However, for examining the effectiveness of using the accelerometer for localization, we are not concerned with this. Almost all smart phones can obtain acceleration data in three dimensions, but it is impossible to calculate the distance that a user has moved from this data because of the amount of noise. To detect whether the user is walking based on noisy acceleration data, the system needs to check the data directly and its time frequency. For example, if the user shakes his legs while his smart phone is in his pocket, the system must determine that he is not in fact walking. Fig. 1. presents examples of acceleration while a user is walking and not walking. There seems to be a slight difference between (a) and (b) in that when the user is walking the acceleration changes at a constant frequency. We transformed the composite acceleration data into its frequency components using the Fast Fourier Transform (FFT) , and this clearly shows the difference (Fig. 2.). In generating a classifier based on the transformed data, we found it inadvisable to classify simply according to a threshold and determined that we should utilize supervised learning because of the diversity of situations. We subsequently generated a classifier using a K-nearest neighbor algorithm (K-NN) for the detection.

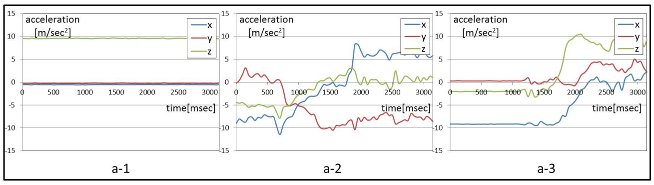

(a) Not walking

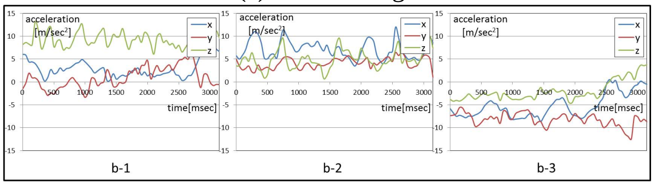

(b) Walking

Fig. 1. Examples of acceleration

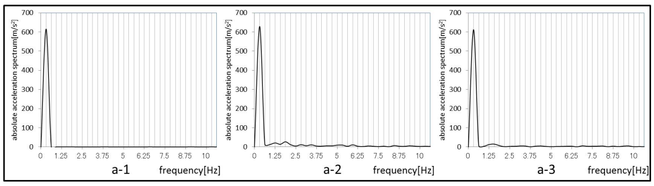

(a) Not walking

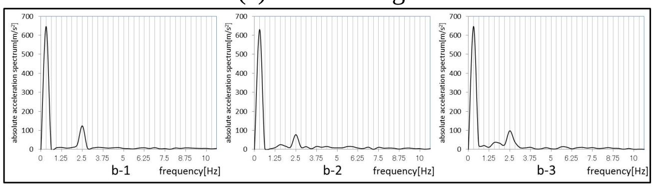

(b) Walking

Fig. 2. Examples of spectrum

Acceleration data obtained at intervals of 50[ms] by a smart phone and transformed into frequency components, which are classified once 64 data have been stored. Therefore the system indicates whether or not a user is walking at intervals of 3.2[s]. The classifier is generated from 200 samples used as a training data set, and evaluated by 200 other samples used as a test data set. Fig. 3. presents the results of this test. According to the K-NN algorithm, an unclassified sample is assigned to the class represented by a majority of its k nearest neighbors in the training data set. With $k = 5$, we achieve a precision of 100.0[%] and recall of 94.0[%] for

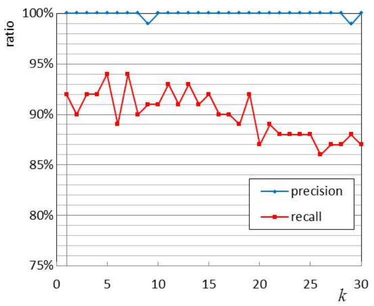

Fig. 3. Precision and recall ratio vs. k

classification of whether or not a user is walking, using the accelerometer in a smart phone.

2.3 Proposed system model

The system estimates position using this classifier and the model of Eq. (2). Consider the set $\mathbf{P}_i$, defined as the set of significant RSSI. $\mathbf{P}_i$ is updated by the following steps:

1. measure RSSI of the ith access point at time $t :\stackrel{\text{def}}{=} p_t$
2. if the classifier determines the user is moving, $\mathbf{P}_i = \{\emptyset\}$
3. $\mathbf{P}_i = \mathbf{P}_i + \{p_t\}$

The number of elements $|\mathbf{P}_i|$ thus varies dynamically, and the average value $\overline{P}_i$ of Eq. (1) is given by

$$\overline{P}_i = \frac{1}{|\mathbf{P}_i|} \sum_{p_t \in \mathbf{P}_i} p_t \quad . \tag{3}$$

Furthermore, $\hat{d}_i$, defined as the distance estimated by RSSI, is

$$\hat{d} = exp\left(\frac{1}{\beta} ln\left(\frac{\bar{P}}{\alpha}\right)\right) \tag{4}$$

by deformatting Eq. (1). Therefore, the localization problem is given by the following:

$$find\ \varphi = (x, y)\ which\ minimizes$$

$$E(\varphi) = \sum_{a_i \in A} w_i^2 \left(\hat{d}_i \quad d_i(\varphi)\right)^2$$

$$where$$

$$\hat{d} = exp\left(\frac{1}{\beta} \ln\left(\frac{\frac{1}{|\mathbf{P}_i|}\sum_{p_t \in \mathbf{P}_i} p_t}{\alpha}\right)\right) \tag{5}$$

3 IMPLEMENTATION FOR EVALUATION

We implemented a localization system using the model given above.

3.1 System configuration

The system consists of a module in the smart phone and a localization server. The smart phone measures the RSSI from multiple access points at even intervals, while in parallel obtaining acceleration information from its accelerometer. The obtained acceleration data are transformed, and then a classifier determines whether or not a user is moving based on data taken at regular intervals by the smart phone. The smart phone sends the RSSI data for multiple access points along with the result of the determination of whether or not the user is moving to the localization server. The server estimates the smart phone's position from the received data using the proposed method and displays the result on the screen.

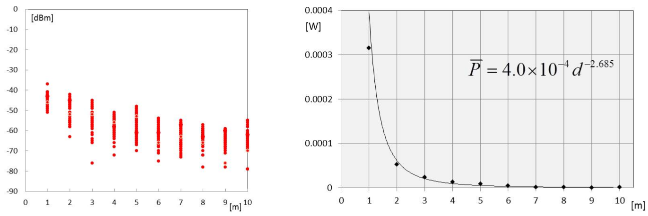

(a) RSSI measurement (b) RSSI propagation model

Fig. 4. RSSI measurement

3.2 Preparatory experiment

We measured the RSSI 100 times at each 1[m] intervals to determine the constants of Eq. (1), . Fig. 4.(a) presents the result. Using the average value for each distance, we determine the constants by the least-squares method after converting the units form dBm to W. In this case, we obtained $\alpha = 4.0 \quad 10^{\ 4}$ and $\beta = 2.685$.

3.3 Solution for least-squares problem

As mentioned above, the localization problem can be viewed as a problem of minimizing a non-linear continuous function with no constraints, or what is called least-squares problem. Several algorithmic solutions for this problem have been proposed, and in this study, we use the Levenberg-Marquardt algorithm[5]. This is a cross between the Gauss-Newton direction and the steepest descent direction, and is the most popular method for least-squares. We need to note, however, that it may not converge to a best fit solution if the initial value is far from the optimum value.

4 EXPERIMENT AND EVALUATION

4.1 Outline of experiment

We conducted an experiment with the system in order to evaluate the effectiveness of the proposed method. In this experiment, we compare the proposed method and the classical method using RSSI that simply uses the last signal to estimate distance. The room in which the experiment was conducted is a space of 8.75[m] by 9.4[m], and there are many desks in the room. Imagine a user sitting at his desk, the system estimates his position 500 times in two different ways. The experiment was conducted at three positions in the room.

4.2 Result and evaluation

Fig. 5. presents the graphical result of the experiment. The triangle indicates the true position in the room, and the black and red circles indicate the estimated position by the classical and proposed methods. These observations may suggest that the proposed method has a smaller variance than the classical method. In fact, we see from Fig. 6. that the more times the system estimates the position, the smaller the share of error in the position estimated by the proposed

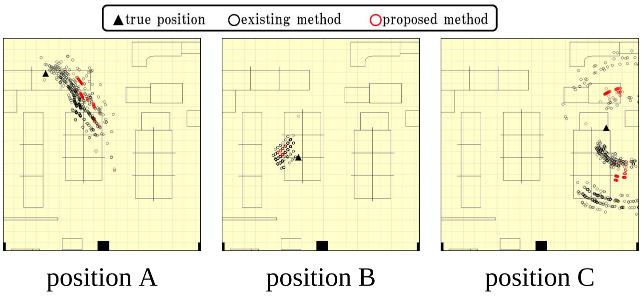

Fig. 5. Graphical result

method becomes. It is reasonable to assume that the influence of any one distance measurement on the estimation becomes small and that the estimation result becomes more accurate as a result of using more measurement data. Note that a position estimated by the proposed method uses only the average value of the overall RSSIs measured before, and not the average position from among all the positions estimated before. Therefore the error in Fig .6. is not an average of overall precious performance either. Something else notable is the earliest few values in the graphs of positions B and C. The values are very high, but this is caused by the Levenberg-Marquardt algorithm. As mentioned in Section 3.3, the initial value is significant for this algorithm, and if it is far from the optimum value, the result may converge to a local optimal solution. We set the initial value of the first estimation to the center of the room and designed the system so that the initial value after the first one is the last estimated value, but it is nevertheless likely that earliest few values converge to a local optimal solution.

In addition, we use the Root Mean Square Error (RMSE) as a numerical measure for evaluation. RMSE is a frequently used measure of the difference between true values and values which are actually observed in the environment being modeled and estimated. Looking at Table 1.,the RMSE of the proposed method is smaller than that of the classical method in all positions, and therefore the proposed method is superior to the classical method, which simply uses the last signal for position estimation.

Table 1. RMSE

	classical	proposed
position A	1.90[m]	1.75[m]
position B	1.01[m]	0.95[m]
position C	1.93[m]	1.74[m]

5 CONCLUSION

This paper proposes a new indoor localization method for smart phones which are becoming more popular. We focused on the fact that smart phones feature an accelerometer, and introduced a classifier that detects whether or not a user is moving into a classical localization method using least-squares. Our experiment clearly demonstrates that the proposed method is superior to the classical method from an RMSE standpoint.

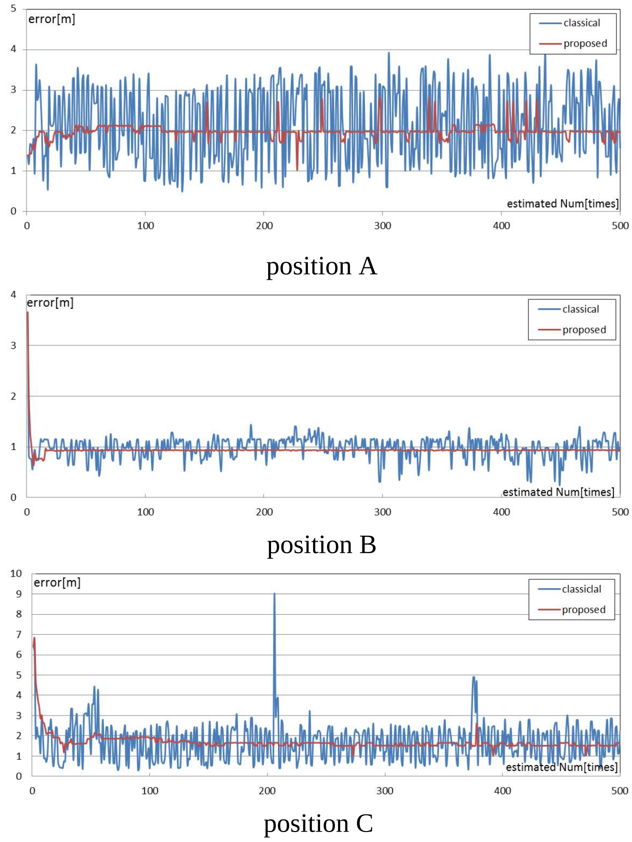

Fig. 6. Comparing error between classical and proposed methods

A future study will combine this classifier with a "finger printing" approach in order to achieve greater accuracy. In this study we used the least-squares approach for indoor localization, but generally, this approach is not so accurate. In fact, though the proposed method achieved greater accuracy than the classical method in our experiment, it did not achieve the required accuracy. Therefore, we need to use another approach superseding the least-squares, e.g. a "finger printing" approach, for indoor localization with smart phones.

REFERENCES

[1] Ekahau,Inc : Ekahau Positioning Engine. http://www.Ekahau.com

[2] HITACHI AirLocation[TM] http://www.hitachi.co.jp/wirelessinfo/products/index.html

[3] S Hara and D Anzai (2009), Use of a Simplified Maximum Likelihood Function in a WLAN-Based Location Estimation. Proc. IEEE Wireless Communications & NetWorking Conference (WCNC) 2009:1167-1172

[4] A Savvides (2001), Dynamic fine-Grained Localization in Ad-Hoc Networks of Sensors. Proc.of 7th Int. Conference on Mobile Computing and Networking:166-179

[5] Marquardt D (1963), An Algorithm for Least-Squares Estimation of Nonlinear Parameters. SIAM J. Appl. Math. Vol. 11:431-441

The Seventeenth International Symposium on Artificial Life and Robotics 2012 (AROB 17th '12),
B-Con Plaza, Beppu, Oita, Japan, January 19-21, 2012

Batch fast update algorithm for incremental association rule discovery

Araya Ariya[1] , Worapoj Kreesuradej[2]

King Mongkut's Institute of Technology Ladkrabang, Thailand

[1]araya_aa@hotmail.com , [2]worapoj@it.kmitl.ac.th

Abstract: When new transactions are inserted into an original database, the existing rules may be change. An incremental association rule mining is an approach to deal with such problem. This paper proposes an algorithm for mining incremental association rules, called batch fast update (BFUP). The proposed algorithm improves the performance of FUP algorithm by reducing a number of scanning times of an original database. The experimental results show that an execution time of BFUP is much faster than that of FUP.

Keywords: Incremental association rules mining, Association rule mining, Data mining

1. INTRODUCTION

An association rule mining, one of the important tasks in data mining, is a well-known research topic that many researchers propose a large number of algorithms for solving association rule discovering problems. This problem was first presented by Agrawal et al [1] which analyzes the behavior of customer purchasing to help business make a decision. The results show co-occurrence buying items called frequent patterns, which can generate interesting rules. From that research, the problem statement of an association rule mining is defined as follows.

Let I = $\{I_1,I_2,\ldots,I_m\}$ be a set of literal items. DB is a database which contains transactions. Each transaction T is a set of items where $T \subseteq I$. Given X is an item and $X \subseteq I$. Each transaction contain X if and only if $X \subseteq T$. Let X and Y are an item where $X \subseteq I$, $Y \subseteq I$ and $X \cap Y \neq 0$. Each set of items , itemsets, is called a frequent itemset if and only if its support is greater than or equal to support threshold s%. It calculates from a number of transactions in DB that contain $X \cup Y$. An association rule can be shown in $X \Rightarrow Y$ form. Each frequent itemset can be made the association rule if and only if it is satisfied by confidence threshold c% which calculates from a number of transactions in DB that contain X and also contain Y. Both s% and c% are specified by user.

After an association rule mining was revealed, it motivated many researchers to extend this research area in a lot of issues. An incremental association rule mining is the one of an association rule mining issue which maintains association rules when new transactions are appended to an original database.

One research issue of an incremental association rule mining is reducing running time of the algorithms by minimizing the number of times to scan an original database. This paper also works on this issue. An algorithm for mining incremental association rules, called batch fast update (BFUP), is proposed. This algorithm has only one original database scanning.

The paper is organized as follows. The literatures of an association rule mining and an incremental association rule mining are reviewed in section 2. The problem statement of an incremental mining on association rule in dynamic database and FUP algorithm are detailed in section 3. The proposed algorithm and its experiment are presented in section 4 and 5 respectively. The paper conclusion and future work are briefed in section 6.

2. RELATED WORK

Mining association rules was first proposed by Agrawal et al [1] which finds a correlation between itemsets in a transaction database. The algorithm has 2 steps: finding frequent itemsets (sometimes they are called large itemsets) and generating rules. Subsequent years, Apriori [2], the most popular algorithm, was proposed to discover frequent itemsets.

When a database, called a dynamic database, is inserted new transactions, frequent itemsets can be changed after inserting new transactions into the dynamic database. Therefore, an association rule discovery algorithm for a dynamic database has to maintain frequent itemsets when new transactions are inserted into the dynamic database.

One approach to find the new frequent itemsets is to rerun Apriori algorithm for the whole transactions of the dynamic database. This approach is not efficient because all the computation done initially at finding out the old large itemsets are wasted and all large itemsets have to be computed again from scratch [3].

Cheung et al [3] proposed fast update algorithm, FUP, to solve a rules maintenance problem by using the previous knowledge to find frequent itemsets in updated database. The concept of FUP is re-using frequent itemsets of previous mining to update with frequent itemsets of an incremental database. Although FUP can decrease a number of candidate itemsets for scanning original database, it still needs to scan an original database k times when new frequent itemsets are found. This can degrade the performance of FUP algorithm.

In our observation, the advantage of FUP are re-using frequent itemsets of a previous mining to prune itemsets which cannot be a frequent itemset in updated database and reducing candidate itemsets to scan in an original database.

However, the disadvantage of FUP is the algorithm needs to scan an original database equal to a size of k frequent itemsets, e.g., if maximum size of k frequent itemsets is k=5, FUP needs to scan an original database for 5 times.

From this problem, this paper proposes an incremental association rule mining algorithm to improve the performance of FUP algorithm by reducing a number of scanning times of an original database.

3. INCREMENTAL ASSOCIATION RULES MINING

3.1 Problem statement

In a dynamic database, new transactions are appended to a database; accordingly, the previous valid rules may be invalid. The problem statement for an incremental association rule is defined as follows.

Let DB is an original database. An increment database db is the new transactions which are inserted into DB. Updated database UD is the combining between original database and increment database, i.e, $UD = DB \cup db$. A number of transactions of an original database, an increment database and an updated database are |DB|, |db| and |UD| = |DB|+|db| respectively.

Before updating activity, L is the frequent itemsets in DB if and only if X.support $\geq s \times |DB|$. After updating activity, L' is the frequent itemsets in updated database if and only if X.support $\geq s \times |UD|$.

According to Tsai et al [4], when news transactions are insert into an original database, an itemset, i.e. X, can be categorized into 4 cases:

Case 1: X is a frequent itemset in both DB and UD

Case 2: X is a frequent itemset in DB and an infrequent itemset in UD

Case 3: X is an infrequent itemset in DB and a frequent itemset in UD

Case 4: X is an infrequent itemset in both DB and UD

Form these cases of itemsets are mentioned above, it is easy to discovered updated frequent itemsets for the itemset of case 1 and 2 because their count in DB and UD are known, therefore, an updating activity is a trivial task. The itemset in case 4 is unimportant because it cannot change an association rule. The most serious case is the 3rd because it needs to rescan an original database for updating its count. Thus, discovering itemsets in case 3 is the most important problem in an incremental association rule mining. In section 3.2, the method to solve that problem is reviewed and section 4, batch fast update algorithm is presented how to improve a performance of FUP.

3.2 FUP algorithm

Apriori [2] is successful for finding frequent itemsets in a database. However, it is unsuitable for mining in dynamic database. Cheung et al [3] have been proposed an incremental algorithm which has a good performance for mining association rules in dynamic database. The concept of FUP is reviewed briefly in this section.

The operation of FUP has 2 phases: 1-iteration and k-iteration where $k \geq 2$. In the first phase, an increment database is scanned for finding candidate 1-itemsets C_1 and its count. After that loser and winner itemsets are found. Finding loser and winner itemsets, C_1 are divided into 2 types: a member and not a member of previous frequent itemsets in an original database. The first type is updated its count and pruned loser itemsets if its updated count is less than s*|UD|. The second type is scanned to an original database if and only if it is a frequent itemset (winner) in an increment database, i.e., its count is greater than or equal to s*|db|. Both types which satisfy by them threshold can be frequent 1-itemsets in updated database L_1'(winner).

The second phase has 3 steps: filtering out loser itemsets, generating candidate k-itemsets $C_{k\geq 2}$ and finding new frequent itemsets. Firstly, FUP filters out losers from L_k (L_k in DB). Given $Y \in L_k$ and $X \in L_{k-1} - L_{k-1}'$, Y is a loser iff $X \in Y$. For the remaining L_k, they are scanned to an increment database and updated their count. Then they are checked for finding a winner or loser itemset similar to the first phase.

Secondly, C_k is generated by using Apriori-gen. Any C_k is pruned if and only if $Y \in C_k$ where Y is the loser from L_k. This step is a key to reduce a number of C_k before scanning an original database. Finally, new frequent itemsets L_k' are found with the same method as the first phase.

4. BATCH FAST UPDATE ALGORITHM

In this section, an algorithm for mining incremental association rules, batch fast update (BFUP) is presented. The proposed algorithm is assumed that two thresholds, minimum support s% and minimum confidence c%, are static. This algorithm needs only one original database pass and infrequent itemsets are not required. The notation used in this section is defined in Table 1.

Table 1. The notation for Batch fast update algorithm

notation	meaning
DB	original database
db	increment database
UD	updated database
s	minimum support
L_k^{DB}	frequent k-itemset in DB
L_k^{UD}	frequent k-itemset in UD
C_k	candidate k-itemset
|DB|	a number of transactions in DB
|db|	a number of transactions in db
|UD|	a number of transactions in UD
X.count	a support of an itemset
Temp_scanDB	itemsets which are scanned in DB

The algorithm has 2 phases: an increment updating phase and a re-scanning original database phase. The first phase is shown in figure 1. At each iteration, an increment database is scanned to find candidate itemsets, i.e., C_k, and their support counts. Basically, candidate itemsets are divided into 2 types: a member and not a member of previous frequent itemsets of an original database. Candidate itemsets of the first type becomes updated frequent itemsets, i.e., L_k^{UD}, if and only if their updated support count is greater than or equal to s*|UD|. Candidate itemsets of the second type are kept in temp_scanDB for rescanning in an original database if and only if their count plus |DB|-1 is greater than s*|UD|. On the other hand, Candidate itemsets of the second type are pruned if and only if their count plus |DB|-1 is less than s*|UD|.

For generating candidate itemset C_k, Apriori-gen is applied. Apriori generates C_k with L_{k-1}*L_{k-1}, whereas BFUP generates C_k with L_k^{UD} * temp_scanDB$_k$.

The second phase of BFUP algorithm is shown in figure 2. After an increment updating phase is ended, all itemsets in temp_scanDB are re-scanned in an original database and updated their support count. Then, all itemsets in temp_scanDB are checked to find updated frequent itemsets. Let X ∊ temp_scanDB, X can be an updated frequent itemset, i.e., L_k^{UD}, if and only if X.count ≥ s*|UD|.

Algorithm 1 An increment updating phase ()

```
Input : db,s,L_k^DB,C_1^DB,|DB|
Output: L_k^UD
|UD|=|DB|+|db|
k = 1
scan db for all X
for all X∈L_1^DB or X∈C_1^DB
   update X.count
   if X.count ≥ s*|UD|
       X → L_k^UD
for all X ∉ L_1^DB or X∉C_1^DB
   if X.count+|DB|-1 ≥ s*|UD|
       X → temp_scanDB
k=2
while (L_k-1^UD ∪ temp_scanDB_k) > 1
   C_k = L_k-1^UD * temp_scanDB_k
   // using Apriori_gen()
   scan db for all C_k
   for all X∈ C_k do
       for all X ∈ L_k^DB
           update X.count
           if X.count ≥  s*|UD|
               X → L_k^UD
       for all X ∉ L_k^DB
           if X.count+|DB|-1 ≥ s*|UD|
               X → temp_scanDB
   k++
end loop
rescan_original()
L_k^UD = L_k^UD ∪ tempL
return L_k^UD
```

Fig. 1. An increment updating phase

Algorithm 2 a re-scanning original database phase ()

```
Input DB, temp_scanDB,s,|UD|
Output tempL
if temp_scanDB ≠ ∅
    scan DB for all X ∊ temp_scanDB
    update X.count
    if X.count ≥ s*|UD|
        X → tempL
endif
return tempL
```

Fig. 2. A re-scanning original database phase

5. EXPERIMENT

The proposed algorithm in this paper aims to improve the performance of FUP. To evaluate the performance of batch fast update (BFUP) algorithm, this algorithm is implemented and tested on a PC with a 2.93 GHz Intel Core i7 and 3 GB main memory. The experiment is tested with 2 synthetic datasets which are generated by using technique in Agrawal [1]. The first dataset is T10I4D100K which has 100,000 transactions. The second dataset is T10I4D50K which has 50,000 transactions. Both datasets are appended by an increment database that has 1,000 transactions.

For the first original database, i.e., T10I4D100K, the experiment is conducted with 0.1%, 0.3% and 0.5% minimum support thresholds. The average of an execution time is shown in table 2 and figure 3 respectively. For comparison, the results are compared with FUP.

Table 2. Average of Execution time for I10T4D100K

min sup	algorithm	execution time (sec.)	a number of frequent itemset	maximum frequent itemset (size of k)
0.1%	FUP	175890.2901	17,127	L_{10}
	BFUP	43580.3014		
0.3%	FUP	19645.1002	1,991	L_7
	BFUP	11678.5801		
0.5%	FUP	9771.1612	862	L_2
	BFUP	9105.8170		

For the second original database, i.e., T10I4D50K, the experiment is conducted with 0.2%, 0.3% and 0.4% minimum support thresholds. The average of an execution time is shown in table 3 and figure 4 respectively.

From the results of the both datasets, they are shown that an execution time of BFUP is much faster than that of FUP. Furthermore, we observe that the more size k is increasing, the execution time between FUP and BFUP is more different.

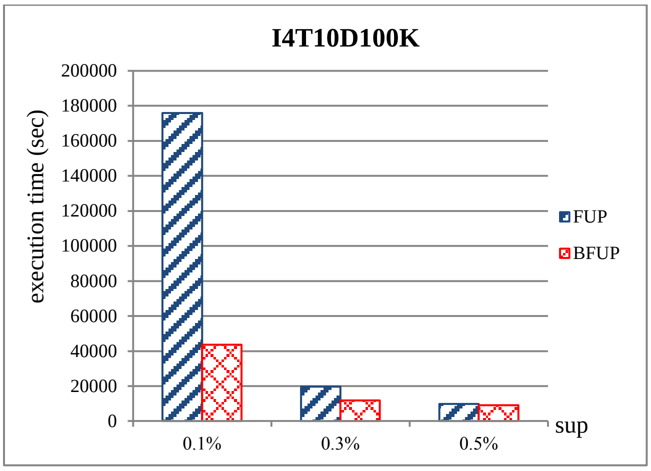

Fig. 3. Execution time comparison for I10T4D100K

Table 3. Average of Execution time for I10T4D50K

min sup	algorithm	execution time (sec.)	a number of frequent itemset	maximum frequent itemset (size of k)
0.2%	FUP	36012.0041	5,307	L_{10}
	BFUP	15402.0908		
0.3%	FUP	17695.8894	1,995	L_7
	BFUP	12906.0013		
0.4%	FUP	12363.9417	1,051	L_3
	BFUP	10866.7162		

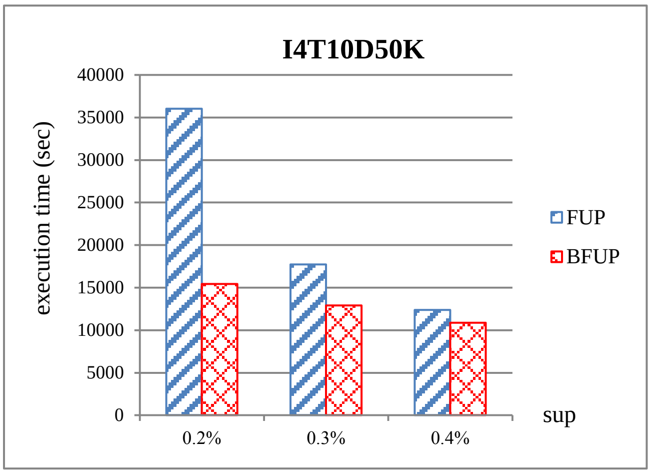

Fig. 4. Execution time comparison for I10T4D50K

6. CONCLUSION

An incremental association rules mining algorithm called batch fast update (BFUP), is proposed. The concept of this algorithm is based from Apriori and FUP algorithm. Although batch fast update algorithm has an execution time better than that of FUP, a large number of temp_scanDB are kept. In the future research, the algorithm for reducing temp_scanDB will be proposed.

7. REFERENCES

[1] Agrawal R, Imielinski T, Swami A (1993), A mining association rules between sets of items in large database, In Proceeding of the ACM SIGMOD Int'l Conf. on Management of Data (ACM SIGMOD'93), Washington, USA, May 1993, pp.207-216.

[2] Agrawal R, Srikant R (1994), Fast algorithm for mining association rules, In Proc. 20th Int. Conf. Very Large DataBases (VLDB'94), Santiago, Chile, September 12-15, 1994, pp.487-499.

[3] Cheung D.W., Han J, Ng V.T., Wong C.Y., Maintenance of Discovered Association rules in Large Databases: An incremental updating technique, In 12th IEEE International Conference on Data Engineering, pp 106-114, 1996.

[4] Tsai Paulry S.M., Lee Chih-Chong, Chen Abree L.P. (2005), An Efficient Approach for Incremental Association Rule Mining, Proceedings of the third Pacific-Asia Conference on Methodologies for Knowledge Discovery and Data Mining, Lecture Notes In Computer Science, Vol. 1574 archieve, 1999.

The Seventeenth International Symposium on Artificial Life and Robotics 2012 (AROB 17th '12),
B-Con Plaza, Beppu, Oita, Japan, January 19-21, 2012

Proposal of method to extract location-related words and to classify location-dependent information

Masaki Sakata[1], Hiroyuki Nishiyama[1]

[1] Graduate School of Sci.and Tech, Tokyou University of Science
Yamazaki 2641, Noda-shi, CHIBA, 278-8510
(Tel: 81-47122-1106, Fax: 81-47122-1106)
(j7411613@ed.tus.ac.jp)

Abstract: In this study, we collected and analyzed tweets on "Twitter" to classify information of categories related to the location to systematically provide information about the location. This method extracts keywords of a high occurrence ratio (location-related words) appearing in tweets from a set of tweets generated at one location. We hypothesized that tweets including location-related words (location-dependent information) contained information related to the location, and classified the information accordingly. This method enables classifying the information related to the location and providing it to users even from information without an address or location.

Keywords: Twitter, location information, location-related word

1 INTRODUCTION

This century is said to be the era of an advanced information society, in which information technology has been developed, such as computers and networks. With the spread of high-performance mobile devices such as smart phones in recent years, we have become able to transmit and receive information anytime, and anywhere. We are thus able to transmit information easily now but have difficulty extracting and obtaining only the information we want from the vast amount of information available. Therefore, we need the ability to identify information proactively, judge its value, and use it suitably. The high-performance mobile devices mentioned above also have a GPS capability, so we can now transmit and receive location information. However, with this GPS capability, even more information has become available to us, so it is even more important that we selectively acquire only the appropriate information. But we hereby have been more needed to acquire appropriate information from the information became more extensive. In the past, we could acquire appropriate information using a keyword search and link structure. But regarding information related to the location, the intensive and provision has not been systematic currently. However, location information has not been widely provided. Although location information is an important factor in categorizing search results, the supply and demand for information is not sufficiently balanced. In this study, we propose a new method of providing location information. We use "Twitter" as a source that includes location information and classify only the tweets that depend on one location from the number of tweets generated. "Twitter"[1] is used as the information because it is able to provide a number of strings with location information attached, strings are obtained from a broad strata of users, and the freshness of the information is good. In 2010, Arakawa et al. proposed methods of acquiring the standard deviation of latitude and longitude for a tweet group, measuring the locational dependence of keywords from the degree of variation in the tweet group, and performing a two-dimensional depth-first search to extract the area with more than a certain percentage of tweet and extracting some locational dependence for the keyword[2]. That enables quantifying the location dependence of the keyword. In the same year, they conducted research on analyzing the string obtained from the location and time information of tweets, and revealed a correlation between the string and the actual input string[3]. Geocoding is a technique for converting geographical information such as station name and address or place name into latitude and longitude coordinates. Using this technique enables obtaining coordinates from information including place names in the text and linking the textual information and coordinates. As an example, there are services such as "maplog"[4] that enables searching the latest blog posts which are written about the range of the map to display. Also, a method to classify messages by category and aggregate similar messages using spatiotemporal information has been proposed by Yamanaka et al[5].

2 SYSTEM DESIGN

Using the geocoding techniques described in the previous section, the categories of information that can be obtained are limited to geographical information. However, there are other categories of information related to the location such as buildings, traffic, and weather. This study attempts to provide only the information of categories related to the location. In this study, the keywords with a high occurrence ratio (location-related words) are extracted from a number of tweets generated on "Twitter" at one location, and location-related words are registered in the database on the server together with location information. We hypothesized that, based on the database created, tweets including location-related words in the text (location-dependent information) contained other information related to the location. Additionally, by repeating the procedure of extracting location-related words and classifying location-dependent information, we thought that extra information (non-location-related words) would be excluded, the number of missed words would be reduced, and the latest information would be provided while responding to location-related words and location-dependent information that varies with time. Also, information is provided by displaying tweets (location-dependent information) in the range of the map for users of this system to display in the browser on the map. The following describes in detail the proposed method for each procedure. In this study, words that have not been determined to be location-related words yet or words for which it is still been unclear whether they are location-related words are referred to as candidate location-related words.

2.1 Extracting location-related words

In this method, tweets including location information are collected. The tweets of Twitter users are collected continuously (can designate a collection area) and are registered in the database together with location information. At the same time, each tweet is morphologically analyzed, and several morphemes generated from a single tweet are registered in the database. Keywords with a high incidence are extracted from a number of tweets generated at one location, and are registered as location-related words in the database. Thus, it is possible to determine location-related words for each area. In addition, location-related words are expected to continue to change constantly with the behavior of Twitter users. However, it is always possible to respond to changing location-related words by constantly repeating the steps from collecting tweets to extracting location-related words, and using only tweets generated in a certain time period. The problem here is how to determine which location tweets are expressed.

2.1.1 Determining the area to which tweets belong

This section describes how to determine which location tweets are indicating. For example, we will consider the situation in Fig. 1. If tweet a was generated at Point X, the tweet could be determined to be indicating Landmark A. A landmark here is a reference point on the map and refers to the name of a station, government office, school, hospital, or post office. In this case, it is possible to identify the area by performing reverse geocoding. Reverse geocoding is a technique to convert the latitude and longitude coordinates for geographical information such as station name and address or place name. However, if it is unclear which location the tweet is indicating like Point Y, it is necessary to know how to resolve the ambiguity. In this method, the area around the tweet generation spot is defined as the area to which the tweet belongs. If the tweet is generated at the red dot in Fig. 2, the range inside the blue circle around the red dot is the tweet area. If the tweet area is partially determined, it is also possible to define the area which an individual morpheme is extracted from the tweet belongs to is equal to the area which the tweet belongs to. Thus, the tweet area is defined by using reverse geocoding and our proposed method together. One more matter must be defined. The tweet area has been determined, but we must determine how to identify location-related words and the area to which they belong from morphemes extracted from several tweets (candidate location-related words).

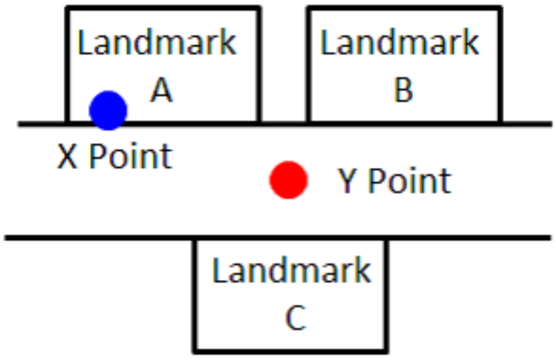

Fig. 1. Subject of tweets: Point X is clear; Point Y is unclear.

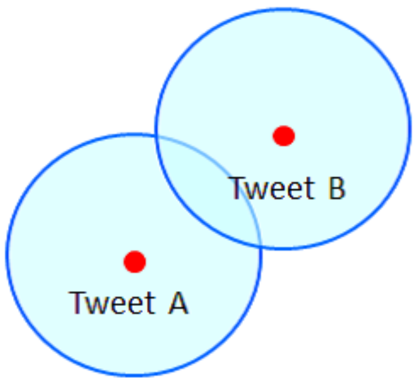

Fig. 2. Area to which tweets belong

2.1.2 Determining location-related words and the area to which they belong

This section describes how to determine the area to which location-related words belong. Even if tweets contain certain location-related words, they can not be location-independent unless they are tweets generated in the area to which location-related words belong. Therefore, how to determine the area to which location-related words belong is important. We will consider focusing on one keyword. The area to which tweets belong is described in the above section. Here, in an area to which a certain location-related word inherently belongs, the tweets including the location-related word should be somewhat dense. Conversely, in an area to which the location-related words inherently should not belong to, generated tweets including the location-related word are few and sparse. If these sparse tweets are removed, the area to which the location-related word belongs can be specified to some extent. For example, assume that tweets including a certain keyword are generated by many users in the positions depicted in Fig. 3. In the area to which a certain location-related word inherently belongs, some of the areas encompassing individual tweets including the location-related word will overlap. In an area to which the location-related word inherently should not belong, there should be few such overlaps. Therefore, only tweets with a specified threshold number of overlaps with other tweets (tweets in the green area in Fig. 3) are adopted, and the tweets with fewer overlaps are removed. Thus, the area is determined by the density of certain candidate location-related words. Pay attention to still being candidate location-related words at phase to have determined the area. When the area is determined, a set of areas composed of several tweets is found (the set of green circles in Fig. 3). If the number of individual tweets composing this set (Fig. 3; three in this example) exceeds a certain number, the word is determined to be a location-related word. Thus, after determining the area in the candidate location-related words phase, the words are determined to be location-related words depending on the number of tweets composing the area. The next section describes how to classify location-dependent information with these location-related words.

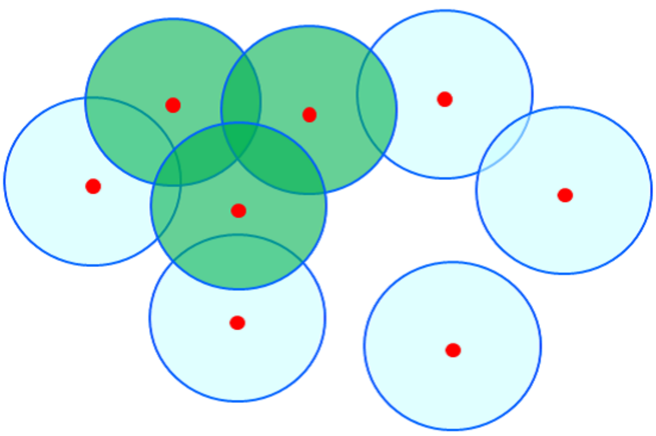

Fig. 3. Area to which location-related words belong

2.2 Classification of location-dependent information

Location-dependent information is classified based on location-related words described in the above section. On the theory that, based on the database created, tweets including keywords determined to be location-related words in the location in the text contained information related to the location, the tweets are acknowledged as location-dependent information. However, this classification rule causes a problem. It can be easy to image that the words expressing a place name and location also become candidate location-related words. In "Twitter," too many tweets express only their own place, such as the Japanese word "nau." Because words expressing a place name and location are also registered as location-related words, tweets expressing only their own place are also acknowledged as location-dependent information. Thus, it is necessary to remove unwanted information from the tweets including location-related words by classifying by means. In this way, location-dependent information is determined from tweets including location-related words in the location in the text by removing unwanted information.

3 IMPLEMENTATION

In this study, Apache is used as a Web server and MySQL is used as the database for the server. The Web server-side programs is implemented using php; the browser-side program, which is a client, is implemented using JavaScript. Tweets on "Twitter" are collected using Twitter API, and location-dependent information is provided to a browser using Google Maps API. Fig. 4 illustrates the system processing flow.

Tweets containing Twitter user location information are collected and registered in the database together with other location information (①). Morphemes generated from the tweets are also registered in the database with location information (②). Location-related words are determined from a set of generated morphemes by the method described in Section 2.1 (③, ④). Using the results, a set of tweets that are already registered in the database is classified (from tweets in the area to which location-related words belong) according to whether it contains location-related words (⑤). Unwanted information described in Section 2.2 is removed from classified tweets by means (⑥). Classification of location-dependent information is complete at this stage, and tweets which include location-dependent information are provided for users of this system by displaying tweets on the map with location information (⑦, ⑧). Fig. 5 presents an example.

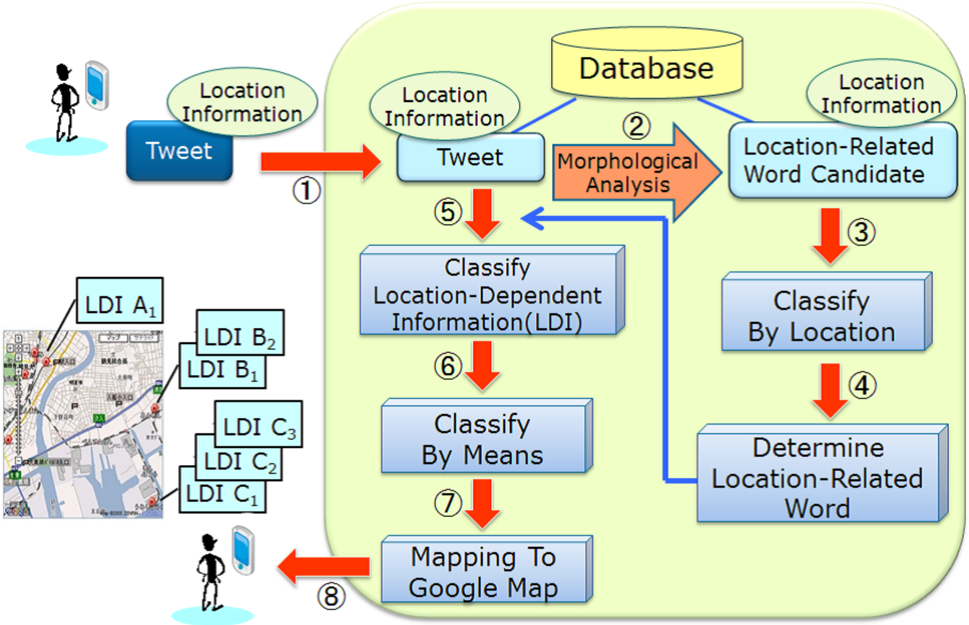

Fig. 4. System flow

This system can be used even from a PC or a smartphone using a browser.

Fig. 5. Example

4 CONCLUSIONS

In this study, we sought to classify only the information of categories related to the location as a systematic method of providing information related to the location. This enables us to classify the information related to the location even from information that cannot be found by conventional methods such as geocoding, not including geographical information such as the address or location. Location-related words change due to changes in the behavior of Twitter users, but if the system is running, this method is able to update location-related words and provide fresh information without the need for analysis. In the future, we will consider extending our method to determine information that users need depending on the content of tweets and location information of Twitter users and to provide location-dependent information focused on the users. We would like to pursue the usefulness of this method further by repeating these extensions of the system.

REFERENCES

[1] Twitter Company:Twitter.http://twitter.com/.

[2] Yutaka Arakawa, Shigeaki Tagashira, Akira Fukuda (2010), Extraction of Location Dependent Words from Twitter Logs (in Japanese). Information Processing Society of Japan SIG Technical Report MBL-55(10):1-6.

[3] Yutaka Arakawa, Shigeaki Tagashira, Akira Fukuda (2010), Relational Analysis between User Context and Input Word on Twitter (in Japanese). Information Processing Society of Japan SIG Technical Report UBI-25(50):1-7.

[4] New Wave Company:maplog.http://maplog.jp/.

[5] Tsutomu Yamanaka, Yuta Tanaka, Yoshinori Hijikata, Shogo Nishida (2010), A Supporting System for Situation Assessment using Text Data with Spatio-temporal Information (in Japanese). journal of Japan Society for Fuzzy Theory and Intelligent Informatics 22(6).

The Seventeenth International Symposium on Artificial Life and Robotics 2012 (AROB 17th '12),
B-Con Plaza, Beppu, Oita, Japan, January 19-21, 2012

Advantages of flexible musculoskeletal robot structure in sensory acquisition

Shuhei Ikemoto[1], Yoichi Nishigori[2], and Koh Hosoda[1]

[1] Graduate School of Information Science and Technology, Osaka University, Osaka, Japan
[2] Graduate School of Engineering, Osaka University, Osaka, Japan
(Tel: 81-06-6879-7739, Fax: 81-06-6879-7750)
(ikemoto@ist.osaka-u.ac.jp)

Abstract: Morphological computation is the concept for which a well-designed hardware can bear part of the computational cost required for robot's control and perception. So far, many musculoskeletal robots have been developed by taking inspiration from human's one and shown superior motion performances. The use of pneumatic artificial muscles (PAMs) has been the key to realize these high performance. Additionally, PAMs have the possibility of being used as sensors for environmental information because they are flexible and backdrivable. In this research, we focus on clarifying how PAMs can contribute to morphological computation of robots driven by these actuators. In particular, we propose an analysis method based on transfer entropy and apply this method to the experimental data acquired by a musculoskeletal robot that opens a door.

Keywords: musculoskeletal robot, pneumatic artificial muscle, transfer entropy

1 INTRODUCTION

Creating a robot inspired from biological systems has been an attractive approach for many researchers in robotics. Especially, human's musculoskeletal system has been often focused because it was optimized to realize intelligent motions during the whole evolutionary history of humans. So far, many musculoskeletal robots that exploit information processing provided by well-designed musculoskeletal structures were proposed. This information processing is called morphological computation and it is one of the key words that symbolize the field of the artificial intelligence paying attention to the embodiment[1].

Artificial pneumatic muscles (PAMs) have been one of most suitable actuators to develop musculoskeletal robots. Thanks to useful features proper of PAMs such as flexibility, backdrivability and high power-to-weight ratio, musculoskeletal robots driven by PAMs have successfully shown superior motion performances[2][3]. Additionally, PAM's state have sometimes been used as a sensor[4] that provides information on the external world and on the state of the robot. This information can be interpreted as proprioceptive information of the musculoskeletal robot and we think that this point is notably important to understand morphological computation in robot's perception. However, in previous researches, the PAM (among the robot's numerous PAMs) that contains important information on the external world was required to be known beforehand and the air-flow to/from such PAM had to be set to zero during the sensing process.

In this research, we focus on morphological computation of musculoskeletal robot's perception using flexibility of PAMs. In particular, in this paper, we aim to show that acquiring environmental information is possible even while the PAM is being driven. Additionally, we don't specify which PAM notably contains environmental information in advance and figure out which PAM is important from the data of all PAMs available in the robot. To this end, we use a musculoskeletal robot arm able to easily open a door by exploiting the morphological computation provided by the flexibility of PAMs. Additionally, we propose an analysis method based on transfer entropy to investigate whether or not PAMs driving the robot arm can contain environmental information. Finally, we apply the proposed method to the data taken in a door-opening task and discuss the analysis results.

2 MUSCULOSKELETAL ROBOT ARM

In this research, we use a musculoskeletal robot arm developed in our research group. This robot arm is driven by PAMs and has several sensors to control and observe the states.

2.1 Hardware design

Fig.1 shows the developed musculoskeletal robot and the configuration of its degrees of freedom. This robot has 7 degrees of freedom(DOF) in its skeletal structure and the configuration is schematically similar to the human's one. For example, the robot arm employs a radioulnar joint and an ellipsoidal joint in the forearm and the wrist, respectively[5]. Fig.2 shows the layout of the PAMs in the robot. The robot is equipped with 17 groups of PAMs for driving its skeletal structure. Because the PAMs have flexibility and backdrivability, the arm can change the posture accordingly to excerting external force. The layout of the PAMs presents similarity with human muscles as well. For example, most of PAMs are configured in the form of antagonistic pairs and there are not only monoarticular muscles but also biarticu-

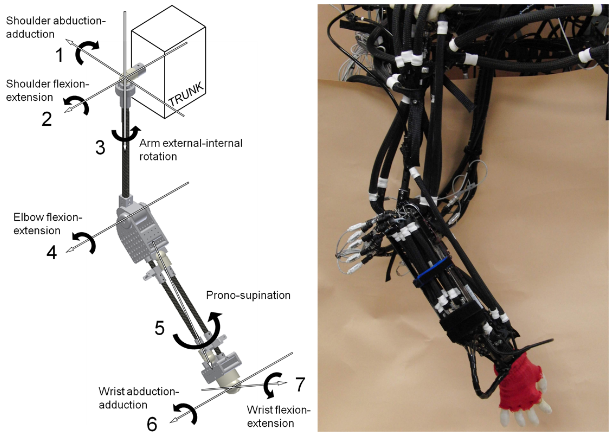

Fig. 1. The 7-DOF musculoskeletal robot arm. The structure is schematically similar to the one of humans and it is driven by PAMs.

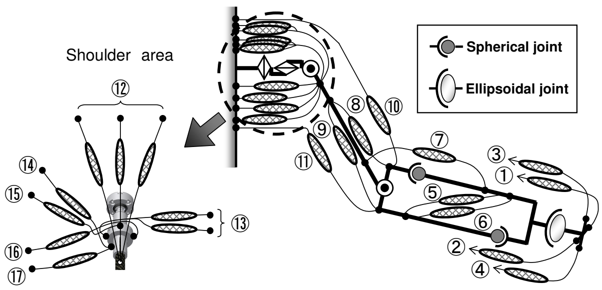

Fig. 2. PAMs layout of the developed pneumatic robot arm. There are 17 different groups of PAMs in the robot arm. Muscles having the same muscle ID are controlled as if they were a single muscle

lar muscles[5]. Additionally, the robot mounts a robot hand driven by PAMs at the end of the arm[6].

In order to investigate whether or not acquiring environmental information from PAMs is possible even if PAMs are being driven, the robot arm was equipped with several kinds of sensors. Since analytical models of PAM's statics have three variables, namely pressure, tension and length, it is obvious that at least two of three variables have to be measured to know the static state[7] of the PAM. In the musculoskeletal robot arm, pressure and tension sensors are available for all PAMs and all PAMs except the robot hand, respectively.

2.2 Control system

So far, many researches have focused on controlling PAMs and the statics was modeled accurately[7]. However, since the analytical models are very complex, it is very difficult to fully consider these models to generate motions of musculoskeletal robots driven by PAMs. Therefore, simple pressure feedback control has been often used[8][9]. In this research, we also adopt a pressure feedback system based on PID control.

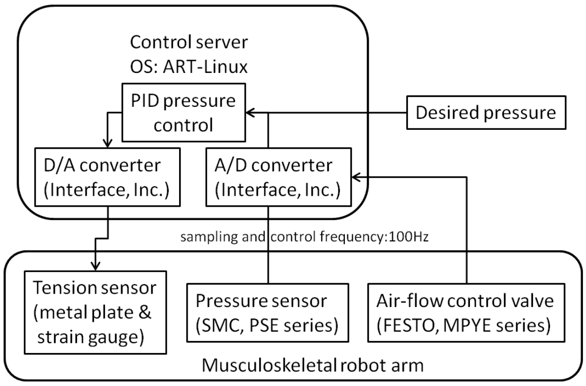

Fig. 3. Control system of the developed musculoskeletal robot.

Fig.3 shows the control system of the robot. Note that all the sensor information and control signal can be recorded during an experiment. For the control server, ART-Linux[1] is employed to ensure realtime data sampling and control. Because the control system shown in Fig.3 needs only the pressure information from all PAMs, the tension sensor information is recorded only for analysis purposes. Actually, the tension sensor information is very important for the analysis because the robot can assume different postures with the same pressures depending on the tensions.

3 MOTION ANALYSIS OF MUSCULOSKELETAL ROBOT

When a musculoskeletal robot is controlled by a time-series of desired pressures, the obtained sensor data has a lot of information about the desired pressures. Therefore, it is required to analyze the differences caused by changes of external force exerted by physical contact and dynamics of the robot. In this research, we focus on transfer entropy to extract these differences.

3.1 Transfer entropy

Transfer entropy is a measure which can quantify nonlinear relationships among stochastically generated time-series of data and a stochastic variable. Intuitively speaking, transfer entropy quantifies dynamic information flow, by measuring how large the influence from a stochastic variable to a time-series of data is.Additionally, transfer entropy can quantify the information flow correctly even in the cases where the two stochastic variables are influenced by another stochastic variables. Recently, transfer entropy has been exploited in

[1] A realtime operating system based on Linux developed by National Institute of Advanced Industrial Science and Technology in Japan: http://www.dh.aist.go.jp/en/research/humanoid/ART-Linux/

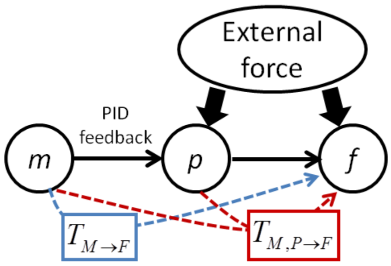

Fig. 4. The schematic relationship among M, P, F and the external force .

the robotics field to find out causalities among robot sensor data[10].

Transfer entropy between two discrete stochastic variables I and J can be defined as:

$$T_{J\to I} = \sum_{i_{n+1},i_n,j_n} P(i_{n+1}, i_n, j_n) \log \frac{P(i_{n+1}|i_n, j_n)}{P(i_{n+1}|i_n)} \quad (1)$$

Where n is a discrete time. This indicates that the transfer entropy is similar to Kullback-Leibler divergence between a probability distribution assuming I has Markov property and a probability distribution assuming I is a subject to J.

3.2 Analysis method

Considering the ideal condition of pressure feedback control, in which the desired pressure M is exactly corresponding to the actual pressure P, the subsidiarity of F to M or P can be expressed by using transfer entropy written as following:

$$\begin{aligned} T_{M\to F} &= \sum_{f_{t+1},f_t,m_t} P(f_{t+1}, f_t, m_t) \log \frac{P(f_{t+1}|f_t, m_t)}{P(f_{t+1}|f_t)} \\ &= T_{P\to F} \quad (2) \\ &= T_{M,P\to F} \end{aligned}$$

As explained in the beginning of this section, the aim of the analysis is investigating the difference caused by changes of external force exerted by physical contact and dynamics of the robot. To this end, we evaluate the difference by using the ideal condition Eq.2 as the baseline.

In order to consider the qualitative meaning of $T_{M\to F}$ and $T_{M,P\to F}$ in the actual condition, we show the relationship among M, P, F and the external force schematically in Fig.4. In the actual condition, the error on the pressure feedback control has to be caused by external force derived from physical contact with the environment and by the dynamics of the robot. As a result, $T_{M\to F}$ and $T_{M,P\to F}$ have to be different. Considering how $T_{M\to F}$ and $T_{M,P\to F}$ change compared to the ideal condition, $T_{M,P\to F}$ is larger than $T_{M\to F}$ in most cases since the M, P will has larger information on the external force than the M alone.

In this paper, we evaluate the difference $T^C_{M,P\to F} = T_{M,P\to F} - T_{M\to F}$ as a measure on how the dynamics of the robot and physical contacts with the environment influence the PAM's states. This measure can be interpreted as the fact that it is possible to subtract the effect of the M because both $T_{M\to F}$ and $T_{M,P\to F}$ contain the information flow from the M to the F.

The $T_{M,P\to F}$ can be written as following:

$$T_{M,P\to F} = \sum_{f_{t+1},f_t,m_t,p_t} P(f_{t+1}, f_t, m_t, p_t) \log \frac{P(f_{t+1}|f_t, m_t, p_t)}{P(f_{t+1}|f_t)} \quad (3)$$

Subtracting $T_{M\to F}$ from Eq.3, $T^C_{M,P\to F}$ can be written as following:

$$\begin{aligned} &T^C_{M,P\to F} = \\ &T_{M,P\to F} - T_{M\to F} = \quad (4) \\ &\sum_{f_{t+1},f_t,m_t,p_t} P(f_{t+1}, f_t, m_t, p_t) \log \frac{P(f_{t+1}|f_t, m_t, p_t)}{P(f_{t+1}|f_t, m_t)} \end{aligned}$$

As explained above, this measure $T^C_{M,P\to F}$ should indicate how external force influences the PAMs. Note that $T^C_{M,P\to F}$ does not have theoretical validity although similar method can be found in related research[10]. Additionally, we note that $T^C_{M,P\to F}$ is applied individually for all PAMs in the robot arm without specifying which PAM should be focused.

4 EXPERIMENT

In this research, we focus on a door-opening task as an example of task in which both exerting and changing external force are present. At first, we will explain about the door-opening task used in the experiment, which can be attained by using the morphological computation of the musculoskeletal robot shown in Fig.1. In the following, we apply the proposed analysis method based on transfer entropy to the data obtained in the door-opening task.

4.1 Door-opening task

The door-opening task is a task in which a robot arm reaches a doorknob, grasps it and opens the door. For the musculoskeletal robot shown in Fig.1, the door-opening task is one of most suitable task to exploit its morphological computation because of the flexibility and backdrivability offered by the PAMs.

Fig.5 shows the sequential snapshots of the robot's motion during door-opening task. The sequence of desired pressures was designed through a trial-and-error process. However, the process is not very complex because it is possible to safely come in contact to the doorknob and move according to the physical constraints imposed by the doorknob easily due to the flexibility of the PAMs. For instance, the rotating and

Fig. 5. The execution of the door-opening task. The developed musculoskeletal robot arm can adaptively grasp and rotate the door knob, and open the door by exploiting its morphological computation.

the opening can be accomplished by inaccurate control because the physical constraints of the door hardly limits the robot motions and guides them to the few available motions when the robot hand is fixed on the doorknob. Since the door-opening consists in a reaching, rotating and opening phase as shown in Fig.5, it is a good example in which the differences previously explained are caused by changes of external force exerted by physical contacts and by the dynamics of the robot.

In addition to the three phases in the door-opening task, we add following three conditions of the task:

1. normal condition (successful trial)
2. locked condition (the door does not open)
3. uncontact condition (failure in reaching the doorknob)

In this paper, we analyze the data obtained in these three conditions. In particular, we investigate how different the $T^C_{M,P\to F}$ are in the three phase of the door-opening task and in the three different conditions.

4.2 Result

For the analysis, 10 trials data were collected for each three conditions. In each trials, the robot arm starts reaching in 0.9 seconds from the beginning of the trial, grasps and rotates the doorknob at 1.0 seconds and pulls it for 3.0 second after the rotation. In comparison with the first condition, the second condition will differ in the second phase and the third condition will be differ after touching the doorknob. It can be assumed that these differences among three conditions and three phases will be observed by $T^C_{M,P\to F}$.

Fig.6 shows the average of $T^C_{M,P\to F}$ value in ten trials of each conditions. The error bar indicates the standard deviation. The left of Fig.6 shows the $T^C_{M,P\to F}$ value for each PAMs in the reaching phase. In the reaching phase, there is no difference among the three conditions except that for the third condition the contact with the doorknob does not occur at the end of the phase. Small differences can be observed in muscle 1, 2, 3 and 4 which drive the wrist of the robot arm as shown in Fig.2. Therefore, the analysis results are reasonable for the reaching phase.

The middle of Fig.6 shows the result for the rotating phase. In this phase, the third condition is very different from the others because it is not physically constrained by the door. From the result, it can be observed that there is a large difference in muscles 6, 7 and 16 between the third condition and the others. Considering the physical meaning of why these $T^C_{M,P\to F}$ values are larger in the third condition, we note that these muscles will get a large reaction force from the know when this is grasped and rotated, if the robot hand is actually fixed on the doorknob. In other words, in the first and the second conditions, the robot motions have to obey the physical constraints imposed by the door. As a consequence, we can assume that the $T^C_{M,P\to F}$ value captured the environmental information reflected in muscle 6, 7 and 16 for the third condition.

The right of Fig.6 shows the results for the opening phase. In this phase, the second condition provides large resistance in moving the arm because the door is locked and does not open. Therefore, the $T^C_{M,P\to F}$ value will be increased in the second condition because the change of the pressure will be more directly easily reflected in the change of the tension. In the right of Fig.6, it can be seen that the $T^C_{M,P\to F}$ values for almost muscles in the second condition are larger than the same values in the first condition. In the third condition, the $T^C_{M,P\to F}$ values of some muscles, such as muscle 8 and 10, are larger than the value for the same quantities in the

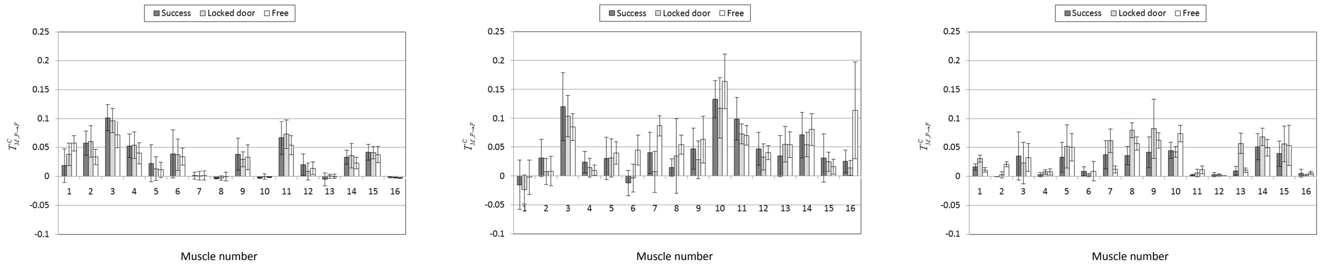

Fig. 6. The $T^C_{M,P\to F}$ in three conditions and three phases.

first condition. This indicates that physical constraints sometimes reduce the resistance of gravity because muscle 8 and 10 mainly bear the weight of the arm in this posture.

Through this experiment, it is qualitatively confirmed that PAMs driving the robot arm can be exploited to extract environmental information such as external force derived from physical contacts with the environment and from the dynamics of the robot. However, this is still a preliminary result that needs to be validated in order to confirm the main concept of this research. Future works will deal with more extensive experiments to validate our hypothesis, supported by the current preliminary results.

5 DISCUSSION AND CONCLUSION

In this research, we focused on morphological computation in a robot's perception that exploits the PAM's features. In particular, we focused on the possibility of PAMs to contribute to morphological computation of robots driven by these actuators. To this end, we proposed an analysis method based on transfer entropy and applied this method to the data taken from an experiment in which a musculoskeletal robot opens a door. As a consequence, it was qualitatively confirmed that the PAMs actuating the musculoskeletal robot arm can be used to obtain environmental information such as physical contacts and the dynamics of the robot even when these are actively actuated. Additionally, it was verified that the analysis method can be applied without specifying beforehand which PAMs should be focused.

The result in this paper can be used for finding out which PAM are useful to learn or improve the musculoskeletal robot's motions. In fact, one of biggest problems to control complex musculoskeletal robots driven by PAMs is the high dimensionality of the state and the motor command spaces derived from the structural complexity. The experiment showed the possibility that few PAMs could be able to generate the robot's motion appropriately and could be used as sensors to extract information on the surrounding environment.

However, the result obtained in this research is still very preliminary. Therefore, it will be necessary to investigate both of the robot's structure and the analysis method for clarifying morphological computation offered by musculoskeletal structures.

REFERENCES

[1] R.eifer and J.Bongard. *how the body shapes the way we think. a new view of intelligence*. MIT Press, 2006.

[2] Ryuma Niiyama, Satoshi Nishikawa, and Yasuo Kuniyoshi. Athlete robot with applied human muscle activation patterns for bipedal running. In *Proc. IEEE-RAS Int. Conf. on Humanoid Robots (Humanoids 2010)*, pages 498–503. Nashville, Tennessee USA, Dec. 2010.

[3] Ryuma Niiyama, Akihiko Nagakubo, and Yasuo Kuniyoshi. Mowgli: A bipedal jumping and landing robot with an artificial musculoskeletal system. In *Proc. IEEE Int. Conf. on Robotics and Automation (ICRA 2007)*, pages 2546–2551 (ThC5.2), Roma, Italy, April 2007.

[4] K. Hosoda, H. Takayama, and T. Takuma. Bouncing monopod with bio-mimetic muscular-skeleton system. In *Intelligent Robots and Systems, 2008. IROS 2008. IEEE/RSJ International Conference on*, pages 3083–3088. IEEE, 2008.

[5] D.A. Neumann and D.L. Wong. *Kinesiology of the musculoskeletal system: foundations for physical rehabilitation*. Mosby St Louis, MO, 2002.

[6] Alejandro Hernandez Arieta and Hiroshi Yokoi. Integration of a multi-d.o.f. individual adaptable with tactile feedback for an emg prosthetic system. *Intelligent Autonomous Systems*, 8:pp.1013–1021, 2004.

[7] C.P. Chou and B. Hannaford. Measurement and modeling of McKibben pneumatic artificial muscles. *IEEE Transactions on Robotics and Automation*, 12(1):90–102, 1996.

[8] B.Tondu, S.Ippolito, J.Guiochet, and A.Daidie. A seven-degrees-of-freedom robot-arm driven by pneumatic artificial muscle for humanoid robots. *The International Journal of Robotics Research*, 24(4):257–274, 2005.

[9] N.Nakamura, M.Sekiguchi, K.Kawashima, T.Fujita, and T.Kagawa. Developing a robot arm using pneumatic artificial rubber muscles. *Power Transmission and Motion Control*, 2002.

[10] Y.Yoshikawa H.Sumioka and M.Asada. Learning of joint attention from detecting causality based on transfer entropy. *Journal of Robotics and Mechatronics*, 20(3):378–385, 2009.

The Seventeenth International Symposium on Artificial Life and Robotics 2012 (AROB 17th '12),
B-Con Plaza, Beppu, Oita, Japan, January 19-21, 2012

Trend Awareness by Value Senses in Home Energy Consumption

Jin Dai[1], Fei Wei[1,3], Shingo Aoki[1], Hiroshi Tsuji[1] , Shuki Inoue[2]
[1]Graduate School of Engineering Osaka Prefecture University Sakai, Osaka, Japan
[2]Energy Use R&D Center of the Kansai Electric Power Co., Inc, Amagasaki, Hyogo, Japan

[3]weifei@mis.cs.osakafu-u.ac.jp

Abstract: To save home energy, we have proposed indirect control based on awareness. One of issues for indirect control is to classify users based on their life style which affects on the transaction of energy consumption. Designing pair-wise comparison among six kinds of value senses (convenience, housework support, healthy life, secure living space, comfort, sustainable environment), this paper proposes the method how to make clusters and then how to clarify the features of cluster in the context of value senses. Using the responses for questionnaire, this paper also describes how the proposed method works.

Keywords: Cluster Analysis; Data Visualization; Energy Saving; Knowledge Management

1 INTRODUCTION

The energy consumption has been a big issue before the miserable disaster of earthquake and tsunami occurred in Japan. Although the industry departments in Japan have paid much attention on this issue since thirty years ago for saving energy and decreasing the volumes of energy consumption, the home energy consumption has been increased because many people prefer comfortable life.

To achieve sustainable development in society, everybody should consider how to save energy in office and at home and public area. There are some ways to bring about a fundamental improvement in energy consumption. For example: 1) to develop intelligent home appliances, 2) to develop new materials for insulated house. Today not only engineers but also consumers are required to bring forth new ideas for saving energy.

One of currently noticeable approach is applying HEMS (Home Energy Management System) under indirect control [1]. Monitoring the status of energy consumption, HEMS tries to raise consumer's awareness of self-control. The Google power meters [2] and the Microsoft hohm [3] are typical examples of HEMS which show graph referring to energy transaction volumes. We have also designed the knowledge management system [4] and the advising method which are under indirect control [5]. The proposal premised on that the similar homes consume about the same amount of energy.

Then how to find out the similar homes? There are some ideas: classifying by consumer/ family property, house property and their life style. Calculating the entropy by the attributes can classify in terms of heavy, general and light consumers which previous research has proposed [6]. However, it cannot find objective boundary between consumers.

This paper focuses on value senses in our daily life. The leverages we used to analysis the responses of questionnaire include pairwise comparison between value senses and energy transaction volumes.

First, we review the background of this research in Chapter 2. Then in Chapter 3 we propose our approach and in Chapter 4 we will describe numerical experimentation. Finally, in Chapter 5 we will conclude our approach and discuss the future work.

2 RELATE WORKS AND PROBLEM DESCRIPTION

2.1 Indirect Control for Saving Energy

First, let us show the statistics of energy consumption. In Japan, as shown in Fig. 1, the volume of energy consumption at industry has been decreasing since thirty years ago. It is because there are variety of regulation and technology innovation.

However, the volume of energy consumption at home has not been decreased but gradually increased even though technology innovation.

It is because people prefer comfortable life and do not pay attention to their consumption: whether they consume energy much or not.

The premise under our research goal is that people change their lifestyle once they are aware of that they consume more energy than others who are similar to them. To save energy, it is expected that they may switch off home appliance if not needed. They may decrease the frequency of bathing. Such action driver is called indirect control [1].

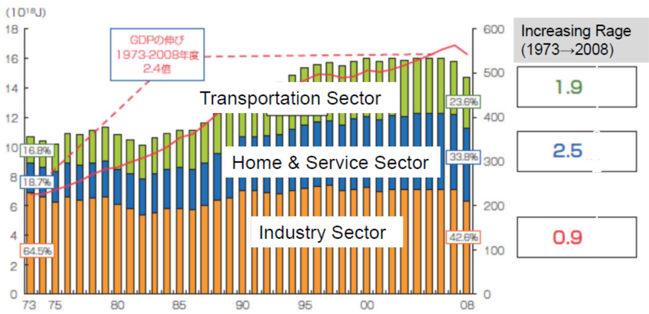

Fig. 1 Trend of Energy Consumption in Japan

As the first step to achieve indirect control, Google power meter [2] and Microsoft hohm [3] are trying to provide the data of their real-time consumption volume by line graph or bar graph to home residents who use them. The smart meter monitors the electric consumption in interval of an hour or sends the central server their consumption at least daily back. However, they do not propose the volume of other energy such as gas and kerosene. Even if one is aware that he consumes much energy than others, he has no chance to know how to improve his life.

On the other hand, the previous research [4] proposed diagnosis system based on knowledge management model. The story for indirect control is as follows:

(1) Collect volumes of recent home energy consumption data with home property including their life environment and life style. Example property includes location, house construction method, frequency of bathing, hour of rising and bedtime.

(2) Classify sample data with their variance by home property. If a classification has a small variance, it becomes useful for notification.

(3) Show consumers their status of energy consumption in the same category homes by visualization technique such as box chart.

(4) Some are notified that they consume energy much. We expect them to improve their daily activity. On the other hand, we expect others who save energy to disclose their idea, motivation, introspection as well as device or artifice.

(5) After the proposed indirect energy load control works well, new sample data should be collected for further energy saving.

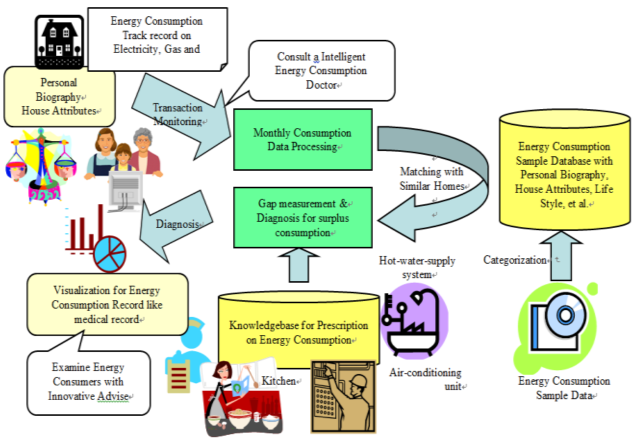

Fig. 2 Overview of KNOTES: Knowledge & Transaction based domestic energy saving support system

We have already designed knowledge management system for second generation of indirect control called KNOTES (Knowledge & Transaction based domestic energy saving support system) [5]. The overview of KNOTES is shown in Fig2.

2.2 Bandwidth of Home Energy Comsumption

In order to make KNOTES work better, the variance of the consumed energy in the same category should be small. To examine if the similar home consume almost the same amount of energy or not, we have collected transaction from two thousands and five hundreds homes with their property [4].

Then main concern is "what is similar?" There are home property such as the family size, generation and occupation. There are also house property such as construction method and size. Further, there is variety of life-style.

Using information entropy theory, we have tried to find out the attributes which affect consumption volume [6]. However, we have not yet gotten clear similarity. Rather it has shown that there are really varieties of homes on energy consumption even if their home property and house property are the same.

In our samples, there are pair-wise comparisons of value sense preference. The prepared value senses are six: convenience, housework support, healthy life, secure living space, comfort, sustainable environment. Therefore, the number of combination is fifteen (6C2). In the following, we will describe how to use the value senses to make category for consumers.

3 VALUE SENSE BASED TREND ANALYSIS

3.1Value Sense Based Cluster Analysis

The pair-wise comparison of value sense is processed as follows: Which is more important for your life: convenience or housework support? The option of answer is 0 (former) or 1 (latter). Then the value senses can be represented by fifteen-dimensional vector whose element is either 0 or 1.

For the vectors, we can apply cluster analysis. Although there is variety of distance functions, we use Euclidean distance. The most similar two samples are combined into one cluster and the same combination is repeated until all samples are combined. It is a kind of hierarchical clustering.

3.2Visualization for Value Sense

In order to clarify the feature of cluster, we propose the VS (Value Sense)-map. VS-map consists of nodes and lines for the preference strength and relations among value senses [7]. Size of node expresses the magnitude of preference. The arrow expresses the priority on preference between nodes.

If there is no priority, the line does not have direction. If there is strong bias between value senses, the line is bold. The flow of drawing up VS-map is illustrated in Fig. 3.

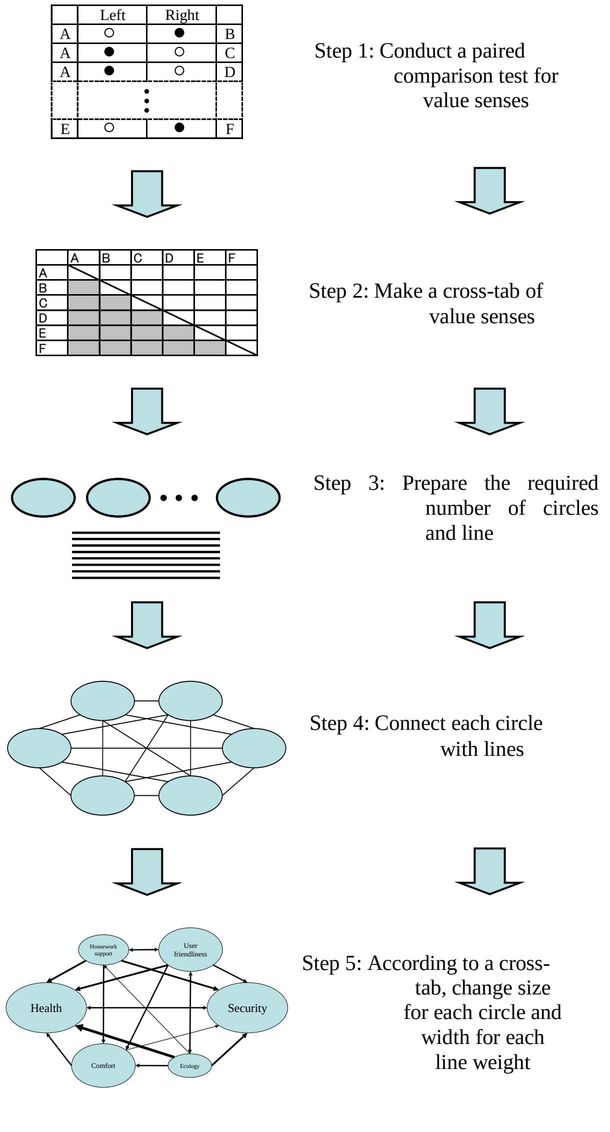

Fig. 3 Flowchart of Creating Value Map

4 NUMERICAL EXPERIMENTATION

4.1 Dataset and Cluster Analysis

To collect at least 13 months transaction data between January, 2007 and December, 2008, we asked 100,000 monitors preliminary if they could disclose them with personal biography, house attributes and life style in January, 2009. Then, we found 2,500 responders who had interest in disclosing their data in a couple of days [4]. The questionnaire consists of thirty categories of questions including energy consumption transaction for 24 months, personal biography and their life style.

Screening the size of family, we have 1,268 samples where more than three persons live in a house. The result of cluster analysis (the number of cluster is ten) is shown if Fig. 4. The basic statistics of clusters are also summarized in Table 1.

The table shows that standard deviation of cluster variance is smaller than that for all samples (2,925.7). It means that value sense based cluster analysis works well for decreasing bandwidth diversity of home energy consumption. It also shows that more than fifty percent of samples are in cluster E14.

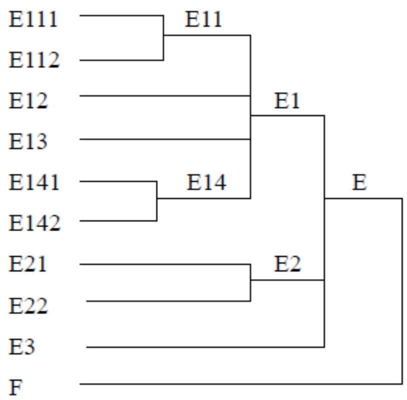

Fig. 4 Cluster Diagram

Table 1 Basic Statistics for Clusters(consumed Joule/year)

Cluster	E111	E112	E12	E13	E141
n	128	144	19	8	284
mean	4,605.1	4,644.4	4,784.2	5,322.4	4,738
Std.	1,959.9	2,295.2	2,234.6	2,616.4	1,912.6
Cluster	E142	E21	E22	E3	F
n	453	52	72	60	48
mean	4,989.6	4,072	4,492.1	4,290	4,031.1
Std.	2,176.9	1,738.2	1,569.8	1,813.7	1,420.4

Total: n=1,268, mean=5,089.2, std.=2,925.7

4.2 Value Map based Discussion

Let us check Fig. 4 again. Hierarchy implies that cluster F is exceptional because there is no subclass. We also found that the average consumption of cluster F(4,031.1) and its standard deviation (1,420.2) are smaller than others as shown in Table 1. It means that the value senses in this cluster relates to the volume of energy consumption in this cluster.

Next, let us check cluster E13 because the average consumption of cluster E13 (5,322.4) is the largest in clusters. Although the number of cluster E13 (8) is smallest, the standard deviation (2,616.4) is largest. It means that the cluster can be also regarded as exceptional and the expected volume of energy consumption in this cluster may be beyond value senses.

Finally, let us check cluster E21 because the average of energy consumption (4,072) is smallest in cluster E. Our concern is how value senses in cluster E21 differs from those in all samples.

The VS-map for all samples, clusters E13, E21 and F are shown in Fig. 5-8. Then we are aware of the followings:

(1) Healthy life is generally preferred over clusters.

(2) Value senses in cluster F is opposite around secure living space. The home which does not take care of secure living space tends to save energy.

(3) Value senses in cluster E13 is not consistent because the directions of arrows are complicated. Then person who does not clear preference among value senses tends to consume much energy.

(4) Person in cluster E21 prefers secure living space as well as sustainable environment. At the same time he does not take care of convenience or housework support.

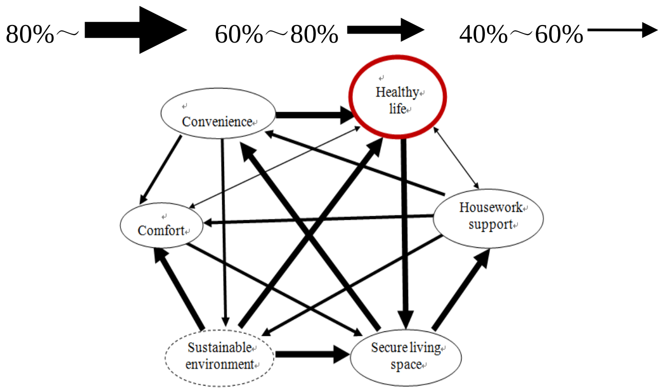

Fig. 5 VS-Map for Typical Clusters (clusters E13)

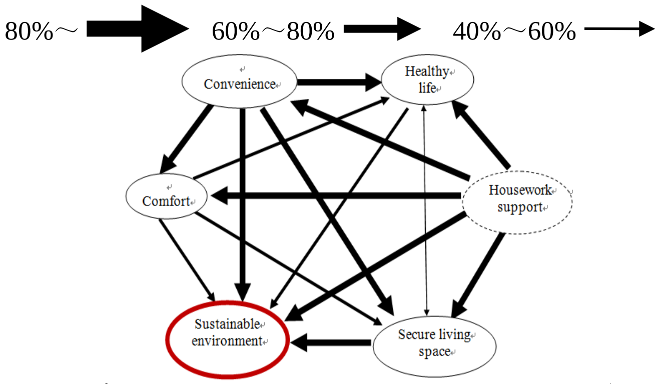

Fig. 6 VS-Map for Typical Clusters (clusters E21)

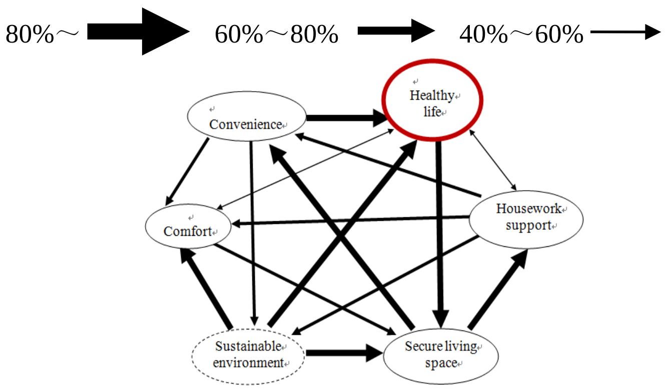

Fig. 7 VS-Map for Typical Clusters (clusters F)

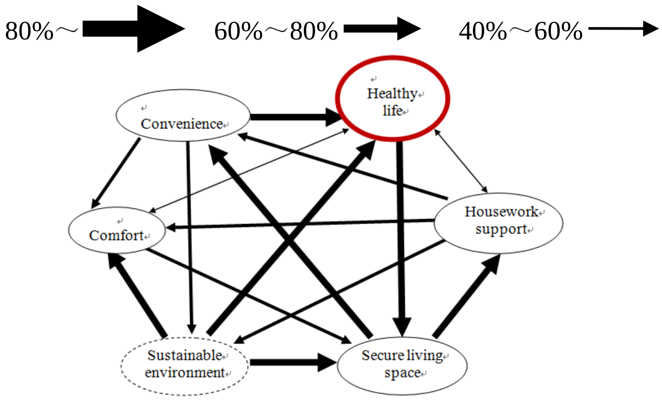

Fig. 8 VS-Map for Typical Clusters (clusters all samples)

5 CONCLUSION

This paper has described indirect control for saving home energy based on awareness. To classify the users, this paper proposed cluster analysis by value senses and introduces the method which visualized the features of the clusters. In our numerical experimentation, there were ten clusters where users in one cluster consumed much energy and those in another cluster consumed less energy.

The features of clusters were visualized by VS-map which shows what kinds of users consume much energy or less. We will develop a knowledge management system which gives awareness and advises for improving our daily life in the near future.

REFERENCES

[1] E. Sugihara (2009), Energy Management and Load Control at Home (in Japanese), Operations Research, Vol. 29, No. 6, pp.329-334.

[2] Google PowerMeter Web sites (2010-12-20 accessed), http://www.google.com/powermeter/.

[3] IMicrosoft hohm Web sites (2010-12-20 accessed), http://www.microsoft-hohm.com/.

[4] S. Inoue, J. Dai, M. Shiba, S. Aoki and H. Tsuji (2010), Knowledge Management Approach for Saving Home Energy Consumption, WCCI 2010 IEEE World Congress on Computational Intelligence, pp.2113-2118.

[5] Hiroki Shigeyoshi, Shuki Inoue, Keniti Tamano, Shingo Aoki, Hiroshi Tsuji, and Tsuyoshi Ueno(2011): Knowledge and Transaction Based Domestic Energy Saving Support System, A. Konig et al. (Eds.), KES 2011, Part IV, LNAI 6884, pp. 242-251, Springer-Verlag Berlin Heidelberg.

[6] M. Shiba, S. Aoki, H. Tsuji ans S. Inoue (2010), Factor Analysis in Home Energy Consumption by Information Entropy and Bayesian Network, Proc. of International Symposium on Aware Compuring, pp.159-165.

[7] [7] H. Tsuji, M. Kojima, A. Takahashi, M. Nakano, S. Aoki, S. Inoue, K. Asari, E. Mimura(2008), Preference Mining on Future Home Energy Consumption, IEEE International Conference on Systems, Man & Cybernetics, IEEE/SMC, pp.3697-3701.

The Seventeenth International Symposium on Artificial Life and Robotics 2012 (AROB 17th '12),
B-Con Plaza, Beppu, Oita, Japan, January 19-21, 2012

Optimal Base-Stock Policy of the Assemble to Order Systems

Shih-Cheng Horng[1], Feng-Yi Yang[2]

[1] Department of Computer Science & Information Engineering, Chaoyang University of Technology
Taichung, Taiwan, R.O.C.
[2] Department of Biomedical Imaging and Radiological Sciences, National Yang-Ming University
Taipei, Taiwan, R.O.C.

[1] schong@cyut.edu.tw
[2] fyyang@ym.edu.tw

Abstract: In this work, an ordinal optimization based evolution algorithm (OOEA) is proposed to solve for a good enough target inventory level of the assemble to order (ATO) system. First, the ATO system is formulated as a combinatorial optimization problem with integer variables that possesses a huge solution space. Next, the genetic algorithm (GA) is used to select *N* excellent solutions from the solution space, where the fitness is evaluated with the radial basis function (RBF) network. Finally, we proceed with the OCBA technique to search for a good enough solution. The proposed OOEA is applied to an ATO system comprising 10 items on 6 products. The good enough target inventory level obtained by the OOEA is promising in the aspects of solution quality and computational efficiency.

Keywords: ordinal optimization, genetic algorithm, radial basis function, optimal computing budget allocation, assemble to order system.

1 INTRODUCTION

Assemble to order (ATO) systems refer to a production strategy in which the customer must first order specified products before the item is manufactured [1]. The main advantage of ATO systems is that customers can quickly receive products customized to meet their requirements. Since the optimal inventory policies for the general ATO systems are not known, heuristic policies such as independent base-stock policies or batch-ordering policies are often used in practice to manage the component inventories. However, there is an exponential growth in the huge solution space as the number of items increases. The huge solution space makes the considered problem very hard for conventional heuristic methods to find near-optimal base-stock policy in a reasonable time.

To overcome the drawback of consuming much computation time for complex ATO systems, we propose an ordinal optimization based evolution algorithm (OOEA) to solve for a good enough target inventory level within a reasonable amount of time. The key idea of the OOEA is to narrow the solution space stage by stage or gradually restrict the search through iterative use of ordinal optimization (OO) theory [2]. The OO theory has been successfully applied to cope with the NP-hard optimization problems such as the wafer probe testing process [3], the cyclic service of the centralized broadband wireless networks [4], and resource allocation of grid computing system [5]. The ATO system operating with a continuous-review base-stock policy can be formulated as a combinatorial optimization problem that possesses a huge solution space and is most suitable for demonstrating the validity of the OOEA.

Therefore, the purpose of this paper is to determine a good enough target inventory level using limited computation time such that the expected total profit per period is maximized. The developed mathematical formulation and simulation procedure can be used for any distributions of arrival processes and production times. The proposed OOEA consists of diversification stage and intensification stage. A radial basis function (RBF) network [6] is firstly treated as a surrogate model to roughly evaluate the objective value of an inventory level. In the diversification stage, the genetic algorithm (GA) [7] is utilized to efficiently select *N* excellent solutions from the solution space where the fitness is evaluated with an RBF network. In the intensification stage, we proceed with the optimal computing budget allocation (OCBA) method [8], which allocates the computing resource and budget by iteratively and adaptively selecting the excellent solutions.

We organize our paper in the following manner. In Section 2, we present a mathematical formulation of a general ATO system. In Section 3,we illustrate the proposed OOEA. In Section 4, the proposed OOEA is applied to an ATO system that comprises 10 items on 6 products. Finally, we draw a conclusion in Section 5.

2 ASSEMBLE TO ORDER SYSTEMS

2.1 Problem Statement

The ATO system consists of a set of h key items and m non-key items from which n products are assembled [9]. Orders for each of n different products arrive according to independent Poisson processes with constant arrival rates $\lambda_i, i = 1,\ldots,n$. Products are made up of a collection of items of different types. Items are either key items or non-key items. If any of the key items are out of stock, then the product order is lost. If all key items are in stock, the order is assembled from all key items and the available non-key items. Product *i* requires $a_{i,j}$ items of type *j*, where *j* ranges from 1 to (*h*+*m*). Each item sold brings a profit p_j, and each item in inventory has a holding cost per unit time of h_j, $j=1,\ldots,h+m$. There are inventory capacities C_j for each item, so that $0 \le x_j \le C_j$, where x_j is the inventory level of item *j*, $j=1,\ldots,h+m$. The production time for each item is truncated normally distributed with mean μ_j and variance σ_j^2, $j=1,\ldots,h+m$, lower bound 0 and upper bound ∞ and is independent of the products' arrival processes.

The ATO system operates with a continuous-review base-stock policy under which each item has a target base stock x_j, $j=1,\ldots,h+m$, and each demand for an item triggers a replenishment order for that item. There are (*h*+*m*) machines, each producing a single type of item. Items are produced one at a time on dedicated machines. We wish to maximize the expected total profit per unit time by selecting the target inventory level for a given arrival rate.

2.2 Mathematical Formulation

The ATO system under the assumed arrival rates for each order can be formulated as follows:

$$\max_{\mathbf{x}\in\Omega} E[f(\mathbf{x})]$$
$$0 \le x_j \le C_j,\ x_j \in Z,\ j=1,\ldots,h+m. \quad (1)$$

where $\mathbf{x}=[x_1 \cdots x_{h+m}]$ denote the vector of inventory level, $E[f(\mathbf{x})]$ denotes the expected total profit per unit time of $\mathbf{x}$. The inequality constraint for each x_j is $0 \le x_j \le C_j$, where the upper bound ensures that we will not go over capacity. Apparently, the solution space is

$$\Omega = \{\mathbf{x}=(x_1,\cdots,x_{h+m}) \mid 0 \le x_j \le C_j,\ x_j \in Z,\ j=1,\ldots,h+m\} \quad (2)$$

where Ω consists of $(C_j+1)^{h+m}$ possible $\mathbf{x}$. Suppose that $h=8$, $m=2$ and $C_j=20$ for $j=1,\ldots,10$, the size of Ω will be 21^{10}, which is very huge. The relationship between inputs and output of ATO stochastic simulated procedures is described in Fig. 1, in which $\mathbf{x}$ and $\boldsymbol{\lambda}$ are the input variables, $f(\mathbf{x})$ is the output objective value, T_w denotes the warm-up period, and $T_{\max}$ denotes the predetermined measurement of time. Each simulation replication should start from a fully stocked system with no orders in production, have a warm-up period of T_w time units, and then capture statistics for the next $T_{\max}-T_w$ time units of operation.

In practice, it is impossible to perform an infinitely long simulation. Thus, the sample mean of the stochastic simulation for a given value of $\mathbf{x}$ is defined as

$$\bar{f}(\mathbf{x}) = \frac{1}{L}\sum_{l=1}^{L} f_l(\mathbf{x}) \quad (3)$$

where L is the total number of simulation replications, $f_l(\mathbf{x})$ denotes the objective value of the lth simulation replication. The $\bar{f}(\mathbf{x})$ is an approximation to $E[f(\mathbf{x})]$, and $\bar{f}(\mathbf{x})$ is asymptotically close to $E[f(\mathbf{x})]$ as L increases. Thus, let $L_e=10^4$ represent the sufficiently large L. In the sequel, we define the exact model of (1) as when $L=L_e$. For the sake of simplicity in expression, we let $\bar{f}_e(\mathbf{x})$ denote the objective value of a given $\mathbf{x}$ computed by exact model.

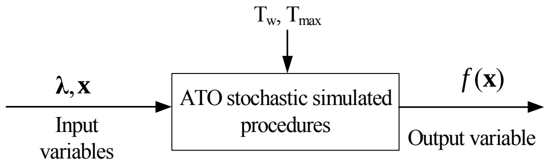

Fig. 1. Relationship between the inputs and the output of ATO stochastic simulated procedures

3 SOLUTION METHOD

3.1 RBF network

The RBF networks are three layer networks including input source nodes, hidden neurons with basis functions, and output neurons with linear activation functions, as shown in Fig. 2 [6].

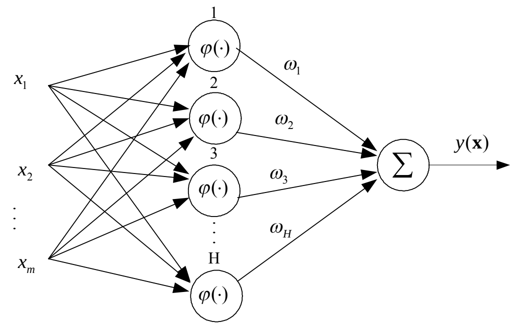

Fig. 2. Structure of an RBF network

An RBF network with a single output can be expressed as follows:

$$y(\mathbf{x}) = \sum_{h=1}^{H} \omega_h \varphi(\|\mathbf{x}-\mathbf{z}_h\|) \quad (4)$$

where $y(\mathbf{x})$ is the objective value of a given $\mathbf{x}$, H is the number of hidden nodes, $\mathbf{z}_h$ are the centers of RBF network, $\varphi(\cdot)$ is a set of RBF, ω_j are weight coefficients, and $\|\cdot\|$ is usually the Euclidean norm. In this work, the Gaussian function is used as the RBF. Once the centers have been chosen and fixed, we use the given *M* samples to find the $\boldsymbol{\omega}=[\omega_1,\ldots,\omega_H]$ by setting up the M equations:

$$\begin{aligned}
&\omega_1\varphi(\|\mathbf{x}^{(1)}-\mathbf{z}_1\|)+\omega_2\varphi(\|\mathbf{x}^{(1)}-\mathbf{z}_2\|)+\ldots+\omega_H\varphi(\|\mathbf{x}^{(1)}-\mathbf{z}_H\|)=y^{(1)}\\
&\omega_1\varphi(\|\mathbf{x}^{(2)}-\mathbf{z}_1\|)+\omega_2\varphi(\|\mathbf{x}^{(2)}-\mathbf{z}_2\|)+\ldots+\omega_H\varphi(\|\mathbf{x}^{(2)}-\mathbf{z}_H\|)=y^{(2)}\\
&\qquad\vdots \qquad\qquad\qquad\qquad\qquad\qquad \vdots\\
&\omega_1\varphi(\|\mathbf{x}^{(M)}-\mathbf{z}_1\|)+\omega_2\varphi(\|\mathbf{x}^{(M)}-\mathbf{z}_2\|)+\ldots+\omega_H\varphi(\|\mathbf{x}^{(M)}-\mathbf{z}_H\|)=y^{(M)}
\end{aligned} \quad (5)$$

The above equations can be solved using the least squares error as long as the vectors $\mathbf{x}^{(i)} \neq \mathbf{x}^{(j)}$, for $i \neq j$. Once we have the weight coefficients and centers, we can evaluate the RBF network at a new sample by using (4) as a guide. We let $F(\mathbf{x}, \boldsymbol{\omega})$ denote the functional output of the trained RBF network of a given $\mathbf{x}$.

3.2. The Genetic Algorithm

GA is a stochastic search algorithm based on the mechanism of natural selection and natural genetics. By the aid of the above effective objective value evaluation model, we can select N excellent solutions from Ω using GA. Assuming an initial random population produced and evaluated, genetic evolution takes place by means of three basic genetic operators: (a) parent selection; (b) crossover; (c) mutation [7]. The chromosome in GA terminology represents a solution $\mathbf{x}$, and each chromosome is encoded by a string of 0s and 1s. Parent selection is a simple procedure whereby two chromosomes are selected from the parent chromosome based on their fitness values. Solutions with high fitness values have a high probability of contributing new offspring to the next generation. The selection rule we used in our approach is a simple roulette-wheel selection. Crossover is an extremely important operator for the GA. It is responsible for the structure recombination and the convergence speed of the GA and is usually applied with relatively high probability denoted as p_c. The chromosomes of the two parents selected are combined to form new chromosomes that inherit segments of information stored in parent chromosomes. The crossover scheme we employed is the single-point crossover. Mutation is the operator responsible for the injection of new information. With a small probability, random bits of the offspring chromosomes flip from 0 to 1 and vice versa and give new characteristics that do not exist in the parent chromosome. In our approach, the mutation operator is applied with a relatively small probability denoted as p_m to every bit of the chromosome.

We randomly selected I chromosomes from Ω to be the initial populations of the GA. The GA is iterated until the maximum iteration count $k_{\max}$ is reached. After reaching the stop criterion, we rank the final generation of these I chromosomes based on their fitness values and pick the top N chromosomes, which form the N excellent solutions.

3.3. The OCBA technique

First, a small number of simulation replications denoted by n_0 is applied to calculate the means and variances of the sample mean of objective value for the N excellent solutions. Let T denote the allowable computing budget for selecting the best solution and n_i denote the number of simulation replications allocated to the i th solution from T. We increase the computing budget by Δ for each iteration, and the criteria of the OCBA technique is to optimally allocate T to n_1, n_2, …, n_N with $n_1 + n_2 + \cdots + n_N = T$, such that the probability of selecting the best solution is maximized. The value of the allowable computing budget is determined by $T = (N \times L_e)/s$, where s is a speed-up factor for corresponding N using the OCBA technique. The OCBA technique can be stated in the following [8].

Step 0. Perform a small number of simulation replications n_0 for all N excellent solutions. Set $l = 0$, $n_1^l = n_0, \ldots, n_N^l = n_0$, and set the value of Δ and T.

Step 1. If $\sum_{i=1}^{N} n_i^l \geq T$, stop and output the best solution $\mathbf{x}^*$ with the maximum number of simulation replications; else, go to Step 2.

Step 2. Increase Δ additional number of simulation replications to $\sum_{i=1}^{N} n_i^l$, and compute the new allocation of simulation replications by $n_j^{l+1} = (\sum_{i=1}^{N} n_i^l + \Delta)/(1 + \alpha_b^l + \sum_{i=1, i \neq j \neq b}^{N} \alpha_i^l)$, $n_b^{l+1} = \alpha_b^l n_j^{l+1}$, and $n_i^{l+1} = \alpha_i^l n_j^{l+1}$ for all $i \neq j \neq b$, where $\alpha_i^l = \left(\frac{\delta_i^l \times (\bar{f}_b^l - \bar{f}_j^l)}{\delta_j^l \times (\bar{f}_b^l - \bar{f}_i^l)} \right)^2$, $\alpha_b^l = \delta_b^l \sqrt{\sum_{i=1, i \neq b}^{N} (\frac{\alpha_i^l}{\delta_i^l})^2}$, $\bar{f}_i^l = \frac{1}{n_i^l} \sum_{k=1}^{n_i^l} f_k(\mathbf{x}_i)$, $\delta_i^l = \sqrt{\frac{1}{n_i^l} \sum_{k=1}^{n_i^l} \left(f_k(\mathbf{x}_i) - \bar{f}_i^l \right)^2}$, $\mathbf{x}_i$ represents the i th excellent solution, $f_k(\mathbf{x}_i)$ denotes the objective value of $\mathbf{x}_i$ at the k th simulation replication, and $b = \arg \max_i \bar{f}_i^l$.

Step 3. Perform additional $\max(0, n_i^{l+1} - n_i^l)$ simulation replications for the i th excellent solution, $i = 1, \ldots, N$. Set $l = l + 1$ and go to Step 1.

3.4 The OOEA

Now, the proposed OOEA can be stated as follows.

Step 1: Randomly select M $\mathbf{x}$'s from Ω. Compute the corresponding $\bar{f}_e(\mathbf{x})$ for each $\mathbf{x}$. Train an RBF network and calculate its $\boldsymbol{\omega}$ using the obtained M input-output pairs, ($\mathbf{x}$, $\bar{f}_e(\mathbf{x})$)'s. Let $F(\mathbf{x}, \boldsymbol{\omega})$ denote the functional output of the trained RBF network.

Step 2: Randomly select I $\mathbf{x}$'s from Ω as the initial population. Apply the GA to these individuals assisted by RBF network, $F(\mathbf{x}, \boldsymbol{\omega})$. After the GA converges, we rank all the final I $\mathbf{x}$'s based on their approximate fatnesses and select the top N $\mathbf{x}$'s to be the excellent solutions.

Step 3: Use the OCBA technique to select the best $\mathbf{x}$ from the N excellent solutions, and this $\mathbf{x}$ is the good enough solution that we seek.

4 TEST RESULTS

To gain more attention from broad readers, we set up a similar example provided in [10] as the application example. The ATO system has six types of product orders (n=6) and ten items including eight key items (h=8) and two non-key items (m=2). Different types of product orders come into the system as Poisson arrival processes with different rates, $\lambda_i, i = 1, \ldots, 6$, and each of them requires a set of key items and a set of non-key items. Each item sold brings a profit, p_j, and each item in inventory has a holding cost per period, h_j, $j = 1, \ldots, 10$. There are inventory capacities for each item, C_j,

$j = 1,\ldots,10$, such that $0 \le x_j \le C_j$, and the production time for each item is normally distributed with mean μ_j and variance σ_j^2, $j = 1,\ldots,10$, truncated at 0. All parameters used are included in Tables 1 and 2. The measurement of time is assumed to start T_w=20 up until $T_{\max}$=70.

Table 1. Parameters related to ten items

Item	1	2	3	4	5	6	7	8	9	10
p_j	1	2	3	4	5	6	7	8	9	10
h_j	2	2	2	2	2	2	2	2	2	2
μ_j	0.15	0.40	0.25	0.15	0.25	0.08	0.13	0.40	0.08	0.13
σ_j	0.0225	0.06	0.0375	0.0225	0.0375	0.012	0.0195	0.06	0.012	0.0195
C_j	20	20	20	20	20	20	20	20	20	20

Table 2. Parameters related to six products

Product	λ_i	Key items								Non-key items	
		$a_{i,1}$	$a_{i,2}$	$a_{i,3}$	$a_{i,4}$	$a_{i,5}$	$a_{i,6}$	$a_{i,7}$	$a_{i,8}$	$a_{i,9}$	$a_{i,10}$
1	4.2	1	0	0	1	0	1	1	0	0	1
2	3.6	1	0	0	0	1	1	1	0	0	1
3	3	0	1	0	1	0	1	0	1	1	1
4	2.4	0	0	1	1	0	1	0	1	1	0
5	1.8	0	0	1	0	1	1	1	0	0	1
6	1.2	0	1	1	1	0	1	0	1	0	0

To construct the surrogate model, we use an RBF network consisting of 10 neurons in input layer, 20 neurons in hidden layer, and 1 neuron in output layer. The 10 neurons in the input layer are for $\mathbf{x}$, and the single output neuron is for $E[f(\mathbf{x})]$. The spread of Gaussian function is set to $\sigma = 1$. The system's condition is the six arrival rates of product orders, $\lambda_i, i = 1,\ldots,6$, which are given in Table 2. For a given system condition, we train the RBF network by randomly selecting M=9604 $\mathbf{x}$'s from the discrete solution space Ω first, then evaluate the corresponding $\bar{f}_e(\mathbf{x})$. We use the above 9604 pairs of $(\mathbf{x}, \bar{f}_e(\mathbf{x}))$'s as the input and output pairs to train the BRF network by calculating its weight coefficients. Once the RBF network is trained, the approximate objective value of $E[f(\mathbf{x})]$ for a given $\mathbf{x}$ can be obtained from the output of RBF network.

We have simulated the OOEA for two cases of N with N=100 and 50. The following parameters are used in GA: I=1000, $p_c = 0.8$, $p_m = 0.03$, and $k_{\max} = 30$. The following parameters are used in OCBA: n_0=20, Δ=20, and $L_e = 10^4$. Since s=25 and 20 corresponding to N=100 and 50, respectively, the parameters T used in OCBA are different in the two cases: T= 40000 and 25000 for N=100 and 50, respectively. The good enough target inventory level $\mathbf{x}^*$, the corresponding $\bar{f}_e(\mathbf{x}^*)$, and the consumed CPU times for the two cases are presented in Table 3. Apparently, as N increases, the corresponding $\bar{f}_e(\mathbf{x}^*)$ increases, however the consumed CPU time also increases. Above all, the CPU times consumed in all cases are within two minutes, which are very fast.

Table 3. The good enough target inventory level $\mathbf{x}^*$, the corresponding $\bar{f}_e(\mathbf{x}^*)$, and the consumed CPU times for the two cases of N

N	s	T	Good enough target inventory level $\mathbf{x}^*$	$\bar{f}_e(\mathbf{x}^*)$	CPU times (minute)
100	25	40000	[3 4 4 13 7 4 4 2 5 8]	237.83	1.91
50	20	25000	[3 7 5 14 9 4 4 2 8 9]	236.06	1.66

5 CONCLUSION

In this work, we have proposed an OOEA to solve for a good enough target inventory level of an ATO system using reasonable computation time. By the aid of the RBF network, the objective value of an inventory level can be roughly evaluated without consuming much computation time. Via stochastic simulation optimization, the arrival processes and production times of ATO system can be from any distributions, and the dimension of the problem can be high.

ACKNOWLEDGMENT

This research work is supported in part by the National Science Council in Taiwan, R.O.C., under grant NSC 100-2221-E-324-006.

REFERENCES

[1] Xiao Y, Chen J, Lee CY (2010), Optimal decisions for assemble-to-order systems with uncertain assembly capacity. Int J Prod Econ 123(1):155-165

[2] Ho YC, Zhao QC, Jia QS (2007), Ordinal Optimization: Soft Optimization for Hard Problems. Springer-Verlag, New York

[3] Horng SC, Lin SS (2009), An ordinal optimization theory based algorithm for a class of simulation optimization problems and application. Expert Syst Appl 36(5):9340-9349

[4] Horng SC, Lin SS (2011), Optimal cyclic service of the centralized broadband wireless networks with k-limited discipline. Simul Model Pract Th 19(1):382-392

[5] Horng SC (2011), Ordinal optimization based approach to the optimal resource allocation of grid computing system. Math Comput Model 54(1-2):519-530

[6] Kumar R, Ganguli R, Omkar SN (2010), Rotorcraft parameter estimation using radial basis function neural network. Appl Math Comput 216(2):584-597

[7] Goldberg DE, Sastry K (2010), Genetic Algorithms: The Design of Innovation. 2nd ed., Springer-Verlag, New York

[8] Chen CH, Lee LH (2010), Stochastic Simulation Optimization: An Optimal Computing Budget Allocation. World Scientific, New Jersey

[9] ElHafsi M (2009), Optimal integrated production and inventory control of an assemble-to-order system with multiple non-unitary demand classes. Eur J Oper Res 194(1):127-142

[10] Hong LJ, Nelson BL (2006), Discrete optimization via simulation using COMPASS. Oper Res 54(1):115-129

The Seventeenth International Symposium on Artificial Life and Robotics 2012 (AROB 17th '12),
B-Con Plaza, Beppu, Oita, Japan, January 19-21, 2012

DNA Sequencing by Max-Min Ant System and Genetic Algorithm

Tao Liu[1] and Michiharu Maeda[2]

Fukuoka Institute of Technology, Fukuoka 811-0295, Japan

[1]mfm10022@bene.fit.ac.jp
[2]maeda@ fit.ac.jp

Abstract: This paper is concerned with DNA sequencing by hybridization. An algorithm that Max-Min Ant System and Genetic Algorithm (MMASGA) is proposed to solve the computational field of sequencing resulting from hybridization experiment. For avoiding the local minimum, MMASGA is based on Max-Min Ant System (MMAS), into which Genetic Algorithm (GA) is added. Before getting into the maximum iteration of MMAS, GA takes place in MMAS. In the numerical evaluation, with the iteration mounting up, the summation of the DNA probe appearance frequency turns more. The accuracy of the solution gotten by MMASGA is higher than MMAS.

Keywords: DNA sequencing, sequencing by hybridization, Max-Min Ant System and Genetic Algorithm.

1 INTRODUCTION

Bioinformatics is the application of computer science and information technology to the field of biology and medicine. DNA sequencing is one of the research objects of the bioinformatics. One of the sequencing methods is sequencing by hybridization (SBH). It is concerned with the computational part of the SBH in this paper. In the case of ideal hybridization experiment, an original DNA sequence can be reconstructed. SBH whose errors are under consideration is regarded as integer program problem and has been formulated. The application of Branch-and-Bound Algorithm for seeking the optimized solution has succeeded, but if there are many errors or the DNA sequence is long, it will take an immense amount of time and the optimized solution cannot be gotten [1].

For seeking the optimized solution Ant Colony Optimization (ACO) has been proposed. ACO is a probabilistic technique for solving computational problems which can be reduced to finding good paths through graphs. Being based on ACO, Max-Min Ant System (MMAS) is proposed and has been applied to the combinatorial optimization problem such as traveling salesman problem (TSP), quadratic assignment problem (QAP), vehicle routing problem (VRP), and internet packet switching.

This paper is concerned with DNA sequencing and Max-Min Ant System and Genetic Algorithm is proposed to solve the computational field of sequencing by hybridization. For avoiding the local solution, the proposed MMASGA is based on MMAS and GA is added into MMAS. Furthermore, by the performance evaluation test, the accuracy of the proposed method is better than the traditional method.

2 Sequencing by Hybridization

2.1 About DNA Sequencing

DNA is a nucleic acid that contains the genetic instructions used in the development and functioning of all known living organisms. The four bases founded in DNA are adenine (A), cytosine (C), guanine (G) and thymine (T). Sequencing by Hybridization is a class of methods for determining the order in which nucleotides occur on a strand of DNA, typically used for looking for small changes relative to a known DNA sequence. The binding of one strand of DNA to its complementary strand in the DNA double-helix is sensitive to even single-base mismatches when the hybrid region is short or if specialized mismatch detection proteins are present. This is exploited in a variety of ways, most notable via DNA chips or microarrays with thousands to billions of synthetic oligonucleotides found in a genome of interest plus many known variations or even all possible single-base variations [3].

In molecular biology, a hybridization probe is a fragment of DNA or RNA of variable length, which is used in DNA or RNA samples to detect the presence of nucleotide sequences (the DNA target) that are complementary to the sequence in the probe. The probe thereby hybridizes to single-stranded nucleic acid whose base sequence allows probe-target base pairing due to complementarity between the probe and target. The labeled probe is first denatured into single stranded DNA (ssDNA) and then hybridized to the target ssDNA immobilized on a membrane [3].

If the gained DNA sequence is ACTCTGG in the hybridization experiment and the probes whose length l is 3 are used, the set of all the probes is {AAA, AAC, AAG… TTT} and the amount of elements is 4^3=64. According to

DNA hybridization, {ACT, CTC, TCT, CTG, TGG} are necessary, as shown in the **Fig.1** [4].

```
ACT
  CTC
   TCT
    CTG
      TGG
---------------
 ACTCTGG
```

Fig. 1. Example of sequencing.

2.2 Formulation

If all the probes aren't recognized, the alphabets below *l*– 1 must overlap in the adjacent probes. And if the wrong probe is not found, several probes must be taken out in the SBH. To deal with all the errors, Blazewics etc. formulated the maximum cardinality found in the SBH below as integer linear programming problem. It is also known as the NP-hard combinatorial optimization problem.

Maximize

$$\sum_{i=1}^{m}\sum_{j=1}^{m} x_{ij} + 1 \qquad (1)$$

Subject to

$$\sum_{i=1}^{m} x_{ik} \le 1, k = 1, \dots, m \qquad (2)$$

$$\sum_{i=1}^{m} x_{ki} \le 1, k = 1, \dots, m \qquad (3)$$

$$\sum_{k=1}^{m}\left(\left|\sum_{i=1}^{m} x_{ki} - \sum_{j=1}^{m} x_{jk}\right|\right) = 2 \qquad (4)$$

$$\sum_{s_k \in s'}\left(\sum_{s_i \in s'} x_{ik} \cdot \sum_{s_j \in s'} x_{ki}\right) < |s'| \qquad (5)$$

$$\forall S' \subset S, S' \neq 0$$

$$\sum_{i=1}^{m}\sum_{j=1}^{m} c_{ij}\, x_{ij} \le n - l \qquad (6)$$

Where m is a cardinality of spectrum, S is a set of probes of cardinality of m, $x_{ij,}$ is a Boolean variable (it is equal 1 if an probe joining vertices i and j is included in the solution; otherwise it is equal to 0), c_{ij} is a cost of a probe joining vertex i with vertex j, and n-*l* is a maximum allowed cost.

Equation (1), to be maximized is equivalent to the number of probes selected. Equation (2) and Equation (3) ensure that each probe included in the solution has at most one immediate successor and one immediate predecessor in the solution path, respectively. Equation (4), the path cannot be the circuit construction. Equation (5), the same probe cannot be used more than twice. Equation (6), a cost connected with the solution is not greater than a given value (equal to n-*l*) [1].

The problem above is one of the kinds that the visited nodes are maximized at the limited distance. For the SBH, distance is the length of the DNA sequence and the nodes are the probes. If the visited nodes get most, the path will be ACT→CTC→TCT→CTG→TGG [4].

3 Ant Colony Optimization and Genetic Algorithm

3.1 Ant Colony Optimization Algorithm

Ant Colony Optimization (ACO) is a population based approach which has been successfully applied to several fields. As the name suggests, ACO has been inspired by the behavior of real ant colonies, in particular, by their foraging behavior. One of its main ideas is the indirect communication among the individuals of a colony of agents, called artificial ants, based on an analogy with trails of a chemical substance, called pheromone, which real ants use for communication. The artificial pheromone trails are a kind of distributed numeric information which is modified by the ants to reflect their experience accumulated while solving a particular problem.

The original idea comes from observing the exploitation of food resources among ants, in which ants' individually limited cognitive abilities have collectively been able to find the shortest path between a food source and the nest. The first ant finds the food source, via any way, then returns to the nest, leaving behind a trail pheromone Ants indiscriminately follow several possible ways, but the strengthening of the runway makes it more attractive as the shortest route. Ants take the shortest route; long portions of other ways lose their trail pheromones. In a series of experiments on a colony of ants with a choice between two unequal length paths leading to a source of food, biologists have observed that ants tended to use the shortest route [5].

The algorithm involves the movement of a colony of ants through the different states of the problem. Thereby, each such ant incrementally constructs a solution to the problem. When an ant completes a solution, or during the construction phase, the ant evaluates the solution and modifies the trail value on the components used in its solution. This pheromone information will direct the search of the future ants.

3.2 Max-Min Ant System

Max-Min Ant System (MMAS) is one kind of the common extensions of ACO. MMAS is that when the pheromones of are updated, the pheromone trails are limited. The added maximum and minimum amounts are $[\tau_{max}, \tau_{min}]$. MMAS thought is the most accurate extension of ACO. MMAS differs in three key aspects from ACO [2].

I. To exploit the best solutions found during an iteration or during the run of the algorithm, after each iteration only one single ant adds pheromone. This ant may be the one which found the best solution in the current iteration (*iteration-best* ant) or the one which found the best solution from the beginning of the trial (*global-best* ant).

II. To avoid stagnation of the search the range of possible pheromone trails on each solution component is limited to an interval [τ_{max},τ_{min}].

III. Additionally, we deliberately initialize the pheromone trails to τ_{max}, achieving in this way a higher exploration of solutions at the start of the algorithm.

The scheme of MMAS algorithm is shown in the **Fig.2.**

procedure MMAS algorithm:
  Set parameters, initialize pheromone trails,
    upper and lower limit of pheromone trails
  while (termination condition not met) **do**
    Construct Solutions
    Apply Local Search
    Update Trails
    Limit Trails
  end
end

Fig.2. The scheme of MMAS algorithm.

3.3 Genetic Algorithm (GA)

A genetic algorithm (GA) is a search heuristic that mimics the process of natural evolution. This heuristic is routinely used to generate useful solutions to optimization and search problems. GAs belong to the larger class of evolutionary algorithms (EA), which generate solutions to optimization problems using techniques inspired by natural evolution, such as inheritance, mutation, selection, and crossover.

GAs are adaptive heuristic search algorithm premised on the evolutionary ideas of natural selection and genetic. The basic concept of GAs is designed to simulate processes in natural system necessary for evolution, specifically those that follow the principles first laid down by Charles Darwin of survival of the fittest. As such they represent an intelligent exploitation of a random search within a defined search space to solve a problem [6].

First pioneered by John Holland in the 60s, Genetic Algorithms has been widely studied, experimented and applied in many fields in engineering worlds. Not only does GA provide an alternative method to solving problem, it consistently outperforms other traditional methods in most of the problems link. Many of the real world problems involved finding optimal parameters, which might prove difficult for traditional methods but ideal for GAs. However, because of its outstanding performance in optimization, GAs have been wrongly regarded as a function optimizer. In fact, there are many ways to view genetic algorithms. Perhaps most users come to GAs looking for a problem solver, but this is a restrictive view

4 Improvement of Max-Min Ant System

It is possible for MMAS to lapse into the local best solution. To raise the precision of MMAS, the problem addressed in this paper is concerned with DNA sequencing and Max-Min Ant System and Genetic Algorithm (MMASGA) is proposed to solve the computational field of sequencing by hybridization. The proposed MMASGA is based on MMAS and GA is added into MMAS. Firstly initial solutions are gotten by MMAS. Then initial solutions of MMAS are treated as the initial solutions of GA in order not to lapse into the local solution. And the method of pheromone secretion is also improved. Only the pheromone of the path of the good solution is raised. After that, inheritance, mutation, selection, and crossover take place and repeat until the termination conditions are fulfilled. Before getting into the maximum search iteration of MMAS, GA takes place in MMAS. The algorithm of MMASGA is shown below. (**Fig.3.**)

procedure MMASGA algorithm:
  Set parameters, initialize pheromone trails,
    upper and lower limit of pheromone trails
  while (termination condition not met) **do**
    Construct Solutions
    Apply Local Search
    while (generation not maximum) **do**
      Inheritance
      Selection
      Crossover
      Mutation
    end
    Update Trails
    Limit Trails
  end
end

Fig.3. The scheme of MMASGA algorithm.

The flow of MMASGA is described below:

I. Initialize the parameters: the maximum iteration T_{max}, the iteration t←0, the initial scatter list, and the initial pheromone trails.

II. The paths are formed randomly and the searched paths are putted into the scatter list. At the same time, a record of the scatter list is made. The initial solutions are made to be the initial generation population of individuals of GA.

III. Until the maximum generation, inheritance, selection, crossover and mutation take place among the individuals.

IV. The probes are calculated and the maximum value is saved.

V. The pheromone trails that construct the solutions are limited and updated. A new record of the scatter list is made.

VI. Set t←t+1. If t = T_{max}, the program terminates, otherwise the program goes to the step Ⅱ.

5 Experimental Results

The parameters of MMASGA are shown in the following description. The set of probes is {CTC, TCT, ACT, TGG, CTG}, the amount of agents is 50, the maximum iteration is 50, the mutation rate is 0.7, and the crossover rate is 0.6.

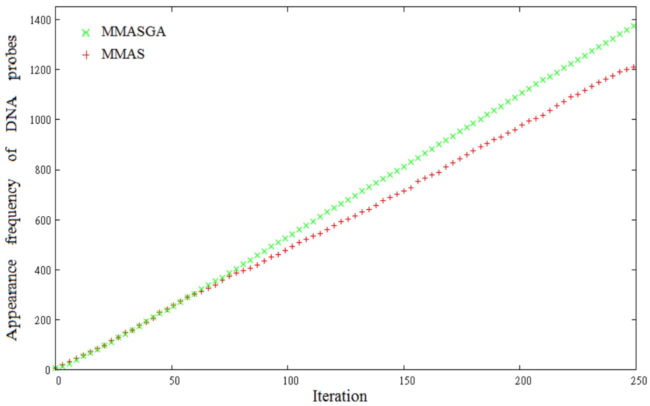

Fig.4. the comparison of performance to MMAS and MMASGA

Table 1. Experimental Results by MMAS and MMASGA

Iteration	MMAS	MMASGA
250	1184	1405
500	2401	3227
1000	4741	6181
10000	47829	79363

The evaluation result is shown above until the iteration counts 250 (**Fig.4.**). The line of × is the result of calculation by MMASGA. The line of + is the result of calculation by MMAS. With the iteration mounting up, the summation of the DNA probe appearance frequency turns more (**Table 1.**). Through the evaluation of the calculation, the accuracy of the solution gotten by proposed MMASGA is higher than MMAS. When the visited nodes get most, the path turns to be ACT→CTC→TCT→CTG→TGG.

6 Conclusion

In the paper, the Max-Min Ant System and Genetic Algorithm for solving a computational phase of the DNA sequencing by hybridization method has been proposed. The algorithm can handle the DNA sequencing with great accuracy. The presented algorithm has been extensively tasted on real, thus computationally hard, DNA sequences. Parameters n (the length of a reconstructed sequence) and l (the length of hybridizing oligonucleotides) chosen for test purposes, had the values used in real experiments. The tests have shown a good performance of the algorithm in presence. With the application of the global search of GA, the precision of MMAS is raised. Future examinations should allow for a further evaluation of the scope of applications of the sequencing approach with the algorithm proposed in this paper with great accuracy.

REFERENCES

[1] J. Blaewicz, P. Formanowicz, M. Kasprzak, W. T. Markiewicz, and J. Weglarz, "DNA sequencing with positive and negative errors," J. Computational Biology, vol.6, pp. 113-123, 1999

[2] T. Stutzle and H. H. Hoos, "MAX-MIN ant system," Future Generation Computer System, vol.16, no.8, pp. 889-914, 2000.

[3] J. Blazewicz, M. Kasprzak, "Complexity of DNA sequencing by hybridization", Theoretical Computer Science 290 (2003). pp. 1459-1473

[4] Makoto Koshino, Takahiro Otani, Daisuke Taka, and Masatoshi Shirayama, " Applying the Max-Min Ant System to the DNA Sequencing and Its Improvement", The Journal of the institute of Electronics, Information and Communication Engineers, vol. J89-D, no. 5, pp. 911-918, 2006.

[5] M. Dorigo and T. Stutzle, Ant Colony Optimization, MIT Press, 2004.

[6] Schmitt, Lothar M, Theory of Genetic Algorithms, Theoretical Computer Science 259, pp. 1–61, 2001.

The Seventeenth International Symposium on Artificial Life and Robotics 2012 (AROB 17th '12),
B-Con Plaza, Beppu, Oita, Japan, January 19-21, 2012

Advanced artificial bee colony algorithm detecting plural acceptable solutions

Masaaki Nishimoto[1], Akihide Utani[1], and Hisao Yamamoto[1]

[1]Tokyo City University, Tokyo 158-8557, Japan
(Tel: 81-3-5707-0104)

[1]autani@tcu.ac.jp

Abstract: In many engineering applications (engineering design problems), since the environment and/or situation of applications may change, it is important to detect plural acceptable solutions (plural acceptable means). As a technique of detecting not a single global optimum solution but plural acceptable solutions, this paper proposes a new optimization algorithm based on advanced Artificial Bee Colony (ABC) algorithm that has the good performance on large scale optimization problems. We evaluate the proposed algorithm through numerical experiments on well-known benchmark functions, such as Rastrigin function and Schwefel function, and discuss its development potential. In numerical experiments, the performances of the proposed algorithm are compared with those of the existing optimization one based on Particle Swarm Optimization (PSO) algorithm for detecting plural acceptable solutions.

Keywords: plural acceptable solutions, swarm intelligence algorithms, artificial bee colony algorithm.

1 INTRODUCTION

The minimization of multimodal functions with many local and global minima is a problem that frequently arises in diverse scientific fields and numerous engineering design problems. This problem is NP-hard in the sense of its computational complexity even in simple cases. As techniques of computing a global minimum of the objective function, many meta-heuristics, which are search algorithms for optimization based on heuristic knowledge, have been proposed. Some well-known representative meta-heuristics are simulated annealing and tabu search which are the traditional optimization algorithms, genetic algorithms and immune algorithms which are classified as evolutionary computation techniques, and ant colony optimization algorithms and particle swarm optimization algorithms [1] which belong to the category of swarm intelligence algorithms.

In meta-heuristics, genetic algorithms and immune algorithms, classified as evolutionary computation techniques, are generally techniques for combination optimization problems. In genetic algorithms and immune algorithms, the variables of continuous type are frequently translated into those of discrete (genetic) type. If there is a dependency between variables, therefore, a promising solution may be destroyed during the solution search process (genetic operation) and the solution search performance may deteriorate. To the contrary, particle swarm optimization algorithm [1] can directly handle the variables of continuous type. Even when there is a dependency between variables, therefore, an efficient and effective solution search can be realized. Recently, particle swarm optimization algorithm is intensively researched because it is superior to the other algorithms on many difficult optimization problems. The ideas that underlie particle swarm optimization algorithm are inspired not by the evolutionary mechanisms encountered in natural selection, but rather by the social behavior of flocking organisms, such as swarms of birds and fish schools. Particle swarm optimization algorithm is a population-based algorithm that exploits a population of individuals to probe promising regions of the search space. The algorithm is simple and allows unconditional application to various optimization problems. However, it has been confirmed that the performance of particle swarm optimization algorithm on large scale optimization problems is not always satisfactory. Therefore, we have proposed a new optimization algorithm based on Artificial Bee Colony (ABC) algorithm [2] that has the good performance on large scale optimization problems [3]. However, in many engineering applications (engineering design problems), since the environment and/or situation of applications may change, it is important to detect plural acceptable solutions (plural acceptable means).

As a technique of detecting not a single global optimum solution but plural acceptable solutions, this paper proposes a new optimization algorithm based on advanced ABC algorithm [3]. We evaluate the proposed algorithm through numerical experiments on well-known benchmark functions, such as Rastrigin function and Schwefel function, and discuss its development potential. In numerical experiments performed, the performances of the proposed algorithm are compared with those of the existing optimization one. The rest of this paper is organized as follows. In Section 2, the proposed algorithm based on advanced ABC algorithm is outlined. In Section 3, the results of numerical experiments are reported. Finally, the paper closes with conclusions in Section 4.

2 PROPOSED ALGORITHM

In the original ABC algorithm, the colony of artificial bees contains three groups of bees: employed bees, onlookers, and scouts. Half of the bees that construct artificial bee colony consist of the employed bees and the rest constitute the onlookers. At the initial state of ABC algorithm, multiple solution search points are randomly set in multidimensional solution search space. For every solution search point, there is only one employed bee, i.e., the number of employed bees is equal to the number of solution search points.

Each employed bee updates its own allocated solution search point in the solution search process. Each onlooker selects one solution search point from the probability based on the fitness value of each solution search point and updates the solution search point chosen. The employed bee of the solution search point that is not undated during the set search iterations becomes a scout and starts to search a new solution search point randomly.

The original ABC algorithm is summarized as follows:

Step 1 (Initialization)

Generate and evaluate the population of solution search points ($\boldsymbol{x}_i$, i=1, ... , SN), where i indicates the solution search point's index. SN is the number of solution search points.

Step 2 (Update of search points by employed bees)

1. Produce and evaluate the new solution search point ($\boldsymbol{v}_i$) on each solution search point ($\boldsymbol{x}_i$) according to the following formula

$$v_{ij} = x_{ij} + \phi_{ij}(x_{ij} - x_{mj}), \quad i = 1,\ldots,SN \tag{1}$$

where $m\in\{1, 2, \ldots, SN\}$ represents randomly chosen solution search point's index and $j\in\{1, 2, \ldots, D\}$ represents randomly chosen variable's index. D is the number of optimization variables. Although m is determined randomly, it has to be different from i. ϕ_{ij} is a random number, uniformly distributed within the interval [-1,1].

2. Apply the greedy selection process between $\boldsymbol{x}_i$ and $\boldsymbol{v}_i$.

Step 3 (Update of search points chosen by onlookers)

1. Compute the probability (P_i) of each solution search point ($\boldsymbol{x}_i$) according to the following formulas

$$fit_i = \begin{cases} \dfrac{1}{1+f(\boldsymbol{x}_i)}, & f(\boldsymbol{x}_i) \geq 0 \\ 1+abs(f(\boldsymbol{x}_i)), & f(\boldsymbol{x}_i) < 0 \end{cases} \quad (i = 1,\ldots,SN) \tag{2}$$

$$P_i = fit_i \Big/ \sum_{n=1}^{SN} fit_n \tag{3}$$

where $f(\boldsymbol{x})$ is the objective function. Each onlooker selects one solution search point ($\boldsymbol{x}_i$) depending on the probability (P_i).

2. Produce and evaluate the new solution search point ($\boldsymbol{v}_i$) on the solution search point ($\boldsymbol{x}_i$) chosen by each onlooker, as in Step2.
3. Apply the greedy selection process between $\boldsymbol{x}_i$ and $\boldsymbol{v}_i$.

Step 4 (Update of solution search points by scouts)

If the solution search point that is not undated during the set search iterations exists, replace it with randomly produced solution search point within solution search space.

Step 5 (Update of best solution)

Memorize the best solution search point.

Step 6 (Judgment of end)

Finish the search when the end condition is satisfied. Otherwise, return to Step 2.

The algorithm of [3] is an advanced ABC algorithm. To detect a global optimum solution effectively, ABC algorithm is improved as follows:

1. Improvement of Eq.(2) to compute fitness value (fit_i)
   To improve the adaptability to various engineering design problems, in the proposed algorithm, the fitness value (fit_i) of each solution search point is computed as follows:

$$fit_i = \begin{cases} \dfrac{1}{f(\boldsymbol{x}_i) - f_{bound}}, & f(\boldsymbol{x}_i) - f_{bound} \geq f_{accuracy} \\ \dfrac{1}{f_{accuracy}}, & f(\boldsymbol{x}_i) - f_{bound} < f_{accuracy} \end{cases} \quad (i = 1,\ldots,SN) \tag{4}$$

   where f_{bound} represents the boundary value of $f(\boldsymbol{x}^+)$ on $\boldsymbol{x}^+$ acceptable as a solution for every problem and $f_{accuracy}$ indicates the exactness of convergence to f_{bound}.
2. Improvement of search point selection by onlookers
   To improve the performance of global solution search, in the proposed algorithm, the solution search is divided into two stages. Each onlooker selects one solution search point out of the high-order α solution search points of fitness value (fit_i) randomly during the first stage of the search.
3. Improvement of reference point (m) in Eq.(1)

To improve the update frequency of each solution search point, the reference point (m) in Eq.(1) is randomly chosen out of the high-order α solution search points of the fitness value (fit_i) during the first stage of the search and is chosen by the roulette selection based on the probability (P_i) of each solution search point $(\boldsymbol{x}_i)$ during the second stage of the search.

In addition, Step 4 (Update of search points by scouts) in the original ABC algorithm is not executed in the algorithm of [3] because the performance of global solution search is improved by the above 2 (Improvement of search point selection by onlookers).

In the proposed algorithm, multiple colonies (swarms) search multiple (plural) acceptable solutions competitively, as in [4].

3 EXPERIMENTAL RESULTS

Through numerical experiments on the following D dimensional benchmark functions, the performances of the proposed algorithm are investigated in detail to verify its effectiveness on large scale optimization problems.

- Rastrigin function

$$\text{min.}\ f_1(\boldsymbol{x}) = \sum_{j=1}^{D} \left\{ x_j^2 - 10 cos(2\pi x_j) + 10 \right\}$$

$$\text{subj. to}\ -5.12 \le x_j \le 5.12, \quad j = 1,...,D$$

$$\boldsymbol{x}^* = (0,...,0), \quad f_1(\boldsymbol{x}^*) = 0$$

- Schwefel function

$$\text{min.}\ f_2(\boldsymbol{x}) = 418.98288727\,D + \sum_{j=1}^{D} - x_j sin(\sqrt{|\,x_j\,|})$$

$$\text{subj. to}\ -512 \le x_j \le 512, \quad j = 1,...,D$$

$$\boldsymbol{x}^* = (420.968750,...,420.968750), \quad f_2(\boldsymbol{x}^*) = 0$$

where $\boldsymbol{x}^*$ of each benchmark function represents a global optimum solution. In **Fig.1**, the landscapes of multimodal functions are illustrated. In the experimental results reported, the proposed algorithm is evaluated through a comparison with the existing optimization one, where the desired number of solutions (m) is set to 3.

First, the fundamental performance of the proposed algorithm is verified through the experimental result on Schwefel function $(D = 2)$. **Fig.2** shows the solution search points on Schwefel function $(D = 2)$. From **Fig.2**, it can be confirmed that three acceptable solutions which include one global optimum solution is accurately detected.

The experimental results obtained by applying the Particle Swarm Optimization algorithm for computing Plural Acceptable Solutions (PSO-PAS) of [4] and the proposed algorithm are arranged in **Tables 1** and **2**. From these experimental results, it can be confirmed that the proposed algorithm is substantially advantageous.

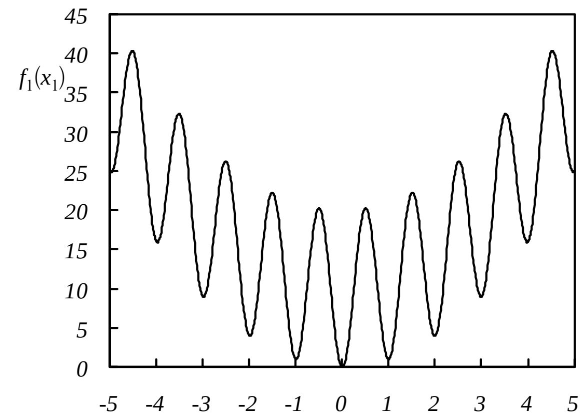

(1) *Rastrigin*

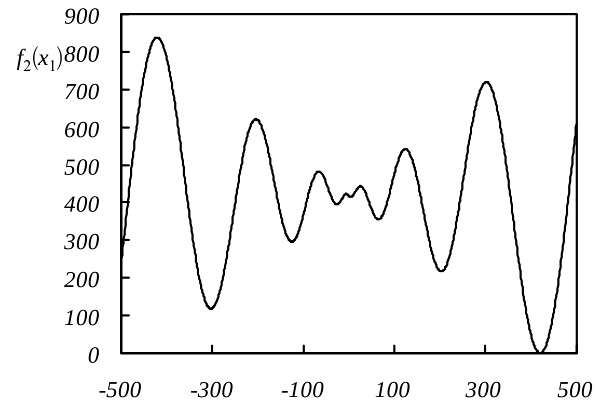

(2) *Schwefel*

Fig.1. Landscapes of multimodal functions $(D = 1)$.

4 CONCLUSION

In this paper, as a technique of detecting not a single global optimum solution but plural acceptable solutions, a new optimization algorithm based on advanced artificial bee colony algorithm [3] has been proposed. In numerical experiments performed on some well-known representative benchmark functions, such as Rastrigin function and Schwefel function, the performances of the proposed algorithm were compared with those of the existing optimization one for detecting plural acceptable solutions [4]. The experimental results indicate that the proposed algorithm is superior to the existing optimization one for detecting plural acceptable solutions [4] and has the development potential as an effective and promising one for many engineering applications (engineering design problems).

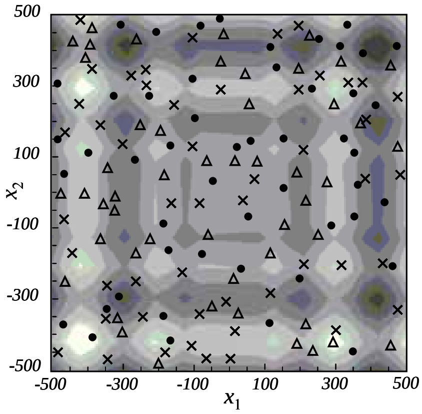

At the initial stage

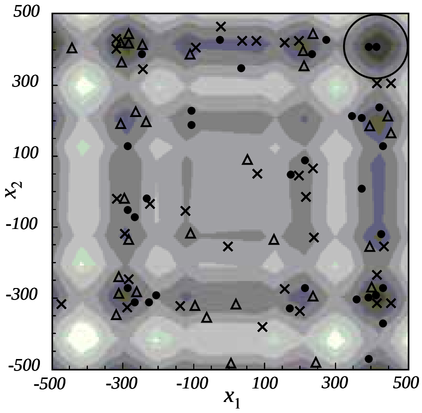

At the first solution detection stage

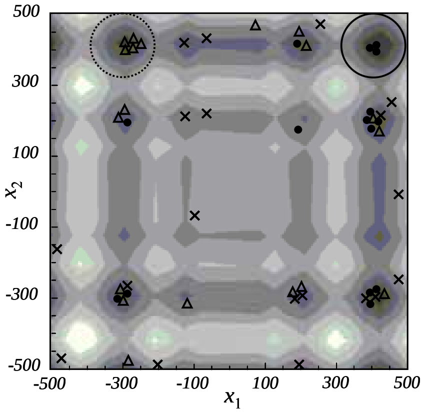

At the second solution detection stage

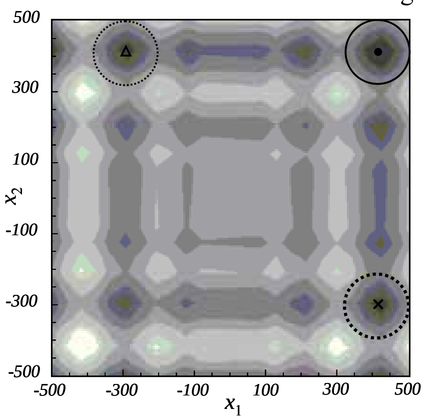

At the final stage

Fig.2. Search points on Schewfel functions ($D = 2$).

Table1. Experimental results (Rastrigin function).

Method	Dim.	Solution1	Solution2	Solution3
PSO-PAS	50	8.63×10^{1}	1.28×10^{2}	1.73×10^{2}
	75	1.88×10^{2}	2.66×10^{2}	3.21×10^{2}
	100	3.12×10^{2}	4.19×10^{2}	5.10×10^{2}
	125	4.30×10^{2}	6.10×10^{2}	7.22×10^{2}
	150	5.32×10^{2}	7.62×10^{2}	8.99×10^{2}
	175	7.04×10^{2}	9.39×10^{2}	1.14×10^{3}
	200	9.42×10^{2}	1.21×10^{3}	1.32×10^{3}
Proposal	50	0.00	9.95×10^{-1}	9.95×10^{-1}
	75	0.00	9.95×10^{-1}	9.95×10^{-1}
	100	0.00	9.95×10^{-1}	9.95×10^{-1}
	125	0.00	9.95×10^{-1}	9.95×10^{-1}
	150	0.00	9.95×10^{-1}	9.95×10^{-1}
	175	1.11×10^{-13}	9.95×10^{-1}	9.95×10^{-1}
	200	3.34×10^{-10}	9.95×10^{-1}	4.28×10^{0}

Table2. Experimental results (Schwefel function).

Method	Dim.	Solution1	Solution2	Solution3
PSO-PAS	50	8.87×10^{4}	9.55×10^{4}	1.02×10^{5}
	75	1.42×10^{5}	1.55×10^{5}	1.78×10^{5}
	100	2.07×10^{5}	2.18×10^{5}	2.33×10^{5}
	125	2.66×10^{5}	2.83×10^{5}	3.06×10^{5}
	150	3.40×10^{5}	3.64×10^{5}	3.94×10^{5}
	175	4.31×10^{5}	4.51×10^{5}	5.02×10^{5}
	200	5.07×10^{5}	——	——
Proposal	50	0.00	1.18×10^{2}	1.18×10^{2}
	75	0.00	1.18×10^{2}	1.18×10^{2}
	100	0.00	1.18×10^{2}	1.18×10^{2}
	125	5.18×10^{2}	7.98×10^{2}	1.05×10^{3}
	150	1.62×10^{3}	1.89×10^{3}	2.17×10^{3}
	175	2.98×10^{3}	3.33×10^{3}	3.61×10^{3}
	200	4.31×10^{3}	4.76×10^{3}	5.15×10^{3}

REFERENCES

[1] J. Kennedy and R.C. Eberhart, Particle swarm optimization, *Proc. of the IEEE International Conference on Neural Networks*, pp.1942-1948, 1995.

[2] D. Karaboga and B. Basturk, A powerful and efficient algorithm for numerical function optimization: artificial bee colony (ABC) algorithm, *J. Global Optimization*, Vol.39, pp.459-471, 2007.

[3] R. Gocho, A. Utani and H. Yamamoto, Improved artificial bee colony algorithm for large-scale optimization problems, *Proc. of the 16th International Symposium on Artificial Life and Robotics*, pp.605-608, 2011.

[4] A. Kumamoto, A. Utani and H. Yamamoto, Advanced particle swarm optimization for computing plural acceptable solutions, *Int. J. Innovative Computing, Information and Control*, Vol.5, No.11(B), pp.4383-44392, 2009.

The Seventeenth International Symposium on Artificial Life and Robotics 2012 (AROB 17th '12),
B-Con Plaza, Beppu, Oita, Japan, January 19-21, 2012

Multi-Objective Optimal Path Selection in the Electric Vehicles

Umair F. Siddiqi[1], Yoichi Shiraichi[1], and Sadiq M. Sait[2]

[1] Department of Production Science & Technology, Gunma University, Ota, Japan
[2] Department of Computer Engineering, King Fahd University of Petroleum & Minerals, Dhahran, Saudi Arabia
(Tel & Fax: +81-276-50-2532)
({umair, siraisi}@emb.cs.gunma-u.ac.jp, sadiq@kfupm.edu.sa)

Abstract: Car navigation systems of the modern vehicles are equipped with an optimal path selection (OPS) unit. The OPS unit is responsible for finding the shortest paths between any source and destination nodes in the road network. In Electric Vehicles (EVs), the purpose of the OPS unit is to find multi-objective shortest paths (MOSP) w.r.t.: (i) Recharging Time, (ii) Distance, and (iii) Travelling Time. This work presents a memory efficient Simulated Evolution (SimE) based algorithm for solving the MOSP problem in EVs. The proposed algorithm uses innovative representation of the solution, and problem-specific goodness and allocation operations. Two different techinques for selecting the recharging stations are also proposed. The performance of the proposed algorithm is compared with NSGA-II, which is a popular population based heuristic for solving the multi-objective optimization problem. The comparsion results show that the proposed algorithm achieves the performance equal to NSGA-II while it requires 2.22 times lesser memory than any population based heuristic.

Keywords: Multi-Objective Optimization, Electric Vehicles, Simulated Evolution

1 INTRODUCTION

Car navigation systems of the modern vehicles are equipped with an optimal path selection unit. The optimal path selection unit is responsible for finding the shortest paths between any source and destination nodes in a road network. The optimization objectives in the internal combustion engine (ICE) based vehicles are: minimizing the distance, travelling time, traffic, etc. The Electric Vehicles (EVs) are also gaining popularity [1]. The optimal path selection in EVs should include minimization of the recharging time. The recharging time of the EVs can generally vary from 10 minutes to 30 minutes and therefore, it is an important factor to be considered in optimal path selection.

The main obstacles in the popularity of the EVs are: (i) Limited battery life, the EVs can travel until the time duration which is equal to the time limit of their batteries without recharging. A general value for the time limit is 2 hours. However, the time limits of the EVs are very small as compared to the ICE based vehicles. (ii) Lack of the infrastructure for the recharging stations. The recharging stations should be placed at regular intervals to ensure that the EVs can travel without any recharging problem. (iii) The recharging time of the EVs is also important. The recharging of the EVs should be performed in minimum possible time like 10 minutes. Many researchers have investigated the feasibility and positioning of the recharging stations [1, 2, 3, 4]. The results of the previous research showed that portable or fixed recharging stations could be placed at suitable places along the road, which ensured that the majority of the EVs could travel without any problem [7]. The rapid recharging technology has enabled full recharging of the EV in 10 minutes. Besides rapid recharging, battery swapping technology is also available which has recharging time as low as 5 minutes. However, battery swapping is expensive to implement than recharging.

The problem of finding optimal path between a source and destination node in the road network is a multi-objective shortest path (MOSP) problem. In this work, the MOSP problem has the following objectives: (i) Minimizing the recharging time, (ii) Minimizing the travelling distance, and (iii) Minimizing the travelling time. The MOSP is an NP-hard discrete optimization problem [5, 6]. The objectives in any multi-objective optimization problem are often contradictory therefore, no one solution can be optimal in all objectives. Therefore, a set of Pareto optimal solutions is found for the multi-objective optimization problem. The Pareto optimal set contains the non-dominated solutions. Evolutionary computation (EC) algorithms have been predominately used to solve multi-objective optimization problems. In many EC algorithms the calculation in any iterations does not depends on the previous iteration. Therefore, they are robust to dynamic changes in the parameter values of the road network like changes in traffic, waiting delay at the recharging stations, etc. The performance of any EC is measured by the number of Pareto optimal solutions it returns and the diversity of the solutions. For practical applications other properties of the EC algorithms like computation time and memory requirements are also very important. The research work in this paper, focused on developing a memory and time efficient EC algorithm for solving the MOSP problems in Electric Vehicles. The objectives of the MOSP problem, can be in contradiction with each other based on the traffic situation or the queues at the recharging stations. For example, when the shortest paths becomes congested then the travelling time on them can exceed the other paths. The proposed algorithm can find MOSP despite the changing traffic conditions. Simulated Evolution (SimE) [9] is a popular EC algorithm which works on only one solution at a time and is therefore, memory efficient than the other population based algorithms like Genetic Algorithms (GA), etc.

This paper proposed a SimE based multi-objectives optimization algorithm for solving the MOSP problem in EVs. The proposed SimE based algorithm has innovative goodness and allocation operations which are tailored for solving the MOSP problem. The performance of the proposed algorithm is compared with a famous heuristic: Non-dominated Sorting Genetic Algorithm (NSGA) -II [8]. The NSGA-II is a population-based algorithm for solving the multi-objective optimization problems. The simulation results show that the proposed algorithm can provide results equal to or better than the NSGA-II while it requires lesser memory than NSGA-II.

This paper is organized as follows: Second section shows the formal description of the problem. Third section contains the detail of the proposed algorithm. Fourth section contains the simulation results and comparison of the proposed algorithm with the other algorithms. The last section contains the conclusion.

2 DESCRIPTION OF THE PROBLEM

2.1 System Overview

In the car navigation system, the driver selects the source and destination nodes of his/her journey. The navigation system finds one or more optimal paths between the source and destination nodes. The navigation systems of the modern vehicles comprise of an embedded system which has interface to the GPS (Global Positioning System). The selection of the optimal path can either be performed independently by each vehicle or the optimal path selection is performed at any centralized station for a group of vehicles.

This work assumes that the optimal path selection is performed independently by the vehicles. Therefore, optimal path selection is performed in the embedded system of the car navigation system and it uses the updated information related to the road network from the GPS. The GPS system can provide the information related to the location of recharging stations and their recharging times to the EVs. The block diagram of the Optimal Path Selection (OPS) unit of an EV is shown in Fig. 1. The figure shows that the OPS unit receives inputs from the GPS and source and destination nodes from the driver. The OPS searches the optimal path based on the provided information and yields one or more optimal paths

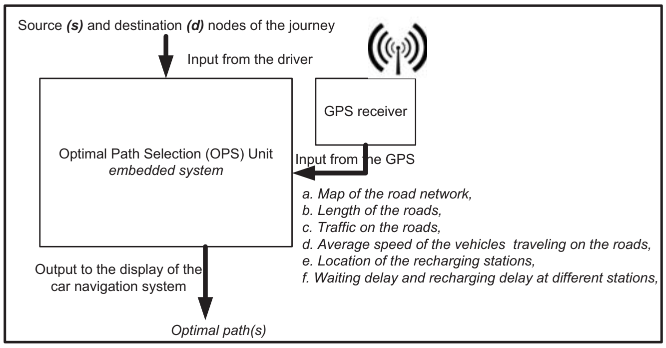

Fig. 1: Block diagram of the Optimal Path Selection (OPS) Unit of the EVs.

Table 1: Properties associated with edges, recharging stations and electric vehicles

Element	Symbol	Description
edge ($e_i \in E$)	$e_i.l$	Length of the edge
	$e_i.S$	Average speed of the EVs
recharging station	$r_j.R_{delay}$	Recharging time per EV
($r_j \in R$)	$r_j.W_{delay}$	Waiting delay per EV due to queuing in it
	$r_j.e$	$e \in E$, s.t. r_j lies along the edge e
	$r_j.p$	Distance of the r_j from the start of $r_j.e$
	$r_j.D$	Travelling time of r_j from the source node
electric vehicle	t_{LIMIT}	The maximum time which the EV can
(EV)		travel without recharging
	s	Source node of the journey
	d	Destination node of the journey
	B_s	The battery level at the source node

to the display unit of the car navigation system.

2.2 Description of the Road Network

Let us consider that in the OPS unit, the electric vehicle is represented as EV and the road network is represented by an undirected graph (G), which is represented as: $G = (V, E, R)$, where V is the set of all vertices or intersections in the road network, E contains the road segments which join the intersections and R contains the recharging stations which exist in the road network. When the road network contains a total of N nodes and M edges, then $V = \{n_0, n_1, ..., n_{N-1}\}$ and $E = \{e_0, e_1, ..e_{M-1}\}$. Any edge $e_i \in E$, $e_i = (n_x, n_y)$, where $n_x \neq n_y$ and $n_x, n_y \in V$. n_x and n_y are the starting and ending nodes of the edge e_i. When the road network contains a total of m recharging stations, then the set R is represented as: $R = \{r_0, r_1, ..., r_{m-1}\}$. The properties associated with the edges, recharging stations and the electric vehicle are shown in Table. 1.

2.3 Description of the Multi-objective Optimization Problem

Let us consider that the solution in the OPS unit is represented as: $P = \{P^A, P^B\}$. P^A stores the edges from E which form a path from the source to the destination node and is represented as: $P^A = \{e_i, e_j, .., e_k\}$, $e_i = (s, n_x)$ and

Input: nodes: u, & v, G=(V,E), N_e= Number of elements in E
Output: Q: A path from u to v nodes.

1: $W = random(M)$
2: Q= Apply Dijkstra's Algorithm (u, v)
3: **return** Q

Fig. 2: Method to find paths: $form\_path(u, v)$.

$e_k = (n_y, d)$, and $s, n_x, n_y, d \in V$. P^B stores the recharging stations from R on which EV should be recharged in order to complete its journey on the path P^A.
The optimization performed in the OPS unit aims to find the paths which are optimized w.r.t. three functions: (i) $f_1(P^B)$, which corresponds to the total recharging time. (ii) $f_2(P^A)$, which corresponds to the total distance and (iii) $f_3(P^A)$, which is the total travelling time. The values of the functions can be computed as follows:

$$f_1(P^B) = \sum_{r_j \in P^B} (r_j.R_{delay} + r_j.W_{delay}) \quad (1)$$

$$f_2(P^A) = \sum_{e_i \in P^A} e_i.l \quad (2)$$

$$f_3(P^A) = \sum_{e_i \in P^A} \frac{e_i.l}{e_i.S} \quad (3)$$

The objective function can be represented as: $Obj(P)$= $Minimize(f_1(P^B), f_2(P^A), f_3(P^A))$. The minimization is performed through the proposed SimE-based algorithm.

3 PROPOSED ALGORITHM

Simulated Evolution (SimE) [9] is a general search strategy for solving a variety of combinatorial optimization problems. The SimE optimization loop consists of the following steps: (i) Evaluation, in which goodness of each element in the population is evaluated. (ii) Selection, in which up-to $n_s\%$ elements in the current solution or P^A having lower goodness values are selected into the set S. (iii) Allocation, in this step the elements in the set S will undergo through the allocation process. The optimization iterations are continued until the stopping criteria which can be the maximum time is reached. This work proposes a design of SimE which has innovative goodness and allocation operations which are tailored for the proposed multi-objective optimization problem. The proposed algorithm stores all non-dominated solutions found during the optimization iterations, which forms its set of Pareto optimal solutions. However, storing only one non-dominated solution which has the maximum value of the hypervolume is sufficient for the proper execution of the proposed algorithm.

In the following the proposed goodness and allocation operations are described in detail. First a method of building a random path from nodes u to v is shown which will be used to build a random path between any two nodes. The algorithm is shown in Fig. 2 and is represented by the function $form\_path(u, v)$. In line 1, W stores M randomly generated integers between $[1, 1000]$. The elements in W are used to assign weights to the edges in E. The Dijkstra's Algorithm finds shortest path w.r.t. the weights assigned to edges in line 1.

3.1 Goodness Function

In SimE, the goodness is defined as the ratio of the estimated minimum cost to the actual cost of the elements. In this work, the solution is represented as $P = \{P^A, P^B\}$. In the Evaluation step, the goodness of all elements in the set P^A is determined. The P^A comprises of a set of edges, and the starting node of the first edge in it is the source node and the ending node of the last edge in it is the destination node. Before goodness calculation is performed, the weights (w_1, w_2, w_3) are assigned to all edges in E. The procedure to assign weights to any edge $e_i \in E$ is shown in Fig. 3.

The weight w_1 corresponds to the average of the recharging and waiting delays of all the recharging stations which exists along the edge e_i. The term in the denominator indicates the total number of recharging stations on any edge [7], which is used to calculate the average. The weight w_2 corresponds to the length of the edge and w_3 corresponds to the travelling time on the edge. The proposed procedure to find the goodness of any edge is shown in Fig. 4. In Fig. 4, the goodness of the edge $e_i \in P^A$ is calculated. The variable r_1 holds the number of edges in P^A which have w_1 value lesser than $e_i.w_1$. Similarly, the variables r_2 and r_3 holds the number of edges in P^A which have w_2 and w_3 values lesser than $e_i.w_2$ and $e_i.w_3$ respectively. At the end, the average of the r_1, r_2 and r_3 variables is calculated.

Input: Any edge $e_i \in P^A$, $P = \{P^A, P^B\}$
Output: $e_i.w_1$, $e_i.w_2$, $e_i.w_3$

$e_i.w_1 = \frac{\sum_{r_j \in R \& r_j.e=e_i} (r_j.R_{delay}+r_j.W_{delay})}{0.05 \times e_i.l}$
$e_i.w_2 = e_i.l$
$e_i.w_3 = \frac{e_i.l}{e_i.S}$
return $\{e_i.w_1, e_i.w_2, e_i.w_3\}$

Fig. 3: Procedure for the assignment of the weights to any edge $e_i \in P^A$.

3.2 Allocation

The selection operation populates the set S by selecting up-to $n_s \times s$ elements from P^A. $n_s \in [0, 1] \in R^+$. The selection operation selects the elements from P^A which are not already selected and have lowest goodness value with probability P_s and any randomly selected element with probability

Input: Any edge $e_i \in P^A$, $P = \{P^A, P^B\}$
Output: $g(e_i)$: goodness of the edge e_i

$r_1 = 0, r_2 = 0, r_3 = 0$
n =Number of elements in P^A
for $j = 0; j < n; j++$ **do**
  if $P^A[j].w_1 > e_i.w_1$ **then**
    r_1++
  end if
  if $P^A[j].w_2 > e_i.w_2$ **then**
    r_2++
  end if
  if $P^A[j].w_3 > e_i.w_3$ **then**
    r_3++
  end if-[]
end for
$g(e_i) = \frac{r_1+r_2+r_3}{3}$
return $g(e_i)$

Fig. 4: Goodness Function $g(e_i)$, $(e_i \in P^A)$.

$P_s - 1$. The allocation operation is applied after the selection operation and it uses the elements in S.

The proposed allocation operation is shown in Fig. 5 using the pseudo code. The variable P_{min} is initialized to P^A. As shown, the allocation operation consists of doubly nested for loops. The outer-most loop executes for N_s number of times and the inner loop executes for each element in S. In the inner loop, an element from S is selected in each iteration. A random sub-path which exists from the starting node of the selected edge to the destination node is created. Then the sub-path is concatenated with the portion of the original solution (i.e., P^A) from the first edge to the edge which lies just before the edge selected from S. The resultant of the sum of the weights (or the square root of the sum of the squares of the three weights) of the new path is calculated and if the value is lesser than the P_{min} then P_{min} is updated to the new solution. At the end of the doubly nested for loops, the path which has minimum value of the resultant of the sum of the weights is returned and P^A is updated.

3.3 Mutation

The mutation operation is applied with probability M_b, In the mutation operation, the complete path which is stored in P^A is replaced by another path from source to destination. The new path is formed using the $form\_path$ function.

3.4 Selection of the Recharging Stations

The travelling limit (t_{LIMIT}) of the EV is the maximum time until which the EV can travel without recharging. Therefore, the EV requires periodic recharging during its journey. The set P^B in P stores the recharging stations on which the EV should be recharged. This subsection

Input: $S = \{x, y, ..., z\}$, $P = \{P^A, P^B\}$, $N_s \in Z^+$
Output: P^A (which is the path after the allocation operation)

s = Number of elements in S, $P_{min} = P^A$
n = Number of elements in P^A
for $i = 0; i < N_s; i++$ **do**
  for $j = 0; j < s; j++$ **do**
    $snode = P^A[S[j]].startnode$, $enode = P^A[n-1].endnode$
    $t1 = FormPath(snode, enode)$
    $t = concatenate\{P^A[0...S[j]-1], t_1\}$
    $v_1 = \sum_{e_i \in t} e_i.w_1$, $v_2 = \sum_{e_i \in t} e_i.w_2$, $v_3 = \sum_{e_i \in t} e_i.w_3$
    $R_1 = \sqrt{v_1^2 + v_2^2 + v_3^2}$
    $v_4 = \sum_{e_i \in P_{min}} e_i.w_1$, $v_5 = \sum_{e_i \in P_{min}} e_i.w_2$, $v_6 = \sum_{e_i \in P_{min}} e_i.w_3$
    $R_2 = \sqrt{v_4^2 + v_5^2 + v_6^2}$
    if $R_1 < R_2$ **then**
      $P_{min} = t$
    end if
  end for
end for
$P^A = P_{min}$
return P^A

Fig. 5: Allocation Operation.

shows the methods of selecting recharging stations for P^B. The proposed methods assumed that P^A is already formed and is not null. Before the recharging stations are selected, the travelling time of all recharging stations which lie along the edges in P^A is determined. For any recharging station $r_j \in P^B$, its travelling time from the source node (s) is stored in $r_j.D$. Equation (4) shows the calculation of the $r_j.D$ value. The equations assumes that r_j lies along e_i and function $pos(e_x)$ returns the position of any edge in the set P^A. $pos(e_x) < pos(e_i)$, if e_x lies before e_i in P^A.

Let us consider: $r_j.e = e_i$, then

$$r_j.D = \sum_{e_x \in P^A \& pos(e_x) < pos(e_i)} \frac{e_x.l}{e_x.S} + \frac{r_j.p}{e_i.S} \tag{4}$$

The proposed work uses two different approaches to select the recharging stations. The first approach is the Last Station Strategy (LSS) and the second approach is the Random Selection Strategy (RSS). In LSS, the recharging station which has travelling time (or D value) closest but not greater than the time which the EV can travel without recharging is selected. The LSS approach is shown using flow chart in Fig. 6(a). In the RSS approach, a recharging station is randomly selected from among the candidate recharging stations. The RSS approach is shown using flow chart in Fig. 6(b). To

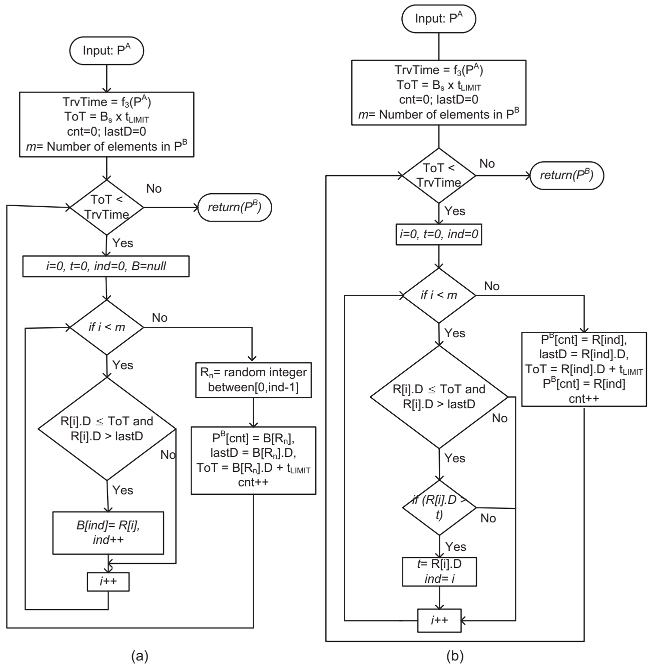

Fig. 6: Selection of recharging stations

populate the set P^B, the proposed algorithm applies both the LSS and RSS techniques. Let us consider that the result from the LSS is P^B and the result from the RSS is P^B.

3.5 Estimation of the Memory Requirements

The SimE works on only one solution. The proposed algorithm creates additional paths which include: Storing a solution which has minimum value of the product: $f_1(P^B) \times f_2(P^A) \times f_3(P^A)$. The allocation operation creates two new paths (t and P_{min}). In the techniques for the selection of recharging stations, the LSS creates one path and RSS creates two paths. The calculation of the number of paths which should be stored in the memory is as follows:
Let us consider that P^A or P^B requires δ units of memory. The maximum memory required is: $mem_{proposed}$= Memory required by the current solution (2δ) + Memory required by the allocation operation (2δ) + Memory required in storing a non-dominated solution (2δ) + memory required in selecting the recharging stations (3δ). Therefore, the total memory requirement is equal to 9δ. For comparison purposes, the minimum memory required by any GA (Genetic Algorithm) is also calculated. The GA stores a population of N elements, and therefore requires: mem_{GA}= $N \times 2\delta$ units of memory. The ratio $\frac{mem_{GA}}{mem_{proposed}} = \frac{2N}{9}$. In GA, the population size i.e. N $\geq$ 10 [8].

4 SIMULATIONS

The proposed algorithm is implemented using Java and its performance is compared with Non-dominated Sorting Genetic Algorithm - II (NSGA-II). The NSGA-II also optimizes paths w.r.t. the recharging time, distance and travelling time. NSGA-II uses the LSS scheme for selecting the recharging stations. The NSGA-II was implemented with population size (N) equal to 10. The ratio $\frac{mem_{GA}}{mem_{proposed}}$= 2.22. In NSGA-II, the population size is 2N, therefore, the ratio becomes 4.44. The proposed algorithm was implemented with parameter values: N_s= 5, i.e., the loop im the Allocation operations executes for five times, and M_b, which is the mutation probability is set to 0.60. The maximum time for the optimization loop is set to 10 seconds in both the proposed algorithm and in NSGA-II. Four road networks $(RG1, RG2, RG3, RG4)$ of different complexities are generated using a research tool [10]. The complexity of the road networks are as: RG1 having 1800 edges and 600 nodes, RG2 having 900 edges and 300 nodes, RG3 having 3400 edges an 1000 nodes, and RG4 having 4700 edges and 1400 nodes. The values to road lengths are randomly assigned to integers between [1, 400] km. The average speed on the edges are assigned to randomly selected integers between [40,120]. The waiting and recharging delay at the recharging stations varies randomly between $[10, 20] \in R$. The maximum time which the EV can travel without recharging is considered to be 2 hours. In any test case the source and destination nodes are randomly selected and the algorithm are used to find the optimum paths between them. On each graph, up-to 20 test problems are executed. In each test problem, the Pareto sets are obtained from both algorithms.

Table 2: Results of the Wilcoxon Rank-Sum tests.

Road Network	p	h	Remarks
$RG1$	0.9031	0	The Hypervolume distributions are same.
$RG2$	0.9676	0	The Hypervolume distributions are same.
$RG3$	0.4567	0	The Hypervolume distributions are same.
$RG4$	0.0858	0	The Hypervolume distributions are same.

The 3D Hypervolume calculation is performed by using the tool [11], which was proposed by Carlos Fonseca et al.. The tool calculates the Hypervolume for the minimization problems. In the Hypervolume calculation, the bounds for the maximum values are considered more than the values in the Pareto Optimal sets. The larger Hypervolume value represents that the Pareto optimal set consists of better solutions. The results are shown using Box-and-Whisker plots in Fig. 7. The box-and-whisker plots, the whiskers are drawn between the minimum and maximum values. The central mark is the median, the edges of the boxes are at the 25th and 75th percentiles. The Wilcoxon Rank Sum test [12] is used to test the null hypothesis, which shows that the Hypervolume distributions obtained from the two algorithms are same. The rank sum test returns p and h values. If $h = 0$, which means that the two distribution are same. p indicates the probability that an element from the first distribution is equal to

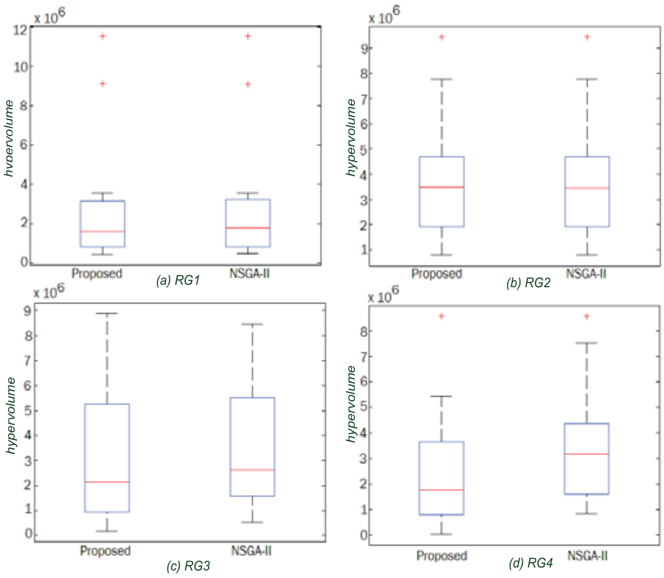

Fig. 7: Box-and-Whisker Plots of the Hypervolumes on different graphs.

the element from the second distribution. The MATLAB's $ranksum$ function is used to apply the rank sum test. The results are shown in Table 2, which shows that the Hypervolumes obtained fromthe proposed algorithm and NSGA-II on different graphs are same. Therefore, the Pareto Optimal solutions obtained from the proposed algorithm are as good as obtained from the NSGA-II.

5 CONCLUSION

In this work, the multi-objective route optimization problem for the Electric Vehicles (EVs) is solved by using the Simulated Evolution (SimE) based algorithm. The optimization objectives are: recharging time, distance and travelling time. Innovative and problem specific Goodness and Allocation operations are being used to achieve better performance. The comparison of the proposed algorithm with NSGA-II, which is a popular GA based heuristic for the multi-optimization problems shows that the proposed algorithm achieves same results as NSGA-II. However, the proposed algorithm requires memory which is 2.2 times lesser than any GA or population based algorithm. This memory size reduction is effective for implementing an embedded hardware.

REFERENCES

[1] Ahmed Y. Saber & Ganesh K. Venayagamoorthy, "One Million Plug-in Electric Vehicles on the Road by 2015," Proceedings of the 12^{th} International IEEE Conference on Intelligent Transportation Systems, St. Lious, MO, USA, Oct. 3-7, 2009.

[2] Medhi E.-Amoli, Kent Choma, & Jason Stefani,"Rapid-Charge Electric-Vehicle Stations," IEEE Transactions of Power Delivery, Vol. 25, No. 3, pp. 1883-1887, July 2010.

[3] Zheng Li, Zafer Sahinoglu, Zhifeng Tao, & K. H. Teo, "Electric Vehicles Network with Nomadic Portable Charging Stations," 2010 IEEE 72^{th} Conference on Vehicular Technology Fall, VTC-2010 Fall, Ottawa, ON, USA, Sept. 6-9, 2010.

[4] Olle Sundstorm & Carl Binding, "Planning Electric-Drive Vehicle Charging under Constrained Grid Conditions," 2010 Internal Conference on Power System Technology, (POWERCON), Zhejiang, China, Oct. 24-28, 2010.

[5] Zbigniew TARAPATA, "Selected Multicriteria Shortest Path Problems: AN Analysis of Complexity, Models and Adoption of Standard Algorithms," Int. J. Appl. Math. Comput. Sci., 2007, Vol. 17, No. 2, 269-287.

[6] M.R. Garey and D. S. Johnson: *Computers and Intractability: A Guide to the Theory of NP-Completeness.*, W. H. Freeman and Co., 1997

[7] Zheng Li, Zafer Sahinoglu, Zhifeng Tao, & K. H. Teo, "Electric Vehicles Network with Nomadic Portable Charging Stations," 2010 IEEE 72^{th} Conference on Vehicular Technology Fall, VTC-2010 Fall, Ottawa, ON, USA, Sept. 6-9, 2010.

[8] Kalyanmoy Deb, Amrit Pratap, Sameer Agarwal, and T. Meyarivan, "A Fast and Elitist Multiobjective Genetic Algorithm: NSGA-II," IEEE Trans. Evolutionary Computation, vol. 6, No. 2, April 2002.

[9] S.M. Sait & H. Youssef, Iterative Computer Algorithms with Applications in Engineering, IEEE Computer Society Press, 1999.

[10] Fabien Viger, Matthieu Latapy, "Efficient and simple generation of random simple connected graphs with prescribed degree sequence," Proc. 11^{th} Conference of Computing and Combinatoric (COCOON 2005), LNCS 3595, pp. 440-449, 2005.

[11] Carlos M. Fonseca, Lus Paquete, and Manuel Lpez-Ibez,"An improved dimension - sweep algorithm for the hypervolume indicator," Proc. 2006 IEEE Congress on Evolutionary Computation (CEC'06), pp. 11571163, Piscataway, NJ, July 2006.

[12] Hollander, M., and D. A. Wolfe, $Nonparametric\ Statistical\ Methods$, John Wiley & Sons, Inc., 1999.

A hybrid evolutionary algorithm for the resource constrained project scheduling problem

Arit Thammano[1] and Ajchara Phu-ang[2]

Computational Intelligence Laboratory
Faculty of Information Technology
King Mongkut's Institute of Technology Ladkrabang
Bangkok, 10520 Thailand
(Tel: (662)723-4964, Fax: (662)723-4910)

[1]arit@it.kmitl.ac.th and [2]s2660603@kmitl.ac.th

Abstract: The resource constrained project scheduling problem (RCPSP) is an NP-hard optimization problem. RCPSP is one of the most important and challenging problem in the project management field. In the past few years, many researches have been proposed for solving the resource constrained project scheduling problem. The objective of this problem is to schedule the activities under the limited amount of the resources so that the project makespan is minimized. This paper proposes a new algorithm for solving RCPSP that combines the concepts of the biological immune system, the simulated annealing algorithm (SA), the tabu search algorithm (TS) and the genetic algorithm (GA) together. The performance of the proposed algorithm is evaluated and compared to the current state of the art metaheuristic algorithms. In this study, the benchmark data sets used in testing the performance of the proposed algorithm are obtained from Project Scheduling Problem Library (PSPLIB). The performance is measured in terms of the average percentage deviation from the critical path lower bound. The experimental results show that the proposed algorithm outperforms the state of the art metaheuristic algorithms on all standard benchmark data sets.

Keywords: Resource constrained project scheduling problem, Metaheuristic, Evolutionary algorithm

1 INTRODUCTION

The resource constrained project scheduling problem (RCPSP) is an NP-hard optimization problem. RCPSP is one of the most important and challenging problem in the project management field. The methods for solving the RCPSP have ranged from exact methods, to heuristic methods, to metaheuristic methods. In recent years, due to the need for solving large realistic project instances, the trend of the research has shifted toward the metaheuristic approaches. The objective of the RCPSP is to schedule the activities under the limited amount of the resources so that the project makespan is minimized [1]. Some metaheuristic methods for solving the RCPSP are reviewed in the following paragraph.

Debels et al [2] proposed a new metaheuristic which combines the scatter search with the electromagnetism optimization heuristic. Tseng and Chen [3] presented a hybrid metaheuristic, named ANGEL, for solving the RCPSP. ANGEL combines ant colony optimization, genetic algorithm and the local search strategy together. A new heuristic algorithm based on filter and fan method has been proposed in [4]. A hybrid metaheuristic algorithm based on the scatter search approach was developed by Ranjbar and Kianfar [5] to solve the RCPSP. Chen et al [6] proposed a hybrid algorithm, called ACOSS, for solving the RCPSP in real-time. The ACOSS algorithm combines a local search strategy, ant colony optimization, and a scatter search in an iterative process.

In this paper, a new hybrid evolutionary algorithm for the RCPSP is proposed. This proposed algorithm combines the concepts of the biological immune system, the simulated annealing algorithm (SA), the tabu search algorithm (TS) and the genetic algorithm (GA) together.

The rest of this paper is organized as follows: Section 2 is the problem definition of the RCPSP. Section 3 presents the proposed algorithm. A brief description of the test sets and the experimental results are given in Section 4. Finally, Section 5 is the conclusion.

2 PROBLEM DEFINITION

The resource constrained project scheduling problem (RCPSP) involves the scheduling of the project activities subject to precedence relations as well as the resource constraints in order to minimize the project duration.

The RCPSP can be stated as follows: A project consists of a set of N activities. Each activity j ($j \in N$) has duration of d_j and requires r_{jk} units of the resource type k. The resource type k has a limited capacity of R_k at any point in time. This means that the sum of the resource requirements for the resource k in any time period cannot exceed R_k. While the activity j is processed, the activity j requires r_{jk} units of the resource type k during every time instant of its non-preemptive duration d_j. In addition, the precedence relation between activities must also be taken into account, not just the resource restrictions.

Fig. 1 is an example of a project which consists of 6 activities (N = 6). Activities 0 and 5 are the dummy activities which represent the start and the end of the project respectively. Activities 1, 2, 3, and 4 are the real activities which require 3, 7, 6, and 2 units of the resource type k.

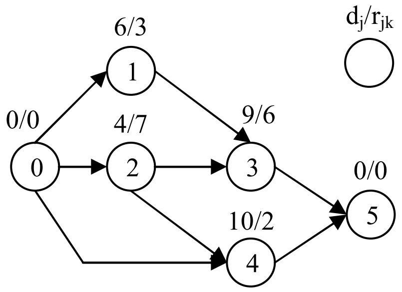

Fig. 1. An example of a project

3 PROPOSED ALGORITHM

The proposed algorithm is based on the concepts of the biological immune system, the simulated annealing algorithm (SA), the tabu search algorithm (TS) and the genetic algorithm (GA). The detailed procedure of the proposed algorithm (Fig. 2) is described as follows:

First, the initial population is generated by using the schedule generation scheme (SGS). The SGS consists of N stages, where N is the number of activities in the project. In each stage, one activity is selected and scheduled at its earliest possible time within the precedence and resource constraints. The SGS process stops when all activities are scheduled.

Second, the negative selection mechanism, to be discussed in Subsection 3.1, is employed to filter out the worst 10 percent of the whole population while the best 90 percent of the population are kept for the crossover process. The crossover operator used in this paper is the permutation encoding crossover (Fig. 3).

Third, the filtered-out chromosomes are forwarded to the TS-SA search algorithm, to be discussed in Subsection 3.2. After performing the TS-SA search, the new chromosomes obtained from the TS-SA search are combined with the new offspring obtained from the crossover operation.

Fourth, the mutation operation is performed on the combined population. The insertion mutation operator proposed by Fogel [7] is employed in this research.

Finally, the stopping criteria are checked. If any of the stopping criteria are met, the algorithm will be terminated. If not, the new population is selected from all solutions available in the current generation, both parents and their offspring; then go back to step 2.

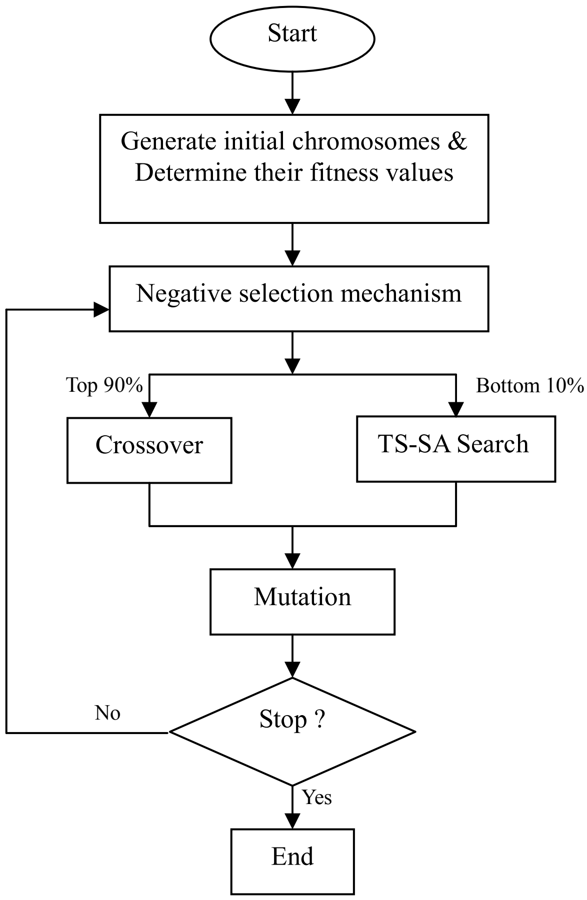

Fig. 2. Proposed algorithm

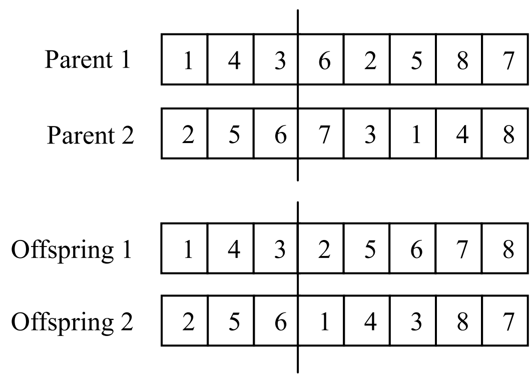

Fig. 3. Example of the permutation encoding crossover

3.1 Negative Selection Mechanism

Negative selection mechanism is inspired by the self/non-self discrimination behavior of the biological immune system. The purpose of the biological immune system is to recognize all cells within the body and categorizes those cells as either self (body cells) or non-self (antigens). When the antigens are found, the T-cells will bind themselves to the antigens and inject poisonous chemicals into them causing their destruction [8]. However, the immune system sometimes becomes dysfunctional by mistaking a body cell for a similar antigen. As a result, the body initiates the destructive operation against its own cells. In order to prevent the above undesirable phenomenon from happening, the negative selection mechanism is employed to remove the T-cells that bind too strongly to the body cells.

This paper employs the negative selection mechanism to remove the worst 10 percent of the whole population.

3.2 TS-SA Search Algorithm

The TS-SA search algorithm is a hybrid between the tabu search algorithm and the simulated annealing algorithm. For each filtered-out chromosome, M neighbor chromosomes are created by randomly mutating two genes in the chromosome. Next, the fittest neighbor is selected according to the tabu restrictions and aspiration criteria. If the best neighbor chromosome is fitter than the current chromosome, the current chromosome is replaced by the best neighbor chromosome. Otherwise, the simulated annealing concept is employed to determine whether the best neighbor chromosome should be accepted for further processing. If the criterion in (1) is met, the best neighbor chromosome will be used for further processing.

$$P(\text{accept}) > \varepsilon \tag{1}$$

$$P(\text{accept}) = \text{Exp}\ [-(E_n - E_c)/T] \tag{2}$$

where E_n is the fitness value of the best neighbor chromosome. E_c is the fitness value of the current chromosome. T is the temperature of the simulated annealing process. In this paper, the initial temperature is set at 90 degree; then the temperature gradually drops until it hits the pre-specified limit, which is 70 degree in this paper.

This TS-SA search is repeated until (1) the temperature of the simulated annealing process falls below a predefined value or (2) the best neighbor chromosome is fitter than the current chromosome.

4 EXPERIMENTAL RESULTS

The performance of the proposed algorithm is evaluated and compared to the current state of the art metaheuristic algorithms. In this study, the benchmark data sets used in testing the performance of the proposed algorithm are obtained from Project Scheduling Problem Library (PSPLIB) [9]. The whole set of projects with 60, 90, and 120 activities (data sets J60, J90, and J120) are considered. The test sets J60 and J90 contain 480 instances with 4 renewable resource types, while the J120 contains 600 instances.

The performance of the proposed model in solving the above mentioned test sets is shown in Table 1. The row labeled with "Sum" contains the sum of the makespans of all problem instances in each test set. The row labeled with "Avg. Dev. CPM (%)" displays the average percentage deviation from the critical path lower bound. The row labeled with "Avg. Dev. LB (%)" reports the average percentage deviation from the currently best known solution. The row labeled with "LB Found" displays the number of problem instances in which the proposed algorithm reports a makespan equal to the currently best known solution.

Table 2 illustrates the comparative results of the proposed algorithm and four of the current state of the art metaheuristic algorithms. In Table 2, the performance is compared in terms of the average percentage deviation from critical path lower bound. The experimental results show that the proposed algorithm outperforms the state of the art metaheuristic algorithms on all benchmark data sets.

Table 1. Experimental Results

	Data Set		
	J60	J90	J120
Sum	38397	45605	74179
Avg. Dev. CPM (%)	10.55%	9.57%	30.54%
Avg. Dev. LB (%)	0.99%	1.34%	4.42%
LB Found	410/480	390/480	291/600

Table 2. Comparative Results

	Average Percentage Deviation from Critical Path Lower Bound		
	J60	J90	J120
Proposed Algorithm	10.55%	9.57%	30.54%
Debels and Vanhoucke (2007) [10]	10.68%	10.35%	30.82%
Ranjbar (2008) [4]	10.56%	10.11%	31.42%
Ranjbar and Kianfar (2009) [5]	10.64%	10.04%	31.49%
Agarwal el al. (2011) [11]	11.29%	11.29%	34.15%

5 CONCLUSION

In this paper, a new metaheuristic algorithm for solving the resource constrained project scheduling problem is proposed. This proposed algorithm is based on the concepts of the biological immune system, the simulated annealing algorithm (SA), the tabu search algorithm (TS) and the genetic algorithm (GA). The experimental results show that the proposed model is capable of providing optimal or near-optimum solutions for all test sets.

REFERENCES

[1] Montoya-Torres JR, Gutierrez-Franco E, Pirachicán-Mayorga C (2010), Project scheduling with limited resources using a genetic algorithm. International Journal of Project Management 28: 619-628

[2] Debels D, Reyck BD, Leus R, Vanhoucke M (2006), A hybrid scatter search/electromagnetism meta-heuristic for project scheduling. European Journal of Operational Research 169: 638-653

[3] Tseng LY, Chen SC (2006), A hybrid metaheuristic for the resource constrained project scheduling problem. European Journal of Operational Research 175: 707-721

[4] Ranjbar M (2008), Solving the resource- constrained project scheduling problem using filter-and-fan approach. Applied Mathematics and Computation 201: 313-318

[5] Ranjbar M, Kianfar F (2009), A hybrid scatter search for the RCPSP. Transaction E: Industrial Engineering 16(1): 11-18

[6] Chen W, Shi YJ, Teng HF, Lan XP, Hu LC (2010), An efficient hybrid algorithm for resource-constrained project scheduling. Information Sciences 180: 1031-1039

[7] Fogel DB (1988), An evolutionary approach to the travelling salesman problem. Biological Cybernetics 60: 139-144

[8] Burke EK, Kendall G (2005), Search Methodologies: Introductory Tutorials in Optimization and Decision Support Techniques. Springer, pp. 375-399

[9] Project Scheduling Problem Library. http://129.187.106.231/psplib

[10] Debels D, Vanhoucke M (2007), A decomposition-based heuristic for the resource-constrained project scheduling problem. Operations Research 55: 457-469

[11] Agarwal A, Colak S, Erenguc S (2011), A neurogenetic approach for the resource-constrained project scheduling problem. Computers & Operations Research 38: 44-50

The Seventeenth International Symposium on Artificial Life and Robotics 2012 (AROB 17th '12),
B-Con Plaza, Beppu, Oita, Japan, January 19-21, 2012

Study on evolution of the artificial flying creature controlled by neuro-evolution

R. Ooe[1], I. Suzuki[2], M. Yamamoto[2], and M. Furukawa[2]

[1]Hokkaido University, Hokkaido 060-0814, Japan
[2]Hokkaido University, Hokkaido 060-0814, Japan
(Tel: 81-11-706-6445, Fax: 81-11-706-6443)

[1]ooe@complex.ist.hokudai.ac.jp

Abstract: In this paper a flight evolutionary simulation of an artificial flying creature (AFC) is described. The three-dimensional motion of the AFC is calculated by the physical engine PhysX and a numerical expression of the simple drag force. The AFC is controlled by an artificial neural network (ANN). The three-layered ANN which has nine input neurons and four output neurons is used for a simulation of the AFC. To evolve ANNs and to have the AFC flight suitably for given target points, a particle swarm optimization (PSO) optimizes parameters of ANNs. The results of evolutionary simulation show that the ability of generalization does not always increase as evolution progresses, and it depends on given tasks of the AFC. It is also shown that the number of situations which the AFC goes through has positive correlation with the ability of generalization.

Keywords: Artificial life, Artificial neural network, Particle swarm optimization, Neuro-evolution, Physical engine

1 INTRODUCTION

Flight is a complex behavior. A sleeping dog can stay on the ground, while a bird not moving its wings can not stay in the sky. Ants can only move on surfaces, which are commonly regarded as the two-dimensional coordinates. On the other hand butterflies can fly freely in the air, the three-dimensional space. So it is interesting to understand the mechanism of flight, however, there are few researches on them.

Compared with flight, walking, jumping and swimming have been studied by many researchers. Sims [1] simulates evolution of the artificial virtual creatures and shows that creatures can acquire morphology and controllers by evolution with the physical interactions. Lipson et al [2]. and Rieffel et al [3]. also show similar results, however, it is a new point that Rieffel uses PhysX, one of physical engines, for calculating motions. In the field of bipedal walking, Allen et al [4]. and Reil et al [5]. show that bipedal robots can jump or walk through evolution. Wu et al [6]. proposes a bird model for computer graphics. This is one of a few studies on flight behaviors, although the evolutionary acquisition of flight is not done in it.

The objective of this study is to show a process in the evolution of flight behavior. In this paper, we describe a numerical simulation of flight evolution by the use of PhysX and drag force calculation. Although this method can calculate the motion faster, it is approximation and not completely accurate. However, we are focusing on the evolutionary process, and we do not deal with verification of the accuracy by experiments in the real world.

The method used for simulation is described in Section Two. Section Three explains a model of the artificial flying creature and how to evolve its controller by neuro-evolution. Section Four shows the evolutionary simulation and its result. Finally, the conclusion is described in Section Five.

2 COMPUTATIONAL METHOD

In order to calculate motion of the artificial flying creatures, we basically use a physical engine. Because it does not support the force which acts objects in a fluid, we use the simple drag force additionally.

2.1 Physical engine

The physical engine is software used for calculation of the multi body dynamics. The most common purpose of the physical engine is to improve reality in three-dimensional computer graphics. In addition, various types of physical simulations can be done easily by the physical engine, so it is used for researches on artificial-life in recent years.

The physical engine can calculate a motion of the complex object which consists of some objects connected by joints. It can also calculate effects of collision and friction and add force to objects. Since these calculations are automatically performed, the physical engine is regarded as a black box.

2.2 Drag force

Objects in a fluid are affected by the fluid via surfaces of the objects. The physical engine does not support this effect of the fluid yet. We use the simple drag force in order to implement the effect in the physical engine. The drag force D is given by

$$D = \frac{1}{2}\rho C_d A \boldsymbol{v}^2 \quad (1)$$

where ρ, C_d, A, and $\boldsymbol{v}$ are fluid density, a drag coefficient, an area of a minute surface, and velocity of the surface.

Although this drag force is a kind of the quasi-steady fluid force and a rough approximation, it is fast and easily combined with the physical engine.

3 MODEL OF THE CREATURE

The artificial flying creature (AFC) is controlled by an artificial neural network (ANN). To optimize parameters of ANNs, we use particle swarm optimization (PSO).

3.1 Artificial flying creature (AFC)

3.1.1 Structure

The AFC in Fig. 1. is similar to a bird. It is composed of four parts: a body, a tail, and two wings. The two wings are rotate on the axes $\boldsymbol{e}_{R1}$ and $\boldsymbol{e}_{L1}$, and on the axes $\boldsymbol{e}_{R2}$ and $\boldsymbol{e}_{L1}$. The tail rotates on the axis $\boldsymbol{e}_{T1}$, and on the axis $\boldsymbol{e}_{T2}$. Each rotation is controlled by an output signal of an ANN. To simplify control of the AFC, rotations of two wings are perfectly symmetrical.

3.1.2 Sensors

The AFC has some virtual sensors. They can measure states of the AFC, and perceive cognitive information. They are used as input signals of ANNs.

3.2 Artificial neural network (ANN)

The AFC has a three layered ANN as a controller. The ANN receives eight input signals from virtual sensors: the pitch and roll angles of the AFC, the forward velocity, the relative angles on the axes $\boldsymbol{e}_{R1}$ and $\boldsymbol{e}_{R2}$, the angular velocity on the axis $\boldsymbol{e}_{R1}$, and the angles relative to a target point. Then the ANN calculates four output signals: the angles on the axes $\boldsymbol{e}_{R1}$, $\boldsymbol{e}_{R2}$, $\boldsymbol{e}_{T1}$, and $\boldsymbol{e}_{T2}$.

3.3 Particle swarm optimization (PSO)

In order to optimize ANNs and control the AFC suitably, we use PSO. The PSO is one of the swarm intelligence and has strong convergence. Each position of a particle represents the parameters of an ANN. The position of the particle i at search step k+1, $\boldsymbol{p}^i_{k+1}$, is calculated by

$$\boldsymbol{v}^i{}_{k+1} = w\boldsymbol{v}^i{}_k + c_1 r_1\left(\boldsymbol{p_d}^i{}_k - \boldsymbol{p}^i{}_k\right) + c_2 r_2\left(\boldsymbol{p_g}{}_k - \boldsymbol{p}^i{}_k\right) \quad (2)$$

and

$$\boldsymbol{p}^i{}_{k+1} = \boldsymbol{p}^i{}_k + \boldsymbol{v}^i{}_{k+1} \quad (3)$$

where w, c_1, and c_2 are coefficients, r_1 and r_2 are uniform random numbers from 0 to 1. $\boldsymbol{p}_d$ is the best position of the particle i, and $\boldsymbol{p}_g$ is the best of all particles.

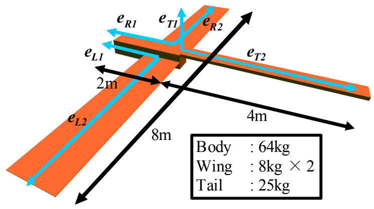

Fig. 1. The artificial flying creature (AFC)

4 EVOLUTION OF FLIGHT TO TARGETS

The AFC evolves to fly to a given target by PSO. We use two different conditions in evolution of the AFC, and then we analyze differences of the process in evolution and the evolved flight to given targets.

4.1 Evolutionary conditions

4.1.1 Common conditions

The AFC is initially placed on the point of (0,200,0) in a static state. Then the AFC starts flying to a target. If the AFC satisfies conditions of termination, the next flight to another target starts, or the next AFC starts flying. The time of numerical integration in PhysX is 1/100 seconds.

We use w = 0.4 and c_1 = c_2 = 2.0 as parameters of PSO. We also use 60 particles, and 2000 search steps of PSO.

4.1.2 Conditions in go-and-stay

In the evolution of "go-and-stay", the AFC evolves to go to only one target given by (200,300,200), and stay there. Each AFC flies for 30 seconds, and then it is evaluated by

$$\sum_{t=0}^{3000} \frac{1}{1 + d_t{}^2} \quad (4)$$

where t and d_t are a time step and a distance from the AFC to the target at time step t.

4.1.3 Conditions in 4-trials

In the evolution of "4-trials", the AFC evolves to go to the four targets given by (200,300,200), (-200,100,200), (-200,300,-200), and (200,100,-200). It does not have to stay around targets. Each AFC flies to a target for 30 seconds at most. If it is situated within 1m from the target, it is considered that the AFC arrives at the target and the flight is terminated. It repeats the flight for a different target four times, and then each is evaluated by

$$\sum_{s=1}^{4} \left\{ \sum_{t=0}^{T_s - 1} \left(\frac{1}{1 + d_{s,t}{}^2} \right) + \sum_{t=T_s}^{3000} 1 \right\} \quad (5)$$

where s, T_s, and $d_{s,t}$ are the number of trials, a time to arrive at a target in trial s, and a distance from the AFC to the target of trial s at time step t.

4.2 Results of evolution

4.2.1 Changing evaluation in evolution

We have done evolutionary simulations 10 times for go-and-stay and 4-trials. Fig. 2. shows changing evaluations at each search step. The result that differences between the maximum values and average values are larger than one between the minimum values and average values shows high variance of these evolutionary simulations.

4.2.2 Evolved flights

Fig. 3. shows the trajectory and snapshot at every second of the most successful flight given by go-and-stay evolution. In this flight, the AFC goes to the target quickly and flies around the target. This satisfies the aim of "go-and-stay". The number of satisfactory flights, however, is only three. The other flights satisfy only the aim of "go", do not satisfy the aim of "stay".

On the other hand, four different patterns of flight are given by 4-trials evolution. The worst flight is to go back and the AFC falls down. The next worse flight is to go to only one or two targets and the AFC falls down. Two better flights are interesting: one gets low evaluation but fully satisfies "go-and-stay", and the other obtains high evaluation but the AFC falls down after arrival. The arriving rate for (200,300,200), (-200,100,200), (-200,300,-200), and (200,100,-200) are 10%, 40%, 0%, and 70% in ten evolutionary simulations. In even the best flight, the AFC arrives at only two targets given by (-200,100,200) and (200,100,-200).

5 ANALYSYS OF EVOLUTIONARY PROCESS

ANNs have properties of generalization, which is the ability to learn many things by little learning. In the case of the AFC, we have defined the ability of generalization as the ability to reach the targets which are not related to the evaluation of the AFC, and then tested the change of the ability of generalization in evolution.

For tests of generalization, 64 target points are set: 32 points are located on circle-1, and the 32 other points are located on circle-2. The radiuses of circle-1 and circle-2 are $200\sqrt{2}$, and the centers of circle-1 and circle-2 are the points of (0,100,0) and (0,300,0). The length for judgment of arrival is 10m, which is larger than 1m in evolution.

Fig. 4. shows the average values of the successful rate of arrival for 64 targets in evolution. The rate of "4-trials" does not decrease as evolution progresses at least, while that of "go-and-stay" obviously decreases after 500 search steps. This result shows that the evolutionary conditions in go-and-stay are not suitable for increasing generalization.

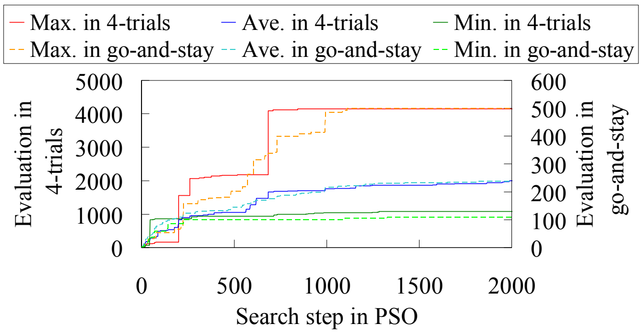

Fig. 2. The change of evaluations in evolution

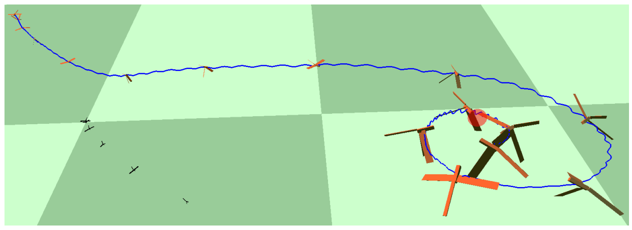

Fig. 3. The most successful flight of go-and-stay

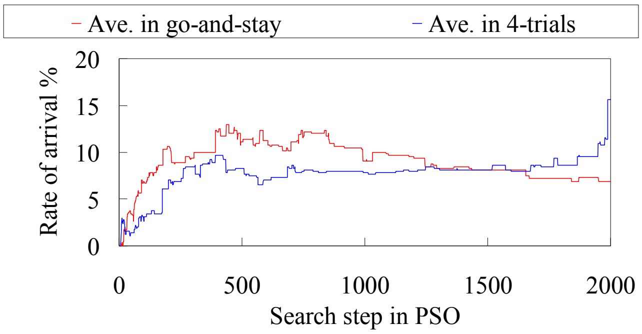

Fig. 4. The successful rate of arrival for 64 targets

We also have counted the "experienced target angles" in evolution of go-and-stay. It is the number of appearing sets of the angles relative to the target in flight. Angles are discretized into integers, and the total number of sets is $360° \times 360° = 129600$.

Fig. 5. shows the relations between the average values of the experienced target angles and the rate of arrival about go-and-stay, and Fig. 6. shows one between the average evaluation and the rate of arrival. Although Fig. 5. shows the relation of monotonic increase, so does not Fig. 6. This result leads us to the idea that increasing the experienced target angles may bring higher successful rate of arrival.

6 EVOLUTION USING TARGET ANGLES

To verify the given hypothesis, we additionally simulate the evolution of the AFC with "experienced target angles". The evolutionary conditions are all the same with that in the evolution of "go-and-stay" but evaluation. The evaluation

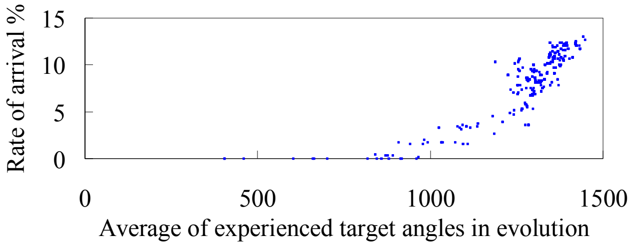

Fig. 5. The relation between the experienced target angles and the rate of arrival in evolution of go-and-stay

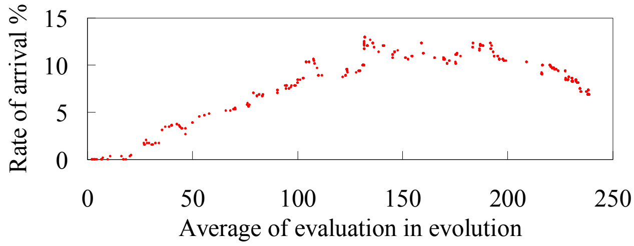

Fig. 6. The relation between the evaluation and the rate of arrival in evolution of go-and-stay

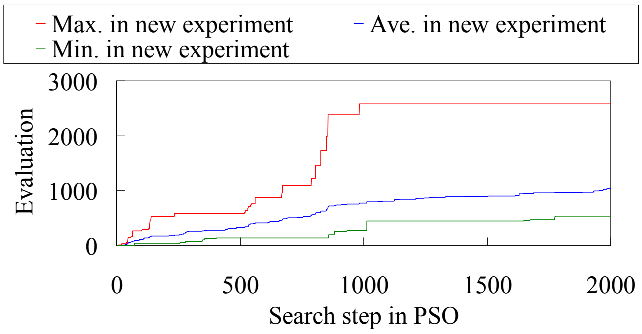

Fig. 7. The change of evaluations in new experiment

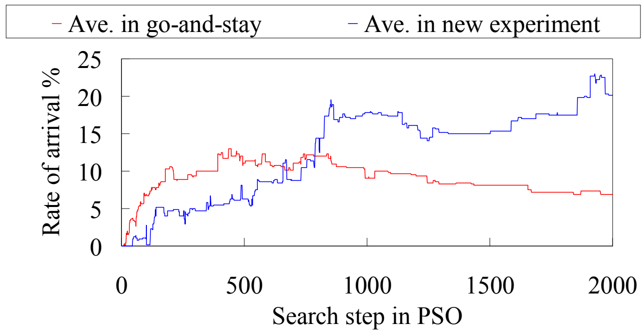

Fig. 8. The successful rate of arrival for 64 targets

of the AFC is given by

$$\left(\sum_{t=0}^{3000}\frac{1}{1+d_t^{\,2}}\right)\left(\frac{100a}{129600}\right)^3 \tag{6}$$

where a is the number of experienced target angles of the AFC. In short, the AFC which has both the ability of "go-and-stay" and more experiences survives by this evaluation.

Fig. 7. shows average evaluations at each search step given by 10 evolutionary simulations. A high variance between each evolution is similar to one of go-and-stay.

Fig. 8. shows the average values of the successful rate of arrival for 64 targets in evolution. The new experiment brings higher rates of arrival at later search steps, and they roughly show the relation of monotonic increase. This result gives support to our hypothesis.

7 CONCLUSION

We have simulated the evolution of the AFC by using PhysX and the drag force calculation. According to two evolutionary conditions, "go-and-stay" and "4-trials", there are some differences in both the evolved flights and the evolutionary processes. A difference in the successful rate of arrival for 64 targets is the most essential: it increases monotonically in the case of 4-trials, while it decreases as evolution progresses in the case of go-and-stay.

A positive correlation between the rate of arrival and the "experienced target angles" suggests that many experiences about angles for targets keep increasing the rate. The new evolution using experienced target angles verifies this hypothesis, and it also shows that indirect factors influence the ability of generalization in evolution. It is a future work to examine whether our theory applies to other cases or not.

REFERENCES

[1] Sims K (1994), Evolving virtual creatures. Proceedings of the 21st annual conference on Computer graphics and interactive techniques, pp.15-22

[2] Lipson H, Pollack J (2000), Automatic design and manufacture of robotic lifeforms. Nature, 406, pp.974-978

[3] Rieffel J, Saunders F, Nadimpalli S et al. (2009), Evolving soft robotic locomotion in PhysX. Proceedings of the 11th Annual Conference Companion on Genetic and Evolutionary Computation Conference (GECCO'09), Montreal, Quebec, Canada, July 8-12, 2009

[4] Allen B, Faloutsos P (2009), Complex networks of simple neurons for bipedal locomotion. Proceedings of 2009 IEEE/RSJ international conference on Intelligent robots and systems (IROS'09), St. Louis, Missouri, USA, Oct 11-15, 2009, pp.4457-4462

[5] Reil T, Husbands P (2002), Evolution of central pattern generators for bipedal walking in a real-time physics environment. IEEE Transactions on evolutionary computation, 6 (2), pp.159-168

[6] Wu J, Popovic Z (2003), Realistic modeling of bird flight animations. Proceedings of ACM SIGGRAPH 2003, San Diego, California, USA, July 29-31, 2003, pp.888-895

The Seventeenth International Symposium on Artificial Life and Robotics 2012 (AROB 17th '12),
B-Con Plaza, Beppu, Oita, Japan, January 19-21, 2012

A new differential artificial bee colony algorithm for large scale optimization problems

Takuya Kagawa[1], Akihide Utani[1], and Hisao Yamamoto[1]

[1]Tokyo City University, Tokyo 158-8557, Japan
(Tel: 81-3-5707-0104)

[1]autani@tcu.ac.jp

Abstract: This paper proposes a novel optimization algorithm based on advanced Artificial Bee Colony (ABC) algorithm that has the good performance on large scale optimization problems named the differential ABC algorithm. In the proposed algorithm, the generation equation of the mutation vector of Differential Evolution (DE) is introduced in advanced ABC algorithm. We evaluate the proposed algorithm through numerical experiments on well-known benchmark functions, such as Rastrigin function, Schwefel function, Ackley function and Griewank function, and discuss its development potential. In numerical experiments performed, the performances of the proposed algorithm are compared with those of the existing optimization ones, such as Particle Swarm Optimization (PSO) algorithm, DE algorithm, ABC algorithm and advanced ABC algorithm.

Keywords: large scale optimization problems, multimodal functions, global optimization, differential evolution, ABC algorithm.

1 INTRODUCTION

The minimization of multimodal functions with many local and global minima is a problem that frequently arises in diverse scientific fields and numerous engineering design problems. This problem is NP-hard in the sense of its computational complexity even in simple cases. As techniques of computing a global minimum of the objective function, many meta-heuristics, which are search algorithms for optimization based on heuristic knowledge, have been proposed. Some well-known representative meta-heuristics are simulated annealing and tabu search which are the traditional optimization algorithms, genetic algorithms and immune algorithms which are classified as evolutionary computation techniques, and ant colony optimization algorithms and particle swarm optimization algorithms [1] which belong to the category of swarm intelligence algorithms.

In meta-heuristics, genetic algorithms and immune algorithms, classified as evolutionary computation techniques, are generally techniques for combination optimization problems. In genetic algorithms and immune algorithms, the variables of continuous type are frequently translated into those of discrete (genetic) type. If there is a dependency between variables, therefore, a promising solution may be destroyed during the solution search process (genetic operation) and the solution search performance may deteriorate. To the contrary, particle swarm optimization algorithm [1] can directly handle the variables of continuous type. Even when there is a dependency between variables, therefore, an efficient and effective solution search can be realized. Recently, particle swarm optimization algorithm is intensively researched because it is superior to the other algorithms on many difficult optimization problems. The ideas that underlie particle swarm optimization algorithm are inspired not by the evolutionary mechanisms encountered in natural selection, but rather by the social behavior of flocking organisms, such as swarms of birds and fish schools. Particle swarm optimization algorithm is a population-based algorithm that exploits a population of individuals to probe promising regions of the search space. The algorithm is simple and allows unconditional application to various optimization problems. However, it has been confirmed that the performance of particle swarm optimization algorithm on large scale optimization problems is not always satisfactory. Therefore, we have proposed a new optimization algorithm based on Artificial Bee Colony (ABC) algorithm [2] that has the good performance on large scale optimization problems [3]. However, for hundreds of dimensional engineering design problems, the improvement of the search performance is moreover required.

This paper proposes a novel optimization algorithm based on advanced ABC algorithm [3] that has the good performance on large scale optimization problems named the differential ABC algorithm. In the proposed algorithm, the generation equation of the mutation vector of Differential Evolution (DE) [4] is introduced in advanced ABC algorithm. We evaluate the proposed algorithm through numerical experiments on well-known benchmark functions, such as Rastrigin function, Schwefel function, Ackley function and Griewank function, and discuss its development potential. In numerical experiments performed, the performances of the proposed algorithm are compared with those of the existing optimization ones. The rest of this paper is organized as follows. In Section 2, the proposed algorithm named the differential ABC algorithm is outlined. In Section 3, the results of numerical experiments are reported. Finally, the paper closes with conclusions in Section 4.

2 PROPOSED ALGORITHM

In the original ABC algorithm, the colony of artificial bees contains three groups of bees: employed bees, onlookers, and scouts. Half of the bees that construct artificial bee colony consist of the employed bees and the rest constitute the onlookers. At the initial state of ABC algorithm, multiple solution search points are randomly set in multidimensional solution search space. For every solution search point, there is only one employed bee, i.e., the number of employed bees is equal to the number of solution search points.

Each employed bee updates its own allocated solution search point in the solution search process. Each onlooker selects one solution search point from the probability based on the fitness value of each solution search point and updates the solution search point chosen. The employed bee of the solution search point that is not undated during the set search iterations becomes a scout and starts to search a new solution search point randomly.

The original ABC algorithm is summarized as follows:

Step 1 (Initialization)

Generate and evaluate the population of solution search points ($\boldsymbol{x}_i$, i=1, ... , SN), where i indicates the solution search point's index. SN is the number of solution search points.

Step 2 (Update of search points by employed bees)

1. Produce and evaluate the new solution search point ($\boldsymbol{v}_i$) on each solution search point ($\boldsymbol{x}_i$) according to the following formula

$$v_{ij} = x_{ij} + \phi_{ij}(x_{ij} - x_{mj}), \quad i = 1,\ldots,SN \tag{1}$$

where $m \in \{1, 2, \ldots, SN\}$ represents randomly chosen solution search point's index and $j \in \{1, 2, \ldots, D\}$ represents randomly chosen variable's index. D is the number of optimization variables. Although m is determined randomly, it has to be different from i. ϕ_{ij} is a random number, uniformly distributed within the interval [-1,1].

2. Apply the greedy selection process between $\boldsymbol{x}_i$ and $\boldsymbol{v}_i$.

Step 3 (Update of search points chosen by onlookers)

1. Compute the probability (P_i) of each solution search point ($\boldsymbol{x}_i$) according to the following formulas

$$fit_i = \begin{cases} \dfrac{1}{1+f(\boldsymbol{x}_i)}, & f(\boldsymbol{x}_i) \geq 0 \\ 1 + abs(f(\boldsymbol{x}_i)), & f(\boldsymbol{x}_i) < 0 \end{cases} \quad (i = 1,\ldots,SN) \tag{2}$$

$$P_i = fit_i \bigg/ \sum_{n=1}^{SN} fit_n \tag{3}$$

where $f(\boldsymbol{x})$ is the objective function. Each onlooker selects one solution search point ($\boldsymbol{x}_i$) depending on the probability (P_i).

2. Produce and evaluate the new solution search point ($\boldsymbol{v}_i$) on the solution search point ($\boldsymbol{x}_i$) chosen by each onlooker, as in Step2.
3. Apply the greedy selection process between $\boldsymbol{x}_i$ and $\boldsymbol{v}_i$.

Step 4 (Update of solution search points by scouts)

If the solution search point that is not undated during the set search iterations exists, replace it with randomly produced solution search point within solution search space.

Step 5 (Update of best solution)

Memorize the best solution search point.

Step 6 (Judgment of end)

Finish the search when the end condition is satisfied. Otherwise, return to Step 2.

The algorithm of [3] is an advanced ABC algorithm. To detect a global optimum solution effectively, ABC algorithm is improved as follows:

1. Improvement of Eq.(2) to compute fitness value (fit_i)
   To improve the adaptability to various engineering design problems, in the proposed algorithm, the fitness value (fit_i) of each solution search point is computed as follows:

$$fit_i = \begin{cases} \dfrac{1}{f(\boldsymbol{x}_i) - f_{bound}}, & f(\boldsymbol{x}_i) - f_{bound} \geq f_{accuracy} \\ \dfrac{1}{f_{accuracy}}, & f(\boldsymbol{x}_i) - f_{bound} < f_{accuracy} \end{cases} \quad (i = 1,\ldots,SN) \tag{4}$$

   where f_{bound} represents the boundary value of $f(\boldsymbol{x}^+)$ on $\boldsymbol{x}^+$ acceptable as a solution for every problem and $f_{accuracy}$ indicates the exactness of convergence to f_{bound}.
2. Improvement of search point selection by onlookers
   To improve the performance of global solution search, in the proposed algorithm, the solution search is divided into two stages. Each onlooker selects one solution search point out of the high-order α solution search points of fitness value (fit_i) randomly during the first stage of the search.
3. Improvement of reference point (m) in Eq.(1)

To improve the update frequency of each solution search point, the reference point (m) in Eq.(1) is randomly chosen out of the high-order α solution search points of the fitness value (fit_i) during the first stage of the search and is chosen by the roulette selection based on the probability (P_i) of each solution search point ($\boldsymbol{x}_i$) during the second stage of the search.

In addition, Step 4 (Update of search points by scouts) in the original ABC algorithm is not executed in the algorithm of [3] because the performance of global solution search is improved by the above 2 (Improvement of search point selection by onlookers).

In the proposed algorithm, the following mutation vector generation equation of Differential Evolution (DE) [4] is introduced for the update of search points by employed bees.

$$\boldsymbol{v}_i = \boldsymbol{x}_{r1} + F(\boldsymbol{x}_{r2} - \boldsymbol{x}_{r3}), \quad i = 1, \dots, SN \tag{5}$$

where $\boldsymbol{x}_{r1}$, $\boldsymbol{x}_{r2}$ and $\boldsymbol{x}_{r3}$ represent the search point's index randomly selected, and F indicates a control parameter determined within the interval [0,1]. The above mutation vector generation equation has the good performance on the global search of multimodal functions. By introducing Eq.(5), it can be expected that the performance of the proposed algorithm is improved.

3 EXPERIMENTAL RESULTS

Through numerical experiments on D dimensional benchmark functions, which are Rastrigin function, Schwefel function, Ackley function and Griewank function, the performances of the proposed algorithm are investigated in detail to verify its effectiveness on large scale optimization problems. In numerical experiments performed, the performances of the proposed algorithm are compared with those of the existing optimization ones.

- Rastrigin function

$$\text{min.}\ f_1(\boldsymbol{x}) = \sum_{j=1}^{D}\left\{x_j^2 - 10\,cos(2\pi x_j) + 10\right\}$$

$$\text{subj. to}\ -5.12 \le x_j \le 5.12, \quad j = 1,\dots,D$$

$$\boldsymbol{x}^* = (0,\dots,0), \quad f_1(\boldsymbol{x}^*) = 0$$

- Schwefel function

$$\text{min.}\ f_2(\boldsymbol{x}) = 418.98288727\,D + \sum_{j=1}^{D} -x_j sin(\sqrt{|x_j|})$$

$$\text{subj. to}\ -512 \le x_j \le 512, \quad j = 1,\dots,D$$

$$\boldsymbol{x}^* = (420.968750,\dots,420.968750), \quad f_2(\boldsymbol{x}^*) = 0$$

- Ackley function

$$\text{min.}\ f_3(\boldsymbol{x}) = 20 + e - 20\,exp\left(-0.2\sqrt{\frac{1}{D}\sum_{j=1}^{D} x_j^2}\right) - exp\left(\frac{1}{D}\sum_{j=1}^{D} cos(2\pi x_j)\right)$$

$$\text{subj. to}\ -30 \le x_j \le 30, \quad j = 1,\dots,D$$

$$\boldsymbol{x}^* = (0,\dots,0), \quad f_3(\boldsymbol{x}^*) = 0$$

- Griewank function

$$\text{min.}\ f_4(\boldsymbol{x}) = \frac{1}{4000}\sum_{j=1}^{D} x_j^2 - \prod_{j=1}^{D} cos\left(\frac{x_j}{\sqrt{j}}\right) + 1$$

$$\text{subj.to}\ -600 \le x_j \le 600, \quad j = 1,\dots,D$$

$$\boldsymbol{x}^* = (0,\dots,0\,), \quad f_4(\boldsymbol{x}^*) = 0$$

where $\boldsymbol{x}^*$ of each benchmark function represents a global optimum solution. In **Fig.1**, the landscapes of multimodal functions are illustrated. The settings which were used in numerical experiments performed are shown in **Table1**. In the experimental results, the proposed algorithm is evaluated through a comparison with existing optimization ones.

Table1 Settings used in the experiments performed.

colony size(N)	*60*
employed bees(SN)	*50% of colony size*
onlookers(N - SN)	*50% of colony size*
Number of iterations	*1000*

The experimental results obtained by applying PSO algorithm, DE algorithm, ABC algorithm, Advanced ABC (AABC) algorithm and the proposed algorithm are arranged in **Tables 2, 3, 4** and **5**. In **Fig.2**, the convergence curves on Rastrigin function (D=100) are shown. From these experimental results, it can be confirmed that the proposed algorithm is substantially advantageous for large scale optimization problems.

4 CONCLUSION

In this paper, a novel optimization algorithm named the differential ABC algorithm has been proposed. In numerical experiments performed on some well-known representative benchmark functions, such as Rastrigin function and Schwefel function, the performances of the proposed algorithm were compared with those of the existing optimization ones. The experimental results indicate that the proposed algorithm is superior to the existing optimization ones for large scale optimization problems.

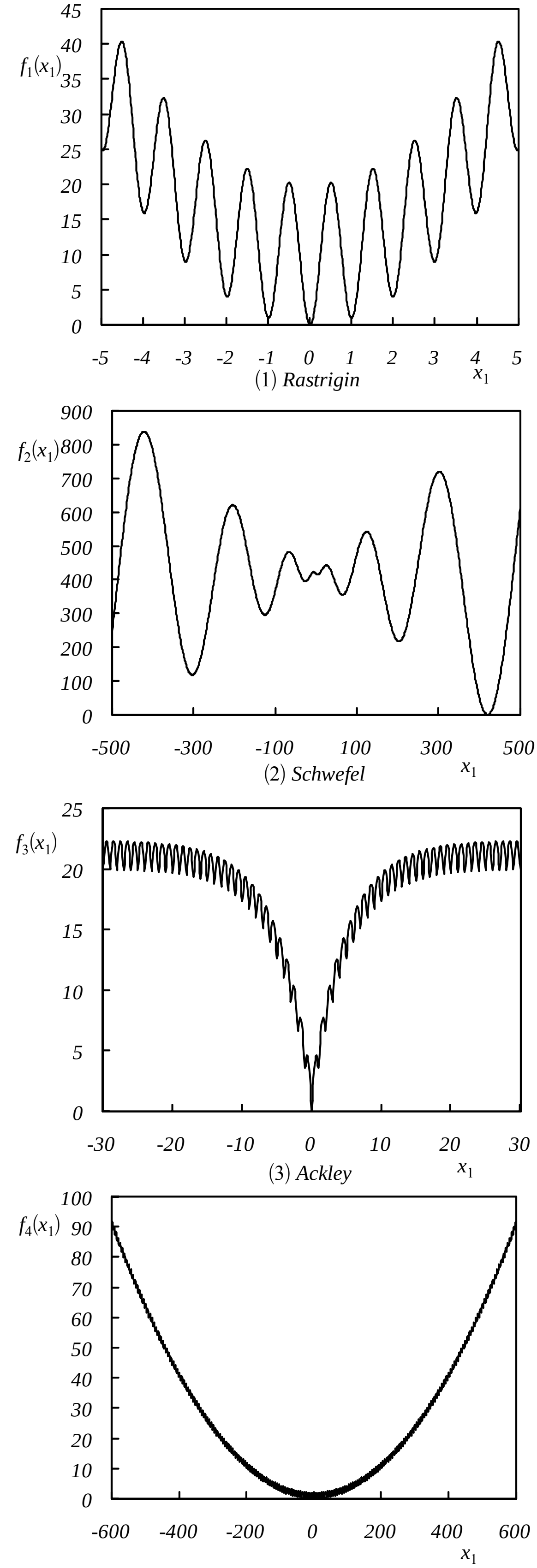

Fig.1. Landscapes of multimodal functions $(D = 1)$.

Table2. Experimental results (Rastrigin function).

Method	Dim.	Best	Ave.	Worst
PSO	50	1.05×10^{2}	1.81×10^{3}	3.14×10^{3}
	75	1.58×10^{2}	2.30×10^{3}	3.26×10^{3}
	100	2.72×10^{2}	3.71×10^{3}	6.10×10^{3}
	150	3.54×10^{2}	6.60×10^{3}	9.31×10^{3}
DE	50	7.62×10^{-2}	4.55×10^{0}	4.23×10^{1}
	75	1.53×10^{1}	8.77×10^{1}	1.81×10^{2}
	100	1.54×10^{2}	2.21×10^{2}	3.22×10^{2}
	150	2.98×10^{2}	5.59×10^{2}	7.38×10^{2}
ABC	50	4.51×10^{-4}	3.53×10^{0}	1.25×10^{1}
	75	4.93×10^{0}	2.42×10^{1}	9.82×10^{1}
	100	6.22×10^{1}	7.16×10^{1}	1.02×10^{2}
	150	1.28×10^{2}	2.77×10^{2}	3.22×10^{2}
AABC	50	2.08×10^{-10}	8.10×10^{-1}	2.99×10^{0}
	75	2.80×10^{0}	8.00×10^{0}	1.57×10^{1}
	100	1.21×10^{1}	1.39×10^{1}	2.92×10^{1}
	150	4.67×10^{1}	5.66×10^{1}	9.53×10^{1}
Proposal	50	3.23×10^{-11}	4.01×10^{-1}	1.99×10^{0}
	75	1.28×10^{-5}	2.33×10^{-1}	1.15×10^{0}
	100	9.96×10^{-1}	2.88×10^{0}	9.50×10^{0}
	150	3.66×10^{1}	5.31×10^{1}	6.30×10^{1}

Table3. Experimental results (Schwefel function).

Method	Dim.	Best	Ave.	Worst
PSO	50	5.39×10^{3}	9.78×10^{3}	1.25×10^{4}
	75	9.20×10^{3}	3.48×10^{4}	4.52×10^{4}
	100	1.92×10^{4}	6.92×10^{4}	9.88×10^{4}
	150	3.35×10^{4}	4.07×10^{5}	5.65×10^{5}
DE	50	1.14×10^{3}	2.24×10^{3}	4.62×10^{3}
	75	6.27×10^{3}	9.87×10^{3}	1.11×10^{4}
	100	1.24×10^{4}	3.45×10^{4}	4.10×10^{4}
	150	5.72×10^{4}	6.70×10^{4}	7.54×10^{4}
ABC	50	8.98×10^{2}	1.30×10^{3}	1.97×10^{3}
	75	2.73×10^{3}	6.01×10^{3}	6.56×10^{3}
	100	6.02×10^{3}	9.31×10^{3}	1.00×10^{4}
	150	9.60×10^{3}	1.62×10^{4}	3.20×10^{4}
AABC	50	1.18×10^{2}	2.03×10^{2}	1.18×10^{3}
	75	1.43×10^{3}	2.39×10^{3}	3.06×10^{3}
	100	2.54×10^{3}	3.03×10^{3}	5.26×10^{3}
	150	6.78×10^{3}	9.02×10^{3}	9.91×10^{3}
Proposal	50	0.00	6.31×10^{1}	2.30×10^{2}
	75	1.90×10^{-6}	7.42×10^{1}	3.44×10^{2}
	100	2.03×10^{-2}	1.48×10^{2}	4.27×10^{2}
	150	1.85×10^{3}	2.53×10^{3}	3.49×10^{3}

Table4. Experimental results (Ackley function).

Method	Dim.	Best	Ave.	Worst
PSO	50	1.82×10^{0}	2.11×10^{1}	2.65×10^{1}
	75	2.54×10^{0}	4.05×10^{1}	6.02×10^{1}
	100	4.84×10^{0}	2.40×10^{2}	4.30×10^{2}
	150	5.79×10^{0}	2.61×10^{2}	8.90×10^{2}
DE	50	9.89×10^{-4}	2.44×10^{-3}	3.56×10^{-3}
	75	2.66×10^{-1}	8.52×10^{-1}	$7.25\times10^{\cdot 0}$
	100	5.26×10^{0}	7.81×10^{0}	8.01×10^{0}
	150	8.59×10^{0}	9.15×10^{0}	9.45×10^{0}
ABC	50	4.74×10^{-4}	1.71×10^{-3}	2.24×10^{-2}
	75	1.30×10^{-1}	7.96×10^{-1}	1.58×10^{0}
	100	1.89×10^{0}	2.49×10^{0}	4.12×10^{0}
	150	4.57×10^{0}	5.75×10^{0}	6.68×10^{0}
AABC	50	3.30×10^{-9}	5.70×10^{-5}	2.21×10^{-3}
	75	1.85×10^{-5}	2.44×10^{-4}	1.55×10^{-3}
	100	1.51×10^{-3}	7.17×10^{-2}	3.74×10^{-1}
	150	1.48×10^{-1}	1.96×10^{-1}	2.46×10^{0}
Proposal	50	1.65×10^{-9}	1.15×10^{-7}	1.37×10^{-6}
	75	8.62×10^{-6}	4.94×10^{-5}	1.67×10^{-4}
	100	9.76×10^{-4}	7.67×10^{-3}	2.41×10^{-2}
	150	8.78×10^{-2}	1.91×10^{-1}	3.93×10^{-1}

Table5. Experimental results (Griewank function).

Method	Dim.	Best	Ave.	Worst
PSO	50	1.23×10^{0}	1.91×10^{1}	2.13×10^{1}
	75	3.89×10^{0}	4.93×10^{1}	9.83×10^{1}
	100	4.01×10^{0}	7.12×10^{1}	1.51×10^{2}
	150	5.99×10^{0}	7.05×10^{1}	1.87×10^{2}
DE	50	5.42×10^{-6}	9.80×10^{-3}	7.30×10^{-2}
	75	5.72×10^{-2}	1.47×10^{-1}	3.89×10^{-1}
	100	4.19×10^{-1}	6.24×10^{-1}	3.83×10^{0}
	150	2.02×10^{0}	3.08×10^{0}	5.31×10^{0}
ABC	50	8.50×10^{-7}	9.21×10^{-3}	3.73×10^{-2}
	75	4.26×10^{-4}	4.57×10^{-2}	1.28×10^{-1}
	100	8.17×10^{-3}	7.94×10^{-2}	5.34×10^{-1}
	150	1.79×10^{-2}	7.17×10^{-1}	9.97×10^{-1}
AABC	50	1.14×10^{-16}	9.13×10^{-5}	4.56×10^{-3}
	75	7.92×10^{-11}	3.61×10^{-3}	6.84×10^{-2}
	100	4.00×10^{-8}	5.49×10^{-3}	3.76×10^{-2}
	150	1.74×10^{-4}	1.68×10^{-2}	2.56×10^{-1}
Proposal	50	1.12×10^{-16}	2.88×10^{-10}	1.75×10^{-9}
	75	5.50×10^{-11}	7.75×10^{-8}	4.71×10^{-7}
	100	1.63×10^{-8}	5.24×10^{-4}	8.84×10^{-3}
	150	1.07×10^{-4}	8.88×10^{-3}	6.63×10^{-2}

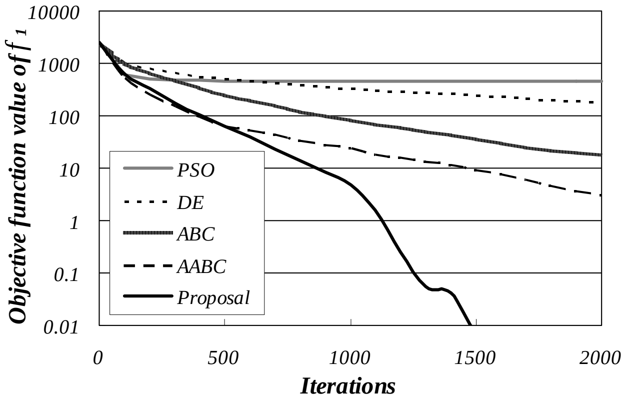

Fig.2. Convergence curves.
[Rastrigin function (D=100)]

REFERENCES

[1] J. Kennedy and R.C. Eberhart, Particle swarm optimization, *Proc. of the IEEE International Conference on Neural Networks*, pp.1942-1948, 1995.

[2] D. Karaboga and B. Basturk, A powerful and efficient algorithm for numerical function optimization: artificial bee colony (ABC) algorithm, *J. Global Optimization*, Vol.39, pp.459-471, 2007.

[3] R. Gocho, A. Utani and H. Yamamoto, Improved artificial bee colony algorithm for large-scale optimization problems, *Proc. of the 16th International Symposium on Artificial Life and Robotics*, pp.605-608, 2011.

[4] R. Storn and K. Price, Differential evolution–A simple and efficient heuristic for global optimization over continuous space, *J. Global Optimization*, Vol.11, pp.341-359, 1997.

The Seventeenth International Symposium on Artificial Life and Robotics 2012 (AROB 17th '12),
B-Con Plaza, Beppu, Oita, Japan, January 19-21, 2012

A generation alternation model for user-system cooperative evolutionary computation

Satoshi Ono[1], Kiyomasa Sakimoto[1], and Shigeru Nakayama[1]

[1] Kagoshima University, Kagoshima, Kagoshima 890-0065, Japan
(Tel: 81-99-285-8453, Fax: 81-99-285-8464)
(ono@ibe.kagoshima-u.ac.jp)

Abstract: User-System Cooperative Evolution (CEUS) is an Evolutionary Computation (EC) method to optimize quantitative and qualitative criteria. In previous work of CEUS, the whole population update is performed at every generation, and the user hardly observes all individuals. This paper proposes a generation alternation model designed for CEUS. The proposed model allows a user to find widely varied individuals in addition to the best individuals by replacing just one individual in a population for each generation, and consequently contributes user's idea generation by enhancing divergent thinking.

Keywords:
user-system cooperative evolution, generation alternation model, interactive evolutionary computation, genetic algorithm

1 INTRODUCTION

Interactive Evolutionary Computation (IEC)[1] faces a dilemma that general Evolutionary Computation (EC) algorithms require much trial and error but IEC can not use a large population and can not iterate so many generations due to user fatigue. To resolve this dilemma, the authors have proposed a method that is a fusion model of IEC and Non-Interactive EC (nIEC)[2]. In this paper we call the above method Cooperative Evolution by User and System (CEUS).

CEUS aims to incorporate user heuristics and/or preference into EC search dynamically. To achieve this, CEUS comprises following two essential functions.

1. CEUS optimizes both qualitative and quantitative objective functions simultaneously:
   CEUS can be regarded as IEC with domain knowledge that can be used to evaluate solutions, or as EC with a qualitative objective function. Designing a fitness function is crucial to find good solutions in real-world problems. But ideal function may not be sufficient to solve such real world problems, and ambiguous complementary subfunctions may be necessary to obtain practical quasi-optimal solutions. Incorporating ambiguous criteria such as user preference particularly makes it difficult to design the fitness function. Various real world problems can therefore be modeled as the problem involving explicit and ambiguous criteria.

2. CEUS has a mechanism to adopt user heuristics and preferences and to estimate user preferences from past user operation:
   To promote the effective use of EC, it is crucial to use large population size and to conduct a search long enough. But excessive user operations must be avoided. CEUS therefore allows a user to dynamically switch the role of EC at any time during the search. For instance, the user lets the system search for a solution like nIEC, and observes the search progress. Whenever the user finds an interesting individual, the user can stop the search, evaluate it, and add a genetic operation to it.

In previous work of CEUS, the whole population update is performed at every generation, and the user hardly observes all individuals. Only the best individuals can be seen by the user because it cannot be updated so frequently except the earlier stage of the search. Varied individuals with a moderate fitness value can be hardly found by the user because such individuals change and are replaced by new ones immediately. Consequently, although CEUS shows good performance to find a solution which can be expected by the user, CEUS was not effective to help the user find unpredictable, varied solutions.

This paper proposes a generation alternation model designed for CEUS. The proposed generation alternation model allows a user to find widely varied individuals in addition to the best individuals by replacing just one individual in a population for each generation. Consequently, the proposed model contributes user's idea generation by enhancing divergent thinking.

Experimental study showed that the proposed generation alternation model helped a user find various solutions not only the best individuals in the population.

2 USER-SYSTEM COOPERATIVE EC

Fig. 1 shows the process flow of CEUS. A typical CEUS search style is that the system searches for solutions by itself at the early stage of the search, and after the system produces some promising individuals the user chooses adequate one

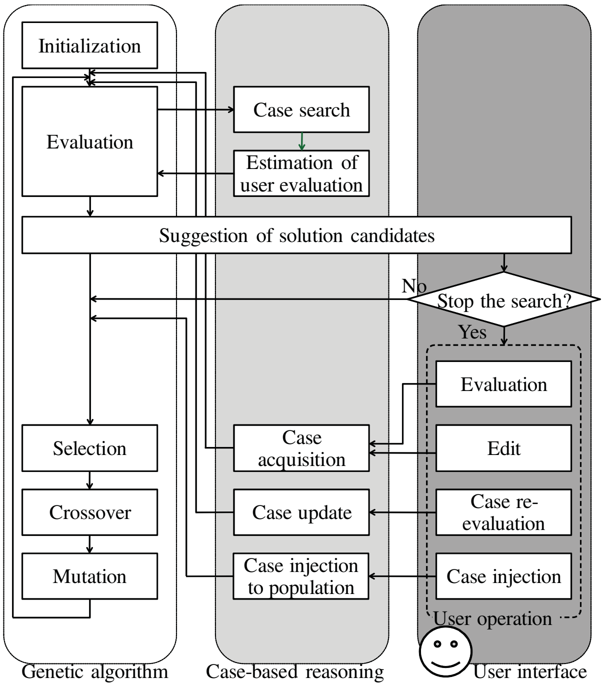

Fig. 1. Process flow of CEUS.

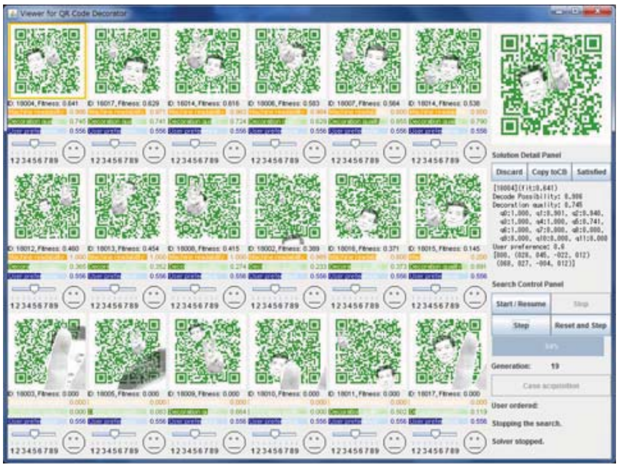

Fig. 2. User interface.

or directly revise them in order to enhance search intensification. nIEC search improves the population based on the chosen or revised individuals.

In CEUS, the user does not have to evaluate individuals at every generation. Unless the user stops the search, the system keeps searching for a solution. Although the user is allowed to concentrate on observing individuals reproduced by the system, it is hard to watch all individuals because the system grinds out individuals. CEUS proposed in [2] adopt simple GA (SGA), and most of individuals are replaced by new offsprings except top elites at every generation.

Therefore, to observe changes on the top elites and a few good individuals is the lowest the user can do. The user can not afford to watch other various individuals, and the user often passes over unpredictable and moderately good individuals. It is important to observe such individuals so that CEUS enhances the user's divergent thinking.

3 PROPOSED GENRATION ALTERNATION MODEL

The generation alternation model for CEUS proposed in this paper aims to increase the chance to discover unpredictable, good solutions. The proposed model is based on the following ideas:

1. **Minimize the gap between generations.**
   Just like Minimal Generation Gap (MGG)[3], one of the generation alternation models to prevent premature convergence, the proposed generation alternation model minimizes the gap between generations. The proposed model replaces only one individual at every generation, whereas MGG replaces two.

2. **Design some rules to choose a parent to be removed and an offspring to be added.** The proposed model generates as many offsprings as population size, and replaces one of the parents by one of the offspring. The parent and the offspring are chosen by rules in order to adjust the balance between search exploitation and exploration based on user preference.

Table 1 shows the generation alternation rules. Rules which have the smaller rule id have the higher priority. R_6 and R_7 are applied by random if none of R_1 to R_5 can be applied.

To esteem user operation and reflect it to the search, R_2 and R_3 removes individuals that are ranked as the minimum priority. R_4 enhances the local search based on user preference.

Although the proposed model can keep diversity by changing only one individual at every generation, bad individuals are hardly removed from the population. R_5, R_6 and R_7 are designed to shake out those individuals.

4 EVALUATION

To verify the effectiveness of the proposed generation alternation model in CEUS, the proposed method is compared with the previous work for CEUS[2] and MGG based method. A two-dimensional barcode decoration problem is used [2]. The problem has three objective functions: machine readability R, decoration quality Q, and user preference P. The readability R and decoration quality Q are quantitative criteria, and fitness F can be calculated by the following

Table 1. Generation alternation rules.

ID	Antecedent	Consequent	
		Deleted	Added
R_1	The parent P_ρ having higher density than T_ρ exists.	P_ρ	Farthest offspring from P_ρ
R_2	Both parent P_0 whose preference was set to 0 and parent P_1 whose preference was set to 1 exist.	P_0	Nearest offspring to P_1
R_3	P_0 exits.	P_0	Farthest offspring from P_0
R_4	Parent P_1, which are evaluated in the current generation, exists.	Parent with the worst preference	Nearest offsping to P_1.
R_5	Fitness of the best offspring O_{best} is greater than the fitness of the best parent P_{best}.	By roulette selection based on inverse fitness value	O_{best}
R_6	—	The worst parent P_{worst}	Offspring O_δ with the maximum improvement from the previous generation
R_7	—	P_{worst}	The nearest offspring to P_{worst}

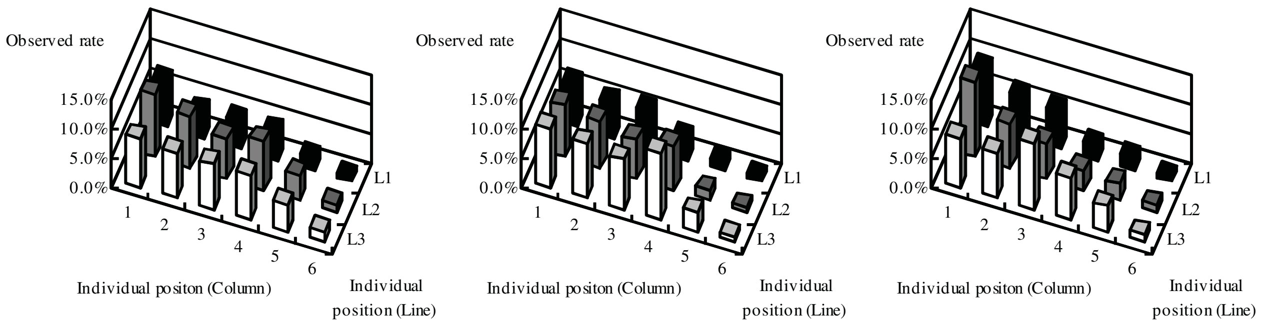

(a) Previous method (Update all) (b) MGG (c) Proposed method (Update one)

Fig. 3. Eye-tracking results.

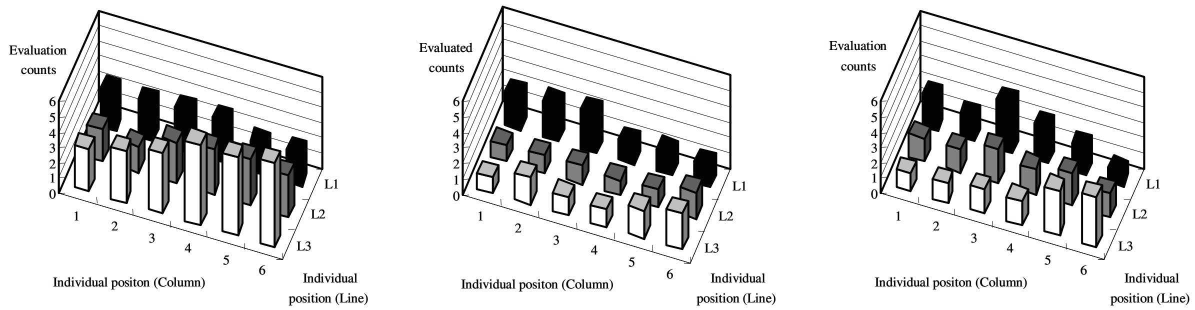

(a) Previous method (Update all) (b) MGG (c) Proposed method (Update one)

Fig. 4. Number of evaluated individuals for each individual position.

equation involving weights $w^{(p)}$, $w^{(q)}$, and $w^{(r)}$.

$$F = R^{w^{(r)}} \times (1 - w^{(p)}) \cdot Q^{w^{(q)}} \times w^{(p)} \cdot P \qquad (1)$$

A system used in this experiment that can show 18 individuals with three lines and six columns as shown in Fig. 2. In this system individuals are sorted by the fitness and placed from top-left to bottom-right.

In this experiment, we tracked user eyes to clarify how the user can see widely varied individuals. Ten examinees tested the above three methods in random order, and answered a questionnaire.

Fig. 3 shows the eye tracking results, and Fig. 4 shows the averaged number of evaluated individuals by the examinees for each individual position. Fig. 3 reveals that individuals in right side columns were hardly watched, and that there was not so much difference between lines in all methods.

According to the questionnaire result, some examinees felt that the proposed model helped to find unpredictable good solutions. Fig. 4 shows that MGG based method and the proposed method urged the examinees to evaluate individuals placed at the second and third lines in addition to elite individuals placed at top-left. Also in the previous method, individuals in the third position seemed evaluated frequently. But this is because the examinees tried to remove bad individuals with much evaluation cost.

There was no significant difference on satisfaction with derived solutions according to the questionnaire result. The fitness of the previous method indicated by "Update all" in Fig. 5 showed the best, and MGG and the proposed method indicated by "Update one" showed worse fitness values. In particular, there seems differences in preference shown in Fig. 5(b), but these results show just transitions of the best solutions and do not imply the satisfaction of the final solutions. Because readability and quality score values of the previous and proposed methods were almost the same, the difference on preference implies that the proposed method tried to reproduce diversified individuals.

5 CONCLUSION

This paper proposes a generation alternation model for CEUS aiming to discover moderately good and unpredictable individuals. Experimental results have shown that MGG and the proposed model helped uses to find such individuals, and that simple eye-tracking was not sufficient to clarify the effectiveness of generation alternation models.

In future we plan to design a simpler rule set, and to analyze the effectiveness of generation alternation models in CEUS.

ACKNOWLEDGEMENT

This work was supported by Grant-in-Aid for Scientific Research (23700272) from the Ministry of Education, Culture, Sports, Science and Technology, Japan.

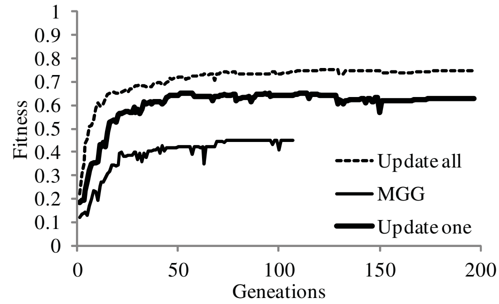

(a) Fitness transitions

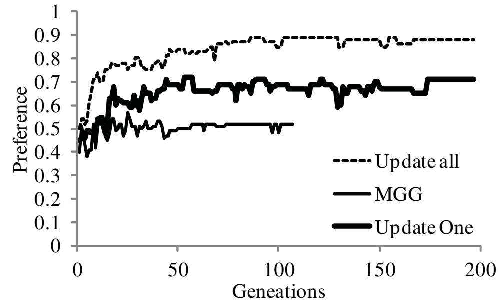

(b) Preference transitions

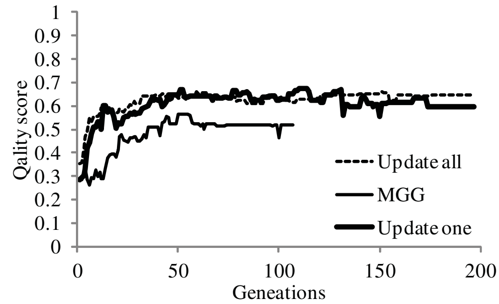

(c) Quality score transitions

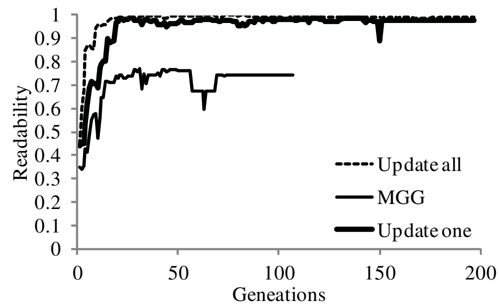

(d) Readability transitions

Fig. 5. Fitness transitions of the best individuals.

REFERENCES

[1] H. Takagi, "Interactive evolutionary computation – fusion of the capabilities of EC optimization and human evaluation," in *Proceedings of the IEEE*, vol. 89, 2001, pp. 1275–1296.

[2] S. Ono and S. Nakayama, "Fusion of interactive and non-interactive evolutionary computation for two-dimensional barcode decoration," in *Proceedings of the 2010 IEEE World Congress on Computational Intelligence (WCCI 2010)*, 2010, pp. 2570–2577.

[3] H. Satoh, M. Yamamura, and S. Kobayashi, "Minimal generation gap model for GAs considering both exploration and exploitation," in *Proceedings of 4th International Conference on Soft Computing*, 1996, pp. 494–497.

The Seventeenth International Symposium on Artificial Life and Robotics 2012 (AROB 17th '12),
B-Con Plaza, Beppu, Oita, Japan, January 19-21, 2012

A neutral evolutionary path-planner

Eivind Samuelsen, Kyrre Harald Glette, and Kazi Shah Nawaz Ripon

Department of Informatics, University of Oslo, Norway
{eivinsam,kyrrehg,ksripon}@ifi.uio.no

Abstract: This paper explores methods for path-planning using evolutionary algorithms. Inspired by research on neutral mutations in evolutionary algorithms, we propose an algorithm based on the idea of introducing redundancy in the solutions, adding explicit neutrality to the evolutionary system. The algorithm introduce explicit neutrality by evolving roadmaps rather than single paths. Since some of the mutation and crossover operators used in conventional evolutionary path-planners are not well suited for this representation, appropriate evolutionary operators will also be explored. The performance of this algorithm on shortest distance path planning problems is compared to a known good genetic algorithm in three different static environments.

Keywords: genetic algorithm, neutrality, path-planning, roadmap

1 INTRODUCTION

Path planning is the problem of finding an optimal obstacle-free path through an environment. In a shortest distance problem, the optimal path is the one going from a start point to a goal point in the shortest possible distance travelled. Many methods have been proposed for solving this optimization problem. They all have certain trade-offs between planning time, robustness, requirements on environment representation and so on. An overview of the most common no-evolutionary methods can be found in [1].

Probabilistic roadmaps (PRMs) are one of the more common methods in path planning. A PRM samples random points in order to simplify the problem and scale well with environment dimensionality. However, it will seldom find optimal solutions unless the amount of samples taken is made impractically large. They also have problems with finding solutions at all in narrow passages and maze-like environments, a problem that to some extent can be remedied by sampling adaptively [2].

Several path-planning methods using evolutionary algorithms (EAs) have also been proposed. A straightforward approach to the shortest distance problem is presented in [3]. Once a good set of solutions has been found by an EA path-planner, it can easily adapt to changes in the environment simply by running the a few more iterations of the algorithm on the updated environment data. However, finding a good set of initial solutions from a set of random solutions can take some time. A remedy for this is to initialize the population with results from a PRM planner has been proposed in [4].

There has recently been some interest in EAs using neutrality and neutral mutations. Neutrality is having redundancy or extra information in the chromosomes so that they can change in ways that do not affect fitness. It is claimed that this can be greatly beneficial to EAs, making them both converge faster to the optimum and also escape local optima more easily. This is inspired by similar theories in biological evolution and some experimental findings, though many of these findings are considered inconclusive by others. A summary of this research can be found in [5].

Although the effects of neutrality in EAs in general are still inconclusive, it is an interesting avenue to explore in solving path-planning problems. One such method is proposed in this paper. Instead of trying to evolve good paths directly, this method tries to evolve good roadmaps for finding paths. We will rank the roadmaps only by the best path found in them by a graph traversal algorithm. Since this ranking does not consider the points in the roadmap that are not part of the resulting path it has explicit neutrality.

2 PROPOSED METHOD

Starting out with a set of PRMs as initial population, our algorithm evolves these roadmaps over many generations. We call this method a roadmap evolver. Roadmaps well suited to find a good path are more likely to survive to the next generation. The nodes that are not on a roadmap's best path can mutate without affecting the roadmap's fitness. This can enable the population to escape local optima more easily.

2.1 Representation and evaluation function

Each chromosome is a set of floating-point vectors that together with the start point and the goal constitute the nodes, or milestones, of a roadmap. If one can draw a straight line between two nodes without intersecting any obstacle, they are connected. A graph traversal algorithm is run to evaluate the chromosomes, finding the best path through it from the start to the goal node.

When an optimal path through the roadmap has been found, the fitness of that path is taken as the fitness of the roadmap. In the experiments done in this paper the path's are optimized for the shortest path. So the fitness of the path is the path's curve length, and the graph traversal is done by A*.

Since not all nodes are necessarily visited during the traversal, the connectivity of the roadmap graph is done dynamically during the graph traversal in order to reduce the number of connectivity checks needed. Still, in general, $O(n^2)$ connectivity checks will be needed in the traversal, where n is the number of nodes in the roadmap.

2.2 Evolutionary operators

The algorithm proposed has a single crossover operator and three mutation operators: nudge, insert and reduce size.

In order to emphasize average-sized children we use a crossover operator similar to uniform crossover: First each point in parent A is given to either child A or child B with equal probability. Then the points in parent B are distributed in the same way. The size of each child is the sum of n coin flips, so it has a binominal distribution. The chromosomes are sets of points and thus inherently unordered. Therefore, there is no need to try to maintain any ordering.

The nudge mutation goes through all the points in a chromosome. Each point has a probability P_{nudge} of being displaced a small distance in some random direction, but only if that displacement does not move the point into or over an obstacle: A normal-distributed vector is added to the point if the straight line between the original point and the point plus the random vector is obstacle-free. If this fails, it is reattempted up to 6 times with a new random vector with increasingly narrow normal distribution. If all attempts fail that point is left unchanged.

The insert mutation tries to add a single point to an individual. A candidate point is generated randomly with uniform probability within the bounds of the environment. If the candidate is obstructed, a short random walk is performed until an unobstructed point is found, or a maximum of three steps are taken. If the candidate is still obstructed, we try it up to 5 more times with different random start points. If no feasible candidate has been found, the operator leaves the individual unchanged.

The reduce size mutation goes through all the points in a chromosome and removes that point with a probability P_{remove} . Thus, on average $n \times P_{\text{remove}}$ points are removed from the set, where n is the original size of the set.

2.3 Initial population and evolutionary process

The population is initialized with N PRMs with an average of N_g non-obstructed nodes in uniform distribution over the environment. If none of the roadmaps give a feasible path from start to a goal then N_g is increased by a constant and N new PRMs are created. This is repeated until at least one initial feasible solution is found.

Each generation is generated as follows: N new individuals are created by crossover. The parents for each crossover operation are selected by simple tournament selection with a tournament size of 2. This is repeated until two different parents have been selected.

All the new individuals are then subjected to mutation. The nudge mutation is performed once, then the insert mutation is performed once with probability P_{insert} . Finally the reduce size mutation is performed. After that, new population is merged with the old. To reduce the population size back to normal, N one-round tournaments are held, and the losing individuals are removed.

Each new individual has P_{insert} points added on average, while $n \times P_{\text{remove}}$ points are removed. This helps the average chromosome size to stay relatively stable, while allowing for variations in order to adapt to different environments.

Table 1: Average run-time, including initialization

Environment	Reference path-planner (per iteration)	Roadmap evolver (per iteration)
"Rocks"	19.0s (10.6ms)	78.3s (174.0ms)
"House"	49.0s (27.2ms)	163.6s (363.6ms)
"Spirals"	25.7s (14.3ms)	131.0s (291.1ms)

3 RESULTS AND DISCUSSION

The algorithm has been tested against a reference path-planner in different environments. The reference algorithm used is similar to the one described in [4], differing mainly in the parameters and selection operators used. It is run with a population size of 40 and a tournament-based selection. It should be noted that the parameters and implementation of the reference algorithm are not fine-tuned or optimized, and can therefore only serve as a general guideline to the performance of a reasonably robust evolutionary path-planner.

The roadmap evolver was run with a population size of 35 and an average initial number of nodes per chromosome of 35 or more. Mutation parameters were set to $P_{\text{nudge}} = 0.2$, $P_{\text{insert}} = 0.4$ and $P_{\text{remove}} = 0.05$.

Three different environments, shown in Fig.1 are tested. Each environment has different characteristics: The "rocky" environment consists of a number of scattered convex shapes, and has a large number of intersecting local optima. The second environment imitates the interior of a single-floor home, and has wall- and corridor-like obstacles, leading to a few, far-apart local optima. The third environment contains two spiral structures and has only one hard-to-find optimum.

The result of 100 runs of each algorithm in each environment is shown in Fig.2. The reference algorithm is run for 1800 iterations, while the roadmap evolver is run for 450 iterations. The large difference in number of iterations is due to differences in run-time per iteration and to differences in how

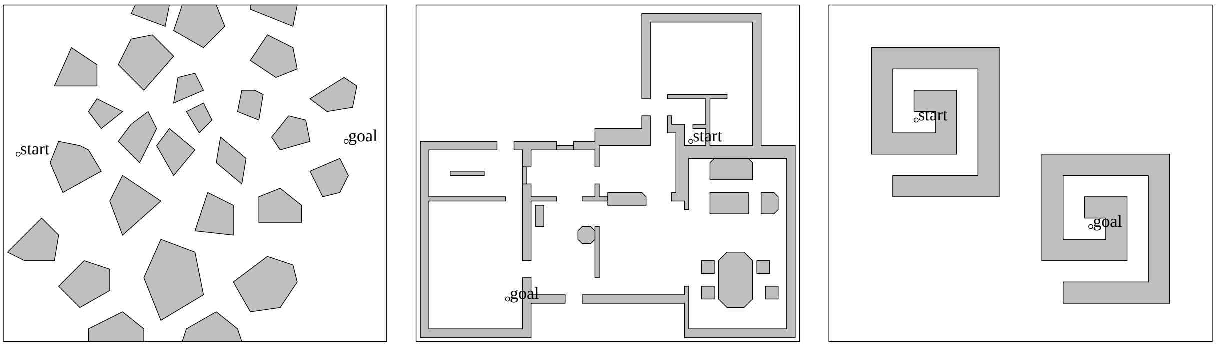

(a) The "rocks" environment (b) The "house" environment (c) The "spirals" environment

Figure 1: The different environments tested

quickly the algorithms converge. The average run-times are shown in Table 1. The average iteration time of the roadmap evolver is more than ten times that of the reference algorithm.

The reference algorithm shows very good performance in the "house" environment, with a good start and little variation. In "rocks" it converges quickly, but seems to get stuck in local optima, because the variation between runs stays high. In the last environment it closes in on the optimum with low variation, but at a very slow pace.

The roadmap evolver has good performance in the "rocks" environment, converging quickly towards a near-optimal solution quickly and with little variation between runs. In the other two environments it closes in on the optimal solution at a good average pace, but the pace is very uneven, with large variations in fitness between runs for many generations.

Compared to the reference algorithm in terms of generations only, the roadmap evolver performs as good or better in both "rocks" and "spirals" environments, but needs more generations to reliably produce near-optimal solutions in the "house" environment. In "rocks" it seems to avoid local optima better, while in "house" it shows signs of jumping out of local optima it have been temporarily stuck in. Note that both algorithms fail to ever find the globally optimal path in the "rocks" environment.

The good performance of the reference algorithm on "house" might be explained by the way the populations are initialized - the reference algorithm guarantees N different feasible solutions, while the roadmap evolver only guarantees at least one.

4 CONCLUSION

In this paper, we proposed a path-planning method using a genetic algorithm that has explicit neutrality. The algorithm was compared to an existing genetic path-planning algorithm that has no neutrality. The proposed algorithm closes in on the optimal solution in comparatively few generations, and shows signs of both avoidance and escape of local minima in a small selection of tested environments. However, run-time performance is poor, most likely because of comparatively high complexity in the fitness function.

The algorithm did display properties expected of a neutral evolutionary system. For future work it would be of interest to examine whether these properties are displayed in other situations too, such as dynamic or partially unknown environments, or path-planning problems with multiple objectives. Initializing the population in the same way as the reference algorithm might increase performance in early generations. Another possibility is developing other different and possibly more efficient neutral path-planning EAs and examine if the same properties appear in them.

REFERENCES

[1] S. LaValle, *Planning algorithms*. Cambridge Univ Pr, 2006.

[2] V. Boor, M. Overmars, and A. van der Stappen, "The gaussian sampling strategy for probabilistic roadmap planners," in *Robotics and Automation, 1999. Proceedings. 1999 IEEE International Conference on*, vol. 2, pp. 1018 –1023 vol.2, 1999.

[3] H. Lin, J. Xiao, and Z. Michalewicz, "Evolutionary algorithm for path planning in mobile robot environment," in *Evolutionary Computation, 1994. IEEE World Congress on Computational Intelligence., Proceedings of the First IEEE Conference on*, pp. 211–216, IEEE, 1994.

[4] M. Naderan-Tahan and M. Manzuri-Shalmani, "Efficient and safe path planning for a mobile robot using genetic algorithm," in *Evolutionary Computation, 2009. CEC '09. IEEE Congress on*, pp. 2091 –2097, may 2009.

[5] E. Galván-López, R. Poli, A. Kattan, M. O'Neill, and A. Brabazon, "Neutrality in evolutionary algorithms... what do we know?," *Evolving Systems*, vol. 2, pp. 145–163, 2011. 10.1007/s12530-011-9030-5.

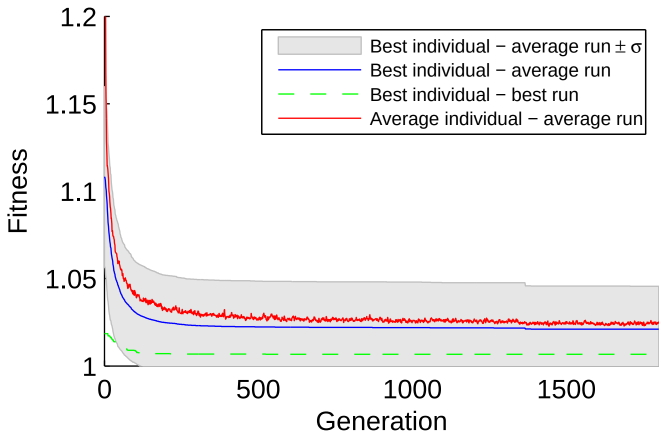

(a) "Rocks" environment - reference path-planner

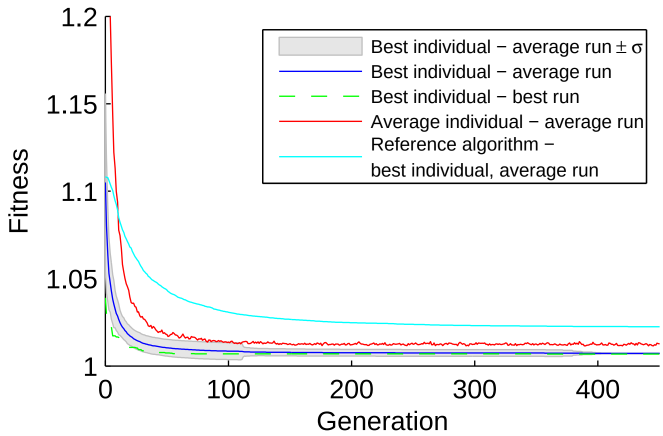

(b) "Rocks" environment - roadmap evolver

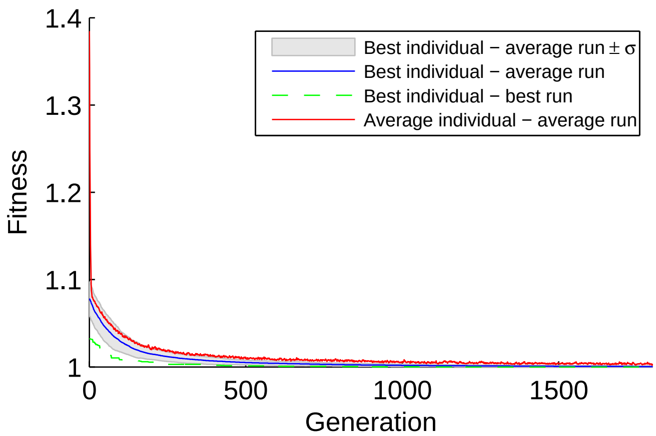

(c) "House" environment - reference path-planner

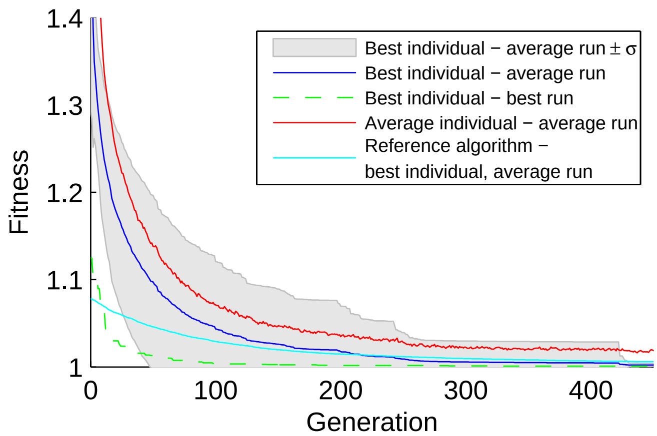

(d) "House" environment - roadmap evolver

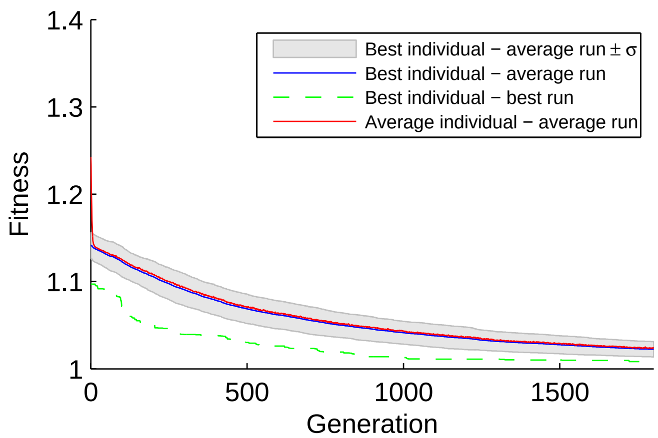

(e) "Spirals" environment - reference path-planner

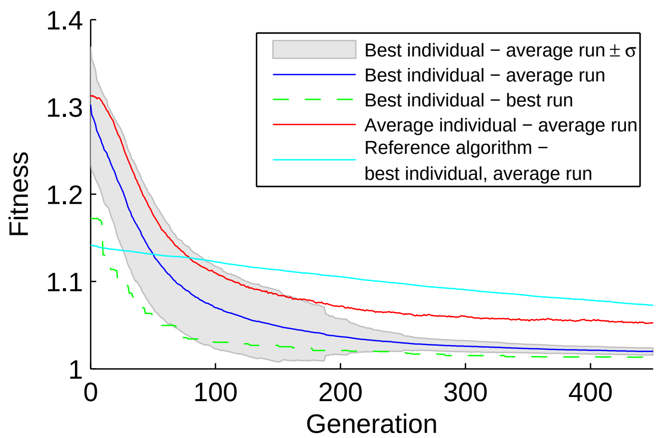

(f) "Spirals" environment - roadmap evolver

Figure 2: Fitness development for each algorithm in each environment. All fitness values are relative to the optimal solution as found by the vismap algorithm. The blue line is the average best fitness for each run. The light grey area around it signifies one standard deviation from that average. The red line is the average fitness of all feasible solutions in the current generation, averaged over all runs. The cyan line in the roadmap evolver plots shows the average best fitness for the reference algorithm for the same iterations.

The Seventeenth International Symposium on Artificial Life and Robotics 2012 (AROB 17th '12),
B-Con Plaza, Beppu, Oita, Japan, January 19-21, 2012

Manipulating a multi-DOF robot manipulator for tasks in home-like environments

Mu-Cheng Hsieh, Po-Ying Tseng, Ming-Shiun Jan, and Kuu-young Young[1]

Department of Electrical Engineering
National Chiao-Tung University, Hsinchu, Taiwan
[1](Tel: 886-3-5712121 ext. 54366, Fax: 886-3-5715998)
[1](kyoung@mail.nctu.edu.tw)

Abstract: As more robots are expected to enter the families to provide assistance soon, many challenging problems shall emerge, when facing the uncertain and varying environments, rather than the organized environments in factories. To date, robots still demand human's assistance when working in home-like environments. To enhance their usefulness, one issue of much interest is how we can effectively operate them for task execution. If not for detailed analysis and program coding, one appealing alternate is to provide a kind of manipulative system for the user to manipulate the robot naturally and efficiently. That motivates us to develop a dextrous manipulation system for multi-DOF robot manipulators based on using the 6-DOF force-reflection joystick. To demonstrate its effectiveness, the developed manipulation system is utilized to govern the robot manipulator for the tasks of water pouring and screw fastening.

Keywords: Manipulation system, Haptic device, Virtual tool, Home-like environment.

1 INTRODUCTION

In the near future, more robots may enter the families to provide assistance. As expected, many challenging problems shall emerge in dealing with the uncertain and varying environments, rather than the organized environments in factories [4]. Up to now, robots still demand human's assistance when working in home-like environments. To enhance their usefulness, one issue of much interest is how we can effectively operate them for task execution. If we are not going to take the load of detailed task analysis and program coding, one alternate is to let the user manipulate the robot via a proper means directly. In other words, an effective manipulation system should be provided for the user to achieve natural and efficient robot governing. As traditional manipulative devices, like teach box, mouse, keyboard, and joystick, may not serve the purpose, we propose developing a dextrous manipulation system for multi-DOF robot manipulators based on using the haptic device.

As the manipulative device, we adopt the 6-DOF force-reflection joystick for the proposed manipulation system, which supports mutual interaction, involves both position and force information, and has the merit in its simplicity and generality. In this manipulation system, we design virtual motion constraints, which are based on the concept of virtual mechanisms and virtual fixtures previously proposed [1,3,7], to confine the movement of the manipulative device in the 3D working space, according to the status of the robot manipulator and task progress. In other words, the virtual motion constraints are designed (i) to help the user recognize the spatial deviation between her/his desired position and the end-effector via a haptic clue, and (ii) to guide her/his movement according to task requirements via some virtual tools. For instance, a virtual ruler can be used to help the user to move the robot along a straight line fast and precisely. The proposed manipulation system thus provides two kinds of virtual motion constraints to assist the user in an interactive and real-time manner. First, a virtual spring is installed between the user and robot manipulator to enhance a virtual linkage between them. In addition, a 3D graphical environment is also implemented to foster the virtual linkage in a visual way. Second, four basic types of virtual tools (point, line, plane, and fixed-rotating-axis) are furnished according to the user's demand on site, but not in a predefined environment or predicted way [2,5]. For demonstration, the manipulation system is utilized to govern the robot manipulator to conduct two kinds of tasks: pour the water between tubes and fasten the screw, both of which demand delicate maneuver. Satisfactory experimental results verify the effectiveness of the proposed manipulation system.

2 PROPOSED MANIPULATION SYSTEM

Fig. 1 illustrates the two major goals of the proposed manipulation system for a multi-DOF manipulator: (i) letting the user feel like she/he is manipulating the robot on site directly when teleoperating the task, and (ii) providing a set of virtual tools that guide the hand movement of the user. Its system block diagram is shown in Fig. 1b, which consists of mainly a 6-DOF haptic device, a virtual linkage, and virtual tools. Via the haptic device, the user sends in the commands, which may be refined by the virtual tools, to govern

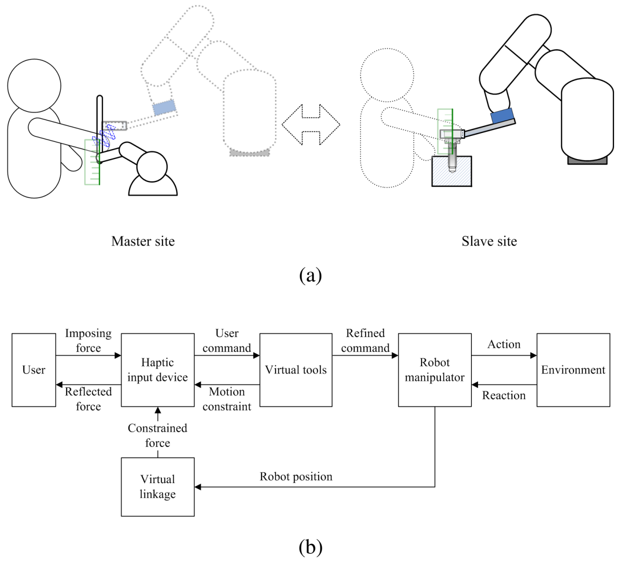

Fig. 1: Proposed manipulation system for a multi-DOF robot manipulator: (a) conceptual diagram and (b) system block diagram.

Fig. 2: The user applies the proposed system to manipulate the real robot manipulator via a haptic input device and 3D graphical environment.

the robot manipulator in the slave site to perform the task in a home-like environment. As the feedback, the robot position, via the virtual linkage and then the haptic device, becomes the reflected force, which is sent back to the user for following manipulation. Meanwhile, the system utilizes the virtual tools to furnish motion constraints for guidance. Based on the descriptions above, the success of the proposed manipulation system mainly depends on proper design of the virtual linkage and virtual tools. The former establishes the human-robot connection for natural and effective manipulation, and the latter provides proper assisting motion constraints along with the progress of task execution.

With the proposed virtual linkage, we intend to create better interaction between the user and robot manipulator, so that the user can perform the manipulation naturally and effectively. Fig. 2 shows a scene in which the user applies the proposed manipulation system to manipulate the real robot manipulator via a haptic input device and 3D graphical environment, which renders the user the linkage status between the master and slave devices in visual way. For the haptic counterpart, we intend to let the user feel like her/his hand holding on the end-effector of the robot manipulator directly. Although direct reflection of the environmental force to the master may yield the user a more realistic feeling, the induced master motion may make system unstable [6]. Therefore, the proposed linkage haptic cue is used to hint the position deviation between the robot manipulator and the desired command, reminding the user that the robot manipulator cannot catch up with the command, in an intuitive and efficient way compared with that provided by the visual information.

To achieve this, we use a simple spring model to generate the constrained force via the force-reflection joystick, serving as a virtual spring that bonds the joystick with the robot manipulator. This constrained force $\mathbf{f}_s(n)$ is formulated as

$$\mathbf{f}_s(n) = K_s(\mathbf{p}_s(n) - \mathbf{p}_u(n)), \tag{1}$$

where K_s stands for the stiffness of the virtual spring, and $\mathbf{p}_s(n)$ and $\mathbf{p}_u(n)$ the position of the end-effector and force-reflection joystick, respectively, both with respect to the coordinate system of the master.

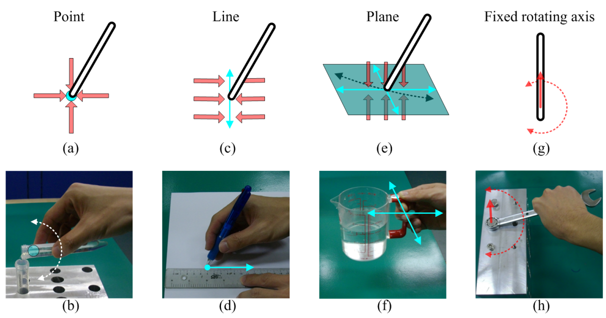

Fig. 3: Proposed virtual tools and their possible applications: (a)-(b) point, (c)-(d) line, (e)-(f) plane, and (g)-(h) fixed-rotating-axis.

To tackle common operations in home-like environments, we design three types of position tools: point, line, and plane, and one type of orientation tool: fixed-rotating-axis. Fig. 3 shows these four virtual tools and their possible applications. The position tools can let the haptic device only move on a point, a line, or a plane, for instance, a point tool for the water pouring task. The orientation tool can let the haptic device maintain a fixed rotating axis for rotation, such as for the screw fastening task. Details of their implementation will be in our following paper.

3 SYSTEM IMPLEMENTATION

As shown in Fig. 2, the proposed manipulation system consists of a 6-DOF Mitsubishi RV-2A robot manipulator, with a mounted end-effector, such as a box-end wrench or gripper, a SensAble Phantom Omni 6-DOF joystick with 3-DOF force feedback, and a personal computer (Intel Core Duo E8400 CPU and 2 GB RAM) for constructing the 3D graphical environment for rendering the virtual robot and virtual tools, in addition to the computation of the haptic feedbacks for both the virtual linkage and virtual tools. To satisfy the requirements from various devices, we use three threads to deal with the haptic data (about 1 kHz), visual data (about 60 Hz), and manipulator control data (about 141 Hz). To match up the workspaces between the haptic device and robot manipulator, the length ratio between these two coordinates is set to be 1:2.

4 EXPERIMENTS

To demonstrate its effectiveness, the proposed manipulation system was utilized to govern the robot manipulator to conduct two kinds of tasks: pour the water between tubes and fasten the screw, both of which demand delicate maneuver. For each experiment, there were two operation modes: with the help of both virtual tools and virtual linkage (mode V) and without those (mode NV). To alleviate the learning effect, eight subjects were first invited to conduct the first experiment, and then another seven subjects for the second one. Moreover, the order of these two operation modes was randomly arranged for the subject. Each subject was asked to achieve two successful trials for each mode. Most of them had no experience in manipulating the robot manipulator using the haptic input device before. Thus, before conducting the trial for each mode, the subject practiced several times to be familiar with the manipulation system.

Fig. 4 shows the setup of the first experiment, in which the robot manipulator was governed to grasp the tube vertically up, which was initially put in the hole on the right rack, and then horizontally moved it to pour the water inside into the tube on the left, and finally put it back to the original location in a reversal sequence. A successful trial should transfer at least 90% of the water. In responding to the operations, mode V provides two line tools for vertical up and down, two plane tools for horizontal leftward and rightward, and one point tool for water-pouring rotation. The experimental results show that, the medians of the execution time for the two modes (NV: 59.2 s and V: 50.0 s), indicating that the virtual tools helped to reduce about 9.2 s (15.5 %); the medians of the traveling path for the two modes (NV: 817 mm and V: 721 mm), indicating a reduction of about 96 mm (11.8 %). Fig. 5 shows the robot trajectories for a specific user as an example. In Fig. 5a, the virtual tools led to quite straight movements in up and down, more smooth movements in a horizontal plane during leftward and rightward, and steady rotation in water pouring. Most of subjects reported that the bonding forces from the virtual linkage and virtual tools did help to maintain stable movements.

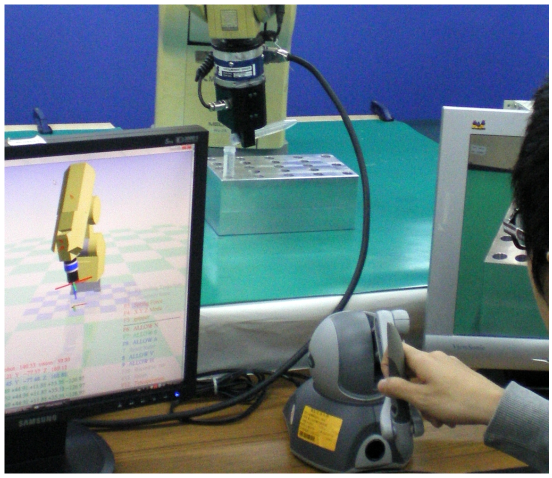

Fig. 4: Water pouring task.

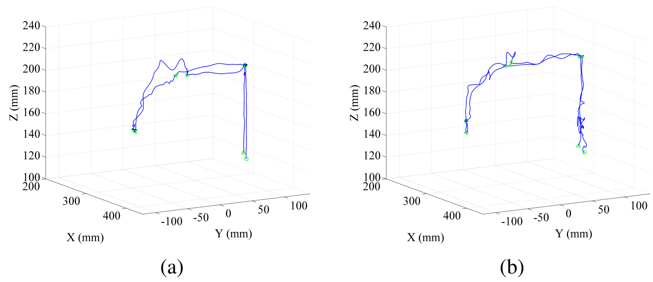

Fig. 5: Robot trajectories of water pouring for a user as an example: (a) with the help of virtual tools and (b) without the help.

The setup for the second experiment is shown in Fig. 2. The robot manipulator was governed to fasten a hexagonal screw via a box-end wrench. The procedure is as follows:

1. Place the box-end wrench over the screw head and pose a proper rotating axis for next step.

2. Rotate the wrench clockwise certain angle to fasten the screw and at the same time keep the rotating axis fixed.

3. Release the wrench from the screw and then rotate the wrench counter-clockwise certain angle.

4. Repeat the steps above until the screw is fastened.

In responding to these steps, the subject can utilize two kinds of virtual tools to assist in the manipulation, described as follows:

- The line tool is used to assist in the straight motion along with the rotating axis, which helps to place the wrench over the screw.

- The orientation tool is used to maintain a fixed rotating axis to prevent the user from inaccurate manipulation.

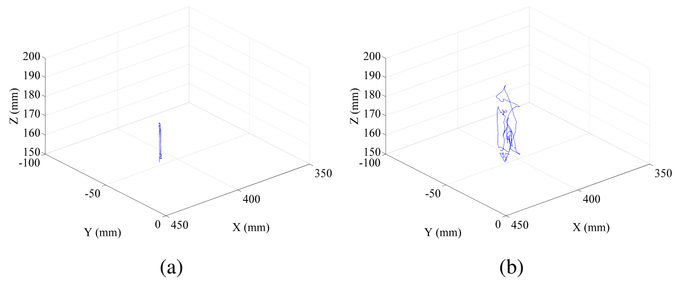

Fig. 6: Robot trajectories of screw fastening for a user as an example: (a) with the help of virtual tools and (b) without the help.

The experimental results show that, the medians of the execution time for the two modes (NV: 33.24 s and V: 25.06 s), indicating the virtual tools helped to reduce about 8.18 s (24.6 $\%$); the medians of the traveling path for the two modes (NV: 216.5 mm and V: 119.6 mm), indicating a reduction of about 96.9 mm (44.8 $\%$). Fig. 6 shows the robot trajectories for a specific user as an example. With the help of the proposed virtual tools, the trajectories in Fig. 6a were straight and more close together, compared with those in Fig. 6b. Furthermore, most of subjects reported that with the help of virtual tools they could place the wrench over the screw and stably fasten it more fast and precisely.

5 CONCLUSION

In this paper, we have proposed an effective manipulation system for multi-DOF robot manipulators based on virtual linkage and virtual tools. The virtual linkage enhances the connection between the user and robot manipulator, and virtual tools are helpful in dealing with the requirements from various tasks. We have applied the proposed manipulation system to conduct two different kinds of tasks, both of which demand delicate maneuver. Satisfactory experimental results have verified its effectiveness. In future works, we plan to enhance the proposed manipulation system, so that it can be applied for more versatile tasks in home-like environments.

ACKNOWLEDGMENT

This work was supported in part by the National Science Council under grant NSC 99-2221-E-009-157.

REFERENCES

[1] Abbott JJ, Marayong P, and Okamura AM (2007), Haptic Virtual Fixtures for Robot-Assisted Manipulation, Robotics Research 28: 49-64.

[2] Forsyth BA and MacLean KE (2006), Predictive Haptic Guidance: Intelligent User Assistance for the Control of Dynamic Tasks. IEEE Transactions on Visualization and Computer Graphics 12(1): 103-113.

[3] Hsieh MC and Young KY (2010), Motion Constraint Design and Implementation for a Multi-Functional Virtual Manipulation System. Mechatronics 20(3): 346-354.

[4] Kemp CC, Edsinger A, and Torres-Jara E (2007), Challenges for Robot Manipulation in Human Environments. IEEE Robotics and Automation Magazine 14(1): 20-29.

[5] Kuang AB, Payandeh S, Zheng B, Henigman F, and MacKenzie CL (2004), Assembling Virtual Fixtures for Guidance in Training Environments, International Symposium on Haptic Interfaces for Virtual Environment and Teleoperator Systems 367-374.

[6] Kuchenbecker KJ and Niemeyer G (2006), Induced Master Motion in Force-Reflecting Teleoperation, Journal of Dynamic Systems, Measurement, and Control 128(4):800-810.

[7] Rosenberg LB (1993), Virtual Fixtures: Perceptual Tools for Telerobotic Manipulation, IEEE Virtual Reality Annual International Symposium 76-82.

The Seventeenth International Symposium on Artificial Life and Robotics 2012 (AROB 17th '12),
B-Con Plaza, Beppu, Oita, Japan, January 19-21, 2012

An Article Retrieval Support System That Accepts Arbitrary Kansei Words

Yuichi Murakami, Shingo Nakamura, and Shuji Hashimoto

Waseda University, Tokyo, 169-8555, Japan
(Tel: 81-3-5286-3233, Fax: 81-3-3202-7523)
yuichi@shalab.phys.waseda.ac.jp, shingo@shalab.phys.waseda.ac.jp, shuji@waseda.jp

Abstract: In most article retrieval systems using Kansei words, there exists a gap between user's Kansei and system's Kansei model. Therefore, it is not always easy to retrieve the desirable articles. The purpose of this paper is to bridge this gap by introducing a novel function to accept arbitrary Kansei words. The parameters related to newly added Kansei words are automatically estimated from articles selected by the user during search. Thereby, the system is customized for individual users, to bridge the gap. In the evaluation experiments, we took actual paintings as the articles, and evaluated the user-satisfaction, accuracy, *novelty* and *serendipity* of the system through actual user operations. Most of users were satisfied with the system and could find unknown desirable articles. Moreover they could often find unexpectedly interested articles.

Keywords: User profiling, Kansei information processing, Cooperative system, Web retrieval

1 INTRODUCTION

Web services are increasing day by day and the demands for e-commerce have also become higher. It is, however, not easy to retrieve a proper article from a lot of articles in web pages. One way of retrieving articles is to use keywords. Especially using adjective keywords called "Kansei words" is effective to represent human feelings and impressions. However, the accuracy of retrieval results is not sufficient due to the gap between user's Kansei and system's Kansei model. Therefore, it takes a long time to retrieve the desirable articles. To bridge this gap, we consider that it is necessary to introduce user profiles, and implementation of the following two functions: 1) to add arbitrary Kansei words freely, 2) to fit system Kansei words to the user's Kansei. Hijikata pointed out that user profiling methods can be classified as either explicit or implicit methods [1]. In the explicit method, users directly input the information about individual taste. In the implicit method, the system estimates the individual taste based on the past user behavior. As examples of explicit method, individual tastes are estimated by the questionnaire in advance [2][3], or by asking users to grade the browsed internet pages on their interest and relevance [4]. Such explicit methods put a strain on users. On the other hand, implicit methods infer individual taste by usage history [5][6]. However, they need enough usage history. Most of studies about Kansei retrieval system took an explicit method. However, we take an implicit method in order not to put a strain on users together with above two functions.

We already proposed the system to fit system Kansei words to the user's Kansei in prepared default Kansei words decided by a system architect [7]. In this paper, we append the function of adding arbitrary Kansei words to the previous system. The proposed system collects articles fitting or non-fitting to the added Kansei word while users search the desirable articles. Utilizing the collected articles, the system estimates the parameters related to the added Kansei words by using the support vector machine (SVM) method. Thereby, users can freely use arbitrary Kansei words, and customize to the own desirable system by editing retrieval criteria as they please. In the result, we expect to improve the satisfaction because users are not tired of the system and the flexibility of retrieval is improved. However, the parameters related to the added Kansei words are learned through user's most desirable article by neural networks because the added Kansei words are often low accuracy.

For the experiments, we developed an article retrieval support system implemented with the proposed method, and employed artistic painting images for article database. We evaluated the user-satisfaction and accuracy through actual operations. We also employed *novelty* and *serendipity* as the evaluation indices [8]. Users have potentially multiple preferences for diverseness of Kansei words [9]. Therefore, these two metrics are useful to measure how much ambiguous or unaware preferences are derived.

2 PROPOSED SYSTEM

Most users wish to search articles not only by given Kansei words but also by suitable their own Kansei words. However, the system cannot prepare all Kansei words in advance because all most of the words and expressions have the potential to be utilized as Kansei words. Therefore, it is important to add arbitrary Kansei words to the system freely. However, the system has to parameterize the arbitrary Kansei word in accordance with all articles, which

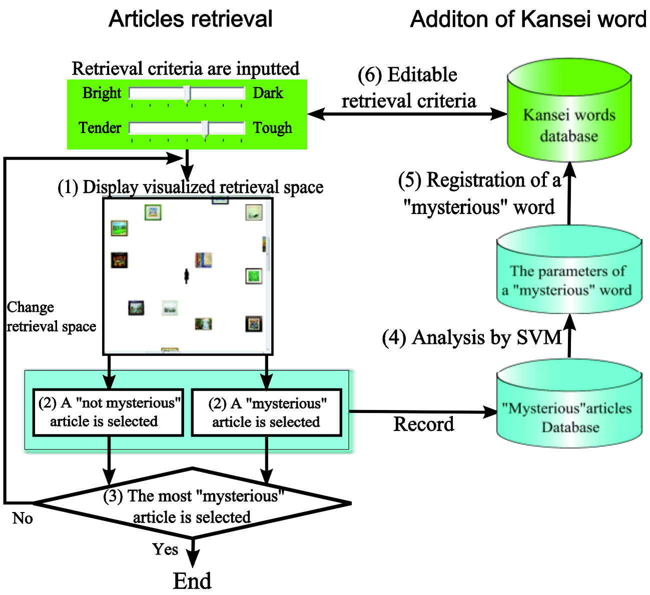

Fig.1. The schematic diagram of proposed system

is laborious. Meanwhile, Mukunoki el al reported that some typical and popular Kansei words can express other Kansei words [9], although it needs images selected by specialists in order to add arbitrary Kansei words. We suggest a new procedure to treat arbitrary Kansei words by utilizing the given default Kansei words.

2.1.1. Registration and usage of arbitrary Kansei words

Fig.1 shows the schematic diagram of the proposed system in case of adding an arbitrary word "mysterious". First, the proposed system needs to find out which articles fit the added Kansei word for users as teacher data for supervised learning. The Kansei retrieval system we proposed before is employed to collect such data efficiently. The previous system can visualize the two-dimensional retrieval space converted from Kansei parameter space by Self Organizing Maps ((1) in Fig.1). Moreover, the user can point not only desirable articles but also undesirable ones. In the case of selecting undesirable articles, the retrieval space is changed to follow the user's tendency. With the help of this system, users repeat the selection of articles fitting or non-fitting to the added Kansei word. This operation continues until users find the most fitting article for the added Kansei word, or select a sufficient number of articles. The user's strain to collect teacher data is minimized because the system concomitantly collects the data while users repeat the selection to find the most desirable article. At this stage, the articles fitting the added Kansei word are scored by +1. On the other hand, the articles not fitting it are scored by -1. After the teacher data are collected enough, the system estimates the parameters of the added Kansei word by SVM. The added Kansei word is registered as retrieval criteria in the same way as the default Kansei words after this procedure. Additionally, the system can also create the new retrieval space concerning the parameters of the added Kansei word. Therefore, the system can create an opportunity to discover unknown desirable articles as unexpectedly interested articles.

2.1.2. Editable retrieval criteria

Users can freely use arbitrary Kansei words added by themselves. Besides, Kansei words added by other users are also available as own retrieval criteria by accessing the database which stores the parameters of each added Kansei word. Users can also eliminate the added Kansei words from retrieval criteria ((6) in Fig.1). Therefore, users are not tired of the system because they can customize the system.

2.1.3. Learn parameters of added Kansei words

The previous system learns user's Kansei based on user's most desirable article with a three-layered perceptron. We extend the previous system to the range of added Kansei words. Learning method is the same as the previous system. The system learns the relationship between the initial input retrieval criteria's parameters including added Kansei words and the finally selected article ones. In other words, the perceptron's input data is the initial position on the visualized retrieval space, and the teacher data is the position of the article finally selected.

3 IMPREMENTATION

We made some experiments to evaluate the usage of the proposed retrieval system for painting images to assist the customers who wish to buy paintings. In the experiments, 135 painting images were stored in the database. They were rated by 20 people with 7-point scale of 8 adjective pairs shown in **Table 1**. The adjective pairs were chosen according to the Inoue's study on Kansei evaluation of paintings [10]. The average of human evaluation was set into the system database in advance as the initial system's Kansei model. The system also allowed users to add arbitrary Kansei words based on this 8 adjective pairs.

We utilized the software library LibSVM for SVMs modeling. We ran a preliminary experiment to avoid over fitting. In the result, we chose C-SVM with RBF kernel. If the teacher data existed only in one side, we chose one-class SVM. Cost parameter and ν parameter were set to 2 and 0.1. Other tool parameters were set to the default values of the LibSVM. The other system parameters and software's composition were conformed to the previous system.

Table 1. Pairs of Kansei word

Pair #	***Kansei Words***	
1	Bright	Dark
2	Tender	Tough
3	Cheerful	Melancholy
4	Fancy	Plain
5	Complicated	Simple
6	Sharp	Dull
7	Warm	Cold
8	Comfortable	Uneasy

4 EVALUATION EXPERIMENTS AND RESULTS

In the evaluation experiments, we employed *novelty* and *serendipity* metrics as the evaluation indices other than the satisfaction or accuracy. They can measure the "non-obviousness" of the retrieval system as an important metrics for user-satisfaction. These metrics indicate whether the recommended item is both unknown and favorite. We evaluated that how many unknown desirable articles about a new Kansei word were recommended. A serendipitous recommendation helps users to find an unexpectedly interested item which might not be discovered in other way. For measuring serendipity, it is necessary to evaluate how the recommended items attract and surprise the user. However, no concrete calculation method has been proposed so far. Therefore, subjective assessment was adopted.

4.2.1. Satisfaction and accuracy

We asked 13 people the accuracy and satisfaction of an arbitrary Kansei word added by themselves. We also asked the accuracy and satisfaction when users utilized Kansei words added by other users. The result is shown in **Fig.2**. Here, we defined "Good" and "Excellent" evaluations mean "be satisfied". We concluded that added Kansei words are useful because over 70% of the users were satisfied with it. Though accuracy of Kansei words added by other users are occasionally inadequate, satisfaction level is high. Interestingly, some users commented "it is fun to feel other user's Kansei though the accuracy is low." Next, we asked the satisfaction of editable retrieval criteria. The result is shown in **Table 2**. Most of the users were satisfied with the function of editable retrieval criteria. We consider that users were satisfied with not only searching user's desirable articles but also customizing the system.

Moreover, we evaluated the function of neural networks. 8 users tried retrieving their preferred paintings five times. Afterward we compared the positions of Kansei learning with the initial positions. **Table 3** shows the average result for 8 users. The first and second columns represent the

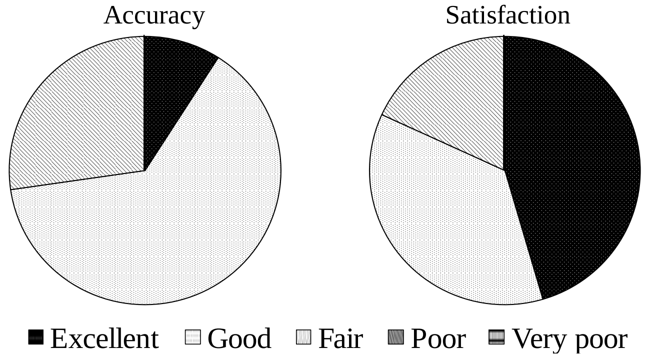

(a) Arbitrary Kansei words added by themselves

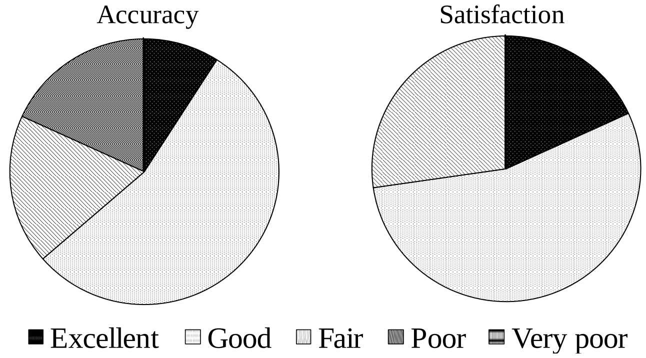

(b) Kansei words added by other users

Fig.2. The accuracy and satisfaction for added Kansei words

Table 2. Editable retrieval criteria

Evaluation	***Excellent***	***Good***	***Fair***	***Poor***	***Very poor***
Rate	23.1%	69.2%	7.7%	0.0%	0.0%

Table 3. Result of by Kansei learning

	Without Kansei learning	***With Kansei learning***	***Difference***
Average (5 times try)	1.00	0.64	-0.36

distance values between the initial position and the finally selected position with Kansei learning. The values are the normalized distance of visualized retrieval space. The third column indicates the difference. The initial position gets about 0.36 closer to the selected article. It can be concluded that the system fits to individual user's preference in the course of using the system even if arbitrary Kansei words are included in retrieval criteria.

4.2.2. Novelty and serendipity

We evaluated the *novelty* and *serendipity*. We asked 10 people to show the articles in the database that fit to the added Kansei word. We then distilled teacher data used for creating a new Kansei word. We consider that these articles are regarded as novel articles because they are

Table 4. The novelty for adding Kansei words

Added Kansei words	*Novelty*		
	Precision	*Recall*	*F value*
mysterious	0.50	0.43	0.46
boisterous	0.33	0.50	0.40
realistic	0.38	0.26	0.31
unusual	0.43	0.20	0.27
disorganized	0.17	0.50	0.25
expansive	0.30	0.13	0.18
enjoyble	0.00	0.00	0.00
likeable	0.29	0.29	0.29
good	0.25	0.16	0.20
beautiful	0.17	0.06	0.09
average	**0.28**	**0.25**	**0.26**

Table 5. The serendipity for adding Kansei words

Evaluation	*Yes*	*Rather yes*	*Yes and no*	*Rather No*	*No*
Rate	38.5%	46.1%	0.0%	7.7%	7.7%

fit to the Kansei word. We evaluated the precision, recall and F value of novel articles. Here, if the values of the new Kansei word by SVM were above 0.85, they were regarded as fitting articles. The result is shown in **Table 4**. The F value of Hijikata's system specialized for novelty is about 0.3. However, the F value of typical system not specialized for novelty is under 0.1 [8]. Therefore, our proposed system showed better results than previous system in novelty. Moreover, the adjectives having high "evaluation factor" (e.g. *likeable*, *good* and *beautiful*) generally is difficult for utilizing as retrieval criteria because there are great differences between individuals. However, users can occasionally find unknown desirable articles.

We also evaluated serendipity by subjective assessment of the proposed system. 13 people tried and the result is shown in **Table 5**. Most of users answered "yes" or "rather yes" about adding arbitrary Kansei words. We consider that the system created a new retrieval space concerning the parameters of the added Kansei word, and an opportunity to find unexpectedly interested articles. In the result, we concluded that users could find unknown desirable articles, and could find unexpectedly interested articles by using the proposed system.

5 CONCLUSION

We have proposed an article retrieval support system that accepts arbitrary Kansei words not to put strain on users. Users can freely add arbitrary Kansei words, and edit retrieval criteria. Moreover, the parameters related to the added Kansei words are learned by neural networks. In the experiments, we confirmed that most of users were satisfied with adding arbitrary Kansei words, and customizing the system. Besides, the accuracy of the system was improved. We also confirmed that users could find unknown desirable articles, and could find unexpectedly interested articles by using the proposed system.

We are trying to apply the developed system for other different article retrievals to examine the universality of the proposed method. In the future, we would like to link physical parameters to Kansei factors, and to implement the automatic indexing of articles.

ACKNOWLEDGMENT

This work was supported in part by the CREST project "Foundation of technology supporting the creation of digital media contents" of JST, and the "Global Robot Academia," Grant-in-Aid for Global COE Program by the Ministry of Education, Culture, Sports, Science and Technology, Japan.

REFERENCES

[1] Hijikata Y. (2004), Implicit user profiling for on demand relevance feedback. Proceedings of the 9th International Conference on Intelligent User Interfaces, pp. 198-205

[2] Sugihara T., Morimoto K. and Kurokawa T. (2004), An Improved Kansei-Based Music Retrieval System with a New Distance in a Kansei Space. Proceedings of the 2004 IEEE International Workshop on Robot and Human Interactive Communication, pp.141-146

[3] Miyakawa A., Ishida T. and Shibata Y. (2008). Visual and Physical Feature Analysis for Kansei Retrieval Method in VR Japanese Crafting Presentation System. Workshops 22nd International Conference on Advanced Information Networking and Applications, pp.477-482

[4] Pazzani M. and Billsus D. (1997), Learning and Revising User Profiles: the Identification of Interesting Web Sites. Machine Learning. 27(3), pp.313-331

[5] Sugiyama K., Hatano K. and Yoshikawa M. (2004), Adaptive Web Search Based on User Profile Constructed without Any Effort from Users. Proc. of WWW'04, pp.675-684

[6] Sakurai Y. and Tsuruta S. (2009), A Searching Method based on Mechanically Learned Subjective Image. Journal of Japan Society for Fuzzy Theory and Intelligent Informatics 21(2), pp. 214-221

[7] Murakami Y., Nakamura S. and Hashimoto S. (2010), An article retrieval support system that learns user's Kansei. User Science and Engineering, 2010 International Conference on, pp.32-37

[8] Hijikata Y., Shimizu T. and Nishida S. (2009), Discovery-oriented Collaborative Filtering for Improving User Satisfaction. 14th ACM International Conference on Intelligent User Interfaces, pp.67-76

[9] Mukunoki M., Tanaka H. and Ikeda K. (2001), An Image Retrieval System Using the Feature Space Consisting of Antonymous Pairs of Adjectives. Transactions of Information Processing Society of Japan 42(7), pp.1914-1921

[10] Inoue M., and Kobayashi T. (1985), The research domain and scale construction of adjective-pairs in a semantic differential method in Japan. The Japanese journal of educational psychology 33(3), pp. 253-260

The Seventeenth International Symposium on Artificial Life and Robotics 2012 (AROB 17th '12),
B-Con Plaza, Beppu, Oita, Japan, January 19-21, 2012

Design of a User-Support System for Vision Information Using a Smart Phone

Hiroyuki Nishiyama[1] and Fumio Mizoguchi[1]

[1] Faculty of Sci. and Tech. Tokyo University of Science
2641 Yamazaki, Noda-shi, CHIBA, 278-8510, Japan
(Tel: +81-47122-1106; Fax: +81-47122-1106)
(hiroyuki@rs.noda.tus.ac.jp, mizo@wisdomtex.com)

Abstract: In this paper, we design a user-support system for vision information using smart phones. When the user takes a picture of a target using the smart phone camera, our system can recognize the image of the target and recommend a suitable service to the user. The system with executes simple image analysis and determines a suitable service for the target image. The simple image analysis can extract 13 parameters (e.g., color information (RGB), number of intersections, depth of intersection, line width, and line depth). We use machine learning to classify the parameters into each service. In our research, we use a Support Vector Machine (SVM) as a learning machine tool. Our system design provides user support for several services such as translation, barcode readers, and diagnosis of skin images and demonstrates the effectiveness of our research.

Keywords: User Support System, Data Mining, Support Vector Machine, Smart Phone

1 INTRODUCTION

Recently, many multifunctional cellular phone terminals, such as smart phones (e.g., Androids and iPhones), have been developed as a result of the evolution of the computer, network infrastructure, and lightweight battery technology. Thus, the number of users is rapidly increasing [5]. The smart phone is equipped with various sensor systems (e.g., an acceleration sensor, an infrared sensor, and a luminosity sensor), besides the camera function. Furthermore, easily programmed applications acquire input from each function. Various research activities and services performed with a smart phone using such features. Examples are the study of service applications such as translation from English to Japanese, barcode readers, recognition of billboards, recognition of facial images, and diagnosis of skin images using visual information from the camera of a smart phone. Examples are the study of the diagnosis service of skin image that recommends cosmetics that are appropriate for the skin condition by transmitting the skin image from the camera function to an analysis server [1, 2] To use these services, a user should select a service application and point the smart phone camera (take a picture) toward the subject of the service, and then receive the information service from the application. However, when the subject size or focus do not match, the user cannot access the service. The user must then retake the picture. Such mistakes are frequently made when a user first accesses an application.

Considering this background, we have designed a user-support system for vision information using smart phones. In our study, when the user takes a picture of a target using the smart phone camera, our system can recognize the image of the target and recommend a suitable service to the user. In addition, our system provides advice by voice and a user interface using a touch panel. When the target image conditions are unsuitable for the service, our system can advise the user directly. The user can then adjust the size of the image target area by operating the touch panel. In our design, we use a design model of a server-client system; a smart phone is used as a client because the smart phone's CPU is not powerful enough to achieve these services, so the services are implemented by server machines. The system with the smart phone as a client executes simple image analysis and determines a suitable service for the target image. To improve its judgments, this system can advise and request input via voice and text to adjust the area of the target image using the touch panel. The simple image analysis can extract 13 parameters (e.g., color information (RGB), number of intersections, depth of intersection, line width, and line depth). We use machine learning to classify the parameters into each service. In our research, we use a Support Vector Machine (SVM) [3] as a learning machine tool.

Our system design provides user support for several services such as translation, barcode readers, and diagnosis of skin images and demonstrates the effectiveness of our research.

2 SUPPORT VECTOR MACHINE

The SVM that is used in our study to determine is a classification technique that uses supervised learning and that can be applied to pattern recognition and regression analysis. The learning algorithm of the SVM is derived from optimization theory, and the learning method introduced by Vapnik [3] calculates a super-plane that separates positive and negative examples as training data. High identification performance can

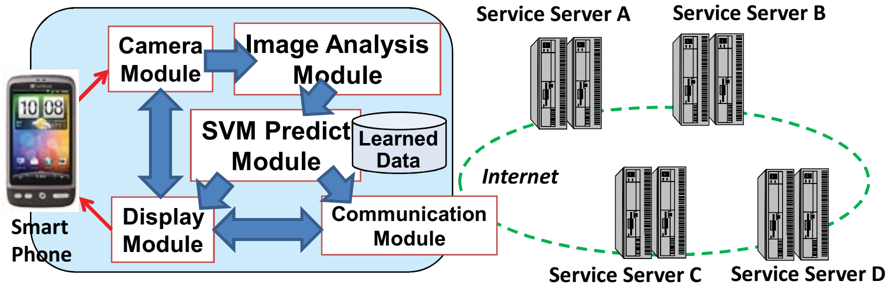

Fig. 1. Structure of the user-support system for vision information using smart phones

be demonstrated by adding the kernel function and margin maximization (e.g., mapping to a higher dimension space by using the nonlinear map, and introducing the kernel function to linear separate by the higher-dimension feature space). The pattern is mapped to the feature space of limited or infinite order, and it is possible to linear separate on the feature space. Thus, the SVM is used in various fields like categorizing text, image recognition, and bioinformatics, and was recently applied to Classification of Web services [4].

In our study, we use the Java version of libsvm [7] that can be implemented on an Android as the SVM and supports also multi-class classification.

3 SMART PHONE

A smart phone is similar to a small laptop computer. However, a smart phone has a telephone call function, and it is easy to carry because it is small and light. Its display is rather small, and it does not have a keyboard. Moreover, the development of an Android smart phone is comparatively easy, because the development language basically conforms to Java in the Android application (Android SDK[6]). In our study, the smart phone (Android) is an HTC Desire SoftBank X06HT (CPU: Qualcomm Snapdragon 1GHz, Internal memory: ROM 512MB/RAM 576MB, OS: Android 2.1 with HTC Sense).

The performance of the assumed smart phone (Android phone) in this study is as follows.

- Camera function

  A picture can be taken using the photography function of the Camera API (android.hardware.Camera) with which the Android phone is equipped. The camera focus when the picture is taken can also be checked using this API. The resolution of the picture changes with the performance of a smart phone; we use a size of 1216x2048 pixels in our research. (If the screen is too small, the accuracy will be affected; if it is too large, the processing speed of the smart phone will be affected.)

- Display function

  The picture and text can be displayed as output on the Android phone, which recognizes a finger touch and drag operation on a display as an input. These functions are provided to build the user interface of AndroidAPI (android.app.Activity).

Additionally, a smart phone is equipped with GPS and various sensor systems (e.g., acceleration sensor, brightness sensor, and temperature sensor) and can use voice annunciation through a speaker.

4 SYSTEM ARCHITECTURE

We have designed a user-support system for vision information using smart phones. When a user takes a picture of a target using the smart phone camera, this system executes simple image analysis and determines a suitable service for the target image. The system's simple image analysis can extract 13 parameters (e.g., color information (RGB), number of intersections, depth of intersection, line width, and line depth). We use machine learning to classify the parameters into each service. In our study, we use a Support Vector Machine (SVM) [3] as a learner, learn information collected with the smart phone beforehand, and judge the target image of newly collected information. The information is gathered and judged in a smart phone, and the learning process can be performed in a smart phone or a personal computer.

Figure 1 depicts the structure of the user-support system for vision information using smart phones. The modules in this system have the following roles.

- The camera module takes a picture using the camera function of the smart phone. This module judges the camera focus when photographing skin.

- The display module provides information to the user by displaying the input information and treats the operation on display as input from the user. This module displays the picture and text when the picture is taken, transmits

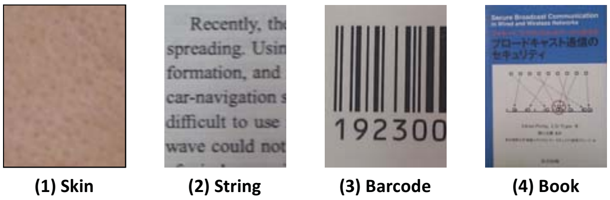

Fig. 2. Samples of parts of the image used by each service. (1) Skin image. (2) String image. (3) Barcode image. (4) Book image.

it to the service server, and provides the diagnostic result. The area of the picture to be transmitted to the service server can be selected using the touch-panel function of the smart phone.

- The image analysis module analyzes the image to extract the parameters from the image data. This image analysis extracts 13 parameters (e.g., color information (RGB), number of intersections, depth of intersection, line width, and line depth (image depth)). The image parameters are used by the SVM prediction module to determine a suitable service.

- The SVM prediction module judges the image parameters using learning data created by our learning tool (see the next section) and determines a suitable service for the target image.

- The communication module transmits information to and receives information from the suitable service server.

5 LEARNING BY SVM

In our study, the SVM creates the learning data of the image for which a suitable service is to be determined, and we implement the SVM prediction module in Fig. 1 by using the learning data. While learning, we collect image data that can be used by several services such as translation, barcode readers, and diagnosis of skin images; analyze each image and extract parameters; and execute parameter classification learning by SVM. We use the Java version of libsvm [7] that can be implemented on an Android as the SVM.

5.1 Extraction of Parameters by Image Analysis

To execute learning with an SVM, we implemented the function of image analysis to extract the parameters from the collected image data (such as Fig. 2) in the smart phone. This image analysis uses the same function implemented for the skin diagnosis service [1]. Processing was reduced to enable analyzing the image more quickly in the smart phone. The

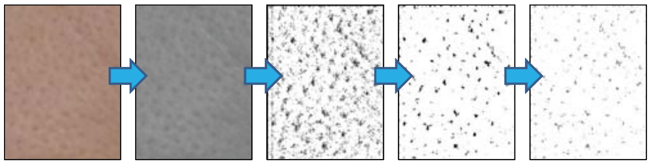

Fig. 3. Image analysis using a skin image. (A) Original image. (B) Gray-scale image. (C) Binary image. (D) Noise reduction. (E) Line image.

Judge	ID0	ID1	ID2		ID12
1	0:489	1:471	2:154	···	12:128
1	0:704	1:676	2:143	···	12:124
2	0:1076	1:1051	2:146	···	12:120
3	0:744	1:726	2:147	···	12:130
3	0:877	1:862	2:170	···	12:128
4	0:1009	1:968	2:129	···	12:152
⋮				⋮	

13 parameters

The number of images

Fig. 4. Parameters used for SVM learning (before scaling)

image analysis process (Fig. 3) first extracts 240 to 320 pixels of the central portion of the acquired image (Fig. 3(A)). Next, the function converts the image into a gray-scale image (Fig. 3(B)), prepares a binary image (Fig. 3(C)), performs noise reduction (Fig. 3(D)), and creates a line image (Fig. 3(E)). This image analysis extracts 13 parameters (e.g., color information (RGB), number of intersections, depth of intersection, line width, and line depth (image depth)). (The skin diagnosis service extracts 45 parameters to recognize the state of the skin image in detail.) The learning data are created by learning these parameters using the SVM.

5.2 Creating Learning Data

To create learning data by applying SVM learning, we collected the images that became training data. There were 100 data images, 25 each for skin, string, barcode, and book images. Next, we extracted the parameters from the collected image data using the image analysis function.

Figure 4 presents data when collected parameters are learned by the SVM. The parameters of one line represent one image. The left-hand numbers (1 to 4) indicate whether the image is skin (1), string (2), barcode (3), or book (4). After scaling, these parameters can be learned by the SVM, and learning data is created. We used the Java version of libsvm [7] that can be implemented on an Android as the SVM and that also supports multiple classifications. We used the Gaussian kernel as a kernel function for SVM learning. Cross validation indicated a learning accuracy of 89.0%.

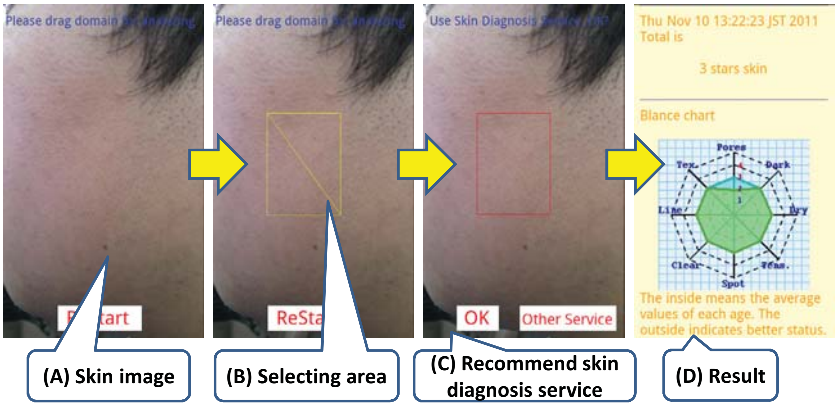

Fig. 5. Process of the user-support system for vision information using the smart phone

6 USER-SUPPORT SYSTEM

In our study, we implemented a user-support system that enabled service judgment based on the created learning data for vision information using smart phones (Fig. 1). We used HTC Desire X06HT (described in paragraph 3) as an Android smart phone. In our study, when the user takes a picture of a target using the smart phone camera, our system can recognize the target image and recommend a suitable service to the user. In addition, our system provides advice by voice and a user interface using a touch panel.

The process flow of the user-support system is presented in Fig. 5. In this figure, this user wants to use a skin diagnosis service. First, when the user photographs his/her own skin using the smart phone via the camera module, our system displays the skin image via the display module (Fig. 5(A)). Next, the user selects the area of the image (Fig. 5(B)) for which the service is to be used. The image analysis module then analyzes the image and extracts the parameters, and the SVM prediction module judges a suitable service. In Fig. 5(C), our system recommends the skin diagnosis service wanted by the user. When the user pushes the "OK" button (Fig. 5(C)), our system transmits the selected image data to the skin diagnosis service server via the communication module. Finally, the result is displayed (Fig. 5(D)). In these processes, our system can advise the user via text and voice while the user is taking a picture, for example, and provide operational advice based on the situation.

With our system, the user can take a picture of a target using the smart phone camera and receive a suitable service recommendation from our user-support system.

7 CONCLUSION

In this paper, we designed a user-support system for vision information using smart phones. When the user takes a picture of a target using the smart phone camera, our system can perform simple image analysis, recognize the target image, and recommend a suitable service to the user. To improve its judgments, this system can advise and request input via voice and text to adjust the area of the target image using the touch panel. We use machine learning with a Support Vector Machine (SVM) to classify the parameters extracted by the simple image analysis into each service. We implemented a user-support system that enabled the judgment based on the created learning data for vision information using smart phones and demonstrated the system's effectiveness.

REFERENCES

[1] H. Hiraishi, F. Mizoguchi: A Cellular Telephone-Based Application for Skin-Grading to Support Cosmetic Sales, IAAI 2003, pp. 19-24, 2003.

[2] H. Nishiyama and F. Mizoguchi: Cognitive Support by Smart Phone - Human Judgment on Cosmetic Skin Analysis Support - , The 10th IEEE International Conference on COGNITIVE INFORMATICS & COGNITIVE COMPUTING: ICCI*CC 2011, 2011.

[3] V. Vapnik: The Nature of Statistical Learning Theory, Springer-Verlag, 1995.

[4] H. Wang, Y. Shi, X. Zhou, Q. Zhou, S. Shao and A. Bouguettaya: Web Service Classification using Support Vector Machine, The Proc. of the 22nd International Conference on Tools with Artificial Intelligence, pp. 3-6, 2010.

[5] Mobile Content Forum: *K-tai white paper 2010*, Impress R&D, 2009. [in Japanese]

[6] Android SDK Guide, http://www.android.com/

[7] C.-C. Chang and C.-J. Lin: LIBSVM: a library for support vector machines, http://www.csie.ntu.edu.tw/ cjlin/libsvm/

The Seventeenth International Symposium on Artificial Life and Robotics 2012 (AROB 17th '12),
B-Con Plaza, Beppu, Oita, Japan, January 19-21, 2012

Producing text and speech from video images of lips movement photographed in speaking Japanese by using mouth shape sequence code
- An experimental system to communicate with hearing impaired persons -

Shiori Kawahata, Eiko Koyama, Tsuyoshi Miyazaki[1], and Fujio Yamamoto[2]

Kanagawa Institute of Technology, Atsugi, Kanagawa 243-0292, Japan
[1]miyazaki@ic.kanagawa-it.ac.jp, [2]yamamoto@ic.kanagawa-it.ac.jp

Abstract: We proposed a method to detect distinctive mouth shapes from images that uttered Japanese. And a method to realize machine lip-reading from the order of detected mouth shapes was proposed. Therefore, we propose a communication system for hearing impaired persons using the machine lip-reading. This system supports the communication with the hearing impaired persons and remote persons using the Twitter. In addition, the input of the message is realized with machine lip-reading because hearing impaired persons have difficulty in utterance by the voice. We also devise the interface which can be operated only with a mouse. We carry out an experiment to send a message which is input with machine lip-reading to the Twitter, and evaluate this system.

Keywords: Hearing impaired persons, Twitter, Lip-reading, Communication

1 INTRODUCTION

For a hearing impaired person, both uttering and hearing a speech are difficult. Therefore, some special means are necessary to communicate with other people. As the one, there are lip-reading. The studies of so-called machine lip-reading using the image recognition technologies are performed. We are studying a method unlike the conventional machine lip-reading. We know that a person having the technology of lip-reading pays its attention to the distinctive mouth shapes and their transition, which appear intermittently during a speech. In our study, such knowledge from a human is used as the logical model for automatically recognizing the mouth shape movement. As the first stage, six kinds of basic mouth shape patterns are defined and expressed as the codes, which are easy to be handled by a computer. The pronunciation of Japanese words and sentences was proved to be expressed by series of such mouth shape codes. We called them MSSC (Mouth Shape Sequence Code) (Miyazaki et al [1]). In the second stage, we enabled the generation of MSSC from a video image, which is taken from the mouth movement of an uttering person (Miyazaki et al [2]). We consider that it is possible to generate a text string from utterance images using the machine lip-reading.

Acquired hearing impaired persons have ability to speak and to hear Japanese. This ability or experience is very useful for machine lipreading. In the hearing impaired persons, there are some persons that have physical disability, too. Therefore, we devise a system that sends a message to the Twitter from Japanese utterance images without using keyboard. We expect that this system is used as communication tools for hearing impaired persons.

In this paper, we describe the system that converts Japanese utterance images into a text message and sends the message to the Twitter. This system adopts the"mentions" to send messages to specific users. We propose the system that supports real-time communication with hearing impaired persons and remote place persons. The outline of this system is shown in Fig. 1.

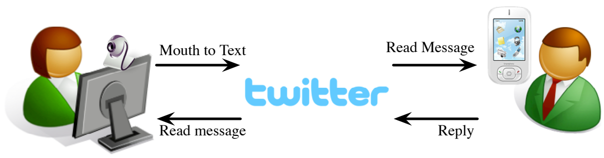

Fig. 1. Outline of this system

2 TWEET USING MACHINE LIP-READING

The block diagram of this system is shown in Fig. 2. This system consists of two subsystems (Part 1 and Part 2). The Part 1 generates MSSC mentioned above, from a video image (sound is not included), which photographed the movement of lips. It is sent to the Part 2 subsystem as text files. The Part 2 is controlled by a "Control window". By the operations on this Control window, Part 1 video picture is displayed, and the MSSC file is received. It is converted into the normal text. For this conversion, we have the pairs of MSSC code and the corresponding text in a phrases database. There is the case that different utterance contents are converted into a same MSSC code because of the principle of this conversion method. Therefore, it is necessary for the sender to choose an appropriate message among the candidates by some means. The chosen message is transmitted to the Twitter as a direct message. The reply text message from the addressee can be confirmed with this GUI screen, too.

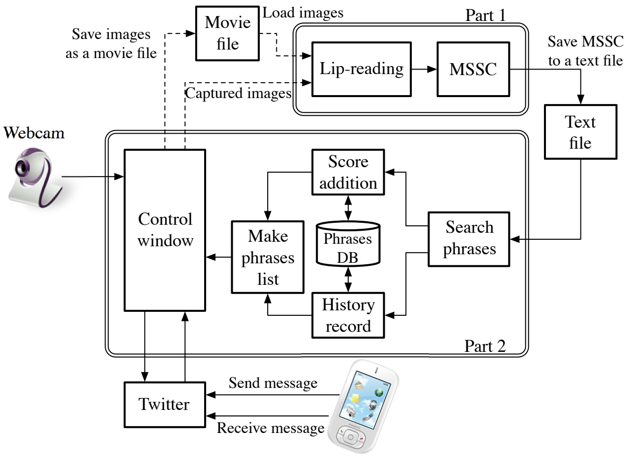

Fig. 2. Block diagram of this system

2.1 Generation of MSSC from utterance images (Part 1)

The lip-reading method which is used in this system is logically materialized knowledge of the lip-reading skill holders and detects distinctive mouth shapes. In the method, five mouth shapes of Japanese vowels and closed mouth shape were defined as "Basic Mouth Shape (BaMS)". We explain the relation between Japanese phones[1] and mouth shapes. A Japanese phone is uttered with only the "Beginning Mouth Shape (BeMS)" or the combination of the BeMS and "End Mouth Shape (EMS)". The BeMS are the mouth shapes which are formed at the beginning of utterance such as "ma", "sa" or "wa". The EMS are the mouth shapes which are formed at the end of utterance. When a Japanese words and phrases are uttered, the sequence of formed mouth shapes is expressed by "Mouth Shpaes Sequence Code (MSSC)". Each mouth shape is defined as $C = \{\mathtt{A}, \mathtt{I}, \mathtt{U}, \mathtt{E}, \mathtt{O}, \mathtt{X}, -\}$, which is called "Mouth Shape Code (MS Code)". Each MS Code corresponds to the mouth shape /a/, /i/, /u/, /e/, /o/ and closed mouth shape, respectively. The last MS Code "−" expresses that the BeMS is not formed. In an MSSC, the odd-numbered codes and the even-numbered codes correspond to MS Codes of BeMS and EMS respectively. For example, the MSSC of "EBINA" (name of a city in Japan) is expressed as "`-EXI-A`". This MSSC shows that a closed mouth shape "`X`" is formed on the second phone "BI".

In the Part 1, similarities between mouth shape image, which is captured by webcam or in movie file, and the BaMS images are calculated. After that, the BeMS terms and the EMS terms are detected from the utterance term using the similarities. Then, an MSSC is generated from the mouth shape of each term (Miyazaki et al [2]). Fig. 3 shows the generation process of MSSC.

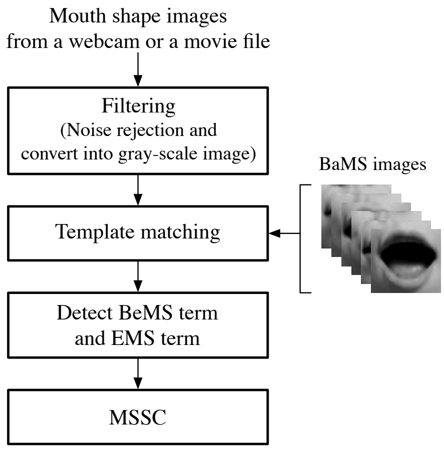

Fig. 3. The generation process of MSSC

2.2 Tweet from an MSSC (Part 2)

In this part, a Japanese phrase that is detected from the Phrases DB is sent to the Twitter (Makice [3]). To detect the phrase, two processes, "Score addition process" and "History record process", are executed. Table 1 shows the Japanese phrases and their MSSC stored in the DB.

After machine lip-reading, the phrase which the user required may not be detected. Therefore, in the Score addition process, points are added to each phrase stored in the DB.

In the History record process, a history count is added to the phrase which is sent to the Twitter. As the result of the two process, some phrases are listed by the score order and the history order. Then, the user selects a phrase from the list, and the phrase is sent to the Twitter.

2.2.1 Score addition process

To add a score to each phrase stored in the DB, each MS Code of MSSC generated in the Part1 is compared with the MS Code of the phrases stored in the DB. The score addition flow is shown in Fig. 4. In the Fig. 4, $c_n(s)$ means a s-th MS Code of MSSC of n-th phrase stored in the DB. $m(s)$ means a s-th MS Code of the MSSC generated in the Part 1 correspondingly.

An example is shown in Table 2. This result shows the case of utterance "Arigato". In the MSSC row, the MS Codes of "Arigato" stored in the DB are shown. In the Result row, the MS Codes that are generated in the Part 1 are shown. The row of *score*1 and *score*2 show the points that are calculated in the Score addition process. For example, the point of *score*1 in the case of $s = 2$ is 1 because of $c_n(2) = m(2)$. The point of *score*1 in the case of $s = 6$ is 0 because of $c_n(6) \neq m(6)$.

[1] The length of voice equivalent of one short syllable is called "mora", and the voice is called "phone".

Table 1. Phrases Database

#	MSSC	Japanese articulation	English meaning
1	-I-U-A-E-IXA-U-A	Itsu kaeri masuka	When do you come home?
2	-IXAUOIE-U-A	Ima doko desuka	Where are you now?
3	-I-X-U-I-A-I-E-U	Kinkyu jitai desu	State of emergency.
4	-A-I-AUO-U	Arigato	Thank you.
5	UA-IXA-I-A	Wakari masita	I've got it.

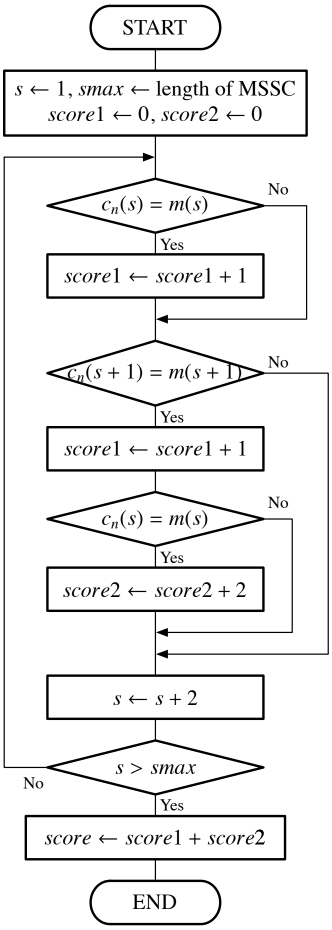

Fig. 4. The flow of Score addition process

About the *score*2, the first point is 2 because of $c_n(1) = m(1)$ and $c_n(2) = m(2)$. The third point is 0 because of $c_n(5) = m(5)$ and $c_n(6) \neq m(6)$.

Then, the total of *score*1 becomes 7 and the total of *score*2 becomes 4. As a result, the score of n-th phrase becomes $score1 + score2$.

2.2.2 History record process

In this process, the count that a phrase is sent to the Twitter is recorded. If some phrases get the same score, the phrase of which the count is greater is listed higher on the Control window. The phrases that are used frequently become easy to be selected.

Table 2. Example of point addition

s	1	2	3	4	5	6	7	8	9	10
MSSC	-	A	-	I	-	A	U	O	-	U
Result	-	A	-	I	-	E	-	O	-	O
*score*1	1	1	1	1	1	0	0	1	1	0
*score*2	2		2		0		0		0	

Firstly, The phrase list is sorted by the history order. Secondly, the list is sorted by the score order and some of top phrases of the list are displayed.

2.3 Control window

We describe the Control window of this system. The window is shown in Fig. 5. Four components are located in this window.

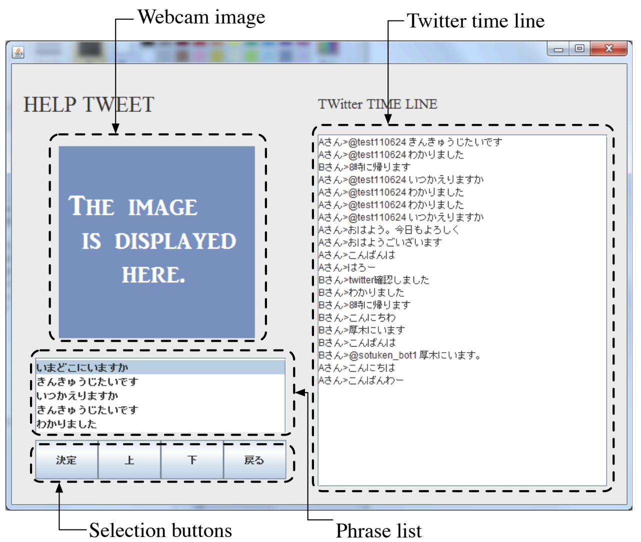

Fig. 5. Control window

The images captured by webcam are shown in the "Webcam image" pane. As the result of machine lip-reading, top five phrases are listed on the "Phrase list" pane. The user select a phrase from the list by using selection button and send a message to the Twitter. The four buttons are "Send", "Upward", "Downward" and "Cancel". After that, the posted message is listed on the top of the "Twitter time line".

Table 3. The detection rate and the ranking

Japanese articulation	English meaning	1st	2nd	3rd	4th	5th
Ashita	tomorrow	83% (1)	100% (1)	83% (1)	100% (1)	33% (2)
Ima	now	75% (1)	50% (1)	75% (1)	75% (1)	75% (1)
Istu	when	75% (1)	50% (2)	75% (1)	50% (2)	100% (1)

3 EXPERIMENTS

We carried out an experiment to convert into Japanese words and phrases from MSSC. The MSSC were generated from images that uttered Japanese. However, we used recorded utterance images.

Firstly, Japanese phrases and their MSSC were stored in the Phrases DB. The stored phrases were “Kyo” (today in English), “Ashita” (tomorrow), “Ima” (now), “Itsu” (when), “Dokoni” (where), “Dokohe” (where), “Imasuka” and “Kaerimasuka”.

During the experiments, the subject uttered phrases without moving head. Furthermore, the mouth shapes before utterance and after utterance assumed closed mouth shape.

3.1 Experimental results

A subject uttered Japanese phrases five times. The phrases were “Ashita”, “Ima” and “Itsu”.

The detection rate of each phrase and its ranking are shown in Table 3. The detection rate shows the ratio that is matching rate of each MSSC stored in the DB and generated in the Part 1. The number in parenthesis shows the ranking.

In most results, the detection rate was higher than 50%, and some of them got 100%. Besides, all phrases were ranked as the 1st or 2nd in the list. Through this experiment, we confirmed that the detection rates differed, though the same phrases were uttered.

4 CONCLUSION

In this paper, we proposed a system for supporting hearing impaired person by using machine lip-reading. An MSSC was generated from the utterance images and was able to be converted into Japanese. Furthermore, the converted Japanese was able to be sent to the Twitter as a message.

If the phrases in the Phrases Database are increased, incorrect phrases may be listed in high-ranking. As a remedy, we have to devise score addition method and examine comparison method of MSSC.

Although the system is only at a very early stage now, we can see that this approach has big possibilities to promote communication between hearing impaired persons and the general people. Additional facilities such as text-to-speech conversion and speech-to-text conversion are also being developed in order to provide more convenient usages. We also plan to improve the precision of the conversion from mouth shape images to readable text.

ACKNOWLEDGEMENTS

This work was supported by the Ministry of Education, Culture, Sports, Science and Technology Grant-in-Aid for Scientific Research (C) 23501176 and Grant-in-Aid for Young Scientists (B) 23700672.

REFERENCES

[1] Miyazaki T, Nakashima T, Ishii N (2011), A Proposal of Mouth Shapes Sequence Code for Japanese Pronunciation. The 12th International Conference on Software Engineering, Artificial Intelligence, Networking and Parallel/Distributed Computing (SNPD 2011), Studies in Computational Intelligence 368, Sydney, Australia, Jul 6-8, 2011, pp. 55-65

[2] Miyazaki T, Nakashima T, Ishii N (2011), A Detection Method of Basic Mouth Shapes from Japanese Utterance Images. Proceedings of the 14th International Conference on Human-Computer Interaction (HCII 2011), Lecture Notes in Computer Science 6761, Orlando, Florida, USA, Jul 9-14, 201, pp. 608-617

[3] Makice K (2009), Twitter API: Up and Running Learn How to Build Applications with the Twitter API. O'Reilly

Development of the Electric Wheelchair Hands-Free Semi-Automatic Control System using the Surface-Electromygram of Facial Muscles.

Yuki Yamashita[1], Hiroki Tamura[1], and Koichi Tanno[1]

[1]University of Miyazaki, Miyazaki 889-2192, Japan
(Tel: 81-985-58-7409)

htamura@cc.miyazaki-u.ac.jp

Abstract: The goal of Human-Computer Interface (or called Human-Robot interface) research is to provide humans with a new communication channel that allows translating people's intention states via a computer into performing specific actions. This paper presents a novel hands-free control system for controlling the electric wheelchair, which is based on Bio-signals as surface electromyogram signals. The Bioelectric signals are picked up from facial muscles then the Bio-signals are passed through an amplifier and a high pass filter. Motion control commands (Forward, Left, Right, Forward to the Right, Forward to the left and Stop) are classified by simple rule. These commands are used for controlling the electric wheelchair. However, it is difficult to safety control and fine control using the biological signal only. In addition, we introduce the semi-automatic control system using the laser range scanner. In this paper, we report the introduction of our proposal systems and our experimental results.

Keywords: Surface Electromyogram Signal, Electric Wheelchair, Motion Control Command Rule, Semi-Automatic Control

1 INTRODUCTION

Surface electromyogram signals (abbr. s-EMG) are detected over the skin surface and are generated by the electrical activity of the muscle fibers during contraction [1]. Moved muscle can be presumed by analyzing s-EMG. S-EMG is used to control artificial leg etc. s-EMG recognition of using the conventional neural network is a method which learns the relation between s-EMG patterns and is reproduced using a neural network. Our previous works [2] [3] [4] showed that technique of integrated EMG is much easier and superior than the fast Fourier transform analysis. Integrated EMG is a running average of the rectification s-EMG.

One of the major challenges for prosthesis or Human-Robot Device development is to produce devices to perfectly mimic their natural counterparts. A very popular approach for prosthesis or Robot control is based on the use of Bio-signals (s-EMG, electroencephalogram (abbr. EEG), electrooculogram .,etc). One of them is s-EMG collected from remnant or normal muscles and use them as control inputs for the artificial limb or Robot Device. As these devices, known as s-EMG-based Hands-Free Wheelchair [5][6][7] use a biological signal to control their movements, it is expected that they should be much easier to control [8]. Other techniques have the method of using gesture [9]. However, the system of gesture is not used by the severely handicapped human.

In this paper, we applied to the electric wheelchair hands-free semi-automatic control system for the severely handicapped human using facial muscles s-EMG pattern recognition system. The six motion control commands (Forward, Left, Right, Forward to the Right, Forward to the left and Stop) are classified by our proposal simple rule. In addition, it is difficult to safety control and fine control of the biological signal only, we introduce the semi-automatic control system using the laser range scanner.

We tried the experiment of driving in the course by using our proposal system. The experimental subjects were five healthy men in twenties whose physique looks like. One person was an expert of the system, and others were the inexperienced person. From their experiments, we showed that the control of our proposal system is easy. In addition, the obstacle evading function was added to our system for the speed control and the stop control. We also tested those control

2 ELECTRIC WHEELCHAIR HANDS-FREE CONTROL SYSTEM USING S-EMG SIGNALS[6][7]

Head movement is a natural form of gesture and can be used to indicate a certain direction [5]. Serious disabled people can't move neck and head, but can get face figures. S-EMG is a way of studying facial muscles activities by recording action potentials from contracting fibres. S-EMG can be detected with surface electrodes. Surface electrodes are easy to apply. This is a non-invasive way to record s-EMG while posing no health and safety risk to the users.

Figure 1 shows the formal scheme for the acquisition and analysis of the s-EMG signal for the control organization and flow of information through the system [6][7]. Our system is based on the five features, 1) surface electrodes, 2) Amplifier (INA114P), 3) High pass filter, 4) Personal Computer for s-EMG signal classification and motion control command output, and 5) Electric Wheelchair Control Box.

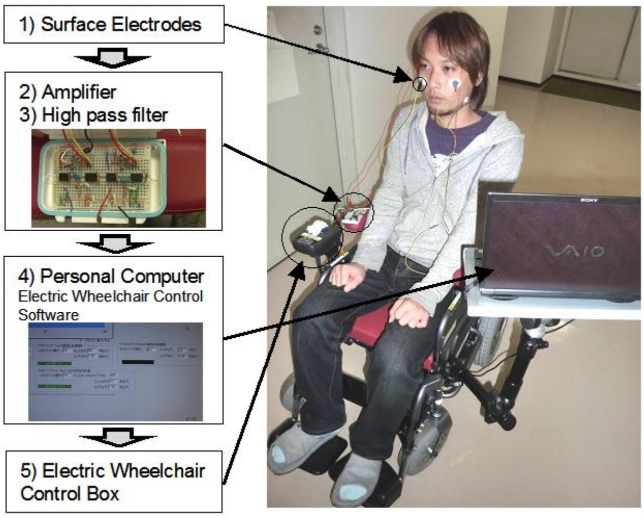

Figure 1. The Flow of Electric Wheelchair Control System using surface s-EMG.

The s-EMG signal detected by surface electrodes is amplified and filtered prior to data acquisition, in order to reduce noise artefacts and enhance spectral components that contain information for data analysis. Two channels of s-EMG signals can be used to recognize face figure movement. 5 Ag/AgCl electrodes are used (two for each channel and one is for ground). In order to remove the DC level and 60 Hz power line noise, the 4th order high pass filter is used. The cutoff frequency of high pass filter is 66.7Hz. In order to effectively filter functions, s-EMG measurement device is used two amplifiers. After filtering and the amplification (about 470 times) stages, the s-EMG signals are digitized (16 bit) and then transferred to the personal computer. The sampling frequency of the measurement data is 1 KHz. And the band is from 0 Hz to 500 Hz. The s-EMG signals are then processed by a classification technique which is based on the combination of 2 class classifier using the threshold. This proposal method is necessary to set the value of threshold of each user. At the finally, the electric wheelchair is controlled by the output command from personal computer using the D/A converter.

The utilized facial movements, motion control command classes and effective channels of bio-signals are defined in Table 1. The electric wheelchair is controlled according to the rule of Table 1. From Table 1, it is easy to select Stop Command in this rule. Because, it is the easiest to perform action to bite and the threshold of the STOP command is smaller than a front command. Therefore, our system is safety, because Stop Command is selected in the false identification case. The inputs for the rules of table 1 classification are given the moving average method process. Moreover, this system doesn't react to the usual blink.

Table 1. The Input Pattern and Classes of Our Rules.

Command	Motion	Active Channel
Turn Right	Wink with right eye	1
Turn Left	Wink with left eye	2
Forward	Bite	1 and 2
Stop	Bite in the state of the Forward, Turn Right and Turn Left Commands	1 and 2 * *These thresholds are smaller than Forward command.
Forward to the Right	Wink with right eye in the state of the Forward Command	1
Forward to the Left	Wink with left eye in the state of the Forward Command	2

3 FUNCTIONAL SAFETY AND SEMI-AUTOMATIC CONTROL

3.1 The Speed Control

The obstacle evading function is important for the safety control of the electric wheelchair. In this paper, we develop the obstacle evasion function using the laser range scanner (HOKUYOU Automatic Co.,Ltd : Classic-URG) for the electric wheelchair safety control. The URG laser range scanner is the most compact obstacle detection sensor with distance measurement principle using laser. Scanning angle of our system is 180° (max 240°). Our system measures the distance by 15° intervals. Figure 2 is image figure.

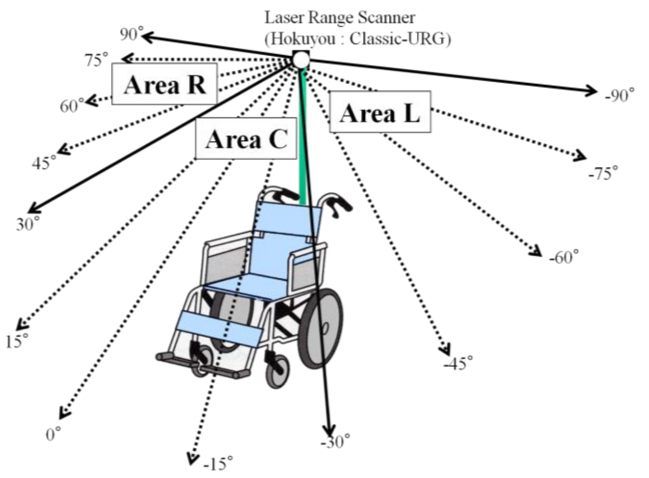

Figure 2. Functional Safety using Laser Range Scanner.

When the obstacle evading function detects the obstacle, our system sounds the alarm and speed control. Speed control is controlled according to the rules of the table 2. Our proposal system could detect about 3.0 meter before obstacle. Our proposal system slows down the speed for evading the obstacle, and wards off a collision. It became easy to evade the obstacle with this function.

Table 2. The Speed Control Rules.

Area R / C / L (0 : no obstacle, 1: obstacle)	Power of Turn Right / Forward / Turn Left (100%:max speed , 0%:stop)
0 /0/ 0	100% / 100% / 100%
0 /0/ 1	100% / 100% / 75%
0 /1/ 0	100% / 75% / 100%
0 /1/ 1	100% / 75% / 75%
1 /0/ 0	75% / 100% / 100%
1 /0/ 1	75% / 100% / 75%
1 /1/ 0	75% / 75% / 100%
1 /1/ 1	75% / 75% / 75%

3.2. The Stop Control

In this subsection, we introduce the safe stop control using the laser range scanner. The electric wheelchair which we developed turns at a radius of 1.5 meter. Therefore, the electric wheelchair cannot work when an obstacle is in the 1.5 meter range. As simple solution, the electric wheelchair stops when a radius of less than 2.0 meters includes an obstacle (Figure 3). Thereby, the electric wheelchair turns safely and can evade an obstacle.

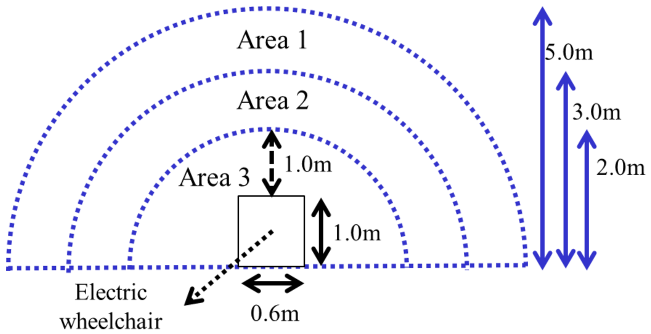

Figure 3. Sensor Measurement Area (Area 1: No control, Area 2: Speed control, Area 3: Stop).

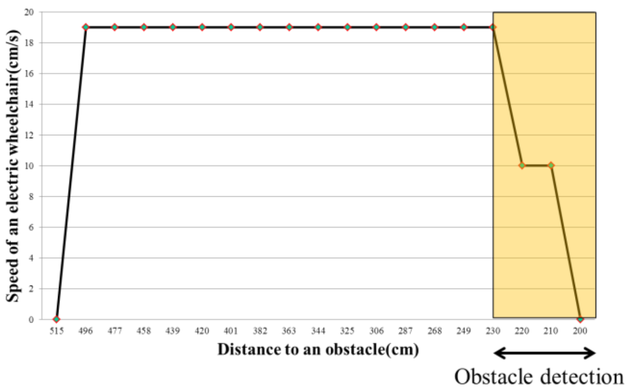

Figure 4. Result of Speed Control Test.

We tried the driving test in the hallway for evaluation of our proposed stop control system. The experiment operated the electric wheelchair toward to wall. The result is shown in Figure 4. From the result, our proposed system was able to detect the obstacle and was able to perform speed control and safe stop.

The electric wheelchair can be controlled in semi-automation by functional safety using laser range scanner. Our proposed system reduces the stress of user. However, our system has still some problems about the discovery of the movement object. These are our future works.

4 EXPERIMENTAL RESULTS

We tried the experiment of driving in the course by using our proposed system. The experimental subjects were five healthy men in twenties whose physique looks similar. One subject was an expert of the system, and others were the inexperienced subject. The driving course is shown in Figure 5. This driving course is about 125 seconds by original electric wheelchair using joystick. The task is to drive the electric wheelchair from position Start to Goal by contraction of facial muscles. The speed of electric wheelchair used low speed (1.0[k meter/hour]). We performed five experimental to each of five subjects. We compare our proposed system by the average time [sec] and the average classification rate [%].

The experimental results are shown in Table 3. The average time of 201 seconds in all, the average classification rate is 98.2 percent. The classification ratio indicates how much the correct command is selected for the total number of commands made by the subjects. From the experiment results, the classification rate of our proposed system and the computer simulation results of paper [10] are similar. The results of inexperienced subjects were almost same as the results of experienced subject. In particular, inexperienced subject S.H has the best results even though the first experiments. The usability of our proposed system was a good result. However, the difference between our proposed system and original electric wheelchair using joystick was 76 seconds.

From these experiments, we think that the control of our proposed system is easy. From these experiment results, the electric wheelchair control system using facial muscles s-EMG is a good system for the severely handicapped human. In addition, we think that the merit of our proposed system does not need a lot of training for user. Moreover, when the obstacle (the road cones) became near, our proposed system was able to be evaded smoothly without Stop command because the speed slowed by the obstacle evasion function. However, this processing reduced the speed.

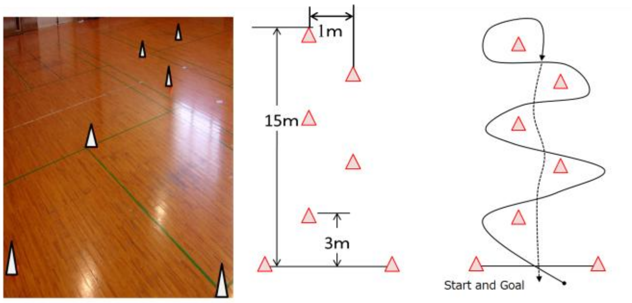

Figure 5. The Driving Course.

Table 3.Experiment Results.

Subject	Time		Classification	
	Average [sec]	Standard deviation	Average [%]	Standard deviation
Experienced subject S.H	188	16.3	94.9 (150/158)	3.07
Inexperienced subject 1 T.B	229	54.1	97.4 (191/196)	2.95
Inexperienced subject 2 T.M	197	20.6	97.5 (196/201)	1.92
Inexperienced subject 3 T.Y	229	13.3	97.2 (243/250)	3.39
Inexperienced subject 4 S.H	164	7.98	100.0 (116/116)	0

5 CONCLUSION

In this paper, we applied to the electric wheelchair hands-free semi-automatic control system for the severely handicapped human using facial muscles s-EMG pattern recognition system. We tried the experiment of driving in the course by using our proposed system. The experimental subjects were five healthy men in twenties whose physique looks like. One person was an expert of the system, and others were the inexperienced person. From these experiments, we showed that the control of our proposed system is easy and our proposed system does not need a lot of training for user.

Our proposed system could also be used by handicapped person without training. Moreover, we think that our proposed system is useful than the system using the EEG signals. In the future works, we plan to develop of algorithm that can be turned more smoothly, improve the obstacle evading function and test the severely handicapped human.

REFERENCES

[1] K. Tomohiro, M. Tadashi, K. Tohru and S. Tsugutake, “Practical Usage of Surface Electromyogram”, Biomechanism Library, 2006.

[2] H. Tamura, D. Okumura, K. Tanno, “A Study of Motion Recognition without FFT from Surface-EMG”, Vol, J90-D No, 9 pp.2652-2655, THE JOURNAL OF IEICE D, 2007. (Japanese)

[3] D. Okumura, H. Tamura, K. Tanno, “Proposal of the Motion Recognition system corresponding Surface-EMG changes”, Proceedings of Forum on Information Technology 2007 (FIT2007) , pp G-022 (CD-ROM), 2007. (Japanese)

[4] H. Tamure, T. Gotoh, D. Okumura, H. Tanaka, K. Tanno “A Study on the s-EMG Pattern Recognition using Neural Network” International Journal of Innovative Computing, Information and Control, Vol.5, No.12 (B) pp.4877-4884, Dec. 2009.

[5] A. Assareh, S. Konjkav, A. Fallah, S.M.P. Firoozabadi, “A New Approach for Navigating Automatic Wheelchairs using EMG signals Feature Extraction and Classification with an Adaptive Controller,” in Proc, The 12th International Conference on Biomedical Engineering, SINGAPORE, Dec. 2005.

[6] H. Tamura, T. Manabe, K. Tanno, Y. Fuse“The electric wheelchair control system using surface-electromygram of facial muscles”,Proc. of World Automation Congress 2010, IFMIP 240, CDROM, (pp.1-6), 2010.

[7] H. Tamura, T. Manabe, T. Goto, Y. Yamashita, K. Tanno“A Study of the Electric Wheelchair Hands-Free Safety Control System using the Surface-Electromygram of Facial Muscles”, Lecture Notes in Computer Science, 6425/ International Conference on Intelligent Robotics and Applications (ICIRA)2010, (2), pp.97-104, 2010.

[8] S.M.P. Firoozabadi, M. Asghari Oskoei and H. Hu, “A Human-Computer Interface based on Forehead Multi-channel Bio-signals to control a virtual wheelchair,” Proceedings of the 14th Iranian Conference on Biomedical Engineering (ICBME), Shahed University, Iran, pp. 272–277, Feb. 2008.

[9] P. Jia, H. H. Hu, T. Lu, and K. Yuan, “Head gesture recognition for hands-free control of an intelligent wheelchair”, Industrial Robot: An. International Journal, 34(1):60–68, 2007.

[10] T. Manabe, H. Tamura, K. Tanno, “The Control Experiments of the Electric Wheelchair using s-EMG of Facial Muscles”, Proceedings of Forum on Information Technology 2009 (FIT2009), pp. K-008 (CD-ROM), 2009.(Japanese)

Upper extremity prosthetics: current status, challenges and future directions

D.S.V Bandara[1], R.A.R.C Gopura[2], K.T.M.U Hemapala[3], and Kazuo Kiguchi[4]

[1,2]Department of Mechanical Engineering, University of Moratuwa, Sri Lanka
[3]Department of Electrical Engineering, University of Moratuwa, Sri Lanka
[4]Department of Advanced Technology Fusion, Saga University, Japan

[1]sanjaya@mech.mrt.ac.lk, [2]gopura@mech.mrt.ac.lk, [3]udayanga@elect.mrt.ac.lk, [4]kiguchi@ieee.org

Abstract: There is a drastic increment of the demand for prosthetic devices over the last few decades. This is caused by the increased amputees because of casualties due to civil wars, injuries due to accidents, *etc*. Therefore, the robotic prostheses are one of the highly interested research areas in recent robotic research. The target is to make sure the amputee gets a better chance to interact with the real world, in spite of the amputation he has. The paper presents the results of a comprehensive literature analysis towards a development of an upper-limb prosthetic arm. This study identifies the methods of prosthetic classification as the segment of application, number of degrees of freedom (DoF), types of applied actuators, types of power transmission methods and control methods. In this study, the upper extremity prosthetic devices are classified based on the segment of application. Thus, they can be mainly classified into shoulder prosthetics, transhumeral and elbow prosthetics, transradial and hand prosthetics. This study considers all the above categories of recent upper extremity prosthetics, and reviews their key technologies by taking state-of-the-art robots as examples.

Keywords: robotic prosthetics, transhumeral, transradial, upper-extremity.

1 INTRODUCTION

A prosthetic is a device that replaces an amputated body part of a person. It is expected to restore the physical appearance and the lost functions of the amputated body part. Limb replacements are taking place at a higher frequency, affected by casualties due to war, accidents, cardiovascular disease, tumors and congenital anomalies.

In 490 B.C., it was a Persian soldier who cut off his own feet in order to escape from a prison and later replaced it with a wooden foot which is the first prosthetic [1]. However, the development and the fabrication of the prosthetics dated back to about 500 years [2]. Recent development of the prosthetics was influenced by the World War I and II, which resulted in a remarkable loss of man power in USA and Europe. In 1948, the concept of Cybernetics, *i.e.*, the study of control and communication between human and machine [3], played a significant role later on for the improvement of the prostheses. Samuel Anderson created the first electrically powered prosthetic arm that uses external power, with the support of the US government and IBM in 1949 [4]. Russians in 1958 developed the first myoelectric arm and soon after, Otto Bock Company came up with a commercially available prosthetic arm for common application which was the first finished versions of the Russian design [4]. The researchers have been making effort to develop a perfect prosthetic system, which will mimic the exact human motion pattern, power requirement and anatomical/cosmetic features.

The advancement of the mechatronic technology over the recent years leads to a number of upper extremity prosthetics both commercially available and still in the research level [6]-[16]. Nevertheless, they are not that popular among the amputees due to their inability to meet the user expectations up to a desired level in real world. Most of them are with poor functional and controlling properties, which is the major, concern of the prosthetic user to loss their interest on the prosthetics [5].

During the last decade number of research work [6]-[11] had been carried out and some of research works are still ongoing. At present, Utah Arm [17], Boston Elbow and Otto Bock [12]-[16], which are commercially available can be considered as the pioneers in this filed. Dean Kamen's Luke Arm, Proto 2 and MANUS-HAND are still at the developing stage [18]. Most of these commercially available prosthetics [16] are capable of generating only few limited degrees of freedoms (DoF): elbow flexion/ extension, forearm pronation/supination, and prehension. Forearm pronation/supination is generated in a terminal device forfeiting the human upper limb anatomy. Therefore, the adaptation of the wearer to the real world might be an extra burden. Some prostheses are developed to generate the functions of the human hand. Touch Bionics's i-Limb [19] is the state-of-the-art upper limb prosthetic and before that it was Otto Bock's SensorHand Speed, which was a basic open and close mechanism only. The dexterity of hand prosthesis is still far from that of the state-of-the-art non-prosthetic mechanical hands, such as the DLR II [20].

Main target of this review paper is to cover brief history, challenges, current status and future developments of upper extremity prosthetic devices. Authors tried to review the state of the art prosthetics developed in the last six years.

Biomechanics of upper-limb toward the development of an upper-limb prosthetic device, challenges to the development of prosthetic limbs, a brief review on the state-of-art upper limb prosthetic limbs and a brief idea on future research directions are presented respectively.

2 BIOMECHANICS OF UPPER EXTREMITY

Before developing a robotic prosthetic device to mimic the upper extremity, a thorough understanding of its physics should be there. Three major components of the upper extremity are shoulder complex, elbow complex and wrist. Shoulder complex is built with three bones: clavicle, scapula and humerus and four articulations. Shoulder can be modeled into a ball-and-socket joint. The proximal part of the humerus, humeral head and the female part of the scapula, glenoid cavity respectively act as the ball. The main motions of the shoulder joint are shoulder flexion/extension, abduction/adduction and internal/ external rotation. During each motion, the position of the centre of rotation of the shoulder joint changes.

Three bones of the arm and the forearm, humerus, radius and ulna are connected to the elbow (radioulnar) joint at the distal part of thehumerus. The ulnohumeral and the radiohumeral articulations are contributing to the motions of the flexion/extension of the forearm. Further, the radioulnar articulation contributes the motions of supination/pronation of the radius and ulnar bones [21].

The wrist is a collection of eight carpal bones. It has two major articulations, radiocarpal and midcarpal based on their functionality. The radiocarpal joint allows motions in two planes: flexion/extension and radial/ulnar deviation of the wrist, which are generated around an instantaneous center. However, the centroide travels in a small path, therefore the displacement of the instantaneous center of rotation is ignored and the axes of rotation for the motions are considered to be fixed. These axes pass through the capitate. Even though the wrist joint motions are considered to be generated with respect to the two axes, some research work [14] has shown that they are generated with respect to four axes. The wrist flexion axis and the extension axis are different, but intersects at a point at capitate. Similarly the radial and ulnar deviation axes are also different and intersect at capitates [22]. The slight offset of the rotational axes of the flexion/extension and the radial/ulnar deviation is approximately 5 mm [22].

3 CHALLENGES

Even though the existing upper limb prosthetic devices are able to cater the amputees' requirements to a certain degree, still there are lot of improvements and design challenges that have to be addressed. They are briefly discussed here. Amputees expect a prosthetic not to be overweight, anthropomorphic in appearance and cosmetics [23] and the functionality of the prosthetic to provide expected motion intentions of the user as a normal human limb. Ultimate objective of a prosthetic limb is to make sure both user and the surroundings do not feel the difference of the amputation which the user is having. In addition, the prosthetic limb should demonstrate a significant decrease in the metabolic demands which will be equivalent to a human being without any amputation, for daily motions.

These expectations are still constrained by different technological barriers which needed to be overcome to develop a perfect prosthetic device. Most of the actuation methods that are being used are heavy and if not they are with limited torque and power. Furthermore, the actuator sizes and the operational behaviors such as smooth and simultaneous motion of joints, noises also should be rectified towards the anthropomorphism. Prehension, grasping or holding of an object is one of the main functions expected from the human hand. It is capable of holding anything and will not effect by the object to be hold. The surface finish, geometry, stiffness or strength of the object will not affect the grasping function of the human hand. All these requirements are not yet integrated at one place.

Further, tactile sensing is another important input from the human upper limb to the robot making a good interaction of the human being with the environment. It helps to make accurate motions which sensory inputs are required. Tactile sensing and force sensing are essential outcomes of a human upper extremity and yet to be developed such a system. Furthermore, the unavailability of proper accessory devices such as power sources with tolerable weight for long time use, material types for more anthropomorphic features, is also a challenge to develop a perfect upper extremity prosthetic. The motions of the robot should to be with required power and the joint movements have to be simultaneous. Since most of the amputees wear the prosthetic more than 8 hours per day [23] the user fatigue is a great concern in prosthetic design. When the actuators are large enough to provide the desired power they may be with a much weight and will be uncomfortable to use for longer time periods. In addition, the concern should be on the prosthetic sockets as well. It should be comfortable enough to wear for a longer period of time. Moreover, different control signals are available for the prosthetic devices. Electromyography (EMG) signals are mostly preferred by most of the researchers since EMG signals directly convey the human motion intention to the control system. However, the amputees have already lost their body part and muscles obviously. It limits the amount of control signals that can be gained through the EMG. This ultimately leads to a limitation of the number of communication channels available for the control of a multi-DoF upper limb prosthesis resulting them to underperform on showing the correct motion intention of the user.

4 REVIEW OF UPPER EXTREMITY PROSTHETICS

In recent years, a number of upper-limb prosthetic devices have been proposed [19], [24]-[33]. Available prosthetic devices can be classified considering different criterion. This study identifies the methods of prosthetic classification as the segment of application, DoF, types of applied actuators, types of power transmission methods and control methods. The methods of classification of prosthetic are shown in Fig. 1(a). Since this paper is mainly focused on application of the robotic upper limb prosthetics, the classification is carried out based on the location of application of the prosthetic. The classification is shown in Fig. 1(b).

Table 2 shows a comparison of existing prosthetic limbs. In the next sub sections recent upper-limb prosthetics are reviewed by explaining their basic designing concepts. They are selected based on their key technological features in their designs. Transhemral prosthetics and elbow prosthetics, Transradial and hand prosthetics are combined together in following subtitles for the ease of the presenting.

4.1 Shoulder Prosthetic Devices

Shoulder prostheses are worn by amputees with shoulder disarticulation. The following section presents the state-of-the art shoulder prosthetics.

4.1.1 DEKAs (DARPAs) Luke Arm [24]

The Luke Arm is the latest upper arm prosthesis developed by Defense Advanced Research Projects Agency (DARPA), designed by Dean Kamen [24]. Its advanced dexterity makes the Luke Arm better than the prosthesis currently in the market. The arm has 18DoF and it is more than the 03DoF other available in arm prosthesis today. In addition, high quality electronics and software allow for fine control of the arm which will allow amputees to perform many complex tasks such as to pluck chocolate-covered coffee beans one by one, pick up a power drill, unlock a door, and shake hands. The Luke arm is modular based, adjustable to use by anyone with any level of amputation since shoulder, elbow, forearm and the hand are independent from each other.

4.1.2 Proto 2 [25]

Proto 2 was launched as one of the phases of a four-year program to create prosthetic arms that can be better imitated natural limbs by Defense Advanced Research Projects Agency (DARPA) [25]. It is built with 100 sensors that connect the natural neural signals of body to the mechanical prosthetic arm making a sensory feedback loop. Thus the wearer interacts with an object and the arm feeds back in real time. The user could get a feeling of where the arm is in space, what object it is touching, whether that object is smooth or rough, how hard the hand is holding it, and what temperature the object is. Further, the motions of Proto 2 are smooth and not with jerks.

4.2 Transhemural & Elbow Prosthetic Devices

These are worn by amputees with elbow disarticulation or transhumeral amputation. State-of-the art transhumeral and elbow prosthetic devices are explained below.

4.2.1 A Gas-Actuated Transhumeral Prosthesis [26]

This is an anthropomorphic 21DoF, 9 degree-of-actuation prosthesis arm for transhumeral amputees. The arm utilizes a monopropellant, hydrogen peroxide as a gas generator to power nine pneumatic type actuators that drive elbow, wrist and a 17DoF compliant hand. The design makes the arm compact. Elbow and wrist joints are integrated with position and force sensing. The prosthesis is expected to approach the dexterity of an anatomical arm and is projected to deliver half of the force and power output of an average human arm. The usage of the gas-type actuators let the arm to achieve better volumetric and gravimetric power density.

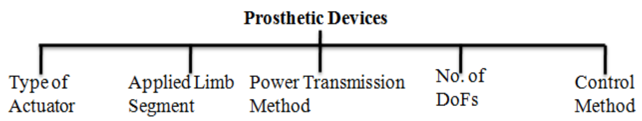

(a) Methods of classification of prosthetic devices

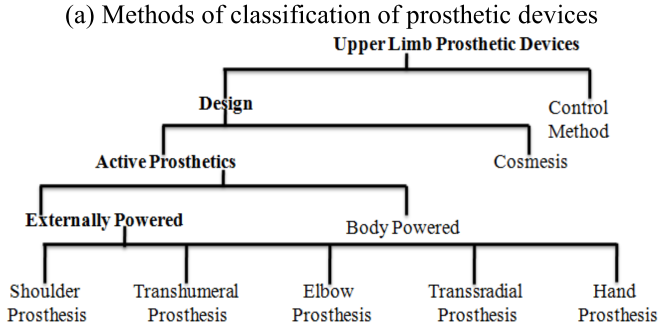

(b) Classification based on applied limb segment

Fig. 1. Classification of Robotic Prosthetic devices

4.2.2 Saga University Prosthetic Arm [27]

The robotic prosthetic arm developed by Saga University is with 05DoF and targets to mimic the human anatomy as much as possible [27]. A T–mechanism is introduced here to mimic the human alike forearm motion and it contributes to the supination/pronation with the introduction of two shafts which act as the ulna and radial bones of the human arm. In order to achieve the objective of prehension, hand with a single DoF is attached to the distal end of the ulna and radial shafts with a ball joint.

4.2.3 MSUM elbow–2 [28]

The prosthetic is mainly capable of providing elbow flexion/extension. In the design the gears are substituted with linkages with ball bearing and by screw ball transmissions, when possible which has been lead to an increment of the mechanical efficiency of the hand [28]. In the initial design the axis of the ball screw is connected to a brushless motor via an epicyclical transmission and a belt-pulley system. The measured overall mechanical efficiency of this system was increased up to 64%. Later as an improvement, the screwball axis is oscillating and is directly connected to a "pancake" brushless motor. This architecture raises the efficiency to over 80%. The prosthetic could be integrated with other mechanisms to develop a transhumeral or shoulder prosthetic.

4.3 Transradial and Hand Prosthetic Devices

Transradial and hand prostheses are worn by amputees with wrist disarticulation or transradial amputation. Below mentioned devices are the state-of-the art transradial and hand prostheses.

4.3.1 Touch Bionics i-Limb [19]

Touch Bionics i-Limb is the first commercially available prosthetic device with five individually powered digits. Its inclusion of a thumb that works like the human thumb, let the hand to achieve different positions, enables important grip configurations [19], many of which have not been available to amputees before. The articulating fingers are able to close tightly around objects. Furthermore, the built-in stall detection for the each individual finger can detect the power cut-off position to the finger. Each individual finger will be locked in the position until the patient triggers an open signal through a muscle signal.

4.3.2 Under-actuated Hand Prosthesis [29]

Nasser *et al* proposed this hand to overcome the drawbacks of commercially available hand prostheses [29]. The hand design is based on an under-actuated 15DoF, 1DoF actuation configuration, fully capable of performing activities of daily living. Each finger is fully independent from each other and adaptable to grasp any object of any geometry. The system is capable of providing safe and reliable grasping without the need for feedback sensors, multiple servos, or any type of data processing. The design is focused towards providing upper limb amputees with the prosthetic hand that is cosmetically appealing, functionally comparable by means of DoFs, weight and cost.

4.3.3 FLUIDHAND III [30]

FLUIDHAND is hand prosthesis with enhanced functionality, cosmetic; enable security, and adaptive grasping as well as aesthetically appealing properties [30]. The combination of flexible fluidic actuators and soft passive elements reduces the required grasping force for a wide range of objects. Further, the enhanced actuator system allows high grasping forces if necessary. Two myoelectrodes in the socket together with the developed controller board and software enable quick selection of the most important grasping patterns. Vibrotactile force feedback and wireless programming and control options complete the characteristics of the FLUIDHAND III.

5 CONCLUSION AND FUTURE DIRECTIONS

This paper briefly reviewed available upper limb prosthesis developed over the recent years. It covers both commercially available upper limb prosthetics and the upper limb prosthetics still in the development stage. Nevertheless, following research goals could be followed for the future developments of a prosthetic device.

A biomechanical investigation should be carried for the upper-limb with and without the state-of-the-art prosthetics to identify the main problems of the state-of-the-art in the field. Using the results of the investigation the goals can be set for the future developments of the prosthetics limb. The goals can be standardized by means of weight, size, durability, actuation speeds, level of activity, and professional needs at a global level. In addition, a proper scheme can be proposed to evaluate the available prosthetic limbs by means of anthropometry, dexterity, user acceptance, etc. A measuring criterion should be defined for each different requirement of a prosthetic in order to achieve the objective of proper evaluation. The metabolic cost of transport (COT), which is the measuring of oxygen consumption and carbon dioxide production of human breathing during a task, can be used to benchmark the future developments of the prosthetic devices. Identification of the factors affecting the COT of a prosthetic user and the direct addressing of them in the designs will give better

Table 1. Comparison of Upper-Limb Prosthetic Devices

Reference	Location of Application	DoF	Actuator	Power Transmission	Special Feature	Control Method/ Input
DARPA's Luke Arm [24]	Shoulder, Elbow, Hand	18	DC Motors	Gear Drives	Adjustable to use for any level of amputation	EMG-TMR foot pad in shoe
Manus Hand [31]	Hand	3	DC Motors	Gear Drives, Geneva Mechanism,	Underactuateddesign principle	EMG
Proto 2 – John Hopkins University [25]	Shoulder and Elbow	25	DC Motors	Tendons	Real time feedback for grasping	EMG- TMR
i-Limb – Touch Bionics [19]	Hand and Fingers	11	DC Motors	Tendons	Five individually powered digits	EMG
Under-actuated Hand Prosthesis [29]	Hand and Fingers	15	Motors	Gears and steel rods	Independent fingers, Adapt to any geometry	Under development
The FLUIDHAND III [30]	Hand and Fingers	8	Fluidic Actuators	Pressurized Fluid	Vibrotactile force feedback	EMG
Prosthetic Arm – SAGA[27]	Elbow and Wrist	5	DC Motors	Cables and Gears	Anatomical Design Approach	EMG
Gas-Actuated Transhumeral Prosthesis[26]	Elbow	21	Pneumatic Actuators	Pressurized Fluid	Half of the force and power of a human arm	Under development
Prosthetic Hand Driven by Shape Memory Alloy Actuators [32]	Hand and Fingers	7	SMA Actuators	Shape Memory Alloys wires	lightweight, multifunctional, silent and cosmetically appealing	EMG
Bebionic Hand [33]	Hand and Fingers	11	DC Motors	Mechanical Links	position sensor to achieve the desired grip pattern	EMG

results. In addition, the existing actuation and power transmission methods have to be developed to meet the requirements towards a perfect prosthetic device. Improvements should be done on under-actuation topologies, artificial muscles and tendons.

To give a better prosthetic handling to the amputee, the number of control inputs has to be increased and more effective pattern recognition methods to extract detailed data from surface EMG signals from the residual muscles have to be invented. Furthermore, the usage of implantable EMG electrodes and the targeted muscle reinnervation also will lead the researchers to get more comfortable with the number of controller inputs available. In addition, mechanomyography (MMG) signals which is the detection of sound produced by contracting muscles and the pressure signals generated due to pressure exerted by the residual limb on the socket are also used as inputs to the control system. With properly developed pattern recognition methods, two or more hybridization of these control methods will ultimately produce a better control method for the prosthetics, which will operate according to the human motion intention.

Electroencephalogram (EEG) signals, which are the measurement of brains spontaneous electrical activity, will also become a control input when used with a proper signal classification mechanism. Furthermore, electrocorticogram (ECoG) signals and spike recordings from the primary motor cortex will also become future trends in prosthetics controlling.

Furthermore, biomechanical energy harvesting methods to harvest energy from body heat and from motions of various parts of the body during walking, such as heel strike; ankle, knee, hip, shoulder, and elbow joint motion; and center of mass vertical motion could be improved to power the prosthetic devices without making the power source and extra burden to the wearer.

ACKNOWLEDGEMENT

The authors gratefully acknowledge the support provided for this research by National Research Council, Sri Lanka from the Grant 11-067.

REFERENCES

[1] History of Prostheses (2009) [online], Available: http://www.uihealthcare.com/depts/medmusem/wallexhibits/body/histofpros/histofpros.html

[2] Thompson G, Lubic D, (2009) The Bionic Arm: New Prosthetic Devices Fuse Man and Machine. in Proc. of Seventh Annual Freshman Conf., pp. 1-8

[3] Wiener N (1948), CYBERNETICS or Control and commu nication in the Animal and the Machine. MIT Press

[4] Meier RH, Atkins DJ (2004), Functional Restoration of Adults and Children with Upper Extremity Amputation. Demos Medical Publishing Inc. New York

[5] Carrozza MC, Dario P, Vecchi F, Roccella S, Zecca M, Sebastiani F (2003), The Cyberhand: On the Design of a Cybernetic Prosthetic Hand Intended to be Interfaced to the Peripheral Nervous System. in Proc. of IEEE/RSJ Int. Conf. on Intelligent Robots and Systems, vol. 3, pp. 2642-2647.

[6] Troncossi M, Castelli VP, Davalli A (2005), Design of Upper Limb Prostheses: A New Subject-Oriented Approach. Journal of Mechanics in Medicine & Biology, vol. 5, no. 2, pp. 387-390

[7] Escudero AZ, Alvarez J, Leiza L (2002), Develop ment of a Parallel Myoelectric Prosthesis for Above Elbow Replacement. in Proc. of Second Joint EMBS/BMES Conf., Houston, TX, USA, pp. 2404-2405

[8] Tsuji T, Fukuda O, Shigeyoshi H, Kaneko M (2000), Bio-Mimetic Impedance Control of an EMG-Controlled Prosthetic Hand. in Proc. of the IEEE/RSJ Intl. Conf. on Intelligent Robots and Systems, pp. 377-382

[9] Fukuda O, Tsuji T, Kaneko M, Otsuka A (2003), A Human-Assisting Manipulator Teleoperated by EMG Signals and Arm Motions. IEEE Trans. on Robotics and Automation, vol. 19, no. 2, pp.210-222

[10] Ito K, Tsuji T, Kato A, Ito M (1992), An EMG Controlled Prosthetic Forearm in Three Degree of Freedom Using Ultrasonic Motors. in Proc. of IEEE Int. Conf. on Engineering and Biology Society,vol.4, pp.1487-1488

[11] Saito Y, Ogawa A, Negoto H, Ohnishi K (2005), Development of Intelligent Prosthetic Hand Adapted to Age and Body Shape. in Proc. of IEEE Int. Conf. on Rehabilitation Robotics, Chicago, USA, pp. 384-389

[12] Lee S, Saridis GN (1984), The Control of a Prosthetic Arm by EMG Pattern Recognition. IEEE Trans. Auto. Contr., vol. 29, pp. 290-302

[13] Jacobson SC, Knutti DF, Johnson RT, Sears HH (1982), Development of the Utah Artificial Arm. IEEE Trans. on Biomedical Engineering, vol. 29, no. 4, pp. 249-269

[14] Scott RN, Parker PA (1988), Myoelectric Prostheses State of the Art. Journal of Medical Eng. and Technology, vol. 12, no. 4, pp. 143-151

[15] Otto Bock Arm Prostheses (2011) [online], Available: http://www.ottobock.com

[16] Toledo C, Leija L, Muñoz R, Vera A, Ramírez A (2009), Upper limb prostheses for amputations above elbow: A review. in Proc. of Int. Conf. on Health Care Exchanges, Mexico, pp. 104-108

[17] Utah Arm 3(UA3): Motion Control /Utah Arm (2011) [online] Available: http://utaharm.com

[18] Allin S, Eckel E, Markham H, Brewer B (2010), Recent Trends in the Development and Evaluation of Assistive Robotic Manipulation Devices. Physical Medicine and Rehabilitation Clinics of North America, vol. 21, no. 1, pp. 59-77

[19] Touch Bionics, The i-Limb Hand, The world's first fully articulating and commercially available bionic hand.(2011) [online], Available: http://94.229.167.224/i-LIMB/introduction

[20] Orabona F, Castellini C, Caputo B, Fiorilla AE, Sandini G (2009), Model adaptation with least-squares SVM for adaptive hand prosthetics. in Proc. of IEEE int. Conf. on Robotics and Automation, Kobe, Japan, pp.2897-2903

[21] Hamill J, Knutzen KM (1995), Functional Anatomy of the Upper-Extremity. in Biomechanical Basis of Human Movement, pp 137-186

[22] Gopura RARC, Kiguchi K (2009), Mechanical Designs of Active Upper Limb Exoskeleton Robots State-of-the-Art and Design Difficulties. in Proc. of IEEE Int. Conf. on Rehabilitation Robotics, Kyoto, Japan, pp.178-187

[23] Pylatiuk C, Schulz S, Doderlein L (2007), Results of an internet survey of myoelectric prosthetic hand users. Journal of Prosth Ortho,vol.19,no. 2 pp.362–370

[24] DARPA's "Luke Arm" Readies for clinical trials (2011) [online], Available: http://www.danshope.com/news/showarticl e.php?article_id=27

[25] A "Manhattan Project" for the Next Generation of Bionic Arms IEEE Spectrum.2009 (2011) [online] http://spectrum.ieee.org/biomedical/bionics/a-manhattan-project for-the-next-gener ation-of-bionic-arms

[26] Fite KB, Withrow TJ, Xiangrong S, Wait KW, Mitchell JE, Goldfarb M (2008), A Gas-Actuated Anthropomorphic Prosthesis for Transhumeral Amputees. IEEETrans.onRobotics, vol.24,pp.159-169

[27] Kundu SK, Kiguchi K, Horikawa E (2008), Design and Control Strategy for a 5 DOF Above-Elbow Prosthetic Arm. Int. Journal of ARM, vol. 09, no. 3, pp. 61-75

[28] Casolo F, Cinquemani S, Cocetta M (2008), Evolution of elbow prosthesis transmission. in Int. Symposium of Mechatronics and Its Applications, pp. 1-6

[29] Nasser S, Rincon D, Rodriguez MN (2006), Design of an Anthropomorphic Underactuated Hand Prosthesis with Passive- Adaptive Grasping Capabilities. in Proc. 2006 Florida Conference on Recent Advances in Robotics, Miami, Florida

[30] Gaiser IN, Pylatiuk C, Schulz S, Oberle R, Werner T (2009), The FLUIDHAND III: A multifunctional Prosthetic Hand. American Academy of Orthotists and Prosthetists, vol. 21 no. 2, pp. 91-96.

[31] Pons JL, Rocon E, Ceres R, Reynaerts D, Saro B, Levin S, Moorleghem WV (2004), The MANUS-HAND Dextrous Robotics Upper Limb Prosthesis: Mechanical and Manipulation Aspects. in Proc. of Int. Conf. on Autonomous Robots2004,vol.16, no.2, pp143–163

[32] Andrianesis K, Tzes A (2008), Design of an Anthropomorphic Prosthetic Hand Driven by Shape Memory Alloy Actuators. in Proc. of IEEE/RAS-EMBS Int. Conf. on Biomedical Robotics and Biomechatronics, Scottsdale, AZ, USA, pp 517-522

[33] Steeper RSL, BeBionic Product Brochure (2011)[online], available: http://www.bebionic.com

The Seventeenth International Symposium on Artificial Life and Robotics 2012 (AROB 17th '12),
B-Con Plaza, Beppu, Oita, Japan, January 19-21, 2012

Wire-driven two fingers robotic hand for operating a touch-sensitive panel

Tatsuro Hakui[1], Yukiharu Yamauchi[1], Sei-ichiro Kamata[2], and Shinnosuke Nakao[2]

[1] Kitakyushu National College of Technology, Kitakyushu, Fukuoka 802-0985, Japan
(Tel: 81-93-964-7297, Fax: 81-93-964-7298)
(yamauchi@kct.ac.jp)
[2] Waseda University Graduate School, Kitakyushu, Fukuoka 808-0135, Japan

Abstract: Previously, we developed a robotic system in collaboration with the Graduate School of Information, Production and Systems, Waseda University, and Shanghai Jiao Tong University. This system, named Ninomiya-kun, can read a book. It is a child-sized humanoid whose head that is equipped with two cameras, and it can communicate with humans via sounds voice and gestures. The image of a printed document, such as a picture book, textbook, or magazine, each of which has a large number of characters, is captured by the cameras, and the characters are extracted from the captured image. Using a built-in computer with character recognition software, the robot translates the extracted characters into spoken words, which are produced by a voice synthesizer. In this paper, we propose a wire-driven robotic hand system for the operation of tablet computers such as the Apple iPad and Sony Tablet, and electronic book readers such as the Amazon Kindle. It has two fingers, each of which has a wire-driven region and a touch pen at the fingertip for operating touch-sensitive panels. We describe the system configuration and wire-driven architecture herein.

Keywords: A wire-driven control, touch-sensitive panel operation, embedded software, robotic hand, two-finger hand

1 INTRODUCTION

Japan has a long and distinguished history of developing robot technologies, and robots reflect certain cultural aspects of Japan. Next-generation robot technologies are expected to be highly advanced; hence, the demand for robots for medical care and living assistance is expected to increase accordingly. Previously, we developed a robotic system in collaboration with the Graduate School of Information, Production and Systems, Waseda University, and Shanghai Jiao Tong University. This system, named Ninomiya-kun, can read a book (Fig.1) [1, 2]. It is a child-sized humanoid whose head is equipped with two cameras, and it can communicate with humans via sounds and gestures [3]. However, it has no legs; hence it cannot move around. The image of a printed document, such as a newspaper, magazine, or catalog, each of which has a large number of words, is captured by the cameras, and the words are extracted from the captured image [5, 6]. Then, the robot reads these words out loud using a voice synthesizer. In addition, it is able to turn the pages of a book. An electronic book reader with a touch-sensitive panel is extremely thin, like a magazine. It is smaller than most paperback books, and it can store hundreds of titles. Moreover, it can potentially revolutionize the struggling newspaper and magazine publishing industry. The objective of the proposed robotic hand system is to operate tablet computers such as the Apple iPad and Sony Tablet, and electronic book readers such as the Amazon Kindle. In this paper, we propose a wire-driven robotic hand system for the operation of tablet computers. It has two fingers, each of which has a wire-driven region and a touch pen at the fingertip for operating touch-sensitive panels of tablet computers. The system consists of three wire-driven actuators (pulse motors), and it is controlled using a personal computer [4, 7]. Some motions of the hand are achieved by embedded software. Each finger consists of three diarthrodial joints. A wire is fastened to each fingertip, and it is driven by each actuator. The fingertips are used for pinch-zoom, tap, and flick operations on a tablet computer in order to read words in a printed document. In this paper, we present the system architecture for realizing flexible wire-driven control, and we describe how the system achieves flexible motions.

Fig. 1. Robotic system Ninomiya-kun

2 SYSTEM STRUCTURE OF NINOMIYA-KUN'S HAND

The robotic system Ninomiya-kun is equipped with a mechanical hand in order to turn the pages of a book. This hand system is driven by a gear, and it has a mechanism of a suction pump for extracting the contents of a page. Figure 2 shows the hand of Ninomiya-kun. Further, a page whose contents are extracted by one hand is turned over, and the page turned over is held with the other hand. However, the following problems are encountered.

1. Unexpected behavior due to transient response.
2. Book damage due to metallic hand operation.
3. In turning a page by the suction pump, we looked like an unique behavior.

Solving these problems will enable us to realize flexible behavior of the robotic hand system.

(a) (b)

Fig. 2. Ninomiya-kun's mechanical hand

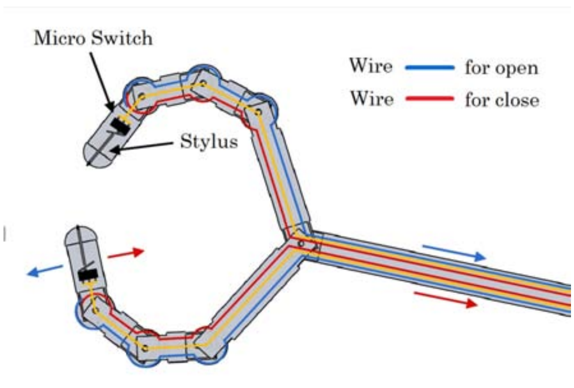

Fig. 3. Wire-driven system used to actuate the hand

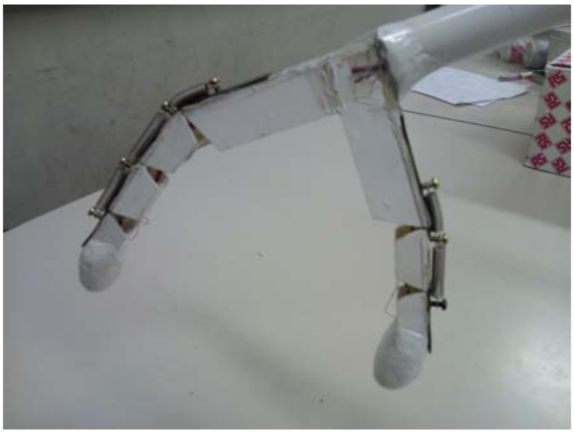

Fig. 4. Test model of wire-driven two-fingered robotic system

3 PROPOSED SYSTEM CONFIGURATION

The two fingers of the robotic hand are operated by two wires through actuators, as shown in Fig. 3. We have focused on designing a wire-driven robotic system [8, 9]. Because its performance is highly dependent on the geometry of the structure, we can easily modify it in order to adapt it to various tasks [10, 11]. The ability to vary the minimal and maximal wire length is crucial because these parameters play an important role in the robot workspace, accuracy, and maximal velocities [12, 13]. This has motivated us to design a coiling system based on an actuator and pulleys. We attempt to realize a system that is made from a plastic material and equipped with a wire-driven two-fingered robotic hand. In the future, this system can be used for operating tablet computers with touch-sensitive panels, such as the Apple iPad. We used a readily available plastic material in order to minimize the weight of the system. Wires were used for operating the fingertips to realize flexible behavior of the robotic hand system. Moreover, such a setup can prevent the positioning error due to gear's backlash . Springs were used for opening and closing the fingers. The test model of the robotic system is shown in Fig. 4.

The developed wire-driven two-fingered robotic system consists of a two-fingered hand, a built-in microcomputer, and a personal computer. Figure 5 shows the system configuration, and Fig. 6 shows its hardware components.

The two-fingered hand has three diarthrodial joints driven by a pulse motor whose rotational speed is defined by the number of the pulses fed by the controlling microcomputer. One extremity of the wire is attached to a fixed point of a fingertip, and from this point, the wire goes alternately to pulleys that are attached to the diarthrodial joints and the finger links. The wire goes from the final pulley of the finger to the actuator. The system is controlled by a personal computer with Linux OS, including electronic circuits that are

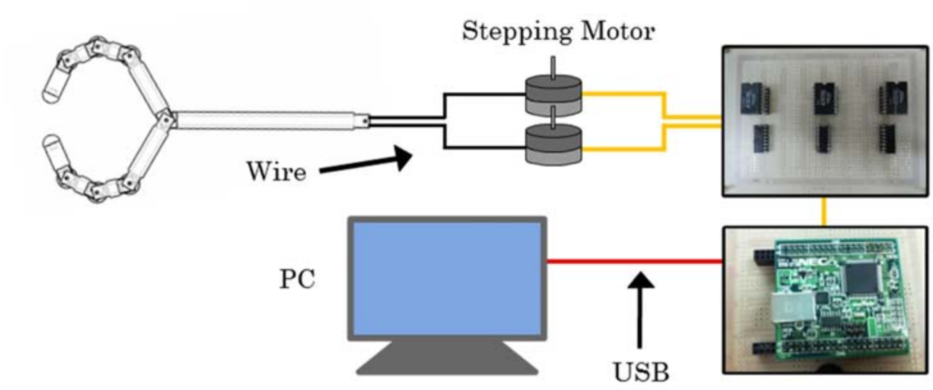

Fig. 5. System configuration

connected to a USB interface.

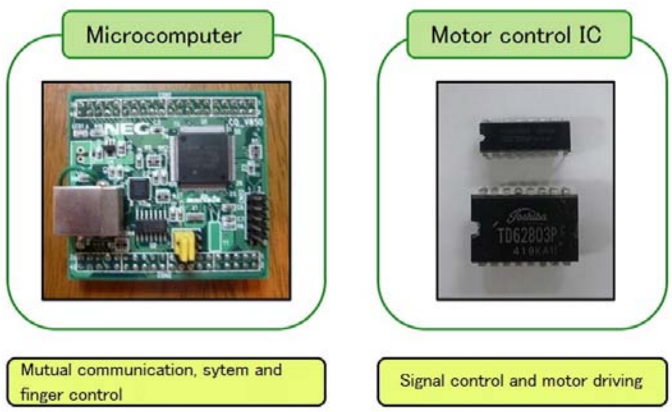

Fig. 6. Hardware components of robotic system

4 EXPERIMENTS

An experiment was conducted using the test model of the robotic system. An iPad and a smartphone placed on a special book stand were operated by the robotic hand. We evaluated the behavior of the driven parts and the system usability for tablet computers. Figure 7 shows a snapshot of the operation. We checked whether the tablet computer could be operated by the motion of the fingers. The following problems were encountered.

1. The finger size is large for operating a tablet computer and a smartphone.
2. The wire-driven mechanism becomes inoperative when the wires break.
3. The restoring force of the springs is insufficient.

5 CONCLUSION

We proposed a wire-driven robotic hand system for the operation of a tablet computer, and we realized a test model made from a plastic material. To evaluate the behavior of the driven parts and the system usability for tablet computers, we devised a strategy based on the light-weight body. This strategy was implemented experimentally using the test model of the two-fingered robotic hand system, and satisfactory results were obtained. Further development of the system is required in order to ensure flexible motion of the fingers. In addition, enhanced behavior of system can be realized by solving the identified problems.

REFERENCES

[1] Y. Komatsubara, Y. Yamauchi, S. Kamata (2008), Recognizing and reading for characters on books (in Japanese). ITE Annual conference 2008

[2] Y. Komatsubara, Y. Yamauchi, S. Kamata (2009), Character segmentation and reading from Japanese character (in Japanese). ITE Annual conference 2009

[3] T. Kawabuchi, Y. Yamauchi, S. Kamata (2010), Technique for Reading documents with multiple better type (in Japanese), SICE Kyushu Annual conference 2010, 203A-4

[4] N. Horii, Y. Yamauchi (2010), Control for a wire-driven humanoid robotic system (in Japanese), SICE Kyushu Annual conference 2010, 102A-3

[5] S. Imamoto, Y.Yamauchi (2011), Head and stem extraction from printed music scores, International Workshop on Target Recognition and Tracking 2011, pp.72

[6] N. Habu, Y.Yamauchi (2011), Printed Japanese characters recognition system, International Workshop on Target Recognition and Tracking 2011, pp.73

(a) Operating iPad

(b) Operating smartphone

Fig. 7. Hand system operating a tablet computer

[7] T. Hakui, Y. Yamauchi (2011), Two-finger robotic hand for a touch panel system, International Workshop on Target Recognition and Tracking 2011, pp.74

[8] E. Shammas, A.Wolf, and H. Choset(2006), Three degrees-of-freedom joint for spatial hyper-redundant robots, Mech. Mach. Theory, vol. 41:170-190

[9] A.Wolf, H. B. Brown, R. Casciola, A. Costa, M. Schwerin, E. Shamas, and H. Choset(2003), A mobile hyper-redundant mechanism for search and rescue tasks, Proc. IEEE/RSJ Int. Conf. Intell. Robots Syst., 2889-2895

[10] G. S. Chirikjian and J. W. Burdick(1995), Kinematically optimal hyperredundant manipulator configurations, IEEE Trans. Robot. Autom., vol. 11(6):794-806

[11] G. S. Chirikjian and J. W. Burdick(1994), A hyper-redundant manipulator, IEEE Robot. Autom. Mag., vol. 1(4):22-29

[12] G. S. Chirikjian and J. W. Burdick(1993), Design and experiments with a 30-DOF robot, Proc. IEEE Int. Conf. Robot. Autom., Atlanta, GA, vol. 3:113-119

[13] C. Wright, A. Johnson, A. Peck, Z. McCord, A. Naaktgeboren, P. Gianfortoni,M. Gonzalez-Rivero, R. Hatton, and H. Choset(2007), Design of a modular snake robot, Proc. IEEE/RSJ Int. Conf. Intell. Robots Syst., 2609-2614

The Seventeenth International Symposium on Artificial Life and Robotics 2012 (AROB 17th '12),
B-Con Plaza, Beppu, Oita, Japan, January 19-21, 2012

Development of a singing robotic system from music scores in real time

Shou Imamoto[1], Yukiharu Yamauchi[1], Sei-ichiro Kamata[2]
Naoto Ohata[2], and Yusuke Murayama[2]

[1] Kitakyushu National College of Technology, Kitakyushu, Fukuoka 802-0985, Japan
(Tel: 81-93-964-7297, Fax: 81-93-964-7298)
(yamauchi@kct.ac.jp)
[2] Waseda University Graduate School, Kitakyushu, Fukuoka 808-0135, Japan

Abstract: In this paper, we propose a novel robotic entertainment system that can read a musical score and sing a song in real time. The objective of this system is to provide on-demand entertainment to onlookers. Previously, we developed a robotic system in collaboration with the Graduate School of Information, Production and Systems, Waseda University, and Shanghai Jiao Tong University. This system, named Ninomiya-kun, can read a book. It is equipped with a camera to read printed material placed on a book stand. In this study, we attempt to realize a robotic system that can sing a song by producing human-like sounds on the basis of notes and words extracted from a music score. Experimental results show that the proposed technique consistently outperforms well-established procedures.

Keywords: Robot vision, entertainment robots, music score recognition, singing robotic system

1 INTRODUCTION

Recently, robotic systems have been enhanced considerably, and they have become an integral part of the manufacturing industry. In addition, robots play an active role in medical care, living assistance, and security. The demand for robots for living assistance is expected to increase with the ongoing development of robotic systems.

Fig. 1. Robotic system Ninomiya-kun

Previously, we developed a robotic system in collaboration with the Graduate School of Information, Production and Systems, Waseda University and Shanghai Jiao Tong University [1, 2]. This system, named Ninomiya-kun (Fig. 1), can read a book. It is a child-sized humanoid that does not have legs; hence, it cannot move around. Further, it is equipped with two cameras for processing visual information and it can communicate with humans via sounds and gestures. It reads text by focusing its camera on printed material, such as a newspaper, magazine, or catalog, which is placed on a special book stand. Using a built-in computer with character recognition software, the robot translates the text into spoken words, which are produced by a voice synthesizer.

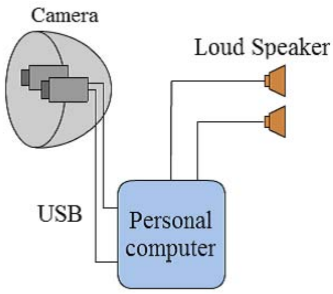

Fig. 2. System configuration of Ninomiya-kun

We have started enhancing Ninomiya-kun with new capabilities, and it must be trained to provide entertainment. It is important for an entertainment system to provide on-demand entertainment to onlookers. Our objective is to develop a robotic system that can read a musical score and sing a song in real time. We attempt to realize a system that can capture a printed music score using the camera installed in its the head, and sing a song by producing human-like sounds on the basis of the notes and words extracted from the captured music score[3, 4]. The input image should be properly processed for the successful recognition of the music score. In the first part of this paper, we discuss an image preprocessing technique for detecting musical notes, and we evaluate its performance. In the second part of this paper, we propose an adaptive technique for recognizing musical notes in order to deal with notes that belong to the same pitch class. Ex-

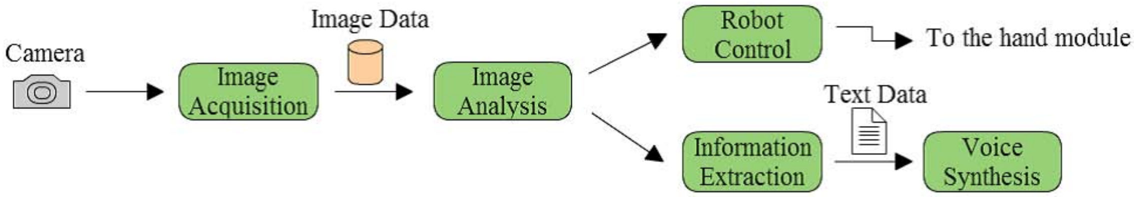

Fig. 3. Structure of the software system

perimental results indicate excellent music score recognition performance.

2 SYSTEM CONFIGURATION

The proposed robotic system has a backpack that consists of three units: a personal computer unit, an image acquisition unit, and a loudspeaker unit, i.e., an electro-acoustic transducer that produces sounds on the basis of the text that is translated into spoken words[11]. It has two hands that are driven by servomotors, enabling it to open a book and turn its pages; the rotational speed and angles of the hands are determined by the personal computer unit. Its head is equipped with two cameras as visual sensors. The video signals recorded by the cameras are transferred to the personal computer unit through the image acquisition unit, which provides high-resolution digitized images. The system configuration is shown in Fig. 2 [12, 13].

3 SOFTWARE CONFIGURATION

In this section, we describe an image processing technique for extracting notes and lyrics from printed music scores. A staff, or stave, is a set of five horizontal lines and four spaces, each of which represents a different musical pitch; it provides important information for musicians. As shown in Fig. 3, the software for the proposed robotic system consists of five modules: the image acquisition module, the image analysis module, the information extraction module, the voice synthesis module, and the robot control module. The image acquisition module captures a score using the camera and the image acquisition unit connected to the personal computer; then, this module performs image strain compensation and image binarization. Next, the image analysis module receives the binarized image and extracts the position of the staff. In the information extraction module, the pitch class of each note (C, C# , D etc.) is determined by the staff position information; in addition, it is determined whether the relative duration of each note is based on the ordering of sounds on a frequency-related scale. Simultaneously, the lyrics that are printed below the staff are extracted in this module. Accordingly, the voice synthesizer in the voice synthesis module produces human-like sounds; when required, requests for a rest period, i.e., is an interval of silence, are sent to the voice synthesis module by the information extraction module [5, 6].

4 EXTRACTION OF HEAD AND STEM

In an automatic music score recognition system, it is very important to extract the heads and stems of notes because these are the most ubiquitous and musically relevant symbols in a score [7, 8]. The objective of the system is to extract note heads quickly and accurately. It acquires the music score continuously in order to extract the heads and stems. In this study, we emphasize on the developmental aspect of the robotic system; hence, we employ a simple score with no chords. Initially, the camera is focused on the beginning of a score, and the score is continuously captured until a rest period is requested. Figure 4 shows the score that is used as a target. The image area that includes the candidates for heads and stems is extracted [9].

Fig. 4. Simple music score with no chords

The image area that includes the candidates for heads and stems is extracted. In order to extract the heads and stems, the stave is extracted by calculating the horizontal histogram of the music score, and the candidates for the areas with the lyrics are detected (Fig. 5). The black elliptical parts of the notes are the note heads; they indicate the note value (i.e., rhythmic duration), and they are extracted according to the relative position in the staff. The height of the head is equal to the interval between the lines in the staff, and the width of the head is 1.2 times its height. A template image is generated for heads whose height is less than the interval between the lines [10]. This template is compared with the overlapped image areas, while the detected stave is erased from the image (Fig. 6). The pitches of the notes are determined according to the position of the extracted heads. In the next step, stems, flags, and accidental notations are detected by template matching.

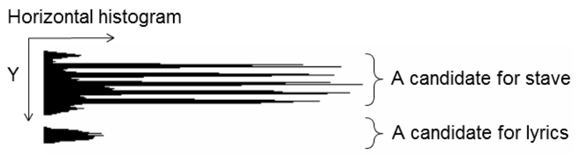

Fig. 5. Histogram of the music score

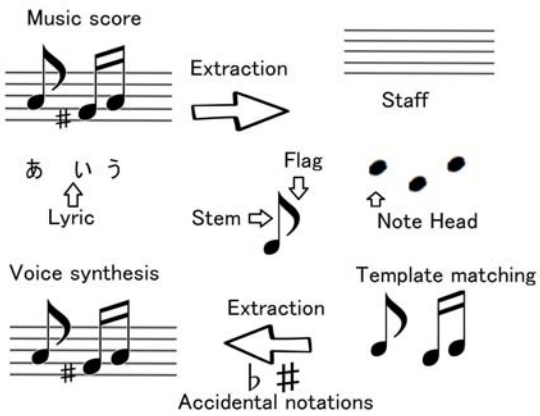

Fig. 6. Procedure for detecting notes

5 EXPERIMENTS

An experiment was conducted using the robotic system Ninomiya-kun. A captured music score is shown in Fig. 7. The robot extracted lyrics and music notes by focusing its camera on a printed music score placed on a special music stand. Fig. 8 (a) shows the recognition process; its side view is shown in Fig. 8 (b). The experiment was conducted as follows. Two music scores were used. One was "Kimigayo,"the national anthem of Japan; it is a short composition. The other was a 30-s extract from "Happiness," a song by the Japanese group Arashi. We used two scores in order to check whether the system is able to sing all the lyrics of different music scores. Figure 9 shows the staff extracted by calculating the histogram of "Kimigayo"; it was extracted with high accuracy. The accuracy of staff extraction from other music scores is more or less the same. The notes in the music scores "Kimigayo" and "Happiness" were detected by the template matching procedure, as shown in Fig. 10. The detected note heads are denoted by red boxes. However, the half notes were not detected, as shown in Fig. 10. A half note is a note having a white elliptical head. The template matching procedure fails to recognize a white note head that should be recognized because the pixel size of the elliptical part is different from that of the template image. We plan to devise ways to improve the accuracy off half notes detection.

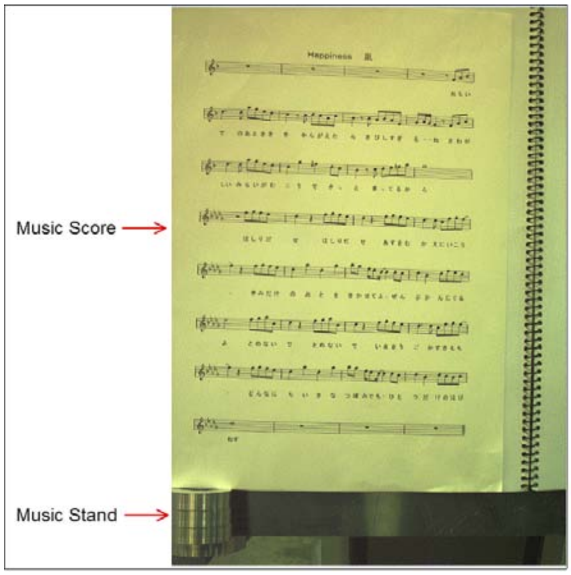

Fig. 7. Music score captured by Ninomiya-kun

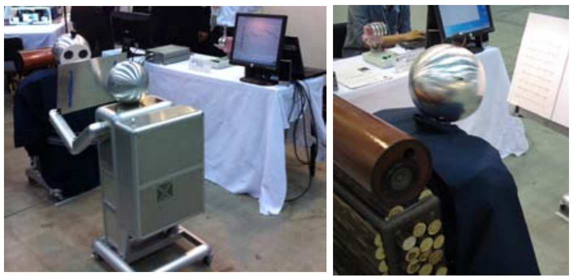

(a) (b)

Fig. 8. Ninomiya-kun extracting lyrics and music notes

6 CONCLUSION

We proposed a novel robotic entertainment system that can extract notes from printed music scores using solely visual information. To realize the recognition of simple music scores, we devised a strategy based on image processing. This strategy was evaluated experimentally using the robotic system Ninomiya-kun, and satisfactory results were obtained. Further development of the software is required in order to realize the recognition of more complex music

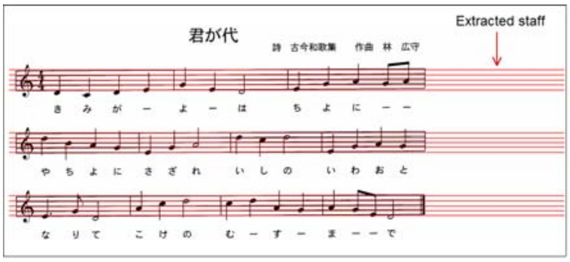

Fig. 9. Extracted staff in "Kimigayo"

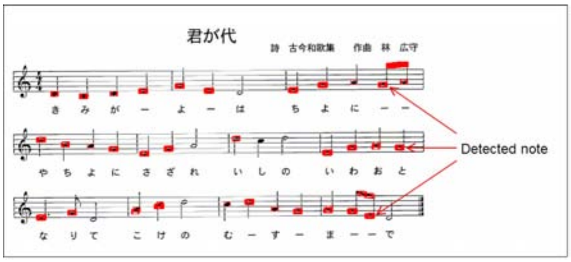

Fig. 10. Detected notes in "Kimigayo"

scores; investigation to this end is currently underway. In addition, a comprehensive evaluation of the recognition procedure remains to be established [14].

REFERENCES

[1] Y. Komatsubara, Y. Yamauchi, S. Kamata (2008), Recognizing and reading for characters on books (in Japanese). ITE Annual conference 2008

[2] Y. Komatsubara, Y. Yamauchi, S. Kamata (2009), Character segmentation and reading from Japanese character (in Japanese). ITE Annual conference 2009

[3] Jaime S. Cardoso, Artur Capela, Ana Rebelo, Carlos Guedes (2008), A connected path approach for staff detection on a music score. ICIP 2008:1005-1008

[4] Arshia Cont (2010), A coupled duration-focused architecture for real-time music-to-score alignment. IEEE Trans. Pattern Analysis and Machine Intelligence, Vol.32, No.6:974-987

[5] J. Keshet, S. Shalev-Shwartz, Y. Singer, and D. Chazan (2007), A large margin algorithm for speech-to-phoneme and music-to-Score alignment. IEEE Trans. Audio, Speech, and Language Processing, Vol.15, No.8:2373-2382

[6] M. Johnson (2005), Capacity and complexity of HMM duration modeling techniques. IEEE Signal Processing Letters, Vol.12, No.5:407-410

[7] L. Rabiner (1989), A tutorial on hidden Markov models and selected applications in speech recognition. Proc. IEEE, Vol.77, No. 2:257-285

[8] C. Raphael (1999), Automatic segmentation of acoustic musical signals using hidden Markov models. IEEE Trans. Pattern Analysis and Machine Intelligence, Vol.21, No.4:360-370

[9] A. Cont (2006), Realtime audio to score alignment for polyphonic music instruments using sparse non-negative constraints and hierarchical HMMS. Proc. IEEE Acoustics, Speech, and Signal Processing

[10] C. Raphael (2006), Aligning music audio with symbolic scores using a hybrid graphical model. Machine Learning, vol. 65:389-409

[11] T. Kawabuchi, Y. Yamauchi, S. Kamata (2010), Technique for Reading documents with multiple better type (in Japanese), SICE Kyushu Annual conference 2010, 203A-4

[12] S. Imamoto, Y.Yamauchi (2011), Head and stem extraction from printed music scores, International Workshop on Target Recognition and Tracking 2011, pp.72

[13] N. Habu, Y.Yamauchi (2011), Printed Japanese characters recognition system, International Workshop on Target Recognition and Tracking 2011, pp.73

[14] T. Hakui, Y. Yamauchi (2011), Two-finger robotic hand for a touch panel system, International Workshop on Target Recognition and Tracking 2011, pp.74

The Seventeenth International Symposium on Artificial Life and Robotics 2012 (AROB 17th '12),
B-Con Plaza, Beppu, Oita, Japan, January 19-21, 2012

Robotic system for reading Japanese characters on a written document in real time

Narumi Habu[1], Yukiharu Yamauchi[1], Sei-ichiro Kamata[2]
Youhei Shinfuku[2], and Takahiro Kawabuchi[1]

[1] Kitakyushu National College of Technology, Kitakyushu, Fukuoka 802-0985, Japan
(Tel: 81-93-964-7297, Fax: 81-93-964-7298)
(yamauchi@kct.ac.jp)
[2] Waseda University Graduate School, Kitakyushu, Fukuoka 808-0135, Japan

Abstract: This paper presents a robotic system in which a robot reads a printed document in Japanese. Currently, Apple's iPad, Amazon's Kindle, Sony Table, and other electronic book readers, are stimulating the electronic book market. These are, essentially smaller versions of personal computers and can be used to send emails, watch movies, or play games. In cooperation with Waseda University Graduate School and Shanghai Jiao Tong University, we have developed a robotic system called Ninomiya-kun that has the ability to read a book. This robotic system is the size of a child and has an appearance resembling a human being. The robot is equipped with two cameras as part of a visual information processing mechanism and can communicate with humans via voice and gestures. It automatically extracts character areas that contain Japanese characters, which are recognized using character recognition procedures. The system configuration is described, as well as the Japanese character recognition procedures performed by the robot. The experimental results are also discussed.

Keywords: Robot vision, entertainment robots, music score recognition, singing robotic system

1 INTRODUCTION

In fictional stories such as movies and cartoons, domestic robots are commonly used to assist humans; for example, Doraemon, a cat-like robot from the future, helps children fulfill their dreams using various secret devices. In a typical episode of this cartoon, whenever the central character becomes a target of bullying or fails in something, Doraemon uses unique technological devices from his belly pouch to help him. In the same way, robots will be working in offices, factories, and homes in the near future.

In 2004, a group of doctors suggested that parents limit their children's contact with TV and computer games. They claimed that TV and computer games reduced children's time for playing outside with their friends and having conversations with their families. They also recommended that parents read picture books to their children. Working in conjunction with Waseda University Graduate School and Shanghai Jiao Tong University, we have jointly developed a robotic system called Ninomiya-kun that can read a book (Fig. 1) [1, 2]. This robotic system is equipped with two cameras on the head and is able to communicate with humans via voice and gestures. It has an appearance that resembles a human being. The image of a printed document such as a picture book, textbook, or magazine, each of which has a large number of characters, is captured with the camera placed on the head, and the characters are extracted from the captured image.

Character recognition software in the robot translates

Fig. 1. Robotic system Ninomiya-kun

these characters into spoken words, which are produced using a voice synthesizer. We have already proposed a book reading robotic system, Ninomiya-kun, by training its TV camera. This system could be applied to reads a book out loud for children or a visually impaired person. In the parents' stead, the proposed system can be used to read picture books to their children. This robotic system automatically extracts areas with Japanese characters, which are recognized by the character recognition application software. It has a character dictionary with a layered structure that has the ability to recognize over 2,000 kanji, hiragana, and katakana characters and can currently read elementary texts. This paper describes the method for segmenting a sentence into Japanese kanji, hiragana, and katakana characters from the image data and retrieving them from the dictionary [3]. The proposed technique can be applied to read printed documents out loud using tablet computers such as Apple's iPad, Amazon's Kindle, Sony Table, or other electronic book readers. In the following, the system configuration is introduced, followed by the procedures for the Japanese character recognition. The experimental results are also discussed.

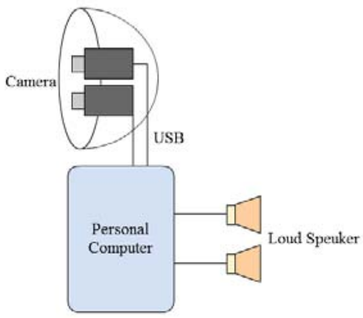

Fig. 2. System configuration of Ninomiya-kun

2 SYSTEM CONFIGURATION

The system configuration of Ninomiya-kun is shown in Fig. 2. This robotic system has three units in the robot's backpack: a personal computer unit, an image capture unit, and a loudspeaker unit, which is an electro-acoustic transducer that produces sound in response to the texts that are translated into spoken words. It has two hands that are driven by servomotors that are used to open a book and turn a page; the rotational speed and angles of the servomotors are given by the controlling personal computer unit [4]. Two cameras on the robots's head are used as visual sensors. The video signals from the cameras are transferred to the personal computer unit through an image acquisition interface unit, which provides digitized images at high resolution [6].

Processing a document to extract its content in an automated fashion is the essential task of this system. The following software modules are used to process a document, as depicted in Fig. 3.

1. The image acquisition module captures a document's image using the camera and the image acquisition unit attached to the personal computer and performs a binarization process on the image.

2. The image analysis module then extracts distinctive characteristics from the document being processed.

3. The information extraction module is a classification stage that identifies the characters and groups them according to certain classes.

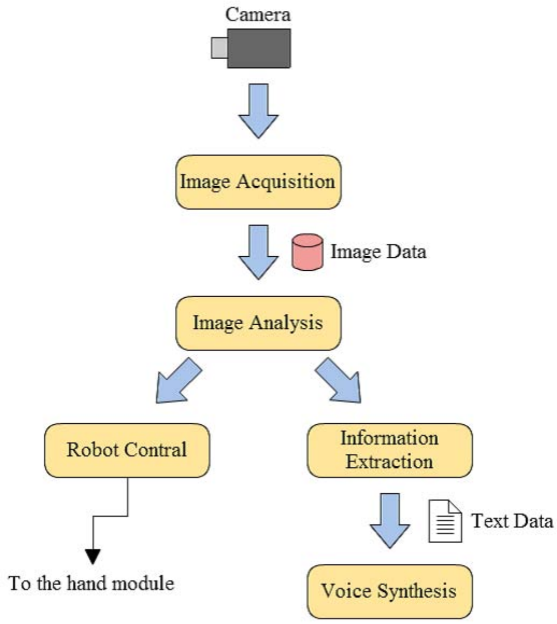

Fig. 3. Structure of software system

4. The voice synthesis module reproduces human voices using a voice synthesizer.

5. The robot control module controls the posture of two cameras and drives the servomotors for the two hands.

3 CHARACTER SEGMENTATION FROM A PRINTED DOCUMENT

This section provides an outline of the image processing and analysis for the character segmentation from the image captured by the camera [7, 8]. Real-time recognition is realized by recognizing the document when the robot opens it and turns a page. However, the recognition depends on an algorithm and the speed of the computer. No delay is caused in the task of reading the document out loud because the character segmentation is carried out in the background. The system needs be fast enough to keep up with this reading task.

3.1 Distortion correction and image processing

Off-line character recognition uses a scanned image. The proposed system uses an image captured by the robot equipped with the camera. When the captured image is used as an input image, there are two differences from the image scanned with a scanner.

1. Image distortion: The image scanned with a scanner has no distorted characters, whereas the image captured by the camera has numerous distorted characters in many cases.

2. Image resolution: The number of pixels that is assigned to a character in the image captured from the camera is considerably smaller than that assigned to a character in the considerably as image from the scanner.

The character recognition algorithm needs to recognize an input image with low resolution. The character distortion must be detected and corrected. Before the correction of a distorted character, an input image is digitized. The digitized image is divided into eight domains, and the histogram for these domains are calculated (Fig. 4).

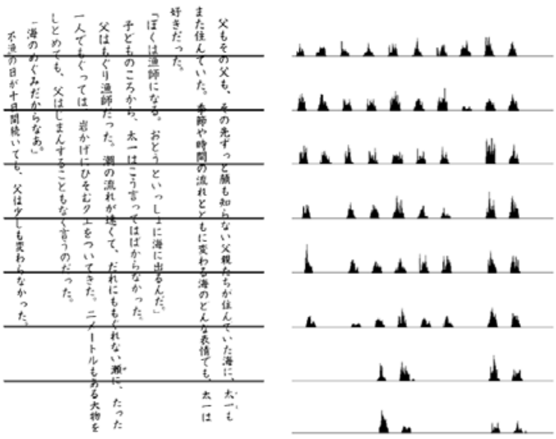

Fig. 4. Divided image and histogram

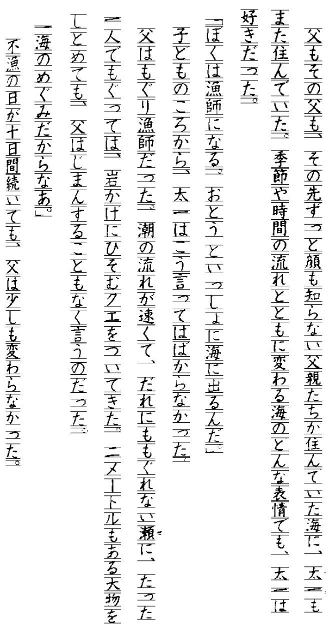

Fig. 5. Results for correction of distorted image

The inclination is calculated by using the histogram of a neighboring domain. In an image without inclination, we focus on the matching in the peak and trough positions in the histogram of the domain. With this matching, one side of the histogram of two neighboring domains is moved from side to side. The position that best matches the peak and trough in the histogram is calculated. The results of this correction are shown in Fig. 5.

3.2 Character segmentation

Next, the procedure for segmenting a character from an input image is described. The segmentation of a character is performed for every other line or column. One line is segmented out, and the segmenting candidate position of the character is calculated from the histogram of the line (Fig. 6 (a)). In the next procedure, the segmented characters merge sequentially from the top character. As an example, we take a case where two segmenting candidate characters are merged. If the length to width ratio is 1:1.2 or less, two candidate characters are merged. The merged case is shown in Fig. 6 (b) and (c). Another case is shown in Fig. 6 (d) and (e).

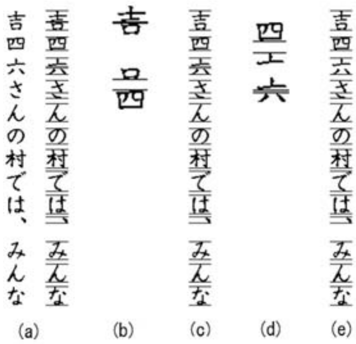

Fig. 6. Merging of two candidate characters

3.3 Feature vector detection

The features for every segmented character are calculated and compared with the system dictionary. The segmented characters differ in size. The outline box of a character is calculated and the size is normalized to 64 × 64 pixels. The directional element feature, which determines the amount of directional change in the outline, is used as a recognition feature. The outline pixels that match four directional changes are detected (Fig. 7).

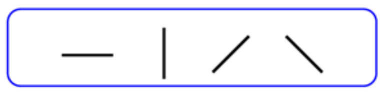

Fig. 7. Four directional changes

An outline from the normalized image is calculated, and 12 kinds of 3 × 3 pixel masked images are used to extract the directional change in the outline (Fig. 8). The mask and outline pixels are measured, and the directional change is given to the outline pixel that matches the mask. The directional change is then compared with the feature vectors stored in the dictionary.

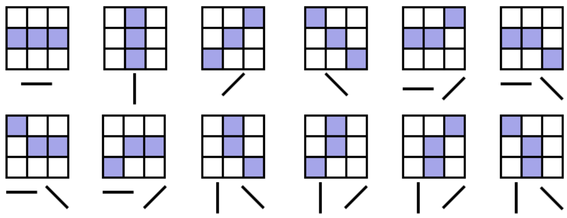

Fig. 8. 12 kinds of masked images

4 EXPERIMENTAL RESULT

An experiment was conducted using the robotic system Ninomiya-kun. A captured document and the character segmentation results are shown in Fig. 9. A portion of the recognition results is shown in Fig. 10. In the experimental results, for a document with 262 characters, 244 characters were correctly recognized.

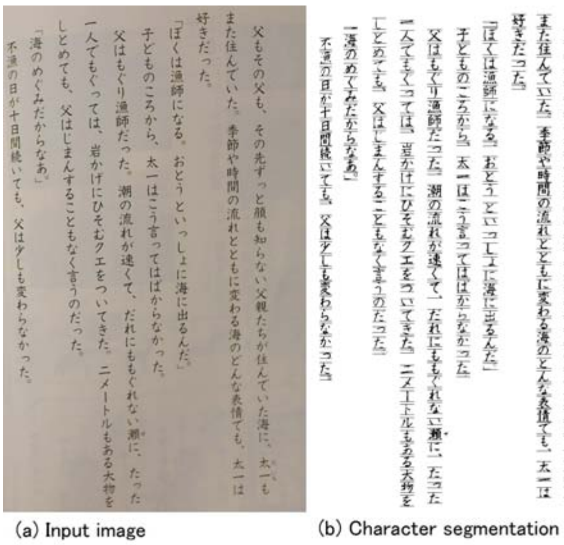

Fig. 9. Input image and character segmentation

5 CONCLUSION

We described a novel robotic entertainment system that can recognize Japanese characters from the a printed document. This system can recognize a printed document with nearly ninety percent accuracy. However, the recognition of a document printed with multiple letter types is difficult. The recognition accuracy is also greatly influenced by the lighting. The system needs to be further developed to improve the recognition accuracy for multiple letter types and the influence of lighting, which are now under investigation [9].

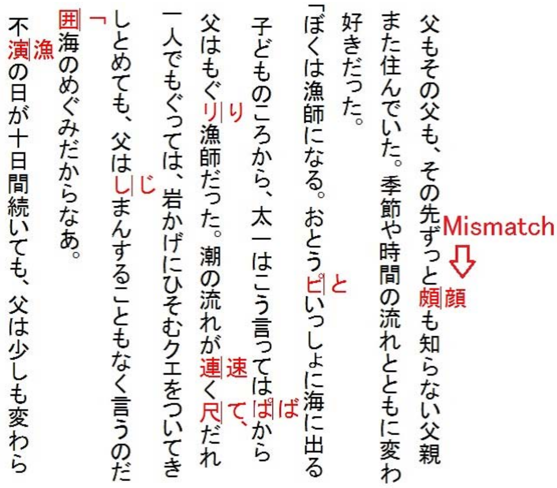

Fig. 10. Experimental results

REFERENCES

[1] Y. Komatsubara, Y. Yamauchi, S. Kamata (2008), Recognizing and reading for characters on books (in Japanese). ITE Annual conference 2008

[2] Y. Komatsubara, Y. Yamauchi, S. Kamata (2009), Character segmentation and reading from Japanese character (in Japanese). ITE Annual conference 2009

[3] T. Kawabuchi, Y. Yamauchi, S. Kamata (2010), Technique for Reading documents with multiple better type (in Japanese), SICE Kyushu Annual conference 2010, 203A-4

[4] S. Akram, M. Dar, A. Quyoum (2010), Document image processing, International Journal of Computer Apprlications, Vol.10, No.5:35-40

[5] Cheng-Lin Liu (2007), Normalization-cooperated gradient feature extraction for handwritten character recognition, IEEE Trans. Pattern Analysis and Machine Intelligence, Vol.29, No.8:1465-1469

[6] S. Imamoto, Y.Yamauchi (2011), Head and stem extraction from printed music scores, International Workshop on Target Recognition and Tracking 2011, pp.72

[7] N. Habu, Y.Yamauchi (2011), Printed Japanese characters recognition system, International Workshop on Target Recognition and Tracking 2011, pp.73

[8] T. Hakui, Y. Yamauchi (2011), Two-finger robotic hand for a touch panel system, International Workshop on Target Recognition and Tracking 2011, pp.74

Eye-Gesture Controlled Intelligent Wheelchair using Electro-Oculography

Satish Ravishankar[1], Govinda Ram Pingali[2], Niyanth Krishna Polisetty[3], Theja Ram Pingali[4],
Dr. Padmaja K.V[5], Avinash Sista[6]

[1,2,3] 7th Semester, Instrumentation Technology Department, R.V. College of Engineering, Bangalore, India
[4] 1st Semester, Instrumentation Technology Department, R.V. College of Engineering, Bangalore, India
[5] Head of Department, Instrumentation Technology, R.V. College of Engineering, Bangalore, India
[6] Senior Design Engineer, IES Division, Mahindra Satyam, Hyderabad, India

[1] satishr@iparadigmshift.com
[2] govindram@iparadigmshift.com
[3] niyanthkp@iparadigmshift.com
[4] dstrp@iparadigmshift.com
[5] padmajakv@rvce.edu.in
[6] avinash_sista@mahindrasatyam.com

Abstract: This paper describes the design and implementation of an eye-gesture controlled electric wheelchair using the technique of Electro-Oculography. This is designed to be used as an intelligent mobility aid for the paralyzed which has features such as tilt detection, obstacle sensing, avoidance and path re-routing. The design employs an embedded control module that processes the bio-electric signals generated by the eye movements to actuate real world events. A microcontroller is used in place of a laptop computer, as the decision making entity, thereby making this an affordable solution. Various safety features are integrated using the control module to make a robust and optimized model.

Keywords: Electro-oculography, eye-gaze tracking, obstacle detection, paralysis, path re-routing, wheelchair

1 INTRODUCTION

Victims of severe paralysis, amputees and other physically challenged are unfairly deprived of an acceptable standard of life. Spinal cord injuries (SCI) and Progressive Motor Neuron Diseases (PMND) could cause a condition known as Quadriplegia which leads to loss of muscle functionality below the neck due to which the subjects are constantly dependant on others for their mobility. In such cases, ocular control is either not affected or affected last. Keeping in mind these constraints in muscle control and disease progression, a cost effective solution is developed in order to assure victims of paralysis a greater degree of independence and better quality of life. The idea involves the design and implementation of an eye-gesture controlled electric wheelchair using the bio-medical technique of Electro-Oculography (EOG).

Of the several methods exist to detect eye-gestures, the physiologies of EOG are better understood. It is simpler to complete the acquisition, feature extraction and analysis of EOG signals [2]. Therefore, EOG based approach is more suited for this application in terms of dependability, accuracy and cost.

Several designs of an EOG based wheelchair have been proposed [3,4]. These designs make use of a laptop computer as the processing and control centre. Other systems that do not employ a laptop have also been proposed but such methods lack intelligence in terms of the systems' awareness of the environment. This paper proposes a modular design of an EOG based Human-Wheelchair interface which incorporates an obstacle detection, avoidance and path re-routing algorithm for reliable navigation using simple and effective ultrasonic range sensors to acquire sensorial information from the ambiance for reliable navigation. Integration of tilt detection into the algorithm is also imperative in order to address the problem of the assembly toppling over at a critical tilt point considering the fact that the user may need to manoeuvre through uneven terrain.

Since the target group comprises of those who require constant medical supervision, Patient Health Monitoring Systems become an indispensable part of the mobility aid. This makes for a well-rounded, complete system that not only assists the user in safe, collision-free mobility but also keeps track of his/her vital statistics, generates alerts and notifications which effect arrival of timely medical attention when required. The intelligence algorithm along with Patient health Monitoring Systems seek to achieve increased reliability and safety.

2 DESIGN AND IMPLEMENTATION

This paper presents an EOG based wheelchair with active collision avoidance and tilt detection. The system architecture has four major parts:

(2.1) EOG signal acquisition
(2.2) Signal conditioning module
(2.3) Wheelchair mechatronics and sensor system
(2.4) Control module and Intelligence Algorithm

Fig. 1 shows the proposed system architecture, and these major parts are illustrated as follows.

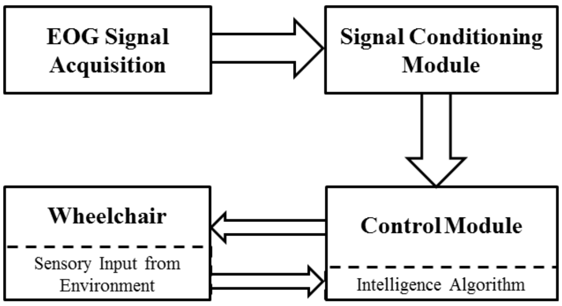

Fig. 1: System Architecture

2.1 EOG Signal Acquisition

Electrooculography (EOG/E.O.G.) is a technique for measuring the resting potential of the retina. The resulting signal is called the electro-oculogram. The main applications are in ophthalmological diagnosis and in recording eye movements. The eye, a seat of resting potential, acts as a dipole in which the anterior pole (cornea of the eye) is positive and the posterior pole (retina of the eye) is negative. This difference in potential can be explained by the metabolic activities in the eye which can be measured by means of EOG. The EOG signal has a magnitude in the range of 100µV to 1000µV with a frequency range of 0 to 30Hz [4].

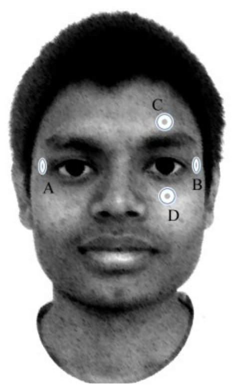

Fig. 2: Electrode Placement

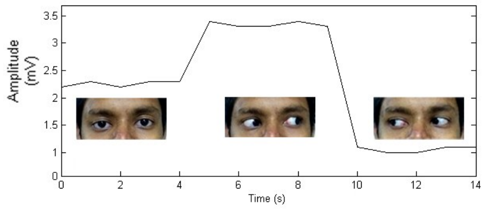

Fig. 3: EOG Horizontal Differential Signal

Silver-Silver Chloride (Ag-AgCl) electrodes are placed on the corners (lateral canthi) of both the eyes to capture the change in EOG signal for lateral eye motion. When the subject’s gaze is to the left, the positive end of the dipole the eye comes closer to the electrode on the left canthus and the negative end to the right canthus.

The vice-versa is observed for the eyes looking towards the right. This is portrayed in Figure 3. In a similar manner, electrodes placed above and below the eyes of the subject can be used to record change in EOG signal for eye-ball motion in the vertical direction (Figure 4). Ideally the difference in potential should be proportional to the sine of the angle the eye produces with respect to the central axis.

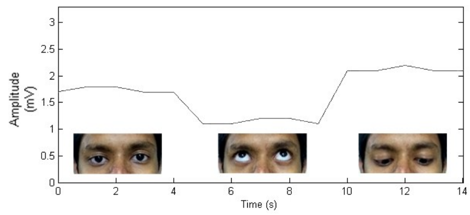

Fig. 4: EOG Vertical Differential Signal

2.2 Signal Conditioning Module

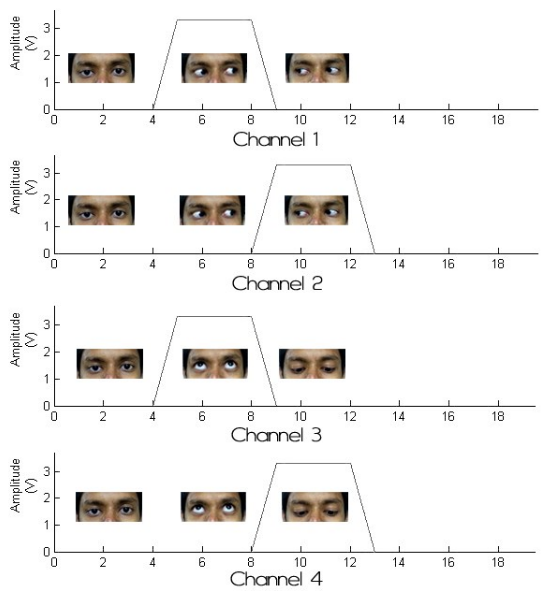

Fig. 5: Digital Input to Microcontroller

The EOG signal is a low voltage range bio-potential signal which can be easily corrupted by noise in the ambiance. It therefore is passed through a signal conditioning module to extract the horizontal and vertical gaze direction.

The signal processing module consists of amplification in two stages using instrumentation amplifiers (AD620) with a gain of 100 and 10 respectively. Noise is cancelled out using a low pass filter of cut off frequency 30Hz. The DC drift is removed using a high pass filter of cut-off frequency 0.16 Hz. A divider circuit is used using high-speed switching diodes and op-amps in inverting and non-inverting stages to achieve four separate channels of signal, one each for up, down, left and right [4].

Therefore eye gaze direction will be detected as a pulse which can be effectively considered a digital HIGH. The absence of such a pulse can be considered a digital LOW. This in effect renders the use of an Analog to Digital converter unnecessary. The output of the signal conditioning module is shown in figure 5.

2.3 Wheelchair and Sensory Input from Environment

The eye-gaze direction and speed control directives form the wheelchair motion commands that are generated by the EOG and signal processing modules are supplied to the microcontroller.

In most cases, an inconsistency exists between the goal direction and the direction of the wheelchair. This is caused due to the presence of obstacles in the motion path and the inability of the driver to navigate past them. Therefore, ultrasonic obstacle detection sensors are strategically placed on the wheelchair body, as shown in figure 6, to sense obstacles and thus aid in manoeuvring around them.

The sensory information is then sent to a microcontroller in the wheelchair which has an obstacle avoidance algorithm programmed. The final decision made by the microcontroller by a combination of eye- commands and sensory input is then sent to the DC motor drives.

As mentioned earlier, the speed of the wheelchair is set based on vertical eye-gaze. Pulse width modulation (PWM) technique is used to change and control the speed of the motors. The PWM signal is generated by the microcontroller placed on the wheelchair.

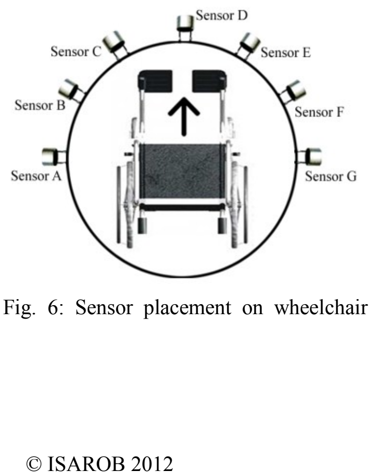

Fig. 6: Sensor placement on wheelchair

PID controllers are used to achieve linear and hence smoother turns.

2.4 Control Module and Intelligence Algorithm

The control module is split into two parts, the User Instruction Processor (UIP) and the Drive Control Module (DCM), each with its own microcontroller. Full duplex wireless communication exists between the two processors.

The microcontroller on the UIP accepts four-channel digital input from the divider module. It can be inferred from figure 5 that a digital HIGH pulse cannot be detected simultaneously in channels 1 and 2 (horizontal) or channels 3 and 4 (vertical). But a combination of horizontal and vertical motion can be detected along with pure horizontal or vertical gestures. This directly implies the UIPs capability of detecting 8 different positions of the eye ball. These various gestures can be used individually or as a combination of two or more, to generate simple or complex patterns.

Let up, down, right and left gaze directions correspond to North (N), South (S), East (E) and West (W) respectively and no pulse correspond to C (for centre). Simple eye gestures such N, S, E and W can be used to perform functions that need immediate execution such as stopping/braking and turning. For example, if the UIP receives a W signal, it makes the drive control decision that will cause a left turn. Similarly, a right turn is executed for E. Most importantly the wheelchair can be stopped/braked immediately for an S pulse. This allows immediate addressing of a user generated braking command.

A sequence of gestures that use combinations such as NW, NE, SW and SE along with N, S, E and W can be used to perform other functions that do not require quick response from the system. For instance, an N pulse followed by NE can be used to increase wheelchair speed and an N pulse followed by NW can be used to reduce wheelchair speed. This method of speed control can be pictured as sliding along a horizontal speed control bar. Also, powering on the system can be done using the following sequence: N-NE-E-SE-S-SW-W-NW-N-C. This pattern resembles a power button on any common household device. Drive control using such patterns are very intuitive and therefore make wheelchair control easy to learn and execute.

A Patient Health Monitoring system is interfaced to the UIP microcontroller which handles patient health stats data as a secondary function. Health monitoring systems are an integral part of the system since members of the target group sometimes require continuous medical supervision.

The drive control decisions made by the UIP are first encoded and then communicated to the DCM wirelessly. Wireless transmission is used to reduce wire clutter and increase modularity of the design. The DCM uses these decisions and sensory input data from the ultrasonic sensors placed on the wheelchair to make the final drive control decision using the intelligence algorithm that resides in the DCM microcontroller.

The intelligence algorithm works on the principle that the drive control decisions made by the UIP are always followed by the wheelchair until an obstacle is detected. Until such a time, the intelligence algorithm works in a transparent mode. The moment an obstacle is sensed by the ultrasonic sensors, the wheelchair is stopped immediately. Let us consider two cases: stationary obstacle and a moving obstacle.

In the case of a stationary obstacle, the wheelchair is firstly stopped. The outputs of all the sensors remain the same as the instant when the wheelchair was stopped even after some time has elapsed. The intelligence algorithm takes the constancy of the sensor outputs to classify the obstacle as stationary. The system now switches to the wall follower mode and generates an auditory alert, a beep for instance that notifies the user of the need for a "wall-follower direction" and remains in a wait state. In the wall follower mode, wheelchair speed control is not necessary and therefore the corresponding control gestures can be used to input wall-follower direction i.e., N followed by NW for left and N followed NE for right. Once the user inputs the desired direction of motion, the wheelchair turns toward the specified direction and navigates around the obstacle in the wall follower mode. To keep the wheelchair in this mode the user looks straight forward (C signal). In case the user needs to break away from the obstacle at any chosen time, he looks away from the obstacle, to the right or left, thus producing a W or E signal respectively which causes the wheelchair to turn away in that direction. This effectively aids the user in navigating around any stationary obstacle and also gives him/her maximum possible control.

A special case of a stationary obstacle is a dead-end. For the system to recognize a dead-end, the minimum requirement is that sensors B, C, D, E and F (figure 6) all output digital high at the same time. In such a situation, the only option of navigation is motion in reverse. Since wheelchair motion in reverse is not advisable for safety reasons, this obstacle is handled by making the wheelchair execute a 180° turn on the spot. Now the control is handed back to the user for further commandeering.

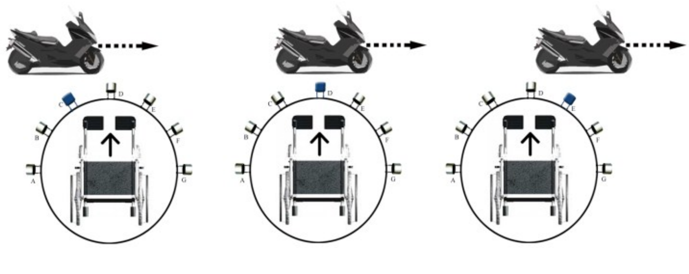

Fig. 7: Moving Obstacle

Now, let us consider a moving obstacle. When an obstacle is detected the wheelchair is immediately halted. The DCM waits to check if the sensor outputs remain the same even after some predefined time period. In this case the sensor outputs do not remain constant but change as the obstacle moves by. In figure 7, when the moving obstacle is first detected sensor C generates a digital HIGH signal as the obstacle is within its pre-set minimum distance. Then the obstacle moves to the right eliciting an active high from sensors D and E sequentially. The intelligence algorithm classifies such an obstacle that causes changing sensor output to be a moving obstacle. In such a case, the wheelchair is halted until the obstacle is beyond the minimum distance setting of all the sensors and is then allowed to move.

A gyroscope is interfaced with the DCM for wheelchair tilt detection. When the user drives through uneven terrain or on a ramp, there is a possibility of the wheelchair toppling over at a critical tilt point. The gyroscope is used to detect tilt angle which is supplied to the DCM microcontroller for processing. When the wheelchair reaches a predefined safe tilt limit, an auditory alert is generated warning the user of the imminent danger of toppling over so as to enable him to take corrective measures and the UIP is informed of this safe tilt limit breach wirelessly.

A GSM modem is also interfaced to the UIP. When the user cannot manoeuver through a region without external help due to excessive tilt or in case the wheelchair has toppled over, an alert in sent via text message to a pre-selected individual who can come to the user's aid. The same can be done to alert the user's doctor/nurse when the Health Monitoring system indicates that the user is in need of medical attention.

The complete functional block diagram of this design is illustrated in Figure 8.

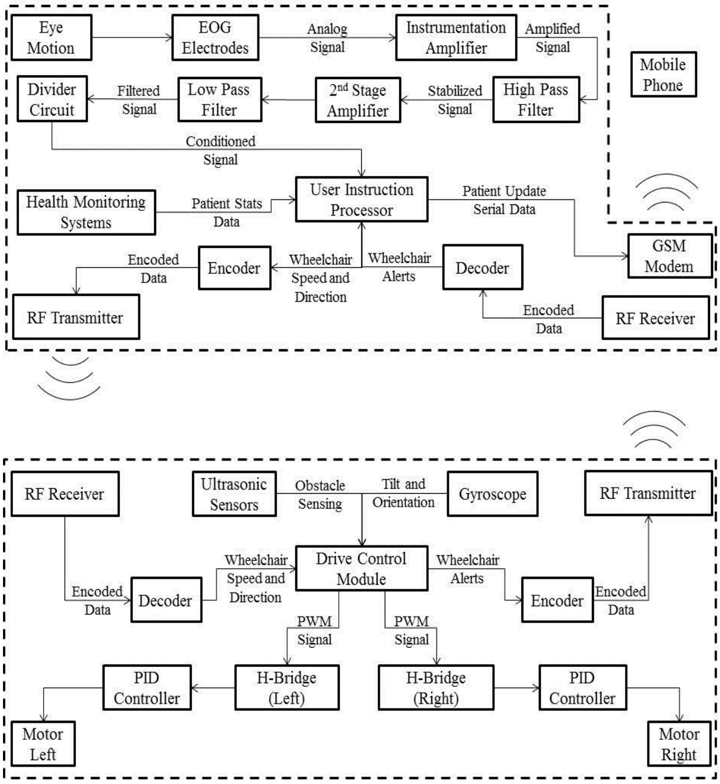

Figure 8: Complete Functional Block Diagram

3 PROPOSED MODEL

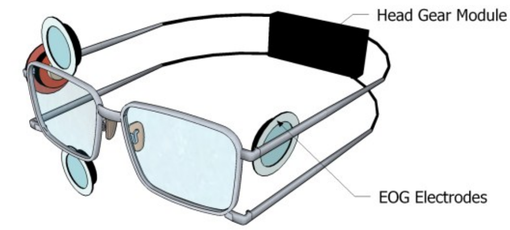

Figure 9: Proposed Head Gear

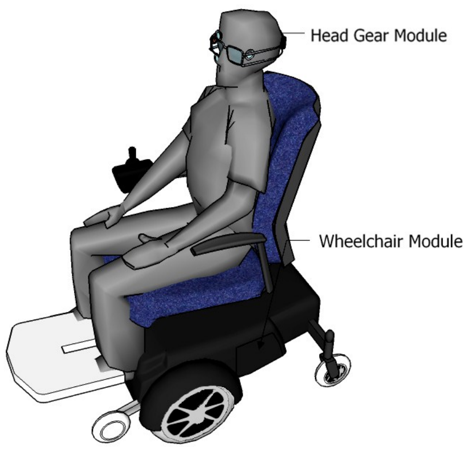

Figure 10: Proposed Wheelchair

4 CONCLUSION

This paper presents a method of eye gesture based wheelchair control using Electro-Oculography. User commands for wheelchair control are obtained from the EOG signal using the signal conditioning module. The extracted commands are processed through the intelligence algorithm that also takes into account ambient obstacle proximity detected by the wheelchair ultrasonic sensors to generate improved collision free drive control. This wheelchair is designed to be an intuitive and cost effective control method. A proof of concept has been successfully developed where the direction of motion of a wireless robot has been controlled using eye gestures (figure 11).

Figure 11: Proof of concept - Control Module (L) and Wireless robot (R)

REFERENCES

[1] Kenji Yamagashi, Junichi Hori and Michio Miyakawa, "Development of EOG-based communication system controlled by eight-directional movements", *Proceedings of the 28th IEEE EMBS Annual Conference*, New York, 2006

[2] Min Lin, Bin Li, "A wireless EOG-based human computer interface", *3rd International Conference on Biomedical Engineering and Informatics*, Shanghai, 2010.

[3] Chung-Hsien Kuo, Yi-Chang Chan, Hung-Chyun Chou, and Jia-Wun Siao, "Eye-glasses based electro-oculography human-wheelchair interface," *Proceedings of the IEEE 2009 International Conference on Systems, Man and Cybernetics*, San Antonio, Texas, Oct 2009.

[4] S.Yathunanthan, L.U.R. Chandrasena, A. Umakanthan, V. Vasuki and S.R. Munasinghe, "Controlling a wheelchair by use of EOG signal," *Proceedings of 4th IEEE International Conference on Information and Automation for Sustainability* , Colombo, Srilanka, 2008

The Seventeenth International Symposium on Artificial Life and Robotics 2012 (AROB 17th '12),
B-Con Plaza, Beppu, Oita, Japan, January 19-21, 2012

Hamming Distance based Gradient Orientation Pattern Matching

Prarinya Siritanawan, and Toshiaki Kondo

Sirindhorn International Institute of Technology, Thammasat University, Thailand
(Tel: +66(0)29869009, Fax: +66(0)29869112-3)
p.siritanawan@gmail.com, tkondo@siit.tu.ac.th

Abstract: This paper presents a novel pattern matching technique for motion estimation and visual tracking under varying illuminations, including a large amount of occlusions. To cope with the illumination problem, we previously proposed a matching technique using gradient orientation information, called gradient orientation pattern matching technique. Unlike conventional image features such as intensities and gradients, gradient orientations are known to be robust to illumination changes. In this paper, we introduce the Hamming distance to the gradient orientation pattern matching as a new similarity metric. Simulation results show that the new proposed method is robust to both illumination changes and a large amount of occlusions compared with existing matching techniques.

Keywords: gradient orientation pattern matching, hamming distance, object tracking, occlusion, template matching

1 INTRODUCTION

The purpose of this paper is to establish the novel pattern matching technique for motion estimation and visual tracking under varying illumination and partial occlusion scenarios. Various object tracking techniques have been proposed in the literature [1]. Most of them assume that illuminations are constant and occlusions are marginal, which does not always hold in real situations. To deal with the illumination variation problem, we previously proposed a matching technique using gradient orientation information, called gradient orientation pattern matching technique (GOPM) [2][3].

Unlike conventional image features such as intensities and gradients, gradient orientation information is far more independent of illumination changes over time. Generally, gradient orientation is extracted from image intensities using the trigonometric functions $\theta = arctan(I_y/I_x)$, where I_x and I_y are partial derivative of the intensity in x and y directions. This trigonometric function is slow and undesirable in the hardware implementation. GOPM technique has exhibited an alternative approach of utilizing unit gradient vectors (UGVs) to avoid the trigonometric function [3]. The efficiency of the matching method on decomposed unit gradient vectors is identical to the matching on the angular values but the calculation is reduced. We have examined it by implementing the technique on a real-time eye tracking [4][5].

For the GOPM, we can employ any traditional similarity metric, such as the sum-of-absolute differences (SAD), the sum-of-squared differences (SSD), zero-mean normalized cross-correlation (ZNCC) and so on. In this paper, we introduce the Hamming distance (HD) to the GOPM as a new similarity metric. The HD is considered robust to the occlusion problem because it is concerned with the number of pixels that match (or do not match) rather than paying attention to the differences between images. For quantitative evaluations, we have created three artificial image sequences using three still images and simulate illumination changes and occlusions in the similar fashion as in [2] and [3]. Furthermore, the new proposed technique has been examined on real video sequences and compares its efficiency over the other matching techniques. Simulation results show that the new proposed method is robust to both illumination changes and a large amount of occlusions compared with existing matching techniques.

2 MATCHING METHODS

2.1 Gradient Orientation Pattern Matching (GOPM)

The method decomposes orthogonal components of unit gradient vectors (UGVs) and performs similarity measurement on x and y gradient component separately. The UGVs could be obtained though the following normalized equations (Eq.(1))

$$\begin{aligned} n_x(x,y) &= I_x(x,y)/\sqrt{I_x^2(x,y)+I_y^2(x,y)+\epsilon} \\ n_y(x,y) &= I_y(x,y)/\sqrt{I_x^2(x,y)+I_y^2(x,y)+\epsilon} \end{aligned} \tag{1}$$

where I_x and I_y are gradient in x and y direction. The ϵ is a small constant added to prevent zero-division during normalization.

Using the unit gradient vectors obtained above, the best matching position is searched for with a full search strategy. In previous work, the similarity metric of GOPM are based on sum-of-absolute difference (SAD) [2] and sum-of-square difference (SSD) [5]. The SSDs for unit gradient vectors are expressed in Eqs. (2) and (3).

$$SSD\_n_x = \sum_{i=1}^{N}\sum_{j=1}^{N}(n_{x1}(x+i,y+j) - n_{x2}(i,j))^2 \quad (2)$$

$$SSD\_n_y = \sum_{j=1}^{N}\sum_{i=1}^{N}(n_{y1}(x+i,y+j) - n_{y2}(i,j))^2 \quad (3)$$

where SSD_n_x and SSD_n_y are results of similarity metric between UGVs of sample image and template at position (x,y). Note that *N* is the block size of matching, n_{x1} and n_{y1} are UGVs of sample image, and n_{x2} and n_{y2} are UGVs of template. The gradient orientation pattern matching (GOPM) is then given by Eq. (4).

$$GOPM(\vec{p},\vec{d}) = SSD\_n_x + SSD\_n_y \quad (4)$$

2.2 Hamming Distance based Gradient Orientation Pattern Matching

In this research, we introduce the Hamming distance (HD) as a new similarity metric of GOPM instead of SSD. General description of HD metric is defined by Eq. (5).

$$HD(x,y) = \sum_{i=1}^{N}\sum_{j=1}^{N} I_1(x+i,y+j) \oplus I_2(i,j) \quad (5)$$

where I_1 is intensity of sample image at position (x,y) and I_2 is intensity of template. Generally HD compares 2 corresponding binary pixels by exclusive OR operator. The technique is widely used in VHDL and Iris recognition [6]. HD concerns the number of pixels that match rather than overall differences and yields better results in occlusion scenarios. To apply HD with non-binary information such as intensities or gradient orientations, the exclusive OR operation would be represented by threshold absolute difference [7].

$$sim(I_1, I_2, (x,y)) = \delta(|I_1(x,y) - I_2(x,y)| > p) \quad (6)$$

Thus, we could derive the Hamming distance of gradient orientations by Eqs. (7) and (8).

$$HD\_n_x(x,y) = \sum_{i=1}^{N}\sum_{j=1}^{N}\delta(|n_{x1} - n_{x2}| > \tau_1) \quad (7)$$

$$HD\_n_y(x,y) = \sum_{i=1}^{N}\sum_{j=1}^{N}\delta(|n_{y1} - n_{y2}| > \tau_2) \quad (8)$$

where τ_1 and τ_2 are certain thresholds. The differences those are higher than thresholds yields distance 1 and 0 in the vice versa. The distances are accumulated over the block area and demonstrate the similarity of that block pattern to the template. After calculating Hamming distance of UGVs, the Hamming distance based gradient orientation pattern matching is then calculated by OR operator as shown in Eq. (9).

$$HDGOPM = HD\_n_x \vee HD\_n_y \quad (9)$$

(a) (b) (c)

Fig. 1. (a) Part of the Lena image, and corresponding gradient orientations in x and y directions, (b) n_x and (c) n_y

3 EXPERIMENTAL RESULTS

In the experiment, we established 3 kinds of simulation: i) Illumination change test, ii) Occlusion problem in illumination change situation, and iii) Testing all of problems out in the video sequences.

In the first three simulations, we create an artificial motion sequence on still image. The standard test images; Lena, Cameraman, and House with size 512 by 512 pixels are used as first frames. The second frames of sequence are then generated by translating the first frames by 5 pixels in both vertical and horizontal direction. To compute the motion vector over the entire scene, we defined 961 blocks in the first frame as reference blocks, and each block have size 16 by 16 pixels. The 961 motion vectors are estimated by measuring the similarity of reference pattern and the pattern in the second frame. The search range in the second frame is set around reference block areas by +/- 8 pixels (32 by 32 pixels search range).

Fig. 2. (a) The standard test image House, (b) the image translated by 55 pixels, and (c) the translated image under non-uniform illumination

3.1 Illumination change test

To simulate the illumination change situation in the artificial motion sequence, we re-simulate the worst case condition of illumination change test in previous research [2][3]. The second frame is translated (5,5) pixels under Gaussian noise with SNR 40dB and non-uniform illumination change of intensities, which the image intensities within vertical and horizontal stripes are rapidly reduced to half and the intensity in the areas where two stripes overlap are reduce to one forth.

Table 1. Successful motion estimation rate (%) under non-uniform illumination change

Image	Standard SSD	GOPM with SSD	GOPM with HD
Lena	21.23	99.89	100
Cameraman	26.74	99.89	100
House	23.10	99.37	100

Successful motion estimation rate (%) of 961 motion vector estimated by standard SSD, GOPM with SSD metric, and HD based GOPM are shown in Table 1. GOPM is obviously overcome lighting change problem (successful rate approximately 99% by SSD similarity metric and 100% successful rate by HD metric). Meanwhile SSD on intensity features is incapable to estimate the motion (successful rates are approximately 20%).

3.2 Occlusion test under illumination change situation

In the second experiment, the second frame of sequences are also translated by (5,5) pixels and 40dB Gaussian noise added. The non-uniform illumination is varied in the same way as in the first experiment. To simulate the occlusion situations in the sequences, the pattern of reference block are then occluded by *mxm* zeros square (Fig. 3), where *m* iterate from 0 to 13, which is approximately 81% covered. The successful motion estimation rates of SSD, GOPM with SSD metric and GOPM with HD metric on each standard test images are plotted against occlusion size over the pattern (Fig. 6). According to the graphs, GOPM with HD metric yields the highest successful motion estimation rates, while the successful rates of GOPM with SSD metric are slightly lower than HD metric. For standard SSD, it is severely fail to estimate the motion vector under the circumstances. This shows the advantage of HD based GOPM under occlusion and non-uniform illumination change.

3.3 Test in video sequences

Finally the last simulation shows the performance of proposed matching technique on the video sequences. In this experiment, the face template is initialized manually in the first frame. The video sequences consisted of 4 different scenarios; *normal* situation, *illumination change* by shot the flashlight in various angle and distance, *occlusion* which an unknown object cover some part of the face and the last scenario is *occlusion problem under illumination change* situation (Fig. 4). As a result, all matching techniques; SSD on intensities, GOPM with SSD metric and GOPM with HD metric could perform a tracking very well under normal situation. However in the case of illumination change, SSD fails

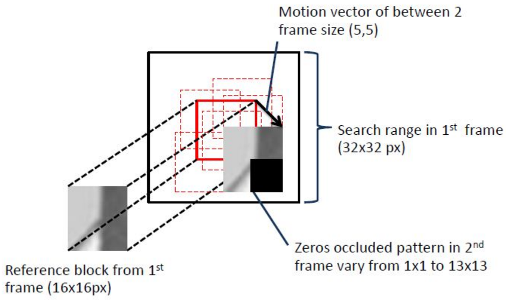

Fig. 3. Motion estimation on artificial motion sequence with (5,5) pixel translation, illumination change, 40dB Gaussian noise and zeros occlusion.

to archive the tracking, while both GOPM with SSD metric and GOPM with HD metric are fine. For occlusion problem (and occlusion under illumination change), only GOPM with HD metric could keep track the object almost of the entire video sequence. The similarity measurement results in Fig. 5 demonstrate the advantage of GOPM with HD metric over other techniques which matching results are disturbed due to the occlusion existence.

Fig. 4. Four real image sequences; constant light without occlusion, irregular lighting without occlusion, constant lighting with occlusion, and irregular lighting with occlusion.

4 CONCLUSION

In this paper, we have proposed a novel pattern matching technique for motion estimation and visual tracking, which combines the advantages of gradient orientation features and Hamming distance metric. Unit gradient vectors are computed from template and input images before measuring the similarity between them using the Hamming distance. The Hamming distance is equivalent to the number of pixels whose unit gradient vectors are similar to each other between the template and images. The proposed method can perform robustly in time-varying lighting conditions with partial occlusions. Our simulation results have shown those advantages over existing matching techniques on both synthetic and real image sequences.

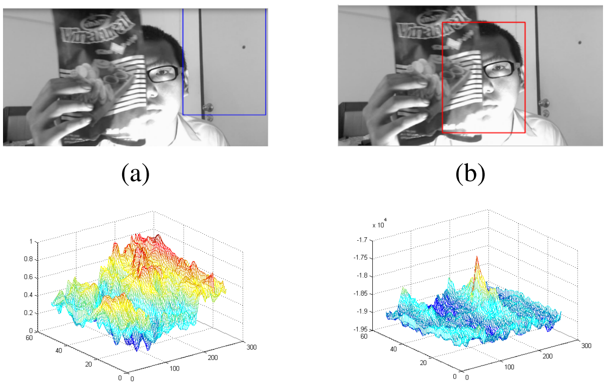

(a) (b) (c) (d)

Fig. 5. Tracking results under irregular lighting with occlusion by (a) GOPM with SSD, (b) GOPM with HD, (c) and (d) the distributions of the corresponding similarity measurements

REFERENCES

[1] Yilmaz A, Javed O, Shah M (2006), Object Tracking: A Survey. ACM Computing Surveys 38(4), Article 13, Dec 2006

[2] Kondo T, Kongprawechnon W (2009), A Block Matching Technique Using Unit Gradient Vectors, Proceedings of MVA2009 IAPR Conference on Machine Vision Applications, Yokohama, Japan, May 20-22, 2009

[3] Kondo T, Kongprawechnon W (2009), A matching technique using gradient orientation patterns, Thammasat Int. J. Sc. Tech. 14(3)

[4] Hotrakool W, Siritanawan P, Kondo T (2010), "Real-time Gradient Orientation Pattern Matching, Proceedings of International Conference on Embedded System and Information Technology, Chaing Mai, Thailand, 2010

[5] Hotrakool W, Siritanawan P, Kondo T, A Real-time Eye-tracking Method using Time-varying Gradient Orientation Patterns, Proceedings of ECTI-CON, Thailand, 2010

[6] Gupta S, Doshi V, Jain A, Iyer S, Iris Recognition System using Biometric Template Matching Technology, JACSA International Journal of Advanced Computer Science and Applications 1(2):24-28

[7] Ofir Pele and Michel Werman, Robust Real-time Pattern Matching Using Bayesian Sequential Hypothesis Testing, IEEE Transaction on Pattern Analysis and Machine Intelligence, August 2008

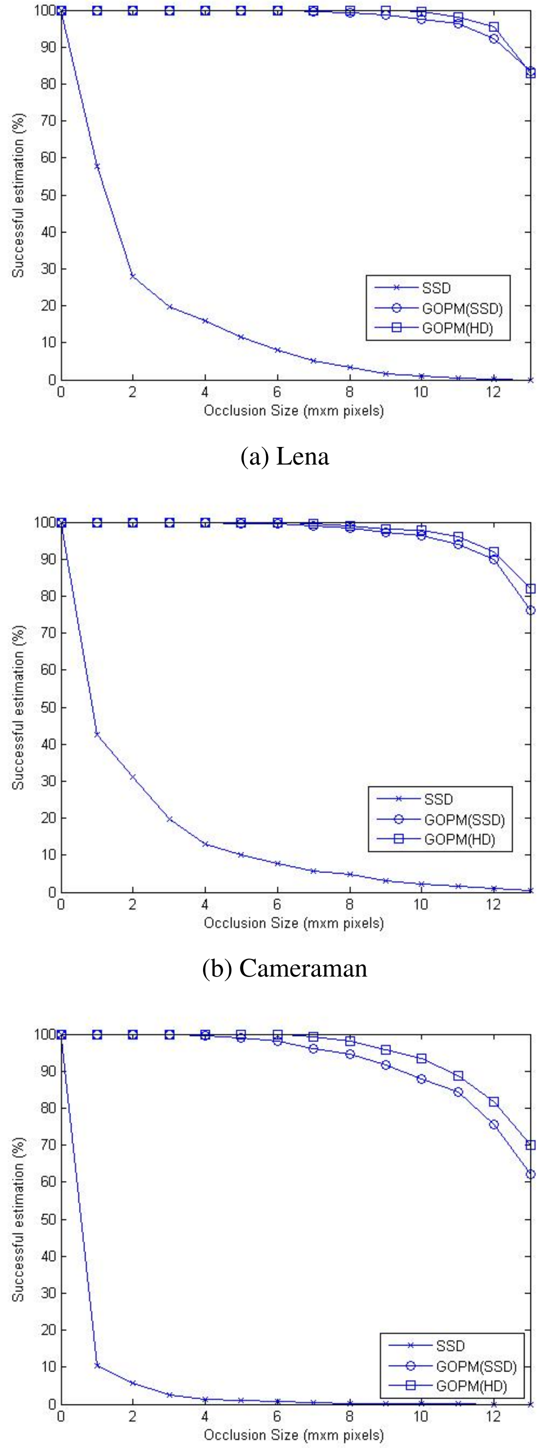

(a) Lena

(b) Cameraman

(c) House

Fig. 6. Successful rate motion estimation of occlusion testing under non-uniform illumination change on artificial motion sequences by using (a) Lena, (b) Cameraman, and (c) House image. The sizes of occlusion block are varied from 0x0 to 13x13 pixels

The Seventeenth International Symposium on Artificial Life and Robotics 2012 (AROB 17th '12),
B-Con Plaza, Beppu, Oita, Japan, January 19-21, 2012

Microscopic image restoration based on tensor factorization of rotated patches

Masayuki Kouno[1], Ken Nakae[1], Shigeyuki Oba[1,2], and Shin Ishii[1]

[1] Graduate School of Informatics, Kyoto University, Gokasho, Uji, Kyoto 611-0011, Japan
[2] PRESTO, Japan Science and Technology Agency
(Tel: 81-774-38-3938, Fax: 81-774-38-3941)
(kouno-m@sys.i.kyoto-u.ac.jp)

Abstract: In microscopic image processing for analyzing biological objects, structural characters of objects such as symmetry and direction can be used as a prior knowledge to improve the result. In this study, we incorporated filamentous character of local structures of neurons into a statistical model of image patches so as to obtain an image processing method based on tensor factorization with image patch rotation. Tensor factorization enabled us to incorporate correlation structure between neighboring pixels, and patch rotation helped us obtain image bases that well reproduce filamentous structures of neurons. We applied the proposed model to a microscopic image and found significant improvement in image restoration performance over existing methods even with smaller number of bases.

Keywords: Image processing, Microscopic image, Tensor factorization, Local feature extraction

1 INTRODUCTION

Statistical modeling of image patches is a standard method to extract local structural features in image processing [1]. Rectangular image patches are cut out from a target image and regarded as random vector-valued samples. Statistical modeling of vector-valued variables provides a general tool for statistical feature extraction, unsupervised learning, and noise reduction by regression, to various application fields, such as natural image recognition, text recognition, and face recognition [2]. On the other hand, such statistical methods may suffer from information loss due to conventional transformation from rectangular image patches into vectors, which would lead to deterioration of image restoration performance. In this study, we try to reduce loss of structural information in microscopic image processing, by introducing the following two strategies: to obtain direction of foreground objects by fitting rotational image patches; and, to handle each fitted image patch as a matrix *(patch height patch width)* rather than a vector.

2 NOTATIONS FOR TENSOR ANALYSIS

In this section, we introduce notations necessary to describe the idea of tensor factorization.

2.1 Tensor & its matricization

Let $\underline{\mathbf{Y}} \in \mathbb{R}^{I_1 \times I_2 \times \cdots \times I_N}$ be an an N-way tensor whose real-valued element $y_{i_1 i_2 \cdots i_N} \in \mathbb{R}$ is indexed by $i_n \in 1, 2, \quad, I_n$ for $1 \quad n \quad N$. Each of $I_1, I_2, \quad, I_N \in \mathbb{N}$ denotes the largest index number for the corresponding mode. A zero-way tensor is represented by a scalar y, a one-way tensor by a vector $\mathbf{y}$, a two-way tensor by a matrix $\mathbf{Y}$, and a three or higher-way tensor by a general tensor $\underline{\mathbf{Y}}$. $||\underline{\mathbf{Y}}||_{\mathrm{F}}^2$ denotes squared Frobenius norm, which is a sum of squared elements of the tensor $\underline{\mathbf{Y}}$.

To operate and illustrate a multi-way tensor, we may rearrange tensor elements to a matrix form, which is called matricization. The mode-n matricization of a tensor $\underline{\mathbf{Y}}$ rearranges the tensor elements as $\mathbf{Y}_{(n)} \in \mathbb{R}^{I_n \times (M_n)}$, where $M_n = I_1 I_2 \quad I_{n\ 1} I_{n+1} \quad I_N$.

2.2 Tensor-matrix product

The mode-n product $(n = 1, 2, \quad, N)$ of a tensor $\underline{\mathbf{G}} \in \mathbb{R}^{J_1 \times J_2 \times \cdots \times J_N}$ and a matrix $\mathbf{A} \in \mathbb{R}^{I_n \times J_n}$, $\underline{\mathbf{Y}} = \underline{\mathbf{G}} \quad_n \mathbf{A}$, is a tensor $\underline{\mathbf{Y}} \in \mathbb{R}^{J_1 \times \cdots \times J_{n-1} \times I_n \times J_{n+1} \times \cdots \times J_N}$ whose elements are given by $y_{j_1 j_2 \cdots j_{n-1} i_n j_{n+1} \cdots j_N} = \sum_{j_n=1}^{J_n} g_{j_1 j_2 \cdots J_N} a_{i_n j_n}$.

Multiplication of a tensor over all modes other than one mode is denoted as $\underline{\mathbf{G}} \quad_{-n} \{\mathbf{A}\} = \underline{\mathbf{G}} \quad_1 \mathbf{A}^{(1)} \quad_{n-1} \mathbf{A}^{(n-1)} \quad_{n+1} \mathbf{A}^{(n+1)} \quad_N \mathbf{A}^{(N)}$ and the resulting tensor has dimensionality $I_1 \quad I_{n\ 1} \quad J_n \quad I_{n+1} \quad I_N$.

3 METHODS

In this section, we present our new image restoration method based on tensor factorization and rotational patches.

3.1 Image restoration incorporating patch rotation

Our image restoration method is a modification of the tensor factorization method proposed by Kim et al. [3]. Their method consisted of two steps; a basis learning step and a basis application step. We added a patch rotation process to both of these steps in order to incorporate symmetric structural features of image patch bases.

In the basis learning step, first, an image patch tensor is generated from an objective image; we obtain p samples of $m \quad m$ rectangular image patches from the full-size image; here, a rectangular image patch is said a foreground one if

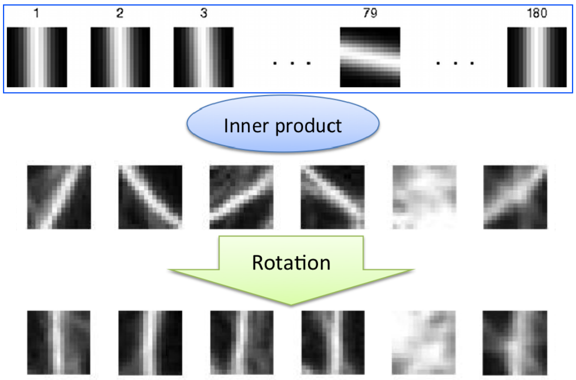

Fig. 1: Template image patch set by hand (leftmost panel) and its rotations (2...180). Foreground image patches before (middle) and after (lower) the rotation process.

its central pixel is brighter than the pre-determined level, or a background one otherwise. p samples of foreground patches are arranged into an $m \times m \times p$ three-way tensor, which is called a *train patch tensor*. Background patches were omitted in the following analysis. We calculate a *basis tensor* $\underline{\mathbf{U}} \in \mathbb{R}^{m \times m \times K}$ as a solution of the minimization problem:

$$\underline{\mathbf{U}} = \underset{(\underline{\mathbf{U}}, \mathbf{V})}{\arg\min} ||\underline{\mathbf{Y}} - \underline{\mathbf{U}} \times_3 \mathbf{V}||_F^2, \qquad (1)$$

where $\mathbf{V}$ is a $p \times K$ mixing matrix such to allow the linear sum of K *basis patches* $\underline{\mathbf{U}}(:,:,k)(k = 1, \cdots, K)$ to well approximate the *train patch tensor* $\underline{\mathbf{Y}}$; that is, the ith patch $\underline{\mathbf{Y}}(:,:,i)$ is well approximated by a linear sum of the basis patches $\sum_k \underline{\mathbf{U}}(:,:,k)\mathbf{V}(i,k)$ for all i. The number K ($< p$) of basis patches should be set appropriately by hand. This minimization problem is solved by three-way tensor factorization and we applied higer order orthogonal iteration (HOOI) algorithm for it, which is explained in detail in section 3.2.

In the basis application process, we restore a noisy image patch $\mathcal{Y}$ and achieve a restored image patch $\hat{\mathcal{Y}}$ by applying the basis tensor $\underline{\mathbf{U}}$ that was obtained in the basis learning step. We assume that an image patch $\mathcal{Y}$ is expressed by linear combination of K basis patches as follows.

$$\begin{aligned}\mathcal{Y} &= \underline{\mathbf{U}} \times_3 \mathbf{v} + \mathbf{E} \\ &= \sum_{k=1}^{K} \underline{\mathbf{U}}(:,:,k) v_k + \mathbf{E},\end{aligned} \qquad (2)$$

where $\underline{\mathbf{U}}(:,:,k)$ is an $m \times m$ matrix that represents the kth basis patch image, $\mathbf{v}$ is K-dimensional weight vector, and $\mathbf{E}$ is an $m \times m$ residual matrix. We calculate the weight vector $\hat{\mathbf{v}}^T = (\hat{v}_1, \cdots, \hat{v}_K)$ that minimizes the residual norm $||\mathbf{E}||_F^2$. Finally, we obtain the restored image patch $\hat{\mathcal{Y}} = \underline{\mathbf{U}} \times_3 \hat{\mathbf{v}}$. The entire image is restored by applying the above restoration process for all patches in the image.

Algorithm HOOI for three-way tensor factorization

Input: $\underline{\mathbf{Y}} \in \mathbb{R}^{I_1 \times I_2 \times I_3}$
Output: n th matrix $\mathbf{A}^{(n)} \in \mathbb{R}^{I_n \times J_n} (n = 1, 2, 3)$ and
a core tensor $\underline{\mathbf{G}} \in \mathbb{R}^{J_1 \times J_2 \times J_3}$
such that $\left|\left|\underline{\mathbf{Y}} - \hat{\underline{\mathbf{Y}}}\right|\right|_F^2$ is minimized.

begin
random initialization for all matrices $\mathbf{A}^{(n)}$
repeat
  for $n = 1$ *to* 3 **do**
    $\underline{\mathbf{W}}^{(n)} = \underline{\mathbf{Y}} \otimes_{-n} \{\mathbf{A}^{(n)T}\}$
    $[\mathbf{A}^{(n)}, \mathbf{\Sigma}^{(n)}, \mathbf{B}^{(n)}] = \mathtt{svds}(\mathbf{W}^{(n)}_{(n)}, J_n)$
  end for
until a stopping criterion is realized
$\underline{\mathbf{G}} = \underline{\mathbf{Y}} \times_1 \mathbf{A}^{(1)^T} \times_2 \mathbf{A}^{(2)^T} \times_3 \mathbf{A}^{(3)^T}$
end

In this study, we introduce a patch rotation process in order to incorporate symmetry in the objective cell structures. First, we prepared a template image (the leftmost panel in Fig. 1), which was set manually to represent a local neural filamentous structure in the vertical direction. Next, we prepared a set of its rotated image templates with rotation angles, 1, 2, ..., 180 degree (Fig. 1). In the patch rotation process, we fit each sampled patch to the vertical template in the following manner; calculate correlation coefficients between the sampled patch and the rotated templates of 180 rotation angles, determine the best rotation angle that maximizes the correlation, and rotate the sampled patch into the inverse direction with the determined rotation angle. In the above procedure, we rotated the template patch 180 times, rather than the sampled patch, in order to reduce the number of total number of rotation operation. Fig. 1 shows some examples of image patches before (middle) and after (lower) the patch rotation.

We applied the patch rotation process to the both of basis learning and basis application steps. Before the basis learning step, we align all image patches to fit the template image, and gather the rotated patches to construct a three-way patch tensor for the basis learning. Before the basis application step, we align each image patch to fit the template image, and restore the central pixel of the result of an application of the base.

Owing to the patch rotation, we can omit trivial variations of foreground patch images that can be generated by the rotation of rectangular spatial cutting windows, and, consequently, we expect that the set of bases reflect variations among neuronal local structures.

3.2 HOOI algorithm for basis learning step

The HOOI algorithm for the three-way tensor factorization in the basis learning step is based on an iterative Al-

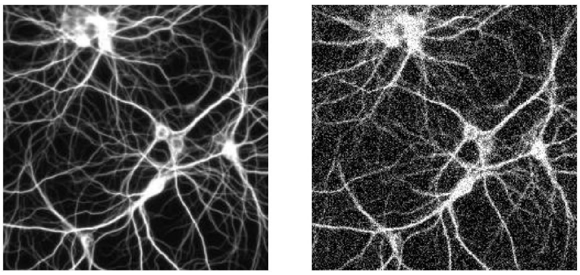

Fig. 2: An original microscopic image (size: 300 300 pixels) taken from `www.greenspine.ca` (Paul De Koninck, Laval University) (left) and a noisy image (right).

ternative Least Squares (ALS) algorithm. In each iteration of ALS, one basis is updated to minimize the residual error while keeping the others fixed, and finally we seek a (locally) optimal solution [4]. An extension of ALS for tensor factorization, HOOI was first introduced by De Lathauwer, De Moor and Vandewalle [4] and recently extended and implemented by Kolda and Bader in their MATLAB Tensor Toolbox[5]. We used this toolbox for tensor factorization in this study.

The HOOI factorizes the $m \quad m \quad p$ patch tensor $\underline{\mathbf{Y}}$ into an $m \quad m \quad K$ core tensor $\underline{\mathbf{G}}$ and three matrices $\mathbf{A}^{(1)}$, $\mathbf{A}^{(2)}$, and $\mathbf{A}^{(3)}$,

$$\underline{\mathbf{Y}} = \underline{\mathbf{G}} \quad {}_1\,\mathbf{A}^{(1)} \quad {}_2\,\mathbf{A}^{(2)} \quad {}_3\,\mathbf{A}^{(3)}. \tag{3}$$

We calculate the basis tensor that is defined in Eq. (1), $\underline{\mathbf{U}} \in \mathbb{R}^{m\times m\times K}$, by using the result of HOOI as follows, $\underline{\mathbf{U}} = \underline{\mathbf{G}} \quad {}_1\,\mathbf{A}^{(1)} \quad {}_2\,\mathbf{A}^{(2)}$.

In the HOOI algorithm, $\texttt{svds}(\mathbf{W}_{(n)}^{(n)})$ denotes a singular value decomposition procedure that decomposes a matrix like $\mathbf{W}_{(n)}^{(n)} = \mathbf{A}^{(n)}\mathbf{\Sigma}^{(n)}\mathbf{B}^{(n)T}$. The cost function $\left|\left|\underline{\mathbf{Y}} \quad \hat{\underline{\mathbf{Y}}}\right|\right|_{\mathrm{F}}^2$ is monitored so that the algorithm is terminated when its difference from that in the last step is smaller than a constant (' a stopping criterion ' on line 8 in the algorithm).

3.3 Image restoration by matrix factorization

We compared the proposed method with simple matrix factorization and two-way tensor factorization. In the case of two-way tensor factorization, the train patch tensor is arranged to an $M \quad p$ matrix, where the column size $M = m^2$ corresponds to the number of pixels in an $m \quad m$ image patch. The M-dimensional patch vector $\mathbf{y}$ is represented by a linear combination of $K(\ll p)$ bases. $\mathbf{y} = \sum_{k=1}^{K} v_k \mathbf{u}_k + \boldsymbol{\varepsilon}$, where $\mathbf{u}_k$ is the kth M-dimensional basis vector, v_k is a scalar weight of the kth basis, and $\boldsymbol{\varepsilon}$ is an M-dimensional residual vector. Let $\mathbf{U} = (\mathbf{u}_1, \quad , \mathbf{u}_K)$ be an $M \quad K$ matrix that gathers all basis vectors $\mathbf{u}_k$. In the basis learning step, we obtain a basis matrix $\mathbf{U}$ that minimizes $||\boldsymbol{\varepsilon}||_{\mathrm{F}}^2$, and, in the basis application step, we calculate $\hat{\mathbf{v}}$ and $\hat{\mathbf{y}} = \mathbf{U}\hat{\mathbf{v}}$.

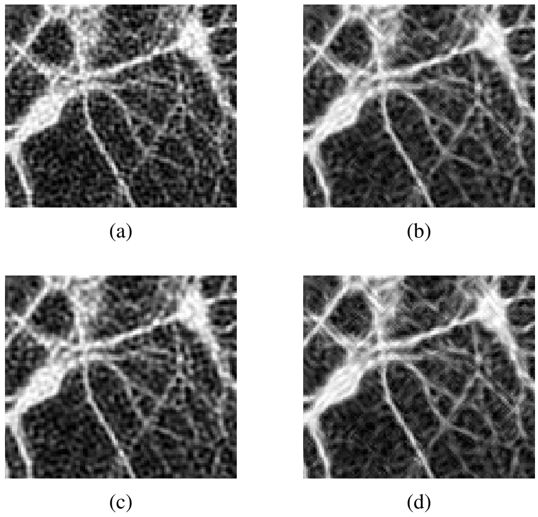

Fig. 3: Restoration by matrix factorization (a) without patch rotation ($K = 64$) and with patch rotation ($K = 52$). Restoration by tensor factorization (c) without patch rotation ($K = 52$) and(d) with patch rotation ($K = 46$).

4 RESULTS

Image restoration performance was compared between tensor factorization and matrix factorization, and between with and without the patch rotation process. A microscopic image of size 300 300 pixels was clipped from the original image (size: 634 800 pixels) of a neuronal network, registered on `www.greenspine.ca` (Paul De Koninck, Laval University) (Fig. 2, left). To examine the restoration performance, we artificially added white Gaussian noise (variance = 0.03) to the neuronal image (Fig. 2, right). Since we know the original image, we can evaluate the image restoration performance by calculating the root mean squared error (RMSE) of pixel brightness between the original and restored images. Since the performance depends on the number of bases, K, the RMSE was calculated with various K values for each method. For the basis learning, we extracted about 17,000 image patches of size 13 13 pixels from the original image before noise addition. Although the original image is not available in the actual image restoration application, we here assumed the basis learning has been accomplished by using clear images prior to the application of our image restoration method. Other possible procedure would be to iterate the basis learning step and image restoration by using the same (possibly noisy) images.

The image restoration results are shown in Fig. 3. The image restored by the tensor factorization with patch rotation obviously exhibited finer fiber structures than those by other methods. Such good restoration performance of the proposed method can be further seen in the numerical results summarized in Fig. 4. Since the performance was largely depen-

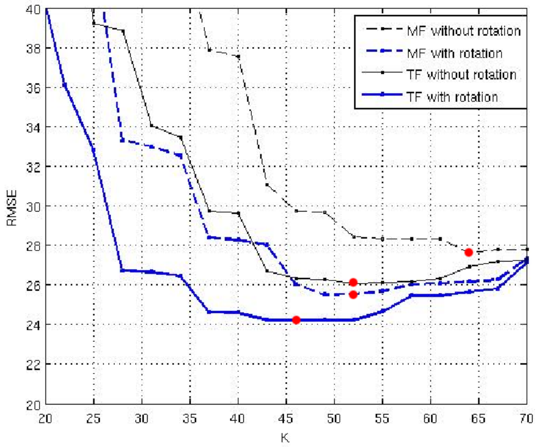

Fig. 4: Comparison of image restoration performance. Horizontal and vertical axes denote the number of bases (K) and the root mean squared restoration error (RMSE), respectively. Solid and chained lines denote the image restoration with and without image patch rotation process, respectively. Thick and thin lines denote the image restoration by means of three-way tensor factorization and matrix factorization, respectively. Red point denotes the best setting of K for each case.

dent on the number of bases, K, we here examined various K values. Although the RMSE of each method became the smallest with an appropriate setting of K, with the best setting being dependent on the method, the proposed method, the tensor factorization with patch rotation, showed the least RMSE value in every setting. In addition, tensor factorization (TF) showed better results that matrix factorization (MF), even though the former employed a smaller K value than the latter.

The advantage of the patch rotation was obvious especially when the number of bases was small. Table 1 shows the RMSE with the best setting of K for various noise levels added to the original image; our proposed method showed the best restoration performance with a smaller number of bases in all cases.

5 CONCLUDING REMARKS

In this study, we proposed an image restoration method based on the three-way tensor factorization of rotated image patches, which is suitable for restoration of microscopic images of biological targets such as neuronal networks. In the simulation experiment using a real image of neuronal network, we found significant performance gain in image restoration due to the two important ingredients of our method, tensor factorization and image patch rotation.

Fluorescence microscopy has a dilemma that increase in the frame rate suffers from larger shot noise, while decrease leads to the lack of information. Thus, a good image restoration technique is important for improving the data acquisition efficacy. For example, if we can restore low resolution images by utilizing basis images created from other high resolution images, the original low resolution images are restored cheaply in a software manner. Applications to 3D images and movies would be important future extensions, and capturing various finer structures of neuronal networks by further modifying our statistical model will also be promising.

Table 1: RMSE comparison for various noise levels added to the original image.

(a) variance $= 0.01$

RMSE	MF	TF
without rotation	18.27 ($K = 70$)	17.48 ($K = 64$)
with rotation	17.28 ($K = 64$)	**16.42** ($K = 55$)

(b) variance $= 0.03$

RMSE	MF	TF
without rotation	27.64 ($K = 64$)	26.09 ($K = 52$)
with rotation	25.51 ($K = 52$)	**24.21** ($K = 46$)

ACKNOWLEDGMENT

This study was supported by Grant-in-Aid for Scientific Research on Innovative Areas: "Mesoscopic neurocircuity: towards understanding of the functional and structural basis of brain information processing" from MEXT, Japan.

REFERENCES

[1] Muresan DD and Parks TW (2003), Adaptive principal components and image denoising. *International Conference on Image Processing*, 1:I–101–4.

[2] Lee DD and Seung HS (1999), Learning the parts of objects by non-negative matrix factorization. *Nature*, 401(6755):788–91.

[3] Kim YD and Choi S (2007), Nonnegative Tucker Decomposition. *IEEE Conference on Computer Vision and Pattern Recognition*, 1–8.

[4] de Lathauwer L, de Moor B, and Vandewalle J (2000), On the Best Rank-1 and Rank-($R_1, R_2, ..., R_N$) Approximation of Higher-Order Tensors. *SIAM Journal on Matrix Analysis and Applications*, 21(4):1324–42.

[5] Bader BW and Kolda TG (2006), Algorithm 862: MATLAB tensor classes for fast algorithm prototyping. *ACM Trans. Mathematical Software*, 32(4):635—53.

The Seventeenth International Symposium on Artificial Life and Robotics 2012 (AROB 17th '12),
B-Con Plaza, Beppu, Oita, Japan, January 19-21, 2012

Robotic applications of a defensible error-aware super-resolution technique

Jeremy Straub[1]

[1]University of North Dakota, Grand Forks, ND 58202, USA
(Tel: 1-701-777-4107, Fax: 1-701-777-3330)

[1]jeremy.straub@und.edu

Abstract: Many robotics applications that rely on computer vision for long-term route planning can benefit from increasing the resolution of the imagery used for that planning. Increased resolution increases the effective planning timeframe and allows the AI planner to consider obstacles that are more distant. As a best-case scenario, a route that might otherwise be taken just to encounter a distant obstacle that requires significant backtracking could be avoided. Super-resolution image enhancement, however, introduces its own problems as it can create false positive and false negative inclusions. Thus, for many applications, basic super resolution is unsuitable for robotic planning applications as the level of accuracy of the enhanced data is unknown. A framework for reporting confidence in super-resolution enhancement is presented in this paper. This approach includes a numeric confidence map along with the super-resolved data. The AI consumer of the enhanced data can, thus, consider both the data as well as the confidence meta-data. This framework is demonstrated and evaluated via an implementation of a database-based super-resolution technique that also supplies confidence map data. Robotic applications are discussed.

Keywords: Image enhancement, super resolution, decision confidence.

1 INTRODUCTION

Robotic control decision-making can have disastrous effects when it is based on inaccurate data. When a failure happens, it is important to be able to ascertain what caused that failure. Many artificial intelligence (AI) techniques, however, make this difficult. Some techniques train on-the-fly resulting in a decision being made with a framework that existed for a single moment-in-time and may never reoccur. While, theoretically, the data, node weightings, and other factors relevant to a decision could be preserved via storage, this is practically problematic – particularly when one considers that a craft that makes a poor decision may be destroyed (as a result of the decision, or otherwise), making the data unavailable for analysis. While this problem is wide-ranging and affects all areas of AI decision making, this paper deals with error that can be introduced via super resolution (the enlargement of images via computer processing) and how this error can be quantified and its potential factored in to the decision making process.

2 BACKGROUND

Numerous approaches to super resolution have been suggested. These approaches can be divided in to two main categories: those which infer data and those which simply piece together existing data. Piecing solutions [e.g., 2, 3, 4, 7] use several images of a scene or subject and take advantage of camera shifts or movement to allow a higher resolution image to be constructed from two or more low-resolution images.

Inference-based super resolution [e.g., 6], alternately, draws on patterns in the image format, prior knowledge or other sources to create an output image that attempts to replicate what would produced by capturing the original scene or subject at the output resolution. Inference-based approaches can be further divided into approaches which attempt to apply an algorithm to a single image to enhance it without additional information and approaches which base the output on both the input image and prior knowledge. All present forms of super resolution only produce approximations of the actual high-resolution image; these approximations can (and usually do, to various extents) include false positive inclusion and false negative exclusion.

Robotic AI control systems use imagery for immediate decision-making and long range planning. Immediate decision-making can include obstacle avoidance, target location and identification, and such. Long range planning uses image analysis for target identification, prediction of traverse-ability and, terrain type.

A short-range perception failure could result in damage to or loss of the robot (due to misjudging the terrain and falling or flipping). This, however, is unlikely as at close range the obstacles are quite large and would be difficult to miss (to the extent where super resolution would generally be unnecessary). Also, other techniques can be used to avoid these perils (such as a scanning laser or whisker, etc.).

At a longer range, however, super resolution is very relevant and the cost of bad information can be significant. Two scenarios deserve consideration. In the first longrage imagery scenario, enhanced imagery is used for route planning. In this instance, detail removal (via super resolution smoothing) can result in obstacles going unrecognized – conversely, it can also result in a preferable path being smoothed over to look no different than near-by obstacles). This may cause the robot to commit to a path which it will later be forced to backtrack from when higher-resolution imagery correctly detects the true nature of the path.

In the second scenario, super-resolved imagery is used for target location and identification. Particularly if the object size is close to the working-block size of the super resolution (for prior knowledge SR systems), it is possible that one complete image is incorrectly replaced with another. A friendly craft may thus be targeted as a foe or a foe incorrectly ignored as a friend.

3 SUPER RESOLUTION TECHNIQUE

The proposed approach makes three important additions to previous super resolution research. It starts with a trained database-based approach with corner matching loosely based on [5]. It adds to this the integration of a commercial database product for storage and searching, weighting of the search based on pattern occurrence training, and the inclusion of a confidence level map with the produced image.

3.1 Training

Training populates the database. Source images are trained to identify patterns starting at each pixel (excluding those on the far right and bottom where the training box size would be cut off by the image edge) in the image, starting from the top left. Figure 1 demonstrates how a given area of the image actually is used to crate numerous training patterns. The number of patterns produced by a given image is N=(H-A)(W-a), where a is the height and width of the pattern size.

Patterns collected in training are stored in the database at three resolutions. They are stored at the full resolution, a medium resolution (which will equate to the resolution of the images to be presented later) and a low resolution which is stored to aid in pattern matching when processing a presented image. The database contains a column for each pixel-location in each pattern size. An index is applied only to the database columns for the low-resolution image, to speed searching later. A temporary index may be incorporated for the high-resolution patterns to speed the training process; however, this should be removed before presenting images for SR.

For each pattern that is sliced from each training image, the database is searched for a match. If a match is found an 'occurrence' counter is incremented and no further work is done. If no match is found, the medium and low versions of the pattern are created via averaging the corresponding pixels of the high-resolution pattern and stored; the occurrence counter for the pattern is set to 1.

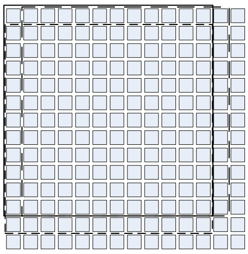

Fig. 1. Source Image Slicing

3.2 Image Enhancement

The image is processed through one medium-size pattern at a time, with a slight overlap. For each location, the medium resolution pattern from the source image is used to make a low-resolution pattern which is used to search the database and identify candidate patterns. Some previous work has attempted to fulfill a particular quota when selecting candidate patterns. In this instance, patterns are searched for based on a maximum difference from the low-resolution pattern (applied on a per-pixel basis). Any patterns which match the criteria are selected for consideration. If a match is not found, the tolerances are increased incrementally until a match is found or a maximum level of tolerance increase is reached. In the case where the search stops without finding a match, the medium resolution pattern is enlarged and placed in to the final image.

If candidates are identified, the medium resolution patterns (associated with the particular small size patterns selected in the search) are then used to select the pattern that will be placed in the final image. The medium patterns are compared to the medium pattern from the presented image and a difference value is computed. They are also compared to the overlap area and a difference value is computed. Finally, the 'occurrence' value stored with each pattern is retrieved. A final merged difference evaluation value is computed:

$$DEV = (a * DM) + (b * DO) - (c * O) \quad (1)$$

where a, b and c are the weighting constants (respectively) for the medium-pattern-difference (D_M), overlap-difference(D_O) and occurrence level (O). The prevailing pattern is placed in to the final image and the confidence map is updated.

3.3 Confidence

For each pattern of pixels placed in to the final image, a corresponding entry is placed in to the confidence map. The map, which is created as an ASCII text file, is depicted visually in figure 4. The confidence value is similar to the DEV used during the enhancement process; however, it is presented as a confidence value (as opposed to a weighted difference). The confidence value is calculated:

$$C=[(w*DM)+((1-w)*DO)]/K * (O/OMax) \qquad (2)$$

where K is the maximum difference possible and O_{Max} is the maximum number of occurrences recorded for a single pattern in the current database (O_{Max} could also be set to an arbitrary value). It is expected that this confidence map can be fed into the AI planning routine and incorporated in its internal route confidence assessment process.

4 TECHNIQUE EVALUATION

A frequently used approach to evaluating super resolution is to compare the SR output image to the original image on a pixel-by-pixel basis. While this approach has the benefit of simplicity, it does not provide a particularly useful metric for evaluating the real-world performance of super resolution. In the case of images that will be viewed by humans, the question (generally) isn't one of whether the image is pixel-perfect, but instead relates to whether the image looks to be of high enough resolution. For example, in super resolving video for recreational viewing (such as in [3]), the objective is not to make the image perfect – but to make sure that the image is believably high-res. In other applications (such as the discussed application of AI decision making or barcode enhancement [e.g., 1]), the smoothness and high-resolution-look of the image are unimportant. What is important, however, is the accurate representation of critical features. To this end, a suitable performance evaluation metric is the correlation of low confidence with error areas. We can't expect the SR algorithm to perfectly enlarge every part of every image, every time but we must be able to ascertain how good each super-resolved image area is in order to include it in decision-making.

4.1 Subjective Visual Evaluation

The visual effect of the super resolution process is, obviously, quite subjective. Further, in an application in robotic guidance, the appearance of the super-resolved image to human observers is secondary to its utility for decision-making. However, as this is a commonly used metric for evaluating super resolution, it is appropriate to discuss it briefly. As figures 2 and 3 demonstrate, the algorithm seems (visually) to perform quite well on pattern-filled areas. Edges, however, can prove difficult. Experimentation using a database trained with the high-resolution version of an image that is presented performs exceptionally well. This, thus, demonstrates that the edge problem is not an issue with the approach (that is, the approach can produce a visually pleasing edge-area) but with the data that is stored during training. Increasing the training set size (using images that have minimal correlation with the image to be presented) also demonstrates improvements, confirming this.

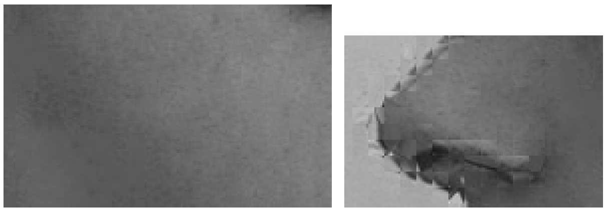

Fig. 2 & 3. Left: Enhanced Face Texture. Right: Pixilation Around

4.2 Pixel Comparison Evaluation

One of the most commonly used methods for evaluating super resolution is to compare the super-resolved image on a pixel-by-pixel basis to the original large-size image. This comparison averaged a 0.9% perfect match. However, given that the images are not black and white, but instead gray scale, it is not prudent to compare only perfect matches (as it is unlikely that a source pattern would have exactly the same shades of grey in pattern – the goal here is to get close). When we apply an error margin of 10% of the color range, the match average jumps to 89.3%. The visual difference of this 10% error margin is barely perceptible. It may, for example, manifest itself as a slightly different shading of an individual's face based on pattern matching of a lighter or darker skinned individual. However, similar effects could easily be caused by lighting in the location of photography or minor skin color change due to tanning, etc.

4.3 Confidence Correlation Evaluation

The evaluation technique that is of greatest interest to AI decision making, however, is confidence correlation. Confidence correlation compares each area of the image to the natural high-resolution image like in pixel comparison evaluation. The error value resulting from this is then compared with the confidence value for the pixel produced for the confidence map (as previously described). The confidence correlation, thus, indicates whether the confidence values should be trusted (while the confidence value indicates the accuracy of the super resolution process).

Confidence correlation is calculated as:

$$L = \frac{\left[\sum \left(\frac{C}{E} \times S\right)\right]}{n} \quad (3)$$

where C is the confidence value from Eq. 2, E is the error discussed in section IV-B, S is a scaling constant and n is the number of observations that are being used to compute the confidence correlation value. We, thus, end up with a scaled average correlation between the confidence and error value.

Confidence correlation was calculated for three cases: high error, medium error and low error. The confidence correlation values obtained through testing appear to be fairly consistent between the different error levels: 0.78, 0.82 and 0.79 for high, medium and low error, respectively.

5 SOURCES OF ERROR

Several sources of possible error were considered. Like most super resolution research, the experimental setup for this research is somewhat contrived. Images from prior facial recognition work were used to train and test the system. The images were headshots against a quasi-consistent background (though the actual color of the background in the images varied, likely due to the impact of lighting and using different cameras for different images). In each image, at least 25% of the image consisted of a lightly patterned background. The presence of this background could potentially increase or decrease accuracy calculations (depending on whether the database contained an exact or very close match) significantly, because of its prevalence. An additional test of two closely cropped face images was performed to assess the potential impact of this. One had a background color that was in the database and the other had a background color that the database was not trained with. While the accuracy metric values differed from the values for presenting the image with the larger background area, they did not fall outside of the range of values generated for testing with backgrounds.

6 CONCLUSION

It appears that a training-driven approach to super-resolution can produce acceptable results when the training and presented images are of similar objects. This would tend to suggest that a general-purpose database could be made that would be able to provide suitable enhancement for a variety of object and background types and which could be supplemented (to provide greater accuracy) with domain-specific databases.

When using a super-resolved image for AI decision-making, the potential error that is inevitably introduced by the super resolution process must be considered. The confidence map has been shown to provide a reasonable estimation of this error that can be considered by the AI as an estimation of the true error (based on comparing the actual high-resolution image to the super resolved one) which is, of course, not available in real world application.

Several topics of future research are suggested from this study. First, it would likely be possible to increase accuracy while reducing database size by storing difference patterns instead of gray scale values in the database. Future research could look at the feasibility of storing a pattern of delta-values from the mean-color-value of the image; [8] has looked at how patterns recur at different levels and thus it is reasonable to assume that they may recur in different shades as well. Second, this same concept could be applied to color images (including the aforementioned change). Finally, it would be prudent to compare the accuracy of decision-making using a higher-resolution super-resolved image with decision-making using a lower resolution image to determine the actual benefit of increasing image resolution.

ACKNOLEDGEMENT

Credit is hereby given to the Massachusetts Institute of Technology and to the Center for Biological and Computational Learning for providing the database of facial images.

REFERENCES

[1] Bailey, Donald G. "Super-resolution of bar codes." *Journal of Electronic Imaging*, 2001: 213-220.

[2] Bishop, Christopher M., and Andrew Blake. "Super-resolution Enhancement of Video." *Proc. Artificial Intelligence and Statistics*, 2003.

[3] Borman, S., and R.L. Stevenson. "Super-resolution from image sequences-a review." *1998 Midwest Symposium on Circuits and Systems*, 1998: 374-378.

[4] Elad, M., and A. Feuer. "Super-resolution reconstruction of image sequences." *IEEE Transactions on Pattern Analysis and Machine Intelligence*, 1999: 817-834.

[5] Freeman, William T., Thouis R. Jones, and Egon C. Pasztor. "Example-Based Super-Resolution." *IEEE Computer Graphics and Applications*, 2002: 56-65.

[6] Glasner, D., S. Bagon, and M Irani. "Super-resolution from a single image." *2009 IEEE 12th International Conference on Computer Vision*, 2009: 349-356.

[7] Irani, M., and S. Peleg. "Super resolution from image sequences." *10th International Conference on Pattern Recognition*, 1990: 115-120 vol. 2.

[8] Wang, Qiang, Xiaoou Tang, and H. Shum. "Patch based blind image super resolution." *Tenth IEEE International Conference on Computer Vision*, 2005: 709-716.

The Seventeenth International Symposium on Artificial Life and Robotics 2012 (AROB 17th '12),
B-Con Plaza, Beppu, Oita, Japan, January 19-21, 2012

A study on situation recognition in wide area by aerial image analysis

Ganwen JIANG [1], Jun YOSHIDA[1], Masayuki KASHIMA[1], Kiminori SATO[1]
and Mutsumi WATANABE[1]
[1] Department of Information Science and Biomedical Engineering, the Graduate School of Science and Engineering,
Kagoshima University, Korimoto 1-21-40, Kagoshima, Kagoshima 890-0065, Japan
(Tel: 81-80-5264-2806)

[1] kyoukinbun@yahoo.co.jp

Abstract: Recently, social security and natural disasters are worrying. In order to solve these problems and to reduce the damage, wide-area monitoring by computer vision is needed. Traditional monitoring systems have many problems that are caused by limited visual field in conventional technique. In this research, the air vehicle system which is to track a particular person indoors and outdoors where there are multiple people exist is proposed. Besides that, the four blades helicopter as a flying robot named AR.Drone is used. On experimental method, Hough transform method, Histogram method, Snakes method and Particle filter method are used in the research. Experimental results indoors and outdoors have shown the effectiveness of the proposed methods. The purpose of the study is to perform a wide area situation recognition and autonomous control of flying robot indoors and outdoors.

Keywords: Hough Transform, Histogram, Snakes, Particle Filter, Computer Vision, Wide Area Monitoring.

1 BACKGROUND

Recently, the number of crime incident at university, bank, convenience stores and so on occurs frequently because of the increase of invasion by intruders. In addition, natural disasters such as volcanic activities and earthquakes occur frequently, which makes damage become worse. For example, 400,000 people were affected by earthquake in Sichuan, China on May 12, 2008 while more than 200,000 people were affected by earthquake in Japan on March 11, 2011 because rescue was not done promptly after disasters (Fig.1.).

Fig.1. Northeast earthquake in Japan

In agricultural sector, it is a subject about how to understand the production status in vast farmland and how to prevent vermin damage. Therefore, the pesticide usage and residue status monitoring is also important.

In order to solve these problems and to reduce the damages, it is important to carry out the wide area monitoring.

2 RELATED RESEARCHES

2.1 The Traditional Monitoring System

As for traditional monitoring system, firstly, it is to detect dynamic objects from image, and to track it. Secondly, it is to understand what is the object classified, and then to understand the structure of the object. The problem of background fluctuation and illumination change the effect of the recognition results. Flowchart of traditional monitoring system is as follows (Table 1.).

Table 1. Flowchart of traditional monitoring system [1]

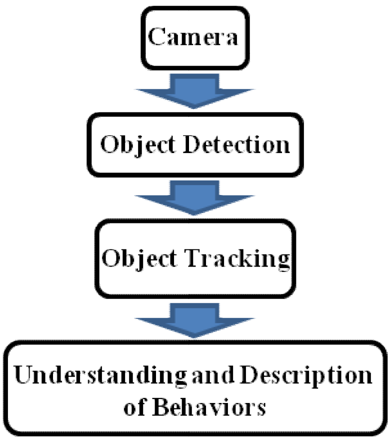

2.2 The problem of conventional method

Typical approaches of automatic monitoring are the background difference method and model method. The background difference method is explained as follows. Beforehand, the background image is taken where dynamic objects do not exist. After that, dynamic object is detected depending on differential results of input image and background image. The robust of technique is influenced by complex environment. Detection accuracy of model method is reduced when part of the body is shielded (Fig.2.).

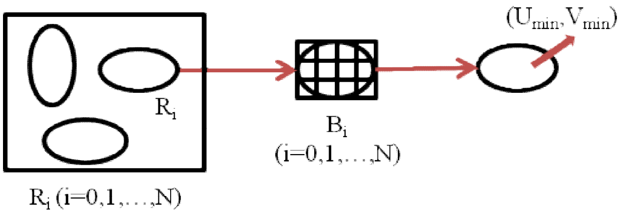

Fig.2. Conventional method [1]

There are many problems that are caused by limited visual field in the traditional monitoring system, such as difficulties to decide the border situation, shielding due to buildings and trees and difficulties to track target object.

On the other hand, in aerial images there are scarcely vision problems and obstacles problems that make it possible to track single or multiple target objects. Besides, it is easy to carry out wide area monitoring. The matter of aerial image is that it has less characteristics of target object and flying robot is likely to be susceptible to wind and weather.

3 AERIAL IMAGE

There are two ways to take aerial image. The first way is to use the retention type robot (balloon robot) and the second way is to use the flying type robot (flying robot). The merits and demerits of both are as follows (Table 2.).

Table 2. merits and demerits of Balloon Robot and Flying Robot

	Merits	Demerits
Balloon Robot	battery is not required	can not track target object
	safety is high	Low degrees of freedom
		susceptible to wind and weather
Flying Robot	can track target object	battery is required
	autonomous co-ntrol is possible	vibration effects image quality

Because the purpose of study is to track target object and the flying robot can be controlled automatically, the flying robot is chosen for this study.

4 PROPOSALS OF STUDY

The air vehicle system which is to track a particular person indoors and outdoors where there are multiple people exist is proposed. The purpose of the study is to perform a wide area situation recognition and autonomous control of flying robot indoors and outdoors. It is to detect a particular person by head of the person as a feature, because the characteristics is few from aerial image, and to track the person detected by head, clothing color and so on as features. As for autonomous control of flying robot, flying robot is controlled by landmark recognition.

There are many types of flying robots such as helicopter type , flying robot with wings and flying robot with blades. In this research, four blades helicopter as a flying robot named AR.Drone shown in left of Figure 3 is used. AR.Drone can be controlled by ipod touch and iphone, because of the Wireless communication function (Fig.3).

Fig.3. Types of the Flying Robot

5 EXPERIMENTAL METHODS

5.1 Experiment for detecting a particular person

Table 3. Flowchart of detecting target object

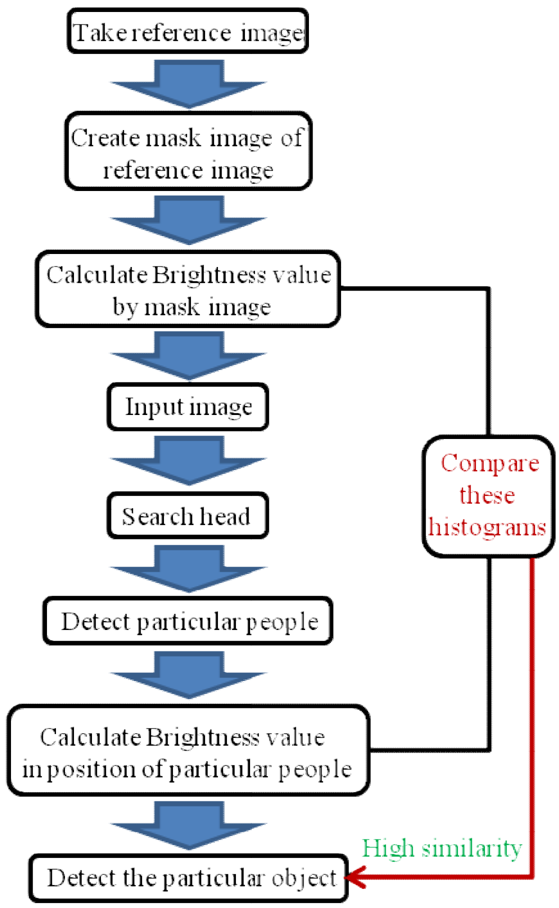

Firstly, the reference image is taken in the same scene and the mask image is created from reference image by the

Photoshop. The size of mask image is the same as the reference image. Secondly, it is to perform the edge extraction on AVI video taken by AR.Drone in the scene. Thirdly, the video processed is done by expansion and smoothing processing. Then, it is to detect the head of person exist by the Hough Transform method (Equation (1)) [2].

$$r^2 = (x_i - centreX)^2 + (Y_i - centreY)^2 \qquad (1)$$

After that, the brightness histogram of the circles detected and mask image above-mentioned are calculated. Additionally, to compare two histograms to decide who is the particular person (Table 3.).

5.2 Experiment for tracking a particular person

Firstly, input the image processed above. Secondly, it is to separate the people detected above and calculate the initial contour of this people. Thirdly, it is to track these people by Snakes method (Equation (2)).

$$E^*_{snake} = \int_0^1 E_{snake}(v(s))ds$$
$$= \int_0^1 E_{\text{int}}(v(s)) + E_{image}(v(s)) + E_{con}(v(s))ds \qquad (2)$$

Where E_{int} represent the internal energy of the spline due to bending, E_{image} gives rise to the image forces, and E_{con} gives rise to the external constraint forces [3].

When snakes failed, it returns to the beginning image, and tracks this people by Particle filter method (Table 4.).

Table 4. Track the particular target object

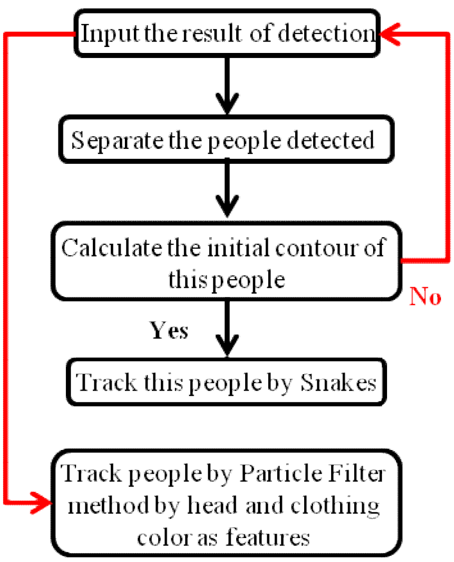

Particle Filters are usually used to estimate Bayesian models. The particle filter aims to estimate the sequence of hidden parameters, xk for k = 0,1,2,3,…, based only on the observed data yk for k = 0,1,2,3,…. All Bayesian estimates of xk follow from the posterior distribution p (xk | y0, y1… yk). In contrast, the MCMC or importance sampling approach would model the full posterior p(x0, x1… xk | y0, y1… yk) [4] [5].

5.3 Autonomous Control of Flying Robot

This part is to recognize landmark and be controlled by landmark. At first, the image is inputted. Secondly, it is to search the landmark, and then to detect the landmark. If landmark is detected successfully, the center is located, and horizontal angle is adjusted. Finally, flying robot draw nearer to object and to recognize it (Table 5.).

Table 5. The method of autonomous control

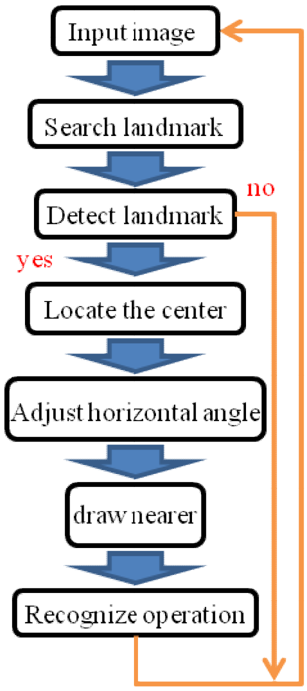

6 EXPERIMENTAL RESULTS

At first, the problem of height restriction is solved. There is a three meters height restriction on AR.Drone. In order to ensure the range of vision and be able to track the objects, this problem has to be noted. In addition, there are two cameras with AR.Drone. They are located at the bottom of AR.Drone and the front of AR.drone. In order to take the front image and bottom image, the problem with switching the camera has been solved (Fig.6.).

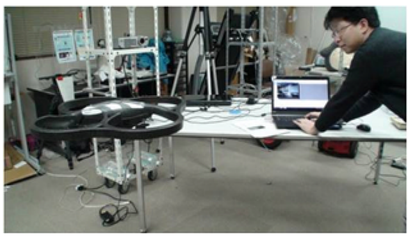

Fig.6. AR.Drone is controlled

6.1 Detect People by Flying Robot

Figure.7 shows the four blades helicopter as flying robot named AR.Drone is controlled by PC. In addition, automatic setting of the thresholds used in Hough Transform method has been achieved (Fig.7).

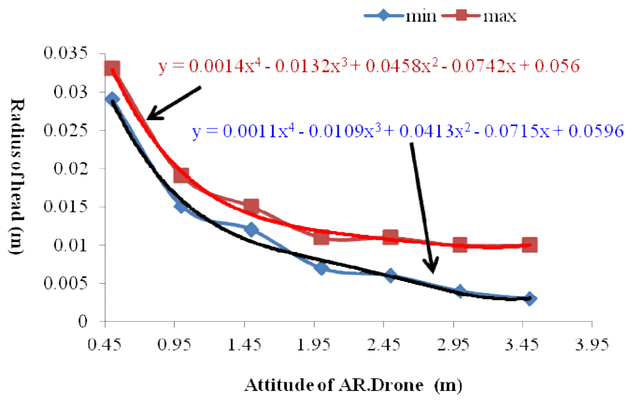

Fig.7. The Relation Between Attitude of AR.Drone and Radius of Head

It shows that particular person is detected by AR.Drone by Hough Transform method and Brightness Histogram method in Figure.8.

Fig.8. Detect person by Hough Transform and Brightness Histogram

The images on the top are without obstacle and the images on the bottom are with obstacle in the scene. Images on the left show people were detected and results are drawn by green rectangles. Images on the middle show results of edge extraction by the Sobel Operator. Images on the right show results of brightness histograms of head.

6.2 Track a Particular Person

The process of tracking person by Snakes method is shown in Figure.9. At first, the initial contour is decided and then parameters of Snakes are fixed by Equation (2) above-mentioned.

6.3 Results of Autonomous Control

Fig.10 is the result of autonomous control. Left image shows AR.Drone is controlled by red object, and right image shows it has detected red object successfully.

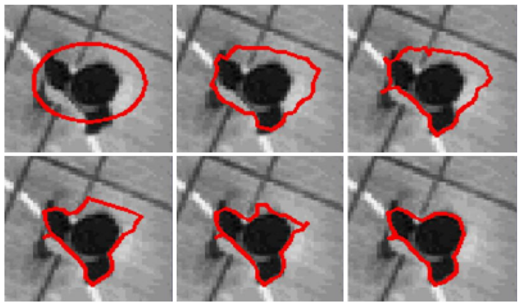

Fig.9. Tracking Process by Snakes Method

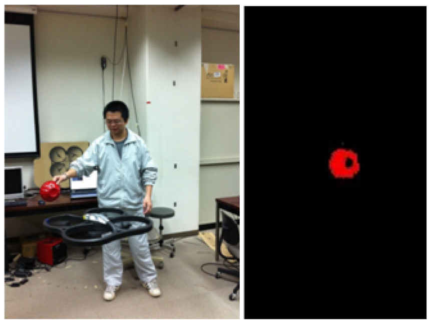

Fig.10. Red Object Recognition

7 CONCLUSION

The study is to detect and track the specific people. We hope that the flying robot is able to track the person by itself. Therefore, it is important to carry out autonomous control on flying robot. We also hope to achieve the aim that flying robot is able to detect and track target object automatically and help the people who wants to be helped.

REFERENCES

[1] Yusuke Itani and Hiroshi Watanabe, "A study on Object Detection in Complex Bankground", IEICE Technical Report PRMU 2006-179 (2006-12).

[2] D.H.Ballard,"Generalizing the Hough transform to detect arbitrary shapes", Volume: 13, Issue: 2, Publisher: Elsevier, Pages: 111-122, Pattern Recognition (1981).

[3] MICHAEL KASS, ANDREW WITKIN, and DEMETRI TERZOPOULOS, "Snakes: Active Contour Models", International Journal of Computer Vision, 321-331 (1988).

[4] A. Korah, J. P. Cances, G. Ferre and V. Meghdadi, "EQUALIZATION BASED ON PARTICLE FILTERING FOR MOBILE STATION RECEIVERS", 15th European Signal Processing Conference (EUSIPCO 2007), Poznan, Poland, September 3-7, 2007.

[5] MICHAEL ISARD AND ANDREW BLAKE, "CONDENSATION—Conditional Density Propagation for Visual Tracking", International Journal of Computer Vision 29(1), 5–28 (1998).

The Seventeenth International Symposium on Artificial Life and Robotics 2012 (AROB 17th '12),
B-Con Plaza, Beppu, Oita, Japan, January 19-21, 2012

Visual IMU in Manhattan-like Enviroments from 2.5D data

Sven Olufs[1] and Markus Vincze[1]

[1] Vienna University of Technology, Automation and Control Institute,
Gusshausstrasse 25-29 / E376, A-1040 Vienna, Austria
(olufs@ieee.org, vincze@acin.tuwien.ac.at)

Abstract: In this paper we presented a novel robust method for a visual IMU in manhattan-like environments i.e. the frequently observed dominance of three mutually orthogonal vanishing directions in man-made environments. Our approach is based on the idea of the separate estimation of the rotational and translational motion based on dense 3D and 2D features. We estimate the Manhattan-like structure by using an MSAC variant that estimates the Manhattan system directly from the 3D data. In contrast to other methods we use only the normal vectors of each voxel rather than estimating it indirectly using plane estimation. In a next step we estimate the translative motion of the robot relative to the Manhattan system using constrained visual odometry. Both rotational and translational motions are fused in a UKF. We show the robustness of our Manhattan-estimation using real world data. In this paper we demonstrate our approach using a Microsoft Kinect, while the approach will work with all kind of 2.5D sensors.

Keywords: Visual IMU, Manhattan-System, Computer Vision

1 INTRODUCTION

The domain of service robotics has become an important and fast growing market in the last decade. While service robotics has become more and more common in the industry domain they are still rare in the home robotics domain. Recent demographic developments in Europe and Japan have shown that there is a need for service robotics in everybody's home due to the elderly society phenomenon. With the home robotics domain we have usually a relative small area (e.g. 100m2), clutter and visually weakly structured environments. To cope with these environments, the use of 2.5D sensors has become quite popular in the last decade. With the recent release of Microsoft's Kinect sensor, the popularity of 2.5D sensors gained a boost. The Kinect sensor is suitable for the task for two reasons: The sensors are cheaper than laser scanners and its offers a depth image at frame rate. The challenge with data from 2.5D data is to cope with noise and uncertainty due to the nature of the sensors. For instance, the quality of 2.5D data from the Kinect depends on the reflection properties of the observed surface and the angle of incidence (assuming Lambert surfaces).

In this paper we propose a novel method to estimate the absolute rotation (namely roll, pitch and yaw) and relative translative motion from 2.5D data by exploiting partial Manhattan-like Geometry of an indoor environment. Manhattan-like structures are the frequently observed dominance of three mutually orthogonal vanishing directions in man-made environments. Many indoor environments can be considered as Manhattan-like since most walls of a room are aligned orthogonally to the ground or quasi Manhattan-like if the walls are not aligned orthogonally to each other. In many cases, furniture is also aligned Manhattan-like to its environment, e.g. a couch or cupboard can be aligned with a wall. Here we emphasize that it is not necessary that the furniture is aligned to all three major axes i.e. even if a table is not aligned to a wall its table surface is usually parallel to the ground.

The novelty of the paper is twofold: First an MSAC variant that directly estimates an Manhattan-system based on normal vectors. In this paper we use it to detect the dominant Manhattan system in the image. The second contribution is a geometric constrained visual odometry in combination with a UKF that exploits kinematic constrains of robot motion. The approach is efficient and robust to noise.

The paper is organized as follows: After a brief discussing on the state of the art, we describe in section 3.1 the proposed approach in two major parts: The first part describes the estimation of the Manhattan system within the 2.5D data. The second part (3.2) presents the constrained visual Odometry. Finally, we give the conclusion and results in section 4.

2 RELATED WORK

Visual odometry is a relative young area in the field of robotics. A poplar approach is the estimation using motion models (top-down). Davison et al. [1] proposed a method where a underlying motion model predicts the position of features to the next frame and updates it with a EKF. This idea was also used by Clipp et al.[2] by using multiple EKF filters or by [3] using more sophist aced features for tracking. Another idea is to use structure from motion techniques

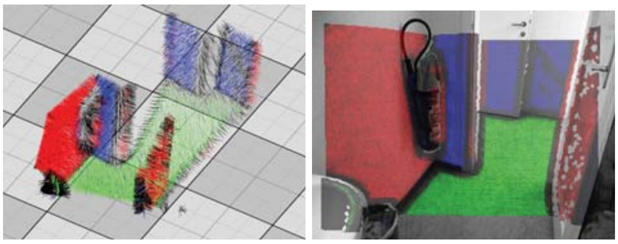

(a) Normal Vectors (b) Image

Figure 1: Estimated Manhattan System of a sample scene. The colors indicate the membership to one of the three major axis.

instead of EKF filter as proposed by Klein et al. [4] or only using spares bundle adjustment Konolige et al. [5] for pose refiement.

The use of the *Manhattan-World* assumption is quite popular in the computer vision literature, for instance, in the use of multi view-reconstruction [6, 7, 8]. Gallup et al. [6] use *Manhattan-World* assumption as prior for plane sweeping i.e. using only orthogonal planes. Furukawa et al. [8] use a similar approach for reconstructing piecewise planar patches and Markov random field formulation for exact planes. Sinha et al. [7] use a similar method, but with a less strict model. Gupta et al. [9] extend the idea by including not a-priory known kinematics on image structure.

3 OUR APPROACH

Our approach consist of three steps: First, we estimate the Manhattan-like structure by using an MSAC variant that estimates the Manhattan system directly from the 3D data. In contrast to other methods we use only the normal vectors of each voxel rather than estimating it indirectly using plane estimation. In a next step we estimate the translative motion of the robot relative to the Manhattan system using constrained visual odometry. Finally we combine both estimates with a unscented Kalman filter to reject implausible motions.

3.1 Manhattan System Estimation

We propose an approach using a variant of the well known Random Sample Consensus (RANSAC) techniques. RANSAC based methods obtain their estimate by randomly selecting coefficients from a given dataset to a known model. The estimation is iterative, in each iteration the number of inlier is counted. After a fixed number of iterations, the model with the most inlier is used as estimate.
The idea is to describe the Manhattan-world as three normal vectors $\vec{N}_1, \vec{N}_2, \vec{N}_3$ one for each axis. We use the normal vectors to express the *orientation* to an axis i.e. the vector is virtually aimed in both directions of the axis. We use a normal vector estimation based on integral images and is a good

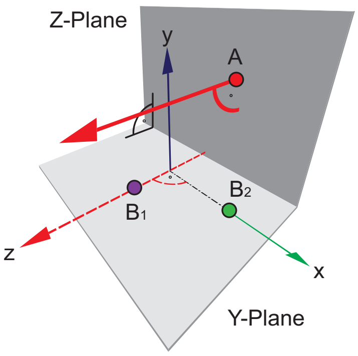

Figure 2: Estimating the Manhattan configuration using three normal vectors and RANSAC methods: A is used as seed for the Manhattan system for the first axis. B_1, B_2 are used to calculate the "roll" of the second axis and the third axis is redundant. Here we assume that A and B_1, B_2 do not share the same orientation plane of the Manhattan system, but that B_1, B_2 does.

trade off of runtime and quality. The normal vector of a voxel counts as an inlier, if the angle to one of the three axis normal vectors is within a certain threshold e.g. 5 degrees. The resulting angle is always between 0-90 degrees, since an axis does not have an orientation like a normal vector. The model is given as follows: Let $\vec{A}, \vec{B}_1, \vec{B}_2 \in V$ randomly selected voxels of the 2.5D grid and $\vec{a}, \vec{b}_1, \vec{b}_2$ its associated normal vectors. The three vectors are calculated with:

$$
\begin{aligned}
\vec{N}_1 &= \vec{a} \\
\vec{N}_2 &= \vec{B}_2 + \vec{a}((\vec{B}_1 - \vec{B}_2) \cdot \vec{a}) - \vec{B}_1 \\
\vec{N}_3 &= \vec{N}_1 \times \vec{N}_2
\end{aligned}
$$

The entire concept is depicted in figure 2: The overall assumption is that A is a point on a Manhattan-like structure for instance on the "Z-Plane". B_1 and B_2 are both on corresponding different Manhattan-like structure for instance the "Y-Plane" or "X-Plane". Since the Manhattan system is redundant to one axis, we only need to calculate two axes e.g. in figure 2 the x axis is redundant. The first vector is given by the normal vector of A itself. The second vector is obtained by shifting the first vector to B_1 and using B_2 as "roll" component. The third vector is the cross product of both previous vectors. This approach generates always a valid Manhattan system using three vectors. Note that we do not check in advance if e.g. B_1 and B_2 are on the same plane, since we have no prior information about planes in the 2.5D data at this step. Such "inplausible configurations" usually generate a Manhattan system with a significant less inliers than a "proper configuration" like in figure 2.

In practice we use MSAC [10] for estimation, an M-

Estimator RANSAC variant: Instead of counting inlier within a specific threshold, we accumulate the error of the model from the original data. The MSAC uses a threshold to specify a maximum error that a voxel belong to the model. Since we assume that we have one dominant Manhattan system we adapt this approach. The idea is to use an additional fixed error if an error exceeds the maximum error. In practice the additional fixed error is significant greater than the measured maximum error according to the threshold. This will raise the probability that the MASC will favor the dominant system rather than a valid random one as long the dominant one is also the largest one in the data. In our setup we use 5 degrees as threshold and 10 times as max constant error. Figure 1 shows an correct estimated Manhattan system.

3.2 Geometric Constratined Visual Odometry

The visual odometry is used to estimate the relative translative motion of the robot to the estimated Manhattan system since the rotation was already obtained on the previous step. We use standard KLT [11] features to track to estimate the motion in the 2.5d data. The tracking is done on the 2D grayscale image using the GPU within $> 1ms$ with Zach et al. [11] implementation. The depth estimation for each point is straight forward, we use the xyz coordinates from the depth data. The motion estimation is done with a one point RANSAC matching with known depth and known correspondence per point. One tracked point is chosen as model i.e. the relative motion of the point in 3D and the previous point while the roation is removed before. As with the standard RANSAC the solution with the most inliers in chosen and used for motion estimation, see figure 3. Only tracked KLT points with valid (non interpolated) depth are used. We use a maximum distance of 10cm for inliers and 50 iterations. The entire runtime for our visual odometry is $> 1ms$.

3.3 Data filtering with UKF

In a first step we track the rational movement and convert it to a angular motion speed for all three angles. The translational part is converted similar to translation speed. In order to cope with either homonymic and non-holonomic robot, we use a motion inertia model, in the fashion of Rao-Blackwellized particle filters [12]. We a central point of mass (like the center of the wheels) as center for all rotations and translational motions. We also assume that the robot is heavy and that a mass lays on top of the center point of mass to prevent that the robot jumpsy up and down in the estimation process. We decompose the six speeds into forces that push the center of mass, plus the gravity (or mass on top) on the center of mass point. Using this sevens force leads to that the UKF filters out implausible motions without expoliting the kinematics to much in detail. We use a straight forward uncended Kalman filter UKF for data fusion, as proposed in various literature e.g. [13]. We don't use an EKF due to it can easly get stuck in local minima, while UKF allows multiple hypothis in the uncended transformation.

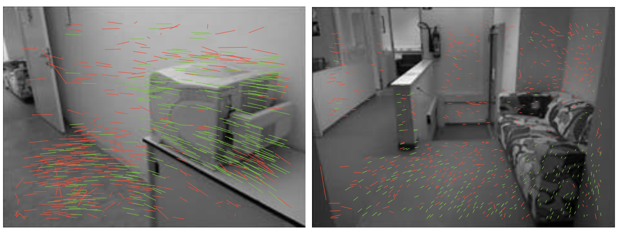

(a) Rotative Motion (b) Translative Motion

Figure 3: Visual Odometry using KLT features and RANSAC motion estimation. Outliers are shown in Red, Inliers in Green

4 CONCLUSION AND RESULTS

In this paper we presented a novel robust method for a visual IMU in manhattan-like environments. Our approach is based on the idea of the separate estimation of the rotational and translational motion based on dense 3D and spares 2D features. The proper estimation depends on the amount of visible structure of the Manhattan system within the 2.5D data. As long structure of two axis is visible a robust estimation is possible. As long as Manhattan structure of one axis is clearly visible in the image, its enough that the second axis is partially visible within the data i.e. at least 1 percent of the data. The use of normal vectors is efficient for Manhattan system estimation, but can be computational expensive. The use of integral image style normal vector estimation is a good trade off of runtime and quality and allows to use the entire data set rather than a sub sampled set. Our implementation of the constrained visual odometry is efficient and simple due to only the translative motion part remains.

The overall rotational error is less than 0.2degree, the relative translative error is less than 2mm within a travelling distance of 10m using a Microsoft Kinect. In contrast to other methods we obtain the absolute rotation to the environment instead of the relative rotation like with Visual SLAM. While our work uses the Kinects as sensor, it is also applyable to all kind of 2.5D sensors. We successful used our approach for mapping with a tilting laser scanner using only our visual IMU.

Experiments have shown that many home and office environments contains Manhattan like structure with all three axis. We want to emphasize that the minimal Manhattan system for our approach are two axis, which is very likely in the most indoor environments. That is usually the ground and a random wall which will be aligned orthogonal in most indoor cases. We figured out that this kind of condition does not hold true in some museums, for instance the Solomon R. Guggenheim Museum in New York.

We also find our Manhattan system estimation every useful in the combination with SLAM in indoor environments. Since our system eliminates to 99.8% the rotation from the data, SLAM has only to deal with the translational mapping error. First experiments with the gmapping package in willow garages Robot Operation System "ROS" have shown improved results with fewer misalignment scans. Due to that gmapping assumes an non-holonomic robot, we had to hack the code to support a psydo-holonomic one.
Our next steps is to relax the Manhattan constrains and to combine our method with SLAM with visual finger prints for place recognition.

ACKNOWLEDGMENT

The research leading to these results has received funding from the European Community's Seventh Framework Program (FP7/2011-2014) under grant agreement no FP7-ICT-2011-7 288146 (HOBBIT)

REFERENCES

[1] Andrew J. Davison, Ian Reid, Nicholas Molton, and Olivier Stasse. Monoslam: Real-time single camera slam. In *IEEE Transactions on Pattern Analysis and Machine Intelligence*, 2007.

[2] B. Clipp, Lim Jongwoo, J.-M. Frahm, and M. Pollefeys. Parallel, real-time visual slam. In *IEEE/RSJ International Conference on Intelligent Robots and Systems (IROS)*, 2010.

[3] D. Schleicher, L.M. Bergasa, R. Barea, E. Lopez, M. Ocaa, J. Nuevo, and P. Fernandez. Real-time stereo visual slam in large-scale environments based on sift fingerprints. In *IEEE International Symposium on Intelligent Signal Processing*, 2007.

[4] Georg Klein and David Murray. Parallel tracking and mapping for small AR workspaces. In *Proc. Sixth IEEE and ACM International Symposium on Mixed and Augmented Reality (ISMAR'07)*, 2007.

[5] Kurt Konolige, Giorgio Grisetti, Rainer Kummerle, Wolfram Burgard, and Benson Limketkai and Régis Vincent. Sparse pose adjustment for 2d mapping. In *IEEE/RSJ International Conference on Intelligent Robots and Systems (IROS)*, 2010.

[6] D. Gallup, J. Frahm, P. Mordohai, Q. Yang, and M. Pollefeys. Real-time plane-sweeping stereo with multiple sweeping directions. In *IEEE Conference on Computer Vision and Pattern Recognition (CVPR)*, 2007.

[7] S. Sinha, D. Steedly, and R. Szeliski. Piecewise planar stereo for image-based rendering. In *International Conference on Computer Vision (ICCV)*, 2009.

[8] Y. Furukawa, B. Curless, S. Seitz, and R. Szeliski. Manhattan-world stereo. In *IEEE Conference on Computer Vision and Pattern Recognition (CVPR)*, 2009.

[9] A. Gupta, A. A. Efros, and M. Hebert. Blocks world revisited: Image understanding using qualitative geometry and mechanics. In *European Conference on Computer Vision (ECCV)*, 2010.

[10] R. I. Hartley A. and Zisserman. *Multiple View Geometry in Computer Vision*. Cambridge University Press, ISBN: 0521540518, second edition, 2004.

[11] C. Zach, D. Gallup, and J.-M. Frahm. Fast gain-adaptive klt tracking on the gpu. In *CVPR Workshop on Visual Computer Vision on GPU's (CVGPU)*, 2008.

[12] Robert Sim and James J. Little. Autonomous vision-based exploration and mapping using hybrid maps and rao-blackwellised particle filters. In *IEEE/RSJ International Conference on Intelligent Robots and Systems (IROS)*, 2006.

[13] S. Thrun, W. Burgard, and D. Fox. *Probabilistic Robotics*. MIT Press, Cambridge MA, first edition, 2005.

Image texture analysis using second order statistical model

Shahera Hossain[1], Seiichi Serikawa[2]

Department of Electrical Engineering, Kyushu Institute of Technology
1-1 Sensui-cho, Tobata, Kitakyushu, 804-8550, Japan
(Tel: 81-80-3907-2228, Fax: 81-97-594-0181)

[1]shaherahossain@yahoo.com

Abstract: Image texture analysis is very crucial research topic for various vision-based applications. In this paper, robust gray-level co-occurrence matrix (GLCM)-based statistical model is explored and exploited for various image texture analysis. After demonstrating the model, experimental analyses are accomplished with datasets to demonstrate the performances of the statistical model. It illustrates that these statistical modules can be very much functional for image texture understanding.**.** Initially, we run our model in some ground-truth images covering few basic patterns, so that we can vividly compare the results on various images on datasets. The experimental dataset is the standard 'building surface dataset', where the experimental results relate the ground-truth data significantly.

Keywords: Co-occurrence matrix, GLCM, Texture analysis.

1 INTRODUCTION

Texture analysis is an attractive area of research because of its wide applicability in many fields. We can define texture as the surface of the objects. Several researchers define texture as a number of combined structurizing elements. Haralick et al. [7] assume texture as a spatial statistical distribution of gray pixels. We know that we can differentiate various image surfaces, objects, etc. A machine usually fails to identify an object based on its surface of similar patterns [10]. In these circumstances, identify complex surface using texture cue from a single image is an intricate problem [10]. In this paper, we explore statistical models for various image texture surfaces in order to develop a robust recognition and classification system. It is known that identification of similar objects under various real-world lightings is very challenging task for a machine/robot vision system. From the experimental results based on our analyzed statistical models, we achieve promising hypothesis by employing a benchmark dataset along with our ground truth dataset for in-depth analysis. To the best of our knowledge, these models in the building dataset along with ground truth analysis have not been undertaken by others.

Section 2 demonstrates some related works of this topic. Section 3 describes the statistical methodology exploiting the Gray Level Co-occurrence Matrix for texture analysis. Then, in Section 4, we illustrate some experimental results using a benchmark dataset. Finally, conclusion is presented in Section 5.

2 RELATED WORK

Texture analysis is very important research area in Machine vision system. Many researchers did their research based on different patterns of texture image. This research is very important for industry, medical experiment, and garments sector for automatic inspection of product. Texture analysis describes a variety of image-analysis techniques that quantify the variation in surface intensity or patterns, including some that are imperceptible to the human visual system. Quality control is important in textile industry. Texture analysis plays an important role in the automated visual inspection of texture images to detect their defects. For this purpose, Ozdemir *et al.* [1] did comparative experiment based on deferent textile sample. Model-based and feature-based methods are implemented and tested for textile images in a laboratory environment. Texture features, such as energy, entropy, contrast, homogeneity, and correlation, are then derived from the co-occurrence matrix. Several works have reported using co-occurrence matrices to detect defects, such as [2-7]. For example in [6], Iivarinen *et al.* applied co-occurrence texture features to detecting defects in paper web where the normal textures have characteristic frequency. Texture analysis is a valuable and adaptable implement in neuro-MR imaging. Texture analysis plays a encouraging role in the medical image interpretation. In some cases, however, statistical or spectral textural features have outperformed visual assessment in discriminating between or among intracranial tumors, as well as in discerning subtle anatomic changes associated with a high risk of seizures in patients with epilepsy.

3 METHOD

We explored the 2nd order statistics, called Gray Level Co-occurrence Matrix (GLCM). It is a way of extracting 2nd order statistical texture features. A GLCM is a matrix where the number of rows and columns is equal to the number of distinct gray levels or pixel values in the image of that surface. GLCM is a matrix that describes the frequency of one gray level appearing in a specified spatial linear relationship with another gray level within the area of investigation [11-12]. Fig. 1 shows the system flow diagram of this work.

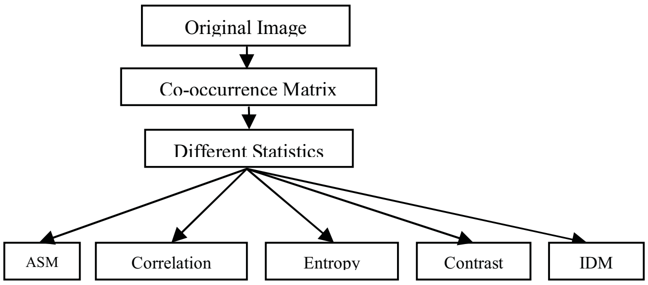

Fig. 1. System flow for this method.

In this paper, we exploit the Gray Level Co-occurrence Matrix (GLCM) for texture analysis. Given an image, each with an intensity, the GLCM is a tabulation of how often different combinations of gray levels co-occur in an image or image section. Texture feature calculations use the contents of the GLCM to give a measure of the variation in intensity (i.e., image texture) at the pixel of interest. Typically, the co-occurrence matrix is computed based on two parameters, which are the relative distance between the pixel pair *d* measured in pixel number and their relative orientation θ. Normally, θ is quantized in four directions (e.g., 0º, 45 º, 90 º and 135 º) [11-12], even though various other combinations could be possible. As our dataset is based on buildings – it is not necessary to explore all different angles. The other parameter *d* is also important. Based on our experiment, we consider *d* as 1. If we have an image that contains *N* gray levels from 0 to *N*–1, and if we consider *f*(*m*,*n*) is the intensity at sample *m*, line *n* of the neighborhood, then we can have the gray level co-occurrence matrix as,

$$p(i,j \mid \Delta x,\Delta y) = WQ(i,j \mid \Delta x,\Delta y) \tag{1}$$

where, $$W = \frac{1}{(M-\Delta x)(N-\Delta y)}$$

$$Q(i,j \mid \Delta x,\Delta y) = \sum_{n=1}^{N-\Delta y}\sum_{m=1}^{M-\Delta x} A$$

where,

$$A = \begin{cases} 1 & \text{if } f(m,n)=i \text{ and } f(m+\Delta x, n+\Delta y)=j \\ 0 & \text{otherwise} \end{cases}$$

The resultant texture images show the pixel-based spatial distribution of magnetic anomalies, associated with elements of subsurface structure, with much higher lateral resolution than the original magnetic images. In this paper, we consider seven different cues based on GLCM texture features. These features are – angular second moment (ASM), contrast, correlation, variance, inverse difference moment, sum entropy and information measures of correlation. The features are thoroughly promising [7].

Angular Second Moment (ASM):

$$ASM = \sum_{i=0}^{N-1}\sum_{j=0}^{N-1} p_{ij}^2 \tag{2}$$

It is also known as energy, uniformity, and uniformity of energy, returns the sum of squared elements in the GLCM. ASM ranges from 0.0 for an image with many classes and little clumping to 1.0 for an image with a single class.

Contrast:

$$Contrast = \sum_{i=0}^{N-1}\sum_{j=0}^{N-1} (i-j)^2 p_{ij} \tag{3}$$

It provides a measure of the intensity contrast between a pixel and its neighbor over the whole image. Contrast is also known as variance and inertia.

Correlation:

$$Corr = \sum_{i=0}^{N-1}\sum_{j=0}^{N-1} \frac{(i-\mu_i)(j-\mu_j)}{\sqrt{(\sigma_i^2)(\sigma_j^2)}} p_{ij} \tag{4}$$

It returns a measure of how correlated a pixel is to its neighbor over the whole image. We also explored *entropy*.

Entropy:

$$Entropy = -\sum_{i=0}^{N-1}\sum_{j=0}^{N-1} p_{ij} \times \log(p_{ij}) \tag{5}$$

It is a statistical measure of randomness that can be used to characterize the texture of the input image. We use he normalized GLCM as it is the joint probability occurrence of pixel pairs with a defined spatial relationship having gray level values of an image.

Inverse difference moment (IDM):

$$IDM = \sum_{i=0}^{N-1}\sum_{j=0}^{N-1} \frac{1}{1+(i-j)^2} p_{ij} \tag{6}$$

The inverse difference moment is another textural measure that attains a maximum value when all the image pixels that are compared have the same value, then yields a strong response at the central locations of the features of interest. IDM ranges from 0.0 for an image that is highly textured to 1.0 for an image that is untextured (such as an image with a single class).

4 EXPERIMENT AND RESULT

In this paper, we present a ground truth analysis for the GLCM-based image features. In Fig. 2, the ground-truth data contains 5 images – full white, strips in black and white – vertical direction and horizontal direction, gray, etc. This dataset shows comparative robust intuition of this concept. We cover different building images to analyze the statistical model features and some frames are shown in Fig. 3.

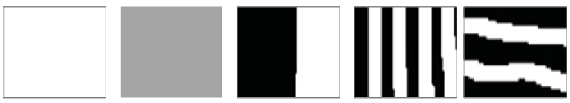

Fig.2 Ground-truth images.

Fig.3 Sample frames for the Building surface dataset.

In Fig. 4, we demonstrate the ASM. We can see that for bld-14, the ASM value is higher than others. We think that bld-14 has less texture elements and the pixels are very similar. The GT data for gt1 and gt2 has similar pattern with higher ASM value. Similarly, Fig. 5 shows contrast for ground-truth (GT) and building dataset. Similar to Fig. 4, it is evident that bld-14 has very less contrast. Contrast is zero when the neighboring pixels have constant values. The bld-6 has higher contrast values.

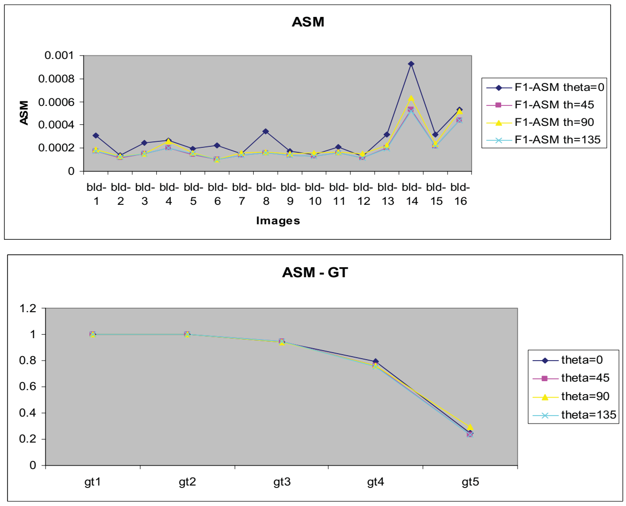

Fig.4 ASM for four angles with ground-truth (GT) and building dataset.

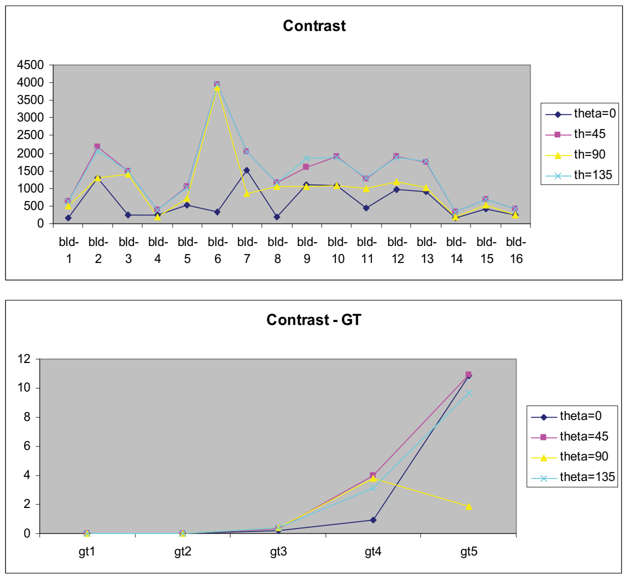

Fig.5 Contrasts evaluation for four angles.

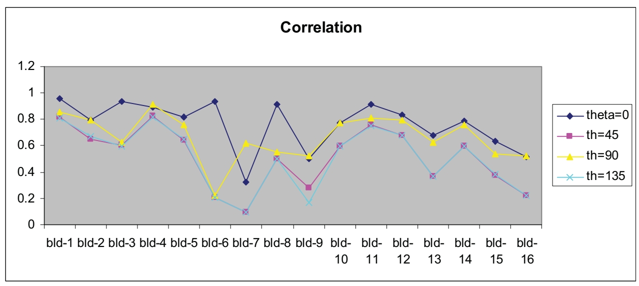

Fig.6 Correlation measures for four angles.

In Fig. 6, correlation measures are analyzed for the building surface dataset. Finally, the inverse difference moment (IDM) is computed as well for four angles for the ground-truth (GT) and building surface images. From the

GT graph in Fig. 7, it is visible that the IDM has higher value when all elements of the image are same. The bld-14 image has higher values for IDM and ASM.

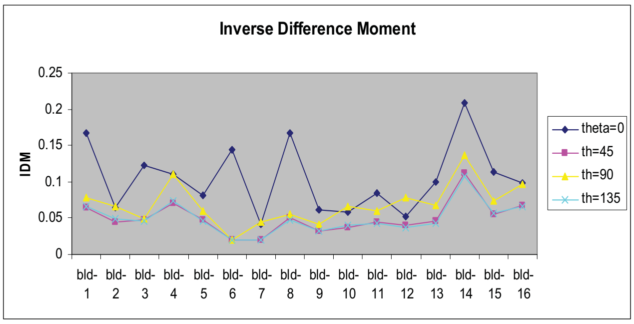

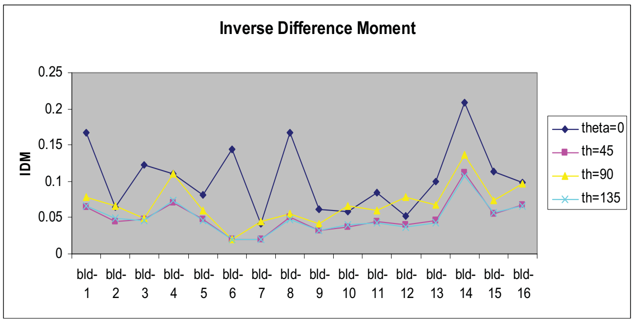

Fig.7 Graph for inverse difference moment.

5 CONCLUSIONS

In this paper, we explored image texture analysis, which is an important area for different real-life applications. Here, we exploited some of the robust gray-level co-occurrence matrix (GLCM)-based statistical measured for various image texture analyses. The gray-level co-occurrence matrix is a way of extracting 2nd order statistical texture features. In this paper, we computed and analyzed the angular second moment (ASM), correlation, contrast and inverse difference moment (IDM) based on the gray-level co-occurrence matrix. After demonstrating the model, we accomplished some experimental analyses by using a dataset to demonstrate the performances of the statistical model. It illustrates that these statistical modules can be very much functional for image texture understanding.. Initially, we ran our model in some ground-truth images covering few basic patterns, so that we can compare the results on various images on datasets. The experimental dataset is the standard 'building surface dataset', where the experimental results relate the ground-truth data significantly. In future, we will extract more features based on GLCM for texture analysis and evaluation, and we will classify various textures by employing classifiers. We will also analyze by using other datasets.

REFERENCES

[1] Ozdemir S, Baykut A, Meylani R, Ercil A, Ertuzun A (1998), Comparative evaluation of texture analysis algorithms for defect inspection of textile products. Int. Conf. on Pattern Recognition, pp.1738-1740.
[2] Bodnarova A, Williams J, Bennamoun M, Kubik K (1997), Optimal textural features for flaw detection in textile materials. IEEE TENCON, PP.307-310.
[3] Siew L, Hodgson R, Wood E (1998), Texture measures for carpet wear assessment. IEEE Trans. on Pattern Analysis and Machine Intelligence 10, pp.92-105.
[4] Iivarinen J, Rauhamaa J, Visa A (1996), Unsupervised segmentation of surface defects. Int. Conf. on Pattern Recognition, pp.356-360.
[5] Shiranita K, Miyajima T, Takiyama R (1998), Determination of meat quality by texture analysis. Pattern Recognition Letters, 19, pp.1319-1324.
[6] Iivarinen J (2000), Surface defect detection with histogram-based texture features. SPIE Intelligent Robots and Computer Vision XIX: Algorithms, Techniques, and Active Vision, pp.140-145.
[7] Haralick R, Shanmugam K, Dinstein I (1973), Textural features for image classification, IEEE Trans. on Systems, Man and Cybernetics, 3, pp.610-621.
[8] Latif-Amet L, Ertuzun A, Ercil A (2000), An efficient method for texture defect detection: Subband domain co-occurrence matrices. Image and Vision Computing, 18(6-7), pp.543-553.
[9] Kassner A, Thornhill R (2010), Texture analysis: a review of neurologic MR imaging applications, AM Journal Neuroradiol ,31, pp.809-16.
[10] Hossain S, Serikawa S (2010), Statistical analysis and psychological evaluation of surfaces under various illumination, Int. Journal of Applied Machines and Materials, 36, pp.422-429.
[11] Baraldi A, Parmiggiani F (1995), An investigation of the textural characteristics associated with GLCM matrix statistical parameters, IEEE Trans. on Geos. and Remote Sensing, 33(2), pp.293-304.
[12] Mokji1 M, Bakar S (2007), Gray level co-occurrence matrix computation based on Haar wavelet, Computer Graphics, Imaging and Visualisation.
[13] Adelson E (2008), Image statistics and surface perception, SPIE-IS&T Electronic Imaging, 6806, pp.1-9.
[14] Dror R, Willisky A, Edelson E (2004), Statistical characterization of real-world illumination, Journal of Vision, 4, pp.821-837.
[15] Koudelka M, Magda S, Belhumeur P, Kriegman D (2003), Acquisition, compression and synthesis of bidirectional texture functions, 3rd Int. Workshop on Texture Analysis and Synthesis.
[16] Sharan L, Li Y, Motoyoshi I, Nishida S, Adelson E (2008), Image statistics for surface reflectance perception, Journal of Optical Society America, 25(4).

Study on the development of the log scaling system based on the machine vision

Jiwu Wang [1], Weijie Gao [1], Fangbo Liao [1],and Sugisaka Masanori [2]

[1] Department of Mechanical and Electrical Engineering, Beijing Jiaotong University, Beijing, China, 100044
[2] Nippon Bunri University, Oita 870-0397, Japan

[1]jwwang@bjtu.edu.cn
[2] ms@alife-robotics.co.jp

Abstract: The conventional log scaling, which is measured with a ruler by manual operation in order to get higher precision, is carried on by more workers working hard for a longer time. With the new developed technique, it is possible to use the machine vision for the log scaling. In order to get satisfactory results for that scaling process, the distance between the log and camera should be measured accurately. At the same time, the environment conditions for image capture will be considered carefully. In this paper, the laser rangefinder is developed to determine the distance between the log and camera automatically. The log scaling based on the machine vision was developed, and its properties were tested with various experiments.

Keywords: Machine vision, Log scaling, Image processing

1 INTRODUCTION

Log scaling is the measurement of the gross and net volume of logs. The primary purpose of scaling is to determine the volume of logs that will be charged at a different price. For the conventional scaling, it is necessary to measure log diameters and lengths first, and some defects will be considered based on an approved set of rules. Generally, a given number of logs will be determined for the gross and net volume in that scaling process. Although there are many methods to scale the volume of a log, such as weight scaling that is frequently used on low value materials or when the weight difference is very small for the similar logs, most of the scaling still performed manually by measuring the diameter and length of the log with a tape measure. The working conditions and physical labor intensity can be improved, but most operations sometimes have to be done in the high places, hot or cold environments. If we can change the manual log scaling operation with some machine operation, the efficiency and accuracy will be improved.

In the railway freight, the logs before scaling are loaded in the carriage as shown in figure 1. Two or three bundles of logs are laid on each carriage with height about 4 meters. Their diameters are different in different carriages. For the big diameter log, there are about ten pieces of logs in each bundle. There will be more than twenty or thirty piece of logs in each bundle if the log diameter is smaller. No matter what type of the log diameter, the height of each bundle is nearly the same (about 4 meters high). Compared with the small diameter log scaling, the scaling is easier for the big diameter log. When a log will be scaling, both sides need be done and the smaller one will be chosen as the scaling result. If it is a small diameter log, it is difficult even to find both sides for that log in that bundle. Moreover, many workers have to climb to higher place to measure. Generally, more than 200 operators work at the same time more than 12 hours for a freight train. The scaling results will also be influenced by human factors etc.

1) Bigger diameter

2) Both bigger and smaller diameter

Figure 1 Illustration of logs with different diameters

Aimed at the various problems of manual log scaling, many researchers try to use machine visions to substitute manual scaling. Although some researchers have applied the image processing technique to the log scaling, the best operation will be the scaling process of machine vision that is the same as manual operation. Because many logs' interface can be taken in an image, we can scale more logs at the same time from one captured picture. If necessary, we can also scale the log one by one based on the machine vision technique. The scaling efficiency can be improved remarkably. Moreover, the captured images can be saved in a database for the systematic management. Certainly they can also be used as the certification for later application. There are many advantages for the machine vision scaling, but the scaling accuracy is determined by such as lighting conditions, video image quality, etc.

When we use machine vision for log scaling, the distance between camera and the log interface should be determined first. Then the log diameter of its interface can be calculated based on the camera focus and previous distance. Now the distance generally is determined with infrared sensors or ultrasonic sensors, etc. Because the distance is longer than the effective range of such sensors and there is a gap among the log interfaces, those sensors can not work robustly. The laser rangefinder sensor can satisfy our requirements, but it is generally expensive. In the machine vision scaling, the image processing technique is used to determine the geometric dimensions of measured objects. Therefore, we can also determine that distance based on the image processing with point laser.

For the manual scaling, workers can find the shortest interface diameter fast based on their experience. If we develop some algorithms of image processing, the process will be complicated and its result will not always be reliable. Because the computer is good at calculation, many diameters in different angles of each interface will be measured and the smallest will be selected as the final result. The experiments showed, it is possible to replace the manual scaling with the computer vision scaling.

1. 2

2 DISTANCE CALCULATION BASED ON IMAGE PROCESSING

For the machine vision scaling, the first step is to decide the distance between the camera and the measured log. Although there are many sensors can be used to get the distance, considering the working conditions, we will use the image processing technique to get that distance. The conventional distance calculation based on image processing should use two cameras. That technique is not appropriate to our applications. In order to get the distance, here a point laser is used.

The relationship between the camera and pint laser is shown in Figure 2. Here, we assume the camera view angle in width direction is λ_x , λ_y is in the height direction, the length between the lens center and laser center is L, the coordinates of the laser center in image plane is P(x,y), θ is the angle between the lens center line and the vertical line from camera center to the laser center line, the image dimension is 2w×2h. Thus we can get the angle β, which is the angle between the connection line from camera center to P(x,y) and the optical axis of the camera.

$\beta = \arctan(\tan(\lambda_y) * (y-h)/h$

Then the distance between the camera and the object point will be:

HY $= L * \tan(\theta - \beta)$

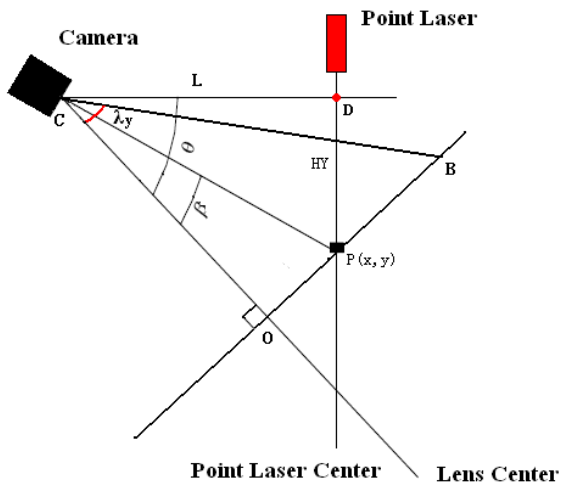

Figure 2 The illustration of distance calculation for image processing

Each paper size should be A4 size (210mm by 297mm). Write the paper in English.

3 EXPERIMENTS

In order to test the system whether it is appropriate for the application of the log scaling, the flowing experiments were carried out.

3.1 Experiments on the distance calculation based on image processing with point laser

If we want to proceed the log scaling based on the image processing, the first step is to get the distance between the camera and some target cross section. According to practical applications' requirements, the distance from 30cm to 300cm is tested.

In the experiment, seven groups of data were verified. We fixed the camera first, then marked seven points which are the distance of 30cm，45cm，85cm，100cm，150cm，300cm to the camera respectively. The test sample and point laser is shown in figure 3. The sample size is w0×h0=15mm×7.6mm. At each marked point, we will calculate the distance from camera to the sample. At the same time, we will also calculate the width and height respectively based on the distance gotten from image processing. Moreover, the relative error will be calculated. All results are listed in the table 1.

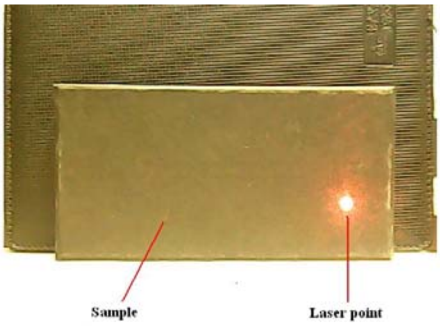

Figure 3 The illustration of the test sample and laser point

Table 1 The comparison between image processing and manual measurement (Unit: cm)

Manual d0	30	45	85	100	150	200	300
Camera d	29.93	44.34	84.16	98.60	146.49	193.54	285.29
(d-d0) /d0	-0.2%	-1.5%	-1%	-1.4%	-2.3%	-3.2%	-4.9%
Width w	14.81	14.75	14.64	14.53	14.91	15.06	14.68
(w-w0) /w0	-1.2%	-1.7%	-2.4%	-3.1%	-0.6%	0.4%	-2.1%
Height h	7.56	7.54	7.51	7.49	7.53	7.67	7.37
(h-h0) /h0	-0.5%	-0.8%	-1.2%	-1.4%	-0.9%	0.9%	-3%

Because the captured image size is 640×480pixels, the resolution is not high enough for objects far from the camera. When the object is put on the 300cm mark, the calculation accuracy of the distance, sample width and height is lower than the near marks to the camera. For our experiment camera, if the distance between camera and sample is controlled less than 100cm, we can get better calculation results based on the image processing. Although the results are also good for the distance from 100cm to 200cm, the edge points of the sample can not be extracted accurately.

3.2. Experiments on the log scaling based on image processing

In order to simulate the practical log scaling, the log cross sections are laid as shown in figure 4. First the distance between the camera and the log cross section is calculated based on the image processing, and its result is 84.76cm.The manual measurement is 85cm, and the relative error is 0.28%.

Figure 4 The illustration of log scaling experiment for distance calculation

The log scaling of the cross section is shown in figure 5. In order to get a more accurate calculation result, the whole cross section is divided equally by six angles, so six diameters can be calculated at the same time. In our experiment, the defect on the cross section will not be considered. Our experiment purpose is to verify the accuracy of the machine vision scaling. Each diameter is calculated based on two intersection points of each line. The initial length of each diameter is shown in the bottom of the figure 5, which are calculated only based on the coordinates on the image plane. When we consider the distance between the camera and log section, the real length will be calculated. The real length is shown in the right upper part of figure 6, which is transformed from the shortest one after the comparison among the above six calculation results. The manual result is 22cm. The image calculation result is 22.096cm, so the relative error is 0.4%. The manual result is also an approximate dimension.

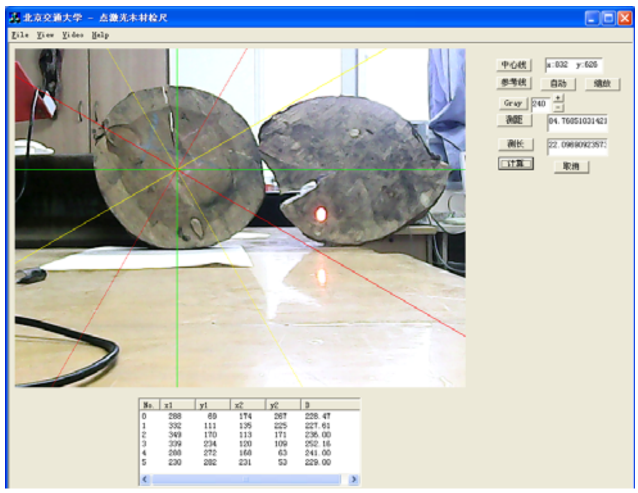

Figure 5 The illustration of the cross section scaling for left sample

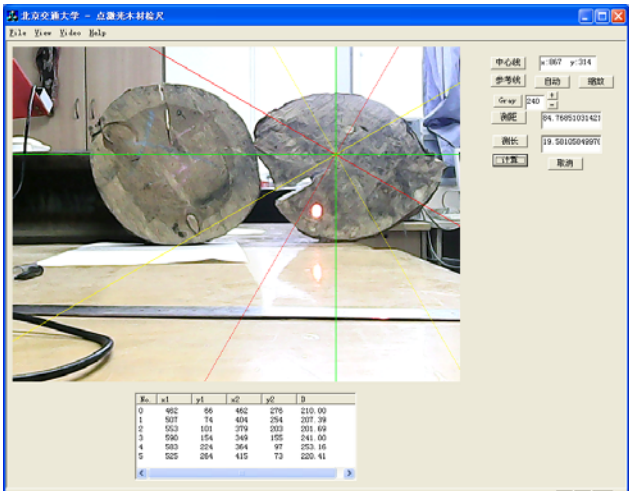

Figure 6 The illustration of the cross section scaling for right sample

In order to verify the machine vision scaling, another similar operation is done with another sample. The manual result is 20cm, and the image processing result is 19.58cm. The relative error is 2.1%. The big error is caused by the irregular cross section. It is difficult to get the shortest diameter by manual scaling.

4 CONCLUSIONS

According to the experiments on the distance calculation and log scaling based on the image processing, we can get following conclusions:

With our designed device, the distance between camera and target object can be calculated. If we want to get more accurate result, the distance can not be too far and the camera should have high resolution.

We can carry out the log scaling with machine vision. With this technique, the single log can be measured automatically, and multiple logs also can be measured in a same image. When we scale multiple logs in one image, their accuracy will be higher if their cross sections are in the same vertical plane. On the other hand, it is better to use camera with higher resolution.

REFERENCES

[1] Jiwu Wang, Weijie Gao, Yisong Wang, Study on the height measurement based on the image processing technique[J].Journal of AROB 16th,Japan January 27-29,2011.

[2] Diao Diandong, Zhai Tongxin, Influence on the wood market with log scaling of non national standard, Chengshi Jianshe Lilun Yanjiu, (Electrical version), 2011.No.18

[3] Chen Zhenfei, Precision analysis for double obser vation station of IRST systems used for passive ranging, Science Technology and Engineering, 2007.3.Vol. 7, No.5:842-844.

Arterial Hemodynamic Analysis on Non-enhanced Magnetic Resonance Angiogram Using Optical Flow

Akiyoshi Yamamoto, Hyoungseop Kim, Joo Kooi Tan and Seiji Ishikawa

Kyushu Institute of Technology, 1-1 Sensui, Tobata, Kitakyushu 804-8550, Japan
(Tel: +81-93-884-3185; Fax: +81-93-861-1159)
(Email address: kim@cntl.kyutech.ac.jp)

Abstract: Peripheral arterial disease (PAD) is caused to the lower extremity atherosclerotic disease. Its diagnosis is needed to obtain much kind of the information of vascular morphology as well as the blood flow information based on hemodynamics. The diagnosis of the PAD using magnetic resonance imaging (MRI) equipment without contrast medium is available as a useful visual screening in clinical practice. In this paper, we propose a novel method for visualizing hemodynamics to arterial images obtained by a non-contrast enhanced magnetic resonance angiography (MRA) based on the Lucas-Kanade optical flow with the image pyramid processing, and satisfied experimental results are obtained.

Keywords: PAD, non-enhanced MRA, Lucas-Kanade optical flow, image pyramid processing

I. INTRODUCTION

Peripheral arterial disease (PAD), also called peripheral vascular disease, is atherosclerosis of the lower extremities causing ischemia. Severe PAD usually requires angioplasty or surgical bypass and may require amputation. Prognosis of this disease is generally good for treatment, although mortality rate is relatively high because coronary artery or cerebrovascular disease often coexists. In order to perform endovascular treatment or surgery, it is necessary to understand the vascular morphology and hemodynamic. In other words, by tracking the amount of blood flowing into the tissue, the treatment strategy is determined for the symptom. In diagnostic imaging for the PAD, computed tomography angiography (CTA) and magnetic resonance angiography (MRA) has seen widespread acceptance as noninvasive vascular diagnosis. When CTA and MRA are performed, however, it is necessary to consider the side effects when using contrast agent and these images are mainly used to diagnosis vascular morphology. On the other hand, non-contrast enhanced MRA is a very useful imaging technique which is obtained by magnetic resonance imaging (MRI). It has various advantages, for example, the ability to provide vascular morphology and hemodynamic without contrast agents. Especially, fresh blood imaging (FBI) method is useful for a non-enhanced MRA to detect a variety of vascular diseases causes of the PAD [1, 2].

The FBI is an electrocardiogram gated non-contrast enhanced MRA technique, which employs arterial signal difference between systole and diastole during a cardiac cycle, i.e. subtraction of the diastolic bright-blood arteries from the systolic black-blood arteries allowed visualization of the arteries by cancelling the veins. According to this experiment, the FBI has some density information corresponding to the cardiac cycle, which may be closely related to blood flow. In other word, the hemodynamic can be expressed by imaging the MRI signal information related to the pulse wave using the image density information during the cardiac cycle phase [3]. Nevertheless, it is difficult to express the direction and the velocity of blood flow on the FBI by using only image density information. In the medical image processing field and computer vision, it is important to develop hemodynamic analysis system. In particular, the vascular systems in human organs are distributed throughout the body, which generates a large number of image data in a single examination. In order to observe blood flow in a wide area may be also required some software for playing a supporting role in diagnosis such as the CAD systems [4]. Many CAD systems have been developed to analyze the internal organs based on CT, and MRI on the medical field [5]. Despite many researchers have developed various image processing techniques for blood flow, the related research papers concerning these techniques are very small, for which MRI imaging technique to acquire the original image are difficult. In addition, since the density information of the image rely on the subjects, determining between the normal region and the noise is also difficult.

A new development of CAD system to visualize hemodynamic using optical flow analysis is presented in this paper. The arterial images are obtained from non-enhanced MRA technique.

II. PROPOSED METHODS

In this section we will present our proposed image preprocessing method for detecting hemodynamic on MR images. Fig.1 shows the procedure of the subtraction for FBI images as an illustration. The FBI image is depicted as white blood in the early-systolic

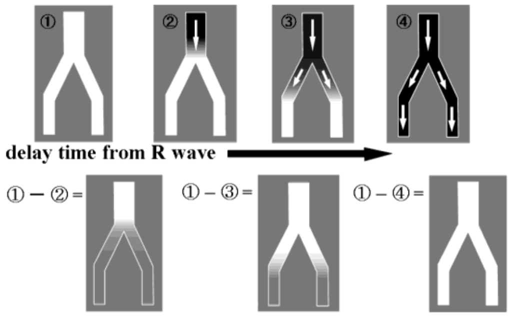

Fig. 1 A subtraction technique using successive MR images

Fig. 2 Examples of MIP images after subtraction

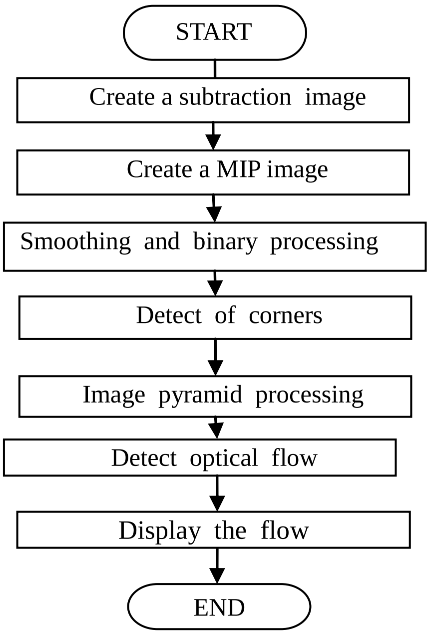

Fig. 3 Flow of procedure

phase, furthermore in the end-systolic phases; these images will become black blood as flows from the central to peripheral. From this result, these vessels are visualized such as angiogram by using subtraction technique as shown in Fig.1.

Fig. 2 gives examples of the maximum intensity projection (MIP) images obtained by the above method. A white area in Fig. 2 shows the blood vessel area. The outline of some image analyzing technique is shown below. Moreover, the overall scheme of the image processing techniques for tracking the region of blood vessels is illustrated in Fig. 3. The method consists of three main steps; detecting corners on the blood vessel region, feature tracking based on the Lucas-Kanade optical flow, and displaying the blood vessel. To acquire flow information on FBI images, some image processing techniques are introduced. In the first step, pre-processing technique such as smoothing and binarization are performed to reduce image noise, and then corners of features point are derived on these images. In the second step, using the Lucas-Kanade optical flow with an image pyramid processing to respond to rapid changes in the flow, velocity fields of the image are performed. In the third step, the estimated velocity vectors in the second step are depicted some arrows on the FBI images.

2.1 Detecting corners using Harris operator

Harris operator [6] is a method to derive feature points based on the correlation of image signal and the operator increase each correlation output value at the feature points of edges and corners. According to Schmid [7], this operator can be high repeatability to detect the points with the similar features. Even if the original image encounter these image transformations such as rotation and enlargement.

Given a point (x, y) and its shift (Δx, Δy), the weighted auto-correlation function is defined as,

$$E(x,y)=\sum_{W}\left[I(x_i,y_i)-I(x_i+\Delta x,y_i+\Delta y)\right]^2. \tag{2.1}$$

Where W is the weighting function. Here we applied the Gaussian function. $I(\Delta x_i,\ \Delta y_i)$ denotes the image function and (x_i, y_i) are the points in the window W centered on (x, y).The shifted image is approximated by a Taylor expansion truncated to the first order terms,

$$I(x_i+\Delta x,y_i+\Delta y)\approx I(x_i,y_i)+\left[I_x(x_i,y_i)I_y(x_i,y_i)\right]\begin{bmatrix}\Delta x\\ \Delta y\end{bmatrix} \tag{2.2}$$

In this study, auto-correlation matrix; $\boldsymbol{M}$, can be expressed as follows:

$$M=\begin{pmatrix}\sum w\left(I_x(x_i,y_i)\right)^2 & \sum wI_x(x_i,y_i)I_y(x_i,y_i)\\ \sum wI_x(x_i,y_i)I_y(x_i,y_i) & \sum w\left(I_y(x_i,y_i)\right)^2\end{pmatrix} \tag{2.3}$$

This can be expressed as the following

$$E(x,y)=(\Delta x,\Delta y)M(\Delta x,\Delta y)^T. \tag{2.4}$$

Two eigenvalues of this matrix $\boldsymbol{M}$ ($\lambda 1$, $\lambda 2$) said that while the highest corner. We use the following formula R rating in order to reduce the computational cost.

$$R=\lambda 1\lambda 2-k(\lambda 1+\lambda 2)=Det(M)-k(TraceM)^2 \tag{2.5}$$

However, when the curvature is k=0.06, there is a feature point (R>0). Feature points of corners with these procedures are utilized for the following optical flow analysis.

2.2 Lucas-Kanade optical flow method for detecting the feature points

The optical flow is a method to detect the motion of the object by determining a flow vector which calculated the velocity of the image from a continuous image sequence in time. The gradient method, optical flow estimation, is calculated motion vectors based on the equation relating the temporal gradient of local characters on the image and a spatial gradient. A basic constraint equation in the gradient method is based on th e condition that the pixel value of any point is no changed when the subject has moved. The equation is calculated as follows. The initial hypothesis in measuring image motion is that the intensity structures of local time-varying image regions are approximately constant under motion for at least a short duration [8]. Formally, if $I(x,y,t)$ is the image intensity function,

$$I(x,y,t) = I(x+\Delta x, y+\Delta y, t+\Delta t) \tag{2.6}$$

where (Δx, Δy) is the displacement of the local image region at $I(x,y,t)$ after time(Δt). Expanding the left-hand side of this equation in Taylor series yields

$$I(x+\Delta x, y+\Delta y, t+\Delta t) = I(x,y,t) + \Delta x\frac{\partial I}{\partial x} + \Delta y\frac{\partial I}{\partial y} + \Delta t\frac{\partial I}{\partial t} + \varepsilon \tag{2.7}$$

where $I_x = \frac{\partial I}{\partial x}, I_y = \frac{\partial I}{\partial y}$ and $I_t = \frac{\partial I}{\partial t}$ are the 1st order partial derivatives of $I(x,y,t)$ and ε. The 2nd and higher order terms are assumed negligible. Subtracting I = (x, y,t) on both sides, ignoring ε and dividing by Δt yields

$$I_x u + I_y v + I_t = 0 \tag{2.8}$$

Where I_x, I_y and I_t are spatio-temporal intensity derivatives and (u, v) is the image velocity. Equation (2.8) is known as the optical flow constraint equation and defines a single local constraint on image motion. However this constraint is not sufficient to compute both components of (u, v) as the optical flow constraint equation is ill-posed because of the reason such as the aperture problem. For this reason, the second constraint condition is added.

In Lucas and Kanade method the second constraint condition is that assume the neighborhood pixels in a small region have the same flow vectors. Under this assumption, the following equation for the k-th pixel is given by

$$I_{xk} u + I_{yk} u = -I_t k \cdot \tag{2.9}$$

The simultaneous equation is solved at a ($n \times n$) pixel of this neighborhood region. A solution of this simultaneous equation is obtained by using weighted least-squares. In order to estimate the optical flow, the window function (5×5) is performed.

2.3 Optical flow analysis using image pyramid

The blood flow in the human body often appears a small motion as well as a large motion in some vessel regions. The Lucas-Kanade optical flow is assumed to be as small and coherent motions; therefore, a large window will be required to detect large motions such as the blood flow. In the case of large and noncoherent motions, however, the large window would break the coherent motion assumption easily. We employed image pyramid to mitigate the problems caused by breaking the assumptions. When a pyramid-shaped a hierarchical structure is created by reducing the original image successively, the image moves accordingly decreases based on these image sizes. The feature points between images in a larger spatial scale with the optical flow are estimated initially, these feature points are then used as initial values between images at the following layer. Since these processes are iterated until the size of the original image, the reliability of the rapid changes in estimated flow is improved.

III. EXPERIMENTAL RESULTS

To acquire blood flow information, we applied automatically proposed method to MRA images obtained by FBI method. Image size is 256 x 256 [pixels] and the image set consists of 60 to 80 slices images per case. Visualizing hemodynamics for the blood flow is performed by utilizing L-K optical flow with the image pyramid processing in order to respond to rapid changes of blood flow. 8 cases experimental results on flow processing, displaying the flow vectors, are shown that the proposed method performed well. The results of the optical flow vectors processing in cardiac cycle are shown in Fig. 4(a), 4(b), and 4(c), respectively.

The flow vectors are generated from the abdominal artery near the heart, and these vectors are viewed as a movement from the external artery to the femoral artery over time. It was possible to display the flow vectors comparable to some antegrade arterial blood flow from the abdominal aorta to the femoral vessels in all cases.

Overall the performance for these flow detection results are evaluated by tested a statistically significant differences between each cardiac cycle times that are detected first moment at the femoral artery and are most often detected flow vectors. An example of a graph measured the velocity of the cardiac cycle in the femoral artery with a velocity measurement method by using MRA technique called the phase shift (PS) is shown in Fig. 5. The results of the cardiac cycle time obtained from the respective first moment obtained by the results of Fig. 5 are shown in Table 1. The result counted the number of vectors at the first moment in the ROI set in the femoral artery. The analysis results of cardiac cycle time obtained from the respective first moment and the cardiac cycle time of the maximum count number are shown in Table 2, respectively.

(a) (b) (c)

Fig. 4 Results of optical flow

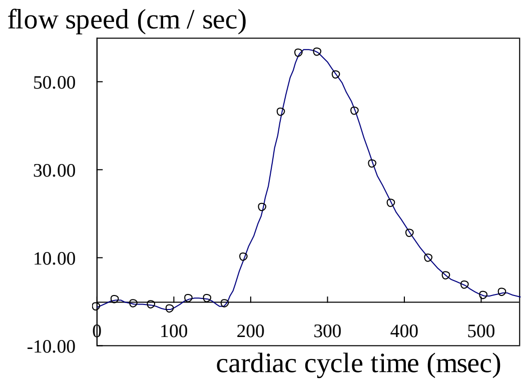

Fig. 5 An example of flow speed measurement using PS

Table 1 Result of calculated times at the first moment to each subject of 8 cases

Subject	First moment (msec)
A	170
B	170
C	155
D	165
E	165
F	160
G	155
H	155

Table 2 Results of cardiac cycle time of 8cases

Subject	maximum count (msec)	first moment (msec)
A	150	170
B	180	170
C	180	155
D	150	165
E	180	165
F	150	160
G	150	155
H	180	155

Based on these results, a significant difference test was performed by Mann-Whitney U test. The results of the analysis of the eight samples are $p = 0.39$ ($p> 0.05$), and there were no statistically significant differences between two groups.

IV. DISCUSSION AND CONCLUSIONS

In this paper, we developed a CAD system to visualize the hemodynamic using arterial images which are obtained from a non-enhanced MRA technique. Due to employ the ideas of subtraction technique between images, after pre-processing such as smoothing and Binarization, a good performance was obtained by using corner detection and analysis of optical flow. From the Table 2, since there were no statistically significant differences between the times of cardiac cycle detected the maximum number of the flow vectors and the time at each first moment of the blood flow, it may be considered that the flow vectors are able to show blood flow in the human body. Therefore, this correlation is considered that the flow vectors indicate a first motion of blood flow in the cardiac cycle. Although, the flow vectors do not necessarily indicate reflection for the speed of blood flow and blood volume. The first motion of blood flow reflects a pulse wave of the blood ejected from the heart. It is predictable from these discussions that the flow vectors obtained by optical flow analysis on the non-enhanced MR angiography images are able to estimate blood flow indirectly.

In order to set the threshold value based on the experience for binarization processing to process image noise, however, it should always be considered a risk that the detection rate of flow depend on the quality of original image. For these reasons, it is necessary to develop a flow detection algorithm without depending on the quality of the original image.

REFERENCES

[1] K. Nakamura, M. Miyazaki, K. Kuroki, A. Yamamoto: "Noncontrast-enhanced peripheral MRA: Technical optimization of flow-spoiled fresh blood imaging for screening peripheral arterial diseases", Magnetic Resonance in Medicine, Vol.65, pp.595–602, 2011.

[2] Miyazaki M, Lee S Lee: "Nonenhanced MR Angiography, Radiology", 248, pp.20-43, 2008.

[3] A. Yamamoto, K. Nakamura, M. Miyazaki, Y. Shioya, S. Kawanami, Y. Matsufuji: "Non-contrast-enhanced MRDSA of peripheral arteries using continuous acquisitions of ECG-Triggered 2D half-Fourier FSE within a cardiac cycle", Proc. International Society of Magnetic Resonance in Medicine, Vol.11, pp.1709, 2003.

[4] J. M. Fitzpatrick, D. L. G. Hill, Y. Shyr et al.: "Visual Assessment of the Accuracy of Retrospective Registration of MR and CT Images of the Brain", IEEE Trans. Med. Imaging, Vol.17, No. 4, pp.517-585, 1998.

[5] S. Busayarat, T. Zrimec: "Detection of bronchopulmonary segments on high-resolution CT preliminary results", IEEE International Symposium on Computer-Based Medical Systems, pp.199-204, 2007.

[6] C. Harris and M. Stephens: A Combined Corner and Edge Detector, Proc. 14th AlveyVision Conference, pp.147-151, 1988.

[7] C. Schmid, R. Mohr, and C. Bauckhage. "Comparing and evaluating interest points." International Conference on Computer Vision, pp. 230-135, 1998.

[8]Lucas, B., and Kanade, T.: "An Iterative Image Regis tration Technique with an Application to Stereo Visio n", Proceedings of the Seventh International Joint Co nference on Artificial intelligence, pp. 674-679, 1981.

The Seventeenth International Symposium on Artificial Life and Robotics 2012 (AROB 17th '12),
B-Con Plaza, Beppu, Oita, Japan, January 19-21, 2012

Reinforcement learning with phased approach for fast learning

Norifumi Hodohara, Yuichi Murakami, Shingo Nakamura and Shuji Hashimoto

Waseda University, Tokyo, 169-8555, Japan
(Tel: 81-3-5286-3233, Fax: 81-3-3202-7523)

nhodohara@shalab.phys.waseda.ac.jp

Abstract: In this paper we consider the reduction of the computational cost of reinforcement learning. When we apply the reinforcement learning to a robot with a large number of DOF, it needs a tremendous amount of time for learning because of the large state space. This problem is called "the curse of dimensionality". To solve the problem, we propose a phased approach on reinforcement learning. In the proposed method, we apply reinforcement learning to a robot with limited DOF at first, then release the restriction and resume the learning from the previous learning result. The computer simulation using arm robots having four and five joints proved the effectiveness of the proposed method. We also conducted an experiment in the case that an obstacle exists around the arm.

Keywords: Arm Robot, Reinforcement Learning, Phased Learning, Q-Learning.

1 INTRODUCTION

In recent years, robots have been expected to work not only in structured environments like factories, but also in different unstructured environments. The reinforcement learning [1], which is able to make robots acquire objective behaviors by themselves, attracts attention as a method to avoid the difficulty of programing of robot behavior in such environments. However, the reinforcement learning has a big problem called "the curse of dimensionality". This means that learning cost gets huge with increased DOF of the robot because the robot's state space exponentially expands.

Previously, some researchers have used the reinforcement learning for a robot with a number of DOF. They have manually given the environmental information to the robot to make the state space as small as possible [2][3]. However, it is workable only under the special conditions, and it is inevitable that learning time must be lengthened when large amount of information to solve a problem is not given in advance.

In this research, we attempt to reduce the learning cost by introducing a phased procedure in applying to a robot with a number of DOF. In this approach, the reinforcement learning is applied to the robot with the limited DOF beforehand, which can reduce the learning cost because the scope of state space gets narrower. Then we release the limitation of the robot's motion and restart the reinforcement learning with the state value of the previous learning result. In this way we expect that the robot learns objective task faster than the standard reinforcement learning starts with the full DOF from the beginning. In this paper, we call the first phase learning "previous learning" and final phase learning "eventual learning". To confirm the feasibility of the proposed method, we applied it to arm robots having four and five joints in the computer simulation. We also experimented in the environment with an obstacle.

2 PROPOSED METHOD

2.1 Reinforcement Learning

In this research, we use the Q-learning, the typical algorithm of reinforcement learning. Here, we briefly introduce the method.

When the agent at step t takes the action a_t based on its current state s_t, the state-action value function $Q(s_t, a_t)$ is updated as follows:

$$Q(s_t, a_t) \leftarrow Q(s_t, a_t) + \alpha[r_{t+1} + \gamma \max_a Q(s_{t+1}, a) - Q(s_t, a_t)] \quad (1)$$

where r_t is the reward the agent receives at step t, α is a learning rate and γ is a discount rate.

We employ the Radial Basis Function (RBF) network [4] for the approximation of the state-action value function. Thereby, Q-values are treated as a continuous function and neighboring state-action values are related in the value space. We use the Gaussian distribution as the RBF and place them in the value space divided into segments uniformly. Therefore, the approximated state-action value function is given by:

$$Q_a(\boldsymbol{s}) = \sum_j w(\boldsymbol{\mu}_j) \exp\left[-\frac{|\boldsymbol{s} - \boldsymbol{\mu}_j|^2}{\sigma^2}\right] \quad (2)$$

where w, $\boldsymbol{\mu}$ and σ^2 are the weight, the average and the variance of the RBF network. The weight w is updated as Q_a gets close to right-side value of (1).

2.2 Phased Approach

Here, we assume that an agent takes two-dimensional state $\boldsymbol{s}=(s_1, s_2)$ for explanation, and introduce an outline of the phased approach, the proposed method in this study. At first, the agent learns with a restricted dimension of state $\boldsymbol{s}$ in the previous learning phase. In this case, s_1 is fixed at constant value s_1', and the agent learns only with variable s_2 as shown in **Fig. 1.** (a). Thereby, the learning cost is reduced because it allows the agent to explore narrow area of the entire state space. However, the learning result exists in the only limited region of the space. Next, we spread out the resultant state value into the whole state space by using the Gaussian distribution function as follows:

$$w(s_1, s_2) = c \cdot w(s_1', s_2) \exp\left[-\frac{(s_1 - s_1')^2}{{\sigma_s}^2}\right] \qquad (3)$$

where ${\sigma_s}^2$ is the variance of the Gaussian and c is the constant for adjusting an effect of the previous learning. The weight of the RBF network w spreads in a direction toward s_1-axis as shown in **Fig. 1.** (b). Finally, after releasing the limitation of state $\boldsymbol{s}$, the agent restarts learning from the expanded result and acquires an optimal behavior in the eventual learning phase.

In this way, we expect that the agent learns objective task faster than simply learns the whole value space from the beginning. This approach can be expanded to the more dimensional cases.

3 ARM ROBOT

Here we introduce an arm robot with multiple joints for the experimentation. The robot is implemented with Open Dynamics Engine (ODE), the free library for simulating physical dynamics. **Fig. 2.** (a) shows the arm robot with four joints and environment created by the ODE. The joints rotate around the z-axis, therefore robot moves only in the xy-plane. Each link can overlap other links. The whole length of the robot is constant regardless of the number of joints and each link length is the same.

As shown in **Fig. 2.** (b), a movable range of the each joint is from -150 to 150 degrees, and each joint rotates 30 degrees clockwise or counter-clockwise in one step. The first joint from the root adopts absolute angle and the other joints adopt relative angle. The agent action a is defined to rotate any one of joints in 30 degrees. The state $\boldsymbol{s}$ is defined as a combination of respective joint angles, thus the number of all the states is 11^n, where the n is the number of joints.

4 EXPERIMENTS

4.1 Experimental setup

We examined both the proposed method and the standard reinforcement learning with the arm robot for comparison. In the experiments of the proposed method, the agent learned with some fixed joints in the previous learning phase as shown in **Fig. 3.** (a). Then, as shown in **Fig. 3.** (b), the agent learned again by using all the joints starting with the value space expanded from the previous learning result as the eventual learning. Meanwhile, the agent began learning with all the joints in the standard reinforcement learning. Both of the methods employed the Q-learning approximated by RBF network.

The robot's task was to reach a target with its tip. The agent received a reward only when the robot accomplished its task. On the other hand, the agent paid a penalty when the robot touched an obstacle. There were two experimental environments; with and without an obstacle. The robot having 2 joints cannot reach the target when the obstacle exists. The robot restarted from an initial position when it reached the task or touched the obstacle. If the obstacle existed, the initial position took the other side of the target across the obstacle. If it didn't exist, the initial position was took randomly.

In the Q-learning, the agent updated its state-action value $Q(s, a)$ at each step. One episode was defined as the robot reaching the target once. However, if the agent

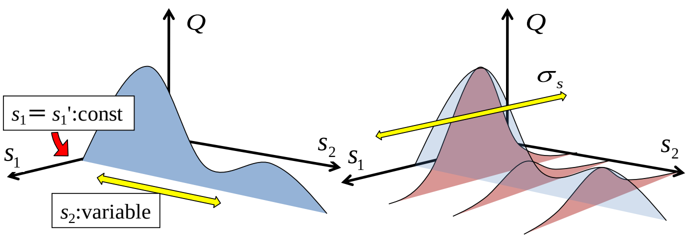

(a) Previous learning (b) Value spreading

Fig. 1. The outline of the phased learning.

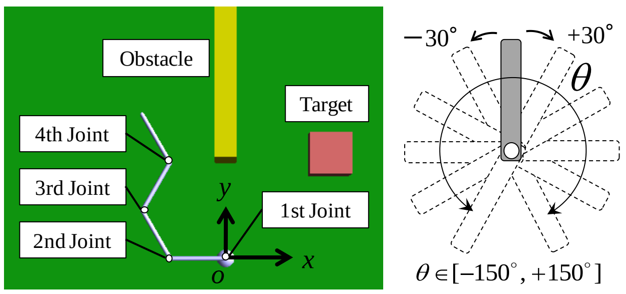

(a) The robot having four joints (b) The movable range

Fig. 2. The arm robot simulated by ODE.

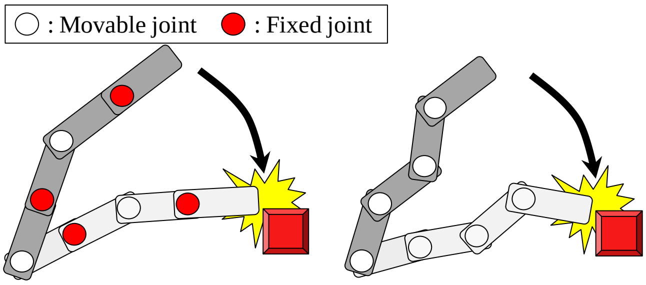

(a) Fixing a part of the joints (b) Moving the all joints

Fig. 3. Applying the proposed method to the arm robot.

couldn't accomplish the task until $N_{\max}$ steps, the next episode started from another initial position. We employed the softmax function as a policy of the agent as follows:

$$\pi(s,a) = \frac{\exp(Q(s,a)/T_B)}{\sum_b \exp(Q(s,b)/T_B)} \tag{6}$$

where $\pi(s, a)$ is the probability distribution of taking the action a based on the state s and T_B is the Boltzmann temperature.

4.2 Configuration

We conducted three experiments to compare the proposed method with the standard reinforcement learning. In the first experiment, we applied our method to the arm robot with four joints in the environment without an obstacle. The agent learned under the condition with fixing the 2nd and 4th joints as the previous learning. Then, the agent restarted the learning as the eventual learning. In the same way, we conducted another two cases: fixing 1st and 3rd joints, and 2nd and 3rd joints. In the second experiment, we utilized the arm robot with five joints without an obstacle. As the previous learning, the agent learned with the robot fixed the 2nd, 4th and 5th joints. In the third experiment, we applied the proposed method to the arm robot with four joints in the environment with an obstacle. The previous learning was conducted with fixing 2nd and 4th joints without the obstacle. The agent then learned with the obstacle in the eventual learning phase. We compared the learning cost of our method with the cost of the standard reinforcement learning.

In each experiment, the agent learned during 50 episodes as the previous learning. The shapes and locations of the target and the obstacle are shown in **Table 1**. The values of these lengths were based on the condition that the whole length of the arm robot was 1 and the origin position was placed at the root of the arm robot. In the Q-learning, a values of the reward and penalty were 1 and -1, and $N_{\max}$ was set to 10,000. The RBFs variance σ^2 equaled 0.01 in the value space divided into 11^n segments. **Table 2.** shows the detail of the other experimental parameters. These parameters were determined empirically by exploratory experiments.

Table 1. The shapes and locations of the target

	Shape	x area	y area
Target	0.20×0.20 Square	[0.40, 0.60]	[0.40, 0.60]
Obstacle	0.10×0.55 Rectangle	[-0.05, 0.05]	[0.45, 1.00]

Table 2. The experimental parameters

	α	γ	T_B	σ_S	c
Previous learning	0.4	0.6	0.005	-	-
4 joints	0.5	0.6	0.005	0.2	0.5
5 joints	0.4	0.8	0.005	0.2	0.1
4 joints with obstacle	0.4	0.8	0.005	0.3	0.2

5 REUSLTS

Fig. 4. shows the step cost of reaching the target at each episode number of each experiments. **Fig. 5.** shows the total cost of steps until the 50th episode finished. The every resultant value is an average of the 100 times experiments.

As shown in **Fig. 4.**, the agent with the proposed method learned the tasks with less steps in all the experiments. Thus the feasibility of the proposed method is confirmed regardless of fixed joints or the number of joints. The eventual learning resultant of our method shows the slow convergence speed in **Fig. 4. (c)**. It is considered that the value around the obstacle which built in the previous learning interrupted the robot to reach the goal target.

As shown in **Fig. 5.**, the number of total steps with phased learning was less than the standard reinforcement learning in all the experiments. Especially, **Fig. 5. (c)** shows higher reduction ratio of total steps than when no obstacle exists. It represented that our proposed method is more efficient in complex environment.

6 CONCLUSION

We have developed an algorithm of reinforcement learning, phased learning. In this method, an agent learned with limited robot's DOF in the previous learning phase. The proposed method allows robots having a number of DOF to learn tasks efficiently. The conducted experiments with arm robots having four and five joints proved the feasibility of the proposed method. However, in the experiment with an obstacle, the proposed method converged slower than standard method. We need to research in detail how the resultant of previous learning affects the eventual learning for further improvement.

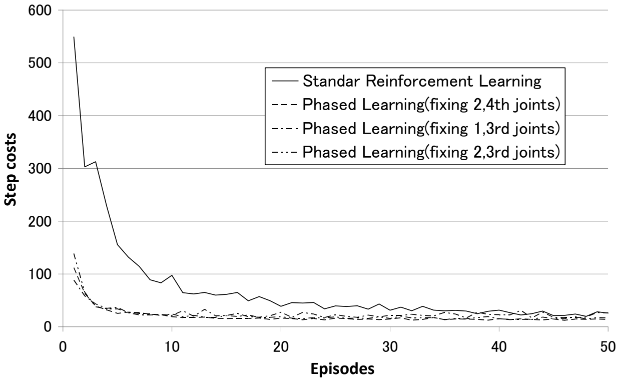

(a)Result on four joints arm robot

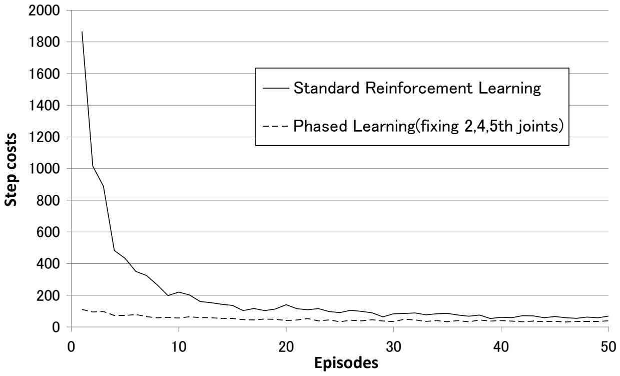

(b)Result on five joints arm robot

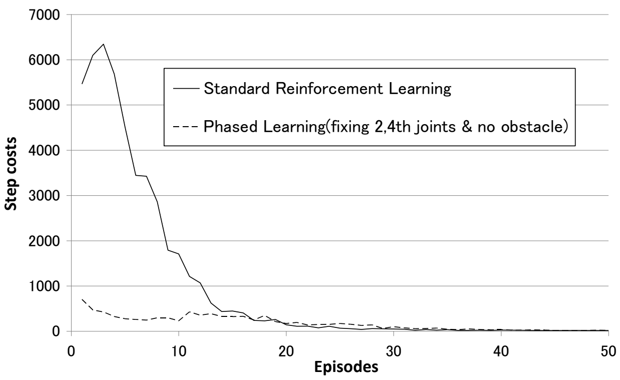

(c)Result on four joints arm robot with an obstacle

Fig. 4. Step costs as a function of episodes.

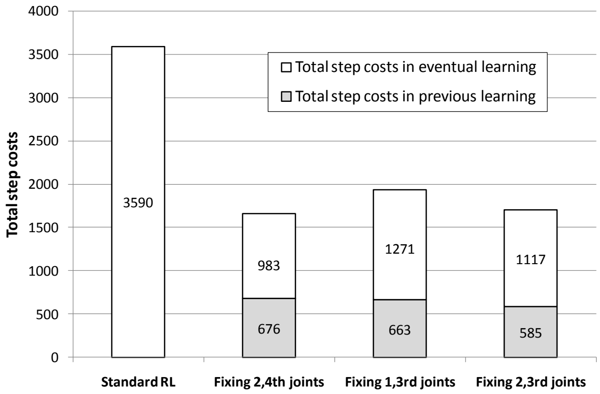

(a) Result on four joints arm robot

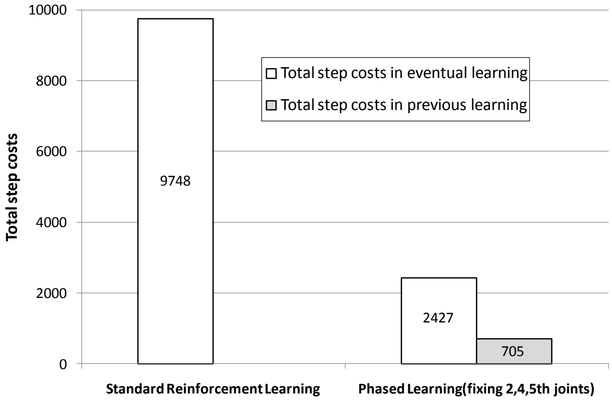

(b) Result on five joints arm robot

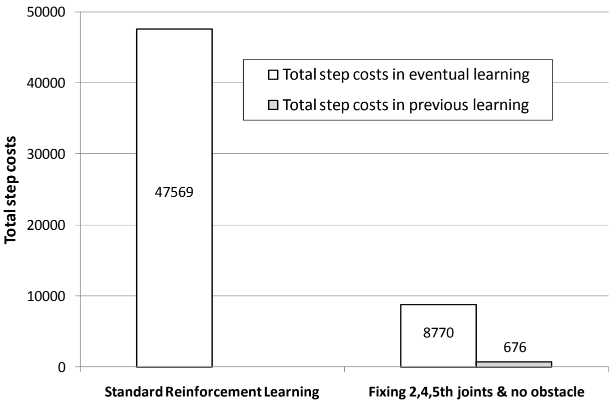

(c) Result on four joints arm robot with an obstacle

Fig. 5. Total step costs during 50 episodes.

ACKNOWLEDGMENT

This work was supported in part by the CREST project "Foundation of technology supporting the creation of digital media contents" of JST, and the "Global Robot Academia," Grant-in-Aid for Global COE Program by the Ministry of Education, Culture, Sports, Science and Technology, Japan.

REFERENCES

[1] Sutton RS, Barto AG (1988), Reinforcement Learning: An Introduction. Cambridge, MA: MIT Press

[2] Takayama A, Ito K, Minamino T(2008), Autonomous control of a snake-like robot using reinforcement learning - Discussion of the role of the mechanical body in abstraction of state-action space. Proc. of IEEE Annual Conference of the IEEE Industrial Electronics Society, pp.1584-1589.

[3] Hara M, Kawabe N, Huang J, Yabuta T(2011), Acquisition of a Gymnast-Like Robotic Giant-Swing Motion by Q-Learning and Improvement of the Repeatability. Journal of Robotics and Mechatronics, Vol.23, No.1, pp.126-136.

[4] Fuchida T, Maehara M, Mori K, Murashima S (2000), A Learning Method of RBF Network using Reinforcement Leaning Method (in Japanese). Technical Report of IEICE, NC99-113, pp.157-163.

The Seventeenth International Symposium on Artificial Life and Robotics 2012 (AROB 17th '12),
B-Con Plaza, Beppu, Oita, Japan, January 19-21, 2012

Identification of continuous-time Hammerstein systems using Gaussian process models trained by particle swarm optimization

Tomohiro Hachino[1] and Shouichi Yamakawa[1]

[1] Kagoshima University, Kagoshima 890-0065, Japan
(Tel & Fax: 81-99-285-8392)
(hachino@eee.kagoshima-u.ac.jp)

Abstract: This paper deals with a nonparametric identification of continuous-time Hammerstein systems using Gaussian process (GP) models. A Hammerstein system consists of a memoryless nonlinear static part followed by a linear dynamic part. The identification model is derived using the GP prior model which is described by the mean function vector and the covariance matrix. This prior model is trained by the separable least-squares approach combining particle swarm optimization with the linear least-squares method to minimize the negative log marginal likelihood of the identification data. Then the nonlinear static part is estimated by the predictive mean function of the GP, and the confidence measure of the estimated nonlinear static part is evaluated by the predictive covariance function of the GP. Simulation results are shown to illustrate the proposed method.

Keywords: continuous-time system, Gaussian process model, Hammerstein system, particle swarm optimization, system identification

1 INTRODUCTION

The Hammerstein system is expressed by a memoryless nonlinear static part followed by a linear dynamic part and has many advantages for control design or stability analysis due to its simple model structure. Numerous identification methods have been proposed for discrete-time Hammerstein systems [1, 2, 3]. Since these approaches are categorized into parametric identification, one needs to use a large number of weighting parameters to describe the nonlinearity and handle a complicated model structure determination. Moreover, no confidence measures for the estimated nonlinear static part are obtained in parametric identification. On the other hand, we have developed a nonparametric identification method based on the Gaussian process (GP) models, which can give the estimated nonlinear function with the confidence measure [4]. However, since most practical systems are usually continuous-time, it is very important to develop an accurate identification method for continuous-time Hammerstein systems.

Therefore, in this paper, we discuss the nonparametric identification of continuous-time Hammerstein systems using the GP model. The identification model is derived using the GP prior model which is described by the mean function vector and the covariance matrix. The prior mean function is represented in linear form of the input and the prior covariance function is expressed by the Gaussian kernel. This prior model is trained by the separable least-squares (LS) approach combining particle swarm optimization (PSO) [5] with the linear LS method to minimize the negative log marginal likelihood of the identification data. PSO is a swarm intelligence optimization technique, which was inspired by the social behavior of a flock of birds or a shoal of fish, and has been empirically shown to be very efficient for optimization. The use of PSO might increase the efficiency of identification due to its simple algorithm. The hyperparameters of the covariance functions and the numerator parameters of the linear dynamic part are represented with the particles and are searched by PSO, while the denominator parameters of the linear dynamic part are estimated by the linear LS method. Then the nonlinear static part is estimated by the predictive mean function of the GP, and the confidence measure of the estimated nonlinear static part is evaluated by the predictive covariance function of the GP. Simulation results show that the accuracy of the proposed method is superior to that of a conventional identification method.

2 STATEMENT OF THE PROBLEM

Consider a single-input, single-output continuous-time nonlinear system described by the Hammerstein model shown in Fig. 1. This system can be mathematically described as

$$\begin{cases} \sum_{i=0}^{n} a_i p^{n-i} y(t) = b_0 x(t) \quad (a_0 = 1) \\ x(t) = f(u(t)) + \epsilon(t) \end{cases} \tag{1}$$

where $u(t)$ and $y(t)$ are input and output signals, respectively. $x(t)$ is intermediate signal that is not accessible for measurement. $f(\cdot)$ is unknown nonlinear function, which is assumed to be stationary and smooth. $\epsilon(t)$ is assumed to be a zero-mean Gaussian noise with variance σ_n^2. $A(p) = \sum_{i=0}^{n} a_i p^{n-i}$ is the denominator polynomial of the linear dynamic part, where p denotes a differential operator. n is assumed to be known.

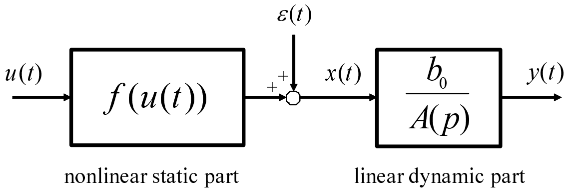

Fig. 1. Continuous-time Hammerstein system

The aim of this paper is to identify the system parameters $\{a_i\}$ and $\{b_j\}$ of the linear dynamic part, and the nonlinear static function $f(\cdot)$ with the confidence measure, from input and output data in the GP framework.

3 IDENTIFICATION MODEL BY THE GP

The following state variable filter $F(p)$ is introduced in order to evaluate higher order derivatives of signals:

$$F(p) = \frac{1}{p^q + \gamma_1 p^{q-1} + \cdots\cdots + \gamma_q} \quad (q > n) \tag{2}$$

Multiplying both sides of Eq. (1) by $F(p)$ yields

$$\begin{cases} \displaystyle\sum_{i=0}^{n} a_i p^{n-i} y^f(t) = b_0 x^f(t) \\ x^f(t) = F(p) f(u(t)) + \epsilon^f(t) \end{cases} \tag{3}$$

where $y^f(t) = F(p)y(t)$, $x^f(t) = F(p)x(t)$ and $\epsilon^f(t) = F(p)\epsilon(t)$. When $F(p)$ has a transport lag characteristic, the filter $F(p)$ and the nonlinear function $f(\cdot)$ are exchangeable and it follows that $F(p)f(u(t)) = f(F(p)u(t)) = f(u^f(t))$. Thus Eq. (3) becomes

$$\begin{cases} \displaystyle\sum_{i=0}^{n} a_i p^{n-i} y^f(t) = b_0 x^f(t) \\ x^f(t) = f(u^f(t)) + \epsilon^f(t) \end{cases} \tag{4}$$

In general the Butterworth filter has approximately a transport lag characteristic for frequencies $\omega \le \omega_c$, where ω_c is the cutoff frequency. Therefore, the Butterworth filter is utilized as the delayed state variable filter $F(p)$ in this paper.

Putting $t = t_1, t_2, \cdots, t_N$ into Eq. (4) yields

$$\boldsymbol{y} = \boldsymbol{A}\boldsymbol{\theta}_a + b_0 \boldsymbol{x} \tag{5}$$

where

$$\begin{aligned} \boldsymbol{y} &= [p^n y^f(t_1), p^n y^f(t_2), \cdots, p^n y^f(t_N)]^{\mathrm{T}} \\ \boldsymbol{x} &= [f(u^f(t_1)) + \epsilon^f(t_1), f(u^f(t_2)) + \epsilon^f(t_2), \\ &\qquad \cdots, f(u^f(t_N)) + \epsilon^f(t_N)]^{\mathrm{T}} \\ \boldsymbol{\theta}_a &= [a_1, a_2, \cdots, a_n]^{\mathrm{T}} \\ \boldsymbol{A} &= \begin{bmatrix} -p^{n-1} y^f(t_1) & \cdots & -y^f(t_1) \\ -p^{n-1} y^f(t_2) & \cdots & -y^f(t_2) \\ \vdots & & \vdots \\ -p^{n-1} y^f(t_N) & \cdots & -y^f(t_N) \end{bmatrix} \end{aligned} \tag{6}$$

A GP is a Gaussian random function and is completely described by its mean function and covariance function. We can regard it as a collection of random variables with a joint multivariable Gaussian distribution. Therefore, the function values $\boldsymbol{f}$ can be represented by the GP:

$$\boldsymbol{f} \sim \mathcal{N}(\boldsymbol{m}(\boldsymbol{u}), \boldsymbol{\Sigma}(\boldsymbol{u}, \boldsymbol{u})) \tag{7}$$

where

$$\begin{aligned} \boldsymbol{f} &= [f(u^f(t_1)), f(u^f(t_2)), \cdots, f(u^f(t_N))]^{\mathrm{T}} \\ \boldsymbol{u} &= [u^f(t_1), u^f(t_2), \cdots, u^f(t_N)]^{\mathrm{T}} \end{aligned} \tag{8}$$

$\boldsymbol{u}$ is the input (variable) of the function $\boldsymbol{f}$, $\boldsymbol{m}(\boldsymbol{u})$ is the mean function vector, and $\boldsymbol{\Sigma}(\boldsymbol{u}, \boldsymbol{u})$ is the covariance matrix. In this paper the mean function is expressed as $m(u^f(t)) = u^f(t)$, i.e., the mean function vector $\boldsymbol{m}(\boldsymbol{u})$ is described as follows:

$$\boldsymbol{m}(\boldsymbol{u}) = \boldsymbol{u} \tag{9}$$

The covariance $\Sigma_{pq} = s(u(t_p), u(t_q))$ is an element of the covariance matrix $\boldsymbol{\Sigma}$, which is a function of $u(t_p)$ and $u(t_q)$. Under the assumption that the nonlinear function $f(\cdot)$ is stationary and smooth, the following Gaussian kernel is utilized in this paper:

$$\begin{aligned} \Sigma_{pq} &= s(u(t_p), u(t_q)) \\ &= \sigma_y^2 \exp\left(-\frac{|u(t_p) - u(t_q)|^2}{2\ell^2}\right) \end{aligned} \tag{10}$$

From Eq. (7), the intermediate signal vector can be written as

$$\boldsymbol{x} \sim \mathcal{N}(\boldsymbol{m}(\boldsymbol{u}), \boldsymbol{K}(\boldsymbol{u}, \boldsymbol{u})) \tag{11}$$

where

$$\begin{aligned} \boldsymbol{K}(\boldsymbol{u}, \boldsymbol{u}) &= \boldsymbol{\Sigma}(\boldsymbol{u}, \boldsymbol{u}) + \sigma_n^2 \boldsymbol{I}_N \\ \boldsymbol{I}_N &: N \times N \ \text{identity matrix} \end{aligned} \tag{12}$$

and $\boldsymbol{\theta}_c = [\sigma_y, \ell, \sigma_n]^{\mathrm{T}}$ is called the *hyperparameter* vector.

Applying the property of the multivariable Gaussian distribution for the linear transformation to Eqs. (5) and (11), the identification model by the GP is derived as

$$\boldsymbol{y} \sim \mathcal{N}(b_0 \boldsymbol{m}(\boldsymbol{u}) + \boldsymbol{A}\boldsymbol{\theta}_a, b_0^2 \boldsymbol{K}(\boldsymbol{u}, \boldsymbol{u})) \tag{13}$$

4 IDENTIFICATION

4.1 Training by PSO

First, the GP prior model is trained by optimizing the unknown parameter vector $\boldsymbol{\theta} = [\boldsymbol{\theta}_a^{\mathrm{T}}, b_0, \boldsymbol{\theta}_c^{\mathrm{T}}]^{\mathrm{T}}$. Although this is a nonlinear optimization problem, we can separate the linear optimization part and the nonlinear optimization part. Therefore, in this paper, we propose a separable LS approach combining PSO with the linear LS method. Only $\boldsymbol{\Omega} = [b_0, \boldsymbol{\theta}_c^{\mathrm{T}}, \omega_c]^{\mathrm{T}}$ is represented with the particles and searched by PSO. The proposed training algorithm is as follows:

Step 1: Initialization

Generate an initial population of Q particles with random positions $\boldsymbol{\Omega}^0_{[i]} = [b_{0[i]}, \boldsymbol{\theta}^{\mathrm{T}}_{c[i]}, \omega_{c[i]}]^{\mathrm{T}}$ and velocities $\boldsymbol{V}^0_{[i]}$ $(i = 1, 2, \cdots, Q)$.

Set the iteration counter l to 0.

Step 2: Filtering of the identification data

Construct Q candidates of the state variable filter using $\omega_{c[i]}$. Calculate the filtered input $u^f_{[i]}(t)$, filtered output $y^f_{[i]}(t)$ and their higher-order derivatives, using each candidate of the state variable filter. Then construct Q candidates of $\boldsymbol{y}_{[i]}$, $\boldsymbol{A}_{[i]}$ and $\boldsymbol{u}_{[i]}$ $(i = 1, 2, \cdots, Q)$.

Step 3: Construction of covariance matrix

Construct Q candidates of covariance matrix $\boldsymbol{K}_{[i]}$ using $\boldsymbol{\theta}_{c[i]}$ $(i = 1, 2, \cdots, Q)$.

Step 4: Estimation of $\boldsymbol{\theta}_{a[i]}$

Estimate Q candidates for $\boldsymbol{\theta}_{a[i]}$ corresponding to $\boldsymbol{\Omega}_{[i]}$ $(i = 1, 2, \cdots, Q)$:

$$\boldsymbol{\theta}_{a[i]} = (\boldsymbol{A}^{\mathrm{T}}_{[i]}\boldsymbol{\mathcal{K}}^{-1}_{[i]}\boldsymbol{A}_{[i]})^{-1}\boldsymbol{A}^{\mathrm{T}}_{[i]}\boldsymbol{\mathcal{K}}^{-1}_{[i]}(\boldsymbol{y}_{[i]} - b_{0[i]}\boldsymbol{u}_{[i]}) \quad (14)$$

where $\boldsymbol{\mathcal{K}}_{[i]} = b^2_{0[i]}\boldsymbol{K}_{[i]}$.

Step 5: Evaluation value calculation

Calculate the negative log marginal likelihood of the identification data:

$$\begin{aligned} J(\boldsymbol{\Omega}^l_{[i]}) &= \frac{1}{2}\log|\boldsymbol{\mathcal{K}}_{[i]}| \\ &+\frac{1}{2}(\boldsymbol{y}_{[i]} - b_{0[i]}\boldsymbol{u}_{[i]} - \boldsymbol{A}_{[i]}\boldsymbol{\theta}_{a[i]})^{\mathrm{T}}\boldsymbol{\mathcal{K}}^{-1}_{[i]} \\ &\times(\boldsymbol{y}_{[i]} - b_{0[i]}\boldsymbol{u}_{[i]} - \boldsymbol{A}_{[i]}\boldsymbol{\theta}_{a[i]}) + \frac{N}{2}\log(2\pi) \end{aligned} \quad (15)$$

Step 6: Update of the best positions $\boldsymbol{pbest}$ and $\boldsymbol{gbest}$

Update $\boldsymbol{pbest}^l_{[i]}$, which is the personal best position, and $\boldsymbol{gbest}^l$, which is the global best position among all particles as follows:

If $l = 0$ then

$$\begin{aligned} &\boldsymbol{pbest}^l_{[i]} = \boldsymbol{\Omega}^l_{[i]} \\ &\boldsymbol{gbest}^l = \boldsymbol{\Omega}^l_{[i_{best}]} \quad i_{best} = arg\min_i J(\boldsymbol{\Omega}^l_{[i]}) \end{aligned} \quad (16)$$

otherwise

$$\boldsymbol{pbest}^l_{[i]} = \begin{cases} \boldsymbol{\Omega}^l_{[i]} & (J(\boldsymbol{\Omega}^l_{[i]}) < J(\boldsymbol{pbest}^{l-1}_{[i]})) \\ \boldsymbol{pbest}^{l-1}_{[i]} & (\text{otherwise}) \end{cases}$$

$$\boldsymbol{gbest}^l = \boldsymbol{pbest}^l_{[i_{best}]} \quad i_{best} = arg\min_i J(\boldsymbol{pbest}^l_{[i]}) \quad (17)$$

Step 7: Update of positions and velocities

Update the particle positions and velocities using Eq. (18):

$$\begin{cases} \boldsymbol{V}^{l+1}_{[i]} = w^l \cdot \boldsymbol{V}^l_{[i]} + c_1 \cdot rand_1() \cdot (\boldsymbol{pbest}^l_{[i]} - \boldsymbol{\Omega}^l_{[i]}) \\ \qquad\qquad + c_2 \cdot rand_2() \cdot (\boldsymbol{gbest}^l - \boldsymbol{\Omega}^l_{[i]}) \\ \boldsymbol{\Omega}^{l+1}_{[i]} = \boldsymbol{\Omega}^l_{[i]} + \boldsymbol{V}^{l+1}_{[i]} \end{cases} \quad (18)$$

where w^l is an inertia factor, c_1 and c_2 are constants representing acceleration coefficients, and $rand_1()$ and $rand_2()$ are uniformly distributed random numbers with amplitude in the range $[0, 1]$.

Step 8: Repetition

Set the iteration counter to $l = l + 1$ and go to Step 2 until the prespecified iteration number l_{max}.

Step 9: Determination of the GP prior model

Determine the vector $\hat{\boldsymbol{\Omega}} = [\hat{b}_0, \hat{\boldsymbol{\theta}}^{\mathrm{T}}_c, \hat{\omega}_c]^{\mathrm{T}}$ and the corresponding denominator parameters of the linear dynamic part $\hat{\boldsymbol{\theta}}_a = [\hat{a}_1, \hat{a}_2, \cdots, \hat{a}_n]^{\mathrm{T}}$ using the best particle position $\boldsymbol{gbest}^{l_{max}}$. Construct the suboptimal prior covariance function:

$$\begin{aligned} &s(u^f(t_p), u^f(t_q)) \\ &\quad = \hat{\sigma}^2_y \exp\left(-\frac{|u^f(t_p) - u^f(t_q)|^2}{2\hat{\ell}^2}\right) \end{aligned} \quad (19)$$

4.2 Estimation of the nonlinear static function

The estimates of the intermediate signal vector $\hat{\boldsymbol{x}}$ can be evaluated as follows:

$$\hat{\boldsymbol{x}} = \frac{1}{\hat{b}_0}(\boldsymbol{y} - \boldsymbol{A}\hat{\boldsymbol{\theta}}_a) \quad (20)$$

Let the test input vector and the corresponding function value vector and intermediate signal vector be $\boldsymbol{u}_*$, $\boldsymbol{f}_*$ and $\boldsymbol{x}_*$, respectively. Then the posterior distribution for $\boldsymbol{f}_*$ is obtained as

$$\boldsymbol{f}_*|\boldsymbol{u}, \hat{\boldsymbol{x}}, \boldsymbol{u}_* \sim \mathcal{N}(\bar{\boldsymbol{f}}_*, cov(\boldsymbol{f}_*)) \quad (21)$$

where $\bar{\boldsymbol{f}}_*$ is the predictive mean vector and $cov(\boldsymbol{f}_*)$ is the predictive covariance matrix, which are given as follows:

$$\begin{aligned} \bar{\boldsymbol{f}}_* &= \boldsymbol{m}(\boldsymbol{u}_*) + \boldsymbol{\Sigma}(\boldsymbol{u}_*, \boldsymbol{u})\boldsymbol{K}^{-1}(\hat{\boldsymbol{x}} - \boldsymbol{m}(\boldsymbol{u})) \\ cov(\boldsymbol{f}_*) &= \boldsymbol{\Sigma}(\boldsymbol{u}_*, \boldsymbol{u}_*) - \boldsymbol{\Sigma}(\boldsymbol{u}_*, \boldsymbol{u})\boldsymbol{K}^{-1}\boldsymbol{\Sigma}(\boldsymbol{u}, \boldsymbol{u}_*) \end{aligned} \quad (22)$$

Thus, the nonlinear static function of the objective system is estimated as

$$\begin{aligned} \hat{f}(u_*(t)) &= m(u_*(t)) \\ &\quad + \boldsymbol{\Sigma}(u_*(t), \boldsymbol{u})\boldsymbol{K}^{-1}(\hat{\boldsymbol{x}} - \boldsymbol{m}(\boldsymbol{u})) \end{aligned} \quad (23)$$

and its covariance function $\hat{s}$ is evaluated as

$$\begin{aligned} \hat{s}(u_*(t_p), u_*(t_q)) &= s(u_*(t_p), u_*(t_q)) \\ &\quad - \boldsymbol{\Sigma}(u_*(t_p), \boldsymbol{u})\boldsymbol{K}^{-1}\boldsymbol{\Sigma}(\boldsymbol{u}, u_*(t_q)) \end{aligned} \quad (24)$$

The predictive covariance function $\hat{k}$ of the intermediate signal is obtained as

$$\hat{k}(u_*(t_p), u_*(t_q)) = \hat{s}(u_*(t_p), u_*(t_q)) + \hat{\sigma}^2_n \delta_{pq} \quad (25)$$

where δ_{pq} is the Kronecker delta, which is 1 if $p = q$ and 0 otherwise. Equations (24) and (25) are used as confidence measures of the estimated nonlinear static function and the intermediate signal, respectively.

5 NUMERICAL SIMULATIONS

Consider a continuous-time Hammerstein system described by

$$\begin{cases} \ddot{y}(t) + a_1\dot{y}(t) + a_2 y(t) = b_0 x(t) \\ x(t) = f(u(t)) + \epsilon(t) \\ a_1 = 3.0, \quad a_2 = 1.5, \quad b_0 = 1.0 \\ f(u(t)) = u(t) + 0.5u^3(t) \end{cases} \tag{26}$$

The output signal is generated by a random signal of band-pass 3.0[rad/s]. The sampling period is taken to be $T = 0.05$[s]. $\epsilon(t)$ is zero-mean Gaussian noise with a standard deviation σ_n of 2.1, which means the noise-to-signal ratio (NSR) is 20%. The number of input and output data is $N = 300$. The design parameters for PSO are chosen as follows: particle size: $Q = 50$, inertia factor: $w^l = w_{max} - (w_{max} - w_{min})l/l_{max}$ $(w_{max} = 0.9, w_{min} = 0.4)$, acceleration coefficients $c_1 = 1.0$, $c_2 = 0.9$, maximum iteration number $l_{max} = 200$.

Estimates of of the parameters in the linear dynamic part are $\hat{a}_1 = 3.072$ and $\hat{a}_2 = 1.490$, respectively, where estimate of b_0 is omitted because the final estimated model is normalized by $\hat{b}_0$. Fig. 2 and Fig. 3 show the estimated nonlinear function and the estimated intermediate signal with the double standard deviation confidence intervals, respectively.

Monte-Carlo simulations of 20 experiments are implemented for the proposed method and conventional RBF-based method. Table 1 shows the mean squares errors between the true outputs and the outputs of the estimated models for various values of σ_n on the average of 20 experiments.

6 CONCLUSIONS

In this paper a novel nonparametric identification method for continuous-time Hammerstein systems has been proposed using the GP model. The GP prior model is trained by the separable LS approach combining the linear LS method with PSO so that the negative log marginal likelihood of the identification data is minimized. The nonlinear static part of the objective Hammerstein system is estimated by the predictive mean function of the GP, and the confidence region of the estimated nonlinear static part is given by the predictive covariance function. Simulation results show that the accuracy of the proposed method is superior to that of a conventional identification method.

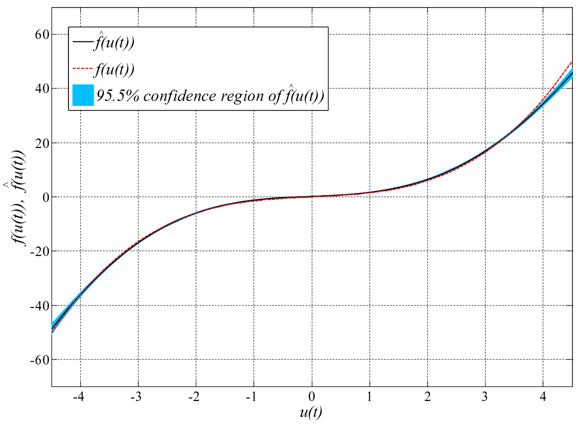

Fig. 2. Estimated nonlinear function

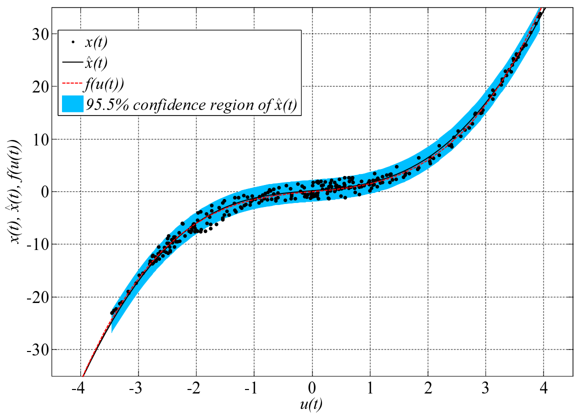

Fig. 3. Estimated intermediate signal

Table 1. Mean squares errors between the true outputs and the outputs of the estimated models

σ_n	NSR [%]	Proposed	RBF-based
1.1	10	2.17e-3	2.26e-3
1.6	15	5.02e-3	6.01e-3
2.1	20	7.41e-3	8.02e-3
2.6	25	1.68e-2	1.99e-2
3.1	30	2.14e-2	2.35e-2

REFERENCES

[1] Al-Duwaish H, Karim M. N (1997), A new method for the identification of Hammerstein model, Automatica, 33(10):1871–1875

[2] Adachi S, Murakami H (1995), Generalized predictive control system design based on non-linear identification by using Hammerstein model (in Japanese), Trans. ISCIE, 8(3):115–121

[3] Hatanaka T, Uosaki K, Koga M (2002), Evolutionary computation approach to Hammerstein model identification, Proc. of the 4th Asian Control Conference :1730–1735

[4] Hachino T, Takata H (2010), Identification of discrete-time Hammerstein systems using Gaussian process model, Journal of Signal Processing, 14(2):129–137

[5] Kennedy J, Eberhart R. C (1995), Particle swarm optimization, Proc. of IEEE International Conference on Neural Networks :1942-1948

Reinforcement learning in dynamic environment -Abstraction of state-action space utilizing properties of the robot body and environment-

Yutaka Takeuchi[1], and Kazuyuki Ito[2]
[1,2]Hosei University, Tokyo 184-8584, Japan
(Tel: 81-42-387-6093, Fax: 81-42-387-6381)

[1] 10r6119@stu.hosei.ac.jp, [2] ito@hosei.ac.jp

Abstract: In this paper, we address the autonomous control of a 3-dimensional snake-like robot through the use of reinforcement learning, and we apply it in a dynamic environment. In general, snake-like robots have high mobility that is realized by many degrees of freedom, and they can move over dynamically shifting environments such as rubble. However, this freedom and flexibility leads to a state explosion problem, and the complexity of the dynamic environment leads to incomplete learning by the robot. To solve these problems, we focus on the properties of the actual operating environment and the dynamics of a mechanical body. We design the body of the robot so that it can abstract small, but necessary state-action space by utilizing these properties, and we make it possible to apply reinforcement learning. To demonstrate the effectiveness of the proposed snake-like robot, we conduct experiments; from the experimental results we conclude that learning is completed within a reasonable time, and that effective behaviors for the robot to adapt itself to an unknown 3-dimensional dynamic environment were realized.

Keywords: Dynamic Environment, Reinforcement Learning, Crawler Robot

1 INTRODUCTION

Recently, robots that have many degrees of freedom have drawn considerable attention. Snake-like robots or robots of serially connected crawlers are typical examples. In general, these robots have high mobility that is realized due to the many degrees of freedom while in motion. So, they can be operated in complex and quick-shifting environments like rubble, and they are expected to be used for practical applications such as rescue operations [1-8].

On the other hand, the application of reinforcement learning for controlling real robots also attracts considerable attention because robots can learn effective behavior by trial-and-error [9]. Therefore, by applying reinforcement learning to a robot with many degrees of freedom, an autonomous robot with high mobility can be realized; such a robot will be very useful for various tasks such as rescue operations. However, conventional reinforcement learning has a serious problem when applied to robots with many degrees of freedom that operate in complex environments. This is known as the state explosion problem. The size of the state-action space increases exponentially with an increase in the robot's degrees of freedom as well as the complexity of the environment. As a result of this increase, learning cannot be completed within a reasonable time limit. In addition, if some part of environment is changed, additional learning is required. So, it is highly difficult to apply reinforcement learning to robots operating in a dynamic environment.

In contrast, animals can learn by trial-and-error in spite of the many degrees of freedom afforded by their bodies and despite the fact that the daily environment that they live in, and contend with, is very complex and dynamic. How animals are able to cope with such a challenging environment is still an open question. But in embodied cognitive science [10], or ecological psychology [11], it is thought that the body plays an important role in realizing adaptive behaviors.

In this paper, we have designed the mechanical body of a robot such that it can abstract state-action space, on the basis of our previous work [12]; this design is expected to solve the problems outlined above. Using the proposed mechanism, the size of the state-action space can be reduced drastically, so that it is possible for the robot to learn in real time. Moreover, the robot's obtained policy is generalized and is applicable without additional learning even if the environment is changed dynamically.

To demonstrate the effectiveness of the proposed mechanism, we conduct experiments. The task of the robot is to learn the effective behavior for moving towards a light source in a dynamic environment. There are many unknown obstacles in the environment, and the obstacles move up and down constantly. The learning process is performed in both the static and dynamic environments, and the obtained policy is applied to other environments as well, where the obstacles are placed in different positions.

2 TASK AND ENVIRONMENT

Fig. 1 shows a dynamic environment. The environment is composed of 24 modules, and each module has two obstacles that move vertically. The range of movement of the obstacles ranges from a height of 5 cm to 12 cm. The dimensions of the environment are 240 cm (length) and 180 cm (width). We employ 5 different modules, as shown Fig. 2, all of which are placed randomly. There is one light source that the robot must move towards, and the aim of the task is to learn effective behavior for homing in on the light source within this 3-dimensional dynamic environment.

Fig. 1. Example of a dynamic operating environment

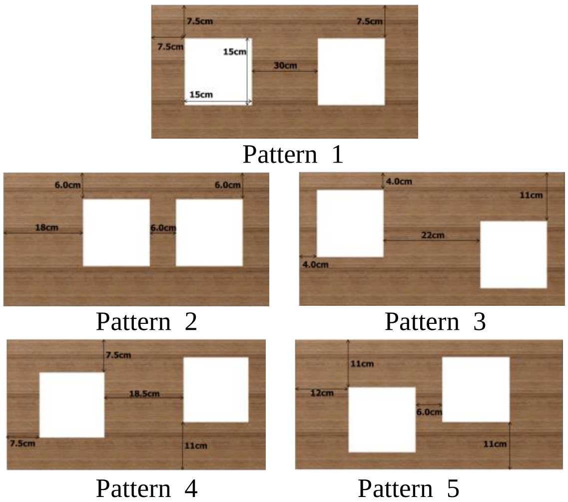

Fig. 2. Layout pattern of the obstacles

3 PROPOSED METHOD

3.1 General framework

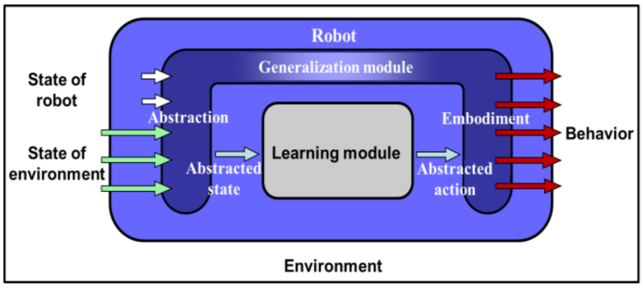

Fig. 3. General framework

Fig. 3 shows the general framework for the abstraction of the state-action space that we proposed in past studies [12, 13]. The robot consists of the generalization module and the learning module. A remarkable concept central to the proposed framework is that the generalization module is realized by the body of the robot itself instead of being implemented in a remote computer. The body is designed such that the necessary calculations for generalization are performed by utilizing the physical properties of the real world. The abstracted information is passed to the learning module in a computer, where the learning process is actually completed, with the selected action being fed back to the generalization module. The generalization module embodies the abstracted action that enables the complex movement of the robot. In the following subsection, we discuss the design the body of a snake-like robot on the basis of this framework.

3.2 Hardware design of body

In this study, we develop a 3-dimensional snake-like robot by improving our previous robot [12]. Fig. 4 shows the mechanism of the robot. The robot is composed of three links that have crawlers. The joints are realized by rubber poles and are moved passively. Two wires are installed on both the sides, and their length can be adjusted by an active pulley that is mounted on the rear end. Upon turning the active pulley, one wire is rolled up while the other wire is loosened. This causes the body of the robot to turn, as shown in Fig. 5.

Due to the passive nature of the joints and the constraining influence of the wires, the robot can adapt to a bumpy and unstable environment. The robot's direction of movement can be controlled by just actuating the active pulley.

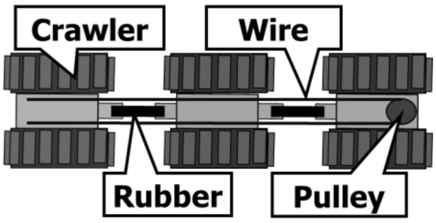

Fig. 4. Outline of robot

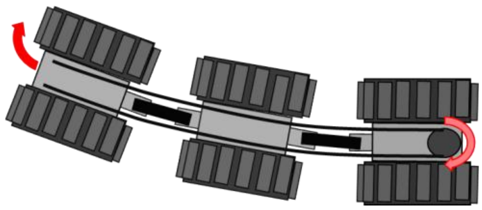

Fig. 5. Mechanism for pulling wires

3.3 Hardware design for sensing

We employ 18 CdS cells for detecting the direction that the light is coming from, as shown in Fig. 6. Each module is composed of 6 CdS cells (Fig. 6 a)), and 3 such modules are embedded on the robot as shown in Fig. 6 b). The CdS cells have directional characteristics and their layout is hemispherical. Therefore, the light direction can be obtained by equation (1):

$$x = \frac{3\sum_{i=1}^{3}(1/R_{i1}) + 2\{\sum_{i=1}^{3}(1/R_{i2}) + \sum_{i=1}^{3}(1/R_{i3})\} + \sum_{i=1}^{3}(1/R_{i4}) + \sum_{i=1}^{3}(1/R_{i5})}{\sum_{j=1}^{6}\sum_{i=1}^{3}(1/R_{ij})} \quad (1)$$

where R_{ij} denotes the electrical resistance of the j-th CdS cell in the i-th module. x represents the center of gravity of the light intensity and is equivalent to the light direction. For more details, please refer to [12].

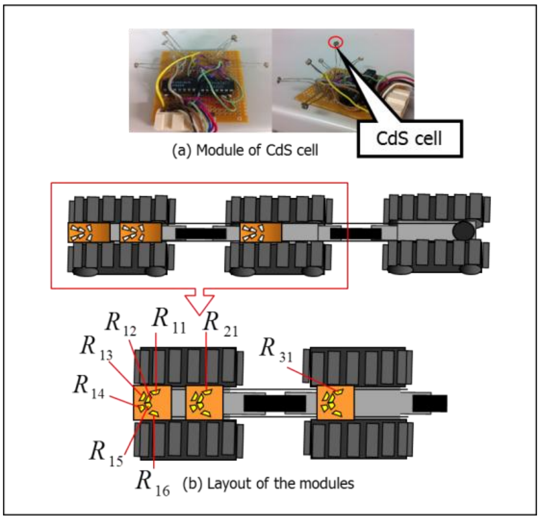

Fig. 6. Sensing system using CdS cells

3.4 Developed robot

Fig. 7 and Table 1 show the developed robot and its specification. The passive joints are realized by using rubber poles. To obtain adequate elasticity, the dimensions of the rubber poles are very important. However, it is very difficult to determine the dimensions theoretically. So, in this paper, these sizes were tuned by preliminary experiments.

Table 1.
Specification of the developed robot

Length	85 cm
Width	13 cm
Height	11 cm
Weight	2 kg

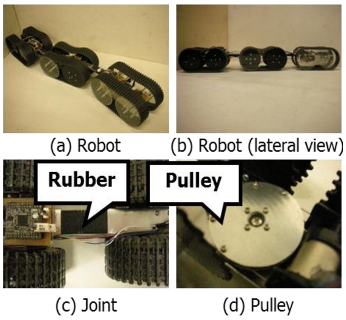

Fig. 7. Developed robot

Fig. 8 shows the result of the preliminary experiment performed for examining the capability of the sensor module. From the results, we find that the horizontal direction of the light can be obtained from the output voltage.

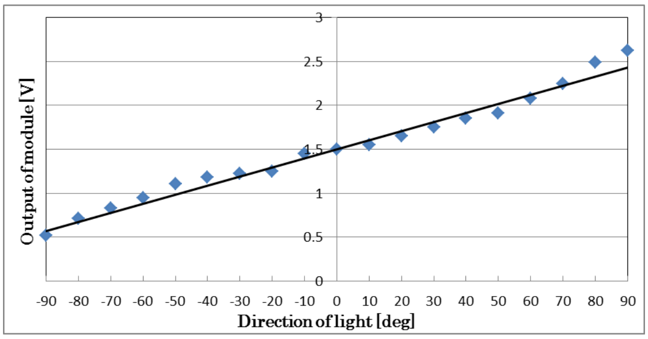

Fig. 8. Output of the sensor module

4 EXPERIMENT

4.1 Setting of reinforcement learning

We employ typical Q-learning [9] as reinforcement learning. Equation (2) represents Q-learning [9].

$$Q(s,a) \leftarrow (1-\alpha)Q(s,a) + \alpha\{r(s,a) + \gamma \max_{a'} Q(s',a')\} \quad (2)$$

where s is the state; a, the action; r, the reward; α, the learning rate; and γ, the discount rate.

We set α as 0.5 and γ as 0.9. The action is selected by using the ε–greedy method, and the probability of random selection of the action is 0.1.

One trial was conducted for a duration of 24 s, and calculations were performed every 0.5 s by using equation (2). Table 2 shows the state of the light direction. The values are the outputs of equation (1). Table 3 shows the state of the body. These values are the angle of the active pulley. Table 4 shows the actions. While the robot is moving towards the light source (the state of the light direction is 2 and the value of the angle of the active pulley is 2), a reward of 100 is assigned. When the robot loses the light source (light source goes out of the perceivable range), a negative reward −100 is assigned. The trial then ends, and the next trial starts.

Table 2.
States of the direction of light

State	Voltage[V]
0	(0.50,1.00]
1	(1.00,1.40]
2	(1.40,1.60]
3	(1.60,2.00]
4	(2.00,2.50]

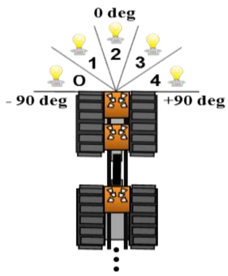

Fig. 9. States of the direction of light

Table 3. States of the body

State	0	1	2	3	4
Degree [deg]	-50	-25	0	25	50
State of robot	Left bend		Straight	Right bend	

Table 4. Action

Action	Motion
0	Turn tail motor by – 25° (Robot will turn left)
1	Hold the tail motor (Maintain state of the body)
2	Turn tail motor by + 25° (Robot will turn right)

4.2 Experiment

The obstacle is placed randomly as shown in Fig. 10, and we conduct the learning process by using a real robot. We consider two cases. One is a static environment where the obstacles do not move. The other is a dynamic environment in which objects move vertically. The learning process is conducted separately for each case.

After the learning process is completed, we apply the policy that is obtained in the static environment to the dynamic environment without additional learning, and we confirm the generalization capabilities of the proposed framework.

Fig. 10. Environment

Fig. 11 shows the learning curves, and Figs. 12 and 13 show the behavior after learning. In both cases, the value of the obtained reward has converged during the 40th trial. This implies that the learning can be completed in a reasonable time. From the result, we conclude that the problem of real-time learning is solved.

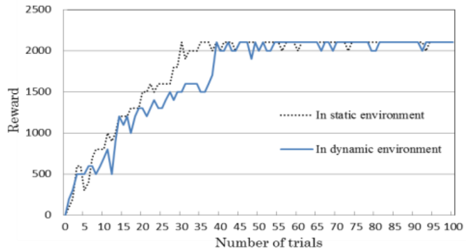

Fig. 11. Learning curve

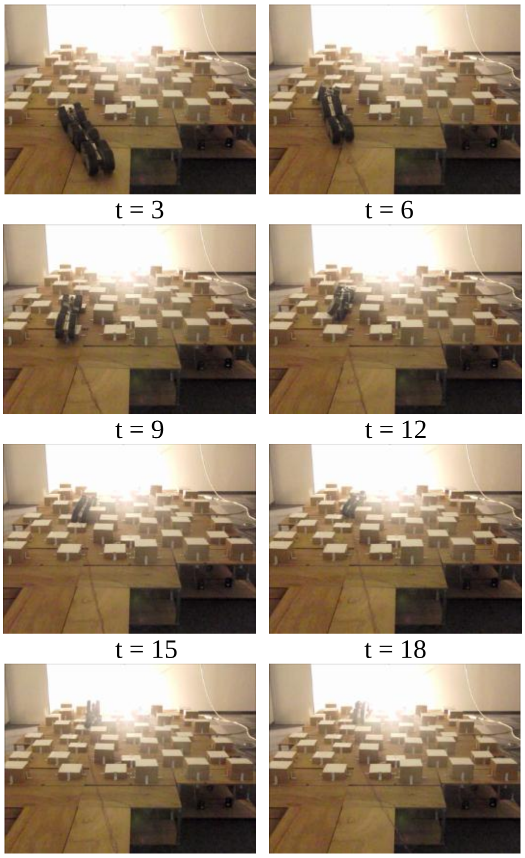

Fig. 12. Behavior after learning (static environment)

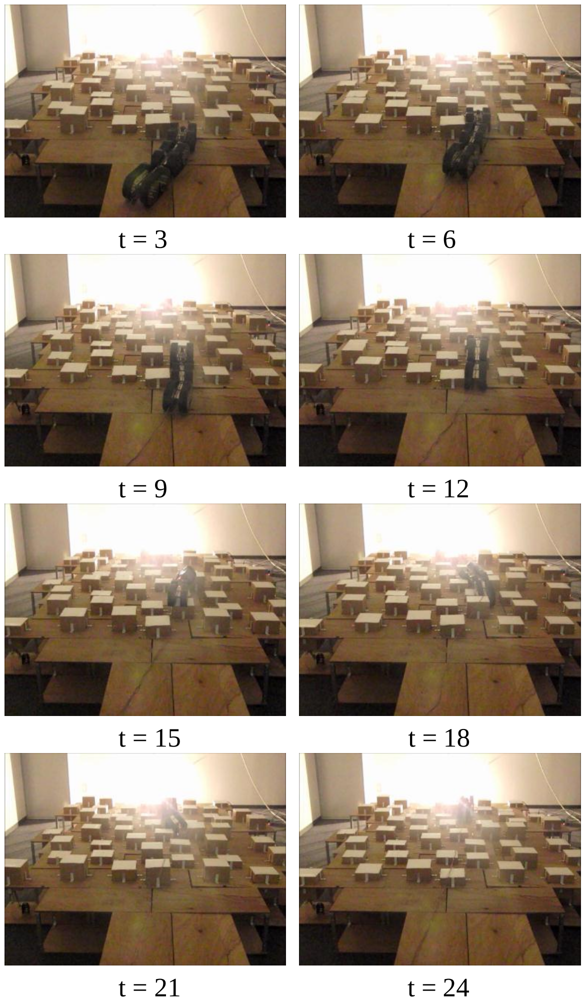

Fig. 13. Behavior after learning (dynamic environment)

Next we consider the generalization capability of the proposed framework. Fig. 14 shows an example of behavior realized by applying the policy obtained in the static environment to the dynamical environment. In this case, there was no additional learning. Nevertheless, the robot could move to the light source. This implies that the obtained policy can be generalized and is applicable to unknown but similar environments without requiring re-learning.

To confirm the generality, we compare state transitions. Fig. 14 shows an example of a state transition graph in the static environment, and Fig. 15 shows one for the dynamic environment.

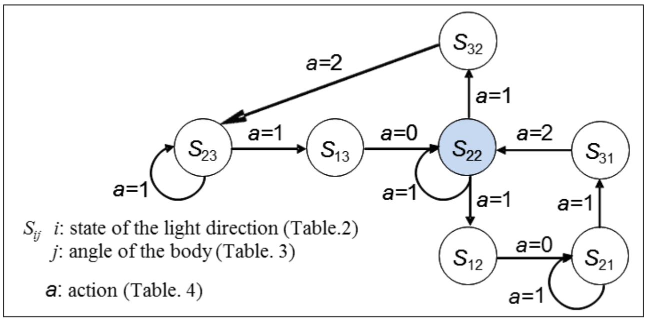

Fig. 14. State transitions in the static environment

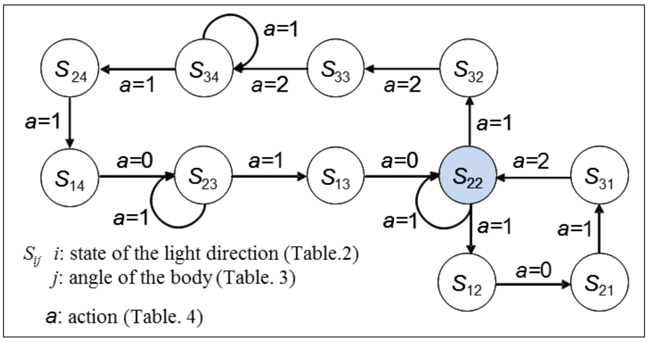

Fig. 15. State transitions in the dynamical environment

5 CONCLUSION

In this study, we examined autonomous control of a multi-crawler robot in a dynamic environment through the use of reinforcement learning. To solve the problems inherent to conventional approaches, which pertain to real-time learning and a lack of generality, we redesigned the mechanical body to abstract state-action space by utilizing the physical properties of the body. To demonstrate the effectiveness of our proposed approach, a prototype robot was developed and experiments were conducted. As a result, the behavior for moving towards a light source was learned within a reasonable time limit and the obtained policy could be generalized.

We conclude that the proposed framework is effective for developing autonomous robots that operate in dynamic environments.

ACKNOWLEDGMENT

This study was partially supported by the Ministry of Education, Culture, Sports, Science and Technology (MEXT) (Grant-in-Aid for Young Scientists (B), 22700156, 2011)

REFERENCES

[1] Arai M, Takayama T, Hirose S (2004), Development of Souryu-III: Connected crawler vehicle for inspection inside narrow and winding spaces, Proc. Int. Conf. Intelligent Robots and Systems, pp.52-57

[2] K. L. Paap, T. Christaller, F. Kirchner (2000), A robot snake to inspect broken buildings, Proc. Int. Conf. Intelligent Robots and Systems, pp.2079-2082

[3] A. Wolf, H. B. Brown, R. Casciola et al (2003), A mobile hyper redundant mechanism for search and rescue tasks, Proc. Int. Conf. Intelligent Robots and Systems, pp.2889-2895

[4] Kamegawa T, Yamasaki T, Igarashi H et al (2004), Development of the snake-like rescue robot "KOHGA," Proc. 2004 IEEE Int. Conf. on Robotics and Automation, pp.5081-5086

[5] Yamada H, Mori M, Hirose S (2007), Stabilization of the head of an undulating snake-like robot, Proc. Int. Conf. Intelligent Robots and Systems, pp.3566-3571

[6] Ito K, Fukumori Y (2006), Autonomous control of a snake-like robot utilizing passive mechanism, Proc. 2006 IEEE Int. Conf. Robotics and Automation, pp.381-386

[7] Ito K, Kamegawa T, Matsuno F (2003), Extended QDSEGA for controlling real robots -Acquisition of locomotion patterns for snake-like robot-, Proc. 2003 IEEE Int. Conf. Robotics and Automation, Sep 14-19, pp.791-796,

[8] Murai R, Ito K, Matsuno F (2006), An intuitive human-robot interface for rescue operation of a 3D snake robot, Proc. 12th IASTED Int. Conf. Robotics and Applications, pp.138-143

[9] Kimura H, Yamashita T, Kobaysahi S (2001), Reinforcement learning of walking behavior for a four-legged robot, Proc. 40th IEEE Conf. Decision and Control, pp.411-416

[10] R. Pfeifer (2001), "Understand Intelligence," The MIT Press, New edition

[11] J. J. Gibson (1987), "The ecological approach to visual perception," Hillsdale, NJ, Lawrence Erlbaum Associates

[12] Ito K, Takayama A, Kobayashi T (2009), "Hardware design of autonomous snake-like robot for reinforcement learning based on environment -Discussion of versatility on different tasks-," The 2009 IEEE/RSJ Int. Conf. Intelligent Robots and Systems, pp.2622-2627

[13] Ito K, Fukumori Y, Takayama A (2007), Autonomous control of real snake-like robot using reinforcement learning -abstraction of state-action space using properties of real world-, Proc. Int. Conf. Intelligent Sensors, Sensor Networks and Information Processing, pp.389-394

The Seventeenth International Symposium on Artificial Life and Robotics 2012 (AROB 17th '12),
B-Con Plaza, Beppu, Oita, Japan, January 19-21, 2012

Intelligent Control Method for Autonomous Vehicle by Fuzzy-Neural Network and Self-position-azimuth Correction

Ryunosuke Takauji[1], Peng Chen[2], and Mitushi Yamashita[3]

[1,2,3]Mie University, Mie 514-8507, Japan
(Tel: 059-231-9592)

[1]511m209@m.mie-u.ac.jp, [2]chen@bio.mie-u.ac.jp, [3]yamasita@bio.mie-u.ac.jp

Abstract: This paper proposes an Intelligent Control Method for Autonomous Vehicle which will roughly-appropriately and automatically recognize and judge the running environment and run along a given orbit without disarray by using Fuzzy-Neural Network (FNN). To realize autonomous running by using FNN, We extracted human's driving knowledge (teaching data for the FNN) from the running data. For acquiring the teaching data for the FNN, the running data are processed and normalized by rough set and defuzzy method. Moreover, we proposes an error correction method called "self-position-azimuth correction" to detect and correct the position and azimuth error between estimated position and actual measured position of the vehicle by using a pole at already-known position. The efficiency of the method has been verified by computer simulations and tests using a model vehicle.

Keywords: Autonomous vehicle, Fuzzy-neural network, Rough set, Self-position-azimuth correction

1 INTRODUCTION

Recently, labor saving in agricultural area is being needed increasingly because of decrease of agricultural workers due to the aging society. The autonomous running for the agricultural vehicle is one of the methods for the labor saving.

The purpose of this research is to construct an intelligent control system by using the fuzzy-neural network (FNN) for an autonomous vehicle which will roughly-appropriately and automatically recognize and judge the running environment and run along a given orbit without disarray.

Though various methods for orbit tracking of the vehicle have been proposed, there are many problems which have not been solved for learning human's driving knowledge and controlling the vehicle quickly as driven by a human driver. To solve these problems, this paper proposes an intelligent control method using fuzzy-neural network and Self-position-azimuth correction.

2 CONSTRUCTION METHOD

2.1 Model vehicle

The model vehicle used for the verification (called RoboCar^{TM}) is shown in fig. 2.1.

The dimensions of the model vehicle are W195.0 mm/D429.0 mm/H212.2 mm.

Speed control and steering angle control can be carried out by the rotary encoder and the servo motor respectively.

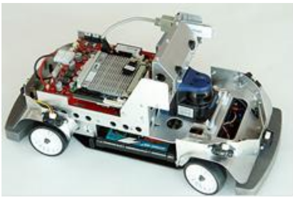

Fig. 2.1. RoboCar

2.2 Setting target orbit

The target orbit is sampled as points expressed by coordinate values which are set with the interval of about 20 cm. The straight line connecting points on the target orbit is regarded as approximate orbit of the target orbit. Also, these points are memorized in the computer of the model vehicle beforehand. The relative distance between the vehicle and point of target orbit are sequentially calculated while running. Then the point with the smallest relative distance is selected as the present target orbit point, the next point of that is regarded as sequential target orbit point. Finally, next point of now target orbit point is next target orbit point.

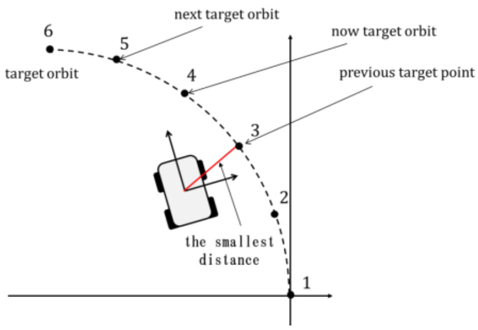

Fig. 2.2. Recognition of target orbit

2.3 Parameters between the vehicle and target orbit

*P*a is the relative distance between the center point of the vehicle and the target orbit. *P*b and *P*c are the relative angle between the direction of the vehicle and the line connected cross point 1 or cross point 2 to the center of the vehicle. Cross point 1 and cross point 2 are the points that the circle centered on the vehicle with the radius 30 cm, 60 cm intersects a target orbit. The vehicle recognizes a relative position by these parameters.

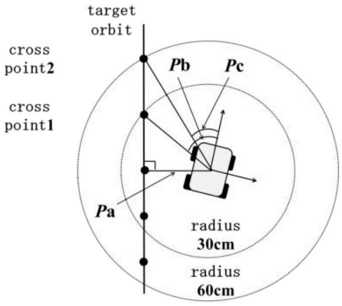

Fig. 2.3. Relative parameters

2.4 Method for extracting driving knowledge

Firstly, the running data is recorded while the vehicle is driven along target orbit by a human driver. *P*a, *P*b, *P*c and steering angle are acquired as the running data. Then, the running data is processed and normalized by rough set and defuzzy method. Human's driving knowledge (teaching data for the FNN) is extracted from the running data.

2.4.1 Normalization

Firstly, we need to normalize *P*a, *P*b, *P*c and steering angle for processing the teaching data by rough set. The range of the normalized relative distance and angle is narrow when the vehicle position is near to the target orbit, else it is wide when the vehicle position is distant from the target orbit. Steering angle is normalized with the interval of 3 degree.

Table 2.1. Range of normalization

Parameters	Pa [cm]	Pb [deg]	Pc [deg]
1	～-30	～-90	～-90
2	-30～-20	-90～-70	-90～-70
3	-20～-10	-70～-55	-70～-55
4	-10～-6	-55～-40	-55～-40
5	-6～-3	-40～-30	-40～-30
6	-3～-1	-30～-20	-30～-20
7	-1～1	-20～-15	-20～-15
8	1～3	-15～-10	-15～-10
9	3～6	-10～-6	-10～-6
10	6～10	-6～-3	-6～-3
11	10～20	-3～-1	-3～-1
12	20～30	-1～1	-1～1
13	30～	1～3	1～3
14		3～6	3～6
15		6～10	6～10
16		10～15	10～15
17		15～20	15～20
18		20～30	20～30
19		30～40	30～40
20		40～55	40～55
21		55～70	55～70
22		70～90	70～90
23		90～	90～

2.4.2 Rough set

In this section, we explain the rough set used this research. As a simple example, the data set is shown in Table. 2.2. *P* (the set of kinds of parameter) is shown by formula (2.1).

Table 2.2. Before rough set

Data No	Parameters P a	b	c	Sk
X1	3	2	1	0
X2	3	4	1	1
X3	1	7	3	0
X4	1	4	1	0
X5	3	4	1	1
X6	1	4	1	1
X7	4	6	2	0
X8	3	2	1	0
X9	4	6	2	1
X10	1	4	1	1

$$P = \{a, b, c\} \tag{2.1}$$

The i^th set of parameter value is shown by formula (2.2).

$$\begin{aligned} &{}^{1}P = \{3,2,1\} \\ &{}^{2}P = \{3,4,1\} \\ &\ldots \\ &{}^{10}P = \{1,4,1\} \end{aligned} \tag{2.2}$$

Approximation space set A is shown by formula (2.3).

$$A = \{r_1, r_2, r_3, r_4, r_5\} \tag{2.3}$$
$$= \{\{X_1, X_8,\}, \{X_2, X_5,\}, \{X_3\}, \{X_4, X_6, X_{10}\}, \{X_7, X_9\}\}$$

Then,

$$\begin{aligned} &r_1 = \{3,2,1\},\ {}^{r1}S = \{0,0\} \\ &r_2 = \{3,4,1\},\ {}^{r2}S = \{1,1\} \\ &r_3 = \{1,7,3\},\ {}^{r3}S = \{0\} \\ &r_4 = \{1,4,1\},\ {}^{r4}S = \{0,1,1\} \\ &r_5 = \{4,6,2\},\ {}^{r5}S = \{0,1\} \end{aligned} \tag{2.4}$$

By formula (2.4), ${}^{S}\beta_{ri}$, uncertainty of measurement to state *S* of equivalent class r_i, are

$$\begin{aligned} &{}^{0}\beta_{r1} = 2/2 = 1{:}100\% \\ &{}^{1}\beta_{r1} = 0/2 = 0{:}0\% \\ &{}^{0}\beta_{r2} = 0/2 = 0{:}0\% \\ &{}^{1}\beta_{r2} = 2/2 = 1{:}100\% \\ &{}^{0}\beta_{r3} = 1/1 = 1{:}100\% \\ &{}^{1}\beta_{r3} = 0/1 = 0\ {:}0\% \\ &{}^{0}\beta_{r4} = 1/3 = 0.33{:}33\% \\ &{}^{1}\beta_{r4} = 2/3 = 0.67{:}67\% \\ &{}^{0}\beta_{r5} = 1/2 = 0.5{:}50\% \\ &{}^{1}\beta_{r5} = 1/2 = 0.5{:}50\% \end{aligned} \tag{2.5}$$

Table 2.3. After rough set

rough sets r_i	Probability		Parameters P		
	${}^{0}\beta_{ri}$	${}^{1}\beta_{ri}$	a	b	c
$r_1=\{X_1^0,X_8^0\}$	100%	0%	3	2	1
$r_2=\{X_2^1,X_5^1\}$	0%	100%	3	4	1
$r_3=\{X_3^0\}$	100%	0%	1	7	3
$r_4=\{X_4^0,X_6^1,X_{10}^1\}$	33%	67%	1	4	1
$r_5=\{X_7^0,X_9^1\}$	50%	50%	4	6	2

2.5 Fuzzy-Neural Network

FNN can control the vehicle automatically and roughly-appropriately recognize and judge the running environment as human driver. Because FNN can output the appropriate results even if the input data have not been learnt beforehand, if we have appropriately made the leaning for the FNN. In this research, the inputs of the FNN are *P*a, *P*b and *P*c, the output of the FNN is steering angle. The construction of the FNN is shown in Fig. 2.4.

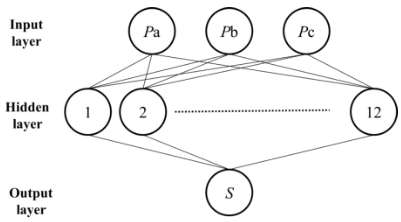

Fig. 2.4. Construction of the FNN

3 POSITION-AZIMUTH CORRECTION

We use the Dead Reckoning Method for the vehicle's positional presumption. But dead reckoning method has the disadvantage that the cumulative error of the vehicle position becomes a big gradually while running. The error is caused by slipping the wheel, etc. To solve this problem, we adopt self-position-azimuth correction using external information. In the verification, a pole (height is 200 mm; diameter is 65 mm) is set at already-known position on the world coordinate system Σ (*x*,*y*). Laser-Range-Finder (LRF) installed on the model vehicle measures a relative distance and angle between the vehicle and a pole. The range of detection of LRF is 5m and 240 degree like Fig. 3.1. Principle of Self-Position-azimuth Correction is shown in Fig. 3.2. $\overrightarrow{W}_{j'1}$ and $\overrightarrow{W}_{j'2}$ are the vector from the center of the vehicle to a pole. Also, the vector $\overrightarrow{W}_{j2-j1}$ can be calculated as follows.

$$\overrightarrow{W}_{j2-j1} = \overrightarrow{W}_{j2} - \overrightarrow{W}_{j1} \tag{2.6}$$

$$\theta_{\mathrm{L3}} = \theta_{\mathrm{L2}} - \theta_{\mathrm{L1}} \tag{2.7}$$

$$\theta_{\mathrm{L4}} = \sin^{-1}\left(\frac{l_2}{l_3} \times \sin\theta_{\mathrm{L3}}\right) \tag{2.8}$$

$$\theta_{\mathrm{G}} = \theta_{\mathrm{L4}} - \theta_{\mathrm{L1}} \tag{2.9}$$

$$R^{-1} = \begin{bmatrix} \cos\theta_{\mathrm{G}} & \sin\theta_{\mathrm{G}} \\ -\sin\theta_{\mathrm{G}} & \cos\theta_{\mathrm{G}} \end{bmatrix} \tag{3.0}$$

$$\vec{G} = \overrightarrow{W}_{j2} - R^{-1}\overrightarrow{W}_{j'2} \tag{3.1}$$

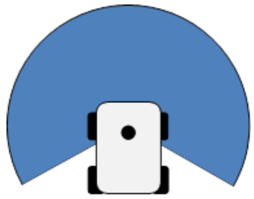

Fig. 3.1. The range of LRF

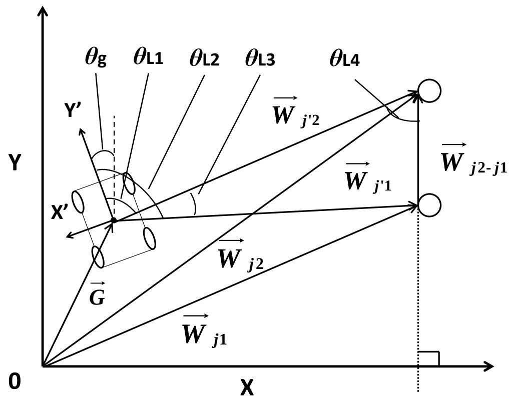

Fig. 3.2. Self-Position-azimuth correction

4. VERIFICATION

4.1 Vehicle communication environment

The model vehicle has Linux and is operated by other PC using access point.

Autonomous running will be operated by installed program.

Fig. 4.1. Communication system

4.2 Method for control of autonomous running

We need to construct the FNN in advance to control the vehicle. For the purpose, the teaching data is acquired by driving the model vehicle by human driver. And the learning for the FNN is done by Back Propagation Algorithm. When autonomous running is executed, the vehicle is controlled by output of the FNN. Output of the FNN is calculated by input *P*a, *P*b and *P*c to the FNN which has learnt the teaching data.

4.3 Acquisition the teaching data

Target orbit are the straight line and half circles with the radius 57.5 cm, 150 cm and 200 cm when we acquire the teaching data for the FNN. The initial positions are shown in Fig. 4.2, Fig. 4.3 when acquiring the teaching data.

The model vehicle's speed is at 10 cm/s. The initial directions are 0, 30 and -30 degrees when the vehicle run along a half circle with the radius 150 cm.

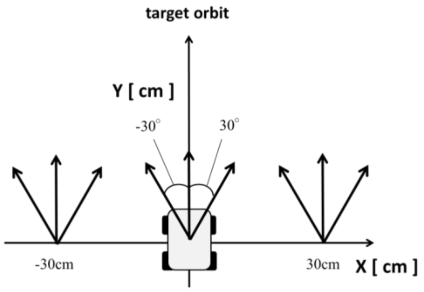

Fig. 4.2. The initial position of the vehicle when the target orbit is straight line

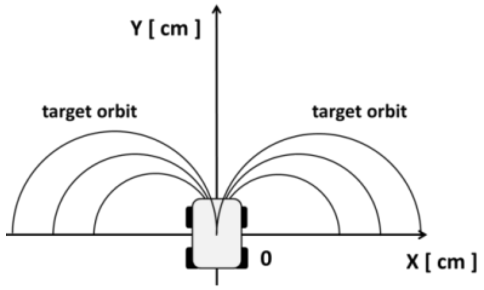

Fig. 4.3. The initial position of the vehicle when the target orbit is a circle

4.4 Running experiment

4.4.1 Verification by simulation

We did the autonomous running simulation using the FNN. The model vehicle's speed was 10 cm/s. The result of the autonomous running simulation is shown in Fig. 4.4, and by the result, the vehicle successfully returned to the straight orbit from the initial position which the FNN has not learnt.

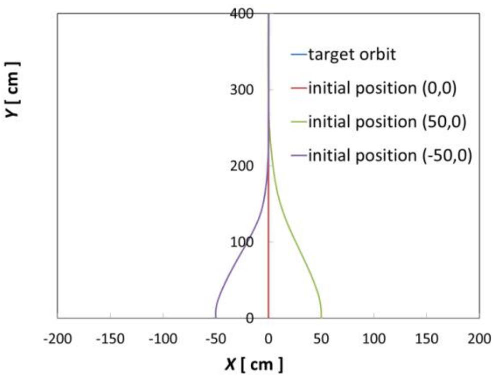

Fig. 4.4. The result of simulation

4.4.2 Verification by the model vehicle

The compound track orbit was set as the target orbit. The vertical straightway section of the target orbit is about 46.2 m, the crosswise straightway section is about 61.9 m, the curve section is a quarter of a circle with the radius 1 m. Also, two poles are set with about 4m intervals. We did the running experiment of the model vehicle. The vehicle's speed was 0.1 m/s, the initial position was (0,0) on the world coordinate system $\Sigma(x,y)$ and the initial direction was 0 degree. The result of running experiment is shown Fig.4.5. The vehicle tended to go to the left side. But the vehicle recognized the position and direction error between the estimated position and actual measured position by Self-position-azimuth correction and returned to the target orbit again. So, the model vehicle can run longer distance than previous experiment results.

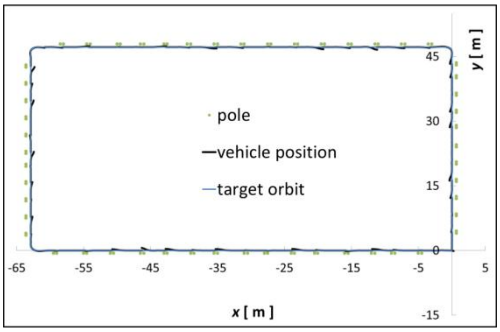

Fig. 4.5. The result of running experiment

5 CONCLUSION

It can be done efficiently to learn the teaching data for the FNN by acquiring the human's driving knowledge from the running data and by processing normalized rough set and defuzzy method even if there is only a small amount of teaching data. It is proved by the verifications that the FNN constructed by these methods can control the vehicle to run along the target orbit while roughly recognize and judge the running environment when the vehicle is in a condition which has not been learnt by the FNN in the vehicle. Also, it is proved that the Self-position-azimuth correction is useful for long distance running. The following problems are considered as the future subjects.

・To install a gyro sensor in the model vehicle and to run automatically in a condition with few poles
・To run automatically at a higher speed than ever
・To establish effective method for avoiding obstacles

REFERENCE

[1] Mukaidono M (1989), Talk of fuzzy (in Japanese). Nikkankougyousinbunsya Co., Ltd.

[2] Yana K, Suzuki Y (1992), Neuro information process technology kaibundousyuppan Co., Ltd. Pp.73-85

[3] Okishio A (1995), Study on the fuzzy navigation of a mobile robot for outdoor works (in Japanese).

The Seventeenth International Symposium on Artificial Life and Robotics 2012 (AROB 17th '12),
B-Con Plaza, Beppu, Oita, Japan, January 19-21, 2012

Learning strategy with neural-networks and reinforcement learning for actual manipulator robot

Shingo Nakamura[1] and Shuji Hashimoto[2]

[1,2]Waseda University, Tokyo 169-8555, Japan
(Tel: 81-3-5286-3233, Fax: 81-3-3202-7523)

[1]shingo@shalab.phys.waseda.ac.jp, [2]shuji@waseda.jp

Abstract: When the bottom-up learning approaches are implemented for mechanical systems, we must face a problem including huge number of trials. They take much time and give hard stress to the actual system. Simulator is often used only for evaluation of the learning method. However, it needs simulator modeling process, and never guarantees repeatability for the actual system. In this study, we are considering a construction of simulator directly from the actual robot with neural-networks. Afterward a constructed simulator is used for reinforcement learning to train a task, and the obtained optimal controller is applied to the actual robot. In this work, we picked up a five-linked manipulator robot, and made it track a ball as a training task. Both learning processes make load against the hardware sufficiently smaller, and the objective controller can be obtained faster than using only actual one.

Keywords: manipulator robot, neural-networks, reinforcement learning, simulator construction.

1 INTRODUCTION

The machine learning method is one of the typical techniques that may provide robots a capability to work in unpredictable and variable human life environment. Until now, many kinds of machine learning method have been proposed and they yield very effective results [1][2]. However, if they are directly applied to the actual machine, they face a problem including huge number of trials, which requires much time and gives stresses against the hardware and then makes a practical application difficult. To avoid such problems, a computational simulator is often employed and performed with a learning method since it permits many trials in short time without physical stresses [3]. However, the simulator utilization for the real system also includes some problems in its construction. Normally, the simulator is manually modeled by differential equation according to the physical law. Consequently, it never makes us completely free from exacting works. Moreover, there is no guarantee that the modeled simulator performance matches the actual machine when its construction is complicated. Hence, we propose a simulator construction directly from the actual hardware. In our method, a simulator learns the relationship between command signal and its resultant state of the hardware. Therefore, if the learning proceeds well, a simulator emulates the hardware behavior certainly, and we are relieved from arduous simulator modeling. After simulator construction, the optimal controller for an objective behavior is trained only with the constructed simulator. Therefore, this process never gives harsh load to the hardware and performs faster than directly using the hardware.

In this paper, we describe a novel method of machine learning using both a simulator and an actual hardware. A simulator of the hardware is directly built from the acquired input and output data of the real hardware and it performs with the neural-networks and the back-propagation learning method without any information of kinematics model. Afterward, the objective controller of the hardware is trained only with the built simulator by the reinforcement learning method. Finally, the optimum controller is applied to the actual hardware. In this manner, the optimal controller is generated via hybrid platform: simulator and hardware, without any knowledge in advance. Here we employed a five-linked manipulator robot as an actual hardware platform, and the only treated properties are state and command signals of actuators assembled into the robot. The task for the robot to train is to track a colored ball. Under these conditions, experiments were conducted and the prosed method was evaluated.

2 BASIC STRATEGY

Fig.1 illustrates a basic structure and process of our method. At first, data of the actual hardware behavior is sampled and collected into a buffer. In this case, data means a set of command and state of the actual hardware, and a resultant state corresponding to the command, which represents the relationship between input and output of the hardware. And then the buffer supplies reference data to

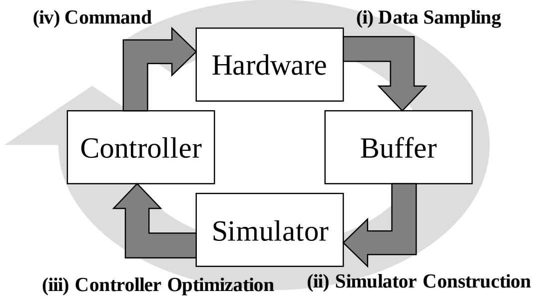

Fig.1. The over view of learning strategy

build a simulator in the appropriate manner. Afterward a controller is trained the optimal control for the objective task using the built simulator. At this time, because of a computational simulator, the hardware does not have to be actually operated and training process performs faster than using the actual hardware. Finally, the optimized controller operates the actual hardware to perform the objective behavior. In this way, the whole process starts from the hardware acting, and the information is returned to the hardware. Based on this structure, we apply to the five-linked manipulator robot to get the optimal task control. The implementation of each process for this problem is explained in the chapter 4.

3 MANIPULATOR ROBOT

In this paper, our method is applied to an actual robot. The robot we employed is a five-linked manipulator robot, composed of five servo motors as shown in Fig.2, and their link relations are illustrated in Fig.3. The motor is digital servo type and performable in serial communication to receive the action command and return the status information. The motor control mode is configured to "speed" mode. Finally the robot hardware consists of such motor, and state and action command of robot mean angle and speed command value for each motor. Specifically, we can just send a speed command value $a = (a_1, a_2, a_3, a_4, a_5)$ to each motor as action command for robot, and observe each motor angle $s = (s_1, s_2, s_3, s_4, s_5)$ as robot state. Some control limitations are given in software level. Every joint is configured to be able to move in range [-π/2, +π/2]. If it is out of the range, it stops until command to move for inside direction comes. Using this platform robot, our method is evaluated by training ball-tracking task.

4 IMPLIMENTATION

As shown in Fig.1, there are four processes in our strategy and their efficient implementation provides a self-

Fig.2. The manipulator robot

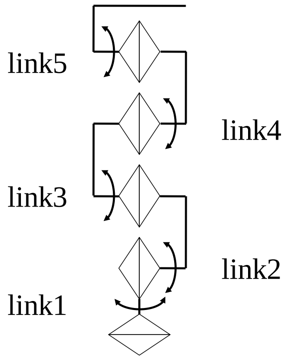

Fig.3. The link structure

learning ability to the system. In this chapter, detailed implementation for the manipulator robot is described.

4.1 Data Collection and Supply

The data sampled from the actual robot is collected into a buffer. In this work, data to collect is a pair information of (s_t, a_t) and $s_{t+\Delta t}$. These mean the robot state s and command a at time t, and its response state s at time $t+\Delta t$. And it is supplied to a simulator for construction. Therefore, the buffer has to keep and supply the suitable data to represent the actual robot.

In order to supply the suitable data to construct a simulator, the limited parameter space $\mathbf{S} \times \mathbf{A}$ is divided into some sub-spaces in a number of $N_S \times N_A$ in similar way. Each sub-space keeps corresponding data. At simulator construction by neural-networks, one sub-space is chosen at random and one sampled data is provided as learning data.

4.2 Simulator Construction

The Multi-Layered Perceptron (MLP) of the neural-networks which is effective for the approximation of a nonlinear function is employed to simulate the hardware. It directly represents the robot behavior. The MLP consists of three layers, i.e. input, hidden and output layer. The MLP is input 10 parameters, namely the manipulator state s_t and command a_t for each motor, while it outputs next robot state $s_{t+\Delta t}$. Each neuron in the output layer is a nonlinear unit expressed with the arctangent sigmoid function whose output is limited in [-1, 1]. Therefore, the output value s_i [-π/2, +π/2] is normalized into [-1, 1].

A simulator has the MLP network inside. In the simulation process, it follows the MLP. The simulator inputs the data set (s, a) at time t, and obtains the normalized difference values in [-1, 1] as an output signal from the MLP. The de-normalized values s is simply represented as the state at time $t+\Delta t$. Fig.4 illustrates the overview of running process of simulation with the MLP.

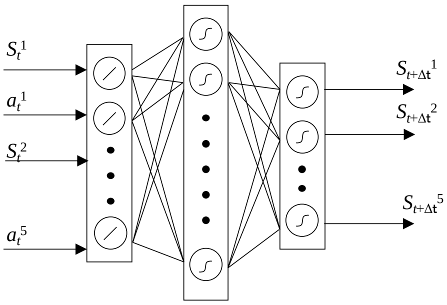

Fig.4. Neural-networks process for robot simulator

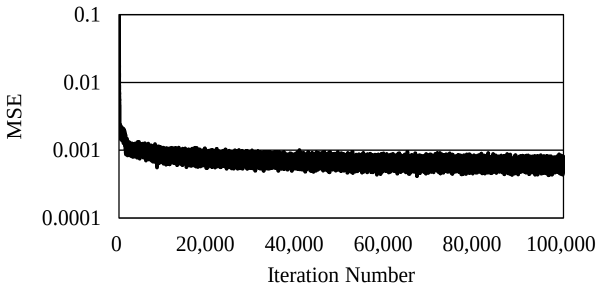

Fig.5. Result of simulator construction learning

And in the process of learning, the teacher data is supplied from the buffer, and the back-propagation method performs.

4.3 Controller Optimization

A controller learns the optimal control using a simulator. Here, we focus on the reinforcement learning [4] to make robot track a ball. In the reinforcement learning, the action is evaluated by the given rewards, and the system learns empirically the optimum action by trials and errors. In this work, we employ the Q-Learning method for the reinforcement learning. This is a typical method of reinforcement learning. When the agent at time t takes the action a_t based on the current state s_t, the state-action value function $Q(s_t, a_t)$ is updated as follows:

$$Q(s_t, a_t) \leftarrow Q(s_t, a_t) + \alpha[r_{t+1} + \gamma \max_a Q(s_{t+1}, a) - Q(s_t, a_t)] \quad (1)$$

where r_t is the reward the agent receives at time t, α is a learning ratio and γ is a discount ratio. In the phase of training, the agent chooses an action randomly. The other hand, it takes the action a where $Q(s_t,a)$ is the max value at state s_t in execution phase. In this way, a controller of the robot explores the optimum action command for each state and then performs tracking the ball.

5 EXPERIMENT AND RESULT

5.1 Data Collection

The target data to train a simulator was sampled from the actual manipulator robot described in the chapter 4. To collect data, an action command a selected in the previously mentioned manner was given with interval Δt = 50 msec. Consequently, the robot moved in the range of motion. The division numbers N_S and N_A for the five-dimensioned state space and action command space were set to 11^5 and 4^5, respectively. This collection process continued for one hour in real world. In other words, 72 thousands sample data were collected.

5.2 Simulator Construction

The learning of the neural-networks was performed by the backpropagation method. The number of neurons in the input, hidden and output layer were 10, 20 and 5, and a target sample data set (s_t, a_t) and $s_{t+\Delta t}$, were randomly took from a divided sub-space, which was selected at uniformly random from whole space. Learning ratio was set to 0.1, and nonlinearity ratio of nonlinear neurons in the MLP was set to 1.0. The number of learning iterations was 10 million times.

This operation was performed just in 10 minutes. Fig.5 shows the mean squared error (MSE) of MLP every one thousand learning. The MSE value decreased until around 1.0×10^{-3}. This means that the accuracy of learning was about 3% in normalized space, namely about 2.6 degree of actual angle.

5.3 Controller Optimization

Learning to track a ball was performed with the obtained simulator in the previous section. The state space **S** and command space **A** was divided into 9 sub-spaces at even intervals and treated as a discrete space for each joint. Hence, whole parameter space **S** × **A** was divided into $5^9\times5^9$ sub-spaces. The 250mm-diameter ball to track was put in the robot-reachable space, and then, task learning processed until the robot touched it or 2,000 steps was done without "touch". Here, "touch" means that the forward point 250 mm from the robot head is inside the ball area. This cycle is defined as "episode" in this experiment. y and z-coordinate value of ball position was fixed, and only x-coordinate value was selected at random for one episode. The controller to optimize was selected, depending on the ball x-coordinate value. Consequently, controllers as many as division number of x-coordinate were prepared. Finally, ball position x was selected at random from [-100, +100]

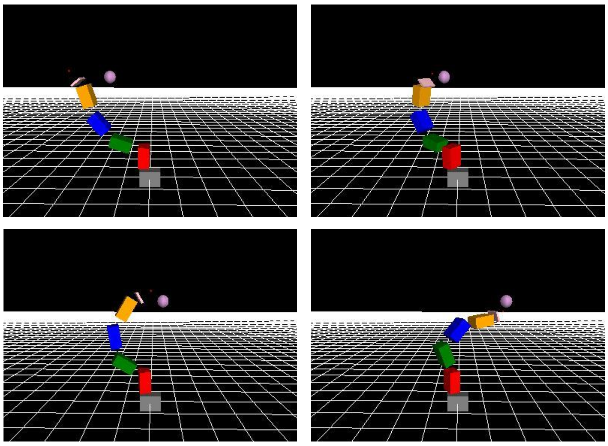

Fig.6. Ball tracking with simulator

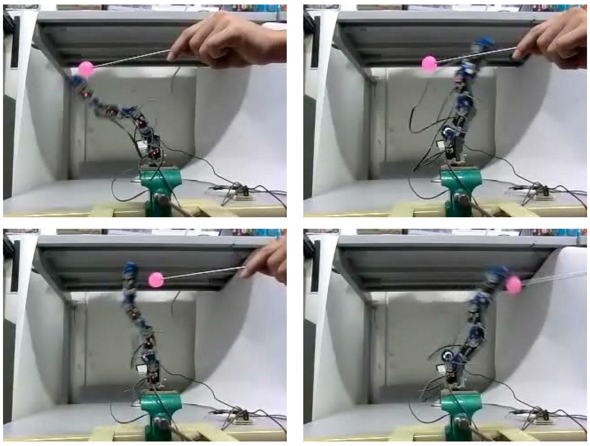

Fig.7. Ball tracking with actual robot

mm, which was divided into 10 areas, y and z were fixed into -32 mm and +192 mm, respectively.

The episodes to learn were repeated a million times in the simulation world. If this operation is executed in the real world, it would take about 28 thousand hours. The reinforcement learning performed according to the formula (1) with interval 50 ms. The parameters α and γ used for the update, were set to 0.1, and 0.9, respectively. The reward 1.0 was given only at the state "touching".

The learning process finished in twelve hours at most, though it would take about three years in the real world. Fig.6 shows the sequential images of ball tracking by simulator. Depending on the target ball position, the corresponding controller was selected and tried to make the robot touch the ball. The moving ball finally made continuous touching into tracking ball.

5.4 Application to actual robot

Finally, we applied the learning result of the previous section to the actual robot controller. In this experiment, the real ball position was detected by image processing in real time. Two web cameras were put around the robot and detect the red ball. The ball positions in camera image were converted into the real world coordinate by the Direct Linear Transformation method.

Fig.7 shows that the sequential images of the actual robot tracking ball. At the beginning of tracking, the robot tried to track the ball correctly. However, it shook more widely than the simulator robot to hold its state. As the ball moved, the robot tried following it. Nevertheless, the robot went down as if it lost the strength. On investigation, the command for the bottom-positioned motor was too weak to lift up self-body though it attempted. These results raise the possibility that accuracy of simulator by the neural-networks was not enough.

6 CONCLUSION

We proposed a novel method of machine learning associating with an actual hardware and its simulator. The simulator of the manipulator robot was constructed by the neural-networks trained with acquired data from the actual hardware without information of the physical law. Afterward, the ball tracking control for the manipulator robot was learned only through the built simulator by the reinforcement learning method. By using the simulator, the reinforcement learning could be finished much faster than using the real hardware without stress. However, when the controller applied to the actual robot, it could not represent the same way of the simulator completely.

Now we have a plan to construct a simulator after some executions of loop flow illustrated in Fig.1. Sampled data information is carried to the hardware controller and data is sampled from hardware cyclically. This is very adaptable process though physical information of target hardware is changed due to deterioration or component exchange. If this is actualized, our method comes more generalized for various machinery systems.

REFERENCES

[1] J. Bongard, V. Zykov, and H. Lipson (2006), Automated synthesis of body schema using multiple sensor modalities, Proceedings of the Int. Conf. on the Simulation and Synthesis of Living Systems

[2] K. Doya, K Samejima, K. Katagiri, and M. Kawato, (2002), Multiple model-based reinforcement learning, Neural Comput., vol.14, no.6, pp.1347-1369

[3] K. Doya (1996), Efficient Nonlinear Control with Actor-Tutor Architecture, Advances in Neural Information Processing System, pp.1012-1018

[4] Sutton RS, Barto AG (1988), Reinforcement Learning: An Introduction. Cambridge, MA: MIT Press

The Seventeenth International Symposium on Artificial Life and Robotics 2012 (AROB 17th '12),
B-Con Plaza, Beppu, Oita, Japan, January 19-21, 2012

A basic study on cooperative behavior of two butterflies inspired by quantum entanglement

Masaki Maezono[1], Ichiro Iimura[2], and Shigeru Nakayama[3]

[1]Kagoshima National College of Technology, Kagoshima 899-5193, Japan
[2]Prefectural University of Kumamoto, Kumamoto 862-8502, Japan
[3]Kagoshima University, Kagoshima 890-0065, Japan
(Tel: 81-995-42-907, Fax: 81-995-42-907)

[1]maezono@kagoshima-ct.ac.jp
[2]iiimura@pu-kumamoto.ac.jp
[3]shignaka@ibe.kagoshima-u.ac.jp

Abstract: Recently, the physical concept of quantum entanglement has been introduced into the two distant insects (butterflies) to cooperatively find each other by the previous study of J. Summhammer. According to his experimental results, we have confirmed that the two butterflies with quantum entanglement may need as little as half of the flight path of independent butterflies to find each other. However, the case where the learning factor, the length of a short straight flight and the threshold of the scent intensity are different between two butterflies has not been clarified in his previous study. Hence we have simulated the cooperation of two butterflies while changing the condition of these parameters. This paper describes the experimental results. We aim at the optimum modeling of cooperative relation of two individuals as the first stage, and the contents in this paper deserve the initial experiment in the case of two distant butterflies which must find each other.

Keywords: cooperative behavior, cooperative action, quantum cooperation, quantum entanglement

1 INTRODUCTION

Recently, the physical concept of quantum mechanical principle such as quantum superposition, quantum interference and quantum entanglement has inspired the information and computer science domain as well as the biology. For example, the physical concept of quantum interference has been brought to Genetic Algorithm by A. Narayanan et al. Quantum superposition has been brought to Evolutionary Algorithm by K.-H. Han et al., too. Regarding quantum entanglement, J. Summhammer has described the possibility of quantum entanglement in the biological domain [1]. He has introduced it into two insects (ants) to cooperatively push a pebble which may be too heavy for one ant, and has introduced it into two distant insects (butterflies) to cooperatively find each other. That is, each of ants/butterflies makes measurements on quantum particles to decide whether to execute certain actions. According to his experimental results, we have confirmed that the two ants with quantum entanglement, i.e., quantum-entangled ants, can push the pebble up to twice as far as independent (classical) ants, and the two butterflies with quantum entanglement, i.e., quantum-entangled butterflies, may need as little as half of the flight path of independent butterflies to find each other. However, the case where important parameters of two ants/butterflies are different each other has not been clarified in his previous study.

As for ants, we have clarified the relation between the force needed to push a pebble, the force of ant1 and the force of ant2 in our previous study. From the experimental results, we have proven that two ants with the bigger difference of force can push the pebble farther in competitive society in both classical ants and quantum-entangled ants [2].

As for butterflies, the relation between the learning factor, the length of a short straight flight and the fraction for threshold of the scent intensity is not yet clarified. In order to clarify the relation among these important parameters, we have simulated the cooperation of two butterflies while changing the condition of these parameters. This paper describes the experimental results. The optimum modeling of cooperative relation is expected by this study. We aim at the optimum modeling of cooperative relation of two individuals as the first stage, and the contents in this paper deserve the initial experiment in the case of two distant butterflies which must find each other.

2 OVERVIEW OF QUANTUM ENTANGLEMENT IN THE PHYSICAL DOMAIN USED IN QUANTUM-ENTANGLED BUTTERFLIES

In this paper we deal with the simplest kind of quantum entanglement. It is the correlation of the angular momentum between two particles of the same kind. The angular momenta of two such particles can easily be measured along different directions. The possible results are then "↑↑", "↓↓", "↑↓", and "↓↑", here "↑" and "↓" are *spin up* and *spin down*, respectively. Quantum theory can only predict the probabilities, $p_{\uparrow\uparrow}$, $p_{\downarrow\downarrow}$, $p_{\uparrow\downarrow}$, and $p_{\downarrow\uparrow}$, for these measurement results. An important state of quantum entanglement, which will be used in butterflies, is the so called *singlet state*. Here, the angular momenta of the two particles are always in the opposite direction each other. Symbolically, this state is written as

$$|\psi\rangle = \frac{|\uparrow\downarrow\rangle - |\downarrow\uparrow\rangle}{\sqrt{2}}. \tag{1}$$

The probabilities for the possible measurement results are

$$p_{\uparrow\uparrow} = p_{\downarrow\downarrow} = \frac{1}{2}\sin^2\left(\frac{\alpha}{2}\right), \tag{2}$$

$$p_{\uparrow\downarrow} = p_{\downarrow\uparrow} = \frac{1}{2}\cos^2\left(\frac{\alpha}{2}\right), \tag{3}$$

where α is the angle between the two chosen directions of measurement.

3 THE MODEL OF QUANTUM-ENTANGLED BUTTERFLIES FINDING EACH OTHER PROPOSED BY J. SUMMHAMMER

J. Summhammer showed the model that two distant butterflies find each other. Two butterflies, which are distant sufficiently each other, are located on the *x*-*y* plane as shown in **Fig. 1**. They can catch only information which is an intensity of scent emanated by other butterfly. Thereby for approaching each other, they must flight respectively to increase the intensity of the scent. The scent has the following character:

- The intensity of the scent emanated by each butterfly drops off as $1/r^2$ where r is the distance from the butterfly.
- The propagation of the scent is very much faster than the speed with which the butterfly, so that each butterfly can notice a change of intensity of the scent at once.
- The direction of the origin of the scent cannot be obtained from physical quantity involved in the scent.

3.1 Flight procedure of a modeled butterfly

As mentioned above, two butterflies can encounter by flying to the direction which increase the intensity of the scent. The algorithm for the flight toward the direction increasing the intensity of the scent is shown below:

[*Step 1*] Choose a direction for a short straight flight.

For the short straight flight, the butterfly chooses the direction randomly, but weighted with a probability distribution of directions. The probability distribution of directions is one which it considers appropriate in view of its experience of change of the scent intensity in the previous short flights. In the beginning, this probability distribution of directions is isotropic.

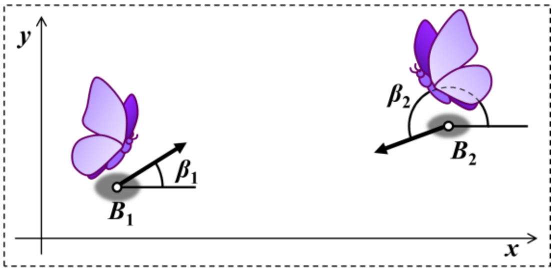

Fig. 1. The example of the flight directions β_1 and β_2 of the butterfly B_1 and the butterfly B_2 on the *x*-*y* plane.

[*Step 2*] Decide whether to really do the short straight flight, or whether to have a little rest.

Independent butterflies decide randomly either the short straight flight or the little rest, respectively. In this case, the probability of each behavior selected is constantly 1/2. On the other hand, the decisions of quantum-entangled butterflies come from quantum measurement which will be explained later. If the butterfly has decided the short flight, that performs a short straight flight of constant length l_f toward the chosen direction, go to *Step 3*. Otherwise, that is, if the butterfly has decided the little rest that does not perform any action, go to *Step 5*.

[*Step 3*] Judge whether the butterfly should fly back or not.

The butterfly measures the scent intensity and compares an increase from the last measurement with a certain threshold. The threshold is taken as a certain fraction f_t of the strongest increase $s_{d\max}$ of the scent intensity encountered in the short flights until then. If the increase s_d is below the threshold ($s_d < f_t \times s_{d\max}$), the butterfly judges this to have been a bad direction and flies back. The butterfly returns to the position before the short flight by flying back. On the other hand, if the increase is above the threshold, the butterfly judges this to have been a good direction and does not fly back.

[*Step 4*] Learn, i.e. update the probability distribution of directions.

Based on the above-mentioned judgment, the probability distribution of directions is updated using a learning factor l. When the butterfly had judged as a good direction, the butterfly enhances the corresponding probability weight by the factor $(1+l)$. This direction is then more likely to be chosen again in one of the next short flights. In contrast, when the butterfly had judged as a bad direction, the butterfly reduces the corresponding probability weight by the factor $(1+l)^{-1}$. This direction is then less likely to be chosen again.

[*Step 5*] Repeat until the butterflies meet each other.

When the distance between two butterflies is less than a certain small value, it is concluded that the two butterflies met each other and this trial is ended. If the distance is still large, return to *Step 1* because the butterfly performs to the next short flight.

3.2 Behavior of the quantum-entangled butterflies

The difference between quantum-entangled butterflies and independent butterflies is shown when the butterfly decides either to really do the short straight flight or to have a little rest (above-mentioned *Step 2*). The independent butterflies decide randomly, whereas the quantum-entangled butterflies decide on the basis of a quantum measurement. The quantum-entangled butterflies share a large number of maximally entangled pairs of spin-1/2 particles, of which each butterfly holds one particle. Here the entangle state is the singlet state. The quantum measurement determines the value of the angular momentum of the particle along the flight direction which is chosen by the butterfly at *Step 1*. If the measurement result is "↑", the butterfly performs the short straight flight. If the result is "↓", the butterfly rests.

Here if we assume a butterfly B_1 chooses β_1 as the flight direction and a butterfly B_2 chooses β_2 as shown in **Fig. 1**, there are the following three possibilities.

Case 1: Both butterflies fly in the direction selected based on self-judgment respectively. This case happens with probabilities

$$p_{\uparrow\uparrow} = \frac{1}{2}\sin^2\left(\frac{\beta_1 - \beta_2}{2}\right), \tag{4}$$

according to Eq. 2.

Case 2: Both butterflies have a little rest. This case happens with probabilities

$$p_{\downarrow\downarrow} = \frac{1}{2}\sin^2\left(\frac{\beta_1 - \beta_2}{2}\right), \tag{5}$$

which is equal to $p_{\uparrow\uparrow}$.

Case 3: One butterfly flies and another rests. This case happens with probabilities

$$p_{\uparrow\downarrow} = p_{\downarrow\uparrow} = \frac{1}{2}\cos^2\left(\frac{\beta_1 - \beta_2}{2}\right), \tag{6}$$

according to Eq. 3.

Note that, when the difference between β_1 and β_2 gets closer to 0, the probability of Case 3 increases. In other words, when the quantum-entangled butterflies choose same direction which does not decrease the distance although both flight, only one butterfly flies frequently.

4 EXPERIMENTAL ANALYSIS

4.1 Method of the experiment

There are the following three important parameters characterizing behavior of the butterfly: the learning factor (l), the length of a short straight flight (l_f) and the fraction for the threshold of the scent intensity (f_t). About each of these three parameters, we have experimented by setting different value between two butterflies. In each following experiment, we have verified the relationship between the total flight distance until two butterflies encounter and the change of the target parameters.

Experiment 1: Varying the learning factor l for two butterflies.

We changed the learning factor l_1 of the butterfly B_1 from 1.00 to 0.00 in -0.05 steps, and also changed l_2 of the butterfly B_2 from 1.00 to 2.00 in +0.05 steps, respectively, where $l_1 + l_2 = 2.00$.

Experiment 2: Varying the flight length l_f for two butterflies.

We changed the flight length $l_{f\,1}$ of the butterfly B_1 from 5.0 to 0.0 in -0.2 steps, and also changed $l_{f\,2}$ of the butterfly B_2 from 5.0 to 10.0 in +0.2 steps, respectively, where $l_{f\,1} + l_{f\,2} = 10.0$.

Experiment 3: Varying the fraction f_t for the threshold of the scent intensity for two butterflies.

We changed the fraction $f_{t\,1}$ of the butterfly B_1 from 0.60 to 0.20 in -0.01 steps, and also changed $f_{t\,2}$ of the butterfly B_2 from 0.60 to 1.00 in +0.01 steps, respectively, where $f_{t\,1} + f_{t\,2} = 1.20$.

We used the default parameters shown in **Table 1** except the target parameters in each experiment.

4.2 Result of learning factor experiment

The experimental result is shown in **Fig. 2**. A solid line shows the average of each trial result by the two quantum-entangled butterflies. A dashed line shows the average of

Table 1. Default parameters used

The learning factor	1.00
The length of a short straight flight	5.0
The fraction for the threshold of the scent intensity	0.60
The direction chosen	16 directions evenly spread over 2π.
The initial distance of two butterflies	1600.0
The distance which can find the another (termination condition)	20.0
The number of trials	1000

each trial result by the two independent butterflies. These are the same also at latter experimental results, which are **Fig. 2** and **Fig. 3**. The graph shows that the equality of the learning factor reduces the number of total flights to encountering of the two butterflies. Especially, this tendency is remarkable on the quantum-entangled butterflies. It is because the probability distributions of directions which change similarly with equal learning factor let the selection frequency of a direction related to cooperative behavior as shown in Eq.4 and Eq.5 increase.

4.3 Result of length of short straight flight experiment

The experimental result is shown in **Fig. 3**. The number of total flights decreases with increase of the difference of the flight length between two butterflies ($l_{f\,2}$ - $l_{f\,1}$). Especially, this tendency is remarkable on the independent butterflies. It is because the difference of ability decreases the opportunity for disturbing each action of uncooperative butterflies. A large value of $l_{f\,2}$ - $l_{f\,1}$ extinguishes mostly the difference from the quantum-entangled butterflies. When one of the two quantum-entangled butterflies is provided the extremely small flight length, success or failure of their approach depends heavily on a behavior of another butterfly. Hence, probably cooperative behavior is no use.

4.4 Result of fraction for threshold of scent intensity experiment

The experimental result is shown in **Fig. 4**. In the case of independent butterflies, the number of total flights decreases with increase of the difference of the fraction for threshold of scent intensity ($f_{t\,2}$ - $f_{t\,1}$) to $f_{t\,1}$= 0.27 and $f_{t\,2}$ = 0.93. On the other hand in the case of the quantum-entangled butterflies, this tendency is not strong; the number of total flights is the minimum at the fractions: $f_{t\,1}$= 0.35 and $f_{t\,2}$ = 0.85. Even if the quantum-entangled butterflies make a cooperative decision whether to fly or to rest, only one butterfly may judge that it is necessary to fly back when the difference of the fractions is quite large. Thereby, the meaning of cooperative behavior by quantum entanglement diminishes.

5 CONCLUSION

In the model of the quantum-entangled butterflies finding each other, we have simulated the model while changing each the three parameter conditions in order to clarify the influence on the performance to find another butterfly. From the each experimental result, we have proven that the conditions to improve the finding performance are the more equivalent learning factor, the

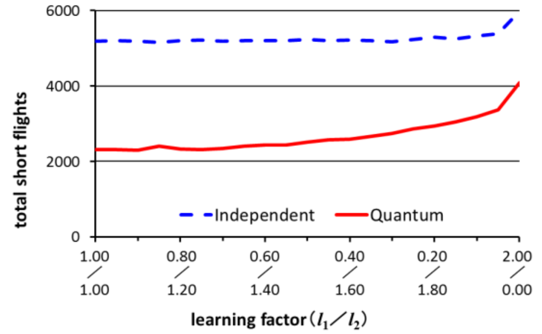

Fig. 2. Total number of short flights needed by the two butterflies to find each other vs. the learning factor l_1 and l_2.

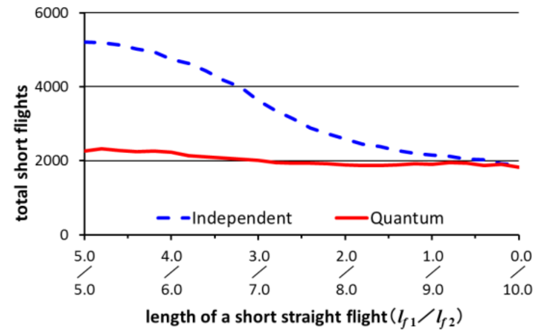

Fig. 3. Total number of short flights needed by the two butterflies to find each other vs. the length of a short straight flight $l_{f\,1}$ and $l_{f\,2}$.

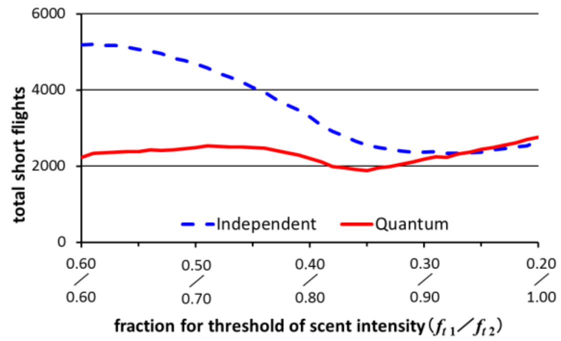

Fig. 4. Total number of short flights needed by the two butterflies to find each other vs. the fraction for threshold of scent intensity $f_{t\,1}$ and $f_{t\,2}$.

bigger difference of the length of a short straight flight, and the bigger difference of the fraction for the threshold of the scent intensity. However, when the difference of each parameter is too large, action of one butterfly is wasted and it may disturb cooperative behavior inspired by quantum entanglement.

REFERENCES

[1] Summhammer J (2006), Quantum cooperation of two insects. arXiv:quant-ph/0503136v2

[2] Nakayama S, Iimura I (2011), Cooperative action in two ants inspired by quantum entanglement state and an interpretation in collective decision making (in Japanese). IPSJ Journal 52(8):2467-2473

The Seventeenth International Symposium on Artificial Life and Robotics 2012 (AROB 17th '12),
B-Con Plaza, Beppu, Oita, Japan, January 19-21, 2012

Importing dynamic planner to BDI agent creating flexible decision-making of policies for selecting robot actions in real world

Megumi Fujita[1], Hiroko Katayama[1], Yuko Ojima[1], and Naoyuki Nide[2]

[1] Graduate School of Nara Women's University, Nara, Nara 630-8506, Japan
[2] Nara Women's University, Nara, Nara 630-8506, Japan
(Tel: +81-742-20-3555, Fax: +81-742-20-3555) (saboten@ics.nara-wu.ac.jp)

Abstract: Our aim is to create a more intelligent form of control for robots that can act autonomously for problem solving in the dynamic environments. The ability to select and modify the action decision policies to achieve the given goals in the most appropriate way as possible, and the easiest and most efficient way of implementation of such policy controls is required. We propose a flexible method for selecting policies of action decision in this paper, using a dynamic planner as the mechanism for determining the policies for action decision making. We proved through experimentation that when a robot cannot achieve its goal using a specific policy, it can modify the given policy to achieve that goal with the use of our method. In particular, for robots in the real world, the error of beliefs due to a false recognition of the sensors may be the reason why a robot cannot achieve its goal, although this situation will not come to light in any simulation. Our method is effective for such situations.

Keywords: Autonomous agent, Intelligent robot, BDI, Real world oriented, Planner

1 INTRODUCTION

With the recent development of advanced robotics, there is a growing expectation for the construction of intelligent robots that can act autonomously by generating plans for achieving their goals in the real world. In particular, such a robot would require the ability to cope with various changes in their environments; for example, when it cannot achieve its goal by using the current plan because of an unexpected change in the real world situation, it must create a new policy of action for achieving its goal.

Our aim is to create such robots using autonomous agents called BDI agents. Since it is now possible to inexpensively and easily obtain small robots, we are currently attempting to equip them with BDI agents and assist them to be able to resolve problems in the real world.

As described in Sec.2, a BDI agent has a native mechanism called "deliberation", which selects a plan to execute immediately from among multiple (currently active) plans for achieving the agent's goals. This mechanism works like the task switching mechanisms of operating systems, and assists the agent in switching goals and gives them a means for easily achieving them. Furthermore, agent designers can separate the codes for switching plans from the codes of the plans themselves. These are part of why the BDI agent is suitable for creating robots that can autonomously solve problems.

However, it would be inadequate to write a deliberation algorithm using the hand-coding manner to achieve a highly flexible switching of plans. A higher-level means to provide a deliberation algorithm is required to infer an appropriate plan depending on the given circumstances of the agents.

In this paper, we propose enhancing the deliberation by introducing a dynamic planner. Human beings normally hold some sort of policy as a higher-level principle for selecting plans for achieving his/her goals, and modify it as necessary to change his/her behavior. Our proposal is to implement this method on an agent using a dynamic planner to decide it's given policy, and therefore, naturally and flexibly enhances the mechanism of the deliberation.

There have been several proposals introducing a planner into a BDI agent ([1, 2, 3]), but they use the planner as a tool that generates plans and provides them to the agents. On the other hand, it is a characteristic point that in our method the dynamic planner works as an effective tool for selecting the action policy of the agent in a dynamic environment. In Sec.4.4, we show that when a robot implemented with this method in our experiment cannot achieve its goal by using the selected plan based on its current action policy, it can change the policy using the dynamic planner and then achieve its goal. Our proposal is effective in that such a property installed in robots is desirable for robots in the real world.

2 BDI AGENTS

A BDI agent[4] is a type of autonomous and rational agent that explicitly has three mental attitudes, beliefs, and desires and intentions (written as B, D and I respectively), and uses their temporal changes in the decision-making process.

When a new goal (desire) arises, a BDI agent selects a usable plan to achieve that goal from the plan library using its belief base ("practical reasoning"), and forms an intention to commit to executing that plan, then adds it to the set of current intentions (active plans). Next, the agent selects a particular intention to execute right now using the belief base (by using a mechanism called "deliberation"), and takes one step to execute it. Subsequently, the agent perceives the environment to update its beliefs, and then updates its intention set (e.g., intentions that have already been achieved are discarded; and if a goal is judged to be impossible to achieve by the current intention for that goal, then that intention is discarded and an alternative intention to achieve the goal is selected[1]). By repeating this sequence of processes as a loop, the agent attempts to achieve its goals.

We use Jason[5], a well-known platform for implementing BDI agents.

3 COOPERATION WITH DYNAMIC PLANNER

In this section, we explain the design of the dynamic planner we propose for use in cooperation with a BDI agent (hereafter called "BDI cooperative dynamic planner"), and explain how it cooperates with the agent.

The BDI cooperative dynamic planner is created by modifying SHOP2[6], a famous hierarchical planner. It uses the planning engine of SHOP2.

Since SHOP2 is designed for static problem solving, when given a goal, it completely decomposes that goal down to a sequence of atomic actions. However, in a dynamic environment, it is impractical to decompose the goal into atomic actions because once the plan is made it may become difficult to proceed with it due to a change in circumstances.

A human being, in a dynamic environment, first makes a rough plan to achieve his/her goal, and when the time comes, he/she decomposes and substantiates the plan more minutely so that it can be directly executed. The BDI cooperative dynamic planner also does the same thing. So, it stops decomposing the plan in the first step of the decomposition process, and accumulates it as a sequence of subgoals. Then, the subgoal at the top of the sequence of subgoals is a goal for the agent, and at this time, the planner decomposes that subgoal into a set of tasks and gives them to the agent who uses them as an action policy for achieving its goals.

If the agent finishes their goal using this policy, it informs the planner, and the planner gives the next subgoal in the sequence to the agent as the next policy. On the other hand, if the agent cannot accomplish the goal using this policy, the planner re-plans under the current condition to create a new action policy and then gives it to the agent.

We implement our planner as a separate program to Jason. The agent running on Jason invokes a sub-process of the planner that stays active until the agent program terminates, and it interacts with the agent using interprocess communications.

[1] Actually, the alternative intention is not selected in this step, but in the next round of a loop.

4 EXAMPLE USING ROBOT

We explain how our proposal is efficient at controlling a robot in the real world using the experiment results in this section.

4.1 Example problem

The example problem for the robot we used in our experiment is to search for treasure in a maze on a grid (Fig.1). Initially, the agent does not have any knowledge about the locations of walls, so each time the agent perceives the existence of a wall, it adds the information about the position of the wall to its belief base. When the robot finds the treasure, it returns back to the initial position. Note that in this experiment, the robot may occasionally collect erroneous information about the positions of walls due to errors in perception caused by the noise of its sensor.

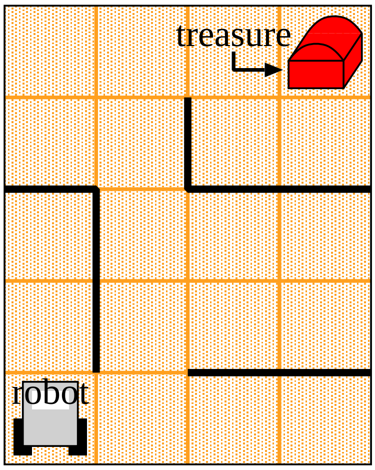

Fig. 1. Map used in our experiment

At first, the robot searches for the treasure while relying on its beliefs about the positions of walls, since it incurs some cost to perceive the walls. However, there are possibilities that the robot is unable to find the treasure due to errors in its beliefs.

If this happens, the robot has to switch to another way of searching while re-perceiving the walls instead of trusting the beliefs about the walls. After that, when the robot finds an unexplored square, it judges that it has escaped the situation of inability to find the treasure, and should switch back to the original way of searching.

4.2 Implementation of atomic actions

The robot we used was a MINDSTORMS NXT developed by the LEGO company. The robot in this experiment is a mobile robot with two front wheels and one rear wheel. It has an ultrasonic sensor in the front to measure the distance to an obstacle (Fig.2).

The NXT fundamentally has only low level commands such as specifying the torque output and receiving an integer signal from the sensor. However, we prepared a higher level of actions, such as "proceed to the next square", "rotate by 90 degrees" and "perceive whether a wall exists", and

The Seventeenth International Symposium on Artificial Life and Robotics 2012 (AROB 17th '12),
B-Con Plaza, Beppu, Oita, Japan, January 19-21, 2012

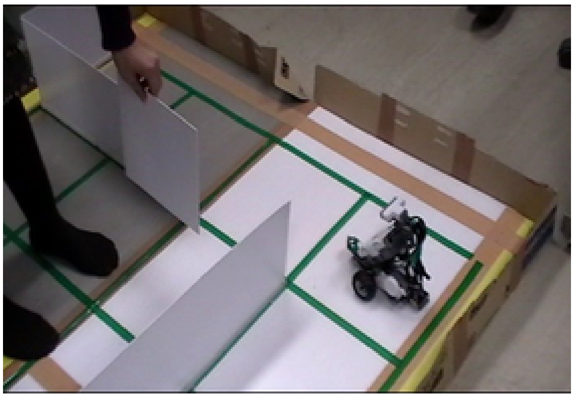

Fig. 2. Schematic layout of our experiment

used them as atomic actions. The merit of this method is that we can separate the low level controls of robots from the plan description of agents. For example, low level robot controls are accompanied by errors due to mechanical inaccuracies with the motors and sensors. If some progress is made with this type of problem, the efficiency of our proposal in this paper improves in conjunction with it, although we do not deal with this topic in this paper.

4.3 Flow of agent program

Let us assume that the agent (robot) has the initial goal of "find the treasure and return to the initial position", and requests an action policy for the subgoal "find treasure" from the planner. The planner creates a "normal search" policy and gives it to the agent. Then, the agent selects a "searching by normal strategy" plan and forms it into an intention.

According to this plan, the agent searches for the treasure while adding (and using) its beliefs about the positions of walls, which is acquired by perception. In this stage, the agent does not repeatedly perceive the places where a wall is believed to exist.

If zero unexplored squares remain, this plan fails. In this case, the agent asks the planner again, and the planner returns a "re-search" action policy. The agent selects a "searching while considering the possibilities of errors with past perceptions" plan, and forms it as a new intention. By following this plan, the agent continues searching while re-perceiving the walls (without relying on the beliefs about the places of walls).

When the agent finds an unexplored square, again it asks the planner for a "normal search" policy. The agent again selects the "searching by normal strategy" plan, makes it an intention, and continues searching in the former way.

After the agent finds the treasure, a "return to the initial position" plan is executed as the next subgoal, which we omit in this paper.

We also omit the actual codes of the agent programs due to space limitations.

4.4 Experimental result

We performed our experiment on a 4 5 grid (Fig.1, 2).

Starting with Fig.1, the agent begins searching using the "normal search" policy described in Sec.4.3.

Meanwhile, to create a situation in which the agent wrongly believes in the existence of a wall, we put an extra wall at a given place in the maze (Fig.3).

Then, the agent continues searching with the erroneous belief in the existence of a wall. When the agent comes that place again, it still believes that there is a wall even after the fake wall has been removed, and does not repeatedly try to perceive it (Fig.4).

The agent goes around all the unexplored squares, and finds that no new routes remain, and thus, it cannot find the treasure. So, the agent asks the planner and switches to the "re-search" policy described in Sec.4.3, and continues searching while re-perceiving in all directions around it (Fig.5).

As a result, the agent finds a new route to the yet unexplored areas (Fig.6). Then, the agent asks the planner, goes back to the "normal search" policy and continues searching until it finds the treasure.

We conducted another experiment in which we place the fake wall on the grid twice. The robot was able to behave properly and find the treasure.

In this regard, we concluded that the robot can deal with the problem of misperception.

5 DISCUSSION

As described in Sec.1, robots in the real world have to change their behaviors according to the various (sometimes unexpected) changes in environments. When an ad-hoc technique, such as the traditional hand-coding method, is used to cope with such problems, there is a tendency for the codes of the plans themselves and the meta-level codes for the switching plans to get mixed up, and the maintainability is then lost.

The BDI agent, as an agent development approach, in comparison with methods such as hand-coding methods, can be regarded as the framework for describing agents using a kind of high-level language. Plans can be described declaratively and in a mutually independent manner, and then explicit codes for switching plans are not necessary. These features are essential for enabling flexible changes in behaviors. Furthermore, the notion of intentions in BDI agents works as a higher-level action decision mechanism and this provides a stable and consistent behavior towards achieving the agent's goals.

In addition, in our method, by leaving the "deliberation" part to the planner, there is no need to procedurally write the deliberation routine, and by only receiving information about the current circumstances from the agent, we can select an

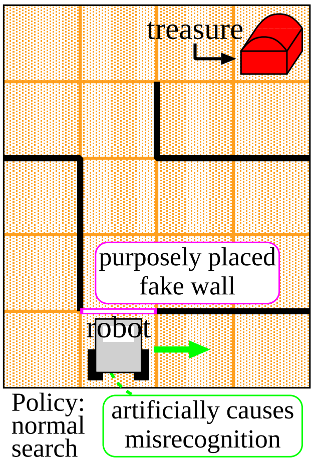

Fig. 3. Producing false recognition of walls

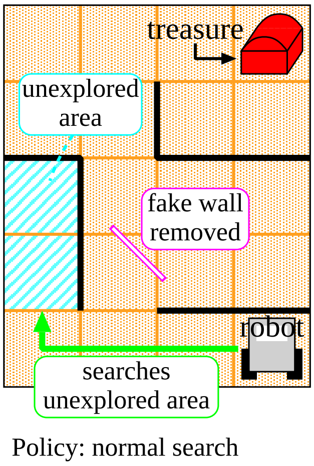

Fig. 4. Continuation of search based on inaccurate belief

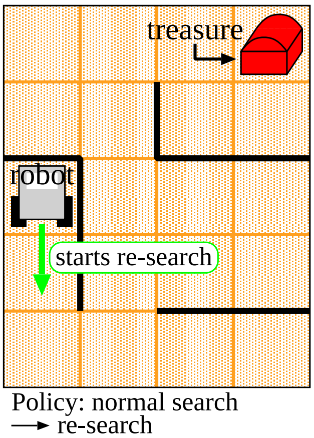

Fig. 5. Being stuck, robot asks planner and switches action policy

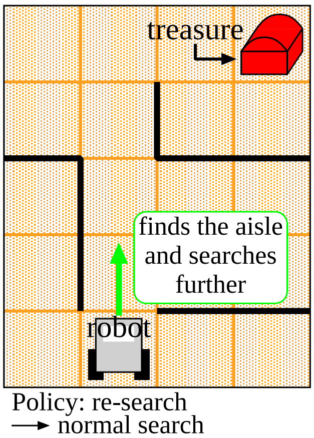

Fig. 6. When unexplored place is found, robot asks planner again, switches policy, and continues searching

appropriate action policy to commit as a plan. Also, when using an efficient planner in large-scale applications, we can expect improvement in the efficiency of selecting plans compared with that from the hand-coding method (though such advantage may be unrealistic in smaller applications such as the experiment discussed in this paper).

Moreover, our method is also a complement to the weakness of Jason as a base of implementation for BDI agents. In Jason, when a plan fails once, the agent can recover by executing a plan for handling that failure, but if the plan for failure fails again, the agent cannot continue to achieve its goal. On the other hand, by using our method, the robot can recover from multiple failures (e.g., misperceptions), as described in Sec.4.4.

Yet another merit of BDI agents is that they have a formalization by using a modal logic named the BDI logic[7], in which not only the demands for the agents but also the behaviors of the agents can be integrally argued. We propose an extension to this by importing the formalization of the planner[8], so there is the future possibility for the formal verification of our method.

6 CONCLUSION

We proposed enhancing the deliberation in BDI agents by introducing a dynamic planner so that an agent can flexibly change its action policy for achieving its goals, and showed that our method is efficient enough for use in robots in the real world through experimentation.

Our future issues include applying this method to a larger task, and introducing the formal verification method introduced in Sec.5.

REFERENCES

[1] A. Walczak, L. Braubach, A. Pokahr, and W. Lamesdorf, "Augmenting BDI Agents with Deliberative Planning Techniques," *The 5th International Workshop on Programming Multiagent Systems (PROMAS-2006)*, pp. 113–127, 2006.

[2] L. de Silva, A. Dekker, and J. Harland, "Planning with Time Limits in BDI Agent Programming Languages," *ACM International Conference Proceeding Series*, vol. 240, pp. 131–139, 2007.

[3] F. R. Meneguzzi, A. F. Zorzo, M. D. C. Móra, and M. Luck, "Incorporating planning into BDI systems," in *Proc. of SCPE 2007*, 2007.

[4] M. P. Singh, A. S. Rao, and M. P. Georgeff, "Formal method in DAI: Logic-Based Representation and Reasoning," in *Multiagent Systems: A Modern Approach to Distributed Artificial Intelligence*, pp. 331–376, The MIT Press, 1999.

[5] R. H. Bordini, J. F. Hübner, and M. Wooldridge, *Programming Multi-Agent Systems in AgentSpeak using Jason*. John Wiley & Sons, 2007.

[6] D. Nau, T.-C. Au, O. Ilghami, U. Kuter, J. W. Murdock, D. Wu, and F. Yaman, "SHOP2: An HTN Planning System," *Journal of Artificial Intelligence Research*, vol. 20, pp. 379–404, 2003.

[7] A. S. Rao and M. P. Georgeff, "Modeling Rational Agents within a BDI-Architecture," in *Proc, of International Conference on Principles of Knowlegde Representation and Reasoning*, pp. 473–484, 1991.

[8] N. Nide, M. Fujita, and S. Takata, "Formalizing combination of dynamic planner and BDI agent," in *Proc. of Joint Agent Workshop and Symposium 2010*, 2010. (in Japanese).

The Seventeenth International Symposium on Artificial Life and Robotics 2012 (AROB 17th '12),
B-Con Plaza, Beppu, Oita, Japan, January 19-21, 2012

Adaptive reinforcement learning based on degree of learning progress

Akihiro Mimura[1] and Shohei Kato[1]

[1] Dept. of Computer Science and Engineering, Graduate School of Engineering, Nagoya Institute of Technology,
Gokiso-cho, Showa-ku, Nagoya, Aichi 466-8555, Japan
(Tel: +81-52-732-5625, Fax: +81-52-732-5625)
({mimura, shohey}@juno.ics.nitech.ac.jp)

Abstract: In this paper, we propose adjustment method named *adaptive learning rate considering learning progress* (ALR-P). The learning rate is a meta parameter that balances trade-off between speed and stability of the learning. Conventionally, designer had to manually set up a fixed learning rate. However, it is difficult for learning agent to adapt dynamic environment with a fixed learning rate. ALR-P enables adaptive adjustment of learning rate based on degree of learning progress for every steps. The degree of learning progress is calculated based on TD-error which is a difference of predicted and observed rewards. Only TD-error which can be calculated easily and simply is used in the ALR-P, so it can be applied into any types of reinforcement learning. We confirm effectiveness of ALR-P under a number of dynamic environments through the maze problem in which the environmental changes occurred.

Keywords: reinforcement learning, learning rate, dynamic environment, adaption, degree of learning progress

1 INTRODUCTION

Recently, there are a lot of researches about robotics using the reinforcement learning. The reinforcement learning is a kind of the machine learning which the learning agent learns and acquires appropriate control rules through the trial and error [1]. Because the learning agent acquires the control rules autonomously, for instance, reinforcement learning is often used for autonomous behavior acquisition of robots [2][3].

However, if meta parameters of the learning such as learning rate and the discount rate are inappropriate, the learning agent cannot behave sufficient performance. In general, the optimal value does not exist in these meta parameters, and the designer should adjust them properly according to the target task and progress of learning. In addition, it is difficult to learn appropriately under dynamic environment. When the reinforcement learning is applied to real environmental problem such as robot control, robustness for environmental change and noise should be taken into consideration. However, a lot of conventional methods are based on the premise that environment is static, and do not take environmental change into consideration.

In this paper, we focus on learning rate, which is one of the meta parameters of the reinforcement learning, and propose the dynamic adjusting method for learning rate.

2 REINFORCEMENT LEARNING

The agent learns control rule by repeating a sequence of taking an action based on action-value (Q-value) and receiving a reward. Q-value is predicted value of the total amount of reward that the agent will receive over the future. The reward indicates what is good in an immediate sense.

Softmax method is used for action selection in this paper, which is often used in many reinforcement learning. Softmax method determines selection probabilities of actions based on Q-values for the corresponding actions. Selection probability of action a in state s is shown as $\Pr(a|s)$, and is determined by the following equation.

$$\Pr(a|s) = \frac{\exp(Q(s,a)/\tau)}{\sum_{a' \in A} \exp(Q(s,a')/\tau)}, \tag{1}$$

where A, $Q(s,a)$, and τ show set of actions that the agent can select in the state s, action-value of the action a in the state s, and the temperature, respectively. The agent receives the reward that is the evaluation value of the selected action from the environment.

The agent dynamically updates the action-value function based on the received rewards. In this paper, we use Q( )-learning [4] as learning algorithm. In Q( )-learning, the action-value function is updated according to the following equation.

$$Q(s,a) \leftarrow Q(s,a) + \quad \delta(s,a)e(s,a), \tag{2}$$

where , $\delta(s,a)$, and $e(s,a)$ show the learning rate, the TD-error of action a in the state s, and the eligibility trace, respectively. TD-error is calculated by the following equation.

$$\delta = r + \gamma \max_{a' \in A'} Q(s',a') - Q(s,a), \tag{3}$$

where r, γ, s', and A' show the reward, the discount rate, the following state after the action a, and set of actions that the agent can select in state s', respectively. Roughly, TD-error indicates the difference of the predicted value and the observed value in the state-action pair. Eligibility trace is index which shows whether the updating of the corresponding Q-value is proper or not.

3 LEARNING RATE

As shown in the Equation (2), a learning rate is a meta parameter which determines updating width of action-value function. Generally, in the case of that the learning rate is high, the progress of learning is fast although the learning is not steady. On the other hand, the learning progresses slowly though the learning is steady in the case of that the learning rate is low. This means that the learning rate is a parameter that balances trade-off between speed and stability of the learning.

In this paper, we propose adjustment method named *adaptive learning rate considering learning progress* (ALR-P). ALR-P adjusts learning rate according to each state (or state-action pair) for every step. The learning in the early stage or environment changes should be progressed speedy even if it can be roughly. because the learning agent have to acquire more proper action-value function as soon as possible in that cases. Meanwhile, the learning in the end stage should be progressed more precisely in order to converge action-value on optimal value in high accuracy. From the above things, the learning rate should be adjusted considering the learning progress; the learning rate should be high to value the learning speed in a state that the action-value cannot be correctly estimated, while the one in a state that the action-value can be correctly estimated should be low to value the stability.

4 ALR-P

ALR-P is a method of adjusting learning rate for every step considering learning progress, and we newly propose *degree of learning progress* in order to realize the adjustment of learning rate in this method. In this method, we focus on TD-error which can be thought a difference of predicted and observed rewards. In a state such as early stages of learning and environmental change, TD-error is high because prediction of reward is not proper. On the other hand, in a state such as converging stages of learning, TD-error is low and approaches 0 because prediction of reward is proper. TD-error changes for every steps, since the suitable learning can be not realized if the learning rate is adjusted based on the each change. Thus, we define the expected value of absolute TD-error as the degree of learning progress, and use the degree of learning progress to adjust the learning rate. The degree of learning progress in state s and action a, $d(s, a)$ is defined by the following equation.

$$d(s, a) := E[|\delta(s, a)|]. \tag{4}$$

Table 1. Q( )-learning applying ALR-P

Initialize $Q(s, a)$ arbitrarily for all s, a
Initialize $e(s, a) = 0$ and $d(s, a) = 0$ for all s, a
Repeat (for each episode):
  Initialize s, a
  Repeat (for each step of episode):
    Choose a' from s' using policy derived from Q (e.g., softmax-method)
    $\delta(s, a) \leftarrow r(s, a) + \gamma \max_{a'} Q(s', a') - Q(s, a)$
    $d(s, a) \leftarrow d(s, a) + \omega[|\delta(s, a)| - d(s, a)]$
    If $d(s, a) > d_m(s, a)$:
      $d_m(s, a) \leftarrow d(s, a)$
    $\alpha = d(s, a)/d_m(s, a)$
    $e(s, a) = 1$
    For all s, a:
      $Q(s, a) \leftarrow Q(s, a) + \alpha\delta e(s, a)$
      $e(s, a) \leftarrow \gamma\lambda e(s, a)$
    $s \leftarrow s'$
    until s is terminal

However, to calculate the expected value, it is necessary to save all history of TD-errors in each state-action pair. Since huge calculation memories and costs are needed for calculating the expected value, it is approximated by the following exponential moving average (EMA).

$$d(s, a) \leftarrow d(s, a) + \omega[|\delta(s, a)| - d(s, a)], \tag{5}$$

where ω shows updating width. By using the EMA, only the present TD-error is required to calculate the degree of learning progress, and the maximum $d(s, a)$ in each state-action pair is saved as $d_m(s, a)$. Using the calculated values from Equation (5), the learning rate   is adjusted by the following equation for every steps.

$$= \frac{d(s, a)}{d_m(s, a)}. \tag{6}$$

Because the learning rate is adjusted based on the degree of learning progress that each state-action pair has, so the learning rate can be adjusted according to the each state-action pair.

In ALR-P, only TD-error is used to calculate the degree of learning progress. Because the TD-error is a simple value generally calculated in existing reinforcement learning methods, it is easy to build ALR-P into almost all reinforcement learning methods such as Q-learning, Sarsa, Actor-Critic and so on. Q( )-learning applying ALR-P is shown in Table 1.

5 ADAPTIVE LEARNING EXPERIMENT

We conduct comparative experiments with ALR-P and conventional methods, and verify effectiveness of ALR-P.

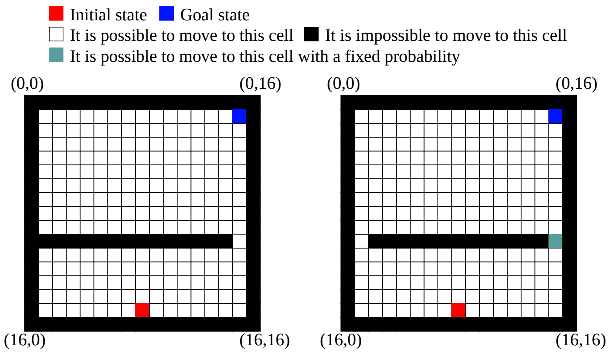

(a) Until 100th episode (b) From 101st episode

Fig. 1. Maze problem

5.1 Maze problem with environmental changes

We apply ALR-P to the maze problems (see Fig. 1) in which the environmental changes are occurred. Each cell shows state, and the coordinates are defined as follows: left-uppermost is $(0, 0)$, right-uppermost is $(0, 16)$, left-lowermost is $(16, 0)$, and right-lowermost is $(16, 16)$. An initial state and a goal state are set to $(15, 8)$ located in lower part of the maze and $(1, 15)$ located in upper-right part, respectively. The environmental changes in this experiment is defined as follows; until 100th episode (Fig. 1(b)), agent can reach goal state by passing through $(10, 15)$, from 101th episode (Fig. 1(b)), $(10, 1)$ is opened up along the left side, and $(10, 15)$ changes whether transition is possible or not with a fixed probability for every steps. And we prepared two transition settings, *Setting A*: agent can through the $(10, 15)$ with a possibility 1/7, and *Setting B*: agent can through the cell with a possibility 1/14. In Setting A, the expected value of sum rewards of right side path which contains $(10, 15)$ is higher than one of the left side path which contains $(10, 1)$. On the other hand, in Setting B, the expected values of sum rewards of both side paths are equivalent.

Comparative methods are RRASP-N [5] and the conventional general methods that learning rate is each fixed to 0.3, 0.5, 0.7, and 0.9. RRASP-N is a method to adjust learning rate to minimize square TD-errors. Q( )-learning is used as learning algorithm, and softmax method is used as action selection rule. This experiment consists of 300 episodes, and one episode is that learning agent reaches in goal state or passes over 100 steps. The agent moves to top, bottom, right, or left cell, and receives reward that is -1 in a step.

5.2 Experimental results

5.2.1 Transition of sum rewards

The above-mentioned experiments were conducted 100 times for the each method. The results shown in Fig. 2 and Fig. 3 indicate that the transition of sum rewards in the Setting A and Setting B, respectively. In Setting A, as comparing the results of the conventional methods that learning rate is each fixed, it was confirmed that advantage by magnitude relation of learning rate is reversed before and after environmental changes. Also in Setting B, there is no conventional method that always keeps advantage without differences of learning rate. Therefore, high learning performance could not be behaved with a stationary learning rate in this problem.

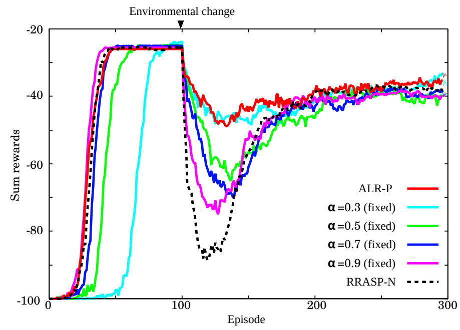

Fig. 2. Transition of sum rewards in the Setting A

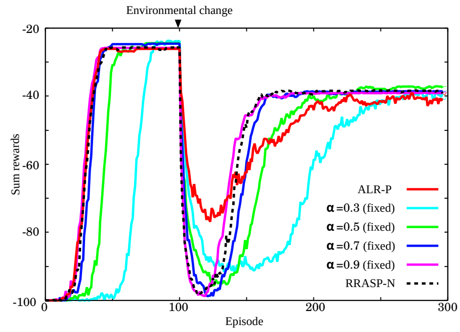

Fig. 3. Transition of sum rewards in the Setting B

From Fig. 2 and Fig. 3, we confirmed that ALR-P behaved high performance, irrespective of environmental changes. Before the environmental changes, ALR-P converged learning fast. After the environmental changes, ALR-P behaved relatively high performance, and progresses learning without greatly reducing sum rewards even though immediately after the environmental changes. On the other hand, RRASP-N was reduced sum rewards greatly in the both settings.

5.2.2 Transition of learning rate

Fig. 4 shows an example of transition of learning rate in state-action pair that state is $(11, 15)$ and action is moving to up. From this figure, we confirm that after environmental changes learning rate was adjusted high again. Because the location of state $(11, 15)$ was near the state in which environmental changes occurred, it is thought that the state was profoundly affected by the environmental changes. ALR-P

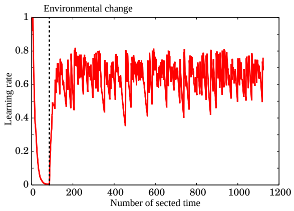

Fig. 4. Transition of learning rate in state-action pair that state is $(11, 15)$ and action is moving to up

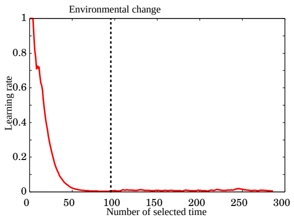

Fig. 5. Transition of learning rate in state-action pair that state is $(15, 8)$ and action is moving to right

Table 2. Success rate of the task and selection path at success episode after environmental changes in the Setting A

Learning rate	Success rate (%)	Selection rate of $(10, 1)$ (%)	Selection rate of $(10, 15)$ (%)
ALR-P	94.25	16.29	83.51
$\alpha = 0.3$ (fixed)	86.08	8.49	91.51
$\alpha = 0.5$ (fixed)	82.59	31.62	68.38
$\alpha = 0.7$ (fixed)	84.43	56.12	43.88
$\alpha = 0.9$ (fixed)	85.16	67.58	32.42
RRASP-N	83.08	84.38	15.62

Table 3. Success rate of the task and selection path at success episode after environmental changes in the Setting B

Learning rate	Success rate (%)	Selection rate of $(10, 1)$ (%)	Selection rate of $(10, 15)$ (%)
ALR-P	83.20	64.67	35.33
$\alpha = 0.3$ (fixed)	62.51	66.06	33.94
$\alpha = 0.5$ (fixed)	75.84	86.26	13.74
$\alpha = 0.7$ (fixed)	81.13	94.99	5.01
$\alpha = 0.9$ (fixed)	84.45	97.21	2.79
RRASP-N	83.08	96.83	3.17

could promote relearning by adjustment of the learning rate according to the variation of TD-error.

Fig. 5 shows an example of transition of learning rate in state-action pair that state is initial state $(15, 8)$ and action is moving to right. From this figure, we confirm that the learning rate was not high even though it was after the environmental changes. Because the location of state $(15, 8)$ was far from the state in which environmental changes occurred, it is thought that the state is not seriously affected by the environmental changes. From these results, it was confirmed that ALR-P could adjust learning rate to appropriate value on each state.

5.2.3 Success rate of task

The results shown in Table 2 and Table 3 indicate that success rate of the task and selection path at success episode after environmental changes in the Setting A and Setting B, respectively. From these tables, we confirm that success rate of ALR-P is relatively higher than other methods in the both settings. The results suggest that ALR-P enables adaptive learning under dynamic environment and has general versatility.

From the tables, we confirmed that ALR-P showed the relatively higher selection rate of $(10, 15)$ than other methods. In Setting B, although expected values of sum rewards of right and left side paths are equivalent, the right side path can be the shortest. Therefore, it can be said that ALR-P not only maintains high success rate, but also searches shorter path.

When RRASP-N is applied, selection rate of $(10, 1)$ is relatively higher than other methods. Thus, it is thought that RRASP-N maintains high success rate by selecting left side path in which environmental change does not occur.

6 CONCLUSION

In this paper, we propose adjustment method named adaptive learning rate considering learning progress (ALR-P). We confirmed that learning agent can adapt to dynamic environment by using ALR-P through maze problem with environmental changes.

For example, in robotic control of humanoids under real world, it is necessary to consider risk such as tumble. ALR-P which can adapt appropriately to dynamic environment is expected to decrease influence of breakdown caused by abrasion of joint, disturbance and so on.

ACKNOWLEDGMENT

This work was supported in part by the Ministry of Education, Science, Sports and Culture, Grant.in.Aid for Scientific Research under grant #20700199.

REFERENCES

[1] Sutton R. S and Barto A. G. (1998). *Reinforcement Learning: An Introduction*. The MIT Press.

[2] Mimura A, Nishibe S, and Kato S. (2011), Kinetic chained throwing humanoid robots by using reinforcement learning. *12th International Symposium on Advanced Intelligent Systems*, pp. 188–191.

[3] Riedmiller M, Gabel T, Hafner R, and Lange S. (2004), Reinforcement learning for robot soccer. *Autonomous Robots*, 27(1), pp.55–73.

[4] Watkins C. J. C. H and Dayan P. (1992), Q-leaning. *Machine Learning*, 8(3-4), pp.279–292.

[5] Noda I. (2010), Adaptation of stepsize parameter to minimize exponential moving average of square error by newton's method. *AAMAS*, pp. M–2–1.

The Seventeenth International Symposium on Artificial Life and Robotics 2012 (AROB 17th '12),
B-Con Plaza, Beppu, Oita, Japan, January 19-21, 2012

Developing reinforcement learning for adaptive co-construction of continuous state and action spaces

Masato Nagayoshi[1], Hajime Murao[2], and Hisashi Tamaki[3]

[1] Niigata College of Nursing, 240, Shinnan, Joetsu 943-0147, Japan
(nagayosi@niigata-cn.ac.jp)
[2] Faculty of Cross-Cultural Studies, Kobe Univ. 1-2-1, Tsurukabuto, Nada-ku, Kobe 657-8501, Japan
(murao@i.cla.kobe-u.ac.jp)
[3] Graduate School of Engineering, Kobe University, Rokko-dai, Nada-ku, Kobe 657-8501, Japan
(tamaki@al.cs.kobe-u.ac.jp)

Abstract: Engineers and researchers are paying more attention to reinforcement learning (RL) as a key technique for realizing adaptive and autonomous decentralized systems. In general, however, it is not easy to put RL into practical use. Our approach mainly deals with the problem of designing state and action spaces. Previously, an adaptive state space construction method which is called a "state space filter" and an adaptive action space construction method which is called "switching RL," have been proposed after the other space has been fixed.
In this paper, we reconstitute these two construction methods as one method by treating the former method and the latter method as a combined method for mimicking an infant's perceptual and motor developments. Then the proposed method is based on introducing and referring to "entropy." In addition, a computational experiment was conducted using a so-called "robot navigation problem" with three-dimentional continuous state space and two-dimensional continuous action space. As a result, the validity of the proposed method has been confirmed.

Keywords: reinforcement learning, adaptive space co-construction, state space design, action space design, entropy

1 INTRODUCTION

Engineers and researchers are paying more attention to reinforcement learning (RL)[1] as a key technique in developing autonomous systems. In general, however, it is not easy to put RL to practical use. Such issues as satisfying the requirements of learning speed, resolving the perceptual aliasing problem, and designing reasonable state and action spaces for an agent, etc., must be resolved. Our approach mainly deals with the problem of designing state and action spaces. By designing suitable state and action spaces adaptively, it can be expected that the other two problems will be resolved simultaneously. Here, the problem of designing state and action spaces involves the following two requirements: (i) to keep the characteristics of the original search space as much as possible in order to seek strategies that lie close to the optimal, and (ii) to reduce the search space as much as possible in order to expedite the learning process. In general, these requirements are in conflict.

Recently an adaptive state space construction method which is called a "state space filter[3]," and an adaptive action space construction method which is called a "switching learning system[4]," have been proposed after the other space has been fixed. Here, we reconstitute these two construction methods as one method by treating them as a combined method for mimicking an infant's perceptual and motor developments The proposed method is to construct state and action spaces adaptively by introducing and referring to the "entropy" as an index of both necessity for the division of the state space in the state and sufficiency for the number of learning opportunities in the state. In addition, a computational experiment was conducted using a so-called "robot navigation problem" with three-dimentional continuous state space and two-dimensional continuous action space.

2 TYPICAL RL METHODS

2.1 Q-learning

Q-learning works by calculating the quality of a state-action combination, namely the Q-value, that gives the expected utility of performing a given action in a given state. By performing an action $a \in \boldsymbol{\mathcal{A}}_{\mathrm{Q}}$, where $\boldsymbol{\mathcal{A}}_{\mathrm{Q}} \subset \boldsymbol{\mathcal{A}}$ is the set of available actions in Q-learning and $\boldsymbol{\mathcal{A}}$ is the action space of the agent, the agent can move from state to state. Each state provides the agent with a reward r. The goal of agent is to maximize its total reward.

The Q-value is updated according to the following formula, when the agent is provided with the reward:

$$Q(s(t\text{-}1), a(t\text{-}1)) \leftarrow Q(s(t\text{-}1), a(t\text{-}1)) + \alpha_{\mathrm{Q}}\{r(t\text{-}1) + \gamma \max_{b \in \boldsymbol{\mathcal{A}}_{\mathrm{Q}}} Q(s(t), b) - Q(s(t\text{-}1), a(t\text{-}1))\} \quad (1)$$

where $Q(s(t\text{-}1), a(t\text{-}1))$ is the Q-value for the state and the action at the time step t-1, $\alpha_{\mathrm{Q}} \in [0, 1]$ is the learning rate of

Q-learning, $\gamma \in [0,1]$ is the discount factor.

The agent selects an action according to the stochastic policy $\pi(a|s)$, which is based on the Q-value. $\pi(a|s)$ specifies the probabilities of taking each action a in each state s. Boltzmann selection, which is one of the typical actionselection methods, is used in this research. Therefore, the policy $\pi(a|s)$ is calculated as

$$\pi(a|s) = \frac{\exp(Q(s,a)/\tau)}{\sum_{b\in\mathcal{A}} \exp(Q(s,b)/\tau)} \tag{2}$$

where τ is a positive parameter labeled temperature.

2.2 Actor-Critic

Actor-critic methods have a separate memory structure in order to represent the policy explicitly independently of the value function. The policy structure is called the "actor," which selects the actions, and the estimated value function is called the "critic," which criticizes the actions made by the actor. The critic is a state-value function. After each action selection, the critic evaluates the new state to determine whether things have gone better or worse than expected. That evaluation is TD-error:

$$\delta(t\text{-}1) = r(t\text{-}1) + \gamma V(s(t)) - V(s(t\text{-}1)) \tag{3}$$

where $V(s)$ is the state value.

Then, $V(s(t\text{-}1))$ is updated according to Eq. 4 in the critic based on this $\delta(t\text{-}1)$. In parallel, it is updated for the stochastic policy $\pi(a|s)$, in the actor.

$$V(s(t\text{-}1)) \leftarrow V(s(t\text{-}1)) + \alpha_{\mathrm{C}}\delta(t\text{-}1) \tag{4}$$

where $\alpha_{\mathrm{C}} \in [0,1]$ is the learning rate of the critic.

It is typical for the normal distribution, shown in Eq. 5, to be used as the stochastic policy in the actor, when actor-critic is applied to a continuous action space[2].

In this case, both the mean $\mu(s)$ and the standard error of the mean $\sigma(s)$ about the normal distribution are calculated using TD-error $\delta(t\text{-}1)$ in the actor, as in Eqs. 6 and 7.

$$\pi(a|s) = \frac{1}{\sigma(s)\sqrt{2\pi}} \exp(\frac{-(a-\mu(s))^2}{2\sigma(s)^2}) \tag{5}$$

$$\mu(s(t\text{-}1)) \leftarrow \mu(s(t\text{-}1)) + \alpha_\mu \delta(t\text{-}1)(a(t\text{-}1) - \mu(s(t\text{-}1))) \tag{6}$$

$$\begin{aligned}\sigma(s(t\text{-}1)) \;\leftarrow\; & \sigma(s(t\text{-}1)) \\ & + \alpha_\sigma \delta(t\text{-}1)((a(t\text{-}1) - \mu(s(t\text{-}1)))^2 - \sigma(s(t\text{-}1))^2)\end{aligned} \tag{7}$$

where $\alpha_\mu \in [0,1], \alpha_\sigma \in [0,1]$ are the learning rate of the mean and the standard error of the mean, respectively. Here, if Eq. 7 is used directly, the standard error could be 0 or a negative value. Therefore it is necessary when setting the standard error to be creative and to specify the range, etc.

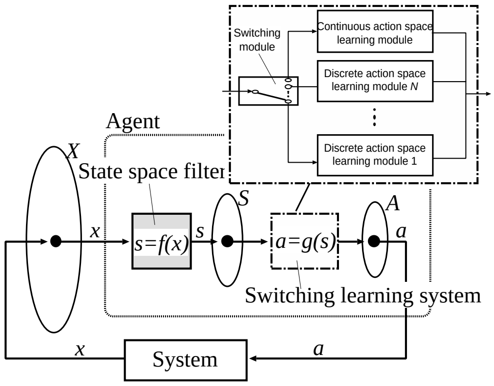

Fig. 1. Proposed development RL model

3 DEVELOPING RL

3.1 Outline of a Computational Model

In this section, we propose developing an RL model to mimic the processes of an infant's perceptual and motor developments. The proposed model is constructed by "state space filter[3]" to mimic the process of perceptual development in which perceptual differentiation progresses as the infant becomes older and more experienced, and a "switching learning system[4]" to mimic the process of motor development in which gross motor skills develop before fine motor skills, as shown in Fig. 1.

This model mimics the process of perceptual development by differentiating the state space gradually from the undifferentiated state space. In parallel, this model also mimics the process of motor development by switching discrete action space learning modules (hereafter called "DA modules") from a more coarse-grained DA module to a more fine-grained DA module, and finally switching to a continuous action space learning module (hereafter called a "CA module").

3.2 State and Action Spaces Construction Method

3.2.1 Basic Idea

A variety of methods can be considered to acquire the state space filter and the switching learning module. Here, we propose a method based on introducing and referring to the entropy, which is defined by action selection probability distributions in a state, and the number of learning opportunities in the state. It is expected that the proposed method (i) is able to learn in parallel the state space filter and the switching learning system, and (ii) does not required specific RL methods for the learning module.

The entropy of action selection probability distributions using Boltzmann selection in a state $H_{\mathrm{D}}(s)$ is defined by

$$H(s) = -(1/\log|\mathcal{A}_{\mathrm{D}}|) \sum_{a\in\mathcal{A}_{\mathrm{D}}} \pi(a|s)\log\pi(a|s) \tag{8}$$

where $\mathcal{A}_{\mathrm{D}}$ is the action space and $|\mathcal{A}_{\mathrm{D}}|$ is the number of available actions of the DA module.

The state space filter is adjusted and the learning module is switched by treating this entropy $H(s)$ as an index of the necessity of division for an inner state s and the action space. In parallel, the learning module is switched by treating this entropy $H(s)$ as an index of sufficiency for the number of learning opportunities in the state.

If the entropy does not get smaller despite the learning module having had a sufficient number of learning opportunities in the inner state, then the state space filter is adjusted by dividing the inner state, and the learning module is switched to a more fine-grained one. In contrast, if the entropy gets small regardless of the number of learning opportunities, the learning module is switched to the CA module because the number of learning opportunities is sufficient.

In this article, Q-learning and actor-critic are applied to the DA module and the CA module, respectively. The learning module is switched in the order of Q-learning with an action space divided evenly into $n, 2n, \cdots, 2^{(N-1)}n$, and finally ending with actor-critic, where N is the number of DA modules.

3.2.2 Adjustment of State Space Filter

If $L(s) > \theta_{\mathrm{L}}$ and $H(s) > \theta_{\mathrm{H}}$, where $L(s)$ is the number of learning opportunities in s, θ_L is a threshold value of the number of learning opportunities, θ_{H} is a threshold value of the entropy, and θ_{L} is set at a sufficiently large number, then the state space filter is adjusted by dividing the range of the input state mapped to the inner state s into two parts for each dimension, and mapping each part to a different inner state. Simultaneously, the learning module is switched. Through this operation, the size of the inner state space increases by $(2^M - 1)$ after being divided, where M is the number of dimensions. Also note that the values of the new $2M$ inner states are the value of the inner state before it was divided.

In addition, after the learning module is switched to the CA module, if $L(s) > \theta_{\mathrm{L}}$, then the state space filter is adjusted by dividing the inner state so that it is more fine-grained.

3.2.3 Switching of Learning Module

If $H(s) > \theta_{\mathrm{H}}$, then the learning module is switched to the CA module because the number of learning opportunities is then sufficient. In the procedure to switch controllers, the result of Q-learning is succeeded by actor-critic and the following procedure is carried out. 1. The state value of the critic, $V(s)$, is initialized by

$$V(s) = \sum_{a \in \boldsymbol{\mathcal{A}}_{\mathrm{Q}}} \pi(a|s) \cdot Q(s,a) \tag{9}$$

2. The normal probability distribution used by the actor is calculated by

$$\mu(s) = \arg\max_{a \in \boldsymbol{\mathcal{A}}_{\mathrm{Q}}} Q(s,a), \tag{10}$$

$$\sigma(s) = |A_{\mathrm{Q}}(\arg\max_{a \in \boldsymbol{\mathcal{A}}_{\mathrm{Q}}} Q(s,a))|/6 \tag{11}$$

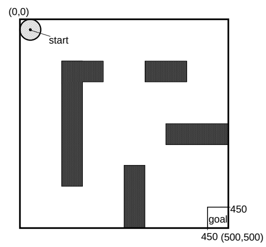

Fig. 2. Robot navigation problem

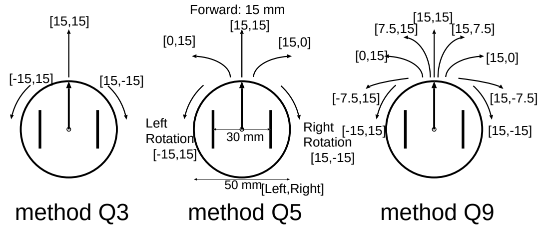

Fig. 3. Available actions of 3 Q-learning methods

where $|A_{\mathrm{Q}}(i)|$ is the range of the action space which represents action i of Q-learning.

If $L(s) > \theta_L$ and $H(s) > \theta_{\mathrm{H}}$, then the learning module is switched to more fine-grained DA module, and finally ends with the CA module. Simultaneously, the state space filter is adjusted.

The Q-values of newly added actions a_i at this time are set according to the following formula :

$$Q(s,i) = \max_{j \in i-1, i+1} Q(s,j) \tag{12}$$

where action $i-1$ and $i+1$ are adjacent to action i. This formula is set in consideration of a more efficient search as well as the idea of the optimistic initial values.

4 COMPUTATIONAL EXAMPLE

4.1 Robot Navigation Problem

The proposed method is applied to a so-called "robot navigation problem" navigating a learning agent from a starting point to a goal area in a continuous state space, as shown in Fig. 2.

Here, the agent has a circular shape (diameter 50 mm), and the continuous space is 500 mm$\times 500$ mm bounded by the external wall, with internal walls as shown in black. The agent can observe the center of its own position and its own direction: $(x_{\mathrm{A}}, y_{\mathrm{A}}, \theta_{\mathrm{A}})$ as the input. The agent has two wheels and can move in any direction, i.e., it can decide right-and-left wheel rotation rates (mm/step): $(\omega_{\mathrm{L}} \in [-15.0, 15.0], \omega_{\mathrm{R}} \in [-15.0, 15.0])$ as the output.

The positive reinforcement signal $r_t = 10$ (reward) is given to the agent only when the center of the agent arrives in the goal area, and the reinforcement signal is $r_t = 0$ at all other steps. The period from when the agent is located at the starting point to when the agent is given a reward, or $100,000$ steps pass away, labeled as 1 episode, is repeated.

4.2 Comparison with adaptive methods

We have confirmed that a combined method of state space filter and switching learning system (hereafter called the "FS" method) shows a better performance than three Q-learning methods where the number of actions is designed to be 3, 5, and 9 (hereafter called the "Q3," "Q5," and "Q9" methods, respectively), and an actor-critic method (hereafter called the "AC" method)with the state space divided evenly into $5 \times 5 \times 8$, $10 \times 10 \times 16$, and $20 \times 20 \times 32$ in this task. Fig. 3 shows the wheel rotation rates on each actions of three Q-learning methods.

In this section, the FS method is compared with three methods using the switching learning system with the state space divided evenly into $5 \times 5 \times 8$, $10 \times 10 \times 16$, and $20 \times 20 \times 32$ (hereafter called the "S5," "S10," and "S20" methods, respectively), and three Q-learning methods, the Q3, Q5, and Q9 methods, using the state space filter (hereafter called the "FQ3," "FQ5," and "FQ9," methods, respectively). Here, an initial state space filter is designed that divides the state space evenly into $5 \times 5 \times 8$ spaces, and the switching learning system is constructed by four learning modules: the "Q3," "Q5," "Q9," and "AC" methods.

All initial Q-values are set at 5.0 as the optimistic initial values[1] for Q-learning methods and the range of $\sigma(x)$ is set at $[0.001, 30.0]$ for the AC method. Here, the maximum limit of $\sigma(x)$ is set so that it becomes the size of the action space: 30.0. Further, the adjustment of the state space filter is assumed until the third attempt in all inner states because it is impossible to evaluate sufficiency for division of the state space.

Computer experiments have been carried out with the parameters shown in Table 1. Here, θ_{H} was set to about 0.359, the maximal value of the entropy when the highest selection probability for one action is 0.9, θ_{L} was set to a large enough number.

The average number of steps required to accomplish the task was observed during learning over 20 simulations with different methods, as described in Fig. 4. The average size of the inner state space was observed during learning over 20 simulations with different methods, as described in Fig. 5.

It can be seen from Fig. 4 that, (1) the FS method showed a worse performance than the FQ3, FQ5, FQ9 and S10 methods with regard to the learning speed, but a better performance than any other methods with regard to the control rule obtained. (2) the S5 method couldn't acquire any proper control rule.

Table 1. Parameters for experiments

Parameter	Value	Parameter	Value
$\alpha_{\mathrm{Q}}, \alpha_{\mathrm{C}}, \alpha_{\mu}, \alpha_{\sigma}$	0.1	γ	0.9
θ_{H}	0.4	τ	0.1
θ_{L}	1000		

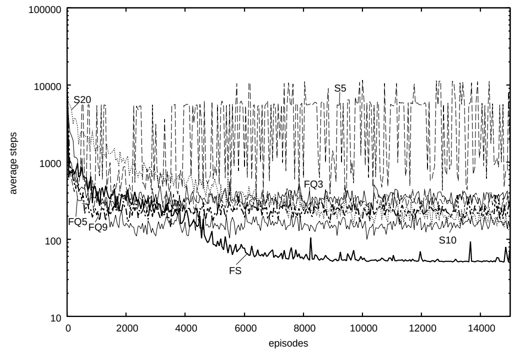

Fig. 4. Required steps

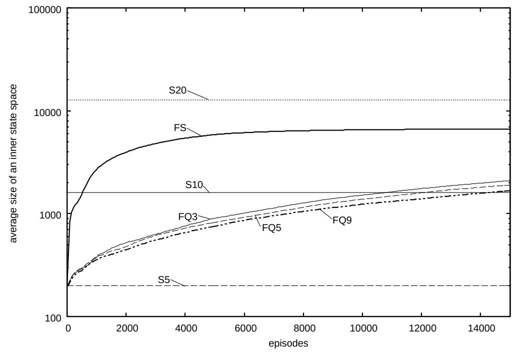

Fig. 5. Size of the inner state space

It can be seen from Fig. 5 that, (1) the FS method is smaller than the S20 method, but larger than any other method except the S20, (2) and is not growing since about 5,000 episode with regard to the size of the inner state space.

Therefore, we have confirmed that the FS method demonstrates better performances than any other method for the robot navigation problem.

5 CONCLUSION

In order to design suitable state and action spaces adaptively, we have proposed the developing RL model, and the state and action spaces co-construction method referring to "entropy." Then, with a computational experiment we confirmed that the combined method of the state space filter and the switching learning system shows better performances than any other method for the robot navigation problem with continuous state and action space.

Our future projects include considering more complicated problems and real-world problems, etc.

REFERENCES

[1] R.S. Sutton and A.G. Barto (1998), Reinforcement Learning, A Bradford Book, MIT Press.

[2] H. Kimura and S. Kobayashi (2000), An Analysis of Actor-Critic Algorithms using Eligibility Traces: Reinforcement Learning with Imperfect Value Functions, JSAI Jour., **15**(2), 267-275 (in Japanese).

[3] M. Nagayoshi, H. Murao, and H. Tamaki (2006), A State Space Filter for Reinforcement Learning, Proc. AROB 11th'06, 615-618(GS1-3).

[4] M. Nagayoshi, H. Murao and H. Tamaki (2010), A Reinforcement Learning with Switching Controllers for Continuous Action Space, Artifi cial Life and Robotics,**15**, 97-100.

Reinforcement learning approach to multi-stage decision making problems with changes in action sets

Takuya Etoh[1], Hirotaka Takano[1], and Junichi Murata[1]

[1] Kyushu University, 744 Motooka, Nishi-ku, Fukuoka, Japan
(Tel: +81-92-802-3675, Fax: +81-92-802-3692)
(etoh@cig.ees.kyushu-u.ac.jp)

Abstract: Multi-stage decision making (MSDM) problems often include changes in practical situations. For example travelling time of a path changes in the path selection problems in road networks. The changes cause risks in adopting solutions to MSDM problems. Therefore, we propose a method for solving MSDM problems considering risks. Reinforcement learning (RL) is adopted as a method for solving those problems, and stochastic changes of action sets are treated. It is necessary to evaluate risks besed on subjective views of decision makers (DMs) because the risk evaluation is by nature subjective and depends on DMs. Therefore, we develop an RL approach to MSDM problems with stochastic changes in sets of alternative actions, which uses new method for evaluating risks of the changes. The effectiveness of the method is illustrated with a road network path selection problem.

Keywords: Multi-stage desicion making, Risk assessment, Subjective occurrence probability, Reinforcement learning

1 INTRODUCTION

In practical situations, there are various Multi-stage decision making (MSDM) problems with changes. For example, in the path selection problem of road network, travelling time of paths changes. There are several optimization methods to solve MSDM problems without changes. In this paper, we adopt Reinforcement Learning (RL), which needs no models of problems for solving MSDM problems [1], and modify RL to MSDM problems with changes.

When MSDM problems include changes, we have to consider risks caused by the changes. In general, risks are evaluated by the occurrence probabilities of changes and costs incurred by the changes. Here, a cost represents the degree of undesirable effect; it does not necessarily indicate an amount of money. In RL, effects of stochastic events are originally evaluated by the expectation, but risks evaluated by the expectation may not fit subjective views of decision makers (DMs). Therefore, a method is necessary for evaluating risk that can incorporate DM's subjective views.

An RL method was reported for solving MSDM problems with changes of state transition probabilities [2] and RL methods for solving MSDM problems with changes of rewards [3, 4]. The former considers states called error states, which are undesirable or dangerous states, and defines risks as probabilities that the agent enters error states. The latter defines risks as variances of rewards or worst-cases of reward changes. Those adopt a weighted sum of expectations of rewards and costs incurred by changes as value functions. In those methods, adjustments of weights reflect DM's subjective views. The determination of the weight values cannot be done intuitively and therefore is not easy. In contrast to those two types of changes, there are also changes of action sets in practical problems. Therefore this type of changes is dealt with in this paper.

The above-mentioned methods need estimates of costs incurred by changes. However, for changes of action sets, estimates of costs incurred by changes cannot be obtained until the learning converges sufficiently, because costs are only evaluated by the difference between the value of the optimal action and the value of the suboptimal action. Therefore, we focus on probabilities at which action sets change, and propose a new method for evaluating risks with DM's subjective views in the form that can fit the RL framework. We assume that probability distributions are known as also assumed in the above-mentioned articles [2, 3, 4].

2 REINFORCEMENT LEARNING

RL is a method for getting optimal action selection policy automatically based on trial-and-error in order to solve complex or unknown problems. Signals used in RL are denoted as follows:

- discrete-time : $t\ (= 0, 1, 2, \ldots)$,
- state of environment at time t : $s_t \in S$,
- action taken by agent at time t : $a_t \in A_{s_t}$,
- reward obtained from environment at time t : r_t,
- policy of agent : $\pi(s, a)$.

In RL, learning is performed by the interaction between the environment and the agent as shown in Fig.1.

First, after the agent takes action a_t at time t, the state s_t transitions to s_{t+1} at next time $t+1$ by the action a_t. As a result, the agent gets the reward r_{t+1}. Second, the agent updates its own policy π, that is strategy of action selection, based on the obtained reward. The agent takes action based on the policy.

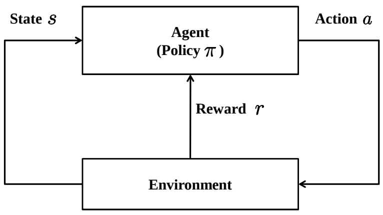

Fig. 1. The interaction between the environment and the agent.

In Fig.1, one cycle is called one step, and sequences of actions and state transitions from starting states to termination states are called an episode.

Because the reward is the only criterion in RL, the agent evaluates merits of actions and states based on the rewards, and those merits are called the values. The action value function is defined as

$$Q^{\pi}(s,a) = E\left[\sum_{k=0}^{\infty} \gamma^k r_{t+1+k} \mid s_t = s, a_t = a, \pi\right]. \quad (1)$$

The equation (1) represents the value of the action $a_t = a$ in the state $s_t = s$ at the time t under the condition that the action is selected by the policy π at time $t+1$ and thereafter. The value is expressed by the expectation of weighted sum of rewards obtained from time $t+1$ to the future.

3 PROPOSED METHOD

3.1 General Problem Setting

We assume Markov decision processes (MDPs). The MDPs include changes of action sets: some of alternative actions become unavailable at certain probabilities in some states. Moreover, there are dependences between occurrences of a number of action changes, and those dependences are described by the conditional probabilities. In this paper, we assume that all of those probabilities are known. Since probabilities that new unknown alternative actions appear are explicitly zero, they do not appear.

3.2 Subjective Occurrence Probability

Risks are evaluated, in general, by occurrence probabilities of changes and costs incurred by changes. When the optimal action becomes unavailable by the change, we have to use a suboptimal action. Therefore, costs are described by difference between the value of the optimal action and the value of the suboptimal action. Occurrence probabilities of changes are assumed to be known, but the costs cannot be obtained until the learning converges sufficiently. Therefore, we consider risk evaluations based on only occurrence probabilities.

Now, consider people who decide to take an umbrella or not after knowing the rainfall forecast. Some people take an umbrella if the rainfall probability is 50 %, but others do not take an umbrella even if the rainfall probability is 50 %. It means that people who take an umbrella consider that it may rain if the rainfall probability is equal to or higher than 50 %, and people who do not take an umbrella consider that it will not rain even if rainfall probability is 50 %. In this way, interpretations of occurrence probabilities vary from person to person.

In this paper, we propose a function $F(p)$ below that can approximate the relationship between objective occurrence probability p and subjective occurrence probability P, and use P as subjective evaluations of the risks,

$$P = F(p) = \frac{1+\exp(\frac{\tau-1}{\sigma})}{\exp(\frac{\tau}{\sigma}) - \exp(\frac{\tau-1}{\sigma})} \frac{\exp(\frac{\tau}{\sigma}) - \exp(\frac{\tau-p}{\sigma})}{1+\exp(\frac{\tau-p}{\sigma})}, \quad (2)$$

where $\tau (0 \leq \tau \leq 1)$ and $\sigma (\sigma \leq 1)$ are parameters reflecting DM's subjective views. Because $F(\tau) = 0.5$ holds, DMs consider that changes will likely to occur if $p \geq \tau$ and consider that chages will not likely to occur if $p < \tau$, that is, the parameter τ means the threshold value. The parameter σ controls the gradient around the threshold value. The curves of equation(2) with various parameter are shown in Fig.2.

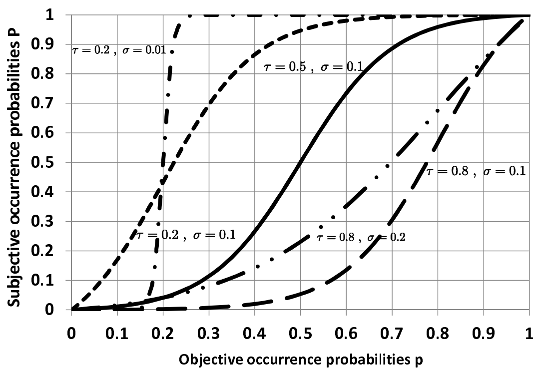

Fig. 2. Subjective occurrence probabilities for objective occurrence probabilities (Function $F(p)$).

3.3 The Compatibility Between the Learning Algorithm and the Risk Evaluation

The value of an action that may become unavailable should be reduced based on DM's subjective interpretations of occurrence probabilities. We multiply the value by a factor $1 - P_t$, where P_t is the subjective probability that the action at time t, a_t becomes unavailable, that is, if the DM interprets that the action will not be available at a high subjective probability ($P_t \simeq 1$), its value is reduced almost to zero. Therefore, the updating equation of Q is defined as

$$Q(s_t, a_t) \leftarrow (1-\alpha)Q(s_t, a_t) \\ +\alpha(1-P_t)\{r_{t+1} + \gamma \max_a Q(s_{t+1}, a)\}. \quad (3)$$

This update formula converges to

$$(1-P_t)\sum_{t=0}^{\infty}(\prod_{j=1}^{k}\gamma(1-P_{t+j}))r_{t+1+k}$$

which is a sum of rewards discounted by not only γ but also $1-P_{t+j}$.

The objective occurrence probabilities p are assumed to be known. But, even if the agent estimates occurrence probabilities, this method is efficient because the convergence of objective occurrence probability estimates is faster than the convergence of value functions.

3.4 Dependence between changes

If there are dependences between changes of action sets for different states, whether a certain action was available or not affects occurrence of changes of other actions which depend on that action. Once we know that a change C_1 has occurred then we can know whether a change C_2 that depends on change C_1 occurs or not with more confidence, i.e. with probability close to 1 or 0. Therefore, when availability of a certain action is known in an episode, we define augmented states x as states including the information. A binary variable f_i is defined which represents the availability of action i: if action i is unavailable, $f_i = 0$, and if action i is available, $f_i = 1$. A vector f is defined as the vector composed of all relevant f_i, and x is defined as $x = \begin{bmatrix} f \\ s \end{bmatrix}$.

Action values $\bar{Q}$ based on augmented states x are updated by

$$\bar{Q}(x_t, a_t) \leftarrow (1-\alpha)\bar{Q}(x_t, a_t) \\ +\alpha(1-P)\{r_{t+1} + \gamma \max_a \bar{Q}(x_{t+1}, a)\}. \quad (4)$$

In each episode, at first, the agent selects actions based on Q. When availability of a certain action that has influences on changes of other actions is known, the agent selects actions based on $\bar{Q}$ until that episode ends. It means that the agent modifies the policy by using real time information.

4 SIMULATIONS

4.1 Problem Setting

We use an example road network shown in Fig.3, where the branches represent road sections and the nodes represent intersections.

In Fig.3, a number in a node is a state number, and a number at the side of a branch is reward obtained by selecting that branch as an action. A large reward is desirable. The starting state is state 0 and the termination state is state 22. $E_{i,j}$ represent an event that an action $a_{i,j}$ moving from node i to node j becomes unavailable.

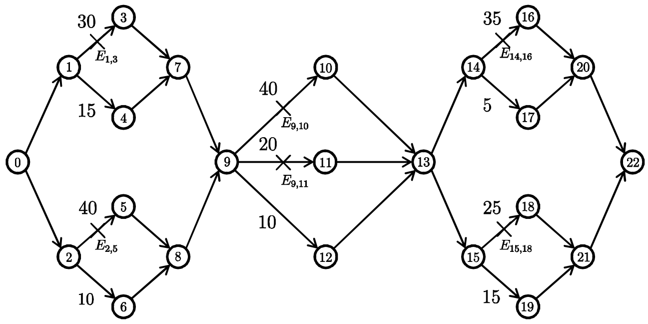

Fig. 3. An example road network.

In branches whose rewards are not explicitly shown, the rewards are all 0 to simplify the problem because those branches are not affected by changes.

Moreover, we assume dependences only between changes of actions selectable in an episode.

For example, we assume that there is dependence between $E_{1,3}$ and any changes except $E_{2,5}$ because the agent can select any changeable actions except $a_{2,5}$ after selecting $a_{1,3}$, but we assume no dependence between $E_{1,3}$ and $E_{2,5}$ since the agent cannot select $a_{2,5}$ after selecting $a_{1,3}$.

4.2 Parameter Setting

Occurrence probabilities of each change in Fig.3 are defined as shown in Table1.

Table 1. Occurrence probabilities.

Probabilities	Conditional event E				
	None	$E_{1,3}$	$E_{2,5}$	$E_{9,10}$	$E_{9,11}$
$P(E_{1,3} \mid E)$	0.35	-	-	-	-
$P(E_{2,5} \mid E)$	0.65	-	-	-	-
$P(E_{9,10} \mid E)$	0.65	0.8	0.2	-	-
$P(E_{9,11} \mid E)$	0.35	0.8	0.8	0.65	-
$P(E_{14,16} \mid E)$	0.65	0.8	0.5	0.2	0.5
$P(E_{15,18} \mid E)$	0.35	0.8	0.5	0.8	0.5

Conditional probabilities given two events, e.g. the conditional probability of $E_{i,j}$ given $E_{k,l}$ and $E_{m,n}$, are not shown in Table1, but we assume that all of these conditional probabilities are 0.5.

We do not treat conditional probabilities given three or more events, and this reason is explained later.

The agent only knows whether actions subject to changes are available or not after trying to take those actions. For example, the occurrence of event $E_{1,3}$ is known after the agent selects an action $a_{1,3}$.

Parameters used in simulations are shown below:
- the number of episode: $10,000,000$,
- the learning rate α: 0.1,
- the discount factor γ: 0.9,
- the method for action selection: $\epsilon-$greedy (ϵ is decreased from 0.5 to 0.05 step by step).

We perform simulations with different parameters in $F(p)$ namely DMs with different subjective interpretation as below:

DM(a) $\tau = 0.5, \sigma = 0.1$,
DM(b) $\tau = 0.3, \sigma = 0.1$,
DM(c) $\tau = 0.5, \sigma = 1$.

Parameter settings of DM(a) and DM(b) correspond to DMs considering that changes are likely to happen when the objective occurrence probabilities equal to or higher than 0.5 and 0.3, respectively because τ is the parameter adjusting threshold values, that is, DM(b) takes more risks than DM(a). DM(a) and DM(c) have the same τ value, but different σ values. DM(c) has gentler slope and therefore does not consider the change is likely to happen until its objective probability well exceeds 0.5.

4.3 Results

Optimal routes based on learned action value functions are shown as belows. ($E_{1,3}$) indicates that the shown route is the optimal route when the occurrence of $E_{1,3}$ is known by selecting $a_{1,3}$.

DM(a) $\tau = 0.5, \sigma = 0.1$
0-1-3-7-9-11-13-15-18-21-22
0-1-4-7-9-12-13-15-19-21-22 ($E_{1,3}$)
0-1-3-7-9-12-13-14-16-20-22 ($E_{9,11}$)
0-1-4-7-9-12-13-14-16-20-22 ($E_{1,3} \cap E_{9,10}$,$E_{1,3} \cap E_{9,11}$)

DM(b) $\tau = 0.3, \sigma = 0.1$
0-1-4-7-9-12-13-15-19-21-22
0-1-4-7-9-12-13-15-19-21-22 ($E_{1,3}, E_{9,11}$)
0-1-4-7-9-12-13-14-16-20-22 ($E_{9,10}$)
0-1-4-7-9-12-13-15-19-21-22 (($E_{1,3} \cap E_{9,10}) \cup (E_{1,3} \cap E_{9,11}$))

DM(c) $\tau = 0.5, \sigma = 1$
0-1-4-7-9-12-13-15-18-21-22
0-1-4-7-9-12-13-15-19-21-22 ($E_{1,3}$)
0-1-4-7-9-12-13-14-16-20-22 ($E_{9,10}$,$E_{9,11}$)
0-1-4-7-9-12-13-14-16-20-22 ($E_{1,3} \cap E_{9,10}$,$E_{1,3} \cap E_{9,11}$)

It is found that DM(a) does not select a branch that becomes unavailable at the probability 0.65 but selects a branch that becomes unavailable at the probability 0.35. Note that unconditional occurrence probabilities are either 0.35 or 0.65 only. Moreover, if $E_{1,3}$ occurs, DM(a) selects a route without changes because all probabilities of changes increase to 0.8. This also shows that DM(a) selects the new optimal routes in response to real time information about the occurrence of changes.

DM(b) and (c) also select appropriate routes for their own subjective risk parameters τ and σ, that is DM(b) selects route in risk averting manor and DM(c) selects route paying less attention to the difference in objective probabilities as compared to DM(a), and DMs select better routes in response to real time information if changes of actions are caused on the way.

We do not treat conditional probabilities given three or more events as described in section 4.2. Simultaneous changes of three or more actions seldomly happen. Therefore, there are few chances that the agent selects actions when three or more events occur. In RL, because action values are updated only after taking those actions, the values of actions under the condition that three or more events occur do not converge. For this reason, we do not consider conditional probabilities given three or more events.

5 CONCLUSIONS

In this paper, we proposed RL approach to obtain the optimal policies in MSDM problems with changes of action sets considering DM's subjective views. It has been shown that the optimal policies are learned which correspond to DM's subjective views.

In contrast to standard RL methods that find the only one optimal policy, the proposed method can select routes in response to real time information during performing actions. This feature is promising in practical applications.

In future work, the issue must be solved that the conditional action values given three or more events do not converge. We have assumed that all probabilities are known, but it is desirable to estimate probabilities by learning.

REFERENCES

[1] Sutton.R.S and Barto.A.G: Reinforcement Learning - An Introduction, The MIT Press (1998).

[2] Peter Geibel and Fritz Wysotzki: Risk-Sensitive Reinforcement Learning Applied to Control under Constraints, Journal of Artificial Intelligence Research 24 81-108 (2005).

[3] Makoto Sato and Shigenobu Kobayashi: Variance-Penalized Reinforcement Learning for Risk-Averese Asset Allocation, Proc. of IDEAL 2000 244-249 (2000).

[4] Takeshi Shibuya: A study on reinforcement learning in unstationary dynamic environments, Proc. of SSI 2010 3B1-2 (2010) (in Japanes).

The Seventeenth International Symposium on Artificial Life and Robotics 2012 (AROB 17th '12),
B-Con Plaza, Beppu, Oita, Japan, January 19-21, 2012

Reduction of learning space by making a choice of sensor information

Yasutaka Kishima[1], Kentarou Kurashige[1], and Toshinobu Numata[1]

[1] Muroran Institute of Technology, Muroran, Hokkaido 050-8585, Japan
(Tel: 81-143-46-5489)
(yasutaka.kishima@gmail.com, kentarou@csse.muroran-it.ac.jp, toshinobu.0122@gmail.com)

Abstract: There are many researches about applying machine learning to robot. Robot uses sensors as input information for learning. When robot performs various task, sensors which are used for each task is important. The reason is important sensors for performing task are different in each task. Robot should use proper sensors for each task. Therefore, we will propose a method which robot can autonomously make a choice of important sensors for each task. We define measure of importance of sensor for task. The measure is coefficient of correlation between sensor value of each sensor and reward on reinforcement learning. Robot decide important sensors based on correlation. Robot reduce learning space based on important sensors. Robot can learn efficiently by reduced learning space.

Keywords: Reduction of learning space, Robotics, Data mining, Reinforcement learning

1 INTRODUCTION

In recent years, robots which have various sensors and actuators are appeared with development of hardware technology. These robots is hoped to use for various task. In order for robot to perform various task, there are many researches about applying machine learning to robot[1]-[3]. Learning for robot is to obtain correspondence between input and output for achieving purpose. The input is information from installed sensors and output is action of robot.

Robot uses sensors as input for learning. The way of use of sensors is important for task. When robot is used for various tasks, installed sensors which are used becomes a problem. The problem is that learning efficiency can be down depend on the way of use of installed sensors in some tasks. Because important sensors for performing task are different. Robot has important sensors and unimportant sensors for a given task. Input of robot is increase for unimportant sensors. When input is increase, the number of corresponding action which agent should learn to input increases. Therefore, learning time increases by using unimportant sensors for learning. As the result learning efficiency is down.

Therefore, robot should learn by using important sensors only for efficient learning. To achieve this, robot should have ability which robot makes a choice of important sensors for task. Our purpose is to propose a system which robot can make a choice of important sensors for any task and robot can learn efficiently by using information from important sensors only.

This system is effective to various task. Robot can make a choice of important sensor for changed task by this system. And information which robot should learn, which is correspondence between information from sensors and action is reduced. As the result, robot can learn efficiently.

2 CONCEPT OF MAKING A CHOICE OF IMPORTANT SENSORS

To make a choice of important sensor, robot needs measure of importance of each sensor for task. We focus on correlation sensor value and degree of achievement of task as the measure of importance of each sensor for task. Many tasks have correlation sensor value and degree of achievement of task. For example, in garbage collection task robot need to approach a garbage to pick up it. Degree of achievement of task is shown distance between the robot and the garbage, and increases as the robot approaches the garbage. There is a correlation between the degree of achievement of the task and distance between robot and the garbage like this.

We show outline on fig.1. Fig.1 shows the case which robot has 2 kinds of sensors, but robot can have more than 2 kinds of sensors. This robot has sensors and ability to act. The robot recognizes environment around the robot by installed sensors. Environment around the robot expressed group of sensor value of each sensor. The robot collects sensor value of each sensor and degree of achievement of task.

When robot act, sensor value of each sensor is changes. Therefore, robot can collect sensor value of each sensor by repeating action. Robot also collects degree of achievement of task. Robot estimates degree of achievement of task based on change of sensor value of each sensor. Environmental information which robot recognizes changes before and after action. Therefore, robot can know whether changed sensor value is good of not for performing task. In example of garbage collection task, focusing on distance sensor for garbage, when move for a garbage, the distance sensor value reduces. When the robot recognize the reduced distance sensor value, the robot can know current distance sensor value is good for performing the garbage collection task.

The robot finds out correlation between sensor value of each sensor and degrees of achievement of task. In fig.1, robot finds out correlation about sensor 1 and sensor 2. There are negative correlation and positive correlation. The robot estimates important sensors which has negative or positive correlation.

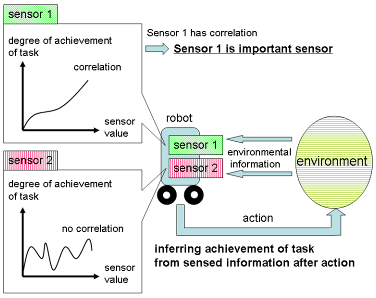

Fig. 1. The outline of making a choice of important sensors

3 PROPOSED SYSTEM ON REINFORCEMENT LEARNING

3.1 Outline of proposed system

The proposed method are used for efficient learning. Therefore, the proposed method is used in combination with a machine learning method. In this paper, we apply reinforcement learning as learning method(RL)[4]. The reason of applying RL is often adopted for experimental robots[5].

We show the system we propose in fig.2. In fig.2, the proposed system is divided into two part. One is the proposed method which robot makes a choice of important sensors. Another is reinforcement learning.

In the proposed method part, robot makes a choice of important sensor for task based on correlations between each sensor and degree of achievement of task. In RL, degree of achievement of task is shown as reward. Robot collects sensor value of each sensor and reward. Robot calculates correlation between each sensor and reward. Then robot decide important sensors based on correlation.

In reinforcement learning, robot learns proper action for task. In this part, there are action evaluation part, creating temporary Q-space based on important sensors part, and action selection part. Action evaluation part is updating evaluation for pair of state and action. State is composed of sensor value of each sensor. In creating temporary Q-space based on important sensors part, robot creates temporary Q-space which is composed of important sensor only. In action selection part, robot select action for recognized state by sensor based on temporary Q-space.

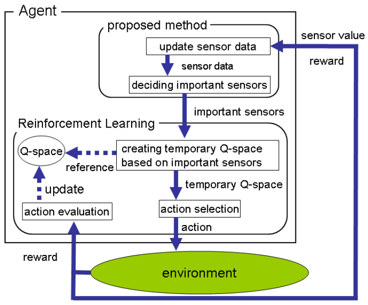

Fig. 2. The outline of proposed system

3.2 Decision of important sensors based on correlation

In proposed method, robot decides important sensors based on correlation between sensor value of each sensor and reward. Robot has sensor value of each sensor and reward which robot has experienced as knowledge. But reward is given for state-action pair. Therefore, there are some reward pattern for a state by an increment of the number of action. In this study, rewards for the state where robot experienced are averaged. Averaged reward at state s is r'_s.

Robot stores sensor value of each sensor and averaged reward as two lists in fig.3 and fig.4. There are state id and sensor value of each sensor in experienced states list. The state id is identification number. The list in fig.3 is an example of experienced states list. There are state id and averaged reward in averaged reward list. The list in fig.4 is an example of averaged reward list.

When robot recognizes state which is not in experienced states list, the robot adds the recognized state. Then robot calculates r'_s and added r'_s, to the averaged reward list. When recognized state is in the experienced states list, robot calculates r'_s and updates r'_s at recognized state in the averaged reward list.

state id	sensor value of sensor 1	sensor value of sensor 2	• • •	sensor value of sensor n
1	s	56	• • •	111
2	23	45	• • •	123
⋮				
m	90	10	• • •	15

Fig. 3. The experienced states list

state id	r'_s
1	111
2	123
⋮	
m	15

Fig. 4. The averaged reward list

Robot calculates coefficient of correlation based on the experienced states list and the averaged reward list. C_j as coefficient of correlation of sensor j and r'_i is calculated by eq.(1).

$$C_j = \frac{\sum_{j=1}^{m}(s_{i,j} - \bar{s}_i)(r'_{,i} - \bar{r'}_i)}{\sqrt{\sum_{j=1}^{m}(s_{i,j} - \bar{s}_i)^2}\sqrt{\sum_{j=1}^{m}(r_{j-\bar{r'}})^2}} \quad (1)$$

The i is identifying number of sensor. The $s_{i,j}$ is sensor value at state id i and sensor id j at the experienced states list. The r_j is averaged reward at state id j in the averaged reward list. The C_i is calculated for each sensor every action. Robot decides important sensor by comparing $|C_i|$ and Th. The Th is threshold to judge important sensor. When the $|C_i|$ is over Th, robot judges sensor as important sensor.

3.3 The way of use of important sensor for learning

Important sensors are used for selection of action in reinforcement learning. Creating temporary Q-space which is composed only important sensor axes by reduction for unimportant sensor axes. Reduction for Q-space is learning space. Reduction for Q-space is to project Q-values in unimportant sensor axes to Q-values in important sensor axes. Fig.5 shows an example of degeneration of Q-space. Important sensor is S_1, unimportant sensor is S_2 in this example. Q-values in S_2 is projected to Q-values in S_1. Projection is addition Q-values in S_2 to Q-values in S_1.

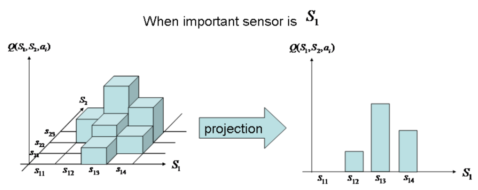

Fig. 5. The projection for temporary Q-space

We formulate based on this outline. Q-value is averaged reward by the number of experience of state-action pair. The number of experience for each state-action pair can be difference. This difference means difference of confidence of Q-value for state-action pair. Therefore, we consider weighted averaging Q-value according to the number of experience. To do this, we estimate total reward based on Q-value and the number of experience for state-action pair. Temporary Q-space is created based on total reward and the number of experience for state-action pair.

Temporary Q-space is used for selection of action at current state. Therefore, we consider projection at only current state of robot. Current state of robot is shown as $S = e_{1,f}, e_{2,g} \ldots, e_{n,z}$. The $e_{1,f}$ means f th sensor value in sensor 1. States of important sensors are shown as $S^{\star} = e_{1,f}, e_{2,g} \cdot \ldots \cdot e_{p,k}$. States of unimportant sensors are shown as $U = e_{p+1,x}, e_{p+2,y} \ldots e_{n,z}$. Total reward of any action at state S ($R(S,a)$) is defined as eq.(2).

$$R(S,a) = R(S^{\star}, U, a) = Q(S,a) \times E(S,a) \qquad (2)$$

The temporary Q-value $Q(S^{\star}, a)$ is defined as eq.(3). The $E(C,U,a)$ is the number of experience of state action pair $(S^{\star}, U, a)$.

$$Q(S^{\star}, a) = \frac{\sum_x \sum_y \cdots \sum_z R_{total}(C,U,a)}{\sum_x \sum_y \cdots \sum_z E(C,U,a)} \qquad (3)$$

We apply ϵ-greedy method for selecting action. The ϵ-greedy method selects the action which has the highest Q-value basically in current state S. But the method selects an action randomly with probability ϵ.

3.4 The action evaluation

We apply weighted averaging method as action evaluation method. The weighted averaging method evaluates by giving weight to reward which robot obtains recently. When current state of robot is S and the selected action is a, Q-value($Q(S,a)$) is updated by eq.(4). The $\alpha$is step size parameter ($0 \leq \alpha \leq 1$).

$$Q(S,a) \leftarrow Q(S,a) + \alpha \left[r - Q(S,a) \right] \qquad (4)$$

4 EXPERIMENT TO CONFIRM EFFECTIVENESS OF THE PROPOSED SYSTEM

4.1 Outline of experiment

In this section, we examine effectiveness of the proposed system on computer simulation. Environment for the experiment is shown fig.6. This environment is grid field u $\times$ u which is surrounded by walls. Length of both walls is u squares. We prepare virtual robot which is called agent. Agent has two distance sensors. One can measure distance between current position of agent and wall A in fig.6. Another can measure distance between current position of agent and wall B. Agent can move up, down, right and left.

In this experiment, agent performs two kinds of task. One is to depart from wall A. Another is to depart from wall A and wall B. Agent can obtain reward according to distance from wall A or both walls. Agent is allocated upper left of environment. When agent move n_{act} times, task is finished.

We confirm effectiveness of the proposed system by comparing the proposed system and ordinary RL. Therefore we prepare two types of agents to compare. One is applied the proposed method. Another is applied the RL only. In the case of the RL only, robot uses all installed sensors. We compare these agents in obtained total reward after moving n_{act} times.

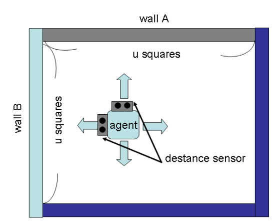

Fig. 6. The environment for the experiment

4.2 The setting of this experiment

We explain about reward for each task and show parameter settings. First, we explain about reward for each task.

In task A, agent can obtain higher reward with increasing the distance between current position of agent and wall A(d_A). Reward of task A is defined in eq.(5).

$$r = d_A \tag{5}$$

In task B, agent can obtain reward based on d_A and the distance between current position of agent and wall B (d_B). Agent can obtain higher reward with increasing both d_A and d_B. Reward of task B is defined in eq.(6)

$$r = d_A + d_B \tag{6}$$

We show parameter settings of this experiment at table.1.

Table 1. The settings of experiment

u	20
n_{act}	20000
ϵ	0.1
α	0.7
initial value of Q-value	0
Th	0.6

4.3 Result and consideration of the experiment

We show result of experiment fig.7 and fig.8. First, we discuss the result about task A. Fig.7 shows obtained reward of agent at each action. The proposed method shows higher convergent of reward than reinforcement learning under 5000 actions. The reason is that robot could select proper sensor for learning by the proposed method. Temporary Q-space has more information than Q-space because of projection of Q-space. The agent using temporary Q-space was easy to select proper action for recognized state.

Next, we discuss the result about task B. Fig.8 shows obtained reward of agent at each action. The proposed method was unstable in early phase of learning(under 5000 actions). The reason is that agent which was applied the proposed method spent times to estimate important sensor. Reward in task B is depend on d_A and d_B. Agent need to collect more sensor and reward data than the case of task A. In early phase of learning, agent selected unimportant sensor because of a lack of sensor and reward data. Therefore reward of agent which was applied the proposed method was lower than agent which was applied reinforcement learning only.

From these result, the proposed method is effective in the case of task which agent uses a part of installed sensor of agent. In the case of task which agent uses all installed sensors of agent, performance of learning in the case of the proposed method is lower than in the case of use of all installed sensors. But agent which is applied the proposed system can change sensors according to importance of each sensor to a task. The agent can learn faster depending on task.

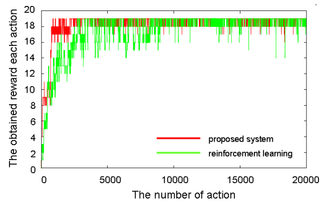

Fig. 7. Obtained reward at each action in task A

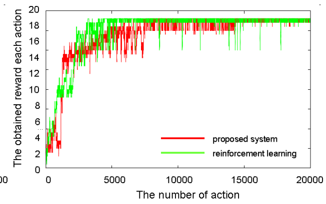

Fig. 8. Obtained reward at each action in task A

5 CONCLUSION

In this paper, we proposed the method which robot makes a choice of important sensors for a task. We constructed a system which is composed proposed method and reinforcement learning. This system is that robot can learn efficiently by the proposed method. We examined effectiveness of the constructed system on simulation. From result of simulation, we confirmed effectiveness of the constructed system and the proposed method. We confirmed robot can learn efficiently by making a choice of important sensors. We will attempt to install this proposed system into actual robot and examine effectiveness as our future work.

REFERENCES

[1] K.merrick, Motivated Learning from Interesting Events: Adaptive, Multitask Learning Agents for Complex Environments, Adaptive Behavior vol.17 no.1 2009, pp.7-27.

[2] Pardowitz.M, Knoop.S, Dillmann.R, .Zollner.R.D,Incremental Learning of Tasks From User Demonstrations, Past Experiences, and Vocal Comments, Systems, Man, and Cybernetics, Part B: Cybernetics, IEEE Transactions on vol.7 No.2 pp.322-332, 2007.

[3] Y.Miyazaki, K.Kurashige, Use of reward - independent knowledge on reinforcement learning for dynamic environment, Proc. of the International Conference on Advanced Computer Science and Information Systems, pp.303-309, Bali, Indonesia, 20th - 23rd Nov. 2010

[4] R.Sutton, A.Barto, Reinforcement Learning, The MIT Press, 1998.

[5] Kober J Person, Oztop E and Peters J, Reinforcement Learning to Adjust Robot Movements to New Situations, Proceedings of the Twenty-Second International Joint Conference on Artificial Intelligence, pp.2650-2655, 2010.

The Seventeenth International Symposium on Artificial Life and Robotics 2012 (AROB 17th '12),
B-Con Plaza, Beppu, Oita, Japan, January 19-21, 2012

An implementation of firefly-inspired network synchronicity without leaders on a group of small wireless devices

Fujio Yamamoto

Kanagawa Institute of Technology, Kanagawa 243-0292, Japan
(Tel: 81-46-291-3181, Fax: 81-46-242-8490)

yamamoto@ic.kanagawa-it.ac.jp

Abstract: Synchronicity observed in a group of fireflies was reconstructed using SunSPOTs. It is based on the software simulation with phase delay model. The main purpose is to provide a method for performing synchronicity among electronic fireflies, rather than obtaining clock synchronization. Some problems arising from the use of real wireless devices, not occurred in the simulation, were addressed and solved. The most important problem was how to send and receive phase delay information among SunSPOTs using real ratio signal. This is not the problem in the simulation because the detection of other flashes can be immediately obtained by simple calculations. The results from the proposed implementation exhibit relatively good synchronicity although its accuracy is not so high. These can be useful to observe synchronous behavior in the biological population without leaders.

Keywords: network synchronicity, sensor network, synchronization

1 INTRODUCTION

Many applications using wireless sensor network technology require time synchronization among each local clock on the devices connected to the network. But it is hard to get an efficient method for it. On the other hand, *synchronicity* is not the same as *time synchronization,* and the both are complementary each other. Synchronicity is considered as the ability to organize simultaneous collective action across a network (Werner-Allen et al [1]). Many research papers on synchronicity inspired by fireflies have been published (Werner-Allen [1], Tyrrell [2], Leidenfrost [3]). However, most of them except Werner-Allen [1] take software simulation, where uncertain behavior and delay in communication are not considered.

In this paper, an implementation method for synchronicity that does not use a centralized signal is presented, and demonstrated on a realistic experimental radio network. This method is based on the synchronicity that has been observed in nature in large populations of fireflies. My paper does not ask for very accurate synchronous behavior because the objective is to demonstrate fireflies' synchronicity on electronic devices. The accuracy of about several milliseconds is good enough to observe flashing of fireflies by human eyes. I proposed a method for synchronicity, and implemented it on the devices as shown below. In the following, at first, flashing behavior of fireflies without leaders is analyzed by a simulation using NetLogo (Wilensky [4], Wilensky [5]). Next, my implementation on a group of SunSPOTs (Smith [6], Simon [7]) is presented. Finally some experimental results are presented.

2 ANALYSIS OF FIREFLY SYNCHRONICITY USING NETLOGO

In the NetLogo's model library, there is an application to simulate behavior of populations of fireflies. It exhibits simultaneous flashing of all the fireflies without leader. I made concise version of it to investigate the mechanism of such synchronous actions. The interface window is illustrated in Fig. 2.1. Some related parameters are set as follows:

[number of fireflies]= 4
[cycle-length] = 6 time ticks
[flash-length] = 2 time ticks
[flashed-to-rest] = 1

Four fireflies are deployed horizontally to one line. They are identified as Firefly-0 (#0), .., Firefly-3 (#3). The distance between adjacent fireflies is set to one (1). This numbering of fireflies is made in round-robin manner, so that the distance between #0 and #3 becomes one. Each firefly tries to adjust its flashing phase to the neighboring one that other emission. It is assumed here that one can receive the emission within the distance 1. The firefly that receives such emission reset its time tick to the value of the flash-length. This resetting occurs only after the flashing and never occurs during its own flashing. Therefore, this makes the receiving firefly delay the phase after its flashing.

Detailed procedures in NetLogo are shown in Fig. 2.2.

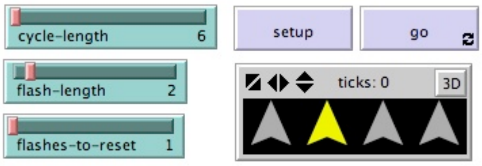

Fig. 2.1 Interfaces in the simulation

```
turtles-own [ clock ] ;; each firefly's clock
to setup
  clear-all
  put-firefly 0 0 3
  put-firefly 1 0 0
  put-firefly 2 0 4
  put-firefly 3 0 5
  ask turtles [recolor]
end
to put-firefly [ix iy iclock] ;; create ordered turtle
  cro 1 [setxy ix iy set clock iclock]
end
to go
  ask turtles [
    increment-clock-upto-cycle-length
    reset-clock-upon-perceiving-other-flash
  ]
  ask turtles [recolor]
  plot-number-of-flashes
  plot-firefly-phase
  tick ;;advance the tick counter by one
end
to increment-clock-upto-cycle-length
  set clock (clock + 1)
  if clock = cycle-length [ set clock 0 ]
end
to reset-clock-upon-perceiving-other-flash
  if  (clock >= flash-length)[ ;; own flash never changed
    if (count turtles in-radius 1 with [color = yellow]
       >= flashes-to-reset) [ set clock flash-length ]
  ]
end
to recolor
  ifelse (clock < flash-length)
    [ set color yellow ] [ set color gray ]
end
```

Fig. 2.2 Procedures in the NetLogo simulation

The results obtained by executing these procedures are illustrated in Fig. 2.3. At the starting point (time tick = 0), four fireflies are in different phase. Only #1 is in flashing interval. The #0 immediately detects the flash from #1 and resets its phase to the value of the flash-length. The same action occurs in the #2. When time tick advances to one, the #1 is still in flashing mode. Therefore, phase delay occurs again in both #0 and #2. When time tick advances to two, the #1 completes its flashing, but the #3 is still in flashing mode. In this situation, both #0 and #2 detects flashing from the #3. This causes the #0 and #2 again reset their phase to the value of flash-length. After that, others affect no fireflies for a while.

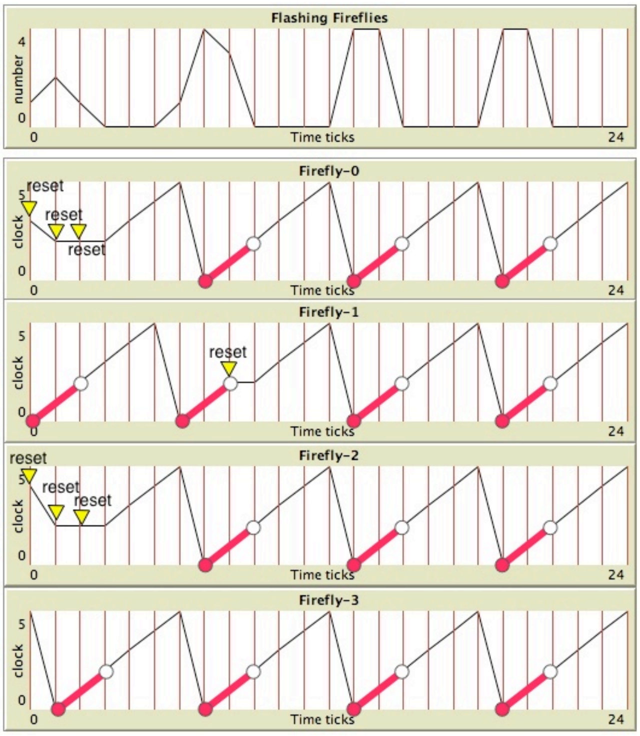

Fig. 2.3 The analysis of the phase delay model

The next notable point is the time when time tick becomes eight. At this point, the #1 detects flashing from either #0 or #2. Therefore, when time tick advances to nine, the #1 resets its phase to the value of flash-length. After the time tick becomes thirteen, all the fireflies exhibit synchronous behavior, and this synchronicity will be continued forever.

3 IMPLEMENTATION OF SYNCHRONICITY ON SUNSPOT

Flashing of fireflies was implemented on a group of small devices with wireless communications. The proposed method for it is based on the NetLogo simulation mentioned above. That is, the phase delay mechanism affecting to the flash cycle, is adopted. However, there are some important issues, which were not appeared in the simulation. They are discussed below.

3.1 Issues in implementation on SunSPOT

The present implementation of the proposed method has been performed on a set of tiny Java machine SunSPOTs Smith [10], Simon [11], Akriboulos [12]. One SunSPOT corresponds to one firefly as illustrated in Fig. 3.1. Each SunSPOT has ZigBee-based radio communication facilities, which exchange clock delay information.

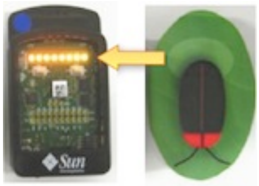

Fig. 3.1 Electronic firefly using SunSPOT

In NetLog simulation the problem of how to detect the flashes of other fireflies does not occur because other nearby flashes are obtained immediately by a simple calculation based on positional information. On the other hand, with SunSPOT, the flash is expressed and emitted by a radio signal, so that other SunSPOTs should be able to receive the flash. Since flashing occurs erratically throughout the population, each SunSPOT generates multiple threads on which other flashes starting at different times can be received.

Another problem is that no global clock exits in the implementation on SunSPOTs differently in the case of NetLogo simulation. In the simulation explained above, all the fireflies refer to one global clock, even though they are in different phases. Namely, as shown in Fig.2.3, all fireflies act based on the common time ticks. Therefore, delay value to synchronize with others always becomes an integer multiples of one time tick. This is not true on SunSPOTs because fireflies must calculate the difference between the starting time of its own flash and the receiving time of other flash by their own local clock. This difference does not necessarily become an integer multiples of one time tick. This implies that synchronicity and time-synchronization are not the same, as shown in the introduction.

3.2 Principles of the implementation

Each firefly on a SunSPOT counts up time ticks in its own clock during the cycle-length. When it reaches the max (i.e. cycle-length), the count is reset to zero. When a firefly becomes time tick zero, it begins flashing and continues it during the flash-length, in which other flashes do not affect the firefly although it can receive other flash. Flashing is realized by broadcasting a packet that has special header. Once the firefly detects other flashes, then it does not receive other flashes for a time. When the firefly receives other flashes, the firefly can calculate the necessary delay time. The delay is the difference between the receiving time of other flash and the starting time of its own flash. The delay is added at the end of the current flash cycle. It is expected that the firefly synchronizes its own flashing at the next cycle with that of the firefly sending the packet.

However, in the real world, several problems can be observed. For example, some pairs of SunSPOTs may maintain fixed value of delay each other for a long time, depending on the startup timing, as shown in the next section. Also, cycle time of each SunSPOT may gradually become disordered. Due to this, synchronicity that is observed may lose accuracy even though essential framework of synchronicity is preserved. In order to settle these problems, it is necessary for a SunSPOT that has been received other flash can get again another flashing signal after several cycles. Such correction seems unavoidable when using many devices with limited timing accuracy.

4 RESULTS AND ANALYSIS

Experiment of this implementation using four to eight SunSPOTs has been performed. The radio output power was set to the minimum so that broadcast range is limited within 20 cm. All the SunSPOTs are aligned into a line. The distance between two SunSPOTs is set to 15 cm. Therefore, each SunSPOT can receive broadcast message only from the neighbors. In this situation, each SunSPOT is started in different time, and human eyes observed the process to the synchronicity. For the group of four SunSPOTs, synchronicity was obtained after two to four cycles. For the group of eight SunSPOTs, it took more cycles but less than six cycles until steady state of synchronicity. Occasionally, disorder of synchronicity was observed. However, the synchronicity was recovered approximately after four to six cycles. Typical two cases observed in the experiment are analyzed in Fig 3.2 and Fig 3.3.

Fig.3.2 shows the group of four SunSPOTs, in which each SunSPOT begins its flashing at random time point. The #1 detects flashing of #2 during its own flashing interval. The delay d1 (difference between the start time of #1 and the start time of #2) was added at the end of the current cycle of #1. This causes synchronicity between #1 and #2 at the next cycle. On the other hand, the #4 detects the second flashing of #3 outside of its flashing interval. The delay d3 (the delay against #3) was added at the end of normal cycle of #4. Any other SunSPOT never disturbed the #2. After two cycles of #1, all four SunSPOTs agreed to synchronize.

Fig.3.3 illustrates different behavior compared to Fig3.2. Note that the cycle-length is changed against the case of Fig. 3.2. to make it easy to explain. One time tick regularly shifts the starting time of three SunSPOTs. The #2 was delayed for d2 (against #1) because #2 detects flashing from #1. By this, the #2 agreed to synchronize with #1. In the same way, #3 tried to synchronize with #2 by adding the delay d1 (against #2) at the end of its cycle. But the #2 and the #3 did not synchronize each other, because the #2 was already delayed for d2. No synchronicity seems to be obtained after that. But at this point, the flag for permission of getting other flash was set as on. (How often this permission is set is indicated as an optional parameter.) Then, reversely, #2 detects the flash from #3, and #1 detect the flash from #2. As a result, all three SunSPOTs went into synchronicity after several time ticks.

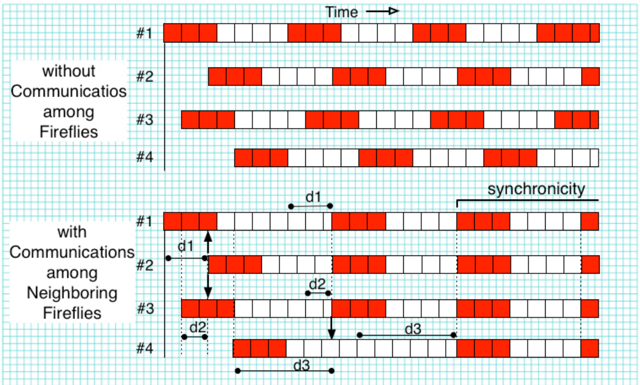

Fig. 3.2 Analysis of randomly started fireflies

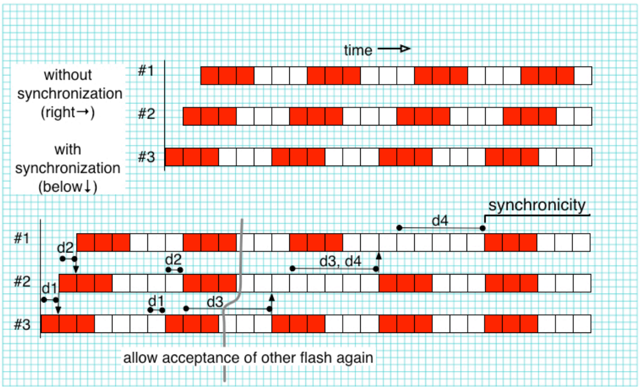

Fig. 3.3 Analysis of regularly started fireflies

5 CONCLUSION

Synchronicity observed in a group of fireflies was reconstructed using four to eight SunSPOTs. It is based on the software simulation with phase delay model. Some problems arising from the use of real wireless devices, not occurred in the simulation, were discussed and solved. The most important problem was how to communicate between SunSPOTs using real ratio signal. This is not the problem in the simulation because the detection of other flashes is immediately obtained by simple calculations. The results from the proposed implementation exhibit relatively good synchronicity although its accuracy is not so high. These can be useful to observe synchronous behavior in the biological population without leaders. Also, it is meaningful to demonstrate the proposed implementation in the education of embedded software development.

ACKNOWLEDGEMENTS

This work was supported by the Ministry of Education, Culture, Sports, Science and Technology Grant-in-Aid for Scientific Research (C) 23501176.

REFERENCES

[1] Werner-Allen G, Tewari G, Pater A, Welsh M and Nagpal R (2005), Firefly-Inspired Sensor Network Synchronicity with Realistic Radio Effects, Proceedings of the 3rd ACM Conference on Embedded Network Sensor Systems (SenSys'05), San Diego, California, pp. 142-153.

[2] Tyrrell A, Auer G (2007), Imposing a Reference Timing onto Firefly Synchronization in Wireless Networks, IEEE 65th Vehicular Technology Conference, VTC2007-Spring. pp. 222 – 226.

[3] Leidenfrost R and Elmenreich W (2009), Firefly Clock Synchronization in an 809.15.4 Wireless Network", EURASIP Journal on Embedded Systems, Volume 2009, Article ID 186406, 17 pages.

[4] Wilensky U (1997), NetLogo Fireflies model, http://ccl.northwestern.edu/netlogo/models/Fireflies, Center for Connected Learning and Computer-Based Modeling, Northwestern University, Evanston, IL.

[5] Wilensky U (1999), "NetLogo", http://ccl.northwestern.edu/netlogo/, Center for Connected Learning and Computer-Based Modeling, Northwestern University, Evanston, IL.

[6] Smith R B (2007), SPOTWorld and the Sun SPOT, Proceedings of the 6th international conference on Information processing in sensor networks, pp. 565-566.

[7] Simon D, Cifuentes C, Cleal D, Daniels J and White D (2006), Java on the bare metal of wireless sensor devices: the squawk Java virtual machine, Proceedings of the 2nd international conference on Virtual execution environments, pp. 78-88.

An Improved Clustering based Monte Carlo Localization Approach For Cooperative Multi-robot Localization

Guanghui Luo[1], Dan Wu[1], and Libing Wu[2]

[1]University of Windsor, Windsor, Ontario, Canada
[2]Wuhan Univeristy, Wuhan, P.R.China
[1]danwu@uwindsor.ca

Abstract: We describe an approach for cooperative multi-robot localization based on Monte Carlo Localization. In our approach, each of the robots maintains its own clustering based MCL algorithm, and communicates with each other whenever it detects another robot. We develop a new information exchange mechanism, which makes use of the information extracted from the clustering component, to synchronize the beliefs of detected robots. By avoiding unnecessary information exchange whenever detection occurs through belief comparison, the proposed approach solves the delayed integration problem which further improves the effectiveness and efficiency of multi-robot localization. This approach has been tested in both real and simulated environments. Compared with single robot localization, the experimental results demonstrate that proposed approach notably improves the performance, especially when the environments are highly symmetric.

Keywords: clustering, MCL, multi-robot localization

I. INTRODUCTION

Mobile robot localization, the process of determining the position and orientation (pose) of a robot within its operating environment from sensor reading, is a prerequisite for subsequent high level navigation tasks. It has been considered as one of the fundamental problems in mobile robotics [6]. The most widely studied localization problems are: Local localization (position tracking), which is to compensate incremental errors in a robot's motion under the assumption that the initial position is known as prior, and the more challenge Global localization, in which the robots are required to estimate their pose by local and incomplete observed information under the condition of uncertain initial position [7].

During the past two decades, most existing work has focused on single robot localization, such as Grid-based approaches [1], Monte Carlo Localization [5, 11], and multi-hypothesis approaches [2]. These approaches have been applied to many different applications in solving localization problem and achieve remarkable successes.

However, more and more researchers are interested in using multiple robots to improve efficiency and robustness. In this paper, we propose an efficient probabilistic approach for cooperative multi-robot localization in indoor environment. Our approach is based on Monte Carlo Localization that has been applied with great practical success to single robot localization. In our approach, the robots, capable of sensing and exchanging information one with another, localize themselves by maintaining their own beliefs which are the proposed clustering based MCL algorithm. Our new developed information exchange mechanism is employed to synchronize each robot's belief whenever one robot detects another in order to speed up the localization process with possible higher accuracy. We utilize the information extracted from the clustering component of the proposed approach which analyzes the distribution of the whole particle set to quantify robot's belief and transfers information across different robots if necessary. We always compare the beliefs of both detected robots before synchronizing their poses' estimate to control information integration. By doing so, we can prevent the localization process from suffering the problem of delayed integration, which means to avoid unnecessary information exchange. In addition, robots themselves are implicitly used as landmarks rather than using only external landmarks, as in other works.

In section II we briefly review previous cooperative localization approaches, the MCL algorithm, and the clustering method. Section III describes details of our proposed method. Section IV presents the experimental results. Finally, section V provides the conclusions and future work.

II. RELATED WORKS

Many robotic applications require that robots work cooperatively in order to perform a certain task [9]. Knowing their global positions is the first step in multi-robot systems.

One early cooperative localization technique with multiple robots was proposed by Kurazume and Nagate [8] ans is known as "portable beacons". The basic underlying idea is that each robot repeats move-and-stop actions and serves as a landmark for the other robots. Only a part of entire robots can move in a certain time instant and this dramatically slows down the overall localization speed.

An EKF-based approach for cooperative multi-robot localization was introduced by Roumeliotis [11]. This approach allows all robots in a group to move simultaneously, and to propagate their state and covariance estimates independently by decomposing the centralized EKF-based cooperative localization into N communicating filters. However, during each update cycle, all robots need to communicate with each other and update the covariance matrix for all pose estimates. The main drawback is that the high cost of computation and communication limits this approach to small robot teams in real-time operation.

Fox and Burgard [4] have proposed a different implementation of cooperative multi-robot localization schema which extends the Monte Carlo Localization (MCL) algorithm. The sample-based version of Markov localization enables localizing mobile robots in any-time fashion. Each robot in the system maintains a probability distribution describing its own pose estimate. When one robot detects another, the "detection model" is used to synchronize the individual robot's beliefs, thereby introducing additional probabilistic constrains which ties one robot's belief to another robot's belief to reduce the uncertainty. This method suffers from the problem of delayed information exchange, which means the information exchange between two detected robots cannot ensure it is always benefit the localization process.

Our proposed approach is a clustering based MCL algorithm for cooperative multi-robot localization. The details of MCL and the related clustering algorithm will be given in this section. We first review some basic concepts in mobile robot localization. The *state* of a robot is defined as the collection of all aspects of the robot and its environment. The state at time t is denote as x_t. The pose of a robot is denoted (x, y, θ), where x and y represent a two-dimensional coordinate and θ represents orientation of the robot. The notion of *belief* is used to represent the robot's internal knowledge about the state of the environment [10]. The expression of belief over state x_t is $bel(x_t) = p(x_t|z_{1:t}, u_{1:t})$. It is a posterior probability over states conditioned on all the past motion data $u_{1:t}$ and all the past measurement data $z_{1:t}$. Localization algorithms based on probabilistic methods have two different components to process these two kinds of data [13]: measurement model, denoted as $p(z_t|x_t)$, and motion model, denoted as $p(x_t|u_t, x_{t-1})$.

A. Monte Carlo Localization

Monte Carlo Localization (MCL) is one of the latest and commonly used probabilistic approaches for single robot localization. MCL is an implementation of Bayes Filter, which represents uncertainty by maintaining a set of weighted samples that are randomly drawn from the probability density [19].

MCL is a recursive algorithm, and Fig. 1 [19] shows one iteration. The inputs of the MCL algorithm are particle set X_{t-1} from previous iteration, control data u_t, measurement data z_t, and the given map m of the environment. Line 1 initializes the particle set $\bar{X}_t$ and X_t. And then for each particle, line 3 do sampling from the motion model, line 4 calculates the importance weight of that particle from the measurement model. Line 7 to line 10 is the resampling phase. The algorithm draws with replacement N particles from the temporary set $\bar{X}_t$. The probability of drawing each particle is given by its importance weight. Finally, the posterior particle set X_t, which contains the particles that with higher importance weights is returned.

Algorithm MCL ($\boldsymbol{X_{t-1}, u_t, z_t, m}$)
1: $\bar{X}_t = X_t = \emptyset$
2: for n =1 to N do
3: $X_t^{[n]}$ = sample_motion_model (u_t, $X_{t-1}^{[n]}$)
4: $w_t^{[n]}$ = measurement_model (z_t, $X_t^{[n]}$, n)
5: $\bar{X}_t = \bar{X}_t + < X_t^{[n]}, w_t^{[n]} >$
6: endfor
7: for n = 1 to N do
8: draw i with probability $\propto w_t^{[i]}$
9: add $x_t^{[i]}$ to X_t
10: endfor
11: Return X_t

Fig. 1. The Monte Carlo Localization (MCL) algorithm [19].

Note that, if MCL finishes successfully, most particles are concentrated on a small region which represents the location of robot, although there is not such a stop condition in the MCL algorithm.

B. Clustering Algorithm BSAS

Clustering is the assignment of a set of observations (particles) into clusters so that observations in the same cluster are similar to each other. Two important parts in almost all clustering algorithms are to select a proximity measure, which measures the dissimilarity between particles or clusters, and the representative of a cluster, which highly depends on the shape of a cluster. As in MCL all poses of particles are represented by a two dimensional coordinate system, it's more effective for us to choose the Euclidean distance measure $d(P_i, P_j) = \sum \sqrt{(x_i - x_j)^2 + (y_i - y_j)^2}$ as our proximity measure. A Compact cluster is what one mostly encounters in MCL, thus the mean point of a cluster is chosen as representative, denoted as $P_{mean} = \frac{1}{N} \sum P_i$, N is the number of particles contained in that cluster.

We choose one of the most efficient clustering methods called Basic Sequential Algorithm Scheme (BSAS) shown in Fig. 2. to be used in the proposed method, because most probabilistic robotics algorithms need real time performance.

The BSAS algorithm takes the whole particle set $X(x_i, \dots x_N)$ that need to be clustered and the user defined threshold of dissimilarity θ as inputs. Line 1 initialize the first cluster, which contains the first particle x_1 presented to the algorithm. From line 2 to line 9 it is a large for loop sequentially going through all the remaining particles. The dissimilarity measures between current particle and every existing cluster is calculated in order to find a minimum one in line 3. From line 4 to line 8, if the minimum measure calculated in line 3 is greater than θ, a new cluster that containing current particle will be created. Otherwise, the considered particle will be assigned to the existing cluster which has the minimum dissimilarity measure to it and update its representative of this cluster.

Algorithm BSAS ($\boldsymbol{X(x_i, \ldots x_N), \theta}$):
1: $m = 1, C_m = \{x_1\}$
2: for *i =2 to N* do
3: find $C_K: d(x_i, C_k) = min_{1\leq j \leq m} d(x_i, C_j)$
4: if $d(x_i, C_k) > \theta$ then
5: $m = m + 1,\ C_m = \{x_i\}$
6: else
7: $C_k \cup \{x_i\}$, update its representative
8: endif
9: endfor

Fig. 2. The Basic Sequential Algorithm Scheme (BSAS) [12].

III. COOPERATIVE CLUSTERING BASED MCL ALGORITHM

Motivated by both the MCL and the BSAS algorithms above, one novel method incorporating clustering into the conventional MCL is proposed for cooperative multi-robot localization in order to further improve the localization performance, as outlined in Fig. 3.

A. MCL+BSAS part

Our proposed approach consists of three parts. In the first part, each robot maintains its own belief by executing the MCL and the BSAS algorithms. The conventional MCL is used and the generated particle set is then supplied to the BSAS algorithm for clustering (the clustering component). By doing so, the proposed approach could monitor the localization process of each robot in real time by making use of the cluster information obtained from BSAS, such as the number of clusters, denoted as n_c, the locations of these clusters, denoted as $pose(a_1, \cdots, a_n)$, the possibility of each cluster represent the true location of the robot. If the percentage p_{max} of particles in the cluster which contains the largest number of particles exceeds a predefined threshold η, then the considered robot is assumed to have been localized, and return the pose of representative of the cluster to be used as a landmark for the other robots. If p_{max} is less than the predefined threshold η, then it indicates the robot fails to localize itself at the moment. The ability that recognizing whether a robot has been l localized or not by itself significantly improves its robustness and autonomy.

B. Detection part

The core idea of multi-robot localization is to let the robot benefit from information collected by others, therefore the interactions between robots is essential to the proposed approach. Robot can perceive other robots in the environment, and then exchange their information with each other if possible to reduce their uncertainty about their external environment. In part 2, the proposed approach manages the behavior of both detected robots in a principled way in order to dealing with the delayed information exchange problem.

Algorithm: Clustering based MCL for multi-robot localizatoin

Part 1:

Initially, each robot executes its own MCL+BSAS to monitor its own pose estimate and cluster information.

If the degree of certainty p_{max} exceeds a predefined threshold η, the considering robot will stop to indicate it has been localized and return its location to be used as landmark for other robots.

Part 2:

When one robot detects another:

(a) If the values of both detected robots' status variables are false, there is no information exchange;

(b) Else there is one robot's status variable is true or both of them are true, then do belief comparison:
  If they are not with the same degree of certainty, do information exchange which use the one with higher certainty to help the other one to refine its pose estimate;
  Else there is no information exchange;

Part 3:

Process of information exchange:

(a) After determining the exchange direction, a predefined distance threshold γ is used to help in refining process:
  Those clusters of the robot with lower certainty, whoever is within the range of predefined distance threshold γ to any clusters of the robot with higher certainty, will be kept;

(b) Return a new set of clusters which will focus on the more possible locations of the robot;

(c) Uniformly resample *N* total particles within the newly returned set of clusters;

Fig. 3. The Clustering based MCL for cooperative multi-robot localization

The behavior is mainly to determine whether to allow an information exchange and the direction of information exchange, with the help of one important Boolean type status variable for each robot described in Fig. 4. Initially, each status variable is set to be "False". During the entire localization process, once a robot has detected any landmark, its status variable will be set to "True", and once a robot has exchanged its belief with another robot, the status variable will be set to "False". If one robot has succeeded in its localization, its Boolean value will always stay in "True"

We manage the detection between robots in two scenarios: (1) in the first scenario, both status variables of two detected robots are false. This scenario includes two situations: (a) both robots have not detected any landmarks yet. Here we can assume that the internal beliefs of both robots about their poses relative to the environment are very blurry.

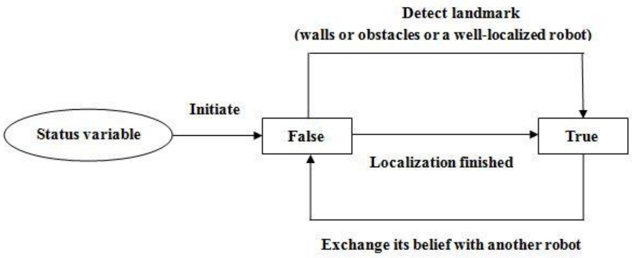

Fig. 4. The status variable diagram.

We skip the information exchanging at the moment since the blurry knowledge will not benefit the localization process. (b) Both robots have already exchanged their beliefs at last encounter or detection, and no landmarks have been observed by both robots yet at current detection. Without a newly observation of landmarks the level of uncertainty will most likely stay the same level or even worse. Normally there is no need to exchange information again. Therefore our approach does not allow the information exchanging under this kind of situations. (2) In the second scenario, there is at least one status variable value is true or both are true. Since perceiving a landmark helps robot gather more information about its environment so it could help in its pose estimate, we consider it as necessary to exchange their beliefs to refine the pose estimates. The direction of refining belief is to use the robot's belief which is with higher certainty about where it is to refine the other with lower centainty about its pose and hence it requires a comparison of the level of certainties about their locations. In order to quantify the belief, our approach makes use of the variable p_{max} extracted from the clustering component. Through comparing of p_{max} of both robots we can find which one is with higher certainty about its position. If they are with the same level of certainty, then we consider it as no need to exchange their information, however, this situation rarely happened in experiments.

Through this strategy our approach makes sure that the information exchange always benefits the localization process.

C. Information exchange part

As mentioned above, each particle or cluster represents one possible position of robot. If two robots detect each other, their estimated poses which are particles or the representatives of clusters should be within a certain distance. Our proposed approach makes use of this geometric relationship to build a mechanism for information exchange. Fig. 5 shows the pseudo code of the process of information exchange. It takes both sets of clusters of robot A and B, and the predefined threshold distance γ as inputs. The direction of information exchange has been determined by part 2, thus, we have two cases: (1) robot A refines robot B from line 1 to 10; (2) vice versa robot B refines robot A. In case 1, line 2 initializes a new set of cluster C'_B. From line 3 to line 8, it is a for loop going through all clusters of robot B. Line 4 calculates the distance between the current cluster of robot B and all clusters of robot A to find the minimum one, if the minimum distance is smaller than the threshold γ, then add it to the set of cluster C'_B. Line 10 uniformly resamples the total number of particles within the newly returned set of clusterC'_B. The process of case 2 is the same as case 1 but with different direction of information exchange.

Information exchange
($C_A(a_1, \cdots, a_m), C_B(b_1, \cdots, b_n), \gamma$):

1: *Case 1: Robot A refines Robot B*
2: $C'_B = \emptyset$
3: for *i =1* to *n* do
4: find $d(b_i, C_A) = min_{1\leq j\leq m} d(x_i, C_j)$
5: if $d(b_i, C_j) < \gamma$ then
6: add b_i to C'_B
7: endif
8: endfor
9: return C'_B
10: uniformly resample particles within C'_B
11: Case 2: Robot B refines Robot A
12: *vice versa*

Fig. 5. The process of information exchange.

IV. EXPERIMENTAL RESULT

Our approach is tested on both real and simulated robots. In both situations, we firstly test the performance of single mobile robot localization, and then apply our approach to multi-robot localization. Three important data: the localization time $t(s)$, the successful rate ε, and the error distance d, will be collected in every experiment. Finally we compare these characteristic results of multi-robot localization with single robot localization, and demonstrate improvement.

A. Experiments Using Real Robots

Fig. 6. Two iRobot Create using in our experiments. The left Create is with black label, while the right one is regular Create.

Fig. 6 shows the two real robots iRobot Create using in our experiments. The experiments are conducted in four different environments shown in Fig. 7. The two Creates started from different locations. The paths of both Create is set to turn left 120° when it bumps to the wall or obstacle, otherwise keep going forward. The total number of particles used to represent the belief of Create is set to 5000. The dissimilarity measure threshold θ is set to 17cm which is the radius of Create. Therefore the shape of each cluster will be the same size as Create. The threshold γ used in the process of information exchange is set to be 60cm since the setup of detection is determined by the range of infrared signals emitted by Virtual wall sensor. Threshold η is set to 70%, which means if the number of particles contained in the largest cluster is equal or larger than 70% of total, the Create will stop to indicate it has been localized. We repeat each experiment 50 times and compare the performance to MCL+BSAS for single robot which ignores robot detections.

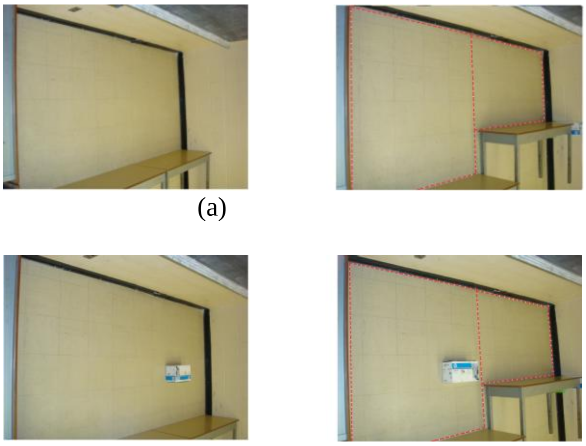

(a)
(b)
(c)
(d)

Fig. 7. Four environments of real robot experiments. (a) A rectangle field with the shape of 300cm×150cm; (b) Two rectangle fields, the left one is 150cm×150cm, the right one is 150cm×100cm; (c) A rectangle field of 300cm×150cm, and an obstacle of 31.5cm×19.5cm placed in the field; (d) Two rectangle fields, the left one is 150cm×150cm, the right one is 150cm×100cm, and an obstacle of 31.5cm×19.5cm placed in the field.

TABLE I.
COMPARE MULTI-ROBOT LOCALIZATION WITH SINGLE ROBOT LOCALIZATION USING CREATE

Environment		***t*** **(s)**	**Time saving (%)**	***ε***	**Increasing of successful rate (%)**
Symmetric	**Single robot**	230.88	37.6%	42%	30%
	Multi robot	144.04		72%	
Asymmetric	**Single robot**	81.6	25.6%	84%	2%
	Multi robot	60.73		86%	
Symmetric with obstacle	**Single robot**	92.62	24.9%	80%	4%
	Multi robot	69.54		84%	
Asymmetric with obstacle	**Single robot**	74.38	30.4%	90%	1%
	Multi robot	51.76		91%	

The results shown in Table I demonstrate that compare to single robot localization, our proposed approach applied in multi-robot localization not only reduces the time for localization, but also increase the successful rate for each robot. We can see without the help of detection of other Create and exchange information between them the time for single robot localization in symmetric environment is 230.88s, and the successful rate is only 42%. With the help of another Create, the results show significant improvement, which reduce the time for localization by 37.6% to 144.04s in average of two Create, and increase the successful rate by 30% to 72%. The large improvement of time saving also shows in the other three environments. However our proposed approach can only increase the successful rates by relatively small ranges in the other three environments. This is because these three environments are very distinctive which means even single Create can achieve high successful rate.

B. Simulation Experiments

The simulation experiments are also implemented in four different environments shown in Fig. 8. Same as in the real robots experiments, both multi-robot localization using our proposed approach and single robot localization have been tested under these four environments. The total number of particles is also 5000. The threshold γ is set to 120 pixels which is the same setup of detection with experiments using Create. The dissimilarity threshold θ is set to be 60 pixels, and threshold η is also set to 70%. We repeat each experiment 50 times.

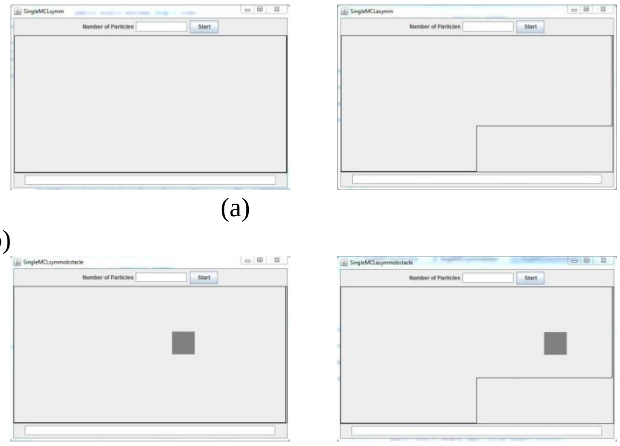

(a)
(b)
(c)
(d)

Fig. 8. Four environments of simulation experiments. (a) A rectangle field of 600×300pixel; (b) Two rectangle fields, the left one is 300×300pixel, the right one is 300×200 pixel; (c) A rectangle field of 600×300pixel, and a gray rectangle obstacle of 50×50pixel placed in the field; (d) Two rectangle fields, the left one is 300×300 pixel, the right one is 300×200pixel, and a gray rectangle obstacle of 50×50pixel placed in the field.

Table II summarizes that our proposed approach can significantly shorten the time for localization in both symmetric environment and featured environments compare with single robot localization. As to the successful rate, it depends on the type of environments. The improvement is obviously while localizing in symmetric environments.

TABLE II

COMPARE MULTI-ROBOT LOCALIZATION WITH SINGLE ROBOT LOCALIZATION IN SIMULATION EXPEIMENTS

Environment		t (s)	Time saving (%)	ε	Increasing of successful rate (%)
Symmetric	Single robot	368.02	70.6%	44%	32%
	Multi robot	109.56		76%	
Asymmetric	Single robot	31.4	28.3%	86%	3%
	Multi robot	22.485		89%	
Symmetric with obstacle	Single robot	33.24	27%	84%	4%
	Multi robot	24.25		88%	
Asymmetric with obstacle	Single robot	28.74	31.6%	92%	1%
	Multi robot	19.65		93%	

C. Study of parameter η

As we mentioned the value of η determines the stop point of each robot's localization which is specified by the minimum percentage of total particles contained in the largest cluster. In this group of experiments, we increase the value of η into 80%, while other parameters stay the same values with previous simulation experiments, to see how it can affect the performance.

TABLE III

COMPARISON OF MULTI-ROBOT LOCALIZATION UNDER TWO VALUES OF η

Environment	Multi robot	t (s)	Time increasing (%)	ε	Increasing of successful rate (%)
Symmetric	η=70%	109.56	18%	76%	2%
	η=80%	129.41		78%	
Asymmetric	η=70%	22.485	14.5%	89%	3%
	η=80%	25.75		92%	
Symmetric with obstacle	η=70%	24.25	16.9%	88%	4%
	η=80%	28.36		92%	
Asymmetric with obstacle	η=70%	19.65	8.5%	93%	1%
	η=80%	21.33		94%	

The results show that a large value of η will take more time to finish the localization process because it requires more information about its external environment to reduce the uncertainty of position estimation. In the mean time, the fact that more particles fall in the largest cluster indicates more likely the pose of representative of this cluster represents the true pose of the robot, which means the successful rate or effectiveness will be increased. However, there is a trade-off between efficiency and effectiveness controlled by η. If η is too big, it will take significantly longer time to localize itself while achieving a relatively small increase of successful rate. On the other hand, if η is too small, despite the rapid reduction of localization time, without guaranteeing the successful rate it will not make any sense to the localization.

V. Conclusion and Future Works

This paper presents a clustering based MCL algorithm for cooperative multi-robot localization, in which all robots moved simultaneously. Each robot maintains its own clustering based MCL algorithm, and communicates with each other whenever it detects another robot. The newly developed mechanism for the communication aims to achieve improve the efficiency and effectiveness of localization process. In addition, the characteristic of without fusion center and the instant communication between two detected robots allow our proposed approach scaling to large group of robots. Compare with single robot localization, experimental results performed in both real and simulated environments demonstrate the improvements in both efficiency and effectiveness of our proposed approach applied in cooperative multi-robot localization.

In the future work, we want to design a more robust way of movement based on already gathered information rather than the simple static path setting. We also want to test our approach on a large group of robots.

ACKNOWLEDGEMENTS The second author would like to thank NSERC for financial support.

REFERENCES

[1] A, Howard, M, J Mataric, and G, S Sukhatme. Cooperative relative localization for mobile robot teams: An ego-centric approach. In Proc. of The naval Reasearch Laboratory Workshop on Multi-Robot Systems (2003), 65-95.
[2] A, Gasparri, S, Panzieri, F, Pascucci, and G, Ulivi. A Hybrid Active Global Localization Algorithm for Mobile Robots. International Conference on Robotics and Automation (April 2007), 10-14.
[3] D, Wu, J, Chen, and Y, Wang. Bring Consciousness to Mobile Robot Being localized. Proceedings of the 2009 IEEE International Conference on Robotics and Biomimetics (741-746 2009).
[4] D, Fox, W, Burgard, H, Kruppa, and S, Thrun. A Probabilistic Approach to Collaborative Multi-robot Localization. Autonomous Robots on Heterogeneous Multi-Robot System, vol.8, no.3 (June 2000), 325-344.
[5] Esha, D Nerurkar, Stergios, I Roumeliotis, and Agostino, Martinelli. Distributed Maximum A Posteriori Estimation for Multi-robot Cooperative Localization. IEEE International Conference on Robotics and Automation (May 12-17 2009), 1402-1409.
[6] H, Hose and H, L Akin. The Reverse Monte Carlo localization algorithm. Robotics and Autonomous Systems (2007), 480-489.
[7] Maja, J Mataric. The robotics primer. The MIT Press, 2007.
[8] P, Trahanias and E, Scordalakis. An efficient sequential clustering method. Pattern Recognition, vol.22(4) (1989), 449-453.
[9] R, Kurazume, S, Nagata, and S, Hirose. Cooperative positioning with multiple robots. In Proc. 1994 IEEE Int. Conf. Robotics and Automation, vol.2 (May 8-13 1994), 1250-1257.
[10] S, Thrun, D, Fox, and W, Burgard. Monte carlo localization with mixture proposal distribution. Proceedings of the AAAI National Conference on Artifical Intelligence (2000), 859-865.
[11] S, I Roumeliotis and G, A Bekey. Distributed multi-robot localization. IEEE Transactions on Robotics and Automation, vol.18, no.5 (October 2002), 781-795.
[12] S, Theodoridis and K, Koutroumbas. Pattern Recognition. Academic Press, 2006.
[13] S, Thrun, W, Burgard, and D, Fox. Probabilistic Robotics. MIT Press, 2006.

The Seventeenth International Symposium on Artificial Life and Robotics 2012 (AROB 17th '12),
B-Con Plaza, Beppu, Oita, Japan, January 19-21, 2012

Soundscape Partitioning to Increase Communication Efficiency in Bird Communities

Reiji Suzuki[1], Charles E. Taylor[2] and Martin L. Cody[2]

[1,2] Gradute School of Information Science, Nagoya University, Furo-cho, Chikusa-ku, Nagoya 464-8601, Japan
[2] Dept. Ecology and Evolutionary Biology, University of California, Los Angeles, Los Angeles, CA, 90095, USA
(Tel/Fax: +81-52-789-4258, e-mail: reiji@nagoya-u.jp)

Abstract: Birds do not always vocalize at random, but may rather divide up sound space in such a manner that they avoid overlap with the songs of other bird species. In effect, a high degree of communication efficiency can be achieved by many simultaneously active vocalists that finely integrate songs with minimal overlap. We describe this phenomenon from several recordings at our principal study location, near Volcano, California. Among the most-studied models for conceptualizing and studying such de-synchronized systems come from scheduling algorithms in computer science, where internet protocols involve packets of information that are broadcast widely; any collisions between them will corrupt the colliding packets so that they need to be resent. We have simulated some of these methods that might be appropriate for the soundscape of bird communities. Some features of these de-synchronized depend on specifics of the algorithms used.

Keywords: Simulated evolution, DESYNC, sound space, resource partitioning, bird song

1 INTRODUCTION

Our laboratory is concerned with developing acoustic sensor arrays so that they will be useful for observing and analyzing bird diversity and behavior. In these studies we observed that birds do not always vocalize at random, but may rather divide up sound space in such a manner that they avoid overlap with the songs of other bird species.

For example, at our primary field site, in a mixed conifer-oak forest near Volcano, CA, we typically encounter 30+ species of birds during a short observation period. Not all of these species sing, but many do, and those who do sing appear to avoid collisions that would occur from singing at the same time. Table 1 shows the amount of time during which we observed 0, 1 or 2+ birds singing at the same time during a recording of approximately 3 minutes on the morning of June 22, 2010. The species singing at this time were: Spotted Towhee (*Pipilo maculatus*); Pacific-slope Flycatcher (*Empidonax difficilis*); Orange-crowned Warbler (*Vermivora celata*); Nashville Warbler (*V. ruficapilla*); Black-throated Gray Warbler (*Dendroica nigrescens*); Hutton's Vireo (*Vireo huttoni*); Red-breasted Nuthatch (*Sitta canadensis*); and Common Bushtit (*Psaltriparus minimus*). From the proportion of the total time each species sang, we can calculate the number of seconds we expect to be vacant (empty), monopolized by a single species, or occupied by the songs of 2+ species, given the species sing independently of each other. What we observed was that less time was vacant or occupied by 2+ species, and more time was monopolized, than expected by chance ($\chi = 14.1$, df = 2, $p < 0.001$).

We believe this avoidance of collisions in soundspace to be typical, if not universal. Others have observed such partitioning, in a variety of locations and species, including Wrentits (*Chamaea fasciata*) and Bewick's Wrens (*Thryomanes bewickii*) [2], Least Flycatchers (*Empidonax minimus*), and Red-eyed Vireos (*Vireo olivaceus*) [3], and a set of four species — Wood Thrush (*Hylocichla mustelina*), Eastern Wood Peewee (*Contopus virens*), Great Crested Flycatcher (*Myiarchus crinitus*), and Ovenbird (*Seiurus aurocapillus*) [4].

Table 1. The observation and expectation of singing behaviors in the recording in a mixed conifer-oak forest near Volcano, CA.

Time	Vacant (0)	Mono (1)	2+	Total
Expectation	102.4	64.8	18.8	186.0
Observation	92.4	85.8	7.9	186.0

In the study reported below we first describe a way to visualize sound space partitioning in a way that may prove to be generally useful, propose some general procedures that the birds might use to avoid collisions, then report on some evolutionary computer simulations that illustrate how these procedures might accomplish what we have observed. Attention is drawn to particulars that might permit experimental determination of just which procedures the birds employ in nature.

2 MATERIALS AND METHODS

Observations plotted in polar coordinates, as used in circular statistics, can help visualization of sound space partitioning. Birds typically sing repeated sequences of phrases, with only a short time between phrases. The entire sequence of phrases constitutes a song [1]. There is then a break of a few seconds, then a new song begins. Examples of some such songs for the species present are available at the web sites for xenon-canto (http://www.xeno-canto.org/) or Macaulay library (http://macaulaylibrary.org/).

Fig. 1 shows polar representations of recordings made at our study site during the mornings of April 19, 2010 (recording 10-21). In this figure the "driver" species was Black-headed Grosbeak (*Pheucticus melanocephalus*), BhGb, in red. Other species singing in the interstices are Orange-crowned Warblers, OcWa, in green and Nashville Warblers, NaWa, in blue. The mean vector of the distribution of singing events for each species is indicated by a bar. Time elapsed since the beginning of the period is indicated around the outside, and number of instances for each time interval by the inner circles. This recordings was made as described in [5], and is posted at our web site, http://taylor0.biology.ucla.edu/al/bioacoustics/. In this recording Black-headed Grosbeaks, were dominant. The average time between starting songs was approximately 7.7 seconds. This was taken as the period of the cycle, as represented around the circumference of the diagram. Time is represented as an angle, taken to be 0 at the beginning of the recording, then progressing to 360 at the end of each period, and then repeated.

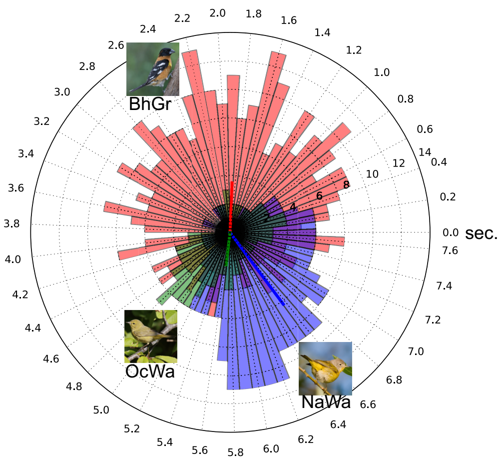

Fig. 1. Circular diagram of de-synchronized singing.

At each 0.1 sec in the recording, we checked whether a species was singing or not, accumulated the number of instances of singing, and represented this number as the radius length in the diagram. This was done separately for each species, then plotted. The average time between song starts usually gave the best representations, but some trial and error adjustments often helped clarity, and is, of course, necessary if there is no dominant species.

There are many procedures the birds might use to partition soundspace. The most-studied models for conceptualizing and studying such desynchronized systems come from scheduling algorithms in computer science, where internet protocols govern packets of information that are broadcast widely, and any collisions between them will corrupt the colliding packets so that they need to be resent. For this study we have simulated three procedures under the assumption that all individuals begin to sing with the shared period T if their songs do not overlap with other songs.

(a) "simple trial and error" If there is no overlap with the songs of others, then that individual will sing again exactly one time period later. But if the song of that individual overlaps at all with the song of another, then that focal individual will change slightly the time it starts its next song with a genetically determined probability p interpreted as its behavioral plasticity. Specifically, it begins to sing the next song with the interval of $T + dt(\ \ DT, DT)$, where $dt(x, y)$ is a random value generated from the uniform distribution on $[x, y]$. Otherwise, it will sing again exactly one time period (T) later.

(b) non persistent CSMA, or "back off" At its time to sing, the focal individual checks whether any other individuals are singing or not. If no one is singing, it begins to, and then decides to sing the next song one time period later. Otherwise (if other birds are singing), it delays its time to sing for the random time $dt(0, DB)$ with a probability p.

(c) DESYNC-based TDMA (Time division multiple access) or just **DESYNCH**. The basic idea of DESYNC algorithm [6] is that each agent modifies its own timing to fire so that it will occur midway between the preceding and the next firing events. We modified this slightly for birds. In our simulations each individual modifies its own timing to sing the next song with a probability p so that the timing gets closer to the relative distance ratio among the mid time point of the preceding (m_p), the focal (m_f) and the next song (m_n) becomes $m_f \quad m_p : m_n \quad m_f = SL_p + SL_f : SL_f + SL_n$ in the future songs. SL_f, SL_n and SL_p are the length of the focal, next and preceding songs respectively. The next timing to sing (t_n) is set in between this desired timing (t_d) and the scheduled timing with the period T (t_s) using an interpolation coefficient DD ($|t_d \quad t_n| : |t_n \quad t_s| = 1 \quad DD : DD$). Otherwise, it will sing again exactly one time period (T) later. This method can be shown to achieve full utilization of the available bandwidth, yet no global clock is required and the algorithm automatically adjusts to any number of participants. These acoustic interactions are conducted until the time reaches $R \quad T$.

For our simulations the population structure and evolutionary process were as follows: We assume S different species and the population of each species is composed of N individuals as shown in Fig. 2. In this example there are three species, with 4 individuals each. The whole population is randomly divided into the N groups of S individuals so that each individual participates in one group and each group includes exactly one individual for each species. The acoustic interaction is conducted among the members of each group independently in order to determine the fitness contribution of each individual. The fitness of each individual is taken to be the total duration during which the focal individual can sing solo (without interference).

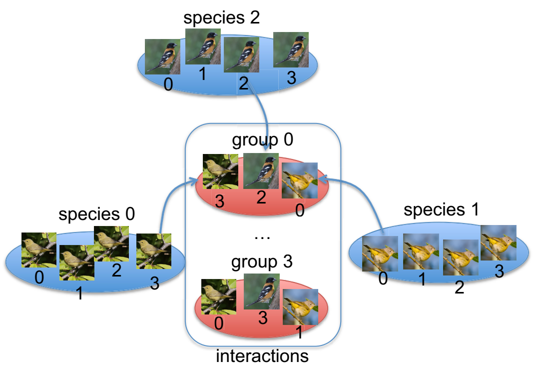

Fig. 2. Population and interaction model for evolution.

We modeled the evolution of the plasticity parameter p. Each individual has its own genetically-determined p that determines its behavior in acoustic interactions. The population of each species is evolved independently according to the genetic algorithm based on selection and mutations. The selection of offspring in the next generation is based on a "roulette wheel selection" according to fitness. For each gene of offspring, a mutation occurs with a small probability p_m, which adds a small random $dt(\quad DM, DM)$ to the current value.

3 RESULTS AND DISCUSSION

For each procedure we conducted experiments with various settings of T for 500 generations using $N = 80, S = 5, R = 30, DT = 7.0, DB = 13.0, DD = 0.5, DM = 0.1$ and $p_m = 0.01$. We assumed the species-specific length of song of the i-th species $SL_i = \{1, 2, 4, 8 \text{ and } 16\}$. The initial population was generated with initial values of p sampled from the uniform distribution over $[0, 1]$. We focused on the effects of T on evolution because it determines the degree of congestion in the acoustic space. Fig. 3 shows the average p in the last generation with the three different temporal avoidance mechanisms. We see that the evolutionary process of plasticity is strongly dependent on the basic temporal avoidance mechanisms and the setting of T.

In the case of (a) "simple trial and error", the plasticity of all species was high when T was large enough. This means that species will generally evolve to avoid temporal overlap of songs in less crowded acoustic spaces. As T decreased, the plasticity of the species with the longest song tended to be small while those of the other species remained high. In other words, the species with the longest song typically evolves to become dominant – what we term the "driver species." The driver species does not change the timing of its song to avoid overlap very much, but keeps its original periodicity, while species with shorter songs adapt to fit into the remaining time segments. Fig. 4 shows examples of interactions among evolved species in three groups with the different temporal avoidance mechanisms when $T = 42$. In this case, we see that the shorter songs randomly fluctuated several times, but they finally fit into the rest of the space left by the driver species with the longest song. This phenomenon can be explained by focusing on the benefit and cost of the adopted temporal avoidance behaviors. In this case, the benefit is to be able to resolve existing overlaps in the future interactions. However, this avoidance can fail and yield another overlap with other songs because of the randomness of the trial and error procedures. Because the effect of this cost is approximately proportional to song length, the species with the longest song is least likely to make timing adjustments and, instead, the species with short songs will make the behavioral adjustments to fit into the soundscape with minimal overlaps.

In the case of (b) "non persistent CSMA", we see that the plasticity of shorter songs converged to higher values as T decreased, while that of the longest song evolved to relatively smaller values although this tendency was not so dramatic as in the previous case. We see from Fig. 4 (b) that the individuals successfully converged to the state with no overlaps by actively delaying their timing to sing in a counterclockwise fashion. The main reason for the evolution of the smaller plasticity of the longest song is not due to the same reason that was observed in case (a). In case (b), the benefit of temporal avoidance is to be able to avoid the overlap with other songs being currently delivered. This benefit is essential for the species with shorter songs because their songs are often completely masked by other longer songs if they do not actively avoid overlap, and vice versa. However, delayed song delivery means that individuals risk losing chances to sing within a limited, finite time span. Thus, the species with the longest song will evolve low plasticity to reduce the cost of avoidance behavior and maximize song delivery opportunities.

In the case of (c) "DESYNC", we see that the plasticity of all species evolved to be high in all conditions of T although p of the longest song was slightly smaller than that of others. This is due to the fact that the p of the longest song evolved to low plasticity in a small number of trials at higher T, implying that somewhat reduced p could be adaptive in those cases. Fig. 4 (c) shows that all individuals actively adjusted their timing to sing in both clockwise and counterclockwise

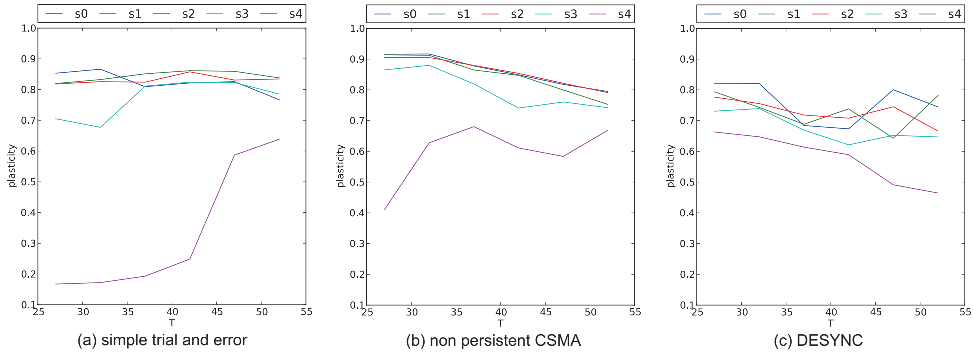

Fig. 3. The average p in the last generation with the three different temporal avoidance mechanisms. Each value is the average over 15 trials.

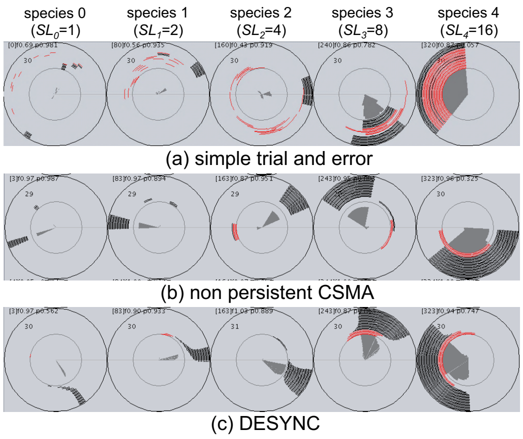

Fig. 4. Examples of interactions with different temporal avoidance procedures when T=42. The five circular diagrams correspond to a group for acoustic interactions. Each diagram represents the singing behavior of an individual. The distribution of its singing events is represented in the inner area in the same way as represented in Fig. 1. The arcs in the outer area show the distribution of songs over the circular time-line where each succeeding period T is arranged from inner- to the outer-most position. Red or black arcs are the songs with or without overlaps, respectively.

manners, and as a result, the population quickly converged to the state with no overlaps. This implies that our modified DESYNC algorithm is adaptive and has almost no cost for adjustment processes. Thus, we did not observe significant effects of the differences in the length of songs on the evolution of the behavioral plasticity of individuals.

4 CONCLUSIONS

We discussed sound space partitioning to increase communication efficiency in bird communities. We described this phenomenon from several recordings, using a way to visualize sound space partitioning based on a circular diagram. We also proposed some general procedures that the birds might use to avoid collisions, then reported on some evolutionary computer simulations that illustrate how the procedures might accomplish what we have observed. The dynamics of soundscape partitioning that emerge as behavioral plasticity evolves to minimize interspecific song overlap are illuminated with our simulation procedures, which can be used to elucidate the communication protocols employed by birds in complex, real-world situations.

REFERENCES

[1] Catchpole, C. K. and Slater, P. J. B. (1995), *Bird Song: Biological Themes and Variations*, Cambridge University Press.

[2] Cody, M. L. and Brown, J. H. (1969), Song asynchrony in neighboring bird species. *Nature*, 222 (5195): 778–780.

[3] Ficken, R. W., Ficken, M. S. and Hailman, J. P. (1974), Temporal pattern shifts to avoid acoustic interference in singing birds. *Science*, 183 (4126): 762–763.

[4] Popp, J. W., Ficken, R. W. and Reinartz, J. A. (1974), Short-term temporal avoidance of interspecific acoustic interference among forest birds. *The Auk*, 102 (4): 744–748.

[5] Kirschel, A. N. G., Cody, M. L. , Harlow, Z. , Promponas, V. J., Vallejo, E. E. and Taylor, C. E. . Territorial dynamics of Mexican Antthrushes revealed by individual recognition of their songs. *Ibis.*, 153:255–268.

[6] Degesys, J., Rose, I. Patel, A. and Nagpal, R. (2007), DESYNC: Self-organizing desynchronization and TDMA on wireless sensor networks. *International Conference on Information Processing in Sensor Networks (IPSN)*, pp. 11–20.

The Seventeenth International Symposium on Artificial Life and Robotics 2012 (AROB 17th '12),
B-Con Plaza, Beppu, Oita, Japan, January 19-21, 2012

A Cooperative Self-localization Method Based on Group Robot Information Sharing

Yuichi Kitazumi, Noriyuki Shinpuku and Kazuo Ishii

Kyushu Institute of Technology, Fukuoka 808-0196, Japan
(Tel: 81-93-695-6012, Fax: 81-93-695-6102)

kitazumi-yuichi@edu.brain.kyutech.ac.jp

Abstract: In the RoboCup MSL (Middle Size League), each robot should be autonomous and have fundamental abilities like obstacle avoidance, path planning, and cooperative behavior. Self-localization is one of the most basic and important functions for mobile robots, especially, multirobot system with cooperative behavior. We aim at improvement of self-localization accuracy of each robot of multirobot system by information sharing. To enhance the robot position accuracy, the soccer ball is used as the common landmark that just one exists in the playing field. In general, measured data, such as distances and angles to the white lines on the field, the ball, have measurement errors in the actual environment, so that we assume that the existence possibility of landmark position follows the Gaussian distribution. In our multirobot system, all robots share the group robot information such as estimated self-location and likelihood, distance and angle to the ball, role (defender, forward) via wireless LAN. Each robot evaluates the position likelihood of the landmark based on the landmark's existence probability. Then each robot corrects its position using fed-back the landmark position. In order to evaluate the efficiency of the proposed method in the real environment, the estimated self-location has been evaluated through experiments using the soccer robots "Musashi".

Keywords: *Multirobot System, Self-Localization, Information Sharing, RoboCup Middle Size League*

1 INTRODUCTION

For autonomous mobile robots, self-localization is one of the most fundamental and important information. Especially, when a multirobot system performs cooperative actions in real-time and actual environment, the importance of self-location increases. In the RoboCup Middle Size League (RoboCup MSL), the self-localization information of each robot is also important information for achieving the cooperative behavior [1][2].

In this research, the RoboCup MSL is selected as the target research platform for development and evaluation of multirobot system and cooperative behaviors, where maximum five robots from a team play soccer game and the collaborations with teammate robots such as pass and role change are inevitable to keep the rules. In the RoboCup MSL, active sensors like laser scanner are also allowed to obtain the surrounding environment, however, the playing field is the flat and simple symmetric environment with few landmark objects and often occupied by many mobile robots, therefore our robots obtain the environmental information mainly from an omni-vision sensor. In the beginning period of MSL, many variations of robots exist and many kinds of sensors are mounted, recently almost robots have an omni-vision system and an omni-directional mobile mechanism to be a holonomic system for easy motion planning [2-5].

Most of MSL robots estimate self-locations and the ball position from images of omni-vision systems using the white lines' position on the field and colored object position [6-8]. In our multirobot system, the distances to white lines are compared with the field model using particle filter and the self-location of each robot is estimated [8-10]. The absolute ball position is obtained by adding the robot self-location and the relative position of the ball from the robot.

We propose a cooperative self-localizing method which use the ball on the soccer field as the common landmark for all teammate robots, and self-locations are corrected by using the estimated absolute ball position by all robots. The proposed system represents the ball position by the existence probability functions for all robots depending on the distance, where the function show high value for the ball-closed robot and low for the robot far from the ball. By combining the probability functions, the ball existence probability map is generated and the proper ball position is estimated. Then, the robot positions and directions are also modified using the estimated ball position.

In experiments, the efficiency of the proposed method with group robot information sharing was evaluated using multirobot system RoboCup MSL by comparing the ball position and robots positions information sharing in real environment, and the experimental results show good improvement of self-locations of Musashi robots.

2 SINGLE ROBOT LOCALIZATION

In the proposed method, each robot estimates its position and direction by the Monte Carlo Localization (MCL) based on the geomagnetic data and the relative distance between the robot and white field lines [6-12]. The origin of the field map is the center of the field and the field is modeled in Cartesian coordinate taking *x* axis to the own goal direction.

The robot's state at time step *t* is represented by $\boldsymbol{x}_t = [r^x_t, r^y_t, {}^a\theta_t]^T$ which consists of its position (r^x_t, r^y_t) and heading ${}^a\theta_t$. The posterior probability $p(\boldsymbol{x}_t|\boldsymbol{y}_{1:t-1})$ is calculated from $\boldsymbol{x}_t$ and time series of observed data $\boldsymbol{y}$. Here, $\boldsymbol{y}_t$ at time step *t* includes 60 relative distances to the closest white line every 6 degrees. In the MCL method, the probability distribution is represented by a set of *N* particles. In our application, each particle has $\boldsymbol{x}_t$ and $\boldsymbol{y}_t$ and the conditional probability $p(\boldsymbol{x}_t|\ \boldsymbol{x}_{t-1},\ \boldsymbol{u}_{t-1})$ is specified by the previous state $\boldsymbol{x}_{t-1}$ and control input $\boldsymbol{u}_{t-1}$. Here, we use odometory data as $\boldsymbol{u}_{t-1}$. In order to apply MSL to self-localizing problem, we assume that the self-location probability follows the Markov decision process, and the posterior probability of current robot state is obtained by the following equation.

$$p(\boldsymbol{x}_t|\boldsymbol{y}_{1:t-1}) = \int p(\boldsymbol{x}_t|\boldsymbol{x}_{t-1}, \boldsymbol{u}_{t-1}) \cdot p(\boldsymbol{x}_{t-1}|\boldsymbol{y}_{1:t-1}) d\boldsymbol{x}_{t-1} \quad (1)$$

Next, as shown in eq.(2), $p(\boldsymbol{x}_t|\boldsymbol{y}_{1:t})$ is updated based on the Bays theorem using likelihood $p(\boldsymbol{y}_t|\boldsymbol{x}_t)$ which is represented as the difference between line distances in each particle and observed data.

$$p(\boldsymbol{x}_t|\boldsymbol{y}_{1:t}) = \frac{p(\boldsymbol{y}_t|\boldsymbol{x}_t) \cdot p(\boldsymbol{x}_t|\boldsymbol{y}_{1:t-1})}{p(\boldsymbol{y}_t|\boldsymbol{y}_{1:t-1})} \quad (2)$$

The robot orientation is estimated from $\boldsymbol{x}_t$, however, the RoboCup MSL environment consists of symmetric and simple surfaces and always two candidate positions exist. That is, MCL has the possibility to select a wrong robot position in the MSL soccer field, called "Kidnapped Problem [13]". To help the problem, the geomagnetic sensor is utilized to have the robot direction. The predicted robot position is calculated by weighted average based on $\boldsymbol{x}_t$ and $p(\boldsymbol{x}_t|\boldsymbol{y}_{1:t})$ as a weight. The self-localization process calculates the estimation iteratively. When the likelihood of estimated position from MCL is lower than a certain threshold (low reliability), the position from dead-reckoning method is adopted.

3 COOPERATIVE SELF LOCALIZATION

In our system, the self-localization is detected based on the visual information and wheel encoder data. Therefore the accuracy of self-localization depends on lighting condition, occlusions by opponent robots, and wheel slipping. In this paper, we consider the feature of multirobot system in RoboCup MSL, and propose a cooperative self-localization method based on information sharing among multirobots. The proposed method is realized by following steps.

Step 1. All robots find the ball and set as the common landmark.

Step 2. All robots share the ball position and self-position via wireless LAN.

Step 3. All robots estimate the proper ball position based on the shared information

Step 4. Using the estimated landmark (ball) position, each robot updates its position.

In this paper, the proper ball estimation of Step 3 is described "Landmark Estimation", and we call the estimated ball position by multi robots "the proper ball position" in followings. Self-position updating of Step 4 is described "Cooperative Self-Localization."

3.1 Landmark Estimation

In RoboCup MSL, many robots has omni-directional camera as an external sensor [5-8]. In this study, we assumed that the robot is equipped the omni-directional sensor and each object position is calculated using the own position and relative distances and angles between the robot and objects.

In general, the localization accuracy of object by the omni-directional camera depends on the distance from camera. In this process, each robot calculates the ball existence probability p^i_d by assuming the Gaussian distribution shown in eq.3. The variables p^x and p^y indicate the *x* and *y* coordinate of an arbitrary point on the soccer field, $\overline{m^i_x}$ and $\overline{m^i_y}$ do the *x* and *y* coordinate of the observed ball position from *i*-th robot ($\boldsymbol{m}^i=[m^i_x, m^i_y]^T$). Here, $\overline{m^i_x}$ and $\overline{m^i_y}$ are calculated as weighted average during *n* steps as shown in eq.4; we used the time-depending weight w_t. The parameters σ^i_d is the weighted variance parameters during *n* steps as shown in eq.5; $\overline{d^i}$ is the weighted average of the relative distance between the *i*-th robot and the ball from eq.6.

$$p^i_d(p^x, p^y) = \prod_{k=x,y} \frac{1}{\sqrt{2\pi\sigma^i_d}} \exp\left(-\frac{\left(p^k - \overline{m}^i_k\right)^2}{2\sigma^i_d} \right) \quad (3)$$

$$\overline{m}^i_{x,y} = \sum_{t=1}^{n} m^i_{x,y}(t) \cdot w_t \Big/ \sum_{t=1}^{n} w_t \quad (4)$$

$$\sigma^i_d = \sum_{t=1}^{n} \left(d^i(t) - \overline{d^i} \right)^2 \cdot w_t \Big/ \sum_{t=1}^{n} w_t \quad (5)$$

$$\overline{d^i} = \sum_{t=1}^{n} d^i(t) \cdot w_t \Big/ \sum_{t=1}^{n} w_t \quad (6)$$

The robot direction is estimated based on the MCL and heading sensor data, however the heading sensor data includes noise from magnetic distortion, so that the existence probability of the ball position p^i_s regarding magnetic compass is set to the Gaussian distribution in eq.7. As shown in Fig. 1, the parameter θ^i shows the angle between two lines; one line is from the *i*-th robot to the ball, and the other line is from the *i*-th robot to arbitrary point. The parameter r^i is the distance from the *i*-th robot to the arbitrary point, and l^i is the length of the arc; the center of the arc is the *i*-th robot position.

The parameter V^i is the weighted variance parameter regarding to the relative ball angle $\overline{\theta^i_{rel}}$ in robot coordinate during n steps as follows in eq.8. $\overline{\theta^i_{rel}}$ is calculated as weighted average during n steps as shown in eq.9. In the eq.10, we define that the variance for p^i_s is sum of the variance of heading sensor θ_{th} and V^i which regarding time. The ball existence probability is distributed along the circular arc, and the probability density takes the maximum value on the straight line L from the robot to the ball.

$$p^i_s\left(l^i\right) = \exp\left(-\frac{{l^i}^2}{2{\sigma^i_s}^2}\right) \quad (7)$$

$$V^i = \sum_{t=1}^{n}\left(\theta^i_{rel}(t) - \overline{\theta^i_{rel}}\right)^2 \cdot w_t \Big/ \sum_{t=1}^{n} w_t \quad (8)$$

$$\overline{\theta^i_{rel}} = \sum_{t=1}^{n} \theta^i_{rel}(t) \cdot w_t \Big/ \sum_{t=1}^{n} w_t \quad (9)$$

$$\sigma^i_s = r^i \cdot \sin\left(\theta_{th} + V^i\right) \quad (10)$$

In the proposed system, the conclusive ball existence probability p^i_{all} is calculated as the product of p^i_d and p^i_s in eq.11. Here, M is the number of robot in our team. Finally, we assume that the proper ball position p^i_{all} is the highest on the soccer field.

$$p^i_{all}\left(p^x, p^y\right) = \frac{1}{2M}\sum_{i=1}^{M}\left\{p^i_d\left(p^x, p^y\right) + p^i_s\left(l^i\right)\right\} \quad (11)$$

3.2 Cooperative Self-Localization

When the robot position has error, the observed ball position will be estimated far from the true ball position. It is desirable that the estimated robot position is adjusted near the true robot position by using the landmark, the ball position, so as to fit the observed ball position to the proper ball position. In the proposed system, we introduced an updating rule for ball position as shown in eq.12. α^i_d means the coefficient for updating the ball position based on the

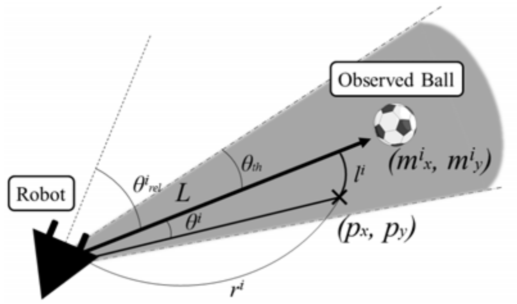

Fig. 1. Definition of existence probability p^i_s

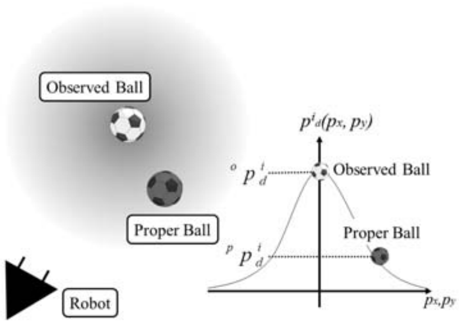

(a) (b)

Fig. 2. Updating coefficient by parallel translation based on $^o p^i_d$ and $^p p^i_d$.

ball existence probability as following eq.13. γ^i_d is dumping factor which follow the feature of omni-directional camera as shown in eq.14. $d_{\min}$ means minimum relative distance between the robot and ball, and we set 0.4 as a $d_{\min}$ in this experiment.

$$\Delta \boldsymbol{m}^i = \alpha^i_d \cdot \gamma^i_d \cdot (\boldsymbol{m}^i_p - \boldsymbol{m}^i_o) \quad (12)$$

$$\alpha^i_d = \frac{{}^o p^i_d - {}^p p^i_d}{{}^o p^i_d} \quad (13)$$

$$\gamma^i_d = \exp\left(d_{\min} - d^i(t)\right) \quad (14)$$

The robot position is also revised by parallel translation based on p^i_d and rotational translation based on p^i_s. $\boldsymbol{R(\theta)} \in \boldsymbol{R}^{3\text{x}3}$ is rotational matrix, and β^i_d means the coefficient for updating the robot angle based on p^i_s. θ_{pro} means the direction of the proper ball position in the robot coordinate. $^o p^i_s$ and $^p p^i_s$ are the observed and the proper ball position reliability regarding the ball angle.

$$\boldsymbol{x}_{t+1} = \boldsymbol{x}_t \cdot \boldsymbol{R}(\Delta\theta^i) + \left[\Delta \boldsymbol{m}^{i^T}, \Delta\theta^i\right]^T \quad (15)$$

$$\Delta\theta^i = \beta^i_d \cdot \left(1 - \gamma^i_d\right) \cdot \left(\theta_{pro} - \theta^i_{rel}\right) \quad (16)$$

$$\beta^i_s = \frac{{}^o p^i_s - {}^p p^i_s}{{}^o p^i_s} \quad (17)$$

Considering the parallel translation updating, let us consider the situation as shown in Fig. 2. Figure 2-(a) shows the observed ball and the proper ball, and the robot calculates the ball position reliability to take high value around observed ball position. ${}^{o}p^{i}_{d}$ and ${}^{p}p^{i}_{d}$ in Fig. 2-(b) are the probabilities of the observed and the proper ball position. Equation 17 is derived in the same way with the position updating. Finally, the robot state is updated by eq.15.

4 EXPERIMENTAL RESULTS

We evaluated the performance of the proposed system used soccer robot "Musashi [14, 15]" as shown in Fig.3 in real environment. In the experiment, five robots are set in the fixed positions as shown in Fig. 4. The ball moves from A(0.00, 0.00) to B(8.50, 0.00) at a speed of 3.0[m/s]. The color calibration was set by human operator, and the lighting condition was constant during experiment. In one experiment, 80 data of self-localization and the absolute ball position were recorded during the approximately 3.0[sec]. Figure 4 shows the position of each robot and the ball on the soccer field. The positions are goalkeeper:(9.00, 0.00), field-player1:(6.00, 3.00), field-player2:(3.00, 3.00), field-player3: (3.00, -3.00) and field-player4: (6.00, -3.00). The direction of the each robot was taken to the opponent goal. In consideration of the time delay in communication between robots, the position information of goalkeeper and the provided position information from field-players to goalkeeper were used for the experiment. Table 1 shows absolute errors of the proper ball position and observed ball position. Table 2 shows absolute robot state errors of self-localization by the single robot (MCL only) and multi robot (Cooperative Self-Localization).

In evaluation of the ball position, we focused on the y axis error e_{bd} of the ball and evaluated by eq.18. Here, N means data amount of self-localization and the absolute ball position, and m^{tr}_{y} and ${}^{n}m^{i}_{y}$ is proper y position of the ball and y position of observed or estimated ball.

$$e_{bd} = \frac{1}{N}\sum_{n=1}^{N}\sqrt{\left(m_y^{tr} - {}^{n}m_y^{i}\right)^2} \qquad (18)$$

The absolute robot state errors e_{rp}, e_{ra} are evaluated by eq.19 and eq.20. r^{ty}_{x}, r^{ty}_{y} and θ^{r} is correct robot state, respectively. And also, ${}^{n}r^{i}_{x}$, ${}^{n}r^{i}_{y}$ and ${}^{n}{}_{a}\theta^{i}$ means robot state at time-step n.

$$e_{rp} = \frac{1}{N}\sum_{n=1}^{N}\sqrt{\left(r_x^{tr} - {}^{n}r_x^{i}\right)^2 + \left(r_y^{tr} - {}^{n}r_y^{i}\right)^2} \qquad (19)$$

Dimensions	Triangle 520[mm], Height 800[mm]
Weight	19.0[kg]
Motor	Maxon DC Motor 70[W] x 3
Motor Driver	Faulhaber MCDC 2805 x 3
Wheel	Omni wheel x 3
Battery	Li-Polymer Battery 25.9[V] 2000[mAh]
Sensors	Omni Camera, Digital Compass

Fig.3. Overview and Specification of "Musashi"

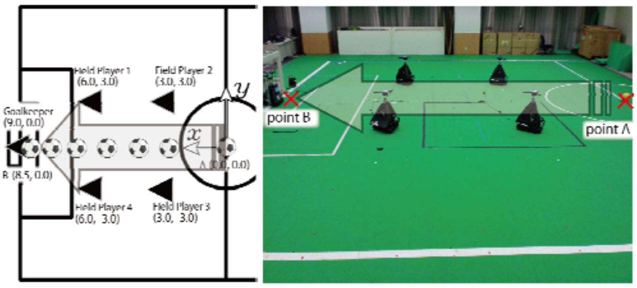

Fig. 4. The experiment condition in dynamic environment

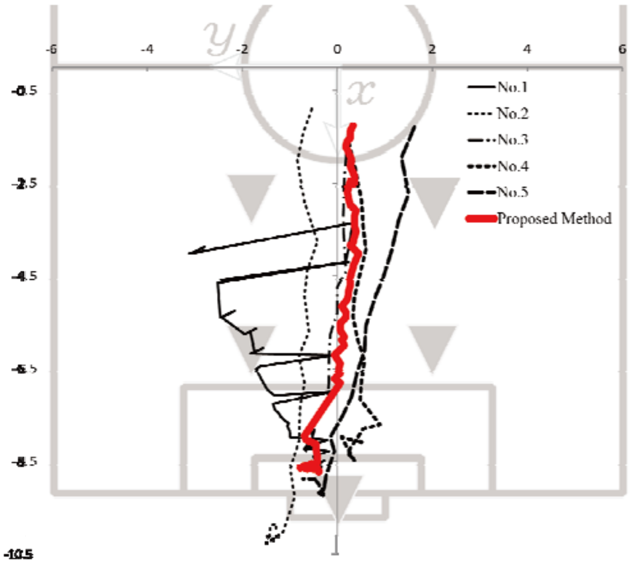

Fig. 5. Orbits of observed ball and proper ball

Table 1. The result of landmark estimation

	No.1 [m]	No.2 [m]	No.3 [m]	No.4 [m]	No.5 [m]	Proposed Method [m]
e_{bd}	1.09	0.91	0.33	0.46	0.61	0.39
SD	0.82	0.31	0.23	0.16	0.44	0.20

Table 2. The result of cooperative self-localization

	Single Localization		Multi Localization	
Position[m]	e_{rp}	SD	e_{rp}	SD
	0.36	0.09	0.34	0.09
Angle[deg]	e_{ra}	SD	e_{ra}	SD
	25.05	9.62	14.54	12.04

$$e_{ra} = \frac{1}{N}\sum_{n=1}^{N}\sqrt{\left(\theta^{tr} - {}_{a}^{n}\theta^{i}\right)^{2}} \qquad (20)$$

In table 1, the absolute observed ball position error of goalkeeper included 1.09[m] in average, and also standard variation (*SD*) was 0.82[m]. As shown in Fig.5, the observed ball position error was reduced when the ball moved until near the robot. The absolute ball position error of landmark estimation showed 0.39[m] in average and *SD* was 0.20[m]. This result indicates the landmark estimation could reduce the absolute ball position error than the absolute observed ball position error of goalkeeper. Table 2 shows the absolute robot state error of cooperative self-localization was smaller than the single robot localization. The absolute robot position error of single robot localization was 0.36[m] in average and *SD* was 0.09[m], and also the aboslute angle error was 25.05[deg] in average and *SD* was 9.62[deg]. In the results of cooperative self-localization, the absolute robot position error was 0.34[m] in average and *SD* was 0.09[m], the absolute angle error was 14.54[deg] in average and *SD* was 12.04[deg]. This result indicates the robot state was guided to the proper robot state, however the standard variation of the observed information affects the result of cooperative self-localization.

5 CONCLUSION

We proposed a cooperative self-localization method based on group robot information sharing using the landmark position and implemented the proposed method to a multirobot system “RoboCup MSL robots”. The performance of the poposed method has been evaluated using five autonomous mobile robots. This experimental results show that the ball estimation based on the information sharing increases the reliability of ball existence. In RoboCup MSL environment, it is mentioned that the reliable ball position can be shared with the robot which cannot observe a ball due to increasing the reliability of the ball position. In addition, cooperative self-localization can adjust the robot positions to the proper position.

As a future work, we apply the proposed method to realize the cooperative behaviors such pass, drible, and shoot.

REFERENCES

[1] H. Matsubara, et al., “History of RoboCup and Prospects of RoboCup-2002”, RSJ, Vol.20, No.1, pp.2-6

[2] S. Monteiro, F. Ribeiro,Paulo Garrido,“Problems and Solutions in Middle Size Robot Soccer – A Review”, Robotica'2001 - Festival Nacional de Robótica, pp.25-28, April 2001, Guimarães, Portugal, 2001.

[3] D. J. H. Bruijnen, et al., “Tech United Eindhoven: Team Description 2010”, RoboCup 2010 in Singapore

[4] M. Gholipuor, et al., “MRL Middle Size Team: 2010 Team Description Paper”, RoboCup 2010 in Singapore

[5] A. J. R.Neves, J. L. Azevedo, et al. “CAMBADA’2010: Team Description Paper”, RoboCup 2010 in Singapore

[6] Martin Lauer, Sascha Lange and Martin Riedmiller, “Calculating the perfect match: An efficient and accurate approach for robot self-localization”, In A. Bredenfield, RoboCup 2005: Robot Soccer World Cup IX, LNCS, Springer, 2005.

[7] A.Merke, S. Welker, and M. Riedmiller, “Line Based robot localization under natural light condition”, In ECAI 2004, Workshop on Agents in Dynamic and Real-Time Environments, Valencia, Spain, 2004

[8] Amir A. F. Nassiraei, Y. Kitazumi, “Hibikino-Musashi Team Description Paper”, RoboCup 2010 in Singapore

[9] Y. Sato, et al., “A Study of Line Based Localization for RoboCup Middle Size League”, Proc. of the 2008 JSME Conference on Robotics and Mechatronics, 2P1-J14, Nagano, Japan, 2008, in Japanese

[10] N. Shinpuku, I. Godler, “Robot Self-Localization Using Particle Filter in RoboCup Middle Size League”, Proc. of the 2010 JSME Conference on Robotics and Mechatronics, 1P1-F26, Asahikawa, Japan, 2010, in Japanese,

[11] S. Thrun, et al., “Robust Monte Carlo Localization for Mobile Robot”, Artificial Intelligence Journal, Vol.128, No.1-2, pp.99-141

[12] F. Dellaert, et al., “Monte Carlo Localization for Mobile Robots”, Proc. of 1999 IEEE International Conference on Robotics and Automation, Vol.2, pp.1322-1328, Detroit, 1999

[13] R. Ueda, et al., “Recovery Methods for Fatal Estimation Errors on Monte Carlo Localization”, Journal of the Robotics Society of Japan, Vol.23, No.4, pp.466-473, 2005, in Japanese

[14] A. A. F. Nassiraei, et al., “Concept of Mechatronics Modular Design for an Autonomous Mobile Soccer Robot”, ICRA2007, pp.178-183, Jacksonville

[15]Y. Takemura, et al., “Auto Color Calibration Algorithm Using Neural Networks and its application to RoboCup Robot Vision”, International Journal of Artificial Intelligence, Vol.7, pp.368-383

Dual layered multi agent system for intentional islanding operation of microgrids

A.L. Kulasekera[1], R.A.R.C. Gopura [2], K.T.M.U. Hemapala[3], N. Perera[4], and Achala Pallegedara[5]

[1,2]Dept. of Mechanical Engineering, University of Moratuwa, Katubedda, Sri Lanka
[3,4]Dept. of Electrical Engineering, University of Moratuwa, Katubedda, Sri Lanka
[5]Dept. of science and technology, Graduate school of science and technology, Saga University, Saga, Japan

[3]udayanga@elect.mrt.ac.lk

Abstract: The paper focuses on proposing a dual layered, multi agent based control system for distributed control of a microgrid aimed at intentional islanding. The architecture consists of two layers; primary layer and secondary layer. The primary layer includes a User agent, a Distributed Generator (DG) agent and a Control agent. The secondary layer consists of a Low Voltage (LV) agent and a Load agent. The Control agent is capable of supervising the secondary layer agents. The proposed multi agent based control architecture is developed using the JADE platform and it is used to control a microgrid simulated in MATLAB/SIMULINK. In order to validate the effectiveness of the proposed method, investigations are carried out for islanding scenarios simulated on the test network. The results of this study show the capability of developing a reliable control mechanism for islanding operation of microgrids based on the proposed concept.

Keywords: distributed control, intentional islanding, microgrid, multi agent systems.

1 INTRODUCTION

Legacy power distribution systems are facing a tough challenge in meeting the needs of the rapidly evolving electricity market. Time is ripe for a smarter grid capable of meeting the present and future power delivery requirements. The looming dangers of climate change is also demanding a paradigm shift from large scale fossil fuel based sources towards small scale lower emission systems. The incorporation of smaller distributed generation (DG) units with maximum renewable energy penetration is vital in meeting all these demands.

This requires the ability to handle active generation and loads, which had not been addressed in existing legacy system designs. Smaller microgrids comprising local generation is a concept put forward to cater this requirement. These microgrids can be operated either in island mode, where the local loads are fully supplied by the local generation, or in grid connected mode, where the microgrid is either exporting or importing power from the main grid.

With the local generation and loads coming into the picture, local distributed control is essential for the local grid stability. Microgrid can survive from an upstream outage in the main grid by switching to island mode and maintaining supply to the most critical local loads. Load shedding has to be carried out rapidly when the microgrid is switched to island mode as the local generation capabilities might be limited.

In order to provide these local distributed control capabilities, development of distributed control systems are essential. Multi Agent Systems (MAS) is a technology coming forward in this aspect. MAS have been developed for a wide range of applications in power systems [1]. The use of MASs in microgrid applications has been evolving over the last decade with considerable amount of work being carried out regarding distributed control applications for microgrids [2].

This paper proposes a novel dual layered MAS capable of distributed control of a microgrid. The MAS is developed in JADE platform and it is used to control a microgrid simulated in MATLAB/SIMULINK. A brief outline of micro grids is presented in section 2. An overview of multi agent systems is presented in section 3. The proposed dual layered multi agent system architecture is presented in section 4. Section 5 describes the simulations carried out and their results. Finally the conclusions are given in section 6.

2 OUTLINE OF MICROGRIDS

Microgrids can be created by embedding small-scale conventional generation units or Non-Conventional Renewable Energy Sources (NCRES) to existing electrical infrastructure. These NCRES can be mini-hydro, solar photo-voltaic (PV), wind, geo-thermal, small internal combustion (IC) engines, biomass or waste-to-energy systems. Such embedded systems will provide the microgrid with DG capabilities. A conceptual model of a microgrid is presented in Fig. 1.

Once an upstream disturbance takes place on the main grid, the microgrid can separate from the main grid at the point of common coupling and isolate the local loads from any outage, providing a higher level of service, with minimum effect to the stability and the integrity of the main grid. This capability of intentional islanding will deliver a higher reliability than legacy power systems [3]. Thereafter, the microgrid has to manage the local loads to make sure that the most critical loads are supplied by the available limited local capacity. This would require priority based load shedding.

3 OVERVIEW OF MULTI AGENT SYSTEMS

Multi agent systems are complex systems composed of several autonomous agents with only local knowledge and limited abilities but are able to interact in order to achieve a global objective [1]. Their ability to act as a container for conventional control methodologies as well as artificial intelligent based techniques and expert systems has become an additional advantage in building hybrid controllers in microgrid.

A MAS in essence is an abstraction of the role of agents in real life into intelligent control systems. These agents are able to act as autonomous social entities which react to changes in their environment and take intuitive actions in order to realize their individual goals. The aim of a multi agent based control system is to apply this individual goal seeking in a manner such that the overall target required by the user is achieved efficiently and effectively as possible.

Since Fast communication facilities such as fiber-optics, 3G, GSM/GPRS have become an integrated part of power systems [4], it is easier and more feasible to integrate multi-agent systems into power system applications.

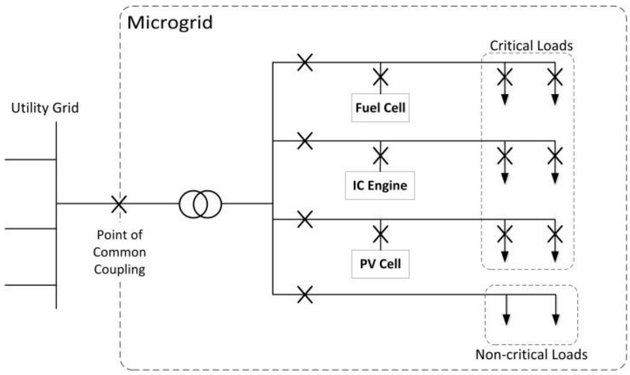

Fig. 1. Conceptual model of a microgrid

In a microgrid, an individual intelligent agent can be assigned to each entity (circuit breaker, generation unit, loads, users etc.). This assignment determines the architecture of the MAS. Several different multi agent architectures have been presented in [5]-[8].

4 DUAL LAYERED ARCHITECTURE OF MULTI AGENT SYSTEM

Fig. 2 shows the conceptual design of the proposed dual layered control architecture for microgrids. The MAS system is developed using the JADE platform [9]. The model presents a dual layer distributed control architecture. The primary layer comprises of three major agents; DG Agent, User Agent and Control Agent. The three major agents will be tasked with sensing and controlling the components of the microgrid. The DG agent will collect the information related to the DG such as; availability, connection status, power rating, energy source availability and cost of energy. The control agent is in control of a secondary layer comprising of a Load agent and a Low Voltage (LV) agent, overseeing the load control and microgrid connection control capabilities.

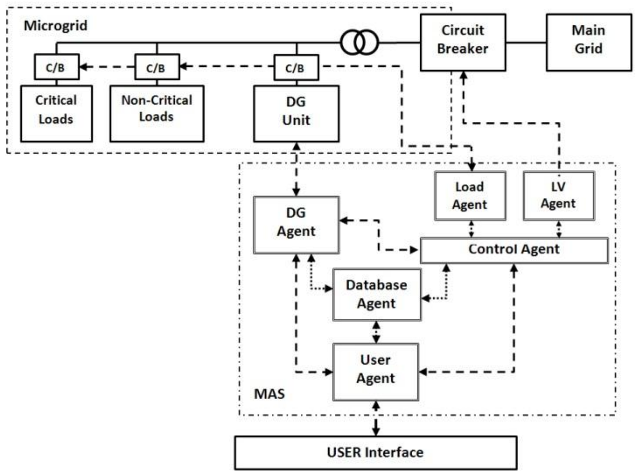

Fig. 2. Dual layered MAS architecture

During an upstream fault, the LV agent will island the microgrid, by tripping the circuit breaker at the point of common coupling, if the Control agent allows it. During island operation the load shedding will be taken care of by the Load agents to ensure that power is delivered to the most critical loads on the priority basis set by the Control agent. This will be implemented by Load agents opening circuit breakers at each of the controlled local loads.

The User agent behaves as the gateway for the user to interact with the system, to obtain real-time information and set system goals. A utility agent acting in the form of a database agent is utilized to store system information and the data and messages shared between the agents. The database agent will also be the access point for data for all the agents and users.

The control agent will be the center of the primary layer holding influence over the DG agent and controlling the LV and Load agents. The control flow chat followed by the control agent is given in Fig. 3. The operation of the control agent during the detection of an upstream outage is described in the next section.

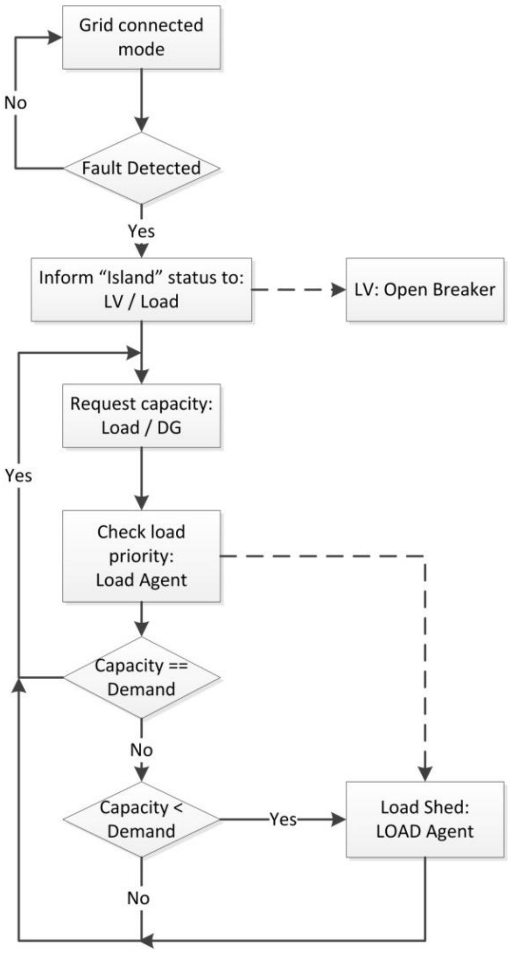

Fig. 3. Control flow chart of Control agent

5 SIMULATION AND RESULTS

The microgrid test bed used for the simulations (Fig. 4) consists of an embedded generator, acting as a DG unit, supplying part of the local demand, and several critical and non-critical loads. It is assumed that the DG unit can operate at full capacity without fuel limitations during any outage. This simulation test bed is modeled using MATLAB/SIMULINK. An external TCP/IP server [10] is used to connect the MAS to the simulated test bed.

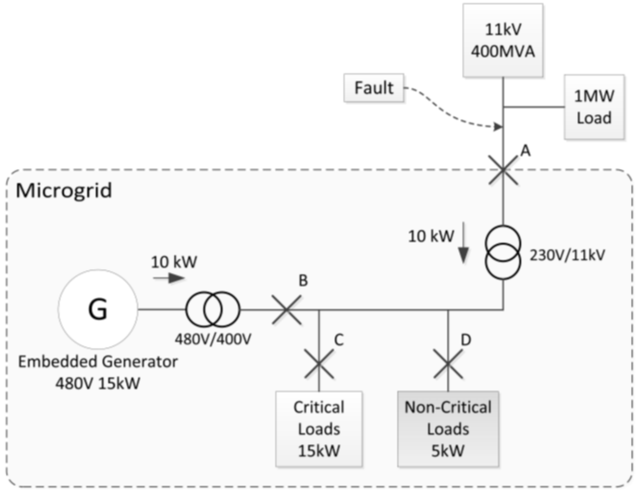

Fig. 4. Microgrid simulation model

The objective of the test setup is to demonstrate the ability of the proposed MAS to island the microgrid after an upstream fault is detected. Initially the microgrid is operating in the grid-connected mode, with the embedded generator is supplying only part of the local loads while the rest is supplied by the utility grid. The demands supplied by the DG and the grid are depicted in Fig. 4. At the beginning of the simulation breakers A, B, C and D are all closed.

While the microgrid is in grid connected mode and upstream fault is introduced at 0.05 s as seen in Fig. 5 and is switched to island mode thereafter. Line-to-line voltages are measured from points C and D shown in Fig. 4.

5.1 Grid connected mode

While the microgrid is in grid-connected mode, the total demand is 20 kW, with 15 kW critical loads and 5 kW non-critical loads. During the grid-connected mode the embedded generator only provides 10 kW output, 50% of the total demand. Another 10 kW is required from the main grid to supply the microgrid.

5.2 Transition period

When the upstream outage is detected at t = 0.05 s the control agent informs the LV agent and the Load agents to switch to island mode operation. Upon receiving the islanding order the LV agent trips the main circuit breaker A, at the point of common coupling, isolating the microgrid from the utility (Fig.5(c)). The Control agent then queries the DG agent and the load agents regarding their available capacities the DG can provide to the microgrid and the power requirements of the connected loads.

As the total load of 20 kW exceeds the available maximum capacity of 15 kW, the control agent commands the load agents to shed the 5 kW non-critical loads to match the DG capacity. Soon as the microgrid is put to island mode the supply to the critical loads is maintained (see Fig. 5(a)). The load agent at the non-critical loads sheds them from the system by opening breaker D (see Fig. 5(b)).

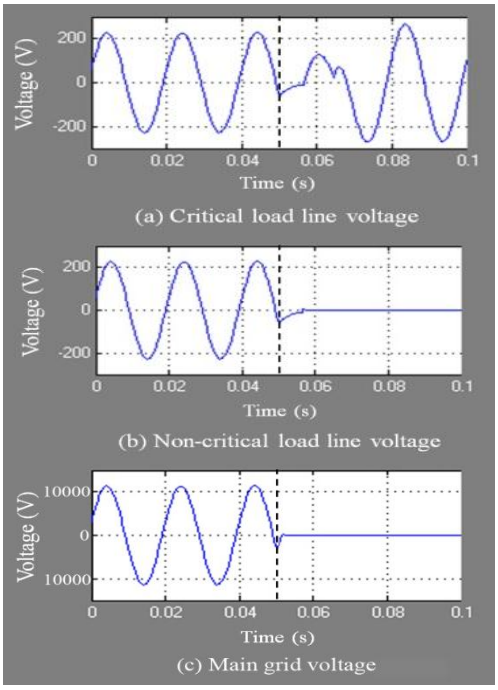

Fig. 5. Simulation results during intentional islanding. (a) Line to line voltage across critical load at 'C', (b) Line to line voltage across the non-critical load at 'D', (c) Line to line voltage at breaker 'A'.

5.3 Islanded mode

At t=0.05s the microgrid is separated from the main grid and the load agents balance the local demand. After the microgrid switches to island mode the total local demand is met by the embedded generator supplying 15 kW.

All agent operations are carried out rapidly, from detecting fault, opening the main breaker, connecting the local source and shedding loads, to stabilize the microgrid within 0.02 s. Therefore the system is able to disconnect from the main utility grid and maintain the supply to the critical loads without suffering a brownout and/or blackout.

6 CONCLUSION

A dual layered MAS for intentional islanding operation of microgrid is proposed in this paper. The agent architecture was developed using the JADE platform. Time domain simulations were carried out using a test system simulated in MATLAB/SIMULINK. The test bed was simulated for 0.1 s with the introduction of an upstream fault at 0.05 s. the MAS was able successfully restore supply within 0.02 s to the critical loads by islanding the microgrid and shedding non-critical loads. The results show the capability of the Multi Agent System to safely island and maintain the supply to its critical loads. These results validate the effectiveness of the MAS in controlling DG units to protect and control a microgrid. In the future the MAS will be implemented on a physical test bed to further validate the results.

ACKNOWLEDGEMENT

The authors gratefully acknowledge the support provided by the Sri Lankan National Science Foundation. (Grant Number RG/2011/ESA/02)

REFERENCES

[1] Mcarthur SDJ, Davidson EM, Catterson VM, et al (2007), Multi-agent systems for power engineering application Part I: Concepts, approaches, and technical challenges, IEEE Trans. on Power Systems, vol. 22, no. 4, pp. 1743-1752.

[2] Kulasekera AL, Gopura RARC, Hemapala KTMU, et al (2011), A Review on Multi-Agent Systems in Microgrid Applications, In: Proceedings of IEEE PES Conference on Innovative Smart Grid Technologies India (ISGT 2011), Kollam, Kerala, India, December 1-3, 2011.

[3] Lasseter RH, Paigi P (2004), Microgrid: A Conceptual Solution, In: Proceedings of IEEE 35th Annual Power Electronics Specialists Conference, (PESC '04), June 20-25, 2004, vol.6, pp. 4285 - 4290

[4] Wissner M (2011), ICT, growth and productivity in the German energy sector - On the way to a smart grid?, Utilities Policy, vol. 19, no. 1, pp. 14-19.

[5] Aung HN, Khambadkone AM, Srinivasan D, et al (2010), Agent-based intelligent control for real-time operation of a microgrid, In: Proceedings of 2010 Joint International Conference on Power Electronics, Drives and Energy Systems & 2010 Power India, New Delhi, India, pp. 1-6.

[6] Zheng W and Cai J (2010), A multi-agent system for distributed energy resources control in microgrid, In: Proceedings of 2010 5th International Conference on Critical Infrastructure (CRIS), Beijing, China, pp. 1-5.

[7] Jian Z, Qian A, Chuanwen J, et al (2009), The application of multi agent system in microgrid coordination control, In: Proceedings of 2009 International Conference on Sustainable Power Generation and Supply, Nanjing, pp. 1-6.

[8] Cai N and Mitra J (2010), A decentralized control architecture for a microgrid with power electronic interfaces, In: Proceedings of 2010 North American Power Symposium, Arlington, TX, USA, pp. 1-8

[9] JADE agent development toolkit (2011) [online], Available: http://www.jade.tilab.com

[10] Zimmermann W (2011), IOlib – Hardware input / output library module for matlab and sim ulink [online], Available: http://www.it.hs-esslingen.de/~zimmerma/software/index_uk.html

Multi-Agent Framework for Kinematics Process of Redundant Multi-Link Robots

Shinya Haramaki[1], Akihiro Hayashi[2], Toshifumi Satake[3] and Mochimitsu Komori[4]

[1]Ariake National College of Technology, Fukuoka 836-8585, Japan
[2]Kyushu Institute of Technology, Fukuoka 820-8502, Japan
[3]Asahikawa National College of Technology, Hokkaido 071-8142, Japan
[4]Kyushu Institute of Technology, Fukuoka 804-8550, Japan
(Tel: 81-944-53-8683, Fax: 81-944-53-8865)

[1]haramaki@ariake-nct.ac.jp

Abstract: This paper proposes a framework of a distributed kinematics process model applied to multi-link robots. In the framework, hardware modules which consists of joints and links are defined as joint components of robotic systems, then kinematics models are composed of a set of the local kinematics Agents (LKAs) which are software module to compute the localized direct and inverse kinematics. Kinematics of robotic systems is resolved by the localized kinematics calculation of LKAs for an end effecter to a target position and an information exchange among LKAs. The proposed framework has been applied to case study of the inverse kinematics problems of 7 degree of freedom redundant multi-link robot manipulator.

Keywords: Kinematics, Redundant, Multi-Link Robot, Multi Agent System

1 INTRODUCTION

The latest decade, practical use of robot technologies has been anticipated not only for industries but also for human life support[1]. Robotic technologies have been cultivated so far within practical industrial applications as a useful article. It is, however, not always in the case of human life support robots because of the complicated versatility of tasks, users, and environments.

Human life environments are not tailored for robots still less than for their work, and robot work would be so versatile. The situation would be also versatile so as that, for example, working situation would differ from the former ever task to be provoked. It could not be estimated so it is eventful. Above all, it is required that a typical robot user who are unfamiliar robotic technologies is able to operate robots under the complicated situation.

In order to deal with these difficulties, intelligent robot is required to provide an appropriate support for robot users who have to operate robots and to make motion planning. The term "intelligent" here refers to induce the change for the variation. Because it is considered that behavior appropriate for variation embodies a sort of intelligent, and that the root of its is to change oneself for the variation.

The purpose of this study is to develop a systematic methodology for intelligent robot system that takes control of itself to make a support for robot users. As the first approach for the purpose, this study investigates a framework of kinematics process model by means of multi-agents system concept (MAS in short). MAS applications has been published in terms of mobile robots[2] and manipulator control[3]. Despite of the kinematics constraint can not be disregarded, MAS based kinematics process is little discussed for universal robotic systems. This paper presents a framework of kinematics process system based on MAS and the detail design of the agents as well as the kinematics sequence. The possible impact of the improved robotic systems is confirmed through the case study.

2 AGENT BASED KINEMATICS PROCESS MODEL

2.1 Framework of kinematics process model

Multi-linked robots are composed of the parts, such as effectors, links, and prismatic or rotational joints. Especially, a pair of joint and adjacent link is a basis of the description of the kinematics properties [4]. This study considers effectors and the pairs of joint/link as a unit component, as illustrated in Figure 1, and corresponds the kinematics process called agent to the unit components. The kinematics solution process is constructed by assembling the agents in accordance with robot mechanism.

There are two types of agents called Local Kinematics Agent (LKA) and Effect Point Agent (EPA). LKA is in charge of the kinematics process for the pairs of joint and link. LKA calculates the rotation angle corresponding to joints for the deviation between the target and the current position of effector, and transmits the joint motion to other LKA located at the tip side of robots. EPA represents the effector, and it calculates the deviation between the current position of effector and its target point.

As shown in Figure 1, the kinematics solution system is configured by associating with the Input/Output relation between LKAs and EPA, and the result of this, LKA and EPA processes are directed by the closed information flow. The kinematics solution is asymptotically obtained as the robot posture in respect to the effector target position.

The feature of this system is to not define explicitly overall direct kinematics model differ from other component type approach[5]. Overall kinematics solution model or function is not formulated until LKM and EPA is related to the each other. Reconfigurable system can be realized by the addition or the remove of LKA.

2.2 Outline of local kinematics

The block diagram of LKA is illustrated in Figure 2. It represents LKA of the j-th joint from the base. LKM consists of main three parts which are called Local Direct Kinematics process, Local Inverse Kinematics process, and Joint State variables.

The Joint State variables are the data to represent joint condition. They are joint position $\mathbf{p}_j$, joint axis $\mathbf{a}_j$ and joint rotation angle θ_j. These values are initialized according to a preliminary position and posture of robots. The Local Inverse Kinematics calculates the rotation angle to be moved for minimizing the deviation between the current position and the target position of effector. The Local Direct Kinematics process consists of two transform operations and a composition operation. The transform operation transforms the Joint State variables in accordance with other joint motion located at the base side. The composition operation composes the motion of oneself and the synthetic motion composed of the previous joints.

For example, the Joint State variables of joint j are transformed by the synthetic motion $\mathbf{R}_j$ and $\mathbf{L}_j$ which are rotation and translation, respectively. Where the motion of joint j is $\mathbf{R}_j$ and $\mathbf{L}_j$, the synthetic motion ${}^1\mathbf{R}_j$, ${}^1\mathbf{L}_j$ is made by composing the motion ${}^1\mathbf{R}_{j-1}$, ${}^1\mathbf{L}_{j-1}$ and the motion $\mathbf{R}_j$, $\mathbf{L}_j$. The synthetic motion is sent to next LKA, and it is composed one after another towards LKAs located at the tip side. EPA refers to effector and its process is the same as LKA in the composition except for the process to obtain the deviation between the current position and the target position of effector instead of Local Inverse Kinematics process. The current position of effecor and the deviation are sent to all of LKA for invoking the Local Inverse Kinematics process.

2.3 Kinematics solution process

The overall kinematics is executed by the successive approximations of LKA process for the deviation calculated by EPA. The local direct kinematics of LKA transforms value of the Joint State variables based on synthetic motion ${}^1\mathbf{R}_{j-1}$ and ${}^1\mathbf{L}_{j-1}$. These are the synthetic motion from the base to joint j-1, for instance in Figure 3. The Joint State variables, therefore, are correctly transformed and the direct kinematics properties are satisfied for the overall robots.

In the j-1degrees of freedom robots, EPA located at j-th from the base transforms the Effector State variables by ${}^1\mathbf{R}_{j-1}$ and ${}^1\mathbf{L}_{j-1}$. The effector position $\mathbf{P}_E$ and the deviation $\Delta\mathbf{P}_G$ sent from EPA to each of LKA and the rotation angle is calculated to minimize the deviation by LKA. The rotation angle accumulates as the joint angle θ_j. When the above processing is repeated at proper times, $\Delta\mathbf{P}_G$ is converged on zero and θ_j is converged on a solution of inverse kinematics problem for the target position $\mathbf{P}_G$.

${}^1\mathbf{R}_{j-1}$, ${}^1\mathbf{L}_{j-1}$, $\mathbf{P}_E$ and $\Delta\mathbf{P}_G$ are obtained from the base side LKA and EPA. Then, ${}^1\mathbf{R}_j$ and ${}^1\mathbf{L}_j$ can be determined from only the Joint State variables Therefore, the direct kinematics can be distributed by LKA. LKA is the same process for all joints. The kinematics process can be composed by attaching or detaching LKA in accordance with the structure of robots and by preliminary Joint State variables.

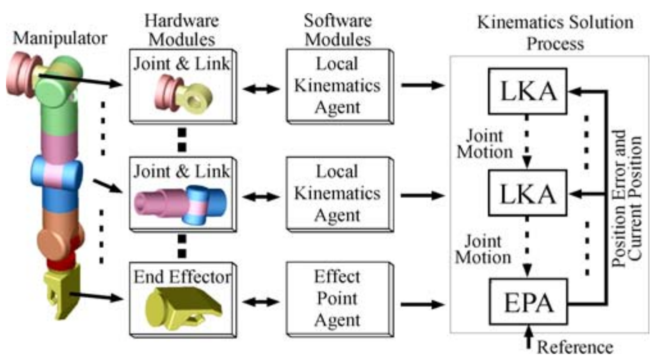

Fig. 1 Agent type kinematics solution model

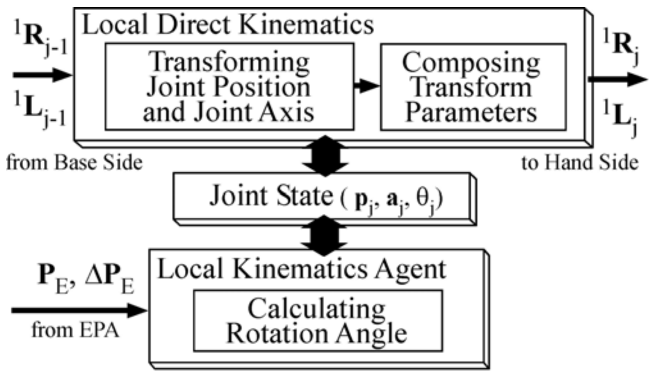

Fig. 2 Block diagram of j-th LKA

The Seventeenth International Symposium on Artificial Life and Robotics 2012 (AROB 17th '12),
B-Con Plaza, Beppu, Oita, Japan, January 19-21, 2012

3 LOCAL KINEMATICS CALCULATION

3.1 Local inverse kinematics

The Local Inverse Kinematics process calculates the deviation angle to minimize the distance between effector and target position. The deviation angle can be represented by the magnitude of vector which is obtained as a joint axis projection of the deviation angle vector. As shown in Figure 4, the deviation angle vector is a plane angle formed between $\mathbf{g}_j$ and $\mathbf{e}_j$. The deviation angle $\Delta\theta_j$ is expressed in the following equation (1).

$$\Delta\theta_j = \begin{cases} 0 & |\mathbf{e}_j \times \mathbf{g}_j| = 0 \\ \mathbf{B}\cdot\mathbf{a}_j \cos^{-1}C & |\mathbf{e}_j \times \mathbf{g}_j| \neq 0 \end{cases} \qquad (1)$$

$$\mathbf{B} = \frac{\mathbf{e}_j \times \mathbf{g}_j}{|\mathbf{e}_j \times \mathbf{g}_j|}, \qquad C = \frac{\mathbf{e}_j \cdot \mathbf{g}_j}{|\mathbf{e}_j|\cdot|\mathbf{g}_j|}$$

$$\mathbf{e}_j = \mathbf{P}_E - \mathbf{p}_j, \qquad \mathbf{g}_j = \mathbf{e}_j + \Delta\mathbf{P}_G$$

Here, $\mathbf{P}_E$ and $\Delta\mathbf{P}_G$ are the information provided from EPA. Also, $\mathbf{e}_j=\mathbf{0}$ and $\mathbf{g}_j=\mathbf{0}$ give singular points of the equation (1), but it is the case of $\mathbf{P}_E+\Delta\mathbf{P}_G=\mathbf{P}_j$ or $\mathbf{P}_E=\mathbf{p}_j$, hence singularity is not noticed in a practical range. Effector motion is a superposition of each joint motion. $\Delta\theta_j$ is approximate value, so, an appropriate proportional constant $K_j(<1)$ is introduced, finally the deviation angle is calculated as $K_j\Delta\theta_j$.

3.2 Local direct kinematics

The local direct kinematics transforms the Joint State variables of LKA in accordance with the synthetic motion sent from the base side LKA. Here, ${}^1\mathbf{R}_{j-1}$ and ${}^1\mathbf{L}_{j-1}$ represent the synthetic motion composed from the base through to the joint j-1. The joint j transforms own Joint State variables by the motion. When the joint position is $\mathbf{P}_j$ and the joint axis is $\mathbf{a}_j$ before transformation, by the motion of ${}^1\mathbf{R}_{j-1}$ and ${}^1\mathbf{L}_{j-1}$, the Joint State variables are transformed as follows.

$$\begin{cases} \tilde{\mathbf{p}}_j = {}^1\mathbf{R}_{j-1}\mathbf{p}_j + {}^1\mathbf{L}_{j-1} \\ \tilde{\mathbf{a}}_j = {}^1\mathbf{R}_{j-1}\mathbf{a}_j \end{cases} \qquad (2)$$

After transformation, for new position $\tilde{\mathbf{p}}_j$ and axis $\tilde{\mathbf{a}}_j$, the rotation $\mathbf{R}_j$ represents as follow from Rodriguez equation when the joint j rotates $\Delta\theta_j$.

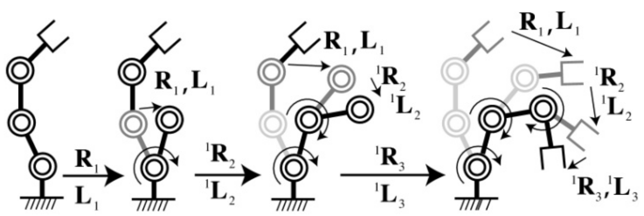

Fig. 3 Direct kinematics calculating process

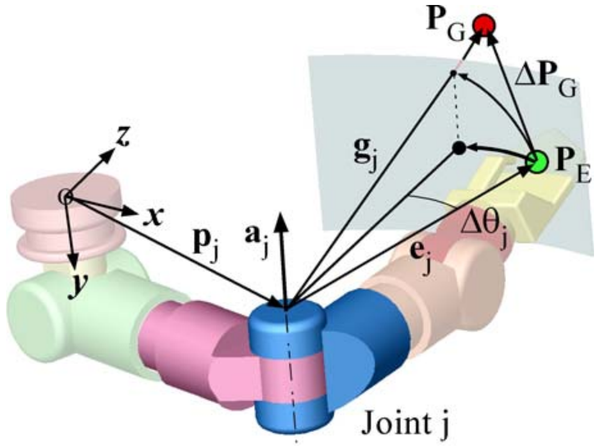

Fig. 4 Schematic of the local inverse kinematics

$$\mathbf{R}_j = \mathbf{E} + [\tilde{\mathbf{a}}_j\times]\sin\Delta\theta_j + [\tilde{\mathbf{a}}_j\times]^2(1-\cos\Delta\theta_j) \qquad (3)$$

Where, $\mathbf{E}$ is a unit matrix, $[\tilde{\mathbf{a}}_j\times]$ is an alternating matrix which is satisfied $\tilde{\mathbf{a}}_j \times \mathbf{p} = [\tilde{\mathbf{a}}_j\times]\mathbf{p}$ with an arbitrary vector $\mathbf{p}$. As shown in Figure 4, $\tilde{\mathbf{a}}_j$ is an axis of rotation passing through $\tilde{\mathbf{p}}_j$. The rotation generated by the joint j with angle $\Delta\theta_j$ transforms an arbitrary point $\mathbf{p}$ and axis $\mathbf{a}$ as follows.

$$\begin{cases} \tilde{\mathbf{p}}_j = \mathbf{R}_j(\mathbf{p}-\tilde{\mathbf{P}}_j) + \tilde{\mathbf{P}}_j = \mathbf{R}_j\mathbf{P} + (\mathbf{E}-\mathbf{R}_j)\tilde{\mathbf{P}}_j \\ \tilde{\mathbf{a}} = \mathbf{R}_j\mathbf{a} \end{cases} \qquad (4)$$

The transformation of $\mathbf{p}$ at equation (4) can be performed by only rotation $\mathbf{R}_j$ around the origin and translation $(\mathbf{E}-\mathbf{R}_j)\tilde{\mathbf{P}}_j$. Consequently, the motion ${}^1\mathbf{R}_j$ and ${}^1\mathbf{L}_j$ which are the composition of $\mathbf{R}_j$, $(\mathbf{E}-\mathbf{R}_j)\tilde{\mathbf{P}}_j$ and ${}^1\mathbf{R}_{j-1}$ and ${}^1\mathbf{L}_{j-1}$ is as follows.

$$\begin{cases} {}^1\mathbf{R}_j = \mathbf{R}_j\,{}^1\mathbf{R}_{j-1} \\ {}^1\mathbf{L}_j = \mathbf{R}_j\,{}^1\mathbf{L}_{j-1} + (\mathbf{E}-\mathbf{R}_j)\tilde{\mathbf{P}}_j \end{cases} \qquad (5)$$

From equation (3) and (4), $\mathbf{R}_j$ and $(\mathbf{E}-\mathbf{R}_j)\tilde{\mathbf{P}}_j$ are determined by only Joint State variables. As ${}^1\mathbf{R}_{j-1}$ and ${}^1\mathbf{L}_{j-1}$ are received from LKA located at the base side, highly independent MAS based kinematics process is available.

4 CASE STUDY

Kinematics solution of 7 d.o.f manipulator

To investigate the proposed framework, the inverse kinematics problem of 7 d.o.f manipulator is executed as illustrated in Figure 5. The initial Joint State variables are show in Figure 5. All of joint angles are set zero at the initial posture, and the end effector is placed on the position (400, 400, 0).

For each iteration by direct and inverse kinematics, the transition of each joint angle is shown in Figure 6. Firstly, some of joint angles had a large value, then these gradually converged a steady value. The transition of position error from the target position is shown in Figure 7. The position error gradually becomes small, after 23 times of iteration processes it is less than 1 mm.

5 CONCLUSION

This paper has presented the framework of kinematics resolution system based on MAS concept and the detail design of the agents as well as the kinematics computation sequence of the system. The feasibility with the possible impact of the improved robot systems has been confirmed through the case study. Conclusions are as follows.

1) Considering a module constructed from joint and link component of robot, defining the Local Kinematics Module (LKA) related to the component and the Effect Point Module (EPA) related to end effector, and the configuration method of a decentralized kinematics calculation model composed of LKA and EPA has proposed.

2) Implementability of decentralizing the calculation of LKA and EPA with respect to each module and calculating the direct and inverse kinematics of manipulator by iterative calculation has been shown.

3) The proposed method has been applied to the inverse kinematics problem of 7 d.o.f manipulator. The computability of the kinematics solution using the proposed calculation model and flexibly with various tasks has been shown.

REFERENCES

[1] Hirokawa J., Matsuhira N., Ogawa H, Wada T.(2 008), Universal Design with Robots, Practice of House -working Task of Home Robot, Journal of the Robotics Society of Japan, vol.26, pp.476-484

[2] Min H., Wang Z.(2009), Distributed Control Alg orithm of Group Escape Behavior for Multiple Mobile Robots, JSME Conference on Robotics and Mechatroni cs, 2A2-F15

[3] Ning, K.(2006), Research on embedded MAS bas ed manipulator control, Industrial Robot An Internation al Journal, vol.33, pp.97-105

[4] Danavit, J. and Hartenberg, R.(1995), A kinemati c notation for lower pair mechanism based on matrices, Transaction of the ASME Jouenal of applied mechani cs Division, pp.215-221

[5] Bi, Z. M., Zang, W. J., Chen, I. M.(2007), Auto mated generation of the D-H parameters for configurati on design of modular manipulators, Robotics and Com puter-Integrated Manufacturing, vol. 23, pp.553-562

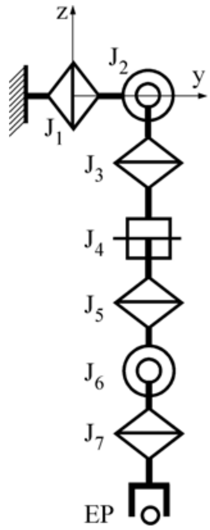

Joint	Initial Joint State	
	Position	Axis
J_1	(0,61.5,0)	(0,-1,0)
J_2	(0,128.5,0)	(1,0,0)
J_3	(0,128.5,-140)	(0,0,1)
J_4	(30,128.5,-270)	(0,-1,0)
J_5	(0,128.5,-385)	(0,0,1)
J_6	0,128.5,-495)	(1,0,0)
J_7	(0,128.5,-573)	(0,0,1)
EP	(0,125,-693)	

Fig. 5 Seven d.o.f manipulator initial configuration

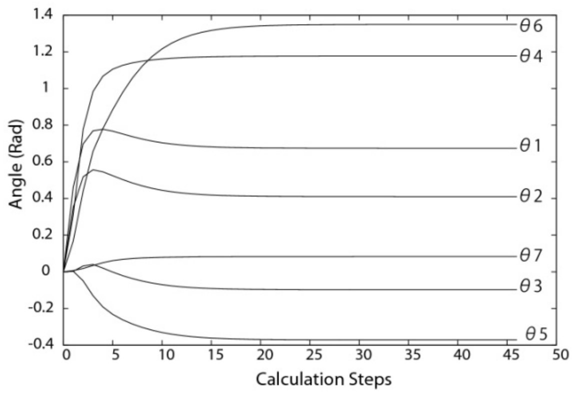

Fig. 6 Calculating result of joint angles

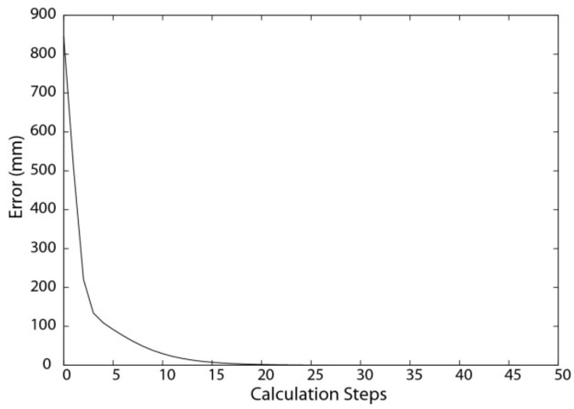

Fig. 7 Position error of end effector

The Seventeenth International Symposium on Artificial Life and Robotics 2012 (AROB 17th '12),
B-Con Plaza, Beppu, Oita, Japan, January 19-21, 2012

Optimizing the Thermoforming of Polypropylene Foam by an Artificial Neural Network

Shih-Jung Liu*, Ting-Ting Wen, and Yau-Zen Chang

Department of Mechanical Engineering
Chang Gung University, Tao-Yuan 333, Taiwan
(Tel: 886-3-2118166, Fax: 886-3-2118558)

*shihjung@mail.cgu.edu.tw

Abstract: In this study, the optimal processing parameters of polypropylene foam thermoforming are obtained by the use of an artificial neural network. Data from tests carried out on a lab-scale thermoforming machine were used to train an artificial neural network, which serves as an inverse model of the process. The inverse model has the desired product dimensions as inputs and the corresponding processing parameters as outputs. The structure, together with the training methods, of the artificial neural network is also investigated. The feasibility of the proposed method is demonstrated by experimental manufacturing of cups with optimal geometry derived from the finite element method. Except the dimension deviation at one location, which amounts to 17.14 %, deviations of the other locations are all below 3.5 %.

Keywords: Polypropylene Foam, Thermoforming, Artificial Neural Network, Optimal Processing Parameters.

1 INTRODUCTION

Thermoforming has become one of the most important polymer processing methods [1]. However, persistent problems in the selection of processing parameters due to the complex interconnected nature of the involved thermal, chemical, friction and visco-elastic phenomena have confounded the overall success of the process. One of the most serious problems is the lack of an adequate method to derive processing parameters with which prescribed product geometry can be obtained. The parameter-selection problem is of great concern, because it is usually linked with high cost and long start-up time. In practice, the trial-and-error method is relied upon with repeated processing runs to achieve required product geometry. This restriction renders uneconomical a small-batch type manufacturing with accurate product shape.

In this work, an effort was made to develop a technique based on ANN to find a set of thermoforming parameters that will produce foamed plastic products in a prescribed geometry. The technique inverts the relation between processing parameters and product dimensions. The inverse model has the desired product dimensions as inputs and the corresponding processing parameters as outputs. The effects of the design factors of the ANNs on the performance of mapping between product dimensions and processing parameters have also been investigated. Finally, experimental manufacturing of cups was used to test the adequacy of the method developed.

2 ARTIFICIAL NEURAL NETWORKS AND THE BACKPROPAGATION LEARNING RULE

ANN (artificial neural network) is one of the proven general-purpose architectures that are able to generate a nonlinear mapping between two sets of data. In this paper, the inverse model is treated as a mapping between the desired product geometry and the corresponding processing parameters, where the former are inputs and the latter are outputs.

The network architecture used for the inverse model problem is the multilayered feedforward neural network (MFNN)[2]. Figure 1 shows an MFNN with two hidden layers, each layer has a synaptic weight matrix W_i, i = 1, 2, 3, defining the connections between the previous layer and the next layer [3-9]. In Figure 1, the connection between the input patterns and the first hidden layer is defined by the weight matrix $W_1 = [w_{ij}^{(1)}] \in \Re^{N_1 \times N_{in}}$, where N_1 is the number of neurons in the first hidden layer and N_{in} is the number of inputs. The connection between the two hidden layers is defined by the weight matrix $W_2 = [w_{ij}^{(2)}] \in \Re^{N_2 \times N_1}$, where N_2 is the number of neurons in the second hidden layer. The last weight matrix $W_3 = [w_{ij}^{(3)}] \in \Re^{N_3 \times N_2}$ defines the connection between output patterns and the second hidden layer, where N_3 is the dimension of output patterns. Given the network input vector $u \in \Re^{N_{in} \times 1}$, the output of the first hidden layer $X_1 \in \Re^{N_1 \times 1}$, which is the input to the second hidden layer, can be written as

$$X_1 = f_1(W_1 . \; u + B_1)$$

where f_1 ( ) is the nonlinear activation function at each neuron in the first hidden layer and $B_1 \in \Re^{N_1 \times 1}$ is the threshold or bias vector of the same layer. The output of the second hidden layer $X_2 \in \Re^{N_2 \times 1}$ can be written as

$$X_2 = f_2 (W_2 . \; X_1 + B_2)$$

where f_2 ( ) is the nonlinear activation function and B_2 is the bias vector of the second hidden layer. The output of the last layer, which is the response of the network $Y = X_3 \in \Re^{N_3 \times 1}$, can be written as

$$Y = X_3 = f_3(W_3.\ \ X_2 + B_3)$$

where f_3 ( ) is the activation function and B_3 is the bias vector of the output layer.

In the following descriptions, the hidden layers of the ANN under study are composed of neurons with a hyperbolic tangent sigmoid activation function defined as:

$$y = f(v) = \tanh(\alpha v) = \frac{e^{\alpha v} - e^{-\alpha v}}{e^{\alpha v} + e^{-\alpha v}} = \frac{1 - e^{-2\alpha v}}{1 + e^{-2\alpha v}}$$

where the value of α is usually set to be 1. Furthermore, the activation function of the output layer is the linear function. That is,

$$Y = W_3.\ \ X_2 + B_3$$

The backpropagation learning algorithm is the most widely used training process for MFNN with differentiable activation functions today. The algorithm is based on the steepest descent gradient principle aiming at the minimization of deviation between the desired network output and the actual output, defined as the scalar positive function

$$E = \sum_{i=1}^{N_3} (d_i - y_i)^2$$

where d_i represents the desired network output and y_i is the actual output of the MLP corresponding to an input pattern. To emphasize relative deviation, the value of E is further tailored to be in a root of mean squared error form in the subsequent discussion:

$$E_{RMS} = \sqrt{\frac{1}{N_3} \sum_{i=1}^{N_3} (d_i - y_i)^2} \qquad \textbf{(1)}$$

On using the backpropagation algorithm, also called the generalized delta rule, we need to find the local error or delta, $\delta_j^{(s)}$, recursively first:

$$\delta_j^{(s)} = [\sum_{h=1}^{N_{s+1}} \delta_h^{(s+1)} \cdot w_{hj}^{(s+1)}] \cdot g_s(\sum_{i=1}^{N_{s-1}} w_{ji}^{(s)} \cdot x_i^{(s-1)} + b_j^{(s)}) \qquad \textbf{(2)}$$

where s = 1, 2 designates the appropriate network layer, g_s( ) represents the first derivation of the activation function f_s( ) in the s-th layer. And $\delta_j(3)$ for the output layer is evaluated as

$$\delta_j^{(3)} = (d_j - y_j) \cdot g_3(\sum_{h=1}^{N_2} w_{jh}{}^{(3)} x_h^{(2)} + b_j)$$

The learning rule for the weight matrix and bias vector is then given by

$$w_{ji}{}^{(s)}(k+1) = w_{ji}{}^{(s)}(k) + \mu \cdot \delta_j^{(s)} \cdot x_i{}^{(s-1)} \qquad (3)$$

$$b_j^{(s)}(k+1) = b_j^{(s)}(k) + \mu \cdot \delta_j^{(s)} \qquad (4)$$

where k denotes time index, s = 1, 2, 3 designates the appropriate network layer. Furthermore, μ in *Eqs 3* and *4* is the corresponding learning rate parameter, which is an important design factor of an MFNN [2].

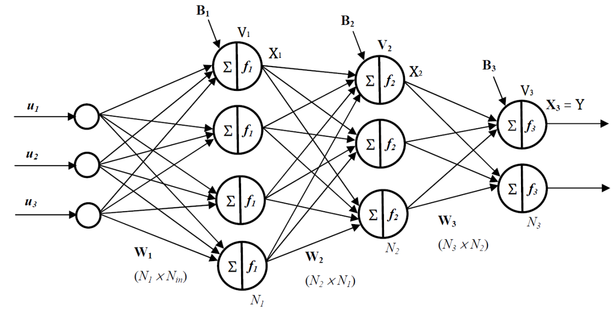

Figure 1. Architecture of a multilayered feedforward neural network (MFNN) with two hidden layers [2].

3 RESULTS AND DISCUSSION

With the network topology and learning rate paramete r being set at optimal values obtained above, Figure 2 shows the convergence history of the RMS prediction error values of the various network outputs. The average training time of a typical run was 12 seconds when executed using a 2.0 GHz Pentium 4 Personal Computer equipped with 1 GB RAM.

We can see that the average RMS error values are all below 0.2. Furthermore, the RMS errors of E and F, that is, the dropping velocity of the assisting plug and the heat transfer coefficient of the assisting plug, can be perfectly reduced below 0.01. We have that the network can fit to the 35 experimental data sets with RMS prediction errors well below 0.02.

Using the training data to assess the network performance can lead to over-fitting. The generalization properties of a neural network cannot be based on the training data alone. Untrained data sets must be used instead to evaluate its generalization capability. We randomly selected 5 experimental data sets, which were not used in the training, as test data sets.

To test the effectiveness of the trained ANN and study fundamental problems associated with inverse model of the thermo forming process, evaluation processes were conducted. The desired cup geometry, which serves as inputs to the ANN, is designed with ANSYS using the Finite Element Method (FEM).

The desired product dimensions were normalized and sent to the trained MFNN to generate outputs. The processing parameters corresponding to the optimal thickness distribution are: A = 187 ^{o}C, B = 91 mm, C = 0.3042 sec, D = 0.02 MPa, E = 222 mm/s, and F = 0.23 W/m·^{o}K (plastic).

Ten cups were manufactured and the average thicknesses of the six sites were obtained. These results are shown graphically in Figure 3. Except the deviation at point 3, which amounts to 17.14 %, dimension deviations of the other points are all below 3.5 % [2].

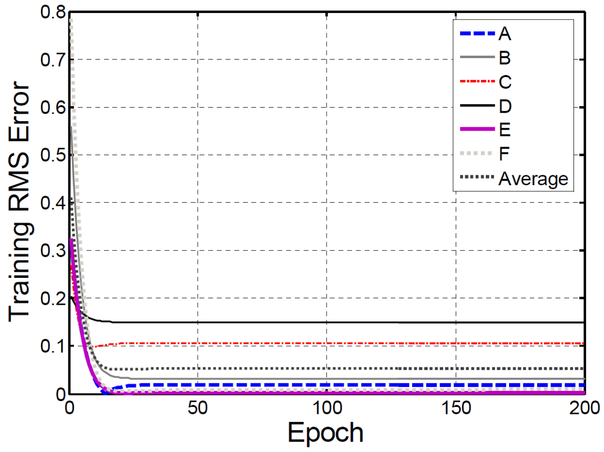

Figure 2. Convergence history of the RMS error values of the training data sets [2].

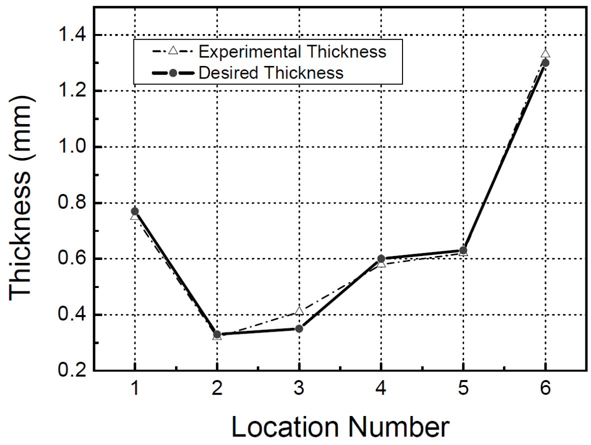

Figure 3. Experimental thickness versus desired thickness [2].

4 CONCLUSION

In this study, inverse model of thermoforming, which is composed of an artificial neural network, has been carried out. Taking thermoforming of the polypropylene foam cups as a specific case, we show in this paper that inverse modeling of a process by a neural network to derive processing parameters is both feasible and practical. This conclusion is justified by experimental results. In addition, inverse model can alleviate the prolonged trial processes required to derive a set of processing parameters corresponding to specified product geometry.

REFERENCES

1. J. L. Throne, Thermoforming, Hanser Publishers, New York (1986).
2. Y.Z. Chang, T.T. Wen, S.J. Liu, Polym. Eng. Sci. 45, 375 (2005)
3. F. M. Ham and I. Kostanic, Principles of Neurocomputing for Science and Engineering, McGraw-Hill (2001).
4. M. M. Gupta, L. Jin, and N. Homma, Static and Dynamic Neural Networks, John Wiley & Sons, Inc (2003).
5. V. Maniezzo, IEEE Trans. on Neural Networks, 51, 39 (1994).
6. D. E. Moriarty and R. Miikkulainen, Evol. Comput., 5, 373 (1997).
7. B. Yang, X.-H. Su, and Y.-D. Wang, the First Int.Conf. on Mach. Learn. and Cybernet. Conf. Proceed., 64 (2002).
8. J. A. Nelder and R. Mead, Comput. J., 7, 308 (1965).
9. W. H. Press, Numerical Recipes in C++: The Art of Scientific Computing, 2nd ed., Cambridge Univ. Press, New York (2002).

The Seventeenth International Symposium on Artificial Life and Robotics 2012 (AROB 17th '12),
B-Con Plaza, Beppu, Oita, Japan, January 19-21, 2012

Situational Judgment System for A Robot in Complex Environments Using Hierarchical Neural Network

Anri Nishimoto, Hitoshi Sori

Tsuyama National College of Technology, Tsuyama, Okayama 708-8509, Japan
(Tel: +81-868-24-8281, Fax: +81-868-24-8281)
(c-anri@tsuyama-ct.ac.jp)

Abstract: Human-beings can prevent crashes by avoiding obstructions when detected it in front of them. At the same time, they can take the best action suitable to the surrounding environment. It is considered that an action control algorithm for a mobile robot is feasible by imitating the above-mentioned action control of human-beings. In this paper, we propose a situational judgment system using a hierarchical neural network. This system outputs the action suitable for a robot to the environment (go straight, go back, turn right, turn left, diagonally forward right, or diagonally forward left). After learning of the system, we mounted the system into the robot and let the robot judge the action in various environments. The experimental results demonstrated that the proposed system was effective for determination of the action of the robot in complex environments.

Keywords: Hierarchical neural network, Robot, Situational judgment

1 INTRODUCTION

Human-beings can prevent crashes by avoiding obstructions when detected it in front of them. At the same time, they can take the best action suitable to the surrounding environment. This is because human-beings can recognize the position and posture of obstructions in relation to those of the person through the use of senses. Therefore it is considered that an action control algorithm for a mobile robot is feasible by imitating the above-mentioned action control of human-beings. In recent year, scientists have been working in research and development of mobile robots with the ability to judge like human-beings'[1].

Until now, we have been developing a situational judgment system that uses a hierarchical neural network(called here, NN)[2, 3]. At first, we developed a situational judgment system that obtains information from a single image(in front of the robot) taken from a CMOS camera mounted in a robot. This process allows the robot to attain 4 correct outputs (go straight, go back, turn right, or turn left) in relation to the environment[4]. However, the situational judgment system could not let the robot judge accurately like a human-beings', because this system only uses one image for input information. We confirmed that the robot mounted this system could not obtain sufficient environmental information from the right side and left side of the robot.

In order to let the robot obtain more environmental information, we have been improving the situational judgment system that obtains information from three images(left side, in front, and right side of the robot) taken from a CMOS camera mounted in a robot[5]. Although the robot was able to obtain more environmental information, outputs of this system were still limited to only 4 outputs. Due to the limitation, the robot was unable to judge similarly to human-beings in complex environments. Accordingly, we confirmed that the improved system was also insufficient as a situational judgment system for a mobile robot.

For this reason, we propose a new situational judgment system with an increase of two extra actions for outputs (diagonally forward right, and diagonally forward left). This proposed system uses a hierarchical NN, and outputs the suitable action to the environment (go straight, go back, turn right, turn left, diagonally forward right, or diagonally forward left). In this paper, we show that the proposed system is effective for determination of the action of the robot in complex environments.

2 SITUATIONAL JUDGMENT SYSTEM

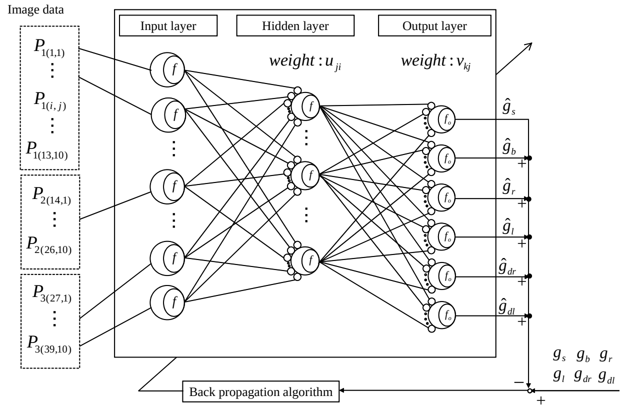

Fig. 1. Situational judgement system

Figure 1 shows the configuration of the proposed situational judgment system using a hierarchical NN. This system inputs images $P_x(i,j)$ that are taken from a CMOS camera mounted in a robot, and outputs the action suitable to the environment (go straight $\hat{g_s}$, go back $\hat{g_b}$, turn right $\hat{g_r}$, turn left $\hat{g_l}$, diagonally forward right $\hat{g_{dr}}$, or diagonally forward left $\hat{g_{dl}}$). Where x is the number of images, i is the number of pixel widths, j is the number of pixel heights.

The NN of the proposed system consists of three layers: input layer, 390 neurons; hidden layer, 195 neurons; and output layer, 6 neurons. In addition, the sigmoid function is used for the nonlinear function of each neuron. Connection weights of the NN are adjusted using a back-propagation algorithm, which is the typical learning technique, so that the sum of square error given by

$$E = \frac{1}{2}\sum\Big\{(g_s-\hat{g_s})^2+(g_b-\hat{g_b})^2+(g_r-\hat{g_r})^2 +(g_l-\hat{g_l})^2+(g_{dr}-\hat{g_{dr}})^2+(g_{dl}-\hat{g_{dl}})^2\Big\} \quad (1)$$

decreases, where g_s, g_b, g_r, g_l, g_{dr}, g_{dl} are the teaching data.

3 IMAGE PROCESSING

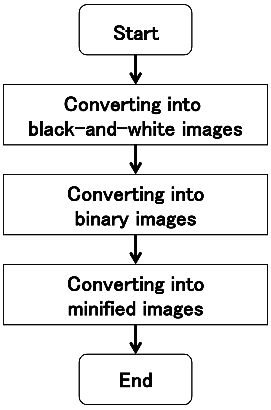

Fig. 2. Flow chart of the image processing

If the amount of input information for the proposed situational judgment system is too much, then the running process of the system will take a lot of time and the proposed situational judgment system will not be able to let a robot judge quickly. Therefore, we use an image processing method to reduce the amount of input information. The proposed situational judgment system inputs processed images by three-step image processing. Figure 2 shows a flow chart of the three-step image processing. At first, the system converts the shot images (colored, 104 pixel widths, and 80 pixel heights) into black-and-white images. Then, the system converts the black-and-white images into binary images. Finally, the system converts the binary images into minified images(13 pixel widths, and 10 pixel heights). These processed images are used to input information for the proposed situational judgment system.

4 LEARNING RESULT

4.1 NN learning

First, we put a robot in environments like Figure 3 and took 108 images of three different directions (6 images each of 6 action patterns) with a camera mounted in the robot. The field of vision of the robot was set to 120 angular degrees for this experiment. These images were used as teaching data, and the proposed situational judgment system was learned. Figure 4 shows some of the images that are used as teaching data.

Figure 5 shows the transition of the sum of square error. After two million iterations, the sum of square error decreased and converged to a constant value of about 0.007.

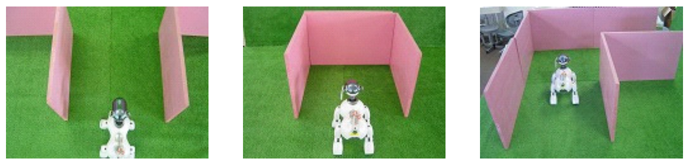

(a) go straight (b) go back (c) turn right

(d) turn left (e) diagonally forward right (f) diagonally forward left

Fig. 3. Example of environments for the NN learning

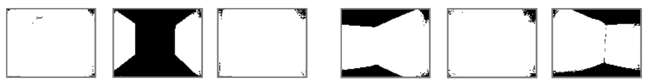

(a) go straight (b) go back

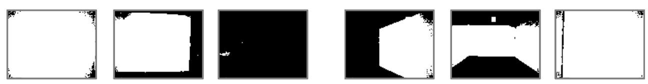

(c) turn right (d) turn left

(e) diagonally forward right (f) diagonally forward left

Fig. 4. Example of images used for the NN learning

4.2 Simulation result

To confirm the reliability of the NN learning results, we carried out simulation experiment by images used as the

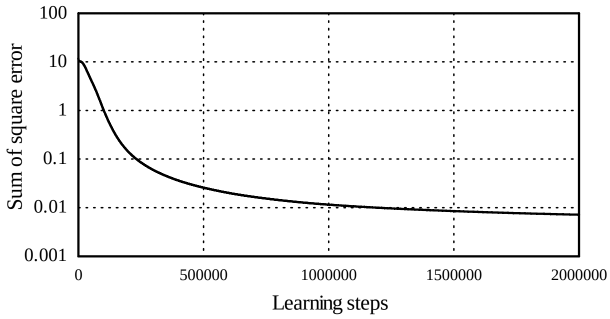

Fig. 5. Transition of the sum of square error

teaching data for the NN learning. Table 1 shows the results of the situational judgment for the simulation experiment. Here, the proposed situational judgment system outputs 6 values from 0 to 1, and the largest value is the best action suitable in each environment. The data values shown in table 1 demonstrate suitable output values for each environment. From these simulation results, we confirmed that the proposed situational judgment system was sufficiently learned.

5 EXPERIMENTAL RESULT IN COMPLEX ENVIRONMENTS

To confirm the usefulness of the proposed situational judgment system, we carried out to let the robot judge the action in complex environments using the learned situational judgment system. The robot mounted the learned system is set in complex environments. Situational judgment results from the robot are displayed on a computer screen using a wireless local area network mounted into the robot as shown in Figure 6. It is important to note that the complex environments are not used as the teaching data for the NN learning.

5.1 Y-junction environment

First, we put the robot in a Y-junction environment shown in Figure 7(a), and let the robot judge the action. Figure 7(b) shows the images shot by the robot in this environment, and

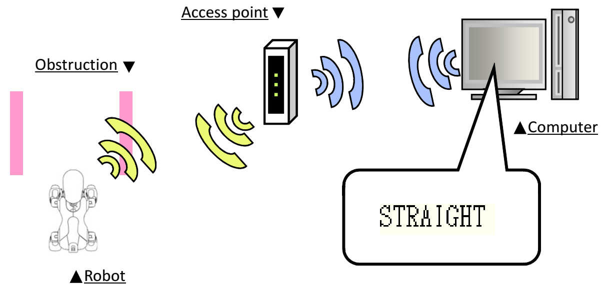

Fig. 6. Experiment system

Figure 7(c) shows the images after the previously-mentioned image processing. Table 2 shows the result of the situational judgment obtained from the robot in this environment.

(a) experimental environment

(b) shot images

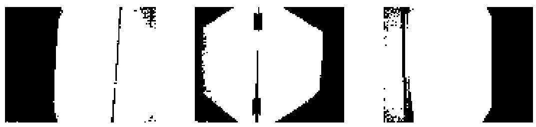

(c) binary images

Fig. 7. Y-junction environment

Table 1. Results of the situational judgment for the simulation experiment

		Result					
		Straight	Back	Right	Left	D-right	D-left
Input image	Straight	**1.000**	0.016	0.004	0.006	0.008	0.010
	Back	0.011	**0.967**	0.000	0.000	0.000	0.012
	Right	0.003	0.006	**0.982**	0.002	0.000	0.002
	Left	0.001	0.000	0.000	**0.973**	0.003	0.013
	D-right	0.000	0.015	0.006	0.001	**0.998**	0.011
	D-left	0.000	0.010	0.000	0.007	0.016	**1.000**

As can be noted from Table 2, the proposed situational judgment system outputted 2 actions(diagonally forward right, and diagonally forward left) suitable to the Y-junction environment. These results clearly demonstrate that this system can output the accurate action in the complex environment.

Table 2. Results of the situational judgment for the Y-juntion environment

	Straight	Back	Right	Left	D-right	D-left
Output	0.000	0.002	0.003	0.001	**0.997**	**0.986**

5.2 Cross road environment

Next, we put the robot in a cross road environment shown in Figure 8(a), and let the robot judge the action. Figure 8(b) shows the images shot by the robot in this environment, and Figure 8(c) shows the images after the image processing. Table 3 shows the result of the situational judgment obtained from the robot in this environment.

From Table 3, the proposed situational judgment system outputted 3 actions(go straight, turn right and turn left) suitable to the cross road environment. Moreover, we confirmed that the robot can obtain complex environment information by the proposed situational judgment system.

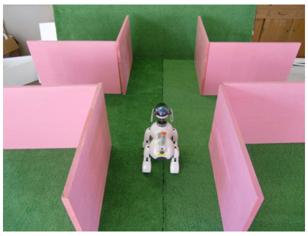

(a) experimental environment

(b) shot images

(c) binary images

Fig. 8. Cross road environment

Table 3. Results of the situational judgment for the cross road environment

	Straight	Back	Right	Left	D-right	D-left
Output	**0.999**	0.183	**0.858**	**0.999**	0.013	0.000

6 CONCLUSION

In this paper, we proposed a situational judgment system using a hierarchical neural network (NN) for a robot. This system outputs the suitable action for the robot to complex environments. The connection weights of the NN are adjusted by the back-propagation algorithm so that the sum of square error decreases to a small value.

To confirm the usefulness of the proposed situational judgment system, we carried out some experiments in complex environments which were not used as the teaching data for the NN learning. From the experiment results, we confirmed that the robot mounted the proposed situational judgment system could output the action similar to a human-beings.

In future works, we plan to construct a running control system for the robot using the proposed situational judgment system. We will target to let the robot run in more complex situations like labyrinth.

REFERENCES

[1] T. Yasuno, T. Kamano, Y. Yamanaka and Y. Son (2004), Motion Control for Autonomous Mobile Robot using Operator's Decision-Making Skill Based on Image Informaiton(in Japanese), IEEJ Industrial Instrumentation and Control, Vol. C-04-89, pp.65-70

[2] M. Hagiwara (1994), Neuro Fuzzy Genetic Algorithm(in Japanese), SangyoTosyo

[3] IEEJ (2002), Learning and the Algorithm(in Japanese), Morikita Publishing

[4] A. Nishimoto and H. Sori (2010), Situational Judgment System for a Quadrupedal Robot Using Hierarchical Neural Network(in Japanese), The Society of Instrument and Control Engineers, Tsuyama District Seminar, pp.17-18

[5] A. Nishimoto and H. Sori (2011), Study of the Situational Judgment System for Robotic Field of View Using a Hierarchical Neural Network(in Japanese), IEEJ 2011 Annual Conference of Electronics, Information and System Society, No.PS4-8, pp.1615-1616

Medical image diagnosis of lung cancer by multi-layered GMDH-type neural network self-selecting functions

Tadashi Kondo[1], Junji Ueno[2], and Shoichiro Takao[3]

[1,2,3]Graduate School of Health Sciences
3-18-15 Kuramoto-cho Tokushima 770-8509 Japan
(Tel: +88-633-9024, Fax: +88-633-9024)

[1]kondo@medsci.tokushima-u.ac.jp

Abstract: In this study, a revised Group Method of Data Handling (GMDH)-type neural network self-selecting optimum neuron architectures is applied to the computer aided image diagnosis (CAD) of lung cancer. The GMDH-type neural network algorithm has an ability of self-selecting optimum neural network architecture from three neural network architectures such as sigmoid function neural network, radial basis function (RBF) neural network and polynomial neural network. The GMDH-type neural network also has abilities of self-selecting the number of layers, the number of neurons in hidden layers and useful input variables. This algorithm is applied to CAD and it is shown that this algorithm is useful for CAD of lung cancer and is very easy to apply practical complex problem because optimum neural network architecture is automatically organized.
Keywords: Neural networks, GMDH, Medical image diagnosis.

1. INTRODUCTION

Group Method of Data Handling (GMDH)-type neural networks and their applications have been proposed in our early works [1],[2]. GMDH-type neural networks can automatically organize neural network architecture by heuristic self-organization method [3],[4], which is a kind of evolutional computation, and they can also determine automatically such structural parameters as the number of layers, the number of neurons in hidden layers and useful input variables.

In this study, a revised GMDH-type neural network algorithm self-selecting optimum neural network architecture is applied to the computer aided image diagnosis (CAD) of lung cancer. In this algorithm, optimum neural network architecture is automatically selected from three neural network architectures such as sigmoid function neural network, RBF neural network and polynomial neural network. Furthermore, structural parameters such as the number of layers, the number of neurons in hidden layers and useful input variables are automatically selected so as to minimize prediction error criterion defined as Akaike's information criterion (AIC) [5] or Prediction Sum of Squares (PSS) [6]. The GMDH-type neural network algorithm is applied to CAD of lung cancer and results show that the revised GMDH-type neural network algorithm is useful for CAD of lung cancer and is very easy to apply practical complex problem because optimum neural network architecture is automatically organized.

2. MULTI-LAYERED GMDH-TYPE NEURAL NETWORK SELF-SELECTING FUNCTION

Revised GMDH-type neural network has a common feedforward multilayered architecture. Figure 1 shows architecture of revised GMDH-type neural network.

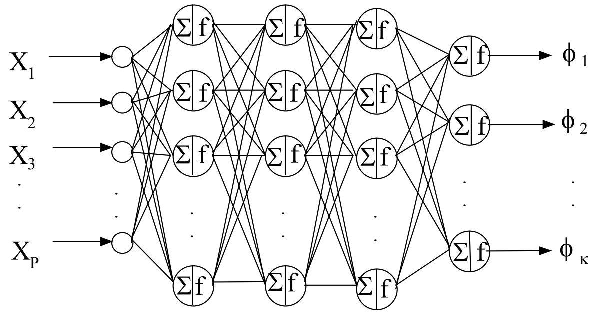

Fig.1 Architecture of revised GMDH-type neural network

2.1 The first layer

$$u_j = x_j \qquad (j=1,2,\ldots,p) \tag{1}$$

where x_j (j=1,2,…,p) are input variables of the nonlinear system, and p is the number of input variables. In the first layer, input variables are set to output variables.

2.2 The second layer

All combinations of r input variables are generated. For each combination, optimum neuron architectures are automatically selected so as to minimize AIC or PSS.

Revised GMDH-type neural network algorithm can select optimum neural network architecture from three neural network architectures such as sigmoid function neural network, RBF neural network and polynomial neural network.

Neuron architectures in each neural network architecture are shown as follows. Neurons are constructed using the first and the second type neuron architectures.

(1) *Sigmoid function neural network*

1) The first type neuron

Σ: (Nonlinear function)

$$z_k=w_1u_i+w_2u_j+w_3u_iu_j+w_4u_i^2+w_5u_j^2+w_6u_i^3+w_7u_i^2u_j+w_8u_iu_j^2+w_9u_j^3-w_0\theta_1 \quad (2)$$

f : (Nonlinear function)

$$y_k=\frac{1}{1+e^{(-z_k)}} \quad (3)$$

2) The second type neuron

Σ: (Linear function)

$$z_k= w_1u_1+w_2u_2+w_3u_3+\cdots+w_ru_r-w_0\theta_1 \quad (r<p) \quad (4)$$

f : (Nonlinear function)

$$y_k=\frac{1}{1+e^{(-z_k)}} \quad (5)$$

(2) *Radial basis function neural network*

1) The first type neuron

Σ: (Nonlinear function)

$$z_k=w_1u_i+w_2u_j+w_3u_iu_j+w_4u_i^2+w_5u_j^2+w_6u_i^3+w_7u_i^2u_j+w_8u_iu_j^2+w_9u_j^3-w_0\theta_1 \quad (6)$$

f : (Nonlinear function)

$$y_k=e^{(-z_k^2)} \quad (7)$$

2) The second type neuron

Σ: (Linear function)

$$z_k= w_1u_1+w_2u_2+w_3u_3+\cdots+w_ru_r-w_0\theta_1 \quad (r<p) \quad (8)$$

f : (Nonlinear function)

$$y_k=e^{(-z_k^2)} \quad (9)$$

(3) *Polynomial neural network*

1) The first type neuron

Σ: (Nonlinear function)

$$z_k=w_1u_i+w_2u_j+w_3u_iu_j+w_4u_i^2+w_5u_j^2+w_6u_i^3+w_7u_i^2u_j+w_8u_iu_j^2+w_9u_j^3-w_0\theta_1 \quad (10)$$

f : (Linear function)

$$y_k=z_k \quad (11)$$

2) The second type neuron

Σ: (Linear function)

$$z_k= w_1u_1+w_2u_2+w_3u_3+\cdots+w_ru_r-w_0\theta_1 \quad (r<p) \quad (12)$$

f : (Linear function)

$$y_k=z_k \quad (13)$$

Here, $\theta_1=1$ and w_i (i=0,1,2,…,9) and w_i (i=0,1,2,…,r) are weights between the first and second layer. Value of r, which is the number of input variables u in each neuron, is set to two for the first type neuron and set to be greater than two and smaller than p for the second type neuron. p is the number of input variables x_i (i=1,2,…,p). Weights w_i (i=0,1,2,…) in each neural network architecture are estimated by stepwise regression analysis [7] using PSS.

[Estimation procedure of weight w_i]

First, values of z_k^{**} are calculated for each neural network architecture as follows.

a)Sigmoid function neural network

$$z_k^{**}=\log_e\left(\frac{\phi'}{1-\phi'}\right) \quad (14)$$

b)RBF neural network

$$z_k^{**}=\sqrt{-\log_e\phi'} \quad (15)$$

c)Polynomial neural network

$$z_k^{**}=\phi \quad (16)$$

where ϕ' is the normalized output variable whose values are between 0 and 1.

Then weights w_i are estimated by stepwise regression analysis [7] which selects useful input variables using AIC or PSS. Only useful variables in Eq.(2), Eq.(4), Eq.(6), Eq.(8), Eq.(10) and Eq.(12) are selected by stepwise regression analysis using AIC or PSS and optimum neuron architectures are organized by selected useful variables.

For each combination, three neuron architectures, which are sigmoid function neuron, RBF neuron and polynomial neuron, are generated and L neurons which minimize PSS are selected for each neuron architecture. From these L selected neurons for each neuron architecture, estimation errors of L neurons are calculated. Then, neural network architecture which has minimum estimation error is selected as revised GMDH-type neural network architecture from three neural network architectures.

After the type of revised GMDH-type neural network architecture is selected, output variables y_k of L selected neurons are set to input variables of neurons in the third layer.

2.3 The third and successive layers

In the second layer, optimum neural network architecture is selected from three neural network architectures. In the third and successive layers, only one neuron architecture, which is sigmoid function neuron or RBF neuron or polynomial neuron, is used for calculation and the same calculation of the second layer is iterated until AIC or PSS values of L neurons with selected neuron architecture stop decreasing. When iterative calculation is terminated, neural network architecture is produced by L selected neurons in each layer.

By using these procedures, the revised GMDH-type neural network self-selecting functions is organized.

3. APPLICATION TO MEDICAL IMAGE DIAGNOSIS OF LUNG CANCER

In this study, the regions of lung cancer were recognized and extracted automatically by using the revised GMDH-type neural network. Multi-detector row CT (MDCT) images of lungs are used in this study. In this application, PSS was used as the prediction error criterion.

3.1 Extraction of candidate image regions of lung cancer.

A lung image shown in Fig. 2 was used for organizing the revised GMDH-type neural network. The statistics of the image densities and x and y coordinates in the neighboring regions, the N×N pixel regions, were used as the image features. Only five parameters namely, mean, standard deviation, variance and x and y coordinates were selected as the useful input variables. The output value of the neural network was zero or one. When N×N pixel region was contained in lung regions, the neural network set the pixel value at the center of the N×N pixel region to one and this pixel was shown as the white point. The neural networks were organized when the values of N were from 3 to 10. It was determined that when N was equal to 4, the neural network architecture had the smallest recognition error. Five useful neurons were selected in each hidden layer. Figure 3 shows the estimation errors of three kinds of neurons in the second layer. The estimation error of the RBF neural network was smallest in three kinds of neurons. The RBF neural network architecture was selected by the revised GMDH-type neural network algorithm. Figure 4 shows the variation of PSS values in the layers. The calculation of the revised GMDH-type neural network was terminated in the eighth layer. The revised GMDH-type neural network outputs the lung image (Fig.5) and the first post-processing analysis of the lung image was carried out. In the first post-processing of the output image, the opening was carried out and small isolated regions were eliminated and the outlines of the lung regions were expanded outside by N/2 pixels. Then, the closing was carried out and the lung regions that did not contain abnormal regions were output. Figure 6 shows the output image after the first post-processing. The output image after the first post-processing was overlapped to the original image (Fig.2) in order to check the accuracy of the image recognition of the lungs as shown in Fig.7. The recognized lung regions are accurate. The lung regions was extracted from the original image using the output image. Figure 8 shows the extracted lung image. The second post-processing such as the opening, closing and so on was carried out in Fig.5 and the lung regions which contained the abnormal regions were obtained as shown in Fig.9. Figure 10 shows the extracted lung image. The candidate image regions of the lung cancer were extracted from Fig.10 using Fig.8 and shown in Fig.11.

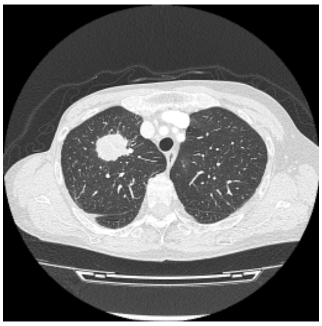

Fig. 2 Original image

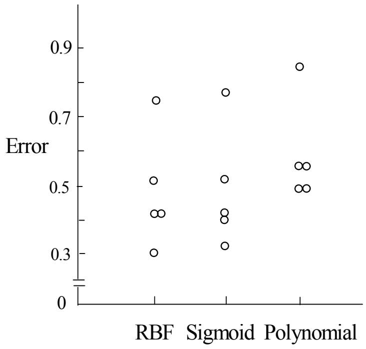

Fig.3 Estimation errors of three kinds of neurons

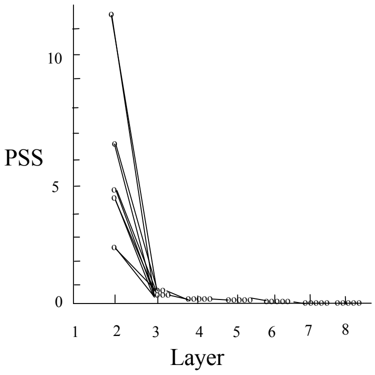

Fig.4 Variation of PSS values

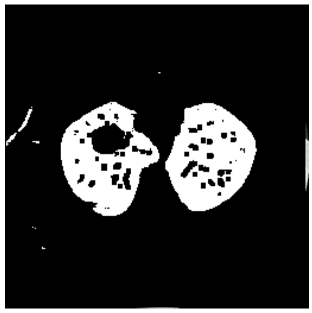

Fig.5 Output image of revised GMDH-type neural network

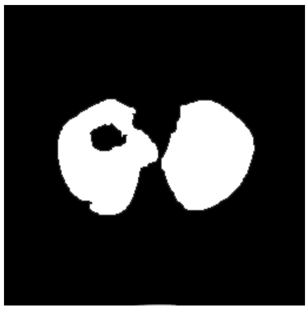

Fig.6 Output image after the first post-processing

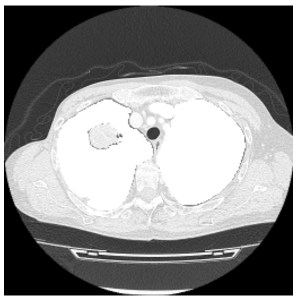

Fig. 7 Overlapped image

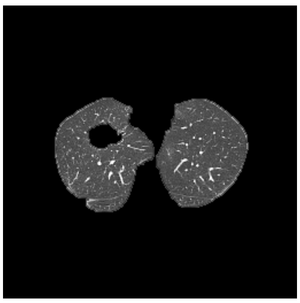

Fig.8 Extracted image of lung regions (1)

Fig. 9 Output image after second post-processing

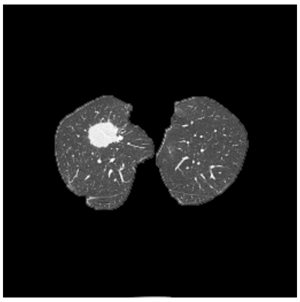

Fig. 10 Extracted image of lung regions (2)

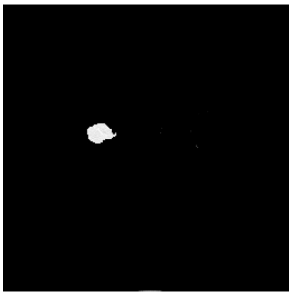

Fig. 11 The candidate image region of lung cancer

3.2 Recognition results of the conventional neural network trained using the back propagation algorithm

A conventional neural network trained using the back propagation algorithm was applied to the same recognition problem and the recognition results were compared with the results obtained using the revised GMDH-type algorithm. The conventional neural network had a three layered architecture and the same five input variables were used in the input layer. The learning calculations of the weights were iterated changing structural parameters such as the number of neurons in the hidden layer and the initial values of the weights. The output images, when the numbers of neurons in the hidden layer (m) are 5, 7 and 9, are shown in Fig.12. These images contain more regions which are not part of the lung and the outlines of the lungs are not extracted with required clarity compared with the output image obtained using the GMDH-type neural network algorithm, which is shown in Fig.5. Note that, in case of the conventional neural network, we obtain many different output images for various structural parameters of the neural network and many iterative calculations of the back propagation are needed for various structural parameters in order to find more accurate neural network architecture.

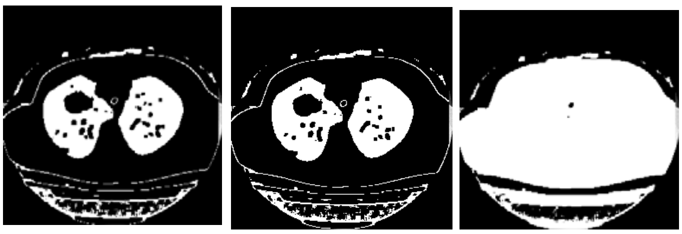

(a) m=5 (b) m=7 (c) m=9

Fig.12 Output images of conventional sigmoid function neural network

4. CONCLUSION

In this paper, the revised GMDH-type neural network algorithm self-selecting functions was applied to the CAD of lung cancer and the results of the revised GMDH-type neural network were compared with those of the conventional sigmoid function neural network trained using the back propagation algorithm. In this revised GMDH-type neural network algorithm, optimum neural network architecture is automatically selected from three neural network architectures such as sigmoid function neural network, RBF neural network and polynomial neural network. Furthermore, structural parameters such as the number of layers, the number of neurons in hidden layers and useful input variables are automatically selected to minimize prediction error criterion defined as AIC or PSS. In the case of the conventional neural network, we obtain many different output images for various structural parameters of the neural network and many iterative calculations of the back propagation are needed for various structural parameters in order to find more accurate neural network architecture. It was shown that the revised GMDH-type neural network algorithm was a useful method for CAD of lung cancer because the neural network architecture is automatically organized so as to minimize the prediction error criterion defined as AIC or PSS.

ACKNOWLEDGEMENT

This work was supported by (JSPS) KAKENHI 22560403.

REFERENCES

[1] T. Kondo and J. Ueno, "Multi-layered GMDH-type neural network self-selecting optimum neural network architecture and its application to 3-dimensional medical image recognition of blood vessels", International Journal of Innovative Computing, Information and Control, vol.4, no.1, pp.175-187, 2008.

[2] T. Kondo, "GMDH neural network algorithm using the heuristic self-organization method and its application to the pattern identification problem", Proc. of the 37th SICE Annual Conference, pp.1143-1148, 1998.

[3] S. J. Farlow ed., Self-organizing methods in modeling, GMDH-type algorithm, New York: Marcel Dekker Inc., 1984.

[4] A. G. Ivakhnenko, "Heuristic self-organization in problems of engineering cybernetics", Automatica, vo.6, no.2, pp.207-219, 1970.

[5] H. Akaike, "A new look at the statistical model identification", IEEE Trans. Automatic Control, vol.AC-19, no.6, pp.716-723, 1974.

[6] H. Tamura, T. Kondo, "Heuristics free group method of data handling algorithm of generating optimum partial polynomials with application to air pollution prediction", Int. J. System Sci., vol.11, no.9, pp.1095-1111, 1980.

[7] N. R. Draper, H. Smith, Applied Regression Analysis, New York: John Wiley and Sons, 1981.

The Seventeenth International Symposium on Artificial Life and Robotics 2012 (AROB 17th '12),
B-Con Plaza, Beppu, Oita, Japan, January 19-21, 2012

The Technique of the Online Learning Method using SOM algorithm for nonlinear SVM

Hiroki Tamura[1], Takeshi Yoshimatsu, and Koichi Tanno

[1] Department of Electrical & Electronic Engineering, University of Miyazaki, 1-1 Gakuen-kibanadai-nishi, Miyazaki-city, Miyazaki, 889-2192, Japan
(Tel: 81-985-58-7409)

[1]htamura@cc.miyazaki-u.ac.jp

Abstract: The support vector machine (SVM) is known as one of the most influential and powerful tools for solving classification and regression problems, but the original SVM does not have an online learning technique. Therefore, many researchers have introduced online learning techniques to the SVM. In a previous article, we proposed an unsupervised online learning method using the technique of the self-organized map for the SVM. In another article, we proposed the midpoint validation method for an improved SVM. We test the performance of the SVM using a combination of the two techniques in this article. In addition, we compare its performance with the original hard margin SVM, and also experiment with our proposed method on surface electromyogram recognition problems with changes in the position of the electrode, and the numerical experiment recognition problem with changes in the time. These experiments showed that our proposed method gave a better performance than the SVM and corresponded to the changing data.

Keywords: Support vector machine, Online learning, Midpoint validation, Pattern classification problem, Surface electromyog ram

1 INTRODUCTION

The support vector machine (SVM) proposed by Cotes and Vapnik is one of the most influential and powerful tools for solving classification problems [1][2][3][4][5].

We studied surface electromyogram (abbr. s-EMG) recognition using the SVM. The purpose was the development of a human interface using an s-EMG. In this study, we considered problems such as the changes in the s-EMG pattern caused by muscle fatigue, and the position of the sensor doing the measurements. In a previous article [6] we proposed the online unsupervised learning method using the technique of a self-organized map for the SVM. Furthermore, the proposed method has a technique for the reconstruction of a SVM.

In addition, we are studying a SVM which is not limited to the recognition of s-EMG. In this study, we pay attention to the problem of the deflection of the separating hyperplane in the input space of a nonlinear SVM, and propose an improved method [7][8]. We call this method the midpoint validation method. This method assumes a midpoint between the classes of training data and an index of the deflection, and moves the separating hyperplane according to the index. This method also has a technique for the reconstruction of a SVM.

These two studies both achieved good results. However, we had not previously combined the two methods. Therefore, we tested the performance of the SVM using a combination of the two techniques. Moreover, we compared its performance with the original hard-margin SVM, Winner Take All model (our previous online method [10]), and also experimented with our proposed method on s-EMG recognition problems with changes in the position of the electrode, and the numerical experiment recognition problem with changes in the time.

2 PROPOSED METHOD

In this section, we introduce the SVM, our online learning method. We also propose a method that combines the online learning method with the midpoint validation method [7][8].

2.1 SVM

A SVM is a mechanical learning system that uses a hypothetical space of linear functions in a high-dimensional feature space. A nonlinear SVM is expressed by Eqs. 1–3. Here, we used the Gaussian kernel given in Eq. 1 as the kernel function, while the SVM decision function g(**x**) and the output of the SVM are as given in Eqs. 2 and 3.

$$K(\mathbf{x},\mathbf{x}_i)=\exp\left(\frac{-\|\mathbf{x}-\mathbf{x}_i\|^2}{2\delta^2}\right) \quad \textbf{(1)}$$

$$g(\mathbf{x})=\sum_{i=1}^{N} w_i K(\mathbf{x},\mathbf{x}_i)+b \quad \textbf{(2)}$$

$$O=sign(g(\mathbf{x})) \quad \textbf{(3)}$$

2.2 Online learning method

In this subsection, we introduce an unsupervised online learning method using the self-organizing map (abbr. SOM) algorithm for the SVM and a restructuring technique.

Let the input space be denoted by $\mathbf{x}_{in} \in$ R. $\mathbf{x}_{in}$ ($in \notin \{i = 1, \ldots, N\}$) is the input vector without the label. The training vectors are included in the kernel function x_i, with $i = 1, \ldots, N$, which belongs to either of the two classes. Therefore, these are given the label $y_i \in \{-1, 1\}$. Each training vector has the same dimensions in input space. The flow of our online learning method is shown in Figs. 1 and 2. The parameter η is an update parameter. The idea of this rule is close to adaptive resonance theory. The parameter s is the Euclidean distance between $\mathbf{x}_{in}$ and each $\mathbf{x}_i$.

Step 1: To find the best mach of the input vector $\mathbf{x}_{in}$ with the training vectors $\mathbf{x}_i$, the Euclidean distance between $\mathbf{x}_{in}$ and each $\mathbf{x}_i$ is computed (Fig. 2a).
Step 2: The following processing (Steps 3-4) are not done to $\mathbf{x}_{in}$ when the label of $\mathbf{x}_{win}$ is not the same as the label of the output result of SVM of $\mathbf{x}_{in}$.
Step 3: To find the best mach of $\mathbf{x}_{win}$ with the training vectors $\mathbf{x}_j$, the Euclidean distance $\mathbf{x}_{win}$, and each $\mathbf{x}_j$ is computed (Fig. 2b).
Step 4: If d_w is condition of the rule of Eq. 4, each $\mathbf{x}_i$ is update according to the learning rule of Eqs. 5 and 6 (Figs. 2c and 2d).
Step 5: Steps 1-4 are done to all input vector.
Step 6: Proposed method repeats *Num* cycles these processing (Steps 1-5) using same inputs vector $\mathbf{x}_{in}$.

$$d_w \leq d_O \qquad (4)$$

$$\mathbf{x}_i^{new} = \mathbf{x}_i^{old} + \eta \cdot f(s)(\mathbf{x}_{in} - \mathbf{x}_i^{old}) \qquad (5)$$

$$f(s) = \begin{cases} \exp(-(3s)^2) \big| y_{win} = y_i & (6.a) \\ 0 \big| y_{win} \neq y_i & (6.b) \end{cases}$$

$$s = \|\mathbf{x}_{in} - \mathbf{x}_i\| \qquad (7)$$

Fig. 1. The flow of the online learning method.

If the SV changes after the update, the SVM is restructured using the updated training vectors. Even if the training vectors change using Steps 1–5, maximizing the margin of the SVM is retained in this restructuring process. In this paper, we first perform the online learning method. Next, we create a SVM with the updated training data. Finally, we perform the midpoint validation method [7][8].

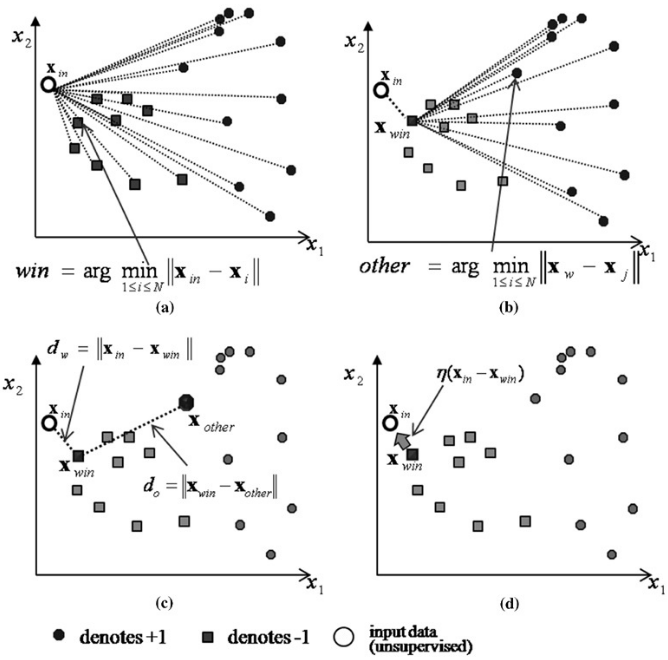

Fig. 2. The flow of the proposed method using SO M. The training vector x_{other} is selected as in (a) and (b). If d_w and d_o are the conditions of the rule in Eq. 4, as in (c), x_{win} is updated using the learning rule in Eq. 5 as in (d).

3 EXPERIMENTS

In this section, the system configuration for experiments on recognizing input data sets changes over time is explained. Next, the system configuration for experiments on recognizing forearm movements using s-EMG is explained. Finally, the results of the computer simulations are described. We compared the performance of the proposed method, Mexican Hat model, Winner Take All (abbr. WTA) model [10], the original hard-margin SVM, and *k*-NN method (form paper [10]). The Mexican Hat model is changed Eq.6.a and b of the proposed method to Eq.8. The WTA model is changed Eq.5 of the proposed method to Eq.9 and not use Eqs.6 and 7.

Mexican Hat model

$$f(s) = \begin{cases} \left(1 - \left(2 \cdot (12s)^2\right)\right) \exp(-(12s)^2) \big| y_{win} = y_i \\ 0 \big| y_{win} \neq y_i \end{cases} \qquad (8)$$

WTA model [10]

$$\mathbf{x}_{win}^{new} = \mathbf{x}_{win}^{old} + \eta \cdot (\mathbf{x}_{in} - \mathbf{x}_{win}^{old}) \qquad (9)$$

3.1 Experimental conditions on numerical

As time-varying input data sets, we created a spiral data sets vary in the two-dimensional space. This is two-class data sets. As class 1, 1000 data were calculated by adding the noise and according to Eqs.10 and 11. As class 2, shifted 180 [deg], 1000 data were created in the same way. In each class, data were divided into training and test data of 900 and 100. In addition, the test data was not chosen from the vicinity of the origin. Shifted 20 [deg] at an angle, 1000 data were created in the same way, in each class. And data were divided into learning and test data of 900 and 100, in each class. Repeat this process 9 times, made 9 data sets.

$$x = 0.1\theta\cos(8\pi\theta) \quad (10)$$

$$y = 0.1\theta\sin(8\pi\theta) \quad (11)$$

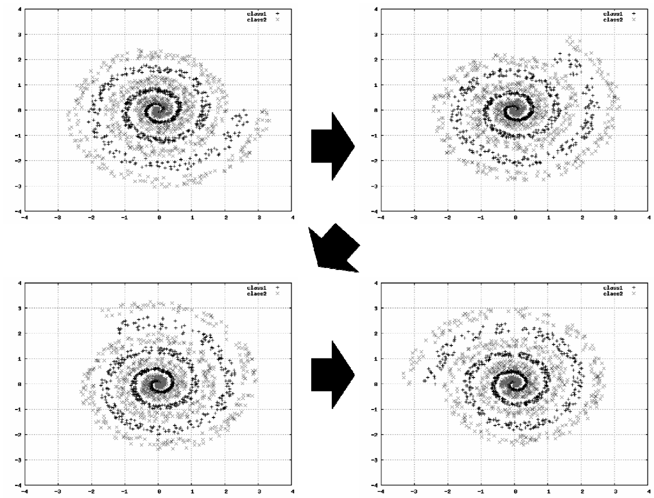

Fig. 3. The spiral data.

3.2 Experiment on numerical

We tested the effectiveness of the proposed method on the spiral recognition problem (Fig.3) that the quantity of the feature changes according to the angle. First, the SVM learn the relation between the coordinate and class from the training data (the training vectors). Next, rotate 20[deg] around the origin. Additional unsupervised learning data (the input vector) are obtained from each class. Last, the recognition rate is calculated from the test data for 100 repeats of each class. The experiments were tested nine times in total by rotating around the origin by 20[deg], 40[deg], 60[deg], 80[deg], 100[deg], 120[deg], 140[deg], 160[deg] and 180[deg]. The basis of the proposed method is the hard-margin SVM using Eq. 1. The Gaussian kernel parameters of the SVM were decided from an evaluation using the training data. Gaussian kernel parameter δ was 0.3. In this experiment, the value of parameter η was 0.1, and the value of *Num* was 1.

3.3 Experimental conditions on forearm muscles

The s-EMG of each movement pattern is measured with electrode sensors, and the quantity of the feature is extracted from the s-EMG. The quantity of the feature is given to the recognition machine as an input, and each movement pattern that generates s-EMG is presumed. The quantity of the feature uses the minimum–maximum values and integration values used by Tamura et al [9]. That article showed that the technique of min–max values and integration values is easier and better than fast Fourier transform processing. The sampling frequency of the measurement data was 1 KHz, and the sampling band was from 0 Hz to 500 Hz.

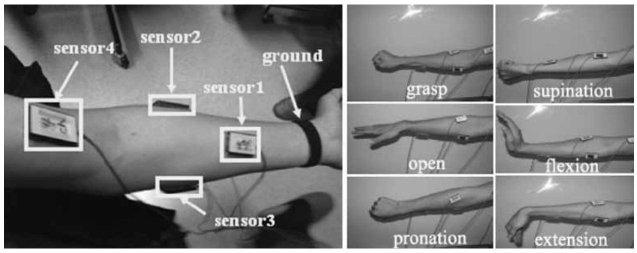

Fig. 4. Image of the forearm motion.

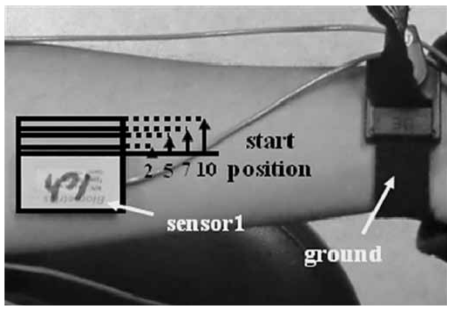

Fig. 5. S-EMG recognition problems with changes in the electrode position (2mm, 5mm, 7mm and 10mm).

3.4 Experiments on forearm muscles

We tested the effectiveness of the proposed method on the s-EMG recognition problem that the quantity of the feature changes according to the position of the electrode. The experimental subjects were three healthy men (T.Y, K.F and S.Y). The subjects sat on a chair. The recognition experiment of the six motion patterns was conducted using s-EMG obtained from four sensors set on the right arm (Fig. 4). Eight inputs were given to the identification machine. The experiments were conducted for 1 day. First, we acquired the training data from the s-EMG concerning the movements of the forearm. Then, the SVM learn the relation between the s-EMG and motion from the training data (the training vectors). Each movement is identified 60 times. Next, the electrode position (sensor 1) is moved 2 mm. Additional unsupervised learning data (the input vector: each motion is repeated 20 or 40 times) are obtained from each movement. Last, the recognition rate is calculated from the test data for 20 repeats of each movement. The measurements were tested four times in total by moving the electrode position by 2 mm, 5 mm, 7 mm, and 10 mm (Fig. 5). The basis of the proposed method is the hard-margin SVM using Eq. 1. The Gaussian kernel parameters of the SVM were decided from an evaluation using the training data. Subject T.Y was 0.7, K.F was 2.0, and S.Y was 0.9. In these experiments, the value of parameter η was 0.1 (on subject T.Y and S.Y) or 0.05 (on subject K.F), and the value of *Num* was 1.

3.5 Experimental result

The results for each simulation method are given in table 1 and 2. In table 1, we show the average success rate of experiment without midpoint validation. From table 1, the proposed method is better than WTA model on result of numeric and subject T.Y. However, Mexican Hat model is worse than the original SVM. Therefore, we consider three methods except the Mexican Hat model. In table 2, we show the average success rate of experiment with midpoint validation. From table 2, the proposed method is better than WTA model on result of numeric and subject T.Y. But, the proposed method is not effective on the subject S.Y. From these results, WTA model had better results, and the proposed method has specialty data and non-specialty data.

Table 1. Average success rate (%) of experiment without Midpoint validation method.

	Numerical	s-EMG		
		T.Y	K.F	S.Y
WTA model	56.3	80.0	**83.3**	**77.7**
Mexican Hat model	53.5	75.8	72.2	59.2
Proposed Method	**66.2**	**85.7**	81.7	72.2
original SVM	50.8	78.5	77.8	76.3

Table 2. Average success rate (%) of experiment with Midpoint validation method.

	Numerical	s-EMG		
		T.Y	K.F	S.Y
WTA model	54.6	81.7	**84.2**	**86.7**
Proposed Method	**68.1**	**86.3**	81.3	70.8
SVM+MV	48.1	77.0	80.8	81.3
k-NN method	-	80.8	82.1	77.7

4 CONCLUSIONS

In this paper, we have proposed a technique of the online learning method using SOM algorithm for nonlinear SVM. The experimental results show that the proposed method is effective in the data which changes uniformly like numerical problem. WTA model is effective in the data which changes irregularly. WTA model is suitable for the recognition problems of s-EMG, because to change irregularly in many cases. The merit of our proposed online method is that the proposed method can be used effectively by setting only one parameter η. The parameter η may be around 0.1. Therefore, the proposed method is useful. In future work, we will experiment on the effectiveness of the proposed method in other problems.

References

[1] Cotes C., Vapnik VN.: Support vector networks. Mach Learn 20(3):273–297 (1995)

[2] Burges CJC.: A tutorial on support vector machines for pattern recognition. Data Mining Knowledge Discovery 2(2) (1998)

[3] Joachims T.: Making large-scale support vector machine learning practical. In: Shoelkopf B, Burges C, Smola A (eds) Advances in kernel methods: support vector learning. pp 169–184 (1999)

[4] Mangasarian OL., Musicant DR.: Active support vector machines. Technical Report 00-04, Data Mining Institute, Computer Sciences Department, University of Wisconsin, Madison (2000)

[5] Mangasarian OL., Musicant DR.: Lagrange support vector machines. J Mach Learn Res 1:161–177 (2001)

[6] Tamura H., Yoshimatu T., Tanno K.: Support vector machines with online unsupervised learning method and its application to s-EMG recognition problems. NOLTA (2010)

[7] Tamura H., Tanno K.: Midpoint-validation method for support vector machine classification. IEICE Trans Inform Syst E91-D(7): 2095–2098 (2008)

[8] Yamashita S., Tamura H., Toyama T., et al.: The effectiveness of midpoint-validation method for support vector machines (in Japanese). Proceedings of Electronics, Information and Systems Conference, IEEJ, CD:GS12-5 (2010)

[9] Tamura H., Gotoh T., Okumura D., et al.: A study on the s-EMG pattern recognition using neural network. Int J Innovative Comput Inform Control 5(12B):4877–4884 (2009)

[10] Shingo Y., Takeshi Y., Hiroki T. and Koichi T.: A study of SVM using the Combination with Online Learning Method and Midpoint-Validation Method. Proc. of AROB2011 (2011)

The Seventeenth International Symposium on Artificial Life and Robotics 2012 (AROB 17th '12),
B-Con Plaza, Beppu, Oita, Japan, January 19-21, 2012

Financial Market Forecasting by Integrating Wavelet Transform and K-means Clustering with Support Vector Machine

Roshan W. D. S[1], Gopura R. A. R. C[1], Jayasekara A. G. B. P[2] and Bandara D. S. V[1]

[1]Department of Mechanical Engineering, University of Moratuwa, Katubedda 10400, Sri Lanka
sameeraroshanuom@gmail.com, gopura@mech.mrt.ac.lk, sanjaya@mech.mrt.ac.lk

[2]Department of Electrical Engineering, University of Moratuwa, Katubedda 10400, Sri Lanka
buddhika@elect.mrt.ac.lk

Abstract: Financial market forecasting is a challenging problem and researchers are still exploring the ways to improve the performance of the existing models. This paper presents a forecasting model by integrating wavelet transform, K-means clustering with support vector machine. At the first stage, noise of the input prices is removed by using wavelet denoising. Wavelet multiresolution analysis is used to decompose the original time series in to multiple details and approximated decompositions. Individual support vector models are trained for each detail part. Approximated part is further analyzed by clustering and training support vector models for each cluster. Finally the forecast is made for the wavelet denoised time series by summing up the forecasts of each support vector model. Results have shown that the proposed model has given the accurate forecast and has the capability to support decisions in real world trading.

Keywords: Support vector machine, wavelet transform, K-means clustering, financial market forecasting.

1 INTRODUCTION

Financial market forecasting has been drawn considerable attention in recent years. Accurate forecast of currencies, indices and commodities has become an important issue in decision making in investments. Forecasting financial time series have become a difficult task because of its noisy, nonstationary characteristics and dependence on lot of economic, political environmental and even psychological factors. Forecasters are trying to develop various forecasting techniques in order to reduce the risk of trading. Neural network has become a good alternative over traditional methods like Random Walk model, Box-Jenkins ARIMA, Hidden Markov model etc., because of its capabilities in nonlinear data analysis and universal function approximation Yu et al [1].

Various neural models such as feed-forward, recurrent, radial basis, probabilistic and Support vector machine (SVM) have been developed and researchers are still exploring the ways to improve the forecasting performance of the neural models. Among those models, SVM that is a new kind of kernel based learning machine based on statistical learning theory, has become a good alternative over other neural architectures because of its structural risk minimization property.

In Roshan et al [2], data preparing and architecture determination has identified as the two main problems in building a model for financial market forecasting and new modeling directions have been explored. At the first stage, noise of the signal and the correlation of the inputs should be removed. Thereafter most influential inputs should be selected for the model. Clustering should be done on selected input space where the inputs with similar statistical features are grouped together. Individual models should be created for each cluster and final model should be an ensemble of all individual models.

Therefore this study is focused on improving the forecasting capability of SVM by integrating wavelet transform and k-means clustering according to the above mentioned modeling direction. Section 2 describes the theoretical background of the SVM, K-means clustering and wavelet transform. The simulation results and discussion are given in section 3. Finally the collusions are given.

2 THEORETICAL BACKGROUND

2.1 Support vector machine

The support vector machine (SVM) was proposed by Vapnik [3] and it is based on the structured risk minimization principle. SVM minimize the upper bound of the generalization error by automatically by estimating optimal VC-dimension h with its nested architecture Hayking [4]. SVM is first proposed for pattern classification of two classes and further extended to multi class pattern classification and regression analysis. The SVM regression function can be stated as follows

$$t = W^T \emptyset(X) + b \qquad (1)$$

Where $\emptyset(X)$ is the nonlinear mapping-function. W and b can be estimated as follows.

$$R(C) = C\frac{1}{n}\sum_{i=1}^{N} L_\varepsilon(r_i, t_i) + \frac{1}{2}\|W\|^2 \qquad (2)$$

Where,

$$L_\varepsilon(r_i, t_i) = \begin{cases} |r_i - t_i| - \varepsilon, & |r_i - t_i| \geq \varepsilon \\ 0, & else \end{cases} \qquad (3)$$

r_i is the actual price at the ith period and t_i is the model prediction. $L_\varepsilon(r_i, t_i)$ is called ε-intensive loss function. Term $C\frac{1}{n}\sum_{i=1}^{N} L_\varepsilon(r_i, t_i)$ is the empirical error and the term $\frac{1}{2}\|W\|^2$ is the measure of the smoothness. Tradeoff between empirical risk and smoothness is controlled by C.

Issue to be resolved is to minimize the empirical risk. We can reformulate this optimization problem by introducing two sets of nonnegative slack variables ε_i and ε_i^*. Then the Eq.(2) is can be transformed in to following constrained optimization.

$$\min_{W,b,\varepsilon_i,\varepsilon_i^*} R(W,\varepsilon_i,\varepsilon_i^*) = \frac{1}{2}W^TW + C\{\sum_{i=1}^{N}(\varepsilon_i + \varepsilon_i^*)\} \quad (4)$$

Subject to,

$$W^t\emptyset(X_i) + b - r_i \leq \varepsilon + \varepsilon_i^*$$

$$r_i - W^t\emptyset(X_i) - b \leq \varepsilon + \varepsilon_i$$

$$\varepsilon_i, \varepsilon_i^* \geq 0$$

Taking Lagrangian and conditions for optimality, model can be represented in dual as follows.

$$f(X,a,a^*) = \sum_{i=1}^{N}(\alpha_i - \alpha_i^*)K(X,X_i) + b \qquad (5)$$

Where α_i and α_i^* are nonzero Lagrangian multipliers which are the solution the dual problem. $K(X,X_i)$ is the kernel function.

$$K(X,X_i) = exp\left\{-\frac{(X-X_i)^2}{\sigma^2}\right\}$$

Radial basis kernel is utilized in this study with empirically obtained near optimal σ and C

2.2 Wavelet transform

Wavelet transform has proven to be highly effective in analyzing noisy and nonstationary time series by number of researchers. Consider real or complex value continues time function $\psi(t)$ with following characteristics.

1. It is integrable to zero

$$\int_{-\infty}^{\infty} \psi(t)\, dt = 0 \qquad (6)$$

2. It is square integrable (has finite energy)

$$\int_{-\infty}^{\infty} |\psi(t)|^2\, dt < \infty \qquad (7)$$

3. Admissibility condition

$$\int_{-\infty}^{\infty} \frac{|\psi'(w)|^2}{w}\, dw < \infty \qquad (8)$$

Where ψ' is fourier transform of ψ

2.2.1 Continuous wavelet transform (CWT)

If a function $\psi(t)$ fulfill above (6), (7), (8) conditions, then the continues wavelet transform can be defined as follows

$$C(a,b) = \int_{-\infty}^{\infty} f(t)\, \Psi_{a,b}(t) dt \qquad (9)$$

Where $\Psi_{a,b}(t) = e^{1/2}\,\Psi\left(\frac{t-b}{a}\right)$ is the mother wavelet. a is scale parameter and b is a translation parameter. The relationship between scale and frequency is that low scales correspond to high frequencies and high scales correspond to low frequencies. CWT has much redundant information of the time series and also takes lot of computation time. There for discrete wavelet transform (DWT) has been introduced to eliminate these shortcomings.

2.2.2. Discrete wavelet transform

Definition of the discrete wavelet transform can be given as follows.

$$C(a,b) = C(j,k) = 2^{\frac{j}{2}}\psi_{j,k}(n) \qquad (10)$$

Parameters a and b are defined as $a = 2^j, b = 2^jk$

2.2.3 Stationary wavelet transform

Discrete wavelet transform suffers from a drawback of shift variance. That means discrete wavelet transform (DWT) of a signal is differ from the DWT of the shifted version of the same signal due to decimation step involved in the DWT Coifman & Donoho [5]. Stationary wavelet transform is designed by removing decimation step in order to avoid shift variance. It is a necessary property for time series analysis. Therefore Stationary wavelet transform has utilized in this study.

2.3 K-means clustering

In statistics and data mining, K-means clustering is a method of cluster analysis. Importance of the clustering input space is, to remove bias variance dilemma and improve overall generalization. K-means clustering is used to partition n observations into k clusters and each observation belongs to the cluster with the nearest mean. Given a set of observations n with m-dimensional real vector, K-means clustering partitions the n observations into k clusters $(k < n)$ and minimize the sum of squares within-each cluster

$$arg\ min \sum_{i=1}^{k} \sum_{X_j \in S_i} \left\| X_j - \mu_i \right\|^2 \qquad (11)$$

where μ_i is the center of the cluster S_i

3 SIMULATION RESULTS

3.1 Forecasting model

In the simulation, model was tested for an actual market condition where new data comes in at every step. In this situation, model has no information what so ever about the next step value. Number of researchers in previous studies has performed financial time series forecasting without taking actual market conditions into consideration. This has led to better testing results but doesn't have capability to make profit in real market conditions

Input selection for financial forecasting often takes a critical place because of the accuracy of the output is entirely depends on the characteristics of inputs. Therefore three types of inputs: time delay price values, simple moving average and exponential moving average, have checked upon the performance of the model. Two moving averages ranges (7 min and 30 min) were tested in the comparison.

Proposed model combines SVM regression, Wavelet decomposition and K-means clustering. Input data is scaled up to reduce the mean squared error of the model. Noise of the input data is further removed by using wavelet denoising, which can be achieved by removing small wavelet coefficients in wavelet decomposition by applying appropriate threshold value, even though averaging methods such as moving averages reduces some amount of noise from the data. Then the approximation and detail parts of the time series have reconstructed separately. Individual SVM models with radial basis kernel and debauchee's wavelet is used for each detailed part.

Radial basis kernel which maps inputs in to an infinite dimensional feature space, has selected according to the Cover's theorem of data mapping Cover [6]. Approximation part is further analyzed by using K-means clustering. Bias variance dilemma is expected to be removed by clustering according to principle of divide and conquer Hayking [7]. Multiple clusters have been created for approximation part of the signal by using K-means clustering. Separate SVM model has created for each cluster. New input vector was assigned to a cluster that has minimum distance from its center and the forecast is made by SVM related to the cluster. Then the output is taken by summing up all SVM models that has been created for detail and approximation parts.

Stationary wavelet transform is highly effective in above steps because of its capabilities in time and frequency localization, orthogonal data mapping and ability to fully reconstruct the original time series. Finally one step ahead and multistep ahead forecast has performed and results were compared with pure SVM regression model and wavelet-SVM regression model.

Pure SVM model has the originally proposed architecture with optimally selected parameters while Wavelet-SVM regression model first decompose original time series in to multiple decompositions and each composition is forecasted using separate SVM regression model and finally results were summed up over all decompositions. Directional statistics (D_stat) and mean squared error (MSE) have used as the performance measures. Model is checked for EUR/USD currency pair which is known to be the most volatile of them all. 1 min values have taken in to the forecast. When removing the noise, 1 min data has the advantage of allowing considerable amount of noise reduction without affecting the profit taking opportunities.

3.2. Results

3.2.1 Pure SVM performance

The results of one step ahead forecast is given in Table 1 and has shown the forecast of pure SVM model is capable of forecasting EUR/USD with great accuracy. But it is only with moving average inputs. Result of the pure SVM is the worst of three models for direct input of time delay data. Even though wavelet denoising has improved the directional performance measure for time series data, it can be clearly seen that wavelet denoising has reduced the accuracy of directional forecast. This is due to the fact that the last few values of the denoised time series are chaotic due to real market conditions. Wavelet transform cannot remove the noise of the values at the edge of the time series. Forecast should be done with those values at every step. Therefore noisy wavelet values at the edge have misled the accuracy of the forecast.

SVM-wavelet model has performed better than pure SVM only when the inputs are past time series data. Again the forecast with moving average inputs is further derogated by wavelet decomposition and wavelet noise reduction. Integration of wavelet transform further increased the error due to the above-mentioned reason.

3.2.2 Importance of the multistep ahead forecast

Even though pure SVM model has shown great accuracy in one step ahead forecasting of moving averages, one step ahead forecasting of moving average data cannot directly used to trade in real markets. It is because of the lag which is an undesirable property of moving average indicators. Therefore one-step forecast accuracy of moving average indicators has no use in real trading systems. However, if the moving average is shifted backwards, the lag will be removed and the cost for removing lag will be a multistep ahead forecast. Chaotic values of the edge of the wavelet coefficients can also be removed by going through same procedure. Again multistep ahead forecast will be needed in order to eliminate the lag. Results of the multistep ahead forecast can be directly used for high frequency trading in real financial markets

3.2.3 Result of multistep ahead forecast.

Results given in the Table 2, shows that the proposed model has outperformed both Pure SVM model and wavelet transformed model in both MSE and D_stat in multistep ahead forecast. Table 2 shows the results for 5 step ahead forecast which was the best performed among multistep forecast. Directional accuracy and MSE of the pure SVM has greatly reduced in the multi-step ahead forecast. Elimination of chaotic values of the wavelet decomposition leads to better directional accuracy of SVM-wavelet model with time series data. Even though 30 min moving average has led to better performance of the model, large period of averaging may has the disadvantage of missing sharp peaks. Thus selection of moving average should be optimized along with the profit of the system.

4 CONCLUSION

This study propose a reliable financial forecasting model by integrating wavelet transform k-means clustering and support vector machine. Even though wavelet transform isn't suitable for single step ahead forecast, it can be highly effective with multistep ahead forecast. Proposed model has the ability to forecast multi step ahead values in with great accuracy. Simple moving average with wavelet noise reduction has over performed other two types of input

Table 1. Single step ahead forecast

Model	Time series data		Simple Moving average		Exponential moving average	
	Direct	Wavelet denoising	Direct	Davelet denoising	Direct	Wavelet denoising
Pure SVM	MSE:1.2278*10e-7 D_stat:42%	MSE:1.2463*10e-7 D_stat:48%	Range:7 MSE:8.3206*10e-9 D_stat:79% Range:30 MSE:8.0944*10e-9 D_stat: 90%	Range:7 MSE:9.3827*10e-9 D_stat:77% Range:30 MSE:8.5179*10e-9 D_stat:87%	Range:7 MSE:9.2117*10e-9 D_stat:71% Range:30 MSE:9 .0204*10e-9 D_stat: 82%	Range:7 MSE:9.0384*10e-9 D_stat:68% Range:30 MSE:7.7411*10e-9 D_stat:84%
SVM-Wavelet model	MSE:3.335*10e-7 D_stat:51%	MSE:5.4623*10e-8 D_stat:64%	Range:7 MSE:2.076*10e-8 D_stat:76% Range:30 MSE:8.2192*10e-9 D_stat:88%	Range:7 MSE:2.3938*10e-8 D_stat:77% Range:30 MSE:1.4058*10e-8 D_stat:88%	Range:7 MSE:1.3290*10e-8 D_stat:70% Range:30 MSE:3.8440*10e-9 D_stat:81%	Range:7 MSE:1.2873*10e-9 D_stat:66% Range:30 MSE:2.14331*10e-9 D_stat:82%
Proposed model	MSE:1.032*10e-7 D_stat:54%	MSE:1.3623*10e-8 D_stat:71%	Range:7 MSE:2.1569*10e-9 D_stat:79% Range:30 MSE:1.2653*10e-9 D_stat:89%	Range:7 MSE:2.5692*10e-9 D_stat:78% Range:30 MSE:1.3506*10e-9 D_stat:89%	Range:7 MSE:2.3526*10e-9 D_stat:71% Range:30 MSE:1.255*10e-10 D_stat:82%	Range:7 MSE:1.9348*10e-10 D_stat:70% Range:30 MSE:0.8047*10e-10 D_stat:83%

Table 2. Multi step ahead forecast (5 steps)

Model	Time series data		Simple Moving average		Exponential moving average	
	Direct	Wavelet denoising	Direct	Wavelet denoising	Direct	Wavelet denoising
Pure SVM	MSE: 1.2658*10e-6 D_stat:44%	MSE: 9.5684*10e-7 D_stat:60%	Range:7 MSE: 1.5437*10e-6 D_stat:65% Range:30 MSE: 1.3268*10e-6 D_stat: 79%	Range:7 MSE: 9.3087*10e-7 D_stat:72% Range:30 MSE: 9.0026*10e-7 D_stat:82%	Range:7 MSE: 1.6789*10e-6 D_stat:63% Range:30 MSE: 1.4869*10e-6 D_stat: 77%	Range:7 MSE: 9.7831*10e-7 D_stat:72% Range:30 MSE: 9.0865*10e-7 D_stat:80%
SVM-wavelet model	MSE: 2.5684*10e-6 D_stat:49%	MSE: 8.4568*10e-7 D_stat:78%	Range:7 MSE: 2.4561*10e-7 D_stat:80% Range:30 MSE:8.2192*10e-8 D_stat:85%	Range:7 MSE: 1.2986*10e-7 D_stat:81% Range:30 MSE: 2.5687*10e-8 D_stat:87%	Range:7 MSE: 2.3658*10e-7 D_stat:79% Range:30 MSE:3.5842 *10e-8 D_stat:84%	Range:7 MSE: 1.96952*10e-7 D_stat:81% Range:30 MSE: 1.8965*10e-8 D_stat:85%
Proposed model	MSE:5.6938 *10e-7 D_stat:52%	MSE: 2.3568*10e-8 D_stat:85%	Range:7 MSE: 5.5147*10e-8 D_stat:81% Range:30 MSE: 9.956*10e-9 D_stat:91%	Range:7 MSE: 2.3614*10e-8 D_stat:85% Range:30 MSE: 8.7695*10e-9 D_stat:93%	Range:7 MSE:6.5387 *10e-8 D_stat:80% Range:30 MSE: 1.3568*10e-9 D_stat:87%	Range:7 MSE:3.068 *10e-8 D_stat:84% Range:30 MSE: 1.069*10e-9 D_stat:89%

based forecasts. Model is tested by simulating real market conditions. Hence it is suitable for decision making in a real trading system. Performance of the model can be further improved by optimizing noise reduction level and threshold, number of clusters, multi-step size, moving average span and SVM parameters.

REFERENCES

[1] Yu, L., Wang, S. & Lai, K.K., 2005. Adaptive smooth Neural Network in foreign exchange rate forecasting. *LNCS*, p.523 – 530.

[2] Roshan, W.D.S., Gopura, R.A.R.C. & Jayasekara, A.G.B.P., 2011. Financial forecasting based on artificial neural networks: Promising directions for modeling. *6th IEEE International Conference on Industrial and Information Systems (ICIIS)*, pp.322 - 327.

[3] Vapnik, V.N., 1995. *The nature of statistical learning theory*. USA: Springer.

[4] Hayking, S., 1999. Committee Machines. In *Neural Networks: A comprehensive foundation, 2nd ed.* NJ, USA: Prentice Hall. Ch. 2.

[5] Coifman, R. & Donoho, D.L., 1995. Translation invariant de-noising. *Lecture Notes in Statistics*, p.125–150.

[6] Cover, T.M., 1965. Geometrical and statistical properties of systems of linear inequalities with application in pattern recognition. *IEEE Transactions on Electronic Computers*, EC-14, pp.326-34.

[7] Hayking, S., 1999. Learning processes. In *Neural Networks: A comprehensive foundation, 2nd ed.* NJ, USA: Prentice Hall. Ch. 2. pp.97-98.

Medical image diagnosis of liver cancer by feedback GMDH-type neural network using knowledge base

Tadashi Kondo[1], Junji Ueno[2], and Shoichiro Takao[3]

[1,2,3]Graduate School of Health Sciences
3-18-15 Kuramoto-cho Tokushima 770-8509 Japan
(Tel: +88-633-9024, Fax: +88-633-9024)
[1]kondo@medsci.tokushima-u.ac.jp

Abstract: A revised Group Method of Data Handling (GMDH)-type neural network algorithm using knowledge base for medical image diagnosis is proposed and is applied to medical image diagnosis of the liver cancer. In this algorithm, the knowledge base for medical image diagnosis is used for organizing the neural network architecture for medical image diagnosis. Furthermore, the revised GMDH-type neural network algorithm has a feedback loop and can identify the characteristics of the medical images accurately using feedback loop calculations. It is shown that the revised GMDH-type neural network is accurate and a useful method for the medical image diagnosis of the liver cancer.
Keywords: Neural networks, GMDH, Medical image diagnosis, Artificial intelligence.

1. INTRODUCTION

The conventional GMDH-type neural network algorithms were proposed in our early works [1],[2]. In this paper, a revised GMDH-type neural network algorithm using knowledge base is proposed and is applied to the medical image diagnosis of liver cancer. In this revised GMDH-type neural network, the knowledge base for medical image diagnosis is used for organizing the neural network architecture. In the knowledge base system, the various kinds of the knowledge such as the medical knowledge, the image processing knowledge and others, are memorized and these knowledge are used to organize the neural network architecture. Furthermore, the revised GMDH-type neural network algorithm has a feedback loop and can identify the characteristics of the medical images accurately using feedback loop calculations. The neural network architecture is selected from three types of neural network architectures such as the sigmoid function type neural network, the radial basis function (RBF) type neural network and the polynomial type neural network using the knowledge base system. Furthermore, the structural parameters such as the number of feedback loops, the number of neurons in the hidden layers and the relevant input variables are automatically selected using heuristic self-organization method [3],[4], which is a kind of evolutional computation, so as to minimize the prediction error criterion defined as Akaike's information criterion (AIC) or Prediction Sum of Squares (PSS)[5].

2. FEEDBACK GMDH-TYPE NEURAL NETWORK USING KNOWLEDGE BASE

Neural network architecture is shown in Fig.1. In this algorithm, the neural network architecture is automatically organized using the knowledge base. The rules in the knowledge base are classified to the following five types.

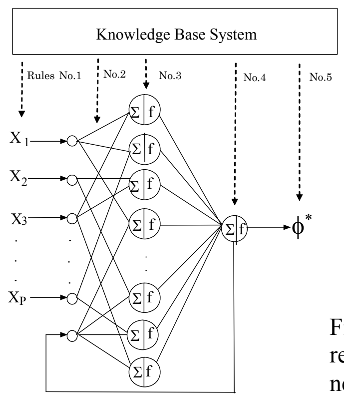

Fig.1 Architecture of revised GMDH-type neural network

2.1 Knowledge base

(1) First type rules.

These rules are concerned with the pre-processing of the original image such as the filtering, the thresh hold processing and so on and the image characteristics of the original image are extracted.

(2) Second type rules.

In the GMDH-type neural network, all combinations of the input variables are generated and the architecture of the neural network is organized using only selected combinations so as to minimize the prediction errors defined as AIC or PSS. In the revised GMDH-type neural network, the combinations of the input variables are controlled using the rules of the knowledge base.

(3) Third type rules.

In the conventional GMDH-type neural network [2], the following seven neuronal architectures are used for organizing neural network to fit the complexity of the nonlinear system. Here, u_i (i =1,2,…,p) and u_j (j =1,2,…,p) show the input variables of the neurons and p is the number of input variables. θ_1=1 and w_i (i=0,1,2,⋯) are weights between the neurons.

1) First type neuron

Σ: (Nonlinear function) $z_k= w_1u_i+w_2u_j+w_3u_iu_j+w_4u_i^2+w_5u_j^2+w_6u_i^3+w_7u_i^2u_j+w_8u_iu_j^2+w_9u_j^3 - w_0\theta_1$ (1)

f : (Nonlinear function) $y_k= 1 / (1+\exp(-z_k))$ (2)

2) Second type neuron

Σ: (Linear function) $z_k= w_1u_1+w_2u_2+w_3u_3+\cdots+w_ru_r - w_0\theta_1$ ($r<p$) (3)

f : (Nonlinear function) $y_k= 1 / (1+\exp(-z_k))$ (4)

3) Third type neuron

Σ: (Nonlinear function) $z_k= w_1u_i+w_2u_j+w_3u_iu_j+w_4u_i^2+w_5u_j^2+w_6u_i^3+w_7u_i^2u_j+w_8u_iu_j^2+w_9u_j^3 - w_0\theta_1$ (5)

f : (Nonlinear function) $y_k= \exp(-z_k^2)$ (6)

4) Fourth type neuron

Σ: (Linear function) $z_k= w_1u_1+w_2u_2+w_3u_3+\cdots+w_ru_r - w_0\theta_1$ ($r<p$) (7)

f : (Nonlinear function) $y_k= \exp(-z_k^2)$ (8)

5) Fifth type neuron

Σ: (Nonlinear function) $z_k= w_1u_i+w_2u_j+w_3u_iu_j+w_4u_i^2+w_5u_j^2+w_6u_i^3+w_7u_i^2u_j+w_8u_iu_j^2+w_9u_j^3 - w_0\theta_1$ (9)

f : (Linear function) $y_k= z_k$ (10)

6) Sixth type neuron

Σ: (Linear function) $z_k= w_1u_1+w_2u_2+w_3u_3+\cdots+w_ru_r - w_0\theta_1$ ($r<p$) (11)

f : (Linear function) $y_k= z_k$ (12)

7) Seventh type neuron

Σ: (Linear function) $z_k= w_1u_1+w_2u_2+w_3u_3+\cdots+w_ru_r - w_0\theta_1$ ($r<p$) (13)

f : (Nonlinear function) $y_k= a_0+a_1z_k+a_2z_k^2+\cdots+a_mz_k^m$ (14)

In the revised GMDH-type neural network, many kinds of the functions can be used as the neuronal architecture and the desirable neuronal architecture in the hidden layer is selected using the third type rules according to the medical or the physical knowledge.

When these rules concerned with the neuronal architecture are not obtained previously, the optimum neuronal architectures fitting the complexity of the nonlinear system are selected automatically so as to minimize the prediction error defined as AIC or PSS.

(4) Fourth type rules.

The neuronal architecture in the output layer is selected using the fourth type rules. When these rules concerned with the neuronal architecture are not obtained previously, the optimum neuronal architectures is selected automatically so as to minimize AIC or PSS.

(5) Fifth type rules.

These rules are concerned with the post-processing of the output images of the neural network. The post-processing such as the closing, the opening and so on are selected using the fifth type rules.

In this paper, we apply the revised GMDH-type neural network to the medical image diagnosis of the liver cancer and the following rules are used in this application.

a) Second type rules.

We do not make the limitations in the combinations of the input variables.

b) Third type rules.

The first type neuronal architecture is used in the hidden layer.

c) Fourth type rules.

The second type neuronal architecture is used in the output layer.

The architecture of the revised GMDH-type neural network is produced concretely using these rules as follows:

2.2 First loop calculation

First, all data are set to the training data. In this study, we used PSS as the prediction error criterion.

(1)Input layer

$u_j=x_j$ (j=1,2,⋯,p) (15)

where x_j (j=1,2,⋯,p) are the input variables of the system, and p is the number of input variables. In the input layer, input variables are set to the output variables.

(2)Hidden layer

All combinations of two variables (u_i,u_j) are generated. For each combination, the neuronal architecture is described by the following equations:

Σ: (Nonlinear function) $z_k= w_1u_i+w_2u_j+w_3u_iu_j+w_4u_i^2+w_5u_j^2+w_6u_i^3+w_7u_i^2u_j+w_8u_iu_j^2+w_9u_j^3 - w_0\theta_1$ (16)

f : (Linear function) $y_k= 1 / (1+\exp(-z_k))$ (17)

where θ_1 =1 and w_i (i=0,1,2,⋯,9) are weights between the input and hidden layer. This neuron is equal to the first type neuron of the conventional GMDH-type neural network. The weights w_i (i=0,1,2,⋯,9) are estimated by using the multiple regression analysis.

This procedure is as follows:

First, the values of z^{**} are calculated by using the following equation:

$$z_k^{**} = \log_e\left(\frac{\phi'}{1-\phi'}\right) \tag{18}$$

where ϕ' is the normalized output variable whose values are between 0 and 1. Then the weights w_i (i=0,1,2,⋯,9) are estimated by using the stepwise regression analysis which selects useful input variables by using the PSS[5].

From these generated neurons, L neurons which minimize the PSS are selected. The output values (y_i) of L

The Seventeenth International Symposium on Artificial Life and Robotics 2012 (AROB 17th '12),
B-Con Plaza, Beppu, Oita, Japan, January 19-21, 2012

selected neurons are set to the input values (u_i) of the neuron in the output layer.

$$u_i = y_i \qquad (i=1,2,\ldots,L) \tag{19}$$

(3)Output layer

The inputs (u_i) of the neuron in the output layer are combined by the following linear function.

$$z = w_0 + \sum_{i=1}^{L} w_i u_i \tag{20}$$

The useful intermediate variables (u_i) are selected by using the stepwise regression analysis in which PSS is used as the variable selection criterion. Then, the estimated output values (z) is used as the feedback value and it is combined with the input variables in the next loop calculation.

2.3 Second and subsequent loop calculations

First, the estimated output value (z) is combined with the input variables and all combinations between the estimated output value (z) and the input variables are generated. The same calculation as the first feedback loop is carried out for each combination. When PSS value of the linear function in (20) does not decrease, the loop calculation is terminated. The output values of the neural network (ϕ^*) are calculated from z as follows:

$$\phi^* = 1 / (1+\exp(-z)) \tag{21}$$

So, in the last feedback loop, the neuronal architecture becomes as follows:

Σ: (Nonlinear function) $\quad z = w_0 + \sum_{i=1}^{L} w_i u_i \quad (22)$

f : (Nonlinear function) $\quad \phi^* = 1 / (1+\exp(-z)) \quad (23)$

This neuron equal to the second type neuron of the conventional GMDH-type neural network.

By using these procedures, the revised GMDH-type neural network can be organized.

3. APPLICATION TO MEDICAL IMAGE DIAGNOSIS OF LIVER CANCER

Multi-detector row CT (MDCT) images of the liver are used in this study.

3.1 Extraction of the candidate image regions of the liver cancer.

A liver image shown in Fig. 2 was used for organizing the revised GMDH-type neural network. By the first type rules, we used the statistics of the image densities and x and y coordinates in the neighboring regions, the $N \times N$ pixel regions, as the image features. As the results, only five parameters namely, mean, standard deviation, variance and x and y coordinates were selected as the useful input variables. The output value of the neural network was zero or one. When $N \times N$ pixel region was contained in the liver region, the neural network set the pixel value at the center of the $N \times N$ pixel region to one and this pixel was shown as the white point. The neural networks were organized when the values of N were from 3 to 10. It was determined that when N was equal to 5, the neural network architecture had the smallest recognition error. Five useful neurons were selected in each hidden layer. Figure 3 shows the variation of PSS values in the layers. The calculation of the revised GMDH-type neural network was terminated in the eighth feedback loop. The PSS value in the first feedback loop was not small but the PSS value was decreased gradually through the feedback loops and the small PSS vale was obtained in the eighth feedback loop. The revised GMDH-type neural network outputs the liver image (Fig.4) and the first post-processing analysis of the liver image was carried out using the fifth type rules. In the first post-processing of the output image, the small isolated regions were eliminated and the outlines of the liver regions were expanded outside by N/2 pixels. Figure 5 shows the output image after the first post-processing. The output image after the first post-processing was overlapped to the original image (Fig.2) in order to check the accuracy of the image recognition as shown in Fig.6. The recognized liver regions are accurate. The liver regions were extracted from the original image using the output image. Figure 7 shows the extracted image of the liver. The second post-processing such as the closing was carried out using the fifth type rules and the liver region which contained the abnormal regions was obtained as shown in Fig.8. Figure 9 shows the extracted image of the liver. The candidate image region of the liver cancer were extracted from Fig.9 using Fig.7 and shown in Fig.10.

Fig.2 Original image

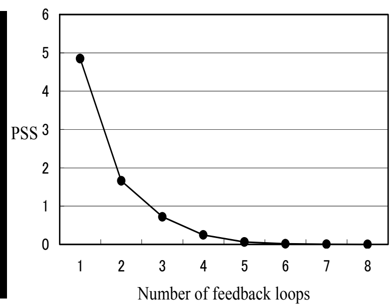

Fig.3 Variation of PSS

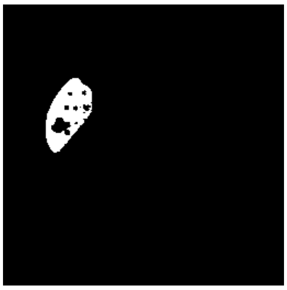

Fig.4 Output image of the neural network

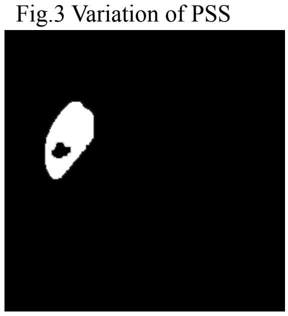

Fig.5 Output image after the first post-processing

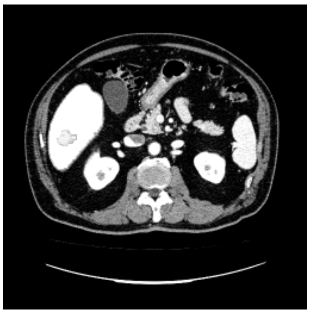

Fig.6 Overlapped image

Fig.7 Extracted image (1)

Fig.8 Output image after the second post-processing

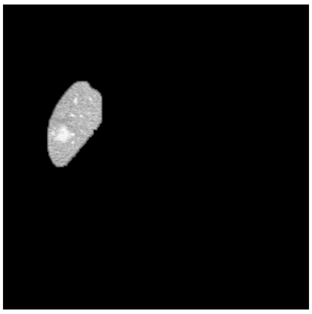

Fig.9 Extracted image (2)

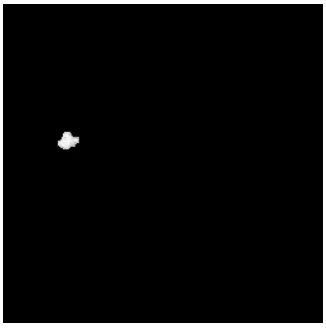

Fig.10 Candidate image region of liver cancer

3.2 Recognition results of the conventional neural network trained using the back propagation algorithm

A conventional neural network trained using the back propagation algorithm was applied to the same recognition problem and the recognition results were compared with the results obtained using the revised GMDH-type algorithm. The conventional neural network had a three layered architecture and the same five input variables were used in the input layer. The learning calculations of the weights were iterated changing structural parameters such as the number of neurons in the hidden layer and the initial values of the weights. The output images, when the numbers of neurons in the hidden layer (m) are 5, 7 and 9, are shown in Fig.11. These images contain more regions which are not part of the liver. Note that, in case of the conventional neural network, we obtain many different output images for various structural parameters of the neural network and many iterative calculations of the back propagation are needed for various structural parameters in order to find more accurate neural network architecture.

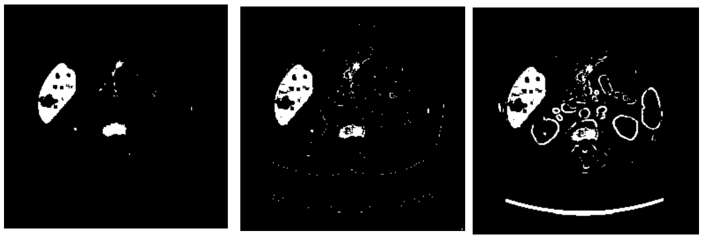

(a) m=5 (b) m=7 (c) m=9

Fig.11 Output images of the conventional sigmoid function neural network

4. CONCLUSION

In this paper, the revised GMDH-type neural network algorithm using knowledge base for the medical image diagnosis was proposed and it was applied to the medical image diagnosis of the liver cancer and the results of revised GMDH-type neural network were compared with those of the conventional sigmoid function neural network trained using the back propagation algorithm. The revised GMDH-type neural network architecture fitting the characteristics of the medical images is organized using the knowledge base for the medical image diagnosis. It was shown that the revised GMDH-type neural network algorithm was accurate and a useful method for the medical image diagnosis of the liver cancer.

ACKNOWLEDGEMENT

This work was supported by (JSPS) KAKENHI 21560428.

REFERENCES

[1] T. Kondo, J. Ueno, "Logistic GMDH-type neural network and its application to identification of X-ray film characteristic curve", *Journal of Advanced Computational Intelligence and Intelligent Informatics,* vol.11, no.3, pp.312-318, 2007.

[2] T. Kondo, "GMDH neural network algorithm using the heuristic self-organization method and its application to the pattern identification problem", *Proc. of the 37th SICE Annual Conference,* pp.1143-1148, 1998.

[3] S.J. Farlow ed., *Self-organizing methods in modeling, GMDH-type algorithm*, Marcel Dekker, Inc., New York, 1984.

[4] A.G. Ivakhnenko, "Heuristic self-organization in problems of engineering cybernetics", *Automatica,* Vol.6, No.2, pp.207-219, 1970.

[5] H. Tamura and T.Kondo, "Heuristics free group method of data handling algorithm of generating optimum partial polynomials with application to air pollution prediction", *Int. J. System Sci.*, Vol.11, No.9, pp.1095-1111, 1980.

The Seventeenth International Symposium on Artificial Life and Robotics 2012 (AROB 17th '12),
B-Con Plaza, Beppu, Oita, Japan, January 19-21, 2012

Large database analysis of out-of-hospital cardiac arrest using ensembled neural networks

Jiann-Shing Shieh[1,5], Yuan-Jang Jiang[1], Huei- Ming Ma[2], Wei-Zen Sun[3], Guan-Wu Jang[4]

[1]*Department of Mechanical Engineering, Yuan Ze University, Taiwan*

[2]*Department of Emergency Medicine, College of Medicine, National Taiwan University, Taiwan*

[3]*Department of Anesthesiology, College of Medicine, National Taiwan University, Taiwan*

[4]*Fire Department, Emergency and Rescue Section, New Taipei City Government, Taiwan.*

[5]*Center for Dynamical Biomarkers and Translational Medicine, National Central University, Taiwan*

(Tel: 886-3-463-8800 ext. 2470; Fax : 886-3-455-8013)

(jsshieh@saturn.yzu.edu.tw)

Abstract: The purpose of this study is to use seven different sensitivity analyses to find out the important variables to establish a comprehensive and objective assessment method. After pre-filtering, we obtained 4095 data for building this ensembled neural networks **(**ENN) model. The data has been divided into 60% data for training, 20% data for validation, and 20% data for testing. The eleven inputs, including response time, on-scene time, patient transfer time, time to cardiopulmonary resuscitation (CPR), CPR on the scene, using drugs, age, gender, using airway, using automated external defibrillator (AED), and trauma type, and one output variable have been selected as ENN model structure. The results have been shown CPR on the scene, using drugs, on-scene time, and using airway in the top four of these 11 important variables. Moreover, these four variables have also been shown significant differences when we use traditional one variable statistics analysis for these variables.

Keywords: Emergency medical system, ensembled neural networks, sensitivity analysis

I. INTRODUCTION

Fire Department, New Taipei City Government started to build a new system of recording pre-hospital cardiopulmonary stop patients' data in 2007. Until June 2011, the system has collected more than 9,000 data of the OHCA (out-of-hospital cardiac arrest) patients, including patients' basic characteristics, emergency treatment, the basic information of ambulance staff and patients' recovery treatment. Therefore, this study will target on analyzing out-of-hospital cardiac arrest patients data, and focus on the distribution of the incident, treatment, and the relationship between survival rate and the relevant characteristics of OHCA patients. Because of many uncertain factors, irregular non-linear characteristics, and the complex relationship of variables, it is difficult to use traditional mathematical equations and analytical methods. Hence, it must more carefully select the characteristics of the method. According to our previous studies [1-3], artificial neuronal network (ANN) is one of the most popular systems to deal with the nonlinear and non-stationary problems. It can be used to model the complex relationships between the inputs and outputs data of the system. An ensembled neural network (ENN) is a learning paradigm where a collection of a number of neural networks is trained for the same task. One theory behind using ENN is that several less accurate networks that are diverse can be combined into a more-accurate ENN. Moreover, we use seven different sensitivity analyses to find out the important variables to establish a comprehensive and objective assessment method. Then, we can understand which variables cause the survival rate or Glasgow Coma Scale (GCS) changes by build a model of ENN.

II. METHODOLOGY

(A) Choosing variables

According to previous research [3,4] and the information recorded in the OHCA patients in Fire Department of New Taipei City Government, the eleven inputs, including response time, on-scene time [3], patient transfer time [4], time to cardiopulmonary resuscitation (CPR), CPR on the scene, using drugs, age, gender, using airway, using automated external defibrillator (AED) [5], and trauma type, and one output variable have been selected as ENN model structure.

(B) Data pre-processing

Although we have 9000 patients in the database, we have only 4,095 complete data in the database after data cleaning. Then we build an ensembled neural network. The data is divided into three parts which were 60% data for training, 20% for validation, 20% for testing as shown in Fig. 1. Testing data do not need to pass through neural network to learn, so we do not sample data by random. The remaining 80% data are divided into 60% of training data and 20% validation data by random sampling. Then we selected topology structure of neural network model, and trial and error can help us for screening each structure [6]. There is a classic topology called pyramid. In many literature records, this method has better convergence and predictability. The pyramid means that the neurons of input layer are more than the neurons of hidden layer, and the neurons of hidden layer is more than the neurons of output layer [7].

(C) ROC analysis

We don't know the performances of model after building neural network model. So we applied ROC (receiver operating characteristic) curve analysis to find out the threshold at each model and estimate the discrimination power of the prediction models. We calculated the sensitivity (SEN), specificity (SPE), positive prediction value (PPV), and negative prediction value (NPV) of each model at the best threshold. Then we use this threshold to separate 0 and 1 for the each output that 0 is death and 1 is alive. Finally, we calculated total accuracy as the discrimination power of the prediction models.

(D) Ensembled neural network model

Although neural network is powerful, it's unstable due to random initial weight problems. Scholars have criticized for this long time. Ensembled neural networks are built by the group of neural networks to solve this problem. The topology structure of ENN is chosen one hidden layer with 8 nodes via trial-and-error method so that we choose 11-8-1 structure for this model. Moreover, the one output variable has been selected 5 different conditions (i.e., 2hr or 24 hr survival rate, or 24hr, 48hr, and 72 hr GCS). Each training data and validation data are used to train 20 networks with different initial weights. Then, 100 artificial neural networks (ANN) have been trained for each network. The learning effect of each network is tested by the testing data to examine the generalization of the network, and the best network in each training data and validation data is selected to be combined into the ensembled model [8, 9] as shown in Fig. 1.

(E) Sensitivity analysis

Sensitivity analysis can find the important parameters in the model. It works by observing the input variables how to impact on the output. We use seven different methods for sensitivity analysis. Firstly. We use the Morris method which is a randomized design that has proved to be an efficient and reliable technique to identify and rank important variables [10, 11]. Secondly, there are three methods to improve Morris method which are set the minimum, maximum, and mean values, while other variables have not changed. The root means square error of the network is assessed. Then the changed of RMSE is calculated. We can rank the input variables by the changed of RMSE. The more important variable is bigger changed. Finally, the rest three methods which are Perturb's method [13], connection weights [14], and Garson algorithm [15], can be seen more details in our previous study [16].

III. RESULTS

We have built five ensembled neural network models for different outputs. After building this ENN model, we use testing data to calculate this five outputs accuracy and the results show the accuracy is 68%, 76%, 80%, 86%, and 89%. The highest accuracy is 72 GCS model of prediction, and we use this model to do seven different sensitivity analysis. Finally, we use vote method to sum these 7 sensitivity methods via adding together the index number of ranked variables in seven methods of sensitivity analysis, and the more important variable has a smaller vote number. The results have been shown CPR on the scene, using drugs, on-scene time, and using airway in the top four of these 11 important variables as shown in Table 1. Moreover, these four variables have also been shown significant differences when we use traditional one variable statistics analysis for these variables.

IV. CONCLUSION

In conclusion, although the results of top four important inputs are consistent with one variable statistics analysis, the result of sensitivity analysis still has not been verified by experts. Hence, a comprehensive discussion with medical doctors who are experts in emergency medical system is still needed, perhaps to refine the ENN model or methods of sensitivity analysis, and certainly to see how widely the model and these methods are applicable.

V. ACKNOWLEDGEMENTS

The authors wish to thank the National Science Council (NSC) of Taiwan (Grant Number NSC 99-2221-E-155-046-MY3) and the Center for Dynamical Biomarkers and Translational Medicine (Grant Number: NSC 99-2911-I-008-100) for supporting this research.

VI. REFERENCES

[1]. Abbod MF, Cheng KY, Cui XR, Huang SJ, Han YY, Shieh JS (2011), Ensembled neural networks for brain death prediction for patients with severe head injury. Biomedical Signal Processing and Control 6: 414-421.

[2]. Liu Q, Cui XR, Abbod MF, Huang SJ, Han YY, Shieh JS (2011), Brain death prediction based on ensembled artificial neural networks in neurosurgical intensive care unit. Journal of the Taiwan Institute of Chemical Engineers 42 (1): 97-107.

[3]. Spaite DW, Valenzuela TD, Meislin HW, Criss EA, Hinsberg P (1993), Prospective validation of a new model for evaluating emergency medical services systems by in-field observation of specific time intervals in prehospital care. Annals of Emergency Medicine 22(4): 638-645.

[4]. Ramanujiam P, Castillo E, Patel E, Vilke G, Wilson MP, Dunford JV (2009), Pre-hospital transport time interval for acute stroke patients. The Journal of Emergency Medicine 37(1): 40-45.

[5]. Balady GJ, Chaitman B, Foster C, Froelicher E, Gordon N, Van Camp S (2002), Automated external defibrillators in health/fitness facilities supplement to the AHA/ACSM Recommendations for Cardiovascular Screening, Staffing, and Emergency Policies at Health/Fitness Facilities. Circulation 105(9): 1147-1150.

[6]. White DA, Sofge DA (1992), Handbook of intelligent control: Neural, Fuzzy, and Adaptive Approaches, New York, NY: Van Nostrand Reinhold.

[7]. Upegui A, Sanchez E (2005), An FPGA platform for on-line topology exploration of spiking neural networks. Microprocessors and Microsystems 29(5): 211-223.

[8]. Hansen LK, Salamon P (1990), Neural Network Ensemble. IEEE Transactions on Pattern Analysis and Machine Intelligence 12(10): 993-1001.

[9]. Krogh A, Vedelsby J (1995), Neural network ensembles, cross validation, and active learning. In: Tesauro G, Touretzkey D, Leen T eds. Advances in Neural Information Processing Systems, 7, Cambridge, MA: MIT Press: 231-238.

[10]. Francos A, Elorza FJ, Bouraoui F, Bidoglio G, Galbiati L (2003), Sensitivity analysis of distributed environmental simulation models: understanding the model behaviour in hydrological studies at the catchment scale. Reliability Engineering and System Safety 79(2): 205-218.

[11]. Zador J, Zsely IG, Turanyi T (2006), Local and global uncertainty analysis of complex chemical kinetic systems. Reliability Engineering and System Safety 91(10): 1232-1240.

[12]. Gevrey M, Dimopoulos I, Lek S (2003), Review and comparison of methods to study the contribution of variables in artificial neural network models. Ecological Modelling 160: 249-264.

[13]. Scardi M, Harding LW (1999), Developing an empirical model of phytoplankton primary production: a neural network case study. Ecological Modelling 120: 213-223.

[14]. Olden JD, Jackson DA (2002), Illuminating the "black box":understanding variable contributions in artificial neural networks. Ecological Modelling 154:135-150.

[15]. Garson GD (1991), Interpreting neural-network connection weights. Artif Intell Expert 6: 47-51.

[16]. Cui XR, Abbod MF, Liu Q, Shieh JS, Chao TY, Hsieh CY, Yang YC (2011), Ensembled artificial neural networks to predict the fitness score for body composition analysis. The Journal of Nutrition, Health and Aging 15 (5): 341-348.

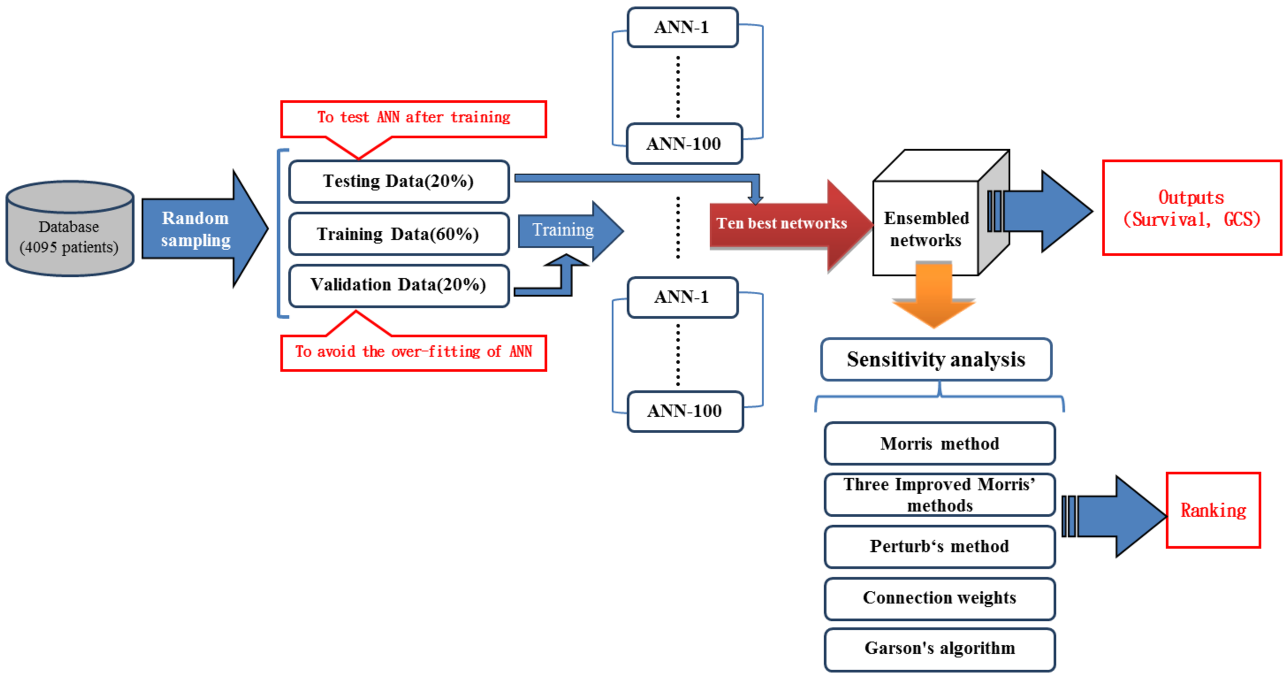

Fig. 1 The flow diagram of ensemble neural networks and sensitivity analysis

Table 1 The ranking of input variables according to seven sensitivity analyses
(Note of Table: SA means sensitive analysis)

Input Variables	SA (Morris Method)	SA_min	SA_mean	SA_max	SA_noise (Perturb Method)	Connect weights	Garson's algorithm	Ranking	One variable statistics analysis
Response time	5	8	7	10	4	7	4	7	$P > 0.05$
On-Scene time	1	4	9	6	1	3	10	3	$P < 0.05$
Patient transfer time	6	7	6	3	9	4	6	6	$P > 0.05$
Time to CPR	11	2	1	1	10	4	11	5	$P > 0.05$
CPR on the scene	3	1	2	2	8	1	1	1	$P < 0.05$
Using drugs	2	3	5	5	6	7	5	2	$P < 0.05$
Age	9	10	11	7	5	4	8	10	$P < 0.05$
Gender	7	6	10	10	3	10	2	9	$P > 0.05$
Using Airway	8	9	3	7	2	2	7	4	$P < 0.05$
Using AED	10	11	8	3	6	9	9	11	$P < 0.05$
Trauma type	4	5	4	9	10	11	3	8	$P < 0.05$

Analog circuit for detecting position of smell based on pheromone source location of silkmoth

Masaki Ihara[1] and Kimihiro Nishio[1]

[1] Tsuyama National College of Technology, 624-1, Numa, Tsuyama, Okayama, 708-8509, Japan
(Tel: 81-868-24-8266)

[1]nishio@tsuyama-ct.ac.jp

Abstract: In this study, we proposed an analog complementary metal oxide semiconductor (CMOS) circuit based on the pheromone source location of the silkmoth. The analog circuit is achieved by the circuit for the threshold processing using the operational amplifier. Since the proposed circuit consists of the smell sensor, five metal oxide semiconductor (MOS) transistors and four resistors, the proposed circuit is simple structure. The test circuit was fabricated on the breadboard by discrete MOS transistors and resistors. The measured results of the test circuit showed that the output voltage becomes large when the smell sensor detects the smell of the target. The output voltage of the test circuit was approximately equal to the output signal of the model based on the pheromone source location of the silkmoth. The measured results showed that the proposed circuit can control the motor. In the future, the novel compact target tracking sensor can be achieved by applying the proposed circuits based on the pheromone source location of the silkmoth and the previous circuit based on the biological vision and auditory systems.

Keywords: analog circuit, pheromone source location, smell detection

1 INTRODUCTION

It is necessary for robotics system, monitoring system and other systems to process information at high speed. High speed processing is easily achieved in the biological system because the information processing is performed in massively parallel nerve networks with a hierarchical structure.

Recently, the simple complementary metal oxide semiconductor (CMOS) circuit for tracking the target [1]-[3] was proposed based on the biological vision and auditory systems. The proposed circuit can capture and track the target by processing information of the image and the sound. However, the circuit cannot track the target in the case that the information of the image and the sound is not acquired.

In such cases, the animal can track the target by using information of the smell. Recently, the model [4],[5] for detecting the position of the smell of the object was proposed based on the pheromone source location of the silkmoth.

In the case that the silkmoth detects the pheromone, the silkmoth goes straight on toward the pheromone source, the silkmoth is turned zigzag, and the silkmoth revolves around the pheromone source. The model was proposed based on such action pattern.

In this study, we proposed an analog CMOS circuit based on the pheromone source location of the silkmoth. The test circuit was fabricated on the breadboard by discrete MOS transistors and resistors. The measured results of the test circuit showed that the output voltage becomes large when the smell sensor detects the smell of the target. The output voltage of the test circuit was approximately equal to the output signal of the model based on the pheromone source location of the silkmoth.

2 MODEL

We describe in this section the pheromone source location of the silkmoth. It is considered that we can propose simple circuit by mimicking the information processing of the insect brain because the construction of the insect brain is simple.

Figure 1 shows the action pattern of the silkmoth for detecting the pheromone source. The silkmoth has the sensor which responds with the pheromone. The sensor generates the constant voltage (pulsed signal) when the pheromone is detected by the sensor.

When the silkmoth detects the pheromone, the silkmoth goes straight on toward the pheromone source until the position *a*. Other sensor responds with the pheromone when the silkmoth arrive at the position *a*.

In the case that the right sensor responds with the pheromone, the silkmoth turns toward the right. In the

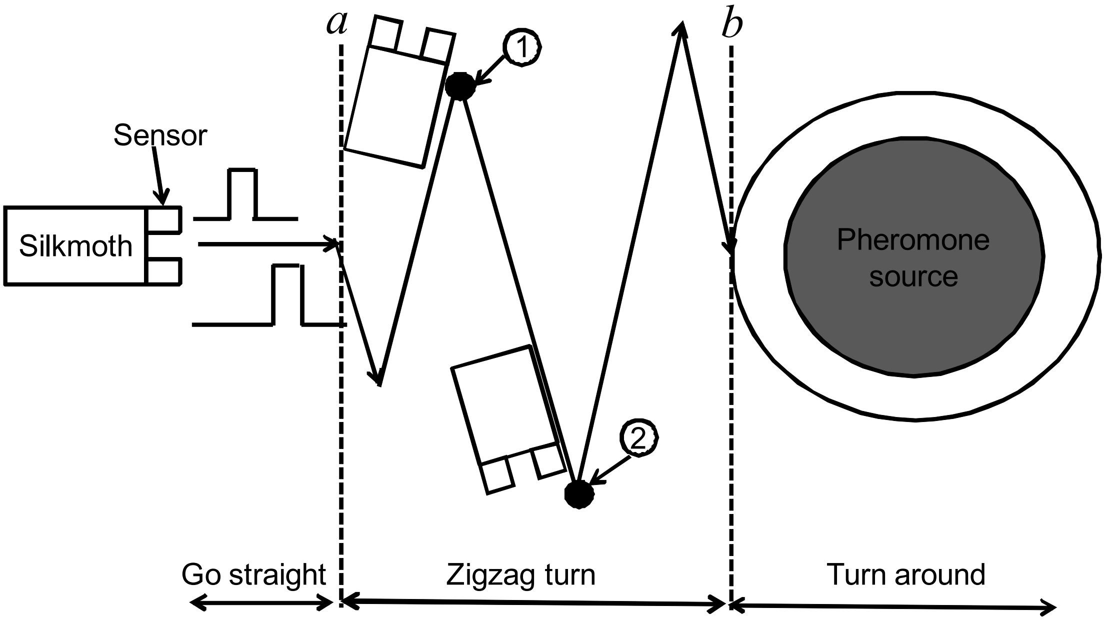

Fig. 1. The action pattern of the silkmoth for detecting the pheromone source

case that the left sensor responds with the pheromone, the silkmoth turns toward the left.

In position 1, the silkmoth turns toward the right since the right sensor responds with the pheromone. In position 2, the silkmoth turns toward the left since the left sensor responds with the pheromone. In the region from position *a* to position *b*, the silkmoth is turned zigzag.

In position *b*, both sensors respond with the pheromone, and the silkmoth detects the pheromone source. Then, the silkmoth revolves around the pheromone sources.

3 CIRCUIT

To realize the action pattern of the silkmoth, we proposed the analog CMOS circuit which outputs the constant voltage (pulsed voltage) when the smell is detected. The proposed circuit is shown in Fig. 2. The analog circuit is achieved by the circuit for the threshold processing using the operational amplifier. Since the proposed circuit consists of the smell sensor, five MOS transistors and four resistors, the proposed circuit is simple structure. The smell sensor is used as the input part. Four resistors are used to set the voltages.

The voltage V_1 is generated by the smell sensor. When the smell sensor detects the smell, V_1 becomes large. The voltage V_2 is set to the constant voltage. V_2 is the threshold voltage.

When V_1 is smaller than V_2, the output voltage V_{out} becomes 0. When V_1 is larger than V_2, V_{out} shows the constant voltage.

Thus, the proposed circuit outputs the constant voltage when the smell sensor detects the smell. By using two proposed circuit, we can develop the compact system which has the same function in Fig. 1.

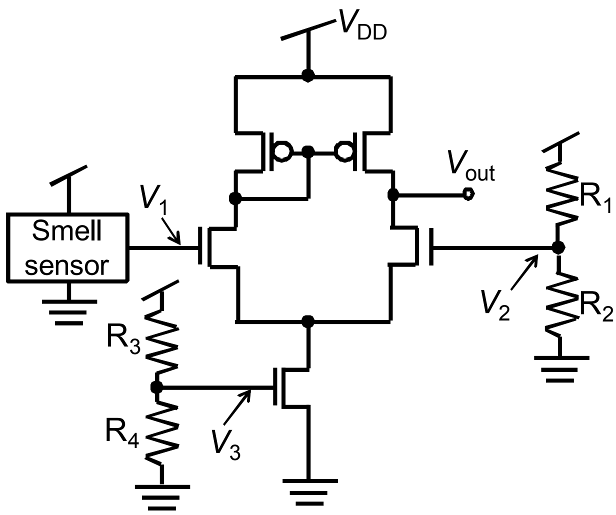

Fig. 2. The proposed circuit

4 MEASURED RESULTS

The test circuit was fabricated on the breadboard by discrete MOS transistors and resistors. Figure 3 shows the photograph of the test circuit. The supply voltage V_{DD} was set to 5 V. By setting to R_1=15 kΩ and R_2=15 kΩ, V_2 was set to 2.5 V. By setting to R_1=3 kΩ and R_2=1 kΩ, V_3 was set to 1.25 V. The ethanol was utilized as the smell source. The distance between the smell sensor and the ethanol was set to 1 m.

Figure 4 shows the output voltage V_{out} of the test circuit. V_{out} becomes the constant voltage (5 V) when the smell sensor detects the smell of the target. The output voltage of the test circuit was approximately equal to the output signal of the model based on the pheromone source location of the silkmoth. Thus, the measured results of the test circuit showed that the proposed circuit can operate normally.

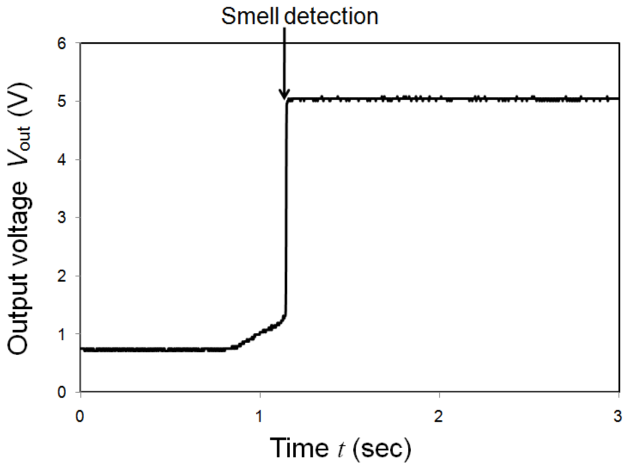

Fig. 4. Measured result of the test circuit

Figure 5 shows the photograph of the test circuit and the motor. The motor is utilized to the system such as the target tracking, mobile robot and others. The motor rotated when the smell sensor detected the smell. It was clarified that the motor can be controlled by the output signal of the proposed circuit.

5 CONCLUSION

We proposed in this study an analog CMOS circuit based on the pheromone source location of the silkmoth. The analog circuit is achieved by the circuit for the threshold processing using the operational amplifier. Since the proposed circuit consists of the smell sensor, five MOS transistors and four resistors, the proposed circuit is simple structure. The smell sensor is input part and four resistors are used to set the voltages. The test circuit was fabricated on the breadboard by discrete MOS transistors and resistors. The measured results of the test circuit showed that the output voltage becomes large when the smell sensor detects the smell of the target. The output voltage of the test circuit was approximately equal to the output signal of the model based on the pheromone source location of the silkmoth. It was clarified from the measured results that the motor can be controlled by the proposed circuit. Thus, we can achieve the novel compact system which has the same functions of the pheromone source location of the silkmoth by using two proposed circuit. In the future, the novel compact target tracking sensor can be achieved by applying the proposed circuits based on the pheromone source location of the silkmoth and

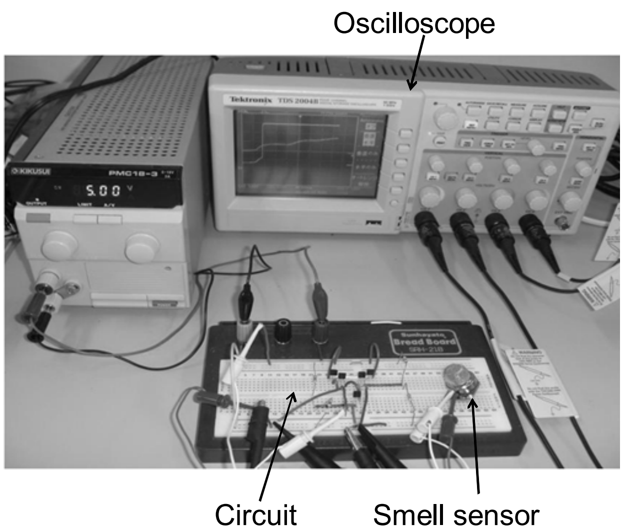

Fig. 3. The photograph of the test circuit

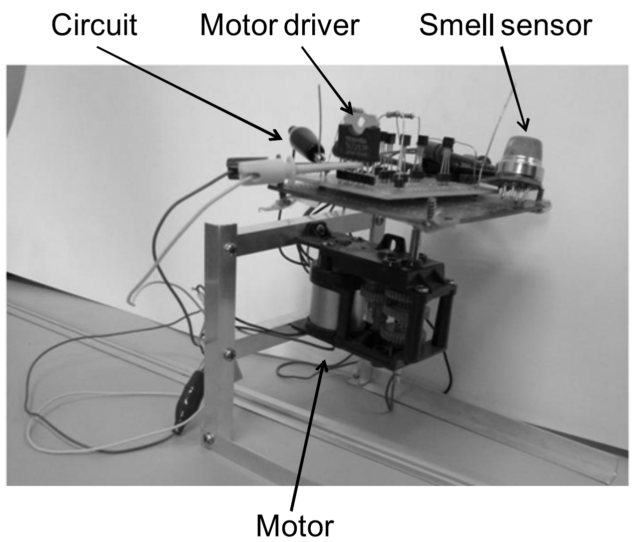

Fig. 5. The photograph of the circuit and the motor

the previous circuit based on the biological vision and auditory systems.

ACKNOWLEDGMENT

This work was partially supported by Japan Society for the Promotion of Science, Grant-in-Aid for Young Scientists (B), 23700222.

REFERENCES

[1] Nishio K, Matsuzaka K (2009), Target tracking system using analog motion detection circuit based on biological vision system. Far East Journal of Electronics and Communications 3:111-124

[2] Nishio K, Yamamoto T (2011), Simple analog-digital motion detection circuit and its application to target tracking system. Artificial Life and Robotics 16:57-60

[3] Nishio K, Tomibe T (2010), Analog-digital circuits for sound localization based on the biological auditory system. Artificial Life and Robotics 15:73-79

[4] Kanzaki R (2009) http://www.fragrancej.co.jp/books/fragrance/305257.html (in Japanese). Fragrance Journal Ltd.

[5] Aihara K, Kanzaki R (2008) http://www.utp.or.jp/bd/978-4-13-062304-9.html (in Japanese). University of Tokyo Press

Discussion of Stability of Adaptive Type Neural Network Direct Controller and Its Folding Behavior

[1]Takayuki Yamada

[1]Ibaraki University, 4-12-1 Nakanarusawa, Hitachi, Ibaraki, 316-8511, Japan
(Tel: +81-294-38-5256, Fax: +81-294-38-5282)

[1]tyamada@mx.ibaraki.ac.jp

Abstract: This paper discusses stability of an adaptive type neural network direct controller in the viewpoint of its folding behavior. First, I discuss the stability for the nonlinear plant and the nonlinear neural network. This discussion confirms that we can include the plant Jacobian problem into the tuning problem of the parameter determining the neural network learning speed. This is because it was confirmed that the direct controller has the folding behavior and the sign of the slope of a part of plant inverse characteristics learned by the neural network dose not change. This means that the sign of the plant Jacobian dose not change. Next, I assume input output relations of the neural network are linear and present the detail of the stability condition. This assumption may not be practical, but it is helpful for understanding of the relationship between the plant Jacobian and the parameter tuning.

Keywords: Neural network, Controller, Learning, Adaptive

I. INTRODUCTION

Many studies have been undertaken in order to apply both the flexibility and the learning capability of neural networks to control systems. We seem to believe that a neural network learns an inverse dynamic of a target plant in a servo level neural network controller application. This is because the target plant dynamics can be cancelled by this learned inverse dynamics if the neural network can learn it. On the other hand, a practical plant generally has a nonlinear dynamics and it is mathematically expressed a many-to-one function whose more than one input values correspond to one output value. There is no inverse function of such function. For this problem, we confirmed that the neural network has the folding behavior in the neural network direct controller through the use of the sine wave as a nonlinear plant.[1] This behavior is that the neural network learns only one branch (; a part of the inverse characteristics and it can be expressed as a one-to-one function mathematically) of the inverse characteristics of the target plant in order to obtain whole plant output. When the neural network realizes such input output mapping, the whole inverse characteristics of the target plant seem to be folded into one branch of the inverse characteristics. This behavior means that we can realize an ideal control system if the neural network can learn only one inverse branch of the plant. Other remarkable point was also confirmed that the sign of the slope of one branch dose not change.[1] That is, the sign of the plant Jacobian (; the derivative of the output with regard to the input) of the branch learned by the neural network of the direct controller dose not change. This fact seems to realize the learning of the neural network direct controller without the direct object plant modeling. The complex structures of the forward and inverse modeling, the feedback error learning and so on are not necessary with regard to realize the neural network learning. However, our previous papers pointed out the possibility of this realization and we did not show the discussion about its stability.

Thus, this paper discusses the stability of the adaptive type neural network direct controller[2] in the viewpoint of the folding behavior. In the second chapter, I discuss the stability for the nonlinear plant and the nonlinear neural network. This discussion confirms that we can include the plant Jacobian problem into the tuning probelm of the parameter determining the neural network learning speed. This is because the sign of the slope of the learned branch dose not change and the sign of the plant Jacobian learned by the neural network of the direct controller dose not change.[1] In the third chapter, I assume the neural network is linear. This assumption may not be practical, but it is helpful for understanding of the relationship between the plant Jacobian and the parameter tuning. This is because this assumption can realize the more details of the stability analysis.

II. LEARNING OF NEURAL NETWORK DIRECT CONTROLLER AND FOLDING BEHAVIOR

Figure 1 shows a structure of the neural network direct controller. As shown in fig.1, the neural network output is the plant input and the learning of the neural network performs so as to minimize the error between the plant output and the desired value (teaching signal). If the learning of the direct controller performs well (equals that the plant output becomes to be the desired value), the neural network of the direct controller obtains a part of the inverse characteristics of the plant dynamics as mentioned in my previous paper.[1]

This paper selects the steepest descent method as the neural network learning rule. It is shown in the following equation.

$$\frac{dW}{dt} = -\eta \frac{\partial J}{\partial W} \tag{1}$$

Where W is the weight of the neural network, η is the parameter determining the learning speed and J is the cost function. This cost function is the square error between the plant output Y and the desired value Yd.

$$\frac{dJ}{dt} = \frac{\partial J}{\partial W}\frac{dW}{dt} \tag{2}$$

If the above equation (2) is satisfied, we can derive the following equation from eq.(1)

$$\frac{dJ}{dt} = -\eta \left(\frac{\partial J}{\partial W}\right)^2 \tag{3}$$

As shown in the above equation, since we can select that the parameter η is the positive value, the cost function J decreases as time progress. That is, the learning rule of the neural network is stable and the plant output becomes to be close to the desired value as time progress because the cost function J is the square error between the plant output and the desired value.

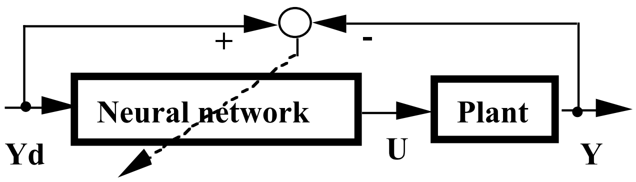

Fig.1 Scheme of neural network direct controller.

If we use an analog hardware as the neural network, we may realize the learning rule of eq.(2). However, most of the neural network controllers use the computer software since it is useful. In this case, the neural network learning rule is expressed as the following equation.

$$W(k+1) = W(k-d) - \eta_0 \frac{\partial J(k)}{\partial W(k-d)} \tag{4}$$

Where k is the sampling number and d is the dead time of the plant. Since this paper selects the adaptive type neural network, the weight of the neural network is changed at every several sampling time as shown in eq.(4). The cost function J(k) is defined as follows;

$$J(k) = \frac{1}{2}\varepsilon^2(k) \tag{5}$$

$$\varepsilon(k) = Yd(k) - Y(k) \tag{6}$$

Where Y is the plant output, Yd is the desired value and ε is the output error between them. Here, when the following eqs.(7) and (8) are assumed, we can obtain eq.(9) from eq.(4).

$$\frac{dW(k-d)}{dt} \cong w(k+1) - w(k-d) \tag{7}$$

$$\frac{dJ(k)}{dt} \cong \frac{\partial J(k)}{\partial W(k-d)}\frac{dW(k-d)}{dt} \tag{8}$$

$$\frac{dJ(k)}{dt} \cong -\eta_0 \left(\frac{\partial J(k)}{\partial W(k-d)}\right)^2 \tag{9}$$

As shown here, although we select the discrete time control system, if the eqs.(7) and (8) are satisfied, the plant output becomes to be close to the desired value as learning progress.

However, it is difficult to realize the learning rule eq.(4) in the direct controller when the plant characteristics is unknown. It is because $(\partial J(k)/\partial W(k-d))$ can not be calculated. As the practical solution, we can use the following equation in the replace of eq.(4).

$$W(k+1) = W(k-d) + \eta\, \varepsilon(k) \frac{\partial U(k-d)}{\partial W(k-d)} \tag{10}$$

Where U is the plant input. It equals the neural network output in the neural network direct controller as shown in fig.1. We must tune the parameter η in the replace of η_0 in eq.(4) and we can calculate eq.(10). It is because $(\partial U(k-d)/\partial W(k-d))$ can be determined by the neural network structure and this is known. The meaning of eq.(10) is explained in the following eq.(11) if eq.(12) is satisfied.

$$\eta = \eta_0 \frac{\partial Y(k)}{\partial U(k-d)} \tag{11}$$

$$\frac{\partial J(k)}{\partial W(k-d)} = \frac{\partial J(k)}{\partial Y(k)}\frac{\partial Y(k)}{\partial U(k-d)}\frac{\partial U(k-d)}{\partial W(k-d)} \tag{12}$$

$$\frac{\partial J(k)}{\partial Y(k)} = -\varepsilon(k) \tag{13}$$

From the similar way of eqs.(7)(8) and (10), we can obtain the following equation.

$$\frac{dJ(k)}{dt} = \eta\, \varepsilon(k) \frac{\partial J(k)}{\partial W(k-d)}\frac{\partial U(k-d)}{\partial W(k-d)} \tag{14}$$

From eqs(11)-(14), the following equation is obtained.

$$\frac{dJ(k)}{dt} = -\eta \frac{\partial Y(k)}{\partial U(k-d)} \left(\varepsilon(k) \frac{\partial U(k-d)}{\partial W(k-d)}\right)^2 \tag{15}$$

Where ($\partial Y(k)/\partial U(k\text{-}d)$) is the derivative of the plant output Y with regard to the plant input U and it is called the plant Jacobian. As shown in eq.(15), if $\eta(\partial Y(k)/\partial U(k\text{-}d))$ is positive, the cost function J decreases as time progress and the plant output becomes to be close to the desired value. That is, the neural network learning is stable and it performs well,

If the plant is linear system, it is well known that the plant Jacobian ($\partial Y(k)/\partial U(k\text{-}d)$ is constant. It is not difficult to tune the parameter η for the linear plant. However, if the plant is nonlinear, the plant Jacobian is not constant and it may be changed from negative to positive or from positive to negative in the neural network learning progress. Thus, the learning rule eq.(10) seems to be not practical because it seems to be difficult to tune the parameter η. However, it was confirmed that the neural network direct controller has the folding behavior.[1] It is not necessary for neural network learning of the direct controller to obtain whole plant inverse characteristics. If the neural network obtains only one branch (a part of the plant inverse characteristics and it is mathematically expressed as one to one function), the plant output matches with the desired value for whole region. The plant Jacobian in eq.(15) is referred to the branch which the neural network must learn. This is because the plant is controlled within this branch. The sign of its slope is not changed because the branch is expressed as one to one function and it monotonously increases or decreases. From eq.(15), the choice of the parameter η is positive or negative to stabilize the neural network learning. It is not so difficult to tune the parameter η.

As shown in eq.(15), the plant Jacobian effect can be included into the tuning of the parameter η and we can use the learning rule eq.(10). However, the assumptions eq.(7) and (8) seem to be strained. In particular, eq.(7) may not be satisfied around the weights which the neural network converge to. In the next section, I discuss the stability condition of the adaptive type neural network direct controller. This discussion uses the assumption that the input output relation of the neural network is linear. It is because it is difficult for the nonlinear neural network to analyze its stability condition, but the discussion of the next session is helpful to understand the plant Jacobian effect and the meaning of the learning rule eq.(10).

III. STABILITY CONDISION OF ADAPTIVE TYPE NEURAL NETWORK DIRECT CONTROLLER

Previous section shows the discussion of the stability of the neural network direct controller and its folding behavior, but the assumption of eqs.(7) & (8) seems to be strained. In order to discuss its stability condition, this section selects a three layer neural network whose neurons have a liner input output relation. This linear assumption may not be practical, but it is helpful for understanding of the neural network stability condition. The neural network is expressed as the following equation by use of this liner assumption.

$$U(k) = \omega^T(k)\ W(k)\ I(k) \tag{16}$$

Where ω is the weight vector between the hidden layer and the output layer, W is the weight matrix between the input layer and the hidden layer and I is the input vector of the neural network.

The following nonlinear plant is selected in this paper.

$$Y(k) = f(Y(k\text{-}d), \bullet\bullet\bullet, Y(k-d-n), U(k-d), \bullet\bullet\bullet, U(k-d-m)) \tag{17}$$

Where n & m are the plant orders and f is the nonlinear function which expresses the plant nonlinearity. The learning rule is derived as the following equations based on eqs.(10)-(13) and the linear assumption.

$$W(k+1) = W(k-d) + \eta\,\varepsilon(k)\omega(k-d)I^T(k-d) \tag{18}$$
$$\omega(k+1) = \omega(k-d) + \eta\,\varepsilon(k)W(k-d)I(k-d) \tag{19}$$

Here, we define the parameter error vector ζ as the following equation.

$$\zeta^T(k) = \omega_0^T\, W_0 - \omega^T(k)\ W(k) \tag{20}$$

Where ω_0 and W_0 are the weight vector and the weight matrix when the neural network is finished to converge.

The following discussion is described about the local stability when the neural network almost converges to the weight vector ω_0 and matrix W_0. From this assumption, the output error is expressed as follows;

$$\varepsilon(k+d) \cong \frac{\partial Y(k+d)}{\partial U(k)} \Delta U(k) \tag{21}$$

Where $\Delta U(k)$ is the difference between the present plant input and the plant input when the neural network is finished to converge. This $\Delta U(k)$ is sufficiently small because of the local stability. We assume the follows;

$$\begin{aligned} \Delta U(k) &\cong (\omega_0 - \omega(k))^T (W_0 - W(k))\ I(k) \\ &\cong (\omega_0^T W_0 - \omega_0^T W(k) - \omega^T(k)\ W_0 + \omega^T(k)\ W(k))\ I(k) \end{aligned} \tag{22}$$

From the local stability, we assume that both ω_0 and W_0 are almost equal to ω and W for the second and third terms of eq.(22). From eqs.(21)(22) and this assumption, we can obtain the following equation.

$$\varepsilon(k+d) = \frac{\partial Y(k+d)}{\partial U(k)} \zeta^T(k) I(k) \tag{23}$$

From the local stability, the output error ε is sufficiently small and ε^2 is almost 0. From this assumption and eqs.(18)(19) & (23), we obtain the following equation.

$$\omega^T(k+1)\, W(k+1) = \omega^T(k-d)\, W(k-d) + \eta \frac{\partial Y(k)}{\partial U(k-d)} \zeta^T(k-d)\, \xi(k-d) \tag{24}$$

$$\xi(k) = I(k)\, \omega^T(k)\, \omega(k)\, I^T(k) + I(k)\, I^T(k)\, W^T(k)\, W(k) \tag{25}$$

From eqs.(20) and (24), the following equation is derived.

$$\zeta^T(k+1) = \zeta^T(k-d)(E - \eta \frac{\partial Y(k)}{\partial U(k-d)} \xi(k-d)) \tag{26}$$

Where E is the identity matrix. When $\phi(k)=\zeta^T(k)\ \zeta\ (k)$ is selected as a candidate of the Lyapunov function, we can obtain the following equation.

$$\Delta\varphi = \varphi(k+1) - \varphi(k-d) = \zeta^T(k-d) Q \zeta(k-d) \tag{27}$$

$$Q = -2\eta\, (\frac{\partial Y(k)}{\partial U(k-d)})\, \xi(k-d) + \eta^2 (\frac{\partial Y(k)}{\partial U(k-d)})^2 \xi(k-d) \xi^T(k-d) \tag{28}$$

Since ξ defined by eq.(25) is the real symmetric matrix whose eigen values are not negative, there is a real orthogonal matrix V so as to $\xi = V^{-1}\beta V$ where β is a diagonal matrix whose diagonal elements are the eigen values of ξ. From eqs.(27) and (28), the following equation is derived.

$$Q = V^{-1}(\eta^2 (\frac{\partial Y(k)}{\partial U(k-d)})^2 \beta^2 - 2\, \eta \frac{\partial Y(k)}{\partial U(k-d)} \beta) V \tag{29}$$

When λ_i is defined by the eigen value of β, λ_i is not negative and the rank of β is 1. That is, the positive λ_i is 1 and this is the maximum eigen value λ_0 which is not 0. From eqs.(27)-(29), when the following equation is satisfied, $\Delta\phi$ is not positive and the neural network controller is stable.

$$0 \le \eta (\frac{\partial Y(k)}{\partial U(k-d)}) \lambda_0 \le 2 \tag{30}$$

As shown in eq.(30), the plant Jacobian ($\partial Y(k)/\partial U(k-d)$) is related to the stable condition. Its sign is important because the parameter η must be changed if its sign is changed in order to stabilize the neural network direct controller. However, my previous paper confirmed that the neural network of the direct controller has the folding behavior. It learns only one branch of the plant inverse in order to express whole plant characteristic. This branch is expressed as one to one function mathematically. The sign of the plant Jacobian is not changed. This is because the branch learned by the neural network monotonously increases or decreases. From eq.(30), it is not necessary to change the sign of the parameter η because λ_0 in eq.(30) is positive.

There is a maximum of absolute value of the plant Jacobian ($\partial Y(k)/\partial U(k-d)$) if the branches learned by the neural network are continuous. If neither this maximum nor λ_0 are not 0, we obtain the following stability condition.

$$0 \le \eta \le \frac{2}{P\lambda_0} \quad (0 < P), \qquad \frac{2}{P\lambda_0} \le \eta \le 0 \quad (0 > P)$$
$$P = \left| \frac{\partial Y(k)}{\partial U(k-d)} \right|_{Max} \tag{31}$$

where P is the maximum of absolute value of the plant Jacobian ($\partial Y(k)/\partial U(k-d)$). As shown in eq.(31), if we tune the parameter η so as to satisfy eq.(31), we can stabilize the neural network direct controller. This is because the maximum eigen value λ_0 is positive and it can be calculated within the neural network learning.

IV. CONCLUSION

This paper discusses the stability of the adaptive type neural network direct controller in the viewpoint of the folding behavior. First, I discuss the stability for the nonlinear plant and the nonlinear neural network. This discussion confirms that we can include the plant Jacobian problem into the tuning problem of the parameter determining the neural network learning speed. This is because the neural network direct controller has the folding behavior. However, the used assumption may be strained around the converged neural network weights. Thus, I assume the input output relation of the neural network is linear and present the more detail of the stability condition of the adaptive type neural network controller.

REFERENCES

[1] Takayuki Yamada, "Remarks on Folding Behavior of Mapping Capability of Neural Network Direct Controller for Many-to-one Plant", Proceedings of AROB 16th '11 (The Sixteenth International Symposium on Artificial Life and Robotics 2011), pp.881-884(2011)

[2] T.Yamada and T.Yabuta, "Some Remarks on characteristics of Direct Neuro-Controller with Regard to Adaptive Control", Transactions of the Society of Instrument and Control Engineers, Vol.27, No.7, pp.784-791(1991)(in Japanese)

The Seventeenth International Symposium on Artificial Life and Robotics 2012 (AROB 17th '12),
B-Con Plaza, Beppu, Oita, Japan, January 19-21, 2012

A Neural Network Strategy for Process Optimization

Shiu-Wan Hung*

Department of Business Administration
National Central University, Tao-Yuan 320 Taiwan
(Tel: 886-3-4250860; Fax: 886-3-4222891)

* shiuwan@mgt.ncu.edu.tw

Abstract: Designing high-quality products/processes at low cost leads to increasing market share and gaining competitive advantage. Thermoforming of plastic sheets has become an important process in industry because of their low cost and good formability. However there are some unsolved problems that confound the overall success of this technique. Nonuniform thickness distribution caused by inappropriate processing condition is one of them. In this study, results of experimentation were used to develop a process model for thermoforming process via a supervised learning back propagation neural network. An "inverse" neural network model was proposed to predict the optimum processing conditions. The network inputs included the thickness distribution at different positions of molded parts. The output of the processing parameters was obtained by neural computing. Good agreement was reached between the computed result by neural network and the experimental data. Optimum processing parameters can thus be obtained by using the neural network scheme we proposed. This provides significant advantages in terms of improved product quality.

Keywords: Polypropylene Foam, Thermoforming, Artificial Neural Network, Optimal Processing Parameters.

1 INTRODUCTION

Manufacturing strategy has been defined as the adoption of courses of action and the allocation of resources necessary for carrying out the goals [1]. Such a broad definition of strategy covers a multitude of decisions how can manufacturing contribute to the competitive advantage of this business. Manufacturing objectives cover such things as cost, quality, delivery and flexibility and usually there are trade-offs between them. Trade-off decisions are also required in a number of key areas in order to support the manufacturing objectives. Production planning/control and product design/engineer- ing are identified within the decision areas. These basic ideas (trade-offs and consistency of objectives/policies) have formed the foundation from which the current understanding of manufacturing strategy has developed.

Designing high-quality products/processes at low cost leads to increasing market share and gaining continuous customer loyalty. Robust design combines the experimental design techniques with quality loss consideration, is an engineering approach of quality improvement that seeks to obtain a lowest cost solution to the product design specification based on the customer's requirement. There is a significant amount of ongoing research in the area of the thermoforming [2] process in industry due to its low cost and good formability. However there are some unsolved problems that confound the overall success of this technique. Nonuniform thickness distribution caused by inappropriate processing condition is one of them. In this study, results of experimentation were used to develop a process strategy for thermoforming process via a supervised learning back propagation neural network. In the process, a thick sheet is clamped in a frame and is heated to a temperature well above its glass transition temperature such that it becomes rubbery and soft. It is then placed over a mold and is stretched to take on the contours of the mold, either by a plug assist or a differential pressure.

An inverse back-propagation neural network [3-5] was proposed to model the thermoforming process of polyethylene terephthalate (PET) materials and to predict the optimum processing parameters. The network inputs included the thickness distribution at different positions of molded parts. The output of processing parameters was obtained by neural computing. The network training was based on 47 sets of training samples and the trained network was tested with 10 sets of the test samples, which were different from the training data. The final goal of this study is to optimize the thermoforming process of PET sheets by using the neural network method, providing significant advantages in terms of improved product quality.

2 EXPERIMENTAL

A neural network is a computer system, which mimics the structure of human brain and imitates intelligent behavior [6]. It consists of many simple and highly connected neurons (processing elements or nodes), and processes information by its dynamic-state response to external inputs. It can deal with the problems of highly dimensional and nonlinear systems. The parallel distributed processing of the neural networks promises high computation rates provided by the massive parallelism, a greater degree of robustness or fault tolerance due to adapt and to continue to improve performance. The learning is based on samples, so it is especially suitable for the complicated process with a nontransparent mechanism. Therefore, neural networks, as one of most active branches of artificial intelligence in recent years, have been widely used in the process industries, including fault diagnosis and pattern recognition, process control and optimization, system modeling, and on-line measurement and prediction.

The earliest embryonic form of neural network was presented by a computer scientist named Rosenblatt (1958). Later, Minski and Papert (1969) claimed that the learning ability of ANN was very limited and could not even complete the basic functions of Exclusive OR gate. Hopfield and Tank (1985) proved that as long as appropriate network architecture was established and calculation of error function was defined, the network would be able to quickly obtain a good approximate solution. Rumelhart and McClelland (1986) were the first researchers to present the back-propagation network, and after that, ANN started to be widely applied to engineering fields such as physics, electronics, electric machinery, automatic control and so on [4,5].

A neural network is composed of many artificial neurons and links and can be formed into various types of network models. With learning, reasonable inference can be generated, making it very suitable to solve complex problems. Meanwhile, its nonlinear model is of high accuracy and has the advantage of accepting logical, numerical, order-relevant and order-irrelevant input, allowing for a wide range of adaptability and application. Currently, the most widely applied model is the Back-propagation Neural Network, a type of supervised learning network that is based on the concept of the gradient descent or steepest descent method, which minimizes the error functions of actual output and expected output. With the addition of hidden layers and the use of smooth and differentiable transfer function, the formula for the weight of the correction network can be derived from the gradient descent or steepest descent method.

In Fig.1 depicting the basic structure of ANN, $X=(x_1, x_2,\dots, x_n)$ is the input layer, and in each layer, the link of neural networks W_{ij} stands for the weight required for Unit *j* in one layer to move to Unit *i* in the previous layer. The functions of each layer are detailed as follows.

1. Input Layer: This represents the input variables of the network, and the numbers of processing units depend on the research problem, with the application of the linear transfer function, i.e., $f(x) = X$.
2. Hidden Layer: This represents the interaction between the processing units, and there is no standard method by which to determine the number of processing units. Generally, the best number can be decided by means of Trial and Error Method. Normally the number of hidden layer units is between (the number of input layer units + the number of output layer units)/2 ~ (the number of input layer units + the number of output layer units) x 2. In addition, due to the application of nonlinear transfer function, the network can either be more than one hidden layer or be designed to be without a hidden layer.
3. Output Layer: This represents the output variables. The number of processing units depends on the question, and the nonlinear transfer function is also used.

(Fig. 1 The structure of ANN)

An "inverse" neural network was proposed for system optimization in this study. Most neural networks use processing parameters as the inputs and molded product qualities as the computed outputs. We allocated inversely, the inputs and outputs in our model; i.e., assigned the product qualities as the inputs and the desired processing parameters as the outputs. The input variables in this research are the measured thickness profiles of molded parts at six different positions. The output variables include five different processing parameters: temperature of the heating pipe, vacuum pressure, plug moving speed, plug displacement, and thermal conductivity of the plug material. Thirteen nodes were selected for the hidden layer, which corresponds to two times the number of input variables plus one; i.e., the network 6-13-5 (six nodes in the input layer, thirteen nodes in the hidden layer, five nodes in the output layer) was chosen as the final structure, using a sigmoid function as its transfer function. By adopting an inverse neural network, we are able to determine the optimum processing parameter sets for the desired thickness profile of the parts.

3 RESULTS AND DISCUSSION

In this report, a model based on the ANN approach was used to predict an optimum setting of thermoforming parameters to achieve the optimum qualitative responses of polypropylene foams. Using the "inverse" neural network proposed in this study, we were able to predict the optimum set of processing parameters for the inputted part thickness distribution. In this study, forty-seven sets of data were used as training samples and the trained neural network was tested by 10 sets of data, which were different from the training samples. The network inputs included the thickness distribution at different positions of molded parts, and the output of the processing parameters was obtained by neural computing. To facilitate the training process, numbers were assigned to different plug materials: 1 for wood covered with woven blanket, 2 for a wood plug, and 3 for a phenol formaldehyde plug. The whole training procedure involved adjusting all weights on connections of the network according to the learning rule. The iteration continued until the computed outputs reached the required precision of agreement to the actual outputs. The test results are in Figs. 2-4 [7]. The results show good agreement to the actual measurement, except for the plug material sample in Fig. 4.

The most valuable result of this research is not only a development of a practical neural network for the thermoforming process of plastic sheets, but also a technique which has been proved to be suitable for modeling and predicting of the thermoforming process. It is valuable for the optimum control of the process and of practical significance to advanced thermoforming processes. Further research is suggested to consider the effect of different thermoplastic materials and assisting plug's geometry and temperature, because they may influence significantly the performance of the thermoforming of thermoplastic materials.

4 CONCLUSIONS

This study has proposed an inverse neural network model to predict optimum processing conditions. The network inputs included the thickness distribution at different positions of molded parts. The output of the processing parameters was obtained by neural computing. Good agreement was reached between the result computed by the neural network and the experimental data. By using the neural network strategy, one is able to optimize the thermoforming process of PET sheets, providing significant advantages in terms of improved product quality.

ACKNOWLEDGEMENT

The National Science Council of Taiwan, R.O.C. under the grant NSCNSC 99-2410-H-008-046-MY3, has supported this work financially.

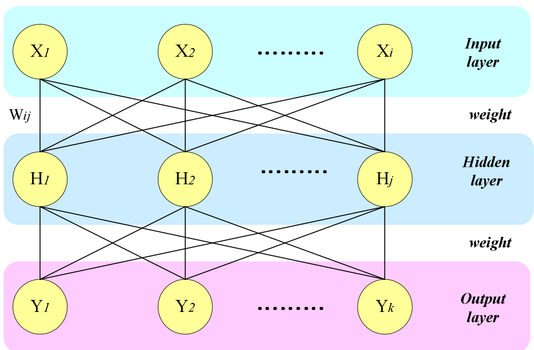

Figure 1 The structure of ANN

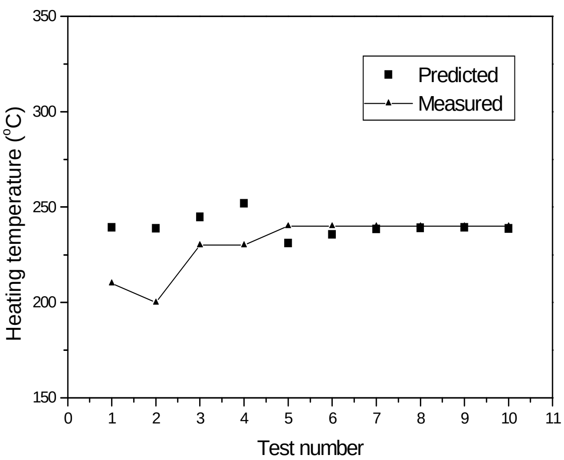

Figure 2. Comparison of predicted heating temperature to actual measurement [7].

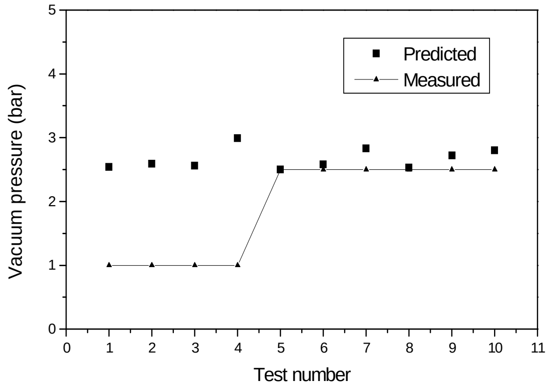

Figure 3. Comparison of predicted vacuum pressure to actual measurement [7].

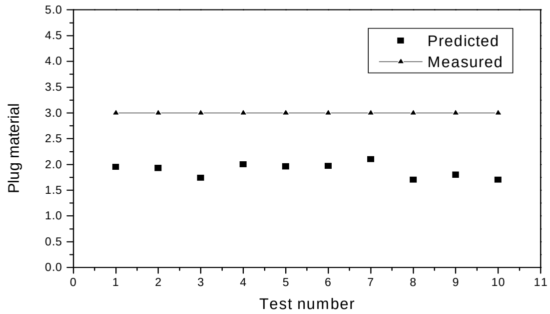

Figure 4. Comparison of predicted plug materials to actual measurement (1: woven blanket, 2: wood, 3: phenol formaldehyde) [7].

REFERENCES

1. M. Chandler, Strategy and Structures: Chapters in the History of the Industrial Enterprise, MIT Press, Cambridge(1962)
2 J.L. Throne, Thermoforming, Hanser Publisher, New York(1986)
3. L.H. Tsoukalas, R.E. Uhrig, Neural Network and Its Applications in Engineering, Wiley, New York(1997)
4. P.K. Simpson, Artificial Neural Systems, Pergamon Press, New York(1990)
5. L. Fausett, Fundamentals of Neural Network, Prentice Hall, New York(1994)
6. Q.Sun, D. Zhang, B. Chen, L.C. Wadsworth, J. Appl. Polym. Sci., **62**, 1605(1998)
7 C. Yang, S. Hung, Modeling and Optimization of a Plastic Thermoforming Process, Journal of Reinforced Plastics and Composites, 23 (1): 109-121, (2004)

The Seventeenth International Symposium on Artificial Life and Robotics 2012 (AROB 17th '12),
B-Con Plaza, Beppu, Oita, Japan, January 19-21, 2012

Handwriting Character Classification Using Freeman's Olfactory KIII Model

Masanao Obayashi*, Shinnosuke Koga*, Ling-Bing Feng*, Takashi Kuremoto*, and Kunikazu Kobayashi*

*Graduate School of Science and Engineering, Yamaguchi University
2-16-2 Tokiwadai, Ube, Yamaguchi, 755-8611, Japan
{m.obayas, n017vk, n007we, wu, koba}@yamaguchi-u.ac.jp)

Abstract: Recently, researches on smell sense that is one of the sensory organs of man have been actively done. The KIII model is one of the olfactory models that is thought out by Freeman referring to a physiological structure of mammal's olfactory system. In this paper, we propose a commonly used feature extraction method that applies Fourier transformation to the behavior of the time series and also propose to use the dynamics of chaotic neuron instead of the Hodgkin-Huxley equation to reduce computation time. Our introduced structure of the chaotic neuron has the simple structure and that it makes possible the chaotic operation same as the Hodgkin-Huxley equation. Paying attention to the point that the human brain does a similar processing to any sense of information, the hand-written image recognition problem that uses the KIII model is adopted as the computation simulation. Through the computer simulation of the handwriting character classification, it is shown that the proposed method is useful in the point of both computation time and the recognition accuracy.

Keywords: Handwriting character classification, Freeman, KIII model, Fourier transformation, Chaotic neuron

I. INTRODUCTION

Recently, according to development of non-invasive measurement techniques (CT, PET, fMRI, NIRS etc.), experimental research on higher-order brain functions has been advancing dramatically and the latest researches have been used in many fields. One of those high-order systems, the olfactory system, has also come to be actively done. As a model of the olfactory system, there is KIII model proposed by Freeman et al. [1][3].

The KIII model has been modeled based on the physiological structure of the mammalian olfactory system, and there are many applications using pattern recognition ability of the olfactory system. For example, J.Fu et. al[2] combined KIII model and the electronic nose with chemical sensors, and applied it to discriminate six typical volatile organic compounds in Chinese wine. The KIII is also applied to Tea Classification problem (Yang et. al[4]), Face Recognition (Li et. al. [6]), On the other hand, response of the olfactory system has a chaotic nature [5][7], it has also attracted many researchers.

In this paper, we apply the KIII model to handwriting character classification. In the application of the KIII model mentioned above, they performed the pattern recognition by using standard deviation of time series response inside the KIII model corresponding to the inputted data which should be discriminated. In this paper, we propose to use Fourier transform as the feature extraction method.

On the other hand, in KIII model, output of the neuron is obtained by solving second order ordinary differential equations and as a result, that leads to the problem that enormous processing time is required. Therefore, in this study, we aim reduction of the processing time, maintaining the chaotic characteristic of each neuron, by adopting the simplified output formula.

II. KIII MODEL

KIII is a recurrent neural network model created by Freeman et al, based on biological olfactory structure [1]. The main parts of the neural olfactory neural system is composed of primary olfactory nerve (PON), olfactory bulb (OB) , anterior nucleus (AON), and prepyriform cortex (PC). According to the anatomic architecture, KIII network is a multi layer neural network model. Fig. 1 shows the structure of the KIII model, in which M, G represent mitral cells and granule

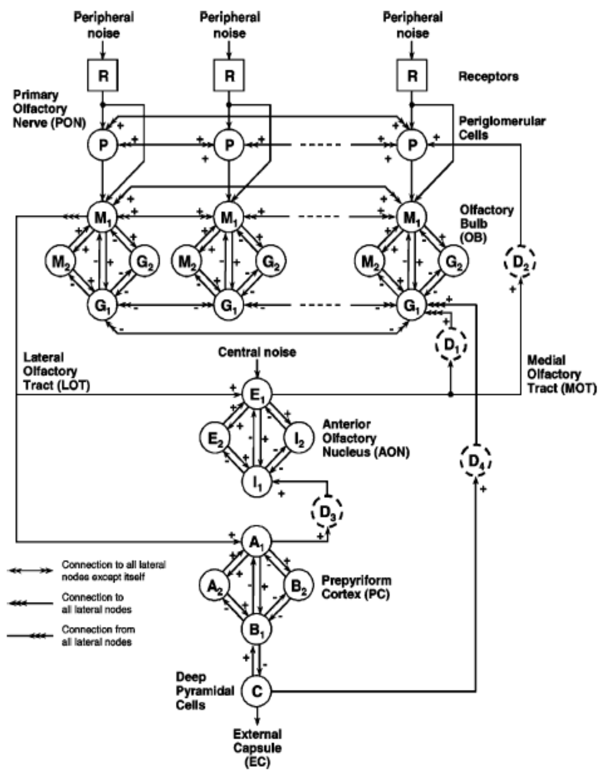

Fig. 1 Structure of the KIII Model (from [5][6])

cells in olfactory bulb.R represents the olfactory receptor, which offers input to the KIII model. E, I, A, B represent excitatory and inhibitory cells in anterior nucleus and prepytiform cortex, respectively. The KIII model based on the olfactory neural system is a high dimensional chaotic network. In this model, the interaction of connected nodes leads to a high-dimensional chaotic attractor. After learning from different patterns, the system will form several low-dimensional local basins[3]. Therefore, the memory for different patterns might be regarded as the formation of the local basins, while the recognition process refers to the transition from one basin to another.

The parameters of the KIII model, such as connection weights between different nodes, were optimized to fulfill features observed in lots of electro-physiological experiments [3]. Every nodes is described as a second order differential equation as follows:

$$\frac{1}{ab}[\ddot{x}_i(t)+(a+b)\dot{x}_i(t)+abx_i(t)]=\sum_{j\neq i}^{N} w_{ij}Q(x_j(t),q_j)+k_i r_i(t),$$

$$Q(x(t),q)=\begin{cases} q\left(1-\exp\left(-\dfrac{\exp(x(t))-1}{q}\right)\right), & x(t)>-x_0 \\ -1, & x(t)\le -x_0 \end{cases}, \qquad (1)$$

$$x_0=-\ln\left(1-q\ln\left(1+\frac{1}{q}\right)\right).$$

$x_i(t)$: state variable of the ith node, w_{ij}: the connection weight from j to ith node, a, b, q: constants derived by the electro-physiological experiments on biological olfactory system. k_i: coefficient as to the effect of the input, $r_i(t)$: input (external stimuli), N: the number of neurons

III. FEATURE EXTRACTION

Usually, when doing pattern recognition using the KIII model in general, we should create a feature vector from the characteristics of the behavior of M1 node dynamics.

Feature extraction by the standard deviation (Commonly used)

The state of OB layer mitral level is used as the strength of activity. The learning process only adjusts connection weights among the mitral. A modified Hebbian learning rule and a habituation rule are employed to KIII model.

When feature data are input to the KIII model with n channels, the behavior of each node is represented as an output time series as shown in Fig. 2. To get the characteristics of the kth channel's state, a value $SD(k)$ is extracted. The period with input patterns is divided into S segments (Fig. 2) and $SD(k)$ is the mean standard deviations of these segments. SD, composed of all the $SD(k)$ in the OB layer, depicts the activities of the all channels.

$$SD(k)=\frac{1}{S}\sum_{r=1}^{s} SD_{kr}, \quad k=1,\ 2,\ \ldots,\ n \quad , \qquad (2)$$

$$SD_m=\frac{1}{n}\sum_{k=1}^{n} SD(k), \quad SD=[SD(1),SD(2),\cdots,SD(n)]. \quad (3)$$

According to the modified Hebbian learning rule Eq. (4), the connection weights are adjusted.

$$\begin{aligned} &\text{IF} \quad SD(i)>(1+K)SD_m \quad \text{AND} \quad SD(j)>(1+K)SD_m \\ &\quad \text{THEN} \quad w'_{ij}=h_{Heb}, \quad w'_{ji}=h_{Heb} \\ &\quad \text{ELSE} \quad w'_{ij}=h_{hab}w_{ij}, \quad w'_{ji}=h_{hab}w_{ji} \end{aligned} \qquad (4)$$

w_{ij}, w'_{ij}: connection weights between M1 nodes before change and after one, respectively, K: bias, h_{Heb} : strengthening coefficient for Hebb learning, h_{hab} : weakening coefficient for refinement learning.

The learning for connecting weights continues while it is under changing.

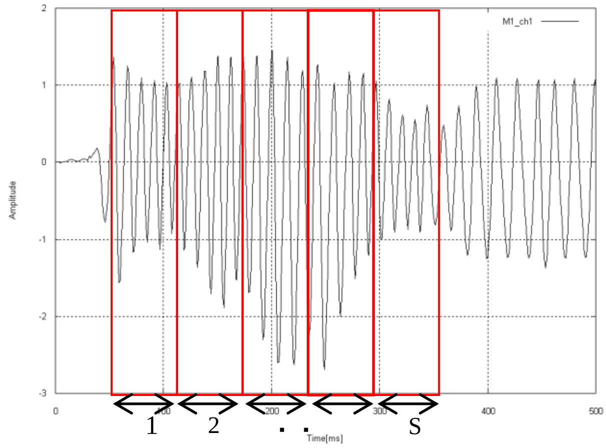

Fig. 2 Example of segmentation in the time-series behavior of the internal state of a M1 node

Fourier transform feature extraction method (Proposed)

Feature vectors are extracted as power spectrum and their frequency obtained by the discrete Fourier transform of time-series data of M1 node as shown in Fig. 3. Which shows an example of the power frequency spectrum.

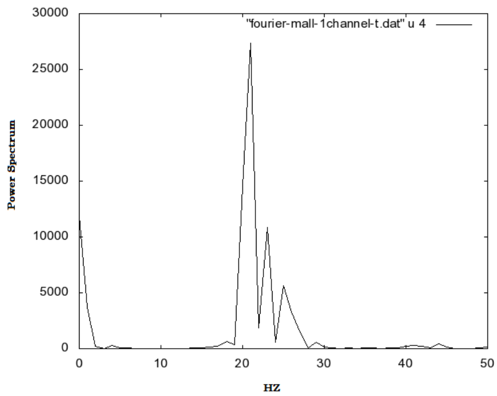

Fig.3 An example of power spectrum

IV. SIMPLIFICATION OF THE OUTPUT NONLINEAR FUNCTION OF THE NODE

The calculation of solutions of second order differential equations for determining the output of the neurons requires enormous processing time. This is a common problem in conventional method. Therefore, to reduce the computation time, we intend to simplify the second order differential equation. Furthermore, to produce chaotic response which are in the response of the above mentioned equations, we propose the two simplified equations referring to dynamics of chaotic neural network (CNN).

Dynamics of Chaotic neural networks

$$y_i(t+1) = ky_i(t) + \sum_{j=1}^{N} \omega_{ij} x_j(t) - \alpha x_i(t) + r_i(t)$$
$$x\ (t+1) = f\left(y(t+1)\right) \quad (5)$$

$y_i(t)$: internal state of the ith neuron, $x_i(t)$: output of the ith neuron, w_{ij}: connection weight from jth neuron to ith neuron, k: refractory decay coefficient, α: constant parameter, $r_i(t)$: input (external stimuli), N: the number of neurons, f: output function of a neuron.

Simplified equation I

$$y_i(t+1) = ky_i(t) + \sum_{j \neq i}^{N} \omega_{ij} Q(x_j(t), q_j) - \alpha x_i(t) + r_i(t)$$
$$x_i(t+1) = \frac{1}{1+\exp\left(-\dfrac{y_i(t+1)}{\varepsilon}\right)} \quad (6)$$

Simplified equation II

$$y_i(t+1) = ky_i(t) + \sum_{j \neq i}^{N} \omega_{ij} x_j(t) - \alpha x_i(t) + r_i(t) \quad (7)$$

V. HANDWRITING CHARACTER CLASSIFICATION

When performing the image pattern recognition using KIII model, there is a question of how to create input vectors of treating the image. In this research, two pre-treatment are carried to create the input vector.

Pixel Average (PA) method

By dividing the image to plural segments and taking the average of each pixel value of split images, we create input vectors which consist of them.

Discrete Cosine Transform (DCT) method

The DCT is one of ways to convert discrete signals into discrete frequency domain. It is mainly used for signal compression, in image processing, that is, the technique has been used in image compression such as

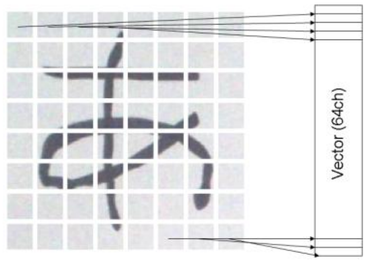

Fig. 4 Example of image segmentation

MPEG and JPEG. Compared to the discrete Fourier transform, this is characterized by the spectrum tend to be concentrated in specific frequencies. In the DCT, the DCT coefficients , that is, features in this research, are calculated by DCT basis functions and they are divided to the DC component (DC) and alternating component (AC). If you make the image DCT transform, the low frequency components (coefficients) are greater, conversely, high-frequency components become so smaller. The formula of DCT is shown in Eq. (8).

$$F_{k,l} = \sum_{j=0}^{N-1}\sum_{i=0}^{N-1} f_{ij}\phi_k[i]\phi_l[j]$$
$$f_{k,l} = \sum_{l=0}^{N-1}\sum_{k=0}^{N-1} F_{kl}\phi_k[i]\phi_l[j] \quad (8)$$
$$\phi_k[i] = \begin{cases} \dfrac{1}{\sqrt{N}} & k=0 \\ \sqrt{\dfrac{2}{N}}\cos\dfrac{(2i+1)k\pi}{2N} & k=1,2,\cdots,N-1 \end{cases}$$

We show the proposed system in Fig. 7.

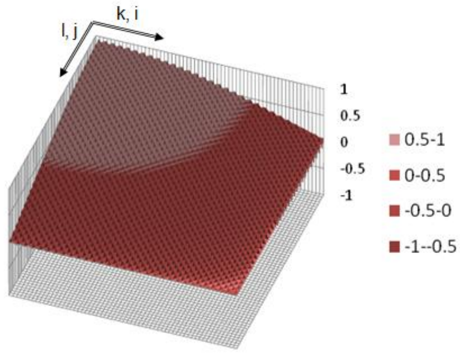

Fig.5 Values of DCT basis function (64×64) $\phi_k[i]\phi_l[i]$

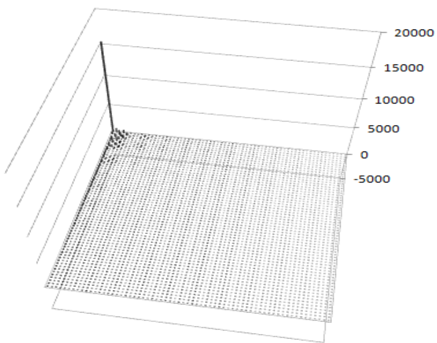

Fig.6 Example of DCT coefficients (64×64)

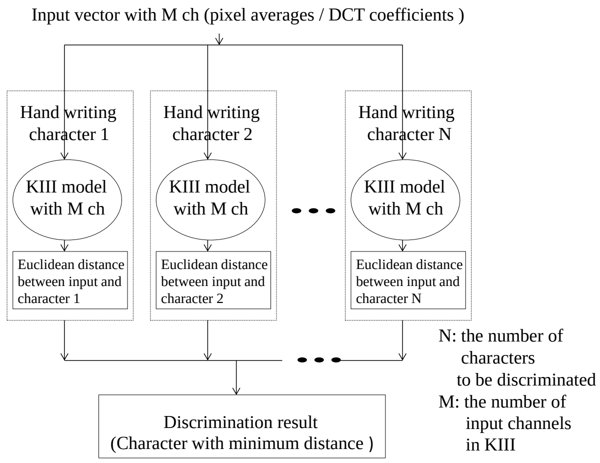

Fig. 7 Hand writing recognition system using KIII model

VI. COMPUTER SIMULATION

We confirm the usefulness of the proposed method under the conditions as follows,

・ Data format：bmp, ・ Data size：512×512
・ Subject：15 (Male), ・The number of channels : 64
・ The number of Japanese characters (refer to Fig.8)：
200 (= 10 males x 4 x 5 characters for training),
100 (= 5 males x 4 x 5 characters for testing)

Fig.8 Examples of hand writing images used in simulation

Simulation 1

We first verify usefulness of the Fourier transform comparing the standard deviation. Simulation results are shown in Table 1. The method using PA & FT is best.

Table 1 Success rates of 2 feature extraction methods

Model / Input feature extraction method	Standard Deviation	Fourier Transform
PA method	89.0%	94.0%
DCT method	84.0%	91.0%

Simulation 2

We next verify usefulness of two cases of simplified output functions of neurons comparing the conventional second-order differential equation. Simulation results are shown in Tables 2, 3 and 4.

Table 2 Success rates of the simplified KIII model I

Model / Input feature extraction method	α＝1.0 in Eqs. (6), (7)		α＝0.35 in Eqs. (6), (7)	
	SD	Fourier	SD	Fourier
PA method	51%	62%	47%	79%
DCT method	27%	58%	37%	62%

Table 3 Success rates of the simplified KIII model II

Model / Input feature extraction method	α＝1.0 in Eqs. (6), (7)		α＝0.35 in Eqs. (6), (7)	
	SD	Fourier	SD	Fourier
PA method	47%	68%	60%	61%
DCT method	40%	59%	34%	69%

Table 4 Computation times among 3 methods

Model	time(sec)
KIII model	3034
Simplified KIII model I	640
Simplified KIII model II	24

VII. DISCUSSION AND CONCLUSION

Recognition result of the feature vector extraction method by the Fourier Transform showed higher recognition rate than the conventional method, the Standard Deviation. In addition, processing times of the simplified two output functions of neurons introduced to make the enormous processing time of KIII model reduce are shortened by 1 / 150 of the conventional for the simplified formula I, 1 / 5 of the conventional for Formula II. However, the recognition rate of both simplified output functions came to be reduced.

Future work is as follows,

● Performance improvement of the proposed method making appropriate trade-off between improving the recognition rate and increasing the processing time, as increasing the number of dimensions of feature vectors.

REFERENCES

[1] Hung-Jen Chang, Walter J. Freeman, Brian C. Burke, Optimization of olfactory model in software to give 1/f power spectra reveals numerical instabilities in solutions governed by aperiodic (chaotic) attractors, Neural Networks 11, pp449-466 (1998)
[2] Jun Fu, Guang Li, Yuqi Qin, Walter J. Freeman, A pattern recognition method for electronic noses based on an olfactory neural network, Sensors and Actuators B 125, pp485-497 (2007)
[3] Chang. H.J., Freeman W.J. Biologically Modeled Noise Stabilizing Neurodynamics for Pattern Recognition. Int J of Bifurcation and Chaos, 8(2) pp.321-345 (1998)
[4] Xinling Yang, Jun Fu, Zhengguo Lou, Liyu Wang, Guang I, Walter J. Freeman, Tea Classification Based on Artifcial Olfaction Using Bionic Olfactory Neural Network, NCS,pp.343-348 (2006)
[5] W.J. Freeman, Simulation of Chaotic EEG Pattern with a Dynamic Model of the Olfactory System, Biol. Cybern. 56,pp.139-150 (1987)
[6] Guang Li, Jin Zhang, You Wang, Walter J. Freeman, Face Recognition Using a Neural Network Simulating Olfactory Systems, LNCS 3972, pp.93-97 (2006)
[7] C.K. Skarda, W.J.Freeman,How brains make chaos in order to make sense of the world, Behavioral And Brain Science, Vol. 10, pp.161-195 (1987)

The Seventeenth International Symposium on Artificial Life and Robotics 2012 (AROB 17th '12),
B-Con Plaza, Beppu, Oita, Japan, January 19-21, 2012

A corner detection technique using unit gradient vectors

Pramuk Boonsieng[1], Toshiaki Kondo, and Waree Kongprawechnon

School of Information, Computer, and Communication,
Sirindhorn International Institute of Technology,
Thammasat University, Bangkok, Thailand
(Tel: 66-2-986-9009, Fax: 66-2-986-9112)

[1]b.pramuk@gmail.com

Abstract: This paper presents a novel method for detecting corners in an image irrespective of the contrast. The corner detection method proposed by Kanade, Lucas, and Tomasi (KLT), Ando, and Harris corner detector are among the most widely used algorithms. They are all based on image gradients. Thus, the performances of those conventional approaches depend on the contrast of images. They work well for high-contrasted patterns, but have a difficulty in detecting low-contrasted corners. To overcome the problem, we propose to use unit gradient vectors (UGVs), instead of gradients, because UGVs are known to be a robust image feature and invariant to image contrast.

Keywords: corner detection, pattern recognition, unit gradient vectors.

1 INTRODUCTION

Corner detection is an important task in the field of digital image processing and computer vision. It finds various applications such as image matching, object recognition, motion estimation, etc [1]. Extracting corners can significantly reduce the computation cost in several applications [2]. Motion estimation also gains an advantage from this corner detection. Motion estimation can be performed correctly in an image area that contains a corner. On the other hand, it is difficult to estimate motions in an area that contains a straight edge boundary because of the so-called aperture problem. Thus, the computational cost can be reduced by performing motion estimation only on the image areas where a corner is present. There are several corner detectors that use image gradients. For instance, the corner detection method proposed by Kanade, Lucas, and Tomasi (KLT) utilizes the smaller eigenvalue of the 2×2 gradient covariance matrix defined locally within an image [3], [4]. Next, Ando's method makes use of the two eigenvalues of the 2×2 gradient covariance matrix [5]. The two eigenvalues are combined into a function in a normalized form. Thirdly, the Harris detector also uses the two eigenvalues [6]. Since these existing methods use image gradients, they depend on image contrast. Thus, they operate properly on high-contrasted corners, but it is truly difficult to detect low-contrasted corners.

In this paper, we propose to substitute unit gradient vectors (UGVs) for image gradients because UGVs is a robust image feature and invariant to image contrast.

2 METHODS

2.1 Kanade-Lucas-Tomasi method

Kanade-Lucas-Tomasi (KLT) or gradient method (GM) rests on the assumption that image intensity is constant overtime.

Let $g(x,y)$ be the image intensities at pixel coordinates (x,y). The gradient vector of $g(x,y)$ are approximated by partial derivatives

$$\begin{cases} g_x(x,y) = g(x,y) * k_x \\ g_y(x,y) = g(x,y) * k_y \end{cases} \tag{1}$$

where the symbol $*$ denotes convolution, and k_x and k_y are first-derivative operators in the x and y directions, respectively. The covariance matrix of the two patterns g_x and g_y is expressed by

$$G = \begin{bmatrix} \Sigma {g_x}^2 & \Sigma g_x g_y \\ \Sigma g_x g_y & \Sigma {g_y}^2 \end{bmatrix} \tag{2}$$

where Σ indicates the integration area in a local 2-D space. By applying PCA to the matrix, G, we obtain two eigenvalues λ_1 and λ_2 where $\lambda_1 > \lambda_2 \geq 0$. The corner is detected when two eigenvalue satisfy the condition $\lambda_1 \approx \lambda_2 \geq 0$.

2.2 Ando corner detection

The Ando method can categorize the image field into an omni-direction of the gradient. It can detect corner by using Eq. (3)

$$Q_{EG} = \frac{4\left(\Sigma g_x{}^2 \cdot \Sigma g_y{}^2 - \Sigma g_x g_y{}^2\right)}{\left(\Sigma g_x{}^2 + \Sigma g_y{}^2\right)^2 + \sigma_{EG}{}^4} \tag{3}$$

$\sigma_{EG}{}^4$ is needed to force the denominator does not equal to zero. The value of Q_{EG} is varied from 0 to 1. If it equals or closes to 1, the gradients are omni-directional. On the other hand, if it equal to 0, the gradients are uni-directional.

2.3 Harris corner detection

The Harris corner detector is widely used in digital image processing and computer vision. It can detect both edges and corners by using Eq. (4)

$$H = det\begin{bmatrix} \Sigma g_x{}^2 & \Sigma g_x g_y \\ \Sigma g_x g_y & \Sigma g_y{}^2 \end{bmatrix} - k \cdot \left(trace\begin{bmatrix} \Sigma g_x{}^2 & \Sigma g_x g_y \\ \Sigma g_x g_y & \Sigma g_y{}^2 \end{bmatrix}\right)^2 \tag{4}$$

where k is a constant. It is normally in between 0.04 and 0.06 [11]. The value of H presents the cornerness of the region. If the value is positive, the gradients are omni-directional, while if it is negative, the gradients are one-directional.

2.4 The proposed method

We propose the unit gradient vectors (UGVs) in place of conventional features such as image intensities and gradients, because UGVs are known to be insensitive under the varying illumination [8], [9].

The unit gradient vectors are computed by dividing gradient vectors by their magnitudes:

$$\begin{cases} n_x(x,y) = g_x(x,y)/\sqrt{g_x{}^2(x,y) + g_y{}^2(x,y)} \\ n_y(x,y) = g_y(x,y)/\sqrt{g_x{}^2(x,y) + g_y{}^2(x,y)} \end{cases} \tag{5}$$

3 RESULTS AND DISCUSSION

For the qualitative evaluation of the corner detection methods, KLT, Ando, Harris corner detector, and the proposed method, the synthetic images are created by generating an 8-bit gray-scale image of size 120 by 120 pixels. The tested image consists of difference 36 intensities levels. It has 25 different contrast corners which are both high and low contrast patterns. The difference of intensity from the top to the bottom of both rows and columns are set from large to small. Zero-noise Gaussian noise is added to test image to generate a noisy image. The signal to noise ratio, SNR, is 40 dB. The size of the block to search the feature is set at 5 by 5 pixels. We search the feature on every single pixel. The tested image is shown in Fig. 1.

We compare the performance of the conventional methods and the proposed method in a pair. We first compared KLT versus the proposed method as show in Fig. 2(a) and 2(b), respectively. The result is scaled from 0 to 1 to simple visualization. The brighter spot respond to the high cornerness on the test image. KLT is high response to the high contrast pattern, in the upper-left of the image, but almost miss the low contrast pattern, in the lower-right of the image as show in Fig. 2(a). The proposed method is high response to the entire corner pattern as show in Fig. 2(b).

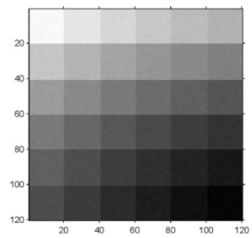

(a)

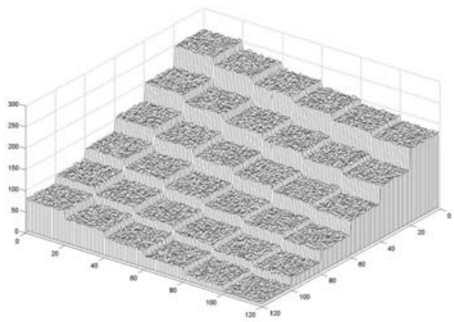

(b)

Fig. 1. (a) A mildly noisy test image. (b) The test image plotted in 3D.

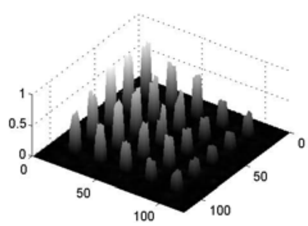

(a)

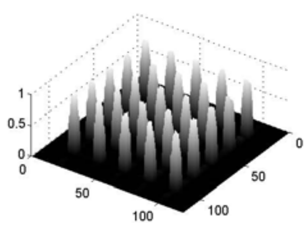

(b)

Fig. 2. Responses to corners by (a) the KLT method and (b) the proposed method.

Secondly, we compared the Ando corner detection with the proposed method as show in Fig. 3. The corners are selected by using Ando method with σ = 900 as shown in Fig. 3(a). The proposed method also uses the same value of σ which used in Ando method but proposed method shows the outer performance that has high response on the low contrast area which Ando has low response.

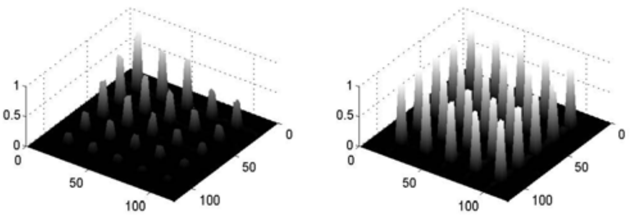

(a) (b)

Fig. 3. Responses to corners by (a) the Ando method, (b) the proposed method.

Next, Harris corner detector is compared with proposed method. The corner is selected by using the Harris corner detector with k = 0.04 as show in Fig. 4(a). Harris can detect both corner and edge in the same time. The white and black pixels respond to the corner and edge, respectively while the gray pixels are shown the flat area. Even it can detect all difference patterns, i.e., corner, edge, and flat area, in the entire image, it almost miss the detection in the low contrast corner. Fig. 4(b) shows the response of the proposed method. It can detect all different patterns especially, also detect the low contrast corner.

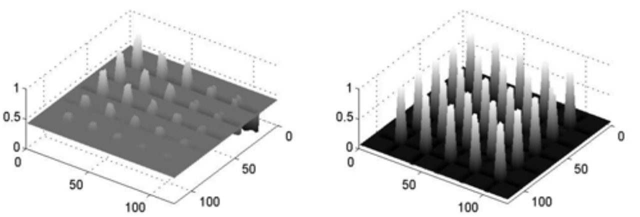

(a) (b)

Fig. 4. Responses to corners by (a) the Harris corner detector and (b) the proposed method.

4 CONCLUSION

This paper presents a comparative study between the popular feature detection methods such as KLT, Ando, and Harris corner detectors, and the proposed method. We introduce the unit gradient vectors in place of conventional image information as gradient. We have shown that the proposed method can detect corners regardless of their contrast. This will lead to stable corner detection under difficult conditions such as irregular illuminations and poor lighting.

ACKNOWLEDGEMENT

This research is supported by the National Research University Project of Thailand Office of Higher Education Commission.

REFERENCES

[1] Li-hui Z, Jie C, Juan Z, et al (2008), The comparison of two typical corner detection algorithms. Second International Symposium on Intelligent Information Technology Application, 2008, pp. 211-215

[2] Pramuk B, Toshiaki K, Waree K (2011), Feature-based gradient orientation structure tensor method, International Conference on Modeling and Simulation Technology, Tokyo, Japan, Oct 22-23, 2011

[3] Tomasi C and Kanade T, Detection and tracking of point features, Carnegie Mellon University Technical Report CMU-CS-91-132, April, 1991

[4] Shi J and Tomasi C, Good features to track. IEEE Conference on Computer Vision and Pattern Recognition, 1994, pp. 593-600

[5] Shigeru A, Image field categorization and edge/corner detection from gradient covariance, IEEE Trans. on Pattern Analysis and Machine Intelligence, vol. 22, no. 2, February, 2000, pp. 179-190

[6] Harris C and Stephens M, A combined corner and edge detector, Proc. 4th Alvey Vision Conf., 1988, pp. 147-151

[7] Pramuk B, Toshiaki K, Waree K (2011), Unit gradient vectors based motion estimation techniques, ECTI Trans. on Electrical Engineering, Electronics, and Communications, vol. 9, no. 2, August, 2011, pp. 246-254

[8] Burgi PY (2004), Motion estimation based on the direction of intensity gradient, Image and Vision Computing, vol. 22, 2004, pp. 637-653

[9] Toshiaki K and Yan H (1999), Automatic human face detection and recognition under non-uniform illumination, Pattern Recognition, vol. 32, 1999, pp. 1707-1718

The Seventeenth International Symposium on Artificial Life and Robotics 2012 (AROB 17th '12),
B-Con Plaza, Beppu, Oita, Japan, January 19-21, 2012

Human Detection Employing the HOG Feature based on Multiple Scale Cells

Yusuke Ehara, Joo Kooi Tan, Seiji Ishikawa, and Takashi Morie

Kyushu Institute of Technology, Kitakyushu 804-8550, Japan

Tel: 093-884-3088, Email: ehara@ss10.cntl.kyutech.ac.jp

Abstract: In this paper, we propose a new human detection method based on local descriptors and machine learning. The HOG feature and RealAdaBoost are well-known methods for detecting humans. However, this technique has shown its limitation because of long processing time due to fixed number of weak-classifiers. To overcome this problem, this paper proposes a HOG based framework using multiple-scale cells for the RealAdaBoost with a variable number of weak-classifiers. The proposed method is faster than existent methods, because it describes more comprehensive intensity gradients and classifies them using low dimension feature vectors. Experimental results show that the proposed method is effective in accuracy and processing time.

Keywords: HOG, Multiple Scale Cells, RealAdaBoost, human detection, machine learning.

1. Introduction

Recently, various techniques for human detection (especially pedestrians) from an image have been developed. These techniques are the main topics in the field of ITS (Intelligent Transport systems) and robot vision. For pedestrian detection, there exist many approaches such as background subtraction, motion based techniques [1], etc. that have been proposed. However, these methods have restrictions in the scenes in which they can be used. For example, some methods can be used only for stationary camera images or only for a moving object. Therefore, using local descriptors and machine learning schemes which can respond to a moving camera and do not have restriction in the detection scene has been gaining spotlights. More especially, the Histograms of Oriented Gradients (HOG) feature proposed by Dalal and Triggs [2] is one of the well-known methods for human detection. The method has robustness to illumination and small shape changes.

There exist a lot of methods based on the HOG feature [3, 4]. For example, Nakashima has proposed Multiple-HOG [5]. Multiple-HOG method is based on using a variable number of divisions on the direction of intensity gradients. Better results have been obtained as compared with conventional methods because of its flexible as well as precise description of the gradients in a cell. However, since the size of a cell is fixed, the amount of information included in one feature vector is limited. Moreover, these methods have the same problem, i.e., long processing time, because HOG needs normalization of every block in an image and the number of weak-classifiers is large and fixed in the RealAdaBoost. If the number of weak-classifiers is reduced, processing time can be faster. Instead, we may might lose high accuracy.

In this paper, we propose a novel human detection method employing the HOG feature based on multiple-scale cells for RealAdaBoost with a variable number of weak-classifiers. By this method, since the size of the edges can be captured more comprehensively, one feature vector contains more information. Therefore, this method can perform at higher speed using few weak-classifiers. Experimental results show that the proposed method is effective in accuracy and in processing time.

2. HOG feature based on Multiple-scale cells

When calculating the HOG feature employing the method proposed by Dalal et al., a cell size is fixed. In this method, we can acquire only the information on a small cell (usually 5×5 pixels) as shown in **Fig. 1(a)**. However, a pedestrian has generally large and strong vertical edges. We propose Multiple-scale-cell HOG feature in this paper. The idea of Multiple-scale-cell HOG is illustrated in Fig. 1(b).

(a) (b)

Fig. 1. Arrangement of a cell in the case of (a) HOG, and (b) Multiple-scale-cell HOG.

The Multiple-size-cell HOG has a variable size of cells. For example, 5×5, 5×20, 20×5 and so on. Moreover a cell-overlap is permitted. Then we can describe the size and the location of an edge comprehensively. The cell size is defined as follows.

$$S_x = \alpha n + C, \qquad S_y = \beta k + C \tag{1}$$

Here S_x is the cell size in the horizontal axis direction, and S_y is the cell size in the vertical direction.

When calculating the HOG feature, block normalization consumes a large part of the processing time, although it assures robustness to lighting condition change. Therefore normalization with every block is not performed in the proposed method. As a substitute, cell overlap is permitted which leads to the use of a larger number of cells.

3. RealAdaBoost with variable number of weak-classifiers

Boosting obtains classifiers of good performance (a strong classifier) by combining many weak-classifiers. The number of weak-classifiers is related to accuracy and processing time. In this paper, we also propose a technique for making the number of weak-classifiers variable. If an image is simple enough to recognize it, such as a road or the sky, we use a small number of weak-classifiers. On the other hand, if an image is complicated, such as roadside trees, we use a large number of weak-classifiers.

First, we train provided data using RealAdaBoost. In RealAdaBoost, the output of a weak-classifier becomes large (positive) when it is a positive sample, and it becomes small (negative) when the sample represents the negative class. Using this characterization during the learning stage of RealAdaBoost, the threshold value is determined by the following formula.

$$th_i = \min\{h_{i,1}, h_{i,2}, \cdots h_{i,N_p}\} \tag{2}$$

Here *i* is the round number, th_i is the threshold in round, h_i is the output value of a weak-classifier in *i* round about a positive sample. N_p is the number of positive samples.

Discrimination is performed using the computed threshold value. The idea of discrimination is illustrated in **Fig. 2**. In Fig. 2, WC_i are weak-classifiers in round i. Even if i have not reached, if the output of weak-classifiers is smaller than a threshold value, calculation will stop at the time. During the image search of a human, the number of weak-classifiers is made variable for every search window as shown in **Fig. 3**.

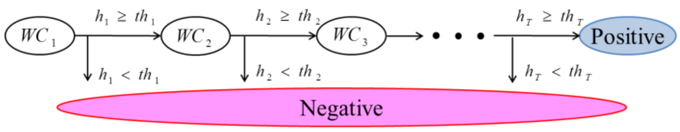

Fig. 2. Variable number of weak-classifiers.

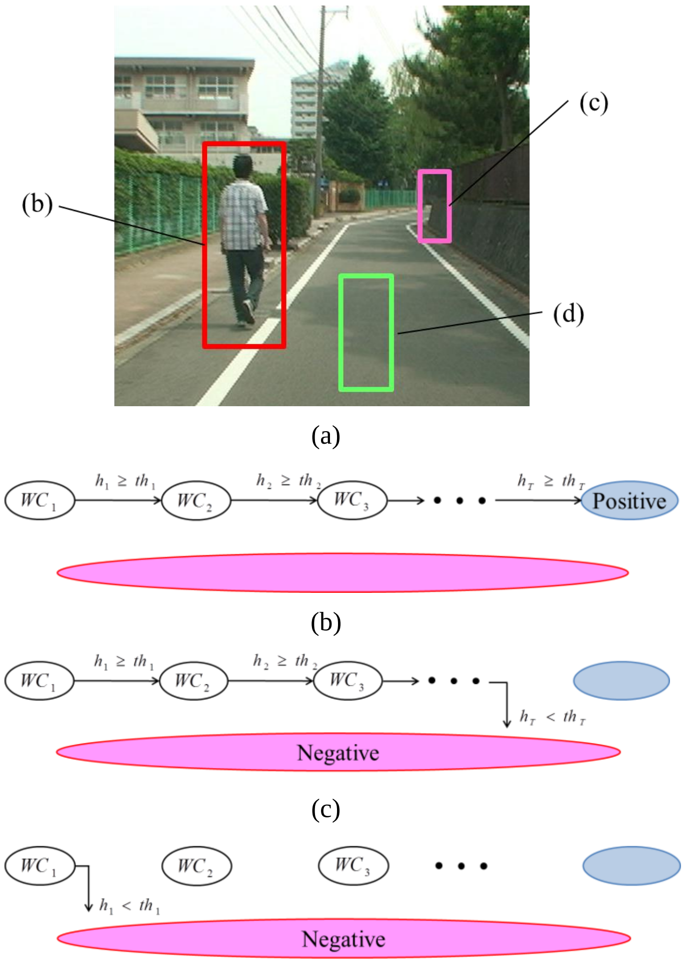

(d)

Fig. 3. The number of weak-classifiers for every search: (a) Input image, (b) positive class, (c) difficult negative class, and (d) easy negative class.

4 EXPERIMENTAL RESULTS

We evaluated the proposed method for human detection by using INRIA Person Dataset. Training data contains 2416/6000(positive/negative) images and test data includes 1126/3000(positive/negative) images. The image size is 30×60 pixels. We compared the proposed method with the conventional method using the HOG feature [1] and RealAdaBoost, and using the Multiple-HOG feature[5] and RealAdaBoost.

The combination of the method in the experiment is shown in a **Table 1**. We compared two previous methods to our proposed schemes. In [1], [5] and our proposed method-1, the number of weak-classifiers is 500. First, the accuracy evaluation experiment of the proposed method (Multiple-scale-cell HOG) was conducted. The DET curve is shown in **Fig. 4**. The DET curve is plotted: True Negative rate is the vertical axis, whereas False Positive rate is the horizontal axis. The method that has its plot in the lowest and the left most area is considered to be the best. Moreover, the accuracy in the case of 500 weak-classifiers is shown in **Table 2**.

Next, we conducted the evaluation experiment of RealAdaBoost with variable number of weak-classifiers. The relationship between the number of weak-classifiers and the rate of an error is shown in **Fig. 5**. The vertical axis represents the error rate. The method that has the lowest plot is the best, which the proposed method-2.

Finally, processing time is compared in **Table 3**. Since processing time differs in a Positive class and a Negative class sample, in the proposed method-2 the processing time of each class is shown separately.

Table 1. The combination of the method in

previous method-1[1]	HOG and RealAdaBoost
previous method-2[5]	Multiple-HOG and RealAdaBoost
proposed method-1	Multiple-scale-cell HOG and RealAdaBoost
proposed method-2	Multiple-scale-cell HOG and RealAdaBoost with variable number of weak-classifiers

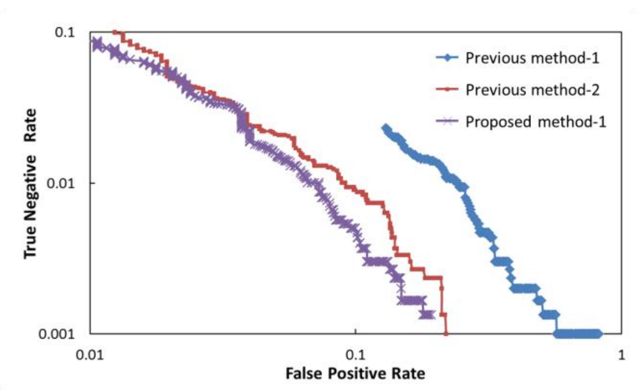

Fig. 4. Accuracy evaluation experiment of Multiple-scale-cell HOG.

Table 2. Detection rate

	Detection Rate[%]
previous method-1	94.15
previous method-2	96.24
proposed method-1	96.32

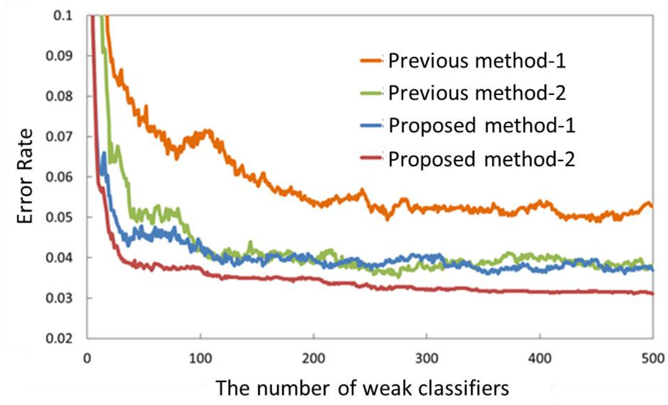

Fig. 5. The relation between the number of weak-classifiers and the error rate.

Table 3. Processing time

	Positive [micro sec]	Negative [micro sec]
previous method-1	152.51	
previous method-2	40.24	
proposed method-1	28.96	
proposed method-2	27.80	0.99

5 DISCUSSION

Fig.4. shows that the proposed method achieved satisfactory accuracy compared with the previous methods. Table 2 also supports this fact. Moreover, the best accuracy was obtained by using Multiple-scale-cell HOG and RealAdaBoost with variable number of weak-classifiers from as shown in Fig.5. It is thought that a satisfactory result is obtained because the probability of FPR was reduced by making the number of weak-classifiers variable.

Moreover, Table 3 showed that the proposed method-2 performed the specified task at a higher speed. This is due to the skipping of the block normalization during the feature vector computation stage. Moreover, during the discrimination stage, it turns out that the negative class can be eliminated at a high speed.

Next, the plot showing the relationship between the number of weak-classifiers and the rate of an error in the first 100 rounds is shown **in Fig. 6**. As shown in Fig. 5, When the number of weak-classifiers is high (~500), the difference in the accuracy of previous methods and Multiple-scale-cell HOG (proposed method-1) is small. However, as shown in Fig. 6, in the first 100 rounds, there is a big difference in the accuracy of two methods. For this reason, within the first 100 rounds, the proposed method can eliminate the negative class samples with high accuracy. This is considered to be based on the contribution of a large scale cell. The amount of information which one feature vector has by using a large scale cell becomes large. Therefore, good accuracy can be acquired when few weak classifiers are used. This is understood also from the feature selection process. The selected edge in three first rounds is shown in **Fig. 7**. It turns out that a large edge is chosen in the first 100 rounds. On the contrary, when the number of weak-classifiers is high, a small edge is chosen. That is, first, its attention is paid to big edge and easy portions, such as a road domain, are eliminated. Next, as Round becomes high, difficult objects, such as a roadside tree, are eliminated using small edge.

6 CONCLUSIONS

We have proposed a method of human detection employing the Multiple-scale-cell HOG and RealAdaBoost with variable number of weak classifiers.

In the experiment, it was checked that it performed higher-speed processing and a better precision than the previous methods. Performance of the method was satisfactory. We are going to apply the method to ITS and robot vision.

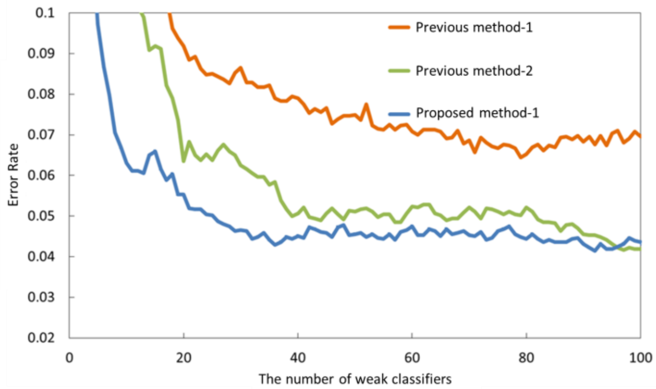

Fig. 6. The relation between the number of weak-classifiers and the error rate in the first 100 rounds.

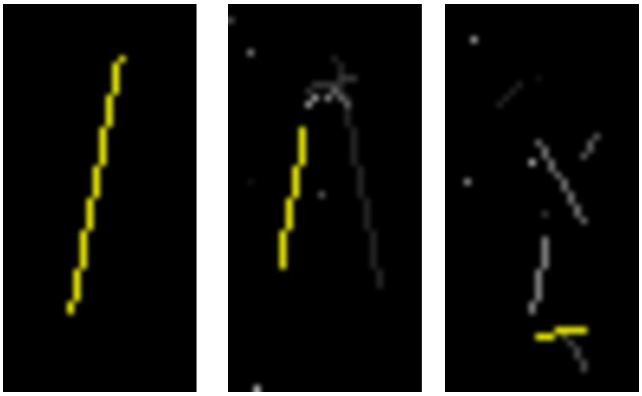

(a) (b) (c)

Fig. 7. Selected edges:(a) Round 1, (b) round 240, and (c) round 499.

ACKNOWLEDGMENT

This work was supported by grant of Regional Innovation Cluster Program and JSPS KAKENHI (22510177).

REFERENCES

[1] Y. Zhang, S. J. Kiselewich, W. A. Bauson, R. Hammoud (2006) Robust moving object detection at distance in the visible spectrum and beyond using a moving camera, Proc. Computer Vision and Pattern Recognition Workshop (CVPRW), 131-139.

[2] N. Dalal, B. Triggs (2005), Histograms of oriented gradients for human detection, Proc. IEEE Conf. on Computer Vision & Pattern Recognition, 886-893.

[3] Q. Zhu, et al. (2006), Fast human detection using a cascade of histograms of oriented gradients, Proc. IEEE Conf. on Computer Vision & Pattern recognition.

[4] Y. Yamauchi, H. Fujiyoshi, T. Yamashita (2008), Human detection by boosting-based co-occurrence feature representation, Meeting on Image Recognition and Understanding.

[5] Y. Nakashima, J. K. Tan, S. Ishikawa, T. Morie (2011), Detecting a human body direction using multiple-HOG, FAST-zero'11.

The Seventeenth International Symposium on Artificial Life and Robotics 2012 (AROB 17th '12),
B-Con Plaza, Beppu, Oita, Japan, January 19-21, 2012

Hash based Early Recognition of Gesture Patterns

Yoshiyasu Ko*, Atsushi Shimada*, Hajime Nagahara*, Rin-ichiro Taniguchi*

* Kyushu University, Fukuoka, Japan
E-mail: {ko,atsushi,nagahara,rin}@limu.ait.kyushu-u.ac.jp

Abstract: We propose an accelerated approach of gesture recognition, "Early Recognition". Early recognition is a method to make a decision of human gesture at their beginning part of it. A gesture consists of a sequential postures. In the training phase, a lot of postures which make the gestures are trained by Self-Organizing Map (SOM). Then, representative postures on the SOM are investigated their contribution ratios for each gesture. Besides, the representative postures are registered into a hash table to realize quick search of a posture in the test phase. When an input gesture is given, a posture in each frame is used as a query and the most similar posture is found from the training samples. Then, if the contribution ratio for a certain gesture exceeds a predefined threshold, the system outputs the gesture label as the recognition result. Through our experiments, we found out that the proposed method outperformed the traditional method in terms of the computational cost and the response speed until the result was determined. Besides, the recognition accuracy of the proposed method was almost the same as the traditional one.

Keywords: Early Recognition, Locality-Sensitive Hashing, Self-Organizing Map

1 INTRODUCTION

Recognizing human gestures plays an important role to realize a man-machine interactive system. We tackle the problem of realizing a seamless interaction required video action game consoles, robotics, remote controller, etc. Generally, a system recognizes a human gesture after the gesture has completely finished. Therefore, if the length of the gesture is long, a user has to wait for the response until the recognition process finishes. That's why general system occurs a large time lag, and loses the smoothness.

In recent years, a new methodology of gesture recognition called "early recognition" has been proposed[1][2]. Early recognition is the method that system determines the recognition result before user's gesture has finished. It gives us very useful solution for the problem of delay of interaction. In the previous approach[3], Self-Organizing Map (SOM)[4][5] is utilized for making a codebook of representative postures from training samples, then contribution ratio of each representative posture is estimated for each gesture class. In recognition process, the best matched representative posture is found from the codebook by searching all nodes of SOM. Therefore, the larger the number of nodes becomes, the longer time search phase takes. Furthermore, if searching takes longer time than a frame rate of input, a system will drop several frames, that may result in lower performance of recognition speed. Generally, the performance depends on the number of nodes, but it requires a large computational cost to find a best matched one.

In this paper, we propose the accelerated approach for searching the best matched node by using Locality-Sensitive Hashing (LSH)[6], in which the computational time does not depend on the size of code book. In the following this paper, we will give a detailed explanation about the proposed method. Besides, the effectiveness of the proposed method becomes clear through the experimental results.

2 PROCESSING FLOW OF PROPOSED METHOD

Proposed method is divided into two processes; training process and recognition process.

2.1 Training Phase

Training process is divided into three steps. Step1 and Step2 are inspired from the previous work by Kawashima *et al*[3]. Flow of this process is explained as follows,

Step 1 Training of Representative Postures

Step 2 Calculation of Contribution Ratio

Step 3 Registration to Hash Table

First, the training sample is clustered by SOM and center vector of each cluster, which is called "representative posture" is output to each neuron of SOM. Secondly, "contribution ratio", which shows how often each representative posture is used for each gesture class is calculated. Finally, sets of representative postures and contribution ratio are registered to hash table. In following subsection, we explain each step in detail.

Step 1 *Training of Representative Postures*

The posture data, which are the skeleton data (Fig.1) sequences of human posture from Microsoft Kinect SDK, are collected as training samples. Each skeleton data has 20 observation points and each observation point

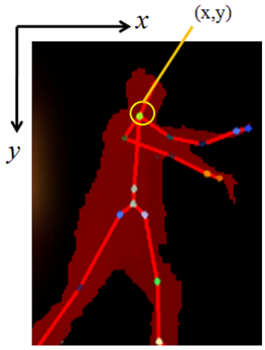

Fig. 1. Skeleton data

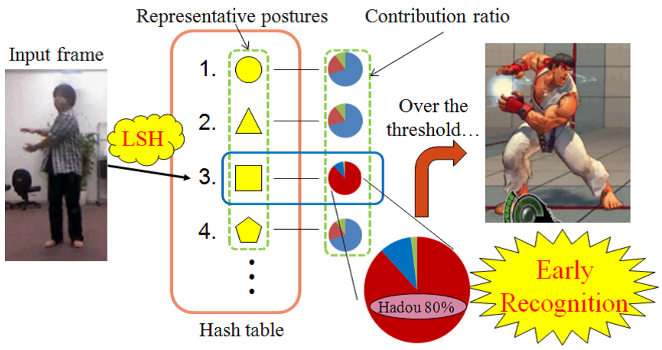

Fig. 2. Flow of Recognition Phase

has 2 dims (x, y) information, so each frame data has 40 dims vectors as information of posture (1 frame = 1/30 sec). Then, that samples of motion's template postures are clustered by SOM and a output center vector of each cluster, which called "representative posture", are registered to each neuron of SOM.

Step 2 *Calculation of Contribution Ratio*

"Contribution Ratio" denotes how often a representative posture is used for each gesture class. The template postures of each motion are input to SOM again and we count the number of times which shows how often the neurons of SOM are used for each gesture class. Then, the ratio of that number of one motion to that of all motions is treated as contribution ratio. In short, The higher value it becomes in only one motion, the more peculiar the posture is to the motion. That ratio is also registered to SOM with each representative posture. Then, the representative posture and the contribution ratio of that are linked by a label number.

Step 3 *Registration to Hash Table*

The representative postures registered to neurons of SOM are registered to hash table. The parameter l and k (Sec.3) need to be selected the proper values because this values are directly relative to the recognition accuracy.

2.2 Recognition Phase

Flow of the recognition phase is shown by Fig.2. The recognition phase is performed frame by frame. In each frame, a best matched posture is searched from all registered representative postures in hash table. If a matched posture is found, its corresponding contribution ratio for each gesture is examined. If a contribution ratio of a certain gesture is higher than a predefined threshold, the system makes final decision of gesture recognition. In other words, the gesture label is the recognition result.

The previous method requires $O(n)$ (n is the number of representative postures) operations to find the best matched posture because of a greedy algorithm. When the n increases, the calculation cost also increases explosively. It is not desirable from the viewpoint of early recognition. Meanwhile, the operation cost of a hash-based approach is not affected by the number of samples. LSH requires $O(kl)$ operations. The values of the k and l are very smaller than n. Moreover, it guarantees a constant operation cost even if the number of postures increases. The search method of LSH is explained in Sec.3.

3 LOCALITY-SENSITIVE HASHING (LSH)

Locality-Sensitive Hashing (LSH) is a kind of approximate nearest neighbor search. Nearest neighbor search needs to calculating distance from query data point to each data point and it takes an enormous amount of time. However, "approximate" nearest neighbor search is the way of finding slate points which are near from query data point. This way can reduce much calculating time because of not requiring to calculate distance between each data points and query data point.

This search method uses "locality-sensitive" hash function. It is the function that the nearer the distance from query data to a data point, the higher value the probability that hash values of both data are matched takes. This function is defined by,

$$h(\boldsymbol{p}) = \left\lfloor \frac{\boldsymbol{a} \cdot \boldsymbol{p} + b}{w} \right\rfloor \tag{1}$$

$\boldsymbol{a}$ is the vector whose value of each element is obtained independently by Gaussian distribution. $\boldsymbol{p}$ is query data, and w is width of hash, b is the real number which is selected in an interval $[0, w]$.

In making search table phase, the k function $g =< h_1, \cdots, h_k >$ is applied for all data points, and the product set of each function's result is obtained. Furthermore, The l group of function $\{g_1, \cdots, g_l\}$ is also applied, and the search table is constructed.

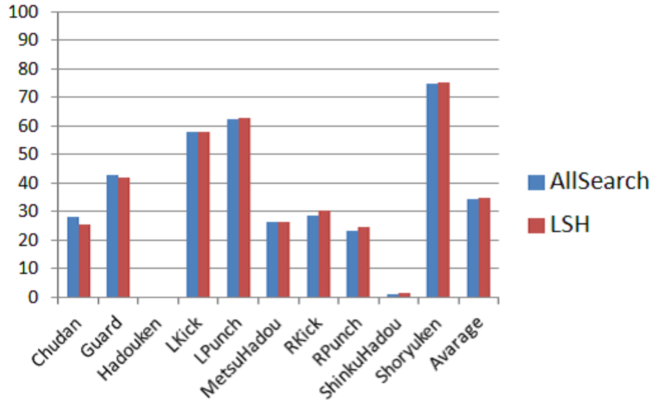

Fig. 3. Recognition Accuracy of 10×10 SOM[%]

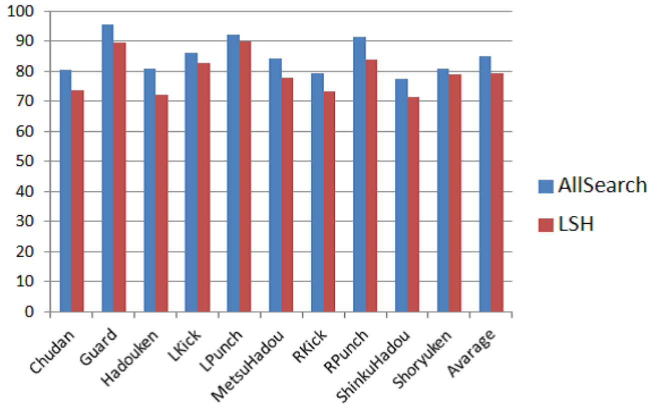

Fig. 4. Recognition Accuracy of 100×100 SOM[%]

In searching phase, when the query vector p is input, the hash value of this vector is calculated and matched product set is searched on each table. Then, the sum of sets of each search result is output as nearest neighbor slate points.

4 EXPERIMENTS

4.1 Preparation

We used the video game software "STREET FIGHTER 4" as the theme of early recognition. Ten kinds of gestures were selected for the experiment. The Kinect sensor captured each gesture at 30fps, which consists of 40-dimensional feature vector (2-dimensional position × 20 points) in each frame. Eight examinees played each gesture 30 times. Therefore, totally 2,400 (30×10×8) samples were collected. These samples were used for 6-fold cross validation in the following evaluation.

The parameters of LSH were set to k =64 and l =5. The size of SOM was changed as 10×10 and 100×100. The threshold to determine the recognition result was set to be 0.6. In other words, if the contribution ratio of the best matched posture exceeded the threshold, the system output

Table 1. Computational Time (sec)

	LSH	All Search
10×10	0.000043	0.00121
100×100	0.000059	0.1031

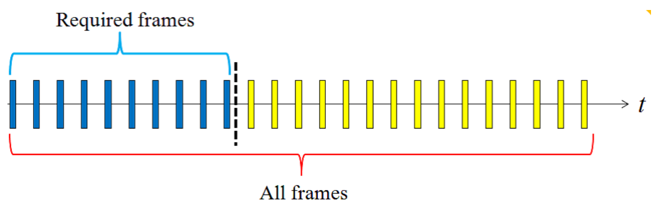

Fig. 5. Definition of Frame Ratio for Recognition (FRR)

the recognition result. In the test phase, if the computational time of each frame exceeded the video rate (i.e. 0.033sec), several frames were skipped (not processed) according to the time. For example, if it took about 0.066sec for each frame, every two frames were used for the evaluation.

4.2 Results

4.2.1 Computational Cost

Table 1 shows the average computational time for finding the best matched posture. In the case of greedy search (all search in the table), the computational time is proportional to the number of neurons. Therefore, the 100×100 size of SOM took about 100 times longer than the 10×10 size of SOM. If we use the 100×100 size of SOM, it will take about 0.1 sec (work at about 10fps). Therefore, every three frames will be used in the online recognition process.

On the other hand, LSH took about 0.00004∼0.00006 sec for each frame, and the computational time was almost constant even if the number of neurons increased. Therefore, we need not skip any frame if the LSH is used for searching the best matched posture.

4.2.2 Accuracy

The recognition accuracy is shown in Fig. 3 and Fig. 4. The horizontal axis shows the label of each gesture and most right is the average of all gestures. The vertical axis means the recognition ratio. We compared two approaches; a greedy search and a LSH-based search. In Fig. 3, the 10×10 size of SOM was used. As discussed above, the computational time was less than 0.033 sec so that any frame was not skipped, but the recognition accuracy was very low for several gesture classes. It makes no sense to reduce the computational time since it results in low accuracy of recognition result.

On the other hand, when the SOM had 100×100 neurons, every three frames were used in the greedy search. The ac-

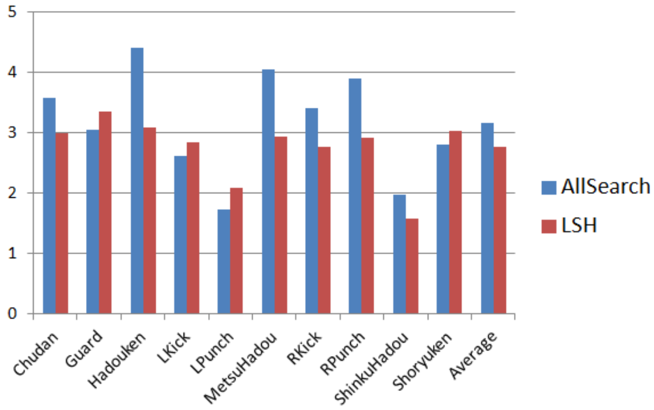

Fig. 6. Frame Ratio for Recognition [%]

curacy of both methods was almost the same. Strictly speaking, however, the accuracy of the greedy search was slightly more than the one of LSH even though the greedy search skipped several frames. We guess the reason as follows. The LSH-based search provides an approximate nearest neighbor search result. Therefore, the found posture is not always the best matched one, and if such a posture unfortunately has a high contribution ratio for a wrong gesture, a wrong label will be output from the system.

4.2.3 Response Speed

One of the most important evaluations is to measure the response speed of the system. In other words, how early the system could output the correct recognition result is evaluated. To measure the response speed, we define the frame ratio for recognition (FRR) as follows.

$$FRR = \frac{\text{\# of required frames}}{\text{\# of all frames}} \times 100 \qquad (2)$$

Fig. 5 supports the explanation of FRR. The FRR evaluates the percentage of the number of frames which are used for recognition to the all frames. Therefore, the smaller value of the FRR is desirable. The evaluation was performed when the system output the correct label only.

Fig. 6 shows the evaluation result of FRR. The FRR of LSH-based method was totally lower than the one of the greedy method. The greedy method skipped several frames in the online recognition process because of its computational time. That's why the FRR becomes higher than LSH-based method, which could investigate all of the input frames.

4.3 Discussion

Through the above experimental results, we found out some advantages of the proposed method. Firstly, the recognition accuracy of the proposed method did not become lower even it reduced the computational cost. Secondly, the response speed was faster than the traditional approach. Therefore, the proposed method realizes two important issues; high accuracy and quick response for input gesture patterns. Finally, the proposed method will work well even if the number of gesture classes increases since the computational cost is independent of the samples.

5 CONCLUSION

We have proposed an accelerated approach of early recognition of human gestures. Self-Organizing Map (SOM) is utilized for learning human gestures and obtaining the representative postures. When we investigate the postures which is the most similar to input posture, if searching all nodes of SOM in previous method is conducted, the computational cost becomes larger in proportion to the number of the representative postures. Moreover, if this phase takes longer time than a frame rate of input, the searching will drop the several frames and give bad effect on the result of recognition. Therefore, we used the Locality-Sensitive Hashing (LSH), which is a kind of approximate nearest neighbor searching, instead of previous method. Through the experiments, we could prove that the accuracy could be kept with much lower computational cost than the previous method. We are now researching the recognition which used the weighting to postures data to improve the recognition accuracy.

REFERENCES

[1] A. Mori, S. Uchida, R. Kurazume, R. Taniguchi, T. Hasegawa and H. Sakoe. “Early recognition and prediction of gestures”. Proc. of International Conference on Pattern Recognition, vol. 3 of 4, pp.560-563, 2006.

[2] S. Uchida, K. Amamoto. “Early Recognition of Sequential Patterns by Classifier Combination”. CD-ROM Proc. of International Conference on Pattern Recognition, 2008.

[3] Manabu Kawashima, Atsushi Shimada, Rin-ichiro Taniguchi : “Early Recognition of Gesture Patterns using Self-Organizing Map”, The Fifth Joint Workshop on Machine Perception and Robotics (MPR2009)

[4] T. Kohonen. “Self-Organization and Associative Memory”. Springer-Verlag, 1989.

[5] Teuvo Kohonen. “Self-Organizing Maps”. Springer Series in Information Science, 1995.

[6] Indyk, Motwani. ”Approximate nearest neighbor: towards removing the curse of dimensionality”. STOC’98, section 4.2

The Seventeenth International Symposium on Artificial Life and Robotics 2012 (AROB 17th '12),
B-Con Plaza, Beppu, Oita, Japan, January 19-21, 2012

Source recognition in acoustic sensor arrays using self-organizing hidden Markov models

Edgar E. Vallejo[1], Julio G. Arriaga[1], and Charles E. Taylor[2]

[1] ITESM Campus Estado de México, Atizapán de Zaragoza, Estado de México, 52926, México
[2] UCLA, Los Angeles, CA, 90095-1606, USA
(Tel: 1-310-825-6850, Fax: 1-310-206-3987)
(taylor@biology.ucla.edu)

Abstract: In this paper, we present a computational model for source recognition in acoustic sensor arrays. The proposed model uses a hybrid method of neural networks to create symbols then hidden Markov models that collectively learn to discriminate sequences of symbols from a collection of recordings from bird species with minimum human intervention. Preliminary simulation results indicate that this model is capable of producing acceptable levels of classification performance.

Keywords: Acoustic sensor arrays, hidden Markov models, bird species classification

1 INTRODUCTION

Over the last few years, we have been engaged in a research program that aims at understanding the capabilities and limitations of sensor arrays in habitat monitoring applications [1]. Particularly, we have developed acoustic sensor arrays for monitoring the diversity and behavior of bird species at several locations in Mexico and in the US. More recently, our research program has evolved towards the application of this technology for understanding the structure and function of bird song.

As part of this study, we have focused on developing robust filters that are able to discriminate bird species, and in some cases, bird individuals with reasonably high accuracy. Specifically, we have explored the use of unsupervised learning methods such as self-organizing maps [11][13], and supervised learning methods such as support vector machines [12], among others. We have had success with the use of hidden Markov models (HMMs) for this problem [9].

We believe that given the appropriate conditions, an array of sensors should be able to self-organize so as to behave as a single ensemble [4][8]. In this idealization, sensors can identify and collectively learn to classify events of interest from an arbitrary acoustic recording stream, with minimal human intervention. This ability is at the core of what is required for achieving adaptive behavior and communication in sensor arrays.

Towards this end, we developed a computational model for source recognition in acoustic sensor arrays. The proposed model uses hidden Markov models that self-organize to discriminate a collection of input sequences with minimal human intervention. We chose HMMs for its ability to discriminate input sequences of arbitrary length, which have proven difficult for alternative classification methods.

Particularly, we introduce a collective learning algorithm that enable a collection of HMMs to learn to classify four different species of antbirds. In the collective learning procedure, a sensor detects an input sequence from the input stream and uses its HMM to determine its corresponding output. The sensor output is then combined with those of its neighbor sensors to produce a consensus output. The sensor then computes the maximum likelihood estimators from these consensus sequences to update its parameters, and the learning process continues.

The overall objective of this self-organizing learning process is to enable HMMs to accurately classify the input sequences and to converge to consistent collective classifications along the array. We used recordings obtained from our field studies in a tropical rainforest in Chiapas, Mexico. From these recordings, we constructed a collection of training sets consisting of tokenized sequences of bird songs.

2 METHODS

2.1 Self-organizing HMMs

In the proposed model, the classification of bird species is produced by hidden Markov models (HMMs). HMMs are extensions of Markov chains in which an observation is a probabilistic function of the state [7].

Formally, a *hidden Markov model* is a 4-tuple (Q, Σ, A, E), where

1. Q is a finite set of states,
2. Σ is an alphabet of symbols,
3. $A = (a_{kl})$ is a $|Q| \times |Q|$ matrix of state transition probabilities,
4. $E = (e_k(b))$ is a $|Q| \times |\Sigma|$ matrix of emission probabilities

Let $M = (Q, \Sigma, A, E)$ be a hidden Markov model. A path $\pi = \pi_1 \ldots \pi_n$ is a sequence of states. The probability that a sequence x of symbols from the alphabet Σ was generated by the path π is

$$P(x|\pi) = \prod_{t=1}^{n} P(x_i|\pi_i)P(\pi_i|\pi_{i+1}) = \prod_{i=1}^{n} e_{\pi_i}(x_i) \cdot a_{\pi_i,\pi_{i+1}}$$

The decoding problem is formulated as to find the optimal path $\pi^* = \arg\max_\pi P(x|\pi)$ for x such that $P(x|\pi)$ is maximized.

The solution of the decoding problem is provided by the Viterbi algorithm [7]. The idea is that the optimal path for the $(i+1)$ prefix $x_1 \ldots x_{i+1}$ of x uses a path for an i-prefix of x that is optimal among the paths ending in an unknown state $\pi_i = k \in Q$.

Define $s_k(i)$ as the probability of the most probable path for the prefix $x_1 \ldots x_i$ that ends with state k ($k \in Q$ and $1 \le i \le n$). Then

$$s_l(i+1) = e_l(x_{i+1}) \cdot \max_{k \in Q}\{s_k \cdot a_{kl}\}$$

Let $M = (Q, \Sigma, A, E)$ be a hidden Markov model and $x = x_1 \cdots x_n$ be a string over the alphabet Σ. The HMM M produces the output o in response to input x, $M(x) = o$, if a sequence of states $\pi = \pi_0 \ldots \pi_n$ exists in Q with the following conditions:

1. π is the optimal path π^* given the sequence x and the hidden Markov model M, and
2. $\pi_i^* = o_i$ ($1 \le i \le n$) is the state of the optimal path π^* given the sequence x and the hidden Markov model M.

2.2 Learning algorithm

For this study, we devised a collective learning algorithm for HMMs. The model comprises a collection of randomly generated HMMs. For each input in the training set, an HMM uses the consensus optimal path of the HMMs in its neighborhood as its target output. The consensus optimal path is obtained from the neighbor HMMs by voting. The maximum likelihood estimators are then computed from the set of target outputs as follows. We count the number of times each particular transition or emission is used in the set of training inputs. Let these be A_{kl} and $E_k(b)$. Then the maximum likelihood estimators for a_{kl} and $e_k(b)$ are given by:

$$a_{kl} = \frac{A_{kl}}{\sum_{l'} A_{kl'}}$$

and

$$e_k(b) = \frac{E_k(b)}{\sum_{b'} E_k(b')}$$

The learning algorithm is described in Table 1.

Table 1. Learning algorithm.

1. Create an initial random set P of HMMs
2. `Do until` number simulation steps N is met
   (a) `For each` HMM $M \in P$ `do`
      i. Select a subset $S \subseteq P$ of HMMs at random
      ii. Compute the output sequence $M'(x) = o$ for each $M' \in S$ and $x \in X$ using the Viterbi algorithm
      iii. Compute the maximum likelihood estimators a_{kl} and $e_k(b)$ from the consensus outputs of S.
      iv. Update the parameters A and E of M to be the maximum likelihood estimators.

   `End for`

`End do`

Table 2. Training set.

label	species	samples
BAS	Barred antshrike	12
DAB	Dusky antbird	12
GAS	Great antshrike	12
MAT	Mexican antthrush	12

2.3 Data set

The samples used in the experiments presented here were provided to us by Martin L. Cody. The dataset consists of songs from four different antbird species that are abundant at the Montes Azules Biosphere Reserve in Chiapas, Mexico. They are listed on Table 2.

The preparation of data proceeded as follows. The songs were segmented using the Raven bird song analysis program [3]. Syllables were identified by small discontinuities in the corresponding spectrogram. Using this procedure, we obtained a collection a syllable samples as listed in Table 3. For each sample, we obtained a series of temporal and spectral measurements using Raven. These parameters were extracted from the sound signal using the short-time Fourier transform (STFT) and selected according to previous studies on bird species classification [3] [6]. These measurements are described in Table 4.

A normalization process was applied to this data because the selected measurements span different orders of magnitude. Such differences might result from how close the subject is to the recorder, for example. Using the mean and the standard deviation of each measurement, we obtained a collection of feature vectors described as z-scores.

The collection of feature vectors describing syllables were classified using a simple competitive learning neural network [5]. Once the syllables have been categorized we proceeded to represent the original songs as strings of symbols using the label from each syllable category. Table 5 shows the string representation of a subset of the songs obtained us-

Table 3. Syllable samples

label	samples
BAS	216
DAB	129
GAS	339
MAT	117

Table 4. Selected features of syllables

parameter	description
Low frequency	The lower frequency bound of the syllable
High frequency	The upper frequency bound of the syllable
Delta time	The duration of the syllable
Max amplitude	The upper amplitude bound of the syllable
Max power	The upper power bound of the syllable

ing a two-unit competitive learning network, with learning constant $\eta = 0.1$ and epochs = 1000.

Similarly, table 6 shows the string representation of a subset of the songs obtained using a four-unit competitive learning network, with learning constant $\eta = 0.1$ and epochs = 1000.

3 EXPERIMENT AND RESULTS

Multiple simulations were conducted using different combinations of parameter values presented in table 7. The following were the major results:

1. HMMs produced a reasonably good categorization performance ($\sim 82\%$) of the training sets.
2. Acceptable numbers of training steps (~ 100) were required for the collection of HMMs to converge to consistent classifications.
3. The description of bird songs using fewer distinct syllables and HMMs with fewer states produced better classification performance.

Table 5. Strings representation of the training set using 2 syllables

label	string
BAS_1	BBBBBBBBBAAAABAAAAAAABA
BAS_2	BBBBAAAAAAAAAAAAAAAAAAAAA
BAS_3	BBBBABBBBAAAAABAAAAABABBA
DAB_1	BAAAAAAAAABBBBB
DAB_2	BAAAAAABBBBBBB
DAB_3	BBAAAAAAAAABBBB
GAS_1	BBBBBBBAAABBABBBABAAAAAABAAABBABBAAAAAB
GAS_2	BBAAAAAABABBABBAAAAAAAAAAAAAAAAAAAAAB
GAS_3	BBBBBBBBBABBAAAAAAAAAAAAAAAAAAAAAAAAB
MAT_1	BBBBBBBBBBBBB
MAT_2	AAAAAAAAAABBB
MAT_3	AAAAAAAAAAAAA

Table 6. Strings representation of the training set using 4 syllables

label	string
BAS_1	DDDAAAAAABAAAAAAAAAABAC
BAS_2	DDDAAAAAAAABBBABBBBBBBAAB
BAS_3	DDDAAAAAAAAABAAAAAAAAAAAC
DAB_1	DBBBBBBBBBDDDDD
DAB_2	DBBBBBBBDDDDDD
DAB_3	DDBBBBBBBBBDDDD
GAS_1	DDDDCCCDCCCCCCCCCCCCBCCACBAACCAAAABACCD
GAS_2	DDACCCCCCBCCCCBCCCCCACAACABBABBBBAAD
GAS_3	DDDCDCCCCCCBCCCCBBBCCBCCAABAABABBBBBCD
MAT_1	DDDDDDDDDDDDD
MAT_2	DBBBBBBDDDBBB
MAT_3	BBBBBBBBBBBBB

Table 7. Parameters for simulations

parameter	value
Simulation steps	100–200
$\|P\|$	128–512
$\|S\|$	8–32
$\|Q\|$	8–16
$\|\Sigma\|$	2-16

To calculate the classification performance we obtain the consensus output sequence from all of the samples in the same category. Then we compute the pairwise similarity of each output sequence produced for each sample in the category with respect to the consensus output sequence of the category.

Table 8 shows the accuracy of classification obtained for the two-syllable experiment using HMMs with 8 states and 100 simulation steps.

Similarly, Table 9 shows the accuracy in classification obtained for the four-syllable experiment using HMMs with 16 states and 200 simulation steps.

4 CONCLUSION

Despite its preliminary character, the results shown here seem to indicate that acceptable categorization of bird species can emerge using self-organizing HMMs. The results also show that the accuracy in classification depends on the number of syllables describing the bird songs. This sug-

Table 8. Simulation results

species	classification
BAS	82%
DAB	86%
GAS	81%
MAT	77%

Table 9. Simulation results

species	classification
BAS	79%
DAB	82%
GAS	78%
MAT	75%

gests the existence of a number that is optimum for accurate species classification. Moreover, categorization requires minimum human intervention in contrast with supervised learning methods. In general, experimental results showed that there is an advantage for simulations in which hidden Markov models posses fewer states.

We think the proposed method could be extended in several ways. For instance, the most relevant in practice would be to use this model for event detection and to identify the species that are sharing the acoustic space, in both the temporal and spectral spaces. This capabilities would enable the technology of sensor arrays to explore important questions in ecology regarding both the inter- and intra- species interaction of birds.

It should be noted that the proposed model has only been tested in a simple simulated setting. We will test the proposed model in real settings in the near future. We believe that self-organizing HMMs hold much promise to contribute for the development of fully automated sensor arrays for habitat monitoring applications.

Acknowledgements

We thank Martin L. Cody for kindly providing to us the recordings of birds vocalizations used in our experiments. This work was supported by the US National Science Foundation, Award No. IIS-1125423. Any opinions, findings and conclusions or recommendations expressed in this publication are those of the authors and do not necessarily reflect the views of the sponsoring agency.

REFERENCES

[1] Blumstein, DT, Mennill, DJ, Clemins, et al (2011) Acoustic monitoring in terrestrial environments using microphone arrays: applications, technological considerations and prospectus. *Journal of Applied Ecology*, Volume 48, Issue 3, pages 758767

[2] Catchpole, C. K., Slater, P. L. B.: *Bird song biological themes and variations.* Cambridge University Press, 1995.

[3] Charif, R. A., Clark, C. W., Fistrup, K. M.: *Raven 1.2 user's manual.* Cornell Laboratory of Ornithology, Ithaca, NY, 2004.

[4] Collier, T. C., Taylor C.E.: Self-Organization in Sensor Networks. *Journal of Parallel and Distributed Computing* 64:7 (2004) pp.866–873.

[5] Hertz, J., Krogh A., Palmer, R. G. (1991) *Introduction to the theory of neural computation*. Addison Wesley, 1991.

[6] Nelson, D. A.: The importance of invariant and distinctive features in species recognition of bird song. *Condor*: Vol. 91, No. 1, pp.120-130,1989.

[7] Rabiner, LR (1989), A tutorial on hidden Markov models and selected applications in speech recognition. *Proceedings of the IEEE* 77: 257–286.

[8] Taylor, C. E.: From cognition in animals to cognition in superorganisms. In M. Bekoff, C. Allen and G. Gurghardt, (eds.), *The Cognitive Animal. Empirical and Theoretical Perspectives on Animal Cognition* The MIT Press, 2002.

[9] Trifa, V., Kirschel, A., Vallejo, EE and CE Taylor (2008). Automated species recognition of antbirds in a Mexican rainforest using hidden Markov models. *J. Acoust. Soc. Am*. Volume 123, Issue 4, pp. 2424-2431.

[10] Vallejo EE and CE Taylor (2004), A simple model for the evolution of a lexicon. In M. Sugisaka, H. Tanaka (eds), *Proceedings of the Ninth International Symposium on Artificial Life and Robotics, AROB9th*.

[11] Vallejo EE, Cody, ML and CE Taylor (2007), Bird species recognition using hierarchical self-organizing maps. In (eds), *Proceedings of the Australian Artificial Life Conference, ACAL 2007*. Springer-Verlag.

[12] Vallejo EE and CE Taylor (2009), Sensor arrays for acoustic monitoring of bird behavior and diversity. Preliminary results on source identification using support vector machines. *Artificial Life and Robotics*. Springer-Verlag.

[13] Vallejo EE and CE Taylor (2010), A self-supervised classifier ensemble for source recognition in acoustic sensor arrays. In (eds), *Proceedings of the Twelfth International Conference on the Simulation of Living Systems, Artificial Life 12*. The MIT Press.

The Seventeenth International Symposium on Artificial Life and Robotics 2012 (AROB 17th '12),
B-Con Plaza, Beppu, Oita, Japan, January 19-21, 2012

Japanese Finger-spelling Recognition Using a Chest-mounted Camera

Akira Nagasue, Joo Kooi Tan, Hyoungseop Kim and Seiji Ishikawa

Kyushu Institute of Technology, Kitakyushu 804-8550, Japan
Tel: 093-884-3191, Email: nagasue@ss10.cntl.kyutech.ac.jp

Abstract: This paper proposes a technique for recognizing Japanese Finger-spelling using a sign language user's chest-mounted camera. Unlike existent systems, the technique employs a sign language user's chest-mounted camera attached to the sign language user himself and recognizes his/her sign language through the captured images of Japanese Finger-spelling. We use a silhouette picture of a hand, and MHI (Motion History Image) for Japanese finger-spelling recognition. The recognition method uses the eigenspace method. Furthermore, in order to recognize Japanese finger-spelling from an animation (image sequence), a character segmentation technique is also proposed. Finally, finger characters are recognized and the performance is shown experimentally.

Keywords: Sign language recognition, Chest-mounted camera, Motion history images, Eigenspace method.

1. INTRODUCTION

Recently, requests on computer-based welfare assistance systems have been increasing. In order to develop these systems, a great number of researches aim the development of automatic Japanese sign language recognition systems using image processing. However, conventional recognition systems deal with those input images obtained from a camera facing a disabled person in hearing and speaking [1] or using many sensors [2, 3]. But, normally, we do not possess this kind of system including a camera in our daily life, since it is hardly the case that we happen to meet such disabled people who wish to talk to us. Thus this kind of system would not spread for practical use in our daily life. On the contrary, if a Japanese sign language user is equipped with such a system, it will definitely improve his/her quality of life (QOL), as he/she can communicate to everyone to whom he/she wishes to do so.

In this paper, we propose a system that is held by a sign language user for recognizing his/her sign language. Unlike existent systems, the proposed system employs a chest-mounted camera shown in **Fig. 1** which is held by a sign language user and recognizes his/her Japanese finger-spelling as shown in **Fig. 2** through the captured images of his/her finger shapes. We think this system can be employed as a new human interface for not only Japanese sign language users but also healthy persons.

2. PROPOSED METHOD

In the first step, we extract a hand area from an image taken from a chest-mounted camera. Next, we recognize the Japanese finger-spelling performed by the user employing the extracted hand area as shown in **Fig. 3**.

Fig. 1. Location of the chest-mounted camera

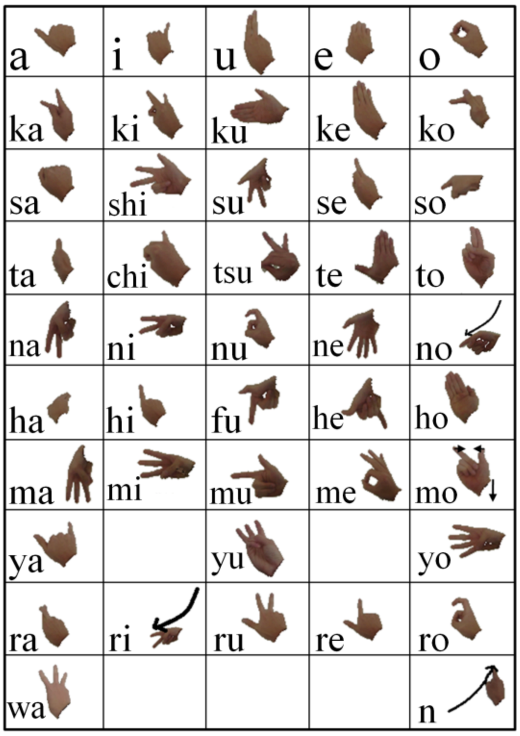

Fig. 2. Japanese finger-spelling list

(a) (b)

Fig. 3. Skin color extraction:
(a) Input image, (b) extracted hand.

2.1 Character recognition

Recognition methods for Japanese finger-spelling are usually composed of a nearest neighbor search in the eigenspace using a hand silhouette for non-moving finger-spelling and nearest neighbor search in eigenspace using a Motion History Image (MHI) [4] and hand silhouettes for moving finger-spelling.

MHI is defined by the following formula.

$$H_\tau(x,y,t)=\begin{cases}\tau & \text{if } D(x,y,t)=1\\ \max(0,H_\tau(x,y,t-1)-1) & \text{otherwise}\end{cases} \quad (1)$$

Here x is the abscissa of an image, y is the ordinate of the image, t expresses time, and τ is a parameter which adjusts time that has passed in the sequence. An example of the expression of a sign language letter by a MHI is shown in **Fig. 4**. Examples of the images used for recognition is shown as well in **Fig. 5**.

Based on this strategy, the recognition of a finger character can be performed regardless of whether motion exists or not.

2.2 Character segmentation

Finger character segmentation in an image sequence is also performed by considering inter-frame difference using hand silhouette images. When the number of moving pixels in the inter-frame difference exceeds a threshold value of motion (Th_M), it is recognized as the frame in which the hand has moved, and when the number of pixels does not exceed the threshold value, it is recognized as the frame which has a stopped (static) hand, i.e., the frame which shows the finger character.

This finger character representation frame is counted. If the number of the frames exceed the threshold value (Th_F), the finger character is recognized as that without a motion. Otherwise it is recognized as that with a motion.

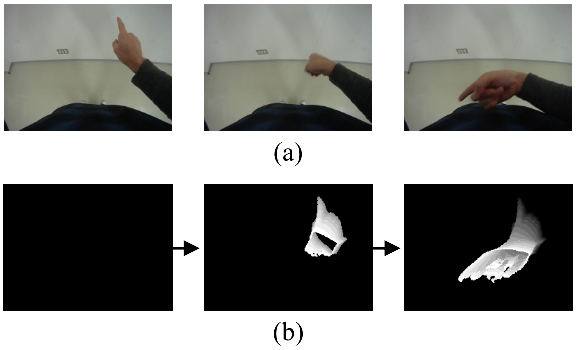

Fig. 4. Examples of MHI: (a) Input images, (b) MHIs.

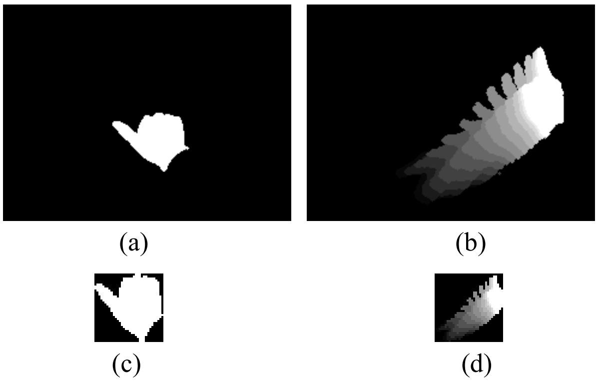

Fig. 5. Examples of database images: (a) Hand silhouette image "a", (b) MHI and hand silhouette image "n", (c) database image "a", (d) database image "n".

3. EXPERIMENTAL RESULTS

3.1 Experiment of Japanese finger-spelling recognition

In the first place, in order to perform the experiment on Japanese finger-spelling recognition, we took the videos of 45 Japanese finger-spelling characters five times. We used four sets for learning, and one set for recognition. This process was repeated five times for one person, and it was repeated with respect to five persons. The recognition rate is computed from the following formula.

$$Recognition\ rate=\frac{CR}{ALL} \quad (2)$$

Here CR is the number of correctly recognized characters, whereas ALL is the number of all characters.

Finally the proposed method achieved 89.1% (1002/1125) of the recognition rate. A detailed result is shown in **Table 1** and **Fig. 6**.

It is thought that incorrect recognition arose in the characters in which the shape or motion are similar with each other, e.g. "no" and "ri". It is shown in **Fig. 7**.

Table 1. Individual recognition rates

	Person A	Person B	Person C	Person D	Person E
Data 1	91.1%	93.3%	75.6%	88.9%	82.2%
Data 2	95.6%	84.4%	91.1%	82.2%	88.9%
Data 3	95.6%	93.3%	88.9%	86.7%	77.8%
Data 4	100.0%	95.6%	95.6%	84.4%	86.7%
Data 5	86.7%	93.3%	91.1%	84.4%	93.3%
Average	93.8%	92.0%	88.4%	85.3%	85.8%

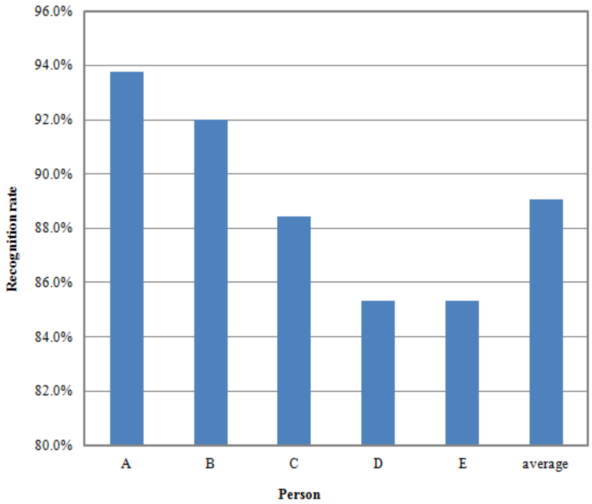

Fig. 6. Average recognition rates of five persons.

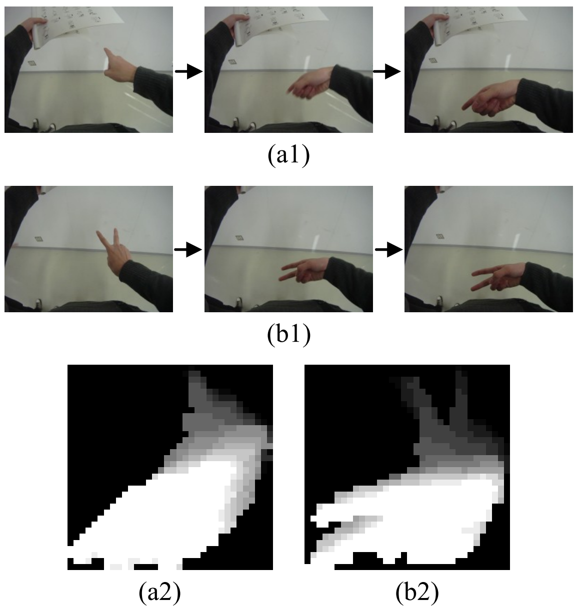

Fig. 7. Examples of similar character:(a1) Input images "no", (b1) input images "ri", (a2) database image "no", (b2) database image "ri".

3.2. Experiment of character segmentation

In the second place, we performed the experiment on character segmentation. We took videos of 6 sentences using Japanese finger-spelling characters four times.
They are 'kon-nichiwa', 'ohayo', 'kore ikura', 'itsu kitano' and 'toki wa kanenari'. An evaluation method is described in the following.

First, the correct answer key-frame which should certainly be contained is set to the character representation section by manual for every character of a text. When the correct answer key-frame is contained in the detected character representation section, it is considered as success (TP: True Positive), and when more than one are contained with the case where it is not contained, it is considered as failure (FP: False Positive). Moreover, the finger character accompanied by a motion or a finger character without a motion is distinguished among success (TP), and success is defined as R (Right). It evaluates using right display rate ($success$) and distinction rate ($decision$). The following formula defines $success$ and $decision$.

$$success = \frac{TP}{NUM} \tag{3}$$

$$decision = \frac{R}{TP} \tag{4}$$

Here NUM is the number of characters in a text.

The proposed method segmented the sentences at a rate of 90.8% ($success$). Among these, 77.8% of the letters were correctly recognized concerning the presence or absence of movement ($decision$).

Since the time to display a character differs from person to person, the existence of a motion in a character has become less discriminative feature. Also, since the motion was distinguished using the number of change pixels, it is thought that the size of the hand being reflected has caused errors. The result of the text recognition using both Japanese finger-spelling recognition method and character segmentation method is shown in **Fig. 8**.

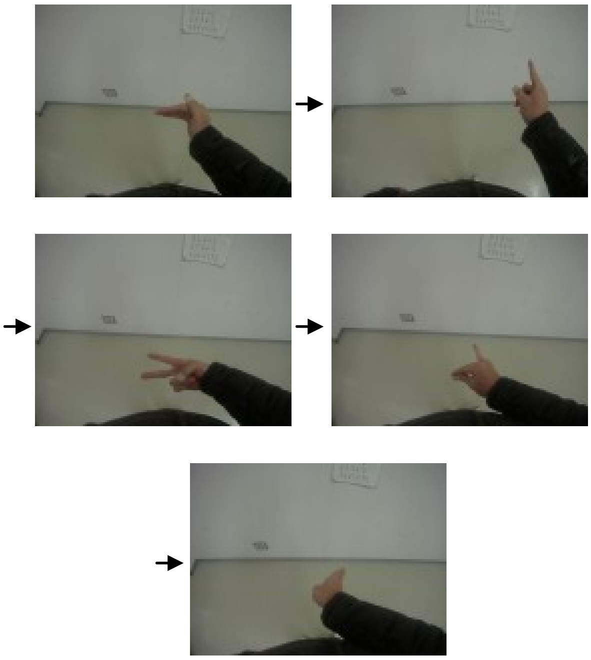

(a)

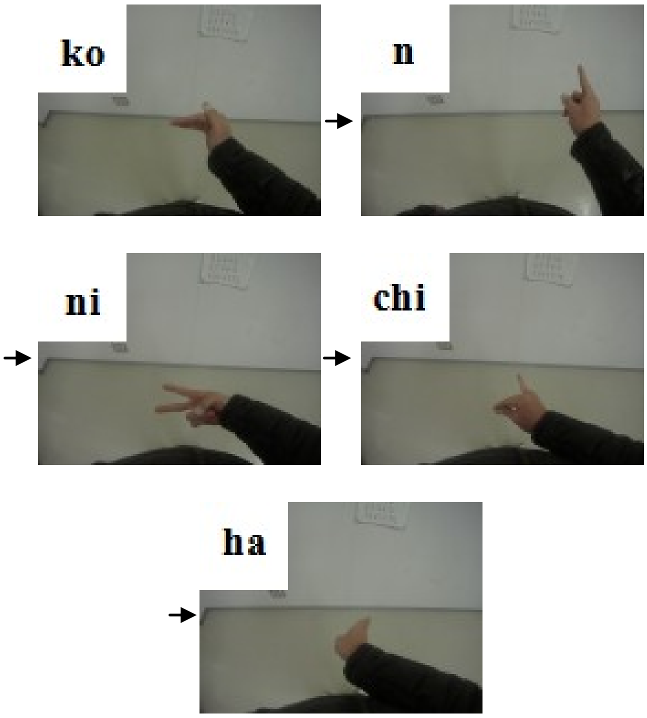

(b)

Fig. 8. The recognition result of "kon-nichiwa": (a) Part of input animation, (b) part of output animation.

4. CONCLUSIONS

We proposed a Japanese finger-spelling recognition method from the chest-mounted camera images of a Japanese sign language user. The performance of the method was satisfactory. However, there still exists a problem in the accuracy of character segmentation. As future work, we are going to improve the character segmentation method. Application to real time recognition is planned and a voice sound and P-sound recognition method will be investigated as well.

REFERENCES

[1] Liwicki, S., Everingham, M. (2009), Automatic recognition of fingerspelled words in British Sign Language. 2009 IEEE Computer Society Conference on Computer Vision and Pattern Recognition, Workshops, pp.50-57.

[2] Brashear, H., Henderson, V., Park K. H., et al (2006), American sign language recognition in game development for deaf children. Proceedings of the 8th International ACM SIGACCESS Conference on Computers and Accessibility, pp.79-86.

[3] Brashear, H., Starner, T., Lukowicz, P., et al (2003), Using multiple sensors for mobile sign language recognition. Seventh IEEE International Symposium, pp.45-52.

[4] Bobick, A. F., Davis, J. W. (2001), The recognition of human movement using temporal templates. IEEE Transactions on Pattern Analysis and Machine Intelligence, Vol.23, No.3, pp.257-267.

ACKNOWLEDGMENT

This work was supported by JSPS KAKENHI (22650022) which is greatly acknowledged.

Development of MEMS micro robot using piezoelectric actuator mechanism

Tatsuya Ogiwara, Kazuto Okazaki, Yutaro Kezuka, Shinpei Yamasaki, Minami Takato, Ken Saito[1]
and Fumio Uchikoba[2]

Nihon University, Chiba 274-8501, Japan
(Tel: +81-47-469-5343, Fax: +81-467-9504)

[1]kensaito@eme.cst.nihon-u.ac.jp
[2]uchikoba@eme.cst.nihon-u.ac.jp

Abstract: This paper presents the MEMS (Micro Electro Mechanical Systems) micro robot using piezoelectric actuator mechanisms. The size of the fabricated micro robot was 3.8, 4.0, 3.5mm, width, length and height, respectively. The basic components of the MEMS micro robot were made from silicon wafer. The micro fabrication of the silicon wafer was done by the MEMS technology. The vibration of the piezoelectric elements was transduced to rotational movement by the piezoelectric actuator mechanisms. Link mechanisms generated the locomotion of the robot from rotational movement. In this paper, continuous movement was achieved by using the piezoelectric actuator mechanism without thermal activation.

Keywords: MEMS, Micro Robot, Piezoelectric Elements.

1 INTRODUCTION

Many studies have been done on micro robots for several applications such as precise manipulations, medical fields, and so on [1, 2]. Although the miniaturization of the robot has been mainly progressed by mechanical machining and assembles, some difficulty has appeared in order to achieve further miniaturization. However, mechanical machining is difficult to fabricate the component which is smaller than 1mm size. Therefore, MEMS (Micro Electro Mechanical Systems) technology which is the micro fabrication technology based on the IC production line has been studied for fabricating the components of the micro robot [3, 4].

We are studying about the micro robot system for the purpose of construct the active system like insects. Insects realize the autonomous operation using the excellent structure and the active brain control. Previously, we constructed the 4.0, 4.0, 3.5 mm, width, length and height size micro robot using MEMS technology [5]. The structure and the step pattern of the robot was emulated those of the insect. The MEMS micro robot was generated locomotion by the rotary type actuator and 6 legs. The rotary type actuator used 4 pieces artificial muscle wires. The artificial muscle wire shrunk at high temperature and extended at low temperature. However, rotary type actuator using artificial muscle wires was difficult to actuate for long periods because thermal generation of the artificial muscle wire was larger than the cooling. In addition, the locomotion speed was limited by the speed of shrunk and extend of the artificial muscle wires.

In this paper, millimeter size piezoelectric actuator mechanism for MEMS micro robot is proposed, though the 6 legs and link mechanisms are same as previous MEMS micro robot. The difference is rotary type actuator. The rotational movement was generated by the piezoelectric actuator. The piezoelectric actuator has the potential of long and fast the locomotion.

2 MECHANISM OF MEMS MICRO ROBOT

2.1 Design of MEMS micro robot

The design of fabricated MEMS micro robot is shown in **Fig. 1.** The size of the MEMS micro robot without piezoelectric elements fabricated by the MEMS technology was designed as 3.8, 4.0, 3.4mm, width, length and height. The MEMS micro robot consisted of the rotary type actuator and the link mechanisms.

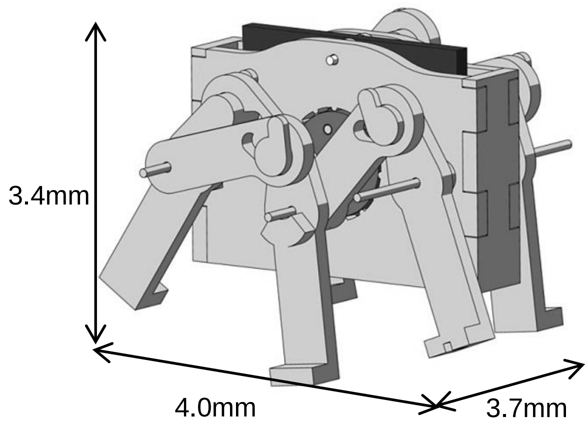

Fig. 1. Design of fabricated MEMS micro robot

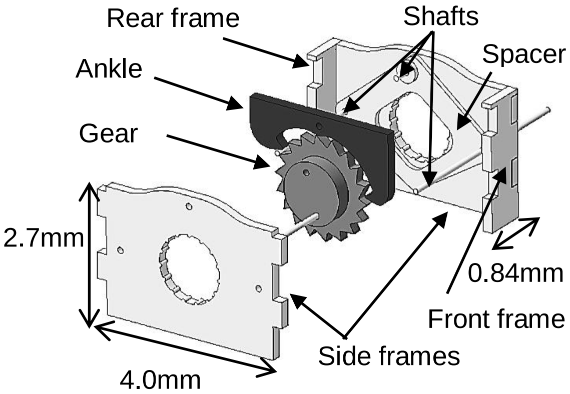

Fig. 2. Design of the rotary type actuator

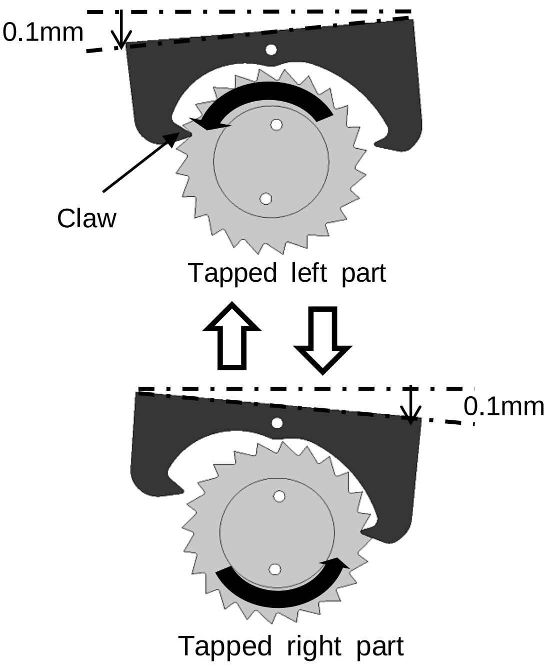

Fig. 3. Rotational mechanism of the ankle and gear

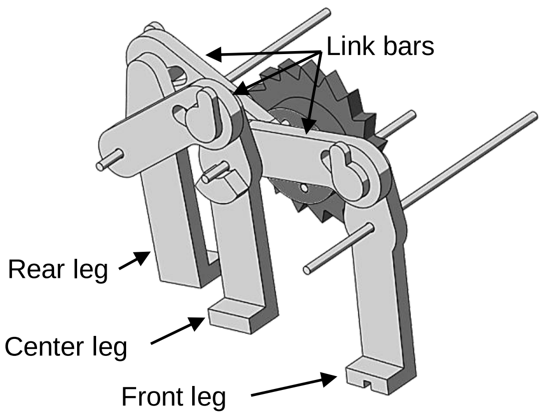

Fig. 4. Design of the link mechanism

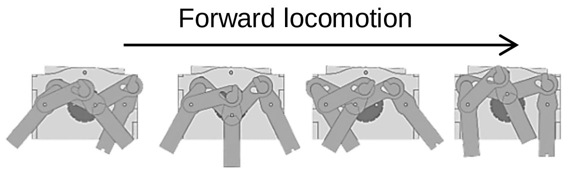

Fig. 5. Schematic diagram of locomotion

The design of the rotary type actuator is shown in **Fig. 2.** The fabrication process of basic components was MEMS technology. The rotary type actuator consisted of frames, an ankle, and a gear. Each frame of micro robot was assembled to join a grooves and tenons. Shafts were fixed in the hole at the top of the side frame. The ankle was connected to the shaft of the side frame. The gear was connected to the hole of the side frame. The displacement of the ankle was designed 0.1mm to generate the rotational movement of the gear.

Fig. 3. shows the mechanism of the ankle and the gear. Alternate tapping the left part and right part of the ankle by piezoelectric elements, and rotational movement of the gear was generated by continuing tapping of the ankle.

Design of the link mechanism is shown in **Fig. 4.** The link mechanism was composed by front legs, center legs, rear legs, and three link bars. The front leg and the rear leg were connected to the center leg by the link bar, respectively. The center leg connected to the gear by the shaft.

Fig. 5. shows the schematic diagram of forward locomotion. The locomotion movement of the micro robot was generated by rotational movement of the gear. The rotational movement was 180 degrees phase shift against the counter side.

2.2 Fabricated Parts

The fabrication process of the micro robot components was based on MEMS technology. The designed shape was formed by the photolithographic process. ICP (Inductively-Coupled plasma) dry etching process realized high aspect ratio machining. The starting materials were silicon wafers with various thicknesses (100, 200, 500μm) which were used depending on the parts.

Fig. 6. shows the fabricated parts of the MEMS micro robot. The gear shaft and the hole in the side frame were designed within the gap of 20μm. The gear shaft and side frame were assembled within the gap 25μm. This gap didn't affect the rotational movement. The link bars and the legs were assembled within the gap 18μm. This gap didn't affect the locomotion.

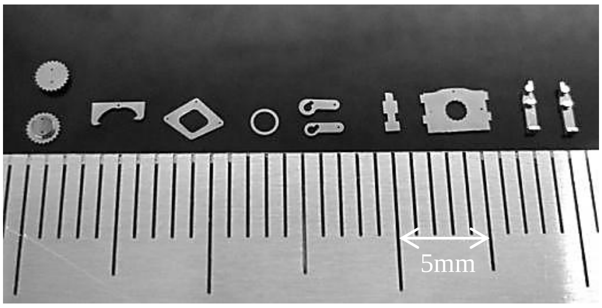

Fig. 6. Fabricated parts of the MEMS micro robot

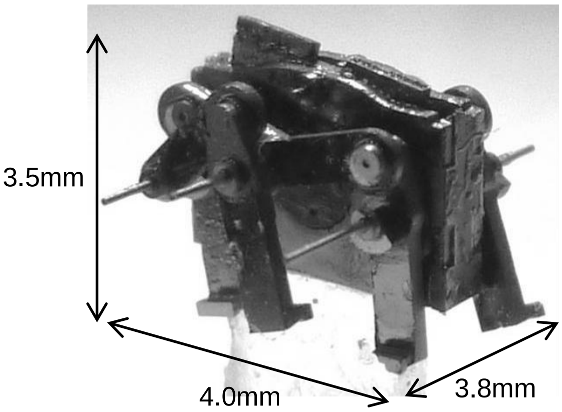

Fig. 7. Fabricated MEMS micro robot

Fig. 7. shows the fabricated MEMS microrobot. The size of the fabricated micro robot was 3.8, 4.0, 3.5mm, width, length and height, respectively.

3 PIEZOELECTRIC ACTUATOR

Schamatic diagram of the piezoelectric actuator is shown in **Fig. 8.** The rotational movement of rotary type actuator was generated by hitting of a pair of hammers using the piezoelectric elements. The piezoelectric elements was 15, 2mm size. The hammer was consisted of piezoelectric elements and a silicon block. The structure of hammer was a cantilever. The rotational movement was 180 degrees phase shift on each side to represent the locomotion of insect. Two hammers were tapping alternate by imputing the anti-phase wave forms. The hammers were connected to the waveform generator and inputted the square wave. The peak to peak voltage was 20V. The frequency of input pulse was based on the resonant frequency of the hammer. The resonant frequency of piezoelectric elements describe as Equation (1). Where f_n is resonance frequency, α_n is resonance frequency constant of cantilever, L is length, E is Young's modulus, I is second moment of area, ρ is density, A.is cross-sectional area.

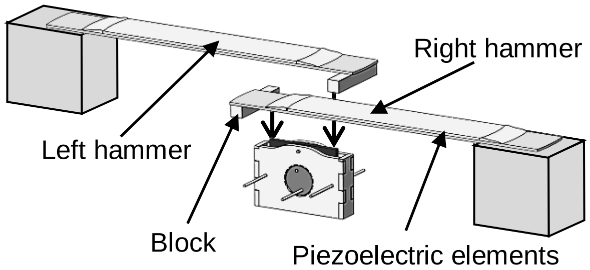

Fig. 8. Schamatic diagram of the piezoelectric actuator

$$f_n = \frac{\alpha_n^2}{2\pi L^2}\sqrt{\frac{EI}{\rho A}} \tag{1}$$

The displacement of piezoelectric elements was maximum when the oscillation mode was ferocity oscillation mode.

The α_n of first oscillation ($\alpha_n = 1.8751$). The calculated resonant frequency of piezoelectric elements was 443Hz. The resonant frequency of hammer was different from piezoelectric element. Therefore, the resonance frequency and displacement of the hammer were measured by laser displacement meter. The input pulse of the hammer was based on the calculated resonant frequency. The maximum displacement of hammer was 395µm. The resonant frequency was 597Hz. A pair of hammers and rotational actuator were assembled and connected to the waveform generator. Therefore, the pulse was inputted to the hammer. The rotational movement was generated by tapping of the hummer. However, the locomotion wasn't generated in the setting parameter. The torque of hammer was not enough to generate the rotational movement of gear. The displacement of the hammer describes as equation (2). Where δ is a displacement of the ankle, P is a weight.

$$\delta = \frac{PL^3}{3EI} \tag{2}$$

The block was used as weights. The mass of the block was regarded as the concentrated load. The displacement of the hammer describe as equation (3). Where m is a mass, g is gravitational.

$$\delta = \frac{mgL^3}{3EI} \tag{3}$$

The displacement of the hammer depends on the number of blocks and lengths of cantilever. The mass of block was 100mg. The mass of the cantilever was increased every 3mg. The block was put on the tip of the hammer. The displacement was measured by laser displacement meter.

Fig. 9. shows the relation of displacement and the mass of hammer. The resonance frequency was changed by varying the mass. Therefore, the resonance frequency of the every measure points was different. This figure shows that the displacement increases in the case of increases the mass.

However, the piezoelectric elements was cracked when the displacement was over 0.9mm. Therefore, the maximum mass was 118mg. The resonant frequency was 235Hz where the displacement was 680μm. As a result, our fabricated robot performed forward locomotion. The locomotion speed was 15mm/min. The proposal piezoelectric actuator mechanism could actuate the rotor for a long period.

4 CONCLUSION

In this paper, we fabricated the 3.8, 4.0, 3.5 mm, width, length, and height size micro robot by MEMS technology. The rotational movement was generated by the rotary type actuator using piezoelectric elements. As a result, the locomotion speed of the robot was 15mm/min. The continuous movement was achieved by using piezoelectric elements without thermal activation.

In the future, we will mount the piezoelectric actuator on the micro robot.

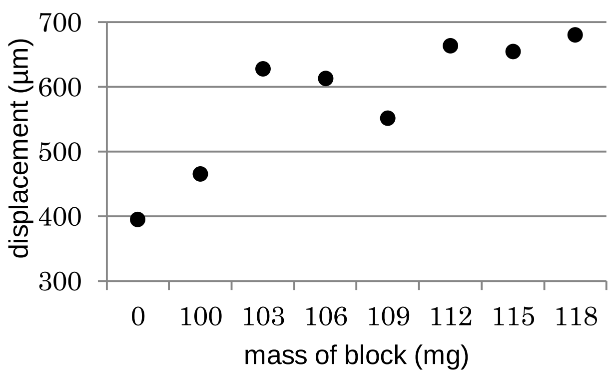

Fig. 9. Relation of displacement and mass of hammer

ACKNOWLEDGEMENTS

The fabrication of the MEMS micro robot was supported by Research Center for Micro Functional Devices, Nihon University.

This study was supported by Nihon University Academic Research Grant (Total research, "11-002"), JSPS KAKENHI (23760243). We appreciate the support.

REFERENCES

[1] P.Saketi (2010), Microrobotic Platform for Manipulation and Flexibility Measurement of Undividual Paper Fibers, IEEE/RSJ International conference on Intelligent Robots and Systems (IROS), pp5762-5767

[2] Andrew T.Baisch (2010), Biologically-Inspired Locomotion of a 2g Hexapod Robot, IEEE/RSJ International conference on Intelligent Robots and Systems (IROS), pp5360-5365

[3] R.J.Wood (2008), The first takeoff of a biologically inspired at-scale robotic insect, IEEE Transactions on Robotics, vol.24, pages 341-347

[4] E. Edqvist, N. Snis, R. Casanova Mohr, O. Scholz, P.Corradi, J. Gao, A. Diéguez, N. Wyrsch and S.Johansson (2009), Evaluation of building technology for mass producible millimeter-sized robots using flexible rinted circuitboards, J. Micromechanics. Microengineering., vol. 19, pp.1-11

[5] K. Okazaki, T. Ogiwara, D. Yang, K. Sakata, K. Saito,Y. Sekine and F. Uchikoba (2011), Development of Pulse Control Type MEMS Micro Robot with Hardware Neural Network, J. Artificial Life and Robotics., vol.16, pp. 229-233

The Seventeenth International Symposium on Artificial Life and Robotics 2012 (AROB 17th '12),
B-Con Plaza, Beppu, Oita, Japan, January 19-21, 2012

Development of an autonomous-drive personal robot "An environment recognition and the position detecting system that used image processing and an LRS"

Katsuhiro Yamamoto, Hideki Ishimaru, and Eiji Hayashi

Department of Mechanical Information Science and Technology
Faculty of Computer Science and System Engineering, Kyushu Institute of Technology
680-4, Kawazu, Iizuka-City, Fukuoka Prefecture, Japan

Abstract: We are developing an autonomous personal robot that will be able to perform practical tasks in a human environment based on information derived from camera images and a laser range sensor(LRS). It is very important that the robot be able to move autonomously in a human environment, and to select a specific target object from among many objects, and these functions will be possible in our system. The robot's environmental recognition system is composed of an autonomous driving system and an object recognition system. First, the autonomous driving system calculates the driving route from the visual information provided by a CCD camera. The robot is driven by this system. The object recognition system proceeds by identifying the specified object using image processing and an LRS, and the robot can grasp the object. An environment recognition system is essential to both of these functions. Here we explain the algorithm by which the robot recognizes the surrounding environment. In addition, we describe the application of this system to our robot, evaluate its performance and discuss our experimental results.

Keywords: Personal robot, monocular camera, Image processing, LRS, Autonomous driving, Object recognition

1. Introduction

In the near future, autonomous driving robots are expected to provide various services in human living environments. To perform these services, the robots will need to grasp the feature of the human environment. Therefore, systems to provide environmental recognition based on image information are being widely studied. However, it is very difficult to recognize all driving environments from image information only; so far, no prospects for such a system have emerged. Therefore, we report on the development of an autonomous personal robot able to perform practical tasks in a human environment based on information derived from camera images and a laser range sensor (LRS), which is used to acquire two-dimensional distance information.

The system for this robot is composed of an autonomous run system for movement and an object recognition system for the recognition and grasping of an object. First, the autonomous run system decides upon a robot driving command based on information in the limited space map. Information such as the placement of walls and barricades is established on to the map, and the data obtained from a CCD camera are compared with the map data. The route is decided, and the robot drives. The object recognition system is composed an object-recognition processing part and a location-information acquisition processing part, both of which use the monocular CCD camera and the LRS. An object is recognized and identified using range information obtained from the LRS in addition to the processed image data provided by the camera. The robot then performs a grasping operation for the object.

2. System view

Our robot has a drive mechanism consisting of two front and two back wheels. The front wheels are attached to a motor that operates the wheels on either side independently, while the back wheels function as castor wheels. This method has the advantage of allowing a small turning radius. To acquire image information, both a single CCD camera with approximately 2,000,000 pixels and an LRS are installed on the head of the robot and can be rotated to all sides by two motors. DC servo motors are used for the robot's drive mechanism, and position and speed control are achieved by the control system of the drive mechanism. The robot also has two arms and hands equipped with sensors, which enable it to respond to the various demands of humans. Finally, an installed wireless LAN can provide remote control for humans. All devices are controlled by a PC, and lead batteries supply the robot's electric power.

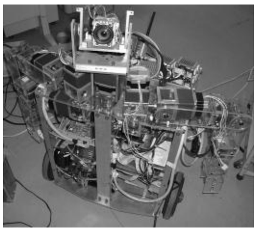

Fig. 1 Our developed robot

3. Specification of the LRS

LRS is a noncontact laser measurement system; our LRS is made by Hokuyo Automatic CO., Ltd. The maximum detection distance of this LRS is 4m. The horizontal plane space is scanned over a 270° angle at intervals of about 0.36° (360°/1024) to detect both the distance and the direction of the target body. This LRS requires a time of only 100 msec for a single scan, and thus a very short distance acquisition time is needed to gain details about the target object recognized with the monocular camera. Fig. 2 shows the externals of the LRS.

Fig. 2 Scanning laser range sensor

4. Autonomous driving system

4.1 System outline

We developed an autonomous driving system for robots that can move in response to image information captured by a monocular CCD camera. It has two subsystems: a route searching system, which decides the course of the robot, and a course correction system, which traces a safe course during the actual run.

4.2 Method for autonomous driving

In this section, we explain the method for autonomous driving. The flow chart for performing autonomous driving is shown in Fig. 3.

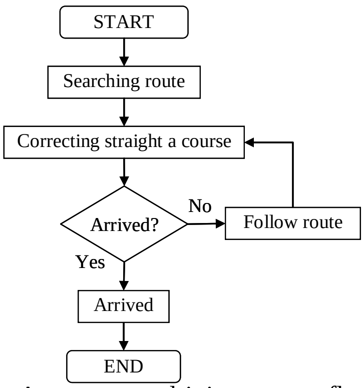

Fig. 3 Autonomous driving system flow chart

I. Route searching system

In this system, the robot searches for routes based on a limited space map. This map includes information such as the start position of the robot, the goal, walls, and danger zones. When there is a wall and an obstacle on the course to a goal, the robot travels along the middle point between them. The robot always takes the shortest route and removes other routes. Fig. 4 shows two routes that were removed because there are objects in the robot's way, and Fig. 5 shows two routes that are correct because they lead the robot around the objects.

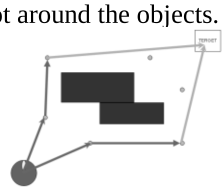

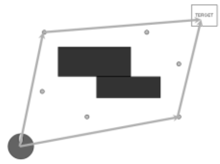

Fig. 4 Removed routes Fig. 5 Correct route

II. Course correction system

Using this system the robot corrects its path by measuring and equalizing the distance on the right and left to prevent it from crashing into a wall.

(i) Data storage

The data consist of the pattern of the slopes of the line on the image, and once calculated, the data are stored in a database. The data are calculated based on the width of the course and the CCD camera angle. The width of the course, direction of the robot, slope of the line and the distance from the center of the course are stored in the database.

(ii) Image processing

The robot acquires the image, and it is processed by edge-based binarization and noise removal. After that, straight lines are extracted, and the image is processed by the Hough transform into straight lines. This process is shown in Fig. 6.

(iii) Self-position correction

The robot estimates its position and direction and corrects the latter by a straight line matched with the data from the database.

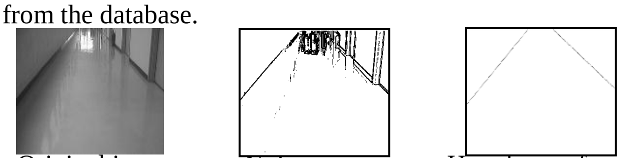

Original image Noise remove Hough transform

Fig. 6 Image processing

4.3 Experiment to evaluate the system evaluation

I. Experiment setup

To evaluate this system, we conducted an experiment at Research building 3F of Kyushu Institute of Technology. The total distance that the robot ran was about 35m, and we verified that its systems worked successfully.

The images used in the experiment were acquired from a camera mounted on the robot. This camera was at a height of 875mm from the floor and its depression angle was 20 degrees.

II. Results of the experiment

The robot could reach the goal thanks to the successful operation of the systems. The course correction system was at work during the run. A picture of the course that the robot followed is shown in Fig. 7. As shown, the course correction system worked, so that robot was able to move around obstacles.

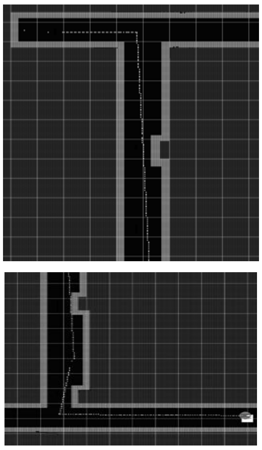

Fig. 7 Results of experiment

5. Object recognition system

5.1 System outline

We developed an object recognition system for robots that can acquire the target object position with image information captured by a monocular CCD camera and range information obtained by an LRS. This system can acquire the object position on the assumption that the object is placed on a desk. The system acquires the location information of the object by using the LRS with the recognized object. Afterwards, the arm is driven based on the location information, and the object can be grasped and held.

5.2 Method for object recognition

In this section, we explain the method for object recognition. The flow chart for the object recognition process is shown in Fig. 8.

I. Object recognition processing

Through object recognition processing, the system can search for objects with image information captured by a monocular CCD camera. The system then searches for the object with the shape and color of the object registered in the database by narrowing the search range to match the camera image step by step. Using this method, objects in the domain can be found. Fig. 9 shows an example of the results of object recognition processing.

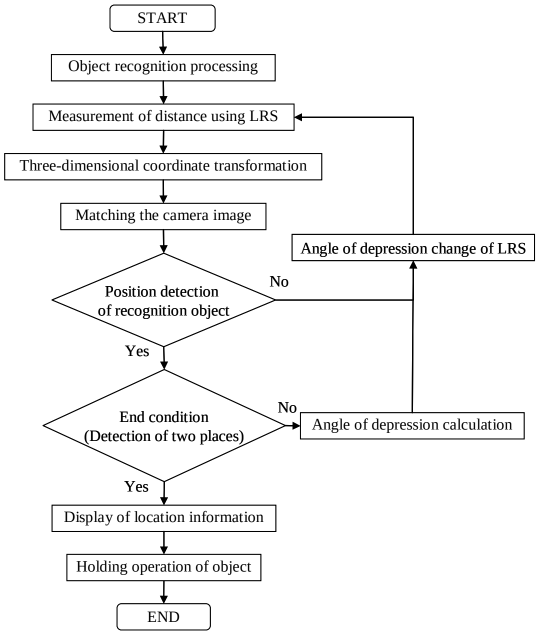

Fig. 8 Object recognition system flow chart

Fig. 9 Object recognition processing

II. Measurement of distance using an LRS

The LRS acquires range information on the object recognized during object recognition processing. The LRS is fixed to the robot head, and moves with the camera. Fig. 10 shows the situation in which the range information is acquired.

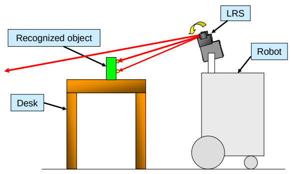

Fig. 10 Position information acquisition

III. Three-dimensional coordinate transformation

The range data of the LRS is range information from the irradiation point to the measurement point of the LRS. Therefore, this range data is converted into three-dimensional coordinates. This conversion is derived in the provided data based on the distance data and the horizontal and perpendicular angles.

IV. Matching the camera image

The system successfully matched the LRS data to the camera image by integrating the camera image with the LRS data.

V. Position detection of the recognized object

The system judges whether the LRS data accurately describes the location information of the object. This involved determining which position of the camera image provides the best measurement point for LRS to detect the object. If the object area recognized in the object recognition processing corresponds to the image coordinates of the LRS measurement point, the measurement can be considered successful. This system acquires three-dimensional coordinates in the vicinity of the center of the object as the location information, provided that the LRS measurement point is at the 60% height level, from the bottom of the object. In addition, to prevent false detection and to provide good, accurate detection, data acquisition is done at a second level on the object (below the 60% mark).

VI. Angle of depression calculation method

The system acquires location information on the object at two places (an upper part and a lower part). After the first set of location information is acquired in the upper part, the angle of depression of the LRS is calculated according to this information. If the distance between the object and the robot can be found, the angle of depression can be calculated from the image information by a geometrical calculation.

VII. Display of location information

When the location information about two places in the recognition object can be acquired, final location information on the object is displayed. Because it is preferable that the acquired positional data reflect the exact position of the object, the area in the center of the two examined places is acquired as the final object location information.

VIII. Recognition of circumference environment

To perform grasping of the recognized object, it is necessary to know the object's circumference. The system acquires the object at center of the camera image, to determine the object's circumference.

VIIII. Grasping operation of object

The target object is located within a certain distance (2 feet) of the robot. Target coordinates are first set in front of the object, based on the acquired object position, and the arm is driven to the coordinates. An image is acquired after the arm arrives, and the remaining drive distance of the arm is calculated from the position of the object and the distance of the hand to the object. The arm is driven again based on the calculated driving amount, and the grasping operation of the object is performed.

5.3 Experiment to evaluate the system

I. Experiment setup

We performed an experiment to evaluate the performance of this system in the grasping operation of an object, in which it searched by object recognition processing. The angle of depression of the camera was set at 10°. Fig. 11 shows the experimental environment when the object was a PET bottle. Its location was on a single-color desk in the laboratory.

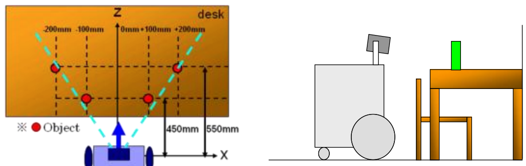

Fig. 11 Experiment environment of the target PET bottle

II. Results of the experiment

As the result of acquiring position information for the PET bottle placed in a variety of places, the maximum error of each set of coordinates was less than 5 mm, and the error in the distance to an object was less than 3%. If the robot is assumed to grasp an object based on this result, we think that it could successfully perform the grasping task.

However, if some parts of the object are hidden, the object recognition may not be able to be carried out correctly. Therefore, it is necessary to improve this system so that it can recognize an object's position based only on some parts of the object.

6. Conclusions

We propose a system that recognizes the driving environment of a robot using image processing and an LRS. This environmental recognition system is composed of an autonomous driving system and an object recognition system. The driving environment of the robot can be processed using these systems, and the behavior pattern of the robot can be expanded within that environment. At present, it is possible for the robot to move in a preselected area, and to locate and grasp a target object. Expansion of the action area and the addition of the transportation operation of the robot with the object are within our sights and will be developed in the future.

The Seventeenth International Symposium on Artificial Life and Robotics 2012 (AROB 17th '12),
B-Con Plaza, Beppu, Oita, Japan, January 19-21, 2012

Design of robotic behavior that imitates animal consciousness: Construction of the user-recognition system

Motoki Yoshida Kei Ueyama Eiji Hayashi

Department of Mechanical Information Science and Technology
Faculty of Computer Science and Systems Engineering, Kyushu Institute of Technology
680-4, Kawazu, Iizuka-City, Fukuoka Prefecture, Japan

***Abstract*:** Our research has been focused on developing a robot with "consciousness" like people or an animal to enhance the user affinity of service robots. Our laboratory previously conceived a model of the mechanism of consciousness and action and a software architecture based on this model that can be used to control the action of a robot, called the Consciousness-Based Architecture (CBA). Here, we built on this model both theoretically and practically. First, we newly theorized a "motivation model" which assumes that certain motives inhere in the actions of sentient beings, and that the motivational processes involved could become part of the robot's determination of action. Our motivation model is based on the dopamine-generating mechanism of sentient beings. Then, as a practical step toward developing an emotionally interactive robot, we developed a user-recognition system using a CCD camera.

***Keywords*:** CBA, Consciousness of the robot, Motivation of the robot, the user recognition

I. INTRODUCTION

At the present time, not only industrial robots but also so-called "service" robots are being quickly developed. There are various types of service robots: business robots, research robots, welfare robots, and domestic robots, to mention a few. The operation of these robots requires not only the basic functions of robots, such as a high level of intellectual activity, but also the function of user compatibility or affinity so that a user can feel close to the robot as a result of its appearance and behavior. User compatibility implies that the user is easily able to operate the given robot, without getting bored with its use, and can easily develop a sense of closeness with it; ultimately, the user can receive the emotional benefits experienced in relationships with other conscious beings.

Although a robot may gain in user compatibility by being genuinely modeled after a face, it is far more challenging to achieve user compatibility through its behavior and actions, including human-like "capricious behavior". The attempt to give robots "consciousness" such as that identified in humans and animals is a part of these requirements.

Our laboratory has studied animals' adjustments to their environments in an attempt to emulate animal behavior. We constructed a hierarchic structural model in which consciousness and behavior were hierarchically related. Based on this model, we developed a software architecture we call Consciousness-based Architecture (CBA). CBA introduces an evaluation function for behavior selection. Here, we elaborate on the evaluation function, using the dopamine-based motivational system as its basis.

For the present study, we developed a robotic arm that has six degrees of freedom, so that the arm could autonomously adjust to a target position. Fig. 1 shows an overview of the robotic arm. The robotic arm that we used has a hand consisting of three fingers in which a small monocular WEB camera is installed. The landmark object is detected in the image acquired by the WEB camera. Previously, as an autonomy action experiment, CBA was applied to the robot arm and the behavior was then inspected.

This paper describes a user-recognition system that can judge a specific person using a CCD camera, and integrates the user-recognition system and CBA. We tested the system to identify target users from among five persons.

Fig. 1 Overview of Robotics arm

Fig. 2 CCD camera

II. SYSTEM STRUCTURE

Fig. 3 shows the appearance of the robot arm, and Fig. 4 shows its degrees of freedom. The robot arm has 7 levels of flexibility {shoulder (Joint1, Joint2), elbow (Joint3, Joint4), wrist (Joint5, Joint6), and finger (Joint7)} at its full length of 450 [mm]. The hand part has 3 fingers with one flexibility; the weight of the main part is about 0.8 kg. A small Web camera, installed at the tip of a robot arm, can recognize the external situation. The web camera and the robot arm's actuator are controlled by USB communication.

Fig. 3 robot arm

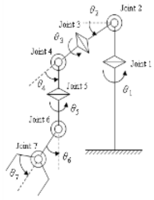

Fig. 4 degree of robot arm

III. AUTONOMOUS BEHAVIOR

1. The motivation of the robot

Most robots are pleasing to people because of their unique movements. However, the action *choices* of robots are too objective in orientation. Action choices that resemble those of subjective human beings and animals are needed to enhance user compatibility. Therefore, we at first considered the structure of sentient action. When an animal, including a human being, takes some action, it can be represented by a flow chart such as "Recognition → Comprehension → Motivation → Action", shown in Fig. 5. On the other hand, the action of the robot tends to eliminates motivation in the simple flow "Recognition (Comprehension) → Action"

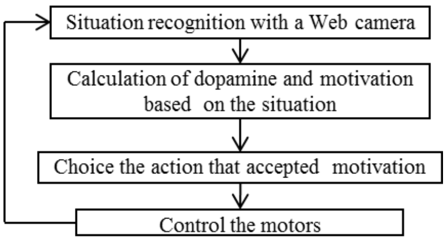

Fig. 5 Flowchart of this system

2. Situation recognition with a Web camera

The first step of the "humanized" robot's system would be to recognize a situation. For this purpose we devised a labeling image (Fig. 6), taken by the Web camera installed on the robot hand. We programmed the system to divide the image into green, blue, and flesh-colored blobs and extract the shape, size, and center of gravity position. From this information and the posture of the robot arm, the robot could recognize the position and its distance from the target-color object. Furthermore, the system memorized the central point for three frames.

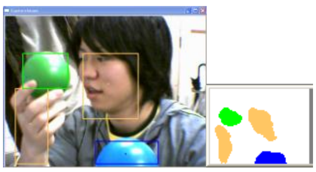

Fig. 6 Web camera image and a labeling image

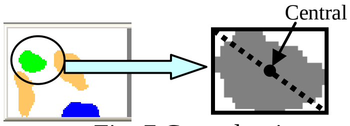

Fig. 7 Central point

3. Calculation of dopamine and motivation based on the situation

When a man and an animal interact, changes occur in the dopamine level in the brain. The dopamine-generating locus was regarded as model for determining the robot's motivation, and was copied for the control model. The control model is shown below. In the graph, sample changes in , ω_n and ζ are shown. T

Rising $y''+2\omega_n\zeta y'+\omega_n^2 y-\omega_n^2 u_{(t)}=0$

Decaying $y=e^{-t/T}$

ω_n : natural angular frequency : earliness of a rising

ζ : braking rate : height of the peak of a rising

T : time constant : attenuation performance

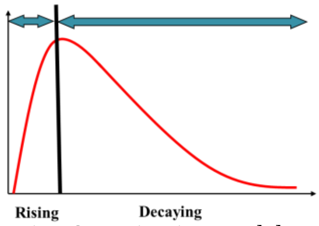

Fig. 8 Motivation model

In the control model dopamine is generated with reference to pleasant or disagreeable stimuli with variables ω_n, and T are determined by the outside environment and the internal state, respectively. Moreover, it is defined by asking for total of the generated dopamine and calculating the secondary delay response in such a way that the total is considered as the input into a robot's motivation.

4. Choice of the action that accepted motivation

The action level was set up by dividing a robot's motivation by a fixed value. In this way, the actions that could be chosen for each action level were limited.

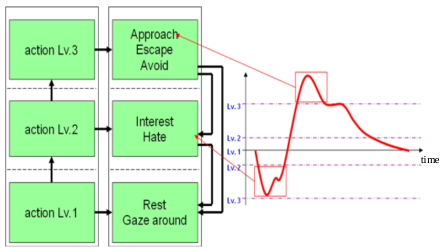

Fig. 9 Choice of the action based on motivation

5. Consciousness architecture (CBA)

Fig. 10 shows a diagram of the hierarchical structure model called CBA (Consciousness-based Architecture) which relates consciousness to behavior hierarchically. The characteristic of this model is that the consciousness field and behavior field are built separately. In a dynamic environment, this model determines the consciousness level appropriate to the environment, and the robot then selects the behavior corresponding to that consciousness level and performs the behavior. This model is characterized in that the consciousness level approaches an upper level so that the robot can select an advanced behavior when certain behavior corresponding to the consciousness level is discouraged by some external environmental factor.

Additionally, an upper-level consciousness can make a choice of a low-level behavior. The mechanism of this model is that it selects the optimum behavior within the low-level behaviors, to achieve the robot's goals.

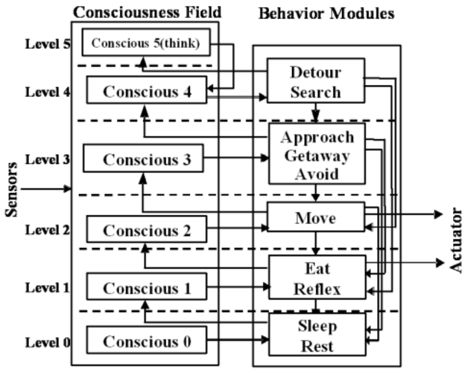

Fig. 10 Consciousness-based Architecture (CBA)

IV. USER-RECOGNITION SYSTEM

4.1. Outline of the system

From an image provided by the CCD camera, the system detects a moving object and carries out a search in its data domain. It pays attention to the shape and color of the object and determines whether it is either a non-human object or a human being. In addition, it detects the parts of person's face and compares each person it encounters with user information on a database. The flow for user recognition is shown in Fig. 11.

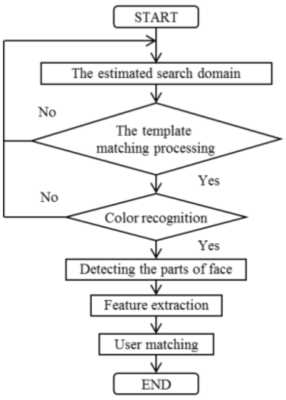

Fig. 12 Difference Image

Fig. 11 System flow Fig. 13 the maximum height

4.2. The estimated search domain

This process estimates the domain of a human being is from the information provided by the differences between the frames.

4.2.1. The detection of height

This system detects the maximum height Y of each X point in the image from the differential image which it acquired from the differences between the frames. The image from these detections is shown in Fig. 12.

4.2.2. Average

This system makes a smooth graph by creating an average by 40 pixels of values of the height Y which it detected at the maximum, because the position sensing of the domain is difficult only at the maximum height Y. An image of average values is shown in Fig. 14.

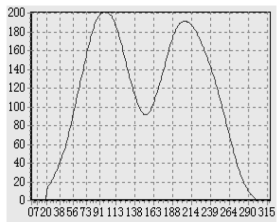

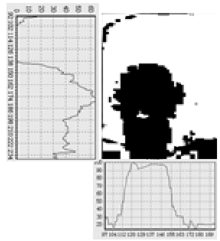

Fig. 14 Graph of the average Fig. 15 Histogram

4.2.3. The detection of the search domain

From the graph, the system detects the part at the top and estimates the position of the human being. Next, it scans from a person's position detects the point below the top or the point that is lower than 1/3 from the height of the person's position. One can assume that a part surrounded by points is a search domain.

4.3. The template-matching processing

When this system begins its operation, it reads the template that imitates the head of a person. The outline acquired in the previous process is compared with the template. The size of the template changes according to the size of the search range. Generally, this process requires a great deal of calculation time. Real-time operation is achieved by reducing the number of comparisons. When the matching rate is higher than the threshold and reaches its maximum, the position is output as the position of a human face.

4.4. Color recognition

An image is difficult to identify using only conventional processing. The system has to finally confirm that the image is that of a human being. Skin color is used to ultimately determine this, using the template-matching process to decide the identity and position of the human image. In this case, color information processing uses the HSV color model.

4.3. Detecting the parts of face

The robot automatically makes a histogram of external color pixels for the X and Y coordinates and judges the position of the face from the histogram. The image of the histogram is shown in Fig. 15.

Then, it detects the eyes and nose of a face through a Gabor filter in a 90 degrees direction.

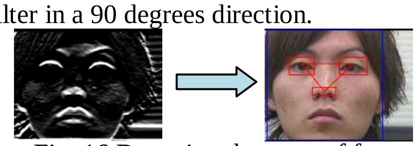

Fig. 16 Detecting the parts of face

Gabor Filter

$$g(x,y,\lambda,\theta,\psi,\sigma,\gamma)=\exp\left(-\frac{x'^2+\gamma^2 y'^2}{2\sigma^2}\right)\cos\left(2\pi\frac{x'}{\lambda}+\psi\right)$$

$$x' = x\cos\theta + y\sin\theta \qquad y' = -x\sin\theta + y\cos\theta$$

λ: The cosine component of wavelength

θ: The direction of the striped pattern on the Gabor function

ψ: A phase offset γ: A aspect ratio

4.4 Feature extraction

As shown in Fig. 17, the distance from a nose to eye is A and the distance between the eyes is B. The robot computes B/A.

It combines and equalizes each image through a Gabor filter pass every 30 degrees. The new image is shown in Fig. 18.

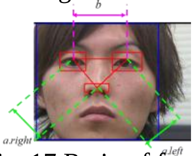

Fig. 17 Ratio of face

Fig. 18 Gabor filter picture

4.5. User matching

It compares the extracted features with the information of the people stored in the database, and checks whether the user is a known person.

V. Experiment

5.1. Experimental method

The system's performance was evaluated with two experiments.

Template matching rate:

1. In whether a user is a particular target person using five different target persons.
2. Matching User A' s template with Users B~E.

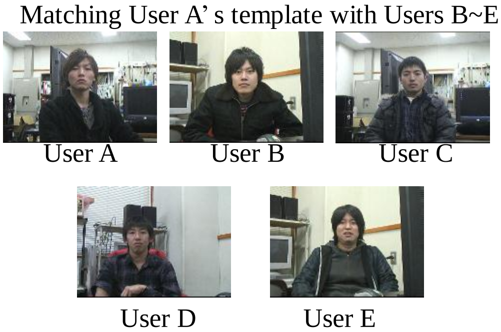

Fig. 19 Objects

5.1. Experiment 1

The result of experiment 1 are shown in Table 1. This system had about a 70 percent recognition rate of the target person. However, since the user's expression always is not the same, the template matching rate can fall.

Tab.1 Result of experiment 1

	User1	User2	User3	User4	User5
1times(%)	77	69	73	70	73
2times(%)	71	73	73	70	76
3times(%)	63	72	68	72	70
4times(%)	72	72	71	71	70
5times(%)	70	71	69	71	50
Average(%)	70.6	71.4	70.8	70.8	67.8

5.2. Experiment 2

The results of experiment 2 are shown in Table 2. When the user differed from the target person, the matching rate dropped below 50 percent.

Tab.2 Result of experiment 2

	User2	User3	User4	User5
1 times(%)	48	47	53	48
2 times(%)	45	41	44	44
3 times(%)	52	41	49	46
4 times(%)	45	43	50	44
5 times(%)	57	46	48	55
Average(%)	47.4	43.6	48.8	46.8

VI. CONCLUSION

In this paper, we created a user-recognition system using a CCD camera. It became possible to identify the target person among 5 different people.

In the future, we will further develop the theoretical and practical tasks needed to design a robot with user affinity, and one that recognizes the user's expression.

VIII. Acknowledgement

This research was partially supported by the Ministry of Education, Science,
Sports and Culture, Grant-in-Aid for Scientific Research, 2011.

IX. References

[1]Seiichi Tanaka, Eiji Hayashi, The recognition of multiple people using an ocellus camera, (AROB 15th ' 2010), Beppu, Oita, Japan, 2010

[2] Kouichirou Kurogi, Eiji Hayashi, Design of robotic behavior that imitates animal consciousness: Emotion expression of robotic arm based on eye ball (AROB 16th ' 2011), Bepu, Oita, Japan, 2011

The Seventeenth International Symposium on Artificial Life and Robotics 2012 (AROB 17th '12),
B-Con Plaza, Beppu, Oita, Japan, January 19-21, 2012

An abductive environment enables teacher's intervention in a robotics class

Ilkka Jormanainen[1], Meurig Beynon[2] and Erkki Sutinen[3]

[1,3] University of Eastern Finland, School of Computing, P.O.Box 111, FI-80101 Joensuu, Finland
[2] University of Warwick, Department of Computer Science, Coventry CV4 7AL, United Kingdom
[1] (Tel: +358 45 872 6228, Fax: +358 251 13 251 7955)

[1]ilkka.jormanainen@uef.fi

Abstract: We propose a novel approach to support teacher's work in an unpredictable learning environment, such as a robotics class. The Conflative Learning Environment (CLE) approach blends the roles of the student, the teacher, and the software developer by taking the diverse users of the learning environments beyond their traditional, fixed roles and blending the users' activities and working environments with each other. We report results from a qualitative study indicating that a novel monitoring environment developed by following the CLE approach helped teachers to recognize students' particular problems better than when observing the students without such support. Results of the study have been used to guide us in the further development of the CLE approach and the monitoring environment.

Keywords: agent, intervention, learning environment, robotics

1 INTRODUCTION

Educational robotics has a recognized status as an attractive tool for modern learning environments. Cheap and highly accessible robotics sets, such as Lego Mindstorms, provide a platform for different kinds of learning scenarios ranging from basic technology education in a primary school to advanced artificial intelligence studies in universities. Learning settings in robotic classes emphasize students' active participation and group-oriented working methods. These kinds of learning settings, especially at an elementary level, however, pose a particular challenge for teachers: How to follow all students' or an individual's activities? Project-based working methods, open-ended tasks, various problem solving strategies, and the iterative nature of robotics projects easily lead the students to take different paths in their work. This makes it difficult for the teacher to detect the students' problems and the right moments for intervention.

Traditionally, intelligent tutoring systems (ITSs) have been used to guide students and teachers in such learning settings. The deductive student modeling approach traditionally used in ITSs is based on pre-defined rules to model and predict students' progress in the learning environment. The systems reveal only the result of a modeling process to the teacher. However, the unpredictable nature of a robotics class requires that the learning environment leaves room for the teacher to explore through *abductive reasoning* what factors actually have led the students to the current situation.

In this paper, we present a *conflative learning environment* (CLE) approach that enables blending of roles. The teacher can adopt a software developer's tasks in his or her own work. This allows the teacher to exploit abductive reasoning to explain observed phenomena in the teaching setting, and to intervene accordingly.

This paper is organized as follows. In the next section, we review previous approaches to tackling the problem of tracking student activities in learning environments where unpredictable events easily take place. We describe how the CLE approach differs from the existing solutions. Then, we present the main findings from a qualitative study that analyzed the use of a monitoring environment built by following the CLE approach.

2 BACKGROUND

In previous research by other authors, the student modeling approaches are mostly theory-driven. The environments, based at least loosely on ITSs, have offered a selection of pre-defined choices by which the monitored data is classified and used for modelling the students. These systems give support for observing the overall progress of all students in the classroom, detecting the problems that the students have, and analyzing the actions of a particular group or even an individual student. Despres and George's research [3] is probably one of the closest to our approach in the educational robotics domain. They describe an intelligent tutoring system that allows the teacher to follow the students' activities in an educational robotics classroom. In the first instance, their system provides support directly to the students, and if that fails, the system reports the difficulties to the teacher as well.

The main difference between the existing and CLE approaches is that, whereas many traditional ITS applications use a theory-based approach for building the learning model, the learning environments based on the CLE approach start from the empirical observations arising from the current learning situation. There are ITSs that apply an empirical approach for building the learner model (for example a multimedia ITS for Geometry by Cooper et. al [2]). However, the learning models in these systems are still at least partially predicted by theoretical assumptions. For example, a given set of features classifies the user's emotional self concept [2].

3 CONFLATIVE LEARNING ENVIRONMENT

A conflative learning environment (CLE) is a novel kind of open and flexible learning environment that was developed based on the observations that the Finnish authors of this paper have gathered during 10 years of running Kids' Club. Kids' Club is a combined after-school robotics and technology club and a living laboratory for designing novel educational technologies in conjunction with their intended users, particularly students and teachers. During the development of the club concept in various school and after-school settings, we have shown that the group-oriented working methods, iterative problem solving processes, group dynamics, and students' different roles in the groups easily lead the groups and individual students to proceed quite differently with their projects. Hence, there is a need for a framework to support the development of learning environments that allow the teacher to explore the learning process deeply.

2.1 Role blending in the CLE approach

The traditional division of the roles in educational technology development processes usually strictly separates the roles of developer, teacher, and learner from each other. Moreover, the tasks undertaken by these process participants usually follow each other in a cycle with predefined steps. The *Empirical Modelling* (EM) approach breaks this division by taking the users of the learning environments beyond their traditional roles and by blending their activities and working environments with each other [1]. In particular, EM has tools that allow the teacher to model students' behavior by his or her observations, thus - to a certain extent - becoming a developer.

The role blending in the CLE approach can take place between the teacher and the developer, the student and the developer, or even between the student and the teacher. The role blending takes place through cyclic processes where the users contribute to building the learning environment gradually by modelling the empirical observations arising from the current learning setting (Figure 1). Modelling is an essential process for a functional learning environment. Traditional learning environments require advanced programming for enhancing the learning environment to match the unexpected, and hence unprogrammed, student behavior. In contrast, EM supports modeling that can be done without interrupting the learning process.

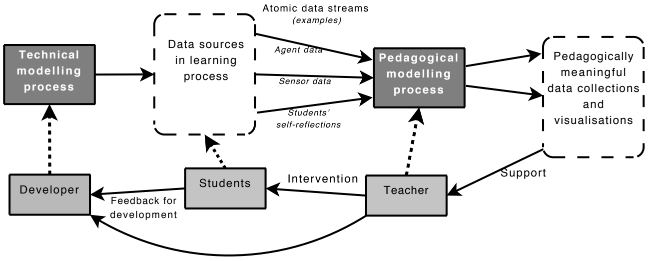

Fig. 1. Example structure of an application based on the CLE approach

2.2 Working processes in the CLE approach

The modelling process in the CLE approach (Figure 1) is based on individual data streams originating from the current learning process. The data can be, for example, information about the users' activities within the learning environment, or automatically collected sensor data, or students' self-reflections about their progress. A learning environment based on the CLE approach should provide appropriate tools for the teachers to process this primary data to obtain pedagogically meaningful collections that can be visualized. As an abstract approach, the CLE does not limit or define the ways in which the user can combine the primary data, or how the observations are presented. A CLE distinguishes development from modelling activities. When building a learning environment by following the CLE approach, there is, indeed, a need to have "traditional" software developers involved. They prepare the tools and the environment so that the users can then make their contribution whilst modelling *as if* in the role of a developer. 'Modelling' means that the users reflect upon their own surrounding and working environment through their observations of the learning environment.

Jormanainen et al proposed in [4] that to make the applications based on the CLE approach more accessible for the users, modelling of the learning process should be divided into two parts. The first part, *technical modeling,* consists of setting up the basic modules of the environment. This part of the modelling process can take place before and even between classes, when the model can be redefined to meet the new requirements. The second part, *pedagogical modelling*, is the process that takes place during the classes. In this part of the modelling process the teacher defines the environment by identifying data collections meaningful for the teaching context and visualizations for the data that the agents collect. It may be that the collections and visualizations of a given instance are not usable elsewhere; for instance, they might depend on the phase at which the students are in their project. To put our work in context, we classify learning environments between the theoretical extremes of *model-based* environments and *modelling-based* environments (Table 1). The model-based environments are traditional ITSs that take deduction as a starting point for the learner's modeling. At the other end, inductive modeling-based environments take empirical observations arising from the current learning setting as a starting point for modeling. It is important to recognize that these are theoretical extremes, and real systems usually fall between these alternatives, for instance, when an abductive approach to modelling is adopted.

Table 1. Model-based and modeling-based learning environments (based on [4])

	Model-based	**Modelling-based**
Modelling approach	Theory-based, deductive	Empirical, inductive
Learning model	Given	Constructed
Adaptation	Black box	Transparent
Roles in the learning community	Separated	Blended
Working environments	Separated	Conflated
Direction of modelling	Top-down	Bottom-up
Modifications to the tools	Through the software development process	On demand in the actual learning situation

4 OPEN MONITORING ENVIRONMENT

To help the teachers working in a robotics class, we have developed an *Open Monitoring Environment* (OME) by following a cyclic process of defining, testing, and evaluating as proposed in the CLE approach [4]. The core idea of the OME is to help the teacher to detect the right moments for intervention in a robotics class and help to build his or her intervention strategies. The students design and build robots with Lego Mindstorms educational robotics sets, and they program the robots by using a visual programming environment. The OME automates data collection from the learning process by utilizing agents to observe students' interactions within the robotics environment [4]. In addition, the OME environment contains a specific modelling environment for the teacher, where he or she can build the model representing the current learning scenario.

5 ANALYZING CLE AND OME

A qualitative analysis of the OME was conducted in a real school setting, where teachers used it for monitoring students' activities in the robotics class. The main focus of the experiment was to address the question: *How does the OME help the teachers who are working in a robotics classroom?* Four teachers and 12 primary school students participated in the study. The participants were divided into two groups of two teachers and six students. During the study, the students worked in pairs for a given robotics task for a period of three hours. Neither teachers nor students had prior familiarity with robotics. The student groups were provided with pre-constructed wheeled robots, and a simple programming task was given to them. The teachers' work during the experiment can be roughly divided into two parts. First, they observed students' actions through the OME environment. When the agents delivered new data to the modelling environment, it was automatically updated to reflect the current situation. Secondly, the teachers used this output to determine when it was appropriate to intervene in students' work (e.g. when they observed a problem). Data collection in the study was conducted in several ways. First, teaching sessions were recorded with a video camera. Second, data produced by the agents based on the students' actions was saved to a database. Third, teachers' actions with the OME were saved to log files. Finally, video-recorded interviews with the teachers were conducted. The research material was analyzed qualitatively. After transcribing the video and interview material, a codebook was built to help the analysis and make the analysis consistent. Before the actual analysis, the reliability of the codebook was tested statistically. Transcribed video and interview material was analyzed by categorizing material according to the codebook with the ATLAS.ti software.

The focus of the qualitative analysis was to identify the opportunities that the OME brings to teachers' work, and to identify the role that EM principles and tools play in implementing an environment based on the CLE approach. The new ideas and teachers' opinions about the additional information that the environment should provide were appreciated as potentially very valuable for improving the OME further. This process is an essential part of the CLE approach. The outcome of the research process serves as an input for the next iteration of technical modelling, and it also helps the researcher to identify ways in which the teacher adopt the role of developer in accordance with the CLE principles.

6 RESULTS

The qualitative analysis of the experiment material shows that the OME helped the teachers to intervene when the students had problems in their robotics exercises. The teachers were able to make informed decisions on what particular issues they would follow from the students' learning process based on the agent data. Furthermore, the teachers were able to recognize students' particular problems through the OME system better than when observing the students without such support. This was especially evident in situations where only one of the teachers was following the students' progress through the OME. In these cases, the teacher in the classroom did not notice that the students were having problems, but another teacher was able to see this through the OME and help the group with the problems. Most of these cases were related to technical problems when the students were unable to upload code to the robot due to the unreliability of the infrared link between the computer and the robot. It was typical for these cases that the students did not ask for help but repeatedly tried to upload the code to the robot, despite the error messages.

7 DISCUSSION

This experiment focused mostly on how the teachers used the OME. It is evident that the OME was beneficial for the teachers especially because they were novices in working with a robotics environment. However, as the idea of the CLE approach is to blend the roles of the teacher and the developer, the issue of being involved in the development was also introduced to the teachers. It was surprising that the teachers actually agreed that they could also develop the environment further if this was a natural part of the work flow. When the teachers looked back on the actual learning process and reflected on how different decisions might have enhanced the quality of the learning process, they identified both key pedagogical issues and ways in which these might be addressed by modifying the learning environment. These issues could then have an impact on the design of a learning environment based on the CLE approach. This means that, by reappraising their decisions, teachers working with the CLE approach blended their traditional role with the role of a system designer.

8 CONCLUSION AND FUTURE WORK

The study reported in this paper gave us more evidence that Empirical Modelling has potential to support role conflation even more deeply than the current implementation of the OME allows. To realize this more effectively in practice, further development is needed to ensure a seamless integration of the EM tools with the learning environment construction process defined by the CLE approach. The analysis of the qualitative data and teacher's work in the classroom guided us in developing a data mining module for the OME [5] to enable automatic processing of agent data. In contrast to traditional data mining applications, a teacher can reconstruct a training set for a data mining algorithm on an on-the-fly basis and apply a new classifier in the environment at any time. The rules associated with the classifier are exposed for the teacher's revision. If the teacher is not satisfied with the resulting classifier, he or she can always modify the rules and changes will be effective immediately. Results from the study indicate that this open data mining process produces pedagogically useful and interpretable information about the students' progress with relatively small datasets [5].

REFERENCES

[1] Beynon W.M, Roe C (2004). Computer Support for Constructionism in Context. In: Proceeding of the Fourth IEEE International Conference on Advanced Learning Technologies, 2004, pp. 216-220.

[2] Cooper D, Arroyo I, Woolf B, Muldner K, Burleson W, Christopherson R. Sensors Model Student Self Concept in the Classroom. In: International Conference on User Modeling and Adaptive Presentation. 2009.

[3] Despres C, George S (2001). Supporting learners' activities in a distance learning environment. International Journal of Continuing Engineering Education and Life Long Learning 11 (3), pp. 261–272.

[4] Jormanainen I, Beynon M, Sutinen, E (2009), Understanding open learning processes in a robotics class. In: Proceeding of the 9th Koli Calling International Conference on Computing Education Research.,pp. 51-54.

[5] Jormanainen I, Sutinen, E (2012). Using Data Mining to Support Teacher's Intervention in a Robotics Class. In: 4th IEEE International Conference on Digital Game and Intelligent Toy Enhanced Learning. Accepted for publication.

A Simplified Approach towards Realizing a 3-D Fax Based On Claytronics

Chetan J and Shrikrishna Upadhyaya
chetanjmurthy@gmail.com , sherlock.krishna@gmail.com
Department of Electronics and Communication, BMS Institute of Technology, Bangalore.

Abstract

In this paper we describe a model approach to realize a three dimensional copy of an object with the help of claytronics. Claytronics is a form of programmable matter that takes the concept of modular robots to a new extreme. Programmable matter refers to a technology that will allow one to control and manipulate three-dimensional physical artifacts (similar to how we already control and manipulate two-dimensional images with computer graphics). In other words, programmable matter will allow us to take a big step beyond virtual reality, to synthetic reality, an environment in which all the objects in a user's environment (including the ones inserted by the computer) are physically realized.

Here we discuss a way to realize a 3D facsimile starting with image/shape acquisition continuing with transmission and finally the process completing with the 3D realization of the target object. We describe the process of image/shape acquisition with two separate methods where the selection of the method is purely dependent on the object. Transmission can be achieved by conventional means. For the object realization we describe an algorithm which can fulfill the purpose.

I. INTRODUCTION

Most of the literature here that is in this section has been sourced directly from earlier papers on claytronics [1], [2]. The idea is to first acquaint the reader with the concept on claytronics.

The whole purpose of claytronics and our work in particular is to create an ensemble of tens or even hundreds of small autonomous robots which could, through coordination, achieve a global effect not possible by any single unit. One of the primary goals of claytronics is to form the basis or a new media type pario. Pario, a logical extension of audio and video, is a media type used to reproduce moving 3D objects in the real world. A direct result is that claytronics must scale to millions of micron-scale units. Having scaling (both in number and size) as a primary design goal impacts the work significantly. This allows us to render physical artifacts with such high fidelity that our senses will easily accept the reproduction for the original. When this goal is achieved we will be able to create an environment, which we call synthetic reality, in which a user can interact with computer generated artifacts as if they were the real thing. Synthetic reality has significant advantages over virtual reality or augmented reality. For example, there is no need for the user to use any form of sensory augmentation, e.g., head mounted displays or haptic feedback devices will be able to see, touch, pick-up, or even use the rendered artifacts.

A futuristic scenario involving claytronics could go like this. An explorer or a naturalist may come across something interesting in his expedition. If the person wishes to communicate this find with fellow scientists he or she can do it by a normal two dimensional image. However if he wants to go beyond that (i.e. communicate not just with X and Y co-ordinates of that object) but involve the 'depth' and 'feel' of the object then Claytronics would be the solution. Using sophisticated image acquisition techniques, the object can be documented. This can be subjected to various processes and then transmitted. At the receiving end using an ensemble of robotic modules a facsimile of the object can be achieved thus the whole process happening in real time.

II. THE PROCESS IN A NUTSHELL

In this section we briefly go over the entire process we plan to achieve. The complete plan and the details do not form a part of the following literature. They are discussed in greater detail in the design section.

To achieve a complete 3D fax machine there are three parts to the system [3]. Shape acquisition, remote transmission, shape reconstruction. This forms the complete loop. Image acquisition can be of two types. For objects whose 3D fax to be obtained has a very small size (the term small here is greatly dependent on the number of claytronic atoms we are in possession of) we have a way of acquiring the image [3] and for objects very much greater than the mass of the ensemble we propose an entirely different way of acquiring the image. While many papers have discussed the former the latter has rarely been given its due. Our belief is that for claytronics to be fully made use of both are very important because many objects we encounter has its size always greater than the mass of the ensemble. While small objects can be sampled by applying the catoms tightly over the surface the big objects can be handled by sophisticated image processing software. In this paper, we briefly describe a method to acquire a 2 dimensional image. Using several 2D images a rough 3D feel can be given to describe. Here again the correctness of the 3D image that is constructed depends on the object and the number of 2D images from which it is constructed. This 3d 'feel' is stripped to its most basic form, points of interest are marked. Further processing is done and this can be transmitted using sophisticated techniques.

After acquisition and transmission comes the shape reconstruction. For reconstruction we start off with a simple co-ordinate feeding message. For convenience purposes we are developing the algorithm for 2-dimensional shapes only. The algorithm can b extended to 3-dimensional objects too, without much difficulty. For implementing the algorithm to the 2-dimensional shapes a very important generalization has to be made. This generalization is like a 'torch bearer'. It holds good for any kind of 2-dimensional shape. The generalization is that all 2-d objects can be described in the form of co-ordinates. This generalization is fairly obvious. In claytronics however the co-ordinates defining is not restricted to the outline or skeleton of the object alone. The co-ordinates here should describe each and every point in the object. A parallel analogy can be made with Digital image processing. These positions/co-ordinates are obtained at the end of the shape acquisition process. And the object can be better described/realized depending on module size. Lesser the module size greater the number of co-ordinates to better assess the object and realize it and greater the module size lesser the number of basic constituents. Therefore the error here is dependent on the size of the module. Alternatively we can even say that error is dependent on the number of co-ordinates. First let us let us go about the task of achieving 3 dimensional rendering of typical ordinary shapes. Once this is achieved moving on to complex shapes is not difficult. As an illustration we take a real life example and illustrate how to achieve it in 2-dimensional XY frame. The same can be extended to the three dimensional frame. At the receiving end the shape formation algorithm is applied and the fax is obtained. For parallel comparison and correction, the 3d image can be reconstructed. This reconstruction however is done by the computer. A big advantage gained here is the degree to which the fax deviates from the original object is always known and repeated iterations can be done to achieve a greater precision.

Additionally, we draw a parallel between image processing and claytronics, and show that both are 'cut from the same cloth'. We will also show you that, certain cases demand a particular kind of approach and in certain other cases we borrow techniques from actual module motion [4].

III. DESIGN

In this section we give a complete detail of the entire process. The advantages and disadvantages are thoroughly debated and possible extensions to the whole idea are added later on. Let us go about each of these processes starting with shape acquisition. As said earlier basically there are two ways in which shape can be acquired. The applications of claytronics using the camera approach are very vast and profound. Particularly multicamera stereo systems can capture dense shape information which can be transmitted in real time using suitable algorithms [6]. Structured light approaches based on scanning lasers can also be used [7], [8]. Alternatively for faxing small objects we can go for contact sensing where the programmable matter reads the shape of an object by direct contact with its surface.

However, here we also focus on the method of capturing of the image by camera for shape acquisition. For the sake of simplicity and understanding we will show it only in two dimensions

1) *Shape acquisition*

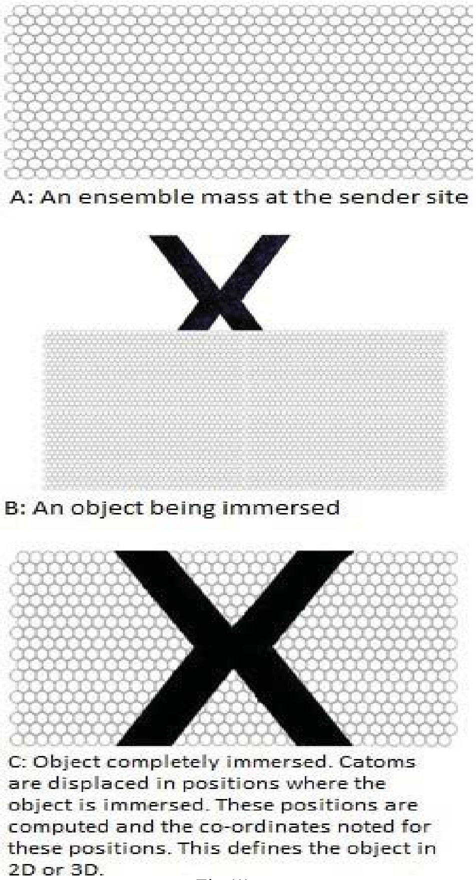

Fig (1)

The process of image acquisition can be done by two techniques. The first is the contact sensing wherein the object is immersed in the ensemble and the catoms can read the shape of the object by direct contact with its surface. This process can be used only for those objects which are small enough to be immersed in the ensemble. Common sense obviously dictates this process cannot be used for buildings, cars, etc. The process starts by immersing the object in the ensemble. When the object is completely immersed and the catoms tightly applied to the object, the ensemble is scanned to recognize which catoms are missing from their regular positions. For effective implementation, the positions of the catoms in default position or when no object is immersed has to be known. This is compared with the catoms whose positions have been displaced i.e. after object immersion. This gives us the co-ordinates that describe the object in space. For proper reconstruction at the receiver side, the coordinates of those positions where the catoms are absent make more sense. Hence the computer now computes the coordinates of the positions where the catoms were displaced. These critical co-ordinates are then transmitted. This process is illustrated in fig.1

A: Picture of a dummy duck

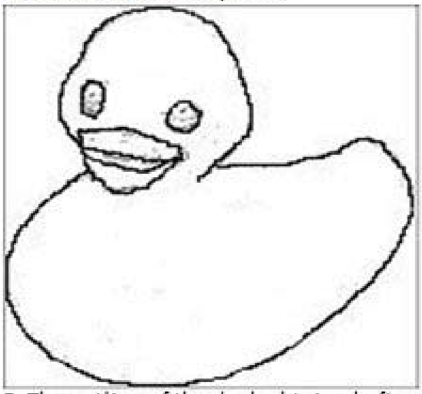

B: The outline of the duck obtained after processing. This method can be used to take 2D images of 3D objects, combine them and after further processing we can get a rough 3D sketch or grid. A simple 2D image is shown for clarity.

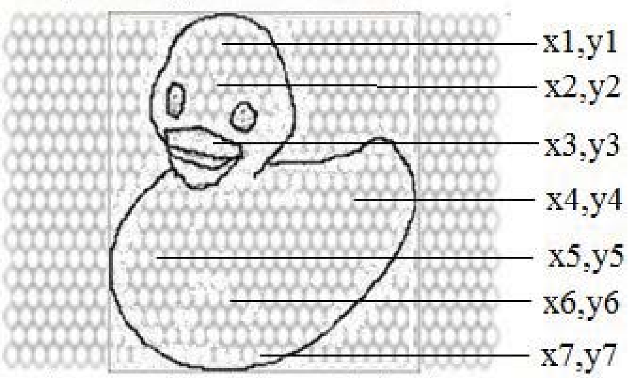

C: The outline of the duck is overlaid on the ensemble. For a 3D realization the surface contour is overlaid on a 3D dimensional ensemble. The computer determines the co-ordinates which form a part of the ensemble. These co-ordinates are then stored or transmitted.

Fig (2)

The second and perhaps a more robust technique which can be used for all types of objects is the non-contact sensing. If the object under consideration is a 2-D object, then a single photograph of the object would suffice. As mentioned it is assumed that the computer knows the coordinates of all the catoms. First the photograph of the object is input to the computer. Describing the process in crude terms, the computer takes the outline of the image and overlays this outline on the virtual ensemble. By simple image comparison the catoms that come inside the overlay or form a part of the overlay can be seen. The co-ordinates of these catoms are then taken and stored. When shape reconstruction is required at the receiving end these co-ordinates are transmitted. The process is illustrated in fig.2.

2) Shape reconstruction

Shape reconstruction is the most important step in claytronics. This can be primarily divided into two stages: the activation stage and the grouping stage. We propose methods to achieve each of these.

Activation

At the end of acquisition the computed set of lattice positions is transmitted and at the receiver site we have these positions. These positions can be the Cartesian Co-ordinates for the required shape to be formed. Depending on the object that we wish realize the number of transmitted co-ordinates may vary. These co-ordinates are stored at the site, till we wish to achieve the realization. Initially the ensemble is powered on, but the catoms are still in the dormant state. The first step is to activate the catoms belonging to the shape to be realized. One way of doing this is illustrated in the figure.

Initially the coordinates are to be fed into the ensemble. Loading several coordinates at a time might result in chaos. So we go for a technique used popularly in networking. We modify it here suitable for our application in claytronics. In claytronics we make the assumption that each module knows its position and location with respect to entire ensemble. Borrowing a technique used in a noiseless channel (stop-and – wait protocol [9]), the receiver sends/feeds one position co-ordinate to the ensemble and stops till it receives a confirmation from the ensemble and then sends the next co-ordinate. We have unilateral communication for the lattice positions but auxiliary ACK (simple tokens of acknowledgement) travel from the other direction. This is different from the arrangement of sending all the co-ordinates to the ensemble at once, in that we add flow control. The step followed is given thus.

-The loading of position co-ordinates is done with the co-ordinates corresponding to least co-ordinates first and then moving on to higher position values in the ascending order.

-Since every module knows its position, when it gets the message with the same co-ordinate it "consumes" that co-ordinate.

-If the co-ordinate it gets is not the same as its position co-ordinate, then it simply acts as a transmission point and passes on the co-ordinate to its neighboring module.

-If same then after consuming the co-ordinate, the module gets activated and for the other co-ordinates it encounters it acts as a transmission point.

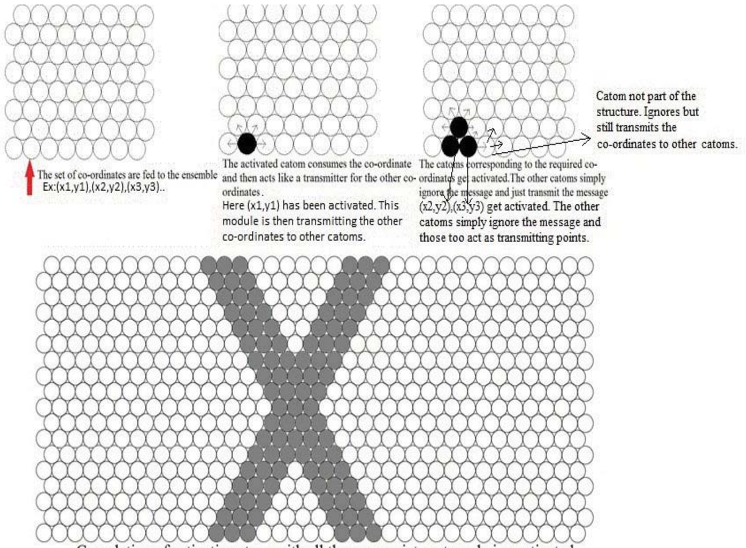

Completion of activation stage with all the appropriate catoms being activated

-The process continues till all the modules that form the part of the shape has been activated. Alternatively till all the co-ordinates have been loaded.

-As seen in fig2 during activation the position co-ordinates are transmitted through the modules like a "chain reaction". This process can never end. A possible solution is that each catom has a memory in that if a catom gets d same co-ordinate the second time it kills it.

At the end of the process the modules which belong to the shape will be activated. The next step in the process is shape formation. A plausible approach has been given below.

Formation

At this point in the process the modules will be activated, the activated modules will have to be bonded. The bonding has to happen between activated modules. Figure illustrates one possible way to do this.

Initially the device initiates the process of bonding by sending a simple initiation message. This occurs the instant when it receives the last ACK frame. The steps involved are given thus.

-The catom which first gets the message will transmit it to its nearest neighbors.

-If the neighbors are activated modules themselves, then it will bond to the catom from which it got a message through the contact patches/points [3]

-If the neighbors are dormant modules the message is simply ignored.

-The bonded module then transmits the message to its nearest neighbors. The whole process continues till all the modules are bonded thus the shape is acquired.

There is the possibility that an already bonded module can get the message again. In such a case the catom simply ignores the message. One more possibility is that a catom might get "bonding message" from two catoms at the same time. Under such a condition the catom can bond to all the catoms or acknowledges the message one by one and bonds to the catom with the smaller X/Y or uses simple math calculations(such as sqrt(x^2 + y^2) and bonds with the least resulting value. This process is illustrated in fig (3).

After the catoms have bonded, the remaining catoms which are not activated are just extracted from the ensemble to obtain the realization of the object by just the catoms. This is shown in the fig (4)

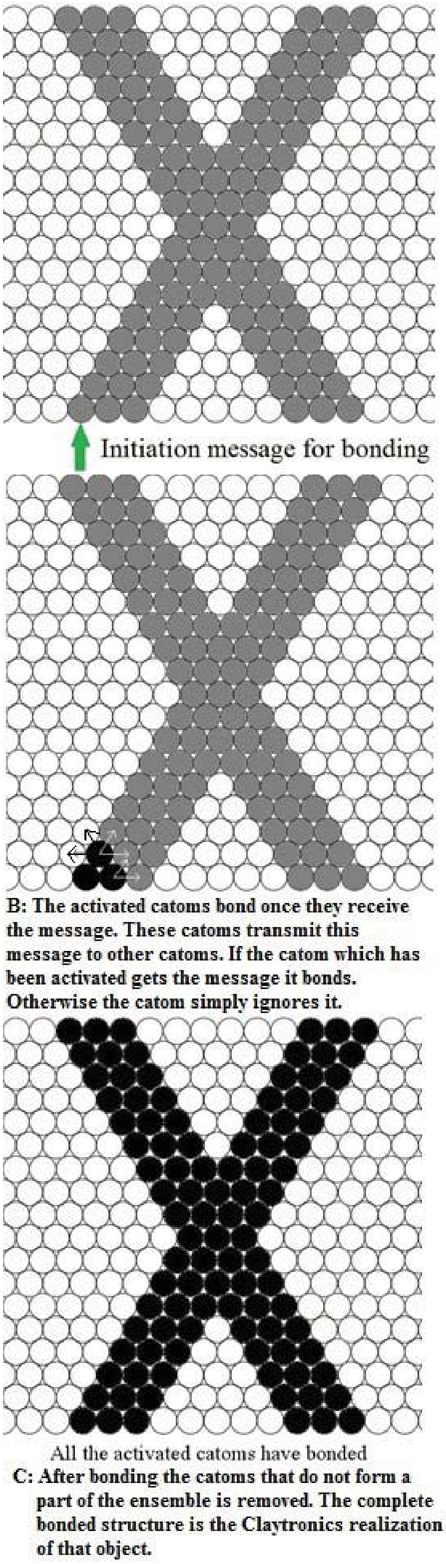

Fig (3)

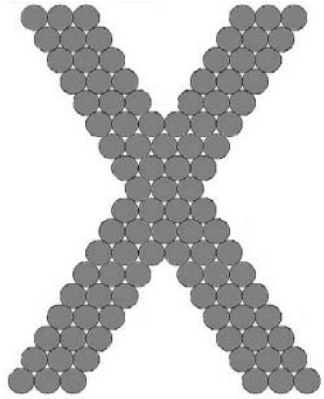

Fig (4)

IV. For 3-D Realization

The whole concept of claytronics can be extended to apply to 3-D objects as well. Here the catom ensemble is assumed to be 3 dimensional. It is also assumed that the computer knows all the coordinates of all the catoms. For image acquisition of a 3-D image, photographs of the object under consideration are taken from different angles. These photographs are then combined using sophisticated techniques to obtain a 3-D photograph of the object [10], [11]. More description of 2D to 3D conversion technique is beyond the scope of this paper. This 3-D image is compared with the ensemble and the coordinates of the catoms which are required are calculated and transmitted.

For shape reconstruction too, the ensemble is assumed to be 3 dimensional. Here the co-ordinates which are transmitted are input to the ensemble. The catoms belonging to the shape to be realized are activated in the same way as the 2-dimensional process. Applying the same principle of stop and wait protocol, the critical coordinates are fed to the ensemble one at a time, each time waiting for an ACK reply to confirm valid transmission. The catoms which aren't activated merely act like transmission paths and route the coordinates to its adjacent catoms. The activated catoms too act like transmission points for the other coordinates. After all the required catoms are energized, the activation stage is complete and the formation stage begins.

In the formation stage the actuation signal is input to a particular catom. This catom broadcasts the bond message to see which of its neighbors are activated. These activated catoms then bond. These bonded catoms individually broadcast the bond message to see which of its neighbors are activated and the process continues.

V. Scope for further development

There are several areas where improvement and research has to be done. In the two image acquisition techniques described, it might not be possible to acquire complete picture of the object and scale it down to the single catom scale. One possible solution may lie in advanced image acquisition techniques where each and every contour can be captured. The time delay involved in activation of certain catoms which are spread far and wide might has to be considered as it might not be insignificant. Efficient algorithms have to be implemented in such cases where the input signal is fed to many catoms instead of a single catom while at the same time achieving the desired result. The paper proposes a technique where the motion or orientation of catoms is not involved. This leads to significant advantages when it comes to power conservation but it might not be feasible in certain situations. For example 3-D realization of an abyss or any object with deep elevation changes, it would involve movement or removal of catoms from certain regions. Another constraint is it might not be possible to implement certain physical structures (for instance where much of the weight is concentrated on the upper half of the structure) with only the activated catoms. Some more additional catoms would also need to be activated to sustain the structure. This algorithm will work effectively for big 3-D realizations but for small 2-D realizations, hole motion algorithms can be used [4], [5]. When these considerations are incorporated into the algorithm, most of the limitations can be overcome and the algorithm would be effective in almost all situations.

VI. References

[1] Seth Copen Goldstein and Todd Mowry, "Claytronics: A Scalable Basis for Future Robots", 2004

[2] Jason Campbell, Padmanabhan Pillai and Seth Copen Goldstein, "The Robot is the Tether: Active, Adaptive Power Routing for Modular Robots with Unary Inter-robot Connectors", 2005

[3] Padmanabhan Pillai, Jason Campbell, Gautam Kedia, Shishir Moudgal, Kaushik Sheth, "A 3D Fax Machine based on Claytronics" , 2006

[4] Preethi Bhat, James Kuffner, Seth Goldstein, Siddhartha Srinivasa, "Hierarchical Motion Planning for Self-reconfigurable Modular Robots", 2006

[5] Michael De Rosa, Seth Goldstein, Peter Lee, Jason Campbell, Padmanabhan Pillai, "Scalable Shape Sculpting via Hole Motion: Motion Planning in Lattice-Constrained Modular Robots", 2006

[6] "Skeleton-Based Data Compression for Multi-Camera Tele-immersion System" Jyh-Ming Lien, Gregorij Kurillo, and Ruzena Bajcsy, 2007

[7]Cyberware, "3d laser scanner", http://www.cyberware.com

[8] XYZ RGB Inc., 3d scanning white paper, http://www.xyzrgb.com/
Html/whitepaper.html

[9]Data communications and networking, fourth edition, Behrouz A. Farouzan

The Seventeenth International Symposium on Artificial Life and Robotics 2012 (AROB 17th '12),
B-Con Plaza, Beppu, Oita, Japan, January 19-21, 2012

A method of teaching a new action to a communication robot through spoken commands

Eiichi Inohira[1] and Yudai Okuda[2]

[1] Kyushu Institute of Technology, Kitakyushu, Fukuoka 808-0196, Japan
(Tel: 81-93-695-6050, Fax: 81-93-695-6050)
(inohira@life.kyutech.ac.jp)
[2] Hoshiden Kyushu Corporation, Kurate, Fukuoka 807-1312, Japan

Abstract: We study on an approach to teach a new action to a communication in spoken commands. It is supposed that these robots are used for household use. Usually, a spoken command corresponds to a predefined action in this type of system. However, it is difficult to prepare many predefined actions to meet user's expectations in any situations. In this paper, we proposed an approach to teaching a new action which is composed of basic actions through spoken commands. And also, we demonstrated our proposed approach through a communication robot PaPeRo, which has a speech recognition system in Japanese. In our experiment, it took approximately 50 seconds to instruct the five combinations of a basic action and an instruction modifier through 10 spoken commands. After teaching the new action, it took approximately 20 seconds to complete a series of stored actions through a single spoken word.

Keywords: Communication robot, speech recognition, teaching

1 INTRODUCTION

There are several researches on service robots communicating with people through spoken dialogue [1, 2, 3]. It is supposed that these robots are used for household use. In general, a spoken command corresponds to a predefined action in this type of system. It means that the robots can perform only a predefined action through spoken commands. Therefore the robots can serve in limited situations. However, a designer is very difficult to prepare many predefined actions in any situations. A user cannot adjust predefined actions without programming according to its expectations. Our solution to this problem is that a user can teach a new action to the robot according to its need. In this paper, we proposed an approach to teaching a new action which is composed of basic actions through spoken commands [5]. And also, we demonstrated our proposed approach through a communication robot PaPeRo [4], which is manufactured by NEC Corporation and has a speech recognition system and speech synthesis in Japanese.

2 OUR PROPOSED TEACHING SYSTEM THROUGH SPOKEN COMMANDS

Our basic idea is that a new complex action is composed of basic actions. It means that a user can teach a new action to a robot via spoken words which describe combination of basic actions. A simplest case is that a robot memorizes a sequence of basic actions. A more complex case is that a robot memorizes a sequence of basic actions and responses to some situations, where a robot is interrupted during acting. A much more complex case is that a robot communicates with a user and modifies apart of a memorized sequence. In stage of practical use, a robot needs to communicate with people via multimodal interfaces such as touch and vision in order to response to contacts with perople and to memorize people and places.

Our proposed teaching system is based on a speech recognition system and a learning system which can store a spoken word corresponding to a sequence of basic actions. Design of our system depends on implementation of the used robot, that is, PaPeRo. Therefore, our implemented teaching system is described in Section 3.

3 EXPERIMENTS

3.1 Overview

In order to perform preliminary experiments to evaluate our proposed approach, we defined the four basic actions (go forward, go backward, turn right, turn left) and the three instruction modifiers (small, middling, big), which specifies magnitude of travel distance or rotation angle in a single action. We prepared a program to store the five combinations of a basic action and an instruction modifier in the robot's memory and to play the new action through a single spoken command. After the robot accepted the spoken command for 'teaching a new action', it waits for a spoken command for basic actions. Next, the robot waits for a spoken command for instruction modifiers. For instance, when a user says, 'go forward', 'big', it means the robot travel long distance forward. Then, a user can give five basic actions to the robot. Here, limitation on the number of stored actions

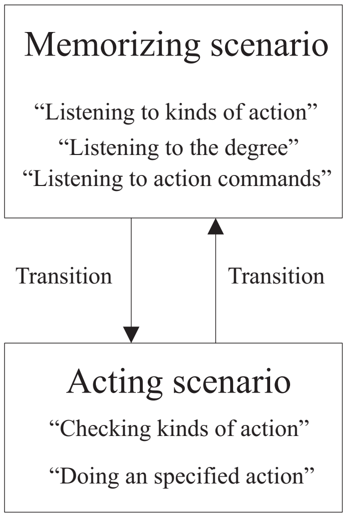

Fig. 1. The teaching scenario

is provisional for preliminary experiment and can be easily changed by modifying the program. After a user taught a new action, the robot can play the new action through a spoken command.

3.2 Experimental setup

PaPeRo has functions of speech recognition and speech synthesis in Japanese. In addition, PaPeRo has two active wheels for moving on a floor and several touch sensors and two cameras, which we do not use in this paper. PaPeRo acts according to a specific scenario, which describes its internal states, external events, robot actions, and state transitions, that is, a finite state machine. We described scenarios to memorize a sequence of basic actions and to invoke a new action. Fig. 1 shows a diagram of the teaching scenario consisting of the memorizing scenario and the acting scenario. In the memorizing scenario, a robot listens to kinds of basic actions and the degree, that is, the instruction modifiers. After memorizing a sequence of basic actions, a robot listens to action commands such as invoking a new action. The acting scenario is prepared in order to travel or turn the robot. The aim of separating scenarios is to remove complex commands to move the robot from the memorizing scenario.

Fig. 2 shows a flow chart of the memorizing scenario. In the memorizing scenario, a robot listens to a pair of kinds of basic actions and the degree until five times. After a robot listens to a pair, it performs an instructed. After a robot memorizes a sequence of the pairs, a robot listens to the action command "all" and performs a new action according to the memorized sequence.

Fig. 3 shows a flow chart of the acting scenario. In the acting scenario, a robot checks if a specified action is travelling or turning. The reason is that the travelling command and the turning command are not the same programmatically.

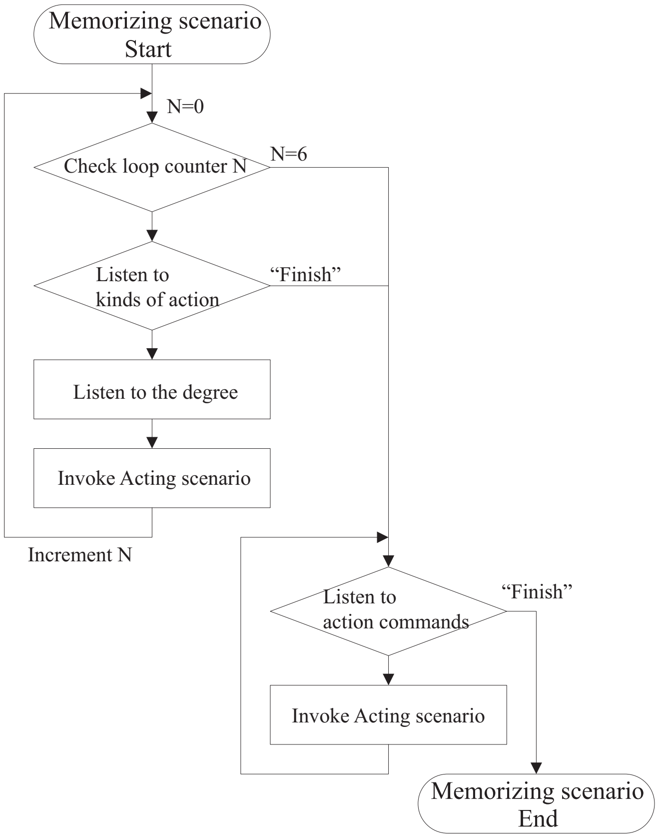

Fig. 2. The memorizing scenario

We defined pairs of a spoken command and a basic actions as shown in Table 1. Table 2 shows definition of instruction modifiers.

3.3 Experimental results

We demonstrated teaching of the new action to travel the robot along a route as shown in Fig. 4. Fig. 5 shows a time chart of our demonstration. We give five pairs of basic actions and instruction modifiers to the robot. The robot memorized the 10 spoken commands as follows:

1. "Go forward" and "ordinarily"
2. "Turn left" and "big"
3. "Go forward" and "big"
4. "Turn right" and "big"
5. "Go backward" and "ordinarily"

Note that a user actually spoke Japanese words in the experiment. After teaching, we give a spoken command "all" to invoke a new action according to memorized sequence of basic commands. A robot performed the new action successfully as shown in Fig. 6.

Table 1. Definition of basic actions

Spoken command	Definition
Go forward	A robot goes forward with constat speed for a specified period
Go backward	A robot goes backward with constat speed for a specified period
Turn right	A robot turns right in the center of its current position by specified rotation angle
Turn left	A robot turns left in the center of its current position by specified rotation angle

Table 2. Definition of instruction modifiers

	Duration [s]		Rotation angle [deg]	
	Go forward	Go backward	Turn right	Turn left
small	1	1	-30	30
ordinarily	3	3	-60	60
big	6	6	-90	90

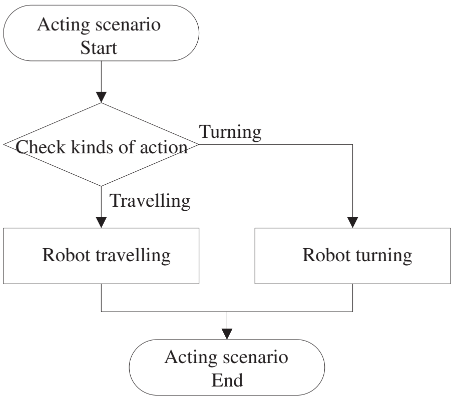

Fig. 3. The acting scenario

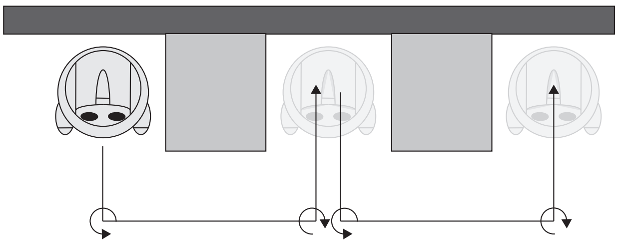

Fig. 4. The travelling route of the robot

In our experiment, it took approximately 50 seconds to instruct the five combinations of a basic action and an instruction modifier through 10 spoken commands. On the other hand, it took approximately 20 seconds to complete a series of stored actions through a single spoken command. We showed that our proposed teaching system realizes to teach a new action to the robot through spoken commands without developing a new program and that teaching a new action via spoken commands is useful for saving time and labor.

4 DISCUSSION

In our demonstration as mentioned above, a robot memorized a sequence of basic actions and instruction modifiers. It means that we realized a simplest teaching system mentioned in Section 2. In the demonstration, it is difficult for us to memorize 10 spoken commands. For instance, when the tenth command is spoken, it is hard for us to recall the first command because we cannot memorize too many commands at a time. Therefore, we need to confirm given basic actions until a certain point before completion of teaching. And also, when a user gives mistaken command to a robot, modification of a taught action is needed. In order to deal with these cases, we need to improve the teaching system as a user smoothly teaches a new action to a robot.

5 CONCLUSION

In this paper, we proposed an approach to teaching a new action which is composed of basic actions through spoken commands. A spoken command corresponds to a predefined action in conventional communication robots. We demonstrated our proposed teaching system through a communication robot PaPeRo, which has a speech recognition system in Japanese. In order to perform preliminary experiments, we defined the four basic actions (go forward, go backward, turn right, turn left) and the three instruction modifiers (small, middling, big). Our teaching system can memorize a squence of basic actions and instruction modifiers via spoken commands and invoke a new action after teaching.

In the future work, we will improve the teaching system in order to deal with modification of a taught action via spoken commands.

REFERENCES

[1] Tikhanoff V, Cangelosi A, Metta G (2011), Integration of speech and action in humanod robots: iCub simu-

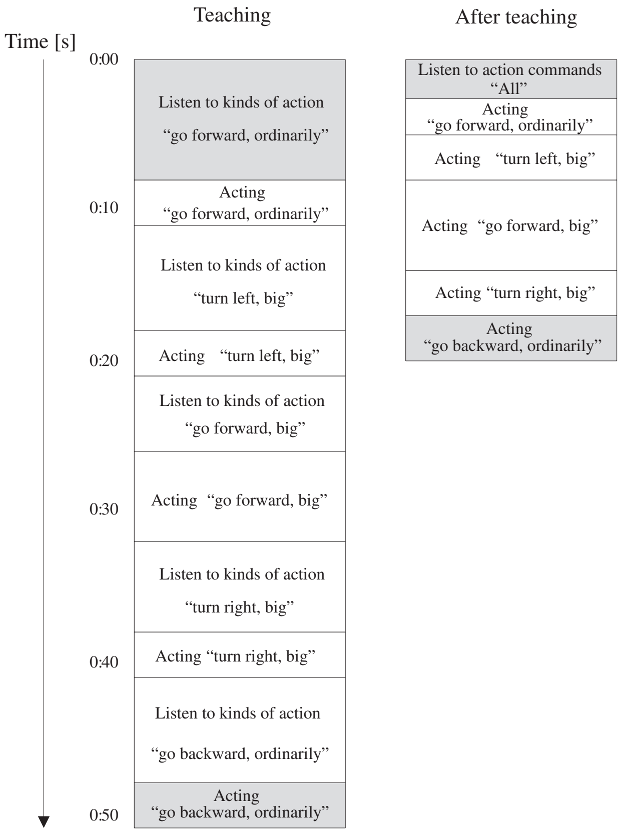

Fig. 5. A time chart of teaching the robot

lation experiments. IEEE trans on Autonomous Mental Development 3(1):17-29

[2] El-Emary IMM, Fezari M, Attoui H (2011), Hidden Markov model/Gaussian mixture models (HMM/GMM) based voice command system: A way to improve the control of remotely operated robot arm TR45. Scientific Research and Essays 6(2):341-350

[3] Budiharto W, Jazidie A, Purwanto D (2010), Indoor Navigation using Adaptive Neuro Fuzzy Controller for Servant Robot. 2010 Second Intl Conf on Computer Engineering and Applications (ICCEA 2010) 582-586

[4] PaPeRo, http://www.nec.co.jp/products/robot/en/index.html

[5] Okuda Y, Inohira E (2010), Acquisition of action by using speech recognition in a communication robot. Proc of the 12th SOFT Kyushu Chapter Annual Conf 67-70

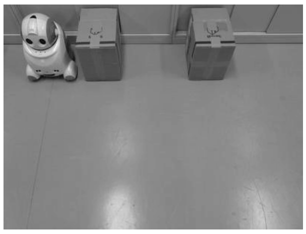

(a) Initial position

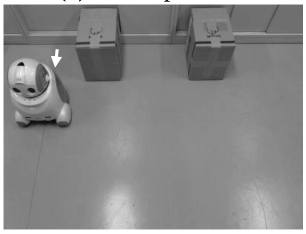

(b) Step 1: "Go forward" and "ordinarily"

(c) Step 2: "Turn left" and "big"

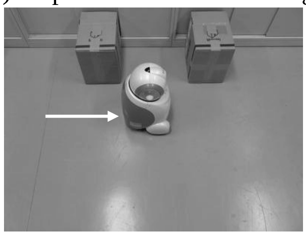

(d) Step 3: "Go forward" and "big"

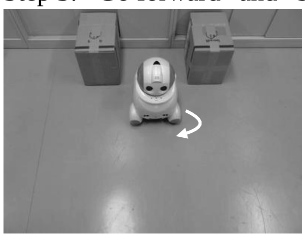

(e) Step 4: "Turn right" and "big"

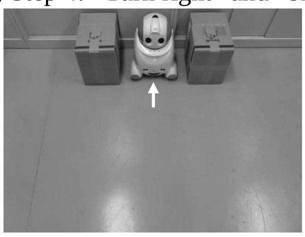

(f) Step 5: "Go forward" and "ordinarily"

Fig. 6. Snapshots of the experiment of teaching the robot

The Seventeenth International Symposium on Artificial Life and Robotics 2012 (AROB 17th '12),
B-Con Plaza, Beppu, Oita, Japan, January 19-21, 2012

Evaluation of the teleoperation system based on force-free control and visual servo control by using different human operator perception: evidence verified by experiments and statistical analysis

Achala Pallegedara[1], Yoshitaka Matsuda[2], Naruto Egashira[3], Takeo Matsumoto[2], Kenta Tsukamoto[2], Takenao Sugi[2] and Satoru Goto[2]

[1] Department of Science and Advanced Technology,
Graduate School of Science and Engineering, Saga University, Saga 840-8502, Japan
[2] Department of Advanced Technology Fusion,
Graduate School of Science and Engineering, Saga University, Saga 840-8502, Japan
(Tel: +81-952-28-8643, Fax: +81-952-28-8666)
(goto@cc.saga-u.ac.jp), (ymatsuda@cc.saga-u.ac.jp)
[3] Department of Control and Information Systems Engineering,
Kurume National College of Technology, Fukuoka 830-8555, Japan
(naruto@kurume-nct.ac.jp)

Abstract: This research considers the teleoperation of an articulated robot arm by means of force-free control and visual servo control over communication channels using Internet technology. The main investigation is carried out to find how effectively improves the accuracy and the effectiveness of the teleoperation after provision of a visual feed back channel to the system. The system accuracy, effectiveness, repeatability, and handleability based on the human operator's skills and operator's cognitive aspects are evaluated by using statistical data analysis and experimental results. Effectiveness of the statistical analysis is assured by increasing number of experiment data and assuming environmental factors and implicit variables maintain to be unchanged.

Keywords: Force-free Control, Teleoperation, Visual Servo Control, Template Matching, Accurate Motion, Rough Motion, Human Operator perception, Correlations, Human cognitive aspects.

1 INTRODUCTION

In many years, telerobotics has been a major concern among researchers. It becomes more focused and justified for space and undersea operations, fire-fighting and rescue operations in battlefronts and disasters, and also for training and entertainment activities. Teleoperation is of utmost importance, when the working site is hazardous, such as nuclear plant activities, land-mine extraction, toxic chemical plant activities and so forth. In recent two decades, Internet has been much popular infrastructure for the communication activities and therefore, researchers use Internet for telerobotic applications as consistent communication platform. The TCP sockets have also been consistently used in many areas in telecommunication so that it gives past track records to be guaranteed as reliable communication with flow control, sequencing and re-transmitting of lost data [1]. The first Internet based telerobotics started as *Goldberg* [2] connecting a SCARA and ASEA IRb-6 type robots to the Internet in 1994. Since then, more researchers found their interest to use Internet for the development of advanced robot teleoperation applications, and remarkable early stage developments are published in [3], [4] and [5].
However, the major concern in Internet technology based teleoperation is that an uncertain transmission delay between human operator in the master side and the teleoperated robot in the slave side. Major contributions to overcome such transmission issues are given in [6]. The *Sheridan's* supervisory control [7] was proposed and it was appreciated in view of stable teleoperation. Supervisory control approach implements an autonomous local feed back loop at the slave manipulator. Remote human operator needs only to send key parameters or few required data to initiate and the slave manipulator, of what just slave manipulator required for planing the trajectories and controlling the manipulator. In this research is also based on a human supervisory control approach.

Figure 1 shows the schematic model representation of an Internet-based supervisory controlled teleoperation system. It also illustrates the main components and the terminologies in the context of a teleoperation systems. In our research, we adopted the same base architecture for experimental teleoperation setup. Moreover, the applicability and effectiveness of the supervisory control in teleoperation is highly depended and affected by the capability of the supervisory control in the master side as well as the local controller of the slave side. The investigation is based on the evaluation of the human operator's skills and cognitive factors on a supervisory control. And how those factors can correlate with an effectiveness of the investigated teleoperation system.

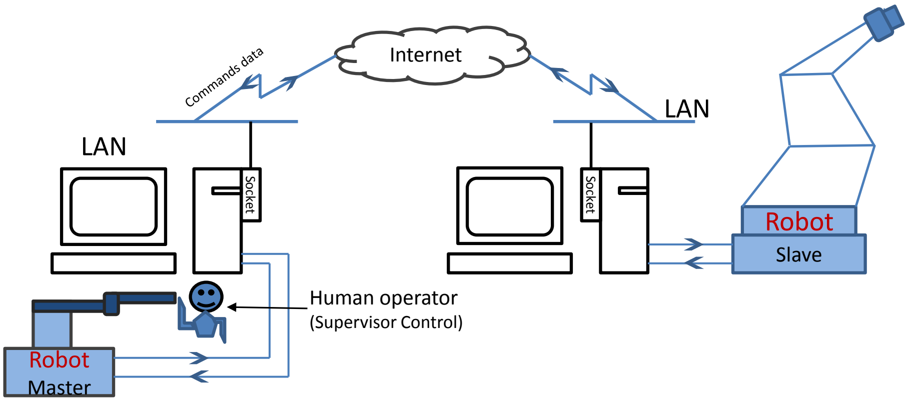

Fig. 1: Schematic diagram of general supervisory controlled semi-autonomous teleoperation system.

The teleoperation system of this research comprises of two different techniques which are attached in to different modules. First one is the force-free control (FFC) which is used to realize the passive motion of robot arm for given external force by human operator. The details of the FFC are described in [8] and references therein. The second one is the image processing module in which template matching (TM) techniques are used to carry out the accurate motion control by means of visual servo control [9]. Experiments were carried out by selecting operators appropriately corresponding to the following three kinds of experiments:

1. Providing camera view feedback to the operator.
2. Giving a guided map including desired path of the target.
3. Both map and visual feedback provided.
4. No additional aid provide (by seeing remote location robot from operational point).

2 TELEOPERATION BY FORCE-FREE CONROL AND VISUAL SERVO CONTROL

Our teleoperation system consists of two different motion control mechanisms. First is to accomplish remote control action by means of human operator assistance, in which FFC method is used. The details of the mechanisms and functions are described in author's work [10]. Figure 2 shows the detailed schematic presentation of the teleoperation system in this paper. The position control can be achieved by two kinds of motions for the reference position of the robot arm, i.e., the rough motion and the accurate motion. For the rough motion, the reference position is generated manually by using the FFC. Second is to accomplish the accurate motion where the reference position is generated automatically by using the vision system based visual servo control (VSC). In order to generate the reference position of the robot arm for the accurate motion, the image obtained from the USB camera is analyzed and processed. The vision system attached to the camera side is responsible for detecting the target position. The reference position data for the robot arm are sent through the network.

After receiving reference position data from the master control, slave robot in the working side moves accordingly as "rough motion." The human operator moves the master robot arm manually until the camera mounted on the working side robot captures the image of the target object. Then system switches to the second control scheme for "accurate motion."

2.1 Force-free control (FFC)

The FFC realizes the passive motion of the robot arm due to external force so that the robot arm can move freely according to the external force. In this teleoperation system FFC control plays an important role by generating reference positions when human operator executes the desired movement on the operational side robot. The generated reference position data is sent to the working side robot via network by using the socket communication TCP/IP [11]. The FFC for passive motion of the robot arm is applied without changes to the robot manufacturer's hardware configurations [12].

2.2 Visual servo control (VSC)

In our teleoperation system, VCS [9] plays an important role by helping working side robot arm to reach the target, after switching from the "rough motion." A general USB camera can be used in the VSC. At each sampling time, image is sent to the image processing in the camera side computer.

The image analysis is done by using template matching (TM) techniques [13, 14], in which, it calculates the position

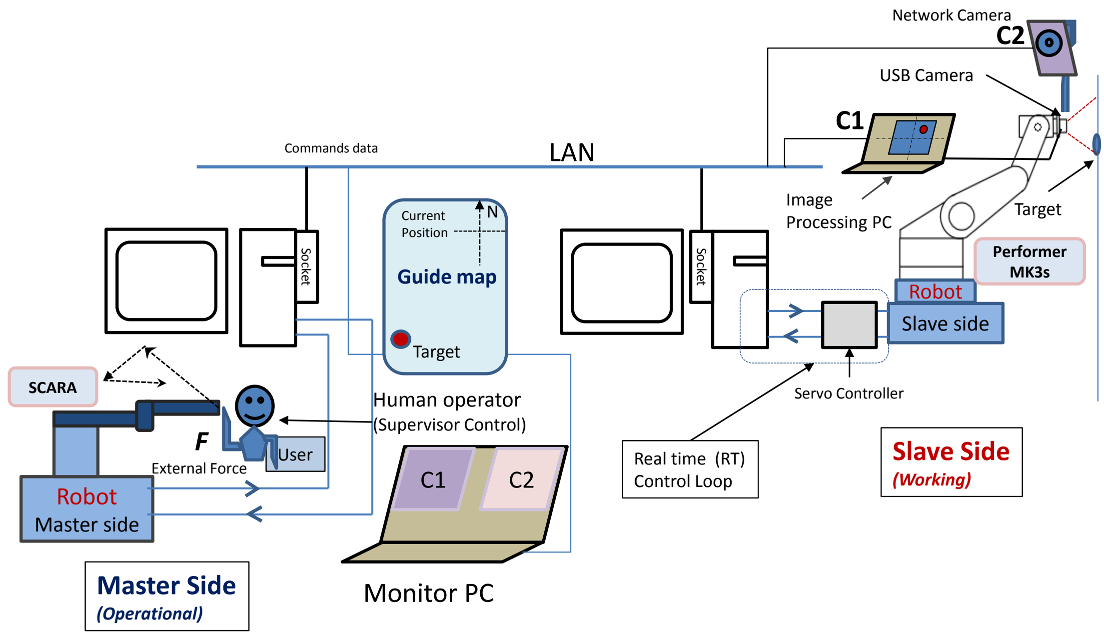

Fig. 2: Schematic overview of the investigated teleoperation system with visual feed back

of the target inside the image. Then, system calculates the corresponding reference position and send it to the working side robot. To apply the template matching algorithm, camera image must be processed at a each sampling so that, robot can reach to the target position. The center of the camera view and the target object at a particular instance of the VSC are calculated in each sampling. And continuously, image is processed and applied the template matching until target would coincides with the center of the camera view.

3 HUMAN OPERATOR'S PERCEPTION

The main objective of this research to investigate the applicability of the system by using different users and scenarios. Therefore, this research is focused on some aspects of the system especially for accuracy, effectiveness, repeatability, handleability and so forth.

In a practical situation no one can guarantee that high skill exclusive operator would be available in all time. Therefore, teleoperation system design is focused to make it as simple to operate even by the average user who does not have prior experience or special skills of operating the system. And also it can be operated with the minimum guidance as shown in Fig. 2. the system would provide the operational assistance by means of online camera views (C1 and C2 in Fig. 2) and the guide map of the target location.

The human operator's responsibility is to manipulate the robot arm in the operational side as to give "rough motion" to the working side robot that would catch the target within its camera view. To investigate the ability of applying the supervisory action by the general user, a larger number of experiments were carried out by providing different means of aid to human user and also sample of users were selected with irrespective of experience, age, field of studies and anthropometry of the body [15].

In general, each human has different levels of cognitive power, persistence, reactive or response time, level of skill for particular area, level of experience, prior knowledge of a particular subject etc. Therefore, any system with human involvement subjects to above mentioned aspects [16]. Due to above mentioned reasons, system is designed in such way that it should be identified the tolerances of those aspects if the system is intended to be applied in real practice.

4 EXPERIMENTAL RESULTS

Figure 2 is illustrated the experimental setup, the robot arm named Performer MK3s with attached USB camera in working side was controlled by the reference position generated in the operational side using SCARA robot. The SCARA is manually operated by a human operator until the target was included in the view of the camera. Then, Performer MK3s is controlled autonomously by the reference position generated in the camera side. As in the Fig. 2, target object is located in the slave side. A Network camera is used to capture the view of the target area and it will give the video feed back to the monitor PC as a camera view $C2$. The SCARA and the MK3s robots are connected to the computers in the master side and the slave side respectively. Image processing is done in the image processing pc $C1$ in the slave side of the system. The arrow marks are given to show the movements of the SCARA robot which are performed by a

Table 1: Experiment data and results for teleoperation using different users

Exp. No.	User No. (Operator)	Skill / Experience. Level	Results (Success or Failed) Direct View	Guide Map	Camera View	Guide & Camera View	Remarks Age-Field of Study (Related or Not)
1	User No.1	High	Success	Success	Success	Success	23 - Related
2	User No.2	High	Success	Success	Success	Success	23 - Related
3	User No.3	High	Success	Success	Success	Success	34 - Related
4	User No.4	Low	Success	Failed	Success	Success	21 - Related
5	User No.5	Low	Success	Failed	Failed	Success	22 - Related
6	User No.6	New	Failed	Failed	Failed	Failed	20 - Non Related
7	User No.7	New	Success	Success	Success	Success	20 - Related
8	User No.8	New	Success	Failed	Success	Success	21 - Non Related
9	User No.9	New	Success	Failed	Failed	Success	21 - Non Related
10	User No.10	New	Success	Success	Success	Success	21 - Non Related
11	User No.11	New	Success	Success	Success	Success	23 - Non Related
12	User No.12	New	Failed	Success	Success	Success	23 - Non Related
13	User No.13	New	Success	Failed	Success	Success	20 - Related
14	User No.14	New	Failed	Failed	Failed	Failed	20 - Related
15	User No.15	New	Failed	Failed	Success	Success	21 - Non Related
16	User No.16	New	Success	Success	Success	Success	21 - Related
17	User No.17	New	Success	Failed	Failed	Success	20 - Non Related
18	User No.18	New	Success	Failed	Success	Success	20 - Non Related
19	User No.19	New	Success	Failed	Success	Success	20 - Related
20	User No.20	New	Success	Failed	Success	Success	21 - Non Related
21	User No.21	New	Success	Success	Success	Success	21 - Non Related
22	User No.1-R	High	Success	Success	Success	Success	23 - Related
23	User No.4-R	Low	Success	Success	Failed	Success	21 - Related
24	User No.9-R	New	Success	Failed	Success	Success	21 - Non Related
25	User No.19-R	New	Failed	Failed	Success	Failed	20 - Related
26	User No.20-R	New	Success	Failed	Failed	Success	21 - Non Related

NB:User No.X-R means Repeat by same user

human operator.

In this experiment, each of the experiments was done by volunteer users as listed in the table 1. The experiments were arranged to get four readings from each user. Users skill level is defined based on the past experience of using the system and ranked them as "High", "Low" and "New" as in the table 1. Four reading were taken form different scenarios of the experiments as listed in the table 1 as follows:

1. "Direct View" is given for an operator manipulate the robot arm by looking at the master side robot directly and no any other aid is given.

2. "Guide Map" is given for an operator manipulates the robot arm by only looking at the site map of the target position as shown in the Fig. 2.

3. "Camera View" is given for an operator manipulates the robot arm by looking at the computer monitor which has camera view of the target location of the working side as shown in the Fig. 2.

4. "Guide and Camera View" is given when operator has both aids of guide map and camera view feed back.

However, communication delays contracted in the system are assumed to be constant for all the scenarios and effects of them are not taken into the account.

The results showed that visual feed back improved the effectiveness of the total teleoperation cycle in regardless of the age and level of experience. However, communication delay on video stream can degrades the decision taking time for performing desired movements by applying external force. Statistical data analysis using the "probability and correlation coefficients" are carried out to verify the results based on how effectively target is reached on different experiment scenarios by different human operators as shown in tables 2 and 3. The "success level" gives the probability of success in each category.

To identify a feasibility of the use of the teleoperation system by different users with different perceptions, thorough investigation are carried out by using unbiased sample of human users. In this investigation, we used 26 different trials of experiments as given in table 1 which denotes the abstract and final information about the total investigation. User age and user's field of studies whether it related to the teleoperation or not are also given under remarks. From the research, We draw main objective that how effectively new user having different perspectives can operate the teleoperation system by using different visual aids such as a video feed back or/and a guide map of the target location.

In addition, a new user was given an introduction prior to begin his trials of experiment. It was found that certain either new or experience users shown energetic and confident interest, and also they wanted to perform more and more trials, however, few of them were found an uncomfort feeling and were lethargic during their turns. Hence, the effectiveness of the supervisory action also depends upon operators instantaneous condition and cognitive aspects of their mind or/and their perspectives regardless of their experience or skills at the time of an experiment [17].

Table 2: Correlation variations with skill level

	Category	Correlation with skill level	Remarks
1	Direct View	-0.2218	Negative
2	Guide map Only	0.1379	Positive
3	Cameras Only	-0.1011	Negative
4	Cameras & Guide	-0.1136	Negative

Table 3: Probability of success variation with category

	Category	Success level %	Remarks (Skilled user)
1	Direct View	80.77	all success
2	Guide map Only	42.31	2 failed
3	Cameras Only	73.1	2 failed
4	Cameras & Guide	88.46	all success

5 DISCUSSION

According to the table 2 guide only scenario is shown positive correlation with skill level. However, all other scenarios, correlation with skill level and success rate have negative correlation. Also it is observed that negative correlation decrease with introduction of camera view, this indicate giving online visual feed back with instruction to the users give better performance. And also introduction of a camera view, it increases the correlation coefficient value between skill level and success rate. Table 3 shows the success probability variation for an each category. Results show that positive increment on a system effectiveness by introducing online camera feed back regardless of a user being an experienced or not. However, experienced users of the system show characteristics that they can handle the system successfully even without an online visual feed back. Moreover, certain amount of users who found difficult to use and manipulate the teleoperation system and results show that success percentage varies when category changes. It is also observed that some users could not be able to manipulate the system in a way that the working robot on desired rough motion towards the target. However, in their second attempt, same users could get succeeded. Therefore, we conclude that system operational functions can easily be understandable for a general user who did not have either any previous interactions or experience on using the system. Since, the sample of users is used for the investigation does not include female users, correlation results might have a high possibility of variation if sample includes female users.

6 CONCLUSION

In this contribution, an investigation is carried out for the teleoperation system to find out how human factors with cognitive aspects affect the system effectiveness and performance when it applies in practice. It is essential that we must test the system with large number of real scenarios to validate the applicability, if the teleoperation system claims to be used in real application. Moreover, especially if a system has human user involvement and which is a critical factor for a fulfillment of final objectives then a sample of users should be selected with a high degree of variation and a sample amount must also be higher. The relevance of the real world application of the teleoperation system, particularly in case of human supervisory involvement, is highlighted from this paper. Finally, by providing a visual feed back for the human user effectively increases an applicability and an effectiveness of the teleoperation system regardless of users' skills, age and relevance to their major field of study. By considering the results, if the user sample number increases nearly up to 100 then, regression analysis can be carried out by using a fitted model for the experimental results.

REFERENCES

[1] Stevens WR (1998), Unix Network Programming, Networking APIs: Sockets and XTI, Upper Saddle River, NJ, Prentice Hall Inc.

[2] Goldberg K (2000), The Robot in the Garden: Telerobotics and Telepistemology in the Age of the Internet, MIT Press, Cambridge, Massachusetts, USA.

[3] Taylor K and Trevelyan J (1995), A Telerobot on The World Wide Web, National Conference of the Australian Robot Association, Melbourne: Australian Robotics Association.

[4] Taylor K and Dalton B (1997), Issues in Internet Telerobotics, International Conference on Field and Service Robotics (FSR 97), Canberra, Australia: The Australian National University, pp. 151-157.

[5] Teresa T and Zhang H (1999), Internet-Based Tele-Manipulation, Proceedings of the 1999 IEEE Canadian Conference on Electrical and Computer Engineering, Shaw Conference Center, Edmonton, Alberta, Canada, pp. 1425-1430.

[6] Conway L, Volz RA and Walker MW (1993), Teleautonomous systems: projecting and coordinating intelligent action at a distance, IEEE Transactions on Robotics and Automation, Vol. 6, No. 2, pp. 146-158.

[7] Sheridan TB (1992), Telerobotics, Automation and Human Supervisory Control, MIT Press, Cambridge, Massachusetts, USA.

[8] Goto S (2010), Teleoperation System of Industrial Articulated Robot Arms by Using Forcefree Control, Robot Manipulators Trends and development, Advanced Robotic Systems International, IN-TECH, Chapter 15, pp. 321-334.

[9] Hutchinson S, Hager GD and Corke PI (1996), A turorial on Visual Servo Control, IEEE Transaction on Robotics and Automation, Vol. 12, No. 5, pp. 651-670.

[10] Pallegedara A, Matsuda Y, Matsumoto T, Tsukamoto K, Egashira N and Goto S (2011), Remote Control of Robot Arms via Network by Force-Free Control Followed Template Matching, Proceedings of the SICE Annual Conference 2011, September 13-18, Tokyo, Japan.

[11] Comer DE and Stevens DL (2001), Internetworking with TCP/IP Vol III: Client-Server Programming And Applications Linux/POSIX Sockets Version, New Jersey, Prentice Hall.

[12] Goto S (2007), Forcefree control for flexible motion of industrial articulated robot arm, Industrial Robotics: Theory, Modeling and Control, Advanced Robotic Systems International, Chapter 30, pp. 813-840, pro literatur Verlag.

[13] Burt PJ, Yen C and Xu X (1982), Local correlation measures for motion analysis: a comparative study, Proceedings of the IEEE Conference on Pattern Recognition and Image Processing, pp. 269274.

[14] Lam SK, Yeong CY, Yew CT, Chai WS and Suandi SA (2010), A Study on Similarity Computations in Template Matching Technique for Identity Verification, International Journal on Computer Science and Engineering, Vol. 02, No. 08, pp. 2659-2665.

[15] Norman DA and Draper SW (1986), User Centered System Design: New Perspectives on Human-Computer Interaction, Lawrence Erlbaum Associates, Hillsdale, New Jersey London.

[16] Howie DE, Janzen ME and Vicente KJ (1996), Research on Factors Influencing Human Cognitive Behaviour (III). CEL Technical Reports Series, CEL No. 96-06.

[17] Hannaman GW, Spurgin AJ and Luckic YD (1985), A model for assessing human cognitive reliability in PRA studies, Proceedings of the IEEE Conference on Human Factors and Power Plants, pp. 343353.

The Seventeenth International Symposium on Artificial Life and Robotics 2012 (AROB 17th '12),
B-Con Plaza, Beppu, Oita, Japan, January 19-21, 2012

Development of flexible joints for a humanoid robot that walks on an oscillating plane

Takehiro Yoneyama[1], Kazuyuki Ito[2]

[1,2] Hosei University, Tokyo 184-8584, Japan
(Tel: 81-42-387-6093, Fax: 81-42-387-6381)

[1] 10r6138@stu.hosei.ac.jp, [2] ito@hosei.ac.jp

Abstract: In this study, we develop flexible joints for a humanoid robot that walks on an oscillating plane and discuss their effectiveness in compensating disturbances. Conventional robots have a rigid frame and are composed of rigid joints driven by geared motors. Therefore, disturbances, which may be caused by external forces from other robots, obstacles, vibration and oscillation of the surface upon which the robot is walking, and so on, are transmitted directly to the robot body, causing the robot to fall. To address this problem, we focus on a flexible mechanism. We develop flexible joints and incorporate them in the waist of a humanoid robot; the experimental task of the robot is to walk on a horizontally oscillating plane until it reaches the desired position. The robot with the proposed flexible joints, reached the goal position despite the fact that the controller was the same as that used for a conventional robot walking on a static plane. From these results, we conclude that our proposed mechanism is effective for humanoid robots that walk on an oscillating plane.

Keywords: Humanoid Robot, Flexible joint, Elasticity

1 INTRODUCTION

In this study, we develop flexible joints for a humanoid robot that walks on an oscillating plane, and discuss their effectiveness in compensating disturbances. In conventional studies, robots have a rigid frame and are composed of rigid joints driven by geared motors. Therefore, disturbances, which may be caused by external forces from other robots, obstacles, vibration and oscillation of the surface upon which the robot is walking, and so on, are transmitted directly to the robot body, causing the robot to fall [1]. To prevent falling, conventional robots require various sensors and a high-spec controller for real-time processing [2]. Nevertheless, it is very difficult for the robot to react quickly and avoid a fall, which prevents robots from operating in unknown dynamic environments. To address this problem, we focus on flexible mechanisms. A flexible mechanism can adapt itself to a rapidly changing environment passively because of its dynamics and physical properties [3-5]. In addition, it requires no sensors and no controllers, because the necessary information is contained within the mechanism itself and the calculation for its control is implicitly performed by its dynamic and physical properties. In our previous study, we developed and confirmed the viability of a flexible joint whose elasticity can be adjusted to adapt to a dynamic environment. The flexible joint presented here compensates for disturbances passively, reducing the load of the controller [6]. However, the previous study was focused on the effectiveness of the flexible joint itself and the performance of the entire robot was not sufficiently discussed. In particular, the subject of autonomous control that would enable a robot to move to a desired position was not addressed.

In this study, we address the topic of autonomous walking by a robot to reach a desired position. We improve our previous flexible mechanism [6], and we develop a humanoid robot that can walk on an oscillating plane to reach a desired position by using a simple autonomous controller that is actually designed for walking on a static plane.

2 TASK AND ENVIRONMENT

For experiments on an oscillating plane, we employ a vibration generator, as shown in Fig.1. The environment measures 1000 mm × 1000 mm. The oscillation amplitude is 50 mm, and, to confirm the frequency response, we vary the frequency from 1.5 Hz to 5.0 Hz.

The task of the robot is to walk toward a target position on the oscillating plane.

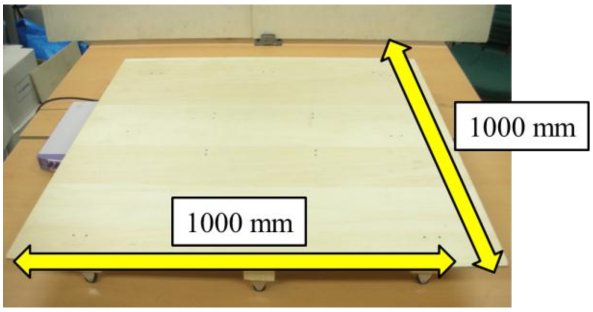

Fig. 1. Oscillating Plane

3 FLEXIBLE JOINT

Fig. 2 shows an illustration of the flexible joint [6]. An upper link and a lower link are brought into contact through the ball bearing and a rubber band. It is possible to for them to interact through the rubber band. If the upper link slides, the rubber cord is pulled and the upper link is pulled back. The length of rubber cord can be adjusted with the servo motor, which causes the rigidity of the flexible joint to change.

Due to the viscoelasticity of rubber, the flexible joint has the characteristics of a low-pass filter. This implies that high-frequency oscillations are removed on account of its dynamic properties.

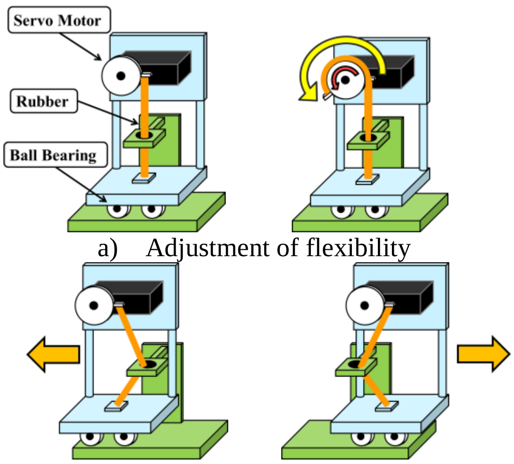

a) Adjustment of flexibility

b) Slide mechanism

Fig. 2. Diagrammatic illustration of the flexible joint

4 DEVELOPED ROBOT

4.1. Humanoid robot

Fig. 3 shows our previous robot [6], and Figs. 4 to 6 show the robot that we discuss in this paper, and Table 1 lists its specifications. In our previous robot, two flexible joints are embedded in each leg, increasing the complexity and the weight. In particular, increase of the legs' weight causes a decrease in the robot's mobility. In this paper, we improve these issues by embedding two flexible joints in the robot's waist. By this mechanism, we reduce the number of the flexible joints and can employ legs with both a simple design and high mobility.

As shown in Fig. 5, the two flexible joints in the robot's waist are at right angles to each other, and can handle two-dimensional horizontal oscillation.

A CCD camera for detecting a target position is installed in the robot's head, and a micro-computer for controlling the servo motors is mounted on the body.

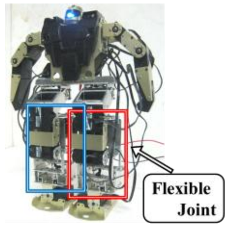

Fig. 3. Previous humanoid robot

Table 1. Details of a humanoid robot

Height	380 mm	Weight	1.78 kg
Width	180 mm	Actuator	KRS-4034HV, KRS-788HV
Depth	130 mm	Degree of freedom	16

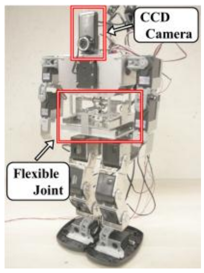

Fig. 4. Humanoid robot

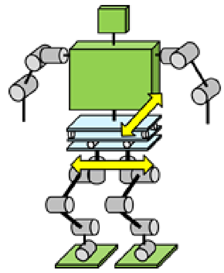

Fig. 5. Sliding direction of the flexible joints

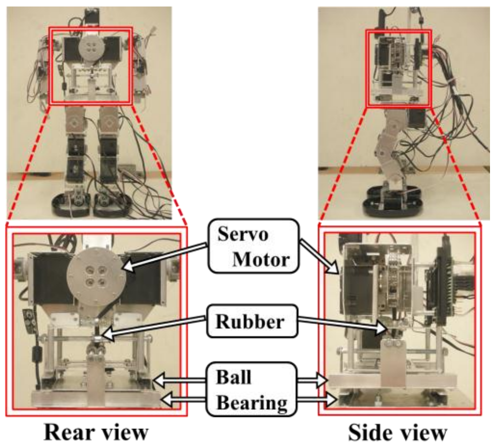

Fig. 6. Developed flexible joint

4.2. Adjustment of the spring constant

Fig. 6 shows the developed flexible joint. The pulling force of the rubber in the horizontal direction F can be approximated by equation (1). As shown in Fig. 7, the elasticity (k of equation (1)) of the flexible joint can be adjusted by rolling up the rubber band through use of the servo motor.

From preliminary experiments, the relation between k and the angle of rotation of the servomotor was given by Fig. 7, and it can be approximated by equation (2).

$$F = -kx \quad (1)$$

$$k = 0.36\frac{\theta}{\pi} + 0.15 \quad (2)$$

k : Constant of spring [N/mm]

θ : Angle of rotation of the servo motor [rad]

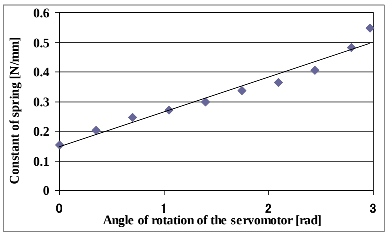

Fig. 7. Constant of spring

4.3. Frequency response of the flexible joint

The motion equation of a flexible joint is shown by equation (3). The frequency response of the flexible joint is shown in Fig. 8. The dotted line represents a high-elasticity (k = 0.50) joint and the solid line represents a low-elasticity (k = 0.15) joint. The cut off frequency of the high-elasticity joint is 7.7 Hz, and that of the low-elasticity joint is 3.7 Hz.

$$M\frac{d^2x}{dt^2} + D\frac{dx}{dt} + kx = f \quad (3)$$

M : Mass [kg]
D : Viscosity resistance [Ns/m]
k : Constant of spring [N/mm]
f : External force [N]

Table 2. Value of parameters

M	D	k (low)	k (high)
0.88 kg	1.00 Ns/m	0.30 N/mm	1.00 N/mm

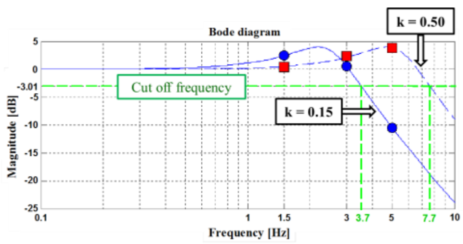

Fig. 8. The frequency response of a flexible joint

5 EXPERIMENT

To demonstrate the effectiveness of the proposed flexible joints, we conduct two experiments. In one experiment, the robot has to stand still on a horizontally oscillating plane, and in the other, the robot is required to walk on the oscillating plane toward a red colored moving target. The target is sensed by a CCD camera, and its image is transmitted to a PC, as shown in Fig. 9. The control signal that causes the robot to start moving to the target is generated by the PC and is transmitted to the micro-computer. The micro-computer generates walking behavior on the basis of the transmitted control signal and the already programmed walking patterns designed for static surfaces. The important point to note is that the oscillation of the surface is not measured and only the walking patterns for a static surface are employed. The oscillation is compensated for by the flexible joints, and hence, the load of the controller is reduced.

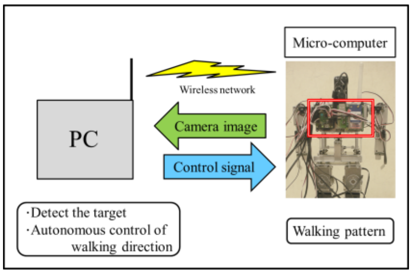

Fig. 9. Intercommunication network

5.1 Experimental Results when the robot stands still

Fig. 10 and Table 3 show the experiment results of standing still. In Fig. 10, the solid line shows the acceleration of the upper body and the broken line shows the acceleration of the plane. Table 3 shows the ratio of the amplitude of the oscillation of the upper body to the amplitude of surface oscillation. From Table 3, we see that sympathetic vibration occurs when the spring constant is low, leading the robot to fall at a frequency of 1.5 Hz. However, the surface oscillation is absorbed when the spring constant is low in cases of higher frequency oscillation, and the oscillation of the upper body of the robot is decreased.

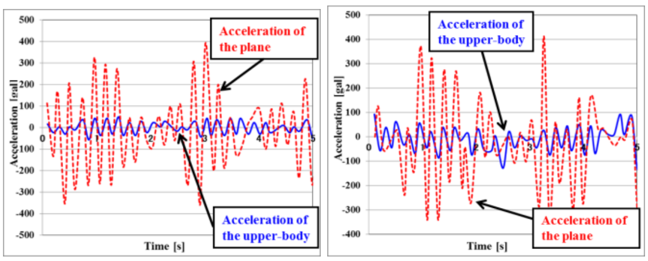

(a) Side to side (b) Front to back

Fig. 10. Result of acceleration (5.0 Hz, k = 0.15)

5.2 Result of the experiment where robot moves to target position

Fig. 11 shows an example of the result. In the case where the constant of the spring is low (k = 0.15), the robot could walk on the oscillating plane and move to the target. On the other hand, in the case where no flexible joints are present (all joints are fixed), the robot falls.

Table 3. Ratio of amplitude (Maximum acceleration of upper body [gal] / Maximum acceleration of ground [gal])

	1.5 Hz		3.0 Hz		5.0 Hz	
	side to side	front to back	side to side	front to back	side to side	front to back
fixing	36 / 36	36 / 36	falling	falling	falling	falling
k = 0.50	38 / 36	38 / 36	falling	falling	falling	falling
k = 0.23	falling	falling	60 / 146	93 / 150	102 / 405	184 / 394
k = 0.15	falling	falling	73 / 148	117 /153	56 / 393	93 / 414

From these results, we can confirm that the developed flexible joint has the characteristic of a low-pass filter, and due to this characteristic, the robot can move to the goal position on the oscillating plane without controllers for handling the oscillation.

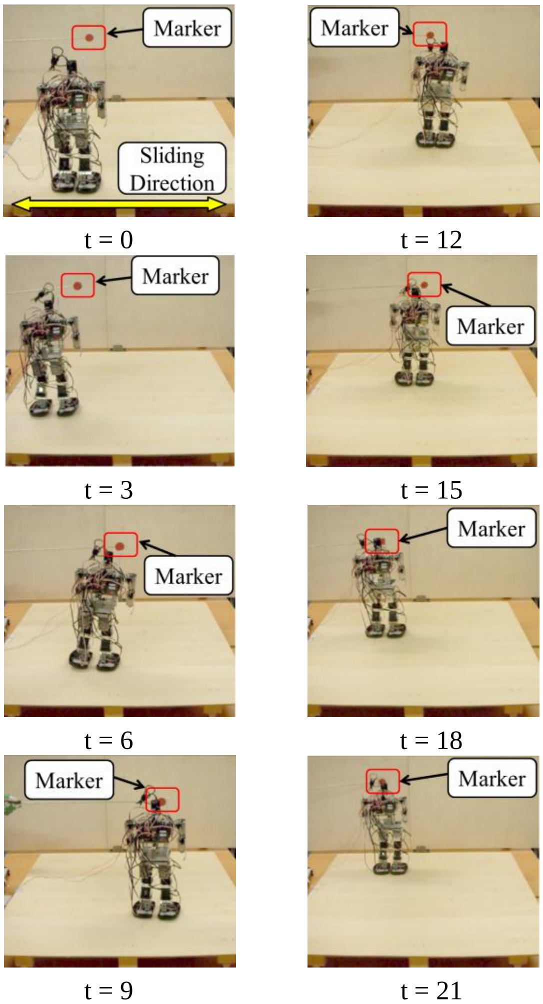

Fig. 11. Walk on the oscillating plane (5.0 Hz, k = 0.15)

6 CONCLUSION

In this study, we developed flexible joints for a humanoid robot that walks on an oscillating plane. By incorporating the flexible joint into the waist of a humanoid robot, we made it possible for the robot to move toward a goal position on a horizontally oscillating plane.

To demonstrate the effectiveness of the developed flexible joint, we conducted two experiments, in which effective walking behaviors were observed.

ACKNOWLEDGMENT

This work was supported by a 2011 Grant-in-Aid for Young Scientists (B), 22700156, from the Ministry of Education, Science, Sports and Culture of Japan.

REFERENCES

[1] Park J, Lee Y, Song J, et al (2008), Safe joint mechanism based on nonlinear stiffness for safe human-robot collision. IEEE International Conference on Robotics and Automation, Vol. 5, pp. 2177-2182

[2] Saiga M, Tomokuni N, Huang J, et al (2005), Analysis of Jumping Performance for a Compact Humanoid with Compliance Control Function (in Japanese). Transactions of the Society of Instrument and Control Engineers, Vol. 41, No. 11, pp. 939-941

[3] Yang J, Hayakawa Y, Oshima K, et al (1995), Adaptive control for Robot Manipulators with Flexible Joints. JSME International Journal. Ser. C, Dynamics, Control, Robotics, Design and Manufacturing, Vol. 38, No. 2, pp. 285-291

[4] Sugaiwa T, Iwata H, Mori H, et al (2008), Visco-Elastic Mechanism Design for Small and Lightweight Flexible Joint Manipulator (in Japanese). Proceedings of the Japan Society of Mechanical Engineers Robotics and Mechatronics Conference, pp.2A1-G02

[5] Dae J, Na Seung Y, Jin Y (2004), Reduction of Disturbance Effects and Sustained Oscillation Using Multi-Sensor Fusion in a Flexible Link System. Annual Conference of IEEE Industrial Electronics Society, Vol. 2 pp. 1540-1545

[6] Yoneyama T, Ito K (2010), Proposal of a flexible translational joint mechanism for humanoid robots. International Conference on Control Automation and Systems, pp. 1034-1039

[7] Wang X, Mills J (2006), Dual-Modal Control of Configuration-Dependent Linkage Vibration in a Smart Parallel Manipulator. IEEE International Conference on Robotics and Automation, Vol. 8, pp. 3544-3549

[8] Politopoulos I, Pham H (2009), Sensitivity of seismically isolated structures. Earthquake Engineering & Structural Dynamics, Vol. 38, No. 8, pp. 989-1007

The Seventeenth International Symposium on Artificial Life and Robotics 2012 (AROB 17th '12),
B-Con Plaza, Beppu, Oita, Japan, January 19-21, 2012

MANUALLY CONTROLLED MANHOLE CLEANING ROBOTIC SYSTEM

Gopal Joshi, Animesh Rana, Venkateshwar.R,
SCHOOL OF ENGINEERING,

VELS UNIVERSITY, CHENNAI, INDIA.

Abstract- ***Aimed at tackling the disadvantages of conventional manhole a new manually controlled manhole cleaning robot system is proposed for performing cleaning work instead of human cleaning manholes that is characteristic of low safety, low efficiency, long time and environmental pollution problems. The robotic system consists of manually controlled suction pump, hydraulic pump station, probe controller, LCD screen for monitoring; windlass, biodegradable bags, disinfectant sprayer. The modular structures have been adopted in the robotic system, which makes it possible to assemble all subsystems in a single unit. This robotic system can reduce the complex mechanism for cleaning the manholes and even provide environmental friendly way of disposing the sludge.***

Keywords: Manually controlled, Eco-friendly, Easy disposal, Safer, Easy use.

I. INTRODUCTION

The basic need of this robotic system is to clean the sludge from manholes. In most of the countries these manholes are being cleaned by humans who put themselves into greater degree of risks. The need of a robotic system which replaces human from cleaning job is quite high in many in most of the countries. This manually controlled robotic system will not only reduce the degree of risk for the people who are associated with this cleaning work but will also provide an eco-friendly way of managing and decomposing these biodegradable wastes. This will minimize the human interference in cleaning work and will make it more safer and easier way of cleaning manholes. It is similar to the systems that are used in cleaning oil tank [1]. The cleaning mechanism used here differs from the conventional oil tank cleaners. The technology proposed here is eco-friendly way of treating the sludge from the manholes which makes this robotic system more reliable and practically feasible.

Fig.1: The above figure shows the basic way cleaning manholes i.e. man entering the manhole risking his life and subjecting him to many bacteria and viruses present in these sludge.

II. SYSTEM REQUIRMENT

In this section, we will review the requirement of manhole cleaning robotic system. Major problem associated with cleaning this manhole is the size of this manhole. The radius of these manholes is extremely small which makes it very difficult for human to go in and clean thus causing injuries. The other problem is people cleaning this manhole come in direct contact with the harmful viruses present in the sludge. All these leads to the requirement of the manually controlled robotic system that helps in solving these mentioned problem and many other problems associated with it.

This manually controlled robotic system works on basic principle suction technique using suction pumps [2], this suction pump induces high pressure inside the manholes breaking the larger particles that are sucked using this induced pressure mechanism. The entire component used in this manually controlled robotic system works on advanced lithium-ion solid polymer electrolyte batteries [3], these high power batteries can be used for portable electronics applications [3]. It consists of touch screen LCD display device which performs dual function of controlling each and every component involved in the working of this system and for keeping track on all the function undergoing in the system. When the power supply is applied to the system, the system gets switched ON and all the controlling features appears on the LCD display. With the help of these controlling features manhole cleaning process is initiated.

There is another problem associated with this manhole cleaning process is proper and eco-friendly method of decomposing this sludge. This sludge from manholes are either dumped in rivers polluting the water body or burning these sludge in open ground causing air pollution and other environmental problem. In order to overcome this problem this robotic system is provided mechanism in which bio-degradable bags are used to fill all the sludge and later these bio-degradable bags are disposed [4] using various disposing methods. These biodegradable-bags are kept in the form rolls, when the controller starts suction process all the sludge from the manhole is sucked and starts filling in these bio-degradable bags. The sludge filled bags are then sealed. As soon as one bag is filled and led out the probe present in the robot pulls out another bag. When cleaning process is completed all sludge filled bags are disposed accordingly.

III. System Overview

A. *Power Source*

The power source which can be used is advanced lithium-ion solid polymer electrolyte batteries [3][6]. These new batteries will utilize new high-energy density anode and cathode active materials developed by SNL and RTI. UBI will incorporate these new materials into an optimized Li-Ion SPE electrode laminate [3].

B. *Suction pump*

The pressure of the suction pump can be manually adjusted according to the requirement. This suction pump works on the mechanism of producing air pressures and absorbing the target [2][6].

C. *Bio-degradable Bags and decomposition*

The purpose of using bio-degradable bag is to reduce pollution, ease the disposal work, prevention of unwanted manual labor. The main material starch and plant fiber for produce the dishware is analyzed in these bags. Biodegradable material is a kind of Green material, which is easily reclaimed and reused, it does not pollute the environment, and it can decompose quickly, there is not insurant to produce after trash [4][6].

Fig.2: Bio-degradable bag roll.

D. *LCD Controller And Display*

The LCD display unit and controller is fixed on the handle bar of the robotic system. This touch screen LCD device has pre-installed application which is used to control all the functional unit of this robotic system.

IV. *Evironment Benefits Of Bio-Degradable Bags*

Biodegradable bags from natural materials, such as vegetable crop derivatives or animal products, sequester CO_2 during the phase when they're growing, only to release CO_2 when they're decomposing, so there is no net gain in carbon dioxide emissions. Under proper conditions biodegradable plastics can degrade where microorganisms can metabolize them.

V. Manually Controlled Manhole Cleaning Robotic System

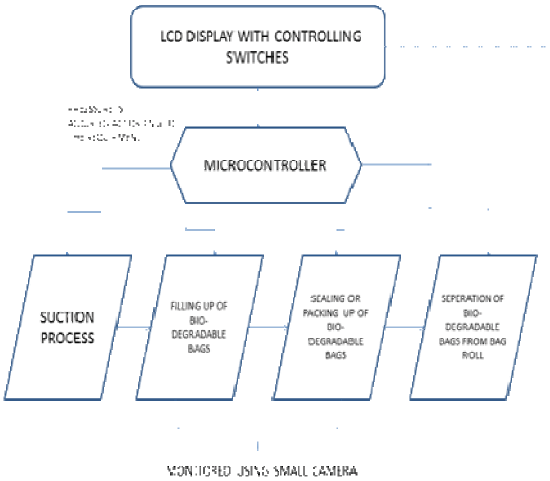

Fig.3 Schematic diagram of working process

VI. Working

The working process of this manually controlled robotics system is done by operator. All the components are controlled by application that can be accessed using touch screen LCD device which is connected to each component. Small camera is fixed inside the circuitry through which entire process can be seen on LCD display. This will help the operator to keep the check on all the process taking place inside the system.

Following process takes place in this system:

A. *Suction process*

*When t*he operator applies the power sources, the suction pump with adjustable pressure gets switched ON and the suction pipe is inserted into the manhole [6]. This inserted suction pipe creates pressure inside the manhole to be cleaned. The smaller sludge particles are easily sucked but it is really difficult to suck relatively larger sludge particle. As this suction pump is provided with adjustable pressure range mechanism, high pressure is induced inside the manhole. Due to this high pressure the larger sludge particles blocking the manholes are disintegrated into smaller particles. These disintegrated particles are then easily sucked by this mounted pressure. The operator continues this process until all the sludge from the manhole is sucked.

B. *Filling process*

The operator then starts the filling process, using two probes bag is pulled from the provide roll of bio-degradable bags. The sludge that is sucked using suction pump is then filled into these bio-degradable bags. These bio-debags are used because it is easy to decompose and environment friendly method of disposal of the sludge. The usage of these bio-degradable bags prevents the disposal of sludge [6] into water bodies or burning them in open ground effecting environment.

C. *Sealing process*

After the sludge is being filled in the bio-degradable bags, the operator switches on the sealing process. In this process, when the bag is completely filled with the sludge it[6] is sealed and lead out.

D. *Disinfecting process*

The robotic system is provided with another section known as disinfecting section. In this section when cleaning process is performed completely some amount of disinfecting chemical is sprayed into the manhole. This sprayed chemical disinfects the manhole.

VIII. PROPOSED MANUALLY CONTROLLED ROBOTIC SYSTEM

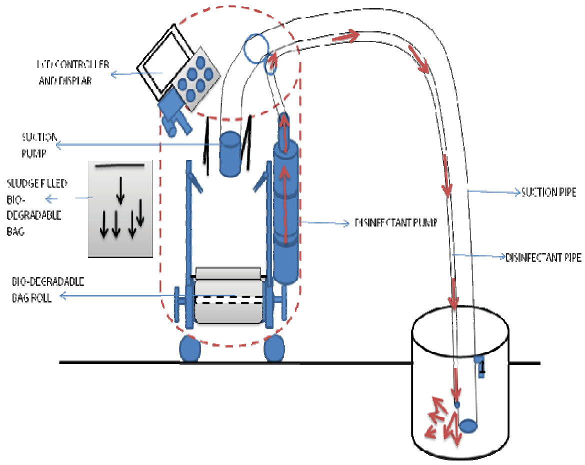

Fig.4 Proposed manually controlled robotic system.

VIII. PROCESS OVERVIEW

In this section the diagrammatical working mechanism of the manhole cleaning process is shown.

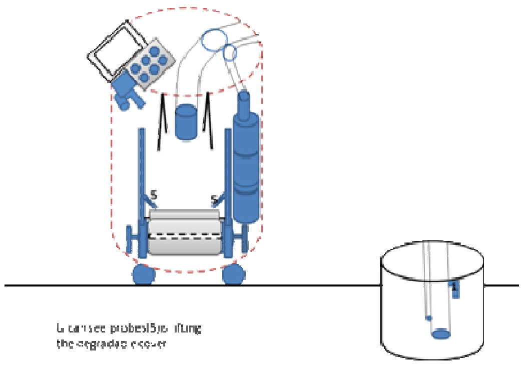

Fig.5.1 Basic Model

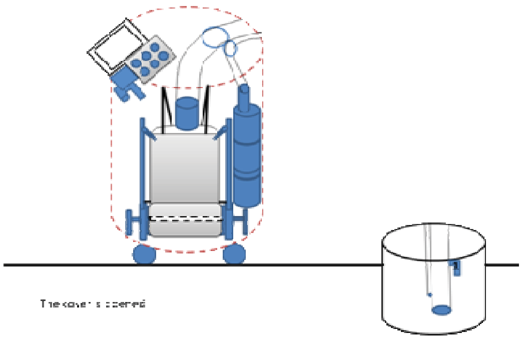

Fig.5.2 Opening of biodegradable bags using probes

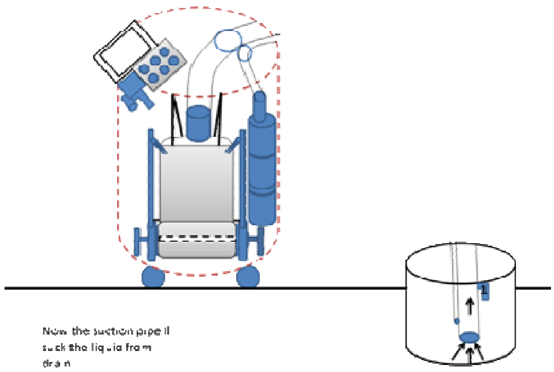

Fig.5.3 Sludge suction operation

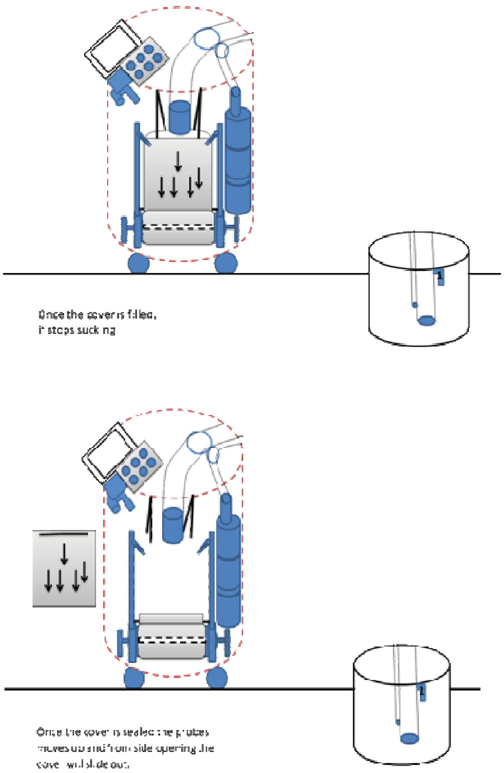

Fig.5.4 Removal of bag for decomposition

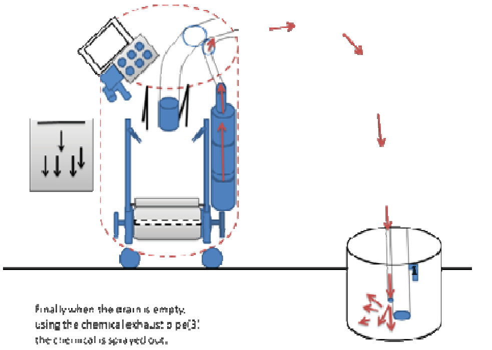

Fig.5.5. Disinfecting process

VIII. Architecture Of Manhole Cleaning Process

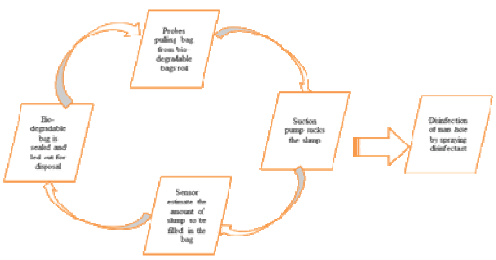

Fig.6 Arcitecture of mahole cleaning process

IX. Conclusion

In this paper we discuss about the use of robotic system to clean manhole. The use of this system will not only make this work simple but it will eco-friendly and safer for the people associated in this cleaning process. Future technologies can make it even more simple and easy to use.

X. FUTURE WORKS

In this paper we have proposed the idea of manually controlled robotic system. We are preparing the prototype of this manually controlled robotic system. Automated version of this robotic system will be done our future work.

References

[1] Deng Sanpeng; Xu Xiaoli; LiChongning; Zhang Xinghui; *Research on the oil tank sludge cleaning robot system, Mechanic Automation and Control Engineering (MACE), 2010 International Conference on 26-28 June 2010 ISBN: 978-1-4244-7737-1, Wuhan*

[2] Hablanian, M. H.; *Performance characteristics of displacement-type vacuum pumps,Massachusetts 02173, Journal of Vacuum Science & Technology A: Vacuum,surfaces, and Films,May1986.*

[3] Teofilo, V.L.; Isaacson, M.J.; Higgins, R.L.; Cuellar, E.A.; *Advanced lithium ion solid polymer electrolyte battery evelopment, Aerospace and Electronic Systems Magazine, IEEE, Nov 1999 Volume: 14 Issue: 11, ISSN: 0885-8985,* 06 August 2002

[4] Xiujie Jia, Jianfeng Li, Fangyi Li, Baokun Wei, *"Analysis of different biodegradable materials and its technique to produce dishware," isee, pp.1-5, 2008 IEEE* International Symposium on Electronics and the Environment, 2008

[5] IEEE Transactions on Computers, : 0018-9340, *IEEE Computer Society,Publication Details: IEEE Transactions on Computers*

[6] Rana, A.; Venkateshwar; Joshi, G.S. Emerging Trends in Robotics and Communication Technologies (INTERACT), 2010, *Manhole cleaning robotic system (MCRS),* International conference on 3-5 Dec. 2010, ISBN: 978-1-4244-9004-2 INSPEC Accession Number: 11822608 ,Chennai

The Seventeenth International Symposium on Artificial Life and Robotics 2012 (AROB 17th '12),
B-Con Plaza, Beppu, Oita, Japan, January 19-21, 2012

An improved Bug-type navigation algorithm for mobile robots

Yi Zhu[1], Tao Zhang[1], Jingyan Song[1], Xiaqin Li[1], Xuedong Chen[2], Masatoshi Nakamura[3]

[1]Department of Automation, School of Information Science and Technology,
Tsinghua University, Beijing 100084, China
(Email: zhu-y07@mails.tsinghua.edu.cn)
[2]School of Mechanical Science and Engineering,
Huazhong University of Science and Technology, Wuhan 430074, China
[3]Research Institute of Systems Control, Saga University, Saga 840-0047, Japan

Abstract: An improved Bug-type navigation algorithm that ensures convergence is proposed in this paper by integrating more heuristic information abstracted from the range data in the authors' previous work. While some similar concepts have been proposed before, the improved algorithm has fully considered many implementation issues that are ignored in the related works and therefore it is more practical than these works. Simulations show that compared with the authors' previous work, the improved algorithm can generate shorter average path length. Experiments on a real robot further verified its practicability.

Keywords: mobile robot; navigation; Bug algorithm; range sensor

1 INTRODUCTION

Autonomous navigation is an important research topic in mobile robotics. In many applications, the workspace is previously unknown and the robot has to utilize the sensory data to decide its motion, which significantly increases the difficulty of navigation. A common problem of many sensor-based navigation algorithms is that the robot may be trapped before reaching the goal when it encounters obstacles with complex boundaries, which is usually termed the local minima problem [1], [2]. Many efforts have been made to solve this problem and a well-known concept is the Bug model [3] which is focused on in this paper.

In the Bug model, the robot is assumed as a point moving in a 2D plane and it has only two motion modes: moving toward the goal and boundary following. It has been proved that if the switching criteria between the two modes are properly designed, the robot can converge to the goal as long as the goal is reachable (otherwise it will report failure). Due to its simplicity and convergence proof, the Bug model has attracted much attention. A series of algorithms have then been proposed based on this model, and they are often termed the Bug algorithms [4]. However, most existing Bug algorithms mainly focus on designing the switch criteria to ensure convergence and optimize the path, but ignore the implementation issues. As a result, the applicability of the algorithm may be affected. Focusing on this problem, we have proposed a new Bug-type algorithm in [5]. This algorithm presents not only a group of new switch criteria, but also a control strategy to implement it on real robots. The control strategy is also valid for many other Bug algorithms. Furthermore, it can generate shorter path than some previous Bug algorithms.

In this paper, the aforementioned algorithm (it is termed the original algorithm below) is further improved by integrating more heuristic information abstracted from the range data to optimize the generated path. The remainder of this paper is arranged as follows: related works are briefly reviewed in Section 2; our work is presented in Section 3 and the experimental studies are presented in Section 4.

2 RELATED WORKS

Since most Bug algorithms can ensure convergence, their performances mainly differ in the path length. Hence how to shorten the generated path is the main problem discussed in most previous works. The most common strategy is to design new switch criteria and our previous work [5] followed this way. Another method is to bypass the obstacles in advance by exploiting the sensory data. This idea firstly appeared in the VisBug algorithm [6], which improves the classical Bug2 algorithm [3] by using range data to find shortcuts of the original path. Based on a similar concept, TangentBug [7] constructs a "local tangent graph" based on the range data in every control cycle to guide the robot. Undoubtedly, exploiting the sensory data is beneficial to navigation. However, these two algorithms assume that any obstacle boundary can be continuously detected. Actually, due to the limited angular resolution, the practical range sensors can only detect the nearest obstacle point in a sector as shown in Fig. 1. Hence it is difficult to well realize these two algorithms since identification errors may occur [4], [8]. In this paper, a concept similar to

VisBug and TangentBug is proposed and integrated in our previous works to further improve its performance. A significant difference is that the angular resolution problem and many other implementation issues have been fully considered in the improved algorithm.

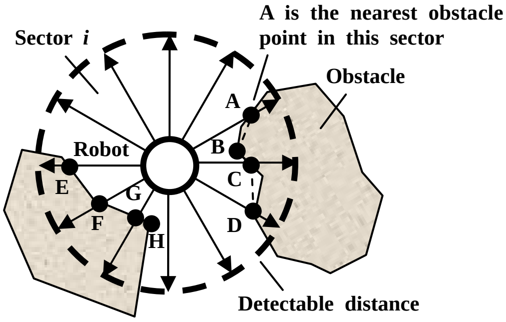

Fig. 1. The angular resolution of the practical range sensors: the robot can only detect eight obstacle points but not two continuous boundaries.

3 THE IMPROVED ALGORITHM

The improved algorithm consists of two reactive motion modes: moving toward the goal (Mode 1) and boundary following (Mode 2). They are respectively described below.

3.1 Motion toward the Goal

In Mode 1, the motion direction is selected by two steps. First, a rough direction θ_R that may lead to an optimal path is selected based on heuristic information abstracted from the range data. Then an exact direction θ_E for obstacle avoidance is calculated based on θ_R. Note that all the angles in this paper refer to the robot-fixed coordinates where the current robot direction is 0° and the angle increases in the anticlockwise direction.

In the first step, the key issue is how to abstract useful heuristic information from the range data. Assumed that the detectable view of the robot is divided into N sectors due to the angular resolution of range sensors as shown in Fig. 1 and each sector is labeled by an integer (a specific sector can be labeled as Sector 1 and the integer increases in the anticlockwise direction), an index set I that contains useful heuristic information can be defined as

$$\left\{ i \mid d_i \neq L \wedge (\left\| \mathbf{O}_i - \mathbf{O}_j \right\| \geq 2(r+D) \vee d_j = L) \wedge d_i < d_j \right\}$$
$$1 \leq i \leq N,\ j = \begin{cases} (i-1) \vee (i+1) & 1 < i < N \\ N \vee (i+1) & i = 1 \\ (i-1) \vee 1 & i = N \end{cases} \qquad (1)$$

where "$\vee$", "$\wedge$" are "logic or" and "logic and", $\mathbf{O}_i$ and d_i are respectively the position of the nearest obstacle point in the i^{th} sector and the distance to this point, r is the robot radius, D is the predefined safe distance to obstacles, L is the detectable distance (if there is no obstacle in the i^{th} sector, $d_i = L$). I contains the indexes of the key obstacle points which are the endpoints of the gaps between different obstacles, e.g., the point A, D, E, H in Fig. 1. A, H are termed "left jump point" and D, E are termed "right jump point". As shown in Fig. 1, if the goal is located in the gaps, the robot can approach it directly. If the goal is located behind any obstacle, the directions of the key obstacle points correspond to the shortest path for bypassing the obstacle.

Based on the above concept, only the goal direction θ_G and the directions indexed by (1) are considered as candidates for θ_R. However, three practical issues should also be considered. First, it is not safe to directly moving to a key obstacle point. Second, it is not wise to select a direction whose corresponding gap is not wide enough to go through. Third, the possible errors caused by the angular resolution and sensor inaccuracy should be considered.

To solve the first problem, the directions indexed by (1) are slightly revised by

$$f(\theta_i) = \begin{cases} \theta_i + \Delta\theta_i & \left\| \mathbf{O}_i - \mathbf{O}_j \right\| \geq 2(r+D) \vee d_j = L \\ \theta_i - \Delta\theta_i & \text{otherwise} \end{cases}$$
$$j = \begin{cases} i+1 & i < N \\ 1 & i = N \end{cases}, \Delta\theta_i = \begin{cases} \arcsin(\dfrac{r+D}{d_i}) & d_i > r+D \\ \arctan(\dfrac{r+D}{d_i}) & d_i \leq r+D \end{cases} \qquad (2)$$

where θ_i is the original direction indexed by (1). An example is shown in Fig. 2. Such a revision can guide the robot to smoothly bypass an obstacle.

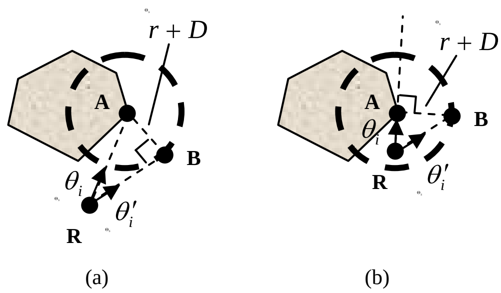

Fig. 2. An example of revising the directions (R is the robot center; A is a right jump point and therefore the direction should be decreased): (a) $d_i > r + D$; (b) $d_i \leq r + D$.

To solve the second problem, a precise method requires expensive computations. Hence a rough method is proposed: if there is no obstacle in a zone near the selected direction, the gap corresponding to this direction is considered as wide enough to go through. An example is shown in Fig. 3.

As to the third problem, due to the angular resolution, the relative position between the robot and the obstacle will affect the judgment of whether an obstacle point is a jump point indexed by (1). As an example shown in Fig. 4 (θ_0 is the minimal detective angle), the robot is initially at R_1 and it judges that B is not a jump point since D_1 is short. However, assumed that the robot moves to the jump point A, when it reaches R$_2$, B may be misjudged as a jump point since D_2 is long enough. Then the robot may move to B, which will cause a zigzag path. To solve this problem, it is required that if the robot selected a left (right) jump point as θ_R in the last cycle, the jump point will be recorded and in the current cycle, the robot can only select θ_R in the left (right) half-side of the vector from the current robot position to this jump point, i.e., the "admissible half-side" shown in Fig. 4. In Addition, the sensor inaccuracy sometimes also affects the judgment. Hence another constraint is added: if the robot selected a left (right) jump point in the last cycle, it cannot select a right (left) jump point in the current cycle unless it have attempted to select right (left) jump point in five successive cycles (one cycle is about 100ms in our experiments).

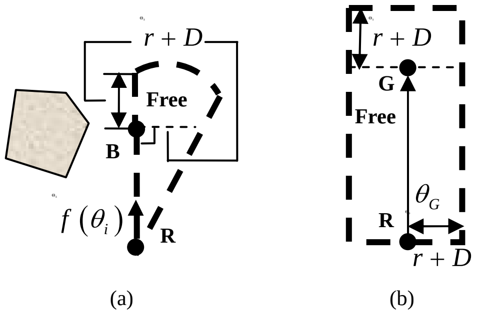

Fig. 3. An example of roughly examining whether a gap is wide enough to go through (B is the same point as shown in Fig. 2; R is the robot center; G is the goal): (a) if the direction is indexed by (1), the examined zone is a sector on the opposite side of the corresponding obstacle; (b) if the direction is the goal direction, the zone is a rectangle.

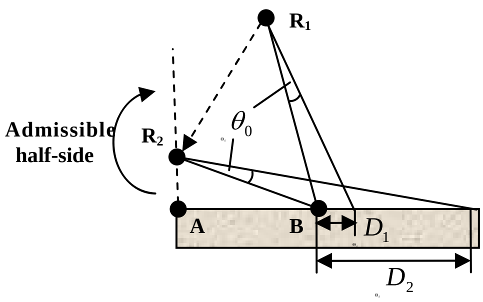

Fig. 4. An example of the misjudgment caused by the angular resolution.

Considering all the issues discussed above, θ_R is finally calculated by

$$\theta_R = \begin{cases} f\left(\theta_{i_0}\right) & I_S \neq \varnothing \wedge \mathrm{C}_1 \\ f\left(\angle\overrightarrow{RO}\right) & I_S \neq \varnothing \wedge \overline{\mathrm{C}}_1 \end{cases}, i_0 = \underset{i \in I_S}{\arg\min}\left\{\left|\theta_i - \theta_G\right|\right\}$$
$$I_S = \left\{i \mid W_i \subset W_{free} \wedge \left|f\left(\theta_i\right) - \theta_G\right| < 90^\circ, i \in I \cup \{N+1\}\right\}$$
$$f\left(\theta_{N+1}\right) = \theta_G, W_{N+1} = W_G \tag{3}$$

where $\angle\overrightarrow{RO}$ is the angle of the vector from the current robot position to the last jump point that has been used as θ_R, f is the map function described in (2), W_i, W_G are respectively the corresponding zone of θ_i and θ_G as shown in Fig. 3, W_{free} is the free workspace, C_1 is satisfied if any following event occurs: i_0 in the current or last cycle indexes the goal direction; both i_0 in the current and last cycle index left or right jump point; no above event has occurred in five successive cycles including the current cycle. In addition, if $I_S = \varnothing$, which implies that there is no collision-free direction for approaching the goal (usually caused by a dead corner and sometimes by the sensor inaccuracy), then $\theta_R \equiv \theta_G$ until the robot switches to the mode of boundary following.

After selecting θ_R, θ_E can be calculated by

$$\theta_E = \underset{\theta \in \Theta}{\arg\min}\left\{\left|\theta - \theta_R\right|\right\}$$
$$\Theta = \left\{\theta \mid \left|\theta - \theta_G\right| < 90^\circ \wedge \theta \in \Theta_S\right\} \tag{4}$$

where Θ_S is the current set of the directions that the robot can keep a safe distance D from obstacles. Note that if $\theta_R = \theta_G$, (4) is degraded to the criterion in the original algorithm [5]. In another word, $\theta_R \equiv \theta_G$ in the original algorithm, but there are more candidates in the improved algorithm and the one that may generate the optimal path according to the heuristic information will be selected.

If $\Theta = \varnothing$, which implies that there is no direction that can both shorten the goal distance and maintain safe for collision avoidance, the robot will switch to Mode 2 after selecting a boundary following direction dir. Such a position is termed a hit-point and each hit-point and the selected dir will be recorded in a list termed Hit-list.

3.2 Boundary Following

Mode 2 is the same as the original algorithm. The concept of finding shortcuts as VisBug and TangentBug are not adopted since it is difficult to always correctly recognize the points in the followed boundary from the range data (we have tried many methods) and it may cause navigation failure. In Mode 2, the robot will record the minimal goal distance d_{Min} and resume Mode 1 once

$$\begin{cases} 0^\circ < \theta_G < 180^\circ \wedge d < d_{\mathrm{Min}} & \text{if } dir = \mathrm{R} \\ -180^\circ < \theta_G < 0^\circ \wedge d < d_{\mathrm{Min}} & \text{if } dir = \mathrm{L} \end{cases} \tag{5}$$

where "L" and "R" represent "left" and "right" to the obstacle, d is the current goal distance. Such a position is termed a leave-point. Additionally, the boundary following direction will be reversed if a previous hit-point (not the current hit-point, i.e., the start point of the current boundary following motion) is met with the same dir as the record in Hit-list (this record is concurrently deleted). Furthermore, if the above event has not occurred after the last time that the robot passed the current hit-point but the current hit-point is met again, the robot can stop and report that the goal is unreachable [5].

3.3 Convergence Analysis

The improved algorithm can be proved to be convergent. A proof sketch is presented below (the detail is omitted due to the limited space).

It can be proved that there are only finite mode switches and the robot can always switch to Mode 1 from Mode 2 if the goal is reachable [5]. Hence the final mode is Mode 1 if the goal is reachable. According to (4), the goal distance always decreases in Mode 1 even if there are misjudgments for selecting θ_R since $|\theta_E - \theta_G| < 90^\circ$. Therefore, the robot can always reach the goal in Mode 1 as long as it is reachable. Otherwise, it will stop and report that the goal is unreachable in Mode 2.

4 EXPERIMENTAL RESULTS

Based on the MobileSim simulation platform and a model of Pioneer3-AT robot, the improved algorithm has been tested in two environments shown in Fig. 5 with 100 randomly selected start/goal points. The two motion modes are realized by the same control strategy proposed in [5]. In all the simulations, the robot has reached the goal, which verifies the convergence of the improved algorithm. For comparison, the original algorithm has also been simulated in the same conditions. As shown in Table 1, the average path length (APL, which is presented as the relative value to the globally shortest path) generated by the improved algorithm is shorter than the original algorithm in both the environments. The reason is that compared with the original algorithm, the improved algorithm can often shorten the path by bypassing the obstacles in advance with the help of the heuristic information abstracted from the range data.

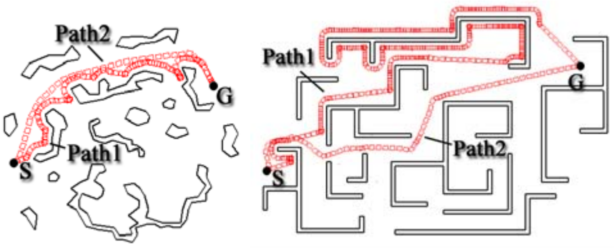

(a) (b)

Fig. 5. Two simulation results (S is the start point; G is the goal; Path1, Path2 are the paths generated by the original and improved algorithm): (a) environments containing scattered obstacles; (b) a maze environment.

TABLE 1 AVERAGE PATH LENGTH (APL) OF THE SIMULATIONS

Environment	Original Algorithm	Improved Algorithm
Scattered Obstacles	1.983	1.409
Maze	2.233	2.108

The improved algorithm has also been implemented on a real Pioneer3-AT robot. An experimental result is presented in Fig. 6: the robot successfully bypasses the obstacles in advance and finally reaches the goal.

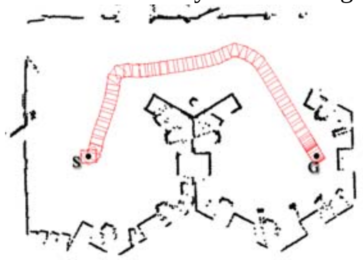

Fig. 6. An experiment on a real robot in an office environment.

5 CONCLUSION

An improved Bug-type algorithm that ensures convergence is proposed in this paper for robot navigation. It improves our previous work [5] by integrating more heuristic information abstracted from the range data to guide the robot. Compared with the similar concepts proposed in VisBug and TangentBug, the improved algorithm is more practical since it has fully considered many implementation issues that are ignored in the these works. Simulations show that it can generate shorter APL than the original algorithm. Experiments on a real robot have further verified its practicability.

REFERENCES

[1] Motlagh O R E, Hong T S, Ismail N (2008), Development of a new minimum avoidance system for a behavior-based mobile robot. Fuzzy Sets Syst. 160: 1929-1946.

[2] Zhang T, Zhu Y, Song J (2010), Real time motion planning for mobile robots by means of artificial potential field method in unknown environment. Ind. Robot 37(4): 384-400.

[3] Lumelsky V, Stepanov A (1987), Path-planning strategies for a point mobile automaton moving amidst unknown obstacles of arbitrary shape. Algorithmica 2: 403-430.

[4] Ng J, Braunl T (2007), Performance comparison of bug navigation algorithms. J. Intell. Robot. Syst. 50: 73-84.

[5] Zhu Y, Zhang T, Song J, Li, X (2010), A new Bug-type navigation algorithm considering practical implementation issues for mobile robots. ROBIO: 531 - 536.

[6] Lumelsky V and Skewis T (1990), Incorporating range sensing in the robot navigation function, IEEE Trans. Syst. Man Cybern. 20(5): 1058-1069.

[7] Kamon I, Rimon E, Rivlin E (1998), TangentBug: a range-sensor-based navigation algorithm. Int. J. Robot. Res. 17(9): 934-953.

[8] Yun X, Tan K-C (1997), A wall-following method for escaping local minima in potential field based motion planning. ICAR: 421-426.

The Seventeenth International Symposium on Artificial Life and Robotics 2012 (AROB 17th '12),
B-Con Plaza, Beppu, Oita, Japan, January 19-21, 2012

Sound source detection robot inspired by water striders

Hiroki NAKATSUKA[1], Kazuyuki ITO[2]

[1,2]Hosei University, Tokyo 184-8584, Japan
(Tel: 81-42-387-6093, Fax: 81-42-387-6381)

[1]hiroki.nakatsuka.2v@stu.hosei.ac.jp

Abstract: In this study, we investigate a position search algorithm inspired by the behavior of a water strider, and we develop a six-legged robot that moves toward a sound source autonomously by using this algorithm. First, we observe the behavior of water striders by using a high-speed camera, and we simplify the observed behavior to obtain some rules. Then, we evaluate the validity and effectiveness of the obtained rules by conducting simulations. Finally, we develop a six-legged robot that is controlled on the basis of the obtained rules. Experimental results show that the developed robot effectively moves toward the sound source.

Keywords: water strider, multi-legged robot, acoustic source localization.

1 Introduction

Recently, robots inspired by living beings such as animals and insects have attracted considerable attention. Living beings are able to adapt to complex real-world scenarios in spite of exhibiting simple behavior because they utilize the properties of their environment; in other words, they realize intelligent behavior by interacting with their environment. Thus, by extending the behavior of living beings to robots, we can control robots effectively using simple algorithms.

In this study, we investigate the behavior of a water strider. A water strider moves toward its prey by sensing ripples produced when its prey falls on the surface of a pond. We observe the behavior of a water strider by using a high-speed camera, and we simplify the observed behavior to obtain some rules for moving toward the prey. Then, we evaluate the validity and effectiveness of the obtained rules by conducting simulations. Finally, we develop a six-legged robot that moves toward a sound source on the basis of the obtained rules, and we demonstrate its effectiveness experimentally.

2 Water strider

We observed the behavior of a water strider by using a high-speed camera. Fig. 1 shows how a water strider moves toward its prey, and Table 1 summarizes the behavior of each leg. Fig. 2 shows the leg numbers.

We found that when a ripple is sensed by one of the water strider's legs, it turns in the direction of that leg, and after turning, it moves forward along a straight line. The turning angle is dependent on the leg by which the ripple is sensed first. The water strider repeats this action until it reaches its prey, as shown in Fig 3.

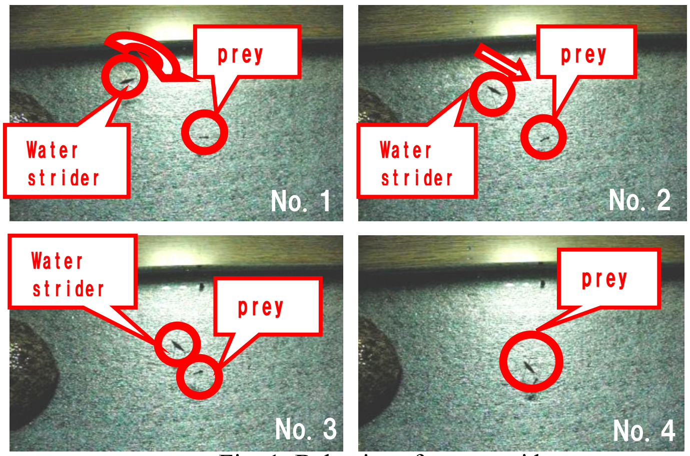

Fig. 1. Behavior of water strider

Table 1. Observed turning angle
(20 observations)

Leg 1		Leg 2		Leg 3	
No. of trial	angle[deg]	No. of trial	angle[deg]	No. of trial	angle[deg]
1	6.0	1	50.0	1	110.0
2	0.0	2	20.0	2	130.0
3	4.0	3	85.0	3	170.0
4	0.0	4	50.0	4	110.0
5	0.0	5	40.0	5	130.0
6	4.0	6	20.0	6	160.0
7	0.0	7	35.0	7	110.0
8	2.0	8	30.0	8	120.0
9	3.0	9	20.0	9	140.0
10	1.0	10	40.0	10	90.0
11	3.0	11	70.0	11	110.0
12	0.0	12	40.0	12	80.0
13	4.0	13	20.0	13	80.0
14	3.0	14	30.0	14	110.0
15	2.0	15	70.0	15	80.0
16	2.0	16	60.0	16	180.0
17	0.0	17	10.0	17	140.0
18	5.0	18	30.0	18	120.0
19	4.0	19	50.0	19	80.0
20	0.0	20	40.0	20	150.0
average	2.2	average	40.5	average	120.0

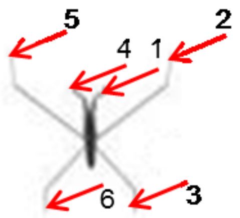

Fig. 2 Leg number

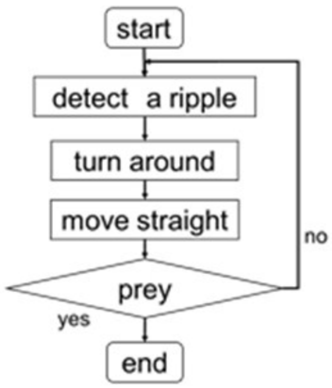

Fig 3. Strategy of water strider

3 Model of water strider

We modeled the water strider by using the following simple rules.

When a leg senses a ripple, the water strider turns in the direction of that leg (The turning angles are listed in Table 2).

Then, it moves forward along a straight line within a certain time period.

This cycle is repeated until the prey is reached.

Table 2. Turning angle

	Leg 1	Leg 2	Leg 3	Leg 4	Leg 5	Leg 6
Turning angle [deg]	2	40	120	-2	-40	-120

Using these rules, the motion of a water strider in time t on a horizontal (xy) plane can be expressed as follows.

$$\theta(t+1)=\theta(t)+\Delta\theta(t) \quad (1)$$

$$x(t+1)=x(t)+v\cos\theta(t) \quad (2)$$

$$y(t+1)=y(t)+v\sin\theta(t) \quad (3)$$

In the equations stated above, x and y denote the position of the water strider, θ denotes its orientation, v denotes its speed (assumed constant), and $\Delta\theta$ denotes its turning angle.

4 Simulation

To evaluate the validity of the simplified model, we conducted simulations. Table 3 lists the simulation parameters, and Fig. 4 shows the simulation results.

Table 3. Simulation parameters

length of water strider [cm]	6
width of water strider [cm]	4.8
speed of water strider [cm/s]	2
interval between ripples [s]	1
speed of ripple [cm/s]	2.5

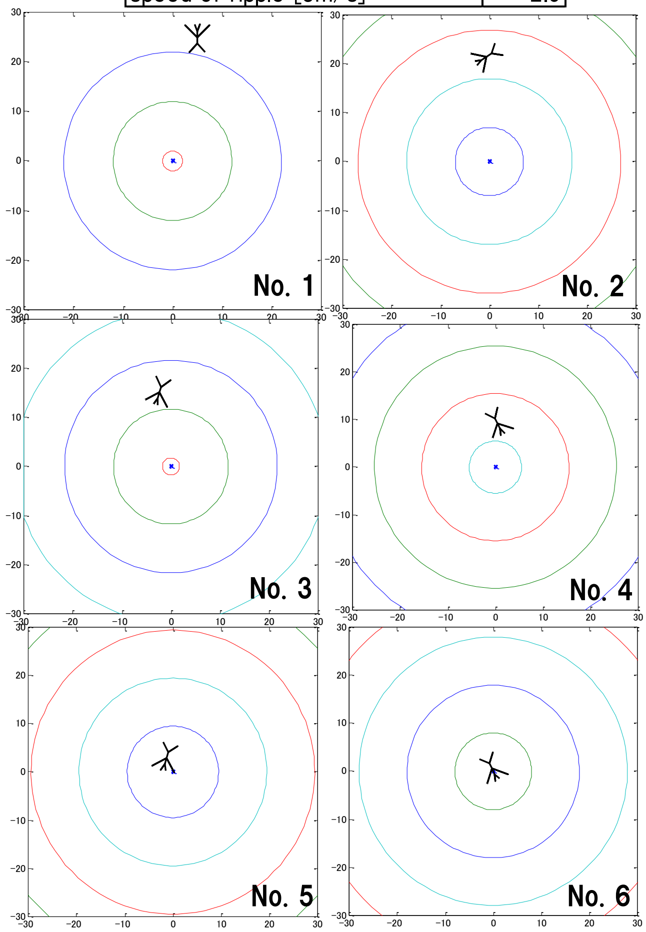

Fig. 4. Simulation results

The results show that the water strider can move toward the ripple source by following the simplified rules.

5 Application to six-legged robot

We developed a six-legged robot, and we adopted the simplified rules to control it.

5.1 Task

Fig. 5 shows the outline of the task. The objective of the task is to move toward the sound source. The position of the sound source is unknown, and the robot moves toward the sound source by using the rules of the water strider.

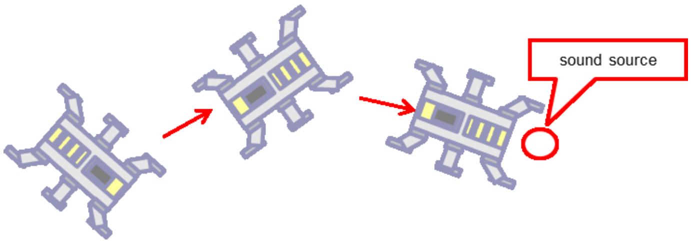

Fig. 5 Task

5.2 Six-legged robot

Fig. 6 shows the developed six-legged robot, and Table 4 lists its specifications. Each leg has two servo motors (Fig. 6 (a)), and it can move from right to left or up and down, as shown in Fig. 7. A microcomputer for controlling the legs is mounted at the center of the body (Fig. 6 (b)). Six microphones are employed to detect sounds; one microphone is attached to each leg (Fig. 6 (c)).

Sound waves from the sound source are detected by the 6 microphones, and the time lag is determined by an electrical circuit (Fig. 6 (d)).

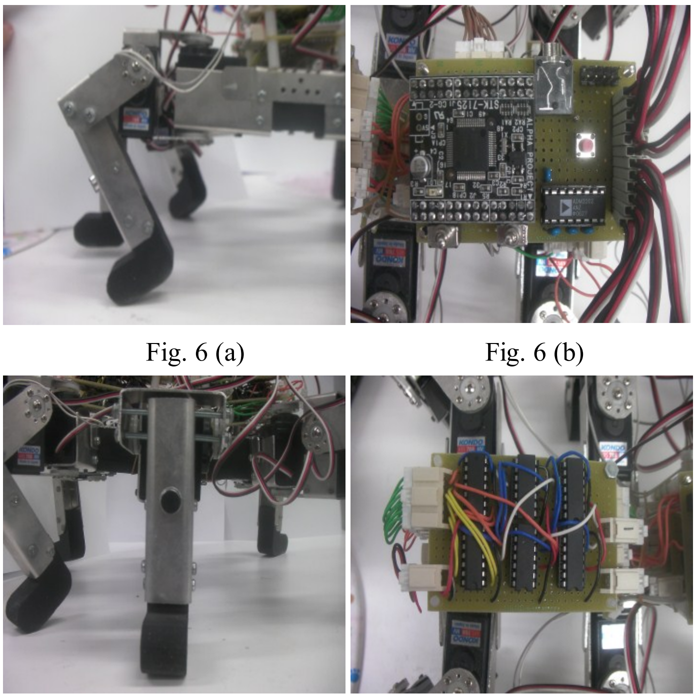

Fig. 6 (a) Fig. 6 (b)

Fig. 6 (c) Fig. 6 (d)

Fig. 6. Six-legged robot

Table 4. Specifications of the robot

Length [mm]	295
Width [mm]	275
Height [mm]	165
Weight [kg]	1.9

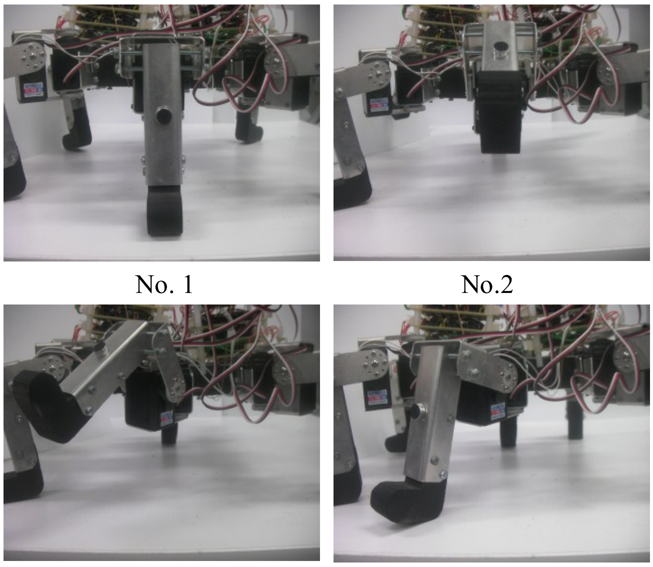

No. 1 No.2

No. 3 No.4

Fig. 7. Motion of leg

Fig. 8 shows the flow of the control signal. The electrical circuit for determining the time lag provides information for identifying the leg that sensed the sound wave first, and this information is passed to the microcomputer. The locomotion pattern for turning and moving along a straight line is pre-programmed in the microcomputer, and the robot moves on the basis of the rules stated in section 3.

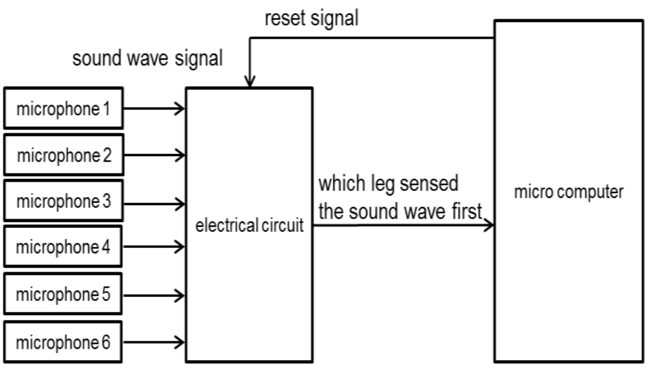

Fig. 8 Flow of control signal

6 Experiment

Experiments were conducted to demonstrate the effectiveness of the proposed framework.

Fig. 9 shows the experimental environment. A participant claps his hands repeatedly, and the robot moves towards him. Fig. 10 shows the realized behavior.

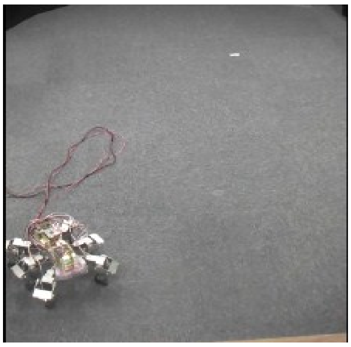

Fig. 9. Experimental environment

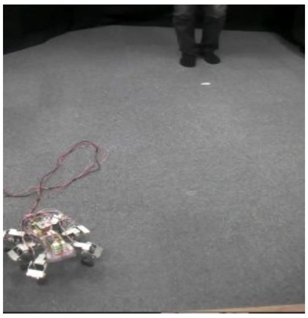

No. 1

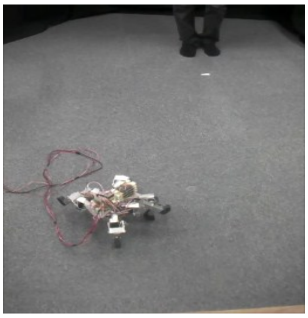

No. 2

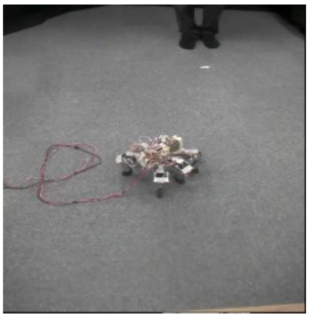

No. 3

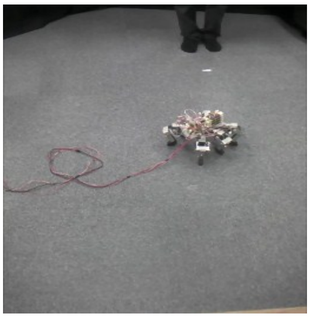

No. 4

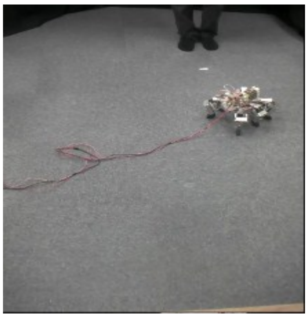

No. 5

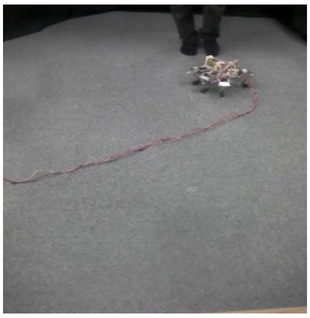

No. 6

Fig. 10. Realized behavior

7 CONCLUSION

In this paper, we investigated the behavior of water striders; we observed their behavior by using a high-speed camera in order to obtain simple rules for determining the prey's position. We evaluated the validity and effectiveness of the obtained rules by conducting simulations, and we adopted the rules to control a six-legged robot. Experiments were conducted using the developed robot, and we confirmed that the robot could move toward the sound source. We can conclude that the rules inspired by the water strider are effective in determining the position of the sound source, even though they are very simple.

In the future, we plan to apply these simple rules to useful practical applications such as search and rescue missions for locating survivors in the event of extensive disasters.

8 Acknowledgment

This study was partially supported by the Ministry of Education, Culture, Sports, Science and Technology (MEXT), Grant-in-Aid for Young Scientists (B), 22700156, 2011.

REFERENCES

[1] O. Ozcan, Han Wang, J.D. Taylor and M. Sitti, "S urface tension driven water strider robot using circular footpads" Robotics and Automation(ICRA), 2010 IEE E International Conference on, 3-7 May 2010, 3799-3 804

[2] H. Takonobu, K. Kodaira and H. Takeda, "Water s trider's muscle arrangement-based robot" Intelligent R obots and Systems, 2005.(IROS 2005).2005 IEEE/RSJ International Conference on, 2-6 Aug 2005, 1754-17 59

[3] K. Suzuki, H. Takanobu, K. Noya, H. Koike and H. Miura, "Water strider robots with microfabricated hydrophobic legs" Intelligent Robots and Systems,200 7.IROS 2007.IEEE/RSJ International Conference on, O ct 29 2007-Nov 2 2007

[4] K. Ito and F. Matsuno, "A Study of Reinforcement Learning for the Robot with Many Degrees of Freedom— Acquisition of Locomotion Patterns for Multi-Legged Robot," In Proc. of IEEE Int. Conf. on Robotics and Automation, 3392–3397, 2002.

[5] Y. Sugimoto, H. Yoshioka and K. Osuka, "Develop ment of Super-multi-legged Passive Dynamic Walking Robot [Jenkka-Ⅲ]" SICE Annual Conference (SICE), 2011 Proceedings of, 13-18 Sept, 2011, 576-579.

The Seventeenth International Symposium on Artificial Life and Robotics 2012 (AROB 17th '12),
B-Con Plaza, Beppu, Oita, Japan, January 19-21, 2012

Stability of Two-Wheeled Mobile Robot Using New Combined Pole-placement Method

Yoko Amano[1]

[1] Nihon University, Koriyama, Fukushima, 963-8642, Japan
(Tel: 81-24-956-8796, Fax: 81-24-956-8796)
(amano@ee.ce.nihon-u.ac.jp)

Abstract: In order to guarantee robotic stability, a new combined pole-placement method is proposed in this paper. The proposed method combines the linear quadratic regulator (LQR) into the pole-placement design. Firstly, a mathematical model of Two-Wheeled Mobile Robot (TWMR) is analytically derived from real TWMR. Secondly, the LQR for TWMR model is designed, and optimal poles can be obtained from the designed LQR. Thirdly, selection conditions of the best poles are the following; 1) the guarantee of convergence speed for TWMR system, 2) the number of vibration times for TWMR, 3) saturation evasion of the control input to TWMR's actuators, 4) the ratio of an imaginary part and a real part is carried out near one of selected poles. The pole-placement method selects the best poles than the optimal poles of LQR. Finally, the stability of the proposed method is confirmed by experiment results.

Keywords: inverted pendulum, linear quadratic regulator, pole placement method, two-wheeled mobile robot

1 INTRODUCTION

Two-wheeled mobile robot (TWMR) always exhibits many problems existing in industrial applications, for example, various nonlinear behaviors under different operation conditions, external disturbances, and physical constraints on some variables. Therefore, the task of on-line control of a highly nonlinear unstable has been a challenge for the modern control field. Since the system behaviors of TWMR including actuator dynamics are highly nonlinear, it is difficult to design a suitable control system that realizes real-time control and accurate balancing control at all time.

On the other hand, many research results of TWMR have been applied to various actual problems for designing walking gaits of humanoid robot, robotic wheelchairs, personal transport systems, and so on. Recently, the control problems of TWMR have been intensively studied due to the challenging demand of fast and precise performance. Besides protecting safety of human and robotic operators, the robotic stability is very important research theme at the longest. There have been many studies on the stable problem, for example, sliding-model control [1], fuzzy switched swing-up control [2], and adaptive control [3] are researched on TWMR. But, these controls are very complex and the response time of the mobile robot system is slower.

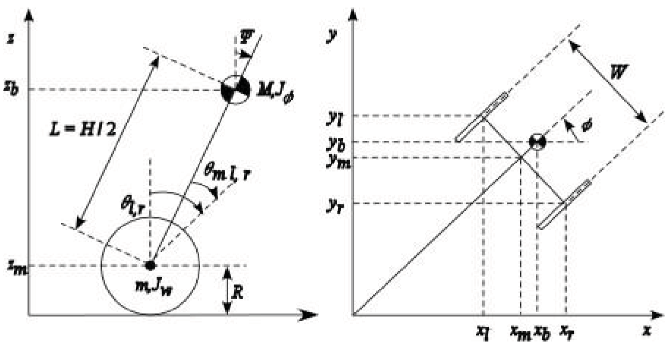

Ψ: body pitch angle, $\theta_{l,r}$: left and right wheel angle, $\theta_{m_{l,r}}$: DC motor angle

Fig.1 Side and plane view of TWMR

2 TWMR'S MODEL

Figure 1 shows side view and plane view of TWMR, the coordinate system shown in Fig.1 is used TWMR model, and physical parameters of TWMR by measurements are shown in Table 1 [4].

We can drive motion equations from TWMR by the Lagrangian method based on the coordinate system shown in Fig.1, the generalized forces F_θ, F_Ψ, F_ϕ can be expressed

Table 1 Physical parameters of TWMR

Gravity acceleration	g=9.81	(m/sec^2)
Wheel weight	m=0.03	(kg)
Wheel radius	R=0.04	(m)
Wheel inertia moment	J_w=mR^2/2	(kgm^2)
Body weight	M=0.6	(kg)
Body width	W=0.14	(m)
Body depth	H=0.144	(m)
Distance between mass and wheel axle	L=H/2	(m)
Body pitch inertia moment	J_Ψ=ML^2/3	(kgm^2)
Body yaw inertia moment	J_ϕ=M(W^2+D^2)/12	(kgm^2)
DC motor inertia moment	J_m=1 $\times 10^{-5}$	(kgm^2)
DC motor resistance	R_m=6.69	(Ω)
DC motor back EMF constant	K_b=0.468	(V sec/rad)
DC motor torque constant	K_t=0.317	(Nm/A)
Gear ratio	n=1	
Friction coef. of body and DC motor	f_m=0.0022	
Friction coef. between wheel and floor	f_w=0	

using the DC motor voltages v_l and v_r.

$$\begin{aligned} F_\theta &= \left[(2m+M)R^2+2J_m+2n^2J_m\right]\ddot{\theta} \\ &\quad +(MLR-2n^2J_m)\ddot{\psi} \qquad (1) \\ F_\psi &= (MLR-2n^2J_m)\ddot{\theta} \\ &\quad +(ML^2+J_\psi+2n^2J_m)\ddot{\psi}-MgL\psi \qquad (2) \\ F_\phi &= \left[\frac{1}{2}mW^2+\frac{W^2}{2R^2}(J_w+n^2J_m)\right]\ddot{\phi} \qquad (3) \end{aligned}$$

here, consider the limit $\Psi \longrightarrow 0$, and neglect the second order term like $\dot{\Psi}^2$.

2.1 State space model

Now, from (1) to (3), we can obtain the following state space model of TWMR.

$$\begin{aligned} \dot{\boldsymbol{x_1}}(t) &= \boldsymbol{A_1}\boldsymbol{x_1}(t)+\boldsymbol{B_1}\boldsymbol{u}(t) \qquad (4) \\ \boldsymbol{y_1}(t) &= \boldsymbol{C_1}\boldsymbol{x_1}(t) \qquad (5) \end{aligned}$$

where, the state variable $\boldsymbol{x_1}(t)$=$[\theta,\psi,\dot{\theta},\dot{\psi}]^T$, the input $\boldsymbol{u}(t)$=$[v_r,v_l]^T$, and the output $\boldsymbol{y_1(t)}$=$[\theta,\psi,\dot{\theta},\dot{\psi}]^T$, the parameter matrices of the state space model (4), (5) describe the following.

$$\boldsymbol{A_1} = \begin{bmatrix} 0 & 0 & 1 & 0 \\ 0 & 0 & 0 & 1 \\ 0 & A_1(3,2) & A_1(3,3) & A_1(3,4) \\ 0 & A_1(4,2) & A_1(4,3) & A_1(4,4) \end{bmatrix} \qquad (6)$$

$$\boldsymbol{B_1} = \begin{bmatrix} 0 & 0 \\ 0 & 0 \\ B_1(3,1) & B_1(3,2) \\ B_1(4,1) & B_1(4,2) \end{bmatrix} \qquad (7)$$

$$\boldsymbol{C_1} = \text{diag}\ [1 \quad 1 \quad 1 \quad 1] \qquad (8)$$

$$\boldsymbol{E} = \begin{bmatrix} E(1,1) & E(1,2) \\ E(2,1) & E(2,2) \end{bmatrix} \qquad (9)$$

$$\begin{aligned} A_1(3,2) &= -\frac{gMLE(1,2)}{\det \boldsymbol{E}} \\ A_1(4,3) &= \frac{gMLE(1,1)}{\det \boldsymbol{E}} \\ A_1(3,3) &= -\frac{2\left[(\beta+f_w)E(2,2)+\beta E(1,2)\right]}{\det \boldsymbol{E}} \\ A_1(3,4) &= \frac{2\left[(\beta+f_w)E(1,2)+\beta E(1,1)\right]}{\det \boldsymbol{E}} \\ A_1(4,3) &= \frac{2\beta\left[E(2,2)+E(1,2)\right]}{\det \boldsymbol{E}} \\ A_1(4,4) &= -\frac{2\beta\left[E(1,1)+E(1,2)\right]}{\det \boldsymbol{E}} \\ B_1(3,1) &= \frac{\alpha\left[E(2,2)+E(1,2)\right]}{\det \boldsymbol{E}} \\ B_1(4,1) &= -\frac{\alpha\left[E(1,1)+E(1,2)\right]}{\det \boldsymbol{E}} \\ \det(\boldsymbol{E}) &= E(1,1)E(2,2)-E(1.2)^2 \end{aligned}$$

$$\begin{aligned} E(1,1) &= (2m+M)R^2+2J_w+2n^2J_m \\ E(1,2) &= MLR-2n^2J_m \\ E(2,1) &= MLR-2n^2J_m \\ E(2,2) &= ML^2+J_\psi+2n^2J_m \end{aligned}$$

$$\alpha=\frac{nK_t}{R_m}, \qquad \beta=\frac{nK_tK_b}{R_m}+f_m$$

2.2 LQR design for TWMR

In this section, LQR design for TWMR is considered as an expansive state space equation. We select θ as a reference state $\boldsymbol{\theta_{ref}}$=$\boldsymbol{C_\theta}\boldsymbol{x}_{1ref}$, and define an error $\boldsymbol{e}(t)$=$\mathrm{C}_\theta\boldsymbol{x}_{1ref}$-$\theta(t)$, $\dot{z}(t)=\mathrm{e}(t)$, then the expansive state space equation can be expressed by

$$\dot{\bar{\boldsymbol{x}}}(t)=\bar{\boldsymbol{A}}\bar{\boldsymbol{x}}(t)+\bar{\boldsymbol{B}}\bar{\boldsymbol{u}}(t) \qquad (10)$$

$$\dot{\bar{\boldsymbol{x}}}(t)=\begin{bmatrix} \dot{\boldsymbol{x}}(t) \\ \dot{\boldsymbol{z}}(t) \end{bmatrix}, \bar{\boldsymbol{A}}=\begin{bmatrix} \boldsymbol{A_1} & 0 \\ 0 & \mathrm{C}_\theta \end{bmatrix},$$

$$\bar{\boldsymbol{B}}=\begin{bmatrix} \boldsymbol{B_1} & 0 \\ 0 & \text{-}\mathrm{C}_\theta \end{bmatrix}, \bar{\boldsymbol{u}}(t)=\begin{bmatrix} \boldsymbol{u}(t) \\ \boldsymbol{x_1}(t) \end{bmatrix}$$

According to an optimal feedback gain matrix $\boldsymbol{K}$ such that the feedback control law

$$\begin{aligned} \bar{\boldsymbol{u}}^*(t) &= -\boldsymbol{K}\bar{\boldsymbol{x}}(t) \qquad (11) \\ &= \begin{bmatrix} -\boldsymbol{k_f} & -\boldsymbol{k_i} \end{bmatrix}\begin{bmatrix} \boldsymbol{x}(t) \\ \boldsymbol{z}(t) \end{bmatrix} \qquad (12) \\ \boldsymbol{K} &= \boldsymbol{R}^{-1}\bar{\boldsymbol{B}}^T\boldsymbol{P} \qquad (13) \end{aligned}$$

minimizes the performance index

$$J = \int_0^\infty (\bar{\boldsymbol{x}}^T(t)\boldsymbol{Q}\bar{\boldsymbol{x}}(t)+\bar{\boldsymbol{u}}^T(t)\boldsymbol{R}\bar{\boldsymbol{u}}(t))dt \qquad (14)$$

subject to the constaint equation (10). Here, matrix $\boldsymbol{P}$ of (13) is the unique positive-definite solution of the associated matrix Riccati Equation

$$\bar{\boldsymbol{A}}^T\boldsymbol{P}+\boldsymbol{P}\bar{\boldsymbol{A}}+\boldsymbol{Q}-\boldsymbol{P}\bar{\boldsymbol{B}}\boldsymbol{R}^{-1}\bar{\boldsymbol{B}}^T\boldsymbol{P}=0 \qquad (15)$$

As stated above, a servo control for TWMR is shown in Fig.2, where $\boldsymbol{C_\theta}$ = diag $[1, \quad 0, \quad 0, \quad 0]$, and the weight matrices $\boldsymbol{Q}$, $\boldsymbol{R}$ of (13) by experimental trial and error.

$$\begin{aligned} \boldsymbol{Q} &= \text{diag}\ [1 \quad 6\times10^5 \quad 1 \quad 1 \quad 4\times10^2] \qquad (16) \\ \boldsymbol{R} &= \text{diag}\ [1\times10^3 \quad 1\times10^3] \qquad (17) \end{aligned}$$

To calculate the LQR problem, and obtain the gain $\boldsymbol{K}$ is

$$\begin{aligned} \boldsymbol{K} &= [k_\theta,\ k_\psi,\ k_{\dot{\theta}},\ k_{\dot{\psi}},\ k_i] \qquad (18) \\ \boldsymbol{K} &= [-0.867,\ -31.931,\ -1.154,\ -2.783,\ -0.446] \end{aligned}$$

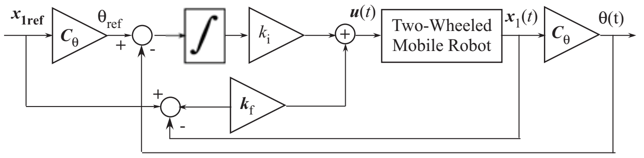

Fig. 2 Servo control system block diagram

3 PROPOSED METHOD

In this section, we present a design proposed method called a combined pole-placement method. We assume that all state variables are measurable and are available for feedback. If the system considered is completely state controllable, then poles of the closed-loop system may be placed at any desired locations by means of state feedback through an appropriate state feedback again matrix.

The present design technique begins with a determination of the desired closed-loop poles based on the transient-response and frequency-response requirements, such as speed, damping ratio, and bandwidth, sa well as steady-state requirements.

3.1 Pole-placement for TWMR

From the expansive state space equation (10) and the optimal control input (11), the closed-loop system can be expressed as

$$\begin{aligned}\dot{\bar{\boldsymbol{x}}}(t) &= \bar{\boldsymbol{A}}\bar{\boldsymbol{x}}(t) - \bar{\boldsymbol{B}}\boldsymbol{K}\bar{\boldsymbol{x}}(t) \\ &= (\bar{\boldsymbol{A}} - \bar{\boldsymbol{B}}\boldsymbol{K})\bar{\boldsymbol{x}}(t) \qquad (19)\end{aligned}$$

The desired characteristic equation is

$$\begin{aligned}|s\boldsymbol{I} - \bar{\boldsymbol{A}} + \bar{\boldsymbol{B}}\boldsymbol{K}| &= (s-p_1)(s-p_2)\cdots(s-p_n) \\ &= s^n + a_{n-1}s^{n-1} + \cdots + a_0 = 0 \qquad (20)\end{aligned}$$

where, p_i (i=1, 2, $\cdots$, n) are poles of the closed-loop system (19). The first step in the pole-placement design approach is to choose the locations of the desired closed-loop poles. The most frequently used approach is to choose such poles on basis of experience in root-locus design, placing a dominant pair of closed-loop poles and choosing other poles so that are far to the left of the dominant closed-loop poles.

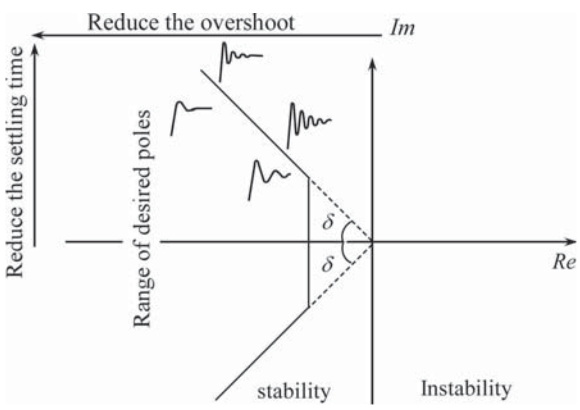

Fig.3 Range of desired poles

We have to note that if the dominant closed-loop poles is far from the $j\omega$-axis, so that the system response becomes very fast, the signals in the system become very large, with the result that system may become nonlinear, this should be avoided and shown in Fig.3.

Another approach is based on LQR approach and determines the desired closed-loop poles such that the system balances between the acceptable response and the amount of control energy required.

In the complex coordinate of Fig.3, an angle $\delta = tan^{-1}(\sqrt{1-\zeta^2}/\zeta)$, here ζ is a damping ratio. For servo control system of robotics, TWMR and so on, $\zeta = 0.6 - 0.8$ and $\delta = 37° - 53°$ have been generally accepted [5].

3.2 Choosing the location of desired closed-loop poles

From $\boldsymbol{K}$ of (18), the pole $\boldsymbol{P_0}$ can be derived and shows the following

$$\boldsymbol{P_0} = [-284.41, -10.92, -1.3 \pm j0.73, -1.47] \qquad (21)$$

We change the damping ratio ζ with 0.05 step from 0.6 to 0.8, and obtain poles $\boldsymbol{P_i}$ $(i = 1, \cdots, 5)$ their feedback gains, the ζ and the natural frequency ω_n are shown in Table 2, 3 and 4, respectively.

Table 2 Closed-loop poles

	p_1	p_2	p_3, p_4	p_5
$\boldsymbol{P_0}$	-284.41	-10.9	$-1.3 \pm j0.73$	-1.47
$\boldsymbol{P_1}$	-284.41	-10.9	$-1.3 \pm j0.96$	-1.47
$\boldsymbol{P_2}$	-284.41	-10.9	$-1.3 \pm j1.15$	-1.47
$\boldsymbol{P_3}$	-284.41	-10.9	$-1.3 \pm j1.31$	-1.47
$\boldsymbol{P_4}$	-284.41	-10.9	$-1.3 \pm j1.51$	-1.47
$\boldsymbol{P_5}$	-284.41	-10.9	$-1.3 \pm j1.73$	-1.47

Table 3 Feedback gains

	k_θ	k_ψ	$k_{\dot{\theta}}$	$k_{\dot{\psi}}$	k_i
$\boldsymbol{P_0}$	-0.867	-31.931	-1.154	-2.783	-0.446
$\boldsymbol{P_1}$	-0.927	-32.059	-1.160	-2.797	-0.524
$\boldsymbol{P_2}$	-0.990	-32.191	-1.167	-2.810	-0.604
$\boldsymbol{P_3}$	-1.051	-32.320	-1.173	-2.823	-0.683
$\boldsymbol{P_4}$	-1.138	-32.506	-1.182	-2.841	-0.796
$\boldsymbol{P_5}$	-1.249	-32.741	-1.193	-2.865	-0.939

Table 4 Damping ratio and Natural frequency

	Damping ratio ζ	Natural frequency ω_n (rad/s)
$\boldsymbol{P_0}$	0.87	1.49
$\boldsymbol{P_1}$	0.80	1.62
$\boldsymbol{P_2}$	0.75	1.74
$\boldsymbol{P_3}$	0.70	1.85
$\boldsymbol{P_4}$	0.65	1.99
$\boldsymbol{P_5}$	0.60	2.16

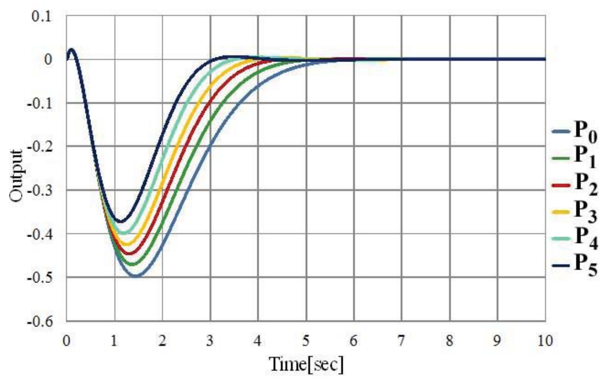

Fig.4 Unit step responses with $\boldsymbol{P_i}$

Figure 4 shows unit step responses of the closed-loop with $\boldsymbol{P_i}$. On the same method, we keep the ζ, and change the real number of the conjugate number $-1.3 \pm j0.73$ with 0.2 step to negative direction. We obtain the good pole $\boldsymbol{P_6} = [-284.4,\ -10.9,\ -1.5 \pm j0.84,\ -1.47]$ with gain margin 5.0 [dB], resonant peak -10.1 [dB], setting time 4.79 (sec.), overshoot -0.41, and $\zeta = 0.87$, $\omega_n = 1.72$ (rad/sec.).

4 EXPERIMENTAL RESULTS

A real TWMR is established practically in our laboratory to illustrate the effectiveness of the proposed method. Using the same parameters shown in Table 1, real stable position experiment is implemented to verify the feasibility of the proposed method with the pole $\boldsymbol{P_6}$ and the LQR method with $\boldsymbol{P_0}$, respectively.

Fig.5 presents the body angle Ψ which tests the stability of TWMR, a small shaking of the body angle with the pole $\boldsymbol{P_6}$ than the pole $\boldsymbol{P_0}$. Fig.6 shows the shifting distance of TWMR at an appointed position. A large distance error using the pole $\boldsymbol{P_0}$ is produced, but, the proposed method with the pole $\boldsymbol{P_6}$ generates very small movement from the appointed position.

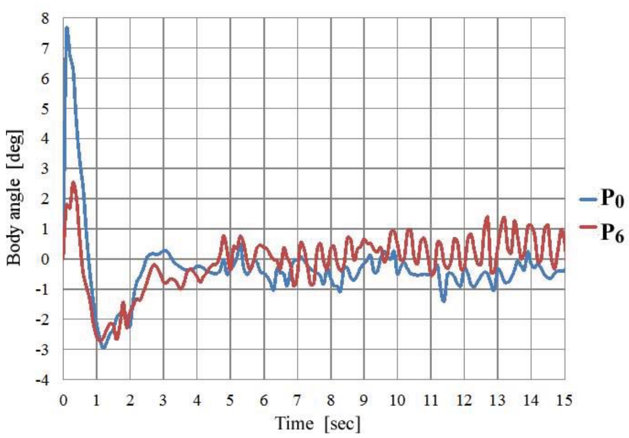

Fig.5 Experimental results of body angle

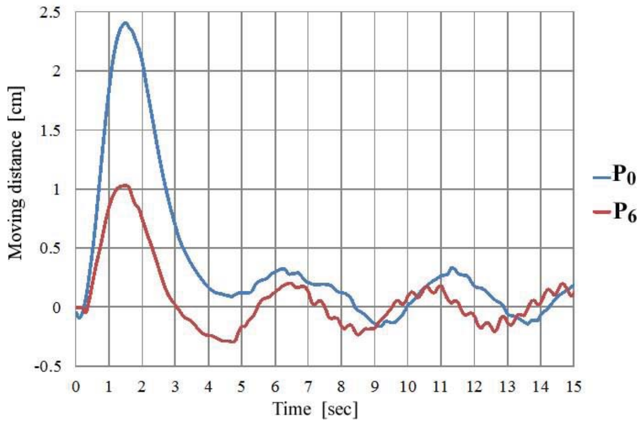

Fig.6 Experimental results of shifting distance

5 CONCLUSION

This paper has implemented the LQR method and pole-placement developmental hardware and software on the real TWMR system, the combined pole-placement method has been newly proposed to control TWMR achieving the desired control behaviors than LQR method.

Finally, the experiment of stable position control was executed using the proposed method and LQR method, the experimental results indeed have verified that the proposed method is effective for the real TWMR system.

REFERENCES

[1] Jian Huang, Zhi-Hong Guan, Takayuki Matsuno, Toshio Fukuda and Kosuke Sekiyama (2011), Sliding-model velocity control of mobile-wheeled inverted-pendulum system, IEEE Trans. Robotics, Vol.26-4, pp. 750-758

[2] Chen-Hao Huang, Wen-June Wang and Chih-Hui Chiu (2011), Design and implementation of fuzzy control on a two-wheel inverted pendulum, IEEE Trans. Ind. Electr. Vol. 58-7, pp. 2988-3001

[3] Zhijun Li and Jun Luo (2009), Adaptive robust dynamic balance and motion control of mobile wheeled inverted pendulums, IEEE Trans. Contr. Syst. Technol. Vol. 17-1, pp. 233-241

[4] Yorihisa Yamanoto (2009), NXTway-GS model-based design, Report of Cybernet systems CO., LTD

[5] Katsuhiko Ogata (2008), MATLAB for Control Engineers, Prentice Hall

The Seventeenth International Symposium on Artificial Life and Robotics 2012 (AROB 17th '12),
B-Con Plaza, Beppu, Oita, Japan, January 19-21, 2012

Phrase and music search engine for musical data

Kentaro Minowa and Eiji Hayashi
Department of Mechanical Information Science and Technology
Faculty of Computer Science and Systems Engineering, Kyushu Institute of Technology
680-4, Kawazu, Iizuka-City, Fukuoka Prefecture, Japan

Abstract: The internet has significantly changed most people's environments. It is possible to search for and obtain information about nearly any subject, and it is possible to purchase many things on the internet. Music files can be purchased, and lyrics can be searched via web services, which is convenient for consumers. However, even if the singer, a part of the musical phrase and the release date are known, a song cannot be accessed if one does not remember the name of the song. If one could enter a sample of the voice, do a search using that voice's length and pitch, find the rhythm and a similarly pitched phrase, it may be possible to determine the name of the song. Therefore, we developed a phrase and music search engine. It searches for a tune from among various tunes, using one phrase of voice data. For the purpose of studying the relationship between tempo and pitch changes related to the frequency of the input voice data, we developed a method using dynamic programming (DP) matching as a way to search for similar phrases. This system converts notes into character strings, runs DP matching using the strings, and calculates the degree of disagreement between these strings. We then use these calculations as an index to determine whether the strings resemble each other.

***Keywords*:** automatic piano, knowledge database, computer music, DP matching

I. INTRODUCTION

The internet has significantly changed most people's environments. It is possible to search for and obtain information about nearly any subject, and it is possible to purchase many things on the internet.

Music purchases are no exception. Previously, CDs were purchased or rented from stores, but now they can be purchased or rented from home. This is convenient for consumers. However, even if the singer, a part of the musical phrase and the release date are known, a song cannot be accessed if one does not remember the name of the song.

On the other hand, related to music performance, we have developed pedal-powered equipment and typing equipment. The problem of fast repetitive typing with the same key and complaints about performance have been solved, and a system in which piano playing takes place automatically has been developed. That system can make use of data when you play piano with MIDI functions and edited data of loudness, the length of the sound, tempo, etc [1]. In addition, studies were conducted two years ago at time of the development of an interactive musical editing system. That system made it possible to perform efficient editing of large music data files. The automatic piano performs the music of the large musical data files. Finding the desired song requires a time-consuming search for the correct musical data. So, we thought it would be useful to have a music information search engine. The system makes an efficient search for the desired song names and musical data, which can reduce the burden on the user.

In this research we developed a system that uses DP matching to search the entire score to look for a match to a given phrase. This system converts notes into character strings and calculates the degree of disagreement between these strings during searching. We use these calculations as an index to determine whether the strings resemble each other.

In this paper, we describe the results of searching for similar phrases using DP matching.

Figure 1.1: View of the automatic piano

II. Musical Editing Support System

2.1 System Architecture

The structure of the system is shown in Figure 2.1. The user edits music via the user's interface on a

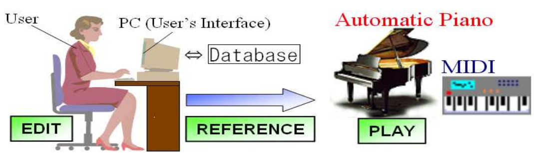

Figure 2.1: Structure of the editing system

computer display. The user can also access a database that has musical grammar, the user's preferences, and so on. As a result, editorial work is reduced and efficient editing becomes possible.

2.2 Performance information

The score is read by the scanner. Scanned data is converted to MusicXML format by the KAWAI Score Maker FX5 program. A database of performance information containing notes, scales, and symbols of music data is created based on the MusicXML data. The created database will be subject to search.

2.2.1 Format of Performance Information

The parameters of performance information are shown in Tables 1 and 2. The automatic piano that we have developed uses a music data structure that is similar to MIDI. We defined performance information, dividing it into two categories: the notes and the pedals. The note information is comprised of the six parameters involved in producing a tone: "Key" (note), "Velo" (velocity), "Gate", "Step", "Bar", and "Time". "Velo" is the dynamics, given by the value of 1–127. "Gate" is the duration of the note in milliseconds. "Step" is the interval of time between notes, and it also exhibits tempo. "Bar" is the vertical line placed on the staff to divide the music into measures.
The pedal information is comprised of four parameters: "Key" (indicating the kind of pedal: "Damper" or "Shifting"), "Velo" (the pedaling quantity), "Time" (the duration for which the pedal is applied)", and "Bar".

Table 2.1: Format of the note information

Parameters	Unit (numerical value)	Resolution	Setting
Key	21~108	Stage 88	Pitch
Velo	1~127	Stage 127	Volume
Gate	ms	1ms	Length
Step	ms	1ms	Interval
Time	ms	1ms	Pronunciation time
Bar	-	-	Bar numbers

Table 2.2: Format of the pedal information

Parameters	Unit (numerical value)	Resolution	Setting
Key	119 or 110	-	119=Damper,110=Shift
Velo	0~127	Stage 128	Position of the pedal
Time	ms	1ms	Pedal operation start time
Bar	-	-	Bar numbers

III. Phrase and music search engine

3.1 System summary

We developed a phrase and music search engine. It searches for one tune from among various tunes using one phrase of voice data. The voice is first inputted; then the interval between the sounds of the inputted voice data is converted back to notes according to the tempo of the music. The system then searches for sequence similarity to the phrase rhythm and notes.

In addition, the pitch of the voice input data was analyzed and pitch changes were calculated. Pitch changes are indicated by the ratio of the pitch of a sound to the pitch of the previous one. By using the change in pitch, we hoped to improve the retrieval accuracy of our system.

3.3 Processing that inputs voice

Voice is input in the shape of waves, as shown in Figure 3.1. The vertical axis of Figure 3.1 shows loudness, and the horizontal axis shows time. By setting a threshold on the vertical axis, the presence of voice can be recognized. The interval of this sound is measured as the time. In other words, as shown in Figure 3.1, the interval of sound is the period between the initial iterative peak and the next sound iterative peak.

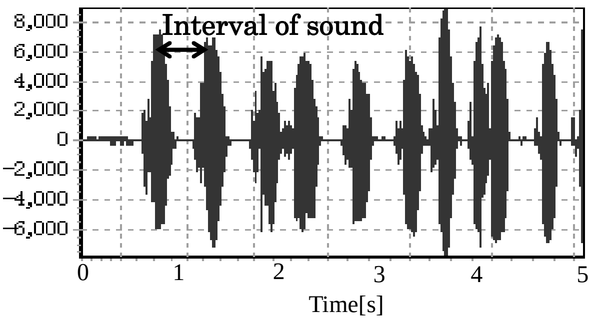

Figure 3.1: Result of sound input

3.4 Converting notes

Measurements of the interval of sound are converted to notes based on the velocity symbol, which appears at the top of the score and represents the number of beats per minute. For example, the indication in Figure 3.2 means 120 quarter note beats per minute. In other words, the length of a quarter note would be 0.5 seconds. The interval of sound is converted into note by using the length of a quarter note.

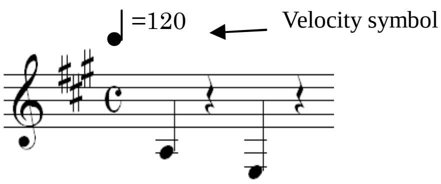

Figure 3.2: Velocity symbol of score

3.5 Frequency analysis of voice data

Pitch is determined by the frequency of the sound, and pitch changes can be determined by the transition of frequency. The voice data frequency analysis is performed using the FFT (fast Fourier transform) algorithm.

Frequency analysis of the voice waveform is conducted for each fixed intervals. And, in one interval, the highest power spectrum frequency is recorded as the main frequency.

IV. Searching for Similar Phrases

As a result of the analysis, it was found that phrases of the same pattern existing in the same tune are performed in a similar expression. In the present study, we used DP matching to search for similar phrases.

4.1 DP matching

DP matching is a technique used widely in the field of speech recognition, bioinformatics and so on. It can calculate the similarity between two words that are different from each other in a number of characters.

In Figure 4.1, the route of minimum cost in each point is taken, and the route with the lowest cost is assumed finally to be the optimal path. The cost at that time is defined as the distance between patterns. In this system, this distance is handled as a threshold to judge whether the phrases are similar to each other.

For example, if the cost moves up or to the right, then it is increased by 1. If it moves to the uppermost level on the right, then it does not increase. Also, if the characters do not correspond in each point, then the cost is increased by 5.

$$g(i,j) = \min\left\{\begin{matrix} g(i-1,j) \\ g(i,j) \\ g(i,j-1) \end{matrix}\right\} + d(i,j)$$

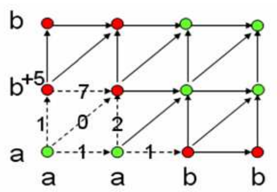

Figure 4.1: DP matching

4.2 Searching with DP matching

In this section we describe a method of searching with DP matching. We had to convert a musical score into character strings (a Note Pattern) before searching for similar phrases. This process is explained below.

4.2.1 Patterning

Each note is expressed by three hexadecimal numbers and patterned using only the digits in the first two decimal places, as shown in Figure 4.2 However, the meanings of these two digits vary. Therefore, to avoid confusion, the second digit is distinguished by applying the letter of the alphabet (V from G).

In addition, the sound frequency obtained in Section 3.5 is made into a pattern. First, the system determines the frequency ratio of two successive sounds, and then the ratio of the frequency is patterned by size, as shown in Figure 4.3

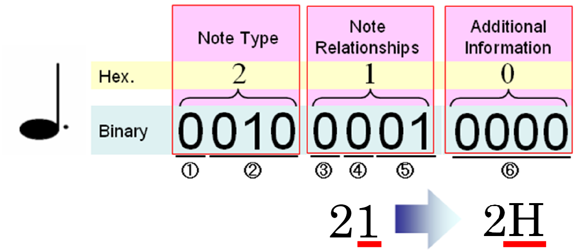

① Note or Rest (0: Note, 1: Rest)
② Note Value (000: A whole note, 001: A half note ...etc)
③ Tie (If the note has a tie then this number is 1.)
④ Ornament
(If the note has an ornament then this number is 1.)
⑤ The number of dots
(Exceptionally, if it is "11" then the note is a tuplet.)
⑥ Additional Information

Figure 4.2: Patterning of notes

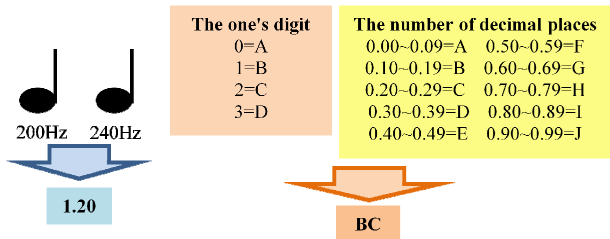

Figure 4.3: Patterning of frequency

4.2.2 The method of searching

A flow chart of a search for a music phrase similar to an input phrase is shown in Figure 4.4.

First, the data of patterned notes column is matched. The phrases with little distance between patterns are searched. Music containing those phrases becomes a search result candidate.

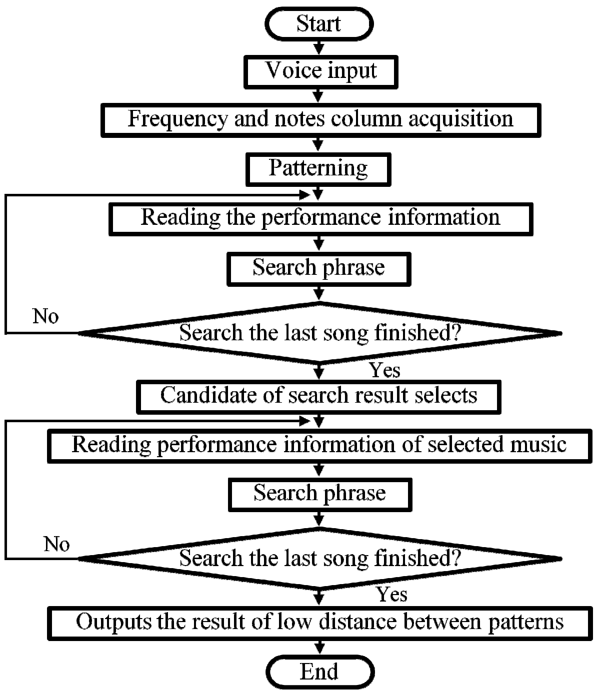

Figure 4.4: The flow of the similar phrase search

Next, the data of patterned sound frequency ratio are matched. Candidates of the search results are narrowed by matching of the frequency ratio.

The search is performed song by song through the database. When the search engine has processed one song, it then proceeds to the next song, continuing to look for the phrase. When the song changes, search engine is change the tempo of the song. And, search phrase is patterned again. After pattern matching in each of two, search result of the lowest distance between patterns is outputted.

V. Retrieval experiment and consideration

We searched for music using the phrase and music search engine. The phrase beginning in bar 59 of "SEKAI NI HITOTU DAKE NO HANA" is sung. The music is searched based on the inputted voice data.

First, the data of the patterned notes column is matched. The system output phrases with a distance of 10 or less. Next, the data of the patterned output phrase frequency ratio is matched. Table 5.1 summarizes the results of the matching. Figure 5.1 represents graphically the difference in the frequency ratio.

A glance at the distance between patterns (Note column) of Table 5.1 will reveal that the phrase beginning in bar 32 of "SEKAI NI HITOTU DAKE NO HANA" and the phrase beginning in bar 59 of the same music are the smallest. However, a search cannot determine the correct one because the two phrases have the same value.

On the other hand, a glance at the distance between patterns (Frequency) of Table 5.1 will reveal that the phrase beginning in bar 32 of "SEKAI" is lower than the phrase beginning in bar 59 of the same music. Thus, in terms of frequency ratios, it is revealed that the phrase begiining in bar 32 is similar to the phrase beginning in bar 59 of "SEKAI NI HITOTU DAKE NO HANA".

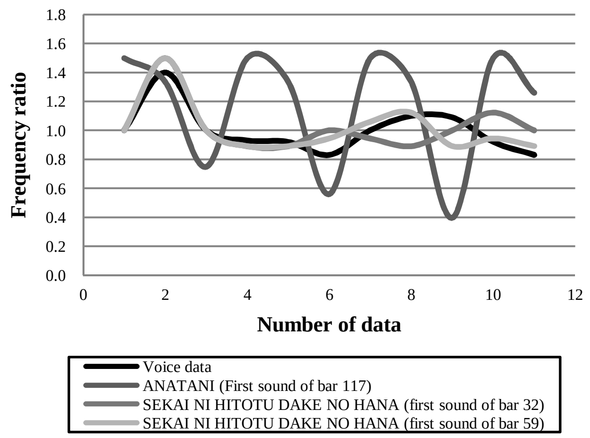

Figure 5.1: Difference in the frequency ratio

Table 5.1: Search result

Name of Music	Bar Number	Note Number	Distance between patterns (Note column)	Distance between patterns (Frequency)
SEKAI NI HITOTU DAKE NO HANA	28	2	10	42
SEKAI NI HITOTU DAKE NO HANA	32	1	5	31
SEKAI NI HITOTU DAKE NO HANA	43	2	10	25
SEKAI NI HITOTU DAKE NO HANA	59	1	5	25
ANATANI	117	1	10	55
ANATANI	118	1	10	55

VI. CONCLUSION

We designed methods of searching for similar phrases using DP matching and combined these functions into a single system.

In the similar phrase search, the system was able to find similar phrases using DP matching in a short time, and it was even possible to find phrases whose resemblance might not be immediately apparent.

In the phrase and music search engine, we developed a system to search for a tune by inputting the data of a voice performing the tune. The interval between the sounds of the inputted voice data is converted to a note according to the tempo of the music. Using this technique, we can search for sequence similarity to a phrase's rhythm and notes. In addition, the search using the patterns of frequency ratio became possible. The search using the patterns of frequency ratio could improve the retrieval accuracy.

In this study, we were able to perform similar phrase searches and searching for a tune by voice. In our future research we will perform evaluations with different pieces of music and will evaluate the existing system.

REFERENCES

[1] Hayashi, E. et al, "Behavior of piano-action in a grand piano.I", Journal of acoustical Society of America, Vol.105, pp.3534-3544, 1999.

[2] Hayashi, E., et al, Interactive musical editing system for supporting human errors and offering personal preferences for an automatic piano, Proc. of the 7th International Symposium on Artificial Life and Robotics, Vol. 2, pp. 513-516, 2002.

[3] Hikisaka, Y., Hayashi, E., et al, Interactive musical editing system for supporting human error and offering personal preferences for an automatic piano –Method of searching for similar phrases with DP matching and inferring performance expression-, Proc. of the 12th International Symposium on Artificial Life and Robotics, GS4-3, 2007.

The Seventeenth International Symposium on Artificial Life and Robotics 2012 (AROB 17th '12),
B-Con Plaza, Beppu, Oita, Japan, January 19-21, 2012

Control of real world complex robots using a biologically inspired algorithm

Fabio DallaLibera[1,2], Shuhei Ikemoto[3], Hiroshi Ishiguro[2], and Koh Hosoda[3]

[1] JSPS Research Fellow / JST ERATO Asada Project / Padua University, Padua 35131, Italy
(fabio.dl@irl.sys.es.osaka-u.ac.jp)
[2] Osaka University, Toyonaka, Osaka 560-8531, Japan
[3] Osaka University, Suita, Osaka 565-0871, Japan

Abstract: Elementary living beings, like bacteria, are able to reach food sources using only limited and very noisy sensory information. In this paper we describe a very simple algorithm inspired from bacteria chemotaxis. We present a Markov chain model for studying the effect of noise on the the behavior of an agent that moves according to this algorithm, and we show that, counterintuitively, the application of noise can increase the expected average performance over a fixed available time. After this theoretical analysis, experiments on real world application of this algorithm are introduced. In particular, we show that the algorithm is able to control a complex robot arm, actuated by 17 McKibben pneumatic artificial muscles, without the need of any model of the robot or of its environment.

Keywords: Robotics, Control techniques, Artificial life

1 INTRODUCTION

Bacteria chemotaxis, the process by which bacteria move toward increasing concentrations of nutrients, is an important topic of the biological field. In particular, the movement of Escherichia Coli (E. Coli) was intensively studied [1]. This bacterium has only two ways of moving, rotating its flagella in clockwise or counterclockwise direction. When the flagella rotate counter-clockwisely they align into a single bundle and the bacterium swims in a straight line. Conversely clockwise rotations break the flagella apart and the bacterium tumbles in place. The bacterium keeps alternating clockwise and counterclockwise rotations. In absence of chemical gradients, the length of the straight line paths, i.e. the counterclockwise rotations, is independent of the direction.

In case of a positive gradient of nutrients, E. Coli reduces its tumbling frequency. In other terms, when the concentration of nutrients increases the bacterium proceeds in the same direction for a longer time. This simple strategy, usually modeled by a biased random walk, is able to drive bacteria to high concentrations of nutrients despite the difficulties in precisely sensing the gradient.

In [2] we proposed a simplified, more generic model for the movement of E. Coli, that we termed *Minimalistic Behavioral Rule* (MBR). Simulations with this model showed that while in most engineering approaches noise is considered as a nuance, that must be filtered to extract the underlying information, noise can actually help bacteria in reaching high concentrations of nutrients.

This paper provides a theoretical analysis of the phenomenon. A Markov chain model is introduced in section 3 to explain the beneficial effect of noise on the movement of an MBR-driven agent. The possibility of employing MBR for the control of complex systems is then shown experimentally by using a robot arm driven by pneumatic actuators (Section 4). Finally, Section 5 concludes the paper by discussing the results.

2 ALGORITHM

As briefly described in the previous section, E. Coli proceeds in the same direction for longer times when the conditions are improving, i.e. when the the concentration of nutrients increases, and proceeds by random walk otherwise. In [2] we defined a very general control algorithm that follows a similar principle. This algorithm, besides being able to explain phenomena regarding bacteria chemotaxis, can be applied for the control of robots, as will be shown in this paper. More formally, the algorithm can be described in the time-discrete domain as follows. Let us denote by E_t an evaluation function (e.g. the concentration of nutrient in the bacteria's case), and by ΔE_t its variation from time $t-1$ to time t. Let us then define a generic motor command $u_t \in \mathbb{R}^n$ that the agent sends to its actuators. The MBR sets u_{t+1} as

$$u_{t+1} = \begin{cases} u_t + \eta R & if\ \Delta E_t \geq 0 \\ random\ selection & otherwise \end{cases}. \quad (1)$$

where $R \in \mathbb{R}^n$ is a random variable, $\eta \in \mathbb{R}$ is a multiplying factor and "random selection" corresponds to randomly picking a motor command in the whole motor command space. Intuitively, MBR tells to change randomly the motor command when the conditions get worse, and keep the current motor command when conditions are improving. In more detail, when the conditions are improving, the motor command is not kept identical to the previous step, but it is slightly modified, with a random perturbation whose inten-

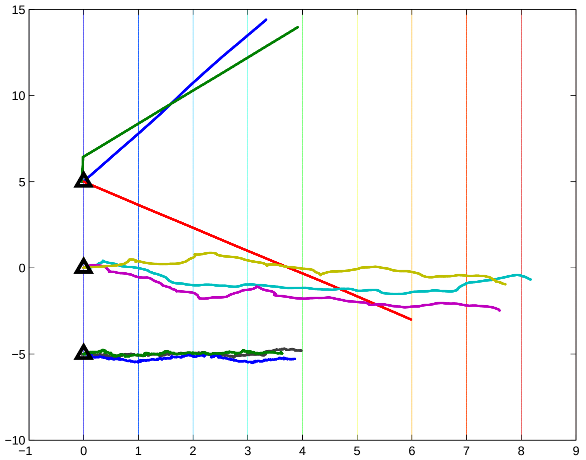

Fig. 1. Paths taken by agents with different values of η: agents starting from $[0,-5]^T$, $[0,0]^T$ and $[0,5]^T$ have, respectively low, medium and high values of η. Each trajectory corresponds to 100 time steps of the agent.

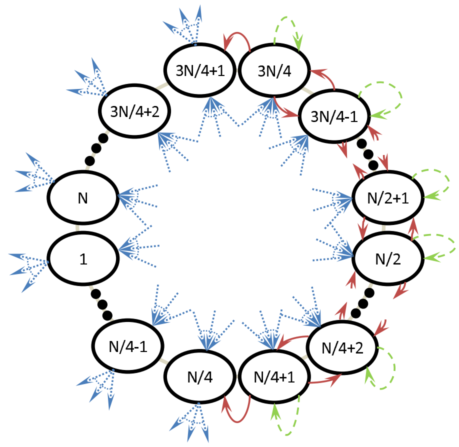

Fig. 2. Representation of the Markov chain. Blue dotted arrows represent the selection of a new node with uniform, $1/N$ probability. Red solid arrows represent transition to the neighboring states with probability v and green dashed arrows indicate loops of probability $1-2v$.

sity is modulated by η. Fig. 1 shows an example of the effect of this random perturbation on the movement of an MBR-controlled agent. Suppose to have an agent that moves on a 2D plane. Let $x \in \mathbb{R}^2$ be the agent position. Assume the agent to move by steps of fixed length s, along the angle indicated by $u_t \in \mathbb{R}$, i.e. $x_{t+1} = x_t + s \cdot [\cos(u_t), sin(u_t)]^T$ and to have an evaluation function that increases along the x axis, i.e. $E_t = [1,0]^T x_t$. If the perturbation η is too small, as for the agents starting from $[0,5]^T$ in Fig. 1, then every motor command u that that bring brings the agent closer to the target, even a very tangential and inefficient one, will be employed for a long time. If the perturbation is too big, as for the agents starting at the bottom of the figure, then the agent keeps changing direction, even when the movement is headed straight to the goal. If the perturbation amplitude η is appropriate, as for the agents starting in the middle of Fig. 1, then the agent will rapidly increase E_t with a good trajectory.

3 THEORETICAL ANALYSIS

In order to understand the reasons of the performance improvement given by an opportune value of $\eta \neq 0$, let us consider again example reported in the previous section. Let us discretize the direction taken by the agent into N possible states of a Markov chain, with the state i, $1 \leq i \leq N$ indicating the probability of taking the directions in the range $\left[-\pi + \frac{2\pi(i-1)}{N}, -\pi + \frac{2\pi+i}{N}\right)$. Let us restrict to the case where transitions due to the perturbation η are limited to neighboring states. In particular, let us assume to transit from a state i to one of its neighbors $i+1$ and $i-1$ with probability v, and remain in the same state with probability $1-2v$, as shown in Fig. 2. We note that only for the states corresponding to directions that lead to an increase of E_t, i.e. the states $\frac{N}{4}+1 \leq i \leq \frac{3N}{4}$, such outward transition to the neighboring states exist. The states corresponding to directions for which $\Delta E_t < 0$, i.e. the directions that imply a random selection in the MBR, have outward transitions that reach each state, including the current state, with probability $1/N$.

The evolution of the probability of the states is described by the following equations. Let us denote by $p_{i,t}$ the probability of being in state i at time t, and by $g = \frac{1-\sum_{i=N/4+1}^{3N/4} p_{i,t}}{N}$ the probability of being selected by random selection when $\Delta E_t < 0$. With these definitions

$$p_{i,t+1} =$$

$$\begin{cases} vp_{i+1,t} + g & if\ i = \frac{N}{4} \\ (1-2v)p_{i,t} + vp_{i+1,t} + g & if\ i = \frac{N}{4}+1 \\ (1-2v)p_{i,t} + v(p_{i+1,t} + p_{i-1,t}) + g & if\ \frac{N}{4}+2 \leq i \leq \frac{3N}{4}-1 \\ (1-2v)p_{i,t} + vp_{i-1,t} + g & if\ i = \frac{3N}{4} \\ vp_{i-1,t} + g & if\ i = \frac{3N}{4}+1 \\ g & otherwise \end{cases} \tag{2}$$

Intuitively, when $v \neq 0$ at every time step there is a "flow of probability" between the nodes. In detail, even starting from a uniform probability of the nodes $p_{i,0} = 1/N$, the nodes $1 \leq i \leq \frac{N}{4}$ and $\frac{3N}{4}+1 \leq i \leq N$ assume a lower probability in one time step. This causes a flow of probability from nodes $\frac{N}{4}+1$ to $\frac{N}{4}$, $\frac{N}{4}+2$ to $\frac{N}{4}+1$, etc. (and, symmetrically, from $\frac{3N}{4}-k$ to $\frac{3N}{4}-k+1$, for $0 \leq k \leq \frac{N}{4}-1$).

Fig. 3 shows the evolution of the probability for different values of v (corresponding, in the MBR, to different values of η) at different time instants t starting from a uniform distribution, i.e. starting from a random direction of the agent. We note that at the beginning a higher value of v is able to "speed up the flow", that makes the distribution peaky around states

$\frac{N}{2}$ and $\frac{N}{2}+1$, corresponding to angles close to 0. As times goes on, however, the distribution becomes more peaky for lower settings of v, as shown in the last panel of Fig. 3.

Let us analyze the chain for $t \to \infty$. The stationary distribution, computed from Eq. 2 and $p_{i,t+1} = p_{i_t}$, is

$$p_{i,t+1} = \begin{cases} \frac{24(n+4)v}{n(8+6n+n^2+96v)} & if i = \frac{N}{4} \wedge i = \frac{3N}{4}+1 \\ \frac{-48i^2+48i(n+1)-12n-9n^2}{n(8+6n+n^2+96v)} & if \frac{N}{4}+1 \leq i \leq \frac{3N}{4} \\ \frac{96v}{n(8+6n+n^2+96v)} & otherwise \end{cases} \tag{3}$$

If we take the derivative with respect to v we find that $\frac{dp_{i,\infty}}{dv}$ is always negative for $\frac{N}{4}+1 \leq i \leq \frac{3N}{4}$ (states that lead to positive ΔE_t) and always positive for the other states (that lead to a negative ΔE_t). In other terms, over short times high values of v are preferable, but as the time available increases, it is more efficient to have a lower value of v. In short, there is a trade-off between the speed with which good

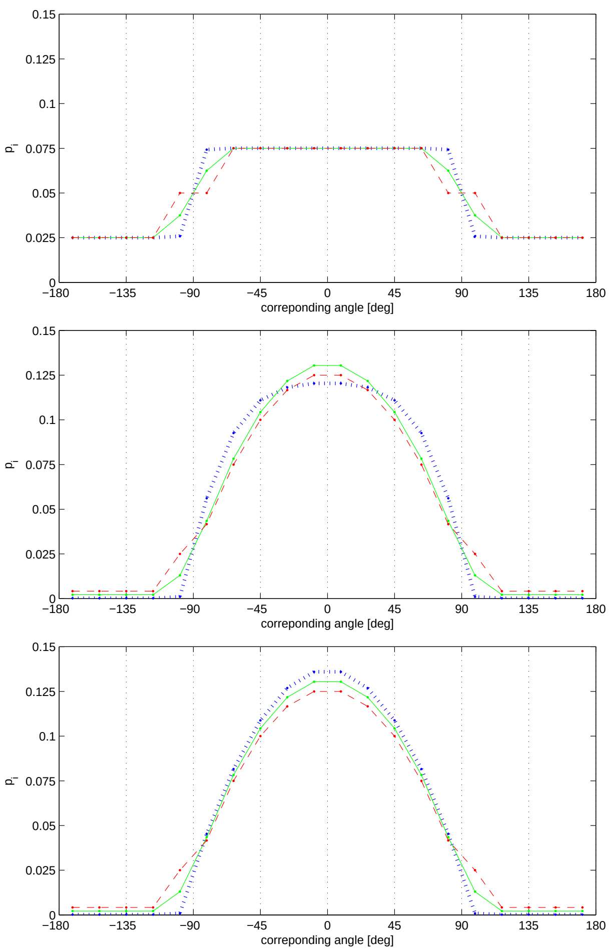

Fig. 3. Probability of a Markov chain of $N = 20$ states starting from a uniform distribution at time $t = 0$. Each panel corresponds to a time instant: $t = 1$ (top panel), $t = 10$ (central panel) and $t = 10^{10}$ (bottom panel). Each panel reports the distribution obtained 3 different values of v: $1/64$ (blue dotted line), $1/4$ (green solid line) and $1/2$ (red dashed line).

motor commands u are chosen, increased by higher values of η, and the precision obtained after a long period, improved by decreasing η. Section 5 will briefly discuss this issue.

These relationships between the noise intensity η, the distribution of the directions taken by the agent and time can be confirmed by numerical simulations of the MBR, with results that resemble the Markov chain approximation here introduced. Actually, the probability density function $p(\theta)$ of taking direction θ is the solution of the following Fredholm integral equation of the second type:

$$\begin{aligned} p(\theta) &= \int_{-\pi/2}^{\pi/2} K(\theta,\phi)p(\phi)d\phi + \frac{1-\int_{-\pi/2}^{\pi/2} p(\phi)d\phi}{2\pi} \\ &= \frac{1}{2\pi} + \int_{-\pi/2}^{\pi/2} (K(\theta,\phi) - \frac{1}{2\pi})p(\phi)d\phi \end{aligned} \tag{4}$$

where K is the probability of taking the direction ϕ when the current direction is θ due to the random perturbation R. For instance, if R is Gaussian, then K is a Von Mises distribution centered in θ, i.e. $K(\theta,\phi) = \frac{e^{cos(\phi-\theta)}}{2\pi I_0(1)}$ with $I_0(x)$ the modified Bessel function of order 0.

However, no closed form can be obtained for $p(\theta)$. The main advantage of the Markov model proposed in this section is thus to allow making predictions on the behavior of an MBR controlled agent, using simple in analytical formulae, without lengthy Monte Carlo simulations.

4 PRACTICAL EXPERIMENTS

Previously reported simulation experiments [3] show that the application of MBR is not restricted to the simple 2D case described beforehand. In particular, it was shown that MBR is able to increase the evaluation function E_t of systems with dynamics

$$x_{t+1} = f(x_t, u_t, \ldots, u_{t-d}) \tag{5}$$

even when $x_t \in \mathbb{R}^n$ $u_t \in \mathbb{R}^m$ with n and m in the order of 40 or more dimensions. It was also shown that the function f can be a nonlinear function of the previous inputs $u_{t-1}, \ldots, u_{t-d}$, and in particular, even when a dead time is present in the system, i.e. $x_{t+1} = f(x_t, u_{t-d})$.

To test the MBR approach in a real world setting, we employed the biologically inspired robot arm shown in Fig. 4. This arm has 7 degrees of freedom driven by 17 McKibben pneumatic muscles. Each muscle is equipped with a pressure sensor, used for closed loop pressure control.

The robot is controlled by setting the variation of the pressure in each of the 17 pneumatic actuators, i.e. $u_t \in \mathbb{R}^{17}$. The task chosen consists in reaching repeatedly three targets in the robot reachable space. These targets are located at the robot's right, left and bottom part of the reachable space.

To verify the robustness of the approach to sensory input noise, we tested three ways of measuring the end effector position, from which the function E_t is computed:

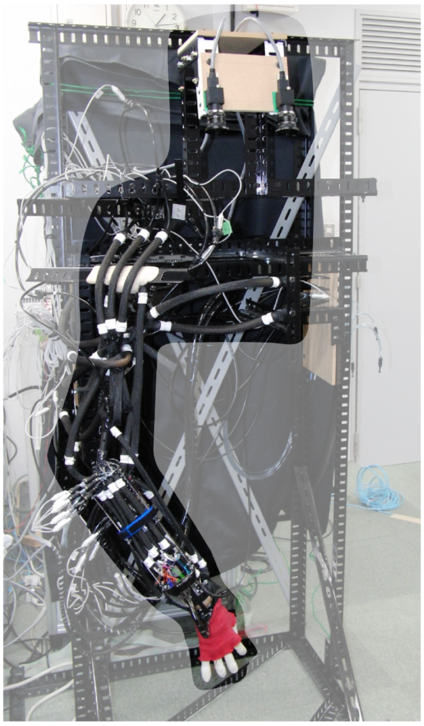

Fig. 4. The robot arm used in the experiment.

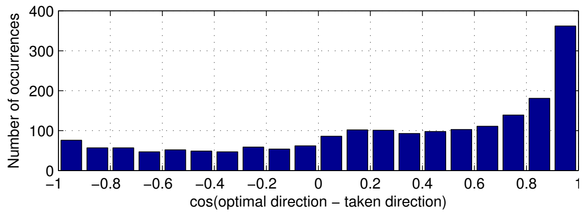

Fig. 5. Frequency of the cosine between the direction taken by the MBR-controlled robot arm and the direction straight to the target location.

1. A four dimensional vector composed by the end-effector centroid in the images of the two cameras mounted on the robot's head.
2. The three dimensional position of the end effector, obtained using stereo computation.
3. A three dimensional position of the end-effector observed by a motion capture system (EvaRT, Motion Analysis Ltd.)

The task could be achieved with all the three types of the information, showing the adaptability and the robustness of the approach. We note that the value of η was chosen empirically, without fine tuning, and kept constant in all the settings. In fact, although not optimal, any $\eta \neq 0$ can be employed for achieving the task.

The real world experiment is different for many points compared with the system analyzed in Section 3: the dimensions of the input command u, of the space x, the mapping between u and x, the noise in the sensory system, etc. Nonetheless, as Fig. 5 shows, the distribution of the cosine between the optimal direction (straight to the target) and the direction taken by the robot during the whole experiment is a decreasing function, as predicted by our simplified model.

5 CONCLUSIONS

In this paper we proposed a Markov chain model to study MBR, a simple, biologically inspired algorithm for robot control. We showed that the algorithm is able to drive a pneumatic robot arm's end-effector to desired targets without any knowledge on the mapping between the control signal u and the resulting evaluation function variation ΔE_t or on the directions taken by the links when each muscle is contracted. We analyzed the distribution of the cosine between the optimal movement and the direction actually taken by the robot, and showed that the probability is a decreasing function of the angle, as predicted by our model, despite the numerous differences between the model and the real world setup.

Future works will need to define policies for changing η online and maximize the performances. We note that starting with a high η and decrease it over time, as in Simulated Annealing, may allow obtaining solutions with high precision (due to a low final η) in a short time (due to an initially high η). However, estimating an appropriate time constant for the adaptation of η is very complex. In fact, this depends on how fast the optimal u changes, which, in turn, depends both on the evaluation function E and on the system dynamics f.

We note that, despite the similarities, MBR presents advantages over classical Simulated Annealing. MBR does not require a good estimation of the evaluation function, but only a binary value specifying if it is increasing or not. Furthermore, it does not need to return to the one state x_t after noticing that x_{t+1} is a less favorable state. This is fundamental when dealing with real word robots of unknown dynamics. Comparison of the two algorithms in real world setups is, however, an important point to be focused in the future.

REFERENCES

[1] J. Adler. The sensing of chemicals by bacteria. *Scientific American*, 234:40–47, 1976.

[2] S. Ikemoto, F. DallaLibera, and H. Ishiguro. Stochastic resonance emergence from a minimalistic behavioral rule. *Journal of Theoretical Biology*, 273(1):179–187, 2011.

[3] F. DallaLibera, S. Ikemoto, T. Minato, H. Ishiguro, E. Menegatti, and E. Pagello. A parameterless biologically inspired control algorithm robust to nonlinearities, dead-times and low-pass filtering effects. In *Proceedings of SIMPAR2010*, pages 362–373.

The Seventeenth International Symposium on Artificial Life and Robotics 2012 (AROB 17th '12),
B-Con Plaza, Beppu, Oita, Japan, January 19-21, 2012

Control method for a redundant robot using stored instances

Yuya Okadome[1], Yutaka Nakamura[1], and Hiroshi Ishiguro[1]

[1] Department of Systems Innovation, Graduate School of Engineering Science, Osaka University, 3-1 Machikaneyama, Toyonaka, Osaka, Japan. okadome.yuya@irl.sys.es.osaka-u.ac.jp

Abstract: A robot operating in a real environment, as opposed to industrial robot working in factory, must have the exibility to cope with disturbances and irregular factors. In this paper, we propose a control method where the control signal is selected from past experiences (stored instances) of a similar situation, according to the evaluation of each instance. We apply our method to the control of a robot with complicated structure, driven by several elastic actuators. Experimental results show that the control of a robot with many DOFs can be achieved by the proposed method.

Keywords: adaptive control, k-nearest neighbor, redundant robot

1 INTRODUCTION

In order for a robot to work in a real environment, the robot has to have the ability to cope with various kinds of situations. A robot with many DOFs is advantageous since it can generate various behaviors, and thus it is expected to have the ability to adapt to various situations. A learning method such as system identi cation or reinforcement learning can be applicable to the control of such a robot; however, this is di cult due to its complexity especially when its dynamics are in uenced by various environmental factors. For example, system identi cation methods using piece-wise linear functions [4][7] to approximate the dynamics of the controlled target have been successfully applied to the control of a robot, but a huge number of pieces becomes necessary to approximate such complex dynamics.

Autonomous learning methods such as reinforcement learning might also be applicable to the control of this type of robot, in principle (e.g. Actor-Critic[1][5] algorithm or Q-Learning[3][6]), but the application becomes di cult in case of controlling a robot with many DOFs. One of the most di cult problems is the increase in the number of parameters to be learned. In order to determine a large number of parameters, it is necessary to obtain a huge number of data (i.e. the curse of dimensionality). Besides, the amount of available data does not increase even though the dimensionality of the dynamics of the target system does increase, resulting in longer operating time and more troubles.

In this paper, we propose a control method using stored instances. In this method, a certain number of instances in the database, similar to the current state, are evaluated based on experience, and one of the instances among them is selected according to this evaluation. The control signal is determined from the selected instance. Since the control signal is determined from the database directly, an explicit modeling of the control target is not necessary. That is, this method is a kind of non-parametric method and uses the knowledge of the system implicitly included in the dataset to determine the output. Note that further knowledge about the system cannot be obtained from the database even if a system identi cation method is used.

2 CONTROL METHOD USING STORED INSTANCES

In this research, we propose a control method where the control signal is directly determined from the stored instances. Since this method does not employ a system identi cation nor a learning method, it is advantageous if the control target has a redundant structure which makes the learning of the system di cult.

2.1 Gathering Instances

To obtain instances for determining the control signal, the robot is controlled by randomly generated control signals at rst. During this procedure, the controller observes the current state of the robot $\boldsymbol{x}(t)$ and output the control signal $\boldsymbol{u}(t)$ at random. A pair consisting of the state and the control signal $\boldsymbol{d}_i = \{\boldsymbol{x}(t=i), \boldsymbol{u}(t=i)\}$ is called "an instance" and added to the database.

Each instance in the database D is denoted by $\boldsymbol{d}_i$ for the understandability of the notation and the database is de ned as a set of instances:

$$D = \{\boldsymbol{d}_i |\ i = 1, 2, \ldots, N\} \quad (1)$$

where N is the number of instances. Note that $\boldsymbol{d}_{i+1}$ is the instance composed by subsequent state and action of the i-th instance $\boldsymbol{d}_i$.

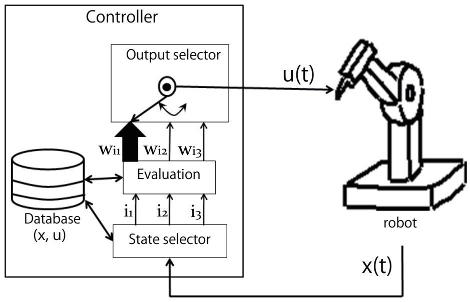

Fig. 1. Block diagram of proposed method

2.2 Control Rule

Fig. 1 shows a block diagram of the proposed method. After the controller observes the state $\boldsymbol{x}(t)$, nearest K neighbors in the database are selected by the "state selector". Indexes of nearest K instances constitute the set "KNN".

We employ a simple evaluation function, where the weight of each instance is determined from the distance between the trajectory starting from each instance in the KNN and the given goal. Thus, the weight of the i-th instance ($i \in KNN$) is de ned as:

$$w_i \quad = \quad \min_{j<p} \{||\boldsymbol{G} \quad \boldsymbol{d}_{i+j}||_2\} \tag{2}$$

where p is the length of the trajectory to be considered in the evaluation, and $\boldsymbol{G}$ denotes the goal state. $||\boldsymbol{G} \quad \boldsymbol{d}_{i+j}||_2$ is the Euclidean distance from the state $\boldsymbol{x}_{i+j}$ of the $i+j$-th instance.

After the evaluation for all instances in KNN, one of the KNN instances is selected by the control signal selector. The probability to select the i-th instance is

$$P(i) = \begin{cases} \frac{\exp(w_i T)}{\sum_{j=1}^{K} \exp(w_j T)} & i \in KNN \\ 0 & \text{otherwise} \end{cases} . \tag{3}$$

T is a parameter called inverse temperature which modi es the probability. When T is large, the instance with maximum weight is selected almost deterministically. On the other hand, when it is small, every instance can be selected with equal probability.

3 CONTROL OF ELASTIC BINARY MANIPULATORS

We applied the proposed method to a control task (reaching task) of a redundant robot (Fig. 2). This robot is a variation of binary manipulators [2] with elastic links.

3.1 Elastic Binary Manipulators

The Elastic Binary Manipulators has several links with a truss-like structure. As seen in Fig. 2, each link (line) and joint (black point) is modeled by a spring damper without mass, and a mass-point, respectively. The control signal to the robot consists of the natural lengths of the links, and changes the equivalent point (posture). In the simulation, the natural lengths of the 12 links represented in the gure by dashed lines can be changed according to the control signal, and the others are xed. The length of each variable link can have a larger or smaller value and the former is 1.5 times longer than the latter.

The force applied to the i-th mass-point is de ned by:

$$\boldsymbol{F}_i \quad = \quad \sum_{j \in C_i} \left\{ \quad k(l_{ij} \quad \bar{l}_{ij}) \frac{\boldsymbol{s}_i \quad \boldsymbol{s}_j}{||\boldsymbol{s}_i \quad \boldsymbol{s}_j||_2} \quad D(\boldsymbol{v}_i \quad \boldsymbol{v}_j) \right\}, \tag{4}$$

$\boldsymbol{s}_\iota$ and $\boldsymbol{v}_\iota$ denote the position and the velocity of the ι-th joint. l_{ij} and $\bar{l}_{ij}$ are the current length and the natural length of the link connecting the i-th and the j-th joints. k and D are the spring and the damping constants.

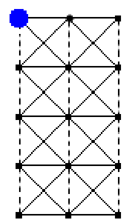

Fig. 2. Structure of the EBM

3.2 Reaching task

The purpose of the reaching task is to move the ende ector (blue point) to the goal position. During the instance-gathering phase (500,000 time steps), 6 links are selected randomly and their natural lengths are altered (small to large/ large to small) every 1,000 time steps. To generate meaningful motions, the control signal is maintained over a certain time period (1,000 time steps).

We conducted experiments with the goal G = (0.2, 0.43). K was set to 5 and T was set to 100 and 1,000. These values were determined by trial and error.

Fig. 3(a) shows the density of state-instances stored in the database visualized by a kernel density estimation method. Fig. 3(b) and Fig. 3(c) show the density of the state while performing the reaching task. The yellow-colored area indicates that the end-e ector stays

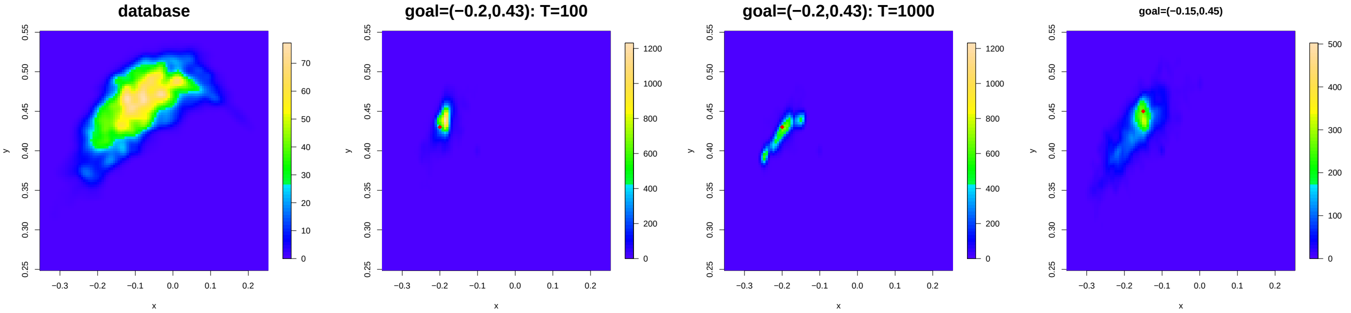

(a) (b) (c) (d) with broken link

Fig. 3. Result of reaching task: Elastic Binary Manipulators

in these areas for a long time. The red point in each gure represents the goal position of the reaching task, and it can be seen that the density concentrates to the area close to the goal in both cases. These results show that our control method allows the robot to achieve the reaching task. The performance of the case $T = 1000$ is worse than that of $T = 100$. This suggests that stochastic choice of control signal makes the robot escape from the local optima.

We conducted an additional experiment to investigate whether our method can exploit the redundancy of the robot (Fig. 3(d)). Even when a controllable link is broken (the natural length is xed), the proposed method allows the robot to achieve the task if there is a link which is able to compensate the broken link.

4 CONTROL OF HUMAN-LIKE ROBOTIC ARM

We applied the proposed method to a control task of a human-like robotic arm (Fig. 4). We conducted a reaching task by this robot.

4.1 Human-Like Robotic Arm

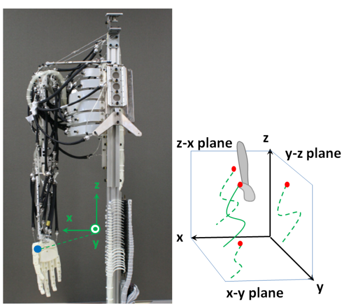

Fig. 4. Human-Like Robotic Arm

The human-like robotic arm consists of 6 links and has a high degree of freedom (9-DOFs). More than 30 pneumatic actuators (arti cial muscles) are connected to these links, and are controlled by 26 air- ow control valves. Each actuator expands (contracts) when the air pressure decreases (increases). Actuators are located at positions similar to those of human muscles. The air ow of each valve monotonically increases according to the control signal, i.e. the output of the D/A converter (output range: 0 6[V]). To control this robotic arm, it is necessary to determine the control signal consisting of 26 analog values depending on the state of the robot.

4.2 Reaching task

The purpose of the reaching task is to move the hand (represented by the blue point in Fig. 4) to the goal position. During the instance-gathering phase (1500[s]), 13 actuators are selected randomly and their input values are altered randomly in every 1[s]. We conducted two experiments with two di erent goals, $G = G1(0, 150, 140)$ and $G2(\ 40, 100, 80)$. In each reaching task, the operation time was 150[s] and the control signal is altered once in 0.5[s]. K and T were set to 10 and $\frac{2}{15}$ by trial and error.

Fig. 5(a) and Fig. 5(b) show the density of the hand position in the database. Fig. 5(c) Fig. 5(f) show the densities of the position of the hand during the reaching tasks projected on the X-Y and X-Z planes. The red point in each gure represents the goal position, and we can see that the density concentrates to the goal in both cases. These results show that our control method allows the robot to achieve the reaching task.

Reaching G2 seems worse than in the case of G1, since the density spreads widely. If there are fewer instances approaching the goal in the database, it is dif- cult to achieve the task since such a instance is often cut o from the k-NN. The reason why reaching G2 is more di cult is that there are fewer instances useful for achieving the task.

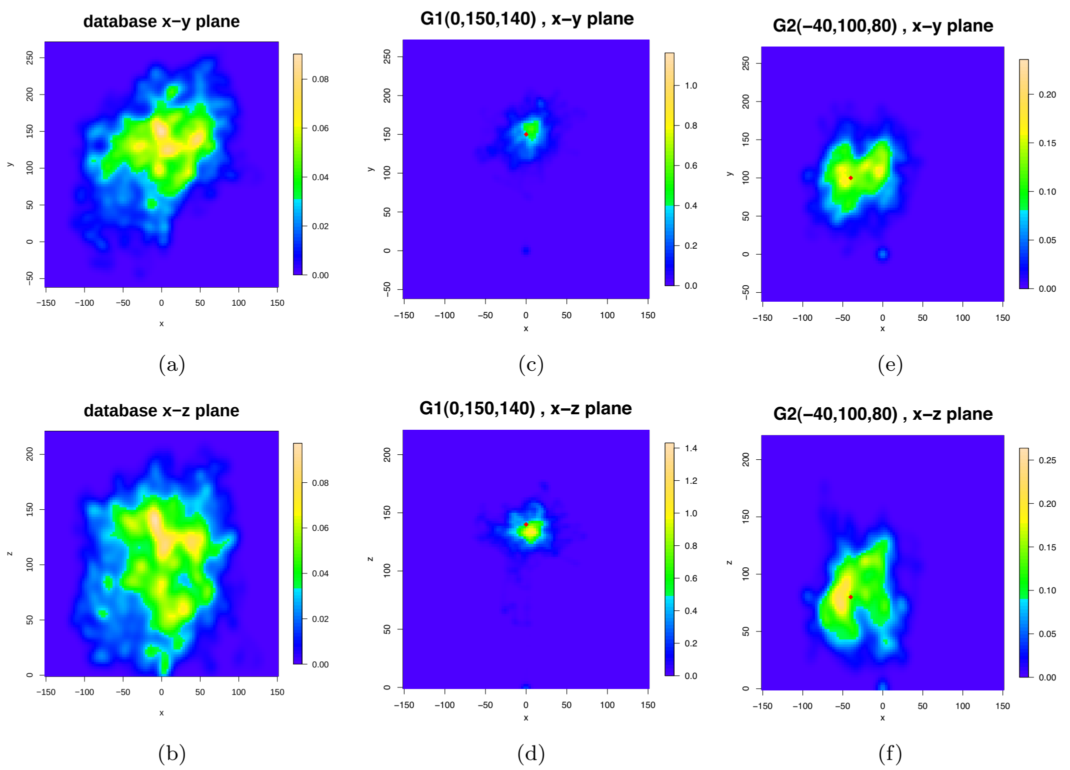

Fig. 5. Result of reaching task: Human-Like Robotic Arm

5 CONCLUSION

In this paper, we proposed a control method using stored instances which does not need an explicit modeling of the control target. We applied the proposed method to the control tasks of redundant robots and showed that the reaching task can be achieved by our method.

One of the problems of our method is performance degradation due to the bias of the distribution of the instance in the database. To overcome this, it might be useful to omit similar instances from the database or employ an importance sampling method. To develop a method for adding the instances in an online manner is also part of our future work.

REFERENCES

[1] H. Kimoto and S. Kobayashi: "An Analysis of Actor/Critic Algorithms using Eligibility Traces: Reinforcement Learning with Imperfect Value Functions" Journal of Japan Society of Arti cial Intelligence, Vol.15, No.2, pp.267-275,2000

[2] Lees, D.S. and Chirikjian, G.S.: "A Combinatorial Approach to Trajectory Planning for Binary Manipulators" Proc of ICRA, pp.2749 – 2754, 1996.

[3] M. Asada, S. Noda, S. Tawaratsumida, and K. Hosoda: "Vision-Based Reinforcement Learning for Purposive Behavior Acquisition." Proc. of ICRA, pp.146–153, 1995.

[4] M. Haruno , D.M.Wolpert, and M. Kawato: "Mosaic: Module selection and identi cation for control," Neural Computation, vol.13, no.10, pp.2201–2220, 2001

[5] Vijaymohan R. Konda and Vivek S. Borkar: "Actor-critic–type learning algorithms for Markov decision processes" SIAM J. Control Optim. Vol. 38, No. 1, pp.94–123, 1999

[6] Watkins, C. J. C. H. and Dayan, P.: "Technical Note: Q-Learning" Machine Learning 8, pp. 279–292, 1992

[7] Y. Tazaki, J. Imura: "Graph-based Model Predictive Control of a Planar Bipedal Walker" 17th International Symposium on Mathematical Theory of Networks and Systems, pp.128–133, Kyoto, Japan, July 24–28, 2006.

Proposal of semiautonomous centipede-like robot for rubbles

Shota KASHIWADA[1], Kazuyuki ITO[2]

[1,2]Hosei University, Tokyo 184-8584, Japan
(Tel: 81-42-387-6093, Fax: 81-42-387-6381)

[1]shota.kashiwada.8j@stu.hosei.ac.jp

Abstract: In this paper, we propose a multi-legged robot that is designed for operating on rubble. Generally, conventional multi-legged robots have many actuators for driving the legs and body. Hence, control in the case of these robots is more complicated than that in the case of crawler robots, and it is very difficult to operate multi-legged robots adaptively in a complex environment like rubble. To solve this problem, we have designed a mechanism of the legged-robot for reducing the controller load by utilizing a passive mechanism. To design the robot, we focus on a centipede. First, we observe the behavior of a centipede by using a high-speed camera, and then, to realize this behavior by a simple mechanism, we propose a multi-legged robot that is realized by connecting many links serially through rubber joints. In this mechanism, every joint has a leg on both sides, and the robot moves regularly like a centipede. The elasticity of the rubber joints compensates for the bumps on the ground. To control the moving direction, wires are installed through the links, and by pulling the wires, the body of the robot can be lifted up or turned. By simply pulling the suitable wires, we can control the moving direction of the robot. We do not have to control many joints individually for crossing bumps. They can move passively and can cross the bumps. To demonstrate the effectiveness of the proposed robot, we have developed a prototype robot and conducted certain experiments. The results show that the robot can move on rubble to desired positions.

Keywords: multi-legged robot, centipede, passive mechanism.

1 Introduction

Recently, robots that operate in complex real environments, for example, rescue robots, agriculture robots, and forestry robots, have attracted considerable attention. Hence, various robots that have high mobility have been developed [1-6]. Usually, conventional robots have many crawlers to realize high mobility and can overcome various obstacles like steps, bumps, and dents. However, crawlers have two disadvantages in a real environment. One is the slip on a low-friction ground like dry sand, and the other is the locking of crawlers owing to the engulfment of wires, long grasses, etc.

On the other hand, legged robots can solve these problems of crawlers and have relatively high mobility in these situations. Therefore, the development of effective multi-legged robots for complex real environments is expected.

However, in general, multi-legged robots have many actuators for driving their legs and body. Hence, control in the case of these robots is more complicated than that in the case of crawler robots, and it is very difficult to operate multi-legged robots autonomously in complex environments like rubble. This is a major disadvantage of multi-legged robots.

In this study, in order to solve this problem, we have designed a mechanism of the legged-robot for reducing the controller load by utilizing the passive mechanism proposed in our previous work [6]. To design the robot, we focus on a centipede. We observe the behavior of a centipede by using a high-speed camera, and then, to realize motions similar to those of a centipede by using a simple mechanism, we propose a multi-legged robot that is realized by connecting many links serially through rubber joints. To demonstrate the effectiveness of the proposed robot, we develop a prototype robot and conduct experiments.

2 Centipede

We observed the behavior of a centipede by using a high-speed camera. Fig. 1 shows a photograph of centipede motion over rubble, and Fig. 2 shows the locomotion pattern.

No. 1 No. 2 No. 3

Fig. 1. Locomotion on rubble

No. 1

No. 2

No. 3

No. 4

Fig. 2. Locomotion pattern

We can see that the legs of the centipede move regularly in wave-like motions from the front to the rear part. However, the legs are not rigid and they adapt to the bumps on the ground while maintaining the wave-like motion. Further, the centipede changes its moving direction by lifting or turning its body. In this study, we aim to realize a similar behavior by using a simple mechanism.

3 Proposed mechanism

Fig. 3 shows the proposed mechanism for realizing the centipede-like behavior.

The multi-legged robot is realized by connecting many links serially through rubber joints (Fig. 3 (a)). Every link has a leg on both sides (Fig. 3 (b)), and each leg has two joints. The legs are moved regularly like those of a centipede by using feedback controllers. To control the moving direction, wires are installed through the links (Fig. 3 (c)), and by pulling the wires, the body of the robot is lifted up or turned as shown in Fig. 4. By simply pulling the suitable wires, we can control the moving direction of the robot. We do not have to control many joints individually for crossing over bumps because the elasticity of the rubber joints compensates for the bumps on the ground. These joints can move passively and can cross the bumps.

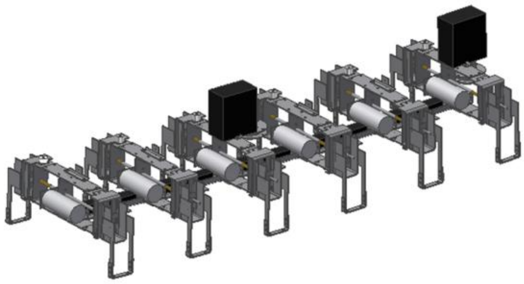

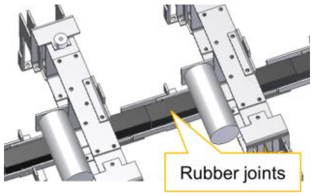

Fig. 3 (a)

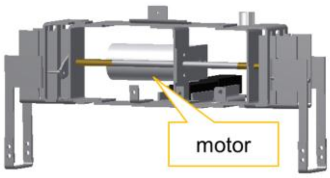

Fig. 3 (b)

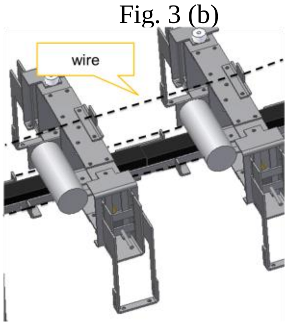

Fig. 3 (c)

Fig. 3. Proposed mechanism

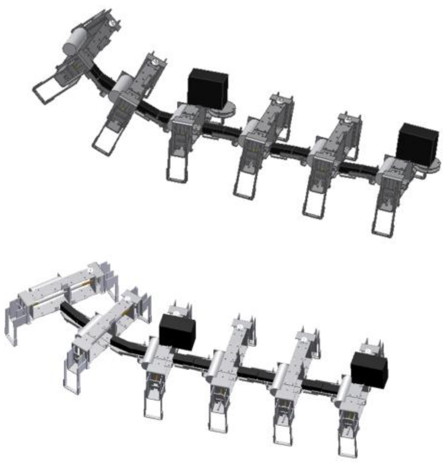

Fig. 4. Control of moving direction

4 Developed robot

We have developed a prototype robot on the basis of the proposed mechanism. Fig. 5 shows the developed robot, and Table 1 presents its specifications.

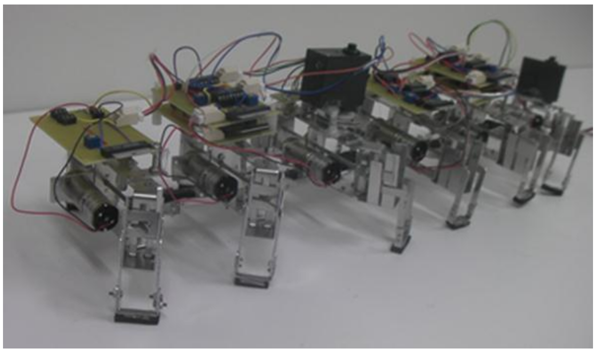

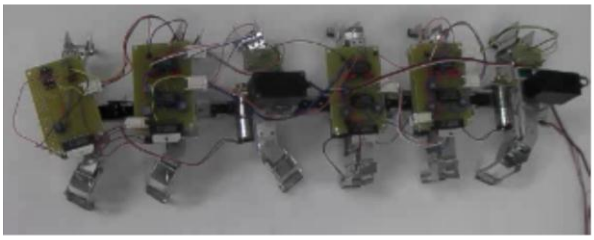

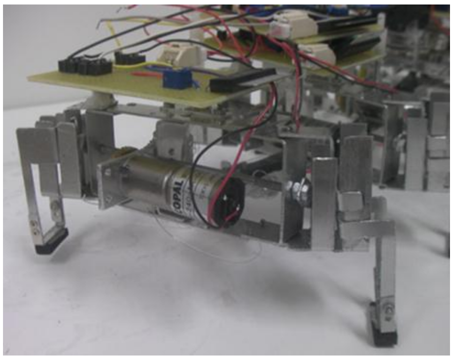

Fig. 5 (a)

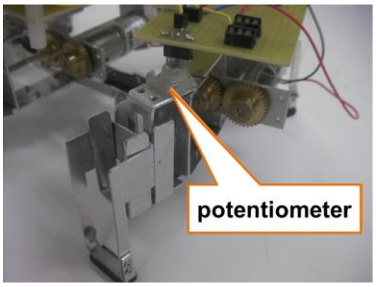

Fig. 5 (b)

Fig. 5. Developed robot

This robot has six links and twelve legs. Each link has two legs that are actuated by one motor (Fig. 5 (a)). The motion of the legs is realized by a link mechanism, as shown in Fig. 6. Each link has one potentiometer (Fig. 5 (b)) to detect the rotating angle, and one controller is employed per link for controlling the phase between the former leg.

Table 4. Specifications of the robot

Length [mm]	420
Width [mm]	150
Height [mm]	80
Weight [kg]	1

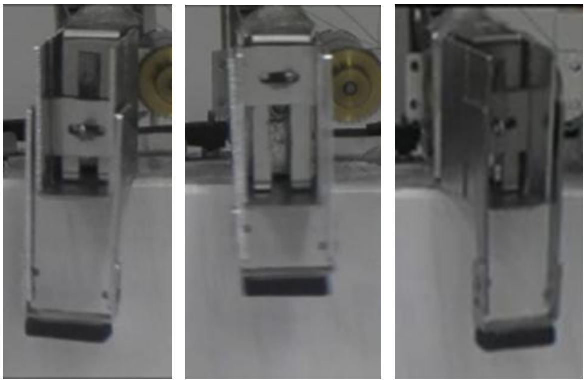

No. 1 No. 2 No. 3

Fig. 6. Link mechanism for legs

5 Experiment

To demonstrate the effectiveness of the proposed mechanism, we carried out experiments.

Fig. 7 shows the locomotion pattern, Fig. 8 shows the movement of the body, and Fig. 9 shows the movement over rubble.

No. 1

No. 2

No. 3

Fig. 7. Locomotion pattern

From Fig. 7, we can confirm that regular movement like that of a centipede is realized.

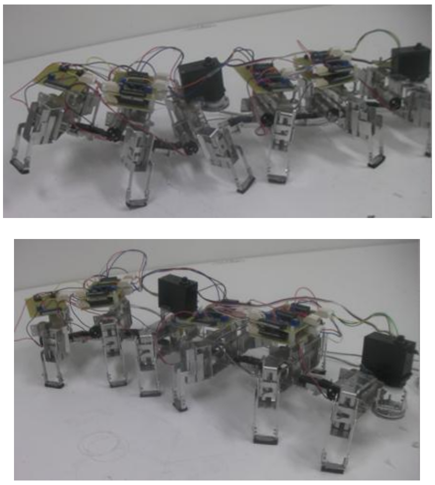

Fig. 8. Movement of robot body

From Fig. 8, we can find that by simply pulling the wire, many degrees of freedom of the body of the robot can be controlled passively and a centipede-like motion can be realized.

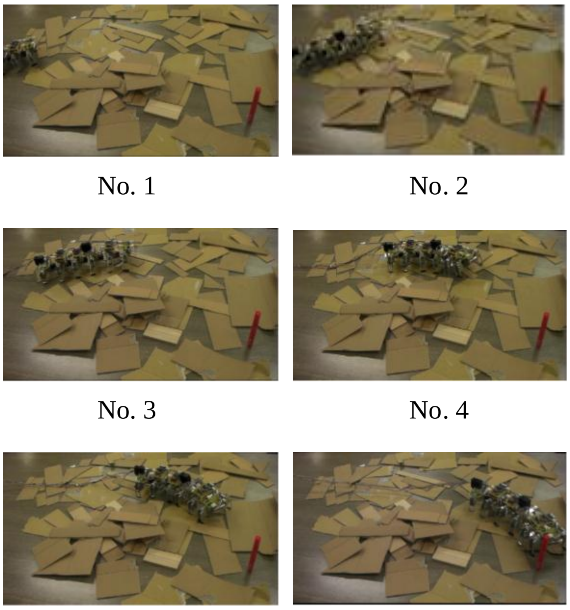

No. 1 No. 2

No. 3 No. 4

No. 5 No. 6

Fig. 9. Movement over rubble

From Fig. 9, we can confirm that the body of the robot moves adaptively to the environment and can move over rubble despite the fact that the operator controls only three wires and many five joints of the body moved autonomously by using the dynamics of the real world.

6 Conclusion

In this study, we designed the mechanism of a legged-robot for reducing the controller load by utilizing a passive mechanism. To design the robot, we focused on a centipede and observed its behavior by using a high-speed camera. To realize centipede-like motions by a simple mechanism, we propose the use of rubber joints. We employed a wire for controlling the body movements. To demonstrate the effectiveness of the proposed mechanism, experiments were conducted, and the behaviors required for moving over rubble were realized.

In a future study, we shall examine the use of the proposed mechanism in practical applications, for example, in a rescue mission for searching for survivors on large disaster sites.

6 Acknowledgment

This study was partially supported by the Ministry of Education, Culture, Sports, Science and Technology (MEXT) through a Grant-in-Aid for Young Scientists (B) (22700156, 2011).

References

[1] M. Arai, T. Takayama, S. Hirose, Development of Souryu- III: Connected Crawler Vehicle for Inspection i nside Narrow and Winding Spaces, Proceedings of IEE E/RSJ International Conference on Intelligent Robots a nd System, Vol.1, 52-57, 2004.

[2] J. Tanaka, K. Suzumori, M. Tanaka, T. Kanada, an d M. Mori, "A Mobile Jack Robot for Rescue Operati on" Proceedings of IEEE International Workshop on Sa fety, Security and Rescue Robotics, 99-104., 2005.

[3] R. Haraguchi, K. Osuka, S. Makita, S. Tadokoro, "The Development of the Mobile Inspection Robot for Rescue Activity, MOIRA2" Proceedings of 12th Intern ational Confence on Advanced Robotics, 498-505, 2005.

[4] H. Miyanaka, N. Wada, T. Kamegawa, N. Sato, S. Tsukui, H. Igarashi, F. Matsuno, Development of an u nit type robot [KOHGA2] with stuck avoidance abilit y" Proceedings of IEEE International Conference on R obotics and Automation, 3877-3882, 2007.

[5] E. Rohmer, K. Ohno, T. Yoshida, K. Nagatani, E. Konayagi, D. Tadokoro, "Integration of a Sub-Crawler s'Autonomous Control in Quince Highly Mobile Rescu e Robot" Proceedings of IEEE/SICE international Symp osium. on System Integration, 78-83, 2010.

[6] H. Maruyama, K. Ito, "Semi-autonomous snake-like robot for search and rescue" Proceedings of 8th IEEE international Workshop on Safety, Security, and Rescu e Robotics, 1-6, 2010.

The Seventeenth International Symposium on Artificial Life and Robotics 2012 (AROB 17th '12),
B-Con Plaza, Beppu, Oita, Japan, January 19-21, 2012

Construction of a sense of force feedback and vision for micro-objects:

Recreate the response and a sense of force of objects

T.Domoto

Graduate School of Computer Science and System Engineering
Kyushu Institute of Technology
680-4, Iizuka City, Fukuoka, Japan, 820-8502
dohmoto@mmcs.mse.kyutech.ac.jp

E. Hayashi

Department of Mechanical Information Science and Technology
Kyushu Institute of Technology
680-4, Iizuka City, Fukuoka, Japan, 820-8502
haya@mse.kyutech.ac.jp

Abstract. The purpose of this research was to develop a combined sense system that uses both force feedback and visual feedback to determine the shape of the microscopic features of a microsample. Efficiency in performing minute procedures would be improved if the operator could have a sense of force while using a manipulator. We used a cantilever to touch a minute object and obtain a reaction force from the degree of bending. We constructed a haptic device that gives a sense of that force to the operator when touching the sample with a cantilever. When the haptic device was used in simulations, the user could feel a force as if he had touched the sample.
Key words: force feedback, haptic interface, simulation.

1. Introduction

Technologies that can accurately perform minute work are now being sought for medical treatment and in the field of manufacturing semiconductors. Such minute work is improved by using micromanipulators, but their operation is difficult because the operator has no sense of force; he or she relies only on sight through a microscope. As a result, a person skilled in the use of this technology is needed for all minute work. The efficiency of minute work would be improved if the operator were able to have a sense of force while using a manipulator.

Here we describe the development of a more efficient system for minute operations. Our aim was to develop a system using not only the sense of sight through a microscope but also a sense of force from the manipulator. For this fundamental research, a system was created to assess the reaction force when a minute sample was touched. A cantilever was used to touch the sample, and the reaction force was obtained from the degree to which the sample bent. In addition, we used a haptic device and amplified the force feedback from a minute sample of a virtual object.

2. System Structure

2-1. System summary

The system structure is shown in Fig. 1a, and a schematic view is shown in Fig. 1b. This system consists of a microscope with an automatic x-y stage, a piezo stage, a feedback stage controller to control the x-y stage, a piezo stage controller, a haptic device for transmitting force feedback (Fig. 2), a cantilever (Fig. 3), and a PC via which the user can control and operate these components. The sample was fixed on the x-y stage by an injector (Fig. 4) and a holding pipette (Fig. 5). When the cantilever, which was fixed to the piezo stage, touched the sample, the operator could maintain the cantilever's position by obtaining the value of the reaction force through the interface. The resolution of the piezo stage is 1 nm.

Fig. 1a. Photograph of the system structure.

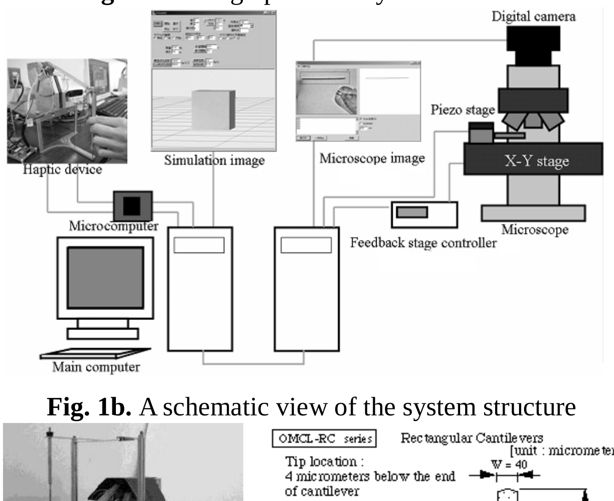

Fig. 1b. A schematic view of the system structure

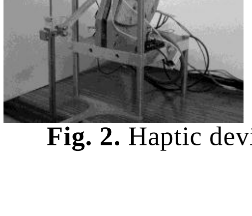

Fig. 2. Haptic device.

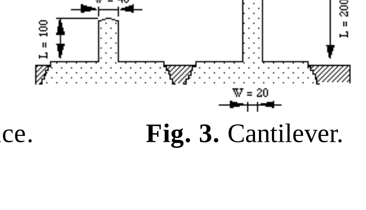

Fig. 3. Cantilever.

Fig. 4. Injector.

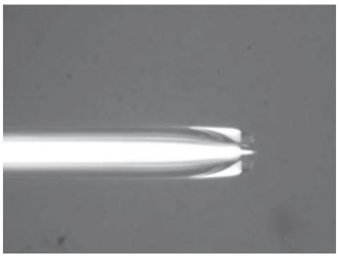

Fig. 5. Tip of holding pipette.

2-2. Haptic device

Figure 6 provides a diagram of the haptic device. It consists primarily of a rotor, a laser, and a position-sensitive device (PSD). We installed a coil on the rotor with a polarity magnet, which generated electromagnetic induction by an electric current and a magnetic force. The angle of the rotor can be measured by the laser and the PSD. The rotor was able to follow any input waveform.

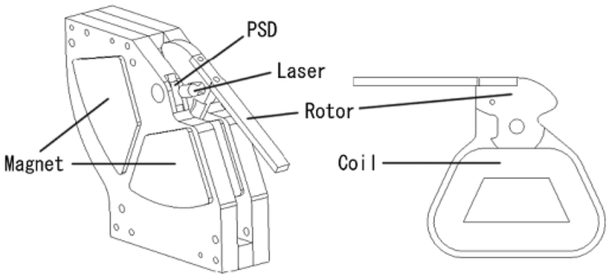

Fig. 6. Diagram of the haptic device.

The actuator is controlled by a servomechanism on the actuator. The system driving the actuator therefore consisted of four actuators: a microcomputer, an inputting AD/DA port, an outputting microcomputer, and a PC outputting order value. The system controls the actuator during each part of the process. Figure 7 shows the structure of the haptic device.

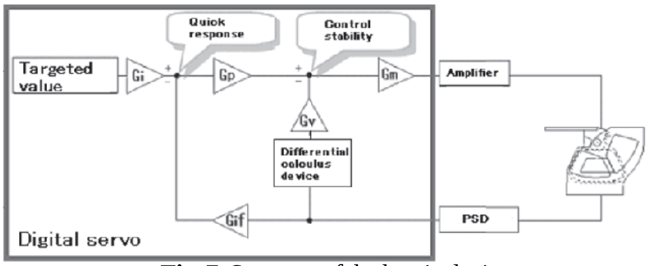

Fig. 7. Structure of the haptic device.

The actuator, whose actions are governed by the PD control, is operated through a digital differential calculus device. A transfer function for the quadratic function system shown in Fig. 8 is provided for the actuator servo system. The role of each parameter of the control system is to adjust the total offset to a master in Gi/Gif, to regulate the item viscosity/resonance point in Gp/Gv, and to regulate the total gain in Gm. Table 1 provides a list of the control parameters of the servomechanism system.

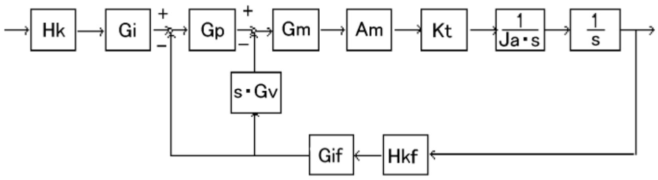

Fig. 8. Block diagram of the servomechanism system.

Table 1 Control parameters of the servomechanism system

Parameter	Reference	Unit
Hk	Position Voltage Constant	18.56 [V/rad]
Hkf	Position Voltage Feedback Constant	18.56 [V/rad]
Am	Amplifier Constant	0.8986 [A/V]
Kt	Torque Constant	0.6141 [Nm/A]
Ja	Moment of Inertia	0.000581 [kg·m]
Gi	Controller Input Gain	1
Gif	Position Feedback Gain	1
Gp	Position Gain	adjusted value
Gv	Velocity Gain	adjusted value
Gm	Manipulation Gain	1

3. Measuring the reaction force

The reaction force was used to calculate the force applied by the minute object. In this experiment, we touched the minute object with the cantilever shown in Fig. 3, and the reaction force was obtained based on the degree of bend of the cantilever. The layout of the experiment is shown in Figs. 7 and 8, and the environment of the experiment is shown in Figs. 9 and 10. Based on this experiment, we were able to determine the reaction force applied by the minute object.

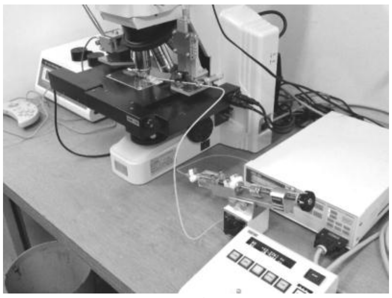

Fig. 9. Environment of the experiment.

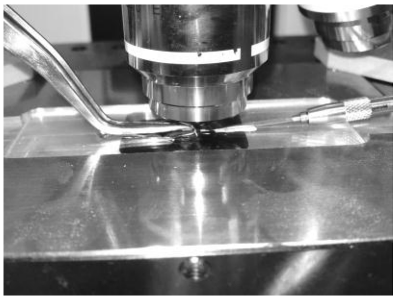

Fig. 10. Close-up of the environment of the experiment.

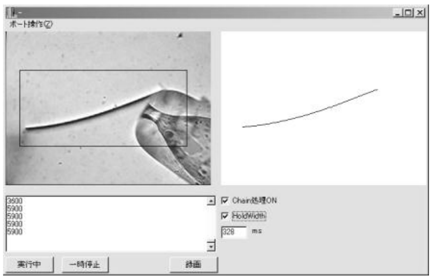

Fig. 11. Cantilever touching the tip of the holding pipette.

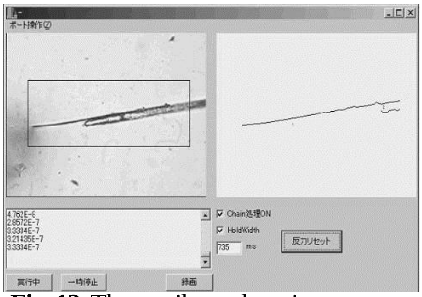

Fig. 12. The cantilever detection program.

Figure 11 shows the cantilever touching the tip of the holding pipette. Figure 12 shows the experiment that measures the reaction force of the downy hair. The image-processing speed of the cantilever was improved by the tracking process. The bend of the cantilever is assumed to be linear-elastic so that Hooke's law may be applied. The restoring force, F, of the bend of the cantilever is given by

$$F = kx \tag{1}$$

where *x* is the compression distance from the equilibrium position, and *k* is the spring constant.

4. Deforming the sample in simulation

In this study, we attempted to build a working system using a microscope, a haptic device, and a simulation. A fundamental element was simulating the deformation of a minute object. Figure 13 shows the graphical user interface (GUI) of the simulator. A graphic tool was created using OpenGL to draw the object and to choose the shape of the sample, for instance, a cube or sphere. The dynamic model of the sample consisted of a spring-mass array of mass points in both the vertical and horizontal directions. An example of the arrangement of mass points is shown in Fig. 14. When a force was applied at a mass point, the simulation calculated the speed of all mass points that had been affected. The image was renewed after every ten calculations.

We defined a spring as having a size but no weight, and a mass point as having a size, a weight, and a rigid body. An arbitrary mass object can be placed on a spring on a bitmap (Fig. 15). In addition, a sample can be seen from various viewpoints, and the deformation of the sample, which is impossible to observe by microscope, can be checked. The shape of this object can be either a cube or a sphere, and any point may be selected as a fixed point or an operating point.

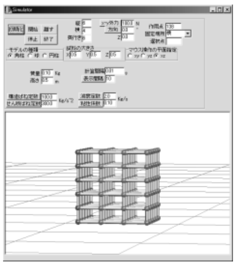

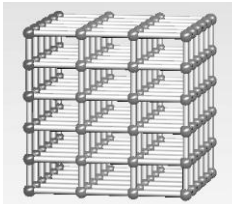

Fig. 13. Simulator.
Fig. 14. Arrangement of mass points

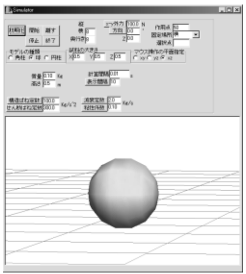

Fig. 15. Placing an arbitrary object on a bitmap.

The calculation method for the displacement of each mass point is based on Newton's equation of motion (Eq. 1) using the Euler method. A mass point is linked to an adjacent mass point at both ends of a spring. When the spring between the mass points is in the equilibrium position, the restoring force, F, is the sum of the elastic force of the construction spring and the shear spring, and the viscous force is given by

$$ma = \Sigma F \tag{2}$$

where m is mass and a is acceleration.

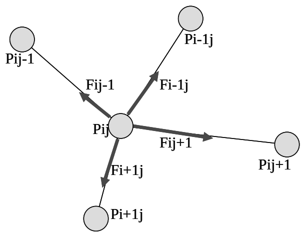

Fig. 16. Elasticity.

ΣF is the sum of the elastic force of the construction spring and shear spring, the viscous force, and the damping force. To obtain F, we divided the restoring force into $F_{damping}$, F_{spring}, and $F_{viscous}$. Equation 2 gives the following equations using the model shown in Fig. 16:

$$F_{spring} = \Sigma F_{ij} \tag{3}$$

$$F_{damping} = -C_d v_i \tag{4}$$

$$F_{viscous} = -C_v (v_i - v_j) \tag{5}$$

$$\Sigma F = F_{spring} + F_{damping} + F_{viscous} \tag{6}$$

where C_d is the damping factor, C_v is viscosity, and v_i and v_j are the velocities.

5. Characteristic measurements and a reappearance experiment for an object

Dynamic and static characteristics of the object were measured and then recreated using the haptic device. The object used this time was silicon manufactured by KYOUTOKAGAKU. The silicon sheet thickness was 2 or 3 [mm]. Each characteristic when silicon was stacked up was measured. Figure17 shows the response of the silicon and the response of the haptic device. Figure18 shows the reaction force of the silicon and the output power of the haptic device.

In the last program, parameters cannot be changed during operation. However, the response of the silicon used for the experiment in this case was could not recreate one parameter, and the sense of force was not linear. Therefore, the program was implemented so that parameters could be changed during operation.

Table 2 shows the frequency, constant of spring, and damping coefficient in each ectopic focus when the dynamic characteristic is recreated. Table 3 shows the frequency and constant of spring in each ectopic focus when the static characteristic is recreated.

The characteristics recreated by the haptic device, and the experiment was evaluated. In this experiment, there was a tendency for a touch feeling close to that of real silicon to be created when the static characteristic was recreated.

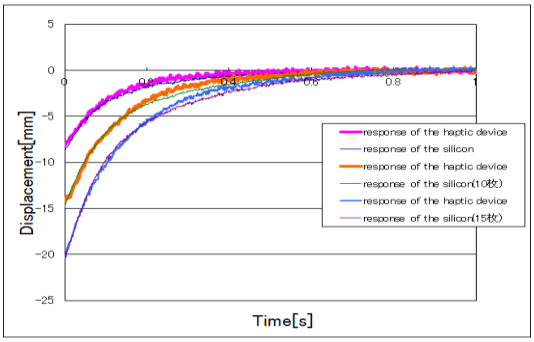

Fig. 17. Unit step response

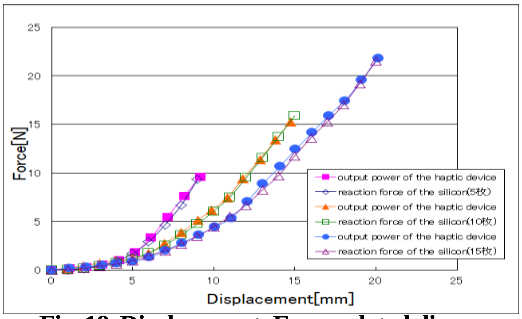

Fig. 18. Displacement_Force related diagram

Table 2. Haptic device parameter with a dynamic characteristic

<table>
<tr><th></th><th colspan="3">5 sheet</th><th colspan="3">10 sheet</th><th colspan="3">15 sheet</th></tr>
<tr><th>displacement[mm]</th><th>frequency[Hz]</th><th>constant of spring[N/mm]</th><th>damping coefficient</th><th>frequency[Hz]</th><th>constant of spring[N/mm]</th><th>damping coefficient</th><th>frequency[Hz]</th><th>constant of spring[N/mm]</th><th>damping coefficient</th></tr>
<tr><td>0</td><td rowspan="2">4.5</td><td rowspan="2">0.0272</td><td rowspan="2">1.6</td><td rowspan="3">4.2</td><td rowspan="3">0.0205</td><td rowspan="3">1.7</td><td rowspan="9">4</td><td rowspan="9">0.0174</td><td rowspan="9">1.7</td></tr>
<tr><td>1</td></tr>
<tr><td>2</td><td rowspan="2">4.5</td><td rowspan="2">0.0272</td><td rowspan="2">1.7</td></tr>
<tr><td>3</td><td rowspan="5">4.2</td><td rowspan="5">0.0205</td><td rowspan="5">1.8</td></tr>
<tr><td>4</td><td rowspan="6">4.5</td><td rowspan="6">0.0272</td><td rowspan="6">1.4</td></tr>
<tr><td>5</td></tr>
<tr><td>6</td></tr>
<tr><td>7</td></tr>
<tr><td>8</td><td rowspan="8">4.2</td><td rowspan="8">0.0205</td><td rowspan="8">1.3</td></tr>
<tr><td>9</td><td rowspan="8">4</td><td rowspan="8">0.0174</td><td rowspan="8">1.8</td></tr>
<tr><td>10</td><td rowspan="11" colspan="3"></td></tr>
<tr><td>11</td></tr>
<tr><td>12</td></tr>
<tr><td>13</td></tr>
<tr><td>14</td></tr>
<tr><td>15</td></tr>
<tr><td>16</td><td rowspan="5" colspan="3"></td></tr>
<tr><td>17</td><td rowspan="4">4</td><td rowspan="4">0.0174</td><td rowspan="4">1.4</td></tr>
<tr><td>18</td></tr>
<tr><td>19</td></tr>
<tr><td>20</td></tr>
</table>

Table 3. Haptic device parameter with a static characteristic

<table>
<tr><th></th><th colspan="2">5 sheet</th><th colspan="2">10 sheet</th><th colspan="2">15 sheet</th></tr>
<tr><th>disaplacement[mm]</th><th>frequency[Hz]</th><th>constant of spring[N/mm]</th><th>frequency[Hz]</th><th>constant of spring[N/mm]</th><th>frequency[Hz]</th><th>constant of spring[N/mm]</th></tr>
<tr><td>0</td><td rowspan="5">9.4</td><td rowspan="5">0.175</td><td rowspan="6">10.6</td><td rowspan="6">0.220</td><td rowspan="7">9.4</td><td rowspan="7">0.175</td></tr>
<tr><td>1</td></tr>
<tr><td>2</td></tr>
<tr><td>3</td></tr>
<tr><td>4</td></tr>
<tr><td>5</td><td rowspan="2">20</td><td rowspan="2">0.782</td></tr>
<tr><td>6</td><td rowspan="5">22.5</td><td rowspan="5">1.01</td></tr>
<tr><td>7</td><td rowspan="3">30</td><td rowspan="3">1.95</td><td rowspan="6">20</td><td rowspan="6">0.782</td></tr>
<tr><td>8</td></tr>
<tr><td>9</td></tr>
<tr><td>10</td><td rowspan="11" colspan="2"></td></tr>
<tr><td>11</td><td rowspan="5">30</td><td rowspan="5">1.95</td></tr>
<tr><td>12</td></tr>
<tr><td>13</td><td rowspan="8">30</td><td rowspan="8">1.95</td></tr>
<tr><td>14</td></tr>
<tr><td>15</td></tr>
<tr><td>16</td><td rowspan="5" colspan="2"></td></tr>
<tr><td>17</td></tr>
<tr><td>18</td></tr>
<tr><td>19</td></tr>
<tr><td>20</td></tr>
</table>

6. Conclusion

In the present study the characteristics of silicon were measured and recreated, and evaluations were carried out with regard to response and sense of force using a haptic device. The touch judging program of the haptic device and sample simulation was implemented. It was found that the spring constants differed greatly with regard to both dynamic and static characteristics in this experiment. The characteristics of various objects will be measured in the future, and The characteristics recreated

Future research should focus on building a system that allows a reaction force to be detected and shown more precisely. Such a system would make it possible to test smaller samples.

7. Acknowledgement

This research was partially supported by the Ministry of Education, Science, Sports and Culture, Grant-in-Aid for Scientific Research, 2011.

References

1. Noda R (2011) Construction of super-micro sense of force feedback and visual for micro objects. Kyushu Institute of Technology. Proceedings of the 15th International Symposium on Artificial Life and Robotics, Beppu, Oita, Japan, 2011

The Seventeenth International Symposium on Artificial Life and Robotics 2012 (AROB 17th '12),
B-Con Plaza, Beppu, Oita, Japan, January 19-21, 2012

Estimate of current state based on experience in POMDP for Reinforcement Learning

Yoshiki Miyazaki[1], Kentarou Kurashige[1]

[1] Muroran Institute of Technology, Hokkaido, Muroran 050-8585, Japan
(Tel: 81-143-46-5400, Fax: 81-143-46-5499)
(s1823084@mmm.muroran-it.ac.jp, kentarou@csse.muroran-it.ac.jp)

Abstract: Recently, reinforcement learning (RL) attracts attention. Because interaction with environment is important on RL, it is necessary to recognize state of robots more accurate. However, in real environment there is incompleteness on recognition by ability lack and noise of sensors. If recognition has incomplete, there is problem that robots cannot learn appropriately because robots cannot distinguish states that robots should originally distinguish. The model including such incompleteness is known as POMDP and we aim to solve the problem learning does not progress appropriately in POMDP. We pay attention to the experience of robots. When robots cannot identify current state uniquely, robots decide current state using current observation, previous recognition state and action. And, by memorizing this state information as internal state, recognizable state increases. In this way, robots can distinguish states which robots cannot distinguish in conventional method and learn appropriately. We show the effectiveness of proposed technique with simulation.

Keywords: Reinforcement Learning, Partially Observable Markov Decision Process, incomplete recognition

1 INTRODUCTION

Now, RL [1] is known as effective technique as one of technique to adapt to environment. RL also attracts attention as technique which is often used in actual robots. On RL, robots learn by interaction with environment. And sensors are necessary for interaction with environment. Robots recognize a situation as a state that robot faces by using sensors. So the recognition by sensors is important for learning.

In RL, most basically model of environment is Markov Decision Process (MDP) [2]. In this environment, it is assumed that the recognition of environment by robots is complete. In other words, robots have enough recognition ability to achieve tasks in MDP. But in real environment, because the ability of sensors is insufficient or sensors have noise, there is often incompleteness for recognition. So, recognized state does not accord with actual situation. Partially Observable Markov Decision Process (POMDP) [3] is model that deals with such incompleteness. In POMDP, robots may recognize different plural situations in real environment as same state. Because robot recognizes different situations as same state, there is possibility that robot cannot learn appropriately for task. So, there are some studies for environment on POMDP [4],[5].

In this paper, we pay attention to using past state and action. And we propose a system coping with incomplete recognition. In proposed system, robot recognizes a current state by using previous state and action. Not always robot recognizes state by using such technique, but robot recognizes current state by using previous state and action at the time that robot recognizes incomplete recognition. Therefore robot needs to recognize whether current state is incomplete recognition. We use experience of robots for recognition of incomplete recognition. In experience on robot, when there is difference on result of same action between same recognized state, incomplete recognition is likely to have occurred. In the case that there is difference from two results of same action on a recognized state, robot define internal state for the state by using previous state and action. And robot can distinguish a state thought to be incomplete recognition by using internal state. Therefore it is possible to consider POMDP to be MDP by using proposed method. And proposed system has four parts: Recognition part, Judgment of incomplete recognition part, Definition of internal state part, and Accumulation of experience part.

In this paper, at first we describe the summary and problems about recognition in POMDP on RL. Secondly we propose the technique of recognition using previous state and action. We will describe four parts of Recognition part, Judgment of incomplete recognition part, Definition of internal state part and Accumulation of experience part. Thirdly, we perform simulation that shows the effectiveness of proposed system. In simulation, we use the maze problem and adapt Q-learning[1] to agent. Moreover, we compare the proposed technique with normal recognition and complete perception. Finally, we describe conclusion and the future work.

2 PROBLEM OF RECOGNITION IN POMDP

2.1 Recognition using sensors on RL

The subjection of our research is a learning agent which has sensors. On RL, at each time period, the agent is in some state $s \in S$ (S is a set of states). But the agent recognizes a state that agent faces through sensors. On recognition based sensors, the agent decides a state by the combination of value of each sensor. Here, $o \in O$ (O is a set of observations) is an observation that agent recognizes through sensors and v_n are value of each sensor. o is expressed in eq.(1), and n is number of sensors agent has.

$$o = \{v_1, v_2, \ldots, v_n\} \tag{1}$$

In the case of the recognition with sensors, the observation is not usually equals to the state in POMDP. And there is a possibility that the agent recognizes two or more another states as a same observation. There are various factors including performance and property of sensors for this reason to cause these, and we think it is difficult to solve the disagreement in the state and observation using only sensors.

In this paper, in case that there is disagreement in the state and the observation, we call this situation as incomplete recognition. And, in case that the observation is same as the state, we call this situation as complete recognition.

2.2 Problem by the incomplete recognition on RL

On RL, agent learn appropriate action based on the observation. Therefor the observation is important. If agent is in incomplete recognition, agent tries to find appropriate action for an observation includes several states (Fig.1). Agent can not learn appropriately, in such case. But incomplete recognition does not become the problem always. When appropriate actions for states included in an observation are the same, agent can learn without problems. In fact, when the appropriate actions for each state included in an observation are different, it adversely affects for learning. In this way, when agent is in incomplete recognition, it is possibility that agent can not learn appropriately. And it is need to distinguish several states included in an observation for such agent.

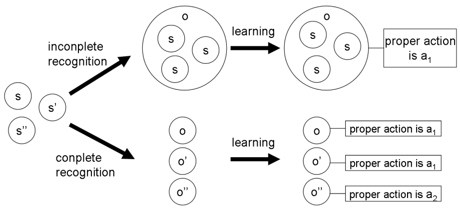

Fig. 1. The relationship of recognition and learning.

3 SUGGESTION OF RECOGNITION TECHNIQUE FOR POMDP

3.1 Estimate of state with previous recognized state and action

When incomplete recognition gives adverse affect for learning, agent should distinguish an recognition state (recognition state is state that agent finally decide) causing incomplete recognition as plural states by subdivision of recognizable state. So, when subdividing an recognition state that is causing the incomplete recognition, we focus on the pair of previous recognition state and action. Specifically when agent is in incomplete recognition at an recognition state, agent subdivides the recognition state by referring to the pair of previous recognition state and action (Fig.2). The subdivided observations are defined new internal state. And this internal state is held as knowledge by addition to X (X is a set of internal states). We define the internal state x in eq.(2). Here, $\hat{o}_t$ is an recognition state at time t, $\hat{o}_{t-1}$ is a recognition state that agent decide at time $t-1$, and a_{t-1} is an action agent takes in $\hat{o}_{t-1}$.

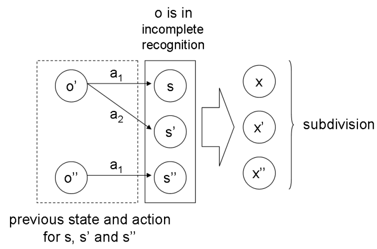

Fig. 2. The conception of estimate of state with previous recognized state and action.

$$x = \{\hat{o}_t, \hat{o}_{t-1}, a_{t-1}\} \tag{2}$$

Agent can recognize current state more particular by referring to previous recognition state and action. However, the number of the internal states that agent should experience increases, if agent subdivides an observation in all situation. It is not desirable that the number of the internal states increases for learning, because it takes much time to learn. In this paper, agent subdivides for the observation that may cause incomplete recognition. Therefore, it is need to judge whether the observation is incomplete recognition for agent. We think the observation includes plural states when a certain observation is incomplete recognition. And in this case, it is thought that different results are shown even if agent takes same action at the observation (Fig.3). Therefore, agent determines an observation that gains different result for same action as situation agent is in incomplete recognition. And we prepare the experience table to compare the results of actions. The proposed system has four original modules:

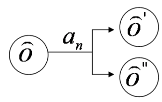

Fig. 3. The problem situation.

Recognition part to decide a internal state by using previous internal state and action, Judgment of incomplete recognition part to determine whether incomplete recognition occurs, Definition of internal state part to subdivide for observation in incomplete recognition, and Accumulation of experience part to saves experience information. And the proposed system also has two conventional modules: Learning part and Choosing action part. We show the construction of proposed system in Fig.4.

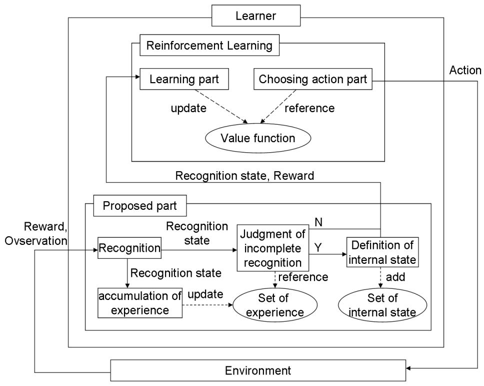

Fig. 4. The construction of proposed system.

3.2 Process of each module

3.2.1 Recognition part

In Recognition, agent decide a recognition state $\hat{o}_t$ by using current observation o_t and previous recognition state $\hat{o}_{t-1}$ and action a_{t-1}. And agent search the internal state x about $\{o_t, \hat{o}_{t-1}, a_{t-1}\}$ in set of internal state X. If agent find the internal state, agent decide x as $\hat{o}_t$. If agent can not fine the internal state, agent decide o_t as $\hat{o}_t$.

3.2.2 Accumulation of experience part

In Accumulation of experience, agent get the experience e as knowledge. This knowledge at time t is expressed in eq.3. And agent add this knowledge to set of experience E.

$$e_t = \{\hat{o}_{t-1}, a_{t-1}, \hat{o}_t\} \tag{3}$$

3.2.3 Judgment of incomplete recognition part

Agent judges whether an recognition state $\hat{o}_t$ is incomplete recognition in following procedures.

- Assume that a_t is an action in $\hat{o}_t$ and $\hat{o}_{t+1}$ is the result of action.
- Search the information about $\{\hat{o}_t, a_t, *\}$ in E
- Assume the found information as $\{\hat{o}_t, a_t, \hat{o}^{'}_{t+1}\}$
- Compare $\hat{o}_{t+1}$ with $\hat{o}^{'}_{t+1}$
- If $\hat{o}_t \neq \hat{o}_{t+1}$, agent judges that $\hat{o}_t$ is incomplete recognition.

3.2.4 Definition of internal state part

When agent subdivides a recognition state $\hat{o}_t$, a new internal state is defined in eq.2. And new internal state defined by eq.2 is add to set of internal state X.

4 SIMULATION USING PROPOSED SYSTEM FOR MAZE PROBLEM

4.1 Outline

We show the proposed system can distinguish the state enough to take task in POMDP through a simulation. We apply proposed system to an agent which recognizes state based on the sensor. And we apply maze problem to the agent with simulation. In the simulation, incomplete recognition happens when an agent decide a state by using only sensors. So the simulation is environment based on POMDP.

In the simulation, we define as one trial to reach a goal, and focus on the number of actions at each trial as the result. In addition, we prepare two agents for comparison. One is an agent deciding a state only with sensors which is same as sensors proposed system has. The other is an agent which has sensor that does not occur incomplete recognition. We unify other conditions for these three agents and apply maze problem and compare the results with these three agents.

4.2 Setting

We show the maze using the simulation in Fig.5. In Fig.5, we assume the coordinate at upper left square as (0,0), and lower right square as (2,2). The start position (●) is (0,2), and goal position ($\star$) is (2,2). In this simulation, agents fall into fatal incomplete recognition in the squares (0,1) and (1,1). Because appropriate action is difference in (1,0) and (1,1), we think it affects learning.

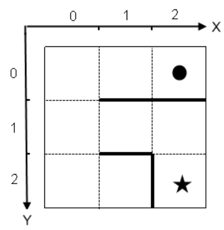

Fig. 5. The maze for simulation.

We prepare three agents (Agent-A, Agent-B, Agent-C). Agent-A and Agent-B has same four sensors. These sensors can recognizes whether there is a wall in front of sensors. Agent-A and Agent-B is set these sensors at vertically and horizontally. In addition Agent-A is applied proposed system. Agent-C own a sensor can know the coordinate in the maze And each agents select an action from four actions :move up, down ,left, right.

In this paper, we apply Q-learning to all agents as learning part. Agents learn based on eq.4 in Q-learning.

$$\begin{aligned} Q(s_t, a_t) \quad &\leftarrow \quad Q(s_t, a_t) + \alpha[r_{t+1} \\ &+ \quad \gamma \max_a Q(s_{t+1}, a) - Q(s_t, a_t)] \end{aligned} \tag{4}$$

$Q(s_t, a_t)$ is action value of a_t in recognized state s_t at time t. r_{t+1} is reward which agent gains in recognized state s_{t+1} at time $t+1$. α and γ are parameters ($0 \leq \alpha, \gamma \leq 1$). And we apply ε-greedy method to all agents as action selection part. When agent select an action, agent take random action by probability of ε and take greedy action by probability of $1-\varepsilon$. We show the parameters in Table 1.

Table 1. Setting for simulation

Reward(only a goal)	100
Total of trial	50
Initial value of Q-value	0.001
Size of maze	3×3
α	0.5
γ	0.7
ε	0.05

4.3 Result and Consideration

We show the result of the simulation in Fig.6. Fig.6 show the number of the actions for reaching the goal every trials for each agent. The X-axis expresses the number of the trials, and the Y-axis is the number of the actions that took for reaching a goal.

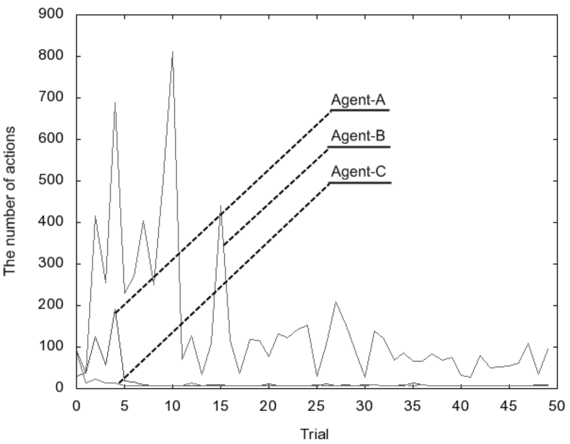

Fig. 6. Comparison of the number of actions each trial about Agent-A,B and C.

In this graph, the number of actions about Agent-B does not converge. Because Agent-B causes incomplete recognition in coordinate of (1,0) and (1,1), the agent can not learn appropriately. And the number of actions about Agent-B is bigger than other agents in all trials. Therefore, we say that incomplete recognition cases adverse affect to learning.

On the other hand, Agent-C does not cause incomplete recognition. Therefore the number of actions about Agent-C is less than Agent-A and B. Agent-C finds the most suitable route to goal by approximately five trials.

We focus on Agent-A. There are trials that there is more number of actions than Agent-C in early period of learning. However, the number of actions about Agent-A and Agent-C is almost same after 7 trials, and we think the proposed system works effectively for incomplete recognition. In proposed system, when agent causes incomplete recognition in coordinate of (1,0) and (1,1), agent distinguishes these state by subdividing the recognized state with previous state and action. Therefor, agent can distinguish enough to learn appropriately.

5 CONCLUSION

In this paper, we focus on the problem of RL in POMDP. There is a problem that agent cases incomplete recognition. And it is possibility that incomplete recognition cases adverse affect for learning. Therefor, agent can not learn appropriately in POMDP. We pay attention to previous recognized state and action for solving this problem. We proposed the recognition technique using not only sensors but also previous recognized state and action. In this way, agent can subdivide the recognized state and learn appropriately. And we proposed the system applied proposed technique to RL. We applied the maze problem to show the usefulness of the proposed system with simulation and we compared with three agents. By this simulation, we showed effectiveness of proposed system for incomplete recognition. In the future, we will apply the proposed system to actual robot.

REFERENCES

[1] Richard S. Sutton and Andrew G. Brato (1998), Reinforcement Learning. The MIT Press

[2] Daniel W. Ttroock (2005), An Introduction to Markov Process, Springer

[3] L.P. Kaelbling, M.L. Littman, A.R. Cassandra (1998), Planning and acting in partially observable stochastic domains. Artificial Intelligence Journal 101: 99-134

[4] E.J. Sondik (1978), The optimal control of partially observable Markov processes over the infinite horizon: Discounted costs. Operations Research 26(2):282-304

[5] K.J. Astrom(1965), Optimal control of Markov decision processes with incomplete state estimation. Journal of Mathematical Analysis and Applications 10:174-205

The Seventeenth International Symposium on Artificial Life and Robotics 2012 (AROB 17th '12),
B-Con Plaza, Beppu, Oita, Japan, January 19-21, 2012

Evolution of locomotion in a simulated quadruped robot and transferral to reality

Kyrre Glette[1], Gordon Klaus[1], Juan Cristobal Zagal[2], and Jim Torresen[1]

[1]University of Oslo, Norway
[2]University of Chile, Chile
[1]{kyrrehg, gordonk, jimtoer}@ifi.uio.no, [2]jczagal@ing.uchile.cl

Abstract: In this paper, we study the suitability of using simulation in the evolution of locomotion in a quadruped robot. The goal of the evolution is to design a control system that produces fast gaits. We evolve gaits in simulation, and then the best controllers are transferred into the real custom built robot and compared with their simulated versions. The results show effective locomotion, with a 1.8 times improvement in speed over earlier results. Finally, we investigate some measures to reduce the difference between simulated and real locomotion.

Keywords: robotics, simulation, genetic algorithms

1 INTRODUCTION

It can be a challenging task to manually design and optimize a control system that enables a robot to walk, particularly an unconventional robot in a complex environment. Evolutionary design allows us to automate this otherwise time consuming and intellectually demanding process [1, 2]. Furthermore, it provides a general procedure that can be applied to various robot morphologies, and can even be used for adapting to changes in the environment or in the robot itself such as damage to or loss of limbs [3]. Importantly, evolution is unconstrained by engineering conventions, and is thus able to find solutions that a human is unlikely to find.

For time-consuming tasks like robotic locomotion, it becomes impractical to perform large-scale evolutions involving tens of thousands of evaluations on the target hardware, due both to time needed and to mechanical wear. For example, in [4], a total of 1217 evaluations were performed on the target hardware, spread across 7 different learning algorithms; and as those authors point out, this number is much smaller than desirable in terms of achieving both high quality results and statistical significance, and certainly took a great deal of time to carry out. (See [5] for another such example.) To overcome this issue, evaluations can instead be performed in a simulator. With sufficient CPU power, many individuals can be evaluated in simulation in the time it would take to evaluate one in reality, while at the same time eliminating mechanical wear and unreliable human intervention.

Due to unavoidable inaccuracies in the simulator, one encounters what is known as the "reality gap" [6], that is, a difference in performance between the simulation and the real system. Despite this problem, reasonable-quality solutions can still be found by evolution which at least qualitatively reflect the behavior predicted by simulation when they are transferred to reality. However, tuning the simulator to reduce the reality gap should do more than just make designs more transferable; we expect it will allow simulated agents to cope with and exploit otherwise inaccurately or completely unrepresented dynamics of the system, thus reshaping or opening up new territory for evolution to explore. Several interesting approaches are currently being explored for dealing with the issue of the reality gap [7, 8, 9, 10].

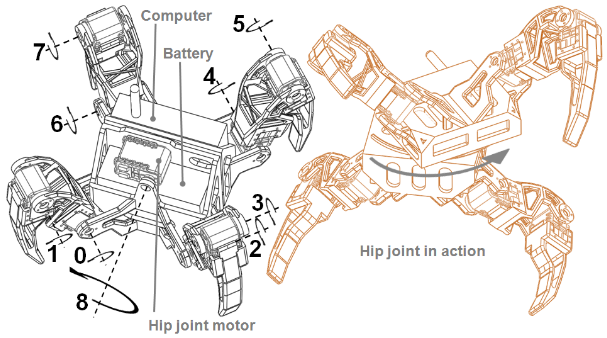

Fig. 1: Schematic view of the robot with the nine joints and associated servos labeled.

In this work, we investigate the suitability of using simulation in the evolution of locomotion in the QuadraTot quadruped robot. The robot has some unconventional characteristics, such as limited motion of the legs and a hip joint allowing the body to twist; see Fig. 1. Given this hardware, the goal of evolution is to design a control system that produces the fastest gait – i.e., the gait that results in the greatest distance covered in a fixed time period. The best controllers that come out of this process are then transferred into the real robot and compared with their simulated versions. Finally, we investigate some measures to reduce the difference between simulated and real locomotion.

2 IMPLEMENTATION

The QuadraTot robot, pictured in Figs. 1 and 2, has 9 joints: two in each leg and one at its center, each actuated by a Dynamixel AX-18A (AX-12A in the "knee" joints) servo. Fully extended, it measures 68 cm across; crouched, 34 cm. With the power supply separate from the body in order to

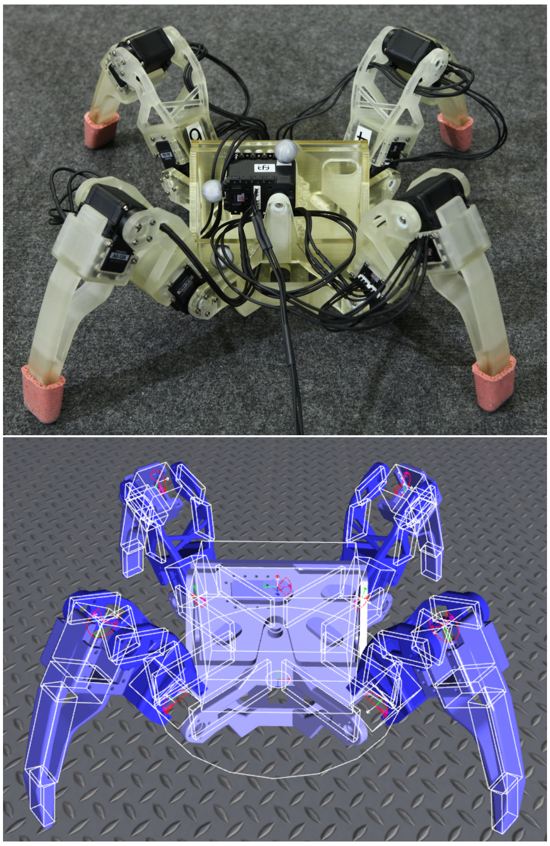

Fig. 2: The robot in reality and in simulation. Note the spherical markers for motion capture on the real robot. The white lines show the shapes for the simulation model.

minimize the strain on the relatively weak servos, the robot weighs 1.4 kg. The body parts[1] were printed on the Objet Connex 500 3D Printing System. One feature was added beyond the original design of the robot: silicone rubber "socks" were attached to its feet to improve traction.

To simulate the dynamics of the QuadraTot robot, we employed the NVIDIA PhysX physics simulation software library. PhysX provides accurate approximations of 3D rigid body motions, collision detection, and motorized joints, to name a few of the features relevant to our work. We built a model of the robot in PhysX to capture the salient aspects of its design such as the lengths of its body parts, positions and types of its joints, and the masses and rough shapes of its parts. The building blocks for the part shapes were boxes of various sizes and orientations. A detailed 3D mesh was presented using OpenGL to make visualization of the simulation more appealing and intuitive. The shapes and the overlying mesh can be seen in Fig. 2. The servos were modeled as motorized revolute joints, where the motor force was proportional to the difference between the actual and target angle; joint parameters were calibrated by observing the response of the real servos.

[1]Available online at `http://creativemachines.cornell.edu/evolved-quadruped-gaits`

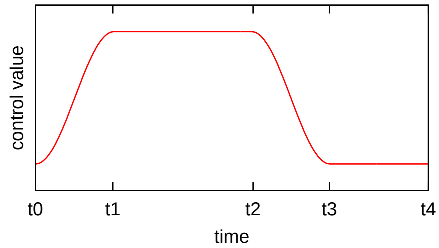

Fig. 3: The motor control function.

To control the motors in each of the robot's joints, we implemented a simple periodic control system consisting of a parameterized smoothed pulse, illustrated in Fig. 3. All controllers operate at the same frequency, but have different curve parameters, as well as individual phase shifts, ϕ. The *attack* parameter decides the time between t_0 and t_1, $pause_0$ the time between t_1 and t_2, *decay* the time between t_2 and t_3, and $pause_1$ the time between t_3 and t_4. The controller output is further parameterized by selecting the *center angle* for the pulse, as well as the *amplitude*.

Our reason for choosing such a simple system is threefold: First, the control system is not the focus of this work; second, in nature, locomotion on flat ground is observed to involve simple periodic motion; and third, the relatively small number of parameters reduces the size of search space for the genetic algorithm (GA), thus speeding up evolution.

For the evolutionary runs, we used the Simple GA method of the GALib software library. The fitness value for the experiments was calculated as the average speed of the robot during the evaluation, i.e., the total distance traveled divided by the simulated evaluation time. The joint parameters were encoded for each of the 9 joints in a binary genome with a total length of 314 bits. A population of 200 individuals was evolved for 300 generations. The bit-flip mutation probability was set to the inverse of the genome length. One point crossover was used with a probability of 0.2.

To observe the motion of the real robot, we employed an infrared camera-based NaturalPoint OptiTrack motion capture system consisting of 8 cameras. Four reflective markers were placed on the robot core to identify its motion. The position of one of these markers, sampled at 60Hz, was logged for the experimental results in the next section.

3 EXPERIMENTAL RESULTS

Where possible, we set simulator parameters to exactly known values, such as the force of gravity and the masses and dimensions of body parts. We set joint angle limits to constrain the motion to a range consistent with the physical robot: the inner joints could swing between -106°and 75°, the outer joints between -141°and 125°, and the hip joint between -53°and 53°. Joint motor forces were set to a very large value. We guessed, rather than measured, the coefficients of static and dynamic friction to both be 1.0. Finally, we chose values for the skin width (i.e., the depth to which

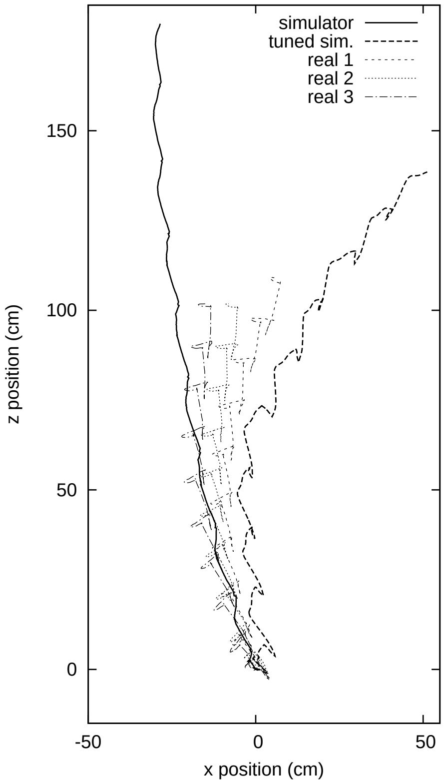

Fig. 4: Horizonal position plot, gait 1 over 10 seconds.

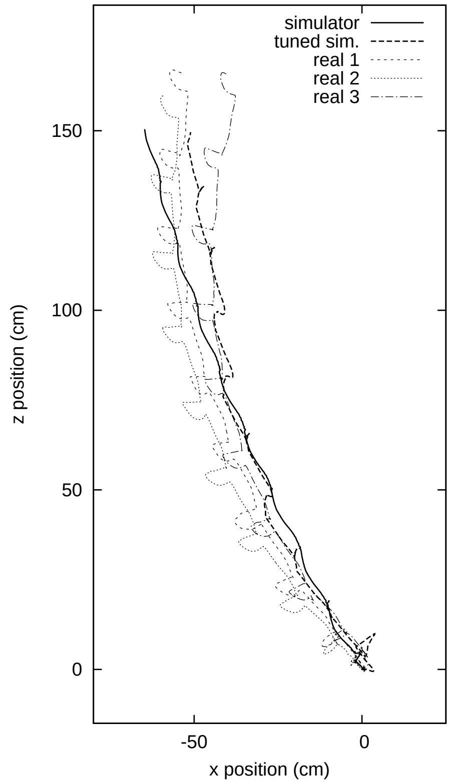

Fig. 5: Horizonal position plot, gait 2 over 10 seconds.

objects are allowed to interpenetrate before being considered to have collided), the joint constraint solver iteration count, and the simulator time step as recommended by the PhysX documentation and from prior experience to 0.05 cm, 200 iterations, and $\frac{1}{60}$ s, respectively.

With the simulator thus configured, we ran the GA to produce some gait patterns, and selected two of the fittest gaits from the final generation based on their qualitatively different strategies. The selected gaits were transferred into the real robot and their positions were recorded[2] for a period of 10 seconds. The resulting gait speeds are compared in Table 1. We then tuned the simulator as an initial attempt to reduce the reality gap for these two gaits. Both static and dynamic friction coefficients were reduced to 0.4. Also, to reproduce a perceived differential slipping tendency in the real robot's feet, anisotropic friction was added such that the feet would slip more easily from side to side (friction coefficients set to 0.1 in this direction) than front to back (friction coefficients set to 0.8 in this direction). Figs. 4 and 5 compare the real and simulated (both before and after tuning) motions for these gaits.

Table 1: Evolved gait speeds

gait	simulated	real (avg 3)
gait 1	18.3 cm/s	10.5 cm/s
gait 2	16.4 cm/s	17.8 cm/s
best in [4]	NA	9.7 cm/s

4 DISCUSSION

We observe from the experiments that the GA found promising gaits given the robot design and the imposed restrictions. The gaits shown in Figs. 4 and 5 employ two different strategies that could be similar to what a human designer might implement: the former is reminiscent of a quadruped animal; and the latter uses a worm-like locomotion strategy where two of the legs serve mostly as support. However, it appears that the solutions could be further tuned to improve performance. The parameter-based model imposed several constraints, including the amount of rotation possible in each joint, thus limiting the range of motion of the limbs. If a greater range of motion were allowed, this would result in both a larger search space and the possibility of exceeding physical limitations; however, the simulator-based approach would be more suitable for this than risking invalid combinations on the target hardware. We noticed that the core joint of the robot was not exploited noticeably in the evolved gaits. This may be due to the fact that its movement was restricted due to frequent motor overload on the real robot. A better simulation of the allowed forces could open up a path towards higher quality gaits.

The observed locomotion speeds were larger than those in found by previous online evolution experiments. Our best

[2] Gait videos: `http://folk.uio.no/kyrrehg/quad`

gait in reality achieved 17.8 cm/s, whereas highest speed found by [4] was only 9.7 cm/s. This difference could be explained by the different control systems and their parameterization or by the larger number of evaluations performed in the evolutionary search with the simulator. Additionally, it should be noted that there are some differences in the experimental setups, in particular with regard to the surface friction and the material used for coating the robot feet, as well as some differences in servo models.

As expected, we observed a difference between the simulated robot behavior and the behavior in the real robot, although it was not as large as anticipated. From the observations of the first gait, the qualitative impression of the behavior is the same, but the real robot turns faster. It seems that this is because of differences in friction between the simulator and reality, which might also account for the more jagged trajectory observed in the position plot. The reality gap observed in the second gait was smaller; although the trajectories were not identical, there was little impact on the final position. We suspect that friction played a smaller role in this gait due to the different contact motion between the legs and the surface, and the initial results from tuning the simulator support this claim. These results indicate that the simulator gives a fairly realistic model of the real robot and that additional tuning is likely to further improve the realism.

We observed during the experiments on the real robot that, after several runs, the motors seemed to lose energy, eventually shutting down with an overload error. We tried to mitigate this problem by disconnecting the power between runs. This should be addressed in future experiments by carefully tuning the model of the motor strengths in the simulator and possibly also instructing the evolution to discourage locomotion which stresses the motors too much.

5 CONCLUSION AND FUTURE WORK

We have developed a simulation environment for an unconventional robot design, where learning has previously only been performed on the real robot. This has allowed design of locomotion through a GA in which evaluations were performed in a simulator, saving time, resources, and wear associated with running EAs on real robots. The results using a simple parametric approach are better than an earlier approach using real world evolution for parametric gaits as well as HyperNEAT. A promising path of future work would be to investigate the use of more sophisticated control algorithms on the proposed evolutionary setup, for even more efficient locomotion. Some of the evolved gaits suffer from the reality gap when transferred to the real robot, whereas others perform closer to the simulated behavior. Tuning of some simulator parameters seems to be one way to improve transferral to reality. Future work should investigate various mechanisms for facilitating the transfer from simulated solutions to real ones, including more sophisticated motion capture of the robot limbs, better and more automated tuning of the simulator, as well as evolving for robustness, e.g. by introducing noise into the simulation.

ACKNOWLEDGEMENTS

The authors would like to thank Jason Yosinski for sharing experience from earlier experiments on the robot as well as providing helpful comments on the paper.

REFERENCES

[1] S. Doncieux, N. Bredeche, and J.-B. Mouret, "Exploring new horizons in evolutionary design of robots," in *Proceedings of the IEEE/RSJ international conference on Intelligent robots and systems (IROS)*, 2009.

[2] I. Harvey, P. Husbands, D. Cliff, A. Thompson, and N. Jakobi, "Evolutionary robotics: the sussex approach," *Robotics and Autonomous Systems*, vol. 20, pp. 205–224, 1997.

[3] H. Lipson, J. C. Bongard, V. Zykov, and E. Malone, "Evolutionary robotics for legged machines: From simulation to physical reality," in *Proceedings of the 9th Int. Conference on Intelligent Autonomous Systems*, pp. 11–18, 2006.

[4] J. Yosinski, J. Clune, D. Hidalgo, S. Nguyen, J. C. Zagal, and H. Lipson, "Evolving robot gaits in hardware: the hyperneat generative encoding vs. parameter optimization.," in *Proceedings of the 20th European Conference on Artificial Life*, pp. 890–897, 2011.

[5] V. Zykov, J. C. Bongard, and H. Lipson, "Evolving dynamic gaits on a physical robot," in *Proceedings of Genetic and Evolutionary Computation Conference, Late Breaking Paper, GECCO*, 2004.

[6] N. Jakobi, P. Husbands, and I. Harvey, "Noise and the reality gap: The use of simulation in evolutionary robotics," in *Advances in Artificial Life: Proc. 3rd European Conference on Artificial Life*, pp. 704–720, Springer-Verlag, 1995.

[7] S. Koos, J.-B. Mouret, and S. Doncieux, "Crossing the reality gap in evolutionary robotics by promoting transferable controllers," in *Proceedings of the 12th annual conference on Genetic and evolutionary computation*, GECCO '10, pp. 119–126, 2010.

[8] J. Zagal, J. Ruiz-del Solar, and P. Vallejos, "Back to reality: Crossing the reality gap in evolutionary robotics," in *Proceedings of IAV 2004, the 5th IFAC Symposium on Intelligent Autonomous Vehicles, Lisbon, Portugal*, 2004.

[9] J. C. Bongard, V. Zykov, and H. Lipson, "Resilient Machines Through Continuous Self-Modeling," *Science*, vol. 314, no. 5802, pp. 1118–1121, 2006.

[10] J. Bongard, "Synthesizing physically-realistic environmental models from robot exploration," in *Proceedings of the 9th European conference on Advances in artificial life*, ECAL'07, pp. 806–815, 2007.

The Seventeenth International Symposium on Artificial Life and Robotics 2012 (AROB 17th '12),
B-Con Plaza, Beppu, Oita, Japan, January 19-21, 2012

A study on the use of tactile instructions for developing robot's motions

Fransiska Basoeki[1,2], Fabio DallaLibera[1,2], Takashi Minato[2,3], and Hiroshi Ishiguro[1,2]

[1] Graduate School of Engineering Science, Osaka University, Toyonaka, Osaka 560-8531, Japan
(fransiska.basoeki@irl.sys.es.osaka-u.ac.jp)
[2] JST ERATO Asada Project, Suita, Osaka 565-0871, Japan
[3] ATR Hiroshi Ishiguro Laboratory, Kyoto 619-0288, Japan

Abstract:
Developing motions for humanoid robots is a time consuming task. However, we note that sport or dance instructors can easily adjust their students' postures by simple touches. This suggests the possibility of exploiting touch for motion development, and allows us to propose a methodology based on this concept. This requires defining how the robot should interpret user's touches. We propose a supervised learning approach for coping this issue, and verify its feasibility experimentally. We then study the data collected by the algorithm, and show that the system is usable both for motion development and as a tool for studying human-robot tactile communication. In particular, considerations on the sparsity that characterize the whole process are presented, and policies for an efficient interpretation of tactile instructions are drawn.

Keywords: humanoid robot, human-robot interaction, touch, tactile communication

1 INTRODUCTION

Humanoid robots often have a high number of degrees of freedom, that makes developing motions challenging. Having robots to do automatic learning of the motion is often impossible. To compensate this, various ways of transferring human knowledge into the robot exists in literature. When the task is known in advance, the programmer may insert his knowledge in the robot's control algorithms, such as in the design of a Central Pattern Generator structure [1]. When the task is only partly known in advance, the programmer can provide modules or motion primitives, as in the Mimesis model [2], while the final user specifies the task motion by composing these elementary modules. Finally, the task may be unknown a priori and in such case the final user must be able to transfer its knowledge to the robot directly, as in Motion retargetting [3] and Kinesthetic demonstration [4].

Our proposed method, Teaching by Touching (TbT), aims to tackle the third case. The idea is to mimic the way sport or dance instructors use touch to correct their students' movements. In conventional approaches [4], robots are completely passive during the learning process. The user is required to force the posture of the robot to the desired one, by application of the necessary forces. Conversely, we propose to equip the robot with knowledge on the meaning of touch instructions, and give it an active role in interpreting the given touch for moving according to the estimated user's intention.

The main issue of such a system lies in the definition of how the touch instruction should be interpreted by the robot. Different approaches exist. The first is to force the user to learn and use a fixed protocol. In this case the robot interpretation algorithms can be very simple. It is sufficient to interpret the instructions according to the mapping. However, the user needs to remember which touch instruction brings the robot to his desired posture, and this may be difficult for inexperienced users. The other way is modeling the way human's communicate through touch. In this case the user can just intuitively provide a touch instruction and the robot will try to interpret the meaning based on all of the available information.

Our system takes the second approach, as explained in the following Section. Section 3 will present the hardware and the system we developed, which can be used both for motion development and for studying the mapping between instructions and desired robot responses. The ability of studying the mapping is important, because it allows extraction of general criteria for the interpretation of tactile instructions, that can be used for the future design of better tactile instruction interpretation algorithms. Section 4 will conclude the paper by summarizing the main results.

2 ALGORITHM

In order to build a model of the mapping between touch instructions and desired responses, data collection of how human interpret touch is necessary. Our system collects these data online, during the motion development itself. In this way no initial model is required, and the model can be progressively refined as the user interacts with the robot.

Fig.1 schematizes the data collection methodology. When the user applies a touch instruction and the robot takes a wrong interpretation, the user notifies the robot that the interpretation is wrong, and shows the correct interpretation by manually moving the robot to the pose as he expected.

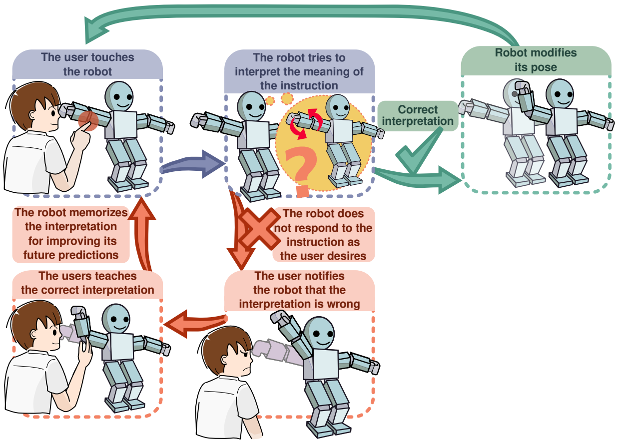

Fig. 1. Teaching by Touching motion development process.

The robot records this example of touch instruction and corresponding desired response into a database, and uses it for improving subsequent interpretations.

The database of collected data is taken as input by a Kernel regression algorithm, used for the computation of the expected meaning of the instructions received. Formally, the input $I \in \mathbb{R}^{n+m+o}$ consists of the touch sensor information $\bar{I} \in \mathbb{R}^n$, where n is the number of sensors, and the context of the robot $\check{I} \in \mathbb{R}^{m+o}$, included becaus it could influence the correct interpretation of the tactile instruction. In our implementation, the context is given by the current position of the m motors and $o = 2$ accelerometer values that represent the robot's spatial orientation. The output is a robot response, properly a rotation angle for each of the motors $M_* \in \mathbb{R}^m$.

The output of the algorithm is defined as $M_* = \sum_{i=1}^{E} \omega(I_*, I_i) M_i$ where E is the number of examples in the database, I_* is the current input from the sensors, I_i is the i-th example input, M_i is the i-th example posture change, and $\omega(I_*, I_i)$ is a kernel function, defined as

$$\omega(I_*, I_i) = \begin{cases} 0 & if\ \exists s : s \in \Psi_i \wedge s \notin \Psi_* \\ \dfrac{\prod_{s\in\Psi_i} \bar{I}_*^{(s)}/\bar{I}_i^{(s)}}{1+\sqrt{\|\check{I}_* - \check{I}_i\|_2^2 + \sum_{s:\notin\Psi_i} (\bar{I}_*^{(s)})^2}} & otherwise \end{cases} \tag{1}$$

with $\bar{I}_i^{(s)}$ denoting the input from the s-th tactile sensor and Ψ_i the set of sensors pushed in the i-th example. This kernel assures that when the sensors are pushed further the joint rotation angles are larger. Its denominator has the role of reducing the influence of the examples that present a context strongly different from the current context $\check{I}_*$. The condition on the set Ψ_* imposes to ignore all the examples relative to the pressure of touch sensors not being pressed in I_*.

The output of the algorithm M_* is used to modify the motion. In particular, the motion of the robot is defined as a set of keyframes F_k that specify the position of all the motors for a certain time t_k of the motion (positions for times $t_k < t < t_{k+1}$ are obtained by linear interpolation of F_k and F_{k+1}). After selecting a time instant t on a GUI, the users can touch the robot, and modify its posture at time t from F_t to to $F_t + M_*$ by simple touches.

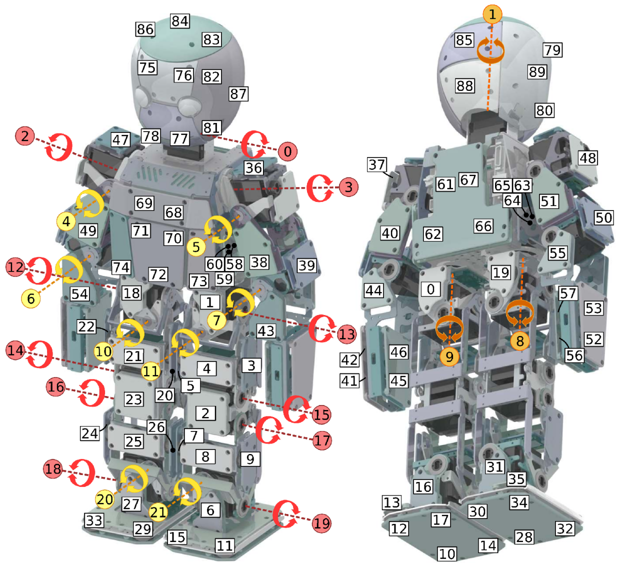

Fig. 2. Diagram of M3 Neony's motors and sensors.

3 EXPERIMENT

To verify the feasibility of the approach, we requested four people that never used the TbT system to develop a motion based on the first half of *Algorithm Exercise*, a dance from a Japanese TV show. The users had a reference motion video, but were allowed to decide when they are done developing the motion.

3.1 Hardware

The experiments were performed with a humanoid robot capable of recognizing touch, M3-Neony [5], a humanoid robot of small size equipped with a high number of tactile sensors developed as a suitable platform for tactile interaction. M3-Neony features 22 41KgF·cm servomotors, 90 tactile sensors (shown in Fig. 2), 3 accelerometers, 2 gyroscopes, 2 cameras and 2 microphones. The tactile sensors are composed of photointerruptors that translate the change of the force applied to the robot into a change in the light received by a phototransistor, as shown in Fig. 3. The experimental setup can be seen in Fig. 4. In particular, a pedal is used to notify the robot that its tactile interpretation is wrong, and allows the user to start providing the correct interpretation, that the robot stores as a (I_i, M_i) couple.

3.2 Results

All the users that attended the experiment performed the task with the proposed system without difficulties, or need for assistance, showing that the system reveals itself to be

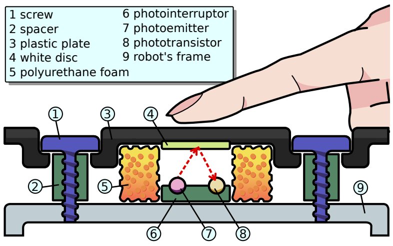

Fig. 3. Schema of tactile sensor structure of M3-Neony.

intuitive for first time users. The development time for the four users was, respectively, 221, 222, 176 and 476 minutes. Direct inspections of video recordings of the interaction show that users spent much time for robot stabilization, beyond our expectations. This confirms experimentally the importance of applying self stabilizing techniques, as the ones in [6], even for the development of quasi-static motions. Future works will introduce the concept of motion stability in the interpretation of tactile instructions, to allow the robot interpret the user's desire of making the robot balanced and let the robot compute the necessary adjustments.

One of the advantages of the systems is, as previously stated, the possibility of studying features of the way users employ touch for teaching. One of the main features that can be noticed by direct data inspection is the sparsity in the tactile interpretation taught by the users. In practice, users mainly touched few sensors and associated interpretations that involve the movement of few motors. As a more quantitative analysis, Table 1 reports the mean over the examples of the Gini index for the sensors ($G(\bar{I}_i)$) and for the motors ($G(Mi)$), $1 \leq i \leq E$.

This strong sparsity suggests us that the mapping between sensors inputs $I_i \in \mathbb{R}^n$ and motors $M_i \in \mathbb{R}^m$ could be sparse as well. To verify this hypothesis, we approximate the mapping with a linear function, and study the effect of enforcing sparsity in the mapping. More specifically, let us consider M_i, $1 \leq i \leq e$. Let us train a linear predictor $B_e \in \mathbb{R}^{m \times n+1}$ such that $M_i \approx B_e \left[\begin{array}{cc} 1 & \bar{I}_i \end{array} \right]^T$ by setting the k-th row of

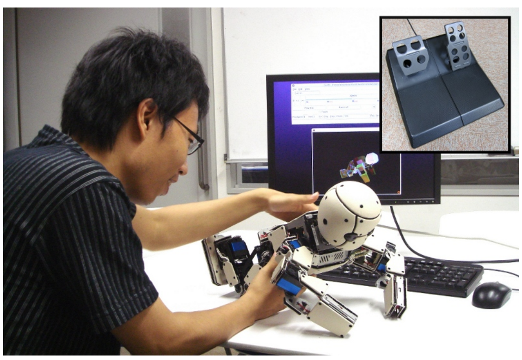

Fig. 4. Experiment environment, inset shows the pedal.

Table 1. Gini Index

	A	B	C	D
$avg_{1 \leq i \leq E} < G(\bar{I}_i)$¿	0.96	0.90	0.98	0.92
$avg_{1 \leq i \leq E} < G(Mi) >$	0.82	0.78	0.87	0.70

$B_e^{(k)}$ as $[b_e^{(k)} \beta_e^{(k)}]$, with $b_e^{(k)} \in \mathbb{R}$ and $\beta_e^{(k)} \in \mathbb{R}^n$ minimizers for the cost function

$$\frac{1}{2N} \sum_{i=1}^{e} \left(M_i^{(k)} - b_e^{(k)} - \beta_e^{(k)} \bar{I}_i \right)^2 + \lambda \left[(1-\alpha) \frac{1}{2} \|\beta_e^k\|_2^2 + \alpha \|\beta_e^k\|_1^2 \right] \quad (2)$$

where $M_i^{(k)}$ is the rotation for the k-th motor in M_i, $\|.\|_2$ denotes the Euclidean norm, $\|.\|_1$ the ℓ_1 norm, $\alpha, \lambda \in \mathbb{R}$ are constants. We note that, as $\alpha \to 0$ the minimization resembles classic linear regression and as $\alpha \to 1$ the minimization favors sparsity [7]. Let us test the generalization capabilities of the predictor by computing the error on the $e+1$-th couple $(\bar{I}_{e+1}, M_{e+1})$, that is, compute the error

$$\varepsilon_e = \left\| M_{e+1} - B_e \left[\begin{array}{c} 1 \\ \bar{I}_{e+1} \end{array} \right] \right\|_2 \quad (3)$$

for different values of α. The average error over $2 \leq e \leq E$ is reported in Fig. 5. The graph clearly shows that increasing the sparsity of the predictor improves the performances, providing support to our hypothesis of strong sparsity in the mapping as well. Previous works [8] showed that the desired responses M_i lie in a subspace of the whole motor subspace, analogously to the tendency for motions of lying in small subspaces of the whole command space [9]. We also found that the two spaces are strongly correlated, i.e. that if we know the frames F_k, $1 \leq k \leq K$ of the motion being developed we can compute the subspace $span < F_1, \ldots F_K > \subsetneq \mathbb{R}^m$ where the M_i have high probability of being located. Motivated by the previous results, we can verify whether also in this case sparsity can improve our predictions. In detail, let us define the matrix

$$\Gamma_{e+1} = \left[\begin{array}{ccc} 1 & \ldots & 1 \\ F_1 & \ldots & F_{K'} \end{array} \right] \quad (4)$$

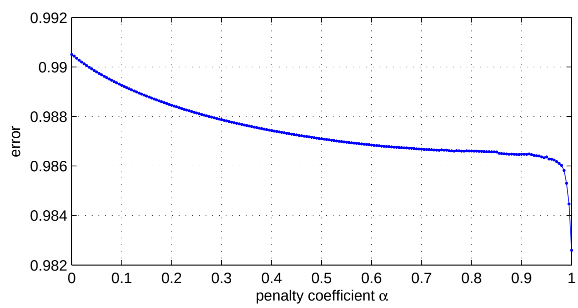

Fig. 5. Average error ε_e for the four users for different values of α.

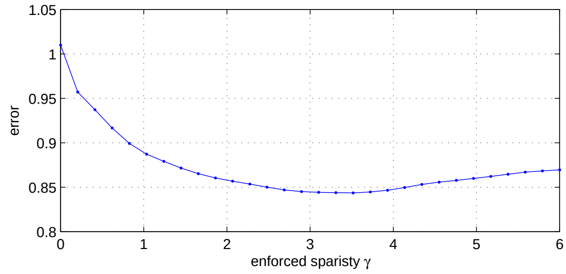

Fig. 6. Average error δ_e for the four users for different values of γ.

of the frames available before the couple $(\bar{I}_{e+1}, M_{e+1})$ is taught. Let us compute B_e and the prediction $p_{e+1} = B_e \left[\begin{array}{cc} 1 & \bar{I}_{e+1} \end{array} \right]^T$ as above, and define ρ_{e+1} as the minimizer of $p_{e+1} - \|\Gamma_{e+1}\rho_{e+1}\|_2^2 + \gamma\|\rho_{e+1}\|_1$. This new value $\rho_{e+1} \in \mathbb{R}^{m+1}$ is essentially a projection on Γ_{e+1} of the prediction p_{e+1}, whose sparsity is enforced increasing γ. Again, we compute the average error

$$\delta_e = \left\| M_{e+1} - \Gamma_{e+1} \left[\begin{array}{c} 1 \\ \bar{I}_{e+1} \end{array} \right] \right\|_2 \tag{5}$$

over the examples, and report the results in Fig. 6. We notice that the best predictions are obtained for $\gamma > 0$, confirming that also in this case sparsity of the projection coefficients can improve our estimates.

4 CONCLUSIONS AND FUTURE WORK

In this paper, we presented a system that allows to teach whole body motions to humanoid robots by physical interaction. Conceptual aspects of the exploitation of touch for motion development were briefly discussed, and a practical system implementation, comprising a small-sized robot equipped with 90 tactile sensors over the whole body was briefly introduced. This system has a two-fold role. On the one side, it allows inexperienced users to develop robot motions. On the other side, it allows studying the way users employ touch to intuitively communicate with robots.

As an example of the possible analysis that can be done on tactile instructions, this paper reports a study on the importance of sparsity in the mapping between pressed sensors and desired robot movements. First, quantitative measures on the sparsity of the input signal (touch sensors pressed) and the output signals (motors that should be moved) were reported. Successively, the possibility of improving the mapping from tactile instructions to motor movements by imposing sparsity was investigated. Finally, the idea of using the frames of the motion itself to improve the prediction on the robot movement was studied. In particular, it was shown that if we restrict the choice to a small subset of them (again, by imposing sparsity in a coefficient vector), then the prediction on the robot movement desired by the user can be improved.

This analysis provides us with important criteria for the design of new algorithms for tactile interpretation. In particular, it tells us that ensuring sparsity can give great performance improvements. For instance, if a neural network is employed for mapping tactile instructions to robot responses, then using rectifying neurons [10], that assure sparsity, appears to be a good choice. Future works will deal with the extension of the analysis reported here and the design of better, more performing algorithms for tactile interpretation based on this analysis.

REFERENCES

[1] L. Righetti and A. Ijspeert. Design methodologies for central pattern generators: an application to crawling humanoids. *Robotic Science and Systems 2006*, pp. 191–198, 2006.

[2] T. Inamura, Y. Nakamura, H. Ezaki, and I. Toshima. Imitation and Primitive Symbol Acquisition of Humanoids by the Integrated Mimesis Loop. *ICRA 2001*, pp. 4208–4213. Seoul, Korea, 2001.

[3] S. Nakaoka, A. Nakazawa, K. Yokoi, H. Hirukawa, and K. Ikeuchi. Generating whole body motions for a biped humanoid robot from captured human dances. *ICRA 2003*, pp. 3905–3910. Taipei, Taiwan, 2003.

[4] M. Hersch, F. Guenter, S. Calinon, and A. Billard. Dynamical System Modulation for Robot Learning via Kinesthetic Demonstrations. *IEEE Transactions on Robotics*, vol. 24(6):pp. 1463–1467, 2008.

[5] T. Minato, F. DallaLibera, S. Yokokawa, Y. Nakamura, H. Ishiguro, and E. Menegatti. A Baby Robot Platform for Cognitive Developmental Robotics. *Workshop on "Synergistic Intelligence" at IROS 2009*. St. Louis, MO, USA, 2009.

[6] Y. Kuroki, B. Blank, T. Mikami, P. Mayeux, A. Miyamoto, R. Playter, K. Nagasaka, M. Raibert, M. Nagano, and J. Yamaguchi. Motion Creating System for A Small Biped Entertainment Robot. *ICRA 2003*, pp. 1394–1399. Taipei, Taiwan, 2003.

[7] J. H. Friedman, T. Hastie, and R. Tibshirani. Regularization Paths for Generalized Linear Models via Coordinate Descent. *Journal of Statistical Software*, vol. 33(1):pp. 1–22, 2010.

[8] F. DallaLibera, F. Basoeki, T. Minato, H. Ishiguro, and E. Menegatti. Teaching By Touching: Interpretation of Tactile Instructions for Motion Development. *IROS 2011*, pp. 3480–3487. San Francisco, CA, USA, 2011.

[9] B. Lim, S. Ra, and F. C. Park. Movement Primitives, Principal Component Analysis, and the Efficient Generation of Natural Motions. *ICRA 2005*, pp. 4630–4635. Barcelona, Spain, 2005.

[10] X. Glorot, A. Bordes, and Y. Bengio. Deep Sparse Rectifier Neural Networks. *Proc. of the 14th Int. Conf. on Artificial Intelligence and Statistics (AISTATS)*, vol. 15 (draft). Sardinia, Italy, 2010.

An intelligent human behavior based automatic accessing control system

ChinLun Lai

Oriental Institute of Technology, Taipei, Taiwan, R.O.C.

fo001@mail.oit.edu.tw

Abstract: In this paper, an innovative intelligent controlling system for automatic door accessing is proposed to improve the drawback of frequent false actions among the existing control systems, while increasing the added values for extra security applications. Through pattern recognition techniques, the proposed system can precisely identify those people with intention of entering and/or leaving the door, and then control opening and closing of this door as a response. The experimental results indicate that our system has the advantages such as high precision, high reliability, and controllability in response to demands. In addition, the product prototype also has the economic benefits of low costs, high added-value, etc. Thus, it is a highly competitive new product.

Keywords: automatic door controlling, behavior analysis, human detection, pattern recognition

1 INTRODUCTION

Automatic door control is convenient and is widely used in many public places such as shores, businesses, transportation stations, airports, and wholesale department stores to eliminate the need of manually opening and closing the doors. However, there exists severe drawback in the existing approaches, ex: they are unable to determine the type and the intention of the detected object. In other words, a puppy or a bicycle passing by will trigger an action to open the door. In addition, even with the help of other technologies they may verify that the object is a person, they are still unable to indentify the intention of the person. For instance, a pedestrian or a person stays close to the door chatting might still trigger the door opening/closing. Frequent false actions not only wastes control and air conditioning energy, but also reduces equipment life time. This calls for the needs of an automatic door control system based on image recognition and intention analysis.

In the proposed method, the action of the door is based on the confirmation that the object is a human body, and movement trajectory indicates his/her intention to access the door. In our approach, an anti-pinch measure has been added to eliminate the false actions among existing systems. We detect the existence of human face other than the human geometric shaped (head, torso) scheme since it is well developed with reasonable detection rate and has the closest resemblance to real human characteristics. In addition, the images can also be saved for latter analysis for the applications such as crime investigation and prevention.

This paper is organized as follows: Section 2 describes the system design concept and related theoretical basis, while the corresponding hardware implementation architecture is described in section 3. Section 4 states the results and the analysis of various field tests of the system prototype, followed by discussions. Finally, the conclusion and future work are made in the last part.

2 THEORETICAL BASIS

2.1 Human face detection

The related researches on human face detection in the past ten years can be classifies into two types: the detection method based on skin color characteristics [1] and the detection method based on the training of human face database [2-4]. The former considers the blocks with the known skin color characteristics in the images as candidate blocks, and then the existence of isosceles triangles formed by eyes and mouth within the blocks can be used to confirm human faces. In the latter method, neural networks [2] or Adaboost [3-4] training methods are used to find human facial features and detect human faces in the established facial image database. The proposed system will use the Adaboost human face detection method to determine the existence of human object.

2.2 Analysis of the object moving trajectory

To determine whether the human object in the monitored areas has the intention to enter the door, the cumulative density function (*CDF*) obtained from tracking the trajectory of the human face movement is used to determine if the person has the intention to enter the door. Thus, this section will be divided into two parts: the tracking of human faces and the estimation of probability distribution of movement trajectory. In the first part, the tracking of human face is realized by comparing if the overlapping area of human face between time t and $t-1$ is smaller than the threshold value. In the second part, the human face moving trajectory of the person with the intention of entering will be estimated to figure probability distribution of x and y axis. Then this probability distribution will be used to establish the probability matrices of the monitored areas to estimate the probability values corresponding to different positions. Finally, this probability value will be used to calculate the cumulative density function corresponding to the movement of each human face to determine whether or not the intention of entering exists.

If a pedestrian within the monitored region (*MR*) has the intention of entering a specific region, there should be characteristics of continuous movement trajectory toward the specific exit/entrance, or looking at the specific exit/entrance with greater time accumulation, etc. Therefore, through the movement trajectory and the spatial position the pedestrians within the monitored regions, in this research the temporal and spatial cumulative probability is calculated and used to determine the intention of entering a specific region. As to the movement trajectories, those pedestrians with the intention of entering the specific region shall gradually move toward the entrance in the process. As to the spatial positions, the position closer to the entrance should be with the higher probability of intention to enter. On the contrary, the position farther to the entrance should be with the lower probability. According to the above description, the probability values of human faces based on their spatial positions within the monitored region is estimated, and then to obtain the cumulative probability in time-space to confirm whether the person has the intention of entering the specific region based on the movement trajectories of the human faces in time.

Since it cannot be predicated from where the pedestrian will enter, in order to obtain the probability of the human face in various positions in space in this research, we assume the center position (x_c^t, y_c^t) of a human face as a random variable. Thus, the movement trajectory of its center point shall have a specific probability distribution during the movement process. First we preset the movement trajectory of the pedestrian from entering the monitored region gradually moving toward the specific exit/entrance, and then according to different starting positions they can be divided into six kinds of entering conditions: upper left, upper right, right above, left, right and lower shift as shown in Fig. 2(a). Then the one-dimensional histograms for x and y and their respective probability distributions can be obtained through vertical and horizontal projection in space, such that the probability value of the human face at various position points within the monitored region can be obtained.

In order to obtain the spatial distribution of the movement trajectories, 20 sets of real movement trajectories data for each different entering condition is calculated, so there are a total of 120 sets of trajectories. Assuming the movement mode of each set is a_i, i=1,…,120, accumulate the 120 sets of movement mode into the statistical image $s = \sum_{i=1}^{120} a_i$. Then the spatial distribution characteristics of movement trajectory can be obtained as shown in Fig. 2(a). Then, the statistical images is projected onto the *x*-axis and *y*-axis in space to obtain the one-dimensional histograms of the vertical and the horizontal spatial characteristics of the movement trajectory, as shown in the blue lines in Fig. 2(b) and 2(c).

Since the one-dimensional histograms generated from the projections of *x*-axis and *y*-axis are the spatial distributions of movement trajectories in the *x*-axis and *y*-axis, this paper uses the estimation method of probability density function (*pdf*) of histogram and the nonlinear least squares curve fitting [5-6] method to estimate the *pdf* of spatial distribution of movement trajectories in the *x*-axis and the *y*-axis respectively. As shown in the experimental results, the probability density function of vertical projection approximates to Gaussian distribution with the average value μ and standard deviation σ as 150 and 1 respectively as shown in (1a). The probability density function of horizontal projection approximates to non-central chi-square distribution with the degree of freedom k as 2 and the non-centrality λ as 23 as shown in (1b).

$$s_v(x) = \frac{1}{\sqrt{2\pi\sigma^2}} e^{(-(x-\mu)/2\sigma^2)} \tag{1a}$$

$$s_h(x;k,\lambda) = \frac{1}{2} e^{-(x+\lambda)/2} (\frac{x}{\lambda})^{k/4-1/2} I_{k/2-1}(\sqrt{\lambda x}) \tag{1b}$$

where the probability distribution functions of (1a) and (1b) are shown in red dotted lines in Fig. 2(b) and (c).

Through the inclusion-exclusion principle [7] of the probability theory, the probability value of human face at each spatial position point is calculated as in (2).

$$p(x_c, y_c) = s_h(x_c) + s_v(y_c) - s_h(x_c) \times s_v(y_c) \tag{2}$$

where $s_h(x_c)$ and $s_v(x_c)$ are the probability values corresponding to the center coordinates of the human face. From (2) the probability matrix (*PM*) of each position point within the monitored region can be obtained. The probability matrix also represents the counter weight values of the various coordinate positions within the monitored space. From the variation of the probability value of the probability matrix, it is observed that the corresponding probability value is larger for position closer to the specific entrance. On the contrary, the corresponding probability value is smaller for position farther away from the specific entrance as shown in Fig. 2(d). Higher gray scale values represent higher probability values.

In order to detect whether or not the movement trajectory of the pedestrian is getting closer to the specific exit/entrance, it is assumed that a pedestrian with the intention of entering will go through τ images after entering the monitored area before getting to the entrance, and the movement trajectory probability of the human face center point of the person should be $p(x_c^i, y_c^i),\ i=1,\ldots,\tau$. Thus, the cumulative distribution function (*cdf*) [7] up to the τ-th image is described as:

$$p_{enter} = \frac{1}{\tau}\sum_{i=1}^{\tau} p(x_c^i, y_c^i) \tag{3}$$

The cumulative probability of the pedestrian up to the τ th image can be obtained by (3). If the pedestrian continues to move toward the exit/entrance gradually or continue to look at the entrance, then the cumulative probability value P_{enter} will exceed the threshold value TH_{PM}, then the intention to enter the specific region can be determined. On the contrary, if this value is smaller than the threshold value, then it's determined that the person does not have the intention to enter, and this case will be excluded. Since the intention of accessing the specific exit/entrance should be greater for the person closer to the exit/entrance, in this research we assume the region with greater than average value μ_{PM} the probability matrix as the main monitored region (*MMR*), and this average value of the probability matrix μ_{PM} will be used as the cumulative threshold value

TH_{PM} to determine if the intention of entering exists. Thus, when the pedestrian is walking toward the specific exit/entrance location gradually, the movement trajectory of the person will fall mostly in the *MMR* (as indicated in the area enclosed by red area in Fig. 2(d)), and the cumulative probability value will become higher along with the accumulation of time and with the center point of human face center approaching the specific exit/entrance. Once it exceeds the threshold value, it's determined that the intention to enter exists and the door will be opened accordingly. Otherwise, it would be determined that the intention to enter did not exist. When the pedestrian continuously looks at the exit/entry within the *MMR*, P_{enter} will exceed the threshold value along with the accumulation of time. Thus, it can also be determined that the intention of entering the specific region exists.

To avoid the pedestrians from being pinched by the closing door before entering/leaving a specific exit/entrance, a modified temporal difference method [8] is adopted to determine whether or not there are moving objects near the exit/entrance, and the determination of whether or not the pedestrian has entered/left the specific region will be used as the basis for activating the door closing procedure.

To confirm whether the pedestrian has entered/left the specific exit/entrance, 1/3 imaging area in front of the exit/entrance is preset to be the anti-pinch monitoring region (*AMG*). The temporal difference method will be used to detect the existence of any foreground within the monitoring region as the basis for activating the door closing procedure.

Temporal difference is to detect the pixel different from the previous moment *t-1* by subtracting two adjacent images in the same image sequence. When this pixel is greater than the threshold value ε, it will be determined as foreground pixel by

$$Fg_i(t) = \begin{cases} 1, & |Fr_i(t) - Fr_i(t-1) > \varepsilon| \\ 0 & , \ otherwise \end{cases} \tag{4}$$

where $Fg_i(t)$ is the foreground pixel at time *t*. $Fr_i(t)$, $Fr_i(t-1)$ are the gray scale values of position *i* in the anti-pinch monitoring region at time *t* and *t-1* respectively.

Assuming the gray scale values of images are of Gaussian distribution, we use twice the standard gray scale value $2\sigma_{t-1}^{AMG}$ of the $Fr_i(t-1)$ anti-pinch monitoring region as the threshold value ε [9] for foreground detection. In order to prevent the pedestrian from repeated entering/leaving of the specific region after entering/leaving the anti-pinch monitoring region, the door closing procedure will be activated with 2-second delay if there is no foreground detected within the anti-pinch monitoring region.

The completed function blocks of the proposed system is presented in Fig. 1.

2.3 Evaluation of system effectiveness

To evaluate the reliability of the system, the total false action probability $ER_{tot}=FRR+FAR$ is defined, while *FAR* is false acceptance rate and *FRR* is false rejection rate. They can be analyzed as follows:

Since the face detection execution speed of this system is 15 frame/second, the human face detection rate (*DR*) is 0.9, the missing rate is *DF=1-DR*. The generally acceptable door opening/closing response time *T* is 2~3 seconds. It can be derived from the above description that the probability of rejection for a pedestrian who wants to enter the door is

$$FRR = \sum_{i=FF}^{TF} C_i^{TF} P(\theta, DF)^i \times [1 - P(\theta, DF)]^{TF-i} \tag{5}$$

where $TF=(Rt*T)$ represents the number of images collected within a specified time period, $FF=(Rt*T)\mu_{PM}$ represents the minimum number of times the human face must be detected, and $P(\theta,DF)$ represents the probability of missed detection of human face within the *MMR*. Under the assumption that *q* and *DF* are independent, the formula can be simplified as

$$P(\theta, DF) = P(\theta) \times DF \tag{6a}$$

$$P(\theta) = \frac{MMR}{MR} \tag{6b}$$

where $P(\theta)$ is area ratio of *MMR* within the monitored area. According to (5), if we preset the door opening response time to be 2 seconds (starting from the detection of the first face with certain distance away from the door), then the *FRR* value should be about 2.193×10^{-6}. If the door response time was set to 3 seconds, the *FRR* value would be less than 6.808×10^{-10}. Generally speaking, it takes about 2~3 seconds for a human body to move from somewhere in front of the door to the entrance to wait for the door to open. Therefore, generally the theoretical false rejection rate should be less than 2 in a million.

On the other hand, it is either the false identifications of facial characteristics (non-human face falsely identified human face) do not possess features of continuous trajectories (random occurrence), or maybe the user only passed by in front of the door. Under these two circumstances the trajectories will be removed during the tracking procedure. That is, there will be no follow-up determination of whether or not the door shall be opened/closed for that target. Therefore, *FAR* can be considered to be 0, and the total false action rate is described by $ER_{tot}=FRR$.

It is observed from the above description that false action rate of this system can be controlled within 2 in a million. Compared with the existing systems (only assuming 1/5 of the *FAR* false action rate), this system has an excellent identification accuracy rate.

3 EXPERIMENTAL RESULT & DISCUSSION

To evaluate the proposed system, A *DM365* platform of *TI*-corp. is selected to implement all the functions. The algorithms developed were programmed in *C* language and were executed under the Linux OS core. The related parameters of the prototype system are as follows: The face detection rate is 0.9. The processing speed is 15 frame/sec. The setup height is 2.2 meters. The angle of depression is 30 degrees. The left and right viewing angles of the image are both 63 degrees. Field tests were conducted in three different locations. The content of related data is presented in table 1.

The experimental results from actual field tests are shown in table 1. Among the experiments of 125 trials in 3 different locations, the number of effective opening, within the default 2 seconds value, was 124. The false rejection rate was 0.008, slightly higher than the theoretically estimated value. In the only case of failure, it was not that the door did not open, just the opening was delayed (the reaction/response time was 4 seconds). Thus, there was actually zero case when a person wanted to enter but was rejected. On the other hand, the number of false acceptance rate due to objects passing by or environmental interference was zero. It is observed that the system effectively overcomes the disadvantage of susceptibility to environmental interference among existing automatic door control systems while retaining the advantages of opening the door effectively and safely.

4 CONCLUSIONS

In this paper, an automatic control system based on the characteristics of human behavior is proposed to replace the existing automatic door control devices. Through image analysis technologies, it is capable of opening the automatic control door after accurate identification of human object with the intention to enter/exit. This way it achieves the goals of added values such as reduction of energy consumption, improved readiness rate of the equipment, and saving of the images of people who entered/exited for future references of other applications. The results of the initial field tests revealed that the developed prototype effectively accomplished the product design specification. It is truly a feasible business product.

REFERENCES

[1] R.L. Hsu, M. Abdel-Mottaleb, and Anil K. Jain, "Face Detection in Color Images," IEEE Transactions on Pattern Analysis and Machine Intelligence, vol. 24, no. 5, pp. 696-706, May 2002.
[2] Henry A. Rowley, Shumeet Baluja, and Takeo Kanade, "Neural Network-Based Face Detection," IEEE Transactions on Pattern Analysis and Machine Intelligence, vol. 20, pp. 23-38, 1998.
[3] Paul Viola, and Michael J. Jones, "Robust Real-Time Face Detection," International Journal of Computer Vision, vol. 57, no. 2, pp. 137-154, 2004.
[4] Rainer Lienhart, and Jochen Maydt, "An Extended Set of Haar-like Features for Rapid Object Detection," Proceedings Of the IEEE International Conference on In Image Processing, vol. 1, pp. 900-903, Sep. 2002.
[5] Scott, David W, "On optimal and data-based histograms," Biometrika, vol. 66, issue 3, pp. 605–610, 1979.
[6] B. W. Silverman, "Density Estimation for Statistics and Data Analysis," 1st ed. London, U.K.: Chapman and Hall, 1986.
[7] Alberto Leon-Garcia, "Probability and Random Processes for Electrical Engineering," Addison-Wesley, 2nd ed., 1994.
[8] Lipton, A. J., H. Fujiyoshi, and R. S. Patil, "Moving target classification and tracking from real-time video," Proceedings of IEEE Workshop Application of Computer Vision, pp. 8-14, 1988.
[9] I. Haritaoglu, David Harwood, and L. S. Davis, "W4:Real-time surveillance of people and their activities," IEEE Transactions Pattern Analysis and Machine intelligence, vol. 22, no. 8, pp. 809–830, August 2000.

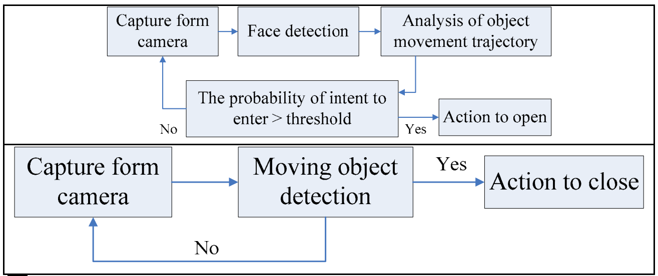

a b **Fig. 1. System flowchart of (a) door opening processes, and (b) closing processes.**

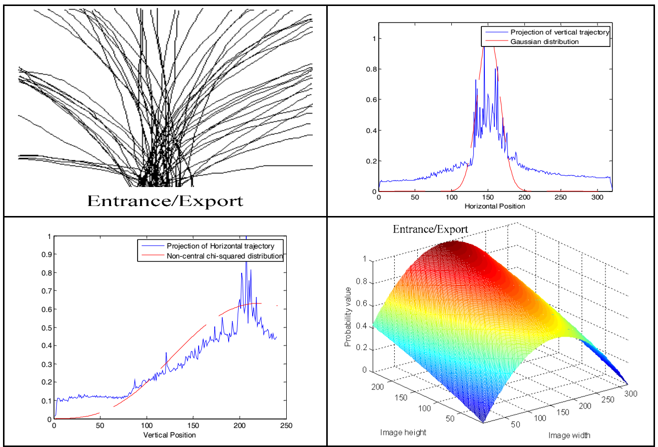

a b c d **Fig. 2. The spatial distribution of trajectory: (a) The movement trajectory, (b) its vertical projection and distribution, (c) the horizontal ones, and (d) corresponding probability matrix.**

Table 1. The False Rejection Rate Results

RESULTS\ LOCATION	TIME (HR)	NO. OF PERSONS	FAILURE COUNT	DETECTION RATE
Yangmei	3	45	0	
Banqiao	4	52	1**	
Yingge	3	28	0	
TOTAL	10	125	1	99.2%
**DOOR DID NOT OPEN AFTER THE DEFAULT TIME HAS BEEN EXCEEDED (2 SECONDS), BUT EVENTUALLY OPENED (ABOUT 4 SECONDS)				

The Seventeenth International Symposium on Artificial Life and Robotics 2012 (AROB 17th '12),
B-Con Plaza, Beppu, Oita, Japan, January 19-21, 2012

Non-contact physical activity estimation method based on electrostatic induction technique

Koichi Kurita

Kochi National College of Technology, Kochi 783-8508, Japan
(Tel: 81-88-864-5547, Fax: 81-88-864-5547)

kurita@ee.kochi-ct.ac.jp

Abstract: We here present a method for measuring human physical activity, which is based on detecting the electrostatic induction current generated by the walking motion under non-contact and non-attached conditions. A theoretical model for the electrostatic induction current generated because of a change in the electric potential of the human body is also proposed. By comparing the obtained electrostatic induction current with the theoretical model, it becomes obvious that this model effectively explains the behavior of the waveform of the electrostatic induction current. The normal walking motions of daily living are recorded using a portable sensor measurement located in an ordinary house. The obtained results show that detailed information regarding physical activity such as a walking cycle can be estimated using our proposed technique. This suggests that the proposed technique, which is based on the detection of the walking signal, can be successfully applied to the estimation of human physical activity.

Keywords: motion detection, electric potential of human body, electrostatic induction current.

1 INTRODUCTION

Physical activity improves health and well-being. The benefits of physical activity for the prevention of cardiovascular disease, cerebral accidents, and some cancers are now well established. These benefits are also enjoyed in old age, where the incidence of many diseases and disabilities increases. Researchers have made numerous attempts to develop methods to measure physical activity. This is because precise measurements of physical activity would allow assessment of physical activity in the same way as a physical activity diary. Estimates of physical activity are often made using self-report measures. However, these have some disadvantages such as the impossibility of estimating activity patterns throughout the day (Davis [1]) and fluctuations in health status (Riki [2]). Therefore, objective measurement methods for physical activity are attracting a great deal of attention as they would overcome the limitations of self-report measures. In particular, measurement of the acceleration of a subject's body provides information on the amount, frequency, and duration of physical activity (Plasqui [3]). An objective physical activity measurement method such as accelerometry can also assess free-living activity. Objective physical activity measurements (Matthews et al [4]) make it obvious that participation in non-exercise physical activity such as housework and stair climbing improves mortality risk.

In particular, it has been noted that walking for exercise is especially effective for long-term weight loss (Ballor [5]), increasing HDL (Fogelholm et al [6]), reducing blood pressure (Dunn et al [7]), and lowering the risk of heart disease and cancer initiation. In the last decade, human walking analysis has attracted much attention from computer vision researchers motivated by its wide application potential. Normally, in vision-based human walking detection, motion features are extracted from image sequences. Subsequently, feature amounts are compared as an identification process. However, in conventional human walking detection methods, experimental conditions such as the distance between the subject and camera, the angle of the camera, and the pixel density of the camera significantly influence the recognition rate of the system. Moreover, the main drawback of these methods is that they cannot detect anything in the dead zone of the camera. Furthermore, many image-processing systems require complex logic to ignore the disturbances caused by the motion of objects other than humans.

Alternatively, body-mounted accelerometers are extensively used for monitoring human motion because these systems are inexpensive compared to an optoelectronic motion capture system. Another advantage of body-mounted accelerometers is that the system is available in an indoor-outdoor space. Additionally, several methods have been presented to measure human activity using various techniques, e.g., an ultrasonic motion analysis system to temporally and spatially measure the amount of human activity, an electromagnetic 3D orientation estimation system that uses the earth's magnetic field, and a wearable ultrasonic motion analysis system. However, in these measurement systems, it is necessary to use some kind of sensor or marker that remains in contact with the subject. Therefore, these methods have not been applied to non-contact detection for human activity measurement.

In this paper, we present a new direction for a human activity estimation technique that does not use a camera or accelerometry. We have developed an effective non-contact technique for the detection of human walking motion using human-generated body charge. This technique involves the detection of an electrostatic induction current on the order of approximately sub-picoamperes flowing through an electrode placed at a distance of 3 m from a subject. The absolute value of the electrostatic induction current depends on the type of footwear and floor material. However, we confirmed that this technique has sufficient sensitivity to detect the electrostatic induction current generated by the walking motion in daily life. This technique effectively explains the behavior of the waveform of the electrostatic induction current flowing through a given measurement electrode using a capacitance model for the human body.

2 PRINCIPLE

The human body is electrically charged during walking (Ficker [8]). In the case of a subject that is standing or walking, we assume that there are two highly resistive layers between the feet of the subject and the floor, as shown in Fig. 1. One layer is the sole of the subject's footwear. The other is the surface of the floor. Capacitance C_{sf} of the feet relative to the ground may be calculated as the sum of capacitance C_s of the sole and capacitance C_f of the floor surface. In addition, C_0 is the capacitance of the rest of the subject's body relative to nearby objects on the floor. Therefore, potential U_B of the human body during walking motion can be expressed as follows:

$$U_B = Q_B \frac{\varepsilon_a S + x C_B}{C_B \varepsilon_a S}. \quad (1)$$

where

$$C_B = C_0 + C_{sf} = C_0 + \frac{C_s C_f}{C_s + C_f}. \quad (2)$$

Q_B is the instantaneous charge of the human body during walking motion, ε_a is the permittivity of the air gap between the sole and floor, and S is the effective sole area at height x above the floor. The induced charge, Q, of a measu rement electrode placed at a certain distance from the subje ct can be expressed as follows:

$$Q = C(U_B - V), \quad (3)$$

where C is the capacitance between the human body and m easurement electrode, and V is the potential of the measure ment electrode. From the above two equations, the induced current, I, flowing through the measurement electrode can b e expressed as follows:

$$I = \frac{dQ}{dt} = C\frac{dU_B}{dt} = CQ_B\left(-\frac{x}{\varepsilon_a S^2}\frac{dS}{dt} + \frac{1}{\varepsilon_a S}\frac{dx}{dt}\right). \quad (4)$$

We assume that the human body is a good conductor. The first term in (4) represents the current induced by the motion of the foot before it is lifted off the floor. The second term represents the current induced by the motion of the foot and leg after the foot is lifted off the floor. The second term is approximately proportional to the velocity of the foot. Therefore, in the case of walking motion near the measurement electrode, it is possible to measure the current generated under perfect non-contact conditions.

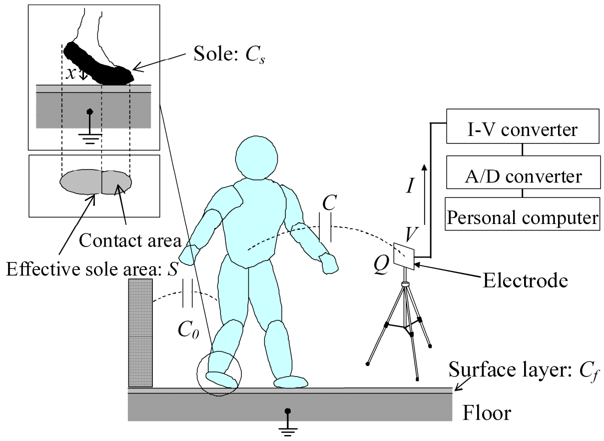

Fig. 1. Schematic of measurement system for detecting walking motion

3 EXPERIMENTAL SYSTEM

A schematic of the measurement system for detecting the electrostatic induction current generated by the changes in the electric potential of a subject's body is shown in Fig. 2. The electrostatic induction current flowing through an electrode placed less than 3 m from the subject's body is converted into voltage using an *I-V* converter with a conversion ratio of 10 V/pA and comprising an operational amplifier (op-amp). The *I–V* converter consists of two low-input-current op-amps, where C_f is 1 pF and R_f is 3 TΩ. The selected low-noise op-amp has an input offset voltage of 40 μV and input offset current of 1 pA. The feedback resistor connected to the op-amp is a hermetically sealed high register that can prevent stray current due to humidity. For such measurements with high input resistance, a conventional guarding method is absolutely imperative for shielding used with op-amps; this prevents stray currents from entering sensitive nodes. Sensitive nodes are completely surrounded by a guard conductor that is kept at the same electric potential as the sensitive node. In addition, induction currents generated by commercial power sources manifest in the form of noise. Therefore, a filtering system with a cutoff frequency of 20 Hz is used. This measurement system is unaffected by the noise from other electronic devices such as mobile phones or microwave ovens. The analog signals are subsequently converted into digital signals using an analog-to-digital (A/D) converter.

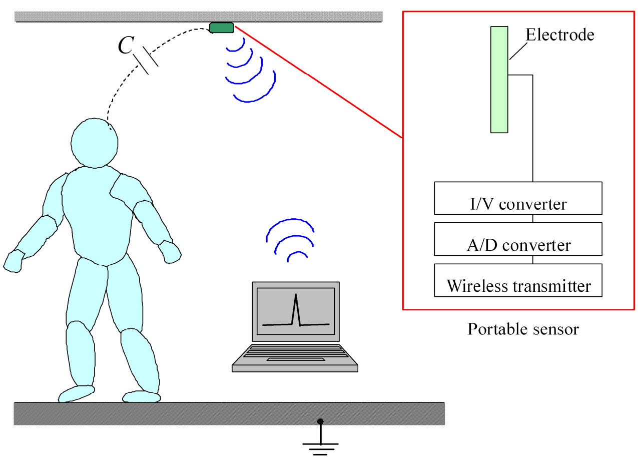

Fig. 2. Schematic of system for detecting walking motion in house by using portable sensor

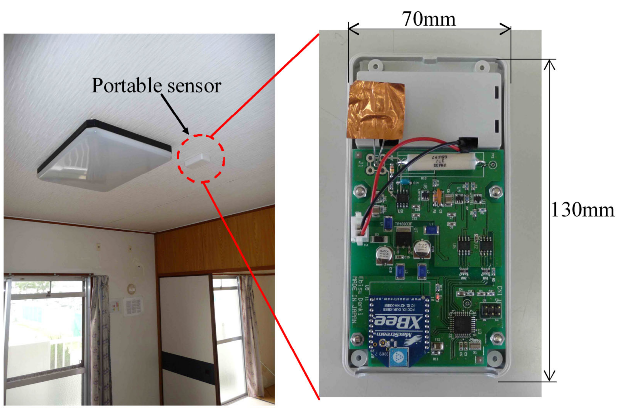

Fig. 3. Photograph of portable sensor

The analog signals are subsequently converted into digital signals using an A/D converter. We used the ZigBee protocol for wireless data transmission to a personal computer from the portable contact detection system. Data were acquired at a sampling frequency of 20 Hz, which is safe given that the actual data transmission rate on ZigBee networks is as low as about 10 kbps. However, this sampling frequency was sufficient for detecting contact events. The measurement electrode is square with a side length of 2 cm. A photograph of the portable detection sensor is shown in Fig. 3.

4 RESULTS AND DISCUSSION

Figure 4 shows the typical waveform of the current generated by the human motion of walking. Cadence components are observed in the resulting waveform for each case. These components indicate the presence of a gait cycle in the walking motion. This gait cycle consists of a combination of alternating swing and stance phases for the left and right feet. The waveform contains cadence component for both feet during bipedal walking; this reveals that the toe of the left foot is lifted off the floor while the heel of the right foot simultaneously comes into contact with the floor. When the toe of the right foot is lifted off the floor, the effective sole area, S, decreases and the distance, x, between the right foot and floor increases continuously. As a result of the walking motion, the current, I, flowing through the measurement electrode increases, as predicted by the first term on the right-hand side of (4). In rapid succession, I decreases, as predicted by the second term on the right-hand side of (4). Furthermore, in the second half of the swing phase, a rapid decrease in x induces a decrease in I, as predicted by the second term on the right-hand side of (4). In rapid succession, I decreases, with an increase in the effective sole area, S, resulting from the heel contact, as predicted by the first term on the right-hand side of (4). Therefore, (4) effectively explains the behavior of the waveform of the electrostatic induction current, I, flowing through the measurement electrode.

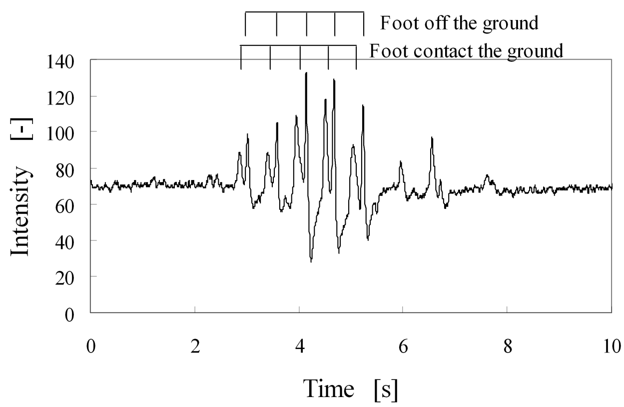

Fig. 4. Typical waveform of current generated by human walking motion

The portable sensor was placed in ceiling of an ordinary house with a wooden floor, as shown in Fig. 3. The subjects were asked to walk normally wearing slippers on a wooden floor. The waveforms of the electrostatic induction currents generated by walking motion are shown in Fig. 5. The change in the intensity of the walking signal obtained by the portable sensor suggests that the subject is drawing closer to the portable sensor and then moving away from it. Therefore, detailed information about physical activity can be estimated using our proposed technique. We have developed an effective non-contact technique for the detection of human physical activity using human-generated body charge.

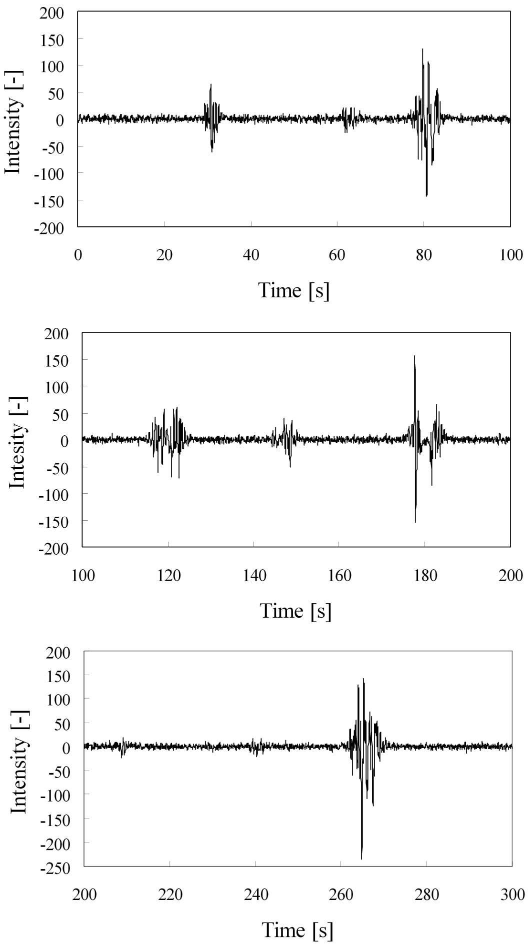

Fig. 5. Waveform of current generated by human walking motion

5 CONCLUSION

This paper described the development of an effective non-contact technique for the detection of human physical activity using human-generated body charge. This technique involves the detection of an electrostatic induction current on the order of approximately sub-picoamperes flowing through an electrode.

We proposed a theoretical model for the electrostatic induction current generated by the walking motion. By comparing the typical waveform of the electrostatic induction current obtained by walking motion with the theoretical model, it became obvious that this model effectively explains the behavior of the waveform of the electrostatic induction current, *I*, flowing through the measurement electrode. The normal walking motions of daily living were obtained using a portable sensor located in an ordinary house. The obtained results showed that detailed information regarding physical activity such as a walking cycle could be estimated using our proposed technique. Therefore, the proposed technique based on the detection of the walking signal can be successfully applied, not only to estimate human physical activity, but also to confirm the safety of an elderly person living alone.

ACKNOWLEDGMENT

This research was partially supported by the SCOPE (Strategic Information and Communications R&D Promotion Programme), 2011.

REFERENCES

[1] Davis MG and Fox KR (2007), Physical activity patterns assessed by accelerometry in older people, Eur. J. Appl. Physiol. 100:581-589

[2] Rikli RE (2000), Reliability, validity, and methodological issues in assessing physical activity in older adults, Res. Q. Exerc. Sport 71:S89-S96

[3] Plasqui G and Westerterp K R (2 0 0 7), Physical activity assessment with accelerometers: an eva luation against doubly labeled water, Obesity 15:2371-2379

[4] Matthews CE et al (2007), Influence of exercise, walking, cycling, and overall nonexercise physical activity on mortality in Chinese women, Am. J. Epidemiol. 165:1343-1350

[5] Ballor DL and Keesev RE (1991), Ameta-analysisi of the factors affecting exercise-induced changes in body mass, fat mass, and fat-free mass in males and females, International Journal of Obesity, 5:717-726

[6] Fogelholm M et al (2000), Effects of walking training on weight management after a very low energy diet in premenopausal obese women: a randomized controlled trial, Archives of Internal Medicine, 160:2177-2184

[7] Dunn AL et al (1999), Comparison of lifestyle and structured interventions to increase physical activity and cardiorespiratory fitness: a randomized trial, Journal of American Medical Association, 281:327-334

[8] Ficker T (2006), Electrification of Human Body by Walking, Journal of Electrostatics, 64:10-16

The Seventeenth International Symposium on Artificial Life and Robotics 2012 (AROB 17th '12),
B-Con Plaza, Beppu, Oita, Japan, January 19-21, 2012

Genetic Algorithm with Cross Paths Detection for Solving Traveling Salesman Problems

Shi-Jim Yen[1], Shih-Yuan Chiu[1] and Sheng-Ta Hsieh[2]

[1] Department of Computer Science and Information Engineering, National Dong Hwa University, Hualien, Taiwan, R.O.C.
[2] Department of Communication Engineering, Oriental Institute of Technology, New Taipei City, Taiwan, R.O.C.

fo013@mail.oit.edu.tw

Abstract: The travelling salesman problem (TSP) is a classic optimization whose goal is to find a shortest route path. In this paper, an improved GA is proposed to solving TSP. For eliminating repeated chromosomes and increasing their diversity, a normalization strategy is proposed. Further, for improving solution searching efficiency, the cross paths detection is also proposed to reduce paths distance. Experiments were conducted on 10 instances of TSPLIB. The results showed that the proposed method exhibits better performance when solving these TSP instances compared to related TSP approaches.

Keywords: cross path detection, genetic algorithm, optimization, traveling salesman problem.

1 INTRODUCTION

The travelling salesman problem (TSP) is a classical NP- hard problem in the field of computer science. In TSP, a set of cities' location will be given and the goal of the problem is try to find a shortest route for visit each city only once.

TSP is used as a benchmark for testing performance of optimization methods. Although there are so many contribution in enhance solution searching ability. Some of them might already be surpassed by novel approaches. In 2007, Shi et al. proposed a particle swarm optimization (PSO) based approach called Discrete PSO [1] for solving TSP. In 2008, Kaur and Murugappan proposed a hybrid genetic algorithm [2]. It combine the nearest neighbor algorithm (NNA) and pure genetic algorithm (GA) for deriving better solutions.

In order to improving optimizer's searching ability and efficiency, this paper presents improved GA to solving TSP. The proposed method is incorporated with the cross path detection to verify and eliminate redundant path for minimizing route solution. The proposed method also involved a normalization strategy to increase diversity of population, which can prevent the solutions from falling into the local optimum and enhance the proposed approach's searching ability.

2 GENETIC ALGORITHM

The basic principles of genetic algorithm (GA) were first introduced by John Holland in 1975[3]. Holland's GA was the first evolutionary computation (EC) paradigm developed and applied. It is for moving from one population of *chromosomes* to a new population by using a kind of Darwin's "natural selection" principle together with the genetics- inspired operators of selection, cross-over, mutation, and inversion [4]. A brief introduction of genetic algorithm will be described.

3 PROPOSED METHOD

Although there are numerous approaches can be applied for solving TSP. Efficiency and robustness of algorithms are still the major issues. In this paper, the nearest neighbor algorithm (NNA) is adopted for initial population. In order to reduce route distance efficiently; the cross paths detection is introduced. Further, the normalization is also involved to keep diversity of population.

3.1 Cross-over

In general, cross-over operation in GA is to generate new offspring. It combines two chromosomes' information which was also generated by chromosomes in a previous generation and evaluated by the cost function. Finally, the better chromosomes will be kept is the population. If a chromosome discovers a new probable solution, its offspring will move closer to it to explore around the region deeply in following cross-over process.

3.2. Mutation

In this paper, mutation is to pick up two dimensions randomly. The chromosome's sequence between the two dimensions will be inversed. For example, there are two randomly selected dimension d_1 and d_2 in a chromosome. The contents (route sequence) between d_1 and $d_{2\,2}$will be re-arrangement.

3.3. Cross Path Detection

The goal of TSP is to find a route as short as possible.

Cross paths in route will serious increase distance in TSP. Although, evolution process of GA will find potential optimal solution. Unfortunately; it still may not be able to avoid such situation. In this paper, a geometry-based method called cross path detection is proposed. For current route, each path will be verified that if it cross to another path. These cross paths will then be eliminated.

Let's use symbol "a-b" denoting the path between city-a and city-b. For example, assuming there are 7 cities in TSP. Assuming the route of these cities is connected according to its serial numbers, and the path between city-1 and city-2 is selected for cross path detection. Thus the path 1-2 need to be compared with 3-4, 4-5, 5-6, 6-7. Note that the path 2-3 and 7-1 need not be compared with 1-2. Due to them will never cross to path 1-2. An example of cross path detection is shown in Fig. 1. In this case, the path 2-5 is cross to path 3-6. Thus, the city-2 will be connected to city-3 and city-5 will be connected to city-6.

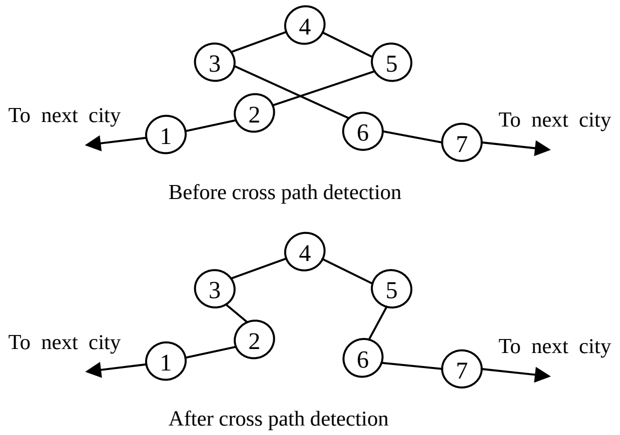

Fig. 1. Example for cross path detection

4 EXPERIMENTS

Ten TSP instances from the TPSLIB [5] were adopted for testing proposed method and compare it to Hybrid Genetic Algorithm [2] and Discrete PSO [1]. The parameters of these methods are set according to their original setting which are listed as following:

- Proposed Method
  The cross-over rate is 1 and the mutation rate is 0.85
- Hybrid Genetic Algorithm
  The cross-over rate is 0.5 and the mutation rate is 0.85
- Discrete PSO
  The inertia weight (w) is 1.49 and the accelerate coefficient (c_1 and c_2) are both 0.72.

All the four population-based optimizer were implemented using MATLAB 2010a. The maximal Number of Function Evaluations (FEs) is set to be 50,000 for all approaches. All algorithms were run 30 times and calculated their mean values and standard deviation for the results.

Table 1. Results of Ten TSP Instances

Instances \ Methods	Proposed method	Hybrid Genetic Algorithm	Discrete PSO
bayg29	9077 ± 6	9128 ± 70	12416 ± 822
st70	694 ± 4	699 ± 8	1141 ± 90
pr76	112749 ± 1544	112959 ± 1708	176556 ± 12538
rat99	1265 ± 5	1248 ± 14	2117 ± 131
eil101	671 ± 5	675 ± 8	996 ± 42
pr107	44494 ± 77	44683 ± 84	97344 ± 14619
ch130	6539 ± 66	6476 ± 99	11278 ± 792
kroA200	30676 ± 66	31479 ± 461	63030 ± 4124
ts225	132412 ± 1024	132647 ± 1243	209885 ± 10579
a280	2856 ± 23	2893 ± 40	4850 ± 23

Table I presents the mean and standard deviation of 30 runs for proposed method, Hybrid Genetic Algorithm and, Discrete PSO on the ten TSP instances. The best results among the four approaches are shown in bold.

From the results, the proposed method performed with better results can be observed. Furthermore, the proposed method surpasses all other algorithms in solving instances of bayg29, st70, pr76, eil101, pr107, kroA200, ts225 and a280. The Hybrid Genetic Algorithm performed better than proposed method on rat99 and ch130.

5 CONCLUSIONS

In this paper, the proposed method has been presented to solve travelling salesman problem (TSP). The cross path detection was adopted for untie the cross paths and for reducing route distance. Ten TSP instances of TSPLIB were selected for experiments. The experiments results show that the proposed method can find better solutions on these benchmarks than related works.

REFERENCES

[1] X. H. Shi, Y.C. Liang, H. P. Lee, C. Lub and Q. X. Wanga, "Particle swarm optimization-based algorithms for TSP and generalized TSP," Information Processing Letters 103, pp. 169-176, 2007.
[2] D. Kaur and M. M. Murugappan, "Performance Enhancement in solving Traveling Salesman Problem using Hybrid Genetic Algorithm," Annual Meeting of the North American In Fuzzy Information Processing Society, pp. 1-6, 2008.
[3] J. H. Holland, Adaptation in Natural and Artificial Systems, University of Michigan Press, 1975.
[4] D. E. Gokdberg, Genetic Algorithms in Search, Optimization & Machine Learning, Addison Wesley, 1989.
[5] http://comopt.ifi.uni-heidelberg.de/software/TSPLIB95/

The Seventeenth International Symposium on Artificial Life and Robotics 2012 (AROB 17th '12),
B-Con Plaza, Beppu, Oita, Japan, January 19-21, 2012

Development of a mechanical safety device for service robots

Yoshihiro Kai[1] and Tatsuya Adachi[2]

[1]Tokai University, Kanagawa 259-1292, Japan
[2]Daitocacao Co., LTD., Kanagawa 259-0151, Japan

[1]kai@tokai.ac.jp

Abstract: In this paper, we present a new safety device to improve the safety of service robots for humans. The safety device consists of only mechanical components without actuators, controllers and batteries. The safety device is attached to each drive-shaft of a robot and locks the drive-shaft after detecting an unexpected robot motion on the basis of the drive-shaft's angular velocity. First, we present the design concept of the safety device. Second, we explain the mechanism of the safety device. Third, we show the developed safety device. Fourth, we experiment by using the developed safety device. Finally, from the experimental results, we discuss the usefulness of the safety device.

Keywords: Human-machine cooperative systems, Human-welfare robotics, Robotics, Safety device, Service robot

1 INTRODUCTION

Recently, there has been a growing interest in service robots which can support human daily activities. In industrial robots, safety of humans is implemented by isolating the robots from humans. However, in service robots, it is not possible to isolate the robots from humans because the robots work within human environments. Therefore, human safety becomes one of the most important issues in service robotics [1]-[4]. In this paper, we present a new safety device to improve human safety. The safety device consists of only mechanical components without actuators, controllers and batteries. The safety device is attached to each drive-shaft of a robot and locks the drive-shaft after detecting an unexpected robot motion on the basis of the drive-shaft's angular velocity. First, we present the design concept of the safety device. Second, we explain the mechanism of the safety device. Third, we show the developed safety device. Fourth, we experiment by using the developed safety device. Finally, from the experimental results, we discuss the usefulness of the safety device.

2 MECHANICAL SAFETY DEVICE

2.1 Characteristics of the Safety Device

The characteristics of the safety device are shown as follows:

(1) If the angular velocity of a drive-shaft (hereinafter referred to as "shaft") exceeds a preset threshold level, then the safety device for the shaft is activated. We call the preset threshold level "detection velocity level".

(2) The detection velocity level is adjustable.

(3) After detecting the unexpected robot motion on the basis of the angular velocity, the safety device switches all motors of the robot off.

(4) After switching off all motors, the safety device locks the shaft.

(5) The lock of the shaft is released by rotating the shaft in a direction opposite to the direction in which the safety device locks the shaft.

(6) The safety device consists of only passive components without actuators, controllers and batteries.

By the above characteristics (1), (3) and (4), we can expect that the safety device prevents high-speed collision between the robot and a human and reduces the collision force (see Fig.1 (i) and (ii)). Furthermore, by (2), we can adjust the detection velocity level according to the requirements for the given task. For example, when the

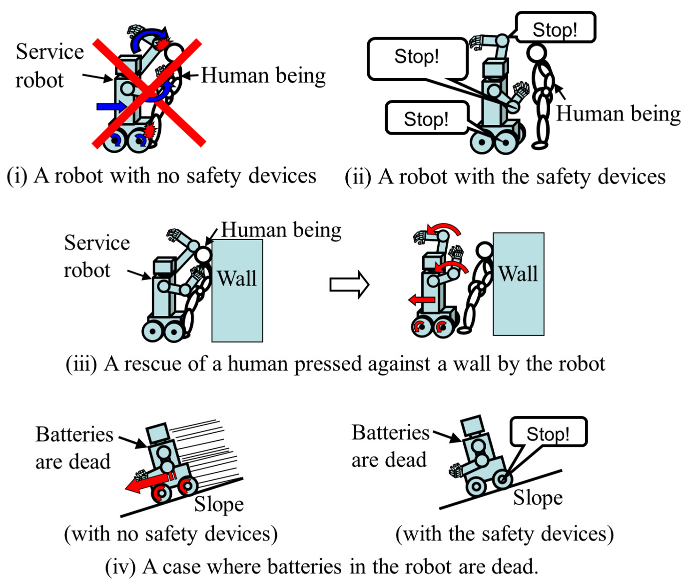

Fig.1 Characteristics of the safety device

robot is required to share workspace with humans in order to support humans, we can set the detection velocity level to low. When the robot is required to perform a high-speed task, we can set the detection velocity level to high and evacuate the robot's workspace. Additionally, by (5), if a human is pressed against a wall by the robot locked by the safety device, we can easily rescue the human by moving the robot in a direction opposite to the direction in which the human is pressed (see Fig.1(iii)). Finally, by (6), even if the batteries in the robot are dead, the safety device can act because it requires no power supply (see Fig.1(iv)).

2.2 Structure and Mechanism of the Safety Device

2.2.1 Structure

Fig.2 shows an example of robots equipped with the safety devices. As shown in Fig.2, the shaft of the robot arm is driven by the motor. In order to lock the shaft in clockwise and counterclockwise directions, two safety devices (one safety device for locking in the clockwise direction and another safety device for locking in the counterclockwise direction) are installed.

Fig.3 shows the structure of the safety device. Gear A, Plate B and Ratchet Wheel A are attached to the shaft of the robot arm. Claw B is attached to Plate B by Pin D. Guide Bar B attached to Claw B is inserted in Guide Hole B of Plate A. The shaft rotates Plate A via the torsion spring. One end of Linear Spring A is connected to Pin B attached to Plate C, and another end is connected to Pin A of Frame B. Plate C has Inner Teeth. Guide Bar A attached to Claw C is inserted to Guide Hole A of Plate C. Gear B meshes with Gear A. A rotary damper is connected to Gear B. Claw A is connected to the axis of the rotary damper. One end of Linear Spring B is connected to Claw A, and another end is connected to Frame A. Frame A is mounted on Frame B. Switch A which can interrupt electric power supply to all motors of the robot is installed at the position of being pressed by Pin C when Plate C is rotated. Fig.4 shows the details of Plate A. The ratchet teeth portion is connected to the plate portion via a spring.

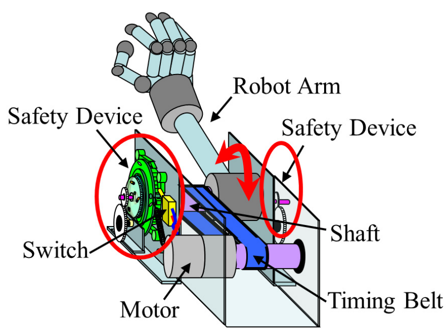

Fig.2 A robot arm with mechanical safety devices

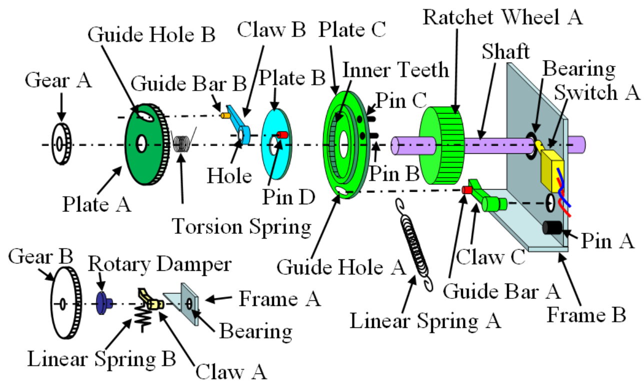

Fig.3 The structure of the mechanical safety device

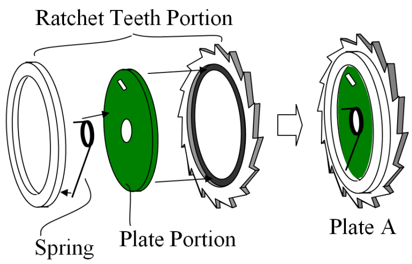

Fig.4 Details of Plate A

2.2.2 Mechanism

(1) Velocity-based detection mechanism

Fig.5 shows the mechanism which mechanically detects the unexpected robot motion on the basis of the angular velocity of the shaft. The damping torque by the rotary damper and the spring torque by Linear Spring B act on Claw A, when Gear B is rotated by Gear A. As the velocity of Gear A (shaft) increases, the damping torque increases. Claw A rotates by the torque difference between the damping torque and the spring torque, and locks Plate A, if the velocity of the shaft exceeds the detection velocity level. The detection velocity level is adjustable by changing the position where the end of Linear Spring B connected to Claw A is attached.

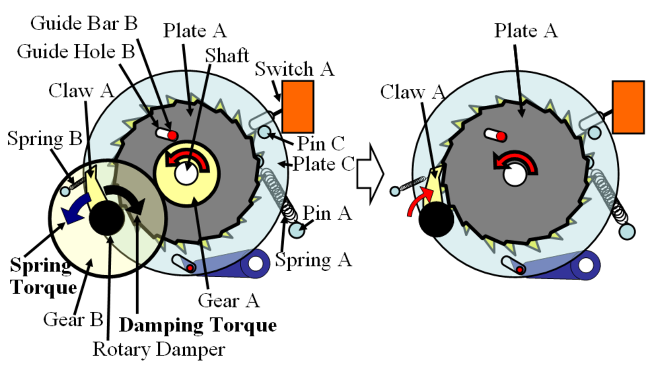

Fig.5 The velocity-based detection mechanism

(2) Shaft-lock mechanism

Fig. 6 shows the mechanism to mechanically lock the shaft. After Plate A was locked, Claw B slides along Guide Hole B of Plate A by the rotation of Plate B and contacts with the inner teeth of Plate C, as shown in Fig. 6(b). After contacting with the inner teeth, Claw B is hooked to the inner teeth and rotates Plate C (Fig. 6(c)). By the rotation of Plate C, Pin C switches off and Claw C moves along Guide Hole A (Fig. 6(d)). After that, Claw C meshes with Ratchet

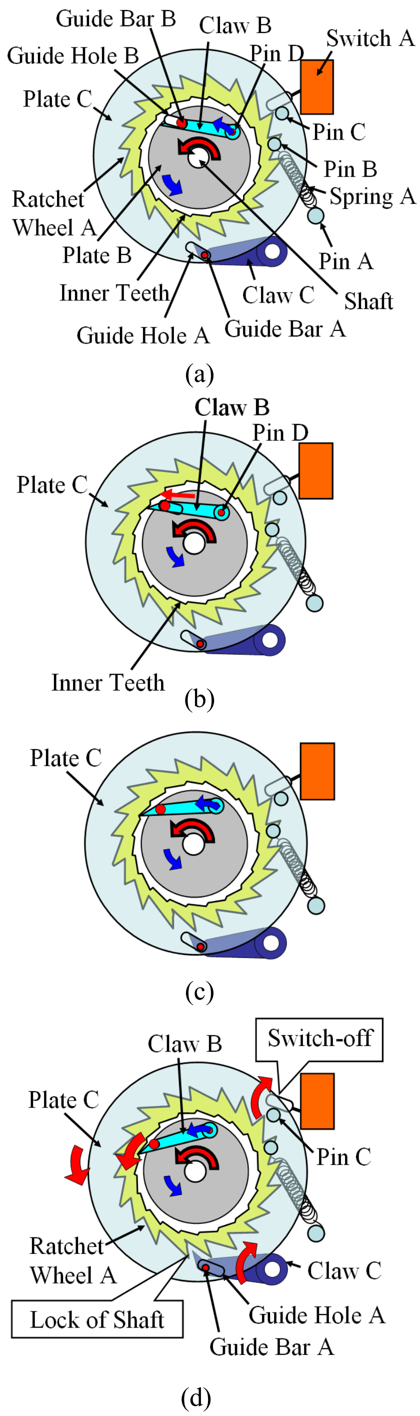

Fig. 6 The shaft-lock mechanism

Wheel A and thus the shaft is locked.

After the shaft is locked, the damping torque acting on Claw A becomes zero. However, if the gravitational torque generated by the arm acts on the shaft in the direction where the safety device is locking (see Fig.7), the lock of the shaft is kept by meshing between Ratchet Wheel A and Claw C. The lock of the shaft is released by moving the arm in the inverse direction.

After the shaft is locked, if the gravitational torque acts in the inverse direction to that of Fig.7 and the velocity of the shaft exceeds the detection velocity level in the inverse direction, the shaft is locked by another safety device for the inverse direction. If the velocity of the shaft does not reach the detection velocity level, the arm slowly falls down and stops in a state of being suspended from the shaft.

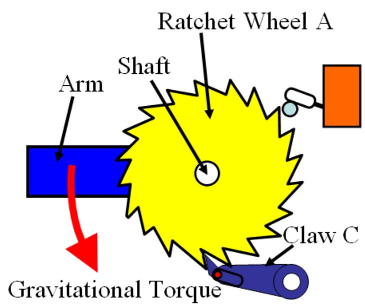

Fig.7 Lock of shaft

(3) Mechanism using three claws

In the above mechanism, in order to be meshed with Ratchet Wheel A and Claw C, it is necessary that the teeth number of Ratchet Wheel A equals the number of inner teeth of Plate C. It is preferred that the rotation angle of Claw B is as short as possible after Claw B contacts with the inner teeth of Plate C. As a method for shorting the rotation angle of Claw B, we can propose increasing the number of inner teeth on Plate C and the number of teeth on Ratchet Wheel A. However, there is a limitation on an increase in the number of inner teeth, because the safety device installed to robot is required to be as compact as possible.

In the following, we explain a mechanism using some claws. By using some claws, the mechanism provides the same advantage as when the teeth number is increased. Fig. 8 illustrates the mechanism in which three claws are used. Each claw is positioned as shown in Fig. 8(a). Lines 1, 2 and 3 trisect each tooth of the inner teeth. If Claw B_1 does not mesh with one of the teeth at the moment of contact, only with the movement of Claw B_2 by one third

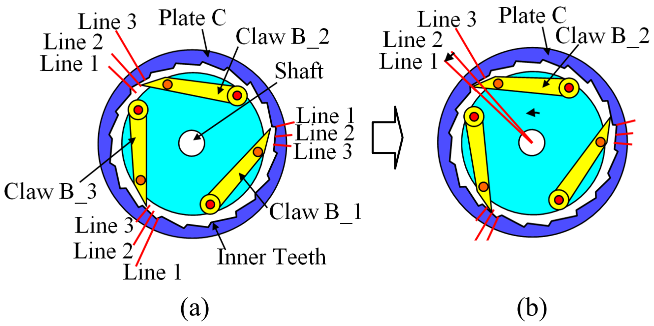

Fig.8 Three claws

of the tooth width, Claw B_2 meshes and rotates Plate C (Fig.8(b)). Note that, in this case, by using the Ratchet Wheel A having three times as many teeth as the inner teeth, Claw C is reliably meshed with the Ratchet Wheel A.

3 EXPERIMENT AND DISCUSSION

We developed the safety device using three claws' mechanism. We experimentally examined whether the shaft is stopped by the developed safety device after the angular velocity of the shaft exceeds the detection velocity level. Fig.9 shows the experimental setup. We attached some markers on the shaft and Claw A, then measured the positions of the markers by using a motion capture system (HAS-500, DITECT Corporation) while increasing the velocity of the shaft by the motor. The sampling frequency of the motion capture system was 200[Hz]. We experimented using a detection velocity level of 2.3 [rad/s]. The number of trials was 10. The angle of Claw A was approximately 0.21[rad] when Claw A locks Plate A.

Fig. 10 shows a typical example of the experimental results. Fig. 10 indicates that the shaft was stopped by the safety device after the angular velocity of the shaft exceeded the detection velocity level. The other results were approximately the same as this result.

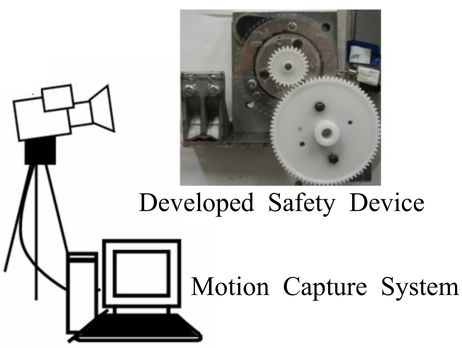

Fig.9 Experimental setup

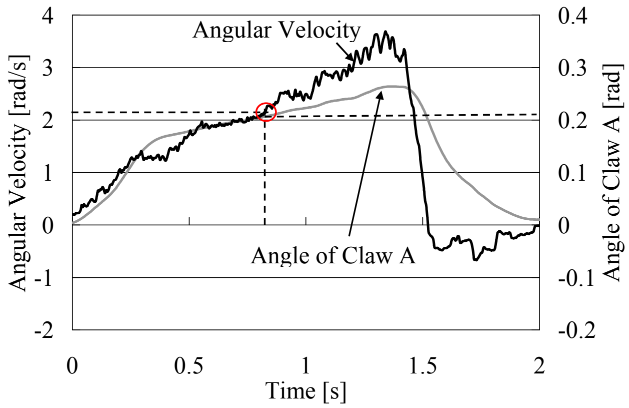

Fig.10 Experimental result

4 CONCLUSION

In this paper, we presented a new safety device to improve the safety of service robots for humans. Furthermore, we designed and developed the safety device. Finally, we experimentally examined the usefulness of the safety device.

ACKNOWLEDGMENT

This work was supported by JSPS KAKENHI (Grant-in-Aid for Scientific Research (C): 21560271).

REFERENCES

[1]Zinn M. et al (2004), Playing It Safe - Human-Friendly Robots, IEEE Robotics and Automation Mag., vol.11, 2004, pp.12-21.

[2]Iwata H., Sugano S. (2009), Design of Anthropomorphic Dexterous Hand with Passive Joints and Sensitive Soft Skins, SI International 2009, pp.129-134.

[3]Kulic D., Croft E. A. (2006), Real-time safety for human-robot interaction, Robotics and Autonomous Systems, 2006, pp.1-12.

[4]Suita K. et al (1995),A Failure-to-Safety "Kyouzon" System with Simple Contact Detection and Stop Capabilities for Safe Human-Autonomous Robot Coexistence, IEEE International Conference on Robotics and Automation, 1995, pp.3089-3096.

The Seventeenth International Symposium on Artificial Life and Robotics 2012 (AROB 17th '12),
B-Con Plaza, Beppu, Oita, Japan, January 19-21, 2012

Improvement by the image processing of the certification of a reconstructed image from Computer-Generated Hologram picked up by digital watermark

Yuki Hirama and Ken-ichi Tanaka

Department of Electronics and Bioinformatics, School of Science and Technology
Meiji University
1-1-1 Higashi-Mita, Tama, Kawasaki, 214-8571, Japan
E-mail: { ce01084, Tanaken }@ise.meiji.ac.jp

ABSTRACT: Computer Generated Hologram (CGH) is made for three dimensional image of a virtual object that difficult to illuminate laser light directly. Even if this CGH deteriorate, it has characteristic that reconstruct is possible. This is a characteristic called the multiplexing that Fourier transform has. This characteristic is paid attention for the purpose of embedding this CGH as digital watermark because it is necessary to deteriorate this CGH. The purpose of this study is to make a computer authenticate CGH which we embedded it as digital watermark and took it out and regenerated. The method of the certification is Phase Only Correlation (POC). This study succeeded in improving the value of this evaluation.

1. INTRODUCTION

Computer Generated Hologram [1]~[3] (CGH) is made for three dimensional image of a virtual object that difficult to illuminate laser light directly. We uses dislocation model of CGH that be made relatively easily because it takes time to reconstruct three dimensional image even if use the fast algorithm. This dislocation model of CGH is demanded by calculating to Fraunhofer diffraction namely disintegration Fourier Transform. Even if this CGH deteriorate, it has characteristic that reconstruct is possible. This characteristic is paid attention for the purpose of embedding this CGH as digital watermark because it is necessary to deteriorate this CGH. This technique is used for the purpose of copyright protecting for digital image The digital watermark to use in this study is a frequency domain type. This technique has the characteristic that the SN ratio of an original image and an embedded image is higher. But this technique has a weak point. When the image which was made by this technique deteriorated, the embedded image not can be taken out. For example, it is the deterioration such as the weighted average filter. Therefore, we do not consider the deterioration of the image which was made by this technique in this study. The purpose of this study is to make a computer authenticate CGH which we embedded it as digital watermark and took it out and regenerated. The method of the certification is Phase Only Correlation (POC). POC is technique in consideration of only the form of the image. This method that pay attention to form includes a fault. It is that a correlation of O and similar form such as Q rises. This study tried improvement by doing image processing before taking the correlation of reconstruct image and original image to improve.

2. METHOD

2.1 MAKING Computer-Generated Hologram

The section explains the principle of the Fourier transform type hologram to use in this paper. For original image f(x,y), we perform a calculation equivalent to Fraunhofer diffraction namely disintegration Fourier Transform. The coordinate system of the original image defines it as (x,y). The coordinate system on the hologram side defines it as (u,v). When we perform this calculation, spectrum information is concentrated in the low frequency domain when we apply it for an original image. It is common to put random phase on original image f(x,y) to distribute this spectrum information for a frequency domain uniformly. Random phase ϕ (x.y) is random numbers of 0 - 2π. In other words, we regard a phase ingredient as important generated complex number information. Therefore, the computer hologram of the Fourier transform type is made by the following expressions.

$$F(u,v) = \frac{1}{\sqrt{N^2}} \sum_{m=0}^{N-1} \sum_{n=0}^{N-1} f(m,n) \phi(x,y) \cdot \exp\left\{ -j \frac{2\pi(mu+nv)}{N} \right\} \tag{2.1.1}$$

In addition, We perform this processing because it is known that gradation characteristics are compatible with the resolution of the reconstruct image by making F(u,v) 2 value by the following methods[4].

$$F'(u,v) \begin{cases} +1 & (\pi/2 \le \left| \arg F_S(u,v) \right|) \\ -1 & (otherwise) \end{cases} \tag{2.1.2}$$

$$F_S(u,v) = \frac{F(u,v)}{\max \left| \mathrm{Re}\left[F(u,v) \right] \right|} \tag{2.1.3}$$

Show the concrete processing result in the next section.

2.2 DIGITAL WATERMARK

This section explain frequency domain embedding type digital watermark to use in this paper. The frequency ingredient embedding type is the digital watermark which paid attention to that a high frequency ingredient of the Fourier transform is hard to look like human eyes. This method can embed CGH as digital watermark without affecting an original image more markedly than the masking type[5]. The information that is embedded by this method is poor at attack of compression father. But, the attack to the image after having embedded it does not consider it in this paper. Because we take first priority whether the certification of the reconstruct image is possible, in this paper use this method. Show below the processing results.

Fig.2.2.1
Original image

Fig 2.2.2
Embedded image
frequency ingredient

Fig 2.2.3
Embedded image
masking type

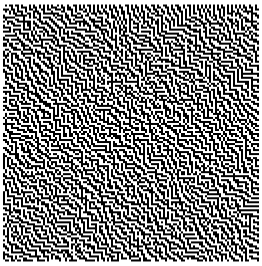

Fig 2.2.4
CGH
original

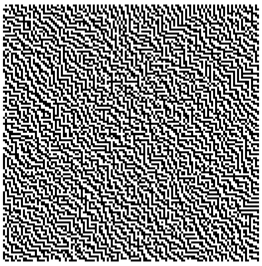

Fig 2.2.5
CGH
picked up

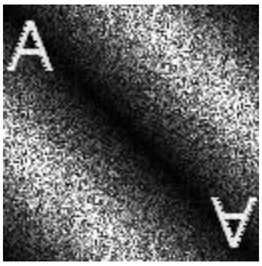

Fig 2.2.6
Reconstructed image
by original CGH

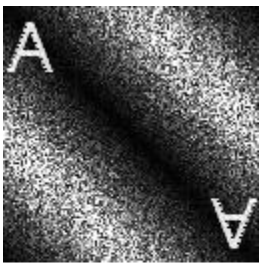

Fig 2.2.7
Reconstructed image
by picked up CGH

This study use the spectrum of the imaginary number to be born in the middle of this processing as a compound key. This is to suppress the deterioration of the image

2.3 PHASE-ONLY CORRELATION

Phase-Only Correlation [6] is a method to calculate a correlation that is made to do normalization to 1 of a provided amplitude ingredient by Fourier transform. Therefore, the method is not affected by the brightness value of the image. In other words the method was pay attention to the shape of the object in the image to compare only the phase ingredient of the image. show below a definition of Phase-Only Correlation.

Two images were put with f(x,y) and g(x,y) each.DFT is Fourier transform, they are as follows.

$$F\ (u,v) = DFT\left[f(x,y)\right] \quad (2.2.1)$$

$$G\ (u,v) = DFT\left[g(x,y)\right] \quad (2.2.1)$$

Phase information and amplitude information was expressed as follows. The amplitude ingredient was regarded as 1

$$F(u,v) = A_F(u,v)\exp(j\ \theta_F(u,v)) \quad (2.2.1)$$

$$G(u,v) = A_G(u,v)\exp(j\ \theta_G(u,v)) \quad (2.2.1)$$

Phase-Only Correlation was defined as follows

$$PH(u,v) = IDFT\left[\frac{F^*(u,v)G(u,v)}{\left|F^*(u,v)G(u,v)\right|}\right] \quad (2.2.1)$$

$F^*(u,v)$ This function is complex conjugate.

2.4 THE IMAGE PROCESSING

1. The pixel level of the image is made a 2 level.(The threshold is 128.)
2. When the value of the attention pixel is clearly higher than the value of the pixel of the circumference, the value of the attention pixel is changed to 0.
3. The image is processed by raster operation until the change of the image disappears.
4. The image is processed by the Laplacian filter. The outline of the letter is extracted in this way.
5. The image which was processed to division into four is used in only a left upper part.

Show below the processing results.

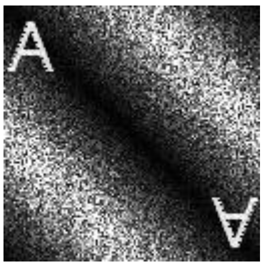

Fig 2.3.1
Before processing

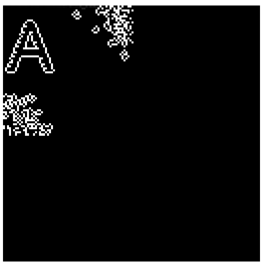

Fig 2.3.2
After processing

3. EXPERIMENT METHOD

1. Prepare the128*128 following images of "A" – "Z" form of the P-Gothic.
2. CGH which was made by a source image is embedded as digital watermark.
3. The embedded image is taken out. The image taken out is reconstructed.
4. The evaluation level by POC of the reconstruct image which nothing is made is compared with the correlative value by POC of the processed reconstruct image.
5. This study assumes the image which showed the highest correlative price a certification image.

4. RESULT

Show below the experiment results. It was revealed that original image and processed reconstruct image became highest. Characteristic examples of the correlative value by POC are "C" that is changed 0.087792897 to 0.150123, "E" that is changed 0.0532826 to 0.107673,"F" that is changed 0.0532826 to 0.094749.

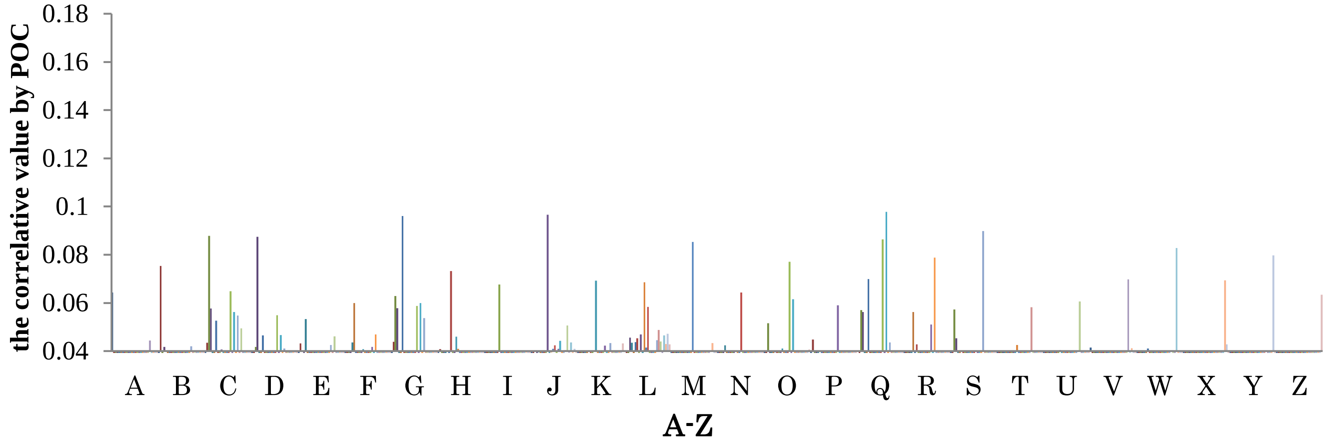

Fig 4.1 original - reconstruct

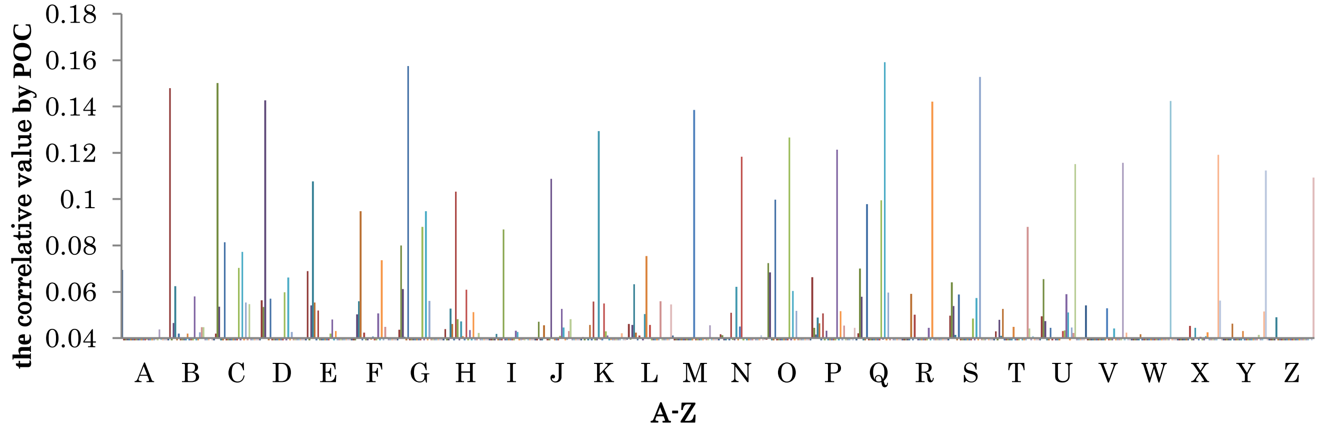

Fig 4.2 original - processed

5. CONSIDERATION

The correlative value by POC improved generally by performing the image processing that paid attention to an outline. The correlative values of character "E" and "F" improved very much. This improvement is able to authenticate it easily by computer. However, the correlative value such as character "A", "I" and "L" did not improve very much. It becomes the future problem to improve these values.

6. REFERENCES

[1] R. Eschbagh: "Comparison of error diffusion method for computer-generated holograms", Appl. Opt., 30, 26, pp.3702-3710(1991)
[2]E. Barnard: "Optimal error diffusion for computer-generated holograms", J. Opt. Soc. Am., A5 pp.1803-1817(1988)
[3]K. Tanak and T. Shimomura: "Three dimensional images reconstruction from computer-generated holograms using error diffusion method", Journal of ITE Vol. 52, No.3, pp. 399-401, 1998.
[4]Yuta Fujita and Ken-ichi Tanaka "Improvement of image reconstructed from Kinoform using error diffusion method"
[5]K.Komatsu and K.Tanaka(2004),Digital-watermarking technology, The institution image electronics engineers of japan (in Japanese)
[6]K.Takahumi ,K.Ito "the Matching of Phase-Only Correlation", Fundamentals of Review, Vol.1, No.1, pp.30~pp40, 2007

The Seventeenth International Symposium on Artificial Life and Robotics 2012 (AROB 17th '12),
B-Con Plaza, Beppu, Oita, Japan, January 19-21, 2012

Improvement of digital halftoning

Hiroki TAKEKAWA and Ken-ichi TANAKA
Department of Science and Technology Meiji University
1-1-1, Higashimita, Tama, Kawasaki, Kanagawa, 214-8571, Japan
E-mail: ce01054@meiji.ac.jp

Abstract: When the image is displayed in the device that there is a limitation in the number of colors and the density value, the half tone processing is a needless technology. Several techniques like the dither method and the error diffusion method[1], etc. are proposed as a well known halftoning. The image evaluation of the processing image by the error diffusion method is superior compared with dither methods. Though, the processing image by the error diffusion method has visual problem. The blur is generated in the edge area. The noise of the striped pattern is generated in area that is low level value change of pixel. This paper, consider improvement the processing image by applying error diffusion algorithm with edge enhancement to using error coefficient corresponding to step edge. It is found that proposed technique process high quality halftoning image compared with error diffusion algorithm with edge enhancement.

Keywords: hlftoning, error diffusion, edge enhancement,

1 Introduction

Error diffusion algorithm with edge enhancement[2] is effect edge enhancement by determined threshold level for each pixel. Though, only this process, it is persisted that the noise of the striped pattern is generated in area that is low level value change of pixel. It is needed to solve this problem taking advantage of the Error diffusion algorithm with edge enhancement. In this paper, we consider the effectiveness that applying error diffusion algorithm with edge enhancement to using error coefficient corresponding to step edge.

2 Error diffusion algorithm with edge enhancement

In this section, describe error diffusion algorithm with edge enhancement briefly. Position of pixel being processed is put with (x, y), the pixel's value is g(x, y), the value that pixel processed is g'(x, y). Then g'(x, y) is as below.

$$g'(x,y)=\begin{Bmatrix}1 & g(x,y)\geq t(x,y)\\ 0 & g(x,y)<t(x,y)\end{Bmatrix} \tag{1}$$

t(x, y) is threshold level for each pixel. Enhancement coefficient is put with k, Standard threshold level is put with t', then t(x, y) is as below.

$$t(x,y)=(1-k)g(x,y)+kt' \tag{2}$$

Quantization error by processed is as below. This quantization error is diffused to neighborhood pixels as below.

$$error(x,y)=g(x,y)-g'(x,y) \tag{3}$$

$$(x',y')=(x',y')+W(x,y)\times error(x,y) \tag{4}$$

W(x, y) is diffusion coefficient that's range is 1 from 0. When k=1, threshold level for each pixel t(x, y) are same as standard threshold level t', it result in several algorithm error diffusion.

3 Reducing stripe noise using proper error coefficient

It is effective to solve the generated noise of the striped pattern that using large size error coefficient in area that is low level value change of pixel[3]. Though, in area pixel's value change high, the distance between the area generate quantization error and the area diffused quantization error is free. This causes the blur is generated in the edge area. Though, it is need to take the following measures.

1) In low level value change of pixel area, large size error coefficient is used.
2) In high level value change of pixel area, near the edge area, small size error coefficient is used.

Next section, describe the algorithm to search high level value change of pixel area to use above method.

4 Detection edge using differential filter

This study, we detect the edge using differential filter to search high level value change of pixel area. Differential filter outputs value change level of pixel as value of pixel, this is effective to search high level value change of pixel area. Differential filter are Fig.1, Fig.2. The value calculated by the differential filter is outputted as value of pixel, the image edge enhanced is displayed. (Fig.3). Value of edge is put with L(x, y), then L(x, y) is as below.

0	0	0
0	1	-1
0	0	0

Fig.1.
Horizontal differential filter ⊿X

0	0	0
0	1	-1
0	0	0

Fig.2.
Vertical differential filter ⊿Y

$$L(x, y) = \sqrt{\triangle X(x, y)^2 + \triangle Y(x, y)^2} \tag{5}$$

Fig.3.
The image edge enhanced

5 Proposed method

It is summarized as follows : the proposed method.

1) The original image is detected the edge in advance.
2) Error diffusion algorithm with edge enhancement applied to the original image.
3) In near the edge area, small size error coefficient (Fig.4) is used. In low level value change of pixel area, large size error coefficient (Fig.5) is used.

It is used as small size error coefficient that is Floyd and Steinberg error coefficient(Fig.4). It is used as large size error coefficient that is original error coefficient(Fig.5). And also, near the edge area is defined as pixel that is detected the edge, and defined as 8 pixels surrounding the edge pixel is detected.

In the case, the quantization error by processed in low level value change of pixel area is diffused to near the edge by large size error coefficient, it is used small error diffusion the pixel.

	x	7/16
1/16	5/16	3/16

Fig.4.
Floyd and Steinberg error coefficient
(x : processed pixel)

				x	128	64	32	16
8	16	32	64	128	64	32	16	8
4	8	16	32	64	32	16	8	4
2	4	8	16	32	16	8	4	2
1	2	4	8	16	8	4	2	1

$\times\left(\frac{1}{930}\right)$

Fig.5.
Original error coefficient
(x : processed pixel)

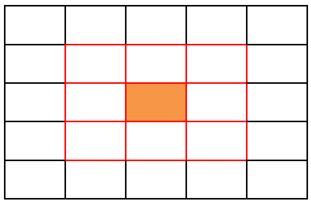

Fig.6.
The areas near the edge.

The pixel edge is detected.

The areas near the edge.

g'(x, y) processed above method is displayed binary as blue, green, red. Error diffusion with edge enhancement algorithm and using error coefficient corresponding to step edge is complete.

6 Result

The original image is Fig.7. This size is 256×256. Value of pixel is 256gradations. It is difficult to judge visual problems like the noise of the striped pattern by numerical evaluation level [4]. There for, these problems are judged by visual. And level deterioration by binary is judged tone reproduction evaluation (MSE) [4], [5]. Standard threshold level is determined by discriminative analysis method [6], [7]. Discriminative analysis method is determiner considering background and object. There for, it is expected superior process in the vicinity monotonic area and edge area. Fig.8 is error diffusion algorithm with edge enhancement. Fig.9 is proposed method.

$$MSE = \frac{1}{MN}\sum (g(x,y) - g'(x,y))^2 \qquad (6)$$

Fig.7. Original image

Fig.8. Error diffusion algorithm with edge enhancement
MSE=22.5074846939085

Fig.9. Proposed method
MSE=22.1088512291146

Fig.9 is superior process in low level value change of pixel area than Fig.7. MSE is superior than Fig.8 of Fig.9 is more. From this, it is effective for tone reproduction evaluation that applying error diffusion algorithm with edge enhancement to using error coefficient corresponding to step edge.

7 Closing

It is effective for decrease the noise of the striped pattern and tone reproduction evaluation, taking advantage of the error diffusion algorithm with edge enhancement that applying error diffusion algorithm with edge enhancement to using error coefficient corresponding to step edge. In addition, it is found evaluation level (MSE) is depended on threshold level from this study. Future study, it is needed to consider that another determination threshold level.

Reference

[1] Floyd,R.W.,and L.Steinberg: "Adaptive Algorithm for Spatial Gray Scale", SID Int. Sym. Digest of Tech. Papers, pp.36-37, (1975)

[2] Eschbach R. and Knox K. T.: "Error diffusion algorithm with edge enhancement", J. Opt. Soc. Am., A8, 8, pp.1844-1850(Aug.1991)

[3] Kazuhisa YANAKA: "Scalable Filter for Error Diffusion", IEICE ,pp.49-52, (2004)

[4] Chihiro HANAOKA and Akira TAGUCHI: "An Error Diffusion Algorithm with Date-dependent Pre-filtering", (May.2005)

[5]Naoki KOBAYASHI, and Hideo SAITOH, :"Halftoning Technique Using Genetic Algorithm", IEICE(D-II). Vol.J78-D-II, no. 10,pp.1450-1459, (Oct. 1995)

[6] Otsu N.: "A Threshold Selection Method from Gray-Level Histograms", IEEE Trans, Syst. Man Cybernet.

SMC-9, 1,pp.62-66 (1979)
[7] Otsu N: "Automatic threshold selection method based on determination and least squarescriterion" (D), IEICE J63-D,4 pp.349-356,(1980)

The Seventeenth International Symposium on Artificial Life and Robotics 2012 (AROB 17th '12),
B-Con Plaza, Beppu, Oita, Japan, January 19-21, 2012

An Improved Differential Evolution for solving Large Scale Global Optimization

Sheng-Ta Hsieh[1], Shih-Yuan Chiu[2] and Shi-Jim Yen[2]

[1] Department of Communication Engineering, Oriental Institute of Technology, New Taipei City, Taiwan, R.O.C.
[2] Department of Computer Science and Information Engineering, National Dong Hwa University, Hualien, Taiwan, R.O.C.

fo013@oit.edu.tw

Abstract: Differential evolution (DE) is a population-based optimization algorithm. The members of population in DE are called parameter vectors. Due to more real-world optimization problems become increasingly complex. Algorithms with more ability and efficiency for searching potential solution are also increasing in demand. Thus, in this paper, an improved DE is proposed for solving large scale global optimization. The proposed method is incorporated with the population manager to eliminate redundant parameter vectors or to hire new ones or to maintain population size according to the solution searching status to make the process more efficient. The proposed method also involves mutation and cross-over for prevent the solutions from falling into the local minimum and enhance searching ability.

Keywords: Differential evolution, population manager, optimization, traveling salesman problem.

1 INTRODUCTION

Due to more real-world optimization problems become increasingly complex. Algorithms with more ability and efficiency for searching potential solution are also increasing in demand. In last four decades, more and more heuristic-based algorithms were proposed for solving numerical optimization, such as genetic algorithm (GA)[1] and particle swarm optimizer (PSO)[2], etc. In 1997, the concept of original differential evolution (DE) was proposed by Storn and Price [3].

Differential evolution (DE) is a population-based optimization algorithm. The members of population in DE are called parameter vectors. There are four common mutation strategies of DE were developed [4][5]and shown as follows.

1. DE/best/1
$$x_n^{child_i} = x_n^{best} + F\left(X_n^{r_1} + X_n^{r_2}\right)$$
2. DE/rand/2
$$x_n^{child_i} = x_n^{r_1} + F_1\left(X_n^{r_2} + X_n^{r_3}\right) + F_2\left(X_n^{r_4} + X_n^{r_5}\right)$$
3. DE/target/1
$$x_n^{child_i} = x_n^{i} + F\left(X_n^{r_1} + X_n^{r_2}\right)$$
4. DE/target to best/1
$$x_n^{child_i} = x_n^{i} + F\left(X_n^{best} + X_n^{r_1}\right)$$

In this paper, an improved DE is proposed for solving large scale global optimization. The proposed method is incorporated with the population manager control population size according to the solution searching status. Also, improved mutation and crossover are involved for prevent the solutions from falling into the local minimum and enhance searching ability.

2 PROPOSED METHOD

The first thing to apply DE for solving different applications is to decide several initial parameters of DE, such as population size. Having more chromosomes can extend the searching space and increase the probability of finding the global optimal solution, but it will require more time in each iteration. The problem is that, until now, there is no way to know what size of population is suitable for solving the current problem. Here, a population manager (PM) is introduced into DE to enhance its searching ability. The PM will increase or decrease population size according to the solution searching status. Thus, the population size in the proposed DE is variable.

2.1 Population Manager

The population manager will increase or decrease particle numbers according to the solution-searching status; thus, the population size in DE is variable. If the particles cannot find a better solution to update the global best solution, particles may be trapped into the local minimum during the searching process or need a competent guide to lead them toward the potential area. Thus, the information (experience) of existing particles may be too little to handle the current solution-searching procedures. Thus, new particles should be added into the population to speedup the solution searching progress.

On the other hand, if particles can find one or more solutions to update the global best solution, the existing particles may too many. For saving some time on finding the global optimal solution, the redundant particles should be expelled from the population to conserve their evolution time for speeding up the solution-searching progress.

2.2. Mutation

In general, mutation is adopted to generate new chromosomes, mutate one or more genes, to save chromosomes that fell into the local minimum using random process, and to explore other potential searching spaces.

In proposed method, mutation is to randomly select a dimension (d_1) of the chromosome i and to perturb it in the range between minimal and maximal solution of another randomly selected dimension (d_2). This will ignore other dimensions but can fine tune the solutions of specific dimensions one by one in the chromosome. To share searching ranges of selected dimensions among particles can generate more potential solutions. In this paper, the mutation rate is increase linearly from 0.001 to 0.01.

2.3. Crossover

In proposed method, crossover is consisted of two parts, one is the same as original DE, and the other is one-cut point cross-over. The activating rate of them is 50-50 in first iteration. After that, the activating rate it will depend on their child's survival rate in previous iteration.

The one-cut-point cross-over is to randomly select a cut-point of particle, and to exchange the right parts of cut-point from two particles. Then, linear combination at the cut-point is performed on particles to generate new solution.

3 EXPERIMENTS

In the experiments, the IEEE CEC 2008 test functions [6], which includes two unimodal and five multimodal functions, were chosen for testing four variants of DE [4][5] and proposed method. Each test functions are set as 500 dimensions and run 25 times and calculated their mean values and standard deviation. The maximum fitness evaluations (FEs) were set as 2,500,000.

The results five variants of DE approaches on the seven test functions with 500D problems are presented in Table I. The real optimal values are also listed on right column of Table I. The best results among the five approaches are shown in bold. From the results, the proposed method surpasses all other algorithms on functions 1, 2, 3, 5, and 6. The DE/best/1 performed better than the proposed on functions 1 and 7. The proposed method can efficiently find better solutions than other algorithms in the same FEs.

4 CONCLUSIONS

In this paper, the proposed method has been presented to solve large scale global numerical optimization problems. The proposed population manager strategy can adjust population size according to its current solution searching state to ensure better (potential) parameter vectors will join the evolution of DE. It also makes DE more robust, prevents parameter vectors from falling into the local minimum. The experiments show that the proposed method can get closer to optimal solutions, and it is more efficient than other variant of DE on the problems studied.

REFERENCES

[1] L. B. Booker, D. E. Gokdberg, and J. H. Holland, Classifier systems and genetic algorithms. Technical report, no. 8, University of Michigan, 1978.

[2] R. C. Eberhart and J. Kennedy, "A new optimizer using particle swarm theory," in Proc. 6th Int. Symp. Micro Mach. Human Sci., Nagoya, Japan, pp. 39–43, 1995.

[3] R. Storn and K. V. Price, "Differential evolution - A simple and Efficient Heuristic for Global Optimization over Continuous Spaces," *Journal of Global Optimization*, vol. 11, mo. 4, pp. 341-359, Dec. 1997.

[4] K. Price, R. Storn, and J. Lampinen, *Differential Evolution - A Practical Approach to Global Optimization*. Berlin, Germany: Springer, 2005.

[5] K. V. Price, "An introduction to differential evolution," in New Ideas in Optimization, D. Corne, M. Dorigo, and V. Glover, Eds. London, U.K.: McGraw-Hill, pp. 79-108, 1999.

[6] http://nical.ustc.edu.cn/conferences/cec2008/lsgo/LSGO.CEC08.Benchmark.rar.

Table I
Experiment Results of 500 Dimensions Problems and Their Optimal Values.

Functions \ Methods	Proposed Method	DE/best/1	DE/target/1	DE/rand/2	DE/target to best/1	Real Optimal Values
f_1	**-4.5000E+02 ±3.9904E-05**	-4.4913E+02 ±5.1040E-01	-3.4633E+02 ±2.1536E+01	-4.4374E+02 ±9.1772E-01	-4.4987E+02 ±2.5957E-02	-450
f_2	**-4.1110E+02 ±1.7628E+00**	-3.6095E+02 ±3.3799E+00	-3.6802E+02 ±1.6044E+00	-3.7015E+02 ±1.2104E+00	-3.7109E+02 ±1.8678E+00	-450
f_3	**1.9389E+03 ±2.1301E+03**	2.7197E+03 ±4.8660E+02	2.0512E+07 ±7.0900E+06	3.4429E+04 ±1.0716E+04	3.0089E+03 ±4.6241E+02	390
f_4	-3.2995E+02 ±9.6550E-03	**-3.2996E+02 ±8.8627E-03**	2.0512E+07 ±7.0900E+06	3.1408E+03 ±1.3488E+02	-1.3606E+02 ±1.4043E+01	-330
f_5	**-1.7983E+02 ±1.7837E-01**	7.7221E+03 ±4.7561E+02	-1.5133E+02 ±4.7245E+00	-1.7592E+02 ±9.4683E-01	1.1096E+03 ±1.1584E+02	-180
f_6	**-1.4000E+02 ±3.0787E-04**	-1.3171E+02 ±4.2650E+00	-1.2070E+02 ±3.9538E-02	-1.2065E+02 ±7.7734E-02	-1.2096E+02 ±6.2450E-02	-140
f_7	-7.4025E+03 ±1.0097E+01	**-7.4042E+03 ±1.2252E+01**	-5.6549E+03 ±7.6434E+01	-4.7831E+03 ±1.2842E+02	-7.3251E+03 ±1.7702E+01	unknown

The Seventeenth International Symposium on Artificial Life and Robotics 2012 (AROB 17th '12),
B-Con Plaza, Beppu, Oita, Japan, January 19-21, 2012

Calibration of Networked Sensors in an Intelligent Space Based on Interactive SLAM

Fumitaka Hashikawa[1], Kazuyuki Morioka[2]

[1,2] Meiji University, Kanagawa 214-8571, Japan
(Tel: +81-44-934-7304, Fax: +81-44-934-7304)

[1]ce01073@meiji.ac.jp, [2]morioka@isc.meiji.ac.jp

Abstract: For human-robot coexistent environments, intelligent spaces including networked laser range sensors, cameras and the other sensing device have been developed. So, we consider the intelligent spaces with Fast-SLAM based on Particle Filter. Especially, on the map construction based on a grid map is more accurate than normal SLAM. However, those methods use only sensing data from the mobile robot to achieve SLAM. In this study, a new method of SLAM, which uses distributed sensors fixed in an environment as intelligent space, is introduced. This method shares information with SLAM of mobile robot. And we introduce calibration method of distributed sensors.

Keywords: mobile robot, SLAM, intelligent space

1 Introduction

Recently, as one of the methods for achievement of human-robot coexistent environments, intelligent space including distributed sensors has been considered [1][2]. In order to build intelligent space and to perform human tracking with distributed sensors, it is required to know positions of distributed sensors in world coordinate system of intelligent space. Then, calibration of distributed sensors must be achieved for development of intelligent spaces. However, it is generally complicated works. Easy calibration method is required for spreading the intelligent space. Especially, since distributed laser range sensors are widely used for human tracking in intelligent spaces, geometrical calibration of many laser range sensors in unified world coordinate system must be achieved. This study focuses on easy calibration of networked laser range sensors.

In this study, structural map building of intelligent space with a mobile robot is exploited for sensor calibration. Maps built by the distributed sensors are compared with the map built in SLAM process of the robot. Then, positions of the distributed sensors are estimated according to matching results.

Also, the map built by the robot is improved accurately according to estimation results of the distributed sensors. This study aims to improve position estimation of the mobile robot itself and the distributed sensors of intelligent space based on interactively communicating each other.

2 Interactive FastSLAM with intelligent space

2.1 Outline

In this study, FastSLAM[3] is used for map building by the mobile robot and localization. SLAM is a method to make a map of the environment, and estimate position of mobile robots simultaneously based on matching between sensing results and environmental maps previously generated. FastSLAM based on particle filter can achieve SLAM with high speed and high accuracy. Especially, grid-based Fast SLAM is more promising. This method includes building a probabilistic grid map based on environment information obtained by a laser range sensor on the mobile robot. Then, the grid map and new sensing results are compared every sampling time, and the grid map is updated. Mobile robot's self-position is also presumed based on this map.

This study considers extending FastSLAM by robot itself to an interactive SLAM with the intelligent space. The interactive SLAM uses grid-maps built by the networked laser range sensors of the intelligent space in addition to grid-maps built by robot itself. When the mobile robot is in the networked sensor's monitoring area, grid maps built by the networked sensors are shared with the mobile robot and used as the constraints of the mobile robot's SLAM. In that case, grid map by networked sensor and sensing results of the mobile robot are compared in each particle in addition to matching with local maps in SLAM process by robot itself with laser sensing results. Particles that match both maps will be preserved as good particles in the FastSLAM. This is effective for improving accuracy of grid maps,

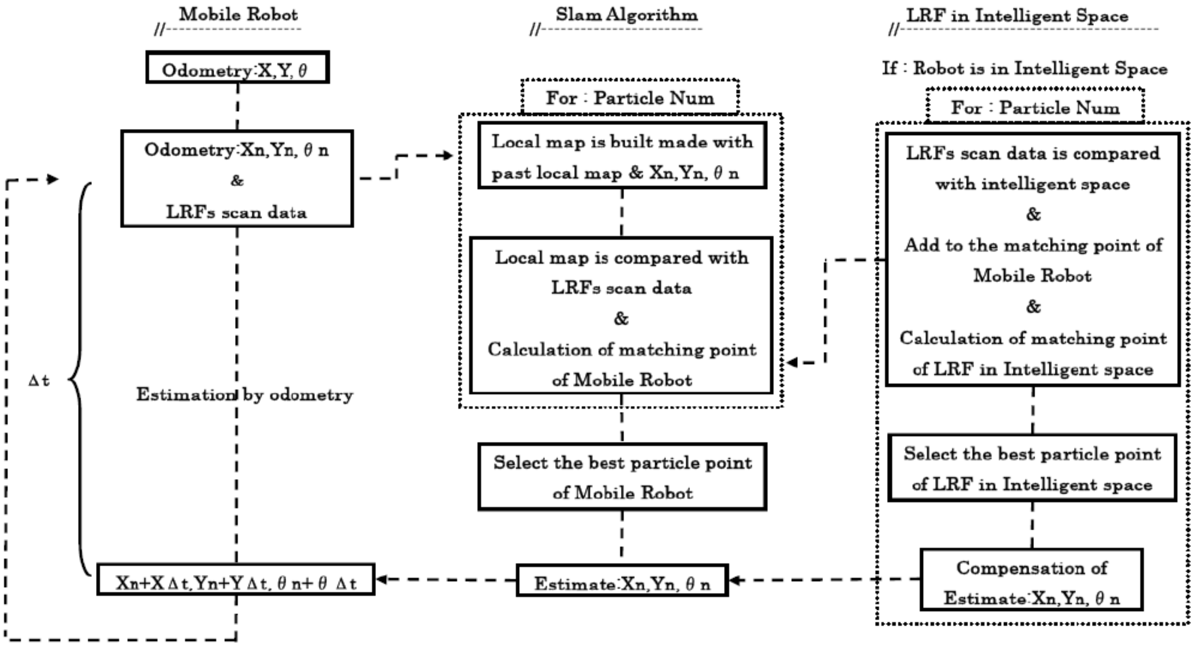

Fig.1 outline of interactive SLAM

because maps built by networked sensors fixed in the environments are integrated to map built by robot itself.

Next, it is assumed that positions of networked sensors in intelligent space are unknown. While interactive SLAM process, positions of networked sensor can be also estimated simultaneously in addition to positions of mobile robots.

2.2 System Configuration

System configuration of interactive SLAM with networked laser range sensors is shown in Fig.1. This system is configured with three processes: mobile robot control including data acquisition, SLAM process of mobile robot itself, mapping with distributed sensor.

In the robot control process, moving distance by odometry and range data by the sensor is measured for every sampling time. The measured data is sent to the SLAM process. At this time, the time stamps of sending data are saved in order to consider calculation time for estimation in the SLAM process. In the SLAM process, Grid Based FastSLAM is exploited for estimating robot positions and maps. Grid Based FastSLAM is based on a particle filter, and robot positions and maps are estimated as state variables. The computed state variable is retransmitted to the robot control process. Robot position in the robot control process is updated with considering the computation time for estimating position in the SLAM process.

Interactive FastSLAM is performed when a mobile robot moves in a monitoring area of a distributed sensor. Then, an occupancy grid map from the distributed sensor and a sensing result from a mobile robot are compared. Although matching between past maps generated by the mobile robot itself and the current sensing data is used for likelihood calculation of a particle in the usual SLAM, comparison with the map of the distributed sensor is also add in the interactive SLAM. Difference between a map estimated by the robot side and a map of the distributed sensor is reflected to estimation result of the interactive SLAM.

2.3 Construction of Grid Map in FastSLAM

Matching between current sensing data by the laser range sensor in the robot and a local map based on past position estimation is performed in map estimation of usual Grid Based FastSLAM. Likelihood is calculated based on the number of sensing points, which matched with the grids with high occupancy probabilities in the local map. This likelihood calculation is performed in each particle of a particle filter. Robot position is estimated by the weighting average based on likelihood of each particle. Fig.2 shows an example of the sensing data by the mobile robot in environment where moving objects, such as humans and the other static objects are exist. Fig.3 shows an example of matching between the sensing data and a local map. In this figure, red points represent grids that the local map and the sensing points are corresponding.

In comparison of Fig.2 and Fig.3, Fig.2 detects the moving objects in the measurement result. Since occupancy grid probabilities matched with any sensing points are updated in the grid map shown in Fig.3, influences of moving objects decrease in map building.

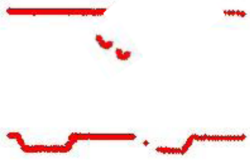

Fig.2 sensing result

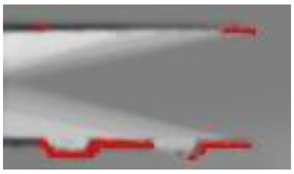

Fig.3 matching of local map and sensing data

2.4 Matching with maps by distributed laser range sensors

In the interactive FastSLAM using intelligent space, when a mobile robot moves into an area of a distributed laser range sensors, likelihood of each particle is computed from comparison with grid maps which the distributed sensors generate in addition to comparison with the local maps which the mobile robot itself generate as mentioned above. That is, when the mobile robot runs in the measuring range of a distributed sensor, it is aimed that accuracies of position and map estimations in SLAM process are improved by evaluating the matching points with the grid map from the distributed sensors. The grid maps of distributed sensors are generated by a method of literature [3]. Fig.4 is an example situation of matching with the map from the sensor fixed in intelligent space. In this figure, red points are current sensing points by the mobile robot. Blue points show the grids, which the map by distributed sensor and the sensing points are corresponded. It is enough when many correspondent points are measured as shown in Fig.4. However, as shown in left figure of Fig.5, there are many cases that correspondent points between the map by the distributed sensor and sensing data are small because of orientation differences between maps and sensing data especially. It means that the number of correspondent points is not enough to evaluate matching with the maps of distributed sensors.

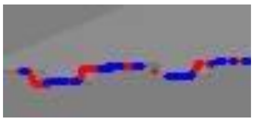

Fig.4 sensing data corresponding to map by a distributed sensor

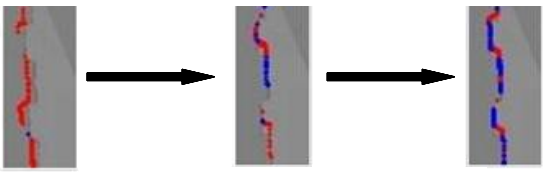

Fig.5 matching correction

So, in this study, orientation differences between maps of distributed sensors and sensing data are used for evaluation of matching. Two grids with the highest occupancy probability in the map of distributed sensor are selected as representative points. In the sensing data observed by the robot side, the points nearest to selected two points are searched. Average errors of two points are reflected to likelihood of each particle. At this time, each particle is also recording slopes of lines between each two points in the grid map or sensing data. State compensation based on the slopes is performed at the update of state variables in the robot side. Both the maps of distributed sensors and the map built by the robot itself are evaluated by performing this process for every cycle of the SLAM process. Matching result is corrected on running of the robot as shown in Fig.5. The number of matching points is shown by blue points increase in this figure. In the monitoring area of distributed sensors, particles, which match with both of the past local map by SLAM and the maps by distributed sensors will be selected as a result.

2.5 Estimating position and orientation of distributed laser range sensors

When positions and orientations of distributed laser range sensors in a world coordinate system are known, position estimation of a mobile robot and accuracy of map building improve according to the map of distributed sensors in the interactive FastSLAM as described above. In this case, the map of distributed sensors becomes constraints in SLAM process. However, when many sensors are distributed in the environment, it becomes a complicated work to know positions and orientations of all sensors in unified world coordinate system. Then, the case, that positions and orientations of distributed sensors are unknown, is considered. This study introduces estimating both positions and orientations of the mobile robot and distributed sensors simultaneously with interactive SLAM.

When a mobile robot enters into an area of distributed sensors, an initial position of the distributed sensor is measured by the mobile robot in the coordinate system of the map generated by the usual SLAM. A measurement result is sent to the distributed sensor. In Grid Based FastSLAM mentioned above, a mobile robot's position and the grid map are used as state variables. In addition to these state variables, positions and postures of distributed sensors are also added as state variables and estimated simultaneously. When the mobile robot runs into the areas of distributed sensors, correction of positions and orientations of distributed sensors are performed.

3 Experiment

As a preliminary experiment on the conditions which positions and orientations of distributed laser range sensors are known, the system of interactive FastSLAM is implemented and the experiment of self-position estimation and map generation was conducted. As experiment environment, the mobile robot moved a squared course in one floor of building of our university. A length of the course is about 100 m. Four distributed sensors were installed in yellow points of Fig.7. Fig.6 shows the map generated by usual FastSLAM only.

On the other hand, Fig.7 is a map built by information sharing with four distributed sensors with the interactive FastSLAM. A part of a red dotted circle in Fig.6 has matching errors when the mobile robot revisited this area. However, an accurate map is shown in a part of a yellow dotted circle in Fig.7, because the robot position and map are obtained by particles, which also matched with the maps from the intelligent space. Fig.8-11 is examples of map matching in the measurement areas of four distributed sensors in the interactive SLAM. These shows find that matching of a sensing result, a map by robot itself, and a map by the distributed sensor is performed in each part. Also, in the case that positions and orientations of distributed sensors are unknown, positions and orientations of the distributed sensors updated to actual values according to robot movement with the similar system.

In this experiment, the number of particle in a particle filter of the interactive SLAM is 50, and the grid size of is set to 50 mm x 50 mm. Pioneer3-DX was used for the mobile robot. UTM30-LX was used for the sensor installed in the robot. URG04-LX was used for the distributed sensors.

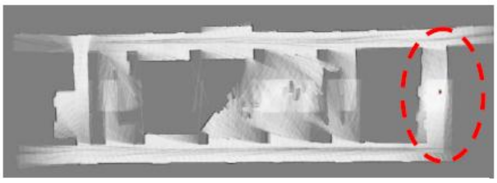

Fig.6 SLAM result (only Mobile robot)

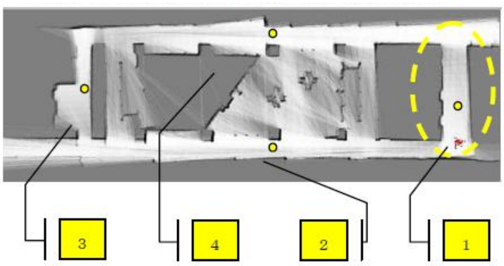

Fig.7 SLAM result (information sharing)

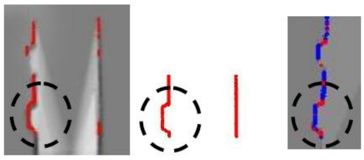

Local Map Sensing result Distributed range finder

Fig.8 Scan matching in "1" of fig.7

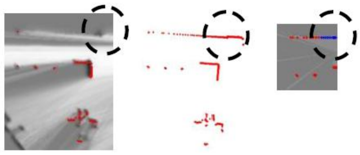

Local Map Sensing result Distributed range finder

Fig.9 Scan matching in "2" of fig.7

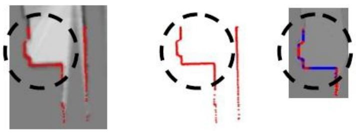

Local Map Sensing result Distributed range finder

Fig.10 Scan matching in "3" of fig.7

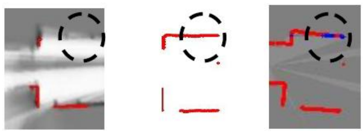

Local Map Sensing result Distributed range finder

Fig.11 Scan matching in "4" of fig.7

4 Conclusion

In this paper, it was shown that it is effective in improving the accuracy of SLAM by using information of distributed laser range sensors in intelligent space in the SLAM problem. This paper also described a possibility that the proposed SLAM is utilizable to estimating positions and orientations of distributed sensors in intelligent space.

References

[1] Joo-Ho Lee, Hideki Hashimoto, (2002) "Intelligent Space - concept and contents", Advanced Robotics, Vol.16, No.3, pp.265-280

[2] Kazuyuki Morioka, and et al., (2004) "Human-following mobile robot in a distributed intelligent sensor network", IEEE Trans. on Industrial Electronics, Vol.51, No.1, pp.229-237

[3] Sebastian Thrun, and et al., (2007) "Probabilistic Robotics", MIT Press, pp.1-483

[4] D. Haehnel, and et al., (2003) "A highly efficient FastSLAM algorithm for generating cyclic maps of large-scale environments from raw laser range measurements", Proc. of IROS

The Seventeenth International Symposium on Artificial Life and Robotics 2012 (AROB 17th '12),
B-Con Plaza, Beppu, Oita, Japan, January 19-21, 2012

Development of Person Identification and Tracking System with Wearable Acceleration Sensors in Intelligent Space

Tomoyasu Takigawa[1], and Kazuyuki Morioka[2]

[1,2]Meiji University, Kanagawa 214-8571, Japan
(Tel: 81-44-934-7304, Fax: 81-44-934-7304)

[1]ce01052@meiji.ac.jp, [2]morioka@isc.meiji.ac.jp

Abstract: This paper proposes a human identification and tracking system with a wearable acceleration sensor and networked laser range scanners in an intelligent space. Human walking activities are measured and associated between laser range scanners and acceleration sensor. In this paper, a proposed person identification system between two types of sensors is described. A module of each sensor is implemented as RT component. The proposed distributed sensor system was developed by integrating these RT components. Information on walking behavior of human is communicated between components and shared in this system. Some experimental results with this system show a possibility of person identification and tracking.

Keywords: Acceleration sensors, Human identification, Human tracking, Intelligent Space, Laser range finders

1 INTRODUCTION

Recently, sensor network for configuring intelligent spaces has been actively studied [1][2]. There are various sensors, such as laser range sensors and cameras installed in the environments or mobile sensors with human in intelligent spaces. Especially, in order to support activities and understand behaviors based on movements of human in the environments, various methods to track the position of human have been proposed. Existing studies can be classified into three types according to properties of sensors.
(1) Vision sensor [3]
System with vision sensors can provide not only human position but also appearance and motion of human. However, they are lacking robustness, because false detections frequently occur due to change in lighting conditions or occlusions by obstacles in the environment.
(2) Laser range finders (LRF) [4]
LRFs have higher reliability and less noise signal because they are not affected by conditions in the environments. However, scan data obtained from laser range scanner cannot get personal identification. Therefore, when tracking multiple people, ambiguity occurs in identifying targets.
(3) Portable sensors [5]
Recently, small devices such as ID tags, acceleration sensors or other sensors have been developed, and they are often installed in mobile phones. Then, humans can easily carry such sensors. ID information can be easily associated to human based on information from mobile sensors. They are effective to ensure individual identification. However, position estimation with these mobile sensors is not accurate. In order to accurate position estimation with only mobile sensors, humans have to wear various kinds of sensors [5].
There are several studies as the solutions for obtaining human ID information and accurate positions simultaneously. Literature [6] shows that ID information can be obtained and human positions can be estimated accurately by integrating touch sensors or pressure sensors installed on the floor and acceleration sensors. Literature [7] shows person tracking and identification based on similarities between angular velocities obtained from gyro sensor with human and estimated by LRFs installed in the environment. In the literature [8], acceleration sensors and cameras installed in the environment are integrated. Correlation between movement of human extracted in images captured from vision sensors and acceleration signals from acceleration sensor with human are calculated.

This study developed a system which performs the person identification, and tracking based on the acceleration sensor with human and laser range scanners installed in the intelligent environment. A module of each sensor is implemented as RT component. The proposed distributed sensor system was developed by integrating these RT components. Information on walking behavior of human is communicated between components and shared in this system. Actually experiments of person identification using this system was performed. Experimental results show the validity of the proposed system. Fig.1 shows a concept of the proposed system.

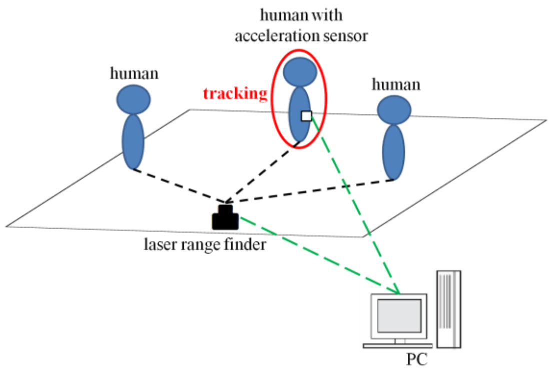

Fig.1 Concept f the study

2 TRACKING AND IDENTIFICATION SYSTEM WITH NETWORKED LASER SENSORS AND WEARABLE ACCELERATION SENSOR

In this study, human walking behaviors are detected in networked laser range scanners in the intelligent space and an acceleration sensor with human respectively. Walking behaviors of two types of sensors are associated according to steps of walking.

2.1 Walking detection using an acceleration sensor

First, the two low-pass filter (LPF, cut-off frequency: 0.5Hz, cut-off frequency: 10Hz) are applied to raw acceleration signals. LPF of 10Hz cut-off is used to eliminate the noise. In addition, DC components are obtained by LPF of 0.5Hz cut-off. DC components are treated as gravitational acceleration components. Fig.2 shows a vertical direction and a forward direction used for analysis of walking motion. If specific changes as shows as Fig.3 were appeared in the measured acceleration data, that motion is detected as "walking". Details of this "walking" detection are described in [9].

2.2 Walking detection using laser range scanners

First, moving objects are extracted by networked laser range sensors installed in the intelligent space calculating difference between current range data and background range data. Then, the position information of only moving objects are detected. Second, hierarchical clustering is applied to the extracted range data. After that, each moving object can be separated and tracked. Fig.4 shows detection and tracking of the human with two legs. If movements of detected human are bigger than threshold amount during a given period, the human is detected as "walking". Details of detecting and tracking human are shown in [10].

2.3 Matching based on walking behaviors

"Walking" behaviors are detected by networked laser range scanners installed in the intelligent space and the acceleration sensor with person. In this study, we focus on the occurrence and duration of walking and stopping. In the matching process, association between behavior detections by laser range scanners and the acceleration sensor are performed. The matching process evaluates whether "walking" behaviors at the same time are detected. A similarity of behaviors between two types of sensors is introduced to evaluate matching. A similarity s_{ij} is calculated with Eq.(1) to each combination of detections by acceleration sensor i and laser scanner j.

$$S_{ij} = 1 - 1/(1 + \exp(l_{ij})) \qquad (1)$$

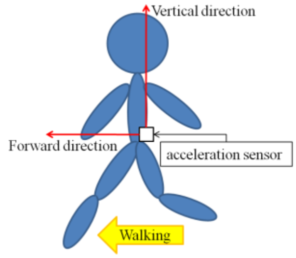

Fig.2 Axis definition of vertical direction and forward direction

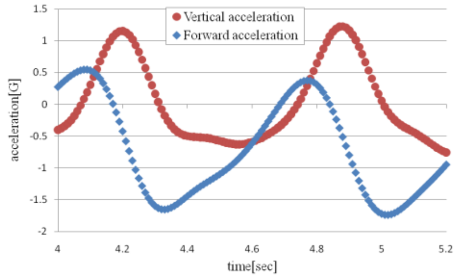

Fig.3 Acceleration change in one cycle walking

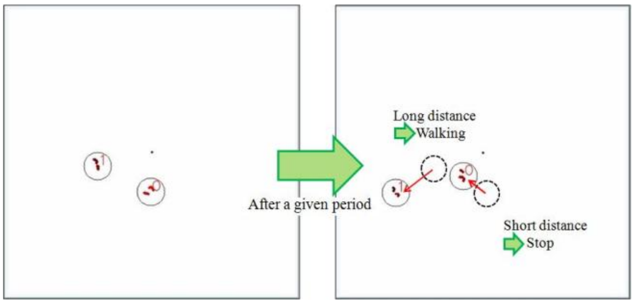

Fig.4 Human tracking and walking detection by laser sensors

l_{ij} changes based on behavior detections. If "walking" or "Stopping" is detected at the same time with both sensors, l_{ij} increases. On the other hand, when different behaviors are detected in both sensors, l_{ij} decreases. Then, a similarity also increases with same behavior and decreases with different behaviors from both sensors. Details of this matching method described in [11].

2.4 System development using RT component

The proposed system which performs walking behavior detection was implemented using RT middleware [12]. Each sensor module described in sections 2.1 or 2.2 was developed as RT component.

First, the component of acceleration sensor is explained. The component of acceleration sensor is executed at a computer set in the intelligent space. In the first operation "on activated", the component of an acceleration sensor reads default settings and connects to an acceleration sensor via Bluetooth from the computer that the component is running. In "on execute" process which it iterates acceleration data acquisition every 0.01 second. LPFs are applied to the acquired acceleration data, and removal of noises and calculation of gravitational acceleration are performed every loop. Acceleration data for calibration of human's forward direction is stored for the first 10 seconds after state transition to "on execute". Then, forward direction calibration is performed using principal component analysis based on acceleration data of the first 10 seconds. After 10 seconds, from two acceleration data, the vertical direction and the forward direction, walking behavior detection of the person with the acceleration sensor is performed. Results of walking behavior detection are transmitted to the other component. Flag "1" for walking behavior, or flag "-1" for stopping behavior as TimedLong type transmitted in this component.

Next, the component of laser range scanner is explained. In the first operation "on activated", the component of laser range scanner acquires range data used as a background. This range data is used for calculation of the background subtraction for extracting moving objects. In "on execute" process, human legs are detected from the moving objects as human. Position data of humans are acquired and the humans are tracked every 0.1 seconds. Walking or stopping detection results received from the component of wearable acceleration sensor is matched with walking or stopping behaviors of each tracking persons detected in the component of laser range scanner. A person with the best similarity is recognized to be a target person.

This system is based on small data communication between two sensor modules. Then, even if those who exist in the intelligent space increase in number, the system is executed by communicating only the information on walking or stopping detections.

Fig. 5 shows the structure of this system. The left is a component of an acceleration sensor. The right is a component of laser range scanner. Advanced components are required to handle many laser range scanners installed in the intelligent space in near future.

3 EXPERIMENT

3.1 System setup

Laser range scanners (Hokuyo Electric Machinery URG-04LX) are set at the height of about 25cm on a smooth floor. The target person wears the sensor (ATR-Promotions WAA-006) with gyro of three axes and acceleration of three axes on the waist. Components including the interface with each sensor and processing of walking detection are developed in each sensor by using the Open Robot Technology Middleware (RT Middleware) of AIST[12].

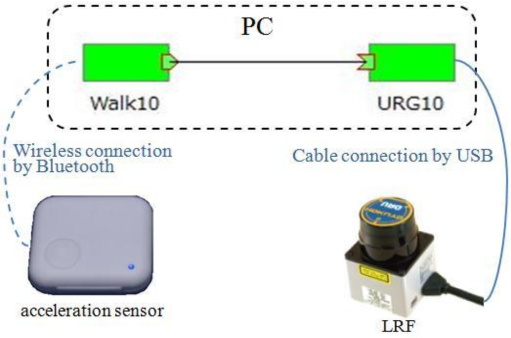

Fig.5 Wire connection figure of a system

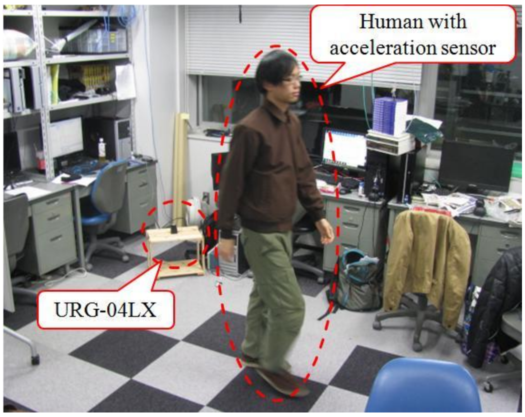

Fig.6 Experimental environment

Detected results of "walking" are communicated between components. Fig.6 shows the experimental environment.

3.2. Experiments of human identification

Experiments on identification of the target human with the acceleration sensor were performed. Five persons with the acceleration sensors walked around in the intelligent space. Laser range sensor is installed in the intelligent space for person tracking. Five persons walked and stopped as shown as Table.1 respectively. Pattern 02 and Pattern 03 are similar behavior. Pattern 04 and Pattern 05 are also similar. The algorithms for detecting correct persons in these similar behaviors are required for person identification. Seconds for walking or stopping were measured by a stopwatch. Fig.7 shows the examples of identification experiments among a target person and non-target persons.

Fig.7 also shows the case of Pattern 03 person. In this figure, the first vertical axis shows the walking distance measured by the laser range scanner, and the second vertical axis shows the number of walking steps detected by the acceleration sensor in [a]. This figure [b] shows similarity changes of all persons using the optimal parameters.

As shown in Fig.7, one of non-target persons performs a similar walking pattern compared with the target person (Pattern 03). In this figure, the similarities of Pattern 01, 04 and 05 were suppressed smaller than the similarities of

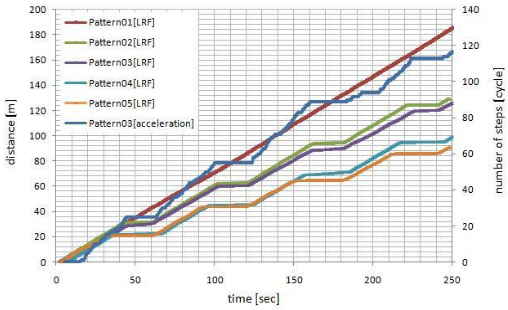

[a] Number of steps measured by acceleration sensor of target person and distance of five persons

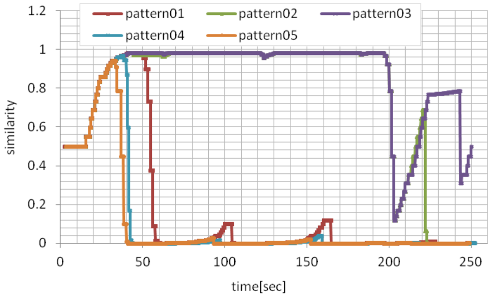

[b] Grade of similarity of five persons

Fig.7 Results of five persons [Target is patturn03]

Pattern 02 and 03 after around 60 sec. Although it took more time to distinguish Pattern 03 with Pattern 02 than the other patterns, the highest similarity was obtained after around 200 sec.

This result introduce the association based on behaviors focused in this study has a possibility to identify a specific person from several persons and track him in high accuracy with laser range sensors in the intelligent space

4 CONCLUSION

This study aimed to identify a specific person with the accurate position measurements by integrating the networked laser range scanners installed in the intelligent space and an acceleration sensor with the person. This paper proposed the identification of a person based on associating the detections of walking behaviors from both sensors. Some experimental results showed the feasibility of the method. Improvement in accuracy of the decision of behavior in each sensor, and how to evaluate the similarity should be reconsidered in order to improve the performance as the future work. Experiments to identify the target from many persons should be performed.

REFERENCES

[1] Joo-Ho Lee, Hideki Hashimoto, "Intelligent Space — concept and contents", Advanced Robotics, Vol.16, No.3, pp.265-280, 2002

[2] Kazuyuki Morioka, Joo-Ho Lee, Hideki Hashimoto, "Human-following mobile robot in a distributed intelligent sensor network", IEEE Transactions on Industrial Electronics, Vol.51, No.1, pp.229-237, 2004

[3] Atsushi Nakazawa, Hirokazu Kato, Shinsaku Hiura, Seiji Inokuchi, "Tracking multiple people using distributed vision systems", IEEE International Conference on Robotics & Automation, pp. 2974-2981, 2002

[4] Jae Hoon Lee, Yong-Shik Kim, Bong Keun Kim, Kohtaro Ohba, Hirohiko Kawata, Akihisa Ohya, Shin'ichi Yuta, "Security Door System Using Human Tracking Method with Laser Range Finders", IEEE International Conference on Mechatronics and Automation, pp. 2060-2065, 2007

[5] Masakatsu Kourogi, Takeshi Kurata, " Personal positioning based on walking locomotion analysis with self-contained sensors and a wearable camera", ISMAR '03 Proceedings of the 2nd IEEE/ACM International Symposium on Mixed and Augmented Reality,pp.103-112, 2003

[6] Tetsushi Ikeda, Hiroshi Ishiguro, Takuichi Nishimura, " People tracking by fusing different kinds of sensors, floor sensosrs and acceleration sensors", IEEE International Conference on Multisensory Fusion and Integration for Intelligent Systems, pp.530-535, 2006

[7] Tetsushi Ikeda, Hiroshi Ishiguro, Dylan F. Glas, Masahiro Shiomi, Takahiro Miyashita, Norihiro Hagita, " Person indenfication by integrating wearable sensors and tracking results from environmental sensors", IEEE International Conference on Robotics and Automation, pp.2637-2642, 2010

[8] Yuichi Maki, Shingo Kagami, Koichi Hashimoto, " Accelerometer Detection in a Camera View Based on Feature Point Tracking", IEEE/SICE International Symposium on System Integration, pp. 448-453, 2010

[9] Tomoyasu Takigawa, Kazuyuki Morioka "Identifying a Person with an Acceleration Sensor Using Tracking System in an Intelligent Space", Advanced Intelligent Mechatronics 2011,pp.7-12, 2011

[10] Yuichi Nakamura, Kazuyuki Morioka, "Human tracking based on direct communication among networked laser range scanners in an intelligent space", The 7th International Conference on Ubiquitous Robots and Ambient Intelligence (URAI2010), pp 534-535, 2010

[11] Tomoyasu Takigawa, Kazuyuki Morioka "I Improvement of Person Identification Rules Based on Walking Behavior Association between Wearable Acceleration Sensors and Intelligent Space", SII2011, 2011 (in press)

[12] Noriaki Ando, Takashi Suehiro, Kosei Kitagaki, Tetsuo Kotoku, Woo-Keun Yoon" RT-middleware: distributed component middleware for RT (robot technology)", Intelligent Robots and Systems 2005, pp.3933 – 3938, 2005

The Seventeenth International Symposium on Artificial Life and Robotics 2012 (AROB 17th '12),
B-Con Plaza, Beppu, Oita, Japan, January 19-21, 2012

Development of Easy Camera Calibration Tool under Unified World Coordinate System Using Online Three-dimensional Reconstruction

Shintaro Kuroiwa[1], Kazuyuki Morioka[2]

[1] Meiji University, Kanagawa 214-8571, Japan
[2] Meiji University, Kanagawa 214-8571, Japan
(Tel: 81-44-934-7171, Fax: 81-44-934-7171)
(ce01033@meiji.ac.jp)

Abstract: Three-dimensional position information is essential in order to give appropriate support for human beings in an intelligent space. Distributed cameras in an intelligent space have to be calibrated for acquisition of three-dimensional position. Since calibration of many cameras is time-consuming, camera calibration method for easy construction of an intelligent space is needed. This paper proposes automatic camera calibration method based on image features and 3D information of minimal calibrated cameras. Image features and 3D positions are shared with uncalibrated cameras via network, and these cameras are calibrated with common image features. In this paper, the first experimental results with SIFT (Scale-Invariant Feature Transform) as image features are shown.

Keywords: camera calibration, stereo camera, 3D reconstruction, mobile robot, intelligent space

1 INTRODUCTION

In recent years, there are many studies on intelligent spaces [1]. Fig.1. shows a concept of the intelligent space for acquiring information on positions and states of robot and person by distributing various sensors and networked cameras in the environment. It is necessary to know three-dimensional geometric relationship between networked cameras and environment in order to achieve various applications based on object positions in intelligent space. In other words, networked cameras must be calibrated geometrically in unified world coordinate system fixed to the environment.

Tsai's calibration method [2] needs to know several corresponding points between three-dimensional world coordinates and two-dimensional coordinates in image plane. Then, these must be measured manually in advance. Zhang's calibration method [3] needs artificial checker pattern. In this method, each camera is calibrated in the different world coordinate system. That is not enough for geometrical calibration of distributed cameras in unified world coordinate system. Since the calibration has to be performed for every camera, it is very time-consuming that human operators calibrate many cameras distributed in the environment with corresponding points or a plane checker pattern as usual. Even if intelligent space is large area, many cameras in the environment are desirable to be calibrated with small manual operation. These cameras must be also calibrated under unified world coordinate system. Camera calibration in unified coordinate system with cooperative positioning system [4] was proposed as a solution of such a problem. In this method, two robot-groups measure three-dimension position each other and move while measuring the other robot positions. On the other hand, geometrical relationship between cameras and environment can be also acquired with Structure from Motion (SFM), such as Parallel Tracking and Mapping (PTAM)[5].

This study introduces a calibration system under unified world coordinate system of networked cameras distributed in the intelligent space. The system uses a portable stereo camera and a mobile robot for calibration. World coordinates of natural corresponding points based on SIFT (Scale-Invariant Feature Transform) [6] are calculated according to localization of the portable stereo camera installed on the mobile robot. The detailed approach is as follows.

Self-position estimation of the mobile robot is used for localization of the portable stereo camera. World coordinates of natural feature points in stereo camera images are calculated using localization results. World coordinates of natural feature points are shared with the uncalibrated network cameras for calibration. However, camera calibration with natural corresponding points based on SIFT often fails. It is caused by that natural corresponding points are concentrated locally and that natural corresponding points include many mis-matched points.

It is desirable that successful calibration is distinguished from unsuccessful one easily by the human operator. In this study, the system for checking calibration conditions online is developed. This system includes matching of SIFT features, calculation of camera parameters, optimization of camera parameters and showing three-dimensional grids for representing calibration results online. Especially, matching of SIFT features take much processing time. In this study, online three-dimensional reconstruction of image features is achieved by fast calculation and matching of SIFT features with GPU.

Accordingly, the human operators of calibration system can calibrate the network cameras distributed in the intelligent space easily by moving the stereo camera on the mobile robot to front of uncalibrated network cameras. In this paper, detailed system configuration and performance of the system will be described.

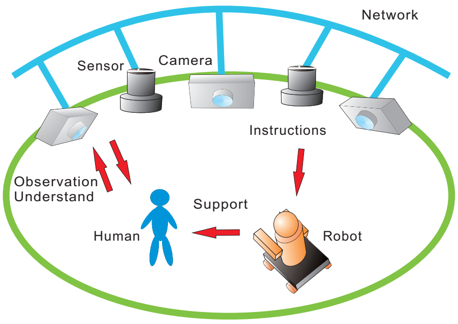

Fig. 1. The concept of the intelligent space

2 EASY CAMERA CALIBRATION SYSTEM

2.1 Proposed System

Fig.2. shows a flow chart of the proposed method. In this study, three-dimensional feature points measured by a portable stereo camera are used for calibration of networked cameras distributed in the intelligent space.

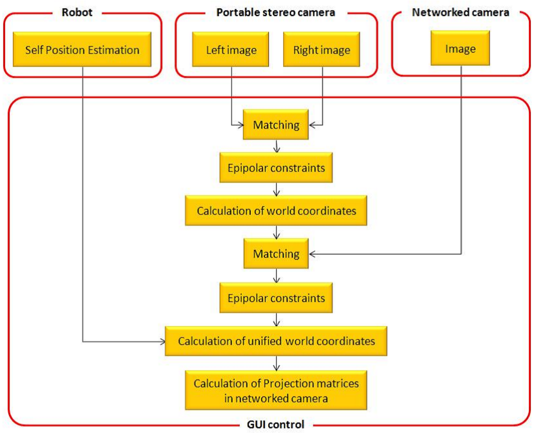

Fig. 2. Flow char t of the proposed method

2.2 Position Estimation of Portable Stereo Camera

A mobile robot with the portable stereo camera is manually controlled so that the view of a stereo camera can overlap with the view of a networked camera. Positions and orientations of the mobile robot are calculated by applying any self-position estimation algorithms of a mobile robot. Then, positions of the portable stereo camera in the unified world coordinate system can be obtained.

2.3 Matching of Feature Points

Matching points between images of a portable stereo camera and an image of a networked camera are calculated using SIFT features. Examples of many matched future points are shown in Fig.3..

However, several mis-matched points are found. These mis-matched points make an accuracy of estimating camera parameters of the networked camera worse. These mis-matched points are removed by a method based on epipolar restraint. Fig.4. shows results of removing mis-matched points in Fig.3..

Fig. 3. Matching of feature points among three images

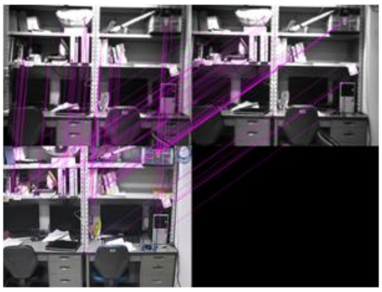

Fig. 4. Matching removed noise among three images

2.4 Positions in Unified World Coordinates

Fig.5. shows a method to calculate three-dimensional positions by the stereo camera in the camera coordinate system. Common feature points extracted by SIFT and epipolar constraints. Then, three-dimensional positions of feature points are calculated from stereo camera images. Of course, a geometrical relationship between left and right cameras of stereo camera is known.

Camera coordinates in the stereo camera must be transformed to unified world coordinate system. Fig.6. shows relationship between the camera coordinate system and the unified world coordinate system. Position estimation results of the mobile robot are applied.

2.5 Calculation of Camera Parameters

Camera parameters of the uncalibrated networked camera are calculated according to unified world coordinates of corresponding feature points between the networked camera and the stereo camera. However, camera parameters calculated

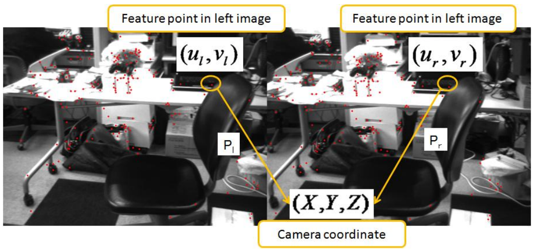

Fig. 5. Position calculation with stereo matching

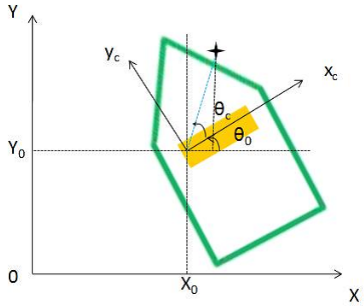

Fig. 6. Transformation between coordinate systems

in this level cannot reconstruct an accurate world coordinate system. Nonlinear optimization called Levenberg-Marquardt algorithm [7] is applied to optimize camera parameters. Details are shown in [8].

3 SYSTEM PERFORMANCE

3.1 Experimental Environment and Systems

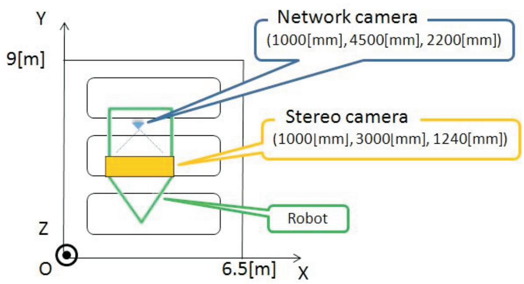

Fig. 7. Experimental environment

Position estimation of a moving stereo camera and calibration of networked cameras in the unified world coordinate system are performed as experiments. Bumblebee2 by Point Grey Research Inc. was used as the stereo camera. Canon VB-300 network camera was arranged in the intelligent space as the uncalibrated cameras for calibration experiment. Pioneer3-DX by MobileRobots Inc. was used as a mobile robot to mount the stereo camera. The stereo camera was calibrated using Zhangfs calibration method. All image sizes of cameras are 640 [pixel]   480 [pixel]. Fig.7. shows a sketch map of experimental environment. The Co-

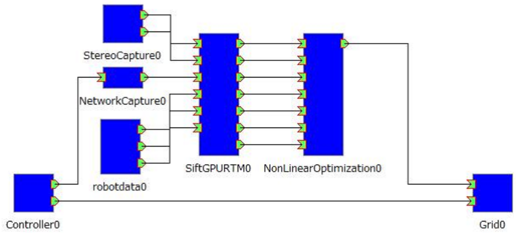

Fig. 8. Connection diagram of the system

ordinates (1000[mm], 4500[mm], 2200[mm]) and the coordinates (1000[mm], 3000[mm], 1240[mm]) mean unified world coordinates of networked camera and stereo camera. Fig.8. shows the connection diagram of this system with RT middleware. All modules of the system are implemented as RT components. A matching component is implemented with GPU processing. Since it achieves high speed matching, it enables to estimate camera parameters online. Camera parameters calculation in the developed system became faster around 30 times than a system with a normal CPU.

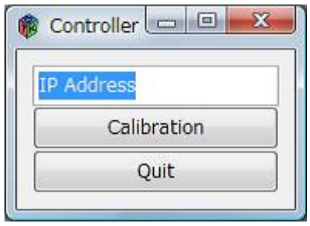

Fig. 9. GUI tool for calibration

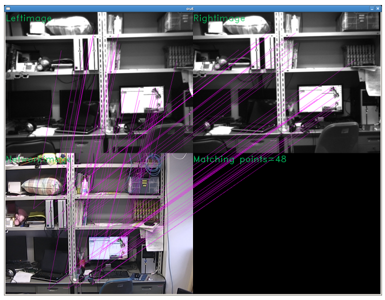

Fig. 10. Matching results

Fig. 11. Result of camera calibration

3.2 Calibration of Networked Cameras

A human operator controls the mobile robot to front of the target camera for making overlaps between the view of a stereo camera and the view of the networked camera. On a screen of computer, matching among the images of stereo camera and the image of networked camera, and three-dimensional reconstruction results are always displayed online. The human operator uses GUI shown in Fig.9. Calibration command is executed with this GUI when the accurate three-dimensional reconstruction results are displayed. Fig.10. shows results of matching. Fig.11. shows an example of three-dimensional reconstruction with calibration results.

3.3 Evaluation Experiment

Fig.12. shows an image of the target networked camera. In this figure, red points are selected and world coordinates of red points in the actual environment are measured manually for evaluations of calculated camera parameters. Green points represent the points projected using the world coordinates of red points and calibrated camera parameters. Errors between red points and green points are calculated. 1. shows the result of evaluation experiment. According to Table 1., there is the great difference between point where an error is small and point where an error is big. It is considered that is caused by that matching points concentrate locally. It can be used for the application like easy Augmented Reality (AR) which does not require highly precise camera calibration. There is room for improvement of this system. Concrete solution is introducing dynamic conditions so that matching points may be dispersively acquired according to a situation.

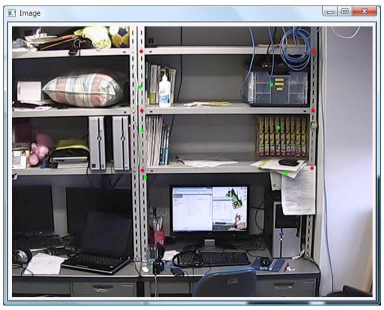

Fig. 12. Points for accuracy evaluation

Table 1. Result of evaluation experiment

Unified World Coordinates			Red		Green		Error
X[mm]	Y[mm]	Z[mm]	u	v	u'	v'	e
1040	470	1300	236	267	231	255	13.00
40	470	1300	486	261	532	251	47.07
1040	470	1650	231	184	230	149	35.01
40	470	1650	472	179	534	149	68.88
1040	470	2000	227	107	229	44	63.03
40	470	2000	460	103	535	44	95.43

4 CONCLUSION

This study proposed the camera calibration system in the unified coordinate system. The camera calibration method is based on estimating the position of the portable stereo camera and matching the feature points between the stereo camera and networked cameras.

REFERENCES

[1] Kazuyuki Morioka, Joo-Ho Lee, Hideki Hashimoto, "Human-following mobile robot in a distributed intelligent sensor network", IEEE Transactions on Industrial Electronics, Vol.51, No.1, pp.229-237, 2004

[2] Zhengyou Zhang, "A Flexible New Technique for Camera Calibration", IEEE Transactions on Pattern Analysis and Machine Intelligence, 22(11):1330-1334, 2000.

[3] Tsai, Roger Y. (1987) gA Versatile Camera Calibration Technique for High- Accuracy 3D Machine Vision Metrology Using Off-the-Shelf TV Cameras and Lenses,ff IEEE Journal of Robotics and Automation, Vol.RA-3, No. 4, August 1987, pp. 323-344.

[4] Tsuyoshi Yokoya, Tsutomu Hasegawa, Ryo Kurazume, Kouji Murakami, "Calibration of Distributed Vision Network in Unified Coordinate System by Mobile Robots", Proc. IEEE Int.Conf. Robotics and Automation, pp. 1412-1417, California, May 19-23,2008

[5] G. Klein and D.W. Murray, "Parallel Tracking and Mapping for Small AR Workspaces", Proc International Symposium on Mixed and Augmented Reality (ISMAR) 2007

[6] D. G. Lowe, gObject recognition from local scaleinvariant featuresh, Proc. of IEEE International Conference on Computer Vision (ICCV), pp.1150-1157, 1999.

[7] William H. Press, Brian P. Flannery, Saul A. Teukolsky, William T. Vetterling, gNumerical Recipes in Ch, Cambridge University Press (1992)

[8] Shintaro Kuroiwa, Kazuyuki Morioka "Calibration of Cameras Distributed in the Intelligent Space Based on Three Dimensional Structure Reconstruction of a Portable Stereo Camera" , Advanced Intelligent Mechatronics (AIM), IEEE/ASME International Conference, pp.1-6 (2011)

Development of a multi-purpose compact board for robot control systems

Mitsuhiro Yamano[1], Shinya Takeda[1], Yuichi Suzukawa[2] and Yu Kakuta[1,]

[1]Yamagata University, Yonezawa-shi 992-8510, Japan
[2]UD Trucks, Ageo-shi 362-8523, Japan
(Tel: 81-238-26-.3238, Fax: 81-238-26-3205)

[1]yamano@yz.yamagata-u.ac.jp

Abstract: This paper presents development of a multi-purpose compact board for robot control systems and its applications. Advanced robot system with many actuators and sensors require complicated control system. Different sensor has different specification of signal output. Advanced robots have to accept many kinds of signals. Prototype robots in the laboratory are often extended and modified for the research. Common computer hardware for many kinds of actuators and sensors contributes to the efficiency of its software development. We have developed the multi-purpose Micro Control Unit (MCU) board that can be used for many kinds of actuators and sensors. The MCU board is designed so that it can be used for many devices and many applications. Two applications of the MCU board are presented to show its effectiveness.

Keywords: Distributed control system, Micro control unit, Robot control system, noise suppression

1 INTRODUCTION

Previously, large-sized computer boards and interface boards are used for control of various robots. These boards are so large that they are not easy to be located in the arms and legs of robots. Lots of long cables are required between the boards and various devices such as sensors and motors.

Recently, performance of small-sized one-chip microcontrollers is increasing. The microcontrollers have the function of CPU, RAM, Digital I/O, A/D converter and so on. Many kinds of microcontroller such as dsPIC by Microhip Technology Inc., H8 by Renesas Electronics Corporation, AVR by Atmel Corporation and ARM architecture are available for robot control.

Various MCU boards for sensing and control have been developed [1][2][3]. Lin at el. developed inertial measurement unit for human body motion tracking [1] and wireless inertial measurement unit for mastication analysis [2]. Faudzi et al. have developed the system using PSoC [3].

We have proposed the control system using a PC and MCUs (Micro Control Units)[4]. The PC are used for calculation of whole robot, and the MCU boards are used for local calculation and digital/analog interface. We also developed MCU boards [4] [5] and they are used in our humanoid robot [4], a robot hand [5], iWalker-2 [6] by Tanaka et al. and Omnidirectional Driving Gear by Tadakuma et al [7]. In this paper, a design and application of a new MCU board are presented. The board is more compact and more convenient than that presented in [5].

2 ROBOT CONTROL SYSTEM USING MCU BOARDS

If a MCU board can be designed for multiple purposes, various robots can be controlled using same boards. For a simple robot with a small number of actuators and sensors, stand-alone MCU board is embedded to control it. For a medium-scale robot, small number of MUC boards can be used for the control using communication standard such as UART (Universal Asynchronous Receiver Transmitter), I2C and SPI(Serial Peripheral Interface). For advanced robots using complicated control algorithms, PC are used for calculation. The advantages of PC are high computing power and wealth of software. The disadvantages of that are its largeness and high consumed power.

Hybrid system using a PC and MCUs are effective for robot control. The PC carries out complicated calculation and MCUs input and output digital/analog signals. Because many kinds of MCU have UART and most PCs have USB (Universal Serial Bus), a PC can communicate with MCUs using USB/UART shown Fig. 1 (a). Many MCUs can be connected with a PC using USB hub and maximum length of USB cables is 5 m. For large-scale robots such as humanoid robots, the control system using a PC, MCUs and RS485 (EIA-485) shown Fig. 1 (b) is effective [4]. Maximum length of RS485 cable is 1.2 km.

RS485 cable can be connected with MCU via RS485/UART converter. Conversion between USB and RS485 is possible by connecting USB/UART converter and UART/RS485 converter.

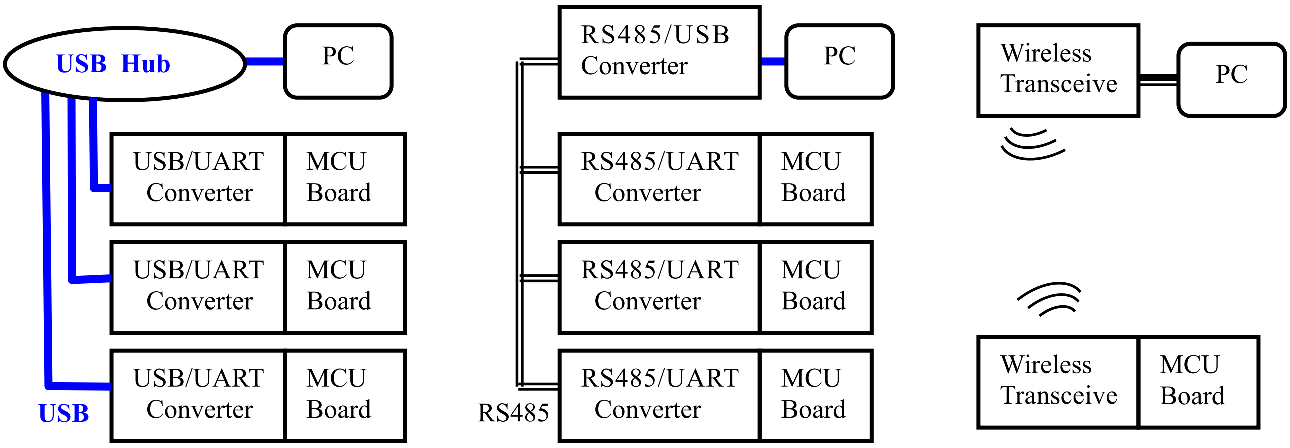

(a) system using USB (b) system using RS485 (c) wireless system

Fig. 1. Sensing and control system using a PC and MCU boards

MCU boards are desired to have the function of wireless communication shown Fig. 1 (c). For example, sensor network system to detect the human behavior is important for the robot control in human environment. Many MCU boards with sensors should be located in rooms. Many long cables for communication of MCU are inconvenient in the rooms. Wireless MCU board is easy to be located in the rooms.

MCUs for robot control are desired to have the many I/O function such as digital I/O, A/D converter, pulse counter, PWM output. A/D converters are used for reading the sensor signals. Pulse counters and PWM modules are used for feedback control of servo motors. D/A converter can be replaced by the integration of PWM and low-pass filter.

3 DESIGN OF MCU BOARD

Considering the requirements written in previous section, we have developed a new MCU board shown in Fig 2. Size of the board is 59 mm by 26 mm. A MCU, linear regulator, DC jack, pin headers, pin sockets for UART and pin sockets for writing program are mounted on a double-sided board. The MCU is dsPIC33FJ128MC204 by Microchip. Most of MCU pins are connected to the pin headers. The basic specification of the board is shown in Table 1. This board can control two DC motors with rotary encoders.

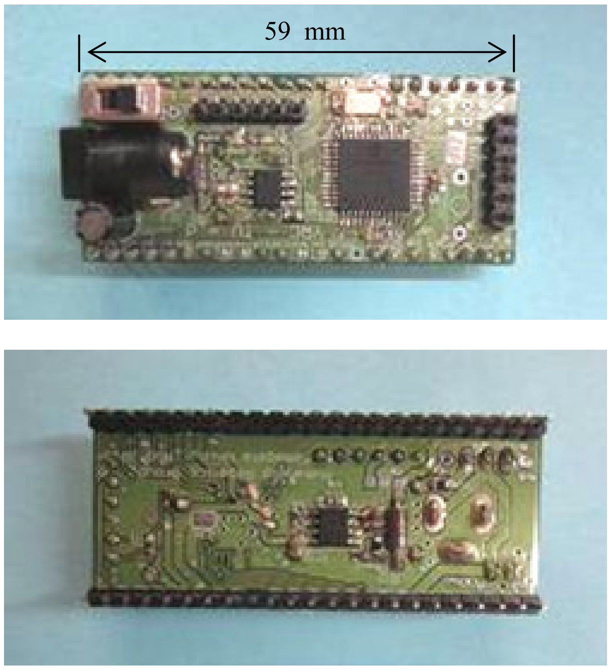

Fig. 2. Top and bottom biew of the MCU board.

Table 1. The specification of the MCU board

function	number of channels	main use
12bit A/D converter	9	Sensors
QEI counter	2	rotary encoders
PWM	8	H-bridge Circuits Analog input drivers
Digital I/O	32	Sensors and actuators
UART	2	USB, RS485, XBee
SPI	2	
I2C	1	

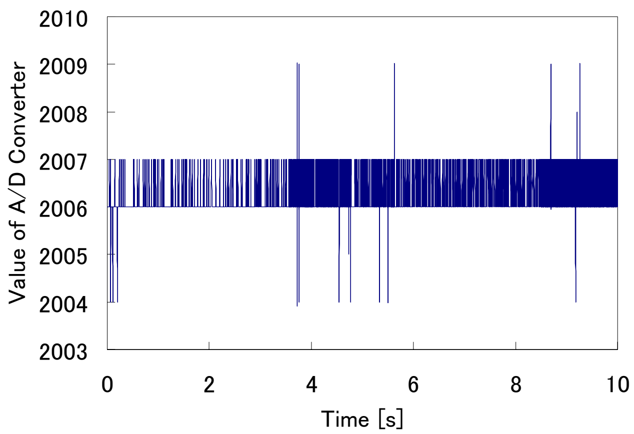

Fig. 3. The result of the experiment.

The pin sockets for UART is designed so that USB/UART converter "FTDI Basic Breakout - 5V" by Sparkfun Electronics or compatible board can be attached to it. The connecter for program writing is designed for the writer of PICkit2 by Microchip. The PICkit2 is connected a PC using a USB cable. Because the pitch of the pin headers is 2.54 mm, the board can be inserted to bread board or 2.54-mm pitch universal board.

The measure against noise is important for MCU board, because the noise have a bad effect on accuracy of A/D converter. To reduce power-supply noise, linear regulator and ferrite bead are utilized. The ground of analog circuit has a single connection to that of digital circuit so that the bad effect of the digital current to analog circuit is reduced.

4 EXPERIMENT

To evaluate the MCU board, we have performed an experiment. In the experiment, voltage of battery cell is measured in order to see the effects of noise. The result of the experiment is shown in Fig. 3. If the effect of the noise is large, variation of the voltage becomes large in the board. In 10 seconds, 4876 times A/D converter data were obtained. Maximum value was 2008 and minimum one was 2004. Most of obtained digital values were 2006 or 2007. Digital value of 2004 was obtained 10 times, 2005 was obtained once, 2008 was obtained once and 2009 was obtained 5 times.

5 APPLICATION OF THE MCU BOARD

We show two application of the MCU board. First one is the system to measure the current of DC servo motors. The photograph of the system is shown in Fig. 4 (a). Motor current is measured by hall effect-based linear current sensor IC. The IC output the voltage signal and the MCU measured the voltage using A/D converter. The values of A/D converter are transmitted to the PC via UART/USB converter.

The other application is sensing system of acceleration and angular velocity with wireless transceiver. The photograph of the system is shown in Fig. 4 (b). The system includes 3-Axis analog output acceleration sensor and analog output vibrational gyroscope. The acceleration sensor is MMA7361LC by Freescale Semiconductor, Inc. and gyroscope is ENC-03R by Murata Manufacturing Co., Ltd. The signals of acceleration sensor and gyroscope are obtained by A/D converter of the MCU. The MCU transmits A/D converter value using UART. For wireless communication, XBee by Digi International Inc. is utilized. XBee receives the data from UART and converts it to wireless signal.

6 CONCLUSION

The development of a multi-purpose compact MCU board has been presented. Requirements of multi-purpose MCU boards have been discussed. The design and specification of the MCU board have been presented. The experimental result of the MCU board shows that variation of A/D converter value is very small when the voltage of battery cell was measured. This result indicates that the bad effect of noise is small. Two applications of the MCU board show that the board can be used for multiple purposes. In future work, we will use the board for the control of a humanoid robot and sensor network systems.

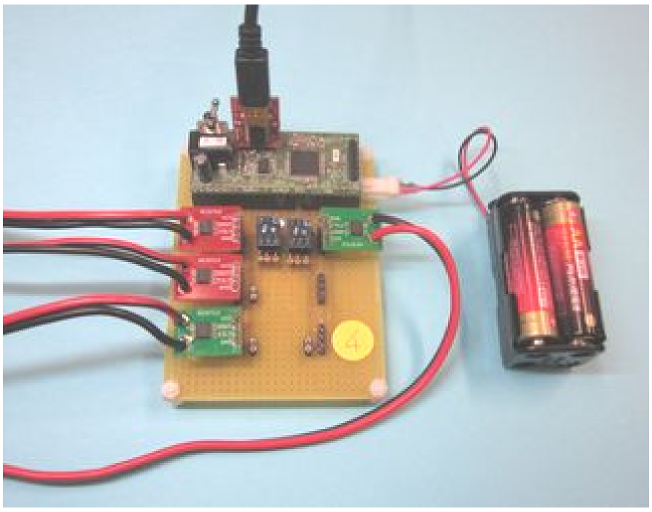

(a) measurement system of motor current

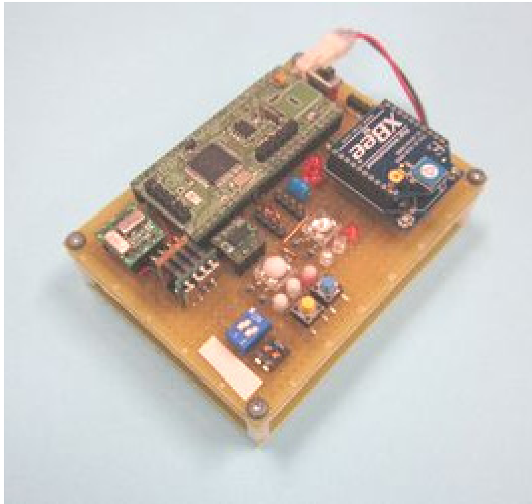

(b) wireless sensor system

Fig. 4 Application of the MCU board.

ACKNOWLEDGMENT

This research was partially supported by Japan Society for the Promotion of Science (KAKENHI 21300040).

REFERENCES

[1] Z. Lin, M. Zecca, S. Sessa, L. Bartolomeo, H. Ishii, K. Itoh, and A. Takanishi, (2010) , Development of an Ultra-miniaturized Inertial Measurement Unit WB-3 for Human Body Motion Tracking. 2010 IEEE/SICE International Symposium on System Integration, pp. 414-419

[2] Z. Lin, IEEE, M. Zecca, S. Sessa, L. Bartolomeo, H. Ishii, K. Itoh, and A. Takanishi(2010), Development of the Miniaturized Wireless Inertial Measurement Unit WB-4: Pilot Test for Mastication Analysis. 2010 IEEE/SICE International Symposium on System Integration, pp. 420-425

[3] Ahmad 'Athif Mohd Faudzi and Koichi Suzumori (2010), Programmable System on Chip Distributed Communication and Control Approach for Human Adaptive Mechanical System. Journal of Computer Science Vol. 6, Issue. 8, pp. 852-861

[4] Mitsuhiro Yamano, Akihiro Ochiai, Yuichi Suzukawa, Hanafiah Yussof, Masahiro Ohka and Yasuo Nasu (2010), Design of a Distributed Control System Using a Personal Computer and Micro Control Units for Humanoid Robots. Journal of Computer Science, Volume 6, Issue 8k, pp. 880-885

[5] Yuichi Suzukawa, Mituhiro Yamano (2010), A Robot Control System Using dsPIC MCU Boards and RT-Middleware (in Japanese). The 28th Annual Conference of the Robotics Society of Japan, CDROM

[6] Toshimasa Tanaka, Takehito Kikuch, Keigo Kobayashi, Kazuhisa Mitobe, Mitsuhiro Yamano, Yuichi Suzukawa (2010) , Development of the 2nd-generation of the intelligently controllable walker (i-Walker2) -Assessment experiment of walking assistance performance of i-Walker 2– (in Japanese). Proceedings of the 2011 JSME Conference on Robotics and Mechatoronics, Japan, CD-ROM

[7] Riichiro Tadakuma, Kenjiro Tadakuma, Kyohei Ioka and Yuichi Tsumaki (2011), Study of the Omnidirectional Driving Gear Mechanism -- Basic Configurations and Performances of Driving Units with Various Curvatures – (in Japanese). Proceedings of 16th Robotics Symposia, Japan, 3B5.

'Cruise-and-Collect' algorithm for an ARM-based autonomous robot

M.N. Zarina[1], M.S Sani Irwan, M.Y. Norhidayah, A. Nur Alisa and M.S. Muzalifah

[1]Fakulti Kej. Elektronik & Kej. Komputer (FKEKK), Universiti Teknikal Malaysia Melaka (UTeM), Melaka, Malaysia
[2]Oita University, Oita 870-1121, Japan
(Tel: +6-06-5552058, Fax: +6-06-5552112)

[1]zarina.noh@utem.edu.my

Abstract: The 'cruise-and-collect' algorithm proposes in this research is intended to be applied for an autonomous robot system. The robot is designed to be used in a sport such as table-tennis, to help the players collect the off-side ball during a game. The controller for the robot system will utilize ARM-based microcontroller chip from Atmel, AT91SAM7S128, as it is the classic ARM7TDMI processor that had marked a great success of ARM processor market. The algorithm is developed via *Flowcode* software which exploits the flowchart as its design entry. The E-block board that has an integrated microcontroller chip is used for the purpose of its hardware prototype and software testing. It is hoped that the development and design process exposed in this research will be benefitted for researchers who are interested in the area of prototype development and robot design, especially via the ARM7TDMI processor platform**.**

Keywords: ARM-based processor, AT91SAM7S128, E-block, *Flowcode*.

1 INTRODUCTION

The concept of autonomous robot reflects that a robot can perform a desired task in an unstructured environment without continuous human guidance, or with minimal human control [1]. Depending on its application, the design approach might cover several modular areas; each carries a certain degree of autonomous in the robot's development.

In developing an autonomous robot for assembly line (typically used in warehouse or factory), the focus is given more to the assembly plan itself [2]. Successful assembly plan ensures that each of the pieces to be assembled in the warehouse is defined clearly in each of its single step. An algorithm related to each of these assembly steps are written such that the robot will perform those task consequently and independently. A feedback scheduling might also be provided in the algorithm to avoid repetition of its assembly step [2]. Compared to the design of an Autonomous Underwater Vehicle (AUV), the focus is more towards the navigational path of the autonomous robot because the robot is moving [3]. In this case, the algorithm design concentrates on collision avoidance and escape route by gathering the object geometries and its relative distance to the robot (reactive system). Furthermore, advancement to the reactive system was proposed, such that a configured database (known surrounding information and maneuver reaction) is added to the component. With this configured database, the reactive system will have additional information that helps the autonomous robot to plan for its navigational path effectively besides its real-time information gathering [3]. Later, the algorithm for autonomous robot navigation was improved, resulting in a real-time hierarchical POMDP (Partially Observable Markov Decision Processes) [4]. This improved algorithm act as a unified framework for autonomous robot navigation in dynamic environment, where it decides for the robot movement in every time step execution. The algorithm also caters for planning, localization and local obstacle avoidance; those are the traditional approach for an autonomous navigational system [2].

2 AUTONOMOUS ROBOT DESIGN ISSUES

Gathering from the literatures [2][3][4], there are several design issues need to be addressed in the development of an autonomous robot. For the purpose of this paper, only two of the design issues will be highlighted. The first issue is the navigational path of the robot; either it is predetermined or unknown. If it is unknown, several sensors need to be listed as part of the feedback circuit in configuring the robot's paths and movements. If it is predetermined, the navigational algorithm needs to be manipulated such that it reflects the predetermined path. The paths need to be clearly specified, so that the robot will be fully autonomous.

Next issue is on the definition of the application of the autonomous robot itself. As such, the algorithm and sensors related need to be configured to perform the required task. The application should also reflect the autonomous robot requirement in its design.

With these two design issues clearly described, the autonomous robot proposed in this research can be developed. Still, the core target in this project will not be forgotten that is, to explore the functionality of ARM-processor platform for robotics application.

3 DEVELOPMENT APPROACH

The prototype of the autonomous robot developed in this research is intended to be used in table-tennis (ping-pong) sport, as a ball-collector (applying the 'cruise-and-collect' algorithm in its system).

The prototype will take a route such that it will cover all the space along its way and collect the ping-pong ball. It is assumed that there is a wall at one side of the navigational path to ease the collecting work and the route is free from any obstacles as in **Fig. 1**. All those mentioned above are the 'cruise' information used in the algorithm of the system in this research.

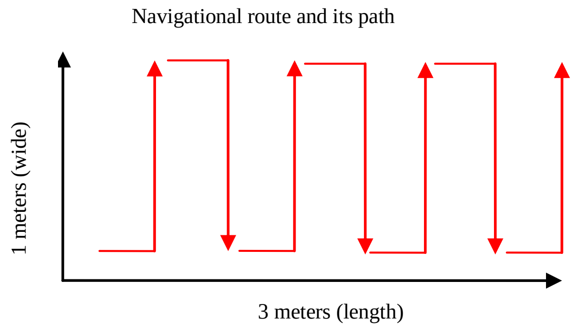

Fig. 1. Navigational path of the autonomous robot

As the application of the autonomous robot in this research is to navigate through its designated route while collecting the ping-pong ball along its way, several sensors needs to be used to realize this system. **Fig. 2** illustrates the block diagram of this autonomous robot prototype.

The Controller Module is the most important part of the autonomous robot as this module consists of the processor unit in the system. The Sensor 1 Module will cater the 'cruise' operation or its navigational route, while the Sensor 2 Module will cater the 'collector' operation. Sensor 3 is of no use at the moment because it is intended to be developed for further enhancement of the system. The 3 sensor modules are the input of the system, to be processed by the Controller Module, in order to produce the respective output to the Cruise Module and Collect Module.

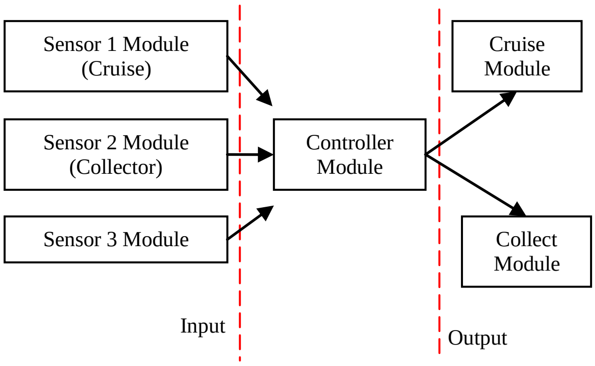

Fig. 2. Block diagram of the autonomous robot prototype

4 ALGORITHM DESIGN

The functional operation of the system is as summarized in the **Fig. 3**. **Fig. 4** detailed the flowchart of the Cruise Module, while **Fig. 5** shows the flowchart of the Collect Module. The Cruise Module inputs consist of 1 switch for prototype On/Off indicator, 1 switch for Start/Stop module and 3 IR sensors to guide the motor in its movement. The IR sensor act as the prototype eyes in order to avoid collision with obstacles in its surrounding. The Collect Module will make use of the same IR sensors in Cruise Module, such that it moves its motor to collect the ball in every turn the prototype made.

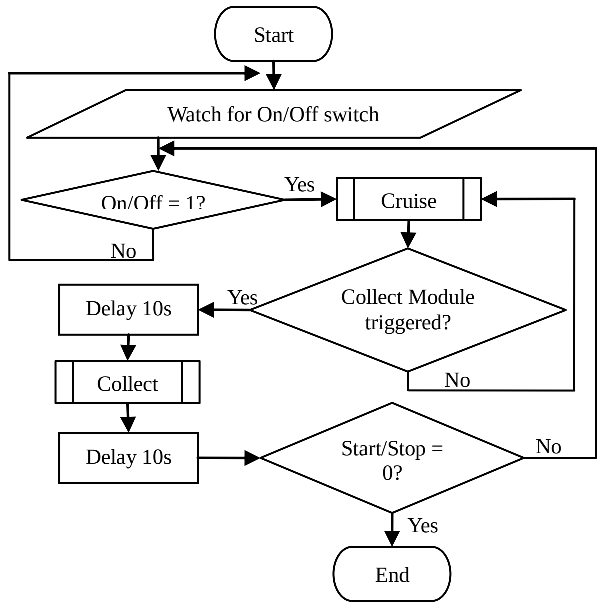

Fig. 3. Flowchart of the system operation

The designed algorithms as shown in the flowcharts are then realized via the *Flowcode* software, software that uses flowcharts as its design entry [5]. The *Flowcode* software has the capability to compile the flowcharts into the user's required form; either into Hex code, C-language code or compiled to the target board in the program. In this project, the designed flowcharts are compiled to its target board, EB031.

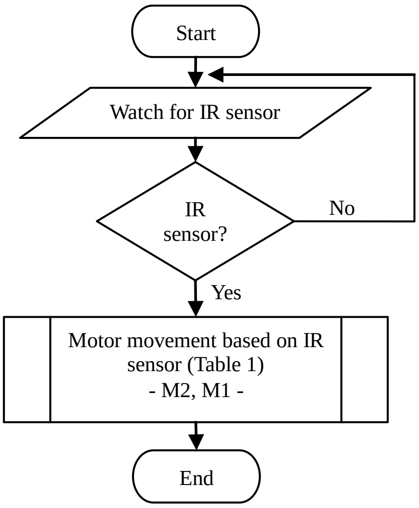

Fig. 4. Flowchart of Cruise Module

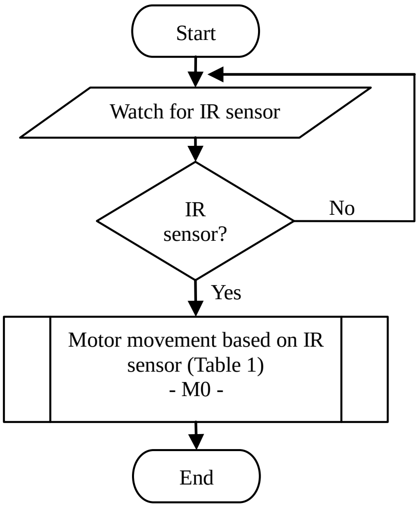

Fig. 5. Flowchart of Collect Module

Table 1. IR sensor and Motor movement

IR Sensor			**Motor**		
IR2	**IR1**	**IR0**	**M2 (Left)**	**M1 (Right)**	**M0**
0	0	0	Forward	Forward	OFF
0	0	1	Forward	Forward	OFF
0	1	0	Reverse	OFF	OFF
0	1	1	OFF	OFF	Forward
* after delay *			OFF	Forward	Reverse
1	0	0	Forward	Forward	OFF
1	0	1	Forward	Forward	OFF
1	1	0	OFF	OFF	Forward
* after delay *			Forward	OFF	Reverse
1	1	1	OFF	OFF	OFF

5 PROTOTYPE TESTING

The autonomous robot in this research is developed via the E-blocks boards, which can be obtained from *Matrix Multimedia Ltd.*, a company based in United Kingdom [5]. Due its low cost and free software download (trial version); these resources are chosen to be applied in this research.

The Controller Module will make use of EB031, an E-block ARM programmer board that is used to load the developed algorithm into the AT91SAM7 microcontroller chip. The microcontroller chip is housed on the removable EB034 board (another E-block), also called as ARM Daughter board. The removable ARM Daughter board allows users to detach the board and have the freedom to develop their own ARM application circuit. Both EB031 and EB034 board are as shown in **Fig. 6**.

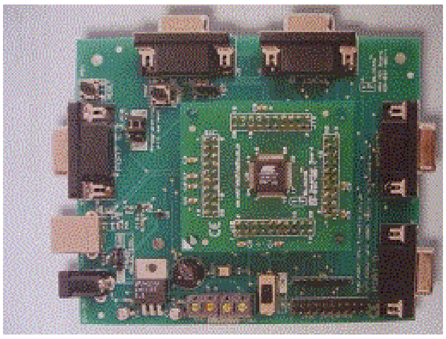

Fig. 6. EB031 and EB034 E-blocks

The supply voltage for EB031 board is an external regulated 6-9V DC supply or powered via the USB port (attached to computer) [6]. The programmer board is connected to any of its required input and output peripherals via its 5 serial ports (Port A, B, C, D and E). In this research, a motor driver board EB022, as shown in **Fig.7** is needed to drive the DC motor for wheel movement [7].

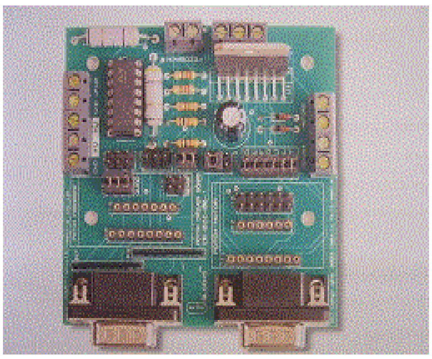

Fig. 7. EB022 E-block

The EB022 board allows users to drive two motors simultaneously and also allow independent PWM control for each motor. This board needs an external supply of minimum 5V and also for the motor power supply in the range of 3.3-24V external DC source.

For the purpose of this paper, the IR sensor status will be simulated via the LED board EB004 (**Fig. 8**) as the intended circuit is still in its development phase at the time of this paper writing. With that, the Collect Module will also be simulated via the LED pattern display.

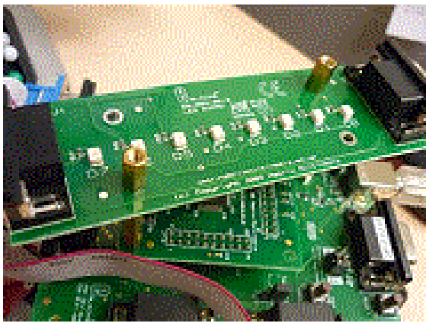

Fig. 8. EB004 E-block

The developed prototype is as shown in **Fig. 9.** With the EB031 and EB034 as the Controller Module, the EB004 will imitate the Collect Module while the EB022 will perform the Cruise Module. In this paper, the IR sensor condition is predetermined in the developed program as the IR sensor circuit is not fully developed at the time of this paper writing.

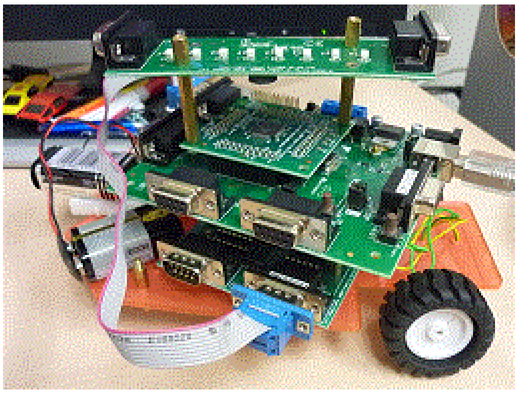

Fig. 9. Autonomous robot prototype

6 OBSERVATION AND CONCLUSION

From the developed prototype, it is observed that with a limited time constraint, researchers or even hobbyist may design their own application and develop the prototype with the use of the E-blocks and *Flowcode* software. The only constraint with the use of E-blocks is that each block must be connected via the serial port or E-block IDC cable if extension to the peripheral connection is needed. However, the removable ARM Daughter board allows customized circuit to be developed, besides restricting the development with only 5 serial ports given on the E-block ARM programmer board.

The 'cruise and collect' algorithm in this research is realized via the flowcharts without the hassles of writing the programming code. In this case, the steps involved in the development phase had been reduced, such that the system designer will only concern on its design requirement, but not the syntax or coding error. The use of flowcharts as the design entry form for the *Flowcode* software help ease the researchers work in testing its prototype. As such, the functional application can be fully tested and verified.

It is hoped that the development tools and design approach exposed in this paper will give the researchers or prototype developers other options in developing their system.

7 ACKNOWLEDGMENT

The authors would like to express the greatest appreciation to the Universiti Teknikal Malaysia Melaka (UTeM) for the continuos support, assistance and help given in completing this research.

REFERENCES

[1] Wikipedia - Autonomous robot (Accessed 2011). Citing Internet sources URL http://en.wikipedia.org/wiki/Autonomous_robot

[2] Daniel E. K. (2004), 'An Approach to Autonomous Robot Assembly', Robotica –Vol. 12, Feb 2004, pp137-155.

[3] Jonathan E., Pedro P., Ben S., David M. L. (2006), 'Design and Evaluation of a Reactive and Deliberative Collision Avoidance and Escape Architecture for Autonomous Robots', Journal of Autonomous Robots, 22 July 2006.

[4] Amalia R., Panos T. (2007), 'Real-time Hierarchical POMDPs for Autonomous Robot Navigation', Robotics and Autonomous Systems, Volume 55, Issue 7, 31 July 2007, pp. 561-571.

[5] Matrix Multimedia Ltd. (Accessed 2011). Citing Internet sources URL http://www.matrixmultimedia.com

[6] Matrix Multimedia Limited (2008), ARM progra mmer and daughter board (EB185-00-1) Technical Data sheet, Document Code: EB185-30-1.

[7] Matrix Multimedia Limited (2006), Motor driver board (EB022-00-1) Datasheet, Document Code: EB022 -30-1.

The Seventeenth International Symposium on Artificial Life and Robotics 2012 (AROB 17th '12),
B-Con Plaza, Beppu, Oita, Japan, January 19-21, 2012

Blood Vessel Extraction for Diabetic Retinopathy

Haniza Yazid[1], Ali AlMejrad[2], M. Rizon[2] and Hamzah Arof[3]

[1]*School of Mechatronic Engineering, Universiti Malaysia Perlis, 02600 Arau, Perlis, Malaysia*

[2]*Department of Biomedical Technology, college of Applied Medical Sciences, King Saud University 11433 Riyadh, Kingdom Saudi Arabia*

[3]*Electrical Engineering Department, University of Malaya, 50603 Kuala Lumpur, Malaysia*

hanizayazid@unimap.edu.my

***Abstract*— Diabetic retinopathy is an eye problem that face by the diabetic's patient. Diabetic Retinopathy (DR) is caused by the changes of the blood vessel in the retina. In the early stage of DR, the blood vessels may swell and leak fluid. However, in the advance stage of DR a new blood vessel that fragile and abnormal may formed and leaks blood to the retina. This can caused vision loss or even blindness. Therefore, this paper proposed to extract the blood vessel based on the peak and valley detection. The proposed methods utilized a green channel image and the inversion image. Next, the resulting images from both methods are combined. Three (3) databases are utilized namely from STructured Analysis of the Retina (STARE), Digital Retina Images for Vessel Extraction (DRIVE) and a database that is acquired from the local hospital.**

***Keywords*— blood vessel, diabetic retinopathy, peaks detection and valley detection.**

I. INTRODUCTION

Blood vessel appearance is a vital indicator in several diagnosis namely diabetic retinopathy, hypertension and arteriosclerosis. In this paper, the main focus is DR. Due to the increasing growth of interest in medical image processing, an automated detection of blood vessel in fundus images for diabetic retinopathy's patient is proposed. Retinopathy is a general term refers to some form of non-inflammatory damage to the eye in the retina. DR can lead to several abnormalities and the abnormalities are not connected to other structure on the retina are microaneurysms (MA), haemorrhages (HR), exudates (EX) and cotton wool spots (CWS). These abnormalities present in the early stage of DR known as Non Profilerative Retinopathy (NPR). Meanwhile, Proliferative Retinopathy (PR) is an advance stage of DR. In PR, a new blood vessel may grow and the new vessels are abnormal and very fragile. By themselves, these blood vessels do not cause symptoms or vision loss. However, if they leak blood, severe vision loss can result.

There are three (3) main methods that can be generally classified for blood vessel detection; window-based, classifier based and tracking based [3]. Kirbas [7] on the other hand did a survey in vessel extraction technique and algorithm. In his paper, 6 categories are classified; pattern recognition techniques, model-based approaches, tracking-based approaches, artificial intelligence-based approaches, neural network-based approaches, and tube-like object detection approaches. For pattern recognition techniques, it have been sub categorised to multi-scale approaches, skeleton-based approaches, region growing approaches, ridge-based approaches, differential geometry-based approaches, matching filters approaches and mathematical morphology schemes. For model-based approaches, three (3) subs have been classified; namely deformable models category, parametric models and generalized cylinders approaches. This paper utilized mathematical morphology that can be categorised in pattern recognition based on Kirbas's survey [7].

Reza [8] proposed to employ Quadtree method to detect the blood vessel in RGB using RGB component. [8] stated that the proposed method can yield true positive fraction values as high as 0.77, which are comparable to or somewhat higher than the results obtained by other known methods. Vallabha [10] utilized scale and orientation selective Gabor filter banks. This proposed method classified the retinal image as mild or severe based on the output obtained by Gabor filter. Localized adaptive thresholding and a multi-window Radon transform are utilized in detecting the vascular system in retinal images. The algorithm was tested with 20 images (10 normal and 10 abnormal) and the result demonstrated that an average positive rate of 86.3% and false positive rate is 3.9% [5, 6]. Meanwhile, local and global features cooperatively to segment the vessel network was proposed by Hoover [3]. Gaussian matched filter is designed and used to locate the center point and width of a vessel in its cross sectional profile. Next, extended Kalman Filter is employed for the optimal linear estimation of the next possible location point. Afterword, branching detection strategy is proposed to check the bifurcation [2]. Jiang [4] proposed a general framework of adaptive local thresholding based on a verification-based multithreshold probing scheme. The proposed method demonstrates a superior performance on normal compared to abnormal. Recently, Xu[11] also proposed to use adaptive thresholding and then extract the large connected component as the large vessels. The residue fragments are classified using Support Vector Machine. The average sensitivity obtained is over 77%. Sukkaew [9] proposed a method applies a Laplacian of Gaussian as a step-edge detector based on the second-order directional derivative to identify locations of the edge of vessels with zero crossings. Chaudhuri proposed two (2) dimensional matched filters to detect the blood vessel [1]. The main focus in this paper is to detect the blood vessel utilizing morphological operation. Three (3) databases are utilized namely the online database known as STARE, DRIVE and a custom database that is acquired from a local hospital. All the databases have different illumination and contrast. These variations are the constraints in previous works. In this paper, the research methodology is present in Section II followed by experimental results in Section III and last but not least the conclusions.

II. RESEARCH METHODOLOGY

Numerous methods have been proposed in previous works. The matched filter, Gabor filter and morphological filtering are the most well-known approach. In this paper, peak and valley detection based on half sphere is proposed. The main different is this proposed method makes use of the inversion of the green channel image to detect the peak. The proposed method for blood vessel detection is illustrated in Fig. 1.

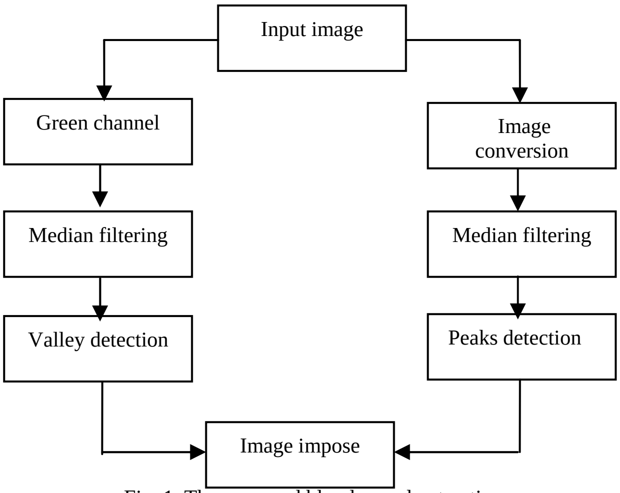

Fig. 1 The proposed blood vessel extraction

A. *Morphology*

Peak detection algorithm is a type of morphological processing. There are several type of structuring element that can be applied such as circle, sphere and square. In this paper, half sphere structuring element is applied.

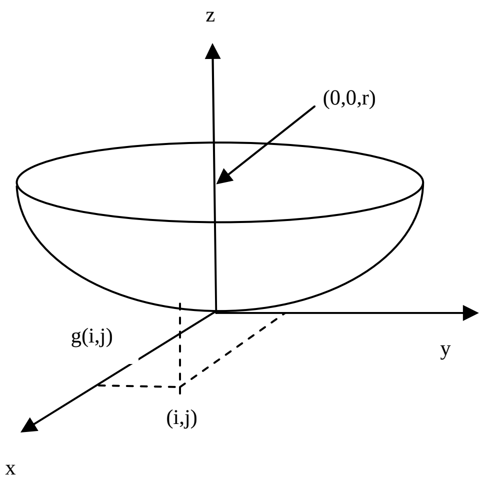

Fig. 2 Half sphere structuring element

If the radius of the sphere is r, G is given by:

$$G = \{ i, j, g(i,j) \} \quad -r \leq i \leq r$$
$$-\left\lfloor \sqrt{r^2 - i^2} \right\rfloor \leq j \leq \left\lfloor \sqrt{r^2 - i^2} \right\rfloor$$

for all i and height;

$$g(i,j) = \left\lfloor r - \sqrt{r^2 - i^2 - j^2} \right\rfloor$$

for all j. where $\lfloor a \rfloor$ denotes the greatest integer smaller than or equal to a real number of G. Given the following definition:

$$I(x,y) \; (0 \leq x \leq m-1, 0 \leq y \leq n-1)$$

- I(x,y): the original image,
- r: radius of the sphere,
- $\lfloor a \rfloor$: the largest integer smaller than or equal to a,
- m,n: is the length and height of the image.
- $\max f(i,j)$ means the maximum of $f(i,j)$ over all the points (i,j) inside G.
- $\min f(i,j)$ means the minimum of $f(i,j)$ over all the points (i,j) inside G.

Peak detection algorithm is an opening morphology. Erosion is performed first then followed by dilation. Peak detection algorithm is simplified as follows;

- Find point (i,j) in half sphere r, find corresponding value of g(i,j)
- Grayscale erosion is performed onto each pixel and obtained R(x,y)
  R(x,y):=max{I(x-1,y-1) + g(i,j)};
- Perform grayscale dilation and obtained D(x,y)
  D(x,y):=min{R(x-1,y-1) - g(i,j)};
- Perform P(x,y) = I(x,y)-D(x,y) for each pixel (x,y)
  P(x,y) = 1 if (x,y) is a peak pixel
  P(x,y) = 0 otherwise
- If P(x,y) >= T for a threshold value T, (x,y) is determined to be a peak.

Valley detection algorithm is a closing morphology. The dilation is performed first followed by erosion. The overall valley detection process is simplified as the following;

- Find point (i,j) in half sphere r, find corresponding value of g(i,j)
- Perform grayscale dilation and obtained D(x,y)
  D(x,y):=max{I(x-1,y-1) + g(i,j)}; (-5<= i <=5)
- Grayscale erosion is performed onto D(x,y) and stored into R(x,y)
  R(x,y):=min{D(x-1,y-1) - g(i,j)};
- Perform V(x,y) = R(x,y) – I(x,y) for each pixel (x,y)
  V(x,y) = 1 if (x,y) is a valley pixel
  V(x,y) = 0 otherwise
- If V(x,y) >= T for a threshold value T, (x,y) is determined to be a valley.

B. *Image impose*

The resulting image from valley detection is imposed to the resulting image obtained from peaks detection. The algorithm to obtain the blood vessel as the following;

If (V[i][j] = valley OR P [i][j] = peak)
*result[i][j] = 255 / *indicate the blood vessel*/*
else
*result[i][j]=0 /*indicate the background*/*

i and j indicate the width and the height of the image meanwhile P[i][j] is an array that hold the peak value. V[i][j] hold the valley value and result[i][j] hold the value after the overall operations.

III. EXPERIMENTAL RESULTS

In this paper three (3) databases are utilized to experiment the proposed methods namely STARE, DRIVE and personal database. The original image is extracted into different channels namely red, green and blue. The red channel is used to extract the retina from the background meanwhile for further process only green channel will be employed. Next, image inversion based on the green channel image is obtained. Fig. 3 and Fig. 4 show the green channel image and the inversion image.

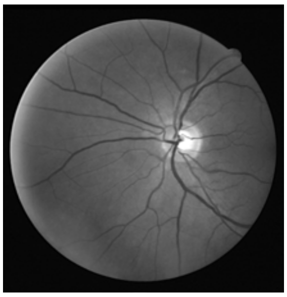

Fig 3 The green channel image

Fig. 4 The inversion image based on the green channel

Median filtering using 3 by 3 windows is utilized to smooth the image without blurring the blood vessel for both images (green channel and inversion image). A large windows size tends to blur the image and eliminate the small vessel information.

In the next process, both images (green channel and inversion image) undergo the peak and valley detection (as explained in Section II). The green channel image will utilize the valley detection method since blood vessel appears in low intensity. On the other hand, in the inversion image, the peaks detection will be employ. The blood vessel appears in high intensity for the inversion image. Both methods tend to detect the blood vessel. However, the inversion image provides more blood vessel information. Fig. 5 and Fig. 6 indicate the resulting image for peak and valley detection.

Fig. 5 Valley detection onto the green channel

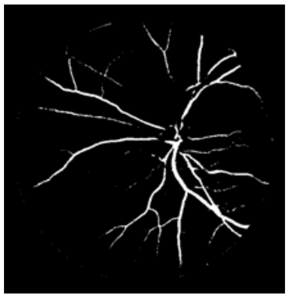

Fig. 6 Peak detection onto the inversion image

In order to acquire the overall blood vessel information, both images are combined as explained in Section II.

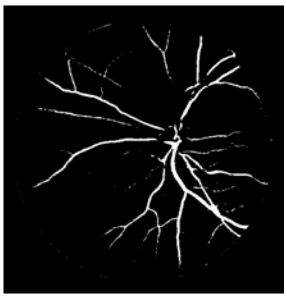

Fig. 7 Combining peaks and valley detection

Fig. 8 indicates the original green images in the left side meanwhile the image after combining the peaks and valley detection is shown in right side.

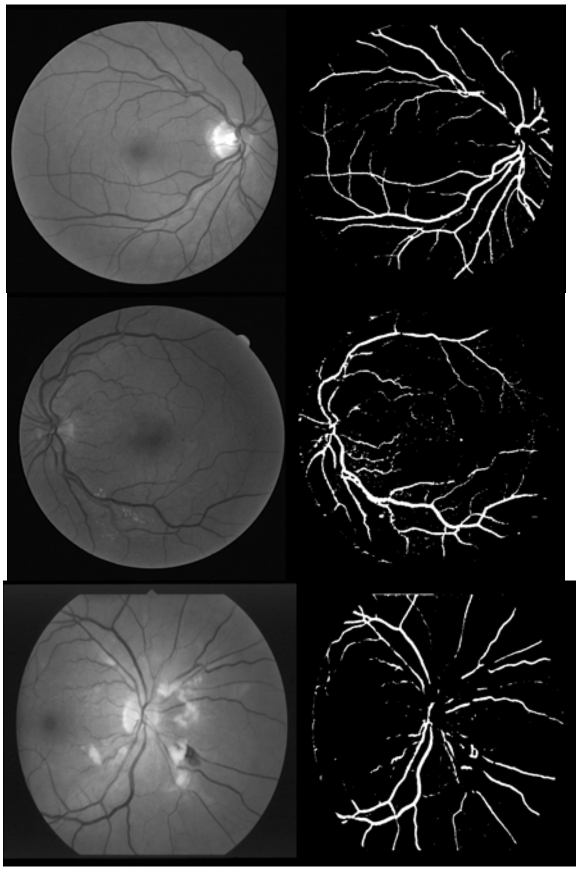

Fig. 8 Original green image (left) and resulting image (right)

Although the resulting image detects the blood vessel but it still fail to detect small vessels. Besides, unrelated information is detected. In the next phase, the image needs to be cleaned by removing the unwanted information and tracking down the missing vessels. However, the mention process above is beyond the scope in this paper.

IV. CONCLUSION

This paper proposed utilizing morphological operation in detecting the blood vessel. Peak and valley detection algorithm based on the green channel image and the inversion image are employed. Then, both resulting images are combined. The result shows that the vessel can be detected using the proposed methods. However, further methods need to be employed to clean the unwanted information and to track down the missing vessels from the previous resulting image.

ACKNOWLEDGMENT

The authors wish to thank the local hospital for assisting the image acquisition process for this research.

REFERENCES

[1] Chauduri, S., Chatterjee, S., Katz, N., Nelson, M., and Goldbaum,M., "Detection of blood vessels in retinal images using two dimensional matched filters". *IEEE Trans. Med. Imag*. vol 8, pp. 263–269, 1989.

[2] Chutatape O, Li H,"A Model-Based Approach for Automated Feature Extraction in Fundus Images". *ICCV 2003*, pp. 394-399.

[3] Hoover, A., Kouznetsova, V., and Goldbaum, M., "Locating blood vessels in retinal images by piecewise threshold probing of a matched filter response". *IEEE Trans. Med Imag*. vol. 19(3), pp. 203–210, 2000.

[4] Jiang, X., and Mojon, D., "Adaptive local thresholding by verification based multithreshold probing with application to vessel detection in retinal images". *IEEE Trans. Pattern Analy.* vol. 254(1), pp.131–137, January 2003.

[5] Katia Estabridis, Rui J. P. de Figueiredo, "Automatic Detection and Diagnosis of Diabetic Retinopathy". *ICIP*, vol. 2, pp. 445-448, 2007.

[6] Katia Estabridis, Rui J. P. de Figueiredo, "Blood Vessel Detection via a Multi-window Parameter Transform". *CBMS 2006*,pp. 424-429

[7] Kirbas, C., and Quek, F., "A review of vessel extraction techniques and algorithms", *ACM Comput. Surv*. vol.32 (2), pp.81–121, 2004.

[8] Reza A.W, C. Eswaran, and Subhas Hati, "Diabetic Retinopathy: A Quadtree based Blood Vessel Detection Algorithm using RGB Components in Fundus Images", *Journal of Medical Systems*, vol. 32, no. 2, pp. 147-155, 2008.

[9] Sukkaew L, Bunyarit Uyyanonvara, Sarah A Barman, Jaruwat Jareanjit, "Automated Vessels Detection on Infant Retinal Images", *International Conference on Control, Automation and Systems (ICCAS2004)*, August 25-27, Bangkok, Thailand, pp. 321-325.

[10] Vallabha D, R. Dorairaj, K. Namuduri, and H.Thompson, "Automated detection and classification of vascular abnormalities in diabetic retinopathy," *Proceedings of Thirty-Eighth Asilomar Conference on Signals, Systems and Computers,* vol. 2, pp. 1625-1629, November 2004.

[11] Xu L, Luo S, "A novel method for blood vessel detection from retinal images", *BioMedical Engineering Online*, vol 9:14, 2010.

Decision tree approach for fault diagnosis of nonlinear

In Soo Lee[1], Jung Hwan Cho[2], Hae Moon Seo[3] and Yoon Seok Nam[4]

[1]School of Electronics and Electrical Engineering, Kyungpook National University, Sangju, 742-711, Korea
(Tel: +82-054-530-1324; Fax: +82-54-530-1320; E-mail: insoolee@knu.ac.kr)
[2]Department of Civil and Environment Engineering, University of Massachusetts Lowell, Lowell, MA 01854, USA
(Tel: +1-978-934-2238; E-mail: junghwan_cho@uml.edu)
[3]Korea Electronics Technology Institute, Gyeonggi-do, 421-742, Korea
(Tel : +82-02-6388-6695; E-mail : bmoons@keti.re.kr)
[4]Division of Information Communication Engineering, Dongguk University, Kyungju, 780-714, Korea
(Tel : +82-54-770-2273; E-mail : ysnam@dongguk.ac.kr)

Abstract: In this paper we proposed a decision tree approach for fault diagnosis of nonlinear systems using tree model CART (classification and regression trees) and MNN (multilayer neural network). In the proposed method, the fault is detected when the errors between the actual system output and the NN nominal system output cross a predetermined threshold. Once a fault in the nonlinear system is detected, CART is used for classifying the fault.

Keywords: CART , fault diagnosis, MNN, nonlinear system

1 INTRODUCTION

There have been many methods for fault diagnosis of the system. These methods fall into two major groups: 1) model free methods, 2) model based methods. The model based fault diagnosis methods are dependent on finding a system mathematical model that defines the relationship between the system inputs and outputs. In practice, however, the mathematical description of the relationship is not easy to obtain due to nonlinearities. To overcome this problem, it is necessary to find the modeling tool of presenting any nonlinear relationship approximately. In recent years, NN(neural network) models have been studied considerably for the fault diagnosis problem [1-3]. Main advantages of the NN model for fault diagnosis applications can be represented by approximating the nonlinear functions and by adaptive learning and parallel processing. Hence this model can be used as a powerful tool for handling nonlinear problems.

This paper presented a decision tree approach for fault diagnosis of nonlinear systems using tree model [4] and MNN [5]. In the proposed method, the fault is detected when the errors between the actual system and the NN nominal system output cross a predetermined threshold. Meanwhile CART is used for classifying the fault. The algorithm contains two main parts: a fault detection part by threshold test and a fault classification part by CART.

2 PROPOSED FAULT DIAGNOSIS METHOD USING NN AND CART

2.1 Fault detection using neural network

Consider a discrete-time nonlinear system,

$$\begin{aligned} y(k+1) = g[\,y(k),\, y(k-1),\, \cdots, y(k-n+1), \\ u(k),\, u(k-1),\, \cdots, u(k-m+1)] + \varepsilon(k) \end{aligned} \quad (1)$$

where $u(k)$ and $y(k)$ are the input and the output at time k , respectively, and $\varepsilon(k)$ is the white noise.

In the proposed method, NN nominal system is utilized to detect the fault in nonlinear system. Therefore, MNN`s with BP learning algorithm is adopted in this study [5].

Fault is detected by the following threshold test

$$J_n(k) = \sum_{i=k-L+1}^{k} e_n^2(i) \; > \; \delta_f \quad (2)$$

where $e_n(k) = y(k) - y_n(k)$ is the error between the nominal system output and actual system output. $y_n(k)$ is the NN nominal system output, δ_f is the predetermined threshold for fault detection, L is moving window length.

If the estimated parameters converge to system parameters, then the error between the system output and estimate NN output has a similar property of the system noise. Thus, the error e_n has a normal distribution. Also, the sum of the normalized square errors in the moving window has a χ_L^2 -distribution with L degrees of freedom as follows:

$$\bar{J}_n(k) = \sum_{i=k-L+1}^{k} \frac{e_n^2(i)}{\sigma^2} \; \sim \; \chi_L^2 \quad (3)$$

If the false-alarm probability limit α is

$$\Pr\Big(\sum_{i=k-L+1}^{k} \frac{e_n^2(i)}{\sigma^2} > \delta^\circ \Big) = \alpha \quad (4)$$

and the threshold is obtained as: $\delta_f = \sigma^2 \delta^\circ$

2.2 Fault classification using decision tree algorithm

The decision tree consists of two parts, tree building and tree pruning. In the stage of tree building the initial state of a decision tree, called the root node, is the first internal node, to which all the patterns of the training set are assigned. If the training example consists of all the same class, then there is only a need for the root node. Conversely, if the training examples at the root node consist of two or more classes, a test node is made that will split the training set into two sub-spaces, or secondary nodes. These can either become terminal nodes, in which a classification is reached, or another test node. The process is recursively repeated until each branch results in a terminal node and a completely discriminating tree is obtained.

The tree obtained by the tree building step may have a large number of branches which substantially increase the tree's complexity. This could lead to encountering the familiar problem of over-fitting and overspecializing toward the training data. If that happens, the tree may not generalize well for new data sets and thus it is necessary to prune the tree to build smaller tree models. CART uses a tree pruning technique based on the principle of minimal cost complexity pruning which is also known as weakest sub-tree shrinking.

3 SIMULATION RESULTS

The nonlinear system is given as

$$y(k) = \cos(3.14\,p_1)\,y(k-1) - 0.7\,y(k-2) + u(k-1) + p_2\,u(k-2) + \varepsilon(k) \tag{5}$$

where, input $u(k) = 0.5\cos(k)$, $\varepsilon(k)$ is white noise with variance $\sigma^2 = 2.56*10^{-4}$, p_1 and p_2 are physical parameters and $p_1 = 0.56$, $p_2 = 0.37$. Here, we choose $\alpha = 0.01$ (1%) and L=30, fault threshold $\delta_f = 0.013$. NNs for fault detection is consists of 4 inputs, one hidden layer with 10 nodes, and one output node. The weights of the NN are adjusted at every time step using a learning rate $\eta = 0.15$, and momentum term $\alpha = 0.1$.

To verify the proposed diagnosis algorithm, one type of fault is the introduced to the system at the 150-th sample number. The following fault is simulated

Fault #1: p_1 is decreased ($p_1 = 0.35$)

The prepared 20 data sets for each system condition (normal, fault #1) were used for training of CART. Fig. 1 shows a classification tree built by CART taking the 15 input data.

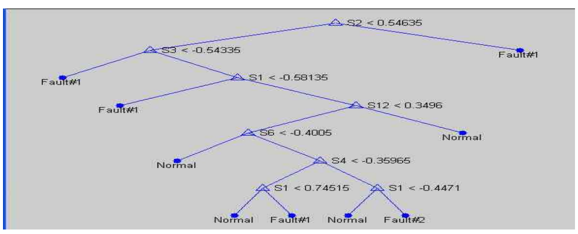

Fig. 1. Trained CART classification tree.

Fig. 2(a) shows the variations of the sum of squares of errors in the moving window, and 2(b) plots fault isolation results by CART. The simulation results show that CART successfully isolates the fault of the nonlinear system.

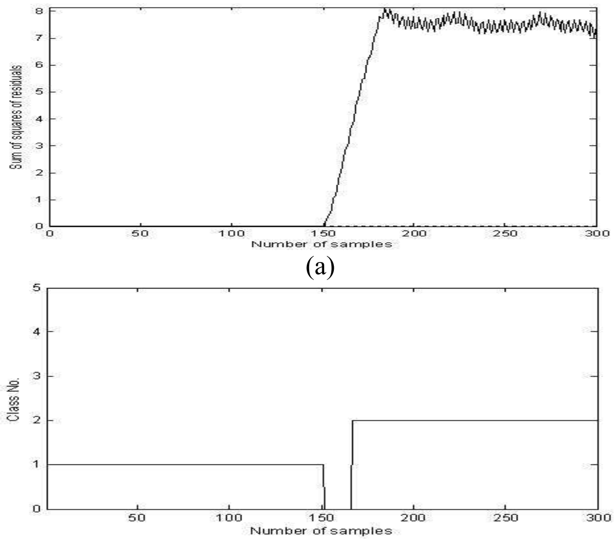

(a)

(b)

Fig. 2. Results of detection and isolation for fault #1.
(a) Change of J_n and fault detection (dashed line: δ_f)
(b) Classification results by CART

4 CONCLUSION

In this work, we develop a fault diagnosis method using CART and MNN to detect and isolate faults in nonlinear systems. The decision tree is proficient at both maintaining the role of dimensionality reduction and at organizing optimally sized classification trees, and therefore it could be a promising approach to diagnose a fault which is occurred in the systems. Simulations are carried out to evaluate the performance of the proposed NN-based diagnosis method.

REFERENCES

[1] M. M. Polycarpou and A. T. Vemuri (1995), Learning methodology for failure detection and accommodation, IEEE Contr. Syst. Mag., 16-24

[2] M. A. Kramer and J. A. Leonard (1990), Diagnosis using backpropagation neural networks-analysis and criticism, Computers Chem. Eng., 14(12): 1323-1338

[3] A. Srinivasan and C. Batur (1994), Hopfield/ART-1 neural network-based fault detection and isolation, IEEE Trans. Neural Networks, 5(6): 890-899

[4] L. Breiman, J.H. Friedman, R.A. Olshen, C.J. Stone (1984), Classification and Regression Trees, Wadsworth Inc., Belmont, CA

[5] D. E. Rumelhart and J. L. McClelland (1986), Parallel d istributed processing: explorations in the microstructure of cognition. vol. 1, MIT Press, Reading, MA

The Seventeenth International Symposium on Artificial Life and Robotics 2012 (AROB 17th '12),
B-Con Plaza, Beppu, Oita, Japan, January 19-21, 2012

A Design of a cost effective Fire Fighting Robot using Intelligent System

Shuddha chowdhury[1], Shuva paul[2], Istiaque islam[3]

[1,2]American International University Bangladesh, Banani,Dhaka,Bangladesh
[3]Islamic University of Technology, Board Bazar, Gazipur-1704, Bangladesh.

[1]shuddha@hotmail.com,[2]paulshuva66@gmail.com,[3]isti9065@yahoo.com

Abstract: We usually read in newspapers about fire accidents and rising death toll rates because of fire related accidents. At times even firemen lose their lives while on rescue operations. We have proposed a model Fire Fighting Robot which has been designed for relief operations with main focus on rescue purposes. Use of robots is growing both on Earth and in space, in large part due to increased capacity for machine intelligence. Robotics defined as a mechanical design that is capable of performing human tasks or behaving in a human-like manner. The Robot is an electrically powered and remotely controlled unmanned vehicle. It is a battery-operated robot on wheels and its primary role is to detect the source of heat and put off flames.

Keywords: Autonomous, Fire Extinguishing, Obstacle detection etc.

1 INTRODUCTION

The Proposed firefighting robot is designed to detect the source of fire with its strong sensor technology integrated with it. We have read some past articles about firefighting robots but we have seen that cost has always been a neglected issue. We have proposed a micro-controller based firefighting robot (ATMEGA-32) [1] which is not only *cost-effective* but also *highly efficient* and *reliable* in its primary purposes. Robotics does not always need to be expensive and it should be designed for mass people. We have carefully chosen our materials surrounded beside us and we want to assemble different technologies for manipulating its main purposes. We have arranged the topics consequently in this paper to maintain the coherence among the discussed topics. Main features of this Robots are-

1. Heat and Smoke Sensor
2. Obstacle Detector
3. Traction System
4. Fire Extinguishing
5. Low battery sensor
6. Wireless Controlling System

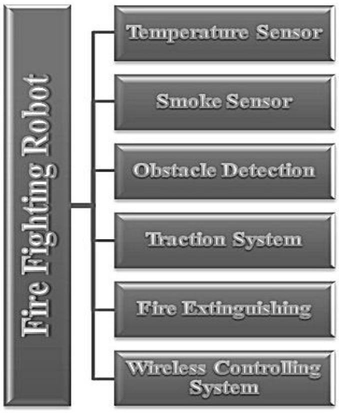

Fig1: Fire Fighting Robot Functions

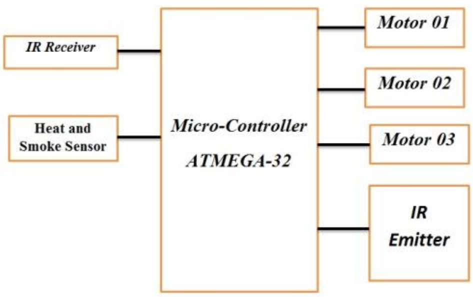

Fig2: Micro-Controller ATMEGA32 pin connection for some parts of the Robot

2 DESIGN

2.1 Heat and Smoke Sensor:

We have used CM-WTK55 as our heat and smoke sensor. The *photoelectric* type smoke part of detector is based on the photoelectric sensing principle [2]. When fire break out and smoke enters the light tight box, the particles of smoke scatter the infrared light, and this scattered light goes into the receiving element, there by emitting an electric current, and while the electric current is up to the fixed extent, the fire alarm will be activated. The fixed temperature heat detector part has stabilized performance, long-term durability and least -malfunction are ensured by employing a bimetal mechanism, which meets UL verification .Its temperature setting is 55°c. [3]

2.2 Obstacle Detection

As we have proposed that our robot is an *autonomous* one it has an efficient system to avoid the obstacles. To detect any kind of obstacles we have used *IR detection system*. We have used IR led for infrared emission .

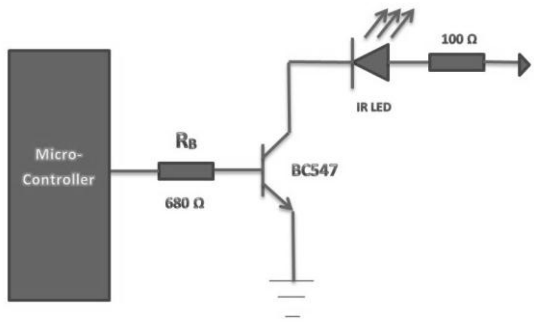

Fig 3: Block diagram of IR emitter

And we have also designed a receiver to receive the reflected IR so that our robot can move avoiding all the obstacles. We placed IR emitter and receiver on the robot in a manner so that it can sense objects and walls surrounding it.

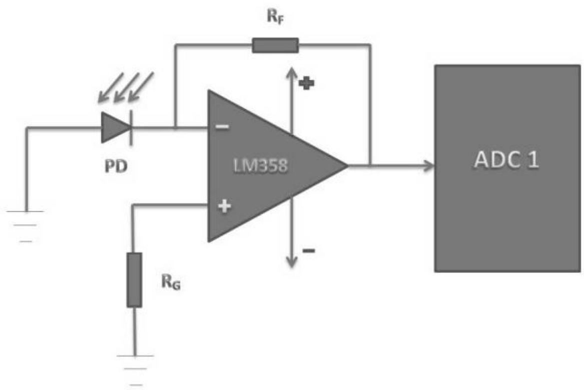

Fig 4: Block diagram of IR receiver

2.3 Traction System:

We have used two *permanent magnet dc motors*. Most of the work, power delivered to the shaft in the form of torque, is done by the permanent magnets. Because power is consumed for only a brief period of time upon each alignment of the permanent magnet and electromagnet, very little power is necessary to run the motor-generator, making it *highly efficient*. The benefits of using permanent magnet dc motors are-wide availability, cost effectiveness, Adequate Power Supply [4]. The movement of our proposed Robot models depends on the rotation of two wheels. If both of the wheels rotate clockwise our robot will move forward. The robot will move backward when both of the wheels rotate anti-clockwise. When the Right side wheel is off, the left side wheel is rotating clockwise, So the robot will turn right at that time and similarly the robot will turn left when the left wheel remains still.

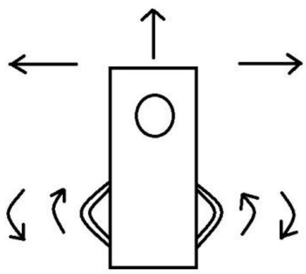

Fig 5: Traction system

2.3.1 Sample programming for traction system

```
Sub Forward

Cls

Lcd "FORWARD"

Pwm1b = 200

Portd.3 = 0

Pwm1a = 200

Portd.6 = 0

End Sub
```

2.4 Wireless Controlling System

We have followed the Manchester coding system for Wireless Controlling. We have modified according to our demand.

2.4.1 Manchester Coding

Manchester coding works on transitions from high to low (bit 0), or low to high (bit 1), the actual width of the pulses doesn't matter particularly (within reason).This is the way the bits are actually sent, a bit 1 is a transition from 0 to 1, and a bit 0 is a transition from 1 to 0 [5].For RF transmission there is a huge possibility in case of receiving a data. So we hane used a *packet system*, where a number of different pieces of information are transmitted after each other in the form of a 'packet', this consists of a number of different sections like header section , address byte, data and checksum.

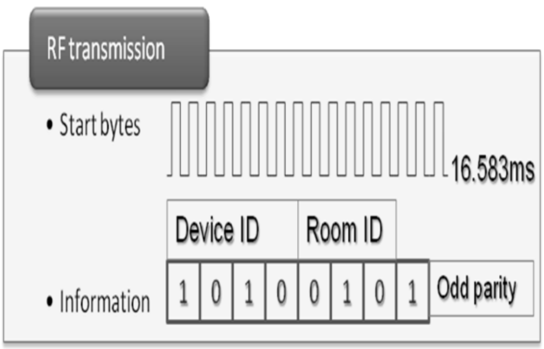

Fig 6: Manchester coding system

The *header* section consits of a row of 20 bit one's followed by a single bit zero.

The long sequence of 1's gives the receiver time to settle and the decoding software time to synchronise.

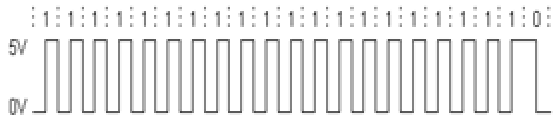

Fig 7: Header

The *address section* consists of the 8 bits of data in the byte, followed by a single bit one, and a single bit zero.

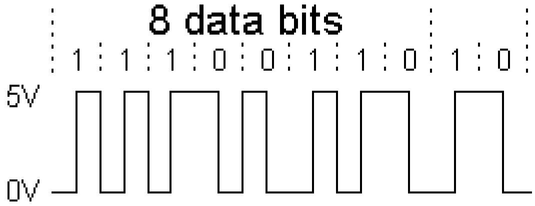

Fig 8: Address byte

Data and checksum are same as address 8 bits.

2.5 Materials

For the robot designing, we used *Aluminium* because it is very strong, light, resistant to corrosion, and affordable. To slow down the heat flow between the outer and inner shells, the gap is filled with rock wool and ceramic paper as insulation material. Most importantly, it is very easy to cut, shape, drill, and bend. Aluminum has a much higher strength to weight ratio. This means that for a mass of aluminum and an equal mass of steel, aluminum would be much stronger. Another important thing about aluminum is that it is resistant to rust. In actuality, aluminum does rust, but it quickly forms an oxidized layer which acts as a protective coating against any further rust. Aluminum has a very high thermal conductivity. We have chosen worm gearing as our gearing because it available, cost effective.

2.6 Low battery sensor

A low battery sensor measures current, voltage from battery, if battery contains lesser voltage or current than standard this circuit will work. A warning alarm will be triggered when battery voltage is lower than the voltage or current level set by the user. As we used 9.6V battery we set the voltage level at 7V, which means this circuit will trigger alarm when the battery voltage is lesser than 7V [6].

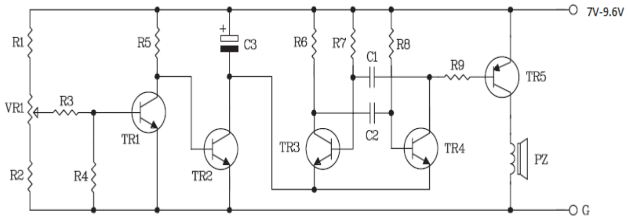

Fig 9: Circuit diagram of low battery sensor

2.7 Power Supply

The power of the robot is supplied by two 9.6 V rechargeable NiCd batteries. The Transmitter battery pack contains NiCd (Nickel-Cadmium chemical composition) rechargeable that provide significantly more energy than comparable AA NiCd batteries. The Battery Pack's cells will provide a constant reliable voltage until they are exhausted. Contrary to popular belief, NiCd batteries do not suffer from any sort of permanent "memory effect". Rechargeable NiCd batteries can be used over and over again for hundreds of battery cycles if properly maintained [7]. However, all batteries will eventually wear out over time.

2.8 Fire Extinguishing

A fire extinguisher or extinguisher is an active fire protection device used to extinguish or control small fires, often in emergency situations**.** For *extinguishing fire* we used *CO_2 and water* [8]. We have placed rotating nozzles in all corner parts of the robot so that it can cover every possible part of a room. Both the extinguishing system will be activated when temperature reaches the set value and smoke is sensed by the sensor. To spray water we used Zodi Outback Gear Zodi 6 Volt which can Pump [9] about 1/2 gallon per minute and weighs only 1lbs.

3 CONCLUSION

Our proposed low cost robot model can move avoiding obstacles and detect fire source without any kind of false alarm. Depending upon the fire intensity it will use the extinguishers attached to it. Our robot can be autonomous and we can also control it by RF transmission. We are currently working on image processing and video feedback system so that we can learn about the inner situation of the room. We are also working on machine learning so that our robot can remember the mistakes and take certain intelligent decision by him. We are trying to make our robot even more cost effective. Our main concern is to make the robot effective in very high temperature. The main deficiency of our proposed robot model is that it is not able decide what kind of extinguisher it would use. We are working on that problem.

4 REFERENCES

[1**]** http://www.atmel.com/atmel/acrobat/doc2503.pdf[2] http://www.pepperl-fuchs.com/global/en/2751.htm
[3]http://www.alibaba.com/productgs/325937404/Combination_heat_and_Smoke_Detector.html
[4]http://pureenergysystems.com/os/EdGrayMotor/PM_PEM_MG/principles/index.html
[5] http://www.winpicprog.co.uk/pic_tutorial12.htm
[6] www.bakatronics.com/shop/item.aspx?itemid=644
[7] http://pvcdrom.pveducation.org/BATTERY/nicads.htm
[8] http://en.wikipedia.org/wiki/Fire_extinguisher
[9]http://www.zodi.com/Dealer/zodidealermedia1067.html

The Seventeenth International Symposium on Artificial Life and Robotics 2012 (AROB 17th '12),
B-Con Plaza, Beppu, Oita, Japan, January 19-21, 2012

Gait analysis using inertial sensor and vision

Tri Nhut Do[1], Young Soo Suh[2]

[1,2]University of Ulsan, Ulsan 680-749, Republic of Korea
(Tel: 82-52-259-1524, Fax: 82-52-259-1524)

[1]trinhutdo@gmail.com
[2]yssuh@ulsan.ac.kr

Abstract: In this paper, a novel method is proposed to analyze the gait using inertial sensor and vision technique. An indirect Kalman filter is used to estimate step length and foot angles. The vision technique provides us vision information which is used to update the Kalman filter. A measurement unit including a camera and inertial sensors is mounted on a shoe. The vision information including position and attitude of a shoe is estimated based on a simple planar landmark system which consists of thousands of markers and be easily expandable. Experiments verify our proposed system is quite accurate, especially in step length measurement. This proposed system is suitable for long distance applications.

Keywords: gait analysis, image processing, inertial sensors, position estimation.

1 INTRODUCTION

Gait analysis [1] involves the measurement of temporal/spatial characteristics (step size and walking speed), kinematics and kinetics. Gait analysis is used for medical purpose, sport analysis and also for entertainment.

In this paper, a new gait analysis system is proposed. A measurement system consisting of a camera and inertial sensors is installed on a shoe. Fiducial markers [2] are printed on paper and placed on the floor. Fiducial markers are used mainly in virtual reality systems. There are many types of markers. Since there are no concerns that complicated backgrounds are mistakenly recognized as markers, we used simple markers in this paper.

When a foot is on floor, the movement is estimated using a camera. When a foot is moving, its movement is estimated using inertial sensors. In an inertial-based foot estimation system, Kalman filters are usually used to estimate foot measurement. For better accuracy, a smoother [3] is used to combine vision data and inertial sensor data.

The paper is organized as follows. In Section 2, formulation problem of the proposed system is given. In Section 3, experimental results are given. Conclusion is given in Section 4.

2 FORMULATION PROBLEM

2.1 Gait analysis system

The gait analysis system consists of a sensor unit on a shoe and fiducial markers on the floor (**Fig. 1. (a)**). A sensor unit consists of a camera (point grey Firefly MV FFMV-03MTM) and inertial sensors (XSens MTi inertial measurement unit).

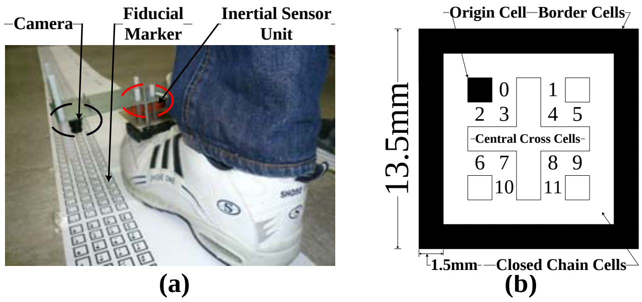

Fig. 1. Gait analysis system and marker's structure

A fiducial marker is similar to ARTag markers [2] and its structure is shown in **Fig. 1(b).** The marker is a nine by nine grid of quadrilateral cells of 1.5 millimeter edge including origin cell, border cells, central-cross cells and closed-chain cells. The marker has twelve bits digital coding system inside. The code bits are distributed along the quadrilateral central-cross in the order from left to right, and from top to bottom. A planar landmark system is generated by N fiducial markers which are composed of a four by M grid of markers as in **Fig. 2.** make it be easily expandable. The marker ID is encode from 0 to $(N-1)$.

2.2 Coordinate frame assignment

There are four coordinate frames in this paper. The world frame is located at the first marker of the planar landmark system. Positions of a foot are expressed in this frame. The navigation frame is used in an inertial navigation algorithm. It has the origin as same as that of the world frame. The camera frame is placed at the pinhole of the camera, where the Z axis perpendicular to the image plane. The last frame is body frame which has three axes coincide with those of inertial sensors. In this paper, it is assumed that three axes of the camera frame and the body frame are the same.

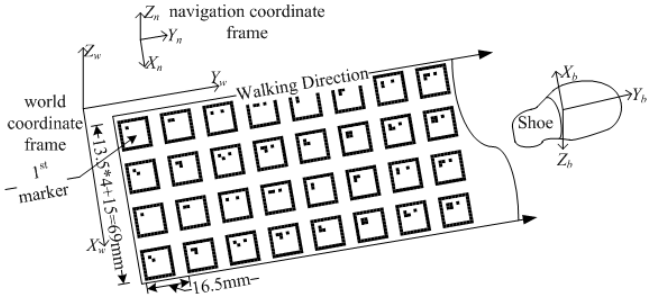

Fig. 2. Planar landmark system and frame assignment

2.3 Position and attitude estimation using markers

When a foot is not moving on the floor, markers in camera image are recognized through an image processing process in which the marker's ID and its outer four corners coordinates are extracted.

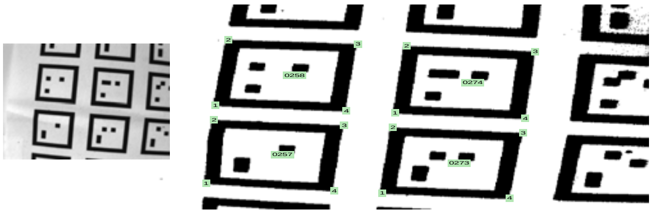

Fig. 3. Origin image and four extracted corners

Position $\left(\hat{r}_{vision}\right)$ and attitude $\left(\hat{C}_{vision}\right)$ of a camera with respect to the world frame are determined using the four corners coordinates and based on the algorithm in [4]. Let r_w be a point expressed in the world frame and r_b be the same point in the body frame. Then the relationship between r_b and r_w is given by

$$r_w = \hat{C}_{vision} r_b + \hat{r}_{vision} \qquad (1)$$

2.4 Position and attitude estimation using inertial data

When a foot is moving, position and attitude are estimated using an inertial navigation algorithm. Firstly, zero velocity intervals are detected [5]. An indirect Kalman filter [6] with state vector $x = \left[q_e \quad v_e \quad r_e\right]'$ is used in forward direction and backward direction. Then a smoother is applied to obtain the best accurate estimation of position and attitude.

3 EXPERIMENTAL RESULT

The camera is firstly calibrated to obtain its intrinsic. In our experiments, the sampling rate of camera and inertial IMU sensors are 30fps and 100Hz, respectively. A person who wears the shoe (**Fig. 1(a)**) is required to free walk along a planar marker system path (**Fig. 2**). Through the experiment shown in **Fig. 4,** it is proved that the position are accurately estimated.

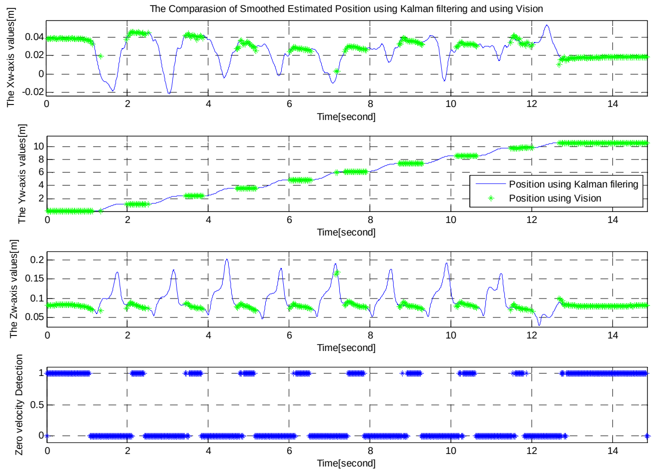

Fig. 4. Position Estimation

4 CONCLUSION

A novel approach was decribed for position and attitude estimation using integration of vision and inertial sensor. In vision, the planar landmark path is easily expandale when longer walking range is need in such application as a clinical gait assessment of patients, parameter estimation of some pedestrian navigation algorithms.

Acknowldegement

This work was supported by Network-based Automation Research Center (NARC) and National Research Foundation of Korea Grant funded by the Korean Government (No. 2011-0002770).

REFERENCES

[1] Whittle, M.W. (2007), Gait analysis: An introduction. 4th edition, Elsevier, Amsterdam, England.

[2] Fiala, M. (2005), Artag, a fiducial marker system using digital techniques. In IEEE Computer Society Conference on Computer Vision and Pattern Recognition, pp. 590-596.

[3] Suh, Y.S.; Do, T.N.; Ro, Y.S.; Kang, H.J. (2010), Smoother for attitude estimation using inertial and magnetic sensors. In IEEE Sensors, Hawaii - USA; pp. 743-746.

[4] Lu, C.-P.; Hager, G.D.; Mjolsness, E. (2000), Fa st and globally convergent pose estimation from video images. IEEE Transactions on Pattern Analysis and Machine Intelligence 22(06):610-622.

[5] Park, S.K.; Suh, Y.S. (2010), A zero velocity detection algorithm using inertial sensors for pedestrian navigation systems. Sensors 10(10):9163-9178.

[6] Suh, Y.S. (2010), Orientation estimation using a quaternion-based indirect kalman filter with adaptive estimation of external acceleration. IEEE Transactions on Instrumentation and Measurment 59(12):3296-3305.

Author Index

Notation of session name: PL: Plenary Speech, IS: Invited Speech,

ISP: Invited Session on Playware, GS: General Session, OS: Organized Session, PS: Poster Session

Note: **P-44** / 1157 = (page no. in Technical Paper Index) / (page no. in Papers)

A

Adachi	Tatsuya	PS1-4	**P-44**/1157
Aihara	Kazuyuki	OS25-4	**P-51**/557
		OS26-1	**P-53**/561
		OS26-3	**P-53**/569
		OS26-4	**P-53**/573
Akaho	Syotaro	OS26-1	**P-53**/561
Aki	Syunsuke	GS6-4	**P-45**/718
Akita	Shohei	OS5-2	**P-47**/146
AlMejrad	Ali	PS1-13	**P-44**/1191
Amano	Yoko	GS28-1	**P-34**/1111
Amari	Shun-ichi	PL2	**P-24**/5
Aoki	Shingo	GS11-3	**P-39**/812
Aonishi	Toru	GS1-3	**P-35**/622
Araki	Hideo	OS3-1	**P-52**/109
		OS3-2	**P-52**/113
		OS3-3	**P-52**/117
		OS3-4	**P-52**/121
Araki	Osamu	OS25-1	**P-51**/545
		OS25-2	**P-51**/549
		OS25-3	**P-51**/553
Arita	Takaya	GS2-4	**P-26**/642
		GS3-3	**P-26**/658
		GS4-2	**P-30**/674
		GS4-3	**P-30**/678
		GS7-2	**P-39**/726
Ariya	Araya	GS10-4	**P-30**/799
Arnold	Solvi Fylgja	GS4-2	**P-30**/674
Arof	Hamzah	PS1-13	**P-44**/1191
Arriaga	Julio G.	GS24-5	**P-33**/1055
Asada	Taro	OS8-2	**P-48**/204
		OS8-3	**P-48**/210
		OS8-4	**P-48**/216
		OS8-5	**P-48**/222
Asano	Hirotoshi	OS27-1	**P-53**/577

B

Bandara	D. S. V	GS22-5	**P-32**/1017
Bandara	Sanjaya Vipula	GS15-2	**P-43**/875
Basoeki	Fransiska	GS29-4	**P-40**/1143
Beynon	Meurig	GS25-4	**P-31**/1075
Bian	Jianling	OS18-1	**P-34**/386
Björnsson	Davíð Þór	ISP4	**P-25**/47
Boonsieng	Pramuk	GS24-2	**P-33**/1044
Botzheim	János	OS23-4	**P-51**/512

C

Cao	Wenjing	GS9-3	**P-28**/779
Cha	Young Chul	OS23-5	**P-52**/516
		OS23-6	**P-52**/520
Chamnongthai	Kosin	OS27-4	**P-53**/592
Chang	Chih-Hung	OS20-5	**P-38**/447
Chang	Hsuan T.	OS20-2	**P-37**/434
Chang	Yau-Zen	GS22-1	**P-32**/1002
Chang	Yi-Chang	OS19-2	**P-38**/406
Chen	Cha'o-Kuang	OS19-5	**P-38**/418
Chen	Changfang	OS17-2	**P-27**/374
Chen	Cheng-Yang	OS20-2	**P-37**/434
Chen	Jhih-Han	OS20-1	**P-37**/430
Chen	Kun-Cheng	OS19-7	**P-39**/426
Chen	Kuo-Ying	OS19-6	**P-38**/422
Chen	Peng	GS19-1	**P-41**/943
Chen	Xuedong	GS27-1	**P-34**/1103
Cheng	Kuo-Sheng	OS19-3	**P-38**/410
Chiang	Huann-Keng	OS19-2	**P-38**/406
Chiu	Shih-Yuan	PS1-3	**P-43**/1155
		PS1-7	**P-44**/1169
Cho	Jung Hwan	PS1-14	**P-44**/1195
Cho	Seung-Yoon	OS23-1	**P-51**/500
Cho	Young Im	OS23-3	**P-51**/508
Chowdhury	Shuddha	PS1-15	**P-44**/1197
Chuang	Wei-Ju	OS19-7	**P-39**/426
Chun	Ho Hwan	OS23-5	**P-52**/516
Chung	Cheng-Yun	OS20-6	**P-38**/451
Cody	Martin L.	GS21-3	**P-30**/985

D

Dai	Fengzhi	OS18-2	**P-34**/390
		OS18-3	**P-34**/394
Dai	Jin	GS11-3	**P-39**/812
DallaLibera	Fabio	GS28-3	**P-35**/1119
		GS29-4	**P-40**/1143
Do	Tri Nhut	PS1-16	**P-45**/1201
Domoto	Tatsuya	GS29-1	**P-40**/1131
Du	Junping	OS17-1	**P-27**/370
		OS17-2	**P-27**/374
		OS17-3	**P-27**/378
		OS17-4	**P-27**/382

E

Ebara	Yasuo	OS21-5	**P-47**/476
Egashira	Naruto	GS26-2	**P-32**/1089
Ehara	Yusuke	GS24-3	**P-33**/1047
Endo	Satoshi	GS7-1	**P-39**/722
Endoh	Taito	OS9-3	**P-42**/234
Eto	Tasuku	OS1-6	**P-46**/85
Etoh	Takuya	GS20-3	**P-39**/967

F

Feng	Liangbing	GS24-1	**P-33**/1040
Fernando	Subha Danushika	GS1-2	**P-35**/618
Friðriksson	Rafn Vídalín	ISP4	**P-25**/47
Fuchida	Takayasu	GS2-3	**P-26**/638
Fujihara	Yutaka	OS18-2	**P-34**/390

Fujimura	Takuro	OS25-2	**P-51**/549
Fujinaka	Toru	OS3-4	**P-52**/121
Fujita	Megumi	GS19-4	**P-41**/955
Fujitani	Yasuhiro	GS8-6	**P-28**/764
Fujiwara	Takeshi	OS15-1	**P-50**/346
		OS15-2	**P-50**/350
		OS15-3	**P-50**/592
Fukaishi	Yuji	OS27-4	**P-53**/150
Fukamachi	Hironori	OS5-3	**P-47**/654
Furukawa	Masashi	GS3-2	**P-26**/838
		GS13-2	**P-27**/141
Furutani	Hiroshi	OS22-4	**P-49**/492

G

Gao	Weijie	GS17-3	**P-40**/922
Gao	Xiang	OS15-2	**P-50**/346
Glette	Kyrre Harald	GS13-5	**P-27**/851
		GS29-3	**P-40**/1139
Gopura	R.A.R.C	GS22-5	**P-32**/1017
Gopura	Ranathunga Arachchilage Ruwan	GS21-5	**P-30**/994
Gopura	Ruwan Chandra	GS15-2	**P-43**/875
Goto	Satoru	GS26-2	**P-32**/1089
Grassia	Filippo	GS7-4	**P-40**/735
Guo	Jr-Hung	OS20-5	**P-38**/447
		OS20-6	**P-38**/451

H

Habib	Maki K.	OS6-1	**P-54**/158
		OS6-3	**P-54**/166
		OS23-2	**P-51**/504
Habu	Narumi	GS15-5	**P-43**/889
Hachino	Tomohiro	GS18-2	**P-37**/934
Hakui	Tatsuro	GS15-3	**P-43**/881
Hanada	Masaki	OS16-1	**P-50**/354
Harada	Hitomi	OS12-3	**P-49**/291
Harada	Koji	OS13-5	**P-37**/317
		OS13-6	**P-37**/321
Haramaki	Shinya	GS21-6	**P-30**/998
Harashima	Fumio	OS23-6	**P-52**/520
Hasama	Masayoshi	OS22-3	**P-49**/488
		OS22-5	**P-49**/496
Hasegawa	Naohiro	OS4-2	**P-47**/129
Hashikawa	Fumitaka	PS1-8	**P-44**/1171
Hashimoto	Kenji	OS24-2	**P-41**/530
Hashimoto	Kiyota	OS2-1	**P-45**/89
		OS2-2	**P-45**/93
		OS2-5	**P-46**/105
Hashimoto	Shuji	GS14-2	**P-36**/859
		GS8-1	**P-28**/739
		GS18-1	**P-37**/930
		GS19-2	**P-41**/947
Hashizume	Yoichiro	OS25-1	**P-51**/545
Hattori	Yuya	GS5-2	**P-31**/690
Hayashi	Akihiro	GS21-6	**P-30**/998
Hayashi	Eiji	GS25-2	**P-31**/1067
		GS25-3	**P-31**/1071
		GS28-2	**P-35**/1115
		GS29-1	**P-40**/1131
Hayashi	Kunioki	GS10-3	**P-29**/795
Hemapala	Manjula Udayanga	GS15-2	**P-43**/875
		GS21-5	**P-30**/994
Heo	Jin Seok	OS20-7	**P-38**/455
Higuchi	Kohji	OS27-4	**P-53**/592
Hirama	Yuki	PS1-5	**P-44**/1161
Hirokawa	Sachio	OS2-1	**P-45**/89
		OS2-3	**P-45**/97
		OS2-4	**P-46**/101
Hitaka	Yasunobu	OS11-5	**P-53**/279
Hodohara	Norifumi	GS18-1	**P-37**/930
Hong	Sinpyo	OS23-5	**P-52**/516
Hong	Tzung-Pei	OS19-4	**P-38**/414
Horng	Shih-Cheng	GS12-1	**P-33**/816
Hosoda	Koh	GS11-2	**P-39**/807
		GS28-3	**P-35**/1119
Hosokawa	Shu	OS27-2	**P-53**/582
		OS27-3	**P-53**/586
Hossain	Shahera	GS17-2	**P-40**/918
Hsia	Kuo-Hsien	OS19-1	**P-38**/402
Hsieh	Mu-Cheng	GS14-1	**P-36**/855
Hsieh	Sheng-Ta	PS1-3	**P-43**/1155
		PS1-7	**P-44**/1169
Huang	Ji-Jer	OS19-3	**P-38**/410
Huang	Ke-Cheng	OS20-1	**P-37**/430
Huang	Tzu-Hsuan	OS21-3	**P-47**/467
Hung	Chung-Wen	OS20-1	**P-37**/430
		OS20-2	**P-37**/434
Hung	Shiu-Wan	GS23-5	**P-42**/1037

I

Iacono	Iolanda	ISP3	**P-25**/43
Ichikawa	Shunta	OS14-2	**P-50**/333
Ide	Hideto	OS27-1	**P-53**/577
Igarashi	Masao	OS16-4	**P-51**/366
Ihara	Masaki	GS23-3	**P-42**/1029
Iida	Kazuki	ISP2	**P-25**/39
Iimura	Ichiro	GS19-3	**P-41**/951
Ikeda	Kosuke	GS8-3	**P-28**/749
Ikeda	Masaaki	OS6-2	**P-54**/162
Ikeda	Satoshi	OS22-4	**P-49**/492
Ikemoto	Shuhei	GS11-2	**P-39**/807
		GS28-3	**P-35**/1119
Imamoto	Shou	GS15-4	**P-43**/885
Inami	Daisuke	OS5-4	**P-47**/154
Inenaga	Sinichi	OS21-2	**P-47**/463
Inohira	Eiichi	GS26-1	**P-32**/1085
Inoue	Hazuki	OS4-2	**P-47**/129
Inoue	Hiromi	OS24-2	**P-41**/530
Inoue	Shuki	GS11-3	**P-39**/812
Ishida	Takeshi	GS3-1	**P-26**/650
Ishida	Yoshiteru	OS13-1	**P-36**/299
		OS13-2	**P-36**/303
		OS13-3	**P-36**/307
		OS13-4	**P-36**/313
		OS13-5	**P-37**/317
		OS13-6	**P-37**/321
		OS13-7	**P-37**/325
		OS14-3	**P-50**/337
		OS14-4	**P-50**/342
Ishiguro	Hiroshi	GS28-3	**P-35**/1119
		GS28-4	**P-35**/1123
		GS29-4	**P-40**/1143
Ishii	Kazuo	GS21-4	**P-30**/989
Ishii	Masahiro	OS10-4	**P-36**/255
Ishii	Shin	GS6-4	**P-45**/718
		GS16-2	**P-29**/902
Ishikawa	Seiji	GS17-4	**P-40**/926
		GS24-3	**P-33**/1047
		GS24-6	**P-33**/1059
Ishimaru	Hideki	GS25-2	**P-31**/1067
Ishitobi	Mitsuaki	OS11-3	**P-52**/271

Islam	Istiaque	PS1-15	**P-44**/1197
Isokawa	Teijiro	GS5-1	**P-31**/686
Ito	Kazuyuki	GS2-2	**P-26**/634
		GS18-3	**P-37**/938
		GS26-3	**P-32**/1095
		GS27-2	**P-34**/1107
		GS28-5	**P-35**/1127
Ito	Kei	OS10-2	**P-35**/246
Ito	Naoharu	OS12-2	**P-49**/287
Ito	Takao	OS22-2	**P-49**/485
		OS22-3	**P-49**/488
		OS22-4	**P-49**/492
		OS22-5	**P-49**/496
Ito	Takuya	GS10-1	**P-29**/787
Itoh	Hidenori	GS3-4	**P-26**/662
Iwabu	Kazuki	GS5-4	**P-31**/701
Iwakiri	Junichi	OS4-3	**P-48**/133
		OS4-4	**P-48**/137
Iwanaga	Saori	OS28-2	**P-29**/604
Iwasaki	Shinya	OS10-4	**P-36**/255
Izumi	Kiyotaka	OS6-2	**P-54**/162
		OS6-4	**P-54**/170

J

J	Chetan	GS25-5	**P-31**/1079
Jan	Ming-Shiun	GS14-1	**P-36**/855
Jang	Guan-Wu	GS23-2	**P-42**/1025
Jayasekara	A.G.B.P	GS22-5	**P-32**/1017
Jeong	Ju-Won	OS20-7	**P-38**/455
Jia	Xiaoqing	OS18-4	**P-34**/398
Jia	Yingmin	OS17-1	**P-27**/370
		OS17-2	**P-27**/374
		OS17-3	**P-27**/378
		OS17-4	**P-27**/382
Jiang	Ganwen	GS16-4	**P-29**/910
Jiang	Yuan-Jang	GS23-2	**P-42**/1025
Jormanainen	Ilkka	GS25-4	**P-31**/1075
Joshi	Gopal	GS26-4	**P-32**/1099
Joshi	Sanjay S.	IS3	**P-24**/18

K

K.V	Padmaja	GS15-6	**P-43**/893
Kagawa	Takuya	GS13-3	**P-27**/842
Kai	Yoshihiro	PS1-4	**P-44**/1157
Kakimoto	Yuta	OS25-2	**P-51**/549
		OS25-3	**P-51**/553
Kaku	Anan	GS8-4	**P-28**/755
Kakudou	Takahisa	OS7-2	**P-54**/184
Kakuta	Yu	PS1-11	**P-44**/1183
Kamata	Sei-ichiro	GS15-3	**P-43**/881
		GS15-4	**P-43**/885
		GS15-5	**P-43**/889
Kambara	Satoshi	GS6-2	**P-45**/710
Kamimura	Atsushi	OS26-2	**P-53**/565
Kamiura	Naotake	GS5-1	**P-31**/686
Kaneko	Hirozumi	GS2-1	**P-26**/630
Kashima	Masayuki	GS16-4	**P-29**/910
Kashiwada	Shota	GS28-5	**P-35**/1127
Katayama	Hiroko	GS19-4	**P-41**/955
Kato	Joji	OS27-2	**P-53**/582
		OS27-3	**P-53**/586
Kato	Masahiko	GS1-4	**P-35**/626
Kato	Norihiko	GS8-6	**P-28**/764
Kato	Ryota	OS8-4	**P-48**/216
Kato	Shohei	GS3-4	**P-26**/662
Kato	Shohei	GS20-1	**P-39**/959
Kato	Tatsuya	OS7-1	**P-54**/180
Katori	Yuichi	OS26-4	**P-53**/573
Katsumata	Yuji	OS13-1	**P-36**/299
Kawabe	Taketoshi	GS8-4	**P-28**/755
		GS9-3	**P-28**/779
		GS9-4	**P-28**/783
Kawabuchi	Takahiro	GS15-5	**P-43**/889
Kawahata	Shiori	GS14-4	**P-36**/867
Kawano	Yoshihiro	OS10-3	**P-36**/251
Kenmochi	Naoya	OS4-3	**P-48**/133
		OS4-4	**P-48**/137
Kezuka	Yutaro	GS25-1	**P-31**/1063
Kibayashi	Ryuuichi	OS21-1	**P-47**/459
Kiguchi	Kazuo	GS15-2	**P-43**/875
Kim	Byung Il	OS23-5	**P-52**/516
Kim	Dong Jin	OS23-5	**P-52**/516
		OS23-6	**P-52**/520
Kim	Eunjin	GS8-5	**P-28**/759
Kim	Hyoungseop	GS17-4	**P-40**/926
		GS24-6	**P-33**/1059
Kim	Sung Mi	OS23-6	**P-52**/520
Kishima	Yasutaka	GS20-4	**P-39**/971
Kishimoto	Yorinori	OS10-1	**P-35**/242
Kitahara	Naoki	OS6-3	**P-54**/166
Kitakaze	Kazuhisa	OS10-1	**P-35**/242
Kitazumi	Yuichi	GS21-4	**P-30**/989
Klaus	Gordon	GS29-3	**P-40**/1139
Ko	Yoshiyasu	GS24-4	**P-33**/1051
Kobayashi	Kengo	GS7-2	**P-39**/726
Kobayashi	Kunikazu	GS6-3	**P-45**/714
		GS24-1	**P-33**/1040
Kobayashi	Tetsuya J.	OS26-2	**P-53**/565
Kobayashi	Yasuhiko	GS5-2	**P-31**/690
Koga	Kiminobu	OS5-1	**P-46**/141
Koga	Shinnosuke	GS24-1	**P-33**/1040
Kohno	Takashi	Tutorial	**P-25**/53
		GS7-4	**P-40**/735
Kojima	Kazuaki	GS4-3	**P-30**/678
Komori	Mochimitsu	GS21-6	**P-30**/998
Kon	Tatsuya	GS2-2	**P-26**/634
Kondo	Tadashi	GS22-3	**P-32**/1009
		GS23-1	**P-42**/1021
Kondo	Toshiaki	GS16-1	**P-29**/898
		GS24-2	**P-33**/1044
Kono	Michio	OS12-1	**P-49**/283
Koro	Chikoto	OS8-5	**P-48**/222
Koshikawa	Shun	OS9-3	**P-42**/234
Kouno	Masayuki	GS16-2	**P-29**/902
Koyama	Eiko	GS14-4	**P-36**/867
Kozawa	Sayuri	OS8-1	**P-48**/200
Kreesuradej	Worapoj	GS10-4	**P-30**/799
Kubo	Masao	OS28-1	**P-29**/600
		OS28-3	**P-29**/608
Kubota	Naoyuki	OS23-4	**P-51**/512
Kubota	Shigeru	GS6-1	**P-45**/706
Kulasekera	Asitha Lakruwan	GS21-5	**P-30**/994
Kunimatsu	Sadaaki	OS11-3	**P-52**/271
Kurashige	Kentarou	GS20-4	**P-39**/971
		GS29-2	**P-40**/1135
Kurata	Koji	GS1-3	**P-35**/622
Kuremoto	Takashi	GS24-1	**P-33**/1040
		GS6-3	**P-45**/714
Kurita	Koichi	PS1-2	**P-43**/1151
Kuroiwa	Shintaro	PS1-10	**P-44**/1179
Kushida	Naoki	OS18-3	**P-34**/394
Küstner	Reinhold	OS12-2	**P-49**/287

Kwak	Youngjoo	OS16-2	**P-50**/358
Kawatsuma	Shinji	IS2	**P-24**/14

L

Lai	ChinLun	PS1-1	**P-43**/1147
Lai	Hsin-Yi	OS19-5	**P-38**/418
Lan	Guo-Cheng	OS19-4	**P-38**/414
Lee	Bong Jin	OS23-5	**P-52**/516
		OS23-6	**P-52**/520
Lee	In Soo	PS1-14	**P-44**/1195
Lee	Ju-Jang	OS23-1	**P-51**/500
Lee	Jung-Ju	OS20-7	**P-38**/455
Lee	Kil Soo	OS23-5	**P-52**/516
		OS23-6	**P-52**/520
Lee	Man Hyung	OS23-5	**P-52**/516
		OS23-6	**P-52**/520
Lee	Yun Ja	OS23-5	**P-52**/516
		OS23-6	**P-52**/520
Levi	Timothée	GS7-4	**P-40**/735
Li	Binyao	OS18-3	**P-34**/394
Li	Bo-Yi	OS20-5	**P-38**/447
Li	Long	OS18-2	**P-34**/390
Li	Xiaqin	GS27-1	**P-34**/1103
Li	Yuan	OS18-2	**P-34**/390
Liao	Fangbo	GS17-3	**P-40**/922
Lien	Shao-Fan	OS19-1	**P-38**/402
Lin	Chien-Chou	OS19-7	**P-39**/426
Lin	Song-Yih	OS19-5	**P-38**/418
Lin	Wei-Cheng	OS19-1	**P-38**/402
Lin	Wen-Bin	OS19-2	**P-38**/406
		OS19-3	**P-38**/410
Liu	Shih-Jung	GS22-1	**P-32**/1002
Liu	Tao	GS12-2	**P-33**/820
Liu	Xiaomin	OS18-1	**P-34**/386
Lu	Cunwei	OS21-4	**P-47**/471
Lu	S.	OS22-2	**P-49**/485
Lu	Yi-Yu	OS19-3	**P-38**/410
Lund	Henrik Hautop	PL1	**P-24**/1
		ISP1	**P-25**/33
		ISP4	**P-25**/47
Luo	Guanghui	GS21-2	**P-30**/979

M

Ma	Huei-Ming	GS23-2	**P-42**/1025
Ma	QingLian	OS5-1	**P-46**/141
Mackin	Kenneth J.	OS9-2	**P-42**/230
		OS9-3	**P-42**/234
		OS9-4	**P-42**/238
		OS10-4	**P-36**/255
		OS16-1	**P-50**/354
		OS16-3	**P-51**/362
Maeda	Michiharu	GS12-2	**P-33**/820
Maeyama	Shoichi	OS7-1	**P-54**/180
		OS7-3	**P-54**/188
		OS7-4	**P-54**/192
		OS7-5	**P-55**/196
Maezono	Masaki	GS19-3	**P-41**/951
Marti	Patrizia	ISP3	**P-25**/43
Matsuda	Noriyuki	GS2-1	**P-26**/630
Matsuda	Yoshitaka	GS26-2	**P-32**/1089
Matsui	Hirokazu	GS8-6	**P-28**/764
Matsui	Nobuyuki	GS5-1	**P-31**/686
Matsuka	Ken	OS13-4	**P-36**/313
Matsumoto	Hirosato	OS21-1	**P-47**/459
Matsumoto	Takeo	GS26-2	**P-32**/1089
Matsuno	Seigo	OS22-3	**P-49**/488
		OS22-5	**P-49**/496
Matsuo	Takashi	OS24-5	**P-41**/541
Matsuo	Takuro	OS4-3	**P-48**/133
Matsushita	Kotaro	OS9-2	**P-42**/230
		OS9-3	**P-42**/234
		OS9-4	**P-42**/238
Matsuura	Yoshinori	OS28-2	**P-29**/604
Md. Zain	Zainah Binti	OS6-4	**P-54**/170
Mehta	Rajiv	OS22-3	**P-49**/488
Mimura	Akihiro	GS20-1	**P-39**/959
Minami	Mamoru	OS6-5	**P-54**/174
Minato	Takashi	GS29-4	**P-40**/1143
Minowa	Kentarou	GS28-2	**P-35**/1115
Miura	Hirokazu	GS2-1	**P-26**/630
Miyake	Syuhei	OS15-2	**P-50**/346
Miyamoto	Kunio	GS3-5	**P-26**/666
Miyata	Ryota	GS1-3	**P-35**/622
Miyazaki	Tsuyoshi	GS14-4	**P-36**/867
Miyazaki	Yoshiki	GS29-2	**P-40**/1135
Mizoguchi	Fumio	GS14-3	**P-36**/863
Mohamed Nor	Mohd Khairi Bin	GS9-1	**P-28**/770
Mokhtari	Ali	OS27-5	**P-53**/596
Moon	Jung Hyun	OS23-6	**P-52**/520
Mori	Hayao	OS16-1	**P-50**/354
Mori	Kazuma	OS16-3	**P-51**/362
Morie	Takashi	GS24-3	**P-33**/1047
Morikawa	Akinobu	OS10-5	**P-36**/259
Morioka	Kazuyuki	PS1-8	**P-44**/1171
		PS1-9	**P-44**/1175
		PS1-10	**P-44**/1179
Motonaka	Kimiko	OS7-3	**P-54**/188
Mukai	Masakazu	GS8-4	**P-28**/755
		GS9-3	**P-28**/779
		GS9-4	**P-28**/783
Mulyono	Nur Budi	OS14-3	**P-50**/337
Murai	Yuki	OS2-2	**P-45**/93
Murakami	Yuichi	GS14-2	**P-36**/859
		GS18-1	**P-37**/930
Murao	Hajime	GS20-2	**P-39**/963
Murata	Junichi	GS20-3	**P-39**/967
Murayama	Yusuke	GS15-4	**P-43**/885
Mutoh	Atsuko	GS3-4	**P-26**/662
Muzalifah	Mohd. Said	PS1-12	**P-44**/1187

N

Nagado	Tsutomu	OS12-1	**P-49**/283
Nagahara	Hajime	GS24-4	**P-33**/1051
Nagai	Isaku	OS6-4	**P-54**/170
		OS7-2	**P-54**/184
		OS7-4	**P-54**/192
Nagai	Yasuo	OS16-3	**P-51**/362
Nagasue	Akira	GS24-6	**P-33**/1059
Nagata	Fusaomi	OS6-1	**P-54**/158
		OS6-3	**P-54**/166
		OS23-2	**P-51**/504
Nagayoshi	Masato	GS20-2	**P-39**/963
Naitoh	Ken	OS24-1	**P-41**/524
		OS24-2	**P-41**/530
Nakae	Ken	GS6-4	**P-45**/718
		GS16-2	**P-29**/902
Nakagama	Yuki	OS12-4	**P-49**/295
Nakakubo	Masato	OS24-5	**P-41**/541
Nakamura	Masatoshi	GS27-1	**P-34**/1103
Nakamura	Shingo	GS14-2	**P-36**/859
		GS18-1	**P-37**/930

Nakamura	Shingo	GS19-2	**P-41**/947
Nakamura	Yoshiaki	OS11-4	**P-53**/275
Nakamura	Yutaka	GS28-4	**P-35**/1123
Nakanishi	Yuu	OS8-3	**P-48**/210
Nakano	Kazushi	OS27-2	**P-53**/582
		OS27-3	**P-53**/586
Nakao	Shinnosuke	GS15-3	**P-43**/881
Nakatsuka	Hiroki	GS27-2	**P-34**/1107
Nakayama	Shigeru	GS13-4	**P-27**/847
		GS19-3	**P-41**/951
Nam	Yoon Seok	PS1-14	**P-44**/1195
Namatame	Akira	OS28-1	**P-29**/600
Narumi	Tomohiro	OS1-1	**P-46**/65
Nide	Naoyuki	GS19-4	**P-41**/955
Niimi	Ayahiko	OS9-1	**P-42**/226
		OS10-2	**P-35**/246
Nishigori	Yoichi	GS11-2	**P-39**/807
Nishikawa	Takaya	OS2-5	**P-46**/105
Nishimoto	Anri	GS22-2	**P-32**/1005
Nishimoto	Masaaki	GS12-3	**P-33**/824
Nishino	Toshimasa	GS8-6	**P-28**/764
Nishio	Kenta	GS2-4	**P-26**/642
Nishio	Kimihiro	GS2-5	**P-26**/646
		GS23-3	**P-42**/1029
Nishiyama	Hiroyuki	GS10-1	**P-29**/787
		GS10-3	**P-29**/795
		GS11-1	**P-39**/803
		GS14-3	**P-36**/863
Nomura	Yoshihiko	GS5-4	**P-31**/701
		GS8-6	**P-28**/764
		OS10-5	**P-36**/259
Norhidayah	Mohamad Yatim	PS1-12	**P-44**/1187
Nugent	Bob	IS1	**P-24**/11
Numata	Toshinobu	GS20-4	**P-39**/971
Nunohiro	Eiji	OS9-2	**P-42**/230
Eiji	Nunohiro	OS9-3	**P-42**/234
		OS9-4	**P-42**/238
		OS16-1	**P-50**/354
		OS16-2	**P-50**/358
		OS16-4	**P-51**/366
Nur Alisa	Ali	PS1-12	**P-44**/1187

O

Oba	Shigeyuki	GS16-2	**P-29**/902
		GS6-2	**P-45**/710
		GS6-4	**P-45**/718
Obana	Hiroaki	GS2-1	**P-26**/630
Obayashi	Masanao	GS24-1	**P-33**/1040
		GS6-3	**P-45**/714
Ogata	Kensuke	OS22-1	**P-48**/480
Ogawa	Jun	GS3-2	**P-26**/654
Ogiwara	Tatsuya	GS25-1	**P-31**/1063
Ohira	Toru	OS24-4	**P-41**/538
Ohnishi	Koji	GS5-3	**P-31**/696
		GS7-3	**P-40**/730
Ohshiro	Masanori	OS9-2	**P-42**/230
		OS9-4	**P-42**/238
Ohta	Naoto	GS15-4	**P-43**/885
Ohta	Yoshihiro	OS27-4	**P-53**/592
Ojima	Yuko	GS19-4	**P-41**/955
Oka	Tetsushi	OS21-1	**P-47**/459
Okada	Makoto	OS2-1	**P-45**/89
		OS2-2	**P-45**/93
Okada	Makoto	OS2-5	**P-46**/105
Okada	Yusuke	OS26-4	**P-53**/573
Okadome	Yuya	GS28-4	**P-35**/1123
Okazaki	Kazuto	GS25-1	**P-31**/1063
Oku	Makito	OS25-4	**P-51**/557
Okubo	Shigenori	GS9-1	**P-28**/770
Okuda	Yudai	GS26-1	**P-32**/1085
Okumura	Katsuhiro	OS1-5	**P-46**/81
Olufs	Sven	GS17-1	**P-40**/914
Omatu	Sigeru	OS3-1	**P-52**/109
		OS3-2	**P-52**/113
		OS3-3	**P-52**/117
		OS3-4	**P-52**/121
Ono	Satoshi	GS13-4	**P-27**/847
Ooe	Ryosuke	GS13-2	**P-27**/838
Oshima	Makoto	GS7-1	**P-39**/722
Otsuka	Akimasa	OS6-1	**P-54**/158
		OS6-3	**P-54**/166
Oya	Masahiro	OS1-3	**P-46**/73
		OS1-4	**P-46**/77
		OS1-5	**P-46**/81
		OS1-6	**P-46**/85

P

Pagliarini	Luigi	ISP1	**P-25**/33
Pallegedara	Achala	GS21-5	**P-30**/994
		GS26-2	**P-32**/1089
Park	Hyung Gyu	OS23-5	**P-52**/516
Park	Jong Geol	OS9-3	**P-42**/234
		OS16-1	**P-50**/354
		OS16-2	**P-50**/358
Paul	Shuva	PS1-15	**P-44**/1197
Perera	Nuwan	GS21-5	**P-30**/994
Phu-ang	Ajchara	GS13-1	**P-27**/834
Pilat	Marcin L.	GS3-3	**P-26**/658
Pingali	Govinda Ram	GS15-6	**P-43**/893
Pingali	Theja Ram	GS15-6	**P-43**/893
Polisetty	Niyanth Krishna	GS15-6	**P-43**/893

Q

Qingquan	Xia	OS22-4	**P-49**/492

R

R	Venkateshwar	GS26-4	**P-32**/1099
Rana	Animesh	GS26-4	**P-32**/1099
Ravishankar	Satish	GS15-6	**P-43**/893
Razali	Saifudin	OS7-5	**P-55**/196
Ripon	Kazi Shah Nawaz	GS13-5	**P-27**/851
Rizon	Mohd	PS1-13	**P-44**/1191
Roshan	W.D.S	GS22-5	**P-32**/1017

S

Saeki	Kouichi	OS22-5	**P-49**/496
Safar	Muhammad Juhairi Aziz	OS7-4	**P-54**/192
Sagami	Takanori	OS27-1	**P-53**/577
Sagara	Shinichi	OS1-1	**P-46**/65
		OS1-2	**P-46**/69
		OS1-3	**P-46**/73
Saighi	Sylvain	GS7-4	**P-40**/735
Sait	Sadiq M.	GS12-4	**P-33**/828
Saito	Ken	GS1-4	**P-35**/626
		GS25-1	**P-31**/1063
Saitoh	Ayumu	GS5-1	**P-31**/686
Sakaguchi	Yuuki	OS5-4	**P-47**/154
Sakai	Toshihiko	OS2-3	**P-45**/97

Sakakibara	Kaoru	OS6-3	**P-54**/166
Sakamoto	Makoto	OS5-1	**P-46**/141
		OS22-3	**P-49**/488
		OS22-4	**P-49**/492
Sakamoto	Ryota	GS5-4	**P-31**/701
		OS10-5	**P-36**/259
Sakata	Masaki	GS11-1	**P-39**/803
Sakimoto	Kiyomasa	GS13-4	**P-27**/847
Sakurai	Naoko	OS15-2	**P-50**/346
		OS15-3	**P-50**/350
Samuelsen	Eivind	GS13-5	**P-27**/851
Sani Irwan	Md. Salim	PS1-12	**P-44**/1187
Sapaty	Peter S.	IS4	**P-25**/24
Satake	Toshifumi	GS21-6	**P-30**/998
Sato	Asaji	OS11-2	**P-52**/267
Sato	Hiroshi	OS28-1	**P-29**/600
		OS28-3	**P-29**/608
Sato	Kiminori	GS16-4	**P-29**/910
Sato	Mikiko	OS4-2	**P-47**/129
Sato	Osamu	OS11-2	**P-52**/267
		OS11-4	**P-53**/275
		OS12-3	**P-49**/291
Sato	Takashi	GS4-4	**P-30**/682
Sato	Tomoki	OS10-2	**P-35**/246
Sato	Yuji	OS4-1	**P-47**/125
		OS4-2	**P-47**/129
		OS5-3	**P-47**/150
		OS5-4	**P-47**/154
Schank	Jeffrey C.	IS3	**P-24**/18
Sekine	Yoshifumi	GS1-4	**P-35**/626
Seo	Hae Moon	PS1-14	**P-44**/1195
Seok	Heo-Jin	OS20-7	**P-38**/455
Serikawa	Seiichi	GS17-2	**P-40**/918
		GS9-2	**P-28**/774
Shen	Chia-Hsing	OS19-6	**P-38**/422
Shibata	Hiroshi	OS1-6	**P-46**/85
Shieh	Jiann-Shing	GS23-2	**P-42**/1025
Shigetomi	Akihito	OS1-2	**P-46**/69
Shimada	Atsushi	GS24-4	**P-33**/1051
Shimada	Hiroki	OS5-2	**P-47**/146
Shimokakimoto	Tomoya	IPS2	**P-25**/39
Shimozawa	Tomoaki	OS1-1	**P-46**/65
		OS1-2	**P-46**/69
Shinfuku	Youhei	GS15-5	**P-43**/889
Shinpuku	Noriyuki	GS21-4	**P-30**/989
Shiraishi	Yoichi	GS12-4	**P-33**/828
Shirakami	Shinichi	OS4-1	**P-47**/125
Shiro	Masanori	OS26-1	**P-53**/561
Siddiqi	Umair Farooq	GS12-4	**P-33**/828
Siritanawan	Prarinya	GS16-1	**P-29**/898
Sista	Avinash	GS15-6	**P-43**/893
Soh	Zu	GS5-2	**P-31**/690
Song	Jingyan	GS27-1	**P-34**/1103
Song	Wei	OS6-5	**P-54**/174
Song	Yu	OS22-5	**P-49**/496
Sori	Hitoshi	GS22-2	**P-32**/1005
Straub	Jeremy	GS16-3	**P-29**/906
		GS8-5	**P-28**/759
Su	Hsu-Shan	OS20-4	**P-37**/443
Su	Juhng-Perng	OS19-1	**P-38**/402
Su	Kuo-Lan	OS20-3	**P-37**/439
		OS20-4	**P-37**/443
		OS20-5	**P-38**/447
		OS20-6	**P-38**/451
Suetsugu	Katsuya	GS3-4	**P-26**/662
Sugi	Takenao	GS26-2	**P-32**/1089
Sugimori	Shunichiro	OS2-2	**P-45**/93
Sugisaka	Masanori	GS17-3	**P-40**/922
		OS18-1	**P-34**/386
		OS18-4	**P-34**/398
Sugita	Kaoru	OS21-2	**P-47**/463
		OS21-3	**P-47**/467
Suh	Young Soo	PS1-16	**P-45**/1201
Sullivan	Chris	IS3	**P-24**/18
Sumi	Kaoru	IS5	**P-25**/30
Sun	Wei-Zen	GS23-2	**P-42**/1025
Susanto	Erwin	OS11-3	**P-52**/271
Sutinen	Erkki	GS25-4	**P-31**/1075
Suzukawa	Yuichi	PS1-11	**P-44**/1183
Suzuki	Hideyuki	OS26-4	**P-53**/573
Suzuki	Ikuo	GS3-2	**P-26**/654
		GS13-2	**P-27**/838
Suzuki	Kenji	ISP2	**P-25**/39
Suzuki	Michiyo	GS5-2	**P-31**/690
Suzuki	Reiji	GS3-3	**P-26**/658
		GS4-2	**P-30**/674
		GS7-2	**P-39**/726
		GS21-3	**P-30**/985
Suzuki	Takahiko	OS2-3	**P-45**/97
Syed Yusoh	Syed Muammar Najib	GS5-4	**P-31**/701

T

Tabuchi	Hitoshi	GS5-1	**P-31**/686
Tabuse	Masayoshi	OS8-1	**P-48**/200
		OS8-2	**P-48**/204
		OS8-3	**P-48**/210
		OS8-4	**P-48**/216
Taira	Yuichiro	OS1-3	**P-46**/73
Takada	Masaaki	OS26-3	**P-53**/569
Takagi	Natsuki	OS1-4	**P-46**/77
Takahashi	Nobuya	OS11-2	**P-52**/267
		OS11-4	**P-53**/275
Takahashi	Tatsuhisa	OS24-5	**P-41**/541
Takano	Hirotaka	GS20-3	**P-39**/967
Takao	Hidenobu	OS24-5	**P-41**/541
Takao	Shoichiro	GS22-3	**P-32**/1009
		GS23-1	**P-42**/1021
Takato	Minami	GS1-4	**P-35**/626
		GS25-1	**P-31**/1063
Takatsuka	Kayoko	OS11-1	**P-52**/263
Takauji	Ryunosuke	GS19-1	**P-41**/943
Takeda	Shinya	PS1-11	**P-44**/1183
Takegami	Eiji	OS27-4	**P-53**/592
Takekawa	Hiroki	PS1-6	**P-44**/1165
Takeuchi	Kazuhiro	OS2-1	**P-45**/89
Takeuchi	Yutaka	GS18-3	**P-37**/938
Taki	Hirokazu	GS2-1	**P-26**/630
Takigawa	Tomoyasu	PS1-9	**P-44**/1175
Tamaki	Hisashi	GS20-2	**P-39**/963
Tamura	Hiroki	GS15-1	**P-43**/871
		GS22-4	**P-32**/1013
Tamura	Tatsuhiro	OS11-3	**P-52**/271
Tamura	Tomotsugu	OS14-1	**P-50**/329
Tan	Joo Kooi	GS17-4	**P-40**/926
		GS24-3	**P-33**/1047
		GS24-6	**P-33**/1059
Tanabe	Kei-Ichi	OS13-7	**P-37**/325
Tanaka	Ken-ichi	PS1-5	**P-44**/1161
		PS1-6	**P-44**/1165
Taniguchi	Rin-ichiro	GS24-4	**P-33**/1051
Tanno	Koichi	GS15-1	**P-43**/871
		GS22-4	**P-32**/1013

Tashiro	Hiroaki	GS4-1	**P-30**/670
Taylor	Charles E.	GS21-3	**P-30**/985
		GS24-5	**P-33**/1055
Termsaithong	Teerasit	OS25-4	**P-51**/557
Thammano	Arit	GS13-1	**P-27**/834
Thi Aung	Kathy	GS2-3	**P-26**/638
Toda	Yuichiro	OS23-4	**P-51**/512
Tokumitsu	Masahiro	OS13-3	**P-36**/307
		OS14-4	**P-50**/342
Tomibe	Takanori	GS2-5	**P-26**/646
Tomioka	Satoshi	OS27-4	**P-53**/592
Tomita	Shigeyuki	OS11-1	**P-52**/263
Tomoda	Nao	OS25-3	**P-51**/553
Torresen	Jim	GS29-3	**P-40**/1139
Tseng	Po-Ying	GS14-1	**P-36**/855
Tseng	Vincent S.	OS19-4	**P-38**/414
Tso	Haw	OS20-3	**P-37**/439
Tsuda	Naoaki	GS8-6	**P-28**/764
Tsuji	Hiroshi	GS11-3	**P-39**/812
Tsuji	Toshio	GS5-2	**P-31**/690
Tsujino	Kazuhiro	OS21-4	**P-47**/471
Tsukamoto	Kenta	GS26-2	**P-32**/1089
Tsuzuruki	Jun	GS1-3	**P-35**/622

U

Uchida	Masafumi	OS27-5	**P-53**/596
Uchida	Yasuo	OS22-4	**P-49**/492
Uchikoba	Fumio	GS1-4	**P-35**/626
		GS25-1	**P-31**/1063
Uchio	Fumitaka	GS2-1	**P-26**/630
Ueda	Takuya	OS13-2	**P-36**/303
Ueno	Junji	GS22-3	**P-32**/1009
		GS23-1	**P-42**/1021
Ueyama	Kei	GS25-3	**P-31**/1071
Umeo	Hiroshi	GS3-5	**P-26**/666
Umezu	Shinjiro	OS24-3	**P-41**/534
Upadhyaya	Shrikrishna	GS25-5	**P-31**/1079
Usui	Shota	OS12-1	**P-49**/283
Utani	Akihide	GS8-2	**P-28**/743
		GS8-3	**P-28**/749
		GS12-3	**P-33**/824
		GS13-3	**P-27**/842

V

Vallejo	Edgar E.	GS24-5	**P-33**/1055
Vincze	Markus	GS17-1	**P-40**/914

W

Wada	Hideki	OS1-5	**P-46**/81
Wang	Dejin	OS18-2	**P-34**/390
		OS18-3	**P-34**/394
Wang	Jiwu	GS17-3	**P-40**/922
Wang	Lixia	OS18-4	**P-34**/398
Wang	Ping	OS17-1	**P-27**/370
Wang	Yazhao	OS17-4	**P-27**/382
Watanabe	Keigo	OS6-1	**P-54**/158
		OS6-2	**P-54**/162
		OS6-3	**P-54**/166
		OS6-4	**P-54**/170
		OS7-1	**P-54**/180
		OS7-2	**P-54**/184
		OS7-3	**P-54**/188
		OS7-4	**P-54**/192
		OS7-5	**P-55**/196
Watanabe	Keigo	OS23-2	**P-51**/504
Watanabe	Kouji	GS6-3	**P-45**/714
Watanabe	Minoru	GS1-1	**P-35**/614
Watanabe	Mutsumi	GS16-4	**P-29**/910
Watanabe	Shin-ichi	OS24-5	**P-41**/541
Watanabe	Yuji	OS14-1	**P-50**/329
		OS14-2	**P-50**/333
Wei	Fei	GS11-3	**P-39**/812
Wen	Ting-Ting	GS22-1	**P-32**/1002
Wimmer	Harald K.	OS12-2	**P-49**/287
Wu	Dan	GS21-2	**P-30**/979
Wu	Libing	GS21-2	**P-30**/979
Wu	Xiaobin	OS2-4	**P-46**/101

X

Xiao	Nan	OS17-3	**P-27**/378
Xue	Chen	OS4-4	**P-48**/137

Y

Yamaba	Hisaaki	OS11-1	**P-52**/263
Yamada	Koichi	GS1-2	**P-35**/618
Yamada	Koji	GS7-1	**P-39**/722
Yamada	Takayoshi	GS4-1	**P-30**/670
Yamada	Takayuki	GS23-4	**P-42**/1033
Yamada	Tomoyuki	OS26-2	**P-53**/565
Yamaguchi	Akihiro	OS28-3	**P-29**/608
Yamaguchi	Daisuke	OS9-1	**P-42**/226
Yamaguchi	Takashi	OS9-3	**P-42**/234
		OS16-3	**P-51**/362
Yamaji	Yuichiro	GS1-1	**P-35**/614
Yamakawa	Shouichi	GS18-2	**P-37**/934
Yamamori	Kunihito	OS4-3	**P-48**/133
		OS4-4	**P-48**/137
		OS5-1	**P-46**/141
Yamamoto	Akiyoshi	GS17-4	**P-40**/926
Yamamoto	Fujio	GS14-4	**P-36**/867
		GS21-1	**P-30**/975
Yamamoto	Hidehiko	GS4-1	**P-30**/670
Yamamoto	Hisao	GS8-2	**P-28**/743
		GS8-3	**P-28**/749
		GS12-3	**P-33**/824
		GS13-3	**P-27**/842
Yamamoto	Katsuhiro	GS25-2	**P-31**/1067
Yamamoto	Masahito	GS3-2	**P-26**/654
		GS13-2	**P-27**/838
Yamano	Mitsuhiro	PS1-11	**P-44**/1183
Yamasaki	Kazuko	OS15-2	**P-50**/346
		OS15-3	**P-50**/350
Yamasaki	Shinpei	GS25-1	**P-31**/1063
Yamashita	Mitushi	GS19-1	**P-41**/943
Yamashita	Yuki	GS15-1	**P-43**/871
Yamauchi	Yukiharu	GS15-3	**P-43**/881
		GS15-4	**P-43**/885
		GS15-5	**P-43**/889
Yamawaki	Akira	GS9-2	**P-28**/774
Yamazaki	Takahiro	OS16-4	**P-51**/366
Yanagimoto	Hidekazu	GS10-2	**P-29**/791
Yang	Feng-Yi	GS12-1	**P-33**/816
Yanou	Akira	OS6-5	**P-54**/174
YAP	Huei Ee	GS8-1	**P-28**/739
Yasuda	Satoshi	GS8-2	**P-28**/743
Yasunaga	Moritoshi	OS5-2	**P-47**/146
Yazid	Haniza	PS1-13	**P-44**/1191
Yeh	Yen-Liang	OS19-6	**P-38**/422
Yen	Shi-Jim	PS1-3	**P-43**/1155

Yen	Shi-Jim	PS1-7	**P-44**/1169
Yim	Sung-Soon	OS23-1	**P-51**/500
Yin	Chengjiu	OS2-3	**P-45**/97
		OS2-4	**P-46**/101
Yokokawa	Akira	GS2-2	**P-26**/634
Yokomichi	Masahiro	OS11-2	**P-52**/267
		OS12-3	**P-49**/291
		OS12-4	**P-49**/295
		OS22-4	**P-49**/492
Yokota	Masao	OS21-2	**P-47**/463
		OS21-3	**P-47**/467
Yonekura	Tatsuhiro	OS10-3	**P-36**/251
Yonemoto	Koichi	OS1-1	**P-46**/65
Yoneyama	Takehiro	GS26-3	**P-32**/1095
Yoshida	Jun	GS16-4	**P-29**/910
Yoshida	Motoki	GS25-3	**P-31**/1071
Yoshihara	Ikuo	OS4-3	**P-48**/133
		OS4-4	**P-48**/137
		OS5-2	**P-47**/146
Yoshimatsu	Takeshi	GS22-4	**P-32**/1013
Yoshimura	Tatsurou	OS28-3	**P-29**/608
Yoshinaga	Tsunehiro	OS22-4	**P-49**/492
Yoshioka	Michifumi	GS10-2	**P-29**/791
Yoshitake	Sho	OS6-1	**P-54**/158
Yoshitake	Toshikazu	OS11-5	**P-53**/279
Yoshitomi	Yasunari	OS8-2	**P-48**/204
		OS8-3	**P-48**/210
		OS8-4	**P-48**/216
		OS8-5	**P-48**/222
Yoshizaki	Saya	OS8-5	**P-48**/222
Yoshizawa	Kousuke	OS15-2	**P-50**/346
		OS15-3	**P-50**/350
Young	Kuu-young	GS14-1	**P-36**/855
Yu	Fashan	OS17-1	**P-27**/370
		OS17-2	**P-27**/374
		OS17-3	**P-27**/378
		OS17-4	**P-27**/382
Yu	Fujia	OS6-5	**P-54**/174
Yu	Kaijiang	GS9-4	**P-28**/783

Z

Zagal	Juan Cristobal	GS29-3	**P-40**/1139
Zarina	Mohd. Noh	PS1-12	**P-44**/1187
Zeng	Jun	OS2-3	**P-45**/97
		OS2-4	**P-46**/101
Zhang	Baolong	OS18-3	**P-34**/394
Zhang	Tao	GS27-1	**P-34**/1103
Zhang	Xueli	OS21-4	**P-47**/471
Zhang	Yu-an	OS5-1	**P-46**/141
Zhao	Huailin	OS18-1	**P-34**/386
		OS18-4	**P-34**/398
Zheng	Zeyu	OS15-2	**P-50**/346
		OS15-3	**P-50**/350
Zhou	Bo	OS1-6	**P-46**/85
Zhou	Chao	OS10-3	**P-36**/251
Zhu	Yi	GS27-1	**P-34**/1103
Zou	Jie-Tong	OS20-3	**P-37**/439
		OS20-6	**P-38**/451

